EIGHTH EDITION

Enhanced DIGITAL VERSION Included

Thrall's Textbook of VETERINARY DIAGNOSTIC RADIOLOGY

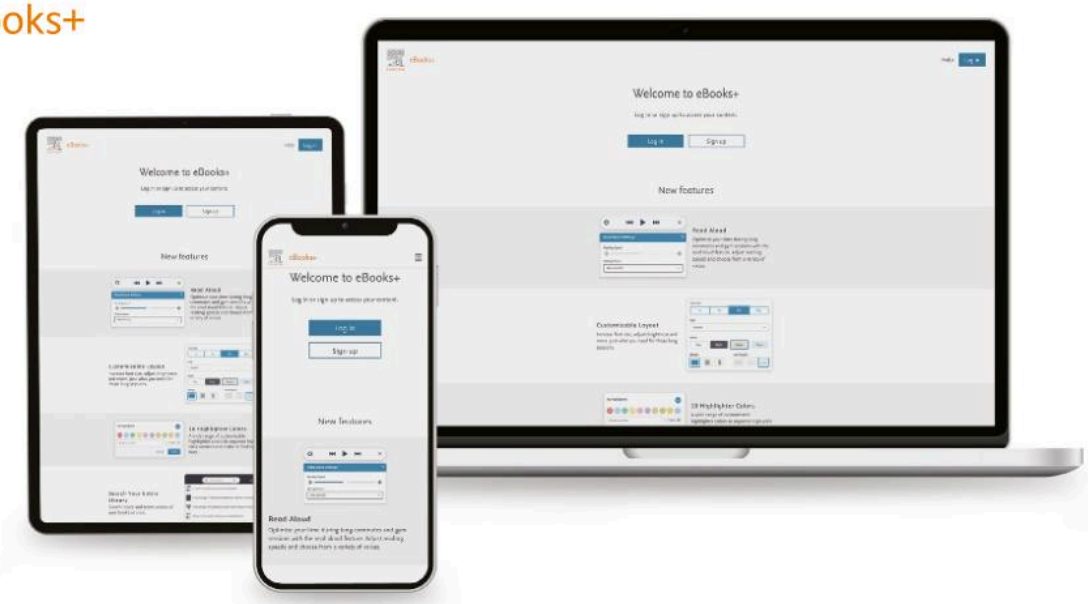


Gabriela S. Seiler
Donald E. Thrall

ELSEVIER

eBooks+

ELSEVIER



Activate your eBook today!

Elsevier eBooks+ allows you to search, browse, make notes, highlight, and have content read aloud.

1. To sign up, visit http://ebooks.health.elsevier.com/
2. Scratch to reveal your code below, and enter in **Redeem Access Code** box
3. Click **Redeem**

Contact Customer Support via
https://service.elsevier.com/app/home/supporthub/elsevierebooksplus/

PLACE PINCODE
STICKER HERE

By buying this genuine product you are guaranteed that Elsevier's high-quality online resources are included in this purchase.

Use of the current edition of the electronic version of this book (eBook) is subject to the terms of the non-transferable, limited license granted at https://www.elsevier.com/legal/elsevier-website-terms-and-conditions. Access to the eBook is limited to the first individual who redeems the access code located on the inside cover of this book at http://ebooks.health.elsevier.com/. The access code is valid for 8 years post publication date. The code may not be transferred to another party.

Thrall's Textbook of

VETERINARY DIAGNOSTIC RADIOLOGY

This page intentionally left blank



EIGHTH EDITION

Thrall's Textbook of VETERINARY DIAGNOSTIC RADIOLOGY

Gabriela S. Seiler Dr.Med.Vet., DECVDI, DACVR
Professor of Radiology
Molecular Biomedical Sciences
North Carolina State University
Raleigh, North Carolina

Donald E. Thrall, DVM, PHD
Emeritus Professor
College of Veterinary Medicine
North Carolina State University
Raleigh, North Carolina
Radiologist
IDEXX Telemedicine Consultants
Clackamas, Oregon



Elsevier
3251 Riverport Lane
St. Louis, Missouri 63043

THRALL'S TEXTBOOK OF VETERINARY DIAGNOSTIC RADIOLOGY,
EIGHTH EDITION ISBN: 978-0-323-93235-6
Copyright © 2025 by Elsevier Inc. All rights are reserved, including those for text and data mining, AI training, and similar technologies.

Publisher's note: Elsevier takes a neutral position with respect to territorial disputes or jurisdictional claims in its published content, including in maps and institutional affiliations.

No part of this publication may be reproduced or transmitted in any form or by any means, electronic or mechanical, including photocopying, recording, or any information storage and retrieval system, without permission in writing from the publisher. Details on how to seek permission, further information about the Publisher's permissions policies and our arrangements with organizations such as the Copyright Clearance Center and the Copyright Licensing Agency, can be found at our website: www.elsevier.com/permissions.

This book and the individual contributions contained in it are protected under copyright by the Publisher (other than as may be noted herein).

Notice

Practitioners and researchers must always rely on their own experience and knowledge in evaluating and using any information, methods, compounds or experiments described herein. Because of rapid advances in the medical sciences, in particular, independent verification of diagnoses and drug dosages should be made. To the fullest extent of the law, no responsibility is assumed by Elsevier, authors, editors or contributors for any injury and/or damage to persons or property as a matter of products liability, negligence or otherwise, or from any use or operation of any methods, products, instructions, or ideas contained in the material herein.

Previous editions copyrighted 2018, 2013, 2007, 2002, 1998, 1994, and 1986.

Executive Content Strategist: Lauren Willis
Content Development Specialist: Casey Potter
Publishing Services Manager: Deepthi Unni
Project Manager: Gayathri S
Design Direction: Ryan Cook

Printed in the United States of America

Last digit is the print number: 9 8 7 6 5 4 3 2 1



List of Contributors

Graeme Allan, DVSc, MVSc, FACVS, DACVR
Veterinary Radiologist
Veterinary Imaging Associates
St Leonards, Sydney
NSW, Australia

Melanie Anderson, DVM, DACVR
Radiologist
Radiology
University of Missouri
Columbia, Missouri

Ryan Appleby, DVM, DACVR
Assistant Professor
Clinical Studies
Ontario Veterinary College
Guelph, Ontario, Canada

Fabrice Audigié, DVM, PhD, HDR, Ass. LA-ECVDI
Professor in Equine Imaging and Locomotor Pathology
Cirale
Ecole Nationale Vétérinaire d'Alfort
Goustranville, France

Myra F. Barrett, DVM, MS, DACVR, DACVR-EDI
Professor of Radiology
Environmental and Radiological Health Sciences
Colorado State University
Fort Collins, Colorado

Clifford Berry III, DVM, DACVR
Associate Clinical Professor
Department of Molecular Biomedical Sciences
North Carolina State University
Apex, North Carolina

Kathryn W. Bills, VMD, DACVR, DACVR-EDI
Associate Professor
Department of Clinical Studies, New Bolton Center
University of Pennsylvania, School of Veterinary Medicine
Kennett Square, Pennsylvania

Elizabeth Biscoe, DVM, DACVR, DACVR-EDI
Equine Veterinary Radiologist
Equine Diagnostic Imaging
Archer, Florida
Veterinary Teleradiologist
VetRad
Worthington, Ohio

Valeria Busoni, DVM, PhD, DECVDI
Associate Professor
Service d'Imagerie Médicale—Clinique Vétérinaire Universitaire
Faculté de Médecine Vétérinaire
Université de Liège
Liège, Belgium

Eli B. Cohen, DVM, DACVR
Founder-Radiologist
Dragonfly Imaging, PLLC
Cary, North Carolina
Adjunct Clinical Professor
Molecular & Biomedical Sciences
NC State College of Veterinary Medicine
Raleigh, North Carolina

Marc-Andre d'Anjou, DMV, DACVR
Veterinary Radiologist
Diagnostic Imaging
Animages Inc.
Longueuil, Québec, Canada

Sarah Davies, BVSc, MS, DACVR
Veterinary Radiologist
Department of Radiology
The Pet Specialists
Terrey Hills, NSW, Australia

Randi Drees, Dr. Med. Vet., PhD, DACVR (Radiology & Radiation Oncology), DipECVDI (add Rad Oncol), MRCVS, CertAVP
Associate Professor
Department of Clinical Science and Services
The Royal Veterinary College
Hatfield, United Kingdom

Wm Tod Drost, DVM, DACVR
Radiologist
Telemedicine
IDEXX
Keswick, Virginia
Executive Director
American College of Veterinary Medicine
Harrisburg, Pennsylvania

Lisa J. Forrest, VMD, DACR, DACVR-RO
Professor
Surgical Sciences
University of Wisconsin-Madison
Madison, Wisconsin
Professor
Carbone Cancer Center
University of Wisconsin-Madison
Madison, Wisconsin

Lorrie Gaschen, DVM, PhD, Dr.Med.Vet, DECVDI
Adjunct Professor of Diagnostic Imaging
Veterinary Clinical Sciences
Louisiana State University
Baton Rouge, Louisiana
Radiologist
VetCT
Cambridge, United Kingdom

Lindsey J. Gilmour, DVM, DACVR, DACVR-EDI
Clinical Associate Professor
Department of Veterinary Large Animal Clinical Sciences
Texas A&M University
College of Veterinary Medicine
College Station, Texas

Christine L. Gremillion, DVM, DACVR, DACVR-EDI
Clinical Assistant Professor
Department of Large Animal Clinical Sciences
Texas A&M University College of Veterinary Medicine and Biomedical Sciences
College Station, Texas

Hock Gan Heng, DMV, MVS, MS, DACVR, DECVDI
Radiologist
VetCT
Cambridge, United Kingdom
Department of Veterinary Clinical Sciences,
Purdue University College of Veterinary
West Lafayette, Indiana

Elodie Huguet, DVM, DACVR
Assistant Professor of Diagnostic Imaging
Small Animal Clinical Sciences
The University of Florida
Micanopy, Florida
IDEXX Teleradiologist
IDEXX Telemedicine Consultants
Clackamas, Oregon

Martha Moon Larson, DVM, MS, DACVR
Professor, Radiology
Department of Small Animal Clinical Sciences
Va-MD College of Veterinary Medicine
Va Tech
Blacksburg, Virginia

Jimmy C. Lattimer, DVM, MS, DACVR, DACVR-RO
Associate Professor
Department of Veterinary Medicine and Surgery
University of Missouri
Columbia, Missouri

Jody E. Lawver, DVM, DACVR, DACVR-EDI
Assistant Professor
Department of Large Animal Clinical Sciences
Michigan State University
East Lansing, Michigan

Wilfried Mai, DVM, MS, PhD, DACVR, DECVDI
Professor
Department of Clinical Sciences and Advanced Medicine
University of Pennsylvania School of Veterinary Medicine
Philadelphia, Pennsylvania

Angela Marolf, DVM, DACVR
Professor and Chair
Department of Veterinary Clinical Sciences
The Ohio State University
Columbus, Ohio

Isabelle Masseau, DVM, PhD, DACVR
Associate Professor
Sciences Cliniques
Université de Montréal
Saint-Hyacinthe, Québec, Canada
Adjunct Professor
Veterinary Medicine & Surgery
University of Missouri
Columbia, Missouri

Federica Morandi, DVM, MS, DECVDI, DACVR
Professor of Radiology
Small Animal Clinical Sciences
University of Tennessee
Knoxville, Tennessee

Dana A. Neelis, DVM, MS, DACVR, DACVR-EDI
Radiologist
Radiology
Neelis Veterinary Imaging
Emmett, Idaho

Nathan C. Nelson, DVM, MS, DACVR, DACVR-EDI
Clinical Professor
Department of Molecular Biomedical Sciences
North Carolina State University
Raleigh, North Carolina

Stephanie G. Nykamp, DVM, MSc, DACVR
Veterinary Radiologist
Vet's Choice Radiology
Northbrook, Illinois

Kathryn L. Phillips, DVM, DACVR, DACVR-EDI
Associate Professor
Veterinary Surgical and Radiological Sciences
UC Davis
Davis, California

Rachel E. Pollard, DVM, PhD, DACVR
Professor Emerita of Diagnostic Imaging
Surgical and Radiological Sciences
University of California, Davis School of Veterinary Medicine
Davis, California

Erin G. Porter, DVM, DACVR, DACVR-EDI
Clinical Associate Professor
Large Animal Clinical Sciences
University of Florida College of Veterinary Medicine
Gainesville, Florida

Elissa K. Randall, DVM, MS, DACVR
Professor Diagnostic Imaging
Environmental and Radiological Health Sciences
Colorado State University
Fort Collins, Colorado

Jennifer A. Reetz, DVM, DACVIM (LA), DACVR
Veterinary Radiologist
Department of Clinical Sciences and Advanced Medicine
School of Veterinary Medicine
University of Pennsylvania
Philadelphia, Pennsylvania

Elizabeth A. Riedesel, DVM, DACVR
Emeritus Professor Retired
Veterinary Clinical Sciences
Iowa State University
Ames, Iowa
Consulting Radiologist
eImaging
Fort Worth, Texas

Ian Robertson, BVSc, DACVR
Emeritus Clinical Professor
Department of Molecular Biomedical Sciences
NC State University
Raleigh, North Carolina
Radiologist
Dragonfly Imaging PLLC
Cary, North Carolina

Federica Rossi, DVM, SRV, DECVDI
Veterinary Radiologist
Diagnostic Imaging
Anicura Clinica Veterinaria dell'Orologio
Sasso Marconi, Italy

Gabriela S. Seiler, Dr.Med.Vet., DECVDI, DACVR
Professor of Radiology
Molecular Biomedical Sciences
North Carolina State University
Raleigh, North Carolina

Kathy A. Spaulding, DVM, DACVR
Clinical Professor Radiology Emeritus—Retired
Department of Veterinary Large Animal Clinical Sciences
Texas A&M University
College Station, Texas

Susanne M. Stieger-Vanegas, Dr. Med. Vet., PhD, DECVDI
Professor, Diagnostic Imaging
Clinical Sciences
Carlson College of Veterinary Medicine
Oregon State University
Corvallis, Oregon

Donald E. Thrall, DVM, PhD, DACVR
Emeritus Professor
College of Veterinary Medicine
North Carolina State University
Raleigh, North Carolina
Radiologist
IDEXX Telemedicine Consultants
Clackamas, Oregon

Elizabeth Acutt, BVSc, MS, DACVR-EDI
Assistant Professor
Department of Large Animal Diagnostic Imaging
School of Veterinary Medicine
University of Pennsylvania
Philadelphia, Pennsylvania

Lenin Arturo Villamizar Martinez, DVM, MS, PhD, DAVDC
Assistant Professor of Veterinary Dentistry and Oral Surgery
Department of Clinical Sciences
North Carolina State University College of Veterinary Medicine
Holly Springs, North Carolina

Andra K. Voges, DVM, DACVR
Clinical Professor
Large Animal Clinical Sciences, Radiology
Texas A&M College of Veterinary Medicine
College Station, Texas

William R. Widmer, DVM, MS, DACVR
Emeritus Professor College of Veterinary Medicine
Veterinary Clinical Sciences
Purdue University
West Lafayette, Indiana
Adjunct Professor, Diagnostic Imaging
College of Veterinary Medicine
Lincoln Memorial University
Harrogate, Tennessee

Preface

The first edition of this text was published in 1986…over 37 years ago. I'm guessing this predates the birth year of some of the authors contributing to this eighth edition. I clearly remember celebrating the release of the first edition with my then Department Head, Arthur Aronson, and a nice bottle of champagne. His support was so critical regarding many of my accomplishments, including this text. Art is no longer with us, but I think of him often. I doubt he would have predicted that this book would survive so many revisions; I know I did not.

I became involved with the first edition solely by chance. It was not something I sought. But, having been presented with the opportunity, I was intrigued and decided to give it a go. I had been involved with an earlier veterinary radiology book, *Carlson's Veterinary Radiology*, along with Drs. Edward Gillette and Jacques Lebel. This was at a time when I thought I knew much more than I did. That book, at least my part, was largely unsuccessful so the opportunity to have a leadership role with another radiology text was a chance at redemption.

When writing this preface for the eighth edition, I looked at my copy of the first edition. What struck me immediately was the extremely poor quality of the illustrations. I remember being reminded of that on numerous occasions and I was quite surprised that a second edition was even requested by the publisher. Fortunately, this problem of poor radiographic reproduction into the print medium has been solved by the greatly increased quality of digital image capture compared to film cassettes. All the images in this text were acquired initially in a digital format, making for the highest quality of reproduction, and select digital images are also available directly on the textbook website.

While numerous things about this book have changed along the way, such as inclusion of CT and MRI concepts and images, normal anatomy, and web-based ancillary materials, the core principles of the book have not. The basis of interpretation used in this textbook remains centered upon description of radiographic abnormalities in terms of roentgen signs—changes in size, shape, location, number, margination, and opacity. Having a firm understanding of roentgen sign description makes one less inclined to make errors by jumping immediately to a diagnosis rather than thoroughly considering radiographic changes in an orderly and efficient manner. The audience also remains the same, with content aimed toward students of imaging at all levels, private practitioners, and to some extent specialists in other fields. Chapters covering the basic principles of interpretation of images of the axial and appendicular skeleton in small and large animals, and the thorax and abdomen in small animals, should be of value to beginning interpreters. These basic chapters offer a framework upon which to base an understanding of more detailed chapters dealing with specific abnormalities. And, as in the second through seventh editions, all chapters in this eighth edition have been either completely rewritten by a new author or thoroughly revised. No chapter has escaped in-depth scrutiny, ensuring that the latest and most accurate information is included.

From the first edition onward, I have always believed that is impossible for one person to prepare a meaningful, comprehensive textbook of veterinary imaging. Thus, as in all previous editions, a group of highly trained specialists in imaging have come together to produce what I think is a magnificent complication of veterinary imaging from the basic to the advanced. I would like to extend my heartfelt thanks to this group of radiologists for taking time from their busy schedules to help create this product.

Nothing lasts forever, including my tenure as Editor of this book. One of my most significant accomplishments while at North Carolina State University was to convince Dr. Gabriela (Gabi) Seiler to join our radiology faculty. Gabi is one of the brightest radiologists that I know, and a wonderful person. She has been extremely productive at North Carolina State University and quickly rose to the rank of Professor. When I was presented with the opportunity of preparing an eighth edition of this book, I knew immediately that I no longer had the stamina for such an immense undertaking. When thinking about a successor, Gabi was the first person who came to mind. I discussed the possibility of assuming Editorship with Gabi and after earnest consideration she agreed to take it on, which was a big relief and a source of great joy for me. As a result, the work you have before you is really a product of Dr. Gabi Seiler and not me. She developed the content for the eighth edition, recruited a cadre of new accomplished authors, and edited much of the text. Although she and I are listed at coeditors, this is Dr. Seiler's book.

From here forward, my involvement with this work will be in name only…*Thrall's Textbook of Veterinary Diagnostic Radiology*. I am honored to have been charged with stewardship of this book for all these years. I trust this eighth edition will be well received and I anticipate many more successful editions under the guidance of Dr. Seiler.

Donald E. Thrall

Acknowledgement

I am deeply honored to be selected as the new editor of the Thrall Textbook of Veterinary Diagnostic Radiology—a truly iconic resource that has profoundly enhanced student learning and remains indispensable for both students and clinicians. I want to acknowledge Dr. Don Thrall's extraordinary achievement in creating and advancing this book to its current 8th edition. I genuinely believe that no one else could have accomplished this, and generations of veterinarians have and will benefit from it. I also deeply appreciate the invaluable contributions of the current and previous authors. Thank you all so much.

Gabriela S. Seiler

Contents

SECTION I

PHYSICS AND PRINCIPLES OF INTERPRETATION

1 **Radiation Protection and Physics of Diagnostic Radiology, 2**
William R. Widmer and Donald E. Thrall

2 **Digital Radiographic Imaging, 22**
Ian Robertson, Donald E. Thrall and Nathan C. Nelson

3 **Physics of Ultrasound Imaging, 40**
Hock Gan Heng and Wm Tod Drost

4 **Principles of Computed Tomography and Magnetic Resonance Imaging, 55**
Marc-André d'Anjou

5 **Contrast Media in Diagnostic Imaging, 76**
Jennifer A. Reetz

6 **Radiographic Interpretation, 90**
Donald E. Thrall

7 **Errors and Pitfalls in Radiographic Interpretation, 100**
Eli B. Cohen

SECTION II

THE AXIAL SKELETON: CANINE, FELINE, AND EQUINE

8 **Radiographic Anatomy of the Axial Skeleton, 110**
Andra K. Voges and Kathy A. Spaulding

9 **Basic Principles of Radiographic Interpretation of the Axial Skeleton, 123**
Donald E. Thrall

10 **Canine and Feline Dental Disease, 137**
Lenin Arturo Villamizar Martinez

11 **The Skull and Nasal Cavities: Canine and Feline, 165**
Lisa J. Forrest

12 **Magnetic Resonance Imaging and Computed Tomographic Features of Brain Disease in Small Animals, 187**
Ian Robertson and Gabriela S. Seiler

13 **The Equine Head, 217**
Nathan C. Nelson

14 **Radiography and Myelography of the Canine and Feline Vertebrae, 244**
William R. Widmer

15 **Magnetic Resonance Imaging and Computed Tomography Features of Canine and Feline Spinal Cord Disease, 279**
Wilfried Mai

SECTION III

THE APPENDICULAR SKELETON: CANINE, FELINE, AND EQUINE

16 **Radiographic Anatomy of the Appendicular Skeleton, 320**
Kathy A. Spaulding and Andra K. Voges

17 **Principles of Radiographic Interpretation of the Appendicular Skeleton and Radiographic Features of Bone Tumors, 348**
Donald E. Thrall

18 **Orthopedic Diseases of Young and Growing Dogs and Cats, 365**
Kathryn L. Phillips

19 **Fracture Healing and Complications, 384**
Gabriela S. Seiler

20 **Radiographic Signs of Joint Disease in Dogs and Cats, 401**
Graeme Allan and Sarah Davies

21 **The Equine Stifle, 428**
Valeria Busoni and Fabrice Audigié

22 **Equine Tarsus, 449**
Jody E. Lawver

23 **Equine Carpus, 470**
Lindsey J. Gilmour

24 **Equine Metacarpus and Metatarsus, 489**
Erin G. Porter

25 **Equine Fetlock Joint, 511**
Kathryn W. Bills

26 **Equine Pastern, 530**
Elizabeth Biscoe and Dana A. Neelis

27 **Equine Foot, 543**
Myra F. Barrett, Elizabeth Acutt and Federica Morandi

SECTION IV

THE THORACIC CAVITY CANINE, FELINE AND EQUINE

28 **Principles of Radiographic Interpretation of the Thorax, 578**
Donald E. Thrall

29 **Canine and Feline Larynx and Trachea, 592**
Randi Drees

30 **Pharynx, Upper Esophageal Sphincter, and Esophagus, 608**
Rachel E. Pollard

31 **Canine and Feline Thoracic Wall, 631**
Gabriela S. Seiler

32 **Canine and Feline Diaphragm, 646**
Elissa K. Randall

33 **Canine and Feline Mediastinum, 662**
Federica Morandi and Donald E. Thrall

34 **Canine and Feline Pleural Space, 686**
Gabriela S. Seiler

35 **Canine and Feline Cardiovascular System, 702**
Elodie Huguet and Clifford Berry

36 **Canine and Feline Lung, 724**
Isabelle Masseau

37 **Equine Thorax, 746**
Stephanie G. Nykamp

SECTION V

ABDOMINAL CAVITY: CANINE AND FELINE

38 **Principles of Radiographic Interpretation of the Abdomen, 764**
Donald E. Thrall

39 **Peritoneal Space, 778**
Susanne M. Stieger-Vanegas

40 **Liver and Spleen, 805**
Martha Moon Larson

41 **Kidneys and Ureters, 837**
Gabriela S. Seiler and Ryan Appleby

42 **Urinary Bladder and Urethra, 860**
Angela Marolf

43 **Prostate Gland, 884**
Jimmy C. Lattimer and Melanie Anderson

44 **Uterus, Ovaries, Vagina, and Testes, 894**
Federica Rossi

45 **Stomach, 923**
Susanne M. Stieger-Vanegas

46 **Small Bowel, 956**
Lorrie Gaschen and Elizabeth A. Riedesel

47 **Large Bowel, 986**
Christine L. Gremillion

Index, 999

Video Table of Contents

Video 4.1. **Image Display.**

Video 4.2. **Computed Tomography.**

Video 29.1. **Sequential DR Images.**

Video 29.2. **Sequential DR Images.**

Video 29.3. **Videofluoroscopic Examination.**

Video 29.4. **Videofluoroscopic Examination.**

Video 29.5. **Videofluoroscopic Examination.**

Video 32.1. **Video Loop of a 3-Year-Old English Bulldog With Chronic Regurgitation for 1 Year.**

Video 32.2. **Ultrasound Video Loop of a 1-Year-Old Cat.**

Video 35.1. **Video of a Normal Beating Heart.**

Video 35.2. **Video of the Heart Base Region of a Dog With Mitral Insufficiency and Tracheal Chondromalacia.**

Video 42.1. **Fluoroscopy of Vaginocystourethrography.**

Video 42.2. **Sonography of the Penile Urethra.**

Video 42.3. **Sonography of the Proximal Urethra.**

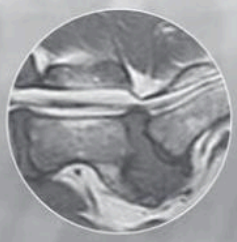
Video 42.4. **Fluoroscopy of Retrograde Urethrography.**

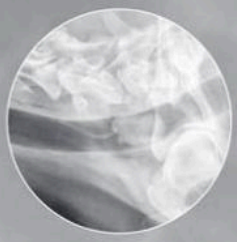
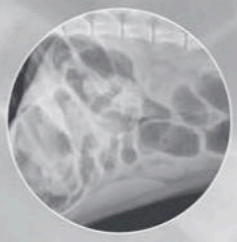
Video 44.1. **Ultrasonographic Findings in Normal Pregnancy - Heart Flick Day 21.**

Video 44.2. **Ultrasonographic Findings in Normal Pregnancy - Heart Flick Day 45.**

SECTION I

Physics and Principles of Interpretation

1 **Radiation Protection and Physics of Diagnostic Radiology**
William R. Widmer • Donald E. Thrall

2 **Digital Radiographic Imaging**
Ian Robertson • Donald E. Thrall • Nathan C. Nelson

3 **Physics of Ultrasound Imaging**
Hock Gan Heng • Wm Tod Drost

4 **Principles of Computed Tomography and Magnetic Resonance Imaging**
Marc-Andre d'Anjou

5 **Contrast Media in Diagnostic Imaging**
Jennifer A. Reetz

6 **Radiographic Interpretation**
Donald E. Thrall

7 **Errors and Pitfalls in Radiographic Interpretation**
Eli B. Cohen

CHAPTER 1

Radiation Protection and Physics of Diagnostic Radiology

William R. Widmer • Donald E. Thrall

X-rays were discovered on November 8, 1895, by Wilhelm Conrad Roentgen, a German physicist (Fig. 1.1).[1] X-rays were immediately used for medical purposes, and many sophisticated applications were soon devised. For example, angiography was described in 1896, only 1 year after the initial discovery of x-rays. Roentgen's finding revolutionized the diagnosis and treatment of disease, and in recognition he was awarded the first Nobel Prize for Physics in 1901. More than 125 years after their discovery, imaging using x-rays is one of the most important and widely used diagnostic tests in people and animals. Despite the advances afforded by diagnostic ultrasound, computed tomography, and magnetic resonance imaging, conventional radiography remains the "workhorse" of veterinary imaging.

BASIC PROPERTIES OF X-RAYS

X-rays and gamma rays are part of the spectrum of electromagnetic (EM) radiation. The only distinction between x-rays and gamma rays is their source; x-rays are produced by electron interactions outside the nucleus, and gamma rays are released from inside the nucleus of unstable atoms having excess energy. There is a false impression that gamma rays are more energetic than x-rays, but this is not universally true. The energy of a gamma ray depends on the amount of energy released by the unstable atom, and the energy of an x-ray depends on the energy of the electron that interacts with the atom. Radiopharmaceuticals used in nuclear imaging generally emit gamma rays with energy similar to x-rays used for diagnostic imaging.



Fig. 1.1 **A,** Wilhelm Conrad Roentgen accidentally discovered x-rays while working with a cathode ray tube containing an inert gas. Roentgen noted that high voltage applied to the tube caused fluorescence of a photographic plate. Roentgen deduced that an unknown, invisible "x" radiation must be produced by the cathode ray tube. **B**, The first known radiograph was made of his wife's hand. (Images in the public domain.)

Table • 1.1

Wavelength and Origin of Common Types of Electromagnetic Radiation.

TYPE OF ELECTROMAGNETIC RADIATION	WAVELENGTH	ORIGIN
Radio waves	1 mm–100 km	Oscillating electrons in antennae
Microwaves	1 mm–1 m	Oscillating electrons in antennae
Infrared	780 nm–1 mm	Electron energy level transition
Visible light	380 nm–700 nm	Electron energy level transition
Ultraviolet	100 nm–400 nm	Electron energy level transition
X-rays	0.1 nm–10 nm	Bremsstrahlung, characteristic
Gamma Rays	1×10^{-6} nm	Nuclear decay

From Bushberg JT, Seibert JA, Leidholdt EM, Jr, et al. *The Essential Physics of Medical Imaging*. 2nd ed. Lippincott Williams & Wilkins; 2012.

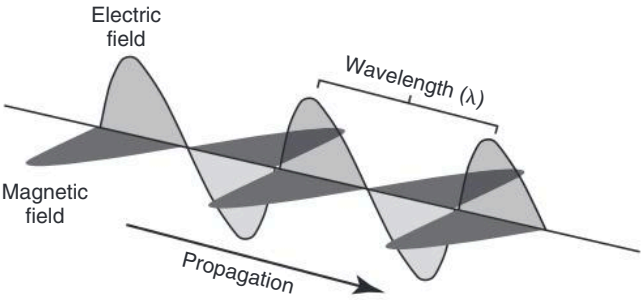


Fig. 1.2 All forms of electromagnetic radiation are characterized by oscillating electric and magnetic fields that move in planes at right angles to each other. Any form of electromagnetic radiation is described by the wavelength, λ, which is the distance between crests, and the frequency, f, which is the number of crests per unit time. The frequency and wavelength determine the specific characteristics of that form of radiation. The velocity (c) of all forms of electromagnetic radiation is the same—the speed of light. The product of wavelength and frequency equals the velocity: $c = f \times \lambda$. Therefore, because velocity is constant, as frequency increases, the wavelength must decrease, and vice versa.

Familiar types of EM radiation other than x-rays and gamma rays include radio waves, radar, microwaves, and visible light (Table 1.1).

EM radiation is a combination of electric and magnetic fields that travel together, oscillating in orthogonal planes in sine-wave fashion (Fig. 1.2). Sine waves are characterized by two related parameters—frequency and wavelength. The velocity of EM radiation is constant, the speed of light, resulting in an inverse relationship between frequency and velocity according to the formula:

$$V = f\lambda$$

- V = speed of light (m/s)
- f = frequency in Hz
- λ = wavelength in m

Properties of x-rays and gamma rays are given in Box 1.1. Some properties of EM radiation cannot be explained adequately by the theories of wave propagation illustrated in Fig. 1.2. Therefore, the *photon* concept was developed to explain the apparent particulate behavior of x-rays and gamma rays. A photon can be considered as a discrete bundle of EM radiation as opposed to a wave. This makes it easier to understand how x-rays create an image or cause radiation damage. In this book, the terms *x-ray* and *photon* are used interchangeably.

Box • 1.1

Properties of X-Rays and Gamma Rays

Have no charge
Have no mass
Travel at the speed of light
Are invisible
Cannot be felt
Travel in a straight line
Cannot be deflected by magnetic fields
Penetrate all matter to some degree
Cause certain substances to fluoresce
Can expose photographic emulsions
Can ionize atoms

The ***energy*** of EM radiation is described according to the formula:

$$\text{Energy} = \text{Planck's constant} \times \frac{\text{speed of light}}{\text{wavelength}}$$

Planck's constant is a proportionality constant between the energy of a photon and its wavelength, and the speed of light is also a constant. Therefore, the energy of EM radiation is inversely proportional to wavelength. The biologic effects of EM radiation are a function of the energy.

The unit of energy for EM radiation is the *electron volt* (eV). One electron volt is the energy gained by one electron as it is accelerated through a potential difference of 1V. On an absolute scale, this is a very small amount of energy. However, x-rays with energy of only 15 eV* can produce ionization of atoms. Ionization occurs when an electron is ejected from the atom, in radiography by an x-ray. This creates an ion pair consisting of the negatively charged electron and the positively charged atom (Fig. 1.3). When x-rays strike a person, they can result in ionizations of DNA, leading to (1) mutations, (2) abortion or fetal abnormalities, (3) susceptibility to disease and shortened life span, (4) carcinogenesis, and (5) cataracts.[2] Therefore, minimizing exposure of personnel working in a radiation environment is critical. Radiation also causes ionizations in patients undergoing medical imaging procedures, but the risk of

*The electron volt (eV) should not be confused with the concept of kilovoltage peak (kVp) applied in an x-ray tube during an exposure; kVp is discussed later in the Production of X-rays section.

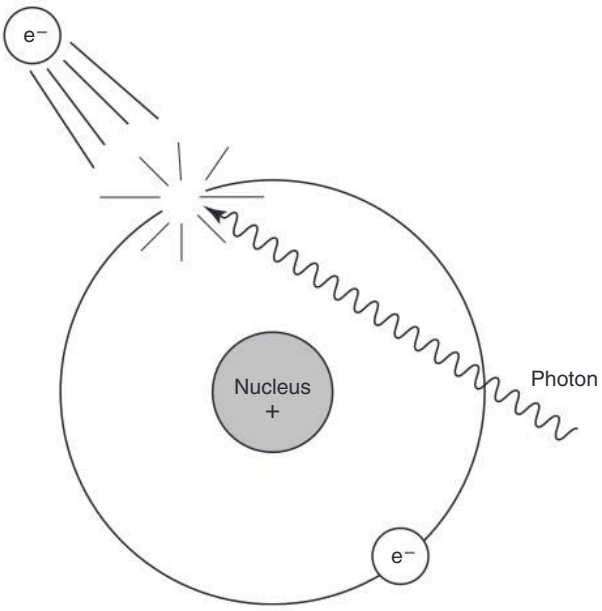


Fig. 1.3 The principle of ionization. A photon ejects an electron from an atom, causing ionization and forming an ion pair, consisting of a negatively charged electron and a positively charged atom. After this ionization event, the photon, depending on its energy, may be completely absorbed, or it may interact with other atoms to produce more ionization. The ejected electron can also interact with biologic molecules, such as DNA, and produce damage. The relative size of the nucleus, electrons, and orbital shells in this figure is not to scale. The "+" symbol in the nucleus designates the normal nuclear positivity created by the presence of positively charged protons. In a neutral atom, this positive charge in the nucleus is balanced by an equal negative charge of orbital electrons.

radiation injury from an imaging procedure is offset by the diagnostic value of the procedure. Radiation workers, on the other hand, are subject to repeated potential low-level exposure and the risk for damage is increased. Also important is the fact that radiation damage to DNA can be amplified biologically because DNA controls cellular processes that extend into subsequent generations of daughter cells. Although only 15 eV of energy is required for ionization of biologic molecules, the energy of x-rays used for medical imaging is much greater. Therefore, each x-ray photon can lead to multiple ionizations in tissue.

The relative risk of biologic injury from x-rays or gamma rays is greater than from other types of EM radiation. For example, the wavelength of visible light is 10,000 times longer than the wavelength of x-rays, and the wavelength of radio waves is even longer (see Table 1.1). Therefore, the energy of light waves and radio waves is many orders of magnitude lower than the energy of x-rays, meaning that light and radio waves do not produce tissue ionization or DNA damage. Other forms of EM radiation, such as microwaves, can lead to biologic damage such as tissue heating but do not lead to molecular ionization.

RADIATION PROTECTION

A goal in diagnostic radiology is to obtain maximum diagnostic information with minimal radiation exposure of the patient, radiology personnel, and general public. This is achievable if guidelines for safe practice are followed and personal protective equipment (PPE) is used. However, because x-rays cannot be seen or felt, it is easy to disregard the danger associated with occupational x-ray exposure (Fig. 1.4). Many veterinarians and technologists have developed a cavalier attitude regarding the hazards associated with ionizing radiation and put themselves at risk, from both medical and legal perspectives. While the use of digital radiograph has vastly improved radiographic quality in veterinary imaging, it has also in many instances led to further disregard for safe radiation practices since the cost and time investment in retakes are minimal.



Fig. 1.4 Careless and unacceptable approach to radiography. The technologist's hands are in the primary x-ray beam. Careless habits such as this are perpetuated because of the stealthy properties of x-rays and lead to unnecessary personnel exposure that could become biologically significant.

Table • 1.2

Radiation Weighting Factor (Quality Factor) for Various Radiation Types.

TYPE OF RADIATION	WEIGHTING FACTOR
X-rays	1
Gamma rays	1
Beta particle (electron)	1
Neutrons	
<10 keV	5
10–100 keV	10
100 keV–2 MeV	20
Alpha particles	20

General principles of radiation protection that can form the basis of a safe workplace are discussed in this chapter. Any specific recommendations regarding radiation safety or protection made in this chapter are subject to overrule by local, state, and/or federal regulations.

Radiation Units

Two related concepts must be understood before radiation units are considered. First, radiation *exposure* and radiation *absorption* are not the same. Some tissues absorb radiation more effectively than others, meaning that exposure to the same amount of radiation will result in different absorbed doses in these tissues. Second, the biologic effect of the same absorbed dose can also be different, being a function of both radiation type and energy. A numeric *weighting factor* or *quality factor* has been derived to estimate the difference in biologic effectiveness of various types of radiation (Table 1.2).

Radiation exposure, radiation absorption, and dose equivalent each have their own unit of measure that was defined originally in the centimeter-gram-second (CGS) system of measures. In 1977, the International System of Units (SI units) was developed in keeping with the trend toward universal adoption

Table • 1.3

Radiation Units.

QUANTITY	CGS[a] UNIT	VALUE	SI[b] UNIT	VALUE
Exposure dose	roentgen	One electrostatic unit of electricity in 1 cubic centimeter of dry air at 0°C and standard atmospheric pressure	roentgen[c]	$2.58 \times 10 - 4$ C/kg
Absorbed dose	rad	100 ergs/g of tissue	gray (Gy)	1 Gy = 1 joule/kg (1 Gy = 100 rads)
Equivalent biologic dose	rem	Dose in rads times weighting factor[d]	sievert (Sv)	Dose in Gy times weighting factor (1 rem = 10 mSv)

[a]CGS, centimeter-gram-second system of units.
[b]International System of Units.
[c]Although the use of roentgen is allowable under the SI system, it is not itself an SI unit, and continued use is strongly discouraged by the National Institute of Standards and Technology.
[d]Weighting factor is a radiation type-specific quantity that compares the ionization density of various types of radiation; see Table 1.2.

of the metric system[3] (Table 1.3). In general, the system of SI units has not been universally adopted in the United States,[4,5] and CGS radiation units are still used, which can be a source of confusion.

Exposure

Radiation exposure is based on the amount of ionization in air that the radiation produces and is quantified by the amount of electrical charge resulting from the ionization. Radiation exposure is expressed in the SI system as coulombs[†] per kilogram of air (C/kg) (see Table 1.3). This SI unit of exposure is cumbersome; thus, an older term of exposure, the roentgen, is still used. One roentgen equals a charge of 2.58 C/kg in air.

Absorbed Dose

The efficiency of x-ray absorption in different materials can vary widely. For example, lead is a much more efficient absorber than water. Therefore, the radiation dose in tissues with different absorption efficiencies will be different when exposed to the same amount of radiation (Fig. 1.5). The SI unit for absorbed dose is the *gray* (Gy). One gray is the amount of radiation leading to absorption of 1 joule[‡]/kg of tissue. Before SI units were accepted, the unit of absorbed dose was the rad, which is equal to 100 ergs[§]/g of tissue (see Table 1.3). The term *rad* is obsolete, but it is so engrained in the radiology lexicon that it has not been replaced universally by the Gy. One gray is equal to 100 rad.

In soft tissue such as muscle, exposure to 1 roentgen amounts to an absorbed dose of approximately 0.9 centigray (cGy) or 0.9 rad. In comparison, bone is a more efficient absorber of x-rays than soft tissue, and exposure to bone of 1 roentgen results in a higher bone-absorbed dose. This difference in absorption between bone and soft tissue may be as great as a factor of 4–5 with low-energy radiation. Differential x-ray absorption between various tissues is the basis of radiographic contrast, and without this difference making a meaningful radiograph would not be possible. As discussed later, the magnitude of the difference between exposure and absorbed dose is the greatest for low energy photons and decreases as photon energy increases.

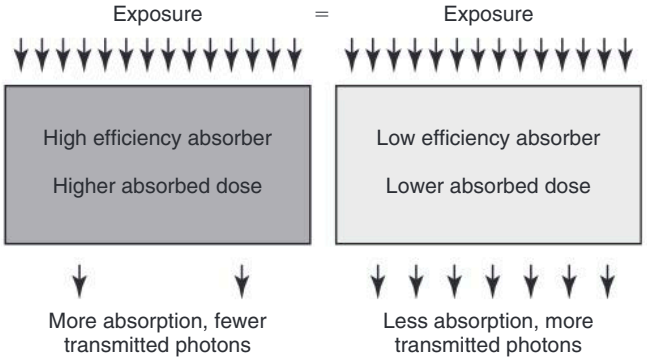


Fig. 1.5 Two materials are exposed to the same number of x-ray photons, represented by the *arrows* at the top. Thus, the exposure dose, in roentgens, or in coulombs per kilogram, is the same for both materials. However, the efficiency of x-ray absorption for the two materials is different. The material on the left is more efficient in absorbing x-rays than the material on the *right*. Therefore, the absorbed dose will be higher in the material on the left even though the exposure dose is the same. One real-life example of this phenomenon is a limb, where bone would be the high-efficiency absorber and fat or muscle the low-efficiency absorber.

Dose Equivalent

As noted earlier, the same absorbed dose, in Gy, from different types of radiation may not produce the same biologic effect. For example, damage from particulate radiation, such as an alpha particle[**] is greater on a Gy-for-Gy basis than damage from the same dose of x-rays (see Table 1.2). This is related to differences in *ionization density* for different types of radiation. A large, heavily charged particle, such as an alpha particle, creates many ionizations that are close together compared to a small lightly charged particle, such as an electron, where ionizations are more widely spaced (Fig. 1.6). The closer the ionizations are to each other, i.e., greater ionization density, the more biologic

[†] A coulomb is the unit of electric charge in the SI units. It is the charge transferred by a constant current of 1 ampere in 1 second.
[‡] The joule is the unit of energy in the SI units. It is the energy exerted by the force of one newton acting to move an object through a distance of 1 m.
[§] The erg is the unit of energy in the CGS system of units. It is the energy exerted by the force of one dyne acting to move an object through a distance of 1 cm.

[**] An alpha particle is a helium nucleus, containing two protons and two neutrons, without orbital electrons. An alpha particle has an electrical charge of 2+ and a mass more than 7000 times larger than that of an electron.

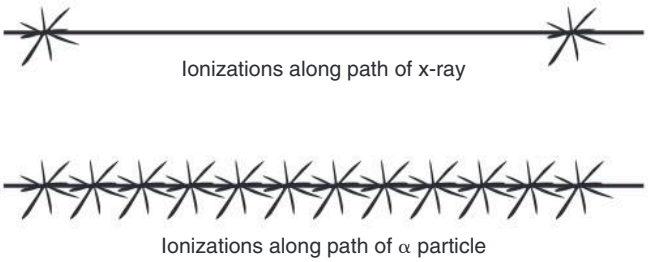


Fig. 1.6 Representation of the ionization density along the paths of an x-ray and an alpha particle. The ionization density along the path of the alpha particle is much higher because of its large mass and 2+ charge. This will lead to greater biologic damage on a Gy-per-Gy basis, and a correction factor will be needed to compare the biologic damage resulting from equal absorbed doses of x-rays versus alpha particles.

damage results from a given dose. Therefore, deposition of 1 Gy from an alpha particle does more biologic damage than deposition of 1 Gy from an x-ray because the ionizations are more clustered. The difference in biologic damage from the same absorbed dose of various radiation types is estimated by the weighting factor, as described earlier (see Table 1.2).

In the SI system, the unit of dose equivalency is the sievert (Sv); the Sv is derived from the product of the absorbed dose in Gy and the weighting factor. Before SI units were accepted, the unit of dose equivalency was the *radiation equivalent in man*, or *rem* (see Table 1.3). The rem was derived from the product of the absorbed dose in rads and the weighting factor, because 1 Gy = 100 rads, 1 Sv = 100 rem.

Radiation Safety

Principles of radiation safety are based on establishment of guidelines to prevent unnecessary exposure of radiation workers and the general public to ionizing radiation. The premise of radiation protection is that some low level of radiation exposure to radiation workers is permissible and will not lead to significant abnormalities or disease. Adverse effects can be classified as either *deterministic* or *stochastic*. Deterministic effects have a threshold. In other words, below some dose there is no effect, but above the threshold dose the severity of the effect is dose related. Radiation-induced cataracts are an example of a deterministic effect. Conversely, stochastic (random) effects have no dose threshold, and the severity of the effect is independent of dose. Radiation-induced cancer is an example of a stochastic effect.[6]

Maximum permissible dose (MPD) is the maximal amount of absorbed radiation that can be delivered to an individual as a whole-body dose or a dose to a specific organ and still be considered safe. The term *safe* in this context means that there is no conclusive evidence that the MPD will lead to harmful immediate or long-term effects to the body as a whole or to any individual structure or organ. Although the effect of very low doses of radiation is not known with certainty, it is safe to assume that any amount of radiation will have some effect and keeping one's dose below the MPD is important. An analogy could be made to smoking a cigarette once a month. There is no evidence that physical damage results from this frequency of smoking, but with increased smoking the probability of physical damage escalates by virtue of a cumulative effect. Unfortunately, an absolute threshold below which damage will definitely not occur has not been established for either cigarette smoking or radiation exposure.

There are multiple levels of bureaucracy regarding the establishment of guidelines for radiation exposure, aimed at avoiding deterministic and stochastic effects. Understanding the mission of all involved organizations can be confusing. Furthermore, different exposure limits are defined for radiation workers versus the general public. These exposure limits vary according to risk versus benefit. For example, the small risk to a member of the general public from being subjected to a radiographic study is outweighed by the benefit of a diagnosis. Likewise, the slightly higher exposure limits allowed for radiation workers are considered acceptable with respect to the missions of the occupation.

The International Commission on Radiological Protection (ICRP) is the primary international body focusing on protection against ionizing radiation. The ICRP is an independent, international, nongovernmental organization. The ICRP provides recommendations and guidance on protection against the risks associated with ionizing radiation. Their recommendations are published approximately four times each year as the journal *Annals of the ICRP*. The whole-body limit for radiation workers set by the ICRP for avoiding stochastic effects is 20 millisievert (mSv) per year, averaged over 5 years, with the provision that dose in any one year should not exceed 50 mSv.[7] The ICRP maintains exposure per quarter should not exceed 12.5 mSv.

In the United States, the National Council on Radiation Protection (NCRP) was chartered by Congress in 1964. Some of the objectives of the NCRP are to develop recommendations about radiation protection and to cooperate with the ICRP. The whole-body limit set for radiation workers by the NCRP for avoiding stochastic effects is 50 mSv per year with a lifetime accumulation not to exceed 10 mSv × age in years.[8] The NCRP also recommends that no occupational exposure occur until the age of 18 years.

The Nuclear Regulatory Commission (NRC) is the agency officially responsible for defining federal exposure standards in the United States. The NRC has adopted the annual radiation dose to adult radiation workers as recommended by the NCRP, a maximum of 50 mSv (5 rem) per year.[9] However, the NRC has not established an upper limit for cumulative exposure because of the uncertainty of such predictions.

The difference in opinion between the NRC and the NCRP regarding the limits for cumulative exposure can be confusing. However, rather than focusing on a specific number for cumulative or annual exposure, the goal should be to minimize any exposure. This is the basis of the ALARA approach, discussed later.

The allowable limit for radiation workers who become pregnant is lower than for nonpregnant radiation workers but ideally should be zero. The monthly exposure limit for the embryo or fetus should not exceed 0.5 mSv (0.05 rem). It is the responsibility of the pregnant radiation worker to notify the supervisor of the pregnancy ***in writing*** so that any change in work habits needed to stay within the recommended dose limit can be implemented.

For the general public, radiation exposure, excluding that related to medical use such as diagnostic imaging and radiation therapy, should not exceed 1 mSv (0.1 rem) per year.

In addition to occupational exposure of radiation workers, the entire population is exposed continually to very low levels of natural and man-made radiation. A revised breakdown of relative exposure of the U.S. public to radiation by various sources was published by the NCRP in 2015 (Fig. 1.7).[10] Revised estimates were needed because in 2006, Americans were exposed to more than seven times as much ionizing radiation from medical procedures as in the early 1980s, mainly due to increases in CT imaging. The number of CT studies performed in human patients doubled between 1997 and 2006.[11] In 2006, medical exposure constituted nearly half of the total radiation exposure of the U.S. population from all sources. The next largest contributor to population exposure was background radiation, mainly from radon gas. The relative level of background radiation varies with geographic location. For

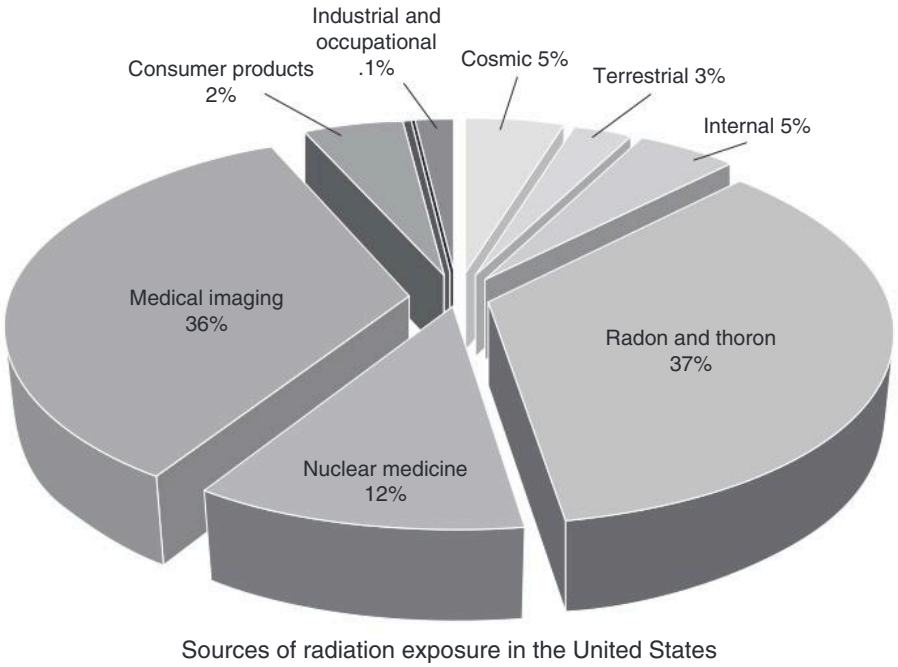


Fig. 1.7 An estimate of sources of exposure dose from ionizing radiation in the United States. (With permission of the National Council on Radiation Protection and Measurements, http://NCRPonline.org.)

example, exposure to cosmic radiation increases at higher elevations, and household radon exposure is greater in the eastern United States. In general, these types of radiation exposures are not considered harmful, providing the use of medical imaging is monitored. The United States Environmental Protection Agency (EPA) provides a calculator that allows estimation of your yearly dose from the most significant sources of ionizing radiation.[††]

Practical Considerations

Technologists assuming the role of radiation workers in veterinary practices must be aware of the risks of radiation. They should be trained in patient positioning for radiography and should be proficient in equipment operation. Technologists should be instructed on the proper use and care of PPE such as lead-impregnated aprons and gloves, and how to adhere to the ALARA (**a**s **l**ow **a**s **r**easonably **a**chievable) principle.[12] The variables used in adhering to ALARA are distance, time, and shielding.

Distance

The distance between personnel in the room and the x-ray tube should be as great as possible because distance is one of the most effective ways of reducing dose. Exposure dose does not change linearly with distance but is dependent on the square of the distance. For example, doubling the distance reduces exposure by a factor of 4, not by a factor of 2. Holding cassettes by hand for equine radiography is discouraged because this can place the employee in the primary beam. Handholding of portable x-ray machines for radiography of the equine distal limb is safe, as long as the machine is adequately shielded.[13] Handholding of companion animals for radiography is permissible, but body parts should be as far from the primary x-ray beam as possible and no part of the body should ever be in the primary beam, regardless of whether protective aprons and gloves are used. With the use of chemical restraint, tape, and sandbags for positioning, it is often possible for the technologist to exit the room during the exposure. Some state veterinary practice acts stipulate that the technologist cannot be in the room during the exposure.

Effective use of beam collimation is another component of distance as this further increases the distance of the technologist from the primary x-ray beam, and also reduces scattered radiation. However, failure to properly collimate the primary x-ray beam is a major error in veterinary radiology. Digital software also allows the visibility of unprotected hands in an image to be cropped out of view (Fig. 1.8).

Time

Time is directly related to the number of images created. Time can be minimized by using sedation or anesthesia for uncooperative patients, or for complicated examinations such as spine or skull studies. Rotation of the technical staff through the radiology service will also dilute any exposure over a larger pool, leading to reduction in individual exposure levels.

Retake examinations also increase personnel dose, and these have likely increased with the increase in digital imaging as retakes are less labor intensive.

Shielding

State building codes require structural shielding to protect personnel and the general public, such as clients in the waiting or examination rooms, from unnecessary radiation exposure. The specific details regarding requisite structural shielding can be obtained from the state radiation protection office.

The most effective PPE for radiation workers is lead-impregnated aprons, gloves, thyroid shields, and eyeglasses. Protective aprons and gloves designed for use in the x-ray room are usually 0.5 mm Pb equivalent. Unfortunately, this equipment is not used consistently. When apron and glove use was monitored in a university setting with video cameras, gloves were used properly in only 46.3% of the studies and leaded eyeglasses were worn only 1.7% of the time.[14] PPE use was also

[††] https://www.epa.gov/radiation/calculate-your-radiation-dose

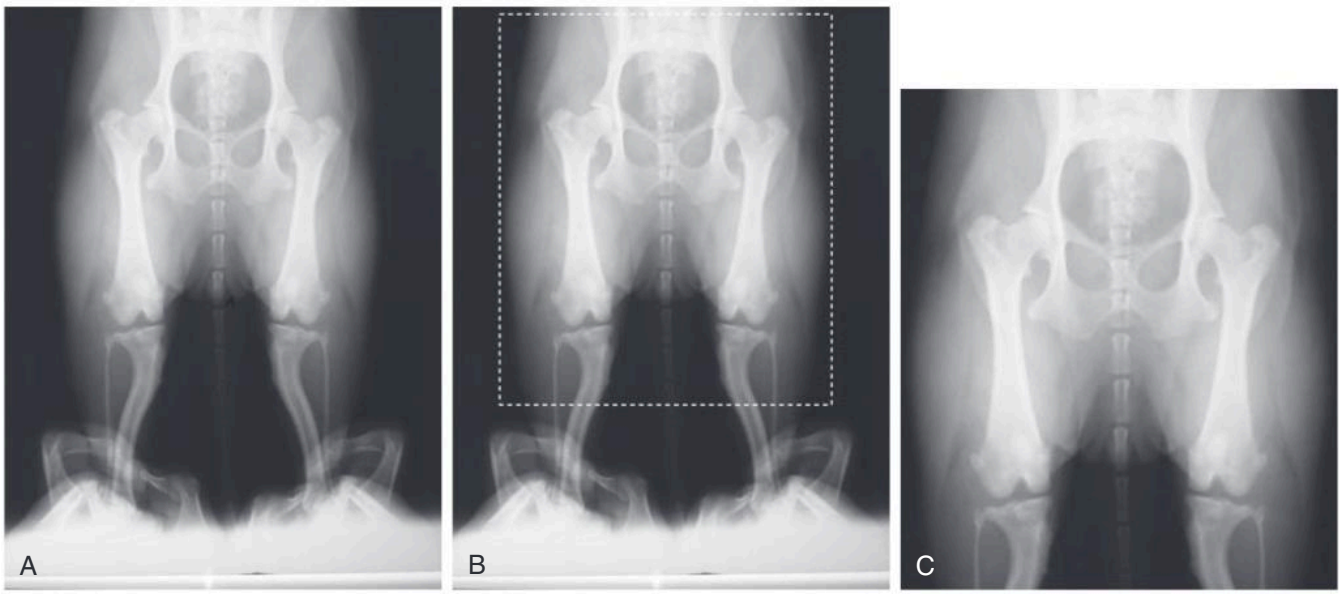


Fig. 1.8 **A,** Ventrodorsal view of a canine pelvis with worker's ungloved hand holding patient's pelvic limbs. **B,** *Dashed line* shows application of software cropping tool. **C,** Cropped image is ready to send to workstation. Daily repetition of this hazardous practice leads to continued overexposure of the hands and wrists, increasing the risk for squamous cell or basal cell carcinomas.

found to be deficient in equine practice.[15] Although not documented, glove use is almost certainly inadequate in private small animal practice (Fig. 1.9A; see Fig. 1.4).

More commonly, when lead gloves are not used, the technologist attempts to keep the unshielded hands outside of the primary beam, thinking that the collimator eliminates radiation exposure in this area. This is not true. There is always enough scattered radiation outside the primary beam to capture an image of parts of the patient or technologist in that area, and this also leads to unnecessary personnel exposure (see Fig. 1.9B). Additionally, the hand will frequently end up in the periphery of the primary beam, leading to even higher exposure. In fact, in Fig. 1.9B the tip of a finger (white arrowhead) is in the edge of the primary beam, but the fingertip is not visible because of overexposure.

Another common mistake is the belief that because lead aprons and gloves are very heavy, they can be used to shield body parts within the primary beam (see Fig. 1.9A). This is also not true. Lead aprons and gloves are designed solely for protecting against scattered radiation and must never be placed in the primary beam because they do not entirely attenuate the x-ray beam. Covering a hand in the primary x-ray beam with an apron or glove is not adequate protection, and the hand will receive unnecessary, excessive radiation (see Fig. 1.9C). The effects of scattered photons from the floor of the x-ray room, or x-ray table, are also usually ignored, but these are important sources of scattered radiation (see Fig. 1.9D). Lastly, radiation protection mittens with a slit in the palm are available. Extending the fingers through the slit facilitates positioning but reduces the amount of overlying protective lead material and leads to excessive extremity dose whether the hand receives primary or secondary radiation.

Aprons and gloves should be placed on racks when not in use. This decreases the risk of creasing and folding that lead to cracking or separation of the protective lead layering. Use of a glove rack also facilitates the evaporation of perspiration that reduces odor. Aprons and gloves should be inspected visually on an annual basis, and any portion that appears physically damaged should be evaluated radiographically for evidence of a crack.

Radiation Supervisor

Identifying a member of the technical staff as a radiation supervisor will optimize the quality of images produced and minimize occupational radiation dose. Having a dedicated radiation protection supervisor provides the technologist with ownership in the process, which will increase quality. The continuity of supervision will contribute to a steady stream of high-quality images and low personnel exposure readings.

The following are some reasonable responsibilities of a radiation supervisor:

- Establish and supervise the implementation of written operating procedures for all employees involved with radiography.
- Periodically review procedures to ensure conformity with local regulations.
- Instruct all personnel in proper radiation protection practices and in efficient and safe equipment operation.
- Oversee conduction of required radiation surveys and keep records of such surveys and tests, including summaries of corrective measures recommended or instituted.
- Routinely observe and periodically test interlock switches and warning signals.
- Ensure that warning signs and signals are properly located.
- Ensure that all equipment is maintained in top-notch working order. Perform annual evaluation of radiation protection equipment.
- Determine the cause of each known or suspected case of excessive abnormal exposure and take steps to prevent its recurrence.
- Train staff in proper radiographic positioning and restraint procedures.
- Radiation safety seminars should be held on a yearly basis to ensure compliance and to educate new personnel.

Personnel Dose Monitoring

Personnel dose monitoring is used to check the adequacy of the radiation safety program, disclose improper radiation protection practices, and detect potentially serious radiation exposure situations. A radiation dosimetry badge is the most commonly used personnel monitoring device. A radiation badge consists of

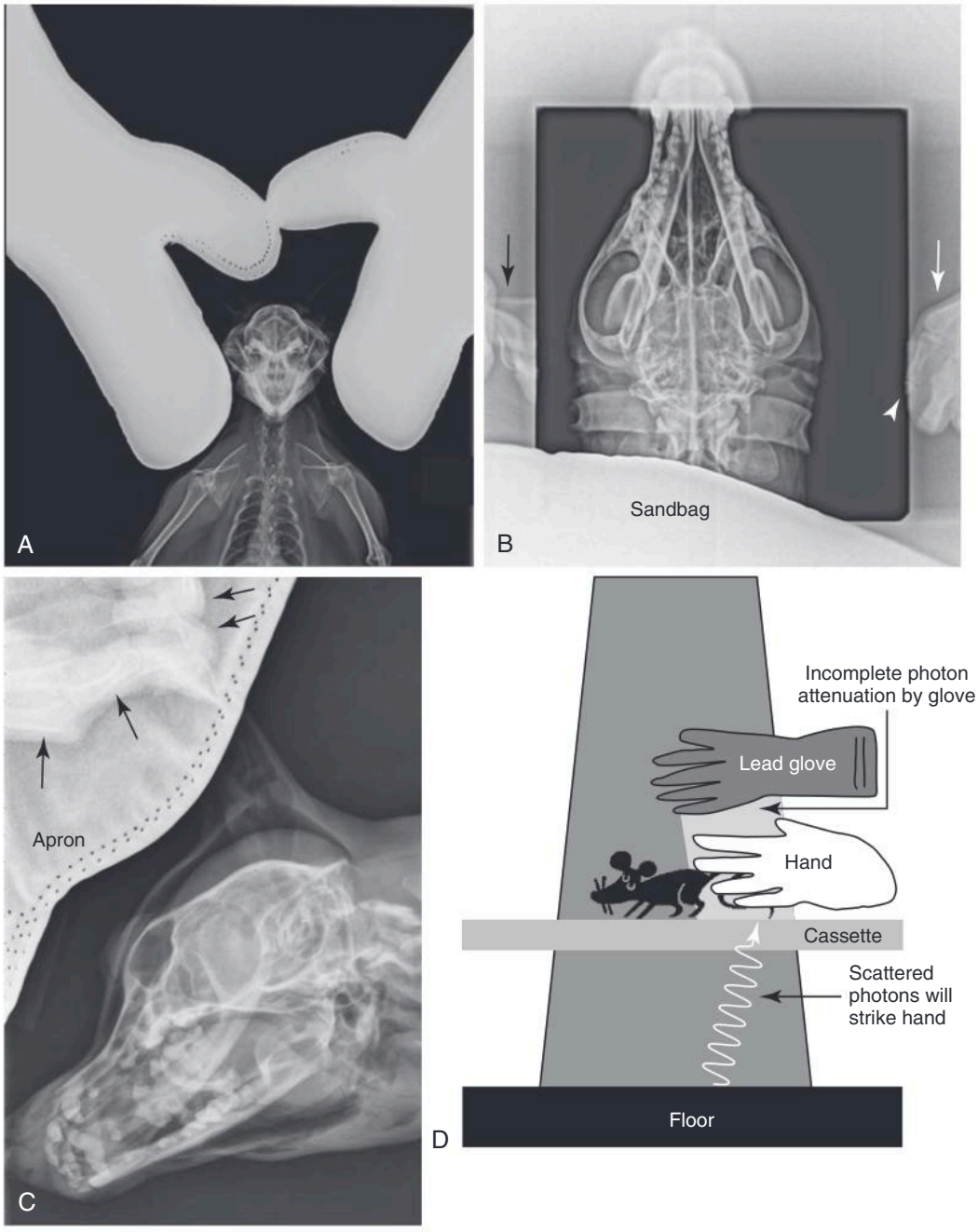


Fig. 1.9 Examples of poor radiation safety practice. **A,** Hands were placed in the primary beam to position this small patient. Although gloves were used, they are not adequate for shielding against the primary x-ray beam and the hands will receive an unacceptable dose. **B,** Dorsoventral skull radiograph of a dog. A sandbag is being used to secure the neck. The technologist is not wearing lead gloves and has grasped the ears of the dog, which are outside of the primary beam, to keep the head in the proper position. The dog's right ear can be seen (*black arrow*). On the left side, the technologist's fingers can also be seen (*white arrow*), because of exposure from radiation outside of the primary beam. The tip of a finger is also in the primary beam (*white arrowhead*). A portion of the technologist's hand can also be seen on the dog's right side, peripheral to the dog's ear but not to the extent that it is identifiable as a hand. The most rostral portion of the dog's nose is also visible outside of the primary beam. **C,** A lateral radiograph of a canine skull was being made. The technologist held the ears in the primary beam with an unprotected hand and then covered their hand with a lead apron, thinking the apron would attenuate the x-rays. It did not. The bones in the technologist's hand are clearly visible (*black arrows*) because of x-rays penetrating the apron. **D,** A small patient is being restrained by an unprotected hand but a lead glove is placed on top of the hand, similar to the situation illustrated in part **C** of this figure. As already stated, this is ineffective because many of the oncoming high-energy photons will penetrate the glove and strike the hand. Also, photons penetrating the cassette and table will strike the floor and be scattered back, also striking the hand. Radiation backscatter is also a reason that the technologist should not sit on the edge of the x-ray table while restraining a patient for radiography. In that instance the scattered photons are going to strike a body part or parts that are more revered than a hand.

a plastic holder, measuring approximately 2 to 3 cm on a side, which has a clip allowing it to be secured to clothing. Modern radiation badges contain either radiation-sensitive aluminum oxide or lithium fluoride crystals. These compounds trap electrons energized by oncoming radiation, and the number of trapped electrons can be quantified and related to the amount of exposure. Radiation badges should be analyzed at least quarterly, but a monthly analysis is preferable so that exposure problems are detected sooner. Badges for declared pregnant workers should be analyzed monthly.

Personnel dose monitoring should be performed in controlled areas for each occupationally exposed individual who has a reasonable possibility of receiving a dose exceeding 10% of the applicable MPD. The radiation badge must be worn only in the workplace and never when the person is exposed to ionizing radiation as part of his or her own medical or dental examinations. The badge is intended to monitor occupational radiation exposure and not medical exposure. If the badge is worn outside of the workplace erroneous readings can result. The radiation badge should be worn on the upper or lower torso. When a protective apron is worn, the radiation badge should be on the outside of the apron for monitoring the radiation environment, but a second radiation badge may also be worn inside the apron when an estimate of body exposure is desired. Anyone occupationally exposed to radiation should have their own badge and radiation badges should never be shared.

Basic Radiation Safety Rules for Diagnostic Radiology

The basic radiation safety rules for diagnostic radiology are:

- Only personnel necessary to complete the procedure should be in the x-ray room at the time of exposure.
- Persons younger than 18 years and pregnant women must not be in the x-ray room during the examination.
- Personnel who assist with radiographic examinations should have a rotating duty roster to minimize exposure to any one person.
- Sandbags, sponges, tape, or other restraining devices should be used for positioning the patient rather than manual restraint.
- Anesthesia or sedation should be used, when possible, to facilitate patient restraint.
- No part of the technologist should be in the primary beam, whether or not protected by gloves or aprons.
- Protective aprons should always be worn when positioning an animal.
- Protective gloves should be worn if hands are near the primary beam.
- Protective glasses should be worn if the work level is heavy or when radiographing large animals. These glasses provide 0.25 mm Pb equivalent protection to the lens.
- Thyroid shields should always be worn. These are "mini-aprons" that are worn around the neck to protect the thyroid gland.
- The primary beam should be collimated so each image has an unexposed border, proving that the primary beam does not exceed the size of the cassette or imaging plate.
- All personnel involved with patient radiography should wear a radiation badge during working hours.
- The radiographic procedure should be planned carefully, and the machine settings double-checked prior to exposure.

PRODUCTION OF X-RAYS

X-rays are produced when high-speed electrons strike metal. For radiography, this occurs in the controlled environment of an x-ray tube. An x-ray tube contains a positively charged target, the anode, and a negatively charged filament, the cathode, within a glass envelope. X-ray tubes provide for acceleration of electrons from their source at the filament to the metal target where x-rays are produced. To create a source of electrons, electric current is passed through the x-ray tube filament raising its temperature in much the same way that an electric current is used to heat the filament of an incandescent lightbulb. The heating allows electrons to "boil" off the surface of the filament, forming a cloud of free, negatively charged, electrons. The number of electrons in the cloud is directly related to the amount of electric current passing through the filament, which is regulated by the milliamperage (mA) control on the x-ray machine control panel (Fig. 1.10). Increasing the mA is analogous to increasing the wattage of a lightbulb. A 100 W bulb has a hotter filament and emits more light rays instantaneously than does a 60 W bulb because more current flows through the filament of a 100 W bulb.

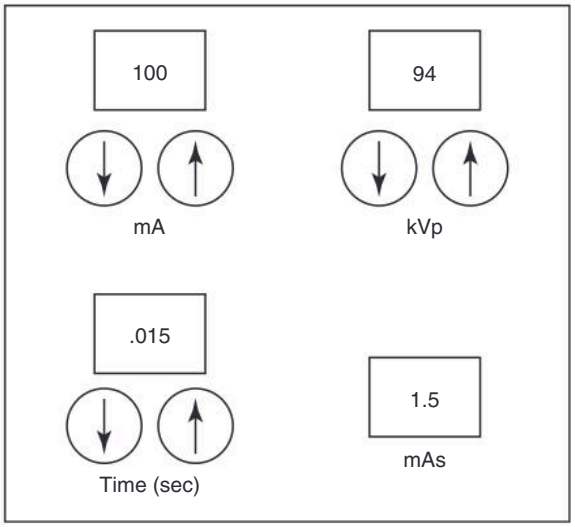


Fig. 1.10 Typical x-ray machine control panel. The time (in seconds), the mA (milliamperes), and the kVp (in kilovolts) are indicated by digital displays and are adjustable individually. As mA and/or time change, the resulting mAs is calculated and displayed automatically.

Electrons produced at the filament are accelerated to the metallic target by applying a voltage differential between the filament and target. As electrons are negatively charged, they will be attracted to the target when the target is positively charged with respect to the filament (opposite charges attract). The energy of the x-rays produced is dependent on the energy of the electrons striking the target. The voltage difference between the filament and target is adjusted with the kilovoltage peak (kVp) control on the x-ray machine control panel (see Fig. 1.10). Increasing kVp increases the voltage difference between the filament and target, and electrons are accelerated to higher velocities and have more kinetic energy when striking the target (Fig. 1.11). Higher energy electrons can produce higher energy x-rays.

X-rays are produced by two mechanisms when electrons strike the target: collisional and radiative interactions. Collisional interactions occur when the oncoming electron hits an orbital electron and ejects it from the target atom. Energy is subsequently released as an x-ray (Fig. 1.12). The energy required to eject an orbital electron is specific to the atom and the shell the orbital electron resides in, and this is called the *binding energy*. Because the binding energy is specific, the x-rays produced by collisional interactions also have specific energies and are termed *characteristic x-rays*—a unique

characteristic of the atom, the shell from which they are ejected, and the source of electron that fills the shell vacancy. X-rays created by collisional interactions account for only a small fraction of the total number of x-rays produced in a diagnostic x-ray tube.

In a radiative interaction (Fig. 1.13), the oncoming electron passes close to the nucleus of the tungsten target atom, attracted by the opposite charge. The oncoming electron does not hit or eject another electron or interact with the target atom in any way, but instead the oncoming electron slows (brakes) as it bends around the nucleus and releases energy in the form of an x-ray. The nucleus of the tungsten atom has a high positive charge due to the presence of 74 positively charged protons. The much smaller electron, with a charge of only −1, is therefore attracted strongly to the nucleus causing the electron to decelerate, or "brake." X-rays generated by a radiative interaction are called *bremsstrahlung* (from the German, translated as *braking radiation*). Braking radiation has a broad spectrum of energies, depending on the energy of the oncoming electron and how much it slows as it bends around the nucleus. The closer to the nucleus the electron travels, the more it curves, the slower it becomes, the more energy it loses, and the more energetic the x-ray produced. Most oncoming electrons undergo multiple braking interactions with the target atoms, and thus a single electron can lead to the production of multiple braking x-rays.

Collisional and radiative processes both contribute to the overall energy spectrum of an x-ray beam (Fig. 1.14), but most x-rays arise from radiative processes. The most energetic x-ray possible in the spectrum will have an energy, in kiloelectron volts (keV), equal to the kVp that was set at the control panel. For a photon to have this maximal energy, an electron must be accelerated from the filament at maximal velocity. This occurs when the voltage between the target and filament is at its maximum (the pattern of voltage fluctuation in the x-ray tube is discussed in the next paragraph). This electron must then lose all of its energy in one radiative interaction. The number of x-ray photons in the spectrum with energy equal to the kVp is very small (see Fig. 1.10). The additional x-rays coming from collisional interactions have specific energies and therefore create peaks at specific points on the curve (see Fig. 1.14).

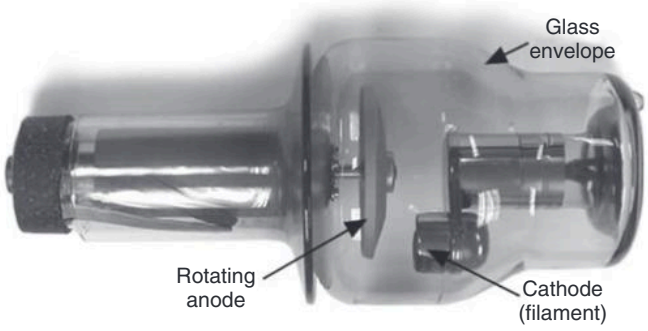


Fig. 1.11 Photograph of an x-ray tube with a rotating anode. The target (anode) rotates at high speed, dissipating heat over a large surface area. Electrons emanate from the filament (cathode). The x-ray tube is encased in a glass envelope from which air has been evacuated. This vacuum prevents electrons from interacting with air molecules when the electrons are accelerated to the target. In the x-ray machine, the x-ray tube is encased in a steel cylinder to control the direction in which x-rays are emitted. (Courtesy of Oak Ridge Associated Universities.)

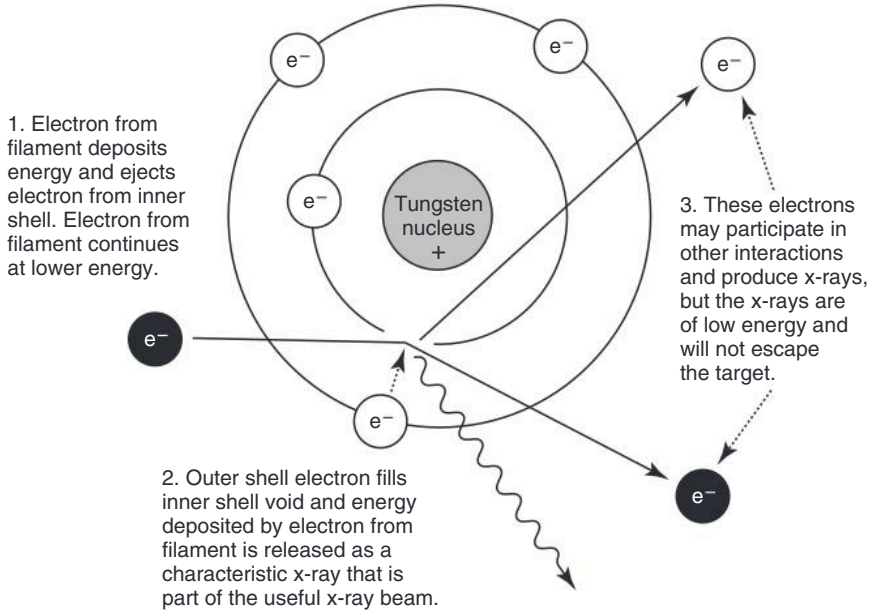


Fig. 1.12 The collisional method of x-ray production. An electron from the filament (shown here in *black* for illustrative purposes) strikes a tungsten atom in the target after being accelerated to high speed through a voltage difference. The oncoming electron deposits energy and ejects an inner shell electron from the target atom. The electron from the filament continues at a different angle, with reduced energy. Atoms with vacancies in electron shells are unstable, and the vacancy is quickly filled by a more peripheral electron. When the electron shell vacancy is filled, the energy deposited by the electron from the filament required to eject the target electron, called the binding energy, is released in the form of a *characteristic* x-ray. The electron ejected from the inner shell and the electron from the filament may continue on and be involved in other interactions and produce additional x-rays, but these x-rays are of low energy and usually do not escape the target. The relative size of the nucleus, electrons, and orbital shells is not to scale. The "+" symbol in the nucleus designates the normal nuclear positivity created by the presence of positively charged protons.

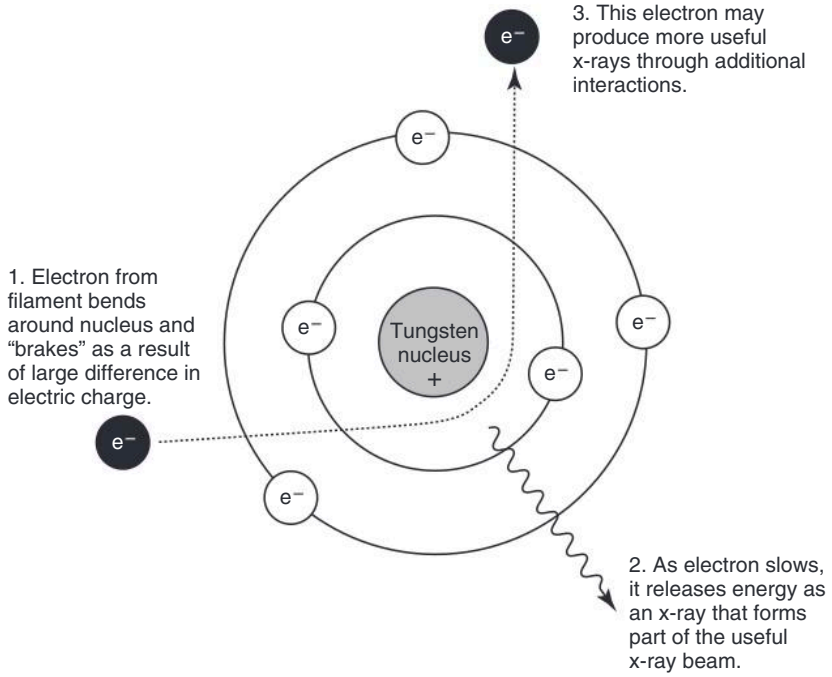


Fig. 1.13 The radiative, or braking, model of x-ray production. An electron from the filament (shown here in *black* for illustrative purposes) changes direction as it nears the nucleus because of the attraction of differing charges. The deflected electron decelerates (brakes) and releases energy in the form of an x-ray. As the deflected electron may pass within various distances of the nucleus, braking radiation has a spectrum of energies. The deflected electron may be involved with additional interactions and produce additional x-rays that contribute to the useful x-ray beam. The relative size of the nucleus, electrons, and orbital shells is not to scale. The "+" symbol in the nucleus designates the normal nuclear positivity created by the presence of positively charged protons.

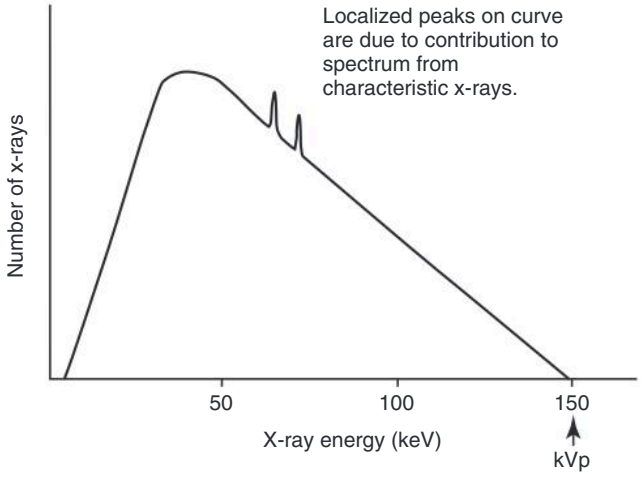


Fig. 1.14 The spectrum of x-ray energies produced by braking and characteristic radiation. The maximum x-ray energy achievable is equal to the kVp (kVp = 150 in this example). For this to occur, an electron must be accelerated at the time when the voltage differential between the filament and target is at the maximum value and then the electron must lose all of its energy in one interaction at the target. As illustrated, the number of x-rays with energy equal to the kVp is very small.

It is important to understand the difference between kVp and keV.[‡‡] The kVp is the maximum voltage applied across the target-filament gap. In the United States, electric current is alternating at 60 Hz (60 cycles per second). Current coming into the x-ray machine is either at 120V or 240V, but this is increased to the selected kVp in a transformer. At a kVp of 80 for example, the 120V or 240V current is increased to 80,000V. The alternating nature of the incoming current results in the voltage difference between the filament and target fluctuating between +kVp and −kVp every 1/60 of a second unless the waveform of the current is modified (Fig. 1.15). The kilo-electron volt (keV), on the other hand, is a unit of energy that describes the energy of either electrons or photons. If the kVp is 100 (100,000V maximum voltage difference between the target and filament), electrons traveling from filament to the target have energies equal to or less than 100 keV (100,000 eV). There are very few electrons having an energy of 100 keV because of the fluctuating nature of the voltage differential as shown in Fig. 1.15; the voltage differential is at the peak value of 100,000V for only an instant in each cycle. So, if an electron is accelerated exactly when the voltage difference between the filament and target is 100,000V, the electron will have, by definition, an energy of 100 keV. If this electron loses all its energy in one single radiative (bremsstrahlung) event, the x-ray created will also have an energy of 100 keV, the same energy as the kVp in the x-ray tube. However, this is very uncommon. Most electrons are accelerated at a voltage lower than the kVp, and most also do not lose all their energy in one braking reaction. This is what leads to the wide spectrum of energies of x-rays present in beam (see Fig. 1.14).

If alternating current (AC) (see Fig. 1.15, *top panel*) is used for x-ray production, the target is positive with respect to the filament only 50% of the time. During the other 50%, the target would be negative with respect to the filament and any free electrons at the surface of the target that might be present because of the high temperature of the target would be attracted to the filament and damage it. To avoid this, the negative phase of the AC is eliminated by a process called *rectification* (see Fig. 1.15, *second* and *third panels*). An in-depth discussion of rectification is beyond the scope of this

[‡‡] An electron volt (eV) is the amount of energy an electron gains as it is accelerated by a potential difference of 1V. 1 keV = 1000 eV.

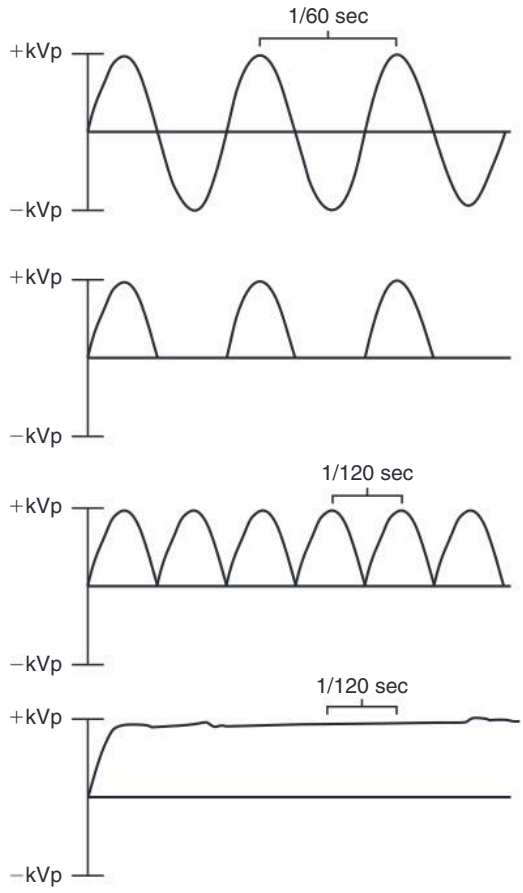


Fig. 1.15 The concept of rectification and the ripple factor. The *upper panel* shows the typical waveform of alternating current in the United States. One complete cycle occurs each 1/60 sec. If this current were used to apply the kVp in the x-ray tube, the target would be positive with respect to the filament, which is desired, only 50% of the time. The other 50% of the time, the filament would be positive with respect to the target. This is a waste of time because electrons are not attracted to the target to produce x-rays when the filament is positive. Also, any free electrons at the target created by heat buildup would travel to the filament, causing damage. The *second panel* illustrates the waveform obtained when current is not allowed to flow during the negative phase of the cycle; this is termed *half-wave rectification*. In this instance, the filament is never positive with respect to the target, but half of each cycle is wasted. Fortunately, there are electronic methods to reverse the polarity of current flow in the negative portion of the cycle leading to the waveform shown in the *third panel*. This is called *full-wave rectification* and results in one useful pulse of current every 1/120 sec. This increases the efficiency of x-ray production by 100%. Now, with what is termed a *high-frequency generator,* electronic circuitry is used to convert alternating current to nearly direct current with little voltage fluctuation during the cycle. The waveform of this current is shown in the *bottom panel*. The target is always positive with respect to the filament and the voltage difference between the filament and target approximates the kVp at all times. Thus, the voltage fluctuation, or the ripple factor, is the lowest with current from a high-frequency generator, and this increases the efficiency of x-ray production significantly.

chapter. What must be understood here is that rectification results in the target always being positive with respect to the filament, despite the use of AC. Thus, electrons travel only from the filament to the target.

X-ray production is a very inefficient process with more than 90% of the energy of the electrons striking the target being converted to heat, not x-rays. Therefore, the target becomes very hot and must be constructed of material with a high melting point. Targets are often made of tungsten, which has a melting point of 3422° C (6192° F). Even with this high melting point, the target in high-output x-ray tubes is designed to rotate

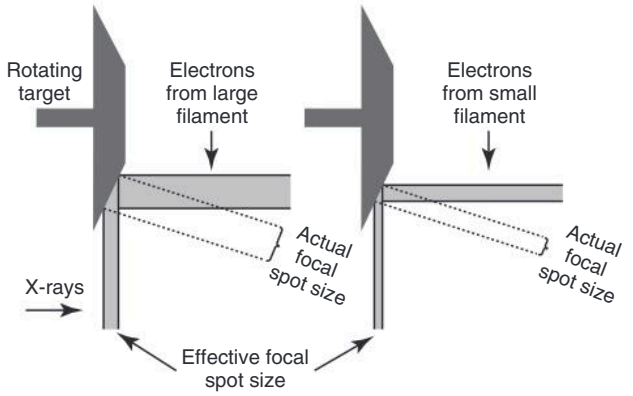


Fig. 1.16 Illustration of the principle of effective focal spot size in an x-ray tube. By angling the edge of the rotating anode, the size of the focal spot from the perspective of the patient appears smaller than it actually is. This facilitates heat distribution. On the *left*, the electrons have emanated from the large filament in the x-ray tube. Although the size of the effective focal spot is reduced compared to the size of the electron stream, the effective focal spot can be reduced even further to improve radiographic detail, as shown on the *right*, by having the electrons emanate from a smaller filament.

to increase the surface area struck by the oncoming electrons. Rotation of the target prevents the target from melting or becoming "pitted," as would happen if electrons struck the same region of a stationary target continually. Tungsten also has a high atomic number (74), which increases the efficiency of x-ray production. The high positive charge of the nucleus of tungsten target atoms leads to more effective braking and bending of electrons from the filament that pass nearby.

The focal spot is the location on the target struck by electrons and is the site of x-ray production. The smaller the focal spot, the better the detail on the radiograph. A practical example of this principle is the sharpness of a shadow cast by a small versus a large light source. A shadow of an object cast by a small light source will be sharper than the shadow cast by a large light source. Therefore, radiographs produced using a small focal spot will have more detail than radiographs produced with a large focal spot. Angling the target is one way to make the focal spot function as being smaller than it really is, creating a small *effective* focal spot, while at the same time maintaining a larger area being struck by electrons to facilitate heat distribution (Fig. 1.16).

Some x-ray tubes have two filaments of different sizes, allowing the technologist to select the size of the filament from which the electrons originate. A smaller filament leads to a smaller effective focal spot. This is illustrated in the right side of Fig. 1.16, where the width of the electron path from the filament has been reduced by 50% by using a smaller filament. As a result, the size of the effective focal spot is also reduced. Reducing focal spot size is useful theoretically when enhanced image detail is necessary, as for radiographing a small bird or reptile. A disadvantage of using the small filament is that higher mA values are not allowed by the electronics, which prevents the filament from overheating and burning out or melting.

As already stated, the number of electrons, and thus the number of x-rays, produced is directly related to the mA setting on the x-ray machine control panel. The number of x-rays produced can also be controlled by the length of time that current is allowed to pass through the filament. The timer on the x-ray machine panel (see Fig. 1.10) controls the length of time current is applied to the filament and is also the time that voltage is applied across the gap between the filament and target of the x-ray tube. X-rays are produced only when a source of electrons and a voltage differential are present across the filament-target gap.

Table • 1.4

Sample of mA and Time Combinations That Result in 5 mAs.

mA	TIME (sec)	mAs
50	0.1	5
100	0.05	5
500	0.01	5
1000	0.005	5

The milliampere second (mAs) is the unit that quantifies the amount of radiation produced and is analogous to leaving a 60 W lightbulb burning twice as long as a 120 W lightbulb. In both instances, the total number of light rays emitted would be roughly the same, although the intensity at any one time would be twice as great for the 120-W bulb. The mAs is the product of mA and time in seconds. A variety of combinations of milliamperage and time can be used to produce the same mAs value and thus the same number of x-rays (Table 1.4).

The x-ray tube is one of the two major components of the x-ray machine, the other being the x-ray generator. The generator has a high-voltage circuit that increases the voltage of the incoming current to provide the large potential voltage difference between the filament and target. The generator also has a low-voltage circuit to provide current to heat the filament. The generator contains a timer to control the time that the filament is hot and the time that the voltage difference is applied between the filament and the target, that is, the *exposure time*. Finally, the generator configures the nature of the cyclic current used in the high-voltage circuit. As already mentioned, one manipulation that is done to increase the efficiency of x-ray production is to reverse the polarity of the negative phase of the 60 Hz AC so that the target is always positive with respect to the filament—that is, full-wave rectification (see Fig. 1.15, *third panel*). This increases the efficiency of x-ray production, but there is still a large amount of time during each phase of the cycle when the voltage is relatively low; in fact, the voltage is at zero every 1/120 second (see Fig. 1.15, *third panel*). Therefore, if the cyclic nature of each cycle could be minimized, there is great opportunity to increase the efficiency of x-ray production. For example, one type of x-ray generator uses a three-phase AC line source (e.g., three voltage sources).[16] Through rectification and staggering of each AC pulse over a 120-degree AC cycle, 2 pulses for each line are produced. Therefore, six electrical pulses are produced over one AC cycle. Despite this improvement, these six pulse generators have largely been replaced by high-frequency generators.

High-frequency generators are the state-of-the-art power source for x-ray tubes. These generators produce nearly constant voltage output (see Fig. 1.15, *bottom panel*). The elimination of the valleys of the voltage waveform increases the efficiency of x-ray output significantly. In a direct comparison of a conventional generator with a high-frequency generator, the high-frequency generator was approximately two times more efficient with a better reproducibility.[17] High-frequency generators are compact, relatively inexpensive, and easily maintained. Therefore, they are the most desired type of x-ray generator and are commonly used in x-ray machines that are manufactured for permanent installation in veterinary practices. Portable units used in the field have voltage waveforms more typical of that shown in the second or third panels of Fig. 1.15. Although conventional generators can be used with digital radiography platforms, high frequency x-ray generators are preferred.

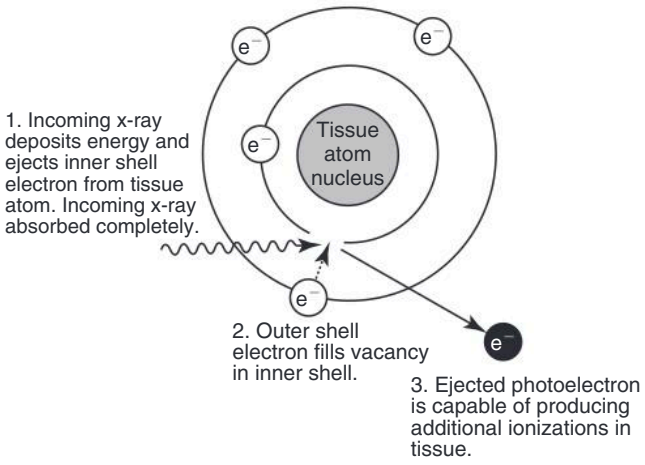


Fig. 1.17 The photoelectric absorption process. An x-ray from the x-ray tube ejects a tissue electron, usually from an inner shell (K shell) of a tissue atom. The incoming x-ray is absorbed completely. The ejected electron, the photoelectron, has sufficient energy to create additional ionizations in tissue but does not contribute in any way to image formation.

INTERACTION OF RADIATION WITH MATTER

To understand how radiographs are produced, it is necessary to understand how photons interact with matter. Photons can interact with matter in one of five possible mechanisms: (1) coherent scattering, (2) photoelectric effect, (3) Compton scattering, (4) pair production, and (5) photodisintegration. Pair production and photodisintegration have no relevance to diagnostic radiology and are not discussed. A basic description of coherent, photoelectric, and Compton processes is given herein; sources for more detailed reading are available.[16]

Coherent Scattering

A photon interacts with an object and the direction of the photon is changed, but the object does not absorb the photon, and the energy of the photon does not change. The fraction of x-rays striking a patient that undergoes coherent scattering is small, approximately 5%. Not only is coherent scattering not useful in the production of the radiograph, but also it is disadvantageous because the scattered photons may strike the x-ray film and degrade image quality, or they may strike the technologist and increase personnel exposure.

Photoelectric Effect

The photoelectric effect is the most important type of radiation interaction with reference to producing a radiograph; this is what results in formation of an image. In a photoelectric interaction, the x-ray striking the patient is absorbed completely (Fig. 1.17), and therefore there are no scattered x-rays to contend with. The complete absorption of the oncoming x-ray leads to reduced exposure of the film or imaging plate under that part of the patient. The absorbed x-ray photon ejects an electron, called a *photoelectron*, from an inner shell of a tissue atom. The photoelectron is eventually absorbed in the patient.

When the vacancy created by ejection of the photoelectron is filled by a peripheral shell electron, a characteristic x-ray is given off.[§§] The energy of characteristic radiation is a function of the atomic number of the atom from which it arises. Because tissue atoms have a low effective atomic number, the energy of characteristic x-rays produced in tissue is very low, and they are

[§§] This is similar in principle to the characteristic x-ray given off in the target of an x-ray tube when the oncoming electron from the filament creates a vacancy in a target atom.

absorbed locally where they contribute to the absorbed dose in the patient being radiographed, but not to production of the radiographic image. This low-energy characteristic x-ray production is not shown in Fig. 1.17.

The probability of a photoelectric interaction increases proportionally to the third power of the atomic number (proportional to Z^3) and decreases proportionally to the third power of the photon energy (proportional to $1/E^3$). The third-power relationship between the photoelectric process and atomic number is very important because it amplifies differences in absorption between various tissues, such as bone versus soft tissue and soft tissue versus fat. If it were not for the third-power atomic number dependence of the photoelectric effect, there would be insufficient differential absorption of x-rays between tissues for the image to have any contrast. That is, all tissues would be of similar radiographic opacity and the radiograph would be useless. The complete absorption of the x-ray in the photoelectric effect, rather than having a scattered photon, is also advantageous because there are no scattered photons to result in fogging of the x-ray film and increased personnel exposure.

The photoelectric effect occurring in the patient should not be confused with collisional x-ray production in the x-ray tube. A characteristic x-ray is produced in both instances because an electron is ejected from an atom in each process, and the void created by the ejected electron being filled by another electron leads to characteristic x-ray production. However, in the photoelectric effect, a photon from the target ejects an electron from an atom in tissue, while in collisional x-ray production, it is a high-energy electron from the filament that ejects the electron from an atom in the target of the x-ray tube. When the vacancy created by the electron ejection is filled, a characteristic x-ray is emitted in both processes. In the case of the photoelectric effect, this x-ray has very low energy because of the low binding energy of inner shell electrons in tissue versus x-ray production where the characteristic x-ray is of much higher energy because of the much higher inner shell binding energy of elections in tungsten, the target material in an x-ray tube.

Compton Scattering

All significant scattered radiation encountered in diagnostic radiology results from Compton scattering. In Compton scattering, an incoming x-ray photon interacts with a peripheral shell electron of a tissue atom. The peripheral shell electron is ejected, and the original photon is scattered at a different angle and at a lower energy (Fig. 1.18). The scattered electron is called either a *Compton electron* or a *recoil electron*. The probability of a Compton reaction is independent of atomic number and depends mainly on the physical density (grams per cubic centimeter) of the tissue. The probability of a Compton interaction increases with increasing photon energy and then decreases at photon energies over 1.02 megaelectron volt (MeV). The independence of Compton scattering on atomic number is disadvantageous with reference to producing a radiograph because all tissues tend to absorb x-rays similarly. For example, the atomic number dependence of photoelectric absorption results in great differences in absorption between tissues such as bone and muscle, and thus good tissue contrast. With Compton absorption being independent of atomic number, differential absorption by different tissue types is diminished, and image contrast is reduced. Thus, if the Compton absorption predominates, the image will have very poor contrast. In good radiographic technique, x-ray beams have an energy in which photoelectric absorption predominates. This maximizes differential x-ray absorption between tissues and image contrast. The photon scattering that occurs with Compton interactions is also disadvantageous because the scattered photons are radiation safety considerations for technologists, and they also degrade the image by producing fog.

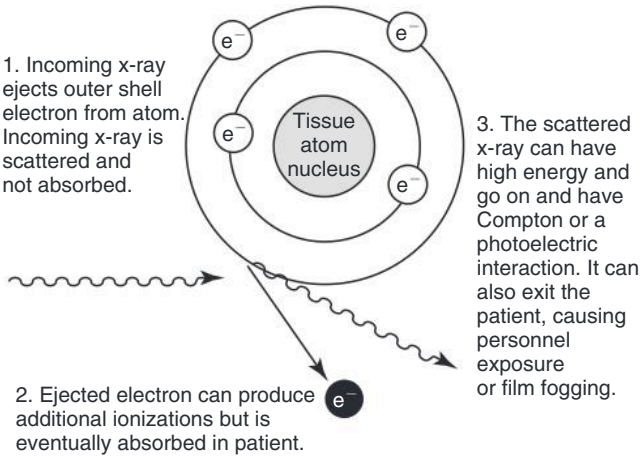


Fig. 1.18 The Compton absorption process. An x-ray produced in the x-ray tube ejects an electron, usually from an outer shell, of a tissue atom. The incoming photon is scattered at an angle and with lower energy but is not absorbed as in the photoelectric process. The energy of the scattered photon is always lower than that of the original photon. The ejected electron and scattered photon may produce additional ionizations and the scattered photon may exit the patient and fog the film or strike personnel.

BASIC CONCEPT OF MAKING A RADIOGRAPH

To make a radiograph, the patient is placed between the x-ray tube and the film cassette or imaging plate (Fig. 1.19). As noted earlier, x-rays produced in a diagnostic x-ray tube have a broad spectrum of energies. Very low-energy x-rays serve no useful purpose because they are all absorbed by the patient and make no useful contribution to the image. Therefore, filters are placed in the x-ray tube housing to remove these very low-energy x-rays from the x-ray beam before they ever strike the patient. The geometric shape of the x-ray beam striking the patient is configured to the size needed by the beam-shaping collimator. In Fig. 1.19, three x-rays pass through the collimator opening. The left x-ray penetrates the patient and will be

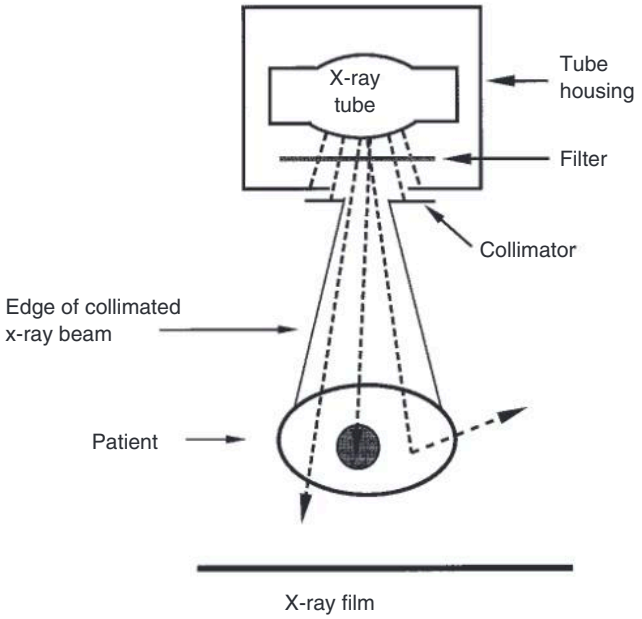


Fig. 1.19 The geometric relation between the x-ray tube, patient, and cassette or imaging plate. A filter in the tube housing removes low-energy x-rays that serve only to increase patient dose. The shape of the beam is configured with a collimator. The fate of three x-rays that pass through the collimator opening and strike the patient is shown. The x-ray on the *left* penetrates the patient and strikes the cassette. The x-ray in the *center* is absorbed by the patient. The x-ray on the *right* is scattered by the patient and could fog the film or contribute to personnel exposure dose.

recorded on the x-ray film. Some fraction of the oncoming x-rays must penetrate the patient and strike the cassette or imaging plate, or no information would be recorded. The middle x-ray hits a structure within the patient and is absorbed. Absorption of some of the x-rays is necessary for the image to have contrast. The x-ray on the right strikes the patient and is scattered. At this direction of scatter, the x-ray may strike a technologist. If the technologist is not wearing a lead apron, lead gloves, or a thyroid shield, they will receive unnecessary radiation dose. If the angle of scatter had been different, the scattered x-ray may have struck the cassette or imaging plate, causing fog and degrading the image.

A radiograph is the image of the internal makeup of an object based on the spatial distribution of x-rays transmitted through the patient. For decades, radiographic images have been recorded on film but as technology has advanced, the pattern of x-rays transmission through a patient is recorded in a digital format. The digital radiograph can then be viewed and manipulated on a computer monitor. The basis of film-based (analog) imaging is discussed briefly in this chapter, and digital radiographic imaging is discussed in Chapter 2.

Film Blackness and Opacity

X-ray film is a photographic film with a light-sensitive emulsion containing silver halide. After exposure to either x-rays or visible light, and film processing, silver halide crystals precipitate and form neutral silver deposits. These deposits are black on processed film. Unexposed crystals are removed during processing, leaving clear areas on the film. Thus, the distribution of precipitated silver determines how black, gray, or clear that part of the film appears. The degree of film blackness is directly related to the number of x-rays striking the film, controlled in part by the mAs (Fig. 1.20).

Film blackness is also affected by the energy of the x-ray beam, which is controlled by the kVp setting. As x-ray energy increases, a greater proportion of the x-rays will penetrate the patient, increasing film blackness (Fig. 1.21).

The distance from the x-ray tube to the film, referred to as the focal spot–film distance (FFD), also affects film blackness. As FFD increases the film blackness decreases because the intensity of x-rays in the x-ray beam (x-rays/unit area) decreases (Fig. 1.22). In most x-ray machines used in small animal practices, the FFD is relatively fixed (~40 inches). However, when using a portable x-ray machine, as in many large animal radiographic settings, the FFD can vary. An incorrect FFD will lead to either overexposure (FFD too short) or underexposure (FFD too long). Changes in FFD are not as important in digital imaging due to the great inherent exposure latitude (see Chapter 2), but a few inches difference in FFD will lead to a marked difference in film blackness, magnified because of the inverse square law:

$$\frac{I_1}{I_2} = \frac{(d_2)^2}{(d_1)^2}$$

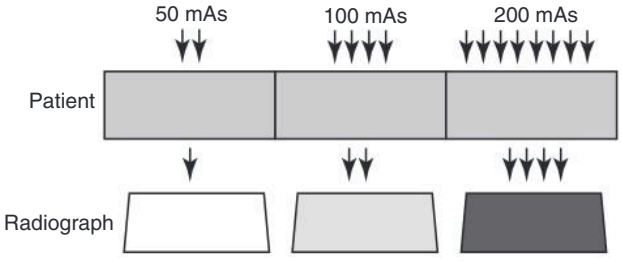


Fig. 1.20 The effect of mAs on the number of x-rays reaching the film, and thus the film blackness. Increasing mAs while keeping the kVp constant will result in more x-rays striking the patient, and then proportionally more will pass through the patient, increasing the blackness of the radiograph. Thus, as mAs is increased, film blackness also increases.

where I is intensity in terms of number of x-rays/unit area, and d is distance. In the equation, I_1 is the intensity at d_1, and I_2 is the intensity at d_2 (Fig. 1.23). For example, if the FFD decreases from 40 to 32 inches, a difference of only 8 inches, exposure increases by slightly over 50% which will result in excessive film blackness (calculation shown online).

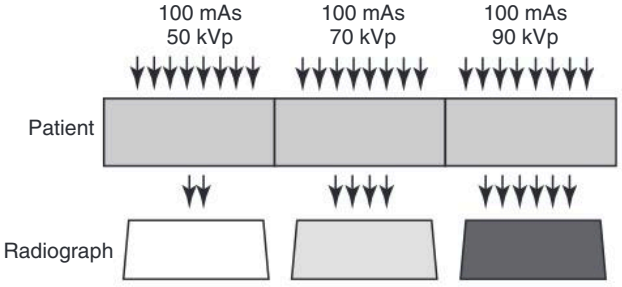


Fig. 1.21 The effect of kVp on the number of x-rays reaching the film, and thus the film blackness. Increasing kVp while keeping mAs constant results in the same number of x-rays being produced, but at higher kVp settings the x-rays have more energy, and a larger fraction will penetrate the patient. This will result in more x-rays hitting the film and an increase in film blackness.

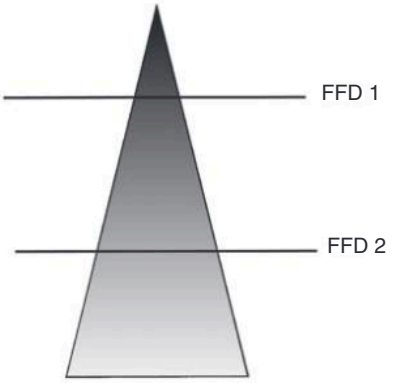


Fig. 1.22 As distance from the focal spot increases, the x-ray intensity in the beam (x-rays/unit area) decreases because of beam divergence. Thus, as focal spot–film distance (*FFD*) increases, film blackness decreases. To obtain film blackness at FFD 2 that is similar to film blackness at FFD 1, the mAs would have to be increased.

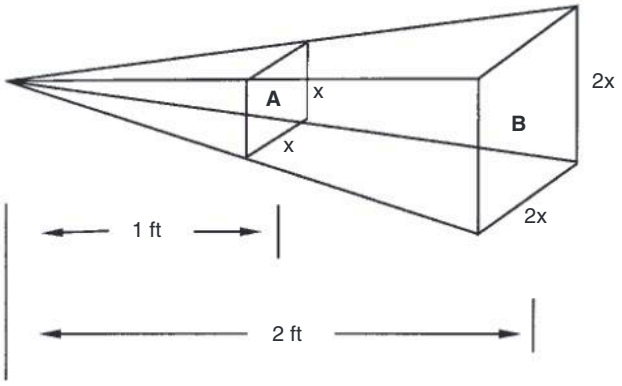


Fig. 1.23 The intensity of an x-ray beam in terms of x-rays/unit area changes with the square of the distance. At a distance of 1 foot, the diverging x-ray beam covers an area represented by square A with each side of dimension x, or an area of (x) times (x) = x^2. At 2 feet, the diverging beam covers an area represented by square B and each side is now twice as long as it was at 1 foot. The area covered by the beam at 2 feet is therefore (2x) times (2x) = $4x^2$, which is four times the area at 1 foot. The intensity falling on the square at 1-foot distance must spread out over an area that is four times as large by the time it reaches the large square at a distance of two feet.

As an example, assume that when an equine limb is radiographed the FFD should be 40 inches, but instead the machine is held too close, at a distance of 32 inches. If we arbitrarily define the x-ray intensity at 40 inches as 100, what change in intensity will result from the error of having the x-ray machine at 32 inches rather than at 40? Thus, in the equation $I_1 = 100$, $d_1 = 40$ inches, $I_2 = ?$, $d_2 = 32$ inches. Substituting, the equation becomes:

$$100/I_2 = (32)^2/(40)^2$$
$$100/I_2 = 1024/2500$$
$$100/I_2 = 0.64$$
$$I_2 = 1.56$$

Therefore, by being 8 inches too close, the exposure to the film is increased by 56%, which leads to observable overexposure.

FACTORS AFFECTING IMAGE DETAIL

Motion

Motion, which leads to image unsharpness, is the biggest enemy of detail in veterinary radiology. Short exposure times are used to minimize the effect of motion. Some x-ray machines are capable of millisecond exposures. When exposure time is very short, the mA must be large; otherwise, the mAs will be too low. Milliampere values up to 1500 can be obtained in some x-ray machines. In private veterinary practices, however, a typical maximum mA value is 300, meaning that exposure time must be longer to obtain suitable film blackness, and motion can become more of a problem.

Focal Spot Size

Some x-ray tubes have an operator selectable focal spot size (see Fig. 1.16). Use of the small focal spot results in improved detail (Fig. 1.24). The disadvantage of the small focal spot is that lower mAs values must be used to prevent the filament from overheating. With a large focal spot, edges of anatomic structures are projected more unsharply than with the small focal spot. This edge unsharpness is termed *penumbra* (see Fig. 1.24). In practice, small focal spots are used rarely because of the associated mAs limitations to prevent filament burn out or melting, as mentioned earlier.

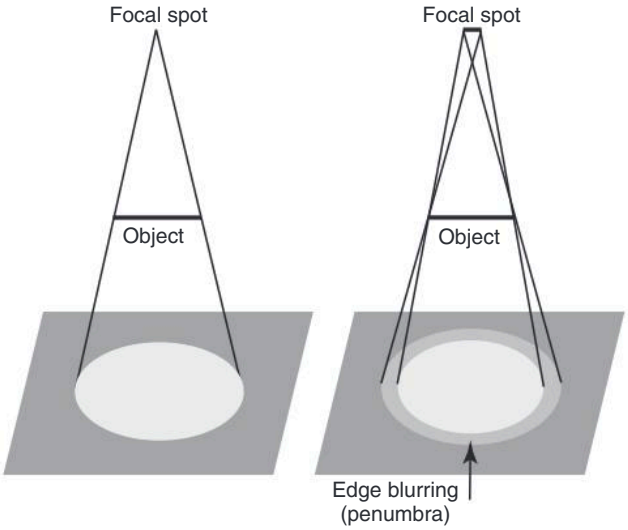


Fig. 1.24 The effect of focal spot size on detail. With a large focal spot, the edge unsharpness, or the penumbra, is larger. This contributes to image unsharpness.

Intensifying Screens

In reality, the x-ray film emulsion is much more sensitive to visible light than to x-rays. Therefore, converting the x-ray energy into visible light via an intensifying screen and then using the visible light to expose the film and create the image is a convenient way to increase the efficiency of radiographic production. For example, it may require 100 mAs to obtain a suitable radiograph when using x-rays to expose film directly, but 1 to 2 mAs might be suitable when an intensifying screen intermediary is used.

Intensifying screens contain phosphorescent crystals that emit light when struck by x-rays (Fig. 1.25). The thicker the crystal layer, the greater the chance of an x-ray being absorbed in the screen and thus more light is produced at any given mAs. But with a thicker layer, there is more light diffusion before hitting the film and degradation in image quality (Figs. 1.26 and 1.27).

Grids

Many digital radiographic systems have processing software that will eliminate the effect of scattered radiation from the patient. However, software may not eliminate enough scattered radiation and scatter must be removed by a *grid.* Grids are also necessary when using film and the patient thickness exceeds 10 cm.

A grid is a flat, rectangular plate with alternating strips of an x-ray absorbent material, such as lead, and an x-ray transparent material, such as fiber, plastic, or aluminum (Fig. 1.28). Some x-rays passing through the patient will be aligned with the transparent material and reach the plate/film (see Fig. 1.28, *photon 2*). Some x-rays interacting with the patient will be scattered at an angle that does not allow them to pass cleanly through the space between the lead strips and they will be absorbed by the lead and not reach the plate/film (see Fig. 1.28, *photon 4*). These scattered x-rays serve only to fog the film. Some primary x-rays also are absorbed by the lead if they strike the lead strips head on (see Fig. 1.28, *photon 1*). Therefore, the mAs must be increased when grids are used to compensate for the portion of the primary x-ray beam absorbed by the lead



Fig. 1.25 The anatomy of an intensifying screen. Intensifying screens are covered with a protective layer. Beneath this is the fluorescent layer, which emits visible light when struck by x-rays. A reflective layer, which lies deep beneath the fluorescent layer, reflects light back in the direction of the x-ray film. The plastic base provides support for the intensifying screen. In the cassette, the x-ray film is in contact with the protective layer, and the protective base is glued to the cassette.

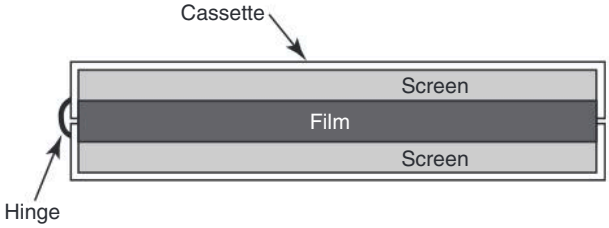


Fig. 1.26 The anatomy of a film-screen cassette. X-ray film is placed in a cassette, sandwiched between two intensifying screens. The use of two intensifying screens increases the efficiency of image production compared to using only one screen. The tradeoff of using two intensifying screens rather than one is a slight loss of detail compared with only one screen. The relative thickness of the film versus intensifying screen is not to scale in this image; in reality the film is much thinner than shown here.

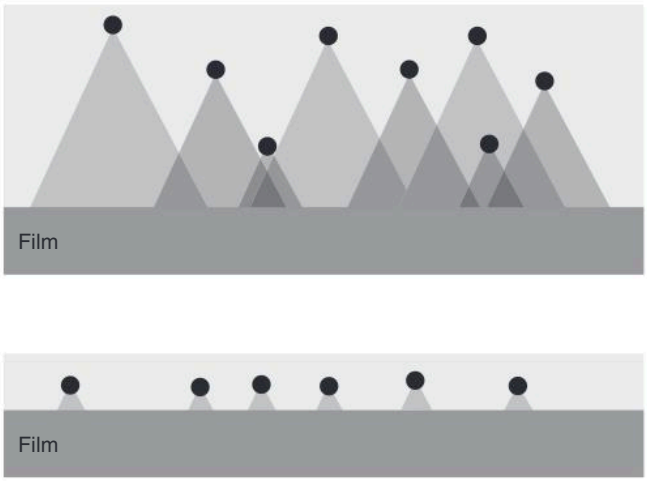


Fig. 1.27 Effect of thickness of the fluorescent layer in an intensifying screen on light diffusion. The fluorescent layer in the top intensifying screen is thicker than in the intensifying screen at the bottom. Phosphorescent crystals are shown in each screen as *small black circles*; there are many more crystals in the thicker fluorescent layer than in the thin layer. In the thicker fluorescent layer, there is more light diffusion from each crystal before striking the film. This will lead to some slight blurring of the image compared with the thinner fluorescent layer at the bottom where there is less light diffusion from each crystal before striking the film. There is also more overlapping of the light emitted from each crystal in the thicker fluorescent layer, which will also contribute to degradation in detail. However, the thicker fluorescent layer requires less radiation (lower mAs) to produce the radiograph than the thinner fluorescent layer, but the detail of the radiograph made using the thicker fluorescent layer will be reduced.

strips. The increase in mAs needed to use a grid is offset by the marked increase in contrast resulting from removal of scattered photons.

The size of each lead strip in Fig. 1.28 has been exaggerated greatly. Typically, a grid contains 80 to 160 lead strips per linear inch. Thus, the lead strips are very thin. Grids with more lead strips per linear inch are preferable because if the lead strips become too thick, they will be visible in the radiograph as radiolucent lines. The radiolucent lines created by the lead strips in a grid can be obscured by causing the grid to oscillate during the radiographic exposure. This blurs the radiolucent lines, rendering them invisible. The device in the x-ray table that causes the grid to oscillate is called the *Bucky,* after its inventor.

Besides the number of lead lines per inch, the grid ratio is another parameter used to describe a grid. The grid ratio describes the relationship of the height of the lead strips (typically up to 5 mm) to the distance between them (typically 0.4 mm or less). That is, if lead strips are five times as high as the space between them, the grid ratio is 5:1 (Fig. 1.29). The higher the grid ratio, the more effective the grid is in absorbing scattered radiation, but the more difficult it will be for primary x-rays to pass through it. This should be apparent by comparing the 5:1 and 8:1 grids in Fig. 1.29. Thus, the higher the grid ratio, the more mAs needed to produce acceptable film blackness. The grid ratio is independent of the number of grid lines per inch. For example, in a 5:1 grid having the same number of lines per inch as an 8:1 grid, the height of the lead strips would have to be lower. In Fig. 1.29, there are more grid lines per inch for the 8:1 grid than for the 5:1 grid. The number of lines per inch determines how conspicuous the lead grid lines will be in a radiograph, assuming that the Bucky is not used. The grid ratio determines the effectiveness of scatter removal. A summary of the relationship of grid lines per inch versus grid ratio is given in Table 1.5.

Note that in Fig. 1.28 the lead and aluminum strips are angled more steeply toward the periphery of the grid. This is

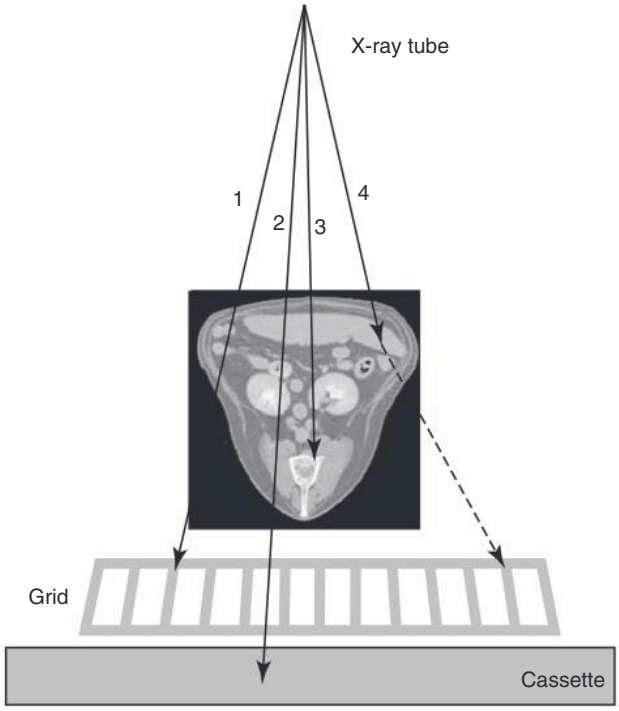


Fig. 1.28 A grid is composed of alternating strips of an x-ray absorbing material, such as lead, and an x-ray transparent material, such as aluminum. The grid is positioned between the patient and the film, usually fixed in the x-ray table, to intercept scattered radiation before it reaches the cassette or imaging plate. The lead strips in this illustration are shown as *gray* regions, and the interposed aluminum strips are shown as the interposed *white* regions. The size of these strips is exaggerated greatly in this drawing. The aluminum absorbs very little radiation, but the lead absorbs nearly all of the x-rays that strike it. Photon 1 penetrates the patient, carrying useful information, but does not reach the cassette because it hits a lead strip and is absorbed. Therefore, a grid does remove useful information, meaning that the mAs must be increased when a grid is used to ensure that adequate numbers of x-rays reach the cassette. Usually, the mAs must be increased by a factor of 2–3. Photon 2 penetrates the patient, carrying useful information, hits an aluminum strip, and is not absorbed so it reaches the cassette. Photon 3 is absorbed in the patient. Differential x-ray absorption, with some x-rays being absorbed and others penetrating the patient, is necessary to create an image. Photon 4 is scattered but strikes a lead strip and is removed by the grid before it hits the cassette. If the grid were not present, this photon would have degraded the image by fogging.

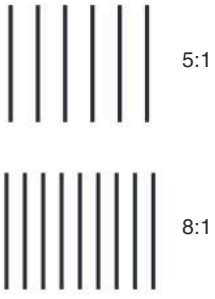


Fig. 1.29 The grid ratio is the ratio of the height of the lead strips, shown here in *black*, to the distance between them. Two grids are shown here. One has a ratio of 5:1 and the other a ratio of 8:1. It is easy to see that more oncoming radiation will be absorbed in the 8:1 grid because the space between the lead strips is thinner. This increases the chance that an incident x-ray will hit a lead strip.

necessary because the divergence of the grid lines must match the divergence of the primary x-ray beam from center to periphery so that the grid does not *cut off* excessive x-rays from the primary beam (Fig. 1.30). Grids constructed with peripheral angulation of the lead strips are called *focused grids*. Focused

Table • 1.5

Criteria Characterizing Grid Efficacy.

CRITERION	DEFINITION	TYPICAL VALUES	INFLUENCE ON RADIOGRAPHIC TECHNIQUE
Lines per inch	Number of lead strips per linear inch of grid	80 lines per inch 100 lines per inch 140 lines per inch	Has no effect on mAs required
Grid ratio	Ratio of height of lead strips to distance between them	5:1 8:1 10:1	Higher grid ratio requires more mAs for comparable film blackness

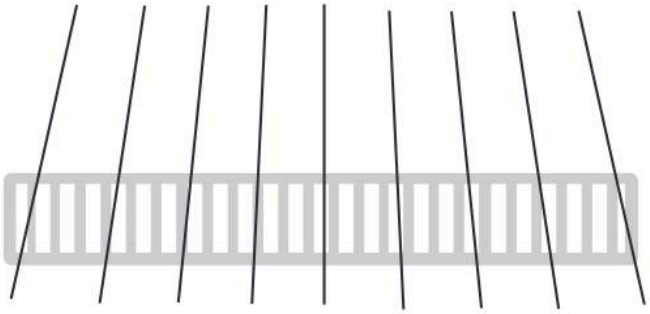


Fig. 1.30 Cutoff of useful radiation because of malalignment of the grid lines to the pattern of x-ray beam divergence. In this example, the lead and aluminum strips in the grid are all vertical. This would be called an *unfocused grid*. The diverging nature of the primary x-ray beam does not match the verticality of the lead and aluminum strips, and many oncoming x-rays are absorbed in the grid, particularly at the edge where the divergence of the x-ray beam is maximal. An unfocused grid would only be functional if the oncoming primary x-ray beam had little or no divergence. This example illustrates the importance of having the geometry of the x-ray beam match the geometry of the grid.

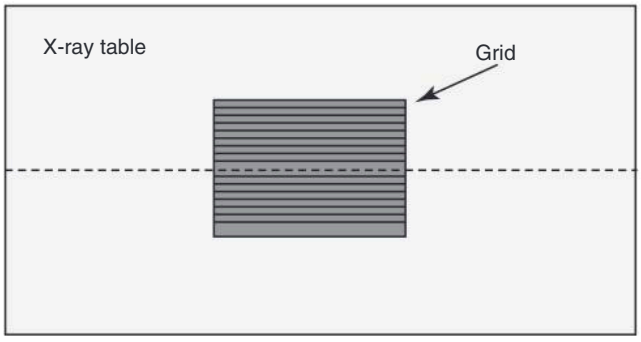


Fig. 1.31 Illustration of proper orientation of the grid with the x-ray table. The grid is centered in the table, and the lead and aluminum strips run parallel with the long axis of the table. If the grid is a focused grid, with angled lead strips, the center of the primary x-ray beam can be positioned anywhere along the dotted line. But if the center of the primary x-ray beam is peripheral to the dotted line, there will be grid cutoff because the divergence of the x-ray beam no longer matches the divergence of the lead strips.

grids must be used within a defined range of FFDs to maintain a parallel relationship between the oncoming x-ray beam and the radiolucent strips.

When a grid is installed into the x-ray table, the grid must be oriented such that the lead strips run parallel with the long axis of the x-ray table (Fig. 1.31). The center of the primary x-ray beam must always be aligned with the centerline of the grid or cutoff will occur because the diverging pattern of the x-ray beam does not match the diverging pattern of the grid lines (Fig. 1.32). The excessive loss of the primary beam caused by positioning the center of the primary x-ray beam peripheral to the center line is called *lateral decentering*.

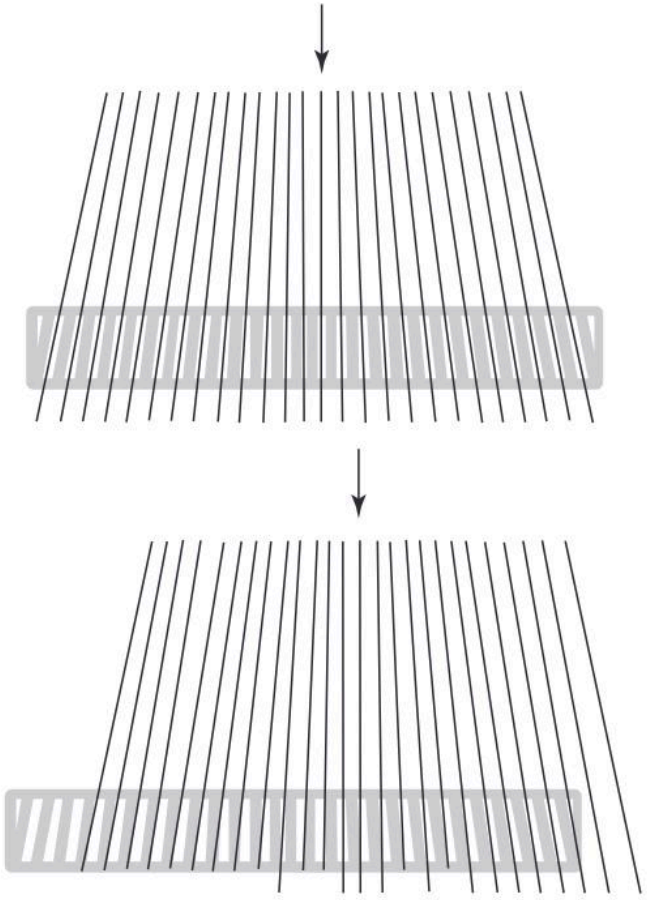


Fig. 1.32 Lateral decentering. When the central ray is centered over a focused grid, the divergence of the x-ray beam matches the divergence of the lead and aluminum strips and a high percentage of the oncoming primary photons pass through the grid. When the central ray is laterally decentered, the divergence of the beam no longer matches the divergence of the lead and aluminum strips in the grid, and the lead strips will absorb more of the primary beam, reducing film blackness. Lateral decentering is the most common grid-induced artifact.

FACTORS AFFECTING CONTRAST

Radiographic contrast refers to the difference in film blackness between structures in the image. If no contrast were present, all parts of the patient would be of the same opacity and individual structures would not be visible. Radiographic contrast in a film image depends mainly on the relationship between kVp and mAs, and the amount of film fogging by scattered x-rays. In a digital system, the contrast is highly dependent on software parameters applied for image processing.

Radiographic Technique

Radiographic contrast refers to the distribution of gray shades in the image and is caused by differential x-ray absorption in

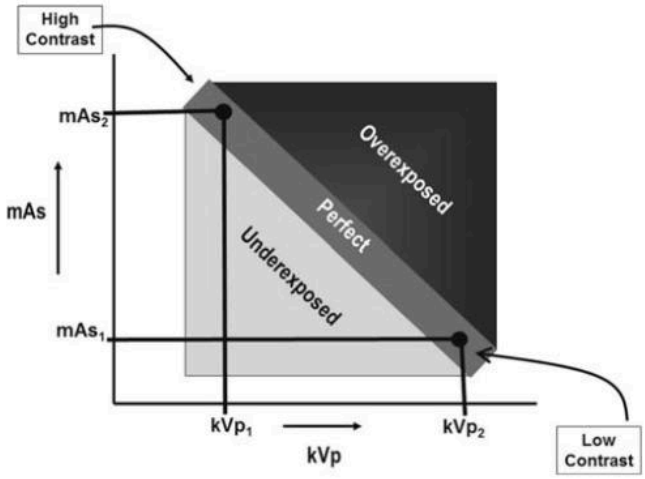


Fig. 1.33 Many combinations of mAs and kVp will produce a perfect radiograph. The term *perfect* is used here to mean a radiograph that is neither underexposed nor overexposed. With low numbers of x-rays, the energy must be high (mAs_1 and kVp_2) so that sufficient numbers reach the film. With many numbers of x-rays, their energy must be low (mAs_2 and kVp_1) or too many will reach the film. Although both of the mAs and kVp combinations shown here will produce adequate film blackness, the contrast of the image will be different. A low mAs and high kVp technique will result in a lower contrast image than one made with a high mAs and low kVp.

various body parts. Radiographic contrast is affected by differences in thickness, physical density, atomic number, and x-ray beam energy. The effects of thickness, physical density, and atomic number on x-ray absorption were covered earlier. The effect of x-ray beam energy (kVp) on contrast is covered in this section.

The ability of an x-ray to penetrate tissue depends on its energy (see Fig. 1.21). X-rays generated at higher kVp values have higher energy. Selecting the kVp setting is one of the most important factors to consider in choosing the exposure factors.[11] For a constant mAs, if the kVp is too low, too few x-rays penetrate the patient, and the radiograph is underexposed (too white), whereas if the kVp is too high, too many x-rays penetrate the patient, and the radiograph is overexposed (too black). The kVp also influences subject contrast. If high mAs values are used (many x-rays generated), then low kVp values must be used to prevent too many of the x-rays from penetrating the patient and reaching the film. If low mAs values are used, then high kVp values must be used so that more of the x-rays penetrate the patient and reach the film (Fig. 1.33).

Even though multiple combinations of mAs and kVp can result in a satisfactory radiograph in terms of film blackness, the contrast of the image will depend on the specific kVp-to-mAs combination selected (Fig. 1.33). In a high-contrast radiograph, also referred to as having a *short scale* of contrast, mostly black and white opacities and very few shades of gray are present. Low-contrast radiographs have a *long scale* of contrast with few blacks and whites but many shades of gray (Fig. 1.34).

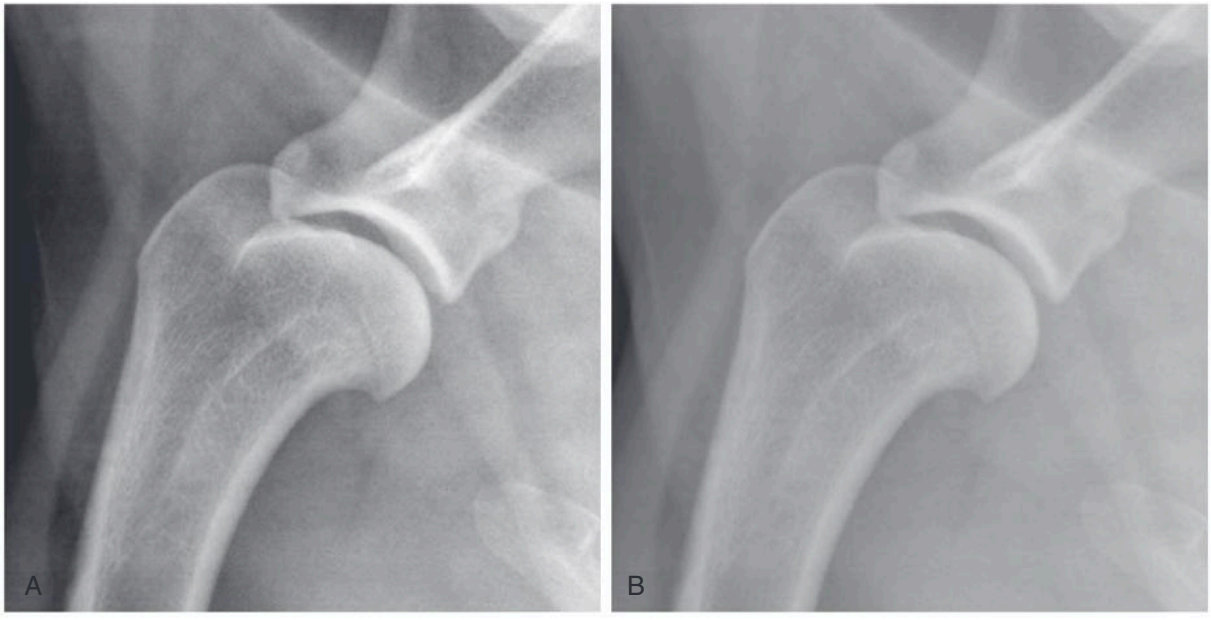


Fig. 1.34 A high-contrast (**A**) and low-contrast (**B**) radiograph of the same canine shoulder. The high-contrast radiograph would be made using a low kVp and high mAs technique, whereas the low-contrast radiograph would be made with a high kVp and low mAs technique. Both radiographs are of acceptable overall film blackness, but the high-contrast image is more useful for assessment of bone architecture. In areas of the body with high inherent contrast, such as the thorax, it would be desirable to use a high kVp—low mAs technique to prevent the radiograph from having too much contrast. Conversely, in areas of the body with low inherent contrast, such as the abdomen, where only fat provides contrast, it would be desirable to use a low kVp—high mAs technique to maximize contrast, and therefore organ discrimination, in the radiograph.

[11] The selection of exposure factors is less critical if one is using a digital radiographic system compared with a film-screen system; this is discussed in detail in Chapter 2.

In general terms, the reason that high mAs–low kVp techniques result in greater radiographic contrast than low mAs–high kVp techniques relates to the relative energies of the x-ray beams produced using these techniques. With the high mAs–low kVp technique, the energy of the x-ray beam is relatively low, and this predisposes to x-rays either being absorbed or not. Using a high mAs–low kVp technique also means that the photoelectric absorption predominates, which is highly dependent on atomic number. Thus, bone will absorb many x-rays whereas soft tissue will absorb fewer, and there will be high contrast between these tissues. This technique is appropriate for abdominal radiography where contrast between soft tissue and fat should be maximized. Conversely, with the low mAs–high kVp technique, the energy of the x-ray beam is higher, and all tissues become less efficient absorbers of x-rays. More photons are absorbed by the Compton process, which is independent of atomic number. Therefore, the differential absorption between bone and soft tissue is minimized, and their radiographic opacity becomes more similar; that is, the radiograph has less contrast. This technique is used for thoracic radiography to decrease the contrast between the ribs and the underlying lung tissue.

REFERENCES

1. Roentgen W. On a new kind of rays. *Vet Radiol Ultrasound*. 1995;36:371–374.
2. Hall E, Giaccia A. *Radiobiology for the Radiologist*. 7th ed. Philadelphia: Lippincott Williams & Wilkins; 2011.
3. NCRP: National Council on Radiation Protection and Measurements. *NCRP Report No. 82—SI Units in Radiation protection and Measurements*. Bethesda: NCRP Publications; 1985.
4. Campion EW. A retreat from SI units. *N Engl J Med*. 1992;327(1):49.
5. Clark DE, Laeseke PF. Systeme international in the ICU in the United States. *Chest*. 2010;137(4):932–937.
6. Hall E, Giaccia A. Radiation carcinogenesis. In: Hall E, Giaccia A, eds. *Radiobiology for the Radiologist*. 7th ed. Philadelphia: Lippincott Williams & Wilkins; 2011.
7. ICRP. Chapters 5 and 6. *Ann ICRP*. 2007;37(2–4):81–123.
8. NCRP: National Council on Radiation Protection and Measurements. *NCRP Report No. 116—limitation of Exposure to Ionizing Radiation*. Bethesda: NCRP Publications; 1993.
9. NRC, Title 10. Chapter 1, Code of federal regulations—energy. Part 20, standards for protection against radiation. In: *United States Nuclear Regulatory Commission Rules and Regulations*. Washington: U.S. Government Printing Office; 1995:20–27.
10. NCRP: National Council on Radiation Protection and Measurements. *NCRP Report No. 160—ionizing Radiation Exposure of the Population of the United States (2009)*. NCRP Publications; 2015.
11. Smth-Bindman R, Miglioritti DL, Larson EB. Rising use of diagnostic medical imaging in a large integrated health system: the use of imaging has skyrocketed in the past decade, but no one patient population or medical condition is responsible. *Health Aff*. 2008;27:1491.
12. NCRP: National Council on Radiation Protection and Measurements. *NCRP Report No. 107—implementation of the Principle of as Low as Reasonably Achievable (ALARA) for Medical and Dental Personnel*. Bethesda: NCRP Publications; 1990.
13. Tyson R, Smiley DC, Pleasant RS, et al. Estimated operator exposure for hand holding portable x-ray units during imaging of the equine distal extremity. *Vet Radiol Ultrasound*. 2011;52:121.
14. Mayer MN, Koehncke NK, Belotta AF, Cheveldae IT, et al. Use of personal protective equipment in a radiology room at a veterinary teaching hospital. *Vet Radiol Ultrasound*. 2018;59:137–146. https://doi.org/10.1111/vru.12583.
15. Belotta A, Mayer MN, Koehncke NK, et al. Survey of self-reported radiation safety practices among North American veterinary technicians involved in equine radiography using portable x-ray equipment. *J Am Vet Med Assoc*. 2021;259:919. –926.
16. Bushberg JT, Seibert JA, Leidholdt Jr EM, et al. *The Essential Physics of Medical Imaging*. 2nd ed. Lippincott Williams & Wilkins; 2012.
17. Barthez PY, et al. Comparison of single-phase and high-frequency generators for x-ray units. *Vet Radiol Ultrasound*. 2002;43(2):118–122.

ELECTRONIC RESOURCES

Additional information related to the content in Chapter 1 can be found online at eBooks.Health.Elsevier.com

- Chapter Quiz



CHAPTER 2

Digital Radiographic Imaging

Ian Robertson • Donald E. Thrall • Nathan C. Nelson

WHAT IS DIGITAL RADIOGRAPHIC IMAGING?

Digital radiographic imaging involves the following steps: (1) electronic measurement of the pattern of x-ray transmission through the patient, (2) conversion of the electronic measurement into a digital computer file, and (3) viewing the digital file on a computer monitor. This process is analogous to acquiring a photograph with a digital camera where the camera records the pattern of colors and intensities irradiating from an object and converts that information to a picture. Digital radiographic imaging is *not* photographing a radiographic film image with a digital camera, nor is it running an analog radiograph through a film scanner to convert the hard copy image into a digital file.

Conventional x-ray machines are used for digital radiography. Thus, to transition from analog to digital imaging, for example, the purchase of a new x-ray machine is usually not necessary. A new x-ray machine purchase could be considered if the existing unit is substandard, or if the hardware associated with the new digital-imaging system is actually housed in the x-ray table. In veterinary medicine, the transition from analog (film-to-screen) radiographic imaging to digital radiographic imaging is nearly complete, with the vast majority of veterinary practices relying on digital rather than analog radiography systems.

Although the price of digital radiography systems has fallen since their initial entry into the veterinary market, there remains substantial capital outlay required in their purchase. Selecting the correct system requires significant time, energy, and planning. All digital systems are not equal, and low-end, less expensive systems may not deliver optimal quality. In the end, the full range of advantages of the digital radiographic environment will not be realized. The old saying "you get what you pay for" is relevant. Unless one is thoroughly versed in digital technology, it is worth hiring a consultant to assist with equipment purchase.

Radiation protection and patient positioning are just as important in digital radiography as they were in analog imaging. Overall, however, the digital transition has improved the quality of radiographic studies acquired in veterinary medicine appreciably. It is critical that those working with or considering the purchase of a digital radiographic system have a thorough understanding of all aspects of this modality.

THE DIGITAL IMAGE FILE

The basis of a digital image is a computer file that contains information relating to a signal that has been measured. In diagnostic medical imaging, the signal can be the pattern of x-ray emission from a patient (radiography), quantification of fan-beam x-ray attenuation by the patient (computed tomography [CT]), the pattern of sound waves reflected by the patient (ultrasound), or the pattern of radiofrequency emission from the patient (magnetic resonance imaging [MRI]).

In diagnostic medical imaging, the computer file is a Digital Imaging and Communications in Medicine (DICOM) format. A DICOM file is a computer file format of the same basic type as .jpeg and .tiff files, and is listed with a .dcm file extension.[1] In addition to the actual image information, every DICOM file contains a large amount of ancillary information stored in what are called *metadata tags*. These tags contain other related information about the image, including the manufacturer of the device that generated the image; the date and time of image acquisition; patient demographic information; acquisition parameters; referrer, practitioner, and operator identifiers; and various other image parameters.[1]

The DICOM file format was derived mainly for consistency to ensure interconnectivity between imaging devices.[2] Without seamless interconnectivity, such as would occur if every vendor encoded the digital radiographic image into a proprietary file format, the convenience of having images in a digital format is reduced greatly. For example, without a standard DICOM file format, images acquired on a digital plate from vendor "A" could be viewed only on software provided by vendor "A." This is a disadvantage because the purchaser might like the features of the hardware but not the features of the software. With the DICOM standard, images created on equipment from vendor "A" can be viewed on a variety of platforms, not only on those from vendor "A." Compliance with formatting digital image files in DICOM format is voluntary. Most reputable vendors realize the advantages of total DICOM compliance, and the DICOM format has become the universal standard in medical imaging, across vendors, modalities, and computer operating systems. It is important that vendor adherence to the DICOM standard be verified before the digital system is purchased, otherwise this tremendous flexibility in viewing and file transmission is lost. The DICOM standard provides for the transmission of medical images from one device to another, such as from the x-ray machine to the server or server to workstation, using a network protocol that runs on top of the existing Internet standard protocol. DICOM images can also be transferred using browser-based technology, and this enhances image portability, particularly when accessing images beyond the local area network.

THE COMPONENTS OF A DIGITAL IMAGE

When the digital file is viewed using appropriate software, discussed later, the digital image comprises individual *pi*cture *el*ements termed *pixels*. The pixels are arranged in a row-by-column matrix. In radiographic, ultrasound, CT, and MRIs, each pixel has a specified shade of gray. The more pixels in a digital file, the greater the matrix size and the larger the file size. Uncompressed digital radiographic image DICOM files are typically in the order of 4 to 12 MB per image, compared to approximately 0.1 MB for a 30-page document (.doc) file and

0.5 MB to 2.0 MB for a high-resolution, color, digital photographic (.jpg) file.

The size of each pixel in a digital image determines the *spatial resolution* of the image, that is, how small of an object can be detected (Fig. 2.1). The hardware provided by the vendor determines the size of the pixel array in a digital radiographic image. In general, more pixels are better, but for any imaging system, there is a point at which more pixels do not result in a superior image. Pixel size (also termed pixel pitch) may be measured in microns or line pairs per mm; guidelines for minimum recommended standards for spatial resolution are available.[3] Although pixel size is important, there are many other hardware and technical factors that ultimately affect the "clinically useful" spatial resolution. Also, detailed later, software manipulation of the raw image file to optimize the displayed image is, within limits, more important than pixel density.

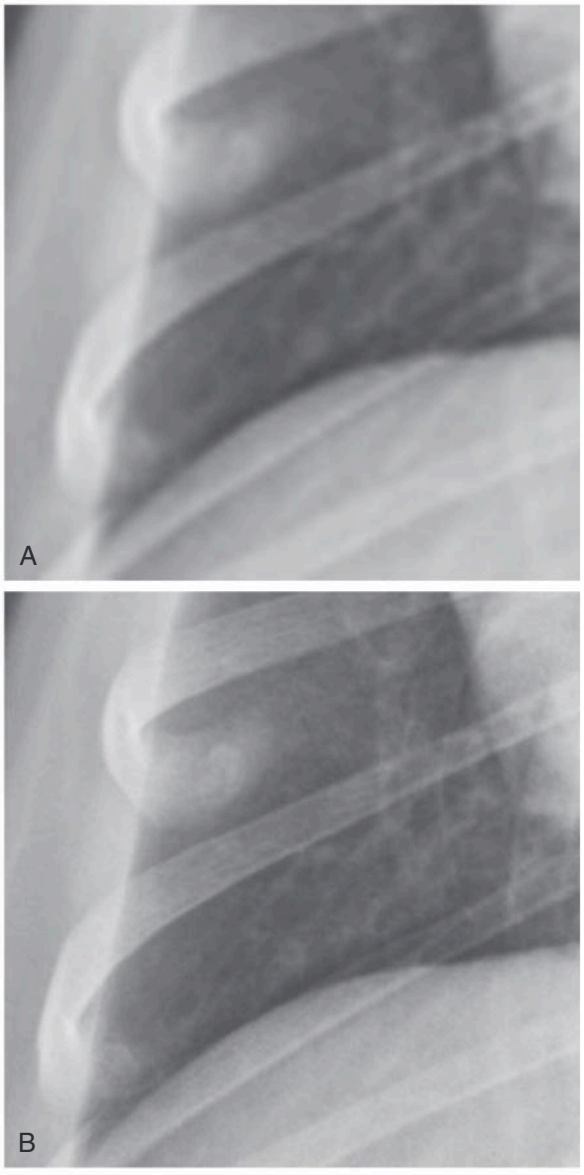


Fig. 2.1 Close-up view of the caudal thorax of a dog. **A,** The resolution of the image is 72 pixels per inch. **B,** The resolution is 300 pixels per inch. The effect of pixel size on image detail is clear with improved resolution due to smaller pixel size in **B**. The requirement for a small pixel size is one reason that digital radiographic image files are very large.

As noted before, in medical digital images, each pixel is assigned a shade of gray. The number of available gray shades for each pixel will influence the contrast of the image. If a pixel can have only a few gray shades, the image can only have a very short scale of contrast (high contrast) because there will be only black pixels, white pixels, and pixels of a few gray shades. If, conversely, there are many gray shade options for each pixel, the scale of contrast can be long. Computer files use binary notation to assign a gray shade to a pixel. In binary notation, the only digits used are 0 and 1. For grayscale assignment, a 0 is assigned black, and a 1 is assigned white; combinations of zeros and ones can be used for various intermediate gray shades. If n equals the number of allowable number of zeroes and ones per pixel, then 2^n is the number of combinations of zeroes and ones, and consequently the number of gray shades that are possible. The more combinations of zeroes and ones, the more gray shades there are possible in each pixel. The number of possible gray shades is referred to as the *bit depth* of the image (Fig. 2.2). Image file size and bit depth are directly related. Without the ability to assign multiple gray shades to each pixel, the image would have no diagnostic value (Fig. 2.3).

DIGITAL RADIOGRAPHY ACQUISITION HARDWARE

There are two main types of digital radiography acquisition hardware: computed radiography (CR) and direct digital radiography (DDR).[4]

As noted, a conventional x-ray tube and x-ray table are used for both CR and DDR applications. The difference between analog and digital imaging is that the film cassette, used for analog imaging, is replaced with a digital recording device to record the distribution of x-rays transmitted through the patient. In CR systems the digital recording device is a cassette that contains a flexible imaging plate, and in DDR systems the digital recording device is a rigid imaging plate or imaging chip (no cassette). Charge-coupled device (CCD) systems, which are a special type of DDR, may require purchase of a new x-ray

Bit depth	Possible pixel values	Number of shades of gray
1	0,1	2
2	00,01,10,11	4
4	0000,0001,0010, 0011,0100,0101 0110,0111,1000, 1001,1010,1011, 1100,1101,1110, 1111	16
8	00000000, 00000001, etc. to 11111111	256
12	000000000000, 000000000001, etc. to 111111111111	4096

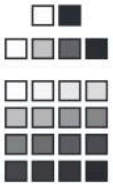


Fig. 2.2 The concept of bit depth. The number of gray shades possible in an image depends on bit depth, which is the range of binary values that can be assigned to a pixel. If only 0 or 1 is possible (bit depth = 1), the pixel can be only black or white. If both 0 and 1 are possible (bit depth = 2), the possible pixel values are 00, 01, 10, and 11, and the pixel can have one of four gray shades. Other possible pixel values can be seen in this figure, along with a representation of the possible grayscale values for bit depths of 1, 2, and 4. The sheer number of possibilities prevents illustrating all grayscale shades for a bit depth greater than 4.

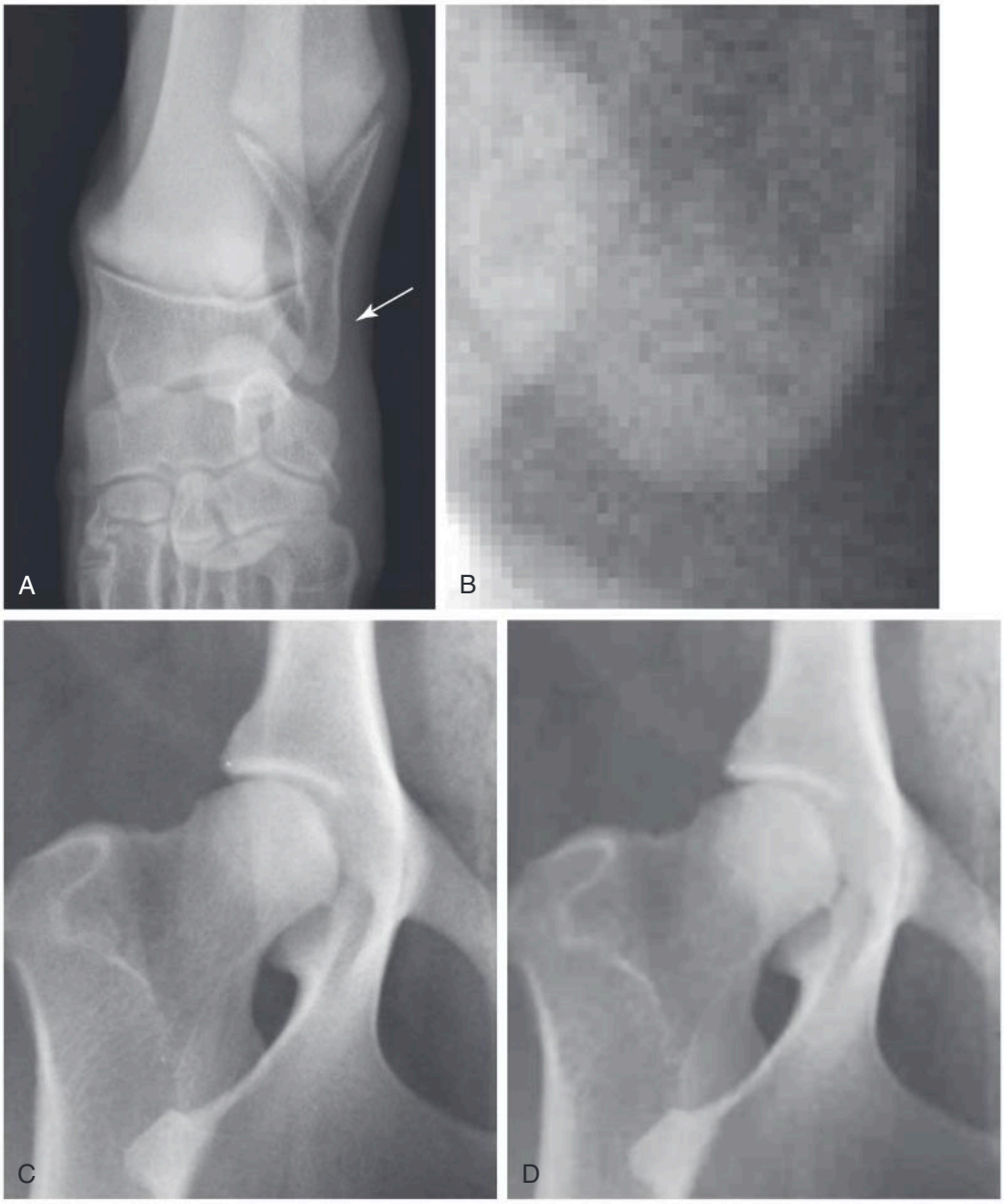


Fig. 2.3 **A,** Craniocaudal radiograph of the distal antebrachium of a dog with a bit depth of 12, meaning that 4096 shades of gray are available for pixel assignment. **B,** Close-up of the styloid process of the ulna (region of *arrow* in **A**). At this magnification, individual pixels are visible, and the large number of gray shades used to create the image can be appreciated. It is easy to see how if the number of gray shades were reduced the contrast in the image would have a very short scale with many blacks and whites but few intermediate gray tones. **C,** The image was acquired at a bit depth of 10. Image **D** was acquired at a bit depth of 8. The inadequate range of gray tones is readily apparent in the 8-bit image.

table because the hardware components are housed in the x-ray table, and it may not be possible to retrofit the new equipment into an existing x-ray table adequately.

Computed Radiography

CR was the earliest digital radiographic system to come on the market. In CR, a cassette that appears outwardly similar to a film cassette is used. The CR cassette does not contain an intensifying screen or x-ray film but instead contains a flexible imaging plate coated with a photostimulable phosphor ([PSP]; Fig. 2.4). In CR, the x-ray attenuation pattern of the patient is temporarily stored as a latent image in the PSP. The latent image is created by changes in electron energy bands that result from x-rays striking the PSP. The latent image is read out optically as photostimulated luminescence when the PSP plate is subsequently stimulated using a scanning laser (Fig. 2.5).[5,6] Therefore, the CR plate must be processed in a plate reader following radiographic exposure (see Fig. 2.4). The processing steps in the CR radiography process are summarized as follows:

- After exposure, the CR cassette is removed from the x-ray table and inserted into the reader.
- The reader automatically removes the PSP plate from the CR cassette.
- The PSP plate is illuminated in the reader by a laser.
- Laser illumination causes visible light to be emitted from the PSP plate.



Fig. 2.4 **A,** Computed radiography (CR) cassette. On external examination, the CR cassette appears similar to a traditional film cassette. **B,** Opened CR cassette. When opened, the photostimulable phosphor (PSP) plate (*asterisk*) is apparent within the CR cassette. **C,** CR reader. The CR cassette (*arrow*) is placed on the reader, which internalizes it and acquires the digital image stored on the PSP. This particular reader is a high-volume, rapid reader suitable for a large facility with high caseload. Smaller footprint, less expensive CR readers are available.

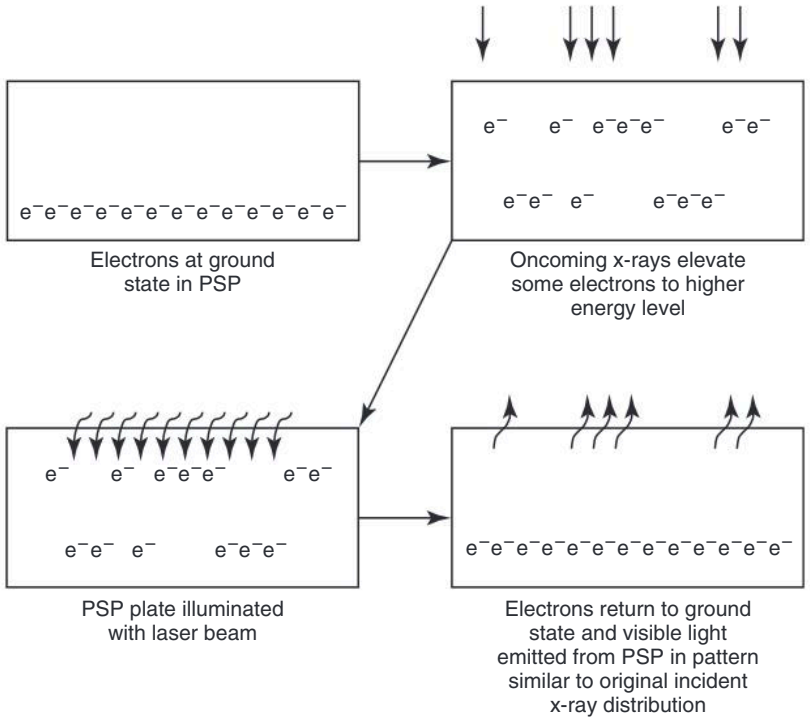


Fig. 2.5 Photostimulable phosphor (*PSP*) plate. Prior to exposure, all electrons reside at a low-energy state. X-rays that exit the patient elevate electrons to a higher energy state in a pattern that represents the distribution of incident x-rays having been transmitted through the patient. When the PSP plate is processed, it is illuminated with a laser that causes the electrons trapped at the higher energy level to return to the ground state; their excess energy is emitted as visible light. The visible light strikes a photomultiplier tube housed in the reader (not shown here) where the light is converted to an electronic signal. The signal is then processed by a computer, and a digital image file is created. The pattern of visible light emission is identical to the pattern of original incident x-ray distribution.

- Emitted visible light strikes a photomultiplier tube where it is converted into electronic signal.
- The electronic signal is digitized and stored as a digital file.
- The PSP plate is exposed to bright white light to make sure all electrons are at ground state in preparation for the next exposure.
- The PSP plate is automatically returned to the cassette in the reader.
- The cassette is ejected from the reader for use on the next patient.

CR remains in widespread use in human imaging but is not as popular in veterinary imaging. There is nothing inherently wrong with CR imaging, and the reason for this relative lack of market penetration is multifactorial. Because the CR plate is handled and manipulated much the same way as an analog film cassette, it may take 1 to 2 minutes for the digital plate to be processed completely in the plate reader, whereas with DDR systems the image is available almost immediately. Because of this, CR does not increase workflow compared with analog imaging. For example, a CR plate reader that can read only one plate at a time is actually slower than a modern automatic x-ray film processor on a per-image basis. While CR cassettes are portable, the reader is typically not mobile and is permanently housed in the veterinary practice. In an ambulatory situation, where x-ray exposures are performed off-site (such as in a horse barn), exposed CR cassettes must be returned to the veterinary practice for processing, preventing rapid evaluation of radiographs in the field. This is a similar workflow as film radiography, so when throughput is not an issue, a good-quality CR system can be perfectly adequate as a replacement for an analog system. One advantage of a CR system is that damaged cassettes can be replaced relatively inexpensively, whereas the cost of replacing a damaged DDR plate, discussed in the next section, is considerably more expensive. Another advantage of CR is that the cassette is not tethered to a computer by a cable as nonwireless digital-imaging plates are. This provides more flexibility and reduces constraints in obtaining nonstandard views, such as images made with a horizontally directed x-ray beam, because the geometric relationship between the x-ray tube and CR plate can be adjusted easily.

Direct Digital Radiography

There are three distinct types of DDR: (1) indirect flat-panel detector system, (2) direct flat-panel detector system, and (3) CCD system. In DDR, the detector replaces the film cassette, and within a few seconds after the radiographic exposure, the digital radiographic image is ready for quality-control evaluation.

Indirect Flat-Panel Detectors

Indirect flat-panel detectors are termed *indirect* because they produce visible light as an intermediate step in image formation. An x-ray intensifying screen, identical in principle to those mentioned in Chapter 1, is used to convert x-ray energy emerging from the patient into visible light.[6,7] The intensifying screen may be comprised of gadolinium oxysulfide or cesium iodide. Cesium iodide innately possess higher efficiency of x-ray detection compared to gadolinium oxysulfide, allowing lower radiation dose and thinner flat-panel device, but comes at a price premium.[8] Regardless of composition, the intensifying screen is layered onto a panel containing an array of tiny photodiodes. Much as with the PSP found in the CR plate, the photodiodes convert visible light emitted from the intensifying screen into an electronic signal that is then read out by a thin-film transistor array and transformed into an electronic file (Fig. 2.6). To have good spatial resolution, the size of each detector element is very small, and a full-size imaging plate measuring approximately 43 cm × 43 cm may have a photodiode matrix of 2600 × 2600. Thus, an indirect flat-panel detector can have 6 to 7 million photodiodes or more. As can be imagined, the electronics needed to record and spatially localize the signal from each photodiode, or pixel, and to also incorporate the photodiode into each detector element is quite complicated. This contributes to the relatively high cost of flat-panel detectors compared with a film-screen cassette system. Indirect flat-panel detectors are commonly capable of a bit depth of 14, meaning there is a grayscale resolution of 16,384 gray shades per pixel.[5] Most digital radiographic systems range in bit depth from 10 to 16 (1024–65,536 shades of gray). Because the human eye can register only 50 to 100 simultaneous shades of gray, even with extreme manipulation of image contrast (postprocessing—see later), there is probably little benefit in generating images with more than 14- to 16-bit depth.

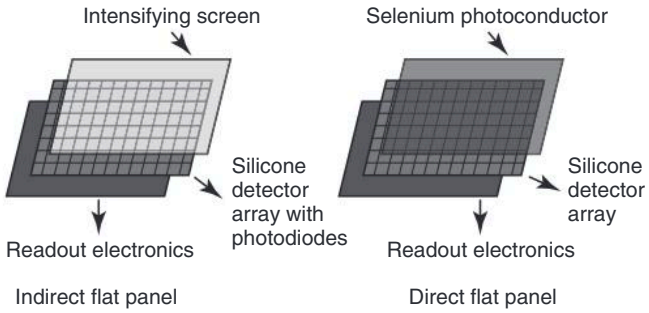


Fig. 2.6 Comparison of the makeup of indirect versus direct flat-panel detectors. With the indirect detector, an x-ray intensifying screen converts oncoming x-ray energy to visible light. The visible light interacts with the detector array, which is composed of small elements that each contain a photodiode and an amorphous selenium detector. The light from the intensifying screen is converted to an electronic signal by the photodiode and then readout by the amorphous selenium detector. Readout electronics maintain spatial resolution and transmit the information to the computer, where it is converted to an electronic file. With the direct detector, there is no light intermediary. The oncoming x-rays strike a selenium photodetector, where the energy is converted to an electronic signal that is collected by the amorphous silicon detector array directly, with subsequent processing by the readout electronics and formation of an electronic file.

Direct Flat-Panel Detectors

In a direct flat-panel detector, there is no visible light intermediary. Oncoming x-rays strike a photoconductor, typically composed of amorphous selenium, which has high efficiency x-ray absorption. Electrons liberated in the selenium layer by the oncoming x-ray beam are collected to form a charge. This charge is then read out directly by the thin-film transistor array, processed by the readout electronics and converted to an electronic file (see Fig. 2.6).[6,7] As with indirect flat-panel detectors, there are millions of detectors in the array, and the pixel matrix is of comparable size, also with a bit depth of 14. Thus, the main difference between indirect and direct flat-panel detectors is the intermediate step of light production from the intensifying screen in indirect systems.

As discussed in Chapter 1, there is some light diffusion within an x-ray intensifying screen. This light diffusion, which can potentially lead to blurring, is a purported disadvantage of indirect flat-panel detectors versus direct flat-panel detectors. However, with modern engineering techniques, and the structure of the crystals in the intensifying screen, the amount of light diffusion that actually occurs in the intensifying screen is minimal and not clinically significant. For all practical purposes, the functionality of modern-day indirect and direct flat-panel detectors is comparable.

Flat-panel systems are increasingly replacing CR systems as the preferred digital radiograph technology in veterinary medicine, given their higher throughput and recent decreases in price. Flat-panel systems can produce diagnostic images with

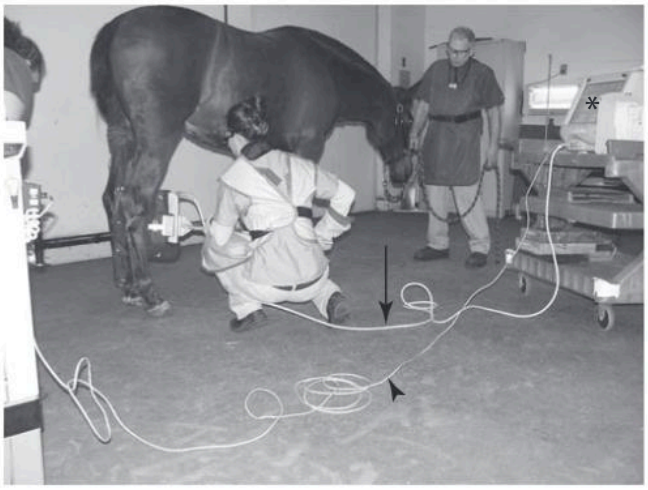


Fig. 2.7 Use of a flat-panel detector during radiography in a horse. Note that a cable (*arrow*) connects the flat-panel detector to an acquisition computer (*asterisk*). A second cable (*arrowhead*) extends from the x-ray tube to the acquisition computer; this cable carries the signal to activate the flat-panel detector when an exposure is made (wireless flat-panel systems and x-ray tubes have eliminated the need for these cables). (Modified with permission from Nelson NC, Zekas LJ, Reese DJ. Digital radiography for the equine practitioner: basic principles and recent advances. *Vet Clin North Am Equine Pract*. 2012;28(3):483–495. https://doi.org/10.1016/j.cveq.2012.08.003. Epub Oct. 18, 2012. PMID: 23177127.)

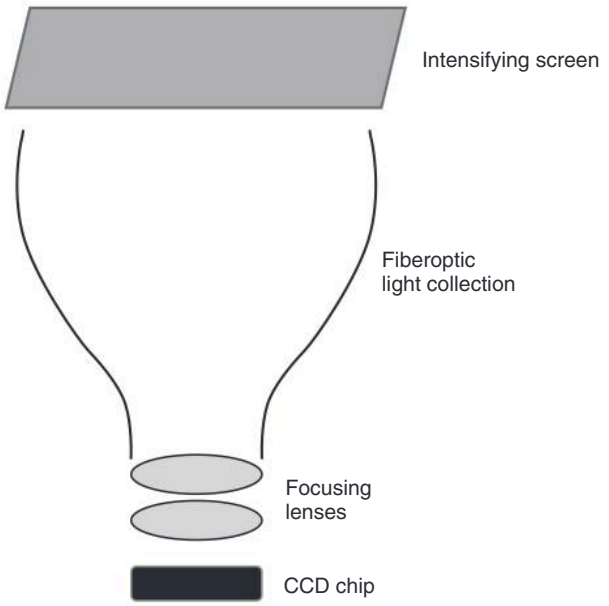


Fig. 2.8 A charge-coupled device (*CCD*) radiography system. X-rays from the patient strike a conventional intensifying screen where the spatial distribution of x-rays is converted to a comparable spatial distribution of visible light. The light is collected using fiberoptics and strikes focusing lenses that direct it onto the light-sensitive CCD chip. Overall image quality is determined mainly by the efficiency of light collection and the quality of the focusing lenses. All of these components are encased in a housing that must be incorporated into the x-ray table. The housing is fixed, which means that the x-ray tube must always be perpendicular to the face of the housing.

lower radiation doses (up to 30% less than CR systems), providing radiation safety benefit to personnel working in the x-ray suite.[9,10] While direct and indirect flat-panel detectors are commonly tethered to a processing computer by a cable, wireless DDR plates are becoming more affordable and widely available (Fig. 2.7). Wireless DDR plates provide particular benefit in the equine setting, where additional cables are a tripping hazard. The recent advent of battery-powered, portable x-ray devices combined with a wireless flat-panel display provides the ultimate in portability and convenience for the equine clinician working in the field.

Additionally, although CR is largely a fully developed technology, material improvements in flat-panel systems continue. Newer flat-panel detectors use a flexible plastic film as the base substrate for the thin-film transistor array, rather than the traditional silicone-based glass substrates currently in use, promising better durability and improved x-ray detection.[11] Newer flat-panel detectors may also allow dynamic digital radiography, allowing rapid capture of multiple sequential images at once.

Charged-Coupled Device

CCD chips are used routinely in video camcorders and digital cameras, but their use in radiographic imaging is less common than either CR or flat-panel DDR radiography. However, some vendors continue to market veterinary radiography systems based on the CCD chip. CCD systems are included in the discussion of DDR because no equipment manipulation is needed between radiographic exposure and image visualization, such as is required in processing a CR cassette.

CCD chips are relatively small compared with a flat-panel detector, being only a few centimeters on each side, compared with up to 43 cm for flat-panel detectors. Although small, there may be millions of pixel elements on the surface of a CCD chip. The CCD chip is sensitive to visible light, not x-rays; this is the basis for their use in camcorders and digital cameras. Thus, for radiography based on CCD technology, a light intermediary is necessary, and this is accomplished by integration of a relatively standard x-ray intensifying screen between the patient and CCD chip. When the CCD chip is exposed to visible light that has been collected and focused from the intensifying screen, the pixels in the CCD chip accumulate electronic charge, which is read out and converted to an electronic file.[6]

The geometry of the CCD system deserves special consideration. Given the small size of the CCD chip, the visible light output from the intensifying screen needs to be focused onto the chip, whereas in an indirect flat-panel detector, the intensifying screen is layered directly onto the detector. Focusing of light from the intensifying screen onto the CCD chip is usually accomplished by integration of fiberoptic light collection and a focusing lens between the intensifying screen and CCD chip (Fig. 2.8). Thus, the quality of the image depends more on the quality of light collection and focusing than on the quality of the CCD chip. Also, there is some loss of light and potentially much light distortion between the intensifying screen and CCD chip, leading to image degradation.

In general, CCD radiography in humans has been reserved for situations where the part being imaged is relatively small (e.g., dental radiography and mammography) and there is less need for light focusing. In veterinary medicine, the parts being radiographed are larger and requirements for focusing more stringent; this can lead to poorer images than obtained with flat-panel detectors, and image quality from CCD systems is considered by many to be inferior to both flat-panel and CR systems. Also, the distance required for collecting and focusing the light from the intensifying screen means that the physical device is large compared with a flat-panel detector. As a result, CCD detectors are housed within the x-ray table. This hardware cannot be retrofitted easily and purchase of a new x-ray machine may be necessary if CCD technology is chosen. The size of the device also limits portability, and there is a requirement for a constant vertical relationship between the x-ray tube and CCD camera. Both of these factors eliminate the possibility of using CCD technology for portable imaging and horizontal

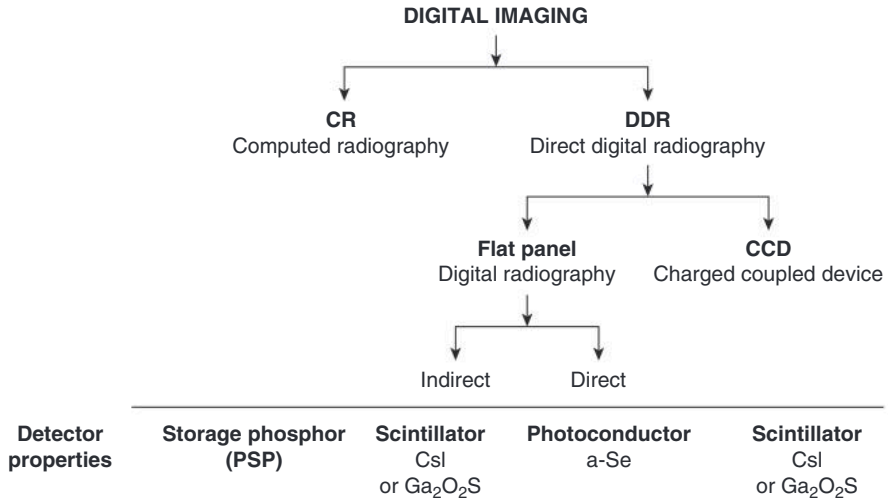


Fig. 2.9 Chart showing the image capture hardware options available in digital imaging. From Lanca L, Silva A. *Digital Imaging Systems for Plain Radiography*. New York: Springer; 2013:9–19.

beam radiography. CCD systems are typically less expensive than flat-panel imaging systems or high-quality CR systems, but image quality is usually inferior. A summary of the various hardware options is shown in Fig. 2.9.[12]

IMAGE PROCESSING AND VIEWING

Regardless of the type of digital radiographic hardware selected, the electronic data are processed by a computer before the final image file is created and displayed. Image file processing and modification occur at a number of points and can be broken down into preprocessing, processing, and postprocessing steps.[13]

Preprocessing of the image is usually beyond the control of the user. Manufacturers apply various corrections to the raw image data to accommodate such things as inhomogeneity in light collection, image distortion by focusing lenses in CCD systems, nonfunctional or dead pixels in the detector, and variation in efficiency between individual detector elements. These preprocessing steps are aimed at eliminating artifacts created by the imaging system itself[13] and are critical to image quality optimization.

The *processing* step is aimed at converting the corrected raw image data to a usable radiographic image. These manipulations, also done on the raw image data, can be controlled to some extent by the user and are aimed at optimizing image contrast, edge enhancement, minimizing image noise, and optimizing other aspects of image presentation.[6,13] These settings are usually configured by the vendor as "presets" or factory default settings, such as *thorax*, *abdomen*, and *extremity*. However, most systems allow customization by the user. Most commonly, the raw data file is not permanently overwritten, and additional image processing can be performed later, if necessary, provided the raw data files have not been deleted. Assessing image quality when the digital image first appears at the QC workstation at the x-ray machine, and making adjustments to optimize image presentation, is part of the "processing" step. Preprocessing and, most importantly, effective image processing are critical, and this functionality is often what sets good vendors and products apart. Progress in digital technology in recent years has centered around improvement in the processing step. Improved algorithms limit the impact of scatter and image noise on the final image, in some case allowing up to 50% reduction in radiation dose necessary to create a diagnostic image.[8,14] The various algorithms and processing techniques are typically proprietary and may vary greatly between products. Once the preprocessing and processing adjustments have been completed, the image is ready for viewing and interpretation. The processed image file is in DICOM format; it may have been converted from another file type. Appropriate header information is inserted, and the study is distributed through the local network to the viewing computer(s) and an appropriate archive. DICOM files, although a graphics file, cannot be viewed directly in programs such as Adobe Photoshop or Microsoft Paint. Rather, they must be viewed with dedicated DICOM file-viewing software. Licenses for this software are typically sold by the hardware vendor and are part of the original purchase package, but some free DICOM viewers are available. The most popular viewers for Apple computers are OsiriX (http://www.osirix-viewer.com) and freeware Horos (https://www.horosproject.org). RadiAnt DICOM viewer (https://www.radiantviewer.com) is a capable, small footprint PC-based viewer with a free trial period, but thereafter requires a paid subscription. ClearCanvas Open Source Project (https://clearcanvas.github.io) is a freeware, open-source PC-based viewer. Which viewing software will be adequate for any particular practice should be considered carefully, and consultation with an expert may be needed to make the best selection.

The functionality of DICOM viewing software represents one of the major advantages of digital radiography. This is the *postprocessing* step of image manipulation, and this is 100% user controlled. DICOM viewers allow images to be magnified and rotated, and the image blackness and contrast can be adjusted independently (Fig. 2.10). Other features are also available, such as viewing multiple images simultaneously and obtaining quantitative measures of area and length. The myriad of image adjustments that can be accomplished is a tremendous advancement over viewing film-based radiographs, which cannot be manipulated at all following their creation. Postprocessing image manipulation does not permanently alter the original image in any way.

Ambient lighting and monitor quality are two important considerations when optimizing image viewing. As ambient light increases, the perceived difference between light and dark on a monitor decreases, and this can affect image interpretation negatively.[15,16] Interestingly, viewing of digital radiographs in a completely dark room with no light other than the monitor light also reduces accuracy.[17] For this reason, computers used

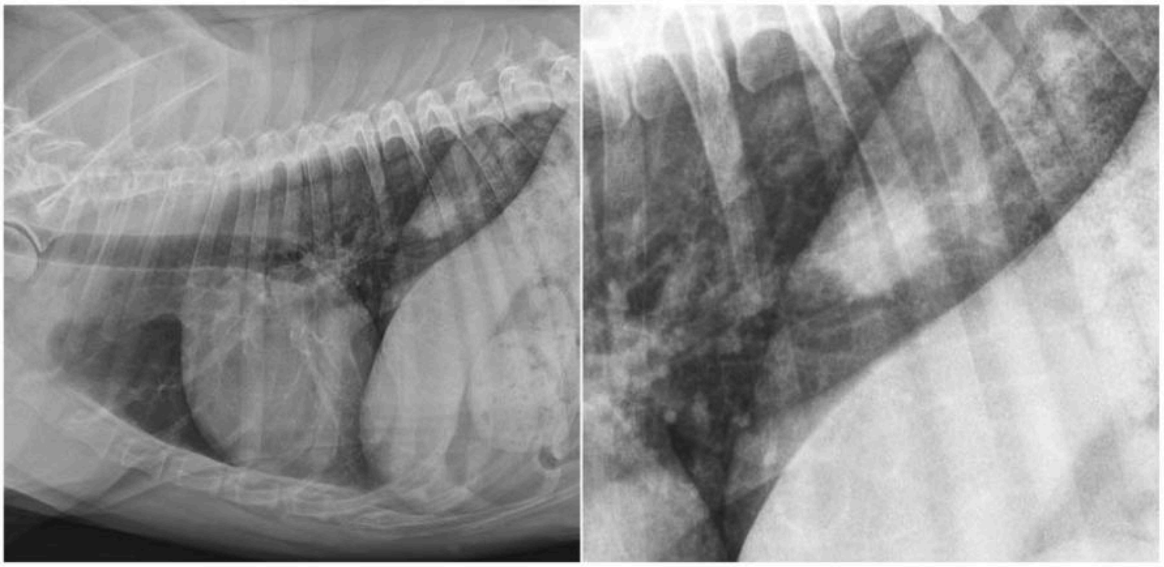


Fig. 2.10 Screen capture from a DICOM viewing program. A left lateral thoracic radiograph is displayed in the *left panel*. In the *right panel*, the same radiograph has been enlarged and the contrast adjusted to increase the conspicuity of a nodule in the caudal lung field.

for primary image interpretation should be in a room with adjustable, or permanently dimmed, lighting but not in total darkness.

Monitor quality is another factor that influences the accuracy of interpretation of digital radiographic images. Both monochrome (black and white) and color liquid-crystal display (LCD) monitors are available, and their technical specifications are highly variable, leading to a wide range of image display quality. Ideally, radiographic images are best viewed on a dedicated medical-grade monochrome LCD monitor.[18] Such monitors are characterized by superior brightness, contrast ratio, and resolution. Monitor brightness relates to how bright a white screen is, and a brighter display enables the user to resolve more shades of gray. Contrast ratio is a measure of the monitor's ability to display true black as black and true white as white. Because LCD technology relies on backlighting, displaying true black is technically challenging, and as a result, LCD monitors with a high contrast ratio are more expensive. Monitor resolution also affects how well digitally captured images appear on the screen. Medical-grade monochrome LCD monitors typically have 3 megapixel resolution or higher. For example, a typical display for such a monitor is 2048 pixels × 1536 pixels, yielding a 3.1-megapixel display. This level of resolution approximates the average resolution of most digital radiographs, which means there is no image downsizing by the graphics card during initial image display. For the user, this means there is no need to routinely magnify images to ensure all the digital information available is evaluated. Unfortunately, medical-grade monochrome LCD monitors are expensive, and their routine use throughout the veterinary imaging environment cannot be justified financially. Consumer-grade color LCD monitors are improving continuously, eroding the diagnostic advantage of more expensive monochrome monitors. However, given the substantial investment that occurs when deploying a digital radiography system, an additional investment to acquire at least one medical-grade monochrome monitor for the primary interpretation of digital radiographic images is justifiable.

Whatever viewing system is chosen, it is important to ensure that monitors are calibrated correctly. Test patterns to assist in monitor calibration are available through the Internet. Medical-grade monochrome LCD monitors should be calibrated using the DICOM grayscale display function standard. LCD monitors lose brightness over time, with consumer-grade monitors affected more rapidly than medical-grade monitors, so brightness should be periodically measured.

DIGITAL VERSUS ANALOG IMAGING

The advantages of digital imaging are quite far reaching, and some have been alluded to in prior sections. It is noteworthy to outline specifically what these advantages are and to expand on those that have not been covered in adequate detail. Advantages of digital radiography are (1) reduced expendable supply cost and elimination of darkroom maintenance; (2) contrast optimization and exposure latitude; (3) image postprocessing, ability to adjust image blackness and contrast after exposure; (4) improved image accessibility and consolidated image storage; (5) enhanced portability enables consultation; (6) use of artificial intelligence, and (7) an opportunity to change the imaging paradigm.

Reduced Expendable Supply Cost and Elimination of Darkroom

In a digital imaging environment, the requirement for purchasing x-ray film, film-filing envelopes, darkroom chemistry, and other related supplies is eliminated. Although these items are not inherently expensive, their use over time as well as the time and effort required for maintenance amount to a considerable sum, which is eliminated in digital imaging. Darkroom errors, such as outdated chemicals, incorrect temperature settings, chemical spills and splashes, and safelight fog or other light leaks, make up a substantial fraction of errors that compromise analog image quality. Additionally, there are increasingly more stringent local government requirements in ensuring personnel safety with respect to darkroom chemicals and fumes and also in the safe disposal of exhausted darkroom chemicals.

Contrast Optimization and Exposure Latitude

When one begins to evaluate digital radiographic images, the initial impression may be that of improved detail when compared with analog film radiographic images. This is a misconception created by the excellent contrast optimization

that characterizes digital radiographs. The detail of an image relates to how small of a structure can be discriminated in the image; this is termed *spatial resolution*. The spatial resolution in a digital or analog radiographic image depends on many factors, some of which apply equally to both analog and digital imaging, but there are a few differences (Box 2.1). In the end, it is the collective effect of these factors that determines the final spatial resolution. The relative inherent spatial resolution from various medical-imaging techniques is provided in Table 2.1.[19] From Table 2.1, it can be seen that the inherent spatial resolution of digital radiographs is roughly half that of analog radiographs; this is the end result of all factors listed in Box 2.1. Although there is a factor of two difference in spatial resolution between analog and digital radiography, this difference is not relevant clinically because the spatial resolution of both analog and digital radiography is excellent. Thus, it is not spatial resolution that sets digital radiography apart. The major factors contributing to the superior image quality of digital radiographs are contrast optimization and exposure latitude.

Because an antiscatter grid can improve both spatial resolution and image contrast, it is worth commenting specifically on their use in digital radiography. Although antiscatter grids can be used in digital radiography, some manufacturers have incorporated a scatter-correction algorithm into the image-processing software that makes grid use unnecessary (Fig. 2.11).[20] Implementation of an antiscatter algorithm avoids the higher milliampere second (mAs) values that are needed to compensate for the presence of an actual grid in the x-ray beam (see Fig. 2.11). The possibility of a grid artifact is also eliminated when grids are not used. Whether or not the end user will be satisfied with the quality of the antiscatter image-processing algorithm will be a matter of individual preference, and the functionality of this feature should be evaluated in any digital system prior to purchase.

Box • 2.1

Factors Contributing to Inherent Spatial Resolution in Digital Versus Analog Radiographs

Digital Radiograph
Focal spot size
Patient scatter
Grid efficiency, if used
Size of crystals in intensifying screen*
Size of detector element in digital plate

Analog Radiograph
Focal spot size
Patient scatter
Grid efficiency, if used
Size of crystals in intensifying screen
Size of light-sensitive crystal in x-ray film emulsion

*For digital radiography, an intensifying screen is used only in indirect flat panels and in CCD systems.

Table • 2.1

Inherent Spatial Resolution of Various Imaging Modalities.

MODALITY	RESOLUTION (mm)
Screen film radiography	0.08
Digital radiography	0.17
Ultrasound imaging (5 megahertz [MHz])	0.30
Computed tomography	0.40
Magnetic resonance imaging	1.00

Modified from Bushberg JT, Seibert JA, Leidholdt Jr. EM, et al. Introduction to medical imaging. In: Bushberg JT, Seibert A, Leidholdt EM, Boone JM, eds. *The Essential Physics of Medical Imaging*. 3rd ed. Philadelphia: Lippincott Williams & Wilkins; 2011:60–68.

Contrast Optimization

Contrast optimization, also termed *contrast resolution*, is a feature of digital radiography that is related to the bit depth of each pixel and the processing software that accompanies the digital-imaging system. The processing software can assign a gray shade to a pixel in a digital image that would have been either black or white in an analog image. This results in more of the image having interpretable gray shades and not appearing over- or underexposed.

With radiographic film, radiographic contrast is associated rigidly with the relationship between kilovoltage peak (kVp) and mAs, as discussed in Chapter 1. Consider the film radiography of a patient where the thickness of various parts of the patient within the primary x-ray beam varies considerably; one example of this would be a lateral radiograph encompassing the caudal abdomen, pelvis, and femurs and stifle joints of a dog. The lumbosacral region of the pelvis is very thick and primarily bone. The caudal abdomen is somewhat thinner and primarily soft tissue. The distal femur and stifle joints are much thinner. When the radiographic technique that is suitable for the average thickness and physical density is selected (e.g., caudal abdomen), the lumbosacral region in the film image will be underexposed and the thinner parts in the film image overexposed because of excessive x-ray transmission. One can think of this result as being caused by the film having a bit depth that is too low to capture all the needed gray shades. The region of the film in the lumbosacral region can only be white, and the region of film in the stifle region can only be black.

With digital radiography, however, the computer can compensate for the wide range of thickness of the patient by assigning a suitable gray shade to pixels in the thick lumbosacral and thin stifle regions, as well as in the caudal abdomen. What this means in practical terms is that in digital imaging, opacity differences associated with variation in thickness are much lower than in analog radiographs (Fig. 2.12). This same principle applies to structures of similar thickness but containing parts that have markedly different physical density, such as massive bones (Fig. 2.13) or air-filled lung (Fig. 2.14). The result is a more pleasing image with more gray shades, with no regions that cannot be assessed because of being over- or underexposed. Making a lateral view of the pelvis of a medium-to-large dog with the pelvic limbs displaced cranially and caudally, as illustrated in Fig. 2.12, is a good field test for contrast optimization software which varies from vendor to vendor.

The terminology used to describe this contrast optimization feature of digital radiographic systems can be confusing. Some have used the term *dynamic range* to mean the same thing as contrast resolution, but there are, in fact, many differing definitions of dynamic range, depending on the system being discussed. The term *dynamic range* has also been used to describe the low dependence of digital-imaging plates on absolute x-ray exposure (kVp and mAs), which in this chapter we call *exposure latitude*.[21] To avoid this confusion, we recommend use of *contrast resolution* or *contrast optimization* to define the ability of an imaging system to display thick and thin regions, and regions of low and high atomic number, suitably in one image, and the term *exposure latitude* to define the ability

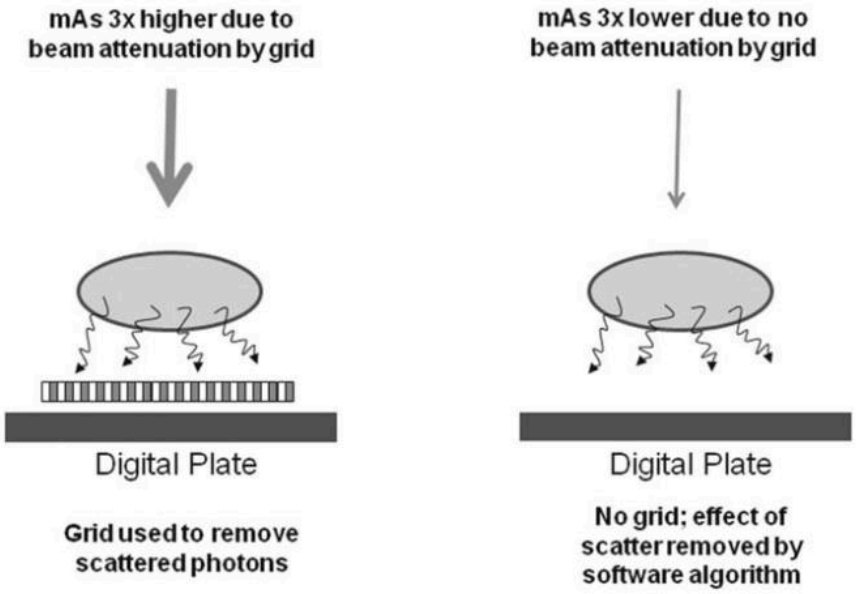


Fig. 2.11 Diagram illustrating the principle of scatter removal by a grid versus a scatter-correction software algorithm. On the *left*, the scattered photons are removed by a grid. This is standard practice in analog radiography and can also be used with computed radiography (CR), direct digital radiography (DDR), and charge-coupled device (CCD) systems. On the *right*, there is no grid, and the effect of the scattered photons has been corrected by a software scatter-correction algorithm. The mAs can be lower on the right because there is no attenuation of the primary beam by the grid. Whether the efficacy of any scatter-correction software will be adequate is subjective and should be field-tested prior to purchase.

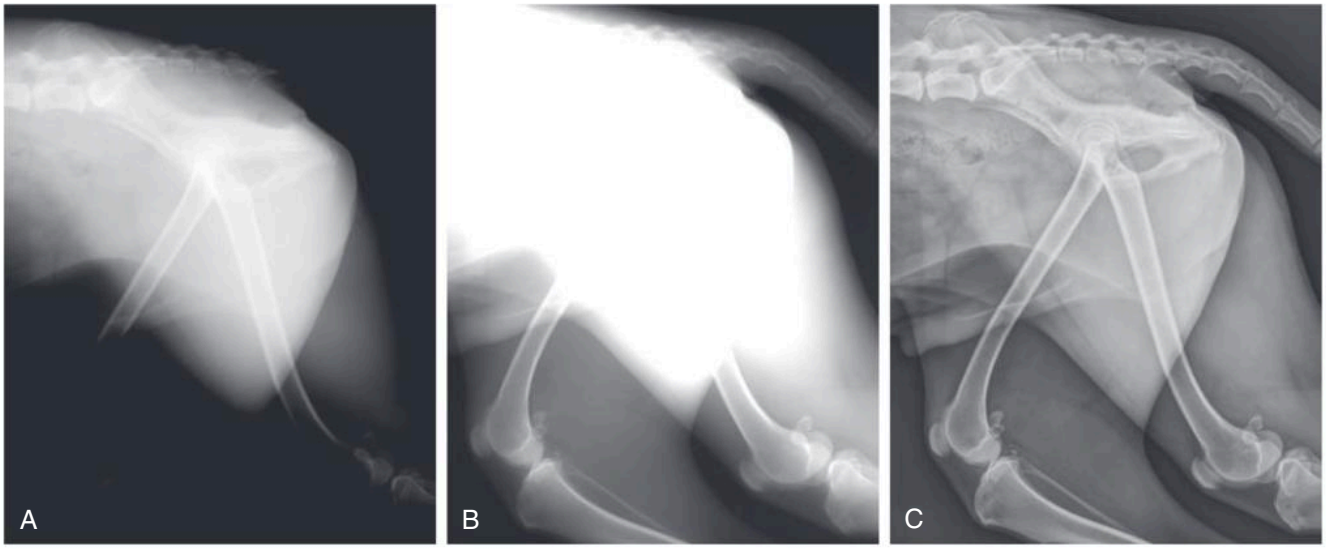


Fig. 2.12 Radiographs illustrating the contrast resolution of digital radiographs versus analog radiographs. **A,** Film radiograph made with exposure factors appropriate for the lumbar spine. The distal aspect of the femurs and the stifles are overexposed because they are thinner and cannot be adequately evaluated. **B,** Film radiograph made with exposure factors appropriate for the stifles. The spine and pelvis are underexposed because they are thicker. **C,** Digital radiograph where both the thick and thin aspects of the patient can be assessed. This wide range of gray shades characterizes the wide contrast resolution of digital radiographs. The ability to assign a gray shade to a pixel is the basis of this wide range of gray shades; this is a feature of the processing software provided by the hardware vendor.

of digital plates to compensate for either high or low kVp-to-mAs combinations that would result in overexposure or underexposure, respectively, in an analog system.

In analog imaging for any given anatomy, image contrast was controlled primarily by kVp, with some contribution from film type and use of an antiscatter grid. If a high contrast image was desired, a low kVp was used, necessitating an increase in mAs to ensure appropriate film blackness. In digital imaging, image contrast is controlled largely by algorithms (and can also be manipulated by the viewer) and as a result, is for the most part, independent of kVp. Therefore, when creating a digital technique chart, the kVp range selected for any given anatomy can be higher than would typically be used for analog imaging. This means a corresponding reduction in mAs. Reducing mAs is always desirable as it reduces the potential for motion artifact, an everyday issue in veterinary radiography.

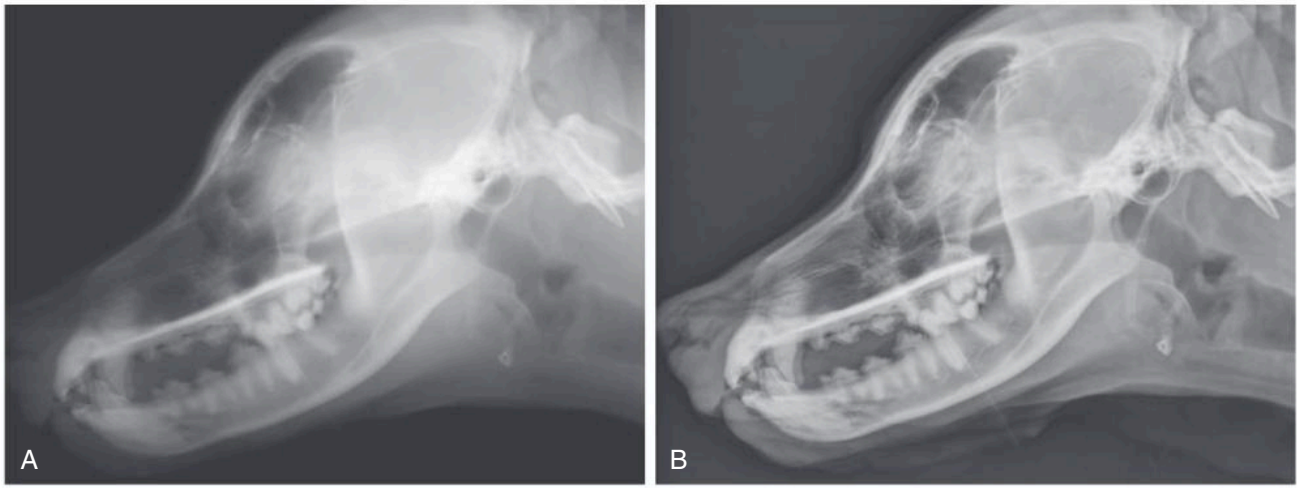


Fig. 2.13 Lateral views of a canine skull made with analog (**A**) and digital (**B**) systems. In **A,** the nasal planum and maxillary structures are overexposed while the temporomandibular joint region is underexposed. Bone underexposure is primarily the result of its increased physical density leading to increased x-ray absorption. In **B,** the image-processing algorithm can compensate for these differences in absorption and assign a more useful gray shade to pixels in soft tissue and bone, leading to an image where thick and thin regions of both bone and soft tissue can be assessed.

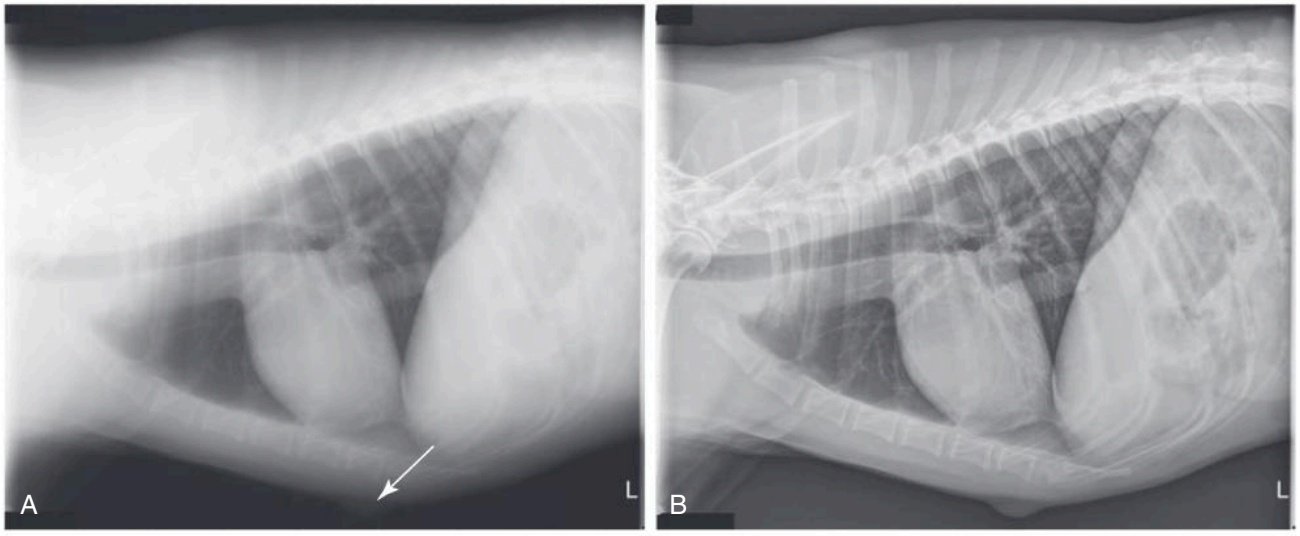


Fig. 2.14 Lateral canine thoracic radiographs of the same patient made with analog (**A**) and digital (**B**) systems. In **A,** the lungs are exposed reasonably and can be interpreted, but the bones, cranial aspect of the abdomen, and paraspinal soft tissues are underexposed, and the periphery of the patient is overexposed. Note the poor visibility of the ventral lipoma because of overexposure (*white arrow* in **A**). The lungs, being of low physical density, absorb few x-rays, and the exposure factors were adjusted for this. The film is incapable of displaying meaningful information in other underexposed or overexposed areas. In **B,** the image-processing algorithm can compensate for the differences in physical density and assign a more useful gray shade to pixels in soft tissue and lung, leading to an image where both can be assessed. Note the increased conspicuity of the small ventral lipoma that was overexposed in the analog image.

Exposure Latitude

The magnitude of the range of radiographic exposures (i.e., the radiographic technique) that can be used to create a diagnostic radiographic image is called *exposure latitude*. With analog radiography, there is only a narrow range of kVp and mAs combinations that will result in satisfactory film blackness, and even then, there will usually be regions of the film image that are too white or too black (see Figs. 2.12, 2.13, and 2.14). Any combination of kVp and mAs outside of the suitable range will result in underexposure or overexposure (Figs. 2.15 and 2.16). With digital plates, exposure latitude is wide and the ability of the processing software to create an image of suitable blackness is much more independent of the kVp and mAs values used (Fig. 2.17; see Fig. 2.16).

One potential disadvantage of the wide exposure latitude that characterizes digital-imaging plates is *exposure creep*, where unnecessarily high exposure factors are not recognized as they would be when using an analog system as overexposure is corrected by the image-processing software.[22,23] The disadvantage of exposure creep is unnecessary patient and personnel exposure to ionizing radiation and increased wear and tear on the x-ray tube. Most digital radiography manufacturers have incorporated an exposure index (EI) metric that enables the user to evaluate the amount of incident radiation that strikes

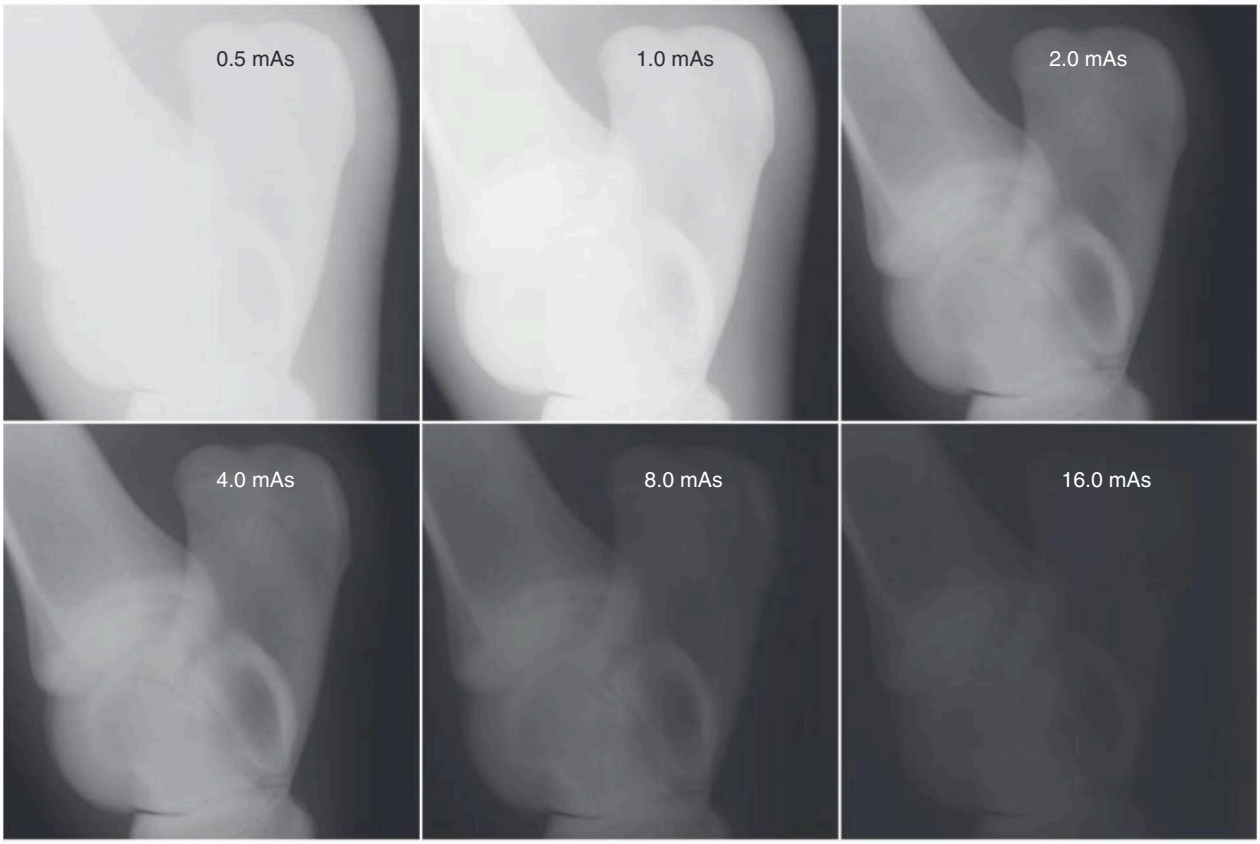


Fig. 2.15 Lateral analog radiographs of an equine tarsus exposed at the same kVp value but at a wide range of mAs values, from 0.5 to 16. At low mAs values, the entire image is underexposed, whereas at high mAs values, the entire image is overexposed. At 2 mAs and 4 mAs the soft tissues can be evaluated, and at 8 mAs the bones can be evaluated. This is an example of the narrow exposure latitude of analog radiography. In daily practice, many poor radiographs are produced because of the selection of incorrect exposure factors.

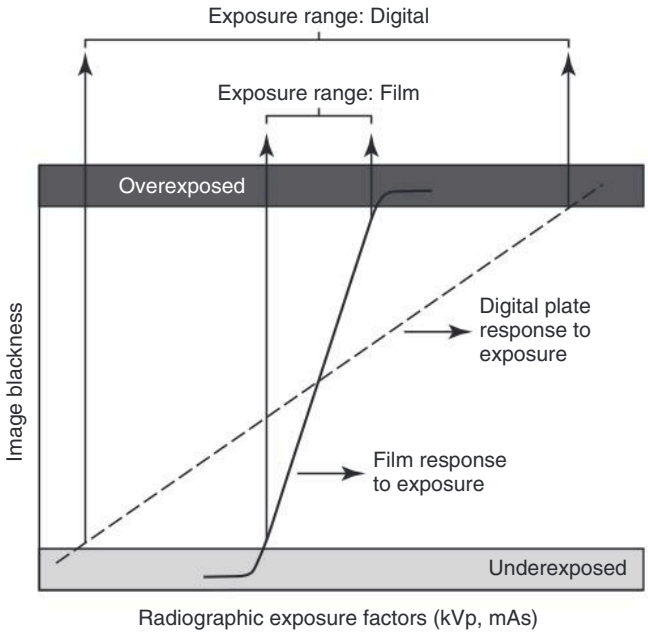


Fig. 2.16 Diagram illustrating the principle of exposure latitude. In this figure, image blackness is plotted as a function of radiographic exposure, that is, kVp and mAs. For film, small changes in kVp and mAs cause dramatic changes in image blackness—the slope of the curve is very steep. There is only a narrow range of exposure that leads to suitable image blackness in an analog system. For digital systems, the slope of the curve is much shallower. This results in many more combinations of kVp and mAs that will result in adequate image blackness. This wide exposure latitude reduces retakes and is a feature of both the hardware and the processing software of the digital-imaging system.

the plate (i.e., the exposure factors). The EI is a measure of radiation striking the relevant image region in a receptor, and an approximate indicator of the x-ray "signal" detected by the digital radiography unit.[24] The EI can be used to judge whether radiographic techniques are too high or too low. However, the EI is only useful if it is monitored routinely. Routine checking of the EI should be part of the quality assurance process used to evaluate the digital-imaging process for every patient.

The transition to digital radiography has led to a dramatic reduction in the number of retakes, especially those related to errors in radiographic exposure.[25] However, the wide exposure latitude that characterizes digital radiography does not mean that underexposure or overexposure is not a problem; these problems still occur, but only at the extremes of exposure factors. With underexposure, the overall image quality may appear satisfactory from a global perspective, but a low EI should prompt a closer inspection of the image which will demonstrate a "grainy" appearance, also known as "quantum mottle." This grainy appearance is caused by high image noise relative to low x-ray signal, created by statistical uncertainty in computer assignment of a gray shade to underexposed regions of the image.[26] This grainy appearance will be obvious on close inspection and could interfere with detection of a subtle lesion, especially those affecting the trabecular pattern of bone (Fig. 2.18). Underexposure requires a repeat radiograph with increased exposure factors. Image noise is particularly responsive to changes in mAs, so if excessive quantum mottle is detected, mAs can be increased until attaining an appropriate EI and satisfactory image noise levels.

Overexposure of digital radiographs does not result in overall film blackening, as with film. The detector elements and processing software are able to compensate electronically for overexposure (excessive x-ray signal), up to a point at which the detector becomes saturated and cannot respond to

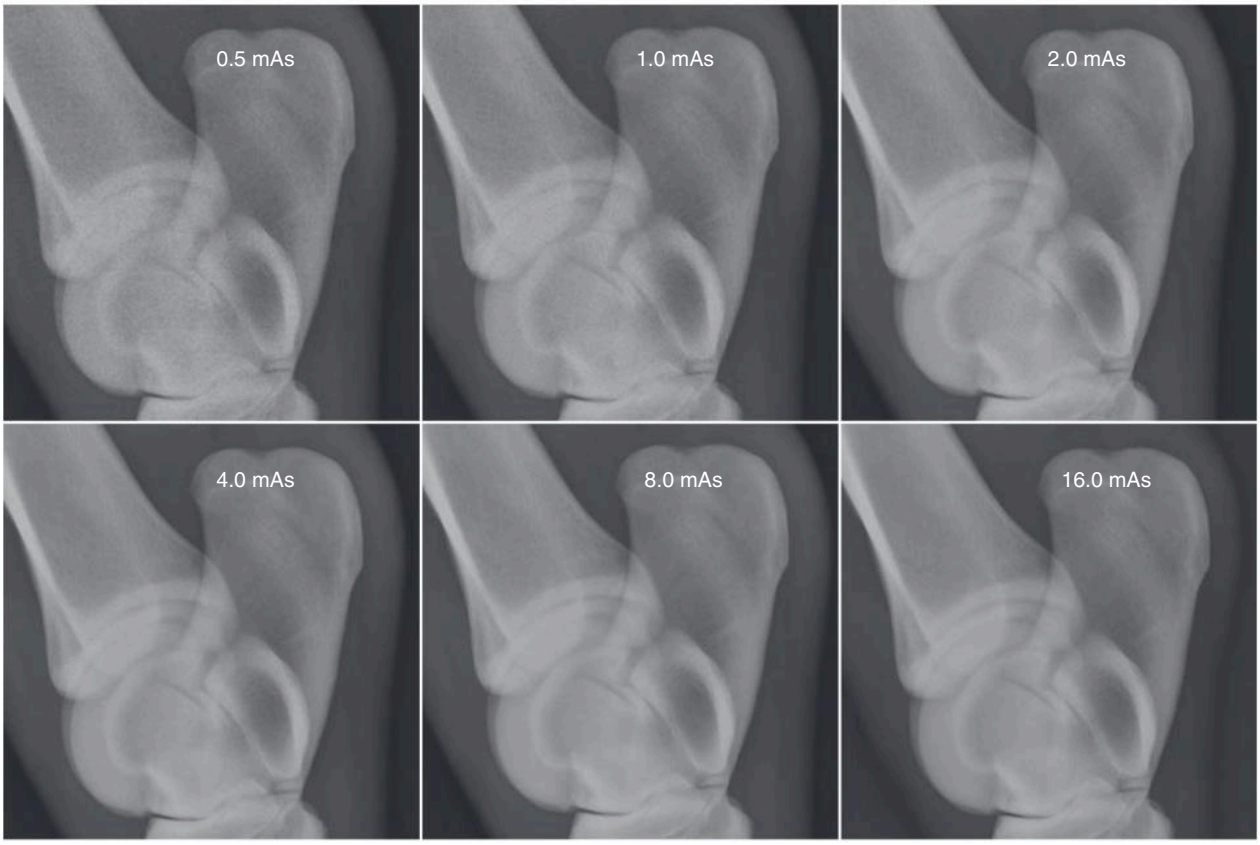


Fig. 2.17 Lateral digital radiographs of the same equine tarsus as in Fig. 2.15, acquired with an indirect flat-panel detector. Note the acceptable film blackness and contrast at all mAs values. This illustrates the reduced dependence of the image blackness and contrast of digital radiographs as a function of radiographic exposure. This wide exposure latitude reduces the number of retakes needed because of the selection of incorrect exposure factors.

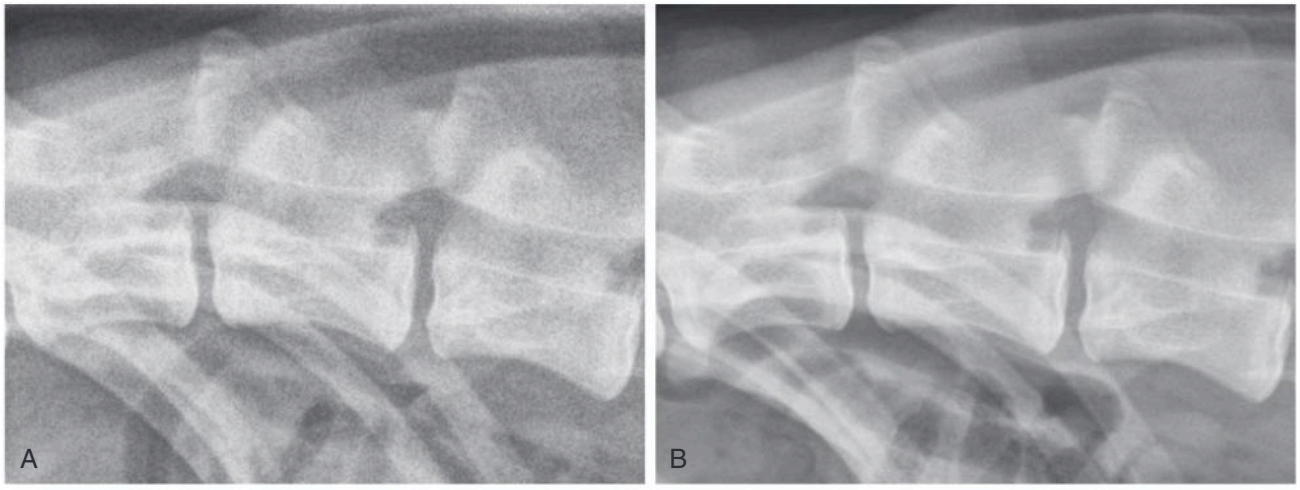


Fig. 2.18 Underexposed (**A**) and properly exposed (**B**) digital radiographs of a portion of the lumbar spine of a dog. In **A,** there is a noticeable grainy appearance to the radiograph because of underexposure. This represents image noise and is created by uncertainty in grayscale assignment to unexposed pixels. In **B,** the grainy appearance has been eliminated by increasing the exposure factors.

additional exposure. At saturation, the computer assigns the maximum pixel value, black, to the pixels that are saturated.[26] This results in some parts of the image being absent or having an abnormal gray shade assignment (Fig. 2.19). Because only portions of the image are overexposed, as compared to the entire image, the overexposed region can be misinterpreted easily as a lesion. Overexposure that results in image saturation necessitates repeating the radiograph using lower exposure values (particularly mAs).

Image Postprocessing

Despite the tremendous contrast resolution of digital radiographs, there is sometimes a desire to make some regions of the final processed image blacker or whiter to facilitate

interpretation. For example, when thoracic radiographic images are produced by the image-processing software, they may have a long scale of contrast that may not be optimal for evaluating the bones in the image. Modifying the image blackness and contrast is accomplished easily with DICOM viewing software, and magnification of regions of the image can also be very useful in detecting small lesions that would be overlooked in an unmagnified digital image or in an analog film image not viewed with a magnifying glass (Fig. 2.20). Most inexperienced interpreters fail to take advantage of the full range of manipulations provided by DICOM viewing software.

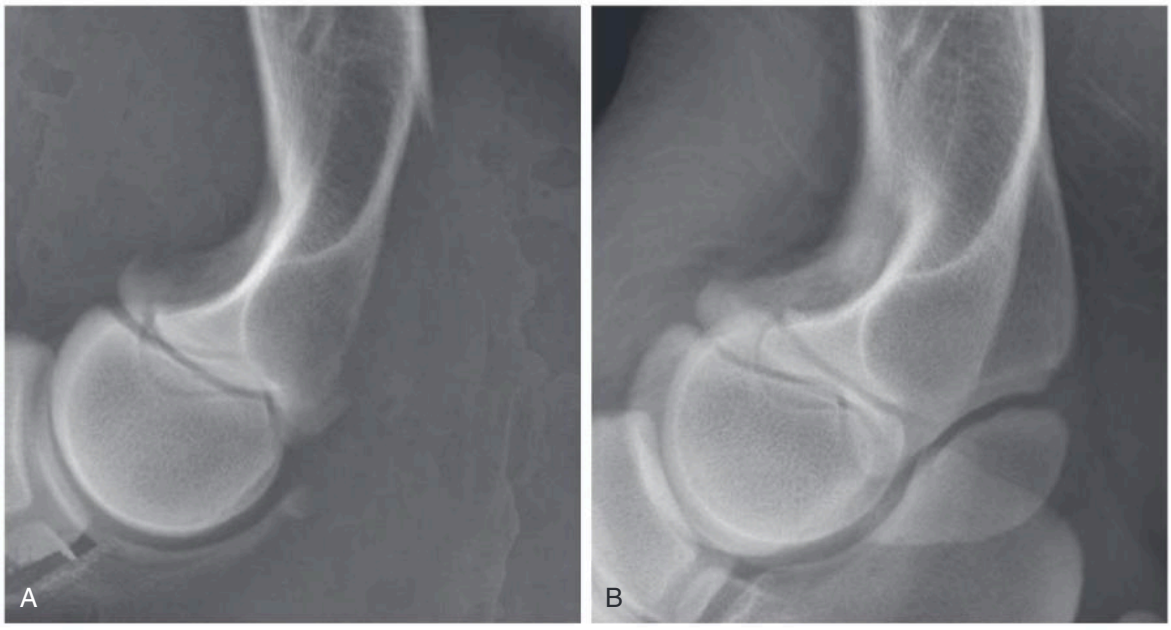


Fig. 2.19 Overexposed (**A**) and properly exposed (**B**) radiograph of the distal humerus of a foal. In **A,** the distocaudal aspect of the humerus, the center of ossification for the medial epicondyle, and the proximal aspect of the ulna are all not visible because of plate saturation in this region created by massive overexposure. In **B,** the missing structures are clearly visible. Missing anatomy caused by plate saturation could easily be interpreted as a pathologic lesion, such as bone lysis.

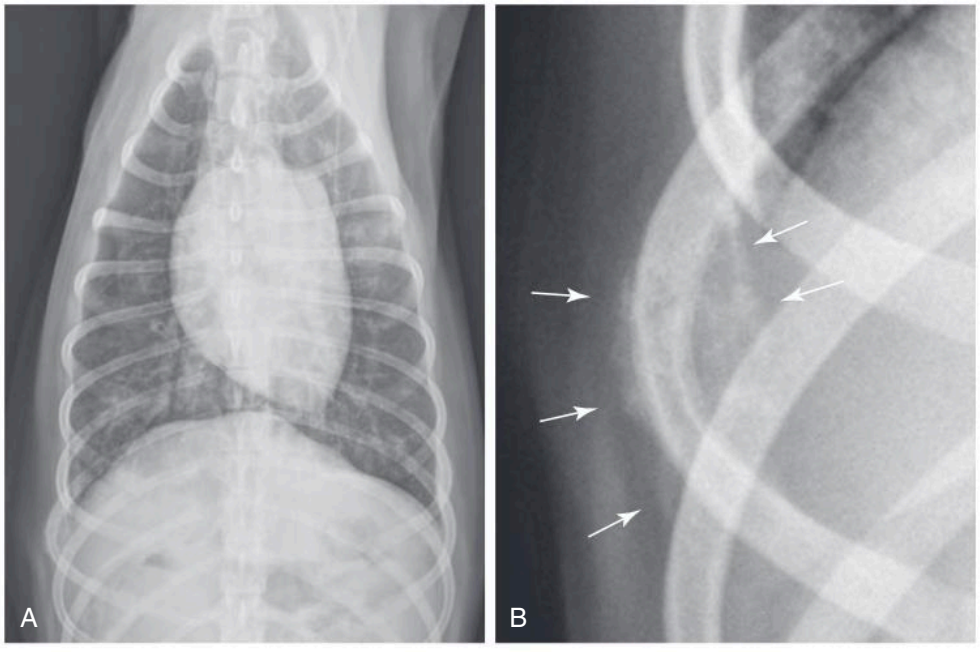


Fig. 2.20 **A,** Ventrodorsal thoracic radiograph of a dog with a scapular tumor. The right forelimb has been removed. This radiograph was part of a series acquired to examine for pulmonary metastasis and, as such, has been processed by the software with a long scale of contrast. There is an aggressive lesion of the right 9th rib. Had the image only been viewed at this magnification, and at this long scale of contrast, this lesion would have likely been overlooked. With digital radiography, the image can be magnified, and every rib examined in detail. Magnification, and making the scale of contrast shorter, greatly increases the conspicuity of the rib lesion, as in **B**. **B,** the irregular periosteal reaction on the right 9th rib is outlined by the *solid white arrows*. The lesion is much more conspicuous with magnification and increased contrast.

Improved Image Accessibility and Consolidated Image Storage

The full advantages of digital imaging are best realized when digital imaging is incorporated into the global practice environment. This means integrating image acquisition and management with the hospital's electronic medical record. In a fully integrated system, radiographic studies are ordered in the electronic medical record. The order appears seamlessly at the x-ray machine computer using functionality known as *DICOM modality worklist*. Selecting the study to be performed from a list of the examinations requested for the day eliminates data entry errors that might result from having to reenter all patient information de novo and improves workflow. When the study has been acquired, appropriate charges are posted automatically in the medical record, and the images are sent to a local server for distribution and archiving. Distribution might include transmission of the images to an off-site radiologist for interpretation, with the radiographic report being entered seamlessly into the patient record after it is completed. The images are viewable through the electronic medical record using either DICOM viewing software, as described previously, or through an Internet browser.

Picture archiving and communication system (PACS) refers to the host of technologies that contribute to the creation, distribution, and archiving of digital images. The basic components of a PACS that might be found in a private veterinary practice are (1) the device, that is, the x-ray machine and the CR or DDR radiography system; (2) a server that acts as the local image archive; (3) workstations that can retrieve images from the server for remote viewing, in the examination room or surgery for example; (4) a local area network for data transfer; (5) an image communication protocol (the DICOM standard); and (6) off-site or cloud-based secure image storage (Fig. 2.21). When purchasing a digital-imaging system, there is often little attention paid to integration of the radiographic hardware and software into the overall hospital environment. This is a mistake and can result in functionality problems that compromise the advantages of transitioning to digital imaging.

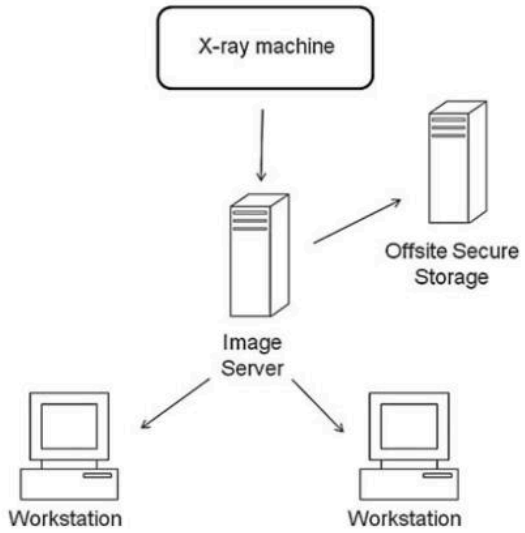


Fig. 2.21 Components of a rudimentary picture archiving and communication system (PACS) system. Images in Digital Imaging and Communications in Medicine (DICOM) format are transferred from the acquisition device, an x-ray machine in this example, to the central server. Images have been assessed by the technical staff for quality prior to being transmitted to the server. The central server must not be relied on as the sole image storage device. Secure off-site image archiving is needed. Clinicians at remote locations, such as the examination room, the intensive care unit (ICU), or surgery, can retrieve images from the server for interpretation and consultation. Images can also be sent from the server to remote locations for additional consultation.

Traditionally, DICOM images have been viewed on a DICOM workstation software that is loaded on the client computer. The images are "downloaded" to the workstation using software that is installed onto the local device, whether it is a MAC or PC operating system.

As discussed previously, the DICOM standard provides for the transmission of medical images from an imaging device or server to a DICOM workstation, using a network protocol that runs on top of the existing Internet standard protocol. There are three important aspects to this connectivity, namely, the application entity (AE) title, port, and internet protocol (IP) address or full registered host name of the computer. Typically, the "DICOM" address of the destination to which you wish to send images can be configured in modality, server, and workstation software. The DICOM transfer protocol uses nonstandard computer ports (usually 104, 4006, and 11112, depending on software). This can make receipt of images using this system problematic if firewall and other security measures are not appropriately configured. Web access to DICOM objects (WADO) is an image transmission protocol that uses http/https to transfer image data, negating some of the network configuration issues inherent in the traditional DICOM connection. DICOM images can also be transferred using browser-based technology, and this enhances image portability, particularly when accessing images beyond the local area network.[27]

The demand for enhanced image portability with minimal delays in transmission is increasing. Clinicians would like to be able to view images on mobile devices, show images to clients in consultation rooms, and provide clients with web links to images and patient data.[28,29] Two significant changes have occurred in medical image management in the last few years that have significantly enhanced image viewing. With the development of the hypertext markup language 5 (HTML5) standard for web browsers has come a tremendous opportunity to develop browser-based medical image viewers that do not require complex browser plug-ins or programs that need to be installed locally on the client computer (so called *thick client configuration*). These new viewers, known as *zero footprint viewers*, require only an HTML5-compatible browser, and many of these viewers have all the functionality of dedicated DICOM workstation software that would otherwise need to be loaded on the client computer. These viewers are browser and operating system agnostic, meaning that they work equally as well in any of the modern browses (Google Chrome, Safari, Microsoft Edge, Mozilla Firefox), running on modern Windows or Apple operating systems and also on iOS and Android devices. In addition to being browser based, they may also be a mobile device "app." There are many advantages to this technology. First, some browser plug-ins pose an increased security risk. As a result of the enhanced functionality of HTML5 and potential security issues associated with Java, browser-based viewers that use Java as a plug-in are losing popularity. Second, DICOM workstations and older browser-based viewers require the images to be downloaded; this takes time, particularly if the study is large and there is poor bandwidth. Third, most older, browser-based viewers are OS and browser specific and DICOM workstations are usually OS specific; this reduces convenience. The programs require downloading and installing (many are not free), and there is always some degree of program upkeep required. These complexities are eliminated by HTML5 zero footprint viewers.

Whereas historically, medical image archives have been limited to the DICOM file format, modern medical archives are designed to archive all types of file formats in addition to DICOM. Many other medical services in addition to diagnostic imaging generate images which should be archived in the medical record. Ophthalmologic, dermatologic, endoscopic,

and arthroscopic photographs and movies are such examples. Additionally, scanned hard copy documents can be an integral part of the patient's medical record and need to be archived. Typical file formats for such medical data include .tiff, .jpeg, .pdf, and .mp4. With the advent of vendor neutral archives (VNAs), all images related to a medical record can be archived in one resource whether they were acquired by diagnostic imaging, or any other service. The term *vendor neutral archive* is somewhat of a misnomer, the important point is not that the archive is vendor neutral, but rather it is file format agnostic. Some modern HTML5 medical image viewers can display these non-DICOM format files as readily as those in DICOM format, meaning that only one interface is needed to view a variety of patient data. In human imaging the deployment of an "enterprise viewer" (defined as a thin-client or zero-client application used on any off-the-shelf device to distribute, display, and manipulate multi-specialty image, video, audio, and scanned documents stored in separate centralized archives) is becoming increasingly popular.[28]

With digital radiography, space costs for filing cabinets and cost of film envelopes and film cataloging are eliminated. Also eliminated is the problem of lost or destroyed radiographs. Digital radiographs are stored as digital files on an image server, an integral part of the PACS. A common mistake, however, is relying on only one primary storage device to archive the collection of digital radiographic files. Storing digital files on a single archive, typically on a single hard disk drive on one server, is not adequate because the hard drive can fail. Also, any other component of the server can also fail and lead to corrupt data, or the server can be destroyed during a physical disaster such as fire or flood. Storage using a redundant array of independent disks (RAID), where data are distributed over multiple disks such that if one disk fails, data integrity is preserved, is an absolute minimum for hardware redundancy. Data storage using RAID is much safer than relying on a single hard disk drive. However, although a RAID configuration does protect against individual hard drive failure, it does not protect against other hardware failures, including RAID controllers and other critical components of a server. Additionally, the data are still subject to loss through server damage during a physical disaster, an unprotected power surge, or corruption through a computer virus. The best solution is redundant off-site duplication and storage where digital radiographic data are duplicated and transferred to an off-site computer on a regular basis, preferably daily, for safe storage.

Cloud storage is commonplace in today's environment and while it is common to have a small image archive in the house, most PACS are configured such that either the primary archive is cloud-based or all studies are sent to the cloud for backup and disaster recovery.

Enhanced Portability Enables Consultation

It is difficult for most practicing veterinarians to become totally competent in radiographic interpretation. The volume of information and the nearly endless variation in how disease manifests radiographically is simply too much. Getting a second opinion on radiographic studies has been employed for decades. Analog film images were either hand-carried to a specialist, if one was lucky enough to be sufficiently close, or sent to the expert by mail or courier. The expert would interpret these images, usually telephone the veterinarian with the results, and prepare a written report that would be returned to the veterinarian along with the radiographs.

With the explosion of digital radiography in veterinary medicine, veterinary teleradiology was born. Teleradiology is a type of telemedicine that involves the electronic transmission of radiological images from one location to another for the purposes of interpretation and/or consultation with a specialist.[30] Veterinary teleradiology was first introduced commercially in the early 1990s with limited success, mostly influenced by slow Internet speeds and large file sizes, but has grown dramatically in recent years, reflecting the recent growth of the broader veterinary telemedicine market.[30–33] It is worth noting that while telemedicine is a valuable tool that augments patient care, it does not replace the patient-client relationship, and should be viewed as a supplemental service.[32]

DICOM files are large, and transmission as an email attachment can be problematic. For teleradiology consultation to work smoothly, a method of direct DICOM transfer needs to be established; this is why it is so important to ensure that the vendor of the digital radiography equipment has configured its DICOM file format appropriately. Currently, the practice of teleradiology in veterinary medicine is widespread because of the availability of broadband Internet connections, image compression, and economically priced PACS and DICOM software.[31] Also, there are many teleradiology service providers throughout the world who have teleradiographic interpretation as their primary mission. These advancements have made turnaround time very short and STAT interpretations possible.

Artificial Intelligence

Artificial intelligence (AI) is a broad term that describes a situation where a computer system performs tasks that mimic human intelligence or serves an analytical role typically satisfied by humans.[34] The field of AI has rapidly progressed in the last 20 years and has now entered the veterinary market, with vendors actively advertising AI systems that provide interpretation input on radiographs in dogs and cats.[34] In human medicine, AI imaging interpretation is bound by FDA regulations, and implementation must include strict proof of design and accuracy.[35] As a result, AI imaging interpretation tends to be narrow-focus and task specific, and often provides computer-aided diagnosis or computer-aided detection tools, rather than all-encompassing or definitive image interpretation.

In comparison, there is no regulatory framework limiting AI in veterinary medicine. Proof of efficacy is not required before a veterinary vendor can offer an AI tool. Whereas AI provides great promise and likely will result in eventual improvements in veterinary practice, the benefits of AI and proof of efficacy are not currently known. The quality of an AI model is heavily influenced by the quality of AI training and validation data used to build the AI model.[36] This type of information is not readily available for commercially available veterinary AI products. The individual veterinary practitioner who implements these tools should be aware of these limitations when evaluating a potential AI interpretation tool. This is a rapidly developing market; individual research publications evaluating AI tools in veterinary medicine have begun to appear, but more are necessary before evidence of efficacy is available.[34–39]

An Opportunity to Change the Imaging Paradigm

Veterinary medicine can be a competitive enterprise, especially in times of economic downturn. Also, pet owners are highly educated and have a wealth of information at their fingertips that they use to help make decisions regarding medical care for their pet. Being perceived as having a modern contemporary practice environment can help maintain and increase a healthy client base regardless of economic and client-education factors. Having digital radiography is one way that practices are viewed as being progressive, and being able to provide high-quality radiographic services can bolster one's professional persona.

The transition to digital radiography can help alleviate problems with radiographic exposure, and darkroom errors are also eliminated. Positioning and selecting the correct radiographic views will not be solved automatically by the transition to digital radiography, but with a digital system, the economic cost of making these modifications is insignificant. For example, with film imaging, many veterinarians were reluctant to obtain

all needed views routinely, three projections of the thorax for example, because of the increased cost of expendable supplies required to do so. Radiographic studies should be priced on an examination basis, not on a per-image or per-view basis. The fee should be set such that the practice makes a profit, all necessary views are included, and the quality standards are acceptable.

Similarly, offering teleradiology consultation signals that a veterinary practice has adopted modern medical technology services. Telemedicine benefits all parties; the improved diagnostic ability improves quality of care for the owner and pet and is an additional service that can be advertised and charged by the veterinarian. The benefits of teleradiology can only be realized if high-quality, well-positioned radiographs are submitted for evaluation. Even the most experienced radiologist cannot provide meaningful consultation if the radiographs are marred by artifact, are poorly positioned, or do not focus on the area of interest.

ARTIFACTS

As with all medical-imaging modalities, there is potential for digital radiographic imaging artifacts. An artifact is an unwanted, usually non-patient-related anomaly in the image that may or may not compromise image interpretation. These occur in both CR and DDR systems and are unique from those encountered in analog film radiography. Overexposure and underexposure and how these differ in appearance from exposure errors in analog radiography were described previously. The discussion of other imaging artifacts that are observed in digital radiography is beyond the scope of this chapter, but excellent references are available.[26,40]

REFERENCES

1. Graham RN, Perriss RW, Scarsbrook AF. DICOM demystified: a review of digital file formats and their use in radiological practice. *Clin Radiol*. 2005;60:1133–1140.
2. Wright MA, Ballance D, Robertson ID, et al. Introduction to DICOM for the practicing veterinarian. *Vet Radiol Ultrasound*. 2008;49:S14–S18.
3. ACVR. Image resolution & DICOM guidelines. https://acvr.org/dashboard/resources/image-resolution-dicom-guidelines/. Accessed 9/1/2022.
4. Widmer WR. Acquisition hardware for digital imaging. *Vet Radiol Ultrasound*. 2008;49:S2–S8.
5. Watt KN, Yan K, DeCrescenzo G, et al. The physics of computed radiography: measurements of pulse height spectra of photostimulable phosphor screens using prompt luminescence. *Med Phys*. 2005;32:3589–3598.
6. Bushberg JT, Selbert JA, Leidholdt Jr EM. *The Essential Physics of Medical Imaging*. Philadelphia: Lippincott Williams & Wilkins; 2002.
7. Cowen AR, Kengyelics SM, Davies AG. Solid-state, flat-panel, digital radiography detectors and their physical imaging characteristics. *Clin Radiol*. 2008;63:487–498.
8. Knight SP. Contemporary research in digital radiography. *J Med Radiat Sci*. 2020;67:254–256.
9. Roch P, Celier D, Dessaud C, et al. Using diagnostic reference levels to evaluate the improvement of patient dose optimisation and the influence of recent technologies in radiography and computed radiography. *Eur J Radiol*. 2018;98:68–74.
10. DeMaio DN, Herrmann T, Noble LB, et al. Best practices in digital radiography. *Radiol Technol*. 2019;91:198–201.
11. Fornell D. *Advances in DR X-ray Technology at RSNA 2019*; 2020. https://www.itnonline.com/article/advances-dr-x-ray-technology-rsna-2019. Accessed 9/1/2022, 2022.
12. Lanca L, Silva A. *Digital Imaging Systems for Plain Radiography*. New York: Springer; 2013:9–19.
13. Lo WY, Puchalski SM. Digital image processing. *Vet Radiol Ultrasound*. 2008;49:S42–47.
14. Feghali JA, Chambers G, Delepierre J, et al. New image quality and dose reduction technique for pediatric digital radiography. *Diagn Interv Imaging*. 2021;102:463–470.
15. Goo JM, Choi JY, Im JG, et al. Effect of monitor luminance and ambient light on observer performance in soft-copy reading of digital chest radiographs. *Radiology*. 2004;232:762–766.
16. Pollard BJ, Samei E, Chawla AS, et al. The effects of ambient lighting in chest radiology reading rooms. *J Digit Imaging*. 2012;25:520–526.
17. Brennan PC, McEntee M, Evanoff M, et al. Ambient lighting: effect of illumination on soft-copy viewing of radiographs of the wrist. *AJR Am J Roentgenol*. 2007;188:W177–W180.
18. Krupinski EA, Kallergi M. Choosing a radiology workstation: technical and clinical considerations. *Radiology*. 2007;242:671–682.
19. Bushberg JT, Seibert JA, Leidholdt Jr EM. *Essential Physical Medical Imaging*. 2nd ed. Philadelphia: Lippincott Williams & Wilkins; 2002.
20. Lo WY, Hornof WJ, Zwingenberger AL, et al. Multiscale image processing and antiscatter grids in digital radiography. *Vet Radiol Ultrasound*. 2009;50:569–576.
21. Korner M, Weber CH, Wirth S, et al. Advances in digital radiography: physical principles and system overview. *Radiographics*. 2007;27:675–686.
22. Shepard SJ, Wang J, Flynn M, et al. An exposure indicator for digital radiography: AAPM Task Group 116 (executive summary). *Med Phys*. 2009;36:2898–2914.
23. Butler ML, Rainford L, Last J, et al. Are exposure index values consistent in clinical practice? A multi-manufacturer investigation. *Radiat Prot Dosimetry*. 2010;139:371–374.
24. Don S, Whiting BR, Rutz LJ, et al. New exposure indicators for digital radiography simplified for radiologists and technologists. *AJR Am J Roentgenol*. 2012;199:1337–1341.
25. Akhtar W, Aslam M, Ali A, et al. Film retakes in digital and conventional radiography. *J Coll Physicians Surg Pak*. 2008;18:151–153.
26. Drost WT, Reese DJ, Hornof WJ. Digital radiography artifacts. *Vet Radiol Ultrasound*. 2008;49:S48–S56.
27. Lipton P, Nagy P, Sevinc G. Leveraging internet technologies with DICOM WADO. *J Digit Imaging*. 2012;25:646–652.
28. Roth CJ, Lannum LM, Dennison DK, et al. The current state and path forward for enterprise image viewing: HIMSS-SIIM Collaborative White Paper. *J Digit Imaging*. 2016;29:567–573.
29. Roth CJ, Lannum LM, Joseph CL. Enterprise imaging governance: HIMSS-SIIM collaborative white paper. *J Digit Imaging*. 2016;29:539–546.
30. AVMA. *Veterinary Telehealth: The Basics*; 2022. https://www.avma.org/resources-tools/animal-health-and-welfare/telehealth-telemedicine-veterinary-practice/veterinary-telehealth-basics. Accessed 9/1/2022.
31. Poteet BA. Veterinary teleradiology. *Vet Radiol Ultrasound*. 2008;49:S33–S36.
32. Drummond A. *Regarding Veterinary-Client-Patient Relationship and Telemedicine*. California Veterinary Medical Board; 2019. https://www.vmb.ca.gov/meetings/materials/072019item11c.pdf.
33. AVMA. *Telehealth & Telemedicine in Veterinary Practice*; 2022. https://www.avma.org/resources-tools/animal-health-and-welfare/telehealth-telemedicine-veterinary-practice. Accessed 9/1/2022.
34. Appleby RB, Basran PS. Artificial intelligence in veterinary medicine. *J Am Vet Med Assoc*. 2022;260:819–824.

35. Hosny A, Parmar C, Quackenbush J, et al. Artificial intelligence in radiology. *Nat Rev Cancer*. 2018;18:500–510.
36. Basran PS, Appleby RB. The unmet potential of artificial intelligence in veterinary medicine. *Am J Vet Res*. 2022;83:385–392.
37. Hur B, Hardefeldt LY, Verspoor K, et al. Overcoming challenges in extracting prescribing habits from veterinary clinics using big data and deep learning. *Aust Vet J*. 2022;100:220–222.
38. Awaysheh A, Wilcke J, Elvinger F, et al. Identifying free-text features to improve automated classification of structured histopathology reports for feline small intestinal disease. *J Vet Diagn Invest*. 2018;30:211–217.
39. Kim E, Fischetti AJ, Sreetharan P, et al. Comparison of artificial intelligence to the veterinary radiologist's diagnosis of canine cardiogenic pulmonary edema. *Vet Radiol Ultrasound*. 2022;63:292–297.
40. Jimenez DA, Armbrust LJ, O'Brien RT, et al. Artifacts in digital radiography. *Vet Radiol Ultrasound*. 2008;49:321–332.

ELECTRONIC RESOURCES

Additional information related to the content in Chapter 2 can be found online at eBooks.Health.Elsevier.com

- Chapter Quiz



CHAPTER 3

Physics of Ultrasound Imaging

Hock Gan Heng • Wm Tod Drost

Diagnostic ultrasound is a widely used, indispensable diagnostic imaging modality that does not use electromagnetic radiation. An understanding of the physics of ultrasound is important because it helps explain some of the limitations of the modality and the artifacts encountered. In this chapter, the physical principles of ultrasound waves, the interactions of ultrasound waves with matter, transducers, Doppler techniques, and ultrasound artifacts are discussed.

PHYSICAL PRINCIPLES OF ULTRASOUND WAVES

Sound travels in waves and transmits energy by alternating regions of low pressure (rarefaction) and high pressure (compression).[1-3] Unlike light and radio waves, sound waves require a medium through which to travel.[4,5] Frequency, wavelength, and velocity are parameters used to describe sound waves; these terms are also used in reference to electromagnetic radiation.

Frequency is the number of times a wave is repeated per second. One wave or cycle occurs when pressure starts at a normal value, increases to a high value, decreases (passing the normal value) to a low value, and then returns to normal. A cycle may also be defined as the combination of compression and successive rarefaction.[3] Frequency is expressed in hertz (Hz), where 1 Hz equals one cycle per second. Sound greater than 20,000 Hz (0.02 MHz) is defined as ultrasound.[3,4] In diagnostic ultrasound, the frequencies are typically between 2 megahertz (MHz) and 15 MHz (1 MHz = 1,000,000 Hz).

Wavelength is the distance traveled by a sound wave in one cycle. In ultrasonography, wavelength is expressed in millimeters (mm). Wavelength is important for image resolution.

Velocity is the rate at which sound travels through an acoustic medium; it is determined by the physical density (mass per unit volume) and stiffness (hardness) of the acoustic medium.[1,3] As a rule, velocity is highest in solids, lower in liquids, and the lowest in gases. Within soft tissue, the average velocity of sound is 1.54 mm/μs (1540 m/s).[1-4] The velocity of sound in soft tissue is important because ultrasound machines use this constant velocity for all calculations.

Velocity is related to frequency and wavelength of a sound wave in the following equation:

$$\text{Velocity (mm/}\mu\text{s)} = \text{Frequency (MHz)} \times \text{Wavelength (mm)}$$

ULTRASOUND WAVE INTERACTION WITH MATTER

Acoustic impedance of a tissue is the product of the tissue's physical density and sound velocity within the tissue.[3] Changes in acoustic impedance from one tissue to another determine how much of the sound wave is reflected and how much is transmitted into the second tissue. The amplitude of the returning echo, which is what is used to make the image, is proportional to the difference in acoustic impedance in two adjacent tissues or substances. If two tissues have the same acoustic impedance, then no echo is created. If a large difference in acoustic impedance exists between two tissues, then almost all the sound is reflected in an echo.[1,3] Almost all sound is reflected at soft tissue/gas and soft tissue/bone interfaces. Thus, little or no sound passes these boundaries. Hence, the speed of sound in bone and gas-filled lung is not important clinically. This nearly total sound reflection creates an acoustic void, or *shadow*, deep to the tissue interface. Without placement of acoustic coupling gel between the patient and transducer, the soft tissue/gas interface created by gas trapped between the skin and transducer would prevent imaging because of reflection of all sound waves and no transmission of sound waves into the body.

Angle of incidence is the angle at which a sound wave encounters a medium. If the angle of incidence is perpendicular (90 degrees) to the reflector, the reflected portion of the sound wave travels 180 degrees opposite to the direction of the initial sound wave, returning to the transducer, and the transmitted portion of the sound wave continues in the same direction as the initial sound wave. If the angle of incidence is not perpendicular, then the angle of reflectance equals the angle of incidence. Any sound wave that is not reflected toward the transducer will not be recorded. A key fact is that the amount of reflected and transmitted sound depends on the *difference in acoustic impedance* of the two media.

An ultrasound beam is attenuated (loses strength), as it travels through a medium. The amount of attenuation is determined by the distance traveled and the frequency of the sound wave. High-frequency sound waves are attenuated more than low-frequency sound waves. Attenuation of the sound wave involves three components: absorption, reflection, and scattering.[1-3]

Absorption is the conversion of the mechanical energy of sound waves to heat.[2,3] Absorption is the dominant component of attenuation of sound in soft tissue.[2,3] However, the relative amount of sound absorbed is quite low, and the temperature change is insignificant and imperceptible.

Reflection of the sound beam contributes to attenuation. As the sound wave encounters tissue interfaces of different acoustic impedance, a reflection is generated. Only reflections that return to the transducer are used for image formation.

Scattering is independent of frequency and occurs when sound waves encounter small, irregular surfaces. This occurs mainly within the parenchyma of organs and is responsible for the echotexture of internal organs.[2,3]

TRANSDUCERS

In ultrasound imaging, transducers contain piezoelectric crystals that convert electric current into sound waves.[2,6] As an electric charge is applied to a piezoelectric crystal, the material deforms and creates a sound wave. Conversely, when sound waves are applied to piezoelectric crystals, they produce an electric signal. Therefore, the same crystal is used to send and receive sound waves.[3] For typical ultrasound imaging, the transducer emits sound waves less than 1% of the time and receives sound waves more than 99% of the time.[7] The pulse repetition frequency (PRF) is the number of times this pattern of sending and receiving is repeated within 1 second.[3] The length of space in one pulse of ultrasound is called the spatial pulse length (SPL). If a sound wave has a wavelength of 0.5 mm and three pulses are sent each time, the SPL is 1.5 mm. SPL is important for axial resolution, with shorter SPL resulting in better axial resolution.

Ultrasound transducers come in many shapes and sizes. The selection of a transducer depends on the physical properties of the transducer and the anatomic region to be imaged.

Electronic transducers, also called *array transducers*, are composed of several small elements in various arrangements. The elements may be arranged in a line or rectangle (linear array), in a curved line (convex array), or in concentric ring fashion (annular array).[8] The elements that compose these transducers are electronically fired in various sequences to create different-shaped fields of view (e.g., rectangular, wedge) and to focus the sound beam at specific depths.

Images made using a sector transducer are pie shaped (Fig. 3.1A), and images made using a linear transducer are rectangular (see Fig. 3.1B). The *footprint* of a transducer is the amount of the transducer that contacts the patient and linear transducers usually have larger footprints than sector transducer. For thoracic imaging, sector-shaped transducers are preferable because images must be acquired intercostally. For abdominal imaging, the use of sector or linear transducers is often dictated by the anatomic structure being imaged and the size of the patient. In most instances, more than one transducer is used during a single examination.

Resolution is the ability of an ultrasound machine to distinguish echoes based on space, time, and strength.[6] Axial resolution is the ability to distinguish two separate reflectors along the direction in which the sound wave is traveling and is equal to half the SPL. When two reflectors are separated by a distance that is greater than half the SPL, the echoes from these two reflectors do not overlap as they return to the transducer and are displayed as separate echoes. If the distance between the reflectors is less than half the SPL, the returning echoes overlap and are displayed as a single echo. Because transducers with higher frequency have a shorter SPL, axial resolution is improved.

Lateral resolution is the ability to distinguish two separate reflectors perpendicular to the direction in which the sound wave is traveling.[6] This is determined by the width of the ultrasound beam.[6] To recognize the objects discretely, the ultrasound beam must be narrower than the distance between the objects. The width of an ultrasound beam decreases with increasing frequency. In a focused ultrasound beam, where the width of the beam is restricted, the lateral resolution is best at the focal point of the ultrasound beam because this is the narrowest part of the beam.[6]

Depth of sound-wave penetration into the body varies inversely with sound wave frequency. Higher-frequency transducers are best for structures that are close to the surface while lower-frequency transducers are best for deeper structures. As a guide, one can begin with a higher-frequency transducer because it has better resolution (higher image quality) and then

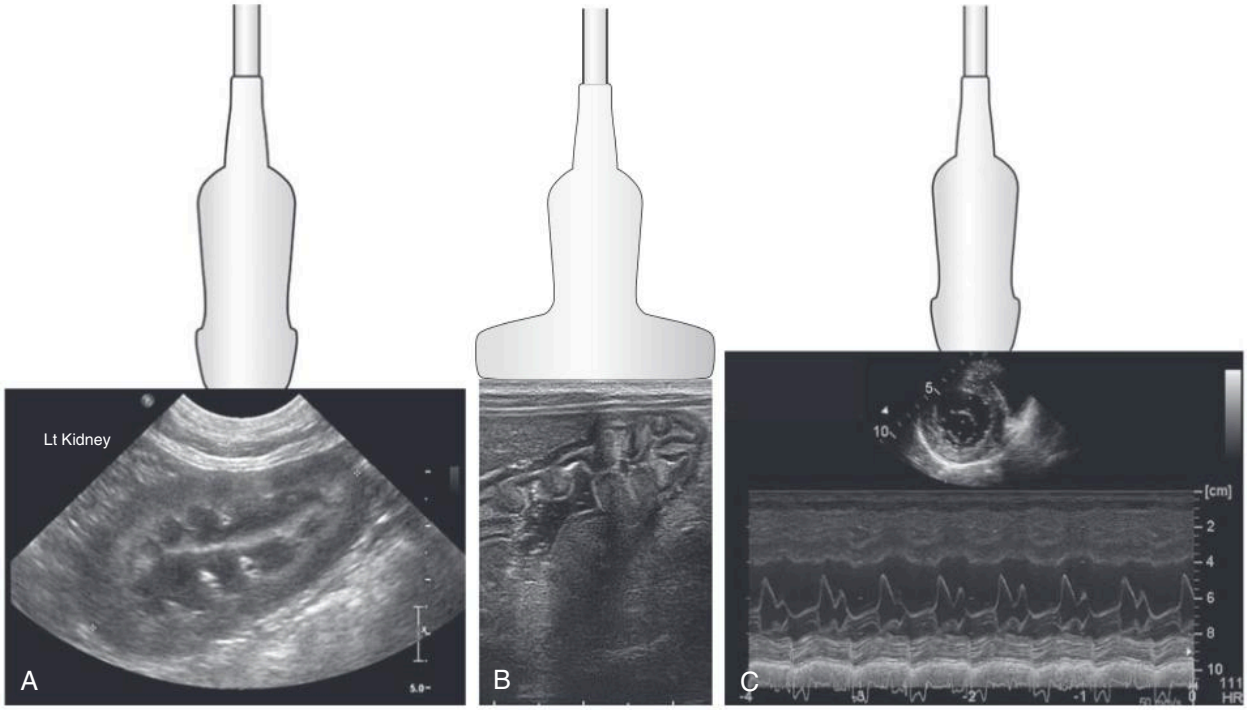


Fig. 3.1 **A,** B-mode sagittal ultrasound image of a canine left kidney made using a curved array transducer. Note the pie-shaped image produced by this type of transducer. The transducer points to the cranial of the patient (indicated by the ■ symbol at the *left* side of the screen). Thus, the cranial pole of the kidney is at the *left* side of the screen and the caudal pole of the kidney is at the right side of the screen. **B,** Image of a feline stomach made using a linear array transducer. Note the rectangular image. **C**, M-mode image depicting movement of the mitral valve. At the top of the image is a B-mode, short-axis image of the left ventricle at the level of the mitral valve. The *dotted line* in the middle of the B-mode image marks the location of the M-mode tracing on the bottom of the image. The M-mode tracing depicts the movement of the mitral valve and left ventricle over time. An electrocardiograph tracing is superimposed in the bottom of the image.

switch to a lower-frequency transducer if deeper structures are not imaged well.

New Technologies in Ultrasound

These technologies are incorporated in most of the newer ultrasound machines and influence the image quality greatly. Thus, knowing the basics and adjusting these features when scanning patients will help improve lesion conspicuity.

Broad bandwidth technology allows for transducers to emit a wide range of frequencies. This allows the user to select various frequencies from the same transducer.[6] A modern broadband 4 MHz transducer can emit frequencies between 1 and 7 MHz.[9] The broadband frequency transducers improve near-field resolution by using the higher frequency of the spectrum and far-field resolution by using the lower frequency of the spectrum. Additionally, axial resolution is improved because these transducers use shorter SPLs.[9]

Harmonic imaging improves normal organ and lesion conspicuity.[9] Harmonics are integer multiples of the frequency of the transmitted ultrasound pulse.[10] If the transmitted frequency (the fundamental frequency or first harmonic) is 4 MHz (F), then the second harmonic is 8 MHz (2F), and the third harmonic is 12 MHz (3F), and so forth.[2,3,9,10] During the interaction of sound waves and tissue, weak echoes are generated at harmonic frequencies.[4] When the echoes return to the ultrasound machine operating in harmonic mode, bandpass filters are applied to reject frequencies that are outside of the specific range.[4,11] For harmonic imaging, the bandpass filter can remove the fundamental frequency allowing the second harmonic frequencies to pass.[10] This results in improved image quality because of three fundamental factors.[11] First, the primary beam is much narrower, improving lateral resolution. Second, some artifacts (discussed later) are reduced or eliminated because the extra beams are not sufficiently strong to generate harmonics. Third, the harmonic beam is generated at a depth beyond where some of the artifactual problems occur, thus reducing image degradation and reducing noise in the near field of the image.

Spatial compounding is a composite image generated by combining multiple frames from ultrasound beams that are angled in different directions.[2,4,11-13] The sound waves from electronic transducers can be steered in multiple directions without moving the transducer. The multiple angles increase the probability of the sound wave encountering a reflector at a 90-degree angle.[5,11] The frames from different angles are compounded and displayed as a single image. Compound images were perceived to have improved contrast resolution, border definition, and/or increased signal-to-noise ratio compared with noncompounded images.[2,13] The number of frames for spatial compounding are an odd number, 3, 5, 7, 9, and so on. The higher the number of frames, the better the spatial resolution and image quality. Generally, a linear transducer has a higher number of frames for spatial compounding. This control is important as spatial compound imaging reduces shadowing artifact, which is used to recognize high attenuating structures such as renal calculi. Turning off spatial compound imaging may help the operator identify the renal calculi (see Fig. 3.7B,D)[2,4]

DISPLAY

Image formation is based on the pulse echo principle.[2,14] The electric signals generated from the returning echoes are amplified to form the final image. When the initial burst of sound is sent into the tissue, a timer is started to determine the amount of time it takes to receive echoes. The elapsed time from sending to receiving is directly related to the distance traveled by the sound wave.[14] The ultrasound machine assumes a constant rate for the velocity of sound (1.54 mm/μs), and because time is recorded, distance can easily be calculated.

Two modes of echo display are used commonly in ultrasonography: brightness mode (B-mode, B scan, or grayscale) and motion mode (M-mode). B-mode is used commonly in both abdominal and cardiac imaging. M-mode is used only for echocardiography.[3]

B-mode images are composed of a collection of dots that correspond to the amplitude or strength of the returning echo.[11] These dots are displayed on a black background, and the brightness or grayscale of the dot is highest (whitest) for the strongest returning echoes. The depth of the structure returning the echoes determines the position of the dots. Multiple thin scan lines make up a complete image so that B-mode images look like a slice of tissue (see Fig. 3.1A,B).[1]

M-mode records a thin section of an ultrasound image over time (see Fig. 3.1C). The region for M-mode imaging is chosen using a B-mode image; the selected M-mode region is usually represented on the screen as a line. Once the M-mode cursor is in the desired location, M-mode is activated. On an M-mode image, the depth of the image is displayed on the vertical axis, and time is displayed on the horizontal axis. The brightness of the dots is proportional to the strength of the returning echoes, as in B-mode. When holding the transducer stationary, the examiner can evaluate how structures move over time. M-mode imaging is used most commonly in echocardiography to evaluate the function of the ventricles and heart valves.

In B-mode imaging, the displayed organs vary with the orientation of the structures being imaged and the position of the transducer. Generally, the transducer should point to cranial with the left side of the screen representing cranial in longitudinal and sagittal orientation (see Fig. 3.1A) and to the right of the patient in transverse orientation. For cardiac imaging, the right side of the screen is cranial in long-axis images. The portion of the image closest to the transducer, the top of the screen, is called the *near field* and the opposite side is called the *far field*.

BASIC SCANNER CONTROLS

Gain affects the amplification of the returning echoes within the receiver. There are two types of gain: general gain and time gain compensation (TGC) that could be adjusted.

General gain: Increasing or decreasing the gain increases or decreases the overall brightness of the image; this should be adjusted at the beginning of each scan. If the gain is too low, the subtle parenchymal detail of tissue is lost. If the gain is too high, contrast resolution is lost due to overall bright image.[11]

Time gain compensation (TGC): Because sound waves lose intensity (attenuation) as they travel in tissue, echoes returning from deeper tissues are weaker than echoes returning from tissues closer to the transducer. To make an image uniform in brightness, amplification of the echoes from deeper tissues to a greater degree than echoes from shallow tissues is helpful. TGC controls allow the user to adjust the gain in selected regions/depth of the image.[11] Typically, an ultrasound machine has a series of slider-bars that control gain to echoes that emanate from various depths. The top sliders control gain for structures in the near field and bottom sliders for gain in the far field (Fig. 3.2). Overall, gain should be adjusted first, then specific regions of the image using the TGC.[11]

Frequency: The highest frequency available to penetrate to the depth of interest should be used because this helps to increase the axial resolution of the image. Thus, using a linear transducer with higher frequency for superficial

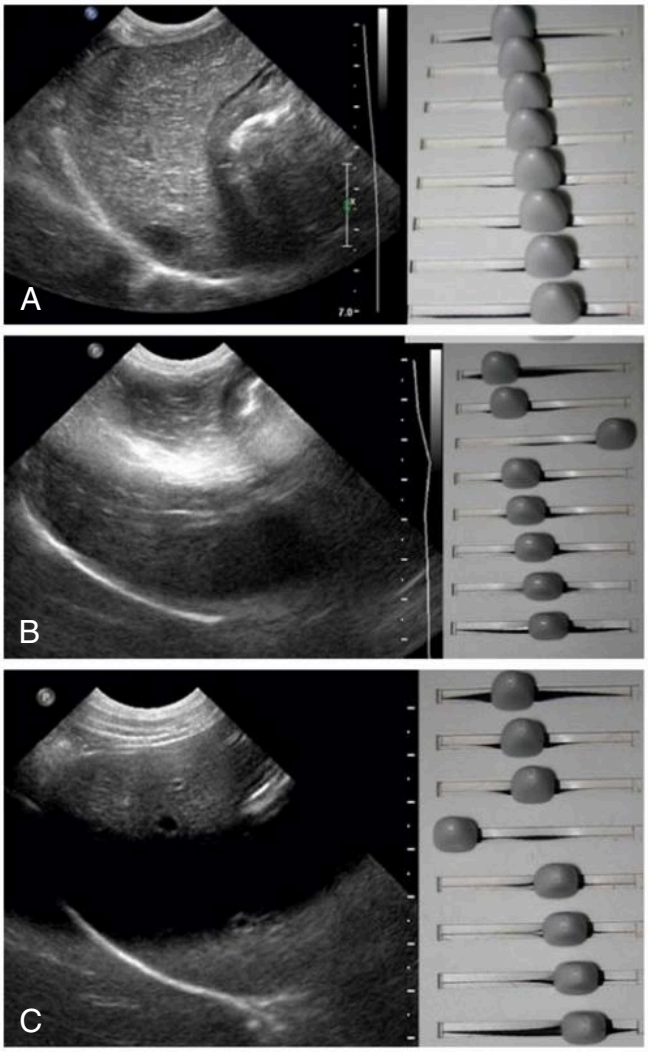


Fig. 3.2 **A,** Ultrasound image of a canine liver using a correct time gain compensation. **B,** The time gain compensation at the third zone was incorrectly overcompensated causing a hyperechoic band in the region. **C,** The time gain compensation at the fourth zone was undercompensated causing hypoechoic band in the region.

structures, such as the gastrointestinal tract, will provide a study with better imaging quality.

Focal point or region: The focal point or region should be adjusted to the region of interest as this will help to increase the lateral resolution. This will also make the identification of abnormality easier. In most ultrasound machines, a single or multiple focal points can be selected. However, the frame rate will be slower when the number of focal points increases. Thus, the use of a single focal point is encouraged. In some ultrasound machines, there is no focal point, and a region/range of focus is present.

Depth of field: The depth of field will determine the displayed size of the organs examined. As a norm, the depth of field should be adjusted so the image of organ is as large as possible to fill the monitor once the structure is identified.

PRINCIPLES OF INTERPRETATION

Echogenicity relates to the relative brightness of a structure. Anechoic structures have no echoes and appear black. When the echogenicity of two structures is compared, the darker structure is hypoechoic, and the brighter structure is hyperechoic. If the structures have the same degree of brightness, they are isoechoic to each other. Because tissue derangements result in changes in echogenicity, it is important to know the relative echogenicity of each abdominal organ. Box 3.1 lists abdominal organs in order of relative echogenicity; however, there is some variability of normal particularly in renal cortex echogenicity.[15] Detecting diffuse changes in echogenicity of a whole organ is difficult, and accurate detection is related to the experience of the sonographer. Machine settings and transducer selection may alter the echogenicity of an organ. Thus, internal organ auto referencing, or multiple abdominal organs, may be compared to determine organ echogenicity.[16] Focal changes in echogenicity are easier to detect because the adjacent normal parenchyma can be compared (Fig. 3.3).

Box • 3.1

General Guidelines of Relative Echogenicity of Commonly Encountered Structures in Order of Decreasing Echogenicity

Bone, gas, organ boundaries
Structural fat, vessel walls
Renal sinus
Prostate (intact male)
Spleen
Storage fat
Liver
Renal cortex
Muscle
Renal medulla
Prostate (neutered male)
Bile, urine

From Park RD, Nyland TG, Lattimer JC, et al. B-Mode Gray-scale ultrasound — imaging artifacts and interpretation principles. Vet Radiol. 1981;22:204–210.

DOPPLER TECHNIQUES

The Doppler technique is used in the investigation of blood flow direction and velocity. There are a few different techniques that are based on the Doppler principles.[17]

Doppler Principle

The pitch of a train whistle or a siren changes as the source of the sound approaches or moves away from the listener. The change in pitch, or sound-wave frequency, is called the *Doppler shift*. This principle has been applied to medical sonography, allowing imaging of the direction and velocity of blood flow. The Doppler effect is named for Johann Christian Andreas Doppler, an Austrian mathematician and physicist, who first proposed the effect in 1842.

In ultrasonography, the change in sound frequency is caused by a moving reflector, most commonly red blood cells. The Doppler shift is the frequency difference between the incident sound waves and the reflected sound waves and is described by the following formula[17]:

$$f_D = (2 \times f_O \times U_{RBC})/c \qquad \text{(Eq. 3.1)}$$

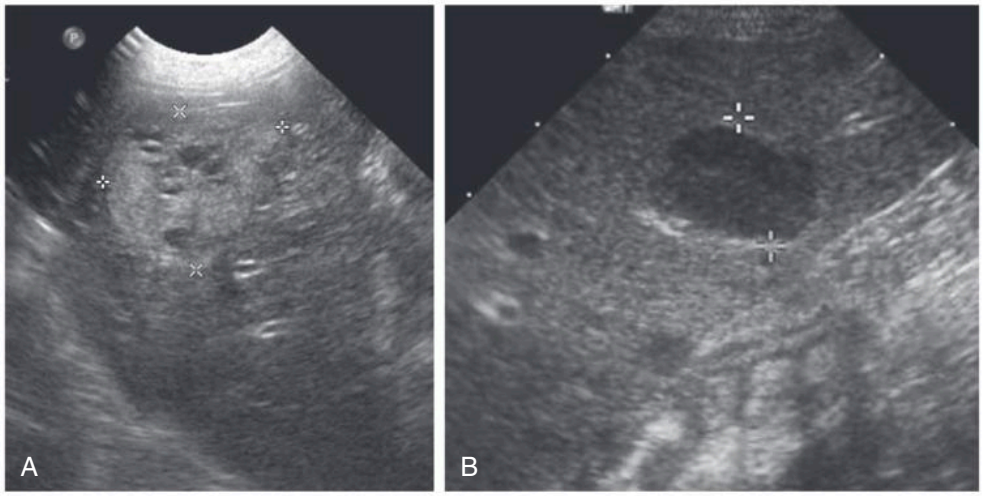


Fig. 3.3 Long-axis ultrasound images of the liver. **A,** A hyperechoic nodule in the liver of a dog indicated by calipers. **B,** A hypoechoic nodule in the liver of a dog, indicated by calipers.

where f_D is the frequency of Doppler shift, f_O is the original frequency; U_{RBC} is the velocity of red blood cells; and c is the speed of sound in soft tissue. The frequency of Doppler shift, recorded in Hz (versus MHz used for sonographic imaging), is in the audible range. Hence, ultrasound machines emit sound related to the Doppler shift.

It is assumed in Eq. 3.1 that the sound waves are parallel to the direction of blood flow. Realistically, when sound waves strike blood vessels, the sound waves are rarely parallel to the direction of flow. The Doppler angle is the angle between the blood-flow direction and the sound wave direction.[18] Without accounting for the Doppler angle, the Doppler shift is underestimated.[18] This is very important for quantification of blood flow. Accounting for the Doppler angle, the velocity of blood flow is calculated by the following formula[19]:

$$U_{RBC} = (f_D \times c)/(2 \times f_O \times \cos\theta)$$

where U_{RBC} is the velocity of red blood cells, f_D is the frequency of Doppler shift, c is the speed of sound in soft tissue, f_O is the original frequency, *cos* is cosine, and θ is the Doppler angle.

Doppler shift cannot be measured if the Doppler angle is 90 degrees because the cosine of a 90-degree angle is 0, and division by 0 is not possible. The Doppler angle θ should be less than 60 degrees for the velocity to be considered accurate,[20] with angles between 30 and 60 degrees being easiest to image.[17]

DOPPLER MODES

Four Doppler modes are discussed: (1) continuous-wave Doppler, (2) pulsed-wave Doppler, (3) color Doppler, and (4) power Doppler.

Continuous-wave Doppler is performed by using two separate crystals housed in one transducer.[17] One crystal emits sound continuously, and the second receives echoes continuously. Continuous-wave Doppler is highly accurate for measuring the Doppler shift. Compared with pulsed-wave Doppler, much higher velocities can be recorded with continuous-wave Doppler because of the continuous signal sampling. The crystal emitting the sound does not have to wait to receive echoes because the second crystal handles the echo-receiving task. However, with continuous-wave Doppler, all Doppler shifts along the path of the sound wave are measured, making differentiation of blood-flow velocity from two blood vessels in the path of the sound wave impossible. This mode is commonly used in echocardiography.

Pulsed-wave Doppler is performed by using the same crystal for sending and receiving sound.[21] Pulsed-wave Doppler is used in combination with B-mode imaging; this is termed *duplex Doppler* (Fig. 3.4A).[17] A blood vessel is selected in the B-mode image for Doppler interrogation, and an electronic region of frequency sampling, called the *gate*, is positioned in the blood vessel. In Fig. 3.4A, the gate, the two parallel lines, is in the aorta. The electronic gate is the only area from which echoes are accepted for flow quantification. Being able to select a blood vessel for interrogation visually is a benefit of pulsed-wave Doppler. This is commonly used in measuring portal vein velocity.
A spectral tracing is produced with both continuous- and pulsed-wave Doppler. The tracing records the velocity and direction of blood flow as a function of time (see Fig. 3.4A). Tracing above the baseline represents blood flow toward the transducer, and tracing below the baseline represents blood flow away from the transducer.[20] If the blood-flow velocity within the sample area is homogenous, the spectral tracing will be thin (see Fig. 3.4A) with an empty area under the curve. Spectral broadening is caused by turbulence or variable speed blood flow and refers to the thickness of the spectral tracing.[17] If a large range of blood-flow velocity is present within the sample area, the spectral tracing will be broad and the area under the curve is filled in. Alternatively, spectral broadening can occur if the transducer is close to the blood vessel, resulting in multiple ultrasound beam angles between the transducer and blood vessel.[17] Spectral tracing is routinely performed in echocardiography to assess blood flow direction and measure velocity.

Color Doppler is a variation of pulsed-wave Doppler.[17] Blood-flow velocity is recorded in multiple regions within an image, and the mean velocities are color-coded. The user determines the size and location of the color Doppler region of interest, which can be much larger than the sample gate used for pulsed-wave Doppler. Color-coded

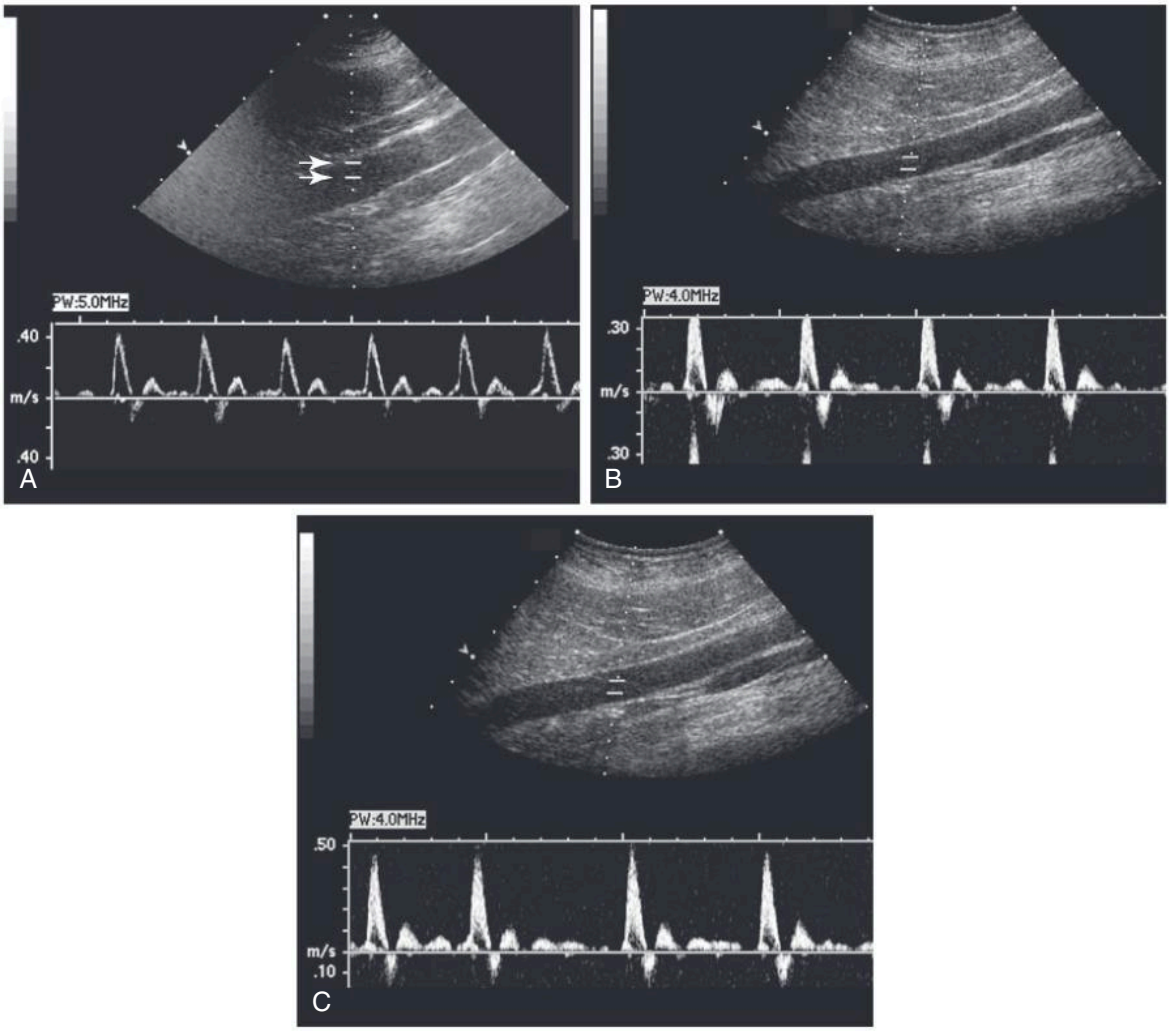


Fig. 3.4 **A,** Duplex Doppler ultrasound image illustrating pulsed-wave Doppler interrogation of a canine aorta. The B-mode image, in the near field, shows placement of the pulsed-wave Doppler gate (*parallel lines, white arrows*) in the central aspect of the aorta. This is the region in which blood-flow velocity is measured. The pulsed-wave Doppler spectral tracing is in the far field. The *solid white line* in the center of the spectral tracing represents the baseline where blood flow = 0 m/s. Signal above baseline represents flow toward the transducer, whereas signal below the baseline represents flow away from the transducer. The velocity scale on the *left* ranges from 0 to 0.40 m/s toward the transducer and 0 to 0.40 m/s away from the transducer. The pulsatile velocity tracing is typical of an artery. **B,** Aliasing of the spectral tracing is noted by the peaks of the "tall spike" being displayed on the bottom of the spectral tracing. The scale indicates that the highest velocity is 0.30 m/s. Because the peak velocity of blood flow within the aorta is greater than 0.30 m/s, the computer displays the tracing on the other end of the scale. Aliasing is corrected (see **A**) by increasing the scale, which increases the pulse repetition frequency (PRF). Note that the width of the spectral tracing in **B** is wider than in **A**. This is caused by more homogeneous velocity of blood flow within the pulsed-wave Doppler gate in part **A**. **C,** Aliasing is corrected by changing the range of velocities displayed; this is also called adjusting the baseline. The velocity range displayed is now from 0.20 m/s away from the transducer to 0.50 m/s toward the transducer compared with part **B**, and aliasing has been eliminated.

information is superimposed on the grayscale B-mode image within the region of interest (Fig. 3.5). Red and blue hues are used commonly for color Doppler. One color indicates net blood flow toward the transducer (most commonly red), and the other color in the reference scale indicates net blood flow away from the transducer (most commonly blue). Velocity of flow is indicated by the intensity or hue of the color. Limitations of color Doppler include that only mean velocity is displayed and that the maximum velocity that can be displayed is limited. Color Doppler is angle dependent so that no Doppler shift is recorded when blood flow is 90 degrees to the transducer. Color Doppler is useful to determine the presence or absence, direction, speed, and/or character of blood flow.[19]

Power Doppler is a signal-processing method that analyzes the total strength of the Doppler signal. This could be related to the direction of the blood flow (directional power Doppler) or ignoring direction of blow flood (nondirectional power Doppler).[17,21,22] This is determined by the concentration of the moving red blood cells. With power Doppler, a color map of the Doppler shift will be created, where the hue and brightness of the color represent the power of the Doppler signal. Power Doppler information

is superimposed on the grayscale B-mode image, and a color-coded reference scale is displayed on the ultrasound machine monitor when the machine is in power Doppler mode. Orange hues are commonly used for nondirectional power Doppler. Compared with color Doppler, power Doppler detects very-low-velocity blood flow and small blood vessels; it is essentially angle independent and not prone to aliasing artifact.[17,21]

Microvascular Imaging

Microvascular imaging is a recent ultrasound imaging technique that helps to show low-velocity and small-diameter blood vessel flow. This is sensitive in detecting slow blood flow in small blood vessels (Fig. 3.6). The name of this technology varies by the manufacturers, such as superb microvascular imaging (SMI), microvascular flow imaging (MVI), B-Flow, S-Flow, XFlow, Fine Flow, and MicroCPA. Evaluation of the clinical utility of this microvascular imaging in the veterinary literature is lacking as this is a very new technology.

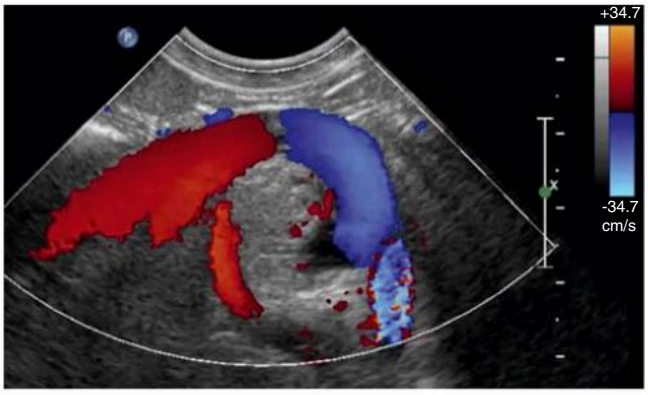


Fig. 3.5 Color Doppler image of a curved blood vessel in a dog. The colors are assigned by the ultrasound machine and are related to the direction of blood flow. According to the color scale, *red* represents blood flowing toward the transducer, and *blue* represents blood flowing away from the transducer (*red* is at the near field at the region of +34.7 cm/s and *blue* is at far field at the region of −34.7 cm/s). The direction of the blood flow in this blood vessel is from left to right. Due to the black and white nature of the picture, the direction of the flow is difficult to identify in this image. Note there is an area of color void in the center, because the blood vessel is at 90 degrees to the direction of the Doppler signal.

Contrast-Enhanced Ultrasound

Contrast-enhanced ultrasound is a technology for detection of intravenously injected contrast media in various organs. Ultrasound contrast media consist of gas-filled lipid spheres (microbubbles) that markedly enhance the ultrasound signal (see Chapter 5). Ultrasound contrast media, for the most part, stay strictly intravascular and are small enough to pass through the pulmonary circulation. Contrast-enhanced ultrasound is used to measure blood volume and tissue perfusion, and evaluate lesion characteristics of an organ.[23,24] This is one of the noninvasive ways to provide more information that may help to differentiate benign and malignant lesions, for example in the liver. The availability of the contrast media, the cost of the contrast media, and the approval for veterinary usage limit the clinical application in veterinary medicine in some countries.

Ultrasound Elastography

Ultrasound elastography evaluates the tissue elasticity/stiffness and helps predict the pathology of the organs. There are different technologies in ultrasound elastography, such as strain elastography and shear wave elastography. Detection of the changes in the elasticity of the diseased organs has the potential to improve the sensitivity and specify in differentiating benign versus malignant or clinically important disease. This technology has been used in the clinical setting to evaluate liver, skin nodules, muscles, tendons, lymph nodes, kidneys, and spleen.[25,26] In human medicine, the use of elastography is an established diagnostic procedure for the detection of hepatic fibrosis, portal hypertension, and esophageal varices. However, the use of ultrasound elastography is not a standard protocol in veterinary ultrasound.

ARTIFACTS

Any part of an image that does not accurately represent the anatomy or physiology of a patient is an imaging artifact.[18] In

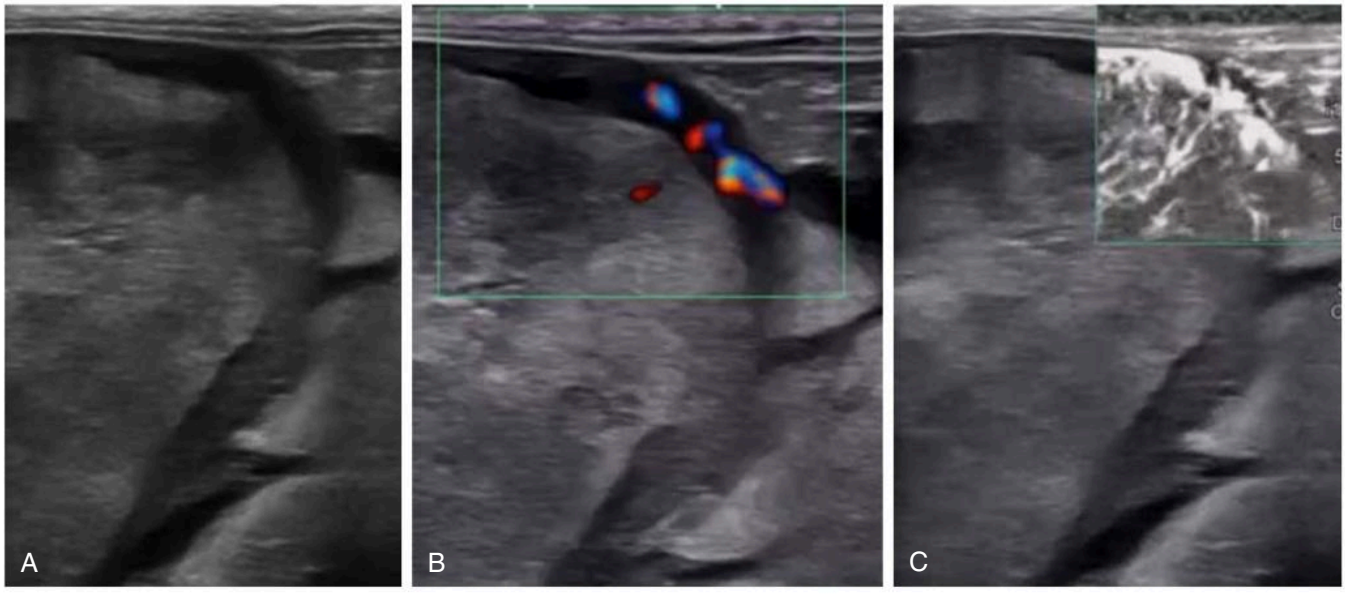


Fig. 3.6 Long-axis ultrasound images of the caudal pole of a feline kidney. **A,** A hypoechoic rim of tissue is present at the peripheral margin of the caudal of the left kidney of a cat. **B,** Directional Power Doppler at a section of this hypoechoic tissue shows moderate blood flow. **C,** Superb microvascular imaging (SMI) shows extensive blood vessels extending from renal cortex into this hypoechoic region.

ultrasound imaging, artifacts are not always undesirable and may enhance evaluation of structures by providing insight regarding the composition of structures.

Before discussing specific artifacts, it is important to remember assumptions that are made when generating an ultrasound image.[21,27,28] These assumptions are as follows:

- Sound waves travel in a straight line.
- Echoes originate only from objects located along the beam axis.
- Echoes return to the transducer after a single reflection.
- The speed of sound in tissue is constant.
- The distance and/or depth to the reflecting or scattering object are proportional to the round-trip travel time of the sound wave.
- The amplitude of returning echoes is related directly to the reflecting or scattering properties of distant objects.
- The energy of a sound wave is attenuated uniformly.

Acoustic shadowing artifacts are regions of decreased echogenicity distal to structures of high reflectivity such as bones or calculi (Fig. 3.7).[21,27-29] In these situations, the primary sound beam is almost completely reflected or absorbed. An insufficient quantity of echoes returned from the location distal to the strong reflector makes these regions appear anechoic (black). The acoustic shadowing artifact is a useful artifact because it gives information about the composition of the structure causing the shadowing. Naturally occurring acoustic shadows are found at soft tissue/bone and soft tissue/gas interfaces, such as in bowel and lung. Pathologic acoustic shadows occur most commonly with renal, cystic, or cholecystic calculi. Many intestinal foreign bodies also cause acoustic shadowing artifact. Acoustic shadowing artifacts are minimized and appear different with spatial compounding.[18,30] When using spatial compounding, a lesion hidden by a shadowing artifact may be identified. Conversely, the composition of a structure may be misinterpreted because it is not shadowing (see Fig. 3.7D).[2]

Acoustic enhancement is a region of increased echogenicity distal to structures of low attenuation, typically fluid. Sound waves traveling through the low attenuating structures have higher remaining intensity, resulting in stronger signal compared with sound waves traveling through adjacent tissues.[21,29] This results in areas of increased echogenicity distal to areas of low attenuation. The two most common sites for acoustic enhancement are distal to the gallbladder and urinary bladder (Fig. 3.8).

Reverberation artifacts occur when the sound waves reflect multiple times between two strong reflectors.[18,27] This violates the assumption that echoes return to the transducer

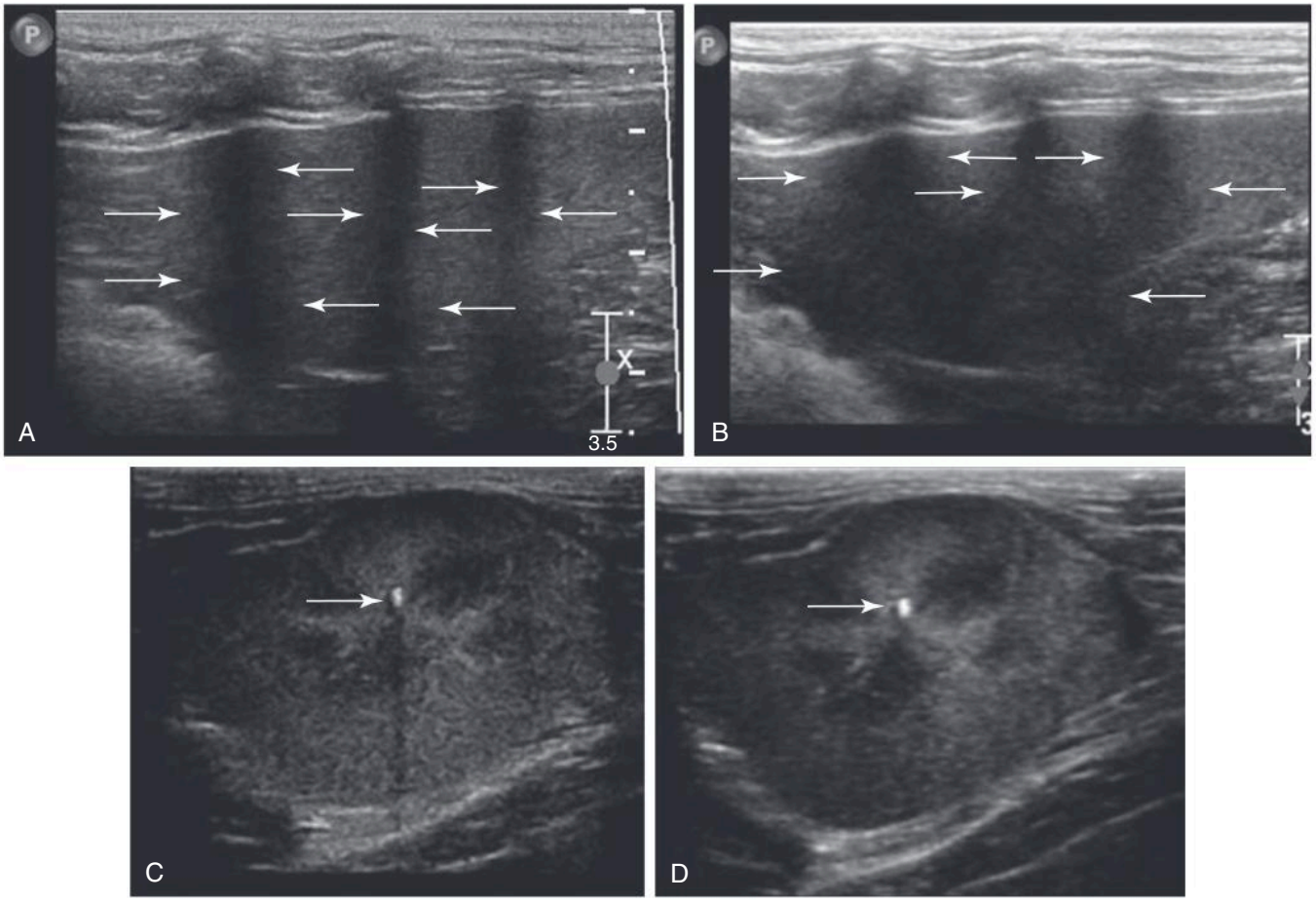


Fig. 3.7 **A** and **B,** Ultrasound images of the spleen. The ribs were between the spleen and transducer causing acoustic shadowing artifact *(white arrows)*. **B,** Note that the acoustic shadowing artifact has a fan shape (spread in the far field) and reduced intensity due to the effect of spatial compounding. **C** and **D,** Ultrasound imaging of a calculus (*white arrow*) in a cat kidney. The acoustic shadowing artifact is clearly seen in **C**. The artifact is not clearly seen in **D** due to spatial compounding. This should not be misinterpreted as absence of a calculus.

after a single reflection.[27] Reverberation occurs when the sound wave encounters an area of high reflectivity, such as bowel gas, and the sound wave is reflected back toward the transducer. When the reflected sound wave encounters the transducer, a portion of it is reflected back into the tissue, where it again encounters the area of high reflectivity. The increased time it takes the sound waves to bounce back and forth until registered as returning echo by the ultrasound system is translated into an echo generated from a deeper depth in multiples of the reverberations. This cycle of bouncing between the transducer and the patient continues many times, resulting in the regularly spaced hyperechoic foci (Fig. 3.9A). The distance between the transducer and the highly reflective surface determines the spacing of the hyperechoic foci. Thus, reverberation artifacts appear as multiple hyperechoic foci that occur at regular intervals.

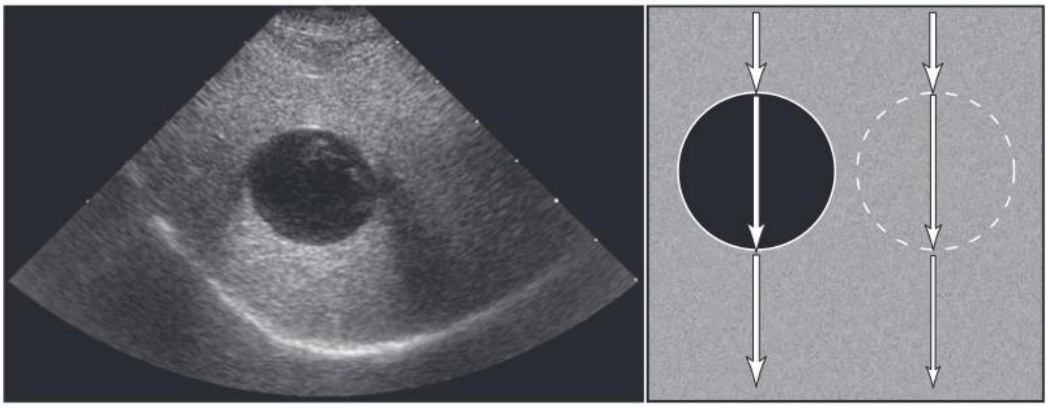


Fig. 3.8 Acoustic enhancement is a region of increased echogenicity beyond structures of low attenuation. In the sonographic image on the *left*, bile in the gallbladder (*black circular structure*) does not attenuate the sound waves as much as the equivalent amount of liver tissue would. This creates acoustic enhancement (*bright area* distal to the gallbladder). The *black triangular area* on the right aspect of the region of acoustic enhancement is an edge-shadowing artifact. In the schematic on the *right*, the left sound wave travels through the liver, then through bile within the gallbladder (*white circle*) and then continues through the liver. The right sound wave travels only through liver. As the left sound wave passes through bile, it is attenuated less than the right sound wave as it travels through liver. Thus, when the left sound wave exits the gallbladder, it has a higher intensity, leading to the return of stronger echoes to the transducer, which creates the distal acoustic enhancement.

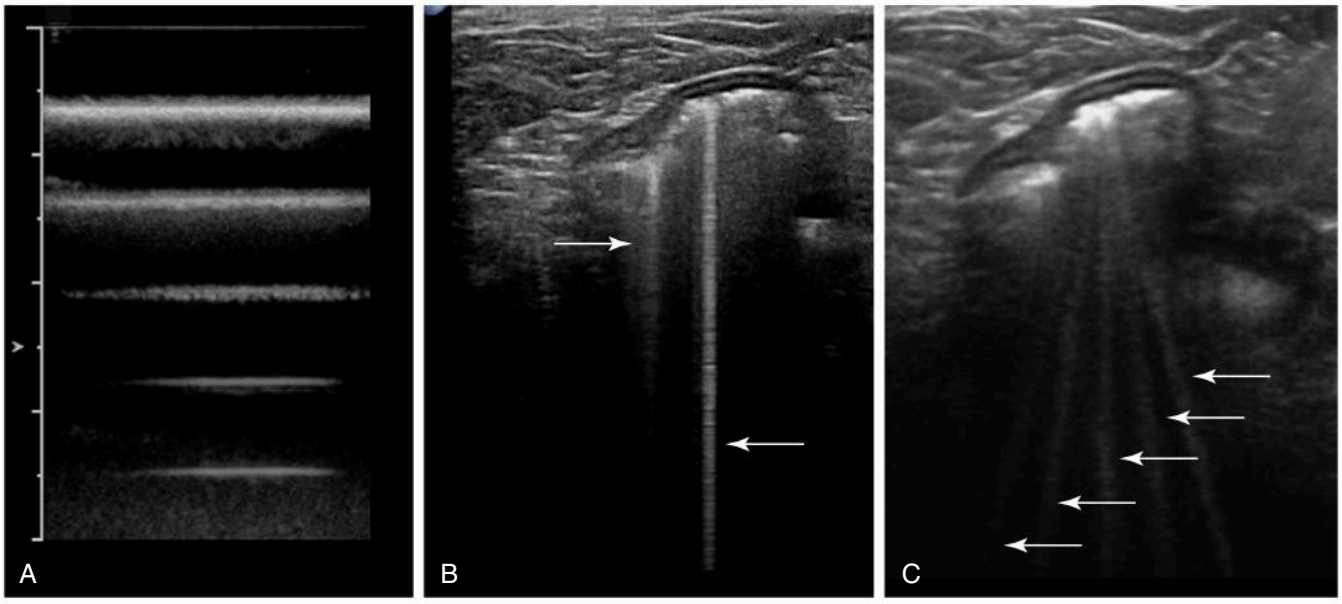


Fig. 3.9 **A,** A reverberation artifact was created by submerging a tongue depressor in a water bath. The actual tongue depressor is the strongest hyperechoic line, closest to the transducer, and the four other hyperechoic lines are reverberation artifacts. Some of the sound waves reflected by the tongue depressor are reflected by the transducer instead of being recorded and then are reflected again by the tongue depressor. The ultrasound machine interprets the twice-reflected signal at a depth of twice the actual distance between the transducer and tongue depressor because the echoes took twice as long to return. The deeper three reverberation artifacts took three, four, and five times as long, respectively, to be recorded by the ultrasound machine and are recorded sequentially farther from the transducer as overall time between recording increases. **B** and **C,** Images of stomach of a dog showing ring-down artifact (*white arrows*). **C,** There is spreading of the ring-down artifact into 5, with reducing intensity due of the spatial compounding.

Comet tail and *ring-down artifacts* are a variation of a reverberation artifact.[27] For comet tail artifacts, the reverberation is caused by two closely spaced, discrete highly reflective surfaces.[21,27] Comet tail artifacts can be created by the front and back of small metallic object such as a pellet or small calculus. On the display, comet tail artifacts are typically thin, hyperechoic bands with a triangular, tapered shape in which the sequential echoes are so close together that they are not seen as separate echoes.[27] Ring-down artifacts are created when ultrasound reverberates within fluid trapped between a tetrahedron of air bubbles.[27,29] This is commonly seen in the gastrointestinal tract. Spatial compound imaging creates a different appearance of the ring-down artifact (see Fig. 3.9B,C).

Mirror-image artifacts appear as duplication of a normal structure on the opposite side of a strong reflector (Fig. 3.10A).[21,18] This violates the assumption that echoes return to the transducer after a single reflection and that sound waves travel in a straight line.[27] This is most encountered when the liver is imaged with the diaphragm/lung interface acting as a highly reflective structure. Apparent duplication of the gallbladder can be used to explain the artifact. Normally, the sound wave sent toward the gallbladder is reflected back to the transducer. For the mirror image gallbladder, the sound from the transducer bounces off the diaphragm/lung interface toward the gallbladder, then instead of reaching the transducer, some sound is reflected off the gallbladder back toward the diaphragm/lung interface where it is reflected again toward the transducer. The sound reflected from the diaphragm/lung interface took longer to return to the transducer; thus, an artificial gallbladder is created at an incorrect location within the patient (see Fig. 3.10B). In the newer generation of ultrasound machines, the mirror image artifacts no longer appear as complete duplication of the organs. In most instances, the mirror image artifact of the gallbladder appears distorted such as smaller, larger, or absent (see Fig. 3.10C).

Side lobes and *grating lobes* are secondary sound beams that emanate in a different direction than the primary sound beam.[27,29,31] Side lobes are associated with all transducers and originate from additional mode vibrations of the piezoelectric crystal. Grating lobes emanate from array transducers. In each instance, these lobes result in an error in positioning of the returning echo (Fig. 3.11A) as the transducer assumes returning

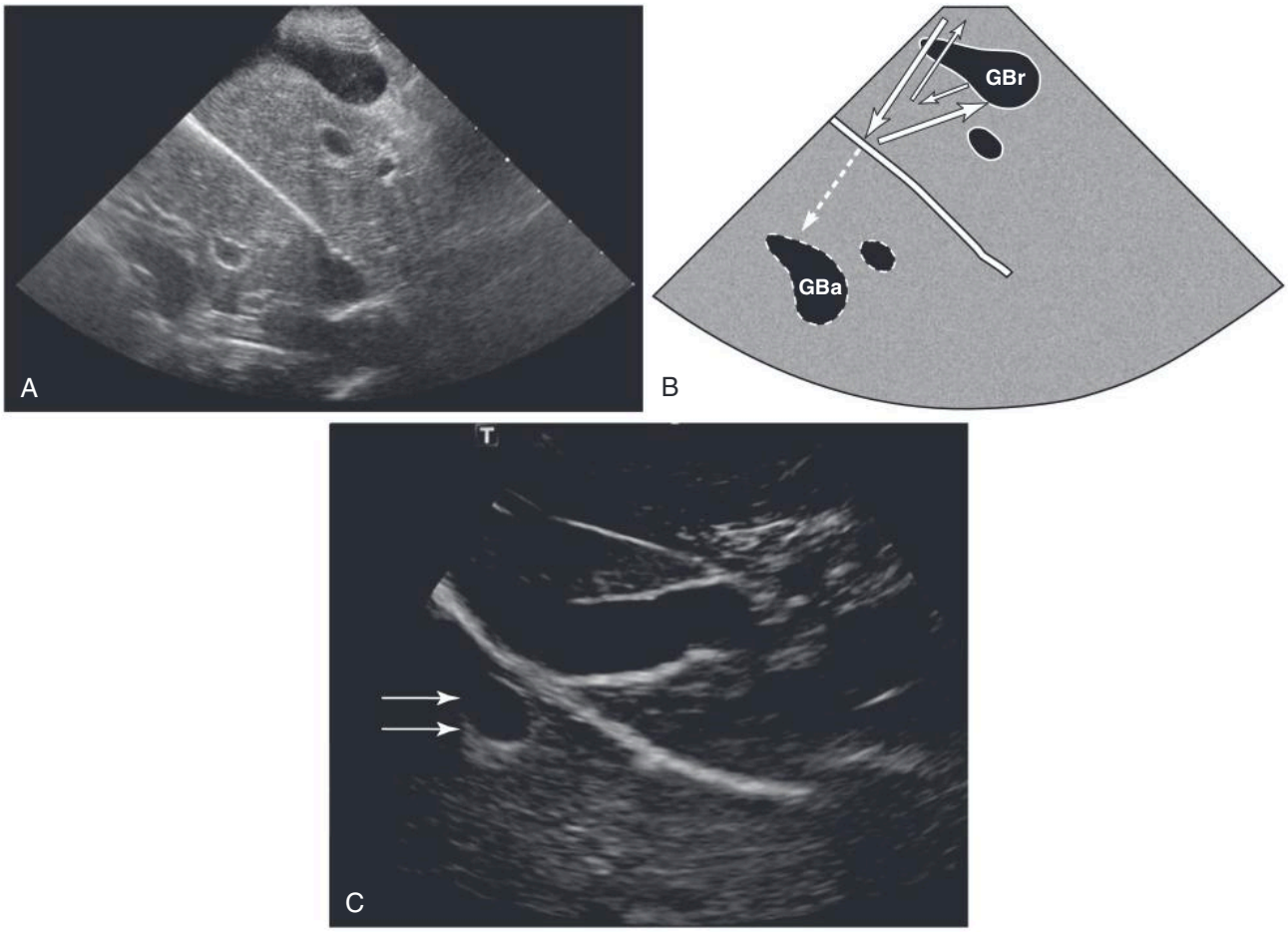


Fig. 3.10 **A,** A mirror image artifact of a canine gallbladder occurred at the lung/diaphragm interface. The real gallbladder (*GBr*) is in the near field, and the artifactual gallbladder is in the far field (*GBa*). The lung/diaphragm interface is the *curved, thin white line* separating the actual gallbladder from the artifactual gallbladder. **B,** The schematic shows the route that the sound wave travels (*white arrows*) to create the image of the artifactual gallbladder. Because the ultrasound machine cannot detect that the sound wave changed direction during its travel, the ultrasound machine assumes another gallbladder (*GBa*) is present below the lung/diaphragm interface. **C,** A mirror image artifact of a feline gallbladder seen in a newer generation of ultrasound machine. Note that the artifactual gallbladder (*white arrows*) is smaller and the shape is different from the actual gallbladder.

echoes are generated along the axis of the primary beam. The side or grating lobes are weaker than the primary sound beam. These lobes must encounter a highly reflective surface and be of sufficient intensity to be noticed.

Slice thickness artifacts are noticed most commonly in association with the urinary bladder and gallbladder. In these structures, slice thickness artifacts mimic the presence of sludge or sediment (see Fig. 3.11B). A primary sound beam, which is three-dimensional, has a certain thickness. When the periphery of the urinary bladder is imaged, part of the thickness of the primary sound beam strikes the bladder wall while the other part strikes anechoic urine. The computer averages these two parts to create the pseudo-sludge. The surface of the pseudo-sludge is usually curved, but the surface of real sludge is

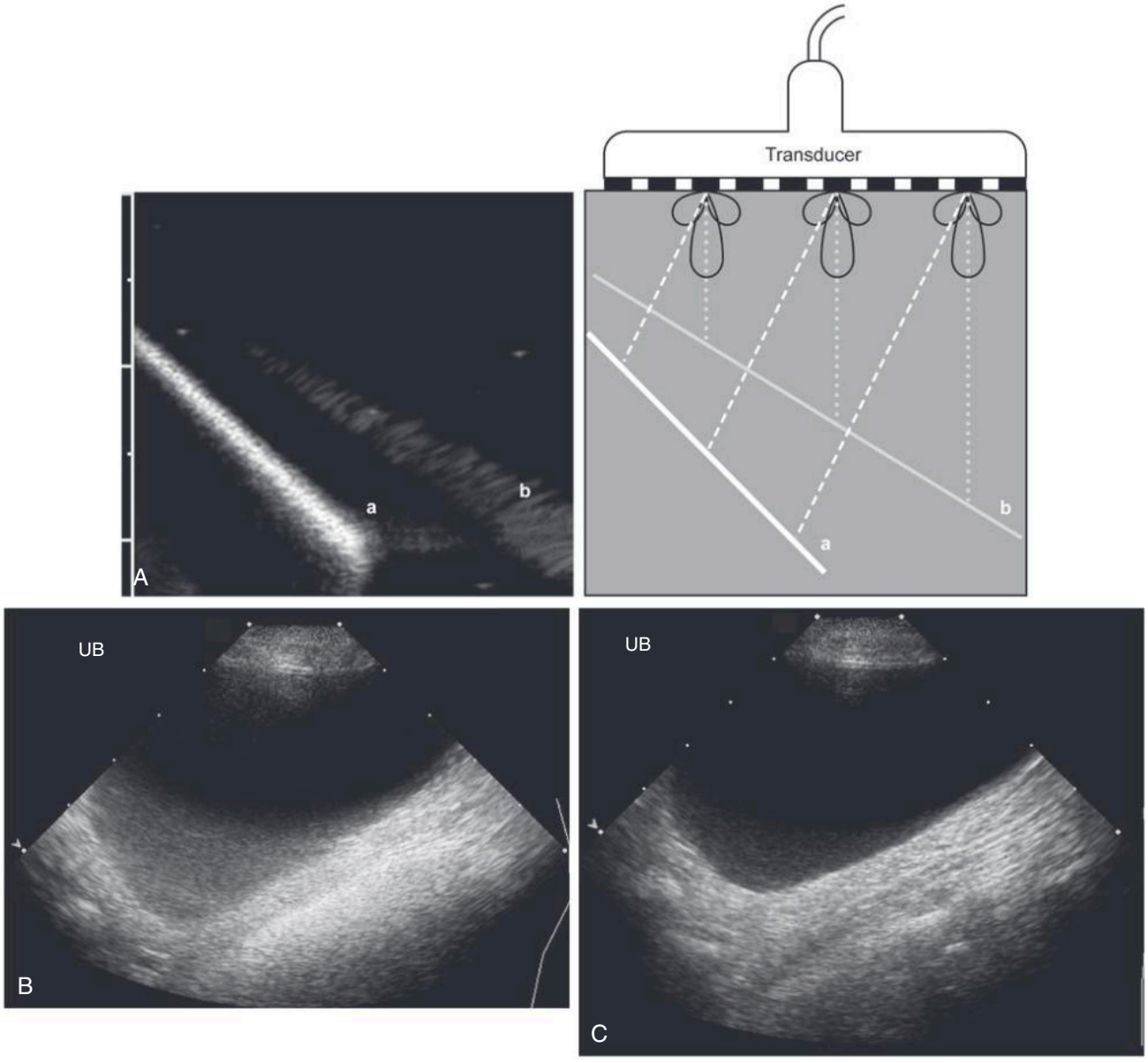


Fig. 3.11 **A,** The image on the *left* was created in a water bath by using a linear array transducer and a tongue depressor. The tongue depressor is the *bright linear structure* closer to the *bottom left* of the image (*a*). The grating lobe artifacts (*b*) are between the transducer (*top right*) and the tongue depressor. The schematic on the *right* shows the grating lobes emitted from selected elements of a linear transducer and how they interact with the tongue depressor (*a*) and create the artifact (*b*). The *angled dotted lines* show the actual path of the grating lobes, and the *vertical dotted lines* illustrate where the ultrasound machine places the image. **B,** An ultrasound image of a canine urinary bladder illustrating slice thickness artifacts. The hypoechoic region in the urinary bladder (left ventral aspect) is created when part of the ultrasound beam images the anechoic urine and part images the isoechoic urinary bladder wall. The two parts of the beam are averaged together to create the hypoechoic region that should not be confused with sediment. **C,** An ultrasound image of the same urinary bladder after altering the angle of insonation slightly. The artifact was reduced. (**A,** Modified from Barthez PY, Leveille R, Scrivani PV. Side lobes and grating lobes artifacts in ultrasound imaging. *Vet Radiol Ultrasound.* 1997;38:387.)

flat. Imaging the bladder from a slightly different angle usually eliminates or reduced the intensity of the artifact (see Fig. 3.11C).

Refraction occurs as the sound wave traverses tissues of different acoustic impedance. As the sound wave moves to the new medium, it is bent. The bending of the sound wave may result in the display of organs in incorrect locations, usually to the side of their actual location.[21,27] Refraction artifacts may lead to measurement errors because organs may appear wider than normal.[27]

Edge-shadowing artifacts are refraction artifacts that are created when sound waves are bent as they encounter a curved surface tangentially.[29] Anechoic regions are present distal to the curved surfaces because of absence of sound waves that have been bent by the curved surface. The edge-shadowing artifact occurs commonly when the kidneys, urinary bladder, or gallbladder is imaged. Edge-shadowing artifact can be eliminated with spatial compounding (Fig. 3.12).[29]

Anisotropic back scattering artifacts is an artifactual alteration of echogenicity of organs or structures due to the orientation of fibrillar or tubular structures such as tendon fibers or renal tubules. This is especially easily seen in the cranial and caudal pole of kidneys in the longitudinal plane as the collagenous basement membranes of renal tubules and medullary rays

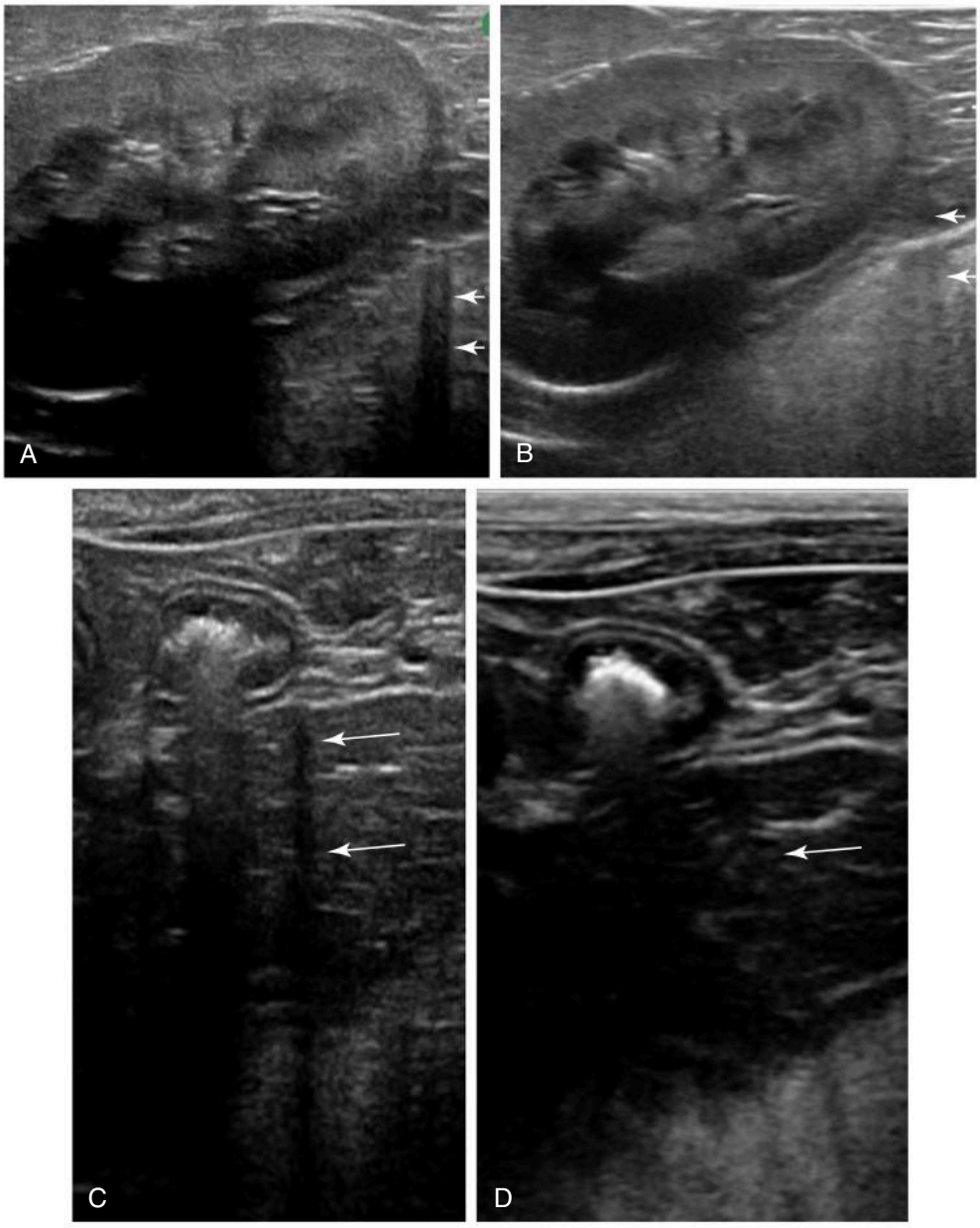


Fig. 3.12 **A** and **C,** Sagittal ultrasound image of a canine kidney and transverse ultrasound image of a canine small intestine illustrating an edge-shadowing artifact caused by sound wave refraction (*white arrows*). As sound waves encounter curved surfaces tangentially, they are bent so that no sound wave is transmitted distal to the curved surface. **B** and **C,** Spreading and reduced intensity of the artifact is due to spatial compounding.

are oriented perpendicular to the ultrasound beam.[32] This artifact should not be mistaken as focal renal fibrosis (Fig. 3.13A,B). The absence of this artifact indicates generalized increased renal echogenicity, and suggestive of feline chronic renal disease (see Fig. 3.13C).[16]

Twinkling artifact is seen with color Doppler ultrasound, which is generated by structures with random, strongly reflective rough surface. This is most commonly seen in the far field of calculi.[33] The intensity of the artifact is dependent of the machine setting, and most obvious when the focal point is located just below the structure, and with decreased PRF. This technology is used to increase the sensitivity and specificity of detection of calculi in the urinary system especially if the calculus is small and does not cause acoustic shadowing artifact in grayscale ultrasound (Fig. 3.14B,D).

Range ambiguity occurs when the PRF is high enough that not all the returning echoes are received before the next sound-wave pulse is sent.[34] Thus, the lagging echoes are misinterpreted as being closer to the transducer than they are. This creates ghost images between the structure of interest and the skin surface. These ghost images may not interfere with image interpretation, especially if the user is aware they exist.

DOPPLER ARTIFACTS

Aliasing is the most common artifact that occurs with pulsed-wave Doppler when the PRF is too low. A portion of the tracing wraps around on the spectral tracing of the Doppler signal (see Fig. 3.4B), to the opposite direction and is therefore displayed on the wrong side of baseline.[21] On a color Doppler image, aliasing is the addition of color from the opposite end of the color scale. The sampling rate of the ultrasound machine needs to be twice the highest Doppler shift frequency of the blood flow.[17] Methods to resolve aliasing including increasing the PRF, decreasing the depth of the Doppler sampling gate, reducing the frequency of the transmitted ultrasound wave, and decreasing the Doppler shift angle (θ).[17]

Typically, the velocity scale may be widened because many ultrasound machines have the PRF of the Doppler unit linked to the scale setting. When using pulsed-wave Doppler, if most of the spectral tracing is on one side of baseline, the baseline can be adjusted to eliminate the aliasing. However, increasing the PRF may lead to *range ambiguity* artifact as described earlier.

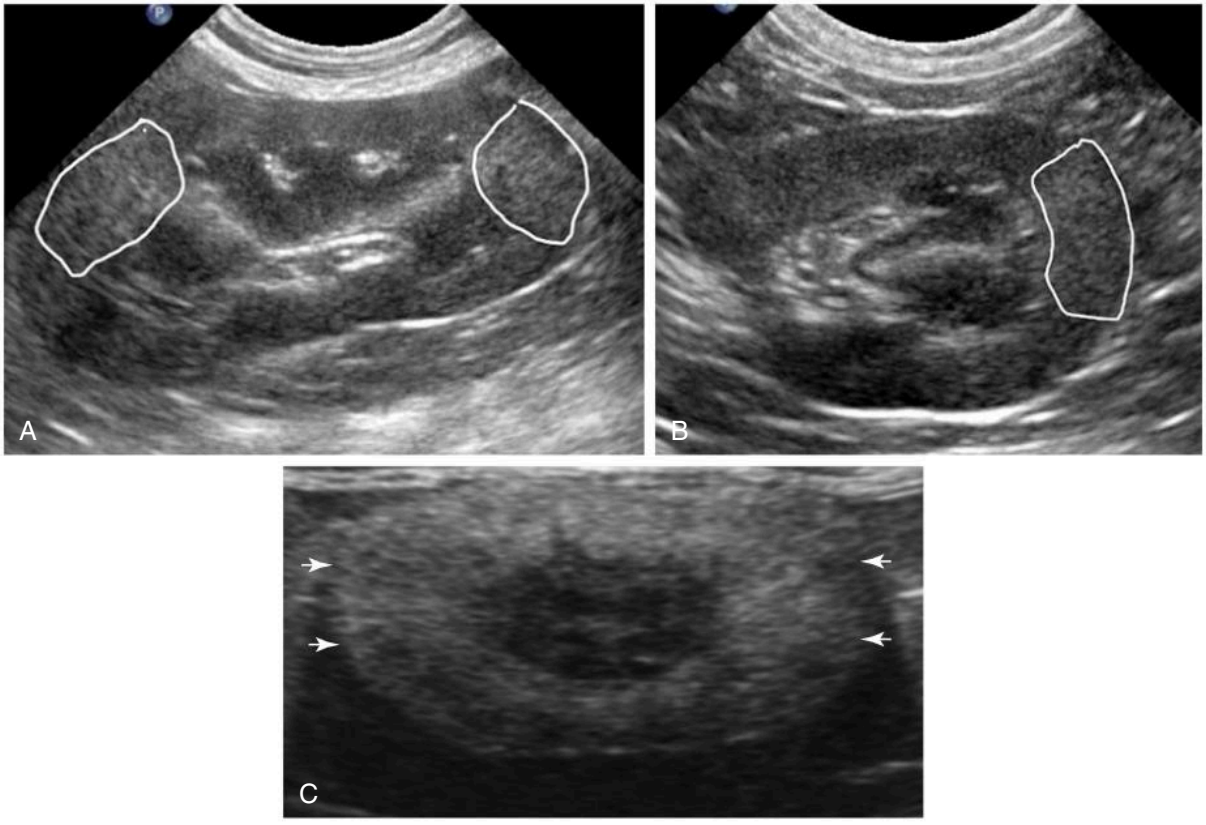


Fig. 3.13 **A,** Sagittal ultrasound image of left kidney of dog. There is artifactual increased echogenicity (anisotropic backscattering artifact) in the cranial and caudal poles of the kidney (areas within *white circles*). **B,** A similar artifactual increased echogenicity is present at the dorsal cortex perpendicular to the ultrasound beam (area within *white circle*). **C,** Sagittal image of left kidney of a cat with advanced renal disease. The anisotropic backscattering artifact (*white arrows*) is absent due to overall increased echogenicity of the renal cortex.

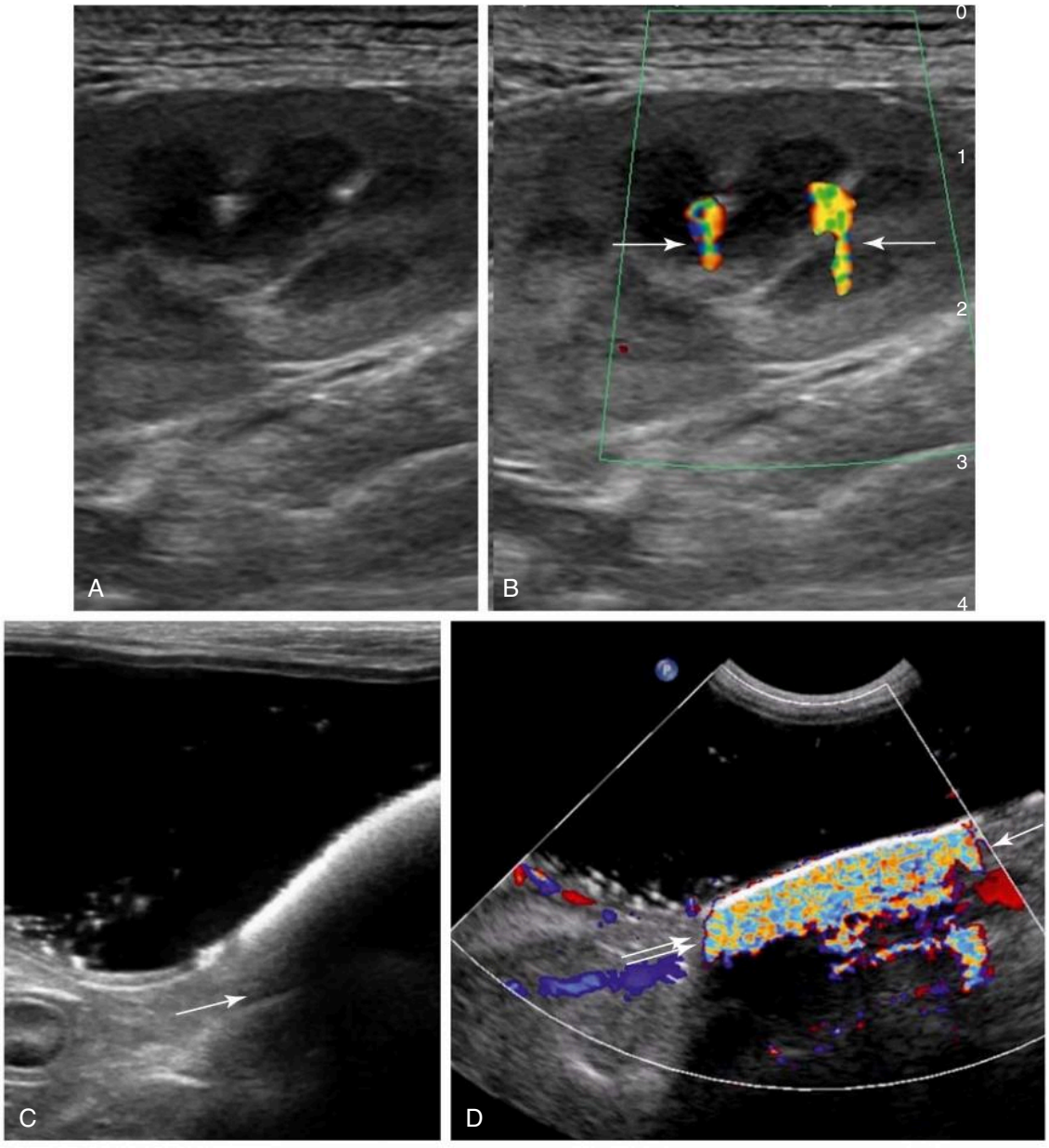


Fig. 3.14 **A,** Hyperechoic foci are present at the diverticula of a left feline kidney. **B,** Twinkling artifact is generated by the calculi seen with color Doppler ultrasound (*white arrows*). **C,** A large amount of gravity dependent hyperechoic calculi is present in the urinary bladder of a cat. The accumulation of the calculi creates a strong distal acoustic shadowing artifact (*white arrow*). **D,** Twinkling artifact is generated with color Doppler ultrasound (*white arrows*).

REFERENCES

1. Curry III TS, Dowdy JE, Murry Jr RC. Ultrasound. In: Curry III TS, Dowdy JE, Murry Jr RC, eds. *Christensen's Physics of Diagnostic Radiology*. Philadelphia: Lea & Febiger; 1990:323–371.
2. Hangiandreou NJ. AAPM/RSNA physics tutorial for residents. Topics in US: B-mode US: basic concepts and new technology. *Radiographics*. 2003;23:1019–1033.
3. Kremkau FW. Ultrasound. In: Kremkau FW, ed. *Sonography: Principles and Instruments*. St. Louis: Elsevier Saunders; 2011:13–39.
4. Lieu D. Ultrasound physics and instrumentation for pathologists. *Arch Pathol Lab Med*. 2010;134:1541–1556.
5. Williams D. The physics of ultrasound. *Anesth Intensive Care Med*. 2012;13:264–268.
6. Kremkau FW. Transducers. In: Kremkau FW, ed. *Sonography: Principles and Instruments*. St. Louis: Elsevier Saunders; 2011:40–68.
7. Martin DJ, Wells ITP, Goodwin CR. Physics of ultrasound. *Anesth Intensive Care Med*. 2015;16:132–135.
8. Kremkau FW, Transducers. *Diagnostic Ultrasound — Principles and Instrumentation*. Philadelphia: W.B. Saunders Company; 1998:79–140.

9. Ziegler L, O'Brien RT. Harmonic ultrasound: a review. *Vet Radiol Ultrasound*. 2002;43:501–509.
10. Anvari A, Forsberg F, Samir AE. A primer on the physical principles of tissue harmonic imaging. *Radiographics*. 2015;35:1955–1964.
11. Kremkau FW. Instruments. In: Kremkau FW, ed. *Sonography: Principles and Instruments*. St. Louis: Elsevier Saunders; 2011:69–124.
12. O'Brien RT, Holmes SP. Recent advances in ultrasound technology. *Clin Tech Small Anim Pract*. 2007;22:93–103.
13. Whatmough C, Guitian J, Baines E, et al. Ultrasound image compounding: effect on perceived image quality. *Vet Radiol Ultrasound*. 2007;48:141–145.
14. Kremkau FW. Introduction. In: Kremkau FW, ed. *Sonography: Principles and Instruments*. St. Louis: Elsevier Saunders; 2011:1–12.
15. Park RD, Nyland TG, Lattimer JC, et al. B-Mode Gray-scale ultrasound – imaging artifacts and interpretation principles. *Vet Radiol*. 1981;22:204–210.
16. Chou PH, Gan HH, Lin FJ, et al. Absence of renal cortical anisotrophic backscattering artifact in feline chronic kidney disease. *Vet Q*. 2021;41, 210-116.
17. Boote EJ. AAPM/RSNA physics tutorial for residents: topics in US: Doppler US techniques: concepts of blood flow detection and flow dynamics. *Radiographics*. 2003;23:1315–1327.
18. Prabhu SJ, Kanal K, Bhargava P, et al. Ultrasound artifacts: classification, applied physics with illustrations, and imaging appearances. *Ultrasound Q*. 2014;30:145–157.
19. Kremkau FW. Doppler principles. In: Kremkau FW, ed. *Sonography: Principles and Instruments*. St. Louis: Elsevier Saunders; 2011:125–175.
20. Wood MM, Romine LE, Lee YK, et al. Spectral Doppler signature waveforms in ultrasonography: a review of normal and abnormal waveforms. *Ultrasound Q*. 2010;26:83–99.
21. Kremkau FW. Artifacts. In: Kremkau FW, ed. *Sonography: Principles and Instruments*. St. Louis: Elsevier Saunders; 2011:176–210.
22. Bude RO, Rubin JM. Power Doppler sonography. *Radiology*. 1996;200:21–23.
23. Nikolina L, Pascaline P, Marco BT, et al. Contrast-enhanced ultrasonography in dogs with inflammatory bowel disease. *J Vet Intern Med*. 2021;35:2167–2176.
24. Banzato T, Rubini G, Orlandi R, et al. Contrast-enhanced ultrasound features of hepatocellular carcinoma in dogs. *Vet Rec*. 2020;186:187.
25. Tamura M, Ohta H, Shimbo G, et al. Usefulness of noninvasive shear wave elastography for the assessment of hepatic fibrosis in dogs with hepatic disease. *J Vet Intern Med*. 2019;33:2067–2074.
26. Seiler GS, Griffith E. Comparisons between elastography stiffness scores for benign versus malignant lymph nodes in dogs and cats. *Vet Radiol Ultrasound*. 2018;59:79–88.
27. Feldman MK, Katyal S, Blackwood MS. US artifacts. *Radiographics*. 2009;29:1179–1189.
28. Shriki J. Ultrasound physics. *Crit Care Clin*. 2014;30:1–24. v.
29. Kirberger RM. Imaging artifacts in diagnostic ultrasound – a review. *Vet Radiol Ultrasound*. 1995;36:297–306.
30. Heng HG, Widmer WR. Appearance of common ultrasound artifacts in conventional vs. spatial compound imaging. *Vet Radiol Ultrasound*. 2010;51:621–627.
31. Barthez PY, Leveille R, Scrivani PV. Side lobes and grating lobes artifacts in ultrasound imaging. *Vet Radiol Ultrasound*. 1997;38:387–393.
32. Ruth JD, Gan HH, Miller MA, et al. Effect of anisotropy and spatial compound imaging on renal cortical echogenicity in dogs. *Vet Radiol Ultrasound*. 2013;54:659–665.
33. Louvet A. Twinkling artifact in small animal color – Doppler sonography. *Vet Radio Ultrasound*. 2006;47:384–390.
34. O'Brien RT, Zagzebski JA, Delaney FA. Ultrasound corner: range ambiguity artifact. *Vet Radiol Ultrasound*. 2001;42:542–545.

ELECTRONIC RESOURCES

Additional information related to the content in Chapter 3 can be found online at eBooks.Health.Elsevier.com.

- Chapter Quiz

CHAPTER 4

Principles of Computed Tomography and Magnetic Resonance Imaging

Marc-André d'Anjou

Computed tomography (CT) and magnetic resonance (MR) imaging have become essential assets to veterinarians in the pursuit of many diagnoses. A general understanding of the physical principles inherent to both modalities is important not only to optimize their use in practice but also to recognize their limitations.

THE ROLE OF COMPUTED TOMOGRAPHY AND MAGNETIC RESONANCE IMAGING IN VETERINARY PRACTICE

CT and MR imaging offer superior diagnostic possibilities over conventional radiography because of two primary advantages, which are their *tomographic nature* and *increased contrast resolution*. Indeed, as opposed to radiographs that represent two-dimensional, or flat, projections of three-dimensional (3D) structures, tissues are examined with CT and MR in thin sections, or slices, thereby eliminating superimposition. Organs and other structures can then be identified more easily and differentiated (Figs. 4.1 and 4.2). Moreover, CT and MR volume datasets can be reformatted in any imaging plane, or as 3D projections (eFig. 4.1), allowing better representation of structural anatomic relationships.

Contrast resolution is the capacity of a system to accurately represent differences in tissue, physical, and/or biochemical characteristics, which are intrinsically linked to x-ray attenuation on CT, or signal intensity on MR imaging. The better the contrast resolution, the more likely subtle variations in tissue components will be displayed as pixels of different shades of gray (Fig. 4.3A). For example, much smaller differences in x-ray attenuation can be detected in CT images when compared to a radiograph.[1,2] This difference is explained by the elimination of scatter that reduces image contrast on radiography and by the use of more sensitive x-ray detectors in CT. As with ultrasonography, pure liquids can be differentiated from soft tissues with CT, which cannot be done with radiographs. MR imaging is recognized even more for its great contrast resolution (see Fig. 4.3B), which can be enhanced by the combined use of different imaging sequences.

Conversely, *spatial resolution*, which corresponds to the minimum resolvable separation between high-contrast objects (see Fig. 4.3A), is more limited with CT and MR imaging, as compared to radiography. The spatial resolution of CT and MR imaging, which is typically linked to the slice thickness, is approximately 0.3 and 1.0 mm,[3] respectively, although technical advances and increased magnetic field strength have contributed to reducing this value for MR imaging. In

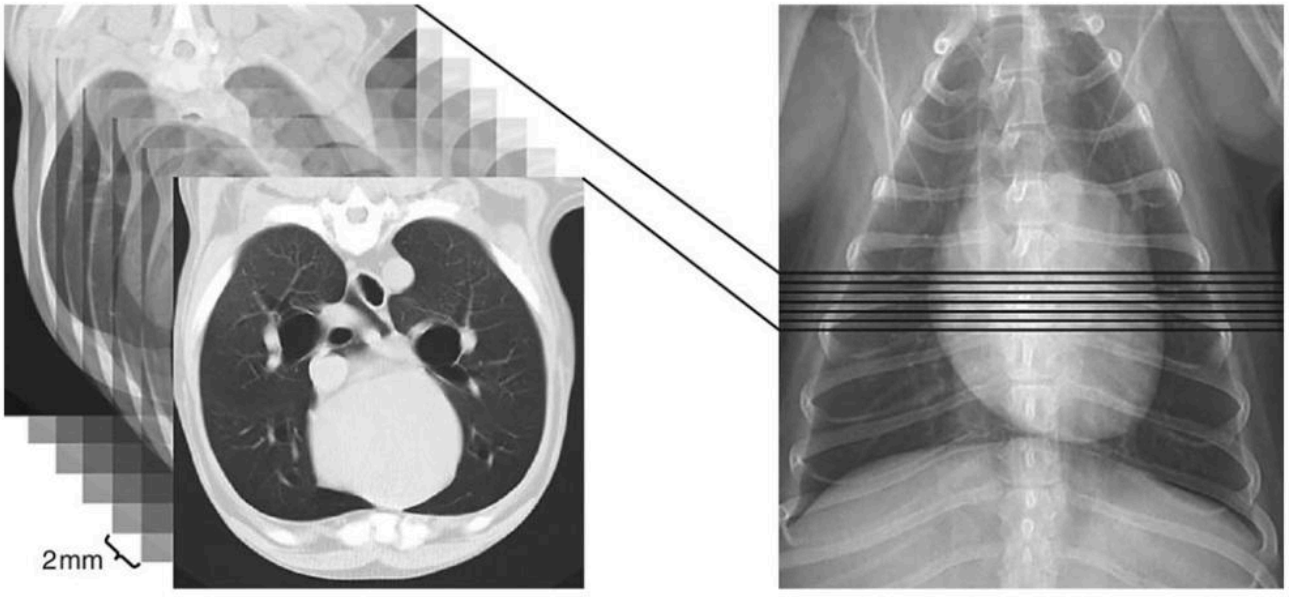


Fig. 4.1 In a computed tomography (CT) study, images are acquired and displayed as sections, or slices, of the body, allowing visualization of structures without superimposition. This fundamental characteristic of tomographic imaging is evident on these contiguous 2-mm-thick images of the thorax of this dog.



eFig. 4.1 Computed tomography (CT) tridimensional (3D) rendering of an arteriovenous malformation (*AVM*) in a young dog presented with ascites and lethargy. This image allows clearly depicting the enlargement of the portal vein (*PV*) and splenic vein (*SV*) due to secondary portal hypertension, as well as the numerous acquired portal shunts in the abdomen. *H,* Heart.

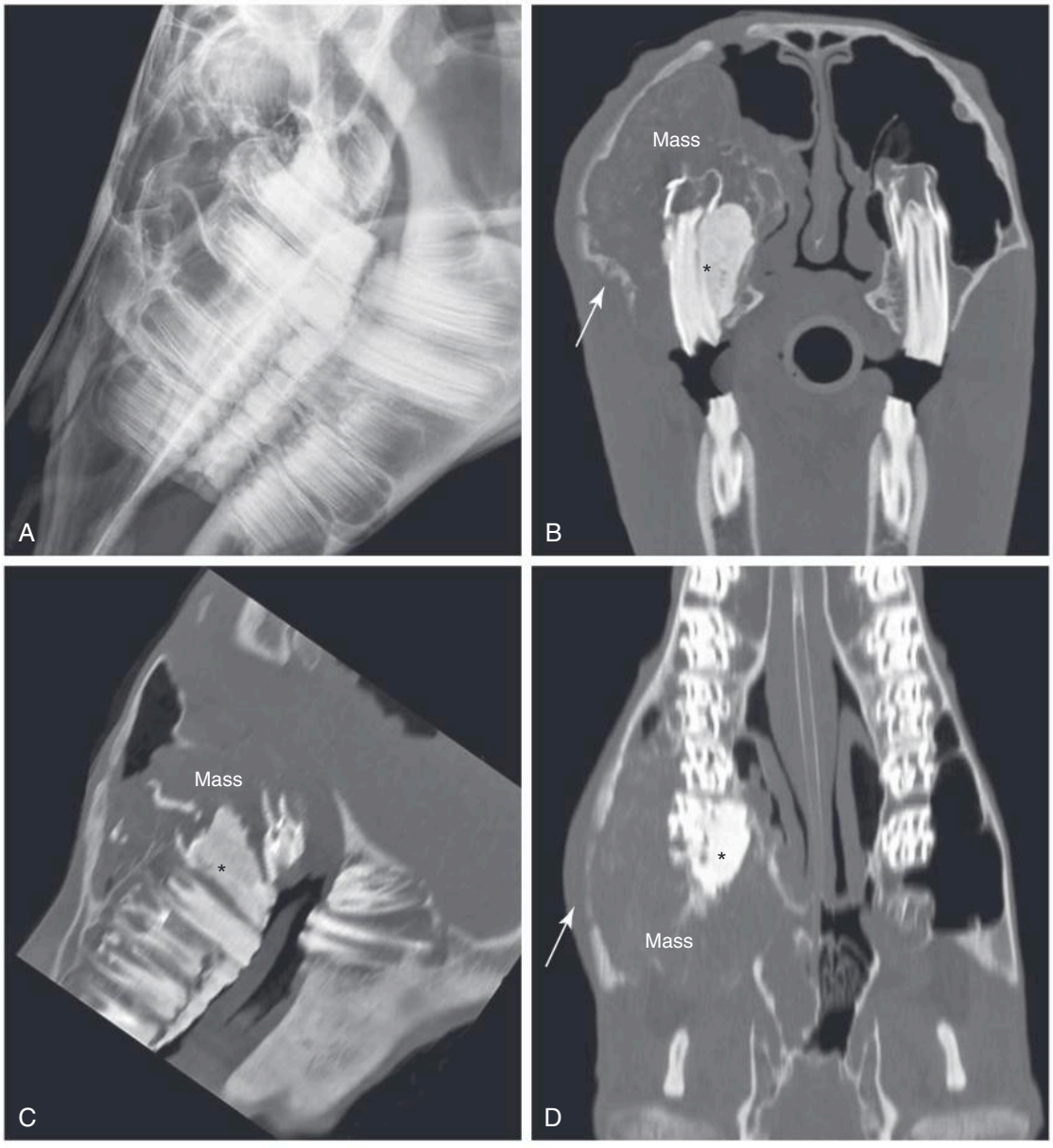


Fig. 4.2 The equine head is anatomically complex with several superimposed structures of variable opacity, making radiographic (**A**) interpretation challenging. In this horse, a large mass associated with maxillary sinus enlargement and bone lysis (*arrows*) is more easily evaluated on transverse (**B**) and reformatted sagittal (**C**) and dorsal (**D**) computed tomography (CT) images. The mass is mainly comprised of soft tissue with a well-de fined mineral component attached to the last molar alveolar bone. An odontoma was con firmed histologically.

comparison, screen-film and digital radiography are associated with a spatial resolution of approximately 0.08 to 0.17 mm,[3] which allows smaller details to be depicted. However, the elimination of superimposition and the superior contrast resolution inherent to CT and MR imaging more than compensate for this limitation in spatial resolution.

IMAGE FORMATION: GENERAL CONCEPTS

CT and MR imaging share several characteristics regarding image formation. Each CT or MR image represents a thin section, or slice, of the body, composed of a matrix filled with small cubical sections, known as *voxels*, or *vo*lume *el*ements. The image is displayed on a flat monitor as a matrix of *pixels*, or *p*icture *el*ements (Fig. 4.4). A voxel associated with greater tissue signal intensity on MR or x-ray attenuation on CT will be displayed as a brighter, or whiter, pixel, whereas lack of signal or x-ray attenuation, such as with air, will appear dark. Although several different values can coexist in each voxel, especially if the voxel is large and if composed of heterogeneous tissue components, only the mean value is expressed and converted to pixel brightness (Fig. 4.5). Hence, both normal and abnormal tissue elements may be combined in a voxel, limiting the resolving capabilities of the modality. Generally, the limiting factor with CT and MR imaging is the slice thickness, which is typically the largest dimension of each voxel. Technical advances in scanners have aimed to reach isotropic resolution, that is, to image sections of tissue with perfectly cubical voxels—the x, y, and z dimensions are the same.[2] Near isotropic resolution has been achieved in multidetector row scanners allowing submillimeter slice generation, which greatly

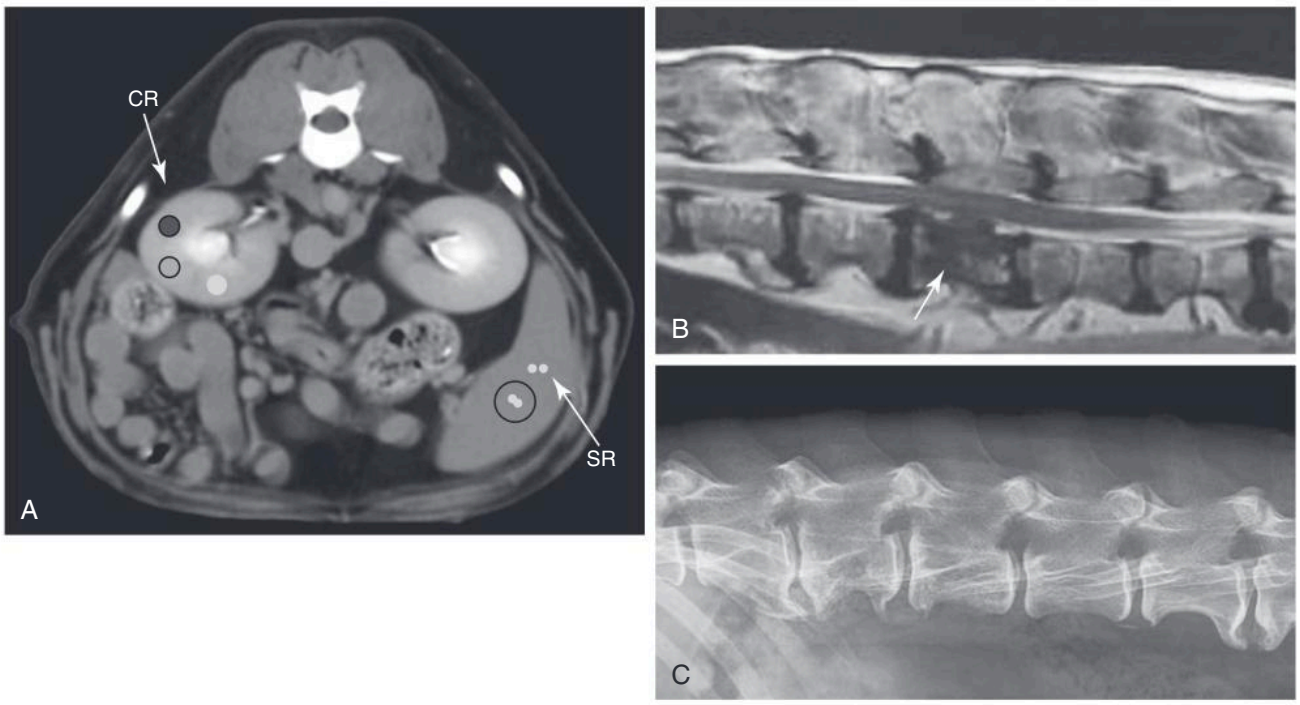


Fig. 4.3 **A,** Schematization of contrast resolution (*CR*) and spatial resolution (*SR*) using a transverse computed tomography (CT) image through the level of the kidneys. Simulated nodules in the right kidney are more easily detected due to the high contrast resolution because their x-ray attenuation characteristics (physical density) differ from the rest of the renal parenchyma. CT offers superior contrast resolution over radiography. In the spleen, the two most dorsal simulated nodules (*arrow*) are visible as independent structures, whereas the more ventral simulated nodules (*circle*) are not visible independently and appear as a single lesion, highlighting the limit of spatial resolution in this image. **B** and **C,** magnetic resonance (MR) imaging is recognized for its outstanding contrast resolution. In this dog with back pain, a malignant neoplasm involving the third lumbar vertebra (*arrow*) is clearly detected with MR imaging (**B**) but was not conspicuous radiographically (**C**).

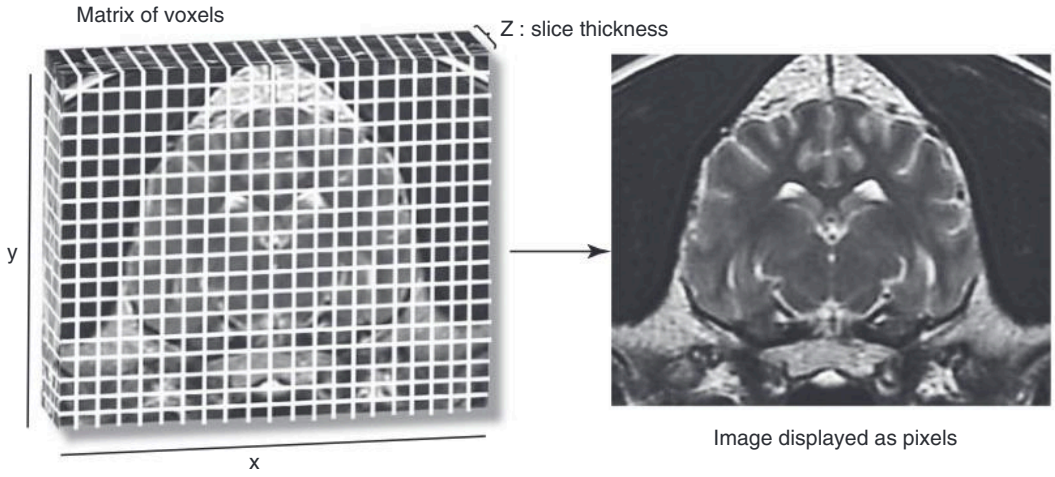


Fig. 4.4 Concept of "voxel-to-pixel" translation in tomographic imaging. The information contained in individual cubes (voxels) of the imaged matrix is displayed as pixels on the computer monitor. Hence, the two-dimensional image is a representation a three-dimensional slab or slice of tissue.

enhances image detail in all planes. Fig. 4.6 illustrates the impact of voxel dimension on image detail.

Among the differences between CT and MR imaging, an important aspect is that image sections can be acquired in any *plane* with MR imaging, including oblique planes (Fig. 4.7). Conversely, with CT, images can be acquired only parallel to the system gantry. Thus, CT images are typically transverse to body parts lying on the table. Fortunately, CT sections are scanned contiguously, forming a volume dataset of millions of tiny cubes, each associated with an attenuation value. It is therefore possible to rearrange, or *reformat*, CT images so that voxels along a plane different than the transverse plane are now displayed as a new matrix of pixels (Fig. 4.8, Video 4.1). This process is known as *multiplanar reformatting*, or *MPR*. These new images can assist in structure recognition, especially for tubular or tortuous structures, and allow more complete assessment (measurements, etc.) of normal and abnormal tissues. Moreover, imaging software can be used to generate 3D

representations through volume or surface rendering methods, helping clinicians, especially those less familiar with tomographic imaging, better understand morphologic changes and plan surgery.

COMPUTED TOMOGRAPHY

In 1979, G. N. Hounsfield and A. M. Cormack were awarded the Nobel Prize in medicine for the development of CT imaging,[1] which was considered by many to be the greatest advance in medicine since the discovery of x-rays. Individual CT images that took several minutes to acquire and reconstruct back then can now be generated in fractions of a second, significantly expanding the range of diagnostic applications while improving patient comfort and reducing motion artifact.

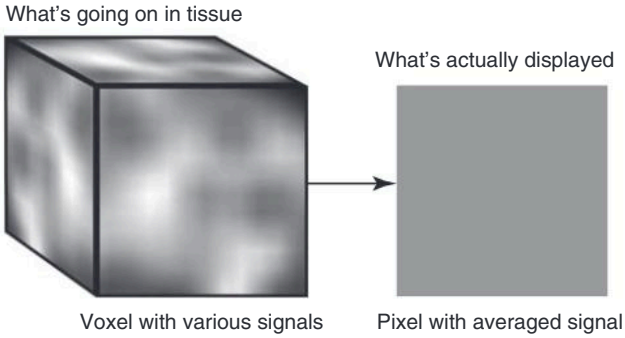


Fig. 4.5 Signal averaging. Although a single voxel may contain tissue of heterogeneous signal intensity, only the average is displayed as a pixel of uniform brightness. More signal in a magnetic resonance image, or increased x-ray attenuation in a computed tomography study, would translate to brighter pixel, whereas lack of signal would be displayed as a dark pixel.

CT technology was based on Radon's mathematic principles developed in 1917, which proved that an image of an object could be produced using an infinite number of projections through that object.[1] With conventional radiographs, orthogonal projections are used to mentally reconstruct anatomic structures in 3D based on the visualization of their shape on perpendicular projections. This process is reliable for simple shapes, but to represent structures with irregular contours accurately, many more radiographic projections are necessary. Now, if thousands of projections could be performed at precise angles, and if x-ray transmission through tissues could be quantified for each of these projections, a sophisticated computer would be able to geometrically *reconstruct* these data and assign specific x-ray transmission values to individual regions of the body. By using a thinly collimated x-ray beam rotating around a patient, slices of tissues can then be computer-generated, each with its own matrix of voxels associated with definite attenuation values. This is the fundamental concept of CT.

Computed Tomography System Geometry

A CT system is mainly composed of a scanning unit (i.e., the *gantry*) with a rotating x-ray emitting tube and a detector system, a patient table, and a console equipped with a sophisticated computer that allows adjusting acquisition parameters and image reconstruction (Fig. 4.9). The rotating x-ray tube is

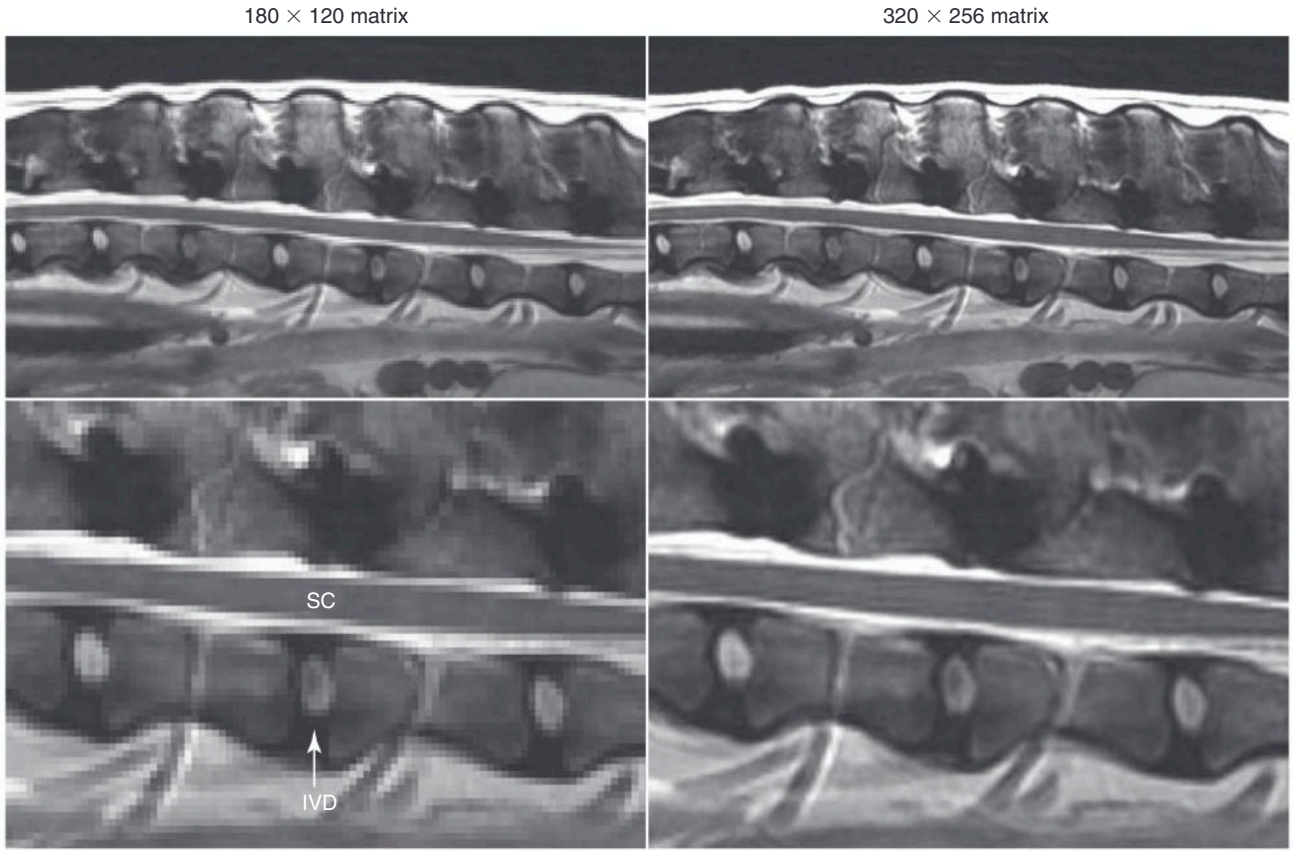


Fig. 4.6 Image matrix and spatial resolution. With a given field of view, a small matrix (180 × 120) contains larger pixels that result in step-like contours. The spinal cord (*SC*) in this dog is smoother in contour when a larger matrix (320 × 256) (i.e., smaller pixels) is used. This superior spatial resolution increases diagnostic accuracy. *IVD,* Intervertebral disc.

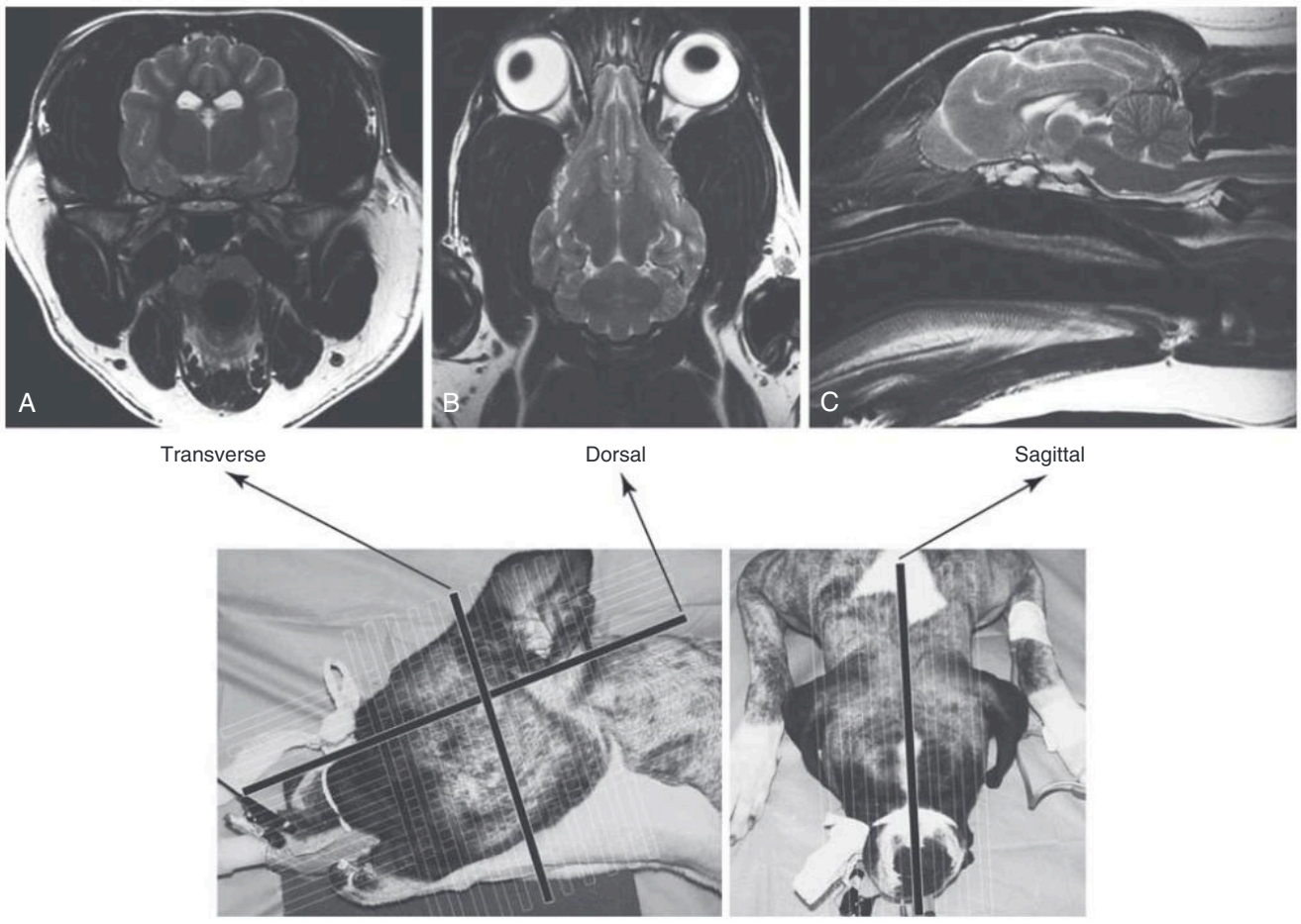


Fig. 4.7 MR images can be acquired in any plane. Transverse (**A**), dorsal (**B**), and sagittal (**C**) planes are typically obtained in most patients, allowing better three-dimensional representation. Image localization is illustrated in the bottom images. Note that all planes can be obtained without having to move the patient.

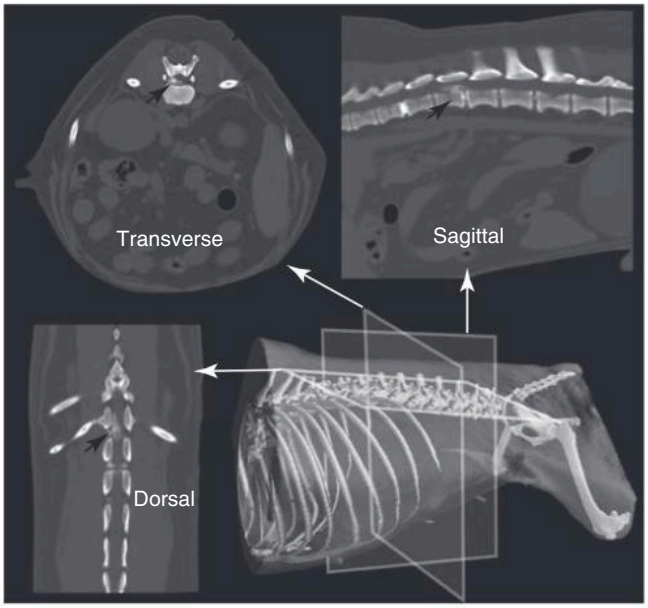


Fig. 4.8 Multiplanar reformatting with computed tomography (CT). Transverse images are obtained initially, but can be reformatted in any plane to help better understand the anatomy. With multidetector CT, thinner sections can be acquired more rapidly, resulting in smoother images with reduced step-like artifacts. The three-dimensional extent of the extruded mineralized disc material is well depicted in all planes (*arrows*).

powerful enough to operate for long periods of time without overheating, thus permitting acquisition of large volumes of data. Modern systems use helical scanning that can rapidly image a large body region without interruption (Fig. 4.10). Rapid tube rotation around the table that simultaneously advances inside the gantry traces a helical path around the patient body, producing a data volume rather than a single slice. Using interpolation methods, flat slices of cubical voxels can be reconstructed from any part of the dataset. Fast scanners reduce motion artifact and allow more precise angiographic procedures with contrast-medium bolus tracking. Advanced scanners that can rapidly acquire sub-millimeter slices generate much smoother images in multiplanar (MP) and 3D reformatting.

The *detector system* also plays an important role in image quality. It converts the incident x-rays that traverse tissue into electronic signals. Ceramic, solid-state detectors have better x-ray absorption and are used in current scanners.[1,4] Each detector is composed of a scintillation crystal that reacts with the incident x-ray and, through an amplification process, generates light that is converted into digital pulses (Fig. 4.11). Detectors are aligned over a semicircular (generally 60 degrees) or annular (360 degrees) array, depending on the system geometry. Annular arrays are stationary, whereas semicircular arrays move synchronously with the opposing x-ray tube (see Fig. 4.9B). CT scanners with multidetector row configurations have become the standard in veterinary hospitals (Fig. 4.12). Such units allow multiple thin contiguous slices to be acquired at a time, an important advantage over previous single-row

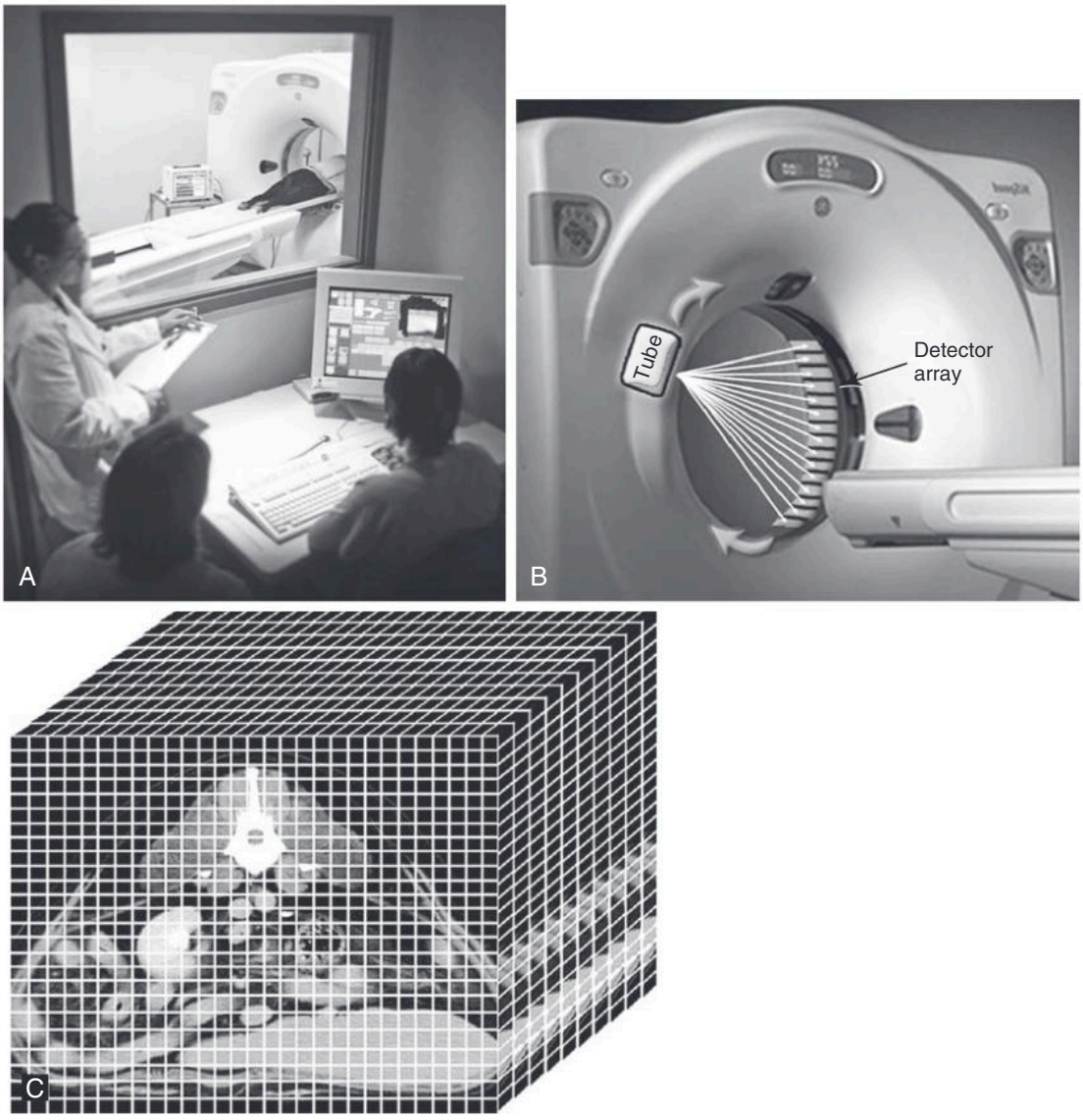


Fig. 4.9 **A,** Typical components of computed tomography (CT). Using a dedicated computer, a technician controls image acquisition and reconstruction. A dog under general anesthesia is observed through a leaded glass window as the CT table advances into the CT gantry. **B,** Most CT scanners are now constructed with a curved array of detectors that rotates around the patient synchronously with the x-ray tube. **C,** The dataset reaching the computer is reconstructed to represent contiguous slices of voxels forming a volume. This volume can then be displayed slice by slice (i.e., transverse images) or reformatted in any plane.

systems. For example, 1-mm-thick slices of a 30-cm-long thorax may require a few seconds to image with a 64-slice scanner, as opposed to a few minutes with a single-row scanner. Images are also more rapidly reconstructed and available for review on the monitor with more recent systems equipped with faster computers. Apart from this significant gain in *temporal resolution* that reduces motion artifacts and tissue misregistration, multidetector row detectors use radiation delivered from x-ray tube more efficiently than single-row detectors.[2] Interscan delays required for tube cooling are significantly reduced with multidetector row systems, allowing for angiographic procedures with multiple series in a short period of time such as those used for portosystemic shunt detection.

Image Formation

The mechanism by which the system reconstructs the data measured by each detector into images as the tube rotates around the patient is sophisticated, yet relatively simple. It starts with the concept of x-ray attenuation, which mainly depends on the electron density of the medium. X-ray attenuation is quantified by measuring the fraction of radiation removed in passing through a given thickness of a specific material, which is based on the *linear attenuation coefficient* (μ) of this material. For image display purposes, x-ray attenuation values calculated by the computer during scanning are expressed as Hounsfield units (HU), normalized to the x-ray attenuation value of water (HU = zero). Any structure or tissue causing more x-ray attenuation than water will have a HU value above zero, whereas any structure or tissue causing less x-ray attenuation than water will have a HU value less than zero (negative). Fig. 4.13 illustrates the range of HU among normal and abnormal tissues. The fact that liquids and soft tissues can be discriminated based on their HU values confirms the greater contrast resolution of CT over radiography.

Other important parameters that are set before image reconstruction include *slice reconstruction interval*, which

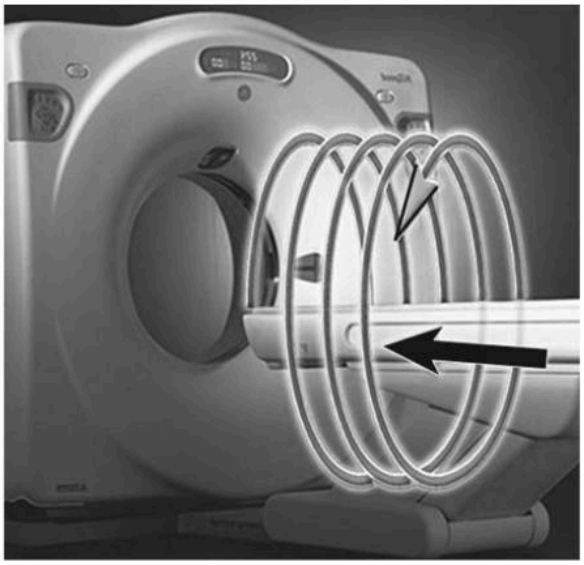


Fig. 4.10 Helical computed tomography (CT). scanning. The table incursion into the gantry as the tube rotates around it results in helicoidal, or spiral, body scanning. This type of acquisition allows images of contiguous sections of tissue, preventing gaps and allowing much faster image acquisition than previous CT generations.

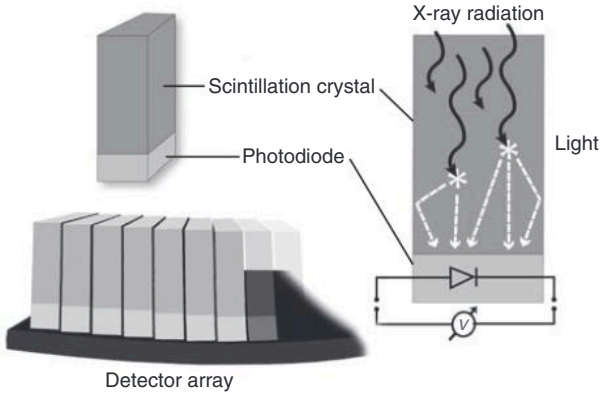


Fig. 4.11 Solid state computed tomography (CT) detectors. X-rays reaching the scintillation crystal generate light photons that are converted to electric current in the photodiode, which is then converted to attenuation values that are used to form the image.

adjusts the proportion of overlap between adjacent slices of tissues used for image reconstruction, and *reconstruction filter*, which determines the level of edge reinforcement applied while processing raw data. These parameters must be set carefully according to the region of interest (ROI). For example, a low-pass filter, commonly known as "standard or soft tissue filter," is recommended when soft tissue contrast must be emphasized, such as in brain imaging, with the downside of creating a blurrier image (Fig. 4.14). "Bone filters," conversely, maximize spatial resolution, but introduce more noise, thus reducing contrast resolution. Such images are sharper but grainier. Intermediate pass filtration may also be used for the reconstruction of smaller soft tissue areas to prevent excessive blurring. Hence, reconstruction filter(s) must be selected according to the size of the body part to be imaged and the content to be highlighted (e.g., soft tissue and/or bone).

Image Display

HU values that can be measured with typical scanners range from approximately −1000 to +3095 HU, for a total of 4096

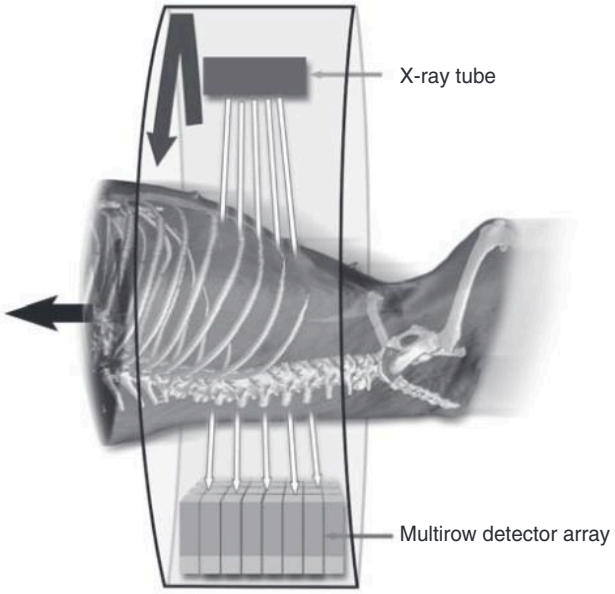


Fig. 4.12 Multidetector (or multislice) computed tomography (CT) scanning. When using more than one row of detectors, larger areas of the body can be imaged during a single tube rotation, allowing faster table advancement, and thus faster scanning. In this illustration there are 8 rows of detectors but newer scanners can contain up to 256 rows, which significantly increases the volume of tissue that can be imaged during one rotation of the x-ray tube.

shades of gray (12 bits of grayscale*). This range of values cannot be resolved by the human eye, which cannot differentiate more than 40 shades of gray.[5] To display and appreciate all tissues composed of variable HU, the *window width* (W) and *level* (L) of the image grayscale can be adjusted, according to the median and range of HU composing the area of interest. The Digital Imaging and Communications in Medicine (DICOM) viewing software allows adjustment of the extent (maximum-to-minimum) of gray shades (W) displayed (i.e., the image *contrast*) and the HU at the center of the window (L) (Fig. 4.15, Video 4.2). W/L must be adapted to the tissues being evaluated and usually requires several adjustments during evaluation of a CT study for all tissues to be evaluated completely.

Interpretation of CT images requires an appropriate understanding of radiographic opacities and anatomy. The attenuation characteristics of tissues can be assessed qualitatively, but also quantitatively. With the DICOM viewing software, HU values are determined precisely after defining a ROI over a selected number of pixels (Fig. 4.16). This can help in distinguishing subtle differences in HU that might not be initially perceived, thus increasing contrast resolution.

Contrast-Enhanced Procedures

The use of iodinated contrast medium has become standard for many CT procedures in veterinary medicine.[6] See Chapter 5 for more information about contrast media used for medical imaging. After an intravenous bolus injection, the distribution of hyperattenuating contrast medium provides information on the perfusion of tissues and integrity of natural barriers, such as the blood–brain barrier. Typically, for nonangiographic procedures, postcontrast scans are performed a few minutes following a bolus injection, to allow contrast medium to pass into the extravascular space. Hence, the HU of a tissue will increase in proportion to the concentration of the contrast medium, the volume of its blood space, and the permeability of its capillary

*See Chapter 2 for a discussion of bit depth.

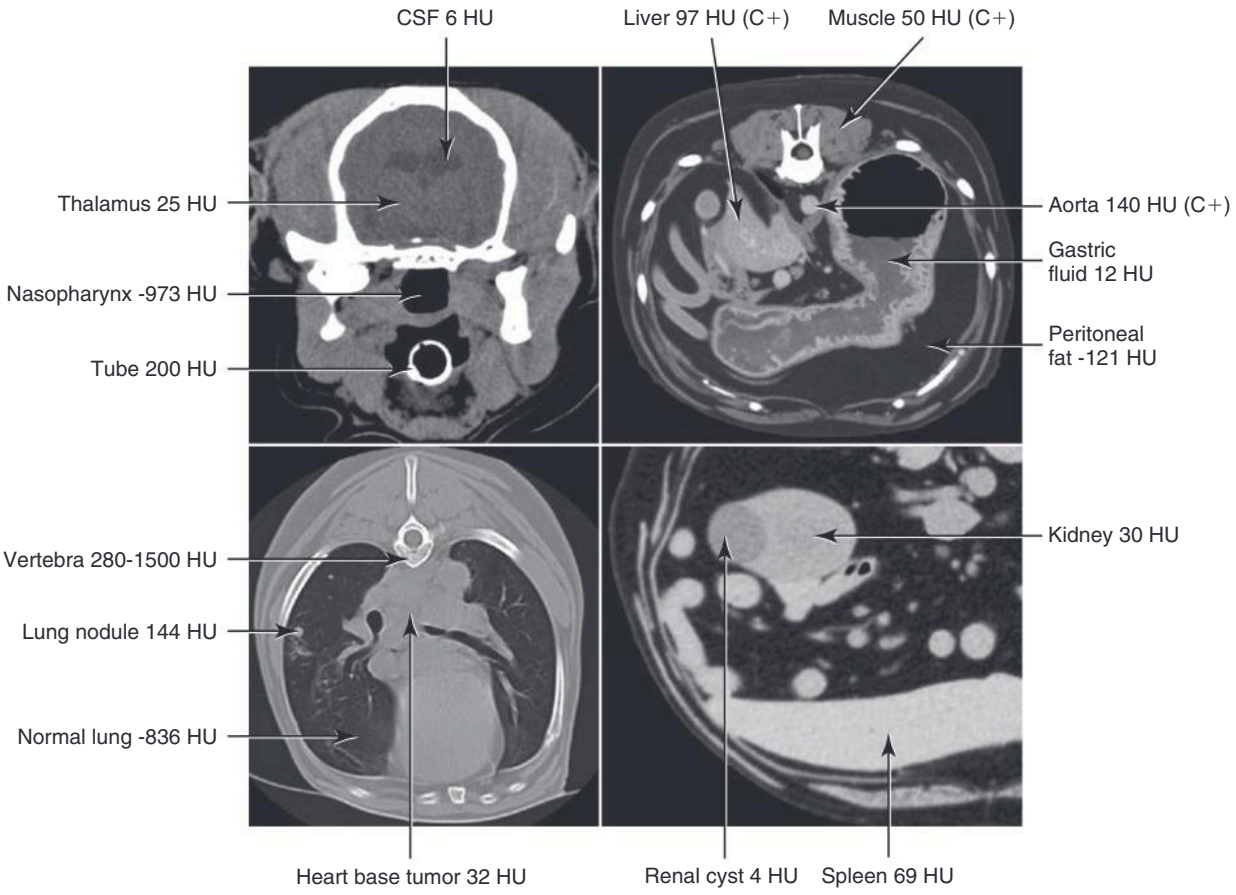


Fig. 4.13 Tissue attenuation (determined as Hounsfield units [*HU*]) can be quantified precisely based on values measured by the CT computer. More subtle differences in attenuation (HU values) are perceived with computed tomography (CT) than radiography, leading to the increasing contrast resolution of CT. For example, the fluid contained in a renal cyst or in the cerebral ventricles can be differentiated from surrounding soft tissue; this is not possible radiographically. Intravenous injection of iodinated contrast medium (C+) increases the HU of vascularized tissues, further increasing the contrast resolution of CT. *CSF,* Cerebrospinal fluid.

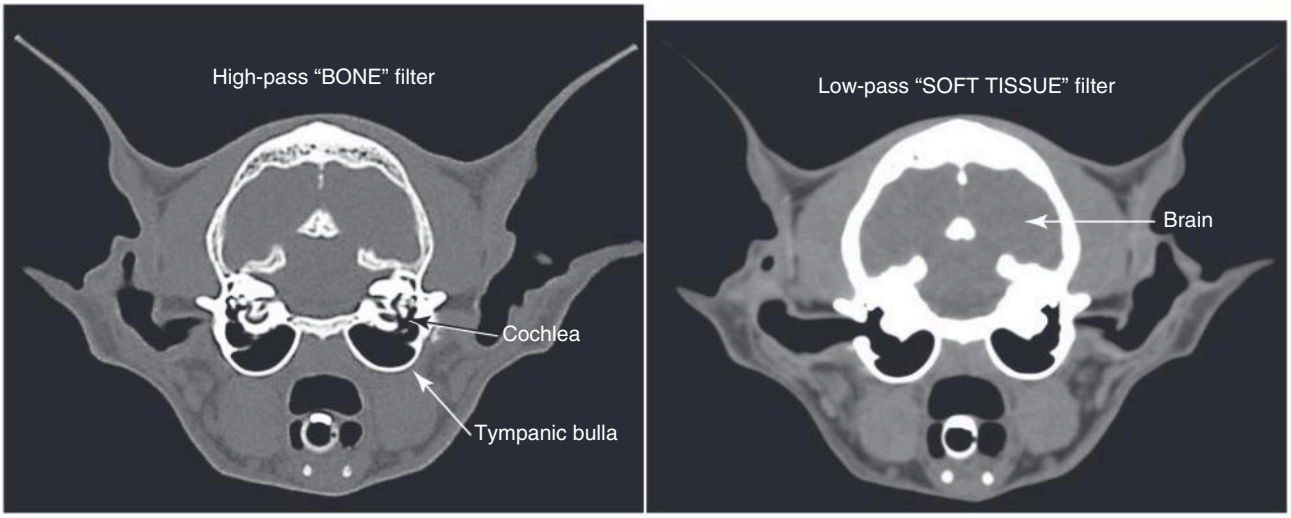


Fig. 4.14 Image reconstruction algorithm. High-pass filtering, also known as "bone filtering," results in sharper images, whereas images reconstructed with low-pass "soft tissue" filter are smoother (or blurrier). The inner ear cochlea is better defined, and the tympanic bulla is thinner with bone filtering, but the brain and other soft tissues of the head are grainier (i.e., noisier) with the same filter. Such filtering is an important part of the image reconstruction steps and requires raw data.

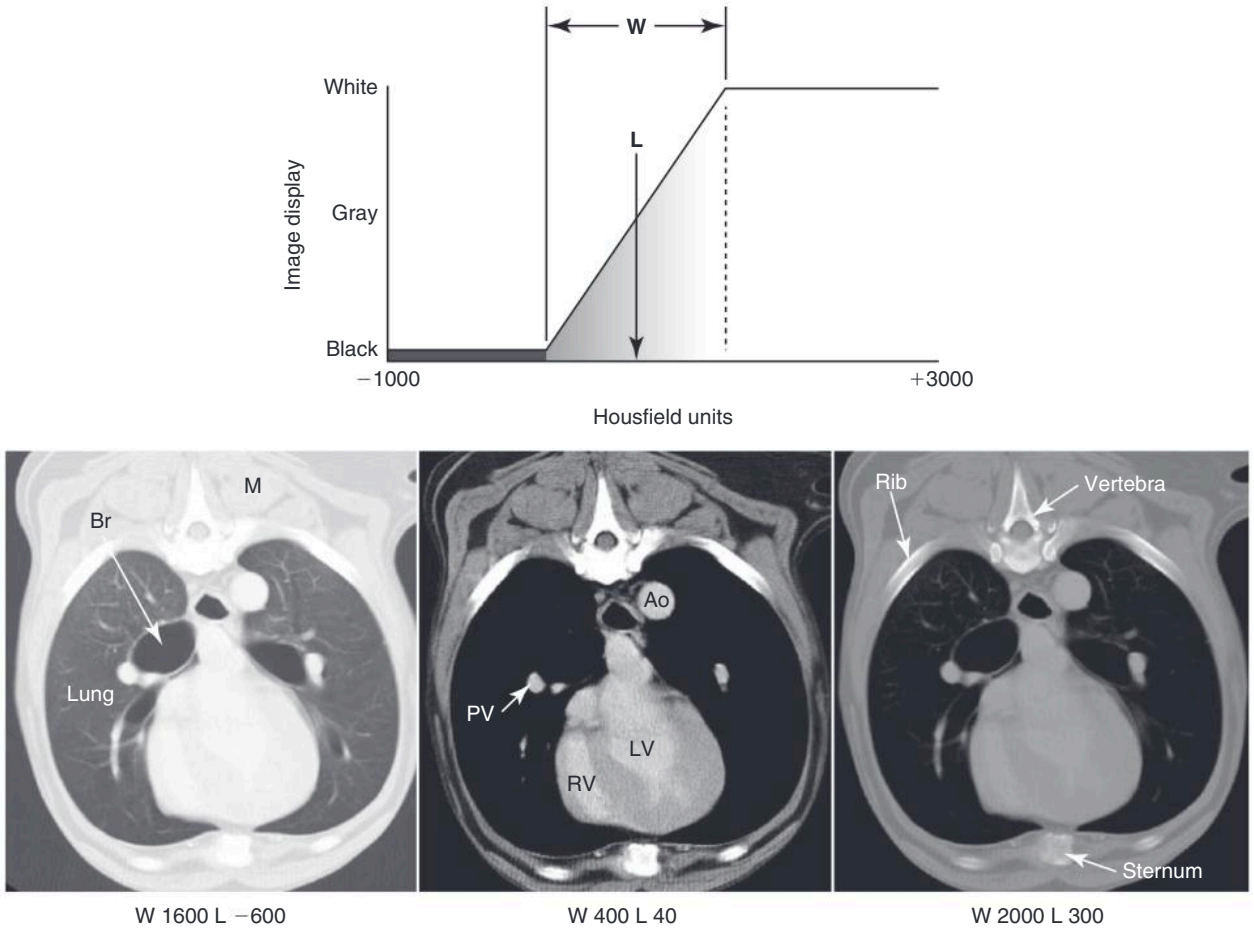


Fig. 4.15 Window width and level adjustments. Because of the limited capacity of the human eye to distinguish different shades of gray, the range of computed tomography (CT) numbers (or Houns field units [HU]) composing the image, from approximately −1000 to +3000, cannot all be displayed at once. With the Digital Imaging and Communications in Medicine (DICOM) viewing software, the window level (*L*) is set at the mean HU of the region of interest, and the window width (*W*) is set to include the range of values to be represented. Practically, L controls the image brightness, and W, the image contrast. A small W, such as 400, will result in a high contrast image. Setting the L to 40 allows better distinction of cardiac chambers filled with diluted contrast medium. Conversely, with these settings, lungs and bone exceed the lower and upper limits of the grayscale and are thus represented with totally black or white pixels, respectively. To assess lung tissue, the W must be widened (1600) and the L must be centered on its mean HU of lung (−600 to −800), whereas bone assessment requires even larger W (2000) and higher L (300). These values must be adapted to the patient. *Ao,* Aorta; *Br,* bronchus; *LV,* left ventricle; *M,* muscle; *PV,* pulmonary vein; *RV,* right ventricle.

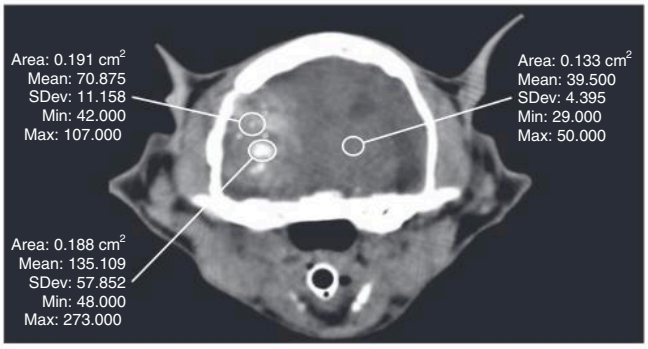
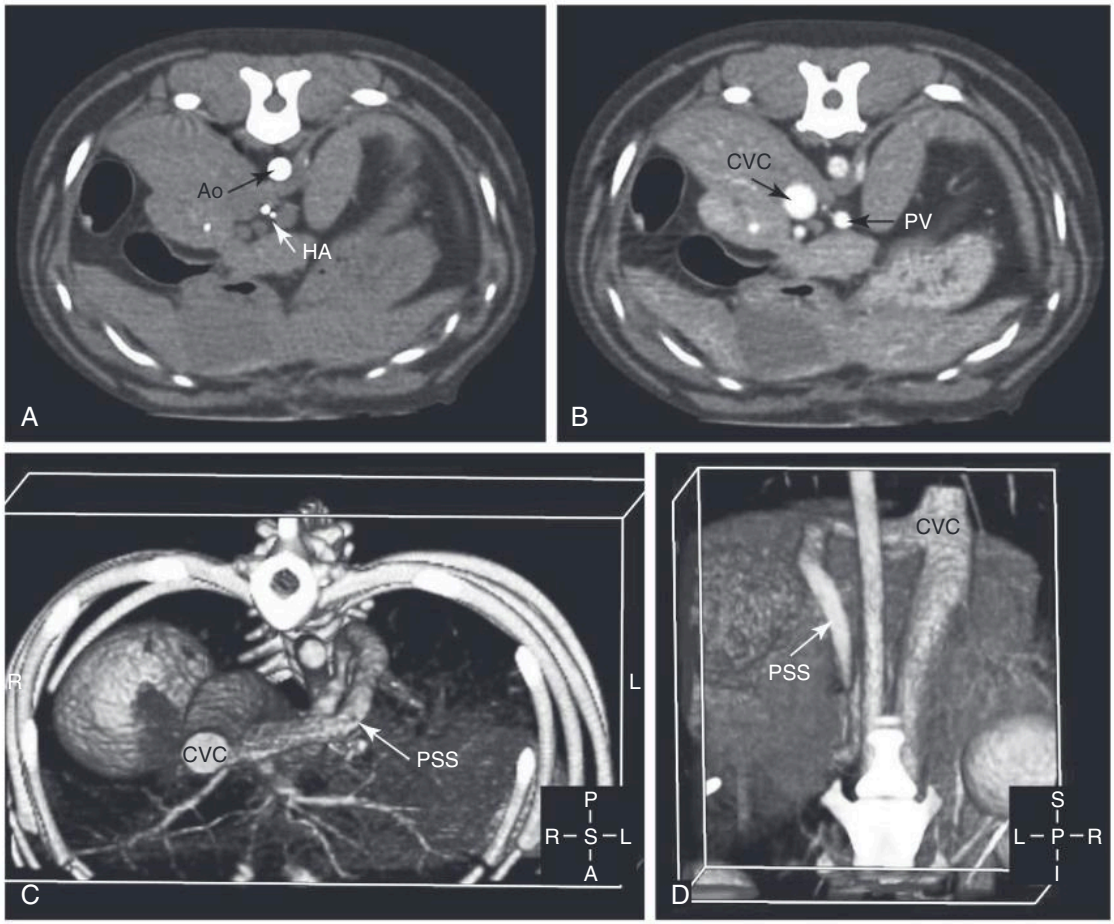


Fig. 4.16 Hounsfield unit (HU) measurements. Differences in HU among normal and pathologic tissues can be determined with the computed tomography (CT) viewing software in specific regions of interest (ROI). Information such as ROI surface area and mean, maximal, and minimal HU is provided. This method allows detection of more subtle differences in HU than what the eye can perceive. In this cat, a mineralized meningioma was identified.

bed.[7] When comparing postcontrast to precontrast CT images, the degree of enhancement can be assessed qualitatively (Fig. 4.17) and quantitatively (see Figs. 4.13 and 4.16). Enhancement characteristics can be used to complement other morphologic observations and increase both sensitivity and specificity of CT examinations.

Angiography represents another important application of CT imaging. CT angiography requires helical scanning and is optimized with multidetector scanners and automated contrast-medium injectors. Scans are performed rapidly after the injection of a contrast-medium bolus and timed according to the vascular phase being examined and its enhancement peak. For example, when injecting into a cephalic vein, contrast medium sequentially reaches the cranial vena cava, right atrium, right ventricle, pulmonary arteries and veins, left atrium and ventricle, aorta and peripheral arteries, before returning to the heart through the vena cava, and to the liver through the portal vein. Precise acquisition timing is required to isolate a group of vessels, which is important when, for example, looking for portosystemic shunts (eFig. 4.2).



eFig. 4.2 Multiphase computed tomography (CT) angiography for portosystemic shunt (*PSS*) detection. **A,** A few seconds after intravenous injection of a bolus of contrast medium, initial scanning highlights the arterial phase of contrast medium distribution. The aorta (*Ao*) and hepatic artery (*HA*) are hyperattenuating. **B,** Shortly thereafter, contrast medium returns through the caudal vena cava (*CVC*) and portal vein (*PV*), while it gradually diminishes in concentration in the aorta. At this point, vascularized tissues are also hyperattenuating. **C** and **D,** Three-dimensional (3D) volume rendering allows a more comprehensive representation of the location and termination of the portosystemic shunt. The 3D image can be moved on the display in any direction and clipped to include only a speci fic region. Here, cranial **(C)** and dorsal **(D)** views are represented.

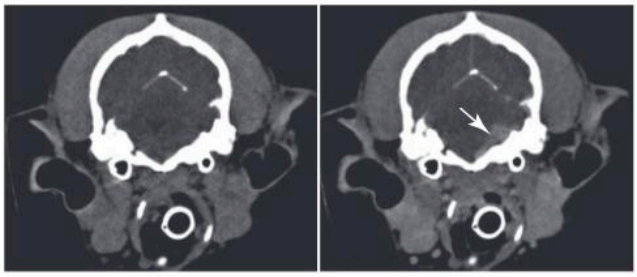


Fig. 4.17 Intravenous injection of iodinated contrast medium increases contrast resolution of computed tomography (CT). In this dog, a contrast-enhancing meningioma (*arrow*), with a broad base along the left temporal bone, was detected only after contrast-medium injection.

Because iodinated contrast medium is eliminated essentially by glomerular filtration, contrast-enhanced CT can also be used to estimate the rate at which this occurs, as well as to assess the renal collecting system.[8]

Risks associated with contrast medium injection are discussed in Chapter 5.

CONE-BEAM COMPUTED TOMOGRAPHY

Cone-beam CT is gaining in popularity in veterinary medicine due to the lower cost of the equipment and installation. Like conventional CT, cone-beam CT consists of an x-ray source, an image detector, a computer, and an image, but uses a cone-shaped x-ray beam as opposed to a collimated fan beam. Use of a cone-beam has the advantage of reducing patient radiation dose, but also leads to increased scatter radiation and reduced contrast-to-noise ratio, which affects image quality. Instead of detectors aligned in row(s), flat panels or image intensifiers are used in cone beam CT technology and these rotate synchronously around the patient through 360 degrees (eFig. 4.3). Cone-beam CT is valuable for the assessment of small head parts and particularly dental structures in dogs and cats as it offers high *spatial resolution*,[9] but its usefulness for larger body regions remains to be determined.

MAGNETIC RESONANCE IMAGING

MR imaging has become an important diagnostic tool in veterinary medicine because of its inherent high-contrast resolution that allows soft tissues to be characterized more sensitively than with CT. The high contrast resolution of MR imaging fundamentally revolves around the electromagnetic properties of hydrogen nuclei (protons), which are abundant in body tissues. Energy transfer to and from these protons can be localized spatially (i.e., in individual voxels) and is the source of image formation. MR imaging can therefore be compared, in a clinical setting, to mapping the distribution of H^+ protons in the water (H_2O) and lipid (CH_2/CH_3) component of tissues. Equipment sophistication and pulse-sequence development are responsible for the growing applicability and accuracy of MR imaging. Although MR imaging is used mainly to investigate neurologic conditions, several other body parts of small and large animals, especially the horse, can be imaged satisfactorily with MR imaging.

Instrumentation

MR systems constitute the most sophisticated equipment in diagnostic imaging, combining electronics, radiofrequency (RF) generators, coils, and gradients that interact with a computer. This combination is necessary for proper tissue excitation and reception and localization of tissue signals. The magnet provides the external magnetic field in which the patient is placed, and its performance is influenced by its field strength, stability, and uniformity. Several types of systems are available, and some of their characteristics will be discussed later. Fig. 4.18 illustrates the main components of the typical MR system.

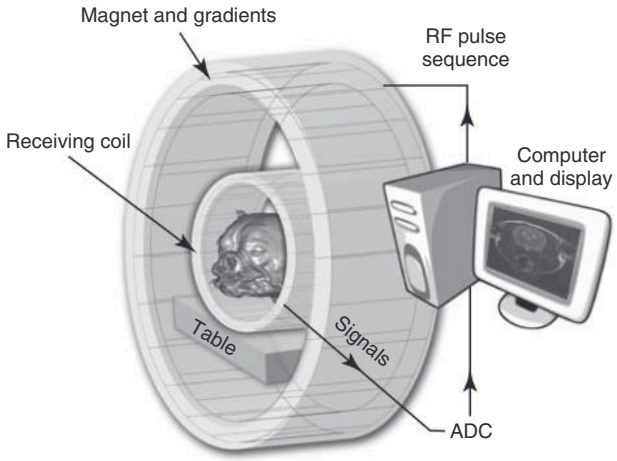


Fig. 4.18 Components of a magnetic resonance (MR) imaging system. The region of the patient to be imaged is placed in the center of the gantry (i.e., maximal magnetic field) and a coil (of variable shape) is placed around or very close to this region. The computer is manipulated to prepare radiofrequency (*RF*) pulse sequences that cause tissue magnetization before signals can be detected as echoes. Different gradients inside the gantry allow localization of individual echoes and are used for gradient-recalled pulse sequences. Analog signals are converted into digital pulses that are transformed into interpretable images. *ADC,* Analog-to-digital converter.

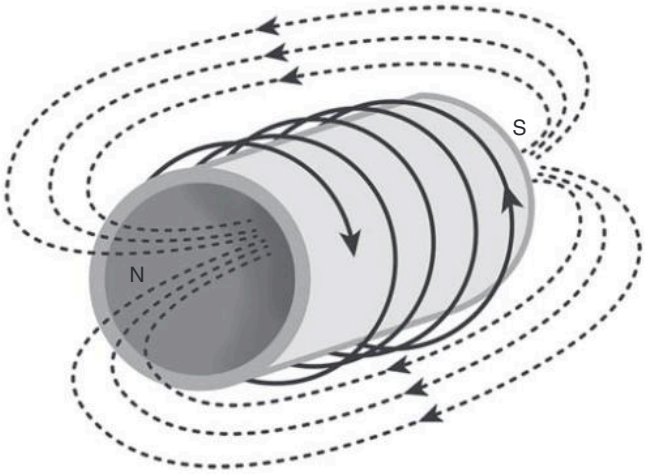
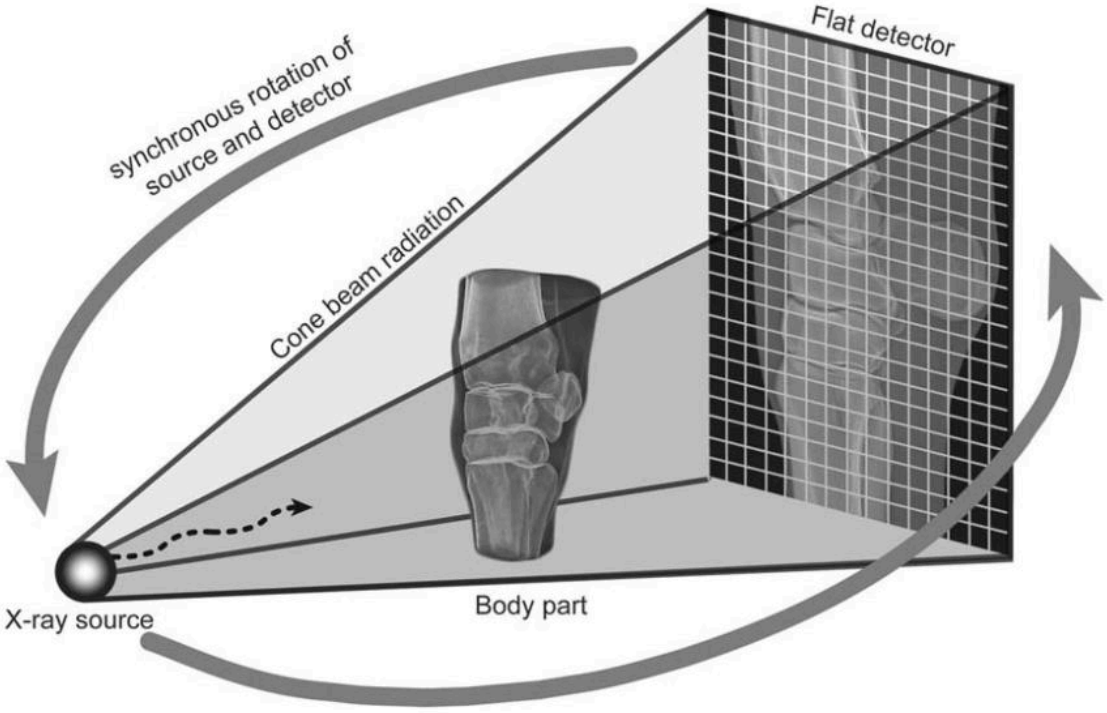


Fig. 4.19 According to Faraday's law of induction, when electronic current travels through a loop of wire, a magnetic field is generated perpendicularly in proportion to the strength of the current. The magnetic field—illustrated here as *curved dashed lines*—is oriented from north (*N*) to south (*S*).

Main Magnetic Field and Radiofrequency Energy

According to Faraday's law of induction, when electronic current travels along a loop of wire, a magnetic field is generated perpendicularly in proportion to the strength of the current (Fig. 4.19).[10] Fundamentally, this is how most MR scanners work, particularly high field-strength systems (magnetic field strength >1 tesla [T]). To generate and maintain such high magnetic fields, superconducting wires are immersed in liquid helium, which serves as cooling agent.



eFig. 4.3 Cone-beam computed tomography. A cone-beam x-ray emitting source rotates around the patient body part synchronously with a flat panel detector, generating a dataset that can be reconstructed in two-dimensional (2D) and three-dimensional (3D) images.

Spins, Excitation, and Relaxation

Each hydrogen proton is positively charged (H^+) and rotates about its axis, like a spinning top. These spinning protons, or *spins*, each act like tiny magnets whose individual magnetization vectors are oriented randomly and cancel out under normal circumstances (Fig. 4.20).

When placed in a strong external magnetic field, spinning protons are forced to align along the axis of this field (B_0), either in the same direction (parallel) or opposite (antiparallel). The magnetic fields of most of these spinning protons cancel out, but a slight excess of protons, which is proportional to the strength of the magnetic field, will be parallel to B_0, producing a *net magnetization* along that axis (see Fig. 4.20). The size of this equilibrium magnetization also depends on the photon density (PD) of tissues present in the field.[10,11]

Influenced by the external B_0 in which they are placed, protons wobble about their axis, a behavior called *precession* (Fig. 4.21).[10,11] This wobbling motion is controlled by application of an external force. The frequency of this precession, also called resonance or *Larmor frequency* (ω_0), is proportional to the main magnetic field strength: $\omega_0 = \gamma B_0$. The constant γ, or *gyromagnetic ratio*, is specific to each type of nuclei. For hydrogen protons, this constant equals 42.6 MHz/T (megahertz per tesla).[10,11]

The phenomenon of precession implies that the magnetization moment of each spinning proton can be broken down into two vector components: one aligned or longitudinal to B_0—the *z*-axis—and one transverse to it, lying on the *xy*-plane (see Fig. 4.21). Although a positive net magnetization is present along the *z*-axis in the equilibrium state, *xy* vector components of spinning protons that precess out of phase cancel out.

By applying a RF pulse that matches the Larmor frequency of the spinning protons, energy can be transferred through a process known as *resonance*. The absorption of this energy by the proton, called *excitation*, causes a state of imbalance. The excited protons jump to a higher energy state during excitation (from parallel to antiparallel), and the macroscopic net magnetization vector flips away from the *z*-axis, toward the *xy*-plane, following a spiral path caused by the precession phenomenon.[10,11] The angle that the net magnetization vector flips away from the *z*-axis is called the *flip angle*, which depends on the strength and duration of the RF pulse. As soon as the RF pulse is stopped, protons will return to their original state of equilibrium in a recovery process called *relaxation* and release and transmit their excess energy.

Whereas the change in longitudinal magnetization is caused by a difference in the number of protons in parallel as opposed to antiparallel states, the transverse magnetization vector growth is caused by protons getting into phase coherence.[10,11] That is, these tiny magnets become globally aligned and precess synchronously. Once the RF current is turned off and relaxation

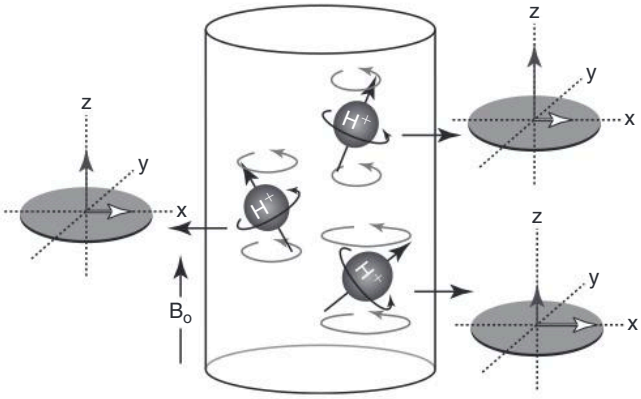


Fig. 4.21 Spin precession. Influenced by the strong external magnetic field, spinning protons wobble about its linear axis, a process called *precession*. The magnetization moment of each spinning proton can be broken down into two vector components: one aligned or longitudinal to B_0—the *z*-axis—and one transverse to it, lying on the *xy*-plane. The relative magnitude of each of these vectors depends on the orientation of the spinning protons in regard to B_0 during the MR imaging sequence process. Notice that as the proton becomes progressively out of alignment with the main magnetic field (B_0), the size of the magnetization vector in the *z*-axis decreases and the size of the magnetization vector in the *xy*-axis increases.

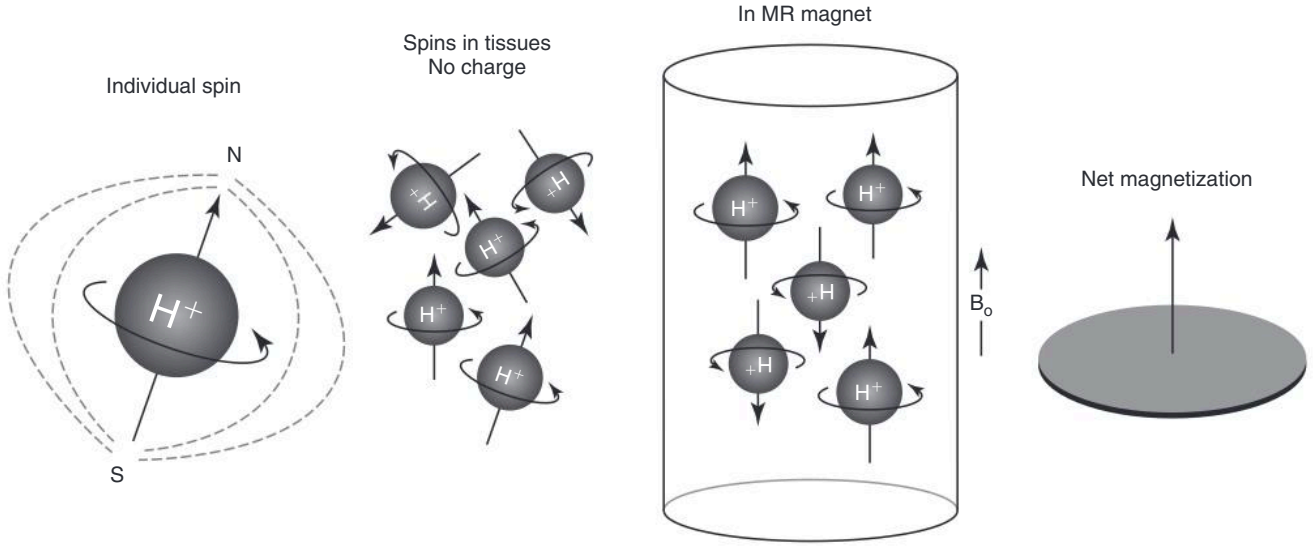


Fig. 4.20 Hydrogen protons (H^+) are used for magnetic resonance (*MR*) imaging because of their abundance in soft tissues and their magnetic characteristics. The positively charged nucleus spins about its axis, generating a very small, local magnetic field, and thus acting as tiny magnet. These protons, or spins, are oriented randomly in tissues under normal conditions so that their magnetic fields cancel out. When placed inside a strong external magnetic field with linear orientation (B_0), these spins are realigned and orient themselves either parallel or antiparallel to this field. A small excess of these spins (proportional to the strength of B_0) are oriented in the parallel direction, thus generating a net magnetization of the tissue. This net magnetization, which at equilibrium is oriented longitudinally, is targeted during imaging sequences.

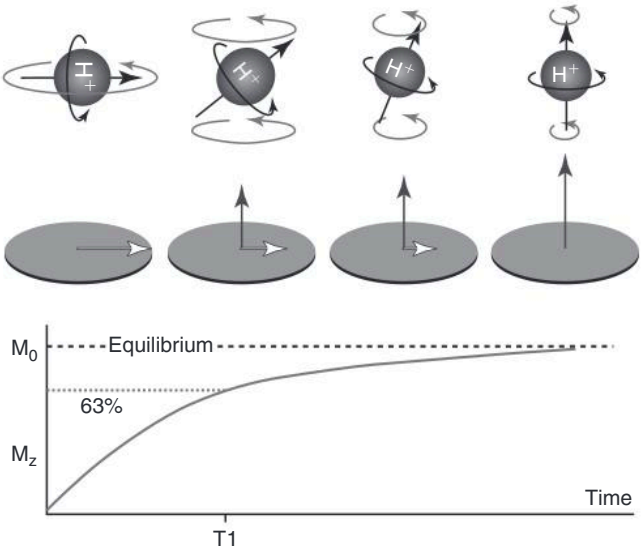


Fig. 4.22 Once the radiofrequency pulse is stopped, the spinning protons immediately start to realign with the main magnetic resonance (MR) magnetic field in the *z*-axis direction transferring their absorbed energy to their molecular environment, also called the lattice. This is T1 relaxation. During this process, the transverse vector component of magnetization (M_z) decreases while the longitudinal component increases to reach an equilibrium (i.e., low-energy state). The T1 time required for the longitudinal magnetization to recover approximately 63% of its original value is called the T1-relaxation time, and is tissue specific. M_0, Longitudinal magnetization at equilibrium state.

begins, two distinct processes occur simultaneously: longitudinal, *T1*, and transverse, *T2*, relaxations. The release of energy from the relaxing protons into their molecular environment, also called the *lattice*, results in more protons returning to the low-energy state, that is, realigned with B_0 (T1 relaxation; Fig. 4.22). At the same time, in-phase spinning protons start interacting with each other, rapidly causing dephasing, and thus eliminating the transverse magnetization vector (T2 relaxation; Fig. 4.23). The rate at which T1 and T2 relaxation occurs is tissue specific and exploitation of these differences is the fundamental source of tissue contrast in MR imaging.

Spin-Echo Sequences

MR images are created once signals arising from excited tissues are detected as echoes by receiving coils, localized spatially, and processed. Because of the differences in T1- and T2-relaxation time between tissues, several technical methods, or *sequences*, can be used to excite and receive signals using RF and gradient pulses, with variable timing and duration. Sequences are divided into two main groups—*spin-echo* and *gradient recalled* sequences. Image interpretation is then based on the evaluation of all sequences obtained in a single examination.

As previously discussed, RF pulses energize tissue protons, which then start to process synchronously, leading to strong transverse magnetization. This process of "flipping" the magnetization away from the *z*-axis is essential to measuring a signal. By placing one or several loops of wire (i.e., *receiving coil*) around the patient, in a plane perpendicular to the transverse axis, the strength of the electronic current induced in the coil is proportional to the transverse magnetic field (Fig. 4.24).

Once the RF pulse is stopped, protons in the *xy*-plane dephase rapidly because of their molecular interactions (i.e., T2 relaxation). In the body, T2 relaxation is accelerated further by the fact that the magnetic field is not perfectly uniform in tissues. Indeed, the magnetic field is slightly stronger in some areas because of the presence of metallic objects, air, or calcium or because of the imperfections of the MR system, for example, 1.505 T for a 1.5 T magnet, and weaker in other parts, for example, 1.495 T.[12] Such inhomogeneities cause protons to rotate at different speeds once the RF pulse is stopped (i.e., some slower than the average and some faster), leading to very rapid dephasing. Thus, instead of decaying according to the specific T2-relaxation time of the tissue, the transverse magnetization decays at a more rapid rate, called *T2** (see Fig. 4.23).

Spin-echo sequences have been developed specifically to eliminate the effect of T2*, the effect caused by magnet inhomogeneities and tissue substances such as calcium. The rationale is simple: By adding a 180-degree RF pulse after the initial 90-degree pulse, protons start rotating effectively in the opposite direction. This effective change in direction allows slow protons, still affected by the same environment inhomogeneities, to become relocated "in front of" faster protons. Shortly thereafter, all protons become coherent again, exponentially increasing transverse magnetization, which peaks at a time called *time of echo* or *TE* (Fig. 4.25; see Fig. 4.23). TE then represents the time between this peak of echo and the initial 90-degree RF pulse. The time it takes for this sequence to be run one time is called the *time to repetition* or *TR* (see Fig. 4.25). For basic pulse sequences, one row of image data is acquired during each TR. Thus, the time required for acquisition of an MR image with a matrix of 256 by 256 pixels (i.e., voxels) takes 256 times TR. With such matrix, a T1-weighted spin-echo image (at 1.5 T) with a TR of 500 ms would take 128 seconds to acquire.

Tissue Contrast

The great diagnostic potential of MR imaging comes from the fact that tissue contrast can be manipulated to enhance anatomy and/or lesion conspicuity. Indeed, by adjusting TE and TR, differences in T1 and T2 relaxation characteristics among tissues can be detected in images (Fig. 4.26).[10,12,13]

Recall that the MR signal that is measured is at its maximum when the transverse magnetization of tissues is completely in phase. When transverse magnetization begins to dephase, the measured MR signal also begins to decrease and becomes null when the transverse magnetization is completely dephased. To detect T2 differences between tissues, time must be allowed for short-T2 tissues to decay enough so that long-T2 tissues are highlighted—that is, high signal at the time of the echo (i.e., at TE). Conversely, maximizing T1 differences requires that the time between subsequent 90-degree RF pulses (i.e., TR) is relatively shorter so that longitudinal recovery of tissues in the *z* direction of short and long T1 is separated. Finally, because T1 and T2 effects occur at the same time, optimizing one necessitates that the other one is inhibited. Hence, *T1-weighting* requires short TR (and short TE), and *T2-weighting* requires long TE (and long TR). If both T1 and T2 effects are inhibited by using long TR and short TE, signal intensities mainly depend on tissue PD, called *proton-density (PD) weighting*. These manipulations result in varying signal intensity (or pixel brightness) levels for the same tissue (Fig. 4.27). Although some tissues can appear similar in one given sequence, they can become quite distinct in another. MR imaging of a body part includes multiple sequences to highlight these tissue differences, but new sequences are developed every day to improve the capacity to identify even more subtle differences.

Magnetic Resonance Signal Localization

Now that the processes of tissue magnetization and echo detection have been discussed, one important feature of MR imaging relates to the ability to determine the precise anatomic location of the signals coming out of tissues. This process is performed by intermittently using three orthogonal linear magnetic gradients that generate short-term variations in

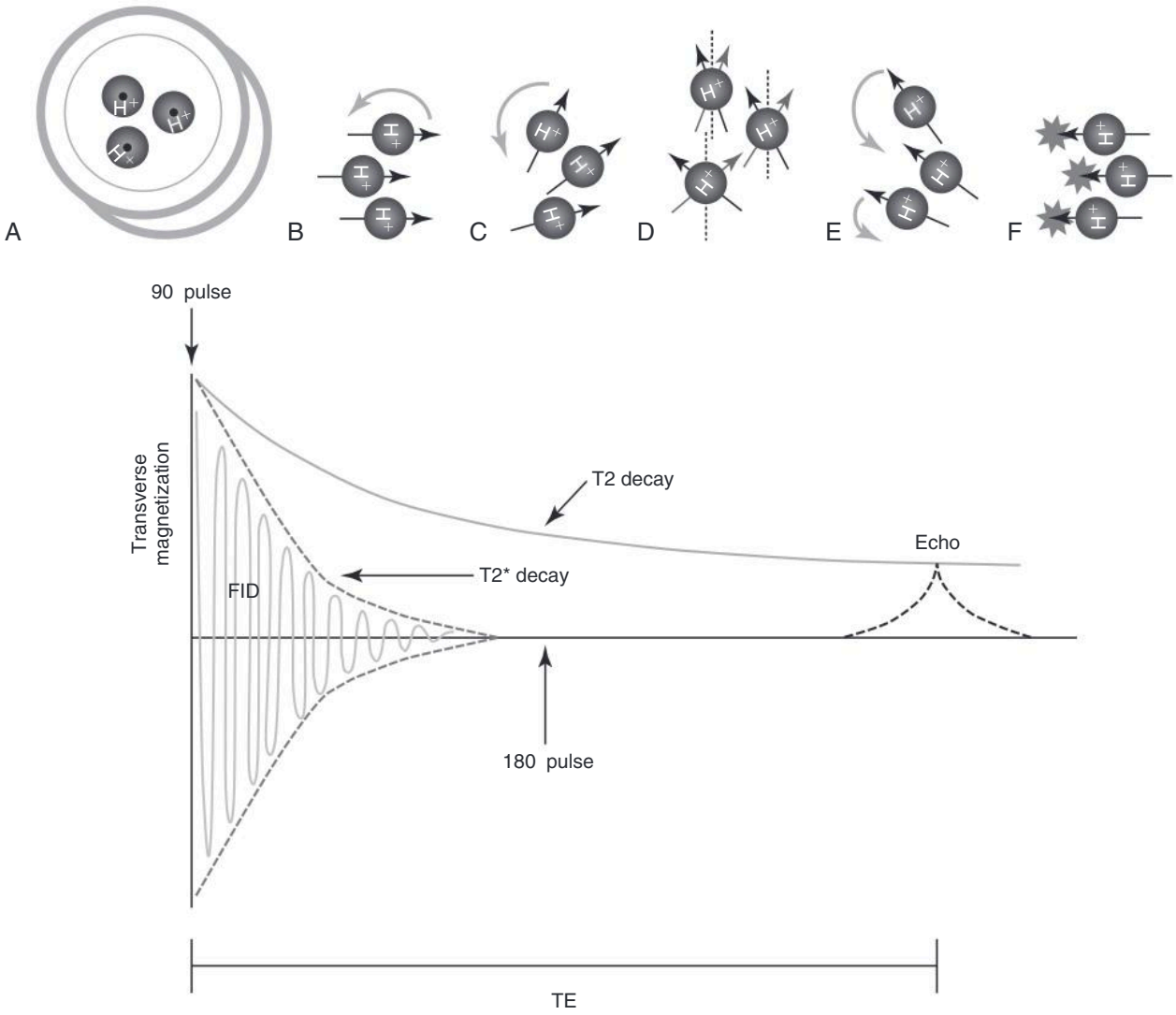


Fig. 4.23 T2 and T2*-relaxation. **A,** When placed in the magnetic resonance (MR) magnet (cylindrical in this case), protons align longitudinally along the axis of its magnetic field. **B,** The first step of a spin-echo sequence consists of a radiofrequency (RF) pulse that flips the magnetization moment of protons toward the transverse plane. This pulse is sometimes referred to as a 90-degree pulse. At this point, protons precess in coherence (i.e., synchronously), which causes strong transverse magnetization in the *xy*-axis. **C,** As soon as the RF pulse is terminated, protons start to dephase because of imperfections in the magnetic field, which is never completely uniform. These slight changes in field uniformity, or field strength, cause protons to precess either more rapidly or less rapidly. This results in rapid loss of transverse net magnetization—called T2* (T2-star) decay, or relaxation. **D,** To counteract the proton dephasing caused by the inhomogeneous magnetic field, another RF pulse is applied to flip back the protons 180 degrees. **E,** Spins rotating more rapidly are then behind slower spins, and as the protons regain coherence the transverse *xy* magnetization regrows (**F**), and ultimately peaks at a time called time *between excitation and echo (TE)*. The rate at which the protons diphase and then rephrase is called the T2-relaxation time, and the amount of signal present at the TE is also tissue dependent. *FID,* Free induction decay.

magnetic field strength across the patient, and therefore the Larmor frequencies of protons.[13] These gradients are produced by additional coiled wires placed in the bore of the magnet, linked to electronic circuitry that is adjusted constantly and precisely through additional *pulses* in the imaging sequence. These gradients are responsible for the tapping or clicking sounds heard during scanning, and the gradient strength influences the anatomic details (i.e., spatial resolution) that can be achieved as well as the speed of image acquisition.

Selection of Spin-Echo Sequences

Several types of spin-echo sequences are available, some used more consistently and others used in more specific circumstances (Fig. 4.28). T1-weighted and T2-weighted sequences are acquired in most patients. In both sequences, multiple 180-degree rephasing pulses are usually applied after the single 90-degree RF pulse during the same TR. This allows more signals to be localized during each TR and speeds up the acquisition process.[12] Spin-echo sequences with more than one 180-degree rephrasing pulse are called *fast spin-echo* or *turbo spin-echo* sequences.

Inversion recovery sequences are used to null the signal from specific tissues or substances, which can help confirm the presence of such components, or improve the conspicuity of nearby tissues with similar signal characteristics. A short inversion time recovery (STIR) sequence is commonly used to

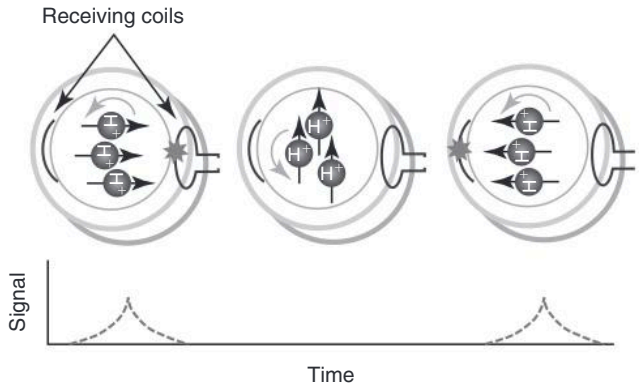


Fig. 4.24 Signal reception. When protons are flipped 90 degrees and precess in phase, they generate a strong transverse magnetization vector, which in turn induces an electric current in loops of wire placed perpendicularly around the body part being imaged. Signals peak when the transverse magnetization vector from the spinning protons is fully perpendicular to each of the wire loop coils and the signal in the coil decreases when the magnetic vector rotates away. Using more loops around the patient increases signal intensity.

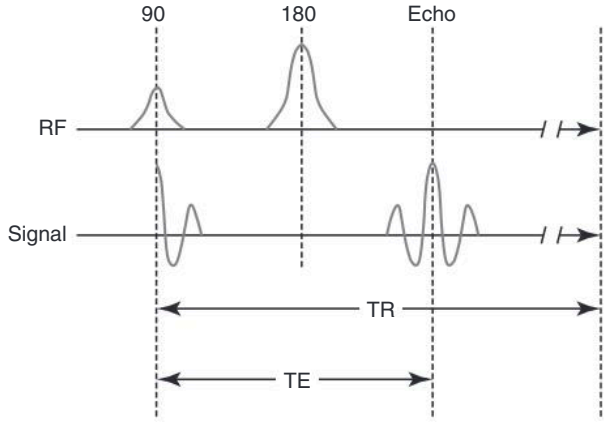


Fig. 4.25 Configuration of a standard spin-echo pulse sequence. Radiofrequency (*RF*) pulses consist of an initial 90-degree pulse followed by a 180-degree pulse. Signals associated with magnetized tissues echo exactly at a time twice that of the 180-degree pulse. The time it takes for this sequence to be run one time is called the *time to repetition (TR). TE,* Time of echo.

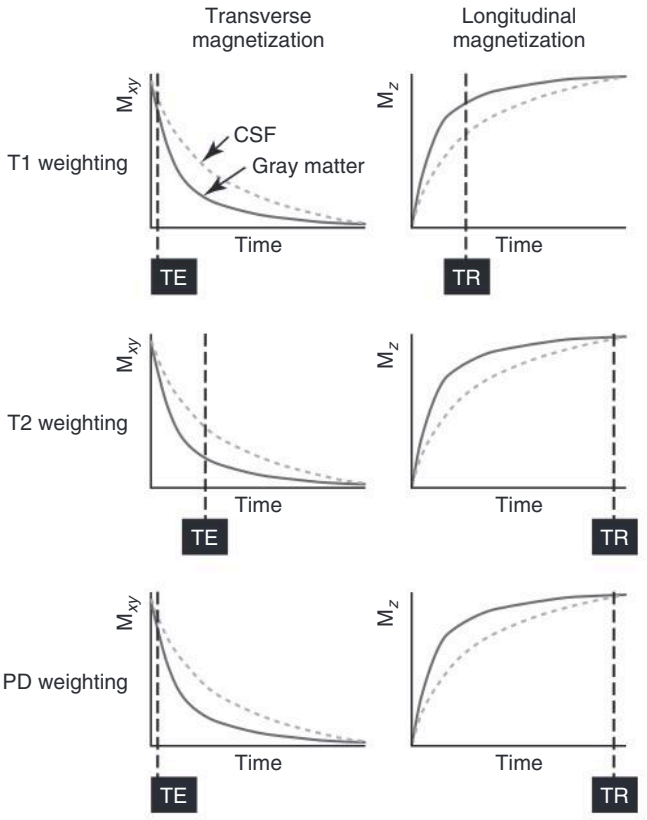


Fig. 4.26 Impact of time of echo (*TE*) and time to repetition (*TR*) on tissue contrast. By adjusting TE and TR, differences in T1- and T2-relaxation characteristics among tissues can be highlighted. By using short TE and short TR, signal echoes from cerebrospinal fluid *(CSF)* and gray matter mainly depend on differences in time for magnetization to regrow in the *z* direction, or longitudinal magnetization (T1 relaxation), as differences in transverse magnetization (T2 relaxation) of CSF and gray matter are negligible. This type of sequence is said to be T1-weighted. If, however, differences in T2 need to be highlighted and differences in T1 inhibited—i.e., T2-weighting—both TE and TR must be prolonged. Finally, using short TE and long TR inhibits both T1 and T2 effects. In that case, T1 and T2 contrast is reduced between CSF and gray matter, and signal intensity is predominantly associated with the density of protons in these tissues. These images have proton-density (*PD*) weighting.

suppress the signal from fat, and because this sequence has T2-weighting, it increases the conspicuity of soft tissue lesions, most of which have prolonged T2 (Fig. 4.29). Unlike chemical fat-signal suppression (discussed later), STIR sequences are not affected by magnetic-field inhomogeneities and therefore result in more uniform fat suppression.[10,11]

Inversion recovery can also be used to null the signal of fluids, such as cerebrospinal fluid (CSF). Such a fluid-attenuated inversion recovery (FLAIR) sequence helps differentiate brain parenchymal lesions from CSF (Fig. 4.30; see Fig. 4.28).[14] For example, a region of increased signal adjacent to a lateral ventricle may not be seen in the T2-weighted spin-echo sequence because of the similar signal characteristics of CSF and tissue water. However, in the FLAIR image, the periventricular lesion may be much more conspicuous because the signal from the free fluid in the ventricle has been nulled (see Fig. 4.30). The FLAIR sequence also aids in confirming a cystic component and the nature of the fluid present. FLAIR sequences are typically used for the brain and can be T2-weighted or T1-weighted and then referred as T2-FLAIR and T1-FLAIR, respectively.[15]

Gradient Recalled Sequences

As opposed to spin-echo sequences, gradient echo sequences use smaller flip angles[†] (i.e., <90 degrees) to start and the 180-degree refocusing RF pulse is not used. Instead, gradients are used to diphase (negative gradient) and rephase (positive gradient) transverse magnetization to generate echoes from tissues. Gradient echo sequences use a shorter TR along with smaller flip angles (i.e., shorter RF pulses), allowing rapid studies with reduced motion artifact, which can be convenient for procedures such as angiography. Gradient echo sequences are also used typically for initial anatomic orientation at the beginning of an examination, so called localizer images.

Although changing the orientation of the gradient allows spinning protons to rephase, field inhomogeneities are not compensated for. Thus, gradient echo sequences with long TEs are T2*-weighted rather than T2-weighted, such as in spin-echo sequences. This also means that gradient echo sequences are more sensitive to magnetic-field inhomogeneity secondary to magnetic susceptibility differences between tissues. Magnetic susceptibility is the property that describes the degree to which

[†]Remember, the flip angle quantifies the amount of deviation of the resting net magnetic vector from the *z*-axis by the first RF pulse.

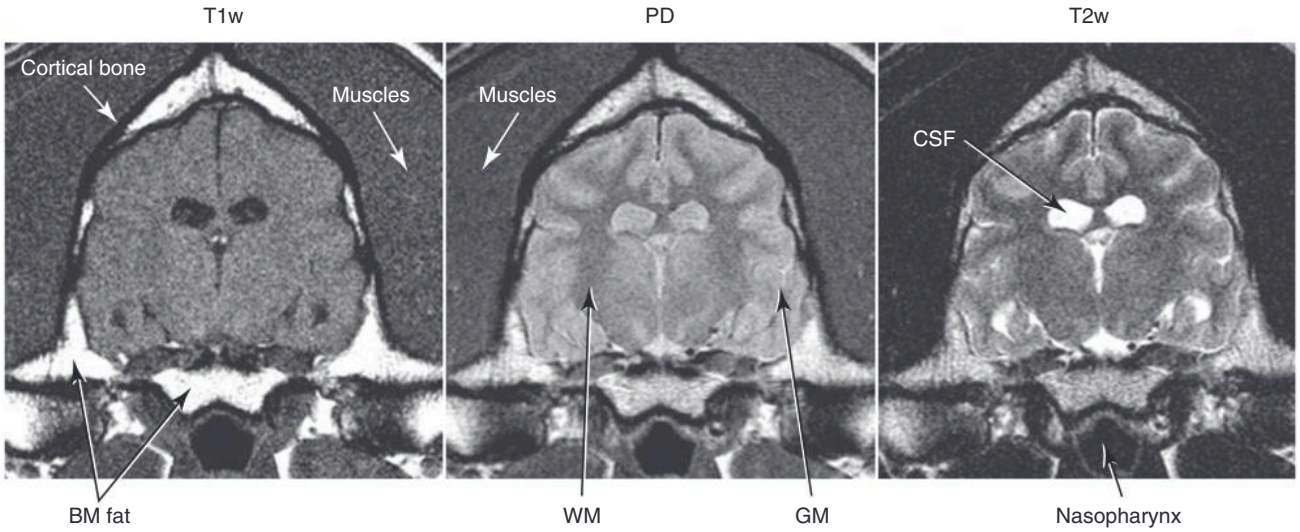


Fig. 4.27 Tissues are associated with variable signal intensity according to the type of weighting. Indeed, cerebrospinal fluid (*CSF*) appears hypointense (dark) in T1-weighting (*T1W*), moderately intense (midgray) in proton-density (*PD*) weighting, and hyperintense (bright) in T2-weighting (*T2W*). Other soft tissue structures also vary in signal intensity between sequences. Normal cortical bone and air are not magnetized enough to generate a signal on any sequence. *BM,* Bone marrow; *GM,* gray matter; *WM,* white matter.

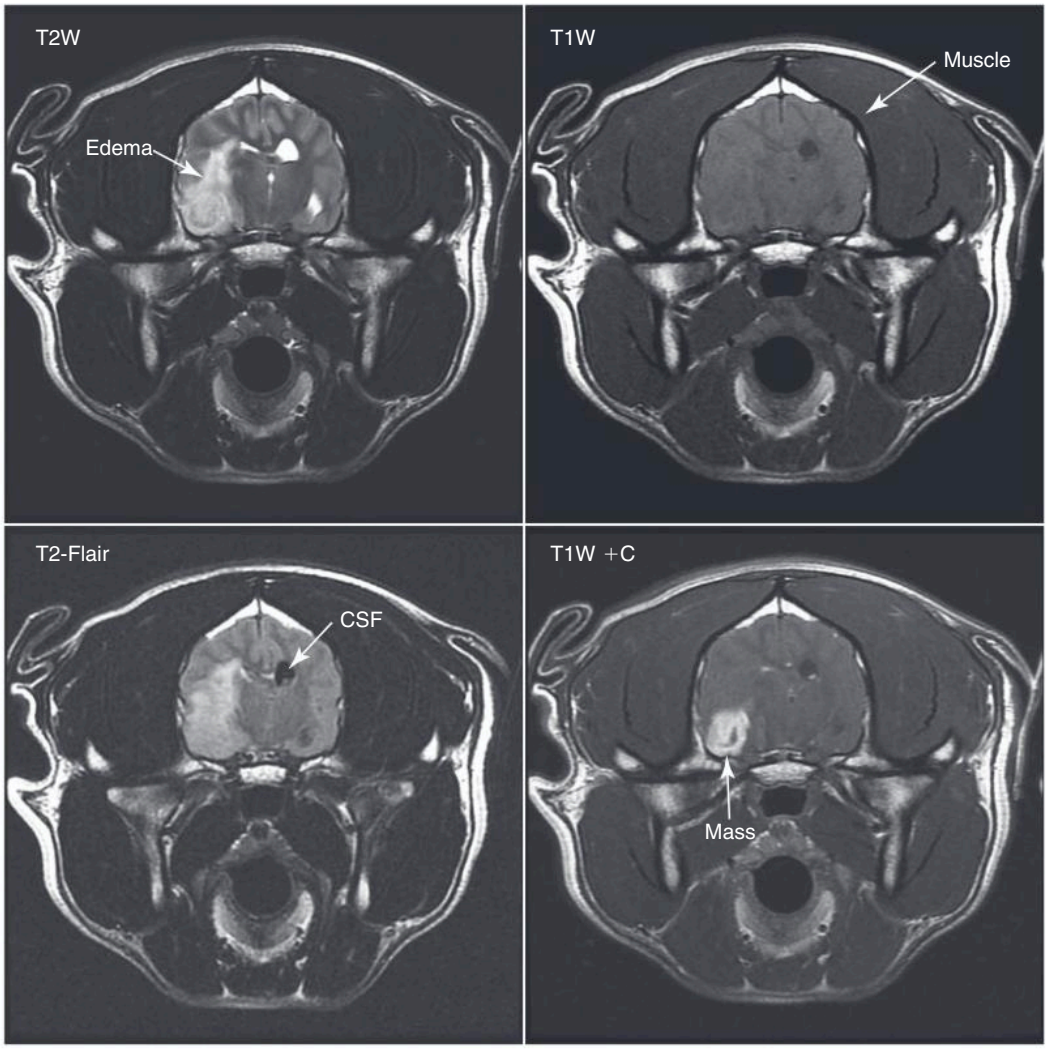


Fig. 4.28 Meningioma in the piriform lobe of a dog. In T2-weighted (*T2W*) images, the mass is hyperintense and also confluent with hyperintense regional vasogenic edema, whereas both the tumor and edema are isointense to the rest of the brain in precontrast T1-weighted (*T1W*) images. Following contrast-medium (gadolinium) injection (*T1W+C*), the mass enhances becoming very hyperintense, except for a central fusiform hypointense area. In a T2W fluid-attenuated inversion recovery (*T2-FLAIR*) sequence (designed to decrease signal coming from pure fluid), the signal from the pure cerebrospinal fluid (*CSF*) is attenuated.

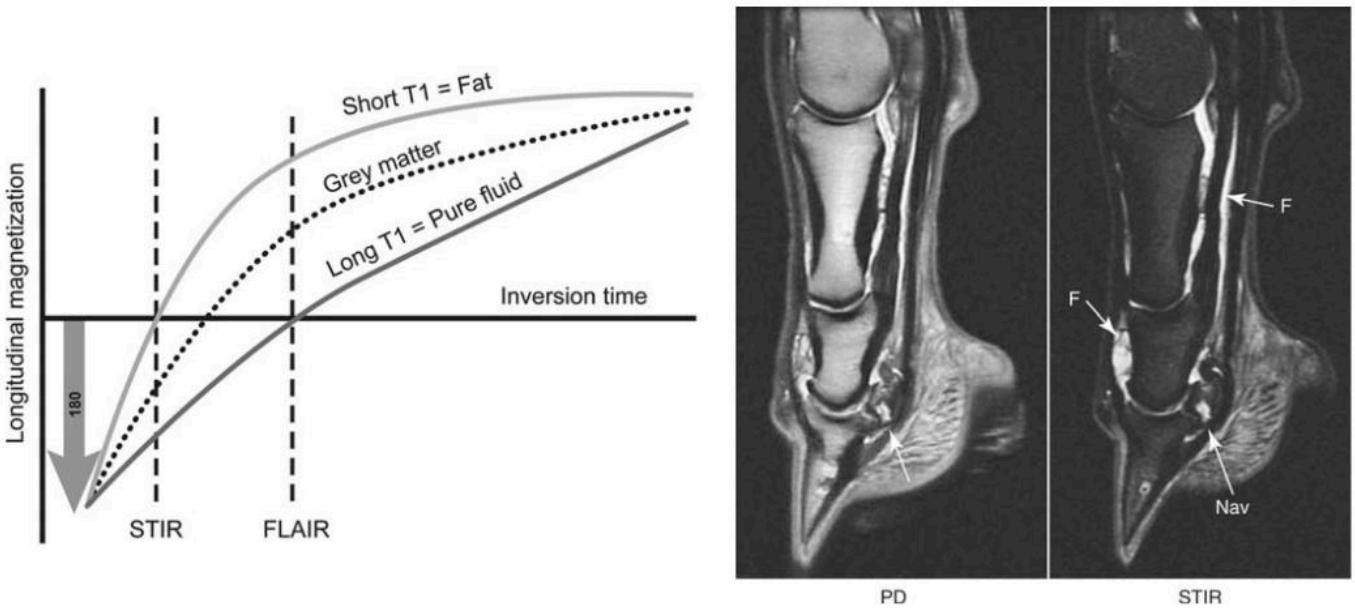


Fig. 4.29 Inversion recovery sequences are used to null the signal from fluids or fat and therefore improve the conspicuity of nearby tissues of similar signal characteristics. This graph illustrates the differences in longitudinal magnetization (T1) recovery rate after a 180-degree pulse is produced, before a regular spin-echo sequence is initiated. The time between the 180-degree pulse and the beginning of the spin-echo sequence is called the inversion time. Fat has very rapid T1-relaxation; therefore, with a short inversion time, the magnetization vector from fat will be in the *xy*-plane and no signal will be recorded in the spin-echo sequence. Sequences with a short inversion time are called *short tau inversion recovery*, or *STIR* sequences. Images on the *right* demonstrate the clinical application of a STIR sequence. By suppressing the signal of fat in the bone marrow, the fluid-filled navicular cyst (*arrow*) becomes more apparent than in the proton-density (*PD*) sequence. Other fluid-filled structures such as synovial fluid (*F*) are also better delineated than on the PD sequence. Because free fluid has a longer T1-relaxation time, the use of a longer inversion time will result in the magnification vector from fluid being in the *xy*-plane and if the spin-echo sequence is initiated now there will be no signal measured from free fluid. Sequences with a longer inversion time are called fluid-attenuated inversion recovery (FLAIR) sequences. FLAIR sequences are mainly used for brain imaging, allowing parenchymal lesions to be better distinguished from normal cerebrospinal fluid (CSF) by eliminating the signal from CSF. See Figs. 4.28 and 4.30.

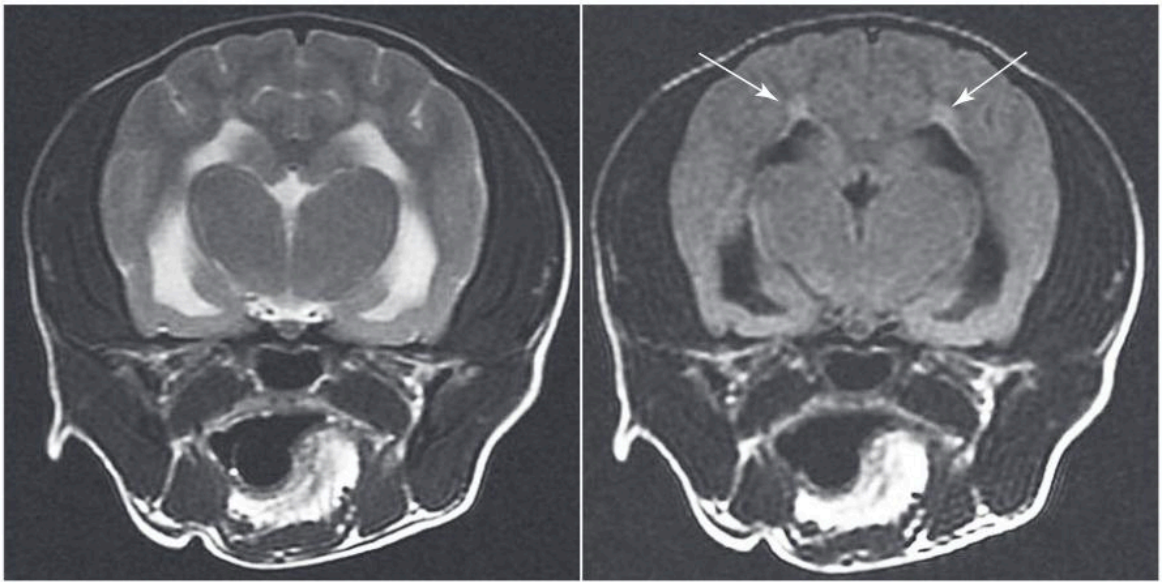


Fig. 4.30 A T2-weighted fluid-attenuated inversion recovery (*T2-FLAIR*) sequence can allow periventricular hyperintensities (*arrows*) to be depicted better than with regular spin-echo T2-weighting (*T2W*) by eliminating the signal from cerebrospinal fluid (CSF). Here, periventricular edema is more evident on T2-FLAIR in this dog with necrotizing encephalitis.

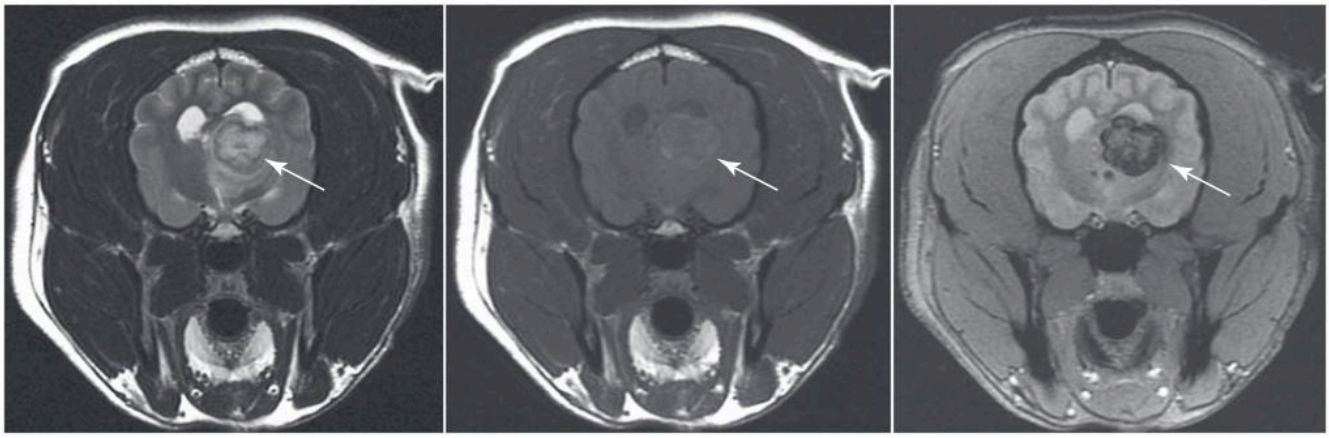


Fig. 4.31 T2* gradient echo (*GRE*) sequences are sensitive to magnetic susceptibility. In this dog with spontaneous brain hemorrhage, the mass lesion (*arrow*) with annular signal void on T2*-GRE in the thalamus corresponds with a susceptibility artifact. The peripheral portion of this lesion appears hyperintense on precontrast T1-weighted fast spin-echo (*T1W-FSE*) and hypointense on T2-weighted FSE (*T2W-FSE*), further confirming the presence of subacute hemorrhage.

these tissues are magnetized when exposed to a magnetic field.[16] Substances can increase (paramagnetic, ferromagnetic) or decrease (diamagnetic) local magnetic field strength and thus exert an effect on nearby spinning protons. Tissues with protons affected by local field inhomogeneity dephase more rapidly, causing signal loss and/or signal misregistration. This phenomenon is even more evident when using a high-field magnet and long TE (e.g., T2*-weighted gradient echo sequence). This concept is exploited for the detection of hemorrhage. Indeed, the iron contained in the hemoglobin increases the local magnetic field substantially, leading to local signal loss and misregistration.[12] T2*-weighted sequences are thus sensitive for detecting hemorrhage (Fig. 4.31).

Several other gradient echo sequences exist, some with more specific application. For example, a spoiled gradient recalled (SPGR) echo sequence highlights articular cartilage (eFig. 4.4),[17] whereas steady state free precession techniques can help depict cranial nerves.[18] It must be pointed out that gradient sequences have specific names that vary among MR imaging system vendors, which can lead to some confusion.[12,19]

Contrast Media

As with CT, contrast media can be injected intravenously for MR imaging to assess the vascular network and tissue perfusion, helping to better detect and characterize pathologic tissues. As opposed to iodinated contrast medium used in CT that increases x-ray attenuation, contrast media commonly used in MR imaging are not meant to be directly visible. Rather, they exert a strong paramagnetic effect that decreases the T2- and T1-relaxation time of protons in vicinity of the contrast medium molecule. Gadolinium-based agents chelated to protective ligands are typically used. At low concentration, such as used in clinical practice, the predominant effect is a shortening of the T1-relaxation time.[10] Thus, tissues accumulating this substance generate greater signal—*contrast-enhance*—on a T1-weighted pulse sequence (Fig. 4.32; see Fig. 4.28). At high gadolinium concentration, T2 shortening may result in a significant decrease in signal intensity noticeable on both T1- and T2-weighted images. This effect can be observed in the bladder as a triple-layer intensity pattern, or pseudolayering.[20]

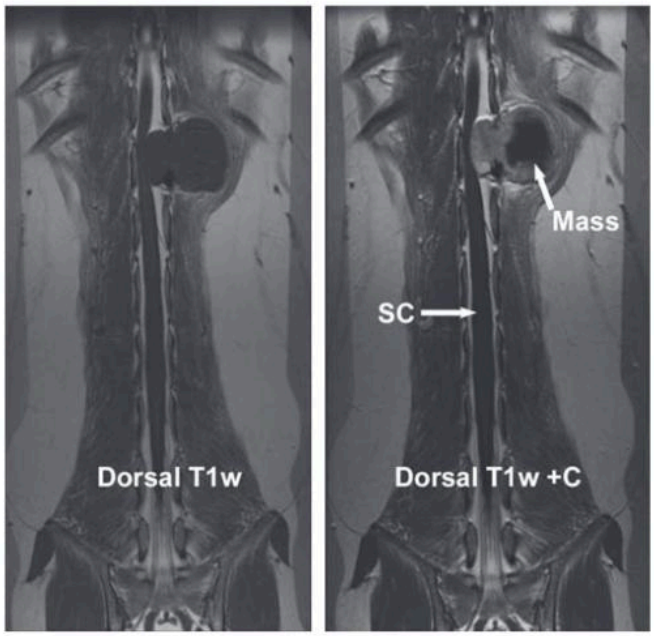
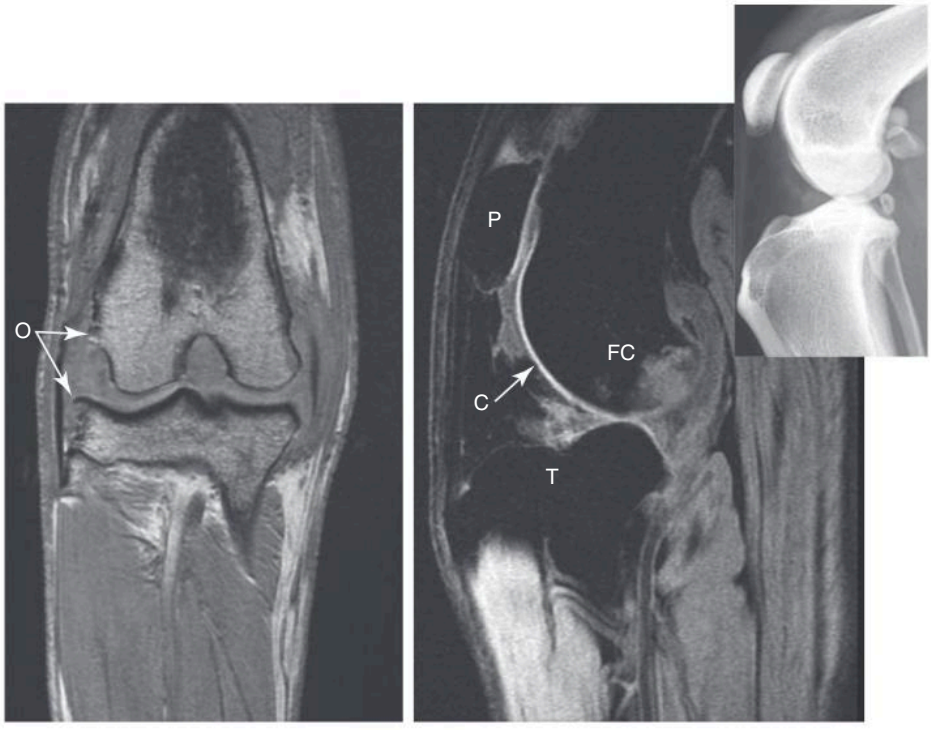


Fig. 4.32 As for computed tomography (CT) imaging, the addition of contrast medium in magnetic resonance (MR) imaging (e.g., gadolinium) increases the contrast resolution of this modality. In this ataxic dog, a large mass is seen in dorsal T1-weighted (*T1W*) images to the *left* of the spine, markedly compressing the spinal cord (*SC*). The periphery of this mass enhances intensity after gadolinium injection (+*C*), as opposed to its central part. An undifferentiated sarcoma with a large cavitary component was diagnosed.

Fat Saturation Sequences

The high signal intensity of adipose tissue on several sequences can limit the visibility of nearby tissues or substances with prolonged T2 relaxation (on T2-weighted sequences) or short T1 relaxation (on T1-weighted sequences). As seen previously, a STIR inversion recovery sequence can be used to attenuate fat signal intensity. Alternatively, fat can be selectively attenuated by exploiting the inherent difference of precessional frequency,



eFig. 4.4 Although spin-echo sequences are predominantly used in magnetic resonance (MR) imaging, gradient echo (*GRE*) sequences are also useful. Osteophytes (*O*) are well demarcated in this dorsal T1-weighted GRE image. In the sagittal spoiled gradient recalled echo sequence acquired with fat saturation (*SPGR + FS*), the articular cartilage (*C*) is well depicted. Joint effusion is also present cranial to the cartilage in this dog with ruptured cranial cruciate ligament and osteoarthritis. *FC,* Femoral condyle; *P,* patella; *T,* tibia.

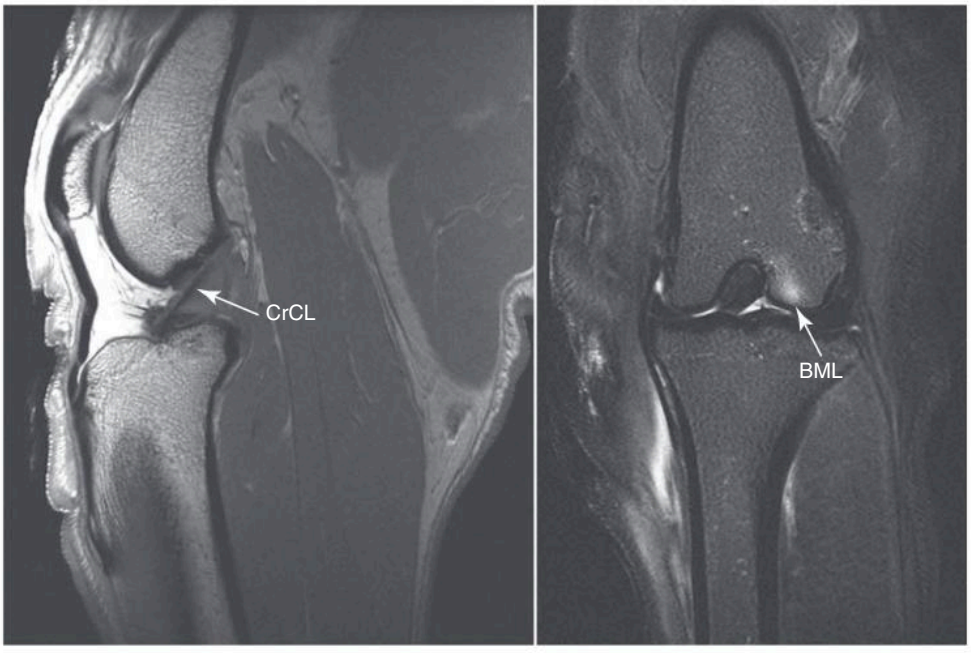


Fig. 4.33 Like short TI inversion recovery (STIR) sequences, chemical fat saturation (*FS*) used with T2-weighting (*T2W*) increases the conspicuity of lesions with prolonged T2 relaxation. A hyperintense bone marrow lesion (*BML*) is identified in the fat suppressed sequence in the lateral femoral condyle of this dog with intact cranial cruciate ligament (*CrCL*). *PD,* Proton density.

or *chemical shift*, that exists between fat and water protons. The magnitude of this difference is 220 Hz at a field strength of 1.5 T. The difference in precessional frequency becomes smaller at lower field strengths; therefore, chemical fat suppression is limited to field strengths of 1.0 Tesla or greater.

As opposed to the 90-degree and 180-degree pulses that have a frequency range large enough to excite both water and lipid protons, *chemical fat saturation* uses a frequency-specific preparation pulse to selectively excite lipid protons, followed by a spoiling gradient pulse that dephases the fat signal. Once the initial fat-specific pulse is produced, the signal generated by the subsequent pulse sequence (spin echo or gradient echo) arises only from nonfatty tissues. If a T2-weighted sequence is employed, tissues with prolonged T2, typically pathologic tissues, become more conspicuous (Fig. 4.33). In combination with gadolinium injection, fat-suppressed T1-weighted sequences maximize the visibility of contrast-enhancing lesions. This can be beneficial for detecting lesions embedded in fat, such as within the epidural or retro-orbital spaces, and in bone marrow, for example.[21] Spinal lesions and abnormal nerves are better recognized (eFig. 4.5).

Other Magnetic Resonance Sequences

Several other imaging sequences can provide important information on the characteristics of tissues. As for chemical fat saturation pulses, most of these sequences are only available with high-field units (>1.0 T).

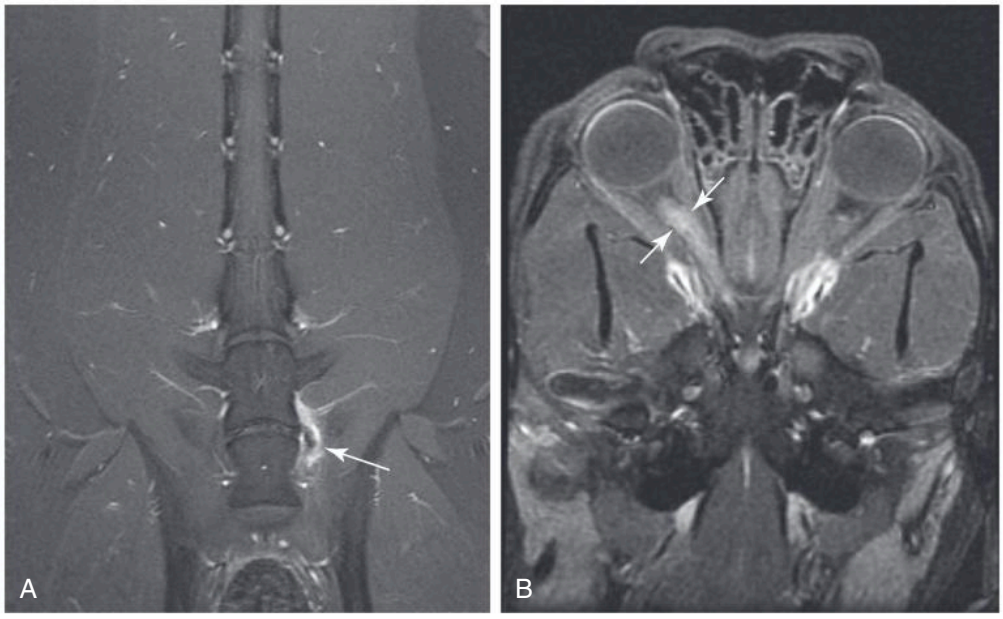
Diffusion-weighted imaging is very sensitive to cytotoxic edema in the early hours of ischemia. Tissue contrast on diffusion-weighted imaging reflects Brownian motion or microscopic movement of water, which is restricted in ischemic tissue.[22] Such technique helps in discriminating early stroke events from structural lesions, such as neoplasia, which can be difficult to differentiate on conventional sequences (Fig. 4.34). *Perfusion-weighted* imaging is another technique that can support a diagnosis of brain infarct.[22] It uses a particular T2*-weighted pulse sequence following a bolus injection of contrast medium such as gadolinium. Images are obtained during the first pass of contrast medium through the capillary beds, which results in susceptibility-induced signal loss that resolves over time. Relative blood flow can then be semiquantified.

Image Quality and Imaging Time

The challenge of imaging animals under anesthesia is to balance image quality and acquisition time. That is, to achieve the most diagnostic examination as quickly as possible. Several parameters are interconnected, making this balance very complex.[23] As discussed earlier, *spatial resolution* dictates the amount of image detail, which influences the ability to clearly see and distinguish anatomic and pathologic structures. Spatial resolution is determined by adjusting slice thickness (voxel depth), field of view (FOV), and matrix size (number of voxels). The height and width of each voxel is determined by the number of rows and columns in the matrix, respectively, divided by the image FOV. The smaller the voxels are, the better the spatial resolution. Conversely, image quality also greatly depends on the amount of signal arising from protons forming each voxel, often described as the signal-to-noise ratio (SNR) of an image. High spatial resolution images, those with small voxels, are then subject to poor SNR. Although it can be tempting to reduce slice thickness or increase matrix size to improve tissue definition, image quality can suffer greatly. SNR can be improved by averaging signal from sequential excitations, which unfortunately increases acquisition time. Technical improvements in software and hardware (high-field magnets, stronger gradients, more sensitive receiving coils, parallel imaging, etc.) have allowed an increase in SNR and spatial resolution at the same time, which is beneficial in small patients (Fig. 4.35).[15,24]

MR Image Artifacts

As with any modality, artifacts can degrade image quality or lead to misdiagnosis. Acknowledgment and comprehension of these artifacts are essential for interpreters.



eFig. 4.5 Contrast enhancement in T1-weighted images is more conspicuous when surrounding fat tissue signal is suppressed. **A,** Dorsal image of the lumbar spine of a dog with left pelvic lameness on which a contrast-enhancing tissue reaction is seen around a hypointense lateralized disc extrusion (*arrow*). **B,** Dorsal image of the head of another dog with optic neuritis (*between arrows*).

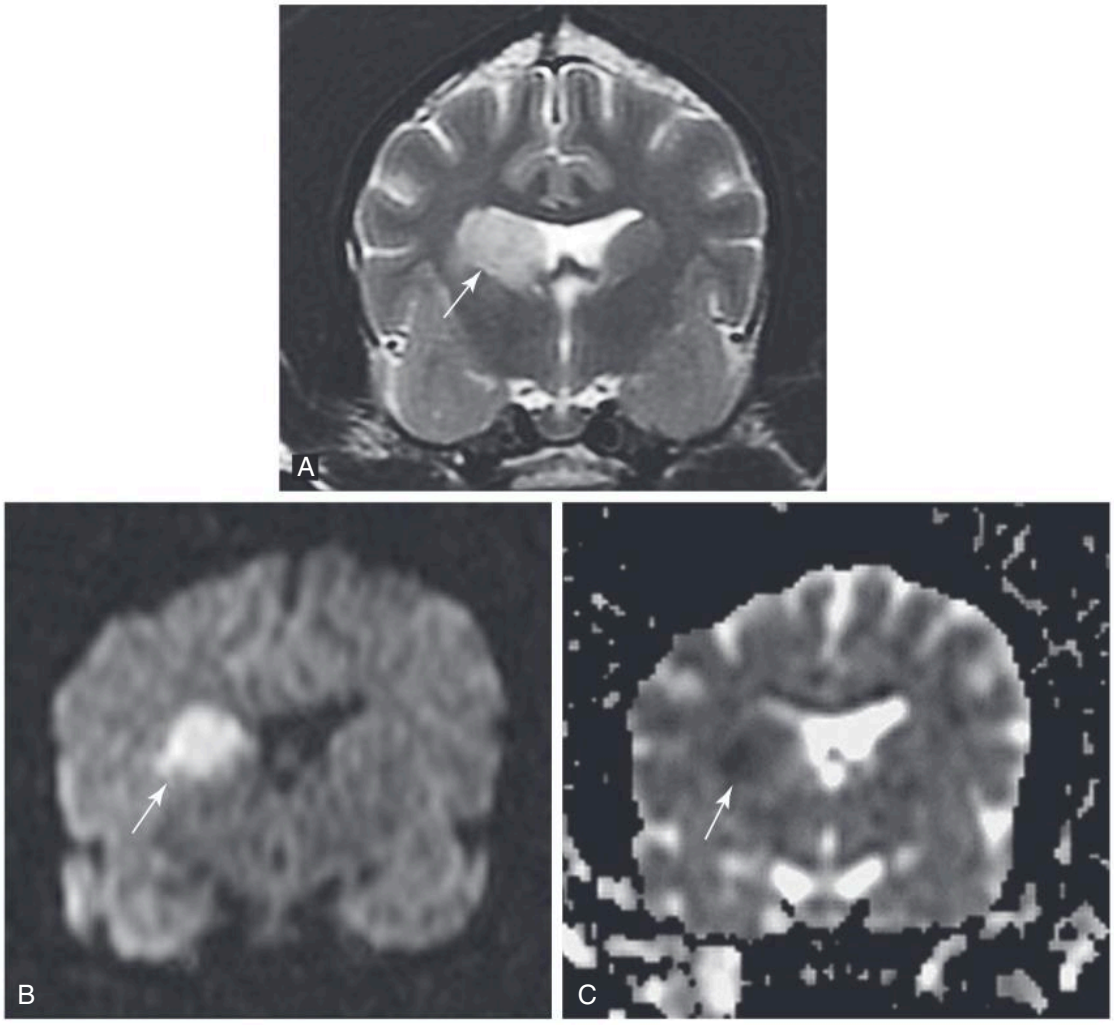
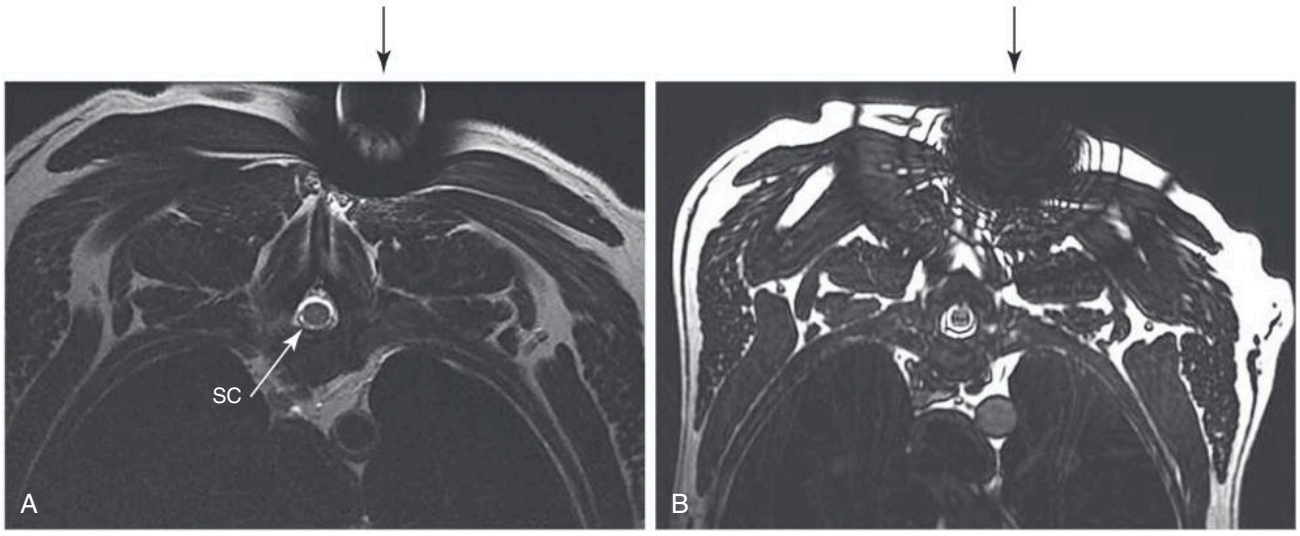


Fig. 4.34 Diffusion-weighted imaging (DWI) is used to confirm early ischemic stroke (*arrow*). The right caudate nucleus is enlarged and hyperintense in transverse T2-weighted fast spin-echo (**A**) and in a diffusion-weighted image (**B**). **C,** In an image of the apparent diffusion coefficient (ADC) the lesion becomes hypointense, indicating restricted water diffusion.

Besides those that can be controlled to a certain degree (e.g., ghosting and aliasing artifacts),[25] artifacts are often related to magnetic susceptibility and are predominant with gradient echo sequences, as discussed previously. Magnetic susceptibility artifacts occur because of local magnetic field inhomogeneity. Structures that substantially affect this homogeneity, such as metallic objects, whether ferrous or not, have strong magnetic susceptibility effects that lead to field distortion.[26] These artifacts appear as geometric image distortion with progressive or abrupt signal void and sharply defined hyperintense boundaries (Fig. 4.36). In veterinary practice, microchips (eFig. 4.6) and orthopedic devices are most often the source of these artifacts, hampering assessment of nearby structures. It may also occur when microscopic metal fragments are left in place when some devices are used during surgery (e.g., drill bits).[16] Other ballistic or gastrointestinal foreign bodies may cause magnetic susceptibility artifacts that can limit the use of MR imaging in these patients significantly, particularly if these objects are ferromagnetic and can therefore migrate because of magnetic attraction. Magnetic susceptibility can also occur at soft tissue/air interfaces. This is typically observed on T2* transverse images obtained at the junction of the frontal sinuses and rostral brain.[26] The magic angle effect is another important MR artifact that can alter the signal intensity of tendons and ligaments in both low- and high-field MR units, mainly described in the distal equine limb.[27] This artifact appears when tendons or ligaments are positioned at specific angles in the magnetic field.

Impact of Magnetic Field Strength

Although high-field (>1.0 T) MR systems are associated with superior SNR and spatial resolution, and offer more advanced imaging protocols, low-field (0.2–0.4 T) units are installed in many veterinary practices, mainly because of lower purchase and maintenance costs.[19] Units can be dedicated veterinary units or produced originally for human use. The limited SNR with these low-field systems is associated with longer scan times and reduced spatial resolution. Also, FOV is generally reduced, which may necessitate moving the patient in the magnet for complete anatomic coverage. Low-field MR imaging is, however, associated with reduced susceptibility artifact, and its open design allows easy access to patients. Also, because of the lower magnetic field strength, accidents associated with the attraction or migration of ferromagnetic objects, located outside or inside the patient, can be prevented more easily. Extremities of horses can also be imaged while the animal is standing using dedicated MR units, which is beneficial.



eFig. 4.6 Identification microchips, which are typically placed in the dorsal subcutaneous fat of the neck in dogs, cause magnetic field distortion and signal voids. The appearance of the susceptibility artifact (*arrow*) varies between sequences. Rings of varying intensity are present in the transverse fast spin-echo T2-weighted image **(A),** whereas several concentric hypointense rings are present in the FIESTA (fast imaging employing steady state acquisition) sequence **(B).** Depending on the magnitude of the artifacts and the size of the neck, the interpretation of a spinal cord (*SC*) abnormality may be hampered

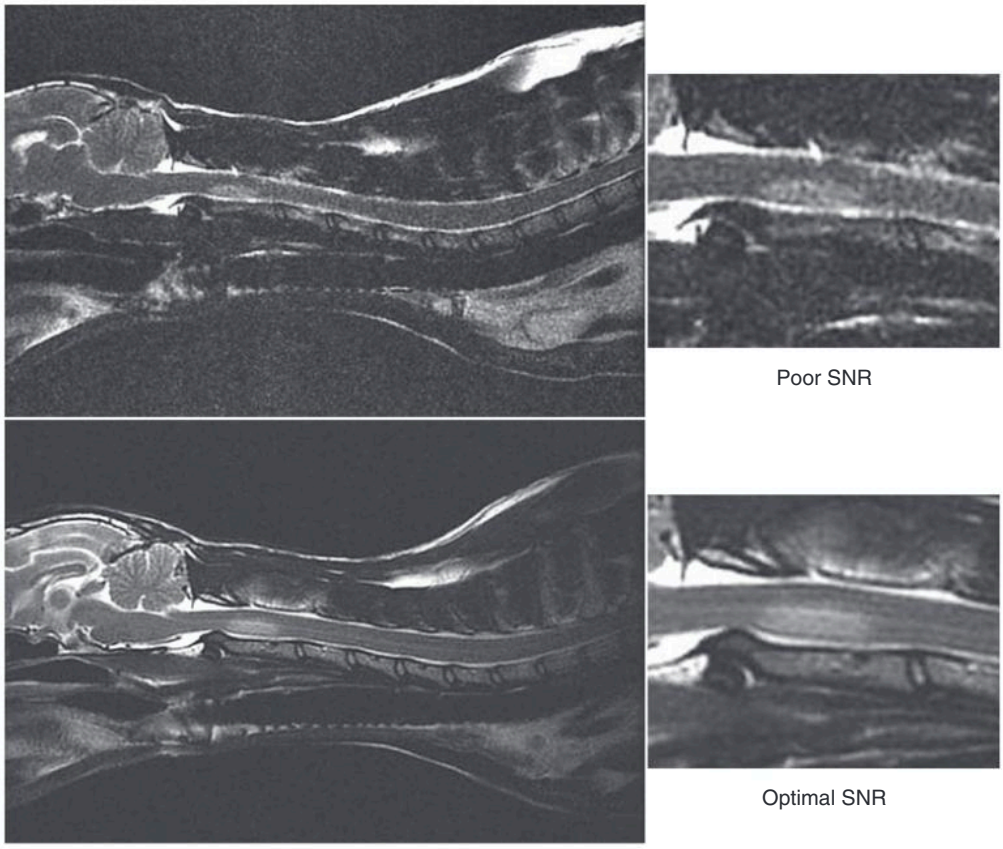


Fig. 4.35 Several factors can influence signal-to-noise (*SNR*) ratio in magnetic resonance (MR) imaging. In this dog, optimal SNR of the cervical spine was obtained after replacing the receiving coil with a more sensitive one (*bottom images*). The initial image with poor SNR is grainier. The ventral spinal cord hyperintensity is better delineated in the bottom image.

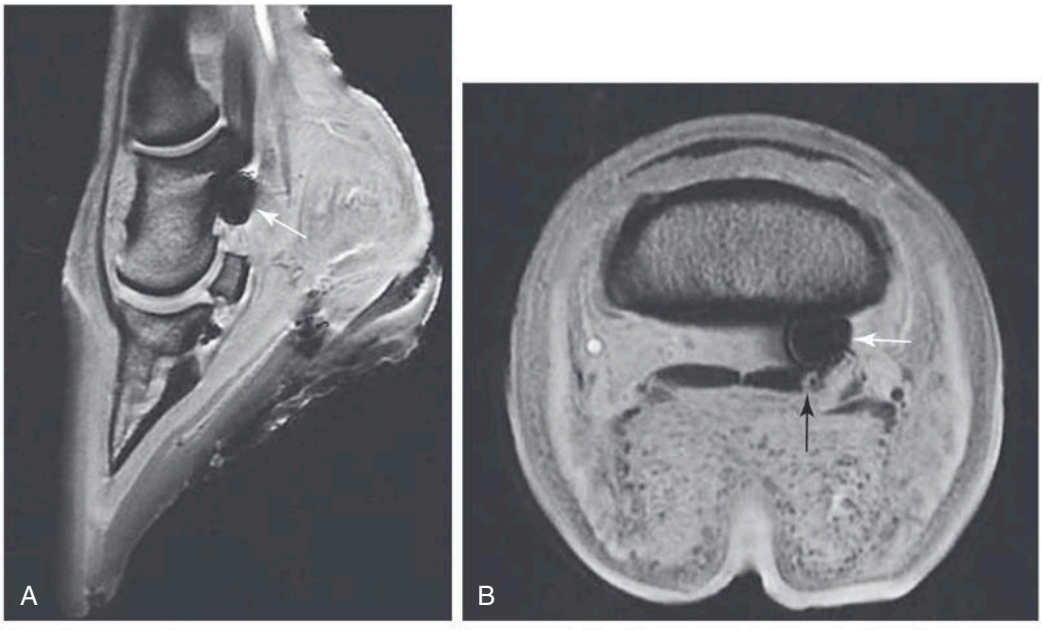


Fig. 4.36 Susceptibility artifact in gradient recalled echo (GRE) sequences. In this equine foot imaged with T1-weighted GRE sequences in sagittal (**A**) and transverse (**B**) planes, there is a sharply demarcated round signal void (*white arrow*), which was the result of a microscopic metallic fragment left in place after a street nail was removed. Note also the damage to the medial lobe of the deep digital flexor tendon (*black arrow*).

REFERENCES

1. Euclid Seeram E. Computed tomography: an overview. In: Euclid Seeram E, ed. *Computed Tomography: Physical Principles, Clinical Applications, and Quality Control*. 4th ed. Burnaby: Elsevier Canada; 2015:1–30.
2. Bushberg J, Seibert J, Leidholdt Jr E, et al. Computed tomography. In: Bushberg J, Seibert J, Leidholdt Jr E, et al., eds. *The Essential Physics of Medical Imaging*. 3rd ed. Philadelphia: Lippincott Williams & Wilkins; 2011:312–374.
3. Bushberg J, Seibert J, Leidholdt Jr E, et al. Introduction to medical imaging. In: Bushberg J, Seibert J, Leidholdt Jr E, et al., eds. *The Essential Physics of Medical Imaging*. 3rd ed. Philadelphia: Lippincott Williams & Wilkins; 2011:3–17.
4. Saunders J, Ohlerth S. CT physics and instrumentation. In: Schwarz T, Saunders J, eds. *Veterinary Computed Tomography*. 1st ed. Oxford: Wiley-Blackwell; 2011.
5. Euclid Seeram E. Physical principles of CT. In: Euclid Seeram E, ed. *Computed Tomography: Physical Principles, Clinical Applications, and Quality Control*. 4th ed. Burnaby: Elsevier Canada; 2015:60.
6. Pollard R, Puchalski S. CT contrast media and applications. In: Schwarz T, Saunders J, eds. *Veterinary Computed Tomography*. 1st ed. Oxford: Wiley-Blackwell; 2011.
7. Miles KA. Tumour angiogenesis and its relation to contrast enhancement on computed tomography: a review. *Eur J Radiol*. 1999;30:198–205.
8. Alexander K, Dunn M, Carmel EN, et al. Clinical application of Patlak plot CT-GFR in animals with upper urinary tract disease. *Vet Radiol Ultrasound*. 2010;51:421–427.
9. Soukup JW, Drees R, Koenig LJ, et al. Comparison of the diagnostic image quality of the canine maxillary dentoalveolar structures obtained by cone beam computed tomography and 64-multidetector row computed tomography. *J Vet Dent*. 2015;32:80–86.
10. McRobbie DW, Moore EA, Graves MJ, et al. In: *MRI from Pictures to Protons*. ed 1. Cambridge: Cambridge University Press; 2003.
11. Mitchell DG, Cohen MS. In: *MRI Principles*. 2nd ed. Philadelphia: Saunders; 2004.
12. Bitar R, Leung G, Perng R, et al. MR pulse sequences: what every radiologist wants to know but is afraid to ask. *Radiographics*. 2006;26:513–537.
13. Balter S. An introduction to the physics of magnetic resonance imaging. *Radiographics*. 1987;7:371–383.
14. Benigni L, Lamb CR. Comparison of fluid-attenuated inversion recovery and T2-weighted magnetic resonance images in dogs and cats with suspected brain disease. *Vet Radiol Ultrasound*. 2005;46:287–292.
15. Robertson ID. Optimal magnetic resonance imaging of the brain. *Vet Radiol Ultrasound*. 2011;52:S15–S22.
16. Freer SR, Scrivani PV. Postoperative susceptibility artifact during magnetic resonance imaging of the vertebral column in two dogs and a cat. *Vet Radiol Ultrasound*. 2008;49:30–34.
17. Olive J, d'Anjou MA, Girard C, et al. Fat-suppressed spoiled gradient-recalled imaging of equine metacarpophalangeal articular cartilage. *Vet Radiol Ultrasound*. 2010;51:107–115.
18. Parry AT, Volk HA. Imaging the cranial nerves. *Vet Radiol Ultrasound*. 2011;52:S32–S41.
19. Konar M, Lang J. Pros and cons of low-field magnetic resonance imaging in veterinary medicine. *Vet Radiol Ultrasound*. 2011;52:S5–S14.
20. Mai W. Pseudolayering artefact on postcontrast magnetic resonance images of the bladder of 18 dogs and three cats. *Vet Rec*. 2008;163:117.
21. d'Anjou MA, Carmel EN, Tidwell AS. Value of fat suppression in gadolinium-enhanced magnetic resonance neuroimaging. *Vet Radiol Ultrasound*. 2011;52:S85–S90.
22. Tidwell AS, Robertson ID. Magnetic resonance imaging of normal and abnormal brain perfusion. *Vet Radiol Ultrasound*. 2011;52:S62–S71.
23. Gavin P, Bagley RS. In: Ames IA, ed. *Practical Small Animal MRI*. 2nd ed. Wiley-Blackwell; 2009.
24. Glockner HU. Parallel MR imaging: a user's guide. *Radiographics*. 2005;25:1279–1297.
25. Cooper JJ, Young BD, Hoffman A, et al. Intracranial magnetic resonance imaging artifacts and pseudolesions in dogs and cats. *Vet Radiol Ultrasound*. 2010;51:587–595.
26. Hecht S, Adams WH, Narak JN, et al. Magnetic resonance imaging susceptibility artifacts due to metallic foreign bodies. *Vet Radiol Ultrasound*. 2011;52(4):409–414 [Epub March 7, 2011].
27. Werpy NM, Ho CP, Kawcak CE. Magic angle effect in normal collateral ligaments of the distal interphalangeal joint in horses imaged with a high-field magnetic resonance imaging system. *Vet Radiol Ultrasound*. 2010;51:2–10.

ELECTRONIC RESOURCES

Additional information related to the content in Chapter 4 can be found online at eBooks.Health.Elsevier.com.

- Chapter Quiz
- Videos

CHAPTER 5

Contrast Media in Diagnostic Imaging

Jennifer A. Reetz

INTRODUCTION

A contrast medium (plural media) is a substance used in medical imaging to change the opacity of a tissue, organ or cavity. By changing the opacity, contrast is increased thereby making tissues, organs, or cavities more conspicuous. Contrast media have applications in radiography, fluoroscopy, ultrasonography, computed tomography (CT), and magnetic resonance imaging (MRI).

RADIOGRAPHIC CONTRAST MEDIA

Radiographic contrast media are characterized as either positive or negative. Positive contrast media (e.g., barium sulfate and iodinated media) result in an increase in radiographic opacity due to increased absorption of x-ray photons (Fig. 5.1). The effective atomic number (Z) of barium (Z = 56) and iodine (Z = 53) is higher than that for soft tissue (Z = 7), which means that there is greater x-ray absorption by barium and iodine through the photoelectric effect and this increases the contrast of the tissues or fluids that contain them. X-ray absorption by barium and iodine is also enhanced by the K-absorption edge (K-edge) effect. The K-edge describes an abrupt increase in photoelectric absorption that occurs when the x-ray beam energy is just beyond the binding energy of inner k-shell electrons. The K-edges of barium (37.4 keV) and iodine (33.2 keV) are near the mean energy of the typical x-ray emission spectrum.[1] Low kVp settings in CT imaging closer to the k-edge of iodine can be used to increase the contrast between enhanced and non-enhanced regions for low dose or delayed postcontrast series.

Negative contrast media, on the other hand, result in a decrease in radiographic opacity due to lower absorption of x-ray photons, rendering the area of interest less radiopaque (more radiolucent) (Fig. 5.2). Typical negative contrast media include room air, CO_2, or NO_2. Sometimes studies combine both positive and negative contrast media and are termed *double-contrast studies*.

When using contrast media in CT (usually iodinated), the concepts are similar in that positive and negative contrast media increase and decrease x-ray beam absorption, respectively, but in CT, grayscale changes are described in terms of attenuation as opposed to opacity because CT images are computed based on quantification of x-ray attenuation. The attenuation values in the acquired voxels are translated into Hounsfield units (HU), which then allows for objective measurements of attenuation changes associated with contrast media (Fig. 5.3).

BARIUM CONTRAST MEDIA

General Information

Barium sulfate ($BaSO_4$) is an insoluble, inert, mineral salt commonly used in gastrointestinal contrast studies. Micropulverized liquid barium preparations are the most common

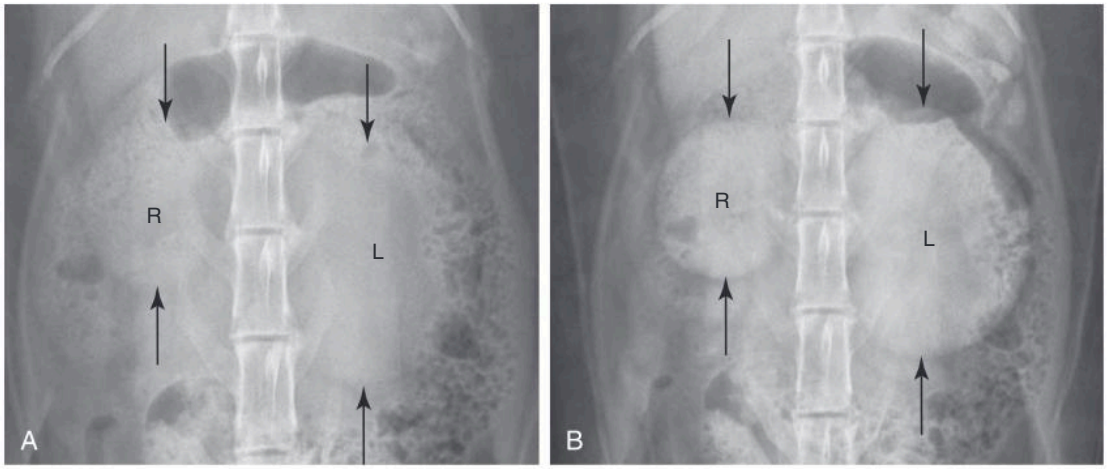


Fig. 5.1 Example of a radiographic positive contrast medium (intravenous excretory urography or IVU). **A**, Survey radiograph of the right (*R*) and left (*L*) kidneys (between *black arrows*) in a cat. Some of the soft tissue opaque renal margins are visible due to contrast provided by fat in the retroperitoneal space, but some portions are indistinct. **B**, Iodinated contrast medium was administered intravenously, and a repeat radiograph obtained almost immediately. Due to the high atomic number of iodine in the contrast medium, there is increased renal radiopacity, which provides additional radiographic contrast such that the renal margins are now clearly visible in their entirety.

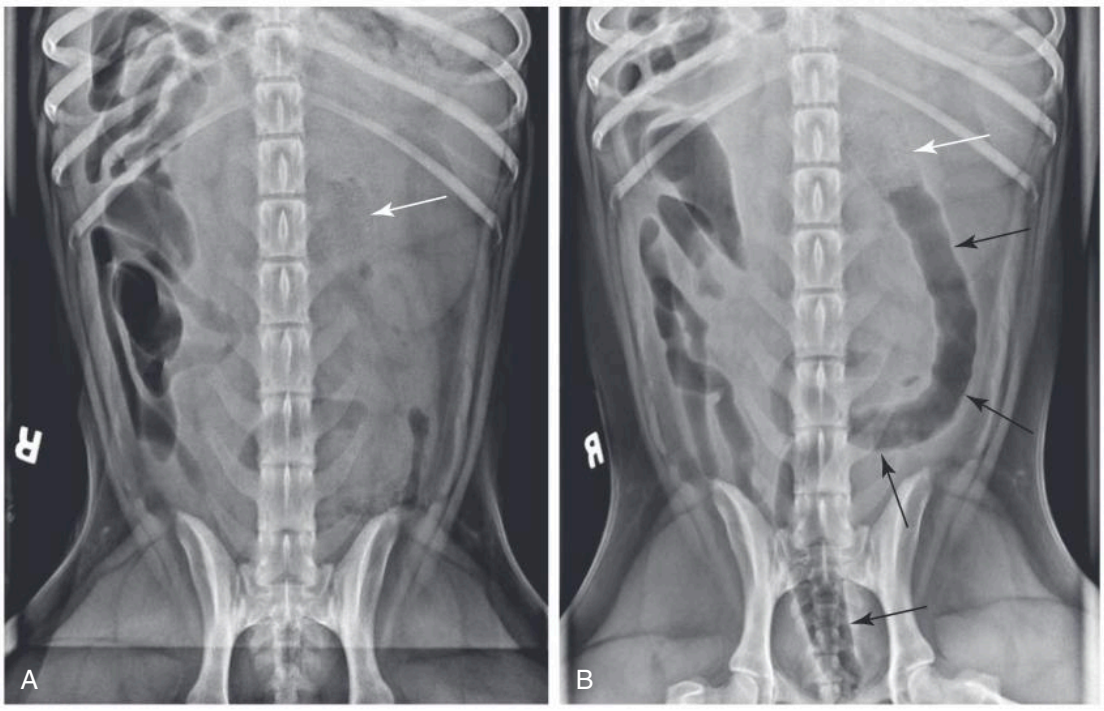


Fig. 5.2 Example of a radiographic negative contrast medium (pneumocolonography performed with room air). **A**, A corn cob foreign body is present within an intestinal segment in the left mid abdomen (*white arrow*) on this ventrodorsal view. Localization of the foreign body to the descending colon vs. jejunum was not possible on this view or the orthogonal view (not shown). **B**, Room air was instilled into the rectum via a red rubber catheter, to delineate the colon. Now that the rectum and descending colon (*black arrows*) contain air, the foreign body can be clearly localized to the colon. The decreased radiopacity (increased radiolucency) of the air-filled colonic lumen provides additional radiographic contrast such that the margins of the foreign body are more readily visible.

formulations used in veterinary medicine. Given the insoluble nature of barium, emulsifiers, stabilizers, and dispersants are added to the barium-water suspension to maintain the barium in suspension (Fig. 5.4).[2] Other barium formulations used in veterinary medicine include barium sulfate powder, barium sulfate paste and barium impregnated polyethylene spheres (BIPS). Barium sulfate powder manually mixed with water can be problematic as the barium particles may sediment and lead to poor quality studies (see Fig. 5.4).[3]

Liquid barium sulfate is the preferred contrast medium for gastrointestinal studies where perforation is not a concern. It allows for a more detailed evaluation of the mucosal surface compared to iodinated water soluble contrast media,[4] and is more resistant to dilution by fluid in the gastrointestinal tract.[5] Double-contrast studies using barium sulfate and room air, as with double-contrast gastrography, allow for more precise mucosal assessment.[6] Interestingly, liquid barium sulfate is sometimes used as a therapeutic agent in patients with acute gastroenteritis to cathartically coat intestinal mucosa and bind bacterial toxins.[7]

The concentration of barium sulfate suspensions is expressed in terms of either weight/volume (w/v) or weight/weight (w/w), which is the percentage of the weight of barium sulfate (grams) relative to the volume (100 mL) or weight (100 g) of the final product, respectively. For example, a liquid barium sulfate suspension labeled as 105% w/v and 58% w/w indicates: 105 g of barium sulfate in 100 mL of the final product (105% w/v) and 58 g of barium sulfate in 100 g of the product (58% w/w). Different concentrations of barium may be used for contrast studies and depending on the baseline concentration of the available barium suspension (e.g., 105% w/v vs. 60% w/v), dilution with water may be needed to achieve the desired concentration.

Adverse Effects

The most serious complication of barium studies is leakage of barium into the mediastinum or abdominal cavity from an esophageal or gastrointestinal perforation.[8] Barium sulfate alone can lead to peritonitis and adhesions,[9] but in association with a gastrointestinal perforation, it may further complicate septic peritonitis through the formation of granulomatous nodules on visceral and parietal surfaces that trap spilled intestinal content and bacteria, thereby contributing to fibrinous adhesions.[10] As with any septic peritonitis, this can be life-threatening and immediate aggressive therapy including surgery is recommended.[10] Similarly, leakage of barium sulfate associated with esophageal perforation can lead to mediastinitis.[8] If a positive contrast study of the gastrointestinal tract is indicated and perforation is of concern, the use of an iodinated, nonionic, water-soluble contrast medium is recommended.

Aspiration of barium following oral administration is another potential complication. Based on knowledge acquired from use of barium sulfate for bronchography, small volumes of barium sulfate aspiration are not problematic owing to its inert nature, and the barium can be cleared from the airways through coughing and the mucociliary apparatus.[5,11] Barium sulfate also undergoes phagocytosis by macrophages and some aspirated barium can remain in the pulmonary interstitium or be translocated to regional lymph nodes.[12] Aspiration of large volumes of barium, however, can result in pneumonia and acute respiratory distress, and ultimately death.[8,13] Other side effects of barium sulfate reported in human beings include allergic reactions, nausea, vomiting, abdominal pain, barolith formation resulting from barium sulfate remaining in the intestine too long, vasovagal reflex (e.g., during colonography), bacteremia (e.g., from barium enema), and intravasation.[5]

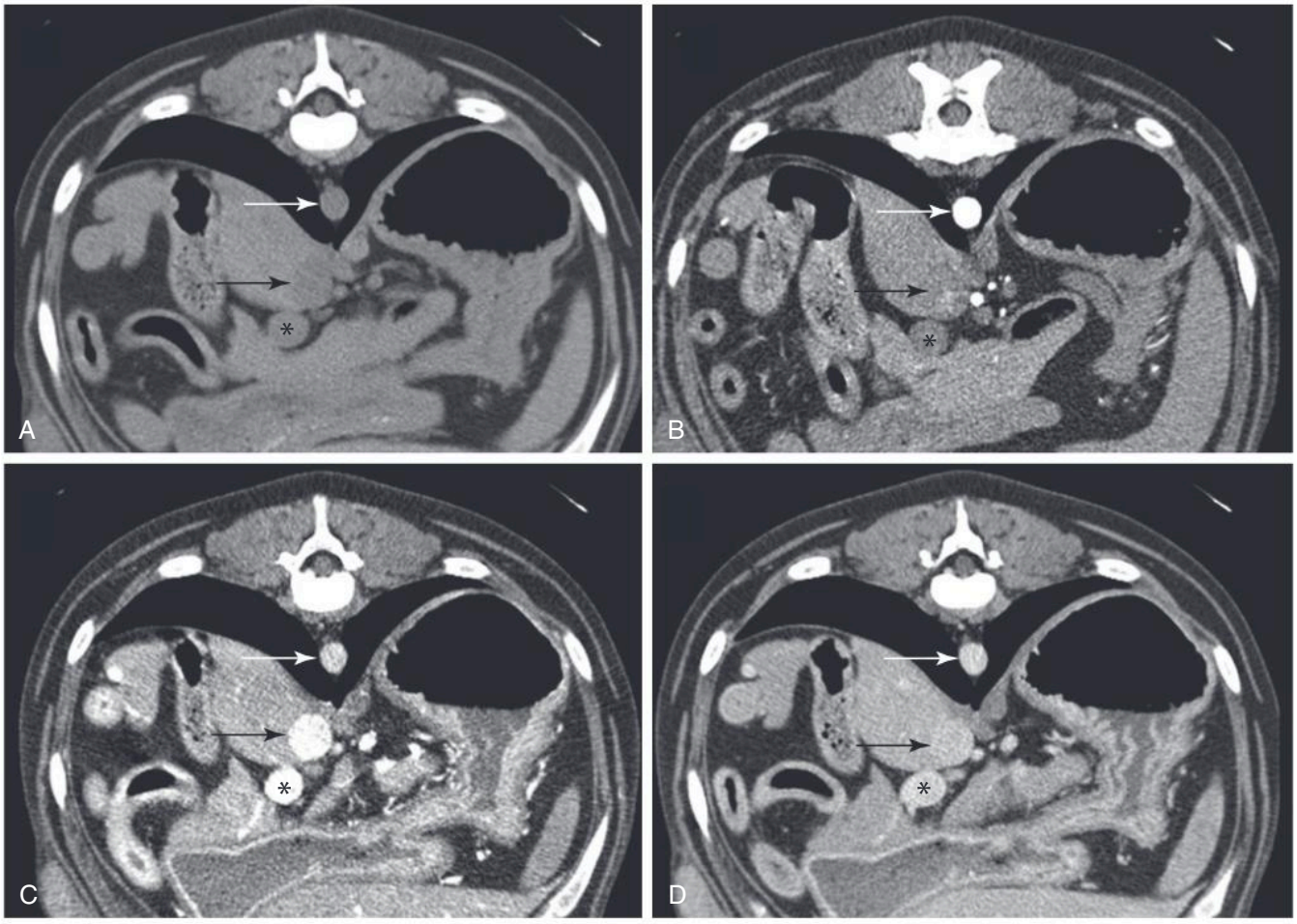


Fig. 5.3 Example of a triple-phase CT angiography to demonstrate changes in vascular attenuation over time after an intravenous bolus of an iodinated contrast medium (iohexol 350 mgI/mL). **A,** Precontrast image of the cranial abdomen. **B,** Arterial phase, with images acquired ~15 seconds after contrast medium injection. The aorta is markedly hyperattenuating relative to the other great vessels, as the contrast medium has not yet reached the venous system. **C,** Venous phase, with images acquired ~80 seconds after contrast injection. The contrast is decreasing in the arterial system and is peaked in the venous system, so that the aorta is less attenuating while the caudal vena cava and portal vein are markedly hyperattenuating. **D,** Delayed phase, with images acquired approximately 120 seconds after contrast medium injection. While all the great vessels are hyperattenuating relative to precontrast images, there is overall less attenuation compared to the arterial and venous phases, as the iodine content in the bloodstream is decreasing. For an objective example, the Houns field units (HU) of the aorta over time are: precontrast = 22.8, arterial phase = 829.00, venous phase 191.60, delayed phase = 160.76. *White arrow,* aorta; *black arrow,* caudal vena cava; *black asterisk,* portal vein.

IODINE-BASED CONTRAST MEDIA

General Information

Iodine-based contrast media are based upon a tri-iodinated benzene ring (Fig. 5.5). There are water-soluble and water-insoluble contrast media, with water-soluble media being the primary ones used in clinical practice. Water-soluble contrast media can be classified based on charge (ionic, nonionic), number of benzene rings (monomer, dimer) and osmolality (high, low, iso-osmolar). Contrast ratio (iodine to solute particle ratio), viscosity, and hydrophilicity (vs. lipophilicity) are other important factors when considering iodinated contrast media. Iodinated contrast media are used in a wide variety of clinical applications in diagnostic imaging, including radiography, fluoroscopy, and CT. Intravascular (IV) administration is the most common route of administration, but other routes exist, such as oral or rectal administration, injection into the urinary system, or intrathecal injection.

Iodinated contrast media normally undergo glomerular filtration and rapid renal excretion after IV administration. Extrarenal excretion pathways exist, most notably biliary excretion. In human beings, extrarenal excretion can occur in patients with renal dysfunction or obstruction, but it can also be seen in normal patients on delayed CT scans (e.g., 24 hours later).[14] Binding of contrast media to serum proteins plays a role in excretion, and with higher protein binding, there is longer plasma retention, which leads to less renal and more biliary excretion.[15] For example, meglumine iotroxate (Biliscopin) has high protein binding; therefore, it can be used for cholecystography after IV administration.[16] Occasionally, renal excretion is seen after oral or rectal contrast administration, as described in normal patients and in those with intestinal mucosal disease, obstruction, or perforation.[17,18]

Properties of Iodinated Contrast Media

Ionic vs. nonionic—Ionic media undergo dissociation into positive and negative ions, whereas nonionic media do not undergo dissociation owing to hydrophilic polar hydroxyl (OH) groups that increase solubility.[19] Ionic media contain

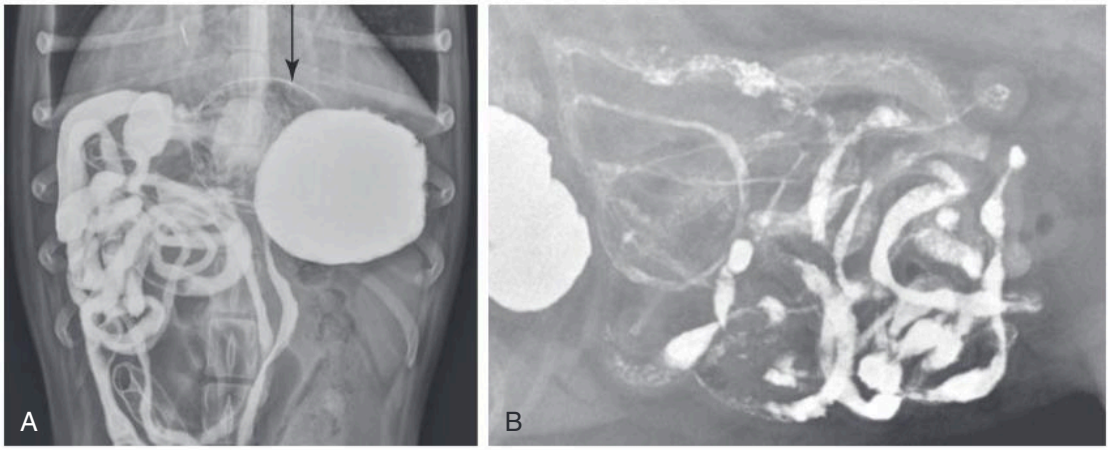


Fig. 5.4 Examples of gastrointestinal studies using liquid barium sulfate. **A**, Upper gastrointestinal study in a dog using commercially available liquid barium sulfate, which is filling part of the stomach and multiple small intestinal segments. There is excellent mucosal coating, which is particularly evident in the gastric body (*black arrow*) where luminal gas highlights the wall. **B**, Upper gastrointestinal study in a dog using barium sulfate powder where the barium in the small intestinal lumen has clumped and come out of suspension. This is termed flocculation and results in very poor mucosal coating.

substances (e.g., sodium, meglumine) that are necessary for improving the solubility of iodine and obtaining physiological pH, but these substances contribute to the higher osmolality of these media as compared to nonionic media (see Fig. 5.5).[19]

Monomers vs. dimers—Monomer contrast media have one tri-iodinated benzene ring whereas dimer contrast media have two rings joined together (see Fig. 5.5). Dimers have a higher concentration of iodine atoms per particles in solution and lower osmolality compared to monomers.

Osmolality—Osmolality is expressed as milliosmole per kilogram of water (mOsm/kg water) and is largely determined by the number of independent particles (molecules, ions) in solution. The dissociative properties of ionic media increase osmolality. Higher iodine concentrations (milligrams of iodine/milliliter of solution, mgI/mL) in any contrast medium (ionic or nonionic) also increases osmolality.[19,20] Ionic monomers are high-osmolality contrast media (Table 5.1), with a much higher osmolality compared to blood (e.g., diatrizoate = 2100 mOsm/kg, blood = 290 mOsm/kg).[21] Nonionic monomers are low-osmolality contrast media, but their osmolality is still two to three times higher than blood (e.g., iohexol 350 mgI/mL = 844 mOsm/kg). The only currently available nonionic dimer contrast medium is iso-osmolar to blood. Osmolality is the main issue related to side effects, with high-osmolality media being associated with more adverse reactions. Osmolality can also affect study quality. For example, fluid will be drawn into the bowel if using a high-osmolar contrast medium for a gastrointestinal contrast study. This will dilute the contrast medium, which then decreases radiographic opacity and lessens the contrast and quality of the study, in addition to potentially leading to dehydration of the patient.

Contrast ratio—This is the number of iodine atoms per number of particles in solution (I/P ratio). Owing to the dissociation of ionic media, there are 2 particles per aliquot of solution as compared to 1 particle for the nonionic media. Therefore, nonionic monomer contrast media have a higher contrast ratio (I/P ratio = 3) compared to ionic monomers (I/P ratio of 1.5). A nonionic dimer has an even higher ratio (I/P ratio = 6) since it contains 6 iodine atoms per 1 solute particle. A higher I/P ratio implies greater opacity, meaning there could be similar contrast enhancement even in the face of a lower contrast medium dose.

Viscosity—Viscosity is the ability of a solution to flow, measured as millipascal × second (mPa·s). High viscosity can make injection of the contrast medium difficult, especially with small-bore IV catheters. The factors that contribute to improving solubility, osmolality, and hydrophilicity inversely affect the viscosity; for example, an iso-osmolar dimer has a higher viscosity compared to a low-osmolar monomer.[20] Viscosity also increases with increasing iodine concentrations and decreases with higher temperatures. Warming contrast media (up to 37°C) prior to administration will decrease viscosity and facilitate injection.[19]

Hydrophilicity vs. lipophilicity—Tri-iodinated benzene rings have an inherent degree of lipophilicity associated with the iodine atoms.[19] On the other hand, hydroxyl groups and nitrogen atoms, which are high in nonionic media, help shield the iodine atoms thereby increasing hydrophilicity (see Fig. 5.5).[22] There is a correlation between lipophilicity and side effects, especially regarding neurotoxicity after intrathecal contrast medium administration.[22,23]

Water-insoluble contrast media—The only available contrast medium in this category is an ethiodized oil medium (Lipiodol), which is commonly added to embolization solutions during interventional radiology procedures, such as thoracic duct embolization in dogs with idiopathic chylothorax.[24]

Adverse Reactions

Adverse reactions associated with water-soluble iodinated contrast media can be acute (occurring within 1 hour of IV injection) or delayed (occurring within hours for up to 1 week).[25] They can be classified by their cause: (1) hypersensitivity reactions (also known as allergic-like, pseudoallergic, or anaphylactic-like reactions), which are dose independent, idiosyncratic, and unpredictable; and (2) physiologic, dose-dependent, nonallergic reactions, which are usually associated with the pharmacological properties of the medium.[18,25]

Hypersensitivity reactions—These reactions are usually acute and range from mild to severe and life-threatening. Most reactions in people are mild and include nausea, vomiting,

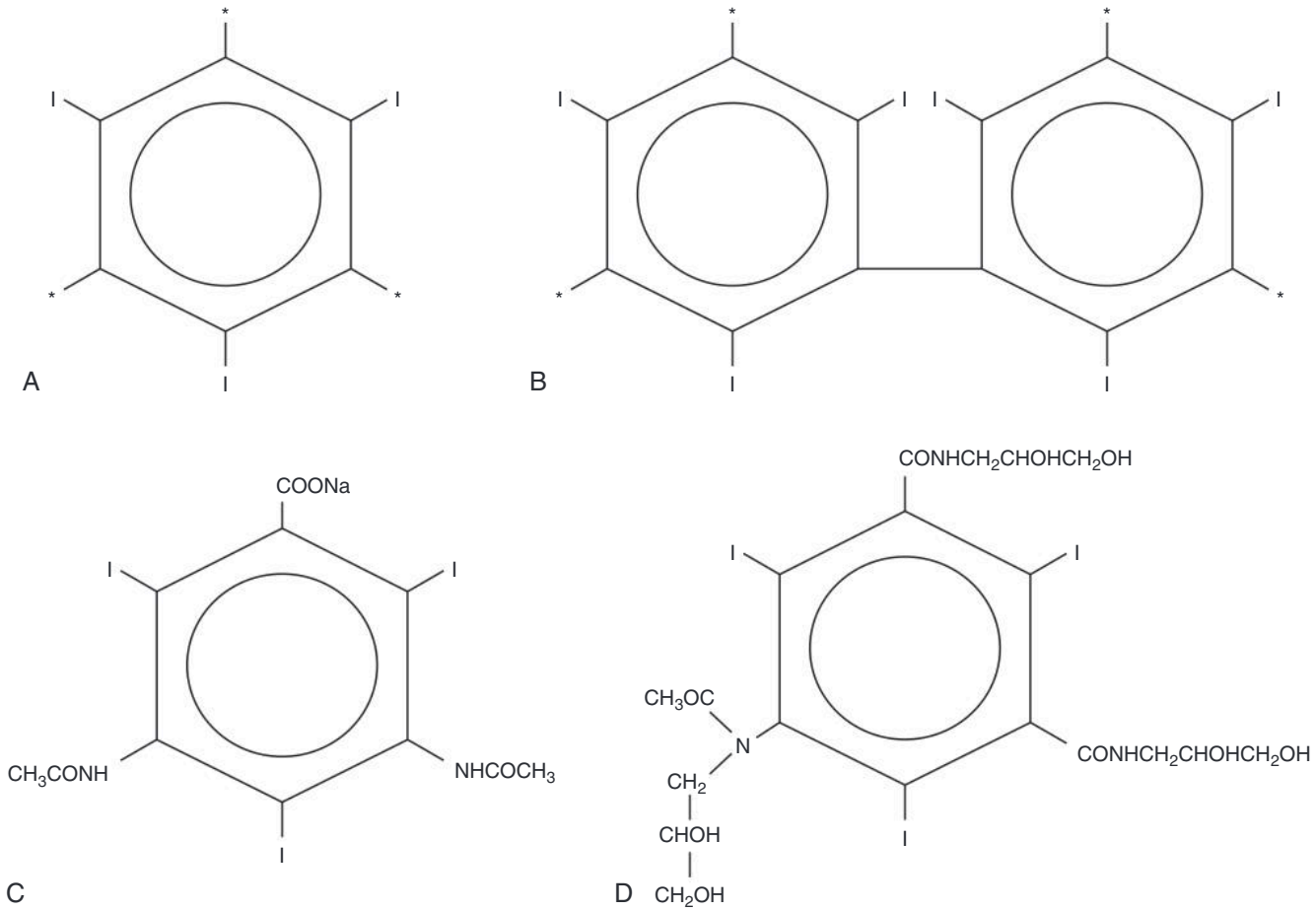


Fig. 5.5 Chemical composition of iodinated contrast media. **A** and **B,** Basic composition of a tri-iodinated monomer (**A**) and dimer (**B**). The *asterisks* (*) indicate the side chains occupied by various contrast media that act to increase solubility (e.g., polar OH groups and sodium or meglumine cations). **C,** Example of an ionic contrast medium (diatrizoate sodium). The sodium ion (COONa) contributes to the high osmolality and the methyl groups (CH_3) contribute to the lipophilicity of ionic contrast media. **D,** Example of a nonionic contrast media (iohexol). The polar OH groups contribute to the hydrophilicity of nonionic contrast media.

or urticaria. More severe reactions, such as bronchospasm, laryngeal edema, hypotensive shock, pulmonary edema, seizures, and cardiopulmonary arrest, can occur. The pathophysiologic mechanisms of these reactions may include histamine release, triggering of the complement cascade, and immune mediated reactions. Many of the reactions are not necessarily a true allergy.[18] The frequency of these reactions is lower with nonionic media;

Table • **5.1**

Currently Available Water-Soluble Iodinated Contrast Media and Their Properties.

CONTRAST MEDIUM	TRADE NAME[a]	STRUCTURE	CHARGE	OSMOLALITY @ 37°C (MOSM/KG WATER)	IODINE CONCENTRATION (MG I/ML)[a]	VISCOSITY @ 37° C (MPA · S)
Diatrizoate	Gastrografin	Monomer	Ionic	High—2100	370	8.4
Iothalamate	Conray	Monomer	Ionic	High—1400	282	4.0
Iohexol	Omnipaque	Monomer	Nonionic	Low—844	350	10.7
Iopamidol	Isovue	Monomer	Nonionic	Low—796	370	9.4
Ioversol	Optiray	Monomer	Nonionic	Low—792	350	9.0
Iopromide	Ultravist	Monomer	Nonionic	Low—774	370	10.0
Ioxilan	Oxilan	Monomer	Nonionic	Low—721	350	8.1
Iomeprol	Iomeron	Monomer	Nonionic	Low—618	350	7.5
Iodixanol	Visipaque	Dimer	Nonionic	Iso-osmolar—290	320	11.8

[a]The list is not all inclusive and various additional formulations (e.g., varied iodine concentrations, different trade names) exist.
From the U.S. Food and Drug Administration and Andreucci M, Faga T, Pisani A. The choice of the iodinated radiographic contrast media to prevent contrast-induced nephropathy. *Adv Nephrol*. 2014. https://doi.org/10.1155/2014/691623.

for example, the prevalence of severe reactions in human beings ranges from 0.05% to 0.22% with ionic media and 0.01% to 0.04% with nonionic media.[25]

Severe, acute hypersensitivity reactions to both ionic and nonionic media have been reported in veterinary medicine. In dogs, reported reactions have included hypotension, hypertension, tachycardia, ventricular premature contractions, bronchospasm, erythema, twitching, periocular edema, and diarrhea.[26–28] Cardiopulmonary arrest has been documented in a cat.[29] Reactions in horses have included bronchospasm, hypotension, sweating, urticaria, and edema.[30,31] A high mortality rate in small birds (45.5%) after CT with contrast medium administration has been reported, although it was not possible to determine whether the birds died because of a contrast medium reaction or because of their underlying illness or anesthesia; regardless, the authors advised cautious use of iodinated contrast media in ill, small birds.[32]

In people, two risk factors for hypersensitivity reactions are a previous reaction to iodinated contrast medium and having asthma or other severe allergies.[18] One study in cats, which included three cats with asthma/chronic bronchitis, did not document any hypersensitivity reactions, but the small number of patients precluded identification of any increased risk of a hypersensitivity reaction with possible predisposing conditions.[33] While almost all acute reactions occur with intravascular use, hypersensitivity reactions in people with extravascular use (e.g., cystography) have been reported.[34] There is potential advantage to premedication with steroids +/- antihistamines in people at higher risk for a hypersensitivity reaction, but breakthrough reactions can still occur and there is no proof that it will reduce the chances of a moderate-to-severe reaction or death.[18,35] Note that given the dose-independent nature of these reactions, a test dose of contrast medium to assess for any possible reactions prior to a full contrast medium dose is not useful.

Delayed adverse reactions in people are predominantly T-cell mediated skin reactions.[18] To date, no delayed reactions have been described in veterinary medicine.

Fatality following iodinated contrast medium use is rare, with an estimation in human beings of 1 in 170,000.[36] In animals, the fatality rate in one source has been estimated at 1 in 80 cases[37]; however, this is an old estimate based on ionic contrast media, and therefore, this number is presumably much lower with the now widespread use of nonionic media. All veterinarians performing contrast studies, though, should be aware of the associated risks and be prepared to provide emergency treatment as required (e.g., IV fluids, epinephrine, atropine, oxygen, diphenhydramine).

Dose-dependent physiologic reactions—Dose-dependent reactions can also range from mild to severe and are related to contrast medium type, concentration, and volume. Since these reactions are generally associated with osmolality and ionicity, low- or iso-osmolar, nonionic media are less likely to induce these reactions compared to high-osmolar, ionic media. Chemotoxicity, associated with lipophilicity and cations (sodium, meglumine), is also worse with ionic media.

Cardiovascular effects—The most common reported effects in veterinary medicine are mild to moderate bradycardia, tachycardia, hypertension, or hypotension, reported in up to 37% of cases.[27,31,33,38–40] Arrhythmias are also possible, especially during coronary arteriography.[41] More severe cardiovascular reactions and arrhythmias have been reported in two dogs, including supraventricular tachycardia and severe tachycardia with isolated ventricular premature contractions.[27]

Cellular and vascular effects—Contrast media can reduce erythrocyte plasticity, which could lead to capillary obstruction and local tissue anoxia, and affect leukocyte migration into tissues, which could dampen immune response, but this of minimal clinical significance.[42,43] Both prothrombotic and anticoagulant effects have been noted after local administration (coronary angiography).[44,45]

Respiratory effects—The most commonly reported effect is either increased or decreased respiratory rate in dogs and decreased respiratory rate in cats.[27] Aspiration of hyperosmolar ionic contrast medium into the lungs can lead to pulmonary edema and severe airway irritation, whereas iso- and low-osmolar contrast medium aspiration is generally tolerated by the lungs.[46,47]

Neurologic effects—Ionic contrast media are no longer approved for use in myelography owing to the higher rate of seizures associated with their chemotoxicity. While there are fewer side effects with nonionic contrast media, they do still occur; for example, the incidence of seizures after myelography in dogs ranges from 3% to 21.4%.[22,23,48–51] Higher total contrast medium dose may lead to a higher incidence of seizures,[49,50] and the authors in one study stated that a maximum contrast medium dose in large dogs should be considered.[49] The rate of seizures is also higher with cerebellomedullary cistern injection compared to lumbar injection in dogs.[48,49] Although osmolality is not the primary reason for neurologic side effects, nonionic media with lower iodine concentration, and therefore lower osmolality, should be used in myelography.[23,52] Note that the dimeric contrast medium iodixanol has been shown to be safe for use in myelography in experimental studies in dogs and cats,[53,54] but it is not approved for intrathecal use in human beings in the United States.

Contrast-induced acute kidney injury (CI-AKI)—Contrast-induced nephropathy (CIN) in human beings is now known as contrast-induced acute kidney injury (CI-AKI). This is a subgroup of contrast-medium-associated acute kidney injury (CA-AKI), which is the broad term for a sudden decrease in kidney function within 48 hours of an IV injection of iodinated contrast medium, whether from direct renal injury due to the contrast medium itself (considered rare) or from causes coincident to contrast medium administration (more common).[35] CI-AKI is likely multifactorial, with possible pathophysiologic mechanisms including (1) direct toxicity to renal tubular cells, (2) alterations in renal microvasculature leading to decreased renal blood flow, (3) reperfusion and subsequent oxidative stress, (4) parenchymal toxicity associated with complement cascade activation and inflammatory cytokines, and (5) toxicity from obstruction of renal tubules by precipitating proteins.[55] These effects are related to osmolality, viscosity, and ionicity. In human beings, the biggest risk factor for CI-AKI is pre-existing severe renal impairment.[56] Other risk factors include but are not limited to dehydration, diabetes, cardiovascular disease, older age, diuretic use, hypertension, and anemia.[35,55] Another potential risk factor is receiving multiple doses of contrast medium in a short time period, and as such, dosing intervals should probably be at least 24 hours apart.[35] High-osmolar, ionic contrast media are associated with higher nephrotoxicity in human beings with underlying renal impairment, but not in those with normal renal function. Contrast medium retention in the kidney (slower transit time of contrast medium through the nephrons) is a risk factor for the development of CI-AKI in human beings.[57] Contrast medium retention was reported in a cat undergoing excretory urography, where a persistent nephrogram phase was noted and then oliguria developed, which resolved after treatment.[58] See Fig. 5.6 for a CT example of contrast medium retention.

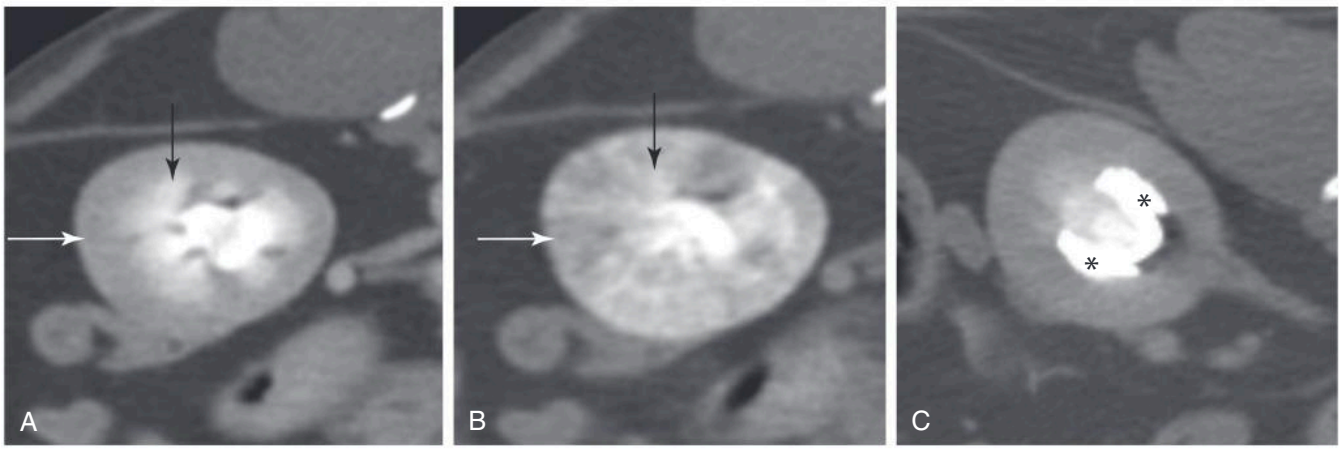


Fig. 5.6 Computed tomography (CT) images in a cat with contrast medium retention (**A, B**) compared to a cat with normal contrast medium excretion (**C**). **A,** Image of the right kidney obtained approximately 2 minutes post-intravascular (IV) injection of iohexol, showing initial normal homogeneous enhancement of the renal cortex (*white arrow*) and medulla (*black arrow*). **B,** Image of the same kidney obtained approximately 15 minutes post-IV contrast injection, showing the development of abnormal, heterogeneous contrast enhancement of the cortex and medulla, consistent with contrast medium retention. The patient was euthanized shortly after the CT, so the clinical relevance of this finding was not determined. Although there was no evidence of renal disease on pre-CT lab work, chronic tubulointerstitial nephritis was present on histopathology, which may or may not have played a role in contrast medium retention. **C**, Comparison image of the right kidney of a normal cat obtained 30 minutes post-IV contrast. Most of the contrast medium is within the renal pelvis (*black asterisks*) as would be expected.

There are reports in veterinary medicine describing CI-AKI/CA-AKI. The largest study included 86 dogs who received mostly nonionic monomers (92 total doses).[59] Seven of the dogs (7.6%) had an increase in serum creatinine (>0.5 mg/dL) within 1 week, two of which developed clinical azotemia. These findings are suggestive of CI-AKI, but other possible contributory factors (e.g., hypotension) were identified. Two dogs and a cat had suspected CI-AKI following CT angiography and transarterial embolization (~24 hours apart) using a nonionic, low-osmolar medium.[60] Potential risk factors in those cases included International Renal Interest Society (IRIS) stage 1 chronic kidney disease, older age, and compensated cardiac disease. Suspected CI-AKI developed in a dog 24 hours post excretory urography using an ionic contrast medium.[61] In healthy beagles receiving IV iohexol 6 to 8 weeks apart, there was a subclinical decrease (17%) in glomerular filtration rate (GFR) after the second injection.[62] Two studies in dogs and cats found a borderline to mild increase in urine protein:creatinine ratio (UPC) within 1 week following IV contrast medium administration, but the clinical relevance of this is unknown.[63,64] These studies suggest that while CI-AKI is uncommon in animals, consideration should be given to monitoring patients for AKI post contrast medium administration, especially in those with pre-existing renal disease or other potential risk factors.

The primary method to decrease the risk of CI-AKI in patients with renal impairment is IV fluids.[35] Also, nonionic contrast media should be used in any patient with evidence of impaired renal function, given their lower nephrotoxicity profile. Contrast studies should not be performed on dehydrated patients, regardless of pre-existing renal status. Cessation of any potentially nephrotoxic drugs should be considered,[56] although this has not been a proven contributor to CI-AKI.[35] Treatment of suspected CI-AKI in human beings primarily involves IV fluid therapy. Other treatments such as diuretics (e.g., furosemide, mannitol) or dopamine have not shown to be useful and could potentially be harmful.[65]

Lower urinary tract effects—There is a report of a dog developing hemorrhagic cystitis after IV contrast medium administration, potentially from longer exposure of the urinary bladder to the contrast medium, owing to partial lower urinary tract obstruction.[66] An experimental study found hemorrhagic and necrotic cystitis/urethritis in dogs and cats after retrograde cystourethrography, but this likely occurred from overdistention of the bladder/urethra and not from the contrast medium itself.[67] If urinalysis is needed, it should be performed prior to iodinated contrast medium administration as alterations in urine specific gravity and urinalysis results can occur.

Effects on thyroid function—Iodinated contrast medium contains a small amount of free iodine and there are rare reports of iodine-induced thyrotoxicosis in susceptible people (e.g., those with hyperthyroidism), which can occur weeks to months after contrast medium administration.[25] Iodinated contrast media are not recommended in people with acute thyroid storm, although a history of hyperthyroidism is not a true contraindication given the rarity of this complication.[35] In cats with hyperthyroidism, there is no information available to suggest that iodinated contrast medium is contraindicated, but based on results in human beings, it seems prudent to avoid iodinated contrast medium in cats with thyroid storm.

The minimal amount of free iodine in these media may still be sufficient to inhibit thyroid uptake of radioactive iodine. A transient decrease in the thyroid:salivary gland uptake of technetium was identified in normal cats 1 day post iohexol administration, although uptake values remained normal.[68] A gap of 14 days between injection of iodinated contrast medium and scintigraphy was recommended to avoid an artificial reduction in technetium uptake. In hyperthyroid cats, low-dose iohexol (65 mI/kg) used for estimating GFR 24 hours prior to I-131 treatment was shown to decrease the absorbed dose of I-131; however, I-131 treatment success rates were similar compared to those cats that did not receive prior iohexol.[69]

Other effects—In human beings, mild physiologic side effects can include flushing, warmth or chills, nasal congestion, nausea, vomiting, anxiety, dizziness, and pain during injection.[8] In veterinary medicine, other reported side effects include vomiting, anxiety, and hyperthermia.[27,50,70]

NEGATIVE CONTRAST MEDIA

Negative contrast media absorb x-ray photons less than soft tissue, thereby decreasing the opacity or attenuation of organs containing them. The most common negative contrast media are room air, CO_2 and NO_2. Both CO_2 and NO_2 are more water soluble than room air, so there is less concern for fatal air embolism, which has been reported after pneumocystography.[71,72] Negative contrast media are most used for gastrointestinal and urinary tract imaging, either alone or in double-contrast studies.

MAGNETIC RESONANCE IMAGING CONTRAST MEDIA

General Information

The primary contrast media used in MRI contain the rare earth metal gadolinium (Gd^{3+}). Gadolinium-based contrast media (GBCM) are paramagnetic, whereby they shorten T1 and T2 relaxation times. Clinically, it is their effect on T1-weighted images that is important, where both normal and abnormal structures may have increased signal (hyperintensity) on postcontrast images as compared to precontrast images (Fig. 5.7). Gadolinium in its free form is toxic, so chelating agents are added to minimize this toxicity. GBCM can be divided into categories, based on the type of ligand (linear or macrocyclic) and ionicity (ionic, nonionic) (Table 5.2). Linear ligands partially wrap around the Gd^{3+} ion, whereas macrocyclic ligands fully surround the ion in a cage-like structure, which gives the macrocyclic contrast media higher stability.[73,74] Higher stability equates to less dissociation and therefore less release of free Gd^{3+} ions into the vasculature and tissues. Ionicity affects osmolality, but this does not have a clinically relevant impact at the standard clinical dose (unlike with water soluble iodinated contrast media), because the total molar amount is lower (1 Gd^{3+} ion vs. 3 iodine ions per molecule).[75]

The ability of gadolinium contrast media to shorten the relaxation time is called relaxivity, which depends on the ligand and other factors such as the protein-binding of the contrast medium, magnetic field strength, and temperature.[73,76] Higher-relaxivity contrast media are more effective in shortening the T1 relaxation time, which allows for a lower contrast medium dose without sacrificing image quality. For example, the newest macrocyclic GBCM (gadopiclenol) can be used at a lower dose in human beings (0.05 mmol/kg vs. the typical dose of 0.1 mmol/kg for other contrast media), without negatively impacting image quality.[77]

GBCMs distribute in the bloodstream and extracellular space with subsequent rapid renal excretion. A few contrast media with higher protein binding are partially excreted by the hepatobiliary system (organ specific contrast media), which means they can serve a dual purpose, with routine early postcontrast (vascular, extracellular tissue phases) and delayed postcontrast (hepatocellular phase) imaging.[76,78–80] GBCMs are typically given IV but intra-articular and intrathecal use has been described in animals.[81–83] Note that while arthrography with GBCMs is commonly performed in human beings, intrathecal use is not approved.

Interestingly, the atomic number ($Z = 64$) of gadolinium renders it radiopaque and GBCMs have been evaluated as an alternative to iodinated media since in standard doses gadolinium is less nephrotoxic.[84] However, since the molar concentrations of iodinated media and GBCMs are different, the x-ray attenuation of iodinated contrast media is about three times that of gadolinium contrast media, and as such, GBCMs are less effective at altering radiographic opacity. To achieve opacification similar to iodinated contrast media, doses of GBCM would need to be increased above standard clinical doses, which will increase nephrotoxicity.[85]

Adverse Reactions

General reactions—Acute adverse reactions to GBCMs in human beings are similar to those with iodinated media, but the incidence is lower.[86] Reactions include hypersensitivity/allergic-like reactions (e.g., urticaria, erythema, bronchospasm, laryngeal edema, hypotensive

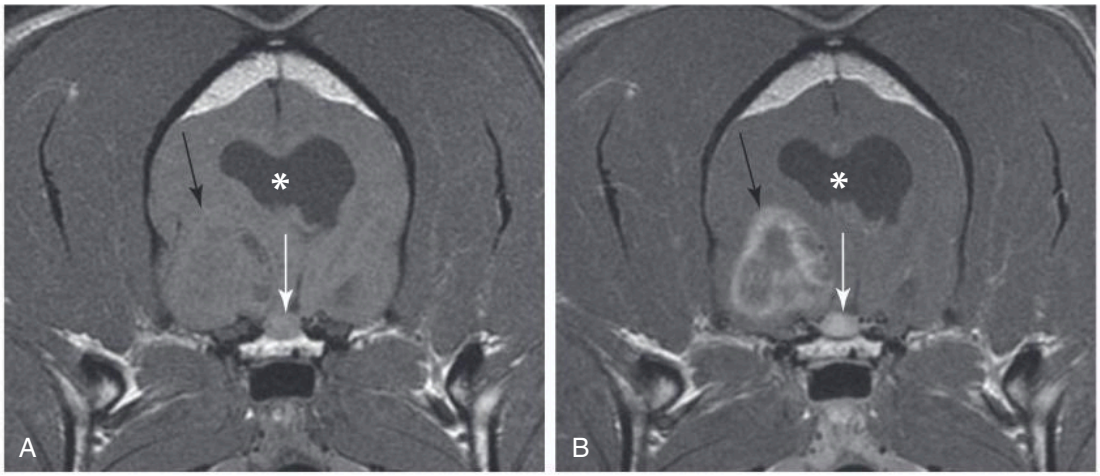


Fig. 5.7 Transverse T1-weighted (T1W) precontrast (**A**) and postcontrast (**B**) magnetic resonance images of the brain in a dog with oligodendroglioma. On both images, the cerebrospinal fluid in the lateral ventricles (*white asterisks*) is hypointense relative to the brain parenchyma due to the longer T1 relaxation time of fluid compared to brain tissue. **A,** The intra-axial mass (*black arrow*) is isointense to mildly hypointense relative to the normal brain, with poor margination. The normal pituitary gland (*white arrow*) is isointense to slightly hyperintense relative to the brain. **B,** Same image post-intravenous (IV) gadolinium-based contrast medium (GBCM) administration showing strong but heterogeneous enhancement (mostly rim enhancement) of the mass, with increased visibility of the margins. Gadolinium shortens the T1 relaxation time, which results in the areas of hyperintensity now present in the mass. Contrast enhancement of an intra-axial mass is due to a disruption in the blood-brain barrier, which can occur in diseases such as neoplasia. The pituitary gland resides outside of the blood-brain barrier and normally displays contrast enhancement as seen here.

Table • 5.2

Classification and Properties of Gadolinium-Based Contrast Media.

CONTRAST MEDIUM	TRADE NAME	CLASS	IONICITY	ORGAN SPECIFIC	EXCRETION PATHWAY	NSF RISK[a]
Gadodiamide	Omniscan	Linear	Nonionic	No	Renal	High
Gadoversetamide	OptiMARK	Linear	Nonionic	No	Renal	High
Gadopentetate dimeglumine	Magnevist	Linear	Ionic	No	Renal	High
Gadobenate dimeglumine	MultiHance	Linear	Ionic	Yes	4%–5% Hepatobiliary + renal	Intermediate
Gadoxetate disodium	Primovist/ Eovist	Linear	Ionic	Yes	50% Hepatobiliary + renal	Intermediate
Gadoterate meglumine	Dotarem/ Artirem	Macrocyclic	Ionic	No	Renal	Low
Gadobutrol	Gadovist/ Gadavist	Macrocyclic	Nonionic	No	Renal	Low
Gadoteridol	ProHance	Macrocyclic	Nonionic	No	Renal	Low
Gadopiclenol	Vueway/ Elucirem	Macrocyclic	Nonionic	No	Renal	Low

NSF, Nephrogenic systemic fibrosis.
[a]This is a rare but very serious adverse reaction in human beings, but it has not been reported in veterinary medicine to date.
From Lohrke J, Frenzel T, Endrikat J, et al. 25 Years of contrast-enhanced MRI: developments, current challenges and future perspectives. *Adv Ther*. 2016;33:1–28.

shock, and cardiopulmonary arrest) and physiologic reactions (e.g., warmth/chills, vomiting, transient dyspnea, and vasovagal reactions).[35,87] Hypersensitivity reactions in human beings are rare, with life-threatening reactions being very rare (0.001%–0.01%).[35] Similar to iodinated contrast media, asthma and other allergies may slightly increase the risk of a hypersensitivity reaction.[35] In dogs and cats, mostly hemodynamic effects have been reported, such as mild alterations in blood pressure, heart rate, and respiratory rates.[27,33,38] In one study of 50 dogs, there were no adverse effects.[88] Mild to severe hypersensitivity reactions have been reported in a total of five dogs and included facial edema, hypotension, tachycardia, body twitching, tachypnea, bronchoconstriction, and severe cardiovascular collapse.[27,89,90] Seizure-like activity, tachycardia, and hypertension occurred in a foal.[91]

Nephrogenic systemic fibrosis (NSF)—NSF is a rare, very late, adverse reaction to gadolinium that results in an irreversible scleroderma-like, fibrosing condition in human beings, leading to impaired renal function.[87] Skin symptoms can develop up to 2 to 3 months or rarely years post GBCM exposure, and signs may initially include pruritis, swelling, and erythema. Later, there is fibrotic thickening of skin and subcutaneous tissues, and in severe reactions, there can be progression to joint contractures, immobility, and rarely organ fibrosis and death.[87] GBCMs are eliminated through the kidneys, and in human beings with normal renal function, the plasma half-life is 1.5 hours. With reduced renal function, the half-life can increase to ≥30 hours, and as such, increased dechelation (release of the Gd^{3+} ion from the contrast medium) may occur.[92] Dechelation results in deposition of free Gd^{3+} into tissues, which can lead to the fibrotic tissue changes. The incidence of NSF is higher with linear GBCMs, and therefore, if the benefits of GBCM usage outweigh the risk in those with renal dysfunction, macrocyclic contrast media are recommended.[35] NSF has not been documented in animals.

Gadolinium deposition in tissues—Gd^{3+} ion deposition can occur in other organs besides the skin, including the brain, bones, and liver. This can even occur in people and animals with normal renal function.[74] T1-weighted (T1W) hyperintensity in the brain, specifically the dentate nucleus and globus pallidus, has been documented in human beings and correlates with the number of times linear GBCMs have been administered.[93] In dogs, there was no evidence of T1W hyperintensity in the brain after multiple injections of a linear GBCM, but small amounts of gadolinium were found in the brain in one dog that had received three GBCM doses.[94] At this time, the consequences of these findings are unknown, but in human beings, there have been recommendations to only use macrocyclic contrast media when possible.

ULTRASOUND CONTRAST MEDIA

General Information

While the use of ultrasound in veterinary medicine is now common, the application of contrast-enhanced ultrasound (CEUS) techniques is less so and is related to varying approval and availability of ultrasound contrast media in different countries. Conventional ultrasound allows for blood flow assessment via Doppler (color, power, microvascular imaging), however, true tissue perfusion at the capillary bed level is only achievable with CEUS. There are many applications for CEUS in animals, including liver, spleen, pancreas, lymph nodes, and intestinal and urogenital tracts. See Fig. 5.8 for an example of how perfusion of a liver nodule can be used to determine whether it is benign or malignant.

Ultrasound contrast media are microbubbles of inert generally insoluble gas stabilized by an outer shell (Table 5.3). The microbubbles are smaller than red blood cells (1–7 um) and therefore can pass through pulmonary capillaries without concern for air embolism.[95] The shell provides microbubble stability, but the microbubbles are eventually destroyed. The primary route of administration is intravenous, although other applications have been described. Most of the ultrasound contrast media are blood pool only, meaning that the microbubbles remain in the blood vessels. There are media that

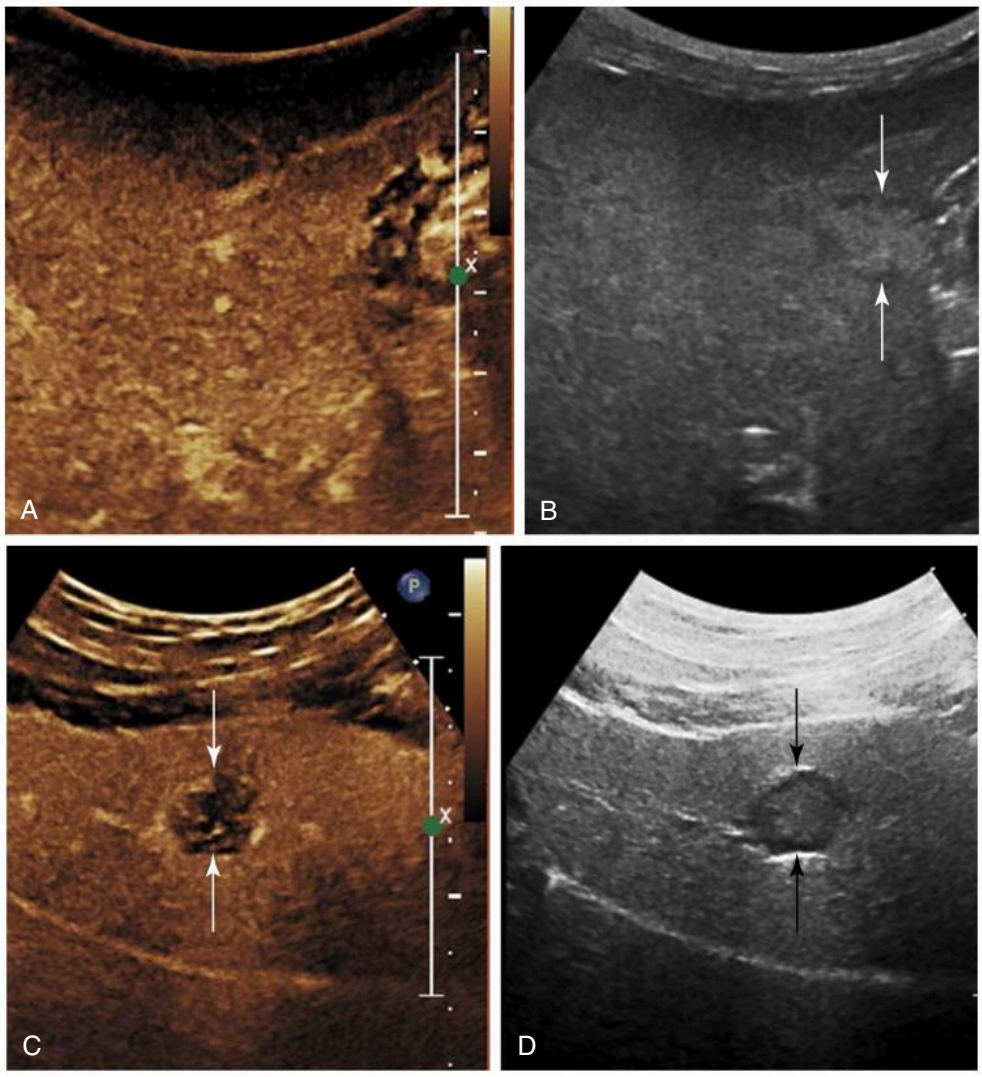


Fig. 5.8 Benign (**A, B**) and malignant (**C, D**) liver nodules examined with contrast enhanced ultrasound using a blood pool only contrast medium. In both sets of images, the B-mode image is on the *right* and the contrast-enhanced image is on the *left*. These are delayed phase images where the microbubbles within the hepatic sinusoids are creating diffuse liver enhancement. Microbubbles are still present in some of the macroscopic vasculature as well. **A—B,** Benign enhancement pattern in a dog with presumptive nodular hyperplasia (no histopathology performed but nodule remained stable for at least 2 years). The heterogeneous target-like nodule (*white arrows*) seen on B-mode is not visible on the contrast enhanced image, as the nodule was isoperfused relative to normal liver parenchyma. **C—D,** Malignant enhancement pattern in a dog with metastatic intestinal carcinoma. The heterogeneous target-like nodule (*black arrows*) seen on B-mode is visible on the contrast enhanced image (*white arrows*), as the nodule is largely hypoperfused relative to normal liver parenchyma. This hypoperfusion is also known as "washout," which is a term that can used to describe the temporal behavior of nodules as compared to adjacent normal liver.

become incorporated into macrophages (e.g., Sonazoid), which allows for delayed phase imaging of the liver and spleen. After microbubble rupture, the gas content is eliminated through the lungs, and the shell components are filtered by the kidneys and eliminated by the liver.[95]

Due to the acoustic impedance of gas, these microbubbles produce marked sound wave scattering and this is the hallmark of CEUS. The behavior of the bubbles is dependent on several parameters, including resonance frequency of the ultrasound beam, focal zone settings, acoustic power, and the inherent properties of the contrast media. Of these, acoustic power is the most important factor affecting microbubble behavior. The power, generally expressed as the mechanical index (MI), is affected by the output of the ultrasound machine, the transmitted frequency, and the attenuation of the ultrasound beam with depth.[96] At very low MI values, the microbubbles will remain relatively static and provide only some scatter. As the MI increases ($\sim<0.2$), the sound waves will cause the microbubbles to oscillate in a linear fashion. These linear echoes are similar to the ultrasound appearance of the adjacent tissue and make differentiation difficult, meaning that normal grayscale or Doppler imaging can be of minimal use. With slightly higher MI ($\sim 0.2—0.5$), the microbubbles will oscillate in a nonlinear fashion and will begin to emit harmonics of the resonance frequency. Adjacent tissue will generally not resonate harmonically, and it is this fact that allows differentiation of the echoes of the microbubbles from the echoes of the tissue. With even further increased MI (>0.5), the microbubbles can oscillate and expand beyond their limits and can be quickly destroyed. This can provide a transient strong nonlinear echo. CEUS generally

Table • 5.3

Currently Available Ultrasound Microbubble Contrast Media and Their Properties.[a]

CONTRAST MEDIUM	GAS TYPE	SHELL TYPE	DISTRIBUTION
Definity	Octofluoropropane	Phospholipid	Blood pool only
Luminity	Octofluoropropane	Phospholipid	Blood pool only
Lumason	Sulfur hexafluoride	Phospholipid	Blood pool only
SonoVue	Sulfur hexafluoride	Phospholipid	Blood pool only
Optison	Perfluoropropane	Albumin	Blood pool only
Sonazoid	Perfluorobutane	Phospholipid	Intravascular + delayed liver/spleen
Visphere[b]	Perfluorocarbon	Phospholipid	Intravascular + delayed liver[†]

[a]Not all contrast media are available in all countries.[b]Contrast medium only available in Taiwan. [†]One exploratory study utilizing this contrast medium did not include imaging of the spleen (Lin LS, Chung CS. Novel contrast medium Visphere™ is feasible for contrast-enhanced ultrasonography in dogs. *Vet Radiol Ultrasound.* 202:61(4):461–470).

assesses signals of the nonlinear oscillation of the bubbles, or the signals produced from their destruction. Harmonic ultrasound techniques can separate the fundamental from the secondary harmonic frequencies and can eliminate background tissue echoes, to enable the usage of only the contrast medium echoes in image formation. This allows for greater evaluation of organ perfusion and their afferent vessels. Harmonic imaging requires specific capabilities of the ultrasound machine and appropriate image analysis programs.

Adverse Reactions

Ultrasound contrast media are generally considered safe and there are no organ-specific toxicities. In human beings, most reactions are mild, such as a warm sensation, itching, nausea, and vomiting. In one study, the incidence of any reaction was 0.125%, with much less frequent serious hypersensitivity reactions at 0.009%.[97] In a multicenter retrospective case study of 488 animals imaged using either SonoVue or Definity, adverse reactions (vomiting, syncope) were reported in about 1% of dogs (4/411) and no cats (0/77).[98] In two of these dogs, however, there were confounding factors that could have caused the clinical signs. Severe hypersensitivity reactions were reported in 2/26 dogs with use of the contrast medium Optison, which was thought to be associated with the human albumin contained within the shell.[99] Based on this study, contrast media containing human albumin should probably be avoided in animals. Overall, when compared to the use of iodinated contrast media, ultrasound contrast media are considered very safe.

Acknowledgment

With special thanks to prior authors of this chapter for their contributions.

REFERENCES

1. Bushberg JT, Seiber JA, Leidholdt EM, Boone JM. *Essential Physics of Medical Imaging.* 4th ed. Philadelphia: Lippincott Williams & Wilkins; 2021.
2. Sireci S. Clinical utility of barium sulfate products. Formulation determines appropriate use. *Appl Radiol.* 2021.
3. Gelfand DW, Ott DJ. Barium sulfate suspensions: an evaluation of available products. *Am J Roentgenol.* 1982;138:935–941.
4. Agut A, Sanchez-Valverde MA, Lasaosa JM, et al. Use of iohexol as a gastrointestinal contrast medium in the dog. *Vet Radiol Ultrasound.* 1993;34:171–177.
5. Saylisoy S, Erturk SM. Gastrointestinal iodinated contrast agents. In: Erturk SM, Ros PR, Ichikawa T, Saylisoy S, eds. *Medical Imaging Contrast Agents: A Clinical Manual.* Switzerland: Springer; 2021.
6. Evans SM, Laufer I. Double gastrography in the normal dog. *Vet Radiol Ultrasound.* 1981;22:2–9.
7. Simpson KW. Diseases of the stomach. In: Ettinger SJ, Feldman EC, eds. *Textbook of Veterinary Internal Medicine.* 7th ed. St Louis Missouri: Saunders; 2010.
8. Beckett KR, Moriarity AK, Langer JM. Safe use of contrast media. What the radiologist needs to know. *Radiographics.* 2015;35:738–750.
9. Westfall RH, Nelson RH, Musselman MM. Barium peritonitis. *Am J Surg.* 1966;112:760–763.
10. Ko JJ, Mann FA. Barium peritonitis in small animals. *J Vet Med Sci.* 2014;76:621–628.
11. Thompson IM, Whittlesey GC, Slovis TL, et al. Evaluation of contrast media for bronchography. *Pediatr Radiol.* 1997;27:598–605.
12. McAlister WH, Askin FB. The effect of some contrast agents in the lung. An experimental study in the rat and dog. *Am J Roentgenol.* 1983;40:245–251.
13. Meola SD, Mazzaferro EM, Wheeler JL, McKiernan B. Medical and surgical management of severe barium aspiration in a dog. *J Vet Emerg Crit Care.* 2008;18:639–645.
14. Yamazaki H, Oi H, Matsushita M, et al. Gallbladder opacification 12–24 h after angiography by CT examination: a multivariate analysis. *Abdom Imaging.* 1996;21:507–511.
15. Lasser EC, Farr RS, Fujimagari T, et al. The significance of protein binding of contrast media in roentgen diagnosis. *Am J Roentgenol.* 1962;87:338–360.
16. Fujita M, Orima A. Effect and safety of meglumine iotroxate for cholangiocystography in normal cats. *Vet Radiol Ultrasound.* 1994;35:79–82.
17. O'Brien T. *Radiographic Diagnosis of Abdominal Disorders of the Dog and Cat: Radiographic Interpretation, Clinical Signs, Pathophysiology.* Philadelphia: Saunders; 1978.
18. Saylisoy S, Erturk SM. Adverse reactions to iodinated contrast agents. In: Erturk SM, Ros PR, Ichikawa T, Saylisoy S, eds. *Medical Imaging Contrast Agents. A Clinical Manual.* Switzerland: Springer; 2021.
19. Speck U. Physicochemical properties of water-soluble contrast media. In: Speck U, ed. *X-Ray Contrast media. Overview, Use and Pharmaceutical Aspects.* Berlin: Springer; 2018.
20. Erol K, Yigitaslan S. Chemistry, physicochemical, properties and pharmacokinetics of iodinated contrast agents. In: Erturk SM, Ros PR, Ichikawa T, Saylisoy S, eds. *Medical*

Imaging Contrast Agents. A Clinical Manual. Switzerland: Springer; 2021.
21. Windberger U, Bartholovitsch A, Plasenzotti R, et al. Whole blood viscosity, plasma viscosity and erythrocyte aggregation in nine mammalian species: reference values and comparison of data. *Exp Physiol*. 2003;88:431.
22. Widmer WR. Iohexol and iopamidol. New contrast media for veterinary myelography. *J Am Vet Med Assoc*. 1989;194: 1714–1716.
23. Widmer WR, Blevins WE. Veterinary myelography. A review of contrast media, adverse effects, and technique. *J Am Anim Hosp Assoc*. 1991;27:163–176.
24. Carvajal JL, Case JB, Grosso FRV, et al. Prospective evaluation of lymphatic embolization as part of the treatment in dogs with presumptive idiopathic chylothorax. *Vet Surg*. 2022;51:O128–O137.
25. Speck U. Risks of contrast media use. In: Speck U, ed. *X-Ray Contrast Media. Overview, Use and Pharmaceutical Aspects*. Berlin: Springer; 2018.
26. Basher KL, Porter IR, Martin-Flores M. Severe (grade IV) hypersensitivity to iodinated contrast agent in an anaesthetized dog. *Can Vet J*. 2019;60:766–769.
27. Scarabelli S, Cripps P, Rioja E, Alderson B. Adverse reactions following administration of contrast media for diagnostic imaging in anaesthetized dogs and cats. A retrospective study. *Vet Anaesth Analg*. 2016;43:502–510.
28. Pollard RE, Pascoe PJ. Severe reaction to intravenous administration of an ionic iodinated contrast agent in two anaesthetized dogs. *J Am Vet Med Assoc*. 2008;233:274–278.
29. Rodrigo-Mocholi D, Willems A, Schauvliege S, et al. Cardiopulmonary arrest in a cat as a result of a suspected anaphylactic reaction to an intravenously administered iodinated contrast agent. *Vet Anaesth Analg*. 2015;42: 554–555.
30. Gunkel CI, Valverde A, Robertson SA, et al. Treatment for a severe reaction to intravenous administration of diatrizoate in an anaesthetized horse. *J Am Vet Med Assoc*. 2004;224: 1143–1146.
31. Pollard RE, Puchalski SM. Reaction to intra-arterial iodinated contrast medium administration in anaesthetized horses. *Vet Radiol Ultrasound*. 2011;52:441–443.
32. McCready JE, Gardhouse SM, Appleby R, Beaufrère H. Mortality rate of birds following intravenous administration of iodinated contrast medium for computed tomography. *J Am Vet Med Assoc*. 2021;259:77–83.
33. Pollard RE, Puchalski SM, Pascoe PJ. Hemodynamic and serum biochemical alterations associated with intravenous administration of three types of contrast media in anaesthetized cats. *Am J Vet Res*. 2008;69:1274–1278.
34. Davis PL. Anaphylactoid reactions to the nonvascular administration of water-soluble iodinated contrast media. *Am J Roentgenol*. 2015;204, 1140–114.
35. *ACR Committee on Drugs and Contrast Media. ACR Manual on Contrast Media*. Reston: American College of Radiology; 2023. https://www.acr.org/-/media/ACR/files/clinical-resources/contrast_media.pdf.
36. Morcos SK, Thomsen HS. Adverse reactions to iodinated contrast media. *Eur Radiol*. 2001;11:1267–1275.
37. Walter PA, Feeney DA, Johnston GR. *Current Veterinary Therapy IX Small Animal Practice*. Philadelphia: Saunders; 1986.
38. Pollard RE, Puchalski SM, Pascoe PJ. Hemodynamic and serum biochemical alterations associated with intravenous administration of three types of contrast media in anaesthetized dogs. *Am J Vet Res*. 2008;69:1268–1273.
39. Vance A, Nelson M, Hofmeister EH. Adverse reactions following administration of an ionic iodinated contrast media in anesthetized dogs. *J Am Anim Hosp Assoc*. 2012;48:172–175.
40. Kan J, Milne M, Tyrrell D, Mansfield C. Lean body weight-adjusted intravenous iodinated contrast dose for abdominal CT in dogs reduces interpatient enhancement variability while providing diagnostic quality organ enhancement. *Vet Radiol Ultrasound*. 2022;63:719–728.
41. Kløw NE, Tande PM, Hevrøy O, Refsum H. Mechanism of ECG changes and arrhythmogenic properties of low osmolality contrast media during coronary arteriography in dog. *Cardiovasc Res*. 1990;24:303–308.
42. Grainger RG. Osmolality of intravascular radiological contrast media. *Br J Radiol*. 1980;53:739.
43. O'Donnell DH, Moloney MA, Bouchier-Hayes DJ, Lee MJ. Iodinated contrast media alter immune responses in pro-inflammatory states. *Acta Radiol*. 2010;51:635–640.
44. Gabelman A, Haberstroh J, Weyrich G. Ionic and non-ionic contrast agent-mediated endothelial injury. *Acta Radiol*. 2001;42:422.
45. Husted SE, Kanstrup H. Thrombotic complications in coronary angioplasty-ionic versus non-ionic low osmolar contrast media. *Acta Radiol*. 1998;39:340–343.
46. Morcos SK. Effects of radiographic contrast media on the lung. *Br J Radiol*. 2003;76:290–295.
47. Davenport D, Cohen MD, Hanna MP, et al. Studies of iodixanol in the rabbit lung and peritoneum. *Pediatr Radiol*. 1999;29:724–730.
48. Barone G, Ziemer LS, Shofer FS, Steinberg SA. Risk factors associated with development of seizures after use of iohexol for myelography in dogs. 182 cases. *J Am Vet Med Assoc*. 2002;220:1499–1502.
49. da Costa RC, Parent JM, Dobson H. Incidence of and risk factors for seizures after myelography performed with iohexol in dogs. 503 cases (2002–2004). *J Am Vet Med Assoc*. 2011;238:1296–1300.
50. Mullen KR, Furness MC, Johnson AL, et al. Adverse reactions in horses that underwent general anesthesia and cervical myelography. *J Vet Intern Med*. 2015;29:954–960.
51. Lexmaulova L, Zatloukal J, Proks P, et al. Incidence of seizures associated with iopamidol or iomeprol myelography in dogs with intervertebral disk disease: 161 cases (2000-2002). *J Vet Emerg Crit Care*. 2009;19:611–616.
52. Fatone G, Lamagna F, Pasolini MP, et al. Myelography in the dog with non-ionic contrast media at different iodine concentrations. *J Small Anim Pract*. 1997;38:292–294.
53. Larsen LE, Heglund IF, Fabian R, et al. Neural tolerability of iodixanol in mice and dogs after single and repeated intracisternal administration. *Acta Radiol Supplementum*. 1995;399:238–243.
54. Ghadiri A, Avizeh R, Faramarzi G. Comparison between iodixanol and iohexol for cervical myelography in cat. *IJVS*. 2015;10:23–29.
55. Perrin T, Descombes e, Cook S. Contrast-induced nephropathy in invasive cardiology. Incidence, pathophysiology, diagnosis, prevention and prognosis. *Swiss Med Wkly*. 2012;142:w13608.
56. Andreucci M, Faga T, Pisani A. The choice of the iodinated radiographic contrast media to prevent contrast-induced nephropathy. *Adv Nephrol*. 2014. https://doi.org/10.1155/2014/691623.
57. Ariyoshi S, Tanabe M, Ito K. Evaluation of the renal parenchymal retention of iodinated contrast agent during follow-up computed tomography performed one day after undergoing contrast-enhanced computed tomography. *Euro J Radiol*. 2020;132:109335.
58. Carr A, Reed A, Pope E. Persistent nephrogram in a cat after intravenous urography. *Vet Radiol Ultrasound*. 1994;35(5):350–354.
59. Goic JB, Koenigshof AM, McGuire LD, et al. A retrospective evaluation of contrast-induced kidney injury in dogs (2006–2012). *J Vet Emerg Crit Care*. 2016;26(5):713–719.

60. Griffin MA, Culp WTN, Palm CA, Poppenga RH. Suspected contrast-induced nephropathy in three sequential patients undergoing computed tomography angiography and transarterial embolization for nonresectable neoplasia. *J Am Vet Med Assoc*. 2021;259:1163–1170.
61. Ihle S, Kostolich M. Acute renal failure associated with contrast medium administration in a dog. *J Am Vet Med Assoc*. 1991;199(7):899–901.
62. Kirberger RM, Cassel N, Carstens A, et al. The effects of repeated intravenous iohexol on renal function in healthy beagles – a preliminary report. *Acta Vet Scand*. 2012;54(1):47.
63. Prüllage ML, Schwendenwein I, Eberspächer-Schweda KS. Does intravenous contrast medium administration result in altered renal biomarkers? A study in clinically stable cats with and without azotemia. *J Feline Med Surg*. 2022;24(6):565–579.
64. Cagnasso F, Bruno B, Bellino C, et al. Alterations of serum biochemical and urinary parameters in a canine population before and after intravenous contrast administration. *Vet Sci*. 2021;8:146.
65. Pasternak JJ, Williamson EE. Clinical pharmacology, uses, and adverse reactions of iodinated contrast agents. A primer for the non-radiologist. *Mayo Clin Proc*. 2012;87:390–402.
66. Devriendt N, van de Velde N, Stock E, et al. Suspected haemorrhagic cystitis in a dog as delayed complication after contrast-enhanced computed tomography. *Vet Rec Case Rep*. 2020. https://doi.org/10.1136/vetreccr-2019-001011.
67. Johnston GR, Stevens JB, Jessen CR, Osborne CA. Complications of retrograde contrast urethrography in dogs and cats. *Am J Vet Res*. 1983;44:1248–1256.
68. Lee WR, Pease AP, Berry CR. The effects of iohexol administration on technetium thyroid scintigraphy in normal cats. *Vet Radiol Ultrasound*. 2010;51:182–185.
69. Peremans K, Vandermeulen E, van Hoek I, et al. Interference of iohexol with radioiodine thyroid uptake in the hyperthyroid cat. *J Feline Med Surg*. 2008;10:460–465.
70. Pollard R, Puchalski S. CT contrast media and applications. In: Schwarz T, Saunders J, eds. *Veterinary Computed Tomography*. West Sussex: John Wiley & Sons; 2011.
71. Ackerman N, Wingfield WE, Corley EA. Fatal air embolism associated with pneumo-urethrography and pneumocystography in a dog. *J Am Vet Med Assoc*. 1972;160:1616–1618.
72. Zontine WJ, Andrews LK. Fatal air embolism as a complication of pneumocystography in two cats. *J Am Vet Rad Soc*. 1978;19:8–11.
73. Yigitaslan S, Erol K. Chemistry, physicochemical properties and pharmacokinetics of gadolinium-based contrast agents. In: Erturk SM, Ros PR, Ichikawa T, Saylisoy S, eds. *Medical Imaging Contrast Agents. A Clinical Manual*. Switzerland: Springer; 2021.
74. Rogosnitzky M, Branch S. Gadolinium-based contrast agent toxicity. a review of known and proposed mechanisms. *Biometals*. 2016;29:365–376.
75. Port M, Idée JM, Medina C, et al. Efficiency, thermodynamic and kinetic stability of marketed gadolinium chelates and their possible clinical consequences. A critical review. *Biometals*. 2008;21:469–490.
76. Lohrke J, Frenzel T, Endrikat J, et al. 25 Years of contrast-enhanced MRI. Developments, current challenges and future perspectives. *Adv Ther*. 2016;33:1–28.
77. Bendszus M, Roberts D, Kolumban B, et al. Dose finding study of gadopiclenol, a new macrocyclic contrast agent, in MRI of central nervous system. *Invest Radiol*. 2020;55:129–137.
78. Marks AL, Hecht S, Stokes JE, et al. Effects of gadoxetate (Eovist) contrast on magnetic resonance imaging characteristics of the liver in clinically healthy dogs. *Vet Radiol Ultrasound*. 2014;55:286–291.
79. Yonetomi D, Kadosawa T, Miyoshi K, et al. Contrast agent Gd-EOB-DTPA (EOB·Primovist®) for low-field magnetic resonance imaging of canine focal liver lesions. *Vet Radiol Ultrasound*. 2012;53:371–380.
80. Constant C, Hecht S, Craig LE, et al. Gadoxetate disodium (GD-EOB-DTPA) on contrast enhanced magnetic resonance imaging characteristics of hepatocellular carcinoma in dogs. *Vet Radiol Ultrasound*. 2016;57:594–600.
81. Muñoz A, Mateo I, Lorenzo V, Martínez J. Imaging diagnosis: traumatic dural tear diagnosed using intrathecal gadopentate dimeglumine. *Vet Radiol Ultrasound*. 2009;50:502–505.
82. Agnello KA, Puchalski SM, Wisner ER, et al. Effect of positioning, scan plane, and arthrography on visibility of periarticular canine shoulder soft tissue structures on magnetic resonance images. *Vet Radiol Ultrasound*. 2008;49:529–539.
83. Schaefer SL, Baumel CA, Gerbig JR, Forrest LJ. Direct magnetic resonance arthrography of the canine shoulder. *Vet Radiol Ultrasound*. 2010;51:391–396.
84. Prince MR, Arnoldus C, Frisoli JK. Nephrotoxicity of high-dose gadolinium compared with iodinated contrast. *J Magn Reson Imaging*. 1996;1:162–166.
85. Heinrich MC, Kuhlmann MK, Kohlbacher S, et al. Cytotoxicity of iodinated and gadolinium-based contrast agents in renal tubular cells at angiographic concentrations: in vitro study. *Radiology*. 2007;242:425–434.
86. Forsting M, Palkowitsch P. Prevalence of acute adverse reactions to gadobutrol—a highly concentrated macrocyclic gadolinium chelate: review of 14,299 patients from observational trials. *Eur J Radiol*. 2010;74(3):e186–e192.
87. Ichikawa S. Gadolinium-based contrast agent toxicity and accumulation. In: Erturk SM, Ros PR, Ichikawa T, Saylisoy S, eds. *Medical Imaging Contrast Agents: A Clinical Manual*. Switzerland: Springer; 2021.
88. Mair AR, Woodley J, Martinez M. Cardiovascular effects of intravenous gadolinium administration to anesthetized dogs undergoing magnetic resonance imaging. *Vet Anaesth Analg*. 2010;37:337–341.
89. Girard NM, Leece EA. Suspected anaphylactoid reaction following intravenous administration of a gadolinium-based contrast agent in three dogs undergoing magnetic resonance imaging. *Vet Anaesth Analg*. 2010;37:352–356.
90. Tucker PK, MacFarlane P. Severe bronchoconstriction as part of a suspected anaphylactic reaction in a dog following administration of gadobutrol. *Vet Record Case Reports*. 2020;8:e001051.
91. Argano M, Hewetson M, Kiviranta AM, Menzies MPL. Seizure-like activity after gadolinium administration in an anaesthetised foal undergoing magnetic resonance imaging. *Vet Record Case Reports*. 2018;6:e000636.
92. Thomsen HS, Morcos SK, Dawson P. Is there a causal relation between the administration of gadolinium based contrast media and the development of nephrogenic systemic fibrosis (NSF)? *Clin Radiol*. 2006;61:905–906.
93. Kanda T, Ishii K, Kawaguchi H, et al. High signal intensity in the dentate nucleus and globus pallidus on unenhanced T1-weighted MR images: relationship with increasing cumulative dose of a gadolinium-based contrast material. *Radiology*. 2014;270:834–841.
94. Richter H, Bücker P, Dunker C, et al. Gadolinium deposition in the brain of dogs after multiple intravenous administrations of linear gadolinium based contrast agents. *PLoS One*. 2020;15:e0227649.

95. Haers H, Saunders J. Review of clinical characteristics and applications of contrast-enhanced ultrasonography in dogs. *J Am Vet Med Assoc.* 2009;234(4):460–470.
96. Correas JM, Bridal L, Lesavre A, et al. Ultrasound contrast agents: properties, principles of action, tolerance, and artifacts. *Eur Radiol.* 2001;11:1316–1328.
97. Piscaglia F, Bolondi L. The safety of Sonovue in abdominal applications: retrospective analysis of 23188 investigations. *Ultrasound Med Biol.* 2006;32:1369–1375.
98. Seiler GS, Brown JC, Reetz JA, et al. Safety of contrast-enhanced ultrasonography in dogs and cats: 488 cases (2002-2011). *J Am Vet Med Assoc.* 2013;242(9):1255–1259.
99. Yamaya Y, Niizeki K, Kim J, et al. Anaphylactoid response to Optison and its effects on pulmonary function in two dogs. 2004. *J Vet Med Sci.* 2004;66:1429–1432.

ELECTRONIC RESOURCES

Additional information related to the content in Chapter 5 can be found online at eBooks.Health.Elsevier.com.

- Chapter Quiz

CHAPTER 6

Radiographic Interpretation

Donald E. Thrall

WHAT IS A RADIOGRAPH?

A radiograph is an image of the distribution of x-rays* that emerge from the patient. When struck by the primary x-ray beam, which is spatially uniform, there is differential absorption of x-rays by the different tissues in the body. This creates nonuniformity in the distribution of x-rays leaving the patient. The character of the nonuniformity is specific to the makeup of the tissue (Fig. 6.1). In normal subjects, the distribution of x-rays exiting the patient has a repeatable pattern, which is recognized as the normal appearance. When looking at radiographs of diseased patients, the examiner is looking for alterations in the distribution of the exiting x-rays that have been created by disease, and also by normal variations in anatomy. Artifacts will also influence the appearance of the final image. With experience, normal appearance and the effects of artifacts are recognized with more confidence, and different appearances of the distribution of exiting x-rays come to be associated with certain diseases. Many sources of normal radiographic anatomy are available to assist with interpretation, including this text, other published material,[1] and online.[2]

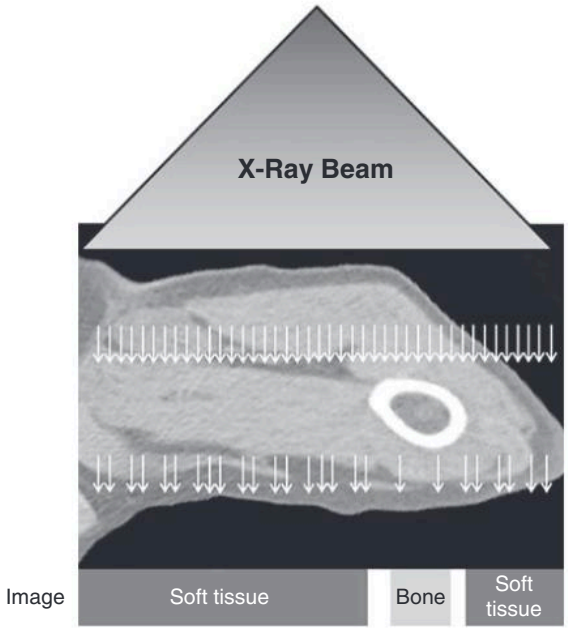


Fig. 6.1 The structure in the image is a transverse computed tomography (CT) image of a canine thigh, which represents a limb being radiographed. The white ring structure is the femur surrounded by muscle with fat in the fascial planes. The primary x-ray beam, represented by the *triangle*, is diverging and uniform. As x-rays (*arrows*) pass through the tissue, some are absorbed and some pass through. X-ray absorption will be relatively homogeneous in the soft tissues but increased in the femur, especially where the x-ray beam strikes the cortex tangentially. This creates a distribution of exiting x-rays that corresponds to the makeup of the thigh. The exiting x-rays are used to create a radiograph.

*Sometimes, the term *x-ray* is used incorrectly as a substitute term for radiograph. The term *x-ray* describes the energy used to create the image, not the radiographic image itself.

HOW X-RAY EXPOSURE IS REPRESENTED IN THE IMAGE

Crucial to proper interpretation of radiographs, and in comprehending radiology reports, is an understanding of the fundamental relationship of x-ray exposure with the degree of blackness or whiteness in the image. Areas of the radiograph that are *black* or *dark gray* are highly exposed regions where many x-rays pass through the patient and strike the imaging plate. Areas of the radiograph that are *white* or *light gray* are less-exposed regions where more x-rays were absorbed by the patient and fewer pass through and fewer strike the plate. Descriptions of blackness and whiteness in a radiograph are described in terms or lucency vs. opacity, respectively. Unfortunately, multiple synonyms are used to describe lucency and opacity (Table 6.1). The term *density or radiographic density* has also been used to describe film blackness and whiteness, i.e., dense = white. However, use of density has fallen out of favor and descriptions based on opacity are preferred.

RADIOGRAPHIC INTERPRETATION

The ability of x-rays to allow us to "see" inside of the body is taken for granted, perhaps because there are many other sophisticated technical advances that are commonplace. But the relatively simple process of using differential x-ray absorption in

Table • 6.1

Terms Used to Describe the Degree of Blackness or Whiteness in a Radiograph.

HIGHLY EXPOSED OR MORE EXPOSED (BLACKER) AREAS	UNEXPOSED OR LESS EXPOSED (WHITER) AREAS
Decreased opacity	Increased opacity
Less opaque	More opaque
Lucent	Opaque
Radiolucent	Radiopaque
Increased radiolucency	Decreased radiolucency



Fig. 6.2 Lateral view of the tibia of a cat. The history specified a lameness of 2 days' duration. The changes on the tibia are extensive, and it is highly unlikely that this extent of new bone formation could have developed over a 2-day interval. This is an example of a history that does not match the radiographic findings. This makes it difficult to assess the significance of the radiographic changes.

the patient to create a radiograph remains a mainstay of diagnostic medicine in both general and specialty practices. Maximizing the potential value of this relatively simple technique still requires constant and ardent attention to detail.

Many factors influence the accuracy of radiographic interpretation. The interpreter must have access to information pertaining to the patient.[3] This includes the signalment, medical history, and the physical abnormalities that are present. The history provided by the owner is often helpful in guiding radiographic interpretation, but the history may also be misleading. Recognizing that radiographic findings may not always agree with the history is a critical step in formulating a correct radiographic assessment (Fig. 6.2).

The physical examination is also very important regarding the identification of the region(s) that should be radiographed and in formulating a preliminary list of rule-outs. Radiographs should never be a substitute for a good physical examination. Also, one might expect radiographs to provide a definitive diagnosis, but more often they lead to a ranking of differential diagnoses, and provide direction for further patient evaluation with other tests or additional imaging.

When obtaining radiographs, it is critical that accurate positioning and proper radiographic technique be used. When compared to film (analog) imaging systems, the extreme exposure latitude that characterizes digital imaging has reduced the number of errors that occur as a result of incorrect kVp and/or mAs settings. However, overexposure and underexposure are still problems, along with poor positioning and lack of proper views. When an owner agrees to have radiographs of their animal made, a contract has been established between the client and veterinarian and implicit in that is the production of adequate images. Unfortunately, many substandard radiographs of animal patients are produced each day. Submission of poor images to a teleradiology service for interpretation by a specialist cannot compensate for errors in radiographic acquisition.

Positioning is not discussed in detail in this book, but the standard views recommended for various areas are outlined in other chapters. One aspect of positioning is important to mention here. It has become common for practices to include the whole body of cats and small dogs in one image, i.e., cat-o-gram and dog-o-gram, respectively. This should be avoided as the anatomy at the cranial and caudal edge of the image will be distorted because these regions are struck by very diverging x-rays. Also, a single radiographic exposure technique will not be optimal for the very different makeup of the thorax vs. abdomen. There is no reason to avoid getting individual studies of both the thorax and abdomen in all patients.

Once suitable radiographs of the patient have been produced, interpretation should be done in a quiet, relatively isolated, environment. This seems obvious, but taking the time to make sure the viewing environment is suitable will pay off with increased accuracy. Concentration and thoroughness are the major determinants of accurate interpretation.

Many of us never receive any instruction in actually how to examine a radiograph. Some people develop a highly accurate examination method whereas others are never able to accomplish this. Everyone will look at radiographs differently. Some look from the periphery to the center, others from the center to the periphery and some haphazardly. Regardless of the examination method, the most important aspect of viewing is to make sure that the entire image is examined. Not finding a lesion is often linked to not looking rather than not seeing. Having a checklist of the regions/structures to be examined will also help in making sure that the entire image is examined. Examples of checklists are included in Chapters 9, 17, 28, and 38.

In addition to examining the overall "real estate" of the image, there is an ancillary examination method that can be useful in evaluating juvenile bone disease. This is called *targeted viewing*. Certain bone diseases have a propensity for certain areas of the skeleton, e.g., osteochondrosis in the caudal humeral head, metaphyseal osteopathy/hypertrophic osteodystrophy (HOD) in the distal radius and ulna, and canine panosteitis in the diaphysis of long bones. Therefore, if during the clinical examination of a young, lame dog, a specific disease is suspected, the commonly affected area should be examined closely in the radiograph. This targeted viewing is ancillary to the general overview and will reduce the incidence of subtle lesions being overlooked.

NAMING AND VIEWING RADIOGRAPHS

There is a systematic naming system for radiographic views that employs standardized terminology (Fig. 6.3). Standardized naming of views allows correct interpretation of radiology reports and implementation of recommendations for additional images. Radiographic views are named according to the location that the central ray of the primary x-ray beam traverses the body part of interest, from point-of-entrance to point-of-exit.[4] For example, an abdominal radiograph made with the dog in dorsal recumbency and an overhead, vertically directed, x-ray beam is a ventrodorsal view. With the dog in ventral recumbency, it is a dorsoventral view. The same method is used for other body parts, with the appropriate directional term applied.

An exception to this system of image nomenclature is that lateral radiographs of the head, neck, thorax, abdomen, and pelvis are usually abbreviated according to side of the body that the patient is lying on, rather than using the more accurate

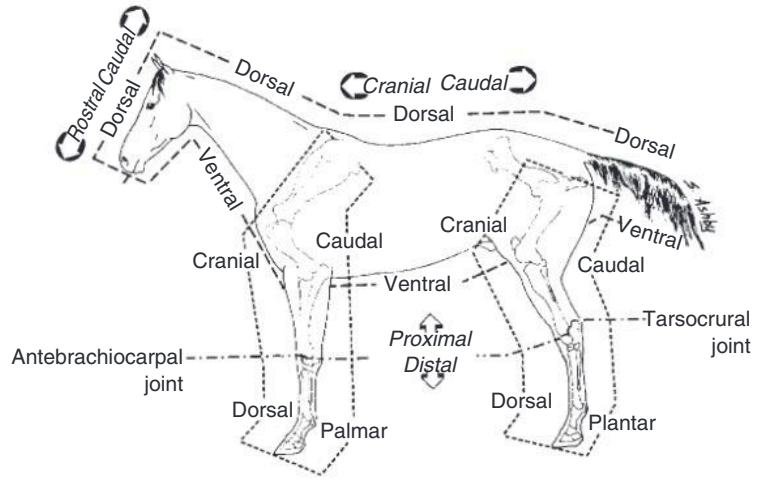


Fig. 6.3 Proper anatomic directional terms as they apply to various parts of the body. (Courtesy Dr. J. E. Smallwood.)

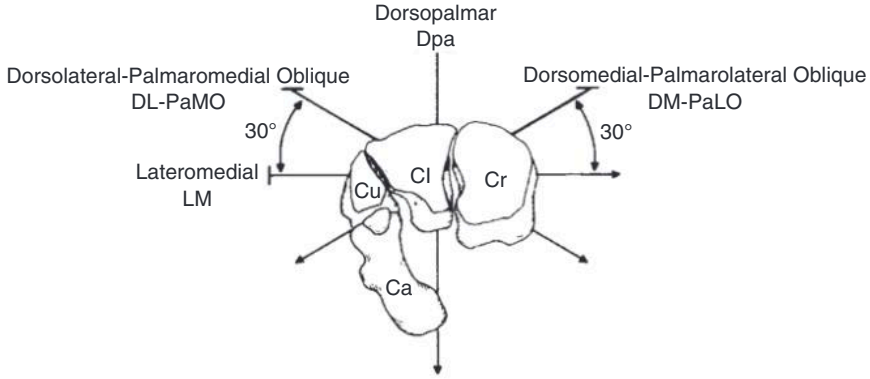


Fig. 6.4 Transverse plane view of the proximal row of equine carpal bones illustrating the principle of naming radiographic projections by the direction of the primary x-ray beam from the point of entrance to the point of exit. (Courtesy Dr. J. E. Smallwood.)

point-of-entrance to point-of-exit method. For example, an abdominal radiograph with the patient lying on the left side is referred to as a left lateral rather than the more correct right-left lateral.

Oblique views are also named by designating the points of entrance and exit (Fig. 6.4). Angles of obliquity can be specified by inserting the number of degrees of obliquity between the directional terms involved. For example, if the dorsolateral palmaromedial oblique (DLPaMO) view in Fig. 6.4 was made by positioning the x-ray tube 60 degrees laterally with respect to dorsal, the designation would be D60LPaMO.

Standardizing the orientation of images for viewing is also important. The brain learns what to expect a certain part to look like when oriented a certain way. Therefore, images should be oriented on the monitor in a predetermined orientation, not randomly. The following has become the standard for image orientation:

- Lateral views of any part are oriented with the cranial (rostral) aspect of the animal pointing to the interpreter's left.
- Ventrodorsal or dorsoventral radiographs of the head, neck, or trunk are oriented with the cranial (rostral) part of the animal pointing up and with the left side of the animal to the interpreter's right.
- Lateromedial or mediolateral radiographs of the extremities, including oblique projections, are oriented with the proximal aspect of the limb pointing up and the cranial or dorsal aspect of the limb to the interpreter's left.
- Caudocranial (plantarodorsal, palmarodorsal) or craniocaudal (dorsopalmar, dorsoplantar) radiographs of the extremities are oriented with the proximal end of the extremity at the top. No convention exists regarding whether the medial or lateral side of the extremity is oriented to the interpreter's right or left.

RADIOGRAPHIC OPACITIES

Various body parts and lesions appear differently in radiographs because a change in the makeup of a tissue will change the x-ray absorption pattern. The extent that a radiograph is able to display differences in blackness or whiteness between various structures is termed *contrast resolution*. Radiographs have poorer contrast resolution than either computed tomography or magnetic resonance images. Therefore, many normal structures and pathologic states that differ only slightly in x-ray absorption will not be able to be identified in radiographs. It takes a relatively large difference in x-ray absorption for a difference in radiographic opacity to be created. As a result, there are only a few distinct differences in radiographic opacity. These opacities are described according to the appearance of only five tissues or objects—*air* (or *gas*), *fat*, *water* (or *fluid* or *soft tissue*), *bone* (or *mineral*), and *metal* (Figs. 6.5 and 6.6). Importantly, a radiographic opacity is not specific for any particular tissue or substance, but only indicates a group of tissues or substances

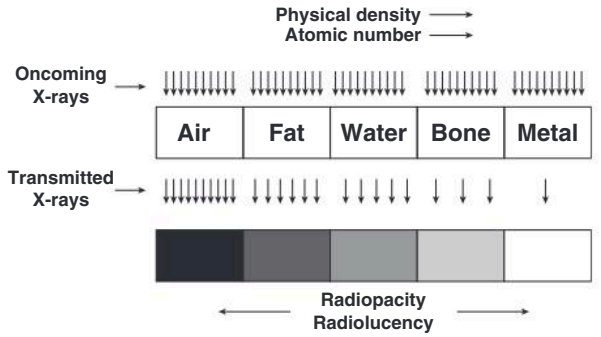


Fig. 6.5 Identical thicknesses of air, fat, water, bone, and metal are struck by an equal number of x-rays. Each material absorbs x-rays differently (differential absorption), depending on the physical density and effective atomic number of the material. This results in five distinct opacities.

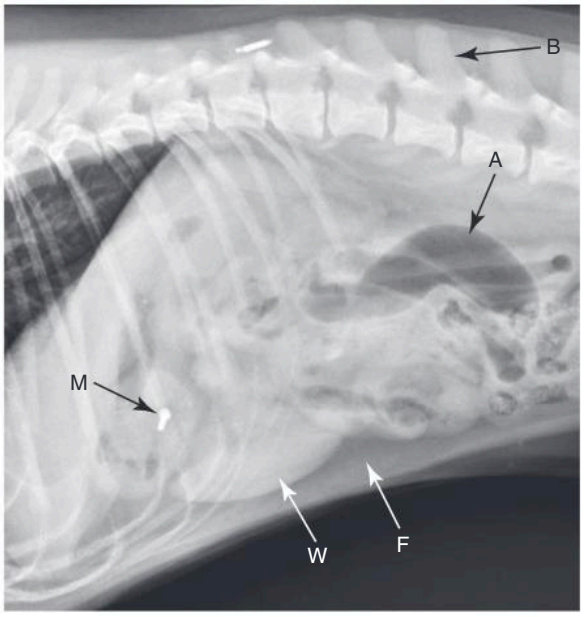


Fig. 6.6 Lateral radiograph of the cranial aspect of the abdomen of a dog. All five radiographic opacities are visible. For example: Air (*A*)—gas in the lumen of the bowel; Fat (*F*)—fat in the omentum; Water (*W*)—the spleen; Bone (*B*)—the spinous process of a vertebra; Metal (*M*)—a foreign body in the stomach. The slightly more radiolucent nature of fat vs. soft tissue is critical in abdominal radiography, as the contrast provided by fat is the reason why most abdominal organs are visible radiographically. Water opacity is a generalization and is also called fluid or soft tissue opacity. Most organs and fluids have this opacity.

that have a similar x-ray attenuation properties (Table 6.2). These five descriptive terms (the five opacities) are used regularly in radiology reports and in conversation to describe radiographic findings.

Thickness also affects radiographic opacity. As thickness increases, the radiopacity will increase (Fig. 6.7). Thus, the five basic opacities are relative, assuming a similar thickness.

RADIOGRAPHIC CONTRAST

An individual structure will not be visible in a radiograph unless there is another structure of a different radiographic opacity that is in contact with it to provide *contrast*. Examples are liver margin visible due to adjacent fat, bone margin visible due to adjacent muscle, and pulmonary vessel margin visible due to adjacent air in the alveoli. Images can have varying degrees of contrast. A *high-contrast* image is one that has mostly blacks and whites and few gray shades, whereas a *low-contrast* image is one that has many gray shades and few blacks and whites (Fig. 6.8). To some extent, this depends on the relative values of kVp vs. mAs, but in digital imaging systems the contrast of the image is affected mainly by the processing algorithm the computer applies to the image data (see Fig. 6.8).

Table • 6.2

Examples of Various Tissues and Substances Having the Same Radiographic Opacity.

RADIOGRAPHIC OPACITY	SUBSTANCES HAVING THAT OPACITY
Air (gas)	Any gas collection present in the body • Air in lung or bowel • Gas in the colon from performing a pneumocolonogram • Nitrogen in a joint from the vacuum phenomenon • Gas from bacterial fermentation • Gas pockets from an injury • Free gas in abdomen after laparotomy • Tissue gas after fracture or joint surgery
Fat	Any tissue composed mainly of fat • Omentum • Mediastinal fat • Intrafascial fat • Falciform fat • Retroperitoneal fat • A lipoma
Water (soft tissue)	Any fluid or soft tissue • Parenchymal organs • Fibrous connective tissue • Muscle • Ligaments • Tendons • Cartilage • Blood • Bile • Cerebrospinal fluid • Urine • Transudate • Exudate • Hematoma • A soft tissue tumor
Bone (mineral)	Any mineralized region • Normal skeletal components • Ingested bone (before digestion) • Periosteal reaction • Dystrophic calcification, as from a calcifying hematoma • Metastatic calcification, as from renal failure
Metal	Anything containing metal • Metallic internal fixation devices • Identification microchip • Bullets or bullet fragments • Ingested foreign material • Horseshoe nails

More pertinent to radiographic interpretation is knowing that the contrast between two structures having the same opacity will be lost if they are in contact, and the borders will not be visible in the image. This is called the silhouette sign (Fig. 6.9) and explains why some normal structures are not visible in radiographs (Fig. 6.10). Also, a regional or complete loss of the border of an organ due to the silhouette sign can also be an important sign of disease (Fig. 6.11). This pathologic loss of a border due to the silhouette sign has also been referred to as *border effacement*. Many other examples of the silhouette sign are provided throughout this book as a part of describing how various diseases appear.

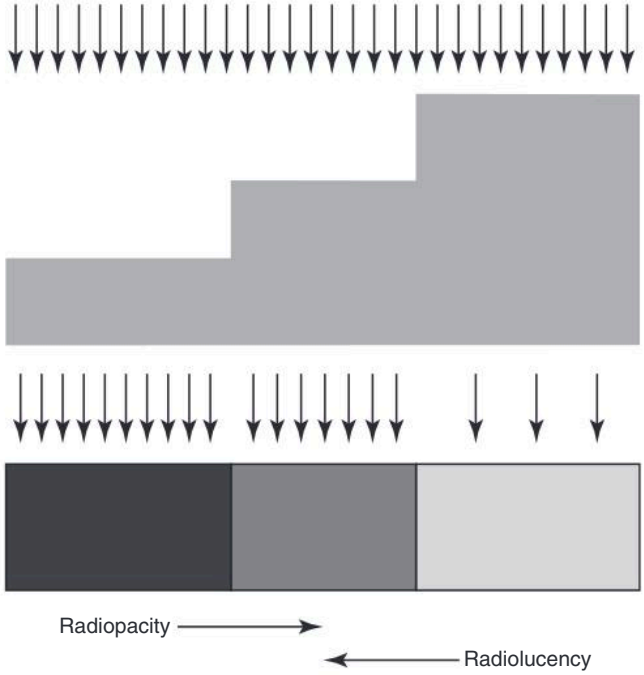


Fig. 6.7 Increasing the thickness of the part increases x-ray absorption and reduces the number of x-rays that pass through. The image will be more opaque under thicker parts of the object or patient.

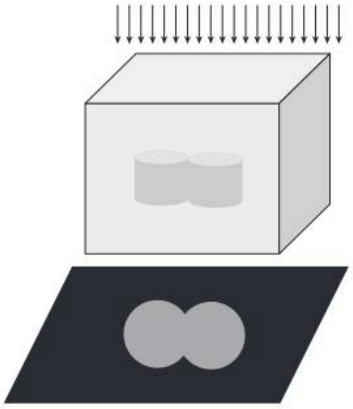


Fig. 6.9 Diagram of the concept of the silhouette sign. The two cylinders have the same radiographic opacity and are in contact. There is no contrasting tissue or substance between them. In the resultant image, the border between the cylinders will not be visible because there is no intervening substance of another radiographic opacity.

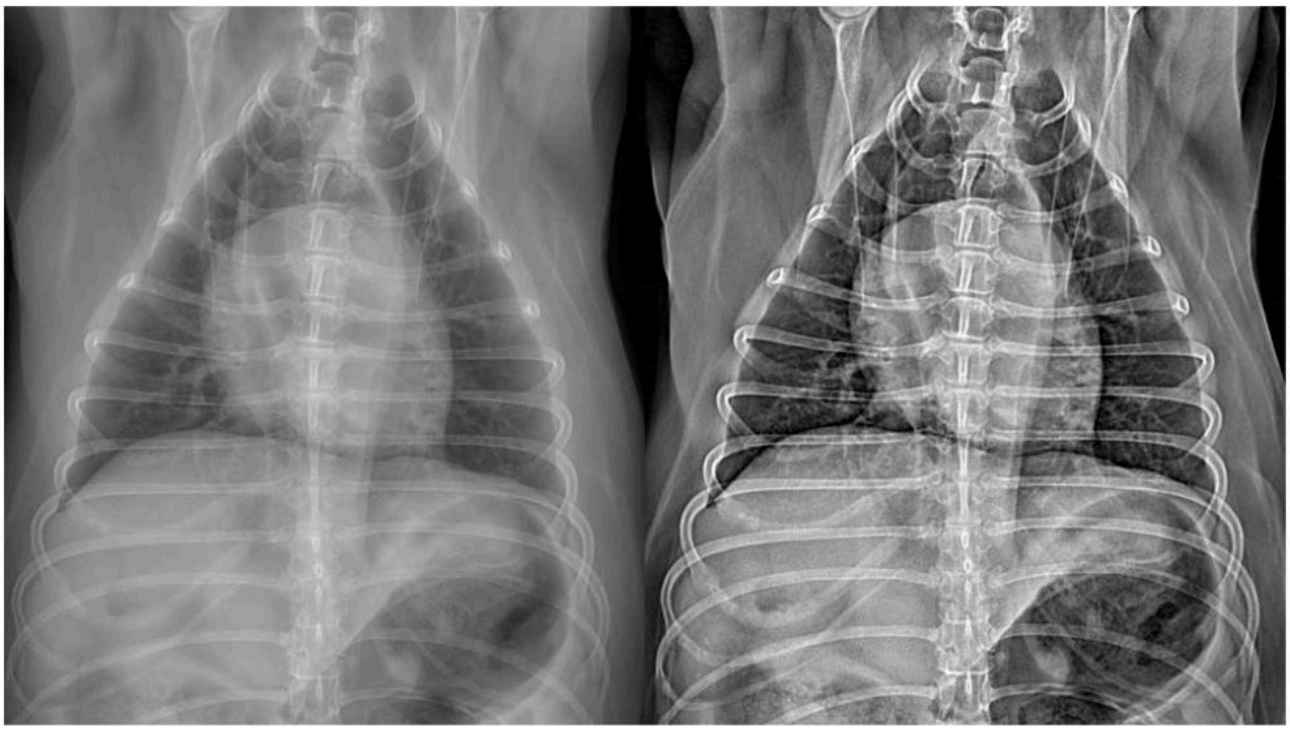


Fig. 6.8 Ventrodorsal digital radiographs of the same dog made using the same mAs and kVp. The image on the *left* was processed with a low contrast algorithm and the one on the *right* with a high contrast algorithm. Note the differences in blacks vs. grays vs. whites between low and high contrast images.

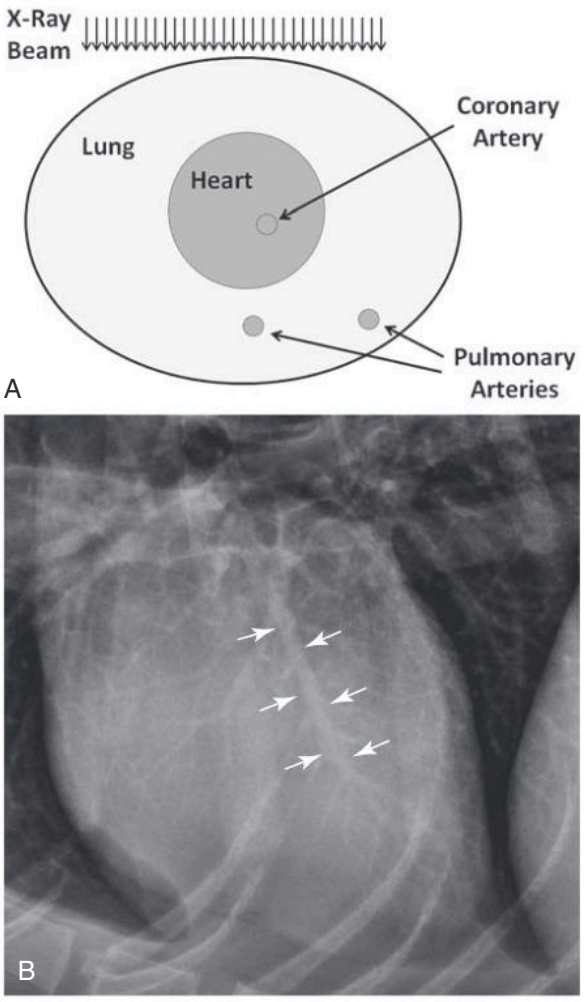


Fig. 6.10 The silhouette sign in action. **A,** Illustration of the x-ray beam striking a lung with two pulmonary arteries and the heart with one coronary artery. In the radiograph, the coronary artery will not be visible because it is surrounded by the myocardium, which has the same radiographic opacity. Both pulmonary arteries will be visible because they are surrounded by air, which provides contrast. **B,** Lateral thoracic radiograph. The vessel superimposed on the heart (*arrows*) is often mistaken for a coronary artery, but this is not possible; it must be a pulmonary vessel surrounded by air.

DESCRIBING ABNORMALITIES

Abnormalities identified in a radiograph must be described in some format and then communicated. This might be in the form of communication with the owner, documenting the findings in the medical record, or in a formal radiographic report. The *Roentgen sign* approach has withstood the test of time as a method for describing radiographic abnormalities. This approach is used throughout this book, in most radiology teaching environments, and by most radiology specialists. The Roentgen sign approach involves describing abnormal radiographic changes using one or more of six terms (Box 6.1), and represents a simple and understandable way to communicate abnormal radiographic findings. Once the Roentgen signs have been compiled, they are considered along with the clinical information to arrive at a list of possible causes, or diseases. This list of possibilities is termed a *gamut*. The mnemonic DAMNITV is an aid to compiling the most reasonable gamuts, and to decrease the chance that an important possibility is not considered. DAMNITV stands for degenerative, anomalous, metabolic, neoplastic, infectious (inflammatory, immune), traumatic, and vascular origins of disease.

RADIOGRAPHIC GEOMETRY

A radiographic image is a two-dimensional representation of a three-dimensional object. One effect of this is a loss of depth perception (Fig. 6.12). Depth perception is improved by acquiring two radiographs at 90 degrees to each other. Such radiographs are termed *orthogonal* radiographs and can be used to mentally reconstruct the third dimension (Fig. 6.13). At least two orthogonal views of a part should be acquired in every radiographic examination. Sometimes even with multiple radiographic views, a more sensitive tomographic[†] modality, such as computed tomography, will be needed to localize a lesion conclusively.

Since patients have thickness, some parts will be closer to the x-ray tube than others when the radiograph is made. The parts closer to the x-ray tube, and further from the plate, will be magnified (Fig. 6.14). As magnification increases, so does image blur (Fig. 6.15). A familiar example of this is the shadow of a hand against a wall cast by a flashlight. The closer the hand gets to the flashlight, the shadow gets larger but is more blurry. The absolute value of the magnification factor can be calculated by dividing the distance from the x-ray focal spot to the plate by the distance from the x-ray focal spot to the part of interest. No matter how the patient is positioned, there will always be some parts that are closer to the x-ray tube than others. Therefore, it is not possible to eliminate magnification from radiographs. This is one reason that patients are always positioned the same and images are always oriented the same…so that the effects of magnification become part of the normal radiographic anatomy.

In addition to there being a difference in distance of various parts of the body from the x-ray tube, the orientation of different parts with respect to the x-ray tube also differs. For an image of an object to accurately represent that object, the object must be parallel to the plate. If the object is angled, the image is distorted and no longer represents the object accurately (Figs. 6.16 and 6.17). As with magnification, it is not possible to eliminate distortion from radiographs as some parts are never parallel to the plate. This is another reason for consistency in patient positioning and image orientation.

Many structures in the patient will overlap relative to the path of the x-ray beam. Thus, in the two-dimensional image, this overlapping either creates an opacity that does not exist in the patient (*summation*) or an opacity that is misplaced and misinterpreted as a lesion (*superimposition*).

Summation is an area of altered opacity occurring when two overlapping objects are in the path of the x-ray beam but are not in contact with each other (Fig. 6.18). Summation creates an opacity that is not actually in the patient. Summation opacities are usually white (opaque) but can be black (lucent). Consider a block of Swiss cheese. When looking at the cheese visually, the holes on the exterior are caused by a cut made through gas bubbles that formed as the cheese fermented. However, there are other gas bubbles completely encased within the block, some of which overlap when viewed from the perspective of the x-ray beam. If the cheese is radiographed, fewer x-rays are absorbed in areas where gas bubbles overlap. The more overlapping bubbles that are present, the greater the number of x-rays that penetrate the cheese and reach the plate (Figs. 6.19 and 6.20). In the Swiss cheese, the summation opacities are radiolucent. In patients, summation usually creates an area of increased opacity. The most common *opaque* summation shadow in patients results from overlapping of the kidneys in a lateral abdominal radiograph. This

[†]A tomographic modality produces images in thin slices, or in a thin plane, which eliminates the problem of spatial localization.

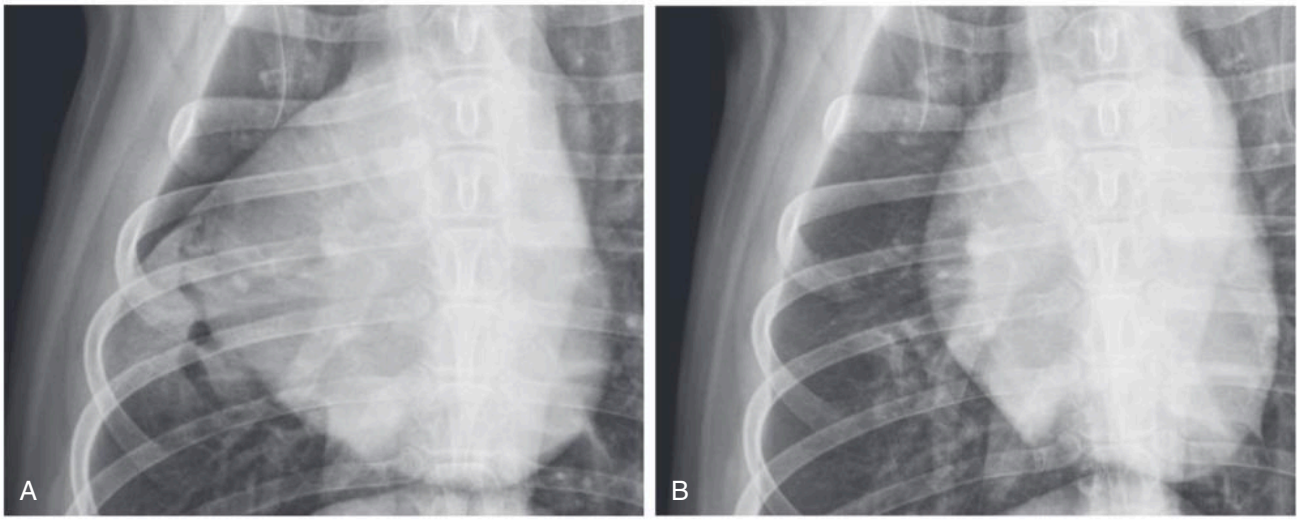


Fig. 6.11 **A,** Ventrodorsal radiograph of a dog with pneumonia in the right middle lung lobe. As the abnormal lung lobe and the cardiac silhouette both have a soft tissue opacity, the border of each is obliterated in the region where they are in contact, and the edge of the heart cannot be discerned. **B,** After resolution of the pneumonia, the true shape and size of the heart can be determined because the heart now touches aerated lung, which provides contrast.

Box • 6.1

Roentgen Signs Used to Describe Radiographic Findings

Size
Shape
Location
Number
Margination
Opacity

leads to an obvious opacity at the intersection of the caudal pole of the right kidney with the cranial pole of the left kidney (Fig. 6.21). Other examples of summation opacities are discussed throughout this book.

Superimposition is the image of an actual structure but the image is in a location where it can be misinterpreted as disease. Of course, there is extensive superimposition of structures in every radiograph, and superimposition opacities are common. As a result of repetitive viewing of radiographs in a standard fashion and using standard patient positioning, most of this superimposition becomes recognized as normal (Figs. 6.22 and 6.23). The intensity of many superimposition opacities seems out of proportion to the small absolute size of the structure, such as in Fig. 6.23. The disproportionate

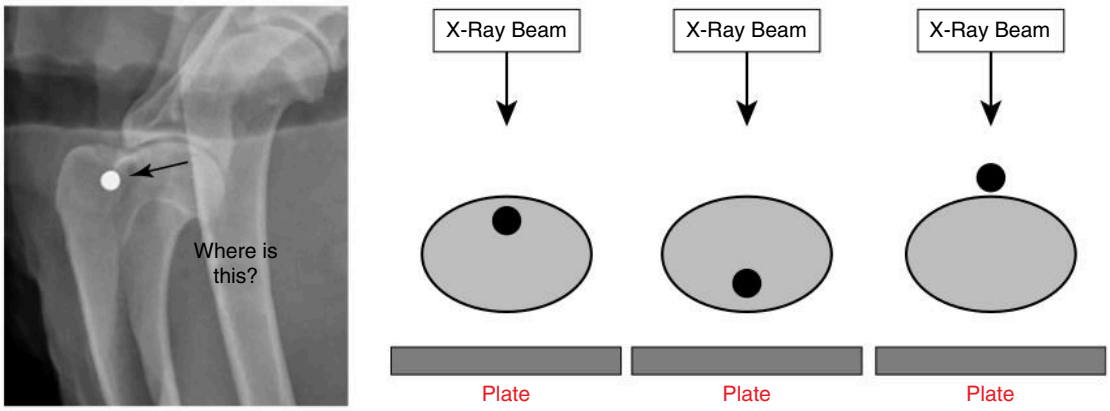


Fig. 6.12 The focal circular metallic opacity visible in the radiograph is a shotgun pellet. From this one view, the location of this pellet cannot be determined. The pellet could be in the patient close to the nondependent surface, in the patient close to the dependent surface, or anywhere in between. The pellet could also be outside of the patient.

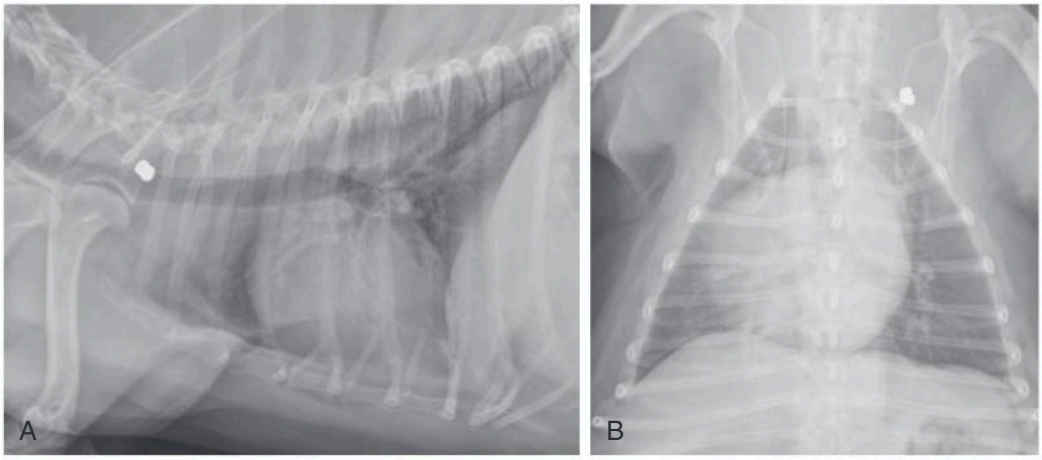


Fig. 6.13 Lateral (**A**) and ventrodorsal (**B**) thoracic radiographs of a dog with an air pellet foreign body. The exact location of the pellet cannot be determined from either image alone. By having these orthogonal radiographs, it can be concluded that the pellet is in the soft tissues just to the *left* of the thoracic inlet.

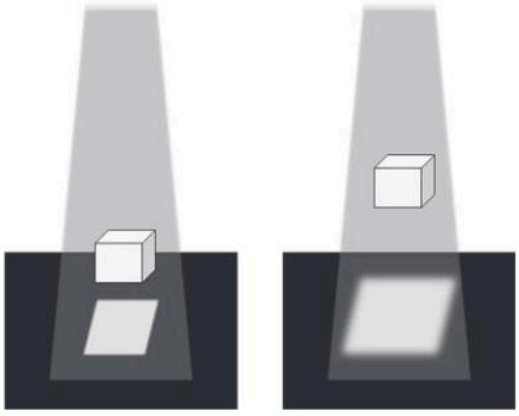


Fig. 6.14 Geometry of magnification. Objects closer to the x-ray tube will be magnified and the border will be less sharp.

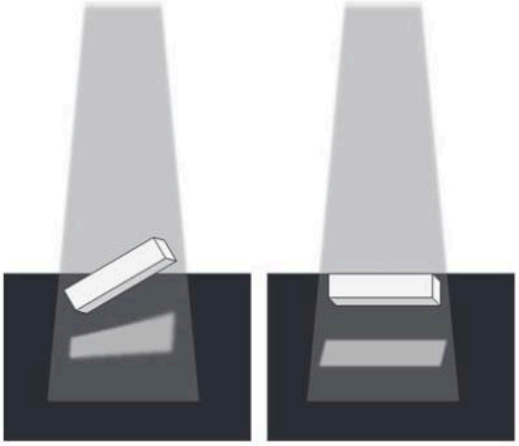


Fig. 6.16 Geometry of distortion. In the *left panel*, the object is not parallel to the plate. Therefore, the part of the object closer to the x-ray tube will be magnified more than the other part. This uneven magnification is termed *distortion*. Greater distortion also increases blur.

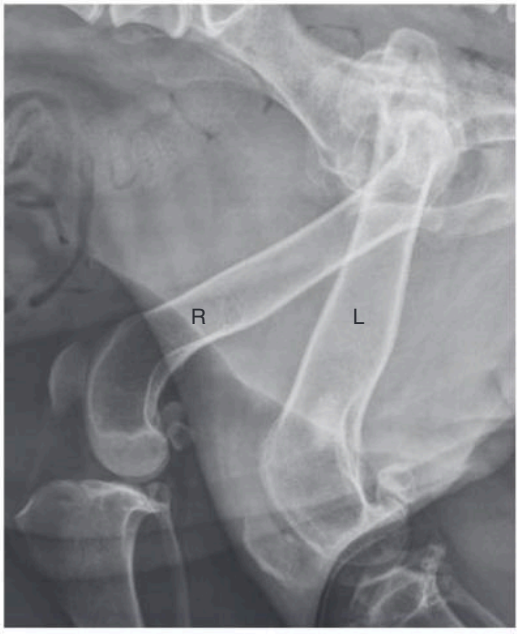


Fig. 6.15 Magnification leads to unsharpness in the image. Lateral view of the pelvis of a dog in right lateral recumbency. This means the right femur (*R*) is closer to the plate, and left femur (*L*) is closer to the x-ray tube. The image of the left femur will be magnified. Note the increased diameter of the left femur compared with the right femur (*R*). The image of the left femur is also less sharp than the image of the right femur.



Fig. 6.17 Ventrodorsal view of the pelvis of a dog with a painful left hip. The left pelvic limb could not be extended because of pain and is angled, with the left stifle farther from the plate than the right. This creates distortion of the left femur making it appear shorter than the right and asymmetrically magnified.

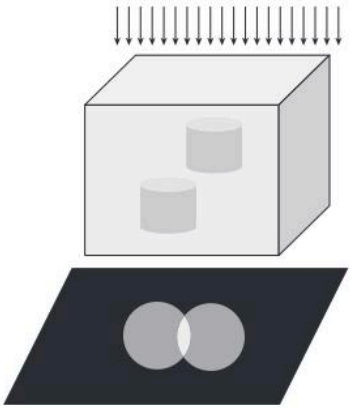


Fig. 6.18 Diagram of the concept of summation. The two cylinders are not in contact but in the region of overlap, there will be increased x-ray absorption that will create a well-defined region of increased opacity in the image that does not exist in the patient.

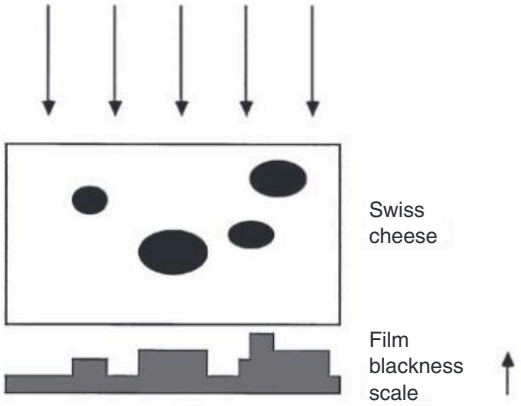


Fig. 6.19 The *rectangle* represents a block of Swiss cheese and the *black ovals* represent gas bubbles. Some of the gas bubbles will overlap from the perspective of the x-ray beam, which is represented by the *arrows*. The two gas bubbles on the *left* will not be superimposed and the larger bubble will create a more radiolucent region. The two bubbles on the *right* overlap partially and in this region the radiolucency is increased over that produced from either bubble alone. This region of increased radiolucency is a summation opacity and does not correspond to any physical part of the cheese.

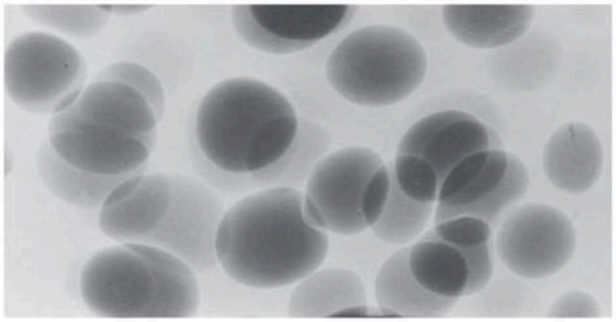


Fig. 6.20 Radiograph of a block of Swiss cheese. There are numerous radiolucent gas bubbles in the cheese. Areas where the bubbles overlap are more radiolucent due to decreased x-ray absorption. Areas where zero, two, three, and four bubbles overlap can be identified. These summation shadows are radiolucent.

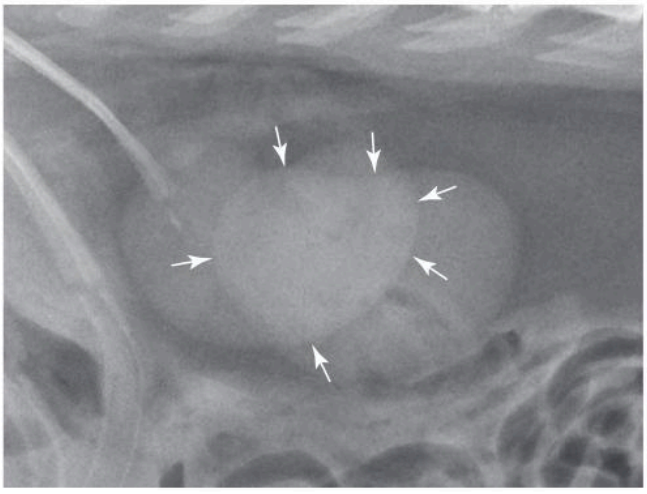


Fig. 6.21 Close-up of the kidneys in a lateral abdominal radiograph of a cat. The kidneys are partially superimposed, resulting in a positive summation shadow (*white arrows*). This opacity could easily be confused with a mass, or with a misshapen kidney. There is no actual structure in the patient with the shape of a summation opacity.

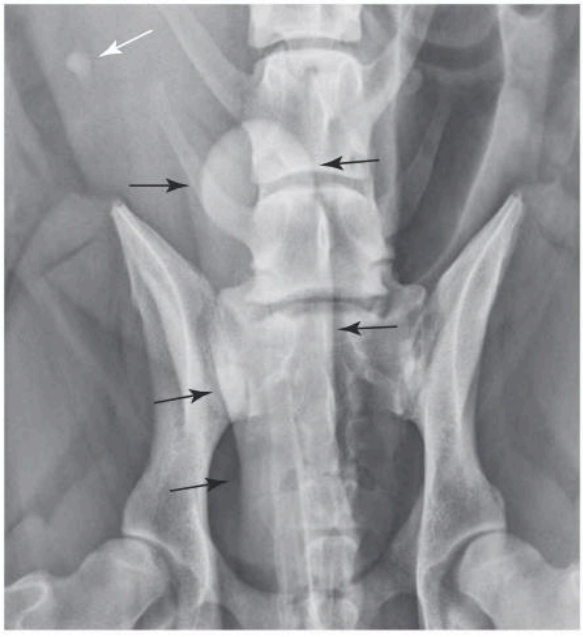


Fig. 6.22 Ventrodorsal radiograph of the caudal abdomen of a male dog. Superimposition of a nipple (*white arrow*) and the prepuce (*black arrows*) have created conspicuous superimposition opacities. These structures are seen commonly and have become recognized as a normal variation.

opacity is due to the structure being surrounded by air and the margin being parallel to the x-ray beam (Fig. 6.24). Many superimposition opacities become recognized as part of the normal spectrum but there are also unique situations where the superimposition opacity could easily be misinterpreted as disease (Figs. 6.25 and 6.26).

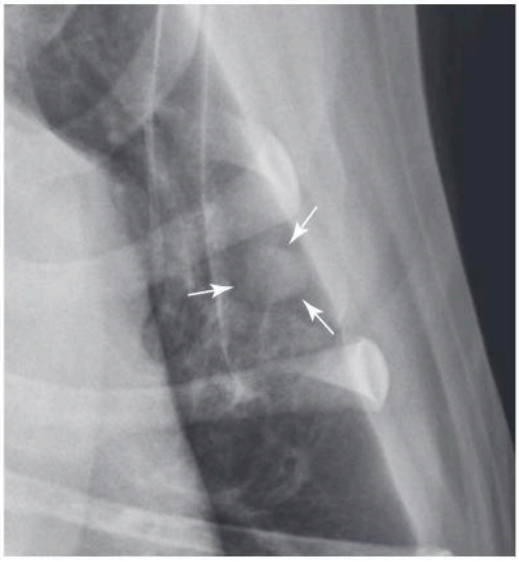


Fig. 6.23 Close-up of a portion of a ventrodorsal thoracic radiograph of a dog. A nipple creates a superimposition opacity (*arrows*) that could be confused with a pulmonary nodule. This particular superimposition artifact occurs commonly and has become recognized as a normal variation. The opacity of the nipple seems out of proportion to its real thickness. This results from air providing contrast against a superficial structure having sides that are parallel to the x-ray beam.

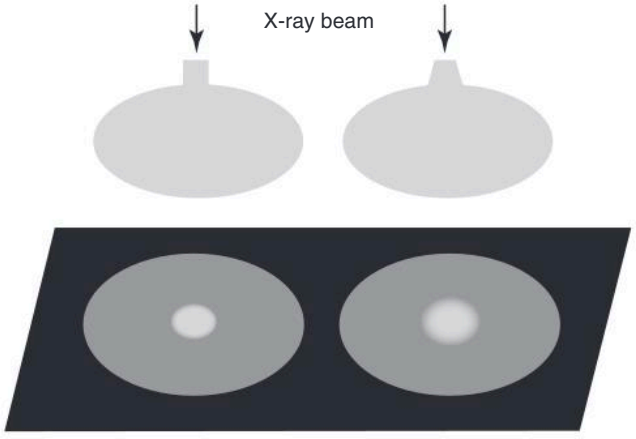


Fig. 6.24 Illustration of why small superficial masses can result in very conspicuous superimposition opacities. On the *left*, the mass has perpendicular sides, is surrounded on all sides by air and the x-ray beam is parallel to the edge of the mass. On the *right*, a comparably sized mass has sloping sides that are not parallel to the primary x-ray beam. This mass will be less conspicuous in the image because the borders are less defined, even though its inherent opacity may be identical.



Fig. 6.25 Lateral view of the caudal aspect of the trunk of a dog. A gastrocnemius fabella is superimposed on the urethra (*black arrow*). This could be misinterpreted as urethral calculus. (Image from Thrall DE, Robertson ID. *Atlas of Normal Radiographic Anatomy and Anatomic Variants in the Dog and Cat*. 3rd ed. St. Louis: Elsevier-Saunders; 2023.)

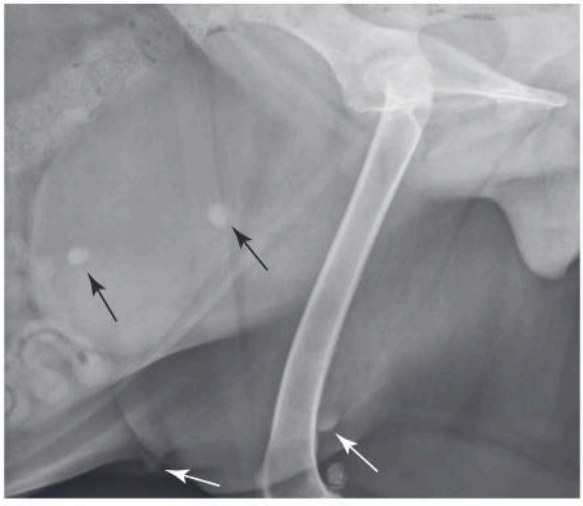


Fig. 6.26 Open-leg lateral view of the femur of a dog. The contralateral femur has been abducted and is dorsal to the trunk. As a result, ventral abdominal soft tissues are also pulled dorsally resulting in two nipples being superimposed on the urinary bladder (*black arrows*), where they could be misinterpreted as cystic calculi. The contralateral nipples are visible ventrally (*white arrows*).

REFERENCES

1. Thrall DE, Robertson ID. *Atlas of Normal Radiographic Anatomy and Anatomic Variants in the Dog and Cat*. 3rd ed. St. Louis: Elsevier-Saunders; 2022.
2. *Imaging Anatomy*. College of Veterinary Medicine, University of Illinois; 2019. https://vetmed.illinois.edu/imaging_anatomy/index.html.
3. Loy CT, Irwig L. Accuracy of diagnostic tests read with and without clinical information: a systematic review. *JAMA*. 2004;292:1602.
4. Smallwood JE, Shively MJ, Rendano VT, et al. A standardized nomenclature for radiographic projections used in veterinary medicine. *Vet Radiol*. 1985;26:2.

ELECTRONIC RESOURCES

Additional information related to the content in Chapter 6 can be found online at eBooks.Health.Elsevier.com.

- Chapter Quiz

CHAPTER 7

Errors and Pitfalls in Radiographic Interpretation

Eli B. Cohen

To recognize and prevent errors and potential pitfalls in any type of image interpretation, it is important to first understand how our eyes and brains work to view and interpret an image. At the core, interpreting images is composed of physical vision (looking at an image), visual perception (what we see), and cognitive decision making (interpreting what we see).[1–3] Different types of errors or pitfalls can occur in each pathway.

HOW WE SEE

Light reaching the eye, or luminance, must occur before we can perceive an image. Luminance is regulated by the amount of light incident on surfaces, reflected or absorbed by those surfaces, and whether there are other conditions in the air or media the light is passing through that can further scatter or interfere with the light.[4] Once light reaches the eye, visual perception can occur. This is the first step in image interpretation, as no analysis of an image can be made before it is viewed. When light strikes the retina, the response is not homogeneous. At the center of the retina is the fovea which contains the largest concentration of cone cells and the largest number of neurons dedicated to it from the primary visual cortex. As a result, the fovea is the portion of the retina with the highest visual acuity and contrast sensitivity. However, the physical world is more complex than can be resolved by the retina and transmitted to the brain, resulting in a compressed signal which is then augmented by memory.[5] In this way, while light signal may strike the retina and activate neurons, what is actually seen or perceived is in part a construction by the observer (Fig. 7.1).[3] This includes mechanisms such as lateral inhibition of the retina, whereby light not only stimulates light receptors of the retina, but also results in inhibition of neighboring light receptors to enhance edge detection. We perceive lateral inhibition as optical illusions known as Mach lines (also called Mach Phenomenon, Mach bands, edge effect), which are bright or dark lines that are not real at the edges of real objects.[5,6] This is just one type of optical illusion, as the light we perceive as a representation of the physical world also relates to the type, number, and depth of surfaces or objects. Our visual system also biases us to perceive the highest luminance in a scene as white, so the background impacts what we focus on (Fig. 7.2).[4] What we see or perceive, therefore, is not an accurate representation of the physical world. Understanding these optical illusions that are always at play can help us to recognize and leverage them to avoid misperception.

Human vision has a large field of view (over 180 degrees), but foveal vision has a small visual angle (1–2 degrees). When viewing images, we either move our eye or head to place objects of interest into foveal vision. When a visual target is at a visual angle of 2 to 30 degrees from us, the eye will move, and when it is more than 30 degrees the head will move.[7–9] This is why most people do not want to sit in the front row of a movie theater, as you have to constantly turn your head to keep the scene in your foveal vision. This is also why it can be helpful to move away from the screen when viewing radiographs (foveate on the forest instead of just a tree). These physical parameters also come into play when considering the layout of a viewing workstation, as a larger number of monitors require greater movement to foveate across all screens.[10]

For our brain to recognize a foveated target, we must fixate or dwell on that target for at least 100 to 300 ms. Beyond this time the retina loses sensitivity, resulting in blurring of the image. To overcome this, the eye makes rapid involuntary movements called saccades which are so fast the visual information during the movement cannot be registered by the brain, and effectively refreshes visual targets on the fovea.[7–9] Eye tracking studies have shown that when we first look at an image, a gist or global impression is formed, then various search patterns are employed to further assess the image.[1,2,10,11] While we seek to foveate targets, studies show that much of an image is not assessed with foveal vision, and peripheral vision is also employed when assessing or comparing targets.[2,3,11] The radiographic description, or findings, in the radiographic report is the representation of the visual search, or what we saw.

HOW WE THINK

Once an image or target is seen or perceived, the cognitive task begins to decide what that image or target means (e.g., normal vs. abnormal). Dual process theory and the Bayesian model are useful ways to think about thinking.

Dual process theory describes thought in terms of system 1 (or type 1) and system 2 (or type 2). System 1 thinking is characterized by decisions that are fast, unconscious, automatic, associative, reflexive, and implicit. These relate to intuition or your gut reaction, and are reliant on reader experience. System 1 is advantageous in that it is a fast process with low effort, does not require working memory, and generates confidence, but is error prone and subject to reader bias. This system relates to how we have evolved to group information into patterns, which become the inherent biases of our minds. System 1 is efficiency at the cost of accuracy and is only accurate under predictable or typical circumstances.[12,13] Consider when you walk into any kind of kitchen, whether it is commercial, residential, or rustic, you instantly register the scene as a kitchen. You do not have to take stock of exactly what is in the kitchen. However, if there is something out of place or unexpected for that pattern, you may not recognize it even if it is relevant (Fig. 7.3).

Conversely, system 2 thinking is characterized by decisions that are slow, conscious, deliberate, reflective, and explicit. This is an analytical and rational process, where we apply rules or methods to reach a decision. System 2 thinking is

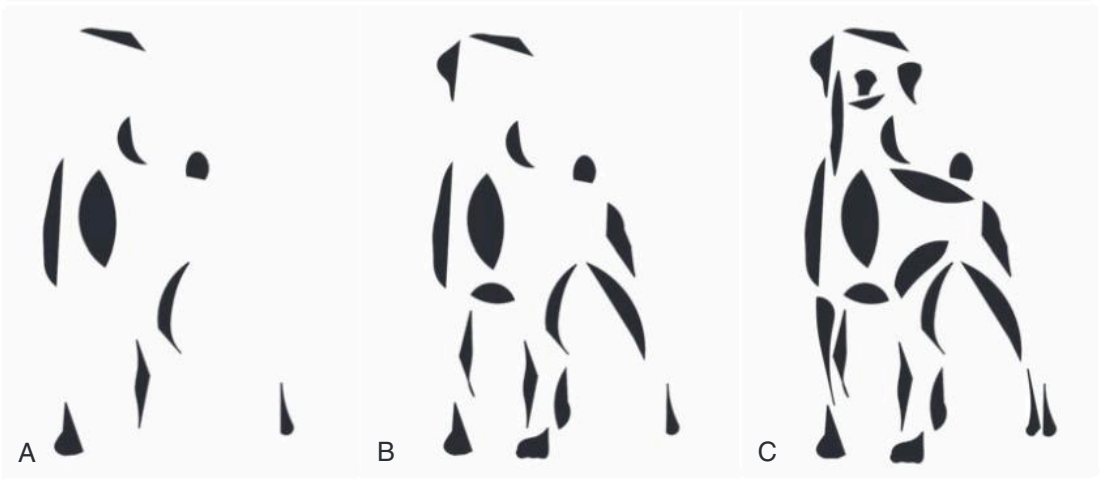


Fig. 7.1 The human brain is very efficient at making predictions and filling in gaps of data using memory (pattern recognition). In which of the images (**A, B, C**) do you identify a floppy eared Doberman? Notice how your mind constructs an image even though it has missing parts.

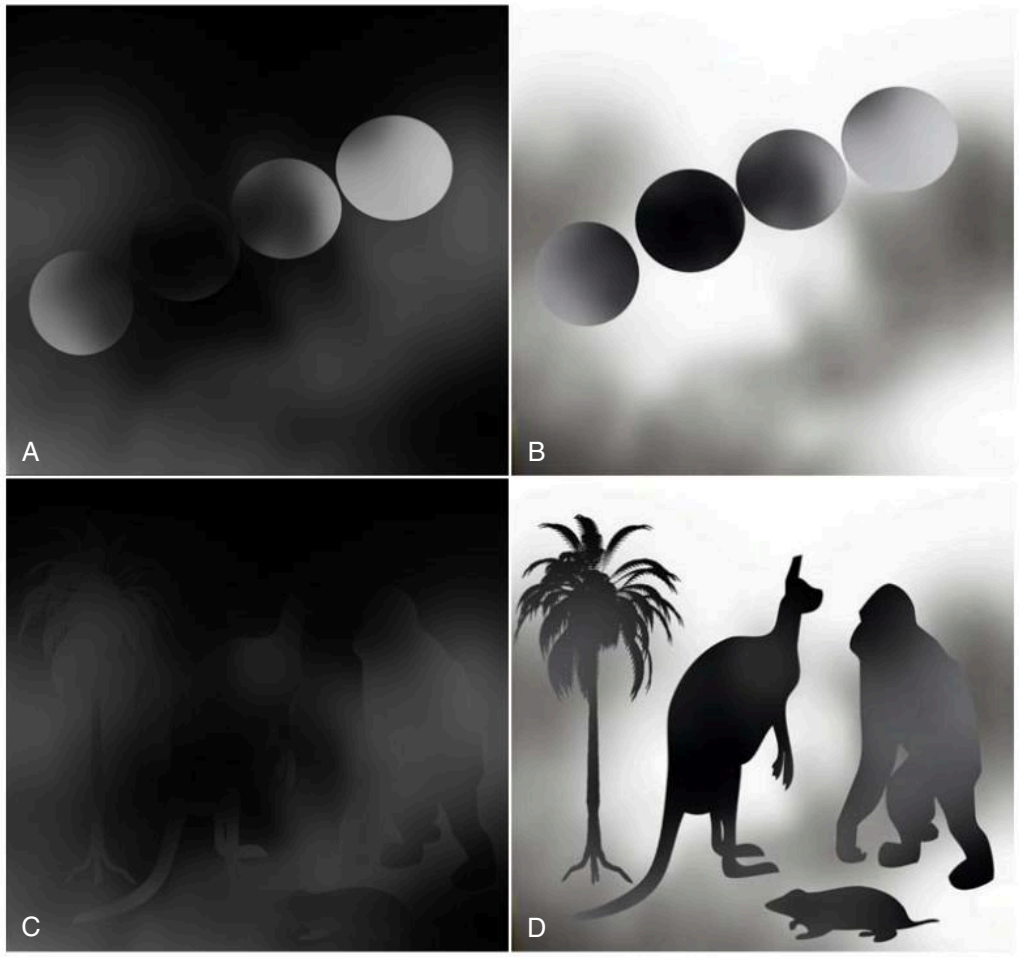


Fig. 7.2 The light or luminance that strikes our retina is not always an accurate representation of what we perceive. Due to interactions within our eye including lateral inhibition, objects in a scene can be perceived differently depending on the surroundings. Believe it or not, the circles (**A, B**) are the exact same shades of gray, and the tree, kangaroo, rat, and gorilla (**C, D**) are the exact same shades of gray. The background tricks us to perceive them as different shades. If you want to check this, cut a small hole in a piece of paper that only allows portions of the figures through, and hold it up to each individual figure to compare between the images. (Modified from Anderson BL, Winawer J. Image segmentation and lightness perception. *Nature*. 2005;434:3.)



Fig. 7.3 Our brains use pattern recognition to efficiently sort data into schema. While this is a very efficient process, it can produce errors. The images show four different types of kitchens, and although they have different types of counters, lighting, and cooking appliances, you probably did not have to think about them being kitchens at all, it was likely automatic. This is type 1 thinking. However, using pattern recognition may have not served you completely; how many kittens did you notice in the images? (Hint: There are nine kittens total to be found). This also illustrates the importance of target knowledge when viewing images.

advantageous because it less error prone but requires working memory and more effort making it slower. System 2 is accuracy at the cost of efficiency.[12] System 2 can challenge the preconceptions of system 1, and avoid falling into the trap of pattern recognition. The SOAP (subjective, objective, assessment, and plan) method is commonly employed in medical records to switch our brain into system 2. This method to think about a patient and their clinical presentation takes time but allows construction of differential diagnoses to accurately weigh available evidence. In diagnostic imaging, system 2 can be seen in search patterns or methods to view an image, and in reporting. Simply having templated prompts for regions of interest (e.g., cardiovascular, pulmonary, pleural, mediastinal, musculoskeletal, extrathoracic) for a thoracic radiograph ensures all regions have been assessed.

We can experience switching from system 1 to system 2 when learning a new language or encountering a word we are unfamiliar with. When we read familiar words and phrases, we often skip words and can still understand the meaning of the sentence. When we encounter an unfamiliar word or phrase, we will sound out the word, breaking it into its component parts (Fig. 7.4). In imaging, people often employ tricks to switch their brains into system 2. For example, over time, when we interpret thoracic radiographs, each view (lateral, ventrodorsal) will become a diagnostic pattern in our brains. This allows increased efficiency over time. Some have advocated flipping a radiograph or digitally inverting the grayscale, particularly when looking for rib fractures or pulmonary nodules. In doing so, they are breaking the image out of the schema of "ventrodorsal thoracic radiograph" or "pulmonary nodules are opaque," to force their brain into system 2 (Fig. 7.5). However, while these tricks may work for a time, performed enough times, they will simply create a new schema, and the same type of errors can again occur. Having a reading method and consciously moving between system 1 and system 2 is a more robust long-term strategy to achieve best accuracy and reduce errors.

Cognition and decision making can also be framed with the Bayesian model. In this way, an output or decision is generated by inputs coded by probabilities. The probability assigned to an input and the resultant output or decision can be related to three functions, likelihood, prior density, and cost. In the context of assessing the lung for metastatic nodules, the likelihood function relates to how likely will the patient have pulmonary nodules. Are they young or old? Do they have a known primary neoplasm? It highlights the importance of patient signalment and pertinent clinical history when our brain calculates this probability. The prior density function in this example relates to how often you have seen pulmonary nodules, be it in any patient or for this specific indication (e.g., pulmonary nodules with mast cell tumor would be uncommon, which could and should affect interpretation). The cost function could relate to the implications of the decision of identifying or missing pulmonary nodules. That decision could

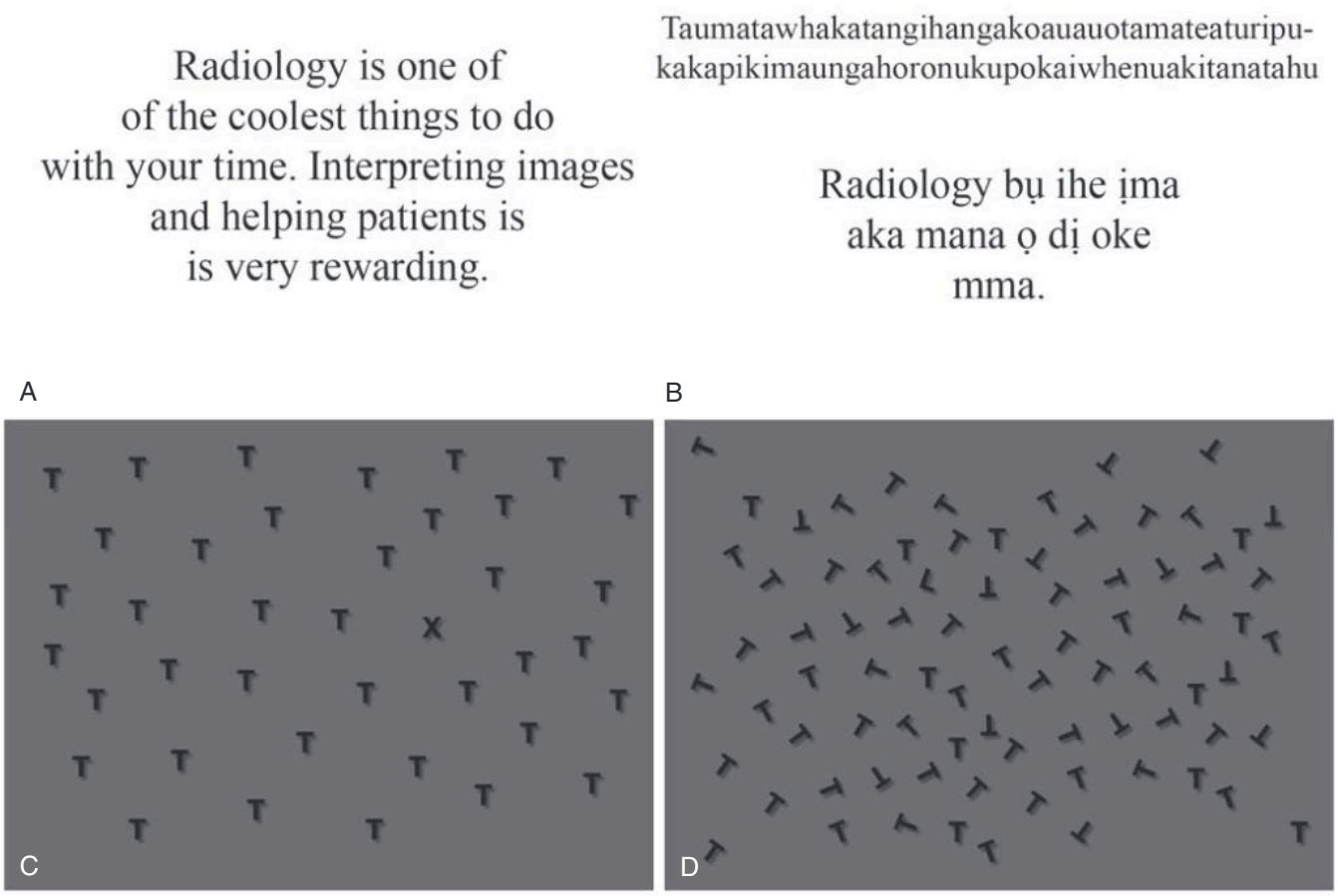


Fig. 7.4 When we encounter words or images that we have seen before (or think we have seen before), we can employ type 1 thinking to efficiently generate a pattern of that word or image. However, when we encounter words or images that are unfamiliar or uncertain, our brains will shift to type 2 thinking, employing speci fic methods to create certainty out of uncertainty. Example **A** was probably not challenging for you to read, and you were likely able to read it very quickly to understand the meaning. In reality, you may have skipped over words or your brain may have made incorrect predictions in order to do so. If you look again, are there any grammar mistakes? In example **B,** the first word is the name of a place in New Zealand. The second phrase are common words but presented in the Igbo language. Likely if you tried to read these and are unfamiliar with this place or the Igbo language, you broke the words into component parts or phonemes, and may have sounded it out, reading the words as you would have as a novice. This is type 2 thinking. In examples **C** and **D,** try to find the one character that is not like the others (one target in a sea of distractors). You likely found the "X" in example **C** quickly without a specific search pattern because it is sufficiently different from the "Ts" (type 1 thinking). Example **D** is more difficult, as the target ("L") is more similar to the distractors ("Ts"). If you did not find it at first, what strategies did you employ? Common methods might be reading left to right, top to bottom, outside-in, inside-out (type 2 thinking).

lead to a specific treatment, euthanasia, or a miss could result in a social cost for how your skill level is perceived. Perhaps you missed a nodule in a prior patient, and now you have increased your sensitivity at the risk of a false positive in order to avoid another "miss." Considering diagnostic imaging within this framework demonstrates that reading a radiograph is a noise and experience limited cognitive task, and highlights places where we can institute practices to reduce error.[7] The radiographic conclusion or opinion in the radiographic report is the representation of the cognitive decision task, or what we think.

ERRORS

Franz Kafka said, "All human errors are impatience, the premature breaking off of what is methodical, and apparent fencing in of the apparent thing." A true diagnostic error (or variance from accuracy) is a result or decision that could result in patient harm, with no scientific data to uphold it. Error severity can be termed negligible (no ill effect), minor (minimal ill effect), moderate (cause short-term ill effect), major (cause long-term ill effect), and extreme (cause severe long-term effect or death).[14] In a literature review over 20 years in human radiology, a rate of 2% to 20% was found for clinically significant or major errors.[15] A diagnostic discrepancy relates to differences in opinions between clinicians, whereby those differing opinions can be justified with available data.[16] Errors leading to incorrect decisions can be thought of within the following framework: prereporting errors, reporting errors, and postreporting errors.

1. Prereporting errors encompass technical factors during imaging acquisition or generation. This could include performing the wrong imaging test, imaging the wrong patient, imaging the wrong region of anatomy, or acquiring nondiagnostic images (poorly positioned, poor technique, image artifacts).[16]

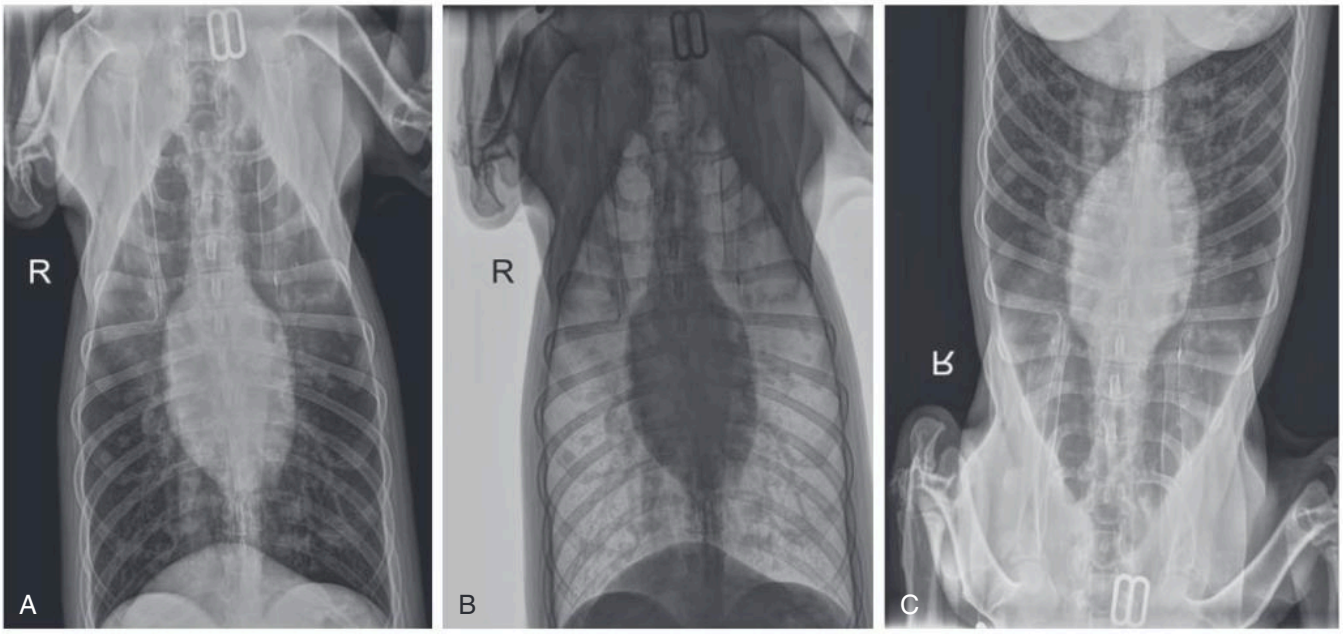


Fig. 7.5 There are tricks one can employ to revert back to a novice brain and break out of pattern recognition. **A, B,** and **C** are the same radiograph, but the grayscale has been inverted in **B,** and the image flipped vertically in **C**. The patient has pulmonary nodules; do you find it easier to see them in one image vs. another? While these tricks may work in the short-term, used enough, our brains will create a new schema of inverted ventrodorsal radiograph or upside down ventrodorsal radiograph, and we will be subject to the same search errors again. A better method is to develop a robust method for searching and interpreting images.

2. Reporting errors encompass errors committed by the reader during assessment, and can be further classified into the following categories:
   a. A search error is one in which we simply "don't see" the lesion, meaning we never physically foveate on it. It is the inability to discriminate embedded targets or a lesion from normal anatomy. Multiple factors lead to search errors.
      i. This can include physical/environmental factors including individual eye anatomy and health, workstation setup (proper monitor resolution and luminance, ambient light, veiling glare, uncluttered interfaces which do not distract attention), image quality (resolution, contrast, motion, positioning), and fatigue (time of day, image volume). Simply having proper/higher luminance monitors results in shorter search time, time to fixate on targets, and dwell time before reaching a decision. Reading performance will also wane later in the day as visual fatigue increases.[1,3,10,11,17]
      ii. Behavioral or systematic factors can also lead to search errors, including inadequate time to search an image, not searching the whole image, and having inadequate target knowledge. Being rushed when reading an image can decrease performance because it can prevent a systematic search. Target knowledge, or knowing what we are looking for, will physically change how we view an image. This highlights the importance of clinical history when interpreting an image.[1–3,11] It can be useful to interpret images without the history first (to limit bias), with a subsequent read after reading the history in order to provide target knowledge.
   b. A fixation error is one in which we "see" the lesion, meaning our eye physically foveates or fixates on a target, but we do not perceive or recognize it consciously. This type of error is directly impacted by training and experience. This is evident when you "see" a lesion only after someone else points it out even though you may have "looked" at it before. You will be better able to recognize that type of lesion on future radiographs.
      i. Fixation errors can also occur secondary to inadequate or incorrect target knowledge, as we are more apt to find what we are looking for. This concept is called inattentive blindness. In a prior study, a series of computed tomography (CT) lung images were provided to expert readers (radiologists) and naïve observers with no medical training. The images had lung nodules, but experimenters also inserted an image of a gorilla 48× larger than a typical nodule into the study. Both groups were asked to count nodules, but were not told to look for gorillas. Some 83% (20/24) of the radiologists did not report seeing the gorilla, even though 60% (12/20) did foveate on it identified with eye tracking (Fig. 7.6). None (0/24) of the naïve observers saw the gorilla. The results show that while expert readers may be less affected by inattentive blindness, both naïve and expert readers are affected by inadequate target knowledge even when a lesion is physically visible. The study also showed the radiologists outperformed the naïve observers in nodule detection (55% vs. 12%), which is the relevant clinical task for a radiologist.[18]
   c. A decision error is one in which we "see" the lesion, fixate, and perceive the lesion, but we do not reach the correct choice (poor judgment).[3] Reaching the correct decision about an image or lesion is directly related to prior training and experience. To reach a decision that pulmonary nodules indicate metastatic neoplasia, one first has to know that neoplasms can metastasize (including to the lung), and ideally there is a clinical history and target knowledge that support

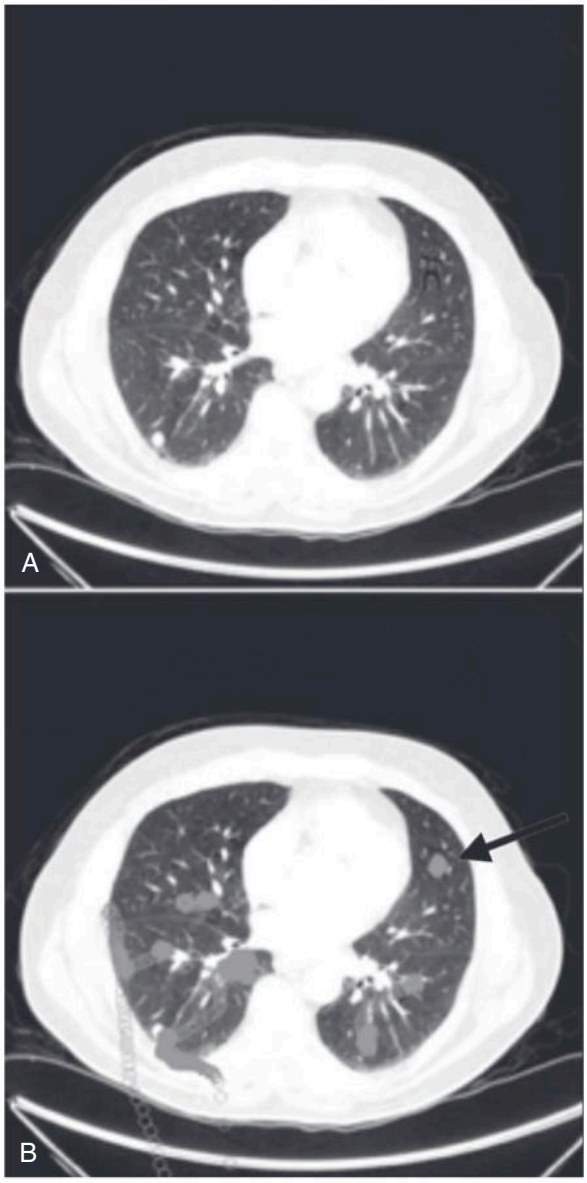


Fig. 7.6 Inattentional blindness is the tendency to miss something you were not looking for or expecting to find. The figure demonstrates this phenomenon, where expert readers (human radiologists), and nonexpert readers were given computed tomography (CT) lung studies to examine and report on pulmonary nodules, but were not told that a small gorilla much larger than a typical nodule would be present in some portions of the studies. Examples **A** and **B** are the same CT lung slice, as presented to the readers (**A**), and with the overlay of where they fixated on using eye tracking (**B**). In **B** it can be seen that the reader looked directly at the gorilla (*light gray dot with black arrow*), but never reported seeing it. In other words, the gorilla was "seen," but not "recognized." Since this is not a real pathology, it was ignored by expert readers even though it was technically "seen." This highlights the importance of target knowledge (knowing what you are looking for). (From Drew T, Vo MLH, Wolfe JM. The invisible gorilla strikes again: sustained inattentional blindness in expert observers. *Psychol Sci*. 2013;24(9):1848-1853.)

that as the correct diagnosis (e.g., the patient is a 12-year-old dog with known splenic hemangiosarcoma). It also requires knowledge and consideration of other differential diagnoses that could result in pulmonary nodules (parasitic granulomas, abscesses, immune mediated granulomas such as eosinophilic bronchopneumopathy), and cognitively filtering what is most likely based not only on the radiographic appearance, but the patient's signalment and clinical history.

d. A thorough list of types of cognitive errors and biases are listed in eTable 7.1, but a few that relate directly to decision error include pattern recognition, prevalence effect, premature closure, satisfaction of search, diagnostic momentum, and automation bias.[19]
   i. Pattern recognition is a tool of system 1 thinking, which is an efficient (although not always accurate) way to recognize a lesion as something you have seen before. Pattern recognition is only accurate under typical circumstances. For example, a cranioventrally distributed alveolar pattern is a common finding in bronchopneumonia/aspiration pneumonia and would be a common diagnosis for a patient

eTable • 7.1

Types of Cognitive Errors and Biases.

COGNITIVE DISPOSITIONS TO RESPOND (ALSO KNOWN AS TYPES OF BIASES AND DIAGNOSTIC ERRORS)		
CDR TYPE	**DESCRIPTION**	**IMAGING EXAMPLE**
Aggregate bias/ fallacy	Believing that aggregated data do not apply to an individual patient.	Ordering an abdominal ultrasound for staging of a patient with an appendicular osteosarcoma, despite data indicating this is an uncommon site of metastasis.
Anchoring	Placing too much weight on information early in the diagnostic process, and not adjusting with new information.	Diagnosing cardiogenic pulmonary edema for a right caudal lung lobe alveolar pattern, in the absence of physical examination features of left-sided congestive heart failure and lack of response to a diuretic trial.
Ascertainment/ Attribution bias	Thinking is shaped by prior expectation (stereotyping).	Presuming a brain lesion is a glioma because the patient is a bulldog, and not considering other differentials.
Automation bias	Tendency to readily accept diagnostic decisions or information from machines, and abdicating human diagnostic oversight. This leads to both errors of commission and omission.	Accepting a diagnosis offered by artificial intelligence without verifying the diagnosis or confirming that the diagnosis is relevant in the context of the clinical history and presentation.
Availability bias	Likelihood of diagnosis is based on what readily comes to mind.	Overdiagnosis of metastatic disease in an oncology practice or underdiagnosis of *Spirocerca lupi* in a nonendemic region.
Base-rate neglect	Ignoring true disease prevalence, inflating or reducing the base-rate, including to avoid missing a rare but significant diagnosis. (Opposite of playing the odds.)	Overconsideration of pythiosis for an intestinal mass in a patient with no access or exposure to fresh water sources.
Commission bias	Tendency toward action opposed to inaction, leading to a false-positive diagnosis or action.	Performing thoracocentesis for pleural effusion on the recommendation of artificial intelligence when no pleural effusion is present.
Confirmation bias	Tendency to seek evidence to support a diagnosis rather than weighing available evidence.	Presuming an aggressive bone lesion in the proximal metaphysis of a Great Dane is osteosarcoma, and not considering other differential diagnoses such as fungal granulomatous disease.
Diagnostic momentum	A diagnosis becomes more definitive as more people or records repeat it.	A patient with multiple repeated radiographs continues to have a bronchial pattern diagnosed because prior reports have diagnosed it, even if one is not present.
Feedback sanction (ignorance trap/ time-delay trap)	When there is a time gap between error and error discovery, the error carries no consequences and corrections cannot be taken.	A patient is euthanized for a diagnosis of a bone tumor, but no biopsy was performed and the apparent lesion was artifact of overexposure.
Framing effect	Diagnosis is influenced by how the patient/problem is framed.	If this patient has an intestinal obstruction, the owners wish to euthanize.
Fundamental attribution error	Tendency to judge or blame patients for their illness.	Presuming a patient on the ultrasound table is being noncompliant, when it cannot remain still because it has vestibular disease.
Gambler's fallacy	The pretest probability of a diagnosis is influenced by prior independent events, presuming the next event will be different. Belief that if a coin comes up heads 10 times in a row, the 11th time is more likely to be tails even though it is similar chance. (Opposite of posterior probability error.)	Seeing 10 patients with cardiogenic pulmonary edema, and assuming the next case will not have cardiogenic pulmonary edema.
Gender/Sex bias	Presuming sex determines diagnosis probability when there is no pathophysiological basis.	Underdiagnosing mammary neoplasia in a male patient.
Hindsight bias	Outcome once known influences realistic assessment of past performance/accuracy.	Being provided cytologic diagnosis of a bone tumor, then convincing yourself you saw the aggressive lesion initially when you did not read it out/it is not visible.

Continued

eTable • 7.1

Types of Cognitive Errors and Biases.—cont'd

COGNITIVE DISPOSITIONS TO RESPOND (ALSO KNOWN AS TYPES OF BIASES AND DIAGNOSTIC ERRORS)		
CDR TYPE	**DESCRIPTION**	**IMAGING EXAMPLE**
Lack of knowledge	A lesion is identified but cannot be accurately interpreted due to lack of clinical history or experiential knowledge about the lesion.	Being unaware that some bones in birds are pneumatized, and misdiagnosing this as pathology.
Omission bias	Tendency toward inaction, leading to a false-negative diagnosis or action.	AI reports radiographs as normal that actually have pulmonary nodules. You do not report the nodules.
Order effects	When information is transferred, we have a bias to remembering the beginning (primacy effect) or the end (recency effect), and all information transferred may not be considered equally.	Receiving a very long clinical history with relevant information in the middle of the history, but only the information at the end is remembered and considered during image assessment.
Outcome bias	Tendency to choose diagnoses that have good outcomes and avoiding diagnoses with bad outcomes.	Underdiagnosing an aggressive bone lesion or pulmonary metastases as they may result in the patient being euthanized.
Overconfidence bias	Tendency to think we know more than we do, placing too much credence on our feelings/ opinions rather than evidence-based information.	Not asking for a second opinion on imaging.
Playing the odds (frequency bias)	When the presentation is ambiguous, the tendency to choose benign diagnoses as being more common, potentially ignoring a more serious diagnosis. (Opposite of base-rate neglect)	Radiographs with stifle joint distention and equivocal subchondral bone lysis, and diagnosing cruciate rupture in lieu of prioritizing a joint centric neoplasm or septic arthritis.
Posterior probability error (prevalence effect)	The pretest probability of a diagnosis is influenced by prior independent events, presuming the next event will be the same. Belief that if a coin comes up heads 10 times in a row, the 11th time is more likely to be heads even though it is similar chance. (Opposite of posterior probability error)	Using radiographs to diagnose cardiogenic pulmonary edema for a patient on three separate events, then diagnosing that on the fourth event when the patient has had a pulmonary thromboembolism.
Premature closure	Accepting a diagnosis before it has been verified, "when a diagnosis is made, thinking stops." Type of tunnel vision.	Identifying an aggressive bone lesion in the diaphysis of a long bone, and missing that there are additional aggressive lesions of vertebrae.
Psych-out error	Patients with behavioral or mental issues may have other conditions missed or have other medical issues misdiagnosed as mental issues.	Presuming a patient's aggression and noncompliance is behavioral, and missing or not considering they may have an androgen producing tumor or brain tumor.
Representativeness restraint	Tendency to look for typical manifestations of disease, at the behest of atypical manifestations of disease "when you hear hoofbeats, don't think zebras."	A patient has a caudodorsal alveolar pattern on radiographs, and you presume this cannot be bronchopneumonia. You have not considered the patient may have had a recent anesthesia and aspiration while in dorsal recumbency.
Satisfaction of search	Tendency to stop searching once something has been found. Type of tunnel vision.	Identifying a pulmonary mass on thoracic radiographs, and missing a humeral periosteal reaction on the edge of the images indicating hypertrophic osteopathy.
Suttons' slip	Tendency to go for the obvious.	Diagnosing an aggressive bone lesion as osteosarcoma in a giant breed dog, and not considering travel history and the possibility of fungal granulomatous disease.
Sunk costs	The more time and finances are invested in a diagnosis, the less likely a clinician will consider alternatives even if the primary diagnosis is not supported by new information.	A patient has had multiple underexposed and underinflated radiographs leading to increase lung opacity, and continued diagnosis of left-sided congestive heart failure. Treatment for heart failure is continued, even though there is no clinical response to the medications and the physical examination is not supportive.

eTable • 7.1

Types of Cognitive Errors and Biases.—cont'd

COGNITIVE DISPOSITIONS TO RESPOND (ALSO KNOWN AS TYPES OF BIASES AND DIAGNOSTIC ERRORS)		
CDR TYPE	**DESCRIPTION**	**IMAGING EXAMPLE**
Triage/patient cueing	Diagnoses can be impacted by how a patient has been previously assessed through the triage process (stable, urgent, emergency, etc.).	Abdominal radiographs are submitted to you STAT with high clinical concern that the patient is obstructed. This may result in you overestimating the patient being obstructed.
Unpacking principle	Failing to acquire all relevant information to reach a diagnosis.	Not acquiring a thorough clinical history that includes travel history to the American Southwest, and therefore failing to consider Coccidiomycosis as a differential diagnosis.
Vertical line failure	Repetitive tasks or diagnoses lead to repetitive inflexible thinking and inconsideration of less common diagnoses. Failure to ask, "what other diagnosis could this be?"	An orthopedic surgeon diagnoses five to six patients per day with cruciate disease based on examination and radiographs, and presumes every case is cruciate disease. This could lead to misdiagnosis of a joint centric neoplasm or pannus.
Visceral bias	How you feel about a patient (or client) may lead to an incorrect decision.	A client is unkempt, and therefore you do not offer advanced imaging such as MRI presuming the client cannot afford that test.
Yin-Yang out	When patients have had extensive workups, the tendency to presume that nothing further can be done and diagnostic effort drops.	A patient has a vague lameness and pain with no apparent answer on radiographs, CT, or MRI. The owner is told nothing further can be done, as opposed to considering serial imaging, infectious disease testing, physical therapy.
Zebra retreat	Avoiding making an uncommon or unusual diagnosis, even when there is supporting evidence.	Ignoring hypertrophic osteopathy on the edge of thoracic radiographs of a patient with a lung tumor, or presuming it is a separate process.

AI, Artificial intelligence; *CT,* computed tomography; *MRI,* magnetic resonance imaging.Data from Goddard P, Leslie A, Jones A, Wakeley C, Kabala J. Error in radiology. *Br J Radiol*. 2001;74:949–951; Onder O, Yarasir Y, Azizova A, Durham G, Onur MR, Ariyurek OM. Errors, discrepancies and underlying bias in radiology with case examples: a pictorial review. *Insights Imaging*. 2021;12:51; Croskerry P. The importance of cognitive errors in diagnosis and strategies to minimize them. *Acad Med*. 2003;78(8):775–780; Croskerry P. Achieving quality in clinical decision making: cognitive strategies and detection of bias. *Acad Merg Med*. 2002;9:1184–1204; Nichols L. Patient cueing, a type of diagnostic error. *Autops Case Rep*. 2016;6(1):27-31.

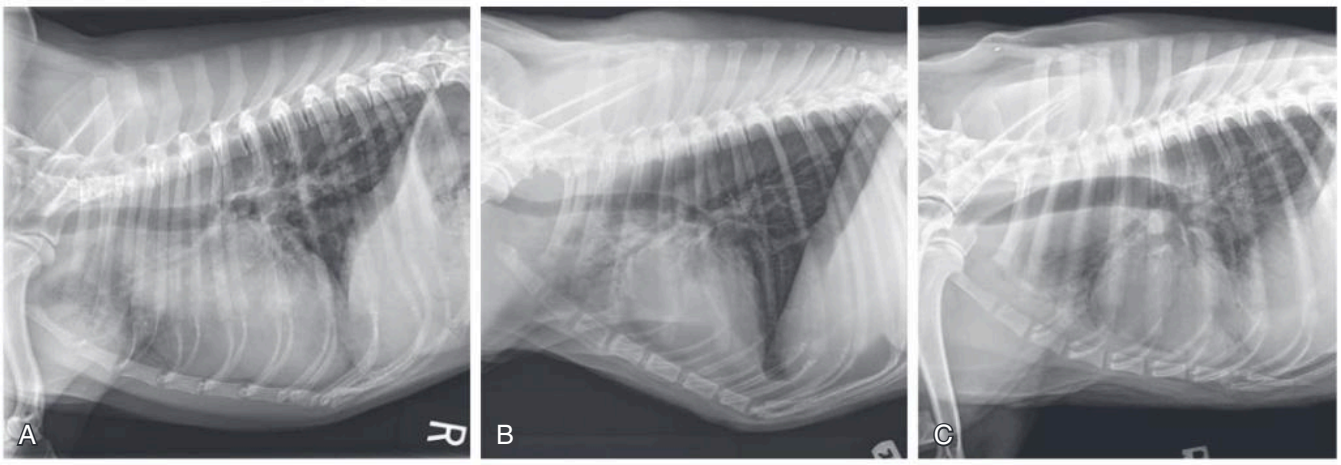


Fig. 7.7 Pattern recognition may work in usual reproducible circumstances but will not work in all situations. Examples **A, B,** and **C** are right lateral thoracic radiographs of patients who all have a ventrally distributed alveolar pattern. This pattern and distribution are commonly seen in bronchopneumonia, which is also a common condition. However, not every ventral alveolar pattern will be pneumonia. There are some other features on these radiographs that may offer clues to other diagnoses. Have a look and decide how you would diagnose these patients on these single views, then read on for the final diagnoses. **A,** Pulmonary infiltrates secondary to pulmonary hypertension. **B,** Bronchopneumonia/aspiration pneumonia. **C,** Bronchopneumonia and pulmonary lymphoma.

with respiratory signs. However, other disease processes can also result in a cranioventral alveolar pattern (Fig. 7.7), and may also result in respiratory signs. While the frequency of other diseases may be less common, they must still be considered.

ii. Frequency of disease also impacts decision making with regard to prevalence effect, whereby lesions you have seen/diagnosed before or are more common are more likely to be diagnosed for subsequent patients. Cranial cruciate ligament rupture is a common diagnosis, and results in increased soft tissue opacity and distention of the stifle joint. While cruciate rupture is much more common than a joint centric neoplasm or septic arthritis in a dog, these other conditions do occur, and other features of an aggressive process may be unconsidered (if they are seen) and a false-positive diagnosis of cruciate rupture may be made.[19]

iii. Premature closure and satisfaction of search can both be considered types of tunnel vision. Premature closure is making a diagnosis such as identifying a lung tumor on thoracic radiographs for a large ovoid soft tissue opacity, but not considering that the patient was recently hit by a car, has a rib fractures, and the "tumor" has a fluid line making a hematocele a more likely diagnosis. This is the cessation of thinking once a diagnosis is made.[19] Satisfaction of search is making a diagnosis (such as esophageal distention consistent with megaesophagus on thoracic radiographs) but discontinuing the search and not identifying that the patient also has pneumonia.[19] This can be thought of as only identifying the tip of the iceberg. An example of these types of errors is demonstrated in Fig. 7.8.

iv. Diagnostic momentum and automation bias can be thought of as types of peer pressure. Diagnostic momentum is peer pressure from human to human and can take the form of another clinician labeling a patient with a certain diagnosis, or that label being present in prior records. There is often reluctance to challenge the correctness of what has been repeated, and a tendency to carry it forward even if the clinical picture no longer fits.[19] An example could be a well-respected radiologist has diagnosed a pathologic bone lesion on prior radiographs, but you think the lesion is more consistent with degenerative change. You may defer to the prior diagnosis instead of asserting what you really think is correct. Automation bias is peer pressure from machine to human, trusting a machine or computer output in replacement of your own



Fig. 7.8 Premature closure and satisfaction of search are types of errors similar to having tunnel vision. A lesion or diagnosis may be seen, and accepted as the full answer, missing other lesions and diagnoses. The ventrodorsal radiograph shown is from a dog who was hit by a car with severe trauma. There is obvious swelling of the right lateral extrathoracic and abdominal soft tissues with gas and intestinal segments indicative of body wall hernia, and there are some right-sided rib luxations and fractures. The swelling certainly draws the eye. However, did you catch/identify all of the left-sided rib fractures?

thought process. This could be accepting a diagnosis provided by artificial intelligence (AI) regardless of the evidence. The result is errors of commission (AI diagnoses pulmonary nodules and you agree even though you do not see nodules) and errors of omission (AI does not identify pulmonary nodules even though present on radiographs, and you do not report them).[20] Studies have shown that we all our susceptible to automation bias regardless of our level of expertise, but there is a protective effect of expertise (experts are less affected by automation bias vs. novices).[21]

e. Intraobserver variability is the variation/accuracy of search, recognition, and decision making by the same person over multiple times points and interobserver variability is the variation/accuracy between separate observers. As humans all the factors mentioned earlier impact accuracy and performance, which is unlikely to be completely consistent and uniform over time (even when evaluating the same images).
   i. Human studies have shown that intraobserver variability can be as high as 20% and interobserver variability as high as 30% to 50%.[22,23] Reader training, experience, and skill directly affect performance, as do physical and environmental factors. You may be less likely to identify pulmonary nodules at the end of the day when you are fatigued or if there are increasing distractions. Even if a nodule or lesion is identified, there could be variation in reporting of size over time, which affects treatment decisions (stable disease, remission, progression).
   ii. In human radiology, studies have shown false-negative rates of 20% to 30%, and false-positive rates of 2% to 15%.[1,3,17,22] More experienced observers will typically have more efficient visual search/fixation/dwell patterns, find lesions faster, process more information, and be more accurate than novice observers.[17,24]

3. Post reporting errors occur during the communication after image interpretation, be it from clinician to clinician, clinician to technician, or clinician to client. These can range from typos or mistakes in the imaging report, particularly if reports generated using voice dictation are not proofread, format or reporting style, lack of or inappropriate recommendations, delayed reporting, or simply misunderstanding between people when the clinical information is exchanged.[16]

ERROR REDUCTION

As humans, we are not infallible, and even the most competent and experienced clinician will occasionally commit an error. While no one is accurate 100% of the time, we can employ strategies to reduce errors, and control variables. As has been related in legal writing surrounding medical errors, this includes reaching and maintaining competence, developing habits of practice, and using proper techniques.[25]

1. Physical factors and limiting distractors/stressors
   a. Having a proper workstation, including high-resolution monitors with appropriate luminance.
   b. Acquiring studies with impeccable technique and positioning whenever possible.
   c. Limiting ambient noise and light (quiet and dark reading room).
   d. Managing fatigue
      i. Taking regular breaks.
      ii. Allow your eyes to accommodate to different distances during breaks.
      iii. Maintaining a manageable workload.
2. Accurate and complete clinical history/target knowledge
   a. Performing a blind read without the clinical history to avoid clinical bias.
   b. Performing an unblinded read with signalment and clinical history for appropriate context and to avoid inattentional blindness.
   c. Availability of prior reports and imaging for comparison when possible.
3. Structured reporting/checklists
   a. Checklists are a way to build system 2 thinking into your practice, providing prompts to ensure the reader has assessed all parts of the imaging study. Checklists have been shown to reduce error, particularly task-focused checklists.[26–28]
4. Double reads/second opinions
   a. Leverage the visual and cognitive resources of more than one person.
   b. Independent second reads can reduce false-negatives but may increase false-positives and interobserver variability. One study showed optimal balance between accuracy and agreement was four independent readings with a reviewer of composite results.[14,20,22,23]
5. Metacognition
   a. Metacognition is thinking about thinking.
   b. Being familiar with the types of errors and biases that can occur allows for error reduction (consciously switching from system 1 to system 2 thinking).[16]
   c. In practice, this could be stopping after interpretation of a set of images, to check that all anatomic regions and parts of the image assessed, the signalment and clinical history considered, and questioning whether the imaging findings fit with the clinical picture.
6. Follow-up/communication
   a. There should be open and effective communication with all members of the medical team, and between the medical team and pet owner.[16]
   b. Clear communication ensures that what was perceived and interpreted is relayed accurately so that treatment steps can reflect those diagnoses.
   c. Communication also allows for feedback and learning from both accurate and inaccurate interpretations.
7. Error assessment
   a. When errors occur, a root cause analysis should be performed.
   b. This allows determination of how/why an error occurred, and whether it was a human or systems error.[14,16]

REFERENCES

1. Krupinski EA. The role of perception in imaging: past and future. *Semin Nucl Med.* 2011;41:392–400.
2. Tuddenham WJ, Calvert WP. Visual search patterns in Roentgen diagnosis. *Radiology*. 1961;76(2):225–226.
3. Tuddenham WJ. Visual search, imaging organization, and reader error in Roentgen diagnosis. *Radiology*. 1962;78(4):694–704.
4. Anderson BL, Winawer J. Image segmentation and lightness perception. *Nature*. 2005;434:3.
5. Papageorges M, Sande R. The Mach phenomenon. *Vet Radiol Ultrasound*. 1990;31(6):274–280.
6. Papageorges M. How the Mach phenomenon and shape affect the radiographic appearance of skeletal structures. *Vet Radiol Ultrasound*. 1991;32(4):191–195.
7. Eckstein MP. Visual search: a retrospective. *J Vis*. 2011;11(5):1–36, 14.
8. Manning D, Ethell SC, Donovan T. Time-dependent observer errors in pulmonary nodule detection. *Br J Radiol*. 2006;79:342–346.

9. Yang GZ, Depmere-Marco L, Hu XP, Rowe A. Visual search: psychophysical models and practical applications. *Image Vis Comput*. 2002;20:291–305.
10. Krupinski EA, Kallergi M. Choosing a radiology workstation: technical and clinical considerations. *Radiology*. 2007;242(3).
11. Kundel HL, Nodine CF, Toto L. Searching for lung nodules: the guidance of visual scanning. *Invest Radiol*. 1991;26(9):777–781.
12. Sowden P, Pringle A, Gabora L. The shifting sands of creative thinking: connections to dual process theory. *Think Reas*. 2015;21(1):4060.
13. McVee MB, Dunsmore K, Gavelek JR. Schema theory revisited. *Rev Educ Res*. 2005;75(4):531–566.
14. Brady A, Laoide RO, McCarthy P. Discrepancy and error in radiology: concepts, causes, consequences. *Ulster Med J*. 2012;81(1):3–9.
15. Goddard P, Leslie A, Jones A, Wakeley C, Kabala J. Error in radiology. *Br J Radiol*. 2001;74:949–951.
16. Onder O, Yarasir Y, Azizova A, Durham G, Onur MR, Ariyurek OM. Errors, discrepancies and underlying bias in radiology with case examples: a pictorial review. *Insights Imaging*. 2021;12:51.
17. Krupinski EA. The importance of perception research in medical imaging. *Radiat Med*. 2000;18(6):329–334.
18. Drew T, Vo MLH, Wolfe JM. The invisible gorilla strikes again: sustained inattentional blindness in expert observers. *Psychol Sci*. 2013, September;24(9):1848–1853.
19. Croskerry P. The importance of cognitive errors in diagnosis and strategies to minimize them. *Acad Med*. 2003;78(8):775–780.
20. Goddard K, Roudsari A, Wyatt JC. Automation Bias: a systematic review of frequency, effect mediators, and mitigators. *J Am Med Assoc*. 2012;19:121–127.
21. Dratsch T, Chen X, Mehrizi MR, et al. Automation bias in mammography: the impact of artificial intelligence BI-RADS suggestions on reader performance. *Radiology*. 2023;307(4):e222176.
22. Yerushalmy J. The statistical assessment of the variability in observer perception and description of roentgenographic pulmonary shadows. *Radiol Clin North Am*. 1969;7:381–392.
23. Kulberg NS, Reshetnikov RV, Novik VP, et al. Inter-observer variability between readers of CT images: all for one and one for all. *Digital Diagnostics*. 2021;2(2):105–118.
24. Nodine CF, Krupinski EA. Perceptual skill, radiology expertise, and visual test performance with NINA and WALDO. *Acad Radiol*. 1998;5:603–612.
25. Caldwell C, Seamone ER. Excusable neglect in malpractice suits against radiologists: a proposed jury introduction to recognize the human condition. *Ann Health Law*. 2007;16:43–77.
26. Al-Khafaji J, Townshend RF, Townsend W, Chopra V, Gupta A. Checklists to reduce diagnostic error: a systematic review of the literature using a human factors framework. *BMJ Open*. 2022;12:e058219.
27. Pronovost P, Needham D, Berenholtz S, et al. An intervention to decrease catheter-related bloodstream infections in the ICU. *N Engl J Med*. 2006;355:2725–2732.
28. Haynes AB, Weiser TG, Berry WR, et al. A surgical safety checklist to reduce morbidity and mortality in a global population. *N Engl J Med*. 2009;360:491–499.

ELECTRONIC RESOURCES

Additional information related to the content in Chapter 7 can be found online at eBooks.Health.Elsevier.com.

- Chapter Quiz

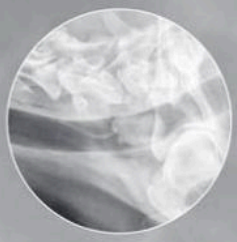


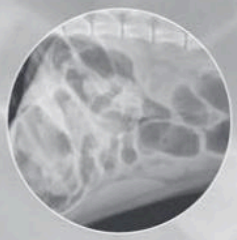
SECTION II











The Axial Skeleton: Canine, Feline, and Equine

8 **Radiographic Anatomy of the Axial Skeleton**
Andra K. Voges • Kathy A. Spaulding

9 **Basic Principles of Radiographic Interpretation of the Axial Skeleton**
Donald E. Thrall

10 **Canine and Feline Dental Disease**
Lenin Arturo Villamizar Martinez

11 **The Skull and Nasal Cavities: Canine and Feline**
Lisa J. Forrest

12 **Magnetic Resonance Imaging and Computed Tomographic Features of Brain Disease in Small Animals**
Ian Robertson • Gabriela S. Seiler

13 **The Equine Head**
Nathan C. Nelson

14 **Radiography and Myelography of the Canine and Feline Vertebrae**
William R. Widmer

15 **Magnetic Resonance Imaging and Computed Tomography Features of Canine and Feline Spinal Cord Disease**
Wilfried Mai

CHAPTER 8

Radiographic Anatomy of the Axial Skeleton

Andra K. Voges • Kathy A. Spaulding

To use the roentgen sign method of recognizing abnormal radiographic findings effectively, an understanding of normal radiographic anatomy for the specific area of interest is necessary. Within the space constraints of a comprehensive veterinary radiology text, this chapter provides a limited reference for the radiographic anatomy of the axial skeleton (Figs. 8.1–8.21). For more detailed information, readers are referred to comprehensive texts on radiographic anatomy.[1–5]

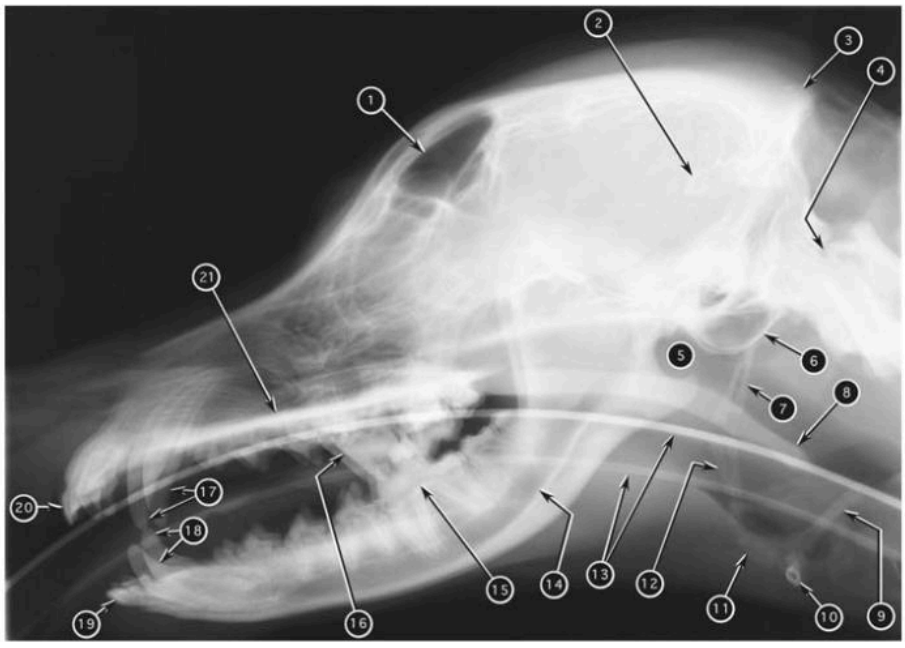


Fig. 8.1 Left–right lateral radiograph of canine head.

1. Frontal sinuses
2. Tentorium osseum cerebelli
3. External occipital protuberance
4. Atlantooccipital joints
5. Air in nasopharynx
6. Tympanic bullae
7. Stylohyoid bones
8. Soft palate
9. Thyrohyoid bones
10. Basihyoid bone
11. Ceratohyoid bones
12. Epihyoid bones
13. Endotracheal tube
14. Inferior alveolar canals of mandibles
15. Inferior first molar teeth (superimposed 309 left/409 right)
16. Superior fourth premolar teeth (superimposed 208 left/108 right)
17. Superior canine teeth (superimposed 204 left/104 right)
18. Inferior canine teeth (superimposed 304 left/404 right)
19. Inferior incisor teeth (superimposed 301, 302, 303 left/401, 402, 403 right)
20. Superior incisor teeth (superimposed 201, 202, 203 left/101, 102, 103 right)
21. Hard palate

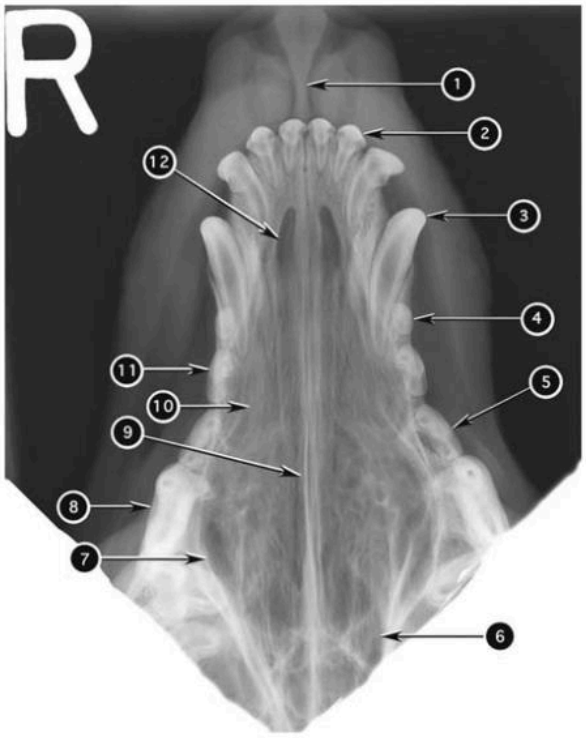


Fig. 8.2 Intraoral dorsoventral radiograph of canine nasal cavity.
1. Cartilaginous nasal septum
2. Superior incisor 2 (202)
3. Superior canine tooth (204)
4. Superior premolar 1 (205)
5. Superior premolar 3 (207)
6. Ethmoidal conchae
7. Maxillary recess
8. Superior premolar 4 (108)
9. Nasal septum
10. Dorsal and ventral nasal conchae
11. Superior premolar 2 (106)
12. Palatine fissure

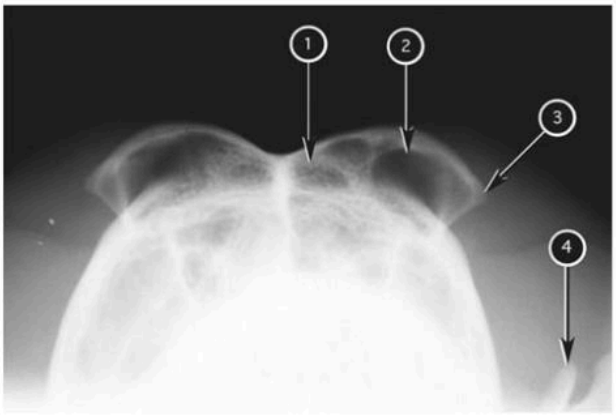


Fig. 8.3 Rostrodorsal-caudodorsal oblique radiograph of canine frontal sinuses.
1. Medial frontal sinus
2. Lateral frontal sinus
3. Zygomatic process of frontal bone
4. Coronoid process of mandible

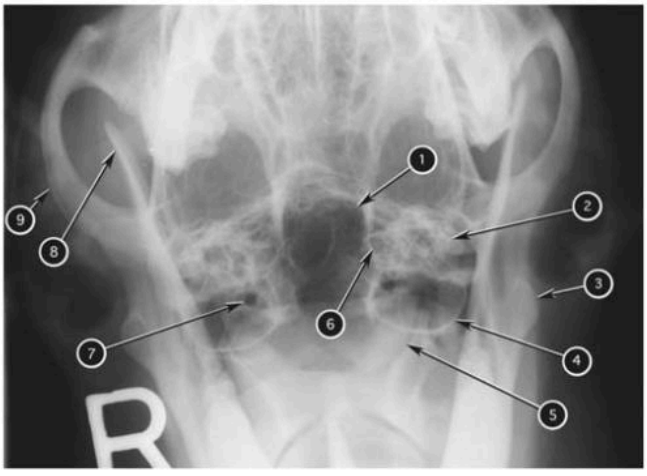


Fig. 8.4 Rostroventral-caudodorsal oblique (open-mouth) radiograph of canine tympanic bullae.
1. Nasopharynx
2. Petrous temporal bone
3. Angular process of mandible
4. Tympanic bulla
5. Atlantooccipital joint
6. Foramen lacerum
7. Jugular foramen|
8. Coronoid process of mandible
9. Zygomatic arch

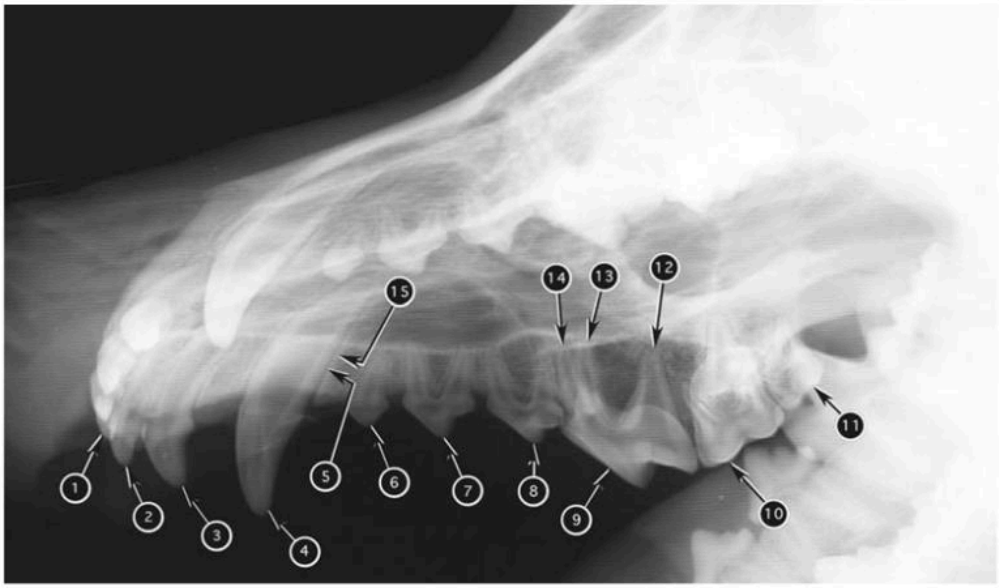
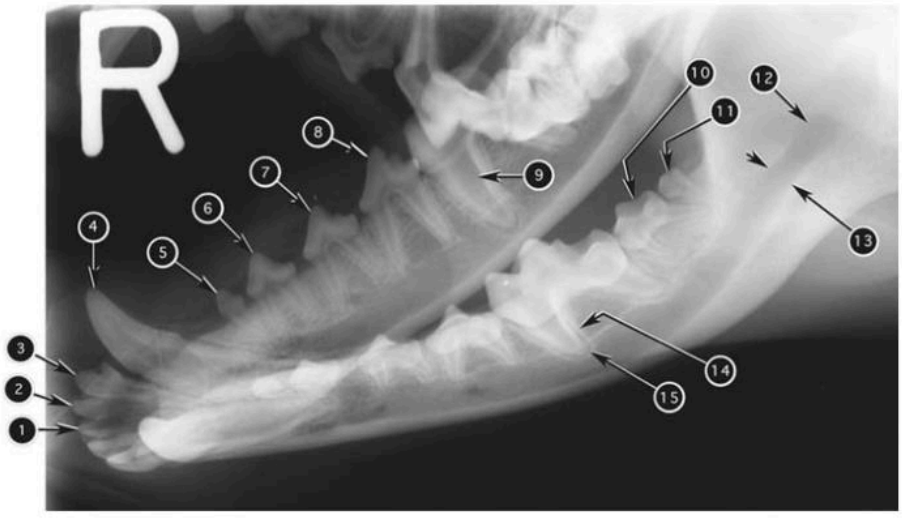


Fig. 8.5 Caudal left ventral/rostral right dorsal oblique radiograph of canine maxillary teeth (right maxilla projected ventrally).

1. Maxillary incisor 1 (101)
2. Maxillary incisor 2 (102)
3. Maxillary incisor 3 (103)
4. Maxillary canine tooth (104)
5. Periodontal ligament
6. Maxillary premolar 1 (105)
7. Maxillary premolar 2 (106)
8. Maxillary premolar 3 (107)
9. Maxillary premolar 4 (108)
10. Maxillary molar 1 (109)
11. Maxillary molar 2 (110)
12. Distal root of maxillary premolar 4 (108)
13. Mesiobuccal root of maxillary premolar 4 (108)
14. Mesiopalatal root of maxillary premolar 4 (108)
15. Cortical bone forming wall of alveolus

Fig. 8.6 Left ventral/right dorsal oblique radiograph of canine mandibular teeth.

1. Right mandibular incisor 1 (401)
2. Right mandibular incisor 2 (402)
3. Right mandibular incisor 3 (403)
4. Right mandibular canine tooth (404)
5. Right mandibular premolar 1 (405)
6. Right mandibular premolar 2 (406)
7. Right mandibular premolar 3 (407)
8. Right mandibular premolar 4 (408)
9. Dental cavity of right mandibular molar 1 (409)
10. Left mandibular molar 2 (310)
11. Left mandibular molar 3 (311)
12. Left mandibular foramen
13. Left mandibular canal
14. Lamina dura (cortical bone forming wall of alveolus) of mesial root of left mandibular molar 1 (309)
15. Periodontal ligament of mesial root of left mandibular molar 1 (309)



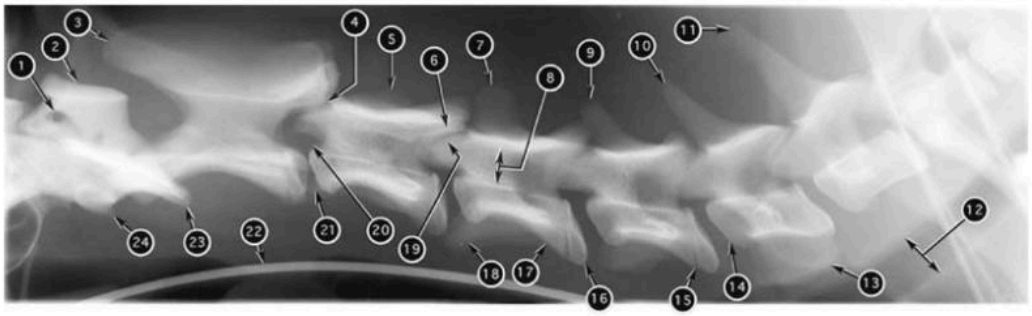


Fig. 8.7 Left-right lateral radiograph of canine cervical vertebrae.

1. Lateral vertebral foramina (left and right) of atlas; emergence of cervical nerve 1
2. Dorsal arch of atlas (C1)
3. Spinous process of axis (C2)
4. Synovial joints between articular processes of C2 and C3
5. Spinous process of C3
6. Caudal articular processes of C3
7. Spinous process of C4
8. Vertebral canal of C4
9. Spinous process of C5
10. Spinous process of C6
11. Spinous process of C7
12. Trachea
13. Expanded ventral laminae of transverse processes of C6
14. Cranial extremity (head) of C6
15. Caudal physis of C5
16. Caudal extremity (fossa) of C4
17. Body of C4
18. Transverse processes of C4
19. Cranial articular processes of C4
20. Intervertebral foramina between C2 and C3
21. Intervertebral disk space between C2 and C3
22. Endotracheal tube
23. Wings (transverse processes) of atlas
24. Ventral tubercle of atlas

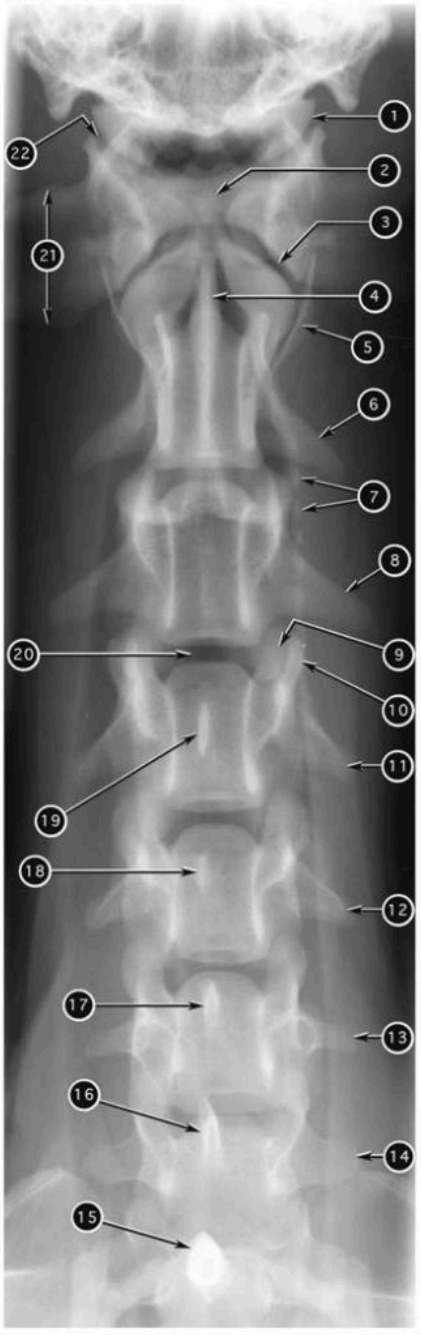


Fig. 8.8 Ventrodorsal radiograph of canine cervical vertebrae.
1. Left occipital condyle
2. Dens of axis
3. Atlantoaxial joint
4. Spinous process of axis
5. Left thyrohyoid bone
6. Left transverse process of axis
7. Tracheal cartilages
8. Left transverse process of C3
9. Left caudal articular process of C3
10. Left cranial articular process of C4
11. Left transverse process of C4
12. Left transverse process of C5
13. Left transverse process of C6
14. Left transverse process of C7
15. Spinous process of T1
16. Spinous process of C7
17. Spinous process of C6
18. Spinous process of C5
19. Spinous process of C4
20. Intervertebral disk space between C3 and C4
21. Right wing of atlas
22. Right atlantooccipital joint

Vetacademy.ir
مجموعه آموزشی پژوهشی وت آکادمی
تلاش #برای_دنیای_بهتر_حیوانات
تیم وت آکادمی
برای دسترسی به تازه ترین آموزش ها و مطالب علمی دامپزشکی؛ وت آکادمی رو فالو کن
سایت مجموعه بزرگ آموزشی پژوهشی وت آکادمی
Vet-academy.ir
صفحه ی اینستاگرام وت آکادمی
@Vetacademy.ir
دسترسی به آرشیو صد گیگ کتاب آموزش دامپزشکی به صورت رایگان
و جزوه های آموزشی در کانال تلگرامی
@Vetfiles
گروه بزرگ تلگرامی، پرسش و پاسخ و آموزش
@VetAcademyGp
صفحه رسمی آپارات وت آکادمی
aparat.com/vetacademy.ir

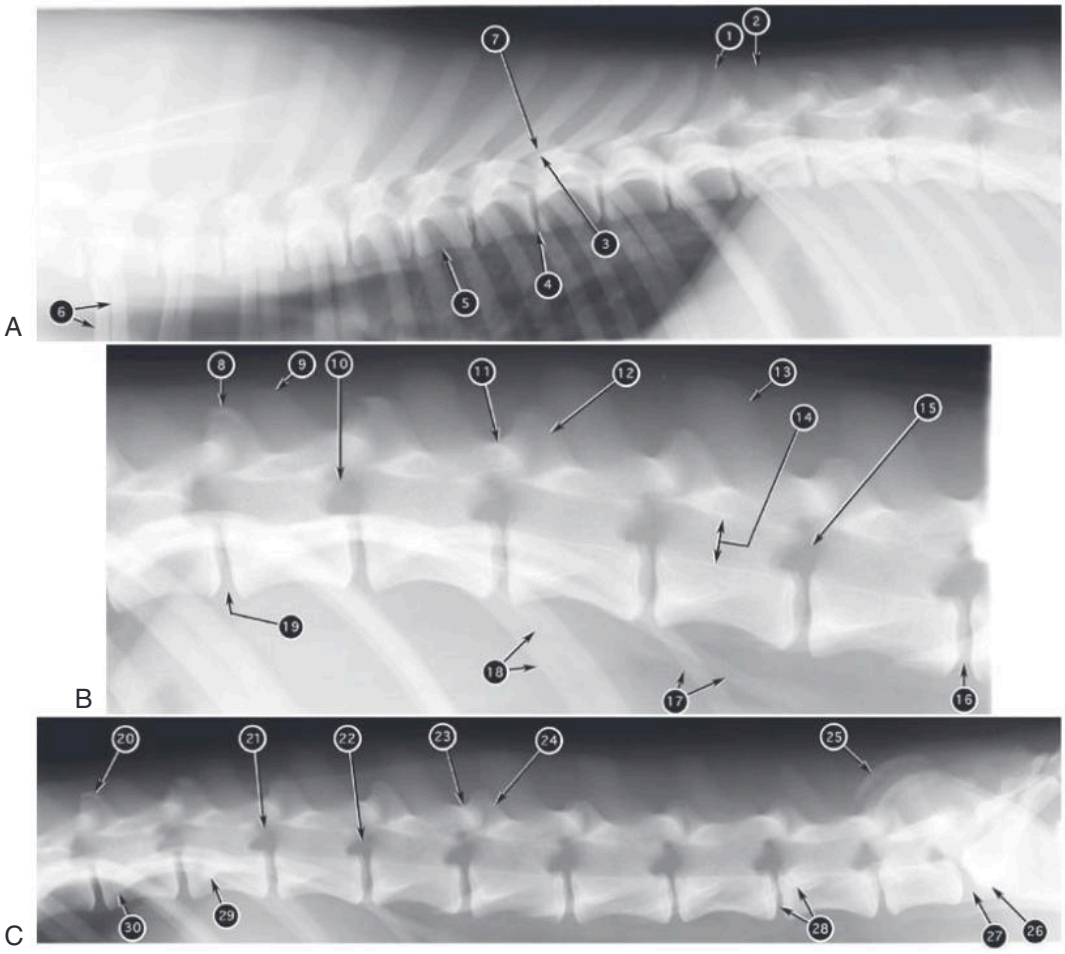


Fig. 8.9 Left-right lateral radiographs of canine thoracic and lumbar vertebrae.

A, Left−right (right) lateral radiograph of thoracic spine.

1. Spinous process of T10
2. Spinous process of T11 (anticlinal vertebra)
3. Cranial articular processes of T8
4. Intervertebral disk space between T7 and T8
5. Body of T6
6. First pair of ribs
7. Caudal articular processes of T7

B, Left−right (right) lateral radiograph of thoracolumbar spine.

8. Mammillary processes atop cranial articular processes of T12
9. Spinous process of T12
10. Accessory processes of T12
11. Caudal articular processes of T13
12. Cranial articular processes of L1
13. Spinous process of L2
14. Vertebral canal of L2
15. Intervertebral foramina between L2 and L3
16. Transverse processes of L4 superimposed over L3−4 intervertebral disk space
17. Thirteenth pair of ribs
18. Twelfth pair of ribs
19. Intervertebral disk space between T11 and T12

C, Left−right (right) lateral radiograph of lumbar spine.

20. Mammillary processes atop cranial articular processes of T12
21. Accessory processes of T13
22. Intervertebral foramina between L1 and L2
23. Caudal articular processes of L2
24. Cranial articular processes of L3
25. Secondary ossification center for crest of ilium
26. Promontory of sacrum
27. Intervertebral disk space between L7 and S1
28. Transverse processes of L6
29. Heads of 13th ribs superimposed on body of T13
30. Heads of 12th ribs superimposed on body of T12

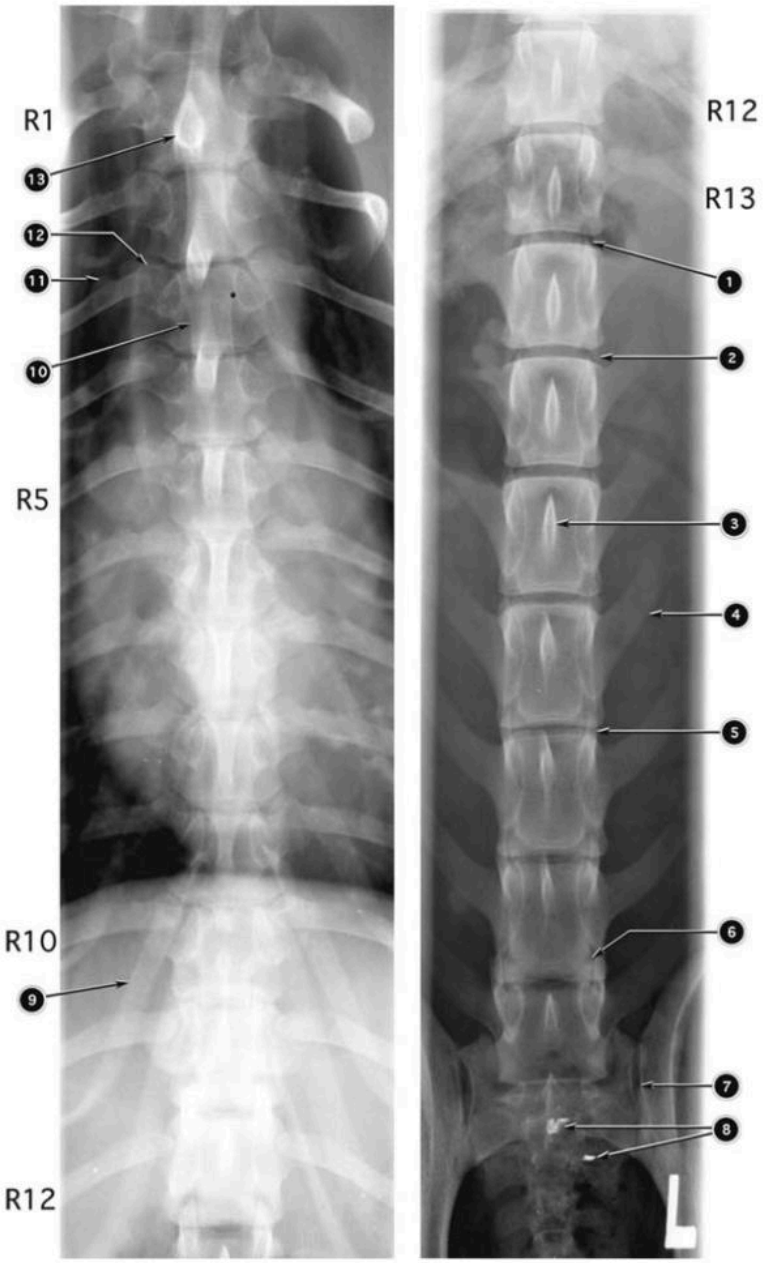


Fig. 8.10 Ventrodorsal radiographs of canine thoracic and lumbar vertebrae. *R,* Rib.

1. Intervertebral disk space between T13 and L1
2. Left accessory process of L2
3. Spinous process of L3
4. Left transverse process of L4
5. Left cranial articular process of L5
6. Left caudal articular process of L6
7. Left sacroiliac joint
8. Metallic foreign bodies in descending colon
9. Costal cartilage of right rib 11
10. Sternum superimposed over vertebrae
11. Tubercle of right rib 3
12. Head of right rib 3, articulating with bodies of vertebrae T2 and T3
13. Spinous process of T1

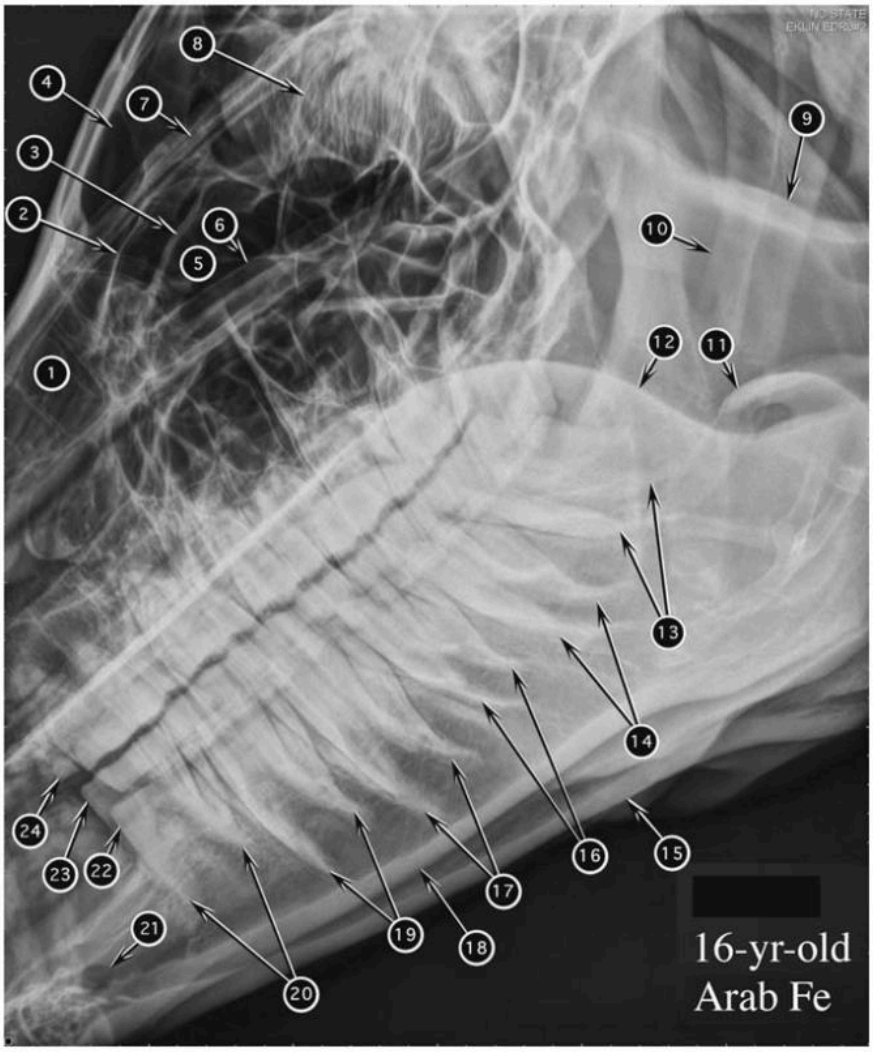


Fig. 8.11 Right-left (left) lateral radiograph of middle region of equine head (16 years old).
1. Dorsal conchal sinuses
2. Septum between left rostral and caudal maxillary sinuses
3. Septum between right rostral and caudal maxillary sinuses
4. Frontal sinuses (communicate with 1)
5. Caudal maxillary sinuses
6. Left infraorbital canal
7. Nasolacrimal ducts
8. Ethmoidal labyrinth
9. Dorsal wall of nasopharynx
10. Left stylohyoid bone
11. Epiglottic cartilage
12. Soft palate resting on root of tongue
13. Roots of right mandibular molar 3 (tooth 411)
14. Roots of right mandibular molar 2 (tooth 410)
15. Ventral border of right mandible
16. Roots of right mandibular molar 1 (tooth 409)
17. Roots of right mandibular premolar 4 (tooth 408)
18. Ventral border of left mandible
19. Roots of right mandibular premolar 3 (tooth 407)
20. Roots of right mandibular premolar 2 (tooth 406)
21. Left mental foramen
22. Right mandibular premolar 2 (tooth 406)
23. Left mandibular premolar 2 (tooth 306)
24. Left and right maxillary premolar 1 (teeth 205 and 105 superimposed)

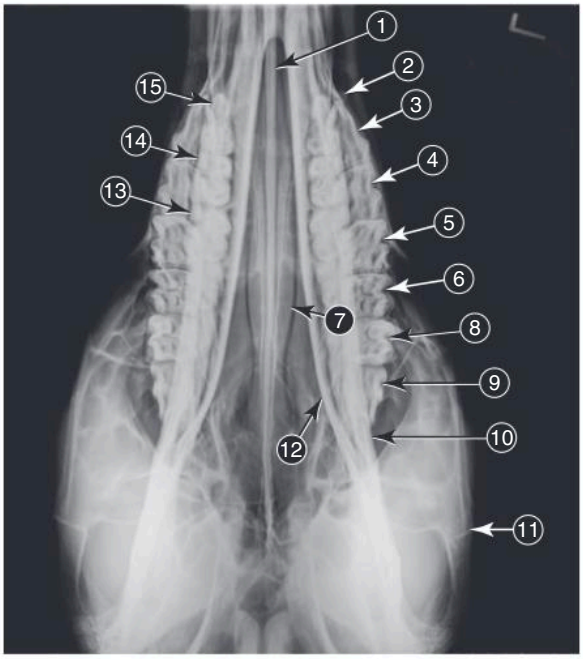


Fig. 8.12 Dorsoventral radiograph of middle region of equine head (16 years old).
1. Cartilaginous nasal septum superimposed on vomer
2. Left maxillary premolar 1 (tooth 205)
3. Left maxillary premolar 2 (tooth 206)
4. Left maxillary premolar 3 (tooth 207)
5. Left maxillary premolar 4 (tooth 208)
6. Left maxillary molar 1 (tooth 209)
7. Mucosa covering left side of nasal septum
8. Left maxillary molar 2 (tooth 210)
9. Left maxillary molar 3 (tooth 211)
10. Lateral surface of left mandible
11. Zygomatic arch
12. Medial surface of left mandible
13. Right mandibular premolar 4 (tooth 408)
14. Right mandibular premolar 3 (tooth 407)
15. Right mandibular premolar 2 (tooth 406)

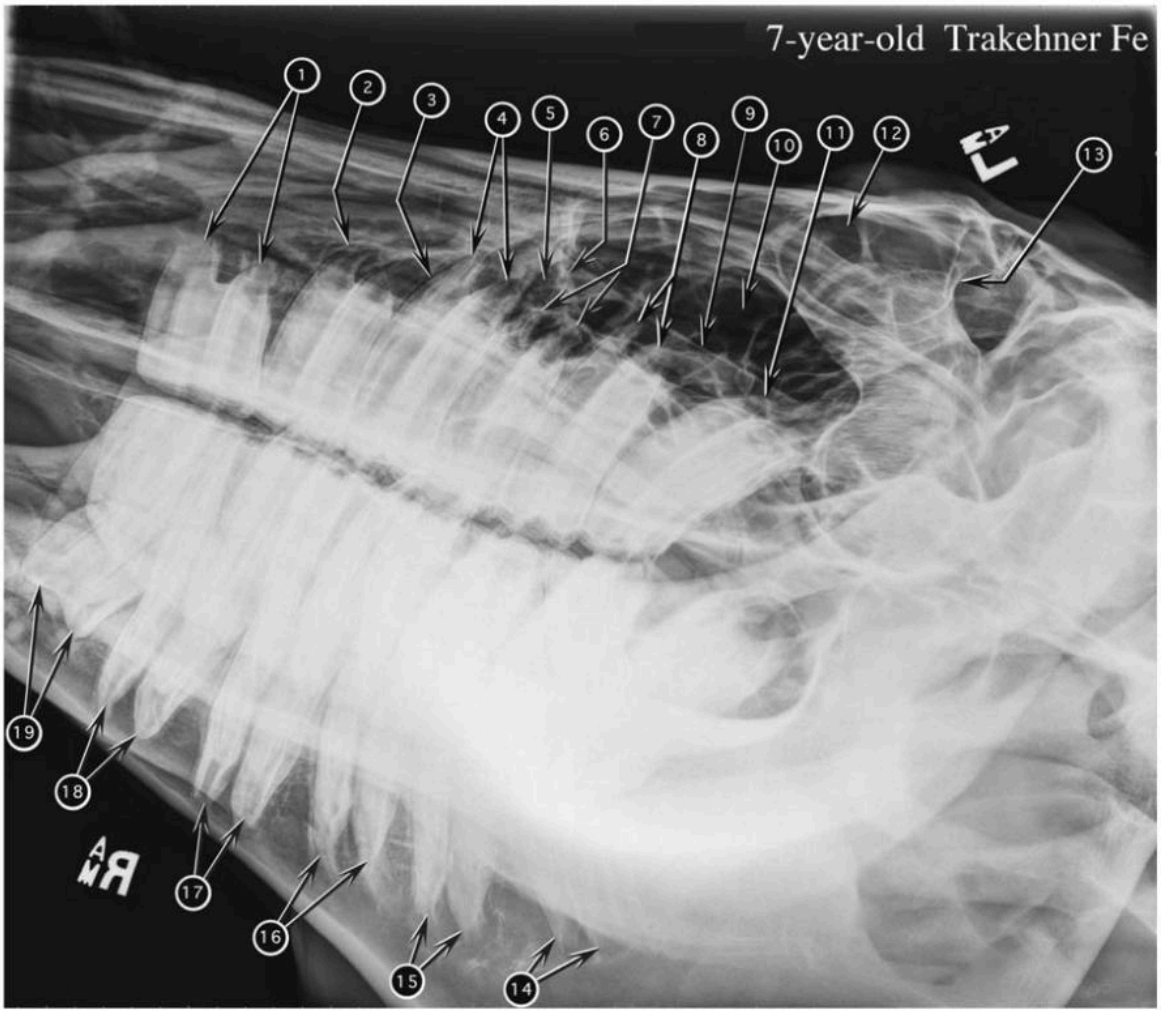


Fig. 8.13 Left ventral-right dorsal oblique (LeV-RtDO) radiograph of middle region of equine head (7 years old).

1. Roots of left maxillary premolar 2 (tooth 206)
2. Roots of left maxillary premolar 3 (tooth 207)
3. Wall of alveolus (*lamina dura dentes*)
4. Roots of left maxillary premolar 4 (tooth 208)
5. Left rostral maxillary sinus
6. Osseous septum separating 5 from 10
7. Roots of left maxillary molar 1 (tooth 209)
8. Roots of left maxillary molar 2 (tooth 210)
9. Left infraorbital canal
10. Left caudal maxillary sinus
11. Roots of left maxillary molar 3 (tooth 211)
12. Left conchofrontal sinus
13. Zygomatic process of left frontal bone
14. Roots of right mandibular molar 3 (tooth 411)
15. Roots of right mandibular molar 2 (tooth 410)
16. Roots of right mandibular molar 1 (tooth 409)
17. Roots of right mandibular premolar 4 (tooth 408)
18. Roots of right mandibular premolar 3 (tooth 407)
19. Roots of right mandibular premolar 2 (tooth 406)

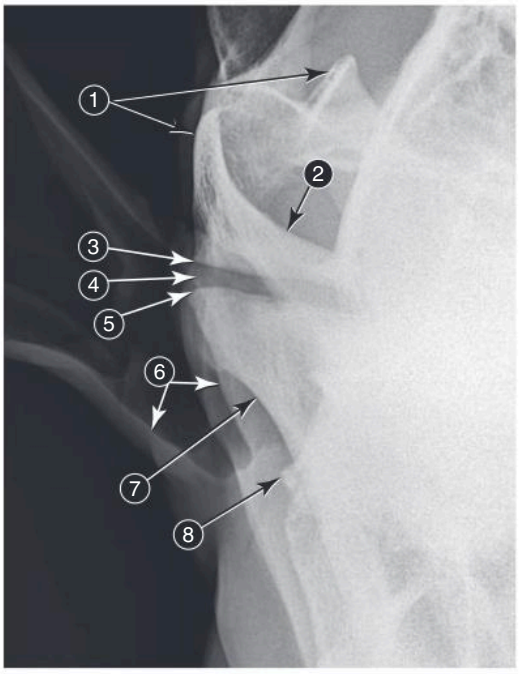


Fig. 8.14 Rostrodorsal-caudoventral oblique (RD-CdVO) radiograph of right equine temporomandibular joint (11 years old).
1. Zygomatic arch
2. Zygomatic process of frontal bone
3. Articular surface of squamous temporal bone
4. Articular disc, which completely divides temporomandibular joint into upper (temporal) and lower (mandibular) compartments
5. Head of mandible
6. Air in cartilaginous part of external acoustic meatus
7. Neck of mandible
8. Caudal lacrimal process projecting from rostromedial edge of orbit

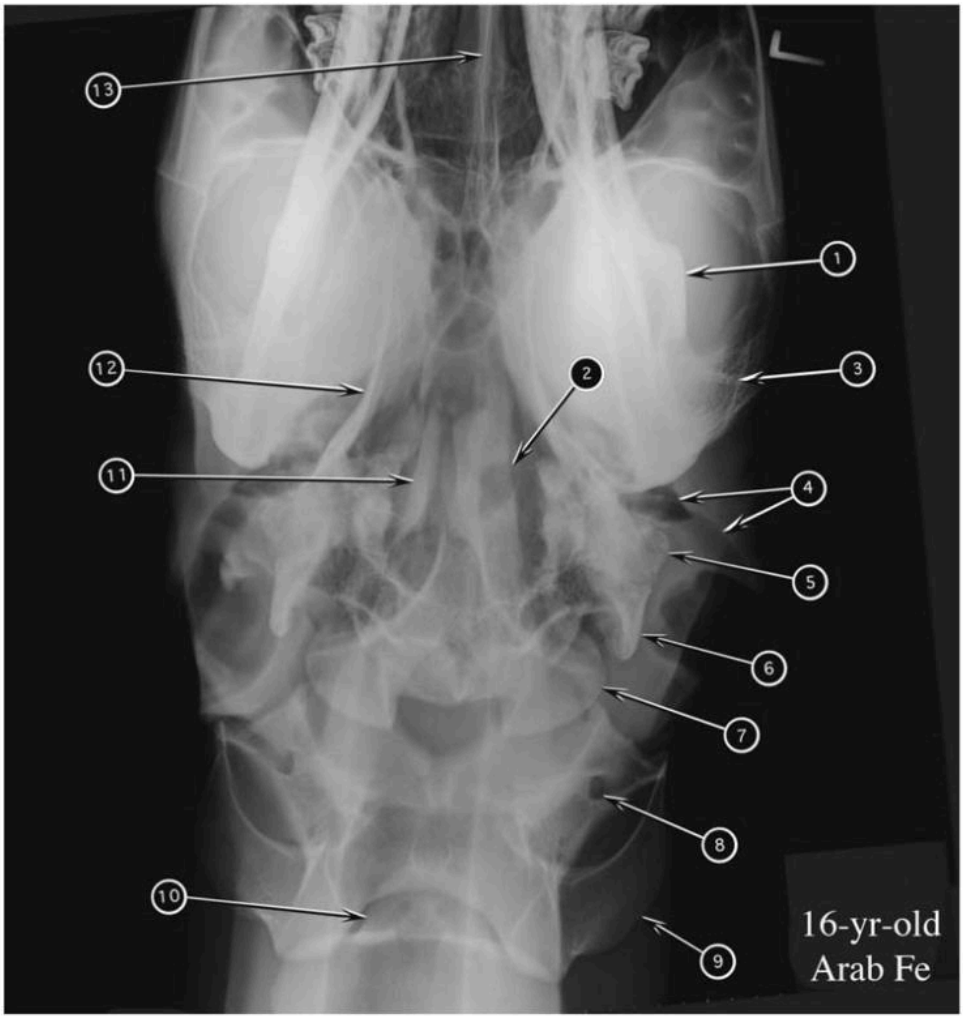


Fig. 8.15 Dorsoventral radiograph of caudal region of equine head (16 years old).
1. Coronoid process of left mandible
2. Left laryngeal ventricle
3. Left temporomandibular joint
4. External ear canal
5. Mastoid process of temporal bone
6. Paracondylar process of occipital bone
7. Occipital condyle
8. Alar foramen of atlas (C1)
9. Wing of atlas (C1)
10. Dens of axis (C2)
11. Right arytenoid cartilage of larynx
12. Right stylohyoid bone
13. Nasal septum

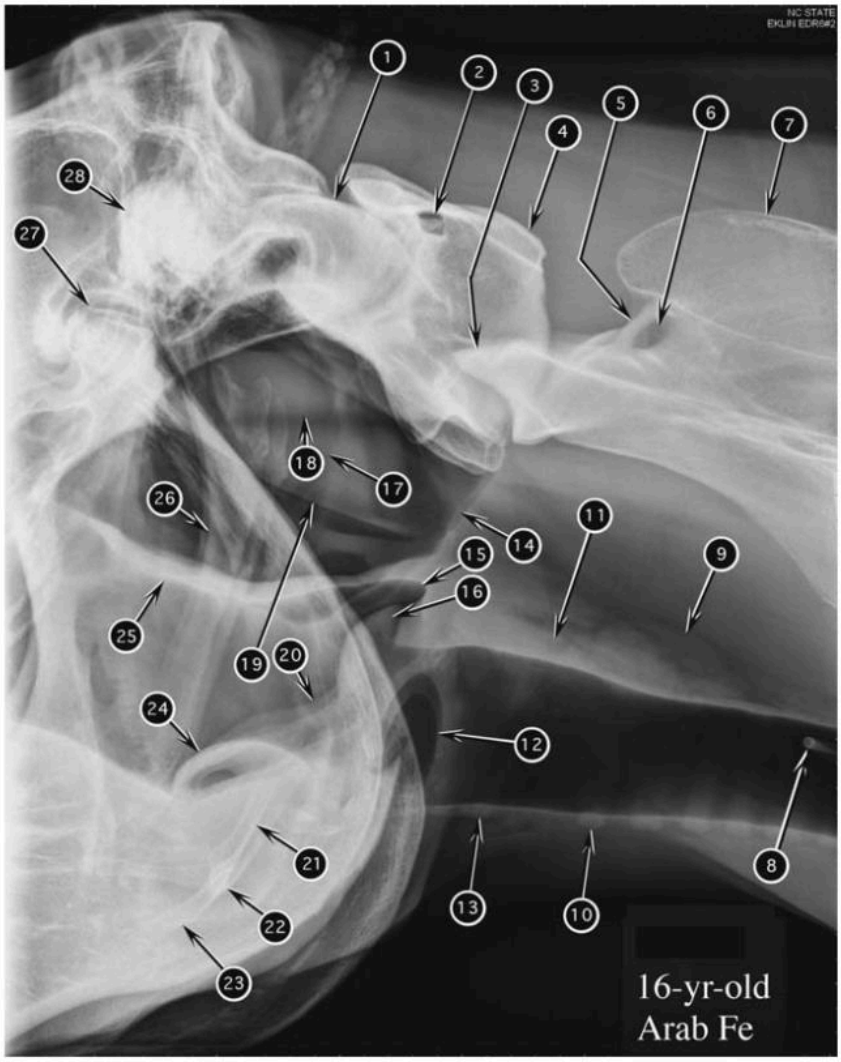


Fig. 8.16 Left–right lateral (right) radiograph of occipital region of equine head (16 years old).
1. Occipital condyles
2. Lateral vertebral foramina of atlas (C1)
3. Dens of axis (C2)
4. Dorsal arch of atlas (C1)
5. Ossified ligaments forming cranial boundary of 6 (not ossified in foals)
6. Lateral vertebral foramina of axis (C2)
7. Spinous process of axis (C2)
8. Catheter in external jugular vein
9. Thyroid gland
10. Tracheal cartilage
11. Lamina of cricoid cartilage
12. Laryngeal ventricles
13. Arch of cricoid cartilage
14. Caudal extent of medial compartments of guttural pouches
15. Laryngopharynx
16. Corniculate processes of arytenoid cartilages
17. Caudal extent of lateral compartments of guttural pouches
18. Rectus capitis ventralis muscle
19. Longus capitis muscles
20. Aryepiglottic folds
21. Thyrohyoid bones
22. Basihyoid bone
23. Lingual process of 22
24. Epiglottic cartilage
25. Dorsal wall of nasopharynx
26. Stylohyoid bones
27. Temporomandibular joints
28. Petrous temporal bones

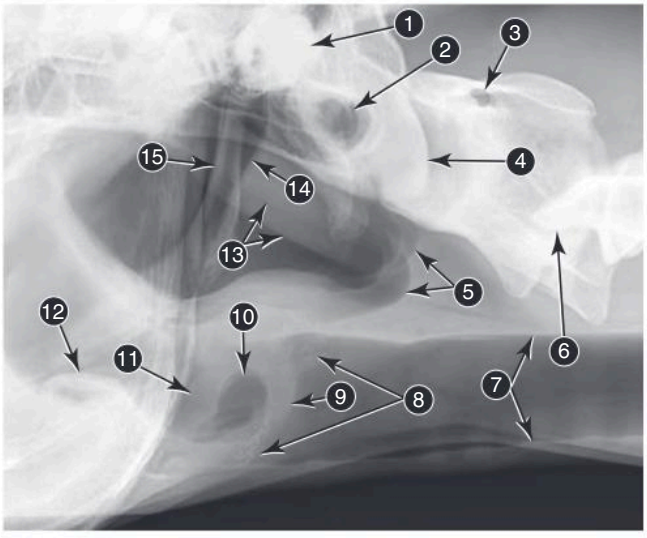


Fig. 8.17 Left–right lateral (right) radiograph of equine guttural pouches and laryngeal area (11 years old).
1. Petrous temporal bones
2. Hypoglossal canals
3. Lateral vertebral foramina of atlas (C1)
4. Occipital condyles
5. Caudal extent of medial compartments of guttural pouches
6. Dens of axis (C2)
7. Air in trachea
8. Early mineralization within thyroid cartilage of larynx[a]
9. Vocal folds
10. Laryngeal ventricles (saccules)
11. Vestibular folds
12. Epiglottis
13. Longus capitis muscles
14. Caudal extent of lateral compartments of guttural pouches
15. Stylohyoid bones

[a]In this horse, the mineralization involves the thyroid cartilage. Mineralization of the laryngeal cartilages in older horses is commonly observed radiographically as an incidental finding, which is not thought to be associated with any clinical problem. However, advanced mineralization of the cricoid or especially arytenoid cartilages may be of clinical concern. (From Tatarniuk, DM, Carmalt, JL, Allen, AL. Induration of the cricoid cartilage complicates prosthetic laryngoplasty in a horse. *Vet Surg.* 2010;39:128–130.)

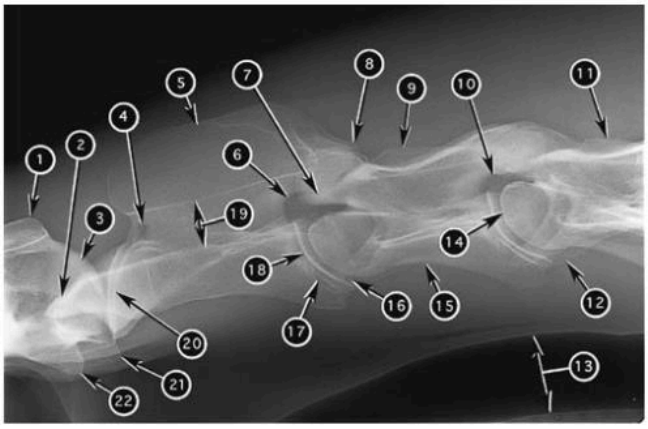


Fig. 8.18 Left–right lateral (right) radiograph of equine cranial cervical vertebrae.

1. Dorsal arch of atlas (C1)
2. Dens of axis (C2)
3. Caudal articular fovea of atlas (C1)
4. Lateral vertebral foramina of axis (C2)
5. Spinous process of axis (C2)
6. Intervertebral foramina between axis (C2) and C3
7. Cranial articular processes of C3
8. Caudal articular processes of axis (C2)
9. Spinous process of C3
10. Intervertebral foramina between C3 and C4
11. Spinous process of C4
12. Transverse processes of C4
13. Trachea
14. Cranial extremity (head) of C4
15. Body of C3
16. Intervertebral disk space between axis (C2) and C3
17. Caudal physis of axis (C2)
18. Caudal extremity (fossa) of axis (C2)
19. Vertebral canal of axis (C2)
20. Cranial articular processes of axis (C2)
21. Wings of atlas (C1)
22. Ventral tubercle of atlas (C1)

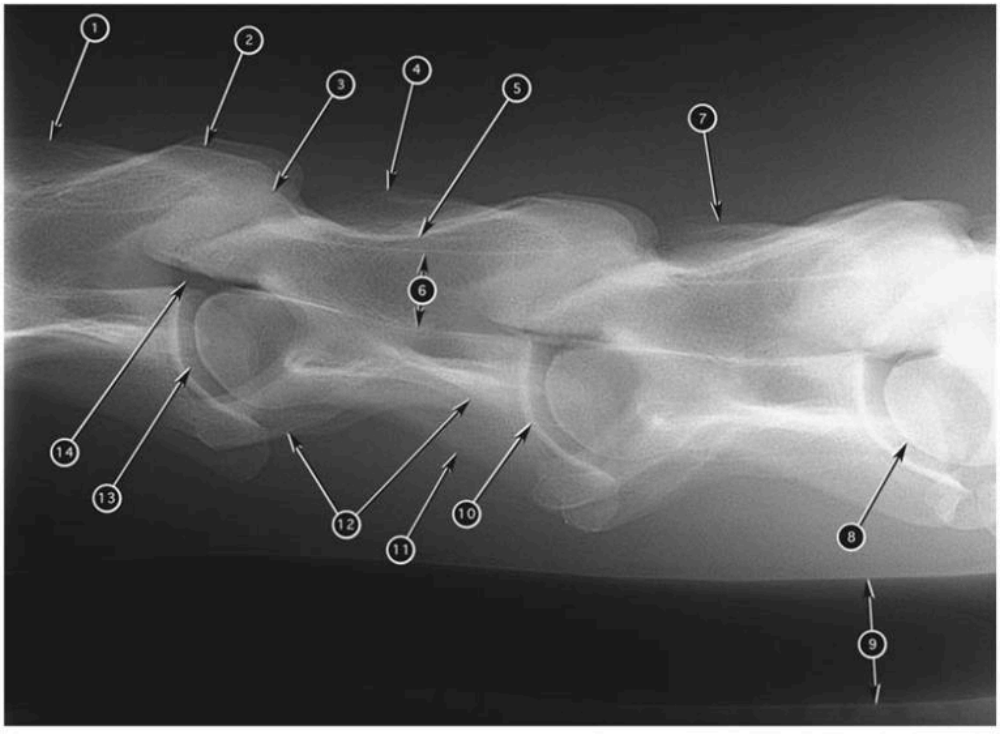


Fig. 8.19 Left–right lateral (right) radiograph of equine middle cervical vertebrae.

1. Spinous process of C3
2. Caudal articular processes of C3
3. Cranial articular processes of C4
4. Spinous process of C4
5. Vertebral arch laminae of C4
6. Vertebral canal of C4
7. Spinous process of C5
8. Cranial extremity (head) of C6
9. Trachea
10. Caudal extremity (fossa) of C4
11. Body of C4
12. Transverse processes of C4
13. Intervertebral disk space between C3 and C4
14. Intervertebral foramina between C3 and C4

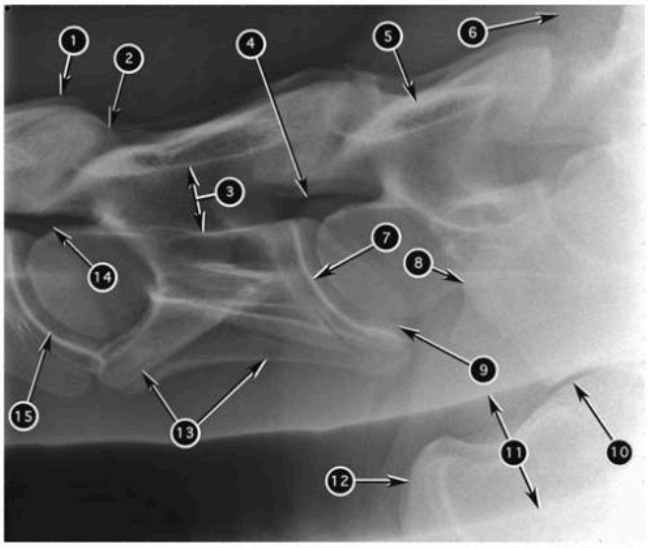


Fig. 8.20 Left–right lateral (right) radiograph of equine caudal cervical vertebrae.
1. Caudal articular processes of C5
2. Cranial articular processes of C6
3. Vertebral canal of C6
4. Intervertebral foramina between C6 and C7
5. Vertebral arch laminae of C7
6. Spinous process of T1
7. Caudal extremity (fossa) of C6
8. Supraglenoid tubercle of scapula
9. Intervertebral disk space between C6 and C7
10. Shoulder joint
11. Trachea
12. Intermediate tubercle of humerus
13. Transverse processes of C6
14. Intervertebral foramina between C5 and C6
15. Intervertebral disk space between C5 and C6

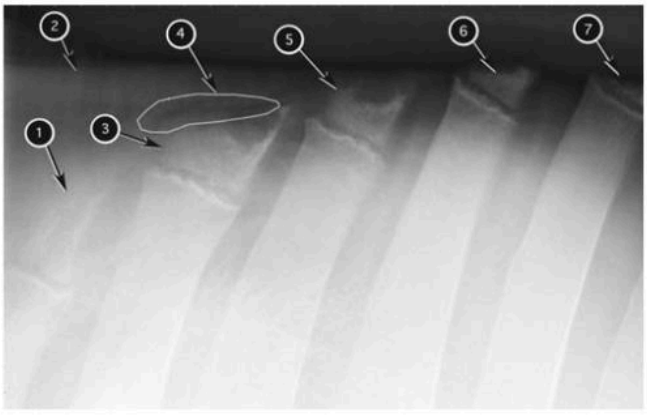


Fig. 8.21 Left–right lateral (right) radiograph of equine withers region.
1. Spinous tuberosity of T2
2. Funiculus nuchae (nuchal ligament)
3. Spinous tuberosity of T3
4. Approximate location of supraspinous bursa
5. Spinous tuberosity of T4
6. Spinous tuberosity of T5
7. Spinous tuberosity of T6

REFERENCES

1. Schebitz HCH. *Atlas of Radiographic Anatomy of the Dog*. Stuttgart, Germany: Parey Verlag; 2005.
2. Schebitz H, Wilkens H. *Atlas of Radiographic Anatomy of the Horse*. 3rd ed. Philadelphia: Saunders; 1978.
3. Thrall D, Robertson ID. *Atlas of normal Radiographic Anatomy and Anatomic Variants in the Dog and Cat*. 3rd ed. St. Louis: Elsevier; 2022.
4. DuPont GA, DeBowes LJ. *Atlas of Dental Radiography in Dogs and Cats*. St. Louis: Saunders-Elsevier; 2009.
5. Smallwood JE, Shively MJ, Rendano VT, et al. A standardized nomenclature for radiographic projections used in veterinary medicine. *Vet Radiol*. 1985;26:2.

CHAPTER 9

Basic Principles of Radiographic Interpretation of the Axial Skeleton

Donald E. Thrall

SKULL

The skull is anatomically complex, therefore the numerous overlapping soft tissue and bone structures result in many abnormalities being inconspicuous radiographically. Also, most intracranial lesions are not visible in radiographs. Therefore, skull radiography is rarely done in small animals in specialty practices, having been replaced by computed tomography (CT) and magnetic resonance imaging (MRI). Skull radiography is more common in small animal general practice and in equine practice but, unfortunately, particularly in dogs and cats, there is a high incidence of technical and positioning errors that negatively affect the diagnostic quality of the study.

Positioning: Dog and Cat

The anatomic complexity of the skull makes it imperative that radiographic positioning be standardized and repeatable; this removes a source of variation caused by obliquity that can complicate radiographic interpretation. At a minimum, obtaining good skull radiographs requires sedation, but general anesthesia is preferable. Making skull radiographs without sedating or anesthesia leads to poor-quality images that cannot be interpreted accurately and is a waste of time, effort, and money.

Lateral and dorsoventral (DV) views comprise the minimum radiographic study of the canine and feline skull but these are rarely adequate without additional views. The DV view is preferred over the ventrodorsal (VD) view, because for the DV view slight downward pressure will facilitate more symmetric positioning as the mandibles will provide a flat, stable surface to support the head (Fig. 9.1). As the dorsal surface of the canine or feline head is rarely flat, symmetric positioning of a VD view is more difficult.

For the lateral view of the skull, the dog or cat cannot be allowed to rest naturally on the x-ray table. The nose will need to be elevated by a positioning sponge in most patients. A sponge may also be needed to elevate the mandibles. The goal is to have left-sided and right-sided structures superimposed perfectly (Fig. 9.2). The positioning devices should be kept free of dirt and debris that can introduce artifacts into the image (see Fig. 9.2). The mouth can be closed or held open with a speculum, preferably a nonmetallic speculum so as not to obscure anatomy. If the disease affects the mandible or maxilla, then there is value in having the mouth open to reduce superimposition.

Because of the anatomic complexity of the skull, many ancillary projections are available to increase the conspicuity of certain regions.[1,2] Some are listed in Table 9.1, and a few examples included (Figs. 9.3–9.9). An ancillary view is not used in every patient but should always be considered depending on the purpose of the radiographic examination. Most ancillary



Fig. 9.1 A perfectly positioned canine dorsoventral (DV) skull radiograph. There is perfect symmetry of left and right sides.



Fig. 9.2 Perfectly positioned lateral canine skull radiograph. The mandibles have been elevated from the x-ray table using a positioning sponge and the tympanic bullae are perfectly superimposed (*black arrow*). Positioning sponges can become soiled and introduce artifacts into the image, as seen here (*white arrow*).

Table • **9.1**

Ancillary Radiographic Projections of the Canine or Feline Skull.

VIEW NO.	PART OF INTEREST	NAME OF PROJECTION	BRIEF DESCRIPTION
1	Frontal sinuses	Rostrocaudal projection of frontal sinuses	Subject in dorsal recumbency. Head flexed 90 degrees to spine such that nose points directly at x-ray tube. Center x-ray beam on frontal sinuses.
2	Right maxillary dental arcade or right tympanic bulla	Open-mouth left 20-degree ventral—right dorsal[a]	Subject in right recumbency. Secure mouth open with speculum. Elevate mandibles 20 degrees with sponge wedge. Center x-ray beam on right maxillary arcade or tympanic bulla.
3	Left maxillary dental arcade or left tympanic bulla	Open-mouth right 20-degree ventral—left dorsal	Subject in left recumbency. Secure mouth open with speculum. Elevate mandibles 20 degrees with sponge wedge. Center x-ray beam on left maxillary arcade or tympanic bulla.
4	Right mandibular dental arcade	Open-mouth left 20-degree dorsal—right ventral	Subject in right recumbency. Secure mouth open with speculum. Elevate maxilla 20 degrees with sponge wedge. Center x-ray beam on right mandibular arcade.
5	Left mandibular dental arcade	Open-mouth right 20-degree dorsal—left ventral	Subject in left recumbency. Secure mouth open with speculum. Elevate maxilla 20 degrees with sponge wedge. Center x-ray beam on left mandibular arcade.
6	Nasal cavity	Open-mouth ventral 20-degree rostral—dorsocaudal	Subject in dorsal recumbency. Secure maxilla against x-ray table such that hard palate is parallel to tabletop. Open mouth widely with speculum or gauze traction on mandible. Angle x-ray beam 20 degrees rostrally and center x-ray beam on hard palate.
7	Nasal cavity	Intraoral dorsoventral	Subject in ventral recumbency. Slide cassette into mouth. Center x-ray beam on dorsal aspect of maxilla.
8	Tympanic bullae	Open-mouth rostrocaudal	Subject in dorsal recumbency. Head flexed 90 degrees to spine such that nose points directly at x-ray tube. Open mouth by retracting maxilla and mandible equally with gauze or tape. Center x-ray beam in back of mouth.
9	Tympanic bullae (cats and brachycephalic dogs)	Rostral 10 degrees ventral —caudodorsal	Subject in dorsal recumbency. Head flexed 90 degrees to spine such that nose points directly at x-ray tube. Angle head/neck 10 degrees caudally, keeping mouth closed. Center x-ray beam at base of skull.
10	Right tympanic bulla/right temporomandibular joint	Left 20 degrees rostral—right caudal	Subject in right recumbency. Elevate nose 20 —30 degrees with sponge. Center x-ray beam on region of temporomandibular joint.
11	Left tympanic bulla/left temporomandibular joint	Right 20 degrees rostral—left caudal	Subject in left recumbency. Elevate nose 20—30 degrees with sponge. Center x-ray beam on region of temporomandibular joint.

[a]Any angle specified in this table for this or any other ancillary skull radiograph is an estimate. This will vary among dogs and should be selected based on visual determination of the angle that results in optimal isolation of the area of interest.

views of the skull require changing the position of the patient while a few require that the x-ray beam be angled (Fig. 9.10). The use of an antiscatter grid will improve image quality in larger patients where the thickness of the skull exceeds approximately 10 cm.

An external marking system must be used to label oblique radiographs of the skull so that the left side can be distinguished reliably from the right side. Both "L" and "R" markers are needed to designate which structures are being projected (Fig. 9.11). If only one marker is used, it is not possible to differentiate left-sided from right-sided structures (Fig. 9.12).

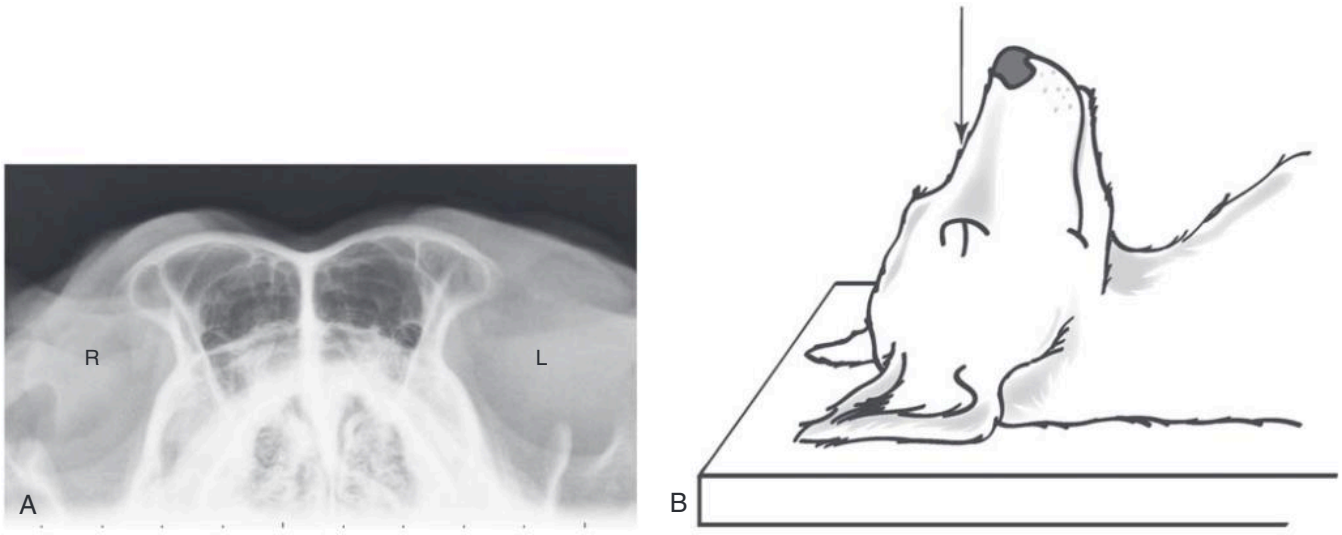


Fig. 9.3 **(A)** Rostrocaudal frontal sinus view in a dog and **(B)** diagram of positioning (see Table 9.1, View No. 1). The patient is in dorsal recumbency with the nose pointing at the x-ray tube. This view provides an unobstructed view of each frontal sinus. It should be kept in mind that brachycephalic dogs and some cats have incompletely developed frontal sinuses. In those patients, the main value of this projection would be to assess the frontal bone itself. *L*, Left side; *R*, right side. (**B,** From Owens JM, Biery DN. *Radiographic Interpretation for the Small Animal Clinician*. Baltimore: Williams & Wilkins; 1999.)

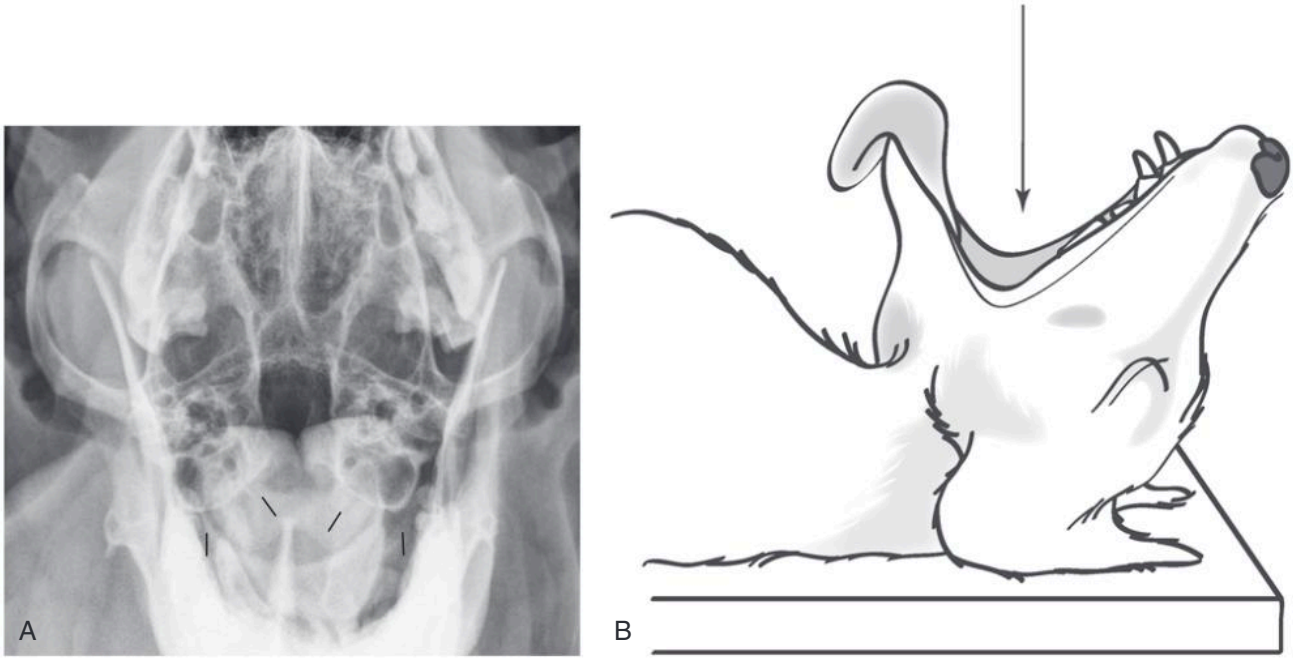


Fig. 9.4 **(A)** Open-mouth rostrocaudal view of the tympanic bullae in a dog and **(B)** diagram of positioning (see Table 9.1, View No. 8 and Fig. 9.10). The patient is in dorsal recumbency with the nose pointing at the x-ray tube. The mouth is held open by retracting the mandible and maxilla with gauze. Centering the x-ray beam in the back of the mouth provides a relatively unobstructed view of the tympanic bullae (*black arrow*). (**B,** From Owens JM, Biery DN. *Radiographic Interpretation for the Small Animal Clinician*. Baltimore: Williams & Wilkins; 1999.)

Positioning: Horse

Sedation is not required for equine skull radiography, but it is recommended to facilitate positioning, especially for the DV view, where the dropped position of the head will make it easier to position the x-ray tube dorsally. Skull radiographs of adult horses are typically acquired with the horse standing.

For the lateral view, the cassette is positioned against the head of the standing horse and a horizontal x-ray beam directed from the opposite side (Fig. 9.13A). The thickness of the equine head leads to radiographic magnification being more pronounced than in the dog or cat. Magnification of a lesion on the side of the head closest to the x-ray tube may result in the lesion not being visible because of blurring. Thus, if the laterality of a lesion is known, the plate should be positioned against that side of the head and the x-ray beam directed from the opposite side. If the laterality of the lesion is not known, it is good practice to obtain both left-right and right-left radiographs to make sure that a lesion is not overlooked because of magnification.



Fig. 9.5 Intraoral dorsoventral (DV) radiograph of maxilla in a dog (see Table 9.1, View No. 7). The patient is in sternal recumbency with the plate inserted into the mouth and the x-ray beam directed onto the dorsal surface of the maxilla. This projection provides an unobstructed view of the nasal cavity. With the increase in digital imaging, this view is used infrequently as the large size of the plate, or computed radiography (CR) cassette, limits the extent that it can be inserted into the mouth. Also, many digital plates are permanently mounted in the x-ray table. The view illustrated in Fig. 9.10 is a more practical substitute.

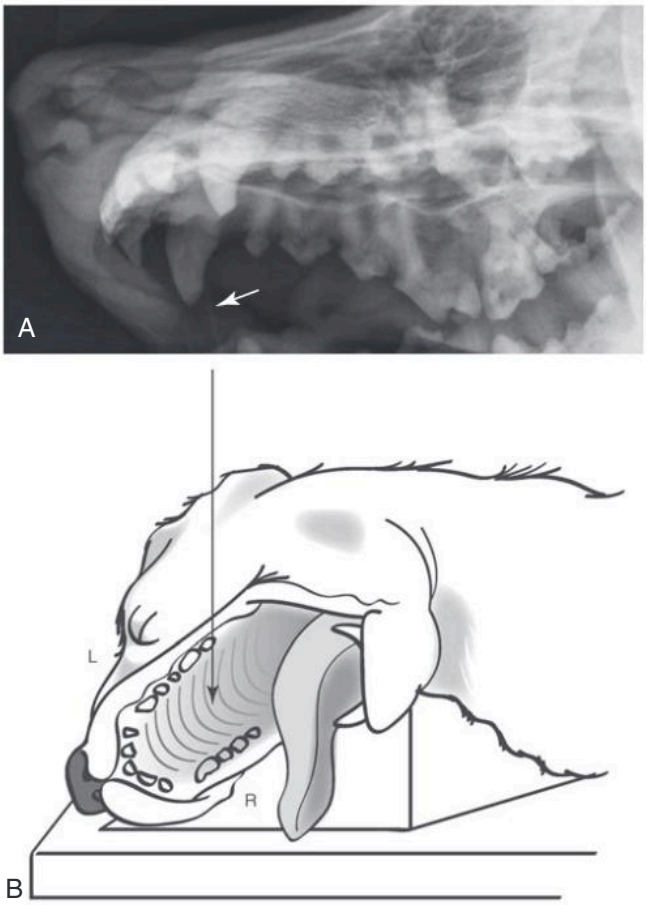


Fig. 9.6 **(A)** Open-mouth, left 20-degree ventral—right dorsal projection of the right maxillary dental arcade in a dog and **(B)** diagram of positioning (see Table 9.1, View No. 2). The patient is in right recumbency and the mouth held open with a speculum. A portion of the plastic speculum is visible in **A** (*white arrow*). The mandibles are elevated 20 degrees from the tabletop with a positioning sponge. This projects the left side of the maxilla dorsal to the right. The x-ray beam, which is vertical to the tabletop, is centered on the right maxillary arcade. This view is mainly used to evaluate bone lesions. For evaluation of teeth, a full mouth dental radiographic study with a small intra-oral plate is preferred. *L*, Left side; *R*, right side. (**B,** From Owens JM, Biery DN. *Radiographic Interpretation for the Small Animal Clinician*. Baltimore: Williams & Wilkins; 1999.)

For the DV view, the plate is ventral to the mandibles and the x-ray beam directed onto the dorsal aspect of the head (see Fig. 9.13B). It is important to keep the x-ray beam perpendicular to the plate. As already noted, sedation is helpful for the DV view because as the horse lowers its head in response to the sedative, dorsal positioning of the x-ray tube is facilitated. Without sedation, one might be able to acquire a DV view of the nasal passage, but a DV view of the calvarium or brain case will usually not be possible. VD views of the skull are not made in the standing horse.

Radiation safety becomes paramount when radiographing the equine head. Positioning the plate by placing it in a plate holder with an extension handle is impractical because of the weight of the plate. This commonly results in motion and blurring of the image. In many practices, equine skull radiographs are acquired by handholding the plate. If this is done, a lead apron, lead gloves, a lead thyroid shield, and lead-impregnated glasses should be worn. The x-ray beam must also be collimated such that the gloved hands, or any other part of the body, are never in the primary x-ray beam.

As in the dog and cat, ancillary oblique views of the equine skull are often needed because of the anatomic complexity. Oblique views are commonly used in the horse to evaluate a nasal passage or a dental arcade (Fig. 9.14). As in the dog and cat, use of properly placed L and R markers is critical to ensure that the structures being projected are identified accurately (Fig. 9.15).

Radiographic Technique

The wide exposure latitude of digital imaging systems means that selecting kVp and mAs values for skull radiography is much less critical than when film-screen technology was used. In digital imaging, many more kVp/mAs combinations will result in a diagnostic image than with film. Exposure latitude also results in the ability to evaluate both the thicker and thinner parts of the skull in the same image; for example, proper exposure of a thicker part does not result in overexposure of a thinner part, and vice versa.

Despite the exposure latitude of digital systems, an inherent problem associated with equine skull radiography is the tendency to overexpose the image (Fig. 9.16). This probably occurs because of a concern that the thick bony components require massive exposure factors for proper imaging.

Ancillary Factors

Although use of an antiscatter grid would be very useful in equine skull radiography, the necessary increase in mAs needed to compensate for the grid may not be possible. Also, a cassette that contains a grid is heavy and difficult to hold steadily by hand, leading to motion and/or grid-line artifacts. A wall-mounted plate holder, discussed subsequently for equine cervical radiographs, is one method to incorporate the use of a grid for equine skull radiography without increasing the risk of motion artifact. A wall-mounted plate holder will also lead to reduced personnel exposure.

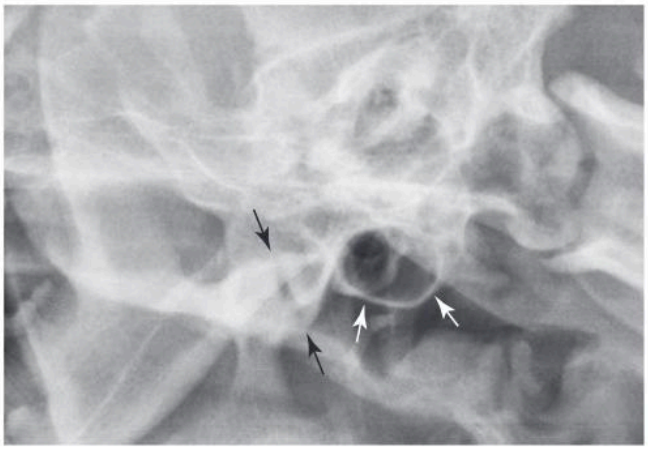


Fig. 9.7 Open-mouth, left 20-degree ventral–right dorsal projection of the right tympanic bulla and temporomandibular joint in a dog (see Table 9.1, View No. 2). This view is identical to that in Fig. 9.6, except the x-ray beam is centered on the middle ear. This allows assessment of the right (dependent) tympanic bulla (*white arrows*) and right temporomandibular joint (*black arrows*). The left (nondependent) tympanic bulla and left temporomandibular joint are projected more dorsally and are superimposed on the skull. Only the right tympanic bulla and temporomandibular joint can be assessed using this positioning. If the left-sided structures are of interest, then the view described in Table 9.1, View No. 3, should be used.

Interpretation Paradigm

The following is a reasonable step-by-step process for interpreting skull radiographs.

- Have adequate radiographic views been obtained according to the clinical problem being assessed? If not, what additional views would help?
- Are there positioning problems that will interfere with interpretation?
- Are the images overexposed or underexposed?
- Has sedation or anesthesia been used? If not, did this affect the usefulness of the radiographs?
- What species or breed characteristics should be considered?
- Are external markers adequate to distinguish between left and right sides?

After these variables have been considered, the images can be scrutinized for abnormalities. The Roentgen sign and DAMNITV (degenerative, anomalous, metabolic, neoplastic, infectious [inflammatory, immune], traumatic, and vascular) methods described in Chapter 6 should be used. In many patients, the cause of the clinical signs will not be found in skull radiographs, or the lesion will be incompletely characterized, and other modalities, such as CT or MRI, will be needed.[3–5] And, even when the lesion is identified, aspiration or biopsy is commonly necessary to obtain a definitive diagnosis.

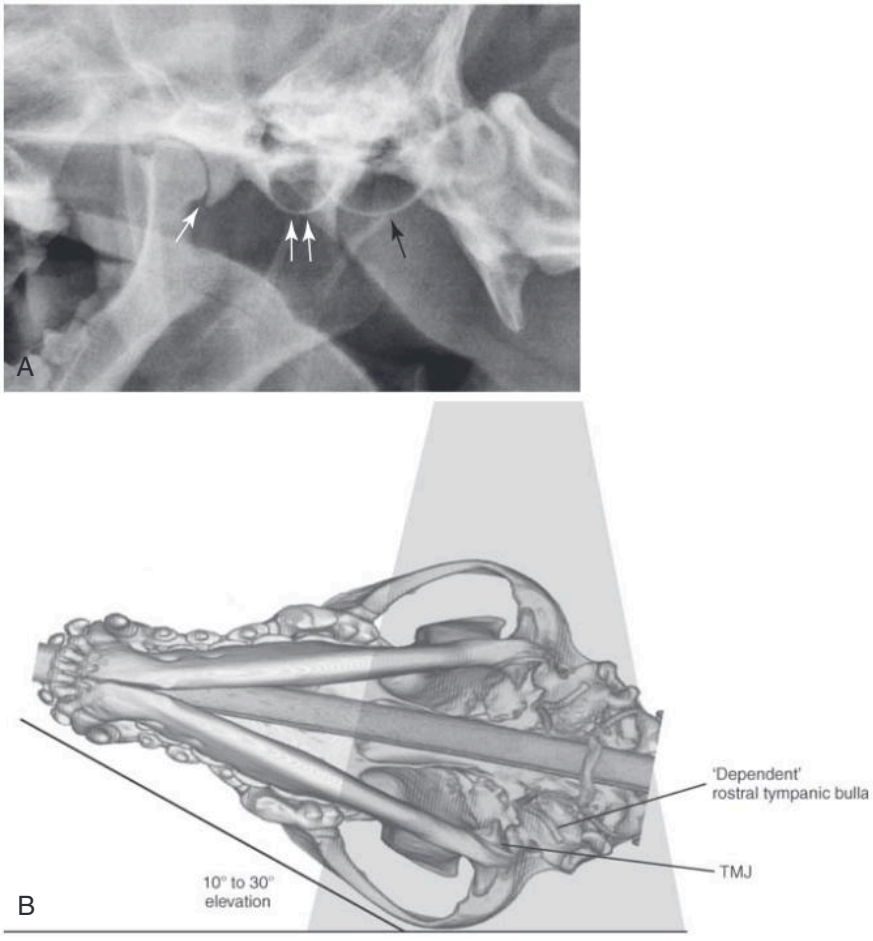


Fig. 9.8 **(A)** Left 20-degree rostral–right caudal projection of the right temporomandibular joint (*single white arrow*) and right tympanic bulla (*double white arrows*) in a dog and **(B)** positioning diagram (see Table 9.1, View No. 10). The patient is in right recumbency, and the tip of the nose is elevated 20 degrees from the tabletop. The x-ray beam is perpendicular to the tabletop and centered on the tympanic bulla. Elevating the nose projects the upper, left, nondependent tympanic bulla (*single black arrow*), caudal to the lower, right, dependent tympanic bulla (*double white arrows*). Compared with Fig. 9.7, the contralateral, nondependent, left tympanic bulla (*black arrow*) is caudal to the one of interest rather than being dorsal. Note that the nondependent, left tympanic bulla is larger because of radiographic magnification. In this view, the nondependent, left temporomandibular joint is superimposed on the region where the tympanic bullae overlap. *TMJ,* Temporomandibular joint. (From Thrall D, Robertson I, eds. *Atlas of Radiographic Anatomy and Normal Anatomic Variants in the Dog and Cat*. 3rd ed. St. Louis: Elsevier; 2023.)

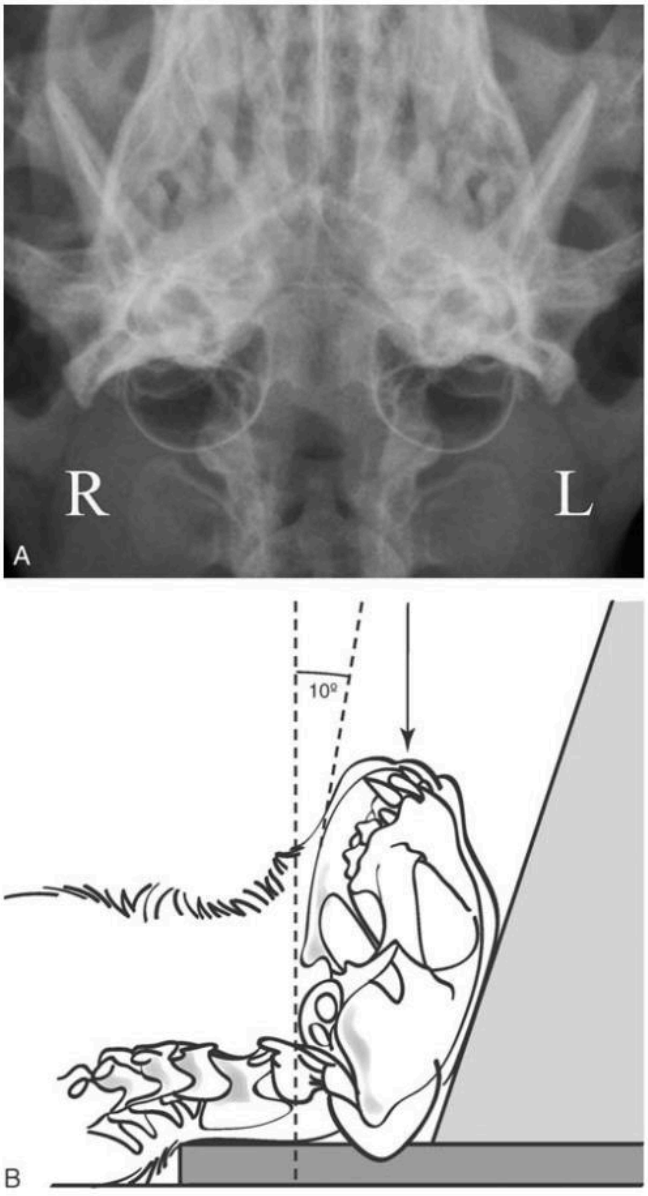


Fig. 9.9 **(A)** Rostral 10-degree ventral–caudodorsal view of the tympanic bullae (*white arrows*) in a cat and **(B)** positioning diagram (see Table 9.1, View No. 9). The patient is in dorsal recumbency with the nose pointing directly at the x-ray tube. The head and neck are extended 10 degrees, and the x-ray beam, which is perpendicular to the tabletop, is centered at the base of the skull. *L,* Left; *R,* right. (From Owens JM, Biery DN. *Radiographic Interpretation for the Small Animal Clinician*. Baltimore: Williams & Wilkins; 1999.)

Experienced radiologists may have a random search pattern, but it is recommended that inexperienced interpreters use an organized approach.[6] Having a mental checklist to guide the interpretation of skull radiographs will reduce the number of errors (Box 9.1).

SPINE

Survey spinal radiographs are acquired commonly in small animal practice due to the high incidence of back pain and pelvic limb paresis, and to rule out root signature as a cause of forelimb lameness. Equine spinal radiographs are obtained less frequently due to the relatively low prevalence of cervical disease and the inability to obtain diagnostic radiographs of the thoracic and lumber spine in adult horses.

There are some unique anatomic features of the spine that should be kept in mind.[1]

- The vertebral formula for the dog and cat is C7 T13 L7 S3 Cd variable.
- The vertebral formula for the horse is C7 T18 L6 S5 Cd15-21.
- There is no intervertebral disc between C1 and C2.
- C1 has large transverse processes.
- C2 has a large spinous process and there is a bony projection from the cranial aspect of the body, the dens.
- C6 has proportionally larger transverse processes in the dog and horse that can serve as an anatomic landmark (Fig. 9.17).
- Thoracic spinous processes in the horse are longer, on a relative basis, than in the dog or cat.
- In the horse, the dorsal aspect of cranial thoracic spinous processes is often highly irregular. This can be confused with an aggressive process or fracture (Fig. 9.18).
- In the dog and cat, the thoracic vertebra with a vertically oriented spinous process is called the *anticlinal vertebrae*; this can be either T10 or T11 (Fig. 9.19).[7]
- Cranial to the anticlinal vertebra, the spinous processes angle caudally, whereas caudal to the anticlinal vertebra, the spinous processes angle cranially.
- The disc space cranial to the anticlinal vertebra is often narrowed; this should not be confused with intervertebral disc disease.
- The ventral cortex of the L3 and/or L4 vertebral bodies in the dog may be indistinct compared with other lumbar vertebrae and this can be confused with effacement from an aggressive process (Fig. 9.20).

Positioning: Dog and Cat

Sedation or general anesthesia is indicated for radiography of the canine or feline spine. The spine is complex anatomically, and it is critical that the patient be positioned symmetrically. Positioning of a dog or cat for spinal radiography is more involved than just laying the patient on the x-ray table (Fig. 9.21).

For most dogs and cats, lateral and VD radiographs will be sufficient for assessing the spine. In lateral views, the goal is to have the sternum and spine in a plane that is parallel to the tabletop. This cannot be accomplished by allowing the subject to lie unrestrained on the x-ray table (Fig. 9.22); the sternum will have to be elevated slightly. In a very few subjects, especially those with a round thorax, it may be necessary to displace the sternum slightly ventrally rather than dorsally. Before radiographing the spine, the patient should be examined to determine in which direction, and by how much, the thorax should be rotated.

Other adjustments may also be necessary. In most dogs and cats, the spine undulates in the plane parallel to the tabletop, and placing pads under sagging regions, such as the cervical spine and caudal lumbar spine cranial to the pelvis, will be necessary to obtain an undistorted image of the spine (Fig. 9.23). This is especially true for the cervical spine, where sagging of the caudal aspect of the cervical spine commonly results in nondiagnostic radiographs unless a positioning sponge is used to eliminate the sagging (Fig. 9.24). The goal is to have the radiograph represent vertebral alignment and the character of the intervertebral disk spaces accurately, and this will not be possible unless the patient is positioned symmetrically.

X-rays in the primary beam diverge from the focal spot, and near the edge of the beam the angled x-rays will distort the vertebrae and disc spaces, despite good positioning of the neck or back. Structures in the center of the beam will not be distorted (Fig. 9.25). To accommodate for x-ray beam divergence, multiple centering points of the primary x-ray beam will be needed for a survey radiographic study of the entire spine, e.g., center at C2, C5, T2, T11, L3, and L6. Obtaining a lateral

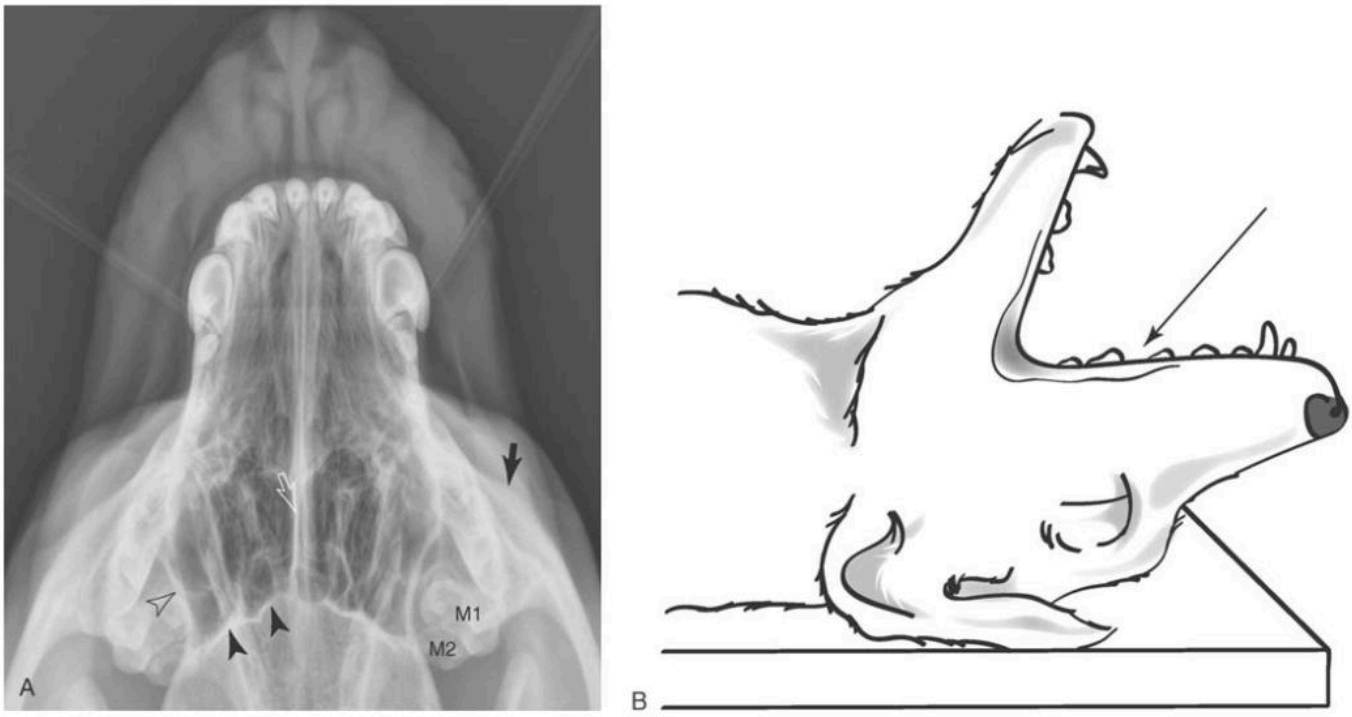


Fig. 9.10 **A,** V20°R-DCdO open-mouth view of the nasal cavity of an 8-month-old mixed breed dog. This view has largely replaced imaging the nasal cavity using an intraoral plate, as shown in Fig. 9.5. Mild, insignificant, distortion of the nasal cavity occurs as a result of the beam angulation. Tape or a small rope is used to hold the maxilla in place and is seen in this image crossing the maxilla just caudal to the canine teeth. The *solid black arrow* is the frontal process of the zygomatic bone. The *solid black arrowhead* is the rostral aspect of the cranial vault. The *hollow black arrowhead* is the lateral margin of the frontal sinus. The *hollow white arrow* is the nasal septum. **B,** Diagram of patient positioning for image **A**. This view should always be included in the radiographic study of a patient with nasal discharge. (**B,** From Owens JM, Biery DN. *Radiographic Interpretation for the Small Animal Clinician*. Baltimore: Williams & Wilkins; 1999.)

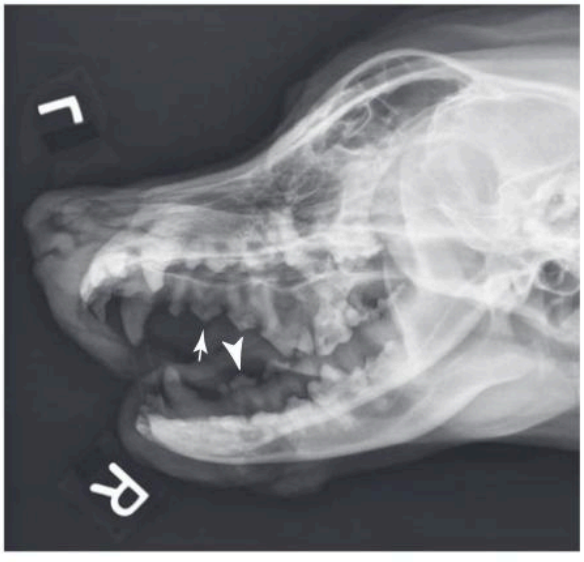


Fig. 9.11 Example of an external marking system for oblique skull radiographs. This is the same positioning as shown in Fig. 9.6. Placing an *L marker* at the top of the image and an *R marker* at the bottom of the image means that the left side of the maxilla and mandible will be dorsal to the right side. This results in the right maxillary dental arcade (*arrow*) and the left mandibular dental arcade (*arrowhead*) being unobstructed.



Fig. 9.12 Oblique radiograph of a canine head. Only one marker has been placed in the field of view. It is not possible from this image to know what this marker means. Does it mean the dog is lying on the *L* side? Is the left mandible or the left maxilla being projected without obstruction? Accurate placement of two markers is required for adequate marking of oblique skull radiographs.

view of the entire thoracic spine or the entire lumbar spine in one image is poor practice because of the distortion that occurs at the periphery of the image.

Spinal radiographs should always be planned in concert with the results from a neurologic examination, where the anatomic location of the lesion has been determined based on neurologic responses and other clinical signs. Thus, in some patients, the radiographic study may be truncated to the cervical spine, T2-

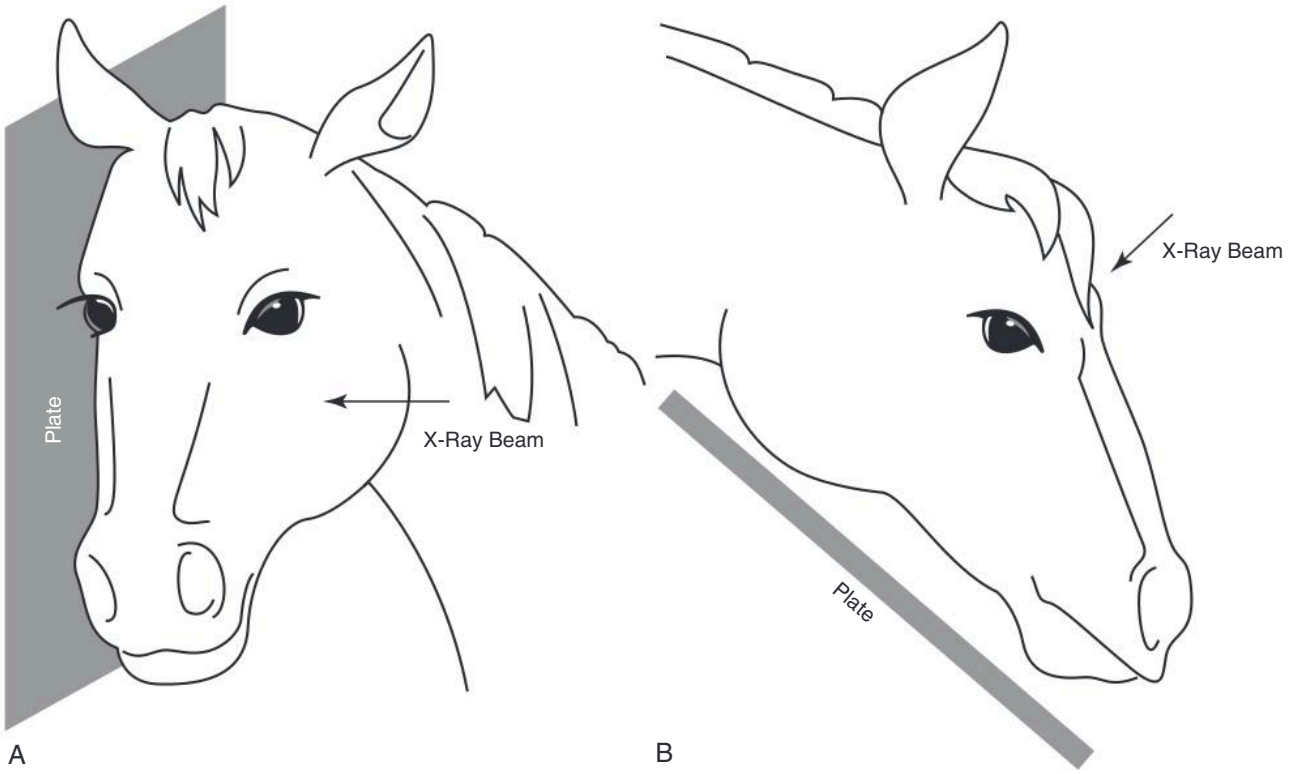


Fig. 9.13 **A,** Positioning for a lateral radiograph of the equine skull. Care must be taken to keep the x-ray beam perpendicular to the plate, particularly if an antiscatter grid is being used. **B,** For the dorsoventral (DV) radiograph, the plate is positioned below the mandibles and the x-ray beam directed onto the dorsal aspect of the head. As with the lateral view, care must be taken to keep the x-ray beam perpendicular to the plate.

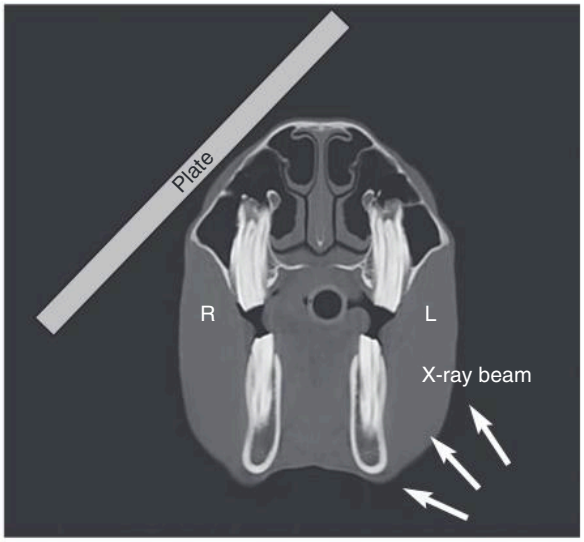


Fig. 9.14 Positioning for a commonly used oblique view of the equine head. In this view, which is a *left 45-degree ventral–right dorsal oblique*, the x-ray beam (*white arrows*) enters from left-ventral and the plate is on the right side perpendicular to the x-ray beam. This will result in an unobstructed view of the ***roots*** of the left maxillary arcade and the right mandibular arcade. The roots of the right maxillary and left mandibular arcades will be superimposed. By keeping this same cassette-beam orientation but moving the x-ray beam more caudal, one can project other structures, such as the left supraorbital process or the left ethmoid region. *L,* Left; *R,* right.



Fig. 9.15 Radiograph acquired using the positioning illustrated in Fig. 9.14. Note the use of both (*L*) and (*R*) markers to reduce confusion. The location of these markers indicates that the left maxillary (*white arrows*) and right mandibular (*black asterisks*) arcades are projected unobstructed. Only the roots of the mandibular teeth are projected unobstructed, and the crowns cannot be seen clearly. The right maxillary and left mandibular arcades are superimposed. Refer to Fig. 9.14 if these points are not clear.



Fig. 9.16 Lateral view of the rostral aspect of an equine skull. Thinner parts are massively overexposed leading to plate saturation and image dropout.

Box • 9.1

Checklist for Interpretation of Skull Radiographs

Calvarium
Tympanic bullae
Temporomandibular joints
Stylohyoid bone and guttural pouches (horse only)
Maxillary and mandibular bone
Maxillary and mandibular teeth
Nasal passage
Sinuses
Laryngopharynx
Soft tissues of the head

L3 spinal cord segments, or lumbosacral region, depending on the results of the neuroanatomic localization.

As discussed in Chapter 6, obtaining orthogonal views of all body parts is needed due to the two-dimensional nature of radiographs. This is especially true in the anatomically complex spine. A scenario where the initial radiographic examination of the spine should be limited to lateral projections is where a spinal fracture or displacement/instability is suspected. In that instance, lateral radiographs should be acquired first and evaluated. If no abnormality is detected, then VD views can be obtained. If an abnormality is detected initially in the lateral views, then the decision can be made to (1) terminate the examination, (2) acquire conventional VD views, or (3) use a horizontal beam to obtain the VD radiograph (Figs. 9.26 and 9.27). A horizontal-beam view of the spine will only be possible if the digital plate is not permanently attached to the x-ray table.

The initial radiographic examination should also be limited to lateral views in dogs with suspected atlantoaxial instability. If instability at C1–C2 is not confirmed in the lateral images, it may be tempting to flex the neck and acquire additional views. This should be undertaken with extreme care and performed either under fluoroscopy or with only minimal flexion as increasing the malalignment will exacerbate spinal cord compression, especially if a dens is present on C2.

Another scenario where lateral views of the spine are often made without additional orthogonal views is in patients being surveyed for discospondylitis. Although lateral views will be the most sensitive for detection of discospondylitis lesions, if there are other abnormalities that mimic the pain from discospondylitis, these can easily be overlooked if orthogonal views are also not acquired.

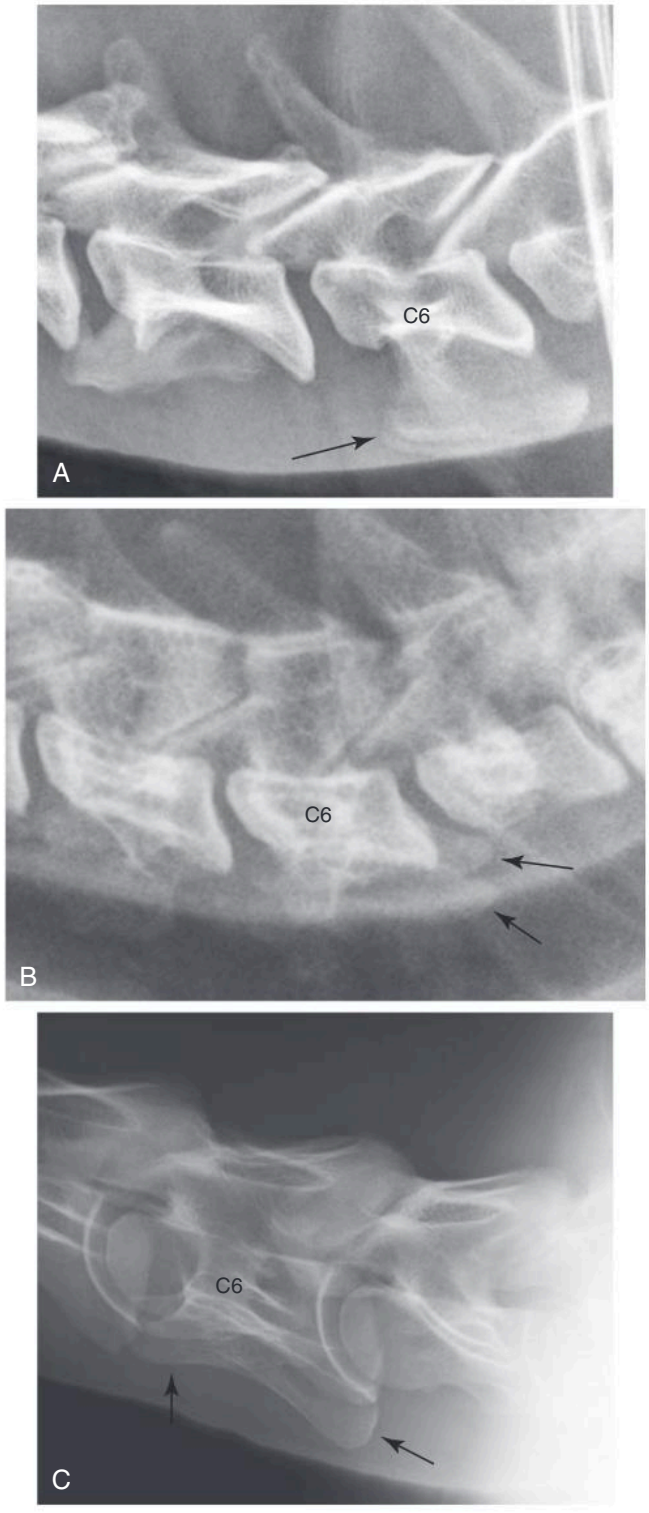


Fig. 9.17 Lateral radiograph of the caudal aspect of the cervical spine in a dog **(A)**, cat **(B)**, and horse **(C)**. In the dog and horse, the transverse processes of C6 (*black arrows*) are larger than on other cervical vertebrae and serve as useful anatomic landmarks. In the cat **(B)**, the transverse processes on C6 are only minimally larger (*black arrows*) and therefore not as useful as an anatomic landmark.

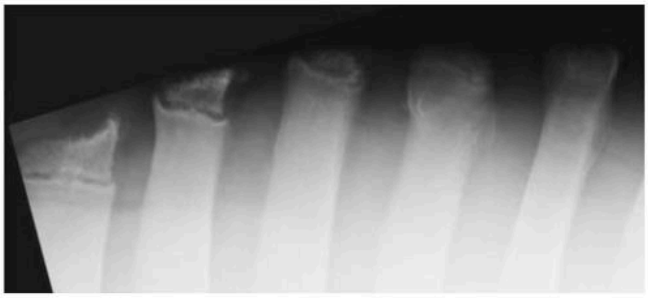


Fig. 9.18 Lateral radiograph of the dorsal aspect of the first few thoracic spinous processes of a horse. Irregular mineralization of the dorsal aspect is often misinterpreted as a fracture. This irregular appearance is not present in all horses. In this horse, some of the spinous processes also have a smooth periosteal reaction; this is also normal.

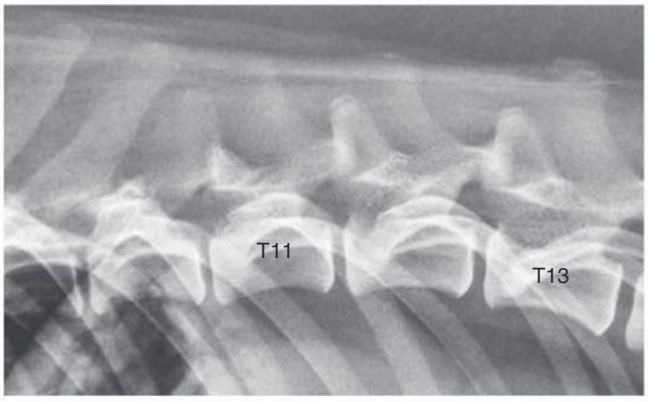


Fig. 9.19 Lateral radiograph of the caudal aspect of the thoracic spine in a dog. The spinous process on T11 is vertical, defining it as the anticlinal vertebra. Cranial to T11 the spinous processes angle caudally, while caudal to T11 the spinous processes angle cranially. (Reprinted with permission from Thrall DE, Robertson ID. *Atlas of Normal Radiographic Anatomy and Anatomic Variants in the Dog and Cat*. 3rd ed. St Louis: Elsevier; 2023.)

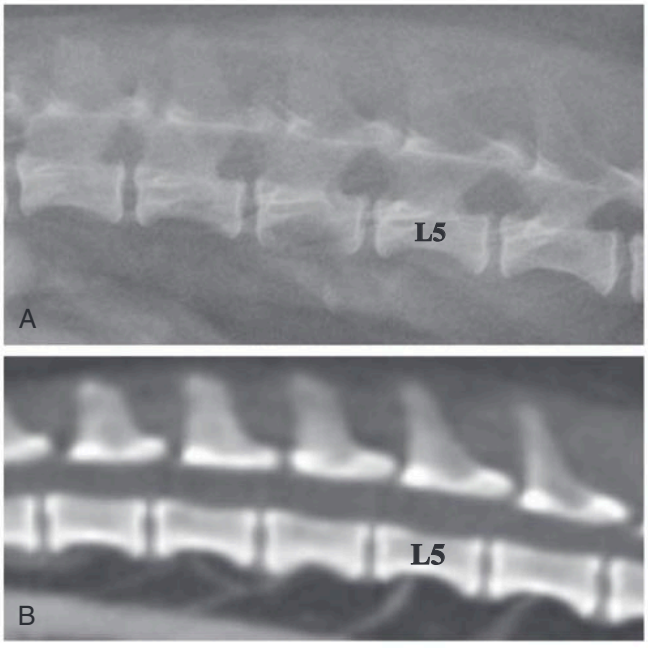


Fig. 9.20 **A,** Radiograph of the lumbar spine of a small dog with an indistinct ventral border of L4 that is highly concerning for effacement from an aggressive process. **B,** Sagittal computed tomography (CT) image of the lumber spine from the same dog as in **A**. The ventral cortex of L4 is not effaced. This illustrates the extent of indistinctness of the ventral cortex of L3 and/or L4 that can occur as normal variation.

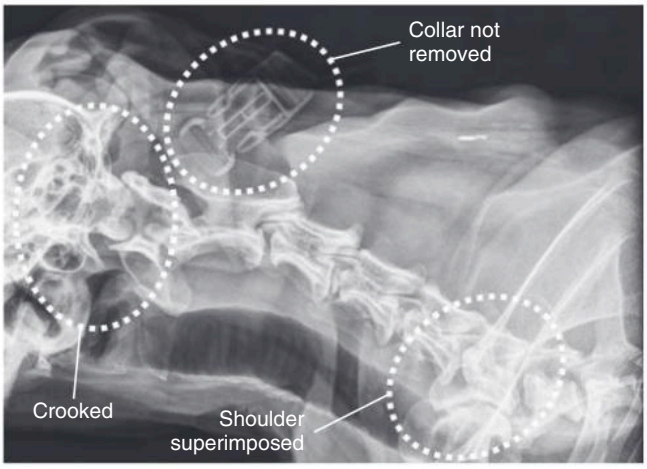


Fig. 9.21 A poorly positioned cervical radiograph that is nearly useless. The patient is crooked, the collar has not been removed, and a shoulder is superimposed on the caudal aspect of the cervical spine. This is a careless approach that wastes time and needlessly increases personnel radiation exposure. The patient and owner deserve higher-quality work.

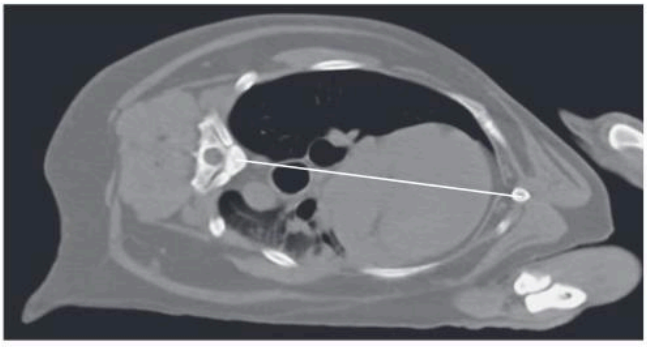


Fig. 9.22 Transverse-computed tomography (CT) image of a canine thorax at the level of the heart. When a dog or cat is allowed to lie on the x-ray table the spine and sternum are in a plane (*white line*) that is not parallel to the x-ray tabletop. For proper positioning of a spinal radiograph of this dog, the sternum would have to be elevated.

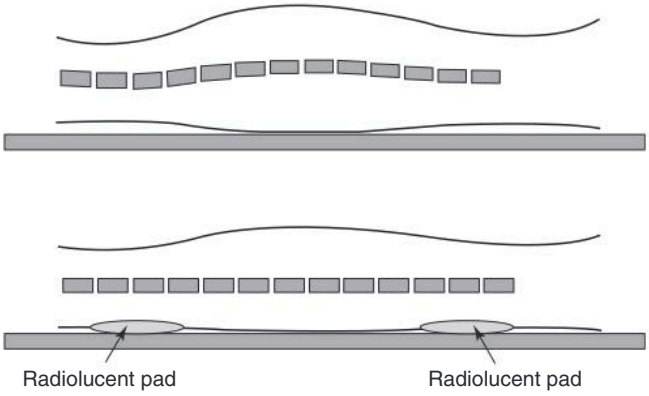


Fig. 9.23 Elevation of sagging portions of the spine leads to improved alignment. In the top panel, the dog is lying unrestrained on the x-ray table; parts of the spine will sag and be distorted in the image. In the bottom panel, sagging portions of the spine are elevated with positioning pads, which will lead to a less distorted lateral projection of the vertebrae. (From Thrall DE, Robertson ID. *Atlas of Normal Radiographic Anatomy and Anatomic Variants in the Dog and Cat*. 3rd ed. St Louis: Elsevier; 2023.)

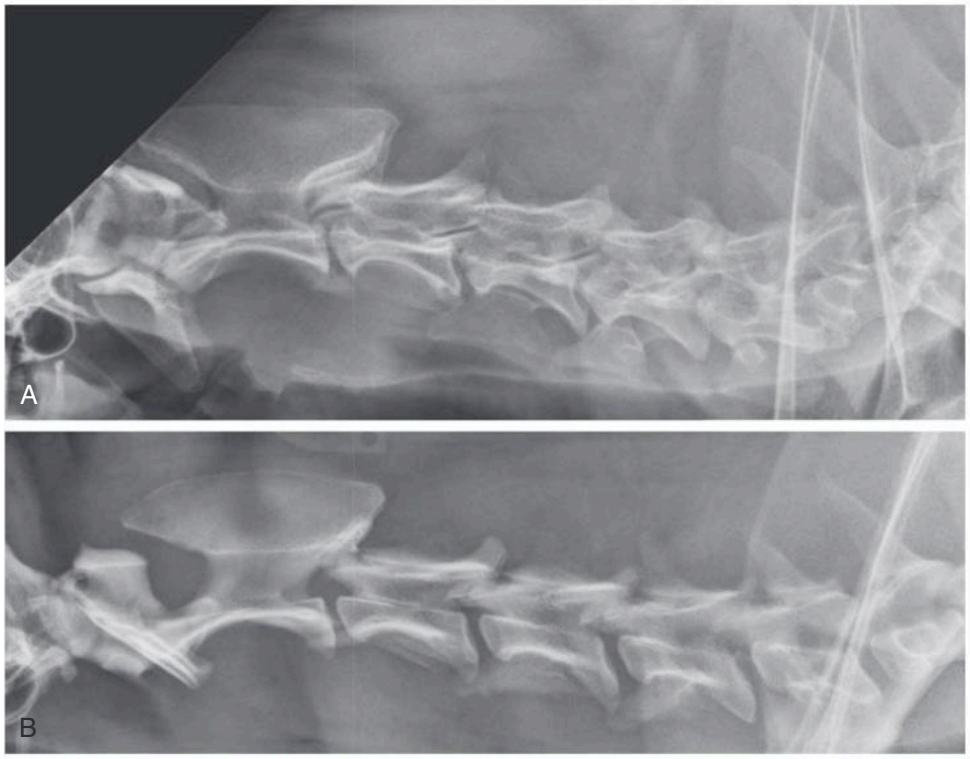


Fig. 9.24 **A,** Lateral radiograph of a canine cervical spine where the natural sagging of the caudal aspect was not corrected with a positioning sponge. Many disc spaces appear narrow but this is a geometric artifact from the sagging. The spine is also rotated; note the relative position of the tympanic bullae and the ventral projection of multiple transverse processes from the cervical vertebrae. **B,** A positioning sponge was placed under the caudal aspect of the cervical spine to correct the sagging. All disc spaces can now be accurately evaluated. The spine is also not rotated.

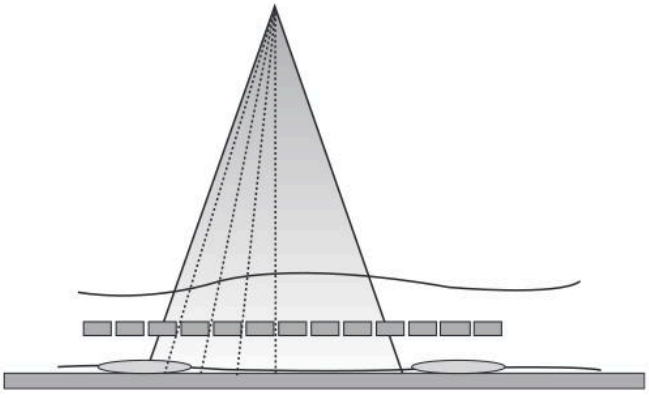


Fig. 9.25 The *gray triangle* represents the diverging x-ray beam. The *dotted lines* represent individual x-rays. The vertical x-ray will pass through the central disk space, and the image of the disk space and the adjacent vertebrae will not be distorted. More peripherally the x-rays are angled, which will lead to an image of the disk space that is narrower than its actual width and the vertebrae in this area will be distorted. (Reprinted with permission from Thrall DE, Robertson ID. *Atlas of Normal Radiographic Anatomy and Anatomic Variants in the Dog and Cat*. 3rd ed. St Louis: Elsevier; 2023.)

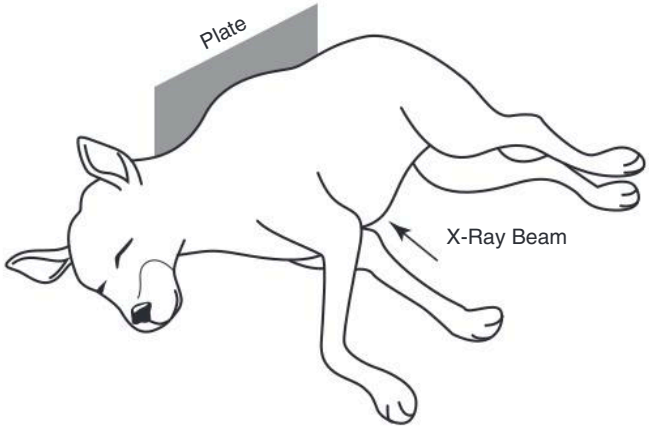


Fig. 9.26 Technique for obtaining a horizontal-beam ventrodorsal radiograph of the spine. In this example, the patient is in right recumbency and the plate is positioned dorsal to the spine, perpendicular to the x-ray table. The x-ray beam is directed horizontally, perpendicular to the plate. It may not be possible to use a grid in this configuration, and this will lead to some reduction in detail. However, the main question is whether there is lateral malalignment at a fracture site, which can usually be answered in spite of the reduced detail created by lack of a grid.

Positioning: Horse

As noted earlier, spinal radiography in the horse is largely confined to the cervical spine, with the horse standing. Sedation is indicated to reduce motion, and the head will drop, making it easier to radiograph the cranial aspect of cervical spine. Equine cervical radiography is usually limited to lateral views. Adequate DV or VD cervical radiographs of the horse cannot be obtained easily. As in small animals, multiple centering points will be needed for survey radiographs of the entire cervical spine, but for a different reason. The length of the equine neck is too great to be imaged with only one location of the plate, and four to five centering points will be needed to image the entire cervical spine.

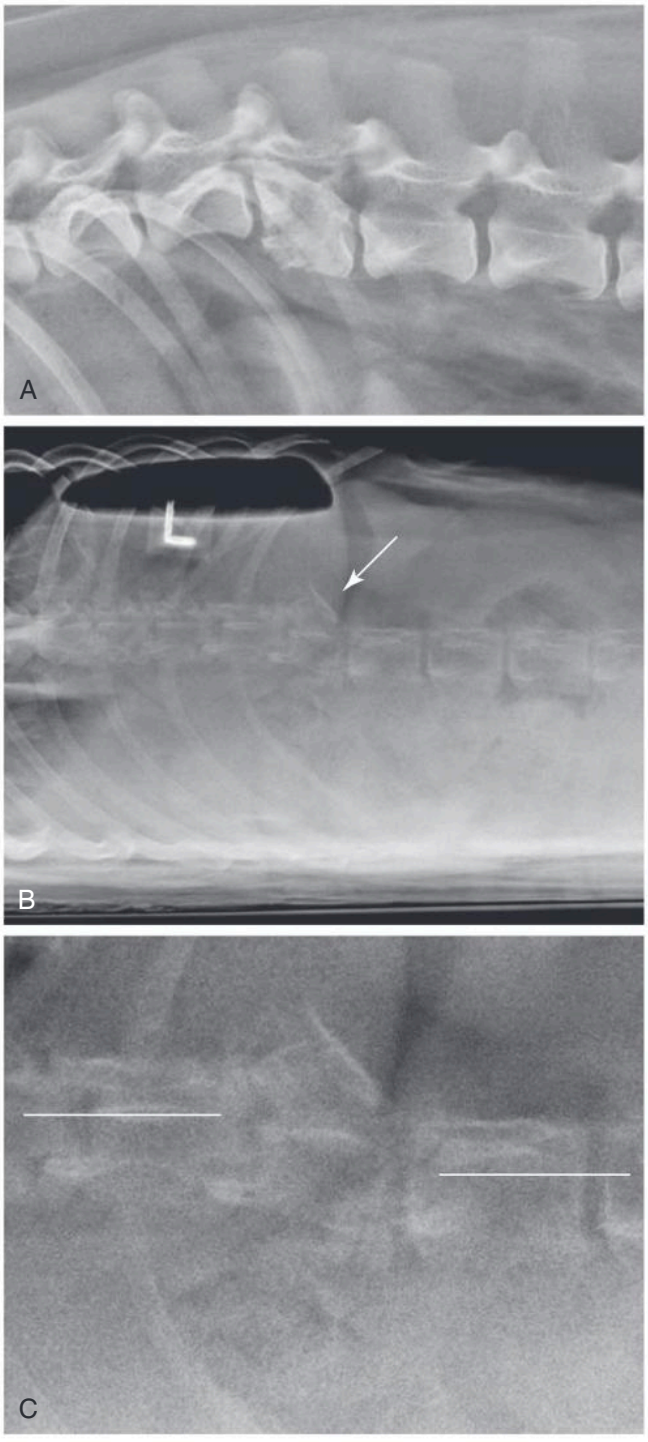


Fig. 9.27 **A,** Lateral radiograph of the thoracolumbar region of an injured dog. There is a comminuted fracture of L1 with cranioventral overriding of the caudal aspect of the vertebral body. This patient should not be put into dorsal recumbency for a ventrodorsal (VD) radiograph because vertebral instability may exacerbate any spinal cord damage that is present. **B,** Horizontal-beam radiograph of the same dog as in **A** using the position illustrated in Fig. 9.26. The large gas bubble is in the fundus of the stomach. The fracture is visible (*arrow*), and there is lateral malalignment. **C,** Close-up of the horizontal-beam image. The *horizontal lines* mark the midsagittal plane of the spine cranial and caudal to the fracture. Lateral malalignment is obvious. The detail of the image if not optimal as a grid was not used but the image is adequate to assess lateral instability. *L*, Left.

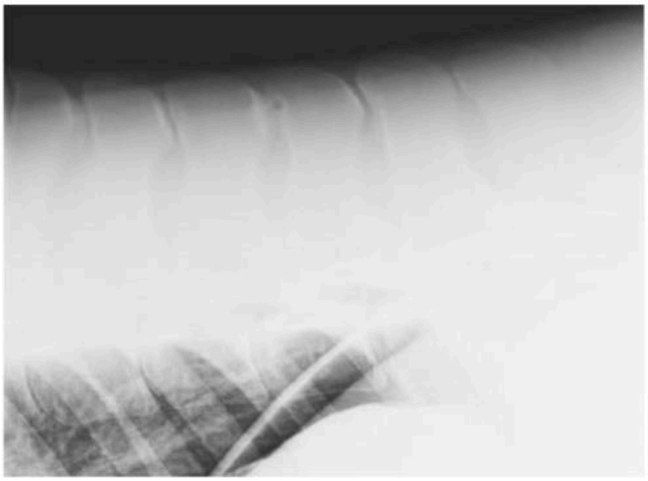


Fig. 9.28 Lateral radiograph of the caudal aspect of an equine thoracic spine. The spinous processes can be assessed, but the caudal thoracic vertebral bodies cannot because of soft tissue superimposition. These spinous processes are remodeled secondary to interference.

The equine thoracic spine is more difficult to assess radiographically than the cervical spine. The thoracic spinous processes can be imaged satisfactorily, but whether thoracic vertebral bodies can be imaged depends on the size of the horse and which thoracic vertebral bodies are of interest. The cranial thoracic vertebral bodies can often be evaluated, but the caudal thoracic vertebral bodies are more difficult to assess because of superimposed soft tissue. Caudal thoracic spinous processes can usually be imaged adequately (Fig. 9.28).

The equine lumbar spine can only be evaluated in very small horses, and usually only in lateral views. The lumbar spine can be assessed in a VD radiograph in small horses, but this requires general anesthesia. Superimposed fecal material will reduce lumbar vertebral detail in VD radiographs, even in small horses.

The cranial aspect of the sacrum cannot be assessed in a lateral radiograph, except in very small horses. The sacrocaudal junction can be seen in most horses in a lateral view. The sacrum can be assessed more thoroughly in a VD radiograph, but this requires general anesthesia. As with the lumbar spine, overlying fecal material will reduce sacral detail in VD radiographs.

Radiographic Technique: Dog and Cat

As in the skull, the wide exposure latitude of digital imaging systems means that selecting kVp and mAs values for spinal radiography is much less critical than when film-screen technology was used. In digital imaging, many more kVp/mAs combinations will result in a diagnostic image than with film. Exposure latitude also results in the ability to evaluate both the thicker and thinner parts of the spine in the same image; e.g., proper exposure of a thicker part does not result in overexposure of a thinner part, and vice versa. Use of an antiscatter grid is recommended if possible but the problems associated with this are the same as mentioned for the skull.

Radiographic Technique: Horse

A wall-mounted plate holder assembly that incorporates a grid greatly facilitates equine spinal radiography (Fig. 9.29). If the x-ray machine is designed to generate high mAs techniques and a wall-mounted plate holder is available, then a grid should be

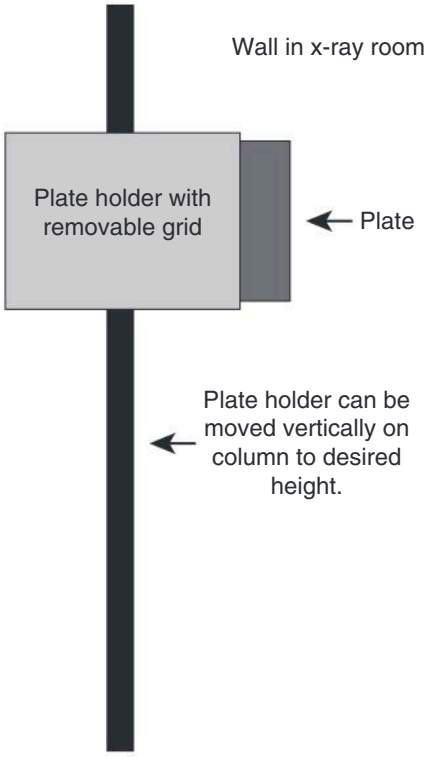


Fig. 9.29 Schematic of the configuration of a wall-mounted plate holder. The plate holder is designed such that an antiscatter grid can be inserted if needed. The plate holder can be raised or lowered on the column to position it at the desired height for the part being radiographed.

used for all spinal radiographs in the horse. The sedated standing horse is simply positioned against the wall-mounted plate holder, which can be raised or lowered to the desired height above the floor of the room, and the radiographic exposure made. These assemblies avoid the need for hand-holding the plate, leading to a reduction in occupational radiation exposure.

Incidental Factors

The most important incidental factors associated with spinal radiography in the dog and cat are breed variation and some congenital anomalies. Congenital transitional vertebral anomalies are common and occur at the cervicothoracic, thoracolumbar, and lumbosacral junctions. In this anomaly, a vertebra at the junction has anatomic characteristics of each adjoining region. The most common cervicothoracic transitional anomaly is the presence of vestigial ribs on C7 (Fig. 9.30). Cervical ribs are not clinically significant in dogs or cats, but in human beings they are sometimes associated with Horner's syndrome.

The most common thoracolumbar transitional anomaly involves asymmetric development of the 13th ribs. There are multiple variations to this anomaly,[1] but the most clinically significant is having a unilateral rib on T13. This anomaly is not significant itself, but can lead to spinal surgery being performed at the wrong location if rib morphology is used to locate the surgical site (Fig. 9.31).

Sacralization of L7 is the most common transitional anomaly at the lumbosacral junction. In this anomaly, one side of L7 has the form of a vertebra with a transverse process while the opposite side has the form of a sacrum and articulates with the ilium (Fig. 9.32). The altered biomechanical loading associated with a lumbosacral transitional anomaly predisposes dogs to lumbosacral disk herniation and nerve root compression.[8,9]

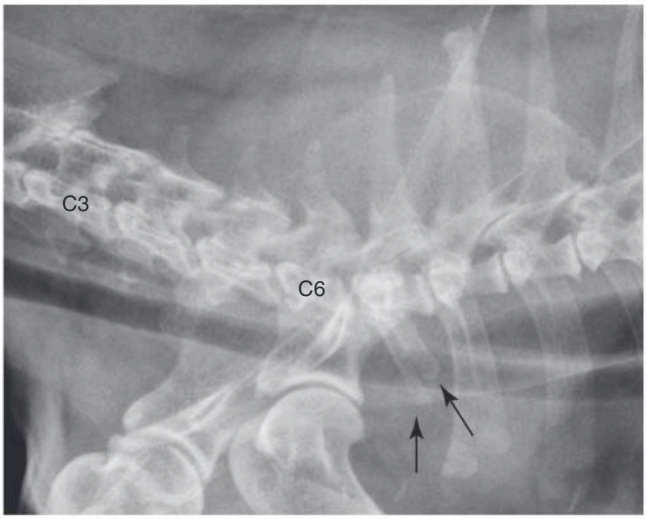


Fig. 9.30 Lateral radiograph of a cat with a cervicothoracic transitional anomaly. Ribs are present on C7. This cat had the normal allotment of 13 thoracic ribs. The 3rd and 6th cervical vertebrae are labeled.

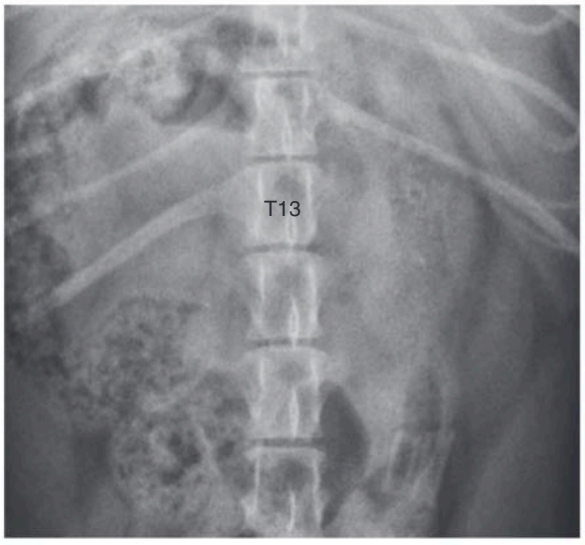


Fig. 9.31 Ventrodorsal radiograph of the thoracolumbar junction of a dog with a transitional anomaly. The right 13th rib developed as a malformed transverse process. The left 13th rib is absent. If ribs were used to locate the site for spinal surgery, it is imperative that the presence of this anomaly be known or the wrong site could be selected.

Interpretation Paradigm

As mentioned, there are relatively few things other than breed variation and congenital anomalies that influence the radiographic appearance of the spine. But because of the complex morphology of the spine, an organized approach is still needed. Assessing whether there is an abnormality in the spinal radiographs of a patient should be the last step in the interpretive process. The following questions should always be considered first:

- Is radiographic technique adequate?
- Are all needed views present?
- Is there a need for additional views?
- Has the study been tailored to the results of neuroanatomic localization?
- Is the positioning adequate, or are there positioning problems that will interfere with interpretation?

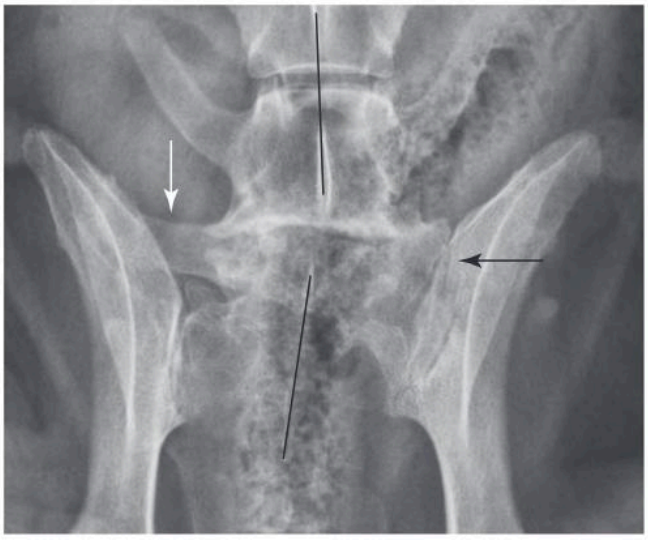


Fig. 9.32 Ventrodorsal radiograph of the lumbosacral region of a dog with sacralization of L7. The right side of L7 has a transverse process (*white arrow*) while the left side of L7 is fused with the ilium (*black arrow*). This anomaly resulted in malalignment of the lumbosacral spinal axis, as indicated by the *black lines*. This malalignment will alter the biomechanical loading of the lumbosacral articulation and coxofemoral joints.

Box • 9.2

Checklist for Interpretation of Spine Radiographs

Number of vertebrae in each anatomic region
Number of ribs in thoracic spine (dog/cats only)
Transitional/congenital anomalies
Vertebral alignment
Symmetry/width of vertebral canal throughout spine
Integrity of neural arch of each vertebra
Vertebral bodies
Intervertebral foramina
Relative size of intervertebral disc spaces
Character of intervertebral discs, e.g. mineralization
Articular processes and articular process joints
Paraspinal soft tissues

- Has a grid been used, and how did this affect the quality of the image? Is there excessive scattered radiation? Are there grid lines?
- Has sedation or anesthesia been used? If not, how did this affect the radiographs?
- What is the species and breed of the patient, and how did this affect the appearance of the images?
- Was the cassette held by hand? Is there motion artifact?
- Are there congenital anomalies that alter the normal appearance of the spine?

After these variables have been considered, the images can be scrutinized for abnormalities. The Roentgen sign and DAMNITV methods described in Chapter 6 should be used. In many patients, the cause of the clinical signs will not be found in spinal radiographs, or the lesion will be incompletely characterized, and other modalities, such as CT or MRI, will be needed.[3–5] And, even when the lesion is identified, aspiration or biopsy is commonly necessary to obtain a definitive diagnosis.

Experienced radiologists may have a random search pattern, but it is recommended that inexperienced interpreters use an organized approach.[6] Having a mental checklist to guide the order of interpretation will reduce the number of errors (Box 9.2).

REFERENCES

1. Thrall D, Robertson I, eds. *Atlas of Radiographic Anatomy and Normal Anatomic Variants in the Dog and Cat.* 3rd ed. St. Louis: Elsevier-Saunders; 2023.
2. Han CM, Hurd CD. *Practical Diagnostic Imaging for the Veterinary Technician.* 3rd ed. Philadelphia: Elsevier-Mosby; 2004.
3. Thrall D, Robertson I, McLeod D, et al. A comparison of radiographic and computed tomographic findings in 31 dogs with malignant nasal cavity tumors. *Vet Radiol Ultrasound.* 1989;30:59.
4. Petite AF, Dennis R. Comparison of radiography and magnetic resonance imaging for evaluating the extent of nasal neoplasia in dogs. *J Small Anim Pract.* 2006;47:529.
5. Rohleder JJ, Jones JC, Duncan RB, et al. Comparative performance of radiography and computed tomography in the diagnosis of middle ear disease in 31 dogs. *Vet Radiol Ultrasound.* 2006;47:45.
6. Halvorsen JG, Swanson D. Interpreting office radiographs. A guide to systematic evaluation. *J Fam Pract.* 1990;31:602.
7. Baines E, Grandage J, Herrtage M, et al. Radiographic definition of the anticlinal vertebra in the dog. *Vet Radiol Ultrasound.* 2009;50:69.
8. Morgan JP, Bahr A, Franti CE, et al. Lumbosacral transitional vertebrae as a predisposing cause of cauda equina syndrome in German shepherd dogs: 161 cases (1987–1990). *J Am Vet Med Assoc.* 1993;202:1877.
9. Fluckiger M, Damur-Djuric N, Hassig M, et al. A lumbosacral transitional vertebra in the dog predisposes to cauda equine syndrome. *Vet Radiol Ultrasound.* 2006;47:39.

ELECTRONIC RESOURCES

Additional information related to the content in Chapter 9 can be found online at eBooks.Health.Elsevier.com.

- Chapter Quiz

CHAPTER 10

Canine and Feline Dental Disease

Lenin Arturo Villamizar Martinez

Diagnostic imaging of the maxillofacial and dentoalveolar structures is critical for pre-, intra-, and postoperative assessment of intraoral and extraoral conditions in dogs and cats.[1,2] Several imaging techniques are available for the veterinary practitioner, from conventional intra- or extraoral radiography to more sophisticated tomographic methods such as computed tomography (CT), magnetic resonance imaging (MRI), and more recently, cone-beam computed tomography (CBCT) (Fig. 10.1).[3–6] This chapter is an introduction to the anatomy of dentoalveolar structures and changes associated with the most common dental abnormalities. It is beyond the scope of this chapter to describe dental radiographic techniques.

Dental radiographs can be performed using an x-ray machine that is mounted to the wall, on a set of wheels or held by hand (Fig. 10.2).[7,8] X-ray dental machines operate at lower mAs values than the other types of dental x-ray equipment (high-frequency x-ray, CT, or CBCT units). However, to comply with the ALARA (as low as reasonably achievable) principle, the operator must leave the room if possible, or be at least 6 feet away from the x-ray source during the dental examination.[9,10] On the other hand, when a handheld x-ray unit is in use, the operator should wear a lead apron and thyroid collar to avoid unnecessary radiation exposure.[11]



Fig. 10.1 Cone-beam computed tomography (CT) mobile unit performing an examination of an adult dog suffering from severe periodontal disease. The device operator remains behind a lead barrier during unit activation to avoid unnecessary radiation exposure.

Dental images were originally acquired with analog dental radiographic film that is available in several sizes for obtaining periapical and occlusal views. Periapical radiographs (sizes 0, 1, and 2) allow evaluation of the entire dental structure and the surrounding bone. In contrast, the occlusal film (size 4) captures intraoral radiographic images of more extensive regions of the maxilla and mandible (Table 10.1).[12,13] Occlusal films may also be used to obtain extraoral views of the more caudal portion of the mandibles and the temporomandibular joints in cats and small dogs.[14–16]

Analog dental films have been largely replaced by direct and indirect digital radiographic systems (see Chapter 2),which improves patient and operator radiation safety since they require shorter exposure times (about 0.1–0.2 seconds) than analog film (0.8 seconds).[7,17]

In the direct system, the solid-state intraoral sensor, mainly available in similar sizes to the analog dental counterpart film sizes 0 and 2, captures the attenuated x-rays after passing through oral tissue. The attenuated photons recorded by the sensor are converted into an electrical signal that is transformed later into a digital signal with a digital-analog converter and transmitted to a computer to form an almost instantaneous radiographic image (Fig. 10.3). One disadvantage of this type of sensor is that it can be easily damaged by a bite if the patient is not under deep sedation or general anesthesia.[17,18]

Indirect systems use reusable photostimulable plates (PSPs) available in sizes 0, 2, 3, and occlusal size 4 to store the latent images formed by the attenuated x-ray beam after passing through the oral tissues. The PSPs must be processed in a dental scanner, where the laser converts the latent image into a digital signal (Fig. 10.4).[7] One of the main disadvantages of PSP is that they can be scratched or bent by teeth, causing artifacts. Therefore, they must be replaced after a certain number of exposures (approximately up to 200 exposures, depending on the manufacturer) to maintain optimal image quality.[18,19]

The radiographic dental examination complements a thorough oral cavity examination and is considered the pillar for assessing the dentoalveolar components and the surrounding maxillary and mandibular bone.[2,20] Dental radiography is preferred over conventional skull radiographs due to the ability to project specific anatomic regions of the dental arcades without excessive overlap between maxillary and mandibular structures. Dental radiography is mainly accomplished intraorally, but the extraoral dental technique may be required when other anatomical structures appear superimposed with the dentoalveolar region (Fig. 10.5).

Intraoral dental radiographs are acquired through bisecting and paralleling techniques. These radiographic techniques allow for obtaining near-isometric projections of the dental



Fig. 10.2 Different types of dental x-ray generators available for veterinary patients. **(A),** Fixed (wall-mounted), **(B)** handheld portable unit, and **(C)** mobile unit mounted on wheels.

Table • **10.1**

X-Ray Dental Film Sizes.

Periapical view film (For assessment of the crown, root, and alveolar bone around the apex)	**Size 0**	(22 × 35 mm)—It can be used in small patients such as cats and small breed dogs
	Size 2	(31 × 41 mm)—Most common film used in veterinary patients for evaluation of dental and periapical structures
Bitewing view film	**Size 3**	(27 × 54 mm)—Used in human dentistry to record the crowns of maxillary and mandibular teeth at once during the assessment of interproximal caries. It can be used in veterinary patients for recording several teeth at once
Film for occlusal view	**Size 4**	(57 × 76 mm)—For periapical view in large or giant breed dogs. Used in veterinary patients for recording larger areas of the mandible or the maxilla

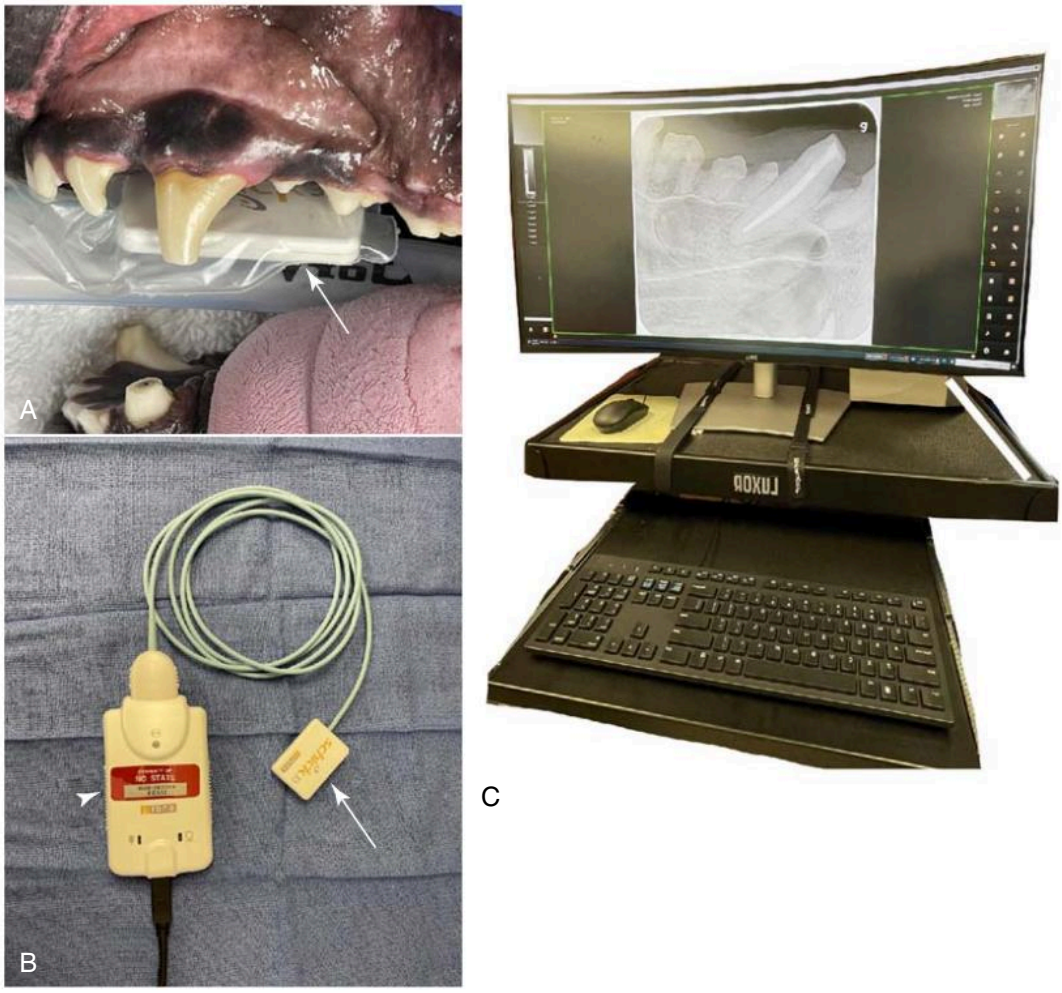


Fig. 10.3 **A,** Solid-state intraoral sensor #2 Dentsply Sirona Schick 33 (*arrow*) during a radiographic assessment of the left maxillary canine tooth of an adult German Shepherd dog affected by severe dental attrition and pulp exposure. **B,** The attenuated x-rays captured in the sensor (*arrow*) are transmitted as an electrical signal to a digital-analog converter (*arrowhead*), where a digital signal is formed. **C,** Afterward, the digital signal is transferred to a computer via a cable with a USB connection to create a diagnostic image using medical imaging software.

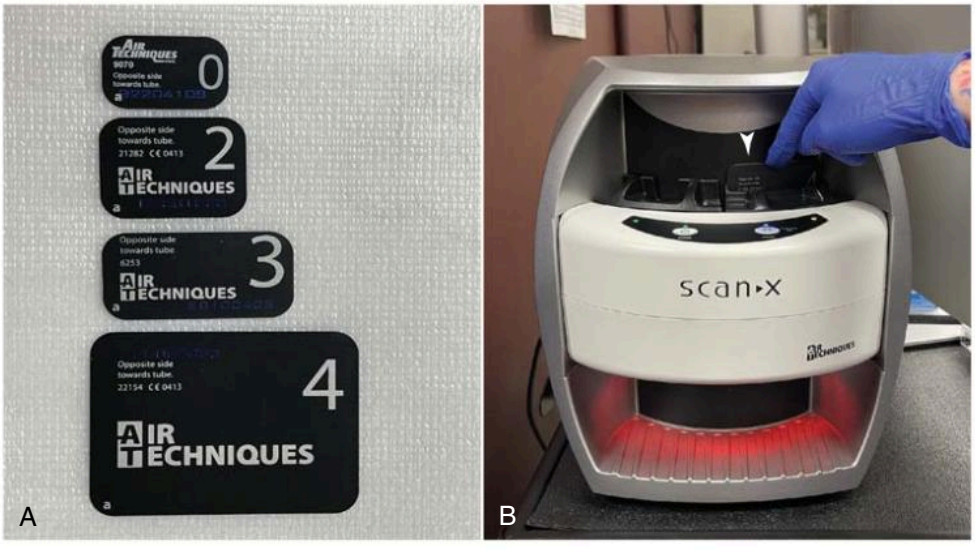


Fig. 10.4 **A,** Periapical #0 and #2, bitewing #3, and occlusal #4 phosphor plates. **B,** Dental scanner. After removing the plastic barrier envelopes, the phosphor plates (*arrowhead*) are carefully manipulated to avoid damage to their surface that may create artifacts in the radiographic image. (ScanX Intraoral Phosphor Plates —Air Techniques).

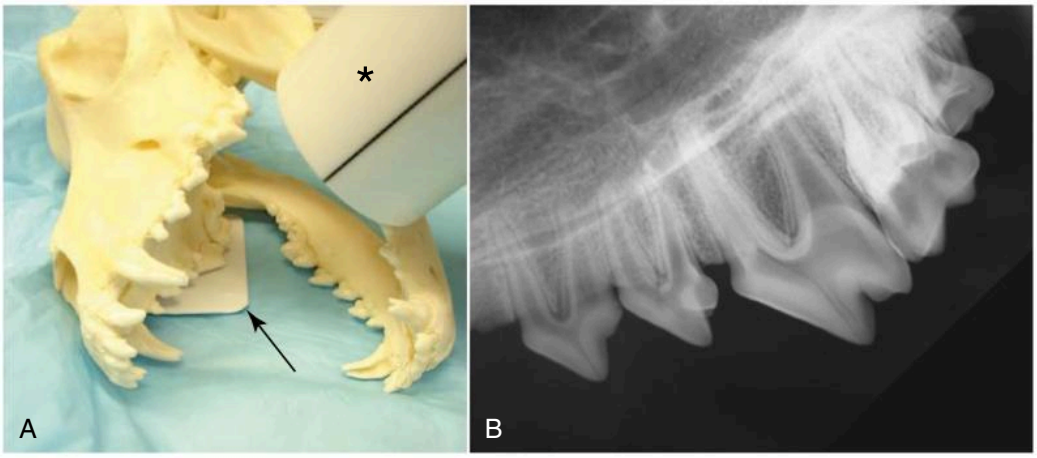


Fig. 10.5 The extraoral dental technique showed in a dog skull produces an open-mouth oblique view. **A,** The film is placed extraoral at the maxillary region (*arrow*). At the same time, the mouth is widely opened to allow exposure to the x-ray beam (*asterisk*) of the anatomical area of interest without overlapping with mandibular structures. **B,** Radiograph of the left maxillary premolar and molar region utilizing the extraoral technique in the same dog skull. This technique helps avoid superimposition between the zygomatic arch and the maxillary teeth, particularly in cats and brachycephalic dogs.

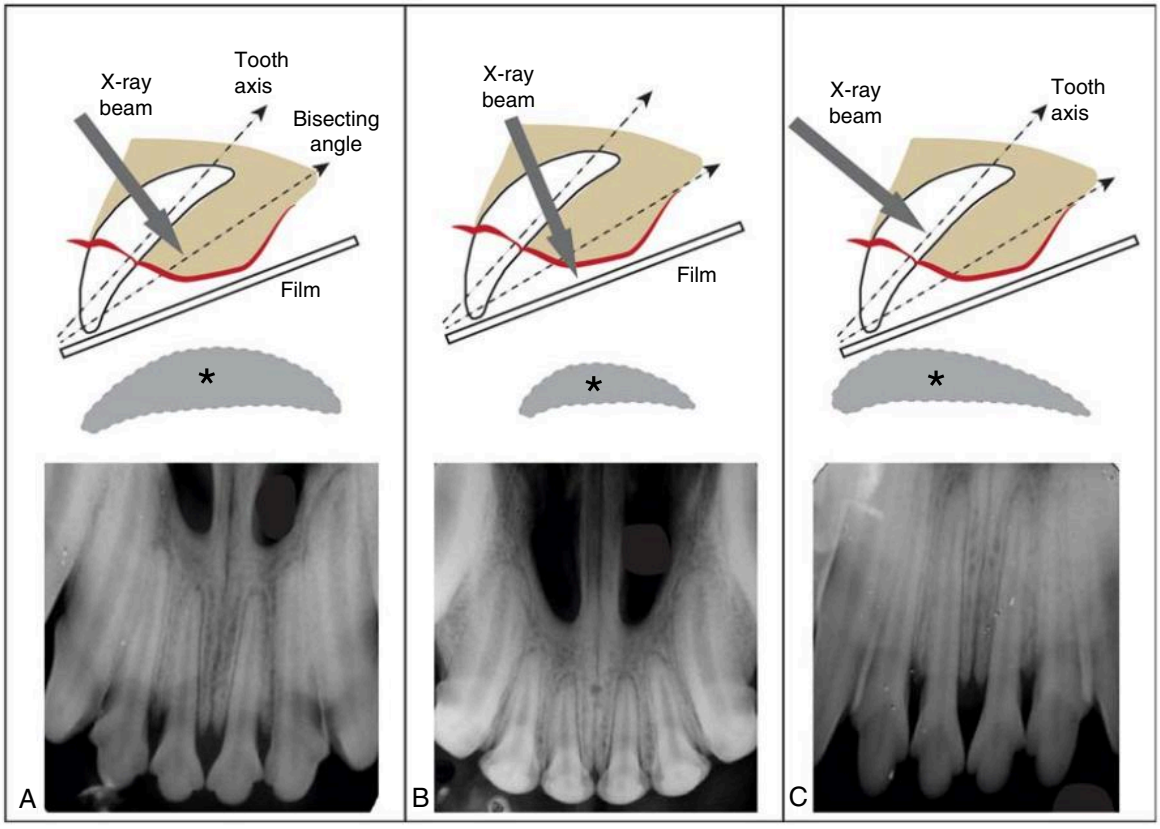


Fig. 10.6 **(A)** Bisecting angle technique, **(B)** foreshortening, and **(C)** elongation of maxillary incisor teeth in an adult dog. A near-isometric view (*asterisk*) is obtained in the bisecting angle by projecting the x-ray beam perpendicular to the bisecting angle. In contrast, if the x-ray beam is projected perpendicular to the film or tooth axis, foreshortening or elongation of the teeth is produced. (Courtesy Lenin A. Villamizar.)

elements without the undesirable imaging effect of elongation or foreshortening of the teeth (Fig. 10.6).[12,13] Another radiographic projection, such as an intraoral dorsoventral view, may help identify nasal cavity disorders associated with inflammatory or neoplastic maxillary conditions (Fig. 10.7).

ANATOMY AND RADIOGRAPHIC INTERPRETATION

The canine and feline skull is composed of bones of the cranium that encase the brain and the bones of the face that support the orbits, the airways related to the nasal cavities, and

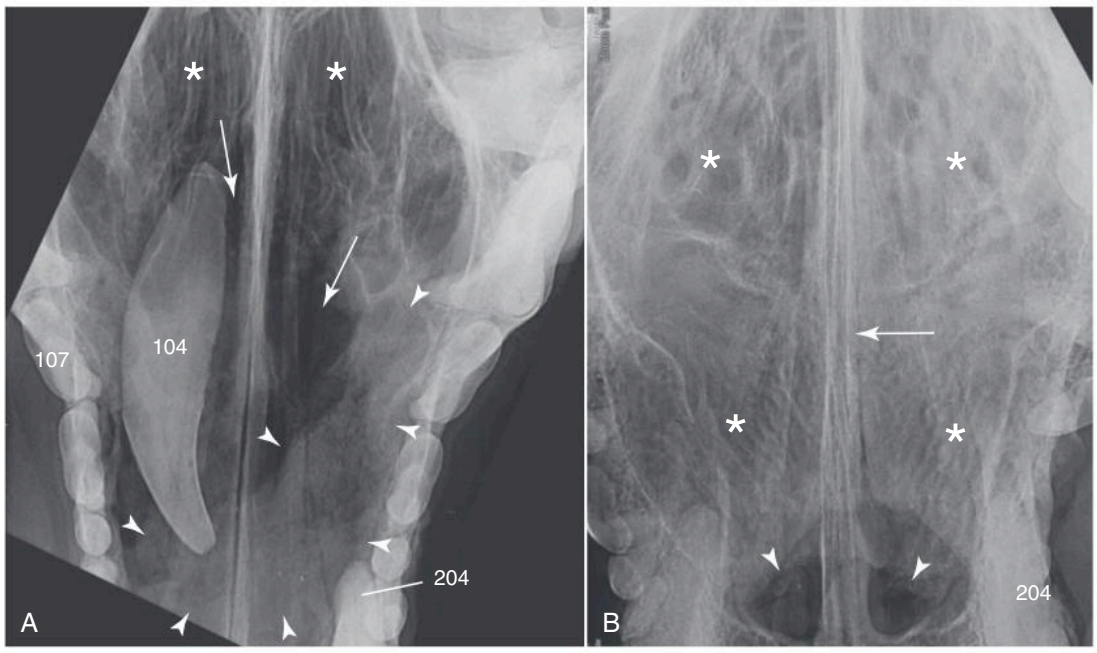


Fig. 10.7 **A,** Dorsoventral intraoral view of a 4-year-old mix-breed dog suffering from chronic nasal discharge. The intraoral radiograph shows the right maxillary tooth (*104*) lodged into the right nasal passage at the level of the right maxillary premolar tooth (*107*). Bilateral opacification (*arrowheads*) and radiolucent areas (*arrows*) suggest a lytic process of the endoturbinates from a chronic inflammatory condition due to an intranasal foreign body. The endoturbinates in the caudal aspect of the nasal passages are preserved (*asterisks*). **(B)** Dorsoventral intraoral view of a 6-year-old boxer displaying normal nasal cavity anatomy. Endoturbinates (*asterisks*), palatine fissures (*arrowheads*), vomer (*arrow*), left maxillary canine tooth (*204*). (Courtesy Lenin A. Villamizar.)

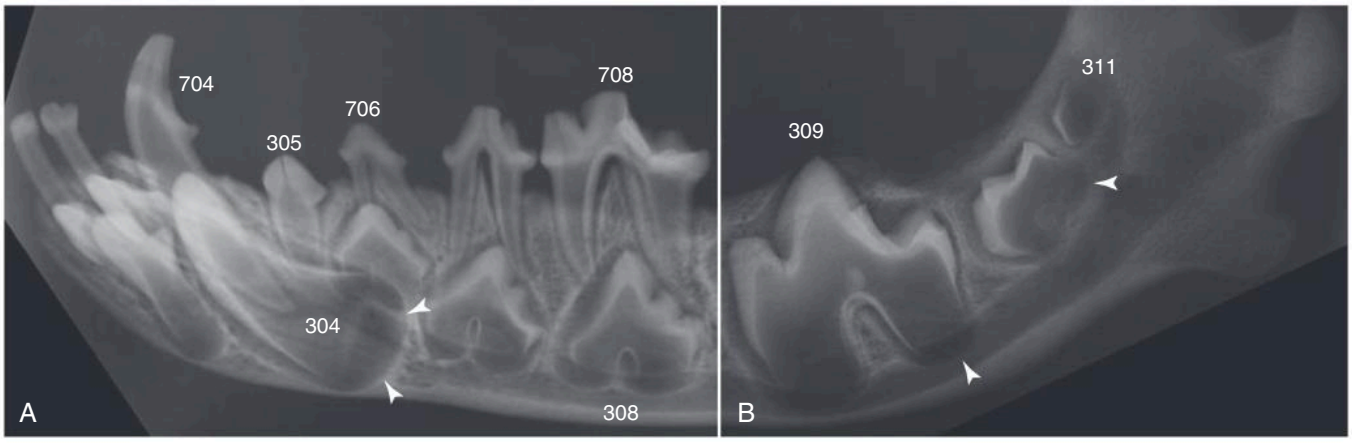


Fig. 10.8 Radiograph of a 4-month-old puppy's developing the **(A)** incisor, canine, and premolar teeth and **(B)** molar teeth. The permanent dentition is underneath the deciduous dentition (*704, 706, 708*). Note the open apex of the permanent teeth (*arrowheads*). The first premolar tooth (*305*) and the molar teeth (*309-311*) do not have deciduous teeth. (Courtesy Lenin A. Villamizar.)

the initial portion of the digestive tract at the oral cavity.[21] In the oral cavity, alveolar processes at the incisive, maxillary, and mandibular bones form alveolar sockets (alveoli), which firmly support the teeth through a fibrous joint known as gomphosis. The tooth and its supporting structures are named the dentoalveolar complex.[21,22]

Dogs and cats have two sets of teeth (deciduous and permanent) characterized by different shapes or types (incisors, canine, premolar, and molar teeth).[22,23] Except for the molar teeth in dogs and cats and the first premolar tooth in the dog, which do not have deciduous counterparts, the eruption of the deciduous teeth typically occurs during the first six to ten weeks of life. On the other hand, permanent dentition starts erupting from 3 months until 6 or 7 months of age (Fig. 10.8).[22,24]

As recommended by the American Veterinary Dental College (AVDC), teeth are correctly named as right or left; maxillary or mandibular; first, second, third, or fourth; incisor, canine, premolar, or molar. The modified Triadan system can be substituted if the full tooth name is not employed. In the modified Triadan system, the dental arcades are divided into quadrants.[25] Then, each tooth in each quadrant is designated a three-digit number from the first incisor teeth in a rostrocaudal direction (Fig. 10.9).[25]

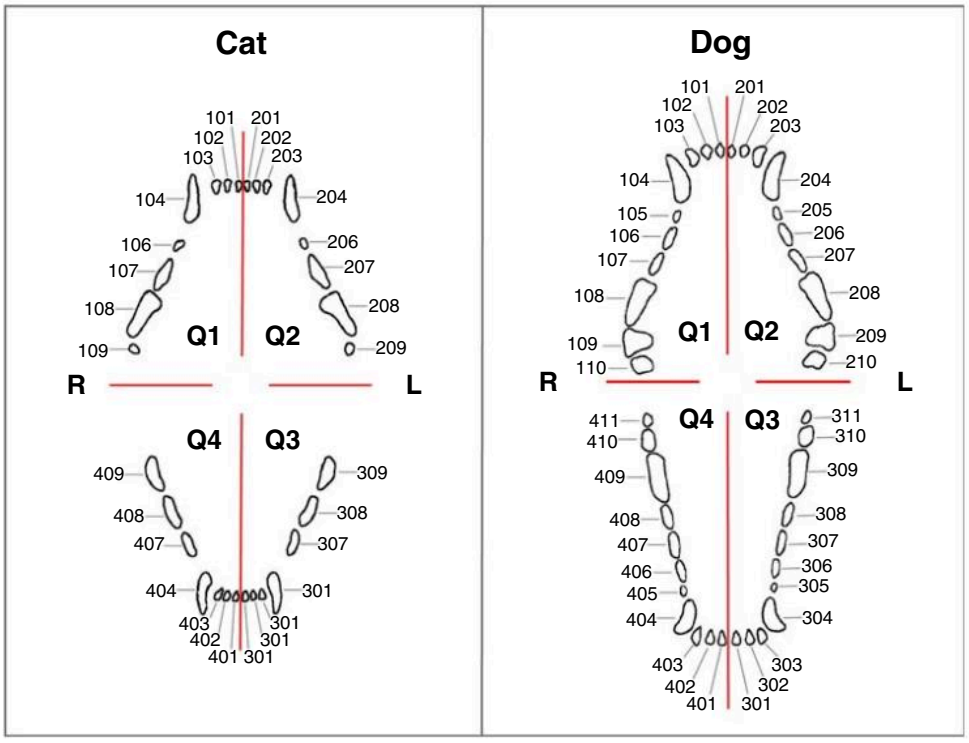


Fig. 10.9 Modified Triadan system in adult cat and dog. The mouth is divided into four quadrants (Q1−Q4) in a clockwise direction where each tooth is numbered with a three-digit number. The first number is associated with the quadrant, and the second and third numbers refer to the tooth position. For deciduous teeth numbering, the first digit for the right maxilla corresponds to "5," the left maxilla to "6," the left mandible to "7," and the right mandible to "8" (e.g., tooth 804: right mandibular deciduous canine tooth).

The intra- and extraoral structures in dogs and cats may be affected by inflammatory, neoplastic, traumatic, developmental, metabolic, congenital, or hereditary disorders. The anatomic complexity of the skull poses a challenge during radiographic interpretation when two-dimensional images of three-dimensional structures are evaluated.[26,27] Knowledge of the dentoalveolar anatomy is critical for understanding alterations of the normal radiographic appearance.

The maxillofacial structures, including the dentoalveolar complex, consist of soft and hard tissues. Depending on the structural chemical composition, each tissue type has a different capacity to attenuate the x-ray beam during a radiographic exam. In this way, highly mineralized structures, such as the enamel, dentin, and alveolar bone, are the most radiopaque areas in the radiograph. At the same time, regions like the pulp cavity, the periodontal ligament space, the gums, and the nasal cavities are less radiopaque (Fig. 10.10).[26–28]

The radiographic assessment of patients undergoing professional dental cleaning includes full-mouth intraoral dental radiographs (Fig. 10.11). However, intraoral views of a specific area may be required if the primary concern and the reason for the consultation are a specific dental structure or region of the oral cavity (e.g., dental fracture). Orthogonal views may be necessary when the dental and maxillofacial structures are superimposed, which can make it challenging to identify a radiographic alteration.[26,27]

Radiographic interpretation of dental radiographs should be systematic. The anatomical structures may be approached from the most general to the most specific to ensure that all relevant information is evaluated. Thus, a general view of the radiopacity and integrity of the maxillary or mandibular bone that supports the teeth, areas of bone lysis or proliferation, and bone morphologic alterations that may be associated with current or past pathologic events should be recorded.[7]

The initial general evaluation can be followed by a more specific assessment of the periodontal structures. This assessment may include[7,12]:

- Identification of alveolar bone loss at the alveolar margin, the periapical and furcation regions
- Widening or absence of the periodontal ligament space
- Loss of the lamina dura, which is the radiographic term for the cribriform plate of the alveolar socket
- Radiopaque or radiolucent areas next to the dental roots

The dental element and its endodontic system can finally be evaluated. Tooth assessment includes[7,29–31]:

- Identification of morphological alterations of the crown and root, unerupted teeth, external tooth resorption, and excessive or missing number of teeth.
- Evaluation of the endodontic system includes comparing the pulp cavity size between permanent teeth in the same patient (e.g., maxillary left vs. right canine), internal tooth resorption, increased radiopacity of the pulp cavity, and periapical lesions associated with tooth fractures or tooth discoloration.

PERIODONTAL DISEASE

Periodontal disease is the most prevalent oral disease in dogs and cats, and is caused by the destructive action of bacterial plaque and its inflammatory effect on the periodontium.[32,33] The periodontium consists of both hard and soft tissue components that support the teeth in the mandibular or maxillary bone. These structures are the alveolar bone, the periodontal ligament, the gums, and the cementum. Teeth suffering from periodontal disease can be associated with gingival bleeding, either spontaneous or during periodontal probing, gingival recession, periodontal pockets, or tooth mobility.[24,32]

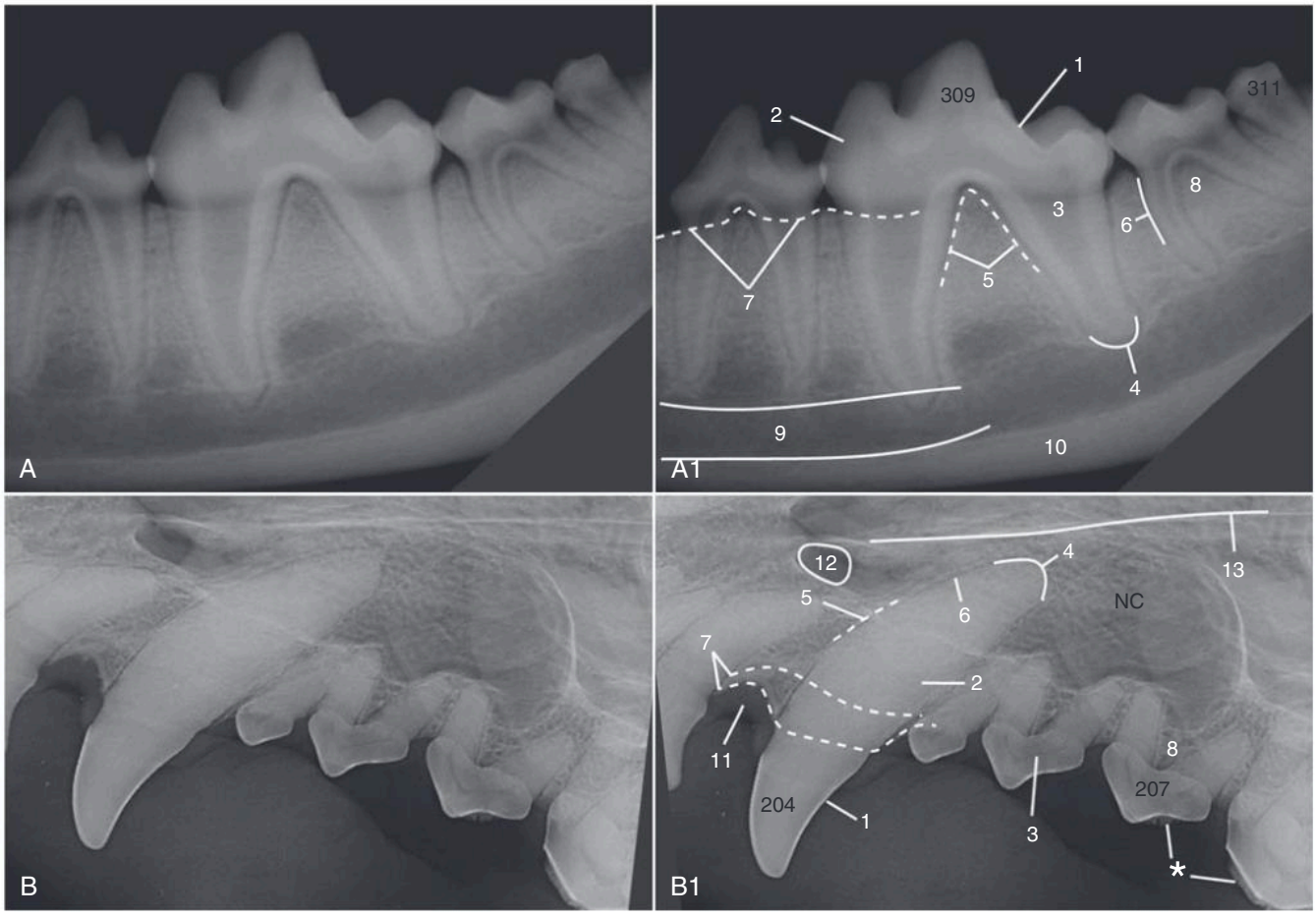


Fig. 10.10 Intraoral parallel technique view of the left mandibular molar teeth region **(A–A1)** and bisecting angle technique view of the left maxillary teeth **(B–B1)** of adult dogs showing the dental, periodontal, and surrounding structures: (1) enamel, (2) dentin, (3) pulp cavity, (4) apex, (5) lamina dura, (6) periodontal ligament space, (7) alveolar margin, (8) interradicular bone, (9) mandibular canal, (10) ventral cortex of the mandible, (11) gingiva, (12) palatine fissure, (13) vomer. Note the *double interrupted lines* in **B1** that correspond to moderate horizontal bone loss at the lingual alveolar margin of the left maxillary canine tooth. *NC,* Nasal cavity; *asterisk,* dental calculus. (Courtesy Lenin A. Villamizar.)

Identifying the radiographic changes in the periodontium associated with periodontal disease is extremely valuable for determining the treatment plan and prognosis. At the initial stage of the disease, the gingival tissue appears edematous due to the presence of bacterial plaque at the gingival sulcus.[34] At this moment, radiographic alterations on the periodontium are not present, as the inflammatory process is limited to soft tissue.

If dental plaque is not removed, the subsequent inflammatory reaction can cause, depending on the stage of the disease, mild, moderate, or advanced alveolar bone loss with destruction of the lamina dura and the periodontal ligament. Radiographic findings associated with periodontal disease may include (Fig. 10.12, eFigs. 10.1–10.3):

- Mild reduction of the alveolar margin height
- Horizontal, oblique, or vertical alveolar bone loss
- Furcation bone loss

Although the cementum can be reabsorbed due to the inflammatory response triggered by periodontitis, this is generally not seen in the radiograph due to the thin nature of the cementum and its similar opacity to dentin.

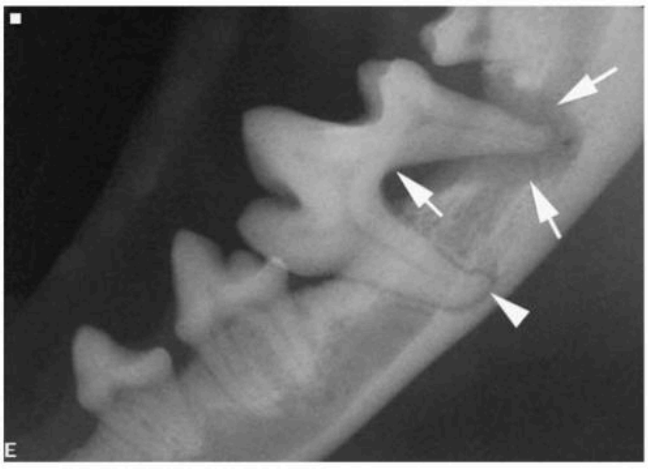
In cats, chronic periodontitis may lead to alveolar bone expansion or alveolar osteitis besides provoking bone loss. This condition is characterized by thickening of the buccal alveolar bone along areas of severe periodontitis.[35,36] Tooth resorption, tooth extrusion, and osteomyelitis of the jaws have also been linked to alveolar bone expansion. Although this can affect any tooth in the cat's mouth, the maxillary canine teeth seem more affected. Clinically, areas with alveolar bone expansion show gingivitis, gum recession, tooth extrusion, tooth mobility, and periodontal infrabony (vertical) pocket formation.[35,37] On dental radiography, the affected area can have a rarifying osseous proliferation or a mottled pattern with prominent trabeculae (Fig. 10.13). In severe cases where the bone lesion has extended beyond the alveolar bone and osteomyelitis is suspected, biopsies should be obtained to rule out a neoplastic process.[35,38,39]

ENDODONTIC DISEASE

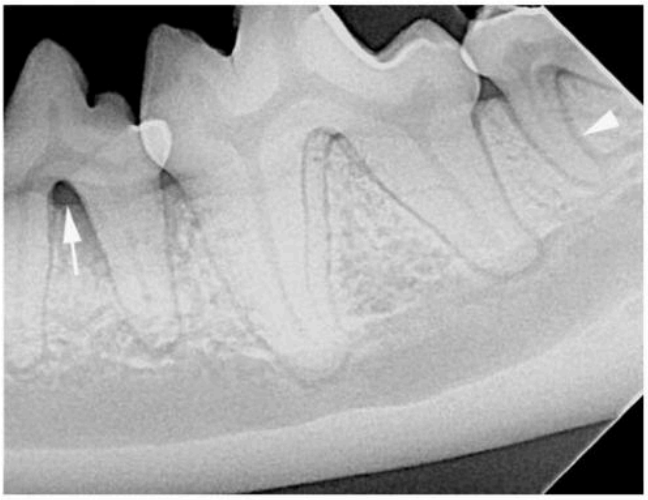
Endodontic disease pertains to any pathologic event affecting the pulp of the tooth. The pulp is an unmineralized dental tissue located in the pulp cavity and is mainly composed of connective tissue, blood vessels, nerves, and dentin-producing cells named odontoblasts.[40,41] The pulp cavity is topographically divided into two areas, the pulp chamber that corresponds to the pulp cavity located in the crown and the root canal that corresponds to the portion of the pulp cavity situated in the root. In multirooted teeth, the most coronal portion of the pulp may slightly protrude into the dentin forming the pulp horns (Fig. 10.14).[7,40]



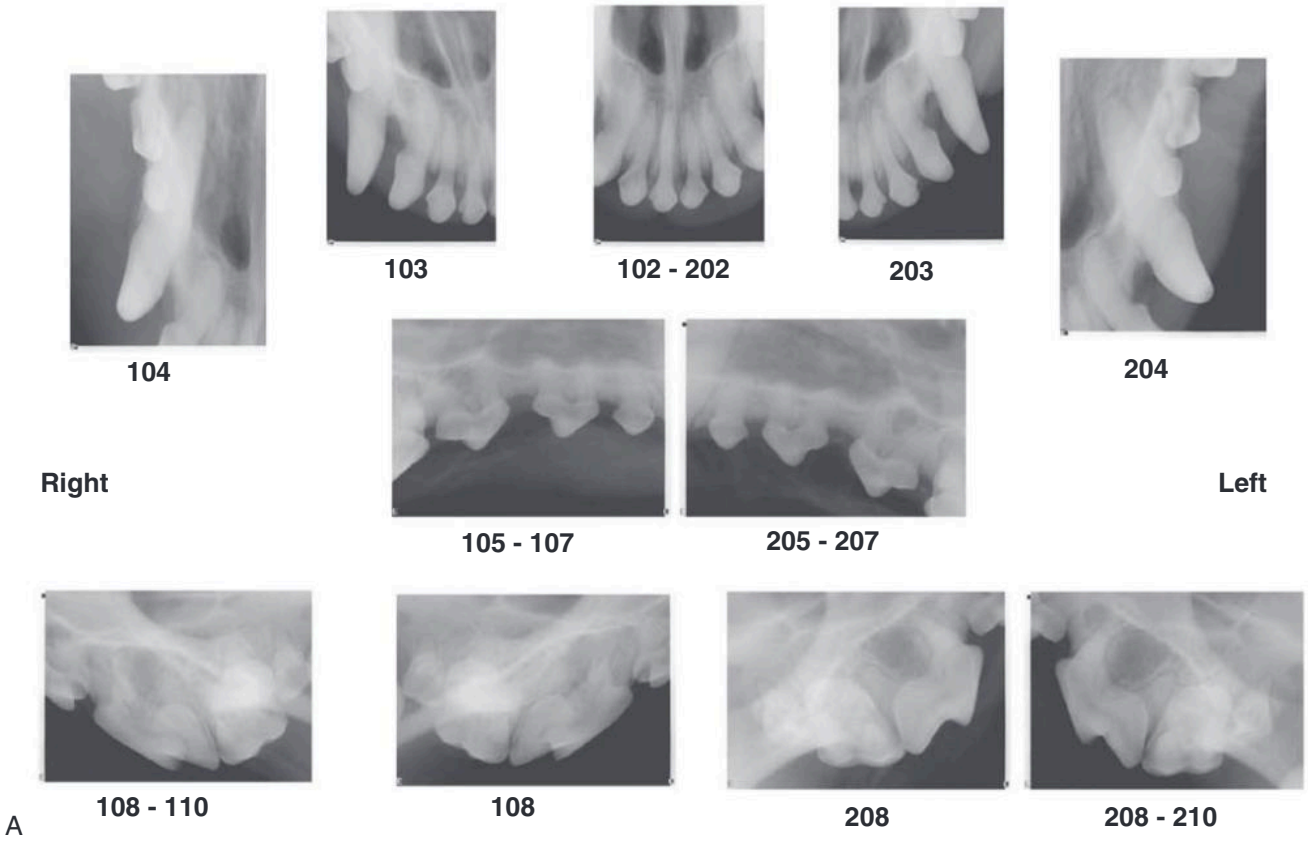
eFig. 10.1 Periodontitis. Horizontal bone loss with furcation exposure of the left maxillary fourth premolar.



eFig. 10.2 Periodontitis. There is severe vertical bone loss characterized by complete loss of attachment of the distal root of the left mandibular first molar with furcation exposure (*white arrows*). There is dilaceration at the mesial root (*white arrowhead*).



eFig. 10.3 Periodontitis. Bone loss at the distal root of the left mandibular fourth premolar with furcation exposure (*white arrow*). Wide periodontal ligament of the mesial root of the second molar (*white arrowhead*). (Courtesy Animal Dental Center, Towson, MD.)



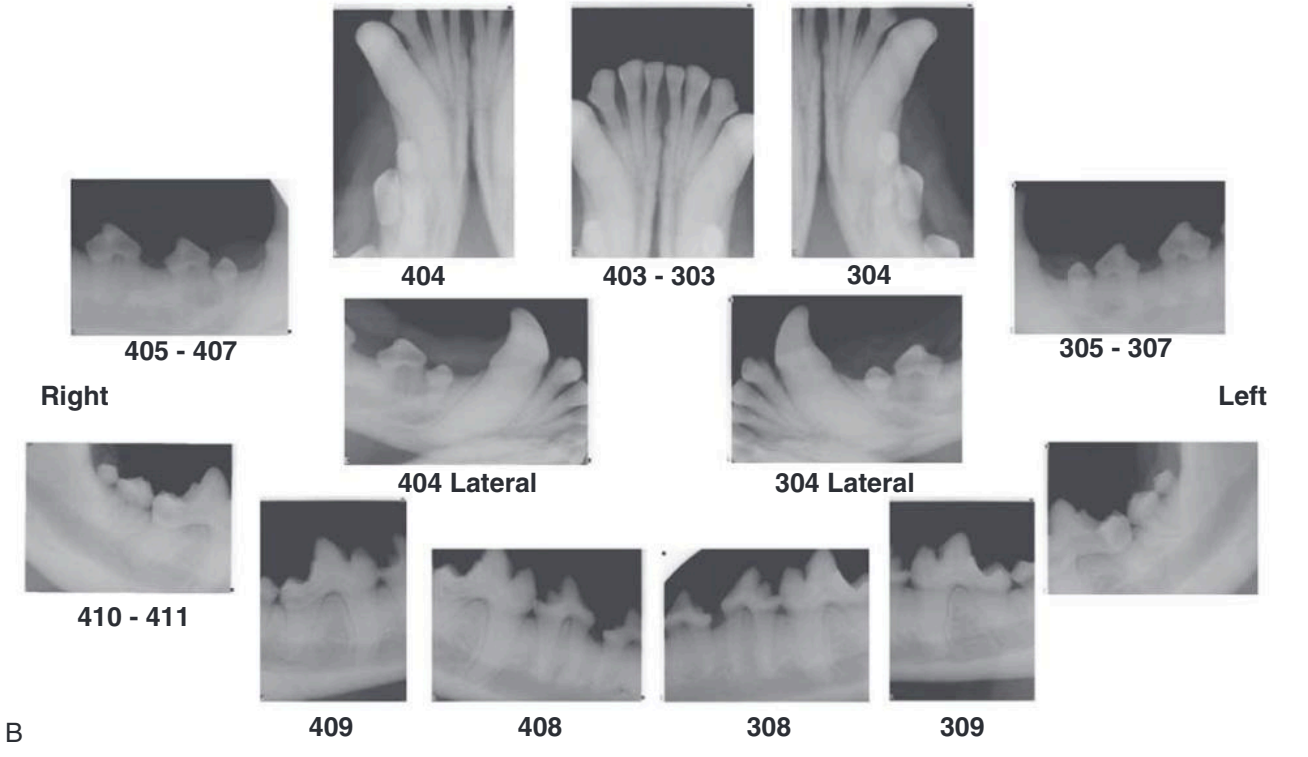


Fig. 10.11 Labially mounted radiographic maxillary **(A)** and mandibular **(B)** set of a dog. This organization of the intraoral radiographs allows the clinician to identify if the radiographs are from the right or left arcades of the patient. Note how the images of the maxillary teeth are pointed down while the mandibular teeth are pointed up.

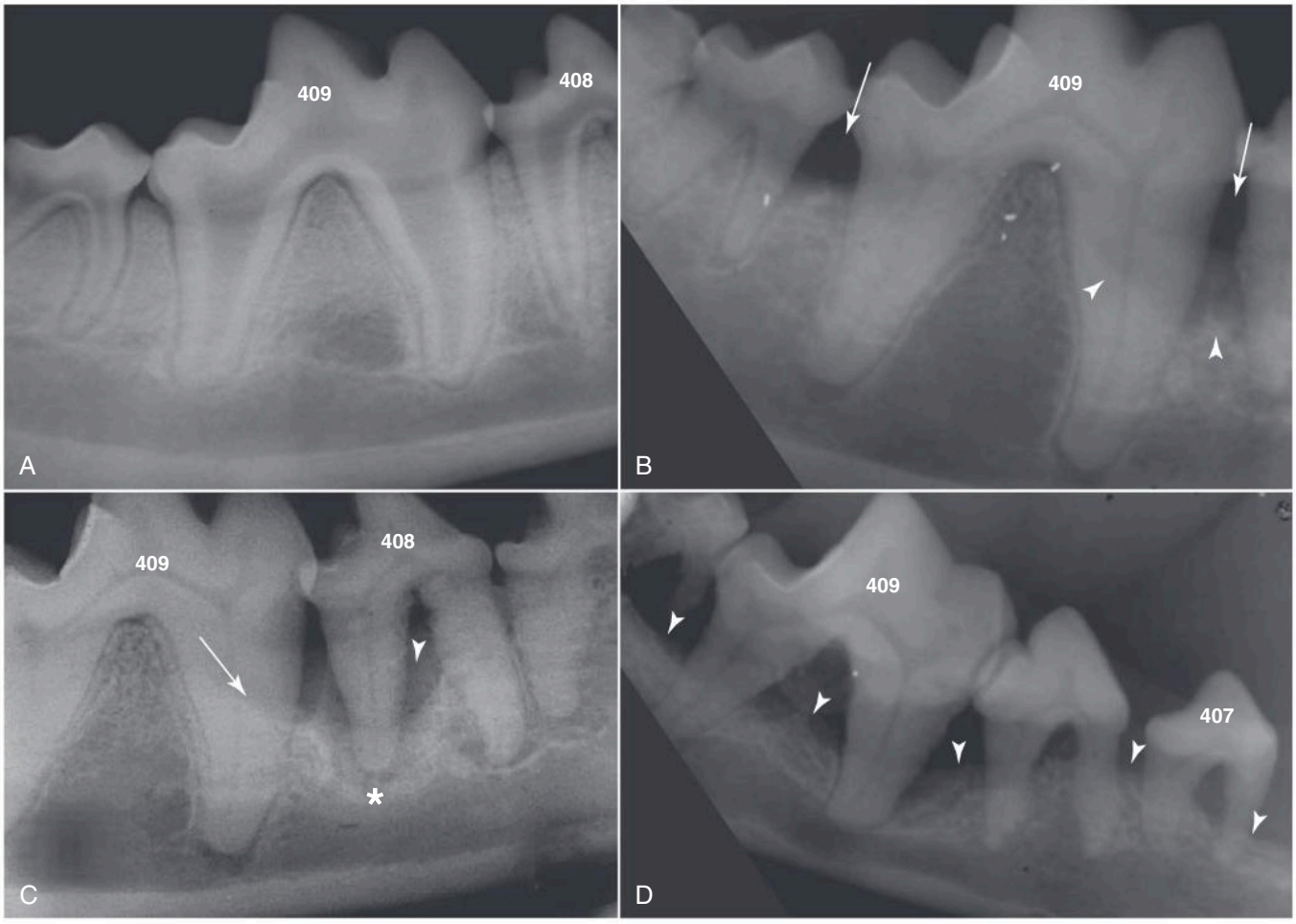


Fig. 10.12 Intraoral parallel technique of the right mandibular teeth in four different adult dogs with normal periodontium **(A)** and several stages of periodontitis: **(B)** mild (*arrows*) and moderate alveolar bone loss between the right mandibular first molar (*409*) and fourth premolar teeth (*arrowheads*). **C,** Severe oblique and vertical (*arrowhead*) alveolar bone loss between 409 and 408. Note the condensing osteitis (*asterisk*) associated with a chronic inflammatory condition. **D,** Severe horizontal bone loss (*arrowheads*) and condensing osteitis.

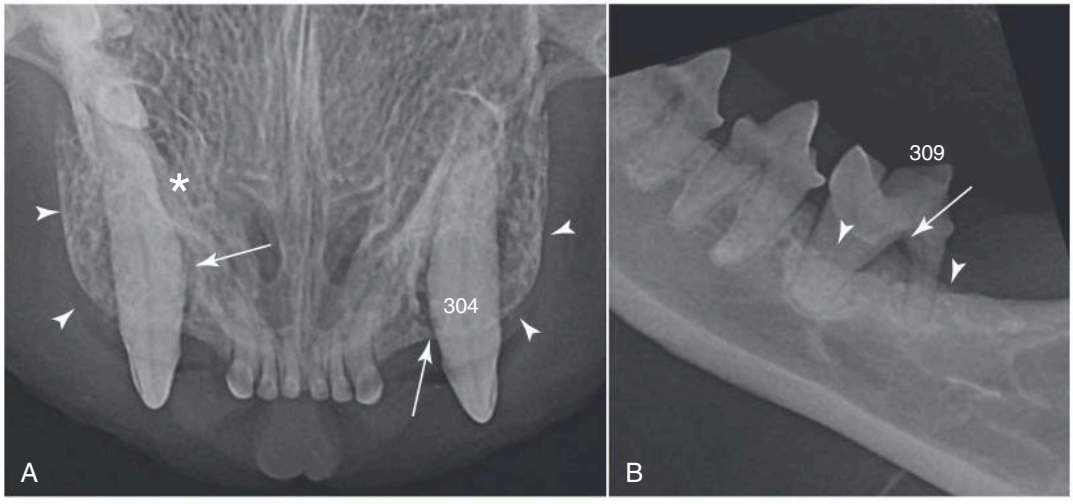


Fig. 10.13 Intraoral bisecting-angle technique occlusal view of the maxilla and parallel technique of the left mandible of an adult cat showing **(A)** bilateral alveolar bone expansion (*arrowheads*), vertical bone loss (*arrows*), and moderate root resorption (*asterisk*). Note the mottled pattern with prominent trabeculae at the buccal aspect of the maxillary canine teeth. **B,** Severe horizontal alveolar bone loss (*arrowheads*) and exposure of the furcation of 309 (*arrow*).

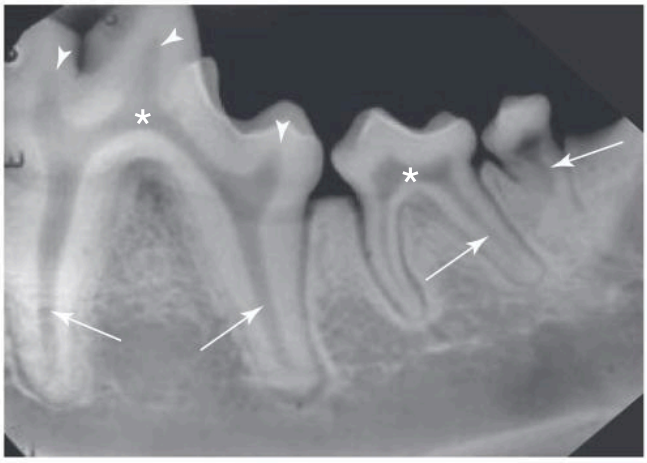


Fig. 10.14 Intraoral radiographs of the right mandibular molar teeth showing the regions of the pulp cavity: pulp chamber (*asterisk*), root canal (*arrows*). In multirooted teeth, the extension of the pulp chamber into the cusp corresponds to the pulp horns (*arrowheads*).

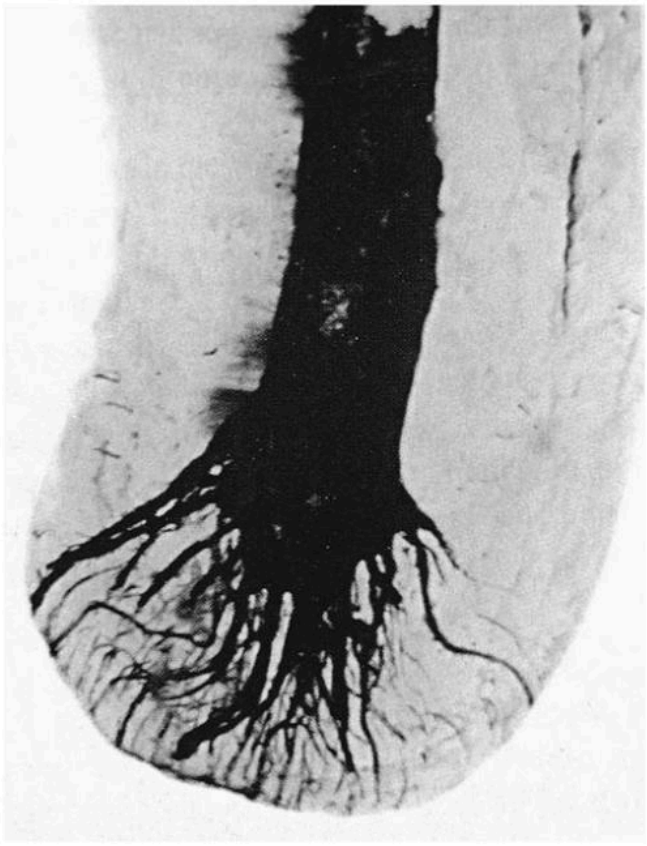


Fig. 10.15 Photomicrograph of the apical delta in a canine tooth. (From Hernandez SZ, Negro VB, Maresca BM. Morphology features of the root canal system of the maxillary fourth premolar and the mandibular first molar in dogs. *J Vet Dent*. 2001;18:9–13.)

The pulp has sensory and nourishment functions that keep the tooth alive, allowing the odontoblasts located at the most outer region of the pulp tissue to build up dentin during the normal development of the tooth. The pulp, and hence the viability of the odontoblast, is supported by arterioles that enter the pulp cavity through the apical delta (Fig. 10.15).[22] The intraoral radiographic approach of the endodontic system includes assessing the size and shape of the pulp cavity and radiographic appearance of the periapical region. Dental radiography allows visibility of the pulp cavity as a narrow radiolucent band in the center of the tooth. In young animals, the pulp cavity is still wide; as the animal ages, this space narrows due to dentin deposition. Asymmetry of the pulp cavity between adjacent or contralateral teeth may indicate pulp necrosis and lack of dentin deposition by odontoblasts (Fig. 10.16).[30,42]

Dentoalveolar injuries such as tooth concussion, subluxation, luxation, or alveolar fracture along the apical portion of the root may also lead to tooth devitalization due to severe pulpitis or disruption of blood supply. Tooth discoloration is the most frequent clinical finding (87%–92%) in teeth suffering from pulp necrosis.[30,42]

Periapical inflammatory lesions associated with endodontic disease may be acute or chronic depending on the host autoimmune response and virulence of the bacteria in the necrotic pulp. During the early stage of the inflammatory lesion, the microflora from the affected pulp triggers an inflammatory response at the apical periodontal ligament and surrounding alveolar bone, known as acute apical periodontitis. Depending on the autoimmune response, pus may form at this stage of the inflammatory process, leading to an apical abscess.[43,44]

Acute apical periodontitis is histologically characterized by the presence of lymphocytes and neutrophils, along with vascular congestion, hyperemia, and edema of the periodontal ligament. Since it is possible that destruction of the mineralized tissues (dentin, cementum, and bone) has not occurred during acute apical periodontitis, the radiographic changes can be limited to widening of the periodontal ligament space only, and radiographic identification can be challenging or underestimated.[44–46]

If the initial inflammatory injury is not resolved, a more chronic inflammatory response occurs with the formation of a periapical granuloma. Radiographically, a periapical granuloma is characterized by ill or well-defined circumscribed radiolucent or radiopaque areas around the tooth apex. During this stage of the inflammatory process, in an attempt to heal, the periapical region is infiltrated by granulation tissue and inflammatory cells such as plasma cells, lymphocytes, and histiocytes.[46,47]

The effect of inflammatory byproducts of a nonvital tooth on the epithelial cells of Malassez located in the periodontal ligament may result in a radicular or periapical cyst formation.[47] Radiographically, a radicular cyst generally corresponds to a single round radiolucent cavitary lesion with a well-defined cortical wall. During the early stage of the periapical cyst, it is challenging to differentiate it from the periapical abscess or granuloma due to its similar osteolytic appearance on dental radiography.[47] Although the radiographic examination may aid in localizing apical periodontitis, histopathology remains the method of choice to identify the type of inflammatory lesion. Histologically, a periapical cyst is associated with an epithelium-lined cavity with an inflamed fibrovascular connective tissue wall.[48,49] Fig. 10.17 depicts the radiographic features of some inflammatory periapical lesions in different patients.

Dental radiography can help identify the origin of the endodontic pathologic condition. In an endo-perio lesion, the endodontic injury from dental trauma leads to the destruction of the periapical periodontal structures. In contrast, in a perio-endo lesion, the endodontic disease results from the invasion of the tooth apex by periodontal microflora from deep periodontal pockets in patients suffering from severe periodontitis (Fig. 10.18).[50,51]

The chevron sign, a nonpathologic radiolucent area that resembles periapical inflammatory lesions, can be observed in

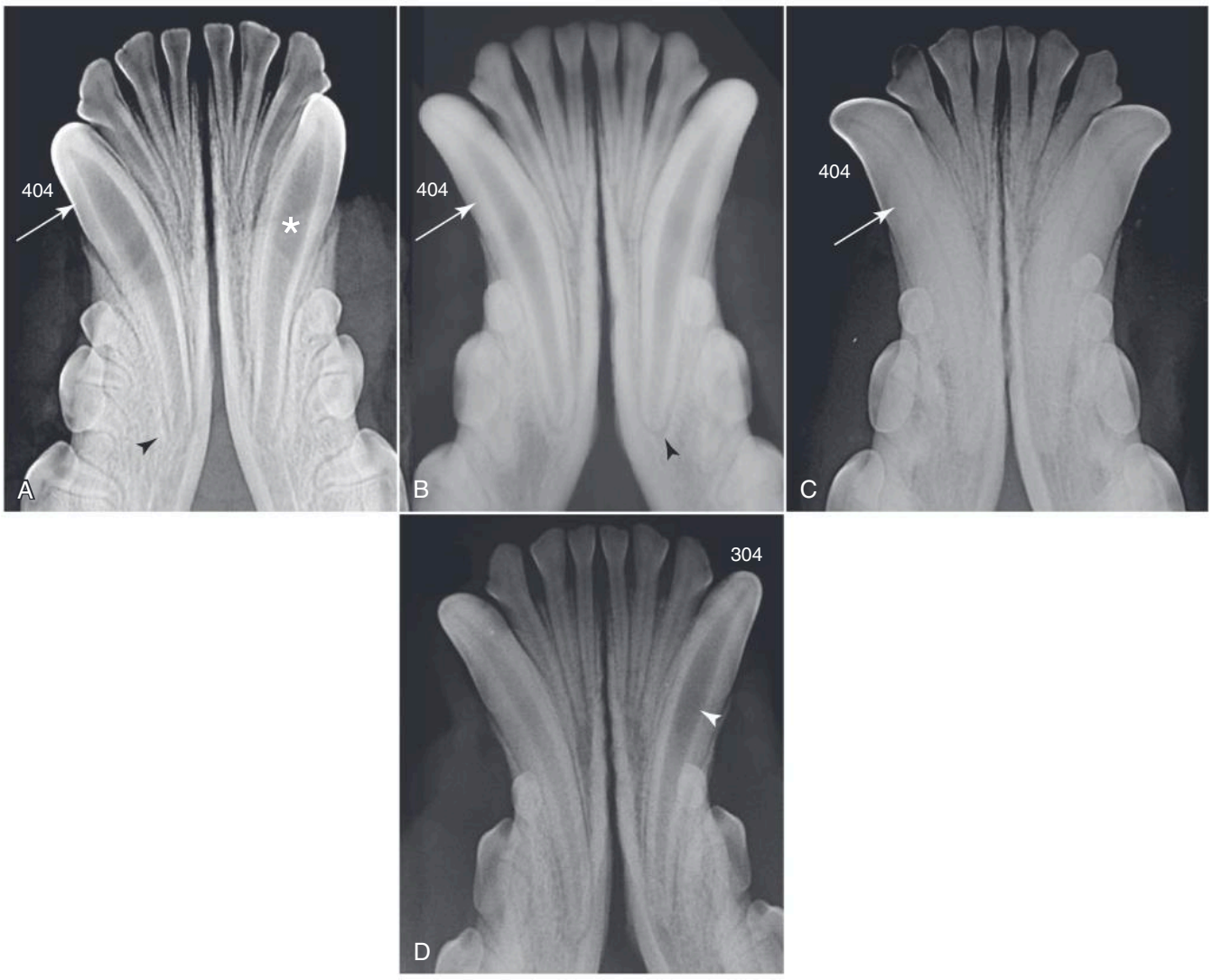


Fig. 10.16 Intraoral occlusal views of the mandibular incisors and canine teeth showing dentin deposition in different age dogs. **A,** 8-month-old Border Collie. Note the open apex (*arrowhead*), the wide pulp cavity (*asterisk*), and the low dentin build-up (*arrow*). **B,** 19-month-old German Shepherd. Note that there is more dentin build-up (*arrow*), and the apex is closed (*arrowhead*). **C,** 11-year mix-breed dog. The pulp cavity appears as a thin radiolucent band with thick dentin walls (*arrow*). **D,** Nonvital *304*. Note the asymmetry between the pulp cavity of the mandibular canine teeth. *304* displays a wider pulp cavity due to a lack of dentin deposition due to pulp necrosis (*arrowhead*).

healthy clinical teeth.[52] Radiographically, this lucency sign may appear as a chevron or V-shape area of decreased radiodensity at the apex of the canine, incisor, and mandibular first molar teeth, as well as the distal root of the maxillary premolar teeth. The chevron sign corresponds to normal trabecular bone and vascular canals projected at the tooth's periapical area (Figs. 10.19 and 10.20).[52] True periapical inflammatory lesions are displayed as more rounded radiolucent areas associated with fractured and discolored teeth or affected by severe periodontal disease.[53]

Internal inflammatory resorption of the inner surface of the pulp cavity is also associated with endodontic disease. As in humans, internal inflammatory resorption is uncommon in dogs. In 224 dogs, only 4.0% had tooth resorption affecting the middle third of the root canal.[31] Although it is unknown why odontoclasts start reabsorbing the dentin, it is suggested that the inflammatory response in a tooth suffering from pulpitis or necrosis leads to self-limiting continuous intraradicular dentin resorption. On dental radiographs, the teeth affected by internal inflammatory resorption display a focal circumscribed, oval, or elongated radiolucent area at the middle third of the root canal.[31,54]

TOOTH RESORPTION

Resorption can affect dogs and cats, ranging from 43% to 53% and 29% to 85%, respectively. This condition is characterized by the progressive destruction of the mineralized components of the tooth, resulting in pulp exposure, dental pain, tooth fracture, and, eventually, tooth loss.[31] Although in dogs and cats, this dental disorder has been associated with inflammatory or neoplastic processes, age, breed, and body weight, and more specifically with chronic excess dietary vitamin D intake in the cat, tooth resorption etiology remains unknown.[35,55,56]

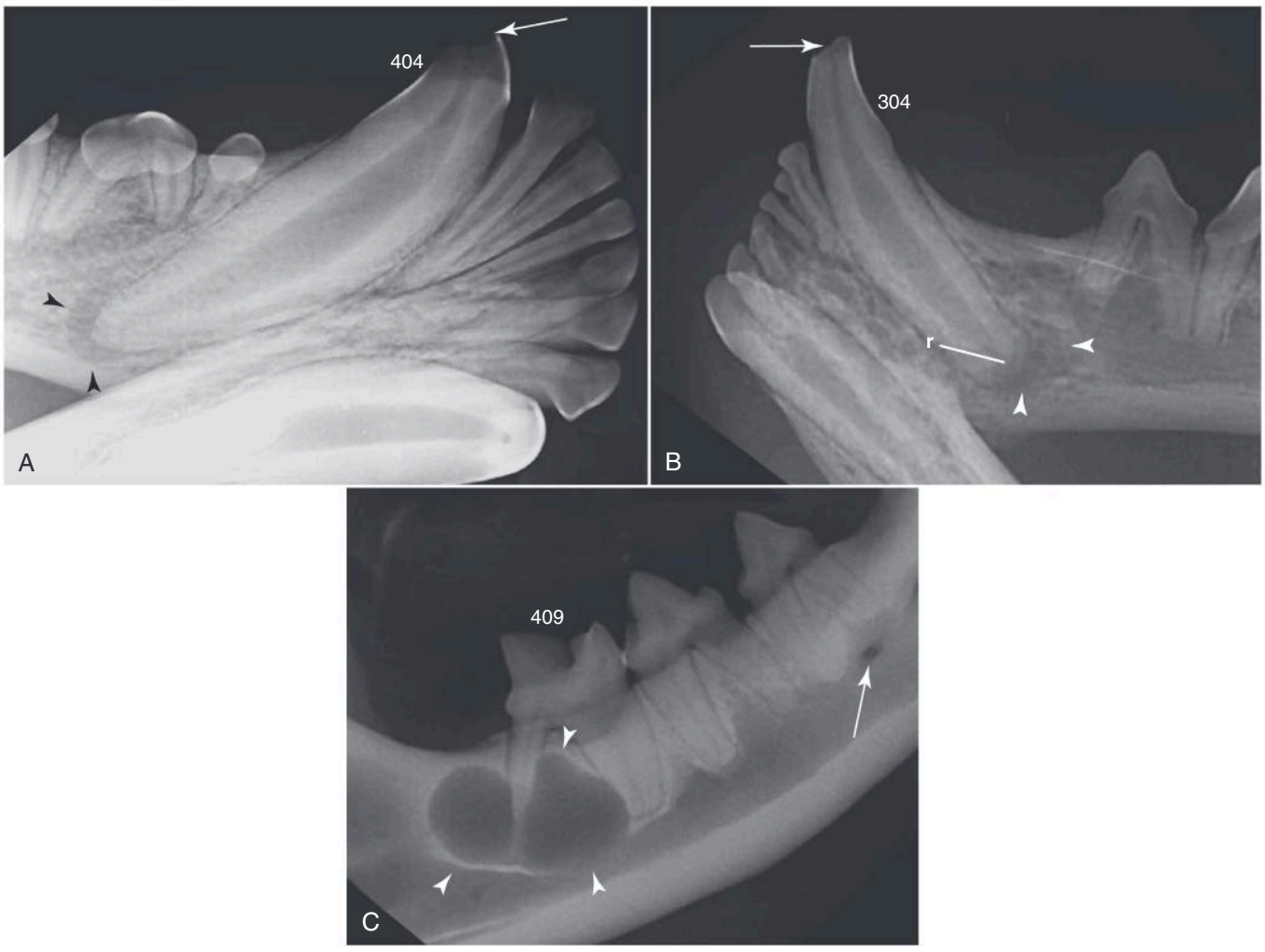


Fig. 10.17 Intraoral radiographs of the right mandibular canine tooth (*404*) of a dog **(A),** left mandibular canine—*304* **(B),** and right mandibular premolar and molar teeth **(C)** in two cats. **A,** Round radiolucent halo at the apex of 404 (*arrowheads*) associated with a complicated crown fracture (*arrow*). **B,** Periapical radiolucent lesion (*arrowheads*) and root resorption (*r*) associated with a complicated crown fracture of *304* (*arrow*). **C,** Radicular cyst observed as a well-defined bilocular radiolucent lesion affecting 409 (*arrowheads*). Distal mental foramen (*arrow*). (Courtesy Dr. Fernanda Lopes, Dentistry and Oral Surgery Service NCSU, College of Veterinary Medicine.)

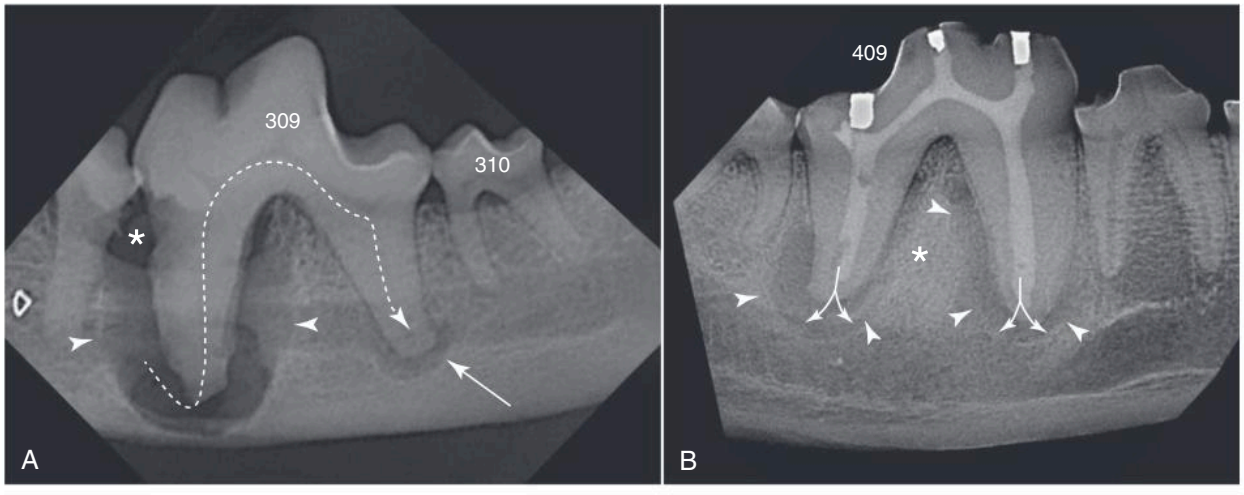


Fig. 10.18 Radiographs of the left **(A)** and right **(B)** mandibular first molar tooth in two dogs. **A,** In a perio-endo lesion, severe periodontitis (*arrowheads*) allows the entrance of bacteria through the apex of the distal root of 309 (*interrupted arrow*), resulting in pulp infection, necrosis, and periapical destruction of the periapical tissue of the mesial root (*arrow*). Note the resorption process at the distal root of 309 due to the inflammatory condition (*asterisk*). **B,** In a tooth with root canal therapy failure, the endo-perio lesion originates from bacteria from the endodontic system. Then the infection invades the periapical tissue (*arrows*), causing severe periodontitis (*arrowheads*). Note the condensing osteitis associated with a chronic inflammatory condition (*asterisk*).

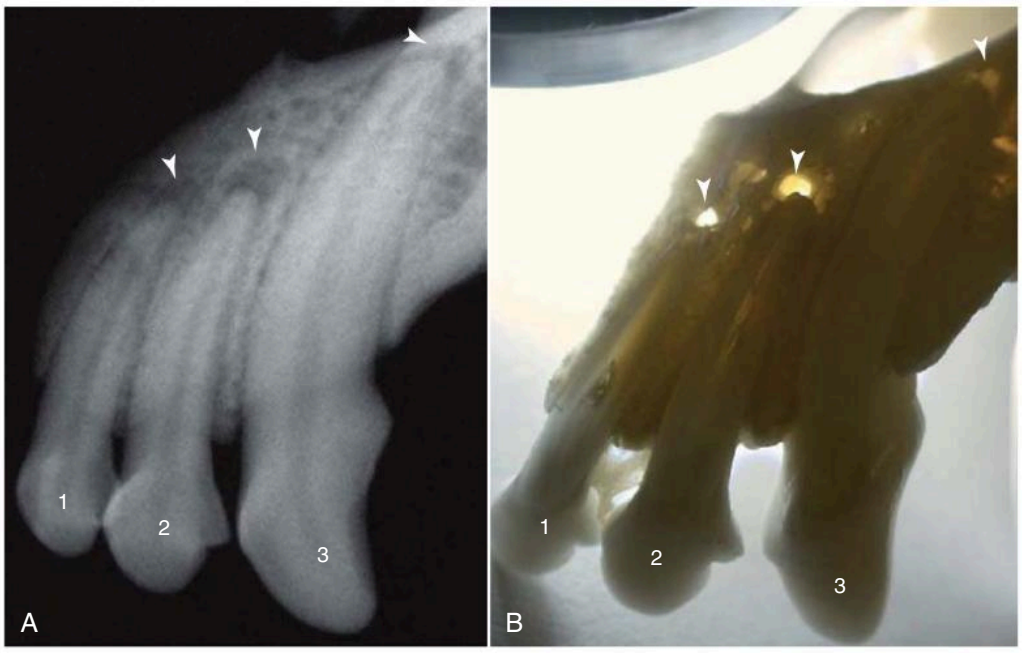


Fig. 10.19 **(A)** Radiograph and **(B)** prepared incisive bone with incisor teeth (*1–3*) showing Chevron-shaped lucencies (*arrowheads*). Chevron lucencies correspond to the normal spongious conformation of the bone that appears superimposed or at the periapical area. (Reproduced with permission from DuPont G, DeBowes L. *Atlas of Dental Radiography in Dogs and Cats*. Saunders, Elsevier; 2009:12.)

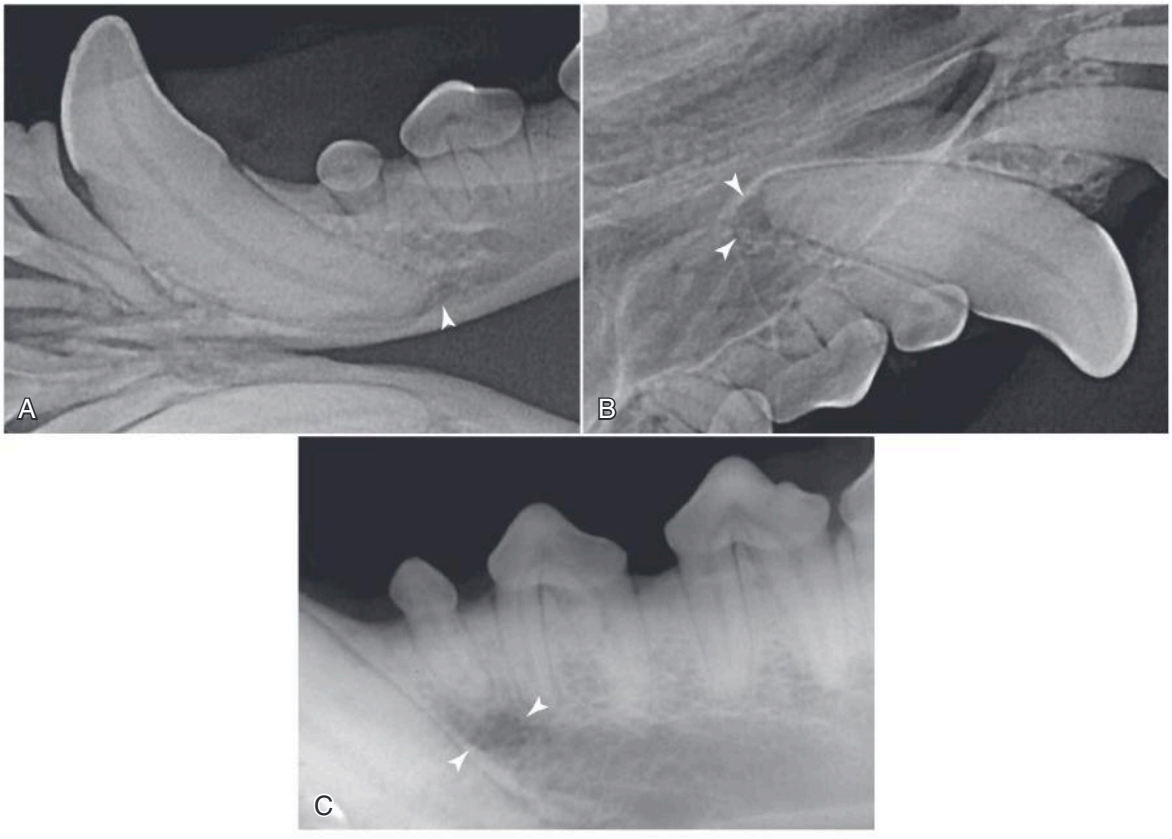


Fig. 10.20 Radiographs of healthy left mandibular **(A)** and right maxillary **(B)** canine teeth in two different dogs with Chevron-shaped lucencies (*arrowheads*). Note the similarity with periapical lesions of endodontic origin. **C,** The middle mental foramen may appear as a periapical lucency if it is projected superimposed or near the apex of the mandibular second premolar (*arrowheads*). Note that the periapical periodontal ligament space and bone appear normal.

Among the most common clinical findings observed during the physical examination in patients suffering from tooth resorption are gingivitis, periodontitis, fracture or loss of dental structure, and, particularly in cats, the presence of granulation tissue at the resorptive lesion location at the cervical region of the tooth.[57,58] Although the physical examination, which includes deep probing of the gingival sulcus and exploring the dental hard tissue under general anesthesia, is mandatory for the initial approach of patients suspected of tooth resorption, intraoral dental radiography is critical to establish the extension of the lesion.[57]

Tooth resorption may be asymptomatic, and clinical manifestations may depend upon the extension and localization of the lesion. Dental destruction associated with tooth resorption can be observed radiographically as a radiolucent region affecting the enamel, cementum, or dentin. However, its radiographic identification depends on the level of destruction of the dental substance. In an early stage of the disease, an incipient resorptive lesion may be radiographically occult. For example, in human beings, more than 30% of enamel demineralization is necessary before it can be detected using conventional dental radiography.[59]

According to the AVDC, tooth resorption is classified as stage 1 to 5, depending on the anatomical location and severity of the lesion (Figs. 10.21 and 10.22) and as type 1 to 3 according to its radiographic appearance (Fig. 10.23).[25] In 2010, the radiographic patterns and types of tooth resorption in dogs were assessed retrospectively, using a classification previously suggested in human beings. External replacement and external inflammatory tooth resorption, homologous lesions to the AVDC type 1 and 2, were the two most common resorptive lesions observed in dogs (Fig. 10.24, eFigs. 10.4–10.11).[31]

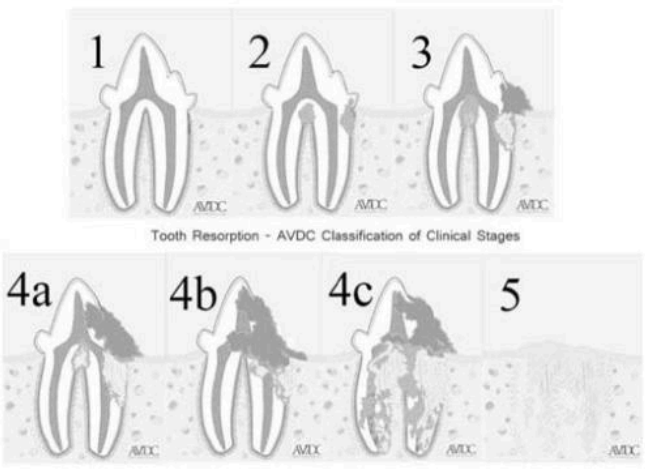


Fig. 10.21 Stages of tooth resorption. *Stage 1,* Mild enamel or cementum destruction. Not detected in dental radiographs. *Stage 2,* Moderate resorption of cementum, or cementum and enamel, extends to the dentin but does not affect the pulp cavity. *Stage 3,* Severe resorption of cementum, or cementum and enamel, with loss of dentin that exposes the pulp cavity. Most of the tooth structure is preserved. *Stage 4a,* Severe resorption of cementum, or cementum and enamel, with loss of dentin that exposes the pulp cavity. Most of the tooth structure of the crown and root is lost in the same proportion. *Stage 4b,* Severe resorption of cementum, or cementum and enamel, with loss of dentin that exposes the pulp cavity. The crown is more affected than the root. *Stage 4c,* Severe resorption of cementum, or cementum and enamel, with loss of dentin that exposes the pulp cavity. The root is more affected than the crown. *Stage 5,* The tooth has been completely reabsorbed, and only remnants of dental structure are observed under a bulged gum. (Reproduced with permission from AVDC Nomenclature.)

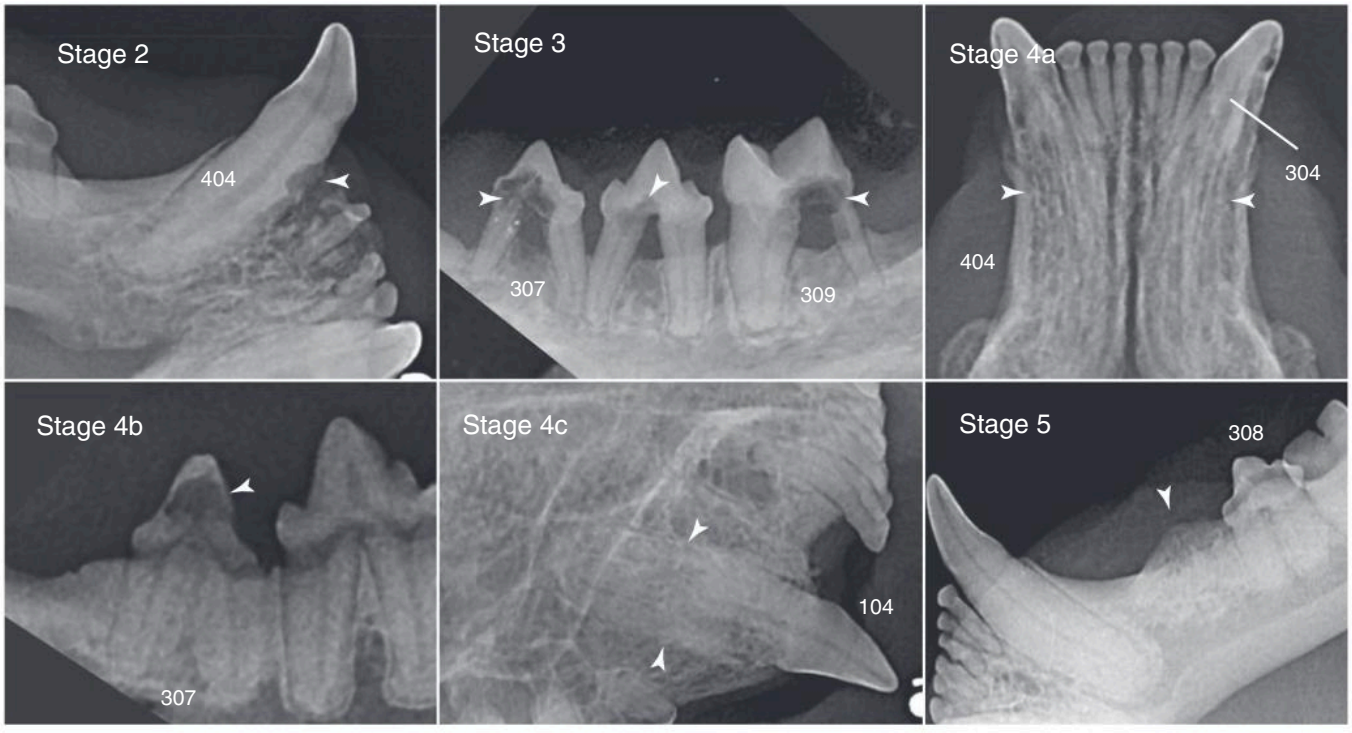
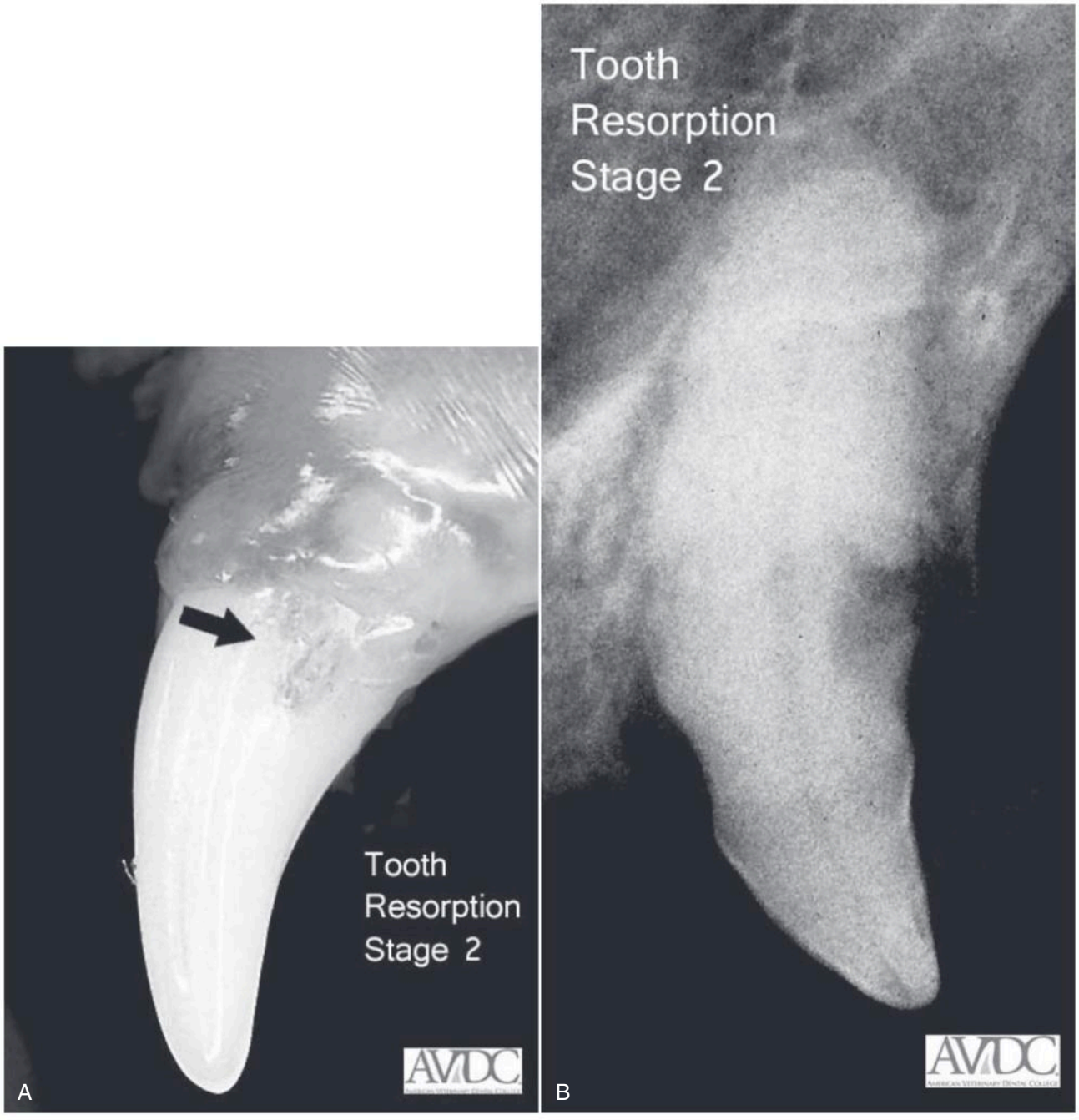
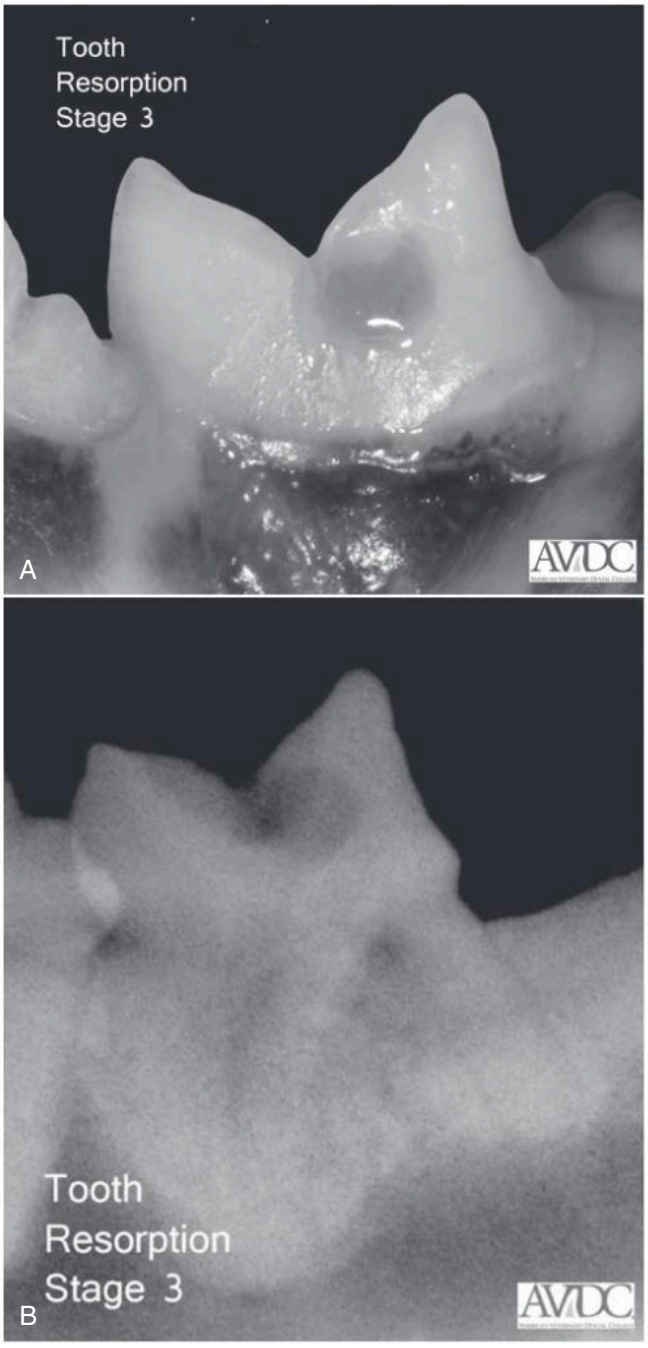


Fig. 10.22 Radiographs of five cats displaying different stages of tooth resorption: *Stage 2* resorption of tooth *404* (*arrowhead*). *Stage 3* resorption of the left mandibular and molar teeth at the level gum line (*arrowheads*) with horizontal bone loss. *Stage 4a* resorption of both mandibular canine teeth (*arrowheads*). *Stage 4b* resorption of *307*. Although both roots are reabsorbing, the crown appears more affected (*arrowhead*). *Stage 4c* resorption of *104*. The root is more affected than the crown (*arrowheads*). *Stage 5* resorption, the left mandibular third premolar tooth (*arrowhead*) appears completely reabsorbed.



eFig. 10.4 **A and B,** Stage 2 resorptive lesion. (Reproduced with permission from AVDC Nomenclature.)



eFig. 10.5 **A,** Photograph. **B,** Dental radiograph of stage 3 resorptive lesion at left mandibular first molar. (Reproduced with permission from AVDC Nomenclature.)



eFig. 10.6 Stage 4a resorptive lesion (crown and root = affected) at left mandibular fourth premolar.



eFig. 10.7 Stage 4b resorptive lesion (crown > root) at left mandibular fourth premolar and first molar. (Courtesy Animal Dental Center, Towson, MD.)



eFig. 10.8 Stage 4c resorptive lesion (root > crown) at left mandibular fourth premolar. (Courtesy Animal Dental Center, Towson, MD.)



eFig. 10.9 Stage 5 resorptive lesion at the right mandibular third premolar.



eFig. 10.10 Type III resorptive lesion. (Reproduced with permission from AVDC Nomenclature.)



eFig. 10.11 Type II resorptive lesion. (Courtesy Animal Dental Center, Towson, MD.)

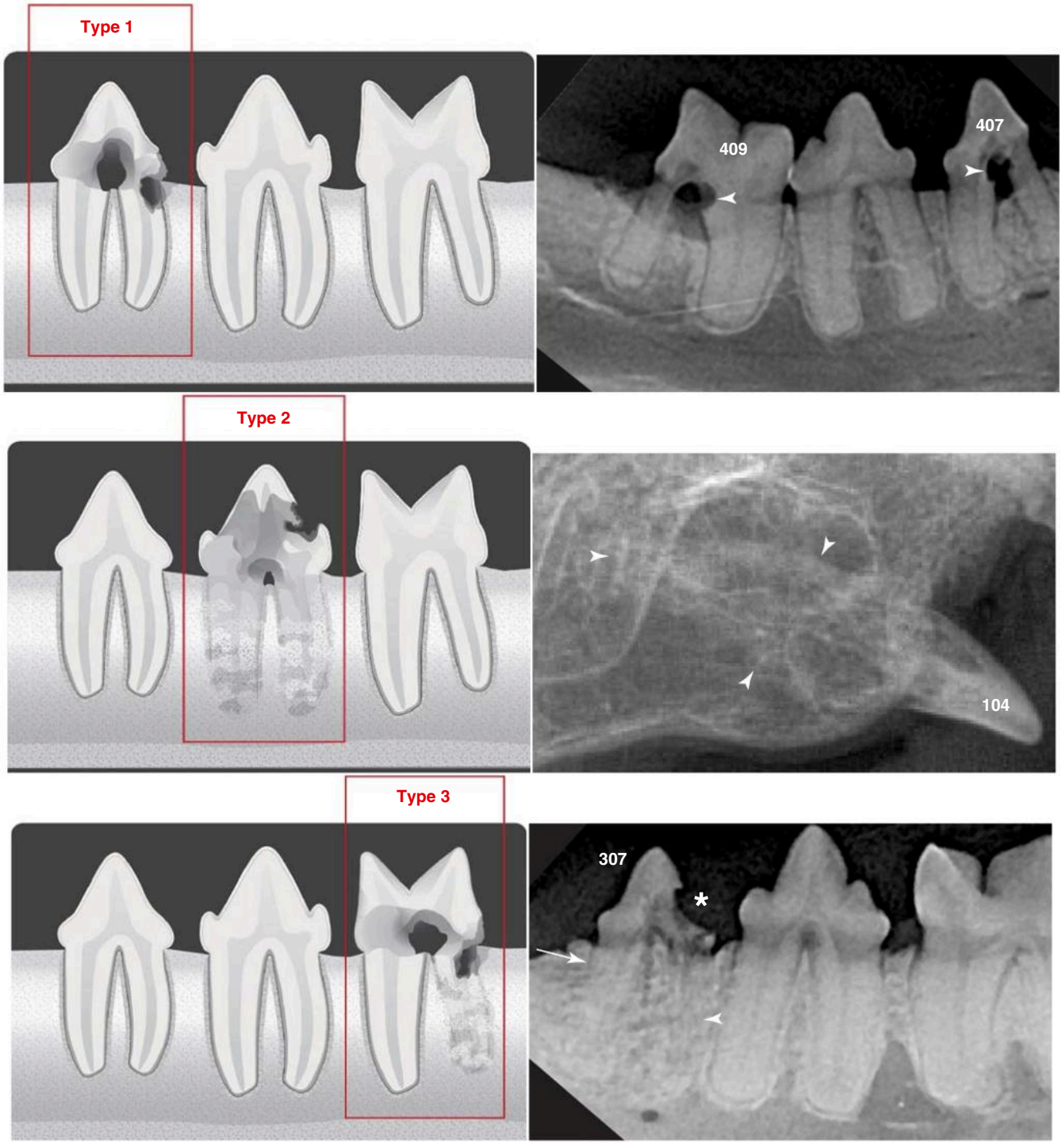


Fig. 10.23 Type resorption according to the radiographic appearance. *Type 1,* Focal or multifocal radiolucent lesions affect the tooth. The radiograph shows normal appearance of the periodontal ligament space and radiopacity of the tooth (*arrowheads*). *Type 2,* Absence of the periodontal ligament with replacement of the root structure by bone (*arrowheads*). *Type 3,* Radiographic features of type 1 and 2 are displayed in the same tooth. Focal or multifocal resorptive lesions may be observed (*asterisk*), with roots presenting intact or reduced periodontal ligament space (*arrow*) and areas of tooth root replacement by bone (*arrowhead*). (©AVDC®, Used with permission.)

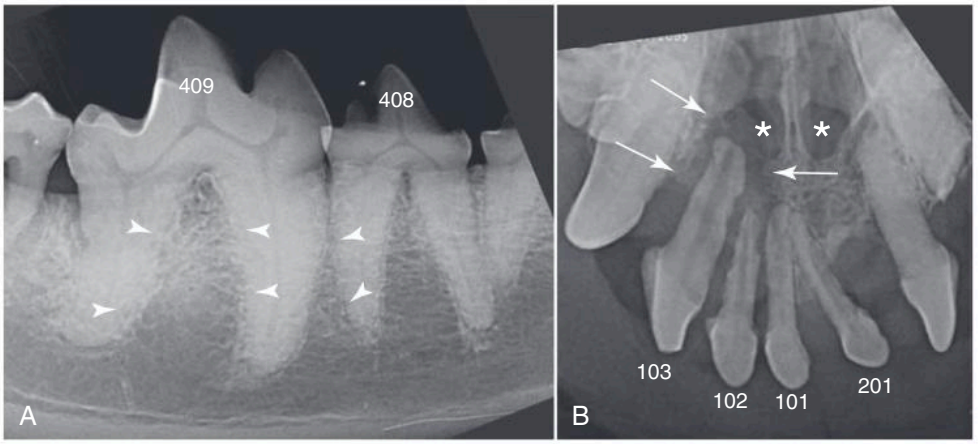


Fig. 10.24 Dental radiographs taken in dogs with **(A)** external replacement and **(B)** external inflammatory tooth resorption. **A,** The absence of periodontal ligament space, loss of dentin, and sclerosis of the adjacent alveolar bone indicate dentoalveolar ankylosis (*arrowheads*). **B,** Inflammatory tooth resorption of the maxillary incisors associated with nonneoplastic periapical lysis (*arrows*). Note the pulp cavity asymmetry of the maxillary incisors indicating pulp necrosis. Palatine fissures (*asterisks*).

DENTOALVEOLAR TRAUMA

Injury of the tooth and the supporting structures in dogs and cats is common. Dentoalveolar trauma has been associated with road traffic accidents, fighting, high-rise falls, and chewing on hard objects or toys.[60,61] Typical clinical findings are loss of dental structures with or without pulp cavity exposure, dental instability, soft tissue laceration (oral or palatal mucosa and gingiva), mandibular or maxillary instability with subsequent dental malocclusion, oral bleeding, ptyalism, and pain. Depending on the severity of the trauma, other maxillofacial structures may be involved (e.g., mandible, temporomandibular joint, maxilla, nasal cavities).[62]

Dental fractures are classified as uncomplicated if the pulp cavity is not exposed to the oral cavity environment or complicated if the pulp cavity is exposed. Depending on the tooth area affected by the trauma, the fractures may be classified as crown, crown-root, or root fractures. In 621 dogs and cats, the most common traumatic dental injury was a complicated crown fracture affecting the mandibular or maxillary canine teeth in young adult dogs and cats. Other trauma-related dentoalveolar disorders are dental concussion, subluxation, luxation, avulsion, and alveolar fracture (Fig. 10.25).[61]

Advanced diagnostic imaging techniques such as CBCT, CT, and MRI are considered the gold standard for assessing maxillofacial trauma. Nevertheless, these diagnostic imaging techniques may have limited availability (Fig. 10.26).[3,63,64] Radiographic assessment of the injured tooth and supporting structures may be made with skull and dental radiography. The latter is preferred for displaying less superimposition of the mineralized structures and better detail of the dentoalveolar complex (Fig. 10.27). The initial evaluation and follow-up of a patient suffering from dentoalveolar trauma must include intraoral dental radiography.

Dental radiography aids in determining the extent of the anatomical damage and the presence of other disorders that may be associated with the current pathology, for example, in a mandibular fracture as a consequence of severe periodontitis or a neoplastic process (Fig. 10.28).[65]

Due to the bidimensional nature of intraoral radiography, more than one radiographic view may be necessary to identify a dentoalveolar fracture. Radiographic characteristics attributed to tooth and alveolar injury may include[66]:

- Alteration of the typical anatomy outline or shape of the tooth
- Tooth displacement from the alveolus socket
- Increase of the radiolucent area of the periodontal ligament
- Loss of continuity of cortical bone
- Change of the alveolar bone shape
- Loss of dental or bone structure

NEOPLASTIC DISORDERS

Benign and malignant neoplasms affect the maxillofacial soft tissues and bones of dogs and cats with an overall incidence of 0.5%. In a retrospective study on dogs and cats, malignant neoplasms accounted for the most common presentation of oral tumors in both species, with a prevalence of 53.6% and 58.1%, respectively. In contrast, benign tumors associated with the dentoalveolar tissues were less frequent, particularly in cats, where incidence ranged between 2.5% and 7.8%.[67,68]

Benign dentoalveolar odontogenic tumors associated with the tooth germ and the periodontium (gingiva, periodontal ligament, cementum, and alveolar bone) are characterized by their slow growth rate and low potential for metastases. Among the most common odontogenic tumors in dogs are the peripheral odontogenic fibroma (POF), previously known as fibromatous and calcifying epulides, and the canine acanthomatous ameloblastoma (CAA), formerly known as acanthomatous epulides. Use of the term *epulis* is discouraged since it is a nonspecific clinical descriptive term associated with any gingival or oral mucosa growth.[25,69] In cats, POF is the most common odontogenic tumor, with a prevalence of 7.8%.[68,70] Although other odontogenic neoplasms, such as the feline inductive odontogenic tumor, cementoblastoma, and odontoma, have been reported in cats, their prevalence is very low.[71–73]

Maxillofacial malignant tumors can appear as a swelling or an ulcerative lesion on the oral mucosa or lip skin that does not heal over time as a regular wound. Malignant neoplasms can be locally aggressive, invade surrounding anatomical structures, and spread to other organs such as lymph nodes and the lungs.

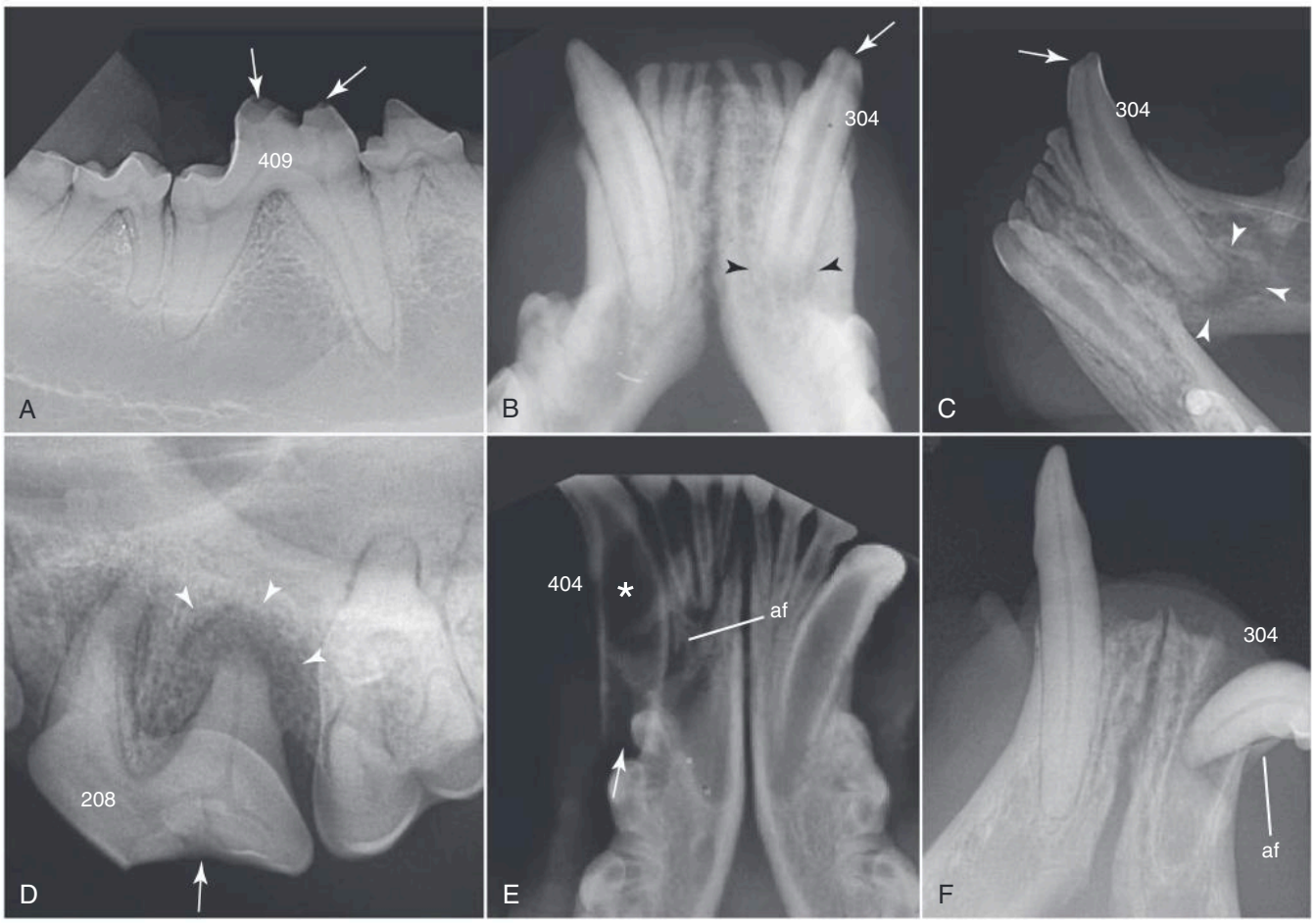


Fig. 10.25 Dental radiographs of different canine and feline patients showing dentoalveolar trauma. **A,** Right mandibular first molar tooth (*409*) with an uncomplicated crown fracture (*arrow*). The loss of enamel and dentin does not extend into the pulp cavity. **B,** Adult cat affected with a complicated crown fracture (*arrow*). Note the resorption of the apex (*arrowheads*). **C,** Complicated crown fracture of the left mandibular canine tooth (*304*) in an adult cat (*arrow*) and periapical lucency (*arrowheads*). **D,** Complicated crown fracture of the left maxillary fourth premolar tooth (*208*) in a dog (*arrow*) and periapical lucency with inflammatory resorption of the apex (*arrowheads*). **E,** Lateral luxation of the right mandibular canine tooth (*404*) in an 8-month-old dog. Note the wide pulp cavity and open apex. **F,** Lateral tooth luxation of the left mandibular canine tooth in an adult cat. *af,* Alveolar bone fracture.

Identifying the type of neoplasia utilizing incisional or excisional biopsy and cancer staging through diagnostic imaging is important for establishing the possible treatment and prognosis. The most common malignant tumor in the dog is malignant melanoma, with an incidence ranging between 27% and 45%, followed by squamous cell carcinoma and fibrosarcoma. In the cat, the most common malignant neoplasm is squamous cell carcinoma, followed by fibrosarcoma.[68,74,75]

Although CT and MRI are the gold-standard diagnostic imaging techniques for assessing maxillofacial neoplastic conditions and cancer staging, veterinary practitioners still widely use intraoral radiography during the initial approach.[76,77] Intraoral radiography may help differentiate between benign and malignant conditions; however, this assumption may be problematic since both tumors may share similar radiographic features.

Benign odontogenic tumors are typically slow-growing disorders characterized by (Fig. 10.29, eFigs. 10.12–10.15)[78]:

- Well-defined smooth borders
- Mild periosteal reaction with cortical bone reaction
- Homogeneous radiopaque, radiolucent, or mixed intratumoral composition
- Possible mass effect with the displacement of adjacent anatomical structures, including the teeth

Odontogenic tumors such as the CAA have also been characterized as being locally aggressive, presenting lytic and proliferative multilocular radiographic patterns.[79]

In contrast, malignant intraoral neoplasms are radiographically characterized by (Fig. 10.30)[80,81]

- Ill-defined borders
- Exuberant proliferative, lytic, or mixed appearance
- Geographic, moth-eaten, or permeative radiolucent areas resulting from bone destruction
- Destruction of the periodontal structures can lead to tooth loss

In addition to diagnostic imaging for evaluation of tumor extension and possible metastasis, incisional biopsy is needed for diagnosing neoplasia since radiographic patterns resembling a neoplastic process may be present in nonneoplastic disorders such as osteonecrosis and osteomyelitis (Fig. 10.31, eFig. 10.16). In cats, about 45% of mandibular lesions resembling an aggressive neoplastic condition were confirmed as osteomyelitis associated with periodontitis or endodontic disease.



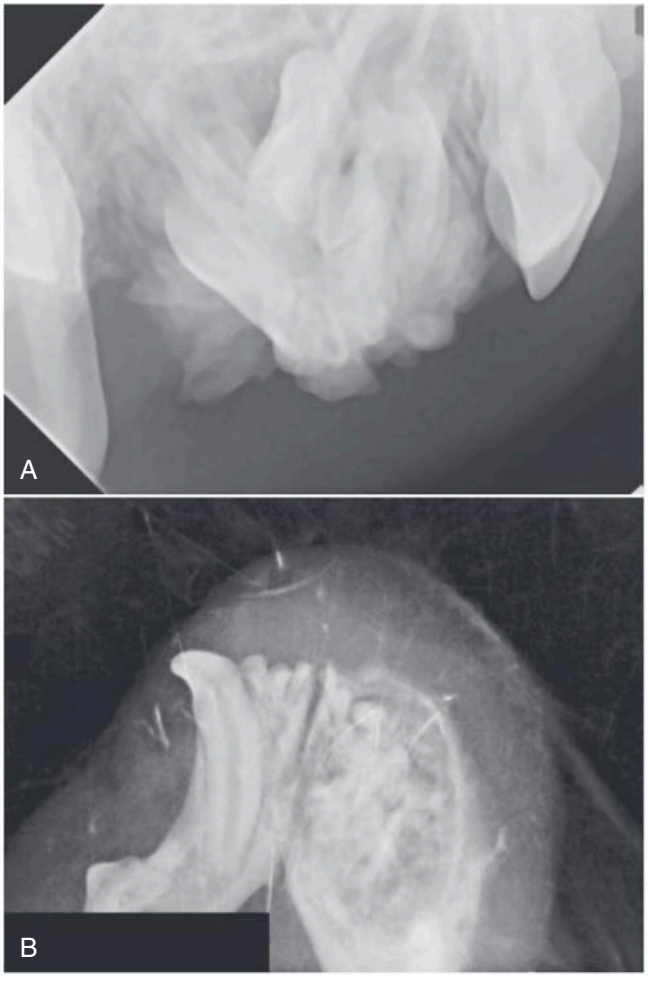
eFig. 10.12 Central (intraosseous) ameloblastoma. (Reproduced with permission from Verstraete FJM. Self-assessment Color Review of Veterinary Dentistry. Ames: Iowa State University Press; 1999.)



eFig. 10.13 Canine acanthomatous ameloblastoma. There is a soft tissue opaque mass with geographic osteolysis in the right rostral mandible. Notice deviation rather than destruction of the dental structures. (Courtesy Animal Dental Center, Towson, MD.)



eFig. 10.14 Peripheral odontogenic fibroma with osseous production adjacent to the right lower canine. (Reproduced with permission from Verstraete FJM. Oral and Maxillofacial Surgery in Dogs and Cats. St Louis: Saunders/Elsevier; 2012.)



eFig. 10.15 **A,** Complex odontoma of the right maxillary fourth premolar in a dog. **B,** Complex odontoma of the left rostral mandible in a feline.



eFig. 10.16 Osteomyelitis secondary to periodontitis in the cat. The rostral mandibles are characterized by a generalized mottled appearance caused by areas of bone destruction. Periosteal proliferation and periapical lucencies at the canine teeth are also present. (Courtesy Animal Dental Center, Towson, MD.)

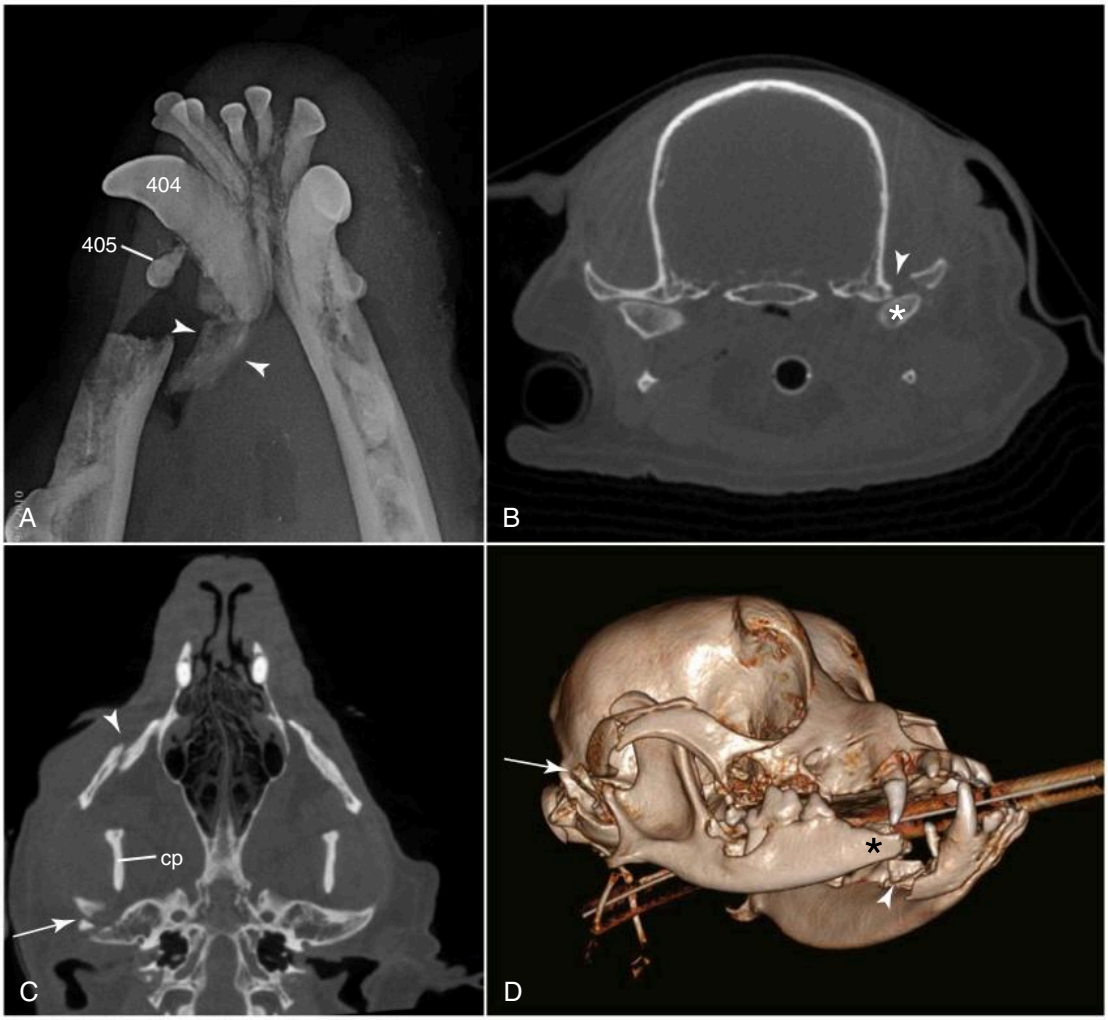


Fig. 10.26 Dental radiograph **(A),** multiplanar cone-beam CT (CBCT) transverse **(B)** and dorsal **(C)** reconstructions, and three-dimensional (3D) rendering **(D)** of a 12-year-old mix-breed dog suffering from maxillofacial trauma. **A,** Right mandibular fracture at the level of the first and second premolar teeth. Note the bone fragment (*arrowheads*) and luxated *405* tooth. **B,** Transverse reconstruction showing a fracture of the left mandibular fossa of the temporal bone (*arrowhead*) and dorso-oblique dislocation of the articular head of the condylar process (*asterisk*). **C,** Dorsal reconstruction showing right maxillary and temporomandibular fractures (*arrowhead and arrow*). *cp,* Coronoid process of the ramus of the mandible. **D,** 3D rendering showing the mandibular fracture (*asterisk*), bone fragment (*arrow*), and right temporomandibular fracture (*arrow*). Advanced diagnostic imaging techniques like CBCT are considered the gold standard for assessing maxillofacial trauma in veterinary patients.

DEVELOPMENTAL ABNORMALITIES OF THE TEETH

Disturbances associated with the number of teeth and roots, the shape of the crown and the root, and malformation of the dental components such as enamel and dentin can have a potential hereditary or congenital origin. Diagnostic imaging of these dental disorders is paramount to determine if surgical intervention is required or, in contrast, monitoring is adequate (Fig. 10.32).

Malocclusion, supernumerary teeth, nonerupted or developmental absence of teeth, and persistent deciduous dentition may have a hereditary origin due to their prevalence in specific breeds of dogs. For example, Yorkshire terriers and Maltese are commonly affected by persistent deciduous dentition, leading to dental malocclusion and severe periodontitis in puppies or young adult dogs.[82] Other dental abnormalities overrepresented in small-breed dogs are root dilaceration and malformation of the mandibular first molar or dens invaginatus. If underestimated or not identified in dental radiography during the first years of the patient's life, an abnormality such as dens invaginatus can result in severe endodontic and periodontic pathoses (Fig. 10.33).[83]

The absence of teeth during physical examination in dogs and cats should be elucidated using dental radiography. The owner must be questioned to establish if the dental structure was previously present or extracted due to dental or periodontal disease. If the dental structure was never clinically present, it is necessary to determine if it remains under the gum as an unerupted tooth.

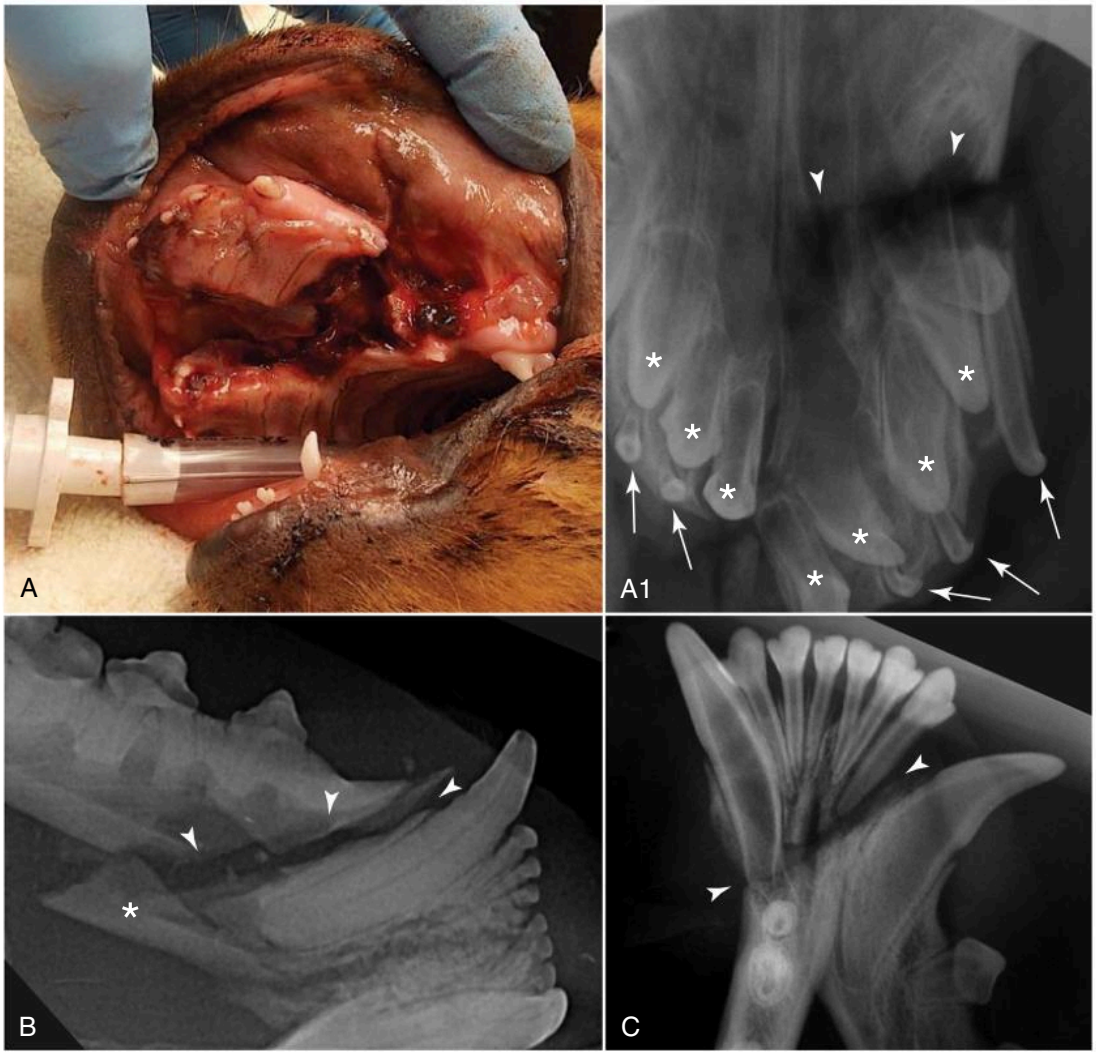


Fig. 10.27 Clinical photograph **(A)** and occlusal dental radiograph **(A1)** of the maxillary region of a 10-week-old Golden Retriever puppy suffering from a dog bite. **A,** Maxillary fracture with palatine, gum, and oral mucosa laceration. Note the nasal cavity exposure. **A1,** The fracture line (*arrowheads*) affects most of the unerupted permanent incisor and canine teeth (*asterisks*). Deciduous dentition (*arrows*). **B,** Comminuted fracture at the distal aspect of the right mandibular canine tooth in an adult cat (*arrowheads*). Bone fragment (*asterisk*). **(C)** Oblique fracture at the rostral aspect of the mandible of a 10-month-old Labrador bulldog. Note the fracture line affecting the apical region of the left mandibular third incisor and the right mandibular canine tooth.

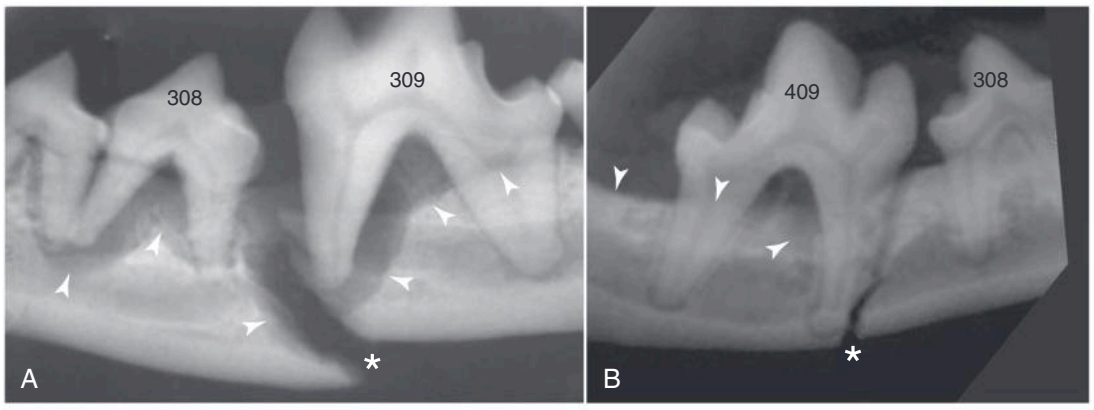


Fig. 10.28 **A and B,** Radiographs of pathologic mandibular fractures (*asterisks*) at the level of the first molar tooth in two different dogs. Note the severe horizontal and vertical bone loss in both patients (*arrowheads*).

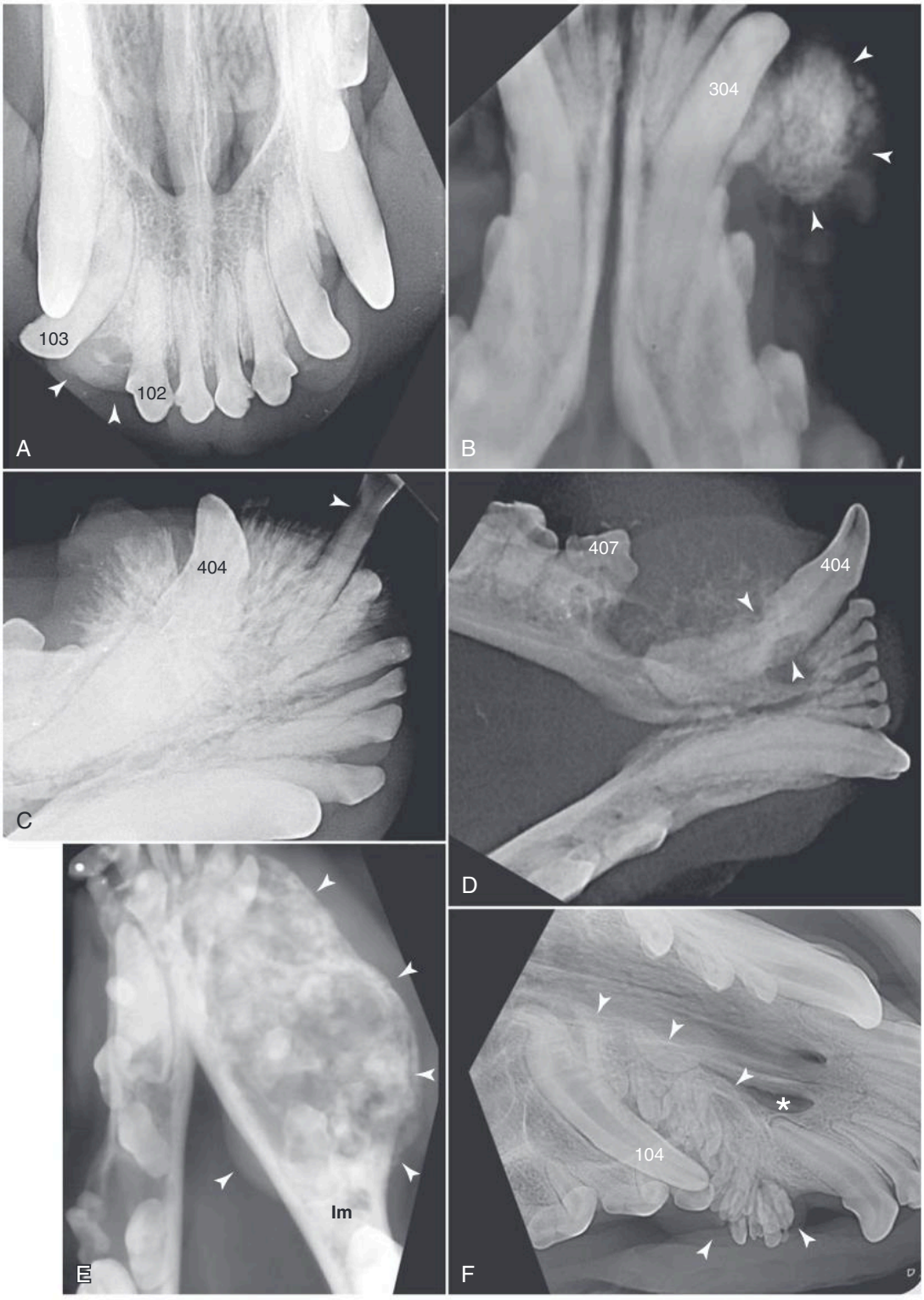


Fig. 10.29 Dental radiographs of different patients affected by benign odontogenic neoplastic processes. **A,** Peripheral odontogenic fibroma in the rostral upper jaw between the incisor teeth *102* and *103* in a 6-year-old dog. Note the soft tissue opacification from the mass and moderate alveolar bone lysis (*arrowheads*). The mass effect displaces the third maxillary incisor (*103*) and increases the interdental space. **B,** Peripheral odontogenic fibroma at the buccal aspect of the left mandibular canine tooth (*304*) in a 5-year-old dog. Note the alveolar bone proliferation and mineralization of the mass (*arrowheads*). **C,** Canine acanthomatous ameloblastoma at the rostral aspect of the right mandible of a 3-year-old Doberman Pinscher dog. Note the spiculated radiographic pattern and the tooth displacement of the third incisor tooth (*arrowhead*). **D,** Amyloid-producing tumor in a 4-year domestic short-hair cat. Note the mass soft tissue opacification, lysis, moderate periosteal reaction, and tooth resorption (*arrowheads*). **E,** Complex odontoma of the left mandible of a dog. A heterogeneous radiographic pattern with radiopaque amorphous dental tissue composition (*arrowheads*). **F,** Compound odontoma of the right maxilla in a dog. Multiple tooth-like structures, called denticles, resemble normal teeth but are disorganized and irregularly shaped (*arrowheads*). Note the malformed apex of the unerupted canine tooth *104*. Palatine fissure (*asterisk*). (**A, C–F,** Courtesy Lenin A. Villamizar. **B,** Courtesy Arizona Veterinary Dental Specialist.)

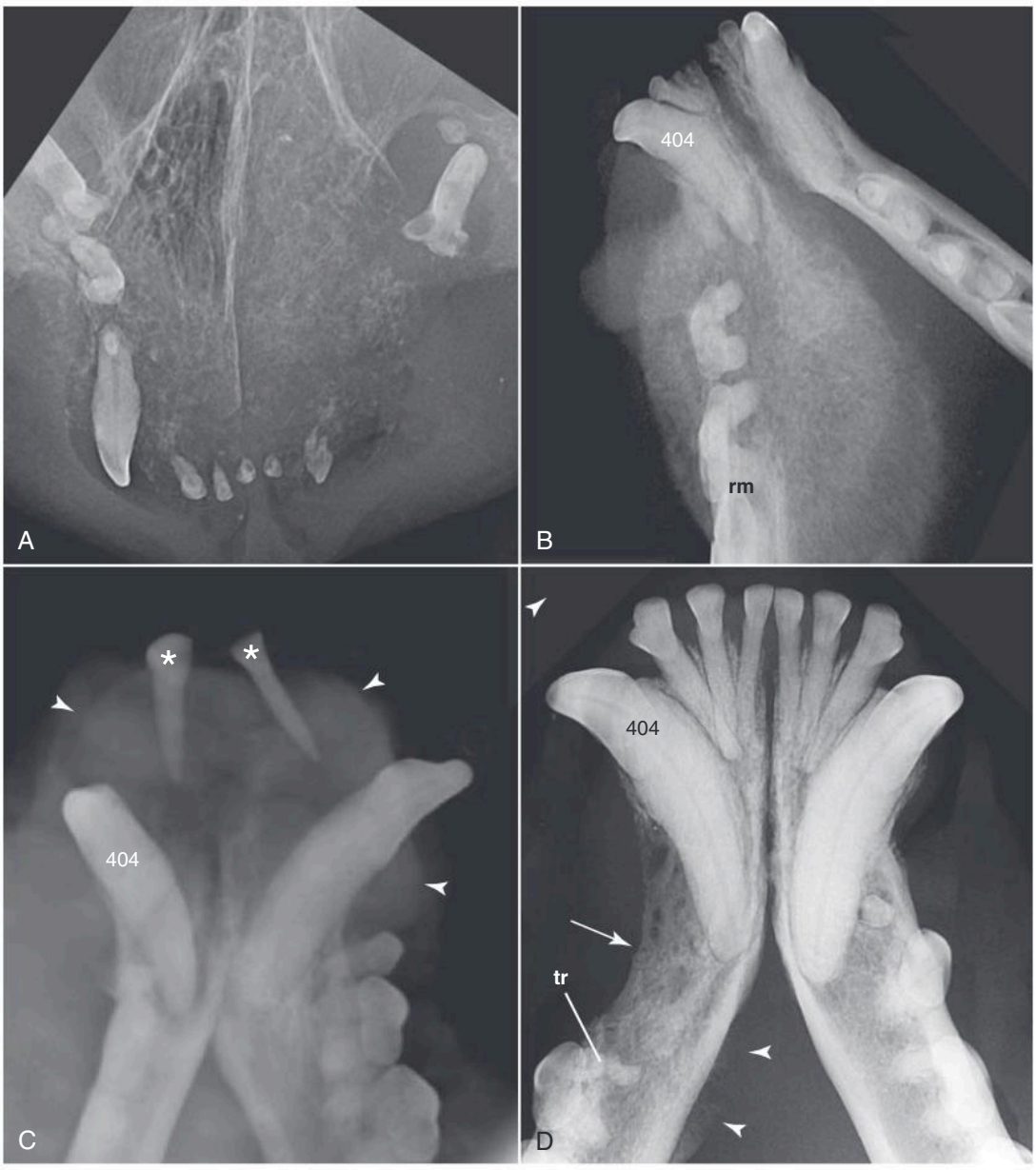


Fig. 10.30 Dental radiographs of different patients affected by malignant neoplastic tumors. **A,** Squamous cell carcinoma causing extensive lysis of the maxilla of a 12-year-old cat. **B,** Squamous cell carcinoma of the right mandible (*rm*) of an adult cat. Note the heterogeneous radiographic pattern, lytic and proliferative caudal to *404*. **C,** Malignant melanoma at the rostral region of the mandible of a 13-year-old dog (*arrowheads*). Observe the extensive bone loss with remnant incisor teeth floating in the soft tissue (*asterisks*). Several incisor teeth are missing as well. **D,** Squamous cell carcinoma in an adult dog at the distal aspect of *404*. Note the moth-eaten appearance of the affected mandible (*arrow*) with mandibular periosteal reaction (*arrowheads*) and tooth resorption (*tr*). (Courtesy Lenin A. Villamizar.)

Unerupted teeth are highly associated with dentigerous cyst formation, which may produce destruction of the surrounding mandibular or maxillary bone.[84] The mandibular first premolar tooth in brachycephalic dog breeds is the most common unerupted tooth. Also, the most common problem associated with unerupted teeth is the dentigerous cyst, with a prevalence of 71.4%.[85] Due to the expansive nature of the dentigerous cyst, intraoral dental radiography may underestimate the extension of the lesion into the mandibular bone or nasal cavity if the maxillary bone is affected. For an accurate assessment of this type of lesion, advanced diagnostic techniques such as CT and CBCT may be required (Fig. 10.34, eFig. 10.17).



eFig. 10.17 Dentigerous cyst at right rostral mandible.

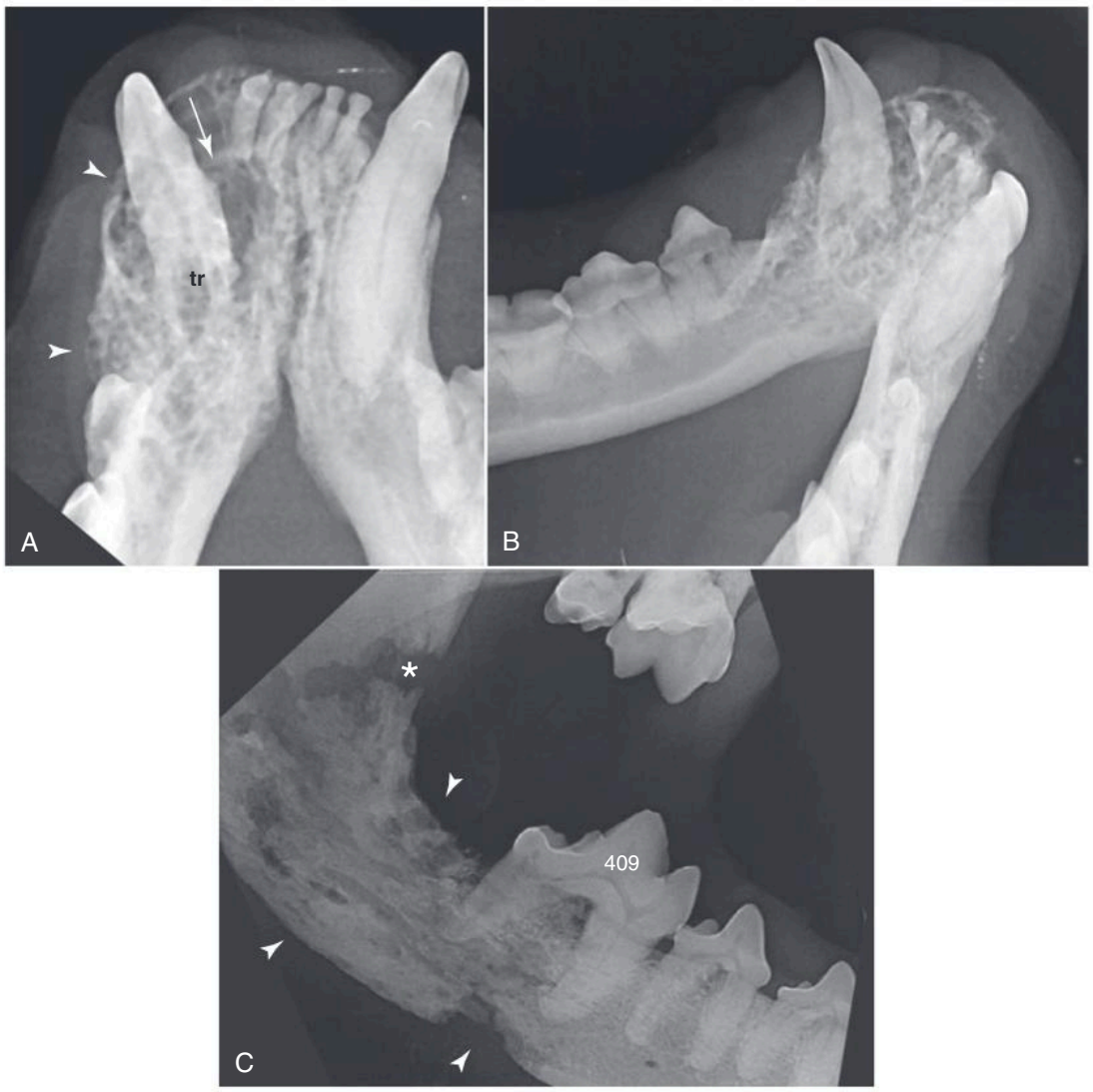


Fig. 10.31 Radiographs of a cat **(A, B)** and a dog **(C)** affected by osteomyelitis. **A, B**, Severe vertical bone loss (*arrows*), bone proliferation (*arrowheads*), and tooth resorption. **C,** Permeative bone destruction (*arrowheads*) of the caudal region of the right mandibular body. A pathological fracture is observed at the angle of the mandible (*asterisk*). *tr,* Tooth resorption.

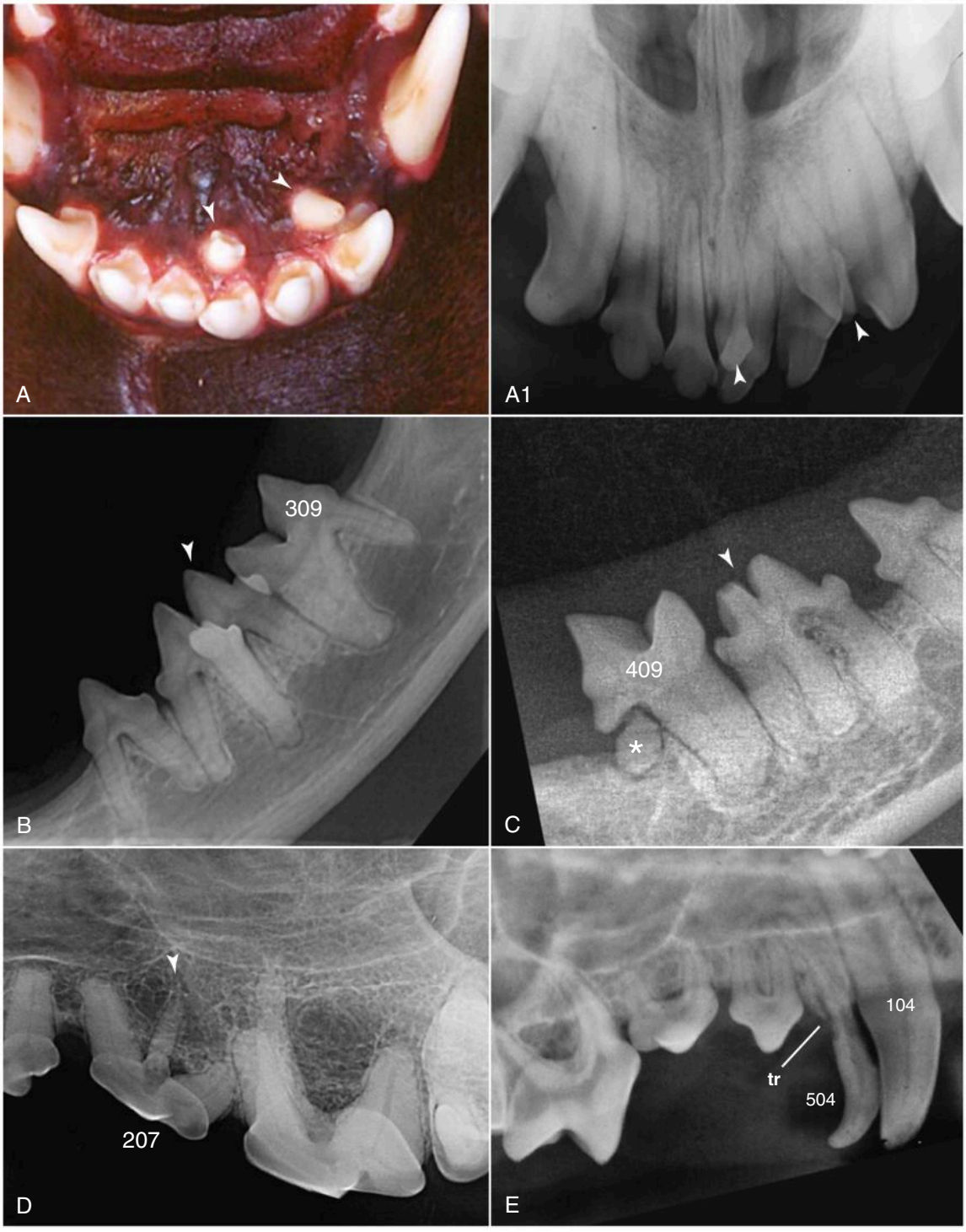


Fig. 10.32 **A, A1,** Clinical photograph and radiograph of a mature dog with supernumerary incisor teeth (*arrowheads*). **B,** Supernumerary premolar tooth in a cat (*arrowhead*). **C,** Gemination and supernumerary root of the right fourth premolar in a cat (*arrowhead*). Root resorption of *409* (*asterisk*). **D,** Supernumerary root of *207* in a mature dog (*arrowhead*). **E,** Right maxillary persistent deciduous tooth in an adult dog (*504*). Note the partial resorption process at the alveolar margin line (*tr*). (**A, A1** Courtesy Dr. Peter P. Emily.)

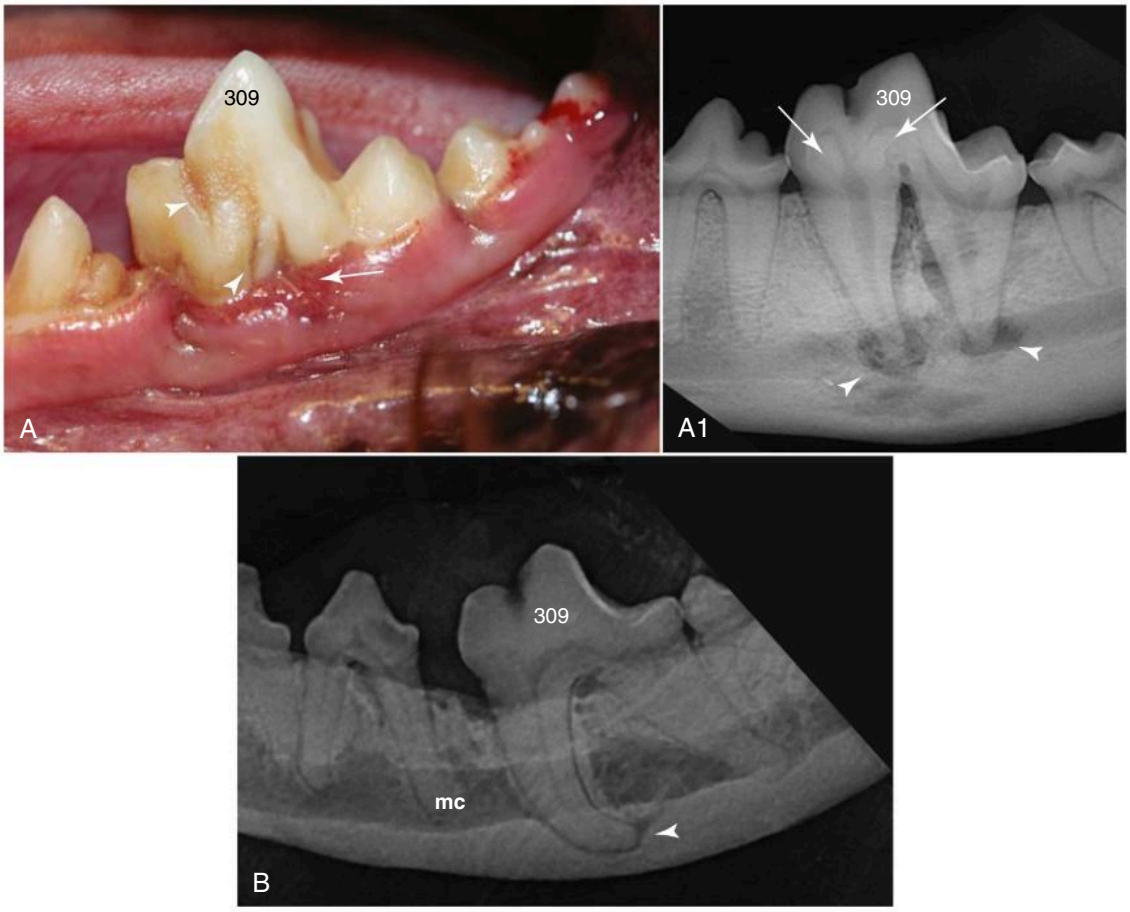


Fig. 10.33 **A, A1,** Clinical photograph and radiograph of dens-in-dente in a Maltese dog (*309*). **A,** Observe the crown malformation (*arrowheads*) and severe gingivitis of *309* (*arrow*). **A1,** Convergent roots of *309*, severe periodontitis, and periapical lucencies (*arrowheads*). Note the radiopaque material at the pulp chamber, resembling a tooth within a tooth (*arrows*). **B,** Dilaceration of the mesial root of *309* (*arrowhead*) in a Chihuahua dog. The dilacerated root extends into the mandible's ventral cortex, overlapping with the mandibular canal (*mc*).



Fig. 10.34 **A, A1,** Clinical photograph and radiograph showing a dentigerous cyst lesion in an adult Boxer dog. **A,** Missing left mandibular first premolar tooth and fluctuant swelling at the adjacent oral mucosa (*asterisk*). **A1,** Nonerupted partially reabsorbed *305* (*arrow*) and locular radiolucent lesion with the presence of a well-defined cortical boundary (*arrowheads*). Note the root resorption of *303* and the bone loss at the mesial root of *307*. **(B, B1)** Extraoral and intraoral clinical photographs, **(B2)** dental radiograph, and **(B3)** three-dimensional (3D) rendering from a cone-beam CT (CBCT) examination in an adult dog affected by a nonerupted canine tooth. **B,** Swelling at the maxillary region (*arrowheads*). **B1,** Missing *204*. **B2,** Nonerupted *204* (*asterisk*) located in the nasal cavity at the level of the second maxillary premolar tooth. **B3,** 3D rendering showing the bone destruction at the maxillary bone (*arrowheads*). (Reproduced with permission from Lenin A. Villamizar.)

Acknowledgment

With special thanks to prior authors of this chapter for their contributions.

REFERENCES

1. Thatcher G. Performing dental procedures in dogs and cats without dental radiographs: malpractice? *Can Vet J*. 2020;61(2):197–200. (Accessed November 8, 2022). /pmc/articles/PMC6973222/.
2. Verstraete FJM, Kass PH, Terpak CH. Diagnostic value of full-mouth radiography in dogs. *Am J Vet Res*. 1998;59(6):686–691. (Accessed August 20, 2020). https://pubmed.ncbi.nlm.nih.gov/9622735/.
3. Heney CM, Arzi B, Kass PH, Hatcher DC, Verstraete FJM. Diagnostic yield of dental radiography and cone-beam computed tomography for the identification of anatomic structures in cats. *Front Vet Sci*. 2019;6(FEB):58. https://doi.org/10.3389/fvets.2019.00058.
4. Roza MR, Silva LAF, Barriviera M, Januário AL, Bezerra ACB, Fioravanti MCS. Cone beam computed tomography and intraoral radiography for diagnosis of dental abnormalities in dogs and cats. *J Vet Sci*. 2011;12(4):387–392. https://doi.org/10.4142/jvs.2011.12.4.387.
5. Villamizar-Martinez LA, Villegas CM, Duailibi E, et al. Morphometry and morphology of the articular surfaces of the medial region of the temporomandibular joint in the Felis catus (domestic cat) - a cone beam computed tomography study. *J Vet Dent*. 2023;40(2):134–142. https://doi.org/10.1177/08987564221141985. In press.
6. Macready DM, Hecht S, Craig LE, Conklin GA. Magnetic resonance imaging features of the temporomandibular joint in normal dogs. *Vet Radiol Ultrasound*. 2010;51(4):436–440. https://doi.org/10.1111/j.1740-8261.2010.01680.x.
7. Villamizar-Martinez LA, Tsugawa AJ. Diagnostic imaging of oral and maxillofacial anatomy and pathology. *Vet Clin North Am – Small Anim Pract*. 2022;52(1):67–105. https://doi.org/10.1016/j.cvsm.2021.08.003.
8. Coffman CR, Brigden GM. Oral and dental imaging equipment and techniques for small animals. *Vet Clin North Am – Small Anim Pract*. 2013;43(3):489–506. https://doi.org/10.1016/j.cvsm.2013.02.007.
9. Lee H, Badal A. A review of doses for dental imaging in 2010–2020 and development of a web dose calculator. *Radiol Res Pract*. 2021;2021:1–18. https://doi.org/10.1155/2021/6924314.
10. National Council on Radiation Protection and Measurements. In: O'Brien C, ed. *NCRP Report No. 177 - Radiation Protection in Dentistry and Oral Maxillofacial Imaging: Recommendations of the National Council on Radiation Protection and Measurements*. Bethesda, MD: NCRP 2020; 2019:18–26. (Accessed November 8, 2022). https://ncrponline.org/shop/reports/report-no-177/.
11. ARIBEX. *Aribex Nomad Pro2 X Ray Operator Manual*. Aribex; Published online 2020:9–12. (Accessed April 25, 2024.) https://archive.org/details/manual_Aribex_Nomad_Pro2_X-Ray_Operator_Manual/page/12/mode/2up.
12. Harvey CE, Emily PP. Oral examination and diagnostic techniques. In: *Small Animal Dentistry*. Mosby-Year Book, Inc.; 1993:29–41.
13. Dental radiology. In: Holmstrom SE, Fitch PF, Eisner ER, eds. *Veterinary Dental Techniques for the Small Animal Practitioner*. 3rd ed. Saunders, Elsevier; 2004:131–174.
14. Villamizar-Martinez LA, Villegas CM, Gioso MA, et al. Radiographic assessment of the feline temporomandibular joint with oblique projections: a preliminary ex vivo study. *J Vet Dent*. 2021;38(4):199–207. https://doi.org/10.1177/08987564211066571.
15. Hammond G, King A, Lapaglia J. Assessment of five oblique radiographic projections of the canine temporomandibular joint. *Vet Radiol Ultrasound*. 2012;53(5):501–506. https://doi.org/10.1111/j.1740-8261.2012.01956.x.
16. Schwarz T, Weller R, Dickie AM, Konar M, Sullivan M. Imaging of the canine and feline temporomandibular joint: a review. *Vet Radiol Ultrasound*. 2002;43(2):85–97. https://doi.org/10.1111/J.1740-8261.2002.TB01656.X.
17. Niemiec BA. Digital dental radiography. *J Vet Dent*. 2007;24(3):192–197. https://doi.org/10.1177/089875640702400311.
18. Villamizar LA, Burgese L, Carvalho VG, Brandão AC, Gioso MA. Uso da radiografia digital na odontologiaveterinária. *Rev Cient Med*. 2010;8(26):447–452. Accessed November 8, 2022 https://pesquisa.bvsalud.org/portal/resource/pt/vti-1578.
19. Bedard A, Davis TD, Angelopoulos C. Storage phosphor plates: how durable are they as a digital dental radiographic system? *J Contemp Dent Pract*. 2004;5(2):057–069. https://doi.org/10.5005/jcdp-5-2-57.
20. Verstraete FJM, Kass PH, Terpak CH. Diagnostic value of full-mouth radiography in cats. *Am J Vet Res*. 1998;59(6):692–695.
21. The skeleton. In: Hermanson JW, de LAEHE, eds. *Miller and Evans' Anatomy of the Dog*. 5th ed. Elsevier; 2020:91–125.
22. Wiggs RB, Lobprise HB. Oral anatomy and physiology. In: Wiggs RB, Lobprise HB, eds. *Veterinary Dentistry Principles & Practice*. 1st ed. Lippincott-Raven; 1997:55–85.
23. Hale FA. Juvenile veterinary dentistry. *Vet Clin North Am – Small Anim Pract*. 2005;35(4 Spec. Iss.):789–817. https://doi.org/10.1016/j.cvsm.2005.02.003.
24. Harvey CE, Emily PP. Function, formation, and anatomy of oral structures in carnivores. In: Harvey CE, Emily PP, eds. *Small Animal Dentistry. Mosby-Year Book*. Inc.; 1993:1–18.
25. Nomenclature. *American Veterinary Dental College*. Published; 2022. (Accessed August 11, 2022). https://avdc.org/avdc-nomenclature/.
26. Gracis M, Harvey CE. Radiographic study of the maxillary canine tooth in mesaticephalic dogs. *J Vet Dent*. 1998;15(2):73–78. https://doi.org/10.1177/089875649801500202.
27. Gracis M. Radiographic study of the maxillary canine tooth of four mesaticephalic cats. *J Vet Dent*. 1999;16(3):115–125. https://doi.org/10.1177/089875649901600303.
28. DuPont GA, DeBowes LJ. Introduction. In: DuPont GA, DeBowes LJ, eds. *Atlas of Dental Radiography in Dogs and Cats*. Saunders, Elsevier; 2009:1–4.
29. Farhadi F, Ruhani MR, Zarandi A. Frequency and pattern of idiopathic osteosclerosis and condensing osteitis lesions in panoramic radiography of Iranian patients. *Dent Res J*. 2016;13(4):322–326. https://doi.org/10.4103/1735-3327.187880.
30. Hale FA. Localized intrinsic staining of teeth due to pulpitis and pulp necrosis in dogs. *J Vet Dent*. 2001;18(1):14–20. https://doi.org/10.1177/089875640101800102.
31. Peralta S, Verstraete FJM, Kass PH. Radiographic evaluation of the types of tooth resorption in dogs. *Am J Vet Res*. 2010;71(7):784–793. https://doi.org/10.2460/ajvr.71.7.784.
32. Harvey CE. Periodontal disease in dogs. Etiopathogenesis, prevalence, and significance. *Vet Clin North Am Small Anim Pract*. 1998;28(5):1111–1128. https://doi.org/10.1016/S0195-5616(98)50105-2.

33. Stella JL, Bauer AE, Croney CC. A cross-sectional study to estimate prevalence of periodontal disease in a population of dogs (*Canis familiaris*) in commercial breeding facilities in Indiana and Illinois. *PLoS One*. 2018;13(1):e0191395. https://doi.org/10.1371/journal.pone.0191395.
34. Harvey CE, Laster L, Shofer F, Miller B. Scoring the full extent of periodontal disease in the dog: development of a Total Mouth Periodontal Score (TMPS) system. *J Vet Dent*. 2008;25(3):176–180. https://doi.org/10.1177/089875640802500303.
35. Bell CM, Soukup JW. Histologic, clinical, and radiologic findings of alveolar bone expansion and osteomyelitis of the jaws in cats. *Vet Pathol*. 2015;52(5):910–918. https://doi.org/10.1177/0300985815591079.
36. D'Astous J. Periodontology: an overview of alveolar bone expansion. *Can Vet J*. 2015;56(3):295–299. (Accessed November 8, 2022). https://www.ncbi.nlm.nih.gov/pmc/articles/PMC4327146/pdf/cvj_03_295.pdf.
37. Lewis JR, Okuda A, Shofer FS, Pachtinger G, Harvey CE, Reiter AM. Significant association between tooth extrusion and tooth resorption in domestic cats. *J Vet Dent*. 2008;25(2):86–95. https://doi.org/10.1177/089875640802500209.
38. Kapatkin AS, Marretta SM, Patnaik AK, Burk RLMR. Mandibular swellings in cats: prospective study of 24 cats. *Am Anim Hosp Assoc*. 1991;27(6):575–580. (Accessed November 14, 2022). https://www.webofscience.com/wos/woscc/full-record/WOS:A1991GV01000001?UT=A1991GV01000001&SID=USW2EC0B12VwAUd6D92ToG9ZBLMlF.
39. Arzi B, Fiani N, Pritchard WB. Diagnostic imaging in veterinary dental practice. *J Am Vet Med Assoc*. 2009;235(10):1149–1151. https://doi.org/10.2460/javma.235.10.1149.
40. Fristad I, Berggreen E. Structure and function of the dentin-pulp complex. In: Hargreaves K, Berman LH, eds. *Cohen's Pathways of the Pulp*. 11th ed. Elsevier; 2016:532–572.
41. Ghannam MG, Bordoni B. *Anatomy, Head and Neck, Pulp (Tooth)*. StatPearls Publishing; 2019. Accessed November 14, 2022 https://www.ncbi.nlm.nih.gov/books/NBK537112/.
42. Feigin K, Bell C, Shope B, Henzel S, Snyder C. Analysis and assessment of pulp vitality of 102 intrinsically stained teeth in dogs. *J Vet Dent*. 2022;39(1):21–33. https://doi.org/10.1177/08987564211060387.
43. Menzies RA, Reiter AM, Lewis JR. Assessment of apical periodontitis in dogs and humans: a review. *J Vet Dent*. 2014;31(1):8–21. https://doi.org/10.1177/089875641403100101.
44. Kovačević M, Tamarut T, Jonjić N, Braut A, Kovačević M. The transition from pulpitis to periapical periodontitis in dogs' teeth. *Aust Endod J*. 2008;34(1):12–18. https://doi.org/10.1111/j.1747-4477.2008.00120.x.
45. Tanomaru-Filho M, Jorge EG, Duarte MAH, Gonçalves M, Guerreiro-Tanomaru JM. Comparative radiographic and histological analyses of periapical lesion development. *Oral Surg Oral Med Oral Pathol Oral Radiol Endod*. 2009;107(3):442–447. https://doi.org/10.1016/J.TRIPLEO.2008.12.009.
46. Marmary Y, Kutiner G. A radiographic survey of periapical jawbone lesions. *Oral Surgery, Oral Med Oral Pathol*. 1986;61(4):405–408. https://doi.org/10.1016/0030-4220(86)90427-5.
47. Lee L. Inflammatory lesions of the jaws. In: White SC, Pharoah M, eds. *Oral Radiology Principles and Interpretation*. 6th ed. 2009:325–342.
48. Verstraete FJM, Zin BP, Kass PH, Cox DP, Jordan RC. Clinical signs and histologic findings in dogs with odontogenic cysts: 41 cases (1995-2010). *J Am Vet Med Assoc*. 2011;239(11):1470–1476. https://doi.org/10.2460/javma.239.11.1470.
49. Murphy B, Bell CM, Soukup JW. Odontogenic cysts. In: Murphy B, Bell CM, Soukup JW, eds. *Veterinary Oral and Maxillofacial Pathology*. 1st ed. John Wiley & Sons, Inc.; 2020:207–215.
50. Al-Fouzan KS. A new classification of endodontic-periodontal lesions. *Int J Dent*. 2014;2014:1–5. https://doi.org/10.1155/2014/919173.
51. Kerns DG, Glickman GN. Endodontic and periodontal interrelationships. In: Cohen S, Hargreaves KM, eds. *Pathways of the Pulp*. 9th ed. Mosby Elsevier; 2006:650–667.
52. Hale FA. The chevron sign. Published 2008. Accessed November 9, 2022. http://www.toothvet.ca/PDFfiles/Chevron.pdf.
53. DuPont GA, DeBowes LJ. Intraoral radiographic anatomy of the dog. In: DuPont GA, DeBowes LJ, eds. *Atlas of Dental Radiography in Dogs and Cats*. Saunders, Elsevier; 2009:6–80.
54. Mittal S, Kumar T, Mittal S, Sharma J. "Internal root resorption: an endodontic challenge": a case series. *J Conserv Dent*. 2014;17(6):590–593. https://doi.org/10.4103/0972-0707.144612.
55. Reiter AM, Lyon KF, Nachreiner RF, Shofer FS. Evaluation of calciotropic hormones in cats with odontoclastic resorptive lesions. *Am J Vet Res*. 2005;66(8):1446–1452. https://doi.org/10.2460/AJVR.2005.66.1446.
56. Nemec A, Arzi B, Murphy B, Kass PH, Verstraete FJM. Prevalence and types of tooth resorption in dogs with oral tumors. *Am J Vet Res*. 2012;73(7):1057–1066. https://doi.org/10.2460/ajvr.73.7.1057.
57. Reiter AM, Lewis JR, Okuda A. Update on the etiology of tooth resorption in domestic cats. *Vet Clin North Am – Small Anim Pract*. 2005;35(4 Spec. Iss.):913–942. https://doi.org/10.1016/j.cvsm.2005.03.006.
58. Vapalahti K, Neittaanmäki H, Lohi H, Virtala A-M. Feline tooth resorption findings from a questionnaire survey on 8115 Finnish cats and a case-control study for a more defined population drawn from the survey. Published online *bioRxiv*. July 14, 2021. https://doi.org/10.1101/2021.01.22.427753, 2021.01.22.427753.
59. Önem E, Baksi BG, Şen BH, Söğüt Ö, Mert A. Diagnostic accuracy of proximal enamel subsurface demineralization and its relationship with calcium loss and lesion depth. *Dentomaxillofac Radiol*. 2012;41(4):285–293. https://doi.org/10.1259/dmfr/55879293.
60. Soltero-Rivera M, Elliott MI, Hast MW, et al. Fracture limits of maxillary fourth premolar teeth in domestic dogs under applied forces. *Front Vet Sci*. 2019;5(JAN):339. https://doi.org/10.3389/fvets.2018.00339.
61. Soukup JW, Hetzel S, Paul A. Classification and epidemiology of traumatic dentoalveolar injuries in dogs and cats: 959 injuries in 660 patient visits (2004–2012). *J Vet Dent*. 2015;32(1):6–14. https://doi.org/10.1177/089875641503200101.
62. Lopes FM, Gioso MA, Ferro DG, Leon-Roman MA, Venturini MAFA, Correa HL. Oral fractures in dogs of Brazil – a retrospective study. *J Vet Dent*. 2005;22(2):86–90. https://doi.org/10.1177/089875640502200202.
63. Lee S, Lee K, Kim H, et al. Comparison of dental radiography and computed tomography: measurement of dentoalveolar structures in healthy, small-sized dogs and cats. *J Vet Sci*. 2020;21(5):e75. https://doi.org/10.4142/JVS.2020.21.E75.
64. Chia H, Taney K, Hoover D, Robertson JB, Villamizar-Martinez LA. Localization of the first mandibular molar roots in relationship to the mandibular canal in small breed dogs—a tomography imaging study. *Front Vet Sci*. 2021;8:684763. https://doi.org/10.3389/fvets.2021.684763.
65. Carvalho CM, Rahal SC, Dos Reis Mesquita L, Castilho MS, Kano WT, Mamprim MJ. Mandibulectomy for treatment of

fractures associated with severe periodontal disease. *Can Vet J*. 2015;56(3):292–294. (Accessed November 15, 2022). /pmc/articles/PMC4327145/.
66. Lam EWN. Trauma to teeth and facial structures. In: White, SC.; Pharoah M, ed. Oral Radiology Principles and Interpretation. 6th ed. Mosby Elsevier: 541-561.
67. Cray M, Selmic LE, Ruple A. Demographics of dogs and cats with oral tumors presenting to teaching hospitals: 1996–2017. *J Vet Sci*. 2020;21(5):1–7. https://doi.org/10.4142/jvs.2020.21.e70.
68. Stebbins KE, Morse CC, Goldschmidt MH. Feline oral neoplasia: a ten-year survey. *Vet Pathol*. 1989;26:121–128.
69. Murphy B, Bell CM, Soukup JW. Tumor-like proliferative lesions of the oral mucosa and jaws. In: Murphy B, Bell CM, Soukup JW, eds. *Veterinary Oral and Maxillofacial Pathology*. 1st ed. John Wiley & Sons, Inc.; 2020:185–193.
70. Velázquez-Urgel I, Sánchez MD, Buelow ME, Villamizar-Martinez LA, Reiter AM. Maxillary and mandibular peripheral odontogenic fibromas (fibromatous epulides of periodontal ligament origin) in a cat. *J Vet Dent*. 2018;35(4):251–257. https://doi.org/10.1177/0898756418812100.
71. Villamizar-Martinez LA, Reiter AM, Sánchez MD, Soltero-Rivera MM. Benign cementoblastoma (true cementoma) in a cat. *J Feline Med Surg Open Reports*. 2016;2(1):1–6. https://doi.org/10.1177/2055116915626847.
72. Gardner DG, Dubielzig RR. Feline inductive odontogenic tumor (inductive fibroameloblastoma) – a tumor unique to cats. *J Oral Pathol Med*. 1995;24(4):185–190. https://doi.org/10.1111/j.1600-0714.1995.tb01163.x.
73. Walsh KM, Denholm LJ, Cooper BJ. Epithelial odontogenic tumours in domestic animals. *J Comp Pathol*. 1987;97(5):503–521. https://doi.org/10.1016/0021-9975(87)90002-8.
74. Vos JH, van der Gaag I. Canine and feline oral-pharyngeal tumours. *J Vet Med Ser A*. 1987;34(6):420–427. https://doi.org/10.1111/j.1439-0442.1987.tb00300.x.
75. Nishiya AT, Massoco CO, Felizzola CR, et al. Comparative aspects of canine melanoma. *Vet Sci*. 2016;3(1):7. https://doi.org/10.3390/vetsci3010007.
76. Ghirelli CO, Villamizar LA, Pinto ACBCF. Comparison of standard radiography and computed tomography in 21 dogs with maxillary masses. *J Vet Dent*. 2013;30(2):72–76. https://doi.org/10.1177/089875641303000201.
77. Ravikanth R. MR evaluation of tongue carcinoma in the assessment of depth of invasion with histopathological correlation: a single center experience. *Indian J Radiol Imaging*. 2020;30(2):126–138. https://doi.org/10.4103/ijri.IJRI_286_19.
78. White SC, Pharoah M. Benign tumors of the jaws. In: White SC, Pharoah M, eds. *Oral Radiology Principles and Interpretation*. 6th ed. Mosby Elsevier; 2009:366–403.
79. Tjepkema J, Bell CM, Soukup JW. Presentation, diagnostic imaging, and clinical outcome of conventional ameloblastoma in dogs. *J Vet Dent*. 2020;37(1):6–13. https://doi.org/10.1177/0898756420924847.
80. Mehta K, McBee MP, Mihal DC, England EB. Radiographic analysis of bone tumors: a systematic approach. *Semin Roentgenol*. 2017;52(4):194–208. https://doi.org/10.1053/J.RO.2017.04.002.
81. Wood RE. Malignant diseases of the jaws. In: White SC, Pharoah M, eds. *Oral Radiology Principles and Interpretation*. 6th ed. Mosby Elsevier; 2009:405–427.
82. Gawor J. Hereditary oral disorders in purebred dogs and cats. In: Gawor J, Niemiec B, eds. *The Veterinary Dental Patient*. John Wiley & Sons, Ltd.; 2021:133–138. https://doi.org/10.1002/9781118974674.ch10.
83. Ng KK, Rine S, Choi E, et al. Mandibular carnassial tooth malformations in 6 dogs—micro-computed tomography and histology findings. *Front Vet Sci*. 2019;6:464. https://doi.org/10.3389/fvets.2019.00464.
84. Bellei E, Ferro S, Zini E, Gracis M. A Clinical, radiographic and histological study of unerupted teeth in dogs and cats: 73 cases (2001–2018). *Front Vet Sci*. 2019;6:357. https://doi.org/10.3389/fvets.2019.00357.
85. Babbitt SG, Volker MK, Luskin IR. Incidence of radiographic cystic lesions associated with unerupted teeth in dogs. *J Vet Dent*. 2016;33(4):226–233. https://doi.org/10.1177/0898756416683490.

ELECTRONIC RESOURCES

Additional information related to the content in Chapter 10 can be found online at eBooks.Health.Elsevier.com.

- Chapter Quiz

CHAPTER 11

The Skull and Nasal Cavities: Canine and Feline

Lisa J. Forrest

NORMAL ANATOMY

General Skull

The skull encompasses the brain and houses the sense organs for hearing, equilibrium, sight, smell, and taste. Along with the skull, facial bones provide attachment sites for teeth, tongue, larynx, and muscles.[1] There is pronounced variation in the shape of the skull in the dog. Three terms are used to designate the different shapes. *Dolichocephalic* breeds, such as collie and Russian wolfhound, have long, narrow heads with an extensive nasal cavity from rostral to caudal. *Mesaticephalic* breeds, such as German Shepherd and beagle, have heads of medium proportion (Fig. 11.1). *Brachycephalic* breeds, such as Boston terrier and Pekingese, have short, wide heads. Cats are more uniform in their skull conformation. However, Siamese tend to have increased facial length as compared with Himalayan and Persian breeds.

Calvaria and Associated Structures

The calvaria comprises the bones of the brain case, with the occipital bone forming the base of the skull. The occipital crest is the most dorsocaudal aspect of the skull (see Fig. 11.1), and the occipital condyles are caudoventral as seen on lateral radiographs. The foramen magnum, centered between the occipital condyles, forms an orifice for passage of the spinal cord.

Nasal Passages and Paranasal Sinuses

The nasal passage extends caudally from the external nares to the cribriform plate and nasopharynx. The cribriform plate is a sieve-like partition between the olfactory bulb and nasal passage. The nasal passage is divided in half by the nasal septum and is filled with thinly scrolled conchae (Fig. 11.2). Caudally, the nasal septum is osseous and fuses with the cribriform plate; it becomes cartilaginous as it extends rostrally.[1] The vomer bone is unpaired and forms the caudoventral bony part of the nasal septum. The cartilaginous nasal septum cannot be seen in radiographs, although it can be distinguished in computed tomography (CT) and magnetic resonance (MR) images. Both dogs and cats have frontal sinuses (see Fig. 11.1), lateral maxillary recesses, and small sphenoidal sinuses. These are named for the bones in which they are located.

Tympanic Bullae and Temporomandibular Joint

The tympanic bullae (see Fig. 11.1) form the ventral part of the temporal bone. These air-filled cavities of the middle ear communicate with the nasopharynx via the auditory tube. The temporal bone consists of the petrosal, tympanic, and squamous sections that are fused in the adult. The petrosal portion is medial and dorsal to the tympanic bulla and is composed of dense bone in the mature animal. The squamous portion of the temporal bone extends rostral and lateral to form the zygomatic arch.

The temporomandibular joint (TMJ) is a condylar joint. The temporal portion consists of the zygomatic process of the squamous temporal bone, which forms the mandibular fossa and the retroarticular process. The retroarticular process is the ventral extension of the squamous temporal bone. The mandibular aspect of the joint includes the condyloid process, which articulates with the mandibular fossa. Imaging of the TMJ can be assessed with radiography,[2–4] but CT and MR imaging are preferred (Fig. 11.3).[4–6]

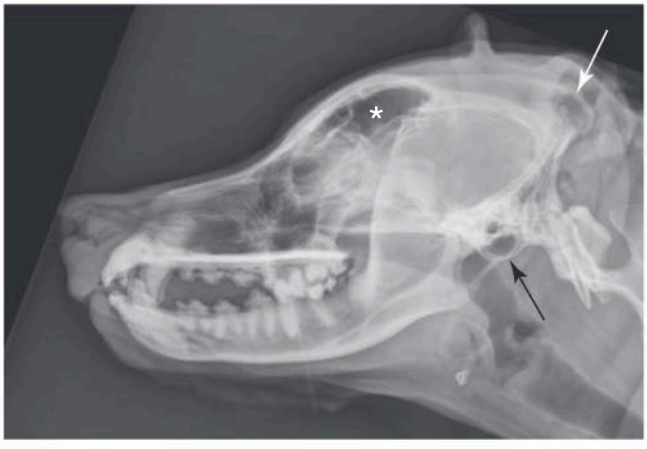


Fig. 11.1 Lateral skull radiograph of a Labrador retriever, which is a mesaticephalic breed. Note the occipital crest (*white arrow*), superimposed frontal sinuses (*asterisk*), and tympanic bullae (*black arrow*).

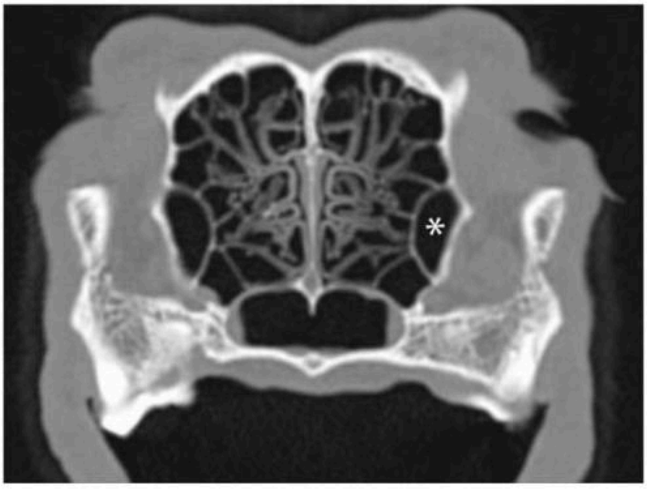


Fig. 11.2 Transverse computed tomography (CT) image at the level of the nasal passage and maxillary recess (*asterisk*), in a bone window (WL = 300, WW = 2800). Note the finely scrolled conchae in the nasal cavity (Chapter 4). *WL,* Window level; *WW,* window width.

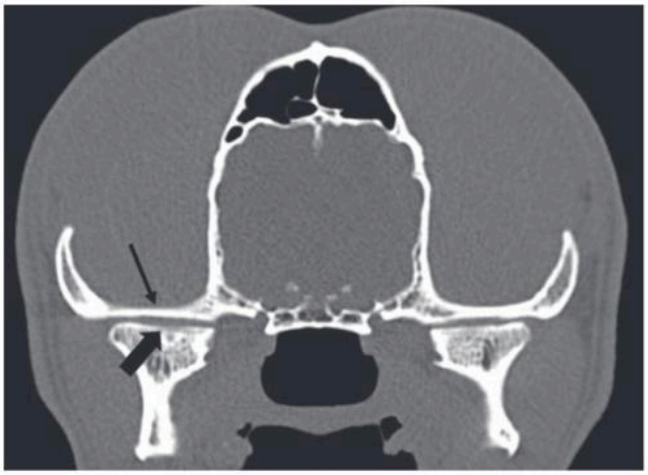


Fig. 11.3 Transverse computed tomography (CT) image at the level of the temporomandibular joint (TMJ) in a bone window (WL = 300, WW = 1500). The *thin black arrow* identifies mandibular fossa of the temporal bone, and the *thick black arrow* identifies the condylar fossa of the mandible, which are the two components of the TMJ.

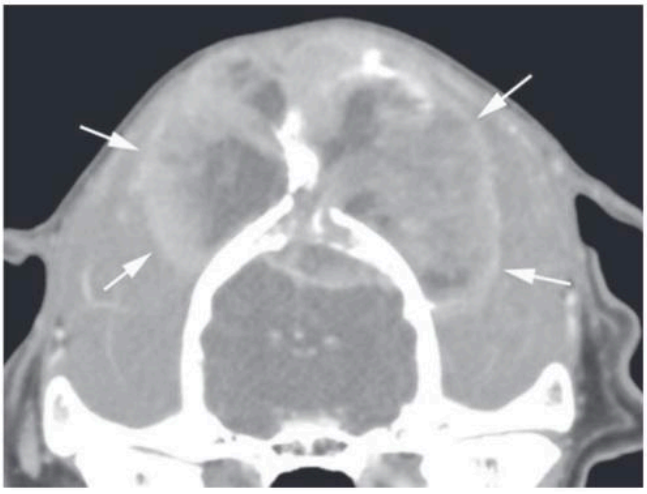


Fig. 11.4 Transverse postcontrast computed tomography (CT) image at the level of the occipital protuberance of a dog with a large soft-tissue sarcoma of the temporal muscles. The *white arrows* delineate the soft-tissue component of the tumor, which is destroying the occipital bone and invading the cranial cavity. This accuracy in tumor staging is impossible from radiographs.

Cross-Sectional Imaging

The cross-sectional imaging techniques of CT and MR imaging are being used more commonly for imaging the head. CT and MR technology provides images without superimposition of structures and better soft tissue delineation compared with radiography (Fig. 11.4).[7] There are several sources describing the normal CT and MR image anatomy of the dog and cat head.[4,6–14]

CONGENITAL ANOMALIES

Hydrocephalus

Hydrocephalus is excessive accumulation of cerebrospinal fluid (CSF) within the ventricular system of the brain. Congenital hydrocephalus occurs secondary to an interruption of CSF flow or defective absorption of CSF.[14–16] Canine breeds affected with congenital hydrocephalus include the Maltese, Yorkshire terrier, English bulldog, Chihuahua, Lhasa Apso, Chinese pug, toy poodle, Pomeranian, Pekingese, Cairn terrier, and Boston terrier.[14,15] Hydrocephalus is less common in cats.[14,16]

Radiographic signs associated with hydrocephalus include (Fig. 11.5):

- Doming of the calvaria and cortical thinning
- Persistent fontanelles
- Homogeneous appearance to the brain, resulting from the loss of normal convolutional skull markings

Radiographs are insensitive for detection and characterization of hydrocephalus, and that information is now acquired using CT or MRI.[15,17] With persistent fontanelles, ultrasound can also be used to assess ventricular size,[17–19] and normal ventricular appearance and size have been quantified in the dog.[17,19,20] The advantage of CT and MRI for evaluating ventricular size is the ability to assess the entire brain for causes of hydrocephalus (Fig. 11.6) (see Chapter 12).

Occipital Dysplasia

Occipital dysplasia (also called keyhole malformation) is the dorsal enlargement of the foramen magnum, secondary to a developmental defect in the occipital bone.[17] The bone defect, which is better assessed using CT than radiography (Fig. 11.7), may be covered by rigid connective tissue to prevent brain prolapse. Occipital dysplasia has been related to clinical neurologic disease and is usually found in miniature and toy breeds.[18,20,21] There is considerable variation in shape of the foramen magnum and occipital dysplasia may be a normal morphologic variation in brachycephalic dogs without clinical signs.[18,22]

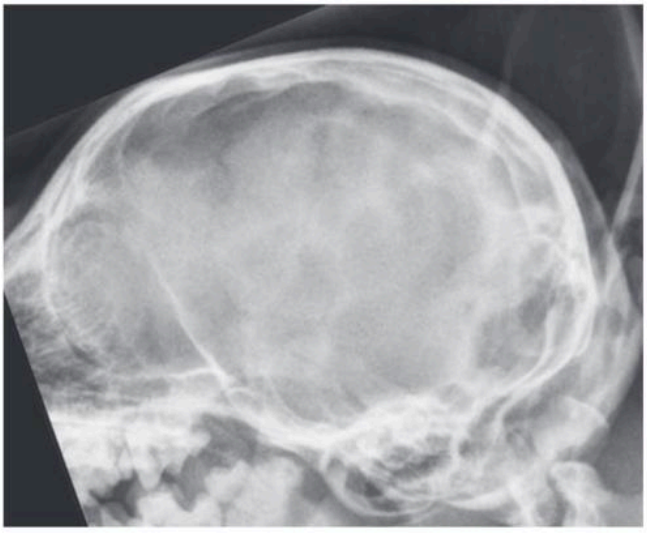


Fig. 11.5 Lateral radiograph of a 19-month-old Papillon with severe hydrocephalus. Note the homogeneous appearance of the calvaria caused by a loss of the normal convolutional skull markings.

Occipital Bone Malformation and Syringomyelia (Chiari-Like Malformation)

Occipital bone malformation may result in overcrowding of the caudal fossa, leading to obstruction of CSF flow, hydrocephalus, and secondary syringomyelia. This hereditary defect, termed *caudal occipital malformation syndrome (COMS)* or *Chiari-like malformation*, is common in the Cavalier King Charles spaniel,[22–25] but is also found in other brachycephalic breeds.[26] Definitive diagnosis is made with MRI,[23] whereby the crowding of the cerebellum in the caudal fossa can be detected. There may be herniation of a portion of the cerebellar vermis (see



Fig. 11.6 Transverse postcontrast T1-weighted magnetic resonance (MR) image of the brain of a dog with a large mass in the third ventricle (*arrow*). This mass has resulted in obstruction to cerebrospinal fluid (CSF) flow and secondary obstructive hydrocephalus. The lateral ventricles (*black* in this MR sequence) are dilated.

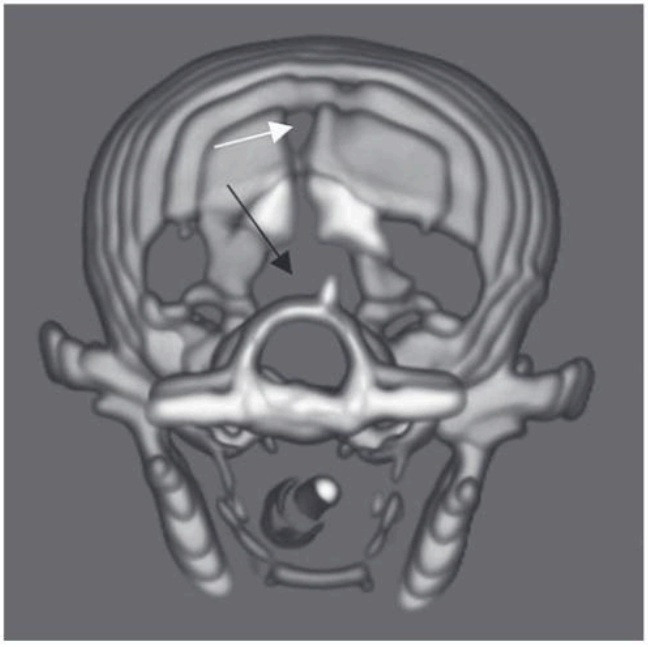


Fig. 11.7 Caudal view of a three-dimensional volume rendering obtained from transverse computed tomography (CT) images of the skull. The foramen magnum should be the approximate size of the vertebral canal of C1. Note the extension of the foramen magnum dorsal to C1 (*black arrow*) and a vertical cleft extending even further dorsally (*white arrow*). Two large dysplastic areas are also visible in the occipital bone to either side of the foramen magnum.

Chapter 12). A positive correlation has been found between foramen magnum size and length of cerebellar herniation.[20,22]

Temporomandibular Joint Dysplasia

Open-mouth jaw locking can be caused by TMJ dysplasia. This congenital condition is uncommon; it is reported most frequently in the Basset Hound but has also been seen in Irish Setters.[27] The open-mouth jaw locking occurs after hyperextension of the jaw, excessive lateral movement of the condyloid process, and subsequent entrapment lateral to the zygomatic arch. Physical entrapment usually occurs on the side opposite from the joint with the most severe dysplastic changes. Yawning often precipitates jaw locking when it results in extreme opening of the mouth.[27] In spaniels, Pekingese, and dachshunds, TMJ dysplasia is an asymptomatic anatomic anomaly.[4,28] Open-mouth jaw locking also occurs in cats,[27,29,30] and CT is routinely used to diagnose TMJ dysplasia, with three-dimensional (3D) reconstructions aiding in surgical planning.[31]

Mucopolysaccharidosis

Mucopolysaccharidoses are a group of hereditary disorders of lysosomal storage, which occur in humans, dogs, cattle, and cats. Mucopolysaccharidosis VI (MPS-VI) is an autosomal recessive lysosomal storage disease recognized in Siamese cats.[32–34] Radiographic skeletal changes in cats with MPS-VI include epiphyseal dysplasia, generalized osteopenia, pectus excavatum, and vertebral and skull changes.[35] Specific skull changes seen on radiographs include shortened nasal conchae, aplasia and hypoplasia of the frontal and sphenoid sinuses, and shortened dimensions to the incisive and maxillary bones.[35] Another form of MPS, MPS-I, has been documented in the domestic short-haired cat,[34] with radiographic skeletal changes that are similar to those in MPS-VI; however, the facial dysmorphia may not be as pronounced as it is in the Siamese.[33] Several different types of MPS have been reported in various dog breeds. MPS in animals has clinical and pathologic manifestations similar to people and therefore represents an excellent model for studying approaches to therapy and care.[32,34,36]

METABOLIC ANOMALIES

Primary or secondary hyperparathyroidism can result in overall decreased bone opacity, sometimes visible on skull radiographs. A parathyroid adenoma or carcinoma, or adenomatous hyperplasia of one or both parathyroid glands, causes primary hyperparathyroidism. This results in excessive synthesis and secretion of parathyroid hormone, which leads to hypercalcemia and subsequent bone resorption.[37–39] Secondary hyperparathyroidism, which includes renal and nutritional secondary hyperparathyroidism, is subsequent to nonendocrine alterations in calcium and phosphorus homeostasis and lead to increased levels of parathyroid hormone and ultimate bone resorption.[40,41]

An early radiographic sign of hyperparathyroidism (primary and secondary) is loss of the lamina dura (Fig. 11.8). This is followed by overall demineralization of the skull bones as the disease progresses (Fig. 11.9, eFig. 11.1). In fact, it is uncommon to see loss of the lamina dura without some concurrent generalized skeletal demineralization. The level of cortical thinning and degree of overall osteolysis and osteomalacia depend on duration and severity of the hyperparathyroidism. Also, because young animals have rapid skeletal turnover, they are affected more severely than older animals. In extreme hyperparathyroidism, demineralization is followed by fibrous tissue hyperplasia, termed *fibrous osteodystrophy*. This uncommon development leads to skull thickening, and particularly by maxillary enlargement, caused by fibrous tissue proliferation.

Ultrasound evaluation of the cervical region can be used to evaluate dogs with hypercalcemia to search for a parathyroid mass.[42] In 210 dogs with primary hyperparathyroidism, a parathyroid mass with a range of 3 to 23 mm in diameter was identified in 129 of 130 dogs that were imaged sonographically.[38] Some 31% of the dogs had cystic calculi, and all were either calcium phosphate or calcium oxalate



eFig. 11.1 Lateral skull radiograph of a 6-year-old dog with chronic renal failure and secondary hyperparathyroidism. The teeth appear very opaque because of the reduction in bone mineral. The lamina dura has been resorbed.

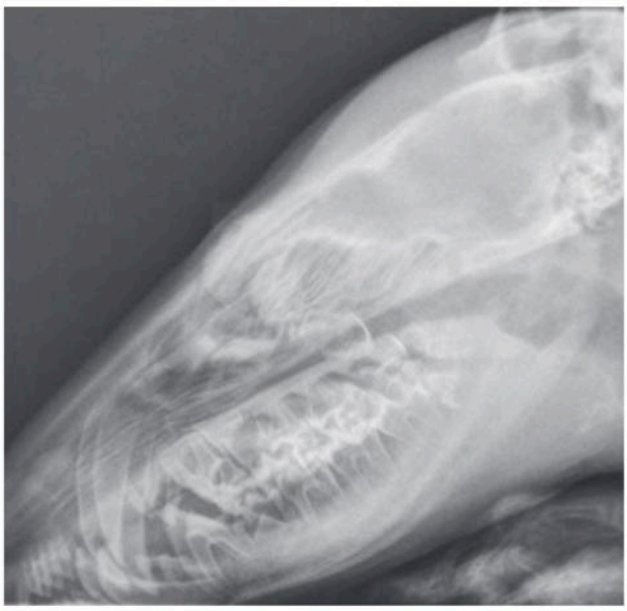


Fig. 11.8 Lateral radiograph of an opossum with nutritional secondary hyperthyroidism. Note the decreased opacity and poor delineation of the skull. This is especially noticeable in the caudal mandibular region, where it is difficult to differentiate the mandible from adjacent soft tissue. Note the lack of visualization of the lamina dura.



Fig. 11.9 Lateral skull radiograph of an 8-year-old poodle with nutritional secondary hyperparathyroidism. Bone opacity is severely generally reduced, and the teeth appear very opaque in comparison. The lamina dura has been resorbed.

(radiopaque).[38] Recent imaging of normal parathyroid glands using ultrasonography, CT, and MRI with improved technology improves the conspicuity of the organ.[43–46] Treatment modalities for primary hyperparathyroidism are surgery and ablation of gland nodules with the latter via ultrasound guidance.[43–47] Keeshond dogs have a genetic predisposition for hyperparathyroidism, and are significantly more likely to have recurrent disease after parathyroidectomy than other breeds.[47]

Thyroid glands on noncontrast CT are hyperattenuating relative to surrounding tissue due to normal iodine concentration.[46] A recent study comparing precontract CT of thyroid glands in brachycephalic dogs and nonbrachycephalic dogs reported significantly lower attenuation values, measured in Hounsfield units (HU), in brachycephalic dogs.[48] Reported ranges for brachycephalic dogs were 69.1 to 108 HU compared to nonbrachycephalic dogs, 75.8 to 121 HU. The authors suggest using different attenuation value ranges for brachycephalic dogs.[48]

Feline acromegaly in diabetic cats can result in bone remodeling of the skull and is caused by chronic excess of growth hormone and insulin-like growth factor-1 (IGF-1).[49–51] Acromegalic cats are generally male neutered, middle to older aged with insulin-resistant diabetes mellitus.[51] Imaging studies using CT and MRI of cats with acromegaly compared with unaffected cats have imaging evidence of a pituitary tumor, increased frontal bone thickness, and evidence of soft tissue accumulation in nasal cavity, sinuses, and pharynx.[49,50] One cat with insulin-resistant diabetes mellitus and elevated IGF-1 levels and a normal pituitary gland did not have imaging evidence of frontal bone or upper airway thickening.[49]

NEOPLASTIC ABNORMALITIES

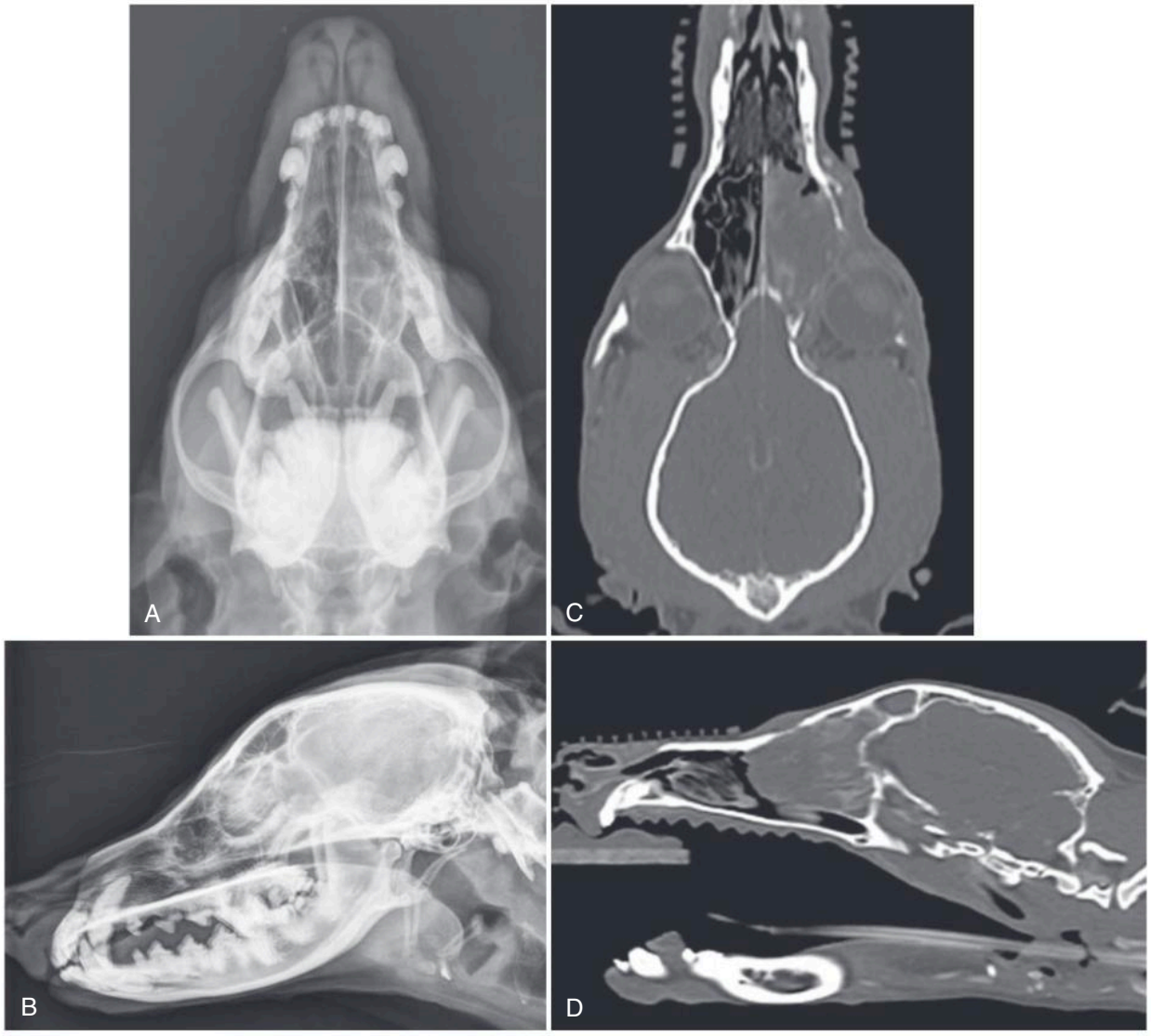
Nasal Tumors

Tumors of the nasal cavity in dogs and cats account for approximately 1% to 2% of all neoplasms.[52,53] These tumors occur in older dogs and cats; approximately two-thirds of nasal tumors are epithelial (adenocarcinoma, squamous cell carcinoma, undifferentiated carcinoma), and the other one-third are mesenchymal (fibrosarcoma, chondrosarcoma, osteosarcoma, undifferentiated sarcoma).[52,53] Intranasal lymphoma also occurs, with a higher prevalence in cats.[52,53] Tumors of the nasal cavity are locally invasive but have a relatively low metastatic potential. External beam radiotherapy is the current treatment of choice,[54–60] with most centers using advanced radiotherapy techniques, such as intensity-modulated radiation therapy, image guidance, and stereotactic radiation therapy.[55,57,58,61–64] With these advanced techniques, tumor dose delivery is improved, and critical adjacent tissues are avoided resulting in reduced treatment side effects.[61,62]

The most useful radiographic views for evaluating nasal disease include the intraoral dorsoventral and/or the open-mouth ventrodorsal view for detailed evaluation of the nasal cavity without superimposition of the mandible (Fig. 11.10, eFig. 11.2). The open-mouth ventrodorsal view is better for cribriform plate assessment, because a radiographic film cassette or digital plate cannot be inserted caudal enough to include the cribriform plate in the intraoral view. The cribriform plate is represented by a V-shaped to C-shaped bony opacity on radiographs, varying according to skull shape (dolichocephalic vs. mesaticephalic and brachycephalic).[65] Evaluation of the cribriform plate is important because nasal tumors often originate from the ethmoid conchae and cribriform plate, and bone lysis detected on radiographs indicates tumor extension into the cranial cavity (see Fig. 11.10A). The rostrocaudal frontal sinus projection is necessary for evaluation of individual frontal sinuses (Fig. 11.11) and is useful especially if CT or MRI is not available.[66]

General anesthesia is an absolute requirement for achieving accurate radiographic positioning, and it facilitates evaluation and comparison of the complex nasal passages. Techniques for obtaining radiographic views of the nasal cavity and paranasal sinuses can be found elsewhere,[68] and they were discussed briefly in Chapter 9. Nasal cavity tumors have an aggressive radiographic appearance; common radiographic features may include[65–73]:

- Increased soft-tissue opacity in the affected nasal cavity, most commonly unilateral but may be bilateral
- Conchae destruction resulting in asymmetry and reduction of the radiopaque conchal outlines
- Destruction of bones adjacent to the nasal cavity



eFig. 11.2 Open-mouth, ventrodorsal **(A)** and lateral **(B)** radiograph of the nasal cavity of a dog with nasal carcinoma. **A,** The caudal aspect of the left nasal cavity is increased in opacity and there is subtle mild reduction of the turbinate detail. **B,** There is a subtle soft tissue bulge dorsal to the maxilla and frontal bones at the level of the ethmoid. Dorsal **(C)** and sagittal **(D)** reformatted computed tomography (CT) images of the same dog. **C,** The soft tissue attenuating mass is visible in the caudal left nasal cavity. There is turbinate destruction in the region of the mass. A focal defect in the left cribriform plate as well as erosion of the medial aspect of the orbit is now apparent but was not visible radiographically. **D,** The nasal mass has caused focal erosion of the maxillary bone and protrudes into the dorsal soft tissue, corresponding to the small soft tissue thickening seen radiographically.



Fig. 11.10 Open-mouth, ventrodorsal radiograph of the nasal cavity of two dogs with a nasal tumor. **A,** On the left, note the increased opacity, loss of conchal detail, and bony destruction of the cribriform plate. The right side of the cribriform plate is intact (*black arrowhead*). **B,** There is increased soft-tissue opacity diffusely throughout the right nasal cavity with effacement of the caudal maxillary and ethmoid turbinates. There is also increased opacity in the right frontal sinus (*black arrows*). The nasal septum appears intact, and there is no evidence of cribriform plate effacement (*black arrowheads*).



Fig. 11.11 Rostrocaudal frontal sinus radiograph of a 7-year-old German Shepherd with a history of epistaxis. Note the increased opacity to the right frontal sinus compared with the left. The increased opacity is nonspecific and could be caused by fluid accumulation or tissue proliferation, or both.

- Deviation and destruction of the bony nasal septum are apparent on radiographs
- Extension of a soft-tissue mass beyond the nasal cavity
- Increased opacity within the frontal sinus, either by tumor extension or by occlusion of nasofrontal communication with subsequent mucus accumulation in the sinus

Aggressive nasal tumors and those with a prolonged duration are more destructive and less confined radiographically, often exhibiting an external soft-tissue mass that represents tumor extension through overlying bone. Conchae destruction and deviation and destruction of the bony nasal septum are apparent on radiographs. Less aggressive tumors and ones that are detected early are difficult to differentiate from rhinitis on radiographs.[65,68] Radiographic confirmation of bone lysis of the cribriform plate and naso-orbital wall is difficult radiographically,[65] and better suited to CT or MRI.

CT has widely replaced radiographs in the assessment of suspected nasal tumors due to its higher sensitivity to subtle lytic changes to the nasal turbinates and osseous nasal boundaries, and ability to better delineate the soft-tissue component of the disease. Radiographic confirmation of bone lysis of the cribriform plate and naso-orbital wall is difficult,[56] and better suited to CT or MRI. CT or MRI is usually necessary to determine if soft tissue in the frontal sinus represents tumor extension or mucus buildup due to reduced drainage. Making this distinction is important for treatment planning.[70] MRI, which is based on the chemical composition of the tissue rather than the electron density, is helpful in distinguishing tumor from mucus in the frontal sinus (Fig. 11.12), but contrast-enhanced CT provides similar information.[70]

CT of the nasal passage is superior to routine radiography for accurate tumor staging (Figs. 11.13 and 11.14, eFig. 11.3)[69] and is useful for attempting to differentiate infection from neoplasia.[11,74,75] It is impossible to determine the stage of a nasal mass adequately from radiographs, and CT is the preferred screening modality for nasal disease. The presence of a mass effect (increased soft tissue in the nasal cavity) along with bone destruction is a hallmark sign of nasal neoplasia in CT as well (see Fig. 11.14). A destructive pattern without a marked mass effect is more typical of *Aspergillus* infection, whereas a mass effect without turbinate destruction is also more typical of infection, although usually not *Aspergillus*.

CT images of patients with nasal cancer are used in computerized radiation therapy planning. Use of CT anatomic information allows optimization of dose distribution across the tumor volume and improved survival with decreased normal tissue side effects.[55–64] MRI of the nasal passage provides excellent, true 3D images of nasal tumors.[70,71,76] Differences in



eFig. 11.3 Transverse computed tomography (CT) image of the nasal cavity of a cat with nasal lymphoma. Abnormal soft tissue attenuating material fills the ventral aspect of both nasal cavities and nasopharyngeal meatus. There is focal destruction of the sphenoethmoidal plate and palatine bone.

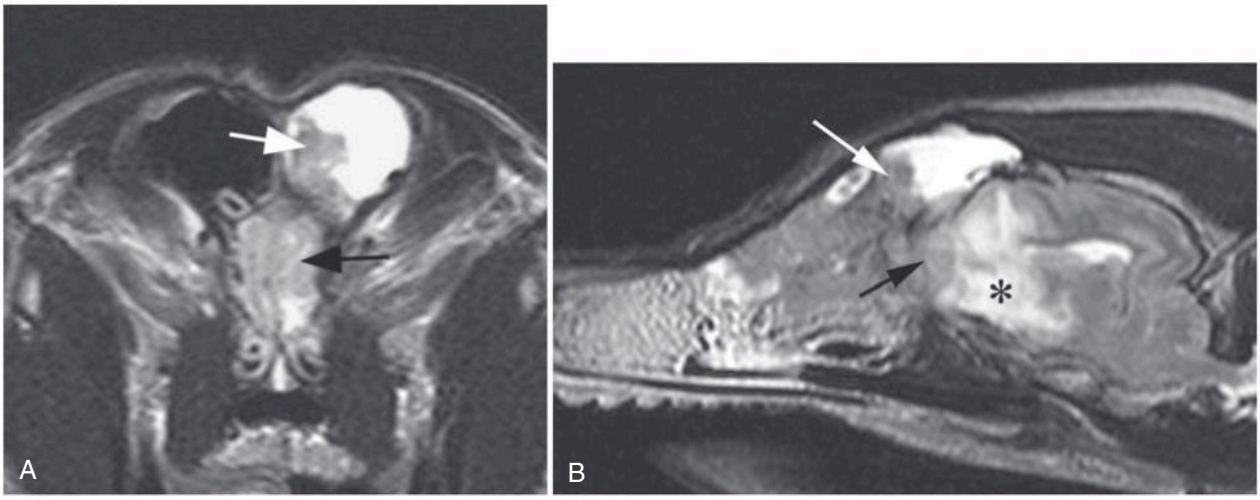


Fig. 11.12 Transverse **(A)** and parasagittal **(B)** fast spin-echo T2-weighted magnetic resonance (MR) images of a dog with a malignant nasal tumor. In **B,** the amorphous tumor mass can be seen in the caudal aspect of the nasal cavity. The tumor has invaded the frontal sinus (*white arrows*), causing obstruction of the nasofrontal communication and resulting in mucus collection in the sinus dorsal and caudal to the tumor. In these T2-weighted images, this mucus has high signal intensity (appears white), and the tumor has less signal intensity. In radiographs, the frontal sinus, the tumor, and the mucus would have the same opacity, making distinction impossible. This tumor has also invaded the cranial cavity (*black arrows*), leading to extensive white matter edema (streaky white signal, *asterisk*) caudal to the tumor in the sagittal view.

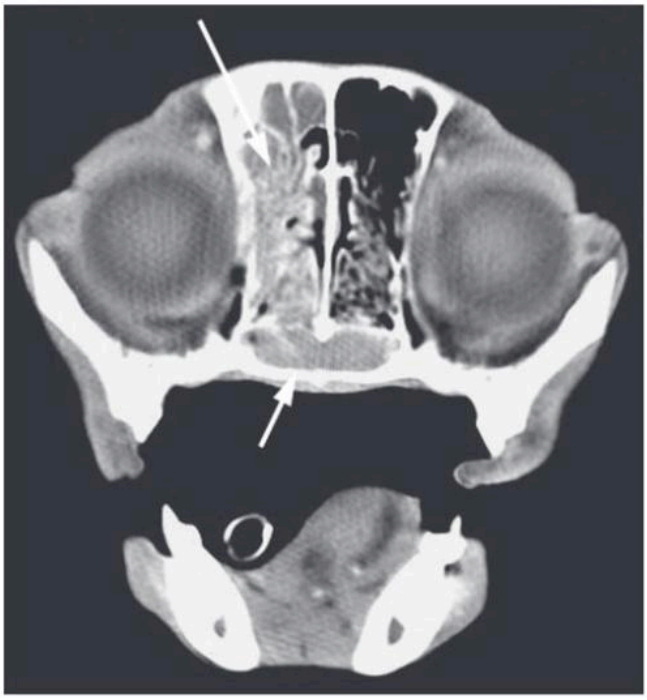


Fig. 11.13 Transverse computed tomography (CT) image of the nasal cavity of a cat with nasal lymphoma at the level of the eyes. Tumor is visible within the nasopharynx (*short white arrow*) and the left nasal cavity (*long white arrow*).

MR signal intensity between sarcomas and carcinomas have been found.[75,76]

Currently, nasal tumors are almost exclusively imaged using CT, which allows better delineation of tumor extent and tumor staging and is used in radiotherapy treatment planning (see Fig. 11.14). Positron emission tomography combined with CT (PET/CT) has been investigated in dogs with spontaneously occurring nasal tumors using ^{18}F-FDG (2-deoxy-2-[18F] fluoro-D-glucose), ^{18}F-FLT (3′-deoxy-3′-fluorothymidine), and ^{61}Cu-ATSM (diacetyl-bis [N^4-methylthiosemicarbazone]).[69–78] In initial studies in 20 dogs, the relationships of glucose metabolism (FDG), cell proliferation (FLT), and cell hypoxia (Cu-ATSM) were generally heterogeneous across both nasal carcinomas and sarcomas.[78] FDG, FLT, and Cu-ATSM imaging were also evaluated with regard to predicting the locations of residual FDG PET uptake in tumors following radiotherapy. Results were variable in that PET imaging could predict locations of residual tumor in some patients, but not others, indicating that not all patients would benefit from a targeted increase in radiotherapy dose based on a single biological target.[77] Studies to find pretreatment imaging agents to predict which patients will benefit from targeted heterogeneous radiotherapy dosing continue in animals and people.

Mandibular and Maxillary Tumors

Tumors of the oral cavity account for approximately 6% to 7% of all canine cancers and 3% of feline cancers.[79,80] Squamous cell carcinoma commonly affects the mandible or maxilla in the dog and cat.[79] Fibrosarcoma[81] and malignant melanoma[79,82] are common in the dog but occur rarely in cats.[82] In the dog, the rostral mandible is a common site for oral squamous cell carcinoma. This tumor has variable bone lysis, and regional or distant metastasis is rare.[79] Oral fibrosarcoma in dogs can affect the maxilla or mandible with a predilection for the palate.[79] In dogs, 82% of squamous cell carcinomas and 78% of fibrosarcomas were characterized radiographically by bone involvement.[79,81] Often, oral fibrosarcoma appears benign histologically, but biologic activity is aggressive. These tumors, often found in the maxilla and mandible of large-breed dogs and commonly in Golden Retrievers, are histologically low-grade yet biologically high-grade aggressive tumors and bone lysis is a common feature.[67] Dogs with oral fibrosarcoma have a lower median survival as compared with those with soft-tissue sarcomas at other sites[83] (Fig. 11.15). In contrast, malignant melanoma occurs in large- and small-breed dogs, commonly metastasizes to regional lymph nodes and lungs, and has variable bone lysis.[82,84] Squamous cell carcinoma in cats affects the mandible or maxilla, causing sclerotic and/or lytic changes to bone[85] (Fig. 11.16, eFig. 11.4). Common CT features of feline squamous cell carcinoma include sublingual and maxillary locations with marked heterogeneous contrast enhancement



eFig. 11.4 **A,** Lateral radiograph of the skull of a cat with focal swelling of the rostral aspect of the mandible. There is irregular, spiculated new bone formation and moth-eaten lysis of the rostral mandible. The diagnosis of squamous cell carcinoma was made histologically. **B,** Ventrodorsal radiograph of a 13-year-old cat with squamous cell carcinoma of the skull. The soft tissues on the region of the right globe are thickened (*arrowheads*). There is diffuse lysis of the right nasal turbinates, right frontal sinus and the right side of the cribriform plate and calvarium (*arrow*).

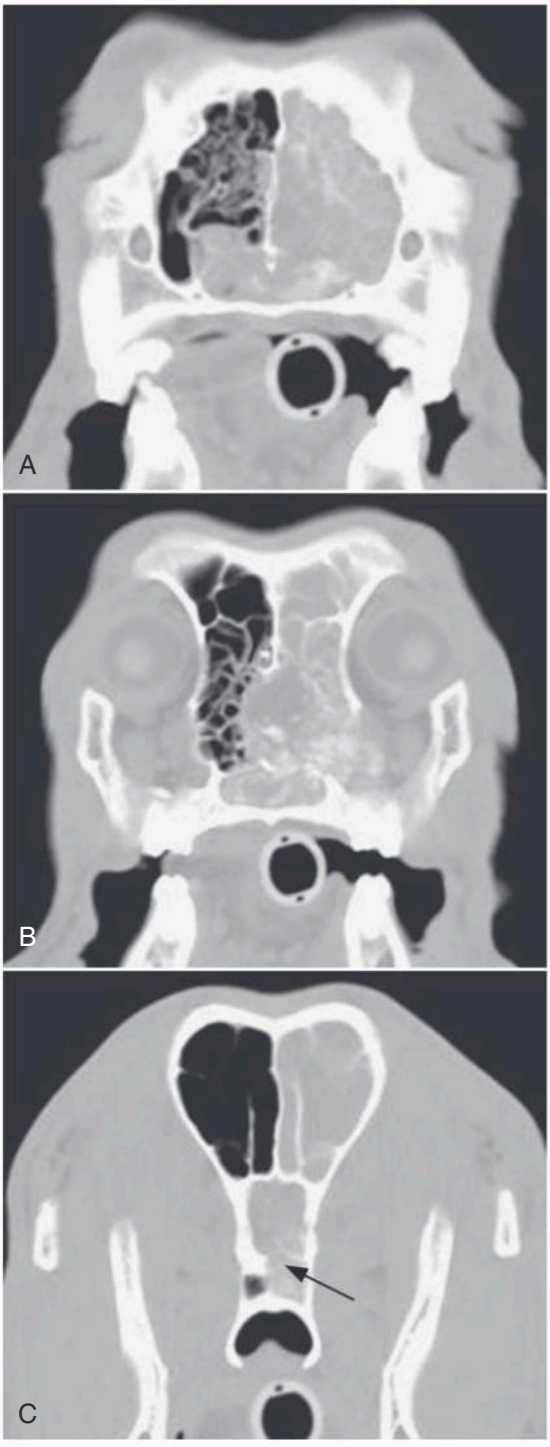


Fig. 11.14 Three transverse computed tomography (CT) images from a dog with a malignant nasal tumor. **A,** Erosion of the vomer with extension of the tumor to the right nasal cavity. **B,** Extension into the left pterygopalatine fossa, across the midline to the right nasal cavity and into the nasopharynx. **C,** Erosion of the cranial vault with intracranial extension (*arrow*). Hyperattenuating material is also present in the left frontal sinus; CT images cannot distinguish tumor extension into the sinus from fluid or mucus collection caused by obstruction of the nasofrontal communication, unless contrast enhancement of tumor extension is seen. This combination of CT abnormalities is characteristic of a malignant nasal tumor. The tumor extensions visible in these CT images would not have been detected in radiographs.



Fig. 11.15 Intraoral dorsoventral radiograph of the maxilla of a dog with a left maxillary gingival mass. In radiographs the mass is visible and contains foci of mineralization (*black arrows*). Distortion of the left incisors and marked bone lysis are also present in this area. Lysis extends caudally (*white arrow*) and blends into normal-appearing conchae. Accurately determining the caudal extent of this tumor with radiographs is impossible; if treatment is undertaken, a computed tomography (CT) study of the maxilla should be acquired to stage the extent of involvement more accurately. Determination of the tumor type from radiographs is also impossible, and a biopsy is needed; however, the appearance of this lesion is most consistent with a malignant gingival tumor. The histologic diagnosis was fibrosarcoma.



Fig. 11.16 Intraoral ventrodorsal radiograph of a cat with a swelling of the left mandible. Note the aggressive mottled appearance of the left rostral mandible. The diagnosis of squamous cell carcinoma was made histologically.

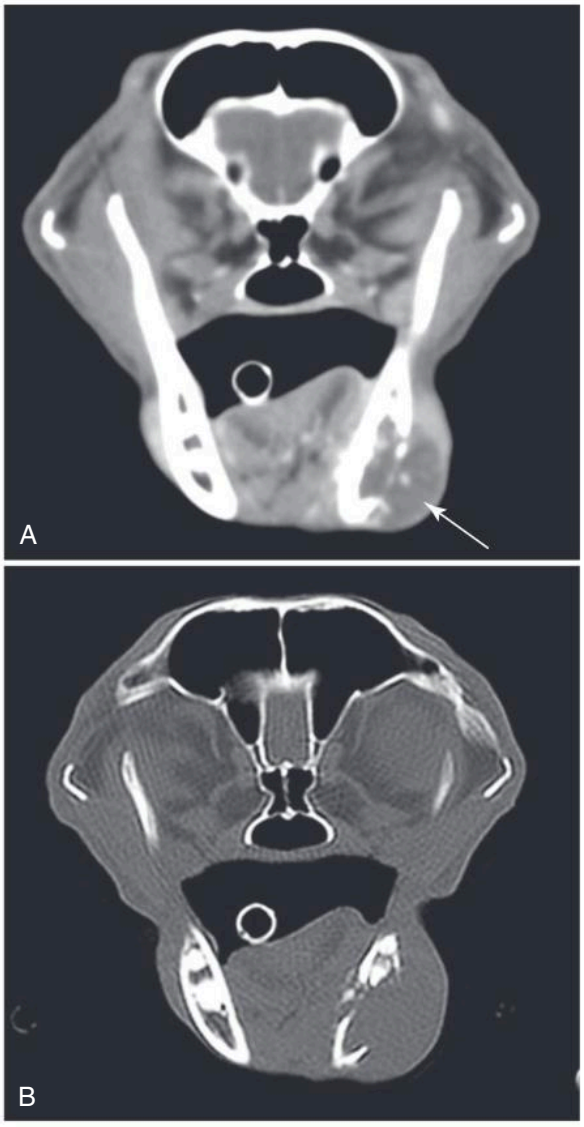


Fig. 11.17 Computed tomography (CT) images of a cat with a left mandibular squamous cell carcinoma. **A,** In the soft-tissue window, post-contrast administration, note the heterogeneous enhancement of the soft tissues (*white arrow*). **B,** In the bone window, note the lysis of the left mandible and loss of teeth.

(Fig. 11.17).[86,87] Flea control products, exposure to tobacco smoke, rural environment, and diet may play a role in development of squamous cell carcinoma in cats.[88,89] Unlike squamous cell carcinoma in the dog, these tumors in cats have a poor prognosis and are less responsive to radiotherapy.[79,85,90,91]

It is impossible to determine the histologic type of an oral tumor from radiographs. Radiographic changes are not dependent on tumor type; some tumors will be lytic, some osteoproductive, and some characterized by a combination of these changes. A sense of biologic aggressiveness can be obtained based on radiographic changes, but a biopsy is necessary for definitive diagnosis. It is also impossible to determine the extent of normal tissue involvement of a tumor from radiographs. If therapy is being considered, either CT or MRI is necessary to accurately determine the extent of tumor involvement.[12,13,92] PET/CT imaging may be more accurate for tumor staging.[93]

Treatment options for oral tumors consist of surgical excision alone, radiotherapy alone, a combination of surgery and radiotherapy,[79,81,82,94,95] photodynamic therapy,[96] and in oral melanoma, vaccine and radiotherapy.[82,97–101] In dogs with oral tumors treated by mandibulectomy or maxillectomy, excellent survival rates are achieved for carcinoma and squamous cell carcinoma, with poorer outcomes noted for sarcomas (fibrosarcoma, osteosarcoma, and malignant melanoma).[79,81,82,101] In dogs with oral fibrosarcoma treated with surgical excision, Golden Retrievers and dogs with incomplete margins were more likely to have local recurrence. However, the overall survival of 24.8 months was increased compared to previous reports of 7 to 12.2 months.[102] In another retrospective study on the outcome of 65 dogs with oral fibrosarcoma, the combination of surgery and radiotherapy provided better median survival (16.5 months) and progression free survival (10 months) over other treatments.[103] Adjuvant chemotherapy in addition to surgery and/or radiotherapy should be considered for oral tumors with the propensity to metastasize.[101,104,105]

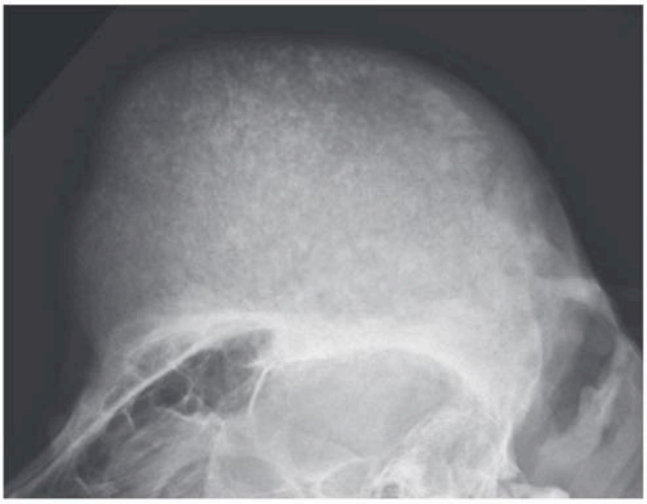


Fig. 11.18 Lateral radiograph of a dog with a dorsal calvarial multilobular osteochondrosarcoma (MLO). The granular appearance is typical of this tumor.

Multilobular Osteochondrosarcoma

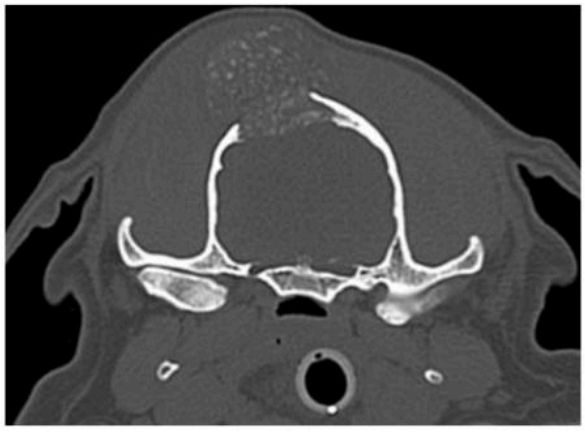
Multilobular osteochondrosarcoma (MLO) is a rare tumor that arises from the skull of dogs. These tumors often arise from the temporo-occipital area, although involvement of the orbit, maxilla, mandible, tympanic bulla, zygomatic arch, and hard palate has been reported.[106–108] An MLO typically has characteristic radiographic features. The margins are well defined, and there can be lysis of adjacent bone.[107] The central core of the tumor comprises a coarse, granular mineral opacity throughout (Fig. 11.18, eFig. 11.5). The granular appearance is also a feature of the CT appearance of MLO (Fig. 11.19). Dogs with MLO are typically older, large-breed dogs.[107] Approximately 50% of dogs experience local recurrence after treatment (surgical excision alone or surgery and radiotherapy), and approximately half develop metastatic disease.[107] CT is superior for the detection of cranial vault invasion (see Fig. 11.19, eFig. 11.6), which is common.[109,110] The features of MLO in MR images have been described in three dogs, all of which had a similar appearance of heterogeneous signal intensity with large regions of contrast enhancement; tumor invasion of soft tissues and brain was well delineated.[111] Time-of-flight MR images are useful to identify cerebral blood flow and for surgical planning.[110]

Other Tumors of the Cranium

Other primary tumors of the cranium include osteosarcoma, osteoma, and osteochondroma. Osteosarcoma is the most



eFig. 11.5 Lateral radiograph of a dog with dorsal calvarial multilobular osteochondrosarcoma (MLO). There is a focal defect in the calvarium caudal to the frontal sinuses. A soft-tissue mass with granular mineralization is present dorsal to this defect.



eFig. 11.6 Transverse computed tomography (CT) image of the same dog as in eFig. 11.5 with dorsal calvarial multilobular osteochondrosarcoma (MLO). There is a focal lysis of the calvarium and there is invasion of the soft-tissue tumor with multifocal granular mineralization causing compression of the brain.

common primary bone tumor, with 10% to 15% arising from the skull. Distribution of canine skull osteosarcoma in 183 dogs was 43.7% maxilla, 32.8% mandible, and 23.5% calvarium, and metastases were rare at diagnosis (3.8%).[105] Multiple treatments were used and median survival for all dogs was 239 days. Dogs treated with surgery had a median survival of 329 days. Surgical excision with tumor-free margins had better local control and longer survival than other treatments.[105] Osteosarcomas arising from the cranial vault do not resemble those from the appendicular skeleton or other skull sites, because they tend to be osteoblastic, have well-defined borders, and contain granular areas of calcification.[107] Osteoma is a slow-growing, benign tumor with a smooth, well-defined border without bony lysis on radiographs and CT. These tumors can arise from the mandible, cranial vault, or sinuses.[112,113]



Fig. 11.19 Computed tomography (CT) image of a dog with a temporal multilobular osteochondrosarcoma (MLO). The granular appearance seen in radiographs is also a feature of the CT appearance of this tumor. The tumor has effaced the temporal bone and extends into the cranial cavity.

Most brain tumors do not have associated survey radiographic findings and are best identified with MRI.[13,114,115] Occasionally, sclerosis of the adjacent calvaria may be noted on routine skull radiographs in cats with meningioma. Calvarial sclerosis is more accurately identified on CT and MRI. These tumors may calcify and cause sclerosis and/or lysis of the adjacent bony calvaria.[115] Imaging of brain tumors is covered in Chapter 4.

INFLAMMATORY AND INFECTIOUS DISORDERS

Nasal Aspergillosis

Nasal aspergillosis is a destructive rhinitis that also typically involves the paranasal sinuses of the dog; it affects younger (<4 years old), nonbrachycephalic dogs more frequently than other types.[116] *Aspergillus* species (primarily *Aspergillus fumigatus*) are common environmental saprophytic fungal organisms.[116] Destructive rhinitis caused by other fungal agents, such as *Penicillium* species, is less common, but *Cryptococcus* species occur in both dogs and cats.[116–118] Nasal blastomycosis can occur in endemic areas. The radiographic appearance of nasal aspergillosis includes (Fig. 11.20, eFig. 11.7)[65,116,119–121]:

- Lysis of conchae with punctate lucencies of bone
- Increased soft-tissue opacity of the nasal cavity is also seen but only focally and not encompassing the entire nasal cavity as it would with neoplastic disease

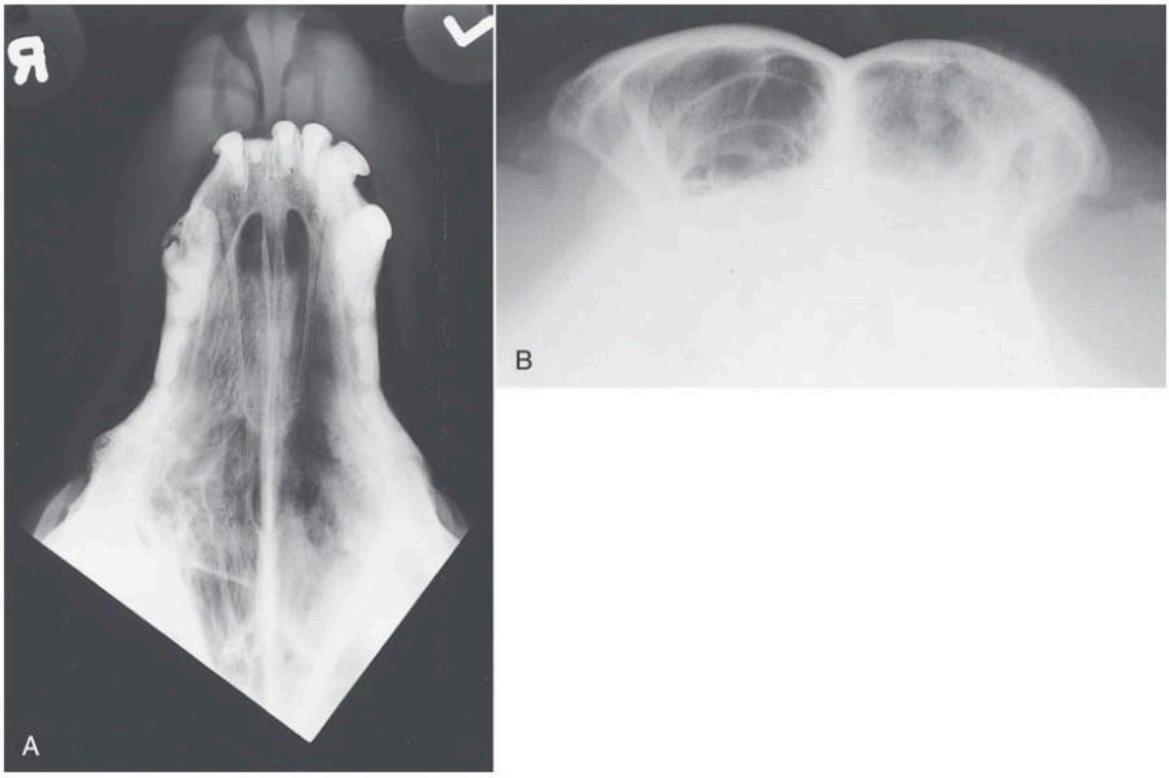
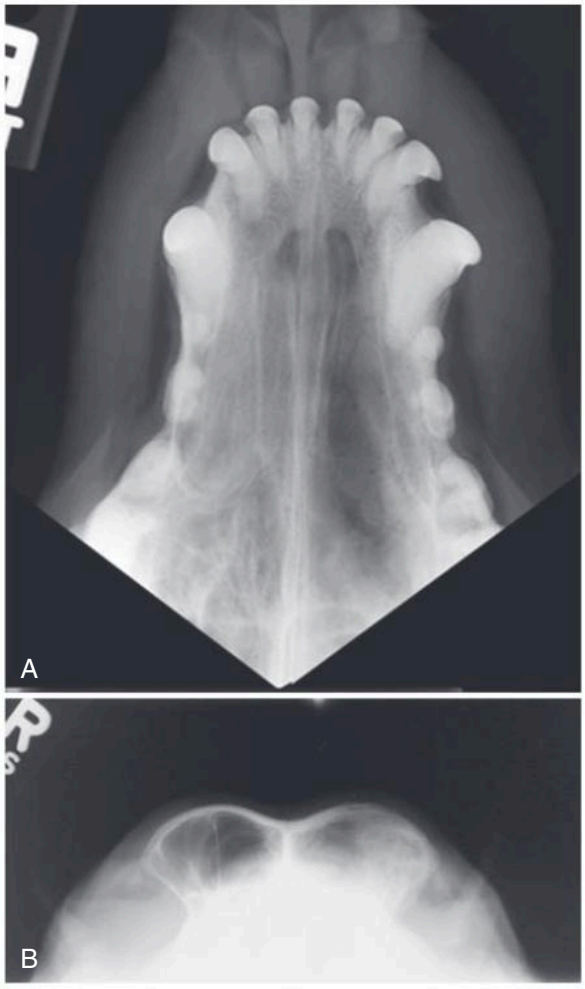


Fig. 11.20 Intraoral dorsoventral maxillary **(A)** and rostrocaudal/frontal sinus **(B)** radiographs of a dog with a 3-month history of nasal discharge. Note the destruction of the nasal conchae in the midportion of the left nasal cavity **(A)** and the increased opacity to the left frontal sinus **(B).** Evidence of frontal-bone irregularity is also present **(B),** indicating destructive sinusitis. Destructive rhinitis secondary to *Aspergillus fumigatus* was diagnosed by culture.



eFig. 11.7 Intraoral dorsoventral maxillary **(A)** and rostrocaudal/frontal sinus **(B)** radiographs of a dog nasal aspergillosis. There is destruction of the left nasal turbinates with reduced opacity of the nasal cavity **(A)** and increased opacity in the left frontal sinus **(B)**. The left frontal bone is thickened medially and partially lytic laterally.

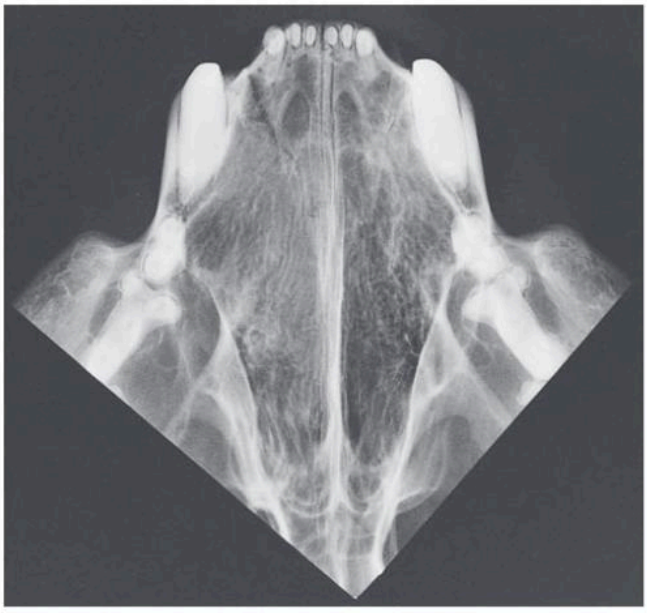


Fig. 11.21 Intraoral, dorsoventral radiograph of a cat with a history of nasal discharge. Note the increased opacity to the right nasal cavity without loss of conchal detail. *Cryptococcus neoformans* was diagnosed by culture.

- Frontal sinus involvement is variable and consists of sinus opacity with or without mottled bone thickening[65,119,120]
- Bony nasal septum erosion or deviation is uncommon except in advanced disease

Nasal aspergillosis is reported in the cat,[121–124] with two distinct anatomical forms: sino-nasal and sino-orbital forms. The sino-orbital form is an invasive mycosis and caused by *Aspergillus felis*, whereas the sino-nasal form can be invasive or noninvasive and commonly caused by *Aspergillus fumigatus* and *Aspergillus niger*.[121,122] *Cryptococcus neoformans*, a fungal infection more commonly seen in cats, can infect the nasal passages, but generally causes a nondestructive hyperplastic rhinitis (Fig. 11.21).[121] Sinonasal fungal disease reported in cats include aspergillosis, cryptococcosis, and hyalohyphomycosis, and clinical signs, age, and CT features can overlap with those found with sinonasal neoplasia.[118,121]

Destructive rhinitis secondary to fungal disease can be difficult to differentiate radiographically from neoplasia. Both diseases cause loss of conchal detail, but a nasal cavity mass effect and invasion of bones surrounding the nasal cavity are more common features of nasal cavity neoplasia.[65,69,120] CT and MRI have been used for evaluating nasal aspergillosis, with cross-sectional imaging modalities superior to radiography due to greater contrast resolution and their tomographic nature (Fig. 11.22). However, diagnosis of fungal disease requires direct visualization of fungal plaques by endoscopy or fungal elements found by cytology or histopathology.[116,119]

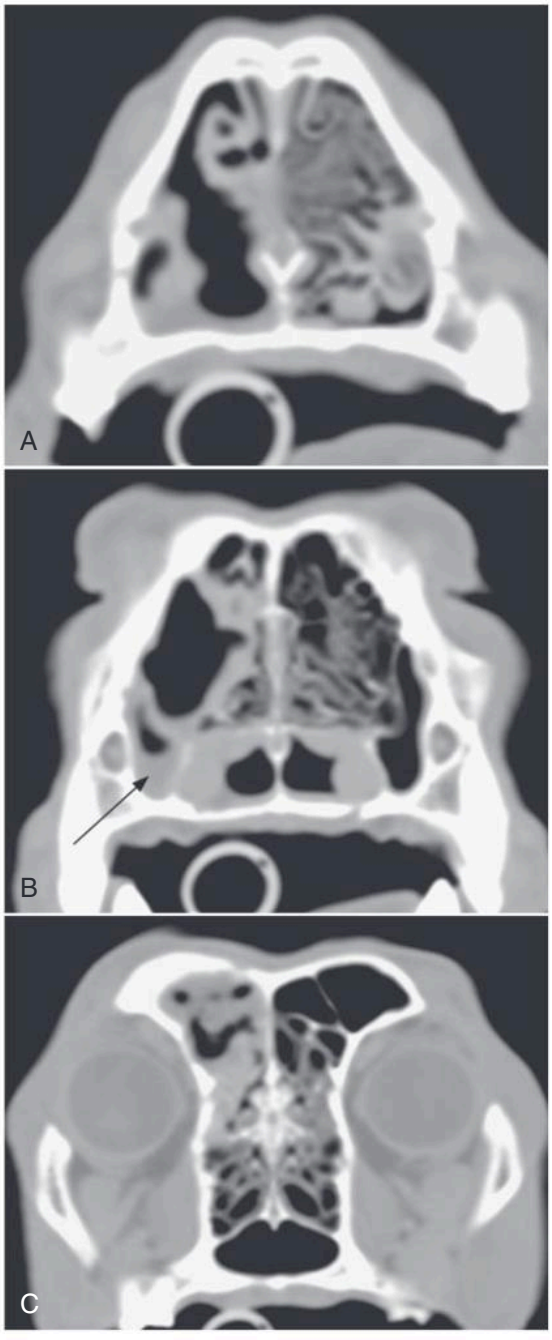


Fig. 11.22 Computed tomographic images of the nasal cavity from a dog with nasal aspergillosis. **A and B,** Destruction of conchae on the right side. Note the normal-appearing left conchae. Residual conchae on the right appear thickened and irregular. **B,** A small amount of fluid (note the meniscus effect, *arrow*) is present in the ventral aspect of the nasal cavity. **C,** There are irregular masses in the right frontal sinus without fluid accumulation, hyperostosis of the lateral aspect of the right frontal sinus, and erosion of the dorsomedial aspect of the right frontal sinus. The finding of conchal destruction and irregular frontal sinus mass effect is much more consistent with nasal aspergillosis than a tumor.

Rhinitis

Rhinitis secondary to bacterial infection, or corticosteroid-responsive rhinitis with lymphoplasmacytic infiltrates, can have a variable radiographic appearance in dogs and cats. Depending on chronicity and severity of rhinitis, destruction of conchae and evidence of bone erosion can occur but it is usually mild and focal.[125–127] Chronic rhinitis and sinusitis in cats are common sequelae to viral upper respiratory tract disease (Fig. 11.23).[126] Radiographic changes are usually bilateral and can range from none in mild infections to an increased opacity of the nasal cavity and frontal sinuses with conchae and vomer bone destruction in severe infections. In 41 dogs with inflammatory nasal disease (aspergillosis vs. lymphoplasmacytic rhinitis), turbinate destruction and hyperintensity on T1-weighted MR images were commonly found with aspergillosis. Turbinate lysis was also found in about half of the dogs with lymphoplasmacytic rhinitis; however, T1-hypointense turbinates were present in more patients.[125]

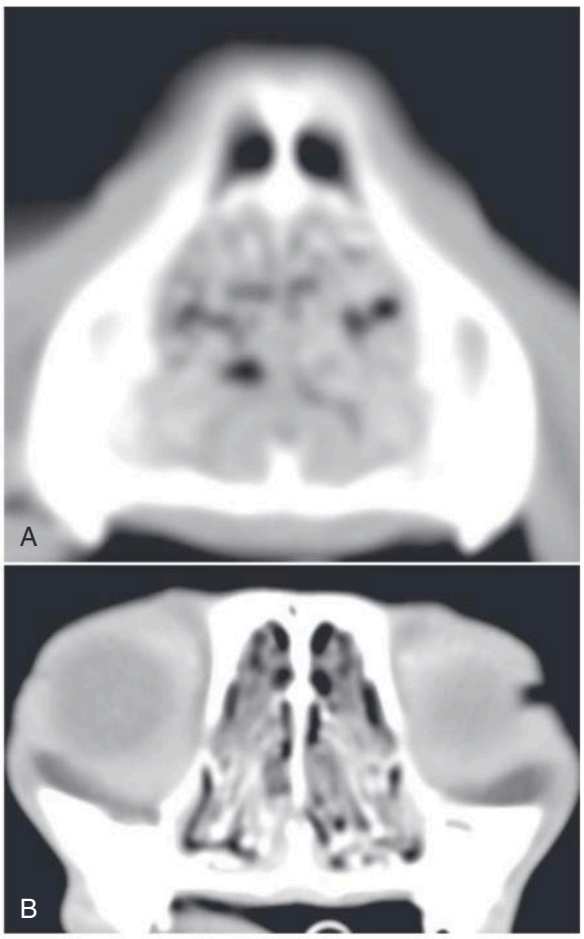


Fig. 11.23 Computed tomography (CT) images of the nasal cavity from a cat with chronic nasal discharge and presumed lower respiratory infection. Amorphous increased opacity in the nasal cavity is visible with indistinct conchal detail **(A and B)** likely caused by edema. This change, without a defined mass effect, and lack of turbinate destruction **(B)** are much more typical of an inflammatory process than a tumor. In radiographs, this change could easily go undetected because of its minor nature.

Nasal Foreign Bodies

Intranasal foreign bodies occur in dogs and cats,[128–131] and foreign plant matter is common in certain environments, for example, grass awns in California. Affected dogs have an acute onset of sneezing and pawing at the nose, and they often have unilateral nasal discharge that may be purulent and malodorous.[128,131] Radiographic findings include:

- Focal increase in soft-tissue opacity
- Focal bone lysis if chronic
- Radiopaque foreign bodies may be visible

CT is more sensitive for identification of foreign bodies than radiography as the findings can be very subtle and focal, but not all foreign objects will be hyperattenuating in CT images.

Otitis

Radiographs are an integral part of the diagnostic workup of a dog or cat presenting with ear disease for evaluation of otitis media. Diagnosis of otitis interna is based on clinical signs and requires CT or MRI for identification. However, in ventrodorsal radiographs, external ear canal stenosis and/or mineralization can often be identified. Otitis media is often secondary to chronic otitis externa. Radiographic findings of otitis media include:

- Increased opacity of the tympanic cavity
- Thickening of the osseous bulla
- In advanced disease, exuberant bone proliferation may involve the petrous temporal bone or the TMJ

The tympanic bullae are best evaluated in lateral oblique and open-mouth radiographic projections (Fig. 11.24). Otitis media can be unilateral; when this occurs, the diagnosis is simplified by a comparison between the two tympanic bullae (see Fig. 11.24). Positioning is crucial when radiography is performed for evaluation of the tympanic bullae; general anesthesia facilitates proper positioning and allows personnel to vacate the room during radiographic exposure. A review of imaging techniques and anatomy for middle ear disease can be found elsewhere.[132–134]

CT is a more sensitive test for evaluation of otitis media,[132–134] but proper technique is necessary to avoid artifactual wall thickening of the bulla on CT images (Fig. 11.25). CT images need to be viewed in a bone and soft-tissue window for complete evaluation (see Chapter 4).[133] Middle ear changes are commonly identified in MR and CT images of dogs with neurologic disease or with subclinical otitis media, and there was no correlation with the signal intensity of material within the middle ear and final diagnosis.[135,136] Evidence of material within the middle ear in MR images of dogs without clinical signs of otitis media was thought to represent subclinical otitis media or fluid accumulation without inflammation,[135,137] whereas in cats, it is thought that obstruction of the auditory tube by sinonasal disease results in effusive tympanic bulla disease seen on CT images.[138] Often, clinical and subclinical ear disease will be identified in cats undergoing CT imaging of the skull. In 310 cats undergoing CT imaging of the skull, 103 had middle ear disease and 34% of these had no clinical evidence of ear disease and most had concurrent nasal disease,[136] consistent with bullous effusion. Middle ear changes in CT in this evaluation were not specific for clinical or subclinical middle ear disease. Although not common, *Aspergillus* otitis has been reported in dogs and cats and is typically unilateral.[139]

Primary secretory otitis media (PSOM) has been described in Cavalier King Charles spaniels.[140] Clinical signs include pain localized to the head and neck and neurologic signs, which are similar to inflammatory central nervous system (CNS) and cervical disc disease, making it difficult to separate this disease from the common neurologic diseases seen in this breed.[140] Abnormalities of the external ear canal and bulging of the tympanic membrane may not be seen clinically, and CT or MRI is necessary for diagnosis. Treatment involves myringotomy and flushing of mucus and mucus plugs, which may need to be repeated. The cause of PSOM is thought to be from the middle ear or auditory tube and may relate to either increased production or decreased drainage of middle ear secretions.[140] An association of trigeminal nerve disease with bulla effusion has been recognized in dogs.[141,142] The trigeminal nerve innervates the muscle that controls opening of the pharyngeal orifice to the auditory tube. The increasing use of CT and MR skull imaging has resulted in documentation of other incidental or subclinical middle ear changes, such as otoliths and hyperostotic tympanic bone spicules in dogs and cats.[143,144]

Feline nasopharyngeal polyps are nonneoplastic growths originating from the mucous membrane of the auditory tube or middle ear.[145,146] Nasopharyngeal polyps generally occur in younger cats and can extend into the external ear canal, the osseous bulla, or the nasopharynx. Although rare, cats can have multiple polyps.[147] Cats may have signs of middle ear disease, rhinitis, or upper airway disease secondary to the space-occupying polyp. Signs of otitis media (increased soft-tissue opacity of the affected bulla) or nasopharyngeal obstruction (Fig. 11.26) may be noted on radiographs. Most feline nasopharyngeal polyps have peripheral contrast enhancement



Fig. 11.24 Dorsoventral **(A)**, rostrocaudal open mouth **(B)**, left 20-degree ventral/right dorsal **(C),** and right 20-degree ventral/left dorsal **(D)** tympanic bulla radiographs of a cat with right chronic otitis media. Compare the normal left tympanic bulla (air-filled, thin, bony rim) with the more opaque, thickened right bulla. The open-mouth radiograph must be interpreted with care, as displacement of the tongue will cause one tympanic bulla to have increased opacity. Here, the right tympanic bulla is more opaque in **B,** but there is also more soft tissue on the right side superimposed on the tympanic bulla. The oblique radiographs are of great value in this instance to assess the opacity of the tympanic bulla further.

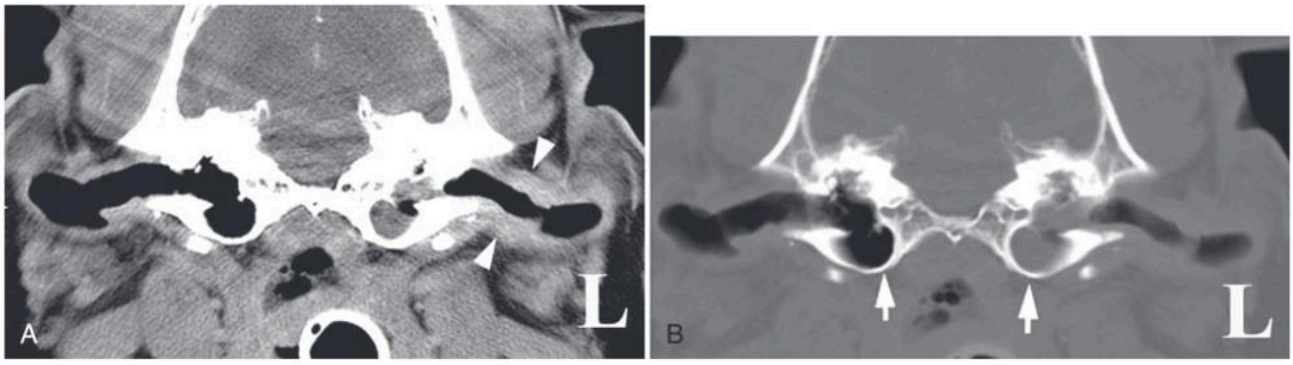


Fig. 11.25 **A,** Transverse computed tomography (CT) image at the level of the ears using a soft-tissue window (WL = 90, WW = 350) of a dog with a slight head tilt to the left. Note the thickened external ear canal (*white arrowheads*) and the soft tissue attenuating material in the left tympanic bulla. **B,** With a bone window (W 2500, L 480) for the same image, the bone thickness is more accurate. Note the tympanic bullae are the same thickness in **B** (*white arrows*), but the wall of the left tympanic bulla appears thicker in **A** due to an artifact associated with use of a soft-tissue window. *L,* Left.

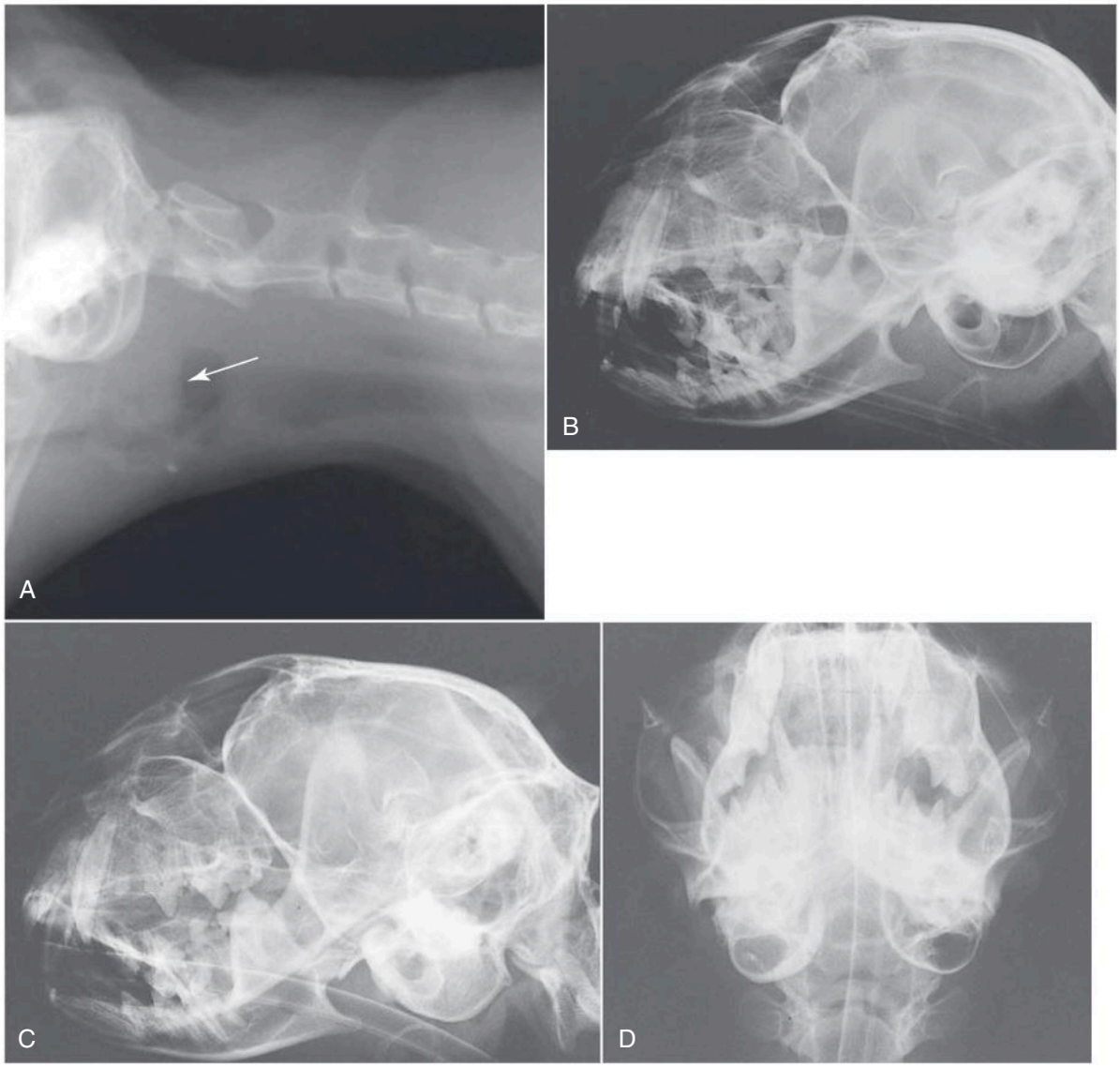


Fig. 11.26 Lateral **(A),** right dorsal-left ventral oblique **(B),** left dorsal-right ventral oblique **(C),** and rostral 10-degree ventral/caudodorsal **(D)** radiographs of a cat with inspiratory dyspnea caused by a nasopharyngeal polyp. Note the soft-tissue nodule in the pharyngeal region on the lateral projection (**A,** *arrow*). Increased opacity and bony thickening of the right tympanic bulla are present in **B, C,** and **D** due to otitis media, likely secondary to auditory tube obstruction by the polyp.

noted on postcontrast CT images, and this is thought to represent superficial inflammation (Fig. 11.27).[148] MRI can also be used to identify inflammatory polyps in cats (Fig. 11.28).[149]

Ear canal tumors occur in dogs and cats. Most often, these tumors are squamous cell carcinoma or mucinous gland adenocarcinoma.[150] Masses obliterate the external ear canal and can cause bone lysis of the adjacent calvaria and osseous bulla (Fig. 11.29). Median survival times for dogs with aural tumors is generally longer than for cats, and treatments usually involve surgery, radiotherapy, or a combination.[150]

Middle ear cholesteatoma, a benign, slowly growing skin cell growth in the middle ear has a distinct CT appearance, being characterized by severe bone changes at the contour of the tympanic bulla, including osteolysis, osteoproliferation and osteosclerosis, expansion of the tympanic cavity, and sclerosis or osteoproliferation of the ipsilateral TMJ and paracondylar process.[151–153] Cholesteatoma can cause lysis of the petrosal part of the temporal bone, leading to intracranial complications. There is usually no appreciable contrast enhancement of the tympanic bulla contents, but ring enhancement may be present (Fig. 11.30, eFig. 11.8).[152,153]

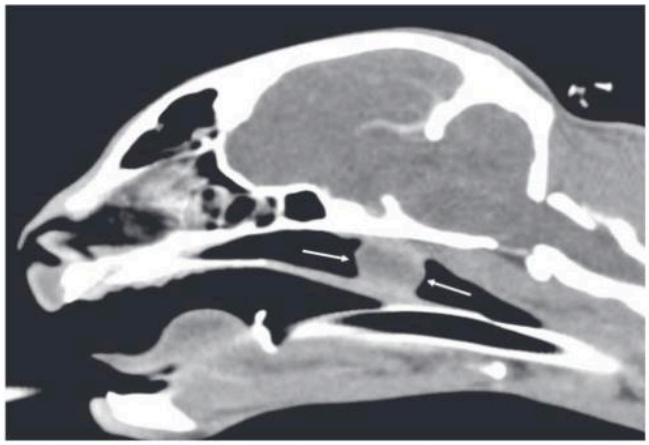


Fig. 11.27 Sagittal reconstructed postcontrast computed tomography (CT) image in a soft-tissue window (WL = 40, WW = 400) of a cat with a nasopharyngeal polyp. Note the peripheral contrast enhancement of the polyp outlined by *white arrows*.



eFig. 11.8 Transverse computed tomography (CT) image at the level of the tympanic bullae of a dog with left cholesteatoma. Note the expansion of the tympanic bulla with irregular thinning of the osseous margins. The tympanic cavity is filled with nonenhancing soft tissue attenuating material.



Fig. 11.28 Transverse **(A, C)** and sagittal reconstructed **(B)** computed tomography (CT) image of the pharyngeal region of a cat with a nasopharyngeal polyp (*white arrows*). In **C,** which is farther caudal than **A,** the polyp had obstructed the left auditory tube, leading to chronic otitis media with expansion and hyperostosis of the tympanic bulla caused by fluid and mucous accumulation.

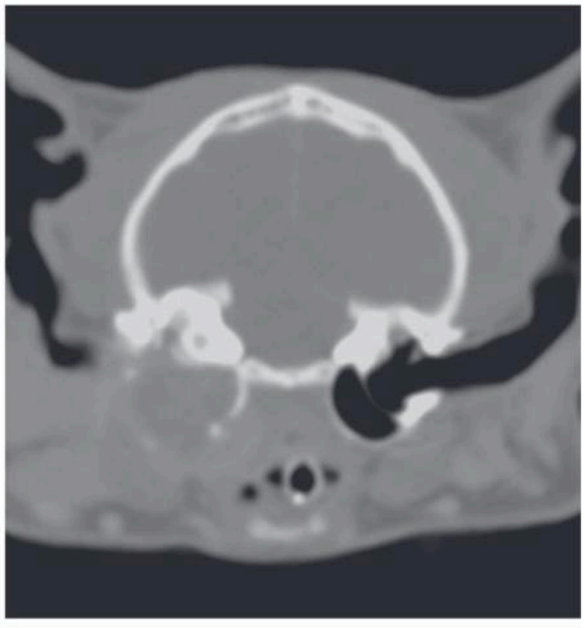


Fig. 11.29 Computed tomography (CT) image of the tympanic bulla region of a cat with a malignant tumor of the left middle ear. Increased tissue or fluid is present in the left tympanic bulla, and there has been expansion of the lateral and ventral aspects of the left tympanic bulla along with bone lysis. This aggressive appearance is typical of a malignant process and should not occur as a result of infection.

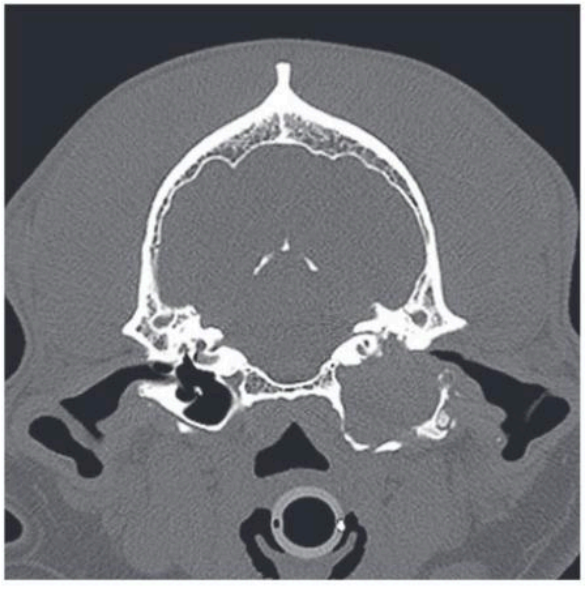


Fig. 11.30 Computed tomography (CT) image of a dog with a left tympanic bulla cholesteatoma. The lesion causes expansion and pressure necrosis of the tympanic bulla.

Masticatory Muscle Myositis

Masticatory muscle myositis is an immune-mediated inflammatory disease where antibodies are formed against type 2M muscle fibers that are present in the temporalis, masseter, and pterygoid muscles. Dogs with this condition often present with a history of lethargy, fever, regional lymphadenopathy, reluctance to eat, and swelling and/or atrophy of the masticatory muscles. The diagnosis is made by detection of antibodies against type 2M fibers in the serum or with histopathology. Cross-sectional imaging can be useful in identifying typical changes and guiding further diagnostics. Typical findings include change in size of the masticatory muscles, and heterogeneous appearance of the musculature with multifocal strong contrast enhancement (Fig. 11.31). The digastric muscle is not affected by the changes. Regional lymphadenopathy is usually present.[154]

TRAUMATIC INJURIES

TMJ luxation can occur in both dogs and cats after external trauma. In the cat, TMJ luxation often occurs after the cat has jumped from a height, and in both dogs and cats, dislocation can occur secondary to vehicular trauma.[155] The TMJ is capable of luxation without fracture because it has considerable lateral sliding movement, and the synchondrosis of the mandibular symphysis allows independent movement of the mandibular rami.[4] Dislocation of the TMJ tends to be in the rostrodorsal direction (Figs. 11.32 and 11.33, eFig. 11.9), because ventrocaudal luxation is prevented by the retroarticular process of the temporal bone.[4] Dogs and cats with TMJ dislocation are unable to close the mouth completely, have dental malocclusion with the mandible displaced to one side, and display excessive salivation.[4] Luxation is most often unilateral; it may

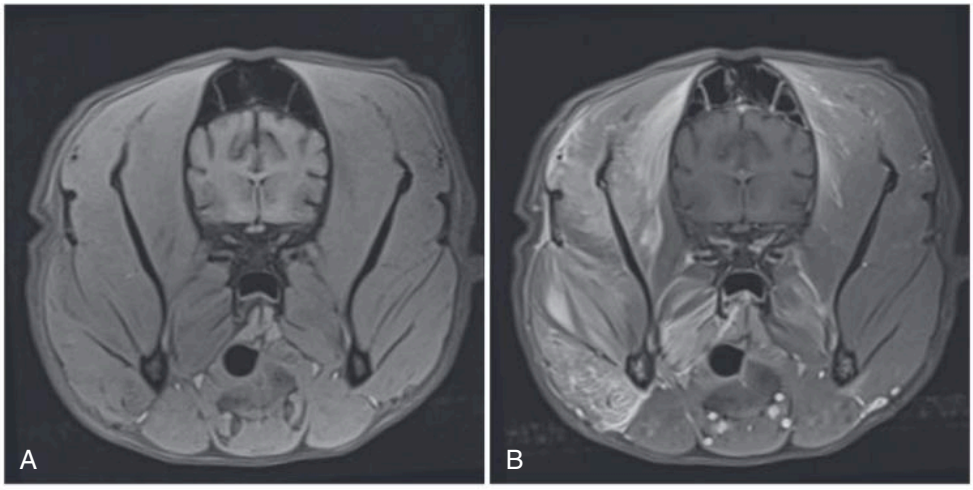


Fig. 11.31 T1-weighted precontrast **(A)** and postcontrast **(B)** transverse MR images of a dog with masticatory muscle myositis. There is marked heterogeneous contrast enhancement of the temporalis, masseter, and pterygoid muscles, worse on the right side. Note that the digastric muscles are not affected.

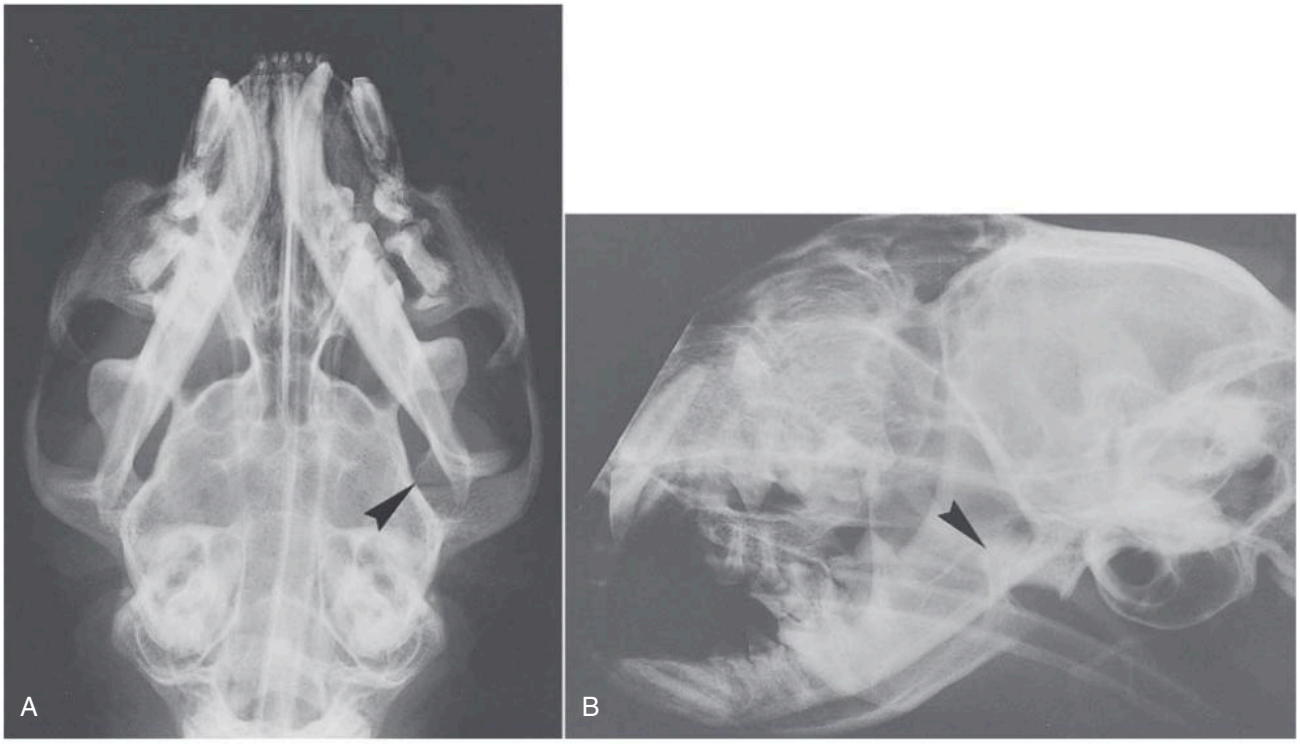
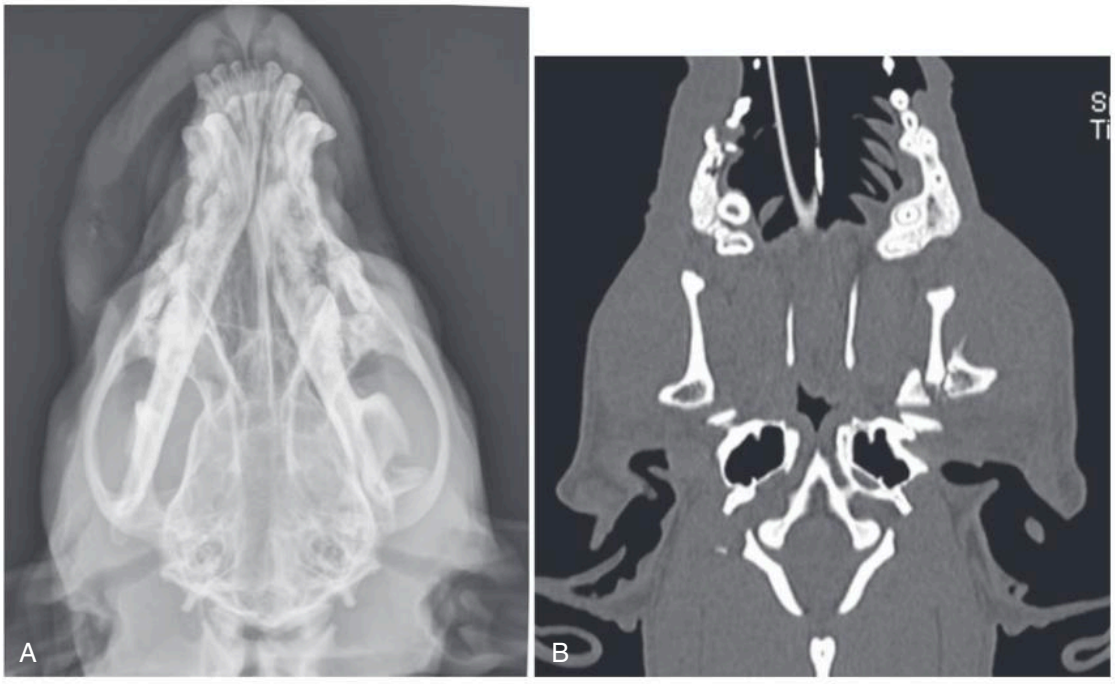


Fig. 11.32 Ventrodorsal **(A)** and right dorsal-left ventral oblique **(B)** radiographs of a 1-year-old domestic shorthair cat with a left temporomandibular luxation. Note the rostral location of the left mandibular condylar process (*arrowhead*) in the ventrodorsal radiograph **(A)**. In the lateral oblique radiograph **(B),** note the rostral and dorsal luxation of the mandibular condylar process (*arrowhead*).



eFig. 11.9 **(A)** Dorsoventral radiograph and **(B)** dorsal reformatted computed tomography (CT) images of a dog who was hit by a car. There is a comminuted fracture of the left temporomandibular joint. A comminuted left mandibular fracture is visible in **(A)** as well. The right muzzle is markedly swollen.

occur alone or with concomitant fractures of the retroarticular process, mandibular fossa, and zygomatic process of the squamous temporal bone or with the condyloid process of the mandible.[4,156]

Radiographic views necessary for evaluating the TMJ include ventrodorsal and 20-degree lateral oblique views in the cat.[4] These views are useful in the dog, but the angle of rotation varies depending on head conformation.[2] A sagittal oblique radiograph, in which the nose is elevated with a foam wedge so that the head is at a 20-degree angle to the cassette from a lateral position, is advocated in dogs as an alternative to lateral oblique views.[2,4] CT imaging provides for more accurate assessment of the TMJ, and it is helpful in diagnosing osteoarthritis, dysplasia, and other disorders.[4,156]

Skull trauma can occur after vehicular collision in dogs and cats. Currently, CT is used most often to image these patients for surgical planning. The ability to perform 3D reconstructions of the region enhances this planning (Fig. 11.34).

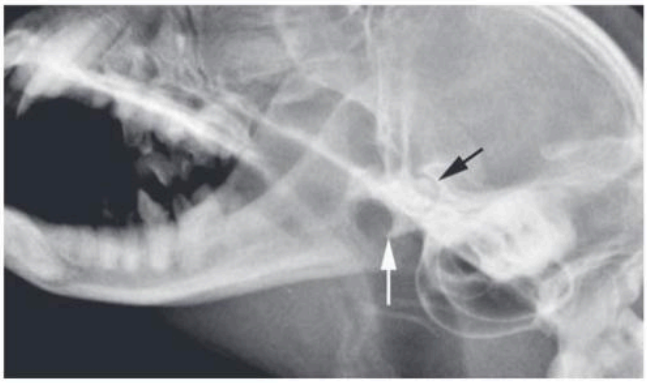


Fig. 11.33 Lateral radiograph of a cat with a unilateral temporomandibular luxation. In the affected joint the articular portion of the mandible is displaced dorsally, leaving an empty appearance to the articular portion of the temporal bone (*white arrow*). In the normal joint, there is good congruity between the articular portions of the mandible and temporal bone (*black arrow*).

MISCELLANEOUS DISEASES

Craniomandibular Osteopathy

Craniomandibular osteopathy (CMO) is a proliferative bone disease that occurs mainly in young West Highland White, Scottish, Cairn, Boston, and other terriers.[4] CMO is occasionally seen in nonterrier breeds. There is a known autosomal recessive inheritance in West Highland White terriers.[157,158] CMO is usually seen in young dogs aged 3 to 8 months; affected dogs have mandibular swelling, prehension difficulties, pain on opening the mouth or with mastication, pyrexia, or combinations of these clinical signs.[4] Bone proliferation can extend to the bullae, mandibular ramus, TMJ, and calvarium occasionally leading to complications.[159]

Radiographically, there is irregular new bone formation in affected areas, primarily the mandible, the tympanic bulla, and the petrous temporal bone (Fig. 11.35). Bone proliferation is often bilateral and may be asymmetric,

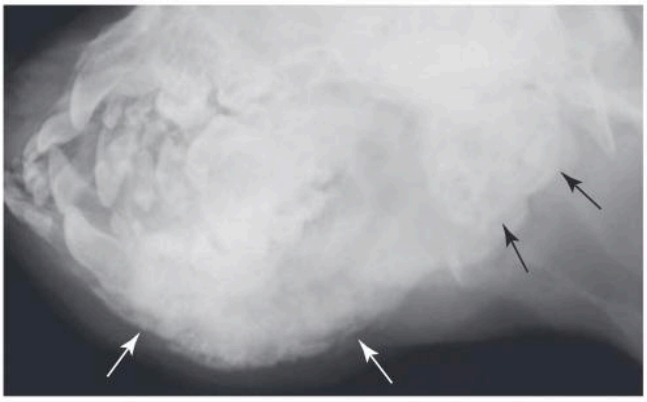


Fig. 11.35 Oblique skull radiograph of a Boston terrier with craniomandibular osteopathy (CMO). There is extensive bone proliferation on the mandibular ramus (*white arrows*), as well as the tympanic bulla (*black arrows*).

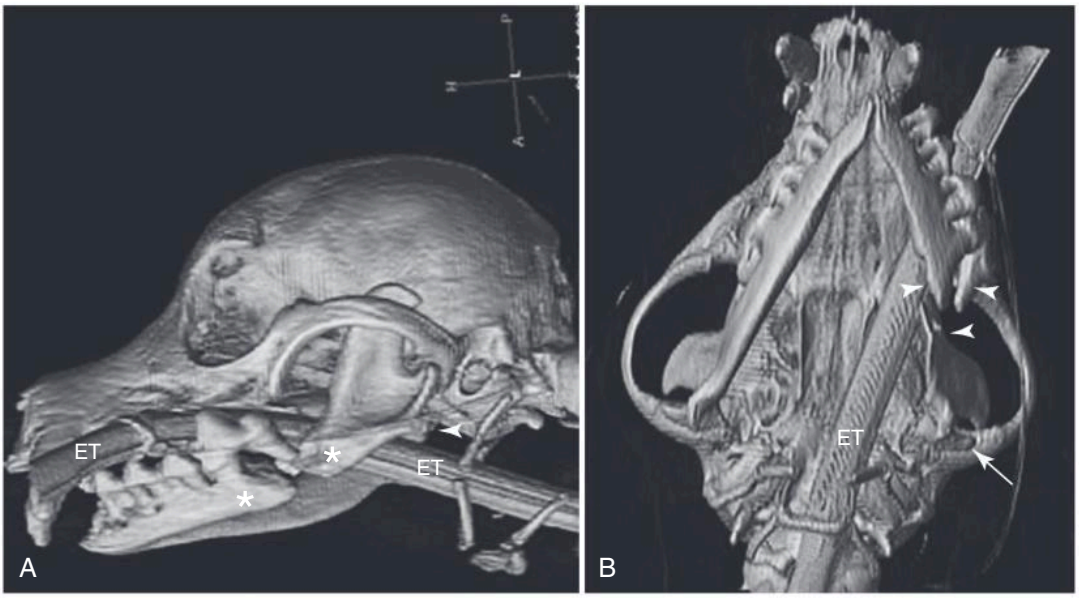


Fig. 11.34 Three-dimensional reconstructed volume rendering of the skull of a dog that sustained a left mandibular fracture. **A,** Left view. Note the obvious fracture fragments of the left mandible (*asterisks*) and that the caudal root of mandibular first molar is no longer embedded in bone. The angular and articular processes of the ramus are ill defined and displaced (*white arrowhead*), indicating probable temporomandibular joint (TMJ) subluxation and possible fracture. **B,** Ventral view. Note three fragments of the fractured left mandible (*white arrowheads*), deviation of the rostral mandible to the left, and caudal displacement of the left mandibular articular process (*white arrow*) indicating TMJ subluxation. *ET,* Endotracheal tube.

although unilateral disease can occur. Bone proliferation can involve the TMJ and can affect jaw movement. Diagnosis is based on signalment and on radiographic findings. Concurrent metaphyseal long-bone changes similar to metaphyseal osteopathy (hypertrophic osteodystrophy [HOD]) have been seen in dogs with CMO, but this is uncommon.[160,161] CMO is a self-limiting disease with unknown etiology. Bone proliferation generally ceases with skeletal maturation (Fig. 11.36).

Calvarial Hyperostosis

Calvarial hyperostotic syndrome resembles canine CMO but is characterized mainly by progressive and often asymmetric skull-bone involvement. The disease affects young male and female Bullmastiff dogs.[161,162] Radiographic findings are smooth thickening of various bones of the calvaria, to various degrees (Fig. 11.37). The smooth bone thickening is dissimilar from the irregular thickening seen in CMO. The etiology of calvarial hyperostosis is unknown.

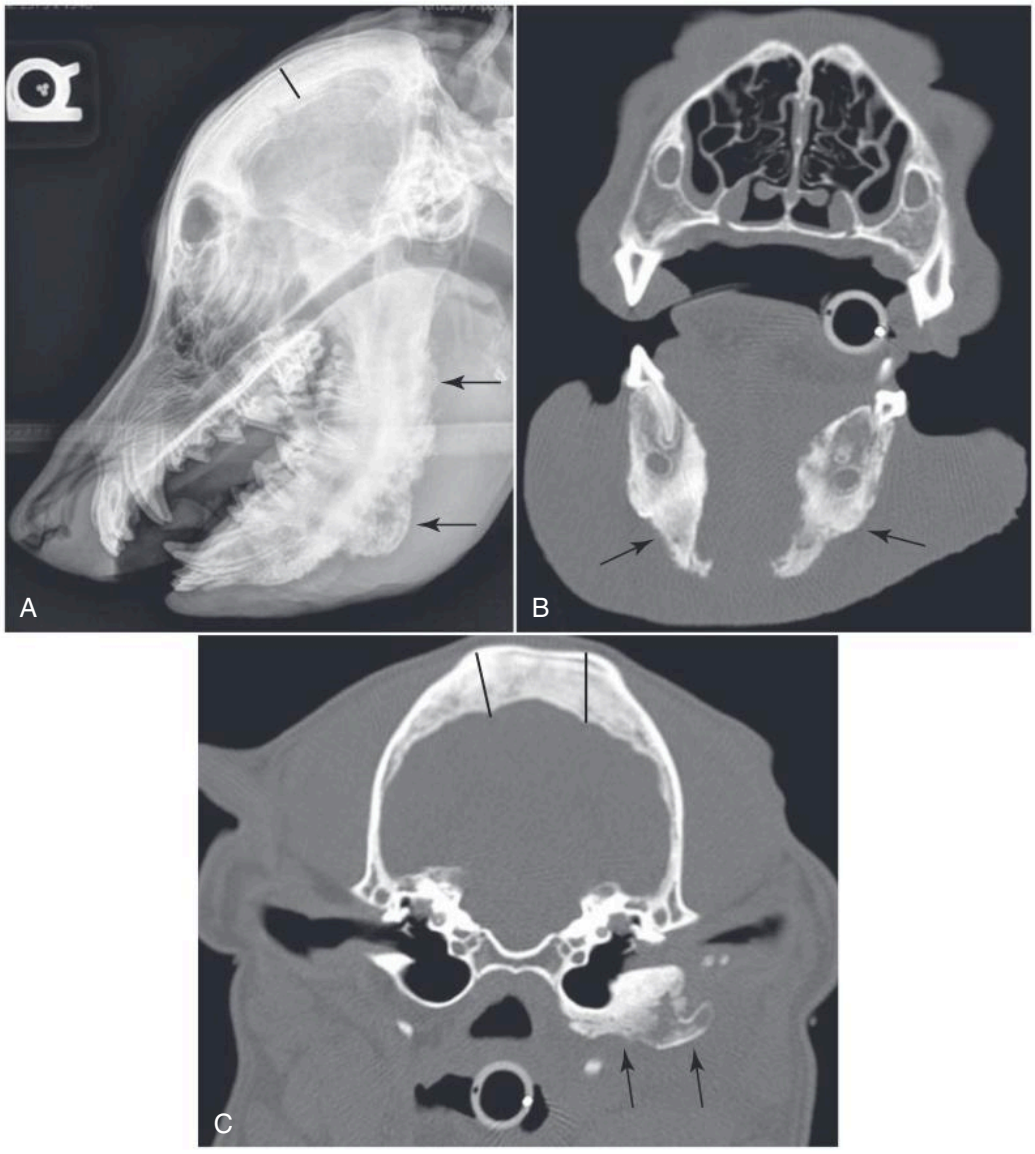


Fig. 11.36 Referral lateral radiograph and CT images of a 6-month-old female Labrador retriever cross with thickened, painful mandible, fever, and chronic hyporexia progressing to anorexia. Clinical signs and bone biopsy consistent with craniomandibular osteopathy (CMO). Right lateral skull image **(A)** and CT images **(B, C)**. In **(A),** note the proliferative bone thickening of the mandible and the calvarium (*black arrows* and *black line*). In **(B),** rostral aspect of skull at level of mandibles, note the smooth bordered and thickened bone attenuation of the mandibles (*black arrows*) and associated soft tissue attenuation. In **(C),** caudal aspect of skull at level of tympanic bullae, note the smooth bordered and thickened bone attenuation of the left bulla, as compared to normal right side (*black arrows*) along with soft tissue attenuation with narrowing of left external ear canal. Note smooth bordered and thickened bone attenuation of dorsal calvarium (*black lines*).



Fig. 11.37 Lateral radiograph of a 6-month-old mastiff. There is smooth thickening of the mandibular, dorsal nasal, and calvarial cortices. Note the small size of the frontal sinuses caused by the peripheral hyperostosis.

REFERENCES

1. Hermanson JW, de Lahunta A, Evans HE. *Miller and Evans' Anatomy of the Dog*. 5th ed. St. Louis: Elsevier; 2020.
2. Dickie AM, Sullivan M. The effect of obliquity on the radiographic appearance of the temporomandibular joint in dogs. *Vet Radiol Ultrasound*. 2001;42(3):205–217.
3. Hammond G, King A, Lapaglia J. Assessment of five oblique radiographic projections of the canine temporomandibular joint. *Vet Radiol Ultrasound*. 2012;53(5):501–506.
4. Schwarz T, Weller R, Dickie AM, Konar M, Sullivan M. Imaging of the canine and feline temporomandibular joint: a review. *Vet Radiol Ultrasound*. 2002;43(2):85–97.
5. Arzi B, Cissell DD, Verstraete FJ, Kass PH, DuRaine GD, Athanasiou KA. Computed tomographic findings in dogs and cats with temporomandibular joint disorders: 58 cases (2006–2011). *J Am Vet Med Assoc*. 2013;242(1):69–75.
6. Macready DM, Hecht S, Craig LE, Conklin GA. Magnetic resonance imaging features of the temporomandibular joint in normal dogs. *Vet Radiol Ultrasound*. 2010;51(4): 436–440.
7. De Rycke LMS JH, Gielen IM, et al. Magnetic resonance imaging, computed tomography, and cross-sectional views of the anatomy of normal nasal cavities and paranasal sinuses in mesaticephalic dogs. *Am J Vet Res*. 2003;64: 1093–1098.
8. Couturier LD C, Ruel Y, Dennis R, Begon D. Anatomical study of cranial nerve emergence and skull foramina in the dog using magnetic resonance imaging and computed tomography. *Vet Radiol Ultrasound*. 2005;46(5):375–383.
9. Gomes E, Degueurce C, Ruel Y, Dennis R, Begon D. Anatomic study of cranial nerve emergence and associated skull foramina in cats using CT and MRI. *Vet Radiol Ultrasound*. 2009;50(4):398–403.
10. Kneissl SP A, Konar M. Low-field magnetic resonance imaging of the canine middle and inner ear. *Vet Radiol Ultrasound*. 2004;45(6):520–552.
11. Lefebvre J, Kuehn NF, Wortinger A. Computed tomography as an aid in the diagnosis of chronic nasal disease in dogs. *J Small Anim Pract*. 2005;46(6):280–285.
12. Schwarz TSJ. *Veterinary Computed Tomography*. West Sussex: UK: Wiley Blackwell; 2011.
13. Wisner ERZ A. *Atlas of Small Animal CT and MRI*. Ames, IA: Wiley Blackwell; 2015.
14. Estey CM. Congenital hydrocephalus. *Vet Clin North Am Small Anim Pract*. 2016;46(2):217–229.
15. Hecht S, Adams WH. MRI of brain disease in veterinary patients part 1: basic principles and congenital brain disorders. *Vet Clin North Am Small Anim Pract*. 2010;40(1):21–38.
16. Thomas WB. Hydrocephalus in dogs and cats. *Vet Clin North Am Small Anim Pract*. 2010;40(1):143–159.
17. Thomas WB. Nonneoplastic disorders of the brain. *Clin Tech Small Anim Pract*. 1999;14(3):125–147.
18. Cerda-Gonzalez S, Dewey CW. Congenital diseases of the craniocervical junction in the dog. *Vet Clin North Am Small Anim Pract*. 2010;40(1):121–141.
19. De Haan CEK SL, Gavin PR, Wendling LR, Griebenow ML. Normal variation in size of the lateral ventricles of the Labrador retriever dog as assessed by magnetic resonance imaging. *Vet Radiol Ultrasound*. 1994;35(2):83–86.
20. Cerda-Gonzalez S, Dewey CW, Scrivani PV, Kline KL. Imaging features of atlanto-occipital overlapping in dogs. *Vet Radiol Ultrasound*. 2009;50(3):264–268.
21. Parry AT, Upjohn MM, Schlegl K, Kneissl S, Lamb CR. Computed tomography variations in morphology of the canine atlas in dogs with and without atlantoaxial subluxation. *Vet Radiol Ultrasound*. 2010;51(6):596–600.
22. Cerda-Gonzalez S, Olby NJ, McCullough S, Pease AP, Broadstone R, Osborne JA. Morphology of the caudal fossa in cavalier king Charles spaniels. *Vet Radiol Ultrasound*. 2009;50(1):37–46.
23. Rusbridge C. Neurological diseases of the cavalier king Charles spaniel. *J Small Anim Pract*. 2005;46(6):265–272.
24. Rusbridge C, Knowler SP. Hereditary aspects of occipital bone hypoplasia and syringomyelia (Chiari type I malformation) in cavalier King Charles spaniels. *Vet Rec*. 2003;153(4):107–112.
25. Rusbridge C, Knowler SP. Inheritance of occipital bone hypoplasia (Chiari type I malformation) in cavalier king Charles spaniels. *J Vet Intern Med*. 2004;18(5):673–678.
26. Freeman AC, Platt SR, Kent M, Huguet E, Rusbridge C, Holmes S. Chiari-like malformation and syringomyelia in American Brussels Griffon dogs. *J Vet Intern Med*. 2014;28(5):1551–1559.
27. Gatineau M, El-Warrak AO, Marretta SM, Kamiya D, Moreau M. Locked jaw syndrome in dogs and cats: 37 cases (1998–2005). *J Vet Dent*. 2008;25(1):16–22.
28. Dickie AM, Schwarz T, Sullivan M. Temporomandibular joint morphology in cavalier king Charles spaniels. *Vet Radiol Ultrasound*. 2002;43(3):260–266.
29. Nutt AE, Anderson T, Gracis M, Doran I, Warren-Smith C, Langley-Hobbs SJ. Open-mouth jaw locking in cats: a literature review and use of CT in three cases. *J Feline Med Surg*. 2018;20(12):1180–1191.
30. Reiter AM. Symphysiotomy, symphysiectomy, and intermandibular arthrodesis in a cat with open-mouth jaw locking—case report and literature review. *J Vet Dent*. 2004;21(3):147–158.
31. Beam RC, Kunz DA, Cook CR, Carson RL, Briscoe P, Cook JL. Use of three-dimensional computed tomography for diagnosis and treatment planning for open-mouth jaw locking in a cat. *J Am Vet Med Assoc*. 2007;230(1):59–63.
32. Crawley AC, Muntz FH, Haskins ME, Jones BR, Hopwood JJ. Prevalence of mucopolysaccharidosis type VI mutations in Siamese cats. *J Vet Intern Med*. 2003;17(4):495–498.
33. Haskins M, Casal M, Ellinwood NM, et al. Animal models for mucopolysaccharidoses and their clinical relevance. *Acta Paediatr Suppl*. 2002;91(439):88–97.
34. Haskins ME. Animal models for mucopolysaccharidosis disorders and their clinical relevance. *Acta Paediatr*. 2007;96(455):56–62.
35. Konde LJT MA, Gaser P, Dial SM, McBiles K, Colgan S, Haskins M. Radiographically visualized skeletal changes associated with mucopolysaccharidosis VI in cats. *Vet Radiol*. 1987;28(6):223–228.

36. Cotugno G, Annunziata P, Tessitore A, et al. Long-term amelioration of feline Mucopolysaccharidosis VI after AAV-mediated liver gene transfer. *Mol Ther*. 2011;19(3):461–469.
37. Bonczynski J. Primary hyperparathyroidism in dogs and cats. *Clin Tech Small Anim Pract*. 2007;22(2):70–74.
38. Feldman EC, Hoar B, Pollard R, Nelson RW. Pretreatment clinical and laboratory findings in dogs with primary hyperparathyroidism: 210 cases (1987–2004). *J Am Vet Med Assoc*. 2005;227(5):756–761.
39. Kumar R, Thompson JR. The regulation of parathyroid hormone secretion and synthesis. *J Am Soc Nephrol*. 2011;22(2):216–224. Epub 2010-12-16.
40. Parker VJ, Harjes LM, Dembek K, Young GS, Chew DJ, Toribio RE. Association of vitamin D metabolites with parathyroid hormone, fibroblast growth factor-23, calcium, and phosphorus in dogs with various stages of chronic kidney disease. *J Vet Intern Med*. 2017;31(3):791–798.
41. Krook LW JP. Nutritional secondary hyperparathyroidism in the animal kingdom: report of two cases. *Clin Imaging*. 2010;34(6):458–461.
42. Wisner ER, Nyland TG. Ultrasonography of the thyroid and parathyroid glands. *Vet Clin North Am Small Anim Pract*. 1998;28(4):973–991.
43. Lautscham E, von Klopmann C, Schaub S, Stengel C, Hartmann A. CT imaging features of the normal parathyroid gland in the dog. *Tierarztl Prax Ausg K Kleintiere Heimtiere*. 2020;48(5):313–320. Epub 2020-10-21.
44. Liles SR, Linder KE, Cain B, Pease AP. Ultrasonography of histologically normal parathyroid glands and thyroid lobules in normocalcemic dogs. *Vet Radiol Ultrasound*. 2010;51(4):447–452.
45. Taeymans O, Dennis R, Saunders JH. Magnetic resonance imaging of the normal canine thyroid gland. *Vet Radiol Ultrasound*. 2008;49(3):238–242.
46. Taeymans O, Schwarz T, Duchateau L, et al. Computed tomographic features of the normal canine thyroid gland. *Vet Radiol Ultrasound*. 2008;49(1):13–19.
47. Thompson D, Skelly B. Prevalence of canine primary hyperparathyroidism recurrence in Keeshond and non-Keeshond dogs after curative parathyroidectomy. *Vet Rec*. 2020;187(11):e93.
48. Amorós O, Espada Y, Vila A, Jiménez A, Novellas R. Precontrast CT attenuation of the thyroid gland is lower in brachycephalic dogs versus non-brachycephalic dogs. *Vet Radiol Ultrasound*. 2021;62(1):54–60.
49. Fischetti AJ, Gisselman K, Peterson ME. CT and MRI evaluation of skull bones and soft tissues in six cats with presumed acromegaly versus 12 unaffected cats. *Vet Radiol Ultrasound*. 2012;53(5):535–539.
50. Lamb CR, Ciasca TC, Mantis P, et al. Computed tomographic signs of acromegaly in 68 diabetic cats with hypersomatotropism. *J Feline Med Surg*. 2014;16(2):99–108.
51. Niessen SJ. Feline acromegaly: an essential differential diagnosis for the difficult diabetic. *J Feline Med Surg*. 2010;12(1):15–23.
52. Malinowski C. Canine and feline nasal neoplasia. *Clin Tech Small Anim Pract*. 2006;21(2):89–94.
53. Ferguson S, Smith KC, Welsh CE, Dobromylskyj MJ. A retrospective study of more than 400 feline nasal biopsy samples in the UK (2006–2013). *J Feline Med Surg*. 2020;22(8):736–743.
54. Nakazawa M, Tomiyasu H, Suzuki K, et al. Efficacy of chemotherapy and palliative hypofractionated radiotherapy for cats with nasal lymphoma. *J Vet Med Sci*. 2021;83(3):456–460.
55. Reczynska AI, LaRue SM, Boss MK, et al. Outcome of stereotactic body radiation for treatment of nasal and nasopharyngeal lymphoma in 32 cats. *J Vet Intern Med*. 2022;36(2):733–742.
56. Giuliano A, Dobson J. Clinical response and survival time of cats with carcinoma of the nasal cavity treated with palliative coarse fractionated radiotherapy. *J Feline Med Surg*. 2020;22(10):922–927.
57. Haney SM, Beaver L, Turrel J, et al. Survival analysis of 97 cats with nasal lymphoma: a multi-institutional retrospective study (1986–2006). *J Vet Intern Med*. 2009;23(2):287–294.
58. Mayer MN, DeWalt JO, Sidhu N, Mauldin GN, Waldner CL. Outcomes and adverse effects associated with stereotactic body radiation therapy in dogs with nasal tumors: 28 cases (2011–2016). *J Am Vet Med Assoc*. 2019;254(5):602–612.
59. Mortier JR, Blackwood L. Treatment of nasal tumours in dogs: a review. *J Small Anim Pract*. 2020;61(7):404–415.
60. Poirier VJ, Koh ESY, Darko J, Fleck A, Pinard C, Vail DM. Patterns of local residual disease and local failure after intensity modulated/image guided radiation therapy for sinonasal tumors in dogs. *J Vet Intern Med*. 2021;35(2):1062–1072.
61. Lawrence JA, Forrest LJ, Turek MM, et al. Proof of principle of ocular sparing in dogs with sinonasal tumors treated with intensity-modulated radiation therapy. *Vet Radiol Ultrasound*. 2010;51(5):561–570.
62. Kubicek L, Milner R, An Q, et al. Outcomes and prognostic factors associated with canine sinonasal tumors treated with curative intent cone-based stereotactic radiosurgery (1999–2013). *Vet Radiol Ultrasound*. 2016;57(3):331–340.
63. Stevens A, Turek M, Vail D, Christensen N, Forrest L. Definitive-intent intensity modulated radiotherapy for modified-Adams' stage 4 canine sinonasal cancer: a retrospective study of 29 cases (2011–2017). *Vet Radiol Ultrasound*. 2020;61(6):718–725.
64. Stiborova K, Meier VS, Takada M, et al. Definitive-intent radiotherapy for sinonasal carcinoma in cats: a multicenter retrospective assessment. *Vet Comp Oncol*. 2020;18(4):626–633.
65. Russo M, Lamb CR, Jakovljevic S. Distinguishing rhinitis and nasal neoplasia by radiography. *Vet Radiol Ultrasound*. 2000;41(2):118–124.
66. Kirberger RM, Fourie SL. An investigation into the usefulness of a rostrocaudal nasal radiographic view in the dog. *J S Afr Vet Assoc*. 2002;73(4):171–176.
67. Ciekot PA, Powers BE, Withrow SJ, Straw RC, Ogilvie GK, LaRue SM. Histologically low-grade, yet biologically high-grade, fibrosarcomas of the mandible and maxilla in dogs: 25 cases (1982–1991). *J Am Vet Med Assoc*. 1994;204(4):610–615.
68. Morris JS, Dunn KJ, Dobson JM, White RA. Radiological assessment of severity of canine nasal tumours and relationship with survival. *J Small Anim Pract*. 1996;37(1):1–6.
69. Adams WM, Kleiter MM, Thrall DE, et al. Prognostic significance of tumor histology and computed tomographic staging for radiation treatment response of canine nasal tumors. *Vet Radiol Ultrasound*. 2009;50(3):330–335.
70. Drees R, Forrest LJ, Chappell R. Comparison of computed tomography and magnetic resonance imaging for the evaluation of canine intranasal neoplasia. *J Small Anim Pract*. 2009;50(7):334–340.
71. Miles MS, Dhaliwal RS, Moore MP, Reed AL. Association of magnetic resonance imaging findings and histologic diagnosis in dogs with nasal disease: 78 cases (2001–2004). *J Am Vet Med Assoc*. 2008;232(12):1844–1849.

72. Miles S, Schwarz T. Canine nasal septum deviation can be a normal variation and correlates with increasing skull indices. *Vet Radiol Ultrasound*. 2020;61(3):279–284.
73. Schwarz T, Sullivan M, Hartung K. Radiographic detection of defects of the nasal boundaries. *Vet Radiol Ultrasound*. 2000;41(3):226–230.
74. Bouyssou S, Hammond GJ, Eivers C. Comparison of CT features of 79 cats with intranasal mass lesions. *J Feline Med Surg*. 2021;23(10):987–995.
75. Tromblee TC, Jones JC, Etue AE, Forrester SD. Association between clinical characteristics, computed tomography characteristics, and histologic diagnosis for cats with sinonasal disease. *Vet Radiol Ultrasound*. 2006;47(3): 241–248.
76. Avner A, Dobson JM, Sales JI, Herrtage ME. Retrospective review of 50 canine nasal tumours evaluated by low-field magnetic resonance imaging. *J Small Anim Pract*. 2008;49(5):233–239.
77. Bradshaw T, Fu R, Bowen S, Zhu J, Forrest L, Jeraj R. Predicting location of recurrence using FDG, FLT, and Cu-ATSM PET in canine sinonasal tumors treated with radiotherapy. *Phys Med Biol*. 2015;60(13):5211–5224.
78. Bradshaw TJ, Bowen SR, Jallow N, Forrest LJ, Jeraj R. Heterogeneity in intratumor correlations of 18F-FDG, 18F-FLT, and 61Cu-ATSM PET in canine sinonasal tumors. *J Nucl Med*. 2013;54(11):1931–1937.
79. Liptak JM. Cancer of the gastrointestinal tract. In: Vail DMT,DH, Liptak JM, eds. *Withrow and MacEwen's Small Animal Clinical Oncology*. 6th ed. St. Louis, MO: Elsevier; 2020:432–491.
80. Mikiewicz M, Paździor-Czapula K, Gesek M, Lemishevskyi V, Otrocka-Domagała I. Canine and feline oral cavity tumours and tumour-like lesions: a retrospective study of 486 cases (2015–2017). *J Comp Pathol*. 2019;172:80–87.
81. Liptak JMC, Christensen NI. Soft tissue sarcomas. In: Vail DMT DH, Liptak JM, eds. *Withrow and MacEwen's Small Animal Clinical Oncology*. 6th ed. St. Louis, MO: Elsevier; 2020:404–431.
82. Bergman PJ, Selmic LE, Kent MS. Melanoma. In: Vail DMT,DH, Liptak JM, eds. *Withrow and MacEwen's Small Animal Clinical Oncology*. 6th ed. St. Louis, MO: Elsevier; 2020:367–381.
83. Forrest LJ, Chun R, Adams WM, Cooley AJ, Vail DM. Postoperative radiotherapy for canine soft tissue sarcoma. *J Vet Intern Med*. 2000;14(6):578–582.
84. Camerino M, Giacobino D, Manassero L, et al. Prognostic impact of bone invasion in canine oral malignant melanoma treated by surgery and anti-CSPG4 vaccination: a retrospective study on 68 cases (2010–2020). *Vet Comp Oncol*. 2022;20(1):189–197.
85. Soltero-Rivera MM, Krick EL, Reiter AM, Brown DC, Lewis JR. Prevalence of regional and distant metastasis in cats with advanced oral squamous cell carcinoma: 49 cases (2005–2011). *J Feline Med Surg*. 2014;16(2):164–169.
86. Gendler A, Lewis JR, Reetz JA, Schwarz T. CT features of oral squamous cell carcinoma in cats: 18 cases (2002–2008). *J Am Vet Med Assoc*. 2010;236(3):319–325.
87. Giacobino D, Camerino M, Riccardo F, et al. Difference in outcome between curative intent vs marginal excision as a first treatment in dogs with oral malignant melanoma and the impact of adjuvant CSPG4-DNA electrovaccination: a retrospective study on 155 cases. *Vet Comp Oncol*. 2021;19(4):651–660.
88. Bertone ER, Snyder LA, Moore AS. Environmental and lifestyle risk factors for oral squamous cell carcinoma in domestic cats. *J Vet Intern Med*. 2003;17(4):557–562.
89. Zaccone R, Renzi A, Chalfon C, et al. Environmental risk factors for the development of oral squamous cell carcinoma in cats. *J Vet Intern Med*. 2022;36(4):1398–1408.
90. Bilgic O, Duda L, Sánchez MD, Lewis JR. Feline oral squamous cell carcinoma: clinical manifestations and literature review. *J Vet Dent*. 2015;32(1):30–40.
91. Poirier VJ, Kaser-Hotz B, Vail DM, Straw RC. Efficacy and toxicity of an accelerated hypofractionated radiation therapy protocol in cats with oral squamous cell carcinoma. *Vet Radiol Ultrasound*. 2013;54(1):81–88.
92. Lee S, Jang Y, Lee G, Jeon S, Kim D, Choi J. CT features of malignant and benign oral tumors in 28 dogs. *Vet Radiol Ultrasound*. 2021;62(5):549–556.
93. Randall EK, Kraft SL, Yoshikawa H, LaRue SM. Evaluation of 18F-FDG PET/CT as a diagnostic imaging and staging tool for feline oral squamous cell carcinoma. *Vet Comp Oncol*. 2016;14(1):28–38.
94. Kawabe M, Mori T, Ito Y, et al. Outcomes of dogs undergoing radiotherapy for treatment of oral malignant melanoma: 111 cases (2006–2012). *J Am Vet Med Assoc*. 2015;247(10):1146–1153.
95. Murphy S, Hayes AM, Blackwood L, Maglennon G, Pattinson H, Sparkes AH. Oral malignant melanoma – the effect of coarse fractionation radiotherapy alone or with adjuvant carboplatin therapy. *Vet Comp Oncol*. 2005;3(4):222–229.
96. McCaw DL, Pope ER, Payne JT, West MK, Tompson RV, Tate D. Treatment of canine oral squamous cell carcinomas with photodynamic therapy. *Br J Cancer*. 2000;82(7):1297–1299.
97. Baja AJ, Kelsey KL, Ruslander DM, Gieger TL, Nolan MW. A retrospective study of 101 dogs with oral melanoma treated with a weekly or biweekly 6 Gy × 6 radiotherapy protocol. *Vet Comp Oncol*. 2022;20(3):623–631.
98. Boston SE, Lu X, Culp WT, et al. Efficacy of systemic adjuvant therapies administered to dogs after excision of oral malignant melanomas: 151 cases (2001–2012). *J Am Vet Med Assoc*. 2014;245(4):401–407.
99. Ottnod JM, Smedley RC, Walshaw R, Hauptman JG, Kiupel M, Obradovich JE. A retrospective analysis of the efficacy of Oncept vaccine for the adjunct treatment of canine oral malignant melanoma. *Vet Comp Oncol*. 2013;11(3):219–229.
100. Proulx DR, Ruslander DM, Dodge RK, et al. A retrospective analysis of 140 dogs with oral melanoma treated with external beam radiation. *Vet Radiol Ultrasound*. 2003;44(3):352–359.
101. Tarone L, Giacobino D, Camerino M, et al. Canine melanoma immunology and immunotherapy: relevance of translational research. *Front Vet Sci*. 2022;9:1–11.
102. Soukup JW, Snyder CJ, Simmons BT, Pinkerton ME, Chun R. Clinical, histologic, and computed tomographic features of oral papillary squamous cell carcinoma in dogs: 9 cases (2008–2011). *J Vet Dent*. 2013;30(1):18–24.
103. Gardner H, Fidel J, Haldorson G, Dernell W, Wheeler B. Canine oral fibrosarcomas: a retrospective analysis of 65 cases (1998–2010). *Vet Comp Oncol*. 2015;13(1):40–47.
104. Riggs J, Adams VJ, Hermer JV, Dobson JM, Murphy S, Ladlow JF. Outcomes following surgical excision or surgical excision combined with adjunctive, hypofractionated radiotherapy in dogs with oral squamous cell carcinoma or fibrosarcoma. *J Am Vet Med Assoc*. 2018;253(1):73–83.
105. Selmic LE, Lafferty MH, Kamstock DA, et al. Outcome and prognostic factors for osteosarcoma of the maxilla, mandible, or calvarium in dogs: 183 cases (1986–2012). *J Am Vet Med Assoc*. 2014;245(8):930–938.

106. Dernell WS, Straw RC, Cooper MF, Powers BE, LaRue SM, Withrow SJ. Multilobular osteochondrosarcoma in 39 dogs: 1979–1993. *J Am Anim Hosp Assoc.* 1998;34(1): 11–18.
107. Ehrhart NP, Christensen NI, Fan TM. Tumors of the skeletal system. In: Vail DMT,DH, Liptak JM, eds. *Withrow and MacEwen's Small Animal Clinical Oncology.* 6th ed. St. Louis, MO: Elsevier; 2020:524–564.
108. Banks TA, Straw RC. Multilobular osteochondrosarcoma of the hard palate in a dog. *Aust Vet J.* 2004;82(7):409–412.
109. Hathcock JT, Newton JC. Computed tomographic characteristics of multilobular tumor of bone involving the cranium in 7 dogs and zygomatic arch in 2 dogs. *Vet Radiol Ultrasound.* 2000;41(3):214–217.
110. Gallegos J, Schwarz T, McAnulty JF. Massive midline occipitotemporal resection of the skull for treatment of multilobular osteochondrosarcoma in two dogs. *J Am Vet Med Assoc.* 2008;233(5):752–757.
111. Lipsitz D, Levitski RE, Berry WL. Magnetic resonance imaging features of multilobular osteochondrosarcoma in 3 dogs. *Vet Radiol Ultrasound.* 2001;42(1):14–19.
112. Volker MK, Luskin IR. Oral osteoma in 6 dogs. *J Vet Dent.* 2014;31(2):88–91.
113. Grozdanic S, Riedesel EA, Ackermann MR. Successful medical treatment of an orbital osteoma in a dog. *Vet Ophthalmol.* 2013;16(2):135–139.
114. Polizopoulou ZS, Koutinas AF, Souftas VD, Kaldrymidou E, Kazakos G, Papadopoulos G. Diagnostic correlation of CT-MRI and histopathology in 10 dogs with brain neoplasms. *J Vet Med A Physiol Pathol Clin Med.* 2004;51(5): 226–231.
115. Motta L, Mandara MT, Skerritt GC. Canine and feline intracranial meningiomas: an updated review. *Vet J.* 2012;192(2):153–165.
116. Sharman MJ, Mansfield CS. Sinonasal aspergillosis in dogs: a review. *J Small Anim Pract.* 2012;53(8):434–444.
117. Cooley S, Galustanian G, Moon A, Summers S. CT findings of nasal cryptococcosis in cats and dogs: a case series. *Vet Radiol Ultrasound.* 2022;63(4):422–429.
118. Trivedi SR, Sykes JE, Cannon MS, et al. Clinical features and epidemiology of cryptococcosis in cats and dogs in California: 93 cases (1988–2010). *J Am Vet Med Assoc.* 2011;239(3):357–369.
119. Saunders JH, Clercx C, Snaps FR, et al. Radiographic, magnetic resonance imaging, computed tomographic, and rhinoscopic features of nasal aspergillosis in dogs. *J Am Vet Med Assoc.* 2004;225(11):1703–1712.
120. Saunders JH, van Bree H. Comparison of radiography and computed tomography for the diagnosis of canine nasal aspergillosis. *Vet Radiol Ultrasound.* 2003;44(4): 414–419.
121. Barrs VR, Beatty JA, Dhand NK, et al. Computed tomographic features of feline sino-nasal and sino-orbital aspergillosis. *Vet J.* 2014;201(2):215–222.
122. Barrs VR, Talbot JJ. Feline aspergillosis. *Vet Clin North Am Small Anim Pract.* 2014;44(1):51–73.
123. Cormack CA, Donahoe SL, Talbot JJ, Beatty JA, Barrs VR. Disseminated invasive aspergillosis caused by *Aspergillus felis* in a cat. *J Vet Intern Med.* 2021;35(5):2395–2400.
124. Karnik K, Reichle JK, Fischetti AJ, Goggin JM. Computed tomographic findings of fungal rhinitis and sinusitis in cats. *Vet Radiol Ultrasound.* 2009;50(1):65–68.
125. Furtado AR, Caine A, Herrtage ME. Diagnostic value of MRI in dogs with inflammatory nasal disease. *J Small Anim Pract.* 2014;55(7):359–363.
126. Roccabianca P, Turchetto S, Ferrari N, et al. Feline lymphoplasmacytic rhinitis (FLPCR): severity of inflammation correlates with reduced mucosal IgA expression. *Vet Immunol Immunopathol.* 2021;234:1–11.
127. Windsor RC, Johnson LR, Herrgesell EJ, De Cock HE. Idiopathic lymphoplasmacytic rhinitis in dogs: 37 cases (1997–2002). *J Am Vet Med Assoc.* 2004;224(12): 1952–1957.
128. Dias MJ, Mouro S, Englar RE, Leal RO. Nasal foreign bodies identified by rhinoscopy in dogs: 42 cases. *J Small Anim Pract.* 2020;61(12):752–756.
129. Fischer MC, Busse C, Adrian AM. Magnetic resonance imaging findings in dogs with orbital inflammation. *J Small Anim Pract.* 2019;60(2):107–115.
130. Lafuma F, Baudin Tréhiou C, Bernardin F, Blond L. Computed tomography may be helpful in discriminating grass awn foreign body rhinitis from non-foreign body rhinitis in dogs. *Vet Radiol Ultrasound.* 2021;62(5):533–540.
131. Moreno-Aguado B, Carrera I, Holdsworth A, Agthe P, Maddox TW, Trevail T. CT findings in 20 dogs and six cats with confirmed nasal foreign bodies. *Vet Radiol Ultrasound.* 2020;61(4):417–426.
132. Belmudes A, Pressanti C, Barthez PY, Castilla-Castaño E, Fabries L, Cadiergues MC. Computed tomographic findings in 205 dogs with clinical signs compatible with middle ear disease: a retrospective study. *Vet Dermatol.* 2018;29(1):45-e20.
133. Bischoff MG, Kneller SK. Diagnostic imaging of the canine and feline ear. *Vet Clin North Am Small Anim Pract.* 2004;34(2):437–458.
134. Rohleder JJ, Jones JC, Duncan RB, Larson MM, Waldron DL, Tromblee T. Comparative performance of radiography and computed tomography in the diagnosis of middle ear disease in 31 dogs. *Vet Radiol Ultrasound.* 2006;47(1):45–52.
135. Owen MC, Lamb CR, Lu D, Targett MP. Material in the middle ear of dogs having magnetic resonance imaging for investigation of neurologic signs. *Vet Radiol Ultrasound.* 2004;45(2):149–155.
136. Shanaman M, Seiler G, Holt DE. Prevalence of clinical and subclinical middle ear disease in cats undergoing computed tomographic scans of the head. *Vet Radiol Ultrasound.* 2012;53(1):76–79.
137. Lorek A, Dennis R, van Dijk J, Bannoehr J. Occult otitis media in dogs with chronic otitis externa – magnetic resonance imaging and association with otoscopic and cytological findings. *Vet Dermatol.* 2020;31(2):146–153.
138. Detweiler DA, Johnson LR, Kass PH, Wisner ER. Computed tomographic evidence of bulla effusion in cats with sinonasal disease: 2001–2004. *J Vet Intern Med.* 2006;20(5):1080–1084.
139. Goodale EC, Outerbridge CA, White SD. Aspergillus otitis in small animals—a retrospective study of 17 cases. *Vet Dermatol.* 2016;27(1):3-e2.
140. Cole LK. Primary secretory otitis media in Cavalier King Charles spaniels. *Vet Clin North Am Small Anim Pract.* 2012;42(6):1137–1142.
141. Kent M, Glass EN, de Lahunta A, Platt SR, Haley A. Prevalence of effusion in the tympanic cavity in dogs with dysfunction of the trigeminal nerve: 18 cases (2004–2013). *J Vet Intern Med.* 2013;27(5):1153–1158.
142. Wessmann A, Hennessey A, Goncalves R, Benigni L, Hammond G, Volk HA. The association of middle ear effusion with trigeminal nerve mass lesions in dogs. *Vet Rec.* 2013;173(18):449.
143. Parzefall B, Rieger A, Volk HA, Maierl J, Brühschwein A, Blutke A. Prevalence and characterization of small tympanic bone spicules and drumstick-like hyperostotic tympanic bone spicules in the middle ear cavity of dogs. *Vet Radiol Ultrasound.* 2015;56(1):25–32.
144. Beck T, Brühschwein A, Meyer-Lindenberg A. Occurrence of tympanic bone spicules and bone crests in domestic cats. *Anat Histol Embryol.* 2020;49(2):216–221.

145. Greci V, Mortellaro CM. Management of otic and nasopharyngeal, and nasal polyps in cats and dogs. *Vet Clin North Am Small Anim Pract.* 2016;46(4):643–661.
146. Swales N, Foster A, Barnard N. Retrospective study of the presentation, diagnosis and management of 16 cats with otitis media not due to nasopharyngeal polyp. *J Feline Med Surg.* 2018;20(12):1082–1086.
147. MacPhail CM, Innocenti CM, Kudnig ST, Veir JK, Lappin MR. Atypical manifestations of feline inflammatory polyps in three cats. *J Feline Med Surg.* 2007;9(3):219–225.
148. Lamb CR, Sibbing K, Priestnall SL. Pathologic basis for rim enhancement observed in computed tomographic images of feline nasopharyngeal polyps. *Vet Radiol Ultrasound.* 2016;57(2):130–136.
149. Tanaka T, Akiyoshi H, Mie K, Nishida H. MRI findings, including diffusion-weighted imaging and apparent diffusion coefficient value, in two cats with nasopharyngeal polyps and one cat with lymphoma. *JFMS Open Rep.* 2018;4(2):1–7.
150. Hauck ML. Tumors of the skin and subcutaneous tissues. In: Vail DM, Thamm DH, Liptak JM, eds. *Withrow and MacEwen's Small Animal Clinical Oncology.* 6th ed. St. Louis, MO: Elsevier; 2020:360–361.
151. Herberger A, Hammond J, Miller A, Olson B. *MRI of a Middle Ear Cholesteatoma in a Cat.* Vet Radiol Ultrasound; 2022.
152. Risselada M. Diagnosis and management of cholesteatomas in dogs. *Vet Clin North Am Small Anim Pract.* 2016;46(4):623–634.
153. Travetti O, Giudice C, Greci V, Lombardo R, Mortellaro CM, Di Giancamillo M. Computed tomography features of middle ear cholesteatoma in dogs. *Vet Radiol Ultrasound.* 2010;51(4):374–379.
154. Reiter AM, Schwarz T. Computed tomographic appearance of masticatory myositis in dogs: 7 cases (1999–2006). *J Am Vet Med Assoc* 2007;231(6).
155. Hecht S, Anderson KM, Castel A, et al. Agreement of magnetic resonance imaging with computed tomography in the assessment for acute skull fractures in a canine and feline cadaver model. *Front Vet Sci.* 2021;8:1–9.
156. Maas CP, Theyse LF. Temporomandibular joint ankylosis in cats and dogs. A report of 10 cases. *Vet Comp Orthop Traumatol.* 2007;20(3):192–197.
157. Padgett GA, Mostosky UV. The mode of inheritance of craniomandibular osteopathy in West Highland White terrier dogs. *Am J Med Genet.* 1986;25(1):9–13.
158. Letko A, Leuthard F, Jagannathan V, et al. Whole genome sequencing indicates heterogeneity of hyperostotic disorders in dogs. *Genes.* 2020;11(2).
159. Beever L, Swinbourne F, Priestnall SL, Ter Haar G, Brockman DJ. Surgical management of chronic otitis secondary to craniomandibular osteopathy in three West Highland white terriers. *J Small Anim Pract.* 2019;60(4):254–260.
160. Matiasovic M, Caine A, Scarpante E, Cherubini GB. Imaging diagnosis-magnetic resonance imaging features of craniomandibular osteopathy in an Airedale Terrier. *Vet Radiol Ultrasound.* 2016;57(3):E27–E29.
161. McConnell JF, Hayes A, Platt SR, Smith KC. Calvarial hyperostosis syndrome in two bullmastiffs. *Vet Radiol Ultrasound.* 2006;47(1):72–77.
162. Pastor KF, Boulay JP, Schelling SH, Carpenter JL. Idiopathic hyperostosis of the calvaria in five young bullmastiffs. *J Am Anim Hosp Assoc.* 2000;36(5):439–445.

ELECTRONIC RESOURCES

Additional information related to the content in Chapter 11 can be found online at eBooks.Health.Elsevier.com.

- Chapter Quiz

CHAPTER 12

Magnetic Resonance Imaging and Computed Tomographic Features of Brain Disease in Small Animals

Ian Robertson • Gabriela S. Seiler

The superior soft tissue contrast of magnetic resonance imaging (MRI) makes it the preferred modality for imaging almost all aspects of intracranial disease, whereas computed tomography (CT) is less sensitive. CT is suitable for brain imaging in trauma cases, as outlined later, and if magnetic resonance (MR) is not available. This chapter is a basic overview of the MR and CT characteristics of common small animal intracranial disorders. A review of the technical details associated with brain imaging in small animals and a more comprehensive review of uncommon disorders is available elsewhere.[1,2]

BASIC MAGNETIC RESONANCE EXAMINATION OF THE BRAIN

A standard MR examination of the canine or feline brain involves the acquisition of multiple pulse sequences in different anatomic planes (Table 12.1). In MR, it is the tissue chemical characteristics that determine the signal intensity in the various sequences. Pulse sequences are selected to assess anatomy and to maximize lesion conspicuity. Images are usually acquired in transverse, sagittal, and dorsal planes (Fig. 12.1).

Rationale for Sequence Selection

In T2-weighted sequences, free fluid (e.g., cerebrospinal fluid [CSF]) is extremely bright/T2 hyperintense. Bright/T2-hyperintense tissues have a longer T2 relaxation (see Chapter 4 for a discussion of T1 and T2 relaxation). Most common pathologic processes, whether neoplastic or inflammatory, result in increased fluid within tissues, and this results in an increase in brightness of the abnormal tissue relative to surrounding normal tissue; the term *increased T2-signal intensity* is commonly used to describe this.

Sometimes it is difficult to identify a T2-hyperintense lesion when it is adjacent to a normal region of high signal, such as adjacent to CSF within the ventricles. With respect to T2-weighted sequences, the signal from free fluid can be eliminated using a fluid-attenuated inversion recovery (FLAIR) sequence. In T2-weighted FLAIR images, free fluid has very low signal, while other hydrated lesions remain bright (Fig. 12.2).[3] Proteinaceous or inflammatory fluid will have less or no signal reduction. The term *nulling* or *null* is used to describe the signal change produced when using an inversion recovery sequence like FLAIR (e.g., the T2 hyperintensity nulls in the FLAIR sequence). A FLAIR sequence may also provide additional information about T2-hyperintense lesions that must be distinguished from CSF, such as cystic meningioma, dermoid and epidermoid cysts, and arachnoid cysts.[4]

In T1-weighted spin-echo sequences, high signal arises from tissues having rapid T1 relaxation, such as fat and methemoglobin. Conversely, fluid and hydrated lesions have reduced signal intensity in T1-weighted images, appearing dark or hypointense. A T1-weighted image is excellent for evaluation of extracranial anatomy, but on its own has poor sensitivity for detection of most intracranial lesions because of their hydrated nature, which leads to low T1 signal. However, blood-brain barrier disruption and regions of altered perfusion can be detected in T1-weighted sequences acquired after the administration of MR contrast medium. The most common MR contrast media are chelated forms of gadolinium, a transitional compound with paramagnetic properties that shorten the T1 relaxation time of tissue in which the material accumulates.[5] Therefore, regions of higher gadolinium concentration will have increased signal (bright) in T1-weighted sequences.

Many pathologic processes in the brain result in some disruption to the blood-brain barrier, often allowing an accumulation of contrast medium after intravenous injection, and thereby increased signal intensity in postcontrast T1-weighted images. Contrast medium should be administered after all other imaging sequences have been acquired, because contrast medium can sometimes affect the appearance of tissues/organs in other sequences.

Certain abnormalities are easier to detect in a specific scan plane, and ensuring these scan planes are part of the routine examination is imperative. For example, a T2-weighted sagittal sequence should be performed routinely to allow better evaluation of the morphology of the midbrain, cerebellum, and caudal brainstem. This is particularly important in the assessment of increased intracranial pressure and caudal fossa crowding.[6]

Table • 12.1

Standard Sequences for Brain Magnetic Resonance Imaging.

SEQUENCE	IMAGE PLANE
T2-weighted spin echo	Transverse and sagittal
T2-FLAIR	Transverse
T1-weighted spin-echo sequence	At least one plane, usually transverse
T2-weighted GRE to assess for hemorrhage	Transverse
T1-weighted spin-echo sequence after administration of contrast medium	Same image plane and acquisition parameters as precontrast, may add image planes
Additional specialized sequences as indicated and available	Depends on indication

FLAIR, Fluid-attenuated inversion recovery; *GRE,* gradient recall echo.

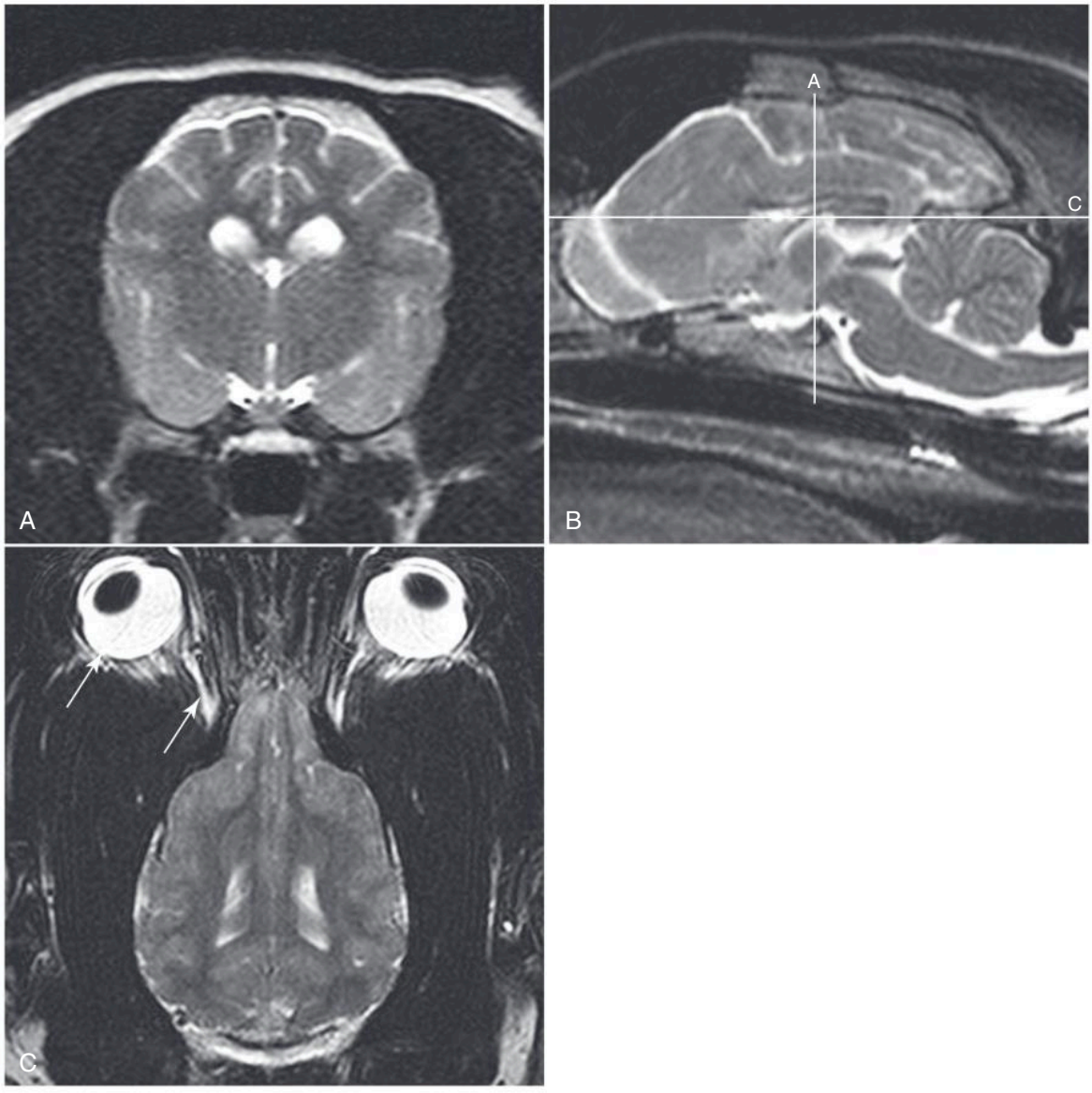


Fig. 12.1 T2-weighted magnetic resonance (MR) images acquired in transverse **(A),** sagittal **(B),** and dorsal planes **(C)**. (Unless specified, "images" refers to conventional spin-echo images.) The sagittal plane image is midline. The locations of the transverse and dorsal plane image are shown in the sagittal plane image. In these T2-weighted images of a normal canine brain, cerebrospinal fluid (CSF) within the ventricles is bright (i.e., has high signal). In **C,** retrobulbar fat and the vitreous humor also have high signal (*white arrows*).

As discussed in Chapter 4, images can be acquired using spin-echo or gradient recall echo (GRE) pulse sequences. GRE images are more susceptible to magnetic field inhomogeneity, and this is exploited when assessing the brain for evidence of chronic hemorrhage (longer than 2–3 days). As hemorrhage is broken down, the magnetic properties of the ferric/ferrous ions in hemoglobin metabolites cause a local field distortion that destroys the MR signal. This appears as a signal void (a black, so-called susceptibility artifact). This is an extremely sensitive indicator of chronic hemorrhage as might occur in patients with intracranial trauma, hemorrhagic tumors, hemorrhagic infarcts, coagulopathies, or hemorrhagic metastasis. The image void is typically much larger than the actual lesion because of blooming (see Hemorrhagic Infarct section).

Putting It All Together

The imaging characteristics of a lesion need to be evaluated in various sequences, so that an accurate assessment of the underlying disease process can be established. For example, a T2-hyperintense region in the brain may represent free fluid such as CSF or brain edema and the two conditions can be differentiated with a T2 FLAIR sequence (see Fig. 12.2). T2 hyperintensity may also represent pathology such as neoplasia which may be contrast enhancing, or necrosis which does not enhance and does not null in a T2-weighted FLAIR sequence (Fig. 12.3). All pulse sequences must be interpreted together to reach the correct conclusion.

Secondary Effects of Focal Intracranial Disease

In addition to altering local signal intensity, brain masses and swelling can also cause major changes to brain morphology. Many masses and the secondary perilesional edema result in brain compression, with a contralateral midline shift, ventricular compression and obstruction, and ultimately either transtentorial and/or cerebellar herniation at the foramen magnum (Fig. 12.4). Herniation of the cingulate gyrus across midline is

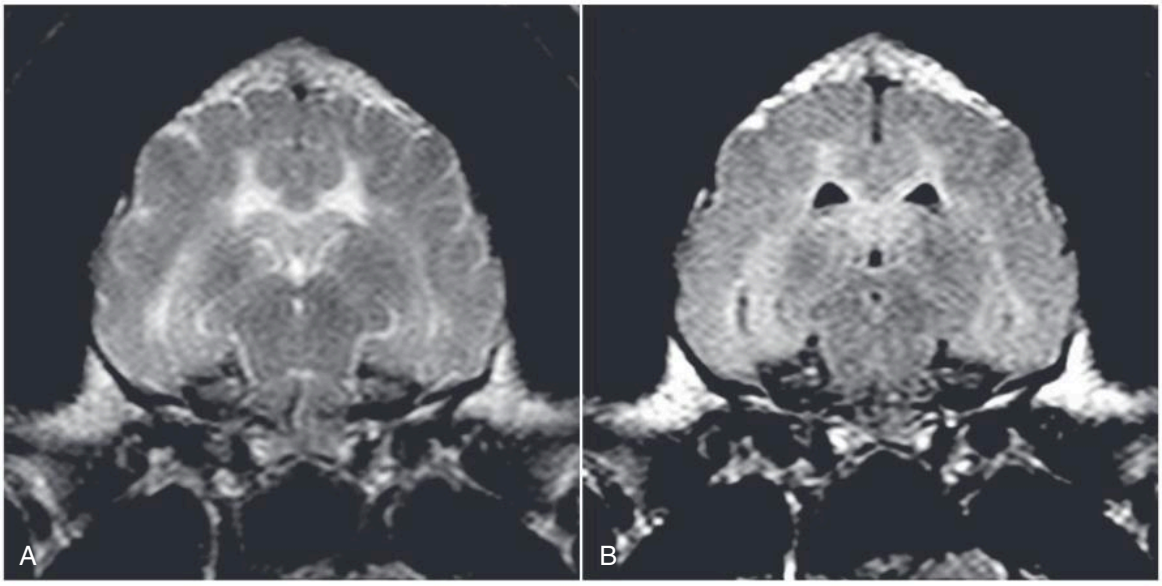


Fig. 12.2 Comparison of T2-weighted spin-echo **(A)** and T2-weighted fluid-attenuated inversion recovery (FLAIR) **(B)** MR images in a dog with leukoencephalitis. In the T2-weighted spin-echo image **(A)**, there is considerable T2-hyperintensity in the ventricular region, but it is impossible to determine whether this is caused by signal from cerebrospinal fluid (CSF) or brain edema or both. Obvious periventricular T2 signal is more conspicuous in the FLAIR image **(B)** as a result of nulling, or elimination, of the high signal from the CSF. Note the lack of signal from CSF in the lateral ventricles in the T2-weighted FLAIR image, as expected.

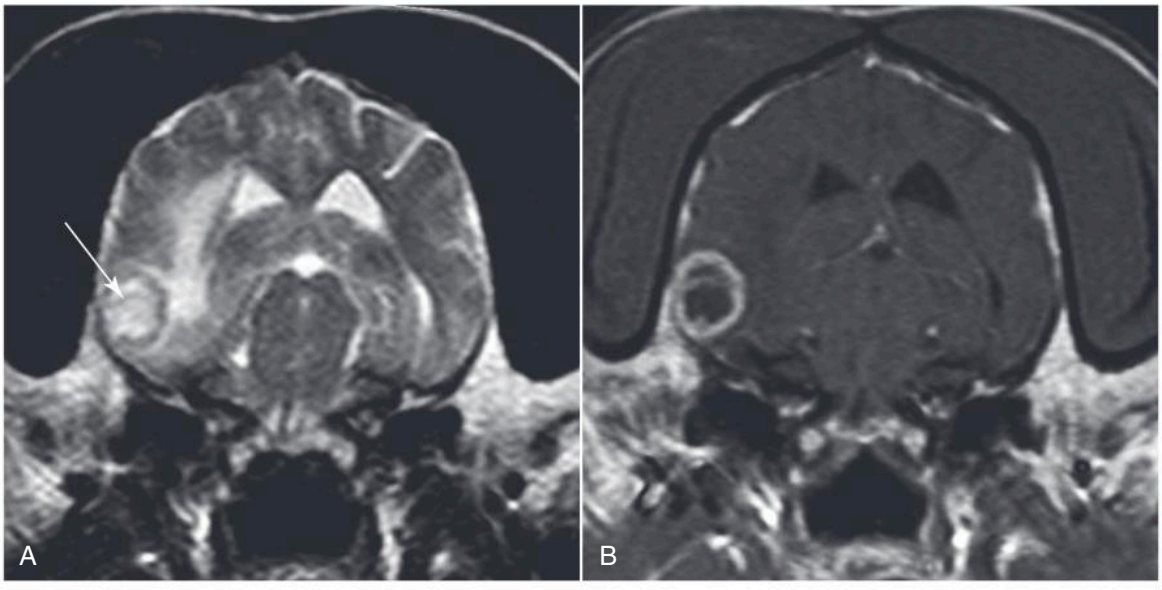


Fig. 12.3 **A,** T2-weighted magnetic resonance (MR) image. There is a focal T2-hyperintense mass (*white arrow*) with a T2-hypointense border surrounded by adjacent wispy regions of T2-hyperintensity consistent with perilesional white matter edema. **B,** Postcontrast T1-weighted image. The T2-hypointense border is now characterized by marked peripheral contrast enhancement, often called *ring enhancement*. The center of the mass does not enhance. In both images, there is a contralateral midline shift as a result of the mass and perilesional edema. Final diagnosis was metastatic hemangiosarcoma, but these signs are not specific for this.

called subfalcine herniation. It is critical not to overlook the signs of cerebellar herniation (Fig. 12.5).

BASIC COMPUTED TOMOGRAPHIC EXAMINATION OF THE BRAIN

CT examination of the brain typically includes acquisition of images in a transverse plane, followed by dorsal and sagittal image reconstructions which do not require acquisition of additional image sequences. The basic principles of CT imaging are outlined in Chapter 4. In most instances, intravenous administration of iodinated contrast medium is required for optimal delineation of normal anatomy outside the blood-brain barrier such as the pituitary gland, choroid plexus, and vasculature. The brain parenchyma itself does not enhance. Differentiation of the gray matter, white matter, and cerebrospinal fluid is possible due to their different attenuation

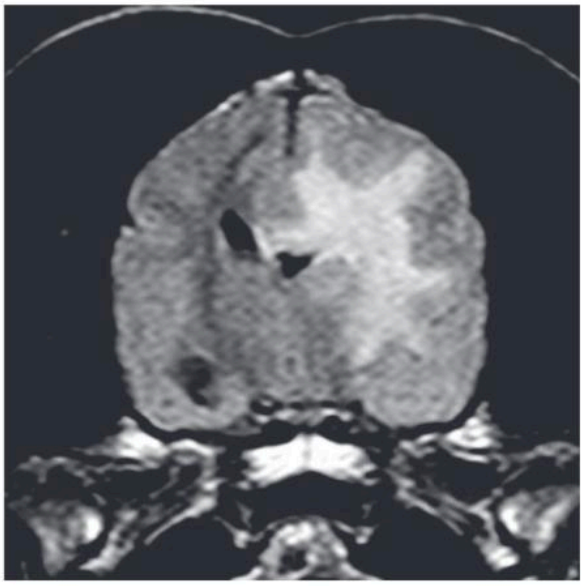


Fig. 12.4 Transverse T2−fluid-attenuated inversion recovery (FLAIR) magnetic resonance (MR) image of a 12-year-old Border collie with a rostrally located meningioma (not seen). In this image, caudal to the mass, there is extensive white-matter edema resulting in compression of the ventricular system and a rightward shift of midline structures. The secondary effects of intracranial masses can be severe and the cause of profound clinical signs unrelated to the primary lesion.

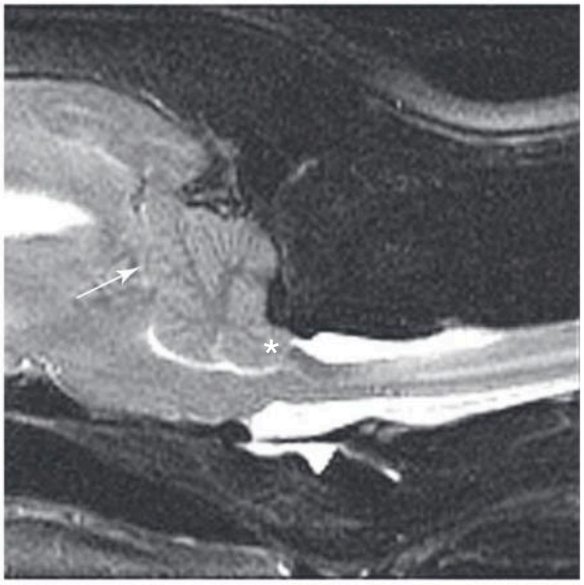


Fig. 12.5 Sagittal T2-weighted magnetic resonance (MR) image of the occipital-cervical junction of a dog with a large forebrain mass (not seen). There is compression of the rostral aspect of the cerebellum (*white arrow*) and herniation of the cerebellar vermis (*asterisk*) into the foramen magnum as a result of increased intracranial pressure. The wispy T2 hyperintensity in the spinal cord is syringohydromyelia, the result of altered cerebrospinal fluid (CSF) flow secondary to brainstem compression. The cranial aspect of the spinal cord is bounded dorsally and ventrally by the highly conspicuous subarachnoid space, containing CSF.

characteristics; however, images have to be viewed in a narrow window to be able to depict the small differences in attenuation. Images should always be viewed in both a bone and soft-tissue window. Contrast medium administration facilitates detection of extra-axial lesions originating outside the brain tissue (meninges, skull). If associated with a breakdown of the blood-brain barrier, intra-axial lesions originating from brain tissue may also be delineated based on an increase in attenuation. Nonenhancing brain lesions, if large enough, can become visible due to an associated mass effect (shift of the falx cerebri, compression of the ventricular system, brain herniation) or presence of hypoattenuating perilesional edema. There are a few indications, namely, trauma with suspected skull fractures and/or intracranial hemorrhage, where contrast medium administration may not be necessary. Imaging the caudal fossa with CT can be particularly challenging due to the artifact of beam hardening from the petrous temporal bone.

Know Normal Anatomy

A working knowledge of normal MR and CT brain anatomy and neuropathophysiologic correlations are prerequisites to characterizing any lesion accurately and correlating it with the clinical signs. Many electronic and hard-copy references for these subjects are available.[7–10]

Developmental Conditions of the Brain

The array of intracranial developmental malformations is well described.[11] Only the most common of these anomalies are discussed here.

Abnormal Fluid Accumulations

Hydrocephalus, the most common developmental anomaly, is the excessive accumulation of CSF within the ventricular system. Hydrocephalus occurs when normal flow is obstructed, when there is overproduction compared to absorption, or when there is brain atrophy. The most common form of hydrocephalus is congenital hydrocephalus, where excessive CSF accumulates before or soon after birth. An inherited malformation of the fluid pathway may be present, or perinatal infection or injury may lead to scarring that affects CSF reabsorption. Less commonly, hydrocephalus occurs in adult patients, usually the result of tumor or infection, which obstructs CSF flow (Fig. 12.6).

The lateral ventricles are usually relatively symmetric, but there is considerable variation in what is considered normal ventricular size, particularly in small-breed dogs.[12]

Agenesis of the septum pellucidum, a thin membrane separating the two cerebral hemispheres and the two lateral ventricles, is a common, typically asymptomatic, finding most frequently seen in larger brachycephalic breeds. In one study, the septum pellucidum was considered intact in only 25% of dogs[13] (Fig. 12.7).

In addition to hydrocephalus, there are other conditions that result in the accumulation of fluid within the cranial vault, the most common being fluid accumulation in the supracollicular region. Three different patterns of supracollicular fluid accumulation have been characterized based on establishing the location of the thin membrane separating the third ventricle from the quadrigeminal cistern.[14] This membrane likely represents the third ventricle wall where the pia mater joins the ependymal layer forming the tela choroidea of the third ventricle.[14] In the first pattern, there is enlargement of the caudodorsal recess of the third ventricle (Fig. 12.8) with the thin membrane separating the third ventricle from the quadrigeminal cistern being displaced caudodorsally. In pattern 2, there is enlargement of both the caudodorsal aspect of the third ventricle and the quadrigeminal cistern and the membrane separating these compartments is visible (Fig. 12.9). In pattern 3, due to enlargement of the quadrigeminal cistern alone, the membrane separating the quadrigeminal cistern and the third ventricle is displaced rostrally.[14] Enlargement of the quadrigeminal cistern results in varying degrees of flattening of the rostrodorsal aspect of the cerebellum (Fig. 12.10).

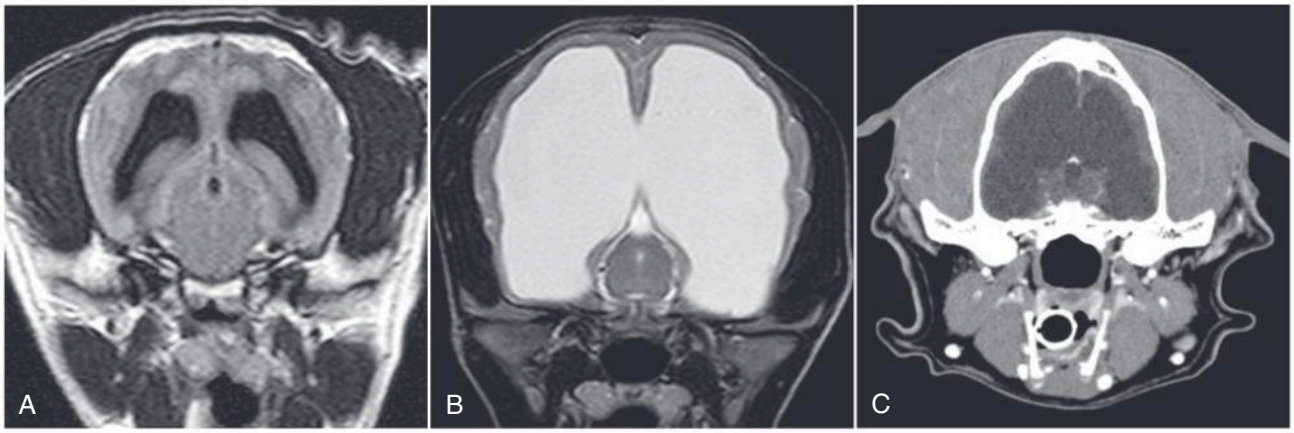


Fig. 12.6 Transverse T2-weighted fluid-attenuated inversion recovery (FLAIR) **(A),** T2-weighted **(B)** MR images, and transverse CT image **(C)** from three dogs with congenital hydrocephalus. The ventricles are much more severely dilated in the dogs in **B** and **C.**

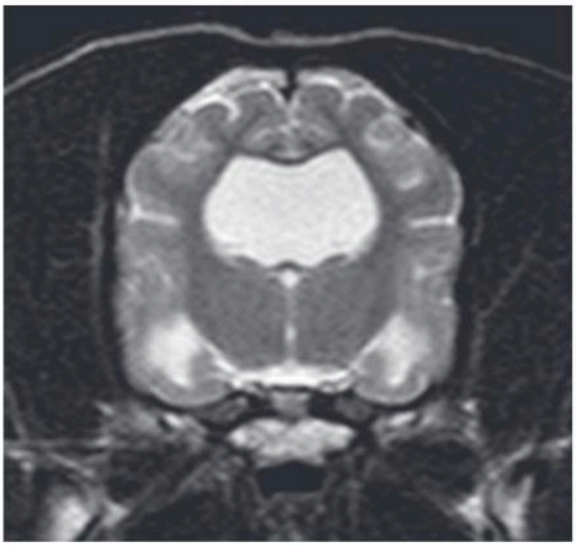


Fig. 12.7 Transverse T2-weighted magnetic resonance (MR) image of a 2-year-old English bulldog. There is a broad midline communication between the lateral ventricles due to agenesis or rupture of the septum pellucidum. Absence of the septum pellucidum is typically asymptomatic.

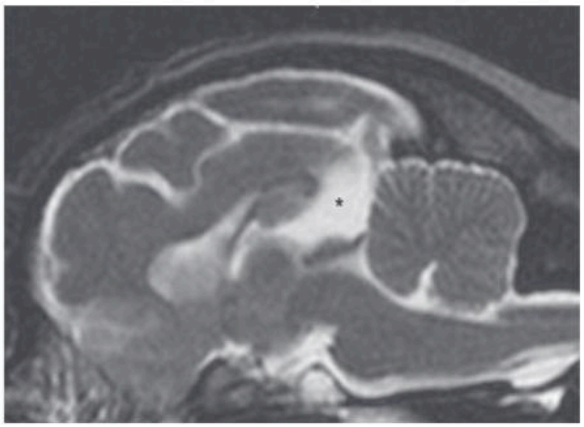


Fig. 12.8 Sagittal T2-weighted magnetic resonance (MR) image of a 15-year-old Lhasa Apso. There is enlargement of the suprapineal recess of the third ventricle, denoted by the *black asterisk.*

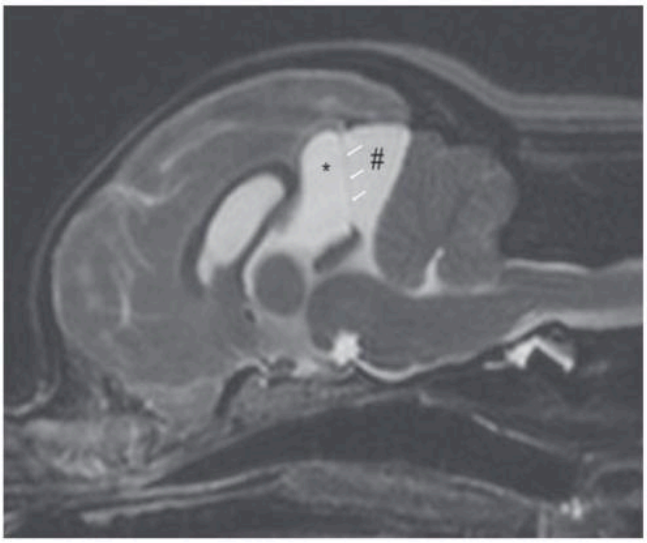


Fig. 12.9 Sagittal T2-weighted magnetic resonance (MR) image of 2-year-old Shih Tzu presenting for seizures. There is a supracollicular fluid accumulation. The line delineated by the *white arrows* is the membrane between an enlarged suprapineal recess of the third ventricle (*black asterisk*) and an enlarged quadrigeminal cistern (*hash sign*).

Other fluid accumulations within the developing brain also occur. Focal fluid accumulations are termed *porencephaly*, whereas extensive fluid accumulations are termed *hydranencephaly.* Developmental porencephaly is due to a focal neuronal migration disorder and results in a gap in the developing cerebral hemisphere. *Encephaloclastic porencephaly* is an all-encompassing term describing cortical loss from various causes, including ischemia, infection, or trauma[15] (Fig. 12.11). These accumulations of fluid usually communicate with the lateral ventricles or the subarachnoid space.

Dandy Walker syndrome is a developmental disorder whereby there is failure of development of the caudoventral aspect of the cerebellar vermis. This results in enlargement of the dorsocaudal aspect of the fourth ventricle (Fig. 12.12). The clinical signs associated with this condition depend on the volume of absent cerebellum. There are a number of manifestations of this condition and a more correct overarching term is probably *Dandy Walker variant.*

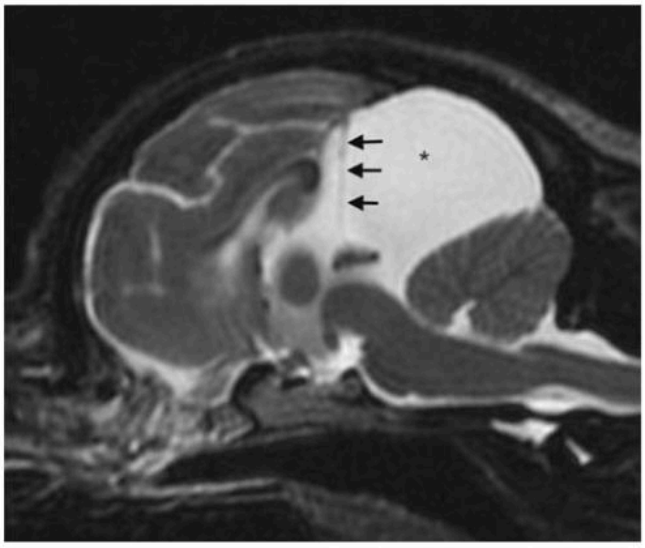


Fig. 12.10 Sagittal T2-weighted magnetic resonance (MR) image of a 13-year-old Pekingese with an acute onset of seizures. There is marked enlargement of the quadrigeminal cistern (*black asterisk*) resulting in flattening of the rostrodorsal aspect of the cerebellum. Despite this, there is no evidence of caudal fossa herniation. This was a pre-existing condition and unrelated to the adult-onset seizures. The membrane between the caudodorsal aspect of the third ventricle and the quadrigeminal cistern is readily evident and is displaced rostrally (*arrows*).

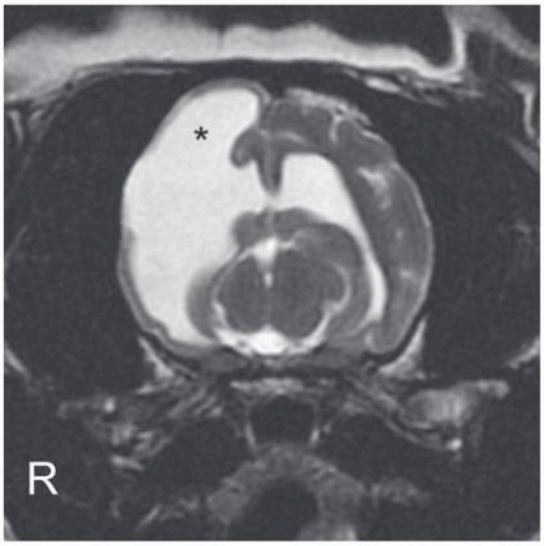


Fig. 12.11 Transverse T2-weighted magnetic resonance (MR) image of an 8-year-old pug with an acute onset of neck pain due to a cervical disc. An incidental finding was right encephaloclastic porencephaly of undetermined etiology. There is expansion of the right lateral ventricle extending to the subarachnoid space (*black asterisk*).

There are a number of uncommon cystic structures that can occur within the cranial vault as a result of incomplete or aberrant separation of the neuroectoderm from the overlying ectodermal tissue. Intracranial epidermoid cysts, intracranial dermoid cysts, Rathke cleft cysts, and craniopharyngiomas originate during gestation from remnants of ectodermal tissue due to defects of neural tube closure.[16] Intracranial epidermoid or dermoid cysts are most commonly located in the fourth ventricle or the cerebellopontine angle (Fig. 12.13). Cystic structures are hypoattenuating in CT images. Signal intensity is variable and dependent on cyst content in MRIs. Cysts with a high lipid content appear hyperintense in T1-weighted and T2-weighed images, whereas cysts with lower lipid content appear T1 hypointense and T2 hyperintense.[17] Dermoid cysts containing adnexa (e.g., hair) may have suspended low intensity foci in all sequences.[18] Cysts often contain protein and keratin and, therefore, do not null in FLAIR sequences. Typically, these complex cysts do not enhance, although ring enhancement may occasionally be present. Rathke cleft cysts and craniopharyngiomas occur in the region of the sella turcica and are typically associated with anomalous development of the pituitary gland.

Other Developmental Morphologic Anomalies

Chiari-like malformation, also called *caudal occipital malformation syndrome (COMS)*, is an all-encompassing term that describes anomalies in the development and morphology of the caudal fossa. This commonly results in crowding of the cerebellum and varying degrees of protrusion of the cerebellum into and through the foramen magnum (Fig. 12.14). The Cavalier King Charles spaniel is the most affected breed, wherein the condition is inherited and thought to affect as much as 95% of the population.[19–22] However, COMS is observed in many other small breeds. MR is commonly used as a screening tool to assist breeding programs in reducing the incidence and severity of COMS. Crowding of the caudal fossa results in protrusion of the caudal cerebellar vermis against or through the foramen magnum. This can result in disruption to CSF flow and an increase in pressure within the spinal cord, leading to the development of fluid-filled cavities within the central and dorsocentral aspect of the spinal cord, termed *syringohydromyelia*. In some patients, syringohydromyelia extends to the thoracic and lumbar spinal cord. There is some association between Chiari-like malformation syndrome and the development of dorsal atlanto-axial bands.[23] While CT is a valuable tool to assess bone pathology, evaluation of the soft tissues of the caudal fossa is limited due to lower contrast resolution and beam hardening artifact. With CT, sagittal reconstructions are most valuable to identify presence of caudal fossa crowding or cerebellar herniation. The accuracy and interobserver agreement for identification of cerebellar herniation and presence of syringomyelia were shown to be higher using high-field MRI compared to multislice CT.[24]

Holoprosencephaly is the failure of the forebrain to bifurcate normally into two discrete cerebral hemispheres. Holoprosencephaly exists in three forms depending on the severity of the malformation, alobar, semilobar, and lobar. Lobar holoprosencephaly has been described in dogs,[25] and dysgenesis/agenesis of the corpus callosum is a feature of this condition. Dogs with developmental abnormalities of the corpus callosum may have hypodipsic hypernatremia. Miniature schnauzers appear to be overrepresented for both dysgenesis of the corpus callosum and lobar holoprosencephaly (Fig. 12.15).

Lissencephaly is an extremely rare condition whereby there is an absence or severe lack of normal gyral formation resulting in a smooth outer surface to the brain (Fig. 12.16). It results from failure of normal neural migration during fetal development. In dogs, the Lhasa Apso is overrepresented, and there may be a genetic predisposition in this breed.[26]

Inherent Disorders in Brain Metabolism

There are many developmental, often breed-specific, inborn errors of brain metabolism that result in MR changes. These conditions, collectively known as *storage diseases*, can result in changes to both brain morphology and signal characteristics due to the abnormal accumulation of one or more products of interrupted metabolic pathways. Mucopolysaccharidosis, neuronal cell lipofuscinosis, cerebellar abiotrophy, and globoid cell leukodystrophy are the most common—albeit rare. There is

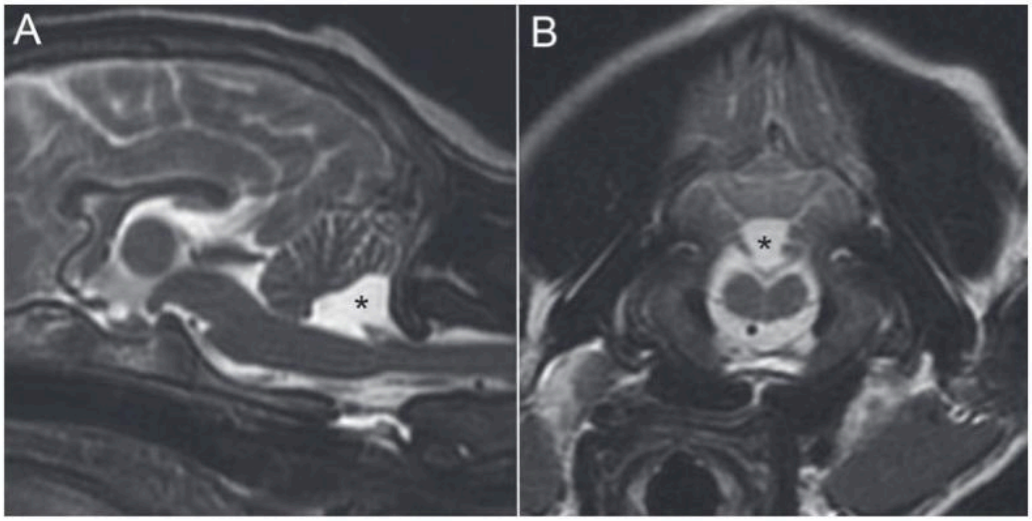


Fig. 12.12 Dandy Walker variant. Sagittal T2-weighted **(A)** and transverse **(B)** magnetic resonance (MR) images of a 4-month-old Labrador retriever puppy with signs of central vestibular disease. Failure of development of the caudoventral aspect of the cerebellar vermis has resulted in an accumulation of fluid, denoted by the *black asterisk.*

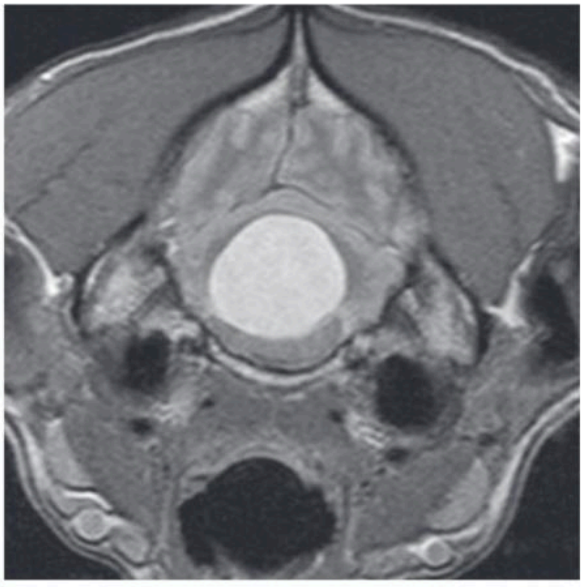


Fig. 12.13 A proton-density (PD)–weighted transverse magnetic resonance (MR) image at the level of the mid aspect of the cerebellum of a 4-year-old mix breed dog. A large spherical cystic mass is present in the fourth ventricle resulting in marked compression and deformation of both the cerebellum and medulla. Histology confirmed an epidermoid cyst.

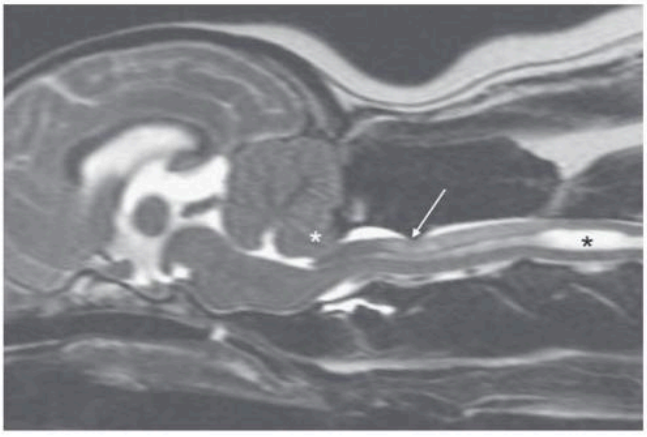


Fig. 12.14 Sagittal T2-weighted magnetic resonance (MR) image of a 4-year-old Cavalier King Charles spaniel. There is crowding of the caudal cerebellar vermis at the foramen magnum (*white asterisk*) and cranial cervical syringohydromyelia (*black asterisk*). There is focal attenuation of the dorsal aspect of the subarachnoid space and a mild indentation in the dorsal aspect of the spinal cord at the caudal aspect of arch of C1 (*white arrow*). This morphology is thought to reflect a dorsal atlanto-axial band and is commonly associated with caudal occipital malformation syndrome. There is mild enlargement of the caudodorsal aspect of the third ventricle.

considerable variation in the appearance of such disorders. Mucopolysaccharidosis and neuronal cell lipofuscinosis typically result in progressive juvenile cortical atrophy and hydrocephalus and an abnormally small corpus callosum, and in the latter, there is often severe peripheral meningeal thickening and enhancement[27] (Fig. 12.17). Cerebellar abiotrophy results in progressive cerebellar atrophy, manifesting as increased conspicuity of the cerebellar folia[28] (Fig. 12.18). Globoid cell leukodystrophy typically results in symmetrical white matter disease, mild hydrocephalus, and symmetrical contrast enhancement of the corpus callosum, internal capsule, and corona radiata.

Nutritional, Metabolic, and Toxic Disorders

There are a number of nutritional disorders that result in morphological signal change within the brain that are detectable with MR. Most commonly, nutritional, toxic, and metabolic disturbances are bilaterally symmetrical. There is considerable overlap in the MR features of many nutritional, metabolic, and toxic disorders, and this confounds the MR assessment. Generally, the presence of lesion symmetry should alert the reader to the possibility of such disorders. Subtle changes in attenuation may be visible with CT imaging; however, in a majority of cases, CT imaging is not sensitive enough and the study will be normal.

Thiamine deficiency results in bilaterally symmetric multifocal abnormalities affecting nuclei of brain and brainstem,

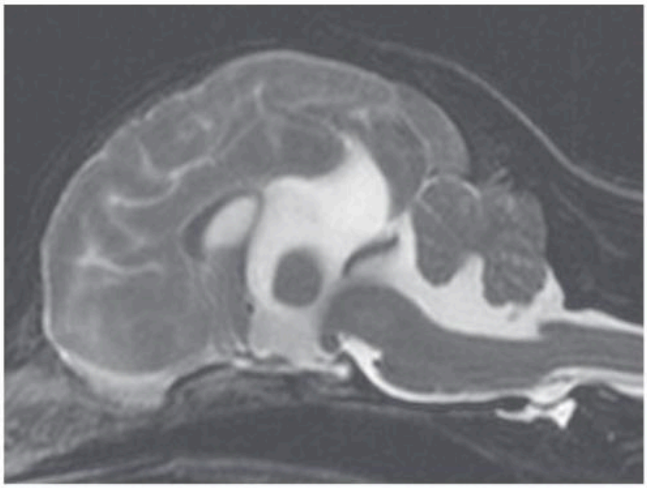


Fig. 12.15 Sagittal T2-weighted magnetic resonance (MR) image of a 2-year-old Chinese Crested dog. There is dysplasia of the caudal aspect of the corpus callosum and with subsequent enlargement of the third ventricle.

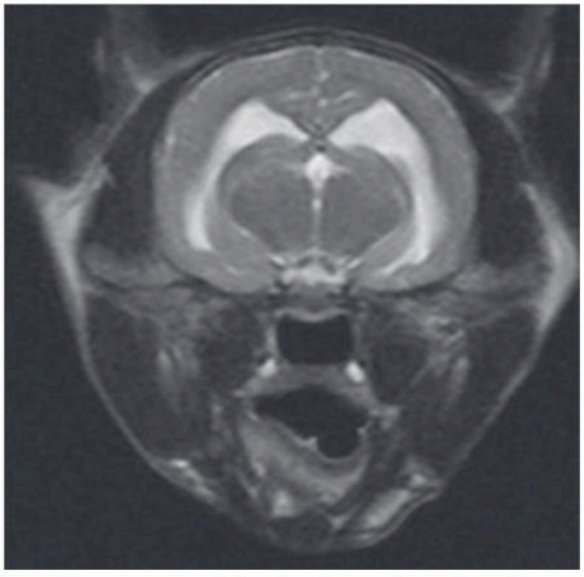


Fig. 12.16 T2 transverse magnetic resonance (MR) image of a 5-month-old domestic medium hair cat with seizures. The surface of the brain is excessively smooth, and there is a paucity of the normal sulci and gyri, which are changes commonly associated with lissencephaly.

including the lateral geniculate nuclei, caudal colliculi, vestibular nuclei, and others[29,30] (Fig. 12.19).

Bilaterally symmetrical T1 hyperintensity in the basal ganglia, specifically the lentiform nuclei, has been observed in human patients with hepatic insufficiency and those receiving total parenteral nutrition and specifically in cats and dogs with hepatic insufficiency associated with portosystemic shunts. The increase in T1 signal is thought due to a buildup of manganese, which is paramagnetic[31] (Fig. 12.20).

There are a number of metabolic disorders that result in intracranial changes that can be detected with MR. A full description of these is beyond the scope of this chapter. One example is subacute necrotizing encephalopathy, which has been documented in the Alaskan husky. This condition closely resembles Leigh syndrome in people and is an incapacitating, ultimately fatal neurodegenerative disorder.[32] The condition has been reported in the Bull terrier[33] and also the Yorkshire terrier. The disorder is characterized by degeneration and necrosis that manifests as bilaterally symmetrical regions of T2 and FLAIR hyperintensity within the central aspect of the thalamus. Additionally, focal T2 hyperintensity has been documented within the midbrain and medulla (Fig. 12.21).

Severe electrolyte disturbances in otherwise normal patients (unrelated to holoprosencephaly) can result in parenchymal changes that manifest with MR detectable changes. Severe hypernatremia can result in a number of symmetrical signal changes, most commonly a bilaterally symmetrical increase in T2 signal in signal at the junction of the internal capsule and lateral margin of the thalamus (Fig. 12.22). In people, this is an uncommon but important postpartum complication.[34]

Inflammatory Conditions

Encephalitis and meningoencephalitis can often be detected using MR, whereas changes may or may not be detectable with CT. Most commonly, cytologic and immunologic analysis of CSF is required to help establish a definitive diagnosis. Meningoencephalitis is typically either infectious or due to dysregulation of the patient's immune system—so-called *immune mediated.* The group of idiopathic noninfectious meningoencephalomyelitides (NIME) includes several subtypes, including steroid responsive meningitis-arteritis (SRMA), eosinophilic meningoencephalitis (EME), granulomatous meningoencephalomyelitis (GME), necrotizing meningoencephalomyelitis (NME), and necrotizing leucoencephalitis (NLE). As SRMA and EME have fairly distinct diagnostic characteristics, the term *meningitis of unknown etiology* (MUE) is used to describe the three specific subtypes that can only be confirmed based on histopathology. These include GME, NME, and NLE.[35]

Generally, immune-mediated brain disease is more common than infectious brain disease.[36] Small breed dogs are more likely to have an immune-mediated etiology and large breed dogs could have either infectious or immune-mediated disease. While there are some breed-specific predispositions and some disorders affect different regions of the brain more commonly, overall, the lesions are patchy or diffuse, T2 and FLAIR hyperintense, T1 iso or hypointense and have variable enhancement—ranging from no enhancement to intense enhancement (Fig. 12.23). The T2 and FLAIR hyperintensity could reflect focal pathology or perilesional edema. In chronic cases, regions of brain necrosis from any etiology may be present, sometimes manifesting as compensatory hydrocephalus, depending on the maturity of the lesion (Fig. 12.24). Encephalitis is often accompanied by meningitis, where there is increased meningeal contrast enhancement.[37] Contrast enhancement is best detected by comparing T1-weighted images acquired before and after contrast medium administration. Not acquiring the precontrast sequence or using different acquisition parameters will invalidate objective assessment of meningeal enhancement. Increased meningeal contrast enhancement and/or multifocal poorly delineated hypoattenuation of the brain tissue with no or mild contrast enhancement may be seen in CT imaging (Fig. 12.25).

Idiopathic hypertrophic pachymeningitis is an uncommon condition whereby there is marked nonspecific thickening and fibrosis of the pachymeninges without extension into the sulci. The Greyhound breed appears overrepresented, and the condition appears to have an immune etiology. The condition should be considered as a possible differential diagnosis for dogs with pachymeningeal thickening and marked enhancement with no identified underlying cause[37] (Fig. 12.26).

Infectious meningoencephalitis includes diseases caused by bacterial, viral, protozoal, rickettsial, fungal, parasitic, and algal agents.[36] Bacterial meningoencephalitis is uncommon and

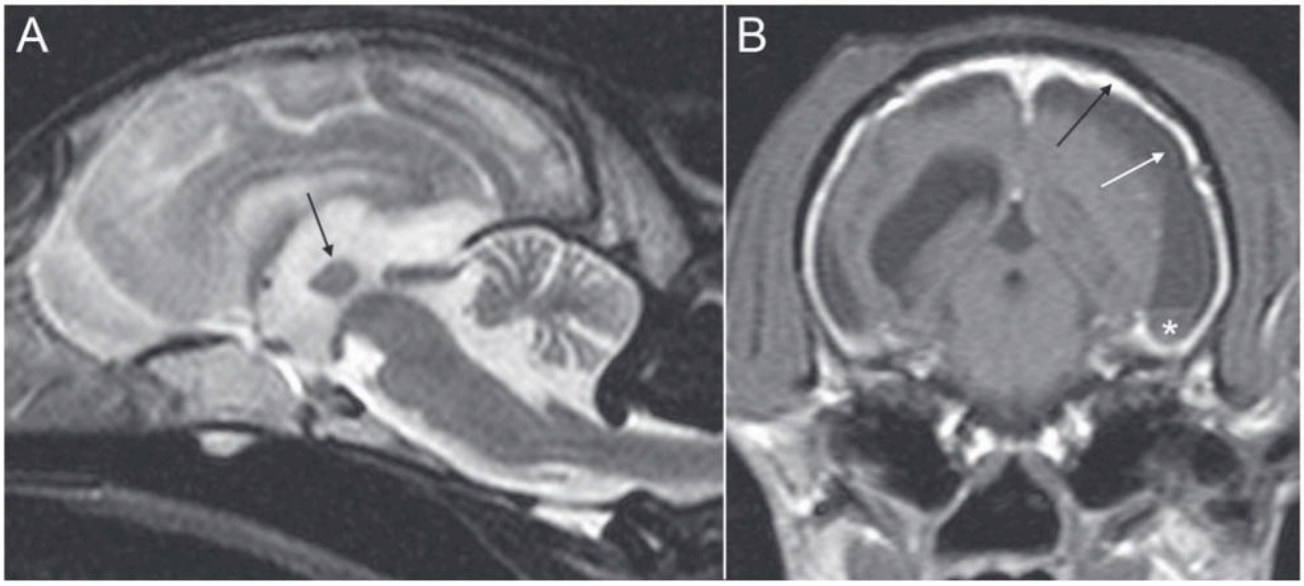


Fig. 12.17 Sagittal T2-weighted image **(A)** and T1-weighted postcontrast magnetic resonance (MR) image **(B)** of an 11-month-old Dachshund with cerebellar and vestibular signs since 6 months of age. Marked atrophy of the interthalamic adhesion is present in **A** (*black arrow*). Atrophy of the cerebellum is also readily evident. In **B,** there is marked pachymeningeal enhancement (*black arrow*) and a large accumulation of peripheral cerebrospinal fluid (CSF) (*white arrow*). A fluid line is evident in the peripheral fluid on the left (*asterisk*). In a gradient echo sequence, the debris in the ventral aspect of the peripheral fluid accumulation had a susceptibility artifact confirming it was hemorrhage. In these instances, hemorrhage is thought to be due to meningeal tearing with progressive brain atrophy.

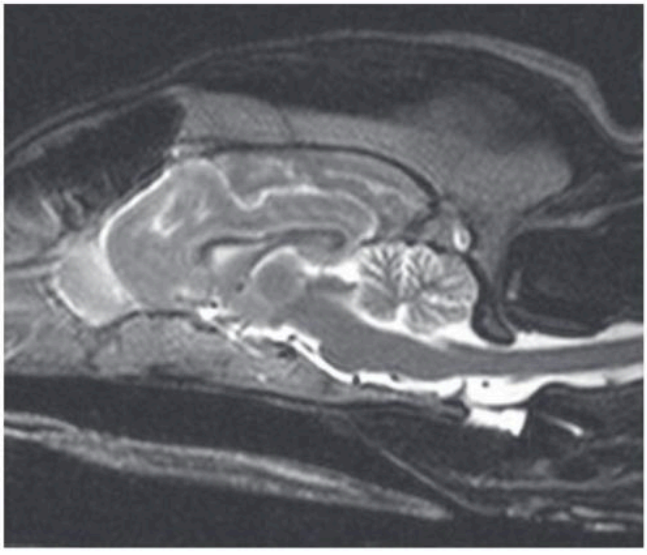


Fig. 12.18 Sagittal T2-weighted magnetic resonance (MR) image of a 4-year-old American bulldog with occasional tremors. Cerebrospinal fluid (CSF) surrounding the atrophic cerebellar folia makes the folia more conspicuous.

when present usually results from extension of a chronic middle ear infection, or chronic sinusitis, or hematogenously (Fig. 12.27). Intracranial feline infectious peritonitis usually causes ependymitis, resulting in marked contrast enhancement of the lining of the ventricular system (Fig. 12.28). Toxoplasmosis and *Neospora* are important infectious disease differentials. Feline ischemic encephalopathy is caused by seasonal transnasal aberrant migration of a *Cuterebra* larva[38,39] (Fig. 12.29). Fungal infections can be region specific and most commonly involve *Cryptococcus neoformans* (feline), *Blastomyces dermatitidis*, and *Coccidioides immitis* and usually manifest as solitary or multifocal T2 hyperintense lesions with variable enhancement.

A normal MR or CT study does not rule out the possibility of inflammatory disease, and evaluation of CSF is required. In 25 patients with CSF alterations consistent with inflammatory brain disease, 24% of the MR studies were normal.[37]

MISCELLANEOUS DISORDERS

Reversible seizure-associated brain edema is typically characterized by nonenhancing T2 and FLAIR hyperintensity with negligible mass effect in patients with a recent history of extensive seizures. The regions most commonly affected are the piriform and temporal lobes.[40] Typically, the changes are bilateral, but changes can also be unilateral and occur elsewhere, including the region of the cingulate gyrus (Fig. 12.30).

Otitis media and interna are important differentials for nystagmus and head tilt. The assessment of inner ear disease is a practical application of using signal differences between T2 and FLAIR sequences to establish a diagnosis.[41] Normal inner ear fluid is T2 hyperintense and should null completely in the T2 FLAIR sequence, similar to CSF. Incomplete nulling suggests altered inner ear fluid content, as occurs with otitis interna (Fig. 12.31). As with all patients with aural disease, close interrogation of the osseous structures and neuroparenchyma is important.

BRAIN NEOPLASIA

Extra-Axial Tumors

Meningiomas are extra-axial tumors of dural origin. They are the most common intracranial tumor in cats and one of the most common in dogs. Meningiomas are usually benign and

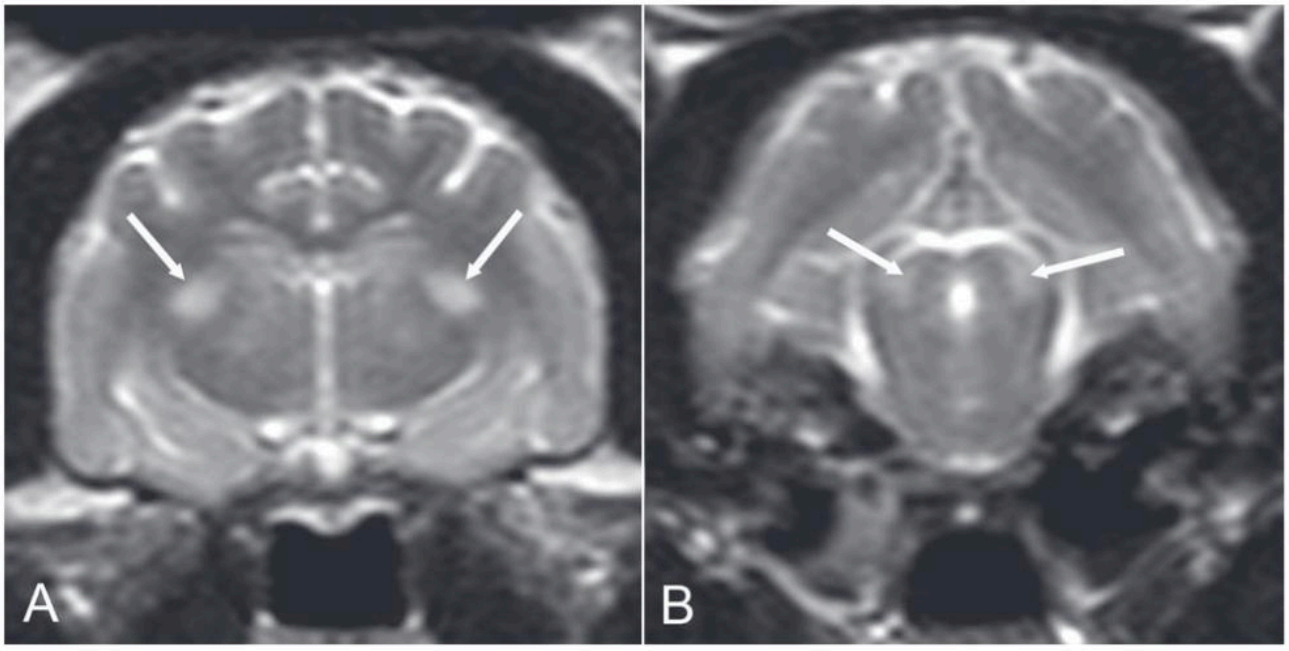


Fig. 12.19 T2-weighted transverse magnetic resonance (MR) images of a 6-year-old domestic short hair cat presenting with a recent history of seizures, ataxia, and vestibular signs. There is bilaterally symmetrical T2 hyperintensity at the level of the thalamus (**A,** *white arrows*) and also in the colliculi (**B,** *white arrows*) due to thiamine deficiency.

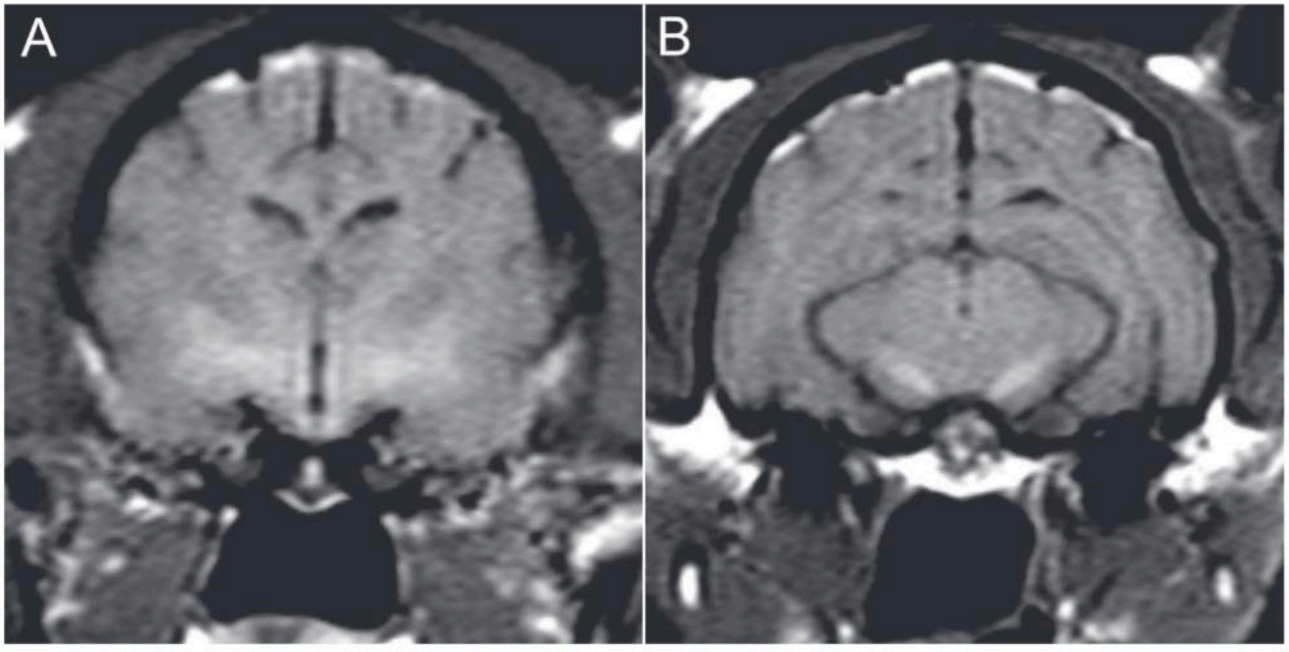


Fig. 12.20 T1-weighted transverse magnetic resonance (MR) images of a 5-year-old domestic short hair cat, at the level of the basal ganglia **(A)** and **(B)** lentiform nuclei. The T1 hyperintensity is thought due to manganese deposition secondary to a portosystemic shunt.

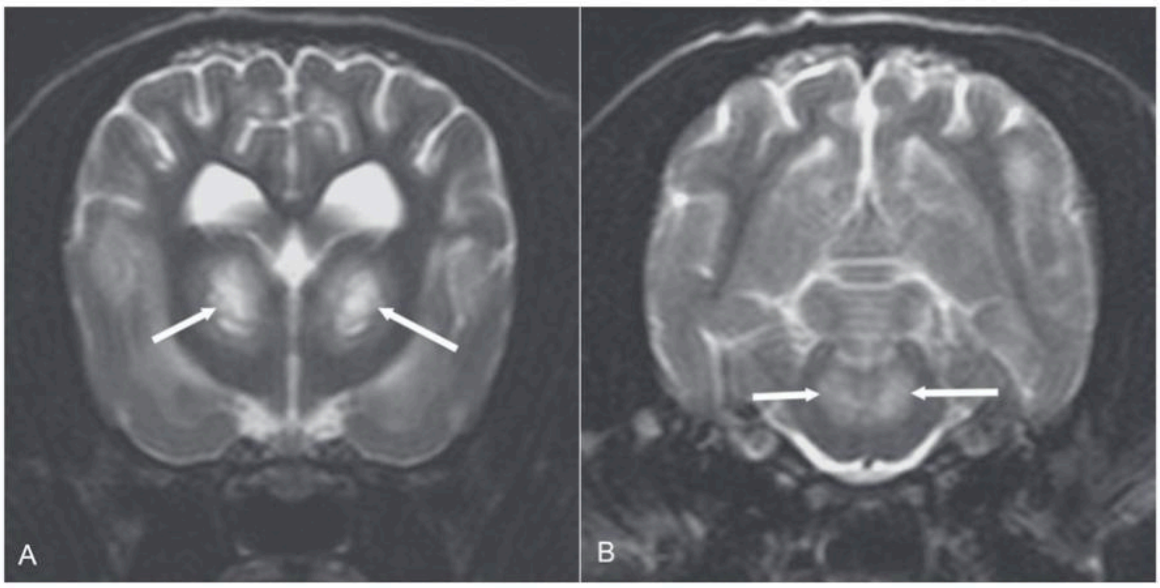


Fig. 12.21 T2-weighted transverse magnetic resonance (MR) image at the level of the thalamus **(A)** and the level of the medulla **(B)** in a 1-year-old Yorkshire terrier. There is bilaterally symmetrical T2 hyperintensity within the central aspect of the thalamus bilaterally (**A,** *white arrows*). There is a bilaterally symmetrical increase in T2 signal intensity within the brainstem at the level of the rostral aspect of the cerebellum (**B,** *white arrows*). Final diagnosis was subacute necrotizing encephalopathy.

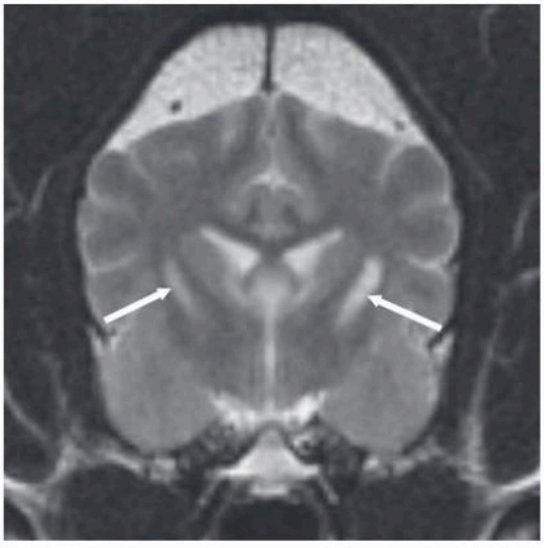


Fig. 12.22 T2-weighed transverse magnetic resonance (MR) image of a 7-year-old mixed-breed dog presenting comatose. The patient was reportedly normal 3 hours earlier. This patient has marked hypernatremia of unknown etiology and responded to fluid therapy. There is bilaterally symmetrical T2 hyperintensity in the white matter tracks adjacent to the thalamus (*white arrow*). The serum sodium in this patient on presentation was more than 180 mEq/L. The changes present in this patient are similar to those reported in people and are sometimes referred to as the *wine glass sign.* (Courtesy Jeff Clarke, DVM, DACVIM [neurology].)

grow slowly. They are variable in size and shape and may be irregular, nodular, ovoid, lobulated, or plaque-like (Fig. 12.31), ranging from a few millimeters to several centimeters in diameter. Meningiomas are often firm and encapsulated, are usually discrete, and may contain mineralization or pockets of fluid (Fig. 12.32). Basal and plaque-like meningiomas are common in the floor of the cranial cavity, especially in the optic chiasm and suprasellar regions. They also occur commonly over the cerebral hemispheres, less commonly in the cerebellopontomedullary region, and rarely in the retrobulbar space, arising from the optic nerve. Multiple meningiomas can occur; this is more common in cats than in dogs. Thickening of bone adjacent to meningiomas, termed *hyperostosis*, may occur, especially in cats (Fig. 12.33). Meningiomas can usually be distinguished from intra-axial tumors because meningiomas are usually peripherally located, or falx-associated broad-based masses that enhance following contrast-medium administration in both CT and MR imaging (see Fig. 12.33). Meningiomas are also often associated with linear contrast enhancement of thickened dura mater adjacent to an extra-axial mass, termed a *dural tail.* In one study, the predictive value of the dural tail sign for meningioma was 94%.[6] It is uncertain whether the dural tail represents neoplastic infiltration beyond the margins of the meningioma or a manifestation of associated inflammation. The amount of disruption to adjacent parenchyma is variable, depending on tumor size and location. Some meningiomas have minimal peripheral edema, although others may have extensive peripheral edema that can result in ventricular compression and brain herniation. An important differential for meningeal enhancement/masses is round cell neoplasia (histiocytic sarcoma and lymphoma).

Choroid Plexus Tumors and Ependymomas

Choroid plexus tumors most commonly occur in the third ventricle and in the lateral recess of the fourth ventricle. The choroid plexus epithelium originates from differentiation of the primitive medullary epithelium and is embryologically related to ependymal cells. Choroid plexus tumors have a tendency to bleed, and exfoliation of choroid plexus cells, from both benign and malignant variants, may occur with subsequent tumor seeding to other areas of the brain or spinal cord through the CSF.[42] Because of the intraventricular location of choroid plexus tumors, obstructive hydrocephalus is common and may be life-threatening. Additionally, some choroid plexus tumors will cause an overproduction of CSF, which exacerbates any

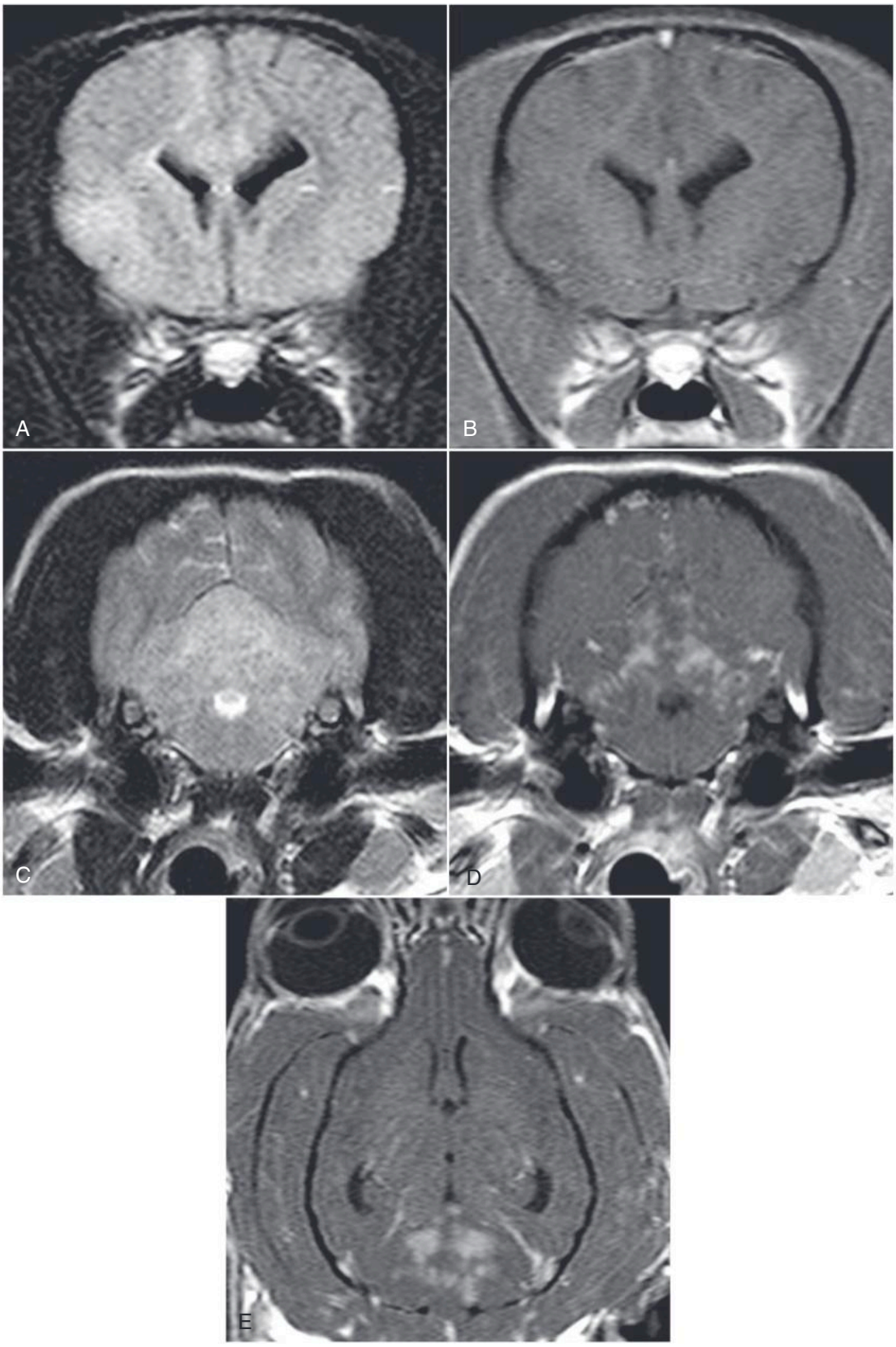


Fig. 12.23 A T2—fluid-attenuated inversion recovery (FLAIR) **(A)** and postcontrast T1-weighted magnetic resonance (MR) image **(B)** of a 4-year-old pug with a history of seizures of progressing severity over a 4-day period. Patchy, ill-defined regions of T2 hyperintensity are present in the right cerebral cortex, most severe in the temporal and parietal lobes. There is minimal mass effect. These regions are mildly T1 hypointense and do not enhance. The most common considerations for these findings are encephalitis, necrotizing encephalitis, and cerebral infarct. On the basis of breed, progressive clinical signs, multifocal distribution of lesions, cerebrospinal fluid (CSF) analysis, and MR findings, necrotizing encephalitis is the most likely diagnosis. **C,** A T2-weighted transverse MR image at the level of the cerebellum, a T1-weighted postcontrast transverse image **(D)** made at the same level as **C,** and a dorsal T1-weighted postcontrast image **(E).** This is a 9-year-old miniature poodle with confirmed granulomatous meningoencephalitis (GME). An ill-defined region of T2-hyperintensity is present in the central aspect of the cerebellum. Multiple patchy regions of contrast enhancement are visible within the cerebellum, as are additional multifocal regions of contrast enhancement, primarily within the corona radiata. The MR findings with GME are variable, and some lesions have minimal contrast enhancement.

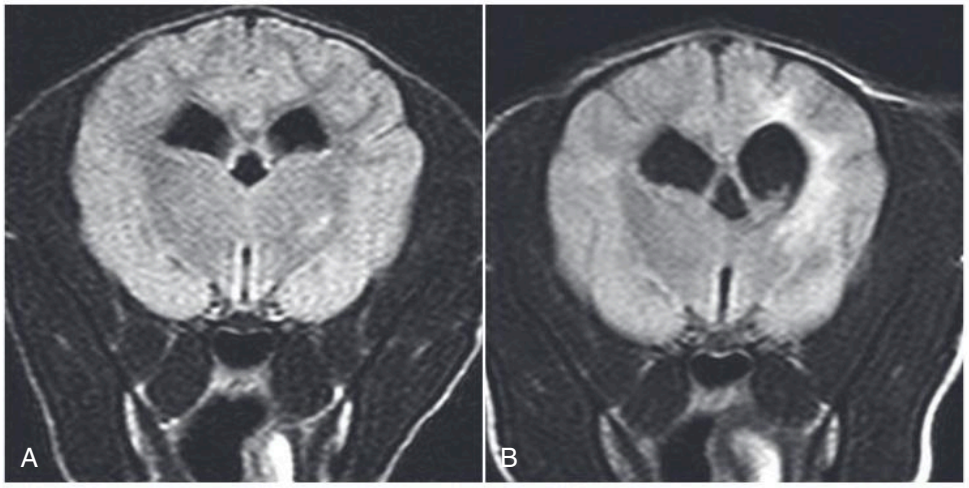


Fig. 12.24 Transverse T2—fluid-attenuated inversion recovery (FLAIR) magnetic resonance (MR) image **(A)** of a 2-year-old Yorkshire terrier and a follow-up image **(B)** at the same level acquired 18 months later. **A,** At presentation, a diagnosis of necrotizing encephalitis was made based on signalment, clinical findings, MR findings, and cerebrospinal fluid (CSF) analysis. In **A,** the ventricular system is mildly enlarged but symmetric. In the later study **B,** the lateral ventricles are larger, asymmetric, and there is a midline shift to the left, toward the side of the larger ventricle. T2 hyperintensity is present in the white matter lateral to the left lateral ventricle. It is likely the ventricular enlargement and midline shift are secondary to parenchymal necrosis; this is often referred to as *compensatory hydrocephalus*. The T2 hyperintensity in **B** did not enhance and, in this patient, reflects unresolved neuropil inflammation.

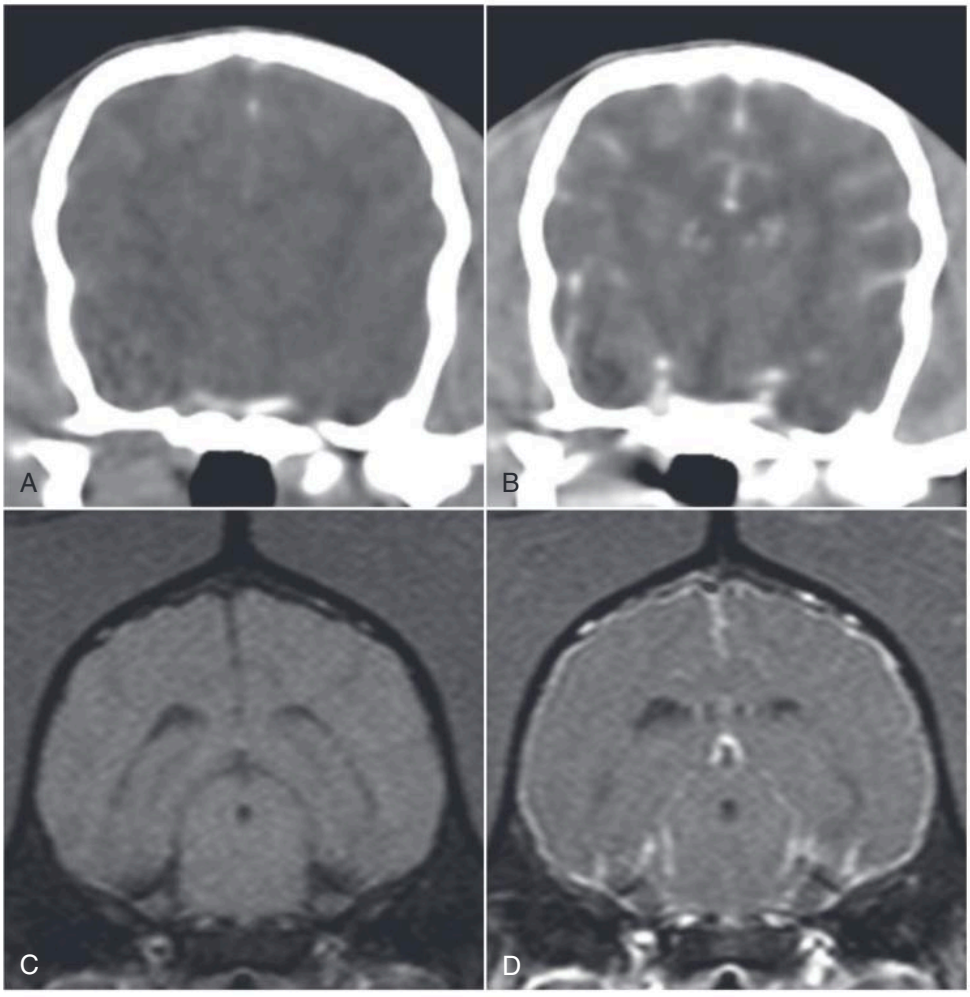


Fig. 12.25 Pre **(A)** and **(B)** postcontrast medium administration transverse computed tomography (CT) images of a 7-year-old Maltese dog with severe meningitis. The meningeal enhancement is readily evident in post-contrast images **(B).** Pre **(C)** and **(D)** postcontrast medium transverse fat saturation magnetic resonance (MR) images of a 5-year-old Labrador with a 4 day history of lethargy, inappetence, ataxia, and dull mentation. There is severe meningeal enhancement. The final (necropsy) diagnosis was immune-mediated lymphoplasmocytic meningoencephalitis.

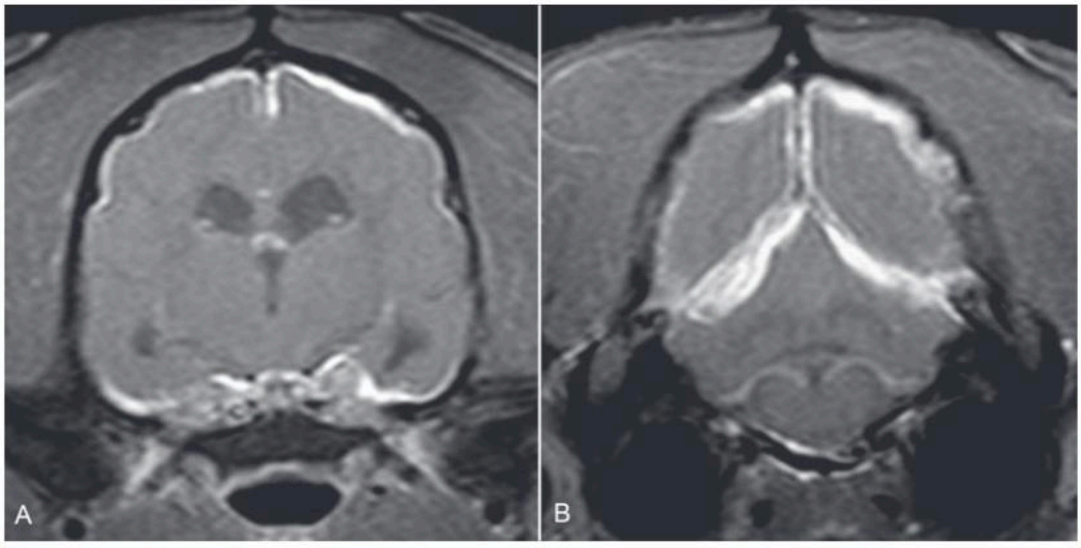


Fig. 12.26 T1-weighted transverse image at level of caudal aspect of the pituitary fossa **(A)** and lateral aperture of the fourth ventricle **(B)** acquired post intravenous contrast medium administration of a 5-year-old Greyhound with a history of progressive cervical pain over many months. There is marked enhancement of the pachymeninges/dura but not of the sulci. The final diagnosis was idiopathic hypertrophic pachymeningitis.

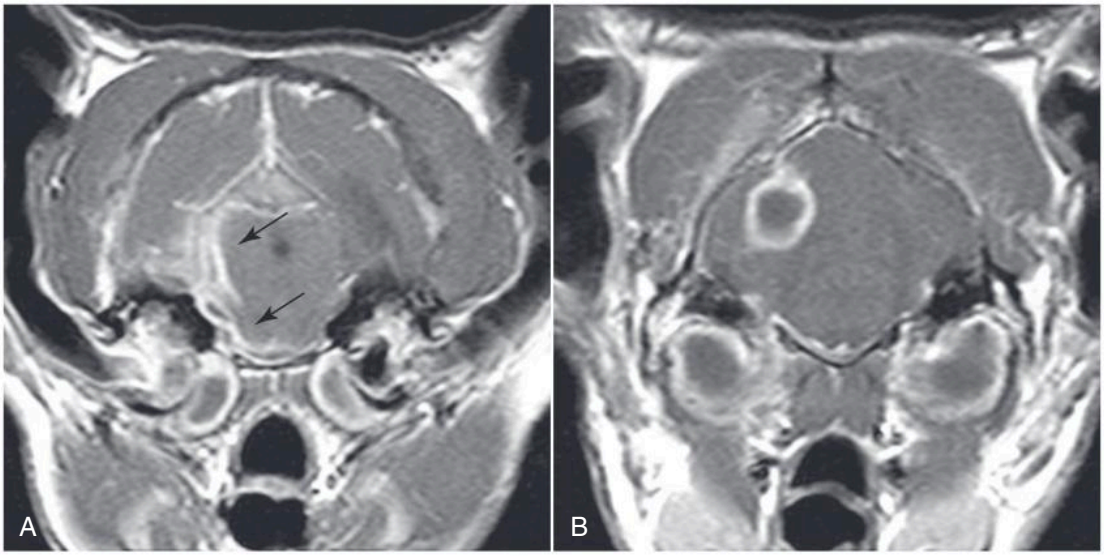


Fig. 12.27 Adjacent transverse T1-weighted postcontrast magnetic resonance (MR) images in a 5-year-old cat with a head tilt and otitis externa. Increased signal intensity in both tympanic bullae is visible. The lining of the bullae is enhanced, but material within either bulla does not enhance. This is consistent with inflammation (exudate in bullae). The meninges adjacent to the right tympanic bulla are characterized by marked contrast enhancement (*arrows* in **A**), and a ring-enhancing mass is present in the right aspect of the cerebellum **(B).** The imaging findings are attributable to otitis media and otitis interna that has progressed to meningoencephalitis and cerebellar abscess.

obstructive process. CSF overproduction can result in massive dilation of the downstream central canal. An important distinguishing feature of choroid plexus tumors is that they are located within a ventricle (Fig. 12.34). Like meningiomas, choroid plexus tumors usually have marked contrast enhancement and sometimes have evidence of hemorrhage and/or dystrophic mineralization. The MR characteristics of intraventricular ependymomas are similar to choroid plexus tumors, but ependymomas are much less common.

Pituitary Tumors

Pituitary tumors are common in dogs but uncommon in cats. They may be nonfunctional or functional. Functional pituitary tumors are typically characterized by pituitary-dependent hyperadrenocorticism (PDH). Up to 60% of dogs with PDH but without neurologic signs have a pituitary tumor 4 to 12 mm in diameter at greatest vertical height.[42] Most pituitary tumors tend to grow dorsocaudally, leading to compression and obliteration of the infundibulum, ventral aspect of the third

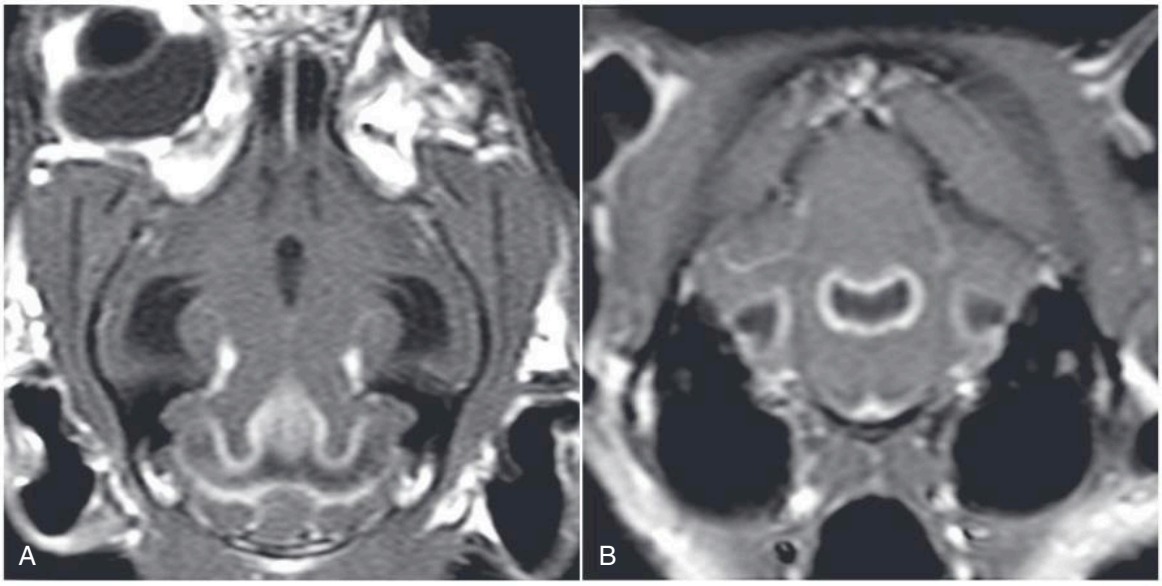


Fig. 12.28 Dorsal **(A)** and transverse **(B)** T1-weighted postcontrast magnetic resonance (MR) images of a cat with feline infectious peritonitis. Intense contrast enhancement of the lining of the ventricular system is present. This is consistent with ependymitis, a common finding in feline infectious peritonitis. The left eye is absent, removed previously as a result of trauma.

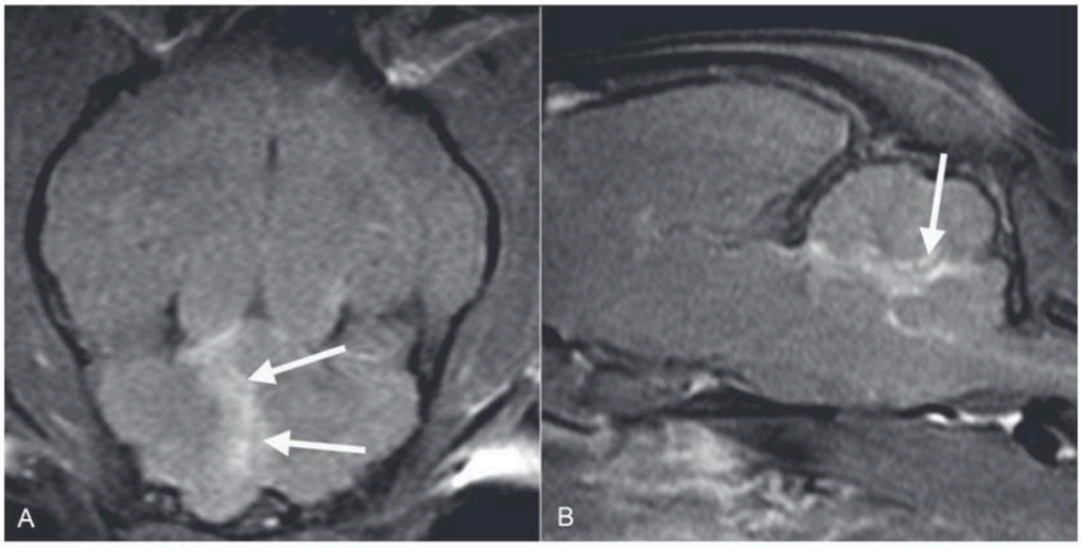


Fig. 12.29 T1-weighted postcontrast dorsal **(A)** and sagittal **(B)** magnetic resonance (MR) images of a 5-year-old indoor/outdoor cat with a recent history of being missing for some days. She was ataxic, anorexic, and depressed. A presumptive diagnosis of feline ischemic encephalopathy (Cuterebra larval migration) was made based on numerous tests, the MR imaging findings and clinical course. There was a curvilinear enhancing region in the frontal lobe (not shown) and a somewhat linear tract of enhancement in the cerebellum (*white arrows*). (Courtesy Heather Jones DVM, DACVIM [neurology].)

ventricle, hypothalamus, and thalamus. They eventually impinge on the internal capsule and optic tracts. MR is useful for visualizing the presence of both microtumors (3–10 mm in diameter) and macrotumors (>10 mm) in dogs with PDH, with or without neurologic signs, especially when endocrine test results are equivocal. Pituitary tumors are always better visualized after contrast medium administration. Usually these tumors have minimal peritumoral edema, uniform contrast enhancement, and well-defined margins (Fig. 12.35). Cystic regions, or evidence of chronic or recent hemorrhage, sometimes extensive, may be present. Pituitary tumors less than 3 mm in diameter may not be visible with MR.

Intra-Axial Tumors: Glioma

Gliomas arise from the neuropil and include astrocytomas, oligodendrogliomas, and glioblastoma multiforme and are particularly common in brachycephalic breeds, such as the Boxer, Boston terrier, and bulldog. Gliomas range in malignancy from

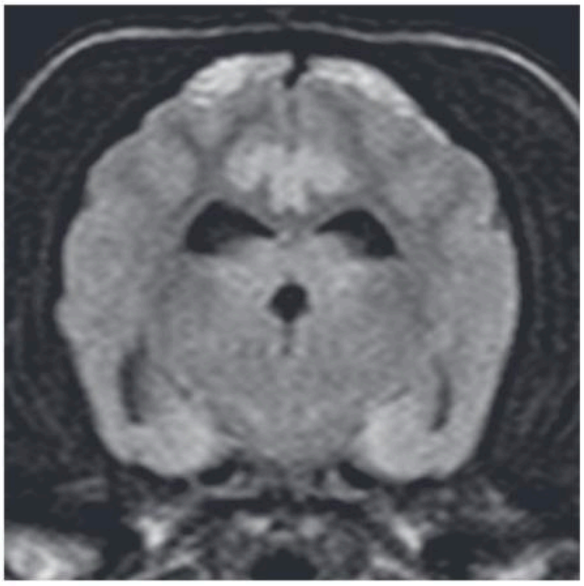


Fig. 12.30 Transverse fluid-attenuated inversion recovery (FLAIR) magnetic resonance (MR) sequence of an 8-year-old beagle with a recent onset of severe cluster seizures. There is FLAIR hyperintensity in the region of the cingulate gyrus, hippocampus, and piriform lobe, bilaterally. The final diagnosis was cryptogenic epilepsy.

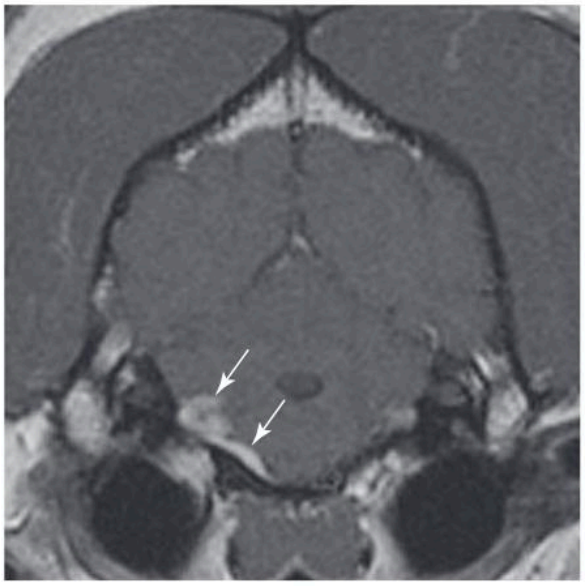


Fig. 12.32 Transverse T1-weighted postcontrast magnetic resonance (MR) image of an 11-year-old Golden retriever. The linear meningeal enhancement (*white arrows*) is a plaque meningioma. Mild ipsilateral temporal muscle atrophy is present, caused by disruption to the adjacent trigeminal nerve nucleus.

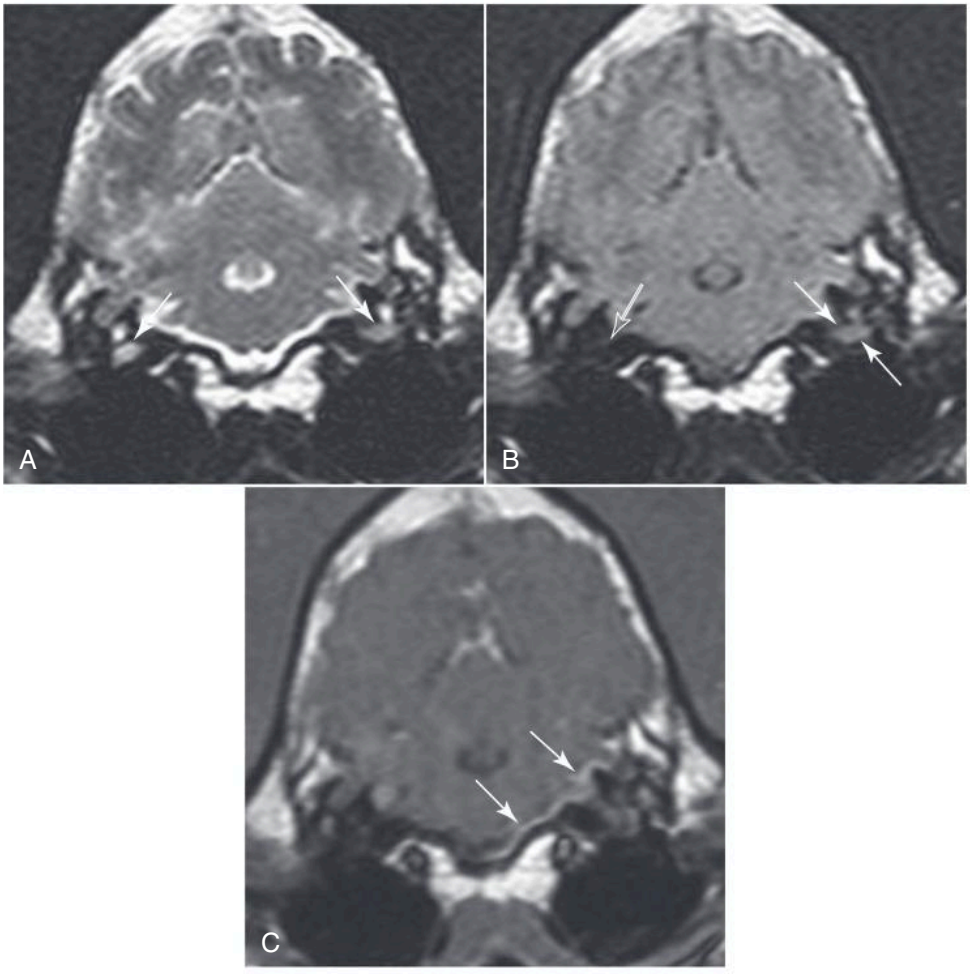


Fig. 12.31 T2 **(A),** fluid-attenuated inversion recovery (FLAIR) **(B),** and T1 postcontrast **(C)** transverse images at the level of the inner ear of a 3-year-old Anatolian shepherd with fever, left head tilt, and nystagmus. In the T2 transverse image **(A)** inner ear fluid signal is similar given subtle positional variation (*solid white arrows*). In the FLAIR sequence, there is incomplete nulling of inner ear fluid on the left (*solid white arrows*) compared to the right (*hollow white arrow*). In **C**, there is increased meningeal enhancement of the meninges adjacent to the bulla (*solid white arrows*). There is no evidence of otitis media. Final diagnosis left otitis interna and septic meningitis.

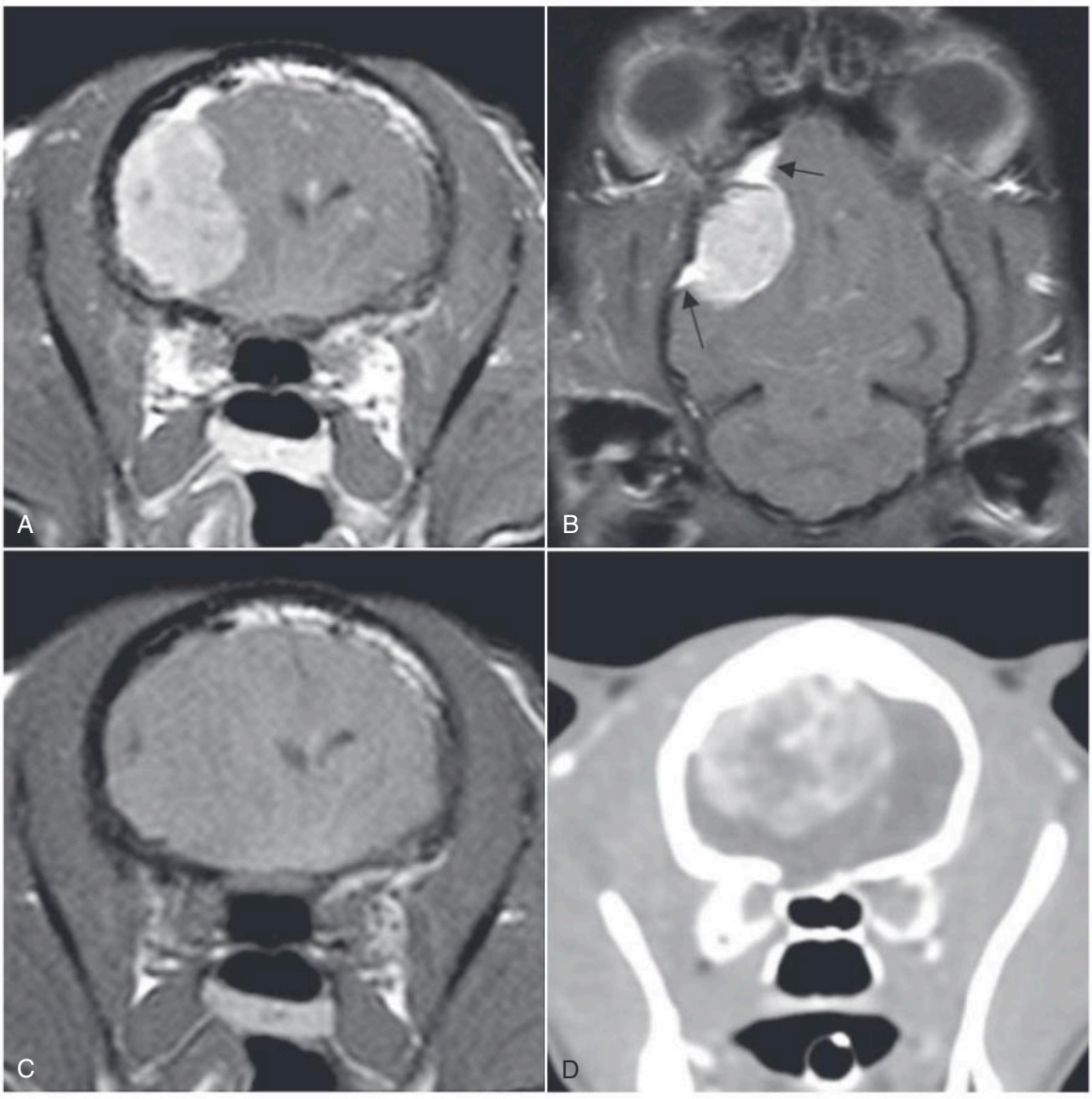


Fig. 12.33 Transverse **(A)** and dorsal **(B)** postcontrast T1-weighted magnetic resonance (MR) images of a feline meningioma. A broad peripheral base and contrast enhancement of the adjacent meninges (*arrows* in **B**) are visible. Dural enhancement in this pattern is termed the *dural tail sign*. **C,** A precontrast T1-weighted transverse image. A midline shift to the left has occurred, and the calvarium on the right is thickened, with replacement of the T1-hyperintense marrow fat with T1-hypointense bone. Calvarial hyperostosis is seen commonly with feline meningioma. **D,** transverse postcontrast computed tomography (CT) image of a feline meningioma. The mass is heterogeneously contrast enhancing and causes a severe midline shift.

low grade and slow growing, to high grade, poorly differentiated highly malignant tumors.

Gliomas vary widely in their MR features. They are often difficult to detect using contrast-enhanced CT imaging of the brain because, unlike meningiomas, many gliomas do not enhance, or enhance only minimally, are often ill-defined, and have varying degrees of perilesional edema (Fig. 12.36). Occasionally, contrast enhancement is not present. A glioma can be difficult to differentiate from a brain abscess and other focal inflammatory conditions of the brain parenchyma,[6] or even from massive infarction.

Gliomatosis cerebri is a rare neoplasm characterized by diffuse and widespread infiltration of the central nervous system by neoplastic glial cells with relative preservation of the neural tissue architecture. It is classified as a malignant (grade III) neuroepithelial tumor of astrocytic origin.[43,44] The MR findings are nonspecific, mimicking many more common conditions, including encephalitis, leukodystrophies, and metabolic encephalopathies. Typically, there may be a diffuse increase in T2 and FLAIR signal throughout regions of the cerebrum with some mass effect but overall relative preservation of the neural morphology and minimal contrast enhancement (Fig. 12.37).

Cranial Nerve Tumors

The terminology given to cranial and spinal nerve and nerve root tumors is confusing because of differing opinions regarding their cell of origin. Although schwannoma, neurilemmoma, and neurofibroma are used interchangeably, the

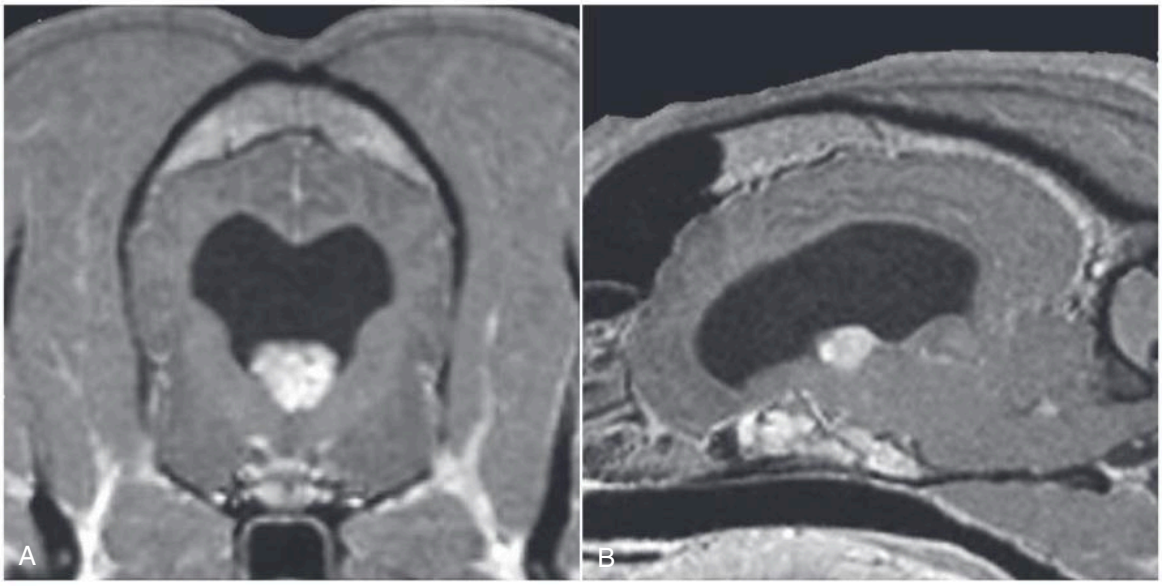


Fig. 12.34 An 8-year-old Boxer with depression and head pressing because of a choroid plexus tumor. In T1-weighted postcontrast magnetic resonance (MR) images (transverse **[A]** and sagittal **[B]**), there is a contrast-enhancing mass in the third ventricle, resulting in obstructive hydrocephalus. The lateral ventricles are enlarged, causing an increase in intracranial pressure and the associated clinical signs.

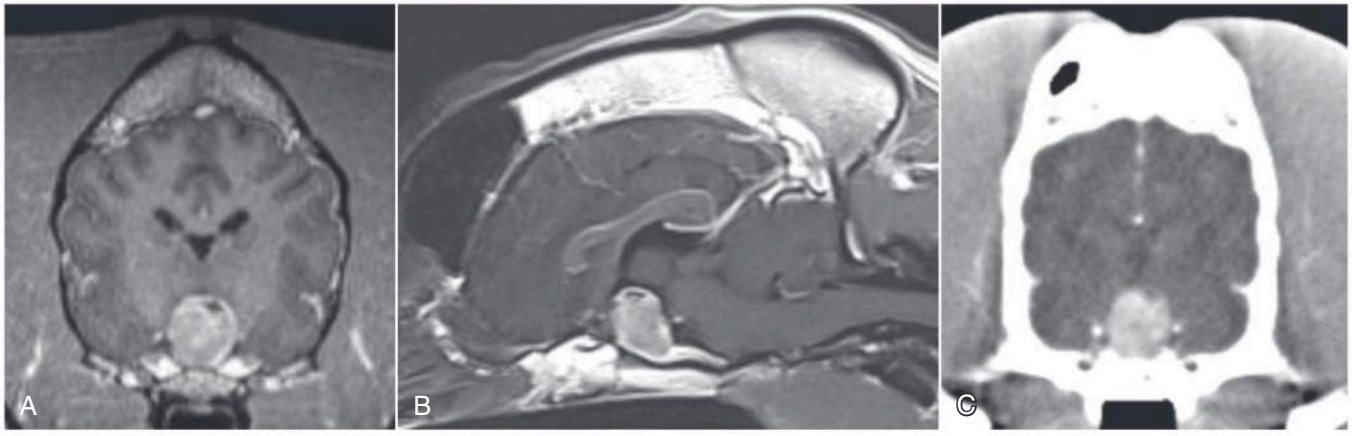


Fig. 12.35 Transverse **(A),** sagittal **(B),** T1-weighted postcontrast magnetic resonance (MR) images and transverse **(C)** contrast-enhanced computed tomography (CT) image of a 12-year-old mix-breed dog with progressive vision loss. The dog was diagnosed with Cushing's disease 2 years ago and medically managed. There is a large contrast-enhancing suprasellar mass causing compression of the hypothalamus. A small cystic area in the left dorsal aspect of the mass presents as focal T1 hypointensity in MR imaging and hypoattenuation in CT images.

designation *malignant (peripheral or cranial) nerve sheath tumor* is recommended, because many of these tumors are malignant and determining the cell of origin (Schwann cell, perineurial cell, fibroblast, etc.) is not possible. Of the cranial nerves, malignant nerve sheath tumors most commonly involve the trigeminal nerve, leading to signs of unilateral trigeminal nerve dysfunction (e.g., unilateral temporalis, masseter, pterygoid, and digastricus muscle atrophy). Cranial nerve sheath tumors are usually either T2 isointense or T2 hyperintense and enhance intensely.[45]

The trigeminal nerve arises at the level of the pons and caudal part of the mesencephalon. The nerve courses rostrally and branches to three divisions (mandibular, maxillary, and ophthalmic) that continue rostrally to exit their respective foramen. Depending on the location of the tumor, foraminal enlargement as a result of pressure remodeling from the expanding tumor can sometimes be seen, and this is an important secondary sign associated with cranial nerve-sheath tumors (Fig. 12.38). Some cranial nerve-sheath tumors are primarily outside the cranial vault and are therefore more easily characterized when fat suppression sequences are used. As discussed in Chapter 4, fat suppression[46] removes the high T1 signal inherent to fat, making normal fat dark. Abnormally contrast-enhancing tissue is more conspicuous when contrasted against a background of dark fat. Fat suppression is possible only on magnets with a field strength of 1 Tesla or greater (Fig. 12.39). In many cases, trigeminal nerve tumors can be difficult to differentiate from trigeminal neuritis. Multiple imaging findings and patient age are considered when prioritizing differentials, but in one paper, all patients with neoplasia had concurrent ipsilateral

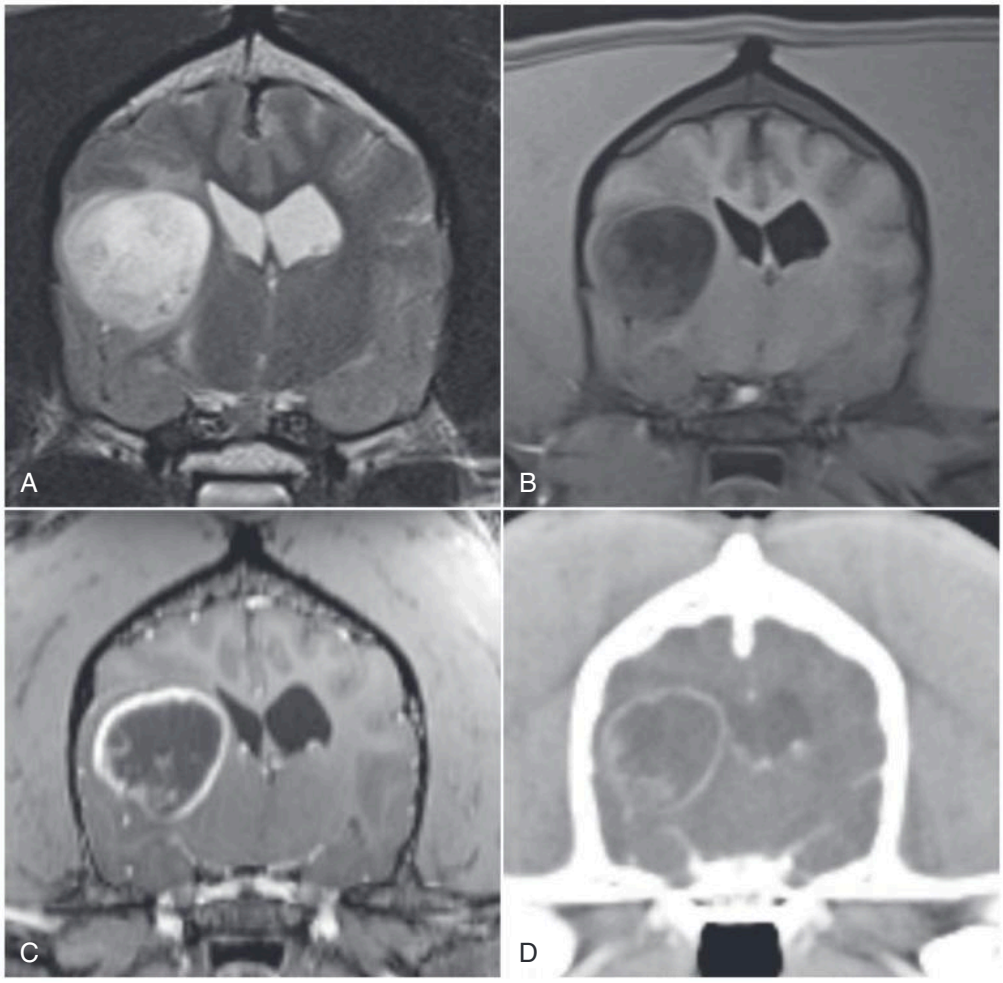


Fig. 12.36 Transverse T2-weighted **(A),** T1-weighted **(B),** T1-weighed postcontrast **(C)** magnetic resonance (MR) images, and a transverse postcontrast **(D)** computed tomography (CT) image of a 9-year-old Boxer with seizures. Within the right temporal lobe, there is a rounded intra-axial mass that causes compression of the right lateral ventricle and a leftward shift of the falx cerebri. The mass is T2 hyperintense and T1 hypointense with strong peripheral contrast enhancement. A thin rim of contrast enhancement is seen in the CT image as well while the center of the mass is hypoattenuating, consistent with a cystic and/or necrotic center. The final diagnosis was oligodendroglioma.

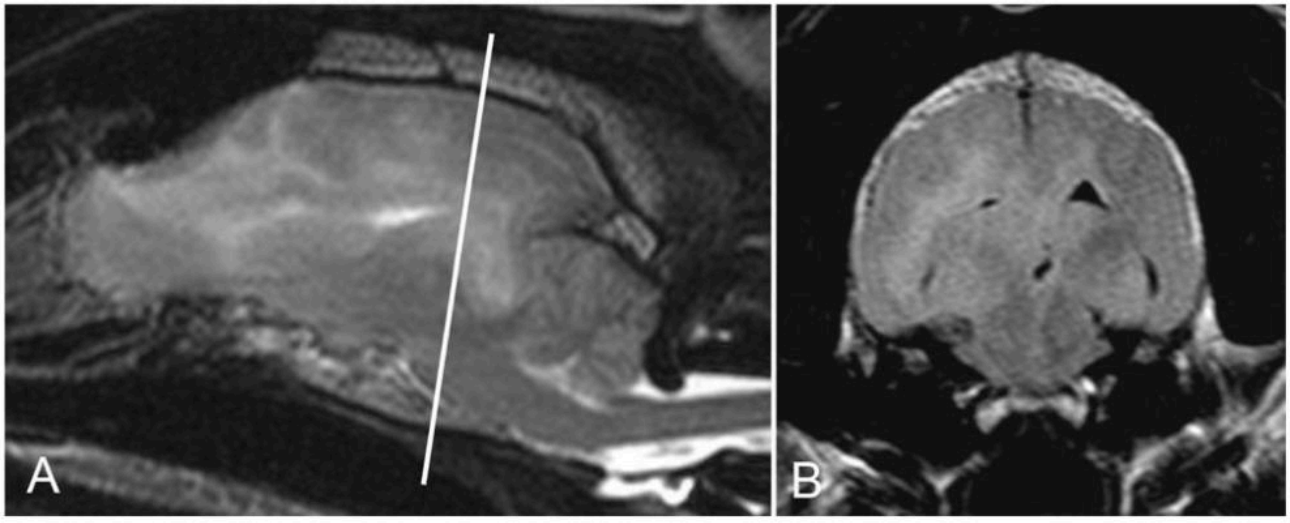


Fig. 12.37 T2-weighted sagittal **(A)** and transverse fluid-attenuated inversion recovery (FLAIR) magnetic resonance (MR) image **(B)** of a 7-year-old Airedale terrier with wide circling and mentation changes for some weeks. The *white line* in **A** is the location of the transverse image **B.** There is a diffuse increase in T2 and FLAIR hyperintensity throughout the cerebral cortex, more extensive on the right. Some attenuation of the caudal aspect of the right lateral ventricle is present. There is subtle leftward shift of midline structures and transtentorial herniation of the right hippocampal gyrus. The differential diagnosis for this pattern is extensive. The final diagnosis was gliomatosis cerebri.

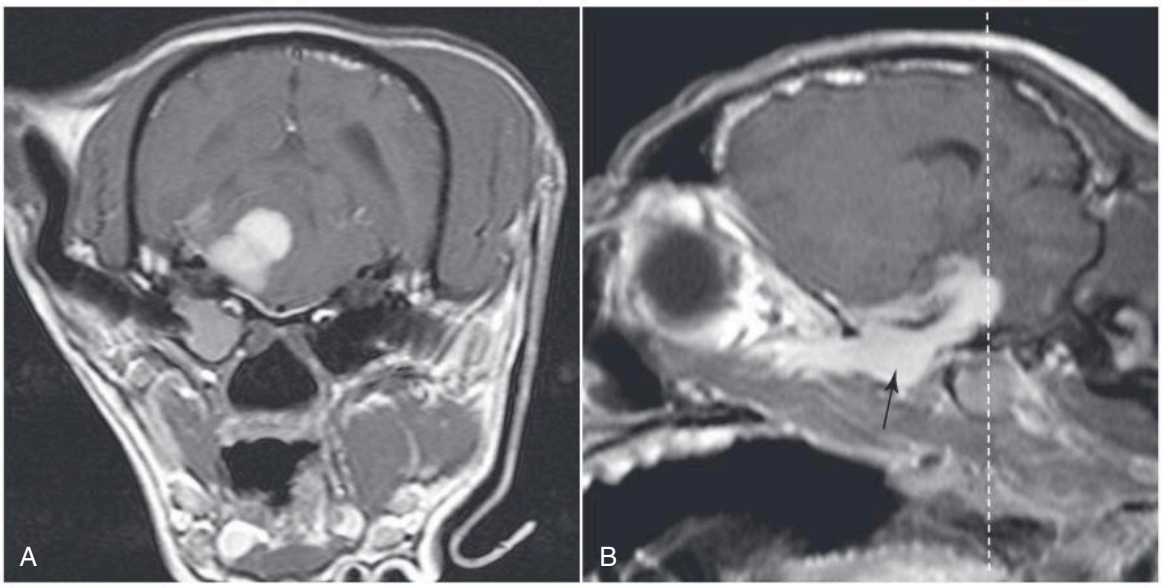


Fig. 12.38 Transverse **(A)** and sagittal **(B)** T1-weighted postcontrast magnetic resonance (MR) images. There is marked atrophy of the temporal musculature on the right side, and an intensely contrast-enhancing tubular mass emanates from the right ventral aspect of the pons and courses rostrally through an enlarged orbital fissure (*arrow* in **B**) to the retrobulbar region. The *vertical dashed line* in **B** designates the location of the transverse image seen in **A.** Final diagnosis was trigeminal nerve sheath tumor. Incidentally, fluid is present in the right tympanic cavity.

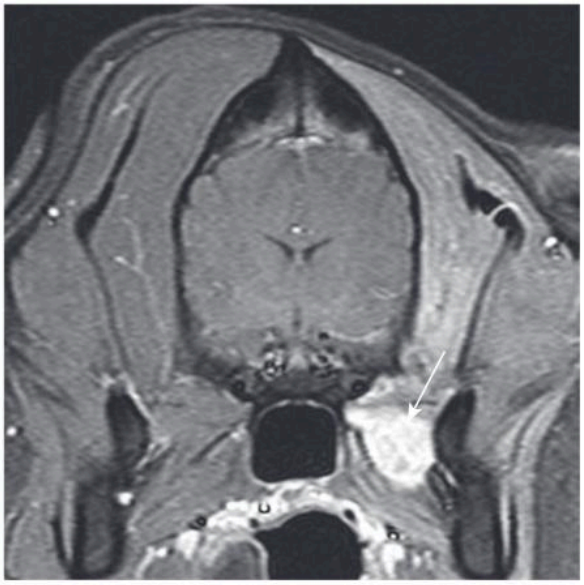


Fig. 12.39 Transverse T1-weighted postcontrast magnetic resonance (MR) image of a 10-year-old mixed-breed dog with left temporal muscle atrophy. In this image, the inherent bright signal from fat has been suppressed, and this increases the conspicuity of the extracranial trigeminal nerve tumor (*arrow*) in this patient. There is increased enhancement of the atrophic left temporal muscles compared to the right. This is commonly seen in muscles affected by neurogenic atrophy and thought to be associated with alterations in autonomic control of vascular and capillary bed secondary to denervation.

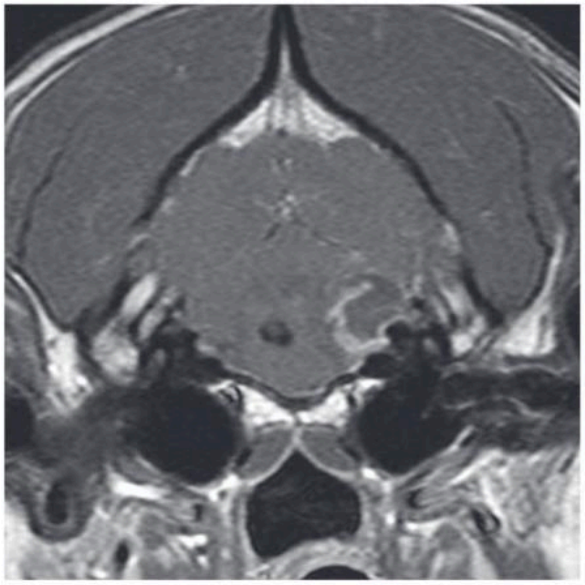


Fig. 12.40 Transverse T1-weighted postcontrast magnetic resonance (MR) image of a 7-year-old Golden retriever. There is a peripherally contrast-enhancing mass at the cerebellopontine angle that appears similar to a cystic meningioma. Extensive peripheral edema and brainstem compression was evident on other sequences. The final diagnosis was histiocytic sarcoma.

noninfectious middle ear effusion, thought due to neurogenic dysfunction of the eustachian tube.[47]

Other Primary Tumors and Metastatic Tumors

A complete review of brain tumors reported in dogs and cats is beyond the scope of this text, and excellent reviews are available.[42,48] Histiocytic sarcoma is an uncommon extra-axial tumor that has imaging characteristics similar to meningioma, including a dural tail[49] (Fig. 12.40); histiocytic sarcoma can also be intra-axial.[50] Meningeal enhancement remote from the tumor epicenter is not an uncommon finding (Fig. 12.41).

Lymphoma is a common tumor both in dogs and cats, manifesting in many ways. With respect to intracranial

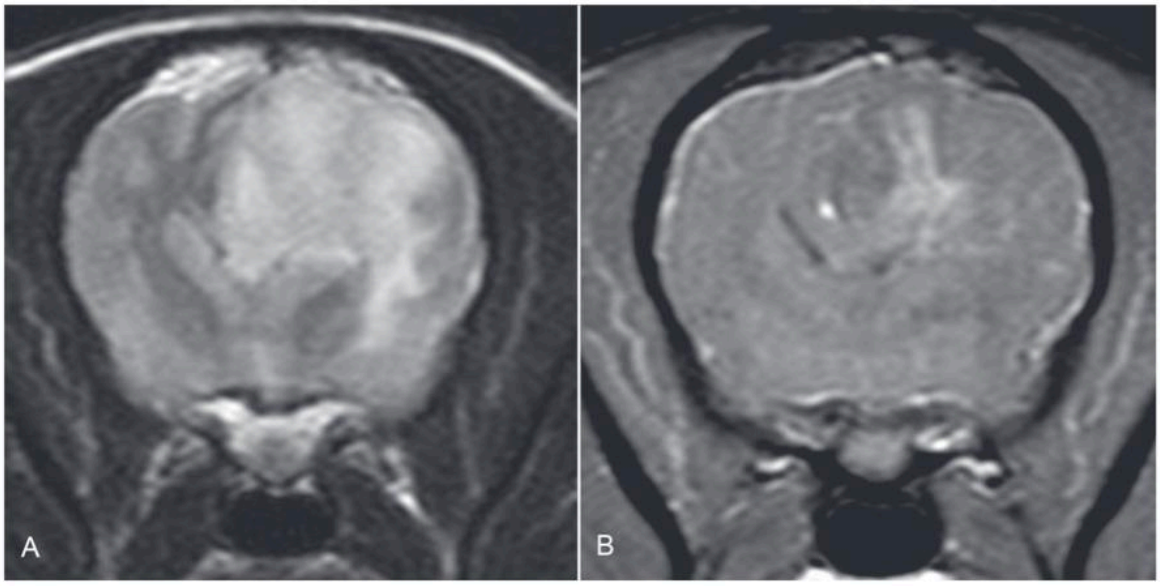


Fig. 12.41 Transverse fluid-attenuated inversion recovery (FLAIR) **(A)** and T1-weighted postcontrast magnetic resonance (MR) image **(B)** at the level of the pituitary gland. The patient is a 12-year-old Schipperke with a recent onset of seizures, depression, and syncope. There is extensive primarily left parietal lobe white matter edema with ventricular compression and a paradoxical midline shift. There is amorphous regional parenchymal enhancement in the region of the presumed mass. The final diagnosis was histiocytic sarcoma. Meningeal enhancement remote from the lesion (in this case right dorsolateral) is not an uncommon finding with histiocytic sarcoma.

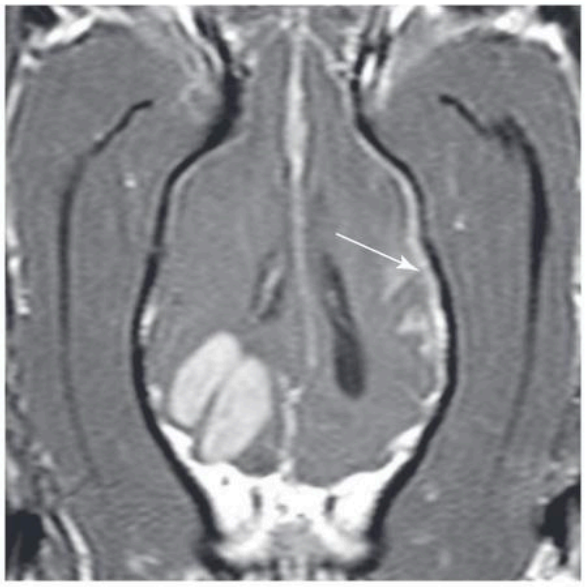


Fig. 12.42 Dorsal T1-weighted postcontrast magnetic resonance (MR) image of a 4-year-old Labrador retriever with lymphoma. There is a lobulated intensely contrasting mass in the occipital lobe that is causing ventricular compression and a leftward shift of midline structures. There is thickening of both the peripheral meninges (particularly on the left, *arrow*) and the falx (rostrally). Mass lesions and meningeal infiltration are common manifestations of intracranial lymphoma in both cats and dogs.

lymphoma, it can be solitary or present in multiple other organs. Typically, lymphoma has at least moderate enhancement and can be asymmetric in distribution (Fig. 12.42) or bilaterally symmetrical (Fig. 12.43).

In one study,[29] brain metastases were as common as primary intracranial tumors, with hemangiosarcoma being the most common metastatic lesion (Fig. 12.44). The brain is not immune to metastases, and secondary intracranial neoplasia is common.

Invasive Extracranial Tumors

Aggressive nasal tumors can extend through the cribriform plate, caudal nasal region, or frontal sinus into the cranial vault, and it is important to include the caudal aspect of the nasal

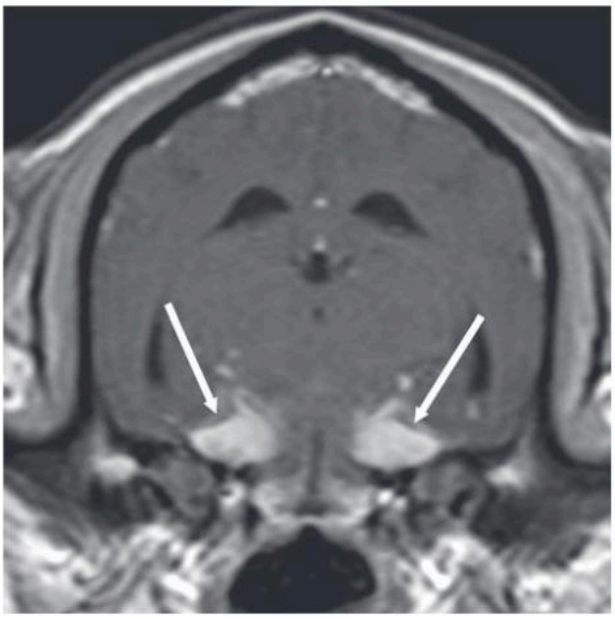


Fig. 12.43 Transverse T1-weighted postcontrast magnetic resonance (MR) image (fat saturation not applied) of a 6-year-old Jack Russell terrier with bilateral temporal muscle wasting and multiple cranial nerve de ficits. The image is at the level of the midbrain. There was marked enhancement extending along the floor of the calvarium bilaterally (*white arrows*). Temporalis muscle wasting and enhancement are evident. Bilateral otitis media is also present, likely secondary to dysfunction of the levator veli palatini muscle. The final diagnosis was lymphoma.

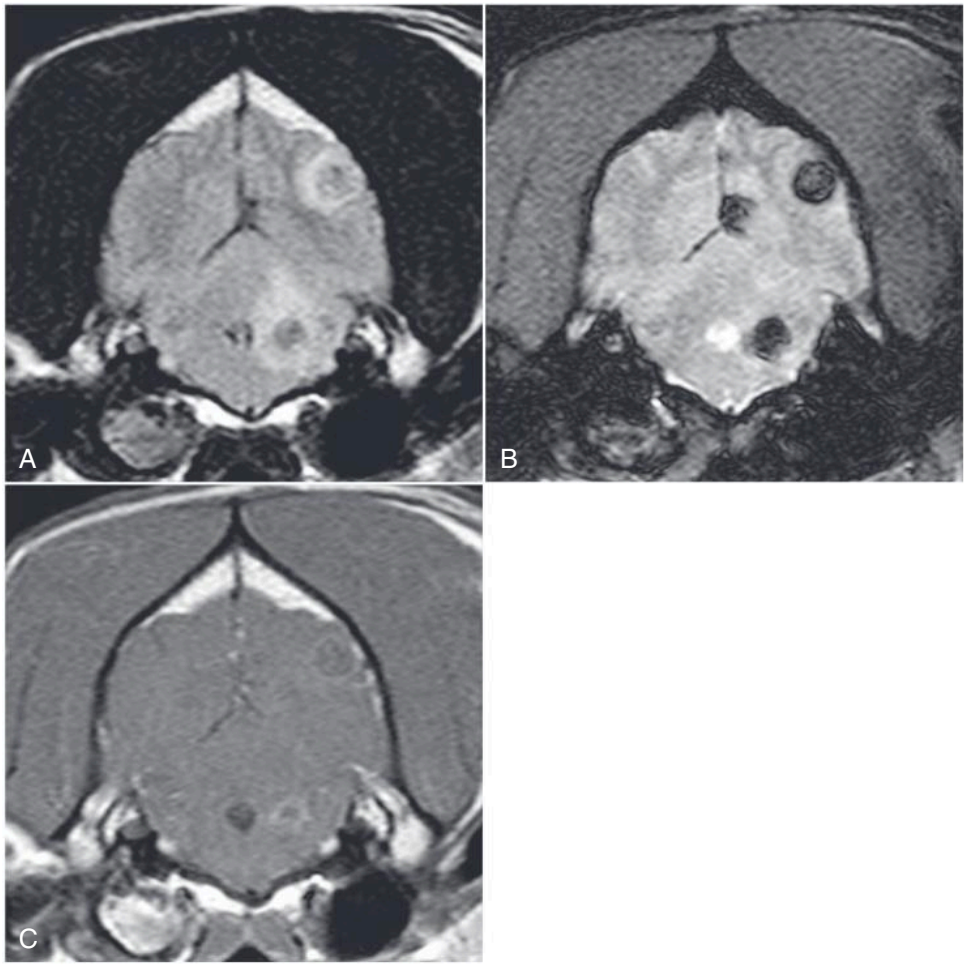


Fig. 12.44 Transverse T2—fluid-attenuated inversion recovery (FLAIR) **(A),** gradient recalled echo (GRE) **(B),** and T1-weighted postcontrast **(C)** magnetic resonance (MR) images of a 9-year-old Golden retriever with metastatic hemangiosarcoma. In **A,** there are two focal hypointense regions with surrounding T2 hyperintensity, presumably edema, in the left occipital lobe and left ventral cerebellum. Minimal mass effect is present. Both lesions have mild peripheral contrast enhancement **(C)** and a susceptibility artifact **(B)** indicating hemorrhage. In **B,** a susceptibility artifact is also present adjacent to the osseous tentorium. This is the border of a similar "out-of-plane" lesion. The imaging characteristics are consistent with both hemorrhagic infarction of some days' duration (approximately >3) and hemorrhagic tumor foci but in this dog were proven to be metastasis. Incidentally, there is right otitis media.

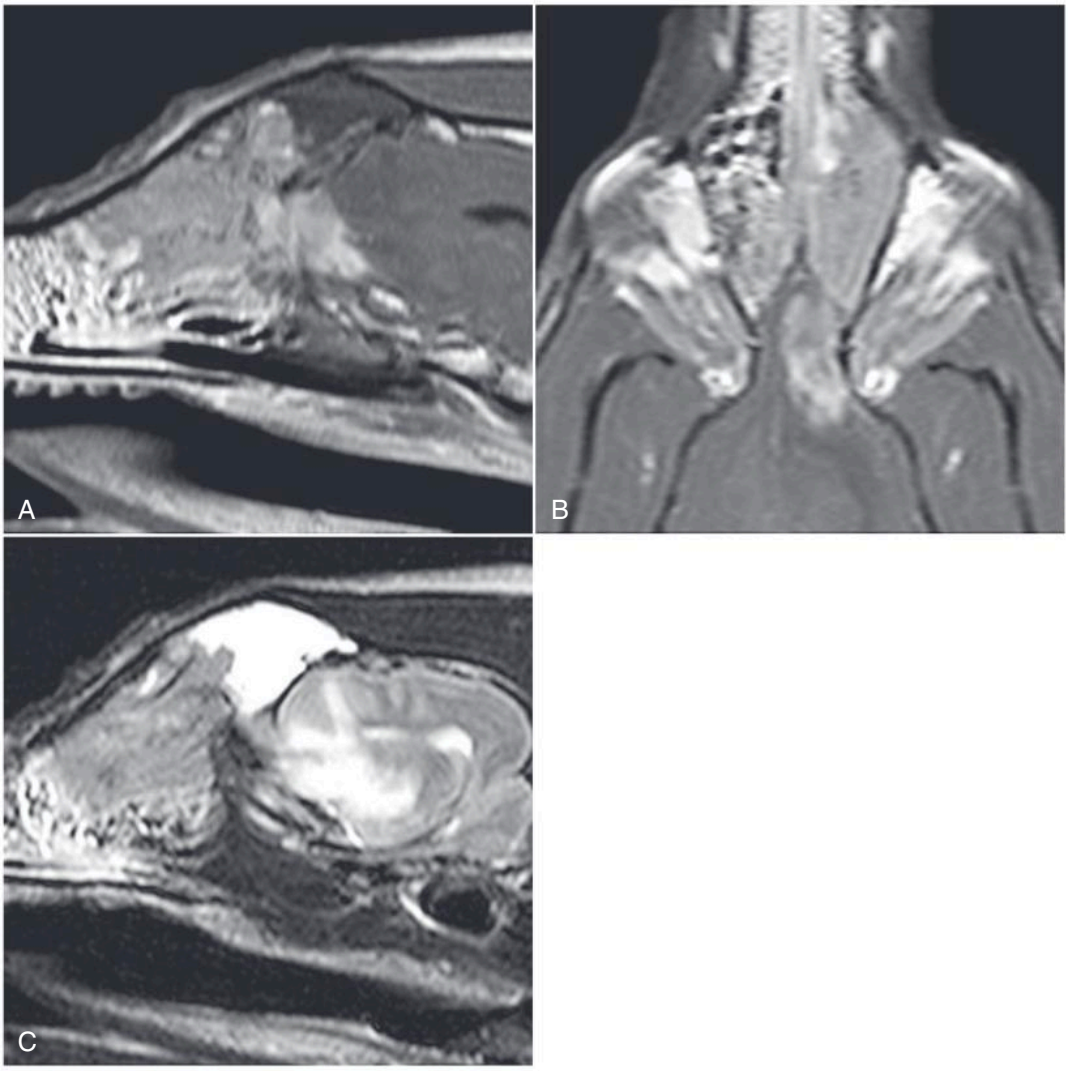


Fig. 12.45 T1-weighted sagittal **(A),** dorsal **(B),** and a T2-weighted sagittal magnetic resonance (MR) image **(C)** of an elderly dog with intermittent epistaxis. A mass is present in the caudal aspect of the left nasal cavity, which extends into the right nasal cavity and also into the rostral fossa. The material in the left frontal sinus is T2 hyperintense **(C)** and T1 isointense **(A)** and does not enhance. On the basis of these signal characteristics, the frontal sinus lesion is more likely to be trapped fluid rather than tumor. Distinguishing mass from trapped fluid cannot be made as easily with contrast-enhanced computed tomography (CT). In the T2-weighted image, extensive white-matter edema is visible as a result of the intracranial extension. The histologic diagnosis was carcinoma.

cavity when imaging the brain (Fig. 12.45). Brain tumors do not commonly extend rostrally through the cribriform plate into the nasal cavity. A rare neural tumor that does traverse the cribriform plate is an olfactory neuroblastoma (esthesioneuroblastoma).[51]

VASCULAR DISRUPTIONS

Occlusive Infarcts

Occlusive brain infarcts are being diagnosed with increasing frequency with MRI but are rarely detectable with CT imaging.[30–32] Infarcts occur most commonly in the cerebellum but also occur in the brainstem and forebrain.

Patients with brain infarction are typically older and present with acute nonprogressive focal neurologic signs. When the brainstem or cerebellum is involved, an important clinical differential is idiopathic peripheral vestibular disease, in which no abnormal MR findings are present. The typical MR characteristics of an acute cerebellar infarct include a triangular or segmental region of T2 hyperintensity that persists in the FLAIR sequence. The shape of the signal change usually closely reflects the territory of the affected artery (Fig. 12.46).

With cerebral infarction, the MR findings may overlap with those of a glioma or focal encephalitis; there is usually ill-defined T2 hyperintensity, T1 hypointensity, no mass effect, and little to no initial contrast enhancement (Fig. 12.47). Typically, after 3 days, regional vascularity increases, particularly at

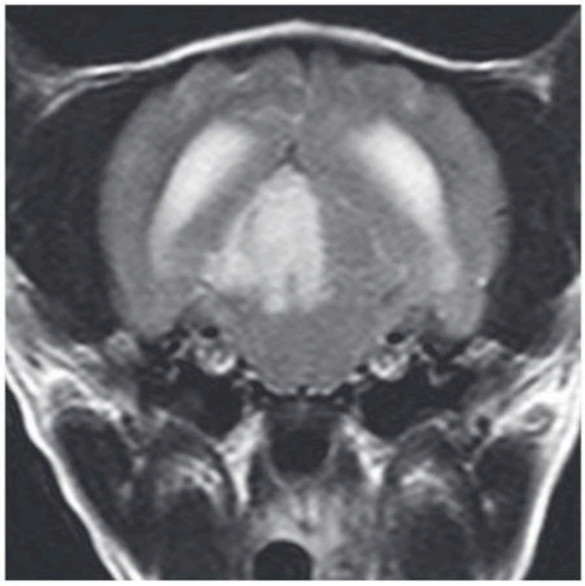


Fig. 12.46 Transverse T2-weighted magnetic resonance (MR) image at the level of the rostral aspect of the cerebellum of an 8-year-old Papillon that developed acute tetraplegia, a right head tilt, and positional vertical nystagmus less than 24 hours previously. The large triangular region of T2 hyperintensity in the right rostral aspect of the cerebellum was mildly T1 hypointense and had no discernible contrast enhancement. The clinical presentation, lesion location, shape, and imaging characteristics are typical of an infarct. This is a particularly large lesion. Diffusion-weighted imaging con firmed restricted water movement, also supporting acute infarction.

the periphery of the lesion.[33] One differentiating feature between infarction and glioma is the initial lack of a mass effect with an infarct. Later, however, a mass effect may develop 3 to 5 days post infarct due to vasogenic edema. Differentiating a cerebral infarct and glioma may not be possible in some patients, and diffusion-weighted MR or follow-up imaging may be necessary. Diffusion imaging quantifies the rate of Brownian motion of water molecules in brain tissue. *Brownian motion* refers to the random movement of molecules. Water molecules are in constant motion, and the rate of movement or diffusion depends on the kinetic energy of the molecules and temperature. In acute infarction, brain cells become overhydrated from failure of the adenosine triphosphate pump, resulting in restricted movement of water (Fig. 12.48). In tumors, water movement is usually less restricted, and tumors will have less evidence of restricted water diffusion. However, restricted water diffusion in an infarct typically only lasts up to 3 to 5 days post infarct, so after this time the ability of diffusion-weighted imaging to distinguish infarct from glioma is lost.

When an occlusive infarct is suspected, the patient should be evaluated for conditions resulting in a hypercoagulable state (e.g., Cushing disease) and loss of antithrombin III.

Hemorrhagic Infarcts

Hemorrhagic infarcts are most commonly associated with hypertension, thrombocytopenia, or other coagulopathies. The MR characteristics may be similar to those for an occlusive infarct (Fig. 12.49). However, the presence of hemorrhage typically results in more signal heterogeneity and larger size of the lesion. The appearance of cerebral hemorrhage changes as the hematoma matures (Table 12.2). The use of standard spin-echo sequences sometimes allows one to estimate the age of a hemorrhagic lesion, based roughly on the signal characteristics. The change in appearance of a hematoma in different sequences over time is related to the magnetic properties of iron within hemoglobin as it transitions through intracellular deoxyhemoglobin to methemoglobin and finally extracellular hemosiderin (Fig. 12.50).

As discussed previously, in comparison to fast (turbo) spin-echo sequences, GRE sequences are more susceptible to magnetic field inhomogeneity created by hemoglobin degradation. Chronic hemorrhage acts like ferromagnetic material, causing pronounced local distortion of the local magnetic field resulting in a signal void (Fig. 12.51; see Figs. 12.44 and 12.49), and for this reason, a GRE sequence should be acquired routinely, even though hemorrhage may not be suspected. Low signal in T2-weighted spin-echo and GRE images is, however, not specific for hemorrhage and may also be seen with mineralization, gas, fibrous tissue, or iron deposits.[33] Susceptibility artifacts in GRE images must be interpreted in light of information gained from all other sequences in the study and the available clinical information.

Trauma

Both MRI and CT can be used to assess patients with head trauma; however, CT is often preferred due to faster acquisition time and excellent ability to detect skull fractures and intracranial hemorrhage in the acute stage. Acute hemorrhage is hyperattenuating to brain tissue in precontrast CT imaging due to the high hemoglobin content. The average Hounsfield units (HUs) of hemorrhage is between 60 and 100, whereas those of gray and white matter are in the range of 30 to 40 and 20 to 30, respectively. Edema may be present as a hypoattenuating halo around the hemorrhagic focus.[52,53] Viewing the CT images in a narrow window is essential to detect subtle changes in attenuation and small foci of hemorrhage (Fig. 12.52).

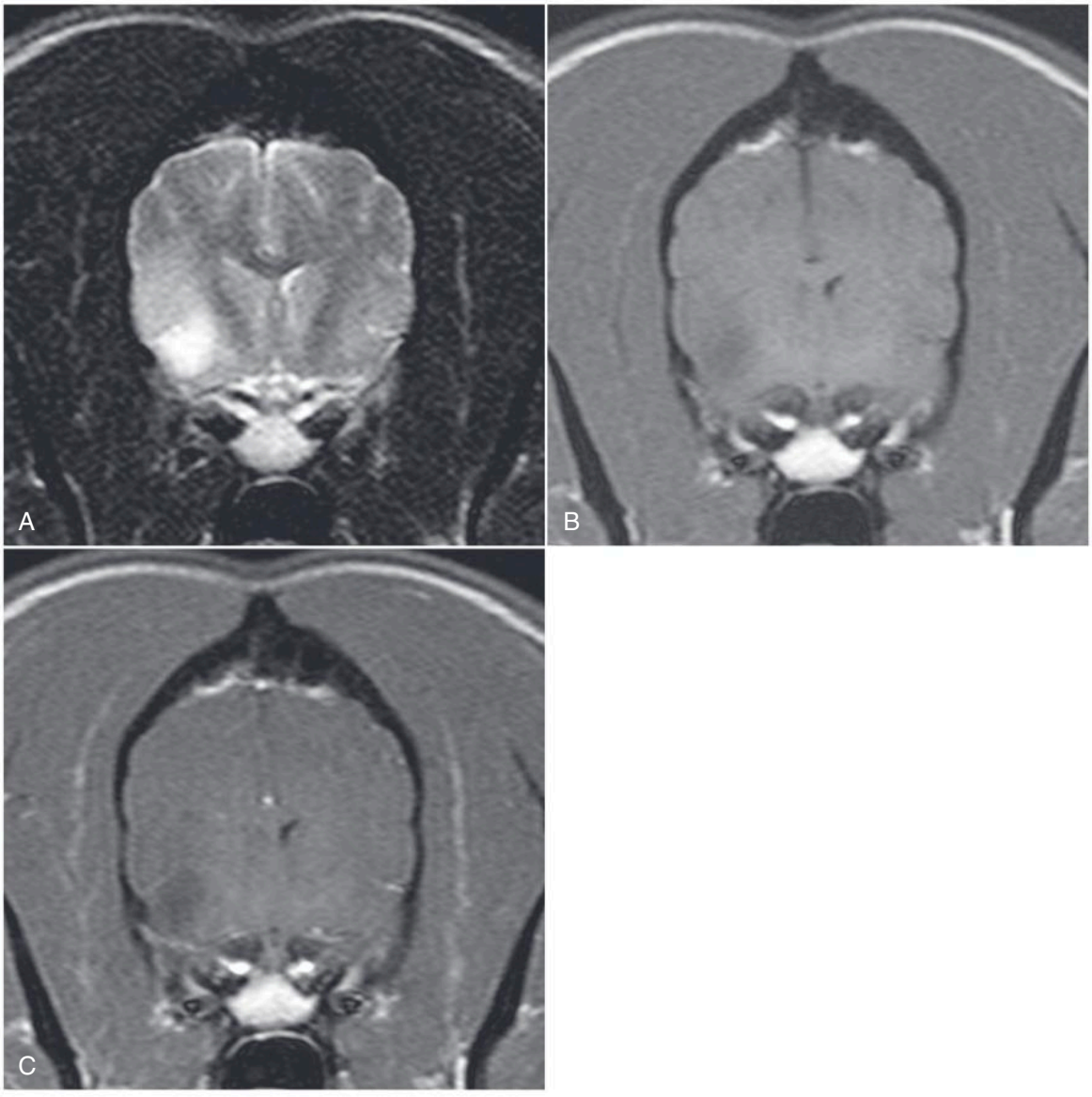


Fig. 12.47 Transverse T2-weighted **(A)** and T1-weighted magnetic resonance (MR) images made before **(B)** and after **(C)** contrast-medium administration in a 10-year-old Labrador retriever with an acute onset of seizures that began 5 days previously. An ill-defined region of T2 hyperintensity is present in the right piriform lobe. The region is T1 hypointense; there is no associated mass effect, and only scant peripheral contrast enhancement. The two most likely differentials are an infarct or a nonenhancing glial cell tumor. The sudden onset of nonprogressive signs is important collaborating history in these patients and helps decide the likelihood of infarction versus glioma. Other considerations for the findings in this patient include necrotizing encephalitis and granulomatous meningoencephalitis (GME), which sometimes has minimal contrast enhancement. Diffusion-weighted imaging can be used to help differentiate these conditions more accurately in the first 1 to 3 days.

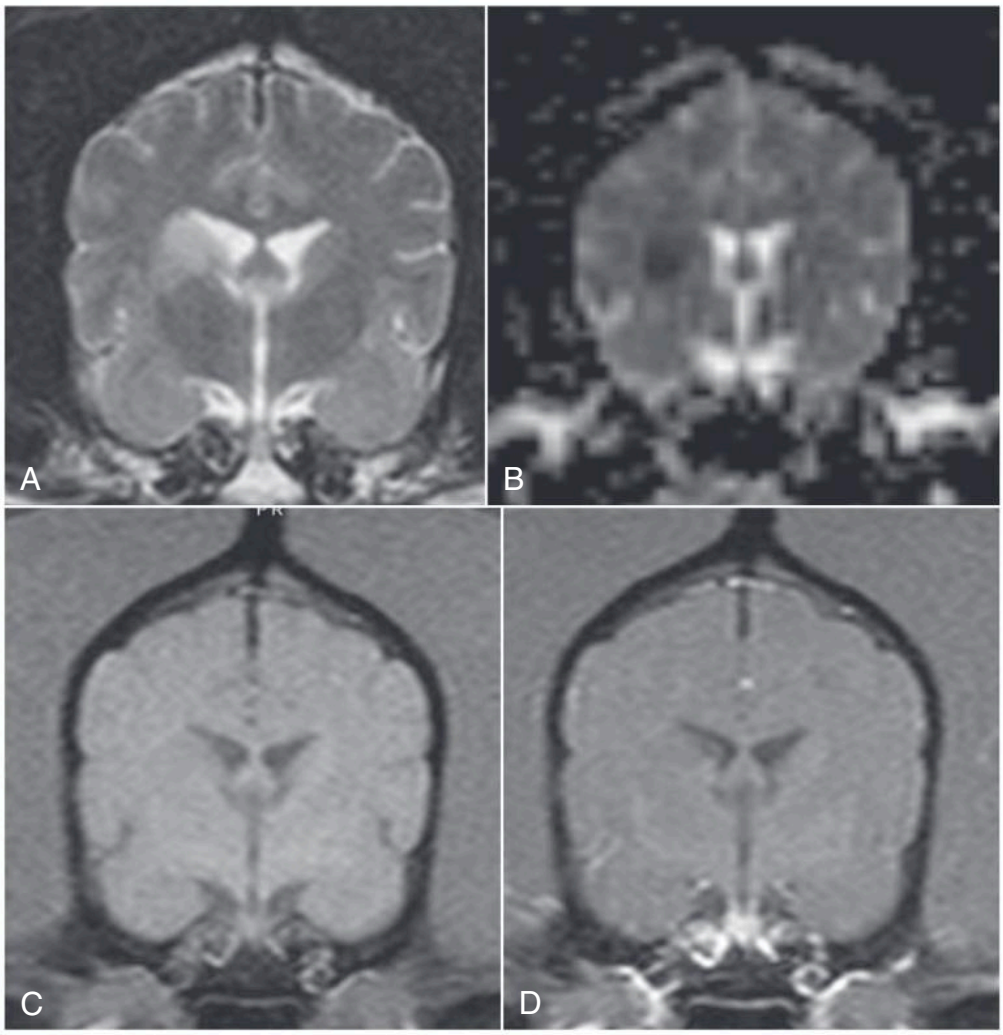


Fig. 12.48 Transverse T2-weighted **(A),** apparent diffusion coefficient (ADC) map **(B),** T1-weighted pre- **(C)** and postcontrast **(D)** images of a 10-year-old standard poodle with acute left hemiparesis. A focal T2 hyperintense, noncontrast-enhancing lesion is seen in the right caudate nucleus. The lesion was hyperintense in diffusion-weighted images and hypointense in ADC maps **(B),** indicating the presence of restricted water diffusion, most consistent with an ischemic cerebrovascular accident.

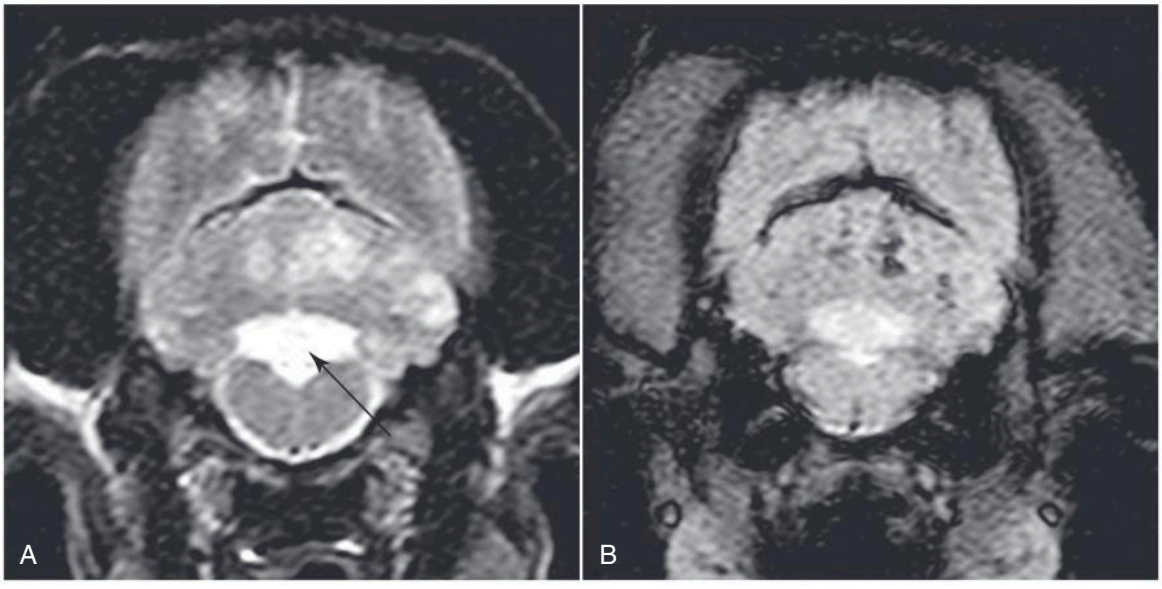


Fig. 12.49 **A,** T2-weighted transverse magnetic resonance (MR) image at the level of the cerebellum. The well-defined region of T2 hyperintensity dorsal to the brainstem (*arrow*) is the fourth ventricle. A region of T2 hyperintensity is present in the central and left aspects of the cerebellum. **B,** T2-weighted gradient recalled echo (GRE) (T2*) MR image at the same level. Hemorrhage is best detected on a GRE sequence because of the magnetic susceptibility effect of hemoglobin breakdown products. The focal regions of signal void are the result of local disruption to the magnetic field because of the magnetic properties of chronic hemorrhage. The size of the signal void does not reflect the size of the hematoma accurately because of blooming artifact.

Table • **12.2**

Classic Magnetic Resonance Appearance of a Maturing Hematoma[a] in Human Central Nervous System Tissue.

PHASE	TIME	HEMOGLOBIN	T1	T2
Hyperacute	<24 hours	Oxyhemoglobin (intracellular)	Isointense or hypointense	Hyperintense
Acute	1–3 days	Deoxyhemoglobin (intracellular)	Isointense or hypointense	Hypointense
Early subacute	>3 days	Methemoglobin (intracellular)	Hyperintense	Hypointense
Late subacute	>7 days	Methemoglobin (extracellular)	Hyperintense	Hyperintense
Chronic	>14 days	Hemosiderin (extracellular)	Isointense or hypointense	Hypointense

[a]There is considerable variation in the appearance of hematomas, and these observations have not been clinically validated fully in dogs. This table should act as guide only.
Modified from Bradley WG Jr. MR appearance of hemorrhage in the brain. *Radiology*. 1993;189:15–26.

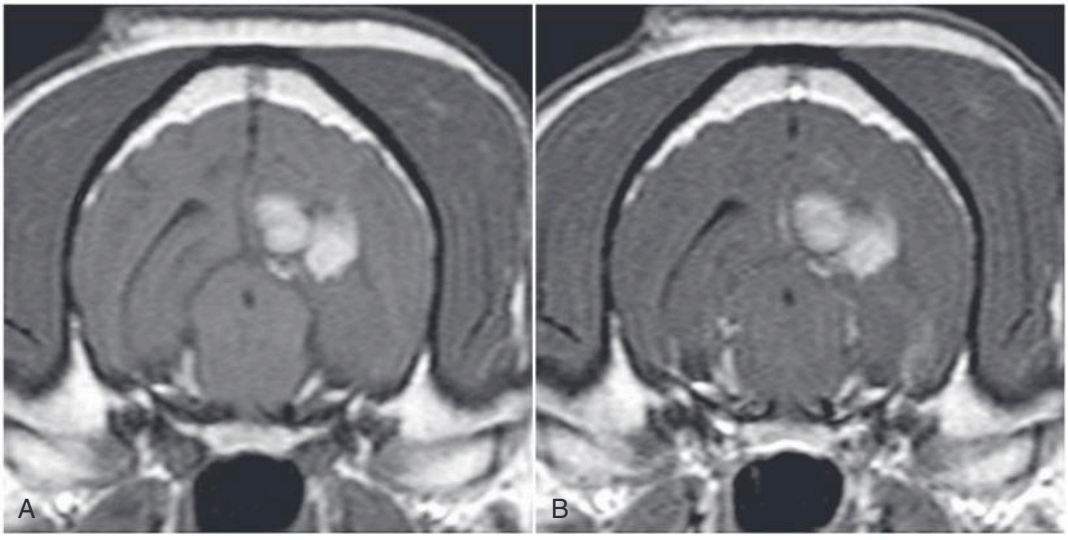


Fig. 12.50 Precontrast **(A)** and postcontrast **(B)** T1-weighted magnetic resonance (MR) images of a 10-year-old spaniel with acute seizures. The precontrast T1-hyperintense region in **A** is hemorrhage of at least 3 days' duration. Both intracellular and extracellular methemoglobins are inherently T1 hyperintense. Other substances that are T1 hyperintense are the normal neurosecretory granules within the pituitary gland, fat, melanin, proteinaceous fluids, and some plasma cell tumors. There is no enhancement of the lesion **(B),** but normal vascular enhancement is apparent adjacent to the lesion.

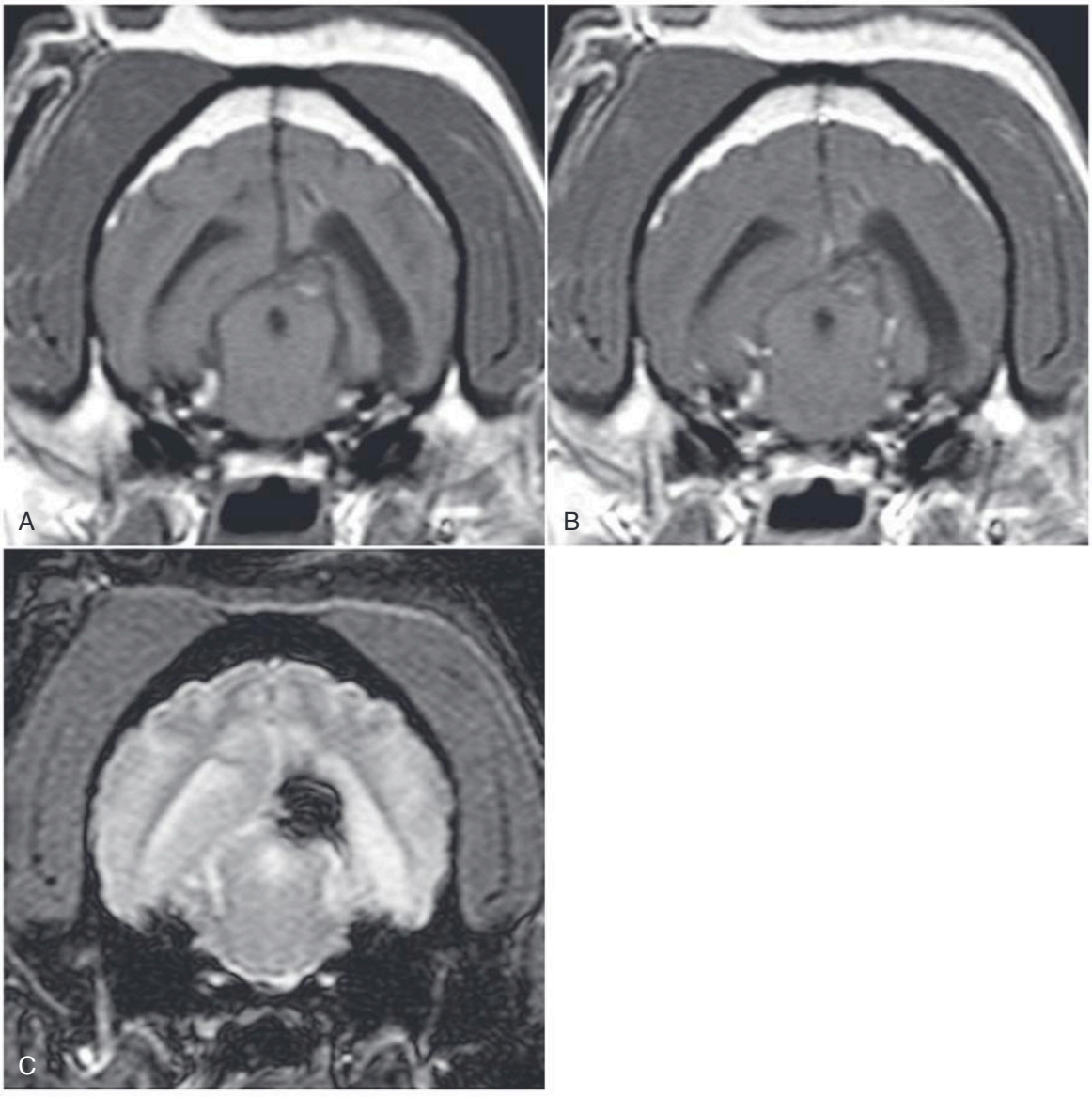


Fig. 12.51 The same dog in Fig. 12.50 imaged 9 months later. The seizures were controlled by medication, and the dog is otherwise normal. T1-weighted magnetic resonance (MR) images made before **(A)** and after **(B)** contrast medium administration. The inherent T1 hyperintensity seen previously is almost completely resolved, indicating a significant reduction in methemoglobin. Focal parenchymal distortion is visible in the region of presumed hemorrhage and adjacent mild left hydrocephalus. The left ventricle is larger than the right because of adjacent parenchymal necrosis and atrophy, so-called *compensatory hydrocephalus.* No abnormal contrast enhancement **(B)** is present. **C,** A T2-weighted gradient recalled echo (GRE) sequence in which there is a large susceptibility artifact as a result of residual hemosiderin. The final diagnosis was hemorrhage associated with a cavernous angioma.

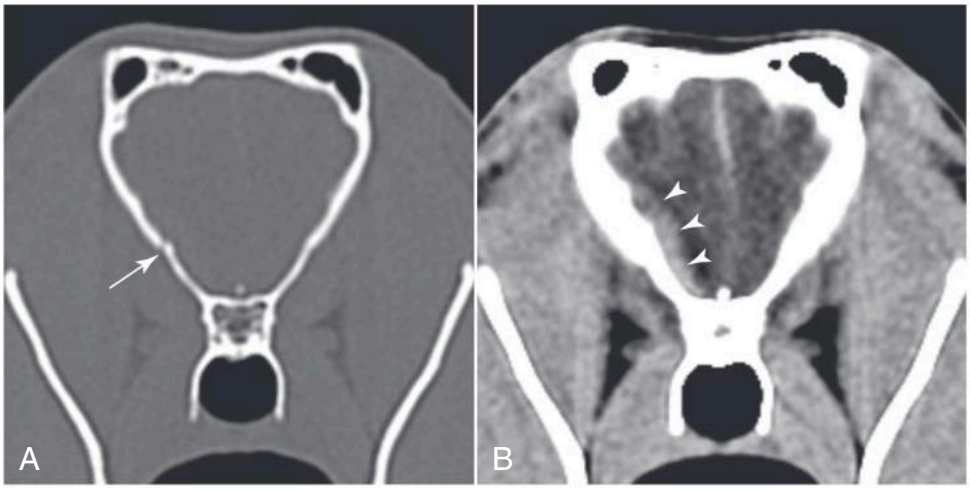


Fig. 12.52 Transverse computed tomography (CT) images in a bone **(A)** and soft-tissue **(B)** window of a Miniature Schnauzer with head trauma. A short oblique hypoattenuating fracture line is seen in the right ventral calvarium (*arrow*). In the same location along the calvarium, there is a band of tissue that is hyperattenuating to the surrounding brain parenchyma (*arrowheads*) consistent with epidural or subdural hemorrhage. There is mild swelling causing a midline shift of the falx cerebri to the left.

REFERENCES

1. Section 2 (Chapters 5.1 to 5.10), MRI of the Brain. In: *Wilfried Mai Editor: Diagnostic MRI of Dogs and Cats*. ed 1. CRC Press; 2018.
2. Hecht, S: B. In T. Schwartz & J. Saunders editors: Veterinary Computed Tomography, ed 1, Wiley-Blackwell 201, p 185.
3. Westbrook C, Kaut Roth C, Talbot J. Pulse sequences. In: Westbrook C, Kaut Roth C, Talbot J, eds. *MRI in Practice*. ed 4. Oxford: Wiley-Blackwell; 2011:140.
4. Benigni L, Lamb CR. Comparison of fluid-attenuated inversion recovery and T2-weighted magnetic resonance images in dogs and cats with suspected brain disease. *Vet Radiol Ultrasound*. 2005;46:287–292.
5. Westbrook C, Kaut Roth C, Talbot J. Contrast agents in MRI. In: Westbrook C, Kaut Roth C, Talbot J, eds. *MRI in Practice*. ed 4. Oxford: Wiley-Blackwell; 2011:372.
6. Cherubini GB, Mantis P, Martinez TA, et al. Utility of magnetic resonance imaging for distinguishing neoplastic from non-neoplastic brain lesions in dogs and cats. *Vet Radiol Ultrasound*. 2005;46:384–387.
7. Leigh EJ, MacKillop E, Robertson ID, et al. Clinical anatomy of the canine brain using magnetic resonance imaging. *Vet Radiol Ultrasound*. 2008;49:113–121.
8. Couturier L, Degueurce C, Ruel Y, et al. Anatomical study of cranial nerve emergence and skull foramina in the dog using magnetic resonance imaging and computed tomography. *Vet Radiol Ultrasound*. 2005;46:375–383.
9. Gomes E, Degueurce C, Ruel Y, et al. Anatomic study of cranial nerve emergence and associated skull foramina in cats using CT and MRI. *Vet Radiol Ultrasound*. 2009;50:398–403.
10. Fletcher TF, Saveraid TC: Canine brain MRI atlas: http://vanat.cvm.umn.edu/mriBrainAtlas. Accessed 1 December 2022.
11. Mackillop E. Magnetic resonance imaging of intracranial malformations in dogs and cats. *Vet Radiol Ultrasound*. 2011;52:42–51.
12. Esteve-Ratsch B, Kneissl S, Gabler C. Comparative evaluation of the ventricles in the Yorkshire Terrier and the German Shepherd dog using low-field MRI. *Vet Radiol Ultrasound*. 2001;42(5):410–413.
13. Ryan CT, Glass EN, Seiler G, et al. Magnetic resonance imaging findings associated with lateral cerebral ventriculomegaly in English Bulldogs. *Vet Radiol Ultrasound*. 2014;55(3):292–299.
14. Bertolini G, Ricciardi M, Caldin M. Multidetector computed tomographic and low-field magnetic resonance imaging anatomy of the quadrigeminal cistern and characterization of supracollicular fluid accumulations in dogs. *Vet Radiol Ultrasound*. 2016;57(3):259–268.
15. Schmidt MJ, Klumpp S, Amort K, et al. Porencephaly in dogs and cats: magnetic resonance imaging findings and clinical signs. *Vet Radiol Ultrasound*. 2012;53(2):142–149.
16. Steinberg T, Matiasek K, Brühschwein A, et al. Imaging diagnosis—intracranial epidermoid cyst in a Doberman pinscher. *Vet Radiol Ultrasound*. 2007;48(3):250–253.
17. Hecht S, Adams WH. MRI of brain disease in veterinary patients part 1: basic principles and congenital brain disorders. *Vet Clin North Am Small Anim Pract*. 2010;40(1):21–38.
18. Targett MP, McInnes E, Dennis R. Magnetic resonance imaging of a medullary dermoid cyst with secondary hydrocephalus in a dog. *Vet Radiol Ultrasound*. 1999;40(1):23–26.
19. Rusbridge C, Knowler SP. Hereditary aspects of occipital bone hypoplasia and syringomyelia (Chiari type I malformation) in cavalier King Charles spaniels. *Vet Rec*. 2003;153(4):107–112.
20. Cerda-Gonzalez S, Olby NJ, McCullough S, et al. Morphology of the caudal fossa in cavalier king Charles spaniels. *Vet Radiol Ultrasound*. 2009;50(1):37–46.
21. Cerda-Gonzalez S, Olby NJ, Griffith EH. Longitudinal study of the relationship among craniocervical morphology, clinical progression, and syringomyelia in a cohort of Cavalier King Charles spaniels. *J Vet Intern Med*. 2016;30(4):1090–1098.
22. Loughin CA. Chiari-like malformation. *Vet Clin North Am Small Anim Pract*. 2016;46:231–242.
23. Cerda-Gonzalez S, Olby NJ, Griffith EH. Dorsal compressive atlantoaxial bands and the craniocervical junction syndrome: association with clinical signs and syringomyelia in mature cavalier King Charles spaniels. *J Vet Intern Med*. 2015;29(3):887–892.
24. Weber SM, Hostnik ET, Drost WT, et al. Comparison of high-field MRI and multidetector CT for grading chiari-like malformation and syringomyelia in cavalier king Charles spaniels. *Vet Radiol Ultrasound*. 2020;61(4):444–452.

25. Shimokawa MT, Iwamoto E, Umeki S, et al. Magnetic resonance imaging and clinical findings in a miniature schnauzer with hypodipsic hypernatremia. *J Vet Med Sci*. 2009;71(10):1387–1391.
26. Lee KI, Lim CY, Kang BT, et al. Clinical and MRI findings of lissencephaly in a mixed breed dog. *J Vet Med Sci*. 2011;73(10):1385–1388.
27. Asakawa MG, Mackillop E, Olby NJ, et al. Imaging diagnosis-neuronal ceroid lipofuscinosis with a chronic subdural hematoma. *Vet Radiol Ultrasound*. 2010;51(2):155–158.
28. Urkasemsin G, Olby NJ. C. hereditary ataxia. *Vet Clin North Am Small Anim Pract*. 2014;44:1075–1089.
29. Snyder M, Lipitz L, Skorupski KA, et al. Secondary intracranial neoplasia in the dog: 177 cases (1986-2003). *J Vet Intern Med*. 2008;22:172–177.
30. Garosi L, McConnell JF, Platt SR, et al. Clinical and topographic magnetic resonance characteristics of suspected brain infarction in 40 dogs. *J Vet Intern Med*. 2006;20:311–321.
31. Rossmeisl JH, Rohleder JJ, Pickett JP, et al. Presumed and confirmed striatocapsular brain infarctions in six dogs. *Vet Ophthalmol*. 2007;10:23–36.
32. Tidwell AS, Robertson ID. Magnetic resonance imaging of normal and abnormal brain perfusion. *Vet Radiol Ultrasound*. 2011;52:62–71.
33. Mulkern RV. Fast imaging techniques. In: Atlas SW, ed. *Magnetic Resonance Imaging Brain Spine*. ed 3. Philadelphia: Lippincott Williams & Wilkins; 2002:178.
34. Sood S, Gupta R, Sharma J, et al. *MRI Spectrum in Acute Toxic and Metabolic Encephalopathies*. Vienna, Austria: European Congress of Radiology; 2014. https://doi.org/10.1594/ecr2014/C-0492.
35. Cornelis I, Van Ham L, Gielen I, De Decker S, Bhatti SFM. Clinical presentation, diagnostic findings, prognostic factors, treatment and outcome in dogs with meningoencephalomyelitis of unknown origin: a review. *Vet J*. 2019;244:37–44.
36. Gonçalves R, De Decker S, Walmsley G, Butterfield S, Maddox TW. Inflammatory disease affecting the central nervous system in dogs: a retrospective study in England (2010–2019). *Frontiers in Veterinary Medicine 27*. 2022. https://doi.org/10.3389/fvets.2021.819945.
37. Lamb CR, Croson PJ, Cappello R, et al. Magnetic resonance imaging findings in 25 dogs with inflammatory cerebrospinal fluid. *Vet Radiol Ultrasound*. 2005;46:17–22.
38. Glass EN, Cornetta AM, Kent M. Clinical and clinicopathologic features in 11 cats with *Cuterebra larvae* myiasis of the central nervous system. *J Vet Intern Med*. 1998;12(5):365–368.
39. Cline JL, Lockaby SB. Pathology in practice: *Aspergillus flavus* mycosis. *J Am Vet Med Assoc*. 2012;241(10):1297–1299.
40. Mellema LM, Koblik PD, Kortz GD, et al. Reversible magnetic resonance imaging abnormalities in dogs following seizures. *Vet Radiol Ultrasound*. 1999;40(6):588–595.
41. Russo M, Covelli EM, Meomartino L, et al. Computed tomographic anatomy of the canine inner and middle ear. *Vet Radiol Ultrasound*. 2005;43(1):22–26.
42. Braund CH, Vite KG: Braund's clinical neurology in small animals: localization, diagnosis and treatment, developmental disorders, *International Veterinary Information Service* (website): http://www.ivis.org/advances/Vite/toc.asp.
43. Martin-Vaquero P, Da Costa RC, Wolk KE, et al. MRI features of gliomatosis cerebri in a dog. *Vet Radiol Ultrasound*. 2012;53:189–192.
44. Porter B, de Lahunta A, Summers B. Gliomatosis cerebri in six dogs. *Vet Pathol*. 2003;40:97–102.
45. Bagley R, Wheeler S, Klopp L, et al. Clinical features of trigeminal nerve-sheath tumor in 10 dogs. *J Am Anim Hosp Assoc*. 1998;34:19–25.
46. Katz ML, Coates JR, Sibigtroth CM, et al. Enzyme replacement therapy attenuates disease progression in a canine model of late-infantile neuronal ceroid lipofuscinosis (CLN2 disease). *J Neurosci Res*. 2014;92:1591–1598.
47. Musso C, Le Boedec K, Gomes E, et al. Diagnostic values of clinical and magnetic resonance findings in presumptive trigeminal Neuropathy: 49 dogs. *J Am Anim Hosp Assoc*. 2020;56:106–113. https://doi.org/10.5326/JAAHA-MS-6997.
48. Wisner ER, Dickinson PJ, Higgins RJ. Magnetic resonance imaging features of canine intracranial neoplasia. *Vet Radiol Ultrasound*. 2011;52:52–61.
49. Tamura S, Tamura Y, Nakamoto Y, et al. MR imaging of histiocytic sarcoma of the canine brain. *Vet Radiol Ultrasound*. 2009;50:178–181.
50. Snyder JM, Shofer FS, Van Winkle TJ, et al. Canine intracranial primary neoplasia: 173 cases (1986-2003). *J Vet Intern Med*. 2006;20:669–675.
51. Söffler C, Hartman A, Gorgas D, et al. Magnetic resonance imaging features of esthesioneuroblastoma in three dogs and one cat. *Tierarztl Prax Ausg K Kleintiere Heimtiere*. 2016;44(5):333–340. https://doi.org/10.15654/TPK-150963. Epub 2016 Jul 7.
52. Platt SR, Radaelli S, McDonnell JJ. Computed tomography after mild head trauma in dogs. *Vet Rec*. 2002;151:243.
53. Chai O, Peery D, Bdolah-Abram T, et al. Computed tomographic findings in dogs with head trauma and development of a novel prognostic computed tomography-based scoring system. *Am J Vet Res*. 2016;78(9):1085–1090.

ELECTRONIC RESOURCES

Additional information related to the content in Chapter 12 can be found online at eBooks.Health.Elsevier.com.

- Chapter Quiz

CHAPTER 13

The Equine Head

Nathan C. Nelson

RADIOLOGY VERSUS OTHER IMAGING MODALITIES

The equine head is composed of numerous overlying structures and complex anatomy, and can be difficult to evaluate completely with radiography. Despite the inherent challenges, radiography remains the mainstay of imaging the equine head due to its widespread availability, low cost, and ability to perform while the patient is standing. The large size of the equine head (which is larger than radiography plates) dictates that projections must be centered over the area of interest. Lateral and dorsoventral (DV) projections are standard, but additional oblique projections may be necessary to optimally evaluate the included anatomy.

The recent advent of standing computed tomography (CT) is revolutionizing imaging of the equine head. The cross-sectional nature of CT removes anatomic superimposition, making it ideally suited to evaluate the complex structures of the equine head. Up until recently, CT examination of the head required anesthesia and dorsal or lateral recumbency, using a special table designed to support the weight of the horse (Fig. 13.1). A number of CT systems now allow standing examinations of the head under sedation alone (see Fig. 13.1). These solutions generally require either a pit with a hydraulic lift to lower the horse to the height of the CT gantry or a lift to elevate the CT scanner.

Magnetic resonance imaging (MRI) of the equine head is rarely performed as it requires general anesthesia and other modalities satisfy most indications for head imaging. The exception is disease of the central nervous system (brain, cranial nerves, and cranial spinal cord), where MRI is the gold standard imaging test. Indications for MRI include imaging the brain, cranial nerves, or inner/middle ear when standing CT is not available or otherwise displays normal structures.

DISEASES OF THE NASAL CAVITY/PARANASAL SINUSES

Radiographic Projections

Maxillary/nasal anatomy is complex (Fig. 13.2). To fully characterize pathology, a minimum of four standard radiographic projections, centered on the sinuses, should be performed in horses with suspected sinus or nasal disease: lateral projection, DV projection, right 30-degree dorsal to left ventral, and left 30-degree dorsal to right ventral obliques.

Sinusitis

Sinusitis is the most common disease of the paranasal sinuses, caused by infection (usually bacterial) within the paranasal sinuses. Affected horses have purulent nasal discharge with a fetid odor and may have facial swelling. In roughly a quarter of horses with sinus disease, there is no history of trauma, dental disease, or other underlying cause for sinusitis, and these are considered cases of *primary sinusitis*. *Secondary sinusitis* occurs when there is a predisposing factor resulting in bacterial infection. Dental disease is the most common cause of secondary sinusitis, although prior facial fractures, cysts, or other masses affecting the nasal cavity may also result in sinusitis. Radiographs or CT are indicated to confirm the presence of sinus fluid, and screen for possible underlying causes of secondary sinusitis. In some cases, CT can discriminate soft tissue masses that might be obscured by fluid on radiography.

Sinusitis causes distinct fluid lines on radiography which are horizontal to the ground (Fig. 13.3, eFig. 13.1). There are two bullae within the nasal conchae rostral to the maxillary sinus: the dorsal and ventral nasal conchal bullae. These bullae may become infected in cases of sinusitis. Chronic empyema of these bullae may serve as a source of chronic, recurrent sinusitis if not treated (Fig. 13.3).[1]

Cysts

Paranasal sinus cysts are the second most common cause of equine secondary sinusitis after dental disease.[2] Their cause is unknown, although there may be an association with ethmoid hematomas given the presence of hemorrhage in cyst walls on histopathologic examination.[3] On radiographs, cysts cause a soft tissue opaque mass within the paranasal sinuses, although it may be gas opaque if internal fluid drains. Cysts can cause mild pressure resorption of regional bones, but rarely cause severe regional lysis. On CT, cysts often have a discrete hyperattenuating wall at their periphery which discriminates cysts from other sinus masses (Fig. 13.4, eFig. 13.2).[4]

Progressive Ethmoid Hematoma (PEH)

PEH is an expansile mass typically arising from the submucosa of the ethmoidal labyrinth, but can occur anywhere within the nasal cavity or paranasal sinuses. The cause is unknown but presumably due to repeated hemorrhage into the submucosa. The result is a mass comprised of blood and fibrous tissue, encapsulated by respiratory epithelium. Radiographs reveal a mass in the area of the ethmoid turbinates (Fig. 13.5, eFig. 13.3). Most PEHs have a characteristic appearance on CT with internal hyperattenuating "swirling" heterogeneity attributable to the presence of hemorrhage or early mineralization in the mass (Fig. 13.6). Unlike radiographs, CT and MR readily identify cribriform plate lysis caused by the PEH, which may preclude some forms of therapy.[5]

Neoplasia

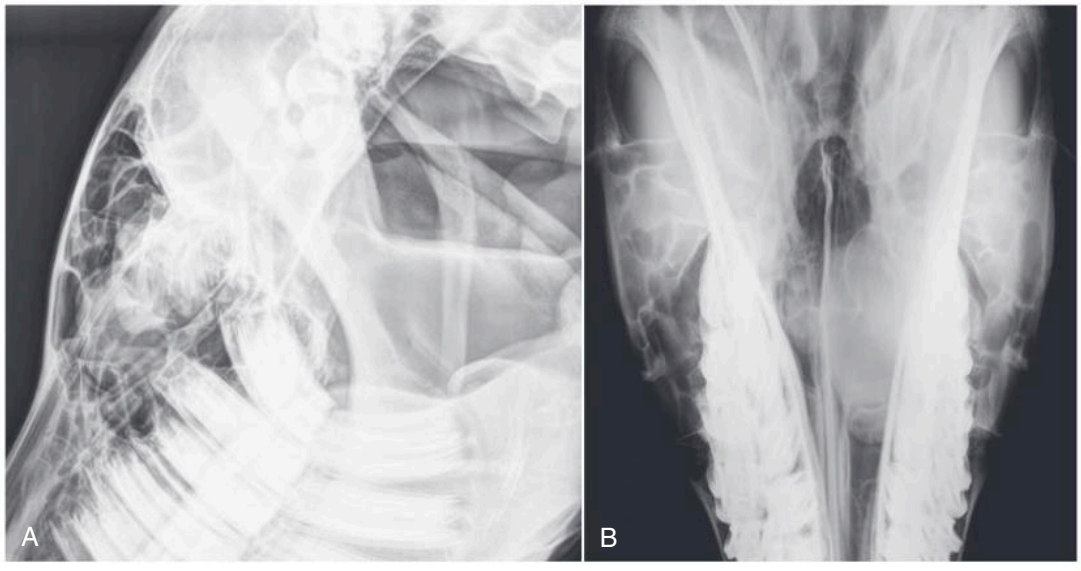
Sinonasal neoplasms are an uncommon cause of sinusitis. Various tumor types are reported, including epithelial tumors (carcinomas of various types), sarcomas such as osteosarcoma and hemangiosarcoma, neuroendocrine tumors/neuroblastoma, hemangiosarcoma, and lymphoid tumors.[6,7] The radiographic appearance of sinonasal neoplasia overlaps with other



eFig. 13.1 Lateral radiograph of a horse with primary sinusitis. Multiple horizontal fluid lines are present within the rostral and caudal maxillary sinuses as well as the conchofrontal sinus. A mild wavemouth is present as well.



eFig. 13.2 Lateral radiograph of a horse with a paranasal sinus cyst. A smoothly marginated lobulated soft tissue structure is seen adjacent to the ethmoid turbinates.



eFig. 13.3 **(A)** Lateral and **(B)** dorsoventral radiographs of a horse with ethmoid hematoma. An expansile, multilobulated soft tissue mass lesion is superimposed with the rostral ethmoid turbinates. The lesion is larger on the left side.

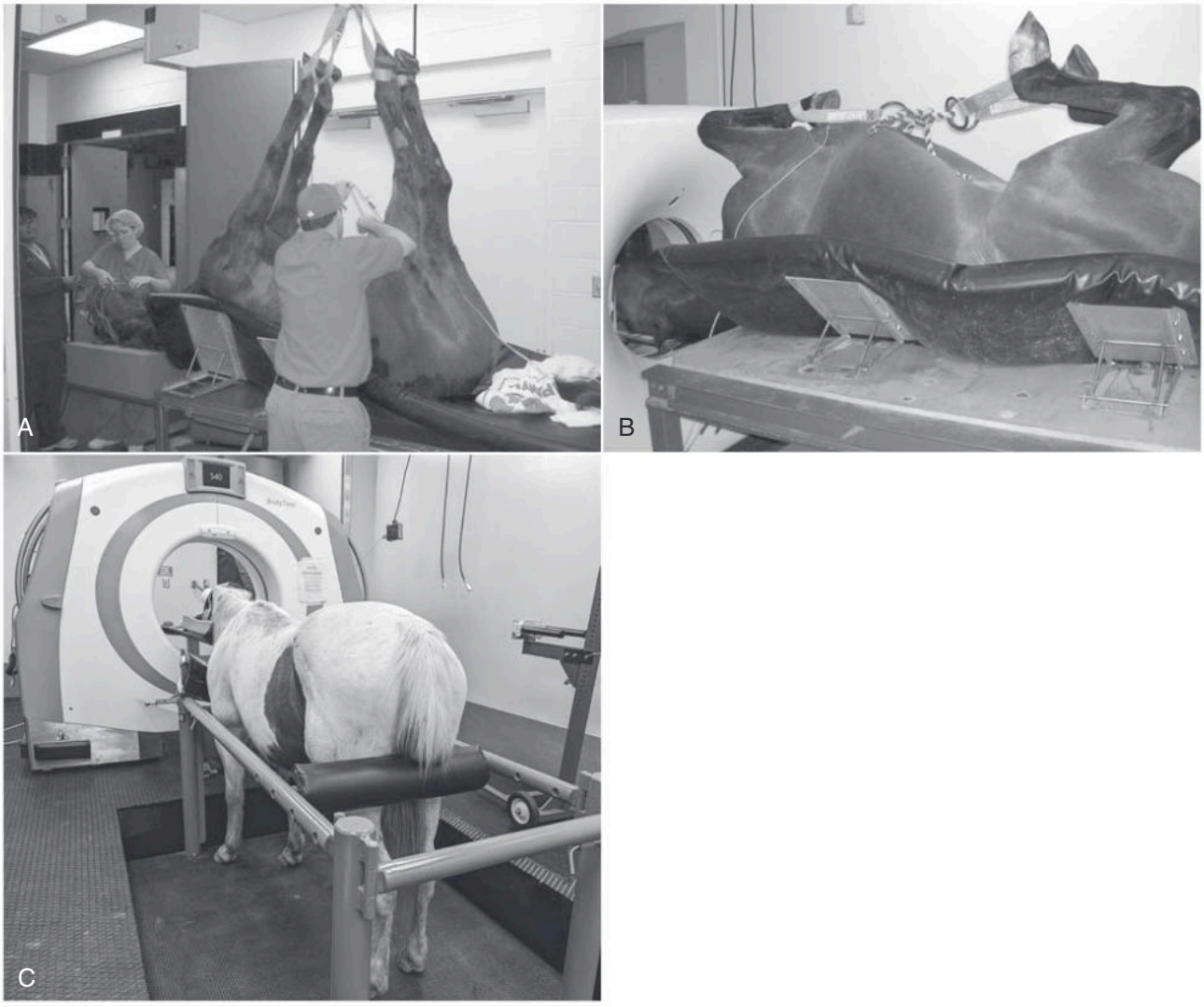


Fig. 13.1 **A,** Anesthetized horse lifted into dorsal recumbency with a hoist and then positioned (**B**) for computed tomography (CT) of the head. **C,** A horse positioned for a standing CT of the head, with the lift lowered below the floor level.

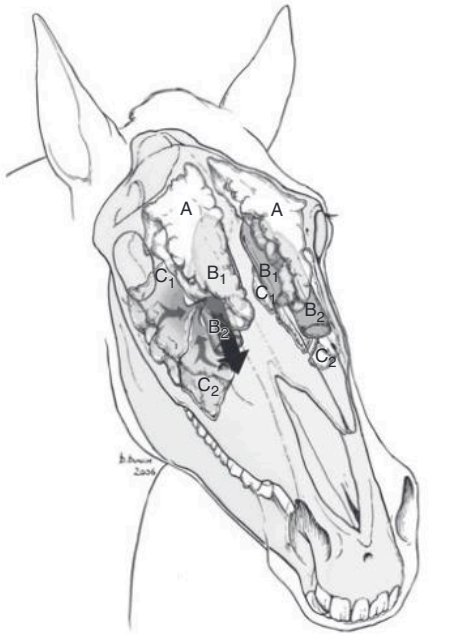


Fig. 13.2 A schematic representation of the equine nasal sinuses and their communications. *A,* Conchofrontal sinus; B_1, dorsal nasal meatus; B_2, middle nasal meatus; C_1, caudal maxillary sinus; C_2, rostral maxillary sinus.



Fig. 13.3 Lateral radiograph showing fluid in the conchofrontal sinus (*arrow*), rostral maxillary sinus (*open arrowhead*), and dorsal and ventral conchal bullae (*closed arrowheads*).

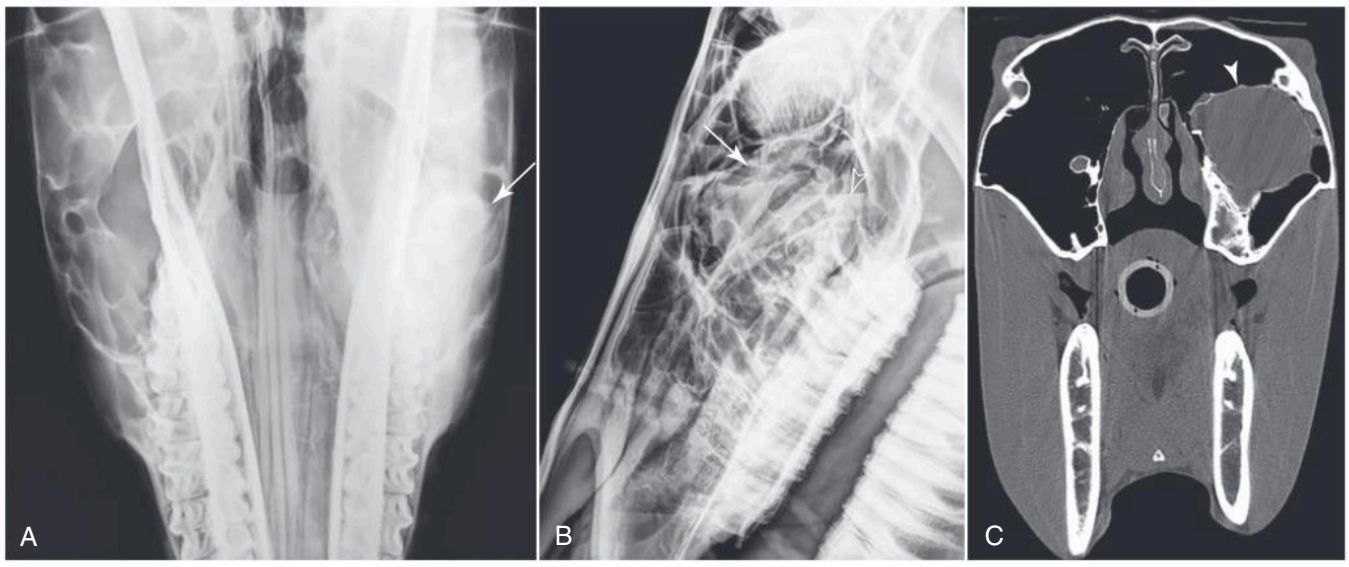


Fig. 13.4 Dorsoventral **(A)** and lateral **(B)** radiographs of a horse with a left paranasal sinus cyst (*arrow*) with effusion in the sinuses (*open arrowhead*). **(C)** Computed tomography (CT) of the same horse showing the mineralized rim of the sinus cyst (*closed arrowhead*).

sinonasal disease such as hematomas or cysts, and radiographs underestimate potential features of malignancy such as bone lysis.[6] Historical and physical examination findings may help prioritize neoplasia as a cause of sinusitis; firm facial swellings or lysis/extension into the hard palate are seen more commonly with neoplastic disease than other causes of paranasal pathology (Fig. 13.7, eFig. 13.4).[8] CT clearly determines regions of bone lysis and MRI best determines invasion of soft tissue structures such as the brain (Fig. 13.8). Extensive regional bone lysis, contrast enhancement of the mass, and extensive osseous production make a neoplastic mass more likely.

Polyps

Polyps are uncommon, benign soft tissue proliferations that occur within the nasal passage or sinuses and likely represent polyploid epithelial proliferation as a response to regional chronic inflammation.[9] On radiographs (Fig. 13.9), polyps are soft tissue masses that have a nonaggressive appearance. They generally do not cause significant bone lysis or production though may cause bone pressure resorption (Fig. 13.10).

DENTAL DISEASE

Normal Dentition

Discussions of equine dentition employ the modified Triadan system, which assigns each tooth a specific number depending on its anatomic quadrant in the mouth (Fig. 13.11). The term "cheek teeth" informally refers to the premolar and molar teeth. The hypsodont (continually erupting) nature of equine teeth means younger horses will have a long reserve crown, which extends further into the sinuses and nasal cavity compared to older horses. Horses between 2 and 4 years of age develop "eruption bumps," sometimes incorrectly referred to as "eruption cysts," over the premolar teeth of the maxilla and mandible. The periapical area of these teeth appears relatively lucent compared to older horses and should not be confused with periapical abscessation (Fig. 13.12). Young horses will have "caps" (retained deciduous teeth) over their mandibular and maxillary teeth when they are between 3 and 5 years of age. The Triadan 05s are small brachydont teeth referred to as "wolf teeth" (Fig. 13.13) that may be retained. Wolf teeth typically do not directly cause clinical signs, but can cause discomfort particularly if they interfere with a bit in the mouth.

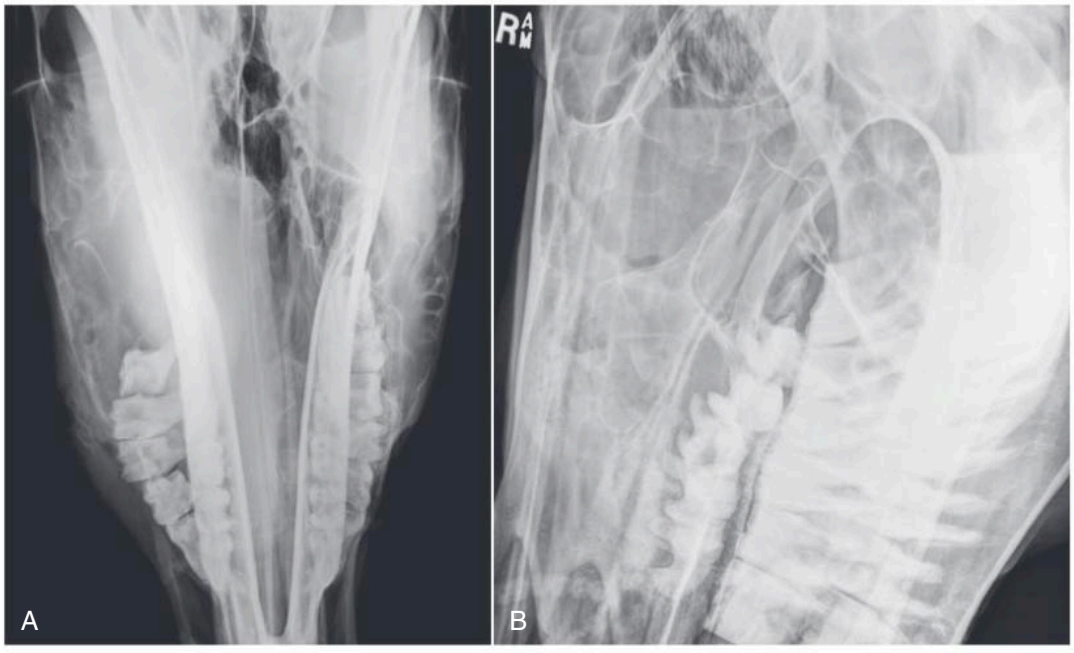
Equine teeth are subjected to high abrasive forces and continual wear, which shapes the occlusal surface of the tooth and ultimately affects the rate of dental attrition. A complete description of equine dental anatomy is beyond the scope of this text. Like brachydont teeth, the equine tooth is constructed of cementum, dentin, and enamel, but unlike the brachydont tooth, the grinding surface is continually worn. The common pulp chamber resides in the apex of the tooth and the pulp horns extend towards the occlusal surface. Deposition of secondary dentin closes these pulp horns as the tooth undergoes normal wear, but there is risk for pulp exposure, infection, and apical abscessation if there is failure of this process. The periodontal space surrounding the tooth should be thin and well defined, and can be difficult to see radiographically compared to CT.

Dental Radiographic Projections

Maxillary cheek teeth: If maxillary premolar/molar dental disease is suspected, the standard projections listed for the maxillary sinuses may be employed, although opening the mouth with a gag during image acquisition facilitates evaluation of the occlusal surfaces. Additional oblique projections are available that better isolate the apices of the maxillary cheek teeth, projecting the palatal root dorsal to the buccal roots: open-mouth right 60-degree ventral to left dorsal oblique and open-mouth left 60-degree ventral to right dorsal oblique (Fig. 13.14). A shallow lateral oblique projection is ideal for evaluation of occlusal abnormalities (wavemouth) (see Fig. 13.14). An offset DV projection (when the mandible is distracted to one side relative to the maxilla) prevents superimposition of the mandibular and maxillary arcades on the DV projection (Fig. 13.15).

Mandibular dental disease: Projections to isolate the mandibular dental apices are similar to those for the maxillary arcade, but centered on the mandible and steeper angles may be necessary to prevent superimposition of the contralateral side.

Maxillary/mandibular incisor disease: Open mouth, intraoral projections allow evaluation of incisor teeth without superimposition of the opposite dental arcade. To acquire these



eFig. 13.4 **(A)** Dorsoventral and **(B)** right oblique radiographs of a horse with histopathologically confirmed squamous cell carcinoma. There is a large soft tissue mass with multiple gas lucencies in the right nasal passages and right paranasal sinuses. A fluid line is visible in the conchofrontal sinus. There is extensive bone destruction of the nasal and maxillary bones. The 106–110 teeth are malaligned with loss of the surrounding alveolar bone and lamina dura. The 111 tooth is missing.

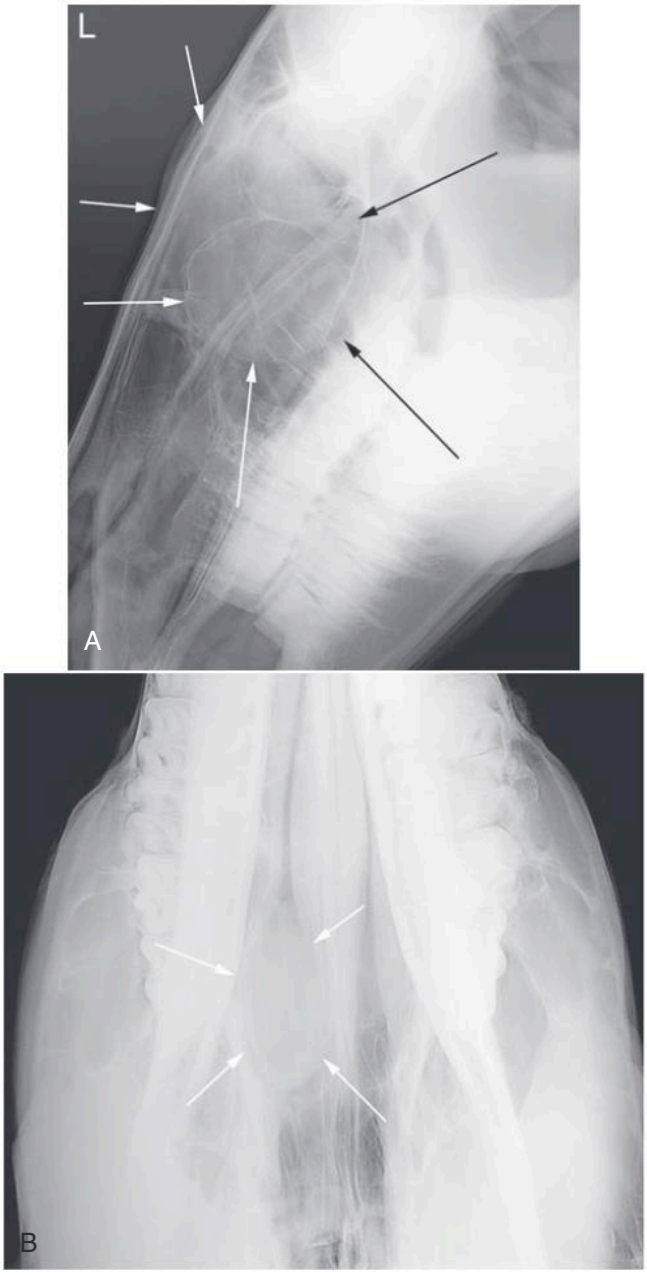


Fig. 13.5 **A,** Lateral radiograph of the head. The ethmoid hematoma (*white* and *black arrows*) is visible in the region of the ethmoid labyrinth. **B,** Dorsoventral radiograph. The lateralized mass (*white arrows*) is in a typical location of an ethmoid hematoma.

projections, a gag is placed in the mouth, and DV and oblique projections acquired (Fig. 13.16).

The complex nature of dental anatomy and pathology precludes an exhaustive review of equine dental disease in this chapter; however, the most common diseases will be discussed later.

Conformational Defects

The occlusal surface may wear in an abnormal pattern. In some cases, the harder enamel folds of the teeth will protrude from the occlusal surface due to differential wear between the enamel and the softer cementum and dentin. These "enamel points" are the most common equine dental disease and cause discomfort during chewing by impinging on regional soft tissues. Enamel points are typically diagnosed on oral examination, but may be apparent on CT imaging or radiographs.

Overwear or fracturing of the occlusal surface of a tooth allows compensatory overgrowth of the opposite tooth, due to loss of the normal rasping that occurs during mastication. In older horses, there can be generalized overgrowth of some teeth of one arcade and undergrowth of the opposing arcade. This results in an occlusal conformation referred to as "wavemouth" (Fig. 13.17).[10]

Cheek Teeth Fractures

Cheek teeth fractures are common, with the 109/209 most commonly affected (see Fig. 13.15). Fractures are most often sagittal in their orientation, and usually extend centrally through the infundibula or more peripherally through the pulp horns. These may lead to pulp exposure and periapical infection if left untreated.

Apical Infections of Cheek Teeth

Periapical cheek tooth infection is a common disorder. Most are caused by blood or lymphatic borne bacterial infection. Pulp exposure, due to imbalance between cheek tooth wear and the formation of secondary dentin or due to dental trauma/fractures, can also lead to infection which ascends to the apical region of the tooth.[10] Regardless of cause, infected teeth are recognized radiographically by surrounding alveolar sclerosis, blunting of tooth roots, and widening of the periodontal space (Fig. 13.18, eFig. 13.5). The interpretation of dental radiographs is challenging; CT greatly improves the specificity when determining which teeth have apical or pulpal infection. The caudal maxillary cheek teeth extend into the paranasal sinuses, so periapical infection can lead to sinusitis. The mandibular and rostral maxillary check teeth do not extend into the sinuses; infection of these teeth can eventually cause fistula formation and a draining tract (Fig. 13.19). Fistulas are more easily identified on CT compared to radiographs (Fig. 13.20).

Odontogenic Tumors

Odontogenic tumors are uncommon and arise from embryonic remnants of the dental lamina.[11] Multiple tumor types occur, including ameloblastoma, ameloblastic carcinomas, and odontomas. There is overlap in the imaging appearance of different tumor types, but all result in an expansile, aggressive lesion centered on the teeth (Fig. 13.21).[11]

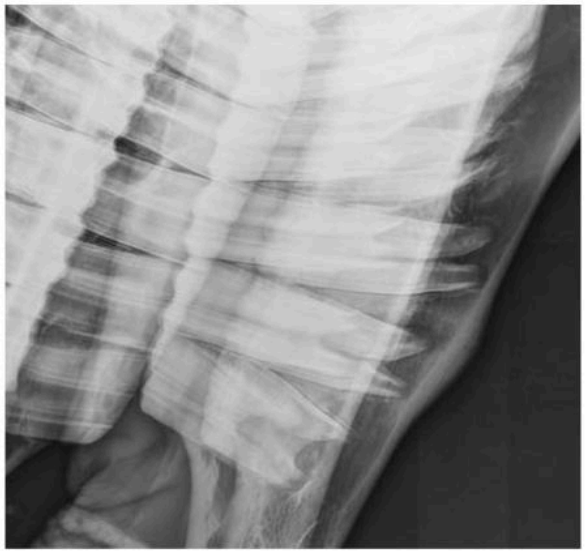
Equine Odontoclastic Tooth Resorption and Hypercementosis (EOTRH)

EOTRH is a common dental disorder predominantly affecting the incisors and canine teeth. It causes various degrees of progressive internal and external root resorption and excessive cemental deposition (Fig. 13.22). EOTRH is recognized most commonly in middle aged and geriatric (<15 years of age) horses, although younger horses can also be affected.[12,13] In one study of horses 10 years and older, 94% of horses had at least minor and 62% had moderate to severe radiographic changes from EOTRH.[14] The etiology is likely multifactorial, and represents a response to periodontal disease or infection, ischemic necrosis, mechanical stress, or genetics.[12] Radiographic findings mimic those on histopathology, with some teeth primarily showing resorptive or proliferative change, but most commonly a mix of both.[12] Hypercementosis results in root and reserve crown enlagement.[13] With the advent of high resolution digital images and increased use of standing CT examination of the head, earlier lesions are being recognized.

NONDENTAL DISEASES OF THE MANDIBLE AND MAXILLA

Bone Cysts

Aneurysmal bone cysts are caused by increased venous pressure and dilatation/rupture of vascular networks, leading to



eFig. 13.5 Oblique view of the left mandible of a horse with a tooth root abscess. There is poorly de fined lysis around the caudal root of the 307 tooth with adjacent sclerosis. There is focal thickening of the mandible subjacent to the tooth root lesion.

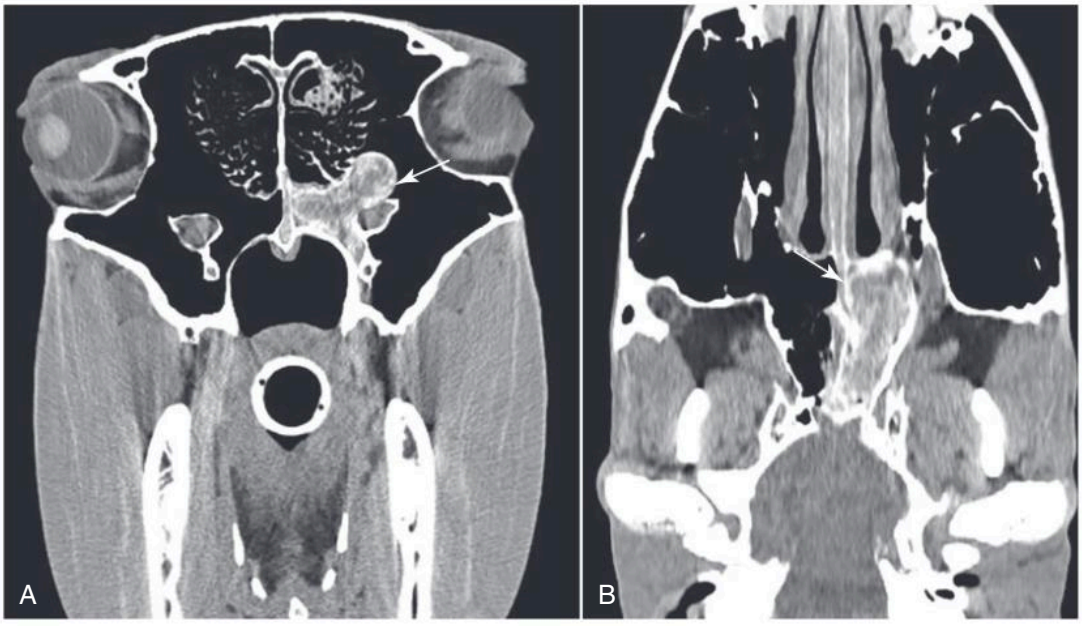


Fig. 13.6 Transverse **(A)** and dorsal **(B)** plane computed tomography (CT) images of an ethmoid hematoma (*arrow*) ventral to the ethmoid turbinates, displaying the characteristic internal swirling hyperattenuating pattern.



Fig. 13.7 Dorsoventral radiograph of a left paranasal sinus carcinoma (*arrows*) showing extensive regional bone lysis, including the nasal septum, extending into the right nasal passage.

cystic growth (Fig. 13.23). They may be idiopathic or occur secondary to other underlying conditions such as fibrous dysplasia or trauma.[15] Radiographically, cysts appear as lucent, multiloculated structures that cause pressure resorption of regional cortical bone and mimic some types of non-proliferative neoplasms (such as ameloblastoma or carcinoma). They may affect the maxilla or the mandible and, while slowly growing, may become very large.[16] Metabolic diseases such as nutritional hyperparathyroidism may cause similar features, such as reduced trabecular and cortical bone density, but are differentiated by the diffuse nature of radiographic abnormalities, compared to bone cysts, which are focal.[17]

Nondentigerous Neoplasia of the Mandible/Maxilla

Mandibular or maxillary neoplasms share many imaging features with bone cysts and tumors of dentigerous origin. Soft tissue neoplasms such as squamous cell carcinoma may invade regional bone, and primary osseous tumors such as fibrosarcoma and osteosarcoma are also reported[18] (Fig. 13.24).

Fibro-osseous Lesions of the Craniofacial Complex

"Fibro-osseous lesions of the craniofacial complex" describe a group of related conditions that result in replacement of normal bone with fibrous connective tissue and mineralization.[19] Within this complex, there are three conditions that share similar histologic features: ossifying fibroma, fibrous dysplasia, and osteoma.[19] Ossifying fibroma is a benign, tumor-like lesion in young (<1 year old) horses that usually affects the mandible, and may occasionally occur in older horses (Fig. 13.25).[20] Radiographically, ossifying fibromas appear similar to other types of soft tissue or osseous neoplasms affecting the mandible, but are usually more mineralized than bone cysts. Fibrous dysplasia also typically occurs in young, growing animals.[19] Histologically, fibrous dysplasia appears similar to other fibro-osseous lesions, but tends to have very little internal mineralization and appears cyst-like. It may also be more diffuse than mass-like.[16] Osteomas most commonly occur on the mandible and rarely in the paranasal sinuses and characterized by benign peripheral cortical proliferation (Fig. 13.26).[19]

Suture Exostosis

Sutures of the equine skull should completely fuse/ossify between 3 months and 5 years of age.[21] Suture exostosis describes swelling and proliferation at the sutures and has numerous other names including suture periostitis and suture separation.[22] The cause is unknown, but likely results from instability or prior injury/facial trauma. On radiographs, soft tissue swelling precedes bone proliferation surrounding a suture line. The suture line appears wider and more radiolucent

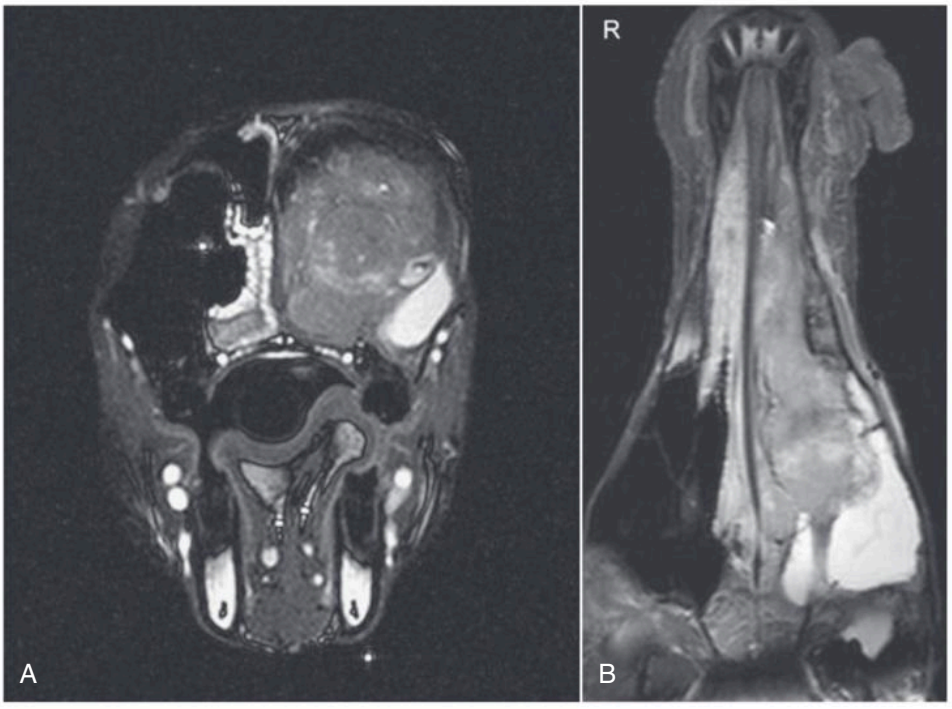


Fig. 13.8 T2-weighted magnetic resonance (MR) images in transverse **(A)** and dorsal **(B)** planes. The regions of very high signal (*white*) signify collections of fluid adjacent to a lymphoid nasal neoplasm.

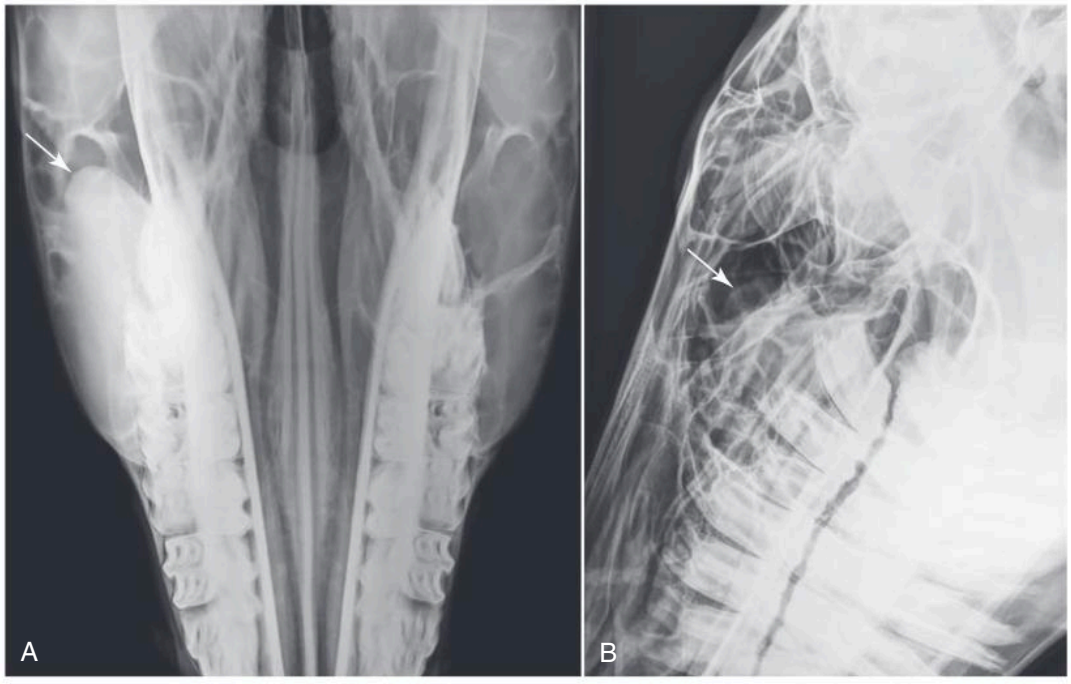


Fig. 13.9 Dorsoventral **(A)** and oblique **(B)** radiographs of a polyp in the right maxillary sinuses (*arrow*).

(Fig. 13.27).[22] The nasofrontal suture is most commonly affected, resulting in a transverse nonpainful firm swelling on the dorsum of the head rostral to the eyes. Nasolacrimal, maxillolacrimal, and/or frontolacrimal sutures may also be involved. With frontal or lacrimal bone involvement, epiphora may develop due to nasolacrimal duct occlusion.[21]

Temporomandibular Joint (TMJ) Abnormalities

The DV projection displays both mandibular condyles simultaneously, but additional oblique projections allow more complete evaluation of the TMJ on radiographs (Fig. 13.28).[23–25] Even with oblique projections, radiographs are insensitive to most TMJ pathology. CT better identifies subtle TMJ

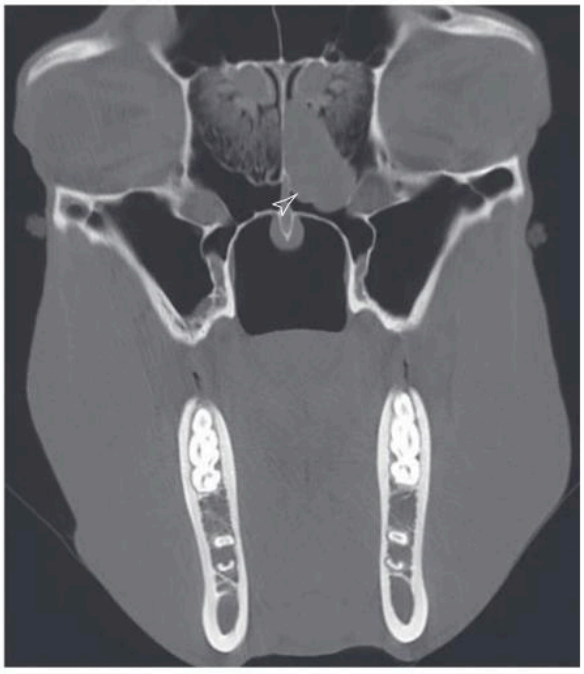


Fig. 13.10 Transverse computed tomography (CT) image of a polyp (*open arrowhead*) in the left sphenoid recess and ethmoid turbinate region causing local turbinate resorption.

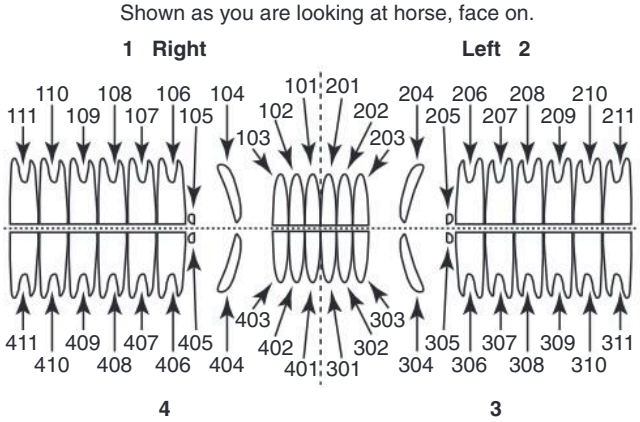


Fig. 13.11 The Triadan numbering system in the horse. The first digit indicates the arcade, the last two digits the specific tooth. (From Baker GJ, Easley J, eds. *Equine Dentistry*. 2nd ed. Philadelphia: Elsevier; 2005.)

abnormalities such as nondisplaced fractures, cyst-like lesions, and mineralization within the intra-articular disc. Most TMJ abnormalities identified on CT are not associated with clinical symptoms (Fig. 13.29).[26]

Fractures

The exposed, ventral position of the mandible predisposes it to fractures from kicks or collisions. Rostral mandible/maxillary fractures tend to be open due to the lack of regional soft tissue surrounding the bone.[27] Fractures through the caudal maxillary or frontal bones commonly result in hemorrhage in the paranasal sinuses (Fig. 13.30). Radiographs underestimate the complexity of facial trauma. CT provides more exact information regarding fracture conformation and dental involvement and better detects complications such as sequestration or delayed bone healing.[28]

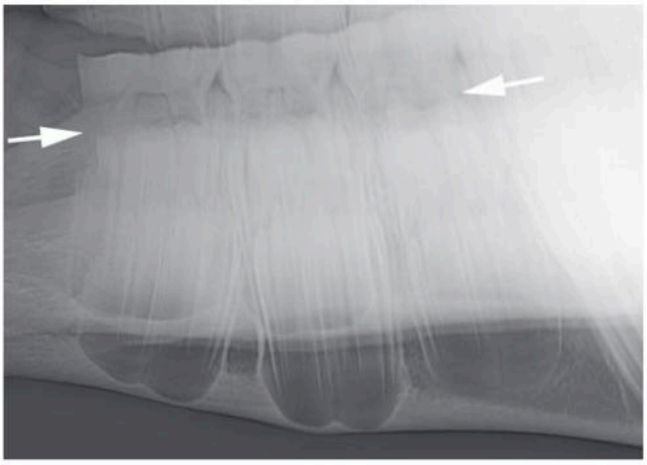


Fig. 13.12 Left 10-degree dorsal-right ventral radiograph of the rostral premolar area of a 2-year-old Oldenburg. Deciduous premolars have not yet been shed. *Arrows* indicate the plane between the deciduous premolars (caps) and permanent premolars. Note the normal expansile, radiolucent region around the roots of the permanent premolar teeth.



Fig. 13.13 Lateral skull radiograph. The maxillary and mandibular first premolars, or wolf teeth, are present (*black arrows*).

GUTTURAL POUCH

Due to the ease and ready availability of guttural pouch endoscopy, radiographs are rarely performed as a primary diagnostic test for guttural pouch disease. Instead, abnormalities of the guttural pouch may be seen "incidentally" when evaluating skull radiographs or CT for other reasons. Radiographs to evaluate the maxilla or mandible typically include only the rostral aspect of the guttural pouch. Complete radiographic examination of the guttural pouch consists of DV and lateral projections centered on the area.

Guttural Pouch Fluid

Lateral projections demonstrate fluid in the guttural pouch as a horizontal gas-fluid interface (Fig. 13.31). Guttural pouch empyema is the accumulation of purulent material in one or both guttural pouches due to bacterial infection of the upper respiratory tract, and assumed to be due to *Streptococcus equi var*

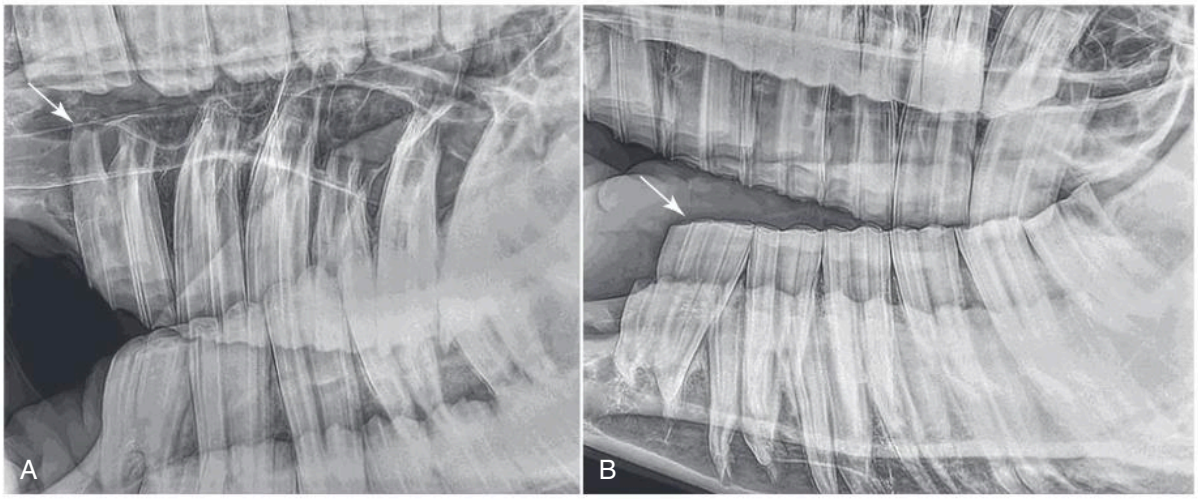


Fig. 13.14 **A,** Right 60-degree ventral-left dorsal oblique used to demonstrate the apices of the maxillary cheek teeth (*arrow*). **B,** Right 25-degree dorsal-left ventral oblique used to identify the occlusal margin of the mandibular arcade (*arrow*).

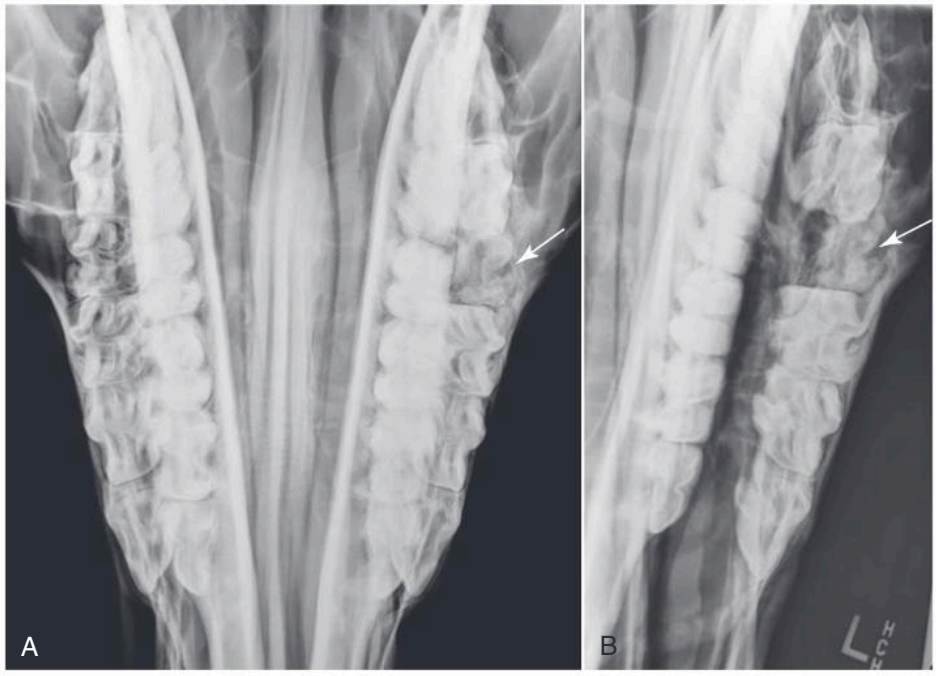


Fig. 13.15 **A,** Standard dorsoventral radiograph of the skull. Pathology of the 209 (*arrow*) is difficult to identify as it partially superimposes the mandible. **B,** With the offset dorsoventral (DV) radiograph, the mandible is distracted away from the maxilla, and it is apparent the buccal aspect of 209 is absent from prior fracture.

equi ("strangles") infection until proven otherwise.[29] Trauma can also result in guttural pouch hemorrhage, particularly if there are fractures to the base of the skull.

Chondroids

Chronic empyema becomes viscous and inspissated. With further dehydration, the exudate forms rounded chondroids, which can become chronic and act as a nidus for recurrent infection.[29] Affected horses typically have a history of upper respiratory tract infections, but occasionally chondroids may be found unexpectedly in horses without a compatible history or clinical signs. On radiographs, chondroids cause discrete, rounded masses in the dependent portion of the guttural pouch, though occasionally may be poorly defined (Fig. 13.32).

Guttural Pouch Masses

The medial retropharyngeal lymph nodes are immediately ventral to the rostral aspect of the guttural pouch; when enlarged, these lymph nodes may protrude into the guttural pouch and cause a mass effect that is visible on radiographs (Fig. 13.33).

Neoplasia rarely affects the guttural pouch, although in severe cases, melanoma may protrude into the guttural pouch from the adjacent soft tissues.[30] Other reported tumors of the

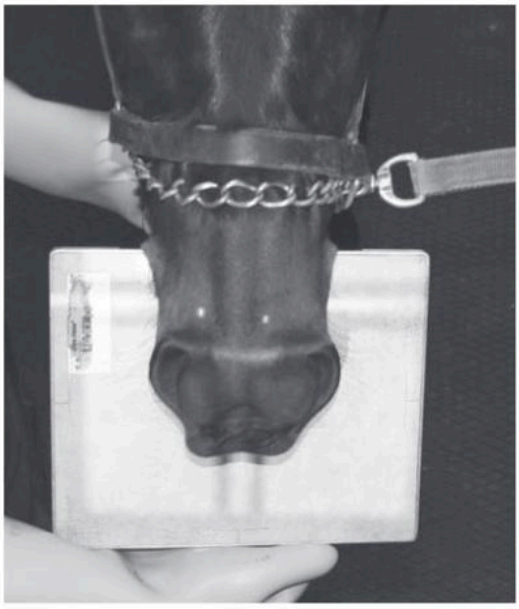


Fig. 13.16 The position for an intraoral, dorsoventral radiograph to evaluate the rostral aspect of the incisive bone.



Fig. 13.17 Left 45-degree dorsal-right ventral oblique radiograph of the head of a 41-year-old pony. Note the irregular occlusive surface of the teeth, termed *wave mouth*, usually seen in older animals because of improper dental care.

guttural pouch include hemangiosarcoma, squamous cell carcinoma, and fibroma.[31]

Tympany

Guttural pouch tympany is a unilateral or bilateral severe distension of the guttural pouches with air, occurring in foals between birth and 1 year of age. The cause is unknown, although a congenital defect or inflammation may prevent gas from exiting the guttural pouch. Arabian and Paint horse foals have a breed predisposition.[29] Radiographs show a severe distension of the guttural pouch with gas (Fig. 13.34).

Trauma

The guttural pouch is well protected from direct trauma due to its location ventral to the calvarium and medial to the caudal mandible. The basilar skull is composed of the basisphenoid bone that articulates caudally with the basioccipital bone and is immediately dorsal to the guttural pouch. Multiple flexors of the head, the largest being the longus capitis muscle, insert on the basilar skull. Basilar skull fractures occur sequential to a horse rearing up and falling backwards, directly striking the poll causing hyperextension of the head. Hyperextension exerts acute traction to the basilar skull musculature, causing fracturing usually at the junction of basisphenoid and basioccipital bones (Fig. 13.35). These fractures may be minimally displaced, complicating radiographic diagnosis, but the resultant hemorrhage fills the guttural pouch and is readily apparent on lateral radiographs. Fluid within the guttural pouch of a patient with recent head trauma should alert the clinician to the possibility of basilar skull fractures.

LARYNX/UPPER AIRWAY

Most laryngeal diseases are diagnosed through direct inspection with endoscopy at rest and during exercise on a treadmill or with a portable videoendoscopy system. Radiography, ultrasound, or CT is performed if imaging of the deeper laryngeal tissues is desired.

Laryngeal Mineralization

Five cartilages comprise the larynx (the epiglottis, thyroid cartilage, cricoid cartilage, and left/right arytenoid cartilages).[32] Laryngeal cartilages and regional muscles are soft tissue opaque; however, the ventral portion of the thyroid cartilage is reliably mineralized (Fig. 13.36).[33] Variable cricoid and arytenoid cartilage mineralization is also commonly identified. Despite earlier suggestions that arytenoid mineralization indicates the presence of arytenoid pathology, more recent research suggests arytenoid mineralization is an incidental finding and not indicative of significant underlying disease.[34–36]

Palatal Dysfunction

On the lateral projection in a normal horse, the epiglottis is dorsal to the caudal soft palate, with a small gas-filled gap between them (see Fig. 13.36). Some horses develop palatal dysfunction, consisting of dorsal displacement of the soft palate (DDSP) and palatal instability (PI).[37] With DDSP, the soft palate shifts dorsal to the epiglottis and is often a dynamic process resulting in upper airway noise and exercise intolerance.[32] PI is a dynamic "billowing" of the soft palate during high airflow situations and often precedes DDSP, but is rarely recognized radiographically without induction of high-performance/high-airflow situations. The etiologies of DDSP and PI are poorly understood but may be related to neuromuscular dysfunction of the intrinsic soft palate muscles or abnormal movement of the laryngohyoid apparatus.[37] Diagnosis of DDSP is usually made during high-speed treadmill endoscopic examination (as displacement may only occur during exercise), but lateral radiographs display displacements that persist at rest (Fig. 13.37).

Epiglottic Masses

The epiglottis can develop different mass-like thickenings, including subepiglottic granulomas, subepiglottic cysts, abscesses, and epiglottitis that may be apparent radiographically.[38,39] The distribution of epiglottic thickening depends on the underlying lesion. Subepiglottic cysts and granulomas arise ventral to the epiglottis, and result in an abnormal fullness to the tissues in this area causing loss of the gas that typically separates the palate from epiglottis (Fig. 13.38).

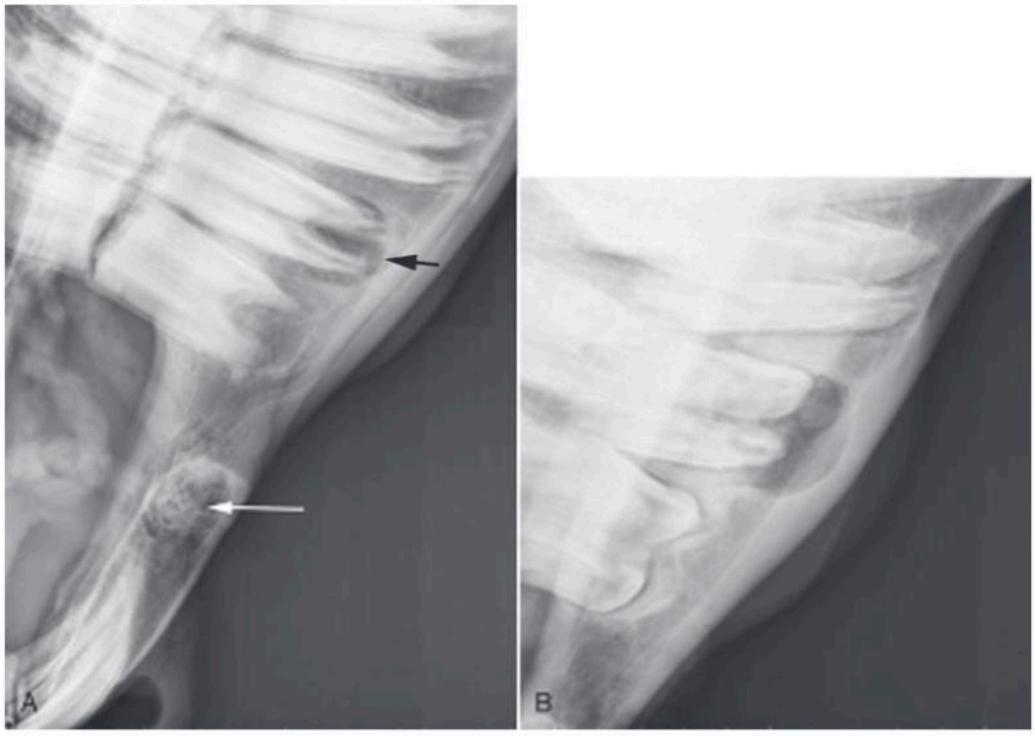


Fig. 13.18 Lateral **(A)** and right 45-degree dorsal-left ventral oblique **(B)** radiographs of the rostral aspect of the head of a horse with a tooth root abscess. **A,** A region of lysis is present around the roots of one of the third mandibular premolars (*black arrow*). The rope halter *(white arrow)* is superimposed over the symphyseal region; care must be taken to avoid misinterpretation of a halter as a lesion. **B,** In the oblique view, it is clear that the lysis is localized to the right arcade. Note the irregularity of the rostral root of the right third mandibular premolar.

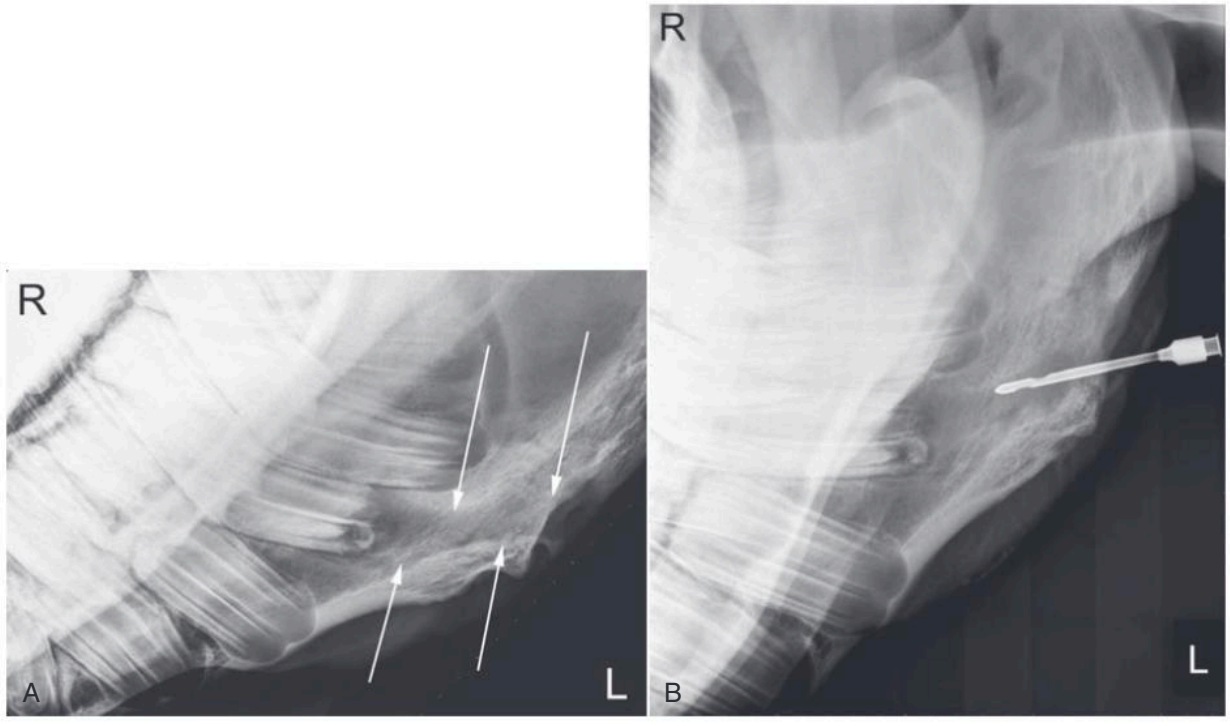


Fig. 13.19 Right 45-degree dorsal-left ventral oblique radiograph without **(A)** and with **(B)** a cannula present in a draining tract from the ventral aspect of the mandible. A mandibular tooth root abscess is present with a well-margined radiolucent tract is visible in the body of the mandible (*arrows*).

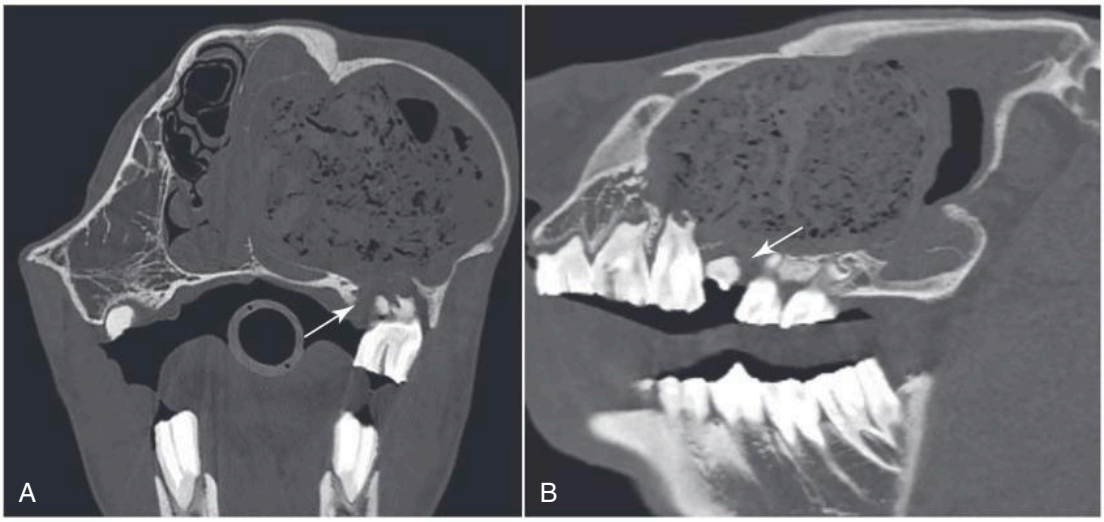


Fig. 13.20 Transverse **(A)** and sagittal **(B)** computed tomography (CT) images of an orosinus fistula (*arrow*). There is a large amount of feed material packed in the sinus causing expansion of the adjacent maxillary bone.



Fig. 13.21 Transverse computed tomography (CT) image of an ameloblastoma, causing a mass effect in the ventral sinus and nasal cavity, centered on the left maxillary cheek teeth. This mass has mineralization within it and is blunting adjacent tooth roots.

Epiglottic Entrapment

Epiglottic entrapment is the most common epiglottic abnormality in racehorses and mature nonracehorses.[38,40] The normal subepiglottic mucosa extends to the peripheral aspect of the epiglottis, but in some cases becomes positioned above the dorsal epiglottic surface causing a continuous surface with the adjacent aryepiglottic folds.[41] Entrapment is typically diagnosed on endoscopy, but may be identified on lateral laryngeal radiographs as a blunted/shortened appearance to the epiglottis (Fig. 13.39, eFig. 13.6).

EAR/HYOID APPARATUS

Temporohyoid Osteoarthropathy

The temporohyoid joint is a permanent synchondrosis between the proximal stylohyoid bone and petrous temporal bone. Older horses can develop bone proliferation at this articulation referred to as temporohyoid osteoarthropathy (THO), which may be clinically silent, although in some horses results in head shaking/rubbing, difficulty chewing, or other behavioral issues. The cause is unknown, but is primarily degenerative in nature, as it occurs more commonly in older horses.[42,43] The temporohyoid articulation is best evaluated on DV and paired rostral oblique radiographic projections centered on the region, as the lateral projection superimposes the left and right sides (Fig. 13.40).

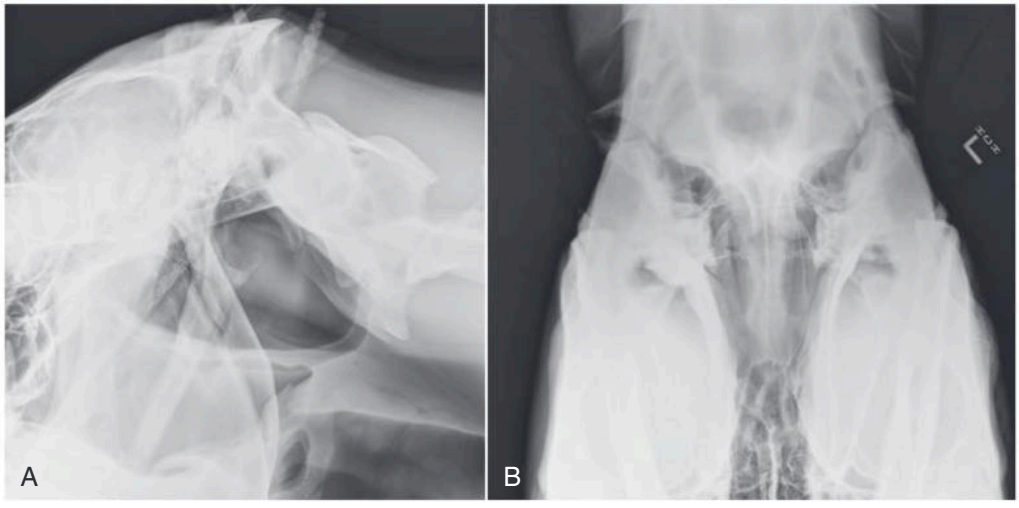
On radiographs and CT, THO is defined by bone proliferation which ranges between subtle and exuberant (Fig. 13.41). The associated stylohyoid bone will become diffusely, progressively thickened as a response to increased stresses from restricted mobility of the temporohyoid joint. Early/mild degenerative changes are much more readily identified with CT compared to radiography. If severe, ankylosis forms between the stylohyoid and temporal bones, increasing the risk of fracture of one or both of these bones during normal tongue movement (Fig. 13.42, eFig. 13.7).[44]

Dentigerous Cysts

Dentigerous cysts (also referred to as heterotopic polyodontia) are congenital defects during prenatal development that result in ectopic dental tissue.[45] This results in tooth-like material that develops in an abnormal location, often near the base of the ear (hence the colloquial name "ear tooth") but can occur elsewhere in the sinuses or cranium. Their lining produces mucoid discharge, which can lead to a chronic draining tract. Imaging demonstrates dental-like tissue in an abnormal location. This abnormal tissue may resemble teeth, with opaque areas containing enamel-like material, although sometimes the mineralization is amorphous and less well formed (Fig. 13.43). CT is better suited for surgical planning, particularly when the cyst is in an atypical location other than the base of the ear.



eFig. 13.6 Lateral radiograph of the laryngeal region of a Quarter horse with epiglottic entrapment. The epiglottis is thickened with round, blunted margins.



eFig. 13.7 Lateral **(A)** and dorsoventral **(B)** radiographs of a horse with temporohyoid osteoarthropathy. There is smoothly margined bone proliferation in the region of the right temporohyoid joint and right tympanic bulla. The right stylohyoid bone is moderately thickened at the articulation with the temporal bone. There is no fracture visible.

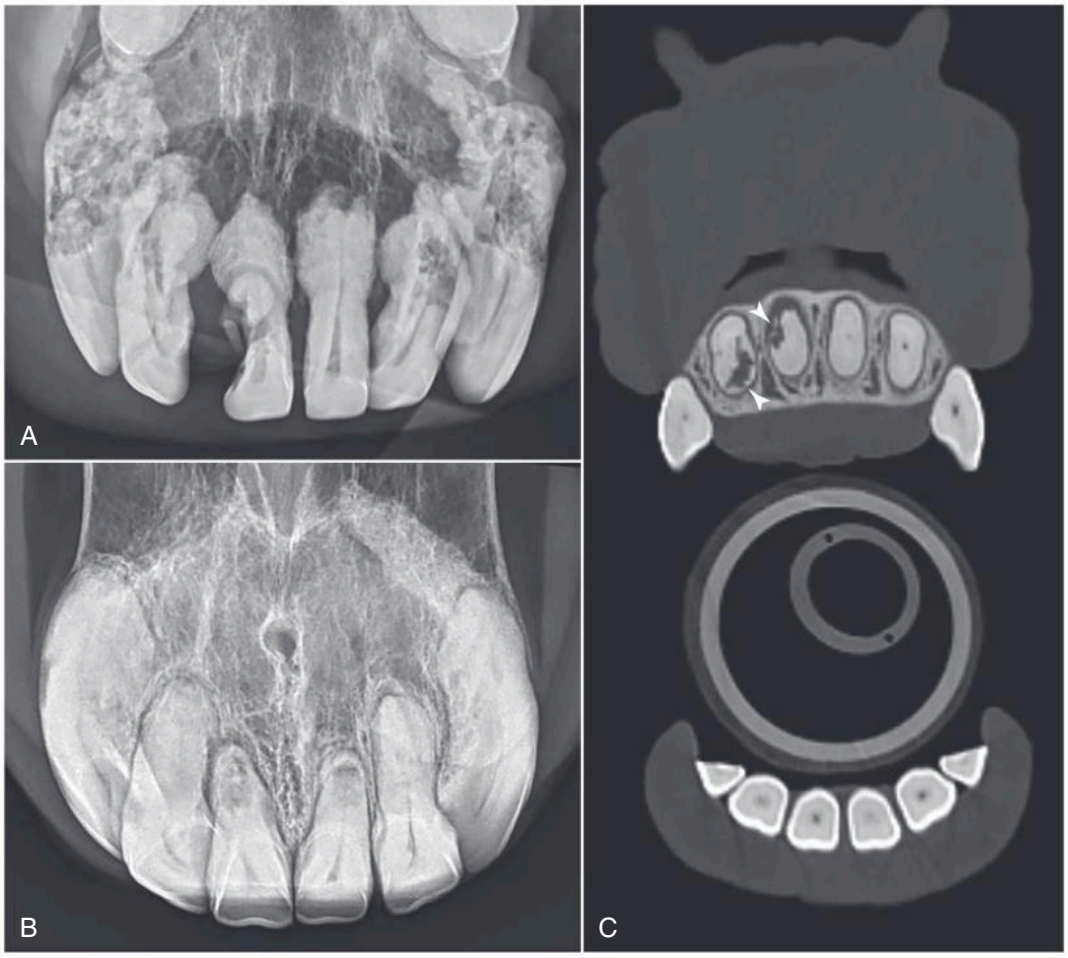


Fig. 13.22 Intraoral radiographs of the maxillary incisors in two horses with equine odontoclastic tooth resorption and hypercementosis (EOTRH). The horse in **(A)** has mixed hypercementosis and resorption, and the horse in **(B)** is primarily characterized by hypercementosis. Computed tomography (CT) identifies more areas of early and subtle resorption (*arrowheads*) compared to radiographs **(C)**.

BRAIN

CT or MRI of the brain is less commonly performed in horses compared to small animals, although is an important part of the diagnostic approach to neurologic equine patients in some cases.[46] When a brain disorder is suspected, the decision to proceed with MRI or CT depends on a combination of factors. MRI is the best modality to demonstrate brain pathology, but anesthesia is necessary. For that reason, MRI may be reserved as a "last test" in horses after collection/analysis of cerebrospinal fluid and other imaging tests (such as standing CT or radiography) have been performed, even though those are low yield in comparison.

Inflammatory Brain Disease

A variety of infectious inflammatory conditions may affect the brain, including equine protozoal myeloencephalopathy and viral encephalitides. They cause an inflammatory pattern, including multifocal T2 hyperintensity in the brain parenchyma and various degrees of contrast enhancement (Fig. 13.44). Abscesses are focal masses that contain central fluid, some degree of regional hemorrhage, and strong contrast enhancement. They may be associated with traumatic injury to the head, and their presence more easily identified on CT compared to other inflammatory brain conditions (Fig. 13.45).[47]

Neoplastic Brain Disease

Primary brain parenchymal neoplasms are rare in the horse. Given the paucity of tumors, the prevalence of different tumor types is unknown, and generally limited to intermittent case reports, although ependymomas tend to be the most commonly reported.[48] In comparison, benign adenomas or hyperplasia of the pituitary pars intermedia are common tumors in horses and result in pituitary pars intermedia dysfunction (PPID).[49] These benign, functional tumors cause hyperadrenocorticism and secondary clinical signs such as hirsutism and secondary diabetes mellitus. The normal pituitary gland can be seen in horses on postcontrast CT and on MRI, with normal size ranges typically less than approximately 10 to 12 mm in height.[50,51] In horses with PPID, the pituitary gland will appear both increased in height and width than nonaffected horses, and on MRI may have heterogeneous signal characteristics (Fig. 13.46).[52]

Cholesterol Granulomas

Cholesterol granulomas (also called cholesterolinic granulomas) are benign, non-neoplastic masses that arise from the choroid

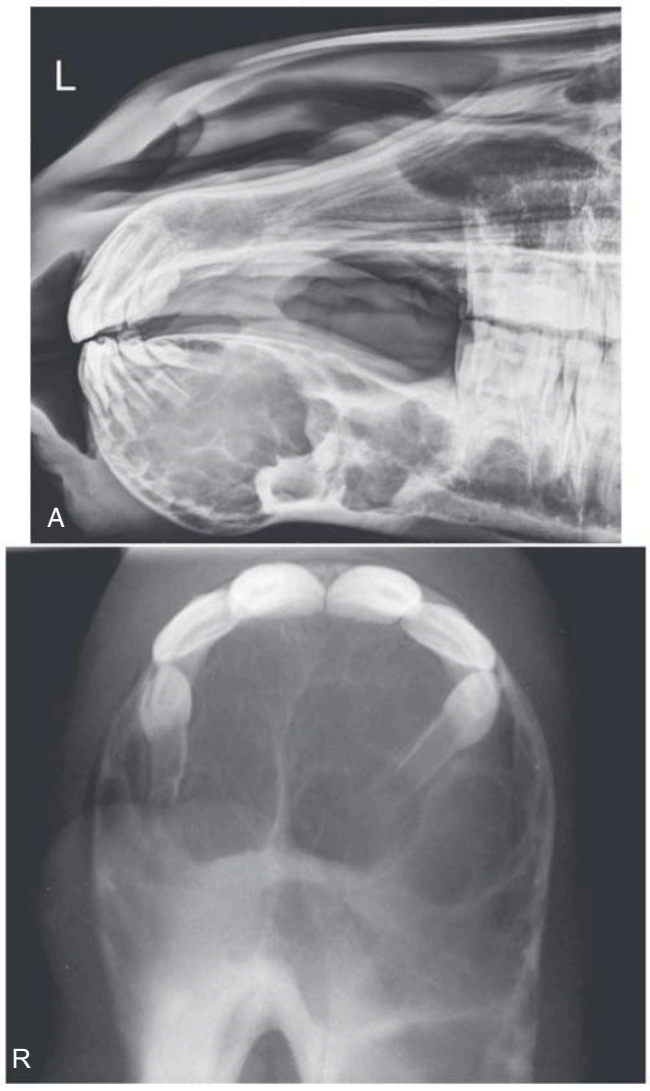


Fig. 13.23 Lateral **(A)** and ventrodorsal **(B)** intraoral radiographs of the rostral aspect of the mandible in a 7-month-old thoroughbred with an expansile, relatively nonaggressive appearing lesion caused by an aneurysmal bone cyst.

plexus, most commonly in the lateral ventricles, though the fourth ventricles may also be involved. Their exact etiology is unknown, but likely result from chronic/intermittent vascular congestion and secondary hemorrhage. This releases cholesterol from erythrocytes which acts as a foreign body inciting a granulomatous, mineralizing response.[53] They are very common, being present in up to 20% of older horses, and rarely cause clinical signs, although can cause ataxia, blindness, depression, and somnolence when large.[53,54] They have a characteristic appearance on CT, being relatively hyperattenuating to adjacent parenchyma with Hounsfield units (HU) values that indicate the presence of mineralization (Fig. 13.47).

Traumatic Brain Injury

Traumatic brain injury (TBI) in horses is usually due to blunt force trauma or occasionally penetrating injuries.[55] Blunt force trauma from rearing and falling over backwards is the most common cause of injury (especially common in younger horses) but TBI also occurs from struggling after being cast, kick injuries, and injuries during anesthetic recovery.[55,56] The choice of imaging modality in cases of head trauma depends on cost and availability, as well as the capability of the patient to stand or recover from anesthesia. Radiographs are less sensitive for skull fractures compared to MRI/CT, and do not directly image the brain. CT is particularly useful in detecting hematoma formation, as the high proteinaceous and hemoglobin content of acute hemorrhage renders it hyperattenuating on precontrast images (Fig. 13.48).

OTHER CONDITIONS OF THE HEAD

Other Fractures

Due to the uncertain nature of head trauma, fractures may occur anywhere in the head, beyond those previously discussed in this chapter. Horses have a complete bony orbit, comprised of the frontal, lacrimal, zygomatic, and temporal bones.[57] Radiographs or CTs are indicated in horses with orbital fractures to determine whether there is sinus or nasal involvement, with most fractures in this area requiring a combination of medical and surgical therapy.[57] Multiple oblique radiographs at varied, steep angles may be necessary to better characterize fractures in this location (Fig. 13.49).

The paracondylar processes are bilateral, long osseous structures caudal to the bulla extending ventrally from the occipital region. Multiple muscles involved with deglutition and opening

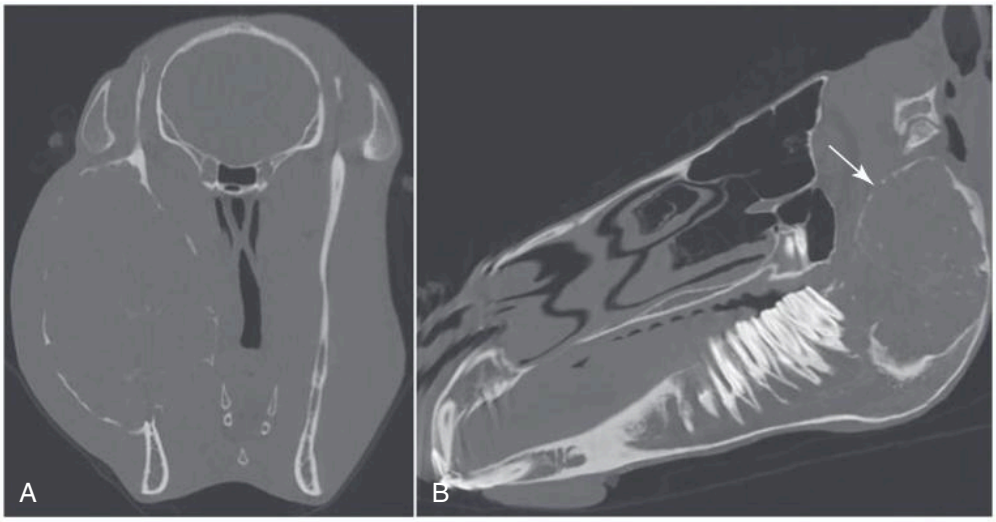


Fig. 13.24 Transverse **(A)** and sagittal **(B)** computed tomography (CT) image of a horse with mandibular fibrosarcoma (*arrows*) causing marked expansion and lysis of the right mandibular ramus.

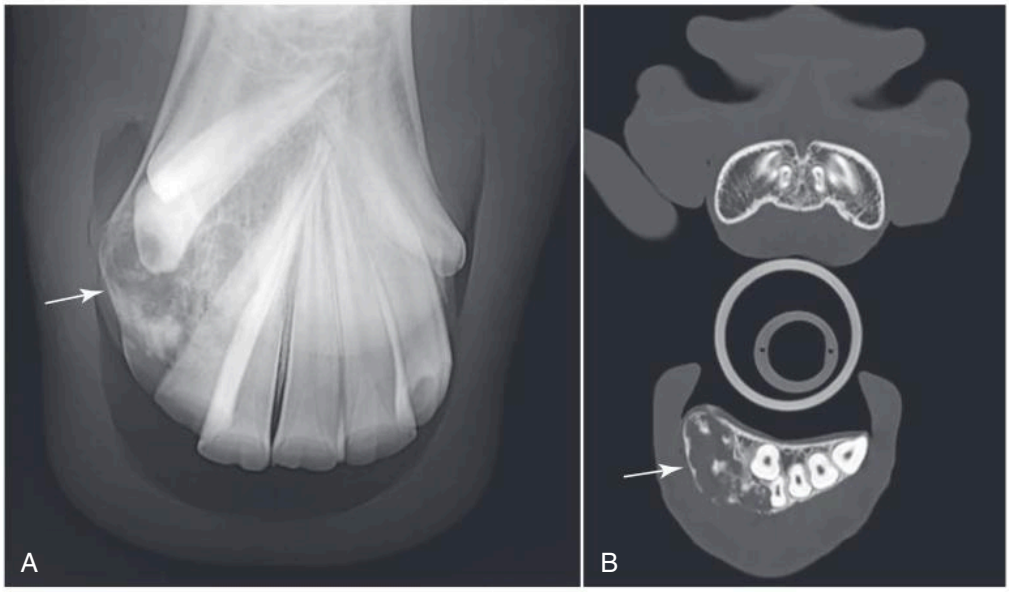


Fig. 13.25 Intraoral mandibular radiograph **(A)** and transverse computed tomography (CT) image **(B)** of an ossifying fibroma (*arrows*). The lesion causes expansion and mixed bone loss and proliferation of the rostral mandible.

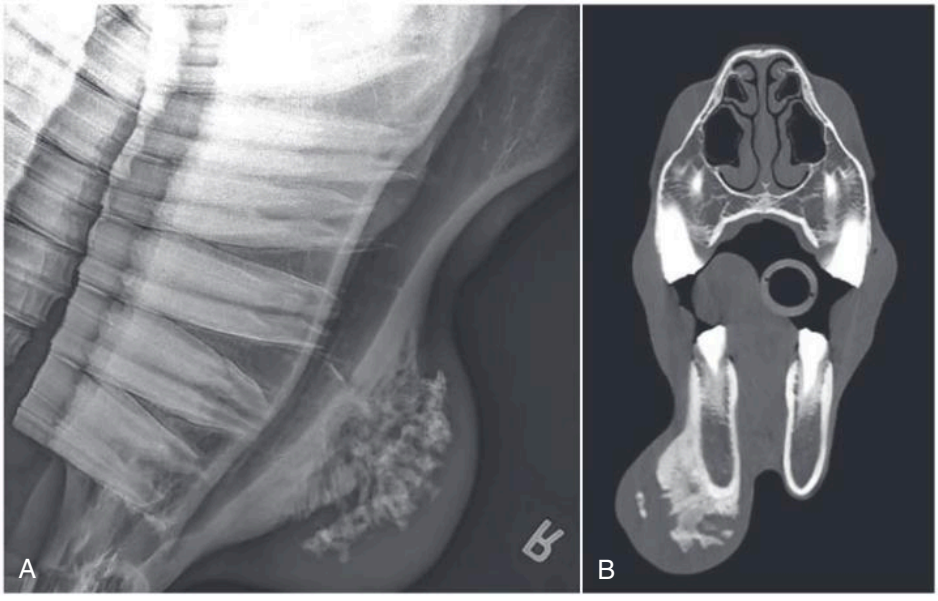


Fig. 13.26 **A,** Oblique radiograph of the right mandible showing a proliferative lesion and thickening of the mandibular cortex that was biopsied as an osteoma. The computed tomography (CT) image **(B)** more clearly shows the lack of medullary involvement.

the mouth arise on these processes.[58] Trauma to the base of the skull can fracture the paracondylar processes. There may be neurological signs (such as facial nerve paralysis given the proximity to the paracondylar process of the facial canal and stylomastoid foramen where the facial nerve emerges), but these fractures may also be seen incidentally in clinically normal horses, presumably from prior healed or unrecognized trauma. Paracondylar process fractures may be difficult to recognize as they superimpose with the complex anatomy of the skull base, and often easiest seen on the DV projection by comparing the fractured process to the contralateral side. CT provides more sensitive detection of small or nondisplaced fractures (Fig. 13.50).

Melanomas

Melanomas are common neoplasms in horses (representing up to 15% of equine neoplasms) with a known genetic predisposition to the gray horse.[30] While they occur in multiple locations, including the perineal/tail base region, they are also frequently seen on the head. They may be superficial in nature, and affect the eyelids and ears, but also occur deeper within the head and can affect lymph nodes, sinuses, guttural pouch, and salivary tissue. Most melanomas are pigmented due to a high concentration of melanin. The presence of melanin results in characteristic high attenuation values on CT compared to adjacent soft tissue structures (Fig. 13.51).[30]

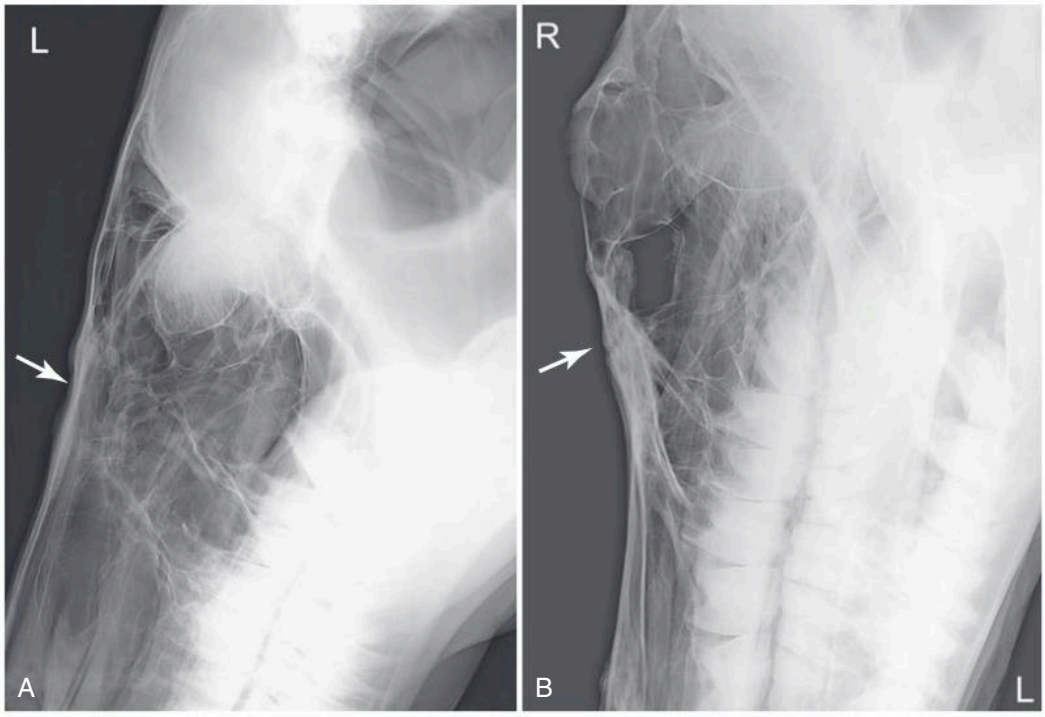


Fig. 13.27 Right-left **(A)** and left rostrodorsal-right caudoventral oblique **(B)** radiographs. There is nasofrontal suture separation at the rostral aspect of the frontal bone causing increased bone opacity (*arrows*).



Fig. 13.28 Rostral 45-degree ventral 30-degree lateral-caudodorsolateral oblique radiograph of a normal temporomandibular joint (*arrow*).

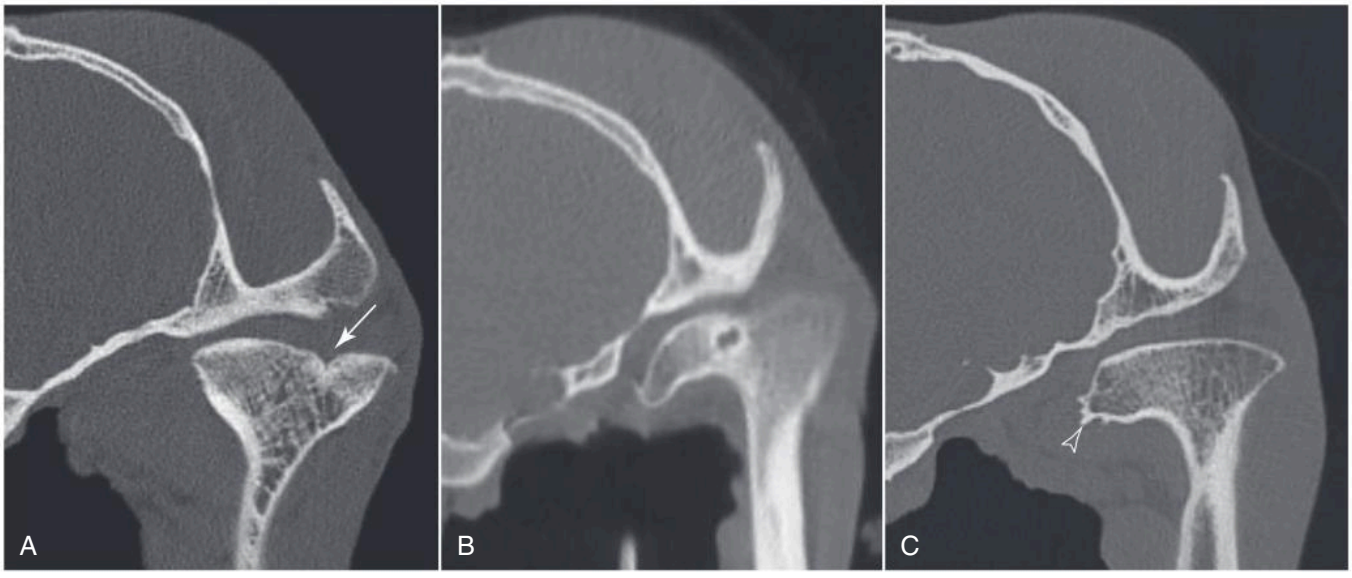


Fig. 13.29 Transverse computed tomography (CT) images showing variations of the mandibular condyle. **A,** Small indentation on the condylar articular surface (*arrow*). **B,** A cyst-like lesion in the mandibular condyle. **C,** Small irregularities along the medial condylar margin (*open arrowhead*).

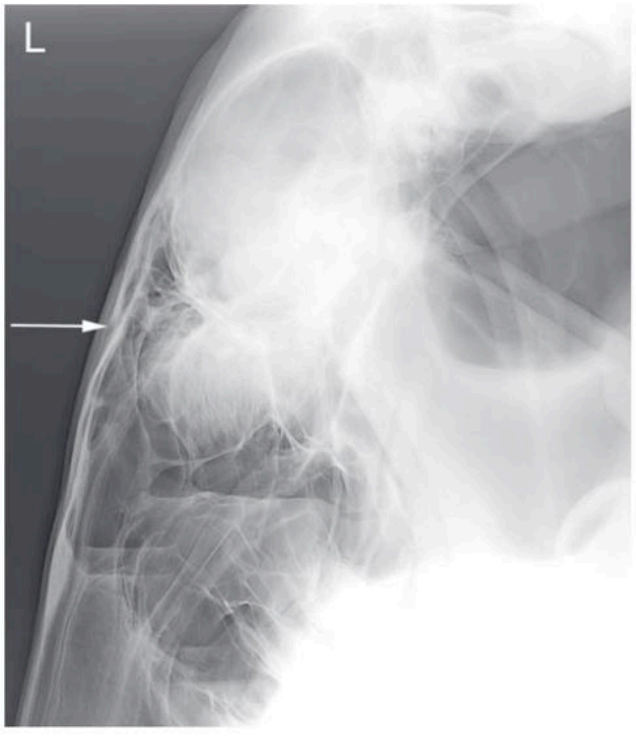


Fig. 13.30 Lateral radiograph of a depression fracture of the frontal bone (*arrow*). Fluid lines due to hemorrhage are also present in the conchofrontal, caudal maxillary, and rostral maxillary sinuses.



Fig. 13.31 Lateral radiograph of guttural pouch empyema with a distinct fluid line (*arrow*). Small superimposed gas bubbles (*arrowheads*) represent abscesses within adjacent soft tissues.

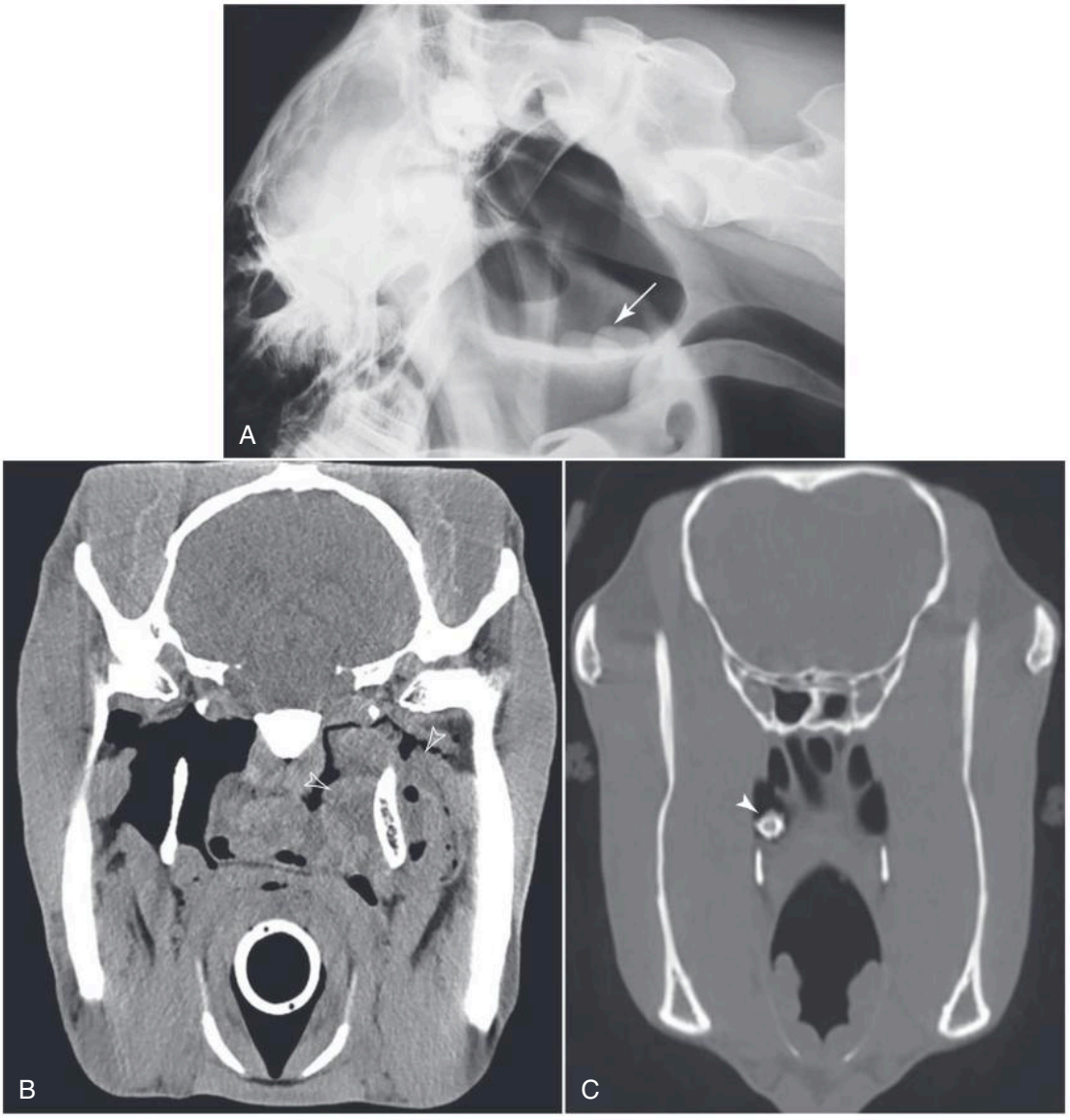


Fig. 13.32 **A,** Lateral radiograph showing two chondroids (*arrow*) in the guttural pouches. **B,** Transverse computed tomography (CT) showing inspissated pus (*open arrowheads*) of a horse with strangles, representing early chondroid formation. **C,** Transverse CT showing a chronic, mineralized chondroid in the guttural pouch (*closed arrowhead*).



Fig. 13.33 Lateral radiograph showing enlarged medial retropharyngeal lymph nodes (*arrowheads*) causing a broad-based soft tissue bulge into the guttural pouches.



Fig. 13.34 Lateral radiograph of the cranial cervical region in a 2-month-old quarter horse with guttural pouch tympany. Note the elongated appearance of the guttural pouch that extends beyond its normal anatomic limit of the caudal margin of the first cervical vertebra.

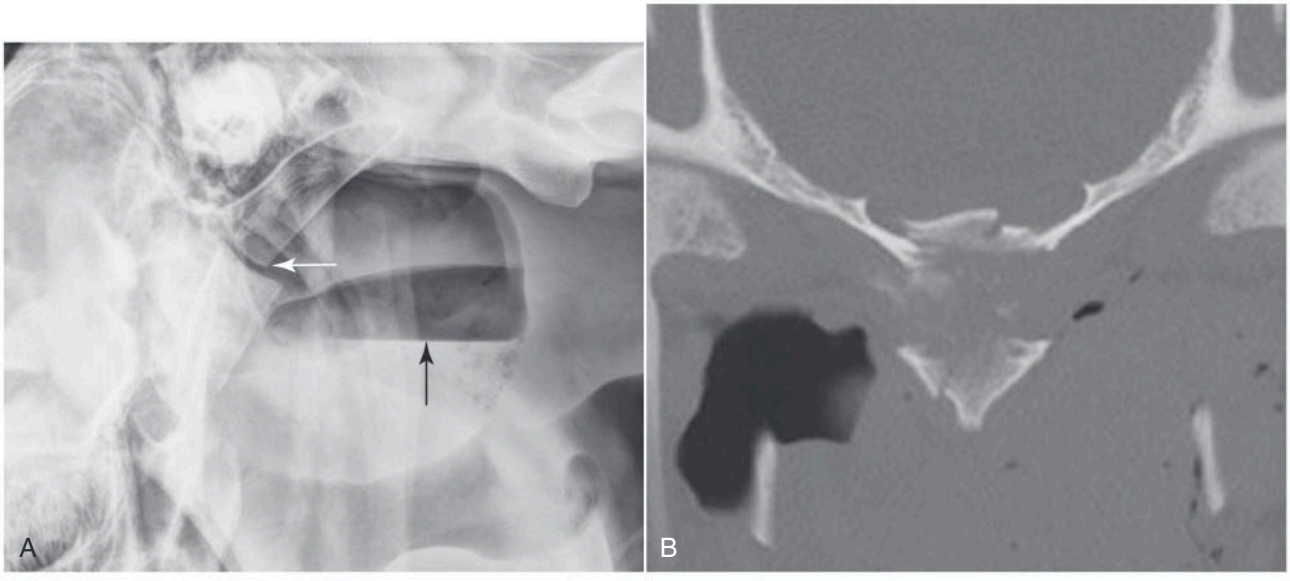


Fig. 13.35 **A,** Lateral radiograph of the head in an 8-month-old Hanoverian that sustained a fall. The basioccipital bone (*white arrow*) is displaced dorsally in relation to the basisphenoid bone. The guttural pouch is partially filled with a soft tissue-fluid opacity that compresses the nasopharynx. A gas/fluid interface is also present (*black arrow*), caused by hemorrhage, a result of avulsion of the ventral skull muscles and fracture of the skull base. Small gas bubbles are visible just caudal to the *black arrow*; this suggests an avulsion of the ventral aspect of the sphenoid sinus with release of air. **B,** Computed tomography (CT) examination thorough the basisphenoid region in another horse with a comminuted basisphenoid-basioccipital fracture.

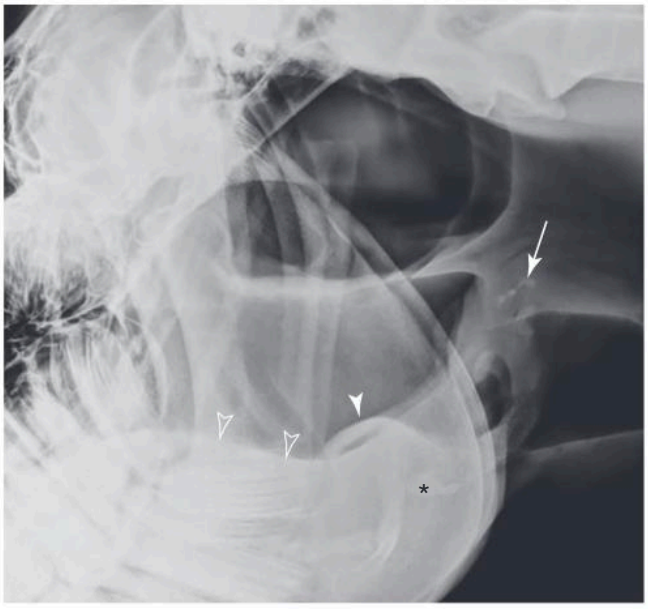


Fig. 13.36 Lateral radiograph showing the tip of the epiglottis (*closed arrowhead*) appropriately dorsal to the soft palate (*open arrowheads*). There is mineralization of the dorsal arytenoid region (*arrow*) and base of the laryngeal cartilages (*asterisk*).



Fig. 13.38 Lateral radiograph of the laryngeal region of a subepiglottic mass (*black arrows*) displacing the epiglottis dorsally; this was a cyst.



Fig. 13.37 Lateral radiograph of the laryngeal region. The epiglottis is ventral to the soft palate (*black arrows*), indicating a dorsally displaced soft palate.

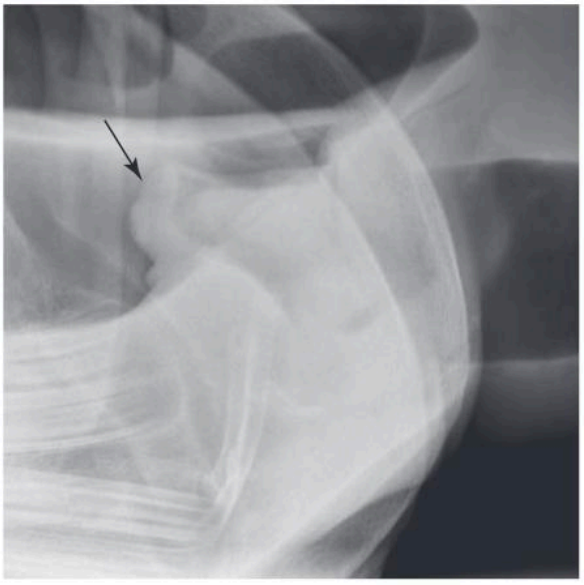


Fig. 13.39 Lateral radiograph of the laryngeal region of a horse with epiglottic entrapment. Note the blunt appearance of the epiglottis (*black arrow*) and the conspicuous aryepiglottic fold.

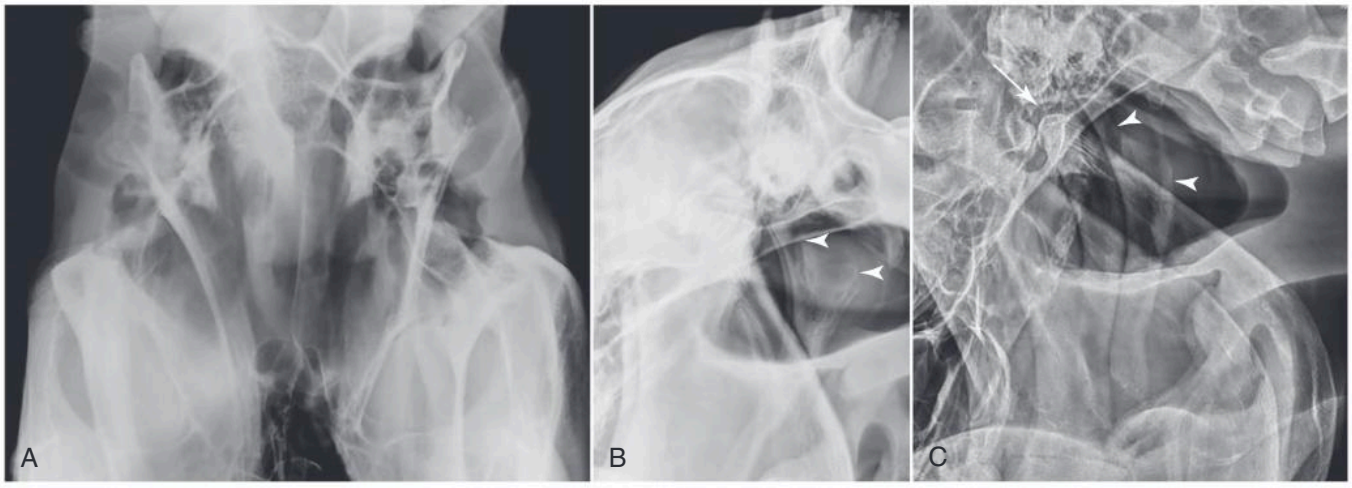


Fig. 13.40 Dorsoventral **(A)**, lateral **(B)**, and lateral 10-degree rostral-laterocaudal oblique **(C)** showing the normal temporomandibular joint (*arrow*) and proximal stylohyoid bone (*arrowheads*). On the lateral projection, the left and right stylohyoid bones are superimposed.

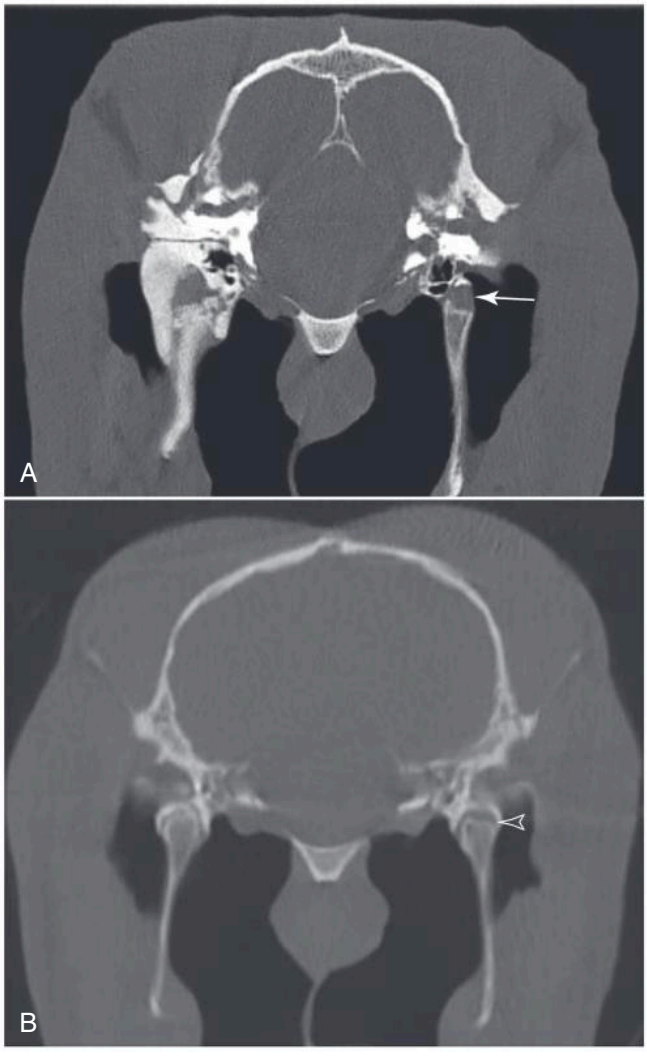


Fig. 13.41 Computed tomography (CT) images of a horse with unilateral severe temporohyoid osteoarthropathy (THO) **(A)** and mild bilateral THO **(B)**. The normal temporohyoid joint (*arrow*) has nonmineralized tympanohyoid cartilage (*arrow*) between the bulla and stylohyoid bone. The contralateral temporohyoid joint in **A** has severe bridging proliferation characteristic of severe THO. The other affected horse **(B)** has mild bilateral mineralization of the tympanohyoid cartilage (*arrowhead*).



Fig. 13.42 Radiograph **(A)**, sagittal **(B)**, and transverse **(C)** computed tomography (CT) images of a horse with severe temporohyoid osteoarthropathy resulting in stylohyoid diffuse thickening (*arrows*) and chronic fractures (*open arrowheads*). CT better demonstrates the presence of fractures.

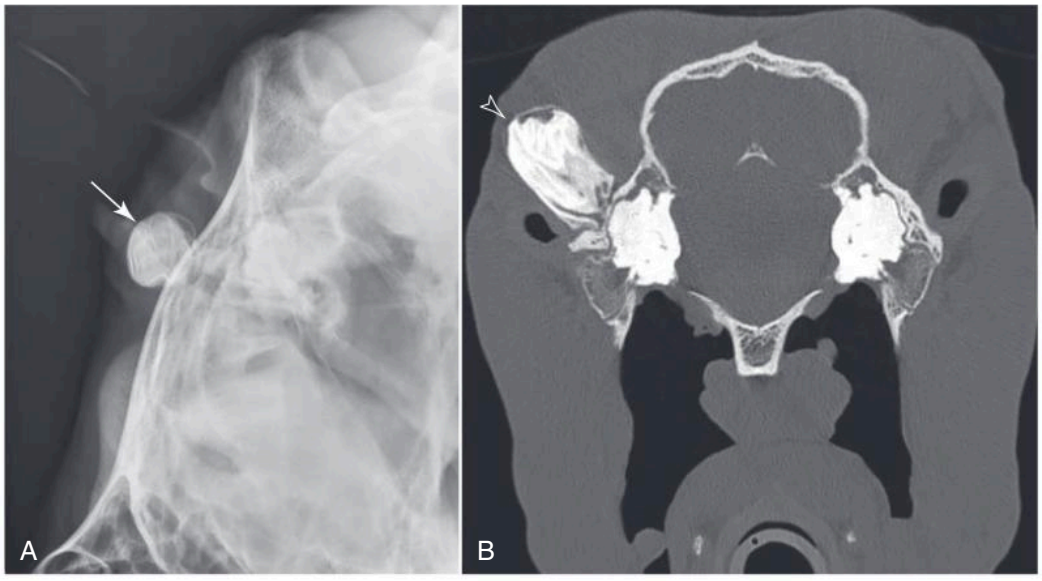


Fig. 13.43 Oblique radiograph of the right ear **(A)** and computed tomography (CT) **(B)** showing a dentigerous cyst. On the radiograph the dentigerous cyst is superimposed with the pinna (*arrow*) with the inner tooth-like structure more apparent on the CT (*open arrowhead*).

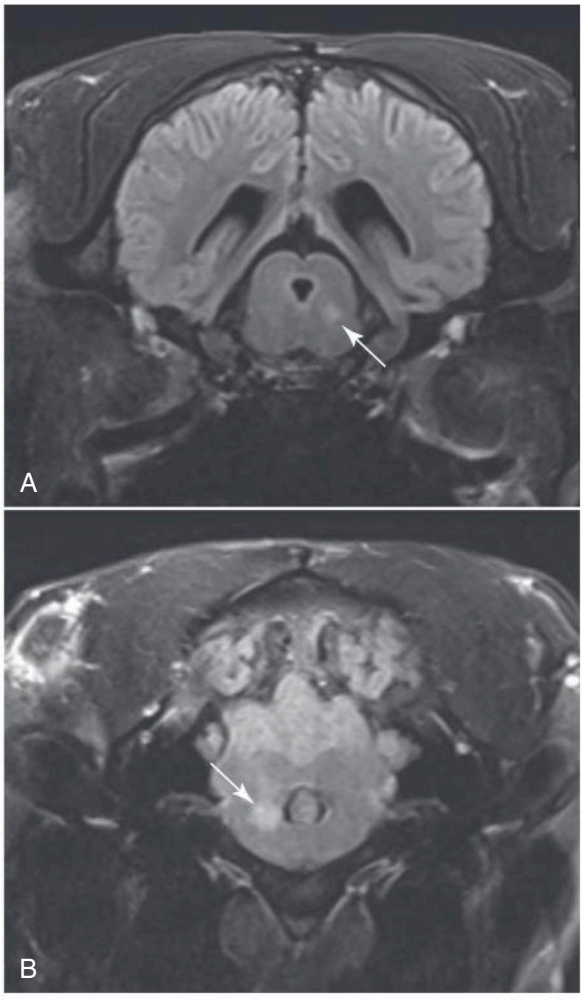


Fig. 13.44 A and B, Transverse fluid-attenuated inversion recovery (FLAIR) images of a horse with equine protozoal myeloencephalitis showing multifocal hyperintensities within the brainstem (*arrows*).



Fig. 13.45 Contrast-enhanced transverse computed tomography (CT) image of the brain. There is a depression fracture of the right parietal bone (*white arrowhead*) and a ring-enhancing lesion within the brain (*white arrows*). The ring-enhancing lesion is the vascular capsule of a brain abscess caused by penetrating trauma.

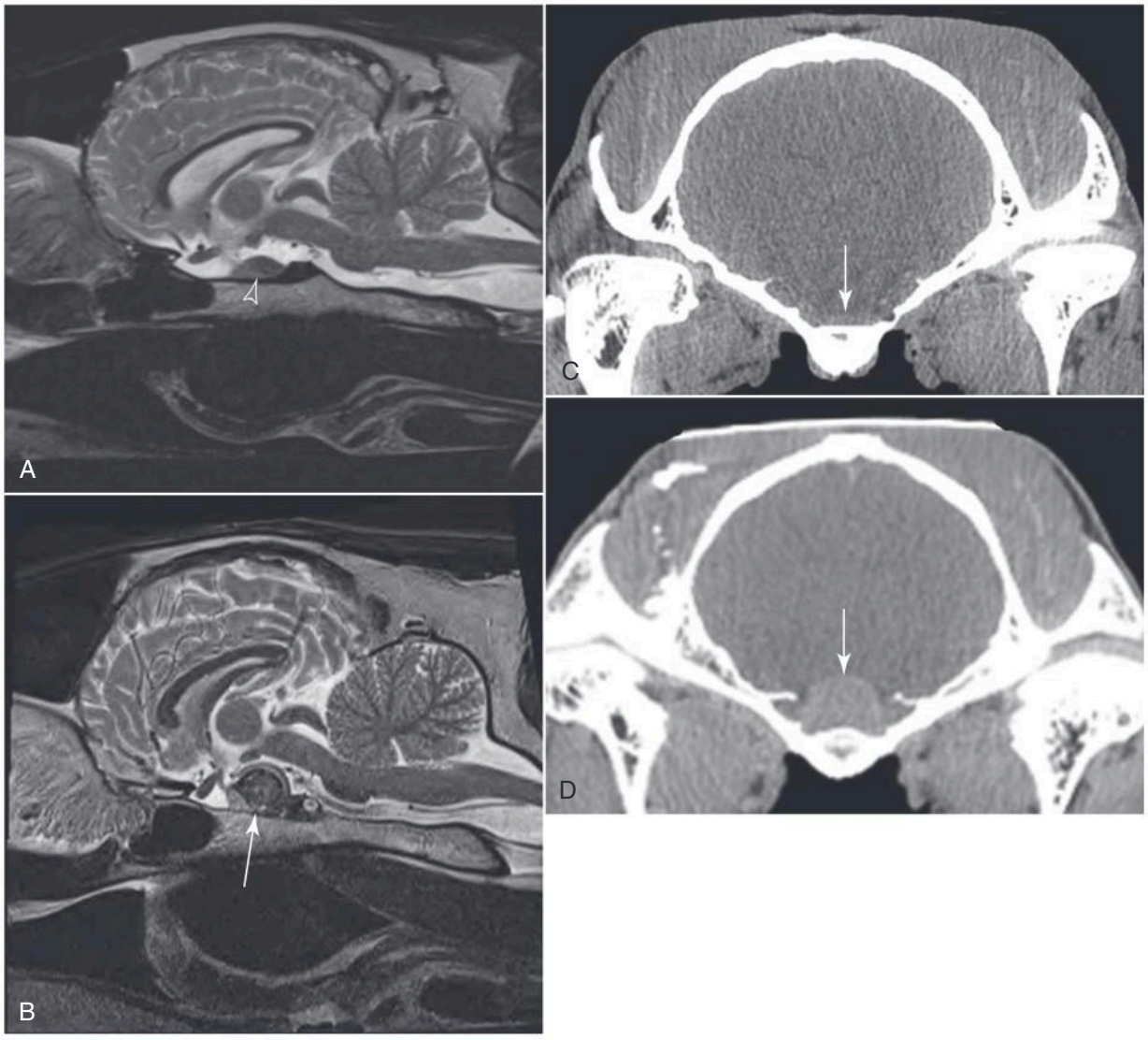


Fig. 13.46 Sagittal T2-weighted magnetic resonance imaging (MRI) image of the brain in a normal horse **(A)** and a horse with hyperadrenocorticism **(B)**. The normal pituitary gland (*arrowhead*) is homogenously hypointense. The affected pituitary gland (*arrow*) is enlarged and hypointense. The low-signal area is likely secondary to increased dopamine, which is paramagnetic and causes a susceptibility artifact on gradient recalled echo sequences. No evidence of hemorrhage was found histopathologically. Transverse postcontrast computed tomography (CT) image of the brain in a normal horse **(C)** and a horse with hyperadrenocorticism **(D)**. There is diffuse enlargement of the pituitary gland in the affected horse (*arrows*).

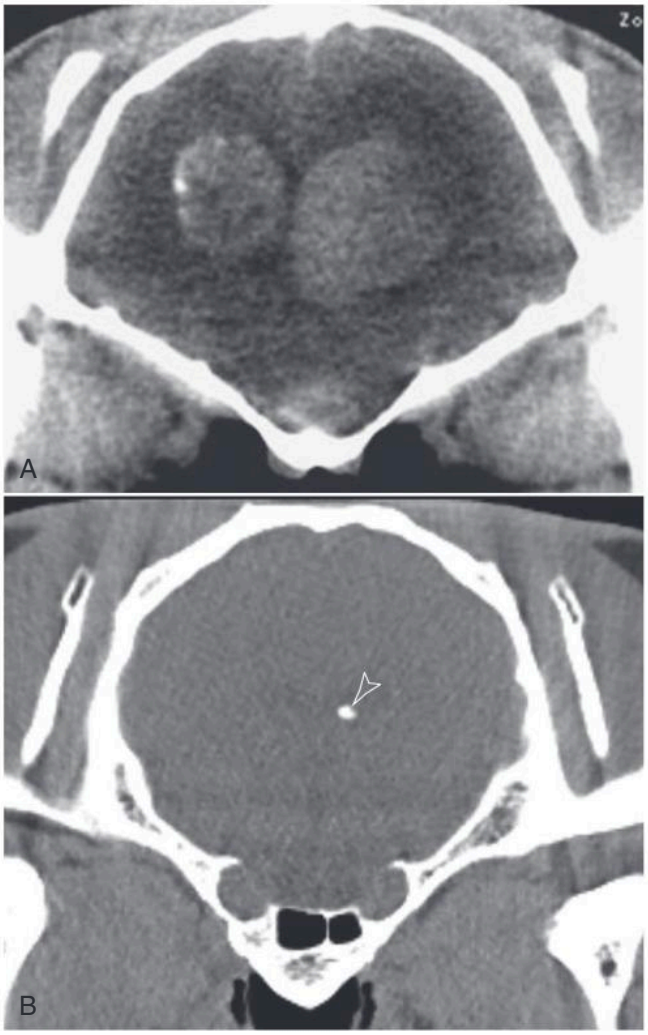


Fig. 13.47 Transverse computed tomography (CT) images of a horse with bilateral very large cholesterol granulomas **(A)** and a horse with a small unilateral granuloma (**B,** *open arrowhead*). The small granulomas are much more commonly seen.

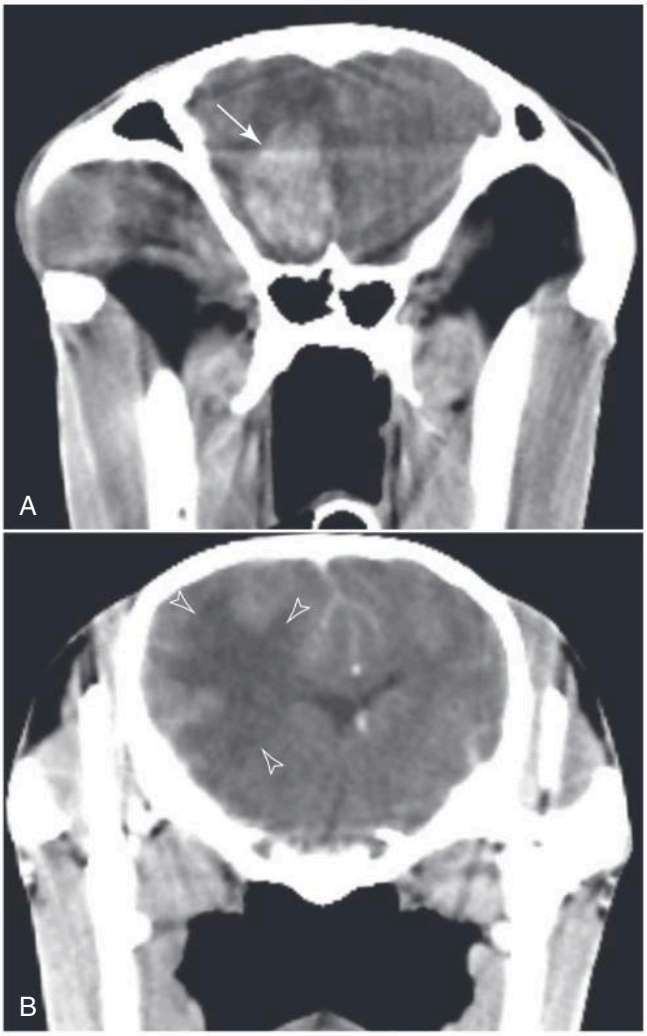


Fig. 13.48 Transverse computed tomography (CT) images of a horse with head trauma showing a large hyperattenuating hematoma in the right forebrain (**A,** *arrow*). There is extensive vasogenic edema caudal to this (**B,** *open arrowheads*) characterized by hypoattenuation and expansion of the white matter tracts.

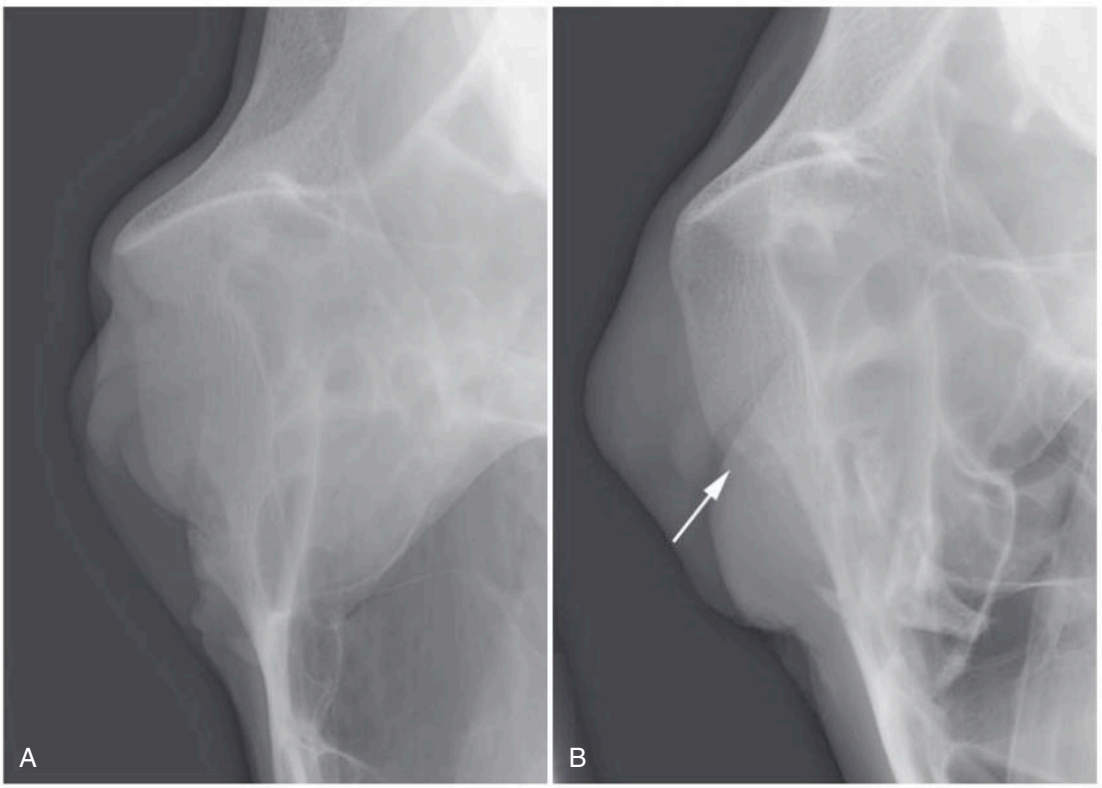


Fig. 13.49 Oblique radiographs of a normal left supraorbital process **(A)** and a right **(B)** supraorbital process with multiple fractures (*arrow*). These images are from the same horse.

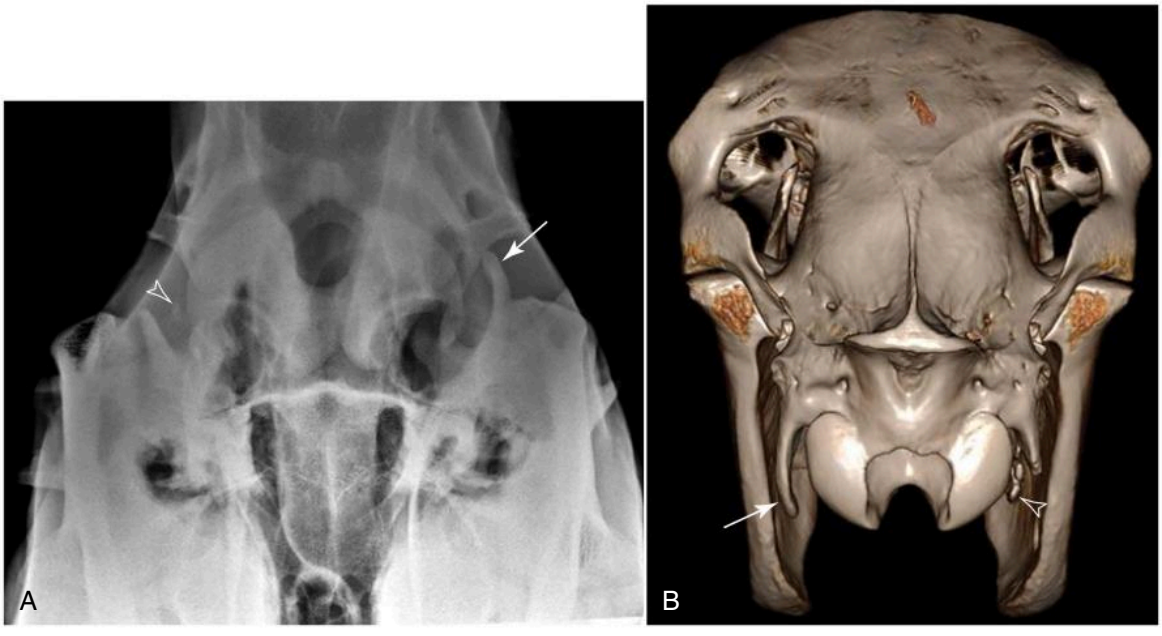


Fig. 13.50 Dorsoventral radiograph **(A)** and three-dimensional, computed tomography (CT) image **(B)** of a horse with a paracondylar process fracture (*open arrowheads*) made most apparent when compared to the normal side (*arrows*). The fracture is more readily identified on the CT image.

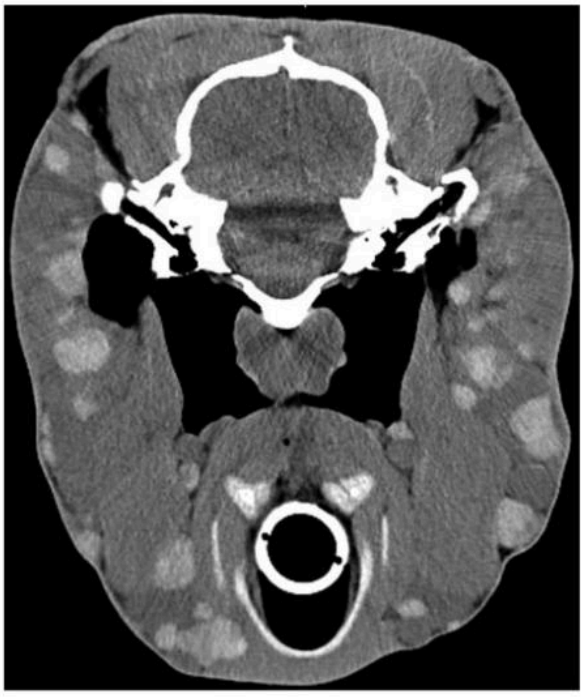


Fig. 13.51 Computed tomography (CT) image without intravenous contrast agent showing numerous hyperattenuating nodules throughout the soft tissues of the head, consistent with melanomas.

Acknowledgment

With special thanks to prior authors of this chapter for their contributions.

REFERENCES

1. Dixon PM, Froydenlund T, Luiti T, et al. Empyema of the nasal conchal bulla as a cause of chronic unilateral nasal discharge in the horse: 10 cases (2013–2014). *Equine Vet J*. 2015;47:445–449.
2. Fenner MF, Verwilghen D, Townsend N, et al. Paranasal sinus cysts in the horse: complications related to their presence and surgical treatment in 37 cases. *Equine Vet J*. 2019;51:57–63.
3. Woodford NS, Lane JG. Long-term retrospective study of 52 horses with sinunasal cysts. *Equine Vet J*. 2006;38: 198–202.
4. Ostrowska J, Lindstrom L, Toth T, et al. Computed tomography characteristics of equine paranasal sinus cysts. *Equine Vet J*. 2020;52:538–546.
5. Textor JA, Puchalski SM, Affolter VK, et al. Results of computed tomography in horses with ethmoid hematoma: 16 cases (1993-2005). *JAVMA-J Am Vet Med A*. 2012;240:1338–1344.
6. Cissell DD, Wisner ER, Textor J, et al. Computed tomographic appearance of equine sinonasal neoplasia. *Vet Radiol Ultrasound*. 2012;53:245–251.
7. Head KW, Dixon PM. Equine nasal and paranasal sinus tumours. Part 1: review of the literature and tumour classification. *Vet J*. 1999;157:261–278.
8. Dixon PM, Parkin TD, Collins N, et al. Historical and clinical features of 200 cases of equine sinus disease. *Vet Rec*. 2011;169:439.
9. Tremaine WH, Clarke CJ, Dixon PM. Histopathological findings in equine sinonasal disorders. *Equine Vet J*. 1999;31:296–303.
10. Dixon PM, Dacre I. A review of equine dental disorders. *Vet J*. 2005;169:165–187.
11. Morgan RE, Fiske-Jackson AR, Hellige M, et al. Equine odontogenic tumors: clinical presentation, CT findings, and outcome in 11 horses. *Vet Radiol Ultrasoun*. 2019;60: 502–512.
12. Limone LE. Update on equine odontoclastic tooth resorption and hypercementosis. *Vet Clin North Am Equine Pract*. 2020;36:671–689.
13. James O. Equine odontoclastic tooth resorption and hypercementosis. *J Vet Dent*. 2022;39:346–357.
14. Rehrl S, Schroder W, Muller C, et al. Radiological prevalence of equine odontoclastic tooth resorption and hypercementosis. *Equine Vet J*. 2018;50:481–487.
15. David F, Levingstone TJ, Schneeweiss W, et al. Enhanced bone healing using collagen-hydroxyapatite scaffold implantation in the treatment of a large multiloculated mandibular aneurysmal bone cyst in a thoroughbred filly. *J Tissue Eng Regen Med*. 2015;9:1193–1199.
16. Lamb CR, Schelling SH. Congenital aneurysmal bone cyst in the mandible of a foal. *Equine Vet J*. 1989;21:130–132.
17. Mendoza FJ, Toribio RE, Perez-Ecija A. Nutritional secondary hyperparathyroidism in equids: overview and new insights. *Equine Vet Educ*. 2017;29:558–563.
18. Leitzen E, Stumpf S, Zimmermann C, et al. A rare case of vascular proliferation in the mandible of a juvenile horse. *Front Vet Sci*. 2020;7:573540.
19. Nottle BF, Tatarniuk DM, Caldwell FJ, et al. Fibro-osseous lesions of the craniofacial complex in horses: 30 cases (2001–2019). *Vet Surg*. 2021;50:383–392.
20. Sponseller BA, Caston SS, Winter MD, et al. What is your diagnosis? Chronic juvenile ossifying fibroma. *J Am Vet Med Assoc*. 2006;229:1727–1728.
21. Bonilla AG, Wilson K, Santschi EM. Suture exostosis with concurrent nasal septum chondrosarcoma in a horse. *Equine Vet Educ*. 2015;27:579–584.
22. Verwilghen D, Easley J, Zwick T, et al. Equine suture exostosis: a review of cases from a multicenter retrospective study. *Vet Sci*. 2022;9.
23. Ebling AJ, McKnight AL, Seiler G, et al. A complementary radiographic projection of the equine temporomandibular joint. *Vet Radiol Ultrasound*. 2009;50:385–391.
24. Townsend NB, Cotton JC, Barakzai SZ. A tangential radiographic projection for investigation of the equine temporomandibular joint. *Vet Surg*. 2009;38:601–606.
25. Ramzan PH, Marr CM, Meehan J, et al. Novel oblique radiographic projection of the temporomandibular articulation of horses. *Vet Rec*. 2008;162:714–716.
26. Carmalt JL, Kneissl S, Rawlinson JE, et al. Computed tomographic appearance of the temporomandibular joint in 1018 asymptomatic horses: a multi-institution study. *Vet Radiol Ultrasound*. 2016;57:237–245.
27. Rizk A, Hamed M. The use of cerclage wire for surgical repair of unilateral rostral mandibular fracture in horses. *Iran J Vet Res*. 2018;19:123–127.
28. Huggons NA, Bell RJW, Puchalski SM. Radiography and computed tomography in the diagnosis of nonneoplastic equine mandibular disease. *Vet Radiol Ultrasoun*. 2011;52:53–60.
29. Freeman DE. Update on disorders and treatment of the guttural pouch. *Vet Clin N Am-Equine*. 2015;31:63–89.
30. Dixon J, Smith K, Perkins J, et al. Computed tomographic appearance of melanomas in the equine head: 13 cases. *Vet Radiol Ultrasoun*. 2016;57:246–252.
31. Hance SR, Bertone AL. Neoplasia. *Vet Clin N Am-Equine*. 1993;9:213–234.
32. McCarrel TM, Woodie JB. Update on laryngeal disorders and treatment. *Vet Clin North Am Equine Pract*. 2015;31:13–26.

33. Virgin JE, Holcombe SJ, Caron JP, et al. Laryngeal advancement surgery improves swallowing function in a reversible equine dysphagia model. *Equine Vet J*. 2016;48:362–367.
34. Bowkett-Pritchard C, Morgan RE. Laryngeal dysplasia: computed tomographic findings in an Oldenburg mare. *Equine Vet Educ*. 2023;35:26–30.
35. Orsini PG, Raker CW, Reid CF, et al. Xeroradiographic evaluation of the equine larynx. *Am J Vet Res*. 1989;50: 845–849.
36. Garrett KS, Embertson RM, Woodie JB, et al. Ultrasound features of arytenoid chondritis in Thoroughbred horses. *Equine Vet J*. 2013;45:598–603.
37. Barakzai SZ, Hawkes CS. Dorsal displacement of the soft palate and palatal instability. *Equine Vet Educ*. 2010;22:253–264.
38. Aitken MR, Parente EJ. Epiglottic abnormalities in mature nonracehorses: 23 cases (1990–2009). *Javma-J Am Vet Med A*. 2011;238:1634–1638.
39. Hawkins JF, Tulleners EP. Epiglottitis in horses: 20 cases (1988-1993). *J Am Vet Med Assoc*. 1994;205:1577–1580.
40. Saulez MN, Gummow B. Prevalence of pharyngeal, laryngeal and tracheal disorders in thoroughbred racehorses, and effect on performance. *Vet Rec*. 2009;165: 431–435.
41. Ducharme NG, Rossignol F. Larynx In: Auer JA, Stick JG, eds. *Equine Surgery*. 5th ed. St. Louis: Elsevier; 759.
42. Naylor RJ, Perkins JD, Allen S, et al. Histopathology and computed tomography of age-associated degeneration of the equine temporohyoid joint. *Equine Vet J*. 2010;42: 425–430.
43. Walker AM, Sellon DC, Cornelisse CJ, et al. Temporohyoid osteoarthropathy in 33 horses (1993–2000). *J Vet Intern Med*. 2002;16:697–703.
44. Pownder S, Scrivani PV, Bezuidenhout A, et al. Computed tomography of temporal bone fractures and temporal region anatomy in horses. *J Vet Intern Med*. 2010;24: 398–406.
45. Ruby JL, Scrivani PV, Thompson MS. What is your diagnosis? *Javma-J Am Vet Med A*. 2015;247:1097–1099.
46. Garrett KS. Special diagnostic techniques in equine neurology (radiography, ultrasonography, computed tomography, and magnetic resonance imaging). *Vet Clin North Am Equine Pract*. 2022;38:171–188.
47. Scrivani PV. Advanced imaging of the nervous system in the horse. *Vet Clin North Am Equine Pract*. 2011;27:439–453.
48. Cavasin JP, Miller AD, Duhamel GE. Intracerebral astrocytoma in a horse. *J Comp Pathol*. 2020;177:1–4.
49. van der Kolk JH, Heinrichs M, van Amerongen JD, et al. Evaluation of pituitary gland anatomy and histopathologic findings in clinically normal horses and horses and ponies with pituitary pars intermedia adenoma. *Am J Vet Res*. 2004;65:1701–1707.
50. Hobbs KJ, Porter E, Wait C, et al. Magnetic resonance imaging of the normal equine pituitary gland. *Vet Radiol Ultrasound*. 2022;63:450–455.
51. McKlveen TL, Jones JC, Sponenberg DP, et al. Assessment of the accuracy of computed tomography for measurement of normal equine pituitary glands. *Am J Vet Res*. 2003;64:1387–1394.
52. Pease AP, Schott 2nd HC, Howey EB, et al. Computed tomographic findings in the pituitary gland and brain of horses with pituitary pars intermedia dysfunction. *J Vet Intern Med*. 2011;25:1144–1151.
53. Tofflemire KL, Whitley RD, Wong DM, et al. Episodic blindness and ataxia in a horse with cholesterinic granulomas. *Vet Ophthalmol*. 2013;16:149–152.
54. Jackson CA, deLahunta A, Dykes NL, et al. Neurological manifestation of cholesterinic granulomas in three horses. *Vet Rec*. 1994;135:228–230.
55. Nout-Lomas YS. Traumatic nervous system injury. *Vet Clin North Am Equine Pract*. 2022;38:363–377.
56. Feary DJ, Magdesian KG, Aleman MA, et al. Traumatic brain injury in horses: 34 cases (1994–2004). *J Am Vet Med Assoc*. 2007;231:259–266.
57. Gerding JC, Clode A, Gilger BC, et al. Equine orbital fractures: a review of 18 cases (2006–2013). *Vet Ophthalmol*. 2014;1:97–106, 17 Suppl.
58. Lischer CJ, Walliser U, Witzmann P, et al. Fracture of the paracondylar process in four horses: advantages of CT imaging. *Equine Vet J*. 2005;37:483–487.

ELECTRONIC RESOURCES

Additional information related to the content in Chapter 13 can be found online at eBooks.Health.Elsevier.com.

- Chapter Quiz

CHAPTER 14

Radiography and Myelography of the Canine and Feline Vertebrae

William R. Widmer

Spinal pain and spinal neuropathy are common problems in small animal practice. This leads to the vertebral column being one of the more frequently imaged anatomic regions. Computed tomography (CT) and magnetic resonance imaging (MRI) are the modalities of choice for full characterization of abnormalities of the vertebrae and spinal cord in small animals. Many conditions including intervertebral disc disease; various myelopathies; and tumors of the spinal cord, meninges, and vertebral column cannot be completely characterized with a conventional survey radiographic examination. However, judicious use of conventional radiography can provide valuable, cost-effective information regarding numerous conditions of the vertebral column, and survey radiographs should always be made before pursuing advanced imaging. Survey radiographs may or may not lead to identification of the cause of the pain or neuropathy; but, especially in older patients, they are rarely normal. Therefore, it is important to have not only an appreciation for the types of spinal abnormalities that can be diagnosed radiographically but also to understand the significance of commonly encountered changes that may not be related directly to the clinical signs. The focus of this chapter is on vertebral diseases that can be imaged effectively with conventional radiography and myelography (including CT myelography), and the significance of commonly encountered incidental findings. Radiographic abnormalities will be supplemented with CT and/or magnetic resonance (MR) images where appropriate. Advanced imaging related specifically to the spinal cord is covered in Chapter 15.

Radiographic technique plays a vital role in radiography of the vertebral column.[1] Suboptimal information occurs when positioning is inaccurate, multiple centered images are not made, and images do not have adequate spatial resolution. Chemical restraint is absolutely necessary for accurate positioning and should be used unless prohibited by the patient's condition. Technical information relating to spinal radiography is discussed in detail in Chapter 9.

ANATOMIC CONSIDERATIONS

A vertebra consists of the body, also referred to as a *centrum*, and the vertebral arch (Fig. 14.1).[1,2] The vertebral arch is composed of paired right and left pedicles and laminae and the unpaired spinous process. The vertebral arch bounds the vertebral canal, which houses the spinal cord. The articular processes of the lamina form the synovial joints along the dorsum of the vertebral column (Fig. 14.2). The articular process joints are diarthrodial (synovial) joints, being composed of articular processes covered with articular cartilage, a synovial membrane and capsule, and contain synovial fluid. They provide dorsal mechanical stabilization of the vertebral column.

Other than the first cervical vertebra, each vertebral body is narrowed centrally and has cranial and caudal endplates that

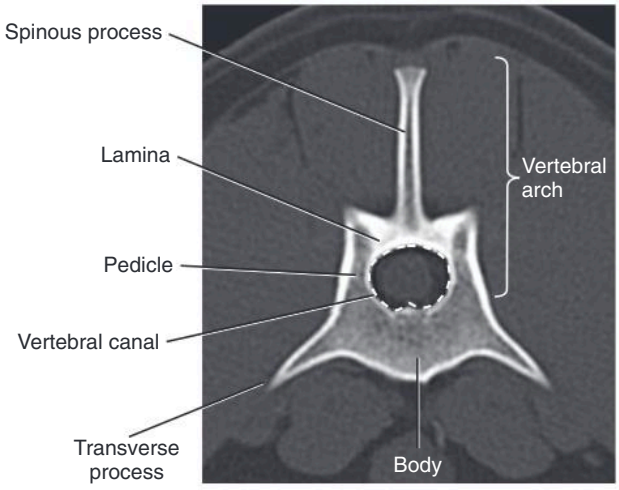


Fig. 14.1 Transverse computed tomography (CT) image of a lumbar vertebra. The core components common to all vertebrae are identified. (From Thrall DE, Robertson ID. *Textbook of Normal Radiographic Anatomy and Normal Anatomic Variants in the Dog and Cat*. 2nd ed. St. Louis: Saunders; 2016.)

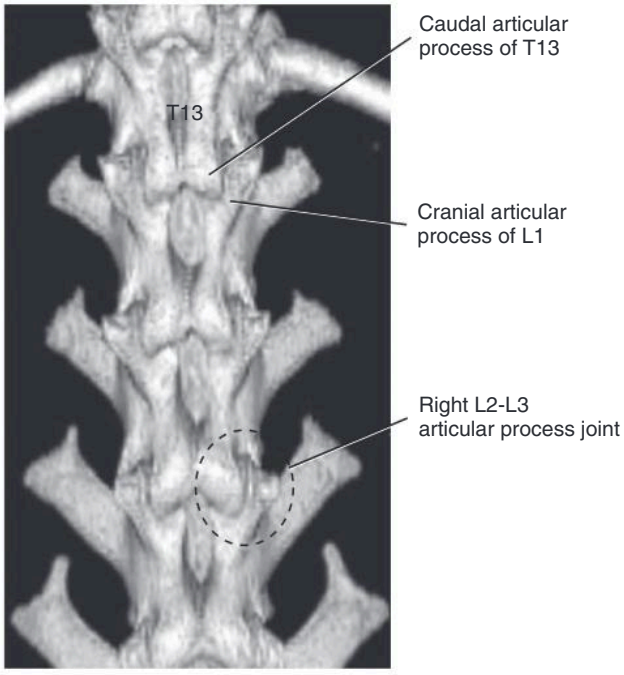


Fig. 14.2 Dorsal view of a three-dimensional rendering of the cranial aspect of the lumbar spine of a dog. The morphology of the articular processes and how they form the dorsal articular process joint can be seen in this rendering. *T13*, Thirteenth vertebral body.

unite with an interposed intervertebral disc. The anatomic structure of C1 (atlas) and C2 (axis) is complex and differs widely from the remainder of the vertebrae (Fig. 14.3).[1–5] C1 has a well-developed vertebral arch, but the body is rudimentary with no distinct vertebral body, endplates, or spinous process, and the cranial and caudal articular processes are convex. C1 articulates cranially with the occipital condyles, forming the atlantooccipital joint, and caudally with C2, forming the atlantoaxial joint. The *wings* of C1 are extensive transverse processes that project laterally and serve as attachments for numerous cervical muscles. The lateral and transverse foramina contain the paired vertebral arteries. C2 has an elongated vertebral body and a massive spinous process. The dens is a finger-like projection extending cranially from the vertebral body of C2 into the cranioventral aspect of the vertebral canal. The dens originates from the intercentrum of C1, but during development, it attaches to C2 and lies within the vertebral canal of C1. C2 has a small transverse process, two cranial articular processes that articulate with the fovea of the atlas, and a caudal endplate.

The sacrum is also much different morphologically than a prototypical vertebra. It is broad in the transverse plane, consists of three fused vertebrae, and articulates cranially with the seventh lumbar vertebra, caudally with the first caudal vertebra, and laterally with the ilium on each side, forming the sacroiliac joints.[1,2] The spinous processes of the sacrum are fused, making up the median sacral crest, and the sacral wing has a large facet for the sacroiliac articulation. The sacroiliac joint is a combined synovial and cartilaginous joint capable of only limited motion due to thick ventral and dorsal ligaments. Multiple foramina are present dorsally and along the pelvic surface of the sacrum, allowing for passage of spinal nerves and blood vessels. There are 6 to 23 caudal vertebrae in most dogs and cats typically have 20 to 24 caudal vertebrae.[6] Cranially, the caudal vertebrae are similar to the lumbar elements; caudal to Cd6, they become elongated and lack a vertebral arch. Y-shaped hemal arches are present ventrally on Cd4-Cd6 and protect the median coccygeal artery, which lies ventral to the vertebral centra.

Important soft-tissue structures of the vertebral column include various ligaments, intervertebral discs, and the

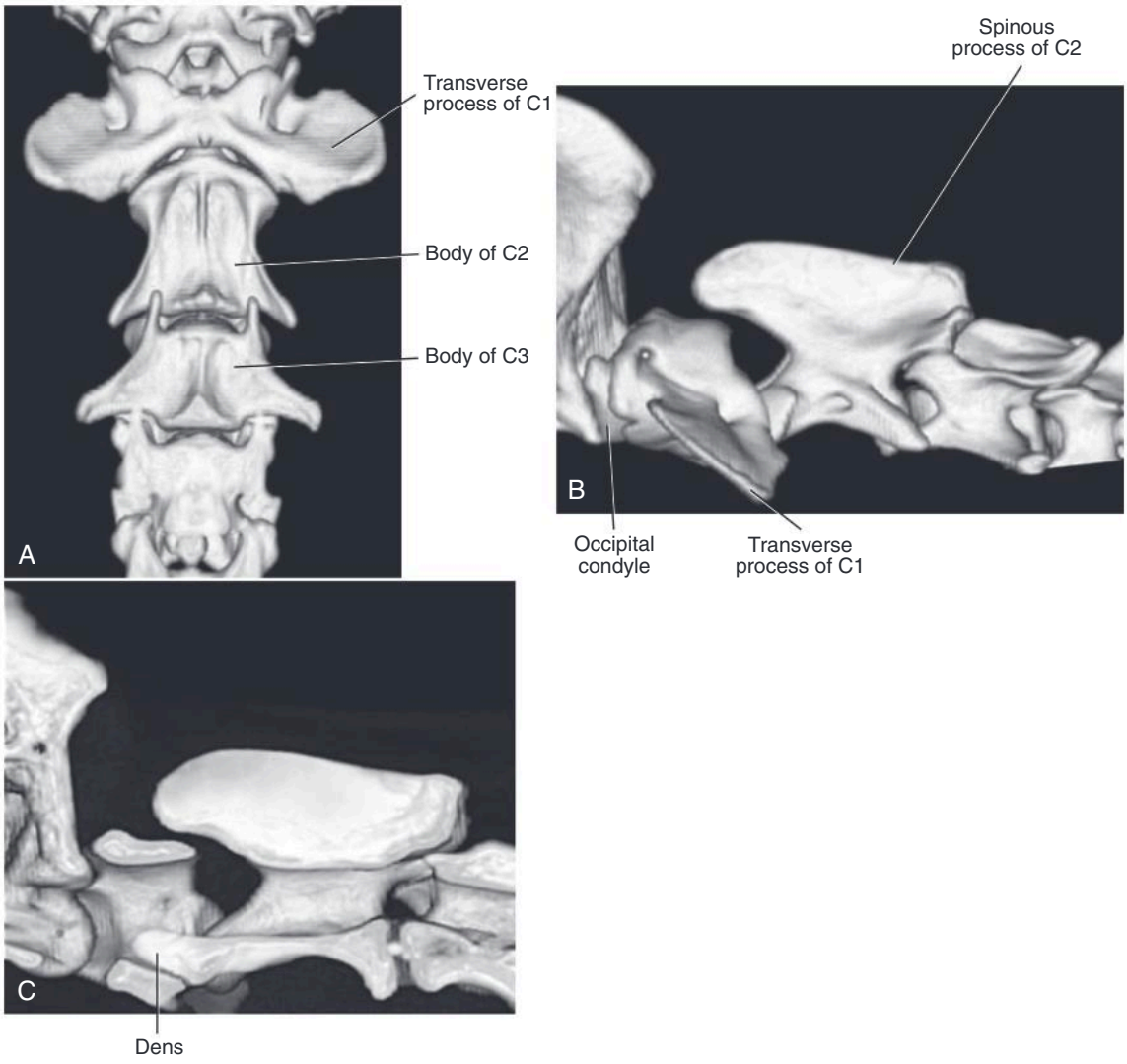


Fig. 14.3 **A,** Ventral view of a three-dimensional rendering of the cranial aspect of the cervical spine of a dog. Note the large transverse processes, called *the wings*, of C1. **B,** Lateral view of a three-dimensional rendering of the cranial aspect of the cervical spine of a dog. The distinctive shape of C1 and C2 versus other cervical vertebrae is obvious. Note the articulation of C1 with the occipital condyles and the large spinous process of C2. **C,** Midsagittal plane through a three-dimensional rendering of the cranial aspect of the cervical spine of a dog. Note the extension of the dens into the ventral aspect of the vertebral canal of C1. Note also the relationship of the cranial aspect of C1 with the occipital condyle.

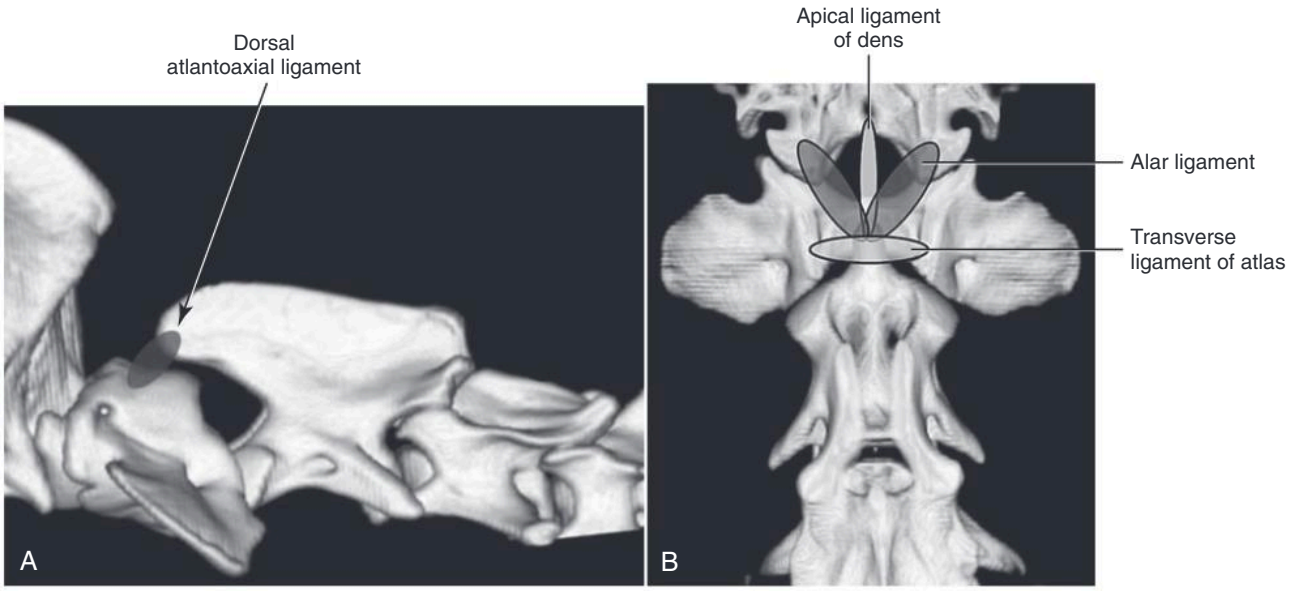


Fig. 14.4 **A,** Lateral view of a three-dimensional rendering of the cranial aspect of the cervical spine in a dog. Note the position of the dorsal atlantoaxial ligament. **B,** Dorsal view of a three-dimensional rendering of the cranial aspect of the cervical spine in a dog. The dorsal lamina of C1 and C2 has been removed to allow visualization of the ligaments on the floor of the vertebral canal. Note how the apical ligament of the dens along with its alar branches and the transverse ligament of the atlas provide stabilization of the atlantoaxial joint.

retinaculum of the articular process joints.[7] Maintaining stability of the atlantoaxial joint is particularly important given the potential for the dens to damage the spinal cord if displaced dorsally. This stabilization is provided by the short, dorsal atlantoaxial ligament, the apical ligament of the dens with its alar branches, and the transverse ligament of the atlas (Fig. 14.4).

In the dog, the nuchal ligament extends from the spinous process of the axis to the spinous processes of the first three thoracic vertebrae and is continued caudally as the supraspinous ligament. It prevents abnormal separation of the spinous processes during flexion. Short interspinous ligaments join each spinous process, adding additional support to the vertebral column. There are also short interarcuate ligaments that contain yellow elastic fibers, which bridge each vertebral arch dorsally. Collectively, these short ligaments have been referred to as the *ligamentum flavum.* These ligaments are difficult to visualize with drawings; thus, see multiplanar MR images in eFig. 14.1A for a better anatomical understanding. There is no nuchal ligament in the cat.

The dorsal longitudinal ligament lies on the floor of the vertebral canal and extends from the dens to the sacrum (Fig. 14.5). The *intercapital* ligaments are short, transverse fibrous bands that lie ventral to the dorsal longitudinal ligament, joining contralateral rib heads between T2 and T11. These ligaments buttress the dorsal part of the annulus cranial to T11 and lead to a reduced incidence of disc herniation between T1 and T11.[7,8]

The ventral longitudinal ligament is smaller than the dorsal longitudinal ligament and spans the ventral surface of the vertebral column (see Fig. 14.5). The annulus fibrosus of each intervertebral disc has oblique fibers that course from one endplate to the next, serving as ligaments.

The intervertebral disc is composed of a tough outer annulus fibrosus, which contains the gelatinous, inner nucleus pulposus (see Fig. 14.5).[7,8] The disc forms a cartilaginous joint between vertebral segments (except at C1–C2 and the sacrum where intervertebral discs are not present) and thus functions as a hydraulic shock absorber. Shock absorption is dependent on a hydrated, deformable nucleus and an intact, elastic annulus.[7]

Compared to canine vertebral, feline vertebra have a shorter body (centrum), narrower intervertebral disc spaces, and more prominent lumbar transverse processes (eFig. 14.2).

A summary of the most important anatomic considerations of the canine and feline vertebrae relative to radiographic interpretation is provided in Box 14.1.[9–11]

ANOMALIES OF THE VERTEBRAL COLUMN

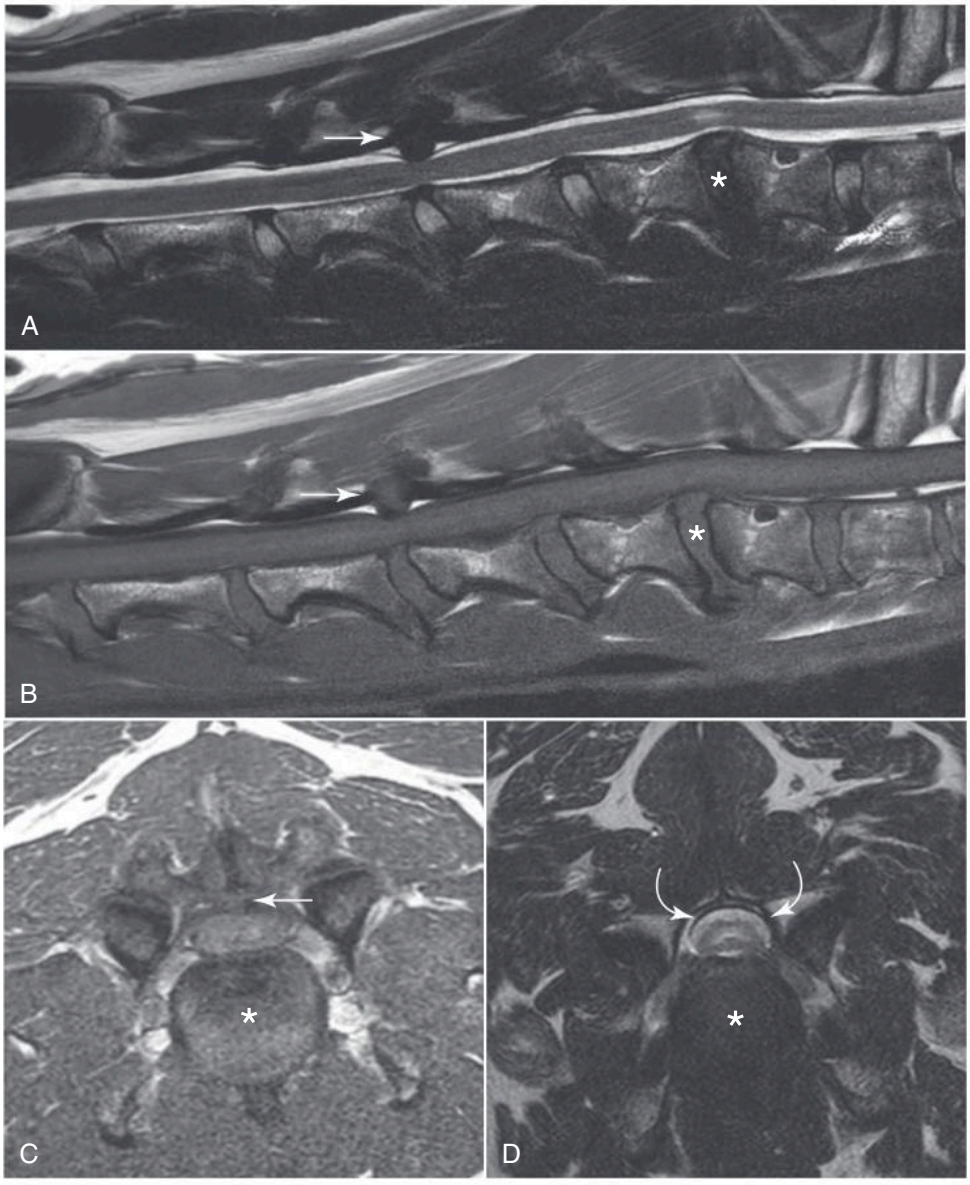
Anomalies of the vertebral column are common and include congenital and developmental malformations.[12,13] Many of these abnormalities are normal variants and have no clinical importance. Additional information on normal variants can be found in Thrall and Robertson.[1]

Block Vertebrae

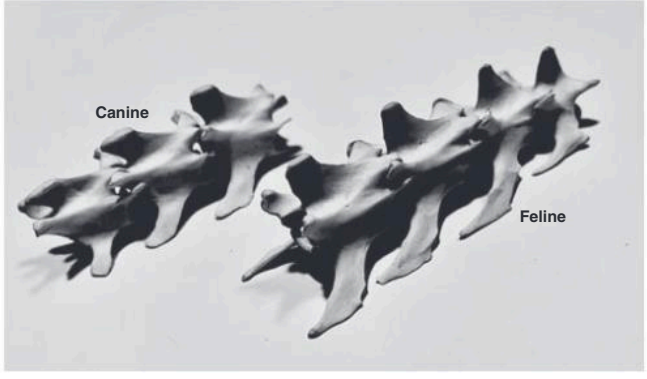
A block vertebra results from fusion of two or more adjacent vertebral bodies. The vertebral arches may also be fused, or they may be unaffected (Fig. 14.6, eFig. 14.3).[1] The disc space between a block vertebra often appears radiographically as a thin radiolucent line but may not be visible at all if the fusion is complete. Block vertebrae are most common in the cervical region, but they also occur in the lumbar spine. Biomechanically, block vertebrae may act as a fulcrum, leading to altered and increased loading immediately adjacent to the fusion. This has been hypothesized to increase the risk of disc disease at adjacent sites (see eFig. 14.3) and has also been implicated in leading to atlantoaxial subluxation.[14] The fused sacral vertebrae are a normal type of block vertebra.

Hemivertebrae

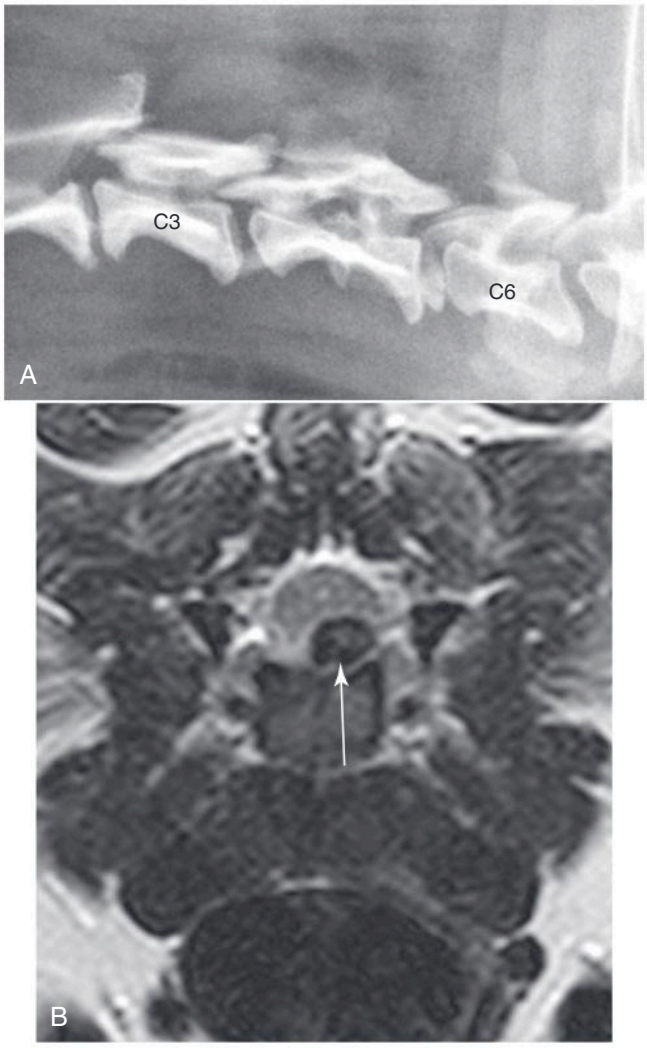
Hemivertebrae are the result of failure of the development and eventual ossification of part of a vertebra, usually the body.[1,12,15] The shape of a hemivertebra depends on the area that fails to develop. A wedge-shaped vertebra is seen on the lateral projection when the ventral aspect of the vertebral body is developed incompletely (Fig. 14.7). When this occurs, the vertebral column often acquires a kyphotic configuration that can lead to extradural compression of the spinal cord. Not all



eFig. 14.1 Magnetic resonance (MR) images showing the arcuate ligaments and ligamentum flavum. Sagittal T2-weighted **(A)** and T1-weighted **(B)** and transverse **(C** and **D)** MR images from an 8-year-old Doberman pinscher diagnosed with cervical spondylomyelopathy. **A and B,** The normally thin interarcuate ligaments making up the *ligamentum flavum* have undergone hypertrophy at C4−C5 (*arrows*), compressing the spinal cord. There is also cord compression from intervertebral disc protrusion at C6−C7 (*asterisks*). **C,** Transverse T1-weighted image showing ligamentum flavum hypertrophy and cord compression (*arrow*). The cord is also compressed by the protruding intervertebral disk (*asterisk*). **D,** T2-weighted image depicting a normal interarcuate ligament dorsal to the spinal cord (*arrows*). The intervertebral disk (*asterisk*) has an annular bulge. (Images courtesy Ronaldo C. da Costa, DVM Ronaldo C. da Costa, DMV, MSc, PhD, The Ohio State University, reproduced with permission.)



eFig. 14.2 Canine and feline vertebrae. Feline vertebrae have longer bodies (centra) and more prominent transverse processes than canine vertebrae.



eFig. 14.3 **A,** Lateral cervical radiograph of a dog with a block vertebra affecting C4—C5. The vertebral bodies and arches are fused. There is no disc space between the fused vertebrae. Note the mineralized disc at C5—C6. The biomechanics of normal neck function are altered by the block vertebra, often leading to degeneration of the intervertebral disc at adjacent interspaces. **B,** Transverse T2-weighted magnetic resonance (MR) image acquired at the level of the cranial aspect of C6. There is a large amount of hypointense disc material (*arrow*) in the left ventral aspect of the vertebral canal that is causing moderate extradural spinal cord compression. Degeneration and herniation of the C5—C6 disc was likely predisposed by altered loading associated with the block vertebra. *C3,* Third cervical vertebra; *C6,* sixth cervical vertebra.

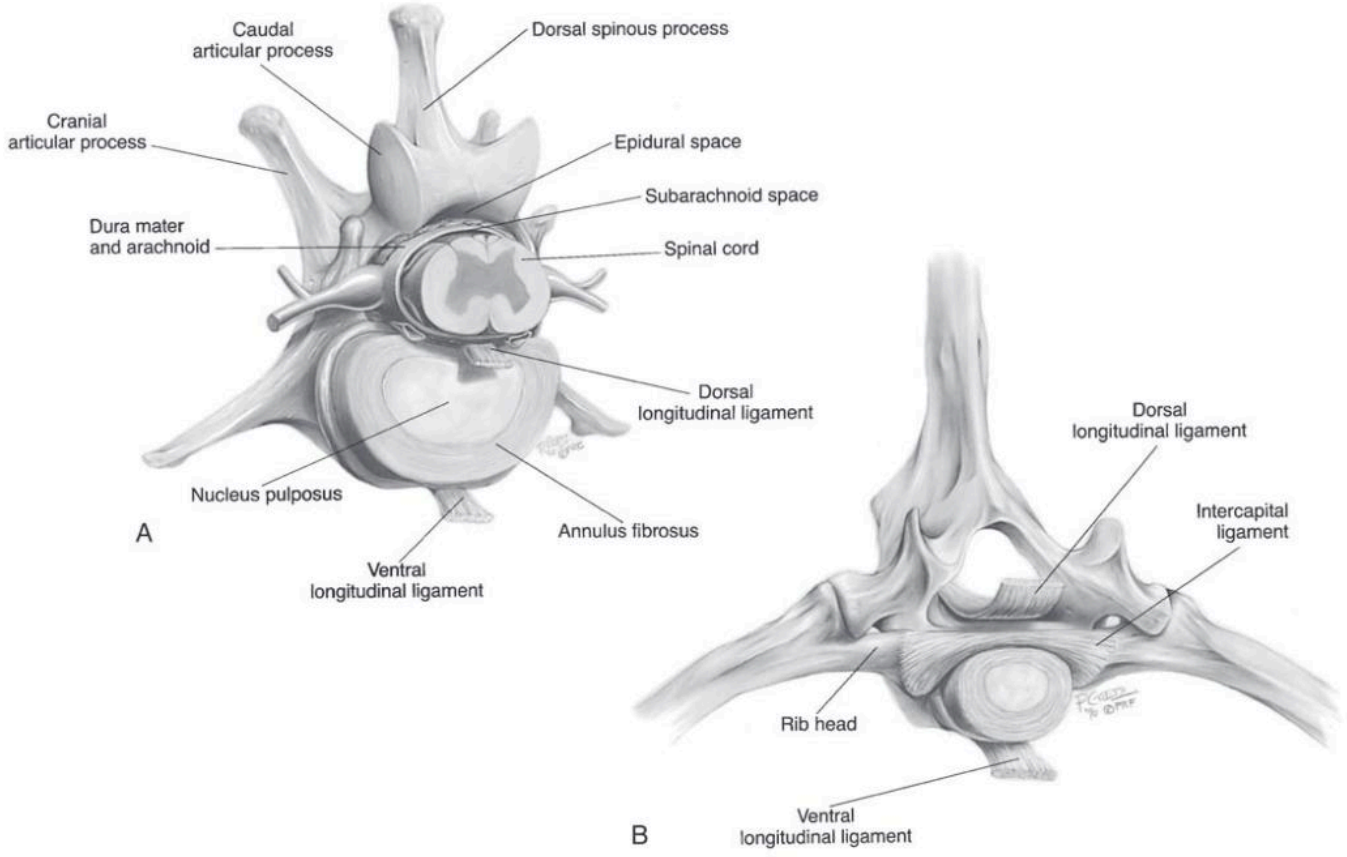


Fig. 14.5 Anatomic components of a typical lumbar vertebra **(A)** and a typical thoracic vertebra and articulation with ribs **(B)**. (Modified from Evans HE, Christensen, JC. *Miller's Anatomy of the Dog*. 2nd ed. Philadelphia: Saunders; 1979.)

Box • **14.1**

Summary of Important Anatomic Features of the Vertebral Column in Small Animals

- Vertebral formulae
  - Dog: C7 T13 L7 S3 Cd6-Cd23
  - Cat: C7 T13 L7 S3 Cd18-Cd21
- The articular processes of adjacent vertebrae overlap, with the cranial articular process lying ventral to the caudal articular process of an adjacent vertebra.
  - In the cervical region, the articular processes are oriented in an oblique plane, summating the intervertebral foramina and vertebral canal.
  - In the lumbar region, the articular processes lie in a dorsal plane and do not summate the foramina and canal.
- C1—C2 does not have an intervertebral disc.
- The dens is usually masked on a true lateral projection but is easily recognized on a lateral view made with slight axial rotation (obliquity).
- The spinous processes of C1 and C2 normally are in close proximity, and the dorsal laminae are nearly parallel, on the lateral projection. This normal relationship is important in recognizing atlantoaxial subluxation.
- C6 is distinguished by large transverse process.
- The intervertebral disc spaces of the cervical vertebrae become progressively wider between C2—C3 and C6—C7.
- T1 has a pronounced spinous process compared with C7.
- T11 is the anticlinal vertebra in most dogs; however, T10 may also be designated the anticlinal vertebra.
- The T10—T11 intervertebral disc space is narrower than adjacent disc spaces in most dogs.
- The ventral aspect of the bodies of L3 and L4 are entheses for the diaphragmatic crura and may be indistinct, especially in large dogs.

From Walker MA. The vertebrae—canine and feline. In: Thrall DE, ed. Textbook of Veterinary Diagnostic Radiology. 4th ed. St. Louis: Saunders; 2002:98—109; Baines EQ, Grandage J, Herritage ME, et al. Radiographic definition of the anticlinal vertebra in the dog. Vet Radiol Ultrasound. 2009;50:69—73.

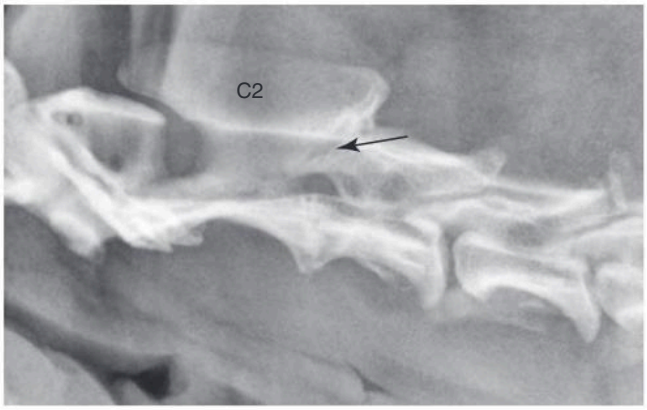


Fig. 14.6 Lateral radiograph of a dog with a block vertebra affecting C2–C3. The intervertebral disc space appears as a thin vertical radiolucent line. A radiolucent line is also visible dorsally at the dorsal articular process joint (*arrow*). These lines signify that complete fusion has not occurred in this dog although there is still increased risk of altered loading of the intervertebral disc at C3–C4, immediately caudal to the fusion.

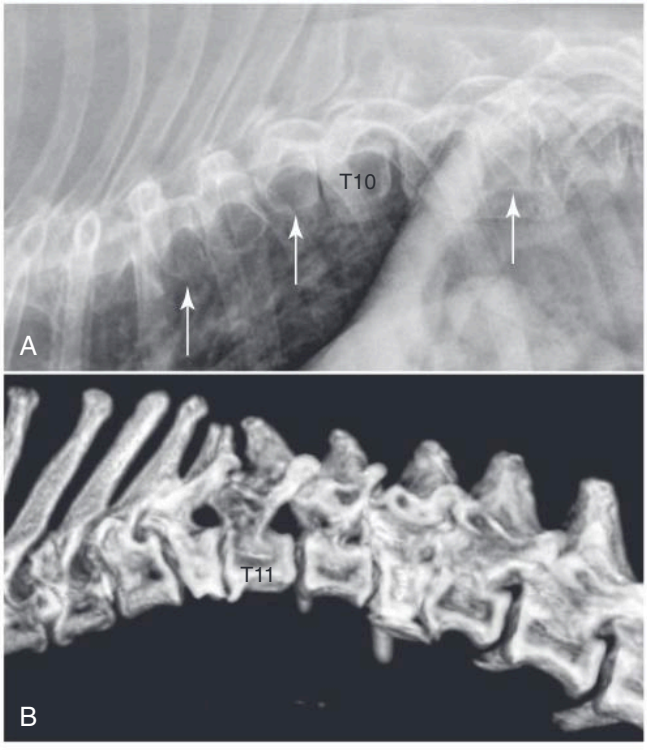


Fig. 14.7 **A,** Lateral thoracic radiograph of a bulldog with multiple hemivertebrae (*white arrows*). **B,** Lateral view of a three-dimensional rendering of the spine of another bulldog. There are hemivertebrae at T10 and T13. *T10,* Tenth thoracic vertebral body; *T11,* eleventh thoracic vertebral body.

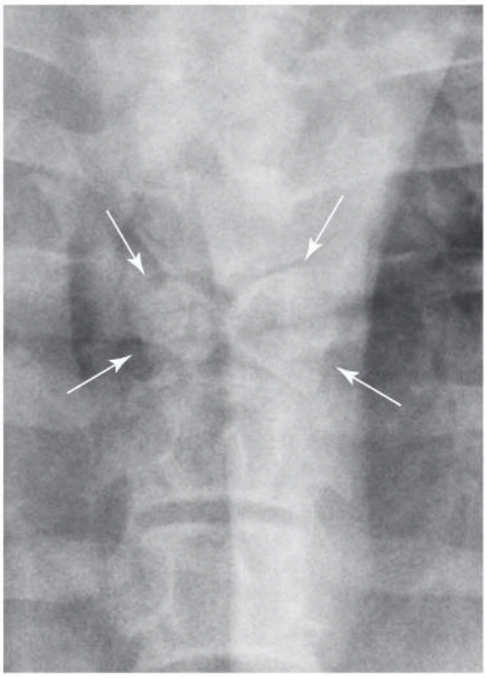


Fig. 14.8 Ventrodorsal (VD) radiograph of the caudal aspect for the thoracic spine in a bulldog. A butterfly anomaly is present (*arrows*).

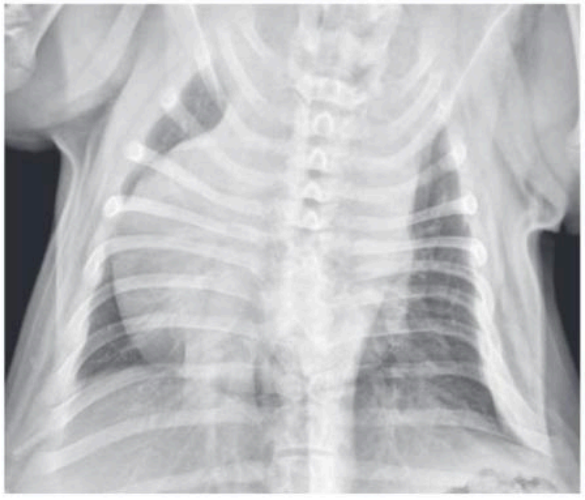


Fig. 14.9 Ventrodorsal (VD) radiograph of a bulldog with multiple thoracic hemivertebrae. The abnormal vertebrae have resulted in thoracic spine foreshortening with secondary crowding of the ribs. This is most noticeable in the left hemithorax.

hemivertebrae are significant clinically, and MRI is required to determine if hemivertebrae are the cause of a spinal neuropathy. A butterfly-shaped vertebra occurs when the midaspect of the body fails to develop, this is best seen on the ventrodorsal (VD) projection[16] (Fig. 14.8). Decreased rib spacing on the VD projection is an important clue that hemivertebrae are present (Fig. 14.9). A hemivertebra should not be confused with a compression fracture; their multiplicity and occurrence in a brachycephalic breed are helpful in this distinction. Also, hemivertebrae have a smoothly marginated cortex, whereas vertebrae affected with a compression fracture have a disrupted margin. The bulldog, French bulldog, Boston terrier, pug and other screw-tail breeds are most affected with hemivertebrae.[12,13]

Transitional Vertebrae

Vertebrae that have characteristics of two different anatomic divisions are known as *transitional vertebrae.*[1,12,17] These anomalies usually involve the vertebral arch rather than the body and occur at cervicothoracic, thoracolumbar, and lumbosacral junctions. The main clinical significance of transitional vertebral anomalies relates to the use of the most caudal ribs as a landmark to identify a site of spinal decompressive surgery. T13 may have malformed, hypoplastic, or absent ribs. L1 may also have ribs, and they may be symmetric or asymmetric. If the most caudal ribs are asymmetric, then surgery can be performed at the incorrect site unless the asymmetry is

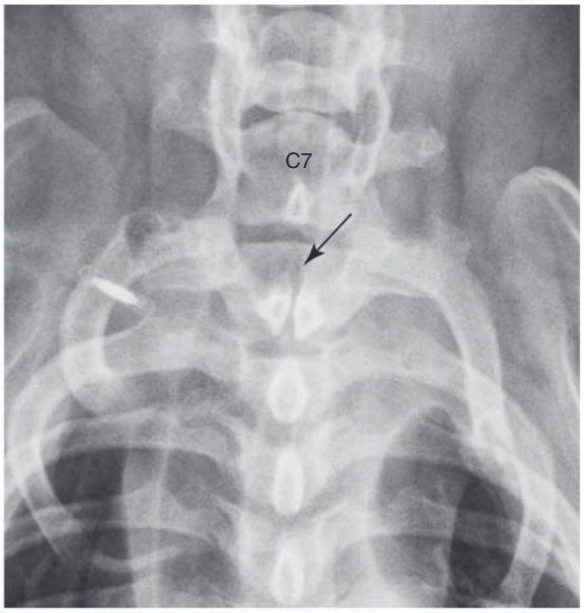


Fig. 14.10 Ventrodorsal (VD) thoracic radiograph of a dog with spina bifida. T1 is characterized by a split spinous process (*arrow*). *C7,* Seventh cervical vertebral body.

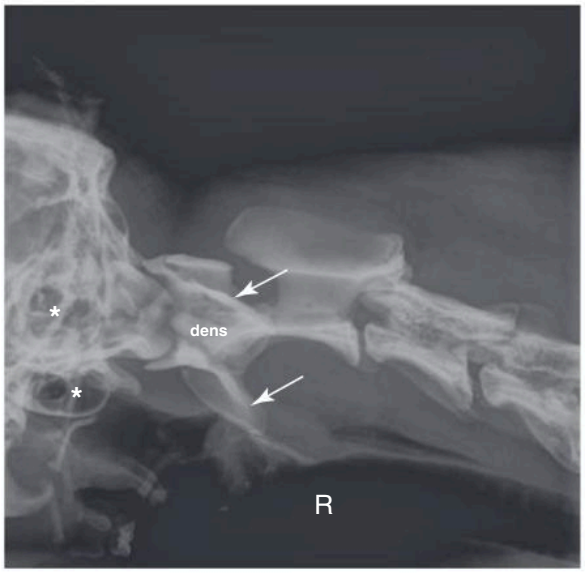


Fig. 14.11 Lateral cervical radiograph of a normal dog. The patient was placed in lateral recumbency and the head and neck were allowed to fall into a natural position on the table; e.g., the head was not rotated into true lateral positioning with the bulla and atlas wings superimposed. *Asterisks* mark the tympanic bullae and the wings of the atlas are denoted by *arrows*. This projection allows good visualization of the dens compared to the standard lateral view where the dens is summated by the lateral masses of the atlas.

recognized. Therefore, the entire spine should be radiographed, or included in CT or MR images, to be certain the thoracolumbar vertebrae are enumerated correctly prior to surgery. Another significant feature of transitional anomalies is the increased incidence of lumbosacral disc disease and nerve root compression that occurs in dogs with a lumbosacral transitional malformation.[18] This relates to the altered, asymmetrical lumbosacral loading that leads to disc degeneration, instability, spondylosis, and nerve root compression. Lumbosacral transitional vertebrae have been established as a risk factor for lumbosacral stenosis in cats.[19] Cats with nontraumatic lumbosacral abnormalities, including absence of L7, transitional vertebra, and L7-S1 degeneration, were at increased risk for constipation and megacolon.[20]

Spina Bifida

Spina bifida results from the lack of development of the vertebral arch and may be associated with neural tube defects—that is, meningocele or meningomyelocele.[1] Typically, there is a cleft in the dorsal part of the vertebral arch and absence or splitting of the spinous process. If the defect in the neural arch is large, a meningocele or meningomyelocele may develop. The most common radiographic manifestation of spina bifida is a split spinous process (Fig. 14.10). There is rarely a neural tube defect in dogs with thoracic spina bifida. At the lumbosacral junction, however, the morphologic derangements are often more severe with absent spinous process, laminar defect, and neural tube defect (eFig. 14.4). MRI is preferred for characterizing the presence and extent of any neural tube defect (see eFig. 14.4). Spina bifida is most common in bulldogs and Manx cats.[13,21]

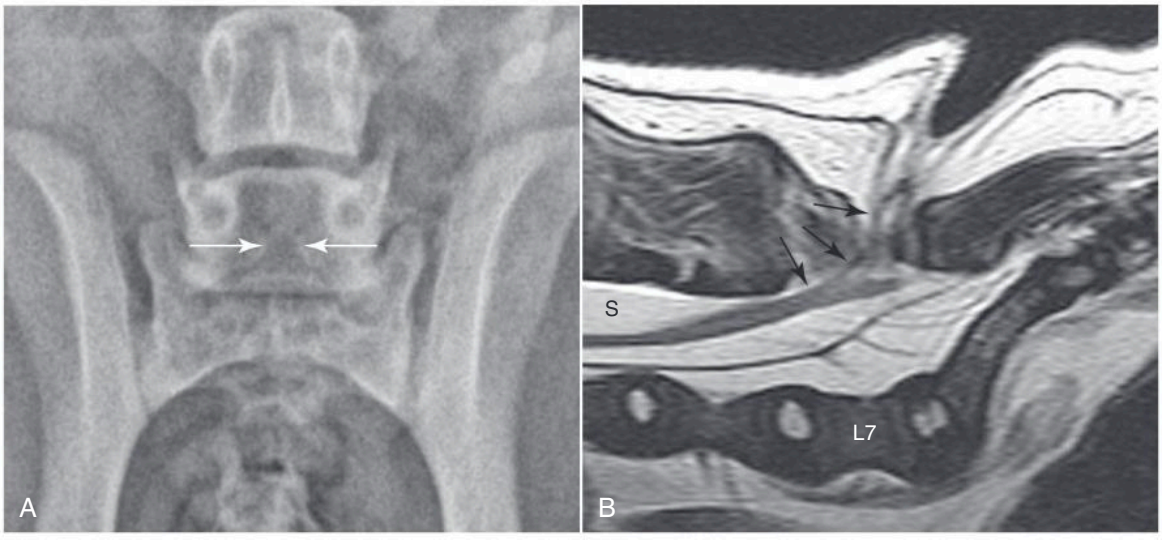
Atlantoaxial Subluxation

In atlantoaxial subluxation, the axis (C2) is displaced dorsally with respect to the atlas (C1), causing extradural compression of the spinal cord. Atlantoaxial subluxation can be a result of either congenital malformation or trauma.[13,21,22] With congenital malformation, the dens is often absent or incompletely ossified,[23] and there may be deficiencies in the ligaments that support the atlantoaxial joint and prevent flexion (see Fig. 14.4). The clinical signs may be acute with trauma or chronic with congenital malformation and are characterized mainly by pain and cervical neuropathy.

A variety of lesions may occur in association with atlantoaxial subluxation, and a working knowledge of the components of the atlantoaxial region is needed for radiographic interpretation.[1,2] Malformation or rupture of the transverse ligament of the atlas frequently leads to atlantoaxial subluxation. This ligament bridges the ventral aspect of the vertebral arch and stabilizes the dens, preventing the rostral aspect of the axis from impinging on the spinal cord (see Fig. 14.4B). A short apical ligament connects the tip of the dens with the occiput along with the alar ligaments (see Fig. 14.4B). A short, dorsal atlantoaxial ligament is also present dorsally (see Fig. 14.4A). Atlantoaxial subluxation caused by congenital predisposition is most common in toy breed dogs, such as the Yorkshire terrier, but acquired atlantoaxial subluxation can occur in any breed.

Atlantoaxial subluxation is best diagnosed radiographically on a lateral projection of the cranial aspect of the cervical spine. When subluxation is suspected, the patient should be handled carefully, especially when tetraparetic, and the head and neck should not be flexed, because this could exacerbate spinal cord damage, especially if the dens is present. On a routine lateral radiograph, the dens is masked by the sheer mass of the atlas. Making a left 15- to 30-degree ventral/right dorsal radiograph will reduce osseous superimposition on the dens and help identify fractures and malformations. A similar radiographic projection can often be made if there is no attempt to obtain a true lateral projection, for example, allowing the axial rotation of the head and neck ventrally (Fig. 14.11). Even with this projection, small fractures may not be apparent. VD projections can also be made, but there is the risk of exacerbating the spinal cord compression, especially in anesthetized patients. The VD projection is unnecessary to confirm atlantoaxial subluxation. The lateral radiographic view is usually diagnostic and two typical findings should be identified:

- If subluxation is present, the axis is displaced dorsally, widening the distance between the vertebral arch of the



eFig. 14.4 **A,** Ventrodorsal (VD) radiograph of a dog with spina bifida. There is no spinous process on L7, and the lamina has a dorsal defect (*white arrows*). **B,** Sagittal T2-weighted magnetic resonance (MR) image of the dog in **A**. Nerve roots (*black arrows*) track dorsally through the laminar defect. There is a large syrinx (*S*) in the caudal aspect of the lumbar spinal cord. *L7,* Seventh lumbar vertebral body.

atlas and the spinous process of the axis. Atlantoaxial instability is characterized by a decreased C1–C2 overlap.[24]

- Most important, the normal linear relationship between the dorsal lamina of the atlas and the dorsal lamina of the axis becomes angular (Fig. 14.12).

Multiple indices to evaluate the relationship between the lamina of C1 and C2 have been described.[24] CT is useful for assessing the morphology of the atlantoaxial junction if surgical stabilization is contemplated (see Fig. 14.12).

Incomplete Ossification of the Atlas

Three centers of ossification fuse to form the atlas and this process is normally complete by approximately 4 months of age. Incomplete ossification can lead to osseous defects at the junction of the centers of ossification and may lead to instability and atlantoaxial subluxation. Surgical stabilization may be necessary in dogs with clinical signs (Fig. 14.13).[25]

Cervical Spondylomyelopathy

Cervical spondylomyelopathy is included under anomalies because anomalous development of vertebrae or inadequate soft tissue stabilization is likely to play a role in manifestation of clinical signs. Cervical spondylomyelopathy encompasses a variety of pathologic changes that are not all seen in every affected animal.[21,26–30] Abnormalities include malformation of the vertebral body and articular processes, malarticulation, instability and malalignment, and stenosis of the vertebral canal. Secondary changes involve dorsal longitudinal ligament and ligamentum flavum hypertrophy and Hansen type II disc protrusion and/or herniation. The end result and cause of clinical signs are static or dynamic extradural cervical spinal cord compression.

The pathophysiology of canine spondylopathy is complex and understood incompletely.[26–28,31] There is debate as to whether vertebral changes are caused by strict malformation of

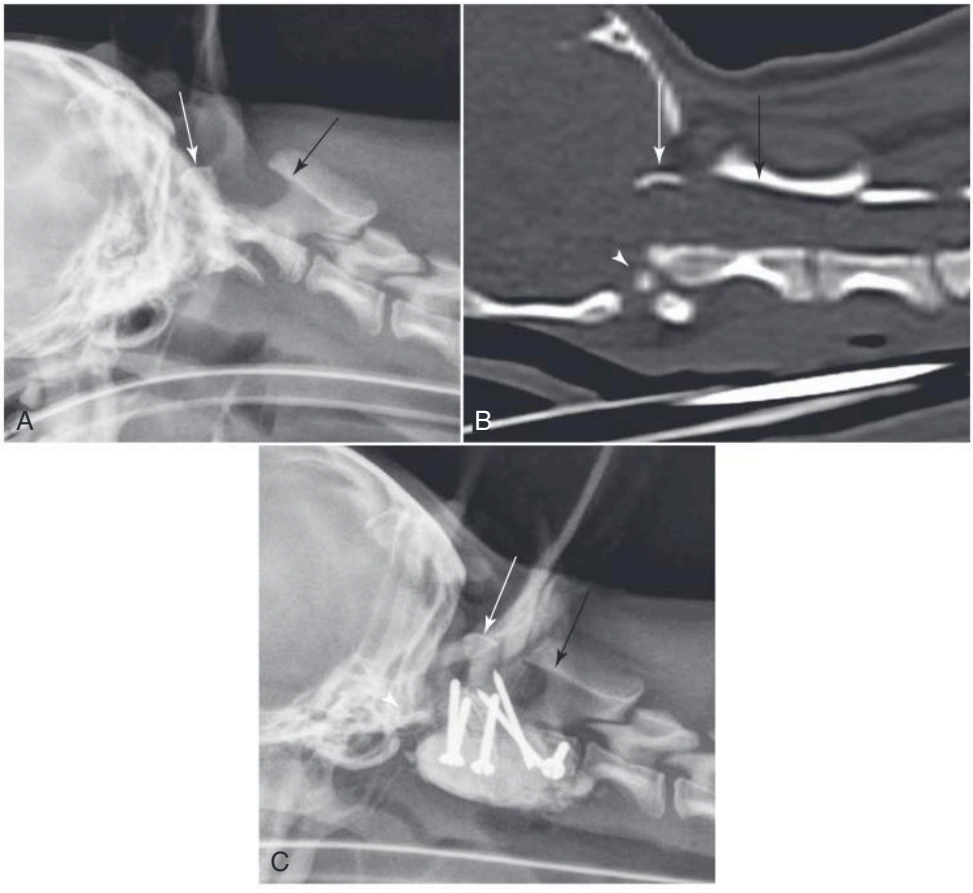


Fig. 14.12 **A,** Lateral radiograph of the cranial aspect of the cervical spine of a dog with an atlantoaxial subluxation. The key to diagnosing atlantoaxial subluxation radiographically is to assess the angular relationship between the lamina of these two vertebrae. Clearly in this dog, the lamina of the atlas (*white arrow*) is not parallel with the lamina of the axis (*black arrow*). A parallel, or nearly parallel, relationship between these structures is normal, whereas a nonparallel relationship indicates malalignment. **B,** Sagittally reformatted computed tomography (CT) image of the cranial aspect of the cervical spine of the dog in **A**. The atlantoaxial subluxation has been reduced spontaneously during positioning of the dog for the CT study. The dorsal lamina of the atlas (*white arrow*) and dorsal lamina of the axis (*black arrow*) are parallel, although there may be some cranial displacement of C2. There is a small avulsion fracture of the apical aspect of the dens (*white arrowhead*) that likely contributed to the instability and subluxation. **C,** Postoperative radiograph of the dog in **A**. Screws and pins have been inserted into the body and transverse processes of C1 and the body of C2 and embedded in methylmethacrylate. The dorsal laminae of the atlas (*white arrow*) and axis (*black arrow*) are nearly parallel. This is a normal angular relationship of these laminae.

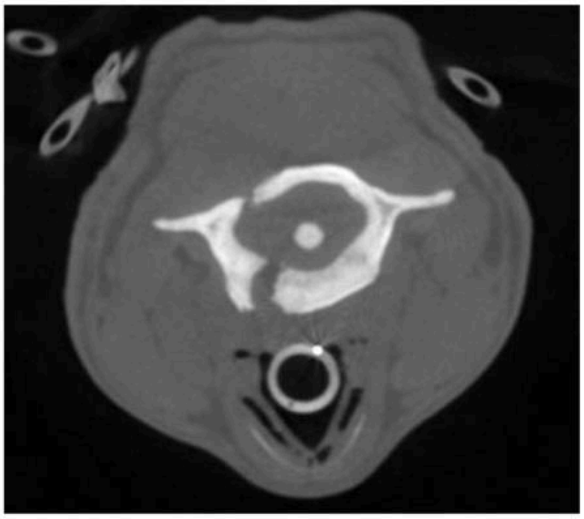


Fig. 14.13 Transverse computed tomography (CT) image of the atlas of a dog with incomplete ossification. There is a focal defect in the body and lamina of the C1 vertebra with mild dislocation of the separated segment. The dens is visible as a round osseous structure in the ventral aspect of the vertebral canal.

the vertebrae or result from remodeling due to underlying instability of the vertebral column. Because of the uncertain etiology, there are multiple synonyms for this condition, including cervical spondylomyelopathy, cervical spondylopathy, cervical vertebral malformation-malarticulation, cervical vertebral stenotic myelopathy, and wobbler syndrome, with the latter arising from the fact that affected animals are often ataxic with a wobbling or swaying gait. No term is accepted universally.[21,28] *Cervical spondylomyelopathy* is used in this discussion.

Cervical spondylomyelopathy is common in young Great Danes and mature Doberman pinschers, but there are many other large breeds that can be affected.[26–28] In the Doberman pinscher, vertebral canal stenosis, Hansen type II disc protrusion and/or herniation, and dorsal annulus fibrosus and dorsal longitudinal ligament hypertrophy are common.[27–30] Affected vertebrae sometimes have cranioventral flattening because of abnormal formation or remodeling. There can also be stenosis of the vertebral canal that results from underdevelopment of the pedicles (Fig. 14.14). This can result in the vertebral canal appearing cone shaped over the length of a vertebra, with it being narrower at the cranial aspect of the vertebra.[26,28]

Cervical spondylomyelopathy in the Great Dane is characterized primarily by articular process malformation and hyperostosis. The hyperostotic articular processes commonly extend medially and ventrally into the vertebral canal and cause extradural spinal cord compression (Fig. 14.15, eFig. 14.5). Vertebral measurements made from the mediolateral projection have been used to assess cervical spondylomyelopathy in Doberman pinschers.[32] Because the pathologic changes between Doberman pinschers and Great Danes often differ, a new method of vertebral mensuration has been proposed in Great Danes, using the VD projection.[33] This method uses the ratio of the distance between the articular process joints versus vertebral body width to screen for suspected cervical spondylomyelopathy. The rationale for this method is that hypertrophy of the articular process joints resulting in dorsolateral canal stenosis is a fundamental change in the Great Dane and is best recognized on the VD projection.

Although the differences in the manifestation of cervical spondylomyelopathy in the Doberman pinscher versus the Great Dane have been described,[27–30] it is important to realize that any individual dog of these breeds or others can have any combination of the changes described.

As should be apparent from Figs. 14.14 and 14.15, survey radiographic changes of cervical spondylomyelopathy may be sufficient to suggest the diagnosis, but conventional myelography, CT, CT myelography, and MRI are necessary to evaluate the location and severity of compressive extradural lesions. MRI is the modality of choice, because it allows assessment of the integrity of the spinal cord in addition to providing for identification of the osseous changes, disc herniation or protrusion, ligamentous hypertrophy, and synovial cyst formation (see Figs. 14.14 and 14.15).[34,35] Although controversial, obtaining myelographic projections with linear traction, flexion, and extension of the cervical spine, in addition to conventional projections, has been advocated to identify the presence of dynamic compression.[26,30] Although these maneuvers might provide insight for surgical decision making, flexion and extension place the anesthetized patient at risk for exacerbation of spinal cord damage. Linear traction, as illustrated in Fig. 14.14, is not likely to be harmful, but its clinical value is questionable. Table 14.1 provides a summary of imaging signs of cervical spondylomyelopathy.

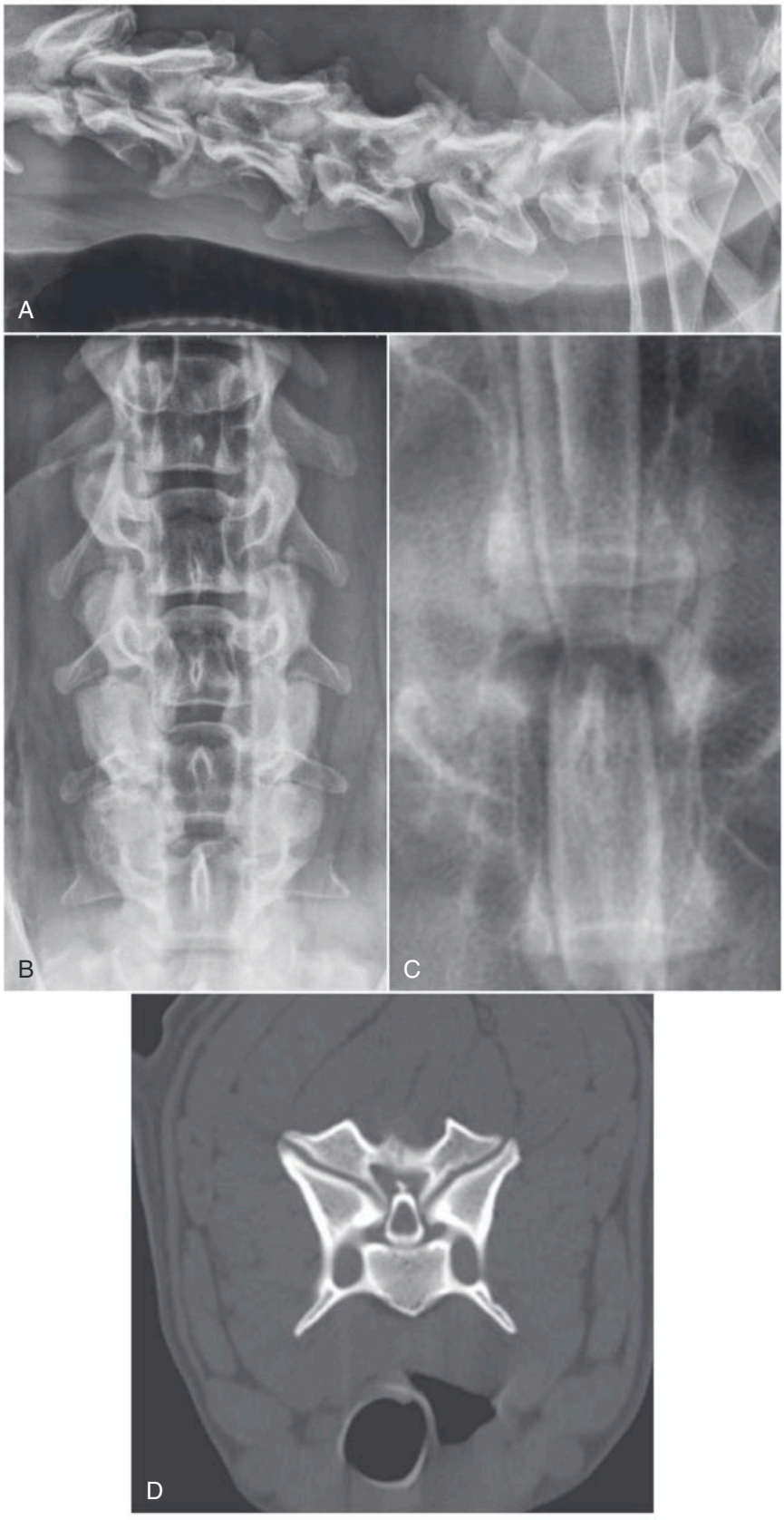
FRACTURE AND LUXATION

Vertebral fracture is usually a result of being hit by a motor vehicle, falling, or gunshot injury.[36] Many vertebral fractures and luxations occur at regional junctions, for example, atlantooccipital, atlantoaxial, cervicothoracic, thoracolumbar, and so forth.[37–39] These junctions may be more subject to flexion-extension and torsion and axial loading compared with the vertebrae within a region. Radiographic features of vertebral fractures include asymmetry, specifically of the articular processes and endplates; displacement of a vertebra with respect to adjoining vertebrae (malalignment); and comminution of the endplate or body. Any fracture has the potential to cause narrowing of the vertebral canal and spinal cord contusion and/or compression. Shortening of the vertebral body and spinal malignment are often seen with compression fractures of the thoracic vertebrae and L7 (Fig. 14.16).[40]

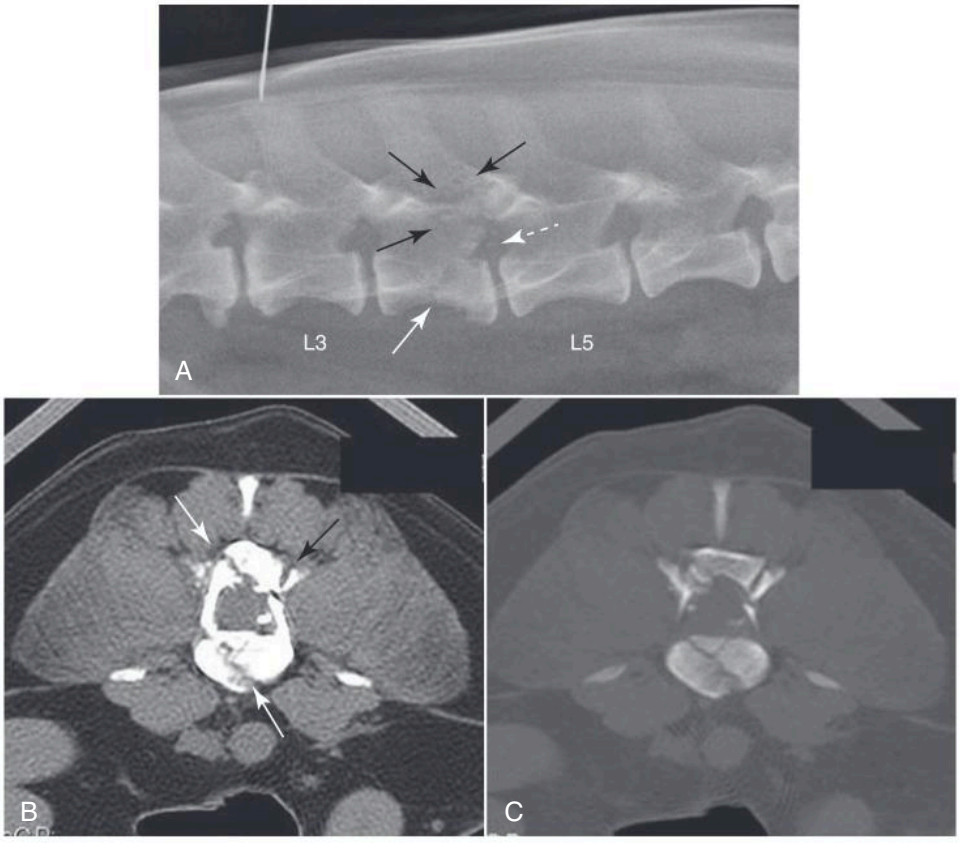
Radiographic evaluation of patients with suspected vertebral fractures is limited by summation and failure to obtain accurate positioning or an adequate number of projections. Patients with vertebral column trauma are frequently unstable and medically unable to receive chemical restraint. In addition, maneuvers to obtain correct positioning may be detrimental to existing spinal trauma, especially VD projections. Flexion, extension, and traction should never be used in animals with spinal trauma. One approach is first to obtain only lateral projections of the spine of patients with a suspected vertebral fracture without or with minimal sedation to avoid further instability after muscle relaxation. If a suspected fracture is seen, a horizontally directed x-ray beam can be used to obtain VD projections. This principle was discussed and illustrated in Chapter 9.

Because of its tomographic nature, CT is superior to radiography for identifying and characterizing vertebral fractures (Fig. 14.17, eFigs. 14.6 and 14.7). In 30 dogs with acute spinal trauma, radiographic sensitivity for fractures and luxations was only 72% and 77%, respectively, and fracture fragments within the vertebral canal and narrowing of the vertebral canal were often unrecognized.[41]

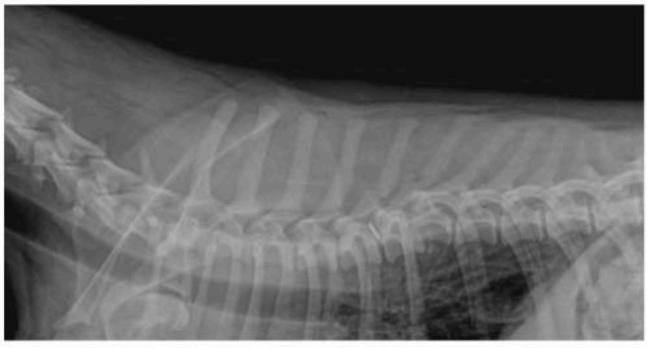
A three-compartment approach has been advocated for evaluating the severity and instability of vertebral fractures and luxations.[36,41] The vertebra is divided into three areas: dorsal, middle, and ventral. The dorsal compartment contains the



eFig. 14.5 Lateral **(A)** and ventrodorsal **(B)** radiographs, ventrodorsal myelogram **(C)**, and transverse computed tomography (CT) myelographic image **(D)** of the caudal cervical spine of a Great Dane with cervical spondylomyelopathy. Radiographically **(A** and **B)**, the articular process joints are enlarged and irregular, but the presence and degree of spinal cord compression cannot be determined. Latero-lateral narrowing of the spinal cord is seen in the myelogram **(C)**. CT-myelography provides the best assessment of the extent of spinal cord compression. The enlarged articular process joints cause dorsolateral spinal cord compression with a resulting triangular appearance of the spinal cord **(D)**.



eFig. 14.6 Lumbar fracture in a dog with lumbar pain after being hit by a car. **A,** Zoomed area of a lateral radiograph of the lumbar region. Note open trabecular bone pattern in lamina pedicles of L4 (*black arrows*). There is discontinuity of the centrum of L4 consistent with a fracture line (*white arrow*). Fracture fragments are seen within the intervertebral foramen (*dasbed white arrow*). These changes are easily overlooked if images on a digital display are not zoomed for interpretation. Incidental findings include narrowing of the intervertebral disc space, endplate sclerosis, and ventral enthesophytes at L2—L3. A needle was placed at the dorsal spinous process of L3 to mark the area of pain detected on neurologic examination. **B** and **C,** Follow-up computed tomography (CT) study of the same dog as in **A**. **B,** Transverse plane image with soft tissue window setting and 2-mm slice thickness. There is extensive comminution consistent with a *burst* fracture of L4. *Arrows* depict multiple fractures through the centrum and vertebral arch. A fragment is also apparent within the vertebral canal. **C,** Same CT image slice as in **B** with bone window setting. Compared to **B,** fracture margins are better defined due to superior image sharpness. However, both image windows are useful as the soft tissue window is superior for assessing soft tissue injury common with spinal fractures.



eFig. 14.7 Lateral radiograph of a dog presented after being hit by a car. T7 is dorsally displaced relative to T6 and a small osseous fragment is seen ventral to T7. The spinous processes of T5 and T6 are fractured. A ventrodorsal projection would be needed to fully assess the injury as lateral displacement may not be visible in this image.

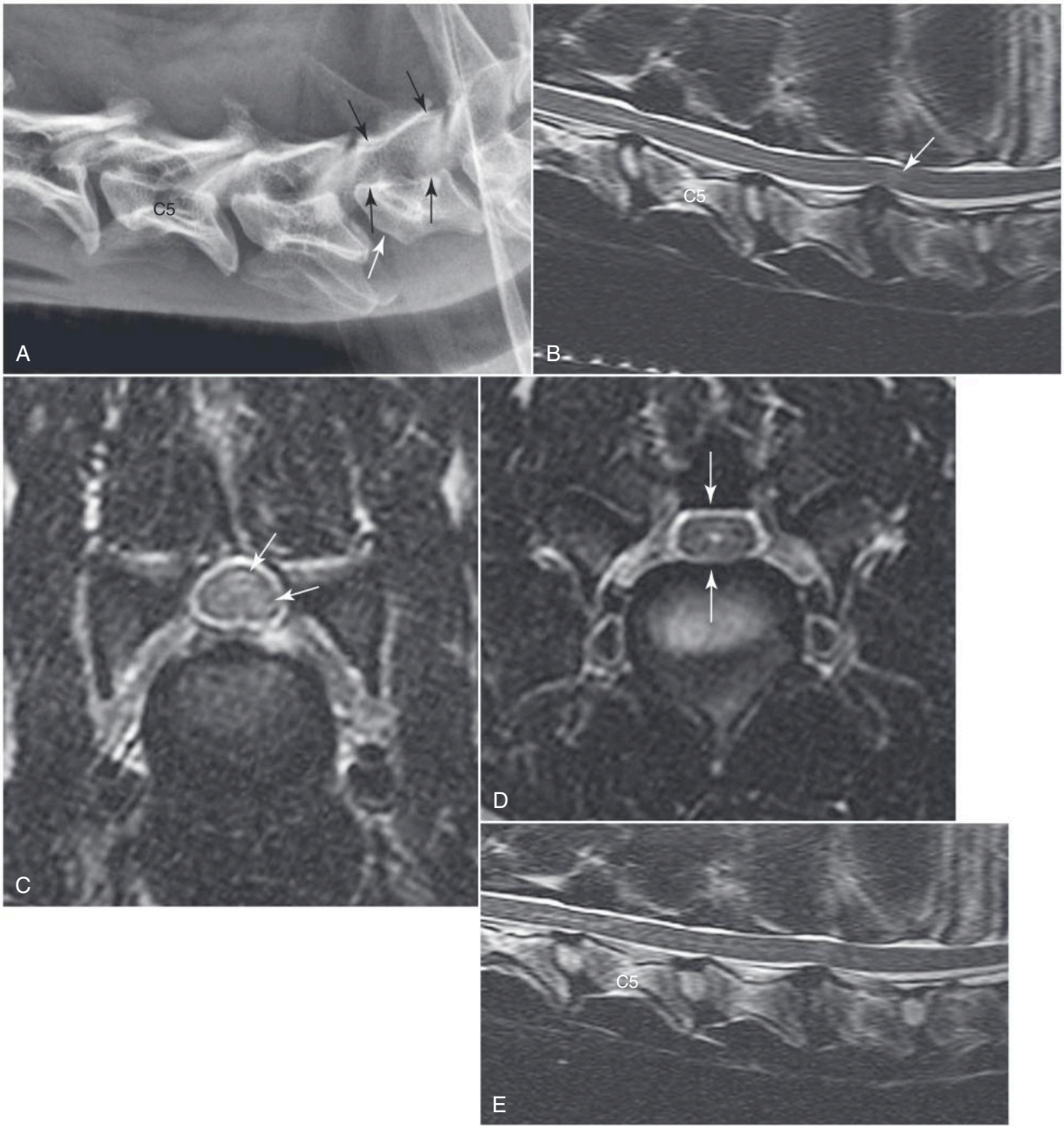


Fig. 14.14 Images from a 6-year-old Doberman pinscher with clinical signs of cervical spondylomyelopathy. **A,** Lateral cervical radiograph. The cranioventral aspect of C7 is flat (*white arrow*). The diameter of the vertebral canal is narrower, or cone shaped, at the cranial aspect of C7 than at the caudal aspect of C7 (*black arrows*). **B,** Sagittal T2-weighted image. There is a hypointense mass in the ventral aspect of the vertebral canal at C6—C7 that is causing extradural spinal cord compression; this is consistent with disc protrusion and/or hypertrophy of the dorsal longitudinal ligament as a result of chronic instability. The spinal cord has a faint area of T2 hyperintensity (*white arrow*) consistent with bruising from the chronic compression. There also is narrowing of the spinal cord at C4—C5. **C,** Transverse T2-weighted image of the spinal cord at C6—C7. There is only mild spinal cord compression, but the intramedullary T2 hyperintensity caused by chronic compression is obvious (*white arrows*). For comparison, the signal of the spinal cord in **D** is normal. **D,** Transverse T2-weighted images of the spinal cord at C4—C5. There is extradural compression of the spinal cord (*white arrows*) because of laminar malformation with secondary vertebral canal stenosis. The signal of the spinal cord is normal; compare this spinal cord signal to the bruised spinal cord in **C**. This compression at C4—C5 was not detected radiographically. **E,** T2-weighted sagittal image acquired with traction placed on the head. The amount of extradural spinal cord compression at C6—C7 is reduced compared with that present in **A,** which was made without traction. In cervical spondylomyelopathy, traction-responsive compression is attributed to hypertrophy of the dorsal longitudinal ligament rather than disc herniation. This has implications for the type of corrective surgery to be done. *C5,* Fifth cervical vertebral body.

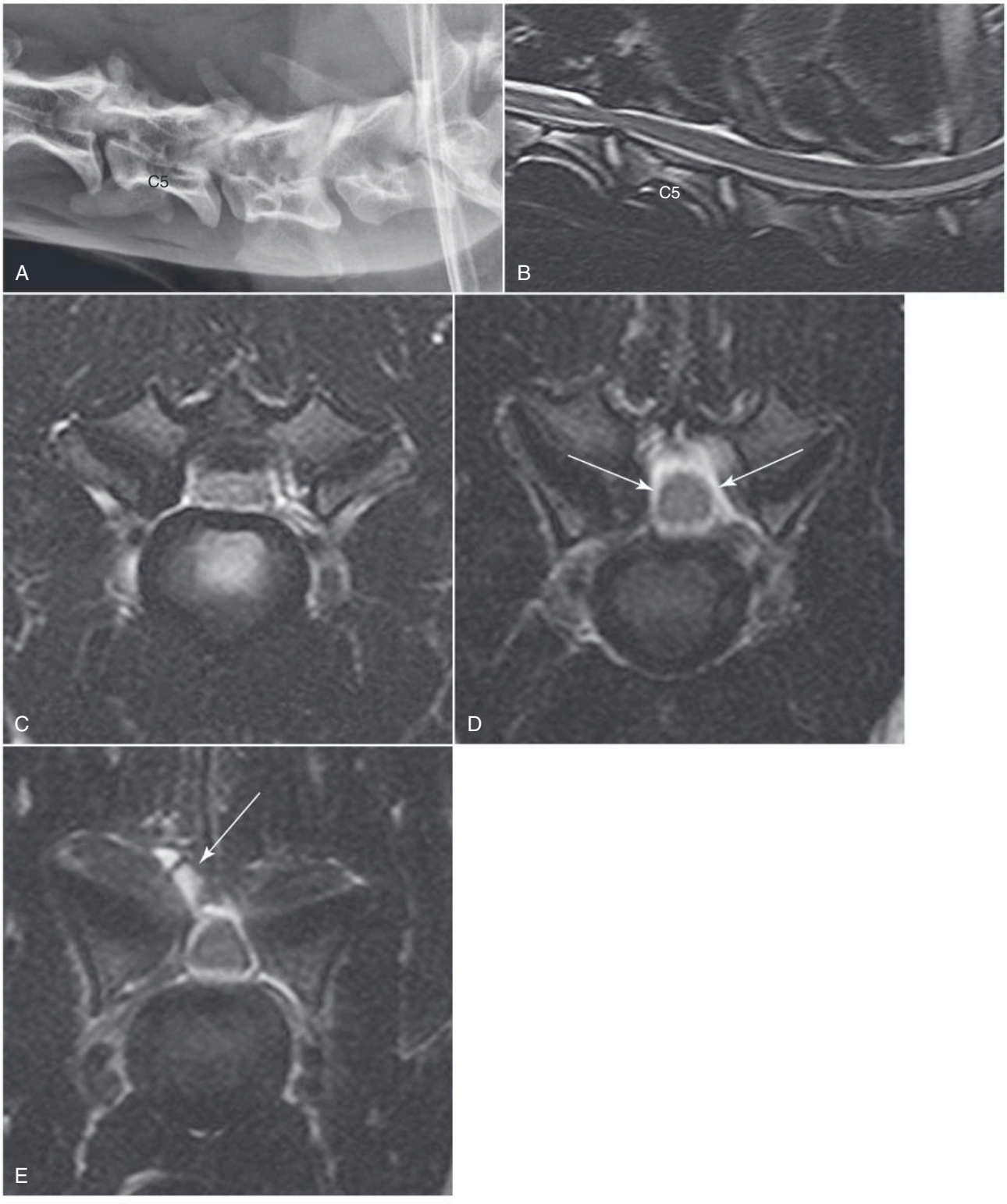


Fig. 14.15 Images from a 2-year-old Great Dane with clinical signs of cervical spondylomyelopathy. **A,** Lateral cervical radiograph. There is moderate to pronounced articular process degenerative joint disease at C4—C5, C5—C6, C6—C7, and C7—T1. These changes occur commonly as a consequence of articular process malformation or instability, or both. What cannot be determined from cervical radiographs is whether the articular process malformation is impinging on the vertebral canal. **B,** T2-weighted sagittal image of the cervical spine. There is mild ventral and marked dorsal extradural compression of the spinal cord at C4—C5. The dorsal compression is typical of laminar malformation leading to vertebral canal narrowing. **C,** Transverse T2-weighted image at C4—C5. The dorsal compression from the laminar malformation is obvious. **D,** Transverse T2-weighted image at C5—C6. At this site, there is bilateral vertebral canal narrowing with extradural spinal cord compression (*white arrows*) that results from the hyperostotic malformed articular processes extending into the vertebral canal. **E,** Transverse T2-weighted image at C6—C7. As at C5—C6, there is articular process malformation and hyperostosis that extends into the vertebral canal and causes extradural spinal cord compression. There is also an articular process synovial cyst (*white arrow*). Synovial cysts develop secondary to the degenerative joint disease and, if large enough, they can extend into the vertebral canal and contribute to the extradural spinal cord compression; in this dog, this cyst is not causing neural compression. The lateral vertebral canal narrowing seen at C5—C6 and C6—C7 was not apparent radiographically. *C5,* Fifth cervical vertebral body.

Table • 14.1

Summary of Typical Imaging Signs of Cervical Spondylomyelopathy.

ABNORMALITY	RADIOGRAPHY	MYELOGRAPHY	COMPUTED TOMOGRAPHY[A]	MAGNETIC RESONANCE[B]
Vertebral body malformation	√	√	√	√
Vertebral canal stenosis	√	√	√	√
Vertebral malalignment	√	√	√	√
Vertebral tipping	√	√	√	√
Articular process remodeling	√	√	√	√
Disc degeneration/prolapse	—	√	√	√
Extradural spinal cord compression	—	√	√	√
Ligamentum flavum, interarcuate ligament, or joint capsule hypertrophy	—	—	—	√

[a]Identifying vertebral malformation, tipping and malignant, is dependent on obtaining sagittal MR images or high-quality sagittally reformatted computed tomography images. Stenosis is apparent on transverse images.
[b]Magnetic resonance is true multiplanar imaging, and it is assumed that dorsal and sagittal, as well as transverse, images are acquired.

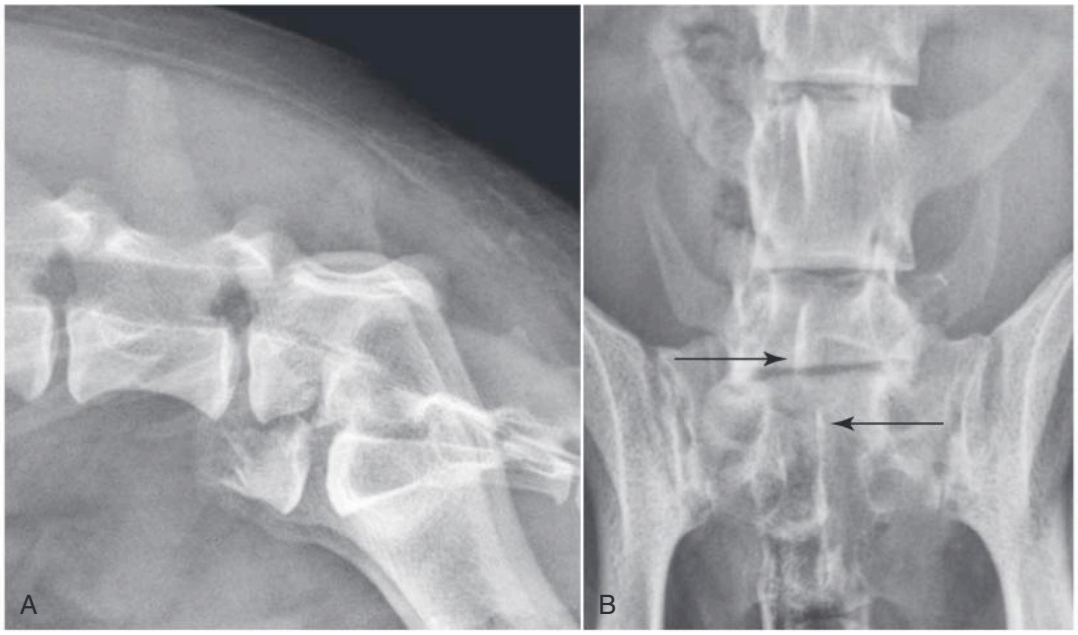


Fig. 14.16 Lateral **(A)** and ventrodorsal (VD) **(B)** radiographs of a dog with a comminuted L7 fracture. In **A,** the caudal fragment is displaced ventrally and cranially because of contraction of the spinal hypaxial muscles. The fracture is obvious in the lateral view. In **B,** L7 is foreshortened; and unless this is recognized, the fracture would be missed if the lateral view were not available. There is slight sagittal malalignment of the spinous processes of L7 and S1 (*black arrow*s) because of axial rotation of the caudal fragment, but this is subtle.

vertebral arch, articular processes, and supportive ligaments; the middle compartment contains spinal cord, dorsal longitudinal ligament, annulus fibrosus, and the dorsal margin of the body; and the ventral compartment includes the remainder of the vertebral body, the annulus, and the ventral longitudinal ligament. If more than one compartment is involved, the fracture-luxation is likely unstable and requires stabilization.[36]

With vertebral fractures and luxations, soft-tissue injury is invariably present and may involve the spinal cord, intervertebral discs, ligaments, and joint capsules. Blunt trauma-induced supraphysiologic forces can result in herniation of the nucleus pulposus of a normal disc (so-called *acute nonprogressive nucleus pulposus extrusion* [ANNPE]). CT, or preferably MRI, should be considered in all animals with vertebral injury, especially if spinal cord impingement is suspected clinically.

INTERVERTEBRAL DISC DISEASE

Clinical signs of intervertebral disc disease result from extension of disc material into the vertebral canal, compressing the spinal cord or spinal nerve roots.[42,43] Descriptive terms used relative to disc lesions are overlapping and include *protrusion, hernia, extrusion, expulsion,* and *prolapse*. The distinction among these lesions cannot be made with conventional radiography and can be difficult even with CT and MRI or at

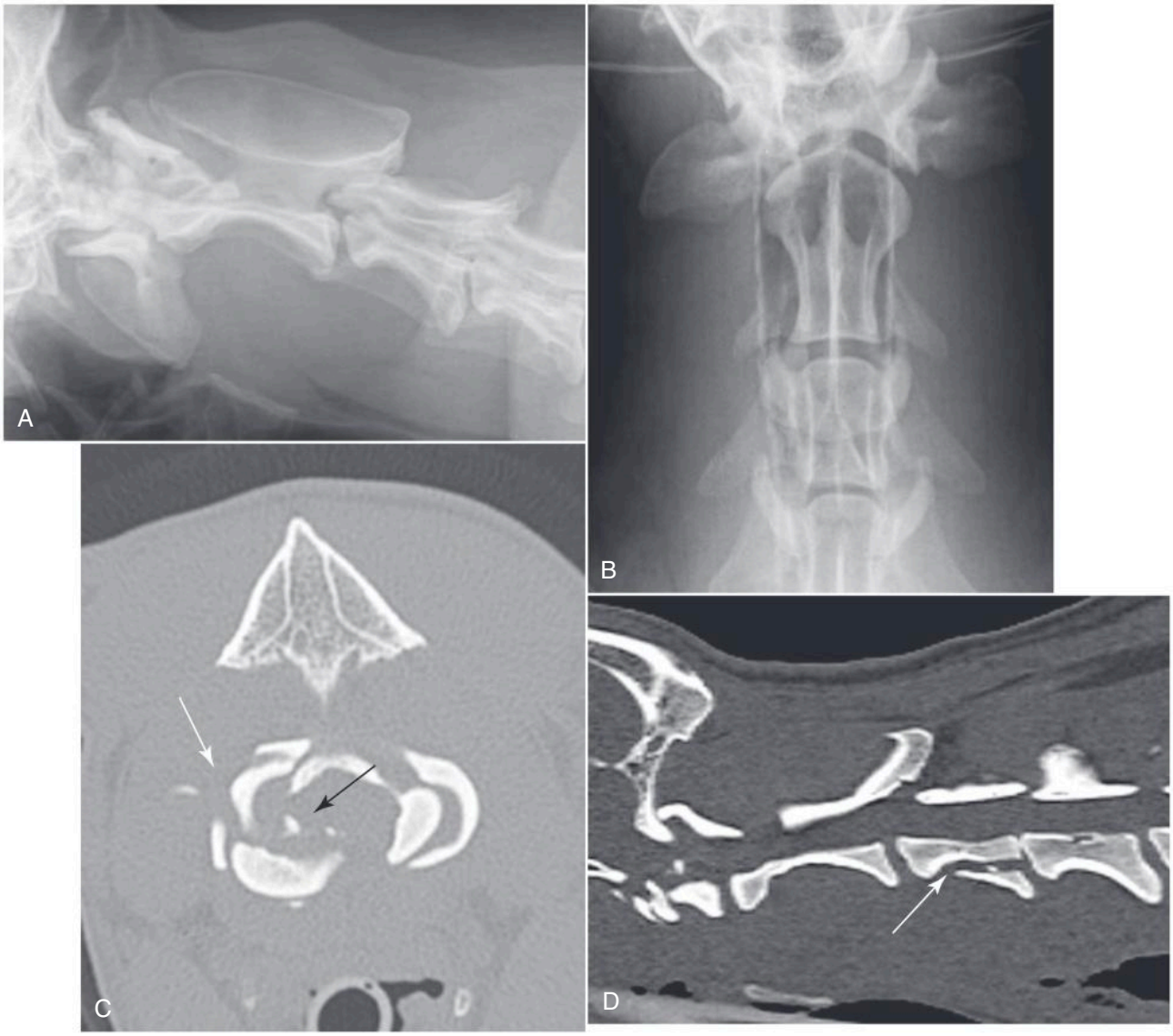


Fig. 14.17 Lateral **(A)** and ventrodorsal (VD) **(B)** radiographs of a dog that was hit by a car. There are severe neurologic signs pointing to a cervical spinal cord injury. In the lateral view, there is narrowing of the C3–C4 disc space and mild subluxation with mild dorsal displacement of the cranial aspect of C4 with respect to C3. The atlas looks very abnormal, but this region is rotated and cannot be assessed. Misdiagnosis of a C1 fracture is common in malpositioned cervical radiographs. In the VD view, there is angulation at the atlanto-occipital articulation, but specific injuries cannot be identified. In a transverse computed tomography (CT) image of the atlanto-occipital junction **(C)**, there are obvious fractures of the occipital bone (*black arrow*) and C1 (*white arrow*). In a sagittally reconstructed cervical image **(D)**, there is also an obvious fracture of C3 (*white arrow*). CT was needed in this dog to identify the traumatic bone injuries accurately.

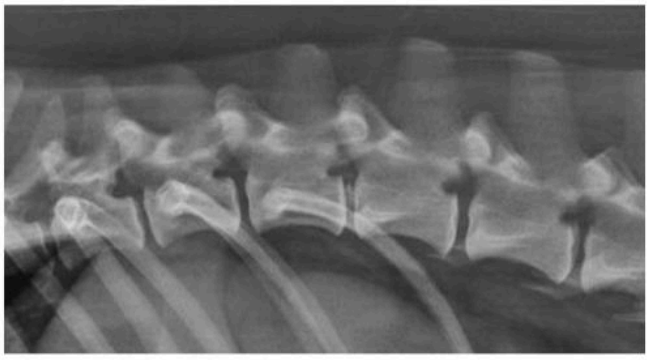
surgery. *Herniation* will be used here to describe any discal mass that is impinging on the spinal cord or spinal nerve roots. Up-to-date classification schemes and nomenclature for intervertebral disc disease are afforded by cross-sectional imaging with CT and MRI, and discussed in Chapter 15. An extensive review of various imaging methods used for intervertebral disc disease has been recently published.[44]

Chondrodystrophic breeds are most commonly affected,[45] but intervertebral disc disease can occur in any breed, including Doberman pinschers with cervical spondylomyelopathy and German shepherds with cauda equina syndrome. Common sites of disc herniation are C2–C3, C3–C4, T12–T13, and T13–L1. Although clinical signs of intervertebral disc disease are uncommon in cats, cervical disc degeneration frequently occurs in cats older than 6 years old.[43]

The sensitivity and specificity of survey radiography to determine the site and severity of disc herniation are poor compared with CT and MRI. Currently, the most important use of survey radiography in animals with signs of intervertebral disc disease is ruling out other conditions, such as a fracture, luxation, or aggressive bone lesions.

Radiographic signs consistent with intervertebral disc disease include one or more of the following[46]:

- Narrowing of the intervertebral disc space
- Narrowing of the intervertebral articular process joint space
- A small intervertebral foramen
- Increased opacity within the intervertebral foramen
- Mineralized disc material within the vertebral canal (Fig. 14.18, eFig. 14.8).



eFig. 14.8 Lateral radiograph of the thoracolumbar spine of a dog with intervertebral disc disease. The T13–L1 intervertebral disc space is narrowed. The intervertebral foramen is narrowed as well and increased in opacity. Some mineralized disc material is visible within the disc space. These findings are not conclusive for a spinal cord compressive lesion being present at this site, and advanced imaging such as computed tomography (CT) or magnetic resonance imaging (MRI) or, if not available, myelography will be needed to evaluate the spinal cord.

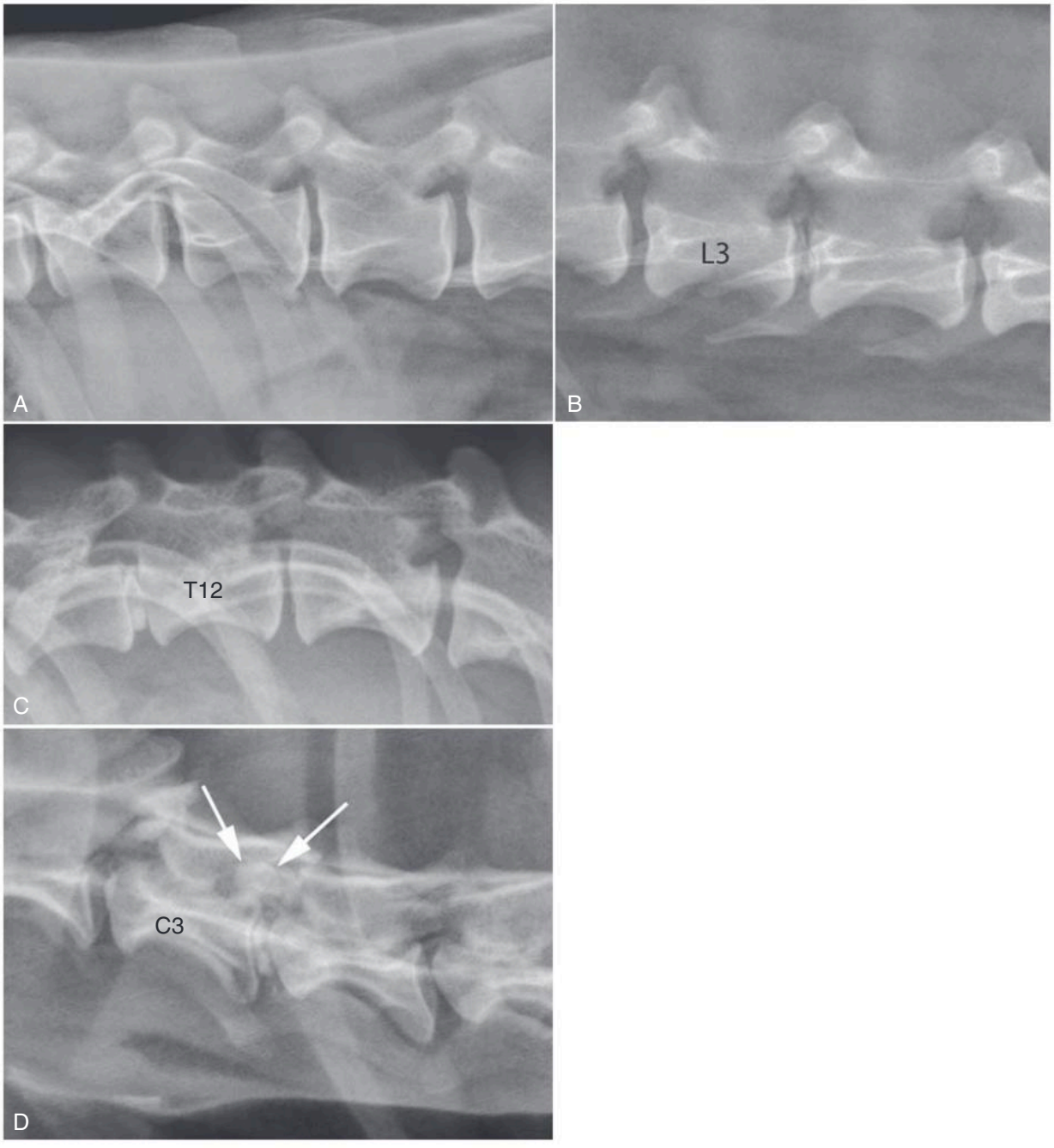


Fig. 14.18 Survey radiographic signs of intervertebral disc disease. **A,** The intervertebral disc space, intervertebral foramen, and dorsal articular process joint space at L1—L2 are all decreased in size compared with adjacent vertebrae. These signs result from vertebrae adjacent to the disc herniation moving closer together. Mild spondylosis deformans is present at L1—L2. **B,** Mineralization of the disc at L3—L4 and mineralized material superimposed over the intervertebral foramen, consistent with mineralized disc material in the vertebral canal. The disc at L3—L4 has not herniated completely; some residual disc material remains between the vertebral endplates. The intervertebral foramen at L3—L4 is slightly smaller than the foramen at L4—L5. **C,** The intervertebral disc space, intervertebral foramen, and dorsal articular process joint space at T12—T13 are all decreased in size compared with adjacent vertebrae. As in **A,** these signs are caused by vertebrae adjacent to the affected disc moving closer together. There is in situ mineralization of the disc at T11—T12. This is not important clinically and signifies only degeneration of the disc. **D,** Mineralization of the disc at C3—C4, with a narrow disc space. The cervical articular processes are larger than in the thoracic or lumbar region and are typically superimposed on the intervertebral foramina, making assessment of cervical foramina more difficult. However, a large mineralized opacity is visible in a position consistent with it being in the vertebral canal (*white arrows*). Confirmation that this opacity is within the vertebral canal requires additional images or modalities. *C3,* Third cervical vertebral body; *L3,* third lumbar vertebral body; *T12,* twelfth thoracic vertebral body.

Careful radiographic technique is critical for interpretation of these changes, keeping in mind that some patients presenting with clinical signs of disc disease may not have any radiographic changes.[47] While narrowing of disc spaces is the most reliable survey sign of disc herniation, false-positives are common.[48] For example, in normalcy, disc spaces at T10–T11 and L5–L6 are usually narrower than adjacent disc spaces. Following hemilaminectomy or fenestration, disc spaces may be narrow in asymptomatic animals. Midsize to large-breed dogs with chronic intervertebral disc disease may have multiple narrowed disc spaces that do not correlate with the neurologic examination. Small intervertebral foramina and narrowed articular process joint spaces are merely a result of partial collapse of the space between two vertebrae and may not be associated with disc hernation. Increased opacity of the intervertebral foramen is caused by either extruded disc material in the vertebral canal or local inflammation of epidural fat at the site of extrusion. This change is evident only on a true lateral projection with exact superimposition of both lateral margins of both intervertebral foramina. Discal mineralization within the intervertebral disc space, so-called *mineralization in situ*, is indicative of intervertebral disc degeneration but does not confirm that this particular disc is causing a clinical problem. Most herniated disc material is nonmineralized or lacks sufficient mineral content to be detected on survey radiographs, whereas the superior contrast resolution of CT allows detection of both nonmineralized and low-mineral-content herniated disc material.[49] Myelographic technique and interpretative principles for the diagnosis of disc herniation are described later.

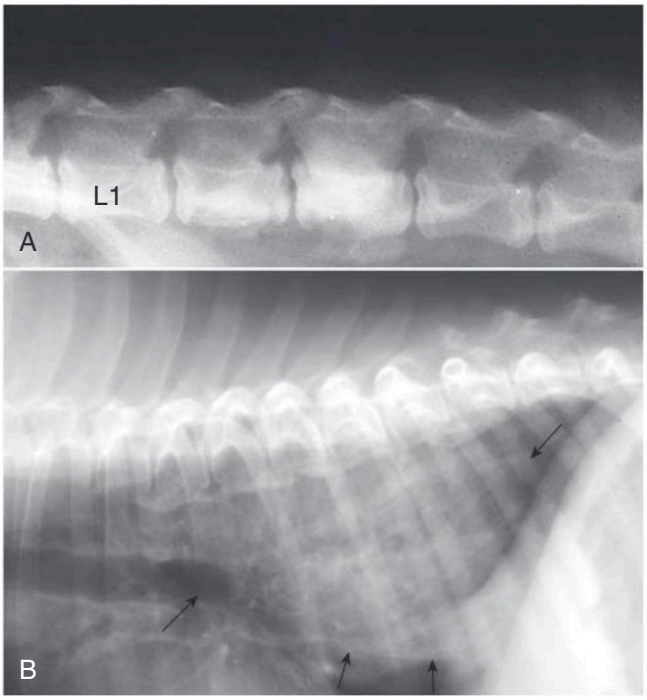


Fig. 14.19 Radiographic signs of spondylitis. **A,** Radiograph of patient with plant awn-induced spondylitis; note increased opacity of the vertebral bodies of L2 and L3 and periosteal reaction. **B,** Lateral radiograph of a dog with *Spirocerca lupi* infection. There is an irregular periosteal response along ventral borders of the thoracic vertebra. Note that the new bone is not centered at the ventral aspect of the disc space, as would be expected in spondylosis. An indistinct soft tissue esophageal mass is present ventral to this area (*arrows*). *L1,* First lumbar vertebral body. (**B,** Courtesy Dr. R. M. Kirberger, University of Pretoria, South Africa.)

INFLAMMATORY CONDITIONS

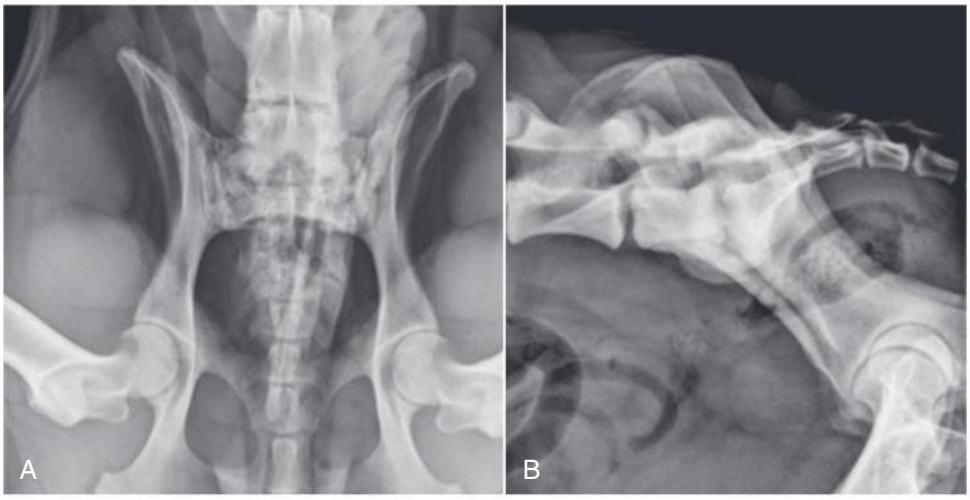
Spondylitis, Vertebral Osteomyelitis, and Vertebral Physitis

Spondylitis is a nonspecific term referring to inflammation of the vertebrae. *Vertebral osteomyelitis* has also been used synonymously with spondylitis when osteomyelitis of the vertebral body is present. Spondylitis should not be confused with *spondylosis*, or *spondylosis deformans*, a degenerative condition of the vertebral column. Common causes of spondylitis include microbial infection, plant awn migration, and infection with *Spirocerca lupi*.[50–58] Paraspinal abscesses may extend to the spine and cause spondylitis.[59] Radiographic changes are mainly those of increased opacity of the vertebral body with an irregular periosteal reaction. With osteomyelitis, radiographic features include an aggressive bone response with patchy lysis of the vertebral bodies and an irregular periosteal response[51–53] (Fig. 14.19). Parasite-induced spondylitis caused by *S. lupi* infection results in osseous proliferation of the ventral aspect of the vertebral bodies of T8–T11.[56] Metastatic neoplasia can cause similar periosteal lesions.[50]

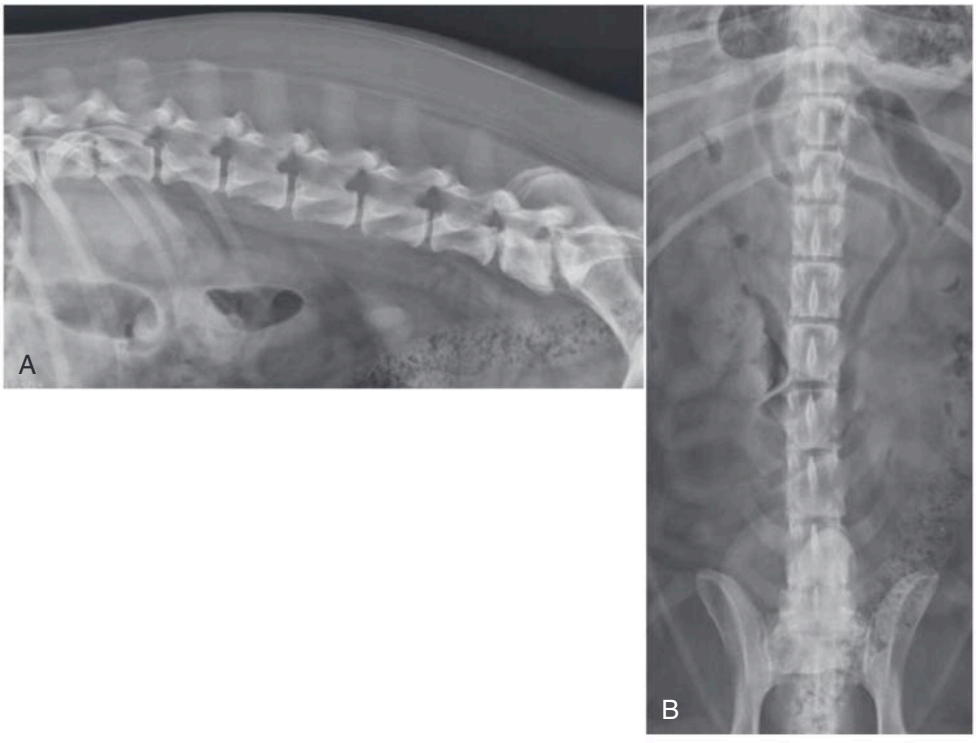
Vertebral physitis occurs in young dogs, and initial radiographic signs include osteolysis of the physeal zone of the affected vertebrae with sparing of the endplates.[60] With progression, there is collapse of the cranial or caudal aspect of the vertebral body and endplate sclerosis. Sepsis is the proposed cause because of hematogenous localization in the slow-flowing capillaries of the vertebral physis. *Acinetobacter* and *Enterococci* species have been isolated from vertebral biopsy material.[60]

Discospondylitis

Discospondylitis is inflammation of an intervertebral disc and its adjacent vertebral endplates.[57,58,61,62] There is also paraspinal soft tissue infection, but this is not detected radiographically. The etiology involves hematogenous spread of microorganisms from distant sites, frequently associated with genitourinary infections and occasionally paraspinal abscess or foreign body migration.[57,62,63] Middle-aged, large-breed dogs are affected commonly, and single or multiple intervertebral discs and adjacent endplates may be involved. Common isolates include *Staphylococcus, Streptococcus, Brucella* species, and *Escherichia coli*, although numerous other bacterial species and yeasts have been isolated.[57,58,62,63] Discospondylitis caused by aspergillosis is mainly seen in German shepherd dogs, possibly associated with the breed's documented immunoglobulin A (IgA) immunodeficiencies.[64] Discospondylitis is less common in cats but has a similar etiopathogenesis.[61] Initial radiographic features include irregular endplate lysis with extension into the vertebral body (Fig. 14.20, eFigs. 14.9 and 14.10). Later, there is collapse of the intervertebral disc space, sclerosis peripheral to the endplate lysis, ventral enthesophyte production, and in some instances subluxation (see Fig. 14.20B). Resolved discospondylitis may have the same appearance as spondylosis deformans (discussed later); usually, the disc space is collapsed at this point. Clinical features of discospondylitis can include fever, leukocytosis, paresthesia, paresis, and rarely paralysis.[57–59,62,63] Meningitis is possible if the inflammatory process extends into the vertebral canal and enters the subarachnoid space.[62] Diagnosis is based on clinical signs and presence of lysis of the vertebral endplates. Radiographic changes of discospondylitis lag behind changes that are apparent in MR images; thus, negative radiographs do not rule out a diagnosis of discospondylitis.[62,65] In a study of juvenile dogs with discospondylitis, CT and ultrasonography were used to identify abnormal discs prior to the onset of typical radiographic changes. The earliest radiographic sign of discospondylitis in juvenile dogs was disc space narrowing.[66]



eFig. 14.9 Ventrodorsal **(A)** and lateral **(B)** radiographs of a dog with discospondylitis at the lumbosacral junction. The endplates are irregularly marginated with focal lysis and adjacent sclerosis. There is ventral new bone formation.



eFig. 14.10 Lateral **(A)** and ventrodorsal **(B)** radiographs of the lumbar spine of a Border Collie with discospondylitis. There is lysis of the vertebral endplates at T13–L1, L6–L7, and L7–S1 with adjacent sclerosis and ventral new bone formation.

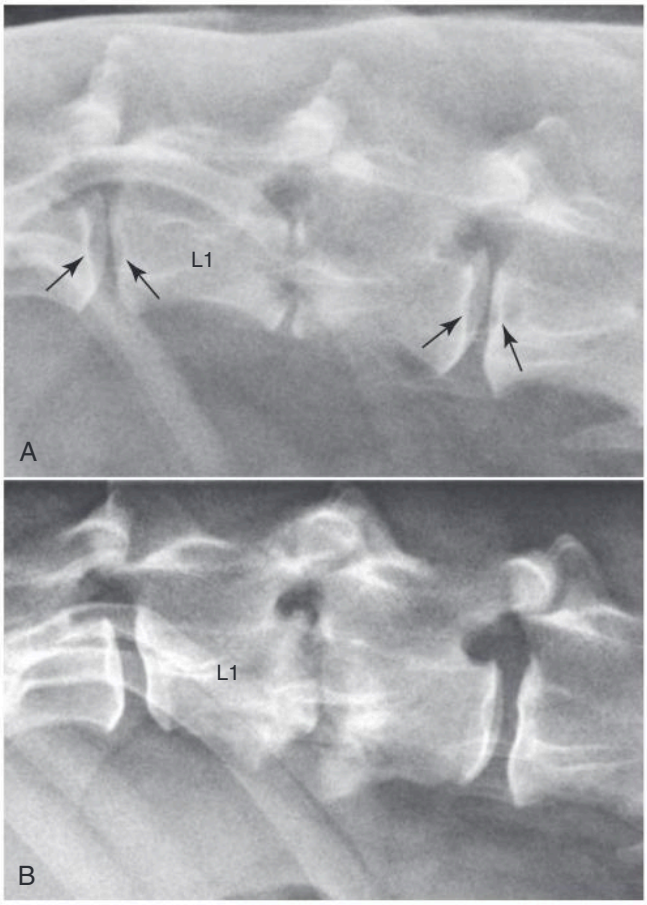


Fig. 14.20 **A,** Lateral radiograph of a dog with acute discospondylitis at L1—L2. There is endplate lysis but no evidence of new bone formation. The disc space at L1—L2 is also narrow, signifying that the disc is herniated, although the location of the disc material cannot be determined. The disc material may be in the vertebral canal, lateral to the disc, or even within the vertebral body as a result of herniation through the diseased endplate. Note the discrete linear opacity associated with a normal endplate (*arrows*). These discrete opacities are absent at L1—L2, and this absence is a clue that the endplates at this site have been effaced. **B,** Lateral radiograph of the same patient made 6 weeks later is characterized by more extensive lysis of the vertebral endplates and sclerosis of the vertebral body adjacent to the endplates. Early changes of spondylosis deformans are also present, and ventral enthesophytes are developing. There is mild subluxation at L1—L2, with L2 being displaced slightly ventrally. The intervertebral foramen at L1—L2 is small because of the disc being herniated and the vertebrae moving closer together.

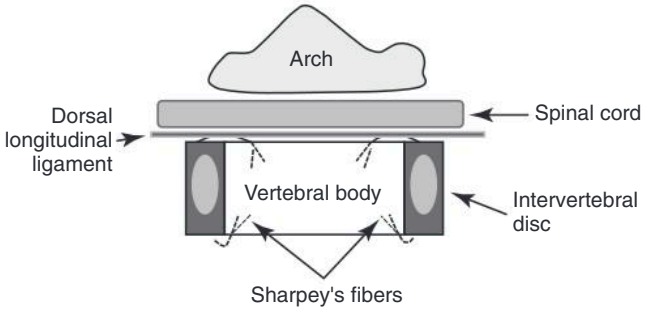


Fig. 14.21 Graphic of the lateral aspect of a typical vertebra and attachments (entheses) of the annulus fibrosis to the vertebral endplate and dorsal longitudinal ligament. Sharpey's fibers are a continuation of annular collagen fibers originating in the annulus and are firmly anchored in the cortical bone of the vertebral endplate. Stimuli of these attachments have been postulated to initiate osseous proliferation at the ventral and lateral margins of endplates in animals with spondylosis deformans.

DEGENERATIVE CONDITIONS

Spondylosis Deformans

Spondylosis is defined as ankylosis of a vertebral joint.[67] The term *spondylosis deformans* is preferred, because it addresses the spectrum of changes associated with this degenerative condition more completely. Spondylosis deformans is common in dogs, especially boxers and large-breed dogs, and it tends to be most prevalent in the thoracolumbar and lumbosacral region.[68–71] Most dogs will eventually develop radiographic criteria of spondylosis deformans. Clinicians should be aware that spondylosis deformans is not an inflammatory process but rather a disease of the attachments of the vertebral joints, which involves the fibers joining the intervertebral discs to the vertebral endplates.[71,72] The outer rim of the annulus fibrosus has strong circumferential attachments to the vertebral endplate with Sharpey's fibers, which are enmeshed in cortical bone (Fig. 14.21). The annulus fibrosus is also anchored to the dorsal longitudinal ligaments by short fibers, adding stability to the vertebral column. The intervertebral disc acts as a thick-walled pressure vessel that is subject to dynamic loading and deformation during locomotion.[73] The exact cause of spondylosis deformans is unknown, but etiopathogenesis might include repetitive trauma, instability, normal aging and wear and tear, and hereditary predisposition.[70,71] However, convincing evidence of a hereditary component was not found in studies of boxer dogs.[74,75] Presently accepted theory states that disruption of Sharpey's fibers is the initiator, leading to radiographically evident osseous proliferation or *enthesopathy* of the margins of the endplate (see Fig. 14.21).[72,73] Eventually, ventral vertebral enthesophytes can bridge the intervertebral disc space at single or multiple sites, leading to fusion. In the thoracolumbar column, fusion leads to increased stress and strain of adjacent vertebral junctions and may result in disc herniation. Radiographic findings may also include endplate thickening and narrowing of the intervertebral disc space, which is possibly related to concurrent disc degeneration and loss of elasticity of the disc[70,71] (Fig. 14.22). It should be noted that dorsal and dorsolateral enthesophytes can form, but these may not be seen on conventional orthogonal radiographic studies because of superimposition on adjacent structures.[76]

Whether or not disc degeneration is a factor in the development of spondylosis deformans is unclear. In dogs, type II intervertebral disc disease may be part of the pathogenesis of spondylosis deformans (Fig. 14.23).[77] Tears of the annulus may occur in dogs with spondylosis deformans, predisposing to type II-disc protrusion. Most clinicians and radiologists agree that spondylosis deformans is clinically insignificant, unless a concurrent herniated disc is present, or if there is impingement on the spinal cord or spinal nerve roots. Nerve root compression from spondylosis is rare except in lumbosacral instability where foraminal impingement results from dorsal extension of the enthesophytes.

Osteoarthritis of the Dorsal Intervertebral Articular Process Joints

The synovial joints of the vertebral column are composed of the articular processes of adjoining vertebrae and are subject to degeneration or osteoarthritis as is any other synovial joint.[1] Typical radiographic changes include remodeling of the articular processes, osteophytosis, and thinning of the joint space. These changes are best seen on lateral radiographs (Fig. 14.24). Although osteoarthritis of the articular process joints can be seen concomitantly with spondylosis deformans, these are separate entities. No specific clinical signs have been attributed

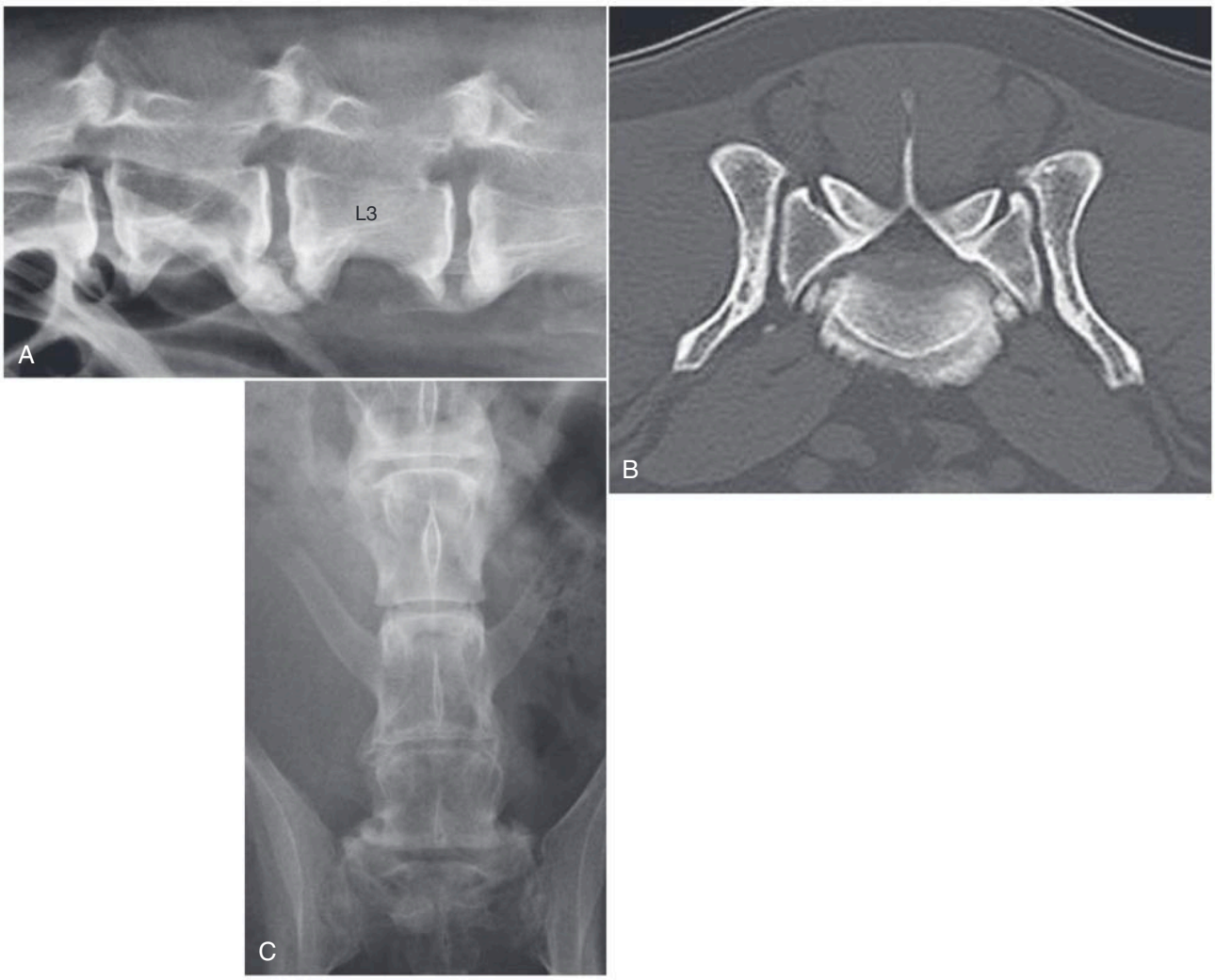


Fig. 14.22 **A,** Lateral radiograph of the lumbar spine. There are ventral enthesophytes at L1—L2, L2—L3, and L3—L4. There is endplate sclerosis of the cranial aspect of L4. The radiolucent region between the ventral enthesophytes at L2—L3 is often confused with a fracture, but this is only a region where the enthesophytes are approaching each other and have not fused. This gap may eventually fuse completely. **B,** Transverse computed tomography (CT) image of a dog with spondylosis. There is ventral osseous proliferation without impingement of the vertebral canal. Note that the dorsal intervertebral articular process joints are unaffected. **C,** Ventrodorsal (VD) radiograph of a dog with spondylosis that has resulted in lateral enthesophytes at L4—L5, L6—L7, and L7—S1. Lateral enthesophytes are rarely of clinical importance because their location is ventral to the spinal cord and nerve roots. *L3,* Third lumbar vertebral body.

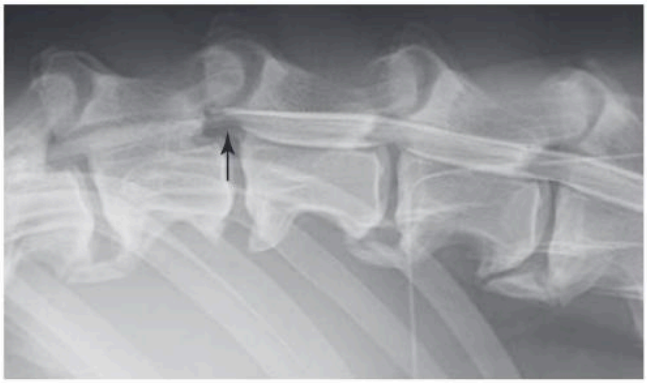


Fig. 14.23 Lateral myelogram of a dog with ataxia and loss of conscious proprioception of the pelvic limbs. There is extensive ventral enthesophyte formation at multiple sites. There is dorsal displacement of the contrast medium in the ventral aspect of the subarachnoid space (*arrow*) at T13—L1, and extradural spinal cord compression secondary to a type II intervertebral disc protrusion. The disc herniation, and not the advanced spondylosis deformans, was responsible for clinical signs.

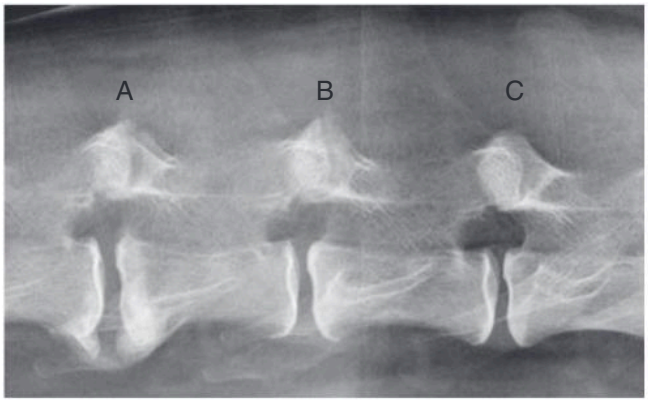


Fig. 14.24 Lateral radiograph of a dog with articular process degenerative joint disease. The joint *C* is normal. The joint *A* has subchondral sclerosis and mild osteophyte formation. The joint *B* is narrow with large osteophytes. Because of the limited motion of these joints, clinical signs of degenerative joint disease are rarely present; however, in some instances, enlarged articular processes may impinge the spinal cord dorsally, causing neurologic signs. Synovial cysts may also impinge the spinal cord laterally as previously discussed.

to articular process degenerative joint disease in dogs, with the exception of instances where there is articular process hypertrophy in dogs with cervical spondylomyelopathy. Synovial cysts, as previously discussed, may develop with osteoarthritis and cause compression of the spinal cord. Osteoarthritis of the articular processes is seen rarely in cats.

Cauda Equina Syndrome

The lumbosacral junction is unique because of its structure, relatively wide range of mobility, and the fact that it houses nerve roots of the caudal aspect of the spinal cord. The terminal part of the spinal cord is the conus medullaris and contains sacral and caudal segments.[78] In dogs, the spinal cord terminates near the level of L6 or L7, depending on breed,[79] and at L7 in cats.[80] The *cauda equina* refers specifically to the collection of nerve roots that lie within the vertebral canal caudal to the termination of the spinal cord.[81] These nerve roots stream caudally from their respective sacrocaudal cord segment, exiting the vertebral canal through intervertebral foramina, caudal to their origin in the spinal cord. This is because the spinal cord is shorter than the vertebral column insofar as they have differential fetal growth rates. Therefore, the spinal nerves descending from the L7 spinal cord segment exit the vertebral canal at the L7-S1 intervertebral foramina and are lateral to the remainder of the cauda equina.

Numerous degenerative, inflammatory, traumatic, and neoplastic conditions can affect the lumbosacrum of dogs and cats and result in pain, neural dysfunction, and exercise restriction.[82,83] Because most of these conditions involve the cauda equina, the term *cauda equina syndrome* has been applied. Other terms used in conjunction with cauda equina syndrome include *lumbosacral disease, lumbosacral stenosis* and *degenerative lumbosacral stenosis, lumbosacral malarticulation malformation, lumbosacral instability*, and others.[9,82,84] In most instances, there is compression, inflammation, ischemia, and/or disruption of the cauda equina.[84] Specific conditions causing cauda equina syndrome are also numerous.[9,82–87] Degenerative lesions are common in dogs and include intervertebral disc disease, instability of the lumbosacrum, stenosis from remodeling changes associated with spondylosis deformans, and impingement from capsulitis or ligamentous hypertrophy because of osteoarthritis of the articular process joints[82] (Fig. 14.25, eFig. 14.11).

Lumbosacral fractures, discospondylitis, and neoplasms including nerve sheath tumors and bone and soft tissue sarcomas have the potential to cause signs of cauda equina syndrome (Fig. 14.26). An osteochondrosis-like lesion of the sacral endplate causing intervertebral disc prolapse and compression of the cauda equina has been reported in German shepherd dogs.[86] Elongation of the dorsal sacral lamina in dogs with transitional vertebra also predisposes to lumbosacral stenosis and cauda equina pain in German shepherds.[18,88] Cauda equina syndrome is uncommon in cats, but sacrocaudal trauma or a *tail pull injury* with avulsion of the cauda equina may be confused with typical signs of cauda equina syndrome.[82]

MRI and CT are the modalities of choice for imaging the lumbosacral region.[84,87] However, conventional radiography can be useful for an initial evaluation of dogs and cats with signs of cauda equina syndrome. Conditions that produce osseous lesions (e.g., discospondylitis, subluxation, stenosis of the vertebral canal, osseous neoplasia, etc.) may be identified on lateral and VD radiographs. Soft tissue lesions of the lumbosacrum, such as prolapse of the intervertebral disc, hypertrophy of ligaments and joint capsules, soft tissue neoplasia, or nerve root entrapment, are not identified; thus, conventional radiographic evaluation is subject to a false-negative result.[84]

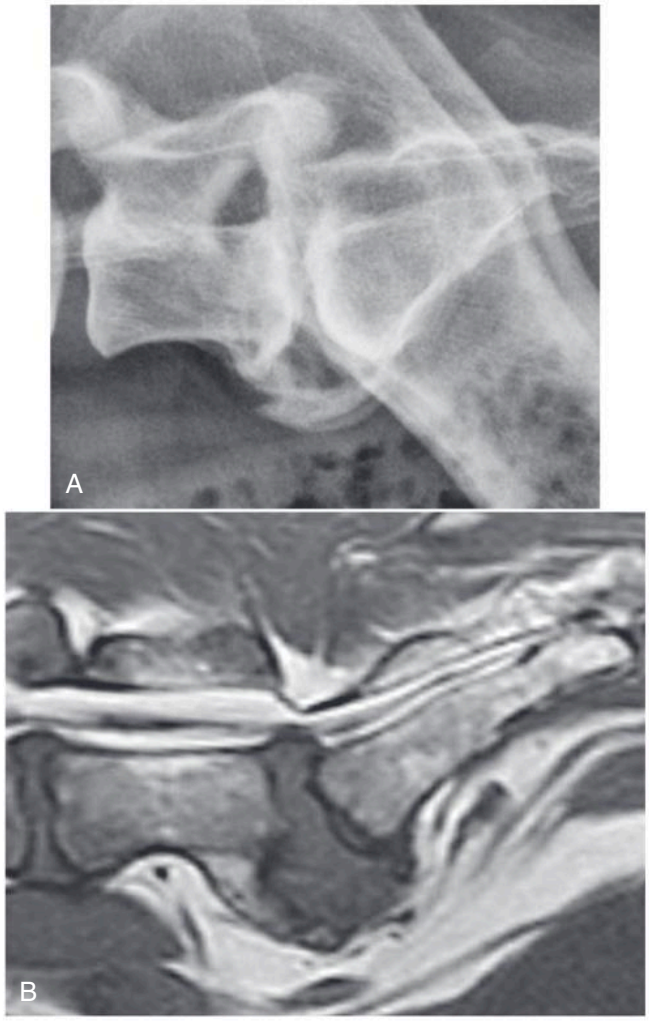


Fig. 14.25 **A,** Lateral radiograph of the lumbosacrum of a dog with chronic lumbosacral pain. There is narrowing of the intervertebral disc space, mild dorsal displacement of L7 with respect to the sacrum, and remodeling of the endplates. The displacement of S1 can lead to entrapment of spinal nerves (cauda equina) but can be seen in asymptomatic dogs as well. Concurrent disc herniation that adds to the compression. Conformation of this change is best accomplished with either magnetic resonance (MR) or computed tomography (CT) imaging. **B,** T1-weighted sagittal MR image of a different animal with similar signs. There is protrusion of the intervertebral disc at L7–S1 and extradural compression of the nerve roots in the vertebral canal.

Positional radiography,[89] myelography,[90,91] epidurography,[91] and discography[92] are helpful for diagnosis of lumbosacral disease; however, these invasive modalities, particularly epidurography and discography, are rarely used since the availability of MRI and CT. Before employing myelography, it should be noted that the dural sac has a variable termination and may not extend to the lumbosacral junction; therefore, a soft tissue lesion, such as a herniated disc, may not be detected.

VERTEBRAL NEOPLASIA

The vertebrae are affected commonly by primary or metastatic neoplasia.[93,94] Pain and/or neuropathy can result, depending on the location and extent of the tumor. Large to medium breeds



eFig. 14.11 Lateral radiograph of the lumbosacral junction of a dog with lumbosacral pain. The disc space is narrowed and there is bridging spondylosis deformans present as well as endplate sclerosis. Increased opacity of the intervertebral foramen may represent herniated disc material, superimposed lateralized spondylosis deformans, or superimposed sacroiliac joints. It is impossible to determine radiographically if this dog has compression of the nerve roots of the cauda equina to cause the clinical signs.

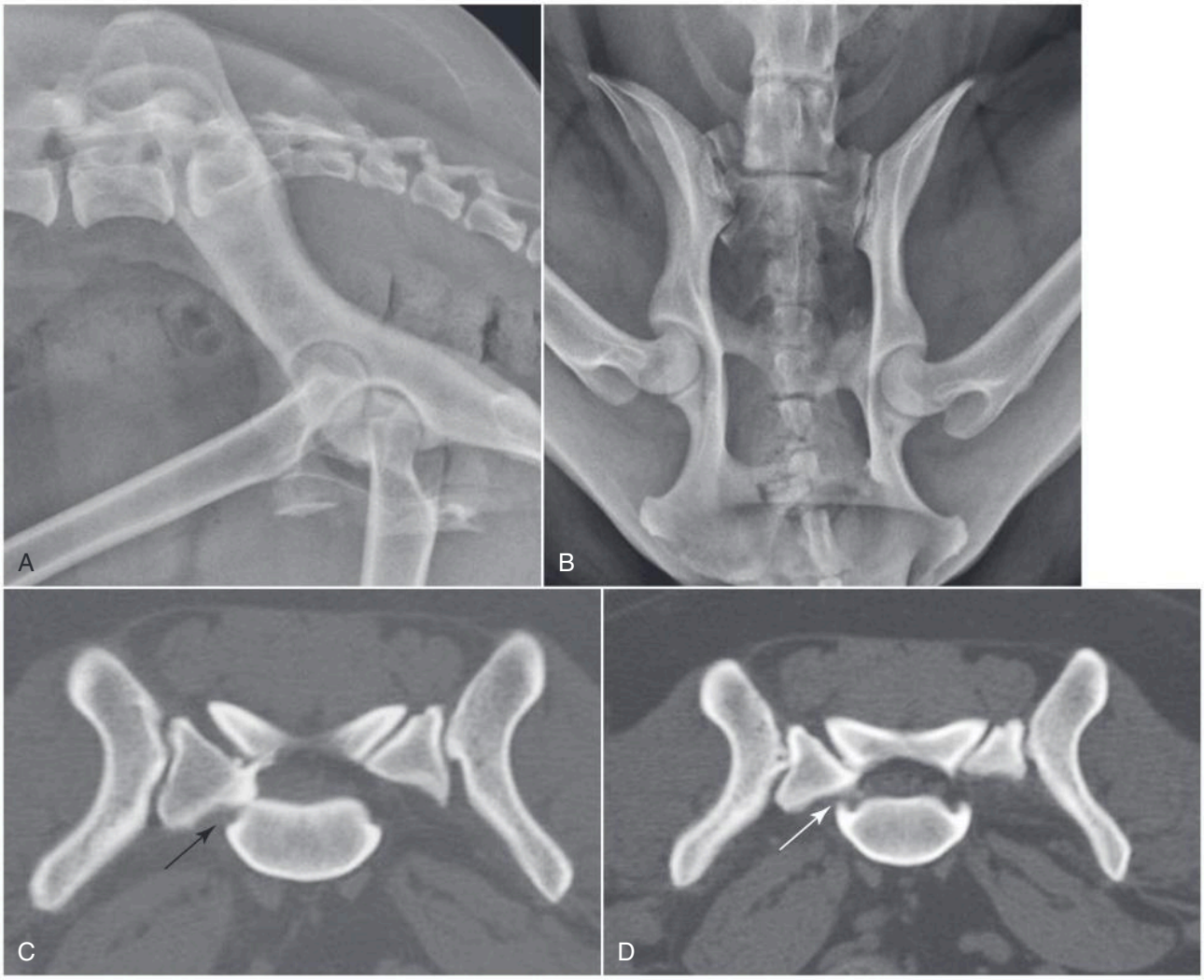
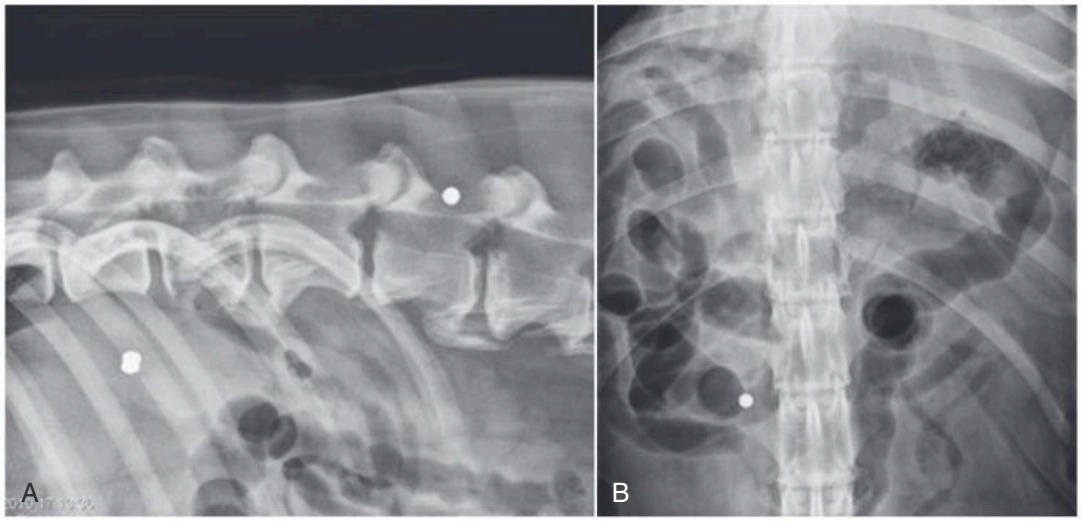


Fig. 14.26 Images of a dog that was hit by a car and presented with right pelvic limb paresis and pain. **A,** Lateral radiograph. There are pubic and ischial fractures. **B,** Ventrodorsal (VD) radiograph. There is an oblique fracture of the right sacral wing with mild displacement; pubic and ischial fractures are also present, although these changes are not striking. Transverse plane computed tomography (CT) images **(C** and **D)** of the same animal confirm that the right sacral fracture is segmental and has narrowed the right intervertebral foramen at L7–S1 (*black and white arrows*), compressing the nerve roots as they exit the vertebral canal. This illustrates the value of cross-sectional imaging in evaluating patients with cauda equina syndrome.

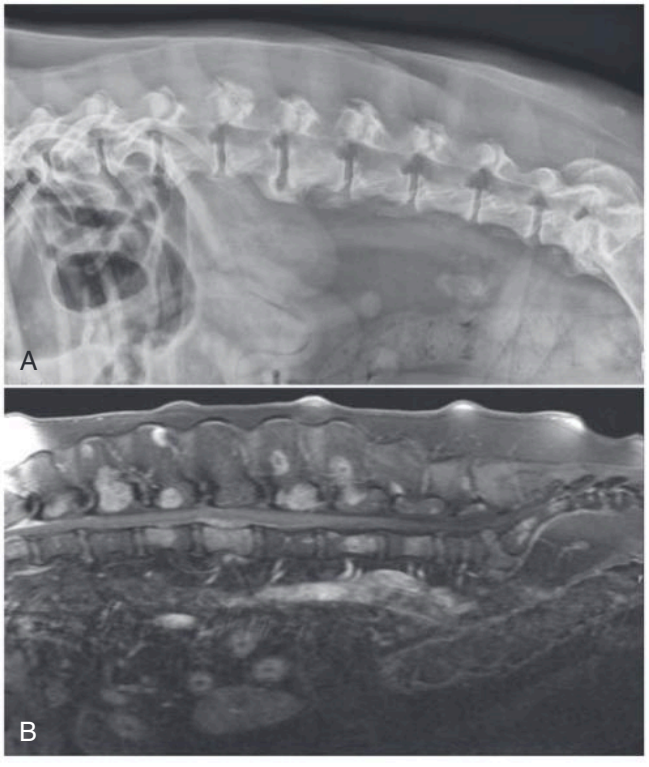
are overrepresented, and most animals are 7 years old or older. Sarcomas, including osteosarcoma, chondrosarcoma, hemangiosarcoma, and fibrosarcoma are the most common primary vertebral neoplasms in dogs and cats. Multiple myeloma, plasmacytoma, and lymphoma also affect vertebrae. In 61 canine vertebral tumors, the most common site for primary neoplasia was the thoracic area, whereas most metastatic neoplasms were found in the lumbar area.[93] Metastatic neoplasia is more common than primary vertebral neoplasia, and carcinomas and sarcomas are the most common cell type.[93,94] The preceding classification does not include tumors originating from the meninges or spinal cord, although some neoplasms cause local invasion of the vertebra and/or osseous remodeling of the vertebral foramen

Radiographic signs of vertebral neoplasia are typical of an aggressive bone response and include bone lysis, new bone production, and pathologic fracture (Fig. 14.27, eFig. 14.12). Metastatic neoplasms cannot be differentiated reliably from primary neoplasms based on radiographic findings; however, primary neoplasms frequently involve only one vertebra, whereas many metastatic neoplasms are polyostotic. Multiple myeloma and lymphoma frequently cause multiple focal osteolytic lesions in the vertebral processes that are easily recognized on conventional radiographs (Fig. 14.28, eFig. 14.13). However, these changes are not pathognomonic. Additionally, normal old dogs and cats may have a coarse trabecular pattern, especially in the spinous process C2, that should not be confused with a neoplastic lesion.

It is vital to remember that significant loss of calcified osseous matrix must be present before a destructive lesion is evident radiographically. In people, metastatic lesions within the trabecular bone must be at least 1.5 cm in diameter and have 50% to 75% loss of local calcium before being detected on survey radiographs.[95] CT and MRI are superior for determining the extent and soft tissue changes associated with vertebral neoplasms and essential for decision making and staging before therapy. CT is more sensitive for identifying bone loss than conventional radiography. Table 14.2 summarizes the salient features of inflammatory and degenerative conditions of the vertebrae.



eFig. 14.12 Lateral **(A)** and ventrodorsal **(B)** radiographs of a dog with an aggressive lesion of T13. The vertebral body is foreshortened compared with the adjacent vertebrae due to a pathologic compression fracture. The vertebral body and pedicles are heterogeneous and decreased in opacity. The outline of the vertebral canal is interrupted.



eFig. 14.13 Lateral radiograph **(A)** and sagittal MR STIR (short tau inversion recovery) sequence **(B)** of a dog with multiple myeloma. On the radiograph **(A)**, the vertebral body of L3 is increased in opacity and the ventral outline of the vertebral canal is interrupted. The base of the spinous process L1 is heterogeneous as well with abnormal trabecular pattern. Multiple additional hyperintense lesions are seen in the MR image, which is much more sensitive for detection of neoplastic lesions **(B)**.

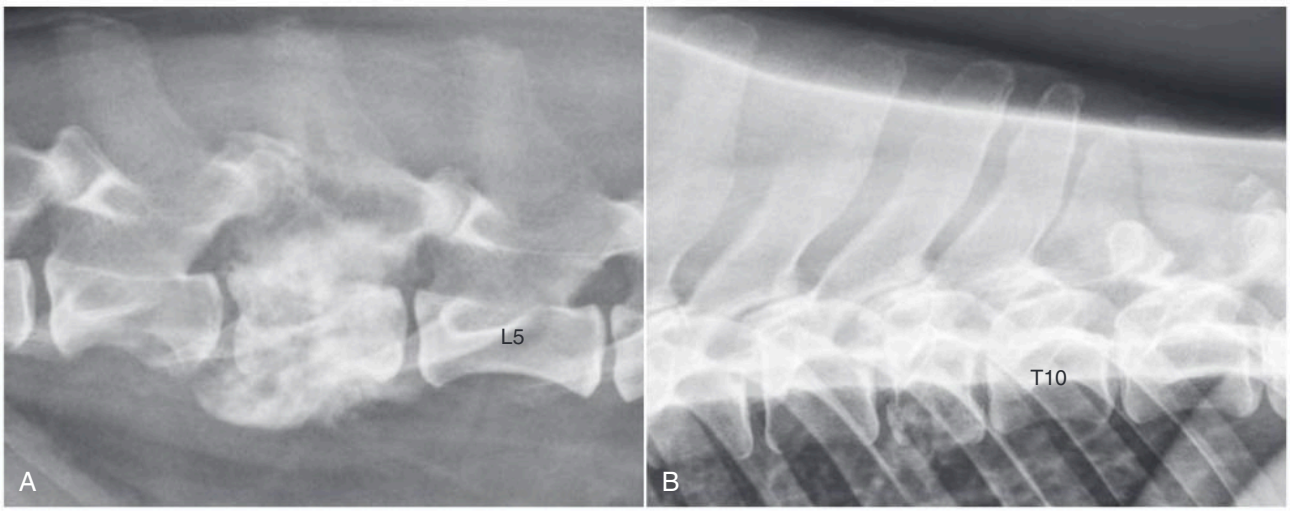


Fig. 14.27 **A,** Lateral radiograph of a dog with a tumor of L4. There are regions of lysis in the vertebral arch and the body, and there is also active new bone formation on the ventral aspect of the body. **B,** Lateral radiograph of a dog with a compression fracture of T9 caused by metastatic cancer. The body is heterogeneously lytic and foreshortened with multiple areas of cortical effacement. Each of these lesions is characterized as aggressive radiographically. *L5*, Fifth lumbar vertebral body; *T10,* tenth thoracic vertebral body.



Fig. 14.28 Lateral cervical radiograph of a dog with multiple myeloma. There are numerous regions of bone lysis in the cervical spine, affecting C2—C5.

METABOLIC AND UNCLASSIFIED CONDITIONS

Disseminated Idiopathic Skeletal Hyperostosis

Disseminated idiopathic skeletal hyperostosis (DISH) is recognized infrequently in dogs and has been reported in a cat.[96] Principal radiographic features include extensive linear new bone formation along the ventrolateral aspect of the vertebral column and ankylosis (Fig. 14.29). Although these changes appear similar to advanced spondylosis deformans, DISH is likely a separate entity; the predominant excessive ventral distribution supports this contention. In the dog, seven criteria have been proposed to help distinguish DISH from spondylosis deformans.[97]

1. Bridging ossification along ventral and lateral aspects of three contiguous vertebral bodies
2. Relative preservation of disc-space width within involved areas and absence of changes of degenerative disc disease,

Table • **14.2**

Radiographic Features of Inflammatory Conditions of the Vertebral Column.

CONDITION	OSSEOUS PRODUCTION	OSTEOLYSIS	NARROWED DISC SPACE
Spondylitis	+; vertebral body	–	–
Vertebral osteomyelitis	+; vertebral body	+; vertebral body	–
Vertebral physitis	+; vertebral endplate	+; vertebral physis	–
Discospondylitis	+; vertebral body and endplate	+; endplate erosion	+

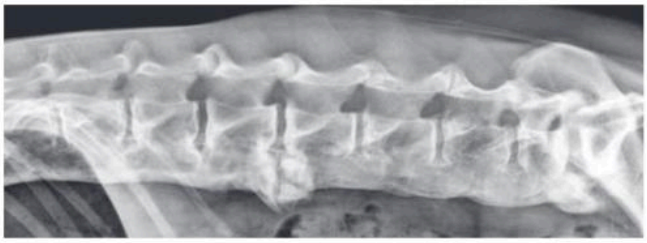


Fig. 14.29 Lateral radiograph of a dog with extensive bridging ventral spondylosis that is consistent with disseminated idiopathic skeletal hyperostosis.

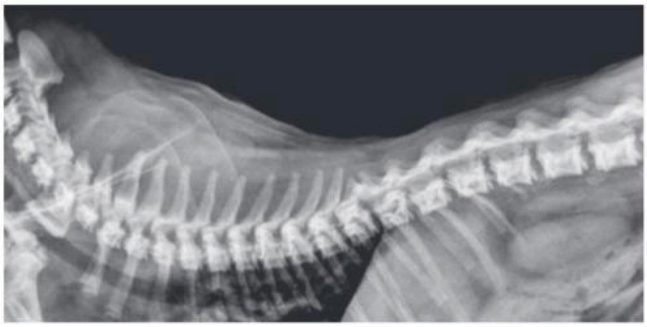


Fig. 14.30 Lateral radiograph of a cat with mucopolysaccharidosis. There is extensive remodeling and shape change of the cervical and thoracic vertebrae. Note the small and irregularly mineralized vertebral epiphyses, typical of this condition.

such as endplate sclerosis, nuclear calcification, or localized spondylosis deformans
3. Osteoarthritis of the dorsal intervertebral process joints
4. Pseudoarthrosis of the spinous processes
5. Enthesopathy of soft tissue attachments in both axial and appendicular skeleton
6. Osteophytes, sclerosis, and ankylosis of the sacroiliac joints
7. Ankylosis of the symphysis pubis

It is suggested that at least four of the seven criteria be present for confirmation of DISH in dogs.[97]

Mucopolysaccharidosis

Radiographic changes of mucopolysaccharidosis type VI in cats include multiple skeletal abnormalities.[98] In the vertebral column, principal changes are remodeling, and shape change of the vertebra, spondylosis deformans, and abnormal development of the dens. These changes are primarily a manifestation of vertebral epiphyseal dysplasia (Fig. 14.30). Changes in the appendicular skeleton include epiphyseal dysplasia of long bones, abnormal nasal conchal development, and coxofemoral subluxation.

Osteopenia

Nutritional secondary hyperparathyroidism can result in generalized bone loss with cortical and trabecular thinning of the vertebra and pathologic fracture (Fig. 14.31). As with radiographically evident metastatic lesions, considerable bone loss must be present to recognize osteopenic conditions. In humans, 30% to 60% of bone matrix must be lost for radiographic detection in metabolic bone diseases.[99] Although senile osteopenia and osteopenia secondary to other endocrinopathies have been described,[9] the degree of bone loss is usually insufficient for detection on survey radiographs of the vertebral column.

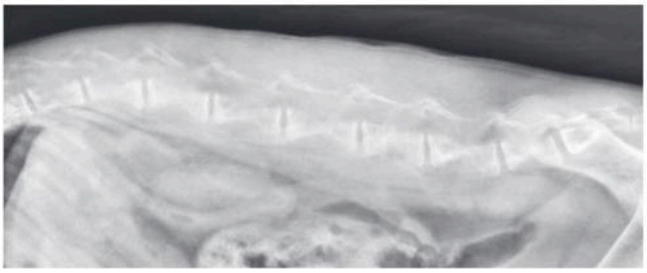


Fig. 14.31 Lateral radiograph of a cat with nutritional secondary hyperparathyroidism. There is marked generalized osteopenia with reduction in bone opacity. The normal high contrast between bone and soft tissue has been lost.

MYELOGRAPHY

Myelography is valuable for identifying extradural compressive lesions but rarely provides meaningful information about the condition of the spinal cord. For this reason, it has largely been replaced by CT and MRI. MRI is noninvasive, and intrathecal injection of contrast medium is unnecessary. However, MRI is not universally available for veterinary patients and may be too expensive for some pet owners. Therefore, conventional myelography and CT-myelography are still viable modalities for use in high-quality practices and referral centers without access to MRI.[44,49]

Common indications for myelography include (1) confirming and localizing spinal cord compression due to intervertebral disc herniation, (2) defining the extent of spinal cord impingement from fractures and luxations, (3) identifying a suspected extradural compressive or intramedullary spinal cord lesion when survey radiographs are normal.

Technique

Myelographic technique is well described[48,100–103]; therefore, a summary is presented here. Myelography is always performed under aseptic conditions, and with the animal under general anesthesia. An accurate survey radiographic or CT study serves as a baseline and should always precede myelography. Nonionic iodinated contrast media such as iohexol (Omnipaque, 240 mgI/mL) are safe and efficacious, and are the contrast media of choice for small animal myelography. Under no circumstances should ionic iodinated benzoic acid derivatives such as diatrizoate or iothalamate salts be used for myelography. Serious side effects with ionic media include seizures, intensification of preexisting neurologic signs, or even death. Nonionic contrast media are relatively safe for myelography if solutions are near iso-osmolal, and careful technique is used. Maintenance intravenous fluid administration during and after myelography speeds contrast medium elimination by the kidneys, helping reduce side effects.

The full-spine dosage is approximately 0.45 mL/kg and the regional dosage is approximately 0.30 mL/kg.[100] These dosages are only guidelines and it is important to administer sufficient contrast medium to fill the subarachnoid space in the region of interest. Contrast medium can be diluted for CT-myelography. A 22-gauge spinal needle with stylet is preferred for myelography because it has a short bevel, which increases the likelihood that the needle will be positioned in the thin subarachnoid space. The stylet is kept in place during subarachnoid puncture to minimize damage if the spinal cord is pierced and to prevent tissue from clogging the needle lumen.

Lumbar myelography is routinely performed because lumbar punctures are relatively safe compared to cervical punctures. The subarachnoid space ends blindly; therefore; the lumbar

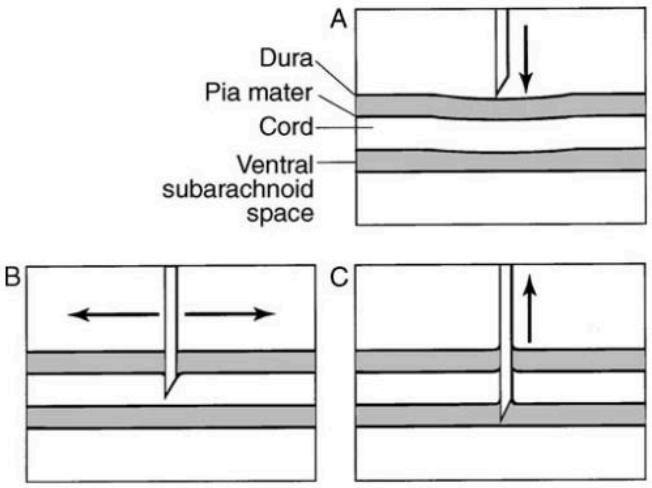


Fig. 14.32 Lumbar puncture may cause mechanical damage to the neural tissue. **A,** Compression of the spinal cord by resistance of the tough dura. **B,** Compression is released as the needle tip passes through the dura, entering the spinal cord. Horizontal movement must be minimized to avoid spinal cord damage. **C,** The needle is retracted slightly (1−2 mm) after it has reached the ventral aspect of the vertebral canal, reducing the chance of epidural injection. (Reproduced with permission from Widmer WR, Blevins WE. Veterinary myelography: a review of contrast media, adverse effects, and technique. *J Am Anim Hosp Assoc.* 1991;19:755.)

injection usually allows contrast medium to be forced cranially past extradural lesions and intramedullary swellings. With a cervical injection, contrast medium tends to flow rostrally into the ventricular system rather than flowing past extradural lesions and cord swellings.[35] Therefore, only the cranial aspect of a compressive lesion is identified with cervical injection myelography. Even in normalcy, full-spine myelograms are rarely achieved with cervical punctures and limited to the cervical vertebral region. Flow of contrast medium into the ventricular system can enhance neurotoxic effects, an additional disadvantage of cervical myelography.

Lumbar myelography is performed by puncture of the ventral subarachnoid space, preferably at L5−6 or L6−7, but L4−5 can be used if injection at these sites cannot be made successfully. Injection at L4−5 should be avoided because of the greater chance for injury to the lumbar intumescence of the spinal cord by the needle. Transneural passage of the needle is necessary for needle placement on the ventral aspect of the subarachnoid space and invariably damages the spinal cord or nerve roots. This can be minimized by keeping the stylet in place and avoiding horizontal movement of the needle during puncture. However, the dorsal aspect of the spinal cord is compressed 2 to 3 mm ventrally as the needle tip is resisted by the tough dura (Fig. 14.32).[103] The animal is placed in lateral recumbency and either of two methods can be used to puncture the subarachnoid space.[100] With the paramedian approach, the needle is inserted slightly caudolateral to the spinous process of L6 or L7 and is directed cranioventrally at a 45-degree angle, through the interarcuate space. The median approach requires insertion of the needle just cranial to the spinous process of L5 or L6, at a 90-degree angle to the vertebral column. When performing lumbar myelography, it can be advantageous to obtain a first lateral radiograph during injection to maximize contrast medium flow past a compressive lesion. Once the needle is removed, lateral VD and oblique VD radiographs should be obtained immediately to again maximize contrast medium volume near a compressive lesion.

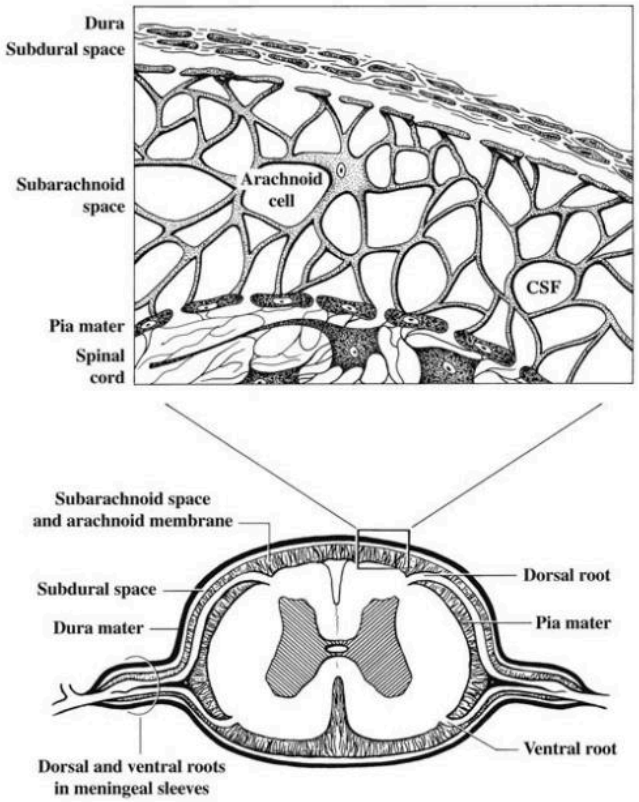


Fig. 14.33 Anatomic relationship (*transverse plane*) of spinal cord, meningeal layers, and subarachnoid space. *Inset* shows microscopic structure of a segment of the meninges and cord. *CSF,* Cerebrospinal fluid. (Modified from Hoerlein BF. *Canine Neurology: Diagnosis and Treatment*. 3rd ed. Philadelphia: WB Saunders; 1978. This figure was redrawn by the Medical Illustration Unit at the Purdue University College of Veterinary Medicine with credits to B.F. Hoerlein.)

Interpretive Principles

Knowing the relationship of the spinal cord to the meninges, epidural space, and vertebral canal is essential for accurate myelography interpretation (Fig. 14.33). This relationship is important for proper localization of vertebral canal mass lesions with respect to the dura, whether interpreting a myelogram or CT/MR images. CT myelography is advantageous over standard myelography because transverse plane images are acquired, thus summation is not a problem. If needed, sagittal and dorsal plane reconstructions can be made, increasing diagnostic information.

The normal conventional myelogram is typified by a sharply marginated, thin line of contrast medium in the subarachnoid space (Figs. 14.34 and 14.35). Small-breed dogs and cats tend to have relatively large spinal cords, and as a result, a thin subarachnoid space[24] (see Fig. 14.34C,D). The ventral aspect of the epidural (extradural) space is normally wide in the caudal cervical region, giving the false impression of spinal cord displacement. The dorsal aspect of the subarachnoid space is widest at the C1−C2 level and tends to be wider than the corresponding ventral aspect of the subarachnoid space in the thoracolumbar region. Small filling defects often seen dorsal to the cervical discs are caused by hypertrophy of the dorsal longitudinal ligament or the annulus fibrosus (see Fig. 14.34) but are not indicative of spinal cord compression if the dorsal subarachnoid space is normal. Clinically significant subarachnoid space filling defects should be accompanied by thinning of the opposite aspect of the contrast medium column or

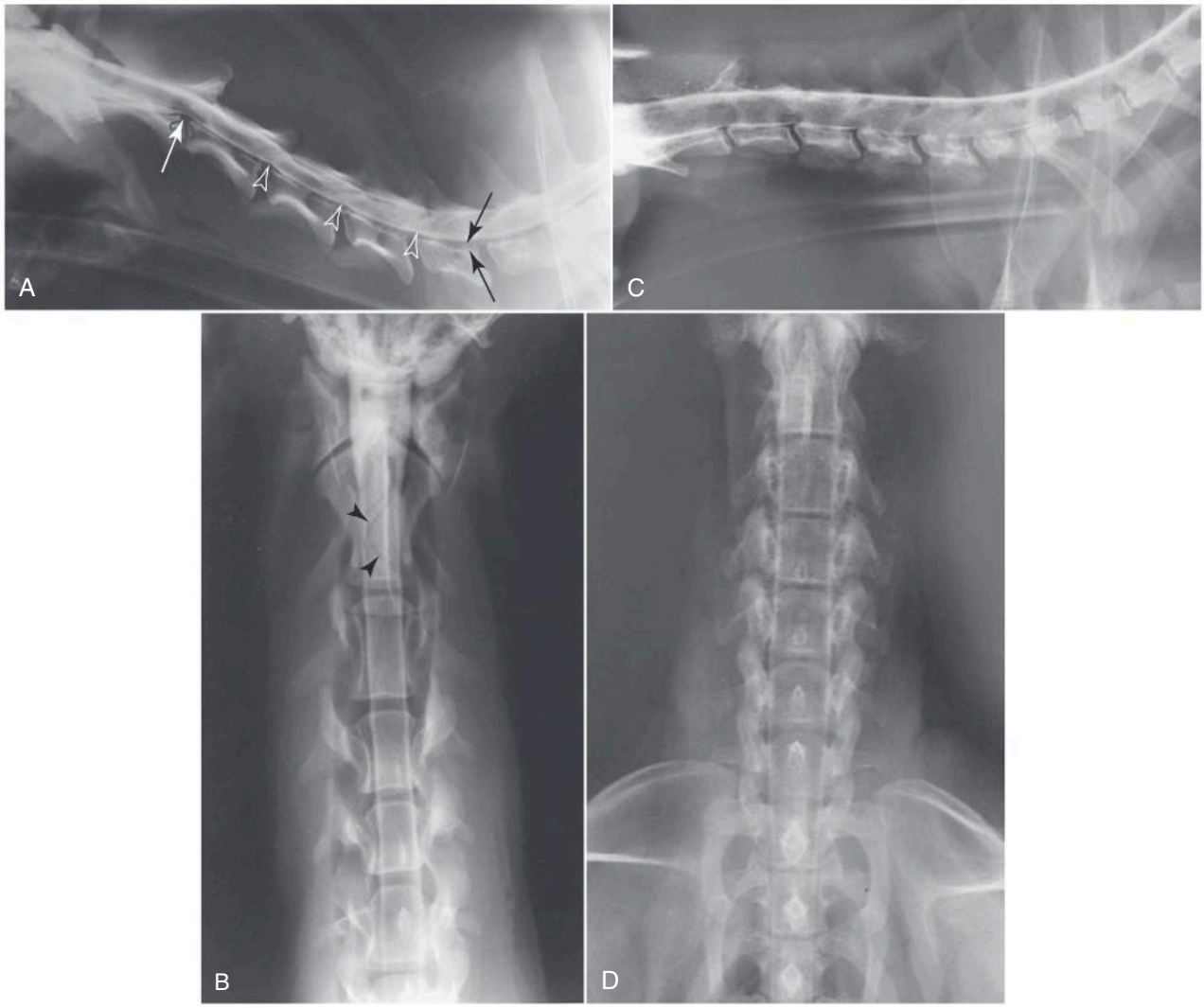


Fig. 14.34 Normal cervical myelogram. **A,** In a dog, on the lateral radiograph the subarachnoid space is wide cranially and thin caudally. Soft tissues (dorsal longitudinal ligament or annulus) normally cause thinning of the ventral aspect of the subarachnoid space C2–C3 (*large white arrow*) and should not be confused with disc herniation. Smaller indentations (*small white arrows*) are also seen in normal dogs. The epidural space is widest dorsal to C6–C7 (*closed black arrows*). **B,** In a dog, on the ventrodorsal radiograph, a serpentine subarachnoid filling defect (*black arrowheads*) is caused by the basilar artery. The subarachnoid space is also wider cranially. Note poor filling of the subarachnoid space in the caudal cervical region, which is caused by the effect of dependency. **C and D,** In the cat, the spinal cord is relatively wide and occupies a large percentage of the vertebral canal. As a result, the subarachnoid space is thin and conforms closely to the margins of the vertebral canal; this can give a false impression of cord swelling.

evidence of spinal cord compression. The thoracic spinal cord lacks an intumescence and is smaller than the cervical and lumbosacral regions of the spinal cord. Although the canine spinal cord typically terminates at L5–6, the contrast medium-filled dural sac often extends beyond the lumbosacral junction (see Fig. 14.35).[102] CT myelograms are typified by an opaque symmetrical ring surrounding the spinal cord (Fig. 14.36). The epidural space is well seen and easily distinguished due to the superior contrast resolution of CT. CT myelograms are excellent for determining the laterality of an extradural lesion such as a herniated disc, aiding the surgeon's decision on right versus left hemilaminectomy.

The abnormal myelogram is characterized by changes in the size and location of the opacified subarachnoid space, and in the width and opacity of the spinal cord. Myelographic lesions can be grouped into the following patterns: extradural lesions, intradural-extramedullary lesions, intramedullary swelling, and intramedullary opacification (Fig. 14.37 and Table 14.3).[102]

Several technical factors affecting myelographic quality and interpretation have been previously detailed (Fig. 14.38).[104] However, two issues are worthy of mention. (1) Epidural injection is problematic with lumbar punctures because contrast medium may leak around the needle punctures in the dura and can obscure the subarachnoid space, limiting interpretation. While this may render a conventional myelogram useless, a follow-up CT study can distinguish between the epidural spill versus and the subarachnoid space, salvaging the procedure. (2) Occasionally, the central canal of the spinal cord is visible after injecting contrast medium vial lumbar puncture. Presence of contrast medium in the central canal occurs when the needle shaft is placed in the central canal or when the central canal communicates with the subarachnoid space at the level of the conus medullaris.[105] In the former instance, contrast medium is presumed to leak back along the needle, especially during rapid injection.[105] "Canalograms" are most likely to occur when puncture is made at L4–5, where the spinal cord–to–vertebral

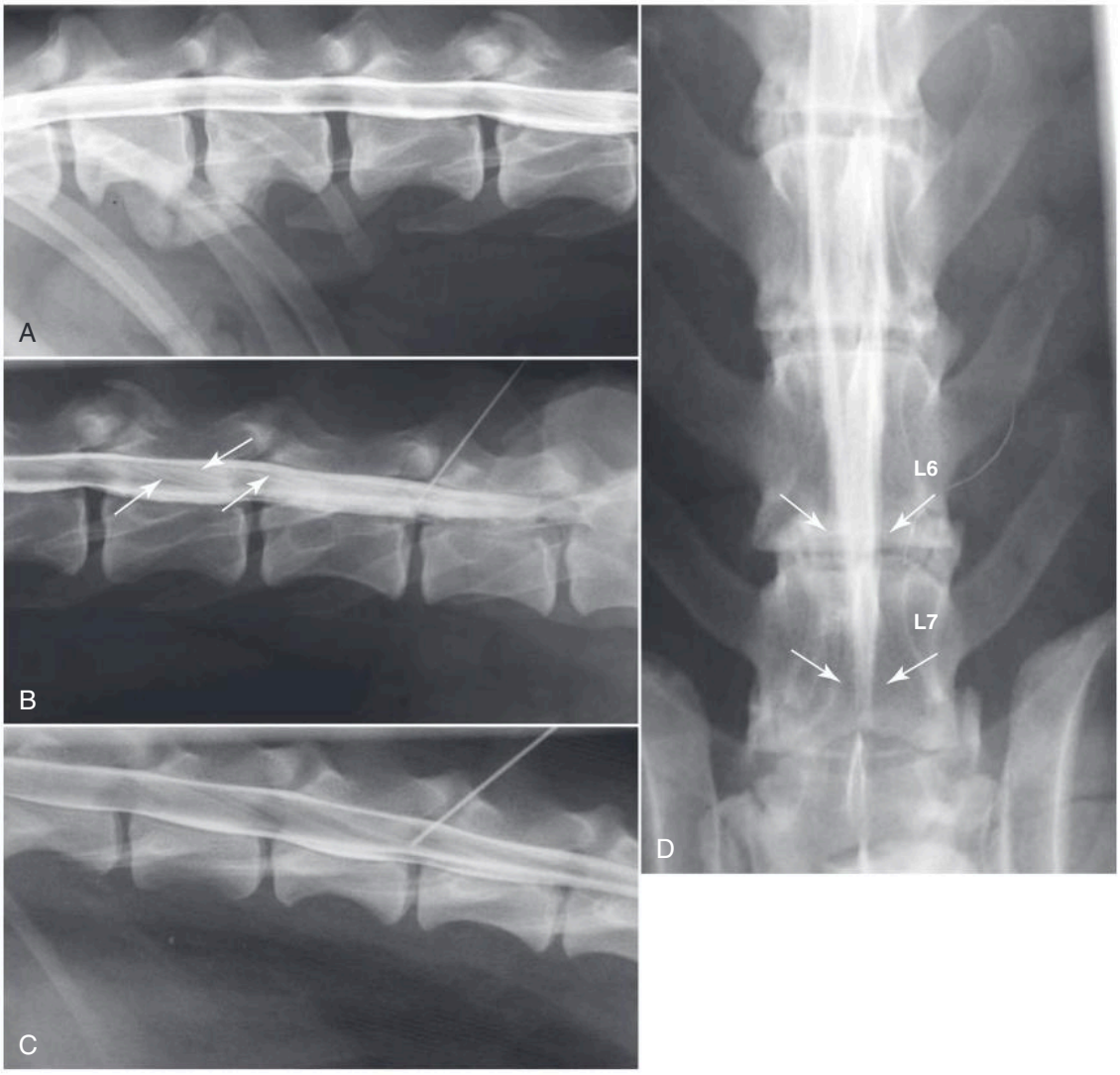


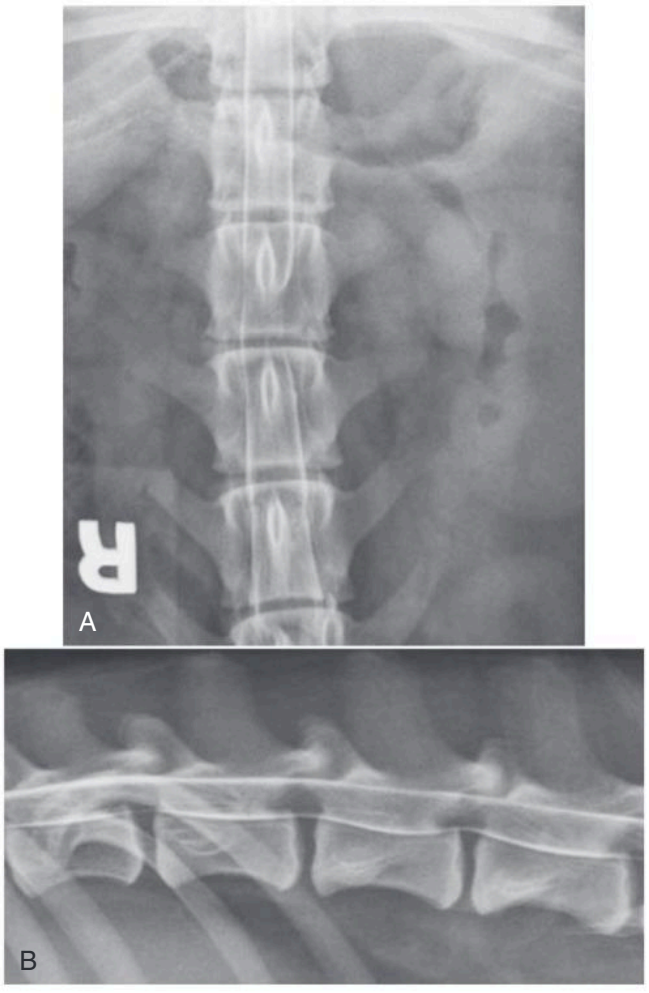
Fig. 14.35 Normal lumbar myelogram. **A,** Lateral myelogram centered at the cranial lumbar area. The dorsal and ventral subarachnoid space is well-filled with contrast medium and there is no epidural opacification. **B,** Lateral myelogram centered at the caudal lumbar area with a puncture at L5—L6. The subarachnoid space terminates at L6—L7. A puncture at L6—L7 would likely have placed the tip of the needle ventral to the thin terminal subarachnoid space and resulted in epidural leakage of contrast medium. Linear filling defects (*arrows*) are due to spinal nerves exiting the spinal cord, a normal finding in good quality study. **C,** Ventrodorsal myelogram centered at the caudal lumbar area with a L4—L5 puncture. Puncture should not be attempted cranial to this area and may cause significant cord injury. **D,** Ventrodorsal myelogram of the same dog as in **C**. The terminal subarachnoid space is thin (*arrows*) and would be difficult to puncture at L6—L7 or L7—S1.

canal ratio is large. The presence of contrast medium in a normal appearing central canal should not be confused with focal, indistinct opacification of the cord typical of myelomalacia. Enlargement of the central canal is associated with hydromyelia. The central canal may also become opacified when severe trauma or neoplasia disrupts the spinal cord parenchyma.

Intervertebral Disc Herniation

An extradural, and in some instances an intramedullary, pattern may result from disc herniation (Box 14.2).[102,106]

Disc herniation typically causes an extradural lesion characterized by thinning and dorsal deviation of the ventral aspect of the subarachnoid space in the lateral radiograph and compensatory widening of the spinal cord in the VD radiograph if the disc material is located in the ventral vertebral canal (Fig. 14.39).[104] On the lateral radiograph, the spinal cord is compressed and is deviated away from the site of disc herniation. The aspect of the contrast medium column adjacent to the herniation tends to be dome shaped, and the opposite side of the contrast medium column is narrowed by the displaced spinal cord. When herniated disc material is slightly lateral to the midline, a split, or forked, appearance to the contrast medium column may be seen on the lateral projection (see Fig. 14.39C). This finding should not be confused with an intradural-extramedullary lesion (see eFig. 14.14).[104,107]



eFig. 14.14 Ventrodorsal **(A)** and lateral **(B)** myelographic images of the thoracolumbar junction of a dog with disc herniation. A left-sided extradural compressive lesion is visible at L2–L3 in the ventrodorsal projection **(A)**, whereas only subtle thinning of the contrast medium in the dorsal and ventral subarachnoid space can be appreciated in the lateral view **(B)**.

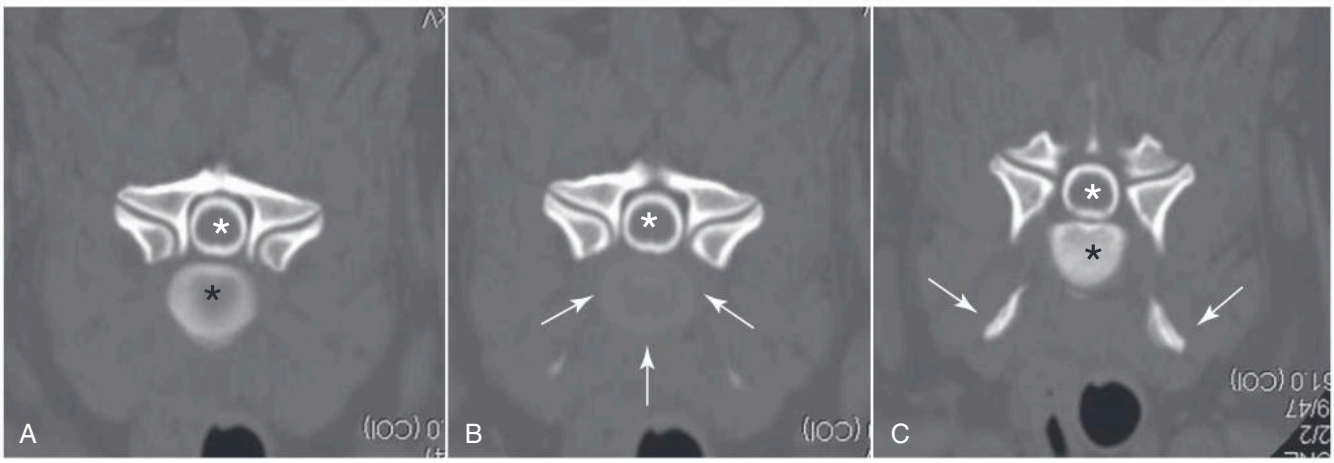


Fig. 14.36 Normal canine postmyelographic computed tomography (CT) transverse images made with a bone algorithm and 3-mm slice thickness. **A,** C2—C3 junction showing caudal endplate of C2 (*black asterisk*) and spinal cord (*white asterisk*) surrounded by contrast medium in the subarachnoid space. The epidural space is the circumferential area between opacified subarachnoid space and the vertebral canal. **B,** CT images made at the C2—C3 intervertebral disc space. *Arrows* delineate normal intervertebral disc, which has similar attenuation of surrounding soft tissue. Spinal cord (*white asterisk*) is surrounded by contrast medium in the subarachnoid space. **C,** CT images made at the C2—C3 junction showing cranial end-plate of C3 (*black asterisk*) and spinal cord (*white asterisk*) surrounded by contrast medium in the subarachnoid space. *Arrows* identify transverse processes of C3.

In type I herniation, an intramedullary pattern may be present due to severe spinal cord swelling. Swelling due to edema may obscure the classic extradural appearance of an extruded disc. Displacement of the subarachnoid space due to intramedullary swelling differs from that of extradural compression. With intramedullary swelling, the subarachnoid space is thin and displaced abaxially in all projections (Fig. 14.40). In some instances, severe spinal cord swelling may completely obliterate the subarachnoid space (see Fig. 14.40C).

If intramedullary swelling is present, slight axial deviation of the subarachnoid space somewhere within the region of spinal cord swelling suggests the site of an extradural discal mass (see Fig. 14.40B). This important clue is often found on only one radiographic projection but can help determine the site for surgical exploration and decompression. If CT is available, postmyelographic imaging can routinely depict the exact site of extradural compression when severe intramedullary swelling is present. It should be kept in mind that hemorrhage from rupture of the ventral vertebral veins is a complication of acute disc extrusion and the resultant hematoma may cause an extradural mass lesion.

Oblique radiographic projections should be obtained during every myelographic study because they frequently provide useful information. If disc material is located lateral to midline, the lateral and VD radiographs will be characterized by only a widened appearance to the spinal cord, whereas in oblique radiographic projections (VL-DR [ventral 25-degree left—dorsal right oblique] and VR-DL [ventral-25 degree right—dorsal left oblique]), an extradural pattern will be seen (Fig. 14.41). In some instances, both left and right lateral radiographic projections are needed for accurate identification of an extradural lesion.[108]

The gradual onset of type II disc protrusion tends to minimize spinal cord swelling, resulting in an extradural myelographic pattern (Fig. 14.42). Chronic changes, including hypertrophy of the annulus fibrosus, ligamentum flavum, and joint capsule of the dorsal intervertebral articular process joint, cause circumferential compression of the spinal cord ("hourglass appearance"). Type II protrusion is part of the cervical vertebral malformation-instability (wobbler) and lumbosacral stenosis-instability (cauda equina) syndromes of large-breed dogs.[82,109]

Acute noncompressive nucleus pulposus extrusion (ANNPE) is typified by an intramedullary myelographic pattern. Contrast medium uptake in the spinal cord can be a sign of cord penetration by the extruded disc material (Fig. 14.43).

Arachnoid Diverticula

Arachnoid diverticula are benign cyst-like areas in the subarachnoid space that may cause extramedullary compression and neural signs.[110–112] Histologically, these are not true cysts because they are not lined with epithelial cells. The cause of arachnoid diverticula is unknown, but a congenital or acquired etiology is possible. Resistance to cerebrospinal fluid (CSF)

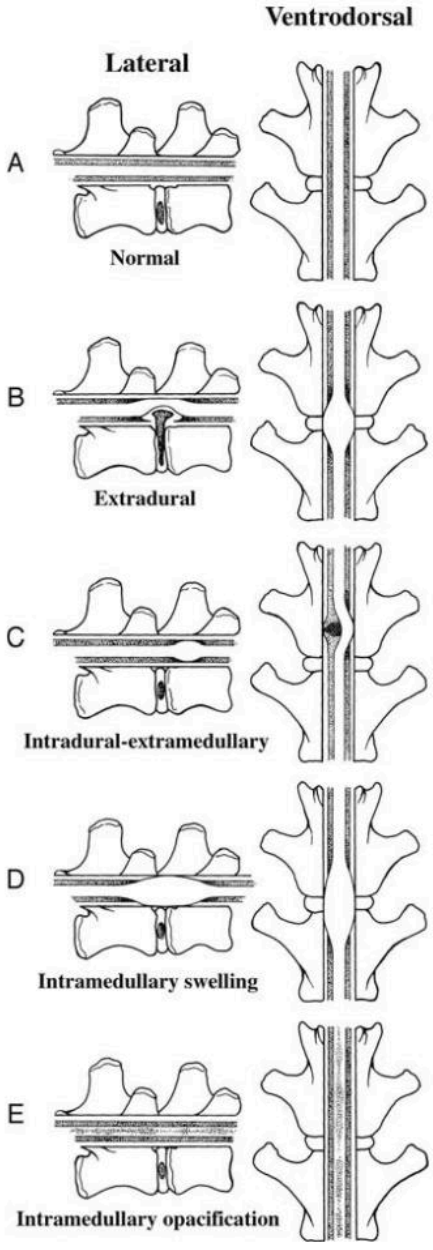


Fig. 14.37 Classification of myelographic lesions. **A,** Normal. **B,** Extradural. An aspect of the contrast medium column is displaced toward the center of the vertebral canal and often thinned or obliterated on one radiographic projection. On the orthogonal projection, the spinal cord may appear widened with peripheral displacement of the subarachnoid space because of an increase in spinal cord diameter caused by the compression. **C,** Intradural-extramedullary mass lesion within the subarachnoid space causes a filling defect in at least one projection. On the orthogonal projection, spinal cord swelling may be present depending on the size of the mass. As the contrast medium abuts the mass in the subarachnoid space, it flares around the mass and has been described as having the appearance of a *golf tee*. **D,** Intramedullary swelling. The spinal cord is swollen, causing thinning and obliteration of the subarachnoid space on both myelographic projections. **E,** Intramedullary opacification. Opacification of the spinal cord parenchyma is caused by the presence of contrast medium. This may be secondary to myelomalacia, which allows intramedullary diffusion of contrast medium. Opacification of the central canal differs and should not be confused with myelomalacia.

Table • **14.3**

Diagnostic Possibilities Associated With Myelographic Patterns.

PATTERN	DIAGNOSIS
Extradural	Intervertebral disc herniation
	Ligamentous hypertrophy
	Hematoma/hemorrhage
	Neoplasia (vertebral or epidural soft tissue)
	Vertebral fracture/dislocation
Intradural-extramedullary	Neoplasia (nerve sheath tumors, meningioma)
	Lateralized extradural masses, such as discs, may give the appearance of an intradural-extramedullary lesion
	Arachnoid diverticulum
Intramedullary swelling	Spinal cord edema or hemorrhage
	Neoplasia (neural, metastatic discrete cell, e.g., granulomatous meningoencephalitis)
	Ischemic myelopathy
Intramedullary opacification	Myelomalacia
	Hematomyelia, spinal cord perforation by high-velocity disc extrusion
Normal	Degenerative myelopathy[a]
	Ischemic myelopathy
	Myelitis
	Meningitis

[a]It is the author's opinion that cord size may be decreased in some dogs with degenerative myelopathy. However, this evidence based studies are lacking, thus this is an anecdotal observation.

flow, possibly induced by trauma, resulting in back pressure and dilation of the subarachnoid space, has been implicated as a cause in older animals. With arachnoid diverticula, survey radiographic examination is usually normal. After myelography, contrast medium fills the "cystic" area, defining abrupt dilation of the subarachnoid contrast medium and compression of the adjacent spinal cord (Fig. 14.44) Recognition of the intradural-extramedullary location of arachnoid cysts is important so that they can be differentiated from nonsurgical intramedullary lesions such as hydromyelia or syringomyelia. The intradural-extramedullary sign in this instance differs from that of a mass lesion (e.g., neurofibroma) in which a filling defect is present as well as subarachnoid dilation. Arachnoid diverticula that arise from causes other than previous trauma or surgery are commonly located in the dorsal aspect of the cervical subarachnoid space.[113]

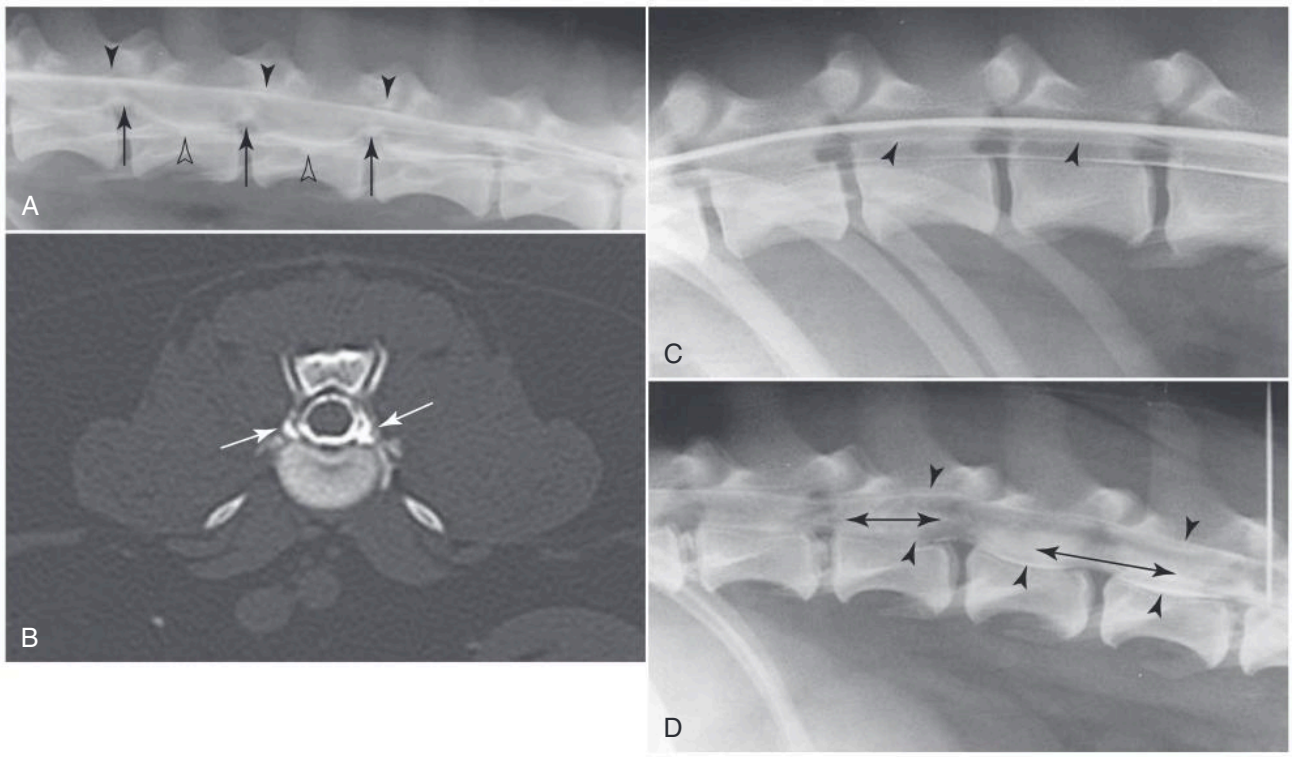


Fig. 14.38 Technical factors affecting myelographic quality. **A**, Moderate epidural leakage after lumbar myelography at L5–L6. Epidural contrast medium is recognized ventrally by the appearance of opacified vertebral venous sinuses (*large closed arrows*) and dorsally by opacification dorsal to the subarachnoid space (*small closed arrows*). Opacified depressions in the vertebral bodies contain the basivertebral veins (*open black arrows*). Epidural contrast medium summates with the subarachnoid space limiting interpretation. **B,** Follow-up computed tomography (CT) study reduces the effect of summation from epidural leakage (*arrows*). Due to the cross-sectional nature of CT, the subarachnoid space is still visualized and interpretation is possible. **C,** Opacification of the central canal (*arrows*) occurs when communication exists between the central canal and the subarachnoid space. **D,** Myelomalacia is typified by diffusion of contrast medium into the spinal cord parenchyma (*double-headed arrows*). Intramedullary swelling is also present, and the subarachnoid space is thin (*arrowheads*).

Box • **14.2**

Myelographic Signs of Intervertebral Disc Disease

Extradural Pattern

- Deviation and thinning of subarachnoid contrast medium at intervertebral disc space (ventral, dorsal, or lateral)
- Forked subarachnoid contrast medium (false intradural-extramedually sign) if disc is lateralized
- Spinal cord displacement
- Spinal cord compression (compensatory displacement flattens cord owing to extradural mass, mimics cord swelling)
- "Hourglass" subarachnoid space filling defect

Intramedullary Pattern

- Uniform spinal cord swelling caused by edema; subarachnoid contrast medium displaced, thin, or absent
- Opacification of spinal cord parenchyma

Synovial Cysts

Synovial cysts secondary to osteoarthritis of the dorsal intervertebral process joints may cause extradural signs and are most frequently seen in the cervical and lumbar areas (Fig. 14.45). Protrusion of the synovial membrane may cause the formation of a para-articular cavity filled with synovial fluid, leading to extradural compression of the cord and nerve roots.[112,113]

Neoplasia

Neoplasms of the meninges may cause intradural/extramedullary myelographic patterns, including meningiomas and nerve sheath tumors (neurofibromas, neurofibrosarcomas, and Schwannomas and nephroblastomas) (Fig. 14.46). Other tumors are possible, including metastatic tumors. Lymphomas and histiocytic sarcoma may cause any type of myelographic pattern, including an extradural pattern (Fig. 14.47). Tumors of the spinal cord usually cause cord swelling and an intramedullary myelographic pattern.

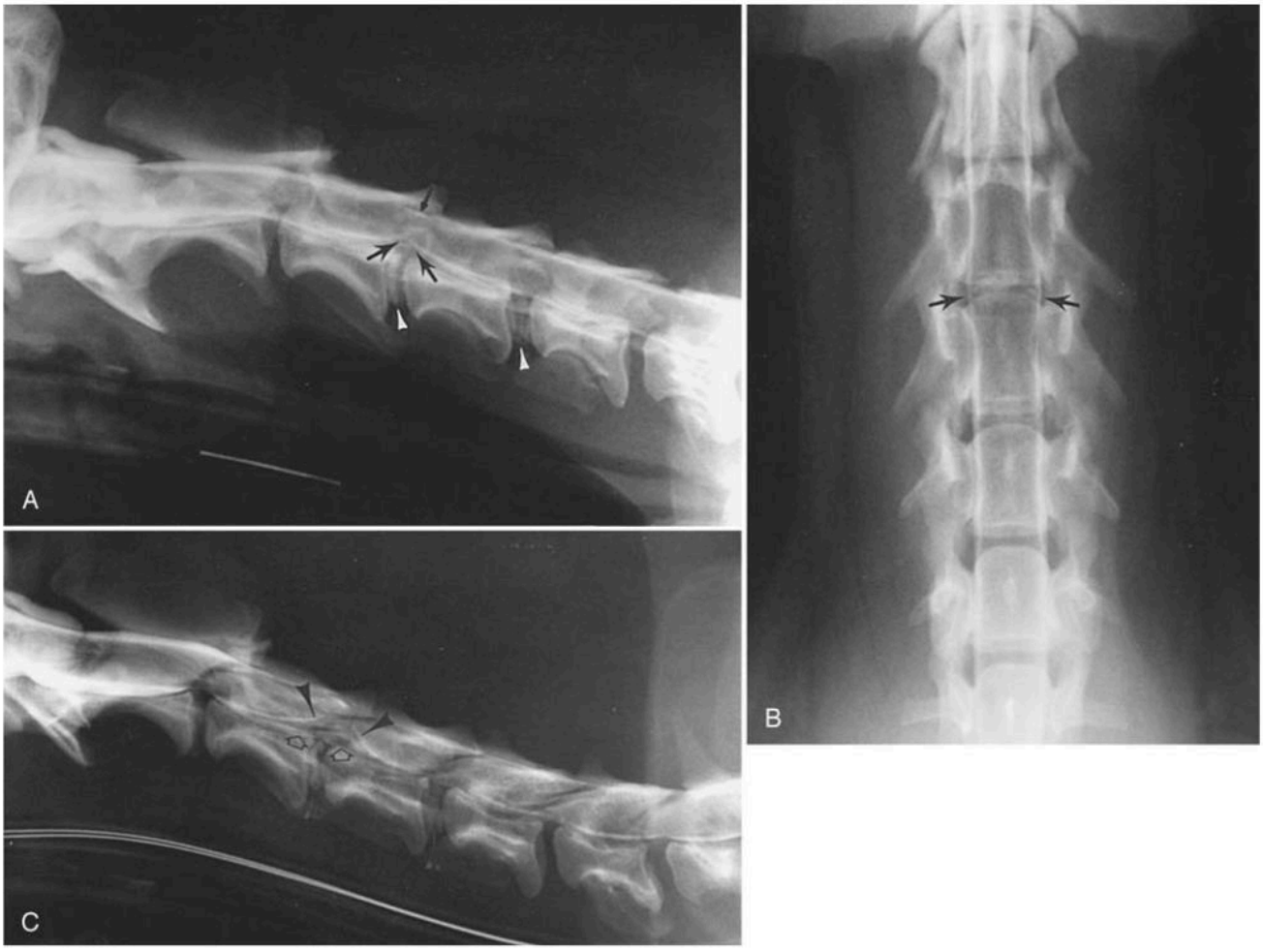


Fig. 14.39 Extradural lesions caused by a type I intervertebral disc herniation at C3–C4 are visible. **A,** Lateral myelogram. Dorsal deviation of the ventral aspect of the subarachnoid space is visible (*large arrows*). The dorsal aspect of the subarachnoid space is thin owing to displacement of the spinal cord (*small arrow*). Note mineralized disc material remaining in situ (*white arrowheads*). **B,** Ventrodorsal myelogram. Spinal cord swelling is typified by thinning and peripheral deviation of the subarachnoid space at C3–C4 (*arrows*). **C,** Forked appearance of the ventral aspect of the subarachnoid space is caused by the x-ray beam striking two tangents of the subarachnoid space. The extruded disc material is located lateral to the midline, causing the ventral aspect of the contrast medium column to appear as a *double line* on the lateral radiograph (*open arrows*). The double line is not seen in **A** because of a slight difference in patient positioning.

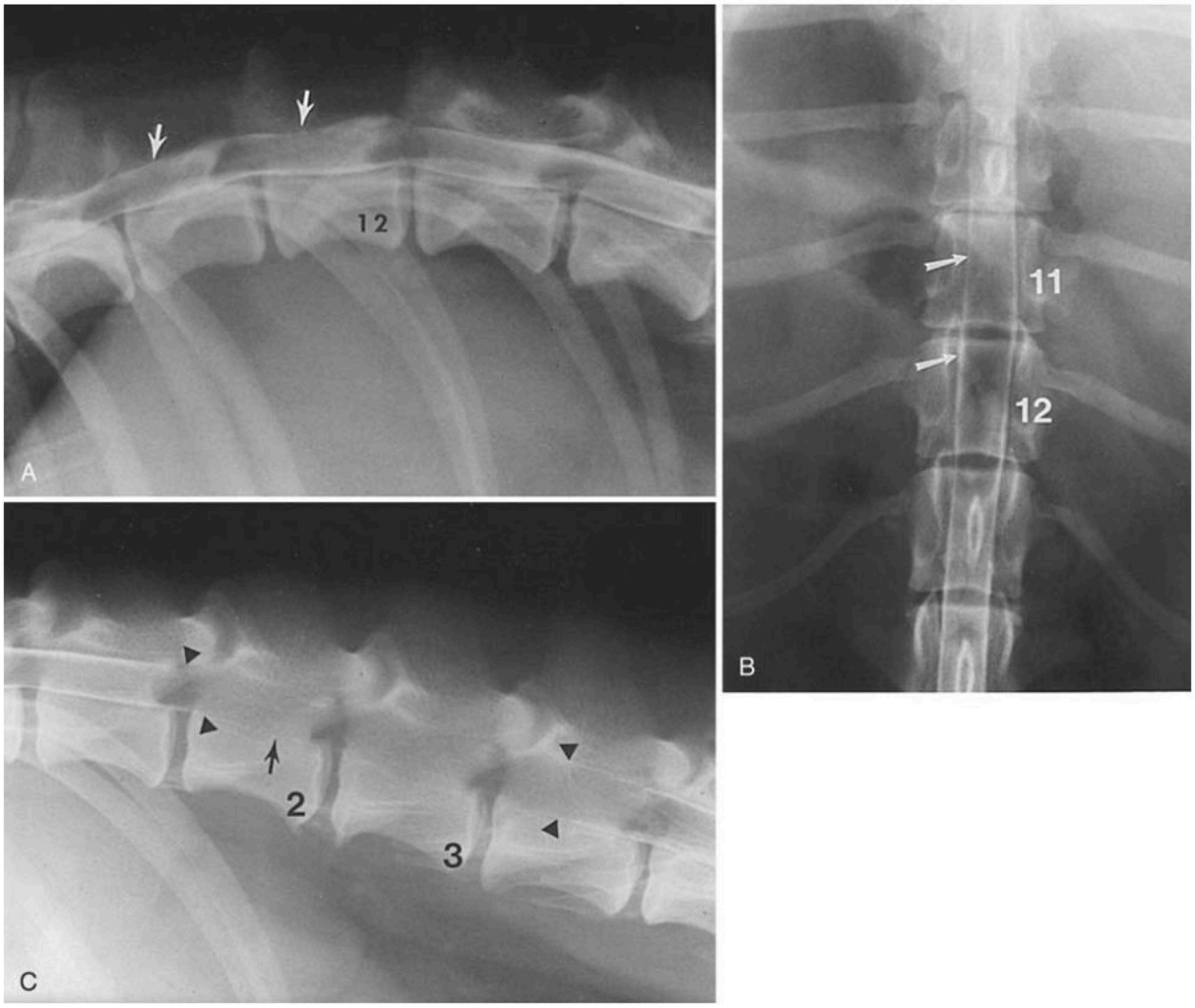


Fig. 14.40 Type I disc prolapse with intramedullary pattern. **A,** Lateral myelogram. Intramedullary swelling and a thin subarachnoid space (*arrows*) at T11—T12 are visible. **B,** Ventrodorsal myelogram of the dog in **A**. The spinal cord is wide at T11—T12; note the central shift of the right aspect of the contrast medium column (*arrows*), which indicates lateralization of the prolapse. In this instance, the surgeon may elect to perform a right hemilaminectomy. Intervertebral disc herniation at T11—T12 was confirmed at surgery. **C,** With severe intramedullary swelling, the contrast medium column may be totally obliterated (*arrowheads*), masking the extradural component of the lesion on all myelographic views. Intervertebral disc herniation at L2—L3 was confirmed at surgery.

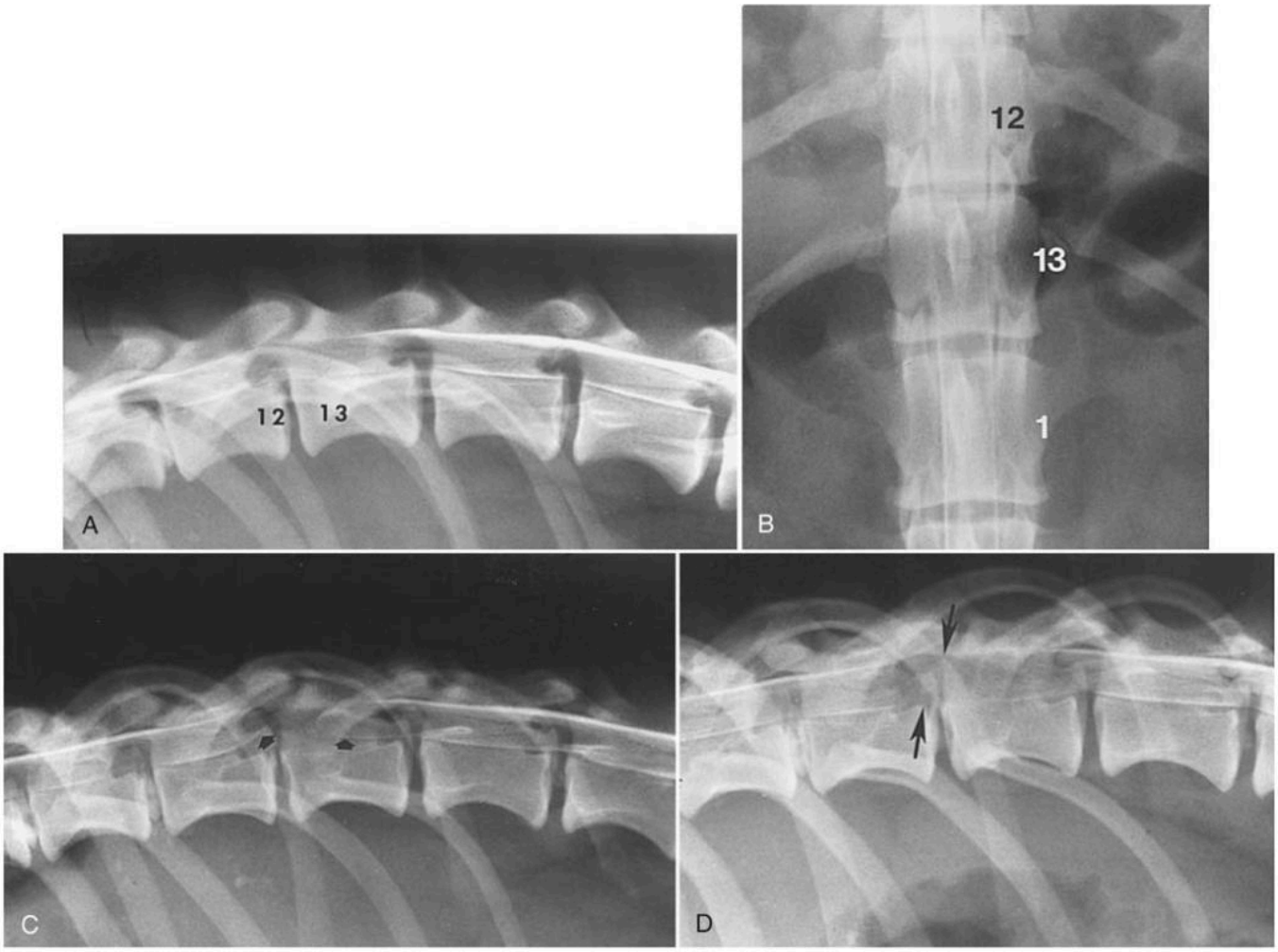


Fig. 14.41 Type I ventrolateral disc herniation. **A and B,** Lateral and ventrodorsal myelograms showing signs of mild intramedullary swelling, but the site of disc herniation is not evident. **C,** On a ventral 65-degree right dorsal to left oblique projection, an extradural mass effect is visible, typified by subarachnoid space thinning and deviation from disc material (*black arrowheads*). **D,** On a ventral 65-degree left dorsal to right oblique projection (orthogonal to **C**), marked intramedullary swelling is present (*black arrows*). The extradural and intramedullary lesions are best recognized on the oblique projections because the x-ray beam is striking each lesion tangentially.

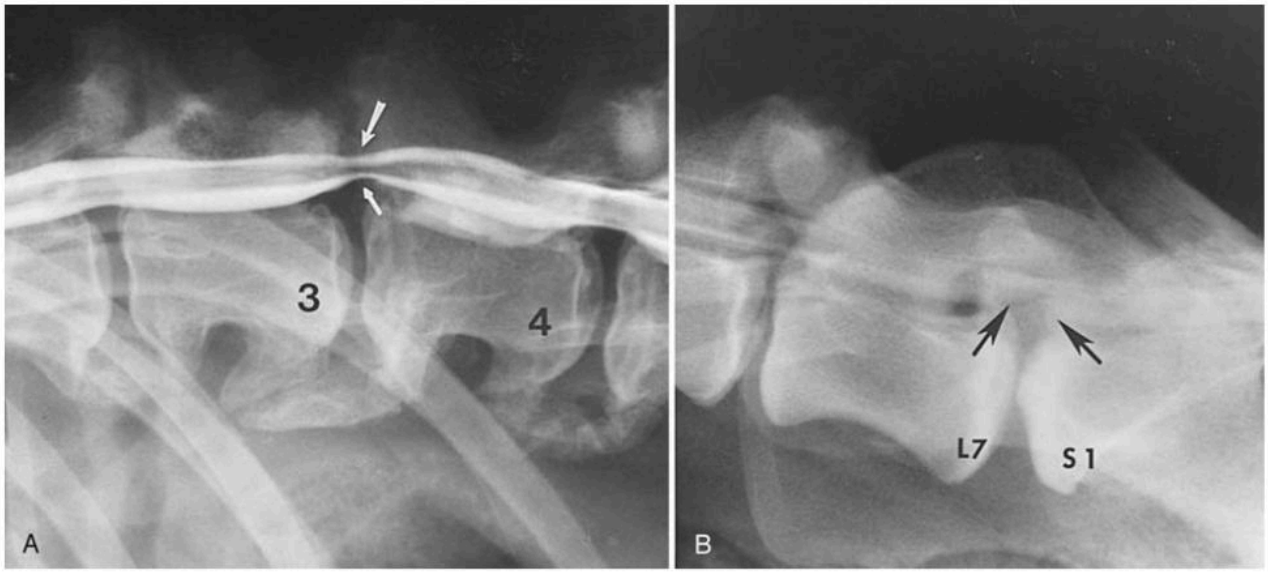


Fig. 14.42 Type II disc protrusion. **A,** Extradural mass effect caused by disc protrusion at L3–L4 (*arrows*). The hourglass appearance, a long-term change, is a result of disc protrusion and hypertrophy of the ventral longitudinal ligament, the annulus fibrosus, and the ligamentum flavum. Long-term degenerative changes of the vertebra are also present (spondylosis deformans and articular process degenerative joint disease). **B,** Disc protrusion at L7–S1. Note the narrowed intervertebral disc space and deviation of the dural sac (*arrows*).

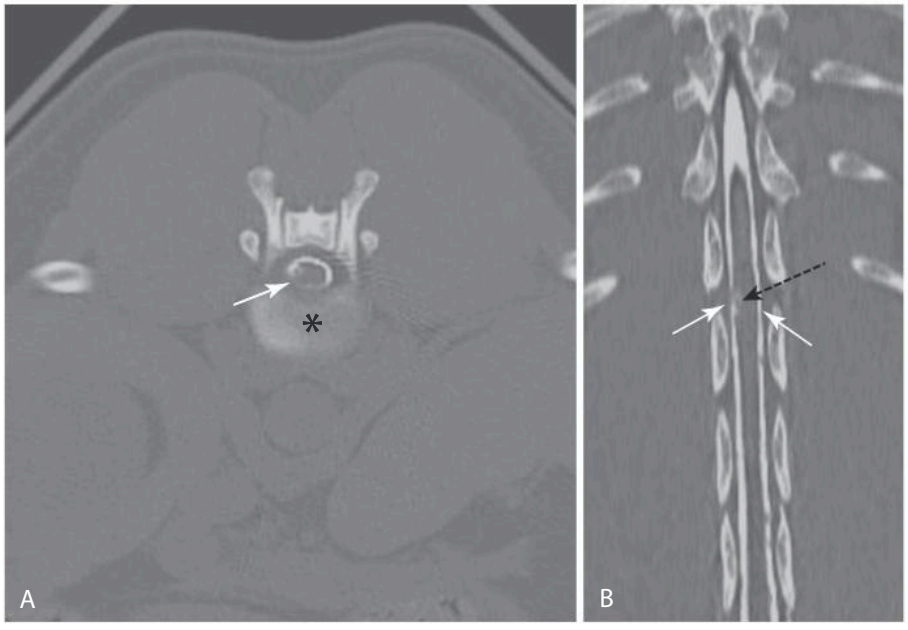


Fig. 14.43 Acute noncompressive nucleus pulposus extrusion in a 6-year-old female spayed Labrador retriever. While running in the yard yelped and became acute nonambulatory on the right pelvic limb and weak on the left. Postmyelographic computed tomography (CT) images were obtained after non-contrast CT imaging was inconclusive. **A,** Transverse postmyelographic CT image at the level of T13–L1. The subarachnoid contrast medium is attenuated ventrolaterally (*arrow*). *Asterisk* denotes intervertebral disc. **B,** Dorsal plane reformatted CT image. *White arrows* reveal thinning of lateral contrast columns consistent with spinal cord swelling. *Dashed black arrow* points toward area of uptake by the spinal cord indicating penetration of the pia by explosive forces from herniation of normal nucleus pulposus. (Images courtesy Gabriela Seiler, North Carolina State University College of Veterinary Medicine, with permission.)

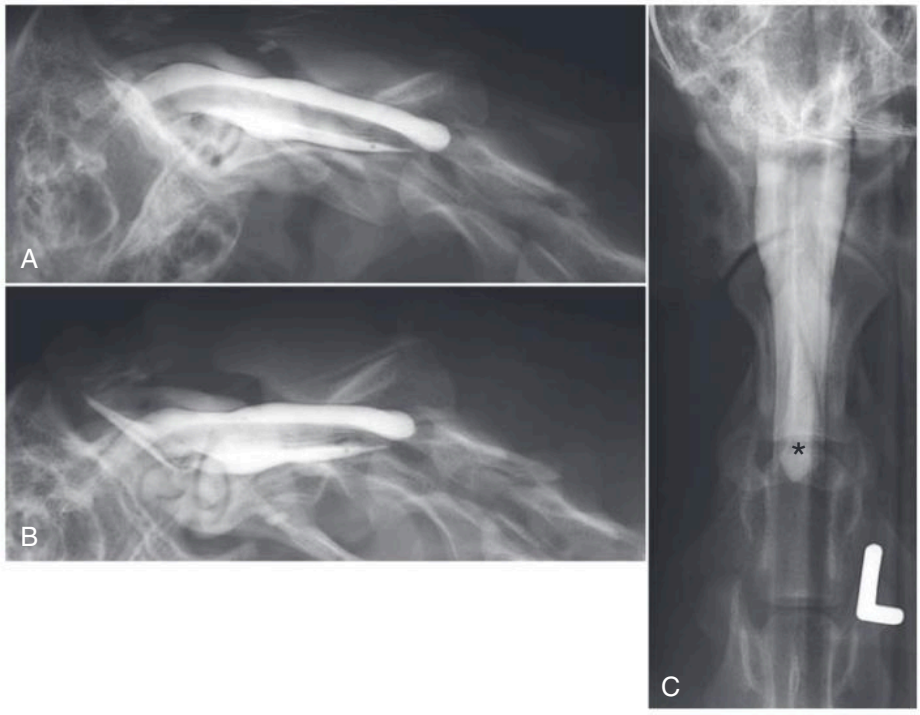


Fig. 14.44 Arachnoid diverticulum in a 3-year-old Rottweiler with cervical pain. **A and B,** 90-degree orthogonal oblique positioned myelograms of the atlantoaxial area following cervical myelography. These images are approximately 15 degrees from true lateral positioning and were made to maximize the diverticulum. An intradural extramedullary pattern is present. The opacified subarachnoid diverticulum is identified by *asterisks*. Note narrowing of cervical spinal cord at C2–C3. **C,** Ventrodorsal myelogram. Note blunted subarachnoid diverticulum (*asterisk*). The spinal cord is summated by the wide dorsal contrast column seen in **A**. (Images courtesy Gabriela Seiler, DVM, PhD, North Carolina State University College of Veterinary Medicine, with permission.)

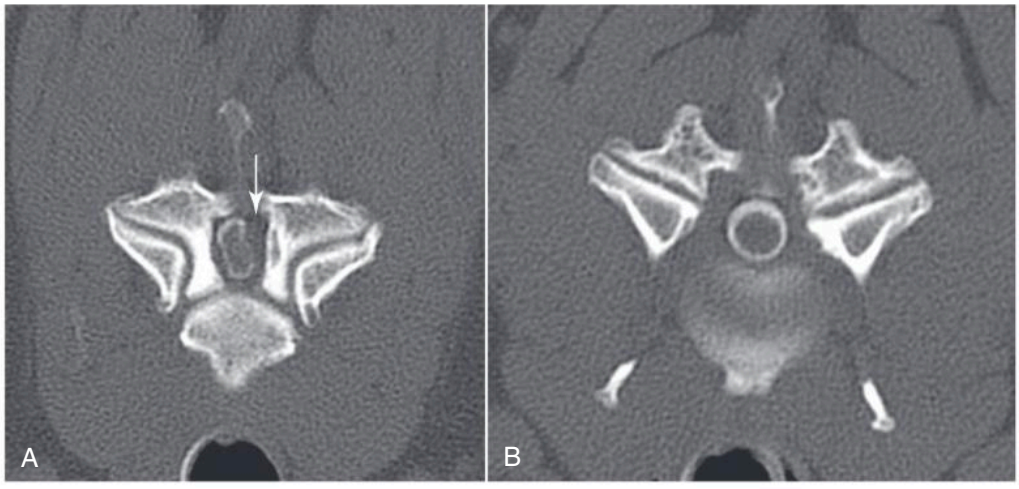


Fig. 14.45 Synovial cyst in a Great Dane with cervical spondylomyelopathy and a synovial cyst. Postmyelographic computed tomography (CT) images were obtained. **A,** Note the thickened/remodeled articular process and the cyst compressing the spinal cord (*arrow*) at C5–C6. **B,** Transverse postmyelographic CT image at C4–C5 showing a normal region for comparison. (Images are courtesy Ronaldo C. da Costa, DVM, MSc, PhD, The Ohio State University, with permission.)

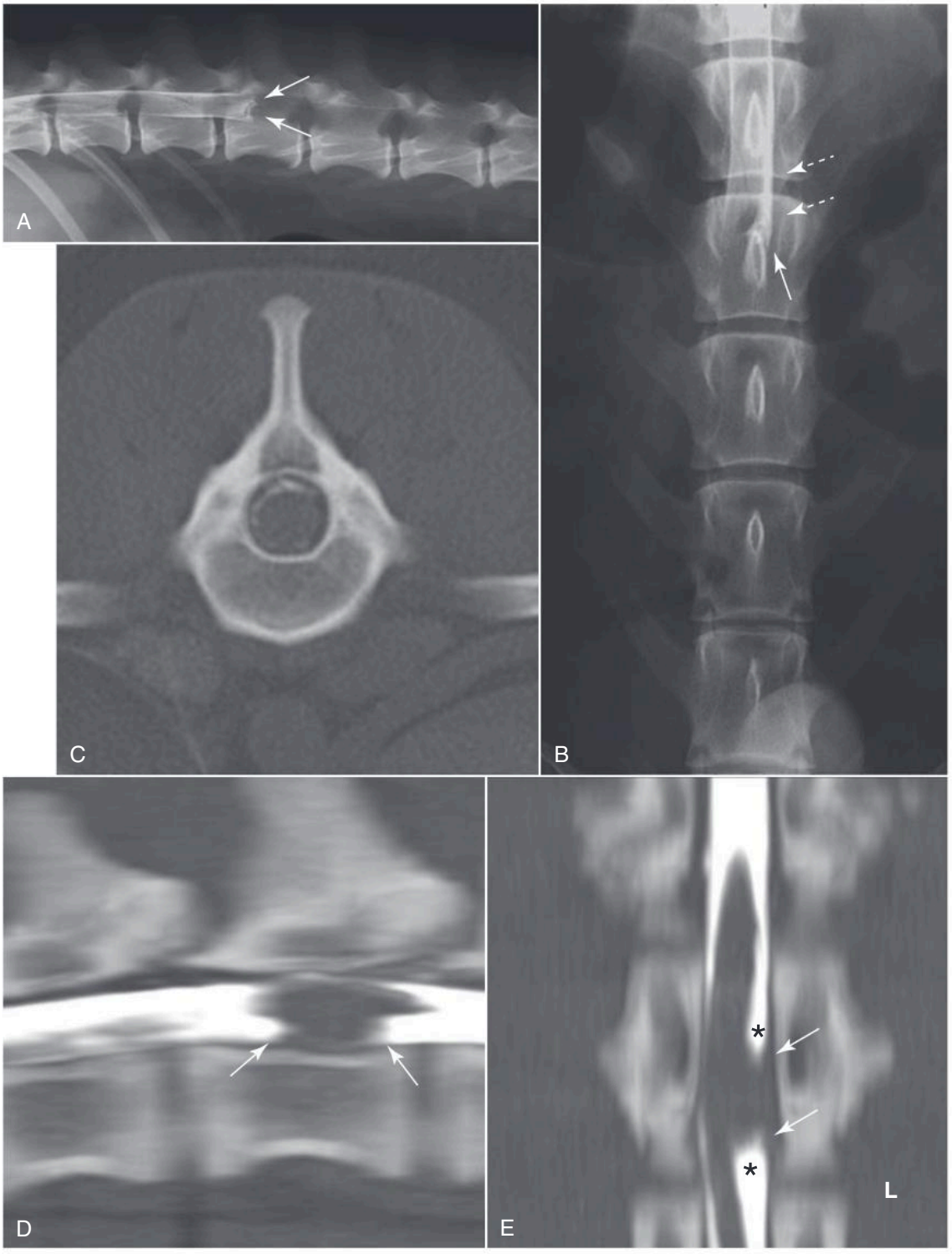


Fig. 14.46 Extraskeletal osteosarcoma in a 3-year-old mixed-breed dog with left pelvic limb monoparesis and decreased patellar reflex. Lateral **(A)** and ventrodorsal **(B)** myelograms are typified by an intradural extramedullary pattern. **A,** There is abrupt cessation of flow of contrast medium caudally at L3 (*arrows*). **B,** The spinal cord has undergone slight axial shift (*dotted arrows*) and the left subarachnoid space is widened as it ends in a blunted appearance. This blunted appearance has been referred to as a "golf tee" pattern as it suggests an intradural mass has caused a filling defect in the subarachnoid space. However, this pattern is not uniformly present with intradural lesions. Transverse **(A)**, sagittal **(D)** and dorsal **(E)** postmyelographic CT images of a dog with an intradural lesion. **C,** Transverse CT slice through L3 showing poor contrast medium filling of the subarachnoid space. **D,** Sagittal reformat at L3. *Arrows* show blunting of contrast medium. **E,** *Asterisks* indicate the widening of the subarachnoid space before it ends bluntly in the dorsal reformatted image.

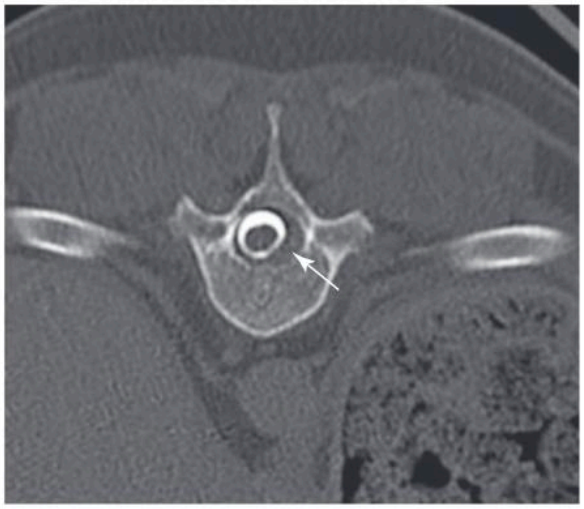


Fig. 14.47 Spinal lymphoma in an old mixed-breed dog with a 3-month history of slowly progressive intermittent cervical pain with a thoracic limb root signature sign. Transverse postmyelographic computed tomography (CT) image of a thoracic vertebra. The *arrow* denotes an extradural hypoattenuating mass displacing the subarachnoid contrast medium and the spinal cord. Additional extradural lesions were found in the cervical region.

Acknowledgment

With special thanks to prior authors of this chapter for their contributions.

REFERENCES

1. Thrall DE, Robertson ID. The spine. In: *Atlas of Normal Radiographic Anatomy and Anatomic Variants of the Dog and Cat*. 3rd ed. St Louis: Saunders; 2023.
2. Evans HE. Chapter 4. The skeleton. In: *Miller's Anatomy of the Dog*. 3rd ed. Philadelphia: Saunders; 1993:166–180.
3. Watson AG. *Phylogeny and Development of the Atlas-Axis Complex in the Dog, Master's Thesis*. Ithaca, NY: Cornell University; 1981.
4. Watson AG. Prenatal development of the composite occipito-atlanto-axial synovial joint cavity in the dog. *Anat Rec*. 1986;216:423–433.
5. Watson AG, Evans HE, DeLahunta A. Ossification of the atlas-axis complex in the dog. *Anat Histol Embryol*. 1986;15:122–138.
6. Evans HE. Chapter 4. The skeleton. In: *Miller's Anatomy of the Dog*. 3rd ed. Philadelphia: Saunders; 1993:178.
7. Evans HE. Chapter 4. The skeleton. In: *Miller's Anatomy of the Dog*. 3rd ed. Philadelphia: Saunders; 1993:225–231.
8. Shores A. Intervertebral disc syndrome in the dog. Part I. Pathophysiology and management. *Compend Contin Educ Pract Vet*. 1981;7:639.
9. Walker MA. The vertebrae—canine and feline. In: Thrall DE, ed. *Textbook of Veterinary Diagnostic Radiology*. ed 4. St Louis: Saunders; 2002:98–109.
10. Macpherson J, Ye Y. The cat vertebral column: stance configuration and range of motion. *Exp Brain Res*. 1998;119:324–332. https://doi.org/10.1007/s002210050348.
11. Baines EQ, Grandage J, Herritage ME, et al. Radiographic definition of the anticlinal vertebra in the dog. *Vet Radiol Ultrasound*. 2009;50:69–73.
12. Morgan JP. Congenital anomalies of the vertebral column of the dog: a study of the incidence and significance based on a radiographic and morphologic study. *J Am Vet Radiol Soc*. 1968;9:21–29.
13. Bailey CS, Morgan JP. Congenital spinal malformations. *Vet Clin North Am Small Anim Pract*. 1992;72:985–1015.
14. Lin JL, Coolman BR. Atlantoaxial subluxation in two dogs with cervical block vertebrae. *J Am Anim Hosp Assoc*. 2009;45:305–310.
15. Done SH, Drew RA, Robins GM, et al. Hemivertebra in the dog: clinical and pathological observations. *Vet Rec*. 1975;14:313–317.
16. Muller F, O'Rahilly R, Benson DR. The early origin of vertebral anomalies, as illustrated by a "butterfly" vertebra. *J Anat*. 1986;149:157–169.
17. Damur-Djuric N, Steffen F, Hassig M, et al. Lumbosacral transitional vertebrae in dogs: classification, prevalence and association with sacroiliac morphology. *Vet Radiol Ultrasound*. 2006;47:32–38.
18. Fluckiger M, Damur-Djuric N, Hassig M, et al. A lumbosacral transitional vertebra in the dog predisposes to caudal equina syndrome. *Vet Radiol Ultrasound*. 2006;47:39–44.
19. Harris G, Ball J, De Decker S. Lumbosacral transitional vertebrae in cats and its relationship to lumbosacral vertebral canal stenosis. *J Feline Med Surg*. 2019;21(4):286–292.
20. Thanaboonnipat C, Kumjumroon K, Boonkwang K, Tangsutthichai N, Sukserm W, Choisunirachon N. Radiographic lumbosacral vertebral abnormalities and constipation in cats. *Vet World*. 2021;14(2):492–498.
21. Lorenz MD, Kornegay JN. *Handbook of Veterinary Neurology*. 4th ed. St Louis: Saunders; 2004:164–189.
22. Cook JR, Oliver JE. Atlantoaxial luxation in the dog. *Compend Contin Educ Pract Vet*. 1981;3:242–252.
23. Watson AG, DeLahunta A. Atlantoaxial subluxation and absence of a transverse ligament of the atlas in dog. *J Am Vet Med Assoc*. 1989;195:235–237.
24. Cummings KR, Vilaplana Grosso F, Moore GE, et al. Radiographic indices for the diagnosis of atlantoaxial instability in toy breed dogs. *Vet Radiol Ultrasound*. 2018;59(6):667–676.
25. Warren-Smith C, Kneissl S, Benigni L, et al. Incomplete ossification of the atlas in dogs with cervical signs. *Vet Radiol Ultrasound*. 2009;50(6):635–638.
26. Lincoln JD. Cervical vertebral malformation/malarticulation syndrome in large dogs. *Vet Clin North Am Small Anim Pract*. 1992;22:923–935.
27. Seim HB, Withrow SJ. Pathophysiology and diagnosis of caudal cervical spondylo-myelopathy with emphasis on the Doberman pinscher. *J Am Anim Hosp Assoc*. 1982;18:241.
28. Van Gundy T. Canine wobbler syndrome. Part I: pathophysiology and diagnosis. *Compend Contin Educ Pract Vet*. 1989;11:269.
29. Selcer B, Oliver J. Cervical spondylopathy: wobbler syndrome in dogs. *J Am Anim Hosp Assoc*. 1975;11:175–179.
30. Seim H. Diagnosis and treatment of cervical vertebral instability-malformation syndromes. In: Bonagura JD, ed. *Kirk's Current Veterinary Therapy XIII: Small Animal Practice*. Philadelphia: Saunders; 2000:992–1000.
31. Headhammer A, Wu F, Krook L, et al. Over nutrition and skeletal disease. An experimental study in growing Great Dane dogs. *Cornell Vet*. 1974;64(suppl 5):58.
32. Drost WT, Lehenbauer TW, Reeves J. Mensuration of cervical vertebral ratios in Doberman pinschers and Great Danes. *Vet Radiol Ultrasound*. 2002;43:124–231.
33. Martin-Valuero P, Da Costa R. Evaluation of traditional and novel radiographic vertebral ratios in Great Danes with versus without cervical spondylomyelopathy. *Vet Radiol Ultrasound*. 2014;55:448–495.
34. Lipsitz D, Levitski RE, Chauvet AE, et al. Magnetic resonance features of cervical stenotic myelopathy in 21 dogs. *Vet Radiol Ultrasound*. 2001;42:20–27.

35. Da Costa RC, Parent J, Dobson H. Comparison of magnetic resonance imaging and myelography in 18 Doberman pinscher dogs with cervical spondylo-myelopathy. *Vet Radiol Ultrasound*. 2006;47:523–531.
36. Shores A. Spinal trauma. Pathophysiology and management of traumatic spinal injuries. *Vet Clin North Am Small Anim Pract*. 1992;22:859–867.
37. Matthiesen DT. Thoracolumbar spinal fractures and luxations: surgical management. *Compend Cont Educ Pract Vet*. 1983;5:867.
38. Walker TL, Tomlinson J, Sorjonen DC, et al. Diseases of the spinal column. In: Slatter DH, ed. *Textbook of Small Animal Surgery*. Philadelphia: Saunders; 1985:1367.
39. Watters DH, Blevins WE, Wallace LJ. Cervical vertebral fractures in 56 dogs: a retrospective study. *J Am Anim Hosp Assoc*. 1999;35:135–146.
40. Slocum B, Rudy RL. Fractures of the seventh lumbar vertebra in the dog. *J Am Anim Hosp Assoc*. 1975;11:67.
41. Kinns J, Mai W, Seiler G, et al. Radiographic sensitivity and negative predictive value for acute canine spinal trauma. *Vet Radiol Ultrasound*. 2006;47:563–570.
42. Hoerlein BF. *Philadelphia. Canine Neurology: Diagnosis and Treatment*. 3rd ed. Saunders; 1978:470–560.
43. DeLahunta A, ed. *Veterinary Neuroanatomy and Clinical Neurology*. 2nd ed. Philadelphia: Saunders; 1983:186–188.
44. da Costa RC, De Decker S, Lewis MJ, Volk H. Canine Spinal Cord Injury Consortium (CANSORT-SCI): diagnostic imaging in intervertebral disc disease. *Front Vet Sci*. 2020;7:588338. https://doi.org/10.3389/fvets.2020.588338.
45. Priester W. Canine intervertebral disc disease—occurrence by age, breed, and sex among 8,117 cases. *Theriogenology*. 1976;6:93–303.
46. Chang Y, Dennis R, Platt SR, et al. Magnetic resonance imaging of traumatic intervertebral disc extension in dogs. *Vet Rec*. 2007;160:795–799.
47. Fen J. Olby NJ and the canine spinal cord injury consortium (CANSORT-SCI): classification of intervertebral disc disease. *Front Vet Sci*. 2020;7:579025.
48. Lamb CN, Nichols A, Targett P, Mannion P. Accuracy of survey radiographic diagnosis of intervertebral disc protrusion in dogs. *Vet Rad Ultrasound*. 2002;43:222–228.
49. Robertson ID, Thrall DE. Imaging dogs with suspected disc herniation: pros and cons of myelography, computed tomography and magnetic resonance, Vet Radiol Ultrasound. 2011;52(suppl 1):S81–S84.
50. Owens JM, Biery DN. Spine. In: Owens JM, Biery DN, eds. *Radiographic Interpretation for the Small Animal Clinician*. 2nd ed. Philadelphia: Williams & Wilkins; 1999:143–144.
51. Hugnet C, Marrou B, Dally C, et al. Osteomyelitis and discospondylitis due to *Scedosporium apiospermum* in a dog. *J Vet Diagn Invest*. 2009;21:120–123.
52. Csébi P, Jakab C, Jánoski K. Vertebral osteomyelitis and meningitis caused by *Pasteurella canis* in a dog—clinicopathological case report. *Acta Vet Hung*. 2010;58:13–21.
53. La Croix JA. Vertebral body osteomyelitis: case report. *J Am Vet Rad Soc*. 1973;14:17–21.
54. Kuwamura M, Ide M, Yamate J, et al. Systemic candidiasis in a dog, developing spondylitis. *J Vet Med Sci*. 2006;68:1117–1119.
55. Johnston DE, Summers BA. Osteomyelitis of the lumbar vertebrae in dogs caused by grass-seed-foreign bodies. *Aust Vet J*. 1971;47:289.
56. van der Merwe L, Kirberger RM, Clift S, et al. *Spirocerca lupi* infection in the dog: a review. *Vet J*. 2008;176:294–309.
57. Thomas WB. Discospondylitis and other vertebral infections. *Vet Clin North Am Small Anim Pract*. 2000;30:169–182.
58. DeLahunta A. Small animal spinal cord disease. In: DeLahunta A, ed. *Veterinary Neuroanatomy and Clinical Neurology*. 2nd ed. Philadelphia: Saunders; 1983:190.
59. Naughton JF, Tucker R, Bagley RS. Radiographic diagnosis-paraspinal abscess in a dog. *Vet Radiol Ultrasound*. 2005;46:23–26.
60. Jimenez MM, O'Callaghan MW. Vertebral physitis: a radiographic diagnosis to be separated from discospondylitis, a preliminary report. *Vet Radiol Ultrasound*. 1995;36:188–195.
61. Packer RA, Coates JR, Cook CR, et al. Sublumbar abscess and discospondylitis in a cat. *Vet Radiol Ultrasound*. 2005;46:396–399.
62. Tipold A, Stein VM. Inflammatory diseases of the small animal spine. *Vet Clin North Am Small Anim Pract*. 2010;40:871–879.
63. Moore MP. Discospondylitis. *Vet Clin North Am Small Anim Pract*. 1992;22:1027–1033.
64. Schultz RM, Johnson EG, Wisner ER, et al. Clinicopathologic and diagnostic imaging characteristics of systemic aspergillosis in 30 dogs. *J Vet Intern Med*. 2008;22(4):851–859.
65. Carrera I, Sullivan M, McConnell F, et al. Magnetic resonance features of discospondylitis in dogs. *Vet Radiol Ultrasound*. 2011;52:125–131.
66. Kirberger RM. Early diagnostic imaging findings in juvenile dogs with presumed diskospondylitis: 10 cases (2008–2014). *J Am Vet Med Assoc*. 2016;249:539–546.
67. *Dorland's Illustrated Medical Dictionary*. 28th ed. Philadelphia: Saunders; 1994:1564.
68. Morgan JP. Spondylosis deformans in the dog. *Acta Orthop Scand Suppl*. 1967;96:7–87.
69. Morgan JP, Biery DN. Spondylosis deformans. In: Newton CD, ed. *Textbook of Small Animal Orthopaedics*. Philadelphia: Lippincott Williams & Wilkins; 1985:733–738.
70. Morgan JP. Spondylosis deformans in the dog: its radiographic appearance. *J Am Vet Radiol Soc*. 1967;8:17.
71. Morgan JP, Miyabayashi T. Degenerative changes in the vertebral column of the dog: common radiographic findings. *Vet Radiol Ultrasound*. 1988;29:72–77.
72. Resnick D. Degenerative disease of the spine. In: Resnick D, ed. *Bone and Joint Imaging*. 2nd ed. Philadelphia: Saunders; 1996:355.
73. Hulkins DW, Meakin JR. Relationship between structure and mechanical function of the tissues of the intervertebral joint. *Am Zool*. 2000;40:42–52.
74. Carnier P, Gallo L, Sturaro E, et al. Prevalence of spondylosis deformans and estimates of genetic parameters for the degree of osteophytes development in Italian boxer dogs. *J Anim Sci*. 2004;82:85–92.
75. Langeland M, Lingaas F. Spondylosis deformans in the boxer: estimates of heritability. *J Small Anim Pract*. 1995;36:166–169.
76. Breit S, Kunzel W. The position and shape of osteophyte formations at canine vertebral endplates and its influence on radiographic diagnosis. *Anat Histol Embryol*. 2001;30:179–184.
77. Levine GJ, Levine JM, Walker MA, et al. Evaluation of the association between spondylosis deformans and clinical signs of intervertebral disc disease in dogs: 172 cases (1999–2000). *J Am Vet Med Assoc*. 2006;228:96–100.
78. Fletcher TF. Chapter 16. Spinal cord and meninges. In: Evans HE, ed. *Miller's Anatomy of the Dog*. ed 3. Philadelphia: Saunders; 1993:804–806.
79. Morgan JP, Atilola M, Bailey CS. Vertebral canal and spinal cord mensuration. A comparative study and its effect on lumbosacral myelography in the dachshund and German shepherd dog. *J Am Vet Med Assoc*. 1987;191:951–957.

80. Pardo AD, Morgan JP. Myelography in the cat: a comparison of cisternal versus lumbar puncture, using metrizamide. *Vet Radiol*. 1988;29:89–95.
81. *Dorland's Illustrated Medical Dictionary*. 28th ed. Philadelphia: Saunders; 1994:280.
82. Wheeler SJ. Lumbosacral disease. *Vet Clin North Am small Anim Pract*. 1992;22:937–950.
83. Lenehan TM. Canine caudal equina syndrome. *Comp Cont Educ Pract Vet*. 1983;5:941–950.
84. Ramirez O, Thrall DE. A review of imaging techniques for canine cauda equina syndrome. *Vet Radiol Ultrasound*. 1998;39:283–296.
85. Jones JC, Sorjonen DC, Simpson ST, et al. Comparison between computed tomographic and surgical finding in 9 large breed dogs with lumbosacral stenosis. *Vet Radiol Ultrasound*. 1996;37:247–256.
86. Lang J, Hani H, Schwalder P. A sacral lesion resembling osteochondrosis in the German shepherd dog. *Vet Radiol Ultrasound*. 1992;33:69–76.
87. Adams WH, Daniel GB, Pardo AD, et al. Magnetic resonance imaging of the caudal lumbar and lumbosacral spine in 13 dogs (1990–1993). *Vet Radiol Ultrasound*. 1995;36:3–13.
88. Seiler GS, Hani H, Busato AR, et al. Facet joint geometry and intervertebral disk degeneration in the L5-S1 region of the vertebral column in German shepherd dogs. *Am J Vet Res*. 2002;63:86–90.
89. Lang J. Flexion-extension myelography canine caudal equina. *Vet Radiol Ultrasound*. 1988;29:242–257.
90. Widmer WR, Thrall DE. Canine and feline intervertebral disc disease, myelography, and spinal cord disease. In: Thrall DE, ed. *Textbook of Veterinary Diagnostic Radiology*. 5th ed. St Louis: Saunders; 2007:194–219.
91. Roberts RE, Selcer BA. Myelography and epidurography. *Vet Clin North Am small Anim Pract*. 1993;23:307–329.
92. Barthez PY, Morgan JP, Lipstiz D. Discography and epidurography for evaluation of the lumbosacral junction in dogs with cauda equina syndrome. *Vet Radiol Ultrasound*. 1994;35:152–157.
93. Morgan JP, Ackerman N, Bailey CS. Vertebral tumors in the dog: a clinical radiologic and pathologic study of 61 primary and secondary lesions. *Vet Radiol Ultrasound*. 1980;21:197–212.
94. Luttgen PL. Neoplasms of the spine. *Vet Clin North Am Small Anim Pract*. 1992;22:973–984.
95. Edelstyn GA, Gillespie PJ, Grebbel FS. The radiological demonstration of osseous metastasis: experimental observations. *Clin Radiol*. 1967;18:158.
96. Bossens K, Bhatti S, Van Soens I, et al. Diffuse idiopathic skeletal hyperostosis of the spine in a nine-year-old cat. *J Small Anim Pract*. 2016;57:33–35.
97. Morgan JP, Stavenborn M. Disseminated idiopathic skeletal hyperostosis (DISH) in a dog. *Vet Radiol Ultrasound*. 1991;32:65–70.
98. Konde LJ, Thrall MA, Gasper P, et al. Radiographically visualized skeletal changes associated with mucopolysaccharidosis VI in cats. *Vet Radiol Ultrasound*. 1987;28:223–228.
99. Harris WH, Heaney RP. Skeletal renewal and metabolic bone disease. *N Engl J Med*. 1969;280(4):193–202.
100. Widmer WR, Blevins WE. Veterinary myelography: a review of contrast media, adverse effects and technique. *J Am Anim Hosp Assoc*. 1991;27:163–177.
101. Olby NJ, Dyce J, Houlton JEF. Correlation of plain radiographic and lumbar myelographic findings in thoracolumbar disc disease. *J Small Anim Pract*. 1994;35:345–350.
102. Roberts RE, Selcer BA. Myelography and epidurography. *Vet Clin North Am Small Anim Pract*. 1993;23:307–329.
103. Tilmant L, Ackerman N, Spencer CP. Mechanical aspects of subarachnoid space puncture in the dog. *Vet Radiol*. 1984;25:227–232.
104. Lamb CR. Common difficulties with myelographic diagnosis of acute intervertebral disc disease in the. dog. *J Small Anim Pract*. 1994;35:549–558.
105. Kirberger RM, Wrigley R. Myelography in the dog: a review of patients with contrast medium in the central canal. *Vet Radiol*. 1993;3:253–258.
106. Burk RL. Problems in the radiographic interpretation of intervertebral disc disease in the dog. *Probl Vet Med Intervert Disc Dis*. 1989;1:381–481.
107. Kirberger RM, Roos CJ, Lubbe AM. The radiological diagnosis of thoracolumbar disc disease in the dachshund. *Vet Radiol Ultrasound*. 1992;33:255–261.
108. Matteucci ML, Ramirez 3rd O, Thrall DE. Radiographic diagnosis: effect of right vs. left lateral recumbency on myelographic appearance of a lateralized extradural mass. *Vet Radiol Ultrasound*. 1999;40:351–352.
109. Mattoon JS, Koblik PD. Quantitative survey radiographic evaluation of the lumbosacral spine of normal dogs and dogs with degenerative lumbosacral stenosis. *Vet Radiol Ultrasound*. 1993;34:194–206.
110. Cambridge AJ, Bagley RS, Britt LG, et al. Radiographic diagnosis: arachnoid cyst in a dog. *Vet Radiol Ultrasound*. 1997;38:434.
111. Bentley JF, Simpson ST, Hathcock JT. Spinal arachnoid cyst in a dog. *J Am Anim Hosp Assoc*. 1991;27:549.
112. da Costa RC, Cook LB. Cystic abnormalities of the spinal cord and vertebral column. *Vet Clin Small Anim*. 2016;46:277–293.
113. Lowrie ML, Platt SR, Garosi LS. Extramedullary spinal cysts in dogs. *Vet Surg*. 2014;43:650–662.

ELECTRONIC RESOURCES

Additional information related to the content in Chapter 14 can be found online at eBooks.Health.Elsevier.com.

- Chapter Quiz

CHAPTER 15

Magnetic Resonance Imaging and Computed Tomography Features of Canine and Feline Spinal Cord Disease

Wilfried Mai

Computed tomography (CT) and magnetic resonance imaging (MRI) are used routinely in the investigation of spinal diseases in the dog and cat.[1,2] They are both superior to radiography in the diagnosis of most spinal conditions. MRI has a better overall diagnostic sensitivity than CT and can be used to diagnose virtually all conditions of the spine. However, there are patients in which CT is still the preferred method, for example, vertebral trauma caused by a gunshot wherein metallic foreign material is present that would cause considerable artifact in magnetic resonance (MR) images, or for the diagnosis of subtle bone lesions, such as vertebral subluxation or fractures. Although a number of spinal conditions can be diagnosed with radiographs (e.g., discospondylitis), CT and MRI may still be warranted to better assess the extent of the condition, which may be important for diagnostic or therapeutic purposes. Earlier diagnosis of some conditions may also be permitted by CT or MRI.

NORMAL APPEARANCE OF THE SPINE ON COMPUTED TOMOGRAPHY AND MAGNETIC RESONANCE IMAGING

Normal Anatomy

A schematic representation of the components of the vertebrae and main ligaments of the spine is shown in Fig. 15.1. The longitudinal ligaments of the vertebral column provide dorsal and ventral support for the intervertebral discs.[3] The dorsal longitudinal ligament lies on the floor of the vertebral canal. In the cervical region, it is wide and thick, which explains why lateral disc extrusion leading to radiculopathy, or root signature, is more common in the cervical region than other spinal regions. In the thoracolumbar area, the dorsal longitudinal ligament is thinner and centered on the midline allowing dorsal protrusion of disc material leading to spinal cord compression. The intercapital ligaments are short, transverse fibrous bands that lie ventral to the dorsal longitudinal ligament, joining left-to-right rib heads between T2 and T11.[3] They, therefore, buttress the dorsal part of the annulus fibrosus cranial to T11, reducing the probability of dorsal disc protrusion in this region. The ventral longitudinal ligament spans the ventral surface of the vertebral column.[3] The yellow ligaments *(ligamentum flavum)*, also called *interarcuate ligaments*, are loose, thin, elastic sheets that bridge the space between the arches of adjacent vertebrae.[3] Another ligament of interest, recently described, is the meningovertebral ligament, which forms a continuous attachment between the ventral surface of the dura mater and dorsal aspect of the vertebral bodies and intervertebral discs, attaching to the dorsal longitudinal ligament. This ligament creates an anatomic barrier which can cause some pathological lesions in the ventral epidural space to have a bilobed shape on cross-sectional imaging.[4]

The spinal cord and spinal nerve roots lie in the vertebral canal, which is formed by the juxtaposition of all the individual vertebral foramina of the spine. The spinal cord begins at the foramen magnum and terminates caudally at the *conus medullaris*, around L6. The actual termination is caudal to L6 in smaller breeds of dogs and cats, whereas it is cranial to L6 in larger canine breeds.[5] Normal segmental widening of the spinal cord is present at the cervical and lumbar intumescences, and this should not be mistaken for pathologic cord swelling.[3] Spinal cord segments and vertebrae have the same numeric designation, with the exception of spinal cord segment C8, but the location of each spinal cord segment is usually cranial to the corresponding vertebral segment.[3] The ratio between the diameter of the spinal cord and the diameter of the vertebral canal varies between dog breeds, being higher in dachshunds and in other chondrodystrophic breeds in general versus non-chondrodystrophic breeds.[6]

The spinal cord is surrounded by the meninges (see Fig. 15.2). The pia mater is the innermost meningeal layer; it is firmly attached to the spinal cord and highly vascular.[7] The arachnoid membrane is next, and the dura mater is the outermost meningeal layer. The arachnoid and dura are attached closely to each other by a layer of dural border cells.[7] The subarachnoid space lies between the arachnoid and pia mater and contains cerebrospinal fluid (CSF) and arachnoid trabeculae that attach the arachnoid to the pia mater. The epidural space is peripheral to the dura mater and contains fat and the internal vertebral venous plexus.[7] The nerve roots exit through the intervertebral foramina. The collection of spinal nerve roots in the lumbosacral area is known as the *cauda equina.* CSF is found in the spinal subarachnoid space, which begins at the foramen magnum, where it communicates with the intracranial subarachnoid space, and ends caudally at the *filum terminale* near the lumbosacral junction. CSF is also found in the central canal of the spinal cord, which communicates with the fourth ventricle cranially and terminates caudally blindly at the *conus medullaris* or in some subjects is continuous with the lumbar subarachnoid space (see Figs. 15.1 and 15.2).[3]

Computed Tomography

On CT, cortical bone is thin and of uniformly high attenuation with smooth margins. Cancellous bone has a lacy or honeycomb appearance (Fig. 15.3). All components of the vertebra (laminae, pedicles, body, foramina, basivertebral venous canal, bony processes) are well visualized with CT. At the midportion of the body, the basivertebral venous canal is visible as a Y-shaped lucency, and a small dorsally projecting ridge of bone is present within the ventral floor of the vertebral foramen at this site (see Fig. 15.3; see also Fig. 15.10).[8] The articular process joints are diarthrodial joints with a thin, smooth subchondral bone; the articular processes are separated by a hypoattenuating space corresponding to synovial fluid and

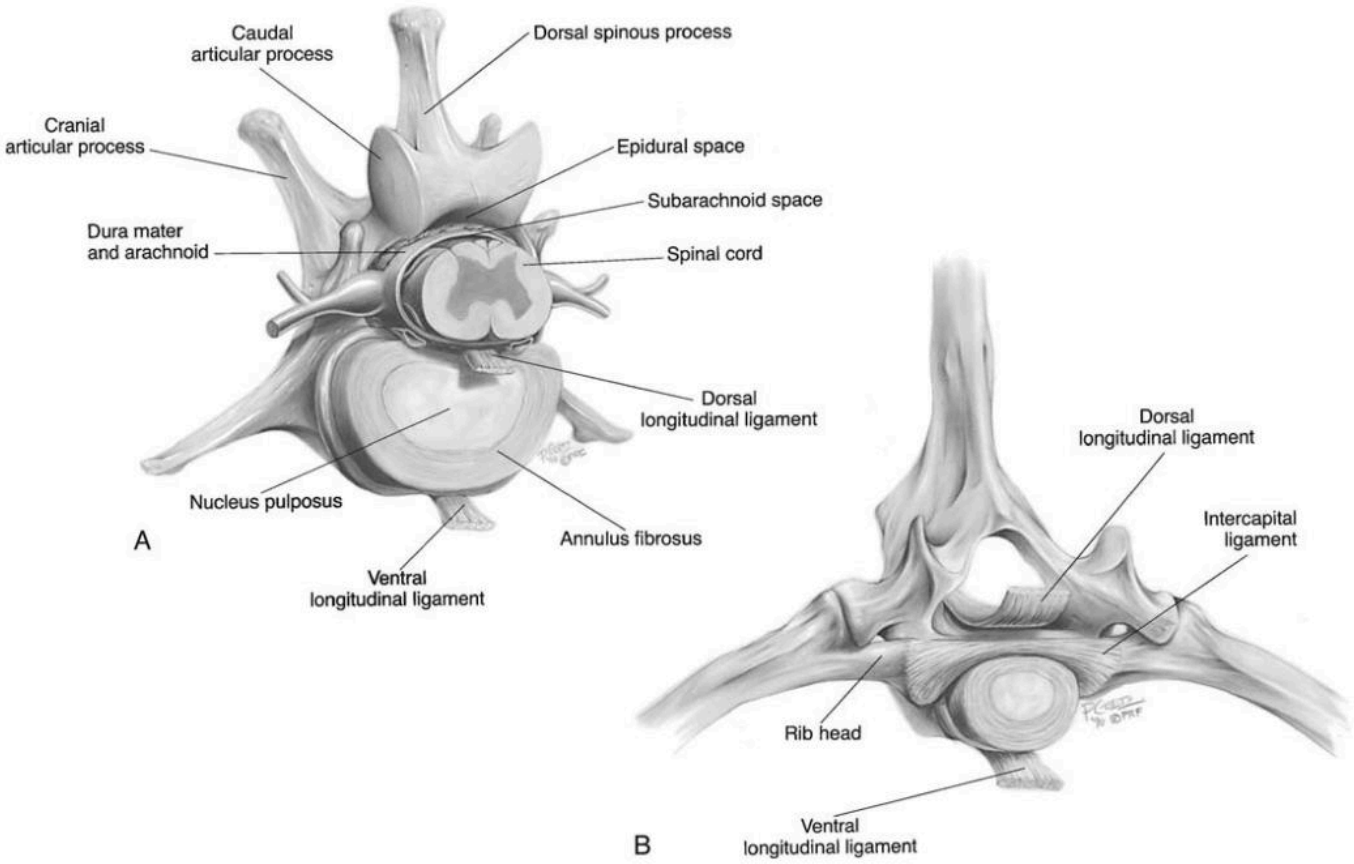


Fig. 15.1 Anatomic components of a typical lumbar vertebra **(A)** and a typical thoracic vertebra and articulation with ribs **(B).** (Modified from Evans HE, Christensen JC. *Miller's Anatomy of the Dog*. 2nd ed. Philadelphia: Saunders; 1979.)

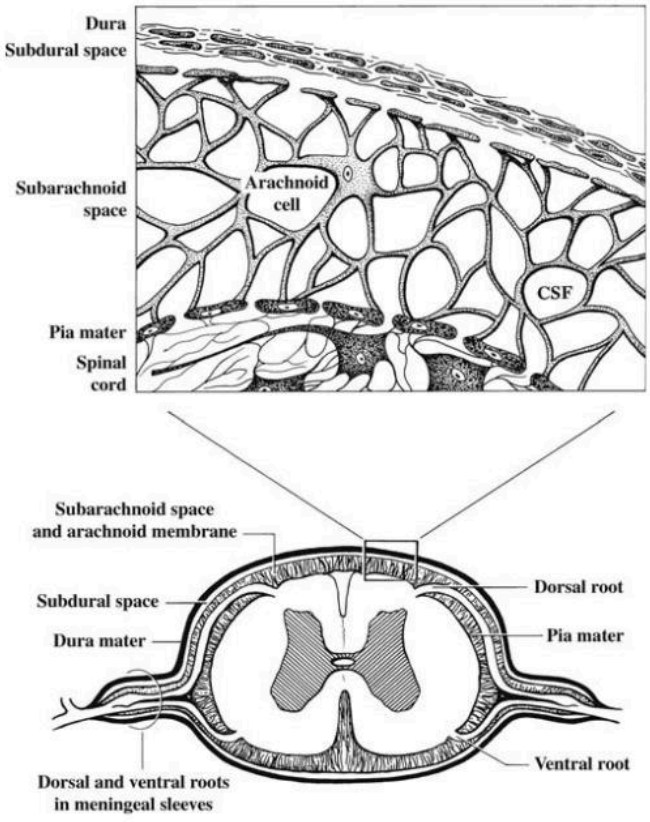


Fig. 15.2 Anatomic relation (transverse plane) of spinal cord, meningeal layers, and subarachnoid space. *Inset* shows microscopic structure of a segment of the meninges and spinal cord. *CSF,* Cerebrospinal fluid. (Modified from Hoerlein BF. *Canine Neurology: Diagnosis and Treatment*. 3rd ed. Philadelphia: Saunders; 1978.)

articular cartilage. On transverse images centered at the disc spaces, the combined margins of the dorsal aspect of the annulus of the intervertebral disc and dorsal longitudinal ligament and ventral aspect of the annulus and ventral longitudinal ligament appear as elliptical soft tissue attenuating structures. Occasionally, the interarcuate ligament *(ligamentum flavum)* is seen as a curvilinear opacity spanning the dorsal laminae and blending with the joint capsule of the articular process joints. The ventral, dorsal, interspinous, and intertransverse ligaments are not resolved from surrounding structures. Epidural fat is hypoattenuating with respect to the soft tissue structures of the vertebral canal. The combination of the spinal cord, blood vessels, subarachnoid space with CSF, and meninges forms a round to oval soft tissue attenuating structure in the middle of the vertebral canal that is surrounded by a rim of hypoattenuating epidural fat (see Fig. 15.3). Nerve roots can be seen as circular or linear soft tissue attenuating structures, depending on their orientation in the scan plane.

When CT is performed after myelography, the thecal sac is hyperattenuating, allowing for more accurate differentiation among intramedullary, intradural, and extradural conditions. CT myelography can be achieved by injecting iodinated contrast medium in the subarachnoid space at 25% of the regular myelographic dose.[9] This allows excellent delineation of the spinal cord and is useful in characterizing compressive lesions or spinal cord atrophy. The normal cross-section of the cervical spinal cord is kidney shaped and slightly larger at C6 to C7. In the thoracic area, there is a dramatic reduction of the spinal cord diameter, and it is also more round.[9]

Magnetic Resonance Imaging

On MRI, cortical bone appears as a black shell around the vertebra on all pulse sequences.[10]

On T1-weighted (T1W) images, epidural fat and paraspinal fat are hyperintense to the spinal cord, whereas the intervertebral discs have medium signal intensity (Fig. 15.4).[10] The

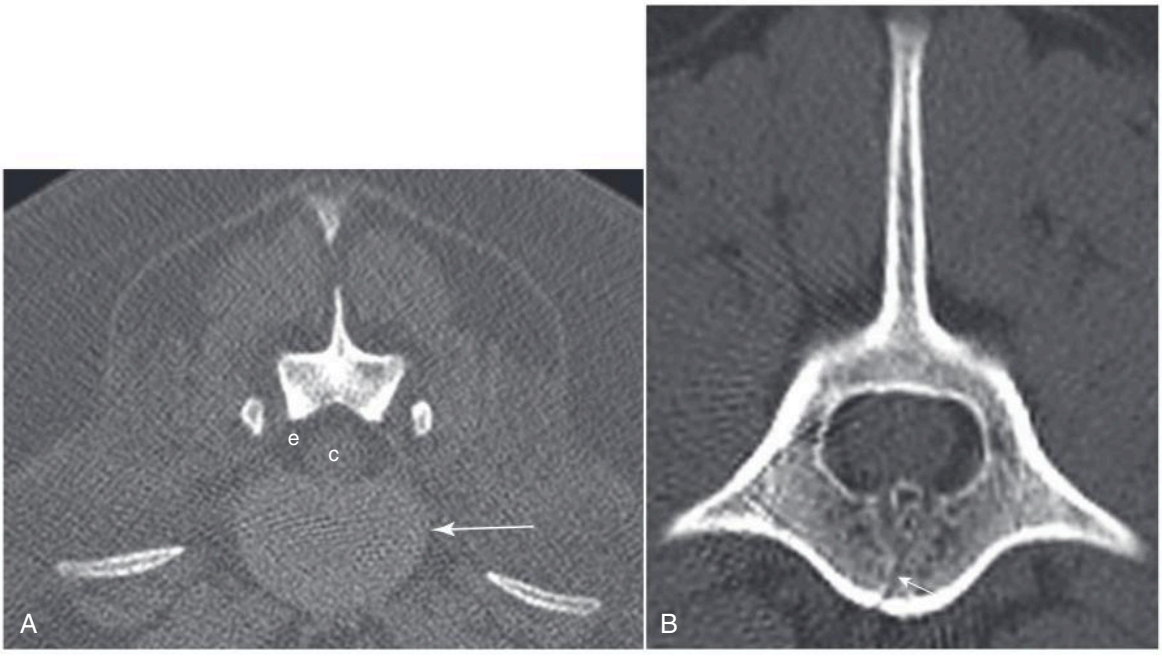


Fig. 15.3 **A,** Transverse computed tomography (CT) image at the level of a lumbar intervertebral disc space: the intervertebral disc is indicated by the *white arrow*. The spinal cord together with the meninges and subarachnoid space form an oval soft tissue attenuating structure in the middle of the vertebral canal (*c*). The epidural fat (*e*) is hypoattenuating and surrounds the spinal cord and meninges. **B,** Transverse CT image in the midportion of the vertebral body. Note the basivertebral venous canal (*white arrow*). The cortical bone forms a homogeneous hyperattenuating boundary around the vertebra, whereas the cancellous bone has a lacy appearance.

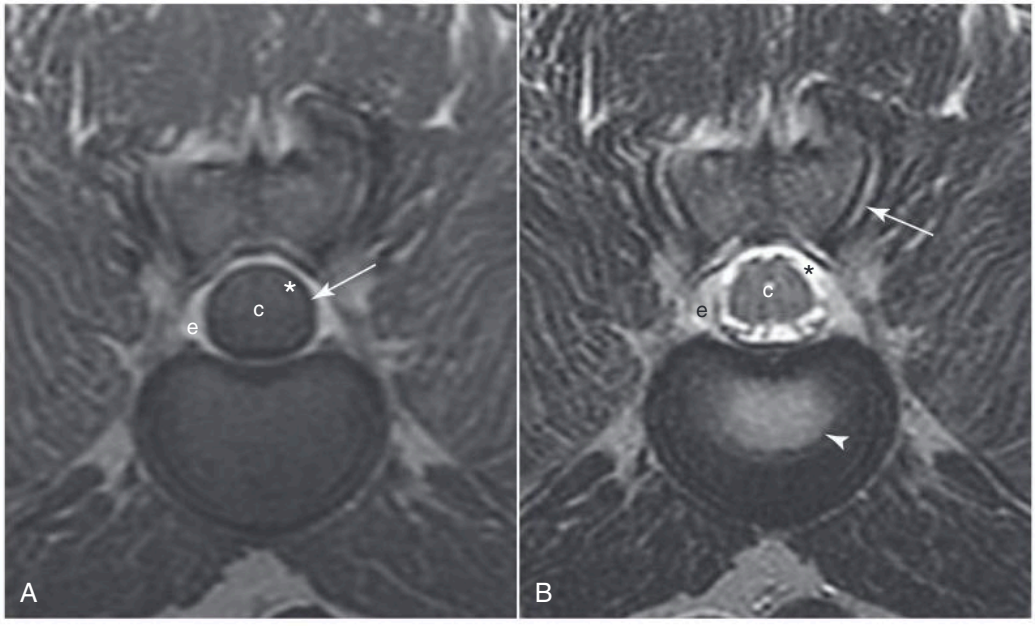


Fig. 15.4 Transverse T1-weighted **(A)** and T2-weighted image **(B)** centered at the L3—L4 intervertebral disc space in a normal dog. The spinal cord (*c*) is in the middle of the vertebral canal. The epidural fat (*e*) is hyperintense on both images. In the T1-weighted image **(A)**, the cerebrospinal fluid (CSF) signal (*asterisk*) is barely distinguished from the spinal cord. A hypointense rim around the spinal cord and CSF represents a combination of the meninges and chemical shift artifact (*white arrow*). In the T2-weighted image **(B)**, the hyperintense CSF forms a bright ring around the spinal cord (*asterisk*). Synovial fluid in the articular process joints forms a thin linear hyperintense signal between the articular processes (*white arrow*). The cortical bone of the articular processes forms a black linear curved structure. The *nucleus pulposus* is the hyperintense signal in the middle of the disc (*white arrowhead*).

hyperintense epidural fat provides contrast for other spinal structures. The spinal cord, nerve roots, and bone marrow are isointense or slightly hypointense to the intervertebral discs. A low-signal shell around the spinal cord represents a combination of CSF in the subarachnoid space, chemical shift artifact, and meningeal structures.[10] The dorsal and ventral longitudinal ligaments, as well as the *ligamentum flavum*, are visible only in the intervertebral areas where they are separated



Fig. 15.5 T2-weighted image centered at L5 in a normal dog. The hyperintense cerebrospinal fluid (CSF) within the dural sac is indicated by (*asterisk*). The extremity of the spinal cord and intradural nerve roots are visible (*black arrow*) in the dural sac, which forms a hypointense rim around the CSF (*white arrowhead*). The epidural fat around the dural sac (*e*) is less hyperintense than CSF. Extradural nerve roots are visible as focal hypointensities *(white arrows)* in the epidural space.

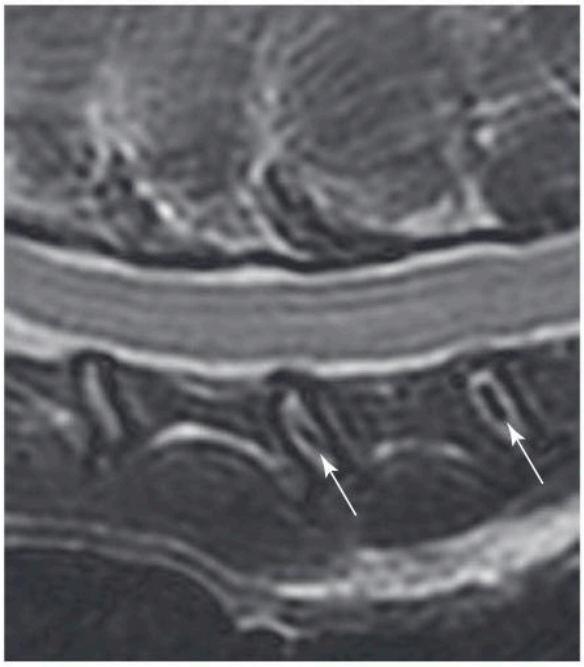


Fig. 15.6 Sagittal T2-weighted image of the caudal aspect of the cervical spine in a dog. Formation of hypointense clefts in the *nucleus pulposus* (*white arrows*) are signs of intervertebral disc degeneration, with reduced water content.

from the bone; they are of low signal intensity.[10] The joint capsule and synovial fluid of the articular process joints are not visible. The internal vertebral venous plexus consists of two symmetric hypointense oval structures, sharply marginated, located ventral to the spinal cord in the midbody regions and diverging slightly from the ventral location at the level of the intervertebral disc spaces.

On T2-weighted (T2W) images, normal intervertebral discs have a high signal because of high water content in the *nucleus pulposus* and inner portion of the *annulus fibrosus* (see Fig. 15.4).[10,11] The epidural fat and paraspinal fat are still hyperintense, and the spinal cord and nerve roots are hypointense (Fig. 15.5). The bone marrow is hypointense compared with fat and is isointense or hypointense to the spinal cord. Depending on the amount of T2 weighting, the CSF in the subarachnoid space forms a thin hyperintense shell around the cord.[10] Sequences with a very heavy T2 weighting, such as single-shot fast spin echo (SSFSE) or half-Fourier acquisition single-shot turbo spin-echo (HASTE), enhance the signal from CSF while suppressing the signal from background tissue, giving a natural myelographic effect.[12,13]

INTERVERTEBRAL DISC DISEASE

The Normal Intervertebral Disc

Intervertebral discs are made of a peripheral *annulus fibrosus* and a central *nucleus pulposus*.[11] The disc lies in close contact with the cartilaginous vertebral endplates with fibers from the *nucleus pulposus* and *annulus fibrosus* being interwoven with the collagen fibers of the cartilaginous endplates and bony trabeculae.[10]

Both the annulus and the nucleus are made of fibrocartilage but differ in the amount of collagen and ground substance.[14] There is more collagen and less ground substance in the annulus than in the nucleus. The ground substance is composed of hyaluronic acid and glycosaminoglycans that hold water because of their strong negative charge.[14] A normal *nucleus pulposus* has a gelatinous consistency. Water, bound to large proteoglycan molecules, is the principal component of the *nucleus pulposus* (80%–88%).[15] The normally very bright signal of the *nucleus pulposus* on T2W images is caused by the long T2 relaxation time of water (see Fig. 15.4).[11]

Classification of Intervertebral Disc Disease

Apart from trauma causing extrusion of nondegenerated (hydrated) disc material (see section on Compressive and Noncompressive Hydrated Nucleus Pulposus Extrusion), degeneration of the intervertebral disc occurs before clinically significant intervertebral disc disease (IVDD).[11] Degenerative IVDD was first classified by Hansen.[16] Hansen type I IVDD is herniation of the *nucleus pulposus* through annular fibers with subsequent extrusion of nuclear material into the vertebral canal. Type I IVDD is more common in chondrodystrophic dogs. The degenerative process leading to type I herniation involves shifting concentrations of glycosaminoglycan, loss of water and proteoglycan content, and increased collagen content. The disc becomes more cartilaginous, and its nucleus becomes more granular, often mineralizes, and loses its hydroelastic shock-absorbing qualities (Fig. 15.6). The degenerative process starts early in life, and herniation is observed in younger animals (2–7 years old, with a peak incidence at 4–5 years old).

Hansen type II IVDD is an annular protrusion caused by shifting of the central nuclear material and is commonly associated with fibroid degeneration. Type II herniation is usually observed in nonchondrodystrophic dogs, and the degenerative process starts later in life, with herniation usually observed at approximately 8 to 10 years old.

With more detailed imaging of the patterns of disc herniation that can be appreciated with MRI, IVDD can be divided into several categories based on appearance more than physiopathology.[17–19] Classification systems have evolved over the years as we learned more about the variable imaging features of disc disease.[20] Fig. 15.7 describes a proposed classification of IVDD. General features include:

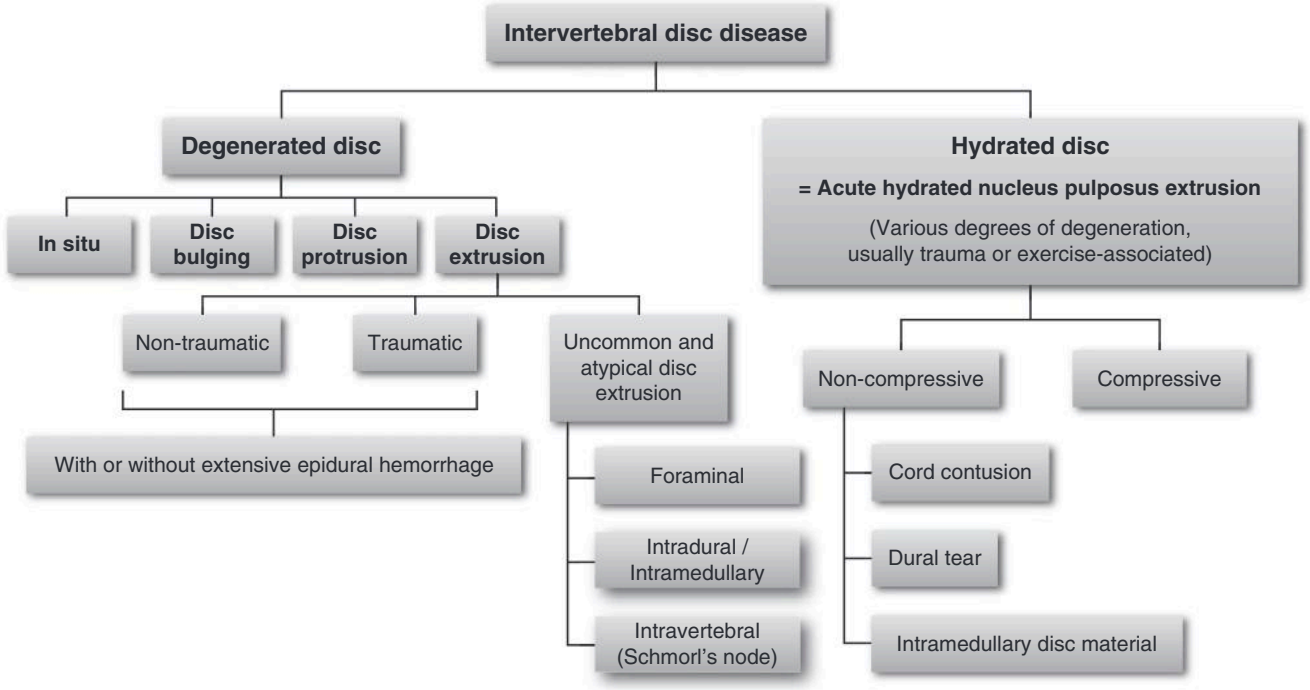
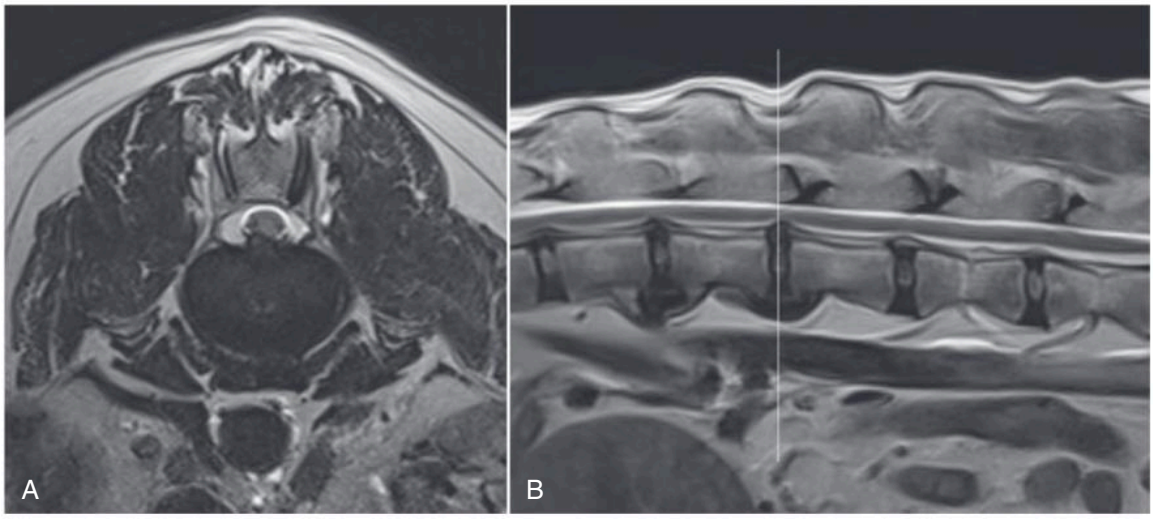


Fig. 15.7 Diagram of a proposed classification for intervertebral disc disease (IVDD) in dogs and cats.

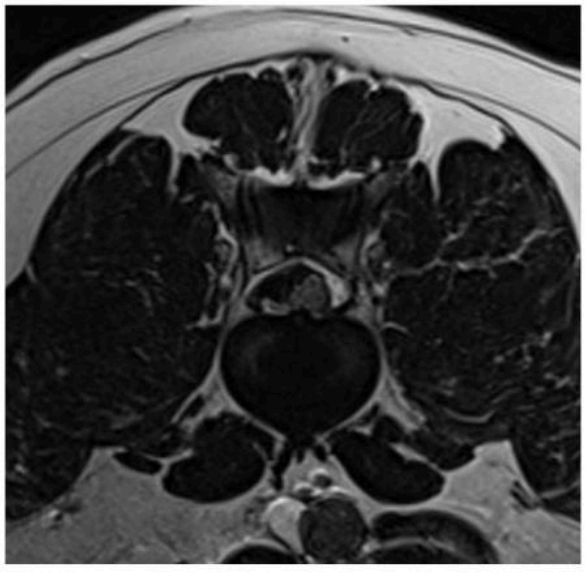


Fig. 15.8 Transverse T2-weighted image of a cervical intervertebral disc space in a dog. There is a Hansen type II disc herniation with protruding hypointense disc material (*white arrow*) causing mild left ventral spinal cord compression.

- A bulging disc corresponds to circumferential extension of the disc beyond the margins of the vertebral endplates.
- A protruding disc is the partial extension of the nucleus and inner annulus through disrupted fibers of the outer annulus but without complete rupture of the outer annulus (Hansen type II). The presence of partial rather than complete intervertebral disc degeneration, midline herniation, and/or multiple herniations makes protrusion more likely than extrusion (Fig. 15.8, eFig. 15.1).[18,19]
- An extruded disc represents true herniation (Hansen type I), where portions of the nucleus and inner annulus traverse through all the layers of the outer annulus and form a focal extradural mass deviating epidural fat and, depending on the size of the herniation, the subarachnoid space and spinal cord (Fig. 15.9, eFig. 15.2). This herniated disc material can detach completely from the disc where it originates and form a free extradural mass, with various degrees of dispersion.[17] The presence of a single intervertebral disc herniation, complete disc degeneration, lateralized herniation, and/or dispersion of the intervertebral disc material makes disc extrusion more likely than protrusion.[18,19] In some animals, the extruded material can lacerate the internal vertebral venous plexus resulting in disc-associated extensive epidural hemorrhage.[21,22]
- Hydrated traumatic disc herniation: If a disc with a normally hydrated *nucleus pulposus* is placed under extreme stress, the dorsal *annulus fibrosus* may rupture, and some of the normal jelly-like *nucleus pulposus* may explode into the vertebral canal and cause spinal cord contusion or dural tears.[23] Because the nucleus material is normally hydrated (although possibly with some degree of degeneration), it diffuses in the peridural fat, leaving only the secondary changes attributable to acute spinal cord contusion with little or no spinal cord compression.[15] In some patients, the herniated disc material can penetrate the spinal cord parenchyma.[24–26] Several terms have been used to describe this syndrome, including *traumatic disc prolapse, traumatic disc herniation, disc explosion, noncompressive nucleus pulposus extrusion, Hansen type III disc disease, high-velocity-low-volume disc disease, traumatic intervertebral disc extrusion, missile disc,* and *acute noncompressive nucleus pulposus extrusion.*[15,27] The term *Hansen type III disc disease* is discouraged because this type of herniation was never described by Hansen. Such herniations are associated most commonly with trauma (such as a road traffic accident or running into an obstacle) but can also be associated with vigorous exercise.[28] In some patients, the herniated hydrated disc



eFig. 15.1 Transverse **(A)** and sagittal **(B)** T2-weighted images of a dog with Hansen type II disc herniation. The location of the transverse slice in **A** is indicated by a *line* in **B**. Hypointense protruded disc material causes mild right ventral spinal cord compression.



eFig. 15.2 Transverse T2-weighted image of a dog with Hansen type I disc herniation. Hypointense extruded disc material is present on the right lateral and dorsolateral aspect of the spinal cord causing compression.

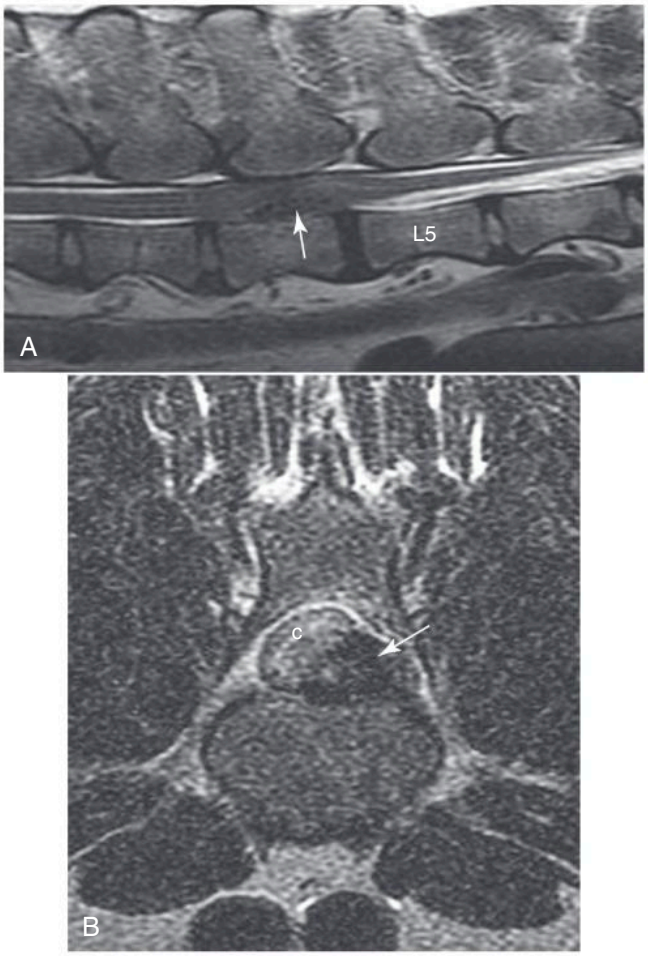


Fig. 15.9 Sagittal **(A)** and transverse **(B)** T2-weighted images in a dog with Hansen type I disc herniation at L4 to L5. The longitudinal extent of the hypointense extruded disc material *(white arrow)* is apparent on the sagittal image. The L4 to L5 disc is markedly hypointense, consistent with degeneration. On the transverse image **(B)**, the hypointense extruded disc material (*white arrow*) causes marked left ventral compression of the spinal cord (*c*).

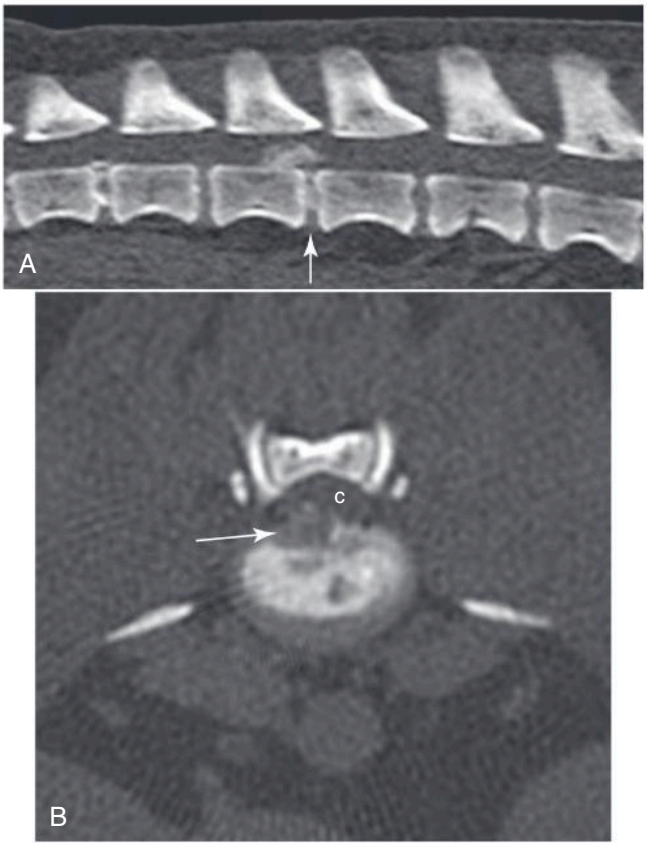


Fig. 15.10 Computed tomography (CT) without intrathecal contrast medium in a dachshund with acute intervertebral disc herniation. **A,** Sagittal reformatted image. Note the hyperattenuating disc material dorsal to the affected narrowed disc space (*white arrow*). Extruded disc material extends cranial to the affected disc space. Mineralized disc material is seen in this space and at two intervertebral disc spaces cranial to this. **B,** Transverse image centered on the affected disc space. There is hyperattenuating material (*white arrow*) in the vertebral canal that causes ventral right-sided spinal cord (*c*) compression.

material may cause focal extradural compression of the spinal cord,[29–31] a condition that may have previously been erroneously referred to as *discal cyst.*[32–34]

Computed Tomography of Intervertebral Disc Disease

CT of the spine for assessing the intervertebral disc should be obtained using thin slices (1–2 mm), low pitch (<2), and a medium-frequency image-reconstruction algorithm.[35] When CT is used in the assessment of the spinal cord, subarachnoid injection of iodinated contrast medium is often performed concurrently, because the spinal cord is often not clearly visible on CT images. Obviously, the use of CT with subarachnoid contrast medium invalidates the potential advantage of diagnosing disc herniation without the side effects associated with myelography, although the dose of contrast medium for CT myelography is less than that for myelography.

CT without intrathecal injection of iodinated contrast medium for detection of IVDD has been evaluated in chondrodystrophic dogs, which are likely to have some degree of mineralization of the herniated material.[36] On CT, vertebrae can be identified as thoracic or lumbar without difficulty based on the presence of ribs or transverse processes. The location of any particular image, therefore, can be identified by counting sequential vertebrae or by using scout images depicting slice location. Acquiring lateral and ventrodorsal scout images reduces the risk of missing a vertebral malformation that could affect accurate localization of individual disc spaces at surgery. This is important, because 10% of dachshunds have transitional anomalies that lead to deranged vertebral anatomy.[37] If the scout images are not of sufficient quality to identify vertebral abnormalities, it may be useful to obtain a routine survey radiograph before performing the CT scan. In chondrodystrophic breeds, CT is excellent at identifying herniated disc material and provides accurate information as far as location, laterality, and extent of spinal cord compression (Fig. 15.10). In chondrodystrophic dogs, acute herniation leads to either a large focal amount of markedly hyperattenuating material (~200 Hounsfield units [HU]) compressing the spinal cord or to more diffuse and less hyperattenuating material (~60 HU) causing less severe spinal cord compression. In the latter instance, the material in the vertebral canal corresponds to areas of epidural hemorrhage. In chronic disc herniation, the attenuation of the herniated material is higher than that of acutely herniated disc material (~700 HU) because the herniated material continues to mineralize after acute herniation.[36] Some pitfalls exist when interpreting CT images. For example, a round focus of mineralization is seen occasionally on transverse images dorsal to the vertebral bodies. This focus has been thought to represent mineralization of the dorsal longitudinal ligament,[36] which fans out to a thin sheet over the intervertebral disc space but

narrows to a circular midline structure over the vertebral body. However, this focal hyperattenuation is more likely a transverse image of the small bony ridge between the dorsal vertebral foramina (Fig. 15.11). This hyperattenuation can be mistaken for disc material.

Although conventional CT is adequate for the diagnosis and localization of mineralized disc extrusions in chondrodystrophic breeds, CT myelography is often necessary for diagnosis if no lesion is identified in a chondrodystrophic dog, if paraplegia is present because of concurrent extradural compression and spinal cord swelling, or if the dog is nonchondrodystrophic.[38]

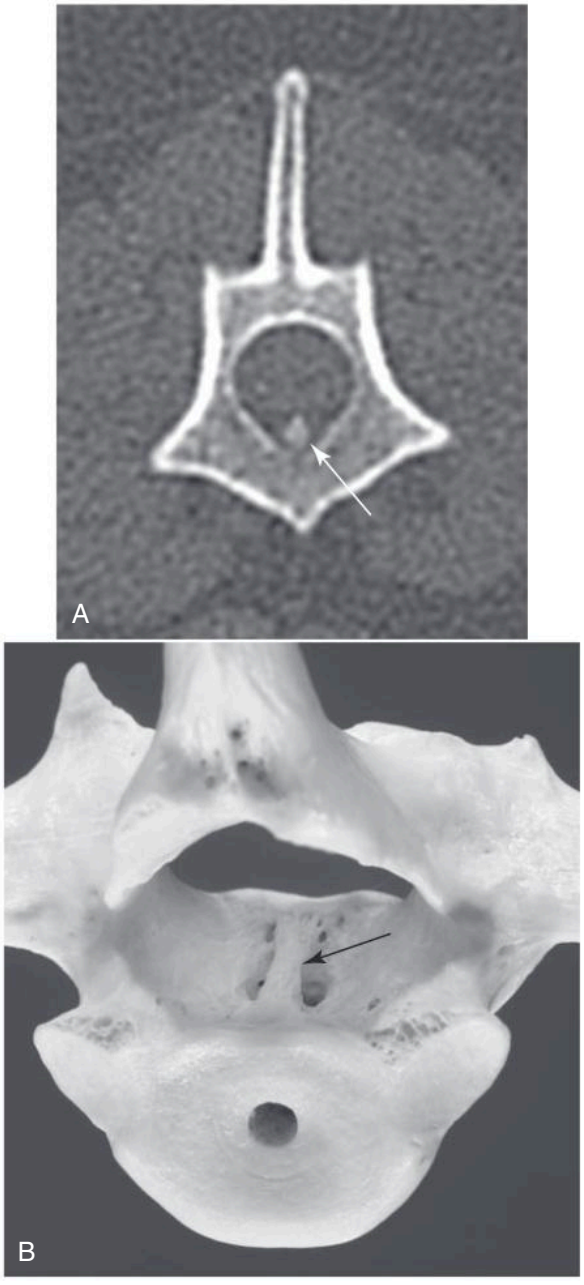


Fig. 15.11 Transverse computed tomography (CT) image **(A)** and photograph **(B)** of a canine vertebra. There is a focal hyperattenuation dorsal to the vertebral body (*white arrow* in **A**) that is created by the bony bridge covering a portion of the dorsal foramina (*black arrow* in **B**). This hyperattenuation is confused with mineralization of the dorsal longitudinal ligament and herniated disc material but is a normal finding. The hole in the end-plate in **B** is a drill hole; this drilling did not disturb the normal appearance of the dorsal foramina.

Magnetic Resonance Imaging of Intervertebral Disc Disease

Although there may be no improvement in patient outcome when using MRI for the diagnosis of IVDD,[39] it is the method of choice for presurgical diagnosis, because it is noninvasive and provides superior anatomic detail, as well as potential prognostic indicators (e.g., myelomalacia). MRI is also more accurate than conventional CT in differentiating disc extrusion from protrusion and also has overall higher sensitivity.[40] Differences in surgical planning based on MRI versus CT were reported in chondrodystrophic dogs with thoracolumbar disc extrusion, with variations in site (but not side) of approach and size of laminectomy. Surgeries planned based on MRI images may result in larger laminectomy windows than when planned with CT, although the clinical implication of this is unknown at this time.[41]

Diagnosis of IVDD is made from magnetic resonance (MR) images when the following signs are seen:

- Extradural compression of the spinal cord centered at the level of an intervertebral disc (Fig. 15.12; see also Fig. 15.9): This is recognized by a loss of signal from the epidural fat and a change in the shape of the spinal cord, as well as a change in the normal ovoid shape of the disc, and is best appreciated on transverse images (see Fig. 15.8).
- Degeneration of the disc (loss of T2-hyperintense signal from the disc).
- Narrowing of the intervertebral disc space: This is usually best evaluated on sagittal T1W images.[42]

MRI is accurate in determining the location and craniocaudal length of extruded intervertebral disc material. T2W images are more reliable in determining the extent of the compressive material.[43] Heavily T2W sequences, such as SSFSE, provide a myelographic effect by enhancing the signal of the CSF and

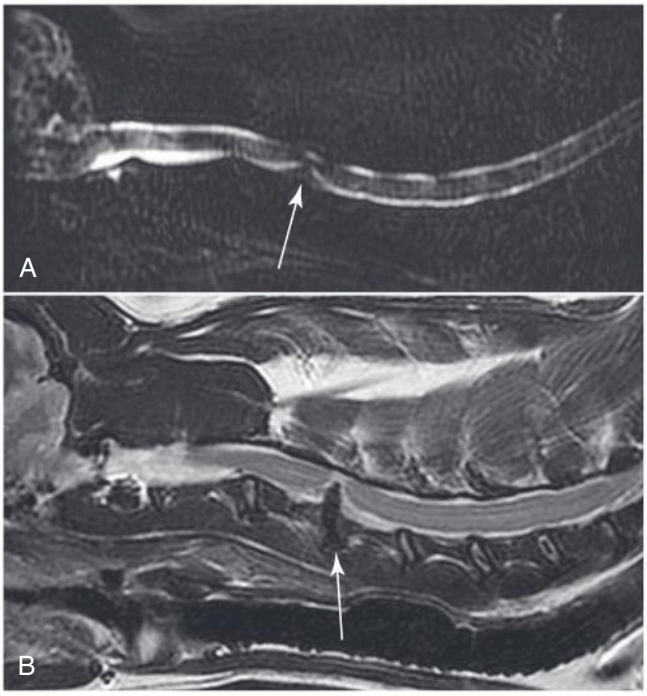


Fig. 15.12 Sagittal single-shot fast spin echo (SSFSE) slab (T2 myelogram) **(A)** and sagittal T2-weighted image **(B)** in a dog with disc herniation at C3–C4. The area of spinal cord compression is obvious on the T2 myelogram (*white arrow*). On the sagittal T2-weighted image, hypointense material is seen extruded from the disc at C3–C4, causing marked ventral spinal cord compression. The disc has lost its normal hyperintense signal (*white arrow*).

suppressing the signal from other structures, and it can be used to quickly spot areas of cord compression based on identification of interruption and/or deviation of the CSF column (see Fig. 15.12).[12]

Epidural hemorrhage and inflammation associated with disc extrusion can be detected with MRI.[44] Hemorrhage typically results from laceration of the internal vertebral venous plexus by the extruded disc, and can extend longitudinally far from the original extrusion site; some authors refer to this variation as "disc extrusion with extensive epidural hemorrhage."[21,22] These changes are observed more commonly when there has been migration of disc material. French bulldogs may be at higher risk.[45] The signal intensity of these epidural lesions is variable, appearing hyperintense to the spinal cord or heterogeneous on T2W images, and hyper-, hypo-, or isointense to the spinal cord on T1W images.[44] This variation likely reflects changes in magnetic properties depending on the age of the hemorrhage and amount of disc-associated inflammation as well as alterations in epidural fat. Gradient recalled echo T2*W pulse sequences are sensitive to the paramagnetic properties of deoxyhemoglobin and methemoglobin, and hemorrhage or hematomas in the epidural space create hypointensities as a result of susceptibility artifact (Fig. 15.13).[46] Contrast enhancement of epidural hemorrhage is common, although it is not associated histopathologically with actual inflammation. In some dogs, these secondary epidural changes can mask the extruded disc material. Altogether, these features can cause erroneous diagnosis of a tumor, and this variability needs to be taken into account when interpreting MR images in dogs with acute neurologic presentation. Some studies did not observe differences in clinical outcome in dogs with epidural hemorrhage or inflammation compared with dogs without these changes,[44] although recent studies suggested that dogs with epidural hemorrhage may have worse clinical outcome, particularly in medium- to large-breed dogs and with increasing longitudinal extension of hemorrhage.[22,45]

Regardless of whether epidural hemorrhage or inflammation is present, contrast enhancement of the compressive extradural disc material occurs in approximately 50% of dogs with disc extrusion (Fig. 15.14).[44,47] Meningeal contrast enhancement adjacent to extruded extradural disc material also occurs in up to 40% of patients (Fig. 15.15).[47]

Changes in signal intensity of the paraspinal muscles can be seen in dogs with disc extrusion, including patchy T2W/short tau inversion recovery (STIR) hyperintensities, and T1W hypointensities with variable contrast enhancement. They correlate with areas of muscle fiber degeneration, edema, inflammation, and necrosis.[48–50] Their clinical significance is unknown, with some studies reporting association with degree of neurologic deficits,[50] while others did not find such association.[49] Myosteatosis (pathologic infiltration of skeletal muscle with fat) can cause T1W and T2W increased signal intensity of paraspinal muscles but is questionably associated with disc herniation in dogs, and is not convincingly a prognostic factor.[51,52]

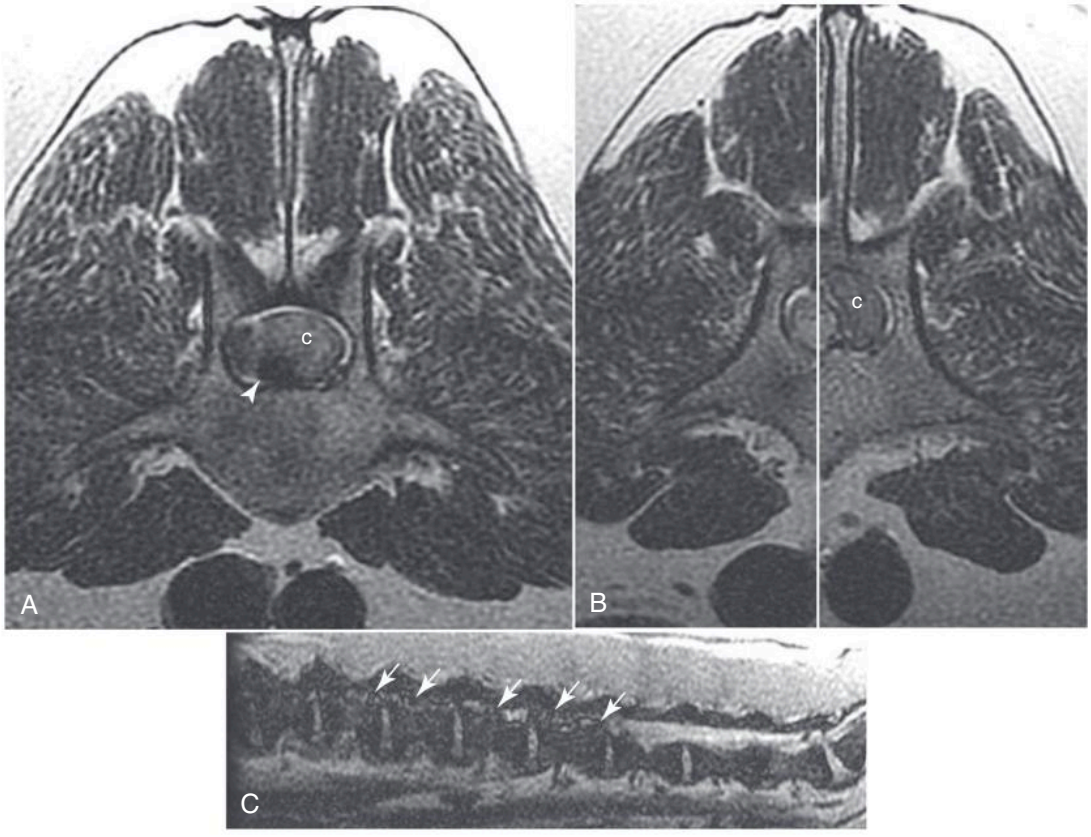


Fig. 15.13 Acute disc herniation at L4–L5 in a dog. Transverse spin echo T2-weighted image at L4–L5 **(A)** and a few millimeters cranial to this **(B)** and a parasagittal T2-weighted gradient recalled echo image **(C)**. The imaging plane in **C** is indicated by the vertical line in **B**. Extruded disc material (*white arrowhead*) compresses the spinal cord (*c*) in **A**. Cranial to this, there is a long strand of tissue that is hyperintense to the spinal cord and compressing it, as seen in **B**. There are multiple susceptibility artifacts in the gradient recalled echo image centered on this tissue (*white arrows*, **C**) consistent with hemorrhage extending over several vertebral bodies. Extensive epidural hemorrhage was present surgically.

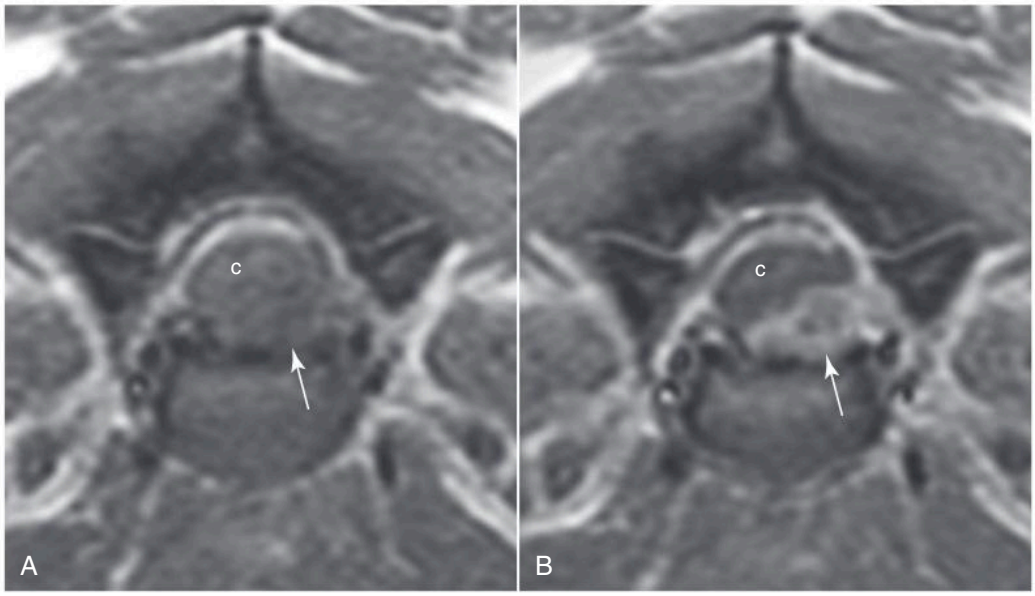


Fig. 15.14 Transverse precontrast **(A)** and postcontrast **(B)** T1-weighted images in a dog with disc herniation. The spinal cord (*c*) is compressed by left ventral extradural disc material, and this material is enhancing after contrast medium injection (*white arrows*). This is common and should not be misinterpreted as evidence of an extradural tumor. (Reproduced with permission from Suran JN, Durham A, Mai W, et al. Contrast enhancement of extradural compressive material on magnetic resonance imaging. *Vet Radiol Ultrasound.* 2011;52:10–16.)

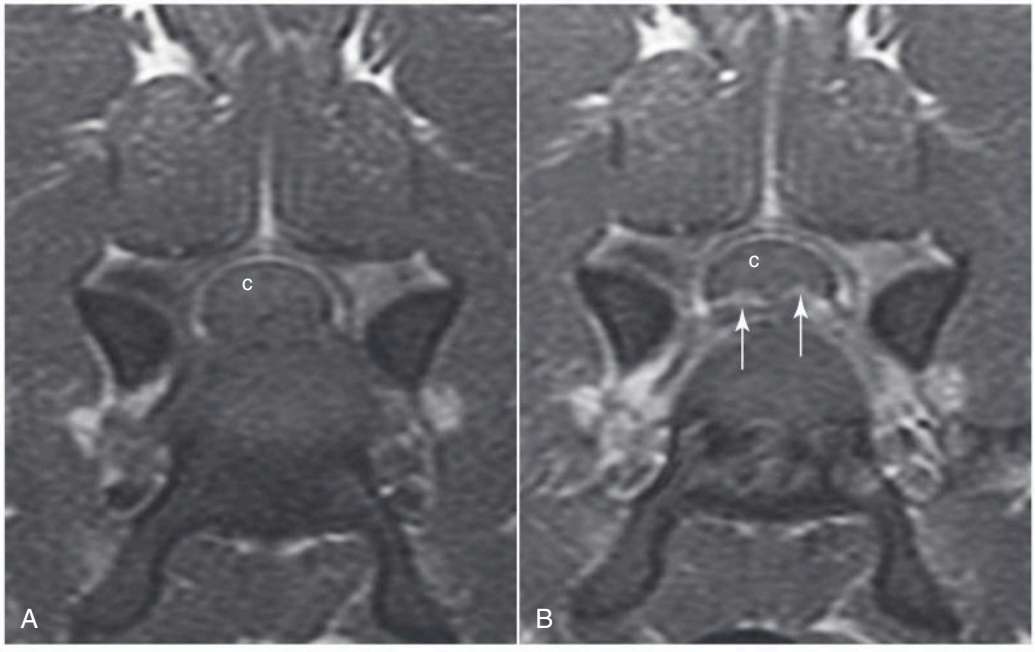


Fig. 15.15 Transverse precontrast **(A)** and postcontrast **(B)** T1-weighted images in a dog with disc herniation. The spinal cord (*c*) is compressed by ventral extradural disc material. Ventral meningeal enhancement is present after contrast medium injection (*white arrows*). (Reproduced with permission from Suran JN, Durham A, Mai W, et al. Contrast enhancement of extradural compressive material on magnetic resonance imaging. *Vet Radiol Ultrasound.* 2011;52:10–16.)

Regional Characteristics of Intervertebral Disc Disease

Cervical Intervertebral Disc Disease

Cervical IVDD accounts for 14% to 16% of IVDD in dogs.[53] Cervical disc extrusion is common in small-breed dogs, especially dachshunds and beagles, but is also seen in large-breed dogs, especially Labrador retrievers, German shepherd dogs, Rottweilers, and Dalmatians.[54,55] In small-breed dogs, the most common sites of herniation are C2–C3, C3–C4, and C4–C5, whereas in large-breed dogs, the most common sites are C4–C5 and C6–C7.[54,55] The amount of compressive myelopathy occurring with cervical IVDD is typically less than with thoracolumbar disc herniation, because the dorsal longitudinal ligament is wider in the cervical area than the thoracolumbar region. Cervical disc herniation also occurs most commonly in the dorsolateral direction, between the dorsal longitudinal ligament and vertebral venous sinus, thereby causing nerve root

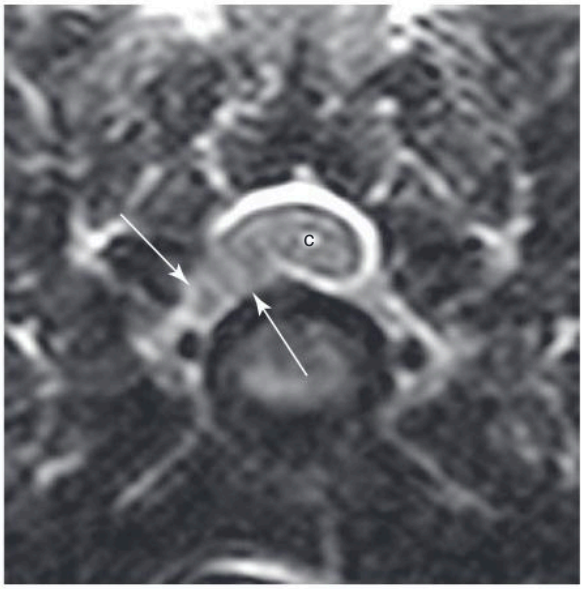


Fig. 15.16 Transverse T2-weighted image of a dog with a foraminal disc herniation at C5–C6. There is disc material in the right ventral aspect of the vertebral canal and in the right foramen (*white arrows*). The disc material is also compressing the spinal cord (*c*).

compression with root signature and cervical pain (Fig. 15.16, eFig. 15.3). Also, some studies found that the cervical spinal cord occupies a smaller proportion of the vertebral canal so that the degree of compression caused by an equal volume of herniated disc material is less than in the thoracolumbar area.[53] A recent study in French bulldogs, however, found an inverse relationship, with a smaller epidural space in the cervical compared to the thoracolumbar region.[56] In the cervical area, there may be a correlation between the degree of spinal cord compression caused by disc herniation and the neurologic grade at time of imaging; however, there is no correlation with outcome after surgery.[53]

Thoracolumbar Intervertebral Disc Disease

The most commonly affected discs in the thoracolumbar region are T12–T13 and T13–L1.[57] Cranial thoracic disc herniation causing spinal cord compression has been reported to be more common in German shepherd dogs compared to other large-breed dogs, especially at T2–T3, T3–T4, and T4–T5.[58–60] Therefore, it is important to include the cranial thoracic spine (including T2–T3) when imaging dogs of this breed with T3–L3 myelopathy.

In dogs with neurologic deficits caused by thoracolumbar disc extrusion (Hansen type I), there is no definitive association between the degree of spinal cord compression as defined on T2W transverse images and the neurologic grade at presentation or outcome after surgery.[57,61] However, the length over which the spinal cord is compressed is associated with the neurologic grade at presentation but not with outcome.[62] In dogs with paraplegia because of acute thoracolumbar disc extrusion, areas of spinal cord hyperintensity on T2W series are often present (Fig. 15.17). The development of intramedullary T2 hyperintensity following disc herniation is associated with more severe neurologic deficits at presentation.[44,47,62] Areas of intramedullary T2 hyperintensity that exceed the length of L2 on sagittal images have been associated with a poor outcome in approximately 50% of patients.[63] This feature has been reported to be a better predictor of poor outcome than loss of deep pain perception,[63,64] and it is independent from the severity of neurologic signs at presentation.[62] However, more recent studies at higher field strength (3 Tesla) did not find an association between length of T2W hyperintensity and recovery of motor function.[65]

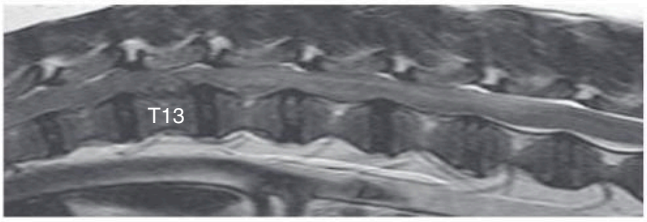


Fig. 15.17 Sagittal T2-weighted image of a dog with disc herniation at T12–T13. There is a heterogeneous mass dorsal to T13 that represents migrated disc material and hemorrhage. Caudal to this lesion, there is diffuse intramedullary T2 hyperintensity consistent with edema and inflammation.

Sacrocaudal Disc Herniation

There has been an anecdotal report of sacrocaudal disc extrusion causing tail pain and problems with defecation, with resolution of these clinical signs after surgical correction. MRI and CT can be useful in confirming the presence of extruded disc material in the sacrocaudal canal.[66,67]

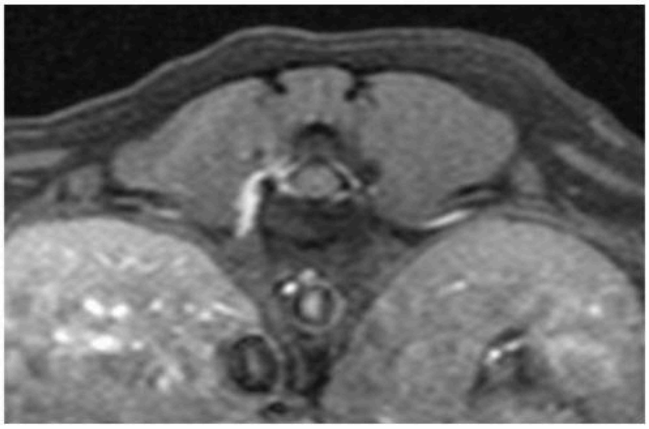
Lumbosacral Stenosis

Degenerative lumbosacral stenosis is an abnormal narrowing of the L5–S3 vertebral canal or intervertebral foramina, with compression of the cauda equina and/or its blood supply.[68] Degenerative lumbosacral stenosis is characterized by intervertebral disc degeneration, intervertebral disc protrusion, bone proliferation on the vertebral endplates and articular processes, vertebral subluxation, and hypertrophy of the articular process joint capsule and interarcuate ligament *(ligamentum flavum).*[68] Acute lumbosacral disc extrusion is much less common but carries an excellent postsurgical prognosis.[69] CT and MRI are both excellent for characterizing degenerative lumbosacral stenosis in dogs.[8,10,68,70–75] In dogs with clinical signs of cauda equina syndrome, CT changes include loss of epidural fat, increased soft tissue opacity in the intervertebral foramen, bulging of the intervertebral disc, spondylosis, thecal sac displacement, narrowed intervertebral foramen, narrowed vertebral canal, thickened articular processes, articular process subluxation, and articular process osteophytosis. On sagittal images, a step between the floor of the vertebral foramen of L7 and the floor of the vertebral foramen of S1 is often seen (Figs. 15.18 and 15.19, eFig. 15.4).[75] Enhancement of the soft tissue compressive material is often observed after injection of contrast medium, and this feature should not be interpreted as evidence of a tumor.[68] Compression should be suspected in sites where there is increased perineural soft tissue material with absence of epidural fat.[70,74] Interpretation of CT changes in the lumbosacral area must be made with caution, because some changes can be present in dogs free of clinical signs and, therefore, insignificant clinically. In particular, idiopathic lumbosacral stenosis and loss of perineural fat have been reported in dogs with no clinical signs.[71] In addition, only slight to fair agreement was found when comparing the results of CT or MRI of the lumbosacral spine to surgery.[75]

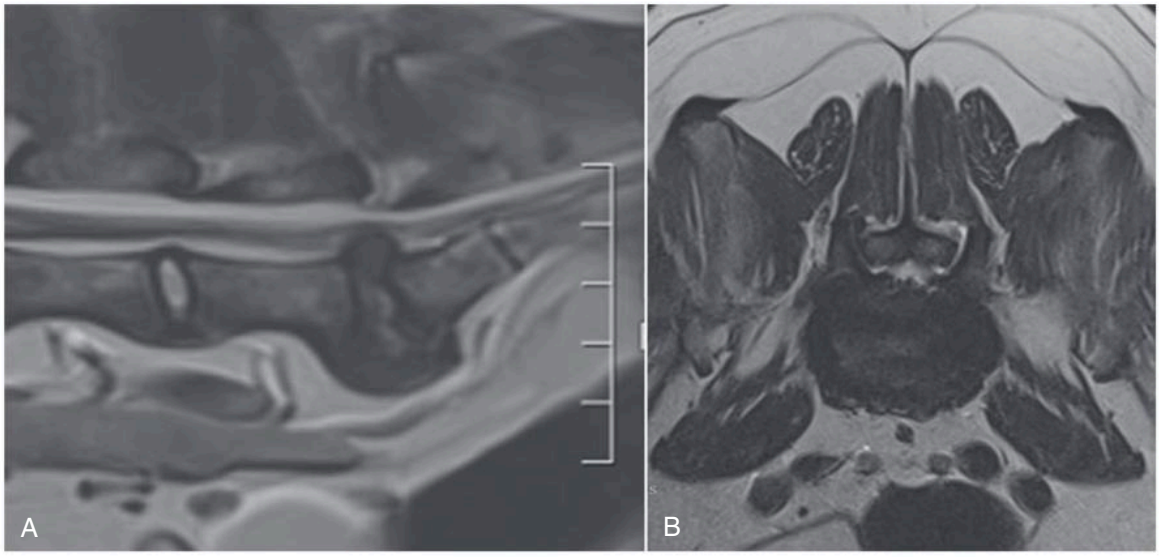
For both CT and MRI, there does not appear to be an association between imaging findings and clinical outcome after surgery in working dogs with clinical signs of degenerative lumbosacral stenosis.[68] Late postsurgical CT and MRI changes are common in dogs that underwent dorsal laminectomy for treatment of lumbosacral stenosis, importantly even in dogs with improved clinical status: such changes include ongoing nerve compression, enhancement of the L7 nerves, lumbosacral intervertebral joints, and paraspinal soft tissues.[76]

Foraminal and Far Lateral Disc Extrusion

With the increasing availability of MRI, clinical foraminal disc extrusion has been recognized more often.[77–79] In the cervical spine, the most common affected sites are C6–C7 and C5–C6.[77] There are also reports of foraminal or extraforaminal



eFig. 15.3 Transverse T1-weighted, fat-saturated image of a dog with right foraminal disc herniation at T13–L1. Round, hypointense disc material is located within the right intervertebral foramen and is outlined by surrounding hyperintense contrast enhancement.



eFig. 15.4 Sagittal **(A)** and transverse **(B)** T2-weighted images of the lumbosacral junction of a German shepherd dog with degenerative lumbosacral stenosis. The lumbosacral disc is hypointense and bulges circumferentially from the disc space. The ventral epidural fat is obliterated by the protruded disc material causing stenosis of the vertebral canal and impingement of the nerve roots of the *cauda equina*.

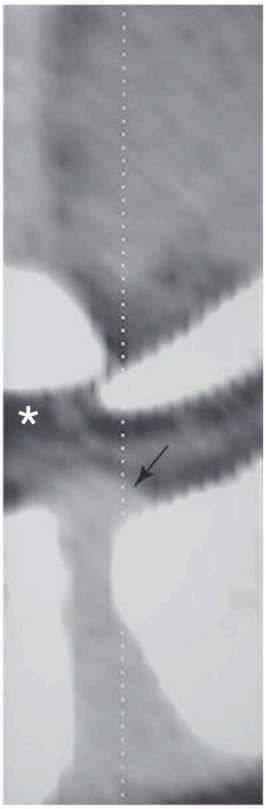


Fig. 15.18 Sagittal reformatted computed tomography (CT) image of the L7 to S1 junction in a dog with clinical signs of lumbosacral disease. There is bulging of the intervertebral disc (*black arrow*) causing mild nerve root compression. Peridural fat is still present in the area indicated by the hypoattenuating material (*asterisk*) around the nerves. There is a slight step between the floor of the vertebral canal of L7 and that of S1, indicating lumbosacral subluxation and/or instability.

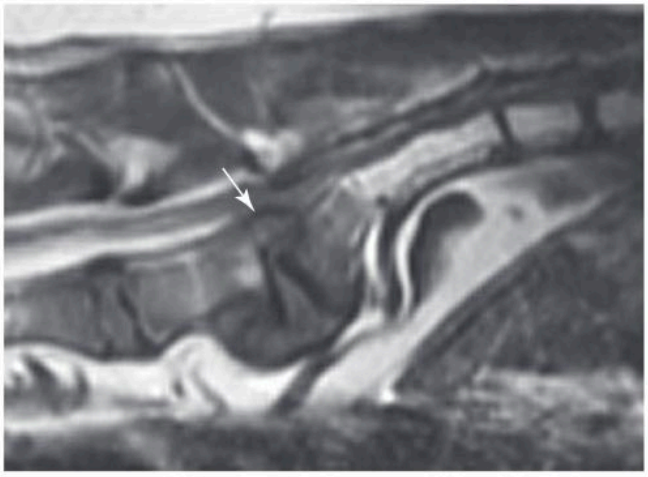


Fig. 15.19 Sagittal T1-weighted image of the caudal lumbar area in a German shepherd with clinical signs of lumbosacral disease. There is a step between the floor of the vertebral canal of L7 and that of S1 indicating lumbosacral subluxation and/or instability. Bulging disc material (*white arrow*) is present dorsal to the lumbosacral disc space causing attenuation of the hyperintense epidural fat. The combined effects of the subluxation and bulging disc are causing stenosis of the vertebral canal with nerve root compression. Ventral spondylosis is present at L7 to S1.

("far lateral") disc herniation in the thoracolumbar or lumbosacral segments, with the most common affected sites being L5–L6 and L6–L7.[78–80] MRI is a more appropriate tool for this diagnosis, due to its excellent soft tissue contrast. Careful examination of transverse images across the disc space and intervertebral foramina is important for correct identification of this condition. Gradient echo images can be useful, because they allow better contrast between the venous sinus and intervertebral disc. On sagittal images, the affected disc has often decreased signal intensity on T2W images. In the cervical spine, differentiation between foraminal stenosis due to foraminal disc extrusion and overgrowth of the articular process can prove challenging.[77] Transverse images show T2-hypointense material associated with the affected disc extruded in a dorsolateral direction and causing impingement of the nerve roots in the foramen or lateral to it. Contrast enhancement of the nerve roots as well as around the compressive lesion is reported.[79,80] Occasionally, foraminal disc extrusion can cause ganglioneuritis,[81] when disc fragments extruded in the foramen induce mechanical and chemical damage to the perineurium of the nerve sheath, and/or penetrate into the nerve root leading to inflammatory changes. These changes can cause thickening of the nerve root and ganglion, with the disc material possibly contributing to the impression of a soft tissue mass in the area. At MRI, these changes appear as a tubular space-occupying lesion in the intervertebral foramen, which is T1-isointense, T2-hyperintense compared to the contralateral nerve, with strong contrast enhancement.[81] Such lesions can easily be mistaken for a peripheral nerve sheath tumor.

Noncompressive Hydrated Nucleus Pulposus Extrusion

Occasionally, disc extrusion occurs without significant preexisting degenerative disc disease when a relatively healthy disc is subjected to a brief excessive force. Such extrusions occur typically during performance of strenuous exercise or following trauma. Names applied to this syndrome were outlined previously in the Classification of Intervertebral Disc Disease section.[15,23,26–28,82–85] Typically, the condition is characterized by an acute, often asymmetric myelopathy that is nonprogressive after the first 24 hours.[27,86] In the majority of cases, this type of herniation is noncompressive, and spinal cord lesions result from contusion rather than compression, with a clinical presentation very similar to primary ischemic myelopathy.[27,86,87]

On MRI, acute noncompressive intervertebral disc extrusion is characterized by the following[15,27,86,88]:

- Focal intramedullary T2 hyperintensity overlying an intervertebral disc: The area of maximal hyperintensity is usually just dorsal to the affected intervertebral disc but can sometimes be seen just cranial or caudal to the disc space. The longitudinal extension of the intramedullary hyperintensity is usually more focal than with ischemic myelopathy, which has a similar clinical presentation (Fig. 15.20).[15,27,86]
- This intramedullary lesion is usually isointense on T1W images and does not enhance after gadolinium injection, although occasional focal precontrast T1W hyper- or hypointensity and mild postcontrast enhancement may be present.[15,27,86]
- There is reduction in volume and signal intensity of the *nucleus pulposus* of the corresponding disc on T2W images (see Fig. 15.20).
- A narrowed intervertebral disc space is seen on sagittal images.
- There is extraneous material or heterogeneous signal changes within the epidural space dorsal to the affected disc space with absence of or minimal spinal cord compression.
- A communicating T2-hyperintense and/or T1-hypointense tract can occasionally be seen traversing the dorsal annulus between the residual *nucleus pulposus* and the vertebral canal.[15]

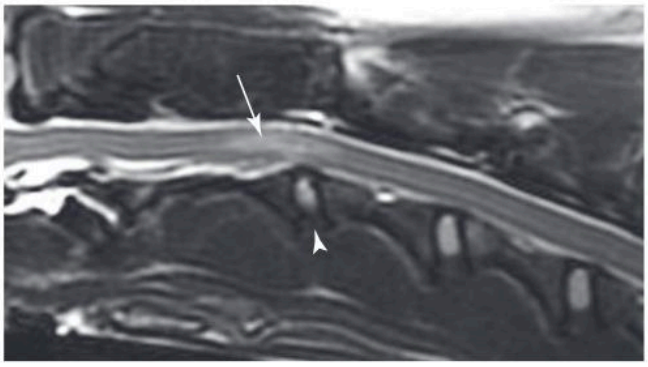


Fig. 15.20 Sagittal T2-weighted image of a dog that ran into a tree and sustained acute noncompressive intervertebral disc extrusion. There is mild loss of volume of the *nucleus pulposus* at C2–C3 (*white arrowhead*) and ill-defined intramedullary T2 hyperintensity (*white arrow*) overlying this space consistent with edema caused by spinal cord contusion. There is no spinal cord compression.

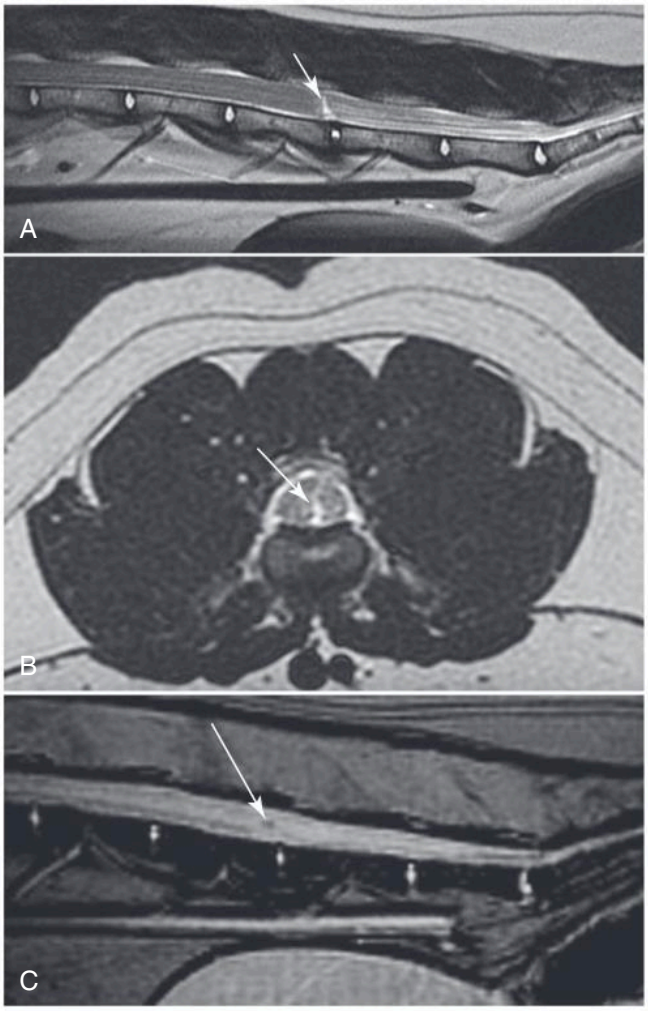


Fig. 15.21 Acute noncompressive intervertebral disc extrusion at L5–L6 in a cat. **A,** T2-weighted sagittal image. **B,** Transverse T2-weighted image centered at L5–L6. **C,** Sagittal gradient recalled echo image matching the location in **A**. A hyperintense intramedullary linear tract extends from the disc space in **A** and **B** (*white arrows*) consistent with intramedullary extrusion of disc material after perforation of the dura mater. Note the loss of volume of the *nucleus pulposus* at L5–L6. A hypointense intramedullary lesion consistent with hemorrhage (*white arrow*) is present in the gradient recalled echo image.

The acutely extruded disc material most commonly damages the spinal cord through contusion without penetrating the dura, but occasionally it can cause a dural tear and penetrate the spinal cord.[23,26,82,84,85] In these instances, a vertical intramedullary linear T2-hyperintense lesion crosses the spinal cord and is contiguous ventrally with the intervertebral disc space (Fig. 15.21, eFig. 15.5). Areas of hypointensity can be seen associated with that tract in gradient recalled echo images because of hemorrhage.[26,85]

Up to 33% of affected patients with acute noncompressive hydrated *nucleus pulposus* extrusion have an unsuccessful outcome.[27] Prognostic factors of unsuccessful outcome include severity of neurologic signs at presentation, percentage of cross-sectional area of the intramedullary lesion on transverse T2W images, and presence of intramedullary hemorrhage. An intramedullary cross-sectional area of the T2-hyperintense lesion exceeding 90% of the spinal cord area is associated with a 92% chance of an unsuccessful outcome.[27]

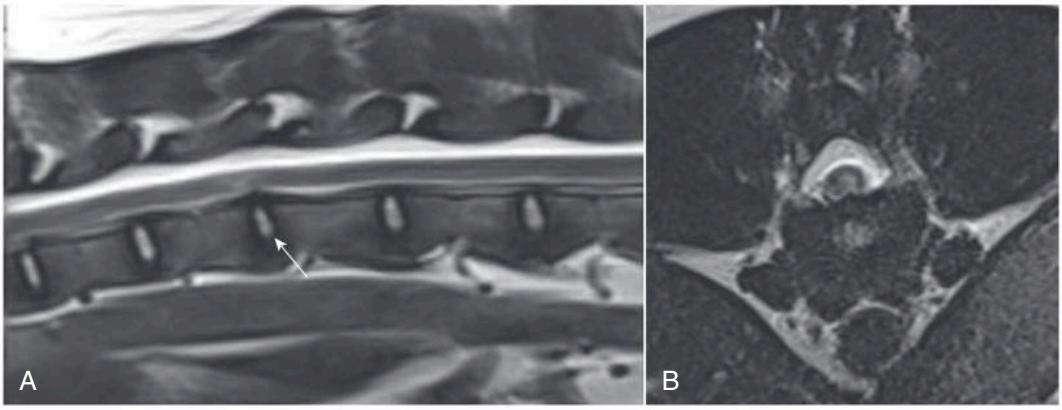
On CT myelography, acute traumatic or exercise-induced disc extrusion can be associated with narrowing of the affected disc space, seen on sagittal or dorsal reformatted images, with evidence of a small amount of minimally compressive extradural material at the level of the disc with spinal cord swelling adjacent to these areas. When the extruded disc material causes rupture of the dura, small leaks of iodinated contrast medium can be seen extending from the subarachnoid space into the epidural space.[89] Leakage of contrast medium into the intervertebral disc in patients with disc-associated dural rupture can be seen with application of spinal traction during conventional myelography.[84] On CT performed after myelography, presence of intramedullary contrast medium can also be seen in patients with intramedullary extrusion.[24]

Compressive Hydrated Nucleus Pulposus Extrusion

In some cases, the extruded hydrated disc material accumulates focally in the epidural space and causes spinal cord compression.[29–31] In this case, the neurological deficits are more severe, and the pain less severe than with other compressive myelopathies.[30]

The MRI features of the compressive form of the disease include the following (Fig. 15.22)[29–31,33,34,90]:

- Space-occupying T2-hyperintense material ventral to the spinal cord, on midline and centered immediately dorsal to a slightly narrowed intervertebral disc space (most commonly C4–C5, C3–C4, C5–C6), causing ventral compression and dorsal displacement of the spinal cord centered at the intervertebral disc space.
- On sagittal T2W images, this extruded material has an elongated shape and is difficult to distinguish from the hyperintense epidural fat and CSF, because it has similar signal intensity. On transverse T2W images centered on the affected disc space, the extruded material lies symmetrically on the midline, ventral to the spinal cord, and often has a characteristic "seagull" shape. That shape is presumed to be due to the presence of the meningovertebral ligament, which creates a midline longitudinal anatomic barrier that confers the gelatinous extruded material that bilobed shape.[4]
- On T2-fluid-attenuated inversion recovery (FLAIR) images, the extruded material typically retains a hyperintense signal,[33,34] but sometimes it is suppressed.[34,90]
- Focal intramedullary T2W hyperintensity dorsal to the affected disc, which is T1W isointense and nonenhancing after gadolinium injection.
- This focal intramedullary T2W hyperintensity is usually iso- to hyperintense on T2*W images, consistent with spinal cord contusion.
- There is inconstant mild diffuse[29] or peripheral[33,34] contrast enhancement of the extruded material.



eFig. 15.5 Sagittal **(A)** and transverse **(B)** T2-weighted images of a dog with acute noncompressive intervertebral disc extrusion at L1—L2. The nucleus pulposus of the L1—L2 disc (*arrow*) is reduced in volume but remains hydrated and T2 hyperintense. Focal irregularity of the annulus fibrosus and T2 hyperintensity of the spinal cord at this level is consistent with disc extrusion and resulting spinal cord contusion.

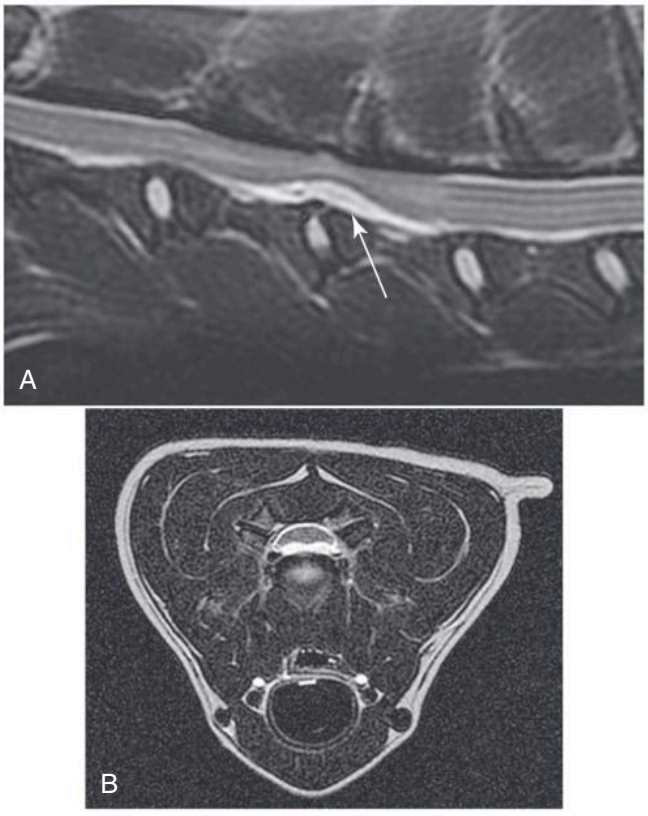


Fig. 15.22 **A,** Sagittal T2-weighted image in a dog with an acute compressive hydrated *nucleus pulposus* extrusion at C4–C5. Note the mild degenerative changes in the disc at C4–C5 with reduced size and signal of the *nucleus pulposus*. The compressive hydrated disc material appears as a broad-based T2-hyperintense structure (*white arrow*) present dorsal to the C4–C5 space that causes ventral spinal cord compression. Intramedullary T2 hyperintensity at that level is consistent with edema. A fluid-filled cystic structure was found during surgery in the ventral epidural space associated with the C4–C5 disc. **B,** Transverse T2-weighted image of the cervical spine in another dog with an acute compressive hydrated *nucleus pulposus* extrusion at C3–C4. Note the seagull pattern caused by the extruded disc material in the ventral epidural space causing marked ventral spinal cord compression.

Intradural And Intramedullary Disc Herniation

Occasionally, extruded disc material can cause laceration of the dura mater and end up in the intradural/extramedullary compartment or in the intramedullary compartment.[26,91–93] During CT myelography, leakage of iodinated contrast material in the epidural space can be seen, and in cases of intradural location of the extruded disc material, focal expansion of the subarachnoid space with a filling defect can be observed.[93] At MRI, in cases of intramedullary disc extrusion, one may observe a linear tract in the spinal cord parenchyma dorsal to the disc space, which is T2-hyperintense, T1-hypointense and with susceptibility artifacts on T2*W images due to parenchymal hemorrhage, often with enhancement on postcontrast T1W images. A thin cleft in the dorsal annulus of the affected disc may also be noted on transverse images.[92] In cases of intradural but extramedullary disc extrusion, a characteristic "Y-sign" has been reported on T2W sagittal images appearing as a hyperintense horizontal Y pattern along the cranial and/or caudal edge of the hypointense compressive disc material; it is thought that this pattern is due to a cleft forming between the dura mater and arachnoid membrane expanding the subdural space.[91] A "beak sign" is also reported, although less commonly, and seen as a triangular hypointense lesion dorsal to the disc and causing cord compression, with occasionally peripheral enhancement on postcontrast T1W series.[91]

CERVICAL SPONDYLOMYELOPATHY

Cervical spondylomyelopathy refers to a collection of disorders of the caudal cervical spine in large-breed dogs resulting in progressive and chronic spinal cord compression. Other terminology used for this condition includes *wobbler disease, cervical vertebral instability, cervical spondylopathy, cervical spondylolisthesis*, and *cervical vertebral malformation-malarticulation*.[94] The clinical signs range from cervical hyperesthesia to tetraplegia, with the most common being a gait disturbance.[94–101]

Pathologic changes observed with cervical spondylomyelopathy include the following[94]:

- Stenosis of the vertebral canal because of malaligned or misshapen vertebral bodies and/or abnormal, hypertrophied articular processes
- Hansen type II disc protrusion alone or in combination with hypertrophy of the dorsal longitudinal ligament resulting in ventral compression of the spinal cord
- Hypertrophy of the interarcuate ligament *(ligamentum flavum)* and the joint capsule of the articular process joints, resulting in dorsal and dorsolateral spinal cord compression
- Osteoarthrosis of the articular processes with excessive soft tissue proliferation and synovial cyst formation also potentially causing dorsolateral spinal cord compression.

Cervical spondylomyelopathy is seen most commonly in Great Danes and Doberman pinschers but also occurs in other large and giant breeds. In middle-aged to older Doberman pinschers, the most common lesion is Hansen type II disc protrusion and hypertrophy of the ligamentum flavum (interarcuate ligament); this condition is often referred to as "disc-associated cervical spondylomyelopathy."[102] In young Doberman pinschers, Great Danes, and other large-breed dogs (such as older German shepherds[103] or Bernese mountain dogs[104]), the disease is more of the stenotic type myelopathy, caused by hypertrophy and degenerative changes of the articular processes and *ligamentum flavum* hypertrophy, which, combined, cause reduction in the size of the vertebral canal; this condition is often referred to as "osseous-associated cervical spondylomyelopathy."[103,105–107] Clinical signs associated with these conditions usually develop at around 2 to 3 years of age, although juvenile presentation is occasionally seen and mostly of the osseous-associated type.[108]

Both CT, with or without myelography, and MRI provide useful information for diagnosis of this condition; however, there is considerable intermethod and interobserver variability in the information gathered from these imaging modalities, and they may be considered as complementary to each other for a thorough evaluation in a given patient.[95,100,109]

Intermethod and interobserver variability is less pronounced for disc-associated cervical spondylomyelopathy as opposed to the stenotic-type myelopathy.[95,100,109]

Computed Tomography of Cervical Spondylomyelopathy

Noncontrast CT is not very useful in the diagnosis of cervical spondylomyelopathy. It allows assessment of the bone abnormalities, such as articular process hypertrophy, malalignment, and spondylosis, but performs poorly in identifying and grade the location of spinal cord compression correctly and does not

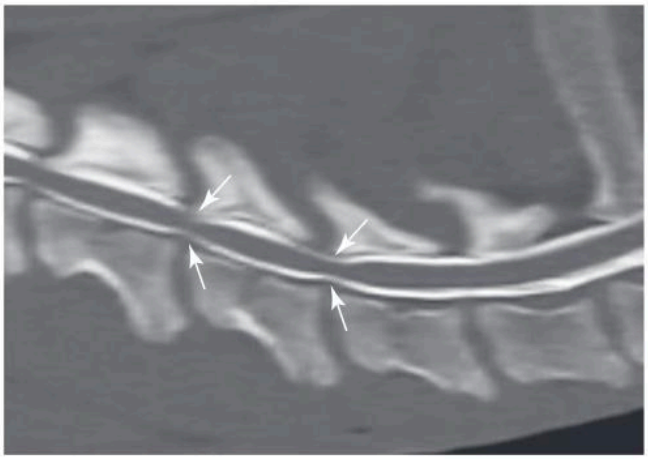


Fig. 15.23 Sagittal reformatted computed tomography (CT) myelogram in a dog with caudal cervical spondylomyelopathy. Note the dorsal and ventral spinal cord compression at C4–C5 and C5–C6 (*white arrows*) because of a combination of ligamentum flavum hypertrophy and dorsal longitudinal ligament hypertrophy with disc bulging. (Image courtesy Dr. Paul Barthez, Clinique Vétérinaire des Halles, Strasbourg, France.)

allow identification of spinal cord atrophy that may be of prognostic value. With CT myelography, conversely, there is excellent delineation of the spinal cord and characterization of the areas of compression (Figs. 15.23 and 15.24). CT myelography provides more information than conventional myelography on the exact location and degree of spinal cord compression. In particular, spinal cord atrophy can be distinguished with CT from reversible spinal cord compression. A further advantage of CT myelography is the superior contrast resolution, which can provide diagnostic images with very little contrast medium in the subarachnoid space.[9] In the Doberman pinscher, several patterns of spinal cord compression have been described on CT[9]:

- Central spinal cord deformity occurs, which most of the time is caused by bulging of the *annulus fibrosus* and occasionally by *nucleus pulposus* extrusion.
- Asymmetric spinal cord compression with intervertebral foramen impingement is caused by unilateral disc protrusion.
- Spinal cord atrophy is characterized by a reduction in the cross-sectional area of the spinal cord, together with relative widening of the subarachnoid space. The atrophic spinal cord can assume an abnormal shape, from a flattened appearance to triangular. It is unclear if spinal cord atrophy is a prognostic indicator of poor outcome, although there are reports of histologic damage, which is likely irreversible, in spinal cords with such a pattern on CT myelography.[9]

The use of traction can provide information on the dynamic nature of spinal cord compression when comparing images in neutral versus stressed positions; sagittal reformatted images are especially useful for this purpose (Fig. 15.25).

Magnetic Resonance Imaging of Cervical Spondylomyelopathy

MRI is accurate in imaging the changes associated with cervical spondylomyelopathy.[95–97,99–101,109–111] Compared with conventional myelography, MRI is more accurate in predicting the site, severity, and nature of the spinal cord compression. Using myelography can lead to an underestimate in the severity of spinal cord compression.[95] MRI is also better than myelography in locating the sites of compressive lesions.[95]

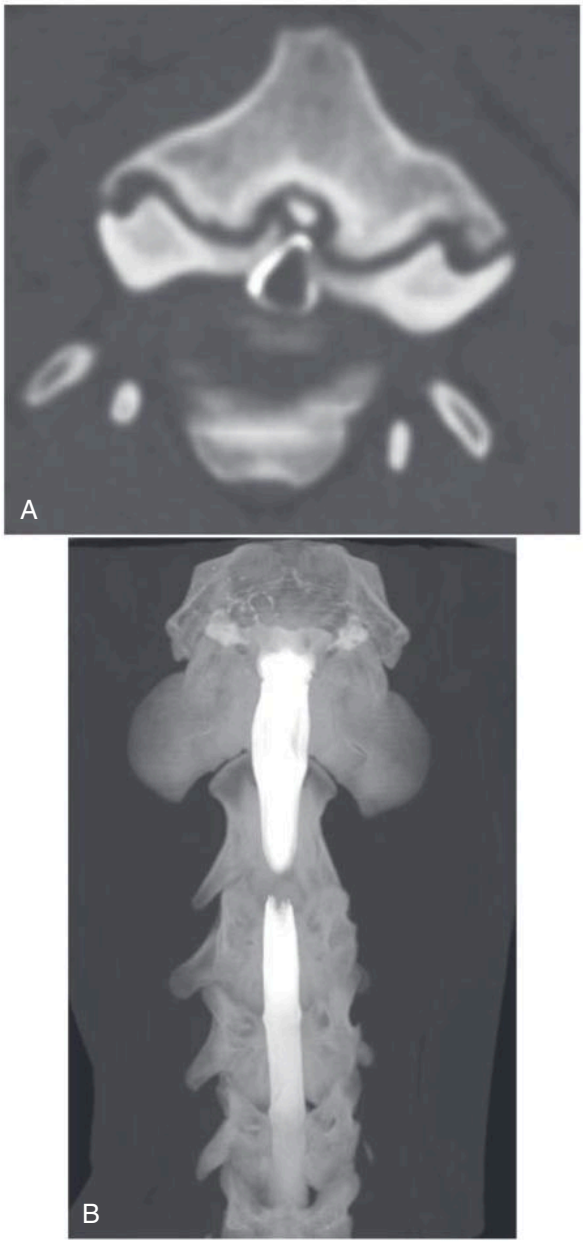


Fig. 15.24 Computed tomography (CT) myelography in a 7-month-old Great Dane with osseous-associated cervical spondylomyelopathy. **A,** Transverse image centered at C2–C3. **B,** Dorsal subvolume maximum intensity projection. There is severe hypertrophy of the articular processes causing marked dorsolateral spinal cord compression at C2–C3. (Image courtesy Dr. Paul Barthez, Dierenkliniek Causus, Oudenburg, Belgium.)

With disc-associated cervical spondylomyelopathy, seen in middle-aged or older Doberman pinschers, the disease is characterized by:

- Disc degeneration, disc bulging, and/or herniation causing spinal cord compression
- *Ligamentum flavum* hypertrophy causing dorsal spinal cord compression
- Alterations in spinal cord signal intensity
- Vertebral body abnormalities and spondylosis

The presence of alterations in spinal cord signal intensity is a reliable indicator of clinically relevant spinal cord compression,[95,97] although this has occasionally been reported in the

caudal cervical spine of clinically normal dogs.[110] However, such T2 hyperintensities do not seem to correlate to prognosis.[96] What is causing the T2 hyperintensity of the gray matter in the spinal cord of affected dogs is not clearly established, but possible reasons include loss of nerve cells, gliosis, and edema. White matter T2 hyperintensity can be caused by demyelination, edema, and Wallerian degeneration. When areas of corresponding T1 hypointensity are present, more severe changes, such as necrosis, myelomalacia, and spongiform changes, may be suspected.[96] There may be a positive correlation between severity of cord compression and neurologic grade; however, multilevel compression is not associated with worse deficits.[102] Dynamic studies with traction MRI have questionable accuracy in identifying the static or dynamic nature of the compression.[95,112]

With osseous-associated cervical spondylomyelopathy, seen in younger Doberman pinschers and giant-breed dogs such as Great Danes, there appears to be a weak correlation between neurologic grade and severity of spinal cord compression, number of affected sites, and presence of T2W spinal cord hyperintensity.[105] The MRI abnormalities seen with this condition include the following[94,99–101]:

- Degenerative changes of the intervertebral discs are seen as decreased signal intensity on T2W images, especially at C6–C7 and C5–C6.
- Hypertrophy of the dorsal longitudinal ligament and osteoarthrosis of the articular process from C3–C4 to C7–T1 is seen, with the most common sites being C4–C5, C5–C6, and C6–C7. These compressive structures appear T1 and T2 hypointense, and spinal cord deformity can be seen on sagittal/parasagittal and transverse images. These abnormalities can cause unilateral or bilateral dorsolateral spinal cord compression, which is best identified on transverse images (Fig. 15.26).

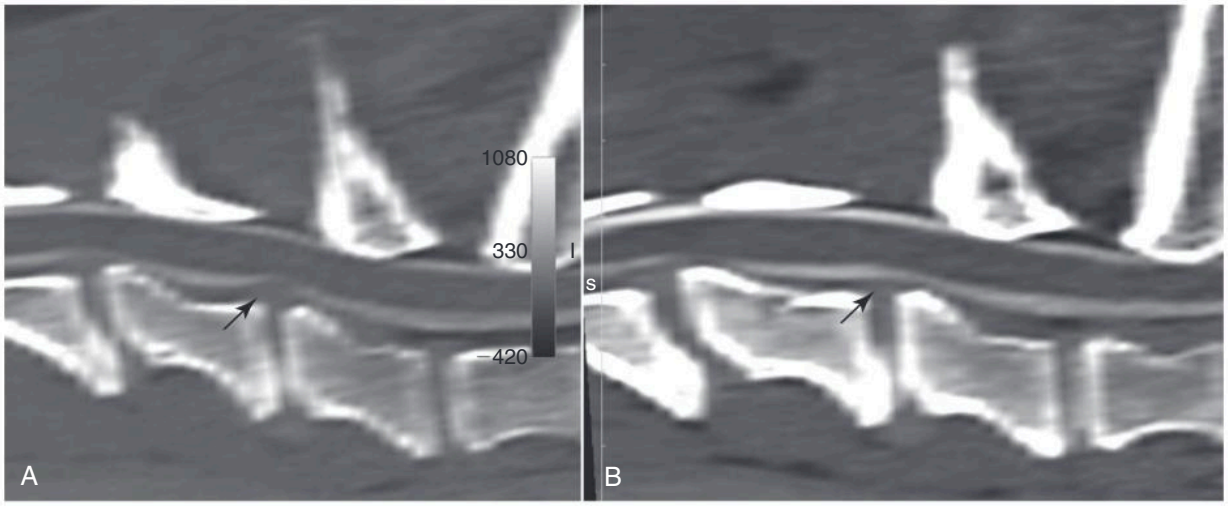


Fig. 15.25 Sagittal reformatted computed tomography (CT)-myelographic images of the caudal cervical spine of a middle-aged Doberman pinscher with disc-associated cervical spondylomyelopathy. **A** shows neutral position, and there is ventral spinal cord compression caused by a bulging disc and/or dorsal longitudinal ligament hypertrophy (*black arrow*). **B** was obtained during cervical traction, and there is reduction in spinal cord compression (*black arrow*), thereby characterizing the dynamic nature of the compression. (Image courtesy Dr. Laurent Couturier, Azur Vet, Cagnes sur Mer, France.)

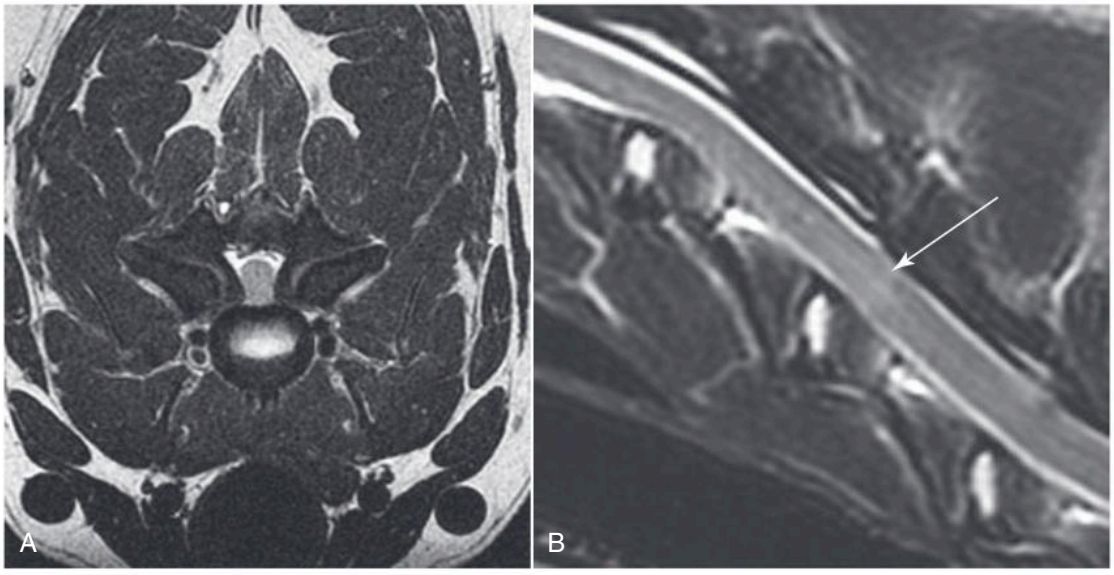


Fig. 15.26 Transverse **(A)** and sagittal **(B)** T2-weighted images in a Great Dane with osseous-associated cervical spondylomyelopathy at C3 to C4. There is marked hypertrophy of the articular processes causing lateral spinal cord compression. There is intramedullary T2 hyperintensity in the sagittal image (*white arrow*). This hyperintensity can help determine the clinical significance of the cervical anomalies.

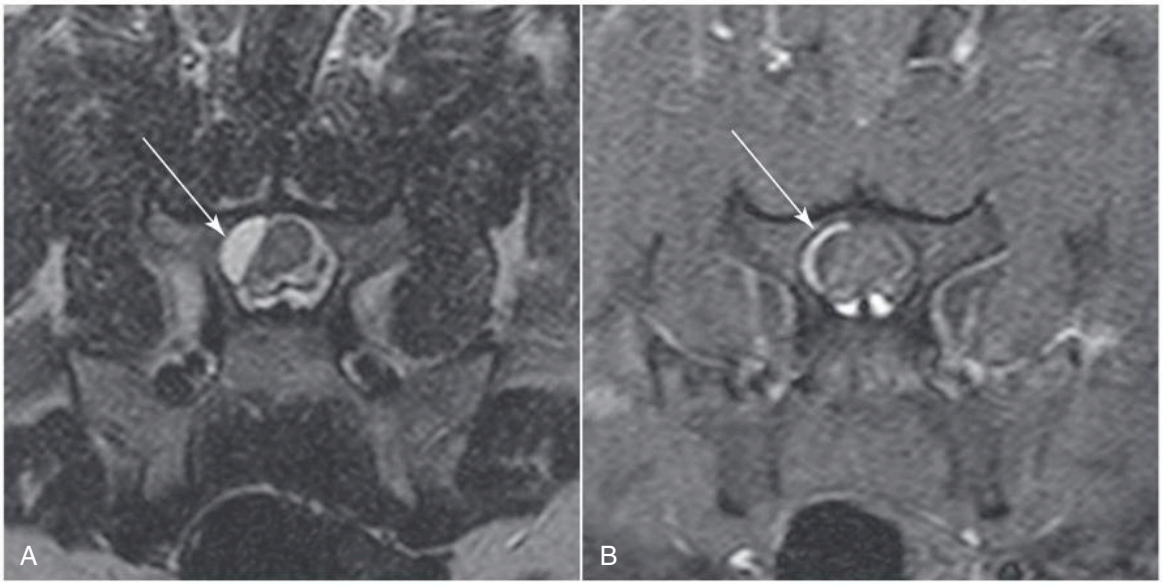


Fig. 15.27 T2-weighted **(A)** and postcontrast, fat-suppressed, T1-weighted **(B)** transverse images of a dog with cervical spondylomyelopathy. There is a large synovial cyst (*white arrow* in **A**) arising from a degenerate articular process joint that is causing moderate spinal cord compression. The joint itself is caudal to this image plane because the cyst has bulged cranially. Following contrast medium administration, there is enhancement of the wall of the cyst (*white arrow* in **B**).

- Intramedullary T2 hyperintensity is associated with areas of spinal cord compression (see Fig. 15.26).
- Synovial cysts are identified as T1-hypointense, T2-hyperintense structures associated with the articular processes and sometimes contributing to dorsolateral spinal cord compression (Fig. 15.27). The wall of these cysts occasionally enhances after gadolinium injection.
- Occasional disc protrusion (Hansen type II) contributes to ventral spinal cord compression, especially at C6–C7.
- Kinematic MRI may reveal an increased number of compressive lesions and changes in site of the most compressive lesion on images obtained in extension vs. neutral positioning.[113]

There is a high incidence of MRI abnormalities of the cervical vertebral column in clinically normal large-breed dogs; these have been documented in Doberman pinschers and foxhounds and include complete disc degeneration, spinal cord compression, vertebral body abnormalities, and even intramedullary T2 hyperintensity.[110] In clinically normal Great Danes, foraminal stenosis (sometimes severe), and less commonly spinal cord compression have been reported.[99] Therefore, caution should be exercised when attributing clinical signs to structural abnormalities seen on MR images. Also, there can be significant variability in the assessment and interpretation of MRI abnormalities across observers in dogs with disc-associated wobbler syndrome so that interpretation of imaging results must be made with caution.[110]

CYSTIC CHANGES OF THE SPINE

Several types of intraspinal cyst-like changes occur in dogs; the most common being arachnoid diverticula, epidermoid/dermoid cysts, articular process synovial, and ganglion cysts. Uncommon cystic changes include perineurial or perineural cysts, also called *Tarlov cysts*, which originate from the dorsal nerve root and ganglion sheath, close to the point where the pia and arachnoid membrane differentiate into endoneurium and perineurium, respectively. Unlike arachnoid diverticula, they are extradural lesions filled with CSF and contain neural structures pertaining to the nerve root and ganglion.[114,115] Cysts of ligamentous or discal origin are extremely rare. Cyst-like changes associated with the intervertebral disc, similar to the "discal cysts" seen in humans, are rarely described in the thoracolumbar spine of dogs and are called "discal pseudocysts."[116,117]

Spinal Arachnoid Diverticula

Spinal arachnoid diverticula are a rare cause of spinal cord compression in dogs and rarely reported in cats.[13,118–138] In dogs, they are located in the subarachnoid space, lined by arachnoid and pia mater, and communicate freely with CSF in the subarachnoid space. Because no true epithelial lining is present, the term *arachnoid diverticula* is used here. These lesions are often congenital but can be associated with spinal cord trauma, IVDD, or previous arachnoiditis.

The most common location is in the cranial cervical or caudal thoracic region. These lesions are usually single but can be multiple. They are most commonly dorsal or dorsolateral to the spinal cord but can be ventral occasionally. Rottweilers are likely to be predisposed to cervical arachnoid diverticula, and pug dogs seem to have a high incidence of thoracolumbar arachnoid diverticula. In pugs, there may be an association between development of arachnoid diverticula and aplasia of the caudal articular processes in the caudal thoracic spine. In addition, in this breed,[139] a familial form of the condition has been reported in the cervical spine.[132]

In CT without contrast medium, there is a hypoattenuating lesion causing spinal cord compression. Diagnosis is established after subarachnoid injection of contrast medium leads to pooling of contrast medium in the diverticulum. Sagittal reformatted images allow recognition of the typical teardrop shape of the lesion.

On MRI, a discrete T1-hypointense region contiguous with the subarachnoid space is present adjacent to the spinal cord (usually dorsal). This lesion is T2 hyperintense and usually suppressed with FLAIR techniques, although a lack of suppression on T2-FLAIR has been reported,[127] and may reflect that occasionally the fluid in the diverticulum is of different chemical composition than CSF, as has been described in intracranial arachnoid cysts in people.[140] Heavily T2W pulse sequences such as HASTE or SSFSE, which highlight fluid-filled spaces

while suppressing background signal, have been reported to increase the sensitivity of MRI for the identification of arachnoid diverticula in dogs.[13]

The diagnosis is usually most obvious on sagittal images where the typical teardrop shape of these lesions is apparent (Fig. 15.28). The spinal cord is compressed to various degrees at the level of the diverticulum. CSF pulsation within the diverticulum can lead to spinal cord edema from the repetitive concussion, or there may be syrinx formation because of altered CSF flow in the region of the diverticulum (Fig. 15.29, eFig. 15.6). MRI is superior to CT myelography for the diagnosis of spinal arachnoid diverticula in the rare instance where the diverticulum does not communicate with the subarachnoid space.

Epidermoid and Dermoid Cysts or Sinuses

Epidermoid and dermoid cysts and sinuses are caused by failure of separation of the surface ectoderm (forming the epidermis) and neuroectoderm (forming the nervous system) during embryogenesis. They have a complex wall and contain both epidermoid tissue and adnexa. They can be associated with the dermal, ocular, and central nervous system (CNS), and the most common CNS manifestation is of a sinus connection with the skin surface that may extend into the vertebral canal to affect the spinal cord ("dermoid sinus").[141] As opposed to sinuses, epidermoid and dermoid cysts do not have an opening onto the midline surface of the skin.[142] With epidermoid cysts or sinuses, the wall of the lesion consists of stratified squamous epithelium, supported by connective tissue stroma. Keratin squames are found within the lesion along with a few inflammatory cells. Dermoid cysts and sinuses differ from epidermoid cysts because the dermoid cyst contains other features of skin, such as sweat glands, hair follicles, and sebaceous glands.

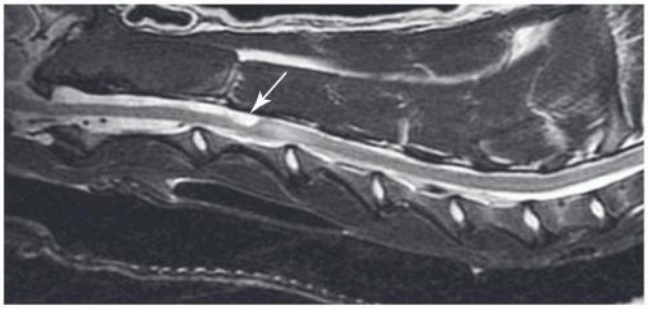


Fig. 15.28 T2-weighted sagittal image in a dog several months after diagnosis of meningitis caused by *Cryptococcus* infection. There is a spinal arachnoid diverticulum (*white arrow*) dorsal to C3 forming a typical teardrop-shaped hyperintense structure dorsal to the spinal cord.

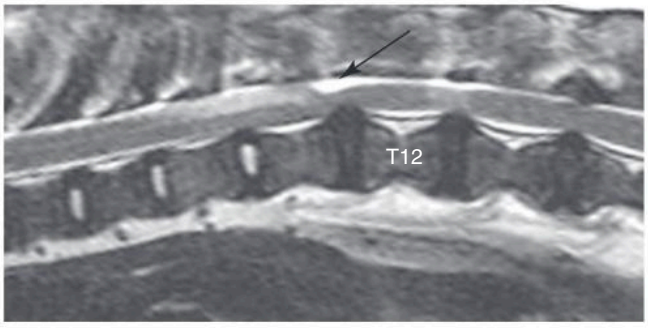


Fig. 15.29 Sagittal T2-weighted image of a dog with a dorsal arachnoid diverticulum (*arrow*) at T11 to T12. There is a region of intramedullary T2 hyperintensity just cranial to the diverticulum that likely represents early syringomyelia because of altered cerebrospinal fluid (CSF) flow.

Epidermoid and dermoid cysts confined strictly to the CNS without a cutaneous or subcutaneous tract develop from skin-determining ectoderm, which remains attached to mesoderm and as the neural tube closes becomes surrounded by the meninges.[143] In such instances, no tract or sinus is present in the dorsal paraspinal soft tissue or skin.[143]

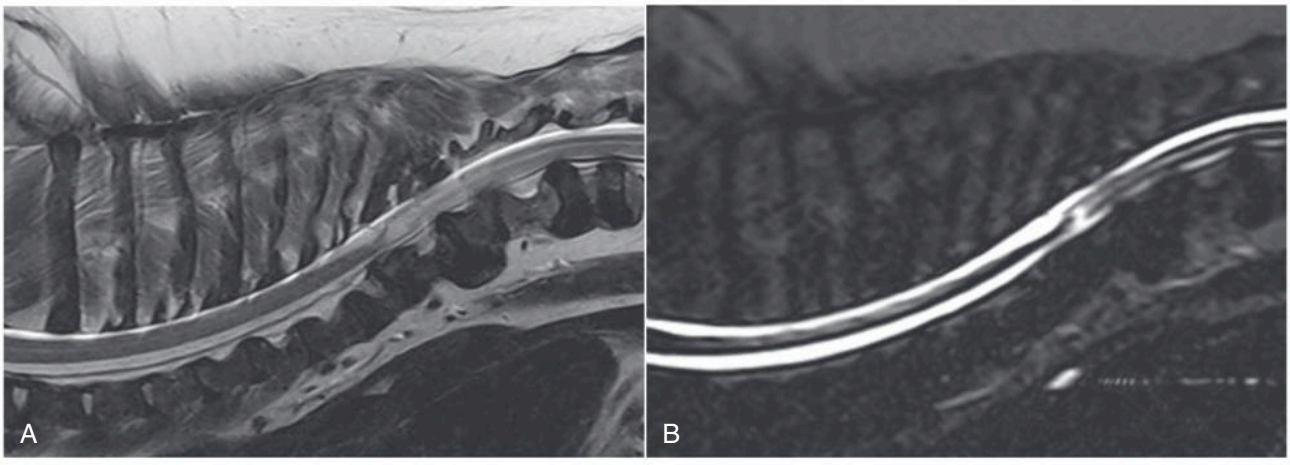
Spinal dermoid sinuses fall into one of six categories, depending on how deep the connecting tract penetrates[144]:

- Type I: Tubular sac extending from the skin to the supraspinous or nuchal ligament
- Type II: More superficial tract, with a deep fibrous strand connecting to the supraspinous or nuchal ligament
- Type III: Superficial tract with no connection to the supraspinous or nuchal ligament
- Type IV: Deep tract that communicates with the vertebral canal and is attached to the dura mater
- Type V: True dermoid "cyst," with a closed capsule and no deeper connection or opening to the skin
- Type VI: Deep tract that extends to the supraspinous or nuchal ligament and continues deeper as a fibrous strand that connects to the dura mater

Only types IV and VI may be associated with neurologic signs, due to their relationship with the dura mater; in these cases, neurologic signs can be the result of infection (abscessation, meningitis, meningomyelitis, and so on), compression of the spinal cord due to progressive enlargement of the deeper portion of the tract with accumulated debris (hair follicles, sebum, keratin, desquamated epithelial cells), tethering of the spinal cord,[144] and syringomyelia.[144]

There are only a few reports on the use of CT and MRI in the diagnosis and presurgical assessment of epidermoid and dermoid cysts in dogs. CT imaging can allow detection of a communication with the vertebral canal through a defect in the vertebral arch, with subsequent spinal cord compression and displacement.[145,146]

The MRI abnormalities reported with spinal dermoid sinus include a focal invagination of the cutaneous tissues toward the spinous processes corresponding to the clinically palpable lesion (Fig. 15.30). Deep to that area, there may be a focal rounded or lenticular subcutaneous lesion, corresponding to the main cavity of the sinus, followed by a tubular tract extending ventrally to a variable depth, depending on the type of dermoid sinus. The lumen of the sinus and its tract is often filled with sebum, keratin debris, and hair, resulting in a variable and unpredictable MR signal. Compared to muscles, the lesions tend to be T2-hyperintense to muscles, whereas T1W signal is more variable (hypo-, iso-, hyperintense).[147–149] Areas that are hyperintense on both T1W and T2W images may correspond to lipid lining.[147] In a report where gadolinium contrast medium was administered intravenously, only minimal enhancement was seen.[147] In a patient where the sinus was abscessed, the lesion was markedly T2-hyperintense and T1-hypointense with a hypointense wall on both T1W and T2W images, suggestive of a thick capsule.[142] In types IV and VI, which have a dural connection, additional signs may include a linear, somewhat tortuous tract of variable signal intensity, extending deep to the skin toward the spine and entering the vertebral canal, connecting with the dura mater, usually through an interarcuate space, and in some instances through a defect of the dorsal arch (schisis).[147,149–151] Concurrent vertebral malformations may be present, such as *spina bifida*, vertebral blocks, partial fusion of adjacent spinous processes, and incomplete dorsal lamina.[144,147,149–151] Such anomalies seem to be more commonly associated with dermoid sinuses that have connection with the dura mater, and therefore their identification should trigger a careful examination of the meninges, subarachnoid space, and spinal cord in that general area. Focal dorsal tenting of the meninges of the spinal cord, due to the dural connection pulling the dura dorsally, may be



eFig. 15.6 Sagittal T2-weighted **(A)** and half-Fourier single-shot turbo spin echo (HASTE) sequence **(B)** of a French bulldog with a dorsal arachnoid diverticulum at T8 to T9. The diverticulum presents as markedly T2 hyperintense focal widening of the subarachnoid space, best seen in the HASTE sequence **(B)**. The spinal cord is T2 hyperintense cranial to the diverticulum, thought to represent edema secondary to pulsation of cerebrospinal fluid (CSF) within the diverticulum. Generalized degenerative disc disease and vertebral malformations are also present.

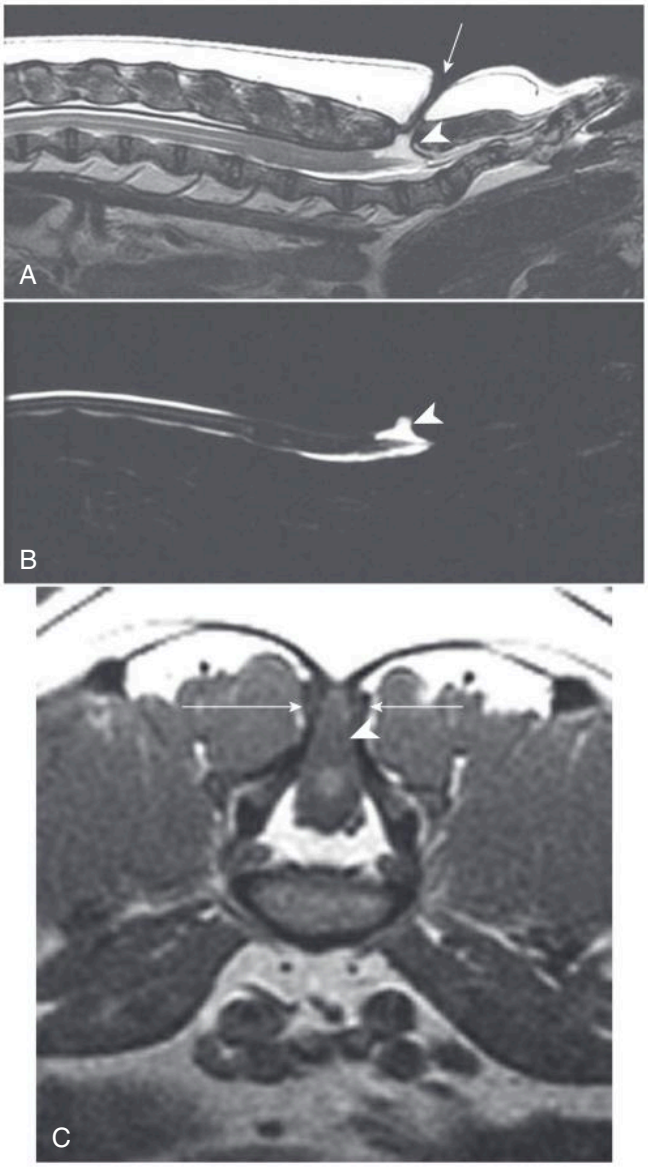


Fig. 15.30 Dermoid sinus and meningocele in a 1-year-old French bulldog. This was an incidental finding as the dog was imaged with MRI because of acute paraplegia due to an intervertebral disc extrusion at L5—L6 (causing the cord swelling seen in the caudal lumbar area). Sagittal T2-weighted **(A)**, sagittal single-shot fast spin echo (SSFSE) "T2-myelogram" **(B)**, and transverse T2-weighted **(C)** images are presented. On the T2-weighted sagittal image, a focal invagination of the cutaneous surface is seen at the level of the lumbosacral region (**A,** *white arrow*) extending towards a split spinous process as seen on the transverse image (**B,** *black arrows*) consistent with spina bifida. A flame-like dorsal expansion of the subarachnoid space is seen on all images (*arrowheads*) directed towards the dermoid sinus consistent with a concurrent meningocele.

seen. In instances of tenting, the dorsal subarachnoid space is focally widened and assumes a characteristic triangular shape on transverse images.[147,150] In instances of tethering, there is dorsal displacement of the spinal cord at the level of the sinus.[144] There may be syringomyelia adjacent to the dural connection, likely associated with focal alterations of the CSF flow dynamics caused by the dural connection or concurrent adhesions or vertebral anomalies.[144] In rare instances, extension of the distal end of the sinus through the dura mater forms a progressively enlarging, debris-filled blind-ended cystic component that appears as an intradural-extramedullary T2-hyperintense mass lesion compressing/displacing the spinal cord.[149]

The MR or CT appearance of strictly intramedullary epidermoid and dermoid cysts has not been reported in dogs or cats, although there is a report of a dermoid cyst in the medulla oblongata of a dog. That lesion was heterogeneous but predominantly hyperintense on both T1W and T2W images with no contrast enhancement.[141]

Articular Process Cysts

Cysts associated with the articular process are extradural fluid-filled round or oval well-defined structures that develop as a result of degeneration of the articular process joint.[115,152–155] They are divided histologically into (1) synovial cysts lined by synovium-like epithelial cells resulting from outpouching of synovial membrane through weakened capsular tissue and (2) ganglion cysts, which are the result of mucinous degeneration of periarticular connective tissue and which do not have a synovial lining. From clinical and imaging perspectives, the two entities are indistinguishable and can therefore be grouped under the terminology *articular process cyst*.[154]

Clinical signs associated with articular process cysts vary from pain to ataxia and tetra- or paraparesis, although in a number of instances, the clinical signs are not attributable to the cyst, but to other causes of spinal cord compression, such as disc herniation, articular process hypertrophy, and vertebral instability. These articular process cysts appear to be more common in large- to giant-breed dogs.[115,152–155] In giant-breed dogs, the cysts tend to be multiple and located in the cervical spine and more common in young dogs.[153] In large-breed dogs, cysts are more commonly found in the thoracolumbar or lumbosacral area in young adults and older dogs.[115,152–155] The cysts can be single or multiple and present at one or several locations.

On MRI, these lesions have the characteristic signal of a fluid-filled lesion appearing as well-defined round lesions associated with the articular processes and are T1 hypointense and T2 hyperintense (Fig. 15.31).[115,152,154,155]

Discal Pseudocyst

Although initial reports of compressive myelopathy due to so-called "discal cysts"[33,34] were deemed to more likely represent compressive forms of hydrated *nucleus pulposus* extrusions in subsequent studies,[32] a rare condition resembling discal cysts seen in humans has been reported.[116,117] These are seen in the thoracolumbar region of medium- to large-breed dogs presenting with acute to subacute neurologic deficits. At MRI, they form rounded to oval-shaped, ventral to ventrolateral extradural compressive lesions arising from the dorsal aspect of the intervertebral disc; they are iso-/hypointense on T1W images, mostly hyperintense on T2W images, with a thin enhancing capsule on postcontrast images and occasional enhancement of the content of the cyst-like lesion. Histologically, the wall of the lesions consists of dense fibrous connective tissue containing clusters of chondroid cells accompanied by notochordal cells with no nerve tissue or disc material; due to the lack of an epithelial lining, discal pseudocyst is a preferred terminology for these lesions.

SPINAL TUMORS

Spinal tumors can be classified on the basis of their location relative to the dura mater and can be described as intramedullary, intradural-extramedullary, or extradural.[156] Most extradural tumors are malignant tumors of constituents of the vertebral column, such as the vertebrae or the soft tissues within or surrounding the vertebral column. Intradural-extramedullary tumors are mostly nerve sheath tumors and meningiomas. Intramedullary neoplasms are usually of glial cell origin, such as astrocytomas or ependymomas, but multicentric

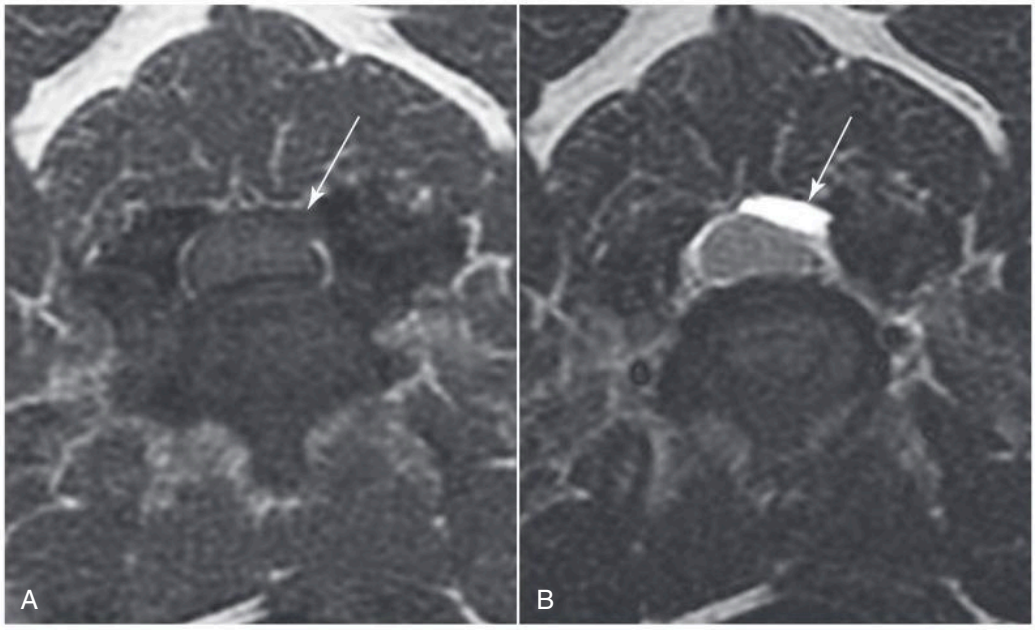


Fig. 15.31 Transverse T1-weighted **(A)** and T2-weighted **(B)** images at C3 to C4 in a dog with a left-sided articular process cyst. The cyst (*white arrows*) is T1 hypointense and markedly T2 hyperintense because of its fluid content. In this dog, the cyst caused mild left dorsolateral spinal cord compression.

non-neural neoplasia (such as, lymphoma) or metastatic lesions (such as, hemangiosarcoma) also occur.

Extradural Tumors

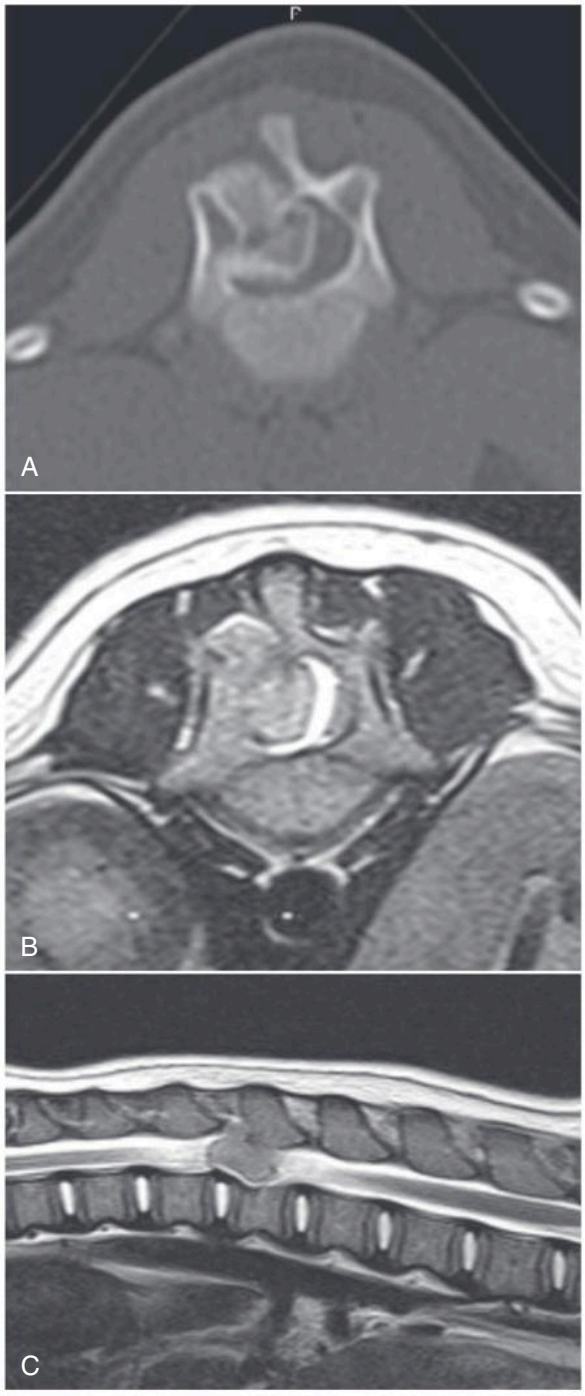
The most common extradural spinal cord tumors in dogs include osteosarcoma and chondrosarcoma.[157] In cats, extradural lymphosarcoma is also frequent.[158,159] Solitary or disseminated histiocytic sarcoma can also affect the vertebrae and cause spinal cord compression.[160] Other disseminated canine tumors with possible vertebral involvement include lymphosarcoma and multiple myeloma.[157] Metastatic vertebral tumors are also common, in particular prostatic carcinoma or transitional cell carcinoma of the bladder and urethra in dogs.[157] Tumors of the paravertebral soft tissues or extradural soft tissue components of the vertebral canal are also possible, and local invasion can cause spinal cord compression. Examples include soft tissue sarcoma, infiltrative lipoma,[161–165] extradural lymphosarcoma, mast cell tumor (primary or metastatic), and hemangiosarcoma.[166–171]

Both MRI and CT are more sensitive than radiography in detecting vertebral lesions and in particular bone lysis that is not apparent radiographically can be demonstrated readily using CT. Vertebral canal tumors can be difficult to localize to the intradural, extradural, or intramedullary compartments on noncontrast CT images.[172] Injection of intravenous contrast medium and, more important, CT myelography are more precise for determining the location of masses in the vertebral canal with respect to the dura. MRI is also good for localizing these lesions; however, with MRI, it is more difficult to localize vertebral canal masses with respect to the dura because of lower spatial resolution.[173] There are no specific CT or MRI features that are associated with a specific tumor type.[172,173]

Vertebral tumors produce variable degrees of bone lysis or proliferation, which is detected easily on CT images (Fig. 15.32, eFig. 15.7). On MR images, alteration of the shape of the affected vertebra can be seen, as well as disruption of the normally hypointense vertebral cortex (Fig. 15.33). In MR images, periosteal reaction appears as hypointense material surrounding the lesion in the affected vertebra. The signal intensity of the lesion itself varies between patients and depends on tumor type. For example, vertebral osteosarcoma has been reported to have T2W heterogeneous signal, with heterogeneous contrast enhancement and osteolysis.[166,174] However, relevant conclusions cannot be drawn as to what the signal intensity of a specific tumor type would be. Most vertebral tumors are monostotic; however, polyostotic lesions are possible in cases of metastatic neoplasia (e.g., from prostatic carcinoma or bladder urothelial carcinoma, metastatic mast cell neoplasia[170]), as well as in cases of bone marrow neoplasia such as multiple myeloma.[175] With multiple myeloma, multiple



Fig. 15.32 Transverse computed tomography (CT)-myelographic image of the thoracic spine in a dog with a vertebral osteochondroma. There is a large proliferative lesion arising from the vertebral arch that causes marked stenosis of the vertebral canal and left dorsolateral compression of the spinal cord (*c*). The subarachnoid space filled with iodinated contrast medium is indicated by the *white arrow*.



eFig. 15.7 Transverse computed tomography image **(A)**, transverse T2-weighted **(B)**, and sagittal T2-weighted magnetic resonance **(C)** images of a 2-month-old Golden retriever with paraparesis. A smoothly margined osseous mass is associated with the right L1 lamina and pedicle and causes severe vertebral canal stenosis and spinal cord compression. The spinal cord is displaced to the left. Osteochondroma was con firmed histopathologically.

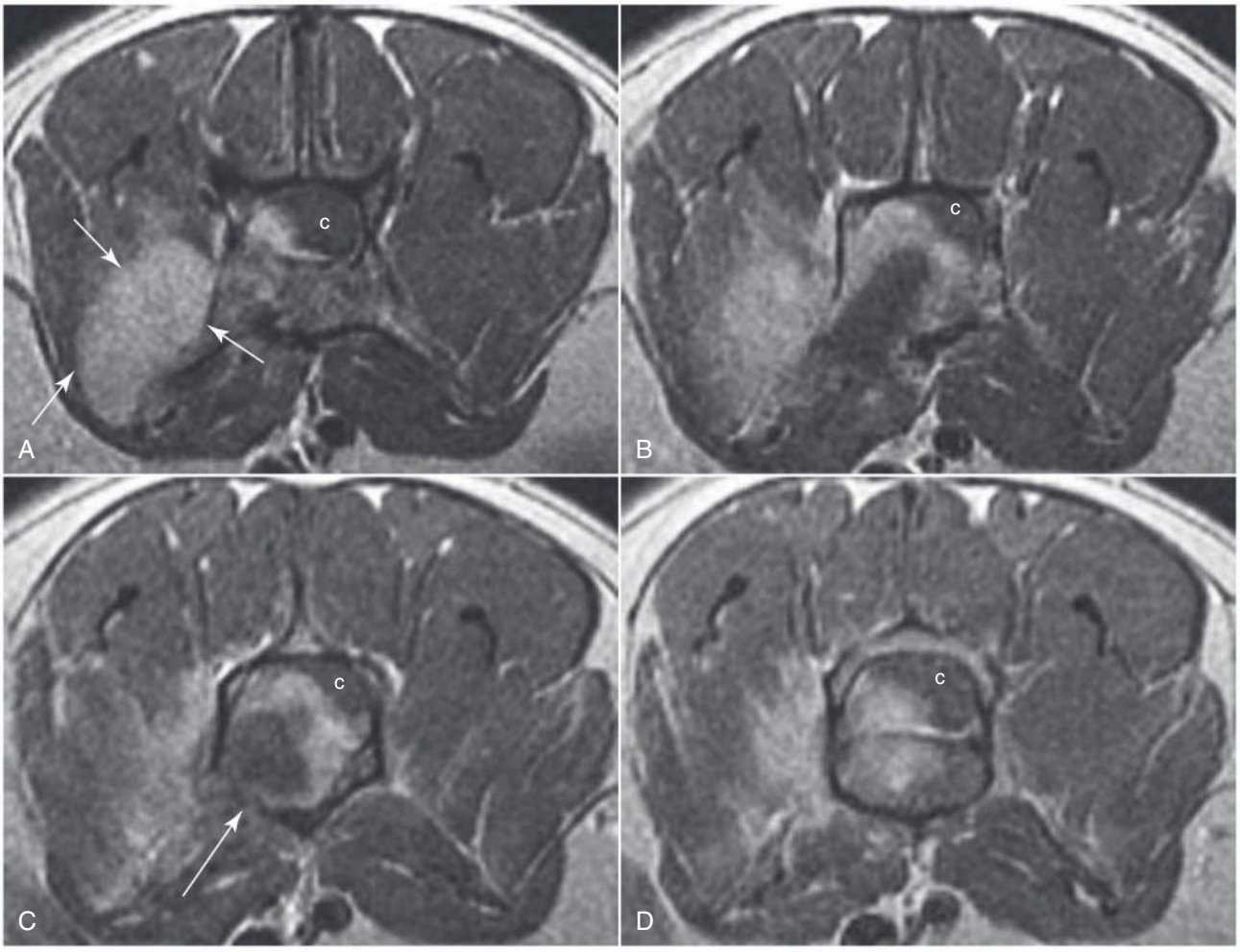


Fig. 15.33 Invasive paravertebral fibrosarcoma in a cat. Successive transverse T1-weighted postcontrast images in the lumbar spine. There is a hyperintense mass (**A,** *arrows*) in the right paraspinal muscles that invades the vertebra **(B)**, destroying the normally hypointense cortex (**C,** *white arrow*) and entering the vertebral canal to cause spinal cord *(c)* compression **(B, C, D)**.

vertebral lesions are seen, which are typically hyper- to isointense on T2W and T1W images, hyperintense on STIR, with variable but homogeneous contrast enhancement. The vertebral lesions are typically expansile, with preservation of the cortical margin.[175] Fat-suppression images are useful for differentiating bone marrow fat accumulation from true lesions. Both appear hyperintense on T1W and T2W images; but with fat suppression, fat signal will decrease but tumor will remain bright (Fig. 15.34).[176,177]

Paravertebral soft tissue tumors can also be imaged well with CT and MRI and can be recognized before they become visible radiographically. MRI and CT also allow assessment of surgical resectability and can be used for radiation-therapy planning.

Infiltrative lipomas have specific imaging characteristics. When in a paravertebral location, an infiltrative lipoma can invade the vertebral canal and cause neurologic signs. On CT imaging, infiltrative lipomas are characteristically hypoattenuating, which is similar to normal fat.[161,164] On MRI, infiltrative lipomas are T1- and T2-hyperintense, and fat-suppression techniques are useful to confirm their fatty composition (Fig. 15.35, eFig. 15.8).[162,163,165]

Intradural-Extramedullary Tumors

One-third of spinal tumors are intradural/extramedullary, and in dogs, these are mainly meningiomas and nerve sheath tumors.[178] Other rare intradural tumors, such as nephroblastoma,

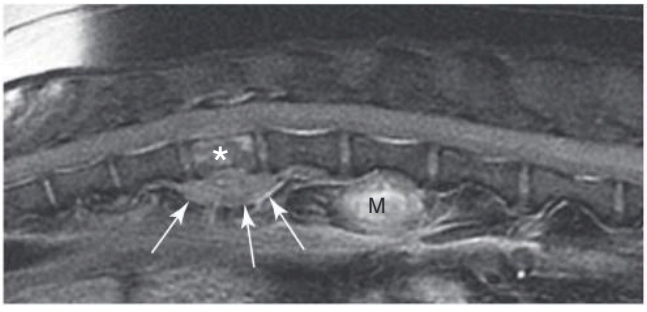
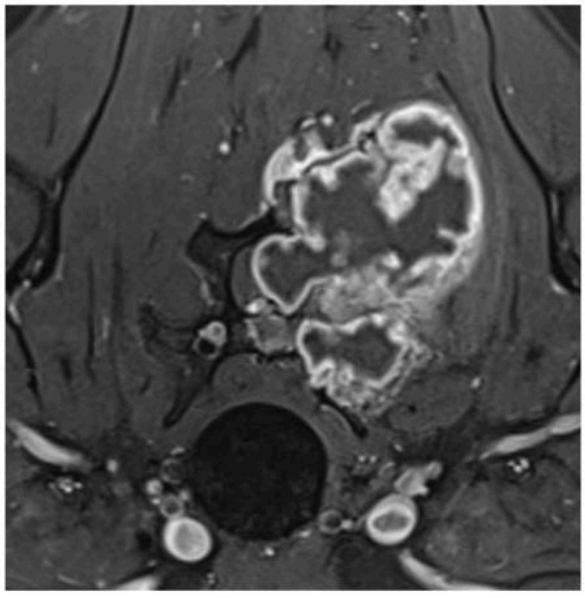


Fig. 15.34 Sagittal postcontrast fat-saturated T1-weighted image of the spine in a dog with metastatic hepatic carcinoma. A hyperintense signal is noted in the vertebral body (*asterisk*), suggesting metastatic tumor. Hyperintense neoplastic proliferation is present ventral to this vertebra (*white arrows*). A metastatic sublumbar periaortic lymph node (*M*) is also present. Fat-suppressed pulse sequences optimize vertebral lesion detection by suppressing the hyperintense signal from fat that may obscure mildly enhancing lesions.

are reported in dogs.[179–186] In cats, the most common intradural/extramedullary tumor is lymphosarcoma, although most of these also have an extradural component.[158,159]

Peripheral Nerve Sheath Tumors

Peripheral nerve sheath tumors can be intradural/extramedullary or extradural. Most are found in the brachial plexus



eFig. 15.8 Transverse T1-weighted fat-saturated postcontrast image of a 7-year-old German shepherd dog with tetraparesis. A large peripherally contrast enhancing mass is centered at the left pedicle of C6 and is invading the vertebral canal, causing severe spinal cord compression. Cytology was consistent with sarcoma, with a primary suspicion of chondrosarcoma.

and as such are located in the axilla.[187–190] If involving the vertebral column, they can have an intradural component and can be difficult to differentiate from intradural lesions, such as meningiomas.

Detection of peripheral nerve sheath tumors with CT can be difficult and depends on detecting soft tissue asymmetry, because they often have attenuating properties similar to muscle. Small or diffuse peripheral nerve sheath tumors may be subtle and hard to detect, and it can also be difficult to assess nerve structures that are oriented obliquely to the transverse CT imaging plane. CT changes associated with peripheral nerve sheath tumors include unilateral muscle atrophy, presence of a soft tissue mass that is isoattenuating to surrounding muscles, and contrast enhancement that is either uniform, patchy, or rim-like.[190] The mass occasionally tracks in a linear fashion into a neighboring intervertebral foramen and can invade the vertebral canal (Fig. 15.36). Invasion into the thoracic cavity can also be seen. Masses as small as 1 cm can be identified on CT.[190]

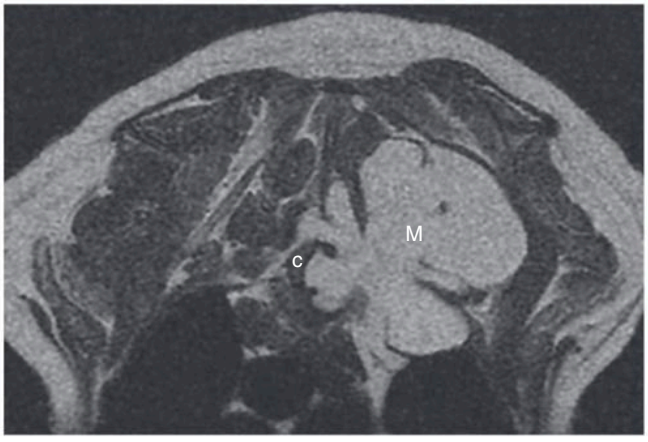


Fig. 15.35 Transverse T1-weighted images of a dog with an infiltrative lipoma in the left paraspinal area. There is a lobulated hyperintense mass (*M*) in the left paraspinal area that is causing vertebral effacement and spinal cord (*c*) compression. Note that the signal of the tumor is identical to the signal of the dorsal subcutaneous fat.

With MRI, multiple sequences in various planes are necessary to identify and stage peripheral nerve sheath tumors and depict their relationship to the surrounding structures, especially the intervertebral foramen and spinal cord.[187] Imaging should be performed with perfect positioning of the patient usually in dorsal recumbency with symmetric positioning of the limbs.[187] Peripheral nerve sheath tumors can be focal masses or diffuse thickening of affected nerves (Figs. 15.37 and 15.38, eFig. 15.9).[187–189] Whether the tumor is mass-like or diffuse, proximal extension of the lesion into the intervertebral foramen and vertebral canal is possible, and this feature is important to detect because it affects whether the tumor can be excised completely. Compared to surrounding skeletal muscles, the tumor is usually T2-hyperintense, although mixed signal intensity is possible (see Fig. 15.37).[42,187–189] Short tau inversion recovery (STIR) pulse sequences, which reduce the signal from fat, are useful in increasing the conspicuity of the tumor.[176,187] Fat saturation on postcontrast images helps identify the tumor by increasing the contrast of enhancing tumor against the background (see Fig. 15.37). The tumor is most commonly T1 isointense on precontrast images but can be hyperintense or of mixed signal intensity. Most tumors have mild to strong contrast enhancement.[176,187] Additional changes seen include ipsilateral muscle atrophy. The atrophic muscles often have abnormal signal, including T2 and T1 hyperintensity, and possible mild contrast enhancement; these changes are consistent with neurogenic atrophy, edema, fat infiltration, and fibrosis.[187]

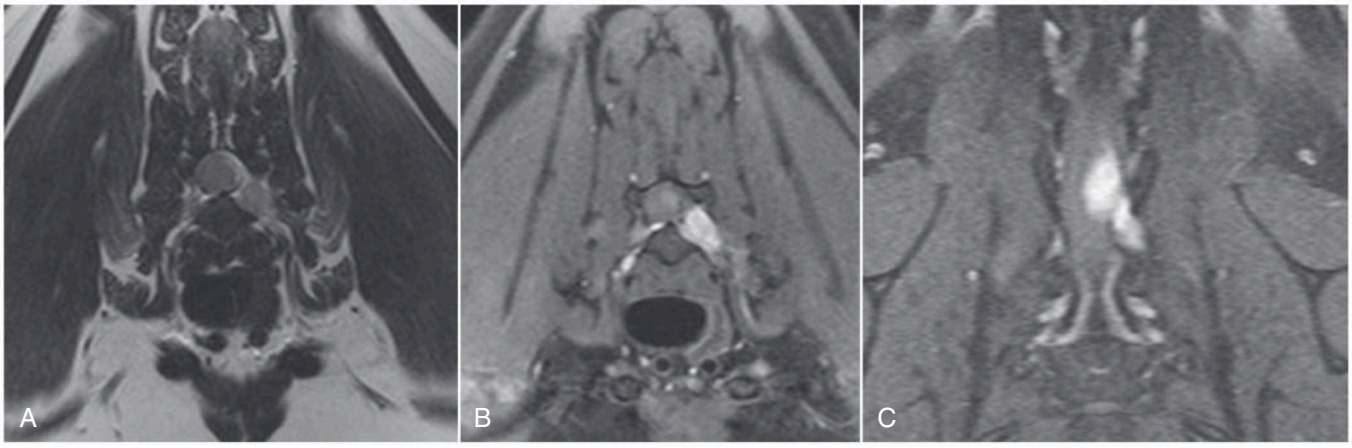
Meningioma

Meningiomas are slowly growing tumors of the meninges that cause neurologic deficits primarily by compression of the spinal cord. Although they can occasionally grow in the epidural space, most meningiomas in dogs and cats are intradural/extramedullary lesions.[191–195] The most common locations are cranial cervical and lumbar regions.[193] Meningiomas are usually single, but multifocal meningiomas are seen occasionally.[193]

On CT myelography, meningiomas appear as an intradural/extramedullary mass, causing a filling defect in the column of contrast medium. A golf-tee sign, similar to the one observed on conventional myelography, appears when the contrast medium diverges to encompass the mass in the subarachnoid space. The golf-tee sign is the hallmark of an intradural/extramedullary



Fig. 15.36 Transverse **(A)** and dorsal **(B)** reformatted postcontrast computed tomography (CT) images at the level of the L5–L6 intervertebral disc space in a dog with a nerve root tumor at L5–L6. Note that the right intervertebral foramen is wide compared with the left. There is a soft tissue mass obliterating the right intervertebral foramen at L5–L6 (*asterisk*) and extending outside in the form of an elongated mass that has contrast enhancement (*white arrows*).



eFig. 15.9 Transverse T2-weighted **(A)**, transverse fat-saturated postcontrast T1-weighted **(B)**, and dorsal fat-saturated postcontrast T1-weighted **(C)** images in a dog with a nerve sheath tumor of the left C8 spinal nerve. The nerve root is enlarged within the vertebral foramen and is strongly contrast enhancing. Contrast-enhancing neoplastic tissue extends into the vertebral canal best seen in **C**.

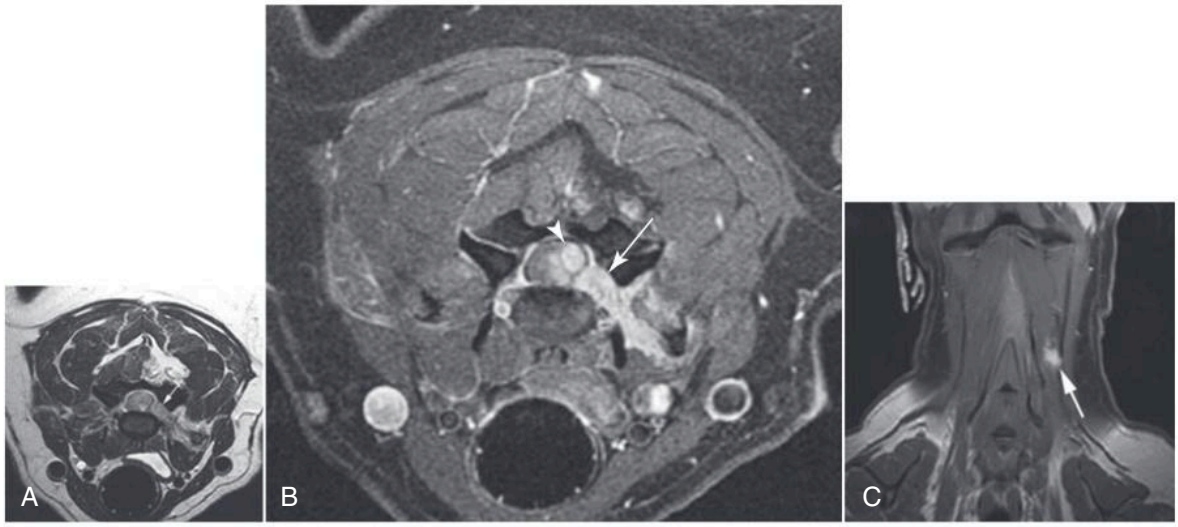


Fig. 15.37 Transverse T2-weighted **(A)**, transverse fat-saturated postcontrast T1-weighted **(B)**, and dorsal fat-saturated postcontrast T1-weighted **(C)** images in a dog with a nerve sheath tumor in the left C3−C4 intervertebral foramen. There is a soft tissue tumor obliterating the left intervertebral foramen at C3−C4 (**A,** *white arrow*). The tumor is nearly isointense to spinal cord and extends peripheral to the foramen in the form of an elongated mass. There is marked diffuse contrast enhancement of the tumor (**B,** *white arrow*). The tumor tracks along the nerve path in the paraspinal muscles (**C,** *white arrow*). An intradural component was apparent on the postcontrast images (*white arrowhead,* **B**).

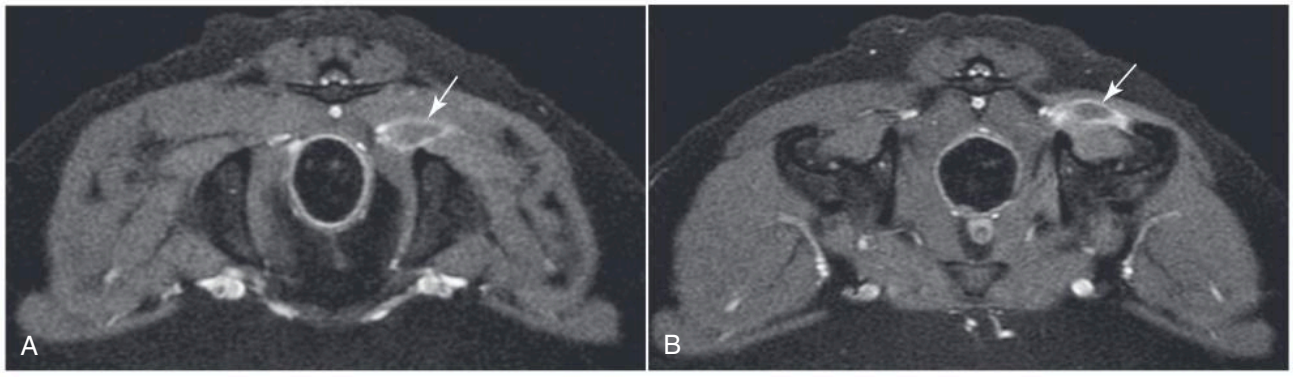


Fig. 15.38 **A and B,** Transverse fat-saturated postcontrast T1-weighted images in a cat with a large extradural sciatic nerve tumor. There is muscle atrophy on the left side. The tumor is slightly hypointense with strong peripheral contrast enhancement (*white arrow*) and follows the path of the sciatic nerve. Fat saturation facilitates the recognition of the abnormal enhancing tissue on postcontrast series.

lesion and is appreciated best on CT when reformatted sagittal and dorsal images are obtained. If iodinated contrast medium is injected intravenously, there may be enhancement of the mass.[193]

On MRI, meningiomas appear as focal masses that are usually hyperintense to the spinal cord on T2W images, and isointense to hypointense to the spinal cord on precontrast T1W images. However, T2 hypointensity and T1 hyperintensity have also been reported.[173,192,193] After gadolinium injection, meningiomas usually have moderate to strong well-defined contrast enhancement.[192,193] Features that help in determining the intradural/extramedullary location include the following[192]:

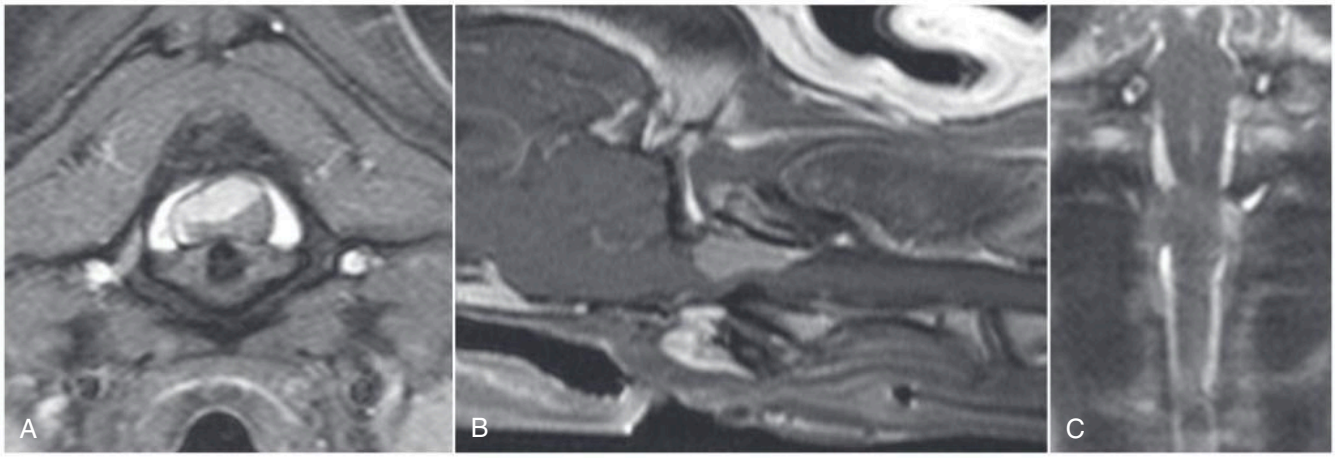
- The broad-based dural margin is seen on at least one of the imaging planes (Fig. 15.39, eFig. 15.10).
- The gradual expansion of the subarachnoid space cranial and caudal to the mass that can be detected on T2W images, especially in the dorsal plane, creates a golf-tee sign similar to that observed with conventional myelography or CT myelography. Heavily T2W MR pulse sequences (T2-myelograms) can be useful in recognizing this sign.[12,173]

An MRI feature often associated with spinal meningiomas is the dural tail sign, which is seen as strong linear enhancement of the border of the tumor confluent with the adjacent meninges (see Fig. 15.39).[192] Confusion with a nerve sheath tumor is possible when the meningioma is located within or exits the intervertebral foramen.[192]

Nephroblastoma

This is a rare tumor typically occurring in young dogs (<3 years old), with German shepherd dogs possibly predisposed.[179–186] The tumor is intradural/extramedullary and located consistently between T10 and L2. It is thought that the tumor arises from ectopic embryonic remnants of renal tissue. A single mass is usually present, although there are rare reports of intraspinal metastases.[186]

On noncontrast CT, swelling of the spinal cord with obliteration of the epidural fat is observed in the affected area; however, the intradural nature of the lesion can only be determined with CT myelography. Even then, it can be difficult to tell if the tumor is intradural/extramedullary or intramedullary, especially because the tumor can invade the spinal cord.



eFig. 15.10 Transverse (**A**) and sagittal (**B**) T1-weighted postcontrast images and dorsal (**C**) half-Fourier single-shot turbo spin echo (HASTE) image of a Boxer with meningioma at the level of C1. The mass is strongly contrast enhancing and well delineated. The spinal cord is ventrally displaced and severely compressed. The mass is intradural in location, causing widening and abrupt termination in the CSF at the right cranial aspect of the mass (**C**).

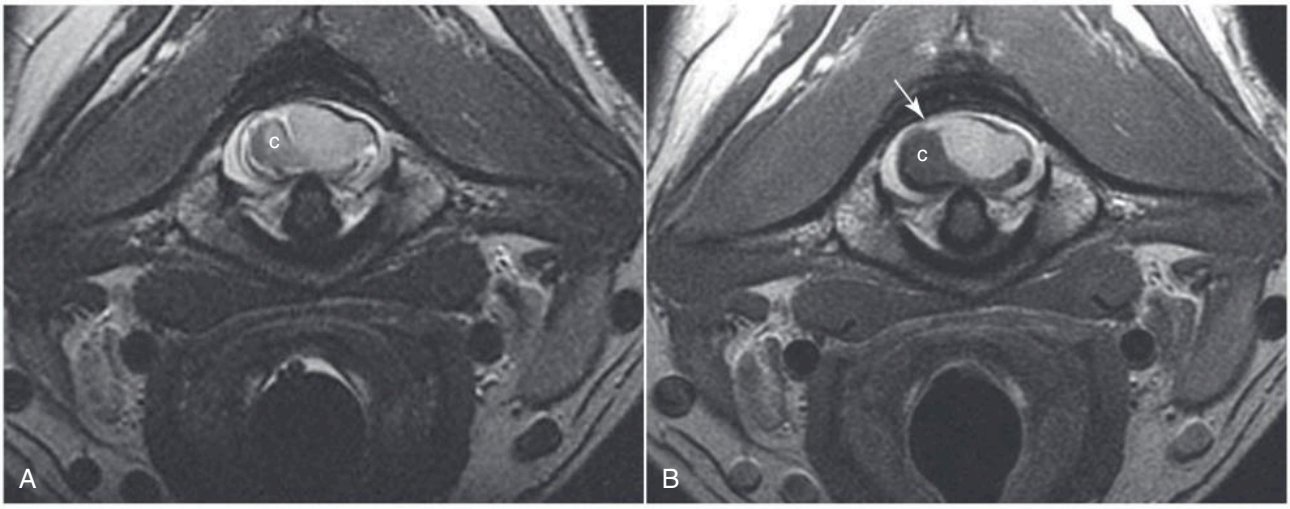


Fig. 15.39 Transverse T2-weighted **(A)** and postcontrast T1-weighted **(B)** images at the level of C1 in a dog with a meningioma. There is an intradural mass in the left dorsal aspect of the subarachnoid space that is broad-based toward the dura and is causing severe spinal cord *(c)* compression. After contrast medium injection **(B)** the mass is markedly and homogeneously contrast enhancing, and a dural tail (*white arrow*) is present on the dorsal right margin of the mass.

On MRI, the tumor is isointense to the spinal cord in T2W images, but it may have heterogeneous signal.[181,183–185] The mass is also usually isointense to the spinal cord on T1W images, but there is moderate to strong contrast enhancement.[181,183–185] Transverse and dorsal images allow the peripheral location of the mass in the dural sac to be detected, often with a broad base toward the meninges. Widening of the subarachnoid space cranial or caudal to the mass (golf-tee sign) can be present and help determine its intradural location. However, this sign is not present consistently, and, as with CT, it can be difficult to determine the intradural/extramedullary origin of the mass, especially when the tumor invades the spinal cord (Fig. 15.40).[185]

Intramedullary Tumors

Intramedullary tumors are rare in dogs and cats, and they can be primary or metastatic.[156] In a retrospective study, the most common canine primary intramedullary tumor was ependymoma, followed by astrocytoma, and less commonly nephroblastoma, chordoma, oligodendroglioma, and teratoma.[196] The most common metastatic lesions were transitional cell carcinoma and hemangiosarcoma, with less common metastatic lesions including pheochromocytoma, mammary/pancreatic/prostatic carcinoma, and sarcoma of unknown etiology.[196] Intramedullary neoplasia is even less common in cats, and most are glial cell tumors (most commonly astrocytomas, but also ependymomas and oligodendrogliomas).[158,197,198] They seem to be more common in the cervical spinal cord.[158,197,198]

CT is poorly sensitive for diagnosis of intramedullary tumors; focal cord swelling may be seen, with variable degrees of parenchymal enhancement on postcontrast series. Reports of the MRI appearance of intramedullary neoplasms are scarce in the veterinary literature. Astrocytomas and oligodendrogliomas form ovoid to elliptical mass lesions that are well marginated, located eccentrically in the spinal cord causing variable degrees of spinal cord swelling; the lesions are T1 iso- to hypointense, T2 and STIR hyperintense, and moderately contrast enhancing.[196] Ependymomas appear as elongated fusiform to ellipsoid lesions with a central location in the spinal cord, and sometimes a multifocal distribution along the neuraxis; they are T1 isointense, T2 hyperintense and strongly contrast enhancing; on sagittal T2W or T2*W images, a hypointense curved area may be seen along the cranial and caudal margins of the lesion due to chronic hemorrhage, and has been referred to as a "cap sign."[196,199]

Tumors With Variable Spinal Distribution

Some types of spinal tumors may have variable distributions and can involve several compartments simultaneously (extradural, intradural/extramedullary, and intramedullary). The most common tumors with this behavior are histiocytic sarcoma, lymphoma, and hemangiosarcoma.

Histiocytic Sarcoma

Histiocytes are a category of leukocytes that occur in many tissues throughout the body. They are derived from stem cell precursors and differentiate into cells of the monocyte/macrophage lineage or dendritic cell lineage.[200] Histiocytic sarcoma is due to neoplastic transformation of interstitial dendritic cells, with the exception of a hematophagocytic variant, which occurs within the splenic red pulp and arises from macrophages.[201] Histiocytic sarcoma can be localized (most commonly as a soft tissue mass along the limbs), or disseminated, affecting multiple organ systems, including the spleen, liver, lungs, lymph nodes, bone marrow, and CNS.[201] The spinal cord can be secondarily affected in histiocytic sarcoma arising from a vertebra. This has been reported more commonly in the disseminated form than the localized form.[160] Such lesions can cause extradural spinal cord compression when they invade into the vertebral canal. They may arise from the soft tissues around the bone and invade bone secondarily, or they may grow initially within the bone marrow and extend to the cortex and adjacent soft tissues. The appearance is similar to that of other aggressive vertebral neoplasm, with bone lysis and soft tissue proliferation.

Direct involvement of the CNS can occur both in the disseminated form of histiocytic sarcoma and as an entity isolated to the CNS ("primary CNS histiocytic sarcoma"). In both cases, all parts of the neuraxis can be affected.[200–203] Retrievers and Pembroke Welsh corgis may be predisposed to CNS involvement with histiocytic sarcoma, with corgis possibly predisposed to the primary CNS form.[201] Histopathologically, neoplastic infiltration in the subarachnoid space and leptomeninges with infiltration into the white matter of the spinal cord and nerve roots is commonly found. Meningeal infiltration is consistently seen; even lesions that appear intramedullary on

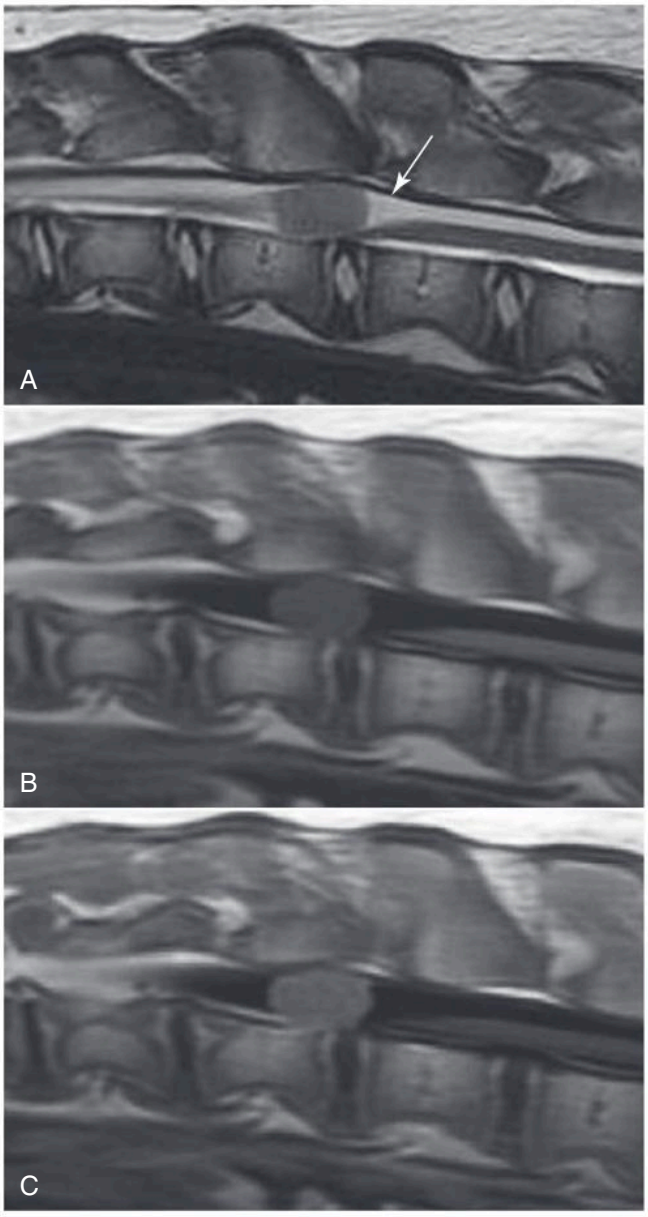


Fig. 15.40 Sagittal T2-weighted **(A)**, T1-weighted with fluid-attenuated inversion recovery (FLAIR) **(B)**, and postcontrast T1-weighted FLAIR **(C)** images of a young dog with a nephroblastoma. There is an ovoid intradural mass at the level of L1. It is isointense to the spinal cord on precontrast images, and there is strong contrast enhancement. Focal widening of the subarachnoid space is present caudal and cranial to the mass, forming a golf-tee sign (*white arrow* in **A**); the cerebrospinal fluid (CSF) in the subarachnoid space is T2 hyperintense and T1 hypointense. (Images courtesy Dr. Shannon Holmes, University of Georgia.)

MRI typically have some form of meningeal association histopathologically.[201–203]

Various MRI features of CNS histiocytic sarcoma can be seen,[200–202] including focal or multifocal intramedullary and/or intradural/extramedullary mass(es) lesion(s), most commonly isointense (less commonly hypo- or hyperintense) on T1W images, hyperintense or of mixed signal intensity on T2W images, hyperintense on STIR, with moderate to marked contrast enhancement after gadolinium injection. Ill-defined diffuse intramedullary T2 hyperintensity with loss of the epidural fat and gray/white matter definition may also be seen, with moderate parenchymal contrast enhancement after gadolinium injection and mild diffuse meningeal enhancement. Meningeal enhancement in the vicinity of focal mass lesions, sometimes with a dural tail sign, may also be seen; this meningeal enhancement often extends over long distances from the mass lesion, and isolated areas of meningeal enhancement away and separate from the mass lesion is also possible, suggestive metastatic spread of the condition through the subarachnoid space. In some cases, the only abnormality can be meningeal enhancement without a mass lesion (leptomeningeal histiocytic sarcoma). MRI features of spinal histiocytic sarcoma, such as focal mass lesions, meningeal thickening, and enhancement, can also be seen with other neoplasms (such as, lymphoma) or rare tumors (such as, meningeal oligodendrogliomatosis) and are therefore nonspecific. Intradural/extramedullary masses with dural tail can also be seen with meningioma.

Lymphoma

In both dogs and cats, lymphoma may involve many tissues outside of the lymphatic system, including the CNS. Spinal lymphoma can be secondary or primary, based on whether neoplastic lymphocytes are or not identified in other organ systems, respectively. Clinical signs depend on the distribution of the lesions in the CNS and on the presence and extent of other organ systems involvement.

In cats, lymphoma is the most common tumor affecting the spinal cord.[158,159] Affected cats are typically young, with short duration of clinical signs.[158,204,205] In that species, the most common location of spinal lymphoma is extradural, or mixed extra- and intradural (affecting the leptomeninges and/or the spinal cord).[158,205] Exclusive intradural location is rare.[158] Extramedullary hematopoietic tissue has been cited as the possible anlage for the development of primary lymphoma of the spine.[205] Involvement of other organ systems is common in cats with spinal lymphoma, with bone marrow and kidneys being more commonly affected.[158,204,205] In some case series, affected cats had lesions in multiple regions of the CNS, including the brain,[158] whereas in other series, single epidural lesions were more common.[205] At MRI, feline spinal lymphoma manifests as both intradural and extradural lesions, often affecting multiple compartments including the paraspinal tissues; the lumbar and lumbosacral regions are more commonly affected.[167,168,206] Lesions are ill-defined, hypointense on T1W images, hyperintense on T2W images, with homogeneous, often strong enhancement on postcontrast T1W images.[167,168,206] Another study where MRI was used reports intramedullary location of lymphoma in less than half the cases of spinal lymphoma, although it does not describe details on their MRI appearance.[207] Pathologic studies are in agreement with these imaging reports, reporting involvement of both extra- and intradural structures, including the spinal cord parenchyma and nerve roots.[159] There are also reports on specific infiltration of the nerves of the brachial plexus, forming mass-like lesions of the affected plexus, resembling a peripheral nerve sheath tumor, and extending into the subarachnoid space and spinal cord parenchyma proximally.[188,205] The MRI appearance of these lesions has not been reported, but one should keep this in mind when identifying mass-like lesions infiltrating the brachial plexus and extending into the vertebral canal in cats.

In dogs, lymphoma is one of the most common neoplasms, and the multicentric form accounts for about 80% of cases. In this species, lymphoma can affect the epidural tissues of the vertebral canal, vertebrae, nerve roots, paraspinal soft tissues, and less commonly the spinal cord (although the spinal cord is commonly affected secondary to compression by extradural neoplastic infiltrates).[173,206,208–214] At MRI, canine spinal lymphoma causes multifocal disease more commonly than focal disease.[208] There is common simultaneous regional involvement of multiple spinal compartments (vertebrae, paraspinal soft tissues, epidural space).[208,210,213,214] The paraspinal lesions

are often ill defined. The vertebral canal and paraspinal components can be seen to communicate through the intervertebral foramens. There are variable degrees of spinal cord compression by the epidural component of the neoplasm.[208,213,214] Signal characteristics are similar for the lesions in the paraspinal and vertebral canal areas, being T1 iso- to hypointense, T2 and STIR hyperintense, moderately to strongly contrast enhancing.[208] In some cases, the lesions can be hyperintense on T1W precontrast images.[173,214] Heterogeneous signal on T2W images, with hypo- and hyperintense areas, is also reported,[213] as well as isointensity to surrounding muscles.[173] Visible vertebral lesions may involve none, one, several, or all vertebrae, and consist of patchy hyperintense areas on T2W images, which unlike fat, remain hyperintense on STIR images. In one case series, vertebral cortical involvement was not observed, even when paravertebral and epidural infiltration around the affected vertebrae was present[208]; however, other reports have described changes in shape of the affected vertebra with cortical involvement, seen as T2W and STIR hyperintense signal with enhancement on T1W postcontrast images, disrupting the normal hypointense signal of the cortex.[210] Cortical involvement has also been reported in pathologic studies.[211] Visible vertebral bone marrow involvement on MRI is not necessarily present, even in cases of simultaneous paravertebral and epidural infiltration.[213,214] Depending on the cellularity of the infiltrate, vertebral bone marrow involvement with lymphoma may be present even in the absence of changes in MRI signal, including on fat-suppressed images.[215] Leptomeningeal involvement with enhancement on postcontrast images is also reported,[206] as well as involvement of the nerve roots and spinal cord parenchyma.[212] Due to the multicentric nature of this tumor, additional lesions may be seen in the field of view, including lymphadenopathy, hepatomegaly, splenomegaly, and splenic nodules.

Hemangiosarcoma

Hemangiosarcoma is a malignant neoplasm of vascular endothelial origin and can arise from any vascular tissue. Spinal hemangiosarcoma has been reported in dogs, either in the intramedullary location,[173,196,216] or extradural location. The extradural form can arise from the vertebrae,[217,218] accounting for about 2% to 3% of primary bone tumors of the vertebral column in dogs. Rarely, hemangiosarcoma can affect the epidural space.[171,219] Intramedullary hemangiosarcoma is usually metastatic,[196,216] while the vertebral and the rare epidural forms are typically primary tumors.[166,169,220] Intradural/extramedullary hemangiosarcoma has only been reported once.[221]

MRI features of primary vertebral hemangiosarcoma include monostotic or segmental polyostotic lesions affecting several consecutive vertebrae. Signal intensity is variable and heterogeneous and signal voids due to susceptibility artifacts may be seen on T2*W images. Signal enhancement is usually strong and heterogeneous, and cortical lysis with extension into the vertebral canal and paraspinal tissues is common.[166,169,220]

At MRI, epidural or intramedullary hemangiosarcoma typically shows a focal mass lesion, usually well defined, that is either in the epidural location causing spinal cord compression, or intramedullary.[171,173,196,216,219] Epidural lesions are isolated (primary tumor),[169,171] whereas intramedullary lesions, being metastatic, can be multifocal.[196] The signal of the mass is typically hyperintense to normal spinal cord parenchyma on T2W images (homogeneous or heterogeneous), hyperintense on STIR images, isointense to hyperintense on T1W precontrast images, and moderately to strongly contrast enhancing (sometimes rim-like).[169,171] Signal voids associated with hemorrhage can be seen within the lesion on T2*W gradient echo images or susceptibility weighted imaging.[216] The spontaneous hyperintensity on T1W images may also reflect the presence of blood degradation products.

MYELOMALACIA

Myelomalacia corresponds to gross softening of the spinal cord resulting from hemorrhagic necrosis.[222,223] It can occur following acute spinal cord injury and is caused by extensive damage to intramedullary vasculature. A core of necrosis may extend cranially and caudally from the level of the spinal cord injury, typically in the base of the dorsal funiculi. A small proportion of dogs with acute disc extrusion will have diffuse myelomalacia, often called *ascending* or *descending myelomalacia.*[223] Myelomalacia can affect up to 10% of dogs with acute disc extrusion that exhibit paraplegia and loss of deep pain perception.[223] The prognosis for patients with myelomalacia is usually poor, but improvement is possible in focal disease. Therefore, MRI is useful in determining prognosis by providing information about the extent of involvement.

On MRI, myelomalacia is characterized by diffuse swelling of the spinal cord that is recognized by loss of visualization of the hyperintense signal from CSF and fat around the spinal cord on T2W images. There is diffuse patchy T2 hyperintensity of the spinal cord (Fig. 15.41) that extends over the length of several vertebral bodies. The affected spinal cord parenchyma is isointense to normal spinal cord on T1W images.[222] Areas of hypointensity associated with spinal cord hemorrhage may be visible in T2*W gradient recalled echo images.[223] In addition to the areas of T2 hyperintensity, areas of T2 hypointensity may be detected at high field strengths because of deoxyhemoglobin in hemorrhagic spinal cord foci.[222,223] Studies have suggested that in dogs with thoracolumbar disc herniation, a longitudinal extent of spinal cord parenchyma T2W hyperintensity higher than 4.5 to 6 times the length of L2 vertebral body could be a predictor of developing ascending/descending myelomalacia.[222,224] A length of CSF signal attenuation on HASTE/SSFSE pulse sequences ("T2-myelogram") >7.4 times the length of L2 vertebral body has also been reported as a predictive MRI criterion,[225] and some studies have found this criterion as more reliable than the length of parenchymal T2W hyperintensity.[226] Another recent study found that the length of parenchymal T2 hyperintensity was not a useful predictor for future development of myelomalacia in dogs with severe neurologic deficits who are not exhibiting clinical signs of myelomalacia.[227] Absence of T2W spinal cord hyperintensity, however, does not rule out future development of myelomalacia particularly if imaging occurs less than 24 hours after onset of paraplegia.[224,226,228,229]



Fig. 15.41 Sagittal T2-weighted image of the lumbar spine in a dog with acute disc herniation at L5–L6 and secondary ascending myelomalacia. There is an ill-defined patchy intramedullary T2 hyperintensity in visible segments of the lumbar spinal cord.

VASCULAR PATHOLOGY

Ischemic Myelopathy

The most common cause of spinal cord ischemia and infarction in dogs and cats is fibrocartilaginous embolism from the *nucleus pulposus* of the intervertebral disc.[86,87,230–235] In cats, hyaline degeneration of the ventral spinal artery has also been reported as a predisposing factor.[233] In dogs other causes include thromboembolism; a hypercoagulable state; vasculopathy; and parasitic, septic, or neoplastic embolization.[230]

The typical clinical presentation is a sudden, frequently asymmetric, mono-, hemi-, or tetraparesis or tetraplegia.[236] Spinal cord thromboembolism is usually nonpainful and nonprogressive after the first 24 hours.[86,230–232] MRI is useful in recognizing changes associated with ischemic myelopathy and differentiating it from other conditions with similar clinical presentations, such as spinal trauma or intervertebral disc herniation.

Typically, there is a focal T2-hyperintense intramedullary lesion that is either T1 hypointense or T1 isointense. On transverse images, the lesion is usually asymmetric (Fig. 15.42, eFig. 15.11). The infarct can sometimes have variable contrast enhancement during the first week.[86,230,231] The lesion involves mostly gray matter, although a large number of dogs also have some white matter involvement. Focal areas of hypointensity suggestive of hemorrhage are identified occasionally on T2*W gradient recalled echo images or susceptibility-weighted imaging. Reduced field-of-view diffusion weighted imaging can help detect areas of restricted diffusion due to cytotoxic edema secondary to ischemia: these appear bright on diffusion-weighted images and dark on apparent diffusion coefficient maps.[237]

The imaging appearance of ischemic myelopathy can be somewhat similar to that seen with acute non-compressive hydrated nucleus pulposus extrusion, however with ischemic myelopathy the T2W hyperintense parenchymal lesions are typically not directly dorsal to an intervertebral disc, and have a more pronounced longitudinal extent; in addition, the epidural space is normal with ischemic myelopathy, whereas heterogeneous signal is often seen in the epidural space adjacent to the lesion with hydrated disc extrusion, due to diffusion of the extruded disc material mixed with the epidural fat. No abnormalities are seen on MR images in approximately 20% of patients. This usually happens when dogs are imaged less than 72 hours after onset of clinical signs.[231] The incidence of abnormal MRI findings is higher in nonambulatory dogs with higher neurologic scores than mildly affected dogs.[231] Dogs with clinically suspected ischemic myelopathy and no MRI changes have a good clinical outcome.[231]

On average, the length of the spinal cord T2 hyperintensity observed on sagittal MR images in dogs with ischemic myelopathy is approximately 1.8 times the length of C6 for cervical or cervicothoracic lesions and 2.2 times the length of L2 for thoracolumbar and lumbosacral lesions. There is an association between the length of spinal cord affected and severity of clinical signs.[231] A lesion-length—to—vertebral-length ratio greater than 2.0 has a sensitivity of 100% in predicting a poor clinical outcome.[231] The percentage cross-sectional area of the spinal cord with T2 hyperintensity is also associated with the severity of the clinical signs.[231] A percentage cross-sectional area of the lesion of more than 67% has a sensitivity of 100% in predicting poor clinical outcome.[231]

Vertebral Venous Plexus Pathology

Enlargement of the cervical vertebral venous system, including of the internal vertebral plexus causing spinal cord compression, has been reported in dogs, particularly sighthounds, although the etiology is unknown.[238] Enlargement of the internal vertebral plexus due to thrombosis or neoplastic infiltration with lymphoma and causing spinal cord compression has also been reported.[239,240]

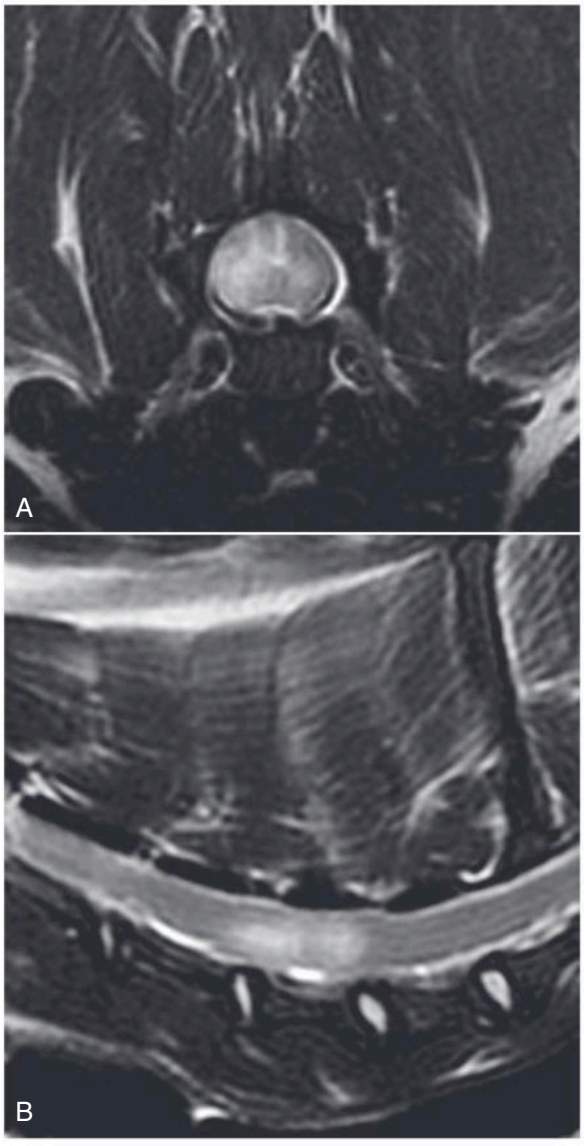
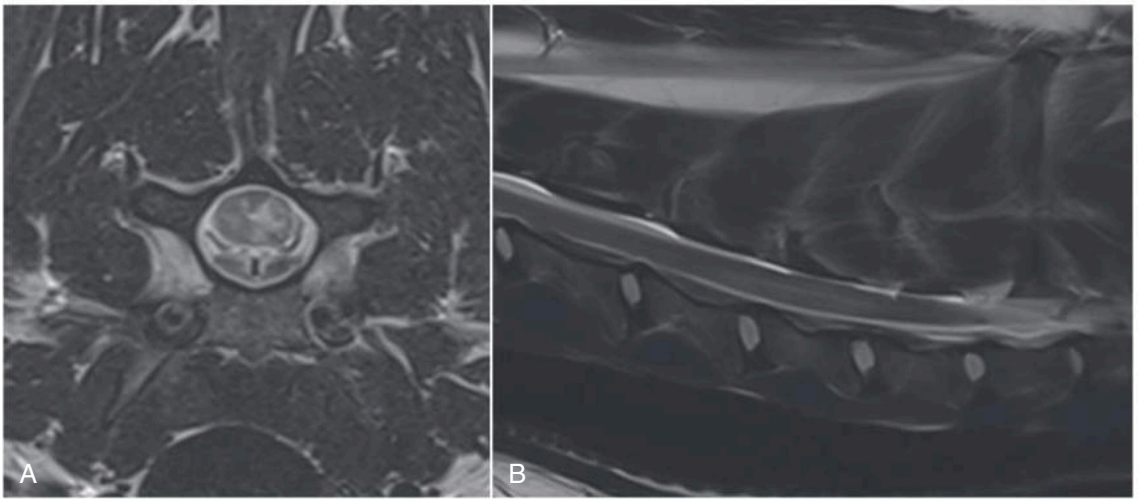


Fig. 15.42 Presumed fibrocartilaginous embolism in a dog. Transverse **(A)** and sagittal **(B)** T2-weighted images. There is a hazy focal hyperintense signal in the spinal cord that is asymmetric on the transverse image, involving both gray and white matter on the right and the ventral gray matter on the left. The intervertebral discs in the vicinity were normal, and there is no compression of the spinal cord. Clinical signs were acute and nonprogressive.

Spinal Hemorrhage

Intraparenchymal spinal cord hemorrhage most commonly occurs secondary to underlying pathology such as ischemic myelopathy, cord contusion such as secondary to disc herniation or trauma, coagulopathy, or neoplasia, particularly hemangiosarcoma.[169,216] Spontaneous intraparenchymal hemorrhage (primary hematomyelia) has been rarely reported in dogs.[241] Spinal cord hemorrhage may be difficult to identify at CT; however, areas of hyperattenuation in the spinal cord may be detected, particularly when using relatively narrow windows. MRI is more sensitive to detect spinal cord hemorrhage, especially when using pulse-sequences sensitive to such changes such as T2*W or susceptibility-weighted imaging (SWI).[216] On these pulse sequences, the byproducts of hemoglobin cause susceptibility artifacts that show up as areas of signal void with various degrees of blooming.[216]

Extraparenchymal hemorrhage can have an extradural (epidural) or more rarely intradural location. Focal hyperacute



eFig. 15.11 Presumed fibrocartilaginous embolism in a dog. Transverse **(A)** and sagittal **(B)** T2-weighted images. There is increased signal intensity of the left lateral aspect of the spinal cord predominantly involving gray matter. The subjacent intervertebral discs are normal in volume and there is no spinal cord compression. Clinical signs were acute and resolved within a few days.

Vetacademy.ir
مجموعه آموزشی پژوهشی
وت آکادمی
تلاش
#برای_دنیای_بهتر_حیوانات
تیم وت آکادمی
برای دسترسی به تازه ترین آموزش ها و
مطالب علمی دامپزشکی؛ وت آکادمی رو فالو کن
سایت مجموعه بزرگ آموزشی پژوهشی وت آکادمی
Vet-academy.ir
صفحه ی اینستاگرام وت آکادمی
@Vetacademy.ir
دسترسی به آرشیو صد گیگ کتاب آموزش دامپزشکی به صورت رایگان
و جزوه های آموزشی در کانال تلگرامی
@Vetfiles
گروه بزرگ تلگرامی، پرسش و پاسخ و آموزش
@VetAcademyGp
صفحه رسمی آپارات وت آکادمی
aparat.com/vetacademy.ir

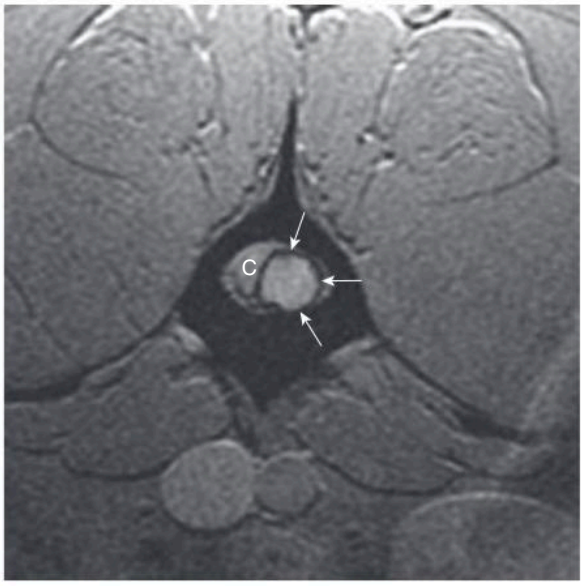


Fig. 15.43 Spontaneous epidural hematoma in a 4-year-old mixed-breed female dog presenting with acute paraplegia with no history of trauma. On this T2*-weighted gradient echo transverse image at the level of L4 vertebral body, there is a rounded extradural lesion (*arrows*) that is causing severe compression of the spinal cord (*c*). A rim of signal void is seen around the lesion consistent with hemorrhage.

intradural extramedullary hemorrhage causing cord compression has been reported in a dog with presumed steroid-responsive meningitis arteritis; the lesion was rounded, iso- to slightly T1W hyperintense and hyperintense on T2W, gradient echo, and T2-FLAIR, with strong homogeneous enhancement on postcontrast T1W images; the hyperintense signal on gradient echo was attributed to peracute arterial bleeding, characterized by high concentration of diamagnetic oxyhemoglobin in the erythrocytes (as opposed to the paramagnetic byproducts of hemoglobin degradation seen in later stages of hemorrhage).[242] Spontaneous extraparenchymal hematomas causing spinal cord compression have been reported in dogs.[243] They are most commonly extradural, rarely intradural. They present as compressive, variably shaped lesions that are T2W-hyperintense, iso- to mildly T1W-hyperintense, with susceptibility artifacts on T2*W images and rare contrast enhancement (Fig. 15.43). Laceration of the internal vertebral plexus secondary to disc extrusion can also cause epidural hemorrhage and contribute to spinal cord compression and inflammatory changes; these were described in the paragraph covering disc herniation.[22,44,45]

SPINAL TRAUMA

Acute spinal trauma can cause unstable spinal injuries that have the potential to lead to failure of the vertebral column to protect the spinal cord and nerve roots from severe insult. Resultant myelopathy and radiculopathy can lead to temporary or permanent paralysis. Rapid and accurate evaluation of the vertebral column and the status of the spinal cord facilitate appropriate treatment and a better-informed prognosis. Radiography is inadequate to rule out acute vertebral fractures and subluxations and is a poor diagnostic tool to assess the stability of spinal fractures. Survey radiography also cannot be used reliably to detect compressive lesions. CT is recommended in patients with a high clinical suspicion of acute fracture and is superior to radiography in the traumatized patient.[244] Multidetector scanners now provide the ability to obtain 1 mm or submillimeter CT images in a short time, and to perform high-quality multiplanar

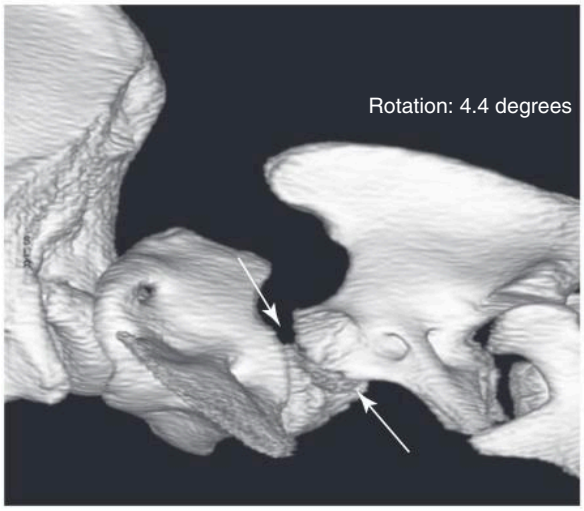


Fig. 15.44 Fracture of the cranial extremity of C2 in a dog. Three-dimensional volume rendering of the cranial cervical spine where the mildly displaced complete transverse fracture of the cranial apex of C2 (*white arrows*) can be seen.

reformatted images with surface and volume rendering (Fig. 15.44). This enables depiction of complex fractures in a three-dimensional format that can assist in surgical planning.[2] The short acquisition time makes it possible to perform a CT study with the anesthetized or sedated patient strapped to a spinal board, thus protecting against further damage.[244]

In canine spinal trauma, MRI can provide helpful information on the location and extent of damage to supportive soft tissue structures and can enable assessment of spinal cord injury in dogs with suspected vertebral instability associated with fracture or subluxation.[245] However, comparative studies between MRI and CT found limited agreement between the two techniques for vertebral fractures, with up to 79% of fractures missed at MRI. Therefore, MRI and CT may be seen as complementary techniques to assess spinal trauma.[246]

INFLAMMATORY/INFECTIOUS CONDITIONS

Discospondylitis

Discospondylitis is infection of two adjacent vertebral endplates and the associated intervertebral disc; *Staphylococcus* spp. is the most frequently isolated organism. Traditionally, discospondylitis was diagnosed based on characteristic radiographic changes together with laboratory findings. A limitation of radiography is the delay of up to a few weeks between the onset of clinical signs and detection of radiographic changes. There is also a discrepancy between clinical and radiographic improvement during recovery.[247]

CT and MRI can be used to confirm a tentative diagnosis of discospondylitis.[248–255] CT features include adjacent endplates erosion, multifocal lytic changes extending into the vertebral bodies, periosteal proliferation adjacent to the affected disc, narrowing or collapse of the disc space.[256] Dorsal and sagittal reformatting is important to identify subtle endplate changes, particularly in juvenile dogs where the only initial change may be a narrowed disc space without significant endplates changes.[257] Compared with CT, MRI can assess the soft tissue components of the vertebral canal including the epidural structures and spinal cord, and thereby provide additional information on degree of involvement of these structures and presence and degree of spinal cord compression. MRI can reveal changes suggestive of discospondylitis in dogs that have normal radiographs, thereby allowing an earlier diagnosis in dogs with supportive clinical signs but equivocal radiographs (Fig. 15.45).[248]

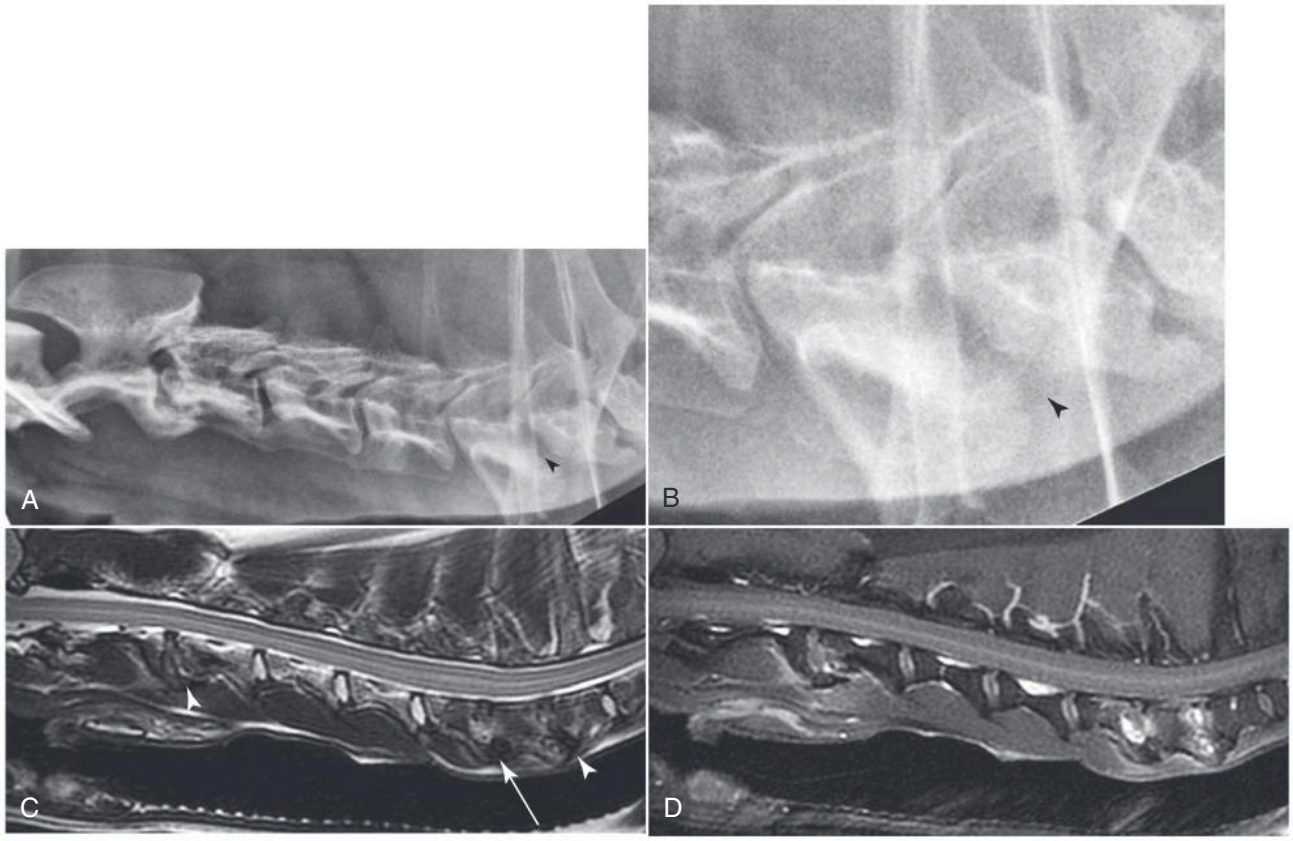


Fig. 15.45 Lateral radiograph of the cervical spine **(A)**, close-up radiograph of C6−C7 **(B)**, sagittal T2-weighted **(C)**, and postcontrast fat saturated T1-weighted **(D)** images in a dog with fever and cervical pain. Characteristic radiographic changes consistent with discospondylitis were present at C6−C7 (*black arrowheads* in **A** and **B**). On the magnetic resonance images, there was irregularity and lysis of the cortical bone around that space (*white arrow* in **C**), and the bone marrow of C6 and C7 has a mixture of increased and decreased intensity on T2-weighted images **(C)**. However, additional lesions are present at C2−C3 and C7−T1 that are also characterized by loss of integrity of the endplates and abnormal bone marrow signal in the vertebral bodies with loss of the normal structure of the intervertebral disc spaces (*white arrowheads* in **C**). On the postcontrast fat-saturated T1-weighted images **(D)**, there is enhancement of the vertebral bodies around the endplates of these three spaces, as well as of the paravertebral soft tissues ventral to the disc spaces, indicative of inflammation. These changes are consistent with discospondylitis, not only at C6−C7 but also at C2−C3 and C7−T1. Lesions of discospondylitis can be detected earlier with MR images than with radiography.

Typical MRI changes seen with discospondylitis include the following (see Fig. 15.45)[248−252,255,257,258]:

- Abnormal T1 hypointensity and T2 hypointensity of adjacent endplates and bone marrow; these lesions are hyperintense on T2W STIR images
- Hyperintense disc on T2W images
- Contrast enhancement of the intervertebral disc, vertebral endplates, and paravertebral soft tissues
- Endplate erosion is usually present, but in early stages where endplate erosion is absent, the only change may be T2 and STIR hyperintensity of bone marrow adjacent to the end-plates
- Spinal cord compression caused by extension of the infection to the epidural space
- Vertebral subluxation on sagittal images

Discospondylitis caused by *Brucella canis* infection has been reported to cause imaging changes that may be unique to this etiology; affected dogs are often young with multifocal lesions. Smooth, round, central endplate lytic changes, defined as "hole punch" lesions, can be seen on sagittal images and vertebral physitis or spondylitis without discitis may be seen; these can be identified as hyperintense vertebral lesions affecting the vertebral bodies on T2W or STIR images, with enhancement on postcontrast T1W images (best appreciated with fat saturation). Paravertebral inflammation with similar signal characteristics is also frequently seen.[259]

Spinal Epidural Empyema

Spinal epidural empyema is presence of a suppurative lesion in the epidural space.[255,260−263] The clinical signs include fever, pain, and progressive neurologic dysfunction. Spinal empyema is relatively rare in dogs. Causes include extension of adjacent osteomyelitis or discospondylitis or hematogenous spread.

On noncontrast CT, an epidural mass is suspected based on lack of visualization of hypoattenuating epidural fat around the spinal cord, but the epidural mass is best identified with CT myelography.[261,262] Intrathecal contrast medium injection can facilitate spread of the infection in the subarachnoid space because of iatrogenic contamination.

MRI is better for diagnosing spinal empyema, because it does not require subarachnoid injection of contrast medium.[255,260,263] Spinal empyema appears as a well-defined epidural mass in the dorsal or ventral aspect of the vertebral canal. The lesion forms a high or mixed signal mass on T2W images but is usually T1-hypointense. A peripheral, rim-like pattern of contrast enhancement or a diffuse pattern of

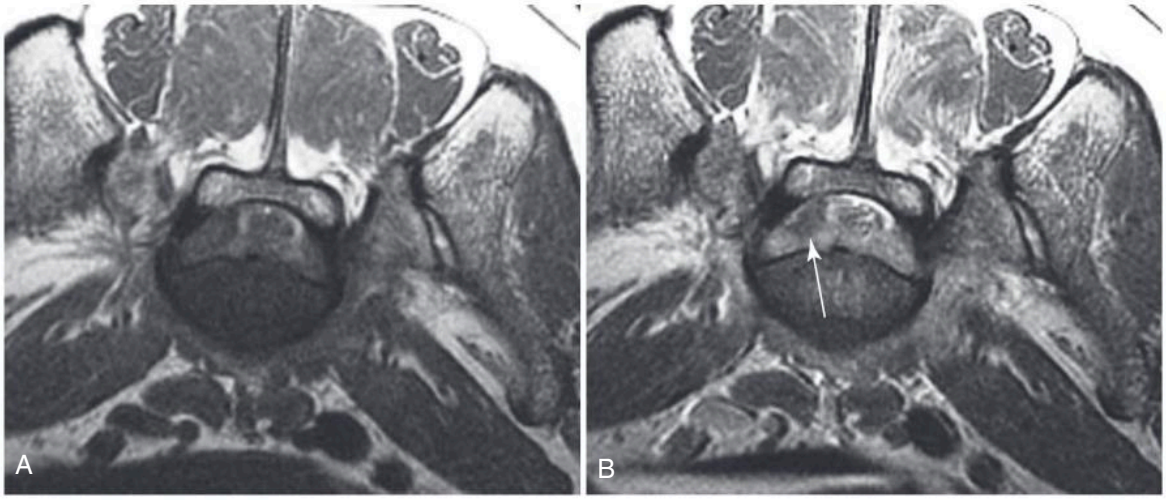


Fig. 15.46 Precontrast **(A)** and postcontrast **(B)** transverse T1-weighted images in the lumbosacral area in a dog with lumbosacral discospondylitis and spinal epidural empyema. The vertebral canal is filled with heterogeneous material that enhances irregularly, with a hypointense nonenhancing area on the right consistent with fluid collection (*white arrow*). Epidural empyema caused by extension of the infectious process from the disc space into the caudal lumbar vertebral canal was confirmed at surgery.

enhancement can be noted (Fig. 15.46). If T2*W gradient recalled echo images are acquired, focal hypointense areas consistent with hemorrhage may be present. Hyperintense lesions in the gray matter of the spinal cord adjacent to the epidural mass can be seen, which may be caused by compression of the spinal cord by the mass or by vascular compromise.[260]

Meningomyelitis

Meningitis and myelitis can have an infectious or noninfectious origin.[264–272] Infectious agents in dogs include viruses (e.g., canine distemper), bacteria (e.g., *Staphylococcus*, *Pasteurella*, *Actinomyces*, and *Nocardia* spp.), fungi (e.g., *Cryptococcus*, *Blastomyces*, *Histoplasma*, and *Coccidioides* spp.), Rickettsiae (e.g., *Ehrlichia* spp., *Rickettsia rickettsii*), protozoa (e.g., *Toxoplasma gondii*, *Neospora caninum*), parasites (e.g., *Dirofilaria immitis*, *Angiostrongylus* spp.), and rarely algae (e.g., *Prototheca wickerhamii*, *Prototheca zopfii*).[267] In cats, feline infectious peritonitis and toxoplasmosis have been reported.[207]

Noninfectious causes of canine meningomyelitis include granulomatous meningoencephalomyelitis, pyogranulomatous meningoencephalomyelitis, and steroid-responsive meningitis arteritis.[265–267,270–272]

CT changes in dogs with meningomyelitis include spinal cord swelling, spinal cord hypoattenuation, and occasionally intramedullary or meningeal contrast enhancement.[266]

General MRI findings in dogs and cats with meningomyelitis include irregular areas of intramedullary T2 hyperintensity (Fig. 15.47), which are isointense or hypointense on precontrast T1W images and have various degrees of contrast enhancement.[264,265,267] Meningeal enhancement may or may not be present. The use of fat suppression on postcontrast spinal images is important in animals with a clinical suspicion of inflammatory pathology, as it may facilitate the recognition of subtle meningeal enhancement.[176,273]

Cervical MRI abnormalities are quite common in dogs with steroid-responsive meningitis arteritis, and include T1W postcontrast enhancement of the meninges, synovium of the articular process joints, and paravertebral muscles with less commonly spinal cord parenchymal enhancement.[273]

Intradural hemorrhage causing cord compression has also been reported (see "Spinal Hemorrhage" section).[242]

In general, MRI changes of meningomyelitis are nonspecific, and other conditions (such as myelomalacia, ischemic myelopathy, or some neoplastic conditions such as histiocytic sarcoma[202] or lymphosarcoma[207,264]) can produce similar changes. Therefore, correlation with clinical signs and laboratory test results is necessary.

VERTEBRAL ANOMALIES

Congenital anomalies of the spine that can be assessed with CT or MRI include atlantoaxial malformation, hemivertebrae, block vertebrae, butterfly vertebrae, transitional vertebrae, and spina bifida (see Fig. 15.30). Most of these anomalies can be diagnosed radiographically (see Chapter 14); however, CT and MRI can provide important additional information. CT provides a better understanding of the bony abnormality and spatial relationship between the abnormal and adjacent vertebrae and effect of the anomaly on the vertebral canal and intervertebral foramina (Fig. 15.48). MRI is indicated when assessment of the spinal cord and associated nerve roots is desired, especially when the consequences of the vertebral anomalies need to be assessed. For example, spina bifida can be associated with focal anomalies of the spinal cord and meninges in the form of a meningocele or myelomeningocele (see Fig. 15.30).[274]

Dysplasia or aplasia of the caudal articular processes in the thoracic spine is common in some breeds such as French and English bulldogs and even more so in pugs.[275] In pugs, several studies have suggested that the condition can be associated with spinal cord pathology in the caudal thoracic spine,[139,276–279] although some studies have questioned that association.[275,280] The spectrum of evidence in that breed, however, suggests that spinal instability associated with the malformation can lead to constrictive myelopathy (dorsal or circumferential) secondary to meningeal fibrosis, and development of compressive arachnoid diverticulum cranial to the constriction.[139,276–279] Concurrent spinal cord compression by disc herniation has also been described.[278] The absence or hypoplasia of the caudal articular processes is best

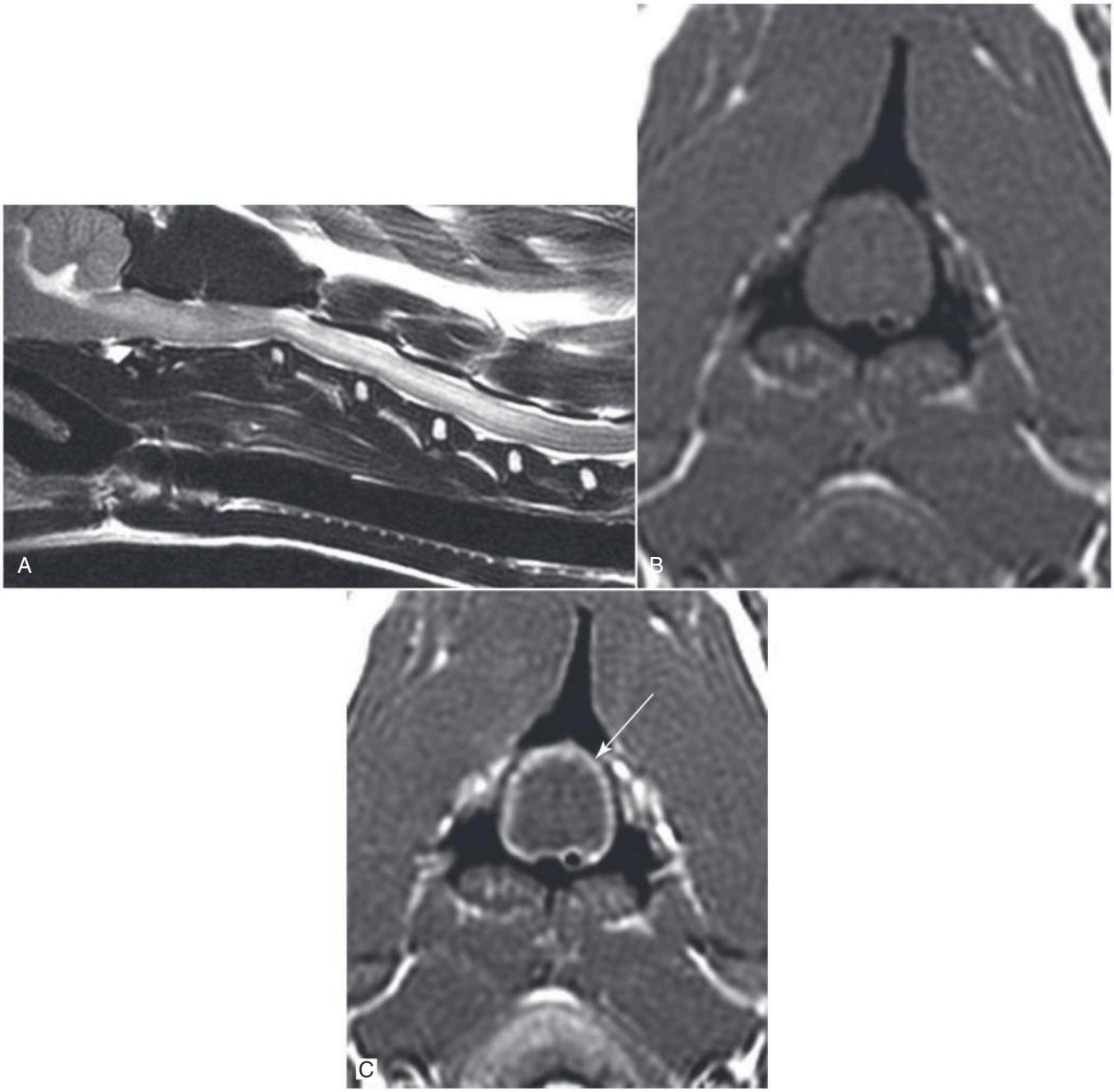


Fig. 15.47 Sagittal T2-weighted **(A)**, transverse precontrast T1-weighted **(B)**, and transverse postcontrast T1-weighted **(C)** images at the level of C2 in a dog with meningomyelitis caused by *Cryptococcus* infection. On the T2-weighted image, extensive ill-defined areas of T2 hyperintensity are present **(A)**. On the postcontrast T1-weighted image, there is strong contrast enhancement (**C,** *white arrow*) of the meninges compared with the precontrast image at the same level **(B)**.

demonstrated with CT given its exquisite bony detail (Fig. 15.49). However, the secondary spinal cord pathology is best demonstrated by MRI. Arachnoid diverticula are easily identified with MRI (see earlier). Meningeal fibrosis causes irregular margination of the subarachnoid space best seen on T2W images, and enhancing meningeal thickening on T1W postcontrast images, located either dorsally or circumferentially.[139,276–279] Focal T2W spinal cord parenchyma hyperintensity is commonly seen. Some studies also reported ventral extradural compression that is V-shaped on transverse images, corresponding histopathologically to areas of fibrosis and chondroid metaplasia.[277]

SYRINGOMYELIA

Syringomyelia is the development of fluid-filled cavities in the spinal cord. It can be caused by various primary problems, including abnormalities of the caudal fossa (Chiari-like malformations), but also other conditions, such as a quadrigeminal cistern cyst, tethered spinal cord, trauma, arachnoiditis, and neoplasia. Any condition that results in altered CSF flow in the caudal fossa of the skull or in the vertebral column can result in the development of a syrinx.[130,281–309]

Chiari-like malformation is common in the Cavalier King Charles spaniel but is reported in other breeds as well.[310] The

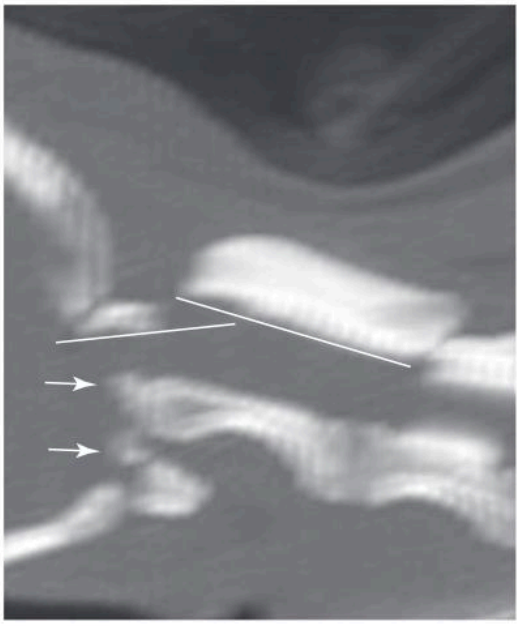


Fig. 15.48 Reformatted sagittal computed tomography (CT) image of the cranial aspect of the cervical spine, in a dog with atlantoaxial instability. The dorsal lamina of C1 is not aligned with the dorsal aspect of the vertebral canal of C2 (*lines*) indicating subluxation. Small bone fragments are associated with the dens (*white arrows*).

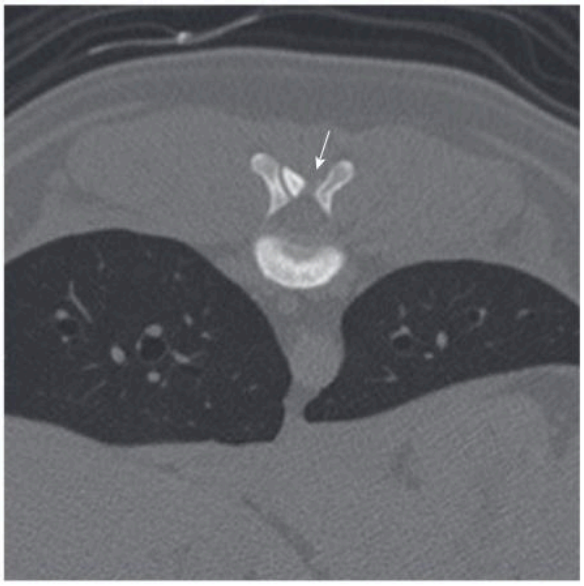


Fig. 15.49 Transverse CT image in a bone window at the level of T11–T12 in a 7-year-old pug. There is complete aplasia of the left caudal articular process of T11 (*arrow*).

basioccipital bone is presumed to be short, resulting in a reduced caudal fossa volume. This causes the caudal aspect of the cerebellar vermis and medulla to extend into or through the foramen magnum causing obstruction of CSF flow. CSF displaced by each systolic cycle through the compressed subarachnoid space results in a high-velocity jet, and this causes an abnormal pressure differential between the spinal cord and subarachnoid space in the cervical area.[289,290,293,303] There is a relative increase in intramedullary pressure and decrease in subarachnoid pressure, the consequence of which is repeated mechanical distention of the spinal cord. This in turn results in fluid accumulation in the spinal cord, with cavitation and

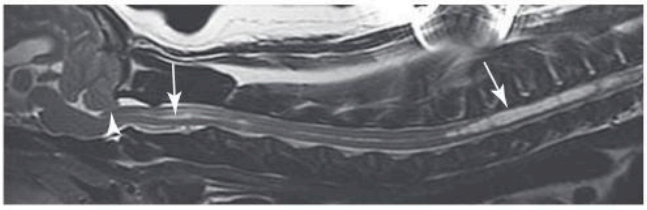


Fig. 15.50 Sagittal T2-weighted image of the caudal brain and cervical spine in a Cavalier King Charles spaniel with Chiari-like malformation and syringomyelia. The caudal fossa is small, causing overcrowding and caudal herniation of the cerebellum into the foramen magnum (*white arrowhead*). There are multiple areas of elongated irregular dilation of the central canal (*white arrows*) in the cervical and cranial thoracic aspects of the spinal cord that form a long syrinx, more pronounced in the thoracic spine.

accumulation of extracellular fluid that coalesces eventually into elongated cavities and syrinx formation; these cavities are commonly separate from the central canal.[289,303]

MRI is a good modality to assess the presence and extent of the syrinx.[284] The syrinx may take the form of a cavity or be complex with septations. A portion of the central canal is usually involved at some level. The longitudinal extent of the syrinx can be evaluated on sagittal images, appearing T2-hyperintense and T1-hypointense (Fig. 15.50). In Chiari-like malformation, the cerebellar vermis and medulla extend into or through the foramen magnum, which is occluded with little or no CSF around neural structures. The magnitude of cerebellar herniation is not correlated with severity. There is typically ventricular dilatation. The cranial cervical and cranial thoracic segments of the spinal cord are typically the most severely affected by the syrinx. Maximum syrinx width is the strongest predictor of pain, scratching behavior, and scoliosis; 95% of Cavalier King Charles spaniels with a maximum syrinx width of 0.64 cm or more will have associated clinical signs,[302] although myelopathic signs develop as soon as the syrinx reaches 4 mm width.[311] Larger syringes with involvement of the dorsal horns of the gray matter of the spinal cord and asymmetrical appearance on transverse images may be associated with persistent neuropathic pain, although the relative contribution of the asymmetry and syrinx size is controversial.[302,312]

REFERENCES

1. Gavin PR. Growth of clinical veterinary magnetic resonance imaging. *Vet Radiol Ultrasound*. 2011;52:S2–S4.
2. Robertson I, Thrall DE. Imaging dogs with suspected disc herniation: pros and cons of myelography, computed tomography, and magnetic resonance. *Vet Radiol Ultrasound*. 2011;52:S81–S84.
3. Evans H. *Miller's Anatomy of the Dog*. 3rd ed. Philadelphia: WB Saunders; 1993.
4. Kent M, Glass EN, Song RB, et al. Anatomic description and clinical relevance of the meningovertebral ligament in dogs. *J Am Vet Med Assoc*. 2019;255:687–694.
5. Pardo A, Morgan J. Myelography in the cat: a comparison of cisternal versus lumbar puncture, using metrizamide. *Vet Radiol*. 1988;29:89.
6. Morgan JP, Atilola M, Bailey CS. Vertebral canal and spinal cord mensuration: a comparative study of its effect on lumbosacral myelography in the dachshund and German shepherd dog. *J Am Vet Med Assoc*. 1987;191:951–957.
7. Scrivani PV, Barthez PY, Leveille R, et al. Subdural injection of contrast medium during cervical myelography. *Vet Radiol Ultrasound*. 1997;38:267–271.
8. Jones JC, Cartee RE, Bartels JE. Computed tomographic anatomy of the canine lumbosacral spine. *Vet Radiol Ultrasound*. 1995;36:91–99.

9. Sharp NJH, Med BV, Cofone M, et al. Computed tomography in the evaluation of caudal cervical spondylomyelopathy of the Doberman Pinscher. *Vet Radiol Ultrasound*. 1995;36:100–108.
10. Adams WH, Daniel GB, Pardo AD, et al. Magnetic resonance imaging of the caudal lumbar and lumbosacral spine in 13 dogs (1990–1993). *Vet Radiol Ultrasound*. 1995;36:3–13.
11. Seiler G, Hani H, Scheidegger J, et al. Staging of lumbar intervertebral disc degeneration in nonchondrodystrophic dogs using low-field magnetic resonance imaging. *Vet Radiol Ultrasound*. 2003;44:179–184.
12. Pease A, Sullivan S, Olby N, et al. Value of a single-shot turbo spin-echo pulse sequence for assessing the architecture of the subarachnoid space and the constitutive nature of cerebrospinal fluid. *Vet Radiol Ultrasound*. 2006;47:254–259.
13. Seiler GS, Robertson ID, Mai W, et al. Usefulness of a half-Fourier acquisition single-shot turbo spin-echo pulse sequence in identifying arachnoid diverticula in dogs. *Vet Radiol Ultrasound*. 2012;53:157–161.
14. Adams WH. The spine. *Clin Tech Sm Anim Pract*. 1999;14:148–159.
15. Chang Y, Dennis R, Platt SR, et al. Magnetic resonance imaging of traumatic intervertebral disc extension in dogs. *Vet Rec*. 2007;160:795–799.
16. Hansen H. A pathologic-anatomical study on disc degeneration in the dog. *Acta Orthop Scand*. 1952;Suppl.
17. Besalti O, Pekcan Z, Sirin YS, et al. Magnetic resonance imaging findings in dogs with thoracolumbar intervertebral disk disease: 69 cases (1997–2005). *J Am Vet Med Assoc*. 2006;228:902–908.
18. De Decker S, Gomes SA, Packer RM, et al. Evaluation of magnetic resonance imaging guidelines for differentiation between thoracolumbar intervertebral disk extrusions and intervertebral disk protrusions in dogs. *Vet Radiol Ultrasound*. 2016;57:526–533.
19. Gomes SA, Volk HA, Packer RM, et al. Clinical and magnetic resonance imaging characteristics of thoracolumbar intervertebral disk extrusions and protrusions in large breed dogs. *Vet Radiol Ultrasound*. 2016;57:417–426.
20. Fenn J, Olby NJ. Consortium. CSCI: classification of intervertebral disc disease. *Front Vet Sci*. 2020;7:579025.
21. Tartarelli CL, Baroni M, Borghi M. Thoracolumbar disc extrusion associated with extensive epidural haemorrhage: a retrospective study of 23 dogs. *J Small Anim Pract*. 2005;46:485–490.
22. Woelfel CW, Robertson JB, Mariani CL, et al. Outcomes and prognostic indicators in 59 paraplegic medium to large breed dogs with extensive epidural hemorrhage secondary to thoracolumbar disc extrusion. *Vet Surg*. 2021;50:527–536.
23. Hay CW, Muir P. Tearing of the dura mater in three dogs. *Vet Rec*. 2000;146:279–282.
24. Kent M, Holmes S, Cohen ELI, et al. CT myelography in a dog with intramedullary intervertebral disc herniation. *Vet Radiol Ultrasound*. 2011;52:185–187.
25. Kitagawa M, Okada M, Kanayama K, et al. Identification of ventrolateral intramedullary intervertebral disc herniation in a dog. *J S Afr Vet Assoc*. 2012;83:103.
26. McConnell JF, Garosi LS. Intramedullary intervertebral disk extrusion in a cat. *Vet Radiol Ultrasound*. 2004;45:327–330.
27. De Risio L, Adams V, Dennis R, et al. Association of clinical and magnetic resonance imaging findings with outcome in dogs with presumptive acute noncompressive nucleus pulposus extrusion: 42 cases (2000–2007). *J Am Vet Med Assoc*. 2009;234:495–504.
28. McKee WM, Downes CJ, Pink JJ, et al. Presumptive exercise-associated peracute thoracolumbar disc extrusion in 48 dogs. *Vet Rec*. 2010;166:523–528.
29. Beltran E, Dennis R, Doyle V, et al. Clinical and magnetic resonance imaging features of canine compressive cervical myelopathy with suspected hydrated nucleus pulposus extrusion. *J Small Anim Pract*. 2012;53:101–107.
30. Hamilton T, Glass E, Drobatz K, et al. Severity of spinal cord dysfunction and pain associated with hydrated nucleus pulposus extrusion in dogs. *Vet Comp Orthop Traumatol*. 2014;27:313–318.
31. Manunta ML, Evangelisti MA, Bergknut N, et al. Hydrated nucleus pulposus herniation in seven dogs. *Vet J*. 2015;203:342–344.
32. Falzone C. Canine acute cervical myelopathy: hydrated nucleus pulposus extrusion or intraspinal discal cysts? *Vet Surg*. 2017;46:376–380.
33. Kang BJ, Jung Y, Park S, et al. Discal cysts of the cervical spine in two dogs. *J Vet Sci*. 2015;16:543–545.
34. Konar M, Lang J, Fluhmann G, et al. Ventral intraspinal cysts associated with the intervertebral disc: magnetic resonance imaging observations in seven dogs. *Vet Surg*. 2008;37:94–101.
35. Drees R, Dennison SE, Keuler NS, et al. Computed tomographic imaging protocol for the canine cervical and lumbar spine. *Vet Radiol Ultrasound*. 2009;50:74–79.
36. Olby NJ, Munana KR, Sharp NJ, et al. The computed tomographic appearance of acute thoracolumbar intervertebral disc herniations in dogs. *Vet Radiol Ultrasound*. 2000;41:396–402.
37. Olby NJ, Dyce J, Houlton JEF. Correlation of plain radiographic and lumbar myelographic findings with surgical findings in thoracolumbar disc disease. *J Small Anim Pract*. 1994;35:345–350.
38. Dennison SE, Drees R, Rylander H, et al. Evaluation of different computed tomography techniques and myelography for the diagnosis of acute canine myelopathy. *Vet Radiol Ultrasound*. 2010;51:254–258.
39. Parry AT, Harris A, Upjohn MM, et al. Does choice of imaging modality affect outcome in dogs with thoracolumbar spinal conditions? *J Small Anim Pract*. 2010;51:312–317.
40. Cooper JJ, Young BD, Griffin JF, Fosgate GT. Comparison between noncontrast computed tomography and magnetic resonance imaging for detection and characterization of thoracolumbar myelopathy caused by intervertebral disk herniation in dogs. *Vet Radiol Ultrasound*. 2014;55:182–189.
41. Noyes JA, Thomovsky SA, Chen AV, et al. Magnetic resonance imaging versus computed tomography to plan hemilaminectomies in chondrodystrophic dogs with intervertebral disc extrusion. *Vet Surg*. 2017;46:1025–1031.
42. Levitski RE, Lipsitz D, Chauvet AE. Magnetic resonance imaging of the cervical spine in 27 dogs. *Vet Radiol Ultrasound*. 1999;40:332–341.
43. Naude SH, Lambrechts NE, Wagner WM, et al. Association of preoperative magnetic resonance imaging findings with surgical features in Dachshunds with thoracolumbar intervertebral disk extrusion. *J Am Vet Med Assoc*. 2008;232:702–708.
44. Mateo I, Lorenzo V, Foradada L, et al. Clinical, pathologic, and magnetic resonance imaging characteristics of canine disc extrusion accompanied by epidural hemorrhage or inflammation. *Vet Radiol Ultrasound*. 2011;52:17–24.
45. Bridges J, Windsor R, Stewart SD, et al. Prevalence and clinical features of thoracolumbar intervertebral disc-associated epidural hemorrhage in dogs. *J Vet Intern Med*. 2022;36:1365–1372.

46. Tidwell AS, Specht A, Blaeser L, et al. Magnetic resonance imaging features of extradural hematomas associated with intervertebral disc herniation in a dog. *Vet Radiol Ultrasound*. 2002;43:319–324.
47. Suran JN, Durham A, Mai W, et al. Contrast enhancement of extradural compressive material on magnetic resonance imaging. *Vet Radiol Ultrasound*. 2011;52:10–16.
48. Furtado ARR, Cherubini GB, Taeymans O. Low-field magnetic resonance changes in the paravertebral musculature of dogs with acute intervertebral disc extrusion. *J Small Anim Pract*. 2019;60:367–373.
49. Morrison EJ, Baron-Chapman ML, Chalkley M. MRI T2/STIR epaxial muscle hyperintensity in some dogs with intervertebral disc extrusion corresponds to histologic patterns of muscle degeneration and inflammation. *Vet Radiol Ultrasound*. 2021;62:150–160.
50. Trampus P, Goepfert C, Welle M, et al. Magnetic resonance imaging signal alterations in paraspinal muscles in dogs with acute thoracolumbar intervertebral disk extrusion. *Front Vet Sci*. 2018;5:16.
51. Beale CC, Secrest SA. MRI assessment of epaxial myosteatosis in dogs with intervertebral disc extrusions and associations with patient factors and outcome. *Vet Radiol Ultrasound*. 2021;62:687–696.
52. Lerer A, Nykamp SG, Harriss AB, et al. MRI-based relationships between spine pathology, intervertebral disc degeneration, and muscle fatty infiltration in chondrodystrophic and non-chondrodystrophic dogs. *Spine J*. 2015;15:2433–2439.
53. Ryan TM, Platt SR, Llabres-Diaz FJ, et al. Detection of spinal cord compression in dogs with cervical intervertebral disc disease by magnetic resonance imaging. *Vet Rec*. 2008;163:11–15.
54. Cherrone KL, Dewey CW, Coates JR, et al. A retrospective comparison of cervical intervertebral disk disease in nonchondrodystrophic large dogs versus small dogs. *J Am Anim Hosp Assoc*. 2004;40:316–320.
55. Hillman RB, Kengeri SS, Waters DJ. Reevaluation of predictive factors for complete recovery in dogs with nonambulatory tetraparesis secondary to cervical disk herniation. *J Am Anim Hosp Assoc*. 2009;45:155–163.
56. Silva S, Genain MA, Khan S, et al. The spinal cord-to-vertebral canal area ratio measured with computed tomography is lower in the thoracolumbar than the cervical region in French bulldogs. *J Am Vet Med Assoc*. 2022:1–4.
57. Penning V, Platt SR, Dennis R, et al. Association of spinal cord compression seen on magnetic resonance imaging with clinical outcome in 67 dogs with thoracolumbar intervertebral disc extrusion. *J Small Anim Pract*. 2006;47:644–650.
58. Gaitero L, Anor S. Cranial thoracic disc protrusions in three German Shepherd dogs. *Vet J*. 2009;182:349–351.
59. Gaitero L, Nykamp S, Daniel R, et al. Comparison between cranial thoracic intervertebral disc herniations in German shepherd dogs and other large breed dogs. *Vet Radiol Ultrasound*. 2013;54:133–138.
60. Jaderlund KJ, Hansson K, Lindberg R, et al. T3-T4 disc herniation in a German shepherd dog. *Vet Rec*. 2002;151:769–770.
61. Israel SK, Levine JM, Kerwin SC, et al. The relative sensitivity of computed tomography and myelography for identification of thoracolumbar intervertebral disk herniations in dogs. *Vet Radiol Ultrasound*. 2009;50:247–252.
62. Levine JM, Fosgate GT, Chen AV, et al. Magnetic resonance imaging in dogs with neurologic impairment due to acute thoracic and lumbar intervertebral disk herniation. *J Vet Intern Med*. 2009;23:1220–1226.
63. Ito D, Matsunaga S, Jeffery ND, et al. Prognostic value of magnetic resonance imaging in dogs with paraplegia caused by thoracolumbar intervertebral disk extrusion: 77 cases (2000–2003). *J Am Vet Med Assoc*. 2005;227:1454–1460.
64. Ruddle TL, Allen DA, Schertel ER, et al. Outcome and prognostic factors in non-ambulatory Hansen Type I intervertebral disc extrusions: 308 cases. *Vet Comp Orthop Traumatol*. 2006;19:29–34.
65. Wang-Leandro A, Siedenburg JS, Hobert MK, et al. Comparison of preoperative quantitative magnetic resonance imaging and clinical assessment of deep pain perception as prognostic tools for early recovery of motor function in paraplegic dogs with intervertebral disk herniations. *J Vet Intern Med*. 2017;31:842–848.
66. Freeman P. Sacrococcygeal intervertebral disc extrusion in a dachshund. *Vet Rec*. 2010;167:618–619.
67. Lawson CM, Reichle JK, McKlveen T, et al. Imaging findings in dogs with caudal intervertebral disc herniation. *Vet Radiol Ultrasound*. 2011;52:487–491.
68. Jones JC, Banfield CM, Ward DL. Association between postoperative outcome and results of magnetic resonance imaging and computed tomography in working dogs with degenerative lumbosacral stenosis. *J Am Vet Med Assoc*. 2000;216:1769–1774.
69. Bresciani L, Trevail R, Clarke S, et al. Lumbosacral intervertebral disk extrusions in 13 dogs. *Vet Surg*. 2021;50:823–832.
70. Jones EC, Sorjonen DC, Simpson ST, et al. Comparison between computed tomographic and surgical findings in nine large-breed dogs with lumbosacral stenosis. *Vet Radiol Ultrasound*. 1996;37:247–256.
71. Jones JC, Inzana KD. Subclinical CT abnormalities in the lumbosacral spine of older large-breed dogs. *Vet Radiol Ultrasound*. 2000;41:19–26.
72. Jones JC, Wilson ME, Bartels JE. A review of high resolution computed tomography and a proposed technique for regional examination of the canine lumbosacral spine. *Vet Radiol Ultrasound*. 1994;35:339–346.
73. Jones JC, Wright JC, Bartels JE. Computed tomographic morphometry of the lumbosacral spine of dogs. *Am J Vet Res*. 1995;56:1125–1132.
74. Ramirez 3rd O, Thrall DE. A review of imaging techniques for canine cauda equina syndrome. *Vet Radiol Ultrasound*. 1998;39:283–296.
75. Suwankong N, Voorhout G, Hazewinkel HA, et al. Agreement between computed tomography, magnetic resonance imaging, and surgical findings in dogs with degenerative lumbosacral stenosis. *J Am Vet Med Assoc*. 2006;229:1924–1929.
76. Rapp M, Ley CJ, Hansson K, et al. Postoperative computed tomography and low-field magnetic resonance imaging findings in dogs with degenerative lumbosacral stenosis treated by dorsal laminectomy. *Vet Comp Orthop Traumatol*. 2017;30:143–152.
77. Bersan E, McConnell F, Trevail R, et al. Cervical intervertebral foraminal disc extrusion in dogs: clinical presentation, MRI characteristics and outcome after medical management. *Vet Rec*. 2015;176:597.
78. Chambers JN, Selcer BA, Sullivan SA, et al. Diagnosis of lateralized lumbosacral disk herniation with magnetic resonance imaging. *J Am Anim Hosp Assoc*. 1997;33:296–299.
79. Fadda A, Lang J, Forterre F. Far lateral lumbar disc extrusion: MRI findings and surgical treatment. *Vet Comp Orthop Traumatol*. 2013;26:318–322.

80. Silva S, Guevar J, Jose-Lopez R, et al. Clinical signs, MRI findings and long-term outcomes of foraminal and far lateral thoracolumbar intervertebral disc herniations in dogs. *Vet Rec*. 2022;190:e1529.
81. Mouradian-Darby AE, Young BD, Griffin JF, et al. Lymphocytic ganglioneuritis secondary to intervertebral disc extrusion in a dog. *J Small Anim Pract*. 2014;55:471–474.
82. Liptak JM, Allan GS, Krockenberger MB, et al. Radiographic diagnosis: intramedullary extrusion of an intervertebral disc. *Vet Radiol Ultrasound*. 2002;43:272–274.
83. Lu D, Lamb CR, Wesselingh K, et al. Acute intervertebral disc extrusion in a cat: clinical and MRI findings. *J Feline Med Surg*. 2002;4:65–68.
84. McKee WM, Downes CJ. Rupture of the dura mater in two dogs caused by the peracute extrusion of a cervical disc. *Vet Rec*. 2008;162:479–481.
85. Sanders SG, Bagley RS, Gavin PR. Intramedullary spinal cord damage associated with intervertebral disk material in a dog. *J Am Vet Med Assoc*. 2002;221:1594–1596, 1574-1595.
86. De Risio L. A Review of fibrocartilaginous embolic myelopathy and different types of peracute non-compressive intervertebral disk extrusions in dogs and cats. *Front Vet Sci*. 2015;2:24.
87. Fenn J, Drees R, Volk HA, et al. Inter- and intraobserver agreement for diagnosing presumptive ischemic myelopathy and acute noncompressive nucleus pulposus extrusion in dogs using magnetic resonance imaging. *Vet Radiol Ultrasound*. 2015;57:33–40.
88. Chow K, Beatty JA, Voss K, et al. Probable lumbar acute non-compressive nucleus pulposus extrusion in a cat with acute onset paraparesis. *J Feline Med Surg*. 2012;14:764–767.
89. Packer RA, Frank PM, Chambers JN. Traumatic subarachnoid-pleural fistula in a dog. *Vet Radiol Ultrasound*. 2004;45:523–527.
90. Kamishina H, Ogawa H, Katayama M, et al. Spontaneous regression of a cervical intraspinal cyst in a dog. *J Vet Med Sci*. 2010;72:349–352.
91. Casado D, Fernandes R, Lourinho F, et al. Magnetic resonance imaging features of canine intradural/extramedullary intervertebral disc extrusion in seven cases. *Front Vet Sci*. 2022;9:1003042.
92. Kim J, Kim H, Hwang J, et al. Preliminary study of presumptive intradural-intramedullary intervertebral disc extrusion in 20 dogs. *J Vet Sci*. 2020;21:e52.
93. Tamura S, Doi S, Tamura Y, et al. Thoracolumbar intradural disc herniation in eight dogs: clinical, low-field magnetic resonance imaging, and computed tomographic myelography findings. *Vet Radiol Ultrasound*. 2015;56:160–167.
94. Lipsitz D, Levitski RE, Chauvet AE, et al. Magnetic resonance imaging features of cervical stenotic myelopathy in 21 dogs. *Vet Radiol Ultrasound*. 2001;42:20–27.
95. da Costa RC, Parent J, Dobson H, et al. Comparison of magnetic resonance imaging and myelography in 18 Doberman pinscher dogs with cervical spondylomyelopathy. *Vet Radiol Ultrasound*. 2006;47:523–531.
96. da Costa RC, Parent JM. One-year clinical and magnetic resonance imaging follow-up of Doberman Pinschers with cervical spondylomyelopathy treated medically or surgically. *J Am Vet Med Assoc*. 2007;231:243–250.
97. da Costa RC, Parent JM, Partlow G, et al. Morphologic and morphometric magnetic resonance imaging features of Doberman Pinschers with and without clinical signs of cervical spondylomyelopathy. *Am J Vet Res*. 2006;67:1601–1612.
98. da Costa RC, Samii VF. Advanced imaging of the spine in small animals. *Vet Clin North Am Small Anim Pract*. 2010;40:765–790.
99. Martin-Vaquero P, da Costa RC. Magnetic resonance imaging features of Great Danes with and without clinical signs of cervical spondylomyelopathy. *J Am Vet Med Assoc*. 2014;245:393–400.
100. Martin-Vaquero P, da Costa RC, Drost WT. Comparison of noncontrast computed tomography and high-field magnetic resonance imaging in the evaluation of Great Danes with cervical spondylomyelopathy. *Vet Radiol Ultrasound*. 2014;55:496–505.
101. Martin-Vaquero P, da Costa RC, Lima CG. Cervical spondylomyelopathy in Great Danes: a magnetic resonance imaging morphometric study. *Vet J*. 2014;201:64–71.
102. Bonelli MA, da Costa L, da Costa RC. Magnetic resonance imaging and neurological findings in dogs with disc-associated cervical spondylomyelopathy: a case series. *BMC Vet Res*. 2021;17:145.
103. Bonelli MA, da Costa RC. Neurologic and magnetic resonance imaging features of German shepherd dogs with cervical spondylomyelopathy: 10 cases (2006–2018). *J Am Vet Med Assoc*. 2019;255:1263–1269.
104. Eagleson JS, Diaz J, Platt SR, et al. Cervical vertebral malformation-malarticulation syndrome in the Bernese mountain dog: clinical and magnetic resonance imaging features. *J Small Anim Pract*. 2009;50:186–193.
105. Bonelli MA, da Costa L, da Costa RC. Association of neurologic signs with high-field MRI findings in 100 dogs with osseous-associated cervical spondylomyelopathy. *Vet Radiol Ultrasound*. 2021;62:678–686.
106. Nye C, Hostnik E, Parker E, et al. Long-term clinical and magnetic resonance imaging follow-up of dogs with osseous-associated cervical spondylomyelopathy. *J Vet Intern Med*. 2020;34:2012–2020.
107. Vansteenkiste D, Martin-Vaquero P, Bonelli M, et al. Long-term computed tomography follow-up in Great Danes with or without signs of osseous-associated cervical Spondylomyelopathy. *BMC Vet Res*. 2019;15:90.
108. de Albuquerque Bonelli M, da Costa RC. Clinical and magnetic resonance imaging characterization of cervical spondylomyelopathy in juvenile dogs. *J Vet Intern Med*. 2019;33:2160–2166.
109. De Decker S, Gielen IM, Duchateau L, et al. Intraobserver, interobserver, and intermethod agreement for results of myelography, computed tomography-myelography, and low-field magnetic resonance imaging in dogs with disk-associated wobbler syndrome. *J Am Vet Med Assoc*. 2011;238:1601–1608.
110. De Decker S, Gielen IM, Duchateau L, et al. Low-field magnetic resonance imaging findings of the caudal portion of the cervical region in clinically normal Doberman Pinschers and Foxhounds. *Am J Vet Res*. 2010;71:428–434.
111. De Decker S, Gielen IMVL, Duchateau L, et al. Intraobserver and interobserver agreement for results of low-field magnetic resonance imaging in dogs with and without clinical signs of disk-associated wobbler syndrome. *J Am Vet Med Assoc*. 2011;238:74–80.
112. Penderis J, Dennis R. Use of traction during magnetic resonance imaging of caudal cervical spondylomyelopathy ("wobbler syndrome") in the dog. *Vet Radiol Ultrasound*. 2004;45:216–219.
113. Provencher M, Habing A, Moore SA, et al. Kinematic magnetic resonance imaging for evaluation of disc-associated cervical spondylomyelopathy in Doberman pinschers. *J Vet Intern Med*. 2016;30:1121–1128.

114. Burke JF, Thawani JP, Berger I, et al. Microsurgical treatment of sacral perineural (Tarlov) cysts: case series and review of the literature. *J Neurosurg Spine*. 2016:1–8.
115. Lowrie ML, Platt SR, Garosi LS. Extramedullary spinal cysts in dogs. *Vet Surg*. 2014;43:650–662.
116. Fiorentino E, Gasparinetti N, Falzone C. Clinical, magnetic resonance imaging and histologic findings of canine thoracolumbar discal pseudocyst: 8 cases (2014–2019). *J Small Anim Pract*. 2021;62:28–32.
117. Penning VA, Benigni L, Steeves E, et al. Imaging diagnosis—degenerative intraspinal cyst associated with an intervertebral disc. *Vet Radiol Ultrasound*. 2007;48:424–427.
118. Dyce J, Herrtage ME, Houlton JEF, et al. Canine spinal 'arachnoid cysts. *J Small Anim Pract*. 1991;32:433–437.
119. Foss KD, Berry WL. What is your neurologic diagnosis? Spinal arachnoid cysts. *J Am Vet Med Assoc*. 2009;234:1009–1011.
120. Frykman OF. Spinal arachnoid cyst in four dogs: diagnosis, surgical, treatment and follow-up results. *J Small Anim Pract*. 1999;40.
121. Galloway AM, Curtis NC, Sommerlad SF, et al. Correlative imaging findings in seven dogs and one cat with spinal arachnoid cysts. *Vet Radiol Ultrasound*. 1999;40:445–452.
122. Gnirs K, Ruel Y, Blot S, et al. Spinal subarachnoid cysts in 13 dogs. *Vet Radiol Ultrasound*. 2003;44:402–408.
123. Goncalves R, Hammond G, Penderis J. Imaging diagnosis: erroneous localization of spinal arachnoid cyst. *Vet Radiol Ultrasound*. 2008;49:460–463.
124. Hashizume CT. Cervical spinal arachnoid cyst in a dog. *Can Vet J*. 2000;41:225–227.
125. Itamoto K. A case involving a dog with a cervical arachnoid cyst treated with marsupilization surgery. *J Jpn Vet Med Assoc*. 2010;63:375–378.
126. Jurina K, Grevel V. Spinal arachnoid pseudocysts in 10 Rottweilers. *J Small Anim Pract*. 2004;45:9–15.
127. Mauler DA, De Decker S, De Risio L, et al. Signalment, clinical presentation, and diagnostic findings in 122 dogs with spinal arachnoid diverticula. *J Vet Intern Med*. 2014;28:175–181.
128. McKee WM, Renwick PW. Marsupialisation of an arachnoid cyst in a dog. *J Small Anim Pract*. 1994;35:108–111.
129. Ness MG. Spinal arachnoid cysts in two Shih Tzu littermates. *Vet Rec*. 1998;142:515–516.
130. Oxley W, Pink J. Amelioration of caudal thoracic syringohydromyelia following surgical management of an adjacent arachnoid cyst. *J Small Anim Pract*. 2012;53:67–72.
131. Parker AJ, Adams WM, Zachary JF. Spinal arachnoid cysts in the dog. *J Am Anim Hosp Assoc*. 1983;19:1001–1008.
132. Rohdin C, Nyman HT, Wohlsein P, et al. Cervical spinal intradural arachnoid cysts in related, young pugs. *J Small Anim Pract*. 2014;55:229–234.
133. Rylander H, Lipsitz D, Berry WL, et al. Retrospective analysis of spinal arachnoid cysts in 14 dogs. *J Vet Intern Med*. 2002;16:690–696.
134. Sessums KB, Ducote JM, American College of Veterinary R. What is your diagnosis? Spinal arachnoid cysts. *J Am Vet Med Assoc*. 2006;228:1019–1020.
135. Shamir MH, Shahar R, Aizenberg I. Subarachnoid cyst in a cat. *J Am Anim Hosp Assoc*. 1997;33:123–125.
136. Skeen TM, Olby NJ, Munana KR, et al. Spinal arachnoid cysts in 17 dogs. *J Am Anim Hosp Assoc*. 2003;39:271–282.
137. Vignoli M, Rossi F, Sarli G. Spinal subarachnoid cyst in a cat. *Vet Radiol Ultrasound*. 1999;40:116–119.
138. Webb AA. Intradural spinal arachnoid cyst in a dog. *Can Vet J*. 1999;40:588–589.
139. Driver CJ, Rose J, Tauro A, et al. Magnetic resonance image findings in pug dogs with thoracolumbar myelopathy and concurrent caudal articular process dysplasia. *BMC Vet Res*. 2019;15:182.
140. Berle M, Wester KG, Ulvik RJ, et al. Arachnoid cysts do not contain cerebrospinal fluid: a comparative chemical analysis of arachnoid cyst fluid and cerebrospinal fluid in adults. *Cerebrospinal Fluid Res*. 2010;7:8.
141. Targett MP, McInnes E, Dennis R. Magnetic resonance imaging of a medullary dermoid cyst with secondary hydrocephalus in a dog. *Vet Radiol Ultrasound*. 1999;40:23–26.
142. Davies ESS, Fransson BA, Gavin PR. A confusing magnetic resonance imaging observation complicating surgery for a dermoid cyst in a Rhodesian ridgeback. *Vet Radiol Ultrasound*. 2004;45:307–309.
143. Shamir MH, Lichovsky D, Aizenberg I, et al. Partial surgical removal of an intramedullary epidermoid cyst from the spinal cord of a dog. *J Small Anim Pract*. 1999;40:439–442.
144. Kiviranta AM, Lappalainen AK, Hagner K, et al. Dermoid sinus and spina bifida in three dogs and a cat. *J Small Anim Pract*. 2011;52:319–324.
145. Fatone G, Brunetti A, Lamagna F, et al. Dermoid sinus and spinal malformations in a Yorkshire terrier: diagnosis and follow-up. *J Small Anim Pract*. 1995;36:178–180.
146. Jones S, Adin C, Thompson E, et al. Computed tomography for the diagnosis and characterization of dermoid sinuses in two dogs. *J Am Anim Hosp Assoc*. 2019;55:e55403.
147. Fleming JM, Platt SR, Kent M, et al. Cervical dermoid sinus in a cat: case presentation and review of the literature. *J Feline Med Surg*. 2011;13:992–996.
148. Rahal S, Mortari AC, Yamashita S, et al. Magnetic resonance imaging in the diagnosis of type 1 dermoid sinus in two Rhodesian ridgeback dogs. *Can Vet J*. 2008;49:871–876.
149. Tong T, Simpson DJ. Case report: spinal dermoid sinus in a Burmese cat with paraparesis. *Aust Vet J*. 2009;87:450–454.
150. Bowens AL, Ducote JM, Early PJ. What is your neurologic diagnosis? Type IV dermoid sinus (pilonidal sinus) in the region of the fourth thoracic vertebra. *J Am Vet Med Assoc*. 2005;227:713–715.
151. Motta L, Skerritt G, Denk D, et al. Dermoid sinus type IV associated with spina bifida in a young Victorian bulldog. *Vet Rec*. 2012;170:127.
152. da Costa RC, Cook LB. Cystic Abnormalities of the spinal cord and vertebral column. *Vet Clin North Am Small Anim Pract*. 2015.
153. Dickinson PJ, Sturges BK, Berry WL, et al. Extradural spinal synovial cysts in nine dogs. *J Small Anim Pract*. 2001;42:502–509.
154. Sale CS, Smith KC. Extradural spinal juxtafacet (synovial) cysts in three dogs. *J Small Anim Pract*. 2007;48:116–119.
155. Webb AA, Pharr JW, Lew LJ, et al. MR imaging findings in a dog with lumbar ganglion cysts. *Vet Radiol Ultrasound*. 2001;42:9–13.
156. Bagley RS. Spinal neoplasms in small animals. *Vet Clin North Am Small Anim Pract*. 2010;40:915–927.
157. Morgan JP, Ackerman N, Bailey CS, et al. Vertebral tumors in the dog: a clinical, radiologic, and pathologic study of 61 primary and secondary lesions. *Vet Radiol*. 1980;21:197–212.
158. Marioni-Henry K, Van Winkle TJ, Smith SH, et al. Tumors affecting the spinal cord of cats: 85 cases (1980–2005). *J Am Vet Med Assoc*. 2008;232:237–243.

159. Marioni-Henry K, Vite CH, Newton AL, et al. Prevalence of diseases of the spinal cord of cats. *J Vet Intern Med*. 2004;18:851–858.
160. Schultz RM, Puchalski SM, Kent M, et al. Skeletal lesions of histiocytic sarcoma in nineteen dogs. *Vet Radiol Ultrasound*. 2007;48:539–543.
161. Agut A, Anson A, Navarro A, et al. Imaging diagnosis-infiltrative lipoma causing spinal cord and lumbar nerve root compression in a dog. *Vet Radiol Ultrasound*. 2013;54:381–383.
162. Hobert MK, Brauer C, Dziallas P, et al. Infiltrative lipoma compressing the spinal cord in 2 large-breed dogs. *Can Vet J*. 2013;54:74–78.
163. Kim HJ, Chang HS, Choi CB, et al. Infiltrative lipoma in cervical bones in a dog. *J Vet Med Sci*. 2005;67:1043–1046.
164. McEntee MC, Thrall DE. Computed tomographic imaging of infiltrative lipoma in 22 dogs. *Vet Radiol Ultrasound*. 2001;42:221–225.
165. Morgan LW, Toal R, Siemering G, et al. Imaging diagnosis—infiltrative lipoma causing spinal cord compression in a dog. *Vet Radiol Ultrasound*. 2007;48:35–37.
166. Auger M, Hecht S, Springer CM. Magnetic resonance imaging features of extradural spinal neoplasia in 60 dogs and seven cats. *Front Vet Sci*. 2020;7:610490.
167. Durand A, Keenihan E, Schweizer D, et al. Clinical and magnetic resonance imaging features of lymphoma involving the nervous system in cats. *J Vet Intern Med*. 2022;36:679–693.
168. Lorenzo V, Ribeiro J, Bernardini M, et al. Clinical and magnetic resonance imaging features, and pathological findings of spinal lymphoma in 27 cats. *Front Vet Sci*. 2022;9:980414.
169. Mallol C, Gutierrez-Quintana R, Hammond G, et al. MRI features of canine hemangiosarcoma affecting the central nervous system. *Vet Radiol Ultrasound*. 2022;63:185–196.
170. Moore TW, Bentley RT, Moore SA, et al. Spinal mast cell tumors in dogs: imaging features and clinical outcome of four cases. *Vet Radiol Ultrasound*. 2017;58:44–52.
171. Paek M, Glass E, Kent M, et al. Primary lumbar extradural hemangiosarcoma in a dog. *J Am Anim Hosp Assoc*. 2015;51:191–196.
172. Drost WT, Love NE, Berry CR. Comparison of radiography, myelography, and computed tomography for the evaluation of canine vertebral and spinal cord tumors in sixteen dogs. *Vet Radiol Ultrasound*. 1996;37:28–33.
173. Kippenes H, Gavin PR, Bagley RS, et al. Magnetic resonance imaging features of tumors of the spine and spinal cord in dogs. *Vet Radiol Ultrasound*. 1999;40:627–633.
174. Tam C, Hecht S, Mai W, et al. Cranial and vertebral osteosarcoma commonly has T2 signal heterogeneity, contrast enhancement, and osteolysis on MRI: a case series of 35 dogs. *Vet Radiol Ultrasound*. 2022;63:552–562.
175. Wyatt S, De Risio L, Driver C, et al. Neurological signs and MRI findings in 12 dogs with multiple myeloma. *Vet Radiol Ultrasound*. 2019;60:409–415.
176. D'Anjou MA. Carmel EN, Tidwell AS: value of fat suppression in gadolinium-enhanced magnetic resonance neuroimaging. *Vet Radiol Ultrasound*. 2011;52:S85–90.
177. Dennis R. Optimal magnetic resonance imaging of the spine. *Vet Radiol Ultrasound*. 2011;52:S72–S80.
178. Wheeler SJ, Sharp NJH. Neurological deficits in multiple limbs: spinal disorders. In: Wheeler SJ, ed. *Manual of Small Animal Neurology*. 2nd ed. Cheltenham. British Small Animal Veterinary Association; 1995:143–158.
179. Brewer DM, Cerda-Gonzalez S, Dewey CW, et al. Spinal cord nephroblastoma in dogs: 11 cases (1985–2007). *J Am Vet Med Assoc*. 2011;238:618–624.
180. Gasser AM, Bush WW, Smith S, et al. Extradural spinal, bone marrow, and renal nephroblastoma. *J Am Anim Hosp Assoc*. 2003;39:80–85.
181. Liebel FX, Rossmeisl Jr JH, Lanz OI, et al. Canine spinal nephroblastoma: long-term outcomes associated with treatment of 10 cases (1996–2009). *Vet Surg*. 2011;40:244–252.
182. Macri NP, Van Alstine W, Coolman RA. Canine spinal nephroblastoma. *J Am Anim Hosp Assoc*. 1997;33:302–306.
183. McConnell JF, Garosi LS, Dennis R, et al. Imaging of a spinal nephroblastoma in a dog. *Vet Radiol Ultrasound*. 2003;44:537–541.
184. Nakade T, Inoue A, Shimazaki H, et al. Spinal nephroblastoma in a miniature Dachshund. *J Vet Med Sci*. 2006;68:1383–1385.
185. Sale CS, Skerritt GC, Smith KC. Spinal nephroblastoma in a crossbreed dog. *J Small Anim Pract*. 2004;45:267–271.
186. Terrell SP, Platt SR, Chrisman CL, et al. Possible intraspinal metastasis of a canine spinal cord nephroblastoma. *Vet Pathol*. 2000;37:94–97.
187. Kraft S, Ehrhart EJ, Gall D, et al. Magnetic resonance imaging characteristics of peripheral nerve sheath tumors of the canine brachial plexus in 18 dogs. *Vet Radiol Ultrasound*. 2007;48:1–7.
188. Linzmann H, Brunnberg L, Gruber AD, et al. A neurotropic lymphoma in the brachial plexus of a cat. *J Feline Med Surg*. 2009;11:522–524.
189. Mellanby RJ, Jeffery ND, Baines EA, et al. Magnetic resonance imaging in the diagnosis of lymphoma involving the brachial plexus in a cat. *Vet Radiol Ultrasound*. 2003;44:522–525.
190. Rudich SR, Feeney DA, Anderson KL, et al. Computed tomography of masses of the brachial plexus and contributing nerve roots in dogs. *Vet Radiol Ultrasound*. 2004;45:46–50.
191. Jose-Lopez R, de la Fuente C, Pumarola M, et al. Spinal meningiomas in dogs: description of 8 cases including a novel radiological and histopathological presentation. *Can Vet J*. 2013;54:948–954.
192. McDonnell JJ, Tidwell AS, Faissler D, et al. Magnetic resonance imaging features of cervical spinal cord meningiomas. *Vet Radiol Ultrasound*. 2005;46:368–374.
193. Petersen SA, Sturges BK, Dickinson PJ, et al. Canine intraspinal meningiomas: imaging features, histopathologic classification, and long-term outcome in 34 dogs. *J Vet Intern Med*. 2008;22:946–953.
194. Wall M, Platt S, Selcer B, et al. Multifocal spinal papillary meningioma in a dog. *Vet Radiol Ultrasound*. 2005;46:309–312.
195. Yeomans SM. Short paper – extensive spinal meningioma in a young dog. *J Comp Pathol*. 2000;122:303–306.
196. Pancotto TE, Rossmeisl Jr JH, Zimmerman K, et al. Intramedullary spinal cord neoplasia in 53 dogs (1990–2010): distribution, clinicopathologic characteristics, and clinical behavior. *J Vet Intern Med*. 2013;27:1500–1508.
197. Hammond JJ, deLahunta A, Glass EN, et al. Feline spinal cord gliomas: clinicopathologic and diagnostic features of seven cases. *J Vet Diagn Invest*. 2014;26:513–520.
198. Tamura S, Hori Y, Tamura Y, et al. Long-term follow-up of surgical treatment of spinal anaplastic astrocytoma in a cat. *J Feline Med Surg*. 2013;15:921–926.
199. Gibson AM, Rosser MF, de Oliveira CR, et al. Magnetic resonance imaging findings and antemortem cytologic diagnosis of intramedullary spinal cord ependymoma in a dog. *J Am Vet Med Assoc*. 2021;259:1446–1451.

200. Taylor A, Eichelberger B, Hodo C, et al. Imaging diagnosis—spinal cord histiocytic sarcoma in a dog. *Vet Radiol Ultrasound*. 2015;56:E17–E20.
201. Mariani CL, Jennings MK, Olby NJ, et al. Histiocytic sarcoma with central nervous system involvement in dogs: 19 cases (2006–2012). *J Vet Intern Med*. 2015;29:607–613.
202. Tzipory L, Vernau KM, Sturges BK, et al. Antemortem diagnosis of localized central nervous system histiocytic sarcoma in 2 dogs. *J Vet Intern Med*. 2009;23:369–374.
203. Uchida K, Morozumi M, Yamaguchi R, et al. Diffuse leptomeningeal malignant histiocytosis in the brain and spinal cord of a Tibetan terrier. *Vet Pathol*. 2001;38: 219–222.
204. Bradshaw JM, Pearson GR, Gruffydd-Jones TJ. A retrospective study of 286 cases of neurological disorders of the cat. *J Comp Pathol*. 2004;131:112–120.
205. Lane SB, Kornegay JN, Duncan JR, et al. Feline spinal lymphosarcoma: a retrospective evaluation of 23 cats. *J Vet Intern Med*. 1994;8:99–104.
206. Palus V, Volk HA, Lamb CR, et al. MRI features of CNS lymphoma in dogs and cats. *Vet Radiol Ultrasound*. 2012;53:44–49.
207. Goncalves R, Platt SR, Llabres-Diaz FJ, et al. Clinical and magnetic resonance imaging findings in 92 cats with clinical signs of spinal cord disease. *J Feline Med Surg*. 2009;11:53–59.
208. Allett B, Hecht S. Magnetic resonance imaging findings in the spine of six dogs diagnosed with lymphoma. *Vet Radiol Ultrasound*. 2016;57:154–161.
209. Bush WW, Throop JL, McManus PM, et al. Intravascular lymphoma involving the central and peripheral nervous systems in a dog. *J Am Anim Hosp Assoc*. 2003;39:90–96.
210. Kornder J, Platt SR, Eagleson J, et al. Imaging diagnosis – vertebral polyostotic lymphoma in a geriatric dog. *Vet Radiol Ultrasound*. 2015.
211. Lamagna B, Lamagna F, Meomartino L, et al. Polyostotic lymphoma with vertebral involvement and spinal extradural compression in a dog. *J Am Anim Hosp Assoc*. 2006;42:71–76.
212. Long SN, Johnston PE, Anderson TJ. Primary T-cell lymphoma of the central nervous system in a dog. *J Am Vet Med Assoc*. 2001;218:719–722.
213. Ortega M, Castillo-Alcala F. Hind-limb paresis in a dog with paralumbar solitary T-cell lymphoma. *Can Vet J*. 2010;51:480–484.
214. Veraa S, Dijkman R, Meij BP, et al. Comparative imaging of spinal extradural lymphoma in a Bordeaux dog. *Can Vet J*. 2010;51:519–521.
215. Feeney DA, Sharkey LC, Steward SM, et al. Applicability of 3T body MRI in assessment of nonfocal bone marrow involvement of hematopoietic neoplasia in dogs. *J Vet Intern Med*. 2013;27:1165–1171.
216. Hammond LJ, Hecht S. Susceptibility artifacts on T2*-weighted magnetic resonance imaging of the canine and feline spine. *Vet Radiol Ultrasound*. 2015;56:398–406.
217. Mackenzie GB, Bellah JR, Threatte RM. What is your diagnosis? Hemangiosarcoma of the cervical vertebrae. *J Am Vet Med Assoc*. 2003;222:1075–1076.
218. Reed AL, Payne JT, Aronson E. What is your diagnosis? Primary hemangiosarcoma of the sixth lumbar vertebra in a dog. *J Am Vet Med Assoc*. 1994;204:1749–1750.
219. de la Fuente C, Pumarola M, Anor S. Imaging diagnosis—spinal epidural hemangiosarcoma in a dog. *Vet Radiol Ultrasound*. 2014;55:424–427.
220. Perez-Martinez C, Regueiro-Purrinos M, Fernandez-Martinez B, et al. Magnetic resonance imaging and immunohistochemistry of primary vertebral hemangiosarcoma in a dog and implications for diagnosis and therapy. *Can Vet J*. 2016;57:1247–1250.
221. Kutara K, Maeta N, Kanda T, et al. Magnetic resonance imaging findings of an intradural extramedullary hemangiosarcoma in a dog. *J Vet Med Sci*. 2019;81:1527–1532.
222. Okada M, Kitagawa M, Ito D, et al. Magnetic resonance imaging features and clinical signs associated with presumptive and confirmed progressive myelomalacia in dogs: 12 cases (1997–2008). *J Am Vet Med Assoc*. 2010;237:1160–1165.
223. Platt SR, McConnell JF, Bestbier M. Magnetic resonance imaging characteristics of ascending hemorrhagic myelomalacia in a dog. *Vet Radiol Ultrasound*. 2006;47:78–82.
224. Balducci F, Canal S, Contiero B, et al. Prevalence and risk factors for presumptive ascending/descending myelomalacia in dogs after thoracolumbar intervertebral disk herniation. *J Vet Intern Med*. 2017;31:498–504.
225. Gilmour LJ, Jeffery ND, Miles K, et al. Single-shot turbo spin echo pulse sequence findings in dogs with and without progressive myelomalacia. *Vet Radiol Ultrasound*. 2017;58:197–205.
226. Castel A, Olby NJ, Mariani CL, et al. Clinical characteristics of dogs with progressive myelomalacia following acute intervertebral disc extrusion. *J Vet Intern Med*. 2017;31:1782–1789.
227. Cordle KJ, Seiler GS, Barnes D, et al. MRI features can help to confirm a diagnosis of progressive myelomalacia, but may not be accurate in dogs lacking characteristic clinical signs at the time of imaging. *Vet Radiol Ultrasound*. 2023;64:283–293.
228. da Costa RC, De Decker S, Lewis MJ, et al. Diagnostic imaging in intervertebral disc disease. *Front Vet Sci*. 2020;7:588338.
229. Olby NJ, da Costa RC, Levine JM, et al. Prognostic factors in canine acute intervertebral disc disease. *Front Vet Sci*. 2020;7:596059.
230. Abramson CJ, Garosi L, Platt SR, et al. Magnetic resonance imaging appearance of suspected ischemic myelopathy in dogs. *Vet Radiol Ultrasound*. 2005;46:225–229.
231. De Risio L, Adams V, Dennis R, et al. Magnetic resonance imaging findings and clinical associations in 52 dogs with suspected ischemic myelopathy. *J Vet Intern Med*. 2007;21:1290–1298.
232. De Risio L, Adams V, Dennis R, et al. Association of clinical and magnetic resonance imaging findings with outcome in dogs suspected to have ischemic myelopathy: 50 cases (2000–2006). *J Am Vet Med Assoc*. 2008;233:129–135.
233. Rylander H, Eminaga S, Palus V, et al. Feline ischemic myelopathy and encephalopathy secondary to hyaline arteriopathy in five cats. *J Feline Med Surg*. 2014;16: 832–839.
234. Simpson KM, De Risio L, Theobald A, et al. Feline ischaemic myelopathy with a predilection for the cranial cervical spinal cord in older cats. *J Feline Med Surg*. 2014;16:1001–1006.
235. Theobald A, Volk HA, Dennis R, et al. Clinical outcome in 19 cats with clinical and magnetic resonance imaging diagnosis of ischaemic myelopathy (2000–2011). *J Feline Med Surg*. 2013;15:132–141.
236. MacKay AD, Rusbridge C, Sparkes AH, et al. MRI characteristics of suspected acute spinal cord infarction in two cats, and a review of the literature. *J Feline Med Surg*. 2005;7:101–107.
237. Mai W. Reduced field-of-view diffusion-weighted MRI can identify restricted diffusion in the spinal cord of dogs and cats with presumptive clinical and high-field MRI diagnosis of acute ischemic myelopathy. *Vet Radiol Ultrasound*. 2020;61:688–695.
238. Vernon JC, Durand A, Guevar J, et al. Vertebral venous system abnormalities identified with magnetic resonance imaging in sighthounds. *Vet Radiol Ultrasound*. 2017.

239. Gilbert S, Brooks-Brownlie H, Cardy T. MRI characteristics of ventral vertebral venous plexus occlusion due to lymphoma in a large breed dog. *Vet Radiol Ultrasound*. 2022.
240. Rhue KE, Taylor AR, Cole RC, et al. Bilateral vertebral venous sinus thrombosis causing cervical spinal cord compression in a dog. *Front Vet Sci*. 2017;4:8.
241. Barker A, Williams JM, Chen A, et al. Suspected primary hematomyelia in 3 dogs. *Can Vet J*. 2015;56:278–284.
242. Wang-Leandro A, Huenerfauth EI, Heissl K, et al. MRI findings of early-stage hyperacute hemorrhage causing extramedullary compression of the cervical spinal cord in a dog with suspected steroid-responsive meningitis-arteritis. *Front Vet Sci*. 2017;4:161.
243. Hague DW, Joslyn S, Bush WW, et al. Clinical, magnetic resonance imaging, and histopathologic findings in 6 dogs with surgically resected extraparenchymal spinal cord hematomas. *J Vet Intern Med*. 2015;29:225–230.
244. Kinns J, Mai W, Seiler G, et al. Radiographic sensitivity and negative predictive value for acute canine spinal trauma. *Vet Radiol Ultrasound*. 2006;47:563–570.
245. Johnson P, Beltran E, Dennis R, et al. Magnetic resonance imaging characteristics of suspected vertebral instability associated with fracture or subluxation in eleven dogs. *Vet Radiol Ultrasound*. 2012;53:552–559.
246. Gallastegui A, Davies E, Zwingenberger AL, et al. MRI has limited agreement with CT in the evaluation of vertebral fractures of the canine trauma patient. *Vet Radiol Ultrasound*. 2019;60:533–542.
247. Shamir MH, Tavor N, Aizenberg T. Radiographic findings during recovery from discospondylitis. *Vet Radiol Ultrasound*. 2001;42:496–503.
248. Carrera I, Sullivan M, McConnell F, et al. Magnetic resonance imaging features of discospondylitis in dogs. *Vet Radiol Ultrasound*. 2011;52:125–131.
249. Cherubini GB, Cappello R, Lu D, et al. MRI findings in a dog with discospondylitis caused by *Bordetella* species. *J Small Anim Pract*. 2004;45:417–420.
250. Gendron K, Doherr MG, Gavin P, et al. Magnetic resonance imaging characterization of vertebral endplate changes in the dog. *Vet Radiol Ultrasound*. 2012;53:50–56.
251. Gonzalo-Orden JM, Altonaga JR, Orden MA, et al. Magnetic resonance, computed tomographic and radiologic findings in a dog with discospondylitis. *Vet Radiol Ultrasound*. 2000;41:142–144.
252. Harris JM, Chen AV, Tucker RL, et al. Clinical features and magnetic resonance imaging characteristics of diskospondylitis in dogs: 23 cases (1997–2010). *J Am Vet Med Assoc*. 2013;242:359–365.
253. Kraft SL, Mussman JM, Smith T, et al. Magnetic resonance imaging of presumptive lumbosacral discospondylitis in a dog. *Vet Radiol Ultrasound*. 1998;39:9–13.
254. Lipscomb VJ, Muir P. Magnetic resonance imaging of a dog with sciatic nerve root signature. *Vet Rec*. 2000;147:393–394.
255. Plessas IN, Jull P, Volk HA. A case of canine discospondylitis and epidural empyema due to *Salmonella* species. *Can Vet J*. 2013;54:595–598.
256. Gomes SA, Targett M, Lowrie M. Computed tomography features of discospondylitis in dogs. *J Vet Intern Med*. 2022;36:2123–2131.
257. Kirberger RM. Early diagnostic imaging findings in juvenile dogs with presumed diskospondylitis: 10 cases (2008–2014). *J Am Vet Med Assoc*. 2016;249:539–546.
258. Gomes SA, Behr S, Garosi LS, et al. Imaging features of discospondylitis in cats. *J Feline Med Surg*. 2020;22:631–640.
259. Long C, Burgers E, Copple C, et al. *Brucella canis* discospondylitis in 33 dogs. *Front Vet Sci*. 2022;9:1043610.
260. De Stefani A, Garosi LS, McConnell FJ, et al. Magnetic resonance imaging features of spinal epidural empyema in five dogs. *Vet Radiol Ultrasound*. 2008;49:135–140.
261. Granger N, Hidalgo A, Leperlier D, et al. Successful treatment of cervical spinal epidural empyema secondary to grass awn migration in a cat. *J Feline Med Surg*. 2007;9:340–345.
262. Nykamp SG, Steffey MA, Scrivani PV, et al. Computed tomographic appearance of epidural empyema in a dog. *Can Vet J*. 2003;44:729–731.
263. Whitty CC, Milner HR, Oram B. Use of magnetic resonance imaging in the diagnosis of spinal empyema caused by a migrating grass awn in a dog. *N Z Vet J*. 2013;61:115–118.
264. Alves L, Gorgas D, Vandevelde M, et al. Segmental meningomyelitis in 2 cats caused by *Toxoplasma gondii*. *J Vet Intern Med*. 2011;25:148–152.
265. Cherubini GB, Platt SR, Anderson TJ, et al. Characteristics of magnetic resonance images of granulomatous meningoencephalomyelitis in 11 dogs. *Vet Rec*. 2006;159:110–115.
266. Griffin JF, Levine JM, Levine GJ, et al. Meningomyelitis in dogs: a retrospective review of 28 cases (1999 to 2007). *J Small Anim Pract*. 2008;49:509–517.
267. Parry AT, Penning VA, Smith KC, et al. Imaging diagnosis—necrotizing meningomyelitis and polyarthritis. *Vet Radiol Ultrasound*. 2009;50:412–415.
268. Radaelli ST, Platt SR. Bacterial meningoencephalomyelitis in dogs: a retrospective study of 23 cases (1990–1999). *J Vet Intern Med*. 2002;16:159–163.
269. Snook ER, Baker DG, Bauer RW. Verminous myelitis in a pit bull puppy. *J Vet Diagn Invest*. 2009;21:400–402.
270. Tipold A. Diagnosis of inflammatory and infectious diseases of the central nervous system in dogs: a retrospective study. *J Vet Intern Med*. 1995;9:304–314.
271. Tipold A, Schatzberg SJ. An update on steroid responsive meningitis-arteritis. *J Small Anim Pract*. 2010;51:150–154.
272. Tipold A, Stein VM. Inflammatory diseases of the spine in small animals. *Vet Clin North Am Small Anim Pract*. 2010;40:871–879.
273. Remelli C, Martello A, Valentini A, et al. Magnetic resonance imaging highlights the meningeal involvement in steroid responsive meningitis-arteritis and suggests the inflammation of the surrounding tissues (70 cases). *Front Vet Sci*. 2022;9:957278.
274. Fingeroth JM, Johnson GC, Burt JK, et al. Neuroradiographic diagnosis and surgical repair of tethered cord syndrome in an English bulldog with spina bifida and myeloschisis. *J Am Vet Med Assoc*. 1989;194:1300–1302.
275. Bertram S, Ter Haar G, De Decker S. Caudal articular process dysplasia of thoracic vertebrae in neurologically normal French bulldogs, English bulldogs, and pugs: prevalence and characteristics. *Vet Radiol Ultrasound*. 2018;59:396–404.
276. Longo S, Gomes SA, Lowrie M. Previously unreported magnetic resonance findings of subarachnoid fibrosis leading to constrictive myelopathy in a pug. *J Small Anim Pract*. 2019;60:324.
277. Lourinho F, Holdsworth A, McConnell JF, et al. Clinical features and MRI characteristics of presumptive constrictive myelopathy in 27 pugs. *Vet Radiol Ultrasound*. 2020;61:545–554.
278. Nishida H, Nakata K, Maeda S, et al. Prevalence and pattern of thoracolumbar caudal articular process anomalies and intervertebral disk herniations in pugs. *J Vet Med Sci*. 2019;81:906–910.
279. Rohdin C, Ljungvall I, Haggstrom J, et al. Thoracolumbar meningeal fibrosis in pugs. *J Vet Intern Med*. 2020;34:797–807.

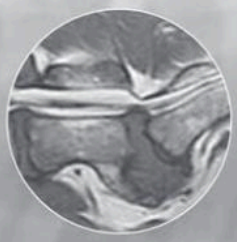
280. Rohdin C, Haggstrom J, Ljungvall I, et al. Presence of thoracic and lumbar vertebral malformations in pugs with and without chronic neurological deficits. *Vet J*. 2018;241:24–30.
281. Carruthers H, Rusbridge C, Dube MP, et al. Association between cervical and intracranial dimensions and syringomyelia in the cavalier King Charles spaniel. *J Small Anim Pract*. 2009;50:394–398.
282. Cerda-Gonzalez S, Bibi KF, Gifford AT, et al. Magnetic resonance imaging-based measures of atlas position: relationship to canine atlantooccipital overlapping, syringomyelia and clinical signs. *Vet J*. 2016.
283. Cerda-Gonzalez S, Olby NJ, Griffith EH. Dorsal compressive atlantoaxial bands and the craniocervical junction syndrome: association with clinical signs and syringomyelia in mature cavalier King Charles spaniels. *J Vet Intern Med*. 2015;29:887–892.
284. Couturier J, Rault D, Cauzinille L. Chiari-like malformation and syringomyelia in normal cavalier King Charles spaniels: a multiple diagnostic imaging approach. *J Small Anim Pract*. 2008;49:438–443.
285. da Costa RC, Parent JM, Poma R, et al. Cervical syringohydromyelia secondary to a brainstem tumor in a dog. *J Am Vet Med Assoc*. 2004;225:1061–1064, 1048.
286. Driver CJ, De Risio L, Hamilton S, et al. Changes over time in craniocerebral morphology and syringomyelia in cavalier King Charles spaniels with Chiari-like malformation. *BMC Vet Res*. 2012;8:215.
287. Driver CJ, Rusbridge C, Cross HR, et al. Relationship of brain parenchyma within the caudal cranial fossa and ventricle size to syringomyelia in cavalier King Charles spaniels. *J Small Anim Pract*. 2010;51:382–386.
288. Driver CJ, Rusbridge C, McGonnell IM, et al. Morphometric assessment of cranial volumes in age-matched Cavalier King Charles spaniels with and without syringomyelia. *Vet Rec*. 2010;167:978–979.
289. Driver CJ, Volk HA, Rusbridge C, et al. An update on the pathogenesis of syringomyelia secondary to Chiari-like malformations in dogs. *Vet J*. 2013;198:551–559.
290. Driver CJ, Watts V, Bunck AC, et al. Assessment of cerebellar pulsation in dogs with and without Chiari-like malformation and syringomyelia using cardiac-gated cine magnetic resonance imaging. *Vet J*. 2013;198:88–91.
291. Fenn J, Schmidt MJ, Simpson H, et al. Venous sinus volume in the caudal cranial fossa in Cavalier King Charles spaniels with syringomyelia. *Vet J*. 2013;197:896–897.
292. Freeman AC, Platt SR, Kent M, et al. Chiari-like malformation and syringomyelia in American Brussels Griffon dogs. *J Vet Intern Med*. 2014;28:1551–1559.
293. Greitz D. Unraveling the riddle of syringomyelia. *Neurosurg Rev*. 2006;29:251–263. discussion 264.
294. Hu HZ, Rusbridge C, Constantino-Casas F, et al. Histopathological investigation of syringomyelia in the cavalier king Charles spaniel. *J Comp Pathol*. 2012;146:192–201.
295. Jung DI, Park C, Kang BT, et al. Acquired cervical syringomyelia secondary to a brainstem meningioma in a Maltese dog. *J Vet Med Sci*. 2006;68:1235–1238.
296. Kirberger RM, Jacobson LS, Davies JV, et al. Hydromyelia in the dog. *Vet Radiol Ultrasound*. 1997;38:30–38.
297. Kromhout K, van Bree H, Broeckx BJ, et al. Low-field magnetic resonance imaging and multislice computed tomography for the detection of cervical syringomyelia in dogs. *J Vet Intern Med*. 2015;29:1354–1359.
298. Loderstedt S, Benigni L, Chandler K, et al. Distribution of syringomyelia along the entire spinal cord in clinically affected Cavalier King Charles Spaniels. *Vet J*. 2011;190:359–363.
299. MacKillop E, Schatzberg SJ, De Lahunta A. Intracranial epidermoid cyst and syringohydromyelia in a dog. *Vet Radiol Ultrasound*. 2006;47:339–344.
300. Plessas IN, Rusbridge C, Driver CJ, et al. Long-term outcome of Cavalier King Charles spaniel dogs with clinical signs associated with Chiari-like malformation and syringomyelia. *Vet Rec*. 2012;171:501.
301. Rusbridge C. Chiari-like malformation with syringomyelia in the Cavalier King Charles spaniel: long-term outcome after surgical management. *Vet Surg*. 2007;36:396–405.
302. Rusbridge C, Carruthers H, Dube MP, et al. Syringomyelia in cavalier King Charles spaniels: the relationship between syrinx dimensions and pain. *J Small Anim Pract*. 2007;48:432–436.
303. Rusbridge C, Greitz D, Iskandar BJ. Syringomyelia: current concepts in pathogenesis, diagnosis, and treatment. *J Vet Intern Med*. 2006;20:469–479.
304. Rusbridge C, Knowler SP. Coexistence of occipital dysplasia and occipital hypoplasia/syringomyelia in the cavalier King Charles spaniel. *J Small Anim Pract*. 2006;47:603–606.
305. Schmidt MJ, Kramer M, Ondreka N. Comparison of the relative occipital bone volume between Cavalier King Charles spaniels with and without syringohydromyelia and French bulldogs. *Vet Radiol Ultrasound*. 2012;53:540–544.
306. Schmidt MJ, Ondreka N, Sauerbrey M, et al. Volume reduction of the jugular foramina in cavalier king Charles spaniels with syringomyelia. *BMC Vet Res*. 2012;8:158.
307. Scrivani PV, Thompson MS, Winegardner KR, et al. Association between frontal-sinus size and syringohydromyelia in small-breed dogs. *Am J Vet Res*. 2007;68:610–613.
308. Shaw TA, McGonnell IM, Driver CJ, et al. Increase in cerebellar volume in Cavalier King Charles Spaniels with Chiari-like malformation and its role in the development of syringomyelia. *PLoS One*. 2012;7:e33660.
309. Wolfe KC, Poma R. Syringomyelia in the Cavalier King Charles Spaniel (CKCS) dog. *Can Vet J*. 2010;51:95–102.
310. Rusbridge C, Knowler SP, Pieterse L, et al. Chiari-like malformation in the Griffon Bruxellois. *J Small Anim Pract*. 2009;50:386–393.
311. Rusbridge C, Stringer F, Knowler SP. Clinical application of diagnostic imaging of Chiari-like malformation and syringomyelia. *Front Vet Sci*. 2018;5:280.
312. Schmidt MJ, Roth J, Ondreka N, et al. A potential role for substance P and interleukin-6 in the cerebrospinal fluid of Cavalier King Charles Spaniels with neuropathic pain. *J Vet Intern Med*. 2013;27:530–535.

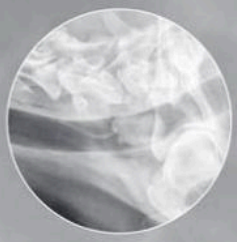
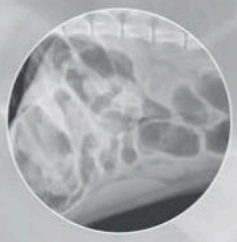
ELECTRONIC RESOURCES

Additional information related to the content in Chapter 15 can be found online at eBooks.Health.Elsevier.com.

- Chapter Quiz

This page intentionally left blank

SECTION III

The Appendicular Skeleton: Canine, Feline, and Equine

16 **Radiographic Anatomy of the Appendicular Skeleton**
Kathy A. Spaulding • Andra K. Voges

17 **Principles of Radiographic Interpretation of the Appendicular Skeleton and Radiographic Features of Bone Tumors**
Donald E. Thrall

18 **Orthopedic Diseases of Young and Growing Dogs and Cats**
Kathryn L. Phillips

19 **Fracture Healing and Complications**
Gabriela S. Seiler

20 **Radiographic Signs of Joint Disease in Dogs and Cats**
Graeme Allan • Sarah Davies

21 **The Equine Stifle**
Valeria Busoni • Fabrice Audigié

22 **Equine Tarsus**
Jody E. Lawver

23 **Equine Carpus**
Lindsey J. Gilmour

24 **Equine Metacarpus and Metatarsus**
Erin G. Porter

25 **Equine Fetlock Joint**
Kathryn W. Bills

26 **Equine Pastern**
Elizabeth Biscoe • Dana A. Neelis

27 **Equine Foot**
Myra F. Barrett • Elizabeth Acutt • Federica Morandi

CHAPTER 16

Radiographic Anatomy of the Appendicular Skeleton

Kathy A. Spaulding and Andra K. Voges

To use the roentgen sign method of recognizing abnormal radiographic findings effectively, an understanding of normal radiographic anatomy for the specific area of interest is necessary. The purpose of this chapter is to provide a limited reference for the radiographic anatomy of the appendicular skeleton. Refer to comprehensive textbooks on gross and radiographic anatomy for more detailed information.[1–7]

The radiographic nomenclature used in this chapter was approved by the American College of Veterinary Radiology in 1983.[8] Some equine images in this chapter (Figs. 16.30–16.49 and 16.54–16.57) have been taken from previous publications and are reproduced here with permission of the journals and authors.[9-11]

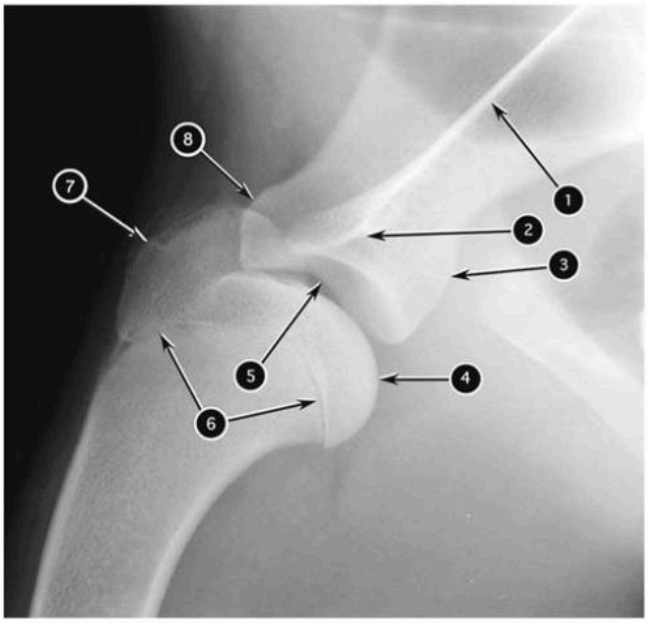


Fig. 16.1 Mediolateral (lateral) radiograph of canine shoulder joint.
1. Spine of scapula
2. Acromion of scapula
3. Infraglenoid tubercle of scapula
4. Head of humerus
5. Glenoid cavity of scapula
6. Proximal physis of humerus
7. Greater tubercle of humerus
8. Supraglenoid tubercle of scapula

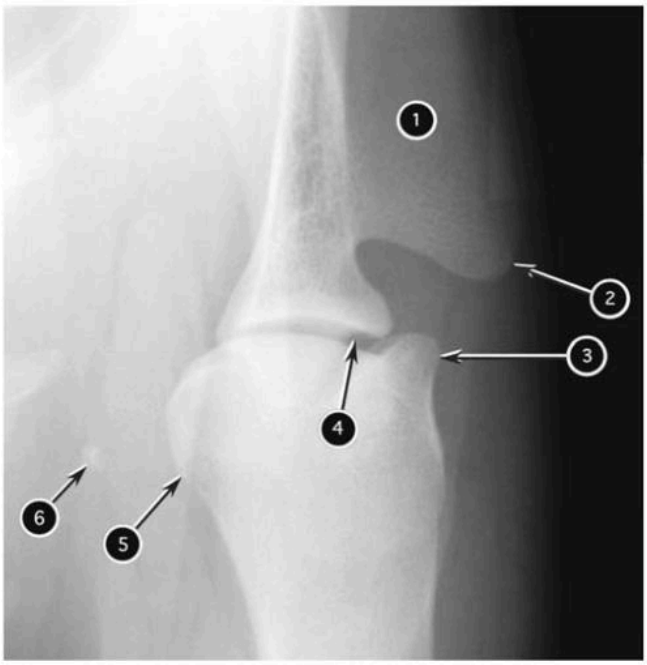


Fig. 16.2 Caudocranial radiograph of canine shoulder joint.
1. Spine of scapula
2. Acromion of scapula
3. Greater tubercle of humerus
4. Humeral (scapulohumeral) joint
5. Lesser tubercle of humerus
6. Clavicle

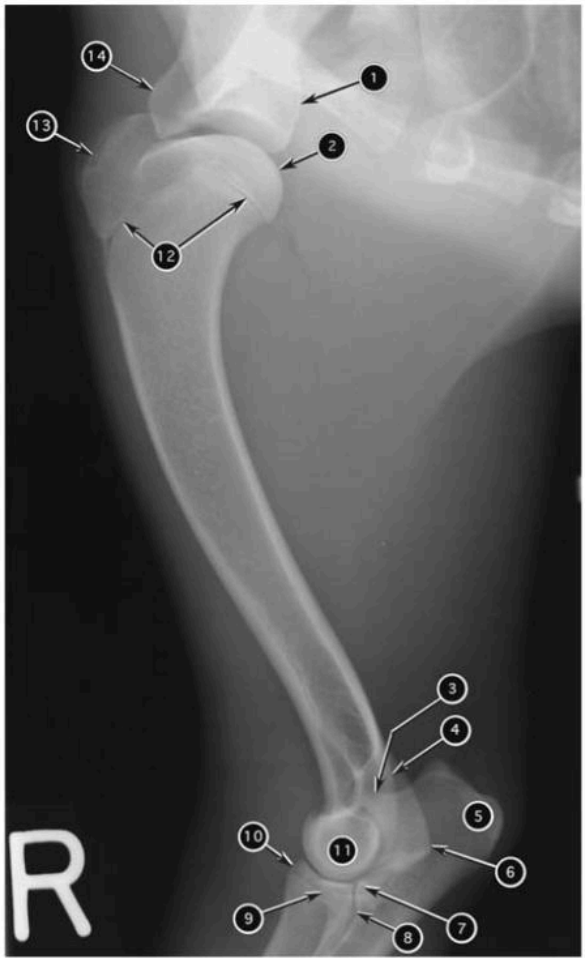


Fig. 16.3 Mediolateral (lateral) radiograph of canine humerus.
1. Infraglenoid tubercle of scapula
2. Head of humerus
3. Anconeal process of ulna
4. Lateral epicondyle of humerus
5. Tuber olecrani
6. Medial epicondyle of humerus
7. Lateral coronoid process of ulna
8. Proximal radioulnar joint
9. Medial coronoid process of ulna
10. Head of radius
11. Condyle of humerus
12. Proximal physis of humerus
13. Greater tubercle of humerus
14. Supraglenoid tubercle of scapula

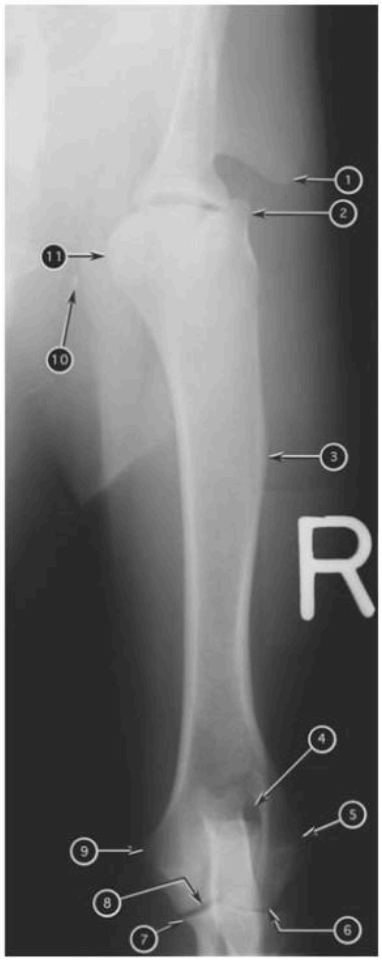


Fig. 16.4 Caudocranial radiograph of canine humerus.
1. Acromion of scapula
2. Greater tubercle of humerus
3. Deltoid tuberosity
4. Supratrochlear foramen of humerus
5. Lateral epicondyle of humerus
6. Capitulum of humeral condyle
7. Medial coronoid process of ulna
8. Trochlea of humeral condyle
9. Medial epicondyle of humerus
10. Clavicle
11. Lesser tubercle of humerus

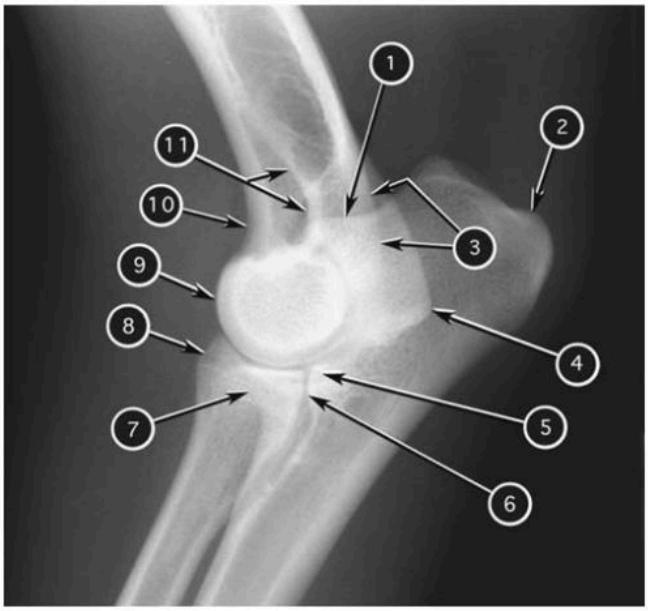


Fig. 16.5 Mediolateral (lateral) radiograph of canine elbow joint.
1. Anconeal process of ulna
2. Tuber olecrani of ulna
3. Caudal border of lateral epicondyle of humerus
4. Caudal border of medial epicondyle of humerus
5. Lateral coronoid process of ulna
6. Proximal radioulnar joint
7. Medial coronoid process of ulna
8. Head of radius
9. Condyle of humerus
10. Cranial border of medial epicondyle of humerus
11. Cranial border of lateral epicondyle of humerus

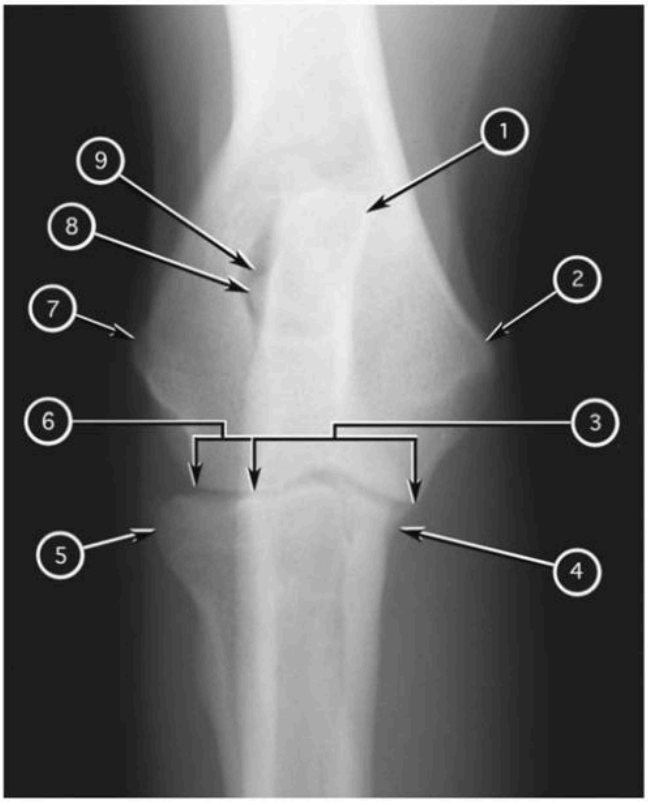


Fig. 16.7 Craniocaudal radiograph of canine elbow joint.
1. Tuber olecrani of ulna
2. Medial epicondyle of humerus
3. Trochlea of humeral condyle
4. Medial coronoid process of ulna
5. Head of radius
6. Capitulum of humeral condyle
7. Lateral epicondyle of humerus
8. Anconeal process of ulna
9. Supratrochlear foramen of humerus

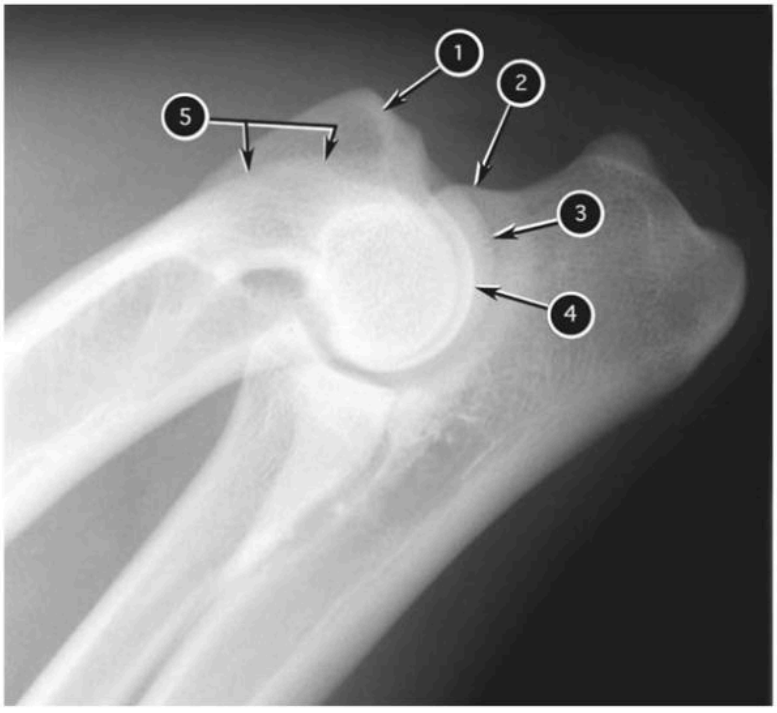


Fig. 16.6 Flexed mediolateral (lateral) radiograph of canine elbow joint.
1. Medial epicondyle of humerus
2. Anconeal process of ulna
3. Medial part of humeral condyle
4. Lateral part of humeral condyle
5. Caudal border of lateral epicondyle of humerus

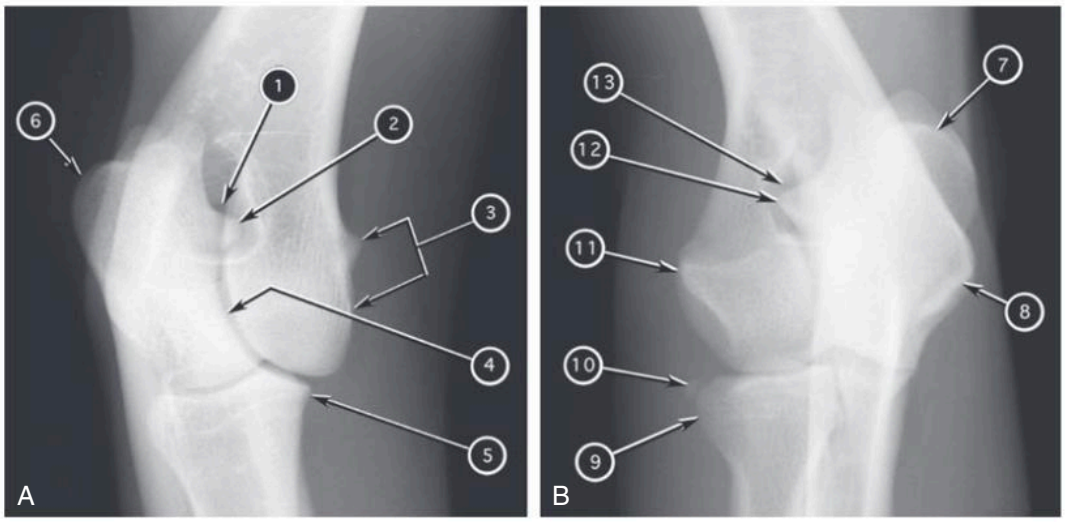


Fig. 16.8 Craniolateral-caudomedial oblique **(A)** and craniomedial-caudolateral oblique **(B)** radiographs of canine elbow joint.

1. Supratrochlear foramen of humerus
2. Anconeal process of ulna
3. Medial epicondyle of humerus
4. Trochlear notch of ulna
5. Medial coronoid process of ulna
6. Tuber olecrani of ulna
7. Tuber olecrani of ulna
8. Medial epicondyle of humerus
9. Head of radius
10. Sesamoid bone of supinator muscle (inconstant)
11. Lateral epicondyle of humerus
12. Anconeal process of ulna
13. Supratrochlear foramen of humerus



Fig. 16.9 Mediolateral (lateral) radiograph of canine antebrachium.
1. Tuber olecrani of ulna
2. Lateral epicondyle of humerus
3. Medial epicondyle of humerus
4. Proximal radioulnar joint
5. Body of ulna
6. Distal metaphysis of ulna
7. Distal epiphysis of ulna
8. Accessory carpal bone
9. Carpal pad
10. Antebrachiocarpal joint
11. Distal epiphysis of radius
12. Distal physis of radius
13. Distal metaphysis of radius
14. Body of radius
15. Neck of radius
16. Head of radius
17. Elbow (cubital) joint
18. Condyle of humerus



Fig. 16.10 Craniocaudal radiograph of canine antebrachium.
1. Medial epicondyle of humerus
2. Medial coronoid process of ulna
3. Body of radius
4. Distal metaphysis of radius
5. Distal epiphysis of radius
6. Intermedioradial carpal bone
7. Sesamoid bone of abductor pollicis longus
8. Ulnar carpal bone
9. Distal epiphysis (styloid process) of ulna
10. Distal metaphysis of ulna
11. Body of ulna
12. Head of radius
13. Elbow (cubital) joint
14. Lateral epicondyle of humerus

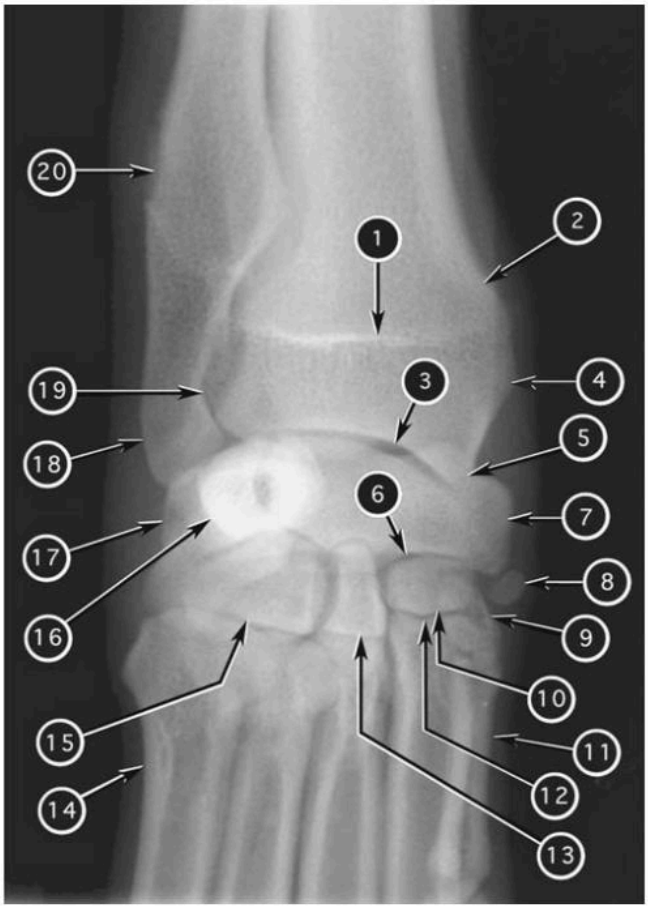


Fig. 16.11 Dorsopalmar radiograph of canine carpus.
1. Distal physis of radius
2. Distal metaphysis of radius
3. Antebrachiocarpal joint
4. Distal epiphysis of radius
5. Styloid process (medial) of radius
6. Middle carpal joint
7. Intermedioradial carpal bone
8. Sesamoid bone of abductor pollicis longus
9. First carpal bone
10. Second carpal bone
11. First metacarpal bone
12. Carpometacarpal joint
13. Third carpal bone
14. Fifth metacarpal bone
15. Fourth carpal bone
16. Accessory carpal bone
17. Ulnar carpal bone
18. Distal epiphysis (styloid process) of ulna
19. Distal radioulnar joint
20. Distal metaphysis of ulna



Fig. 16.12 Mediolateral (lateral) radiograph of canine carpus.
1. Distal epiphysis (styloid process) of ulna
2. Accessory carpal bone
3. Ulnar carpal bone
4. Carpal pad
5. Proximal sesamoid bone of first digit
6. Proximal phalanx of first digit
7. Carpometacarpal joint
8. Middle carpal joint
9. Antebrachiocarpal joint
10. Distal epiphysis of radius



Fig. 16.13 Dorsolateral-palmaromedial oblique radiograph of canine manus.
1. Distal radioulnar joint
2. Accessory carpal bone
3. Ulnar carpal bone
4. Base of metacarpal bone 5
5. First carpal bone
6. Second carpal bone
7. Middle carpal joint
8. Intermedioradial carpal bone
9. Antebrachiocarpal joint

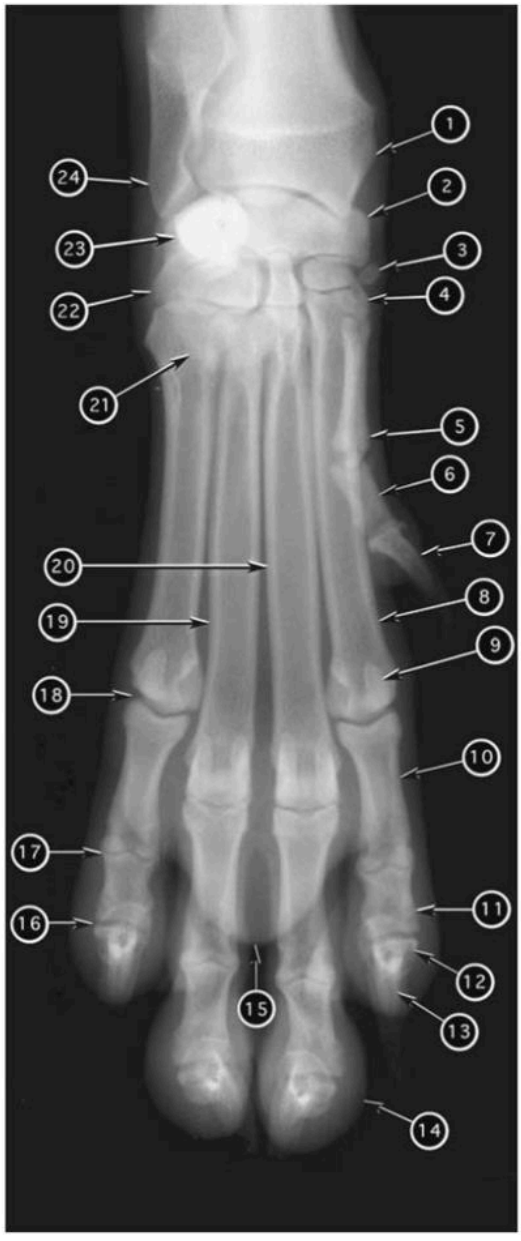


Fig. 16.14 Dorsopalmar radiograph of canine manus.
1. Distal epiphysis of radius
2. Intermedioradial carpal bone
3. Sesamoid bone of abductor pollicis longus
4. First carpal bone
5. Metacarpal bone 1
6. Proximal phalanx of digit 1
7. Distal phalanx of digit 1
8. Second metacarpal bone
9. Abaxial proximal sesamoid bone of digit 2
10. Proximal phalanx of digit 2
11. Middle phalanx of digit 2
12. Unguicular (ungual) crest of distal phalanx of digit 2
13. Unguicular (ungual) process of distal phalanx of digit 2
14. Digital pad of digit 3
15. Metacarpal pad
16. Distal interphalangeal joint of digit 5
17. Proximal interphalangeal joint of digit 5
18. Metacarpophalangeal joint of digit 5
19. Fourth metacarpal bone
20. Third metacarpal bone
21. Carpal pad
22. Ulnar carpal bone
23. Accessory carpal bone
24. Distal epiphysis (styloid process) of ulna



Fig. 16.15 Mediolateral (lateral) radiograph of canine manus.
1. Distal epiphysis (styloid process) of ulna
2. Accessory carpal bone
3. Ulnar carpal bone
4. Carpal pad
5. Proximal sesamoid bone of digit 1
6. Distal phalanx of digit 1
7. Dorsal sesamoid bone
8. Antebrachiocarpal joint
9. Distal epiphysis of radius



Fig. 16.16 Palmaromedial-dorsolateral oblique radiograph of canine manus.
1. Distal epiphysis (styloid process) of ulna
2. Accessory carpal bone
3. Ulnar carpal bone
4. Body of metacarpal bone 5
5. Abaxial proximal sesamoid bone of digit 5
6. Middle phalanx of digit 5
7. Metacarpal pad
8. Digital pad of digit 4
9. Flexor tubercle of distal phalanx of digit 4
10. Unguicular (ungual) crest of distal phalanx of digit 4
11. Unguicular (ungual) process of distal phalanx digit 3
12. Proximal phalanx of digit 2
13. Dorsal sesamoid bone of digit 2
14. Middle carpal joint

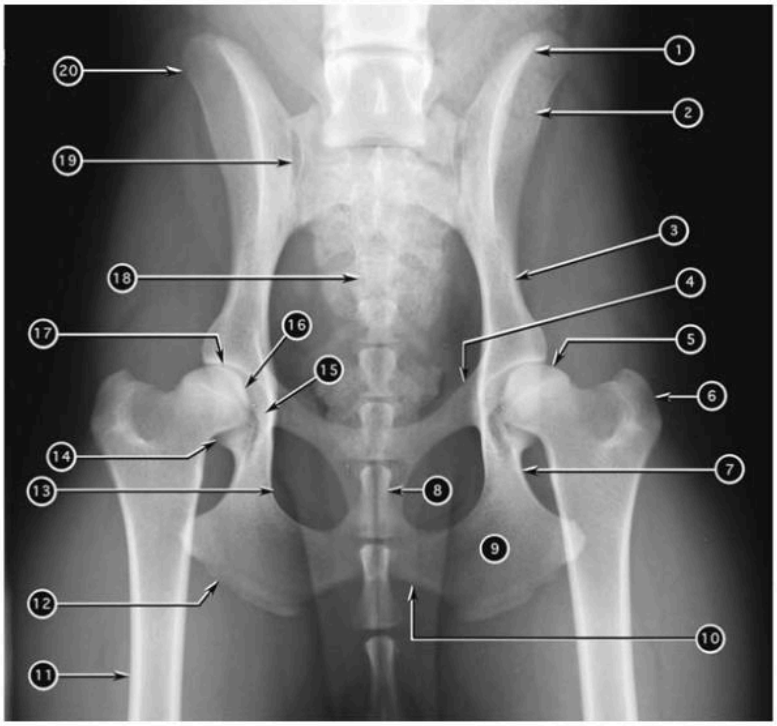


Fig. 16.17 Ventrodorsal radiographs of canine pelvis.
1. Crest of left ilium
2. Wing of left ilium
3. Body of left ilium
4. Body of left pubis
5. Head of left femur
6. Greater trochanter of left femur
7. Body of left ischium
8. Caudal vertebra 4
9. Table of left ischium
10. Ischial arch
11. Body of right femur
12. Right tuber ischiadicum (ischiatic tuberosity)
13. Right obturator foramen
14. Caudodorsal aspect of lunate surface of acetabulum
15. Acetabular fossa
16. Fovea capitis of right femur
17. Cranioventral aspect of lunate surface of acetabulum
18. Sacral vertebra 3
19. Right sacroiliac joint
20. Right tuber coxae (cranioventral iliac spine)

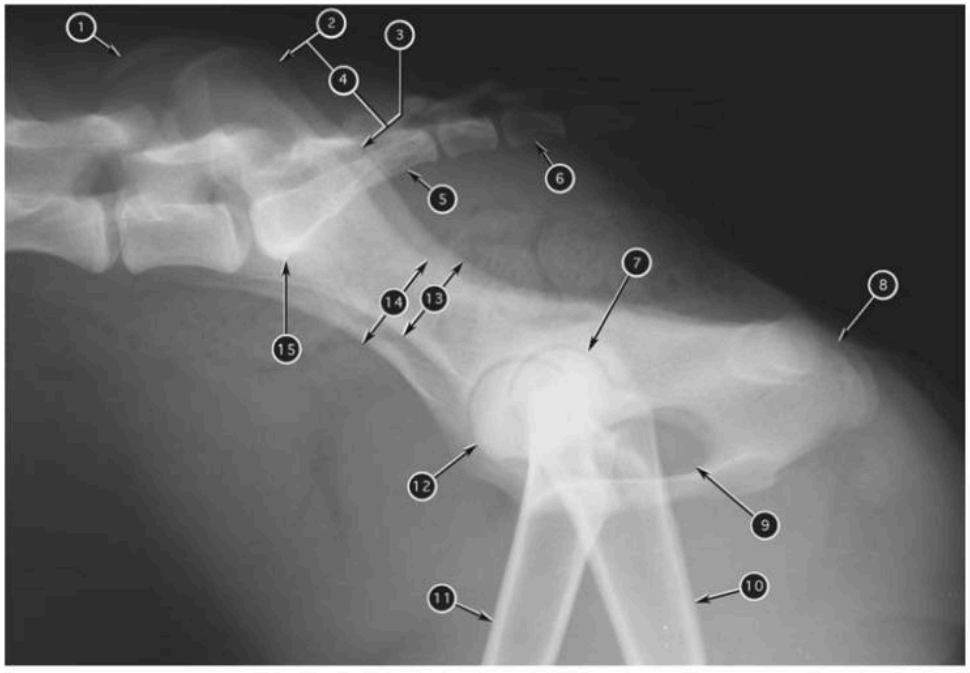


Fig. 16.18 Right-left lateral (left lateral) radiograph of canine pelvis.
1. Crest of right ilium (more magnified)
2. Craniodorsal iliac spine
3. Caudodorsal iliac spine
4. Left tuber sacrale (less magnified)
5. Sacral vertebra 3
6. Caudal vertebra 2
7. Left coxal joint (less magnified)
8. Superimposed right and left tubera ischiadica (ischiatic tuberosities)
9. Superimposed right and left obturator foramina
10. Body (diaphysis) of right femur (more magnified and less distinct margins)
11. Body (diaphysis) of left femur (less magnified)
12. Head of right femur (more magnified)
13. Body of left ilium (less magnified)
14. Body of right ilium (more magnified)
15. Promontory of sacrum

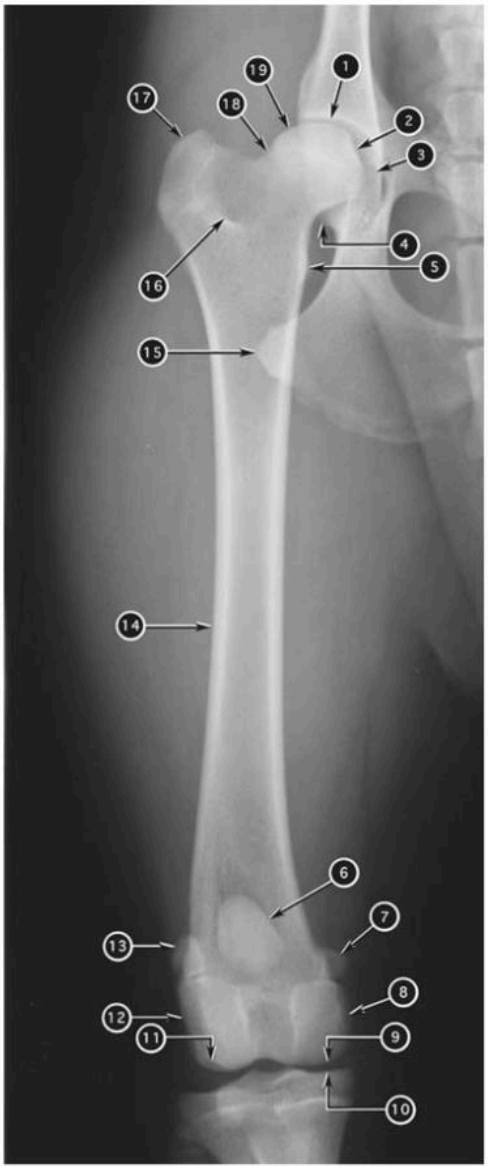


Fig. 16.19 Craniocaudal radiograph of canine femur.
1. Cranioventral aspect of lunate surface of acetabulum
2. Fovea capitis of femur
3. Acetabular fossa
4. Caudodorsal aspect of lunate surface of acetabulum
5. Lesser trochanter of femur
6. Patella
7. Medial sesamoid of gastrocnemius muscle
8. Medial epicondyle of femur
9. Medial condyle of femur
10. Medial condyle of tibia
11. Extensor fossa of femur
12. Lateral epicondyle of femur
13. Lateral sesamoid of gastrocnemius muscle
14. Body of femur
15. Tuber ischiadicum (ischiatic tuberosity)
16. Trochanteric fossa of femur
17. Greater trochanter of femur
18. Neck of femur
19. Head of femur

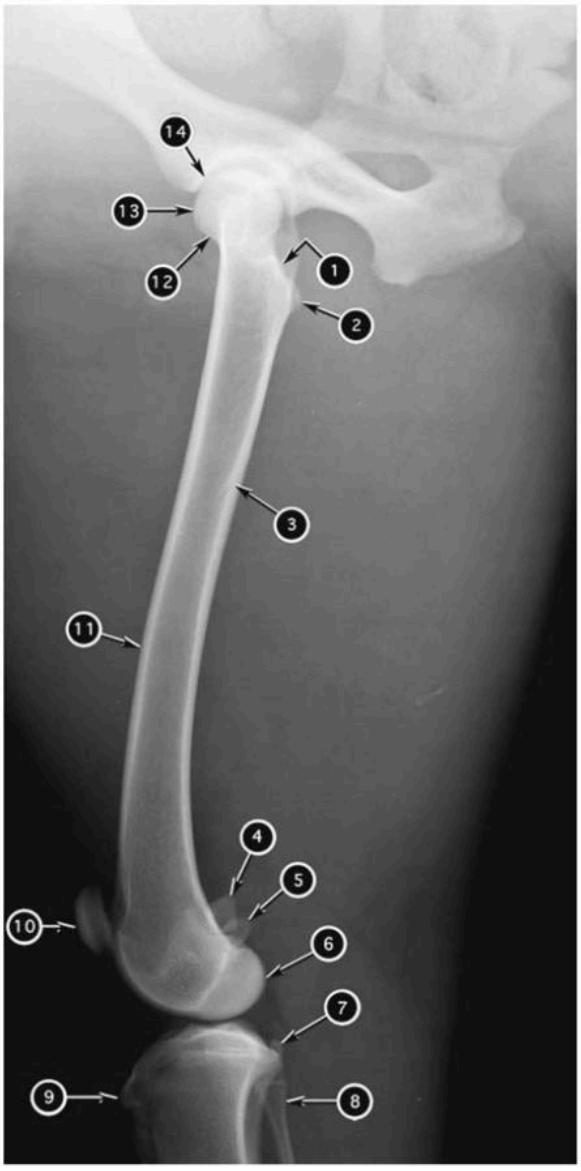


Fig. 16.20 Mediolateral (lateral) radiograph of canine femur.
1. Trochanteric fossa of femur
2. Lesser trochanter of femur
3. Nutrient canal of femur
4. Lateral sesamoid of gastrocnemius muscle
5. Medial sesamoid of gastrocnemius muscle
6. Medial and lateral condyles of femur
7. Sesamoid bone of popliteus muscle
8. Fibula
9. Tibial tuberosity
10. Patella
11. Body of femur
12. Neck of femur
13. Head of femur
14. Craniodorsal aspect of lunate surface of acetabulum

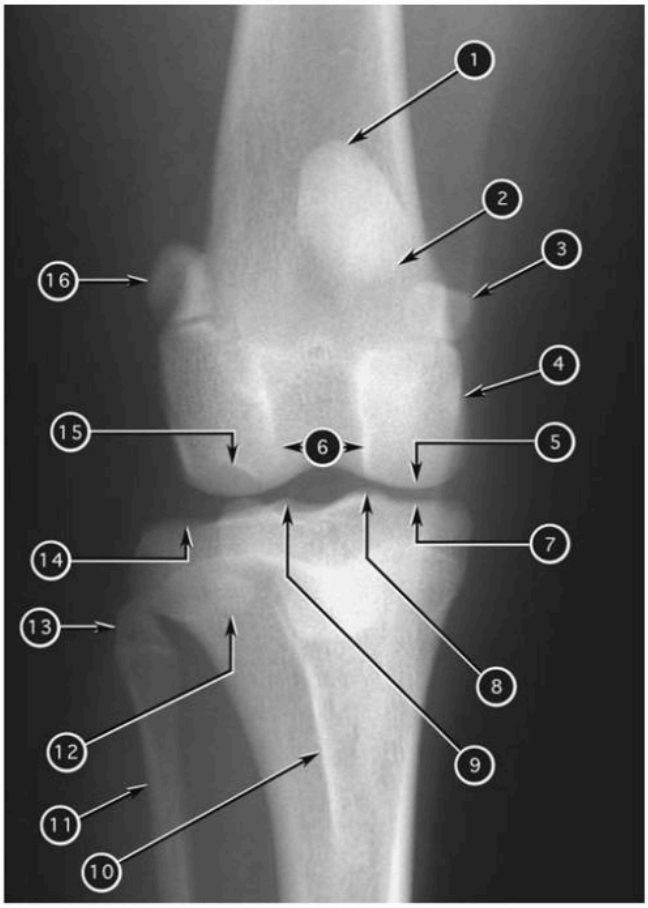


Fig. 16.21 Craniocaudal radiograph of canine stifle joint.
1. Base of patella
2. Apex of patella
3. Medial sesamoid of gastrocnemius muscle
4. Medial epicondyle of femur
5. Medial condyle of femur
6. Intercondylar fossa of femur
7. Medial condyle of tibia
8. Medial tubercle of intercondylar eminence
9. Lateral tubercle of intercondylar eminence
10. Cranial border of tibia
11. Body of fibula
12. Sesamoid bone of popliteus muscle
13. Head of fibula
14. Lateral condyle of tibia
15. Extensor fossa of femur
16. Lateral sesamoid of gastrocnemius

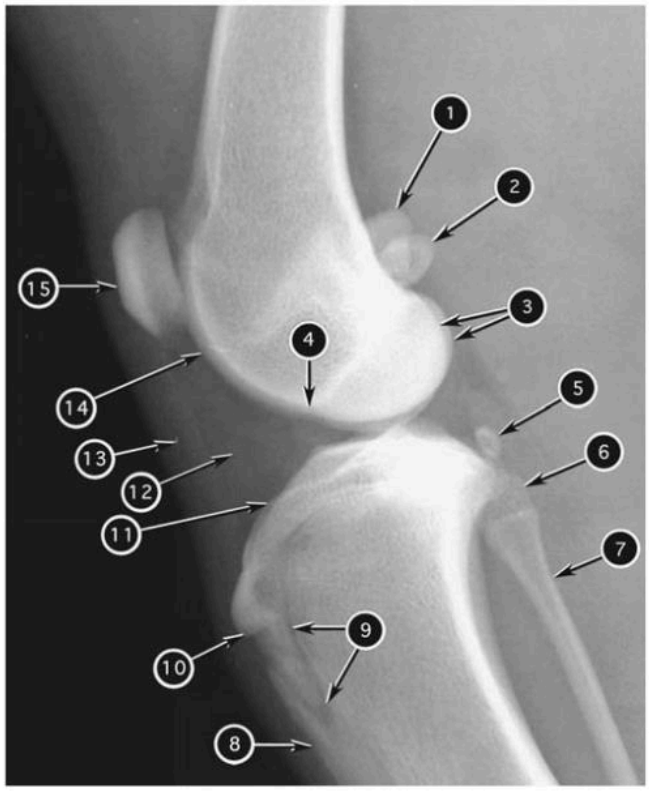


Fig. 16.22 Mediolateral (lateral) radiograph of canine stifle joint.
1. Lateral sesamoid of gastrocnemius muscle
2. Medial sesamoid of gastrocnemius muscle
3. Medial and lateral condyles of femur
4. Extensor fossa of femur
5. Sesamoid bone of popliteus muscle
6. Head of fibula
7. Body of fibula
8. Cranial border of tibia
9. Cartilage between tibial tuberosity and body of tibia
10. Tibial tuberosity
11. Cranial intercondylar area of tibia
12. Infrapatellar fat body (pad)
13. Patellar ligament
14. Superimposed ridges of femoral trochlea
15. Patella

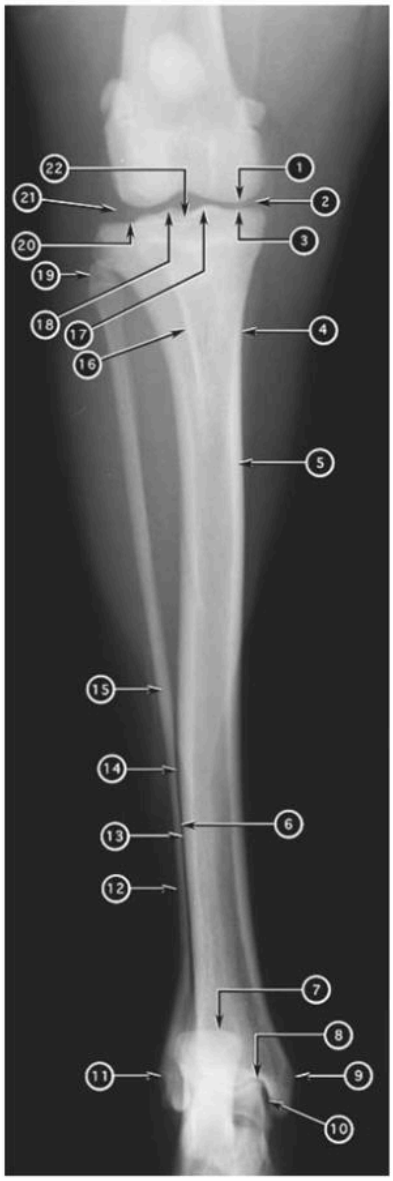


Fig. 16.23 Craniocaudal radiograph of canine crus.
1. Medial condyle of femur
2. Medial meniscus
3. Medial condyle of tibia
4. Medial border of tibia
5. Body of tibia (diaphysis)
6. Medial surface of fibula (faces tibia)
7. Calcaneal tuber
8. Medial groove of tibial cochlea
9. Medial malleolus of tibia
10. Medial aspect of tarsocrural joint
11. Lateral malleolus of fibula
12. Lateral surface of fibula
13. Lateral border of tibia (faces fibula)
14. Interosseous membrane
15. Body of fibula (diaphysis)
16. Cranial border of tibia
17. Medial tubercle of intercondylar eminence
18. Lateral tubercle of intercondylar eminence
19. Head of fibula
20. Lateral condyle of tibia
21. Lateral meniscus
22. Central intercondylar area of tibia



Fig. 16.24 Mediolateral (lateral) radiograph of canine crus.
1. Lateral sesamoid of gastrocnemius muscle
2. Medial sesamoid of gastrocnemius muscle
3. Medial condyle of femur
4. Lateral condyle of femur
5. Sesamoid bone of popliteus muscle
6. Head of fibula
7. Body of fibula (diaphysis)
8. Tarsocrural joint (talocrural, tibiotarsal)
9. Calcaneal tuber
10. Proximal intertarsal joint
11. Trochlea of talus
12. Body of fibula superimposed on tibia (diaphysis)
13. Cranial border of tibia
14. Cartilage between tibial tuberosity and body of tibia
15. Tibial tuberosity
16. Extensor fossa of femur



Fig. 16.25 Mediolateral (lateral) radiograph of canine tarsus.
1. Calcaneal tuber
2. Body of calcaneus
3. Fourth tarsal bone
4. Metatarsal bone 1
5. Superimposed metatarsal bone 2 through metatarsal bone 5
6. Tarsometatarsal joints
7. Third tarsal bone
8. Distal intertarsal joint
9. Central tarsal bone
10. Proximal intertarsal joint
11. Trochlea of the talus
12. Tarsocrural joint

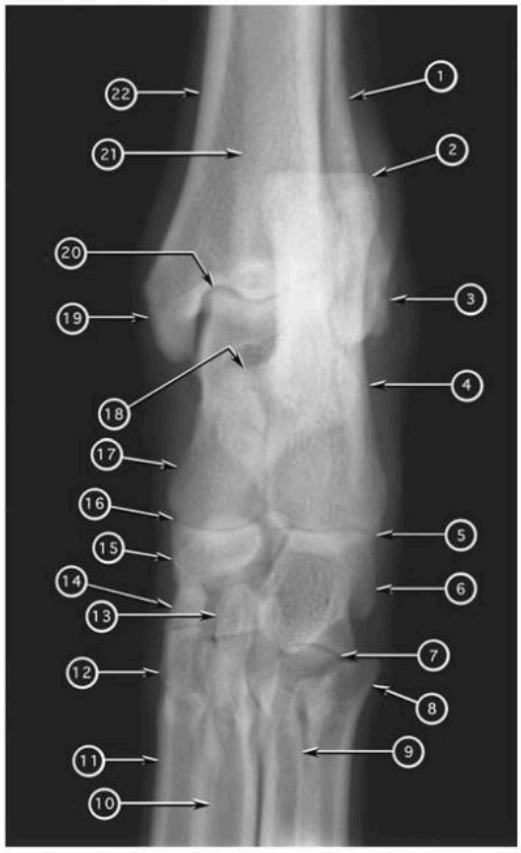


Fig. 16.26 Dorsoplantar radiograph of canine tarsus.
1. Body of fibula (distal diaphysis)
2. Calcaneal tuber
3. Lateral malleolus of fibula
4. Body of calcaneus
5. Proximal intertarsal (calcaneoquartal) joint
6. Fourth tarsal bone
7. Tarsometatarsal joints
8. Base of metatarsal bone 5
9. Metatarsal bone 4
10. Metatarsal bone 3
11. Metatarsal bone 2
12. Metatarsal bone 1
13. Third tarsal bone
14. Superimposed first tarsal bone and second tarsal bone
15. Central tarsal bone
16. Proximal intertarsal (talocalcaneocentral) joint
17. Talus
18. Sustentaculum tali of calcaneus
19. Medial malleolus of tibia
20. Tarsocrural joint (talocrural, tibiotarsal)
21. Common calcanean tendon superimposed on tibia
22. Body of tibia (distal diaphysis)



Fig. 16.27 Dorsolateral-plantaromedial oblique radiograph of canine tarsus.
1. Calcaneal tuber
2. Proximal intertarsal (calcaneoquartal) joint
3. Fourth tarsal bone
4. Tarsometatarsal joints
5. Base of metatarsal bone 5
6. Metatarsal bone 4
7. Metatarsal bone 3
8. Metatarsal bone 2
9. Distal intertarsal joint
10. Central tarsal bone
11. Proximal intertarsal (talocalcaneocentral) joint
12. Sustentaculum tali of calcaneus
13. Medial malleolus of tibia
14. Tarsocrural joint (talocrural, tibiotarsal)

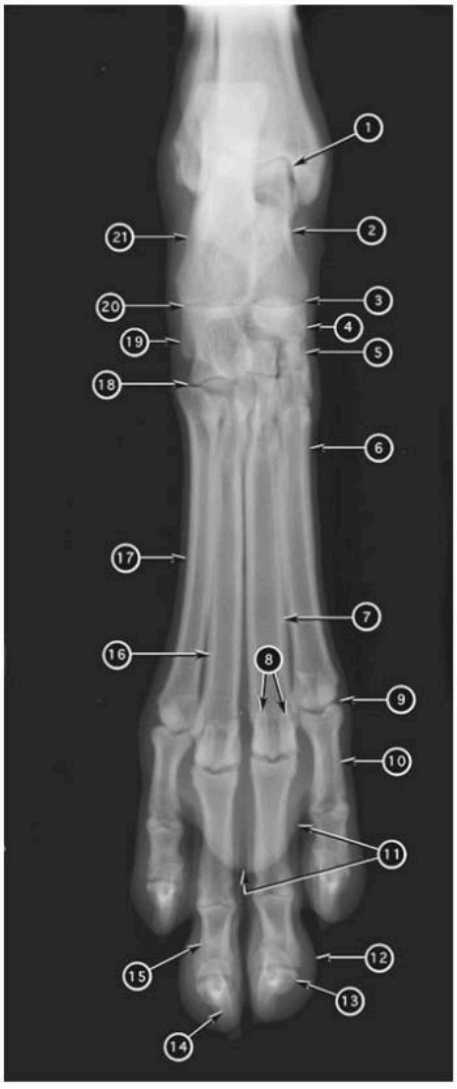


Fig. 16.28 Dorsoplantar radiograph of canine pes.
1. Tarsocrural joint (talocrural, tibiotarsal)
2. Talus
3. Proximal intertarsal (talocalcaneocentral) joint
4. Central tarsal bone
5. Superimposed tarsal bones 1 and 2
6. Metatarsal bone 2
7. Metatarsal bone 3
8. Proximal sesamoid bones of digit 3
9. Metatarsophalangeal joint of digit 2
10. Proximal phalanx of digit 2
11. Metatarsal pad
12. Digital pad of digit 3
13. Distal phalanx of digit 3
14. Unguicular (ungual) process of distal phalanx of digit 4
15. Middle phalanx of digit 4
16. Metatarsal bone 4
17. Metatarsal bone 5
18. Tarsometatarsal joints
19. Fourth tarsal bone
20. Proximal intertarsal (calcaneoquartal) joint
21. Calcaneus



Fig. 16.29 Mediolateral (lateral) radiograph of canine pes with digits spread.

1. Superficial digital flexor (SDF) tendon
2. Calcaneal tuber
3. Calcaneus
4. Proximal intertarsal (calcaneoquartal) joint
5. Tarsal bone 4
6. Base of metatarsal bone 5
7. Body of metatarsal bone 5
8. Proximal sesamoid bones of digit 5
9. Proximal phalanx of digit 5
10. Tape used in positioning
11. Metatarsal pad
12. Distal interphalangeal joint of digit 4
13. Flexor tubercle of distal phalanx of digit 4
14. Middle phalanx of digit 4
15. Unguicular (ungual) process of distal phalanx of digit 3
16. Unguicular (ungual) crest of distal phalanx of digit 3
17. Proximal interphalangeal joint of digit 4
18. Metatarsophalangeal joint of digit 4
19. Tarsometatarsal joints
20. Distal intertarsal joint
21. Proximal intertarsal (talocalcaneocentral) joint
22. Trochlea of talus
23. Tarsocrural joint (talocrural, tibiotarsal)

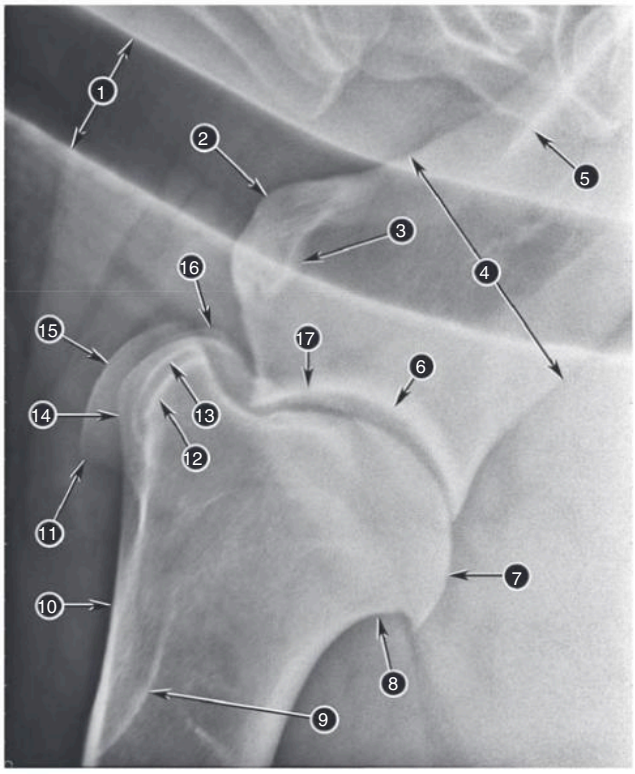


Fig. 16.30 Mediolateral (lateral) radiograph of equine shoulder joint.

1. Air in trachea
2. Supraglenoid tubercle of scapula
3. Coracoid process of scapula
4. Neck of scapula
5. Spine of scapula
6. Medial edge of glenoid fossa
7. Head of humerus
8. Neck of humerus
9. Deltoid tuberosity of humerus
10. Cranial surface of humerus
11. Distal end of intermediate tubercle
12. Floor of lateral part of intertubercular groove
13. Floor of medial part of intertubercular groove
14. Cranial part of lesser tubercle
15. Intermediate tubercle of humerus
16. Cranial part of greater tubercle
17. Glenoid notch in medial edge of glenoid fossa

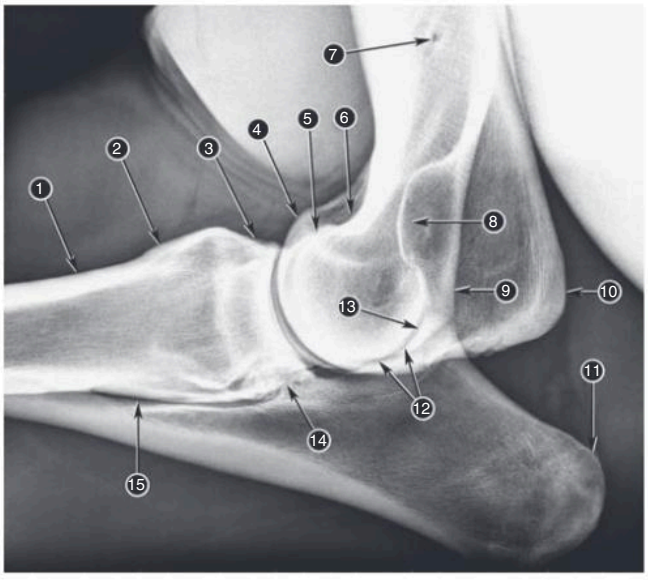


Fig. 16.31 Mediolateral (lateral) radiograph of equine elbow joint.
1. Body of radius (diaphysis)
2. Radial tuberosity
3. Head of radius
4. Trochlea of humeral condyle (medial)
5. Capitulum of humeral condyle (lateral)
6. Radial fossa of humerus
7. Nutrient canal of humerus (medial)
8. Olecranon fossa of humerus
9. Lateral epicondyle of humerus
10. Medial epicondyle of humerus
11. Tuber olecrani
12. Trochlear notch of ulna
13. Anconeal process of ulna
14. Proximal radioulnar joint
15. Proximal interosseous space

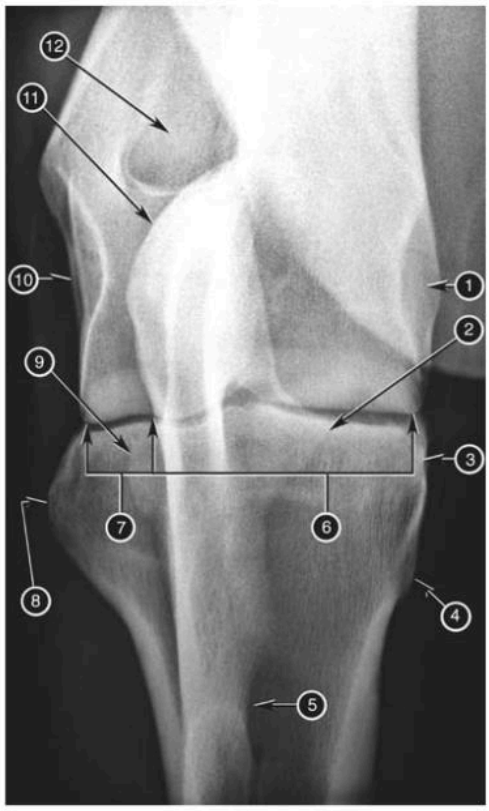


Fig. 16.32 Craniocaudal radiograph of equine elbow joint.
1. Medial epicondyle of humerus
2. Medial coronoid process of ulna
3. Head of radius
4. Radial tuberosity
5. Proximal interosseous space
6. Trochlea of humeral condyle
7. Capitulum of humeral condyle
8. Eminence for lateral collateral ligament
9. Lateral coronoid process of ulna
10. Lateral epicondyle of humerus
11. Tuber olecrani
12. Olecranon fossa of humerus

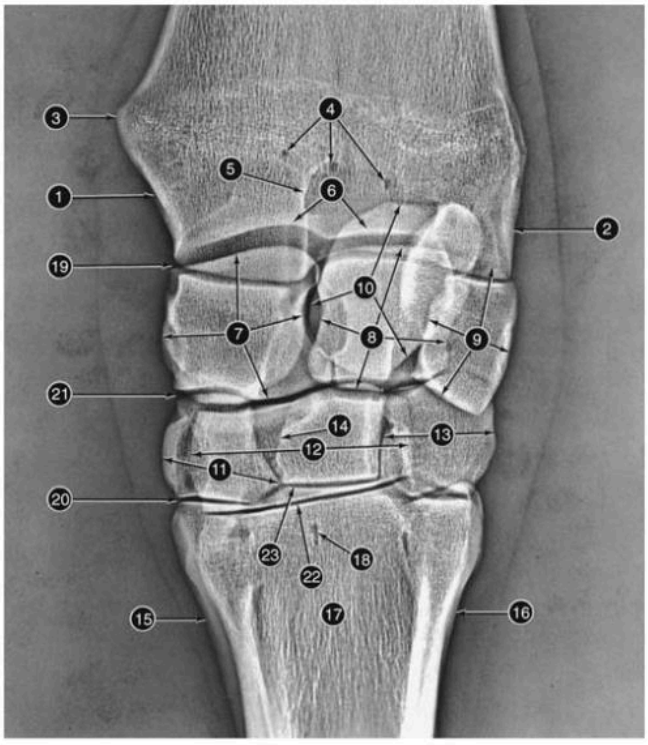


Fig. 16.33 Dorsopalmar xeroradiograph of left equine carpus.
1. Medial styloid process of radius
2. Lateral styloid process of ulna
3. Projection at proximomedial aspect of medial styloid process of radius
4. Vascular channels
5. Caudolateral border of medial styloid process of radius
6. Junction of carpal articular surface with cranial surface of radius
7. Radial carpal bone
8. Intermediate carpal bone
9. Ulnar carpal bone
10. Accessory carpal bone
11. Second carpal bone
12. Third carpal bone
13. Fourth carpal bone
14. Medial border of palmar process of carpal bone 3
15. Metacarpal bone 2
16. Metacarpal bone 4
17. Metacarpal bone 3
18. Vascular channel
19. Antebrachiocarpal joint
20. Carpometacarpal joints
21. Middle carpal joint
22. Shadow cast by dorsal aspects of carpometacarpal joints
23. Shadow cast by palmar aspects of carpometacarpal joints

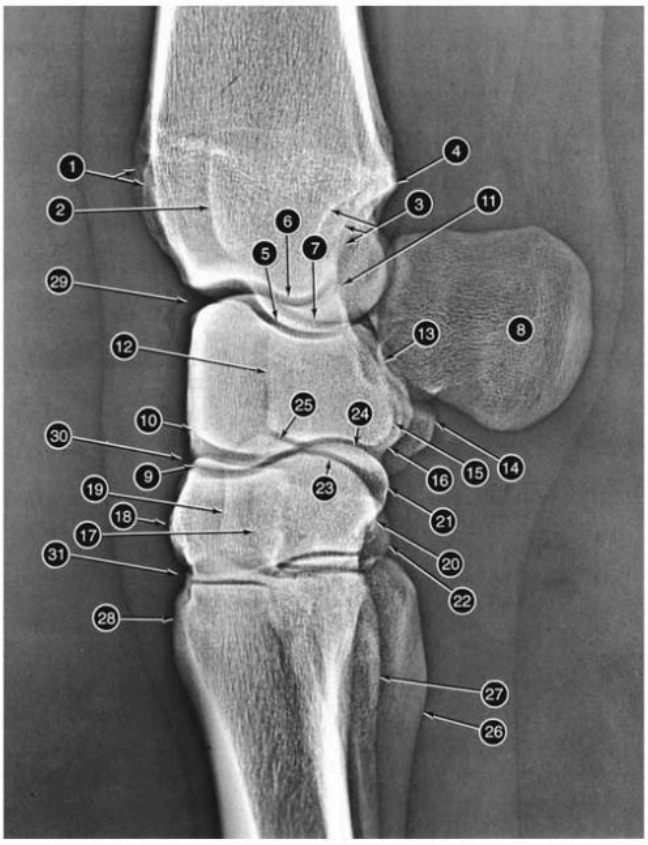


Fig. 16.34 Lateromedial (lateral) xeroradiograph of left equine carpus.
1. Ridges on cranial surface of radius
2. Ridge adjacent to lateral border of common digital extensor tendon
3. Caudal border of radial trochlea
4. Transverse crest of radius
5. Medial part of carpal articular surface
6. Intermediate part of carpal articular surface
7. Lateral part of carpal articular surface
8. Accessory carpal bone
9. Dorsodistal border of radial carpal bone
10. Dorsodistal border of intermediate carpal bone
11. Proximal process of intermediate carpal bone
12. Dorsal surface of ulnar carpal bone
13. Articulation of accessory carpal bone with ulnar carpal bone
14. Palmar border of ulnar carpal bone
15. Palmar border of intermediate carpal bone
16. Palmar border of radial carpal bone
17. Dorsal border of second carpal bone
18. Dorsal border of third carpal bone
19. Dorsal border of fourth carpal bone
20. Palmar border of second carpal bone
21. Palmar border of third carpal bone
22. Palmar border of fourth carpal bone
23. Proximal border of second carpal bone
24. Proximal border of third carpal bone
25. Proximal border of fourth carpal bone
26. Metacarpal bone 4
27. Metacarpal bone 2
28. Metacarpal tuberosity
29. Antebrachiocarpal joint
30. Middle carpal joint
31. Carpometacarpal joints

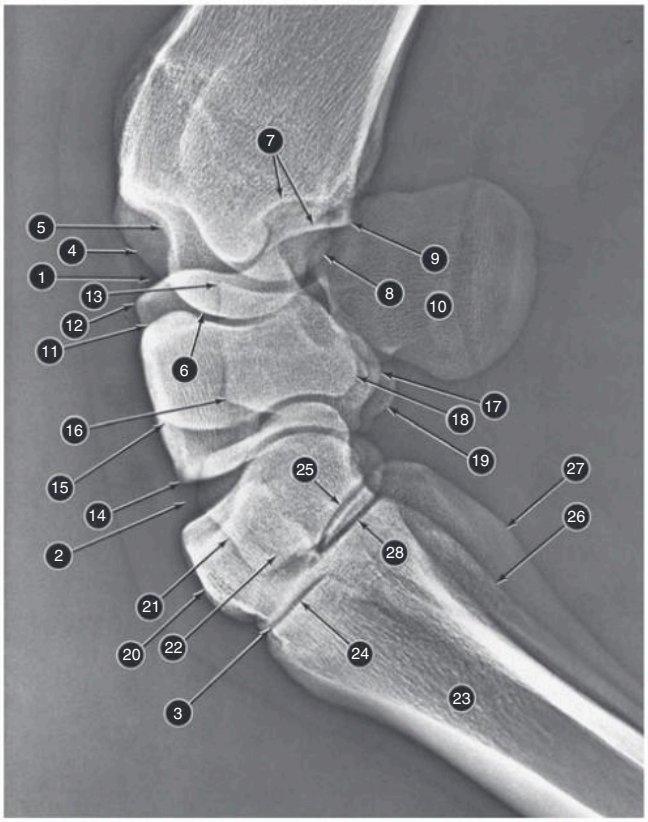


Fig. 16.35 Flexed lateromedial (lateral) xeroradiograph of left equine carpus.

1. Antebrachiocarpal joint
2. Middle carpal joint
3. Carpometacarpal joints
4. Medial border of medial part of carpal articular surface
5. Lateral border of medial part of carpal articular surface
6. Medial styloid process
7. Shadows from caudal aspect of intermediate part of radial trochlea
8. Lateral styloid process
9. Transverse crest of radius
10. Accessory carpal bone
11. Dorsoproximal border of radial carpal bone
12. Dorsoproximal border of intermediate carpal bone
13. Dorsoproximal border of ulnar carpal bone
14. Dorsodistal border of radial carpal bone (isolated)
15. Dorsodistal border of intermediate carpal bone
16. Dorsodistal border of ulnar carpal bone
17. Palmar border of radial carpal bone
18. Palmar border of intermediate carpal bone
19. Palmar border of ulnar carpal bone
20. Dorsal border of third carpal bone
21. Dorsal border of fourth carpal bone
22. Dorsal border of second carpal bone
23. Metacarpal bone 3
24. Third carpometacarpal joint
25. Second carpometacarpal joint
26. Metacarpal bone 2
27. Metacarpal bone 4
28. Fourth carpometacarpal joint

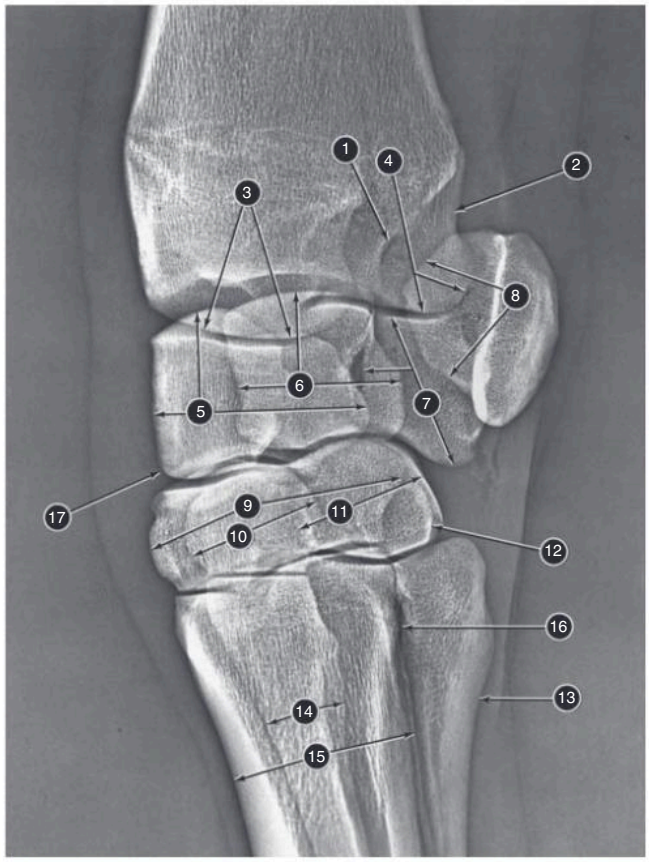


Fig. 16.36 Dorsolateral-palmaromedial oblique xeroradiograph of left equine carpus.

1. Radiolucent area at line of fusion between lateral styloid process and radius
2. Lateral styloid process
3. Medial part of radial trochlea
4. Lateral styloid process
5. Radial carpal bone
6. Intermediate carpal bone
7. Ulnar carpal bone
8. Articulations of accessory carpal bone with lateral styloid process and ulnar carpal bone
9. Third carpal bone
10. Second carpal bone
11. Fourth carpal bone
12. Palmar projection of fourth carpal bone
13. Metacarpal bone 4
14. Metacarpal bone 2
15. Metacarpal bone 3
16. Location of metacarpal interosseous ligaments
17. Distal aspect of dorsomedial border of radial carpal bone (isolated)

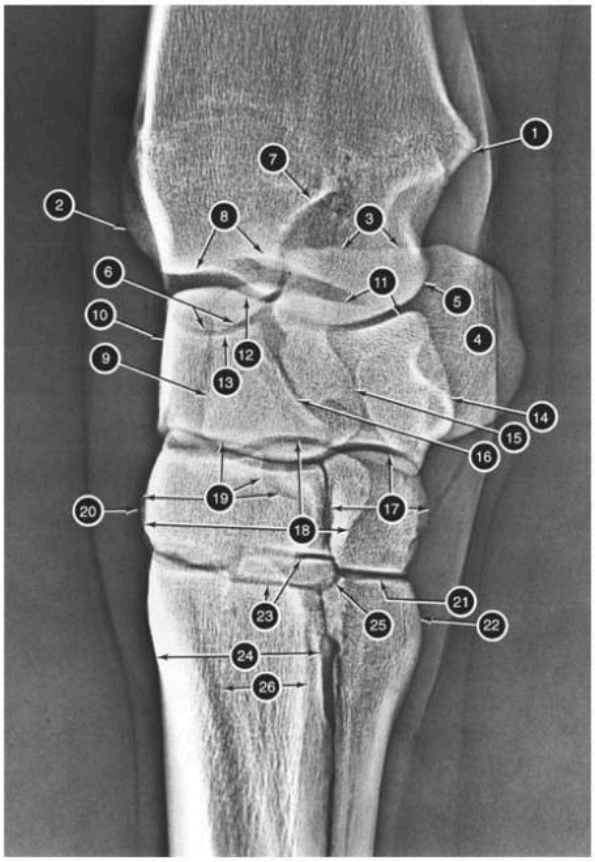


Fig. 16.37 Dorsomedial-palmarolateral oblique xeroradiograph of left equine carpus.
1. Projection of radius for attachment of medial collateral ligament
2. Ridge that forms lateral border of groove for common digital extensor tendon
3. Proximal border of accessory carpal bone
4. Accessory carpal bone
5. Medial styloid process of radius
6. Lateral styloid process
7. Ridge on caudal aspect of radius
8. Ridge at junction of cranial surface of radius with carpal articular surface
9. Dorsolateral border of radial carpal bone
10. Dorsolateral borders of ulnar and intermediate carpal bones
11. Proximal surface of radial carpal bone
12. Proximal surface of intermediate carpal bone
13. Proximal surface of ulnar carpal bone
14. Palmaromedial border of radial carpal bone
15. Palmaromedial border of intermediate carpal bone
16. Palmaromedial border of ulnar carpal bone
17. Second carpal bone
18. Third carpal bone
19. Fourth carpal bone
20. Dorsolateral borders of third and fourth carpal bones
21. Articulation between second carpal bone and metacarpal bone 2
22. Metacarpal bone 2
23. Articulation between third carpal bone and metacarpal bone 3
24. Metacarpal bone 3
25. Inconstant articulation between third carpal bone and metacarpal bone 2
26. Metacarpal bone 4

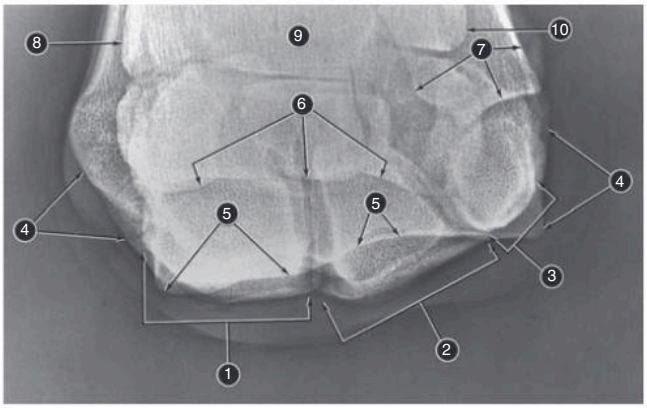


Fig. 16.38 Dorsoproximal-dorsodistal oblique xeroradiograph of proximal row of equine carpal bones.
1. Dorsal surface of radial carpal bone
2. Dorsal surface of intermediate carpal bone
3. Dorsal surface of ulnar carpal bone
4. Radius
5. Carpal articular surface of radial trochlea
6. Dorsal surfaces of distal carpal bones
7. Accessory carpal bone
8. Metacarpal bone 2
9. Metacarpal bone 3
10. Metacarpal bone 4

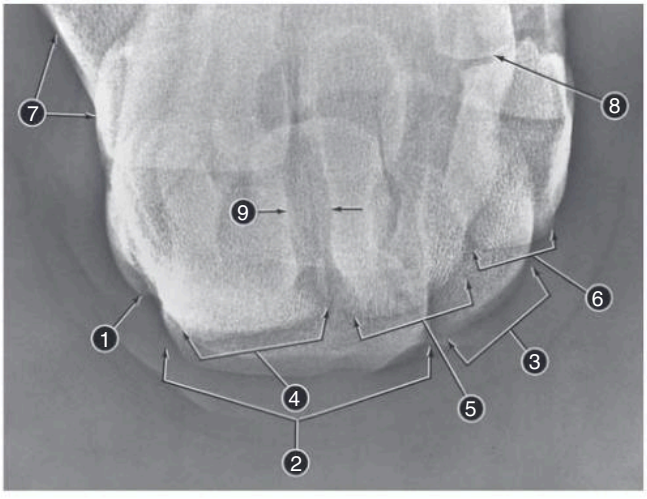


Fig. 16.39 Dorsoproximal-dorsodistal oblique xeroradiograph of distal row of equine carpal bones.
1. Dorsal surface of second carpal bone
2. Dorsal surface of third carpal bone
3. Dorsal surface of fourth carpal bone
4. Dorsal surface of radial carpal bone
5. Dorsal surface of intermediate carpal bone
6. Dorsal surface of ulnar carpal bone
7. Radius
8. Accessory carpal bone
9. Interosseous space between radial and intermediate carpal bones

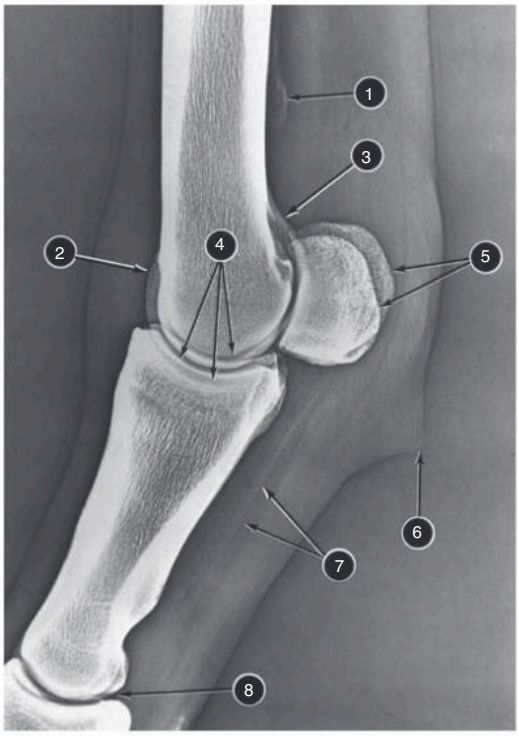


Fig. 16.40 Lateromedial (lateral) xeroradiograph of left equine metacarpophalangeal joint.
1. Distal end (head) of small metacarpal bone
2. Dorsal part of sagittal ridge of metacarpal bone 3
3. Palmar part of sagittal ridge of metacarpal bone 3
4. Metacarpophalangeal joint
5. Proximal sesamoid bones
6. Ergot
7. Straight sesamoid ligament
8. Proximal interphalangeal joint

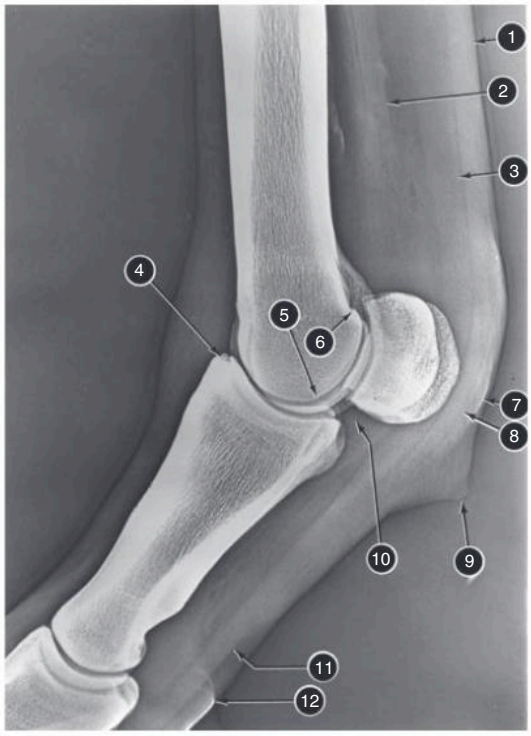


Fig. 16.41 Lateromedial (lateral) xeroradiograph of left equine metacarpophalangeal joint with right limb lifted to increase weight on left limb.
1. Superficial digital flexor tendon
2. Interosseus
3. Deep digital flexor tendon
4. Dorsoproximal aspect of proximal phalanx
5. Subtle transverse ridge on head of metacarpal bone 3
6. Distinct transverse ridge at palmar edge of articular surface
7. Palmar annular ligament of metacarpophalangeal joint
8. Superficial digital flexor tendon
9. Ergot
10. Increased distance between proximal sesamoid bones and proximal phalanx (see Fig. 16.40)
11. Deep distal flexor tendon
12. Distal digital annular ligament

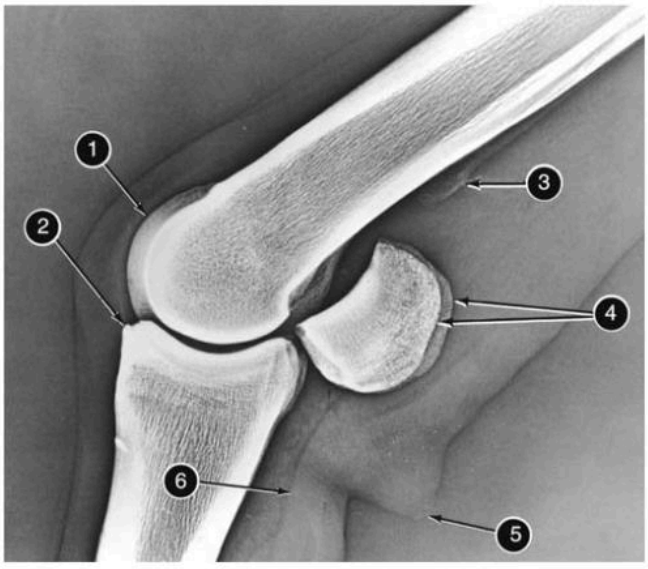


Fig. 16.42 Flexed lateromedial (lateral) xeroradiograph of left equine metacarpophalangeal joint.
1. Sagittal ridge on head of metacarpal bone 3
2. Dorsoproximal aspect of proximal phalanx
3. Distal end of small metacarpal bone
4. Proximal sesamoid bones
5. Ergot
6. Deep digital flexor tendon

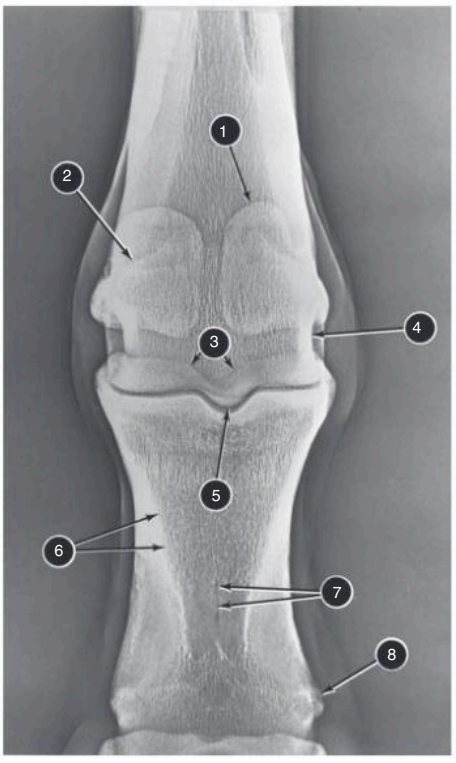


Fig. 16.43 Dorsoproximal-palmarodistal oblique xeroradiograph of left equine metacarpophalangeal joint.
1. Lateral proximal sesamoid bone
2. Depression in interosseus (abaxial) surface of medial proximal sesamoid bone for attachment of interosseus tendon
3. Palmaroproximal edge of proximal phalanx
4. Depression in metacarpal bone 3 for attachment of lateral collateral ligament of metacarpophalangeal joint
5. Sagittal ridge on head of metacarpal bone 3
6. Area of oblique ridge on palmar surface of proximal phalanx for attachment oblique sesamoid ligament
7. Nutrient canal through dorsal cortex of proximal phalanx
8. Lateral distal collateral tubercle of proximal phalanx

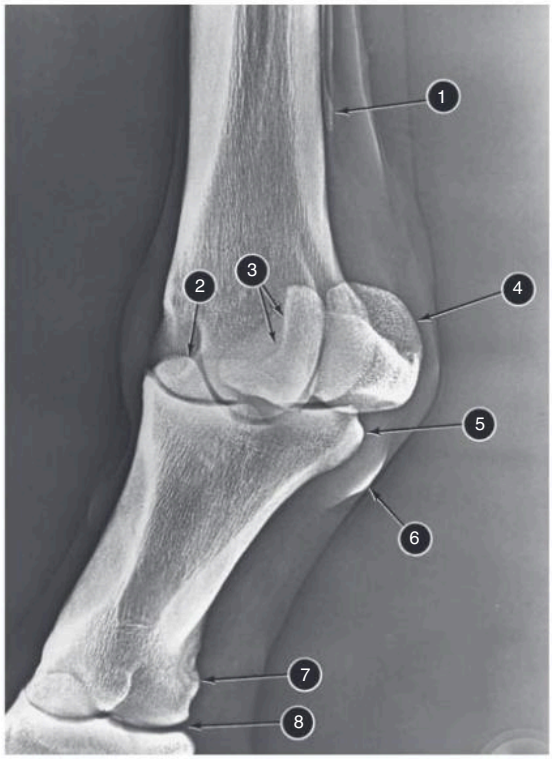


Fig. 16.44 Dorsolateral-palmaromedial oblique xeroradiograph of left equine metacarpophalangeal joint.
1. Distal end of metacarpal bone 4
2. Dorsoproximal aspect of proximal phalanx
3. Depression in interosseus surface of medial proximal sesamoid bone for attachment of interosseus tendon
4. Palmaroabaxial border of lateral proximal sesamoid bone
5. Lateral proximal collateral tubercle of proximal phalanx
6. Ergot
7. Lateral distal collateral tubercle of proximal phalanx
8. Proximal interphalangeal joint

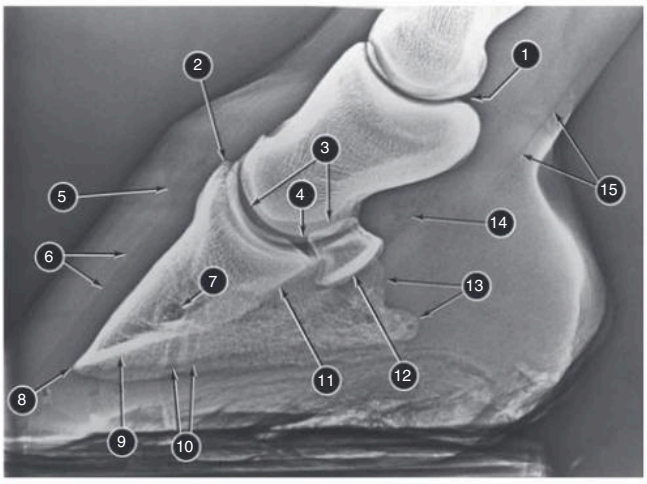


Fig. 16.45 Lateromedial (lateral) xeroradiograph of left equine foredigit.
1. Proximal interphalangeal joint
2. Extensor process of distal phalanx
3. Distal interphalangeal joint
4. Part of distal interphalangeal joint that extends between distal phalanx and the distal sesamoid (navicular) bone
5. Proximal extent of tubular horn forming stratum medium of hoof wall
6. Junction of stratum medium and laminar horn of stratum internum
7. Transverse part of sole canal of distal phalanx; accommodates terminal arch of digital vessels
8. Sole border of distal phalanx
9. Planum cuneatum (sole surface) of distal phalanx
10. Vascular channels extending from sole canal to sole border of distal phalanx
11. Flexor surface of distal phalanx
12. Flexor surface of navicular bone
13. Superimposed medial and lateral palmar processes of distal phalanx
14. Radiolucent areas created by fat within synovial folds
15. Borders of deep digital flexor tendon; defined by fat within synovial folds of digital sheath

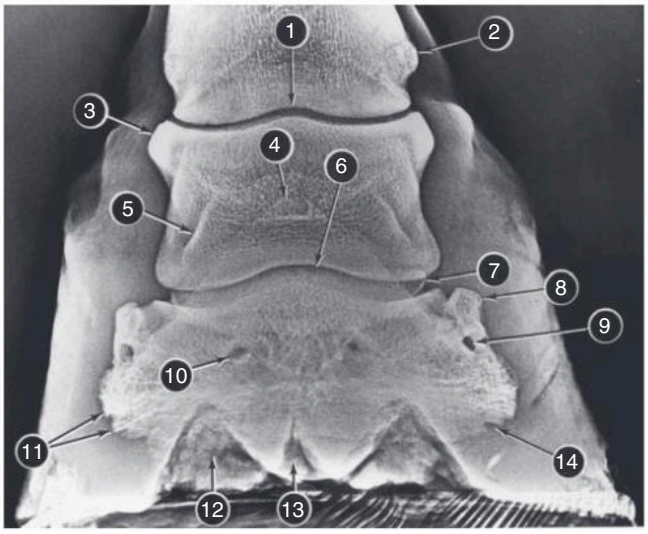


Fig. 16.46 Dorsopalmar xeroradiograph of left equine foredigit.

1. Proximal interphalangeal joint
2. Lateral distal collateral tubercle of proximal phalanx
3. Medial proximal collateral tubercle of middle phalanx
4. Extensor process of distal phalanx
5. Wall of depression in middle phalanx for attachment of medial collateral ligament of distal interphalangeal joint
6. Distal interphalangeal joint
7. Lateral extremity of navicular bone
8. Lateral palmar process of distal phalanx
9. Foramen in lateral palmar process of distal phalanx that accommodates dorsal branches of digital vessels
10. Medial sole foramen of distal phalanx; receives digital vessels as they enter sole canal
11. Sole border of distal phalanx; typically irregular because of notches for vascular channels
12. Medial collateral groove of frog
13. Central groove of frog
14. Notch in sole border associated with vascular channel from sole canal of distal phalanx

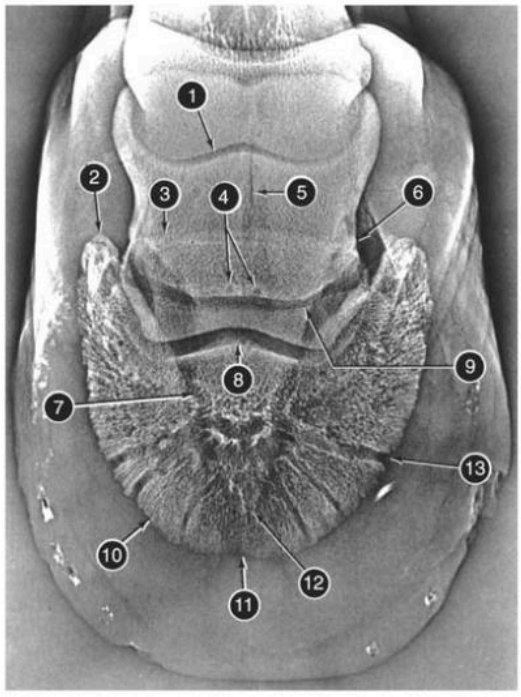


Fig. 16.47 Dorsal 65-degree proximal-palmarodistal oblique xeroradiograph of left equine foredigit.

1. Proximal interphalangeal joint
2. Medial palmar process of distal phalanx
3. Proximal border of navicular bone
4. Vascular foramina and synovial fossae along distal border of navicular bone
5. Air within central groove of frog
6. Lateral extremity of navicular bone
7. Sole canal of distal phalanx
8. Distal interphalangeal joint
9. Articulation of distal phalanx with navicular bone; part of distal interphalangeal joint
10. Sole border of distal phalanx
11. Crena marginis solaris
12. Apex of frog
13. Vascular channel from sole canal to sole border of distal phalanx

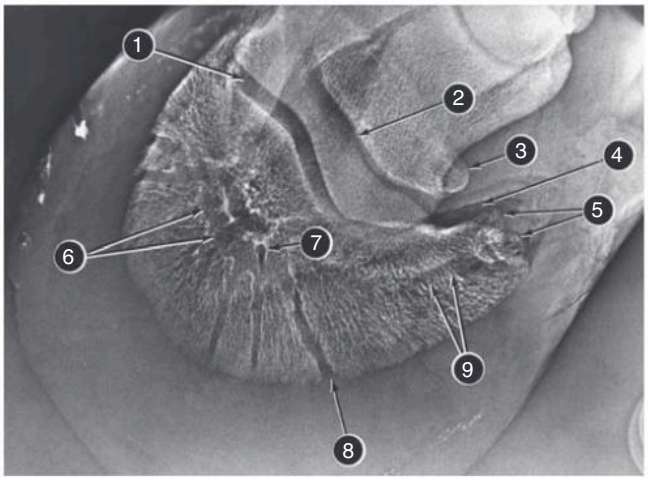


Fig. 16.48 Dorsoproximolateral-palmarodistomedial oblique xeroradiograph of left equine foredigit.
1. Distal interphalangeal joint
2. Articulation of distal phalanx with navicular bone; part of distal interphalangeal joint
3. Lateral extremity of navicular bone
4. Air within lateral collateral groove of frog
5. Lateral palmar process of distal phalanx
6. Sole canal of distal phalanx
7. End-on perspective of vascular channel from sole canal to parietal surface of distal phalanx
8. Vascular channel from sole canal to sole border of distal phalanx
9. Lateral parietal groove of distal phalanx; accommodates dorsal branches of digital vessel

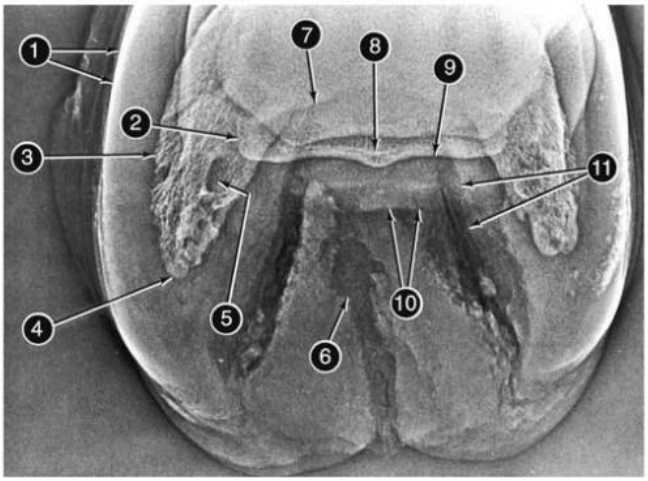


Fig. 16.49 Palmaroproximal-palmarodistal oblique xeroradiograph of left equine foredigit.
1. Proximal border of hoof wall
2. Lateral extremity of navicular bone
3. Sole border of distal phalanx
4. Lateral palmar process of distal phalanx
5. Foramen of lateral palmar process
6. Air within central groove of frog
7. Articulation of middle phalanx with navicular bone; part of distal interphalangeal joint
8. Sagittal ridge of navicular bone
9. Flexor surface of navicular bone
10. Deep digital flexor tendon
11. Air within medial collateral groove of frog

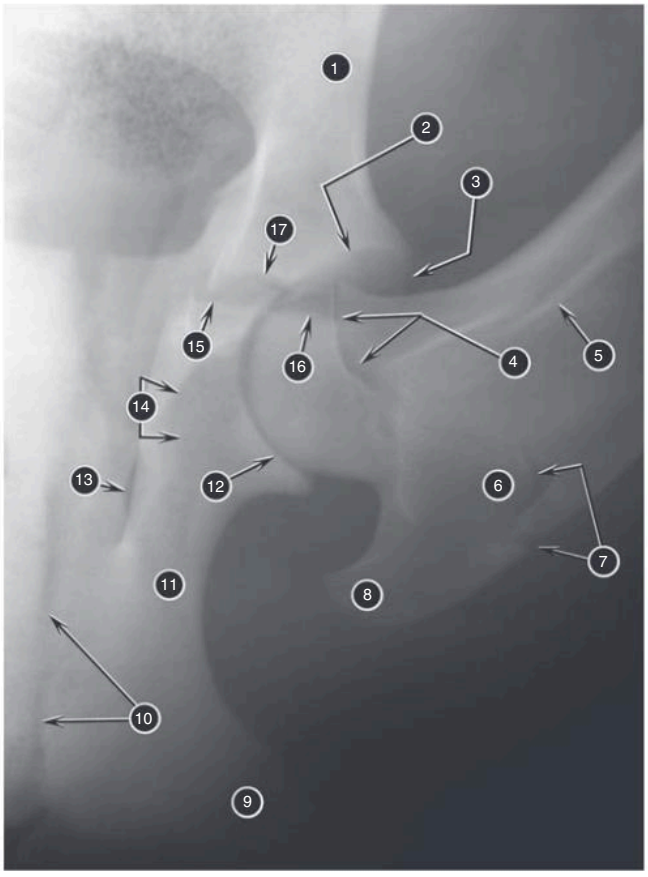


Fig. 16.50 Ventromedial-dorsolateral oblique radiograph of equine hip joint (8 months old).
1. Body of ilium
2. Cranioventral border of acetabulum
3. Craniodorsal border of acetabulum
4. Proximal physis (epiphyseal cartilage) of femur
5. Shadow created by caudal edge of lesser trochanter
6. Radiolucent area created by trochanteric fossa of femur
7. Cartilaginous junction between greater trochanter and femoral body
8. Greater trochanter of femur, caudal part
9. Tuber ischiadicum (ischiatic tuberosity)
10. Cartilaginous pelvic symphysis
11. Body of ischium
12. Caudoventral border of acetabulum
13. Obturator foramen
14. Radiolucent area created by acetabular fossa
15. Radiolucent area created by groove on ventral surface of pubis for accessory ligament of femoral head
16. Radiolucent area created by fovea capitis of femoral head
17. Cranial edge of acetabular notch

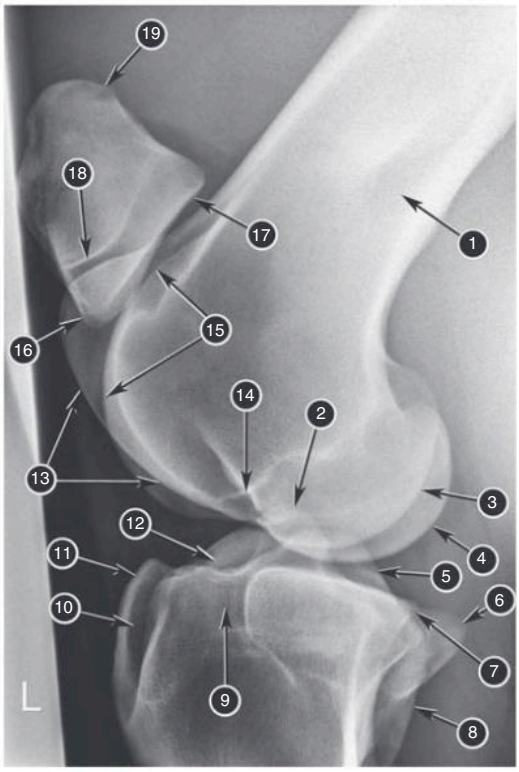


Fig. 16.51 Lateromedial (lateral) radiograph of equine stifle joint.
1. Supracondylar fossa of femur for origin of superficial digital flexor and gastrocnemius muscles
2. Medial tubercle of intercondylar eminence
3. Lateral condyle of femur
4. Medial condyle of femur
5. Lateral tubercle of intercondylar eminence
6. Lateral condyle of tibia
7. Medial condyle of tibia
8. Fibula
9. Extensor groove of tibia
10. Groove for intermediate patellar ligament
11. Lateral part of tibial tuberosity
12. Cranial intercondylar area of tibia
13. Medial ridge of femoral trochlea
14. Extensor fossa of femur
15. Lateral ridge of femoral trochlea
16. Apex of patella
17. Articular surface of patella, gliding part
18. Articular surface of patella, resting part
19. Base of patella

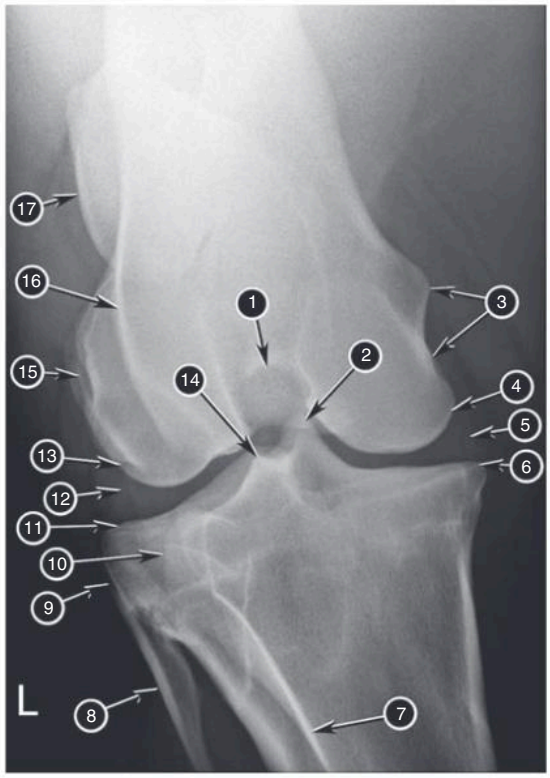


Fig. 16.52 Caudocranial radiograph of equine stifle joint.
1. Intercondylar fossa of femur
2. Medial tubercle of intercondylar eminence
3. Medial epicondyle of femur
4. Medial condyle of femur
5. Medial meniscus and femorotibial joint
6. Medial condyle of tibia
7. Cranial margin of tibia
8. Body of fibula (proximal diaphysis)
9. Head of fibula
10. Lateral part of tibial tuberosity
11. Lateral condyle of tibia
12. Lateral meniscus and femorotibial joint
13. Depression for origin of popliteus muscle
14. Lateral tubercle of intercondylar eminence
15. Lateral epicondyle of femur
16. Lateral ridge of femoral trochlea
17. Patella

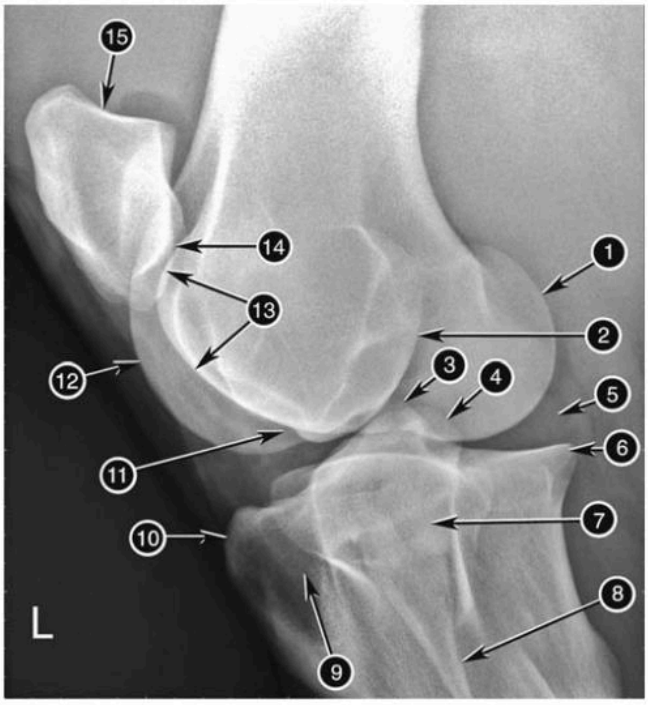


Fig. 16.53 Caudolateral-craniomedial oblique radiograph of equine stifle joint.

1. Medial condyle of femur
2. Lateral condyle of femur
3. Medial tubercle of intercondylar eminence
4. Lateral tubercle of intercondylar eminence
5. Medial meniscus and femorotibial joint
6. Medial condyle of tibia
7. Head of fibula
8. Body of fibula (proximal diaphysis)
9. Extensor groove of tibia
10. Tibial tuberosity
11. Extensor fossa of femur
12. Lateral ridge of femoral trochlea
13. Groove of femoral trochlea
14. Femoropatellar joint
15. Patella

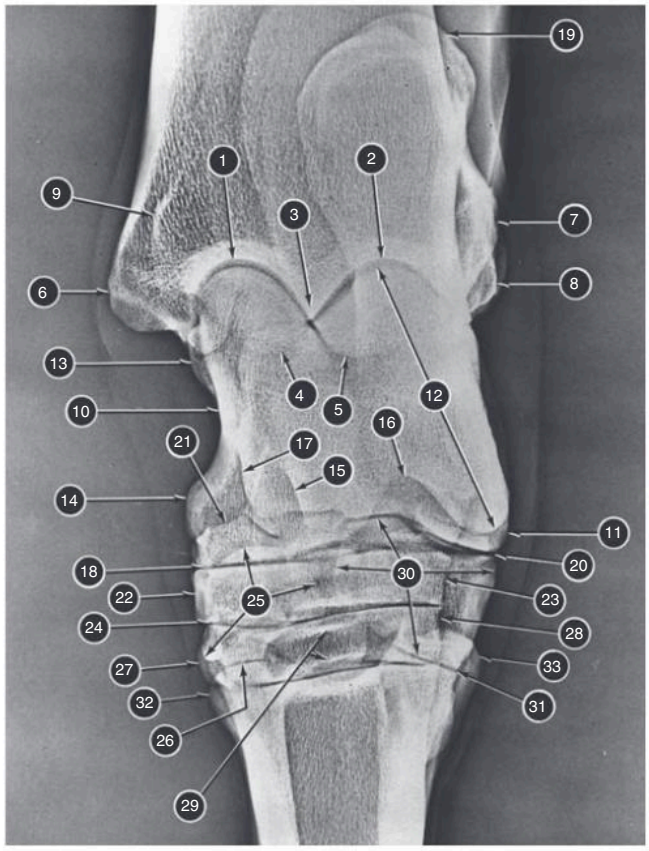


Fig. 16.54 Dorsoplantar xeroradiograph of left equine tarsus.

1. Medial groove of tibial cochlea
2. Lateral groove of tibial cochlea
3. Oblique ridge separating medial and lateral grooves of tibial cochlea
4. Pointed caudal end of oblique ridge
5. Rounded cranial end of oblique ridge
6. Medial malleolus
7. Caudal part of lateral malleolus
8. Cranial part of lateral malleolus
9. Radiopaque shadow
10. Talus
11. Calcaneus
12. Lateral ridge of trochlea tali
13. Proximal tubercle of talus
14. Distal tubercle of talus
15. Medial ridge of trochlea tali
16. Groove between lateral and medial ridges of trochlea tali
17. Medial edge of sustentaculum tali
18. Proximal intertarsal (talocalcaneocentral) joint
19. Tuber calcanei
20. Proximal intertarsal (calcaneoquartal) joint
21. Proximoplantar aspect of central tarsal bone
22. Medial aspect of central tarsal bone
23. Lateral aspect of central tarsal bone
24. Distal intertarsal (centrodistal) joint
25. Fused first and second tarsal bones
26. Articulation between first and second tarsal bones and metatarsal bone 2
27. Medial aspect of third tarsal bone
28. Lateral aspect of third tarsal bone
29. Radiopaque lines produced by walls of nonarticular depressions on third tarsal bone
30. Fourth tarsal bone
31. Tarsometatarsal joints (also articulation between first and second tarsal bones and metatarsal bone 2)
32. Base of metatarsal bone 2
33. Base of metatarsal bone 4

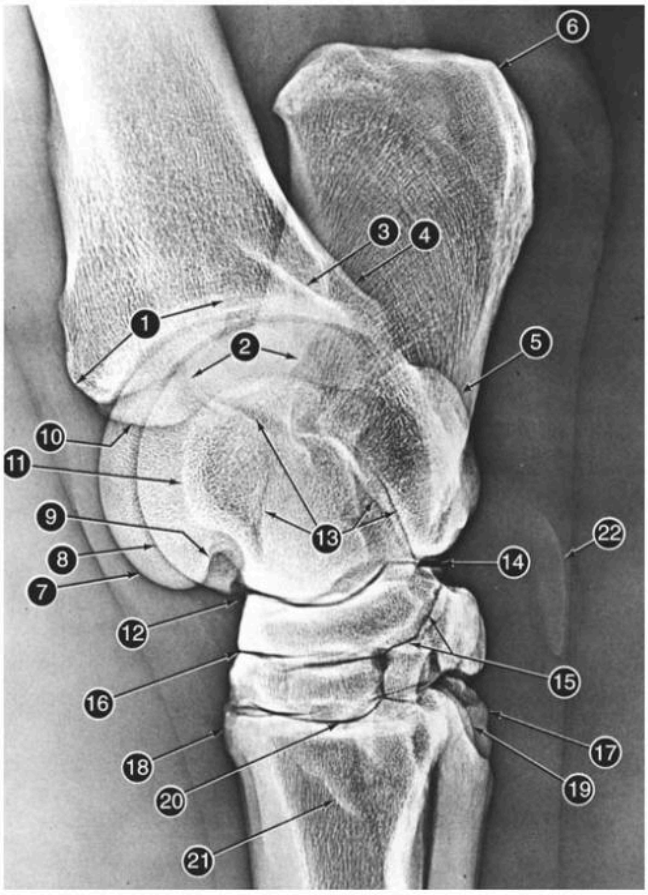


Fig. 16.55 Lateromedial (lateral) xeroradiograph of left equine tarsus.
1. Lateral malleolus
2. Medial malleolus
3. Radiopaque line produced by ridge on caudal surface of tibia
4. Medial part of caudal surface of tibia
5. Sustentaculum tali
6. Tuber calcanei
7. Lateral ridge of trochlea tali
8. Medial ridge of trochlea tali
9. Larger notch associated with lateral ridge of trochlea tali
10. Intermediate part of tibial cochlea
11. Groove of trochlea tali
12. Proximal intertarsal joint
13. Articular facets between talus and calcaneus
14. Plantar aspect of proximal intertarsal joint
15. Articulation between central tarsal bone and fused first and second tarsal bones
16. Distal intertarsal joint
17. Base of metatarsal bone 2
18. Base of metatarsal bone 3
19. Base of metatarsal bone 4
20. Tarsometatarsal joint
21. Groove on metatarsal bone 3 for dorsal metatarsal artery 3
22. Chestnut (torus tarseus)

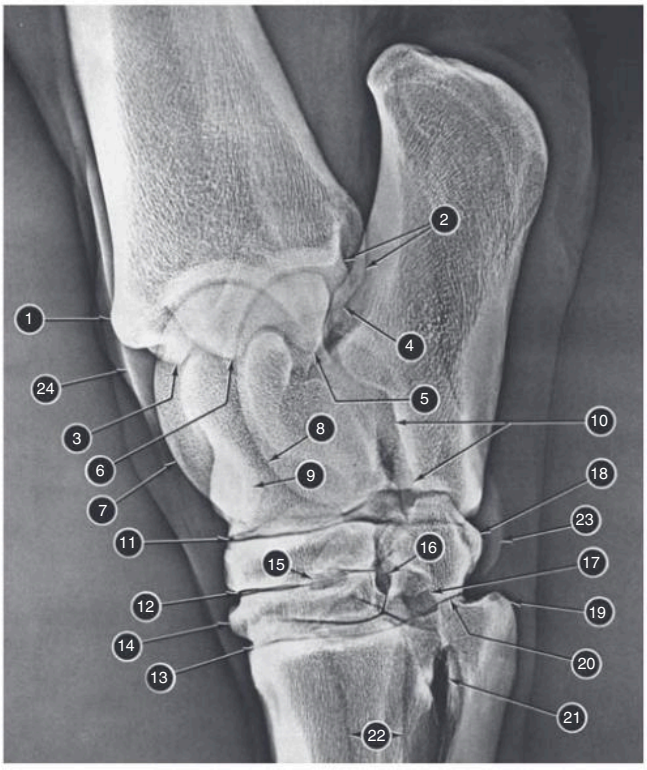


Fig. 16.56 Dorsolateral-plantaromedial oblique xeroradiograph of left equine tarsus.
1. Cranial aspect of medial malleolus
2. Shadows produced by borders of groove in lateral malleolus
3. Distal projection of medial malleolus
4. Distal projection of lateral malleolus
5. Caudal aspect of intermediate ridge of tibial cochlea
6. Cranial aspect of intermediate ridge of tibial cochlea
7. Medial ridge of trochlea tali
8. Lateral ridge of trochlea tali
9. Radiopaque area produced by distal tubercle of talus
10. Sinus tarsi
11. Dorsomedial aspect of proximal intertarsal joint
12. Dorsomedial aspect of distal intertarsal joint
13. Dorsomedial aspect of third tarsometatarsal joint
14. Ridge on dorsomedial aspect of third tarsal bone
15. Nonarticular area between central tarsal bone and third tarsal bone
16. Dorsal opening of tarsal canal
17. Plantar opening of tarsal canal
18. Plantar tuberosity on fourth tarsal bone
19. Base of metatarsal bone 4
20. Articulation between fourth tarsal bone and metatarsal bone 4
21. Interosseous space between metatarsal bones 3 and 4
22. Metatarsal bone 2
23. Chestnut
24. Tendons crossing flexor surface of tarsus

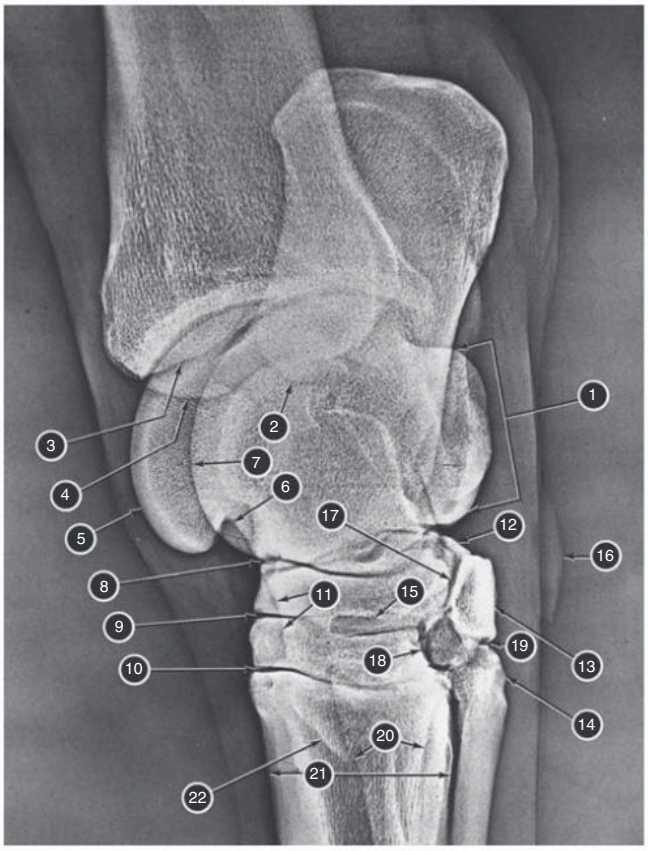


Fig. 16.57 Dorsomedial-plantarolateral oblique xeroradiograph of left equine tarsus.

1. Sustentaculum tali
2. Distal extremity of medial malleolus
3. Distal extremity of lateral malleolus
4. Intermediate ridge of tibial cochlea
5. Lateral ridge of trochlea tali
6. Notch distal to lateral ridge of trochlea tali
7. Medial ridge of trochlea tali
8. Dorsolateral aspect of proximal intertarsal joint
9. Dorsolateral aspect of distal intertarsal joint
10. Dorsolateral aspect of third tarsometatarsal joint
11. Dorsal aspect of fourth tarsal bone
12. Plantaromedial aspect of central tarsal bone
13. Plantaromedial aspect of fused first and second tarsal bones
14. Plantaromedial aspect of metatarsal bone 2
15. Nonarticular depression between central tarsal bone and third tarsal bone
16. Chestnut
17. Articulation between fused first and second tarsal bones and central tarsal bone
18. Articulation between fused first and second tarsal bones and third tarsal bone
19. Articulation between fused first and second tarsal bones and metacarpal bone 2
20. Metacarpal bone
21. Metacarpal bone 3
22. Radiopaque line produced by border of groove for dorsal metatarsal artery 3

REFERENCES

1. Evans HE. *Miller's Anatomy of the Dog*. 3rd ed. Philadelphia: W. B. Saunders Co; 1993.
2. Waibl H, Mayrhofer E, Matis U, et al. *Atlas of Radiographic Anatomy of the Dog*. Stuttgart: Parey Verlag; 2005.
3. Schebitz H, Wilkens H. *Atlas of Radiographic Anatomy of the Horse*. 3rd ed. Philadelphia: Saunders; 1978.
4. Denoix JM. In: *The Equine Distal Limb. An Atlas of Clinical Anatomy and Comparative Imaging*. Boca Raton: CRC Press; 2000.
5. Schebitz H, Wilkens H. *Atlas of Radiographic Anatomy of the Dog and Cat*. 4th ed. Philadelphia: W.B. Saunders Co; 1986.
6. Thrall D, Robertson ID. *Atlas of Normal Radiographic Anatomy and Anatomic Variants in the Dog and Cat*. 2nd ed. St Louis: Elsevier; 2016.
7. Coulson A, Lewis N. *An Atlas of Interpretative Radiographic Anatomy of the Dog and Cat*. 2nd ed. Ames: Blackwell Publishing; 2008.
8. Smallwood JE, Shively MJ, Rendano VT, et al. A standardized nomenclature for radiographic projections used in veterinary medicine. *Vet Radiol*. 1985;26:2.
9. Smallwood JE, Shively MJ. Radiographic and xeroradiographic anatomy of the equine carpus. *Equine Pract*. 1979;1:22.
10. Smallwood JE, Holladay SD. Xeroradiographic anatomy of the equine digit and metacarpophalangeal region. *Vet Radiol*. 1987;28:166.
11. Shively MJ, Smallwood JE. Radiographic and xeroradiographic anatomy of the equine tarsus. *Equine Pract*. 1980;2:19.

CHAPTER 17

Principles of Radiographic Interpretation of the Appendicular Skeleton and Radiographic Features of Bone Tumors

Donald E. Thrall

POSITIONING: DOG AND CAT

Radiographic examination of extremities in dogs and cats should consist of a minimum of two orthogonal projections, a lateral view and a craniocaudal* view. The radiographic field of view should include the joints proximal and distal to the bone of interest. If a joint is being investigated, the primary x-ray beam should be centered on that joint. Occasionally, especially for complex joints like the carpus and tarsus, there are views in addition to the standard orthogonal views that are used for further clarification. These *oblique* views allow evaluation of an edge that is not projected in the standard view. Oblique views are discussed later in the section on equine positioning as they are used more frequently in the horse than in the dog or cat.

There are a few highly specific ancillary projections in dogs that allow evaluation of the edge of surfaces that cannot be assessed in the conventional views. Examples include a cranioproximal/craniodistal view of the bicipital groove for changes associated with bicipital tenosynovitis (Fig. 17.1A) and a flexed dorsoplantar view of the canine tarsus for evaluation of the trochlea of talus without superimposition of calcaneus, for changes associated with osteochondrosis of the talus (see Fig. 17.1B). These specific views are provided only as examples of how changing the orientation of the x-ray beam can lead to projection of clinically important surfaces that cannot be assessed adequately in more standard views. These ancillary views, and others, are discussed throughout the textbook where appropriate.[1]

POSITIONING: HORSE

One aspect of equine radiography that deserves special mention is the common practice of holding the plate by hand. Equine extremity radiographs are almost always acquired with the horse in a standing position, and holding the plate by hand is convenient. However, handholding the plate increases the chance that radiation safety practices will be compromised. Individuals holding a plate by hand should wear protective lead aprons and lead gloves, as well as a thyroid shield and protective lead glasses. And the positioning must be such that no part of the holder is in the primary x-ray beam.

The use of a plate holder for equine extremity radiography is encouraged because it will minimize occupational radiation exposure. A plate holder secures the plate and has an extension handle so that the hands are distant from the primary x-ray beam. A potential disadvantage of a plate holder is the strength needed to position the plate properly.

There are very few instances in the horse where two orthogonal views of a limb will suffice. Two orthogonal views might be adequate for examining the radius or tibia, but even in those sites, *oblique* views are often needed for completeness. Oblique views are intended to project *edges* of a joint or region that cannot be evaluated in standard orthogonal views. More than the edge of a structure can be assessed in any radiograph, but important edge lesions can be overlooked unless they are projected at the periphery of the part. Oblique views maximize the chances of detecting an edge lesion in a complex joint. In oblique views, the point of entrance of the primary x-ray beam is typically moved 30 to 45 degrees medial or 30 to 45 degrees lateral to the point of entrance used for a conventional view. The geometry of oblique projections can be confusing, and this will be explained using the equine carpus as a model (Table 17.1, Figs. 17.2–17.5).†

In a dorsopalmar view of the carpus, the x-ray beam strikes the dorsal surface and the medial and lateral edges are projected in an unobstructed fashion (see Fig. 17.2). A palmarodorsal view would be similar.

In a lateromedial view of the carpus, the x-ray beam strikes the lateral surface, and the dorsal and palmar edges are projected in an unobstructed fashion (see Fig. 17.3). A mediolateral view would be similar.

In a dorsolateral-palmaromedial view of the carpus, the x-ray beam strikes the dorsolateral surface (between the true dorsal and lateral surfaces) with the dorsomedial and palmarolateral edges projected in an unobstructed fashion (see Fig. 17.4). A palmaromedial-dorsolateral view would be similar.

In a dorsomedial-palmarolateral view of the carpus, the x-ray beam strikes the dorsomedial surface with the dorsolateral and palmaromedial edges projected in an unobstructed fashion (see Fig. 17.5). A palmarolateral-dorsomedial view would be similar.

AGGRESSIVE VERSUS NONAGGRESSIVE BONE LESIONS

The principle of using roentgen signs to describe radiographic abnormalities was introduced in Chapter 6, and this method is applicable to describing bone lesions located anywhere in the body. However, in addition to describing a bone lesion according to roentgen signs, an important distinction is whether the bone lesion is caused by an aggressive process, such as a tumor or infection, versus a nonaggressive process, such as a bone cyst. Determining whether a bone lesion is aggressive will

*The term *craniocaudal* applies to a view of a limb where the x-ray beam strikes the front of the limb proximal to the antebrachiocarpal or tarsocrural joint. Views distal to these points would be termed *dorsopalmar* and *dorsoplantar*, respectively. A caudocranial (or palmarodorsal or plantarodorsal) view would be comparable.

†In Figs. 17.2 through 17.5, the imaging plate is oriented perpendicular to the primary x-ray beam, but the plate is not shown for the sake of clarity.

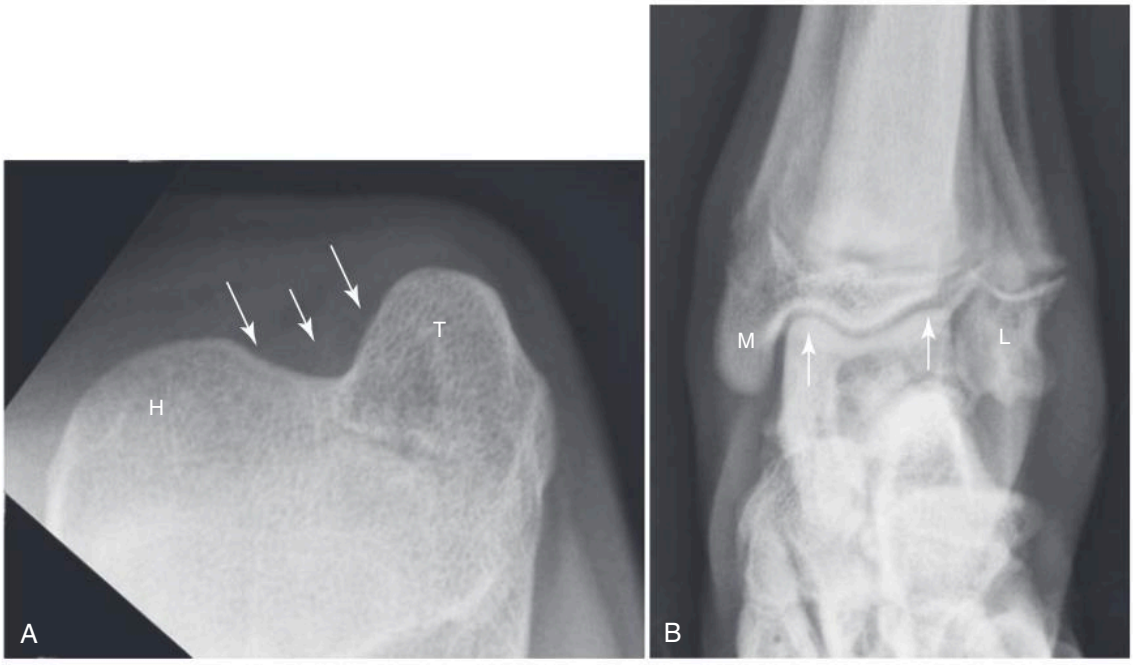


Fig. 17.1 **A,** Cranioproximal/craniodistal view of the proximal humerus to project the bicipital groove (*white arrows*). *H*, Humeral head; *T*, greater tubercle. **B,** Flexed dorsoplantar view of the canine tarsus to project the trochlea of the talus (*white arrows*) without superimposition of the calcaneus. *H,* Humeral head; *L,* lateral malleolus; *M,* medial malleolus; *T,* greater tubercle.

Table • **17.1**

Summary of Edges Projected in Oblique Radiographs.

PROJECTION	STRIKE POINT OF PRIMARY X-RAY BEAM	EDGES PROJECTED
Dorsopalmar	Dorsal	Lateral and medial
Dorsoplantar	Dorsal	Lateral and medial
Craniocaudal	Cranial	Lateral and medial
Palmarodorsal	Palmar	Lateral and medial
Plantarodorsal	Plantar	Lateral and medial
Caudocranial	Caudal	Lateral and medial
Lateromedial	Lateral	Dorsal and palmar, or dorsal and plantar, or cranial and caudal
Mediolateral	Medial	Dorsal and palmar, or dorsal and plantar, or cranial and caudal
Dorsolateral/palmaromedial	Dorsolateral	Dorsomedial and palmarolateral
Palmaromedial/dorsolateral	Palmaromedial	Dorsomedial and palmarolateral
Dorsolateral/plantaromedial	Dorsolateral	Dorsomedial and plantarolateral
Plantaromedial/dorsolateral	Plantaromedial	Dorsomedial and plantarolateral
Craniolateral/caudomedial	Craniolateral	Craniomedial and caudolateral
Caudomedial/craniolateral	Caudomedial	Craniomedial and caudolateral
Dorsomedial/palmarolateral	Dorsomedial	Dorsolateral and palmaromedial
Palmaromedial/dorsomedial	Palmaromedial	Dorsolateral and palmaromedial
Dorsomedial/plantarolateral	Dorsomedial	Dorsolateral and palmaromedial
Plantarolateral/dorsomedial	Plantarolateral	Dorsolateral and palmaromedial

be helpful in directing patient management. For example, a nonaggressive bone lesion could be evaluated sequentially over time for any change. However, sequential evaluation of an aggressive lesion, which is often due to a tumor or an infections process, could jeopardize the patient. Also, if an aggressive bone lesion is present, thoracic radiographs are indicated and an aspirate or biopsy should also be considered. Distinguishing an aggressive from a nonaggressive bone lesion involves the consideration of several specific factors other than basic roentgen signs.

Three criteria are used to determine whether a bone lesion is aggressive: (1) the integrity of the cortex, (2) the character of any periosteal reaction, and (3) the distinctness of the boundary between the bone lesion and the normal bone, called the

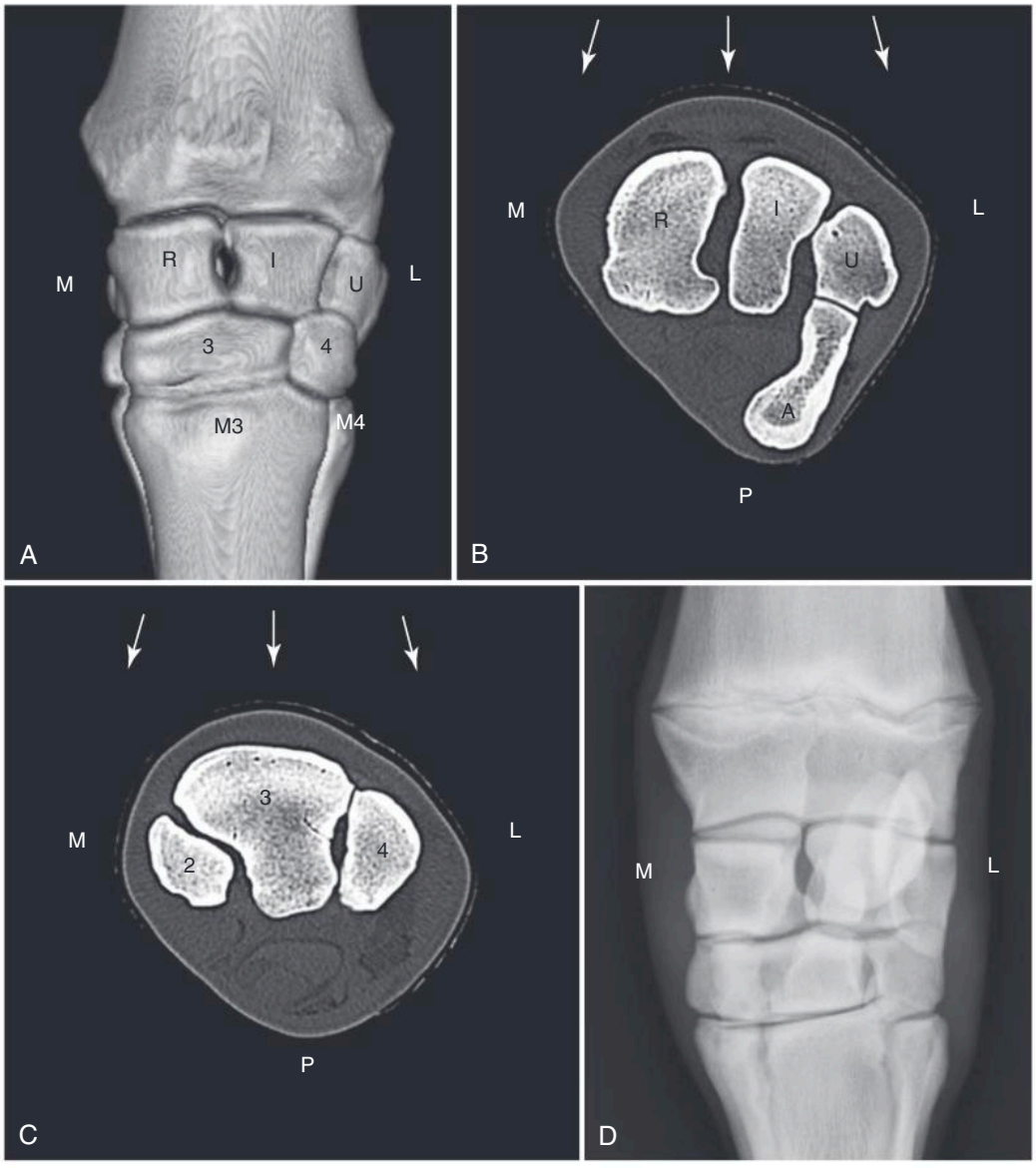


Fig. 17.2 Anatomy of a dorsopalmar radiograph of the equine carpus. **A,** Three-dimensional volume-rendered computed tomography (CT) image of an equine carpus from a dorsal perspective. **B,** Transverse CT image of an equine carpus through the proximal row of carpal bones. **C,** Transverse CT image of an equine carpus through the distal row of carpal bones. **D,** Dorsopalmar equine carpal radiograph. In **B** and **C,** the *white arrows* indicate the direction of the primary x-ray beam. For a dorsopalmar projection, the x-ray beam strikes the dorsal surface of the carpus and the medial and lateral edges of the carpus will be projected. *2,* Second carpal bone; *3,* third carpal bone; *4,* fourth carpal bone; *A,* accessory carpal bone; *I,* intermediate carpal bone; *L,* lateral; *M,* medial; *M3,* third metacarpal bone; *M4,* fourth metacarpal bone; *P,* palmar; *R,* radial carpal bone; *U,* ulnar carpal bone.

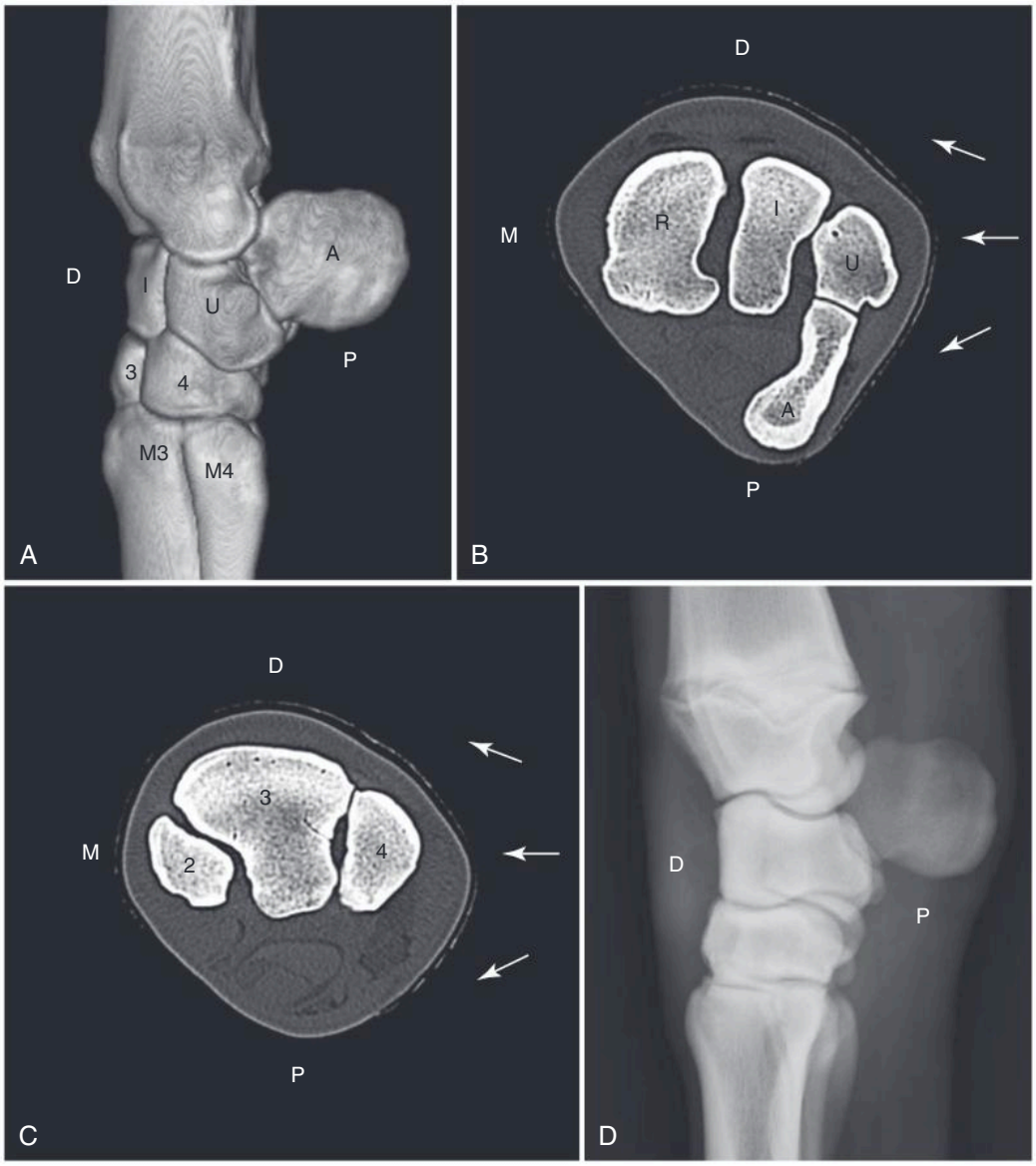


Fig. 17.3 Anatomy of a lateromedial radiograph of the equine carpus. **A,** Three-dimensional volume-rendered computed tomography (CT) image of an equine carpus from a lateral perspective. **B,** Transverse CT image of an equine carpus through the proximal row of carpal bones. **C,** Transverse CT image of an equine carpus through the distal row of carpal bones. **D,** Lateromedial equine carpal radiograph. In **B** and **C,** the *white arrows* indicate the direction of the primary x-ray beam. For a lateromedial projection, the x-ray beam strikes the lateral surface of the carpus and the dorsal and palmar edges of the carpus will be projected. *2,* Second carpal bone; *3,* third carpal bone; *4,* fourth carpal bone; *A,* accessory carpal bone; *D,* dorsal; *I,* intermediate carpal bone; *M,* medial; *M3,* third metacarpal bone; *M4,* fourth metacarpal bone; *P,* palmar; *R,* radial carpal bone; *U,* ulnar carpal bone.



Fig. 17.4 Anatomy of a dorsolateral-palmaromedial radiograph of the equine carpus. **A,** Three-dimensional volume-rendered computed tomography (CT) image of an equine carpus from a dorsolateral perspective. **B,** Transverse CT image of an equine carpus through the proximal row of carpal bones. **C,** Transverse CT image of an equine carpus through the distal row of carpal bones. **D,** Dorsolateral-palmaromedial equine carpal radiograph. In **B** and **C,** the *white arrows* indicate the direction of the primary x-ray beam. For a dorsolateral/palmaromedial radiograph, the x-ray beam strikes the dorsolateral surface of the carpus, and the dorsomedial and palmarolateral edges of the carpus will be projected. *2,* Second carpal bone; *3,* third carpal bone; *4,* fourth carpal bone; *A,* accessory carpal bone; *D,* dorsal; *DM,* dorsomedial; *I,* intermediate carpal bone; *L,* lateral; *M,* medial; *M3,* third metacarpal bone; *M4,* fourth metacarpal bone; *P,* palmar; *PL,* palmarolateral; *PM,* palmaromedial; *R,* radial carpal bone; *U,* ulnar carpal bone.

transition zone (Table 17.2). An aggressive bone lesion will have either an area of cortex destruction **and/or** an active periosteal reaction **and/or** an indistinct transition zone. Therefore, only one criterion of aggressiveness is needed to fulfill the definition of aggressiveness. Importantly, whether a lesion is primarily radiolucent (loss of bone) or radiopaque (production of bone) has no bearing on whether the lesion is aggressive.

Destruction of the Cortex

For cortex destruction, also referred to as *cortex effacement*, to be apparent radiographically, the region of destruction must be hit tangentially by the primary x-ray beam. In other words, the *edge* of the cortex destruction must be visible radiographically, and this depends on the orientation of the cortical destruction with the primary x-ray beam (Figs. 17.6–17.8). If the cortex destruction is not projected tangentially, the affected region of bone will appear more radiolucent, but a discrete area of cortex destruction will not be identified.

Not all bone destruction involves the cortex. Bone loss can be totally within the medullary cavity with preservation of the cortex. Purely medullary bone loss does not mean that the lesion is not aggressive; it means only that one feature of lesion aggressiveness (i.e., cortical destruction) is not present.

A subclassification of bone lysis into geographic, moth-eaten, and permeative patterns has been described.[2] Geographic bone lysis is a large, relatively well-defined region

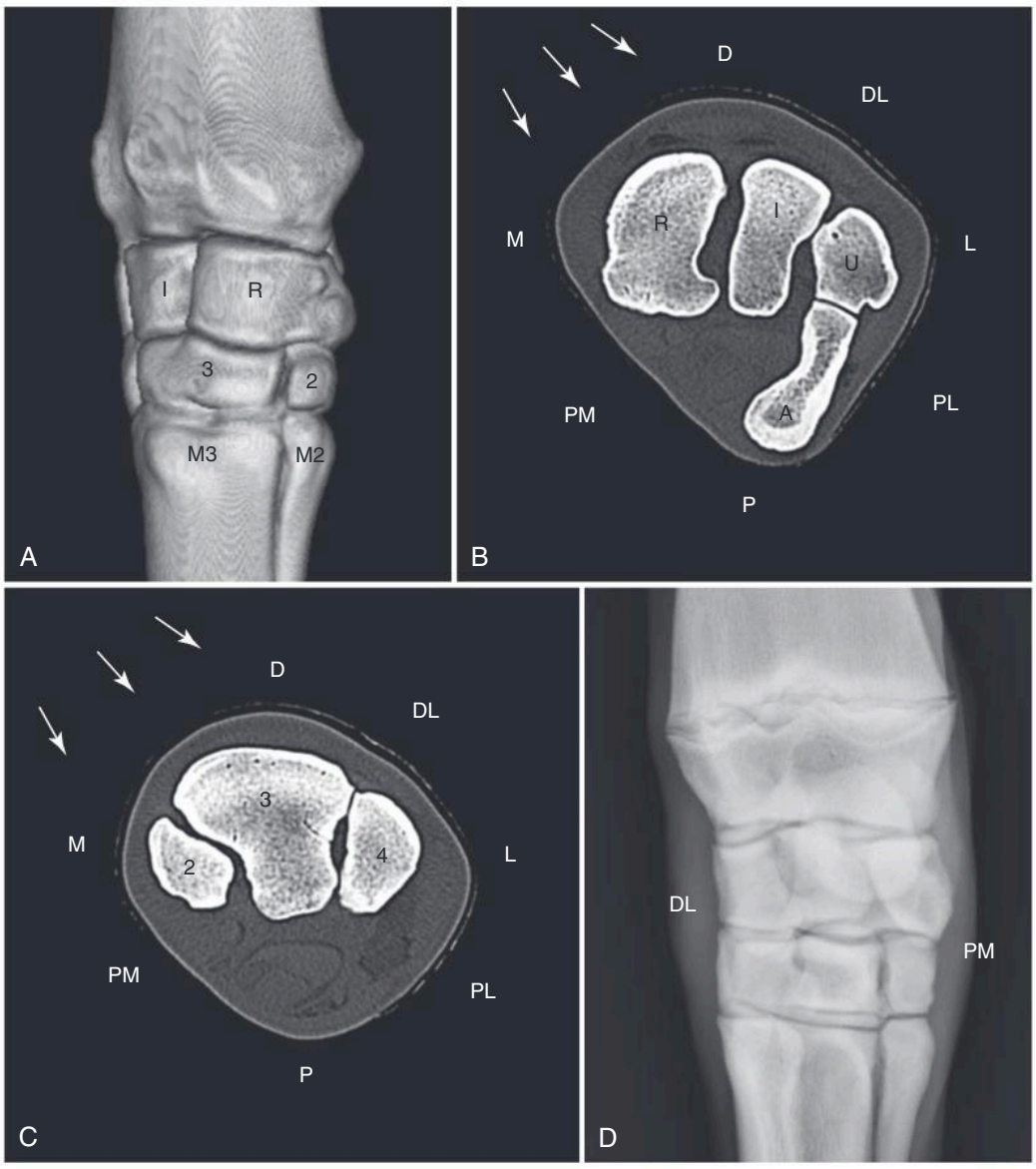


Fig. 17.5 Anatomy of a dorsomedial-palmarolateral radiograph of the equine carpus. **A,** Three-dimensional volume-rendered computed tomography (CT) image of an equine carpus from a dorsomedial perspective. **B,** Transverse CT image of an equine carpus through the proximal row of carpal bones. **C,** Transverse CT image of an equine carpus through the distal row of carpal bones. **D,** Dorsomedial-palmarolateral equine carpal radiograph. In **B** and **C,** the *white arrows* indicate the direction of the primary x-ray beam. For a dorsomedial/palmarolateral projection, the x-ray beam strikes the dorsomedial surface of the carpus, and the dorsolateral and palmaromedial edges of the carpus will be projected. *2,* Second carpal bone; *3,* third carpal bone; *4,* fourth carpal bone; *A,* accessory carpal bone; *D,* dorsal; *DL,* dorsolateral; *I,* intermediate carpal bone; *L,* lateral; *M,* medial; *M2,* second metacarpal bone; *M3,* third metacarpal bone; *P,* palmar; *PL,* palmarolateral; *PM,* palmaromedial; *R,* radial carpal bone; *U,* ulnar carpal bone.

Table • **17.2**

Features of Aggressive and Nonaggressive Bone Lesions.

LESION CLASS	CORTICAL DESTRUCTION	PERIOSTEAL REACTION	TRANSITION ZONE
Aggressive	Yes	Active (irregular)	Not distinct
Nonaggressive	None or expansion of cortex without destruction	None or smooth	Distinct

The presence of any one feature of aggressiveness is sufficient to classify the lesion as such; it is not necessary for all three criteria of aggressiveness to be fulfilled.

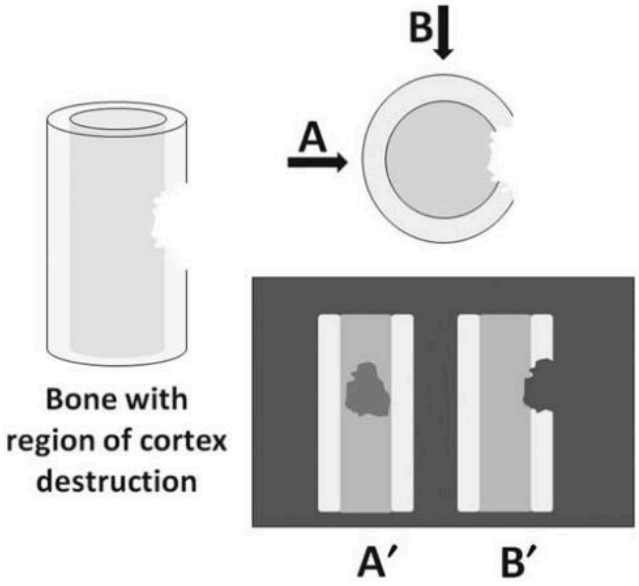


Fig. 17.6 Diagram illustrating the effect of x-ray beam orientation on appearance of cortex destruction. The drawing on the *left* is a bone with a region of cortex destruction. At the *top right* is a cross-section of the bone through the region of cortex destruction. Two orientations of the x-ray beam are shown. In orientation *A*, the x-ray beam strikes the cortex destruction *en face*. In orientation *B*, the x-ray beam strikes the cortex destruction *tangentially*. At the *bottom right* is a diagram of the radiograph resulting from each orientation. In *A′*, the cortex defect will appear as a region of decreased opacity in the center of the bone but the actual defect will not be apparent. In *B′*, the cortex defect is apparent because the defect has been struck tangentially by the x-ray beam. This reemphasizes the importance of having at least two projections of each part being radiographed.

of bone loss (Fig. 17.9). Moth-eaten and permeative patterns of bone lysis are similar and describe the presence of multiple smaller foci, or a less well-defined permeating pattern, of bone lysis (Figs. 17.10 and 17.11). It has been suggested that geographic bone lysis characterizes a less aggressive bone lesion than either moth-eaten or permeative lysis.[2] However, this is not always true and whether a lesion is aggressive should be based only on the criteria noted in Table 17.2. These patterns of lysis should be reserved for descriptive purposes only, as in communication or reports.

In a nonaggressive bone lesion, the cortex may be uninvolved, or it may be expanded without destruction (Fig. 17.12).

Periosteal Reaction

Periosteal bone proliferation is most commonly caused by elevation of the periosteum or regional hyperemia causing activation of bone-forming mesenchymal cells (Fig. 17.13). An active periosteal reaction is a feature of an aggressive bone lesion and is one where the margin of the periosteal reaction is *irregular*, not smooth. There are various degrees of periosteal reactivity and almost innumerable specific appearances of an active periosteal reaction. The presence of an *irregular margin* is the clue that the periosteal reaction is active. Any evidence of periosteal irregularity is consistent with an aggressive bone lesion (Figs. 17.14–17.16). In comparison, a nonaggressive periosteal reaction is characterized by a smooth edge to the periosteal new bone growth (Figs. 17.17 and 17.18) due to remodeling of the periosteal surface after a previous insult or a very slowly proceeding disease process. A smooth periosteal reaction does not mean that the lesion is not aggressive as there may be another finding that characterizes the lesion as aggressive. For example, a lesion with a smooth periosteal reaction but an indistinct transition zone would still be aggressive, as in Fig. 17.17.

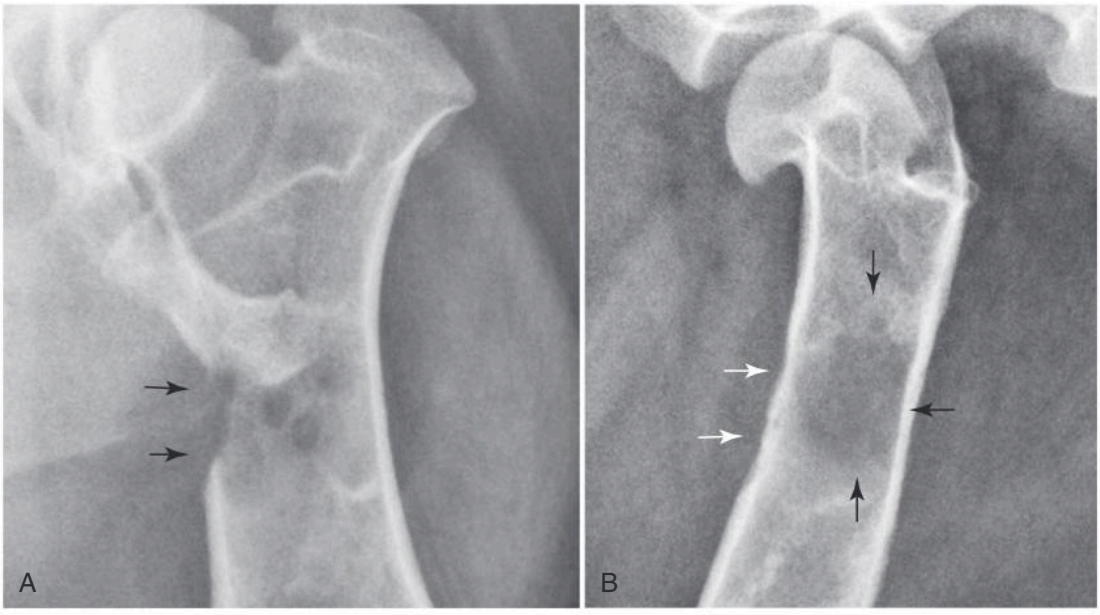


Fig. 17.7 Craniocaudal **(A)** and lateral **(B)** radiographs of the femur of a dog with region of cortex destruction due to metastatic carcinoma. In **A,** the x-ray beam strikes the cortex destruction tangentially (*black arrows*). In **B,** the cortex destruction is superimposed on the bone (*black arrows*) and is not specifically identified. The cranial cortex is irregular (*white arrows*) but is not completely effaced.

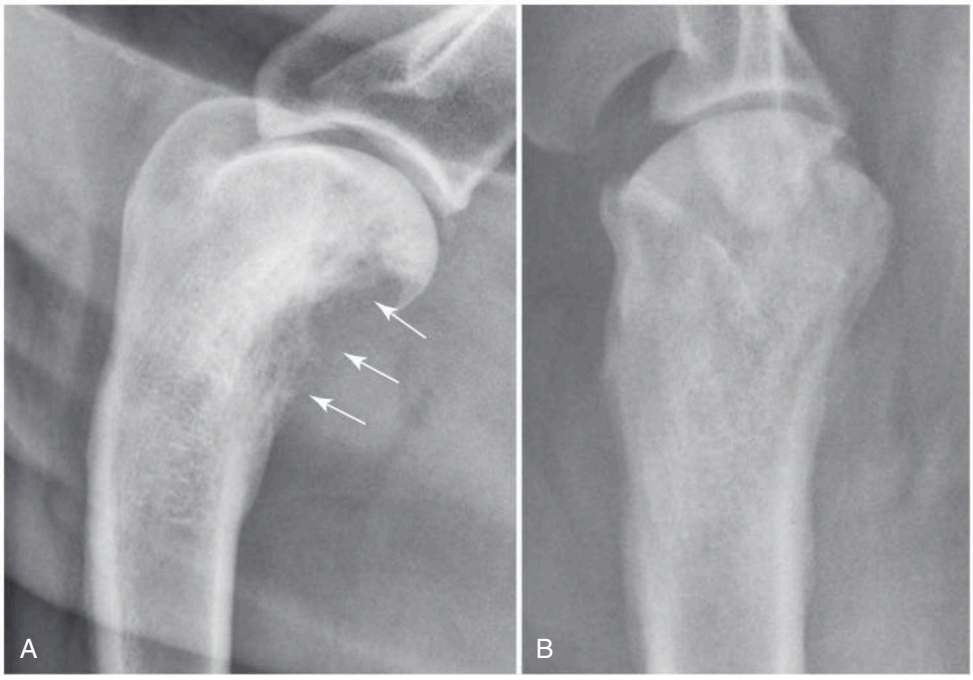


Fig. 17.8 Lateral **(A)** and caudocranial **(B)** views of the proximal aspect of the humerus of a dog with a region of cortex destruction due to osteosarcoma. In **A,** there is obvious destruction of the caudal aspect of the cortex (*white arrows*). In **B,** the cortex destruction is not evident because it is superimposed on the bone.



Fig. 17.9 Lateral radiograph of the distal metacarpus of a horse. There is a large region of geographic bone lysis in the third metacarpal bone (*black arrows*). This lesion has a well-defined transition zone (*black arrows*).

Transition Zone

The character of the junction of the bone lesion with the adjacent normal bone is termed the *transition zone*. The transition zone is typically evaluated in the medullary cavity of the bone. The host bone is usually able to contain a nonaggressive process by forming a sclerotic rim around any area of diseased bone, and the transition zone between the lesion and



Fig. 17.10 Craniocaudal view of the proximal femur of a cat where multiple small areas of moth-eaten lysis are present. The border of these lesions is not well defined, and this is an aggressive process.

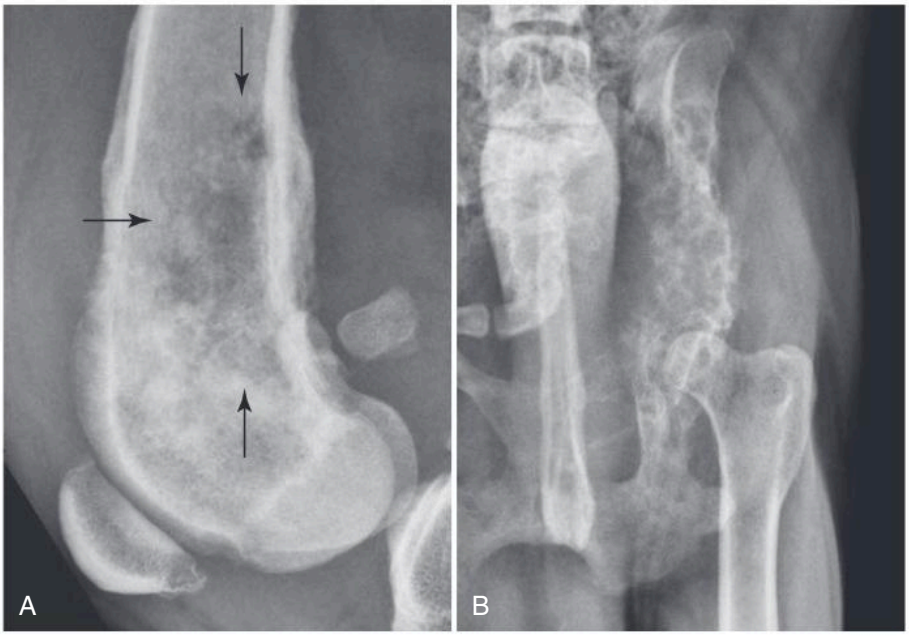


Fig. 17.11 Lateral radiograph of the distal femur in a dog **(A)** and ventrodorsal radiograph of the left hemipelvis of a dog **(B)** with each characterized by permeative lysis. In **A,** the region of lysis is poorly defined (*black arrows*). There is also a sclerotic component and a periosteal reaction. In **B,** the medial cortex of the ilium is also destroyed.



Fig. 17.12 Craniocaudal radiograph of the antebrachium of a dog with a nonaggressive lesion in the ulna. There is expansion of the cortex but not destruction; the edge of the expanded cortex is smooth. There is no active periosteal reaction. Also, the demarcation between abnormal and normal bone, the transition zone, is distinct (*black arrows*).

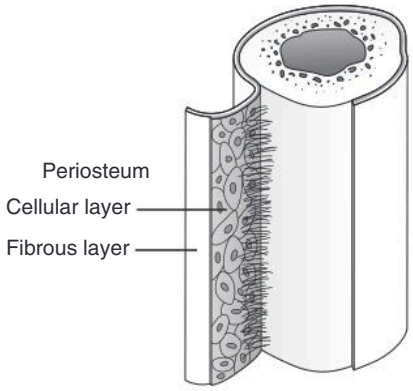


Fig. 17.13 Illustration of the different layers of the periosteum. A cellular layer with mesenchymal cells which have the potential to be activated to produce new bone is covered by a fibrous layer.

the host bone will be easy to define radiographically (Fig. 17.19, see Fig. 17.12). In aggressive bone lesions, the host bone is unable to contain the lesion as the ongoing disease process does not allow for mineral deposition to contain the lesion, and there is no demarcation between the lesion and the host bone (Fig. 17.20, see Fig. 17.17).

As already noted, it is not necessary for a lesion to have all three radiographic features of aggressiveness (cortical destruction, active periosteal reaction, and an indistinct transition zone) to be characterized as aggressive. Any single criterion is sufficient. Moreover, the combined radiographic features of the aggressiveness of a bone lesion are a continuum from a minor alteration in cortex integrity, periosteal response, or transition zone, to major alterations in all three parameters. Importantly, there is not a clinically significant correlation between the number of aggressive features of a lesion, or the extent of their aggressiveness, and the biologic behavior of the lesion. In other words, low radiographic aggressiveness does not mean low biologic aggressiveness. But, importantly, the absence of radiographic evidence of aggressiveness usually means no biologic aggressiveness. Finally, as already mentioned, the categorization of aggressiveness does not take into account whether the lesion is primarily productive or primarily destructive.

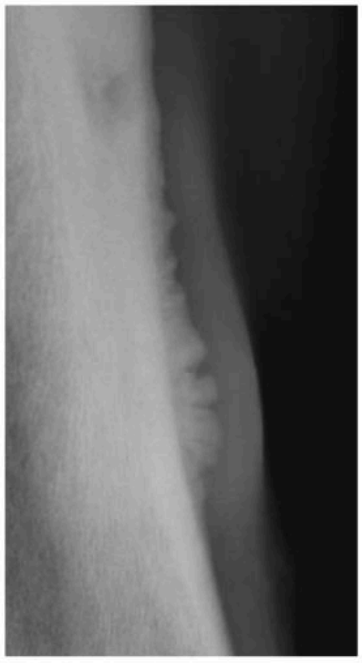


Fig. 17.14 An active periosteal reaction on the radius of a horse with a nondisplaced fracture; the fracture line is not visible in this image. Normal callus is not irregular, and this active periosteal reaction was due to osteomyelitis.

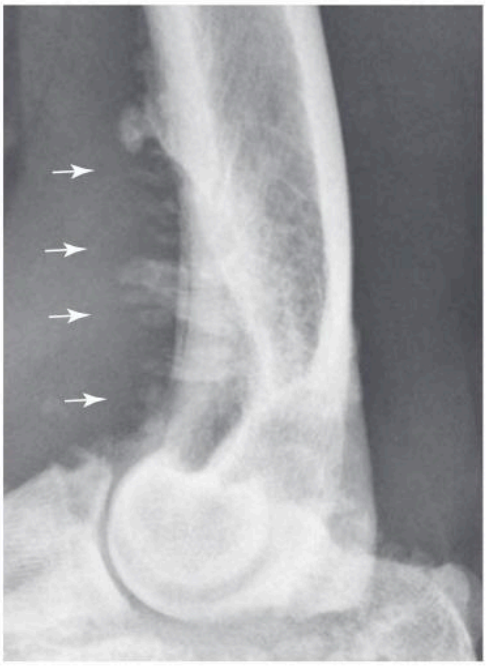


Fig. 17.16 Lateral radiograph of the distal humerus of a dog with an osteosarcoma. There is an active, irregular, periosteal reaction on the humerus (*white arrows*).



Fig. 17.15 Lateral radiograph of the distal antebrachium of a dog with radial osteosarcoma. There is an active, irregular, periosteal reaction on the radius (*white arrows*). The transition zone between the proximal end of the radial lesion and normal bone in the radius is also poorly defined.



Fig. 17.17 Lateral radiograph of the antebrachium of a 7-month-old German shepherd with canine panosteitis.‡ The panosteitis resulted in poorly defined, increased bone opacity in the medullary cavity of the radius that has an indistinct transition zone, but in this dog, there is also a smooth periosteal reaction on the radius.

‡Canine panosteitis is discussed in Chapter 18.



Fig. 17.18 Lateral radiograph of a femur. There is a healed malunion midshaft fracture. There is exuberant smooth periosteal reaction cranial and caudal to the healed fracture representing normal fracture callus.

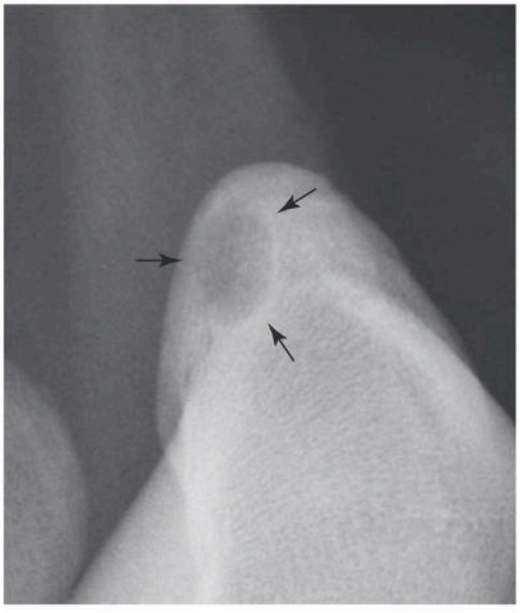


Fig. 17.19 Plantaroproximal-plantarodistal view of an equine calcaneus. There is a well-defined region of bone loss and the edge of the lesion is sharply defined (*black arrows*). This is an example of a well-defined transition zone. There are no other signs of aggressiveness—that is, no cortex destruction and no active periosteal reaction.



Fig. 17.20 Lateral radiograph of the distal femur of a dog with an osteosarcoma. At the proximal extent of the lesion, it is impossible to identify the point at which the abnormal bone ends and the normal bone begins. This is an indistinct transition zone. An active periosteal reaction is also present.

Causes of an Aggressive Lesion

If an aggressive bone lesion is identified, the DAMNITV (degenerative, anomalous, metabolic, neoplastic, infectious [inflammatory, immune], traumatic, and vascular) approach should be used to formulate the list of possible causes. Of most concern is whether the lesion is neoplastic or infectious. A definitive distinction between neoplastic and infectious bone lesions is impossible by radiographic means. However, the radiographic features of the bone lesion, such as the number of bones involved and the location of the lesions within the bones, along with the signalment, history, and physical and laboratory findings can be used to prioritize the possible causes (Table 17.3). Nevertheless, a biopsy or fine-needle aspirate with histopathologic or cytologic evaluation and possibly microbiologic culture is almost always needed for the definitive diagnosis of any aggressive bone lesion where a diagnosis cannot be assumed from the clinical scenario.

Primary Bone Tumors

There are many types of primary bone tumors in the dog, but osteosarcoma is the most common. Canine osteosarcoma is usually characterized by a single (monostotic) aggressive bone lesion originating in the metaphysis.[3] The age distribution of canine osteosarcoma is bimodal with a small peak in incidence at approximately 2 years of age and then a larger peak in incidence later in adult life.[3] Age distribution in cats is not bimodal and osteosarcoma typically occurs in older cats.[4] Most primary bone tumors enlarge from the metaphysis into the epiphysis or diaphysis, or both. Common osteosarcoma sites in the forelimb are the proximal humerus and the distal radius (away from the elbow), and in the hindlimb the distal femur and proximal tibia (toward the stifle). Tumors in the distal tibia are also relatively common. However, a primary bone tumor can arise at any location in either the axial or appendicular skeleton. Primary

Table • 17.3

Common Features of Neoplastic and Infectious Bone Disease in the Appendicular Skeleton of Small Animals[a].

CRITERION	PRIMARY BONE TUMOR	METASTATIC BONE TUMOR	MYCOTIC OSTEOMYELITIS	BACTERIAL OSTEOMYELITIS: HEMATOGENOUS	BACTERIAL OSTEOMYELITIS: INOCULATION
Patient age	Usually old but occurs in young dogs	Old	Young to middle age	Young	Any
Mono- or polyostotic	Monostotic	Polyostotic[b]	Polyostotic[a,b]	Polyostotic	Monostotic or adjacent bones
Location in bone	Metaphysis[c]	Metaphysis or diaphysis	Metaphysis	Metaphysis	Anywhere
Likelihood of columnar periosteal reaction	+	−	−	−	+++

[a]Tabular features are only guidelines, and findings in individual patients may vary. Features are also based on the experience of the author and have not been substantiated by evidence-based investigations.
[b]The axial skeleton may also be affected.[c]Epiphyseal and diaphyseal tumors also occur.



Fig. 17.21 An aggressive lytic lesion (osteosarcoma) in the craniodistal aspect of the radius. There is marked cortex destruction and a poorly defined transition zone between the lytic lesion and normal bone.



Fig. 17.22 A predominantly productive, or sclerotic, aggressive lesion (osteosarcoma) in the distal diaphysis and metaphysis of the femur. This lesion is composed mainly of smoothly marginated new bone, but there is the lack of a sharp transition zone between normal and abnormal bone.

bone tumors do not often cross joints or invade adjacent bones but both can occur as the tumor enlarges. Appendicular osteosarcomas may be primarily lytic (Fig. 17.21), primarily productive (also termed *blastic* or *sclerotic*) (Fig. 17.22), or, most commonly, mixed, with both lytic and productive features (Fig. 17.23).

Occasionally, osteosarcoma develops secondary to bone infarction, either idiopathic bone infarction[5] or bone infarction secondary to chronic bone trauma such as surgical intervention with placement of a prosthetic joint or other implants.[6–8] Other, less common primary bone tumors include fibrosarcoma and chondrosarcoma.[3] Chondrosarcoma is most commonly located in flat bones such as the ribs and scapula.

Metastatic Bone Tumors

Any malignant tumor has the potential to metastasize to the skeleton, but in general bone metastasis from carcinomas is more common than from sarcomas. In dogs, mammary and lung cancers are a common source of bone metastasis. Metastatic tumor sites in the skeleton arise hematogeneously, which usually leads to a polyostotic distribution, either in the axial and/or appendicular skeleton (Fig. 17.24). The lesion distribution is metaphyseal or diaphyseal through the nutrient foramen,



Fig. 17.23 A mixed lytic and productive aggressive lesion (osteosarcoma) in the distal femoral metaphysis and epiphysis. There is an active, irregular, periosteal reaction (*black arrows*) and an indistinct transition zone proximally between normal and abnormal bone. The femoral cortex is thin but not effaced.

and most common sites are in the axial skeleton, such as vertebrae and ribs, and the proximal extent of long bones.[9]

Subungual Tumors Versus Subungual Infections

It is essentially impossible to differentiate between infectious and neoplastic bone lesions in the digit by radiographic means. The most common canine subungual tumors are squamous cell carcinoma and melanoma (Fig. 17.25), commonly occurring in large-breed dogs with black hair coats.[10] Inflammatory conditions of the digit are also common. The development of an aggressive digital lesion is equally frequent with neoplastic and inflammatory conditions. Digital tumors typically involve a single digit; however, a syndrome of metastasis of pulmonary tumors to multiple digits, termed the *lung-digit syndrome*, occurs in cats (Fig. 17.26).[11]

Fungal Bone Infections

Fungal osteomyelitis is another cause of an aggressive bone lesion in dogs. Fungal osteomyelitis typically involves large-breed young adult dogs,[12] and in the United States is most commonly found in geographic areas where predisposing fungi are endemic, such as the southeast (blastomycosis) and the southwest (coccidioidomycosis). However, infected dogs may relocate to nonendemic areas where the index of suspicion for fungal infections is low, and lack of suspicion may delay the diagnosis.

Fungal osteomyelitis is generally of hematogenous origin, leading to involvement of multiple bones (polyostotic

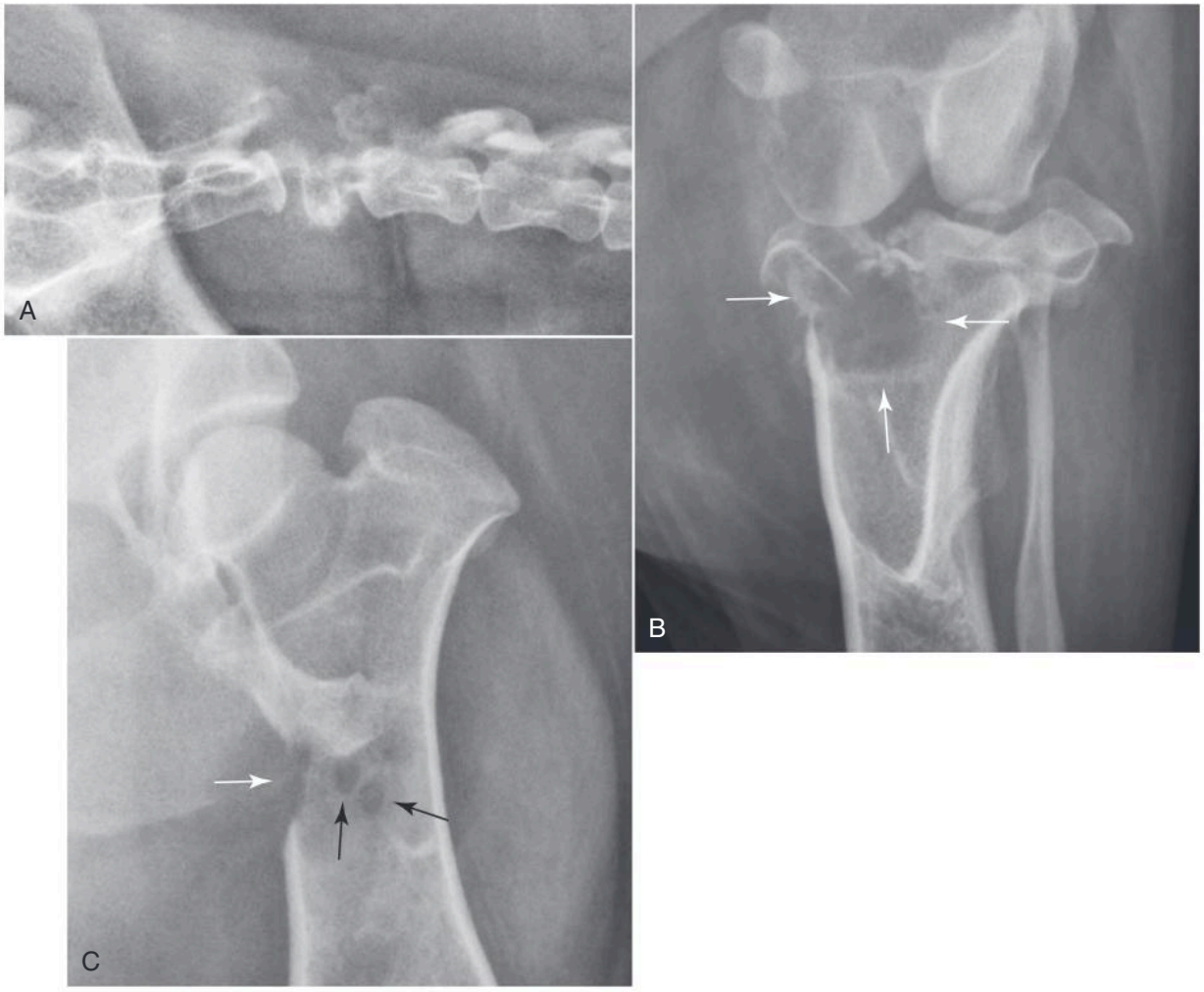


Fig. 17.24 Radiographs of a dog with metastatic round cell tumor. **A,** The first caudal vertebra is collapsed due to tumor effacement. **B,** There is a large lytic lesion in the proximal tibia (*white arrows*) that has caused cortical effacement and collapse of the medial tibial condyle. **C,** There is a large region of cortical lysis (*white arrow*) and multiple regions of moth-eaten lysis in the proximal aspect of the left femur (*black arrows*).

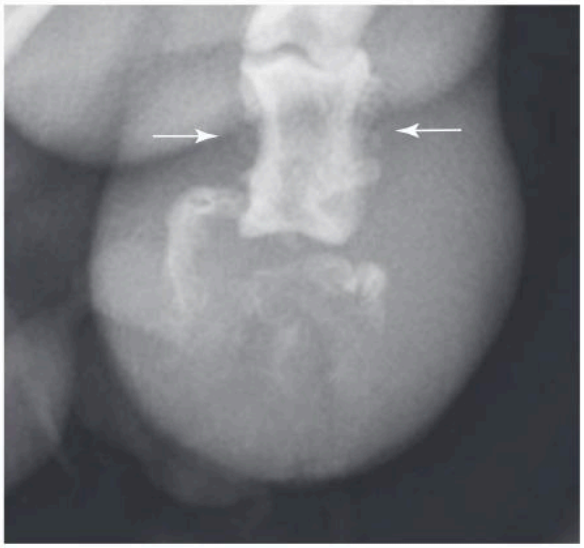


Fig. 17.25 Radiograph of the fifth digit of a dog. The digit is swollen, and there is extensive lysis of the distal phalanx. Histopathologic assessment will be needed for a definitive diagnosis. The diagnosis is squamous cell carcinoma. There is an active periosteal reaction on the middle phalanx of this digit (*white arrows*). This may be because of periosteal irritation from the soft tissue mass, but tumor invasion cannot be ruled out.



Fig. 17.26 **A,** Lateral thoracic radiograph of a 9-year-old cat with a large cavitary tumor (*white arrows*) in the caudal lung. This tumor is typical of a primary lung tumor. Dorsoplantar radiographs of the right **(B)** and left **(C)** pes of the same cat. In **B,** there is marked swelling of the third digit and nearly complete effacement of the middle and distal phalanges. In **C,** there is complete lysis of the distal phalanx of the second digit, and the digit is swollen. Development of multiple sites of digital metastases is sometimes observed in feline patients with primary lung tumors. This has been termed the lung-digit syndrome.

distribution). Fungal osteomyelitis should be considered in any dog with polyostotic aggressive bone lesions (Figs. 17.27). As with all aggressive bone lesions, biopsy and possibly microbiologic testing will be necessary for final diagnosis.

Fungal osteomyelitis can sometimes result in a monostotic aggressive lesion in the metaphysis (Fig. 17.28), as commonly occurs with a primary bone tumor. Thus, any monostotic metaphyseal aggressive lesion should be biopsied/aspirated, or the patient tested for specific fungal disease, before a course of therapy is selected. Other radiographic abnormalities, such as lung lesions or mediastinal lymphadenopathy, may favor a fungal infection, but other testing is still necessary for a definitive diagnosis.

Bacterial Bone Infections

Bacterial osteomyelitis is more common than fungal osteomyelitis, and in dogs and cats is usually acquired by direct inoculation as from an open fracture, a bite wound, or surgery.[13] Hematogenous bacterial osteomyelitis is relatively uncommon in dogs and cats, but can occur, particularly in skeletally immature, potentially immune-compromised, dogs. Bacterial osteomyelitis resulting from direct inoculation obviously has no predilection for skeletal localization and lesions develop at the site of injury. Therefore, bacterial osteomyelitis in dogs and cats usually involves one limb, but more than one bone may be involved. Bacterial osteomyelitis rarely causes a monostotic aggressive bone lesion. Bacterial osteomyelitis is covered in Chapter 19.

Protozoal Bone Infections

Hepatozoonosis is a rare protozoal infection that may cause polyostotic aggressive lesions.[14] Hepatozoon infections have been diagnosed in dogs throughout the world. Most infections occur in the southern portion of the United States. Radiographically, lesions are mainly periosteal and range from irregular periosteal proliferation to smooth laminar thickening of the periosteum. Lesions can occur in the axial or appendicular skeleton.[15] The smooth periosteal reaction form can be misleading because one does not typically associate smooth periosteal reaction with disseminated bone infection.

Although neoplasia and infection are the two most important considerations for an aggressive bone lesion, there are many other clinical entities that result in an aggressive bone lesion. In these instances, the diagnosis is usually made radiographically, in combination with the clinical scenario, rather than with an aspirate or biopsy. Some examples are canine panosteitis and metaphyseal osteopathy (hypertrophic osteodystrophy). For example, in Fig. 17.17 the increase in bone opacity in the medullary cavity would be classified as aggressive due to the lack of a distinct transition zone. However, the appearance of this lesion in the medullary cavity of a long bone in a 7-month-old German shepherd is so characteristic of canine panosteitis that other possibilities are not considered, and a biopsy or thoracic radiographs are not indicated.

Incidental Factors

The most significant incidental factors associated with appendicular radiography in the dog and cat are breed variation and common congenital anomalies. There are fewer incidental factors that influence the appearance of equine appendicular radiographs. The extent of the normal variation and anomalies

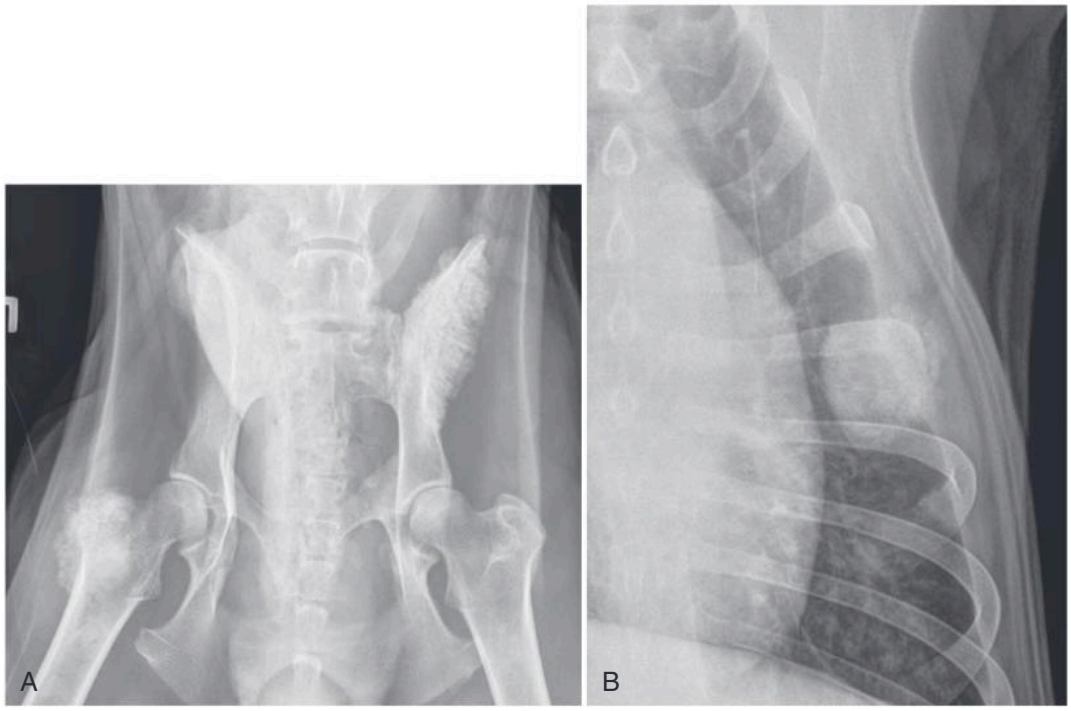


Fig. 17.27 Pelvic **(A)** and thoracic **(B)** radiographs from a 4-year-old pit bull. Aggressive lesions are present in the left ilium, proximal right femur and left fifth rib. Mycotic osteomyelitis is the main consideration for this distribution of aggressive bone lesions. A primary bone tumor would be considered for any of these lesions independently but not in combination. Metastatic neoplasia could have this appearance. Diagnosis: coccidioidomycosis.

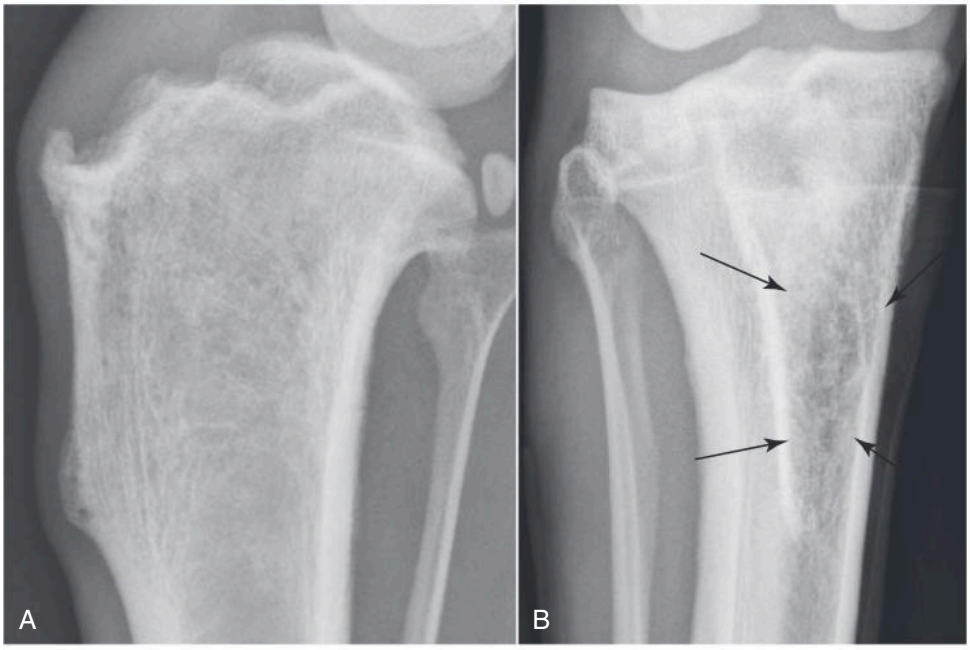


Fig. 17.28 Lateral **(A)** and craniocaudal **(B)** views of the proximal tibia of a 2-year-old Great Dane. In **A,** there is moth-eaten lysis of the proximal tibia. In **B,** there is a region of permeative lysis (*black arrows*) with an indistinct transition zone. This monostotic aggressive lesion is consistent with an osteosarcoma, even in a 2-year-old dog, but was caused by blastomycosis infection.

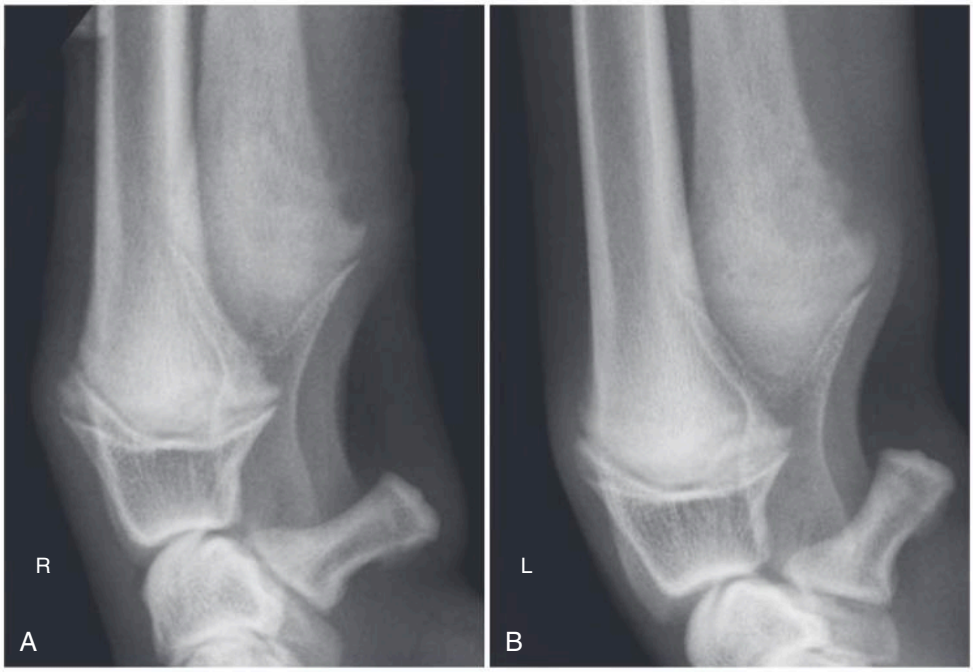


Fig. 17.29 Lateral radiograph **(A)** of the right distal antebrachium of a 5-month-old Irish setter with a right forelimb lameness and pain on carpal palpation. There is an irregular appearance to the distal ulna, especially caudally. It would be easy to misinterpret this as an aggressive lesion, but this is the normal cutback zone resulting from remodeling of the distal ulna as it elongates. If one does not remember that this is a normal finding in young, rapidly growing dogs, radiographing the contralateral left carpal region **(B)** and finding the same appearance lessens the chance that this is a significant lesion.

that may be encountered in the appendicular skeleton of dogs and cats is great and cannot be covered adequately here. Comprehensive references are available.[1] The concept of radiographing the contralateral limb for comparative purposes when a questionable finding is encountered is valuable (Fig. 17.29).

Interpretation Paradigm

Like in all body systems, an organized approach to radiographic interpretation of the appendicular skeleton is needed. This begins with an overview of technique, according the following questions, followed by evaluation for abnormalities.

Are the radiographic views adequate, and are all of the views that are needed present?
Are oblique or other ancillary views needed?
Do the views correspond to the clinical localization of the lesion?
Are the radiographic technique and positioning adequate?
Has a grid been used? Did this affect the quality of the image?
Has sedation or anesthesia been used? If not, how will this affect the utility of the radiographs?
What is the species and breed of the patient?
Was a horizontally directed x-ray beam used with handholding of the cassette or a wall-mounted cassette holder?
Was the cassette held by hand? Is there motion artifact?
Has the joint above and below the location of a suspected bone lesion been included in the imaging study?
Will radiographs of the contralateral limb be helpful?
What congenital anomalies are present that alter the normal appearance of the bone but may not be clinically significant?

After these variables have been considered, the images can be scrutinized for abnormalities. The roentgen sign and DAMNITV methods described in Chapter 6 should be used, along with an assessment of lesion aggressiveness. Unfortunately, bone is very limited in its response to injury. There will be either more or less bone than normal, a periosteal response will be either present or not, and the soft tissues will be either involved or not. Thus, the distribution within the skeleton and the assessment of the patient signalment become extremely important factors in formulating a reasonable differential diagnosis and for formulating a plan (Table 17.4). Regardless, especially for aggressive bone lesions, cytologic and/or microbiologic testing of a tissue sample, from bone or other involved tissue, will be needed for definitive diagnosis.

Experienced radiologists may have a random search pattern, but it is recommended that inexperienced interpreters use an organized approach.[7] Having a mental checklist to guide the order of interpretation will reduce the number of errors (Box 17.1).

In addition to a general examination of the images, it is also helpful to scrutinize appendicular radiographs with a preconception of what disease might be found in a particular region in a particular patient. This is particularly true in young canine and feline patients, where developmental and juvenile bone diseases are often characterized by very specific findings. This is defined as *targeted viewing* and was introduced earlier (see Chapter 6). Examples of targeted viewing are close examination of the (1) proximal margin of the anconeal process in dogs at risk of having elbow dysplasia, (2) proximal margin of the medial ridge of the talus in dogs at risk for tarsal osteochondrosis, and (3) distal radial and ulnar metaphysis in young dogs at risk for hypertrophic osteodystrophy. It is critical that targeted viewing be used as an *ancillary* method. It is a way of double checking that all possibilities have been addressed. Assessing radiographs with only a preconceived idea of what will be present will invariably lead to overlooked lesions and missed diagnoses.

Table • 17.4

Summary of Selected Orthopedic Diseases in Small Animals by Skeletal Distribution and Patient Demographics.

DISEASE	MONOSTOTIC OR POLYOSTOTIC	LOCATION IN BONE	DEMOGRAPHICS
Primary bone cancer	Monostotic	Metaphyseal	Older patients
Metastatic bone cancer	Polyostotic	Metaphyseal or diaphyseal	Older patients
Mycotic osteomyelitis	Polyostotic	Metaphyseal	Middle-aged patients
Bacterial osteomyelitis—hematogenous	Polyostotic	Metaphyseal or diaphyseal	Young patients
Bacterial osteomyelitis—traumatic	Monostotic	Anywhere	Variable
Metabolic bone disease	Polyostotic	Metaphyseal or epiphyseal	Young patients
Panosteitis	Polyostotic	Diaphyseal	Young patients
Hypertrophic osteodystrophy (HOD)	Polyostotic	Metaphyseal	Young patients
Osteochondrosis	Polyostotic	Epiphyseal	Young patients
Hypertrophic osteopathy (HO)	Polyostotic	Epiphyseal and metaphyseal then diaphyseal	Older patients

These data are generalizations and will not apply to all patients.

Box • 17.1

Checklist for Interpretation of Appendicular Skeletal Radiographs

Number of bones involved
Region of bone involved; epiphysis vs. metaphysis vs. diaphysis vs. multiple
Joint involvement
Overall bone opacity
Integrity of the cortex
Presence or absence of a smooth or irregular periosteal reaction
Shape of bones
Character of any transition zone
Character of adjacent soft tissues

REFERENCES

1. Thrall D, Robertson I. *Atlas of Normal Radiographic Anatomy and Anatomic Variants in the Dog and Cat*. 3rd ed. St Louis: Saunders/Elsevier; 2023.
2. O'Donnell P. Evaluation of focal bone lesions: basic principles and clinical scenarios. *Imaging*. 2003;15(4):298–323.
3. Chun R. Common malignant musculoskeletal neoplasms of dogs and cats. *Vet Clin North Am Small Anim Pract*. 2005;35(5):1155–1167.
4. Heldmann E, Anderson M, Wagner-Mann C. Feline osteosarcoma: 145 cases (1990–1995). *J Am Anim Hosp Assoc*. 2000;36(6):518–521.
5. Jimenez IA, Pool Jr RR, Gabrielson KL. Canine idiopathic arteriopathy, appendicular bone infarcts, and neoplastic transformation of bone infarcts in 108 dogs (*Canis lupus familiaris*). *Comp Med*. 2022;72(5):306–319.
6. Marcellin-Little DJ, DeYoung DJ, Thrall DE, Merrill CL. Osteosarcoma at the site of bone infarction associated with total hip arthroplasty in a dog. *Vet Surg*. 1999;28(1):54–60.
7. Sebestyen P, Marcellin-Little DJ, DeYoung BA. Femoral medullary infarction secondary to canine total hip arthroplasty. *Vet Surg*. 2000;29(3):227–236.
8. Arthur EG, Arthur GL, Keeler MR, Bryan JN. Risk of osteosarcoma in dogs after open fracture fixation. *Vet Surg*. 2016;45(1):30–35.
9. Trost ME, Inkelmann MA, Galiza GJN, Silva TM, Kommers GD. Occurrence of tumours metastatic to bones and multicentric tumours with skeletal involvement in dogs. *J Comp Pathol*. 2014;150(1):8–17.
10. Henry CJ, Whitley EM, Tyler JW, Ogilvie GK, Norris A, et al. Canine digital tumors: a veterinary cooperative oncology group retrospective study of 64 dogs. *J Vet Intern Med*. 2005;19(5):720–724.
11. Goldfinch N, Argyle DJ. Feline lung-digit syndrome: unusual metastatic patterns of primary lung tumours in cats. *J Feline Med Surg*. 2012;14(3):202–208.
12. Kerl ME. Update on canine and feline fungal diseases. *Vet Clin North Am Small Anim Pract*. 2003;33(4):721–747.
13. Gieling F, Peters S, Erichsen C, Richards RG, Zeiter S, Moriarty TF. Bacterial osteomyelitis in veterinary orthopaedics: pathophysiology, clinical presentation and advances in treatment across multiple species. *Vet J*. 2019;250:44–54.
14. Ewing SA, Panciera RJ. American canine hepatozoonosis. *Clin Microbiol Rev*. 2003;16(4):688–697.
15. Drost WT, Cummings CA, Mathew JS, Panciera RJ, Ko JCH. Determination of time of onset and location of early skeletal lesions in young dogs experimentally infected with *Hepatozoon americanum* using bone scintigraphy. *Vet Radiol Ultrasound*. 2003;44(1):86–91.

ELECTRONIC RESOURCES

Additional information related to the content in Chapter 17 can be found online at eBooks.Health.Elsevier.com.

- Chapter Quiz

CHAPTER 18

Orthopedic Diseases of Young and Growing Dogs and Cats

Kathryn L. Phillips

Developmental orthopedic disease is a grouping of variable diseases tied together by the population that they affect. This chapter reviews the basic pathophysiology and radiographic appearance of the more common developmental orthopedic diseases in dogs and cats. There are a few trends across this diverse grouping. The lesions are often generalized or at least bilaterally symmetric, for example, affecting all the epiphyses as with congenital hypothyroidism, or all the physes as with rickets, or mirroring lesions on both thoracic or both pelvic limbs as with hypertrophic osteodystrophy (HOD) and osteochondrosis (OC). Because these diseases have known predilection sites, the anatomic distribution of the lesions can be used to make the diagnosis or at least limit the differential list. In this chapter the diseases are grouped based on their anatomic distribution (Table 18.1).

Degenerative joint disease is a common sequela to developmental disorders of the immature skeleton, particularly when the primary lesion involves joints or produces limb deformity. Adult patients will frequently present with lameness attributable to the secondary degenerative joint disease. Advanced degenerative changes can mask the original developmental lesion on radiographs.

DISORDERS PRIMARILY AFFECTING JOINTS

Osteochondrosis and Osteochondrosis Dissecans

Osteochondrosis (OC) is a common cause of lameness in young, rapidly growing, large-breed dogs. Clinical signs usually develop between 6 and 9 months of age. OC occurs from epiphyseal cartilage necrosis, resulting in a failure of normal endochondral ossification. If the vascular bed of the adjacent subchondral bone can envelop and bypass the region of cartilage necrosis, endochondral ossification may resume without development of a clinical lesion. Otherwise, focal failure of endochondral ossification leads to divots within the subchondral bone and progressive chondromalacia may lead to development of clefts or fissures extending from the surface of the cartilage to the subchondral bone. The terms *osteochondrosis* and *osteochondritis* have both been historically used in the literature. Osteochondritis implies inflammation, and inflammation is not a component of the primary developmental disease and the term is therefore not used in this chapter.[1] Osteochondrosis (OC) is further characterized into osteochondrosis dissecans (OCD) when there is a complete fissure through the cartilage creating a flap. As chondral flaps and fragments are of soft tissue opacity, they cannot be radiographically identified. However, when they become ossified and an osteochondral fragment is radiographically apparent, the term *osteochondrosis dissecans* is more specific.

OC occurs at specific anatomic locations and is frequently bilaterally symmetric; thus, if an OC lesion is identified, radiographs of the contralateral limb should be performed. It is rare for a lesion to occur outside of the predilection sites. In dogs the predilection sites are caudal aspect of the humeral head, distomedial humeral trochlea, lateral and medial femoral condyles, and the medial and lateral trochlear ridges of the talus.

Radiographic Signs

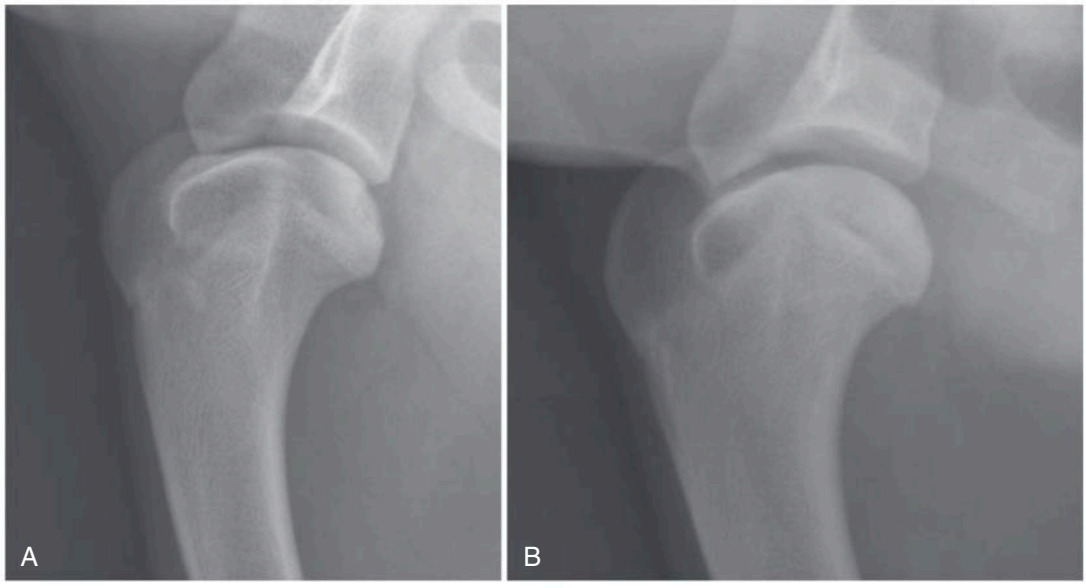
Radiographic findings of OC include flattening or concavity of the affected subchondral bone surface with or without subchondral bone sclerosis. This may result in nonuniformity and apparent widening of the joint space. When mineralized, a cartilage flap is sometimes seen within the subchondral defect, and separate osteochondral fragments (joint mice) may migrate within the joint space. Fragments that have migrated often adhere to the synovial lining and may become vascularized and continue to mineralize and enlarge over time. Joint effusion or joint capsule thickening may present as a localized region of soft tissue thickening centered on the affected joint. A subchondral bone defect is occasionally seen involving the articular surface opposite the primary lesion. These defects are called *kissing lesions*. Degenerative joint disease is a common sequel to OC.

Detection of lesions on the caudal humeral head can be difficult as this surface is spherical in shape and the beam must be tangential to the subchondral bone divot to be detected. If a lesion is not identified but clinically suspected, obtaining additional lateral views in varying degrees of supination can aid in detection of focal subchondral bone flattening. OC of the lateral trochlea of the talus can be obscured by superimposition of the calcaneus in the dorsoplantar view. In this instance, a dorsolateral-plantaromedial oblique[2] or a flexed dorsoplantar view can be acquired to provide an unobstructed view of the lesion. In the stifle, the fossa for the origin of the long digital extensor muscle is sometimes mistaken for a lateral femoral condyle OC lesion because it is superimposed on the dorsolateral aspect of the condyle on both the lateromedial and the caudocranial views (Figs. 18.1–18.3, eFig. 18.1).

When a nonmineralized cartilage fragment is present, intra-articular contrast medium (arthrography) can be used to outline the flap if contrast medium dissects between the fragment and the underlying subchondral bone. Arthrography can be performed in conjunction with radiographs or computed tomography (CT) but is infrequently performed as it adds little to the clinical diagnosis, is not as sensitive as arthroscopy, and the presence of a cartilage flap does not change the surgical plan.[3]

Elbow Dysplasia

Dysplasia is the abnormal growth or development of an organ or structure. There are many ways for the elbow joint to be dysplastic; however, there is a triad of common developmental diseases that are encountered so frequently that the term *elbow dysplasia* is used clinically to refer to them. They include ununited anconeal process, medial coronoid process disease of the ulna, and OC of the distomedial aspect of the humeral



eFig. 18.1 Shoulder osteochondrosis in a 2-year-old Border collie. **A,** Left shoulder: a large subchondral defect with adjacent sclerosis is present on the caudal humeral head. An ovoid mineralized fragment has migrated into the biceps tendon sheath and is visible superimposed over the cranial aspect of the humeral metaphysis. **B,** Right shoulder joint of the same dog: a shallower defect with adjacent subchondral sclerosis is visible on the caudal humeral head.

Table • **18.1**

Juvenile Orthopedic Diseases of Dogs and Cats Based on Anatomic Location.

ANATOMIC LOCATION	DISEASE	ROUGH ESTIMATE OF FREQUENCY OF OCCURRENCE	SPECIES
Diseases primarily affecting joints	Osteochondrosis	Frequent	Large-breed dogs
	Osteochondrosis dissecans		
	Ununited anconeal process	Moderate	Large-breed dogs
	Medial coronoid disease	Extremely frequent	Dogs
	Congenital radial head luxation	Occasional	Bulldogs and chondrodystrophic dogs
	Hip dysplasia	Extremely frequent	Dogs and cats
	Aseptic necrosis of the femoral head	Occasional	Toy breed dogs
	Congenital hypothyroidism	Occasional	Cats and dogs
	Mucopolysaccharidosis	Rare	Cats and dogs
Epiphyseal dysplasia	Multiple epiphyseal dysplasia	Extremely rare	Reported in dogs
	Spontaneous capital physeal fractures of cats	Occasional	Male cats ~2 years of age
	Incomplete ossification of the humeral condyle	Occasional	Dogs
Diseases of the physis	Rickets	Rare	Dogs and cats
	Osteochondrodysplasia of Scottish fold cats	Breed specific	Scottish fold cats
	Breed specific chondrodysplasias	Rare	Dogs
	Hypertrophic osteodystrophy	Moderate	Large-breed dogs
	Multiple cartilaginous exostosis	Rare	Dogs
Disease of the metaphysis	Retained cartilaginous core	Moderate—often not clinical	Dogs
	Panosteitis	Moderate	Large-breed dogs
	Nutritional secondary hyperparathyroidism	Occasional	Dogs, cats, and exotics
Disease of the diaphysis	Osteogenesis imperfecta	Rare	Dogs
Generalized bone disorders	Osteopetrosis	Rare	Cats and dogs
	Knees and teeth syndrome	Rare	Cats

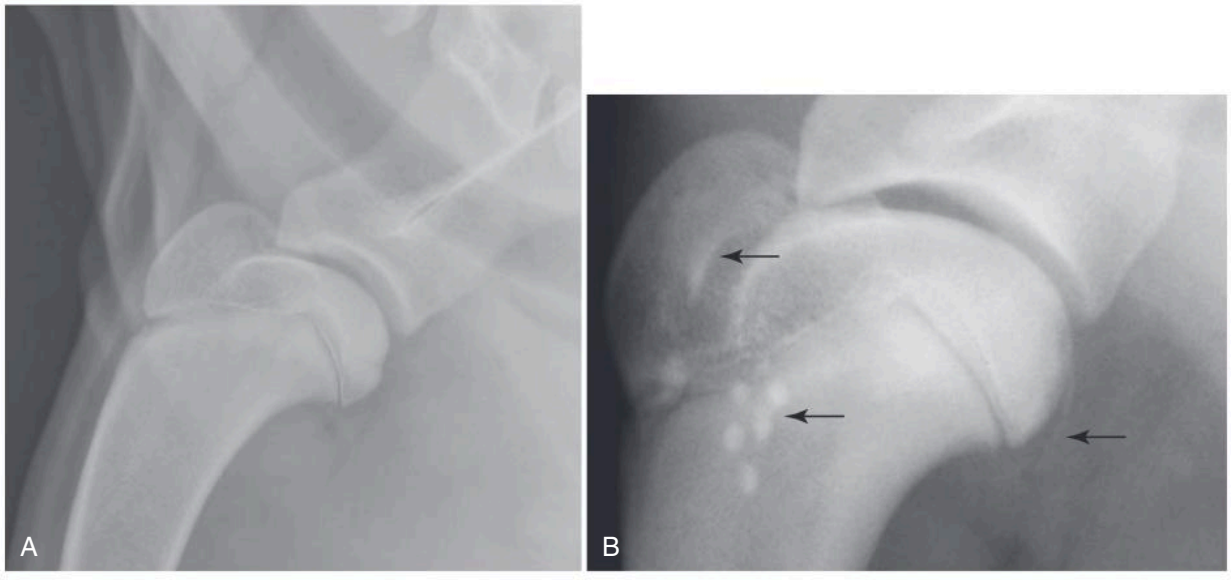


Fig. 18.1 Shoulder osteochondrosis **(A)** and osteochondrosis dissecans **(B)**. The lesions are characterized by concave lucencies of the humeral head and variable surrounding sclerosis. These lesions can sometimes be missed on a straight lateral view due to the rounded surface of the humeral head and several slightly oblique lateral views can be obtained with the limb in varying degrees of internal rotation (pronation). In image **B,** there is a thin flap of mineralized cartilage along the caudal humeral head (*black arrow*) as well as several osteochondral fragments within the bicipital bursa (*black arrows*). In dogs the bicipital bursa and shoulder joint freely communicate. Osteochondral fragments from the humeral head can migrate into the bicipital bursa.

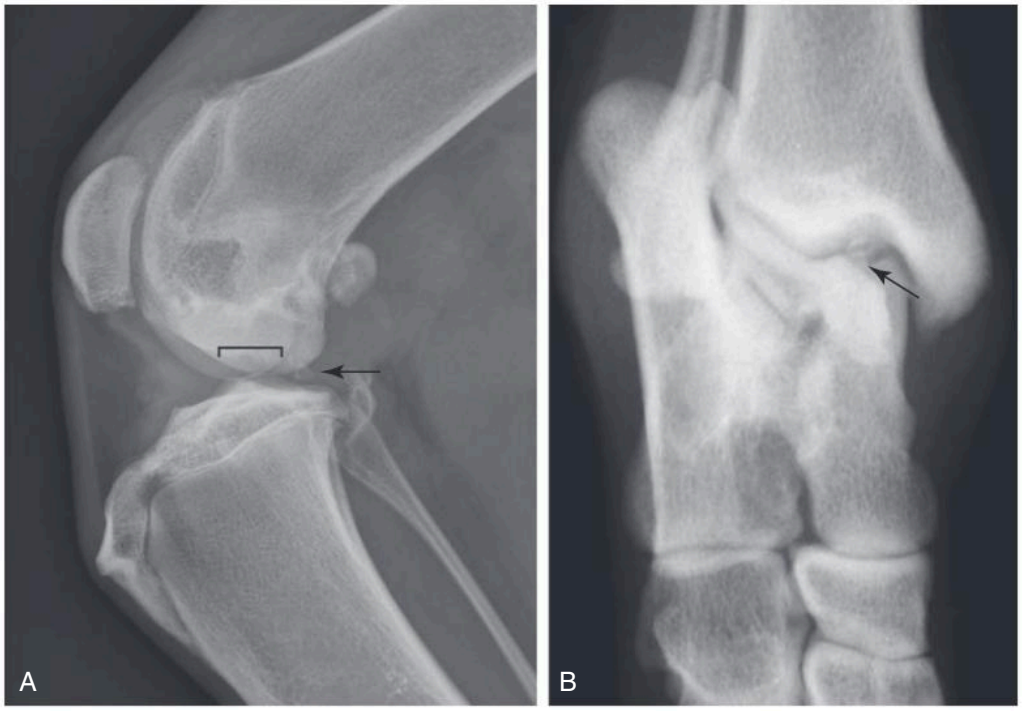


Fig. 18.2 Osteochondrosis dissecans. **A,** Lateral radiograph of the stifle. There is joint effusion. There is an irregularly margined divot so that one of the distal femoral condyles no longer has a round shape (indicated with *brackets*). There is an adjacent osteochondral fragment (*arrow*) in the caudal aspect of the joint. On the dorsoplantar view of the tarsus **(B)**, there is a divot in the medial trochlear ridge of the talus with a rounded osteochondral fragment (*arrow*).

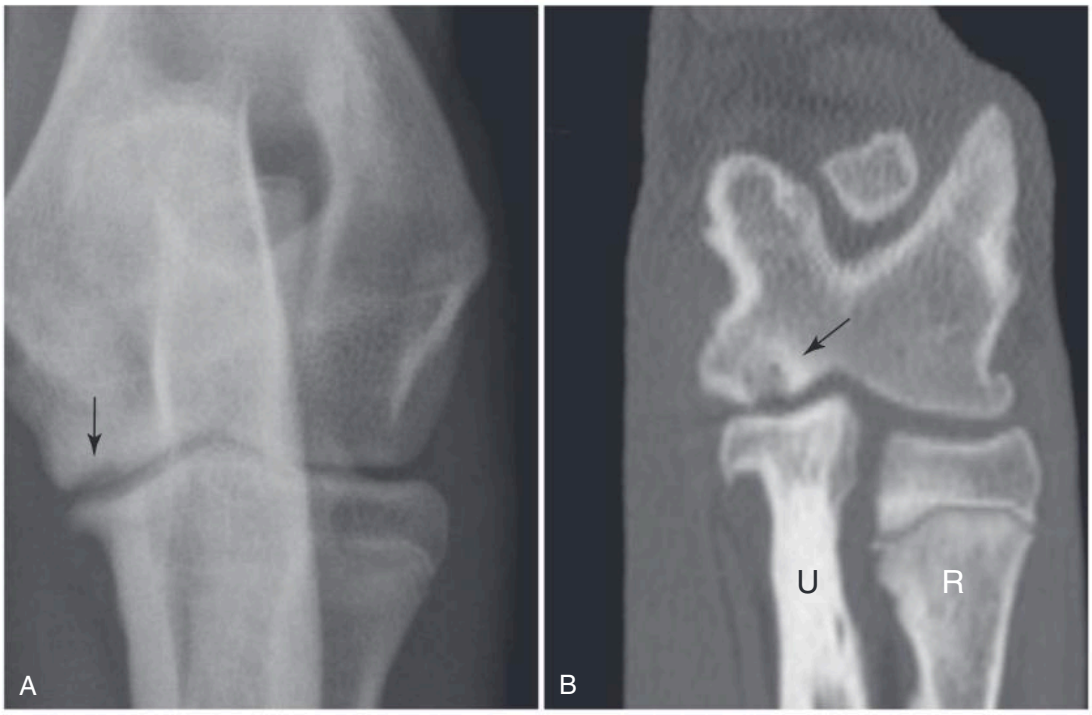


Fig. 18.3 Osteochondrosis of the medial humeral trochlea on radiographs **(A)** and dorsal plane computed tomography (CT) image **(B)**. This is characterized by a well-defined concavity (*arrows*) that can be difficult to identify with radiographs alone due to superimposition.

trochlea (see Osteochondrosis and Osteochondrosis Dissecans section earlier). Elbow joint incongruity is frequently included in the term *elbow dysplasia* as a fourth category. However, joint incongruity is also implicated as the overarching cause for all of the lesions included in elbow dysplasia. When there is disparity between any of the three bones, such as asynchronous growth of the radius and ulna or an elliptically shaped ulnar notch, the result is nonuniform contact of articulating surfaces,



Fig. 18.4 A flexed lateral radiograph of the elbow with an ununited anconeal process. The *arrow* indicates the gap between the anconeal process and the olecranon.

which then leads to cartilage damage, medial coronoid process disease, or ununited anconeal processes. This is typically a bilateral disease, and a patient can have one, two, or all three of the primary lesions simultaneously. A radiographic study of the elbow includes a neutral lateral, a flexed lateral, and a craniocaudal radiograph of both elbow joints. The flexed lateral radiograph facilitates visibility of new bone formation on the proximal margin of the anconeal process and detection of ununited anconeal process since the medial humeral epicondyle is not superimposed. However, flexing the elbow induces a mild degree of rotation that can partially obscure the medial coronoid margin. A slight craniolateral to caudomedial (pronating the limb 15–25 degrees) view can be used to highlight the craniomedial margin and thus the medial coronoid and medial humeral trochlea. CT is now used routinely to evaluate the elbow joint and is more sensitive than survey radiography for detecting medial coronoid disease.

Ununited Anconeal Process

Ununited anconeal processes are a disease of large-breed dogs. A number of large-breed dogs have a normal separate center of ossification at the anconeal process during development.[4,5] Small, separate centers of ossification can be seen radiographically in puppies starting at 13 weeks of age. The anconeal process should be fused normally to the olecranon of the ulna by 150 days (5 months) of age.

Radiographic Signs

The primary radiographic finding is best seen on the flexed lateral view and consists of a radiolucent line separating the anconeal process from the olecranon in dogs older than 150 days (Fig. 18.4, eFig. 18.2). This lucent line is at the base of the anconeal process and can be sharply defined or it may appear irregular and of variable width. Degenerative joint disease of the elbow is a common sequel, and periarticular new bone production from osteoarthrosis may partially obscure the lucency between the ulna and the anconeal process.

Medial Coronoid Process Disease

Medial coronoid process disease is the most common developmental disorder involving the elbow joint and one of the most common causes for thoracic limb lameness in dogs. Medial coronoid process disease includes fragmentation as well as sclerosis and remodeling of the medial coronoid process. It affects medium- and large-breed dogs primarily and has a significantly higher incidence in males. Clinical signs may be apparent as early as 4 to 6 months of age. Radiographic visibility of the medial coronoid is hampered by superimposition of the radius (Fig. 18.5, eFig. 18.3). In most instances, the radiographic diagnosis of fragmented medial coronoid process is made indirectly through recognition of degenerative changes that accompany the primary lesion.

Radiographic Signs

Primary radiographic signs include an abnormal contour or poor definition of the cranial margin of the medial coronoid process on the lateral view. Often the margin, which is radiographically distinct in normal dogs, cannot be followed proximally to the articular surface in affected animals. On the craniocaudal view, the medial margin of the medial coronoid process may appear blunted, rounded, or tipped distally. A separate osseous body, representing the fragmented coronoid process, is seen rarely. Joint incongruity or subluxation may also be present and appears as a stair-step lesion between the ulna and the radial head on the lateral view. However, caution should be used to prevent overinterpretation of this finding. On the lateral view, the normal overlapping lucent lines representing the complex elbow joint margins can be confused with joint incongruity if there is any proximal to distal or vice versa obliquity present.[6,7] Secondary degenerative joint disease is frequent even in young patients. Osteophyte formation on the proximal margin of the anconeal process is one of the earliest signs of degenerative joint disease. Subchondral bone sclerosis also develops along the distal border of the trochlear notch in the region of the lateral coronoid process.[7–10] These secondary findings are best appreciated on the lateral view. A large osteophyte may arise from the medial coronoid margin on the craniocaudal view in addition to the more generalized osteophyte production.

Congenital Radial Head Luxation

Congenital caudolateral radial head luxation has been reported in a variety of dog breeds including bull-dogs, Bouvier de Flandres, Shih Tzu, and Afghan hounds.[11] Affected puppies present with mild forelimb lameness first noticed at 3 to 4 months of age with physical examination findings of pain and reduced range of motion in the affected elbow.

Radiographic Signs

Caudal and lateral luxation of the radius relative to the distal humerus is the primary radiographic finding (Fig. 18.6). The radial epiphysis may appear convex because articulation with the humeral condyle has not resulted in normal development. The articulation of the humerus with the ulna is typically normal and there is no evidence of trauma.

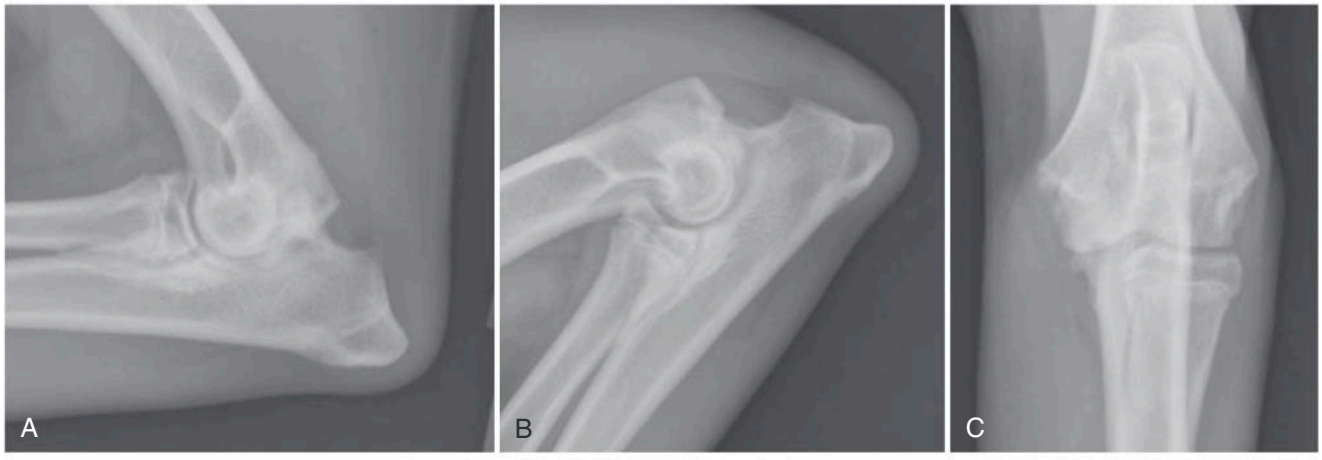
Hip Dysplasia

Hip dysplasia is an extremely common disease caused by abnormal development of the coxofemoral joints. It is a disease that ranges from mild alterations in gait and mobility to debilitating lameness. The majority of the clinical signs are caused by secondary osteoarthritis. Hip dysplasia mainly occurs in large-breed dogs, but it can also affect small dogs and cats.

Canine hip dysplasia is a polygenic inherited disease that is influenced by environmental factors. It is a disease that is not detectable at birth but during growth laxity of the joint develops. As the animal moves, the joints subluxate resulting in altered biomechanical forces on the articular surfaces. Without normal forces applied, the acetabulum does not develop a normal cup-like shape and the femoral head is flattened. This incongruity leads to arthritis later in life.[12] Heritability is a



eFig. 18.2 Ununited anconeal process. *Arrowheads* outline the anconeal process, which is separate from the proximal ulna. The bone margins at the site of separation are smooth and sclerotic, indicating chronicity.



eFig. 18.3 Fragmented medial coronoid process and associated degenerative joint disease. **A,** Lateral view of the elbow joint. The medial coronoid process is blunted proximally. New bone formation consistent with degenerative joint disease is visible on the dorsal surface of the anconeal process and on the radial head. **B,** Flexed lateral view. The coronoid process is blunted and an ovoid mineral opacity structure cranial to it, superimposed over the proximal radius, may represent a dislocated fragment. **C,** Craniocaudal view. Osseous proliferation is visible on the anconeal process and medial humeral epicondyle. A small radiolucent defect in the medial aspect of the humeral trochlea may represent secondary subchondral bone erosion ("kissing lesion") or an osteochondral defect.



Fig. 18.5 Fragmented medial coronoid process. **A,** Lateral view of a normal elbow. The cranial edge of the medial coronoid process (*black arrow*) has a distinct margin that is superimposed on the head of the radius. The proximal margin of the anconeal process (*white arrow*) is also distinct despite being superimposed on the medial and lateral epicondyles of the humerus. **B,** Fragmented medial coronoid process with degenerative joint disease. The margins of the medial coronoid are indistinct compared with those in **A**. There are osteophytes along the proximal margin of the anconeal process (*white arrow*). Subchondral bone sclerosis is also present adjacent to the ulnar notch (*black arrow*). **C,** An osteophyte arises from the medial margin of the ulna on a craniocaudal view (*white arrow*). This osteophyte should not be misinterpreted as the coronoid fragment. **D,** Fragmentation of the medial coronoid process can occasionally be seen on a craniolateral-caudomedial view (*arrow*). **E,** Computed tomography image of the elbow from a dog with a fragmented medial coronoid process and degenerative joint disease. The fragmented coronoid process (*black arrow*) is easily seen. In addition, the basilar part of the coronoid process is sclerotic and remodeled.

numeric estimate of how much a particular trait is controlled by the genotype; a heritability of 1 indicates that the trait is completely genetically controlled and 0 indicates the trait is not genetically influenced. Heritability numbers have been calculated for different breeds of dogs based on hip scores from ventrodorsal radiographs. This results in a range of heritability numbers for different breeds of dogs, from 0.11 in Boxers to 0.43 in German shepherd dogs.[13] However, hip laxity as measured by the distraction index (DI) has a higher genetic correlation. Heritability estimates for hip laxity are 0.46 in



Fig. 18.6 Congenital radial head luxation in a 6-month-old English bulldog. The radial head does not articulate with the distal humeral condyle (*white arrow*). There is no evidence of trauma and the distal radial and ulnar physes appear normal.

German shepherd dogs and Labradors, 0.64 in Golden Retrievers, and 0.85 in Estrela mountain dogs.[14] The higher the heritability estimates, the greater effect selective breeding programs will have on minimizing this disease. Environmental factors do not cause hip dysplasia, but multiple environmental factors are implicated in the phenotypic expression of hip dysplasia. Limiting caloric intake throughout life has been shown to decrease prevalence of hip dysplasia and delay onset and severity of osteoarthritis.[15]

Radiographic Signs

Heavy sedation or anesthesia is extremely helpful in obtaining perfectly symmetrically positioned pelvic radiographs.

Ventrodorsal radiographs are obtained with the hips extended and the pelvic limbs parallel and supinated so that the patellae overlie the trochlear grooves. The radiograph should be centered at the pelvis, and include the entirety of both femora and two lumbar vertebrae. The goal is to have a symmetric view of the pelvis; if there is axial rotation, one acetabular cup will falsely look shallower than the other.

In a normal coxofemoral joint, the femoral head is round and fits perfectly in the acetabular cup and the dorsal acetabular rim covers more than 50% of the femoral head. The joint space is symmetric around the femoral head (Fig. 18.7). With hip dysplasia, the acetabular cup is shallower than normal and the dorsal acetabular rim covers less than 50% of the femoral head.

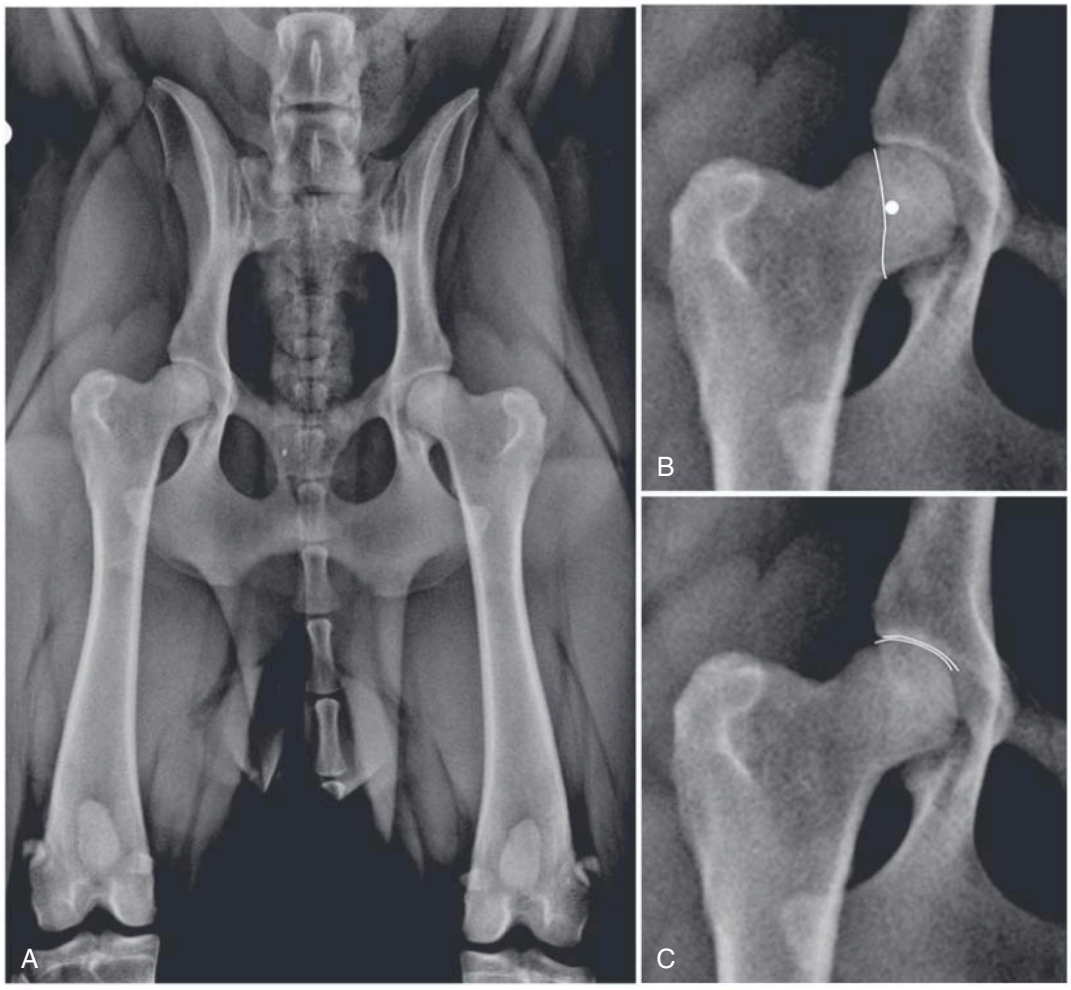


Fig. 18.7 A ventrodorsal radiograph of a dog with normal hips. The patient is well positioned with a symmetric pelvis **(A)**. The dorsal acetabular rim is outlined, and the center of the femoral head is covered by the dorsal acetabular rim **(B)**. The joint is congruent as the joint margins in the cranial one-third of the joint are parallel **(C)**.

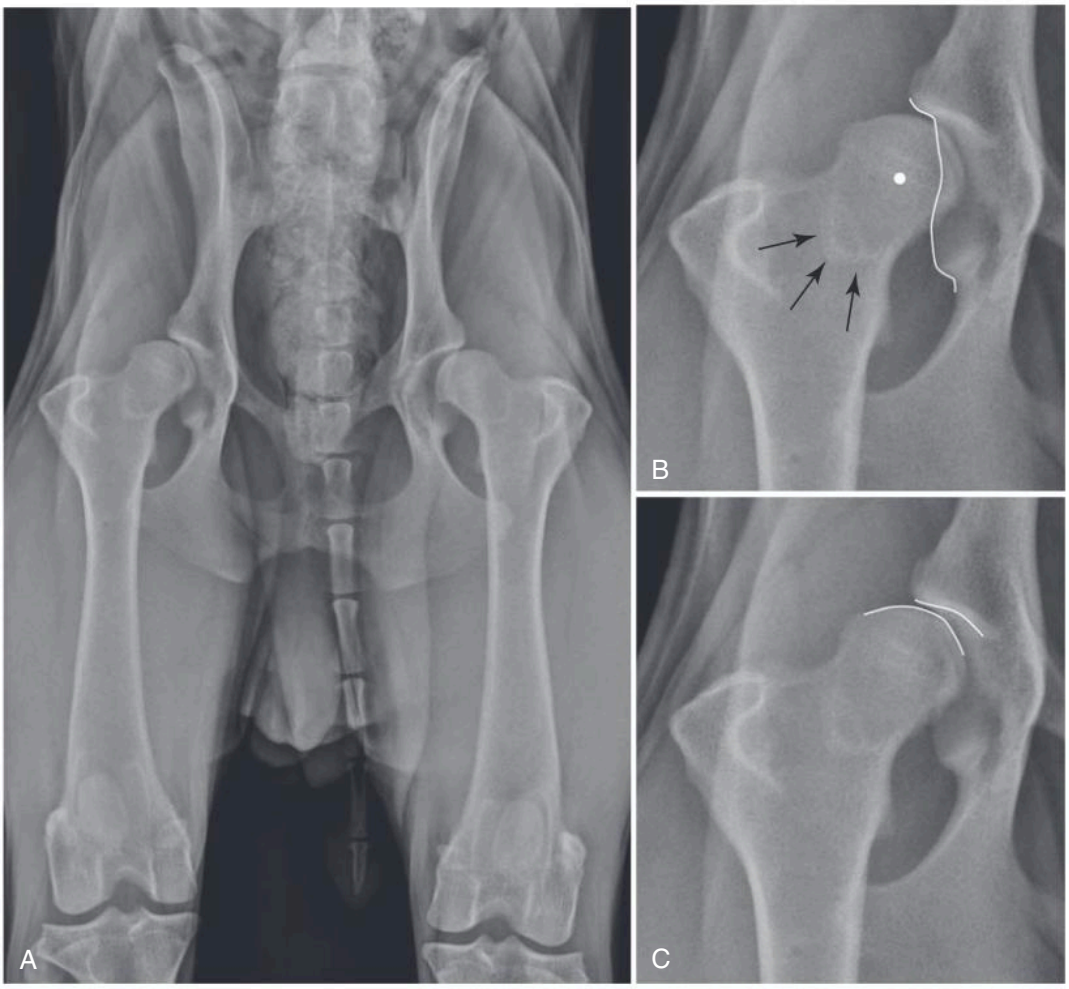


Fig. 18.8 Image **A** is a ventrodorsal radiograph of a dog with hip dysplasia. The dorsal acetabular rim is outlined in image **B**; the center of the femoral head is not covered by the dorsal acetabular rim. The joint is not congruent (**C)** as the joint margins in the cranial aspect of the joint are not parallel and create a wedge-shaped joint space. There is a curvilinear thin line of enthesophytes at the joint capsule insertion of the femoral neck indicated by the *arrows*.

The joint will be incongruent, and the joint margins are no longer parallel along the cranial one-third of the joint. The caudal portion of the joint is not evaluated because of a normal divot of the acetabular fossa and the flattening created by the fovea capitis on the femoral head (Fig. 18.8). Degenerative joint disease is common in patients with hip dysplasia and can be present in young animals. An early indication of degenerative joint disease is a curvilinear line of enthesophytes along the caudolateral margin of the femoral neck at the insertion of the joint capsule, called a *Morgan's line*[16] (see Fig. 18.8, eFig. 18.4). Other signs of degenerative joint disease include a circumferential ring of osteophytes around the femoral head and osteophytes at margins of the acetabulum. The osteophytes and enthesophytes can get quite large encircling the femoral neck, making it appear thicker. In severe disease with eburnation of the femoral head, the head can get sclerotic and angular in shape.

Hip dysplasia in cats will appear as shallow acetabula. The osteophytes have predilection site for the cranial border of the acetabulum, and unlike dogs, cats have little remodeling around the femoral neck.[17]

Distraction techniques are used to measure hip laxity. Several ways of performing distraction views have been reported, but the most common method is the PennHIP method. The patient is in dorsal recumbency, and a specially shaped distraction device is placed between the femurs which are in a neutral position relative to the acetabulum and pointing upwards at a right angle to simulate the dog standing. The device is used as a fulcrum to distract the femoral heads from the acetabulum as the femurs are pressed against the bars of the distraction device. The DI is calculated by drawing a circle of best fit around the femoral head and a second circle of best fit of the acetabulum, then measuring the distance from the center of both of these circles divided by the radius of the circle of the femoral head (Fig. 18.9). The smaller the DI, the less laxity is present. The DIs vary for different breeds of dogs. The PennHIP group has collected data on thousands of dogs and is commercially available. The PennHIP method has inherent advantages over the extended hip method of evaluating the coxofemoral joints. First, it quantifies joint laxity, which is generally accepted as the beginning of a chain of events that culminates in coxofemoral degenerative joint disease. Second, the examination can be performed on young dogs. The predictive value of the DI is constant after 6 months of age, thereby providing valuable information to breeders at an early age when selecting their stock. Third, the technique predicts a DI below which degenerative changes are unlikely to occur. Conversely, the DI and the subsequent development of degenerative joint disease appear to have a direct relation when the DI is greater than 0.3 (for German shepherd dogs) or 0.4 (for Labrador Retrievers and Rottweilers).



eFig. 18.4 Ventrodorsal radiograph of a dog with hip dysplasia. Both femoral heads are subluxated and coverage by the acetabulum is less than 50%. There is flattening of the femoral heads and the femoral necks are thickened. A curvilinear sclerotic line extending across the femoral neck is consistent with enthesophytosis (Morgan's line). The acetabular rims are remodeled, flattened, and sclerotic.

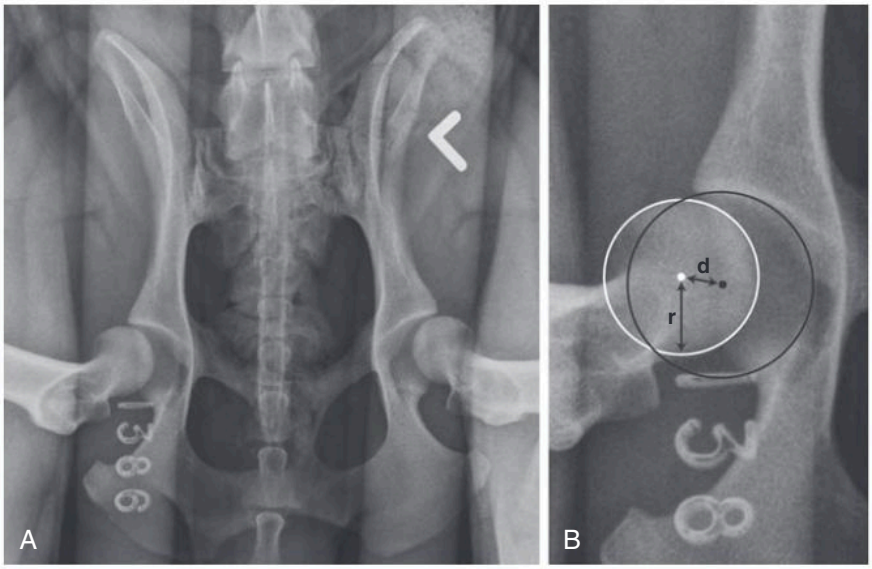


Fig. 18.9 Figure **A** demonstrates a PennHIP distraction view of the coxofemoral joints to assess joint laxity. Figure **B** demonstrates how the distraction index = d/r is determined.

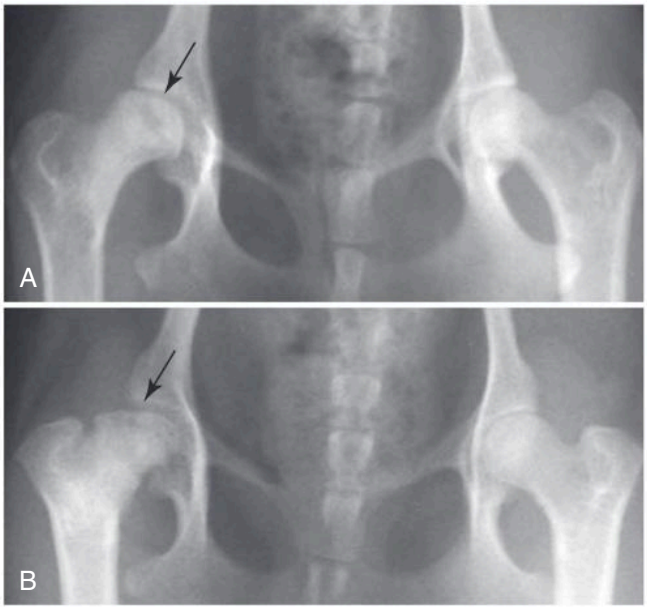


Fig. 18.10 Serial radiographs of a patient with aseptic necrosis of the right femoral head (*arrows*). Image **A** is earlier in the disease process, overtime the femoral head becomes flattened and progressively deformed **(B)**. The left femoral head is normal and remains round in shape.

Aseptic Necrosis of the Femoral Head (Legg-Calvé-Perthes Disease)

Aseptic necrosis of the femoral head occurs in adolescent toy and small-breed dogs (Fig. 18.10, eFig. 18.5). Compromised blood supply to the femoral capital epiphysis causes necrosis of subchondral bone while overlying articular cartilage continues to grow. Revascularization occurs in an attempt to repair the defect, and removal of necrotic bone causes decreased opacity in the affected femoral head. Incomplete removal of necrotic bone and invasion of granulation tissue interferes with healing, resulting in a misshapen femoral head of nonuniform opacity.[18]

Radiographic Signs

As with many of the other developmental skeletal disorders, the radiographic findings of aseptic necrosis of the femoral head vary with the duration of the lesion. Radiographs of the hip joints may appear normal early in the course of the disease. As the disease progresses, lucencies can be detected within the subchondral bone within the femoral head. Areas of decreased opacity may also appear in both the femoral epiphysis and the metaphysis. Flattening and irregularity of the femoral head and neck become apparent as the affected bone remodels and collapses on itself. Remodeling of the femoral head may cause coxofemoral joint space widening and subluxation. Fragmentation of the femoral head may eventually occur from pathologic fracture. Muscle atrophy and radiographic findings associated with degenerative joint disease usually develop. Radiographic evaluation of both hips is indicated because this disease may be bilateral.

EPIPHYSEAL DYSPLASIA

Congenital Hypothyroidism

Congenital hypothyroidism is an uncommon developmental disorder that has been reported in cats, Boxers, Scottish deerhounds, Giant Schnauzers, Affenpinschers, and Great Danes and is caused by thyroid aplasia or hypoplasia (Fig. 18.11, eFigs. 18.6 and 18.7).[19–21] Clinically, the animals are disproportionate, short-limbed dwarves with bowed limbs and long necks and trunks. After identifying an epiphyseal dysplasia radiographically, the diagnosis can be confirmed by measuring thyroid and thyroid stimulating hormone concentrations.

Radiographic Signs

Radiographic findings consist of epiphyseal dysplasia that appears as reduced or delayed ossification of the epiphyseal cartilage model. This is seen most easily in the proximal tibia and the humeral and femoral condyles. Cuboid bone ossification in the carpus and tarsus is also delayed. Vertebral bodies are shorter than normal as a result of endplate dysplasia. The skull may appear shorter and broader than normal. Degenerative joint disease may be seen as a sequel.

Mucopolysaccharidosis

Mucopolysaccharidosis represents a loosely related group of uncommon autosomal recessive inherited disorders that result in a reduction or absence of glycosaminoglycan catabolism. Lysosomal degradation of these mucopolysaccharides is



eFig. 18.5 Aseptic necrosis of the left femoral head. The femoral head is irregularly margined, heterogeneously decreased in opacity and flattened. The right femoral head is normal.



eFig. 18.6 Congenital hypothyroidism in a skeletally immature dog. Mineralization of the long bone epiphyses and cuboid bones of the carpus is markedly reduced. (From Saunders H. The radiographic appearance of canine congenital hypothyroidism: skeletal changes with delayed treatment. *Vet Radiol*. 1991;32:171.)



eFig. 18.7 Lateral radiograph of the lumbar spine of a 2.5-year-old mix-breed dog with congenital hypothyroidism. The vertebral endplates are incompletely formed and the physes remain open. The vertebrae are overall shortened.

necessary for normal growth in developing animals and the abnormal metabolism leads to chronic, progressive, multisystemic disease. More than 10 forms are recognized in people, each produced by a different enzyme defect. Many of these have also been identified in dogs and cats.[22–24] The best-studied animal form is the feline form of mucopolysaccharidosis VI (MPS-VI). It causes polyarthropathies because of faulty cartilage formation. The morphologic appearance of affected cats ranges from normal to short-legged dwarfs with facial dysmorphism. Feline MPS-VI has two genotypes. The least affected phenotype ranges from being physically and clinically normal to having degenerative joint disease of the shoulder and stifle joints. The classic form produces phenotypic features of dwarfism and facial dysmorphia. These cats tend to have lameness and develop hind limb paresis. The diagnosis is confirmed by an MPS urine spot test that looks for the presence of undegraded glycosaminoglycans in the urine.

Radiographic Signs

Radiographic changes of mucopolysaccharidosis involve both the axial and the appendicular skeleton. Generalized epiphyseal dysplasia is present, involving long bones and vertebral endplates. Severely affected animals are osteopenic. Findings include delayed and incomplete mineralization of the epiphyseal cartilage model. Ossified regions of the epiphyses are smaller than normal and have a nonuniform opacity with a granular appearance. Vertebral bodies appear cuboid and shorter than normal (Fig. 18.12, eFig. 18.8). The maxilla is short and flattened; the frontal sinuses may be small or absent. Progressive degenerative joint disease occurs as a result of the epiphyseal malformations. Coxofemoral subluxation or luxation may result from femoral head epiphysis remodeling. Ventral bridging spondylosis is seen in older animals.



Fig. 18.11 A lateral radiograph of an 11-week-old kitten. The image was obtained for the patient's obstipation but demonstrates epiphyseal dysplasia affecting all epiphyses and endplates, and delayed ossification of the cuboidal and sesamoid bones from congenital hypothyroidism.

Multiple Epiphyseal Dysplasia

Multiple epiphyseal dysplasia is described in people where at least five different familial mutations have been identified and result in variation of inappropriately mineralized epiphyses. Multiple epiphyseal dysplasia is very rare, with only sporadic reports in veterinary medicine including a cohort of Beagles reported in the 1970s and a retrospective evaluation that yielded 19 cases from 10 different litters of Hygenhund, Dunker, Golden Retriever, and English pointers. The breeding of two affected Beagle dogs yielded an autosomal recessive pattern of inheritance.[25–27] The dogs are normal at birth and by 5 to 8 months of age the puppies are chronically lame. Some have angular limb deformities. The disease is characterized by failure of ossification of the epiphyses, apophyses, cuboidal bones, and sesamoids. Affected individuals have delayed growth and never reach normal size. This is a diagnosis of exclusion as specific genetic mutations are not known in dogs. Epiphyseal dysplasia is diagnosed radiographically and the more common causes including congenital hypothyroidism and mucopolysaccharidosis are excluded by measuring serum thyroid concentrations and evaluating for glycosaminoglycans (GAGs) in the urine.

Radiographic Signs

These include stippling of the epiphyses and irregular epiphyseal margins. Affected epiphyses eventually mineralize but are moderately deformed. Aberrant separate centers of ossification that eventually fuse with the normal ossification centers have also been described. Accelerated degenerative joint disease occurs.

DISEASES PRIMARILY AFFECTING THE PHYSIS

Spontaneous Capital Physeal Fracture of Cats

Spontaneous capital physeal fractures are defined as fractures that occur without associated trauma. In cats, spontaneous capital physeal fractures are most commonly seen in male cats

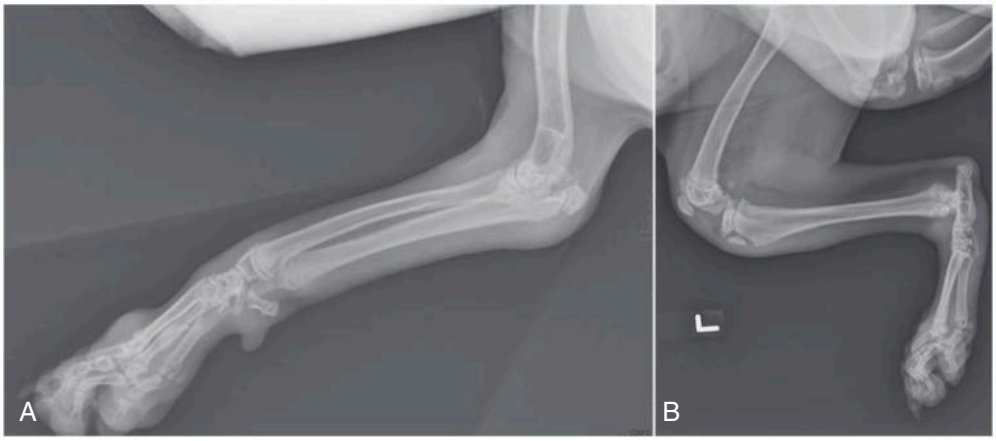
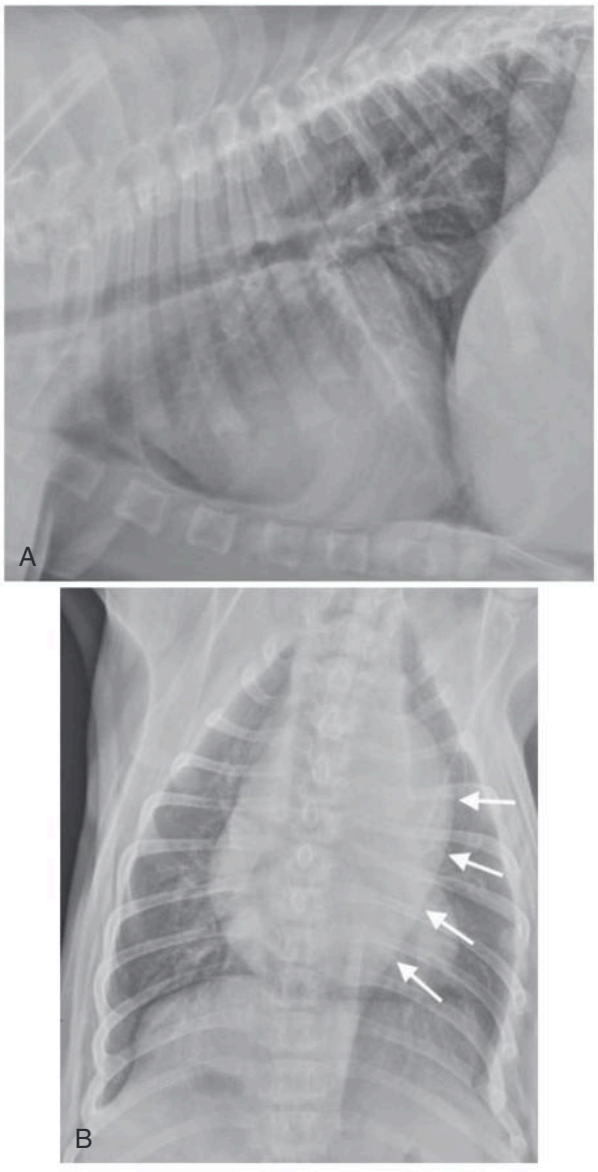


Fig. 18.12 Mucopolysaccharidosis. Lateral radiograph of the elbow **(A)** and of the stifle **(B)** of a 5-month-old Alaskan Malamute puppy with small and irregularly shaped epiphyses.



eFig. 18.8 Lateral **(A)** and dorsoventral **(B)** views of a 5-month-old Alaskan Malamute puppy. There is epiphyseal dysplasia with small, poorly de fined vertebral epiphyses and aneurysmal dilation of the thoracic aorta (outlined by *arrows*). Aortic dilation occurs in some forms of mucopolysaccharidosis, possibly due to alterations in elastin production. The epiphyses are small and irregularly shaped including the vertebral endplates.

and are associated with early neutering, obesity, and delayed capital physeal closure.[28] A relationship between early neutering and delayed physeal closure is proposed and most cats are approximately 2 years of age at time of presentation. Fractures are frequently bilateral although may occur consecutively rather than simultaneously.

Radiographic Signs

The primary radiographic abnormalities include varying degrees of fragment malalignment, femoral head and neck osteolysis, and regional sclerosis (Fig. 18.13, eFig. 18.9). The physeal fracture precedes metaphyseal resorption and the degree of osteolysis and sclerosis of the femoral head and neck progress with chronicity. The ventrodorsal radiograph provides the best evaluation of the capital physis although multiple projections including flexed "frog-legged" and extended leg radiographs may be necessary for diagnosis. Evaluation of the contralateral femoral head and neck is suggested as delayed physeal closure may be evident and bilateral fractures are frequent.



Fig. 18.13 Spontaneous capital physeal fracture in a 23-month-old neutered male cat. The right femoral head is no longer aligned with the femoral neck (*white arrow*). A left-sided femoral head and neck ostectomy was performed previously for capital physeal fracture.

Incomplete Ossification of the Humeral Condyle

Incomplete ossification of the humeral condyle is an inheritable condition of spaniels and French bulldogs resulting in a higher-than-normal incidence of humeral condylar fractures associated with normal physical activity.[29] The incidence of the disorder appears to be higher in males. Sporadic reports have been made of other medium- and large-breed dogs affected by this disorder.[30,31] Two separate centers of ossification in the humeral condyle appear typically by approximately 22 days after birth. The medial and lateral centers of the condyle should fuse by approximately 84 days after birth. Incomplete ossification leads to the presence of a thin fissure separating the medial and lateral halves of the humeral condyle in skeletally mature dogs. The fissure line can be subtle and difficult to detect radiographically, whereas CT is more sensitive. When pathologic fractures occur, approximately half are Y- or T-type fractures affecting the entire epicondylar region; the remainder are limited to fractures of the lateral (35%) or medial (15%) condyle.[29] The incidence of incomplete humeral condylar ossification is high enough that bilateral elbow radiographs or CT should be obtained in any spaniel or French bulldog with a unilateral condylar fracture. An increased incidence of fragmented coronoid processes appears to be associated with this disorder.

Radiographic Signs

The primary radiographic finding in dogs with incomplete humeral condylar ossification is a vertically oriented radiolucent line in the central region of the condyle that may extend from the subchondral bone margin of the trochlea to the distal margin of the supratrochlear foramen (Fig. 18.14). This radiolucency is evident only on the craniocaudal view and may be better seen when the view is obliqued approximately 15 degrees craniomedial to caudolateral, which positions the fissure parallel to the x-ray beam angle. Secondary radiographic signs

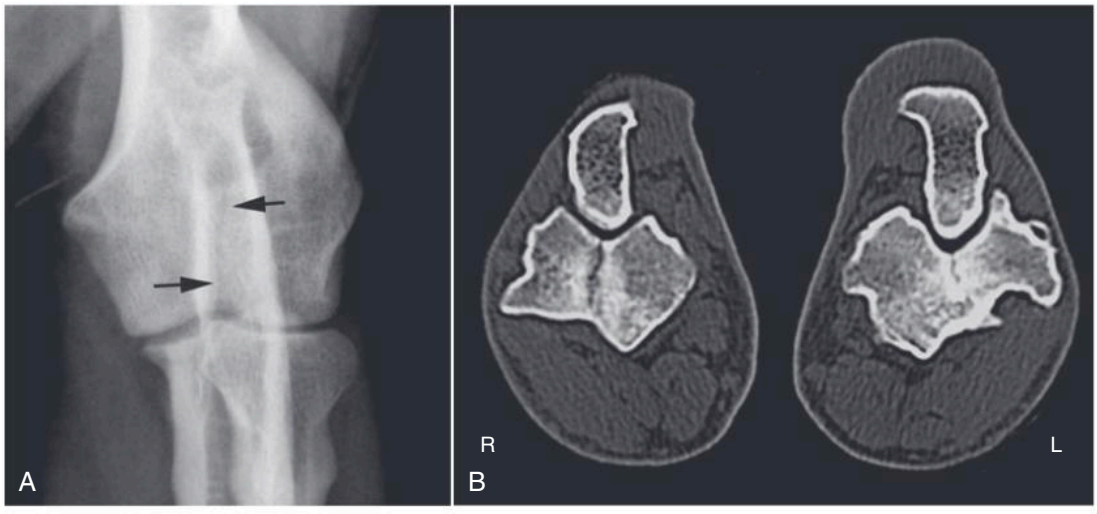
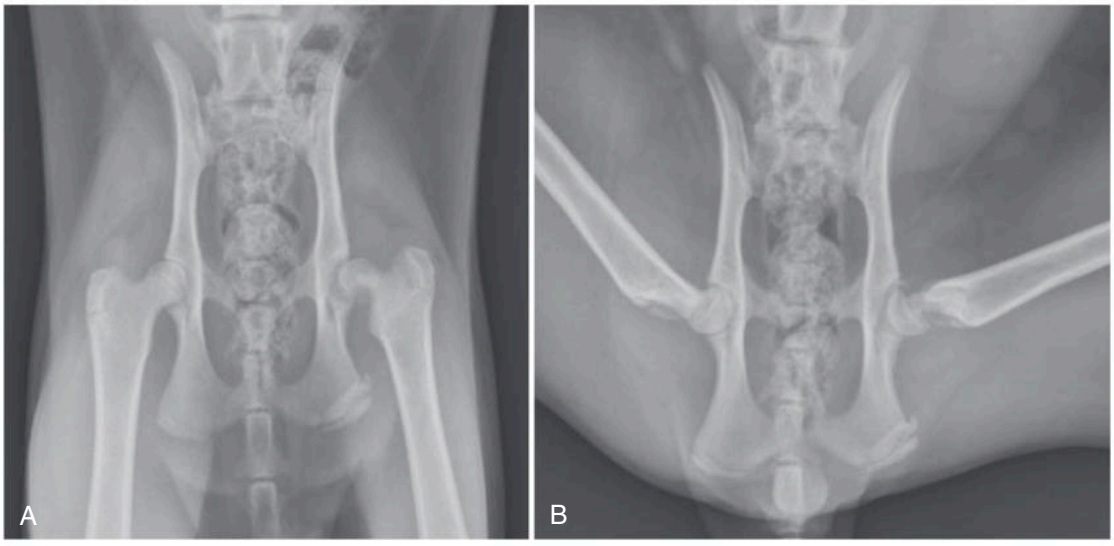


Fig. 18.14 **A,** Incomplete ossification of the humeral condyle. A vertical radiolucent line is present in the distal humeral condyle (*black arrows*). **B,** Computed tomography image of the left and right distal humerus of a dog with incomplete humeral condylar ossification. A sagittally oriented lucent line is evident in each condyle, surrounded by sclerosis of adjacent bone. The ossification deficit is more pronounced in the right humerus.



eFig. 18.9 Spontaneous capital physeal fracture of the left femoral head in a Maine Coon cat. **A,** Extended leg ventrodorsal view. The left femoral neck is thinned and not aligned with the epiphysis of the femoral head. **B,** Flexed (frog-leg) ventrodorsal view. The separation of the femoral epiphysis from the femoral neck is easier to detect in this projection.

include smooth periosteal new bone formation along the lateral and caudal aspect of the humeral epicondylar region. This finding may be a response to chronic instability or incomplete, nondisplaced fracture through the nonossified region. Overt, displaced, pathologic condylar fractures may be present in one or both limbs.

Rickets

Rickets is a rare disease of dogs and cats and is defined as osteomalacia of the physes in juvenile patients due to inadequate vitamin D or heritable disorders affecting vitamin D metabolism or utilization. The decreased vitamin D results in insufficient absorption of calcium and phosphorus from the gastrointestinal (GI) tract. Affected juvenile patients present with hypocalcemia, alopecia, thickening at level of metaphyses, bowing or angular deformities, and lameness. Rickets can be concomitant with secondary hyperparathyroidism as the lack of vitamin D will inhibit GI absorption of calcium. Vitamin D can be manufactured in the skin with ultraviolet light in reptiles, amphibians, birds, and herbivores whereas carnivore dogs and cats obtain vitamin D from dietary sources.[32] Fortunately, rickets from dietary deficiencies is rarely seen in dogs and cats. Hereditary disorders of vitamin D metabolism are sporadically reported in both dogs and cats and are categorized as vitamin D–dependent rickets type I, where there is a deficiency in the enzyme that converts vitamin D to its active form. Type II is also known as hereditary vitamin D–resistant rickets where there is an anomaly of the vitamin D receptor on the target organs.[33]

Radiographic Findings

Radiographic findings of rickets include marked widening of the physes creating large, nonmineralized gaps with flaring and cupping of the adjacent epiphyses and metaphyses (Fig. 18.15, eFig. 18.10). Flared osteochondral junctions along the ribs are called "rachitic rosary" and are usually easily palpated. Diffuse osteopenia with thin cortices may be appreciated and can progress to folding fractures.

Chondrodysplasia and Osteochondral Dysplasia

Chondrodysplasia and osteochondral dysplasia result in short limb disproportionate dwarfism. There are multiple dog breeds (and other species) where short, curved limbs are the breed standard. In fact, the 19 different American Kennel Club chondrodysplastic dog breeds all share a common retrogene that encodes fibroblast growth factor 4 (fgf4).[34] Distinguishing between chondrodystrophic breeds that have been bred for many generations to establish a defect as a breed characteristic and chondrodysplastic dwarves that arise sporadically from normal parents is important. Chondrodysplasia and osteochondrodysplasias as undesirable genetic mutations have been reported in a number of breeds (Table 18.2).[35–41] This category of diseases includes a conglomerate of different genetic mutations. These different causes for chondrodysplasia can appear clinically and radiographically similar with widened physes, flared metaphyses, and angular limb deformities. Further characterization is hampered because specific genetic mutations are not described for many of these examples, and the sporadic nature of both the occurrence and the literature reporting them.

Osteochondrodysplasia of Scottish Fold Cats

A single gene variant in the *TRPV*$_4$ that is autosomal dominant results in the folded ear appearance of the breed and osteochondrodysplasia. The degree of limb deformity and degenerative change is variable and appears worst in individuals that are homozygous dominant for this trait. Heterozygous individuals still have folded ears. When blinded radiologists are asked to evaluate radiographs of heterozygous individuals and of those without the mutation, they are largely able to detect the affected cats, although the heterozygous individuals are much less affected than the extreme examples in Fig. 18.16. Affected animals are shorter than normal, with thick inflexible



Fig. 18.15 Rickets in a 6-month-old female Pomeranian puppy. There is diffuse osteopenia with marked widening of the physis and flaring of the adjacent epiphysis and metaphysis. The puppy did not respond to high doses of oral calcium supplementation and later genome sequencing was performed and an anomaly of the vitamin D receptor ligand-binding domain was identified, compatible with type II/vitamin D-resistant rickets.

Table • **18.2**

Incomplete List of Breed-Specific Chondrodysplasias.

	HERITABILITY	KEY FEATURES	RADIOGRAPHICALLY
Chondrodysplasia of Alaskan Malamutes	Autosomal recessive gene	The skull and spine are not affected	Wide physes, small carpal bones, flared metaphysis
Chondrodysplasia of Norwegian Elkhounds	Autosomal recessive	Front limbs affected more than hind limbs	Similar to the Malamutes, but spine can be affected
Ocular chondrodysplasia of Labrador retrievers	Autosomal recessive	Retinal dysplasia, cataracts	Shortened long bones, asynchronous growth of radius and ulna, large carpal bones, wide ribs



eFig. 18.10 Lateral **(A)** and dorsopalmar **(B)** radiographs of a 6-month-old dog with Rickets. There is severe widening of the physis with flaring of the adjacent metaphysis. The dog had congenital cystic kidney disease.



Fig. 18.16 Scottish fold osteochondral dysplasia. Metatarsal bones are short and misshapen. Phalanges are also affected. Marked secondary degenerative changes are present at all levels from the tarsocrural joint distally. The large mass of new bone in the plantarolateral aspect of the limb contributes to cuboidal bone fusion and tarsal ankylosis.

tail base, splaying of toes, and lack of normal range of motion in carpi and tarsi.

Radiographic Signs

Metaphyses of the metatarsals and metacarpals are distorted and physes are widened. Similar but less pronounced abnormalities are seen involving the phalanges. The metacarpi, metatarsi, and phalanges are shorter than normal resulting in decreased limb length. Caudal vertebrae are reduced in length and have widened endplates. There is accelerated degenerative joint disease. Large enthesophytes can form around joints at points of tendinous origin or insertion (entheses). An ankylosing arthropathy frequently results in fusion of the carpi and tarsi and their articulations with the metacarpi and metatarsi (see Fig. 18.16).[40–43]

DISEASES OF THE METAPHYSIS

Hypertrophic Osteodystrophy

Hypertrophic osteodystrophy (HOD), also called *metaphyseal osteopathy,* is a systemic illness that usually affects large- and giant-breed dogs between the ages of 2 and 7 months. The cause is unknown.[44–47] Clinical signs, including marked pyrexia, diarrhea, footpad hyperkeratosis, leukocytosis, anemia, and pneumonia, are occasionally seen with HOD, lending credibility to the possibility of a systemic infection as a cause for this disease.

Resulting bone lesions are generally bilaterally symmetric and involve the metaphyses of long bones, particularly the distal radius, ulna, and tibia. The costochondral junctions, metacarpal and metatarsal bones, and proximal humerus may also be involved.

Although HOD is self-limiting and resolves after a few weeks, more severe involvement can ultimately result in abnormal/premature physeal closure and subsequent skeletal deformity. Histologically, lesions in the metaphyses consist of a neutrophilic inflammatory response associated with necrosis, hemorrhage, and increased osteoclast numbers. Collapse of necrotic metaphyseal trabecular bone and subperiosteal hemorrhage are also seen.

Radiographic Signs

Early radiographic signs include transversely oriented lucent zones within the metaphysis that are parallel and adjacent to the physes (Fig. 18.17, eFig. 18.11) These are usually best seen in the distal radius and ulna and this appearance is sometimes referred to as the *double physis sign*, although the second radiolucent zone is not actually a physis. A thin margin of subchondral bone sclerosis may parallel the lucent zone and is caused by the collapse of necrotic trabecular bone. Irregular periosteal new bone forms around the metaphysis and is usually distinct and separate from the underlying cortex in the earlier stages of the disease. The extent of new metaphyseal bone formation depends on the severity and duration of the disorder, and such formation may extend to the diaphysis in severely affected dogs (see Fig. 18.17C). Diffuse soft tissue swelling can be seen centered on the metaphyseal regions. Widening, concavity, and increased opacity of the distal rib ends may be present in some dogs.

Osteochondroma, Osteochondromatosis, and Multiple Cartilaginous Exostosis

Osteochondromas may occur in two forms: solitary or multifocal. The multiple form is termed *osteochondromatosis*, also called multiple cartilaginous exostosis. Osteochondroma is a



eFig. 18.11 Hypertrophic osteodystrophy. Lateral **(A)** and dorsopalmar **(B)** views of the distal antebrachium. An irregular radiolucent line is visible proximal to the smoother physeal lines.

benign proliferative disease of bone and cartilage. Hereditary transmission of the disease is suspected in dogs.[48] Any bone that develops by endochondral ossification may be affected and simultaneous involvement in multiple bones is common. Chondrocytes are pushed into the metaphyses and do not differentiate into osteoblasts. Instead, these cartilage islands continue to proliferate as cartilaginous masses that eventually ossify. In dogs, growth usually ceases once the animal has reached maturity resulting in nonpainful bony protuberances throughout the skeleton. The bone lesions are of no clinical significance unless they arise in an area in which function could be compromised, such as the vertebral canal. Most exostoses remain inert once the dog has matured, but malignant transformation has been reported.[49,50] In cats, osteochondromatous lesions typically develop in young adult cats and enlarge progressively throughout the animal's life. The pathogenesis is not fully understood, but it has been associated with feline leukemia virus (FeLV) and other retroviruses.

Radiographic Signs

Rib masses are an amorphous mixture of radiolucency and bone opacity with irregular contours (Fig. 18.18). Long-bone

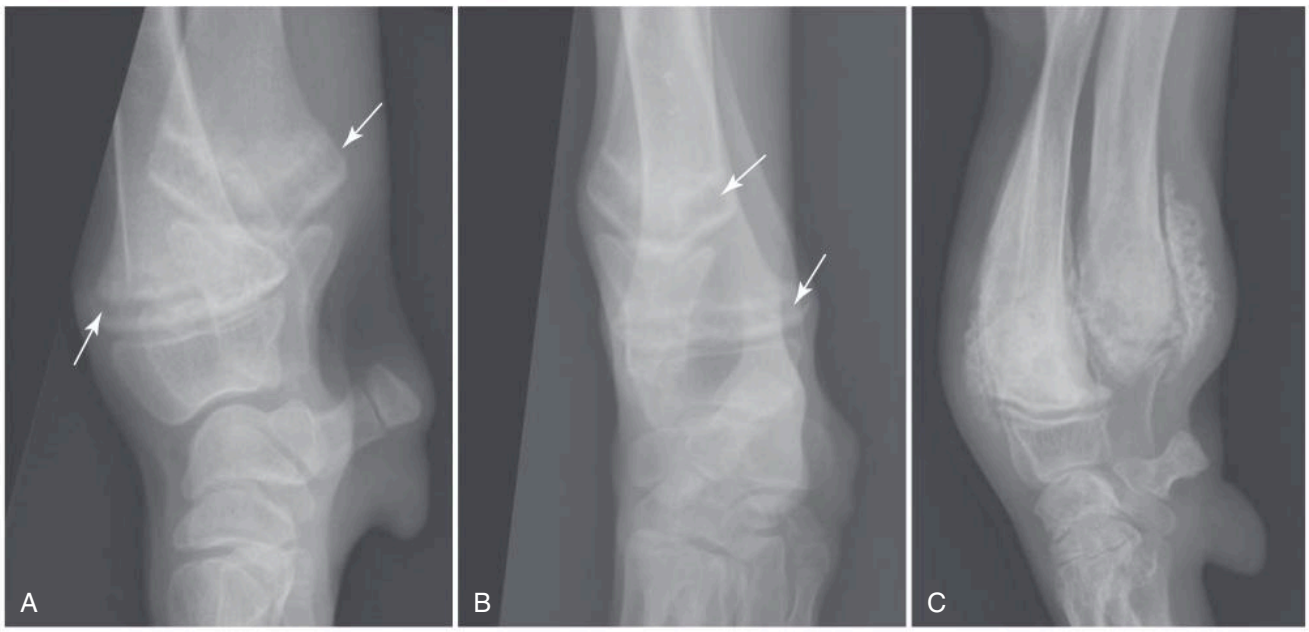


Fig. 18.17 Hypertrophic osteodystrophy. **A and B,** Acute phase. Irregular radiolucent regions are evident in the distal radial and ulnar metaphyses, proximal to the physis (*white arrows*). **C,** Chronic phase. An irregular, palisading periosteal reaction is present.

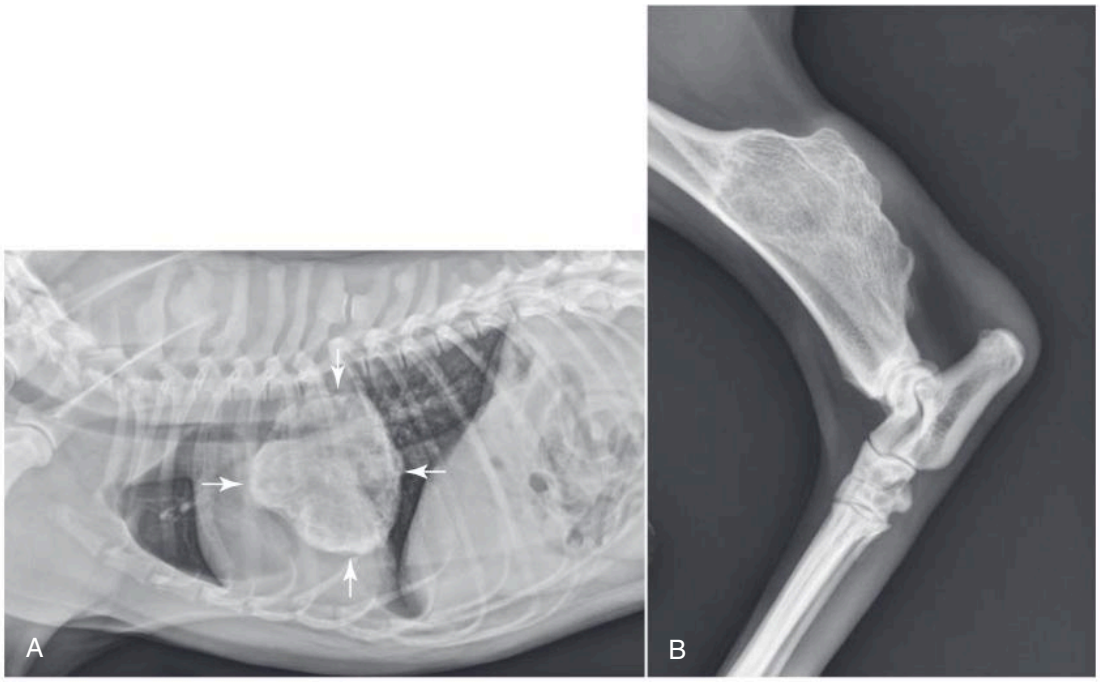


Fig. 18.18 Multiple cartilaginous exostosis. **A,** A large, expansile lesion is present involving the ribs (*white arrows*). The mass has a smoothly margined mineralized rim. Multiple nodular bone masses deform the shape of the thoracic spinous processes. **B,** A large, expansile lesion is present within the distal tibial diaphysis of the same dog.

and vertebral masses tend to be more organized in appearance with radiolucent cartilage and trabecular bone. Cortical bone in the area of the lesion may be present or absent; the bone may be deformed or the exostosis may project externally. The size and shape of exostoses vary.

Retained Cartilage Core

Retained cartilage cores are primarily seen in the distal ulnar metaphysis of large-breed dogs and the proximal tibia.[51] The lesion is caused by a disruption of the normal progression of endochondral ossification with retention of hypertrophied cartilage cells in the central metaphysis. Cartilage retention may cause angular limb deformity from retardation of distal ulnar growth and a resulting mismatch in radial and ulnar elongation, but the lesion is sometimes an incidental finding in otherwise normal dogs.

Radiographic Signs

Radiographic findings include persistence of a radiolucent region in the metaphysis. In the distal ulnar physis, this is flame shaped. In the proximal tibia at the conjunction of the proximal physis and physis of the tibial tuberosity, a focal rounded radiolucency is seen on lateral radiographs (Fig. 18.19).

DISEASE PRIMARILY AFFECTING THE DIAPHYSIS

Panosteitis

Panosteitis is a self-limiting disease that affects the long bones of primarily young, large-breed dogs (Fig. 18.20, eFig. 18.12). Males are affected four times more often than are females. Dogs between the ages of 5 and 12 months are affected most often; however, German shepherd dogs as young as 2 months and as old as 7 years have been reported. Panosteitis lesions may be solitary, affect multiple sites in a single bone, or be multifocal in multiple bones. Although the lesions can affect any part of the diaphysis of a long bone, they often originate and are most pronounced near the nutrient foramen. Bone involvement is often sequential. and the disease may be protracted over several months with lesions resolving in some bones while developing in others. Severity and location of radiographic lesions do not necessarily correlate with the severity of clinical signs and the most clinically affected limb may not have the most



Fig. 18.19 Retained cartilage core in the distal ulna. A triangular radiolucent region is present in the distal ulnar metaphysis (*white arrows*). A thin rim of bone sclerosis is present next to the radiolucency.

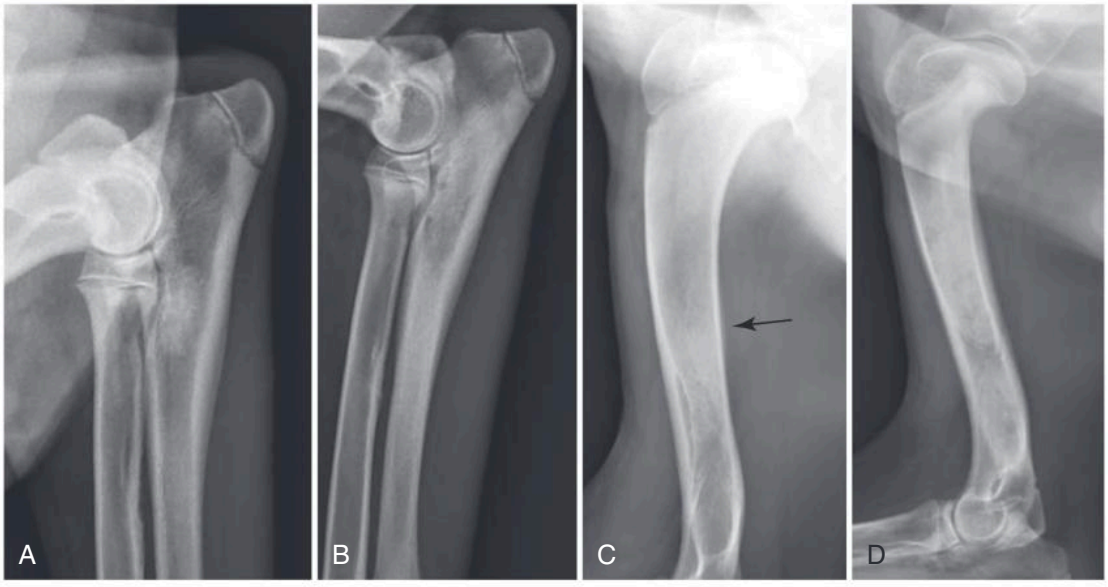
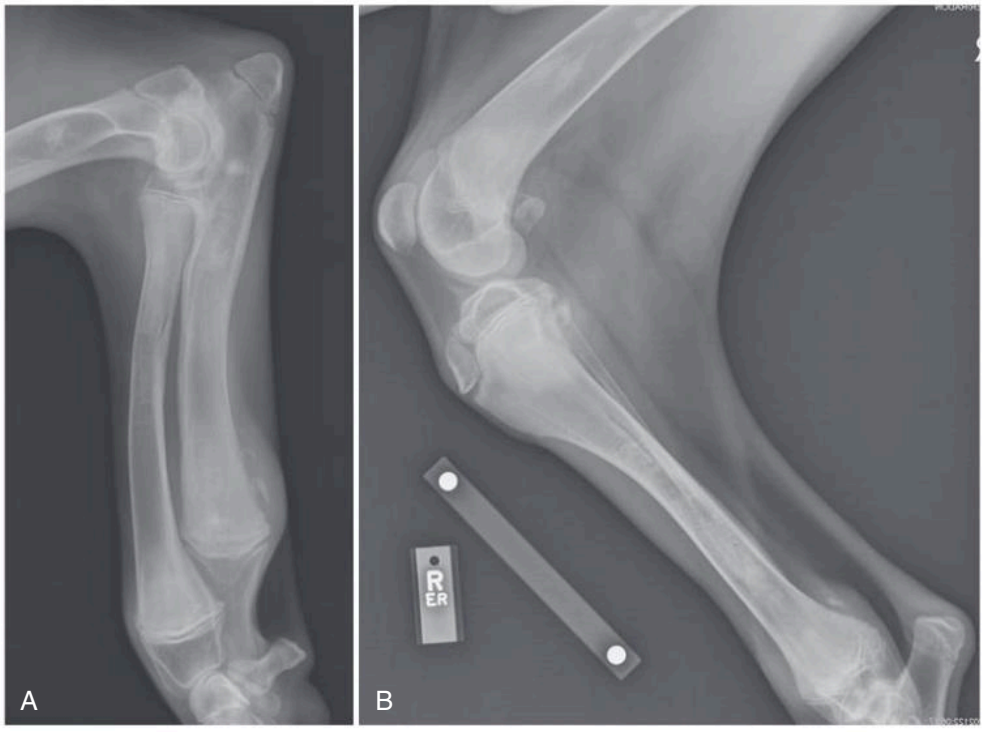


Fig. 18.20 Panosteitis. Left **(A)** and right **(B)** elbows of a 6-month-old canine mix with panosteitis. In **A,** there is a focal increase in medullary opacity in the proximal ulna. This nodular appearance is typical of very early panosteitis. In the right elbow of the dog in **A,** there is more diffuse increased medullary opacity in the ulna, which is typical of a later stage of the disease. **C,** Panosteitis in an 8-month-old canine mix. There is increased medullary opacity in the mid-diaphysis of the humerus at the level of the nutrient foramen, although the foramen is not visible in this dog. Canine panosteitis often begins at the level of the nutrient foramen. There is a focal region of smooth periosteal reaction (*black arrow*) on the caudal aspect of the humerus. **D,** Canine panosteitis in a 6-month-old German shepherd. There is a diffuse increase in medullary opacity in the humerus and an extensive periosteal reaction on the caudal aspect of the humerus.



eFig. 18.12 Lateral radiographs of the antebrachium **(A)** and stifle/crus **(B)** of a 5-month-old Great Dane with panosteitis. Note the multifocal areas of sclerosis in the medullary cavity of the long bones. The dog also has hypertrophic osteodystrophy evidenced by a radiolucent line proximal to the physis. Soft tissue mineralization is seen at the caudal aspect of the distal metaphysis of the ulna and tibia.

pronounced radiographic lesions.[37,38] The term *panosteitis* is a misnomer in that histologically no evidence of an inflammatory response is present. Medullary, endosteal, and periosteal osteoblastic and fibroblastic activity is increased.

Radiographic Signs

Early in the course of the disease, poorly delineated increased opacity starts near the nutrient foramen. As the lesion progresses, medullary opacities become more diffuse and homogeneous. Smooth, continuous periosteal new bone formation develops in the diaphysis of affected bones in one-third to one-half of dogs. Late in the disease, opacities resolve, leaving coarse, thickened trabecular bone that eventually assumes a normal appearance. Cortical thickening may persist as periosteal new bone remodels.

GENERALIZED BONE DISORDERS

Nutritional Secondary Hyperparathyroidism

Nutritional secondary hyperparathyroidism is caused by a diet that is either calcium deficient or calcium and phosphorus imbalanced. Inadequate dietary calcium intake causes an increase in parathyroid hormone. This, in turn, results in bone calcium resorption and generalized osteomalacia. The skeletal changes are diffuse and generalized.[40–42]

Radiographic Signs

Bone opacity is decreased, and cortices may appear abnormally thin. In severely affected animals, bone opacity may be similar to that of soft tissue. A loss of definition of the normally dense dental lamina that surrounds the teeth may also occur. Spinal deformity and pathologic folding fractures of the appendicular and the axial skeleton are common (Fig. 18.21).

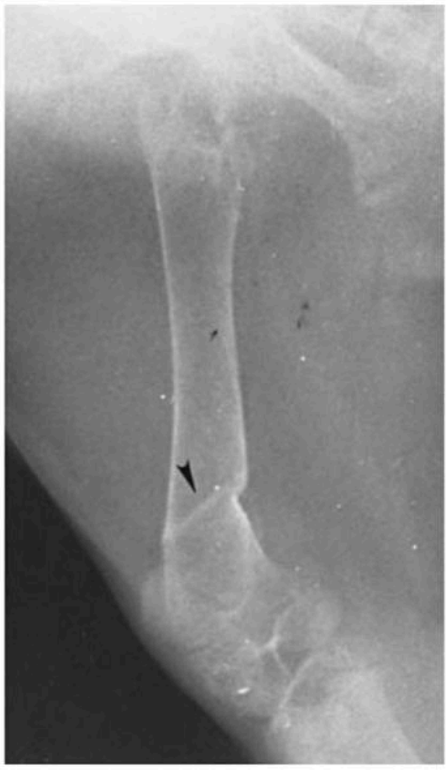


Fig. 18.21 Nutritional secondary hyperparathyroidism. Overall bone opacity is deceased, and the cortices are thin. There is a pathologic folding fracture indicated by the *black arrowhead*.

Osteogenesis Imperfecta

Osteogenesis imperfecta is a rare, brittle bone heritable disease caused by a structural defect in type 1 collagen, which constitutes the majority of the nonmineral bone matrix.[43,44] It has been reported in Dachshunds and Finnish Laphunds. Affected puppies may or may not have stunted growth, multiple reoccurring fractures, and laxity of joints, and the teeth may appear pink. The cortices are thin and contain woven bone with no Haversian canals.

Radiographic Signs

A generalized decrease in bone opacity is present and long bone cortices are thin. Pathologic fractures are common and may be associated with excessively opaque callus formation and medullary sclerosis. The dentin of the teeth is thin. Findings are similar to and can be confused with generalized bone mineral loss from secondary hyperparathyroidism.

Osteopetrosis

Osteopetrosis is a rare, inherited metabolic bone disease that is presumed to be caused by abnormal osteoclast function (Fig. 18.22, eFig. 18.13).[47] Affected animals have a generalized increase in bone opacity specifically affecting medullary cavities. A resulting decrease in the number of normal hematopoietic cells subsequently occurs, leading to myelophthisic anemia.

In cats, varying degrees of osteosclerosis with nonregenerative anemia induced by FeLV have also been reported and the radiographic appearance is identical to that described for osteopetrosis.[46] Until more information is obtained, the finding of generalized osteosclerosis in cats should be considered nonspecific, but viral testing for FeLV should be considered.

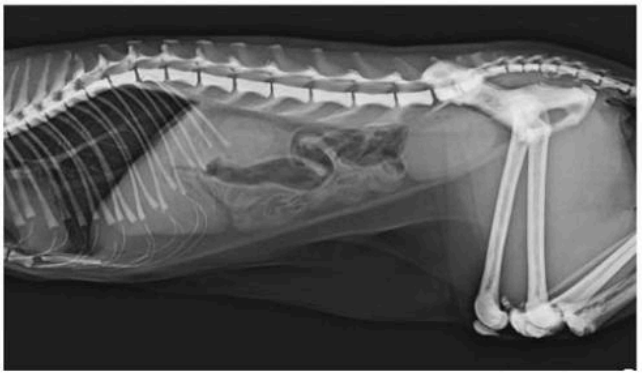


Fig. 18.22 Osteopetrosis in a lateral abdominal radiograph of a 12-year-old cat with nonspecific signs of anorexia and vomiting. Unrelated to the primary complaint there is generalized increased opacity of the axial skeleton and cortical thickening of the appendicular skeleton.

Radiographic Signs

Bone opacity is generally increased, particularly in medullary cavities. The normal trabecular pattern is diminished as a result of the uniform increase in bone opacity and the internal cortical margins become indistinct.

Knees and Teeth Syndrome

Knees and teeth syndrome is a disorder of young cats that develop spontaneous atraumatic patellar fractures. Age of onset of the first fracture ranges from 4 months to 8 years with a mean age of the first patellar fractures at 28 months. Some 78% of these cats develop contralateral patellar fracture. This coincides with persistent deciduous teeth and unerupted permanent teeth. Many of these cats also have spontaneous fractures



eFig. 18.13 Osteopetrosis in a dog. A generalized increase in bone opacity is visible involving the appendicular and the axial skeleton. A loss of corticomedullary junction definition is attributable to increased medullary opacity. In this example, a small distal diaphyseal region of the humeral medullary cavity is not yet affected and appears less opaque than surrounding bone (*white arrow*).

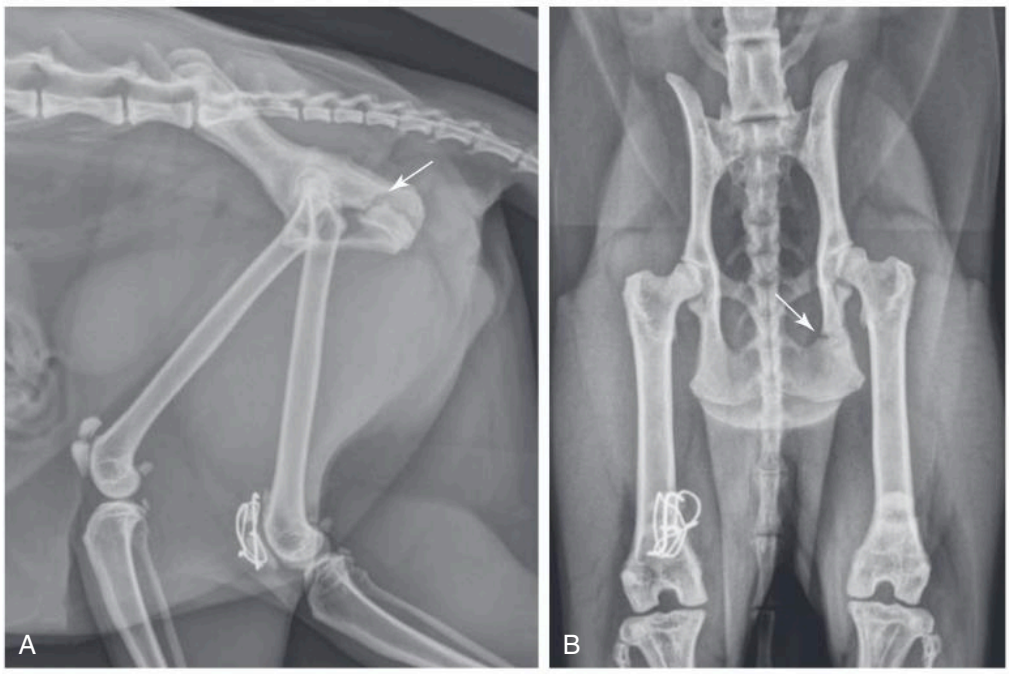


Fig. 18.23 **A,** Lateral and **B,** ventrodorsal radiographs of a domestic shorthaired cat with knee and teeth syndrome. This individual fractured both patellae before 2 years of age and the ischium (*arrows*) at 3 years of age. The right patellar fracture was surgically addressed. The left patellar fracture is a transverse fracture, and the patella is sclerotic.

in other areas including the ischium, tibia, ilium, and calcaneus. An affected individual can have between one and six atraumatic fractures over its lifespan. The etiology that predisposes these cats to fractures is unknown.[48]

Radiographic Signs

The fractures in the patella occur transversely through the middle of the patella or segmentally with more than one fracture. The patellae appear sclerotic radiographically. The pelvic fractures are transverse and they occur through the ischium, acetabulum, and ilium, and unlike traumatic pelvic fractures that tend to occur in groups of three fractures, these cats can have a single fracture (Fig. 18.23).

FOCAL AGENESIS OR MALFORMATIONS

Agenesis and Hypoplasia

Complete agenesis, partial agenesis, or hypoplasia of a long bone may occur. The radius, tibia, and ulna are most often involved, although the metacarpal, metatarsal, and phalangeal bones can also be affected (Fig. 18.24). These anomalies, which can usually be detected at or shortly after birth, may be inherited but are more often a result of in utero environmental factors.

Radiographic Signs

The affected bone or bones are conspicuously absent and the limb is usually malformed and shorter than normal. Limb curvature and joint malformation may also be present.

Polymelia

This general term denotes supernumerary limbs or parts of a limb. Polydactyly, the presence of an excess number of digits, is the most common form of polymelia and is seen most often in cats. A few breeds of dogs, such as the Great Pyrenees, have



Fig. 18.24 Tibial agenesis in a young dog. The tibia is not formed, and the fibula is misshapen. The proximal fibular epiphysis is hypoplastic and poorly mineralized. Tibial agenesis has led to stifle and tarsocrural malformation as well as limb shortening and angular deformity.

also been bred to retain this trait. The anomaly is generally insignificant clinically.

Radiographic Signs

Radiographic signs of polymelia vary according to the bone or bones involved. Polydactyly is a greater-than-normal number of digits, usually arising on the medial side of the limb. Supernumerary digits may include complete or partial metacarpal and metatarsal bones and variable numbers of phalanges (Fig. 18.25).

DISEASES PRIMARILY AFFECTING THE SKULL

Craniomandibular Osteopathy

Craniomandibular osteopathy is a self-limiting disease of puppies. West Highland White terriers are the classic breed although sporadic cases have been described in other breeds of dogs. Puppies are affected between 3 and 8 months of age. The etiology of the disease is unknown. The puppies present for discomfort while eating and pain on opening the mouth. Treatment consists of pain management and providing nutritional support. The disease has also been reported to involve the ulnae and fibulae. The patients can have lameness, palpable thickening of the distal limb, and pain on palpation.[49,50]

Radiographic Signs

These include bilateral enlargement and irregular margins of the mandible. The irregular thickened bone can extend to the tympanic bulla and temporomandibular joint (Fig. 18.26). The ulnae and fibulae may be thickened with a cuff of irregular periosteal reaction similar to chronic HOD.[49,50]

Calvarial Hyperostosis Syndrome

Calvarial hyperostosis is similar to craniomandibular osteopathy but involves the frontal, temporal, and occipital bones. This syndrome is reported in Bullmastiff puppies 5 to 10 months of age. The puppies present with asymmetric firm masses that are painful on palpation and improve or resolve with time. It histologically resembles craniomandibular osteopathy.[52]

Radiographic Signs

These include asymmetric thickening and irregular periosteal reaction of the dorsal calvaria.



Fig. 18.25 Polydactyly in a feline manus. There are six complete digits with a metacarpal bone and three phalanges each.

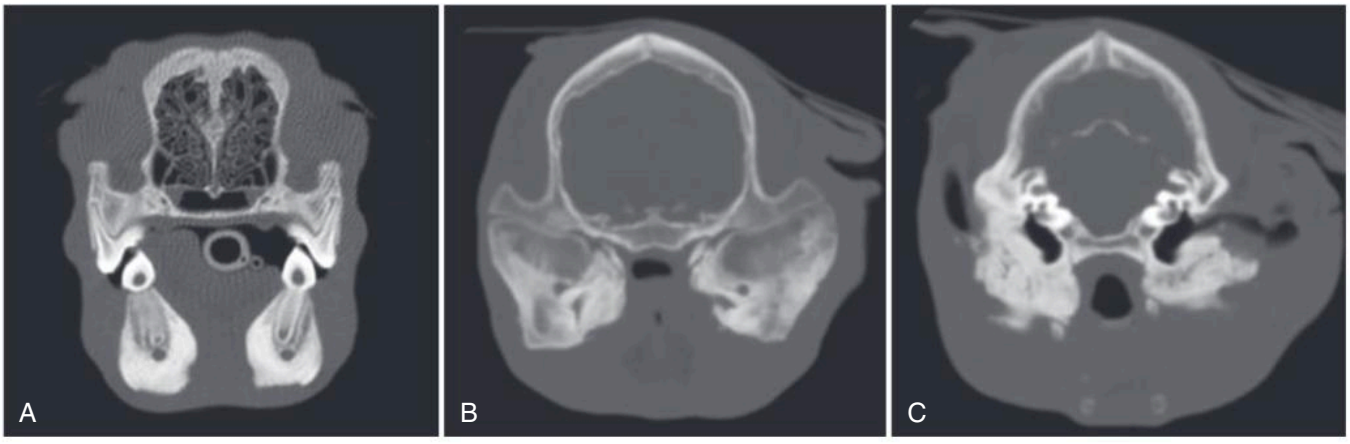


Fig. 18.26 **A,** Transverse computed tomography (CT) image of a 6-month-old female West Highland White terrier with craniomandibular osteopathy characterized by bilaterally symmetric thickening of the mandibles. **B and C,** Transverse CT images of a 1-year-old Golden retriever with severe craniomandibular osteopathy encasing and ankylosing the temporomandibular joints bilaterally **(B)** and surrounding the tympanic bulla **(C)**.

Acknowledgment

With special thanks to prior authors of this chapter for their contributions.

REFERENCES

1. Ytrehus B, Carlson C, Ekman S. Etiology and pathogenesis of osteochondrosis. *Vet Pathol*. 2007;44:429–448.
2. Wisner ER, Berry CR, Morgan JP, et al. Osteochondrosis of the lateral trochlear ridge of the talus in seven rottweiler dogs. *Vet Surg*. 1990;19:435.
3. van Bree HJ, Van Ryssen B. Diagnostic and surgical arthroscopy in osteochondrosis lesions. *Vet Clin North Am Small Anim Pract*. 1998;28:161.
4. Frazho JK, Graham J, Peck JN, et al. Radiographic evaluation of the anconeal process in skeletally immature dogs. *Vet Surg*. 2010;39:829.
5. Nemanic S, Nixon B, Baltzer W. Analysis of risk factors for elbow dysplasia in giant breed dogs. *Vet Comp Orthop Traumatol*. 2016;29(05).
6. Blond L, Dupuis J, Beauregard G, et al. Sensitivity and specificity of radiographic detection of canine elbow incongruence in an in vitro model. *Vet Radiol Ultrasound*. 2005;46:210.
7. Holsworth IG, Wisner ER, Scherrer WE, et al. Accuracy of computerized tomographic evaluation of canine radio-ulnar incongruence in vitro. *Vet Surg*. 2005;34:108.
8. Hornof WJ, Wind AP, Wallack ST, et al. Canine elbow dysplasia. The early radiographic detection of fragmentation of the coronoid process. *Vet Clin North Am Small Anim Pract*. 2000;30:257.
9. Berry C. Evaluation of the canine elbow for fragmented medial coronoid process. *Vet Radiol Ultrasound*. 1992; 33:273.
10. Heidenreich DC, Fourie Y, Barreau P. Presumptive congenital radial head sub-luxation in a Shih Tzu: successful management by radial head osctectomy. *JSAP*. Oct;56(10):626-629.
11. Riser WH. The dysplastic hip joint: radiologic and histologic development. *Vet Pathology*. 1975;12(4):279–305. https://doi.org/10.1177/030098587501200405.
12. King M. Etiopathogenesis of canine hip dysplasia, prevalence, and genetics. *Vet Clin N Am Small Anim Pract*. 2017;47:753–767.
13. Ginja M, Silvestre A, Gonzalo-Orden J, Ferreira A. Diagnosis, genetic control and preventive management of canine hip dysplasia: a review. *Vet J*. 2010;184(3).
14. Smith G, Meyhew P, Kapatkin A, McKelvie P, Shofer F, Grego T. Evaluation of risk factors for degenerative joint disease associated with hip dysplasia in German shepherd dogs, golden retrievers, labrador retrievers and rottweilers. *JAVMA*. 2001;219(12).
15. Powers M, Biery D, Lawler D, et al. Use of the caudolateral curvilinear osteophyte as an early marker for future development of osteoarthritis associated with hip dysplasia in dogs. *JAVMA*. 2004;225(2).
16. Keller G, Reed A, Lattimer J, Corely E. Hip dysplasia: a feline population study. *Vet Radiol Ultrasound*. 1999;40(4).
17. Lee R. Legg-Perthes disease in the dog: the histological and associated radiological changes. *J Am Vet Radiol Assoc*. 1974;15:24.
18. Lieb AS, Grooters AM, Tyler JW, et al. Tetraparesis due to vertebral physeal fracture in an adult dog with congenital hypothyroidism. *J Small Anim Pract*. 1997;38:364.
19. Crowe A. Congenital hypothyroidism in a cat. *Can Vet J*. 2004;45:168.
20. Konde L, Thrall M, Gasper P, et al. Radiographic changes associated with mucopolysaccharidosis in the cat. *Vet Radiol*. 1987;28:223.
21. Rasmussen PG. Multiple epiphyseal dysplasia in a litter of beagle puppies. *J Small Anim Pract*. 1971;12:91.
22. Rasmussen PG. Multiple epiphyseal dysplasia in beagle puppies. *Acta Radiol Suppl*. 1972;319:251.
23. Rorvik A, Teige J, Ottesen N, Lingaas F. Clinical, radiographic and pathologic abnormalities in dogs with multiple epiphyseal dysplasia: 19 cases (1991–2005). *JAVMA*. 2008;233:4.
24. McNicholas WT, Wilkens BE, Blevins WE, et al. Spontaneous femoral capital physeal fractures in adult cats: 26 cases (1996–2001). JAVMA Dec 15:221(12): 1731-1736.
25. Marcellin-Little DJ, DeYoung DJ, Ferris KK, et al. Incomplete ossification of the humeral condyle in spaniels. *Vet Surg*. 1994;23:475.
26. Rovesti GL, Fluckiger M, Margini A, et al. Fragmented coronoid process and incomplete ossification of the humeral condyle in a Rottweiler. *Vet Surg*. 1998;27:354.
27. Gabriel P, Pfeil A, Ludewig E, et al. Magnetic resonance imaging diagnosis: incomplete ossification of the humeral condyle in a German shepherd dog. *J Small Anim Pract*. 2009;50:92.
28. LeVine D, Zhou Y, Ghiloni R, et al. Hereditary 1,25-dihydroxyvitamin D-resistant rickets in Pomeranian dog caused by a novel mutation in the vitamin D receptor gene. *JVIM*. 2009;23:1278–1283.
29. Parker H, VonHoldt B, Pascale Q, et al. An expressed Fdf4 retrogene is associated with breed-defining chondrodysplasia in domestic dogs. *Science*. 2009;325(5943).
30. Bingel SA, Sande RD. Chondrodysplasia in the Norwegian elkhound. *Am J Pathol*. 1982;107:219.
31. Bingel SA, Sande RD, Wight TN. Chondrodysplasia in the Alaskan malamute. Characterization of proteoglycans dissociatively extracted from dwarf growth plates. *Lab Invest*. 1985;53:479.
32. Malik R, Allan GS, Howlett CR, et al. Osteochondrodysplasia in Scottish fold cats. *Aust Vet J*. 1999;77:85.
33. Allan GS. Radiographic features of feline joint diseases. *Vet Clin North Am Small Anim Pract*. 2000;30:281.
34. Rorden C, Griswold M, Moses N, et al. Radiographical survey of osteochondrodysplasia in Scottish fold cats caused by the $TRPV_4$ gene variant. *Hum Genet*. 2021;140.
35. Gandolfi B, Alamri S, Darby W, et al. A dominant $TRPV_4$ variant underlies osteochondrodysplasia in Scottish fold cats. *Oseoarthritis and Cartilage*. 2016;24:8.
36. Muir P, Dubielzig R, Johnson K, et al. Hypertrophic osteodystrophy and calvarial hyperostosis. *Compendium*. 1996;18:143.
37. Baumgartner W, Boyce RW, Weisbrode SE, et al. Histologic and immunocytochemical characterization of canine distemper-associated metaphyseal bone lesions in young dogs following experimental infection. *Vet Pathol*. 1995; 32:702.
38. Franklin MA, Rochat MC, Broaddus KD. Hypertrophic osteodystrophy of the proximal humerus in two dogs. *J Am Anim Hosp Assoc*. 2008;44:342.
39. Gambardella PC, Osborne CA, Stevens JB. Multiple cartilaginous exostoses in the dog. *J Am Vet Med Assoc*. 1975;166:761.
40. Doige C, Pharr J, Withrow S. Chondrosarcoma arising in multiple cartilaginous exostoses in a dog. *J Am Anim Hosp Assoc*. 1978;14:605.
41. Jacobson LS, Kirberger RM. Canine multiple cartilaginous exostoses: unusual manifestations and a review of the literature. *J Am Anim Hosp Assoc*. 1996;32:45.
42. Paek M, Engilges J, Mai W. Prevalence, association with stifle conditions and histopathologic characteristics of tibial tuberosity radiolucencies in dogs. *Vet rad us*. 2013;54(5).
43. Bohning RHJ, Suter PF, Hohn RB, et al. Clinical and radiologic survey of canine panosteitis. *J Am Vet Med Assoc*. 1970;156:870.

44. Voorhout G. Radiographic features of nutritional secondary hyperparathyroidism in the growing dog and cat [in German]. *Tijdschr Diergeneeskd*. 1981;106:317.
45. Campbell BG, Wootton JA, Krook L, et al. Clinical signs and diagnosis of osteogenesis imperfecta in three dogs. *J Am Vet Med Assoc*. 1997;211:183.
46. Seeliger F, Leeb T, Peters M, Bru M, Gmann FM, Trautwen Hewicker-. Osteogenesis imperfecta in two litters of dashhunds. *Vet Pathol*. 2003;40.
47. Hanel RM, Graham JP, Levy JK, et al. Generalized osteosclerosis in a cat. *Vet Radiol Ultrasound*. 2004; 45:318.
48. Reyes N, Longley M, Bailey S, Langley-Hobbs S. Incidence and types of preceding and subsequent fractures in cat with patellar fracture and dental anomaly syndrome. *J Feline Med Surg*. 2019;21(8).
49. Huchkowsky S. Craniomandibular osteopathy in a bullmastiff. *Can Vet J*. 2002;43:11.
50. Hudson J, Montgomery R, Hathcock J, Jarobe J. Computed tomography of craniomandibular osteopathy in a dog. *Vet rad and ultrasound*. 1994;35(2).
51. Johnson KA. Retardation of endochondral ossification at the distal ulnar growth plate in dogs. *Aust Vet J*. 1981;57(10):474–478.
52. Pastor K, Boulay J, Schelling S, Carpenter J. Idiopathic hyperostisis of the calvaria in five young bullmastiffs. *J Am Anim Hosp Assoc*. 2000;36.

ELECTRONIC RESOURCES

Additional information related to the content in Chapter 18 can be found online at eBooks.Health.Elsevier.com.

- Chapter Quiz

CHAPTER 19

Fracture Healing and Complications

Gabriela S. Seiler

PHYSIOLOGY OF BONE DEVELOPMENT AND HEALING

Bones contain three principal cell types: osteoblasts, osteocytes, and osteoclasts. Osteoblasts synthesize the osteoid bone matrix and become osteocytes following mineralization of the osteoid. Osteoclasts are larger cells that reside on the surface of the mineralized matrix and remove both mineral and matrix by secretion of acids and enzymes. In normal bone, the activities of osteoblasts and osteoclasts are coordinated in response to stress (Wolff's law), allowing adaptation of the bone pattern and shape to withstand varying load placed on the bone. Although bone can react to external stimuli or forces, it is slow to react and has limited methods of reaction: bone production, bone resorption, or a combination of production and resorption.[1–3]

The regulation of mineral ions in the serum is controlled mainly by parathyroid hormone, calcitonin, and vitamin D. Parathyroid hormone increases serum calcium by stimulating osteoclastic bone resorption. Calcitonin inhibits the activity of osteoclasts and inhibits intestinal and renal calcium absorption. Vitamin D acts on the intestine to increase absorption of calcium and phosphorus and directly on bone by both mobilization of calcium and phosphorus from previously formed bone and promotion of maturation and mineralization of bone matrix.[1–3]

There are various bone shapes including long, short (cuboid), flat, irregular (such as vertebrae), and sesamoid bones. The structure of the bone can be described as lamellar, which exists as cortical (also called compact) and trabecular (also called cancellous) bone or as woven bone which is a more haphazard organization of the collagen fibers. Specialized connective tissue called *periosteum* surrounds the outer surface of bones and provides protection and nutrition. Long bones are divided into epiphyseal, physeal, metaphyseal, and diaphyseal regions.[1–4]

Normal bone development is similar to post-traumatic remodeling and fracture healing. Therefore, understanding normal bone development is helpful for assessment and optimization of fracture healing. Bone growth occurs through two mechanisms, intramembranous and endochondral ossification. *Intramembranous ossification* is characterized by synthesis of bone directly from osteogenic mesenchymal cells without a cartilage precursor. Most flat bones such as the skull and mandibles are developed this way and intramembranous ossification plays a role in increasing the width of long bones. In *endochondral ossification*, a cartilage model derived from the mesenchyme is formed and subsequently mineralized to form bone. In contrast to intramembranous ossification, mesenchymal cells are stimulated to differentiate into chondrocytes rather than osteoblasts. Endochondral ossification is the primary mechanism to form the appendicular and portions of the axial skeleton such as the vertebrae, ribs, sternebral, and flat bones of the pelvis. Bone remodeling is a continuous process and consists of bone resorption in concert with new bone formation to repair and replace old bone.[1–3] In people, approximately 2% to 3% of the total skeletal mass is thought to be renewed every year through normal remodeling processes.[5–7]

FRACTURE IDENTIFICATION AND DESCRIPTION

Physical examination is an essential first step in the evaluation of fractures and possible complicating factors. Dealing with immediate life-threatening injuries takes precedence over imaging to look for fractures. Identification of open fractures, spinal fractures, and skull fractures requires careful evaluation and methods for temporary stabilization should be available.

Radiography is the most commonly used imaging tool for fracture evaluation in veterinary medicine. At least two orthogonal views of the area in question are essential for adequate evaluation of a potential fracture; otherwise, important information about presence and nature of an injury can be missed (Fig. 19.1). Pain management and sedation are important to minimize patient motion and discomfort during radiography, except in spinal trauma cases where sedation may lead to destabilization and higher risk of spinal cord injury. For long bones, the proximal and distal joints should be included in the view. Horizontal beam radiographs are helpful in patients with spinal injury or instable fractures where moving the patient could be detrimental. Horizontal beam radiography can also be good for optimal imaging of humeral and femoral fractures where imaging with a vertical beam is difficult. In some patients, oblique views are necessary to define or identify a subtle or complex fracture.[8] With minimal displacement, at least part of the fracture plane must be parallel to the x-ray beam for the radiolucent fracture line to be seen (Fig. 19.2). Small stress fractures or incomplete fractures may not have sufficient displacement immediately following the injury to allow detection. Follow-up radiographs in 7 to 10 days may be needed to detect these fractures as the fracture line becomes more conspicuous due to resorption at the fracture fragments.

Computed tomography (CT) imaging is a valuable imaging tool to assess fractures of complex anatomical structures such as the skull and spine, and for surgical planning (Fig. 19.3).[9–13] Fractures are recognized as a radiolucent line or plane traversing the bone with variable amounts of bone fragmentation, displacement of fracture fragments, and soft tissue injury. Knowledge of normal anatomy and normal variations or aberrant anatomic change is critical for accurate interpretation of

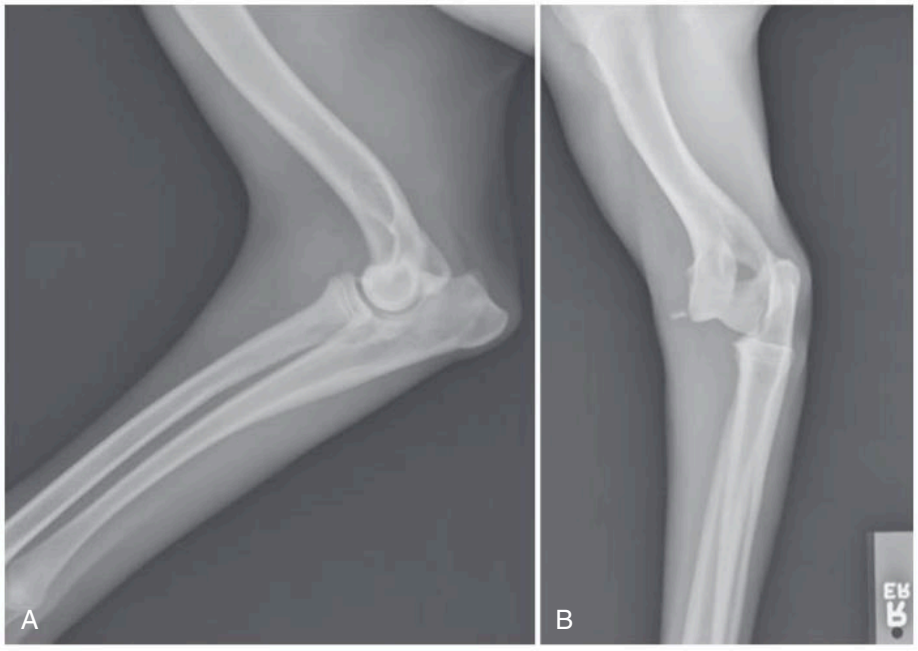


Fig. 19.1 Lateral **(A)** and craniocaudal **(B)** radiographs of the elbow joint of a young hound dog after trauma. Mild joint incongruence and a small osseous body superimposed over the cranial aspect of the radiohumeral joint are visible in the lateral view, whereas joint luxation is and a small fracture fragment are identi fied when adding the craniocaudal view.

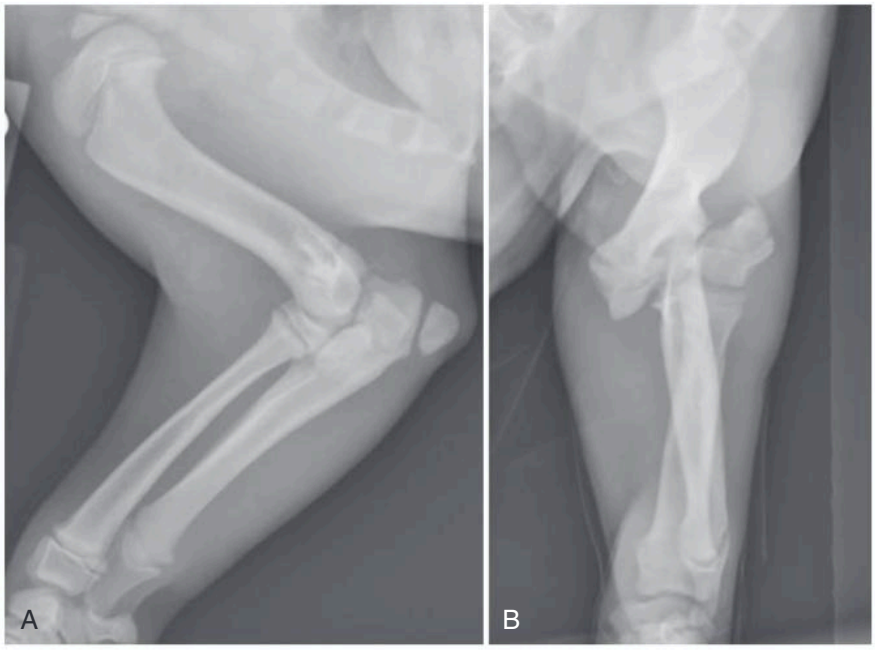


Fig. 19.2 Lateral **(A)** and craniocaudal **(B)** radiographs of the right elbow joint of a 4-month-old French bulldog with a Salter-Harris type IV intercondylar fracture of the distal humerus. The fracture extends through the lateral condyle, physis, and epiphysis into the joint. The fracture is difficult to identify in the lateral view alone.

images. Normal and accessory ossification centers and normal or aberrant nutrient foramina, overlying skin folds, fascial planes, or subcutaneous gas can all mimic fractures.[14,15]

When a fracture is identified, there are several observations that should be considered to optimize fracture assessment and treatment planning.[3]

Location is the first descriptor used in describing a fracture and includes the bone involved and the location in the bone. The location within the bone can be described as diaphyseal, metaphyseal, or epiphyseal. It is important to note the extent of any articular involvement and if there are intra-articular fracture fragments. Concurrent joint luxation or subluxation should be noted



Fig. 19.3 Sagittal (**A,** *left*; **B,** *right*) and dorsal **(C)** plane reconstructed computed tomography (CT) images of the pelvic limbs of a young shepherd mix after unknown trauma. There is a malunion fracture of the left femoral diaphysis and a nonunion fracture of the right femoral neck. Showing the three-dimensional orientation of the fractures is helpful for surgical planning.

as well. If there is growth plate involvement, the Salter-Harris classification system is used, see Box 19.1 (Figs. 19.4–19.6).[16]

Direction of the fracture plane is described as transverse, oblique, longitudinal, or spiral (Figs. 19.7 and 19.8, eFig. 19.1). A fracture can be simple with a single fracture plane, multiple with several fracture planes that are not connecting, or comminuted where there are multiple fragments at a single fracture site (Fig. 19.9, eFig. 19.2). The presence and location of larger fragments should be noted as their presence and degree of displacement may influence treatment choices.

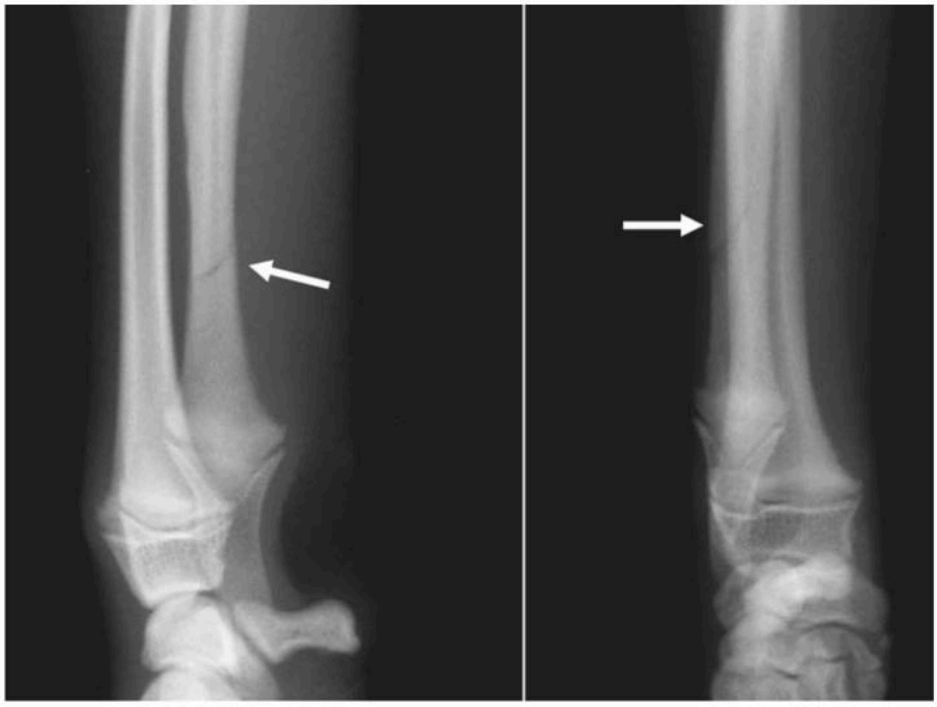
Displacement of fracture fragment components should be mentioned. This is done by noting the location of the distal or caudal fragment relative to the proximal or cranial fragment. Overriding or compression of fracture fragments can result in shortening and increased opacity of the bone at the fracture site; this is particularly important in vertebral fractures. Lengthening of the bone resulting in widening of the fracture gap is uncommon except with avulsion fractures where a piece of bone attached to a tendon or ligament gets pulled away from the bone (Fig. 19.10, eFig. 19.3).

Complete fractures are more common and extend across the entire bone, whereas incomplete fractures involve only a single cortex and are usually very localized. A *greenstick* fracture usually occurs in young animals and is an incomplete fracture of

Box • 19.1

Salter-Harris Classification

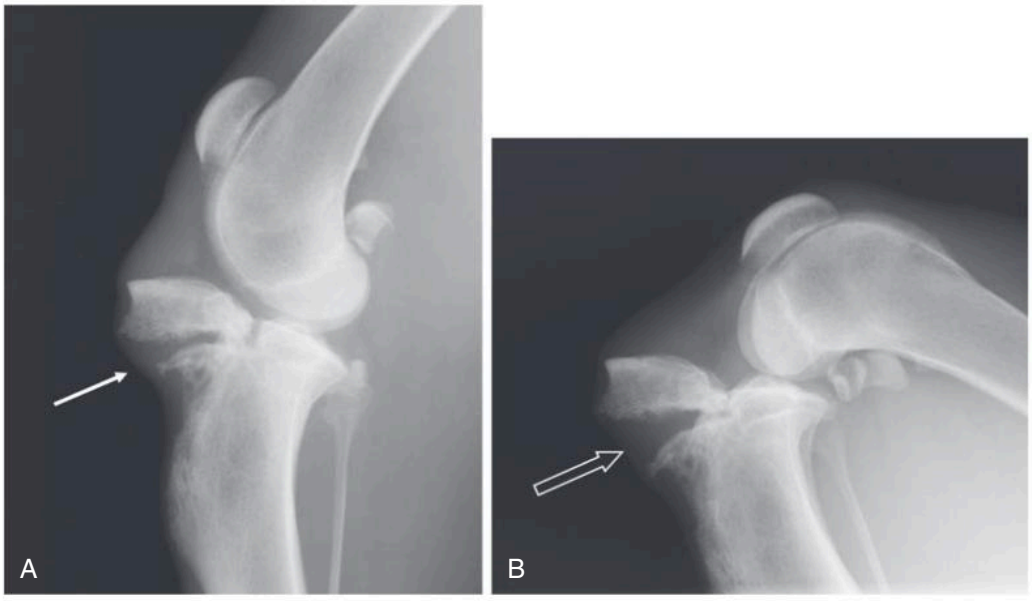
- *Salter-Harris type I*—fracture extends through the physis.
- *Salter-Harris type II*—fractures extends through the physis and a portion of the metaphysis.
- *Salter-Harris type III*—fractures extend through the physis and epiphysis and are usually articular.
- *Salter-Harris type IV*—fractures extend through the epiphysis and cross the physis through the metaphysis. These are usually articular fractures as well.
- *Salter-Harris type V*—crushing or compression fractures that involve the physis. Type V fractures may not be apparent immediately after trauma or could present as increased opacity of the physis without displacement. Comparison with the normal opposite limb may aid in identifying subtle changes. Salter-Harris type V fractures frequently cause premature closure of all or a portion of the physis, leading to angular limb deformities.



eFig. 19.1 Incomplete short oblique fracture of the distal diaphysis of the ulna (*white arrows*).



eFig. 19.2 Severely comminuted distal diaphyseal tibial fracture caused by a ballistic injury. High-velocity projectiles cause severe soft tissue injury in addition to fracture, and this soft tissue injury will delay fracture healing due to vascular disruption. Projectiles may also fragment on contact with bone, as seen here.



eFig. 19.3 **A,** Four-day-old avulsion fracture of tibial tuberosity (*solid arrow*). **B,** In a flexed view, widening of the fracture gap indicates dynamic instability (*open arrow*).

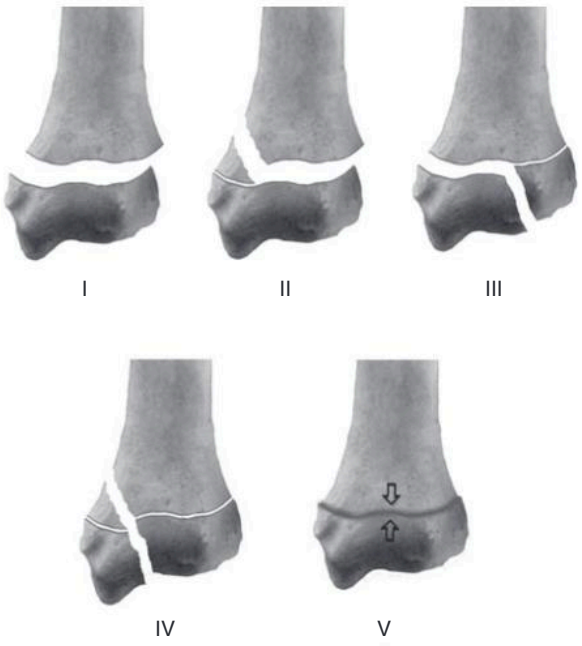


Fig. 19.4 Salter-Harris physeal fracture classification.



Fig. 19.6 Salter-Harris type II fracture of the proximal tibia.



Fig. 19.5 Displaced Salter-Harris type I fracture of the right capital femoral physis.

one side of the bone with bending of the opposite cortex (plastic deformation) (Fig. 19.11). *Fatigue* or *stress* fractures are another type of incomplete fracture. They are typically microfractures caused by repeated trauma over time that exceeds the load capacity of the bone slightly. Stress fractures may not be seen radiographically or may appear as faint, linear, incomplete fractures involving one portion of a bone. Scintigraphy can be used to identify stress fractures when radiographs are normal or inconclusive.[17,18] The term *fissure* is used for thin radiolucent incomplete fracture lines often originating from a complete fracture (see Fig. 19.8, eFig. 19.4). Fissures may develop into complete fractures during repair or during the recovery phase of the injury and are thus important to be recognized.

A fracture is described as open (as opposed to closed) when there is evidence of soft tissue trauma with disruption of the skin surface that could expose the fracture to the outside environment with increased risk of infection. A fracture should always be described as open in presence of subcutaneous emphysema indicating compromise of the skin surface (see Fig. 19.9, eFigs. 19.5 and 19.6).

Chronicity of the fracture is usually known from the history but if uncertain can be estimated radiographically. Acute fractures are characterized by sharp, acute fracture margins without evidence of remodeling and by the presence of soft tissue swelling. A few days after trauma, the fracture margins will be less clearly defined due to resorption and periosteal new bone formation may be noticed.

Pathologic fractures occur if the bone is weakened by preexisting disease such as bone neoplasia or metabolic demineralization, such as hyperparathyroidism. A history of minimal trauma associated with a fracture can be a first indicator that a pathologic fracture may be present. Hints that a fracture is pathologic are reduced bone opacity at the fracture site, cortical thinning, presence of a periosteal reaction with an acute fracture, disturbance in the trabecular pattern, and disproportionate swelling (Figs. 19.12 and 19.13, eFig. 19.7).

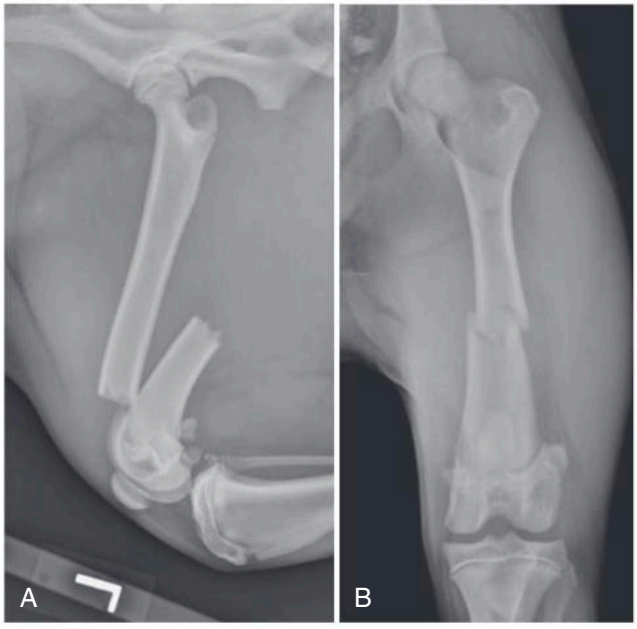


Fig. 19.7 Lateral **(A)** and craniocaudal **(B)** radiographs of an 8-month-old Golden retriever with a transverse fracture of the distal left humeral diaphysis. There is caudal and mild medial displacement of the distal fracture fragment and overriding of the fracture fragments due to contraction of the thigh musculature.

FRACTURE HEALING

Fracture healing involves the same processes as bone growth and remodeling and occurs by two basic methods: direct or primary and indirect or secondary healing. In contrast to the

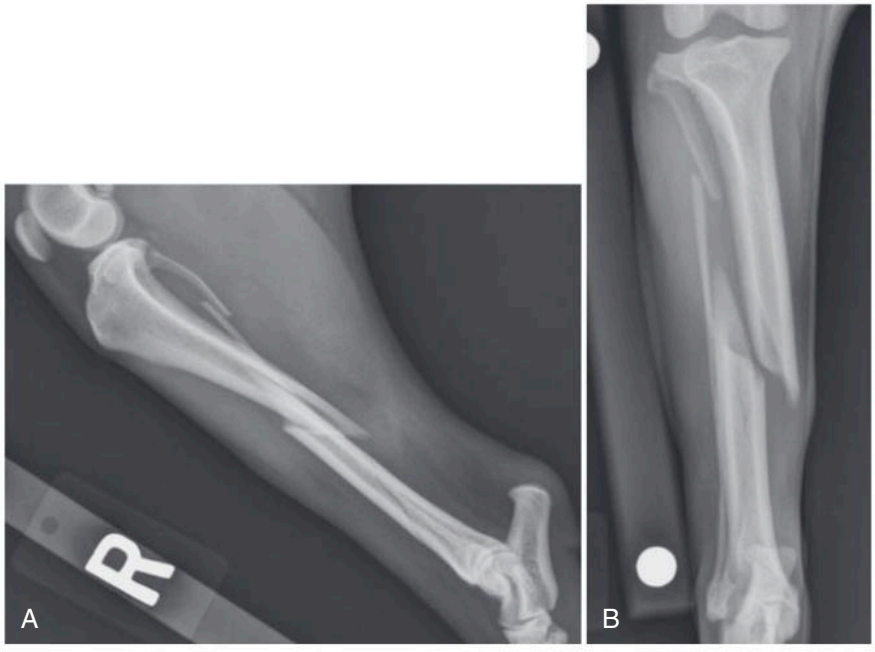
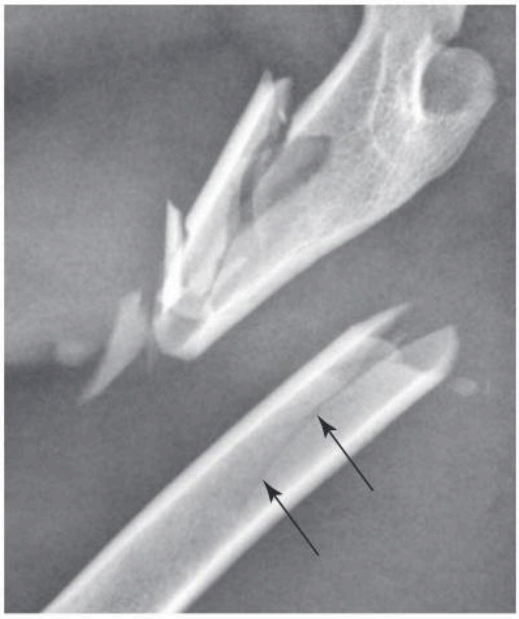


Fig. 19.8 Lateral **(A)** and craniocaudal **(B)** radiographs of a dog with a mid-diaphyseal spiral fracture of the right tibia, and short oblique transverse fracture of the proximal fibular diaphysis. Notice a fissure line that extends distally in a caudoproximal to craniodistal direction.



eFig. 19.4 Lateral view of the proximal aspect of the femur of a dog with a comminuted proximal diaphyseal fracture. There is a fissure fracture extending distally from the main fracture site (*black arrows*). This fissure will affect the type of internal fixation used.



eFig. 19.5 Abrasion-type open articular fractures of the distal tibia and talus (*white arrows*). The medial malleolus and a portion of the medial aspect of the talus are missing because of the abrasive action of the road pavement as the patient was dragged for a short distance after being hit by a car. The soft tissues on the medial aspect are irregular, indicating loss of the soft tissue as well. The tarsocrural joint is open. These fractures are typically open fractures. Blood supply and supportive ligaments in these areas can be severely compromised.



eFig. 19.6 Open transverse distal diaphyseal fractures of the radius and ulna with lateral displacement and mild overriding. The distal end of the proximal radial fracture fragment is outside the soft tissues on the cranial-caudal view, indicating that it is an open fracture (*arrow*). Whether a fracture is open is best judged clinically.



eFig. 19.7 Lateral view of the proximal humerus of a dog with a pathologic fracture (*black arrows*) secondary to an osteosarcoma.

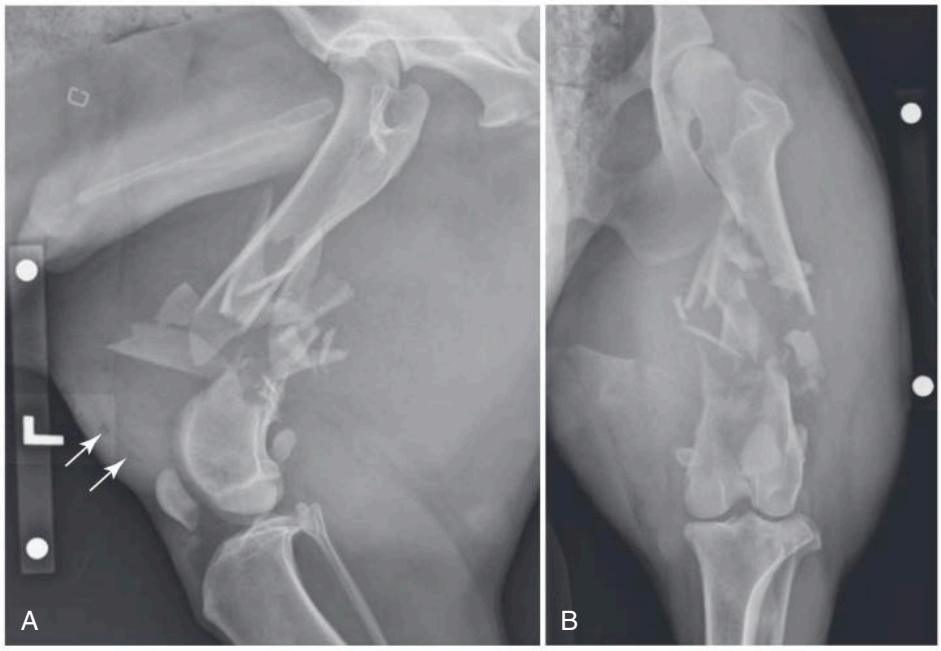


Fig. 19.9 Lateral **(A)** and craniocaudal **(B)** radiographs of a dog with a comminuted fracture of the distal femoral diaphysis and severe soft tissue swelling. Several gas foci along a fascial plane at the cranial aspect of the distal femur (*arrows*) indicate that this is an open fracture.



Fig. 19.10 Avulsion fracture of the tibial tuberosity with proximal displacement of the fragment (*arrow*). A Salter-Harris type II fracture of the proximal tibial physis (*arrowheads*) and a transverse fracture of the proximal fibula are also present.

healing process in many other organs where the reparative tissue is of lesser quality than the original tissue, healing bone is at least as strong, and sometimes stronger, than the original bone.

Direct (primary) bone healing occurs when the gap between fracture fragments is less than 0.01 mm and there is less than 2% strain or motion between the fragments. In direct healing, lamellar bone is formed directly between the two fragments where osteoclasts remove dead bone and osteoblasts follow immediately behind and form new bone. Radiographically, direct bone healing is characterized by slow disappearance of a fracture gap without callus formation. This type of healing is most commonly seen after a corrective osteotomy with reapposition that results in a minimal gap (Fig. 19.14). It is rarely observed in the healing of traumatic fractures.

Indirect (secondary) fracture healing is typical in traumatic fractures. The healing process undergoes several stages that have a different radiographic appearance (Box 19.2). Immediately after the fracture, the inflammatory phase is initiated. Ruptured blood vessels cause hemorrhage and hematoma formation, with associated release of tissue growth factures which stimulate inflammatory cells, osteoprogenitor cells, and osteoclasts which lead a concerted effort in cleaning up, revascularizing, and stabilizing the fracture. The hematoma provides some initial stability to the fracture. Additionally, there is muscle contraction caused by pain which adds stability but, depending on muscle mass, may also further aggravate fracture displacement. Muscle contraction plays an important role in stabilizing spinal fractures and minimizing spinal cord damage. Radiographic changes in the inflammatory phase of fracture healing include soft tissue thickening around an acute fracture which is characterized by sharp fracture margins.

The reparative phase is characterized by reduced swelling and formation of a soft, fibrous callus. The fracture gap is bridged by tissues that are more stress tolerant, with replacement of each tissue type by a more rigid type of tissue until a rigid bridge is formed between the fragments. Granulation tissue can withstand 100% stretching before failure, whereas fibrous tissue can withstand only 10% and bone only 2% deformation before failure.[2] The initial hematoma at a fracture site is replaced by granulation tissue followed by fibrous connective tissue that is replaced by fibrocartilage and then endochondral ossification to produce a bony union.[2,19] Radiographically, in this phase the fracture gap may become more obvious. The fracture margins are not sharp and smooth any longer, and may have a rounded appearance. Clinically, a fibrous callus can form a rigid brace for the bone with a stable fracture before there is a mineralized callus (Fig. 19.15A).



Fig. 19.11 Lateral **(A)** and dorsopalmar **(B)** radiographs of the carpus of a young puppy. There is an incomplete (greenstick) fracture (*arrow*) of the cranial cortex of the distal radial diaphysis.



Fig. 19.12 Aggressive lesion of the distal tibia, characterized by cortical thinning, moth eaten lysis and poor margination. A pathologic fracture extends through the cranial and caudal tibial cortex (*arrows*).



Fig. 19.13 Lateral view of the distal femur of a cat with nutritional secondary hyperparathyroidism. There is a healing malunion fracture of the distal femur. Note the thin cortices and poor contrast between the demineralized bones and adjacent soft tissue.

Wolff's law dictates that bone remodeling adapts to the loads on the bone in *the remodeling phase*.[20] A small degree of motion at the fracture site stimulates formation of an osseous callus which eventually bridges the fracture gap. Osteoblastic bone formation and osteoclastic resorption work together to transform the woven bone of the callus into compact cortical bone, restore the shape of the cortical bone, and reestablish a medullary cavity.

Radiographically, mineralized callus is first visible as a faint mineral opacity between fracture margins, followed by more and more opaque bone deposits and finally a smoothly margined, completely mineralized osseous callus which creates a clinically stable fracture (see Fig. 19.15). The amount of callus is related to the type of fracture, degree of reduction, and fixation. Excessive callus may form in areas of elevation (for example due to subperiosteal hemorrhage) and/or stripping of the

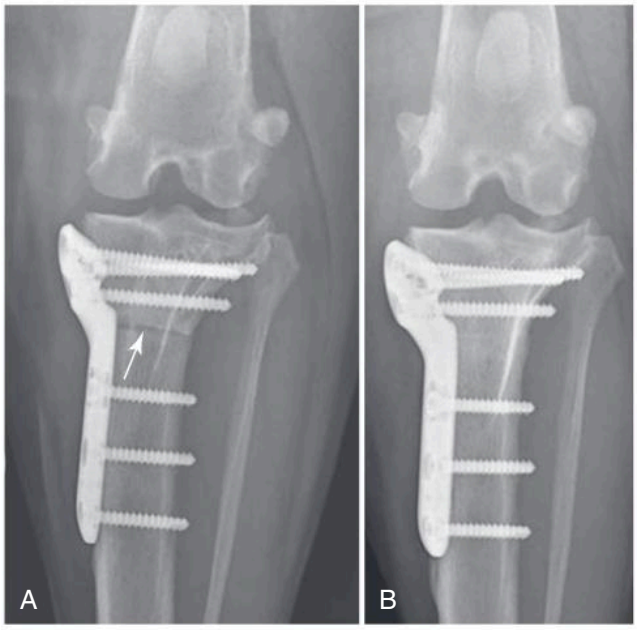


Fig. 19.14 Proximal tibial osteotomy for a tibial plateau leveling osteotomy (TPLO) procedure. Radiographs were obtained after surgery **(A)** and 2 months later **(B)**. The osteotomy site (*arrow*) has healed without callus formation consistent with primary healing.



Fig. 19.15 Spiral fracture of the tibial diaphysis of an 8-month old mixed-breed dog 3 weeks **(A)** and 6 weeks **(B)** after trauma. The fracture was treated with a splint. At 3 weeks, a wide fracture gap is visible, and early callus formation is present starting to bridge the cranial fracture gap. At 6 weeks, there is smooth bridging callus present and the fracture gap is starting to disappear, consistent with normal secondary fracture healing.

Box • **19.2**

Radiographic Appearance of Secondary Fracture Healing

Acute Fracture
Fracture margins are sharp, soft tissue swelling

5 to 10 Days After Reduction
Fracture fragments lose sharp margins due to resorption
Demineralization of fracture fragment ends may result in slight fracture gap widening

10 to 20 Days After Reduction
Formation of endosteal and periosteal callus
Decreasing size of fracture gap
Variable loss in opacity of free fracture fragments

30 Days or More After Reduction
Fracture lines gradually disappear
External callus increases in opacity and remodels

3 Months or More After Reduction
Continued remodeling of external calluses
Trabecular pattern may develop within the callus
Cortical shadow becomes visible through the callus
Medullary cavity continuity gradually reestablished
Cortical remodeling along the lines of stress

periosteum. Findings to support ongoing remodeling include continuity of the cortex across the fracture gap, disappearance of the fracture gap, flattening of the osseous callus, and finally establishment of a near normal bone outline and structure, which can take several months or years to accomplish.

Radiography should not be used as the sole criterion of fracture healing, but the appearance of the fracture should be considered in concert with clinical findings to assess progression and potential complications. The following factors may influence fracture healing and should be considered in the assessment.

Blood Supply

One of the most important prerequisites for normal fracture healing is a normal blood supply. Deficient vascularity may cause complications such as delayed fracture healing or nonunion fracture. Particularly at risk are fractures which are poorly covered by soft tissues and therefore have reduced potential for recruitment of periosteal blood supply, severely comminuted or displaced fractures with disruption of existing blood supply, or fractures with severe tissue damage such as gunshot wounds.[21,22] The incidence of nonunion fractures for example is high in the distal antebrachium of toy breed dogs treated with external coaptation where decreased intraosseous vascular density and minimal soft tissue coverage contribute to the lack of healing.[23] While the blood supply itself cannot be determined radiographically, potential damage can be estimated based on location and appearance of the fracture.

Stability and Anatomic Reduction

Bone healing depends on a certain degree of stability. While a small amount of instability can actually have a stimulating effect on formation of a fibrous and subsequently an osseous callus, too much instability (>5%) is detrimental to fracture healing and may lead to delayed union, malunion, nonunion, or pseudarthrosis formation. Anatomic reduction with a narrow fracture gap improves the chance of direct or rapid indirect fracture healing.[24–27]

Age

Young age is advantageous for fracture healing, and fracture healing progresses at an astonishing pace, occasionally to the detriment of the patient if a fracture is not treated immediately and fibrous tissues have to be broken down to realign fracture fragments with the risk of disrupting fragile blood supply.

Fracture healing progresses slowly in geriatric patients and this has to be taken into account when making treatment and management decisions, and when assessing fractures for normal healing.[28]

Metabolism
The overall metabolism of a patient plays a role and diseases affecting normal bone turnover, such as hyperadrenocorticism, may lead to delays in bone healing.[29,30]

Infection
Infection of the bone or surrounding tissues can disrupt fracture healing directly, or indirectly by causing loosening of the fixation device or necessitating removal of implants before the fracture has healed.

RADIOGRAPHIC EVALUATION OF FRACTURE HEALING AND ASSOCIATED COMPLICATIONS

After treatment, both normal healing and possible complications should be evaluated. At least two orthogonal radiographs are needed to assess reduction and alignment of the fracture after treatment (Fig. 19.16). Radiographs should be repeated every 4 to 6 weeks during the healing process, sooner if clinical signs indicate presence of complications. The "four A" system can be helpful for systematic evaluation of surgical fracture repair, in addition to systematic evaluation of the entire radiograph, including the soft tissues.

- Apposition or reduction of fracture fragments has the goal of restoring the length and shape of the bone.
- Alignment of the affected bone and adjacent joint should be evaluated and changes in alignment over time are signs of instability or implant failure.
- The Apparatus has to be evaluated for size relative to the bone. Cortical engagement of pins and screws and position relative to joint space should be noted; an implant entering a joint space requires surgical revision.
- Activity of new bone formation over time is assessed for presence of callus formation but also for presence bone lysis with implant instability or active bone proliferation indicative of osteomyelitis.

There are many potential complications of fracture healing that should be considered in every follow-up examination.

Stress Protection and Bone Atrophy
A degree of reduced bone density in a fracture site can be caused by insufficient stimulation of bone turnover due to the implant taking up most of the load. Oversized implants are more prone to provide stress protection. Diffuse osteopenia of the affected limb may be noticeable if the limb is not or only lightly used after a fracture, usually associated with disuse muscle atrophy. These changes will resolve once the patient returns to normal activity but is severe can be a predisposition for a stress fracture.

Delayed Union
Delayed union is a subjective classification for a fracture that is not healing within the expected timeframe, this is one of the most common complications of fracture healing. Determination of delayed vs. normal fracture healing is subjective as many factors influence the progression of normal fracture healing as outlined earlier.[31] Radiographically, delayed union is characterized by some signs of fracture healing over time such as resorption of fracture margins, mineralization of the soft tissues bridging the fracture gap while preserving an open medullary cavity at the fracture gap, or nonbridging callus formation (Fig. 19.17).

Nonunion
A nonunion state is reached when a fracture does not have the potential to heal anymore.[32] The diagnosis of nonunion fracture should be made with caution and only when there is strong evidence for it, as it will necessitate a different and often more aggressive treatment approach than a very slowly healing fracture. Radiographically, the most important indicators for a nonunion fracture are lack of progression of fracture healing over time and this typically requires evaluation of the fracture at multiple time points. Smooth, rounded fracture margins with sclerosis of the medullary cavity at the fracture site are suggestive of a nonunion fracture. There are two types of nonunion fractures: viable and nonviable.[2]

Viable (or reactive, vascular) nonunion fractures are characterized by viable active attempts to heal the fracture with

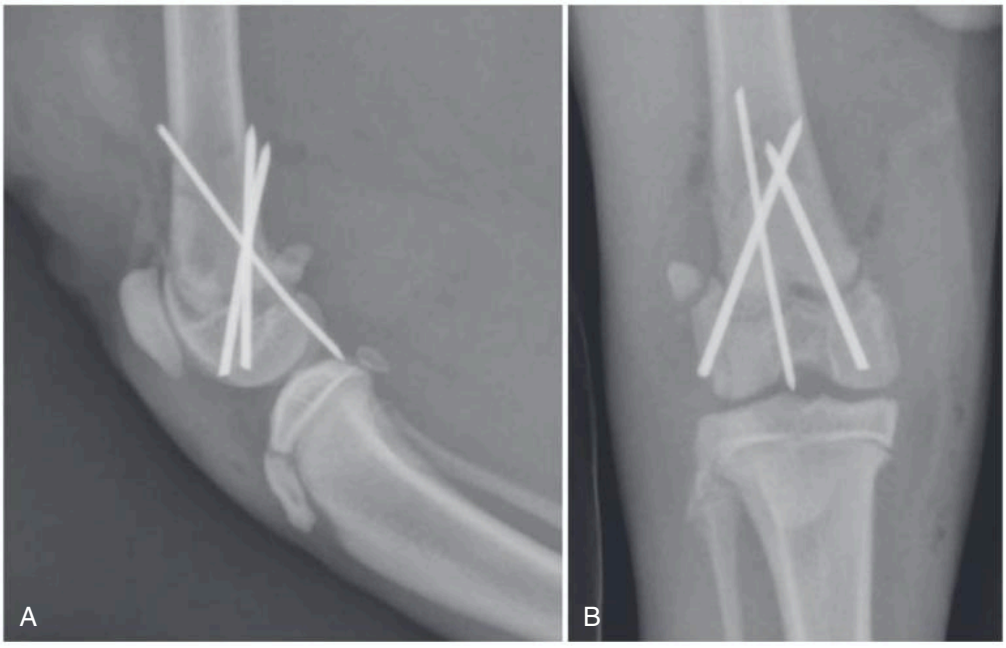


Fig. 19.16 Lateral **(A)** and craniocaudal **(B)** postoperative radiographs of a Salter-Harris type II fracture of the distal femur in a cat. One of the pins extends into the caudal aspect of the stifle joint and had to be replaced.

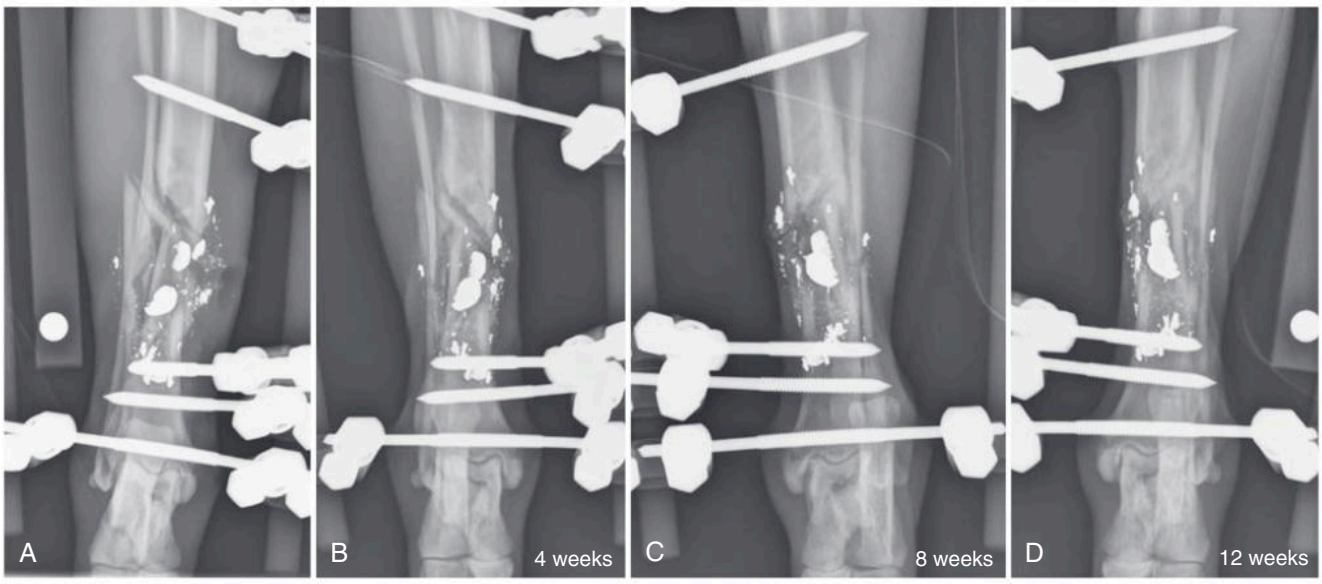


Fig. 19.17 Craniocaudal radiographs of a comminuted fracture of the distal tibia of a 5-year-old dog caused by a gunshot wound, immediately **(A)**, 4 weeks **(B)**, 8 weeks **(C)**, and 12 weeks **(D)** after surgery. The fracture gap is continuously more mineralized, and some callus is slowly added over time. Fracture healing is progressing but at a slow pace consistent with a delayed union, most likely caused by disruption of blood supply due to gunshot trauma.

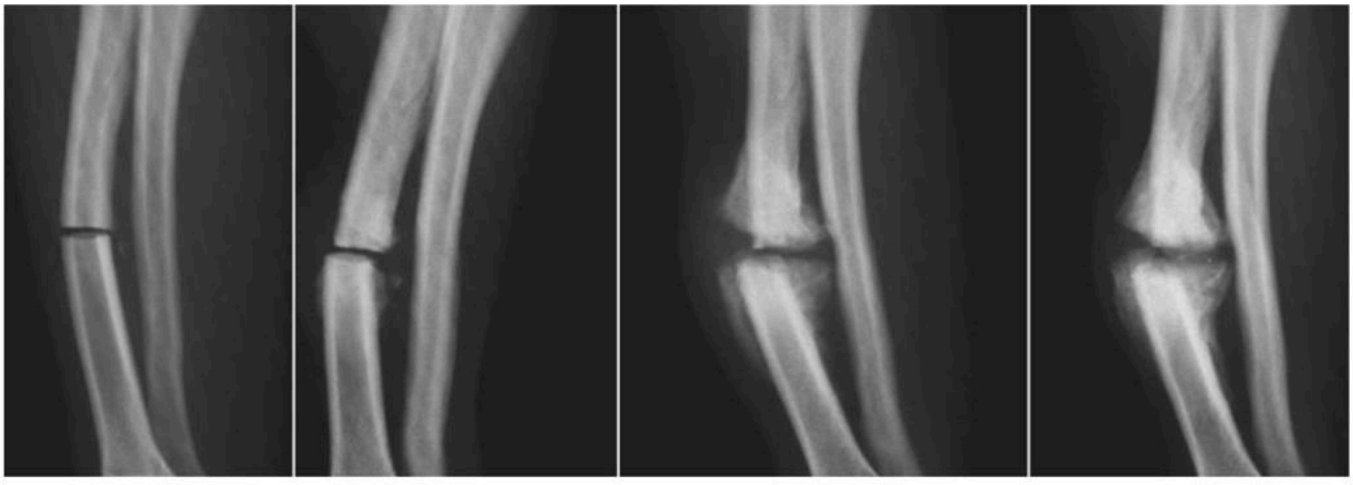


Fig. 19.18 Osteotomy of the radius with lack of fixation develops into a hypertrophic nonunion. Note the exuberant callus around the osteotomy ends with no bridging callus. This appearance is often termed an *elephant foot.*

reactive bone and callus formation. They can be hypertrophic, characterized by abundant callus formation but lack of bridging callus due to excessive motion at the fracture site (Fig. 19.18). Rarely, a pseudoarthrosis may develop because of chronic motion at the fracture site where a fibrous capsule fills with serous fluid (eFig. 19.8). Oligotrophic nonunion fractures have little or no callus with bridging of the fracture fragments by fibrous tissue (Fig. 19.19). These may be difficult to differentiate from a nonviable nonunion fracture because of the lack of callus and reaction at the fracture site. Scintigraphy may be used to detect blood supply to the fracture gap, indicating viable tissue.[33] Generally, some bone reaction at the fragment ends suggests a viable nonunion.

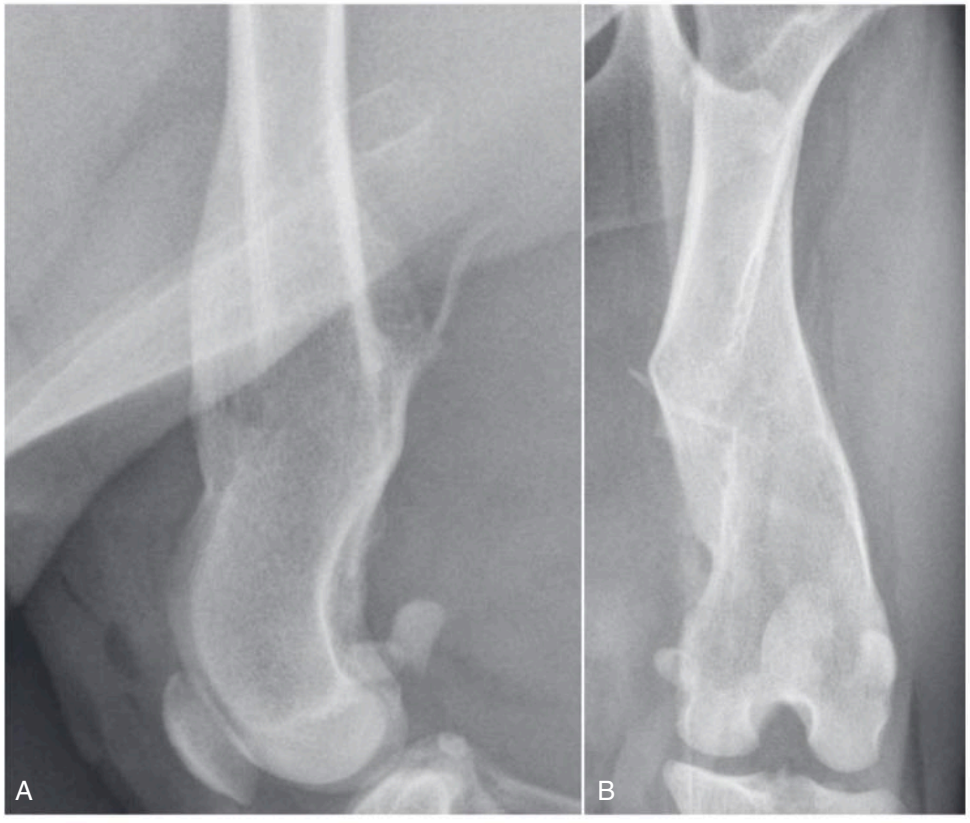
Nonviable nonunion fractures are uncommon and typically occur due to insufficient blood supply at the fracture fragments or an excessive fracture gap between fragments. Nonunion fractures can be dystrophic in nature where there is no bridging callus, a fracture gap, and rounded, sclerotic fracture margins. Necrotic nonunion fractures are associated with sequestrum formation due to complete loss of blood supply; see more details on sequestrum formation later. A large fracture gap that is too wide for bridging callus to form is termed *defect nonunion fracture*. Atrophic nonunion is characterized by thinned, tapering fracture ends without evidence of callus formation and decreased bone opacity, usually a sequela of the other forms of nonviable nonunion fractures. This is most commonly seen in distal antebrachial fractures of toy breeds where there is insufficient blood supply to the fracture (Fig. 19.20).[34,35]

Malunion

Malunion fractures are defined by healing with permanent angular and/or rotational deformity of the affected bone. Malunion can occur due to poor initial reduction and alignment, shifting of fragments during the healing process, implant failure, or premature removal (eFig. 19.9). The clinical relevance of malunion fractures depend on the degree of malunion but also on its influence on associated soft tissue structures such as muscles, tendons, and ligaments which may undergo altered



eFig. 19.8 Hypertrophic nonunion of the femoral mid-diaphysis with pseudoarthrosis. This fracture will not heal without surgical intervention. The dog had an abnormal gait but was not in pain.



eFig. 19.9 Lateral **(A)** and craniocaudal **(B)** views of the femur of a dog with a healed malunion fracture. The distal fragment is angled cranially and displaced laterally. The appearance in the lateral view would be described as a recurvatum malunion and in the craniocaudal view as a translational malunion. Note the larger amount of cranial callus as a result of the loading pattern.

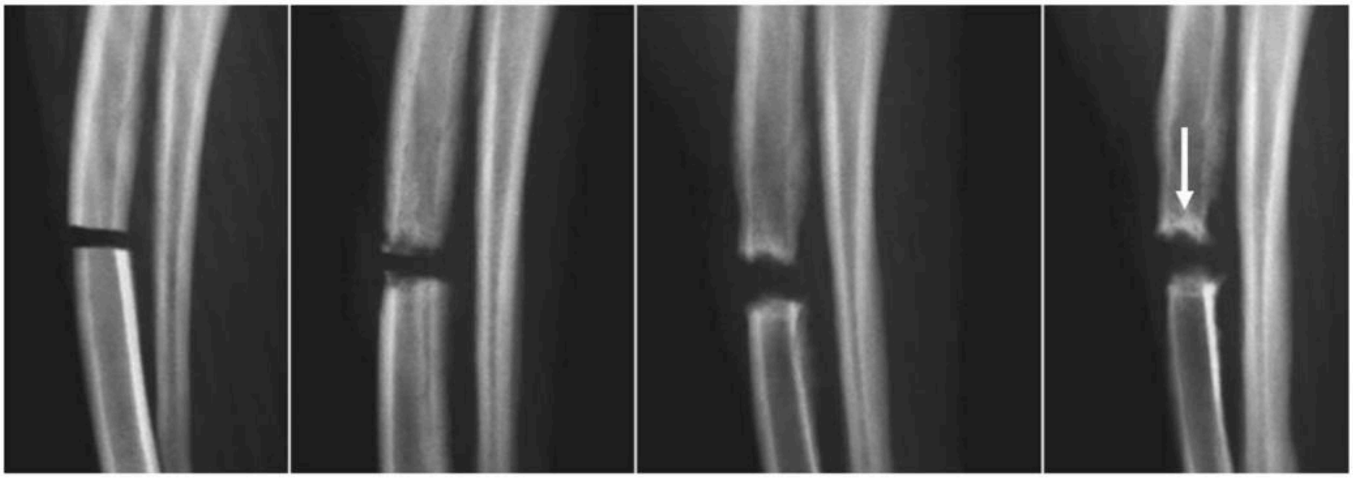


Fig. 19.19 Osteotomy with no fixation develops into an oligotrophic nonunion. Little callus is present at the osteotomy site, with filling in one of the ends of the segments seen as a sclerotic band (*white arrow*).

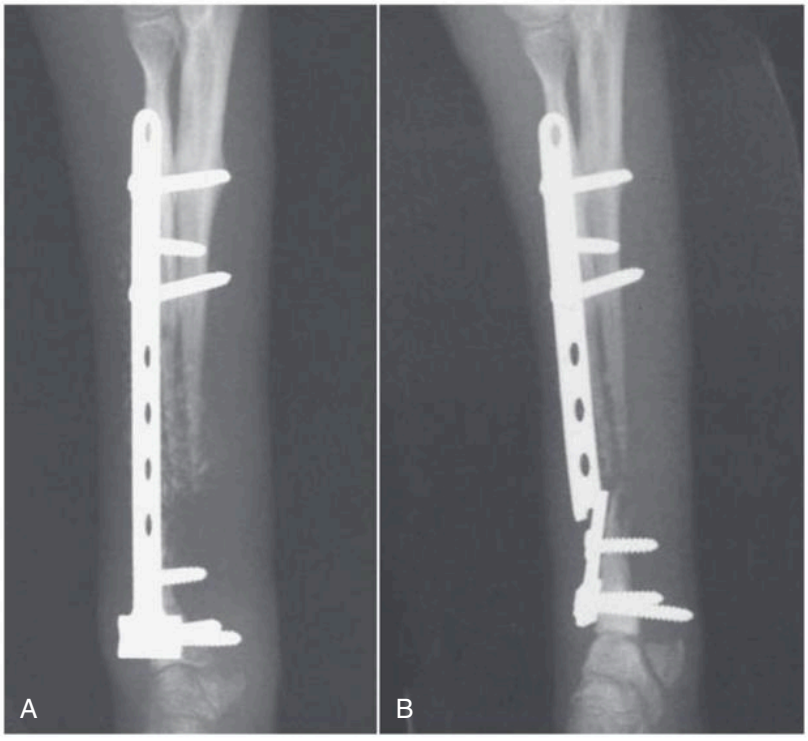
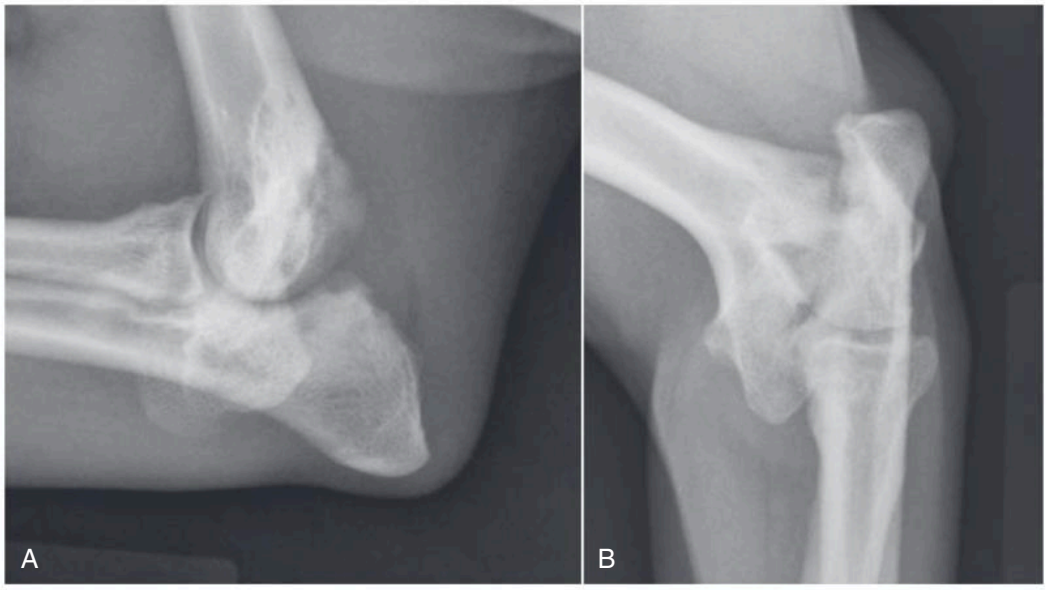


Fig. 19.20 **A,** This toy poodle has atrophic nonunion radial and ulnar fractures at 3 months after the original injury. Note the lack of callus and atrophy of the adjacent ends of the fracture fragments. The small mineral foci overlying the fragments are small islands of cancellous bone grafts placed during fixation. Poor soft tissue environment, including poor blood supply, at the fracture site prevented the formation of callus. **B,** At 4.5 months after the initial injury, bone plate failure from metal fatigue is evident.

stresses and potential injury, as well as adjacent joints (eFig. 19.10). Loadbearing of the bone itself may also be affected in the sense that the main load on the bone may now be shifted from the center to the periphery of the bone. Radiographically, malunion fractures are characterized by abnormal angulation or rotation of the affected bone. Long bone malunion fractures can be classified as *valgus, varus, antecurvatum, recurvatum, torsional,* or *translational* (Fig. 19.21). Cortical thickness may be asymmetrical as one part of the bone may take up more of the load along the axis of force resulting in remodeling and increased cortical thickness (Fig. 19.22).

Implant Instability and Failure

Loosening of fracture of implants can lead to implant failure. Common causes of implant loosening include instability, micromotion of the implants, or infection. Implant motion leads to focal bone resorption around the implant, characterized by a radiolucent area surrounding the implant (Fig. 19.23, eFig. 19.11). This has to be differentiated from an Uberschwinger digital imaging artifact, which is a continuous, thin radiolucent rim around the edges of implants caused by edge enhancement.[36] Resorption due to motion, on the other hand, manifests as asymmetric radiolucency that widens towards the periphery of the bone. Accompanying signs are often soft tissue



eFig. 19.10 Lateral **(A)** and craniocaudal **(B)** radiographs of a dog with a healed malunion intercondylar fracture. The incongruity has led to degenerative joint disease, which is seen best on the lateral view.



eFig. 19.11 The transcondylar lag screw has loosened and migrated laterally (*white arrow*) before bone healing. Consequently, the lateral condylar fracture has formed a malunion, and the intercondylar fracture is a nonunion with malarticulation of the medial aspect of the humeral condyle and the medial coronoid process. The radiolucent zone surrounding the screw likely indicates continued motion. Remodeling of the medial aspect of the humeral condyle and medial coronoid process is advanced, and repair of the nonunion and malunion will not result in a normal joint.

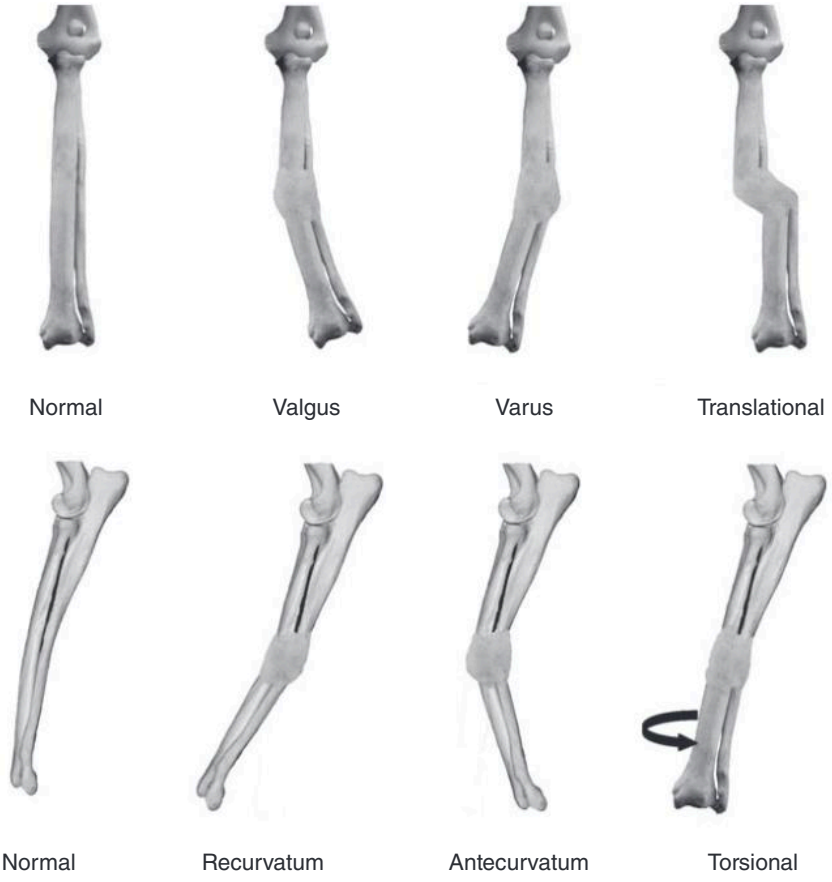


Fig. 19.21 Classification of malunion fractures.

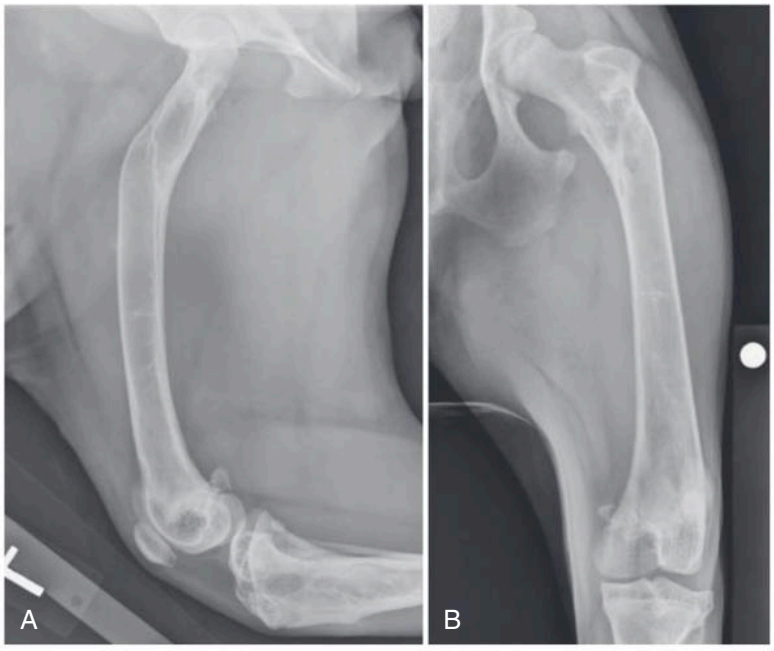


Fig. 19.22 Lateral **(A)** and craniocaudal **(B)** radiographs of a malunion femoral fracture. The fracture has healed but there is abnormal angulation of the proximal femur. Notice that the caudal cortex is thicker due to increased load bearing.



Fig. 19.23 There is uniform peri-implant radiolucency surrounding the most proximal screw (*arrow*) indicating micromotion and loosening of the screw. This is not an Uberschwinger artifact as it is not present at any of the other screws.



Fig. 19.24 Tarsal arthrodesis with implant failure. The medially applied bone plate is fractured at the level of the distal intertarsal joint (*arrow*). There is a wedge-shaped radiolucent area surrounding the tip of the screw placed into the talus (*arrowhead*) caused by motion and implant loosening.

swelling around the implant in question, and movement of the implant relative to the bone it resides in. Comparison of postoperative radiographs with recheck radiographs is therefore helpful to compare the location and position of the implant relative to the bone, of course taking into account potential bone growth in juvenile animals. Care should be taken when obtaining repeat radiographs, to ensure consistent limb positioning and beam centering so that minimal implant motion can be detected with certainty. Fractures of implants are usually relatively easy to recognize radiographically and need to be evaluated based on their potential impact on stability and overall healing capacity of the fracture (Figs. 19.24 and 19.25, eFigs. 19.12 and 19.13).

Angular Limb Deformity

Abnormal, asynchronous bone growth or premature closure of growth plates in immature animals after trauma may lead to angular limb deformity. The most common site for this complication in the dog is premature closure of the distal ulnar physis (eFig. 19.14). The distal ulnar physis appears more susceptible to injury, potentially due to its conical shape that may concentrate forces into the apex of the physis. The initial compressive growth plate injury is often not visible radiographically and the damage is only noted when angular limb deformity develops. Premature closure of the distal ulna leads to cranial bowing of the radius due to continued growth of this bone, and/or distal subluxation of the ulna at the elbow joint. Subluxation of the ulnar carpal joint and valgus deformity of the manus are also common (Fig. 19.26). Premature closure of the distal radial physis is less common and may involve only one side of the physis (eFig. 19.15). Commonly observed sequela of distal radial closure are humeroradial and humeroulnar subluxation, antebrachiocarpal subluxation, and uncommonly, angulation of the manus (Fig. 19.27).

Infection

All fractures have the potential to get infected, given the presence of damaged tissues which can provide a suitable environment for bacterial growth. Poor blood supply and a compromised immune system adds to the risk of infection. Open fractures should always be considered to be contaminated and therefore at a higher risk of infection than a closed fracture, necessitating different treatment decisions.[37–39] Clinical signs of osteomyelitis such as redness, pain, and acute worsening of lameness may be recognized before radiographic signs are present. As infection continues, signs of an aggressive bone lesion including bone lysis, active, irregular, often palisading periosteal reaction and soft tissue swelling will develop (Figs. 19.28 and 19.29, eFig. 19.16). The definitive diagnosis of osteomyelitis is not possible radiographically, and tissue sampling for culture and cytology as needed. A special case of infection includes sequestrum formation, as described in the next paragraph.

Sequestrum

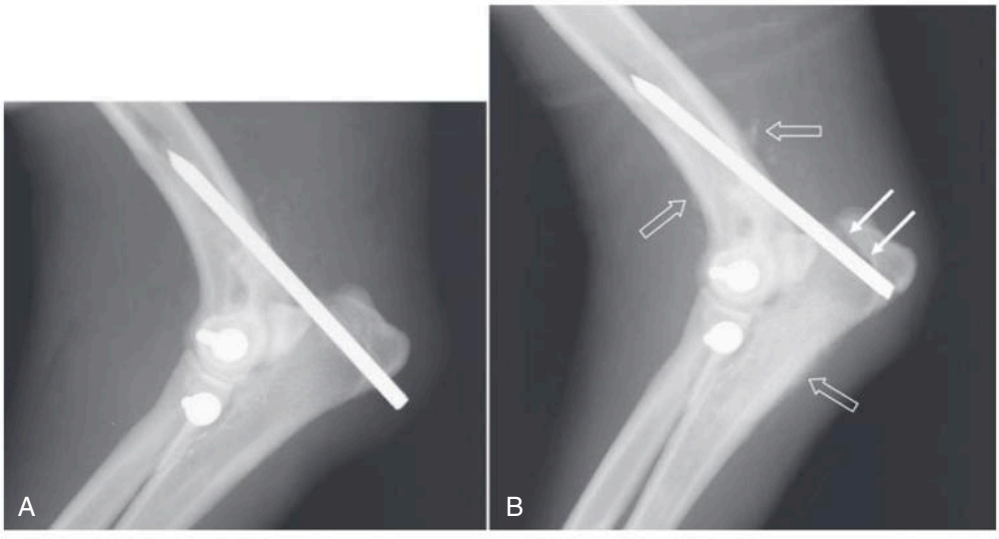
Devitalization of fracture fragments can occur during trauma. It is a normal occurrence that small fracture fragments lose their blood supply and are subsequently resorbed. When larger fracture fragments are devitalized, the devitalized bone or sequestrum creates a reaction with surrounding inflammation and necrosis. A classic sequestrum is recognized as a sharply marginated sclerotic bone fragment (sequestrum) surrounded by or separated from the parent bone by a radiolucent zone that is surrounded by sclerotic bone (involucrum) (see Figs. 19.30 and 19.31). In some instances, a draining tract (cloaca) arises from the radiolucent necrotic area surrounding the sequestrum and extends to the skin surface. Generally, less reaction occurs surrounding a sterile sequestrum; however, determining radiographically whether the sequestrum is infected is not always possible.[40]

Fracture Associated Tumors

Fracture associated sarcomas are defined as sarcomas occurring at a previous fracture site more than 5 years after the original fracture. The pathophysiology of fracture-associated sarcoma is poorly understood. Chronic inflammation and infection at the fracture site with delayed healing as well as implant degradation have been considered as possible causes (Fig. 19.32, eFig. 19.17).[38,41,42]



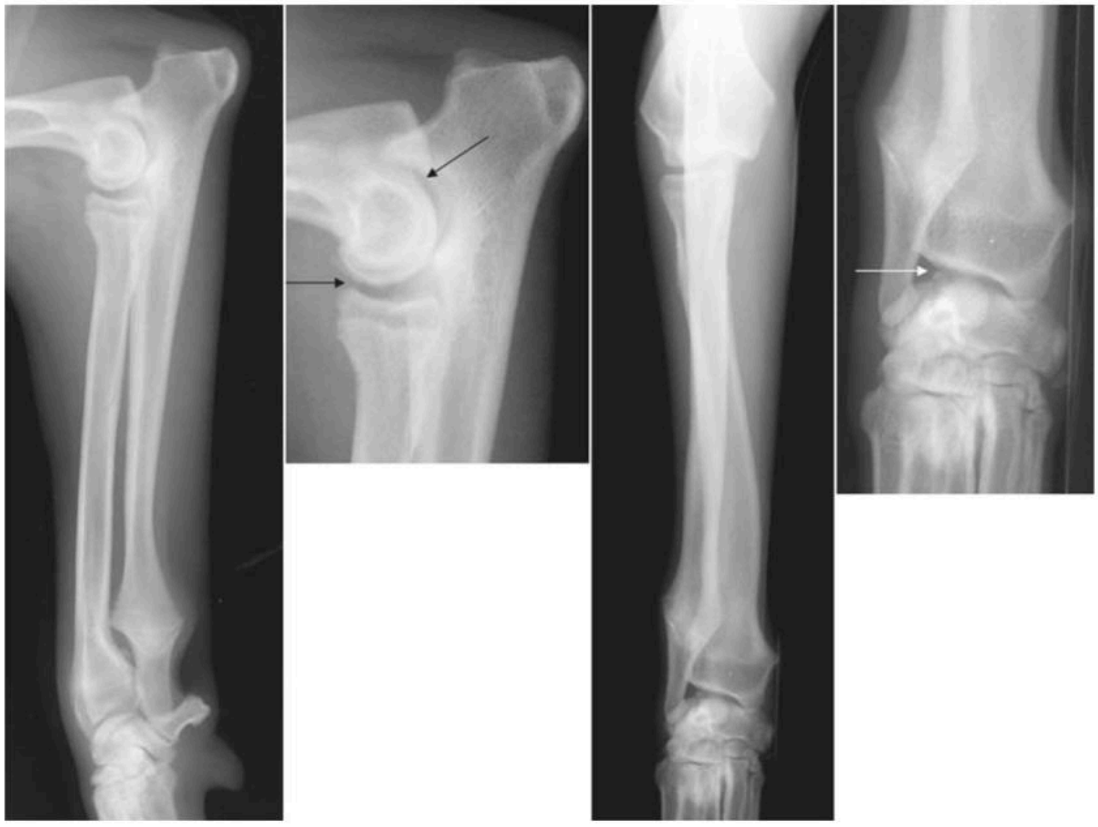
eFig. 19.12 Radiolucencies (*white arrows*) surrounding the fixation pins in the metatarsal bones are a result of infection. Purulent discharge was found around the pins. Note the sclerotic reaction within the metatarsal bones.



eFig. 19.13 Surgery was performed to repair an elbow luxation. **A,** Postoperative lateral radiograph. **B,** Eleven days later, a smoothly marginated radiolucency (*solid white arrows*) surrounding the pin in the proximal ulna is visible, indicating extension and flexion motion of the ulna. The periosteal new bone (*open white arrows*) is a result of trauma to the periosteum during surgery in this case and not an indication of infection.



eFig. 19.14 Premature distal ulnar physeal closure caused by a compression injury to the distal ulnar physis. Cessation of longitudinal growth of the ulna results in predictable changes as the radius continues to grow in length. The lateral view **(A)** shows cranial bowing of radius (*solid arrow*) and distal subluxation of the humeroulnar joint (*open arrow*). The craniocaudal view **(B)** shows valgus angulation of the manus (*solid arrows*).



eFig. 19.15 Antebrachial radiographs of a dog with partial closure of the distal radial physis. The physis has closed laterally. The growth retardation has resulted in subluxation of the lateral aspect of the antebrachiocarpal joint (*white arrow*) and humeroradial and humeroulnar subluxation (*black arrows*). The retarded radial growth results in distal displacement of the radius from the humerus and proximal displacement of the ulna from the humerus. The direction of hmeroulnar subluxation with radial closure is opposite from what is observed in ulnar growth retardation.



eFig. 19.16 Advanced bacterial osteomyelitis after fixation of a distal antebrachial fracture with an external fixator. Note the active periosteal reaction that extends the entire length of the bone. Soft tissue swelling is also present and is important in differentiating septic versus nonseptic periosteal new bone. In addition, the irregular margins of the periosteal reaction are atypical for callus and indicate an aggressive process.



eFig. 19.17 Soft tissue mass (*solid white arrows*) and aggressive periosteal new bone (*open white arrows*) indicating an aggressive bone lesion at and distal to a malunion fracture.

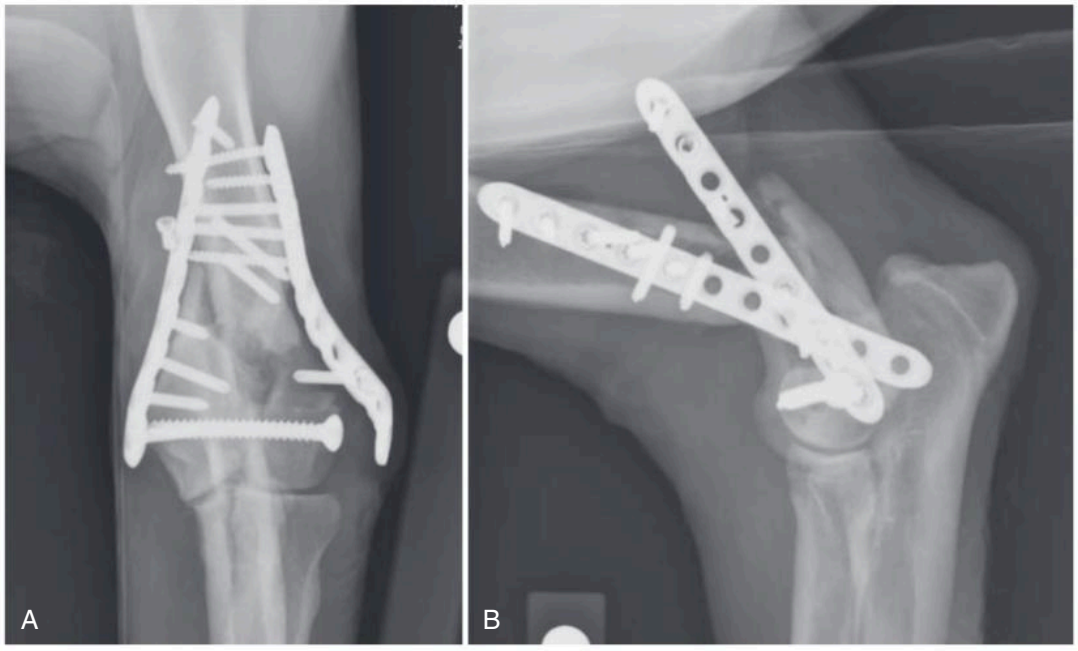


Fig. 19.25 Craniocaudal **(A)** and lateral **(B)** radiographs of a humeral condylar fracture repair with implant failure. The distal portion of the laterally applied bone plate has migrated laterally and there is a large area of radiolucency around the distal most screw that is only partially engaged in the bone. The proximal screws of the medially applied bone plate have fractured, and the plate is removed from the proximal fracture fragment. The fracture is instable with caudal and medial displacement of the distal fracture fragment.

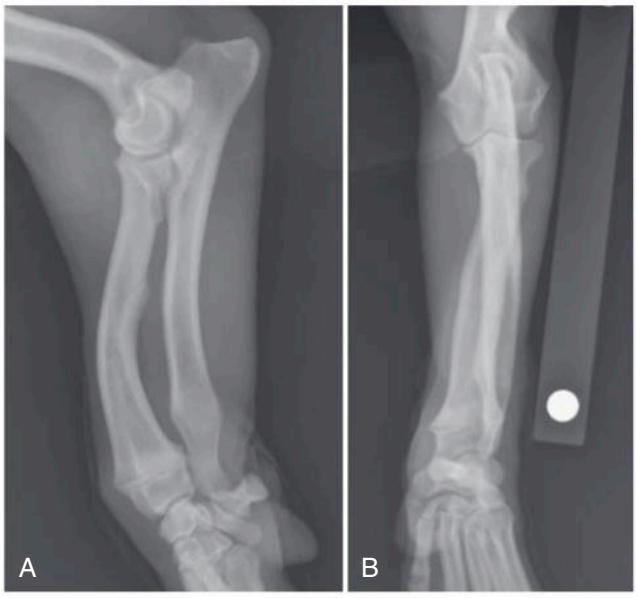


Fig. 19.26 Lateral **(A)** and craniocaudal **(B)** radiographs of the antebrachium of a dog with premature distal ulnar physeal closure which causes shortening of the ulna. Continued growth of the radius results in cranial bowing of the radius and mild carpal valgus.



Fig. 19.27 Lateral **(A)** and craniocaudal **(B)** radiographs of the antebrachium of a dog wtih premature partial distal radial physeal closure. The lateral aspect of the distal radial physis is closed whereas there is still growth medially resulting in valgus deformation at the carpus. The radius is shortened relative to the ulna resulting in elbow joint incongruity.

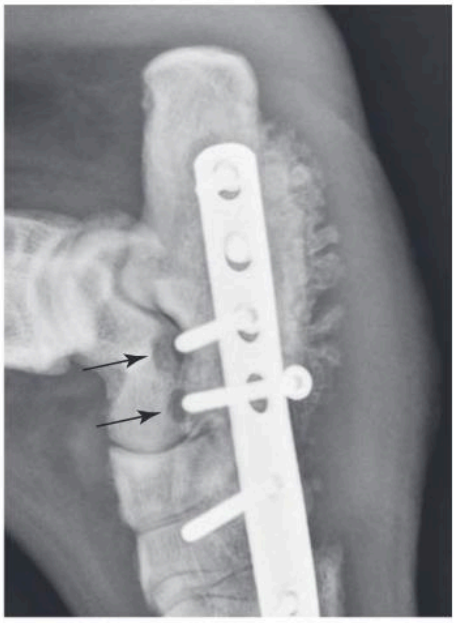


Fig. 19.28 Lateral view of the tarsus of a dog with osteomyelitis. A bone plate is present to provide stabilization of an unstable tarsal joint. There is lysis around the tip of two screws (*black arrows*). The fourth screw from the top is backing out. There is also an irregular active columnar periosteal reaction on the plantar aspect of the calcaneus; this irregular periosteal reaction, which is highly suggestive of osteomyelitis, should never be seen with normal callus. The lysis around the tips of the screws could be caused by motion but considering the columnar periosteal reaction on the calcaneus, screw tract infection is likely.

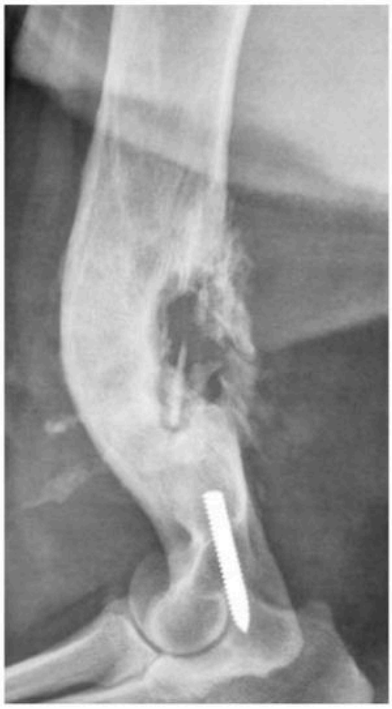


Fig. 19.30 Lateral radiograph of the distal humerus of a dog. There is a healed malunion fracture of the distal humerus with the distal fragment angled caudally (antecurvatum malunion fracture). A piece of a threaded pin is embedded in the distal humerus. There is a sharply margined opaque bone fragment surrounded by a zone of lysis and an active periosteal reaction. The adjacent medullary cavity of the humerus is sclerotic. These are classic findings of a sequestrum with secondary osteomyelitis.

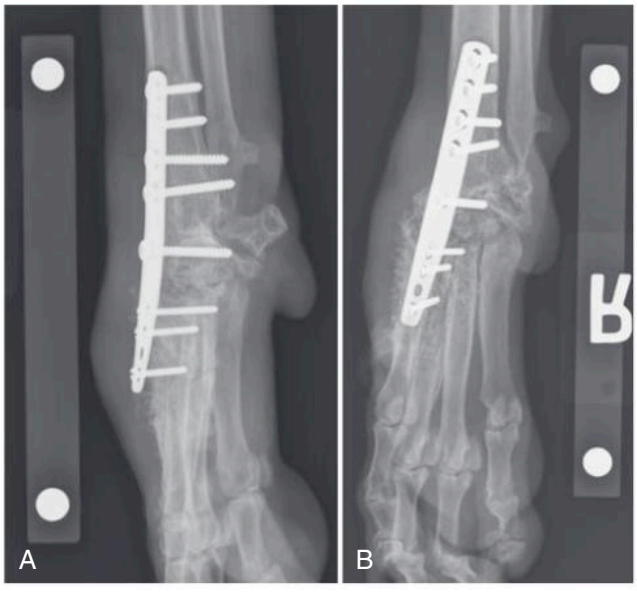


Fig. 19.29 Lateral **(A)** and oblique **(B)** radiograph of the carpus after pancarpal arthrodesis and implant-associated osteomyelitis. The distal most screwhead is disengaged from the plate and the distal aspect of the plate is dorsally displaced. There is spiculated and palisading periosteal reaction along the dorsomedial aspect of the carpus associated with severe soft tissue thickening. There is irregular, palisading periosteal reaction along the cortices of the radius and ulna. There is increased radiolucency surrounding the full pin. The fracture has not healed.



Fig. 19.31 Close-up lateral radiograph of the distal humerus of a dog with an open fracture that was repaired with an external fixator 3 months ago, but an open draining tract remained. The external fixator has been removed. There is a large amount of bridging callus formation. Several angular cortical fragments with no evidence of modeling or periosteal new bone formation are present in the center of the fracture, surrounded by a rim of radiolucency. Bone sequestra were removed surgically.

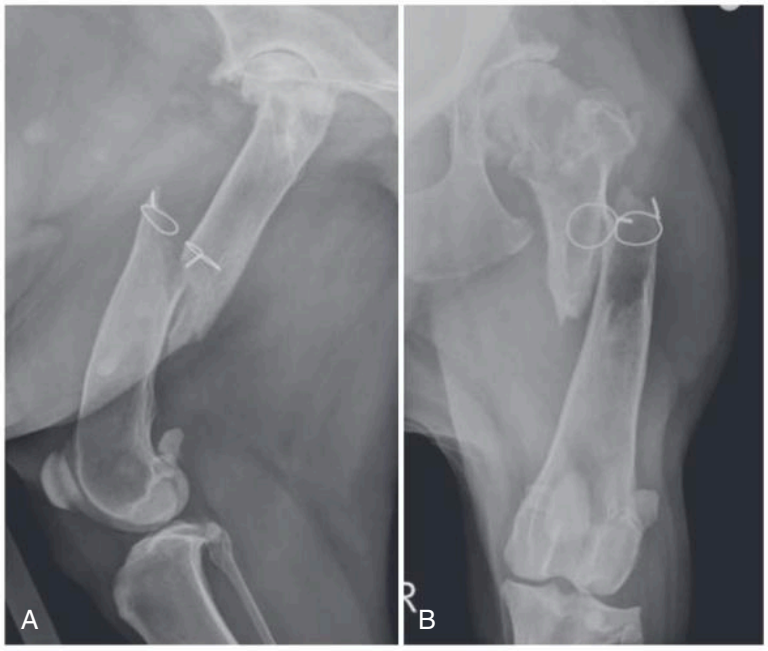


Fig. 19.32 Lateral **(A)** and craniocaudal **(B)** radiographs of the femur of a 12-year-old dog with a pathologic mid-diaphyseal fracture due to osteosarcoma. The dog had a femoral fracture repaired at 2 months of age (see small diameter of cerclage wire). Given the presence of implants and an aggressive lesion in an atypical location for osteosarcoma, implant associated neoplasia was suspected.

Acknowledgment

With special thanks to prior authors of this chapter for their contributions.

REFERENCES

1. Resnick D, Kransdorf MJ. *Bone and Joint Imaging*. 3rd ed. Philadelphia: Elsevier/Saunders; 2005.
2. Slatter D. *Textbook of Small Animal Surgery*. 3rd ed. Vol. 2. Philadelphia: Elsevier/Saunders; 2003.
3. Fossum TW. *Small Animal Surgery*. 5th ed. St Louis: Elsevier/Mosby; 2019.
4. Hedberg EL, Mikos AG. Bone augmentation and repair. In: Buschow KHJ, Cahn RW, Flemings MC, et al., eds. *Encyclopedia of Materials: Science and Technology [Internet]*. Oxford: Elsevier; 2001:782–787.
5. Clarke B. Normal bone anatomy and physiology. *Clin J Am Soc Nephrol*. 2008;3(suppl 3):S131–S139.
6. Palmer RH. External fixators and minimally invasive osteosynthesis in small animal veterinary medicine. *Vet Clin North Am Small Anim Pract*. 2012;42(5):913–934.
7. Elliott DS, Newman KJH, Forward DP, et al. A unified theory of bone healing and nonunion. *Bone Joint Lett J*. 2016;98-B(7):884–891.
8. Sande R. Radiography of orthopedic trauma and fracture repair. *Vet Clin North Am Small Anim Pract*. 1999;29(5):1247–1260.
9. Stieger-Vanegas SM, Senthirajah SKJ, Nemanic S, Baltzer W, Warnock J, Bobe G. Evaluation of the diagnostic accuracy of four-view radiography and conventional computed tomography analysing sacral and pelvic fractures in dogs. *Vet Comp Orthop Traumatol*. 2015;28(3):155–163.
10. Martin TW, LaRue SM, Griffin L. CT characteristics and proposed scoring scheme are predictive of pathologic fracture in dogs with appendicular osteosarcoma treated with stereotactic body radiation therapy. *Vet Radiol Ultrasound*. 2022;63(1):82–90.
11. Kubicek L, Vanderhart D, Wirth K, et al. Association between computed tomographic characteristics and fractures following stereotactic radiosurgery in dogs with appendicular osteosarcoma. *Vet Radiol Ultrasound*. 2016;57(3):321–330.
12. Draffan D, Clements D, Farrell M, Heller J, Bennett D, Carmichael S. The role of computed tomography in the classification and management of pelvic fractures. *Vet Comp Orthop Traumatol*. 2009;22(3):190–197.
13. Strohmeier UW, Harris KP. Humeral intracondylar fissures in French bulldogs. *Vet Rec*. 2021;189(11):e504.
14. Orsini PG, Rendano VT, Sack WO. Ectopic nutrient foramina in the third metatarsal bone of the horse. *Equine Vet J*. 1981;13(2):132–134.
15. Becht JL, Park RD, Kraft SL. Radiographic interpretation of normal skeletal variations and pseudolesions in the equine foot. *Vet Clin North Am Equine Pract*. 2001;17(1):1–18.
16. Salter R, Harris W. Injuries involving the epiphyseal plate. *J Bone Joint Surg*. 1963;45:587.
17. Valdés-Martínez A, Seiler G, Mai W, et al. Quantitative analysis of scintigraphic findings in tibial stress fractures in Thoroughbred racehorses. *Am J Vet Res*. 2008;69(7):886–890.
18. Koblik PD, Hornof WJ, Seeherman HJ. Scintigraphic appearance of stress-induced trauma of the dorsal cortex of the third metacarpal bone in racing Thoroughbred horses: 121 cases (1978–1986). *J Am Vet Med Assoc*. 1988;192(3):390–395.
19. Rockwood CA, Green DP, Heckman JD, et al. *Rockwood and Green's Fractures in Adults*. 7th ed. Philadelphia: Lippincott, Williams & Wilkins; 2009.
20. Frost HM. A 2003 update of bone physiology and Wolff's Law for clinicians. *Angle Orthod*. 2004;74(1):3–15.
21. Karladani AH, Granhed H, Karrholm J, et al. The influence of fracture etiology and type on fracture healing: a review of 104 consecutive tibial shaft fractures. *Arch Orthop Trauma Surg*. 2001;121(6):325–328.

22. Hudson CC, Pozzi A, Lewis DD. Minimally invasive plate osteosynthesis: applications and techniques in dogs and cats. *Vet Comp Orthop Traumatol*. 2009;22(3):175–182.
23. Harasen G. External coaptation of distal radius and ulna fractures. *Can Vet J*. 2003;44(12):101–1011.
24. Epari DR, Schell H, Bail HJ, et al. Instability prolongs the chondral phase during bone healing in sheep. *Bone*. 2006;38(6):864–870.
25. Morgan EF, Gleason RE, Hayward LNM, et al. Mechanotransduction and fracture repair. *J Bone Joint Surg Am*. 2008;90(suppl 1):25–30.
26. Wehner T, Claes L, Niemeyer F. Influence of the fixation stability on the healing time—a numerical study of a patient-specific fracture healing process. *Clin Biomech (Bristol, Avon)*. 2010;25(6):606–612.
27. Lienau J, Schell H, Duda GN, et al. Initial vascularization and tissue differentiation are influenced by fixation stability. *J Orthop Res*. 2005;23(3):639–645.
28. Beale BS. Orthopedic problems in geriatric dogs and cats. *Vet Clin North Am Small Anim Pract*. 2005;35(3):655–674.
29. Follak N, Kloting I, Merk H. Influence of diabetic metabolic state on fracture healing in spontaneously diabetic rats. *Diabetes Metab Res Rev*. 2005;21(3):288–296.
30. Tack LJW, Tatsi C, Stratakis CA, Lodish MB. Effects of glucocorticoids on bone: what we can learn from pediatric endogenous Cushing's syndrome. *Horm Metab Res Horm Stoffwechselforschung Horm Metab*. 2016;48(11):764–770.
31. Piermattei DL, Flo GL, Brinker WO. *Brinker, Piermattei, and Flo's Handbook of Small Animal Orthopedics and Fracture Repair*. 4th ed. Philadelphia: Elsevier/Saunders; 2006.
32. McCartney WT, MacDonald BJ. Incidence of non-union in long bone fractures in 233 cats. *Intern J Appl Res Vet Med*. 2006;4:209.
33. Goggin JM, Hoskinson JJ, Carpenter JW, Roush JK, McLaughlin RM, Anderson DE. Scintigraphic assessment of distal extremity perfusion in 17 patients. *Vet Radiol Ultrasound*. 1997;38(3):211–220.
34. Saikku-Backstrom A, Raiha JE, Valimaa T, et al. Repair of radial fractures in toy breed dogs with self-reinforced biodegradable bone plates, metal screws, and light-weight external coaptation. *Vet Surg*. 2005;34(1):11–17.
35. Welch JA, Boudrieau RJ, DeJardin LM, et al. The intraosseous blood supply of the canine radius: implications for healing of distal fractures in small dogs. *Vet Surg*. 1997;26(1):57–61.
36. Drost WT, Reese DJ, Hornof WJ. Digital radiography artifacts. *Vet Radiol Ultrasound*. 2008;49(1 suppl 1):S48–S56.
37. Gieling F, Peters S, Erichsen C, Richards RG, Zeiter S, Moriarty TF. Bacterial osteomyelitis in veterinary orthopaedics: pathophysiology, clinical presentation and advances in treatment across multiple species. *Vet J*. 2019;250:44–54.
38. Jackson LC, Pacchiana PD. Common complications of fracture repair. *Clin Tech Small Anim Pract*. 2004;19(3):168–179.
39. Metsemakers WJ, Kuehl R, Moriarty TF, et al. Infection after fracture fixation: current surgical and microbiological concepts. *Injury*. 2018;49(3):511–522.
40. Maley JR, Mertens WD, Bahr A. Osteomyelitis-related sequestrum formation in association with the combination tibial plateau leveling osteotomy and cranial closing wedge osteotomy procedure. *Vet Comp Orthop Traumatol*. 2010;23(2):141–147.
41. Stevenson S, Hohn RB, Pohler OE. Fracture-associated sarcoma in the dog. *J Am Vet Med Assoc*. 1982;180(10):1189–1196.
42. Baum JI, Skinner OT, Boston SE. Fracture-associated osteosarcoma of the femur in a cat. *Can Vet J Rev*. 2018;59(10):1096–1098.

ELECTRONIC RESOURCES

Additional information related to the content in Chapter 19 can be found online at eBooks.Health.Elsevier.com.

- Chapter Quiz



CHAPTER 20

Radiographic Signs of Joint Disease in Dogs and Cats

Graeme Allan • Sarah Davies

Most radiographic signs of joint disease are degenerative in nature and nonspecific for the underlying etiology (Box 20.1, Fig. 20.1). Radiographic signs change as joint disease progresses through different phases. Sound knowledge of joint pathophysiology is as important in the diagnosis of joint disease as the ability to make and interpret radiographs of joints.

RADIOGRAPHIC SIGNS OF JOINT DISEASE

Increased Synovial Volume

A moderate increase in joint capsular or intracapsular soft tissue volume may be detected on good-quality radiographs. The joint cartilage, synovial fluid, synovial membrane, and joint capsule cannot be differentiated, because they are all of soft tissue opacity and silhouette with one another. In most joints, an increase in synovial mass appears as periarticular soft tissue swelling, as it can be difficult to differentiate intracapsular from extracapsular soft tissue thickening.

In the stifle, the infrapatellar fat pad may be used to evaluate synovial volume. The normal infrapatellar fat pad is identified readily on lateral stifle radiographs as a relatively radiolucent triangular region immediately caudal to the patellar ligament (Fig. 20.2). When stifle synovial mass increases, either from increased synovial fluid or soft tissue, a combination of inflammatory response and effusion causes the fat pad to be reduced in size and less defined.

Box • **20.1**

Radiographic Signs of Joint Disease

Increased synovial volume
Compressed infrapatellar fat pad
Altered thickness of the joint space
Decreased subchondral bone opacity
Increased subchondral bone opacity
Subchondral bone cyst formation
Altered perichondral bone opacity
Perichondral bony proliferation
Mineralization of joint soft tissues
Intra-articular calcified bodies
Joint displacement or incongruency
Joint malformation
Intra-articular gas

Altered Width of the Joint Space

The joint space is the region of soft tissue opacity between subchondral bone surfaces of opposing weight-bearing surfaces of a joint. This space consists of two layers of articular cartilage separated by a microfilm of synovial fluid. In early joint disease, synovial effusion may cause widening of the joint space. As joint disease progresses, attrition of articular cartilage results in decreased width of the joint space (Fig. 20.3). These changes in joint space width are rarely diagnosed radiographically as small animal patients are not radiographed while bearing weight and also because of inconsistency between the orientation of the primary x-ray beam and joint space.

Decreased Subchondral Bone Opacity and Bone Cyst

Subchondral bone is separated from the synovial fluid by an intact layer of articular cartilage. Any disease that changes the character of synovial fluid, causing the articular cartilage to

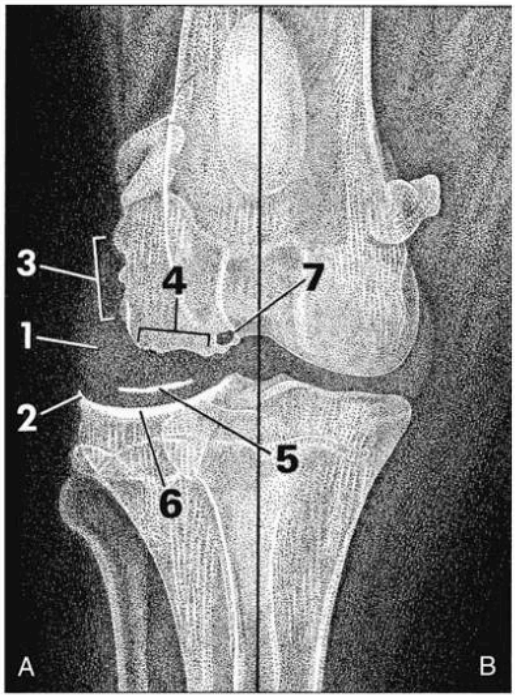


Fig. 20.1 Radiographic signs of joint disease **(A)** compared with a normal joint **(B)**. Increased synovial mass (*1*), perichondral osteophyte (*2*), and enthesophyte formation (*3*) are common radiographic changes. Erosion of the subchondral bone surface (*4*) and joint mice (*5*) are less common, whereas increased subchondral bone opacity (*6*) and subchondral bone cyst formation (*7*) are signs of chronic joint disease.

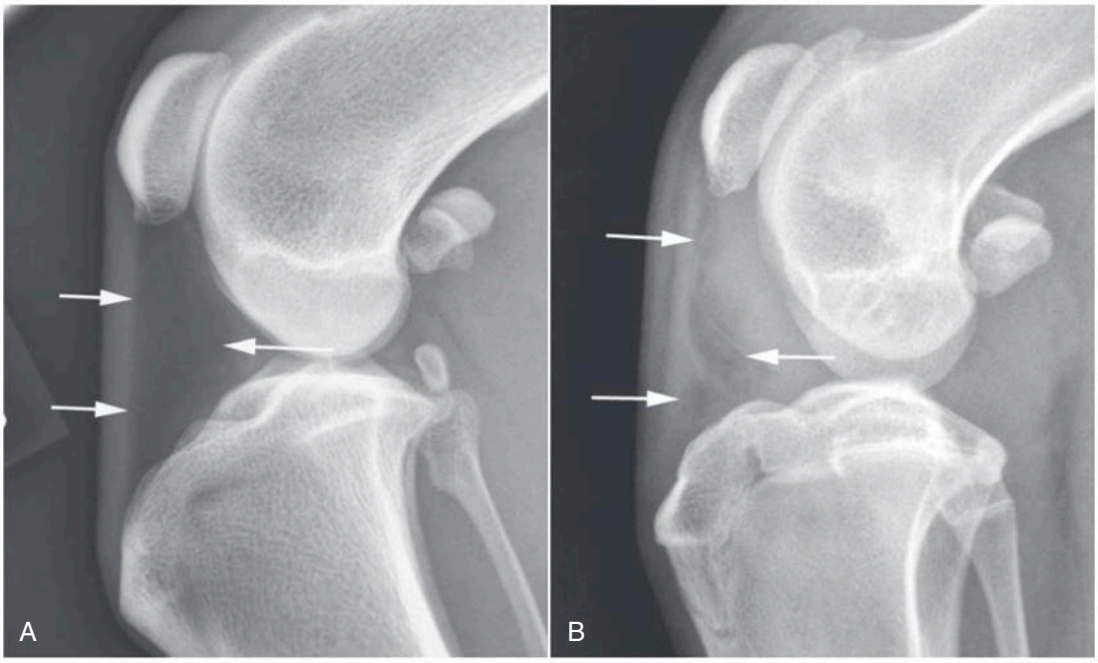


Fig. 20.2 Changes in the shape of the infrapatellar fat pad, located between the *arrows*, is a sensitive indicator of absence **(A)** or presence **(B)** of increased synovial volume in the stifle.

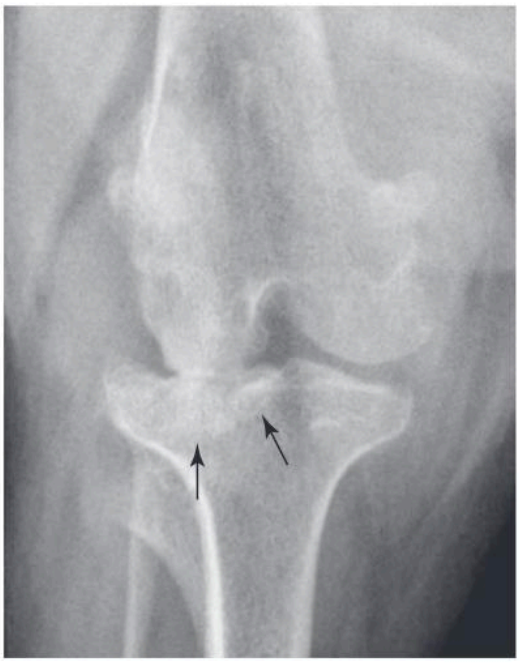


Fig. 20.3 Chronic malalignment of the stifle joint has resulted in narrowing of the lateral aspect of the femorotibial joint, likely because of degeneration of the lateral meniscus. The secondary altered loading of the lateral tibial condyle has resulted in secondary sclerosis (*black arrows*).



Fig. 20.4 Periarticular soft tissue swelling (*white arrows*) and subchondral bone erosion (*white arrowheads*) in the carpus of a dog with an erosive polyarthropathy. (Courtesy Perth Veterinary Specialists, Perth, Australia.)

erode, potentially threatens the integrity of subchondral bone. In inflammatory joint disease, inflammatory exudates may cause pronounced subchondral bone loss. Infectious arthritis may extend into subchondral bone. Subchondral bone loss appears initially as an irregular margin of subchondral bone, but it may extend to cause marked destruction of bone (Fig. 20.4). When bone loss affects smaller carpal and tarsal bones, these small cuboidal bones may be dramatically reduced in mass.

Increased Subchondral Bone Opacity

In benign joint disease such as degenerative joint disease, subchondral bone may be more opaque than normal because of stress remodeling (see Fig. 20.3). Increased subchondral bone opacity usually appears as a subchondral zone sclerosis 1 to 2 mm wide.

Altered Perichondral Bone Opacity

Articular cartilage merges with the synovial membrane at the chondrosynovial junction. This highly vascular membrane is

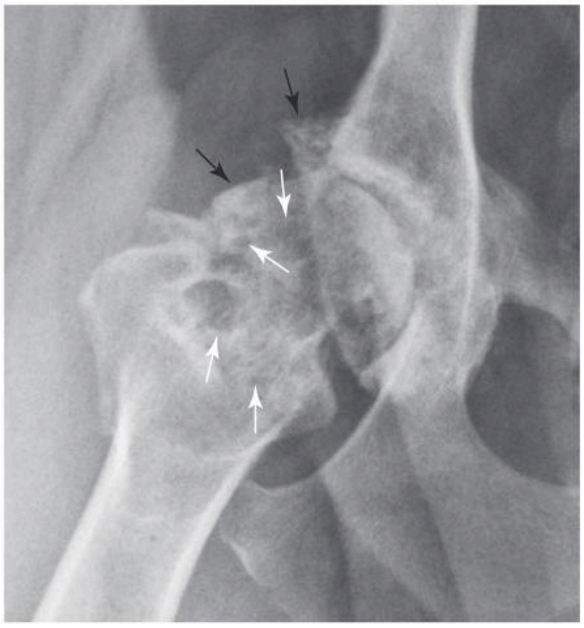


Fig. 20.5 Advanced coxofemoral degenerative joint disease. The femoral neck is thickened, the femoral head is misshapen, and there are numerous osteophytes (*black arrows*). There are multiple small and large radiolucencies (*white arrows*) in the femoral neck because of invasion of bone by hyperplastic synovium.

sensitive to inflammation. Synovial inflammation, or hypertrophy, may result in erosion of bone adjacent to the synovium. Early inflammation causes adjacent bone to appear ragged and spiculated. Longstanding or severe synovial inflammation or hypertrophy may cause pronounced bone erosion (Fig. 20.5).

Articular Soft Tissue Mineralization

Mineralization may occur within the joint capsule, synovial membrane, or synovial fluid as a consequence of chronic joint disease. Occasionally, large accumulations of articular or periarticular calcific material may be observed. Large osteochondromas have been reported within the joints of dogs and cats, and intrameniscal calcification and ossification have been observed in the stifle joints of cats.[1] Pseudogout, or calcium pyrophosphate deposition disease, also causes mineralization of articular and periarticular soft tissues and has been reported in dogs.

Intra-articular Calcified Bodies

Small, well-defined articular and periarticular calcific opacities are occasionally observed in dogs and cats. Such mineralized fragments are sometimes called *joint mice*. Not all such fragments are free within the joint, although they may appear free radiographically; fragments may become adhered to the joint capsule. Articular calcified bodies usually fall into three fairly distinct categories: (1) avulsed fragments of articular or periarticular bone, (2) osteochondral components of a disintegrating joint surface, or (3) small synovial osteochondromas (Table 20.1).[2] They must be differentiated from sesamoid bones.

Joint Displacement or Incongruency

When the normal spatial relation between components of a joint is disturbed, some type of displacement has occurred. A good example is a luxated coxofemoral joint. Other less obvious incongruities, such as the cranial drawer sign in a stifle with a ruptured cranial cruciate ligament and minor elbow incongruity in dogs with elbow dysplasia, can be difficult to see radiographically.[3]

Table • 20.1

Some Common Causes of Calcified Intra-Articular Bodies.

JOINT	ETIOLOGY
Shoulder	Osteochondritis dissecans (OCD) of the head of the humerus
	Mineralization of the bicipital tendon/sheath
	Synovial osteochondroma
	Separate centers of ossification on the glenoid rim
Elbow	Ununited anconeal process
	Fragmented coronoid process
	OCD of the humeral medial condyle
Hip	Avulsion epiphyseal fractures after femoral luxation
	Avascular necrosis of the femoral head
Stifle	OCD of the femoral condyles
	Avulsion fractures of the:
	Origin of the long digital extensor tendon
	Origin or insertion of the cruciate ligaments
	Origin of the popliteus
	Meniscal calcification
	Synovial osteochondroma
	Fragmented or fractured sesamoid bones
Tarsus	OCD of the talus

In all joints, soft tissue periarticular mineralization may occur as a result of degenerative joint disease.

Osteophytes

Osteophytes are bone proliferations covered with fibrocartilage along a joint margin. The proposed pathogenesis of osteophyte formation is that abnormal joint cartilage loading leads to cartilage wear, fibrillation, and loss of cartilage. The products of cartilage degradation mediate synovial hyperplasia and subsequent development of osteophytes.[4,5] Initially, osteophytes consist of cartilage and later become radiographically visible when they become ossified. A fully formed osteophyte is integrated with the subchondral bone and seen as bony outgrowth at the periphery of articular cartilage. Osteophytes occur as a component of degenerative joint disease (see Fig. 20.5).

Entheses and Enthesophytes

An enthesis is the point of insertion of a tendon, ligament, joint capsule, or fascia to bone. During embryogenesis, ligaments and tendons are attached to cartilage, but subsequent metaplasia of fibroblasts at their attachment site results in formation of fibrocartilage. This extends into the tendon or ligament, and endochondral ossification proceeds within the remaining cartilage. Enthesitis is inflammation of the site of tendon or ligament attachment to bone. An enthesophyte is a bony proliferation that develops at an enthesis (Fig. 20.6).[6]

Because enthesophytes and osteophytes appear radiographically similar, confusion in terminology often occurs when referring to these structures on a radiograph. To separate osteophytes around or within joints from enthesophytes, knowing the location of the common entheses is useful information (Figs. 20.6–20.8). In complex joints such as the carpus and tarsus, a large number of intra-articular ligaments are present. Every diarthrodial joint has a joint capsule, and intra-articular and periarticular ligaments and joint capsules insert onto bone at their respective entheses. New bone formations

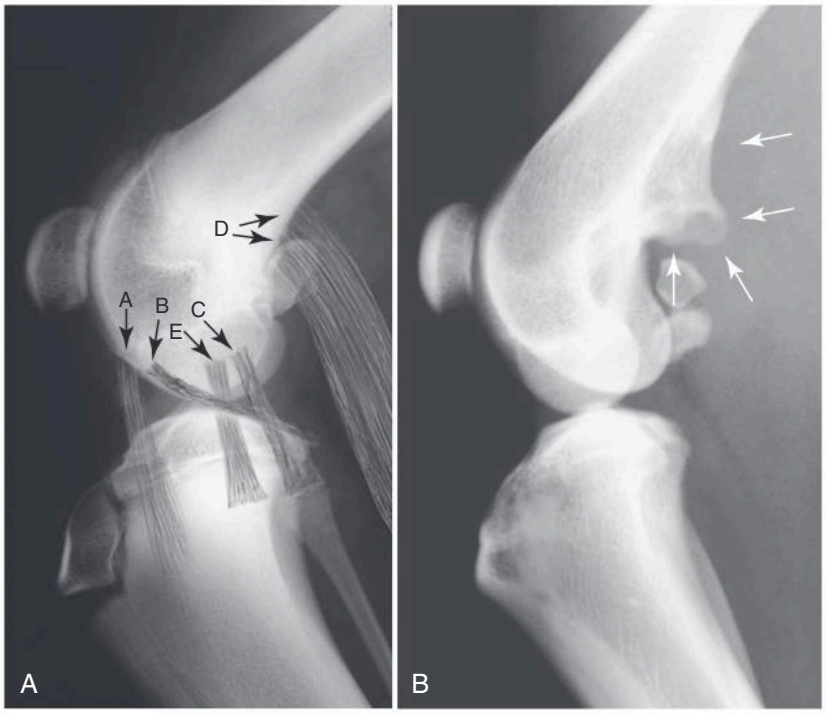


Fig. 20.6 The stifle. **A,** Entheses of origin of the long digital extensor (*A*), popliteus (*B*), lateral collateral ligament (*C*), gastrocnemius (*D*), and medial collateral ligament (*E*). Not depicted are the cranial and caudal cruciate ligaments. **B,** A large enthesophyte arising from the enthesis of origin of the gastrocnemius muscle (*arrows*).

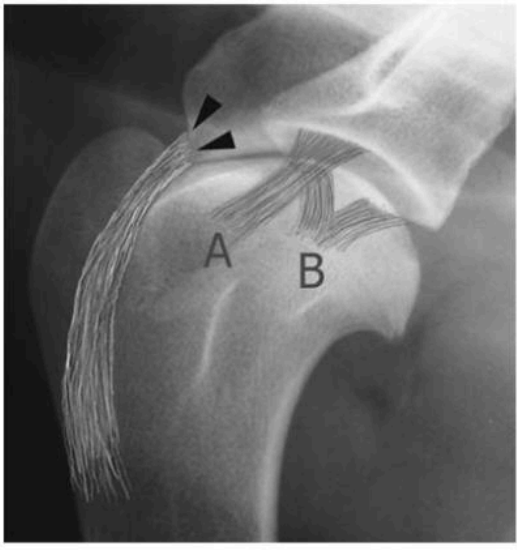


Fig. 20.7 In the scapulohumeral joint the intra-articular tendon of origin of biceps brachii muscle arises from its enthesis (*black arrowheads*) on the supraglenoid tubercle of the scapula. Other entheses around the shoulder are related to the lateral (*A*) and medial (*B*) glenohumeral ligaments and the joint capsule and tendons of insertion of supraspinatus, infraspinatus, and subscapularis muscles (not depicted).



Fig. 20.8 Entheses around the carpus. In addition to the many intra-articular ligaments and the joint capsule (not depicted) are periarticular entheses of extensor carpi radialis and extensor carpi ulnaris (*A*), abductor pollicis longus (*B*), flexor carpi ulnaris (*C*), the check ligaments of the accessory carpal bone (*D*), and flexor carpi radialis (*E*).

arising in or around joints where no known entheses are present are usually referred to as *osteophytes*.

Intra-Articular Gas

Spontaneous or induced gas diffusion into a joint, termed the *vacuum phenomenon*, has been reported in horses and dogs.[7–11] It has also been observed within the intervertebral disc spaces of dogs at sites of disc prolapse. The presence of intra-articular gas is identified more easily during computed tomography (CT) examinations than during radiography.[10] Current theory is that noniatrogenic intra-articular gas represents diffusion of nitrogen from extracellular fluid into an adjacent joint space when negative pressure is present in the joint. This may occur naturally or be induced by applying

Box • **20.2**

Causes of Intra-Articular Gas

Iatrogenic
After arthrotomy/arthroscopy
Negative-contrast arthrography
Arthrocentesis
Tension on joints
PennHIP distraction radiography
Positioning shoulders with OCD for radiography

Trauma
Joint luxation
Penetrating injuries

Infection
Gas-producing microorganisms

Spontaneous
Intervertebral disc disease
Osteoarthritis

OCD, Osteochondritis dissecans.

traction to a joint. Vacuum phenomenon has many causes in dogs and cats (Box 20.2) and is observed when excessive distraction is applied to the coxofemoral joints during distraction radiography and has been reported in 20% of shoulder radiographs in dogs with osteochondritis dissecans (OCD) of the humeral head.[8,9] Gas diffusion is likely induced by traction while positioning the shoulder for OCD examination. Interestingly, gas diffusion was not a feature of normal (non-OCD) contralateral joints of dogs in this series.[8] Positive clinical associations with intra-articular gas include degenerative disc disease, cervical vertebral instability, osteochondrosis, and degenerative joint disease (Fig. 20.9). Intra-articular gas diffuses slowly out of a joint over several hours after normal intra-articular pressure is reestablished.

SESAMOID BONES

Sesamoid bones are located adjacent to the elbow, stifle, tarsus, and the metacarpophalangeal and metatarsophalangeal joints. If sesamoid bones are not identified on a radiograph, they may be absent or be cartilaginous at the time of radiography. The clavicle is present in up to 96% of large dogs and in all cats, but the sesamoids in the iliopubic cartilage were identified in only 11% of one group of greyhounds. In the same group of dogs, the elbow sesamoid, located in the tendon of origin of the supinator, had an incidence of 31%, the lateral plantar tarsometatarsal sesamoid 50%, and the intra-articular tarsometatarsal sesamoid 27%, whereas the popliteal sesamoid is ossified in 84% to 94% of dogs. Sesamoid bones are identified by their size, shape, and location (Figs. 20.10–20.17, Table 20.2). Occasionally, displaced sesamoids are regarded as a sign of muscular or tendinous injury. Although this may be true and has been reported in conjunction with ruptured cruciate ligaments and trauma of the tendon of origin of the popliteus and gastrocnemius,[12] variations in sesamoid location may also occur in the absence of a pathologic condition.

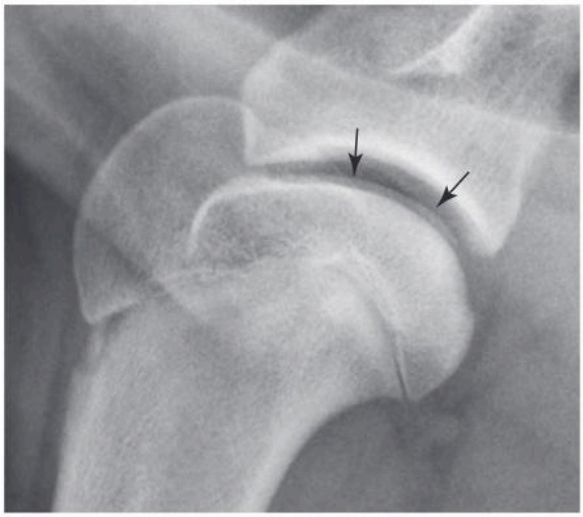


Fig. 20.9 Intra-articular gas is present in the shoulder joint of a dog with osteochondrosis; note the flattening of the caudal aspect of the humeral head. The gas itself is not very conspicuous, but its presence has reduced the opacity of the joint space leading to visualization of the articular cartilage (*black arrows*). If intra-articular gas was not present, the cartilage would not be visible.



Fig. 20.10 Clavicular remnant (*black arrows*) medial to the scapulohumeral joints of a dog.

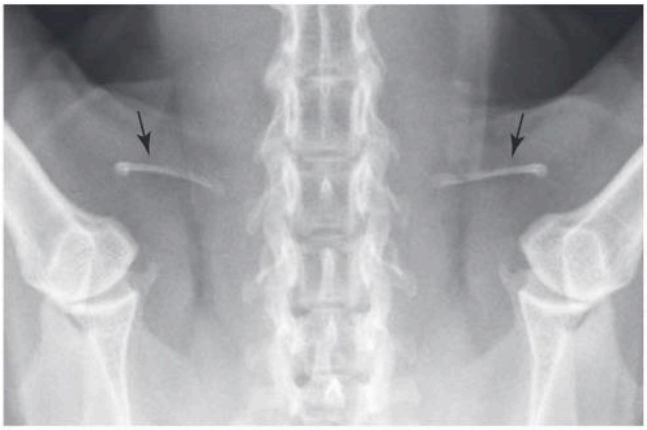


Fig. 20.11 Feline clavicles (*arrows*).

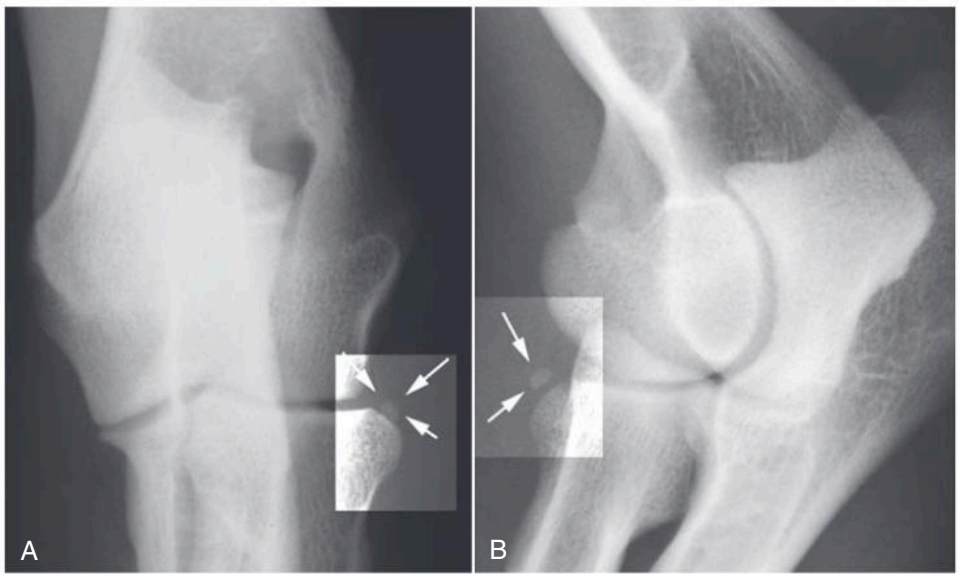


Fig. 20.12 **A and B,** The elbow sesamoid, in the tendon of origin of the supinator, is located adjacent to the craniolateral surface of the head of the radius (*arrows*).

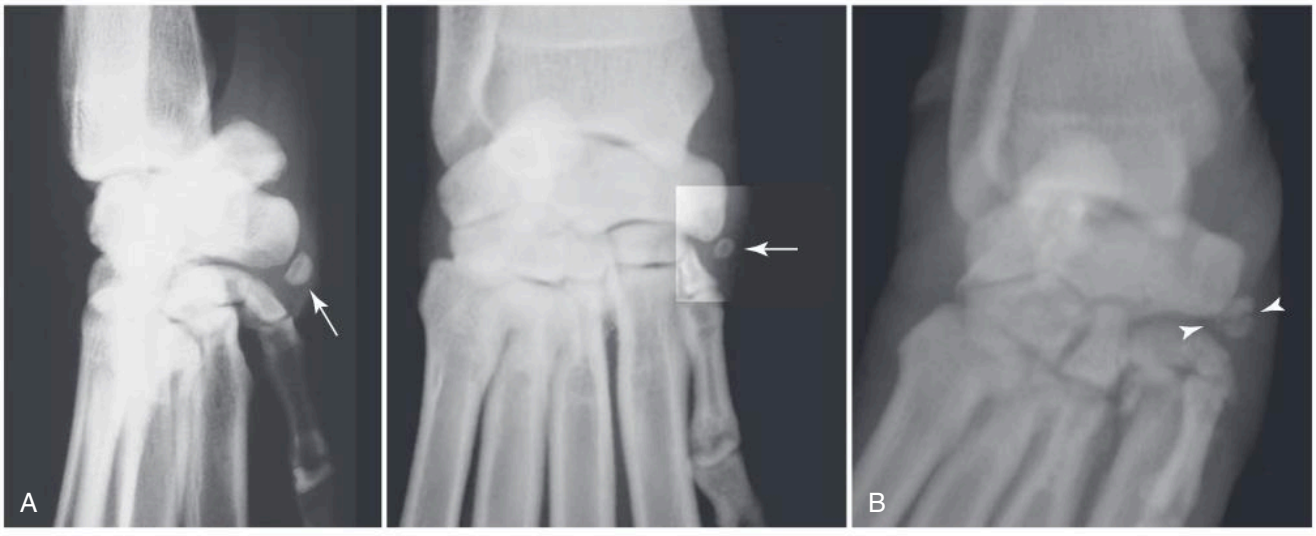


Fig. 20.13 **A,** The sesamoid bone of M. abductor pollicis longus is located in the tendon of the abductor pollicis longus on the medial side of the carpus at the level of the intercarpal articulation (*enhanced box, solid white arrows*). The tendon inserts onto the proximal end of the first digit. **B,** Fractured sesamoid bone of abductor pollicis longus in a patient with complex carpal trauma (*arrowheads*). (**A,** Reproduced with permission from Nicoll R, Allan G, Davies S. Chapter 16: Distal limbs - carpus/tarsus and distally. *BSAVA Manual of Canine and Feline Musculoskeletal Imaging*. Quedgeley, Gloucester, England: BSAVA Publications; 2006. **B,** Courtesy Northside Veterinary Specialists, Sydney, Australia.)

Sesamoid Disease

A syndrome of metacarpophalangeal sesamoid bone fragmentation has been reported in several large breeds of dogs but occurs most commonly in Rottweilers.[13] The underlying cause appears to be osteonecrosis of selected sesamoids, although developmental, traumatic, and degenerative conditions are possible. Eight palmar/plantar sesamoids are present on the four main digits of each of the manus or pes, but sesamoid fragmentation affects mainly the second and seventh palmar sesamoid bones (Fig. 20.18). The incidence has been reported to be as high as 44% in one group of Rottweilers. In another group of 55 Rottweilers, radiographic incidence of sesamoid disease at 12 months old was 73%, with an incidence of clinical signs attributable to sesamoid disease in 65% of affected dogs. Sesamoid disease was identified as the cause of forelimb lameness in 50% of young Rottweilers.[14]

Dorsopalmar radiographs usually allow identification of affected sesamoid bones, but oblique lateral projections with the digits separated by traction may provide additional information. Radiographically, fragmented sesamoid bones appear as a cluster of ossific fragments on the palmar aspect of the joint, adjacent to an unaffected paired sesamoid. Ossicles are usually multiple, with rounded margins that conform to a variety of shapes and sizes (see Fig. 20.18). In racing greyhounds,



Fig. 20.14 The metacarpophalangeal and metatarsophalangeal sesamoids are paired (*white arrowheads*) on the palmar (plantar) surface and single on the dorsal surface (*white and black arrows*). They are numbered from medial to lateral. (Reproduced with permission from Nicoll R, Allan G, Davies S. Chapter 16: Distal limbs - carpus/tarsus and distally. *BSAVA Manual of Canine and Feline Musculoskeletal Imaging*. Quedgeley, Gloucester, England: BSAVA Publications; 2006.)



Fig. 20.15 The iliopubic sesamoids are occasionally seen cranial to the pubic eminence on lateral radiographs of the pelvis of large dogs (*white arrows*).

clearly defined transverse separation of sesamoid bones has been reported, leading to a belief that fracture is the cause of sesamoid fragmentation in this breed.[15]

Although less frequently affected than sesamoids in the manus, fabellae are also prone to fragmentation (Fig. 20.19).

The most common example of sesamoid displacement is luxation of the patella (Fig. 20.20). Patella luxation occurs most frequently in toy dogs and also in Devon Rex cats. Some breeds have an inherited predisposition to patella luxation. Other sesamoid bones are also prone to displacement. Distal displacement of popliteal sesamoids or fabellae can indicate rupture or trauma to their respective tendons, although this is not always true (Fig. 20.21).

DEGENERATIVE JOINT DISEASE

Degenerative joint disease, also termed *osteoarthritis*, is a slowly progressive disease of synovial joints in which synovial effusion and cartilage degradation are key components. It is the most common joint abnormality seen in small animal practice and occurs most frequently in the weight-bearing joints of medium-sized to large dogs, although it may affect any synovial joint of both dogs and cats. The best example of canine degenerative joint disease occurs as a result of canine hip dysplasia. The incidence of hip dysplasia varies from breed to breed and exceeds 50% in many large breeds. The next most frequent locations of degenerative joint disease are the canine shoulder and stifle joints. Signs of shoulder degenerative joint disease were identified in 33% to 50% of groups of dogs surveyed either at necropsy or radiographically; 20% of dogs in another survey had evidence of stifle degenerative joint disease at necropsy.[16]

Degenerative joint disease may be a primary aging change (idiopathic) or occur as a result of a developmental or acquired disorder. Examples of canine developmental disorders include osteochondrosis, elbow incongruity leading to fragmented medial coronoid process, ununited anconeal process, hip dysplasia, patellar luxation, achondroplasia, and conformational

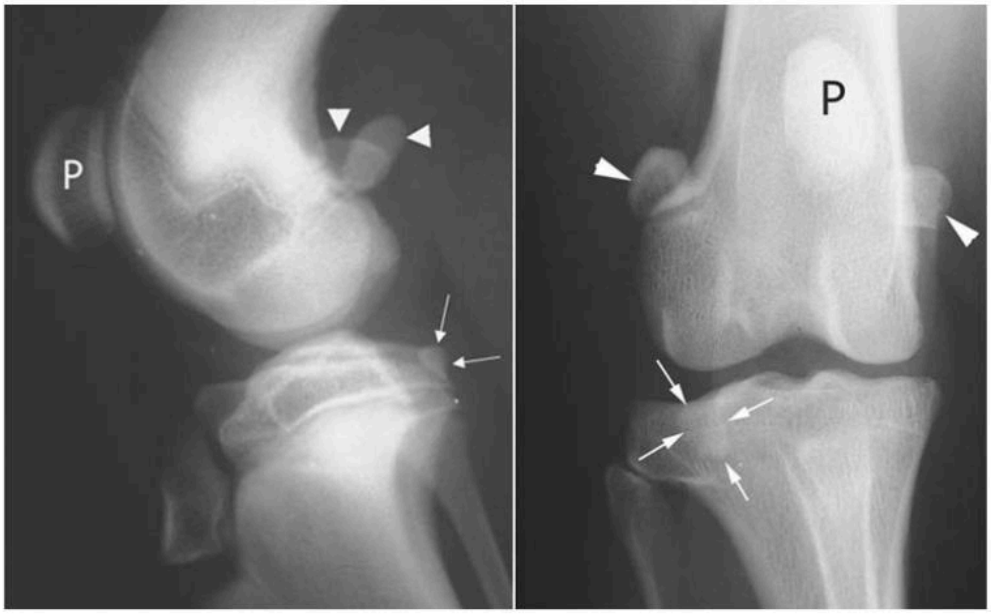


Fig. 20.16 The patella (*P*) is easily identified on the cranial aspect of the femoral condyle. The paired fabellae (*white arrowheads*) are located on the caudal aspect of the femoral condyle, where they lie adjacent to the medial and lateral condyles near the origin of the gastrocnemius. The popliteal sesamoid (*white arrows*) is located caudolaterally, adjacent to the head of the tibia.

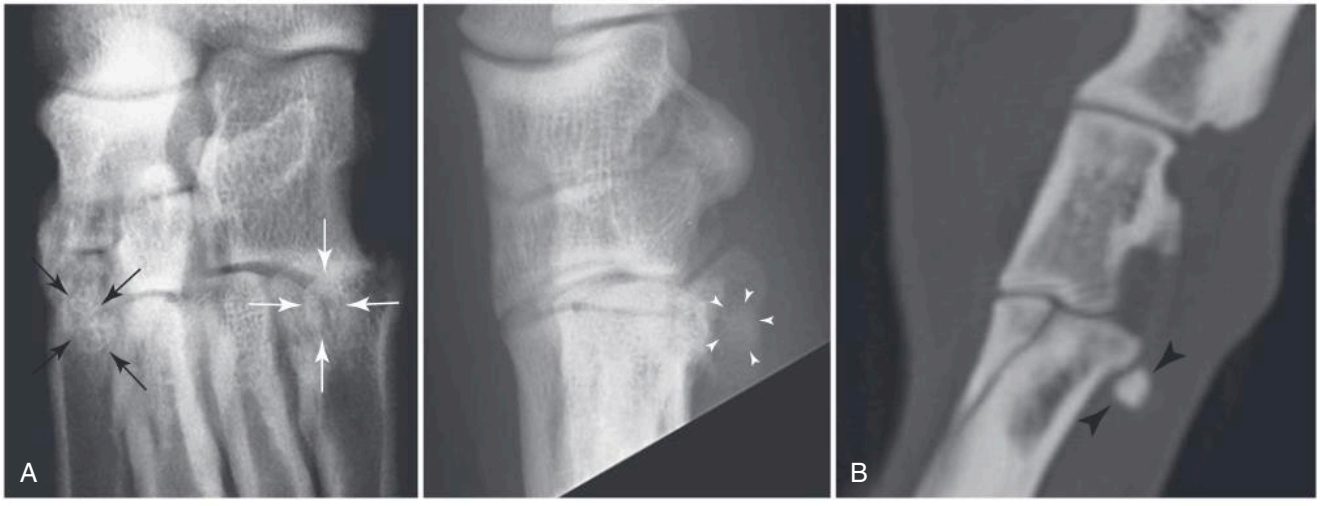


Fig. 20.17 **A,** The lateral tarsometatarsal sesamoid (*white arrows*) and the medially located intra-articular tarsometatarsal sesamoid (*black arrows*) are inconsistently present in dogs and can be difficult to locate. On the lateral image (*right panel*), one can be seen (*white arrowheads*). **B,** Sagittal computed tomography (CT) reformat through the lateral aspect of the tarsus showing the lateral tarsometatarsal sesamoid (*black arrowheads*). (**A,** Reproduced with permission from Nicoll R, Allan G, Davies S. Chapter 16: Distal limbs - carpus/tarsus and distally. *BSAVA Manual of Canine and Feline Musculoskeletal Imaging*. Quedgeley, Gloucester, England: BSAVA Publications: 2006. **B,** Courtesy Northside Veterinary Specialists, Sydney, Australia.)

disorders, such as valgus and varus deformities of the carpus. Acquired disorders capable of causing degenerative joint disease in dogs include trauma, joint instability, epiphyseal aseptic necrosis, recurrent hemarthrosis, and acquired postural or conformational defects, such as joint malalignment after fracture repair.

Radiographic Signs of Progression of Degenerative Joint Disease in Dogs

The stifle is often used to study the progression of canine degenerative joint disease. Initial stages are asymptomatic, and radiographs are usually normal. The first change is mild nonsuppurative synovitis, accompanied by increased synovial mass with alteration of the shape of the infrapatellar fat pad. Focal articular cartilage degeneration follows. The joint space may be wider during this stage; however, this is rarely seen radiographically. As a feature of degenerative joint disease, osteophytosis is progressive and is characterized by the greatest degree of change over time in the canine stifle with naturally occurring instability. When grading stifle degenerative joint disease, evaluating changes in number and size of periarticular osteophytes is more reliable than evaluating subchondral

Table • **20.2**

Sesamoid Bones Visible on Radiographs of Joints of the Canine.

APPENDICULAR SKELETON	JOINT: NAME/LOCATION
Shoulder	Clavicle (medial end of tendinous intersection in the brachiocephalicus) (see Figs. 20.10 and 20.11)
Elbow	Tendon of origin of the supinator (see Fig. 20.12)
Carpus	Tendon of the abductor pollicis longus (see Fig. 20.13)
Metacarpophalangeal	Paired palmar sesamoid bones (located in the tendons of insertion of the interosseous muscles) (see Fig. 20.14)
	Single dorsal sesamoid (located in the extensor tendons)
Coxofemoral	None[a] (see Fig. 20.15)
Femorotibial	Patella (tendon of insertion of the quadriceps femoris) (see Fig. 20.27)
	Sesamoid bones of the gastrocnemius (fabellae)
	Medial head
	Lateral head
	Popliteal sesamoid (tendon of the popliteus)
Tarsus	Lateral plantar tarsometatarsal sesamoid bone (see Fig. 20.17)
	Intra-articular tarsometatarsal sesamoid bone
Metatarsophalangeal	Paired plantar sesamoid bones (see Fig. 20.14)
	Single dorsal sesamoid bone

[a]Sesamoid bone located in the iliopubic cartilage may be seen cranial to the iliopubic eminence.



Fig. 20.18 **A**, Fragmentation of sesamoids 4 and 7 of the manus (*arrows*). **B,** A similar Rottweiler (*white arrows*) has concurrent osteitis of the distal end of a metacarpal bone (*black arrowheads*). **C,** The osteitis was identified as the active lesion using nuclear scintigraphy, and the fragmented sesamoids were not clinically significant. (**B and C,** Courtesy Dr. R. M. Zuber, Gladesville Veterinary Hospital, Sydney, Australia.)

sclerosis, intra-articular mineralization, or synovial effusion.[17,18] Signs of synovial effusion and compression of the infrapatellar fat pad, however, are identifiable radiographic features that often accompany stifle instability.[16]

Osteophyte formation commences as early as 3 days after cranial cruciate ligament transection and can be seen radiographically at the margins of the femoral trochlea as early as 2 weeks after the onset of stifle instability. Initially, osteophytes consist of cartilage, and they do not become visible radiographically until they are ossified. Proximal and distal ends of the trochlear ridges are the earliest sites of osteophyte formation in the stifle. At a later stage, osteophytes develop on the lateral and medial femoral condylar surfaces and tibial condyles, and the patella. Enthesophytes form at points of origin and insertion of cruciate and collateral ligaments subsequent to trochlear ridge osteophytosis.

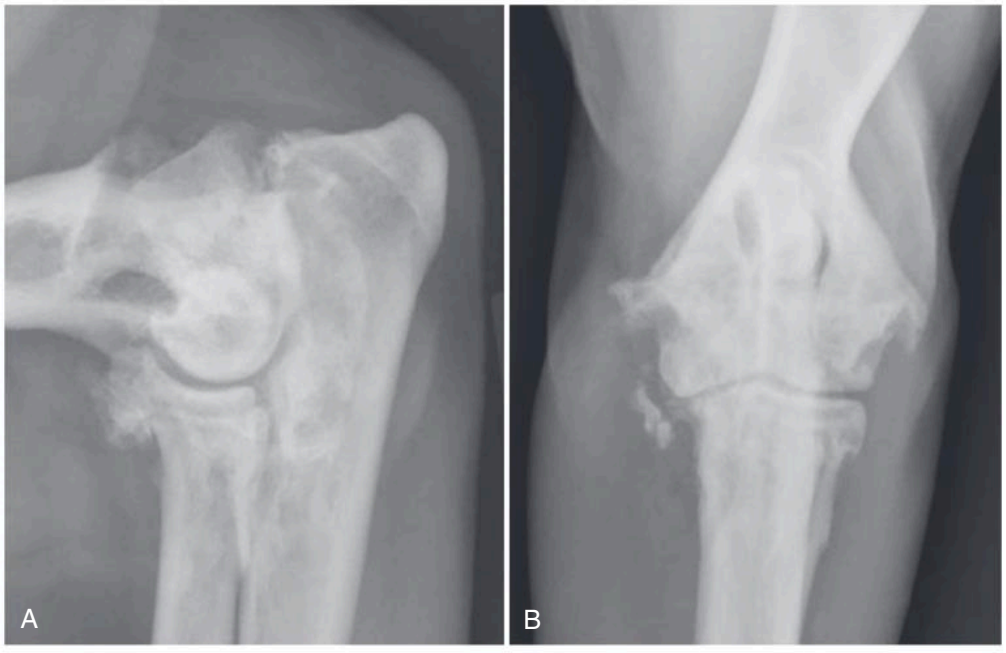
Specific radiographic projections, such as flexed mediolateral, craniomedial-caudolateral, and caudomedial/craniolateral radiographs can be used to facilitate early identification of trochlear ridge osteophytes.[4,17]

In the coxofemoral joint, synovial effusion may cause subluxation. The presence of subluxation is a powerful indicator of the risk of development of coxofemoral degenerative joint disease.[19–21]

Radiographic changes of degenerative joint disease vary according to the stage of disease. The most readily recognizable change is enthesophyte and osteophyte formation, which follows neovascularization of the chondrosynovial junction with resultant fibrocartilage formation. This fibrocartilage collar gradually ossifies with the formation of perichondral new bone (Fig. 20.22, eFig. 20.1). Enthesophytes develop on non–weight-bearing surfaces and are eventually incorporated into adjacent ligamentous or capsular attachments.[16,17]

Thinning of the joint space is observed rarely (see Fig. 20.3). Cartilage damage typically results in stress remodeling and sclerosis of the subchondral bone of the weight-bearing surface (see Fig. 20.3). Subchondral cyst formation, a feature of degenerative joint disease of the human femoral head, has also been observed in joints of small animals (see Fig. 20.5).

Affected joints exhibit decreased range of movement, which results in increased loading of the diminished weight-bearing surface. The combination of increased load, diminished subchondral strength, and loss of shock-absorbing cartilage results in altered shape of the subchondral bone table. This remodeling of subchondral bone is complemented by the addition of



eFig. 20.1 Lateral (A) and craniocaudal (B) radiographs of a dog with osteoarthritis secondary to elbow dysplasia with ununited anconeal process. There is extensive osteophytosis and subchondral sclerosis. Osseous proliferation on the medial and lateral epicondyles is consistent with flexor and extensor enthesopathy.

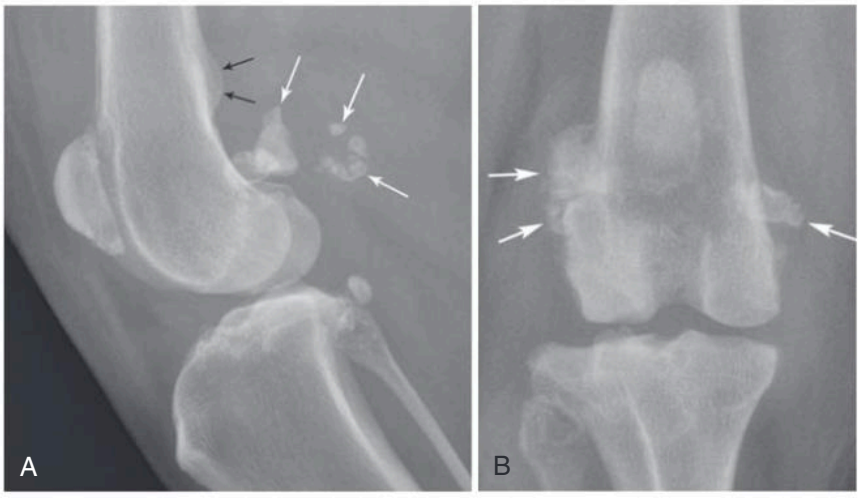


Fig. 20.19 Lateral **(A)** and craniocaudal **(B)** radiographs of a stifle of an adult dog with fragmentation of the fabellae (*white arrows*). Note enthesopathy (*black arrows*) at the origin of the medial and lateral heads of the gastrocnemius muscle.



Fig. 20.20 Medial luxation of the patella in a cat associated with complex joint trauma. On the lateral image, the luxated patella is superimposed on the trochlea of the femoral condyle. (Courtesy Cremorne Veterinary Hospital, Sydney, Australia.)

peripheral new bone in the form of perichondral osteophytes. Altered shape of the osseous components of affected joints is readily identified radiographically. The gamut of radiographic changes seen in degenerative joint disease is outlined in Box 20.3.

Degenerative Joint Disease in Cats

Degenerative joint disease is common in domestic cats.[22] Primary causes of articular cartilage degeneration and consequent degenerative joint disease in cats include the storage disease mucopolysaccharidosis (MPS) and osteochondral dysplasia of Scottish fold cats and age-related degeneration.[23] Postulated secondary causes of feline degenerative joint disease (Fig. 20.23) include developmental and traumatic conditions that alter joint stability, as well as dietary (hypervitaminosis A) causes. Many infectious and immune-based arthropathies alter the integrity of articular cartilage, leading to a cascade of articular changes, with degenerative joint disease as the end result. There is

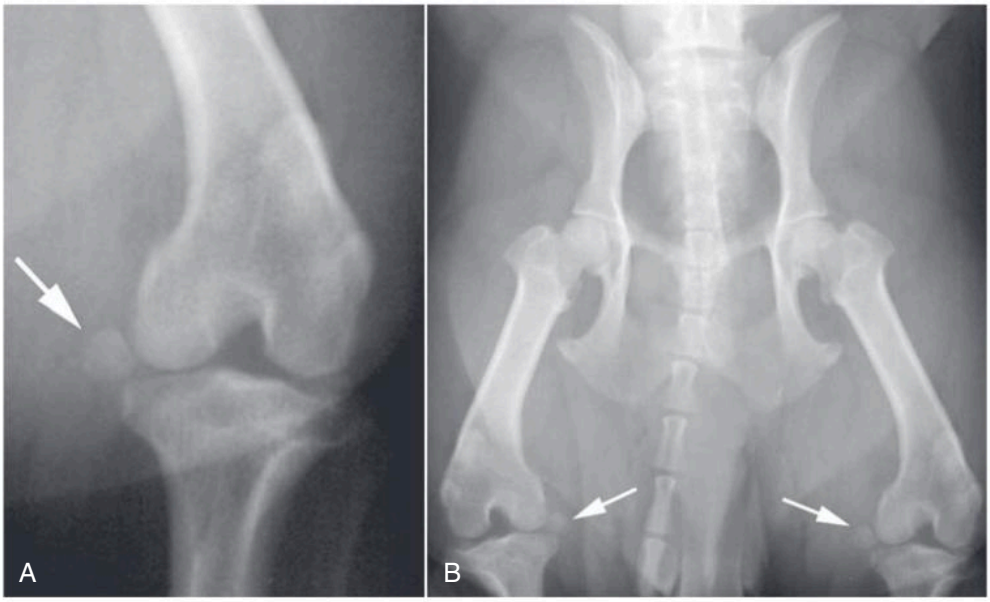


Fig. 20.21 **A,** Distal displacement of the medial fabella (*white arrow*) of the left stifle of a 2-year-old male West Highland White terrier. This may be associated with rupture of the medial head of the gastrocnemius muscle, but this abnormality was bilaterally symmetric (**B,** *white arrows*). This is a common normal variant in this breed. (Courtesy University Veterinary Centre, Sydney, Australia.)



Fig. 20.22 **A and B,** A 7-year-old German shepherd dog had chronic weight-bearing lameness of the right pelvic limb. Perichondral osteophytes and enthesophytes are visible on the patella, distal femur, and proximal tibia. Synovial effusion is also present. **C–E,** Degenerative joint disease in the elbow of a 2-year-old German shepherd. Osteophytes on the cranial aspect of the head of the radius **(C)** and on the medial edge of the medial coronoid process of the ulna **(D)** and enthesophyte formation on the anconeal process **(E)** are degenerative changes often seen secondary to elbow incongruity.

Box • **20.3**

Radiographic Signs of Degenerative Joint Disease

Synovial Effusion
Initial widening, then thinning, of the radiolucent joint space
Perichondral enthesophyte formation of non–weight-bearing surfaces
Increased subchondral bone opacity
Remodeling of subchondral bone
Mineralization of intra-articular and periarticular soft tissues
Subchondral cyst formation

poor correlation between radiographic signs of degenerative joint disease in older cats and degree of clinical lameness.

Cats with uncomplicated degenerative joint disease may be free of clinical signs of joint disease, and radiographic signs of this condition are often discovered accidentally. Most syndromes listed in Box 20.4 are characterized by recognizable clinical signs that are accompanied by appendicular skeletal pain and lameness.

Radiographic signs of degenerative joint disease in cats are similar to those reported in dogs. Periarticular new bone formation as osteophytes or enthesophytes develops around affected joints (see Fig. 20.23). Although articular cartilage is invisible on survey radiographs, remodeling and increased opacity of subchondral bone usually imply changes in joint cartilage. Signs of synovial effusion and/or thickened periarticular soft tissue are seen less commonly in cats than in



Fig. 20.23 Mediolateral **(A)** and craniocaudal **(B)** projections of a feline elbow with marked degenerative joint disease. Exuberant periarticular new bone formation is present around the elbow. (Courtesy Paddington Cat Hospital, Sydney, Australia.)

Box • **20.4**

Causes of Degenerative Joint Disease in Cats

Primary
Scottish fold osteochondrodysplasia
Mucopolysaccharidosis (MPS)
Age-related cartilage degeneration

Secondary
Congenital
Hip dysplasia
Trauma
Traumatic joint instability
Physeal fractures
Infectious/inflammatory
Viral (calicivirus, coronavirus)
Bacterial (bacterial L-form, mycoplasma, bite wounds)
Fungal (cryptococcosis, histoplasmosis)
Nutritional
Hypervitaminosis A
Immune mediated
Rheumatoid arthritis
Progressive proliferative polyarthropathy
Systemic lupus erythematosus (SLE)
Idiopathic polyarthritides

Reproduced with permission from Allan GS. Radiographic features of feline joint diseases. Vet Clin North Am Small Anim Pract. 2000;30:281.

dogs, whereas the incidence of intra-articular soft tissue calcification is more common in cats. Other changes that accompany feline degenerative joint disease include intra-articular and periarticular soft tissue calcification, often ascribed to synovial osteochondromatosis, and prolific periarticular osteophytosis.

Meniscal Ossicles in Cats

Meniscal mineralization is also a common finding in domestic cats (Fig. 20.24). In examining stifle radiographs of 100 cats, 46 had meniscal mineralization detected in one or both stifles.[24] Pain scores were not significantly different between stifles with meniscal mineralization and those without. Thirty-four of 57 cadaver stifles had meniscal mineralization, which was always located in the cranial horn of the medial meniscus. Percentage mineralization of the menisci was significantly correlated with cartilage damage in the medial femoral and tibial condyles. Therefore, feline meniscal mineralization can be associated with medial compartment degenerative joint disease.[24]

A meniscal ossicle is a common finding in large nondomestic cats, such as lions, where it is located in the cranial horn of the medial meniscus.[25]

TRAUMA TO THE JOINT

Trauma Involving the Osseous Components of Joints

A fracture that communicates with a joint space is termed an *articular fracture* (Fig. 20.25). Articular fractures must be diagnosed accurately to ensure appropriate reduction and stabilization. Radiographic examinations should include at a minimum two projections made at right angles to each other. Oblique views should be added, along with projections during flexion, extension, and stress, when needed. These additional projections are of most value when chip or avulsion fractures are suspected or when the osseous structures of interest are superimposed on other osseous structures.

Articular fractures occur most frequently in immature animals because of the incidence of physeal and epiphyseal injury in these patients. Because the proximal femoral physis is intracapsular, all femoral capital physeal fractures are intra-

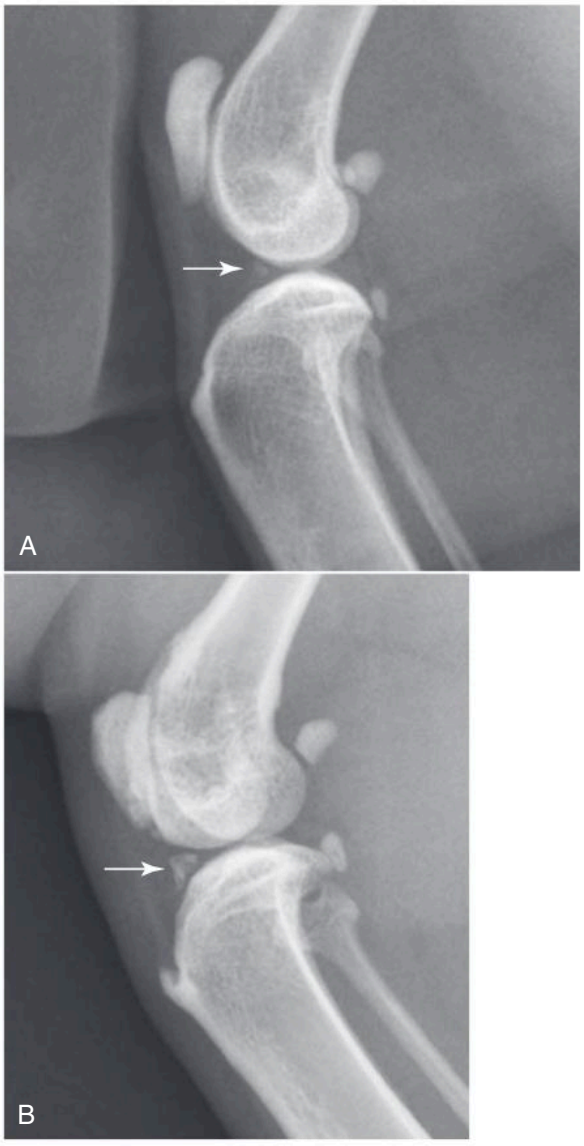


Fig. 20.24 **A,** A small meniscal ossicle in a cat (*white arrow*). **B,** A moderately sized meniscal ossicle in another cat (*white arrow*). There is also an enthesophyte at the patellar ligament attachment site on the proximal tibia.

articular fractures (Fig. 20.26). In other joints, physeal fractures that involve the joint are usually classified as Salter-Harris type III or IV fractures.[26]

Sprains Affecting Joints

Supporting soft tissue structures of joints are not distinctly visible radiographically because they silhouette each other and with adjacent soft tissues. Radiographic features of severe sprains include:

- Periarticular soft tissue swelling
- Avulsion fractures at points of attachment of ligaments, tendons, and capsules to bone (entheses)
- Joint instability or subluxation
- Spatial derangement of the osseous components of a joint

Sprains must be diagnosed promptly. In many instances, appropriate medical or surgical therapy ensures return to normal joint function after moderate to severe sprain injuries. Palpation and manipulation of a sprained joint is usually the best diagnostic tool. Radiographic examination adds information that is useful for treatment planning and also for identifying avulsed osseous fragments. A useful technique for radiographic assessment of a sprained joint is stress radiography (Figs. 20.27 and 20.28). Stress radiography involves the application of force to the joint to demonstrate displacement. Patients need to be heavily sedated or anesthetized for this procedure. The forces applied are the same stresses to which the joint would be subjected in normal daily activity and are defined as compressive, rotational, traction, shear, and wedge forces (Fig. 20.29).[27]

An example of compressive stress is a radiograph of a joint during weight bearing. Ligamentous trauma, as in carpal hyperextension injuries, can be detected by this technique. The cranial drawer sign seen in cranial cruciate ligament trauma is a practical example of a shearing stress. It is stress that is used routinely in clinical examination of the stifle. The same manipulative procedure may be applied to the stifle during radiography to capture the amount of cranial drawer in the image. Traction stress involves pulling the osseous components of the joint away from one another. One application of traction stress involves capital physeal fractures of the femoral head. When traction is applied to the femur in the extended ventrodorsal position, capital physeal fractures are more easily identified.

A technique using traction stress has been described for identifying medial scapulohumeral joint instability in small dogs. With the patient in lateral recumbency, nontraction and traction radiographs are made of the shoulder. A significant increase in joint space has been identified as a sign of medial shoulder instability. Traction and wedge stresses are useful for examining joints for small avulsion fractures and intra-articular joint mice. Unilateral trauma to collateral ligaments of the elbow and stifle may be disclosed with wedge stresses. Because stress radiography requires that personnel hold the patient during x-ray exposure, care must be taken to ensure that appropriate protective clothing is worn.

Tendinopathies, Desmopathies

Injuries to tendons and ligaments are important causes of lameness in dogs and cats and must be distinguished from skeletal and articular causes of lameness. Many tendons and ligaments are intimately associated with joints, lying within them (cruciate ligaments), passing through them (bicipital tendon, long digital extensor tendon), or inserting adjacent to a joint (popliteus tendon). This section includes some of the common desmopathies that occur around joints.

Shoulder

Bicipital Tendon (Biceps Brachii). Gross changes in dogs with bicipital tenosynovitis include synovial effusion, synovial hyperplasia of the bursa, chondromalacia of the intertubercular (bicipital) groove with osteophyte formation at its edges, and metastatic calcification of the biceps tendon. The two latter changes can be seen on survey radiographs of the shoulder (Fig. 20.30) when they occur in affected dogs. Occasionally, discrete mineralized opacities (joint mice) may be seen superimposed on the tendon within the bicipital groove.[28] Ultrasonography, CT and magnetic resonance imaging (MRI) are useful techniques for evaluating the biceps and supraspinatus tendons. Biceps and supraspinatus tendons are closely associated, and enlargement of the supraspinatus tendon can impinge on the biceps tendon within the bicipital groove.



Fig. 20.25 **A,** A 3-year-old German Shorthaired pointer with acute lameness of the left pelvic limb. There is a fracture through the lateral trochlear ridge of the talus (*open black arrow*). **B,** Craniocaudal (*left*) and lateral (*right*) projections of a canine elbow with an intracondylar fracture extending through the medial humeral cortex. There is slight medial displacement of the fragment. Condylar involvement of the fracture is not apparent from the lateral projection. **C,** There are multiple patella fractures (*white arrows*). Note the enthesophyte at the origin of gastrocnemius muscle (*black arrows*). (**A,** Courtesy University Veterinary Centre, Sydney, Australia. **B,** Courtesy North Shore Veterinary Specialist Centre, Sydney, Australia.)

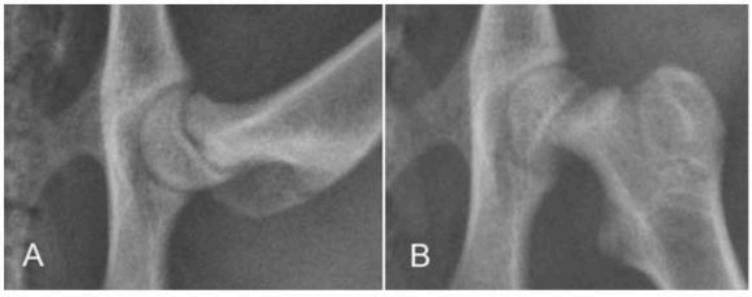


Fig. 20.26 The femoral capital physis appears wider than normal in a flexed (frog-leg) view of the pelvis **(A),** which is confirmed in **B** by rotating the femur into an extended position. This maneuver is useful to con firm this intra-articular fracture.

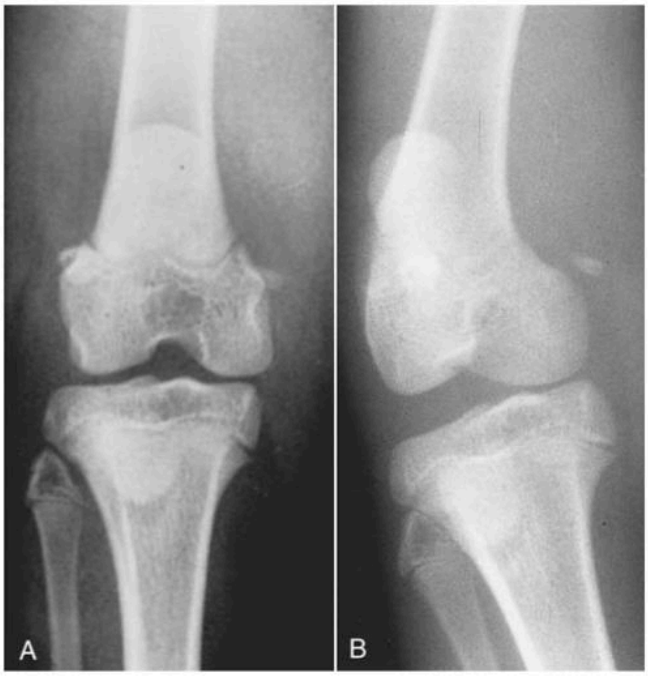


Fig. 20.27 An 8-month-old Burmese cat was lame in the left pelvic limb. A craniocaudal radiograph **(A)** was normal. In a stressed craniocaudal radiograph **(B)**, widening of the lateral aspect of the joint space was discovered. The diagnosis is ruptured lateral collateral ligament.

Ruptured Bicipital Tendon. Bicipital tendinopathy and bursitis may also be evaluated sonographically. In the longitudinal plane, the normal biceps tendon is characterized by an echogenic linear fiber pattern and can be followed from its origin at the supraglenoid tubercle of the scapula to its musculotendinous junction (Fig. 20.31). Ultrasonography may reveal changes in the bicipital tendon or bursa in instances of bursitis and tendonitis (Fig. 20.32). The location of a rupture in the tendon may be identified sonographically.[29] Ultrasonography can also be used to identify the supraspinatus and infraspinatus tendons, the teres minor tendon, and the caudal aspect of the humeral head. Ultrasonography assists in identification of synovial effusion and proliferation within the bicipital bursa, supraspinatus and bicipital tendonitis, dystrophic calcification, and osteochondrosis of the humeral head. It can also be used to assist therapeutic joint or peritendinous injection. MRI has the advantage of superb soft tissue contrast resolution, which is valuable for assessing edema, hemorrhage, and inflammation within tendons and ligaments around joints. Edema-like changes may be visible in the bone at the insertion site of injured tendons and ligaments.

Elbow

Flexor Enthesopathy in Dogs. A mineralized body in the soft tissues distal to, or bone proliferation on, the medial humeral epicondyle are the most common radiographic findings in dogs with flexor enthesopathy (see eFig. 20.1). The margins of the medial humeral epicondyle may be irregular as well. Flexor enthesopathy results from chronic strain of the origin of the



Fig. 20.28 **A,** A neutral lateral radiograph reveals slight incongruity of the distal intertarsal articulation (*arrow*). **B,** Stress radiography revealed the extent and severity of dorsopalmar subluxation in the affected joint, while confirming stability in adjacent articulations.

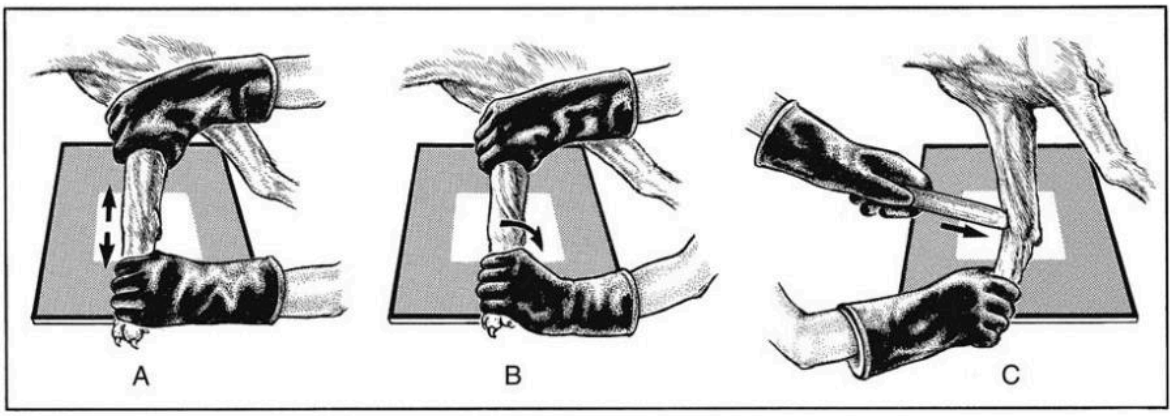


Fig. 20.29 Stress radiography of joints involves the application of traction **(A)**, rotational **(B)**, and wedge **(C)** forces to demonstrate subluxation that may not be evident on standard radiographic projections. (Modified from Farrow CS. Stress radiography: applications in small animal practice. *J Am Vet Med Assoc*. 1982;181:777.)

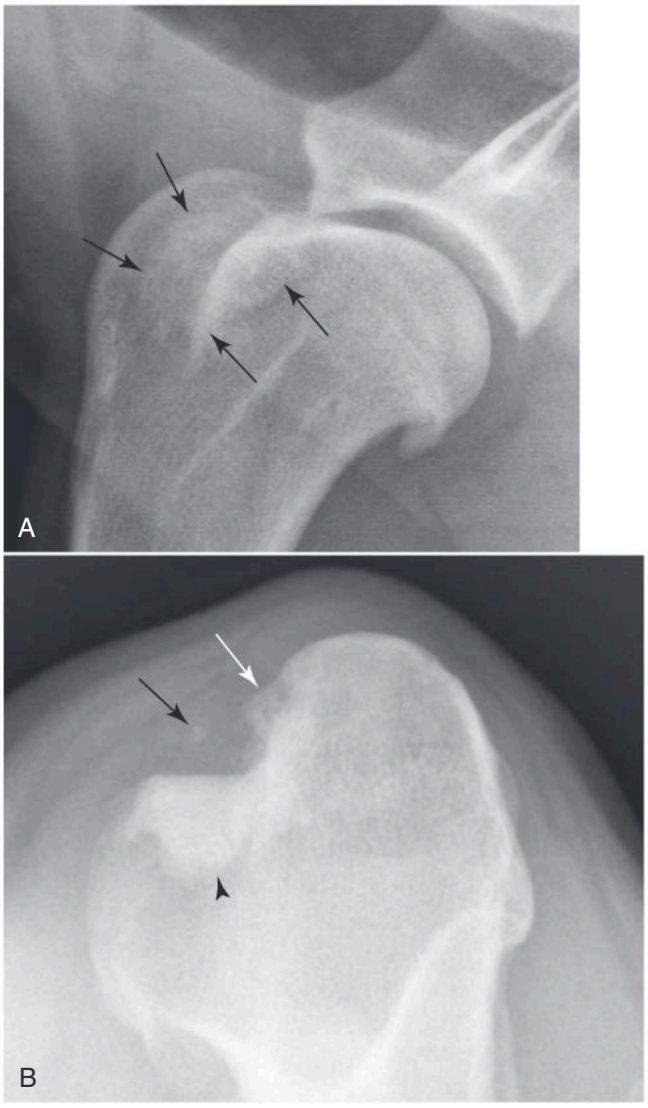


Fig. 20.30 Bicipital tendonitis. **A,** New bone proliferation superimposed on the bicipital groove (*black arrows*) and along the margin of the greater tubercle of the humerus in a dog with bicipital tendonitis. There is also a large osteophyte on the caudal aspect of the humeral head. **B,** A craniproximal/craniodistal (skyline) view of the proximal humerus. There are osteophytes in the bicipital groove (*white arrow*), subchondral sclerosis of the groove (*black arrowhead*), and a focus of mineralization in the biceps tendon (*black arrow*).

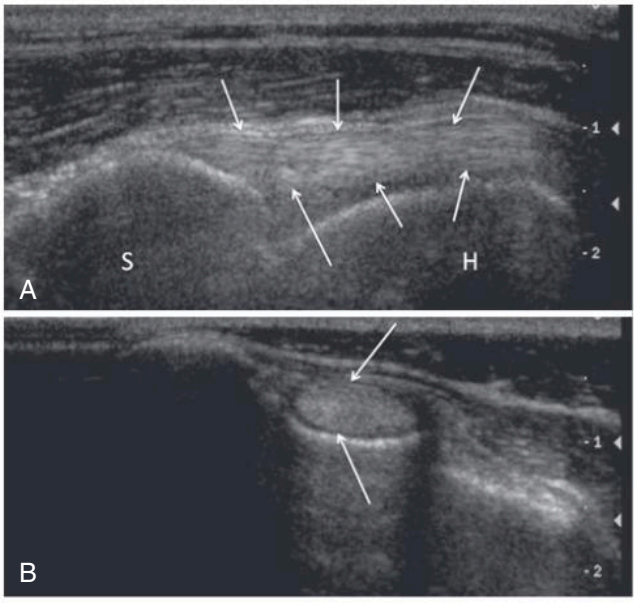


Fig. 20.31 Composite image showing longitudinal **(A)** and cross-sectional **(B)** images of the normal biceps tendon (*arrows*). In a longitudinal plane **(A)**, the tendon is characterized by a linear hyperechoic fiber pattern. The tendon arises from the supraglenoid tubercle of the scapula (*S*) and extends distally within the bicipital groove along the medial border of the humerus (*H*). In cross-section **(B)**, the tendon is a uniformly hyperechoic oval structure surrounded by a thin hypoechoic rim representing slight fluid in the tendon sheath. (Reproduced with permission from Davies S, Allan G, Nicoll R. Joints—general. In: Kirberger R, McEvoy F, eds. *BSAVA Manual of Canine and Feline Musculoskeletal Imaging*. 2nd ed. Gloucester, England: BSAVA; 2016.)

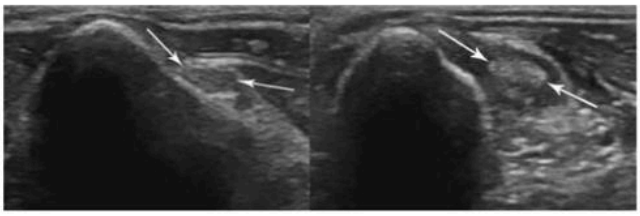


Fig. 20.32 Composite image showing a comparison of normal (*left*) and diseased (*right*) biceps tendons imaged in cross-section in the region of the bicipital groove. *Arrows* indicate the biceps tendon. The abnormal tendon is enlarged, has a slightly irregular outline, and is surrounded by hypoechoic fluid. (Courtesy North Shore Veterinary Specialist Centre, Sydney, Australia.)

carpal and digital flexors, and is often seen in conjunction with elbow degenerative joint disease, particularly due to elbow dysplasia, but can also occur as a primary lesion in dogs with elbow pain.[30]

Medial Epicondylitis in Cats. New bone formation at the medial aspect of the elbow joint at the origin of the humeral head of the flexor carpi ulnaris has been reported in 10% of cats.[31] Bone proliferations may lead to perineural fibrosis and ulnar neuropathy in affected cats. Free joint bodies may be associated with this condition as well (Fig. 20.33).[32]

Carpus

Several important tendons pass close to the carpus or insert onto bones adjacent to it. Osteophytes arising and extending from the medial sulcus of the distal radius follow the path of the tendon of the abductor pollicis longus and are a response to synovitis where the tendon passes over the sulcus. Osteophytosis has been associated with stenosing tenosynovitis of the abductor pollicis longus muscle.[33] These lesions should not be mistaken for aggressive lesions of the distal radius (Fig. 20.34, eFig. 20.2).

The extensor carpi radialis tendon inserts on the dorsal surface of the proximal end of metacarpals 2 and 3. Enthesopathy at the points of insertion can result in new bone formation that can be identified on lateral radiographs of the carpometacarpal region.

The flexor carpi ulnaris tendon inserts on the proximal surface of the accessory carpal bone, and the check ligaments of the accessory carpal bone originate from the distal surface. Again, an enthesopathy can be identified on the proximal and distal surfaces of the accessory carpal bone when an enthesopathy of these tendons and ligaments is present. The tendons



eFig. 20.2 Lateral **(A)** and dorsopalmar **(B)** radiographs of a dog with stenosing tenosynovitis of the abductor pollicis longus muscle. There is soft issue swelling and mineralization along the medial aspect of the carpal joint along the path of the abductor pollicis longus tendon. Osteophytosis is also present along the dorsal margin of the distal radius, the accessory carpal bone and the lateral aspect of the carpus.

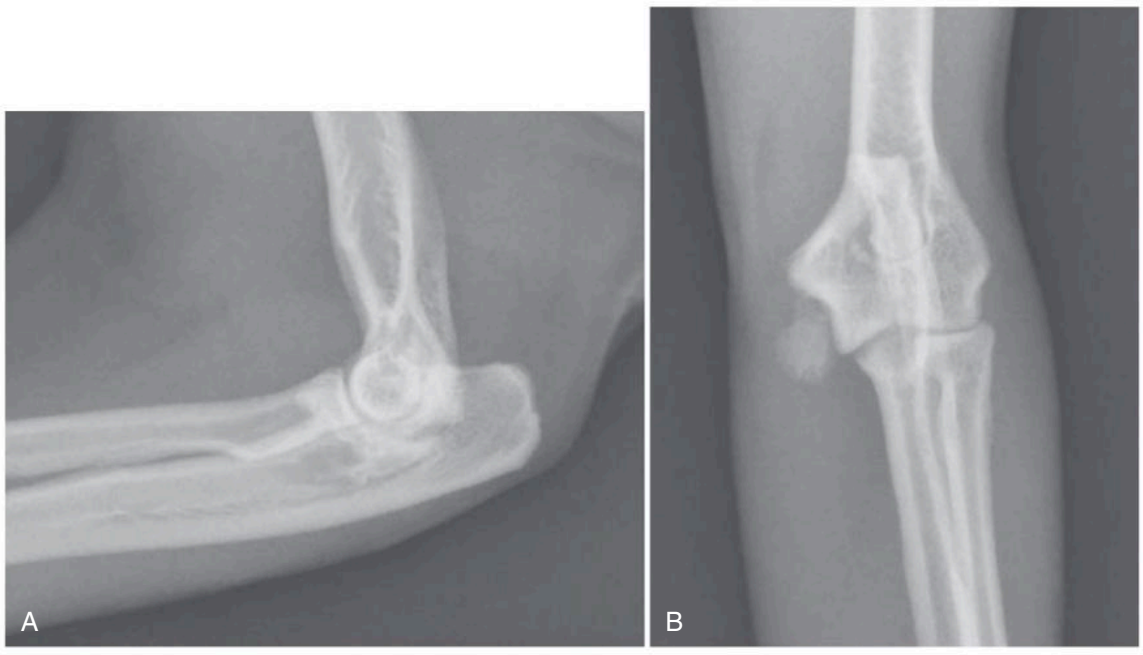


Fig. 20.33 Lateral **(A)** and craniocaudal **(B)** radiographs of a cat with medial epicondylitis. New bone formation is present at the medial aspect of the elbow joint.



Fig. 20.34 Stenosing tenosynovitis of the abductor pollicis longus muscle. There is focal soft tissue swelling at the medial aspect of the carpal joint. Irregular bone proliferation is visible along the medial aspect of the distal radius in the location of the abductor pollicis longus tendon. This should not be confused with an aggressive lesion.

and ligaments around the carpus can be assessed sonographically, as well as by MRI.

Stifle

MRI can be used to assess the structure and integrity of ligaments and tendons of the stifle. Changes in subchondral bone density and signal can be seen with CT and MRI, respectively, at the origin and insertion of the cranial cruciate ligament in patients with cranial cruciate strain. Indications for stifle sonography are limited but could include sonographic guided aspiration of synovial fluid or synovial masses.[34]

Tarsus

The common calcaneal tendon, or Achilles tendon, is composed mainly of the tendons of flexor digitorum superficialis and gastrocnemius muscles, with contribution of tendons from biceps femoris, semitendinosus, and gracilis muscles. It inserts onto the calcaneal tuberosity.[35] Chronic desmopathies of the Achilles tendon cause soft tissue swelling, occasionally containing dystrophic calcification (Fig. 20.35). Ultrasonography enables identification of partial and total ruptures of the deep and superficial structures comprising the Achilles tendon. A dynamic study can be used to assess the relationship between the Achilles tendon and its insertion into the calcaneal tuberosity (Fig. 20.36). Tendinous trauma can be distinguished from muscle trauma.

Hemarthrosis

Intra-articular hemorrhage may occur in dogs with coagulopathies or after joint trauma.[36] Coagulopathies in the dog that may cause hemarthrosis include hemophilia A and B; von Willebrand disease; deficiencies in factors VII, X, and XI; and liver disease. Isolated, infrequent episodes of intra-articular bleeding do not significantly alter joint cartilage integrity. Repeated hemorrhage may lead to severe damage to joint cartilage and subchondral bone. Affected animals have severe non–weight-bearing lameness of affected limbs, and affected joints are swollen and painful. Radiographically, in acute hemarthrosis, there is soft tissue swelling of the joint, which may be extensive.[36] As a consequence of chronic intra-articular hemorrhage, joint cartilage may be eroded and thin and subchondral bone can appear irregular. Repeated injection of whole blood into stifle joints results in remodeling of bones adjacent to the joint. In advanced hemarthrosis, signs similar to degenerative joint disease may be present.

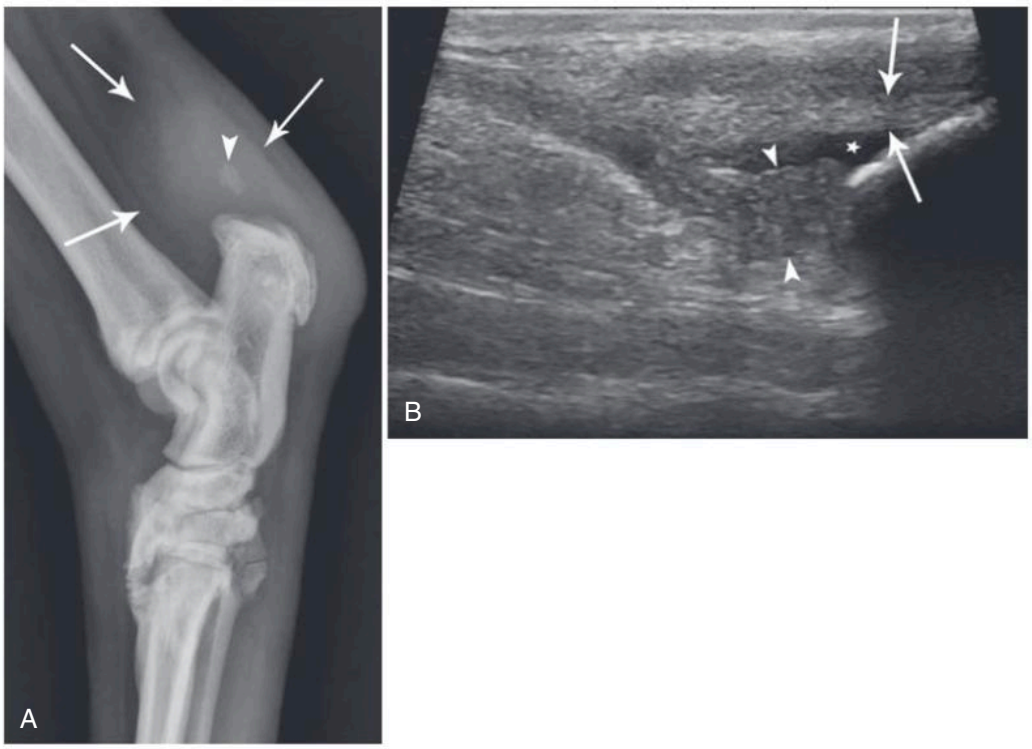


Fig. 20.35 Soft tissue swelling (*arrows*) and dystrophic calcification (*arrowhead*) in the region of the common calcaneal tendon in a dog **(A)**. In the same patient **(B)**, there is sonographic evidence of peritendinous fluid (*star*) and likely fibrinous material (*arrowheads*) in the caudal aspect of the tibiotarsal joint. The gastrocnemius tendon (*arrows*) inserts undisrupted onto the calcaneal tuberosity. (Courtesy North Shore Veterinary Specialist Centre, Sydney, Australia.)

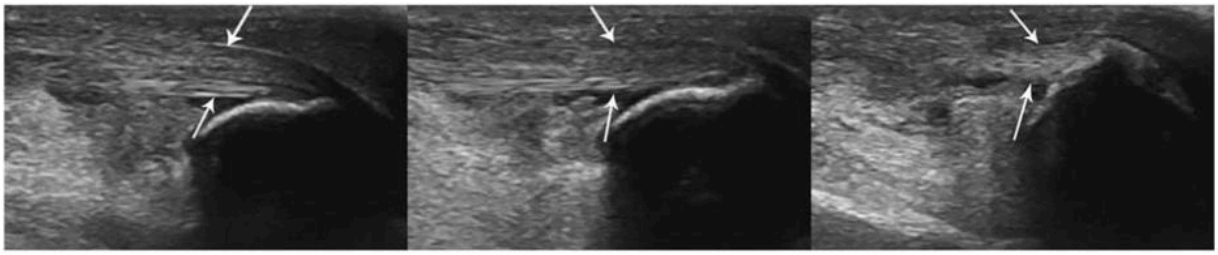


Fig. 20.36 Sonographic study in a dog presented with tarsal swelling after being hit by a car. Sequential images from left to right show progressive extension of the tibiotarsal joint. Attachment of the gastrocnemius tendon (*arrows*) to the calcaneal tuberosity is intact. (Courtesy North Shore Veterinary Specialist Centre, Sydney, Australia.)

THE SYNOVIUM

Villonodular Synovitis

Villonodular synovitis is an intracapsular joint disorder characterized by nodular synovial hyperplasia, which is thought to represent a response to trauma. Experimentally, villonodular synovitis has been reproduced in dogs by repeated intra-articular injections of whole blood. Villonodular synovitis is an established, although uncommon, disorder of people and has also been reported in horses and dogs.[37,38] In dogs, the condition has been identified in the carpus, coxofemoral joint, and stifle. Radiographic signs of villonodular synovitis may be nonspecific but include articular soft tissue swelling alone or with erosion of cortical bone at the chondrosynovial junction (Fig. 20.37). These cortical erosions may appear cyst like, with slightly opaque borders. In severe proximal femoral villonodular synovitis in people, the femoral neck has been described as looking like an apple core. The articular cartilage and subchondral bone are not involved. Differential diagnoses for perichondral erosive lesions, characteristic of villonodular synovitis, include synovial osteochondromatosis, rheumatoid arthritis, and joint neoplasia.

Synovial Osteochondromas

Synovial osteochondromas are islands of cartilage produced by the synovial membrane. Foci of cartilage become pedunculated and may become separated to form loose bodies within the joint. Reports of synovial osteochondromatosis in cats suggest that Burmese cats are overrepresented. The radiographic appearance of mineralized synovial osteochondromas varies. These lesions are usually well-defined, rounded, often multiple intra-articular nodules of calcific opacity (Fig. 20.38). Synovial osteochondromas may also arise from extra-articular foci of synovial tissue (Fig. 20.39).

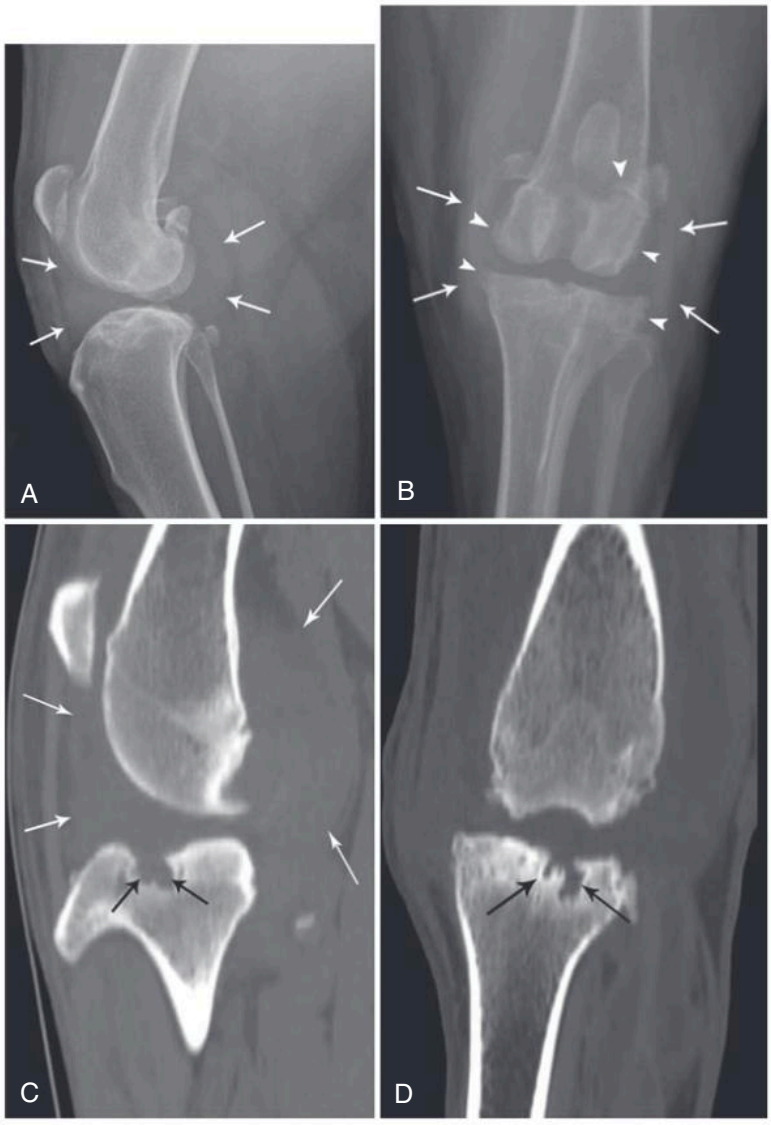


Fig. 20.37 Lateral **(A)** and craniocaudal **(B)** radiographs of the stifle of a dog with a histopathologic diagnosis of villonodular synovitis. There is marked intracapsular soft tissue swelling (*white arrows*) and osteophytes are present on periarticular surfaces (*arrowheads*). Loss of bone (*black arrows*) is detected with computed tomography (CT) in the cranial intercondylar region **(C and D)**. (Courtesy Animal Orthopaedic Specialists, Sydney, Australia.)



Fig. 20.38 A 5-year-old Burmese cat had bilateral stifle enlargement. Extensive lobular mineralization within the stifle joint was evident radiographically. Histologic diagnosis was synovial osteochondroma. (Courtesy Perth Veterinary Specialists, Perth, Australia.)

Synovial osteochondromas have been reported in the dog and the cat.[39,40] Their cause is unknown, but the theory of synovial metaplasia is generally accepted. These lesions have been reported to cause severe lameness in some dogs. Surgical removal of synovial osteochondromas relieves clinical signs of joint pain and lameness.[39] Other conditions in cats in which intra-articular and periarticular mineralization may be confused with synovial osteochondromatosis are mild forms of mucopolysaccharidosis type VI (MPS VI) and hypervitaminosis A.[41]

IMMUNE-MEDIATED POLYARTHROPATHIES

Rheumatoid Arthritis

Rheumatoid arthritis is a severe, progressive, erosive polyarthritis that has been reported in dogs,[42] and a similar condition has been reported in cats.[43] Radiographic changes usually occur in joints of the distal extremities. The stifle and elbow are

affected occasionally. Synovial effusion occurs initially. Radiographs made early are characterized by nonspecific periarticular soft tissue swelling. The joint capsule may be distended. The first radiographic signs of bone involvement may be detected several weeks after the onset of clinical signs. Initial changes are mild, but the radiographic abnormalities become more obvious as the disease advances.

The progression of radiographic changes includes:

1. Subchondral bone destruction and cyst formation (Fig. 20.40)
2. Joint space narrowing
3. Progressive decreased opacity of epiphyses adjacent to affected joints;
4. Destruction of subchondral and perichondral bone
5. Mushrooming of the ends of the metacarpi and metatarsi, which occurs in advanced arthritis and represents collapse of subchondral bone
6. Varying degrees of joint subluxation and luxation (Fig. 20.41, eFig. 20.3)

Other changes more characteristic of degenerative joint disease (osteophytes/enthesophytes, subchondral sclerosis, and calcified periarticular tissues) may also be present.[42]

Systemic Lupus Erythematosus

Systemic lupus erythematosus (SLE) is a multisystemic disease that affects dogs of all breeds, as well as cats. It has a variety of clinical manifestations, including polyarthritis, anemia, nephropathy, skin disease, pericarditis, myocarditis, and lymphadenopathy.[44] Diagnosis of SLE is complicated and is made on the basis of the concurrence of clinical manifestations and serologic evidence. In one study, 121 dogs with a diagnosis of



Fig. 20.39 A 6-year-old male (neutered) Burmese cat had progressive lameness of the right forelimb for 6 weeks. Radiographically, a large, well-defined, ossified mass was visible on the craniomedial aspect of the right elbow. Histologic diagnosis was extra-articular synovial osteochondroma.



Fig. 20.41 Dorsopalmar radiographs of the left **(A)** and right **(B)** manus of a dog with immune-mediated arthropathy. There is subluxation of the left antebrachiocarpal joint and the right carpometacarpal joint. There is also subluxation of distal interphalangeal joint in each manus. Numerous subchondral lytic erosive lesions are present (*white arrows*).

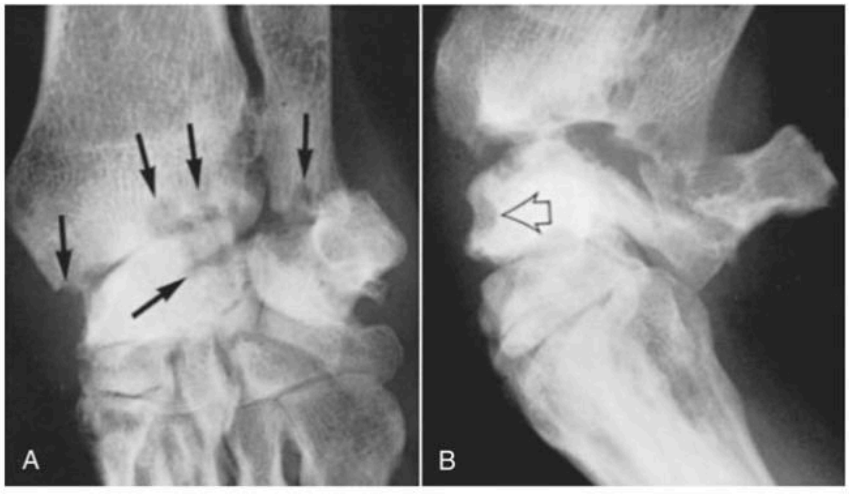


Fig. 20.40 An 8-year-old neutered male corgi crossbreed with rheumatoid arthritis. **A,** Dorsolateral-palmaromedial projection. There is extensive subchondral erosion of the styloid process of the ulna and the articular surfaces of the distal radius and radial carpal bone (*black arrows*). **B,** Lateral projection during flexion. In addition to the changes seen in **A,** note the erosion of the non–weight-bearing dorsal surface of the intermedioradial carpal bone (*open black arrow*). (Courtesy University Veterinary Centre, Sydney, Australia.)



eFig. 20.3 Lateral **(A)** and dorsopalmar **(B)** radiographs of a dog with immune-mediated erosive polyarthropathy. The antebrachiocarpal and proximal interphalangeal joints are subluxated. Multiple areas of subchondral bone lysis are seen in the carpal bones. Soft tissue swelling surrounds the carpal joint.

SLE were reviewed, and joint disease was reported to be the most frequent clinical sign (69%), followed by hematologic (53%), renal (50%), cutaneous (33%), and intrathoracic (17%) manifestations. The arthropathy that occurs in canine SLE is usually effusive but nonerosive. Polyarthritis is typical, but monoarticular arthritis has been reported. Affected joints may be swollen, painful, and warm. The joints most commonly affected are the carpus, tarsus, metatarsus, stifle, and elbow. Radiographic signs are usually absent or are minimal. In chronic SLE, the joint space of affected joints may be narrowed, and the joint capsule is distended. A mild periosteal response has been reported at the junction of joint capsule and bone.

Feline Noninfectious Polyarthritis

Feline noninfectious polyarthritis is a disease of male cats aged 1 to 5 years.[43,45] The polyarthritis can be erosive or nonerosive.[46] There are two types of erosive polyarthritis: (1) the periosteal proliferative form and (2) the erosive form. The erosive form is commonly referred to as *feline rheumatoid arthritis*. A group of nonerosive, effusive polyarthropathies thought to be immune mediated also occur in cats and are associated with a variety of conditions.

Periosteal Proliferative Form

Affected cats have fever, malaise, and stiffness, followed by periarticular soft tissue swelling and regional lymphadenopathy. Radiographic changes may be identified in affected joints after a few weeks. Commonly affected joints are the carpi and tarsi. The stifle, elbow, shoulder, and hip joints are affected to a lesser extent. During the first month, periarticular soft tissue swelling is the predominant sign. Swelling may be either intracapsular or extracapsular. One to 3 months after the onset of clinical signs, periosteal new bone production may be identified at site of joint capsule attachment. During this phase, bone adjacent to affected joints may have decreased opacity and a coarse trabecular pattern. Perichondral new bone formation is pronounced 2 to 3 months after onset of the disease. Extensive enthesopathy may bridge smaller joint spaces. More severe radiographic manifestations include perichondral bone erosion and formation of subchondral cysts. Narrowing of affected joint spaces may occur late.[43] Radiographic signs of the periosteal proliferative form of feline chronic progressive polyarthritis include periarticular soft tissue swelling, periosteal new bone formation, perichondral enthesophyte production, perichondral and subchondral erosion, subchondral cysts, osteopenia of bone adjacent to affected joints, and narrowed joint spaces (Fig. 20.42).

Feline Erosive Polyarthritis

A second, more erosive, form of feline noninfectious polyarthritis has been described; it resembles human rheumatoid arthritis and occurs in older cats.[43] This form is characterized radiographically by severe subchondral bone erosion, perichondral bone erosion, and subchondral cyst formation. Perichondral enthesophyte formation, bone destruction at points of ligamentous insertion to bone, and subluxation of small joints of the extremities also occur. A diagnosis of feline rheumatoid arthritis requires a positive rheumatoid factor test, characteristic histologic changes seen on a synovial biopsy, or both. Both test results are negative in cats with feline proliferative polyarthritis.[46]

Feline Nonerosive Polyarthritis

Two categories of nonerosive polyarthritis have been described in cats.[46] They are feline SLE and idiopathic polyarthritis. Idiopathic polyarthritis has four subtypes: (1) uncomplicated polyarthritis; (2) reactive polyarthritis, associated with a disease process elsewhere in the body; (3) enteropathic polyarthritis, associated with gastrointestinal disease; and (4) malignant-related idiopathic polyarthritis, associated with myeloproliferative disease. Radiography is used to distinguish between erosive and nonerosive forms of feline polyarthritis. The latter group is identified as having periarticular soft tissue swelling, joint capsule distention, and synovial fluid accumulation.



Fig. 20.42 The carpus of a young cat with feline chronic progressive polyarthritis. (Courtesy University Veterinary Centre, Sydney, Australia. Reproduced with permission from Allan GS. Radiographic features of feline joint diseases. *Vet Clin North Am Small Anim Pract*. 2000;30:281.)

Hypertrophic Osteopathy

Hypertrophic osteopathy is a generalized osteoproductive disorder of the periosteum that affects the long and short tubular bones of the extremities. It is usually caused by a thoracic mass or cardiopulmonary disease. Abdominal masses, particularly those of urinary origin, have also been known to cause hypertrophic osteodystrophy. Nonneoplastic causes of hypertrophic osteopathy include inflammatory lung disease (e.g., blastomycosis), intrathoracic foreign bodies, *Dirofilaria immitis* infestation, and spirocercosis. The pathogenesis of hypertrophic osteopathy is understood incompletely. New bone formation typically commences on the distal end of both short and long tubular bones and progresses proximally. Periosteal new bone formation results in cortical thickening. The periosteal surface appears nodular or spiculated when visualized radiographically (Figs. 20.43 and 20.44).

SEPTIC ARTHRITIS

Septic arthritis is diagnosed infrequently in small animals, with the incidence being lower than that of immune-mediated joint disease. Septic arthritis is difficult to diagnose radiographically. Initial radiographic changes are usually limited to joint effusion

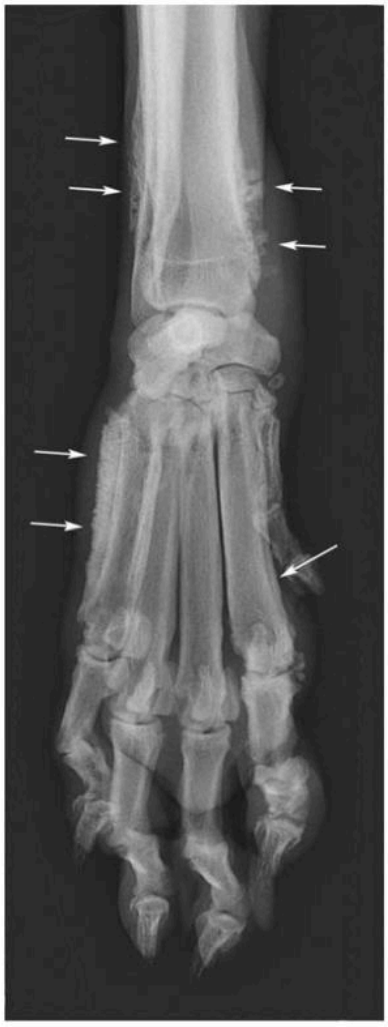


Fig. 20.43 Radiograph of the manus of a dog with hypertrophic osteopathy. There is irregular periosteal reaction (*arrows*) that is most pronounced on the lateral aspect of the fifth metacarpal bone and on the medial aspect of the distal radius. There is less pronounced periosteal reaction on the medial aspect of the manus.



Fig. 20.44 Lateral radiographs of the crus **(A)** and antebrachium **(B)** of a dog with hypertrophic osteopathy that is more advanced than in Fig. 20.46. The abnormal periosteum has progressed to involve the more proximal aspect of the long and short tubular bones.

and periarticular swelling. Ideally, the arthritis should be diagnosed and treated successfully before radiographic changes become apparent.[47] Polyarticular septic arthritis may occur as a result of bacteremia associated with an isolated focus of infection (endocarditis, discospondylitis, or omphalophlebitis) or in conjunction with a systemic disease (as in *Mycoplasma* arthritis, canine leishmaniasis, or feline caliciviral lameness).[48] Polyarticular septic arthritis must be differentiated from immune-mediated joint disease. The former is more likely to affect the larger, more proximal joints of the appendicular skeleton, whereas the latter more commonly affects the joints nearer the distal extremities (Box 20.5). Monoarticular septic arthritis most likely results from extension of focal osteomyelitis into an adjacent joint, direct joint trauma, or foreign body penetration (grass seed awns), or it may occur after joint surgery or intra-articular therapy. Hematogenous dissemination of infection to joints is more common in young animals. Septic arthritis as a complication of surgery, particularly addressing cranial cruciate insufficiency, is more common in older animals.

As already noted, the earliest radiographic changes of septic arthritis are synovial effusion and increased synovial mass, which represent an inflammatory response of the synovium. Soft tissue swelling is usually demarcated by the distended joint capsule. Joint capsule distention is identified more easily in carpal, tarsal, and stifle joints. A useful landmark in the stifle is the infrapatellar fat pad. When the fat pad is compressed cranially, it becomes smaller and unclear, indicating synovial effusion is present. In untreated septic arthritis, joint cartilage destruction follows synovial effusion and is followed by subchondral and perichondral bone destruction (Figs. 20.45 and 20.46, eFig. 20.4, Box 20.6).

Septic arthritis is being identified increasingly in joints that have chronic degenerative joint disease. Initial radiographs are characterized by degenerative joint disease, often leading to inappropriate therapy for the infection. Radiographs made 2 to 4 weeks later reveal more aggressive signs of periosteal new bone formation and intra-articular bone destruction. Septic arthritis should be suspected when acute lameness and joint pain are identified in individual animals whose degenerative joint disease has been controlled previously.

Diagnosis of septic arthritis is based on cytologic assessment of synovial fluid and microbiologic examination of synovial fluid and/or synovium and joint capsule. Radiographic assessment alone has low specificity for septic arthritis, but survey radiographs are useful to rule out other conditions, as well as to follow the progress of a joint infection once a diagnosis of septic arthritis is confirmed.



eFig. 20.4 Septic arthritis, lateral view of the stifle joint. There is moderate intra- and periarticular soft tissue swelling with cranial displacement and compression of the infrapatellar fat pad. There are ill-defined areas of decreased opacity within the femoral condyles with coarse trabecular pattern. Osteophytosis is consistent with degenerative joint disease. A tibial plateau leveling osteotomy (TPLO) plate was previously removed from the tibia; round drill holes are still visible.

Box • **20.5**

Polyarthropathies Affecting the Appendicular Skeleton of Dogs and Cats

- Immune-mediated joint diseases
  - Rheumatoid arthritis
  - Systemic lupus erythematosus (SLE)
  - Feline periosteal proliferative polyarthritis
  - Feline nonerosive immune-mediated polyarthropathy
- Septic arthritis
  - Hematogenous septic arthritis
  - Bacterial or fungal septic arthritis
- Inflammatory arthritides
  - Leishmaniasis
  - Rocky Mountain spotted fever
  - Rickettsia rickettsii
  - Lyme disease
  - *Borrelia burgdorferi*
  - Mycoplasma arthritis
  - Chinese Shar-Pei fever syndrome
  - Feline calicivirus, coronavirus
  - Greyhound polyarthritis
- Hemarthrosis
  - Chronic, recurrent, caused by blood dyscrasias
- Hypervitaminosis A
- Primary degenerative joint disease/osteoarthrosis
- Disseminated idiopathic skeletal hyperostosis syndrome
- Familial or genetic skeletal dysplasias
  - Scottish fold osteochondrodysplasia
  - Feline mucopolysaccharidosis (MPS)
  - Canine hip dysplasia
  - Canine elbow dysplasia
  - Osteochondrosis
- Drug-induced and vaccine-mediated polyarthritis
- Feline osteochondromatosis

Septic Arthritis in Cats

In cats, hematogenously disseminated septic arthritis may be caused by a variety of microorganisms, which include *Mycoplasma gateae*, *Mycoplasma felis*, bacterial L-form infection (*Pasteurella* spp.), calicivirus (transient arthritis in kittens), coronavirus (feline infectious peritonitis), and fungi (cryptococcosis, histoplasmosis). Hematogenously disseminated septic arthritis initially causes a nonerosive polyarthropathy characterized by lameness, synovial effusion, and synovial thickening. Affected cats may be systemically ill. Viremic polyarthropathies tend to be transient, whereas bacterial arthritis can have a protracted course. Direct injection of bacteria from bite wounds can result in mixed infections of microorganisms, which may include anaerobic bacteria.

Septic arthritis from penetrating bite wounds causes lameness that is usually restricted to one joint. Synovial effusion and periarticular soft tissue thickening precede secondary changes (such as, subchondral bone erosion) by weeks or months. CT can facilitate early detection of bone erosions and demonstrate synovitis. Joint infections that extend through the synovium and joint capsule into extracapsular tissue stimulate periosteal new bone formation on bone surfaces adjacent to the joint. Septic arthritis can lead to osteomyelitis in bones on either side of an affected joint.

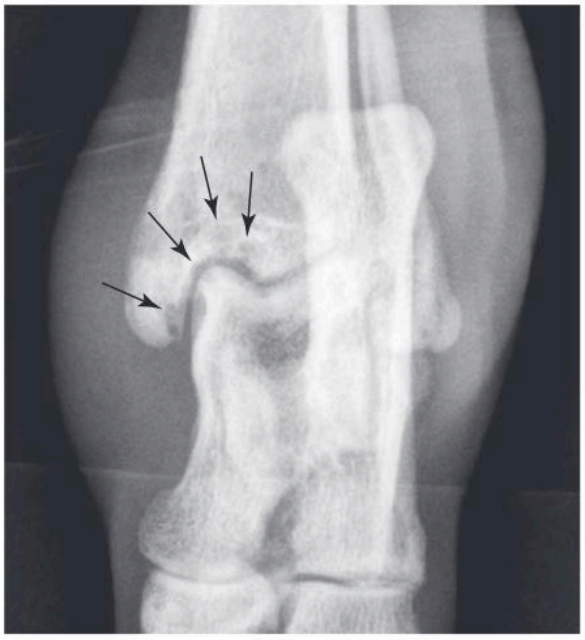


Fig. 20.45 A 1.5-year-old canine mix with lameness and tarsal swelling for 2 weeks. There are focal subchondral lucencies in the distomedial aspect of the tibia (*black arrows*). The swelling is also obvious. Cryptococcus was isolated from synovial fluid.

MISCELLANEOUS POLYARTHROPATHIES

Hypervitaminosis A

Excessive dietary vitamin A produces an ankylosing arthropathy and spondylopathy. Although both dogs and cats can be affected, the disorder is more likely to affect cats. The food mostly associated with hypervitaminosis A is bovine liver, and when fed as an exclusive diet, the clinical syndrome of vitamin A excess can be recognized after a few months. Affected cats become obtunded, apprehensive, reluctant to jump, hypersensitive to neck palpation, and lame. The underlying connective tissue disorder causes vertebral ankylosis and an ankylosing degenerative joint disease of the forelimbs. Recognizable radiographic manifestations of hypervitaminosis A may be seen in as little as 10 weeks after introduction of a diet rich in vitamin A. Changes include ankylosing spondylopathy of the cervical and cranial thoracic vertebral column and periarticular enthesopathy and degenerative joint disease of shoulder and elbow joints (Figs. 20.47 and 20.48). In advanced disease, the additional bone becomes incorporated seamlessly with existing bone so that architecture of the original bones is remodeled completely. Other regions of the vertebral column and other joints of the appendicular skeleton may become involved, but the aforementioned bones and joints appear to be the primary site of bony changes in cats. The ankylosing changes are permanent. They do not resolve once a balanced diet is substituted, but some of the clinical signs of hypervitaminosis A resolve once the dietary imbalance is corrected.

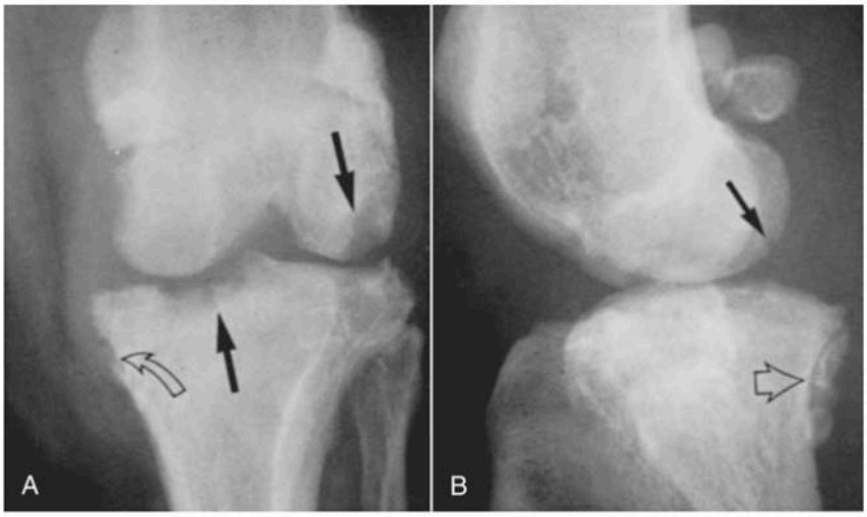


Fig. 20.46 An 8-year-old male Australian cattle dog had stifle swelling and pain that persisted after repair of a ruptured cranial cruciate ligament. **A and B,** Subchondral bone erosion involves the medial condyle of the tibia and the femoral condyles (*solid black arrows*). Periarticular new bone formation is also evident (*open black arrow*). Note the concurrent medial patellar luxation. *Staphylococcus aureus* was isolated from the synovial fluid.

Box • **20.6**

Progression of Radiographic Signs of Infectious Arthritis

- Increased synovial mass indicating synovial effusion and widened radiolucent joint space
- Diminished radiolucent joint space indicating destruction of articular cartilage
- Loss of the smooth surface of the subchondral bone plate; an early sign of infectious penetration of subchondral bone
- Radiolucent signs of destruction of subchondral and perichondral bone usually highlighted by a peripheral border of increased osseous opacity
- In advanced infectious arthritis, weight-bearing surfaces may collapse, causing distortion of joint architecture

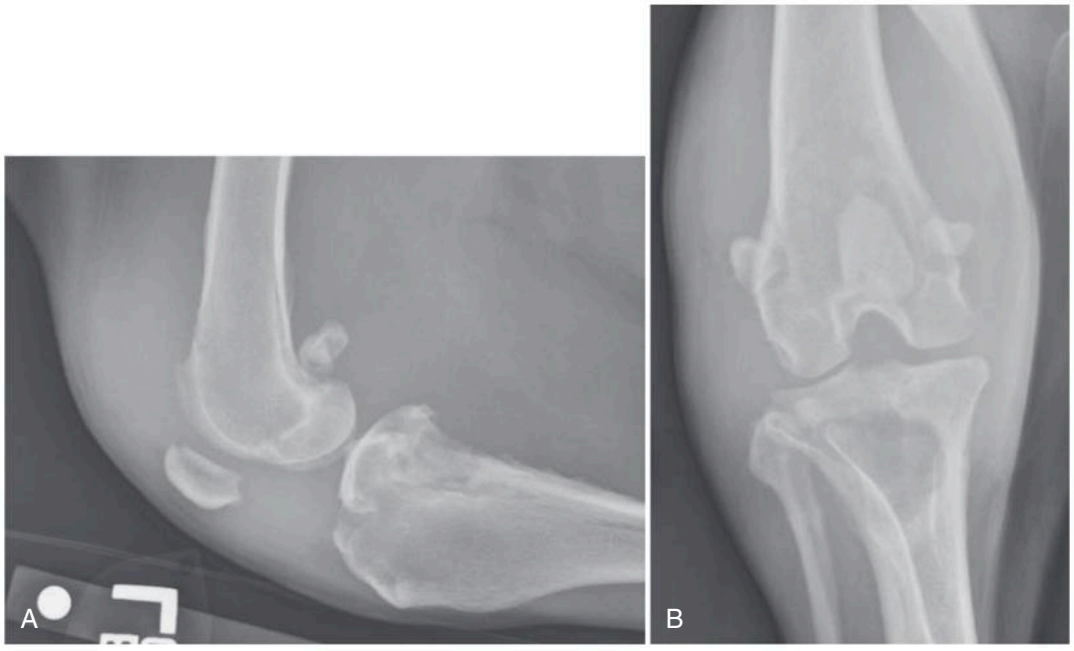


Fig. 20.47 Ankylosing spondylopathy of the cervical and cranial thoracic vertebrae and the sternum of a cat with hypervitaminosis A. (Reproduced with permission from Allan GS. Radiographic features of feline joint diseases. *Vet Clin North Am Small Anim Pract*. 2000;30:281. Courtesy University of Queensland, Brisbane, Australia.)

JOINT NEOPLASIA

Joint tumors are uncommon in dogs and rare in cats.[49,50] The most commonly affected joints are the stifle and elbow in middle-aged, medium-sized to large dogs.[51] The most common tumor types in dogs include histiocytic sarcoma, synovial cell sarcoma, and synovial myxoma. Other types of sarcoma, such as fibrosarcoma or chondrosarcoma, are uncommon.[49] Synovial cell sarcoma arises from primitive mesenchymal precursor cells of the synovial membrane of joints and bursae.[51] Synovial cell sarcomas grow slowly and are first noticeable as a homogeneous soft tissue mass that involves or is near a joint. Portions of the tumor may be calcified, with mineral deposits appearing as hazy and punctate or as linear streaks.

Initial bone involvement usually appears as a spiculated periosteal response followed by ragged erosion of cortical bone adjacent to the tumor. Occasionally, the neoplasm initially appears relatively nonaggressive, mimicking a simple cyst, only to change later into a more extensive and destructive disease (Fig. 20.49, eFig. 20.5). Destruction of cancellous bone may be extensive and most commonly occurs on both sides of the joint. The tumor is locally invasive with a capacity to metastasize.[52] Distant metastasis, particularly to the lungs, occurs in as many as half of reported patients.[51] Histiocytic sarcoma is an aggressive periarticular tumor that can be difficult to differentiate from other joint tumors (Fig. 20.50). It is associated with a high rate of distant metastasis.[53] Bernese mountain dogs and Rottweilers are predisposed and prior joint disease presents an increased risk for development of periarticular histiocytic sarcoma[53] (Fig. 20.51).



eFig. 20.5 Lateral **(A)** and craniocaudal **(B)** radiographs of the stifle joint of a dog with synovial cell sarcoma. A large radiolucent lesion is present in the caudal aspect of the proximal tibia. A mild periosteal reaction surrounds this lesion medially and laterally. Additional radiolucent defects are present in the lateral aspect of the intercondylar fossa of the femur, superimposed on the lateral fabella, and centrally in the distal femur. There is a large soft tissue mass centered on the distal femur within the stifle joint. It is compressing the infrapatellar fat pad distally and displacing the patella cranially. These findings are consistent with a soft tissue joint tumor and associated effusion.

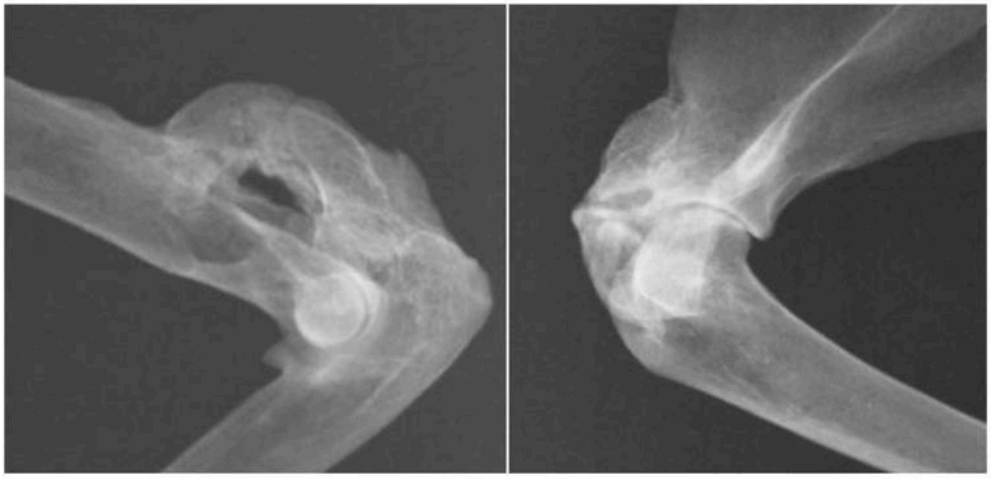


Fig. 20.48 Radiographs of the elbows and a shoulder from the skeleton of a cat that was euthanized because of ankylosing arthropathy caused by hypervitaminosis A.



Fig. 20.49 **A,** A cystic lesion was identified in the distal end of the left ulna (*white arrows*) 6 weeks after the onset of soft tissue swelling around the antebrachiocarpal joint. **B,** The lesion progressed over the succeeding 12 months, by which time a multiloculated cyst-like change was present in the distal radius, ulna, and the proximal row of carpal bones. Histologic diagnosis was synovial cell carcinoma. (Courtesy Dr. P. Young, All Pets Veterinary Hospital, Albury, Australia.)

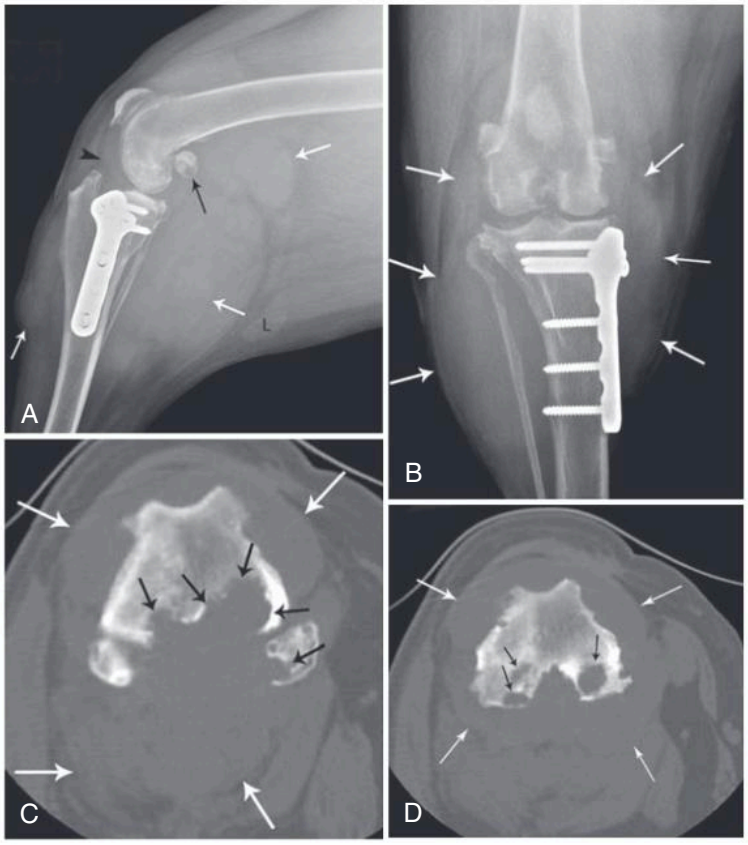


Fig. 20.50 Lateral **(A)** and craniocaudal **(B)** radiographs of the stifle with extensive intracapsular and extracapsular soft tissue swelling. A tibial plateau leveling osteotomy (TPLO) plate is present on the medial aspect of the tibia. *White arrows* indicate the extent of soft tissue swelling. *Black arrowhead* indicates effacement of the infrapatellar fat pad as a sign of increased synovial mass. The distal femur and supracondylar areas have a mottled appearance and lucent foci are present in the fabellae (*black arrow*). The popliteal lymph node is within normal limits for size (*L*). Axial computed tomography (CT) images **(C and D)** show the extent of osteolysis involving the femoral condyles and fabella medial (*black arrows*). Final diagnosis was histiocytic sarcoma. There is no presumed association with the prior TPLO. (Courtesy Animal Orthopaedic Specialists, Sydney, Australia.)

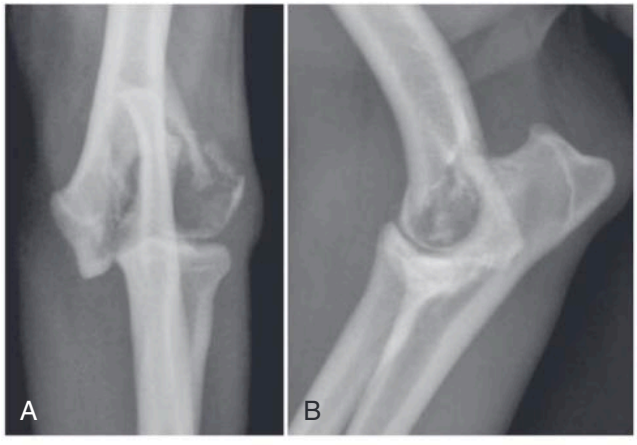


Fig. 20.51 Craniocaudal **(A)** and lateral **(B)** radiographs of a dog with extensive lysis of the lateral aspect of the humeral condyle. There is resulting pathologic fracture in the lateral epicondylar region, extending to involve the joint. Final diagnosis was diffuse mixed cell lymphoma of bone. (Courtesy North Shore Veterinary Specialist Centre, Sydney, Australia.)

REFERENCES

1. Whiting PG, Pool RR. Intrameniscal calcification and ossification in the stifle joints of three domestic cats. *J Am Anim Hosp Assoc*. 1985;21:579.
2. Mahoney PN, Lamb CR. Articular, periarticular and juxtaarticular calcified bodies in the dog and cat: a radiologic review. *Vet Radiol Ultrasound*. 1996;37:3.
3. Mason DR, Schultz KS, Samii VF, et al. Sensitivity of radiographic evaluation of radio-ulnar incongruence in the dog in vivo. *Vet Surg*. 2002;31:125.
4. Widmer WR, Buckwalter KA, Braunstein EM, et al. Radiographic and magnetic resonance-imaging of the stifle joint in experimental osteoarthritis in dogs. *Vet Radiol Ultrasound*. 1994;35:371.
5. Wong SHJ, Chiu KY, Yan CH. Review article: osteophytes. *J Orthopedic Surgery*. 2016;24(3):403–410.
6. McGonagle D, Benjamin M, Marzo-Ortega H, et al. Advances in the understanding of entheseal inflammation. *Curr Rheumatol Rep*. 2002;4:500.
7. Morgan JP. *Radiology of Skeletal Diseases—Principles of Diagnosis in Dogs*. Davis, CA: Veterinary Radiology Associates; 1981:22.

8. van Bree H. Vacuum phenomenon associated with osteochondrosis of the scapulohumeral joint in dogs: 100 cases. *J Am Vet Med Assoc.* 1992;1985–1991(1916):201.
9. *PennHIP Training Manual.* San Diego, CA: Synbiotics Corporation; 1998:22.
10. Hathcock JT. Vacuum phenomenon of the canine spine: CT findings in 3 patients. *Vet Radiol Ultrasound.* 1994;35:285.
11. Weber WJ, Berry CR, Kramer RW. Vacuum phenomenon in 12 dogs. *Vet Radiol Ultrasound.* 1995;36:493.
12. Rendano VT, Dueland R. Variation in location of gastrocnemius sesamoid bones (fabellae) in a dog. *J Am Vet Med Assoc.* 1978;173:200.
13. Cake MA, Read RA. Canine and human sesamoid disease. *Vet Comp Orthop Traumatol.* 1995;8:70.
14. Read RA, Black AP, Armstrong SJ, et al. Incidence and clinical significance of sesamoid disease in Rottweilers. *Vet Rec.* 1992;130:533.
15. Davis PE, Bellenger CR, Turner DM. Fractures of the sesamoid bones in the greyhound. *Aust Vet J.* 1969;45:15.
16. Ljunggren G, Olsson SE. Osteoarthrosis of the shoulder and elbow joints in dogs: a pathologic and radiographic study of necropsy material. *J Am Vet Radiol Soc.* 1975;16:33.
17. Innes JF, Costello M, Barr FJ, et al. Radiographic progression of osteoarthritis of the canine stifle joint: a prospective study. *Vet Radiol Ultrasound.* 2004;45:143.
18. Enomoto M, Baines EA, Roe SC, Marcellin-Little DJ, Lascelles BDX. Defining the rate of, and factors influencing, radiographic progression of osteoarthritis of the canine hip joint. *Vet Record.* 2021;189(10):20–27.
19. Smith GK, Popovitch CA, Gregor TP, et al. Evaluation of risk factors for degenerative joint disease associated with hip dysplasia in dogs. *J Am Vet Med Assoc.* 1995;206:642.
20. Smith GK, Gregor TP, Rhodes WH, et al. Coxofemoral joint laxity from distraction radiography and its contemporaneous and prospective correlation with laxity, subjective score, and evidence of degenerative joint disease from conventional hip-extended radiography in dogs. *Am J Vet Res.* 1993;54:1020.
21. Marshall JL, Olsson SE. Instability of the knee: a long-term experimental study in dogs. *J Bone Joint Surg Am.* 1971;53:1561.
22. Lascelles BDX, Henry JB, Brown J, et al. Cross-sectional study of the prevalence of radiographic degenerative joint disease in domesticated cats. *Vet Surg.* 2010;39:535.
23. Gandolfi B, Alamri S, Darby WG, et al. A dominant TRPV4 variant underlies osteochondrodysplasia in Scottish fold cats. *Osteoarthr Cartil.* 2016;24:1441.
24. Freire M, Brown J, Robertson ID, et al. Meniscal mineralization in domestic cats. *Vet Surg.* 2010;39:545.
25. Walker M, Phalan D, Jensen J, et al. Meniscal ossicles in large non-domestic cats. *Vet Radiol Ultrasound.* 2002;43:249.
26. Salter RB, Harris WR. Injuries involving the epiphyseal plate. *J Bone Joint Surg.* 1963;45:587.
27. Farrow CS. Stress radiography: applications in small animal practice. *J Am Vet Med Assoc.* 1982;181:777.
28. Davidson EB, Griffey SM, Vasseur PB, et al. Histopathological, radiographic, and arthrographic comparison of the biceps tendon in normal dogs and dogs with biceps tenosynovitis. *J Am Anim Hosp Assoc.* 2000;36:522.
29. Kramer M, Gerweng M, Sheppard C, Schimke E. Ultrasonography for the diagnosis of diseases of the tendon and tendon sheath of the biceps brachii muscle. *Vet Surge.* 2001;30(1):64–71.
30. DeBakker E, Saunders JH, vanBree H, Gielen I, Van Ryssen B. Radiographic features of primary and concomitant flexor enthesopathy in the canine elbow. *Vet Radiol Ultrasound.* 2013;54(2):107–113.
31. Streubel R, Geyer H, Montavon PM. Medial humeral epicondylitis in cats. *Vet Surg.* 2012;41(7):795–802.
32. Streubel R, Bilzer T, Grest P, Damur D, Montavon PM. Medial humeral epicondylitis in clinically affected cats. *Vet Surg.* 2015;44(7):905–913.
33. Grundmann S, Montavon PM. Stenosing tenosynovitis of the abductor pollicis longus muscle in dogs. *Vet Comp Orthop Traumatol.* 2001;14:95.
34. Kramer M, Stengel H, Gerwing M, et al. Sonography of the canine stifle. *Vet Radiol Ultrasound.* 1999;40:282.
35. Lamb CR, Duvernois A. Ultrasonographic anatomy of the normal canine calcaneal tendon. *Vet Radiol Ultrasound.* 2005;46(4):326–330.
36. Bellah JR, Weigel JP. Hemarthrosis secondary to suspected warfarin toxicosis in a dog. *J Am Vet Med Assoc.* 1983;182:1126.
37. Mapuvire T, Kandiwa E, Mbiri P, et al. Chronic lymphoplasmacytic villonodular proliferative synovitis in a 10-year-old Jack Russell terrier dog. *Int J Vet Sci Med.* 2020;8(1):100–105.
38. Dempsey LM, Maddox TW, Meiring T, Wustefeld-Janssens B, Comerford EJ. Computed tomography findings of pigmented villonodular synovitis in a dog. *Vet Comp Orthop Traumatol.* 2018;31(4):304–310.
39. Flo GL, Stickle RL, Dunstan RW. Synovial chondrometaplasia in five dogs. *J Am Vet Med Assoc.* 1987;191:1417.
40. Hubler M, Johnson KA, Burling RT, et al. Lesions resembling osteochondromatosis in two cats. *J Small Anim Pract.* 1986;27:181.
41. Crawley AC, Yogalingam G, Muller VJ, et al. Two mutations within a feline mucopolysaccharidosis type VI colony cause three different phenotypes. *J Clin Invest.* 1998;101:109.
42. Bennett D. Immune-based erosive inflammatory joint disease of the dog: canine rheumatoid arthritis: I. Clinical, radiological and laboratory investigations. *J Small Anim Pract.* 1987;28:779.
43. Pedersen NC, Pool RR, O'Brien T. Feline chronic progressive polyarthritis. *Am J Vet Res.* 1980;41:522.
44. Bennett D. Immune-based non-erosive inflammatory joint disease of the dog: I. Canine SLE. *J Small Anim Pract.* 1987;28:871.
45. Moise NS, Crissman JW. Chronic progressive polyarthritis in a cat. *J Am Anim Hosp Assoc.* 1982;18:965.
46. Bennett D, Nash AS. Feline immune-based polyarthritis: a study of thirty-one cases. *J Small Anim Pract.* 1988;29:501.
47. Bennett D, Taylor DJ. Bacterial infective arthritis in the dog. *J Small Anim Pract.* 1988;29:207.
48. Moise NS, Crissman JW, Fairbrother JF, et al. *Mycoplasma gateae* arthritis and tenosynovitis in cats: case report and experimental reproduction of the disease. *Am J Vet Res.* 1983;44:10.
49. Craig LE, Julian ME, Ferracone JD. The diagnosis and prognosis of synovial tumors in dogs: 35 cases. *Vet Pathology.* 2002;39(1):66–73.
50. Silva-Krott IU. Synovial sarcoma in a cat. *J Am Vet Med Assoc.* 1993;203:1430.
51. Vail DM, Powers BE, Getzy DM, et al. Evaluation of prognostic factors for dogs with synovial sarcoma: 36 cases (1986–1991). *J Am Vet Med Assoc.* 1994;205:1300.
52. McGlennon NJ, Houlton JEF, Gorman NT. Synovial sarcoma in the dog—a review. *J Small Anim Pract.* 1988;29:139.
53. Manor EK, Craig LE, Sun X, Cannon CM. Prior joint disease is associated with increased risk of periarticular histiocytic sarcoma in dogs. *Vet Comp Oncol.* 2017;16(1):E83–E88.

ELECTRONIC RESOURCES

Additional information related to the content in Chapter 20 can be found online at eBooks.Health.Elsevier.com.

- Chapter Quiz

CHAPTER 21

The Equine Stifle

Valeria Busoni • Fabrice Audigié

THE STIFLE

Radiographic Examination

Stifle radiographs are acquired frequently in lame patients, presale examinations, and screening radiographic protocols in young horses.[1–3] Most equine radiographic examinations are performed today using digital radiographic (DR) equipment. The greater sensitivity and better dynamic range of DR compared to computed radiographic (CR) systems have led to a significant improvement in quality of stifle radiographs obtained with portable radiographic generators.

Given the large amount of soft tissue in the stifle region, scatter radiation doses to the hands of the detector holder and of the person holding the portable generator may not differ. Lead gloves should therefore be worn by both operators to increase radioprotection.[4] Reducing the number of repeat radiographs is also crucial to increase radioprotection. Because positioning errors are the most common reason for repeat and nondiagnostic radiographs,[5] good knowledge of radiographic technique and anatomy is critical to assess the stifle region.[6]

The lateromedial view is the basic radiographic view of the stifle. The beam is centered 5 to 7 cm proximal to the tibial plateau, between the cranial and middle third of the stifle region. The detector should be vertical to the ground to avoid geometric distortion, and exposure must be sufficient to penetrate the femoral condyles. A lateromedial view of the flexed stifle can be used to examine the cranial and central intercondylar areas of the tibia in more detail.

Depending on the purpose of the radiographic examination or the disease suspected, a caudolateral-craniomedial view and/or a caudocranial view are indicated. The caudolateral-craniomedial view allows good visibility of the two most common sites of disease in the young horse: the lateral femoral trochlear ridge (osteochondrosis site) and the medial femoral condyle (subchondral cyst-like lesion site). Because the femoral condyles are superimposed on the lateromedial view, the caudolateral-craniomedial view is a valuable complement to evaluate the medial femorotibial joint with low exposure factors. The caudolateral-craniomedial view is also helpful for documenting injuries of the articular surface of the patella. The caudocranial view is mainly aimed at the assessment of the femorotibial joints for osteoarthrosis, and it is essential for documenting axial injuries such as enthesopathies or avulsion fractures at the enthesis of the cranial cruciate ligament. The caudocranial view may require the use of a grid for optimal contrast in larger horses, but good diagnostic quality caudocranial radiographs of the stifle can be achieved without a grid with a portable radiographic unit and a DR system if scattering is limited by accurate collimation. This projection should be performed with a 10-degree descending beam to obtain the most accurate assessment of the width of the radiolucent femorotibial joint space, in particular the medial joint space.[7] The caudomedial-craniolateral view requires similar exposure factors to the caudocranial view and is performed less routinely. This projection is also useful to diagnose lateral femorotibial injuries, such as subchondral cyst-like lesions of the lateral femoral condyle and bone remodeling at the proximal or distal insertion of the cranial cruciate ligament.[6] The craniproximal-craniodistal view of the patella is useful when patellar disease is being investigated. This view can be easily obtained with a portable x-ray unit and the required exposure is relatively low.

With the advent of DR systems and their inherently excellent contrast resolution, radiographic evaluation of the soft tissues of the stifle is possible to a certain extent. Lateromedial radiographs of the stifle allow good visualization of the patellar ligaments and the cranial fat pad (Fig. 21.1). Femoropatellar and femorotibial effusions can be suspected on radiographs (see Figs. 21.1 and 21.2). Localization of soft tissue swelling as being extra-articular or intra-articular is possible by evaluating border effacement of patellar ligaments and fat pad displacement (see Fig. 21.1).

Ultrasonography for Supplemental Stifle Imaging

Subchondral cyst-like lesions and tibial or femoral osteophyte formation as a result of osteoarthrosis are the most common radiographic signs of femorotibial disease. Bone fragments, new bone formation, or radiolucent areas at ligament insertions, suggesting avulsion fractures or enthesopathy, may also be seen.[8–10] However, because of the high incidence of soft tissue lesions involving menisci and ligaments, femorotibial pain may be present with no or minor radiographic signs.[8–10] The severity of the lameness, the midterm prognosis for a return to work, or the long-term prognosis for development of osteoarthrosis depends mainly on the severity of articular cartilage and soft tissue damage, in particular meniscal injury.[11,12] A combination of ultrasonographic and radiographic examination is therefore necessary for a routine more complete assessment of the stifle.[9]

Ultrasonography of the weight-bearing stifle allows easy assessment of the femoropatellar and femorotibial synovial recesses, the femoral trochlea, the patellar ligaments, the menisci, the collateral ligaments, and the medial femorotibial joint margins (Fig. 21.3).[13–16] In the flexed stifle, ultrasonography allows evaluation of the cranial horns of the menisci, the cranial meniscotibial ligaments, and a portion of the articular surface of the medial and lateral femoral condyles (see Fig. 21.3).[17,18] Ultrasonography is the first-line modality to diagnose meniscal and cranial meniscotibial ligament damage (see Fig. 21.19), which frequently affects sport and pleasure horses.[19,20] Although specificity is relatively low using arthroscopy as the gold standard,[19] a good correlation between histologic changes and ultrasonographic images has been suggested for meniscal injuries.[21]

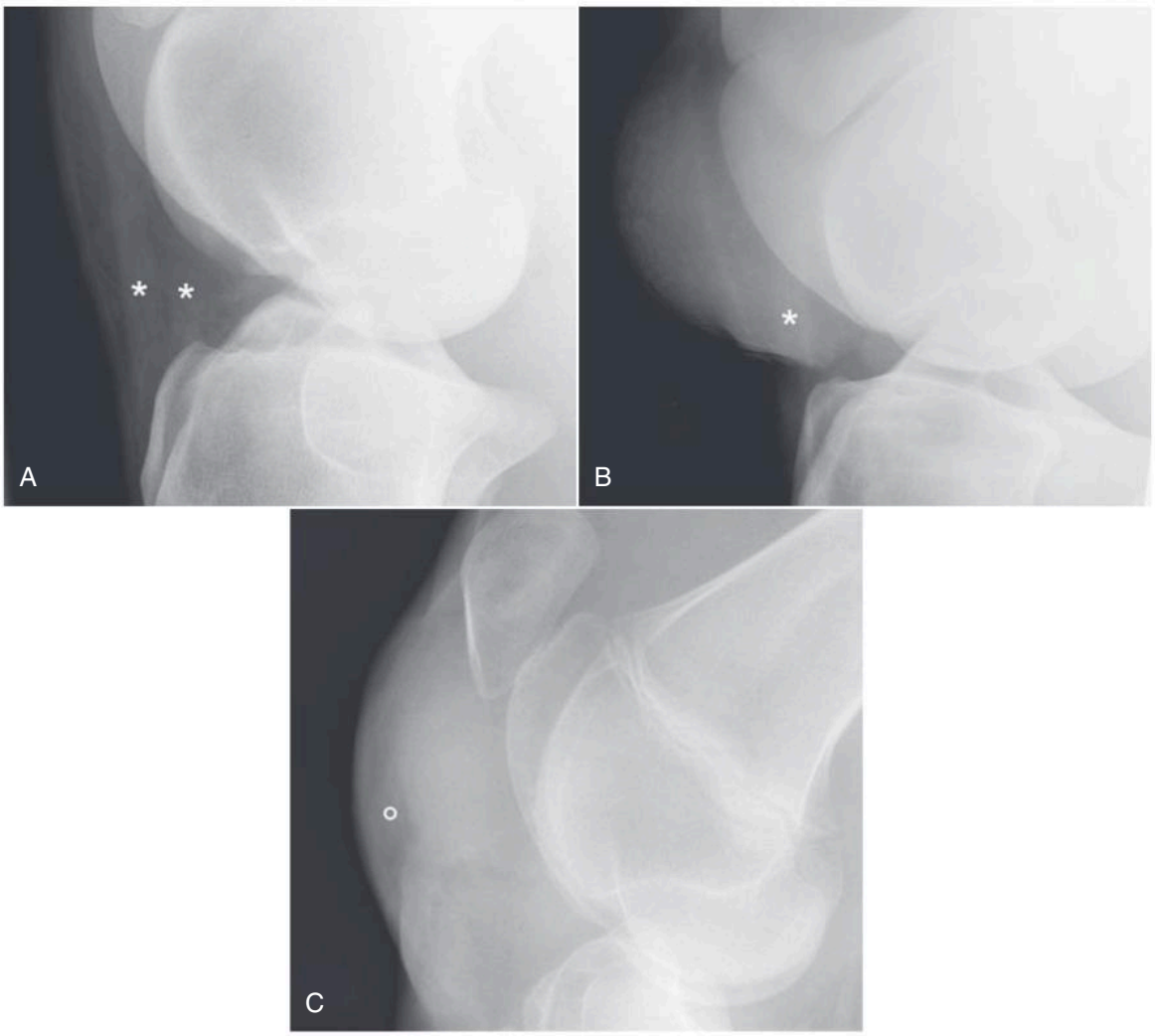


Fig. 21.1 Lateromedial radiographs of three equine stifles. **A,** Normal stifle. The patellar ligaments (*asterisks*) are delineated by the different opacity of the fat pad at the cranial aspect of the joint. **B,** A localized extra-articular soft tissue swelling is present. The middle patellar ligament is still visible (*asterisk*). The horse had an extra-articular abscess. Note that the positioning is not correct for a lateromedial view because it is slightly oblique. **C,** Large soft tissue swelling at the cranial aspect of the stifle. The swelling is intra-articular (femoropatellar and femorotibial), and the patellar ligaments are no longer visible because of border effacement. The fat pad (*open circle*) is displaced cranially.

Advanced Imaging of the Stifle

Because each modality has its limitations depending on lesion location and nature, further comprehensive joint assessment can be carried out using advanced imaging techniques such as computed tomography (CT), CT arthrography and magnetic resonance imaging (MRI).[22–25] The increasing number of large-bore CT machines in equine practice has made the examination of the stifle accessible for all types of horses (Fig. 21.4). The advantage of this modality is the speed of acquisition and the inclusion of both stifle joints allowing the opposite limb to be used as reference in case of unilateral conditions. The short acquisition time also allows the screening of other body parts during the same general anesthesia (for example, other joints of the lame hindlimb in adult horses or both hindlimbs and pelvis in young foals presenting with hematogenous sepsis), and allows the CT examination to be followed by surgical procedures such as arthroscopy. CT examination provides high-resolution three-dimensional (3D) bone imaging while CT-arthrography with intra-articular injection of contrast medium is necessary for an accurate evaluation of articular soft tissues and cartilage.[26,27] Contrary to CT, MRI of the stifle of an adult horse is feasible only in a limited number of magnetic resonance (MR) units. Today, most MR examinations of the stifle are acquired using an open low-field MR unit with a tiltable magnet (see Fig. 21.4).[28] The positioning of the horse in the MR machine remains challenging even in open units and induces compression of the thigh and gluteal muscles of the opposite hindlimb. Therefore, only one stifle can be examined in one session to limit the anesthetic risk and prevent potential anesthetic complications.[28] Knowledge of the 3D anatomy of the stifle is crucial with these modalities and several studies provide reference images.[22,29,30] As documented for other joints, compared to CT, MRI of stifle conditions has the major advantage of documenting soft tissue lesions (including lesions of the articular cartilage) without the use of contrast medium and allows the diagnosis of lesions of the cancellous bone.[26,27] MRI, however, is less sensitive than CT to detect periarticular remodeling and soft tissue mineralization.



Fig. 21.2 Caudolateral-craniomedial radiograph of a 6-month-old colt with severe effusion of the lateral femorotibial joint. A soft tissue opacity band is visible cranial to the femorotibial joint space and the proximal tibia, in the area corresponding to the subextensor recess of the lateral femorotibial joint (*asterisk*).

DISEASES OF THE FEMOROPATELLAR JOINT

Osteochondrosis

The term *juvenile osteochondral conditions (JOCCs)* has been proposed for developmental disorders related to the immature joint or growth plates of young horses based on anatomic and functional considerations.[31] Lesions of the juvenile femoropatellar joint are mainly osteochondral defects and fragmentations of the articular surface of the trochlear ridge.[31] Although these lesions develop early in life, osteochondrosis of the femoropatellar joint is a common radiographic finding in both young and older horses.[1–3,32] Lateromedial or caudolateral-craniomedial views are the best projections to evaluate the femoral trochlea in young horses with synovial distention of the femoropatellar joint. Radiographic signs of osteochondrosis include flattening, irregular subchondral surface, heterogeneous opacity of the trochlear ridge, and presence of bone fragments attached by a radiolucent junction to the bone surface at the cranial aspect of the trochlea (Fig. 21.5). Fragments may also become free and visible far from the trochlear surface (Fig. 21.6, eFig. 21.1). The most common site of osteochondrosis in the equine stifle is the lateral femoral trochlear ridge, especially the middle third.[1–3,32–34] This type of lesion may influence sport and racing performance of affected horses.[34] The trochlear groove may be involved occasionally,[33] with or without associated trochlear ridge involvement. Trochlear groove lesions generally have less clinical significance than ridge defects. Lesions of the medial femoral trochlear ridge are less common (see Fig. 21.3).[3,33,35] Patellar lesions are rare and seen mainly with severe trochlear abnormalities (see eFig. 21.1).[36] An osseous cyst-like lesion has been reported in the proximal medial aspect of the patella in a young horse, but because it was located at the site where most patellar fractures occur, the cause was uncertain.[37]

Considering the age of onset and that osteochondral lesions of the femoral trochlea have the potential to improve between 6 and 18 months, radiographic screening of the stifle for osteochondrosis should not be performed before 12 to 18 months of age.[32,38,39] Because of possible bilateral involvement (see Fig. 21.6, eFig. 21.1), both stifles should always be examined. Because the femoral trochlea cannot be evaluated on the caudocranial view, and the lateromedial and caudolateral-craniomedial views do not allow precise estimation of the mediolateral extent of the lesion, ultrasonographic examination of the cranial aspect of the stifle may be helpful before surgery for a more comprehensive assessment of the extent of the lesion and of articular cartilage damage, and to better define the long-term prognosis (Fig. 21.7). Because of its higher sensitivity compared to radiography, especially for medial trochlear ridge defects, ultrasonography is also useful in horses where radiographic signs are equivocal.[33] Ultrasonography can also be used as a practical, inexpensive, and reliable technique for osteochondrosis screening and to discriminate physiological from pathological events at the lateral femoral trochlear ridge in young foals.[40,41]

Patellar Fragmentation

Patellar fragmentation affects the patellar apex and is seen primarily in horses that have undergone medial patellar desmotomy.[42–44] The fragmentation is the consequence of patellar instability after desmotomy.[42] One or multiple bone fragments may be present (Fig. 21.8). Remodeling of the tibial tuberosity at the insertion of the patellar ligaments and remodeling or enthesopathy of the patella may be present in association with fragmentation of the apex.[42–44] An increase in the angle between the proximal articular surface of the patella and the cranial surface of the femur occurs because of patellar instability following medial patellar desmotomy and may be seen in horses with patellar fragmentation.[42]

For patellar fractures, see the Fractures Involving the Stifle section.

Upward Patellar Fixation

No radiographic sign can be used to confirm the clinical diagnosis of recurrent upward patellar fixation. Radiographic examination of the stifle is recommended to exclude other lesions. Horses with recurrent partial upward patellar fixation may have remodeling of the patellar apex on lateromedial radiographs.[36]

Patellar Luxation

Lateral patellar luxation is an uncommon congenital condition and may be unilateral or bilateral.[45,46] Lateral patellar luxation is often the consequence of femoral trochlear dysplasia with trochlear ridge hypoplasia and a shallow trochlear groove. Lateral patellar luxation may be associated with incomplete ossification of the medial patellar angle.[45] Patellar luxation is recognized in horses of all ages as a cause of a nonpainful gait alteration, more commonly in miniature breeds and ponies.[36,45] Radiographically, lateral patellar luxation appears as a malpositioning of the patella (Fig. 21.9). An increase in the craniocaudal dimension of the patella on the lateromedial view of the stifle is caused by displacement and rotation of the patella compared with the normal axis of the limb. Alteration of the shape of the patella is also frequently observed.[46] Luxation can also be secondary to a traumatic event with possible distal displacement.[47]

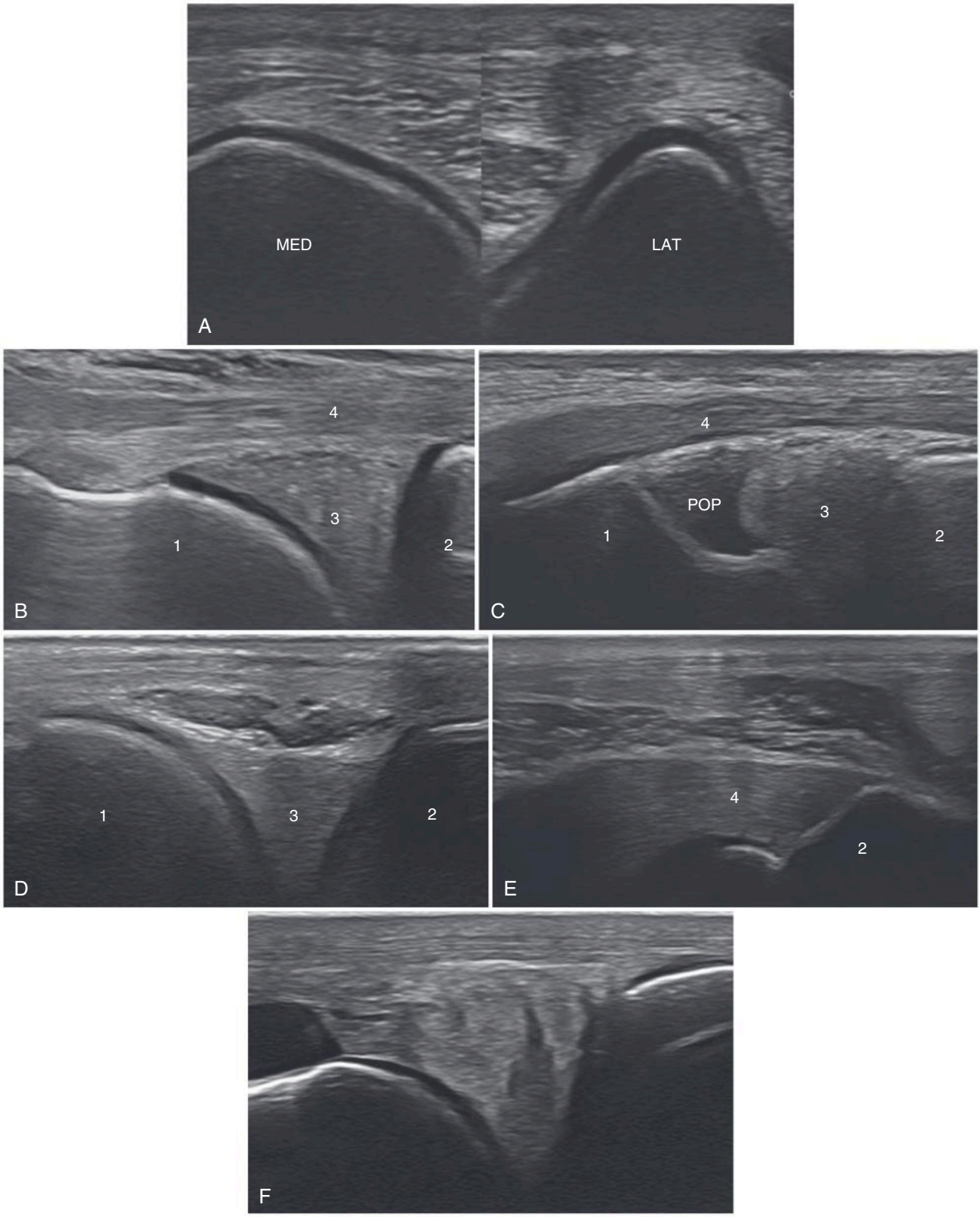


Fig. 21.3 Ultrasound images of the normal equine stifle **(A to E)** and of an equine stifle joint with a meniscal tear **(F)**. Medial is to the *left* in transverse images, proximal is to the *left* in longitudinal images. **A,** Transverse images of the medial (*MED*) and lateral (*LAT*) ridges of the femoral trochlea in a normal horse. The hyperechoic line is the subchondral bone surface. The hypoechoic band that covers the bone is the articular cartilage. **B,** Longitudinal image of the stifle at the medial aspect of the medial femorotibial joint in a normal horse. *1,* Femur; *2,* tibia; *3,* medial meniscus; *4,* medial collateral ligament. **C,** Longitudinal image at the lateral aspect of the lateral femorotibial joint in a normal horse. The hypoechogenicity of the popliteus tendon (*POP*) is caused by the oblique orientation of the fibers in relation to the sound beam. *1,* Femur; *2,* tibia; *3,* lateral meniscus; *4,* lateral collateral ligament. **D–E,** Longitudinal **(D)** and transverse **(E)** images of the flexed stifle obtained at the cranial aspect of the medial femorotibial joint in a normal horse. *1,* Femur; *2,* tibia; *3,* cranial horn of the medial meniscus; *4,* cranial meniscotibial ligament of the medial meniscus inserting on the proximal tibia. **F,** Meniscal tear: a large hypoechoic triangular image crosses the medial meniscus horizontally.



Fig. 21.4 Photographs of a horse under general anesthesia, positioned for advanced imaging of the stifle in a large-bore computed tomography (CT) scan **(A)** and in an open magnetic resonance (MR) unit **(B)**. The placement of the left stifle with respect to the isocenter of the magnet is improved by applying a tension with a rope. Images are acquired using a surface coil placed at the cranial aspect of the stifle.

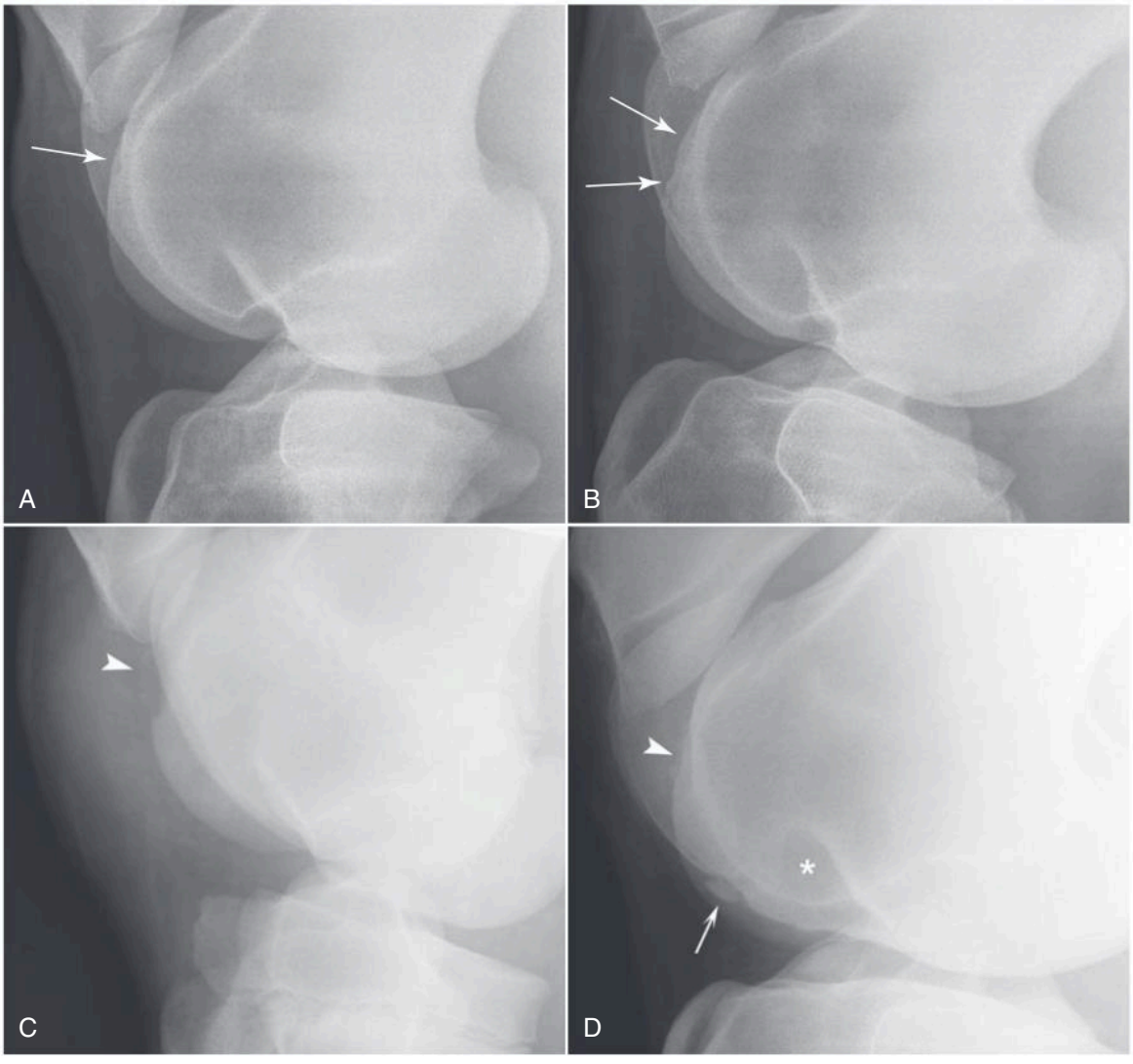


Fig. 21.5 Lateromedial **(A, B, and D)** and caudolateral-craniomedial **(C)** radiographs of the stifle of four horses with osteochondrosis of the femoral trochlea. **A,** The lateral trochlear ridge is flat, and there is a small area of radiolucency in the subchondral bone in its middle third (*white arrow*). **B,** The lateral trochlear ridge is flat, and the subchondral bone has a heterogeneous reduced opacity and an irregular surface in its middle third (*white arrows*). Slight remodeling of the distal aspect of the patella is also present. **C,** The middle third of the lateral femoral trochlear ridge has a large radiolucent defect with small radiopaque fragments located cranial to it (*white arrowhead*). The femoropatellar joint is distended. **D,** The lateral trochlear ridge is flat and irregular in its middle third (*white arrowhead*). The medial trochlear ridge has a bone fragment separated by a radiolucent junction from a defect in the subchondral bone (*white arrow*). The extensor fossa of the distal femur (*asterisk*) is more conspicuous than normal and abnormally delineated cranially. This radiographic finding that can be seen in horses with osteochondrosis, is often associated with severe flattening of the lateral trochlear ridge.



Fig. 21.6 Lateromedial (slightly caudolateral-craniomedial) radiograph of the stifle of a young horse with stifle osteochondrosis. The lateral trochlear ridge is severely dysplastic: the ridge is difficult to distinguish from the trochlear groove, has a wavy contour and a very heterogeneous opacity. A large osteochondral fragment detached from the lateral trochlear ridge has moved to the caudal aspect of the stifle and is visible caudal to the femoral condyles. Note the remodeling of the patellar margins.

Osteomyelitis of the Patella

Chronic osteomyelitis of the patella may develop because of a chronic abscess at the cranial aspect of the stifle.[36] A cranioproximal-craniodistal view of the patella is essential to assess the full extent of involvement (Fig. 21.10). Radiographic signs are periosteal reaction on the cranial patellar surface and areas of reduced opacity within the patella, resulting in a patchy heterogeneous appearance of the patella (see Fig. 21.10). Ultrasonography can help assess concurrent soft tissue infection, localize the abscess, and confirm bone involvement seen as roughening of the bone surface.

DISEASES OF THE FEMOROTIBIAL JOINTS

Subchondral Cyst-Like Lesions

Subchondral cyst-like lesions of the stifle are most frequently juvenile osteoarticular abnormalities but may be seen in horses of any age.[12] Their typical radiographic appearance is a round to oval radiolucent area with well-defined margins within the subchondral bone of the femoral condyles (Fig. 21.11) or, less commonly, the tibial condyles. Subchondral bone cysts may have a distal base of variable extent depending on communication and proximity with the joint space and may be surrounded by a sclerotic rim. The subchondral surface of the femoral condyle is flattened at the level of the cyst. Small bone cysts may be difficult to see within the thick femoral condyle, especially in large horses. Flattening or indentation of the femoral subchondral surface may be the only radiographic sign in some horses.[48,49] Femoral subchondral lesions in young horses may also be seen as more irregularly shaped lucencies (Fig. 21.12). As with trochlear osteochondrosis, femoral juvenile subchondral lesions may evolve until the end of growth. Most shallow lucencies in the medial femoral condyle of immature horses do not change in size but some may fully resolve or, in contrary, develop into a larger cyst-like lesion. Young Thoroughbreds with medial femoral lucencies had less starts as 2-year-olds when compared to their maternal siblings free of stifle pathology.[48] Radiographic signs of degenerative joint disease may be present in older horses with a cyst-like lesion because of chronic synovitis and secondary meniscal damage. Trauma to the medial femorotibial joint may also lead to subchondral bone damage of the medial femoral condyle and induce a radiographically visible radiolucent subchondral cyst-like lesion as synovial fluid is pumped into the subchondral bone.[12] Subchondral cyst-like lesion may also develop in adult horses associated with advanced degenerative femorotibial joint disease (Fig. 21.13). Ultrasonography of the surface of the femoral condyle in the flexed stifle may be used to confirm the lesion[18] (see Fig. 21.13, eFig. 21.2) or to better evaluate cartilage and subchondral defects in horses with subtle radiographic changes.

The most common location for subchondral cyst-like lesions is the weight-bearing area of the medial femoral condyle.[36,50] In the caudocranial view, subchondral lesions affect the central portion of the medial condyle most commonly, but they can also be encountered in the more axial aspect of the medial femoral condyle (see Fig. 21.11C). Osseous cyst-like lesions have also been reported in the caudal aspect of either femoral condyle in foals.[51] This unusual location may be related to a septic origin. An ischemic etiology has also been suggested in condylar lesions of very young foals (Fig. 21.14).[52] Lateral femoral condyle and proximal tibial subchondral lesions are less common than medial femoral condyle lesions (see Fig. 21.11D). A combination of femoral and tibial lesions facing each other or more complex combinations of lesions at different sites may occur, and have a more guarded prognosis (see Fig. 21.12).[36,53,54] Subchondral cyst-like lesions may be difficult to see on slightly underexposed lateromedial radiographs because of superimposition of the femoral condyles. A caudocranial view of optimal exposure and contrast and oblique views are the most useful for confirming and localizing the lesion.

Degenerative Joint Disease

Degenerative joint disease of the femorotibial joint can be a sequel to any stifle injury and is seen commonly in horses with stifle lameness and meniscal damage.[8,10] Involvement of the medial femorotibial joint is more common than involvement of the lateral compartment.[8,36] The most common radiographic signs are remodeling of the tibial and femoral joint margins with production of large-based osteophytes (Fig. 21.15). Tibial osteophytes are usually large with smooth margins, tend to form such that their proximal surface is not in the same plane as the tibial plateau (see Fig. 21.15), and may be difficult to differentiate from the normal tibial margin, especially when the caudocranial view is slightly oblique to the tibial plateau. Femoral osteophytes are seen more commonly on the medial condyle margin. They are usually broad-based and, as tibial osteophytes, their distal surface is not in continuity with the arc of the condylar surface. In some cases, a radiodense osteophytic line may be seen superimposed with the femoral condyle (Fig. 21.16). Narrowing of the femorotibial joint space can be a sign of meniscal damage (thinning, prolapse) or thinning of the articular cartilage of the femorotibial joint in advanced degenerative joint disease (Fig. 21.17, eFig. 21.3). Marked articular cartilage degeneration can be seen following repeated injections of long-acting steroids.[55] Areas of subchondral bone sclerosis and lucencies are mainly seen in advanced articular damage with meniscal injury and prolapse (see Fig. 21.17). These lucencies may lead to acquired



eFig. 21.1 Lateromedial radiograph of the opposite stifle of young horse presented in Fig. 21.6 with bilateral stifle osteochondrosis. A large osteochondral fragment is present at the distal aspect of the lateral trochlear ridge (*arrowheads*). The dorsal aspect of the medial trochlear ridge has an abnormal shape (*arrow*) just proximal to a small bone fragment or mineralization. Note the abnormal shape of the patella and the severe remodeling of its margins.

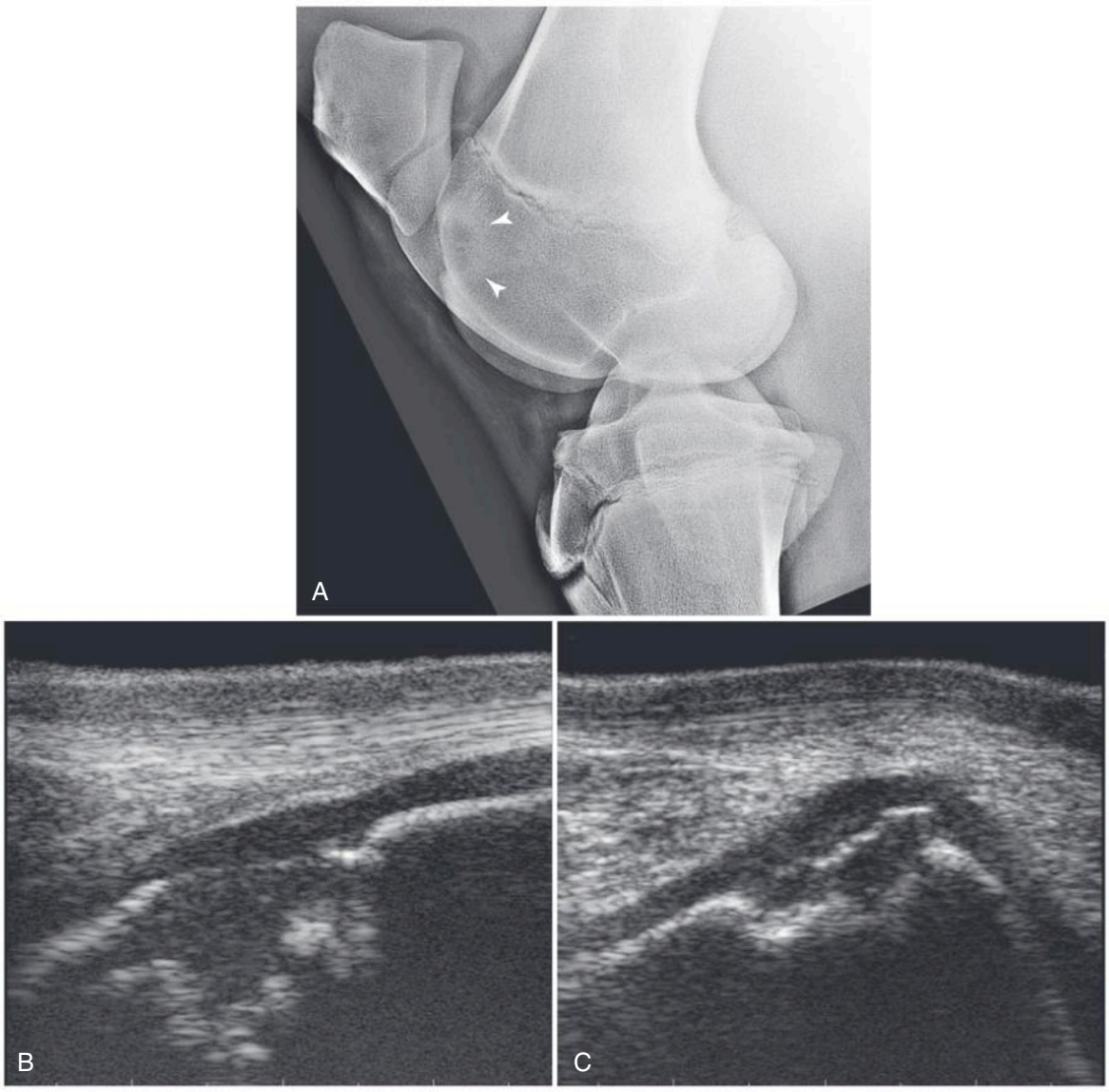


Fig. 21.7 Lateromedial radiograph **(A)** and ultrasound images **(B, C)** of the stifle of a young horse with stifle osteochondrosis. A large defect surrounded by a sclerotic band (*arrowheads*) is visible on the radiograph in the proximal third of the lateral trochlear ridge. In the longitudinal **(B)** and transverse **(C)** ultrasonographic images of the lateral trochlear ridge, the thickness of the hypoechoic cartilage is uneven, and the subchondral bone surface has lost the normal smooth hyperechoic appearance at the site of the defect. The subchondral bone is hypoechoic as not ossified, and the hyperechoic deep limit of the defect is very irregular. Compare this figure to the normal femoral trochlea in Fig. 21.3A,B.

subchondral cyst-like lesions of the stifle. These acquired cyst-like lesions are most frequently found in the medial femoral condyle and in the medial condyle of tibia (see Fig. 21.13)

Meniscal and Meniscotibial Ligament Damage

The menisci, which are of soft tissue opacity on radiographs, occupy, with the articular cartilage, the space between the distal femoral condyles and the proximal tibial plateau. The menisci cannot be seen radiographically. Therefore, meniscal damage can only be suspected on radiographs when calcification is present in the femorotibial joint space or close to it (Fig. 21.18), or on the basis of secondary bone abnormalities, such as radiolucent areas (see Fig. 21.15B, Fig. 21.19), new bone formation, or avulsion fragments at the site of insertion of the cranial meniscotibial ligaments on the proximal tibia (Fig. 21.20).[8] New bone formation cranial to the medial intercondylar eminence of the tibia has been reported as the most frequent radiographic finding in horses with meniscal damage confirmed at arthroscopy (Fig. 21.21).[8] However, when the site of pain responsible for the lameness has been proven to be the stifle, or when distention of the femorotibial joint is present, soft tissue injuries, in particular meniscal damage, should be considered as a cause of lameness in absence of radiographic signs of joint disease.[9,10,17,20,56]



Fig. 21.8 Lateromedial radiograph of the patella of a horse with patellar fragmentation (*asterisk*) after medial patellar desmotomy.

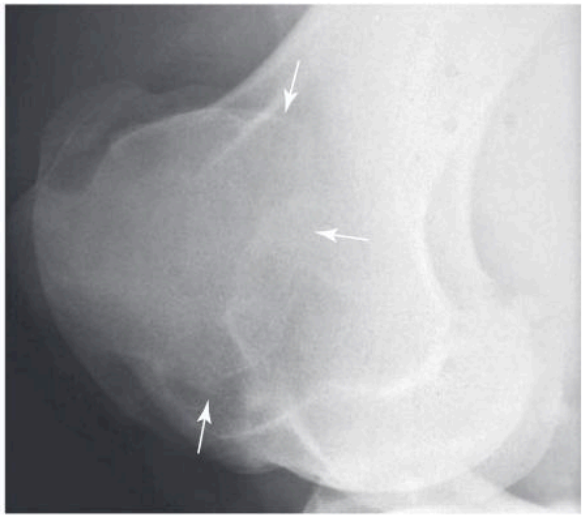


Fig. 21.9 Lateromedial radiograph of the stifle of an adult horse with permanent lateral patellar luxation. The patella (*white arrows*) is superimposed on the femoral trochlea.

The first-line imaging technique to evaluate meniscal and cranial meniscotibial ligament damage is ultrasonography (see Fig. 21.3). Meniscal damage can be seen ultrasonographically as changes in shape (thinning), position (prolapse), and/or echogenicity (hypo- or hyperechoic areas) (see Fig. 21.3F). Hypoechoic stripes seen in menisci of clinically normal horses should not be confused with clinically significant meniscal lesions. Cranial meniscotibial ligaments are assessed on the flexed stifle. Cranial meniscotibial ligament damage can be seen as altered echogenicity and architecture of the ligament

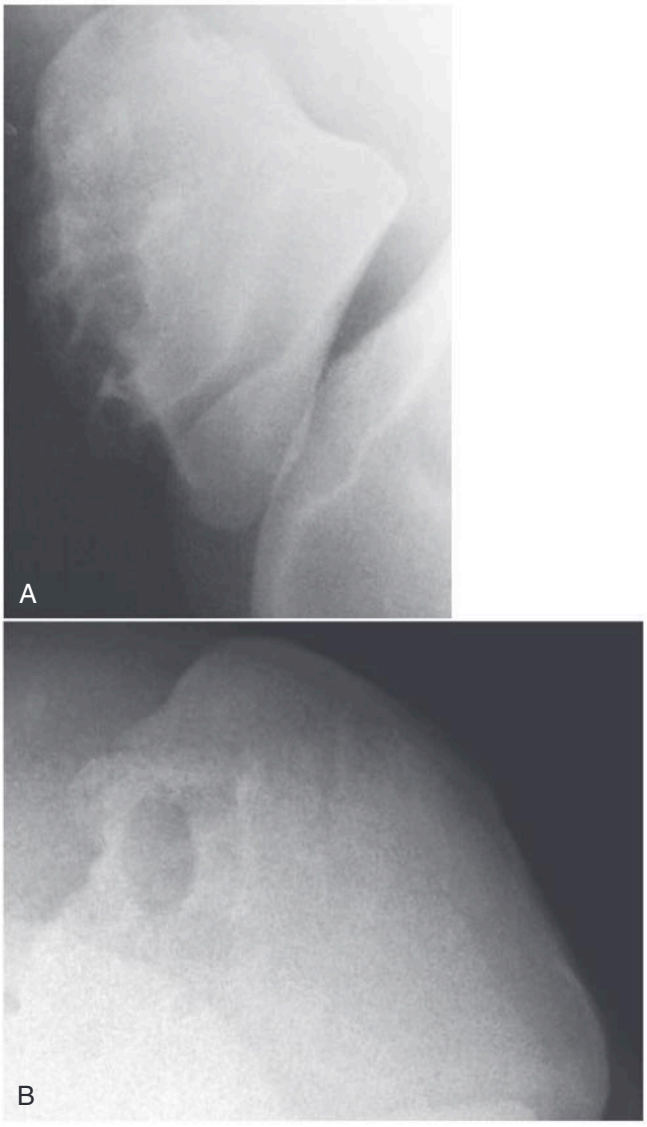


Fig. 21.10 Lateromedial **(A)** and cranioproximal-craniodistal **(B)** radiographs of the patella of a horse with an abscess at the cranial aspect of the stifle and secondary patellar osteomyelitis. The patella is heterogeneous and contains radiolucent areas. The cranial patellar surface is irregular. A large radiolucent defect is seen in the patella in the cranioproximal-craniodistal view.

and is frequently associated with bone surface irregularity as a sign of enthesopathy (see Fig. 21.19D). Concurrently, ultrasonography allows the assessment of all joint compartments and the degree and chronicity of synovitis. When advanced imaging is indicated, MRI and CT arthrography also allow a good assessment of meniscal and meniscotibial ligament damage (see Fig. 21.19C).[26,27]

Cruciate Ligament and Collateral Ligament Damage

Indirect radiographic signs of cruciate ligament damage are radiolucent areas at the ligament insertion sites on the distal femur or bone remodeling at the tibial insertions (Fig. 21.22). In chronic damage, there can be mineralization of the injured ligament.[8] Avulsion of bone at the femoral and tibial cruciate ligament insertions has also been reported.[6,57,58] Fractures of the medial intercondylar eminence are described in association

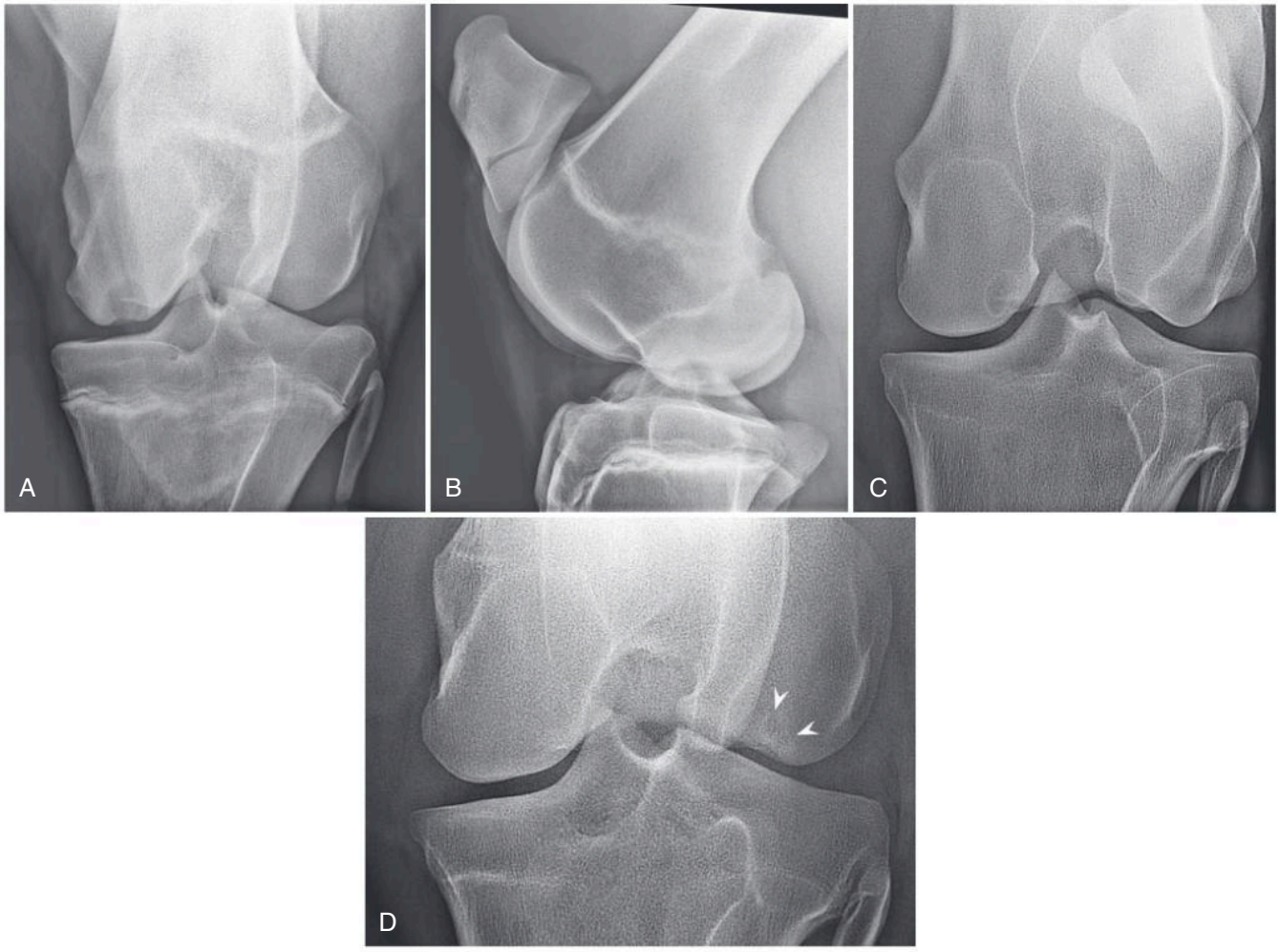


Fig. 21.11 Caudocranial **(A, C, D)** and lateromedial **(B)** radiographs of the stifle of three horses with a subchondral bone cyst. **A and B,** Caudocranial **(A)** and lateromedial **(B)** radiographs of a 2-year-old horse (horse 1). There is a large, half-oval shape, subchondral radiolucency in the medial femoral condyle. Severe surrounding sclerosis and flattening of the condyle are also present. **C,** Caudocranial radiograph of horse 2. An oval, well-marginated radiolucent area surrounded by a thin sclerotic rim is visible in the axial part of the medial femoral condyle. Subchondral cyst-like lesions are more commonly found in the central weight-bearing part of the medial femoral condyle, but this axial location can be observed in some horses. **D,** Caudocranial radiograph of horse 3. Small radiolucent areas surrounded by a faint sclerosis are present in the lateral femoral condyle (*arrowheads*). Subchondral cyst-like lesions of the lateral femoral condyle are in most instances more difficult to see compared with those in the medial condyle because of their smaller size.

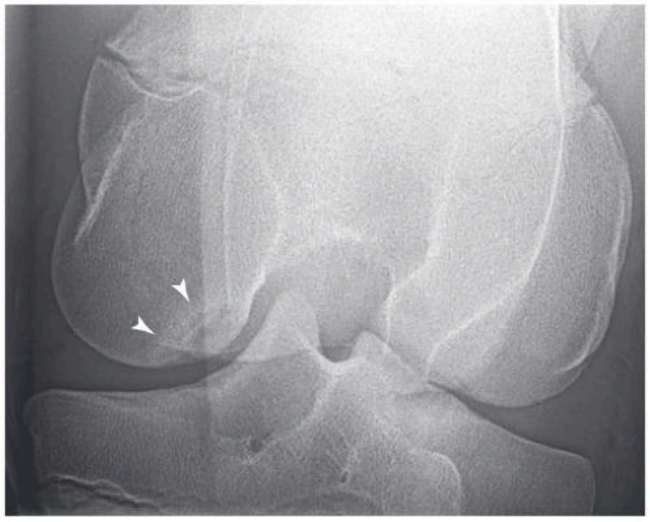


Fig. 21.12 Caudocranial radiograph of a 6-month-old colt with a juvenile subchondral lesion in the medial femoral and tibial condyles. Irregularly marginated band-like subchondral radiolucencies are visible in the axial aspect of the medial femoral condyle, with surrounding sclerosis (*arrowheads*). The condylar subchondral surface is flattened and misshapen at the level of the radiolucencies and there is a subchondral radiolucent band surrounded by sclerosis in the medial tibial condyle in the area facing the femoral lesion. Similar lesions (less visible on this view because of the superimposition of the femoral trochlea) are present in the axial aspect of the lateral femoral and tibial condyles.

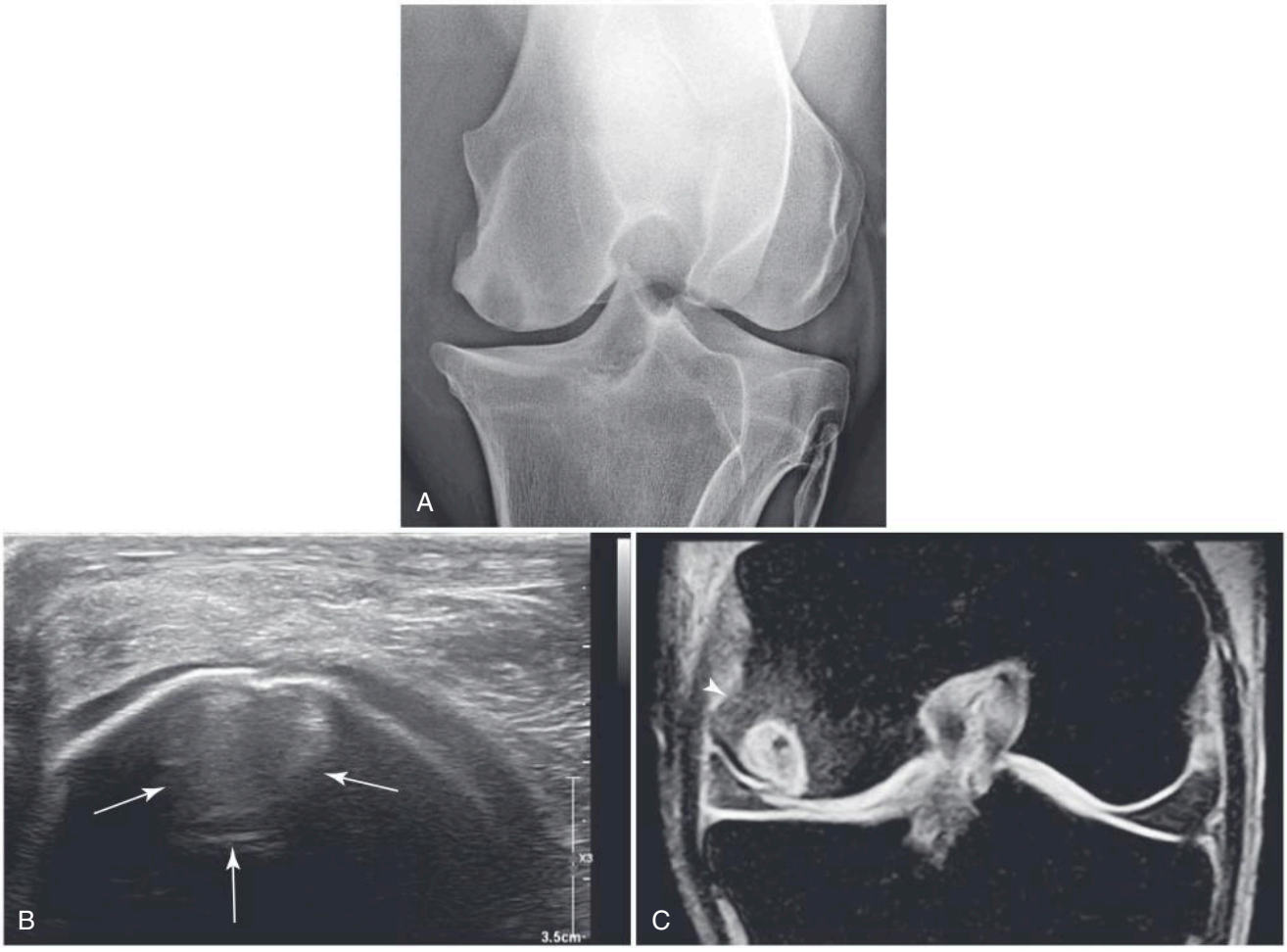


Fig. 21.13 Caudocranial radiograph **(A)**, ultrasound **(B)**, and fat suppressed magnetic resonance (MR) **(C)** images of the stifle of a 6-year-old Thoroughbred performing in jumping racing with an acquired subchondral cyst-like lesion associated with degenerative femorotibial joint disease. On the previous radiographs obtained 4 months before at the onset of the marked hindlimb lameness, the large subchondral cyst-like lesion was not visible. A large cyst-like lesion is now present in the medial femoral condyle **(A, C)**. The cyst is surrounded by sclerosis **(A)** and by a large band of high-signal edema on the MR image **(C)** affecting both the cancellous and compact bone (*arrowhead*). The bone surface of femoral condyle is flattened and irregular **(A–C)**. The cyst is covered by a thinner and altered cartilage layer (hypoechoic band with an increased echogenicity on the US image obtained on the flexed stifle). Note the presence of deep echoes below the subchondral surface at the level of the cyst **(B,** *arrows***)**. The medial meniscus has an abnormal increased and heterogeneous signal on the MR image. Femoral and tibial osteophytes demonstrate degenerative joint disease.

with cranial cruciate ligament damage and have been suggested to be caused by lateral pressure of the medial condyle more than avulsion.[8] Because of the difficulty in visualizing cruciate ligaments with ultrasonography, when available, CT arthrography and MRI should be considered to diagnose cruciate ligament injuries.[26,27]

Collateral ligament damage of the stifle because of acute trauma does not result in any radiographic abnormality except joint swelling. In acute complete traumatic collateral ligament rupture, joint instability can be assessed using a caudocranial projection with the stifle under stress.[9] Ultrasonography allows assessment of the medial and lateral collateral ligaments.[13] Chronic enthesopathy may be visible on caudocranial radiographic views as a change in shape or an increased irregularity of the surface of the medial or lateral femoral epicondyles (Fig. 21.23).

FRACTURES INVOLVING THE STIFLE

Patellar Fractures

Patellar fractures most commonly involve the medial angle of the patella.[59,60] These fractures occur mainly in steeplechase and eventing horses when the flexed joint strikes a fixed fence.[59,60] Concurrent medial patellar fractures and lateral collateral ligament avulsion fractures subsequent to trauma have been described.[61] However, fractures of the medial angle may be incidental and not related to lameness at the time of radiographic examination. These fractures may be suspected on the lateromedial view because of an area of heterogeneously increased opacity in medial patellar angle (Fig. 21.24). A cranioproximal-craniodistal view of the stifle allows confirmation of the diagnosis and a complete assessment of fracture extent and morphology. Patellar fracture may be associated with fractures of



eFig. 21.2 Longitudinal ultrasound image of the medial femoral condyle obtained on the flexed stifle in a horse with a subchondral cyst-like lesion (proximal to the *left*). There is a large V-shape defect in the subchondral bone in the distal aspect of the condyle that corresponds to the cyst-like lesion.



Fig. 21.14 Lateromedial radiograph of the stifle of a 5-month-old Thoroughbred colt with a grade 4/5 lameness showing marked changes in the opacity of the subchondral and adjacent cancellous bone of the lateral femoral condyle extending from its cranial to its caudoproximal aspect. Note the duplication of the caudal articular surface of the lateral femoral condyle compatible with a large osteochondral fragment (*arrowhead*). These changes most likely represent an extensive juvenile osteochondral disease.

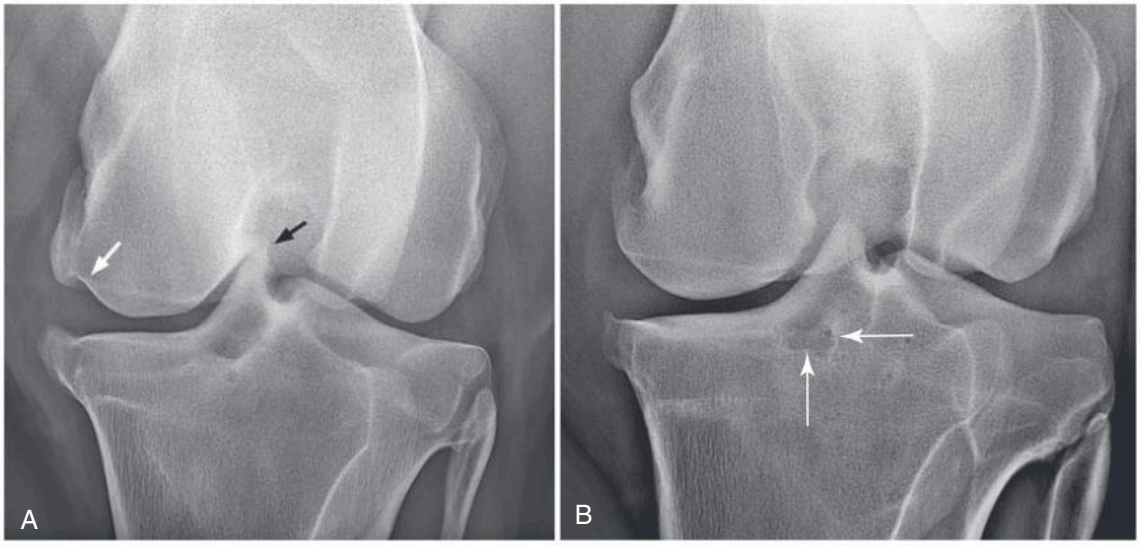


Fig. 21.15 Caudocranial radiographs of the stifle of two horses with meniscal injuries and degenerative joint disease. **A,** Femoral and tibial osteophytes are present on the medial articular margins. Note the change in curvature between the condyle surface and the femoral osteophyte (*white arrow*). Osteophytes are also present on the top of the medial tibial intercondylar eminence and corresponding axial margin of the medial femoral condyle (*black arrow*). **B,** A radiolucent area delineated by a faint sclerotic margin is present in the medial aspect of the cranial intercondylar area at the site of insertion of the cranial meniscotibial ligament (*white arrows*). This radiographic sign indicates a cranial enthesopathy of the medial meniscus. Femoral and tibial osteophytes are also visible. Note the thin horizontal line superimposed over the medial femoral condyle. This line is created by remodeling of the craniomedial margin of the medial femoral condyle and is observed frequently when there is marked-to-severe degenerative joint disease of the medial femorotibial joint (see Fig. 21.16).

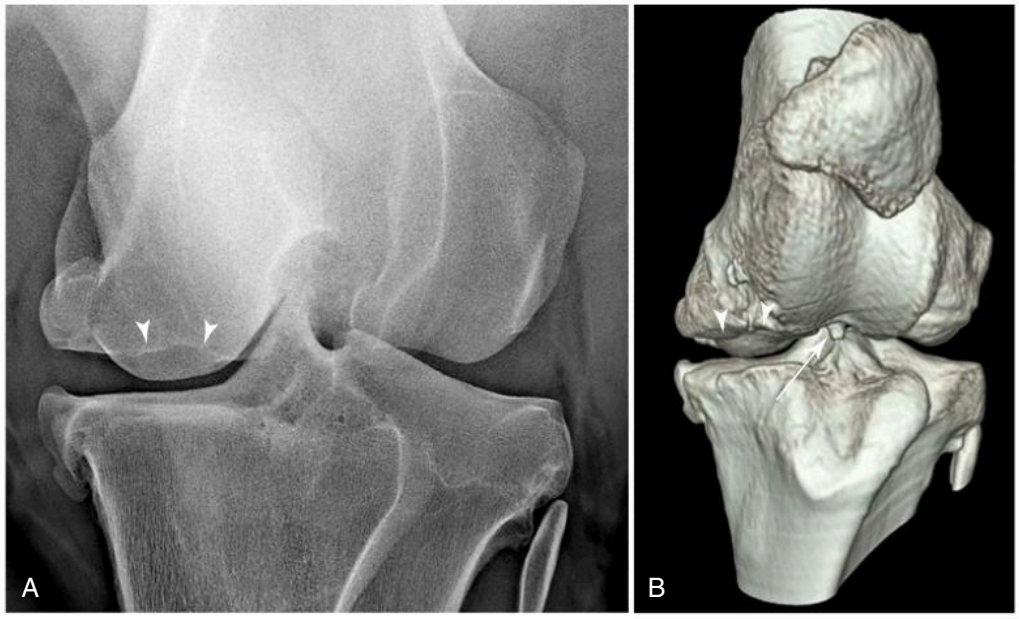
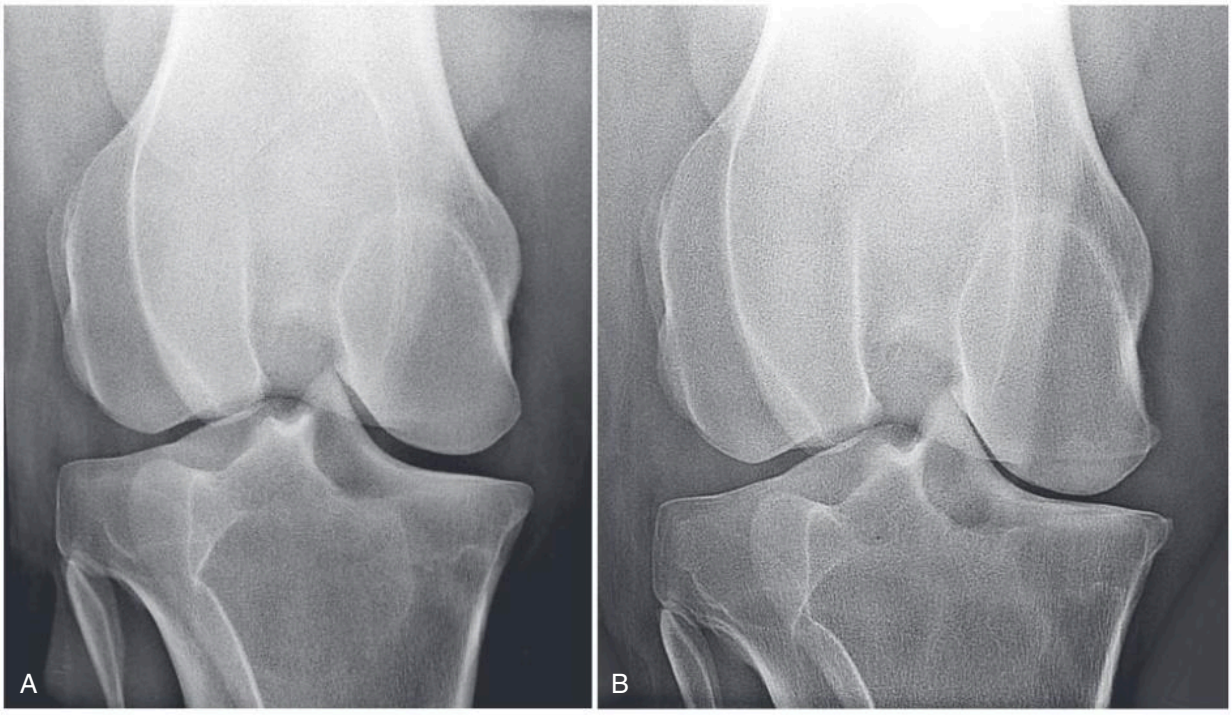


Fig. 21.16 Caudocranial radiograph **(A)** and three-dimensional (3D) volume rendering computed tomography (CT) image **(B)** of the stifle of a horse with advanced medial femorotibial degenerative joint disease. Large broad-based osteophytes are present on the medial femoral and tibial margins. The margin of the femoral osteophyte production extending on the cranial border of the femoral condyle **(B)** creates a thin radiopaque osteophytic line superimposed to the femoral condyle on the caudocranial radiograph **(A, B,** ***arrowheads*****)**. Note the large remodeling of the cranial aspect of the medial intercondylar tubercule **(B,** ***arrow*****)**.



Fig. 21.17 Caudocranial radiograph (close-up view) of the stifle of a horse with severe medial meniscal damage, calcification, and prolapse. The medial femorotibial joint space is narrowed, and the proximal tibial condyle is sclerotic because of a prolapse of the medial meniscus. Calcified meniscal material is present outside the articular space at the medial aspect of the joint. The medial femoral and tibial joint margins have large osteophytes.



eFig. 21.3 Caudocranial view **(A)** of the stifle of 4-year-old French Trotter with a medial collateral desmopathy of the femorotibial joint showing no radiographic abnormalities. Same caudocranial view performs 2.5 years later because of a marked hindlimb lameness **(B)** demonstrating medial femorotibial degenerative joint disease with severe thinning of the joint space and femoral osteophytes. During this period, the horse was able to race with regular injection of corticosteroids in the medial femorotibial joint.

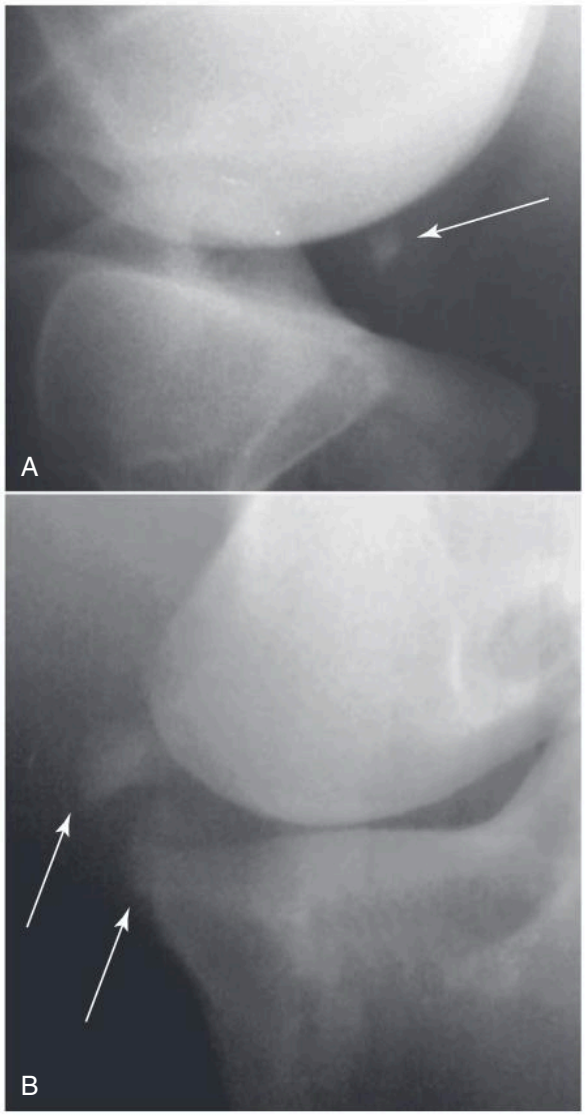


Fig. 21.18 Lateromedial **(A)** and caudocranial **(B)** radiographs (close-up views) of the stifle of two horses with meniscal calcification. **A,** A small radiopaque focus (*white arrow*) is present between the femoral condyle and the caudal aspect of the tibial plateau compatible with calcification in the caudal horn of the medial meniscus. **B,** Two large radiopaque bodies (*white arrows*) at the medial aspect of the medial femorotibial joint correspond to calcified portions of a prolapsed medial meniscus. Note the associated narrowing of the femorotibial joint space.



Fig. 21.19 Caudocranial radiograph **(A)**, computed tomography (CT) **(B)**, fat suppressed magnetic resonance (MR) **(C)**, and ultrasonographic **(D)** images of the stifle of a 11-month-old filly with severe cranial meniscotibial ligament enthesopathy of the lateral meniscus. A large semicircular defect with irregular margins surrounded by severe sclerosis is present in the cranial intercondylar area of the tibia at the site of insertion of the lateral cranial meniscotibial ligament. Note the increased signal around the bone defect in the MR image representing bone edema **(C)** and the presence of small mineralization or bony fragments within the meniscotibial ligament **(B–D)**. The ultrasonographic transverse image obtained at the cranial aspect of the medial femorotibial joint in the flexed stifle shows a hypoechoic area in the deep portion of the ligament and the irregular interrupted hyperechoic bone surface at the site of attachment (*arrow*, compare to normal image in Fig. 21.3D).

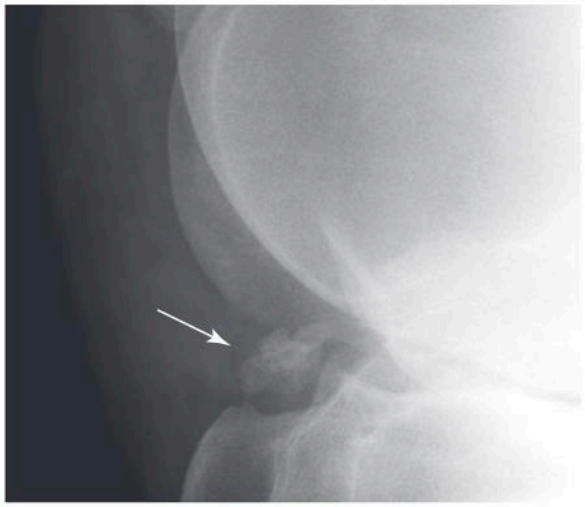


Fig. 21.20 Caudolateral-craniomedial radiograph (close-up view) of the stifle in a horse with severe medial meniscal damage and prolapse. A large bone fragment is visible at the cranial aspect of the femorotibial joint space (*white arrow*), which represents an old avulsion fragment at the cranial meniscotibial ligament attachment.

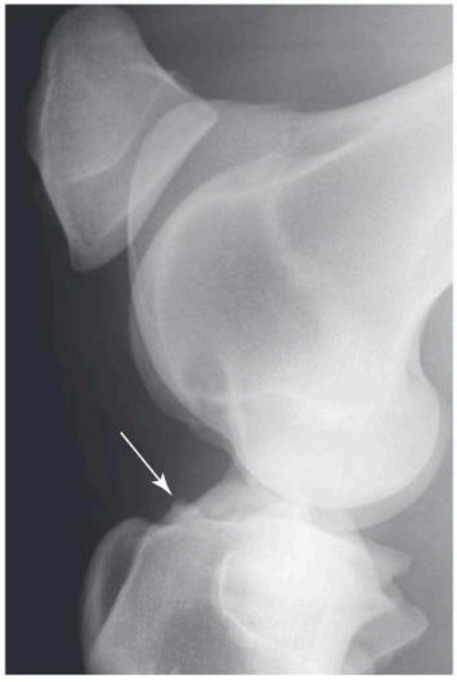


Fig. 21.21 Flexed lateromedial radiograph of an equine stifle. An osseous proliferation is present cranial to the tibial intercondylar eminence (*white arrow*). Ultrasonographically, there was a horizontal fissure and a partial prolapse of the medial meniscus and damage to the medial cranial meniscotibial ligament.

the trochlear ridges of the femur.[36] Ultrasonographic examination adds valuable information in patellar fractures by documenting associated soft tissue injuries and defining the anatomic origin of avulsed fragments, that is, parapatellar fibrocartilages, patellar ligaments, and distal enthesis of the quadriceps femoris muscle.

Tibial and Femoral Fractures

Fractures of the tibial tuberosity are the most commonly reported fractures involving the proximal tibia in adult horses.[36] Trauma with wounds of the tibial tuberosity may lead to sequestrum formation and be associated to lateral patellar ligament damage (Fig. 21.25).[62] In these instances, synovial involvement is uncommon. Fractures involving the intercondylar eminence or the caudal aspect of the proximal tibia are seen in association with cruciate ligament damage and often involve the ligament insertion sites.[57,58,63] The proximal aspect of the tibial diaphysis is the most common site for incomplete fracture of the tibia, which usually begins at the lateral aspect of the bone and spirals distally (eFig. 21.4).[36,64] Radiographic diagnosis of an incomplete fracture may be challenging even if several oblique views are made. Complete rest and repeat radiographs approximately 7 to 10 days after the onset of the acute lameness are indicated. At this stage, the fracture line becomes more visible because of resorption of the fracture margins. In racehorses, tibial fatigue fractures can also be encountered, most commonly in the caudal and proximal metaphyseal region. The most common radiographic signs at

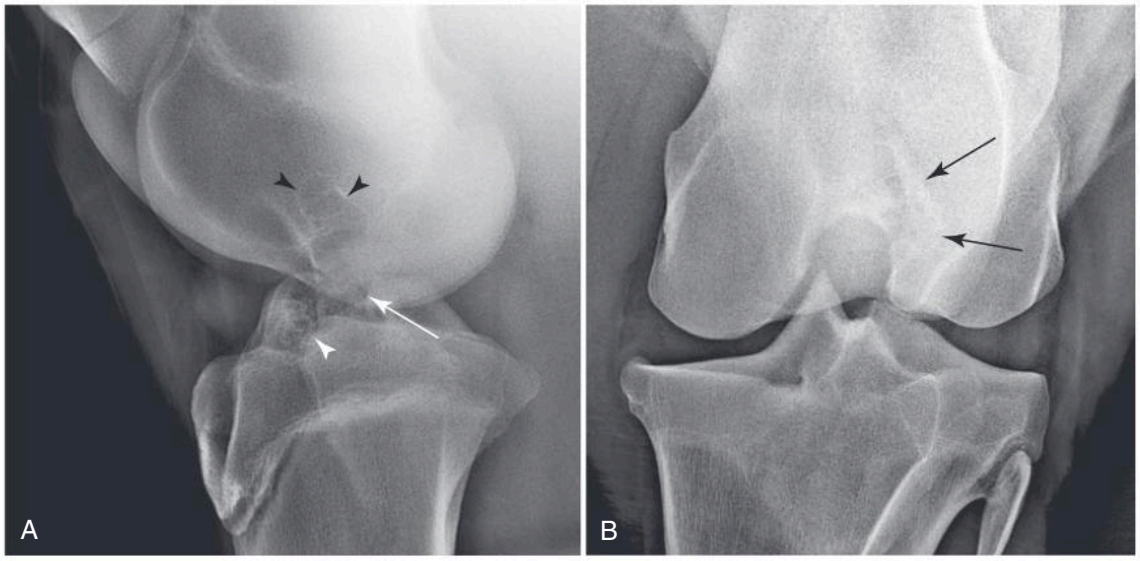


Fig. 21.22 Lateromedial **(A)** and caudocranial **(B)** radiographs of two horses with cruciate ligament injury. **A,** One-year-old colt with a history of trauma 5 months ago. The soft tissue swelling located cranial to the femorotibial joint space without border effacement of the patellar ligaments suggests severe femorotibial joint effusion. Severe opacity changes are visible at the cranial and central tibial intercondylar areas (*white arrowhead*). The caudal aspect of the medial intercondylar eminence is difficult to identify because of increased and heterogeneous opacity seen in the intercondylar area (*white arrow*). In other radiographic views and based on ultrasonographic examination, there were enthesopathies of the cranial meniscotibial ligaments and a fracture of the medial intercondylar eminence suggesting cranial cruciate ligament damage. The large radiolucent area surrounded by a thin sclerotic rim visible in the cranioproximal aspect of the femoral intercondylar fossa (*black arrowheads*) suggests an associated chronic femoral enthesopathy of the caudal cruciate ligament. **B,** Several round coalescing radiolucencies surrounded by sclerosis (*arrows*) are visible at the axial aspect of the lateral femoral condyle in the intercondylar area at the site of femoral attachment of the cranial cruciate ligament and represent the radiographic signs of a severe chronic enthesopathy.



Fig. 21.23 Caudocranial radiograph of the stifle of a horse with a history of previous trauma to the stifle. The medial epicondyle has an irregular surface indicating chronic enthesopathy of the medial collateral ligament (*arrow*). Ultrasound confirmed medial collateral ligament damage by demonstrating a severely enlarged and hypoechoic ligament with loss of its regular fiber architecture.

the site of the stress fracture are periosteal bone proliferation, thickening of the cortical bone, and sclerosis of the adjacent cancellous bone (Fig. 21.26).

Fractures of the femur involving the distal epiphysis are uncommon in adult horses. Trochlear ridge fractures are seen as free sharp fragments and a bone defect in the trochlea or as radiolucent lines in the trochlear ridge in incomplete nondisplaced fractures. These fractures result from direct external trauma and may be associated with patellar fractures.[36] Femoral avulsion fractures of the origin of the common tendon of the peroneus tertius and the extensor digitorum longus are reported in foals (Fig. 21.27).[65,66]

Fibular Fractures

Fibular fractures have been rarely reported as a cause of lameness.[36,67] Care should be taken not to confuse the normal radiolucent line traversing the proximal fibula because of incomplete ossification with a fracture line. Callus formation is a useful radiographic sign of the presence of a fracture.[36,67]

MISCELLANEOUS CONDITIONS INVOLVING THE STIFLE

Calcinosis Circumscripta

Calcinosis circumscripta is localized deposition of calcium in small nodules in subcutaneous tissues or attached to tendons or joint capsules.[68] The lesions of calcinosis circumscripta appear grossly as hard, spherical, nonpainful, subcutaneous, or periarticular swellings. The etiology of calcinosis circumscripta is unknown but thought to be of traumatic origin.[69] In the horse, the predilection site is the lateral aspect of the stifle close to the extensor groove of the tibia.[69] The lesion is visible radiographically as a well-circumscribed, roughly oval accumulation of granular mineral opacities at the lateral aspect of the proximal tibia (Fig. 21.28). Calcinosis circumscripta may be an incidental finding because the lesion rarely causes lameness.[69]

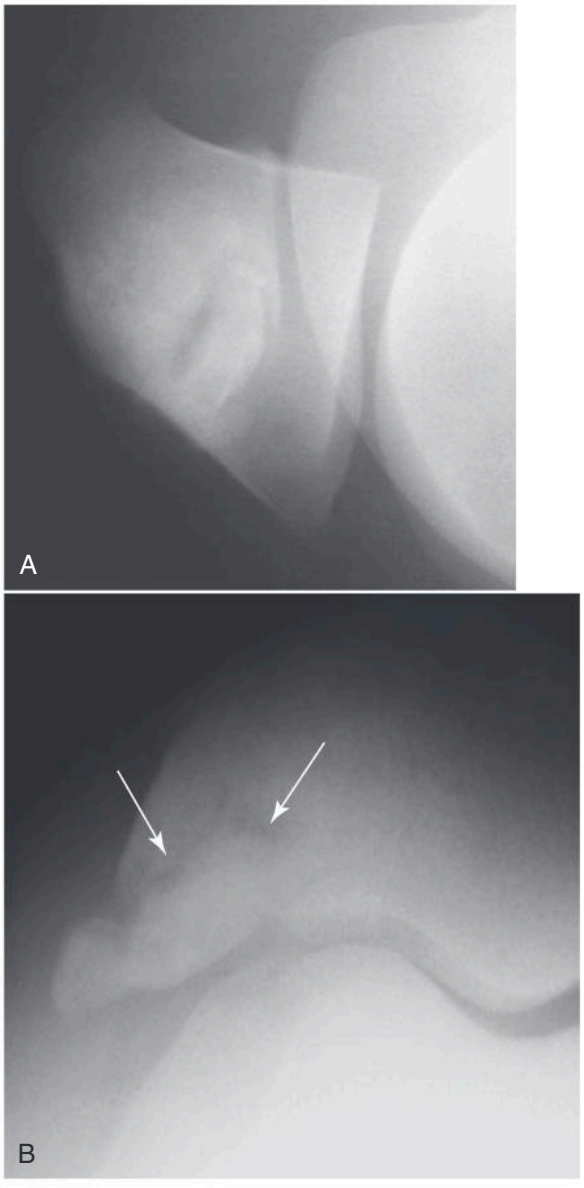


Fig. 21.24 Flexed lateromedial **(A)** and cranioproximal-craniodistal **(B)** radiographs (close-up views) of the stifle of a horse with a chronic nondisplaced fracture of the medial aspect of the patella. **A,** The patella has increased opacity and a radiolucent line at the level of the medial angle. The medial articular surface is irregular and interrupted by the radiolucent line. **B,** The fracture of the medial angle of the patella is seen as an ill-defined radiolucent line (*white arrows*) separating two bone fragments. The fracture involves the medial articular surface of the patella.

Most commonly, there is a firm, nonpainful swelling that has been increasing slowly in size. The lesions are frequently bilateral, and radiographic examination of the contralateral limb is important if surgical removal is considered.

Septic Arthritis and Osteomyelitis

Septic arthritis is inflammation of a joint caused by bacterial invasion and proliferation.[70] Septic arthritis may occur in foals or adult horses. Hematogenous spread is the most common cause of septic arthritis in foals, whereas septic arthritis in adult horses is usually a consequence of penetrating wounds, injection, or surgery.[70]



Fig. 21.25 Lateromedial radiograph of the proximal tibia of a young horse who had a trauma of the stifle with several wounds 3 weeks before. A linear radiopaque fragment is visible at a short distance from the tibia cranially and represents a bone sequestrum detached from the tibial tuberosity. Note the soft tissue swelling at the same level and the bone debris between the sequestrum and the tibia. The cranial surface of the tibial tuberosity is slightly irregular. At ultrasonography the horse had a hypoechoic fistulous tract and a traumatic lesion of the lateral patellar ligament.

Infection of the stifle joint in adult horses is rare. Periarticular infection and abscess after trauma and penetrating wounds is more common than bacterial joint invasion.[70] In foals, the femoropatellar joint and the femorotibial joints are common sites of septic arthritis, and the femur is one of the bones most affected by hematogenous osteomyelitis.[71] Bone changes appear late in the condition in adult horses, whereas they occur earlier in foals. Concurrent septic arthritis and osteomyelitis is common in foals, and foals with osteomyelitis without septic arthritis are usually older.[71] In the same way, foals with a single bone lesion tend to be older than those with multiple bone lesions.[71] Bone changes attributable to osteomyelitis may have a physeal or epiphyseal location in foals and are located differently depending on the joints infected concomitantly. When the femoropatellar joint is affected, osteolysis is mainly seen on the femoral trochlea and/or the patellar articular surface (Fig. 21.29). Subchondral bone abnormalities on the femoral trochlea may be more difficult to assess, because the trochlear ridges normally have an irregular bone surface in young foals during ossification. Femorotibial involvement is often uniaxial (medial or lateral) (Fig. 21.30). Bone involvement is seen as ill-defined radiolucent areas in the subchondral bone of the tibial plateau and/or the femoral condyles, with the medial femoral condyle being affected more commonly.[51,71] Another characteristic of these subchondral radiolucent areas is their potential location in the non–weight-bearing part of the femoral condyles. Physeal osteomyelitis in foals appears as widening of the radiolucent physis and ill-defined physeal margins associated with local swelling. Well-defined radiolucent areas in the subchondral bone may remain evident as long-term sequelae of osteomyelitis when infection is eliminated.



eFig. 21.4 Caudocranial radiograph of the tibial diaphysis of a horse with a 1-week-old incomplete fracture of the tibia. A radiolucent line begins at the lateral aspect of the proximal tibia and spirals distally through the entire tibial diaphysis (*white arrowheads*).

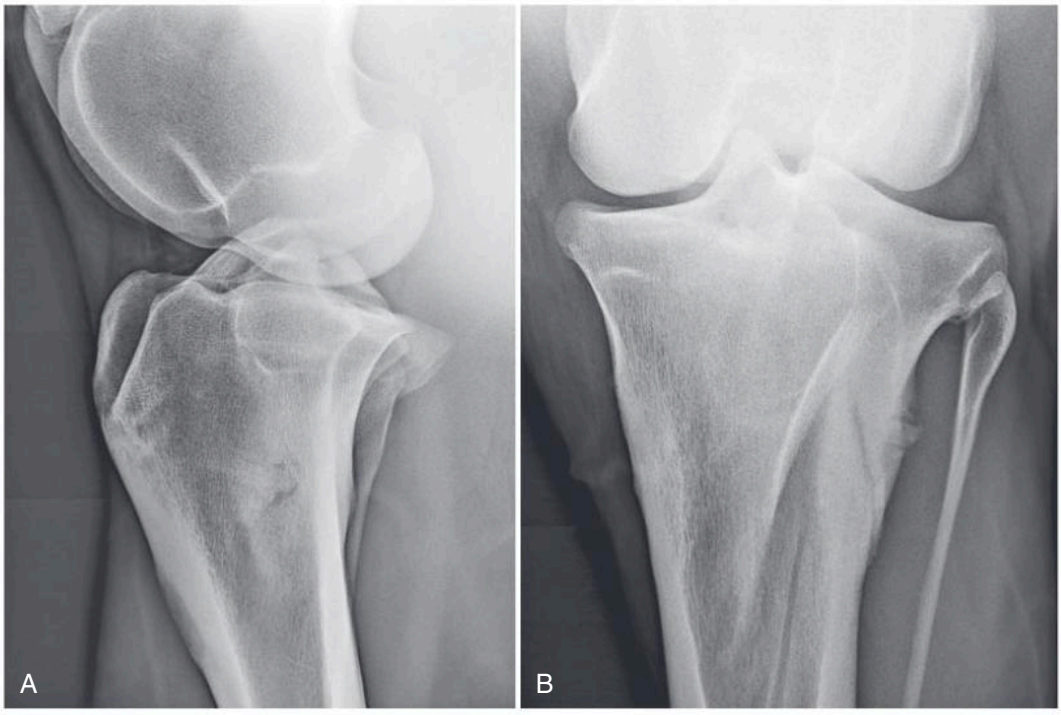


Fig. 21.26 Lateromedial **(A)** and caudocranial **(B)** radiographs of a Thoroughbred horse with a stress fracture of the proximal tibia. The stress fracture is seen as a linear radiolucent line with massive sclerosis of the cancellous bone, thickening of the cortical bone, and focal periosteal bony proliferation in the lateral caudal aspect of the proximal tibial metaphysis.

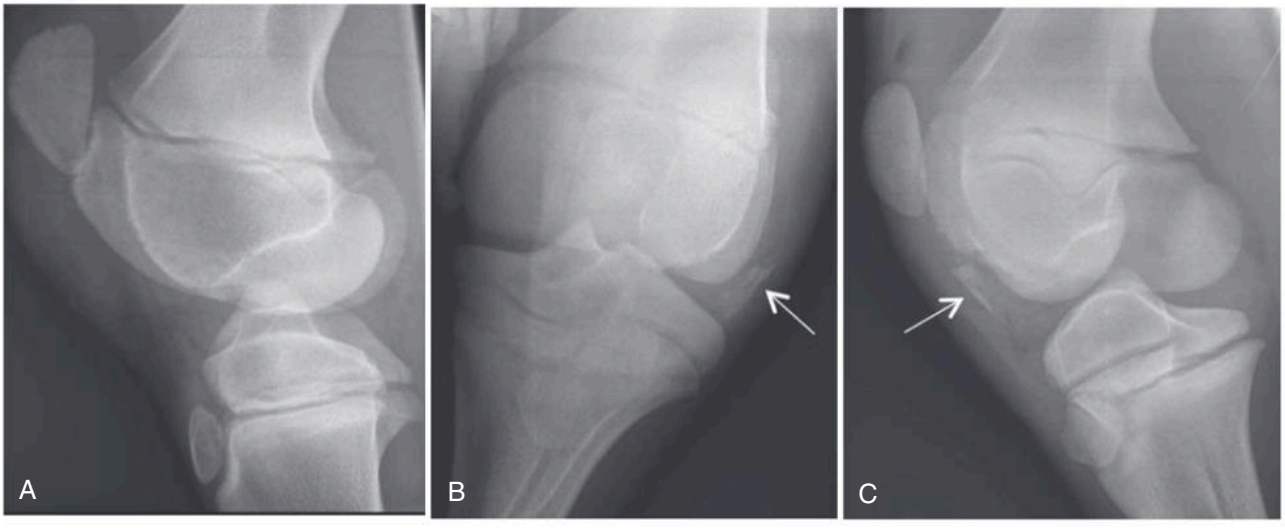


Fig. 21.27 Lateromedial **(A)**, caudocranial **(B)**, and caudolateral-craniomedial oblique **(C)** radiographs of the stifle of a foal with a femoral avulsion fracture at the site of origin of the common tendon of the peroneus tertius and the extensor digitorum longus. Because of its lateral position, the bone fragment is better seen on the caudocranial and on the caudolateral-craniomedial oblique views (*arrows*) but is only visible as a heterogeneous opacity in the area of the extensor fossa superimposed over the femur on the lateromedial radiograph.

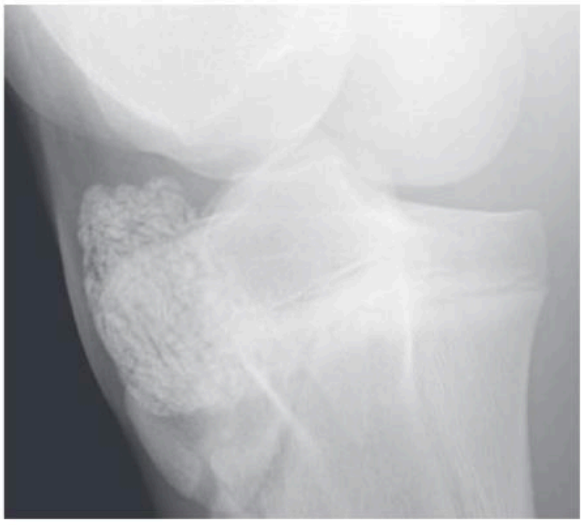


Fig. 21.28 Caudolateral-craniomedial stifle radiograph of a young horse with calcinosis circumscripta. A large cluster of calcified granular material is located at the lateral aspect of the proximal tibia.

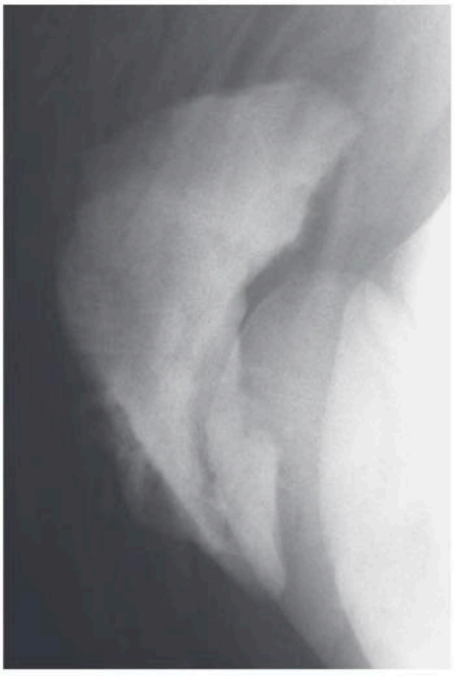


Fig. 21.29 Lateromedial radiograph of the patella of a foal with septic arthritis of the femoropatellar joint. The articular surface of the patella is irregular, and there is severe lysis of the subchondral bone.

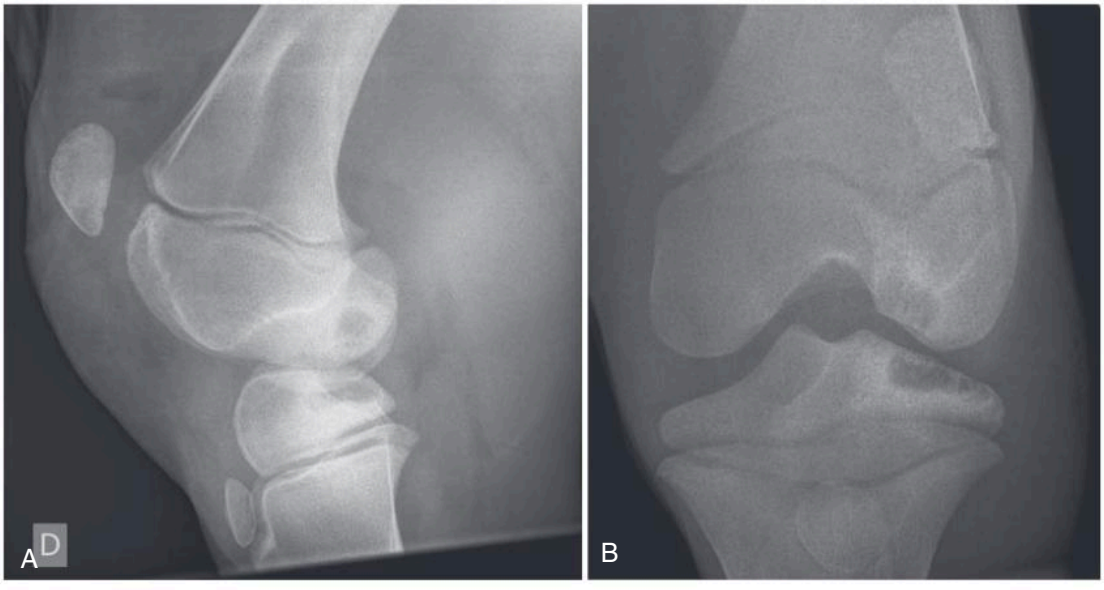


Fig. 21.30 Lateromedial **(A)** and caudocranial **(B)** radiographs of a 4-week-old foal with septic arthritis and osteomyelitis of the stifle. There is severe joint swelling demonstrated by loss of visualization of the middle patellar ligament, lack of visualization of the fat pad, and displacement of the fascial and cutaneous planes. In the caudal aspect of the stifle, two large, slightly heterogeneous, radiolucent areas of infected bone are seen in the axial aspect of the lateral femoral condyle and in the proximal tibia. Surrounding cancellous bone has an increased opacity due to sclerosis.

REFERENCES

1. Preston SA, Zimmel DN, Chmielewski TL, et al. Prevalence of various presale radiographic findings and association of findings with sales price in Thoroughbred yearlings sold in Kentucky. *J Am Vet Med Assoc.* 2010;236(4):440–445.
2. Van Grevenhof EM, Ducro BJ, Van Weeren PR, et al. Prevalence of various radiographic manifestations of osteochondrosis and their correlations between and within joints in Dutch Warmblood horses. *Equine Vet J.* 2009;41(1):11–16.
3. Verwilghen D, Serteyn D, Pille F, et al. Prevalence of radiographic findings in candidate sires (2001–2008). *Vlaams Diergeneeskundig Tijdschrift.* 2009;78:419.
4. Belotta AF, Mayer MN, Waldner CL, et al. X-ray tube operators can be exposed to equal or higher scattered radiation doses to the hand as cassette holders during diagnostic radiographic procedures of the equine vertebral column and limbs. *Am J Vet Res Mar.* 2022 3;83(5):412–418.
5. Jackson MA, Vizard AL, Anderson GA, et al. Identification and prevalence of errors affecting the quality of radiographs submitted to Australian Thoroughbred yearling sale repositories. *Vet Radiol Ultrasound.* 2011;52(3):262–269.
6. Aldrich ED, Goodrich LR, Monahan MK, et al. Radiographic localisation of the entheses of the equine stifle. *Equine Vet J.* 2017;49(4):493–500.
7. Trencart P, Alexander K, De Lasalle J, et al. Radiographic evaluation of the width of the femorotibial joint space in horses. *Am J Vet Res.* 2016;77(2):127–136.
8. Walmsley JP. Diagnosis and treatment of ligamentous and meniscal injuries in the equine stifle. *Vet Clin North Am Equine Pract.* 2005;21(3):651–672.
9. Denoix JM, Audigié F. Imaging of the musculoskeletal system in horses. In: Hinchcliff K, Kaneps AJ, Geor RJ, et al., eds. *Equine Sports Medicine and Surgery—Basic and Clinical Sciences of the Equine Athlete.* Philadelphia: Saunders; 2004:161.
10. De Busscher V, Verwilghen D, Bolen G, et al. Meniscal damage diagnosed by ultrasonography in horses: a retrospective study of 74 femorotibial joint ultrasonographic examinations (2000–2005). *J Equine Vet Sci.* 2006;26:453.
11. Flynn KA, Whitcomb MB. Equine meniscal injuries: a retrospective study of 14 horses. *Proc Am Assoc Equine Pract.* 2002;48:249.
12. Hendrix SM, Baxter GM, McIlwraith CW, et al. Concurrent or sequential development of medial meniscal and subchondral cystic lesions within the medial femorotibial joint in horses (1996–2006). *Equine Vet J.* 2010;42(1):5–9.
13. Coudry V, Denoix JM. Ultrasonography of the femorotibial collateral ligaments of the horse. *Equine Vet Educ.* 2010;17(5):275–279.
14. Denoix JM, Busoni V. Ultrasonography of joints and synovia. In: White NA, Moore JN, eds. *Current Techniques in Equine Surgery and Lameness.* 2nd ed. Philadelphia: Saunders; 1998:643.
15. Hoaglund EL, Barrett MF, Daglish J, et al. Intermediate patellar ligament desmopathy often occurs in conjunction with other stifle abnormalities. *Vet Radiol Ultrasound.* 2019;60(4):416–422.
16. Gottlieb R, Whitcomb MB, Vaughan B, et al. Ultrasonographic appearance of normal and injured lateral patellar ligaments in the equine stifle. *Equine Vet J.* 2016;48(3):299–306.
17. Moiroud CH, Denoix JM. Ultrasound diagnosis of injuries of the cranial meniscotibial ligament of the medial meniscus. *Equine Vet Educ.* 2017;29(11):617–620.
18. Jacquet S, Audigié F, Denoix JM. Ultrasonographic diagnosis of subchondral bone cysts in the medial femoral condyle in horses. *Equine Vet Educ.* 2007;19:47.
19. Cohen JM, Richardson DW, McKnight AL, et al. Long-term outcome in 44 horses with stifle lameness after arthroscopic exploration and debridement. *Vet Surg.* 2009;38(4):543–551.
20. Davis JG, García-López JM. Arthroscopic findings and long-term outcomes in 76 sport horses with meniscal injuries (2008–2018). *Vet Surg.* 2022;51(3):409–417.
21. De Busscher V, Schreder A, Busoni V, et al. Histological study of the horse stifle menisci in relation with ultrasonographic aspect: preliminary study. *Italian J Anat Embryol.* 2006;111:132.
22. Santos MP, Gutierrez-Nibeyro SD, McKnight AL, et al. Gross and histopathologic correlation of low-field magnetic resonance imaging findings in the stifle of asymptomatic horses. *Vet Radiol Ultrasound.* 2015;56(4):407–416.
23. Adrian AM, Barrett MF, Werpy NM, et al. A comparison of arthroscopy to ultrasonography for identification of pathology of the equine stifle. *Equine Vet J.* 2017;49(3):314–321.
24. De Lasalle J, Alexander K, Olive J, et al. Comparisons among radiography, ultrasonography and computed tomography for ex vivo characterization of stifle osteoarthritis in the horse. *Vet Radiol Ultrasound.* 2016;57(5):489–501.
25. Valdés-Martínez A. Computed tomographic arthrography of the equine stifle joint. *Vet Clin North Am Equine Pract.* 2012;28(3):583–598.
26. Aßmann AD, Ohlerth S, Suárez Sánchez-Andráde J, et al. Ex vivo comparison of 3 Tesla magnetic resonance imaging and multidetector computed tomography arthrography to identify artificial soft tissue lesions in equine stifles. *Vet Surg.* 2022;51(4):648–657.
27. Nelson BB, Kawcak CE, Goodrich LR, et al. Comparison between computed tomographic arthrography, radiography, ultrasonography, and arthroscopy for the diagnosis of femorotibial joint disease in western performance horses. *Vet Radiol Ultrasound.* 2016;57(4):387–402.
28. Waselau M, McKnight A, Kasparek A. Magnetic resonance imaging of equine stifles: technique and observations in 76 clinical cases. *Equine Vet Educ.* 2020;32(10):85–91.
29. Daglish J, Frisbie DD, Selberg KT, et al. High field magnetic resonance imaging is comparable with gross anatomy for description of the normal appearance of soft tissues in the equine stifle. *Vet Radiol Ultrasound.* 2018;59(6):721–736.
30. Vekens EV, Bergman EH, Vanderperren K, et al. Computed tomographic anatomy of the equine stifle joint. *Am J Vet Res.* 2011;72(4):512–521.
31. Denoix JM, Jeffcott LB, McIlwraith CW, et al. A review of terminology for equine juvenile osteochondral conditions (JOCC) based on anatomical and functional considerations. *Vet J.* 2013;197(1):29–35.
32. Dik KJ, Enzerink E, Van Weeren PR. Radiographic development of osteochondral abnormalities in the hock and stifle of Dutch Warmblood foals, from age 1 to 11 months. *Equine Vet J.* 1999;31:9–15.
33. Bourzac C, Alexander K, Rossier Y, et al. Comparison of radiography and ultrasonography for the diagnosis of osteochondritis dissecans in the equine femoropatellar joint. *Equine Vet J.* 2009;41(7):685–692.
34. Robert C, Valette JP, Denoix JM. Correlation between routine radiographic findings and early racing career in French trotters. *Equine Vet J Suppl.* 2006;36:473–478.
35. Kane AJ, Park RD, McIlwraith CW, et al. Radiographic changes in Thoroughbred yearlings. Part 1: prevalence at the time of the yearling sales. *Equine Vet J.* 2003;35(4):354–365.

36. Butler JA, Colles CM, Dyson SJ, et al. *Clinical Radiology of the Horse*. 3rd ed. London: Blackwell; 2008.
37. Trostle SS, Casinella LL, Sussman KH, et al. What is your diagnosis? Osseous cystlike lesion of the patella. *J Am Vet Med Assoc*. 2007;230(5):663–664.
38. Jacquet S, Robert C, Valette JP, et al. Evolution of radiological findings detected in the limbs of 321 young horses between the ages of 6 and 18 months. *Vet J*. 2013;197(1):58–64.
39. Santschi EM, Prichard MA, Whitman JL, et al. Stifle radiography in Thoroughbreds from 6 to 18 months of age. *Equine Vet Educ*. 2019;32(10):78–84.
40. Hoey S, O'Sullivan J, Byrne J, et al. Ultrasound screening protocol for osteochondrosis at selected predilection sites in thoroughbred yearlings, Ir. *Vet J*. 2022;75(1):8.
41. Martel G, Crowley D, Olive J, et al. Ultrasonographic screening for subclinical osteochondrosis of the femoral trochlea in foals (28–166 days old): a prospective farm study. *Equine Vet J*. 2018;50(3):312–320.
42. Baccarin RY, Martins EA, Hagen SC, et al. Patellar instability following experimental medial patellar desmotomy in horses. *Vet Comp Orthop Traumatol*. 2009;22(1):27–31.
43. Labens R, Busoni V, Peters F, et al. Ultrasonographic and radiographic diagnosis of patellar fragmentation secondary to bilateral medial patellar ligament desmotomy in a Warmblood gelding. *Equine Vet Educ*. 2005;17:201.
44. McIlwraith CW. Osteochondral fragmentation of the distal aspect of the patella in horses. *Equine Vet J*. 1990;22(3):157–163.
45. Engelbert TA, Tate LP, Richardson DC, et al. Lateral patellar luxation in miniature horses. *Vet Surg*. 1993;22(4):293–297.
46. Pagliara E, Cantatore F, Pallante M, et al. Lateral patellar instability in Standardbred horses at the weanling age: clinical and morphological features in four cases (2017–2019). *Equine Vet Educ*. 2022;34(1):47–53.
47. Hall MS, Jalim SL, Russell TM. Distal luxation of the patella in a horse. *Aust Vet J*. 2010;88(10):396–398.
48. Pérez-Nogués M, Derham A, Marmion J, et al. Progression of shallow medial femoral condyle radiographic lucencies in Thoroughbred repository radiographs and their influence on future racing careers. *Equine Vet J*. 2021;53(2):287–293.
49. Scott GS, Crawford WH, Colahan PT, et al. Arthroscopic findings in the horses with subtle radiographic evidence of osteochondral lesions of the medial femoral condyle: 15 cases (1995–2002). *J Am Vet Med Assoc*. 2004;224(11):1823–1826.
50. Howard RD, McIlwraith CW, Trotter GW. Arthroscopic surgery for subchondral cystic lesions of the medial femoral condyle in horses: 41 cases (1988–1991). *J Am Vet Med Assoc*. 1995;206(6):842–850.
51. Hance SR, Schneider RK, Embertson RM, et al. Lesions of the caudal aspect of the femoral condyles in foals: 20 cases (1980–1990). *J Am Vet Med Assoc*. 1993;202(4):637–646.
52. Haggett EF, Foote AK, Head MJ, et al. Necrosis of the femoral condyles in a four-week-old foal: clinical, imaging and histopathological features. *Equine Vet J*. 2012;41:91–95.
53. Bonilla AG, Bertone AL, Brokken MT, et al. Concurrent or sequential tibial subchondral cystic lesions in 4 horses with medial femoral condyle subchondral cystic lesions. *J Am Vet Med Assoc*. 2016;249(11):1313–1318.
54. Textor JA, Nixon AJ, Lumsden J, et al. Subchondral cystic lesions of the proximal extremity of the tibia in horses: 12 cases (1983–2000). *J Am Vet Med Assoc*. 2001;218(3):408–413.
55. Audigié F. *Unpublished Data*. 2011.
56. Dillenbeck MB, Whitcomb J, Dechant, et al. Ultrasonographic diagnosis of lateral meniscal rupture in two horses with severe lameness. *Equine Vet Educ*. 2022;34(1):21–26.
57. Edwards RB, Nixon AJ. Avulsion of the cranial cruciate ligament insertion in a horse. *Equine Vet J*. 1996;28(4):334–336.
58. Rose PL, Graham JP, Moore I, et al. Imaging diagnosis—caudal cruciate ligament avulsion in a horse. *Vet Radiol Ultrasound*. 2001;42(5):414–416.
59. Dyson S, Wright I, Kold S, et al. Clinical and radiographic features, treatment and outcome in 15 horses with fracture of the medial aspect of the patella. *Equine Vet J*. 1992;24(4):264–268.
60. Dyson SJ. Stifle trauma in the event horse. *Equine Vet Educ*. 1994;6:234.
61. McLellan J, Plevin S, Taylor E. Concurrent patellar fracture and lateral collateral ligament avulsion as a result of trauma in three horses. *J Am Vet Med Assoc*. 2012;240(10):1218–1222.
62. Gottlieb R, Whitcomb MB, Vaughan B, et al. Ultrasonographic appearance of normal and injured lateral patellar ligaments in the equine stifle. *Equine Vet J*. 2016;48(3):299–306.
63. Rubio-Martínez LM, Redding WR, Bladon B, et al. Fracture of the medial intercondylar eminence of the tibia in horses treated by arthroscopic fragment removal (21 horses). *Equine Vet J*. 2018;50(1):60–64.
64. Ross MW. The crus. In: Ross MW, Dyson SJ, eds. *Diagnosis and Management of Lameness in the Horse*. 2nd ed. St Louis: Elsevier/Saunders; 2011:526.
65. Blikslager AT, Bristol DG. Avulsion of the origin of the peroneus tertius tendon in a foal. *J Am Vet Med Assoc*. 1994;204(9):1483–1485.
66. Holcombe SJ, Bertone AL. Avulsion fracture of the origin of the extensor digitorum longus muscle in a foal. *J Am Vet Med Assoc*. 1994;204(10):1652–1654.
67. Engiles JB, Orsini JA, Ross MW. What is your diagnosis? Fracture of the fibula. *J Am Vet Med Assoc*. 2004;224(9):1429–1430.
68. Studdert VP, Gay CC. *Blood DC: Saunders Comprehensive Veterinary Dictionary*. 4th ed. St Louis: Elsevier/Saunders; 2012.
69. Milner PI. Calcinosis Circumscripta in the horse. *Equine Vet Educ*. 2009;21:589.
70. Bertone A. Infectious arthritis. In: Ross MW, Dyson SJ, eds. *Diagnosis and Management of Lameness in the Horse*. 2nd ed. St Louis: Elsevier/Saunders; 2011:677.
71. Neil KM, Axon JE, Begg AP, et al. Retrospective study of 108 foals with septic osteomyelitis. *Aust Vet J*. 2010;88(1–2):4–12.

ELECTRONIC RESOURCES

Additional information related to the content in Chapter 21 can be found online at eBooks.Health.Elsevier.com.

- Chapter Quiz

CHAPTER 22

Equine Tarsus

Jody E. Lawver

TARSAL ANATOMY

The equine tarsus is a complex joint composed of a large centrally located talus that articulates with the tibial cochleae proximally, the calcaneus plantarly and medially, and central and fourth tarsal bones distally. The calcaneus has a large medial rectangular projection, the sustentaculum tali, that forms the osseous boundaries of the tarsal canal for passage of the lateral digital flexor tendon. The elongated calcaneal tuber provides a broad surface for the common calcaneal tendon insertion. The fourth tarsal bone is the largest of the cuboidal bones, located laterally, and spans the height of both the central tarsal and third tarsal bone which are large flat bones stacked upon one another. The smaller first and second tarsal bones are usually fused and located plantaromedially. There are five main joints of the tarsus, including the high motion tibiotarsal (also called tarsocrural) joint and low motion talocalcaneal, talocalcaneal-centroquartal (proximal intertarsal), centrodistal (also called distal intertarsal), and tarsometatarsal joints.[1] The tibiotarsal, talocalcaneal, and proximal intertarsal joints communicate in all horses.[2] The centrodistal and tarsometatarsal joints communicate in approximately a third of horses.

A myriad of tendons and ligaments support and traverse the tarsus. Separation into four quadrants, dorsal, plantar, medial, and lateral, simplifies anatomic understanding (Box 22.1). A recent review of radiographic tarsal soft tissue attachments is available.[3]

Neonatal and Juvenile Tarsus

Normal tarsal cuboidal bones are all present and nearly fully ossified in a skeletally mature foal at birth with only slightly rounded bone margins and mildly widened joint spaces. The talar trochleae should be convex at birth but may have slightly roughed or granular margins. The tibial medial malleolus is incompletely ossified, often with mildly roughened margin but is not a separate apophysis. The tibial lateral malleolus and calcaneal tuber are separate apophyses usually present at birth or shortly after and fuse by 3 months (see Fig. 22.18) and between 16 and 28 months, respectively.[4,5] The third metatarsal bone proximal physis and usually the first and second tarsal bones should be completely fused at birth.[5] The distal tibial physis fuses between 17 and 24 months.[4] Endochondral, apophyseal, and physeal ossification is generally a bilaterally symmetric process and radiographs of both tarsi should be acquired for comparison of questionable abnormalities.

Normal Tarsal Variants and Incidental Findings

- Lateral or medial trochlear ridge of the talus slight flattening or mild focal concavity unassociated with sclerosis and/or fragmentation[6] (Fig. 22.1).
- Medial trochlear talar ridge distal margin varied shape and contour with occasional small rounded osseous fragments, referred to as "dew drop" lesions[1,6] (see Fig. 22.1).
- Fused versus unfused first and second tarsal bones.[4]

TARSAL RADIOGRAPHY

Complete tarsal evaluation requires four projections, including dorsoplantar (DPl), lateromedial (LM, 5°lateroproximal-mediodistal oblique, or 5°LPrMDiO), dorsolateral-plantaromedial (D45°MPlLO, DMPLO, or medial oblique), and dorsomedial-plantarolateral (D60°LPlMO, DLPMO, or lateral oblique) (Box 22.2). Given inherently narrowed distal tarsal joints, the horse should be square and radiographed on a level surface with x-ray beam crosshairs centered on the distal tarsus. When standard views fail to identify the cause of lameness localized to the tarsus,

Box • 22.1

Soft Tissues of the Tarsus Separated Into Compartments

Dorsal Quadrant
- Cranialis tibialis musculotendinous portion with medial (cunean) tendon branch and cunean bursa
- Fibularis (peroneus) tertius ligament with lateral branch
- Talometatarsal ligament (dorsal tarsometatarsal ligament)
- Long digital extensor tendon

Medial Quadrant
- Long and three short (superficial, middle, deep) tibiotarsal collateral ligaments
- Medial digital flexor tendon

Lateral Quadrant
- Long and three short (superficial, middle, deep) tibiotarsal collateral ligaments
- Lateral digital extensor tendon

Plantar Quadrant
- Lateral digital flexor within the tarsal sheath
- Long plantar ligament
- Common calcaneal tendon:
  - Superficial digital flexor, gastrocnemius, accessory ligament (composed of the biceps femoris, semitendinosus, and vestigial soleus)
- Calcaneal bursae (subcutaneous, intertendinous, gastrocnemius calcaneal bursae):
  - Intertendinous and gastrocnemius calcaneal bursae are contiguous in all horses
  - Subcutaneous and intertendinous calcaneal bursae communicate in approximately 40% of horses

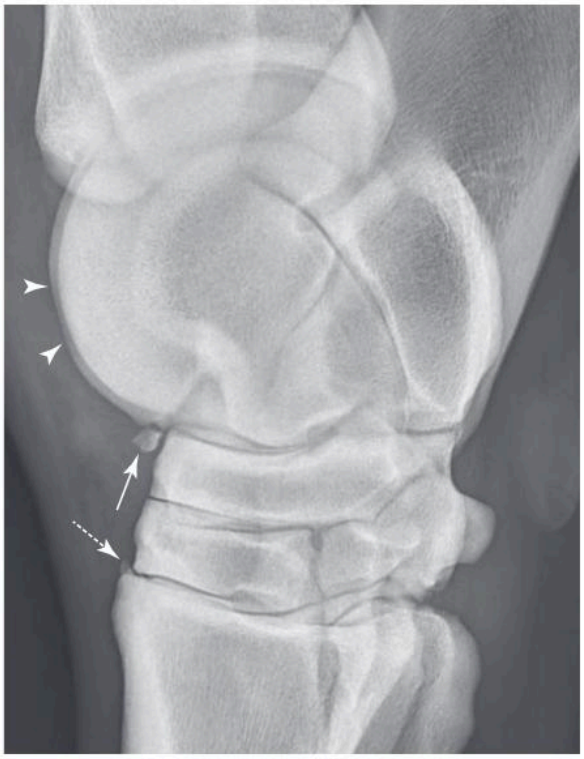


Fig. 22.1 Lateromedial (LM) projection depicting normal variants of slight medial trochlear ridge flattening (*white arrowheads*) and a separate osseous body at the distal medial trochlear ridge (*white arrow*) which should not be mistaken for osteochondrosis. Small, smoothly margined bone proliferation of the dorsal third metatarsal bone (*white dashed arrow*) with smooth margination of the third tarsal bone is generally incidental enthesopathy.

additional oblique and stressed radiographic views often aid lesion characterization (see Box 22.2).

DEVELOPMENTAL OSSEOUS CONDITIONS

Osteochondrosis and Osteochondritis Dissecans

Osteochondrosis (OC) is a common juvenile bone disorder. OC is caused by focal endochondral vascular failures often of unknown etiology,[7] and current investigations of heritable/genetic causes or acquired causes such as sepsis, physiologic or traumatic vascular insult, or metabolic/nutritional imbalances are ongoing.[7,8] Osteochondritis dissecans (OCD) is a condition in which OC leads to the separation of bone and cartilage fragments into the joint resulting in joint inflammation. Separated osteochondral fragments may remain attached or become loose within the joint and may never ossify requiring ultrasound or arthroscopy for identification. OC can occur in any breed, although is most common in Standardbreds (10.5%–35%), Warmbloods (20%), and Thoroughbreds (20%) and uncommon in ponies.[9] Affected yearlings or juvenile horses early in training generally present with variable tibiotarsal joint effusion (bog spavin) and/or variable degrees of lameness. Severity of joint effusion does not always correlate with the degree of lameness. Clinical signs are occasionally absent. Because OC is found in multiple joints in 50% of cases[7] and commonly bilateral, screening radiographs or systematic ultrasound[10] of the contralateral joint and other joints with OC predilection is often performed in racing and performance stock.

The four major tarsal OC predilection sites are within the tibiotarsal joint and include the intermediate cochlear ridge of the tibia (ICRT, also known as DIRT for distal intermediate ridge of the tibia), lateral talar trochlear ridge, medial talar trochlear ridge, and tibial medial malleolus articular margin[11–13] (Figs. 22.2 and 22.3, eFigs. 22.1 and 22.2). DMPLO and D20PLMO are the most helpful projections; thus, acquiring a D20PLMO for evaluation of the medial malleolus articular margin is crucial when evaluating horses for tarsal OC lesions. Other less common OC locations include the proximal weight-bearing portion of the medial trochlear ridge of the talus[14] and medial margin of the intermediate cochlear ridge of the talus[15] (see Fig. 22.2). These unique OC locations often require additional oblique and/or flexed projections for detection. OC of the lateral tibial malleolus and medial proximal tubercle of the talus has been reported although soft tissue avulsion fragments, particularly of the deep collateral ligaments, may mimic OC at these locations.[16]

Tarsal osteochondral lesions identified in young foals with no clinical signs may be monitored for progressive ossification with maturation however bone abnormalities are likely permanent after 5 months of age.[9,17] OC associated with joint effusion or lameness of any aged animal should prompt surgical consultation.

Radiographic features of OC include:

1. Intracapsular swelling of the tibiotarsal joint.
2. Subchondral bone margin flattening, irregularity or concave defect of parent bone generally accompanied by peripheral sclerosis.
3. Faint to well-mineralized rounded osseous fragments, although fragmentation may remain as unossified cartilage requiring ultrasound or arthroscopy for identification.
4. Eventual osteoarthritis (OA).

Fragmentation of the Proximal Talar Tubercle

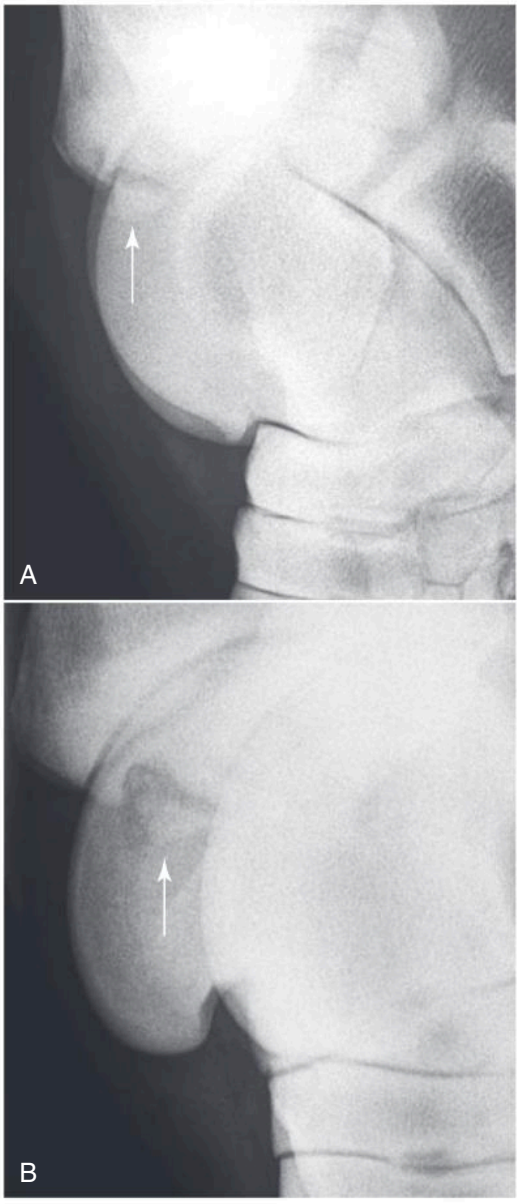
Osseous fragments originating from the proximomedial tubercle of the talus (Fig. 22.4) are more common in Warmbloods and are occasionally bilateral. They may represent an additional site of OC, although trauma to the medial short deep collateral ligament, medial talocalcaneal or tarsal plantar ligament has also been proposed. Medial fragmentation of this tubercle may be more clinically significant compared to plantar fragmentation, as the medial aspect serves as the insertion site of the medial short deep collateral ligament. A calcaneal dorsoplantar skyline projection can improve localization. However, tubercle fragmentation is often incidental in sound horses without tibiotarsal effusion, so its clinical significance should be carefully weighed against other plausible causes.

Subchondral Osseous Cyst-Like Lesions

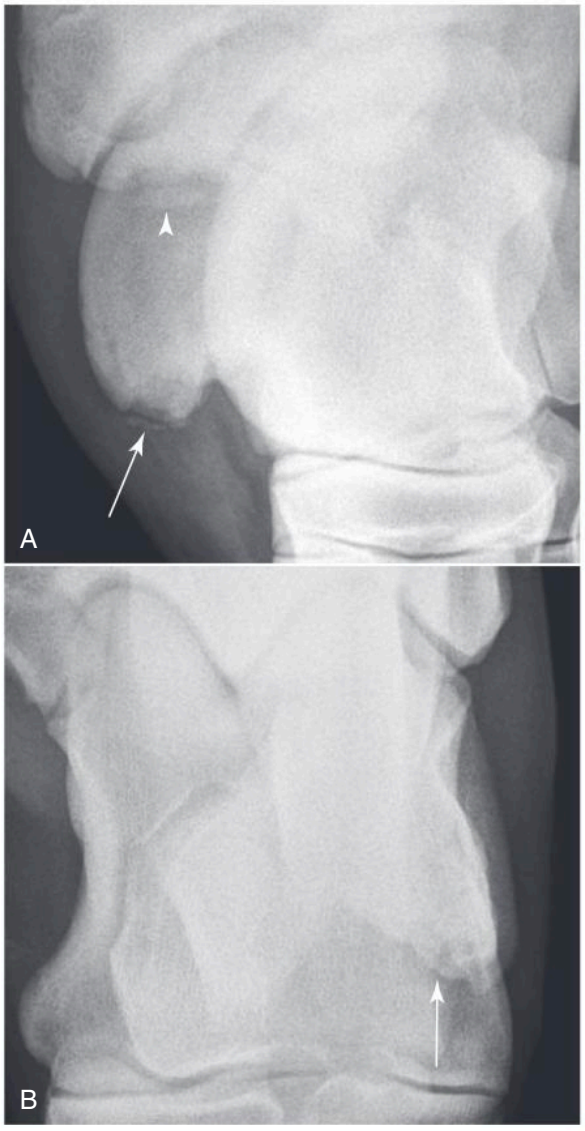
Tarsal subchondral osseous cyst-like lesions (SOCLs) are rare and sparsely reported. They occur in both older and younger horses and may be either developmental or acquired. Possible causes include joint sepsis, trauma to the articular cartilage or underlying bone, or OC. The central and third tarsal bones, talus, and distal tibia are most affected, and horses may be lame or sound, with or without joint effusion. Classically, SOCLs are centrally radiolucent or hyperintense on magnetic resonance imaging (MRI) with intense surrounding regional sclerosis (Fig. 22.5). A flexed lateral projection to remove calcaneal summation may assist in identifying talar[18] (Fig. 22.6, eFig. 22.3) or distal tibial SOCLs since standard radiographs occasionally appear normal. As many SOCLs cause intense sclerosis additional evaluation with computed tomography (CT) or MRI is helpful in differentiating a cyst-like lesion from other causes of sclerosis.[19,20]

Incomplete Cuboidal Bone Ossification (Also Termed *Aseptic Necrosis*)

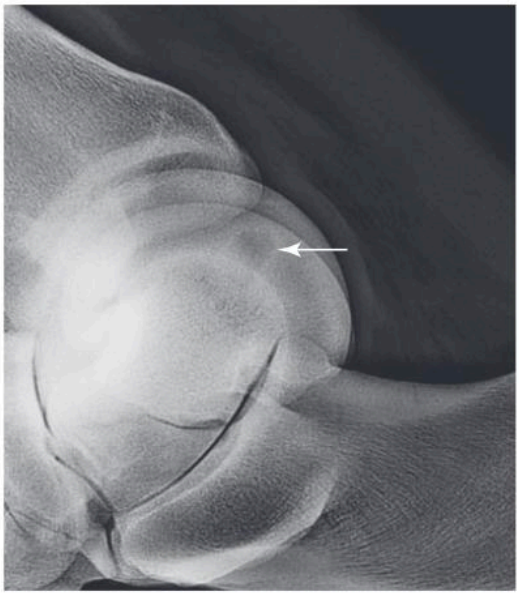
If cuboidal bone ossification is incomplete, typical of premature or dysmature foals, and the foal is allowed to exercise normally, the underdeveloped bones are prone to collapse and crush injury (Fig. 22.7, eFig. 22.4). Wedge shaping that commonly



eFig. 22.1 Lateromedial **(A)** and plantarolateral-dorsomedial **(B)** radiographs of the tarsus of a horse with osteochondrosis of the intermediate ridge of the tibia. A bone fragment is visible distal to a concave defect in the intermediate ridge of the tibial cochlea (*white arrows*). The fragment is easier to see on the plantarolateral-dorsomedial view, because only the lateral trochlear ridge of the talus is superimposed on it.



eFig. 22.2 Plantarolateral-dorsomedial **(A)** and dorsoplantar **(B)** radiographs of the tarsus of a young horse with osteochondrosis of the intermediate ridge of the tibia and the lateral talar ridge. A bone fragment is present adjacent to the intermediate ridge of the tibia on the plantarolateral-dorsomedial oblique view (*white arrowhead*). A defect in the distal extremity of the lateral trochlear ridge is visible on both views (*white arrows*). At this level, the bone surface is irregular, and two thin bony fragments are attached by a radiolucent junction to the edge of the ridge.



eFig. 22.3 Flexed lateromedial radiograph of the tarsus. There is a radiolucent subchondral cyst-like lesion in the weight-bearing portion of the lateral talar ridge (*white arrow*).



eFig. 22.4 Lateromedial radiograph of a 5-day-old foal with incomplete ossification of the tarsal bones. The third tarsal bone is narrower dorsally and has a wedge shape. The tarsometatarsal joint space is uneven and larger dorsally. The opacity of the dorsal portion of the third tarsal bone is heterogeneous, and there are small ill-defined radiolucent areas. This foal had concomitant septic arthritis and osteomyelitis.

Box • **22.2**

Orthogonal, Oblique, and Stressed Radiograph Projections of the Tarsus and Their Uses

Standard Projections

Dorsoplantar (DPl)

- Elevating the generator 5 to 10 degrees proximally will orient the x-ray beam through the lateral joint spaces.
- Generator at 0 degrees horizontal with the long axis of the tarsus better orients the x-ray beam through the medial joint space. Preferred view as most distal tarsal pathology occurs medially.

Lateromedial (5°lateroproximal-mediodistal oblique or 5°LPrMDiO)

- 5 degrees lateral obliquity of the x-ray generator plantar from midsagittal plane is preferred over true 0 degrees LM projections as it will completely superimpose the talar trochlea, improving talocalcaneal joint space evaluation (Fig. 22.2A).

Dorsolateral-plantaromedial (D45°MPlLO, DMPLO, or medial oblique) (Fig. 22.2C).

Dorsomedial-plantarolateral (D60°LPlMO, DLPMO, or lateral oblique) (Fig. 22.2D).

Additional Projections

Dorso20°lateral to plantaromedial oblique (D20°LPlMO)

- Evaluation of the medial malleolar subchondral bone for osteochondrosis (Fig. 22.2B).
- Detection of incomplete sagittal fractures of the talus in racing breeds (Fig. 22.17B).

Flexed plantar 75 degrees proximal- plantarodistal oblique (Flexed Pl75°PrPDiO or calcaneal skyline)

- Improved visualization of the proximal talar tubercle for fragmentation or avulsion (Fig. 22.4E).
- Plantaroproximal view of the sustentaculum tali, tarsal groove and calcaneal tuber for abnormal osseous remodeling or lysis, or mineralization of the lateral digital flexor tendon.
- Highlights a small portion of the plantar medial trochlear ridge and medial aspect of the talocalcaneal joint.

Flexed lateromedial (Flexed LM)

- Offsets tibial cochleae from the weight-bearing portion of the proximal talar trochleae for proximoplantar osteochondral fragments, fractures, or bone remodeling. Adding mild proximal or distal obliquity to the flexion can additionally reduce medial/lateral talar trochlea superimposition augmenting individual evaluation (Fig. 22.6C).
- Assists in identification of distal tarsal luxations (Fig. 22.11).

Flexed dorsoplantar (Flexed DPl)

- Removes superimposition of the talar trochlea from the calcaneus providing orthogonal plane evaluation of individual trochlea and cochlea subchondral bone margins.
- Challenging to perform.

Dorso 30 degrees medial to plantarolateral oblique (D30°MPlLO)

- Offsets proximal talar tubercle from the talus in cases of tubercle fragmentation (Fig. 22.4D).
- In clinically suspected central tarsal bone sagittal fractures, multiple obliques D30-550°MPlLO at 5 to 10 degree intervals may be necessary to align the x-ray beam tangential to the fracture plane (Fig. 22.15C).

Dorsoplantar (DPl) with medial or lateral limb stress

- Confirms pathologic joint space widening of collateral ligament ruptures and/or osseous malalignment indicative of subluxation/luxation (Fig. 22.14C).

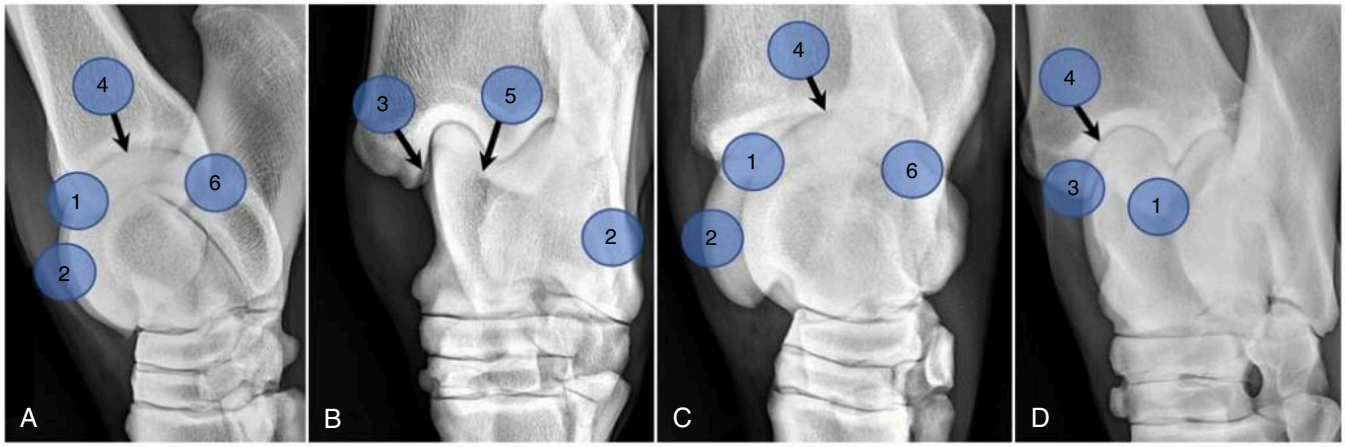


Fig. 22.2 Lateral **(A)**, D20PLMO **(B)**, DMPLO **(C)**, and DPLMO **(D)** normal tarsal radiographs illustrating the predilection sites of osteochondritis dissecans. *1*, Intermediate cochlear ridge of the tibia (ICRT); *2*, lateral talar trochlear ridge; *3*, tibial medial malleolus; *4*, medial talar trochlear ridge (uncommon); *5*, medial margin intermediate cochlear ridge of the tibia (uncommon); *6*, proximal tubercle of the talus (not conclusively osteochondrosis etiology).

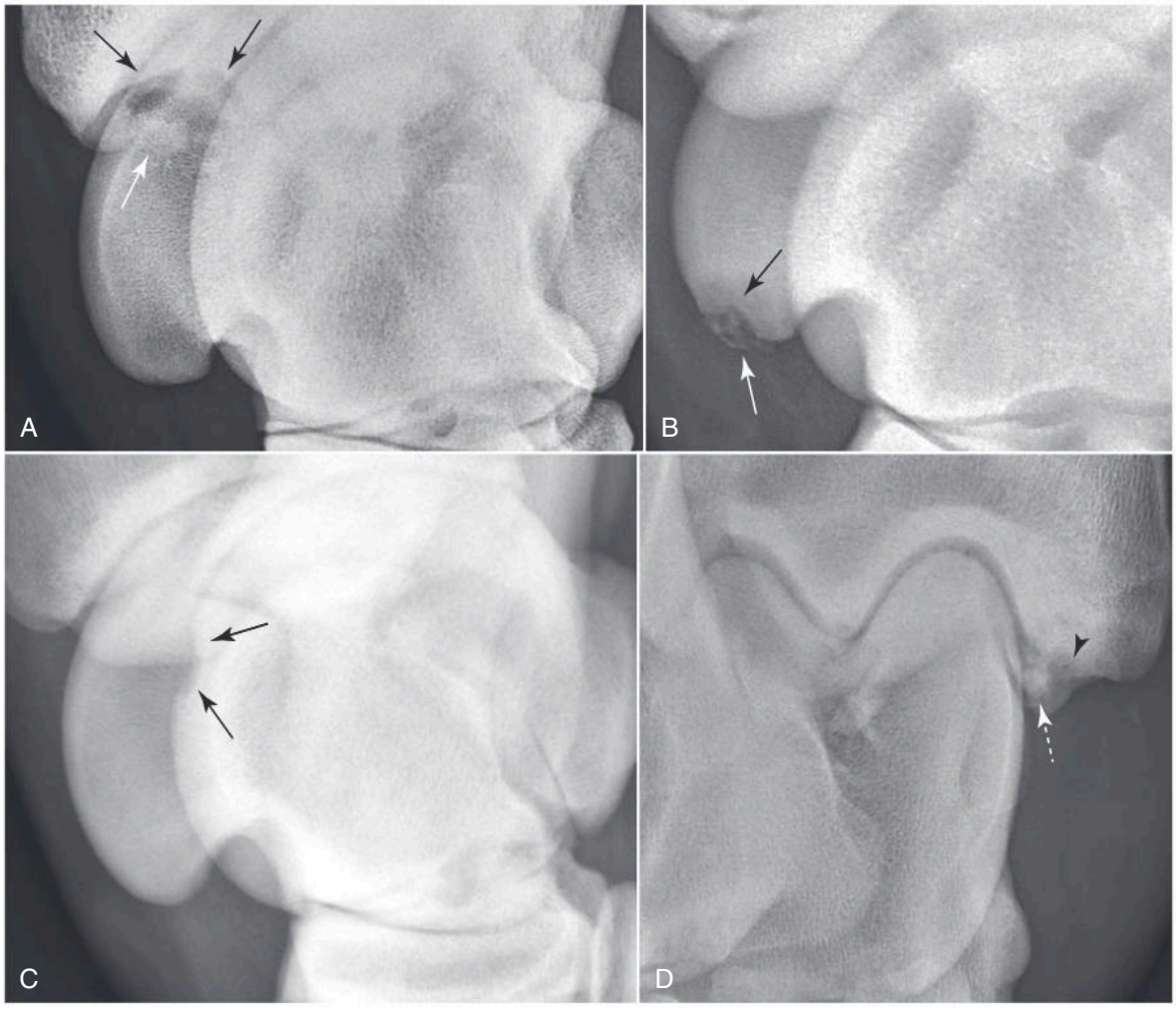


Fig. 22.3 Examples of osteochondritis dissecans (OCD) in four different juvenile horses. DMPLO radiographs of OCD of the intermediate cochlear ridge of the tibia **(A)**, lateral trochlear ridge of the talus **(B)**, and medial trochlear ridge of the talus **(C)** illustrate variable mineralized osteochondral fragments (*white arrows*) adjacent to concave parent bone defects (*black arrows*). An ossified osteochondral fragment was not identified in **(C)** but confirmed ultrasonographically (not shown). **D,** A D20PLMO radiograph is crucial in identification of subtle osteochondral fragments (*white dashed arrow*) associated with OCD of the medial malleolus medial subchondral margin. The adjacent subchondral bone (*black arrowhead*) is lucent and misshapen.

accompanies poorly ossified cuboidal bones may also predispose central and third tarsal bones to dorsal slab fracture in racing breeds.[21] A grading scheme can assist in clinical management and prognostication.[22]

Aseptic Physitis

Aseptic physitis is an inflammatory condition related to abnormal endochondral ossification at the level of the growth plate in rapidly growing horses, generally less than 2 years of age. Inflammatory forms of physitis are generally attributed to rapid growth phase, high nutritional plan, excessive work, trauma, and/or nutritional imbalances. Radiographic features include irregular physeal margins with widening and flaring of the growth plate often with mild soft tissue swelling. The inflammatory form has more uniformly distributed physeal margin irregularity and widening, has less associated soft tissue swelling, and no osteolysis compared to septic physitis.[23] Development of angular limb deformity is less common given more even distribution of inflammation, although development should still be monitored.

Angular Limb Deformity

In neonates, mild valgus and laxity are normal initially and typically self-resolve rapidly with exercise and maturation. Excessive medial (varus) or lateral (valgus) deviation when viewed from behind the horse or abnormally increased ("camped under") or decreased ("camped out") tarsal angle when viewed from the side of the horse strains growth plates, joints, and supporting soft tissues of the limb. These conformational defects may be related to abnormal bone ossification, flexural laxity or contracture, or physitis and can predispose adult horses to osteoarthritis, hoof problems, and soft tissue injury. Orthogonal radiographs performed with large detector plates or increased source-to-object distance to include as much long bone and joints proximal and distal to the tarsus as possible aid in identifying the center point of osseous malformations, articular angles, and secondary osseous pathologies for best therapeutic guidance.

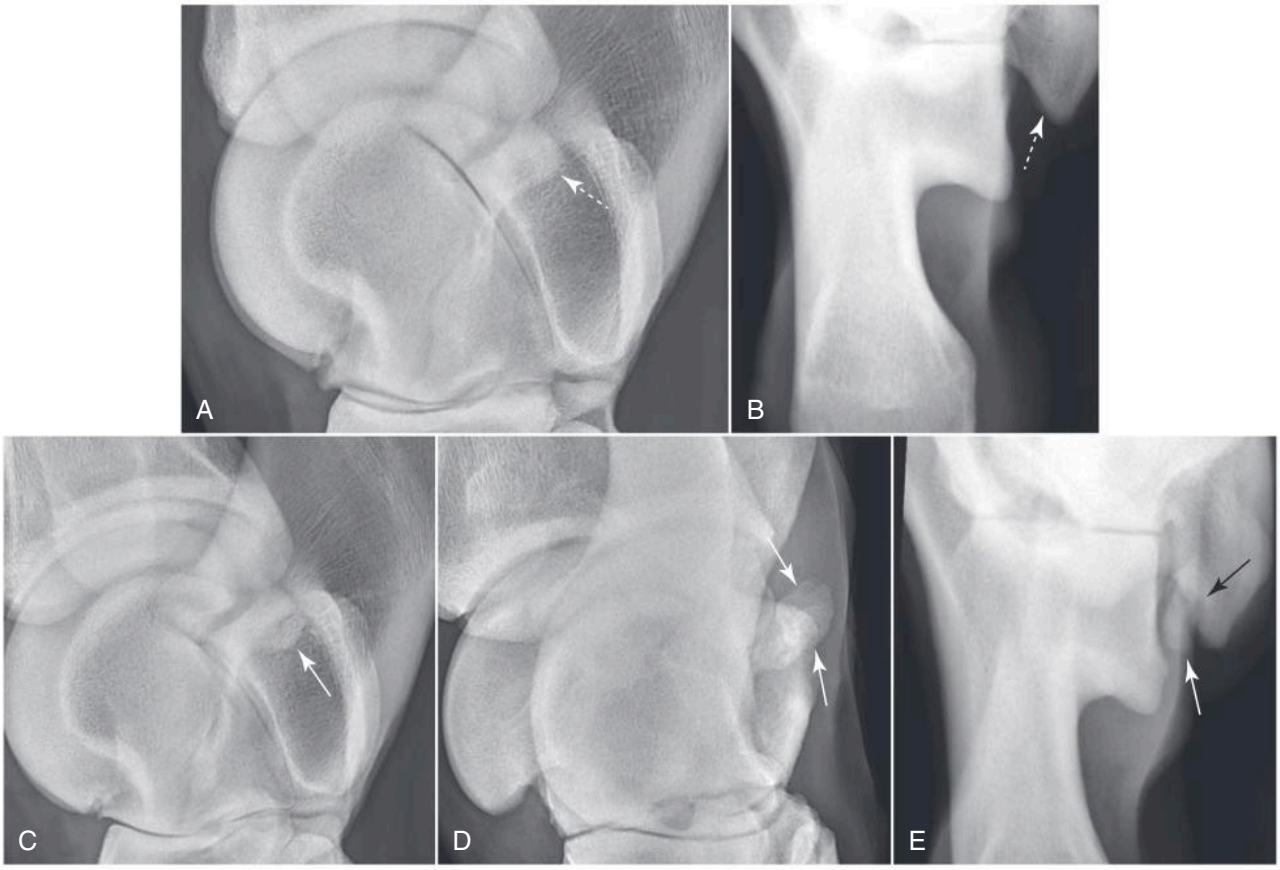


Fig. 22.4 Lateromedial (LM) **(A)** and dorsoproximal calcaneal skyline **(B)** projections of a normal horse highlighting the normal contour of the proximal tubercle of the talus (*white dashed arrows*). LM **(C)**, DM30°PLO **(D)**, and flexed calcaneal skyline **(E)** projections reveal proximal tubercle fragmentation (*white arrows*) in a sound horse without tarsal effusion. The nonstandard projections **(D and E)** reduce bone summation and greatly assist in confirming equivocal fragmentation and better define plantar from medial fragments. In **(E)**, the irregularly margined concave radiolucent defect (*black arrow*) is associated with the medial tubercle margin in the region of the short deep medial collateral ligament insertion.

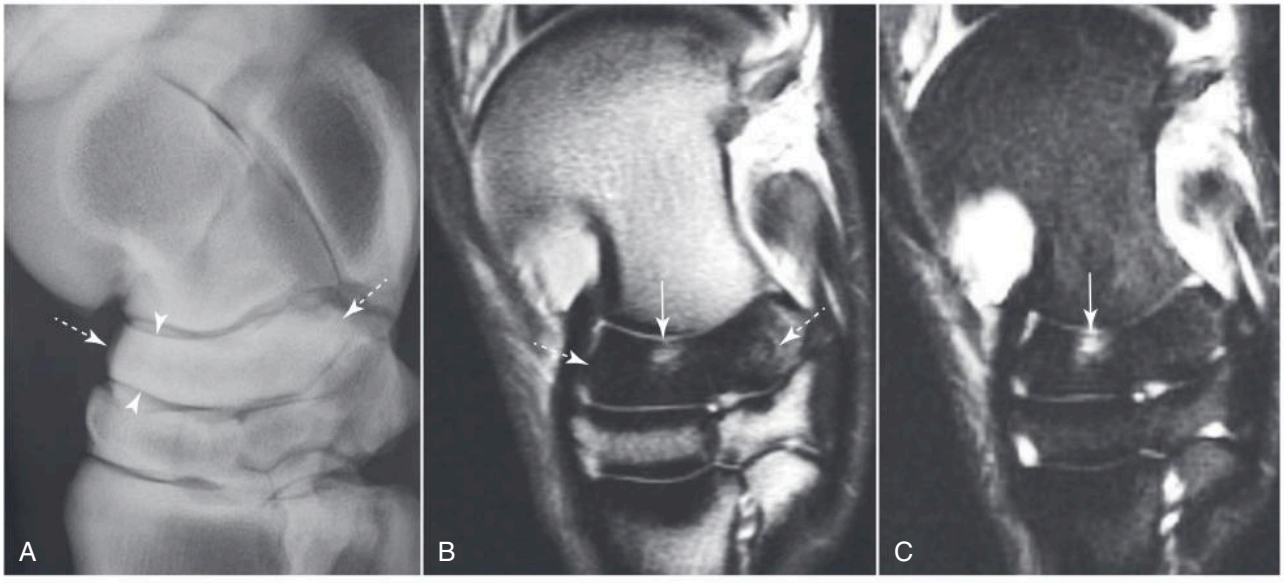


Fig. 22.5 **A,** Lateromedial (LM) radiograph of an 8-year-old Warmblood with one month duration of left pelvic limb lameness localized to the distal tarsus illustrating severe, diffuse central tarsal bone sclerosis (*white dashed arrows* and *white arrowheads*) with near complete effacement of normal trabecular bone. Radiographic sclerosis of this severity lacking other radiographic features of osteoarthritis is generally indicative of significant bone injury as with a chronic slab fracture or osseous cyst-like lesion. 3 Tesla magnetic resonance imaging (MRI) parasagittal proton density **(B)** and additional parasagittal short tau inversion recovery (STIR) **(C)** images confirmed the severe hypointense sclerosis (*white dashed arrows*) and revealed a small hyperintense subchondral osseous cyst-like lesion with ill-defined peripheral bone marrow-like edema (*white arrow*) as the underlying cause.

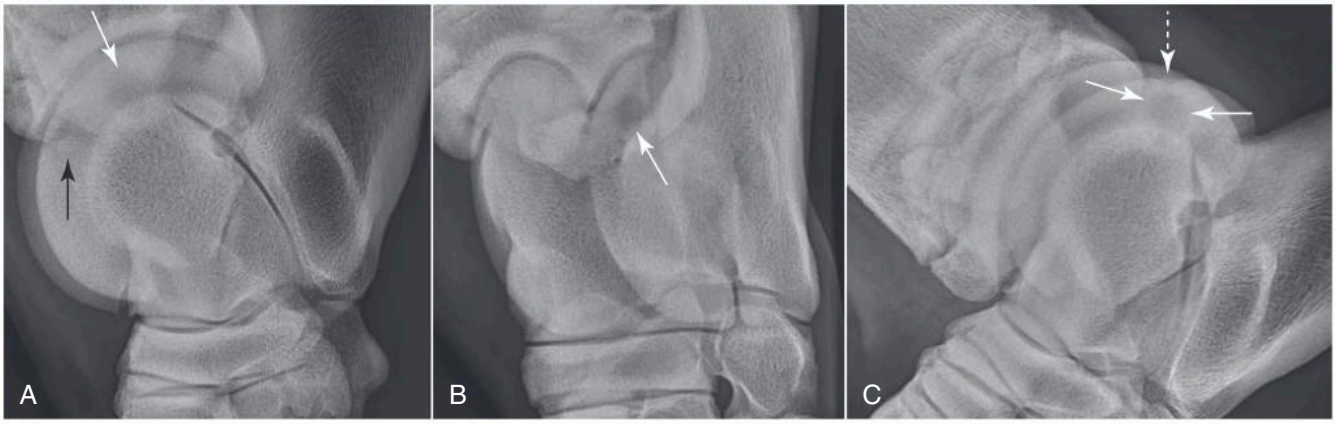


Fig. 22.6 Tarsal images of a 1.5-year-old Arabian colt presenting for tibiotarsal effusion but no lameness. *White arrows* in **A, B, and C** depict a subchondral cyst-like lesion within the lateral trochlea of the talus. In lateromedial (LM) **(A)** (*black arrow*) and DLPMO **(B)** projections, this lesion is summated with the tibial cochlea, but the addition of a flexed lateral projection **(C)** offsets the cochlea from the trochlear ridges confirming the location. A shallow subchondral margin defect (*white dashed arrow*) is also better seen in the flexed lateral projection. Osteochondritis dissecans of the intermediate cochlear ridge of the tibia is also present illustrated by a small osteochondral fragment and adjacent parent bone concave defect.

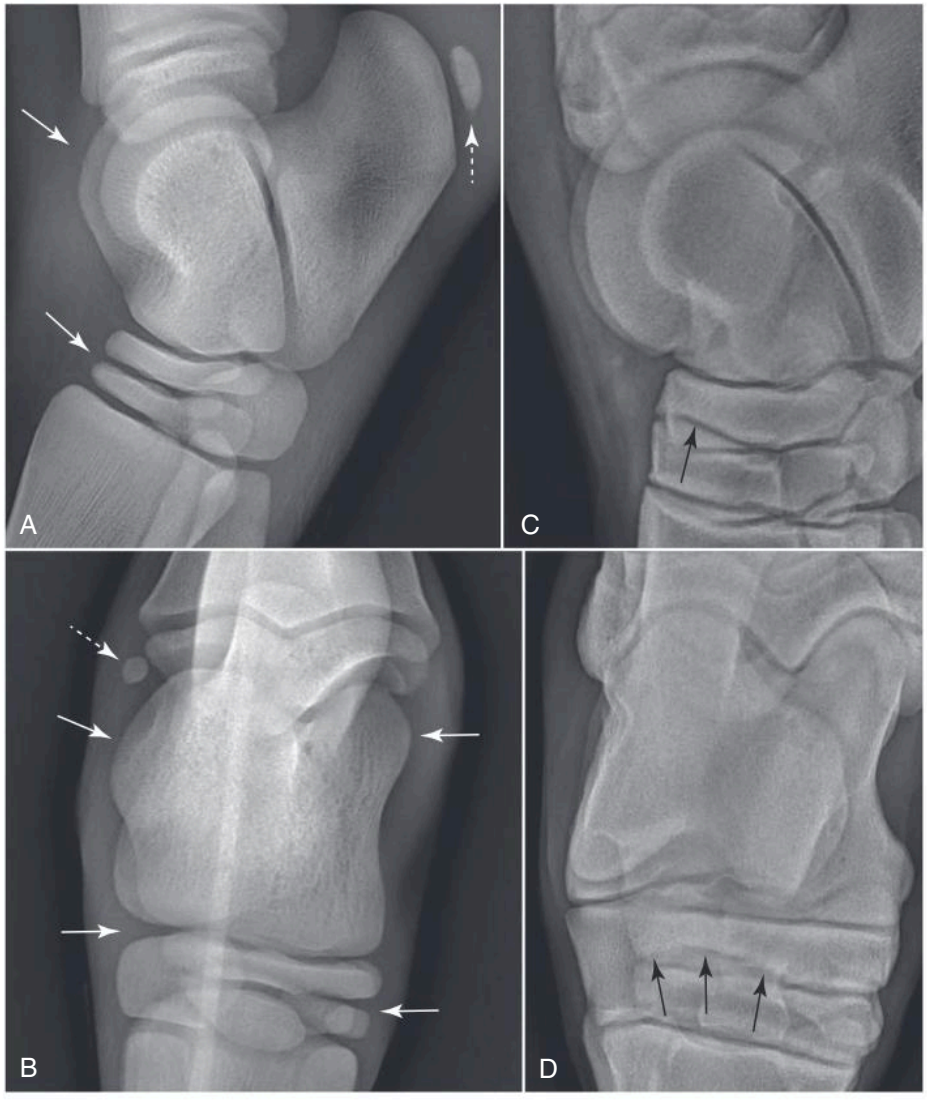


Fig. 22.7 Orthogonal tarsal images of a 3-day-old Arabian filly (336 days gestation) presenting for inability to rise. The filly was small with silky haircoat compatible with dysmaturity. Lateromedial (LM) **(A)** and dorsoplantar (DPl) **(B)** radiographs show rounding of the cuboidal bones and reduced convexity of the talar trochlea with increased joint space (*white arrows*). These findings paired with present cuboidal bones and normally fused proximal metatarsal epiphysis are compatible with grade 3 incomplete ossification. *White dashed arrows* indicate the normal lateral malleolus and calcaneal tuber apophysis separate centers of ossification. Lateral **(C)** and DPl **(D)** radiographs of this same filly at 5 months of age show dorsal wedging and irregular margination of the central tarsal bone ventrolaterally (*black arrows*).

DEGENERATIVE AND ACQUIRED OSSEOUS CONDITIONS

Osteoarthritis (Degenerative Joint Disease, Bone Spavin)

Osteoarthritis (OA) is common in all horse breeds and can occur at any age, with older horses and Icelandic horses more often affected resulting from repetitive, low-grade bone trauma.[24,25] Other inciting causes include ligamentous injury, sepsis, hemarthrosis, conformational faults such as tarsal valgus or increased or decreased tarsal angulation, or underlying bone malformation as with wedge-shaped cuboidal bones.[24] The centrodistal and tarsometatarsal joints are most often affected (Fig. 22.8, eFigs. 22.5 and 22.6), usually dorsomedially although can be dorsolateral in distribution, as commonly seen in Icelandic horses, highlighting the importance of acquiring both DMPLO and DLPMO projections. Lameness severity, duration, and response to flexion examination does not correlate well with the severity of distal tarsal joint radiographic change,[25] emphasizing the importance of diagnostic anesthesia. Well-defined dorsal third metatarsal bone proliferation without other bone changes is generally regarded as incidental enthesopathy[26] (see Fig. 22.1). Tibiotarsal OA is less common[27] and generally secondary to chronic OC, sepsis, or injury to the collateral ligaments, synovium, cartilage, or subchondral bone. It often requires evaluation with ultrasound,[28] cross-sectional imaging,[29] or exploratory arthroscopy[30] if the inciting cause is not radiographically apparent. OA of the tibiotarsal joints (Fig. 22.9) or talocalcaneal joints is generally associated with significant lameness and less responsiveness to medical therapy.[27]

Radiographic features of OA include:

1. Intracapsular soft tissue swelling if tibiotarsal joint affected
2. Periarticular bone proliferation (osteophytes)
3. Subchondral bone resorption/lysis in later stages
4. Possible development of osseous cyst-like lesions
5. Eventual joint space collapse due to cartilage degradation (Fig. 22.10, eFig. 22.7)

Unique to distal tarsal OA, the normal, more radiolucent trabeculation of the central and third tarsal bones is often effaced by radiopaque sclerosis. Additionally, central osteophytes may obscure the interosseous canals and extensive dorsomedial bone proliferation may develop, commonly referred to as "bone spavin."

Tarsal Luxations

Severe torsional trauma as with twisting falls or limb entrapment under a fence often causes collateral ligament rupture resulting in luxation and occurs most commonly in the tarsometatarsal and proximal intertarsal joints. The centrodistal and tibiotarsal joints are less common due to enhanced stability via the fourth tarsal bone and interdigitating tibiotarsal

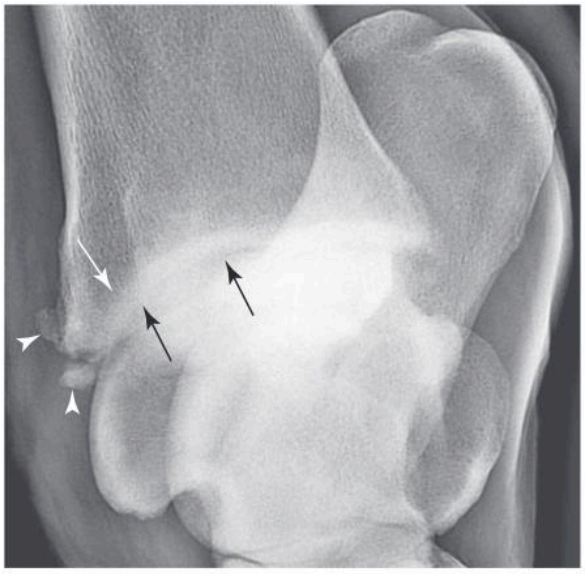


Fig. 22.9 DMPLO projection of a horse 15 months after sustaining a lateral collateral ligament injury. Two rounded osseous fragments are adjacent to the lateral malleolus (*white arrowheads*). The loss of subchondral bone definition (*white arrow*) and radiolucent joint space (*black arrows*) is indicative of severe articular cartilage erosion and severe tibiotarsal osteoarthritis and is associated with severe lameness. (Radiograph courtesy Valeria Busoni and Fabrice Audigie.)

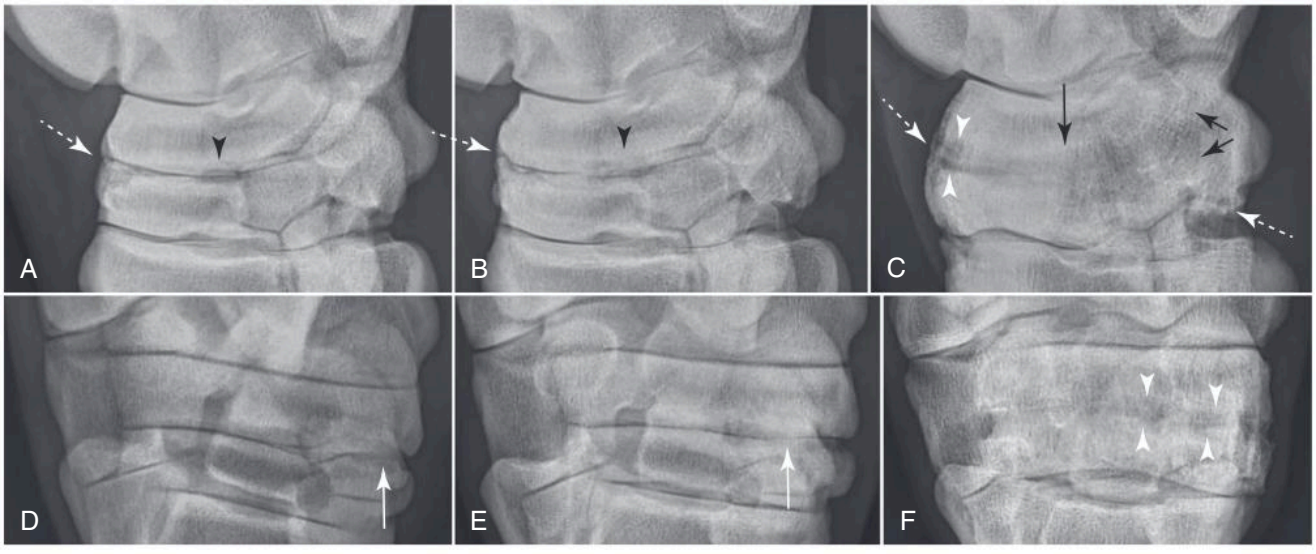
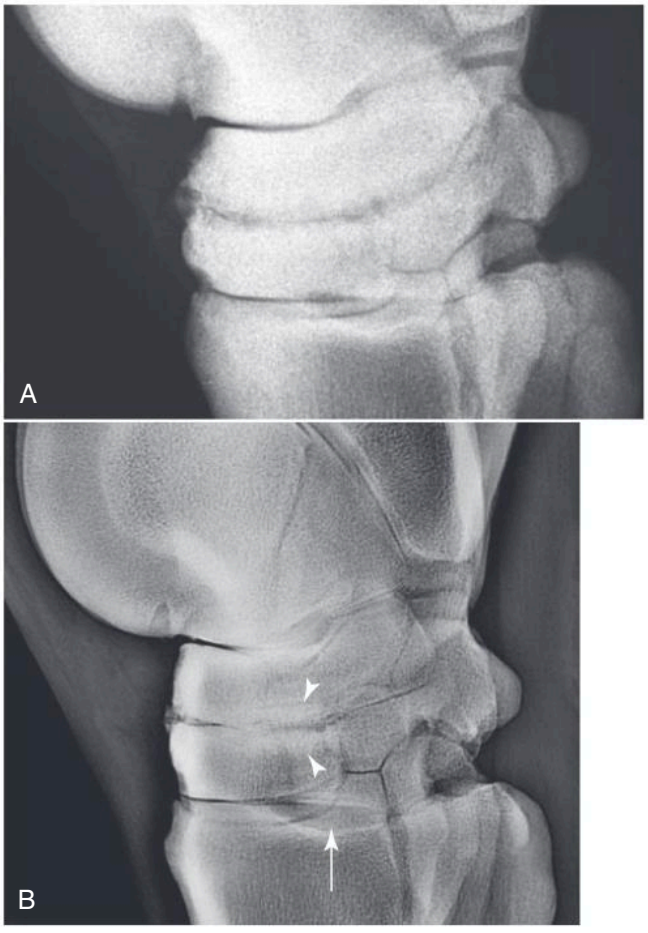


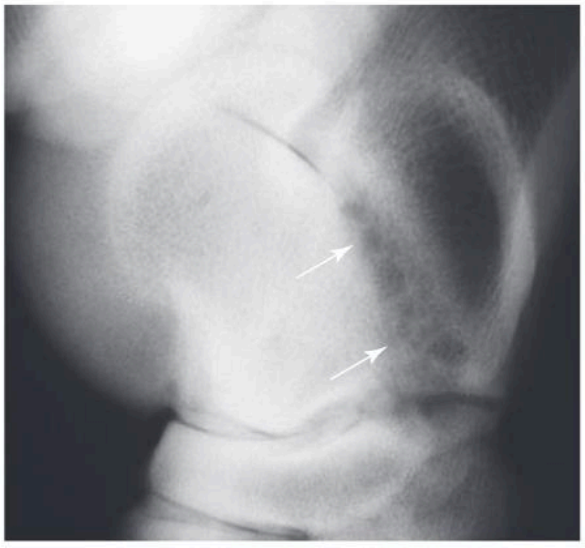
Fig. 22.8 Lateromedial (LM) **(A, B, C)** and dorsoplantar (DPl) **(D, E, F)** radiographs of increasing distal tarsal osteoarthritis severity from left to right. Osteophytes (*white dashed arrows*) and trabecular bone sclerosis, which may obscure the interosseous space (*black arrowheads*), joint space narrowing (*white arrows*), or joint space widening (*white arrowheads*), are classic radiographic features. The horse in **C** and **F** has a wedge-shaped third tarsal bone (*black arrows*).



eFig. 22.5 **A,** Lateromedial tarsal radiograph of a horse with distal intertarsal degenerative joint disease. There is osteophyte formation at the dorsal aspect of the distal intertarsal joint. The joint space seems wide because of radiolucency of the lytic subchondral bone. The trabecular bone of the central and third tarsal bone is sclerotic. **B,** Lateromedial tarsal radiograph of a horse with distal intertarsal degenerative joint disease characterized by thinning of the joint space and osteophyte formation. The interosseous fossa of the joint is hardly visible. The normal radiolucent area surrounded by a thin radiopaque line (compare to the normal appearance in the tarsometatarsal joint [*white arrow*]) is obscured by marked sclerosis of the osseous margins (*white arrowheads*). This finding suggests enthesopathy of the corresponding tarsal interosseous ligament and worsens the clinical prognosis.



eFig. 22.6 Lateromedial radiograph of an endurance (120−160 km) pony referred for back pain and a poor hindlimb dissociation at gallop. There is severe distal intertarsal degenerative disease with a lack of identification of the corresponding joint space. A diffuse radiolucent area is present at the level of the joint space because of the subchondral bone lysis. The cancellous bone of the central and third tarsal bone is sclerotic. Note also a focal subchondral cyst-like lesion in the medial and distal part of the talocalcaneal joint (*arrowhead*).



eFig. 22.7 Lateromedial radiograph of the tarsus in a horse with severe hindlimb lameness and moderate distention of the tarsocrural joint. The distal portion of the talocalcaneal joint appears widened and ill-defined (*white arrows*) because of severe subchondral bone lysis. These findings are indicative of severe talocalcaneal degenerative joint disease.

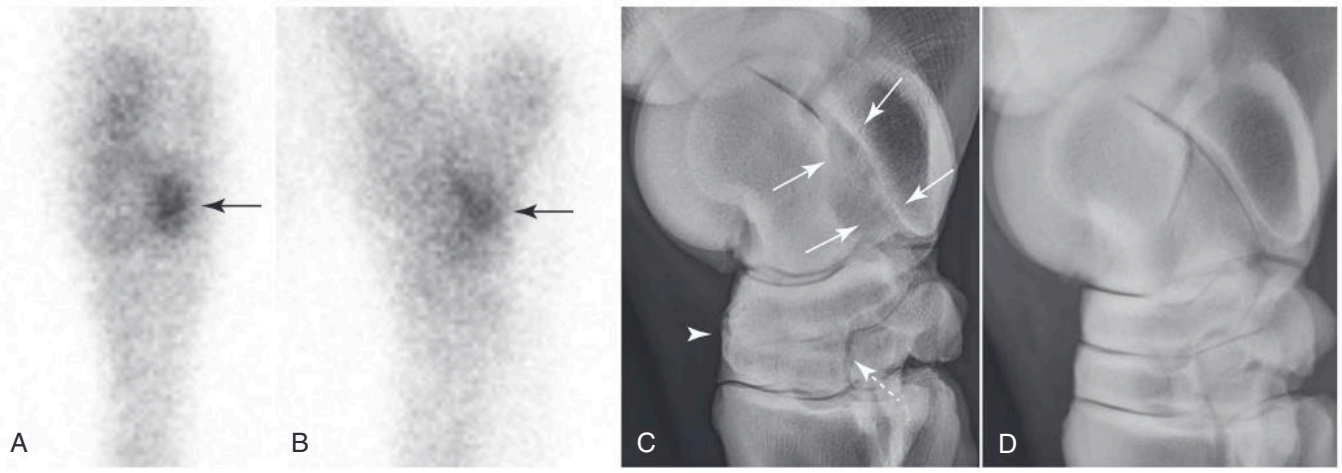


Fig. 22.10 A 15-year-old Warmblood mare with left distal tarsal joint osteoarthritis (OA) negative to diagnostic anesthesia presented for bone scintigraphy. Lateral **(A)** and plantar **(B)** scintigraphic bone phase images show focal radiopharmaceutical uptake plantaromedially in the region of the medial talocalcaneal joint articulation or sustentaculum tali (*black arrows*). Tarsal sheath ultrasound and plantar sustentacular margin in a calcaneal skyline projection were normal. **C,** The lateromedial (LM) tarsal radiograph shows complete collapse of the distomedial talocalcaneal joint with associated ill-defined radiopaque subchondral sclerosis and focal lysis (*white arrows*). The centrodistal joint is also completely collapsed, sclerotic, and dorsally ankylosed (*white arrowhead*) with irregular margins and sclerosis of the centrodistal interosseous canal (*white dashed arrow*). A comparison LM radiograph of normal tarsal joint and interosseous canal spacing is provided **(D)**. In **A,** medial is to the *left;* in **B,** dorsal is the *left.*



Fig. 22.11 A partially flexed lateromedial (LM) radiograph of a 5-year-old Appaloosa gelding with acute non−weight-bearing lameness after getting caught under a trailer stall partition. The central tarsal and metatarsal bones are dorsally displaced resulting in a step defect at the centrodistal joint dorsally (*white arrow*) and severe joint space widening between the third and fused first/second tarsal bones (*black arrow*), consistent with severe subluxation of the centrodistal joint.

articular surfaces, respectively.[31] Radiographically, luxations can spontaneously reduce and may require additional flexed lateral (Fig. 22.11) or dorsoplantar projections with careful medial or lateral stress applied to the distal limb to identify joint space widening and/or incongruency.[31–33]

Tarsal Fractures

Tarsal fractures are generally uncommon due to robust support of collateral ligaments and other peritarsal soft tissues. Catastrophic displaced and/or comminuted fractures of the talus and calcaneus (Fig. 22.12) are most common and carry a grave prognosis. Smaller displaced or minimally displaced fractures or avulsions of the tarsus have better outcomes for survival and possibly athletic career if diagnosed and managed properly and are discussed below.

Tibial Malleolar Fractures

The lateral (Fig. 22.13) and less commonly medial tibial malleoli are the most common tarsal fractures, almost always articular, and occur after kick or fall trauma and/or severe rotational stress when the hoof is fixed to the ground. The long and short medial and lateral collateral ligaments of the tibiotarsal joint originate from the malleoli, and thus, malleolar fractures warrant sonographic assessment of the collateral ligaments. Smaller collateral avulsions tend to respond favorably to surgical removal of the bone fragment.[34] Fractures that are comminuted and involve a significant portion of the collateral ligament surface area, but are too small for fixation, carry an elevated risk of tibiotarsal luxation during the recovery process (Fig. 22.14).

Trochlear Ridge Fractures

These articular fractures are uncommon but generally related to external trauma as with a kick by another horse (see Fig. 22.12). They can be associated with favorable outcomes with expedited surgical intervention.[35]

Incomplete or Minimally Displaced Fractures

These fractures are overall uncommon and can be challenging to detect both clinically and radiographically due to inherent summation of bone and lack of fracture displacement. Incomplete talar, central, and third tarsal bone slab fractures are most common. These types of fractures are often associated with intense surrounding sclerosis and likely represent pathologic fatigue fracture secondary to repetitive or maladaptive bone stress.[36] If available, nuclear scintigraphy is extremely helpful to

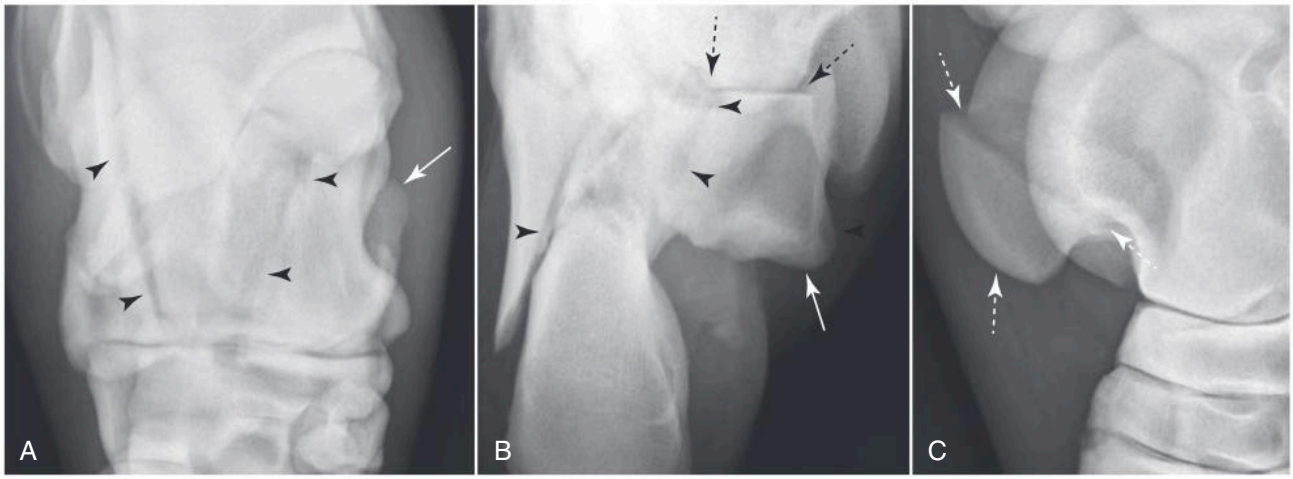


Fig. 22.12 Dorsoplantar (DPl) **(A)** and calcaneal skyline **(B)** radiographs of a 15-year-old Quarter horse stallion presenting for acute toe dragging depicts a closed comminuted articular calcaneal fracture with two minimally displaced radiolucent fracture lines (*black arrowheads*) and lateral deviation of the sustentaculum tali (*white arrows*) illustrated by step defects (*black dashed arrows*) at the medial talocalcaneal joint. **C,** DMPLO image of a different horse with acute tarsal swelling after turnout shows a closed minimally displaced lateral trochlear ridge articular fracture (*white dashed arrows*). Horse **(C)** also has tarsometatarsal joint space narrowing with focal lysis of the proximal third tarsal bone and central tarsal bone sclerosis consistent with distal tarsal osteoarthritis.

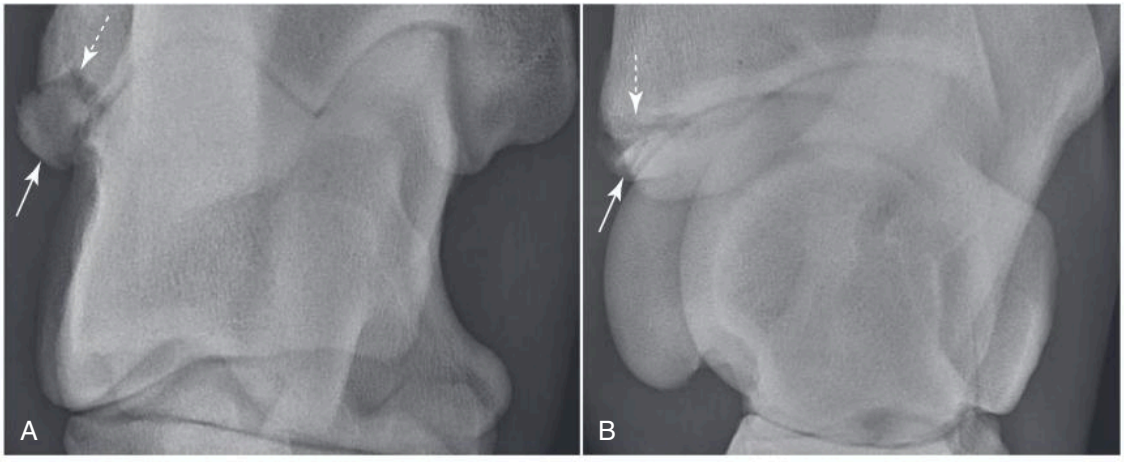


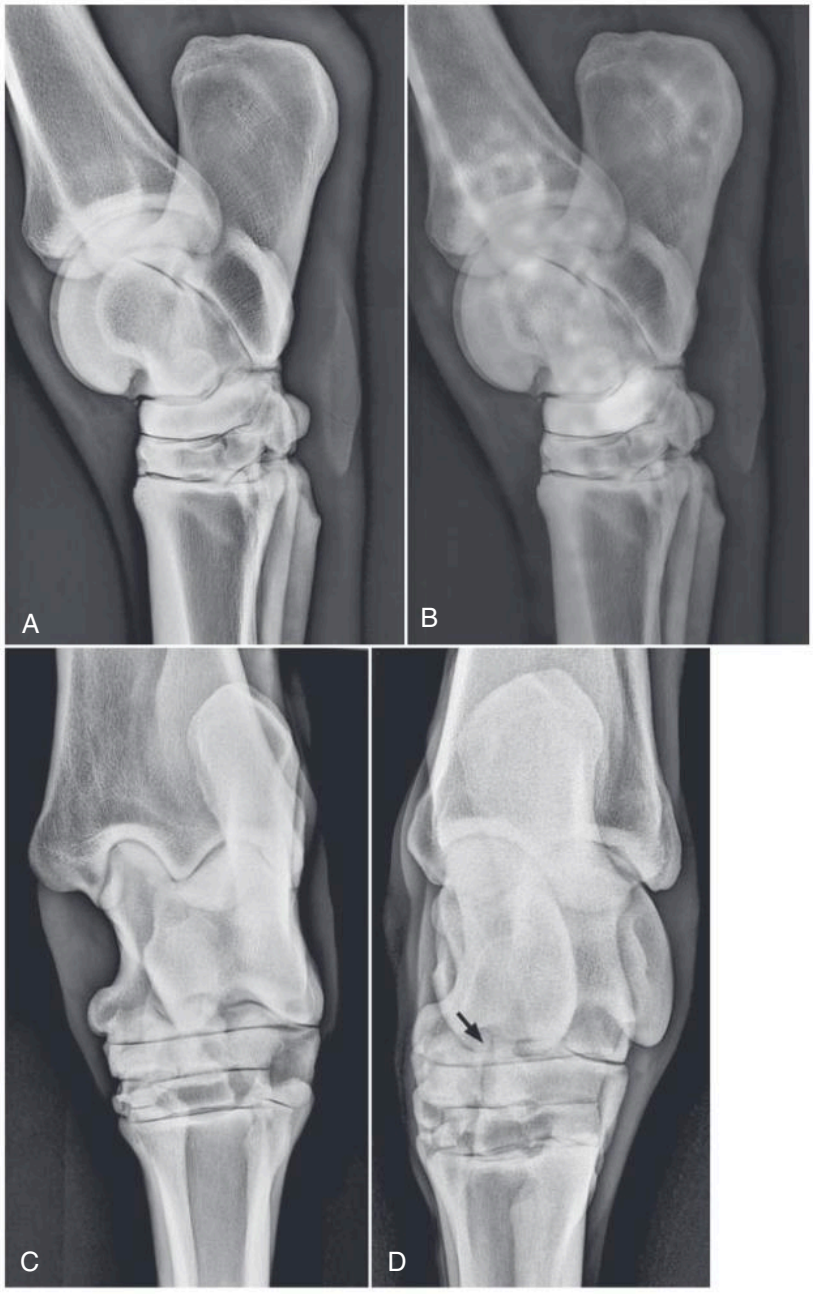
Fig. 22.13 Dorsoplantar (DPl) **(A)** and lateromedial (LM) **(B)** radiographs of a 2-year-old Oldenburg with 2 weeks of tarsal swelling that remained pasture sound. A chronic minimally distolaterally displaced articular avulsion fracture of the lateral malleolus (*white arrows*) is illustrated by rounded and mildly irregular fracture bed margins (*white dashed arrows*).

initially localize or confirm focal, severe radiopharmaceutical uptake of a clinically or radiographically suspected fracture. Cross-sectional imaging with CT or high-field MRI can also confirm fractures although is generally reserved for animals undergoing surgical fixation to avoid catastrophic displacement during anesthetic recovery.

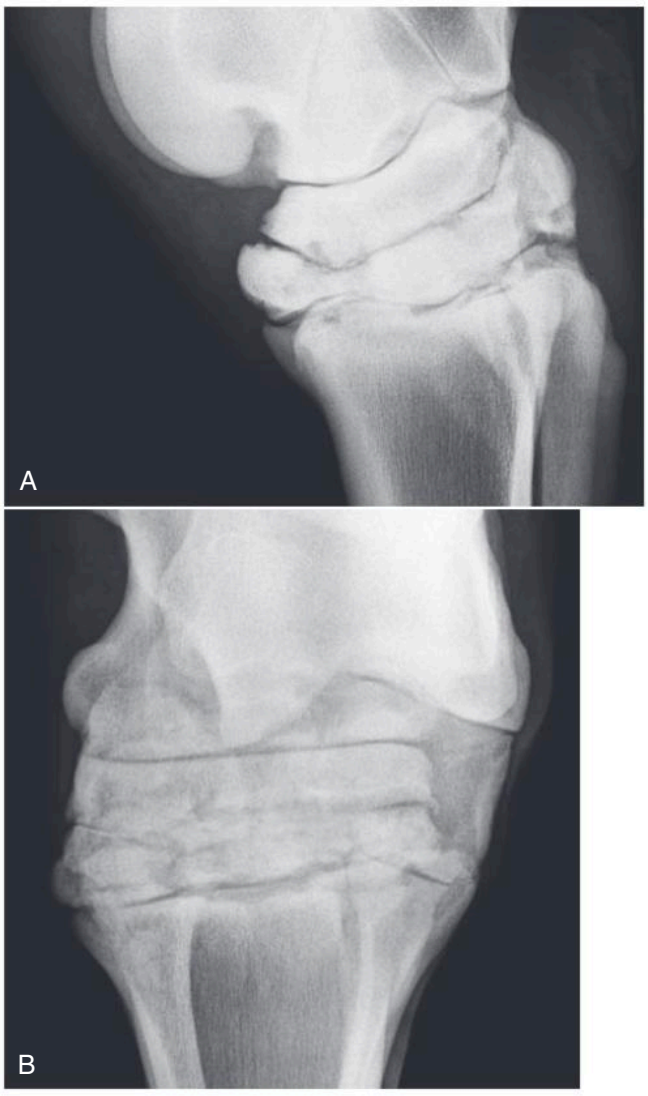
Central Tarsal Bone Sagittal Slab or Comminuted Fracture. Slab fractures are bicortical fractures that are also biarticular. Sagittal slab fractures are uncommon and most prevalent in nonracing breeds. Repetitive dorsomedial loading forces inherent of the equine pelvic limb result in predictable fracture orientation in a dorsomedial to plantarolateral plane, often requiring several DM30-55°PlLO obliques at 5- to 10-degree increments to best align the x-ray beam tangential to the fracture plane[37] (Fig. 22.15, eFig. 22.8).

Third and Central Tarsal Bone Dorsal Slab Fractures. These rare articular fractures occur in racing Thoroughbreds and Standardbreds or rarely during other high-speed work and are attributed to repetitive dorsal bone stress. Wedge-shaped conformation of the cuboidal bones is a suggested risk factor[21] (Fig. 22.16, eFig. 22.9), although fractures at this location occur in horses with and without wedge-shaped conformation.[38] Third tarsal dorsal slab fractures are more common than similar fractures of the central tarsal bone and occur along the dorsolateral aspect of the T3 dorsal facet.[38] Occasionally, dorsal slab fractures are bilateral in distribution.

Incomplete Sagittal Fracture of the Talus. This rare fracture occurs at the proximal aspect of the trochlear groove in racing breeds or, rarely, other breeds competing in speed work often with history of chronic lameness with acute exacerbation shortly after strenuous work. Radiographs are often unremarkable as they are not tangential to the plane of the fracture. Nuclear scintigraphy ideally aided by flexed lateral views to offset the tibia and talus often localizes focal radiopharmaceutical



eFig. 22.8 Lateromedial **(A and B)**, dorsoplantar **(C)**, and dorsomedial/plantarolateral oblique **(D)** radiographs of the tarsus of a 14-year-old showjumper with an acute and severe onset of lameness 3 months ago. The scintigraphic image of the tarsus is superimposed to the lateromedial radiograph in **B**. There is a marked diffuse sclerosis of the central tarsal bone mainly visible on the dorsoplantar view. Note the difference in bone opacity between the central and third tarsal bones, and cancellous bone has almost the same opacity as the subchondral bone plate. There are also small bone fragments at the distal aspect of the medial talar ridge and a dorsal metatarsal bone spur, unrelated to the fracture. The oblique dorsomedial/plantarolateral view demonstrates the presence of a biarticular fracture of the central tarsal bone. Note the fracture line visible on the plantar aspect of the central tarsal bone above the proximal intertarsal joint space (**D,** *arrow*) confirming the dorsomedial/plantarolateral orientation of the fracture and its extension to the most plantar aspect of the bone. Superimposition of the lateral scintigraphic image with the lateromedial radiograph **(B)** shows increased radiopharmaceutical uptake mainly located in the plantar half of the central tarsal bone.



eFig. 22.9 Lateromedial **(A)** and dorsoplantar **(B)** radiographs of the tarsus of a young horse with severe tarsal bone collapse. **A,** The central and third tarsal bones are sclerotic and have an abnormal shape with a severe narrowing of the third tarsal bone in its middle third. As a consequence, the distal intertarsal joint space and tarsometatarsal joint space are not parallel, and the dorsal surface of the distal tarsal row is abnormally convex. There are also areas of radiolucency in the subchondral bone of the distal intertarsal and tarsometatarsal joint, subchondral sclerosis, and a large dorsal bony spur of the proximal metatarsus. **B,** The distal intertarsal joint space and the tarsometatarsal joint space are not parallel as in a normal horse. The distal intertarsal joint space is ill-de fined and irregular.

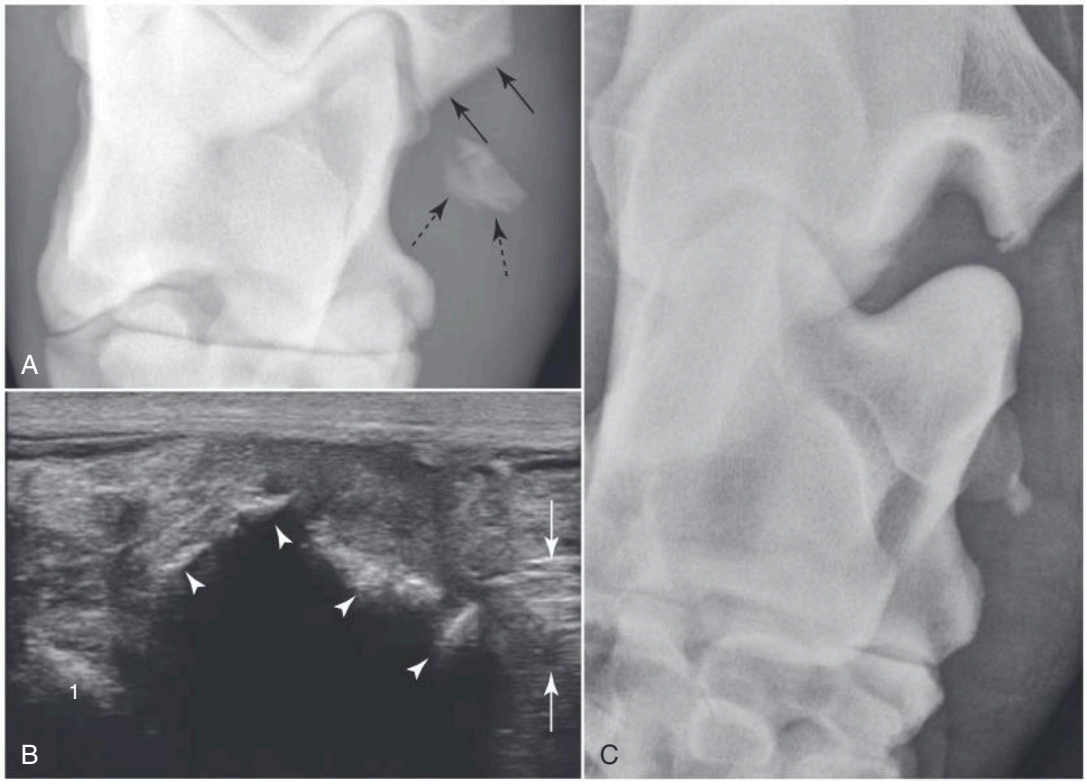


Fig. 22.14 Dorsoplantar (DPl) image **(A)** of a 15-year-old Warmblood gelding with acute 4/5 left pelvic limb lameness and severe tibiotarsal effusion after turnout revealed a large medial malleolus avulsion fracture characterized by severe intracapsular tibiotarsal effusion, blunted misshaping of the medial malleolus (*black arrows*), and at least two large avulsed bone fragments (*black dashed arrows*). The distal fragment location remote from the malleolus results from distraction by short collateral ligaments. **B,** Collateral ligament ultrasound confirmed multiple fragments (*white arrowheads*) retracted from the medial malleolus with a partial portion of the superficial short collateral ligament (*white arrows*) remaining attached to the distal fragment margins. The other short collateral ligaments were not seen due to the degree of soft tissue disruption and shadowing bone fragments. The long collateral ligament was enlarged but intact (not shown) and no clinical joint instability was evident. **C,** During anesthetic recovery for bone fragment removal visible joint instability occurred. Subsequent dorsoplantar image with slight medial stress applied conclusively confirmed progression to a complete medial collateral ligament rupture, evidenced by severe widening of the medial tibiotarsal joint space. *1,* Medial aspect of talus. In **B** proximal is to the *left.* (Ultrasound image courtesy Caitlyn Horne, DVM, DACVSMR.)

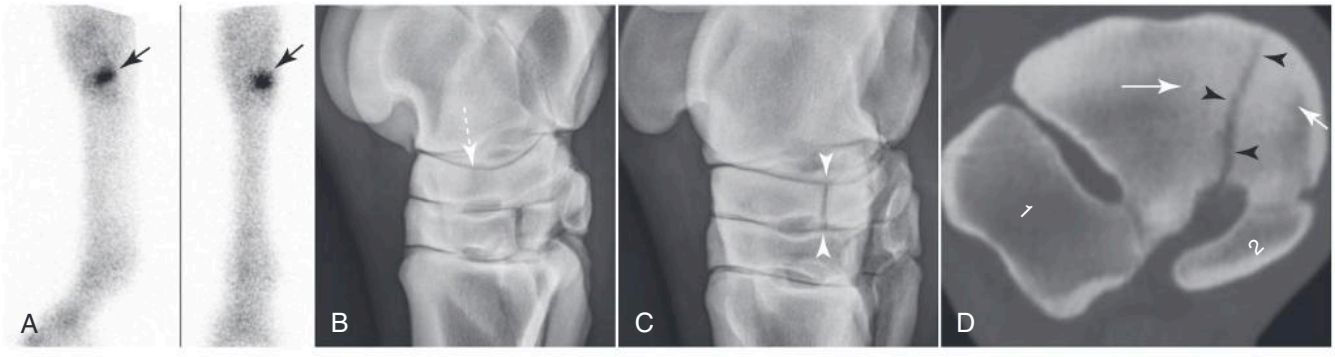


Fig. 22.15 A 14-year-old Oldenburg gelding was referred for 4/5 left pelvic limb lameness with no appreciable swelling or localizable pain after falling at pasture. Pelvis limb bone scintigraphy **(A)** revealed focal intense central tarsal bone radiopharmaceutical uptake (*black arrows*) in lateral (*left*) and plantar (*right*) images supportive of fracture or subchondral bone injury given acute history. Multiple DMPLO radiographs were acquired every 5 to 10 degrees. The standard DMPLO **(B)** faintly delineates a potential fracture line (*white dashed arrow*), subsequently confirmed (*white arrowheads*) by aligning the x-ray beam tangential with the fracture plane via a D55MPLO **(C)**. Computed tomography (CT) was performed for surgical planning. A bone algorithm transverse slice **(D)** illustrates the typical dorsomedial to plantarolateral orientation of these fractures (*black arrowheads*). Note the bordering sclerosis (*white arrows*) surrounding the fracture. *1,* Fourth tarsal bone; *2,* fused first/second tarsal bones. In **D** dorsal is to the *left* in the lateral image and lateral is to the *left* in the plantar image.

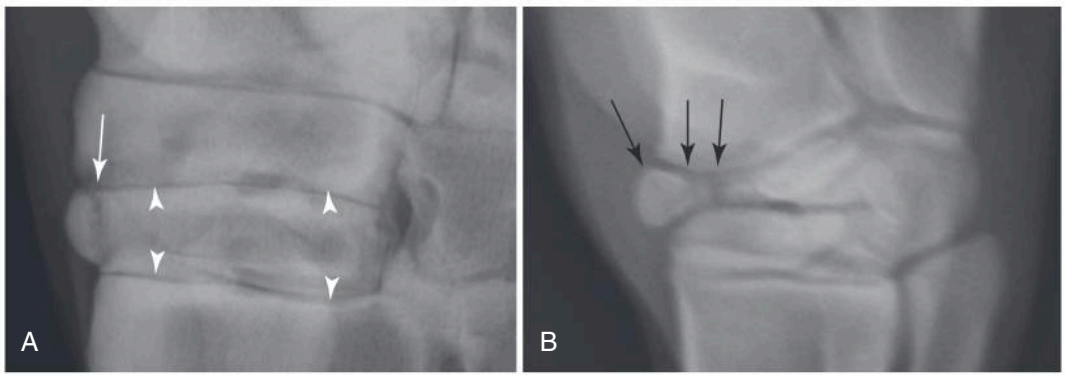


Fig. 22.16 **A,** DLPMO projection in a 9-year-old Warmblood with a 2-week history of left pelvic limb lameness showing a radiolucent nondisplaced third tarsal bone fracture with irregular fracture margins (*white arrow*) indicative of chronicity. Note the third tarsal bone is narrower in dorsal proximodistal height compared to plantar (*white arrowheads*). **B,** Lateromedial (LM) projection of a 2-month-old premature Miniature Pony foal with a history of incomplete cuboidal bone ossification and recent onset distal tarsal swelling. The central tarsal bone is severely wedge-shaped and collapsed centrally with multiple radiolucent fracture lines (*black arrows*) resulting in dorsally displaced fragments and enlargement of the bordering soft tissues.

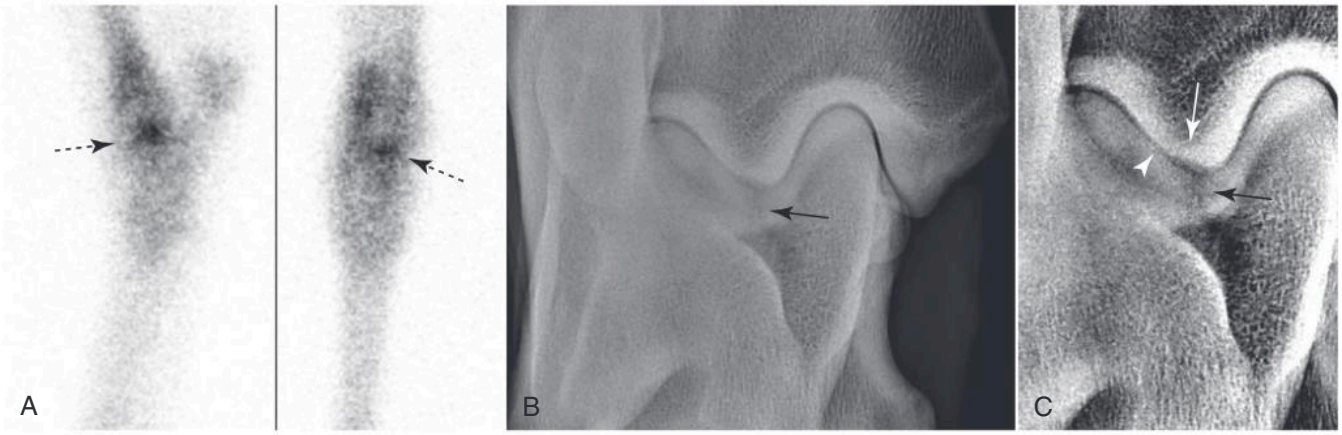


Fig. 22.17 A 3-year-old racing Standardbred in training presented for acute 4/5 left pelvic limb lameness and tibiotarsal effusion. Routine tarsal radiographs were normal. Lateral and plantar bone scintigraphic images **(A)** revealed focal moderate radiopharmaceutical uptake centered on the proximal talus or distal tibia (*black dashed arrows*) compatible with incomplete fracture, subchondral cyst, marrow lesion, or osteochondrosis. More diffuse moderate uptake of the distal tibia was symmetric to the contralateral limb and interpreted as stress remodeling given the level of training. A D20PLMO radiograph **(B)** was acquired showing a subtle incomplete radiolucent fracture line (*black arrows*) coursing the subchondral bone plate of the trochlear groove of the talus, best appreciated with higher image contrast **(C)**. The adjacent intermediate tibial cochlear subchondral bone is also flattened (*white arrow*) with thinning of the normally uniform radiolucent joint space (*white arrowhead*) consistent with cartilage and subchondral bone loss.

uptake to the midproximal talus. Targeted radiography with multiple D10-30°LPMO oblique radiographs often reveals characteristic subchondral linear to curvilinear incomplete fracture that can partially extend into the trabecular bone with surrounding sclerosis[39] (Fig. 22.17). Incomplete fractures can propagate spontaneously and become complete. Incomplete fractures are usually successfully managed with rest.[39]

Osteomyelitis and Septic Arthritis

In mature horses, synovial infection, also termed *synovial sepsis* or *septic arthritis*, is often complicated by osteomyelitis and most often results from local wound or medical procedures such as synovial sampling, intra-articular therapies, or surgery. In foals, septic arthritis more often affects multiple joints via systemic infection and hematogenous inoculation.[40] Within the tarsus the tibiotarsal joint, tarsal sheath, and calcaneal bursae are more commonly infected.[41] The combination of intracapsular and extracapsular soft tissue swelling are clinical findings concerning for synovial sepsis. Osseous structures often remain radiographically normal initially; thus, synovial cytology and culture for confirmation of sepsis are paramount to early diagnosis and appropriate management. In cases with full-thickness wounds, positive contrast radiography can assist in identification of synovial involvement.[41] Joint infections eventually lead to radiographically appreciable lysis of subchondral bone (osteomyelitis), joint collapse, and development of OA. Bone abscessation, sequestra, or cyst-like lesions can also develop and comparative radiographs at 2- to 3-day intervals during treatment are commonly performed to monitor bone integrity. Abnormal osseous findings are a negative prognostic indicator regardless of age or joint affected; however, recent advances in antimicrobial delivery have improved prevention and outcomes.

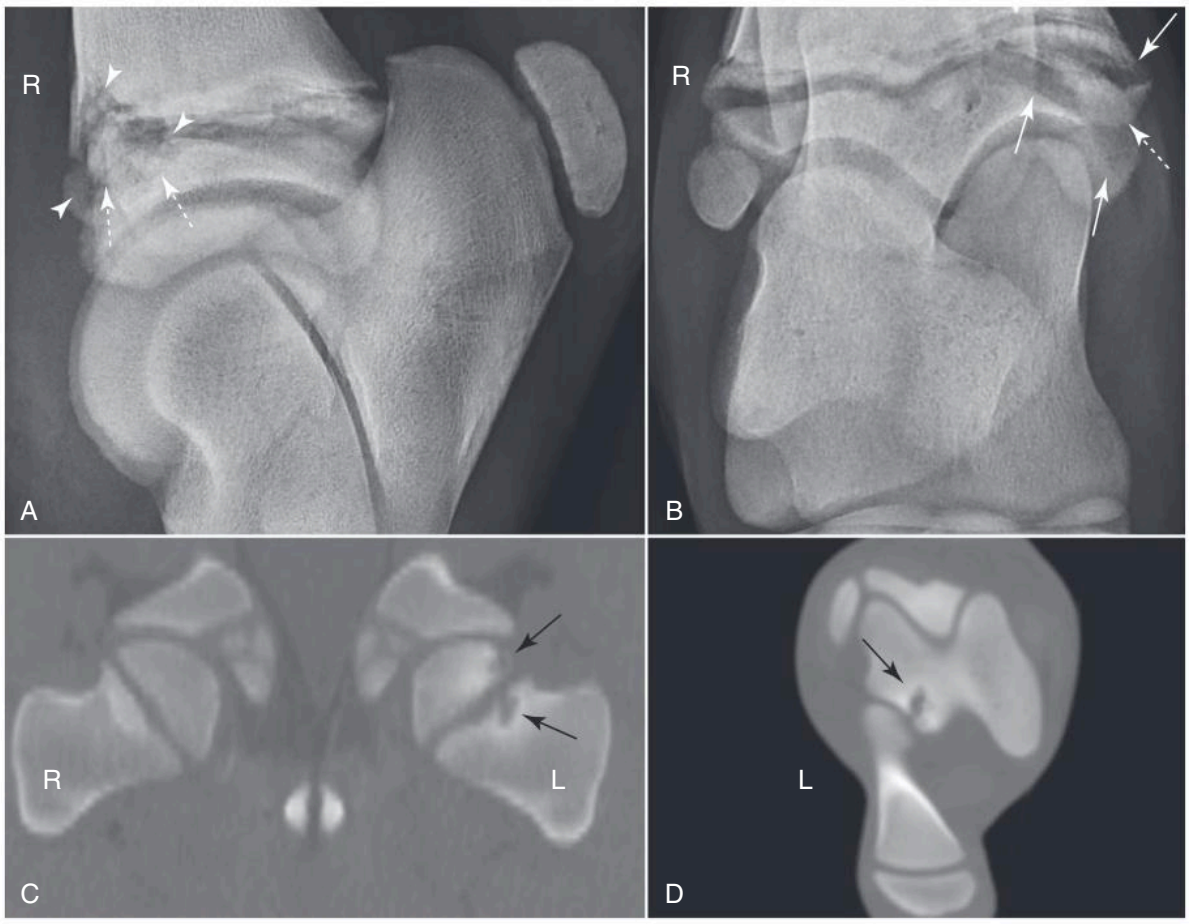


Fig. 22.18 Lateromedial (LM) **(A)** and dorsoplantar (DPl) **(B)** right tarsal radiographs of a 20-day-old Quarter horse filly with fever, right proximal tarsal swelling, and history of failure of passive transfer. The medial physis is widened (*white arrows*) with dorsal epiphyseal and metaphyseal margin irregularity and regional bone lysis (*white arrowheads*) and separation of epiphyseal fragment(s) (*white dashed arrows*) represent osteomyelitis and sequestra formation. A whole-body fan-beam computed tomography (CT) was performed. Dorsal CT bone reformats **(C and D)** revealed additional bone lysis with peripheral hyperattenuating sclerosis in the right proximal femoral physis and left lateral talar trochlea (*black arrows*) which were not suspected clinically. Salmonella was cultured from the right tibiotarsal joint.

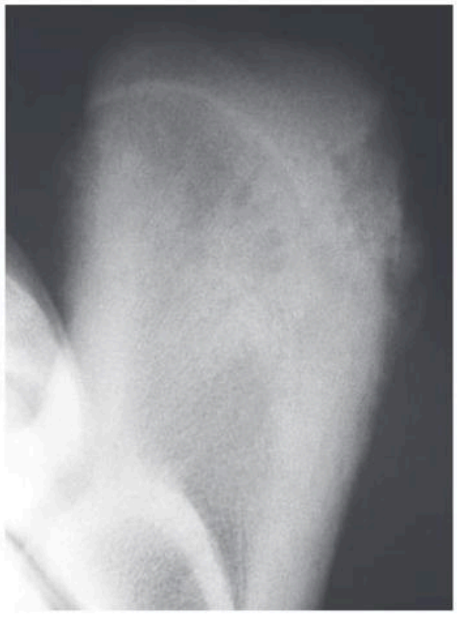
Neonatal Infectious Polyarthritis and Septic Physitis

Certain factors, such as immaturity, dysmaturity, failure of passive transfer, urachal patency, omphalitis, respiratory or gastrointestinal disease, wounds, or malnutrition may increase the risk of bacteremia and joint or growth plate infection in neonates and weanlings. Sepsis is confirmed via joint cytology and culture. CT or MRI, when available, can detect the development of osteomyelitis earlier,[43] as 30% to 50% bone loss is needed before lysis is visible radiographically. Sedated CT (Fig. 22.18), where available, is a growing modality for quickly assessing multiple joints and concomitant infections within the thorax or abdomen in septic foals.[42,43] MRI can reveal characteristic osteomyelitis changes[44] but requires general anesthesia and a longer scan time compared to CT. Serial radiographs 1 to 3 days apart can also be helpful in monitoring for development of osteomyelitis.

Septic physitis is usually seen in foals less than 6 months of age, with risk factors similar to infectious arthritis. As with synovial sepsis, clinical signs and radiographic changes offer a presumptive diagnosis although sampling of the joint fluid or physeal bone abnormality is required for definitive diagnosis and therapeutic guidance. Septic physitis most often affects the distal tibia and is asymmetric compared to aseptic forms[23] generally affecting one side of the growth plate with accompanying discrete regions of radiolysis (see Fig. 22.18). Despite aggressive and early treatment, asymmetric physeal growth may lead to eventual angular limb deformity and maturation should be monitored closely.

Calcaneal Tuber Osteitis/Osteomyelitis and Septic Calcaneal Bursitis

Osteolytic lesions associated with the calcaneal tuber are more often septic than aseptic and often involve the calcaneal bursae as the result of blunt trauma and/or wound, although they can also be hematogenous, especially in foals. Standard tarsal radiographs including a flexed calcaneal skyline projection and ultrasonography of the plantar tarsus aid in complete evaluation of the osseous and soft tissue structures involved. Positive contrast fistulography is recommended if a draining tract is present to better understand the soft tissues involved (Fig. 22.19, eFig. 22.10). Bone lysis and/or sequestra may take one to several weeks to declare themselves radiographically; thus, serial imaging is important. Ultrasound often reveals bursal thickening and anechoic to echogenic effusion and possibly concomitant injury to other components of the



eFig. 22.10 Lateromedial radiograph of the calcaneus of a horse with calcaneal osteomyelitis that developed after a penetrating injury of the point of the tarsus. Several ill-defined radiolucent areas are present in the calcaneus, mainly at its plantar aspect. The surrounding bone is diffusely sclerotic. There is also some marginal irregularity of the dorsal and plantar contours of the calcaneus. No sharp transition zone exists between abnormal and normal bone.

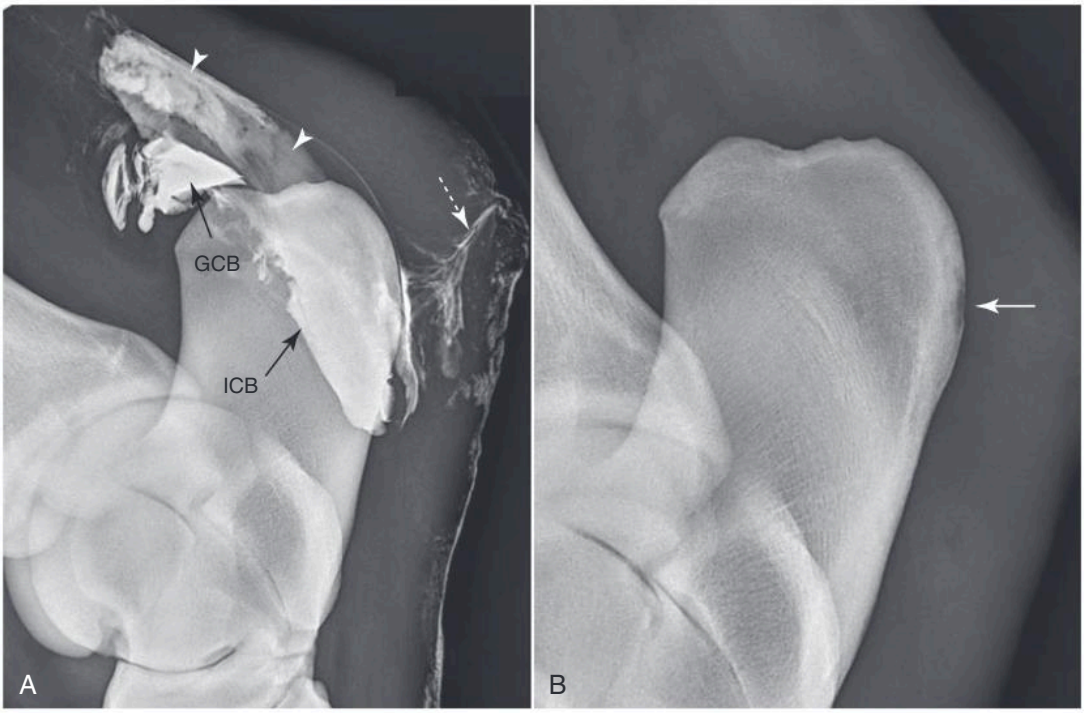


Fig. 22.19 **A,** Lateromedial (LM) tarsal fistulogram radiograph of an 11-year-old Friesian mare with right pelvic limb lameness after sustaining a plantar wound 2 weeks prior. Contrast medium travels from the plantar wound cranially through a draining tract (*white dashed arrow*) before filling the intertendinous (*ICB*) and gastrocnemius (*GCB*) calcaneal bursae and outlining the margins of the gastrocnemius tendon (*white arrowheads*). The bursae and tendon margins are irregular supportive of proliferative bursitis and chronic peritendinous inflammation. Cytology of the calcaneal bursal fluid confirmed septic bursitis. **B,** Recheck lateral radiograph 2 weeks later revealed improved soft tissue swelling but newly developed plantar calcaneal tuber lysis (*white arrow*), consistent with septic osteitis.

common calcaneal tendon, plantar ligaments, tarsal sheath and/or tibiotarsal joint. Septic bursitis combined with tendon injury and/or calcaneal osteitis have poorer reported outcomes.[45,46]

Septic Osteomyelitis and Fragmentation of the Sustentaculum Tali

Similar to the calcaneus, sustentaculum tali lysis is often septic caused by an inciting kick injury, wound, or draining tract at or above the level of the chestnut and can be career or life-ending if not treated early and aggressively.[48] Tarsal sheath effusion may or may not be present. DMPLO and flexed calcaneal skyline views are most helpful often revealing irregular sustentacular margination, osseous proliferation, bone fragmentation or sequestra (Fig. 22.20), and/or fractures. Immediately after injury ultrasound may be normal or show only minimal sheath effusion. Chronic cases generally reveal progressive tarsal sheath thickening and synovial masses often with septations of fluid and adhesions. Depending on injury severity and chronicity the lateral digital flexor tendon may show enlargement with or without fiber disruption and/or margin fibrillation. Prognosis is poor without early and aggressive treatment.[47,48]

SOFT TISSUE CONDITIONS OF THE EQUINE TARSUS

Peritarsal soft tissue injuries often present with visible soft tissue and/or joint swelling and pain to local palpation. Generally, a combination of radiographs and comprehensive ultrasound provide a presumptive or confirmed diagnosis. Intracapsular or extracapsular soft tissue swelling and/or osseous fragmentation or mineralization at entheses are indirect radiographic findings supportive of soft tissue injury within or around a joint.

Medial and Lateral Soft Tissue Injuries

Collateral Ligament Enthesopathy, Desmopathy, and Avulsions

The medial (Fig. 22.21) and lateral (Fig. 22.22) tibiotarsal collateral ligament anatomy is complex, with each composed of one long and three short components (superficial, middle, and deep) with the short ligaments running oblique to nearly perpendicular to the long ligaments.[49,50] Collectively, the collateral ligaments have variable insertions onto the talus, calcaneus, cuboidal, and metatarsal bones to provide robust joint stability.[49,50] In general, when the limb is extended, the long components of the collateral ligaments are under tension while the short components are relaxed and vice versa when the limb is in flexion.[50] Injury of the tibiotarsal collateral ligaments is relatively common[49,51,52] and most often related to supraphysiologic rotational forces during sharp turns or a fall/kick injury, although repetitive cyclic loading may be related to lateral collateral ligament injuries in Standardbred racehorses.[49] Acute injury typically results in severe lameness and extensive joint effusion. Radiographs are often normal aside from intracapsular swelling unless bone avulsion or other fractures occurred. Acute sonographic findings often show characteristic swirling echogenic effusion, supportive of hemarthrosis due to capsular tearing, which often is a concurrent injury with collateral ligament tears.[49] In the chronic phase, synovial distension often progresses to proliferative synovitis with thick multiloculated septae and reduced fluid component. Primary

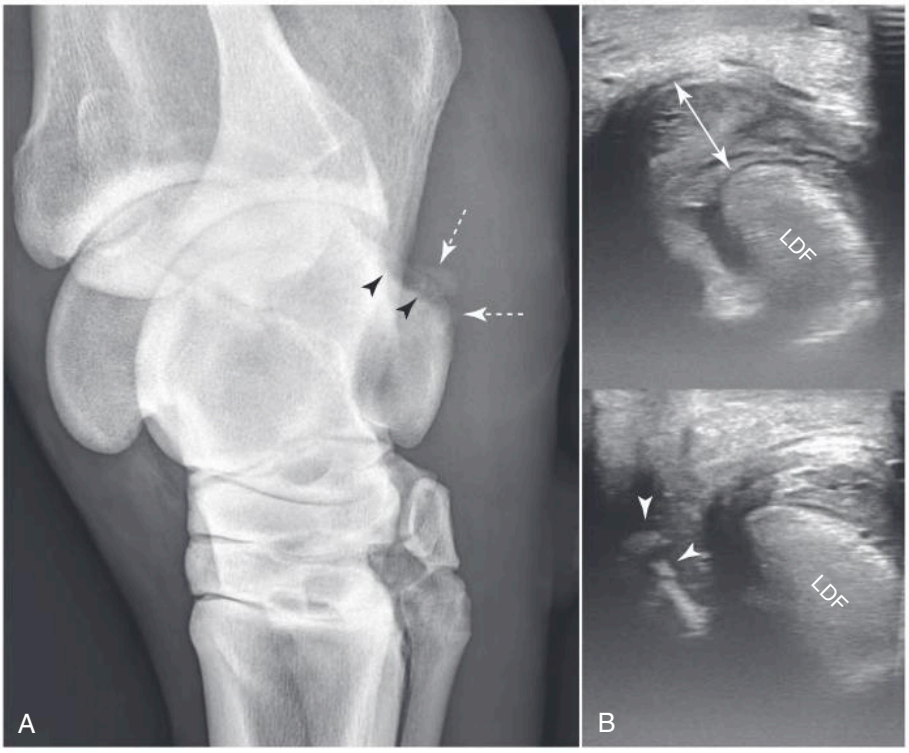


Fig. 22.20 **A,** DMPLO image in a 5-year-old Arabian mare with progressive lameness and plantar swelling 4 weeks after treatment of a plantar hock wound illustrates osteolysis of the proximal sustentaculum tali (*black arrowheads*) with adjacent rounded osseous fragments or sequestra (*white dashed arrows*). **B,** Transverse sonographic imaging of the tarsal sheath revealed severe proliferative sheath mass-like thickening (*white double arrow*) and generalized rounded enlargement of the lateral digital flexor (*LDF*). The sustentaculum plantar margin was discontinuous with multiple small hyperechoic bone fragments (*white arrowheads*). Septic tenovaginitis was confirmed with fluid cytology. In **B** dorsal is to the *left* and medial is to the *top* of the images. (Ultrasound image courtesy Caitlyn Horne, DVM, DACVSMR.)

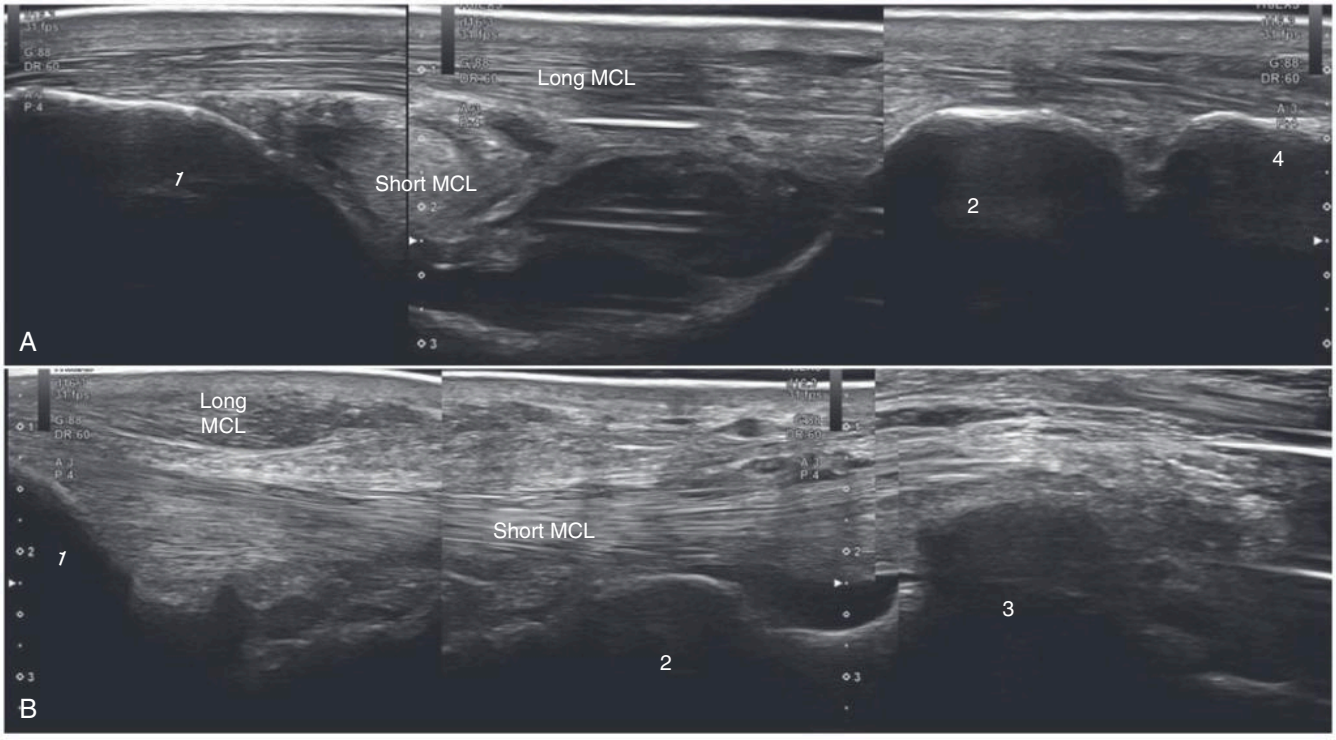


Fig. 22.21 Composite ultrasound images of the medial tibiotarsal collateral ligaments *(MCL).* In image **A,** the ultrasound transducer is aligned parallel to the long axis of the long medial collateral ligament, causing the short collateral ligaments to appear nearly perpendicular to the probe in a short axis (transverse) plane. In **B,** the transducer has been rotated almost 90 degrees to align parallel to the short portion of the collateral ligaments, showcasing the long portion of the collateral in a shorter axis (transverse) plane. *1,* Medial tibial malleolus; *2,* talus; *3,* calcaneus; *4,* central tarsal bone. The variable insertions of the ligaments are not shown. In both **A** and **B,** proximal is to the *left* and medial is to the *top* of the images.

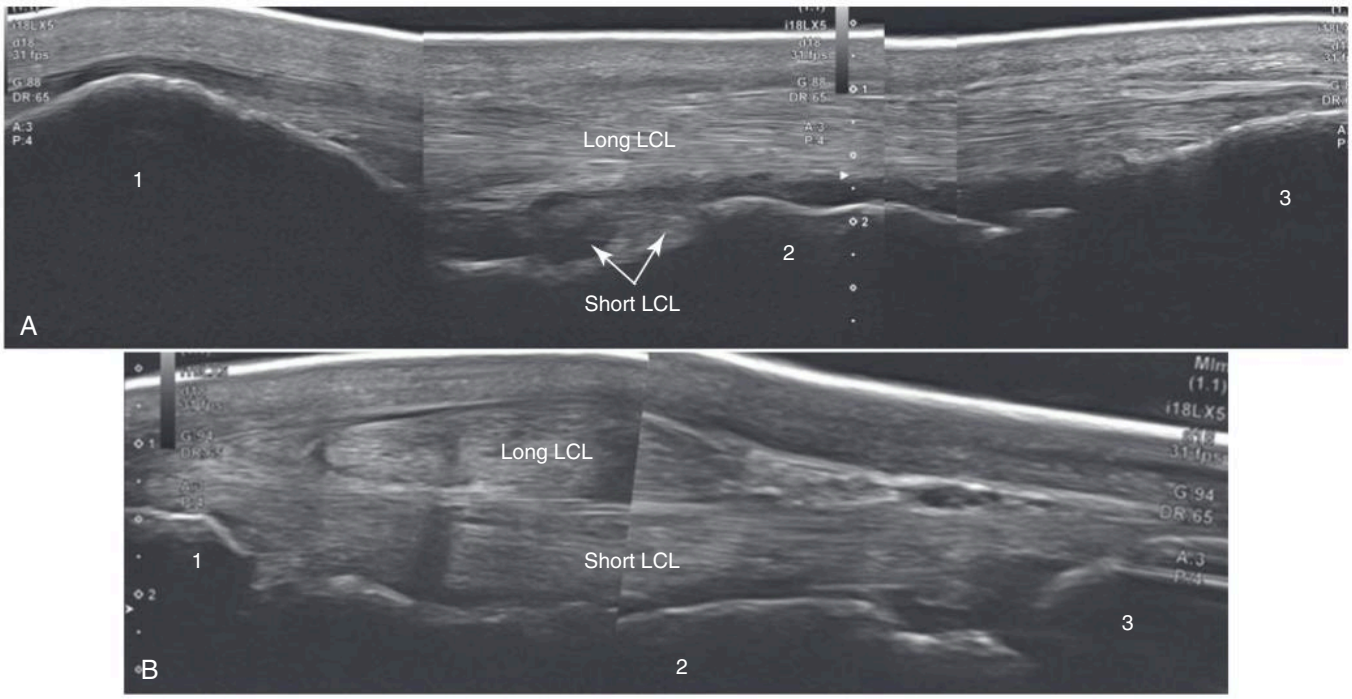


Fig. 22.22 Composite ultrasound images of the lateral tibiotarsal collateral ligament (*LCL*). In image **A,** the ultrasound transducer is positioned parallel to the long axis of the long lateral collateral ligament, resulting in the short lateral collateral ligaments being oriented almost perpendicular to the probe in a short axis (transverse) plane. In **B,** the transducer has been rotated almost 90 degrees to align more parallel to the short portion of the collateral ligaments, showcasing the long portion of the collateral in a shorter axis (transverse) plane. *1,* Medial tibial malleolus; *2,* talus; *3,* calcaneus. The variable insertions of the ligaments are not shown. In both **A** and **B,** proximal is to the *left* and lateral is to the *top* of the images.

collateral desmitis and desmopathies often reveal periligamentous soft tissue thickening and diffuse ligamentous enlargement with variable fiber pattern disorganization. Complete fiber disruption or core lesions are rarely seen.[52] Depending on lesion severity and management osteoarthritis may eventually develop due to joint instability and/or chronic synovitis. Prognosis for return to prior athletic use in horses with tibiotarsal osteoarthritis is generally guarded.[52] As collateral ligament ultrasound is complex and often challenged by severity of effusion or pain response with examination diagnosis of collateral ligament injuries can also be confirmed by high-field MRI (Fig. 22.23), CT arthrography[53] and/or exploratory arthroscopy.[50,54]

Plantar Soft Tissue Injuries

Curb

Prior to routine use of ultrasonography, "curb" was a colloquial term indicative of long plantar ligament (LPL) injury, but today "curb" is used to describe nonspecific soft tissue swelling of the plantar tarsus (Fig. 22.24) with the primary injury requiring sonography or less commonly MRI or CT to fully characterize.

Types of Curb: Long Plantar Desmitis/Desmopathy. The LPL originates along the plantarolateral calcaneus with a broad insertion onto the fourth metatarsal and fourth tarsal bones. Common in racing and Western performance breeds, long plantar injury is more often acute in onset and sonographically associated with focal or diffuse ligament enlargement with fiber disruption or large core lesions.[55,57]

Types of Curb: Plantar Fasciitis (Peritendinous-Periligamentous Inflammation). The plantar fascia is a thin, fibrous fascial layer deep to the skin and superficial to the LPL and superficial digital flexor tendon (SDFT). Plantar fasciitis is inflammation and thickening of this fascia uncomplicated by other tendon or ligament injury. Sonographically, the plantar fascia is thickened with echogenic to heterogeneous soft tissue proliferation with or without fluid accumulation. The cause may be related to fatigue injury from athletic overload and/or exercise in deep footing in endurance and racing breeds, though trauma is more commonly reported in sport horses. Prognosis for plantar fasciitis uncomplicated by tendon or ligament injury is favorable with appropriate rest and rehabilitation.[56] Conversely, fasciitis is generally a component of proximal SDFT or LPL lesions and may be an early indicator of impending tendinous or ligamentous injury.[57]

Types of Curb: Proximal Superficial Digital Flexor Tendonitis/Tendinopathy. The superficial digital flexor originates from the femoral supracondylar fossa as the caudal arm of the reciprocal apparatus. It wraps around the gastrocnemius muscle dorsomedially and forms a fibrocartilaginous cap on the plantar lobe of the tuber calcaneus.[58] Injury to the proximal SDFT along the plantar tarsus results in generalized enlargement with loss of the normal elliptical shape becoming rounder and generally enlarged (see Fig. 22.23). Injury that extends distal to the tarsus is associated with more severe lameness and worsened prognosis.[55]

Superficial Digital Flexor Subluxation/Luxations

Talocalcaneal ligaments secure the fibrocartilaginous cap medially and laterally to the calcaneal tuber, and tears of these ligaments can result in calcaneal bursitis as these structures communicate. Partial tears (Fig. 22.25) cause subluxation without dynamic instability, while full tears result in dynamic luxation of the fibrocartilage. Lateral luxations resulting from a medial tear are more common and offer better outcomes compared to medial luxations. This is due to the lateral stability provided by the gastrocnemius tendon (GT), which encourages

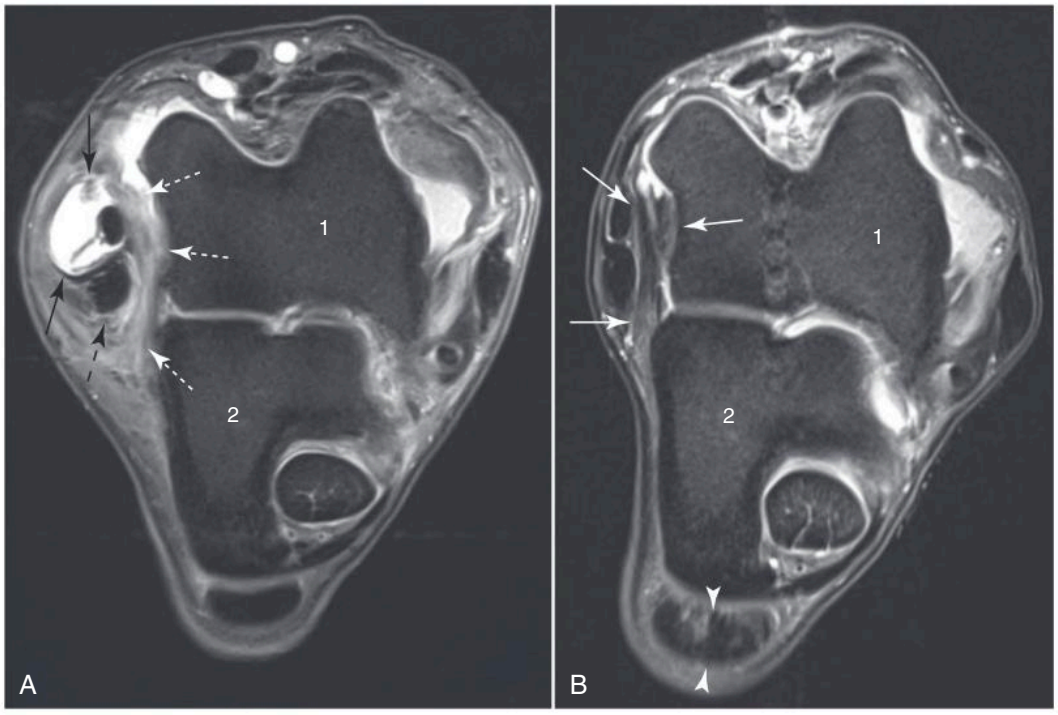


Fig. 22.23 Transverse 3 Tesla magnetic resonance imaging (MRI) proton density fat-suppressed images of disruption of the lateral short collateral ligaments **(A)** and normal contralateral limb comparison **(B)**. In **A,** the short collateral ligaments are enlarged, poorly margined, and not able to be distinguished from one another with disorganized fiber alignment and diffuse hyperintensity (*white dashed arrows*) compared to **B** (*white arrows*). There is also mild enlargement and hyperintense margin fibrillation of the long lateral collateral ligament (*black dashed arrow*), as well as hyperintense fluid signal expanding the lateral digital flexor tendon sheath (*black arrows*). In **B,** multifocal hyperintense tears and moderate diffuse enlargement of the superficial digital flexor tendon was incidentally discovered in the contralateral limb. *1,* Talus; *2,* calcaneus. In both images, lateral is to the *left* and dorsal to the *top* of the image.

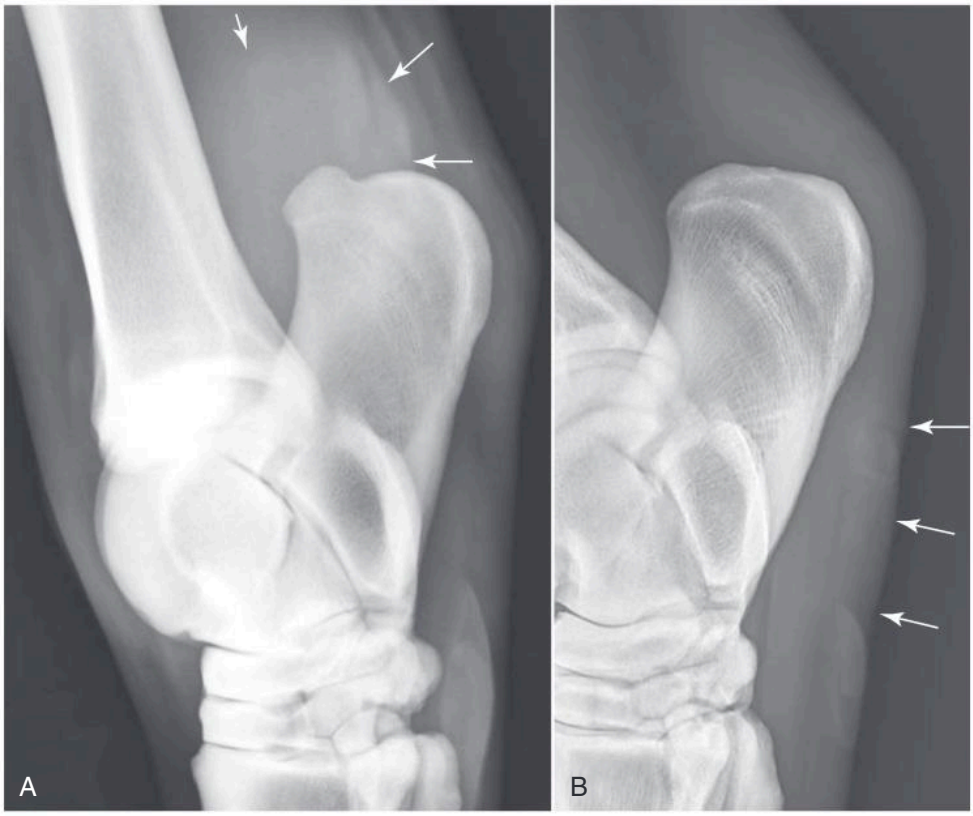


Fig. 22.24 Lateromedial (LM) radiographs showcasing different plantar soft tissue swellings (*white arrows*) of **(A)** severe tarsal sheath effusion ("thoroughpin") and **(B)** plantar fasciitis ("curb"). Specific diagnosis of soft tissue structures involved and therefore prognostication and therapeutic guidance requires ultrasound and occasionally computed tomography (CT) or magnetic resonance imaging (MRI).

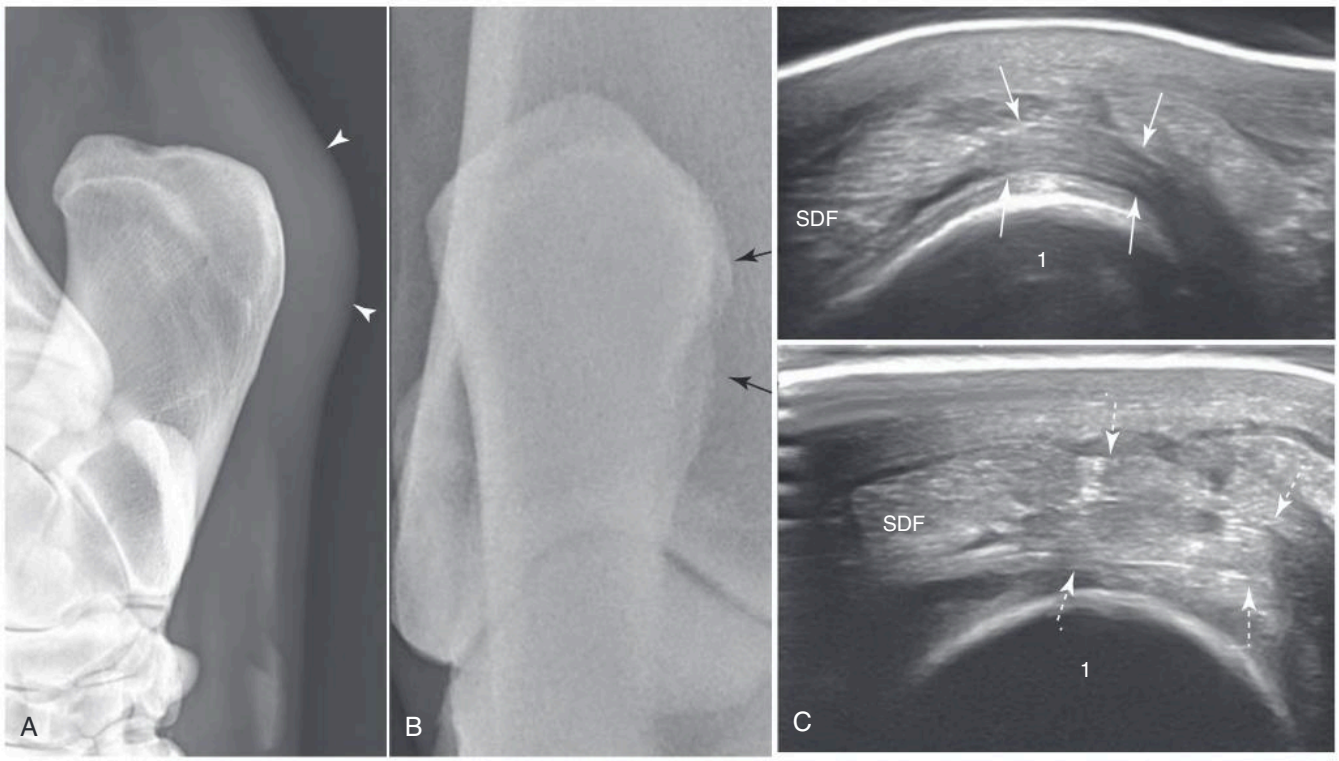


Fig. 22.25 Lateromedial (LM) **(A)** and dorsoplantar (DPl) **(B)** radiographs of a sound 10-year-old Quarter horse with point of hock swelling (*white arrowheads*) showing smooth osseous proliferation along the medial calcaneal tuber (*black arrows*) in the region of the talocalcaneal ligament attachments. Plantar ultrasound (**C,** *bottom* image) revealed medial talocalcaneal ligament enlargement and poor fiber alignment (*white dashed arrows*) with periligamentous thickening indicative of chronic, partial tears. The superficial digital flexor (*SDF*) fibrocartilaginous cap would mildly subluxate from plantar to lateral during tarsal flexion confirming partial medial tear. Contrast to the normal contralateral limb (**C,** *top* image), *white arrows* depict uniform fiber pattern, size, and margination of the medial talocalcaneal ligament. *1,* Calcaneal tuber. In **B,** the *top* of the image is medial, and the *left* of the image is plantar.

the SDFT to remain near the calcaneal tuber. Longitudinal tears through the fibrocartilage can lead to the tuber calcaneus protruding through the cap.[59] Conservative and surgical therapies are both viable options for treatment, with surgery providing improved tendon stability but risks other complications including implant infection.[60]

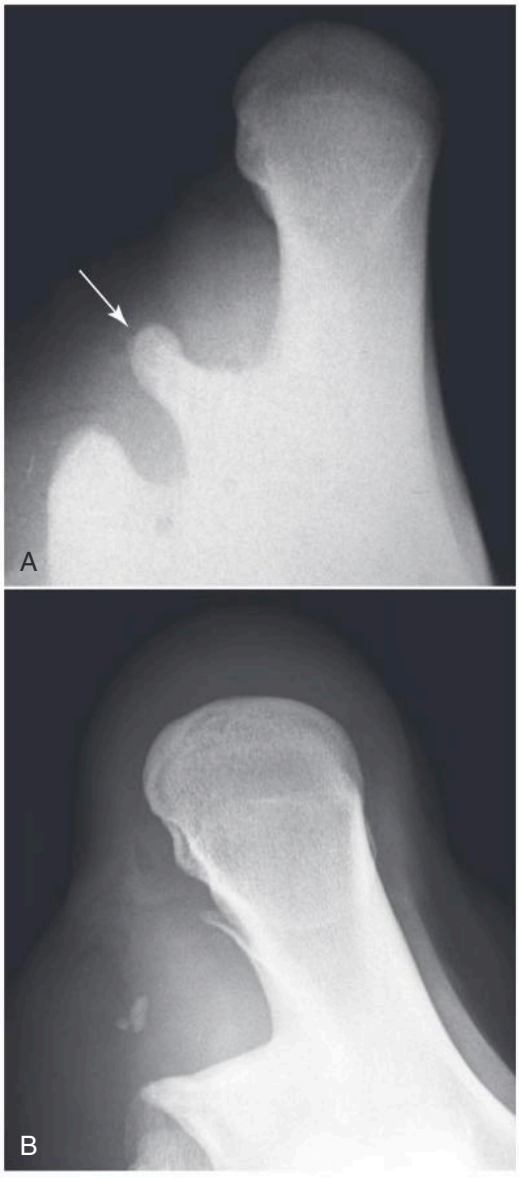
Thoroughpin: Tarsal Sheath Tenosynovitis/ Tenovaginitis

The tarsal sheath is a synovial lining covering the lateral digital flexor (LDF) tendon from the distal tibia to the proximal metatarsus. The tarsal sheath is bounded dorsolaterally by an osseous tarsal groove created by the calcaneal shaft and sustentaculum tali, which is covered by thick fibrocartilage for enhanced tendon gliding. The deep plantar ligament and thick plantar retinaculum (also called the metatarsocalcaneal ligament),[61] respectively, form the dorsodistal and plantaromedial tarsal sheath boundaries. These boundaries prevent distension of the tarsal sheath at the tarsal bone level, but proximal recesses at the level of the common calcaneal tendon can enlarge and cause visible distension (Fig. 22.26, eFig. 22.11), colloquially termed *thoroughpin*. Recurrent tarsal sheath effusion or effusion accompanied by lameness should be taken seriously due to the poorer outcomes associated with both septic or chronic sterile tenosynovitis of the tarsal sheath.[47,48,62] Chronic tarsal sheath effusions in horses are usually a result of tendovaginitis, which affects both the sheath and LDF tendon. Radiographs may reveal soft tissue swelling in the region of the proximal tarsal sheath recesses, mineralization of the tendon or tarsal sheath, and/or sustentacular osseous changes like exostosis, fragmentation, or lysis. Ultrasound can confirm radiographic pathology and provide additional insight into the severity of synovial thickening, the presence of synovial masses or fronds that may form adhesions with the LDF, as well as alterations in the size, shape, or fiber pattern of the LDF (Fig. 22.27).[48] Importantly, some horses with lateral digital flexor tendinopathies do not present with significant effusion or radiographic or ultrasound abnormalities and require intrathecal diagnostic anesthesia and MRI for diagnosis.[62]

False thoroughpin is described as unilocular or multilocular perisynovial fluid distention near but not communicating with the tarsal sheath, tibiotarsal joint, or calcaneal bursae, occurring more commonly along the lateral aspect.[63] Differentiation of a true and false thoroughpin requires contrast radiography or endoscopy to evaluate communication with synovial structures.[64,65]

Gastrocnemius Tendinitis/Tendinopathy

The GT, along with the SDFT, originates from the femoral supercondylar fossa and together they make up the largest fascicles of the common calcaneal tendon. The GT tendon inserts on the plantar lobe of the calcaneal tuber just cranial to the SDFT fibercartilagenous cap. Injury of the GT can occur at various points along its length, such as with avulsion of the femoral origin, myofibril disruption of the muscle body, or tendinous components within the common calcaneal



eFig. 22.11 Plantaroproximal/plantarodistal views of the sustentaculum tali of two horses with aseptic chronic tenosynovitis of the tarsal sheath. **A,** A large, smooth, bony proliferation is present on the medial margin of the sustentaculum tali (*white arrow*). **B,** The soft tissues plantar to the sustentaculum tali are thickened, and two focal areas of mineralization with smooth margins are visible plantar to the sustentaculum tali. These likely represent dystrophic calcifications in the soft tissues. Mild remodeling of the medial margin of the sustentaculum tali and a bony proliferation on the medial surface of the tuber calcanei are also present.

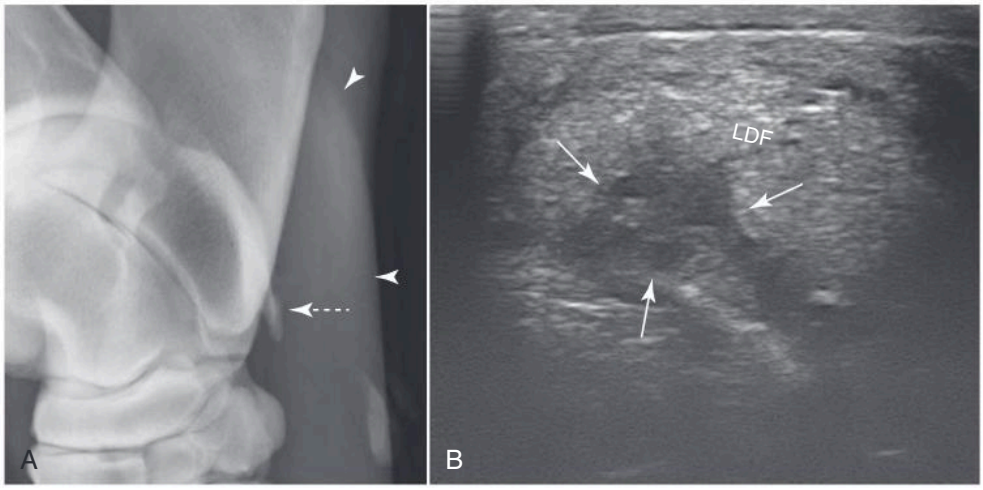


Fig. 22.26 **A,** Lateromedial (LM) radiograph of a 6-year-old Friesian mare with right pelvic limb lameness and progressive plantar tarsal curb-like swelling showing plantar soft tissue convexity (*white arrowheads*) and smoothly margined mineral proliferation distal to the sustentacula tali (*white dashed arrow*). Differentials for the mineral include exostosis or dystrophic mineralization of the tarsal sheath or lateral digital flexor tendon and are often associated with extensive tarsal sheath pathology warranting ultrasound interrogation. **B,** Plantar ultrasound revealed proliferative tarsal sheath effusion along with severe generalized enlargement and central large hypoechoic core lesion (*white arrows*) of the lateral digital extensor just proximal to the chestnut. *LDF,* Lateral digital flexor. (Ultrasound image courtesy Caitlyn Horne, DVM, DACVSMR.)

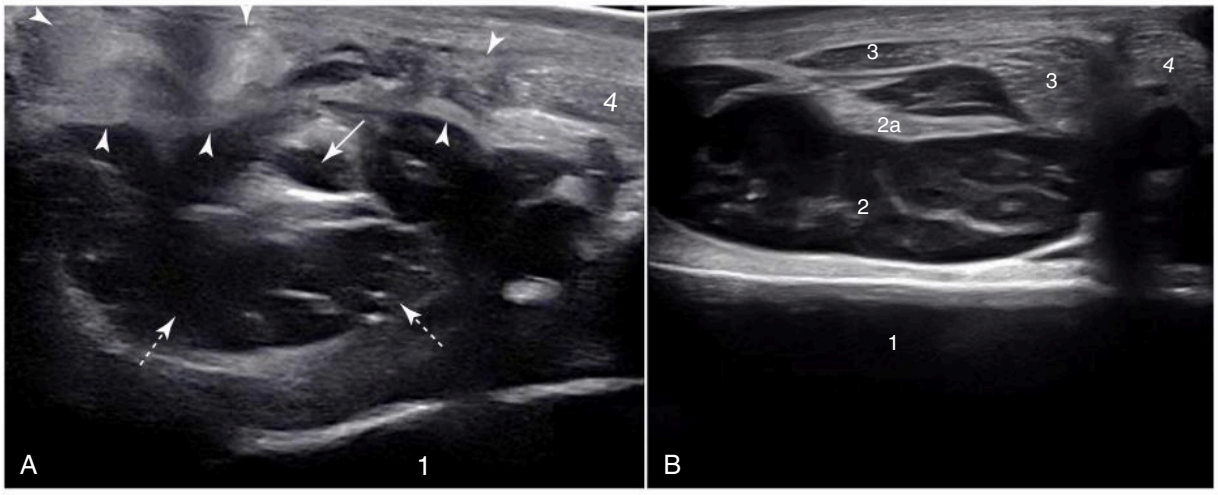


Fig. 22.27 Ultrasound images of a 4-year-old Thoroughbred gelding with recent lameness and dorsal tarsal soft tissue swelling and pain. The tarsus was not able to be extended when the stifle was flexed. In **A and B,** the ultrasound transducer is positioned perpendicular to the long axis of limb just proximal to the tibiotarsal joint, resulting in a short axis (transverse) image of the combined fibularis tertius ligament and cranialis tibialis musculotendinous portion. In **A,** the fibularis tertius ligament (*white arrowheads*) is enlarged and misshapen with complete loss of architecture replaced by heterogeneous tissue and no identifiable normal ligament fibers. The surrounding cranialis tibialis muscle (*white dashed arrows*) is enlarged and rounded with a hypoechoic tear in the central forming tendon (*white arrow*). This clinical picture is compatible with hyperextension injury and severe fibularis tertius desmitis and cranialis tibialis musculotendinitis with small central tear. Compare with the normal contralateral limb in **B**. *1,* Distal tibia; *2,* cranialis tibialis muscular portion; *2a,* cranialis tibialis tendinous portion; *3,* fibularis tertius ligament; *4,* long digital extensor tendon. In both images, medial is to the *left* and cranial is to the *top* of the images.

tendon.[66–68] Ultrasound of the common tendon components, surrounding bursae, and tarsal sheath is important for diagnosis and identification of comorbidities. Ultrasound characteristics of GT tendinitis generally reveal diffuse tendon enlargement and less commonly fiber disruption within the body.[69] The tendon is also prone to complications associated with plantar lacerations and wounds.[70] Injuries of the common calcaneal tendon components particularly if associated with plantar wounds should be evaluated with radiographs, including a flexed calcaneal skyline projection. This is necessary to assess for concurrent calcaneal osteitis, which often indicates a septic process and should be taken seriously given poorer outcomes.[45]

Dorsal Soft Tissue Injuries

Fibularis (Peroneus) Tertius

The fibularis tertius (FT) is entirely tendinous in the horse and represents the cranial arm of the reciprocal apparatus. At the

level of the tibiotarsal joint, the FT traverses the dorsal tarsus forming a tunnel for passage of the cranialis tibialis musculotendinous junction. The FT then bifurcates into smaller dorsal and lateral branches which insert on the dorsal metatarsus and dorsal and lateral distal tarsal bones.[71,72] FT complete or partial rupture—or tendinitis are caused by hyperextension injury or trauma and will present with varying degrees of dorsal tarsal or crus swelling and lameness depending on the severity and location of the injury. While radiographs are indicated to rule out concurrent osseous trauma, ultrasound is paramount and may show tendon enlargement, margin irregularity, and variable degrees of fiber disruption (see Fig. 22.27).[73] Complete rupture results in inappropriate extension of the tarsus when the stifle is flexed.[72] Generally, rupture occurs within the mid- or distal portion, although can occur at the origin resulting in femoropatellar effusion and possibly osseous avulsion.[71,74] Dystrophic mineralization or insertional enthesopathy of the FT is occasionally identified radiographically and generally well tolerated when not associated with other changes.

Long Digital Extensor Tenosynovitis

A synovial sheath envelops the long digital extensor tendon (LoDET) as it traverses the dorsal tarsus and is a palpable structure just lateral to the medial trochlear ridge. The proximal, middle, and distal dorsal tarsal retinaculae are situated between the LoDET and skin and generally prevent visualization of LoDET sheath effusion. Distal to the tarsus, the lateral digital extensor tendon, which also has its own sheath, fuses with the LoDET and travels dorsally along the metatarsus to insert on the distal phalanx. Severing of these tendons once conjoined below the metatarsus has a poorer prognosis than more proximal at the tarsus/metatarsus, where they are separated and the retinacular attachments afford collateral stabilization.[75]

Focal Peritarsal Cellulitis

This is a rare, acute, and painful cellulitis localized to the dorsal tarsus and results in severe, sudden-onset lameness. It is characterized by expansion and increased echogenicity of the subcutaneous and peritendinous structures, with diffuse hypoechoic fluid locules,[76] and may be associated with septic tenosynovitis of the LoDET.[77] Early and aggressive diagnosis and treatment without complications of osteomyelitis or laminitis are associated with favorable outcomes.

Acknowledgment

With special thanks to prior authors of this chapter for their contributions.

REFERENCES

1. Espinosa-Mur P, Cote N, Desjardins MR. Arthroscopic removal of osteochondral fragments in the dorsal pouch of the proximal intertarsal joint in 29 horses. *Vet Surg*. 2018;47(4):555–565.
2. Bell BT, Baker GJ, Foreman JH, Abbott LC. In vivo investigation of communication between the distal intertarsal and tarsometatarsal joints in horses and ponies. *Vet Surg*. 1993;22(4):289–292.
3. Casillas JM, Jacobs CC, Manfredi JM. Radiographic localization of the attachments of soft tissue structures in the tarsal region of horses. *Am J Vet Res*. 2020;81(5):406–415.
4. Butler JR, Colles CM, Dyson SJ, Kold SE. *The tarsus. Clinical Radiology of the Horse*. 4th ed. John Wiley & Sons; 2017:349–398.
5. Rogers CW, Gee EK, Dittmer K. Growth and bone development in the horse: when is a horse skeletally mature? *Animals (Basel)*. 2021;11(3):632.
6. Hinkle FE, Johnson SA, Selberg KT, Barrett MF. A review of normal radiographic variants commonly mistaken for pathological findings in horses. *Equine Vet Educ*. 2020;32(12):664–672.
7. Olstad K, Ekman S, Carlson CS. An update on the pathogenesis of osteochondrosis. *Vet Pathol*. 2015;52(5):785–802.
8. Hendrickson EH, Lykkjen S, Dolvik NI, Olstad K. Prevalence of osteochondral lesions in the fetlock and hock joints of Standardbred horses that survived bacterial infection before 6 months of age. *BMC Vet Res*. 2018;14(1):143.
9. Ortved K. Surgical management of osteochondrosis in foals. *Vet Clin North Am Equine Pract*. 2017;33(2):379–396.
10. Hoey S, O'Sullivan J, Byrne J, Devine S, Toomey W, McAllister H, et al. Ultrasound screening protocol for osteochondrosis at selected predilection sites in Thoroughbred yearlings. *Ir Vet J*. 2022;75(1):3.
11. Grevenhof EM, Ducro BJ, Van Weeren PR, Van Tartwijk JMFM, Van den Belt AJ, Bijma P. Prevalence of various radiographic manifestations of osteochondrosis and their correlations between and within joints in Dutch Warmblood horses. *Equine Vet J*. 2009;41(1):11–16.
12. James O, Payne R, Bathe A, Greet T, Wylie C. Arthroscopy of the dorsal and plantar pouches of the tarsocrural joint for the treatment of osteochondritis dissecans in the horse: clinical features and follow-up. *Vet Surg*. 2016;45(8):1049–1055.
13. Oliver LJ, Baird DK, Baird AN, Moore GE. Prevalence and distribution of radiographically evident lesions on repository films in the hock and stifle joints of yearling Thoroughbred horses in New Zealand. *N Z Vet J*. 2011;59(4):202–209.
14. Simpson CM, Lumsden JM. Unusual osteochondral lesions of the talus in a horse. *Aust Vet J*. 2001;79(11):752–755.
15. Kadic LIM, Rodgerson DH, Newsom LE, Spirito M. Description of a rare osteochondrosis lesion of the medial aspect of the distal intermediate ridge of the tibia in seven Thoroughbred horses (2008-2018). *Vet Radiol Ultrasound*. 2019;60(3):285–290.
16. Espinosa-Mur P, Lacourt M, Alexander K, David F, Laverty S. Fragmentation of the proximal tubercle of the talus in horses: 9 cases (2004–2010). *J Am Vet Med Assoc*. 2013;243(7):984–991.
17. Vanderperren K, Raes E, Van Bree H, Saunders JH. Diagnostic imaging of the equine tarsal region using radiography and ultrasonography. Part 2: bone disorders. *Vet J*. 2009;179(2):188–196.
18. Montgomery LJ, Juzwiak JS. Subchondral cyst-like lesions in the talus of four horses. *Equine Vet Educ*. 2009;21(12):629–636.
19. Dyson S. Lameness associated with mineralization of the central tarsal bone and a small osseous cyst-like lesion in two sport horses. *J Equine Vet Sci*. 2013;33(1):51–56.
20. Garcia-Lopez JM, Kirker-Head CA. Occult subchondral osseous cyst-like lesions of the equine tarsocrural joint. *Vet Surg*. 2004;33(6):557–564.
21. Baird DH, Pilsworth RC. Wedge-shaped conformation of the dorsolateral aspect of the third tarsal bone in the thoroughbred racehorse is associated with development of slab fractures at this site. *Equine Vet J*. 2001;33(7):617–620.
22. Wong DM, Scarratt WK, Maxwell V, Moon VM. Incomplete ossification of the carpal, tarsal, and navicular bones in a dysmature foal. *Equine Vet Educ*. 2003;15(2):72–81.

23. Suarez-Fuentes DG, Tatarniuk D. Clinical and radiographic findings of septic physitis in foals. *Equine Vet Educ*. 2020;32(3):e134–e139.
24. Sprackman L, Dakin SG, May SAWR. Relationship between the shape of the central and third tarsal bones and the presence of tarsal osteoarthritis. *Vet J*. 2015;203(1):94–98.
25. Byam-Cook KL, Singer ER. Is there a relationship between clinical presentation, diagnostic and radiographic findings and outcome in horses with osteoarthritis of the small tarsal joints. *Equine Vet J*. 2009;41(2):118–123.
26. Fairburn A, Dyson S, Murray R. Clinical significance of osseous spurs on the dorsoproximal aspect of the third metatarsal bone. *Equine Vet J*. 2010;42(7):591–599.
27. Smith RK, Dyson SJ, Schramme MC, Head MJ, Payne RJ, Platt D, et al. Osteoarthritis of the talocalcaneal joint in 18 horses. *Equine Vet J*. 2005;37(2):166–171.
28. Raes EV, Vanderperren K, Pille F, Saunders JH. Ultrasonographic findings in 100 horses with tarsal region disorders. *Vet J*. 2010;184(2):201–209.
29. Barrett MF, Selburg KT, Johnson SA, Hersman J, Frisbie DD. High field magnetic resonance imaging contributes to diagnosis of equine distal tarsus and proximal metatarsal lesions: 103 cases. *Vet Radiol Ultrasound*. 2018;59(5):587–596.
30. Barker WHJ, Smith MRW, Minshall GJ, Wright IM. Soft tissue injuries of the tarsocrural joint: a retrospective analysis of 30 cases evaluated arthroscopically. *Equine Vet J*. 2013;45(4):435–441.
31. Keller SA, Furst AE, Kircher P, Ringer S, Kuemmerle JM. Locking compression plate fixation of equine tarsal subluxations. *Vet Surg*. 2015;44(8):949–956.
32. Dowling BA, Dart AJ, Hodgson DR. Surgical treatment of tarsometatarsal joint luxation in a miniature horse foal. *Aust Vet J*. 2000;78(10):683–684.
33. Abuja GA, Bubeck KA, Quinteros DD, Garcia-Lopez JM. Surgical treatment of distal tarsal joint luxations in three horses. *Vet Comp Orthop Traumatol*. 2013.
34. Smith MRW. Fractures of the tibial malleoli. *Equine Vet Educ*. 2012;24(10):503–506.
35. Nixon AJ. *Equine Fracture Repair*. Hoboken: John Wiley & Sons; 2020.
36. Katzman SA, Spriet MP, Beck BR, Barrett MF, Hendrickson DA. Incomplete fracture of the talus secondary to maladaptive stress remodeling in a horse. *J Am Vet Med Assoc*. 2019;254(1):102–108.
37. Gunst S, Chicca FD, Furst AE, Kuemmerle JM. Central tarsal bone fractures in horses not used for racing: computed tomographic configuration and long-term outcome of lag screw fixation. *Equine Vet J*. 2016;48(5):585–589.
38. Steel CM, Collins VL, Hance SR, Adkins AR, Hitchens PL. Prevalence, radiographic resolution and outcomes of slab fractures of the third and central tarsal bones in juvenile Thoroughbred horses. *Aust Vet J*. 2019;97(4):108–115.
39. Davidson EJ, Ross MW, Parente EJ. Incomplete sagittal fractures of the talus in 11 racehorses: outcome. *Equine Vet J*. 2005;37(6):457–461.
40. Wright L, Ekstrom CT, Kristoffersen M, Lindegaard C. Haematogenous septic arthritis in foals: short- and long-term outcome and analysis of factors affecting prognosis. *Equine Vet J*. 2017;29(6):328–336.
41. Bryant HA, Dixon JJ, Weller R, Bolt DM. Use of positive contrast radiography to identify synovial involvement in horses with traumatic limb wounds. *Equine Vet J*. 2019;51(1):20–23.
42. Barba M, Lepage OM. Diagnostic utility of computed tomography imaging in foals: 10 cases (2008–2010). *Equine Vet Educ*. 2013;25(1):29–38.
43. Munsterman AS, Alexander K, Samii VF, Latimer FG. Computed tomography in the diagnosis of septic physitis in two foals. *Equine Vet Educ*. 2007;19(4):200–206.
44. Gaschen L, LeRoux A, Trichel J, Riggs L, Bragulla HH, Rademacher N, et al. Magnetic resonance imaging in foals with infectious arthritis. *Vet Radiol Ultrasound*. 2011;52(6):627–633.
45. Post EM, Singer ER, Clegg PD, Smith RK, Cripps PJ. Retrospective study of 24 cases of septic calcaneal bursitis in the horse. *Equine Vet J*. 2003;35(8):662–668.
46. Isgren CM, Salem SE, Singer ER, Wylie CE, Lipreri G, Graham RJTY, et al. A multi-centre cohort study investigating the outcome of synovial contamination or sepsis of the calcaneal bursae in horses treated by endoscopic lavage and debridement. *Equine Vet J*. 2020;52(3):404–410.
47. Hand DR, Watkins JP, Honnas CM, Kemper D. Osteomyelitis of the sustentaculum tali in horses: 10 cases (1992-1998). *J Am Vet Med Assoc*. 2001;219(3):341–345.
48. Tommasa SD, Scharner D, Brehm W, Troillet A. Disorders of the sustentaculum tali and the medial trochlear ridge of the talus in horses: novel findings and surgical management of five cases. *Vet Rec*. 2021;188(5):e144.
49. Sherlock CE, Eggleston RB, Peroni JF, Parks AH. Desmitis of the medial tarsal collateral ligament in 7 horses. *Equine Vet Educ*. 2012;24(2):72–80.
50. Kummerle JM, Kummer MR. Arthroscopically accessible anatomy of the tarsal collateral ligaments in the horse. *Vet Surg*. 2013;42(3):267–274.
51. Whitcomb M. Ultrasonography of the equine tarsus. *AAEP Proceedings*. 2006;52:13–30.
52. Lamb L, Zubrod C, Hague B, Brakenhoff J, Major M. Clinical outcome of collateral ligament injuries of the tarsus. *Can Vet J*. 2012;53(5):518–524.
53. Raes E, Bergman HJ, Van Ryssen B, Vanderperren K, Stock E, Saunders JH. Computed tomographic features of lesions detected in horses with tarsal lameness. *Equine Vet J*. 2014;46:189–193.
54. Biggi M, Dyson SJ. Use of high-field and low-field magnetic resonance imaging to describe the anatomy of the proximal portion of the tarsal region of nonlame horses. *Am J Vet Res*. 2018;79(3):299–310.
55. Ross MW, Genovese RL. Curb. In: Ross MW, Dyson SJ, eds. *Diagnosis and Management of Lameness in the Horse*. 2nd ed. St. Louis: W.B. Saunders; 2011:792–798.
56. Paris A, Beccati F, Pepe M. Plantar fasciitis in 19 endurance horses: diagnosis, treatment and follow-up. *Equine Vet Educ*. 2020;32(1):1–10.
57. Ross MW, Genovese RL, Reef VB. Curb: a collection of plantar tarsal soft tissue injuries. *AAEP Proceedings*. 2002;48:337–342.
58. Emond AL, Seignour VC, Denoix JM. Ultrasonographic examination of the tuber calcanei area: technique and normal ultrasonographic images. *Equine Vet Educ*. 2022;34(4):192–199.
59. Wright IM, Minshall GJ. Injuries of the calcaneal insertions of the superficial digital flexor tendon in 19 horses. *Equine Vet J*. 2012;44(2):136–142.
60. Federici M, Furst AE, Hoey S, Bichofberger AS. Outcome of conservative and surgical treatment for luxations of the equine superficial digital flexor tendon from the calcaneal tuber. *Equine Vet Educ*. 2019;31(2):49–56.
61. Dyson S, Blunden A, Murray R. Magnetic resonance imaging, gross postmortem, and histological findings for soft tissues of the plantar aspect of the tarsus in normal horses. *Vet Radiol Ultrasound*. 2016;57(2):216–227.
62. Davis W, Caniglia CJ, Lustgarten M, Blackwelder T, Robertson I, Redding RW. Clinical and diagnostic imaging characteristics of lateral digital flexor tendinitis within the

tarsal sheath in four horses. *Vet Radiol Ultrasound*. 2013;54(2):166–173.
63. Dyson SJ. Bursae and other soft tissue swellings. In: Ross MW, Dyson SJ, eds. *Diagnosis and Management of Lameness in the Horse*. Philadelphia: Saunders; 2003:705–708.
64. Vanderperren K, Raes E, Hoegaerts M, Saunders JH. Diagnostic imaging of the equine tarsal region using radiography and ultrasonography. Part 1: the soft tissues. *Vet J*. 2009;182(2):179–187.
65. Minshall GJ, Wright IM. Synoviocoeles associated with the tarsal sheath: description of the lesions and treatment in 15 horses. *Equine Vet J*. 2011;43(1):71–75.
66. Jesty SA, Palmer JE, Parente EJ, Schaer TP, Wilkins PA. Rupture of the gastrocnemius muscle in six foals. *J Am Vet Med Assoc*. 2005;227(12):1965–1968.
67. Swor TM, Schneider RK, Ross MW, Hammer EJ, Tucker RL. Injury to the origin of the gastrocnemius muscle as a possible cause of lameness in four horses. *J Am Vet Med Assoc*. 2001;219(3):215–219.
68. Raes EV, Bergman EHJ, van der Veen H, Vanderperren K, Van der Vekens E, Saunders JH. Comparison of cross-sectional anatomy and computed tomography of the tarsus in horses. *Am J Vet Res*. 2011;72(9):1209–1221.
69. Redding RW. The tarsus. In: Baxter GM, ed. *Adam's and Stashak's Lameness in Horses*. 7th ed. John Wiley & Sons; 2020:657–701.
70. Bertuglia A, Puglisi G. Repair of the Achilles mechanism in a miniature horse. *Equine Vet Educ*. 2005;17(1):3–8.
71. Koenig J, Cruz A, Genovese R, Trostle S. Rupture of the peroneus tertius tendon in 27 horses. *Can Vet J*. 2005;46(6):503–506.
72. Deniox J. Peronius tertius anatomy and lesions. *Equine Vet Educ*. 2007;19(8):416–418.
73. Reimer JA, Ruggles AR, Hopper SA. Sonographic abnormalities of the dorsal tarsal region. In: 55. American Association of Equine Practitioners Proceedings; 2009:458–466.
74. Holcombe SJ, Bertone AL. Avulsion fracture of the origin of the extensor digitorum longus muscle in a foal. *J Am Vet Med Assoc*. 1994;204(11):1652–1653.
75. Elliott CRB, Vasey JR, Russell TM. Transection of the lateral and long digital extensor tendons in racehorses. *Aust Vet J*. 2012;90(1–2):20–23.
76. Pilswoth RC, Head MJ. A study of ten cases of focal peritarsal infection as a cause of severe lameness in the Thoroughbred racehorse: clinical signs, differential diagnosis, treatment and outcome. *Equine Vet J*. 2001;33(4):366–370.
77. Kalka T, Harding PG, Cullimore AM. Focal peritarsal cellulitis with long digital extensor tenosynovitis. *Equine Vet Educ*. 2022;34(5):e228–e233.

ELECTRONIC RESOURCES

Additional information related to the content in Chapter 22 can be found online at eBooks.Health.Elsevier.com

- Chapter Quiz

CHAPTER 23

Equine Carpus

Lindsey J. Gilmour

The equine carpus is a complex anatomical region comprised of seven cuboidal bones that are arranged in two rows to create three main joints: antebrachiocarpal (radiocarpal), middle carpal (intercarpal), and carpometacarpal. The proximal row of cuboidal bones contains the radial, intermediate, and ulnar carpal bones. The accessory carpal bone is situated palmar to and articulates with the radius and ulnar carpal bone. The distal row of cuboidal bones contains the second, third, and fourth carpal bones with inconsistent appearance of first and fifth carpal bones. The bulk of the horse's weight-bearing load falls upon the radial, intermediate, and third carpal bones.[1] Small intercarpal joints between articulating cuboidal bones are stabilized by numerous extracapsular and intracapsular ligaments. Range of motion within the carpus is largely limited to flexion and extension of the antebrachiocarpal and middle carpal joints while the carpometacarpal joint is relatively immobile.[2]

Indications for carpal imaging are similar to those in other areas of the equine limb and include a history of regional trauma, external wounds, soft tissue swelling or palpable thickening, pain or lameness that is relieved with regional or intra-articular diagnostic analgesia, and prepurchase examinations plus screening for incomplete ossification of cuboidal bones in foals with suspected prematurity or dysmaturity.[3] Radiographic findings should always be correlated with a complete patient history, physical and lameness exam findings, and the results of diagnostic analgesia, if performed. The focus of this chapter will be radiography of the equine carpus, which is a practical first step for diagnostic imaging of this region.

RADIOGRAPHIC STUDY ACQUISITION

Soft tissues surrounding the carpal region in a full-sized, adult horse are thin enough that the area can be successfully imaged using a standard portable x-ray machine and image receptor. At minimum, a standard radiographic study of the carpus will include four projections made with the x-ray beam centered on the middle carpal joint in a standing and evenly weight-bearing patient. Projections include dorsopalmar, lateromedial, and paired dorsolateral-palmaromedial (DLPMO) and dorsomedial-palmarolateral oblique (DMPLO) views.[3]

In many patients, the addition of one or more special views to the standard carpal study will further aid in radiographic interpretation. A flexed lateromedial projection is obtained to aid in differentiation of the cuboidal bones as the intermediate and fourth carpal bones will move proximally relative to the radial and third carpal bones, respectively. This view allows supplementary evaluation of articular surfaces and joint spaces. Its high clinical utility leads some clinicians to consider this view part of a standard carpal study.[1] Three additional flexed dorsoproximal-dorsodistal oblique projections, also called tangential or "skyline" views, can be made at increasing angles from the horizontal plane (Fig. 23.1). One or more skyline views can be added to a study for the purpose of enhanced evaluation of the dorsal aspects of the distal row of carpal bones, proximal row of carpal bones, and the distal radius.

Radiographic projections made while stress is manually applied to the carpal joints can be used to diagnose and/or characterize joint subluxation that is otherwise suspected based on clinical examination of a patient. The typical flexed lateral radiographic projection can be considered a stress projection, while others include a lateral view with the carpus held in extension and dorsopalmar views made while lateral or medial bending pressure is applied to the carpus. Stress projections are employed in an attempt to demonstrate abnormal dorsopalmar or mediolateral movements within the carpus that result in joint space widening and asymmetry secondary to partial or complete rupture of the supporting soft tissue structures. Manipulation of unstable joints in this manner is expected to be very painful for the patient. Adequate sedation and analgesia are critical to perform stress radiographs humanely in these cases. Radiation safety should not be compromised, and the diagnostician must ensure that patient and equipment handlers are wearing protective equipment with their hands always positioned outside of the primary x-ray beam.[4]

Carpal lesions are bilateral in many instances. Radiographic examination of both carpi can be especially valuable when investigating an equine patient for stress-related pathology, fractures and osteochondral fragments, and developmental disorders. It is also important to note that normal radiographs do not necessarily indicate lack of osseous or soft tissue pathology. There are many reports where radiographic findings (or lack thereof) conflict with findings of other imaging modalities such as ultrasound, computed tomography, magnetic resonance imaging, and arthroscopy.[1]

NORMAL ANATOMICAL VARIANTS AND INCIDENTAL FINDINGS

Medial and Lateral Protrusions on the Caudal Aspect of Distal Radial Physis

The caudomedial and caudolateral aspects of the distal radius have normal osseous projections at the level of the physis that are highlighted on lateral, DLPMO, and DMPLO projections (Fig. 23.2A). A smooth indentation in the caudal aspect of the distal radial epiphysis known as the radial fossa is also apparent on dorsopalmar projections of the carpus (Fig. 23.2B). These normal features should be recognized to avoid a misdiagnosis.

Vestigial Ulna

In some horses, a vestigial ulna is visible as a thin, mineral opacity separated from the caudolateral aspect of the radius. This structure should not be misinterpreted as periosteal proliferation or other disease[5] (Fig. 23.2C).

Incomplete Fusion of the Lateral Styloid Process

Developmentally, the distal aspect of the ulna becomes the lateral styloid process via a separate center of ossification that fuses with the radial epiphysis by 9 months of age.[1] The lateral styloid process is usually completely fused with the radius in skeletally mature horses. Occasionally, horses may have incomplete fusion that is incidental but results in radiographically visible retention of a small radiolucent zone in the distal radial epiphysis without surrounding sclerosis or bone irregularity. This should not be mistaken for an osseous cyst-like lesion or fracture[6] (Fig. 23.2C).



Fig. 23.1 Skyline projections of the equine carpus. To obtain the three skyline projections of the equine carpus, the carpus is flexed and the image receptor is held parallel to the metacarpus. The x-ray tube is positioned dorsal to the carpus and angled distally at approximately 85 degrees to highlight the dorsodistal aspect of the radius, 55 degrees to highlight the dorsal aspect of the proximal row of carpal bones, and 35 degrees to highlight the dorsal aspect of the distal row of carpal bones. *White lines* represent the x-ray beam angle for each projection.

Variable Appearance of Ulnar Carpal Bone

Lucent regions, irregularities, and variable shapes of the axial, non–weight-bearing surface of the ulnar carpal bone and, sometimes, the adjacent fourth metacarpal bone can be seen on the DLPMO images[5] (Fig. 23.3). These lesions are very rarely associated with lameness or joint effusion and are commonly considered as having low clinical significance despite the likelihood of an early traumatic avulsion of the lateral palmar intercarpal ligament. Radiolucencies on the subchondral, weight-bearing surface of the ulnar carpal bone are sometimes associated with lameness but may also heal before 12 months of age and/or respond to conservative management.[7]

First and Fifth Carpal Bones

Vestigial first and fifth carpal bones are inconsistently present in adult horses and should not be mistaken for osteochondral fragments. In a study of radiologic anatomic variation of the carpus, first carpal bones were found in 29% of horses and fifth carpal bones in 1.4% of horses.[5] The fifth carpal bone is usually smaller than the first carpal bone, although their size is highly variable and either bone may be present in one or both limbs. Occasionally, the first carpal bone is incompletely separated from the second carpal bone. Vestigial first and fifth carpal bones can also be associated with incidental, focal concavities or lucent defects in the adjacent cuboidal and metatarsal bones as a result of variable articulation[5] (Fig. 23.4).

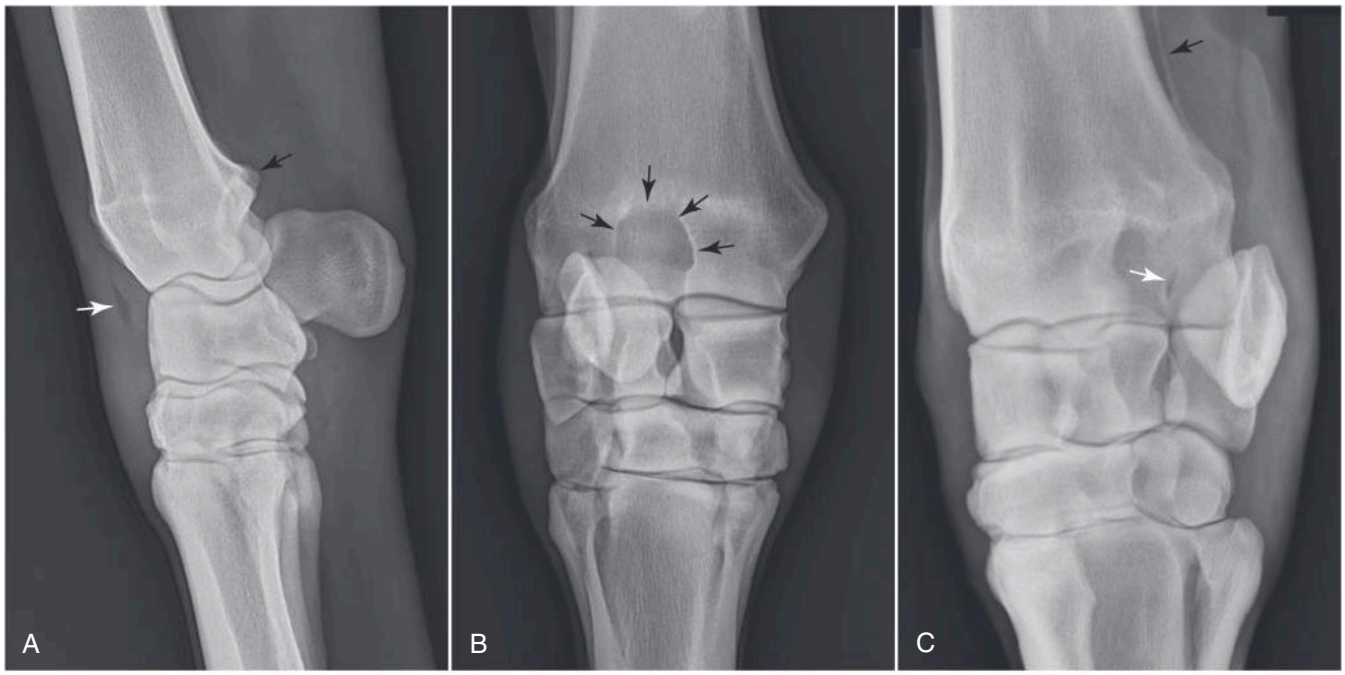


Fig. 23.2 Normal anatomical variants and incidental findings of the distal radius. **A,** Lateral view depicting normal protrusions on the caudodistal radius (*black arrow*) and small dorsal fat pad of the antebrachiocarpal joint (*white arrow*). **B,** Slightly obliqued dorsopalmar projection highlighting the well-defined radial fossa (*black arrows*). **C,** Dorsolateral-palmaromedial oblique (DLPMO) projection of a patient with a vestigial ulna (*black arrow*) represented by a thin, mineral opacity running roughly parallel with the lateral surface of the radius before fusing with it distally. The lateral styloid process of the ulna is also incompletely fused to the radial epiphysis (*white arrow*).

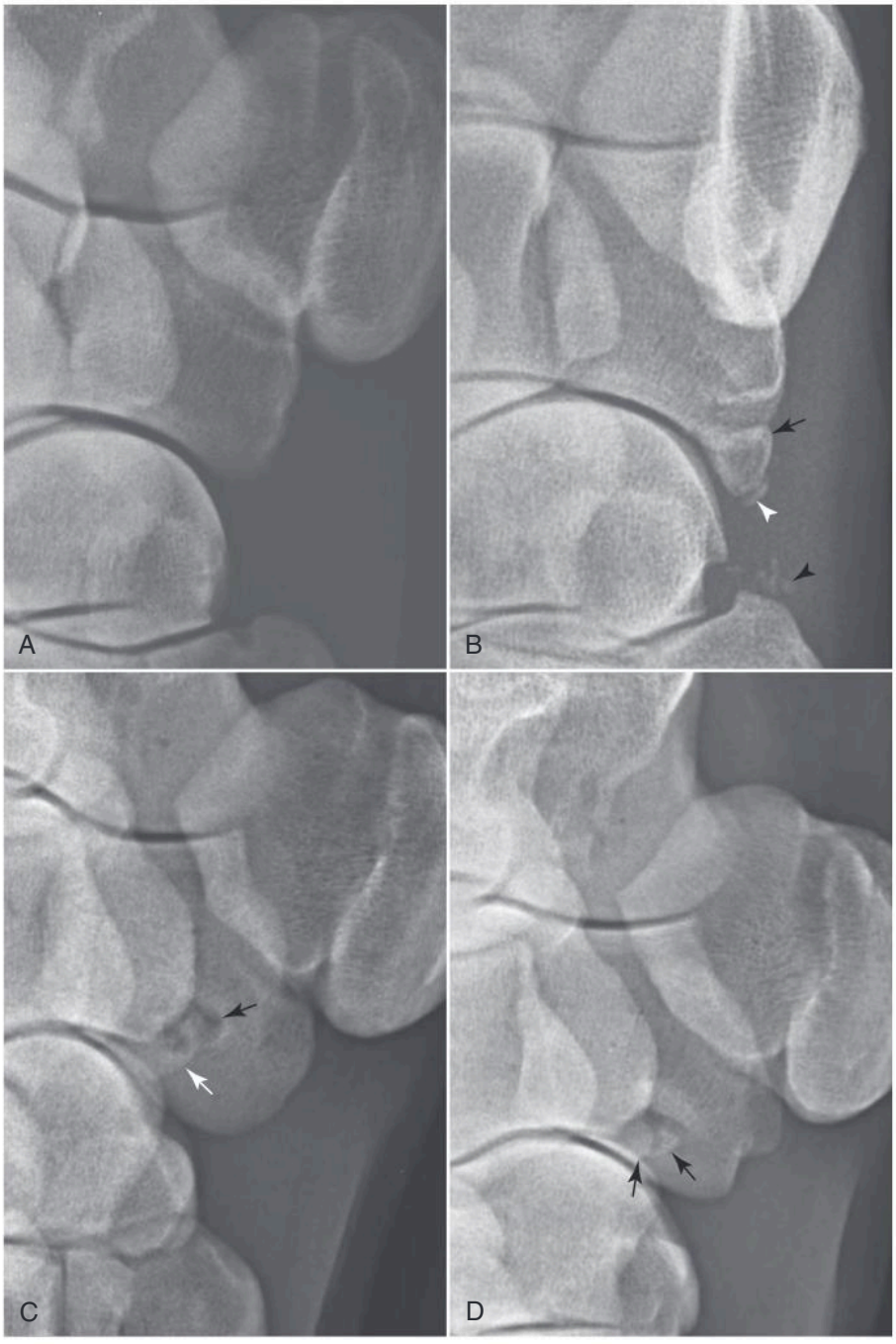


Fig. 23.3 Normal/incidental variants of the ulnar carpal bone on magnified dorsolateral-palmaromedial oblique projections. **A,** Normal/typical ulnar carpal bone. **B,** Atypical configuration of the distal palmar aspect of the ulnar carpal bone (*black arrow*) with a separate center of ossification immediately distal to this (*white arrowhead*). Note also the poorly demarcated mineralization proximal to the base of the fourth metacarpal bone (*black arrowhead*). **C,** There is an osseous cyst-like lesion in the ulnar carpal bone (*black arrow*) with an osseous fragment distal to this (*white arrow*). **D,** There are two well-defined osseous fragments overlying the ulnar carpal bone (*black arrows*) surrounded by a less well-demarcated radiolucent area in the ulnar carpal bone.

RADIOGRAPHIC ABNORMALITIES

Juvenile Orthopedic Conditions

Radiographic examination is useful for both diagnosis of and screening for developmental type orthopedic diseases in young equine patients. Some conditions have the capacity to evolve in patients between 6 and 18 months of age, becoming newly apparent, improved, worsened, or even spontaneously resolved on serial radiographs obtained throughout this timeframe.[8] Therefore, it is important to recognize that use of radiographs for screening purposes at a single time point does have limitations in this population of horses.

Incomplete Ossification

Carpal (and tarsal) cuboidal bones become mineralized via endochondral ossification that occurs in the final 2 to 3 months

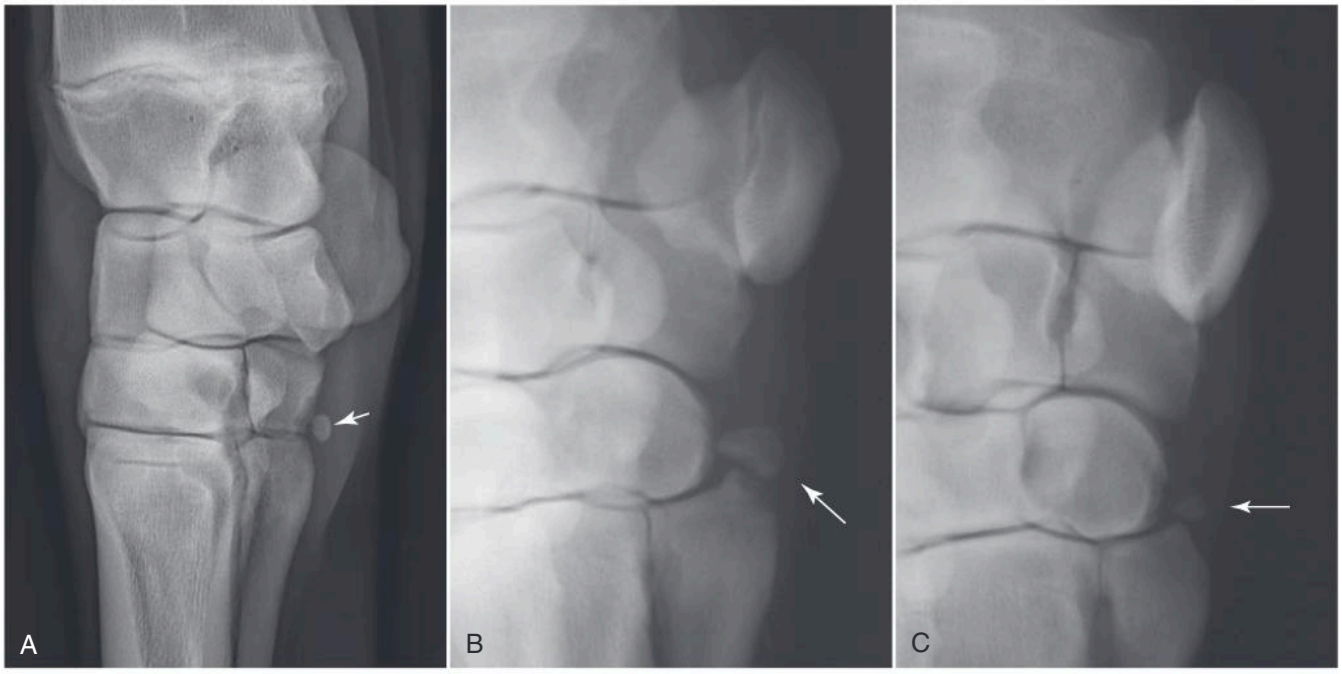


Fig. 23.4 Normal first and fifth carpal bones. **A,** Dorsomedial-palmarolateral view depicting a small, round first carpal bone (*white arrow*) adjacent to a very subtle concavity in the second carpal bone. **B—C,** Magnified dorsolateral-palmaromedial views showing normal variations of a fifth carpal bone (*white arrows*) in two different horses. In **B,** note the associated concavity in the proximal aspect of the fourth metacarpal bone (incidental).

of gestation. Mature carpal bones generally have straight edges with squared corners, congruent joint spaces with uniform width, and a trabecular bone pattern within the medullary cavity. Due to reduced mineralization of the cartilage model, radiographically immature carpal bones have:

- curved corners and rounded contour
- very little medullary trabecular detail
- wide joint spaces without flat apposing bone surfaces (Fig. 23.5A, eFig. 23.1)

Although often associated with neonatal prematurity or dysmaturity in hospitalized foals, variably incomplete ossification of the cuboidal bones has also been reported in a large percentage of full-term, clinically normal foals within 1 week of birth which suggests that cuboidal bone mineralization does not always predictably correlate with gestational length.[7] If a neonatal foal with incomplete ossification of the cuboidal bones is allowed to exercise freely, the relatively soft cartilage model of immature carpal bones can become compressed or crushed, ultimately leading to misshapen bones, angular limb deformity, and/or osteoarthritis later in life (Fig. 23.5B). All of these sequelae can result in reduced athletic performance. Early diagnosis can guide management decisions to favorably reduce the impact of incomplete cuboidal bone ossification.

Physitis/Epiphysitis

Physitis can manifest in the distal radius of young horses up to 2 years old. Physitis may be septic or aseptic in nature, and radiographic features of these two different pathogeneses can overlap. Knowledge of the normal, evolving physeal appearance in growing horses is crucial for radiographic interpretation (Fig. 23.6A). Acquisition of complementary radiographic views of the contralateral limb can be valuable for comparison and diagnosis of physitis. Radiographs have been shown to underestimate the presence and severity of physitis compared to computed tomography.[9]

Sometimes referred to as physeal dysplasia, aseptic physitis is an inflammatory but noninfectious process identified in young horses. It is correlated with nutritional factors and rapid bone growth. Radiographs may be normal in the early stages of physitis, and in more chronic stages may show:

- metaphyseal flaring
- irregularity and widening of the physis
- asymmetry and sclerosis of the metaphysis
- wedge-shaped epiphysis[10] (Fig. 23.6B)

Septic physitis is caused by hematogenous bacterial spread that is most common in younger foals between 1 week and 4 months of age.[10] This process rarely occurs in isolation and is usually associated with septicemia and respiratory, gastrointestinal, or umbilical disease. Foals with failure of passive transfer are at greatest risk for development of septic arthritis and septic physitis. The distinguishing radiographic feature of septic physitis in foals is aggressive osteolysis presenting as a focal irregularity of the physis with irregular radiolucency extending into the adjacent epiphysis and/or metaphysis (Fig. 23.6C). Detection of radiolucency and physeal irregularity is more challenging if the osteolysis extends along the entire length of the physis. The bone adjacent to the physis may be sclerotic and it may have an altered trabecular pattern, flared abaxial contour, and/or periosteal proliferation. Concurrent soft tissue swelling surrounding the affected physis and septic arthritis of the antebrachiocarpal joint or any other synovial joint are other radiographic findings that may be present in foals with septic physitis.[11] Differentiation of aseptic versus septic physitis will be further guided by patient clinical data such as the presence or absence of a fever and other systemic comorbidities.

Angular Limb Deformities

Developmental limb deformities of the carpus are common in young horses and can be congenital or acquired. They are classified into three categories: (1) angular limb deformity in which a portion of the limb is angled medially or laterally from the center line, (2) flexural deformity in which the alignment of the limb is deviated in a cranial or caudal direction, and (3)



eFig. 23.1 Dorsopalmar view of the carpi of a premature newborn foal with incomplete ossification of the carpal cuboidal bones. The cuboidal bones have rounded margins and the joint spaces are increased in width.

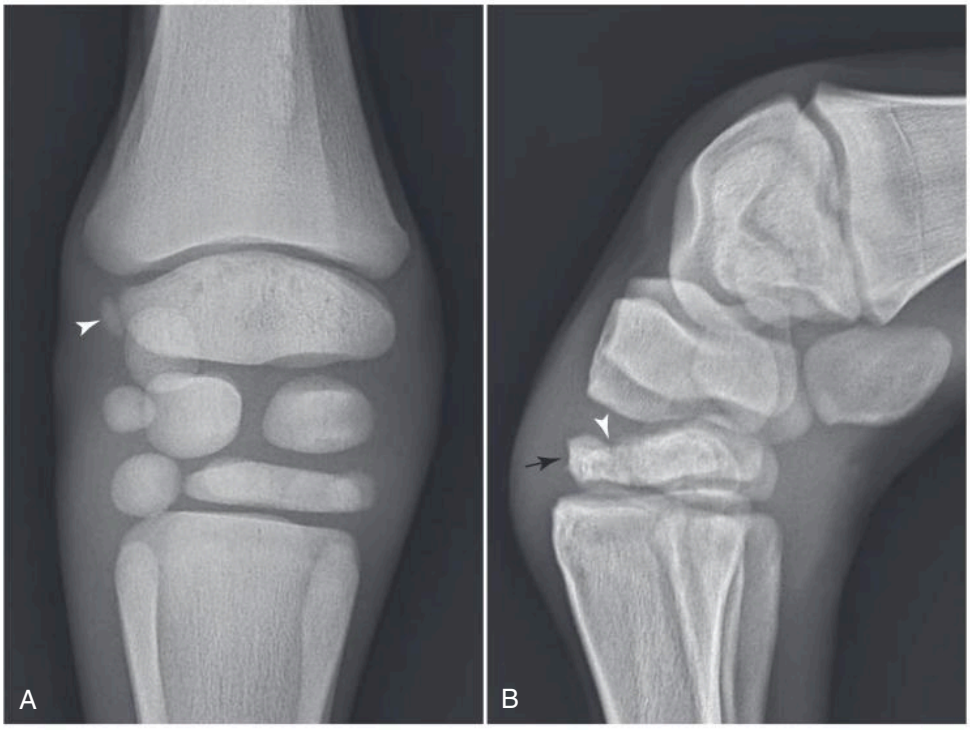


Fig. 23.5 **A,** Dorsopalmar view of a premature, 7-day-old foal with incomplete ossification of the cuboidal bones. Lateral is to the *left.* The carpal bones are small with rounded contours and minimal medullary trabecular bone pattern. Joint spaces are wide. The lateral styloid process of the ulna (*white arrowhead*) is not yet fused to the distal radial epiphysis, which is normal at this age. **B,** Lateral view of a 2-month-old foal presenting for recheck following hospitalization for prematurity and incomplete ossification of cuboidal bones that was diagnosed immediately after birth. Despite aggressive exercise restriction and preventive management, the third carpal bone has become misshapen (*black arrow*) secondary to crushing injury of the immature cartilage model very early in life. There is a secondary fracture of the third carpal bone (*white arrowhead*) which will lead to early osteoarthritis of the middle carpal joint.

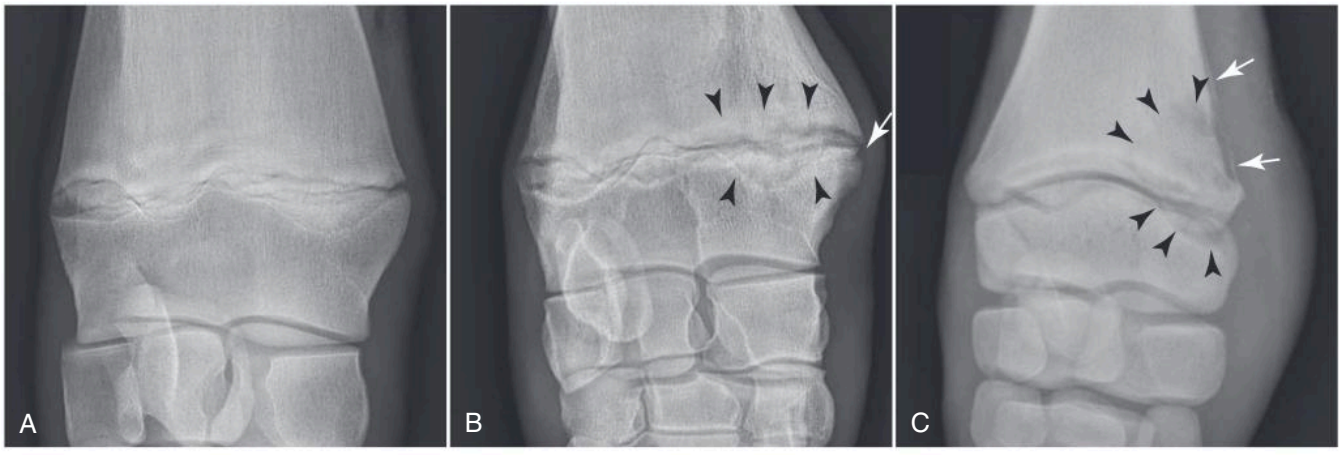


Fig. 23.6 Distal radial physis. Lateral is to the *left.* **A,** Normal distal radial physis. **B,** Aseptic physitis of the distal radius with flaring of the medial metaphysis and epiphysis, mild widening of the medial aspect of the physis (*white arrow*), and mild periphyseal sclerosis (*black arrowheads*). Soft tissues medial to the physis are mildly thickened. **C,** Septic physitis of the distal radius with mild widening of the medial aspect of the physis, a large zone of adjacent metaphyseal and epiphyseal osteolysis (*black arrowheads*), metaphyeal periosteal proliferation (*white arrows*), and moderate overlying soft tissue thickening centered on the medial aspect of distal radial physis.

rotational deformity in which the limb is rotated inward or outward along the axial plane.[12] Rotational deformities most often originate proximal to the carpus. Some cases of angular and flexural limb deformity can be present at birth and self-correct over days to months, although most cases are considered pathologic and benefit from prompt therapy to prevent future lameness and loss of athletic ability.

Carpal angular limb deformities can be a result of collateral ligament laxity and/or asymmetric bone growth in the distal radius, cuboidal bones, or proximal metacarpus. Asymmetric

bone growth is often identified as a sequela of incomplete cuboidal bone ossification and physitis or physeal dysplasia. While standard size image detectors will work, radiographs meant to evaluate for angular limb deformity are best obtained using long image detector plates so that the greatest length of bone proximal and distal to the deformity is captured. Radiographic evidence of carpal valgus and, less commonly, carpal varus can be assessed on dorsopalmar views with bisecting lines drawn through the long axes of the distal radius and the third metacarpal bone (Fig. 23.7, eFig. 23.2). The lines should be parallel and near contiguous in normal horses or intersect at the point of maximal limb deviation in affected horses, which will suggest the underlying origin of the deformity (Table 23.1). The intersecting angle of lines can also be used to estimate severity of the angular limb deformity and to monitor response to therapy. Importantly, angular limb deformities are relatively easy to misinterpret on radiographs if the patient is not fully weight bearing or the limb is otherwise not positioned parallel with the imaging plate. The severity of the angulation can also be falsely elevated on radiographs of sedated foals due to altered weight bearing that sometimes exacerbates joint laxity.[12]

Flexural deformities are characterized by disproportionate length of the bone and musculotendinous unit. Diagnosis is usually straightforward using visual examination and correlated with lateromedial and dorsopalmar radiographic views to evaluate bone alignment and skeletal maturity. Viewed from the lateral side, normal standing conformation of the carpus is straight from the distal radius through the proximal metacarpus. Any dorsal extension or palmar flexion of the carpal joints in a fully weight-bearing animal is considered abnormal[13] (Fig. 23.8).

Table • 23.1

Radiographic Abnormalities Found Concurrently With Angular Limb Deformity Based on the Point of Maximal Limb Deviation.

POINT OF MAXIMAL LIMB DEVIATION	POSSIBLE CONCURRENT RADIOGRAPHIC ABNORMALITIES
Distal radial physis	Asymmetric widening or narrowing of the physis with deviation of the distal limb away from the wider side of the physis due to faster growth on that side
Distal radial epiphysis	Wedge shaped epiphysis, delayed development of the lateral styloid process; distal radial physis and antebrachiocarpal joint are not parallel
Cuboidal bones	Incomplete ossification with osseous collapse or deformity; lines through carpal joint spaces are not parallel (Fig. 23.7)
Antebrachiocarpal, middle carpal, and carpometacarpal joints	Joint spaces not parallel (particularly on radiographs obtained while stress is applied to the medial and lateral aspects of the joint)

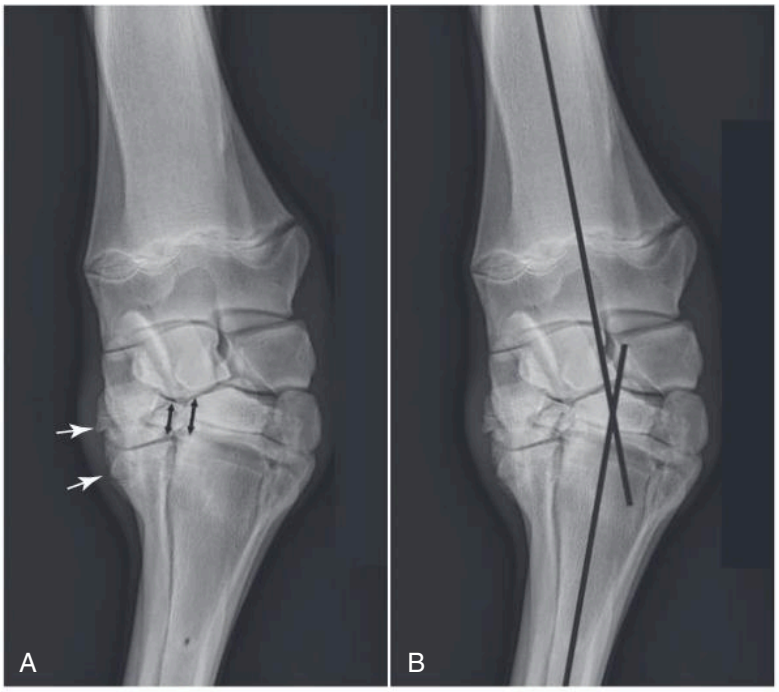


Fig. 23.7 Dorsopalmar views depicting carpal valgus secondary to historical trauma/crushing injury of the third and fourth carpal bones; lateral is to the *left*. **A,** The diaphysis of the third metacarpal bone is angled laterally relative to the distal radius. The distal radial physis is not parallel with the middle carpal or carpometacarpal joints. The lateral aspects of the third carpal bone and the fourth carpal bone are wedge shaped (*black double-headed arrows*). Smooth periarticular new bone (*white arrows*) and associated soft tissue thickening are present along the lateral aspects of the fourth carpal and fourth metacarpal bones. **B,** Same image as in **A** with bisecting lines drawn through the long axes of the distal radius and third metacarpal bones. These lines intersect at the distal row of carpal bones, which is the point of maximal limb deviation.



eFig. 23.2 Dorsopalmar radiographs of a 3-month-old foal with bilateral carpal valgus. The third metacarpal bones are angled laterally relative to the distal radius with a lesser degree of severity compared to the horse presented in Fig. 23.7.



Fig. 23.8 Fully weight-bearing lateral view of a foal with severe flexural limb deformity centered at the carpus secondary to tendon contracture. The antebrachiocarpal and middle carpal joints are flexed. The distal row of carpal bones is dorsally subluxated relative to the proximal row of carpal bones. The radius has a cranially bowed shape. Note that the cuboidal bones have a mildly rounded contour indicative of concurrent incomplete ossification.

Osseous Subchondral Cyst-Like Lesions

Osseous cyst-like lesions, also called subchondral bone cysts, have been reported in several locations within the equine carpus. They are considered to have a multifactorial etiology, the most well accepted of which include osteochondrosis and articular cartilage trauma. While traumatically induced cyst-like lesions are not limited to juvenile patients, the radiographic features are similar and therefore described here. When confirmed radiographically, osseous cyst-like lesions are identified as discrete, well-circumscribed (sometimes termed geographic), radiolucent defects in the subchondral bone that vary in appearance from shallow concavities to large, rounded, or conical cavities that extend deep into the medullary cavity. They may or may not have a visible communicating tract with the articular surface and are often surrounded by sclerosis that can range from a thin and well-defined rim to a more intense and poorly defined zone of mineral opacity. In the carpus, solitary lesions are most commonly found in the ulnar and second carpal bones[14] (Fig. 23.3C,D). These are rarely of clinical significance. Incidental osseous defects may also be identified in the proximal aspect of the second or fourth carpal and metacarpal bones in articulation with vestigial first and fifth carpal bones (Fig. 23.4A,B). The potential for clinical significance increases for carpal cyst-like lesions in the distal radius, radial and third carpal bones, and in lesions along a weight-bearing surface or with articular communication (Fig. 23.9, eFig. 23.3). The clinical significance of osseous cyst-like lesions in the carpus should be correlated with relevant diagnostic analgesia.[15]

Osteochondrosis/Osteochondritis Dissecans

The etiology and pathogenesis of osteochondral lesions in young horses have been widely debated for many years. Most presentations of carpal osteochondral fragmentation are thought to be an effect of microdamage to subchondral bone associated with biomechanical stress and loading rather than a primary failure of endochondral ossification. For this reason,

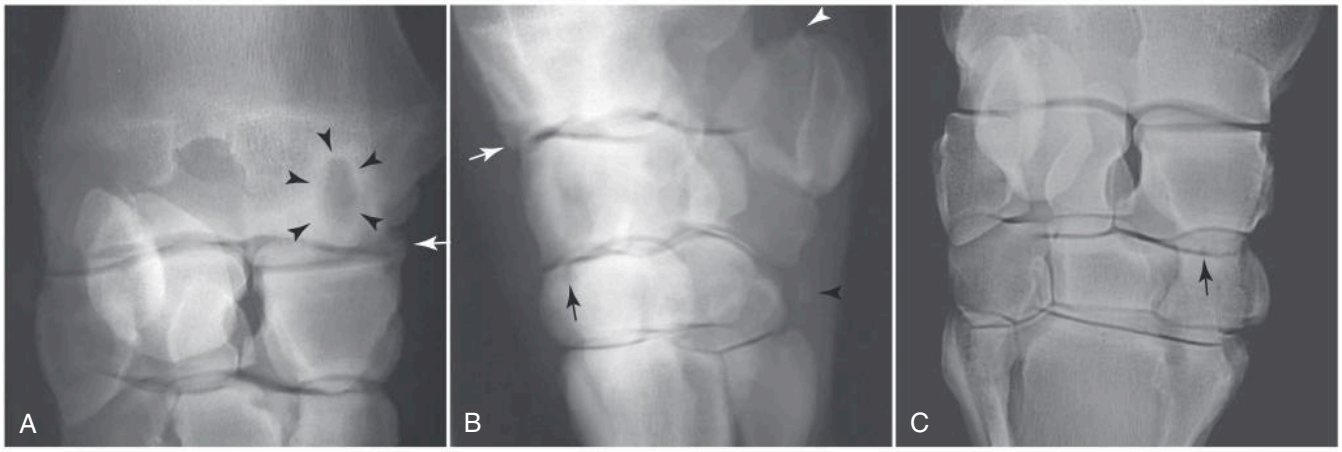


Fig. 23.9 Osseous subchondral cyst-like lesions. **A,** Magnified dorsopalmar projection centered on the antebrachiocarpal joint; lateral is to the left. Note the ovoid, radiolucent cyst-like lesion surrounded by a rim of increased mineral opacity in the distomedial epiphysis of the radius (*black arrowheads*) and secondary periarticular osteophyte formation along the distomedial radius and proximomedial radial carpal bone (*white arrow*). **B,** Dorsolateral-palmaromedial oblique projection of the same carpus in panel **A**. An additional radiolucent cyst-like lesion in the proximal aspect of the third carpal bone (*black arrow*), secondary periarticular osteophytosis along the dorsal aspect of the antebrachiocarpal joint (*white arrow*), and a small osseous projection on the proximal aspect of the accessory carpal bone (*white arrowhead*) are also visible. An incidental vestigial fifth carpal bone is present (*black arrowhead*). **C,** Magnified dorsopalmar projection centered on the middle carpal joint; lateral is to the left. A small osseous cyst-like lesion is present in the second carpal bone (*arrow*) associated with injury to the intercarpal ligament between the second and third carpal bones that was identified on magnetic resonance imaging.



eFig. 23.3 Dorsolateral-palmaromedial oblique radiograph of a Warmblood horse with chronic lameness. Superimposed with the proximal aspect of the radial carpal bone there is a well-de fined round radiolucency with a thin sclerotic rim. A narrow portion of the radiolucency extends toward the articular margin. This lesion is consistent with a cyst-like lesion of the radial carpal bone. Notice also the narrow fusiform shaped vertically oriented radiolucent region associated with the distal lateral radius which most likely represents incomplete fusion of the ulnar styloid process.

osteochondral fragmentation is discussed later in this chapter with traumatic orthopedic conditions.[16,17]

Osteoarthritis/Degenerative Joint Disease

Carpal osteoarthritis has been described as a result of one of two syndromes: stress-induced bone injury of young horses in training and insidious disease in older horses without a correlation to athletic function.[12] In racehorses, carpal osteoarthritis is correlated with osteochondral fragmentation, which is discussed later in this chapter. In non-racehorses, carpal osteoarthritis tends to manifest at a later age and the presence of osteochondral fragments in these horses is more unusual.[18]

Radiographic features of osteoarthritis in the antebrachiocarpal and middle carpal joints are similar to those in other anatomic regions and include:

- periarticular osteophytosis, sclerosis, and/or lucency in the subchondral bone
- intracapsular soft tissue swelling
- joint space narrowing
- new bone proliferation at the sites of joint capsule attachment (Fig. 23.10, eFig. 23.4)

Osteophytes are commonly observed on the dorsal surface of the carpal bones, while the palmar surfaces may be more affected in advanced cases. The normally sharp corners of the cuboidal bones may become rounded and/or radiolucent. Sometimes, mineralized osteochondral fragments are observed within the joint space (Fig. 23.11). Radiolucency or osteolysis of the subchondral bone typically follows articular cartilage loss and results in irregularity of the articular bone surface and joint space narrowing. Distention of the antebrachiocarpal or middle



Fig. 23.10 Radiographic features of antebrachiocarpal joint osteoarthritis in a 13-year-old sport horse with intermittent lameness of the imaged limb. **A,** Dorsopalmar view; lateral is to the *left.* There are osteophytes along the medial and lateral aspect of the radiocarpal joint (*white arrowheads*), rounding of the proximomedial corner of the radial carpal bone, subchondral sclerosis of the radial and ulnar carpal bones (*asterisks*), and intracapsular soft tissue thickening centered on the affected joint (*white arrow*). **B,** Flexed lateral view showing that the osteophytosis is predominantly along the dorsal aspect of the antebrachiocarpal joint including the distal radius and proximal aspects of the intermediate and radial carpal bones (*white arrowheads*). **C,** Dorsolateral-palmaromedial view. Consistent with the other views, the largest osteophytes are dorsomedially located on the distal radius and proximal aspect of the radial carpal bone (*white arrowheads*). Enthesophytes are present on the dorsal aspect of the radial carpal bone (*black arrow*). The intracapsular soft tissue swelling is centered at the joint (*white arrow*). There is a small enthesophyte along the proximal aspect of the accessory carpal bone and a rounded mineral focus in the adjacent soft tissue (*black arrowheads*).

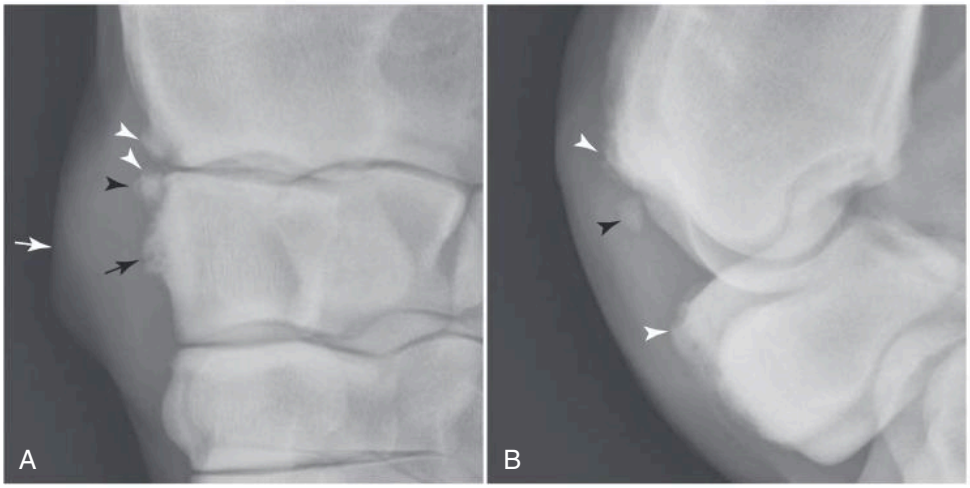


Fig. 23.11 Antebrachiocarpal joint osteoarthritis with intracapsular osteochondral fragment. **A,** Dorsolateral-palmaromedial (DLPMO) projection with a rounded, nondisplaced osteochondral fragment of the dorsal proximomedial aspect of the radial carpal bone (*black arrowhead*), periarticular osteophytosis of the dorsomedial aspect of the joint (*white arrowheads*), enthesopathy along the dorsal aspect of the radial carpal bone (*black arrow*), and intracapsular soft tissue swelling (*white arrow*). **B,** Flexed lateral projection of the same carpus as in **A** that depicts a rounded osteochondral fragment slightly displaced from the distal aspect of the radius (*black arrowhead*) and osteophytosis of the distal radius and proximodorsal intermediate carpal bone (*white arrowheads*).



eFig. 23.4 Dorsopalmar carpal radiograph of a 6-year-old Quarter horse with carpometacarpal osteoarthritis. Lateral is to the right. There are moderate periarticular bone proliferations along the margins of the medial carpometacarpal joint and the metaphyseal margin of the 3rd metacarpal bone. Mild subchondral resorption is present along the medial joint margins. There is mild associated soft tissue swelling.

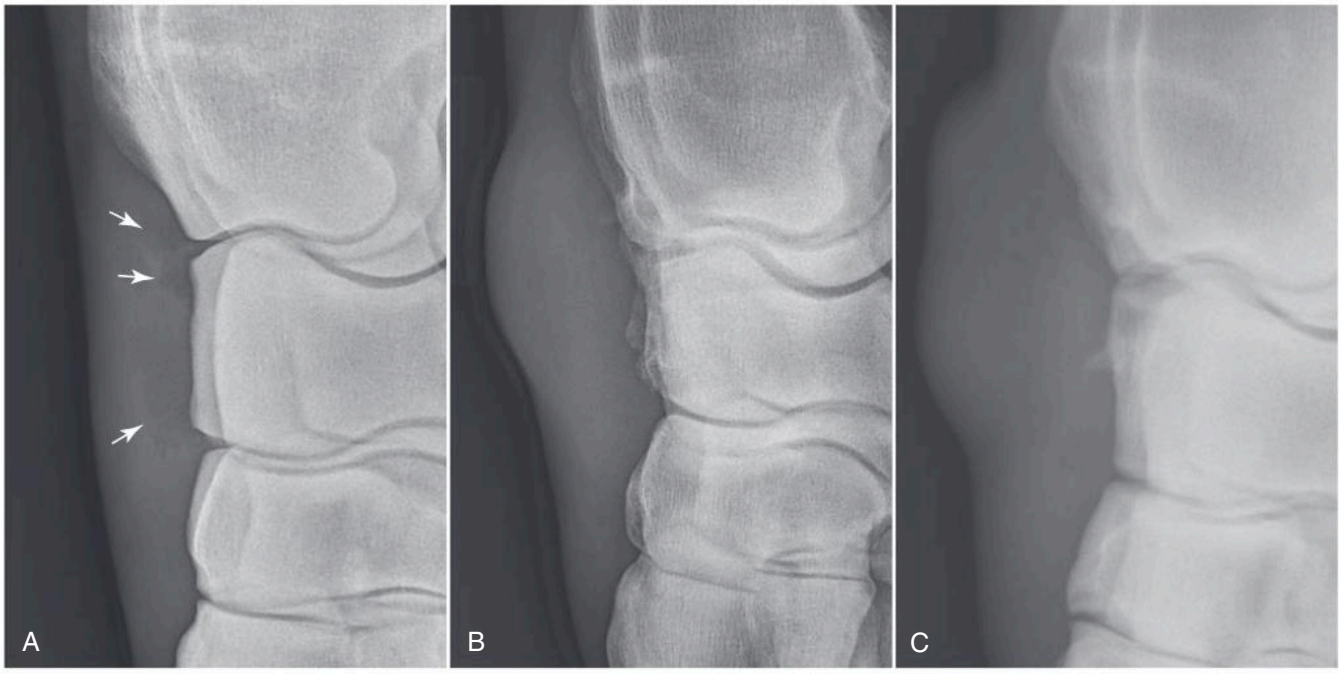


Fig. 23.12 Lateral radiographs of the carpus. **A,** Normal carpus with extracapsular fat accumulation dorsal to the antebrachiocarpal joint and proximal row of carpal bones (*white arrows*). **B and C,** Two different horses with antebrachiocarpal osteoarthritis and effacement of the normal dorsal fat pads.

carpal joint capsules may indicate synovial effusion, synovitis, and/or intracapsular soft tissue injury and is characterized by soft tissue swelling centered over the dorsal aspect of either joint with effacement of its respective radiolucent dorsal fat pad (see Fig. 23.2 and Fig. 23.12).

Likely due to its minimal range of motion, osteoarthritis of the carpometacarpal joint occurs less commonly than that in the antebrachiocarpal or middle carpal joints.[19] Osteoarthritis in this joint is more common in middle-aged and older horses. A subset of carpometacarpal arthritis presents with characteristic bone proliferation along the second carpal bone and proximal aspect of the second metacarpal bone in the expected region of joint capsule and medial collateral ligament attachment. The proliferative bone can extend proximally and partially bridge the medial aspect of the joint, becoming mottled in appearance as the bone mass grows in size. Many horses present with concurrent carpometacarpal joint space narrowing, osteolysis of the proximal aspect of the second metacarpal bone, and intracapsular or extracapsular soft tissue thickening centered over the articulation between the second carpal and metacarpal bones (Fig. 23.13). Some will have involvement of the third carpal and metacarpal bones, radiographic evidence of joint effusion, and also osteophytosis of the middle carpal joint. Radiographic changes in such cases are best evaluated on dorsopalmar and dorsomedial-palmarolateral oblique projections. Carpal range of motion is often decreased and painful, making positioning for flexed lateral radiographic views challenging when attempted. Response to treatment has been reported to be short lived with a poor likelihood that the horse will be able to return to work long term.[19,20]

Septic Arthritis and Osteomyelitis

In adult horses, septic arthritis is most commonly caused by penetrating trauma directly into a joint or extension of infection from periarticular tissues. Iatrogenic infection secondary to joint injections or arthroscopic procedures is also possible.[21] In addition to these causes, foals can also acquire septic arthritis secondary to hematogenous inoculation of the joint resulting from bacteremia. Foals with failure of passive transfer, multisystemic disease, and/or septicemia are at high risk for development of septic arthritis as well as osteomyelitis and physitis.[22,23]

Horses with septic arthritis of the carpus usually present with acute, severe, and rapidly progressive lameness with concurrent heat, pain, and soft tissue swelling over the affected region. The earliest radiographic sign of septic arthritis is often joint effusion with distention of the synovial capsule and/or extracapsular soft tissue swelling, although this can vary depending on the underlying cause of the septic process. Joint effusion can result in widening of the joint space in early stages, while articular cartilage loss leads to joint space narrowing in more advanced stages of disease. Other radiographic features of septic arthritis and osteomyelitis include:

- subchondral radiolucency caused by osteolysis
- increased subchondral bone opacity caused by sclerosis
- extracapsular soft tissue swelling
- progressive bone proliferation with aggressive morphology-like amorphous, palisading, or spiculated patterns (Fig. 23.14).

If there is a suspicion of sepsis, it is essential to evaluate radiographs for osteomyelitis both at the time of initial assessment as well as at follow-up intervals throughout the course of treatment. The presence of carpal osteomyelitis will worsen the prognosis for return to athletic function and therapy may be altered if osteomyelitis is identified. Approximately 30% to 50% reduction in bone opacity is required before osteolysis becomes radiographically visible, making radiographs a relatively insensitive measure for bone loss.[24]

Traumatic Orthopedic Disease

Intra-Articular Fractures

Racehorses are most likely to be affected by traumatic osteochondral injury compared to non-racehorses. Among the three main carpal joints, osteochondral trauma resulting in intra-articular damage is most frequent along the dorsal aspect of

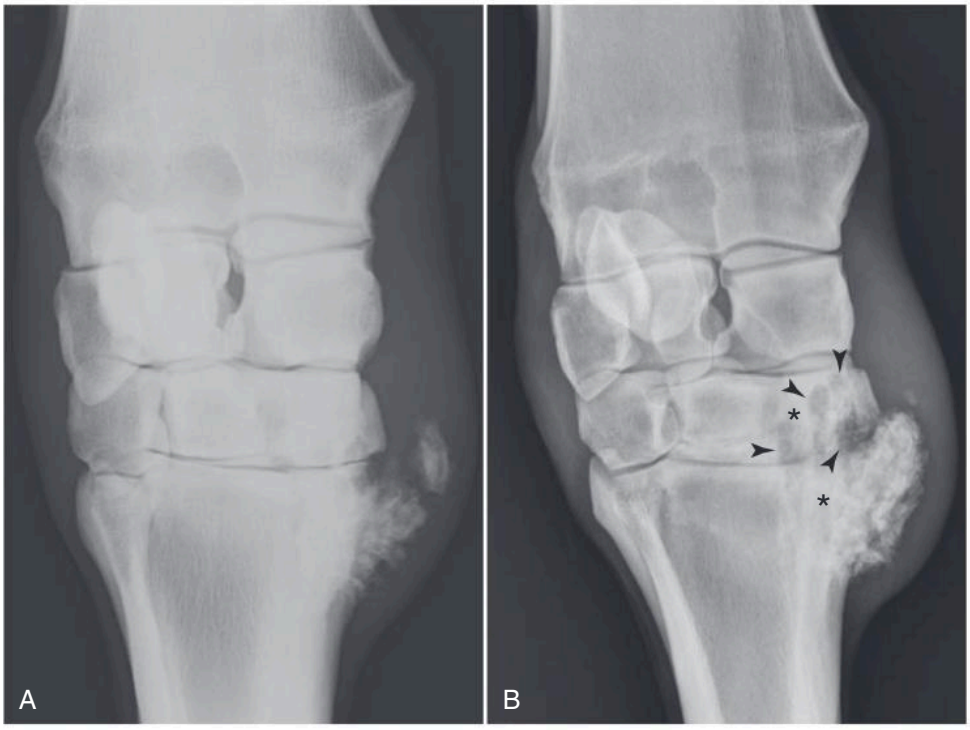


Fig. 23.13 Dorsopalmar projections of carpometacarpal osteoarthritis; lateral is to the *left*. **A,** Adult pony with severe lameness—extensive new bone extends proximally from the level of the medial collateral ligament attachment on the third metacarpal bone. The medial aspect of the carpometacarpal joint is narrowed and there is mild osteophytosis of the distomedial aspect of the second carpal bone. **B,** Adult Quarter horse with visible enlargement of the carpus with associated lameness—there is a mottled mass of bone proliferation extending proximally from the second and third metacarpal bones to the second carpal bone that partially bridges the medial aspect of the carpometacarpal joint. The medial aspect of the joint is narrowed with regions of osteolysis (*black arrowheads*) and sclerosis (*asterisks*) in the second and third carpal and second and third metacarpal bones. Soft tissue thickening centered along the medial aspect of the joint parallels the underlying bone growth.

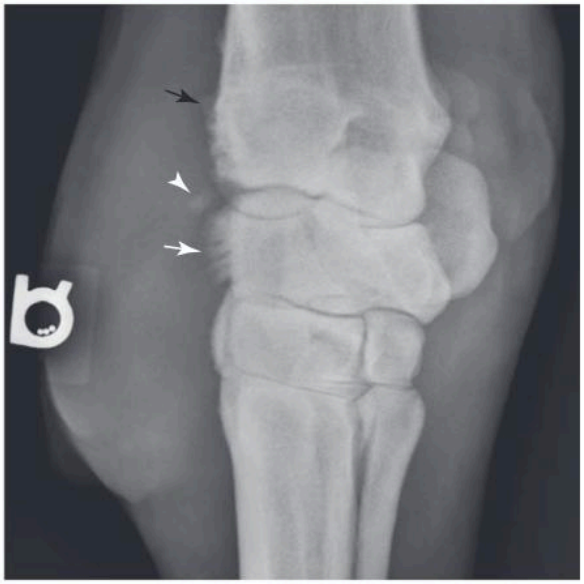


Fig. 23.14 Palmarolateral-dorsomedial projection depicting septic arthritis of the antebrachiocarpal joint. Note the palisading bone proliferation on the dorsal aspect of the ulnar carpal bone (*white arrow*) and massive soft tissue thickening dorsal to the carpus that are consistent with (but not pathognomonic for) a septic process. There is also more rounded osteophytosis of the distal radius (*black arrow*) and a separate mineral structure in the dorsal aspect of the antebrachiocarpal joint (*white arrowhead*).

the middle and antebrachiocarpal joints. Radiographic lesions can include:

- articular cartilage erosion
- osteochondral fragmentation (sometimes called chip fractures)
- slab fractures

Depending on its severity and extent, articular cartilage erosion may be imperceptible on radiographs or may be assumed based on joint space narrowing. Osteochondral fragmentation and slab fractures may be preceded by focal radiolucency indicating collapse of the subchondral bone as well as medullary sclerosis indicating chronic bone injury.

Osteochondral Fragmentation

The pathogenesis of osteochondral fragmentation is generally accepted to involve microdamage of subchondral bone that ultimately leads to separation of necrotic tissue from the original bone margin or separation through the base of new bone growth (osteophytosis). These intracapsular bits of separated bone are often referred to as fragments rather than fractures due to this pathogenesis. Osteochondral fragmentation is a common underlying cause of carpal osteoarthritis and it is also suggested that subchondral bone brittleness associated with osteoarthritis can lead to osteochondral fragmentation.[18] Osteochondral fragmentation in the carpus typically arises from a single articular surface along the dorsal periphery of a carpal bone. Specifically, the dorsodistal aspect of the radial carpal bone is the most common origin site for osteochondral fragments in racing Quarter horses and Thoroughbreds (Fig. 23.15).

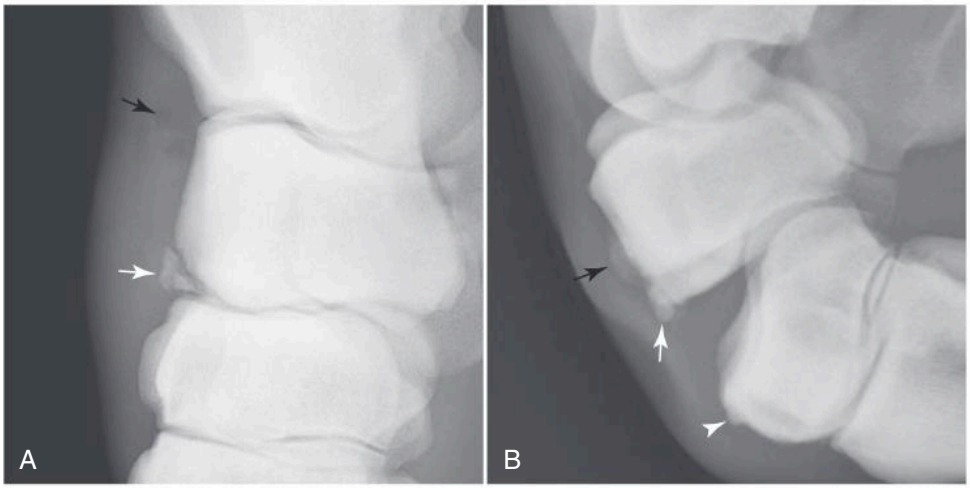


Fig. 23.15 Osteochondral fragments arising from the distal aspect of the radial carpal bone. **A,** Lateral view. A triangular bone fragment is dorsally displaced from the radial carpal bone (*white arrow*) and mild soft tissue swelling is centered over the intercarpal joint. Note the normal fat pad dorsal to the antebrachiocarpal joint (*black arrow*). **B,** Flexed lateral view of a different horse. A small osteochondral fragment summates with the dorsodistal aspect of the radial carpal bone (*white arrow*). There is also smooth new bone formation on the dorsal aspect of the radial carpal bone (*black arrow*) and mild osteophytosis of the proximal aspect of the third carpal bone (*white arrowhead*) consistent with osteoarthritis of the intercarpal joint.

The frequency of osteochondral fragmentation at other carpal sites will vary with breed and performance activity. Some of the most commonly reported sites are the dorsoproximal aspects of the intermediate, radial, and third carpal bones and the distolateral aspect of the radius (Fig. 23.11). Fragments originating within the dorsal aspect of the carpus are commonly seen bilaterally, and fragmentation is frequently identified in conjunction with joint effusion and variable lameness. Fragments within the palmar aspects of the carpal joints may be associated with trauma to the palmar surface of any carpal bone including avulsion of palmar intercarpal ligaments, palmar migration of fragments that originated along the dorsal surface of a carpal bone, or comminuted fractures of any carpal bone. Treatments including arthroscopic fragment removal are routinely recommended because fragments can cause pain, induce synovial inflammation, and hasten the progression of osteoarthritis. The poorest prognosis for return to athletic function is reserved for fragmentation and secondary damage within the middle carpal joint.[2]

Slab Fractures

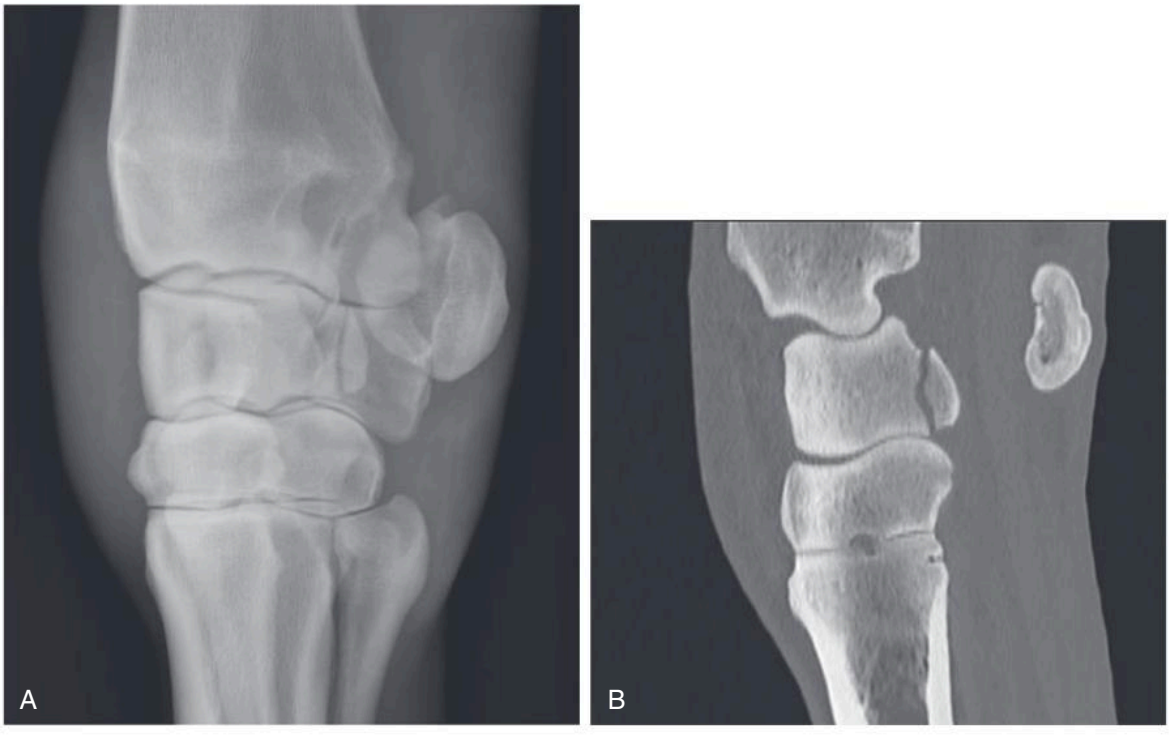
Slab fractures are generally described as being biarticular with fracture lines extending to the proximal and distal articular surfaces of a carpal bone, although incomplete fracture is possible with involvement of only one articular surface. Slab fractures can be simple or comminuted, displaced, or nondisplaced. They can be oriented in a dorsal or, less commonly, a sagittal plane (Fig. 23.16, eFig. 23.5). Dorsal plane fracture fragments are very commonly dorsally displaced to some degree, and this displacement can be reduced when the limb is positioned for flexed lateral radiographs. Axial instability concurrent with displacement can result in "collapse" of a fractured cuboidal bone such that a proximally positioned bone can sink distally into the fracture gap (Fig. 23.17). Sagittal plane slab fractures are inherently more stable and displacement is less common. Slab fractures tend to propagate deeper within the bone compared to the more peripheral location of many osteochondral fragments. Both dorsal and sagittal plane slab fractures are most common in the radial facet of the third carpal bone.[2] Slab fractures are most easily identified on radiographic studies in which the x-ray beam is parallel with the fracture gap. Radiographic identification can be particularly challenging for dorsal plane fractures involving both the radial and intermediate facets of the third carpal bone and incomplete sagittal plane fractures through the radial facet (Fig. 23.18, eFig. 23.6). Some sagittal slab fractures are oriented in a proximolateral-distomedial oblique plane and may be difficult or impossible to detect on standard images and appropriate skyline views. The addition of a special dorsoproximal lateral-palmarodistal medial oblique skyline projection has been shown to increase sensitivity of radiographic detection of these fractures in racehorses with consistent clinical signs.[25] Horses with carpal slab fractures can present with a range of clinical severity from mild lameness to severe, non–weight-bearing lameness. Intracapsular soft tissue opacity may be an effect of hemarthrosis, joint effusion, or synovitis. Conservative management of nondisplaced carpal slab fractures has been reported, although surgical stabilization is more often recommended to restore joint congruity, minimize secondary joint damage, and slow the progression of osteoarthritis. Return to athletic function in racehorses may be possible following surgical fixation of third carpal bone slab fractures. Not surprisingly, the best outcomes are seen in horses lacking severe concurrent or pre-existing joint pathology. Thoroughbreds and Standardbreds with significant fracture displacement, large fragment size associated with a fracture originating deep within the bone, osteolysis of the third carpal bone, and articular cartilage damage at the time of injury have a more guarded prognosis in terms of racing performance following surgical fracture stabilization.[26]

Accessory Carpal Bone Fracture

Accessory carpal bone fractures are relatively uncommon compared to the various fracture/fragment types discussed earlier. Most are oriented in the dorsal plane through the middle



eFig. 23.5 Dorsal-35 degrees proximal-dorsodistal oblique projection (skyline view of the distal row of carpal bones) of a Standardbred horse with a fracture of the third carpal bone. Lateral is to the left. There is moderate sclerosis and decreased trabecular pattern of the third carpal bone. A curvilinear fracture line extends to the dorsal surface of the third carpal bone.



eFig. 23.6 Carpal fractures in a 14-year-old Warmblood horse. **A,** Dorsolateral-palmaromedial radiograph. A slab fracture extends through the palmarolateral aspect of the intermediate carpal bone. The accessory carpal bone is abnormally shaped due to a dorsoproximal margin fracture. **B,** Sagittal reformatted Computed tomography image of the same horse, highlighting the intermediate carpal bone fracture.

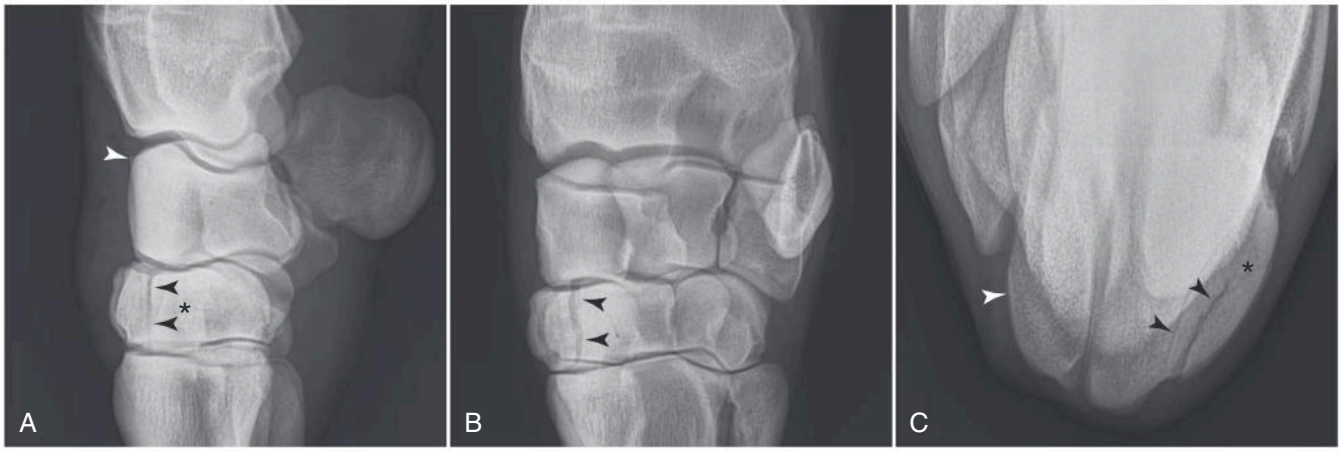


Fig. 23.16 Slab fracture of the third carpal bone in a 4-year-old Thoroughbred racing stallion. **A,** Lateral projection depicting a complete, biarticular radiolucent fracture line traversing the dorsal aspect of the third carpal bone (*black arrowheads*) with mild soft tissue thickening centered dorsal to the intercarpal joint. The dorsal slab fragment of the third carpal bone is slightly dorsally displaced. The dorsal half of the third carpal bone is sclerotic (*asterisk*). A small osteophyte is visible on the dorsoproximal aspect of the intermediate carpal bone (*white arrowhead*). **B,** Dorsolateral-palmaromedial projection better highlighting the fracture line described in **A** (*black arrowheads*). **C,** Dorsal-35 degrees proximal-dorsodistal oblique projection (skyline view of the distal row of carpal bones); lateral is to the *left*. This view confirms the dorsal plane fracture seen as two obliquely oriented radiolucent lines (*black arrowheads*) and the sclerosis that are both within the radial facet of the third carpal bone. Note the relatively reduced trabecular bone pattern and increased mineral opacity of the radial facet (*asterisk*) compared to the fourth carpal bone (*white arrowhead*).



Fig. 23.17 Dorsopalmar radiograph of the carpus; lateral is to the *left*. There are multiple comminuted fractures in the lateral aspect of the carpus including the third and fourth carpal bones. A large part of the fourth carpal bone is laterally/abaxially displaced. The lateral aspect of the carpus including the ulnar carpal bone is distally collapsed into the fracture gap indicating axial instability. Accurate identification of all fractures in this case will be extremely difficult using radiographs alone and computed tomography (CT) of this patient would provide more complete evaluation.

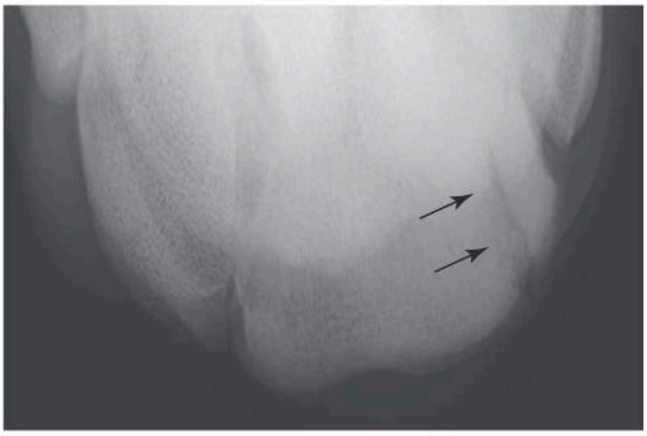


Fig. 23.18 Dorsal-35 degrees proximal-dorsodistal oblique projection (skyline view of the distal row of carpal bones); lateral is to the *left*. An incomplete sagittal plane slab fracture (*black arrows*) and sclerosis in the radial facet of the third carpal bone are present. The fracture margins are indistinct, indicating chronicity. The fracture line was not identified in any other radiographic projection.

of the bone, making the weight bearing and flexed lateromedial radiographic projections most helpful for diagnosis (Fig. 23.19, eFig. 23.7); however, a small proportion of accessory carpal bone fractures are identified in other planes/locations. Complete dorsal plane fractures can be displaced when the limb is positioned for flexed lateral radiographs. A majority of accessory carpal bone fractures are comminuted with communication into the carpal sheath. Sharp fracture fragments of the accessory carpal bone can lacerate the lateral edge of the deep digital flexor tendon and/or migrate distally in the carpal sheath to the mid-metacarpal region. Fragments within the distal aspect of the carpal sheath can usually be imaged with a lateromedial radiograph and/or ultrasound.[2,27] Accessory carpal bone fractures can be treated conservatively or via surgical fragment removal depending on morphology. They are likely to heal with a fibrous union rather than bony callus.[28]

Carpal Luxation/Subluxation

Damage to the joint capsule and/or extracapsular support structures, carpal and proximal metacarpal bone fractures, and



eFig. 23.7 Lateral carpal radiograph of a Quarter horse with accessory carpal bone fracture. Two angular, fragments are present proximal to the accessory carpal bone. Moderate soft tissue swelling surrounds the carpus.

other trauma within the carpal region can lead to joint instability resulting in luxation or subluxation. Although relatively uncommon, luxation and subluxation are usually a result of collateral ligament injury affecting any of the three main carpal joints.[29] More than one joint can be affected concurrently. Luxation and subluxation are diagnosed radiographically as malalignment of the bone column through the carpal region. Malalignment may be identified on standard radiographic projections or may require additional stressed projections where pressure is manually applied to the joints via flexion, extension, and medial or lateral angulation. Radiographs may also reveal intracapsular and/or extracapsular soft tissue swelling, features of osteoarthritis, carpal bone fractures, or osteochondral fragmentation (Fig. 23.20). In some cases, angular limb deformity (varus or valgus) is also present. Lameness associated with carpal subluxation is often severe. Treatment is often initiated with goals of palliative pain management and breeding soundness rather than return to full athletic capability. Radiographic healing of carpal subluxation is centered on the subluxated joint and demonstrated by stabilizing external bone callus formation, enthesopathy at collateral ligament attachment sites, subchondral sclerosis, variable bone erosion or osteopenia, and progressive osteoarthritis. Periarticular fibrous tissue commonly contributes to reduced range of motion in the joint(s) over time.[30]

Sclerosis and New Bone Formation

Carpal Bone Sclerosis

Sclerosis of the carpal bones is generally understood to be an effect of repetitive trauma resulting from abnormal compression of the carpal bones that leads to microdamage of the subchondral bone (i.e., "exercise/stress adaptation mismatch").

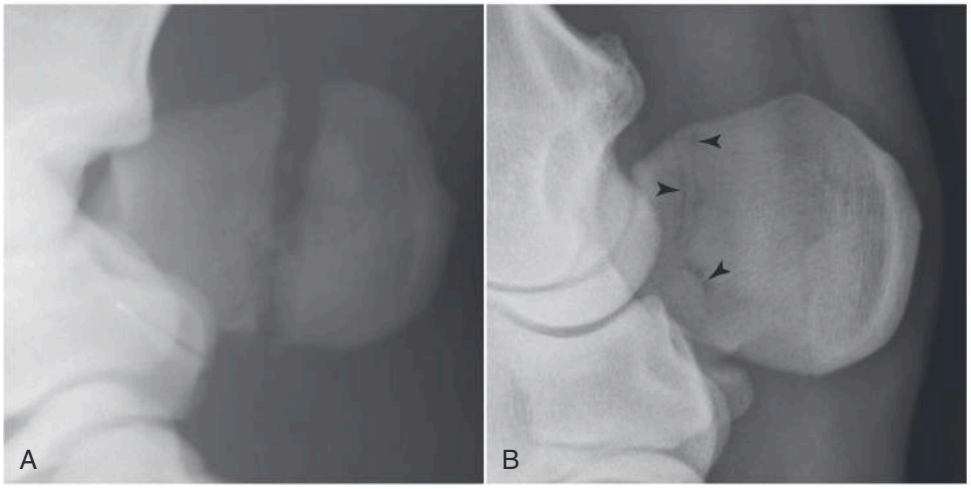


Fig. 23.19 Weight-bearing lateral views of two different horses with accessory carpal bone fracture. **A,** A complete, dorsal plane fracture extends through the middle of the bone. **B,** An incomplete or complete but minimally displaced dorsal plane fracture extends through the dorsal third of the bone (*black arrowheads*). A flexed lateral projection did not cause significant widening of the fracture line or increased displacement in this case.

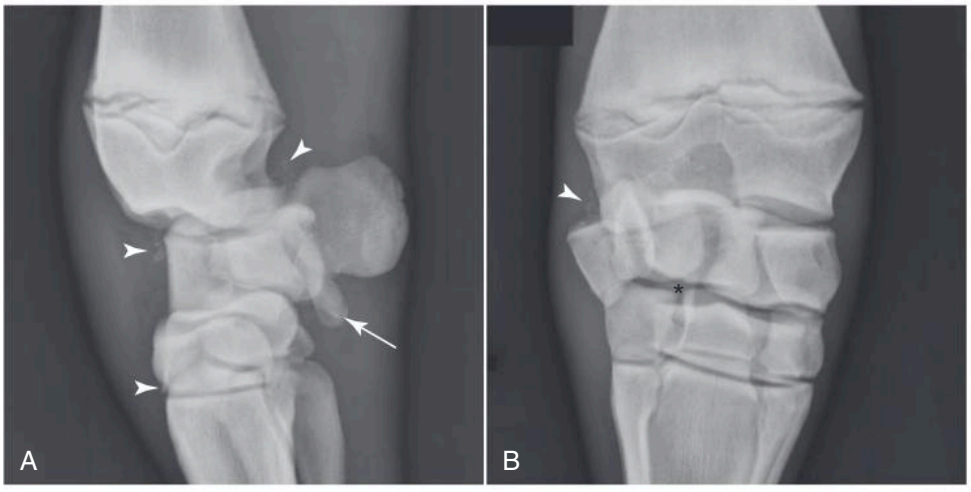


Fig. 23.20 Traumatic antebrachiocarpal joint luxation, biarticular ulnar carpal bone fracture, and numerous avulsion or chip fracture fragments secondary to kick injury in a 6-month-old Quarter horse filly. **A,** Lateral view. The proximal row of carpal bones is displaced palmarly relative to both the distal radius and the distal row of carpal bones. A large, oblong mineral fragment is distally displaced from the ulnar carpal bone (*white arrow*) and there are numerous small mineral fragments within the soft tissues surrounding the carpal bones (*white arrowheads*) consistent with avulsion fragments or chip fractures. Regional soft tissues are thickened. **B,** Dorsopalmar view; lateral is to the *left*. The antebrachiocarpal and middle carpal joints are wide. The ulnar carpal bone is abaxially displaced; its axially positioned fracture fragment is poorly defined on this view but summates with the intercarpal joint (*asterisk*). The lateral aspect of the radial epiphysis is distally collapsed into the fracture gap, further indicating axial instability. Small mineral avulsion fragments or chip fractures are also correlated on this view.

Carpal hyperextension, exercise at extreme speeds or on poor quality footing, inferior conformation, and improper hoof care can all lead to abnormal stresses on the carpal bones. Carpal bone overload results in adaptive increases in bone density and stiffness that is frequently followed by osteochondral fragmentation and/or fractures.[2]

Sclerosis itself is radiographically characterized by loss of distinction between the cortex and medullary cavity. Although sclerosis can be identified on standard radiographic views, assessment of the skyline projections of the proximal and distal row of carpal bones can be particularly helpful. The radial facet of the third carpal bone is the most common carpal site affected by sclerosis. Mild sclerosis of the third carpal bone is relatively common in young racing and sport horses and is sometimes considered an incidental finding because sclerosis does not always correlate with development of pathology, pain, or lameness.[1] Pronounced radiopacity of the medullary cavity with loss of corticomedullary distinction, however, is a sign of maladaptive, stress-related bone remodeling that could predispose the bone to fracture and is therefore considered abnormal. Comparison of the medullary opacity of the third and fourth carpal bones on a dorsal 35-degree proximal-dorsodistal oblique radiograph is a useful technique to determine the extent and severity of carpal bone sclerosis (Fig. 23.21). This view is also used to assess for fractures of the third carpal bone (Figs. 23.16C and 23.18).[3] Further comparison between right and left thoracic limbs is also recommended, as bilateral disease is possible.

Osteochondroma and Other Exostoses (Distal Radius)

An exostosis is defined as a benign bony outgrowth from an existing bone. An osteochondroma is a benign exostosis with a cartilage cap that is most typically found near a physis. The caudodistal surface of the radial metaphysis is the most common site for solitary osteochondroma in the horse, although they have also been described in other locations including the craniodistal radius and caudodistal tibia (Fig. 23.22).[31] Caudally oriented exostoses that are histopathologically different from osteochondromas have also been reported at the level of the caudal distal radial physis (Fig. 23.23A). Both osteochondromas and other exostoses in this area can result in similar clinical syndromes as they protrude caudally to impinge upon or penetrate the carpal sheath. This results in tenosynovitis and effusion, with or without concurrent deep digital flexor injury, secondary to superficial abrasion of the collagen fibers by the bone proliferation (Fig. 23.23B,C). Associated clinical signs of carpal sheath effusion and/or lameness may be constant or intermittent, and arthroscopic removal of the impinging exostoses is reported to result in a good prognosis for the patient's return to athletic activity.[32,33] Lateral and flexed lateral projections are usually most helpful for radiographic diagnosis of exostoses affecting the carpal sheath.

Soft Tissue Abnormalities

Ultrasonography is often more useful in the assessment of soft tissue injury; however, radiographs are used to identify underlying bone trauma and/or signs of chronic enthesopathy at tendon and ligament attachment sites. Extracapsular/extrasynovial swelling tends to be regional and diffuse, extending beyond the expected geographic confines of the joint capsules and tendon sheaths. It is important to recognize that intracapsular (synovial) distension and extracapsular soft tissue swelling can occur concurrently, and radiographic differentiation between intra- or extrasynovial location of soft tissue swelling can be difficult or impossible due to border effacement among these tissues.

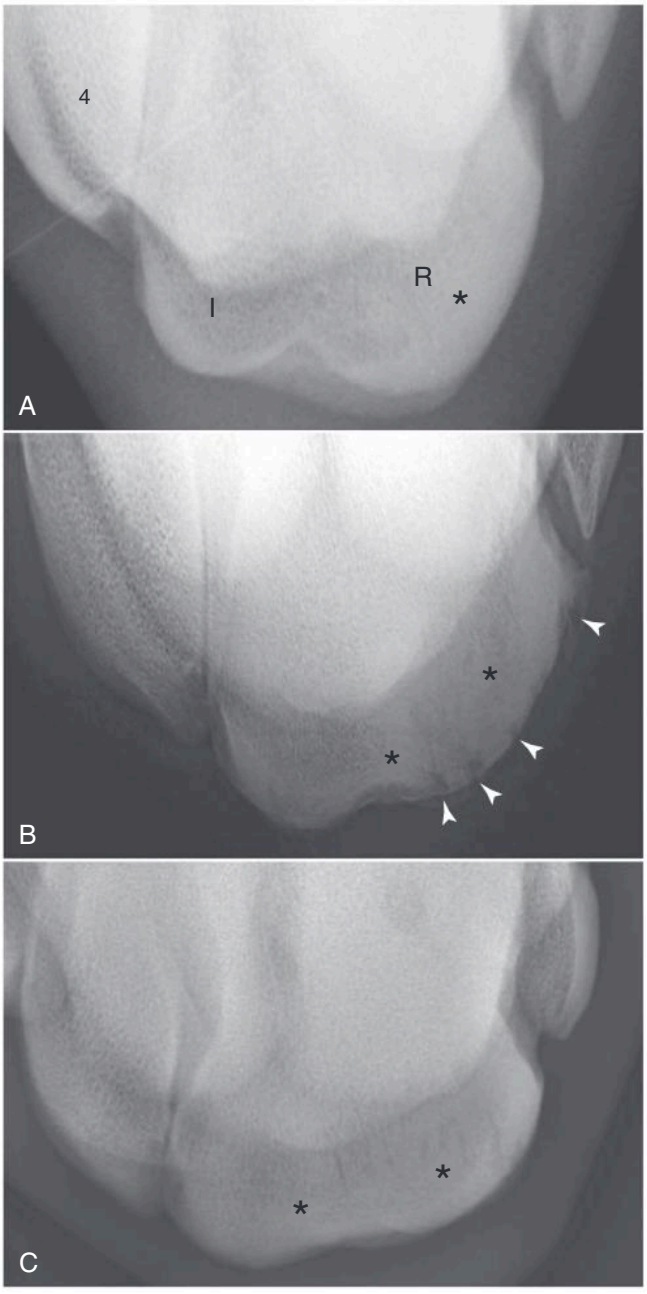


Fig. 23.21 Magnified dorsal-35 degrees proximal-dorsodistal oblique projections (skyline views of the distal row of carpal bones); lateral is to the *left*. In all panels, note the increased mineral opacity/sclerosis of the third carpal bone (*asterisks*). **A,** Compare the sclerosis of the radial facet (*R*) to the more normal trabecular pattern in the intermediate facet (*I*) and fourth carpal bone (*4*). **B,** The third carpal bone is diffusely sclerotic but more so in the radial facet. Note the ill-defined radiolucent areas in the dorsal border of the bone that may be areas of erosion, subchondral bone defects, enlarged vascular channels, or incomplete fractures (*arrowheads*). **C,** The third carpal bone is diffusely sclerotic and faintly striated with radiolucent lines that may be enlarged vascular channels. Both changes are more severe in the radial facet.

Collateral Ligament Injury

Collateral ligament injury often results in soft tissue swelling overlying the affected ligament.[34] Radiographic features of moderate to severe and/or chronic carpal collateral ligament injury that affect the underlying bone or limb alignment might be detectable. While collateral ligament desmopathy is often



Fig. 23.22 Lateral view of the distal radius in a 4-year-old Clydesdale with a solitary osteochondroma of the distal radius. A small, columnar exostosis arises from the caudal aspect of the radius just proximal to the distal radial physis (*white arrows*).

seen in otherwise stable joints, complete rupture of a collateral ligament could result in abnormal laxity, luxation, or subluxation. Horses with collateral ligament injury may present concurrently with avulsion fractures or enthesopathy at the ligament origin and/or insertion sites and osteoarthritis of the carpal joints (Fig. 23.24). Medial collateral ligament injury is reportedly more common than lateral collateral ligament injury in the carpus and may result in development of carpal varus deformity.[35] Radiography is an insensitive diagnostic test for many soft tissue lesions that do not affect the underlying bone, and ultrasound may be beneficial as a complementary imaging modality for collateral ligament injury.

Intercarpal Ligament Desmopathy

Primary injury to the intercarpal ligaments is an uncommon cause of joint effusion and lameness in horses. Carpal luxation or other trauma can also result in secondary injury to these ligaments (Fig. 23.20). Radiographically, intercarpal ligament desmopathy can be associated with intracapsular effusion and enthesopathy along the dorsal aspect of the cuboidal bones.[1] The lateral palmar intercarpal ligament is also sometimes associated with avulsion fragments from its attachment on the ulnar carpal bone as seen on the DLPMO projection.[36] However, fragmentation and lucency in this area have also been described as an incidental finding in horses without lameness or other clinical signs.[7]

Joint Effusion and Synovitis

Radiolucent, perisynovial fat pads are normally visible along the dorsal surface of the antebrachiocarpal and middle carpal joints on lateral projections of the carpus (Fig. 23.12). These fat pads can be obscured in cases of intracapsular effusion or synovitis.

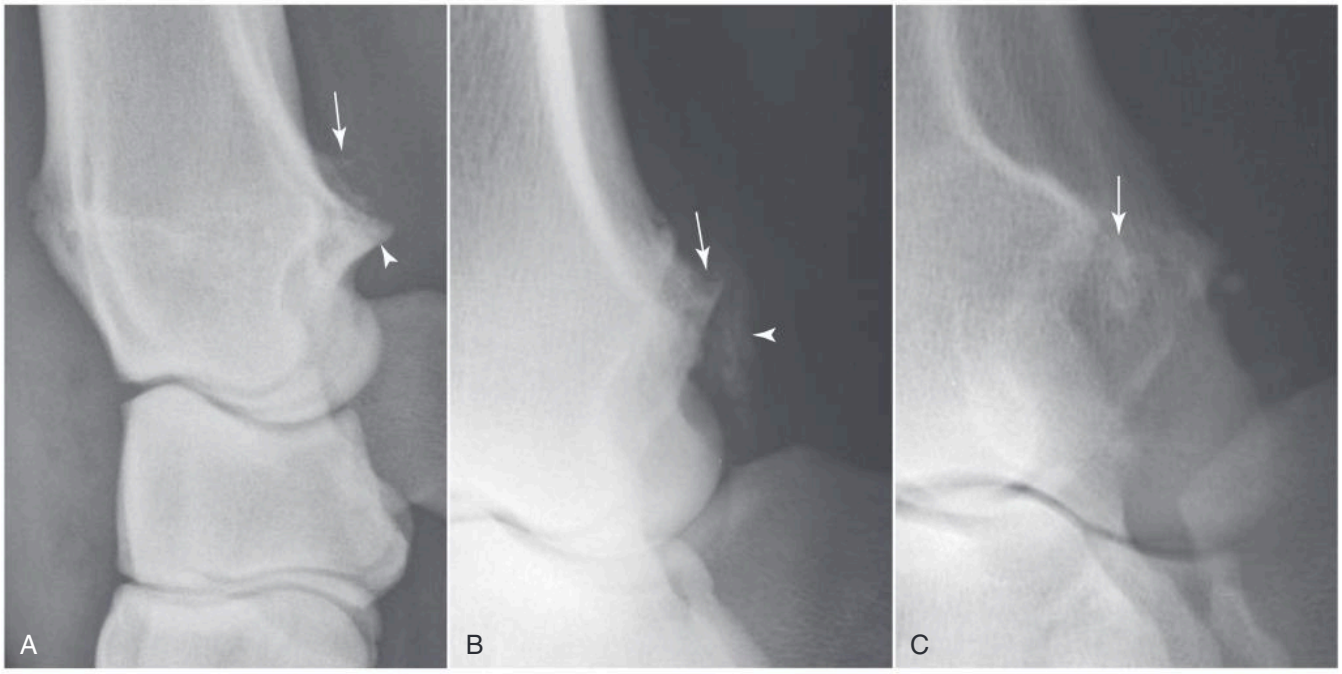


Fig. 23.23 Exostoses of the caudodistal radius. **A,** Lateral view. A pointed osseous projection extends caudally from or just proximal to the closed distal radial physis (*white arrow*). This is distinct from the normal caudomedial and caudolateral projections of the distal radius (*arrowhead*). **B,** Magnified lateral view of a different horse than in panel **A**; Note the exostosis projecting caudally from the level of the distal radial physis (*white arrow*). The roughly linear mineral opacity in the soft tissues caudal to the radius in this region (*arrowhead*) was confirmed sonographically to be dystrophic mineralization within the deep digital flexor tendon, which supports a diagnosis of chronic tendinopathy secondary to impingement. **C,** Dorsolateral-palmaromedial oblique image of the same carpus as in panel **B**. The exostosis (*white arrow*) is between the normal bony prominences on the caudomedial and caudolateral distal radius.



Fig. 23.24 Dorsopalmar view depicting chronic medial collateral ligament injury in a 4-year-old Quarter horse secondary to prior trauma. Lateral is to the *left*. Soft tissues medial to the carpus are thickened and contain several separate mineral fragments (*white arrowheads*) consistent with avulsion fragments of the second carpal and metacarpal bones. The medial/abaxial surface of the second carpal and metacarpal bones is smoothly remodeled. Medial collateral ligament desmitis was confirmed sonographically. Note the less severe soft tissue swelling lateral to the carpus and the punctate mineral opacity abaxial to the fourth carpal bone (*black arrowhead*) that may indicate less severe lateral collateral ligament injury.



Fig. 23.25 Lateral projection of a 3-year-old American Paint horse with severe carpal sheath effusion (*asterisk*) causing effacement of fascial planes. There is a small osteochondroma (*arrowhead*) that was found to be incidental and unlikely to be contributing to the carpal sheath effusion based on sonographic exam. Compare the palmar carpal soft tissues in this horse to the normal region in Fig. 23.2A.

They should be differentiated from subcutaneous gas. Soft tissue enlargement caused by intrasynovial effusion and/or synovitis is typically centered over the affected synovial structure (e.g., joint capsule or tendon sheath).

Carpal Sheath Effusion

The carpal sheath extends from the distal radial metaphysis to the mid-metacarpus, and the concave medial surface of the accessory carpal bone serves as the lateral boundary of the carpal canal.[2] Through this region, the sheath contains the superficial and deep digital flexor tendons. Tenosynovitis and subsequent swelling of the carpal sheath can result from exostoses and osteochondroma of the caudodistal radius, accessory carpal bone fractures, and injury to the superficial and deep digital flexor tendons.[33] Fascial planes along the palmar aspect of the carpus can become obscured with distention of the carpal canal (Fig. 23.25).[1]

Tendinopathy/Tenosynovitis of the Extensor Carpi Radialis, Common Digital Extensor, or Lateral Digital Extensor

Normal carpal extensor tendon sheaths each contain only a small volume of synovial fluid. Vertically oriented soft tissue swelling over the dorsal or dorsolateral aspect of the carpus may indicate tendon sheath effusion and/or tenosynovitis of the extensor carpi radialis, common digital extensor, or lateral digital extensor. Chronic tenosynovitis of the extensor carpi radialis or common digital extensor may result in new bone proliferation along the craniodorsal or craniodorsal and lateral aspect of the distal radius, respectively (Fig. 23.26).[1] New bone



Fig. 23.26 Lateral view of a 12-year-old crossbred gelding obtained 6 weeks after a traumatic extensor carpi radialis injury. Extensive soft tissue swelling is centered over the craniodistal radius proximal to a region of irregular, sharply pointed osseous remodeling on the distal radius (*white arrowheads*). Severe enlargement and disruption of the extensor carpi radialis tendon were identified sonographically with adhesions to the tendon sheath. Note the incidental vestigial ulna (*black arrowhead*), normal bony protuberance on the caudodistal radius (*white arrow*), and summation with the chestnut (*black arrow*).



Fig. 23.27 Dorsolateral-palmaromedial projection depicting a chronic carpal hygroma in a 17-year-old mule. The focal soft tissue swelling centered dorsomedial to the carpometacarpal joint contains two foci of dystrophic mineralization. No communication with the regional synovial structures could be identified and the swelling remained static over the course of several years.

may be smooth or palisading, and concurrent enthesopathy on the dorsal aspect of the radial, intermediate, and third carpal bone is also possible.[37]

Carpal Hygroma, Synovial Hernia, and Synovial Fistula

A carpal hygroma is a nonpainful soft tissue swelling on the dorsal aspect of the carpus that is acquired following trauma or repetitive injury (Fig. 23.27).[38] Hygromata are not connected to synovial structures, although they are sometimes called "false bursae" because it is common to identify subcutaneous fluid accumulation deep to the soft tissue swelling.

Synovial hernias result from a defect in the joint capsule through which a portion of the synovial membrane (and synovial fluid) protrudes. This term is sometimes used synonymously with "synovial cyst" or "synovial ganglia," although the three terms are distinct entities as cysts do not necessarily have a patent communication with the joint cavity and ganglia do not have a synovial lining.[39] Synovial hernias are also typically nonpainful and identified as an incidental finding with contrast radiographs, ultrasound, or magnetic resonance imaging (MRI).

Synovial fistulae are communications between two synovial structures (e.g., joints and tendon sheaths) that are often presumed to be secondary to previous, concurrent trauma to the communicating structures. Fistulous communication between a carpal hygroma, the antebrachiocarpal joint, and the extensor carpi radialis tendon sheath has also been reported.[40]

Soft Tissue Trauma, Draining Tracts, Foreign Bodies

Following acute carpal trauma, radiographs are indicated to identify osseous lesions such as fractures, luxations, and avulsions as well as to assess the region for radiopaque foreign bodies. Hematomas and hemarthrosis can result in extra- and intracapsular soft tissue swelling, respectively. In the chronic stages of healing, soft tissue wounds sometimes develop suppurative draining/fistulous tracts secondary to bone sequestra or foreign material that remains embedded within the soft tissues.

Table • 23.2

Soft Tissue Swellings of the Dorsal Carpus and Their Possible Radiographic Findings Following Intralesional Contrast Medium Injection.

ETIOLOGY OF SOFT TISSUE SWELLING	EXPECTED CONTRAST RADIOGRAPHIC FINDINGS
Carpal hygroma	Contrast medium remains extracapsular and within the soft tissue swelling itself
Synovial hernia	Contrast medium can be detected in an underlying synovial cavity (joint space or tendon sheath); occasionally, contrast movement is restricted by a one-way valve effect and communication between the synovial hernia and underlying synovial cavity cannot be confirmed
Synovial fistula	Contrast medium detected in two communicating synovial structures
Draining tracts	Contrast medium may highlight the tract itself, subcutaneous pockets, foreign bodies, and/or communication between the tract and adjacent synovial cavities

Following survey radiographs, contrast medium can be aseptically injected into hygromas, synovial cavities, and draining tracts to better characterize and aid in differentiation of these various soft tissue lesions of the carpus[41] (Table 23.2).

Calcinosis Circumscripta

Calcinosis circumscripta is a collection of calcium salt deposits in the subcutaneous tissue that manifests radiographically as a granular, mineral opaque mass. This is a variation of dystrophic mineralization that is uncommonly identified at sites of previous soft tissue trauma or chronic irritation, over bony prominences and pressure points, or near joint spaces. Calcinosis circumscripta may be intra- or extracapsular.[42]

Hypertrophic Osteopathy

Hypertrophic osteopathy is characterized most commonly by painful lower limb swelling, stiffness and/or lameness, joint effusion, and/or restricted flexibility of affected joints. Radiographically, the metacarpal and metatarsal bones are affected most commonly with symmetrical, palisading periosteal proliferation along the diaphyses and metaphyses without involvement of the subchondral bone or articular surfaces. This bone proliferation can be seen in other bones including the radius and carpal bones. Similar to what is seen in small animal patients, equine hypertrophic osteopathy occurs in tandem with a variety of intrathoracic and, rarely, intra-abdominal pathology including granulomatous disease, pulmonary abscess, pneumonia, pleural space disease, and neoplasia. The osseous lesions of hypertrophic osteopathy may regress or resolve following treatment of the primary disease process.[43]

Acknowledgment

With special thanks to prior authors of this chapter for their contributions.

REFERENCES

1. Wright IM, Butler JA. Radiography and radiology of the mature carpus. *Equine Vet Educ.* 1996;8:37–42.
2. Wright IM, McIlwraith CW. Fractures of the carpus. In: Wright IM, ed. *Fractures in the Horse.* Hoboken: Wiley-Blackwell; 2022.
3. Butler J. Radiography and radiology of the carpus and proximal aspect of the metacarpus of the horse. *Practice.* 2013;35:85–90.
4. Pilsworth RC. Stress radiographs: when, how and why to use them. *Equine Vet Educ.* 2002;14, 16-16.
5. Simon V, Dyson SJ. Radiologic anatomic variation of the carpus in horses with carpal lameness and control horses. *Vet Radiol Ultrasound.* 2010;51:601–606.
6. Hinkle FE, Johnson SA, Selberg KT, Barrett MF. A review of normal radiographical variants commonly mistaken for pathological findings in horses. *Equine Vet Educ.* 2020;32:664–672.
7. Santschi EM, Prichard MA, Whitman JL, et al. Survey radiography of the carpus and tarsus in neonatal thoroughbred foals and appearance at 6 months of age. *J Equine Vet Sci.* 2018;63:55–60.
8. Jacquet S, Robert C, Valette JP, Denoix JM. Evolution of radiological findings detected in the limbs of 321 young horses between the ages of 6 and 18 months. *Vet J.* 2013;197(1):58–64.
9. Glass K, Watts AE. Septic arthritis, physitis, and osteomyelitis in foals. *Vet Clin North Am Equine Pract.* 2017;33(2):299–314.
10. Tatarniuk DM, Trumble TN, Baxter GM, Ernst NS, McIlwraith CW, Hunt RJ. Lameness in the young horse. In: Baxter GM, ed. *Adams & Stashak's Lameness in Horses.* 7th ed. Hoboken: John Wiley & Sons; 2020.
11. Suarez-Fuentes DG, Tatarniuk DM. Clinical and radiographic findings of septic physitis in foals. *Vet Comp Orthop Traumatol.* 2020;03(02):e134–e139.
12. Stashak TS. Lameness of the proximal limb: the carpus. In: Baxter GM, ed. *Adams & Stashak's Lameness in Horses.* 7th ed. Hoboken: John Wiley & Sons; 2020.
13. Gaughan EM. Flexural limb deformities of the carpus and fetlock in foals. *Vet Clin North Am Equine Pract.* 2017;33(2):331–342.
14. Denoix JM, Jacquet S, Lepeule J, Crevier-Denoix N, Valette JP, Robert C. Radiographic findings of juvenile osteochondral conditions detected in 392 foals using a field radiographic protocol. *Vet J.* 2013;197(1):45–51.
15. Pilsworth R, Head M. Presales radiographic surveys in yearlings 2. Significance of lesions in the carpus, tarsus and stifle. *Practice.* 2010;32:247–253.
16. Graham RJTY, Rosanowski SM, McIlwraith CW. A 10-year study of arthroscopic surgery in racing Thoroughbreds and Quarter Horses with osteochondral fragmentation of the carpus. *Equine Vet J.* 2020;52:225–231.
17. Ramos S, Pinto A, Crespo J, et al. Osteochondrosis (osteochondritis dissecans) in Lusitano horses. *Prevalence and characteristics, J Equine Vet Sci.* 2022;117.
18. Garvican E, Clegg P. Clinical aspects of the equine carpal joints. *Companion Anim.* 2007;12:5–12.
19. Panizzi L, Barber SM, Lang HM, Carmalt JL. Carpometacarpal osteoarthritis in thirty-three horses. *Vet Surg.* 2009;38:998–1005.
20. Malone ED, Les CM, Turner TA. Severe carpometacarpal osteoarthritis in older Arabian horses. *Vet Surg.* 2003;32:191–195.
21. Schneider RK, Bramlage LR, Moore RM, Mecklenburg LM, Kohn CW, Gabel AA. A retrospective study of 192 horses affected with septic arthritis/tenosynovitis. *Equine Vet J.* 1992;24(6):436–442.
22. Steel CM, Hunt AR, Adams PL, et al. Factors associated with prognosis for survival and athletic use in foals with septic arthritis: 93 cases (1987–1994). *J Am Vet Med Assoc.* 1999;215(7):973–977.
23. Hardy J. Etiology, diagnosis, and treatment of septic arthritis, osteitis, and osteomyelitis in foals. *Clin Tech Equine Pract.* 2006;5(4):309–317.
24. Lindegaard C, van Galen G, Aarsvold S, Berg LC, Verwilghen D. Haematogenous septic arthritis, physitis and osteomyelitis in foals. A tutorial review on pathogenesis, diagnosis, treatment and prognosis. Part 1. *Equine Vet Educ.* 2021;33:659–672.
25. Ramzan PHL. A novel radiographic projection for the detection of sagittal plane slab fracture of the equine third carpal bone. *Equine Vet J.* 2019;51(2):258–260.
26. Doering AK, Reesink HL, Luedke LK, et al. Return to racing after surgical management of third carpal bone slab fractures in thoroughbred and Standardbred racehorses. *Vet Surg.* 2019;48:513–523.
27. Minshall GJ, Wright IM. Frontal plane fractures of the accessory carpal bone and implications for the carpal sheath of the digital flexor tendons. *Equine Vet J.* 2014;45(5):579–584.
28. Dyson SJ. Fractures of the accessory carpal bone. *Equine Vet Educ.* 1990;2:188–190.
29. Smith MRW. Management of joint instability. *Equine Vet Educ.* 1990;22(3):112–114.
30. Bailey JV, Barber SM, Fretz PB, Jacobs KA. Subluxation of the carpus in thirteen horses. *Can Vet J.* 1984;25(8):311–314.
31. Russell JW, Hall MS, Kelly GM. Osteochondroma on the cranial aspect of the distal radial metaphysis causing tenosynovitis of the extensor carpi radialis tendon sheath in a horse. *Aust Vet J.* 2017;95(1–2):46–48.
32. Nixon AJ, Schachter BL, Pool RR. Exostoses of the caudal perimeter of the radial physis as a cause of carpal synovial sheath tenosynovitis and lameness in horses: 10 cases (1999–2003). *J Am Vet Med Assoc.* 2004;224(2):264–270.
33. Wright IM, Minshall GJ. Clinical, radiological and ultrasonographic features, treatment and outcome in 22 horses with caudal distal radial osteochondromata. *Equine Vet J.* 2012;44:319–324.
34. Quiney L, Murray R, Dyson S. Management of primary injuries of the medial collateral ligament of the carpus in two horses. *J Equine Vet Sci.* 2020;86.
35. Vanslambrouck LMA, Whitcomb MB, Vaughan B. Ultrasonographic diagnosis of carpal collateral ligament injuries in 20 horses (2000–2015). *Proceedings of the 62nd Annual Convention of the Am Assoc Equine Pract.* 2016;399.
36. Beinlich CP, Nixon AJ. Radiographic and pathologic characterization of lateral palmar intercarpal ligament avulsion fractures in the horse. *Vet Radiol Ultrasound.* 2004;45(6):532–537.
37. Platt D, Wright IM. Chronic tenosynovitis of the carpal extensor tendon sheaths in 15 horses. *Equine Vet J.* 1997;29:11–16.
38. Schramme M, Schumacher J. Management of Bursitis. In: Auer JA, Kümmerle JM, Prange T, Stick JA, eds. *Equine Surgery.* 5th ed. St. Louis: Elsevier; 2019.
39. Lacourt M, MacDonald M, Rossier Y, Laverty S. Equine articular synovial cysts: 16 cases. *Vet Surg.* 2013;42:99–106.
40. Rybar M, Fraser BSL. Surgical repair of synovial fistulae between a carpal hygroma, the tendon sheath of the extensor carpi radialis and the antebrachiocarpal joint in a horse. *Equine Vet Educ.* 2020;32:e100–e105.
41. Lamb CR. Contrast radiography of equine joints, tendon sheaths, and draining tracts. *Vet Clin North Am Equine Pract.* 1991;7(2):241–257.

42. Tóth F, Schumacher J, Newman S. Calcinosis circumscripta in the antebrachiocarpal joint of a horse. *Equine Vet Educ*. 1991;21:584–588.
43. Mair TS, Dyson SJ, Fraser JA, Edwards GB, Hillyer MH, Love S. Hypertrophic osteopathy (Marie's disease) in Equidae: a review of twenty-four cases. *Equine Vet J*. 1996;28:256–262.

ELECTRONIC RESOURCES

Additional information related to the content in Chapter 23 can be found online at eBooks.Health.Elsevier.com.

- Chapter Quiz

CHAPTER 24

Equine Metacarpus and Metatarsus

Erin G. Porter

Throughout this chapter, we will refer to the metacarpus and metatarsus collectively as the metacarpus; however, discussion also applies to the metatarsus unless otherwise specified. Relevant anatomical and pathological differences between the metacarpus and metatarsus will be discussed. In order to obtain high quality radiographs of the metacarpus, appropriate patient positioning and restraint is imperative. The patient should stand with all four limbs squarely positioned and equally weight bearing, and light sedation may be necessary. Comprehensive radiographic evaluation of the metacarpus includes the carpometacarpal joint in collimation proximally, and the metacarpophalangeal joint, distally. Depending on the size of the x-ray detector available, this may require a proximally and distally collimated view of each projection. A standard radiographic series includes dorsopalmar (DP), lateromedial, dorsomedial-palmarolateral oblique (DMPLO), and dorsolateral-palmaromedial oblique (DLPMO) projections. In the pelvic limb, the term *palmar* should be replaced by *plantar*. Additional projections may be indicated based on the history, clinical exam, and available imaging findings and these projections will be further discussed where indicated.

RADIOGRAPHIC ANATOMY AND COMMON VARIANTS

The Third Metacarpal Bone (The Cannon Bone)

The third metacarpal bone lies between the second and fourth metacarpal bones and is the largest of the three bones. When there is partial superimposition of two bones, as is seen in radiography of the metacarpus, a linear lucent line can be seen paralleling the region of superimposition. This phenomenon, known at Mach bands or Mach lines, is due to an optical illusion of edge enhancement created by the observer's retina, and should not be mistaken for a fracture line (Fig. 24.1).[1] While all three metacarpal bones articulate with the distal row of carpal bones to form the carpometacarpal joint, it is only the third metacarpal bone that contributes to the articulation of the metacarpophalangeal joint. The third metatarsal bone is slightly longer than the third metacarpal bone and has a more convex dorsal margin and more palmar angulation of the condyle. The principal nutrient foramen is present in the proximal to middle third of the third metacarpal bone. On the dorsopalmar projection, it is easily identified as a well-defined, oval lucency, but on lateral and oblique projections, it is obliquely oriented in the palmar cortex of the third metacarpal bone, and should not be mistaken for a fracture (Fig. 24.2). On the dorsopalmar projection, a variable number of pinpoint nutrient foramina may be seen in the proximal subchondral bone of the third metacarpal bone, just distal to the carpometacarpal joint (see Fig. 24.2). The palmaroproximal cortex of the third metacarpal bone normally has a coarser trabecular pattern than the remainder of the cortex (see Fig. 24.2). The dorsal cortex of the third metacarpal bone is normally thicker than the palmar cortex, as seen on the lateral projection, which should not be mistaken for pathology. A well-defined exostosis or "bone spur," which may be bilateral, may be present at the dorsoproximal aspect of the third metatarsal bone in up to 25% of horses, and although it is not correlated with lameness, it is more frequently seen concurrent with radiologic abnormalities of the distal tarsal joints (Fig. 24.3).[2] The condyle of the third metacarpal bone consists of medial and lateral parts separated by a sagittal ridge, which is the most distal extension of the condyle and articulates with the sagittal groove of the proximal phalanx. The medial portion of the condyle is mildly larger than the lateral portion, which can be helpful for determining laterality on the dorsopalmar projection if necessary. At birth, the proximal physis of the third metacarpal bone should be completely closed and the distal physis closes at 3 to 6 months of age.

The Second and Fourth Metacarpal and Metatarsal Bones (The Splint Bones)

The second and fourth metacarpal bones are attached to the medial and lateral aspect of the third metacarpal bone by small interosseous ligaments. It is common for these ligaments to



Fig. 24.1 Dorsopalmar radiograph of a metacarpus. Lateral is to the *left*. There is a radiolucent line (*arrows*) on the axial aspect of the fourth metacarpal bone. This is a Mach line artifact created at the margin of the third and fourth metacarpal bones.

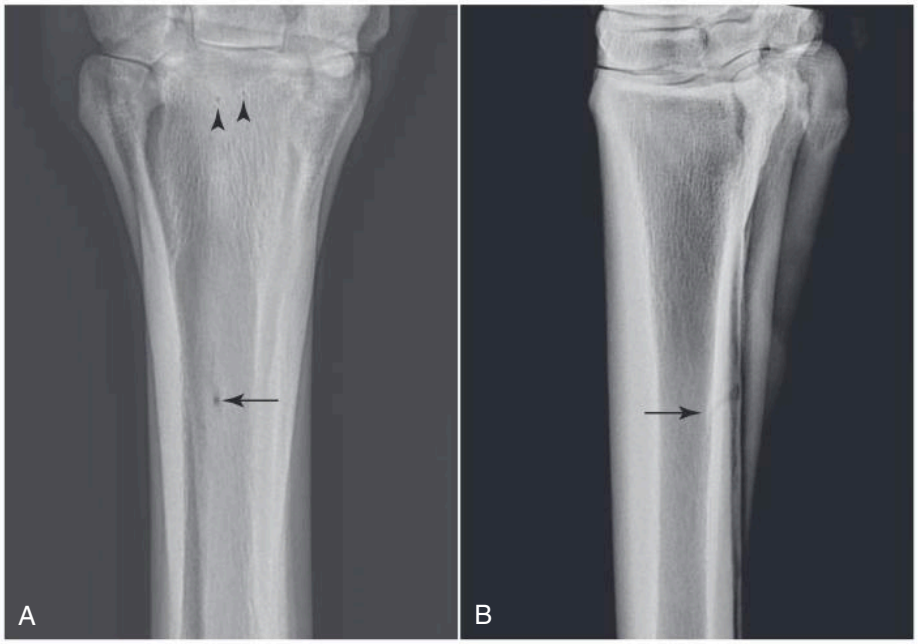


Fig. 24.2 **A,** Dorsopalmar radiograph of the metacarpus. Lateral is to the *left*. The principal nutrient foramen is seen as a well-defined, oval lucency (*arrow*) and pinpoint nutrient foramina are present in the proximal subchondral bone of the third metacarpal bone (*arrowheads*). Note the coarser trabecular pattern of the proximal aspect of the third metacarpal bone. **B,** Lateromedial projection of the metacarpus. Dorsal is to the *left*. The principal nutrient foramen is obliquely oriented in the palmar cortex of the third metacarpal bone and should not be mistaken for a fracture (*arrow*).

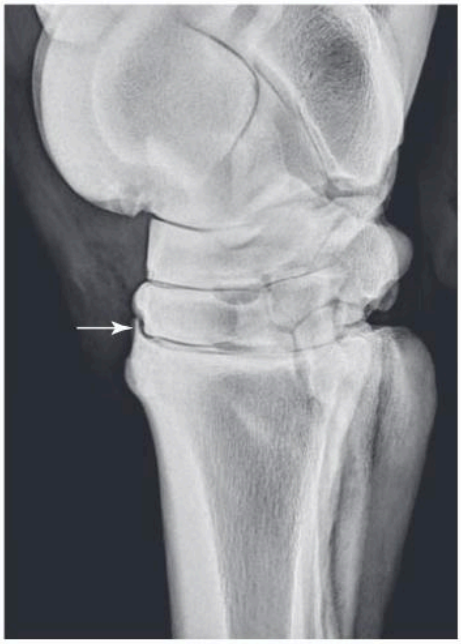


Fig. 24.3 Lateromedial projection of the proximal metatarsus. Dorsal is to the *left*. A well-defined exostosis or "bone spur" is present at the dorsoproximal aspect of the third metatarsal bone (*arrow*). This finding is often incidental and not associated with lameness.

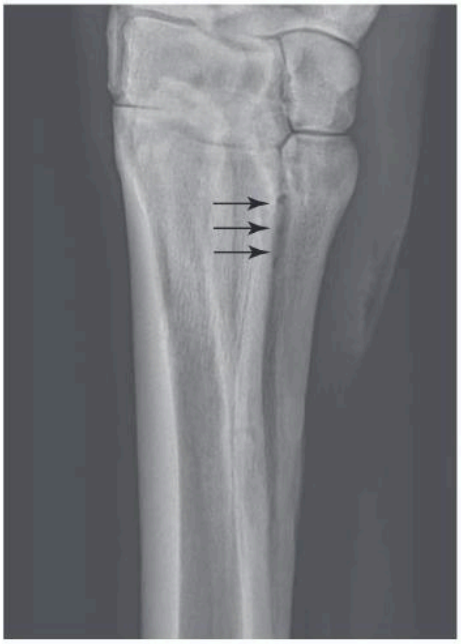


Fig. 24.4 Dorsomedial-palmarolateral oblique projection of the right metacarpus. Dorsal is to the *left*. There is smooth mineralization of the interosseous space between the second and third metacarpal bones (*arrows*). This is a common, incidental finding.

ossify over time, often bilaterally, with the medial interosseous space being more affected (Fig. 24.4).[3] Proximally, the metacarpal bones have a larger base and taper in size along their shaft towards their distal ends or "buttons," which may be bulbous, and can be palpated approximately three-quarters of the way down the metacarpus. In the forelimb, the second metacarpal bone articulates with the second carpal bone as well as a variable portion of the third carpal bone, and the fourth metacarpal bone articulates with the fourth carpal bone (Fig. 24.5). In the hindlimb, the second metatarsal bone articulates with the fused first and second tarsal bones, and the fourth metatarsal bone articulates with the fourth tarsal bone (see Fig. 24.5). In well-positioned, oblique projections of the metacarpus and metatarsus, the interosseous space between

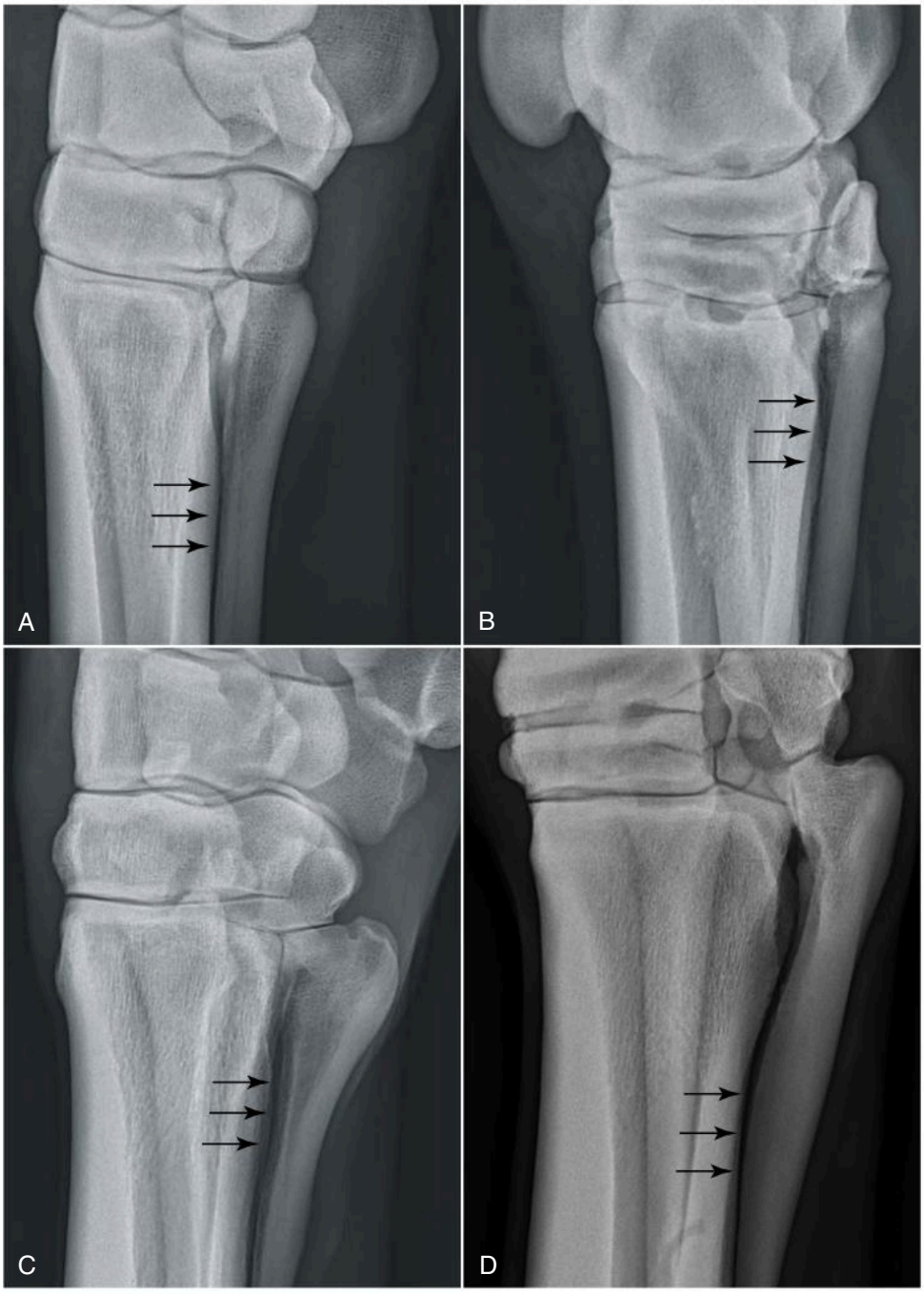


Fig. 24.5 **A,** Dorsomedial-palmarolateral oblique projection of the left proximal metacarpus. Dorsal is to the *left.* The second metacarpal bone articulates with the second and third carpal bone. The interosseous space between the second and third metacarpal bones can be clearly seen. **B,** Dorsomedial-plantarolateral oblique projection of the right proximal metatarsus. Dorsal is to the *left.* The second metatarsal bone can be seen articulating with the fused first and second tarsal bones. The interosseous space between the second and third metatarsal bones can be clearly seen. **C,** Dorsolateral-palmaromedial oblique projection of the left proximal metacarpus. Dorsal is to the *left.* The fourth metacarpal bone articulates with the fourth carpal bone. The interosseous space between the fourth and third metacarpal bones can be clearly seen. **D,** Dorsolateral-plantaromedial oblique projection of the left proximal metatarsus tarsus. Dorsal is to the left. The fourth metatarsal bone can be seen articulating with the fourth tarsal bone. The interosseous space between the fourth and third metatarsal bones can be clearly seen. *Arrows* indicate the interosseous space on all radiographs.

the second and third or fourth and third metacarpal or metatarsal bones is clearly visible (see Fig. 24.5). The fourth metatarsal bone has a prominent base, which can be variably shaped, including having a notched, bilobed or fragmented appearance, often bilaterally, and the base of the fourth metacarpal bone may have a proximal extension or radiolucency (Fig. 24.6).[4] A radiolucent concavity may be seen, in the proximal aspect of the second metacarpal bone, especially when a first carpal bone is present (Fig. 24.7).[4] At birth, the proximal physes of the splint bones should be closed, while the

distal epiphyses are cartilaginous and may appear separated from the body of the splint bone as they ossify, which can be mistaken for a fracture.

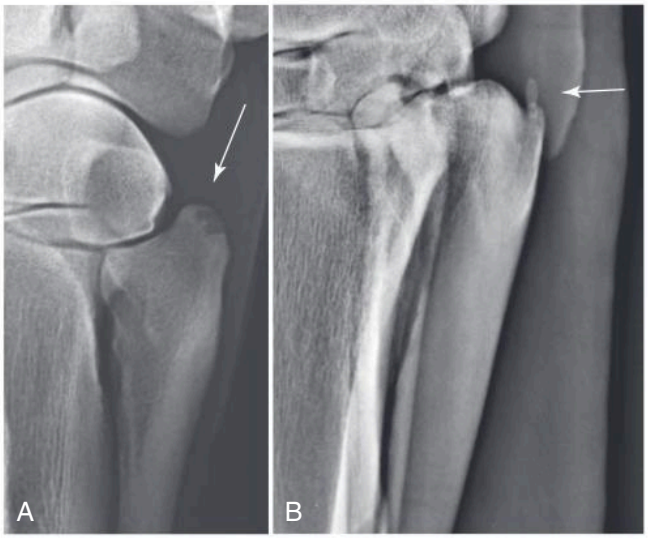


Fig. 24.6 **A,** Dorsolateral-palmaromedial oblique radiograph of a proximal metacarpal region. The base of the fourth metacarpal bone is extended proximally, and there is an ill-defined radiolucent area (*arrow*) in the most proximal aspect. **B,** Dorsolateral-plantaromedial oblique radiograph of the proximal metatarsal region. There is osseous proliferation extending proximally from the plantaroproximal aspect of the fourth metatarsal bone (*arrow*).

Metacarpal Soft Tissues

Multiple tendons, ligaments, and soft tissue structures provide support for the metacarpus and allow for extension and flexion of the digit. The extensor tendons, which lie along the dorsal and lateral aspect of the third metacarpal bone contribute little to the radiographic appearance of the metacarpus and are rarely of clinical relevance. The flexor tendons of the metacarpus include the superficial and deep digital flexor tendons, which run palmar to the third metacarpal bone. At the mid-metacarpus, the deep digital flexor tendon is joined dorsally by an accessory (check) ligament which originates from the palmar carpal ligament and palmar aspect of the third and fourth carpal bones in the forelimb.[5] In the pelvic limb, the accessory ligament of the deep digital flexor tendon originates from the plantar aspect of the ligament between the calcaneus and central and third tarsal bones. It is usually smaller, reportedly absent in 6% of hindlimbs, and has more variable morphology than in the thoracic limb.[6] In the distal third of the metacarpus, between the splint bones and the proximal sesamoid bones, is the manica flexoria, a sleeve that wraps dorsally from the superficial digital flexor tendon and encircles the deep digital flexor tendon to maintain both tendons in a central position within the digital sheath.

The third interosseous muscle (suspensory ligament) originates primarily from the palmar or plantar aspect of the third metacarpal or metatarsal bone. It has smaller attachments on the third carpal and metacarpal bone or fourth tarsal bone, calcaneus, and fourth metatarsal bones, and it is bordered by the splint bones.[5,7–9] The proximal portion of the suspensory ligament is bilobed in the forelimb and somewhat triangular in the hindlimb, and it fuses distally to form a flat, oval body before dividing into branches. In the hindlimb, the proximal

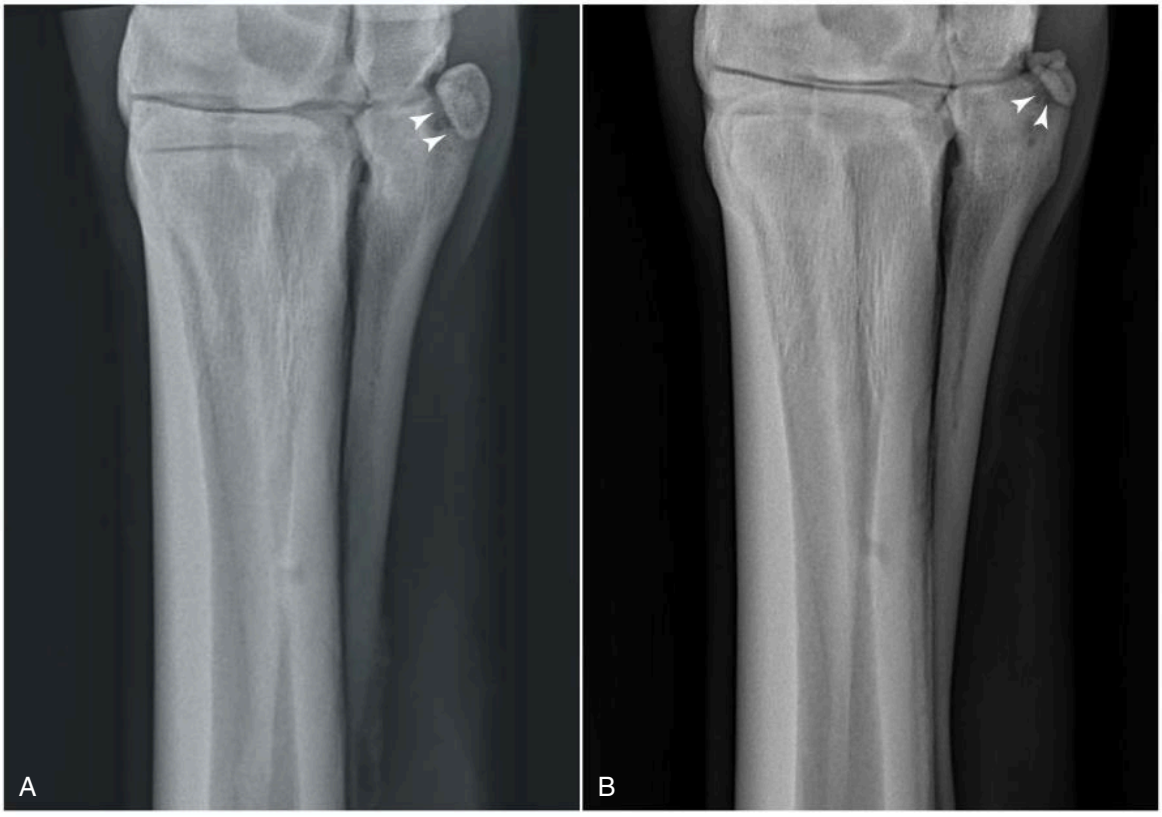


Fig. 24.7 Dorsomedial-palmarolateral oblique projections of the *right* **(A)** and *left* **(B)** proximal metacarpus of the same horse. The palmaroproximal aspect of the second metacarpal bone has a focal, concave margin and radiolucency (*arrowheads*) and a first carpal bone is present bilaterally. The *left* first carpal bone has an incidental, bipartite appearance **(B)**.

aspect of the suspensory ligament is closer to the fourth metatarsal bone with more connective tissue separating it from the second metatarsal bone.[10] A dense band of fascia borders the plantar aspect of the proximal suspensory ligament, connecting to the second and fourth metatarsal bones. In the distal third of the metacarpus, the suspensory ligament body splits into medial and lateral branches which insert on the proximal sesamoid bones. Small, medial and lateral extensor branches wrap dorsally to insert on the extensor tendon. Up to 29.5% of the length of the suspensory ligament branches is subsynovial to the metacarpophalangeal and metatarsophalangeal joints.[11] The suspensory ligament contains variable amounts of fat and muscle, which are typically located in two medial and lateral bundles proximally and become more randomly positioned in a zig-zag pattern within the body of the ligament.[10]

Synovial structures of the metacarpus and metatarsus include the carpal and tarsal sheath, respectively, and the digital flexor tendon sheath. The carpal sheath encircles the superficial and deep digital flexor tendon and accessory ligament of the deep digital flexor tendon and extends to the proximal third of the metacarpus. The tarsal sheath encircles the lateral digital flexor tendon and accessory ligament of the deep digital flexor tendon and extends to the proximal third of the metatarsus. The digital flexor tendon sheath extends from the distal third of the metacarpus to the mid to distal pastern and surrounds the superficial and deep digital flexor tendons.

COMMON RADIOGRAPHIC ABNORMALITIES OF THE METACARPUS

Soft Tissue Structures

When evaluating the metacarpus for soft tissue pathology, it is important to have a thorough understanding of relevant soft tissue anatomy. Due to the limited amount of fat in the metacarpus, soft tissue swelling due to enlargement of the superficial soft tissue structures such as the suspensory ligament branches or superficial digital flexor tendon may be radiographically apparent. Moderate to marked effusion and/or synovitis of the digital flexor tendon sheath may result in the appearance of soft tissue enlargement of the medial and lateral aspect of the distal third of the metacarpus on the DP projection or increased soft tissue opacity between the suspensory ligament branches and digital flexor tendons on the lateral projection (Fig. 24.8). Dystrophic mineralization of soft tissues structures such as the flexor tendons or suspensory ligament branches may be radiographically apparent (see Fig. 24.8).

Soft tissue thickening of the metacarpus may be focal or diffuse. Differentials for focal soft tissue thickening depend on the anatomic location, how extensive the lesion is, and if there is concurrent osseous pathology. Differential diagnoses may include focal edema, hematoma, granuloma formation as secondary to trauma or infectious etiologies such as habronemiasis, fibrosis from prior/chronic soft tissue injury or soft tissue neoplasia (Fig. 24.9). Subcutaneous emphysema may also be seen due to a wound, abscess, or iatrogenic introduction. Thorough evaluation of the osseous structures in the region of the soft tissue pathology is pertinent, and acquiring multiple oblique radiographic projections may be helpful to rule out associated pathology such as sequestrum formation, periosteal proliferation, or osteomyelitis. Differential diagnoses for diffuse soft tissue thickening surrounding the metacarpus may include subcutaneous edema, cellulitis, lymphangitis, and vasculitis and should be prioritized in light of the clinical exam and other imaging findings (see Fig. 24.9).



Fig. 24.8 Lateromedial projection of the right distal metatarsus and metatarsophalangeal joint. Dorsal is to the *left*. Increased soft tissue opacity is present in the region of the digital flexor tendon sheath, plantar to the suspensory ligament branches, and there is focal plantar convexity (*white arrow*) due to marked tenosynovitis. A large amount of soft tissue dystrophic mineralization is seen in the region of the digital sheath (*black arrow*).

Periostitis

Periostitis is inflammation of the periosteum which may result in osseous proliferation and can occur due to trauma, infection, or less commonly, neoplasia. The equine metacarpus is a common location for focal periosteal proliferation due to trauma, as there is a limited amount of fat and soft tissue overlying the bone to provide protection. Radiographic evaluation should be performed when firm, osseous thickening is noted in order to rule out fractures and attempt to differentiate between benign and malignant processes. Although these periosteal reactions are not frequently associated with lameness, they will often have persistently increased radiopharmaceutical uptake when evaluated with nuclear scintigraphy.[12]

Focal regions of osseous proliferation may also be seen at the interosseous space between the metacarpal bones, commonly referred to as "splints."[13] These occur due to trauma to the interosseous ligament or syndesmosis between the metacarpal bones, and are very common, especially in young horses as they are started into work. Splints most commonly develop between the second and third metacarpal bones in the forelimb, and between the third and fourth metatarsal bones in the hindlimb. Splints can be difficult to differentiate from periostitis radiographically and may have a similar clinical presentation. In the initial, active phases, these lesions are often warm and painful upon palpation and may have associated soft tissue swelling. After the inflammation resolves, nonpainful osseous proliferation will persist for an extended period of time. The anatomic location of the periosteal proliferation should be considered even after the inflammatory period resolves as the proliferation may impinge on adjacent soft tissue structures such as the suspensory ligament, causing regional desmopathy and adhesion formation.[14] In these cases,

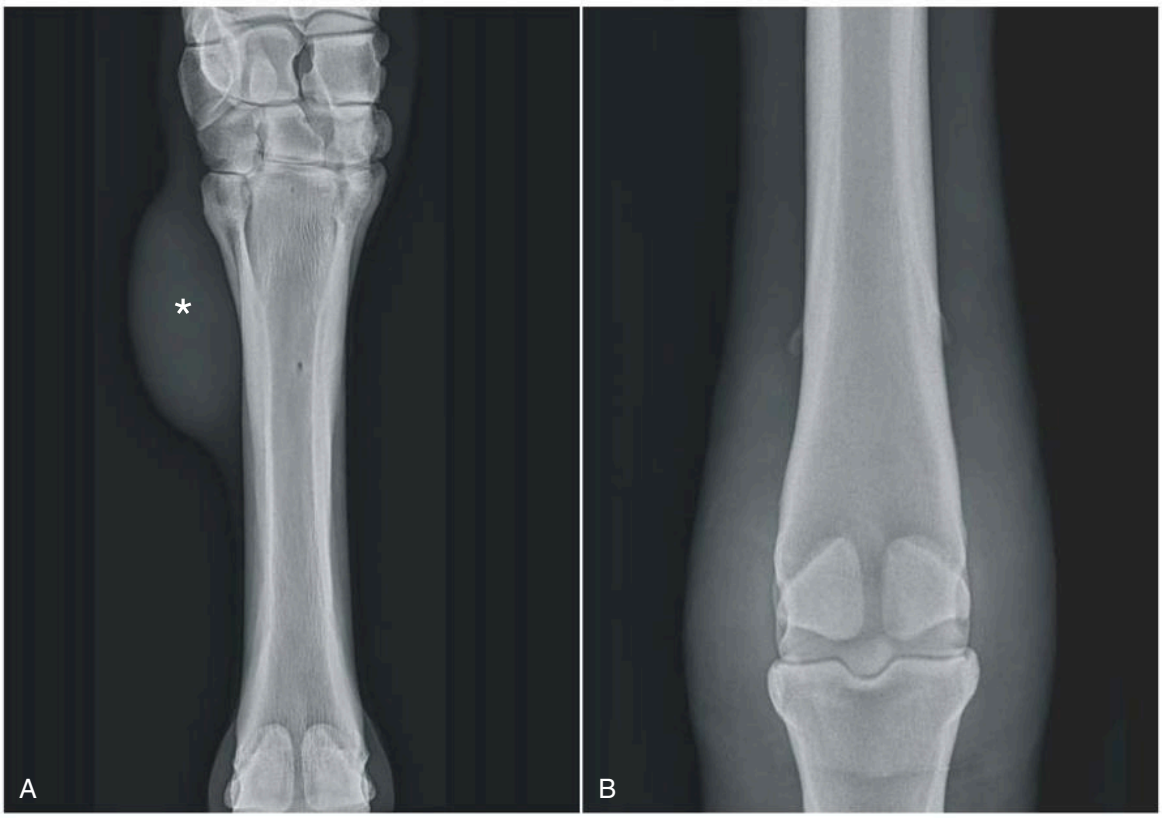


Fig. 24.9 **A,** Dorsopalmar projection of the left metacarpus. Lateral is to the *left.* A large, well-defined soft tissue opaque mass is present along the proximal lateral aspect of the metacarpus (*asterisk*). This lesion was diagnosed as fibrosarcoma. **B,** Dorsoplantar projection of the left distal metatarsus. Lateral is to the *left.* Marked, diffuse soft tissue swelling surrounds the metatarsus, secondary to cellulitis in this case.

ultrasound provides a useful compliment to radiographs for evaluation of concurrent soft tissue pathology. The proliferation may have irregular margins with multiple linear lucent regions, which, when superimposed on the underlying bone, can be difficult to differentiate from fracture formation (Fig. 24.10). Radiographic evaluation should include oblique projections at various angles of obliquity of the metacarpal region as needed to evaluate the interosseous spaces between the metacarpal bones.

Dorsal metacarpal disease, also known as "bucked shins," is a common cause of periostitis, most often seen in 2-year-old Thoroughbred racehorses. It is caused by cyclic fatigue due to excessive compression of the dorsal and dorsomedial aspects of the third metacarpal bone, often bilaterally, and can lead to incomplete (saucer) fractures of the dorsal cortex of the third metacarpal bone. With this disease, the bone undergoes repetitive stress without the necessary amount of time needed to adequately remodel. New, weaker bone is produced at the points of stress on the bone, and the rapid bone formation causes the periosteum to be elevated from the underlying cortex and become inflamed. Diagnosis is often made by the physical exam and history of pain on palpation over the dorsal aspect of the third metacarpal bone and/or soreness after strenuous athletic activity. Radiographic findings may include smooth periosteal proliferation over the dorsal and dorsal medial aspect of the third metacarpal bone and incomplete, dorsal cortical fractures. This region should be carefully evaluated for incomplete fractures (Fig. 24.11).

Hypertrophic osteopathy is a rare condition in horses resulting in symmetrical periosteal proliferation along the diaphysis and metaphysis of long bones, most often affecting the metacarpal and metatarsal bones. This disease process typically occurs in association with other pathology, most commonly intrathoracic disease.[15]

Osteomyelitis and Sequestra

Due to limited fat and soft tissue surrounding the metacarpal bones, this region is especially predisposed to bone trauma, which in some cases, may result in infectious osteitis or osteomyelitis. Radiographically, aggressive processes in bone, such as infection and neoplasia are more likely to result in irregularly margined, ill-defined proliferation and/or lysis with indistinct margins or a long zone of transition between normal and abnormal bone. Sequestrum formation is a common sequela to trauma and infection in the metacarpal region, often affecting the thick dorsal cortex of the third metacarpal bone.[16] Sequestra consist of a central piece of devitalized, sclerotic bone (the sequestrum) which has become separated from the adjacent, healthy bone and surrounded by a radiolucent region consisting of purulent material and granulation tissue encircled by a zone of dense bone (the involucrum). A draining tract (cloaca) may also be present, extending from the sequestrum through the surrounding tissues. The radiographic appearance of sequestra depends on the angle at which it is struck by the x-ray beam (Fig. 24.12, eFig. 24.1). As the sequestrum serves as a nidus for infection, surgical debridement is often necessary to facilitate healing.

Proximal Suspensory Ligament Enthesopathy and Avulsion

Radiographic findings of suspensory ligament enthesopathy may include periosteal proliferation, trabecular or endosteal sclerosis, or osteolysis at the proximal attachment site of the suspensory ligament.[10,17,18] As seen on the dorsopalmar projections, the trabecular pattern of the proximal third metacarpal



eFig. 24.1 Dorsomedial-palmarolateral oblique radiograph of the metacarpus. There is extensive new bone formation on the palmaromedial aspect of the third metacarpal bone. A thin linear bone fragment (sequestrum) is surrounded by an oval radiolucent involucrum. There is surrounding cortical sclerosis. The soft tissues are thickened with irregular skin surface which may represent debris or a wound.

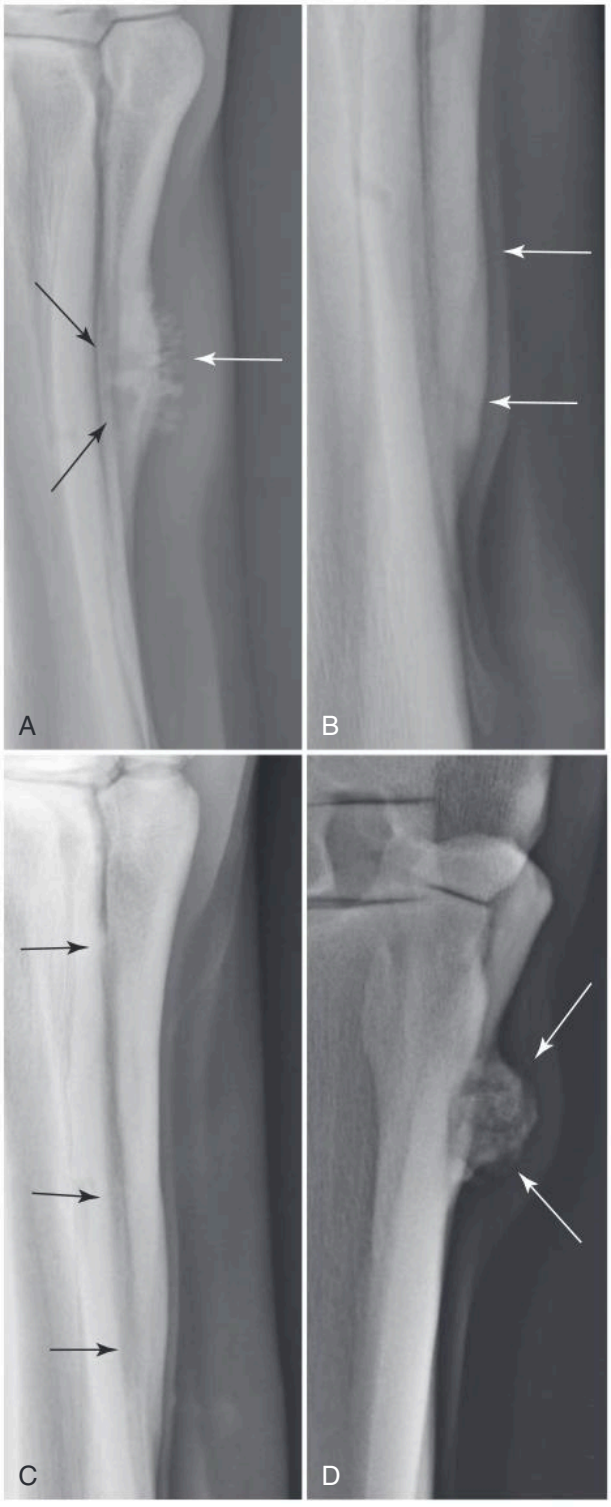


Fig. 24.10 **A,** Dorsomedial-palmarolateral oblique radiograph of the second and third metacarpal bones. The middle one-third of the second metacarpal bone is smoothly enlarged, with irregularly outlined new bone on the palmar aspect of heterogeneous mineral opacity (*white arrow*). Within the second metacarpal bone there are ill-defined radiolucent areas (*black arrows*). Although irregular in appearance, such lesions may not be clinically significant. **B,** Dorsomedial-palmarolateral oblique radiograph of the second and third metacarpal bones. There is a smoothly marginated exostosis (*white arrows*) on the second metacarpal bone of unlikely clinical significance. **C,** Dorsomedial/palmarolateral oblique radiograph of the second and third metacarpal bones. There is mineralization between the two bones in the interosseous space (*black arrows*). This is of unlikely clinical significance. **D,** Dorsoplantar radiograph of a proximal metatarsal region. Lateral is to the *right*. There is a large exostosis of heterogeneous mineral opacity on the lateral aspect of the third metatarsal bone (*white arrows*).

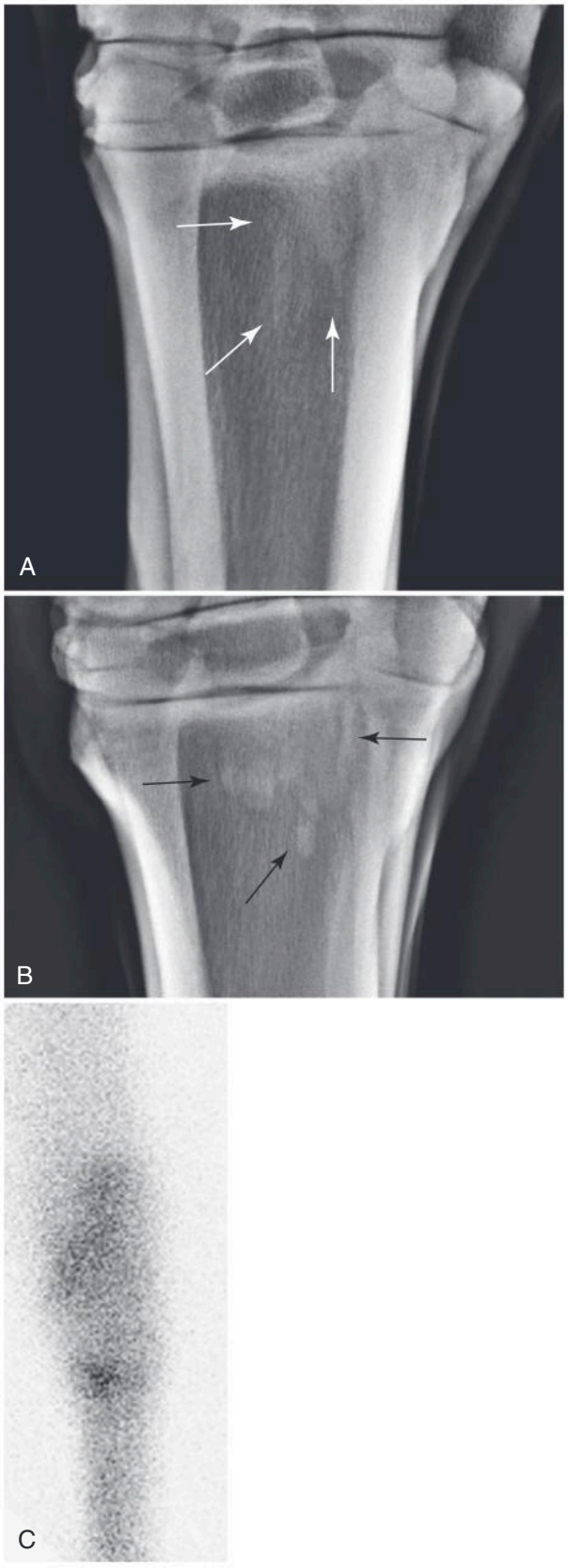
bone normally has a more coarse appearance relative to the remainder of the bone, but the pattern should be uniformly distributed. It is common to see a proximodistally oriented, thin, linear mineral opacity on midline, which may be an incidental finding (Fig. 24.13). Sclerosis of the proximal third metacarpal bone at the attachment of the suspensory ligament may be multifocal or localized to the lateral or medial aspect and can range from mild to severely increased mineral opacity resulting in loss of the normal trabecular bone pattern (Fig. 24.14, eFig. 24.2). Osteolysis may be seen as focal or multifocal regions of decreased mineral opacity at the palmaroproximal cortex of the third metacarpal bone. These radiographic findings may be subtle and more thorough evaluation of the proximal suspensory ligament attachment site may be achieved with collimated projections centered on the proximal one-third of the metacarpus. Abnormal mineral opacity or changes in the trabecular bone pattern will be best seen on the dorsopalmar projection, while endosteal sclerosis and osseous proliferation will be better evaluated on the lateromedial projection. Osseous proliferation or sclerosis at the proximal suspensory ligament attachment site is likely chronic in nature and does not always indicate a source of lameness. When evaluated in Quarter horses, radiographically identified osseous changes on the third metatarsal bone were not predictive of either the presence or severity of proximal suspensory desmopathy, but there was a positive correlation between the severity of radiographic and magnetic resonance imaging (MRI) findings for osseous proliferation and resorption at the ligament attachment site.[19] Avulsion fractures at the attachment site of the suspensory ligament can also occur.[20,21] In these cases, additional projections including collimated dorsopalmar and lateral projections of the proximal aspect of the third metacarpal region can be helpful to better elucidate the fracture line (Fig. 24.15).

Splint Bone Fractures

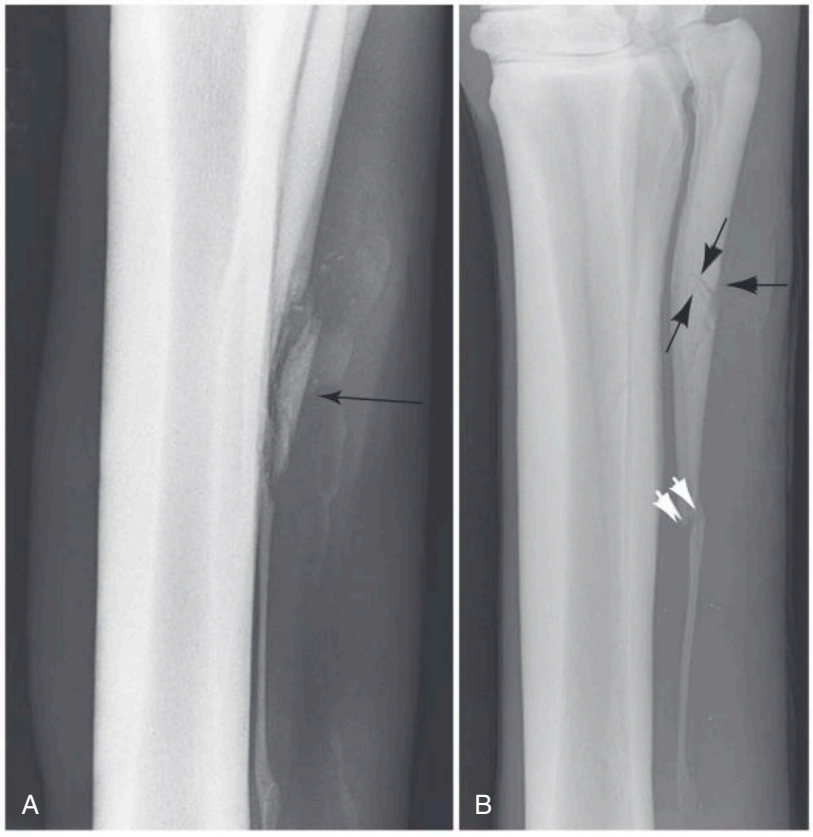
The second and fourth metacarpal and metatarsal bones will be referred to as the splint bones in this section unless otherwise specified. Similar to the third metacarpal bone, the splint bones are particularly prone to external trauma due to their superficial location and limited soft tissue coverage to offer protection. Trauma such as kicks can result in open fractures of the proximal and mid portions of the splint bones, which can lead to osteomyelitis and sequestration. The distal aspect of the splint bones may be abaxially displaced and even fractured in association with desmopathy of the suspensory ligament branches (Fig. 24.16, eFig. 24.3).[22] Nonunion fractures or unfused separate centers of ossifications may be seen in the distal aspects of the splint bones, without clinical relevance. Management of splint fractures depends on the location of the fracture and the weight-bearing status of the bone.[21,23] When a splint bone fracture is clinically suspected, it may be helpful to obtain radiographs at multiple angles of obliquity between lateromedial and dorsopalmar in order to obtain an image with the primary x-ray beam tangential to the fracture margin. Repeated radiographs over time should be evaluated for fracture healing as well as callus development. The position of any excessive callus formation should be taken into consideration as axial protrusion of the callus can impinge upon the suspensory ligament and result in desmopathy and adhesion formation (Fig. 24.17).[14]

Third Metacarpal/Metatarsal Fractures

The third metacarpal bone is a common location for stress fractures in racehorses and sport horses. Stress fractures occur at specific predilection sites along the bone when damage due to repetitive loading accumulates more quickly than can be repaired by the remodeling process. Common stress fractures in the third metacarpal bone include parasagittal groove condylar fractures,[24] sagittally oriented fractures of the palmar, proximal cortex,[25] transversely oriented stress fractures of the palmar, distal cortex,[26] and frontal[27] and sagittal oblique[28]



eFig. 24.2 **A,** Dorsoplantar radiograph of a proximal metatarsal region of a horse with proximal suspensory enthesopathy. Lateral is to the *right.* There is mild diffuse increased radiopacity of the proximolateral aspect of the third metatarsal bone (*white arrows*). **B,** Dorsoplantar radiograph of a proximal metatarsal region of an 8-year-old Warmblood dressage horse with proximal suspensory enthesopathy. Lateral is to the *right.* There are several variably shaped radiopacities superimposed over the proximolateral aspect of the third metatarsal bone (*black arrows*) consistent with entheseous new bone. **C,** Plantar bone/phase scintigraphic image of the tarsus of a 10-year-old horse with lameness localized to the left proximal metatarsal region. A focal region of increased radiopharmaceutical uptake is visible in the proximolateral aspect of the metatarsal area associated with entheseous new bone formation secondary to proximal suspensory desmopathy.



eFig. 24.3 **A,** Dorsomedial/plantarolateral oblique radiograph of the right metatarsal region of a 6-year-old event horse 2 weeks after a kick injury. There is a slightly displaced fracture of the diaphysis of the second metatarsal bone (*black arrow*). **B,** Dorsolateral/plantaromedial oblique image of the right metatarsal region of a 7-year-old event horse several days after injury. There are branching fracture lines at the junction between the proximal and mid thirds of the fourth metatarsal bone (*black arrowheads);* comminution was evident in other views. In addition, there is a simple, slightly displaced, fracture at the junction between the mid and distal thirds of the fourth metatarsal bone (*white arrowheads*).

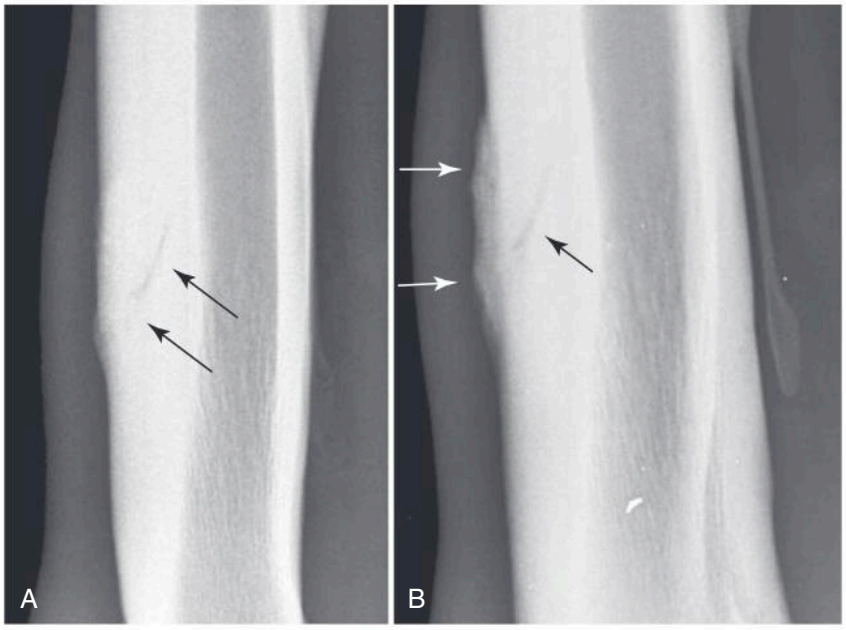


Fig. 24.11 **A,** Lateromedial projection of the mid metacarpus of a 3-year-old Thoroughbred flat racehorse. Dorsal is to the *left.* There is a curved radiolucent line in the dorsal cortex of the third metacarpal bone (*black arrow*s), typical of an incomplete dorsal cortical stress or fatigue fracture with mild overlying soft tissue swelling. **B,** Dorsolateral-palmaromedial oblique radiograph of the mid metacarpal region of the same limb as illustrated in **A**. There is an incomplete dorsal cortical stress fracture (*black arrow*), with extensive periosteal callus (*white arrows*) and overlying soft tissue swelling. There is also a mild endosteal reaction.

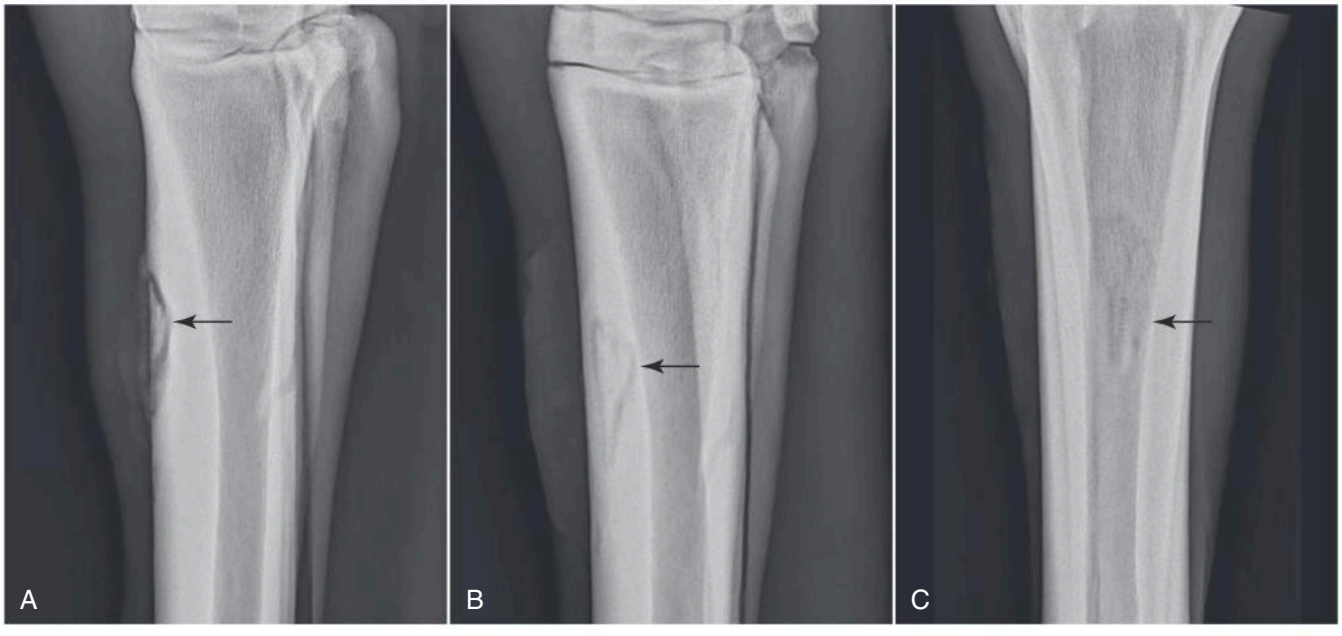


Fig. 24.12 Lateromedial **(A)**, dorsomedial-plantarolateral oblique **(B)**, and dorsoplantar **(C)** projections of the metatarsus. A sequestrum is present on the dorsoproximal aspect of the third metatarsal bone (*arrows*), characterized by a well-defined, thin, oval, sclerotic mineral opacity (sequestrum) surrounded by a radiolucency bordered by sclerotic bone (involucrum), with focal soft tissue thickening and adjacent cutaneous margin irregularity. Note the difference in appearance of the sequestrum depending on the orientation of the x-ray beam relative to the lesion.

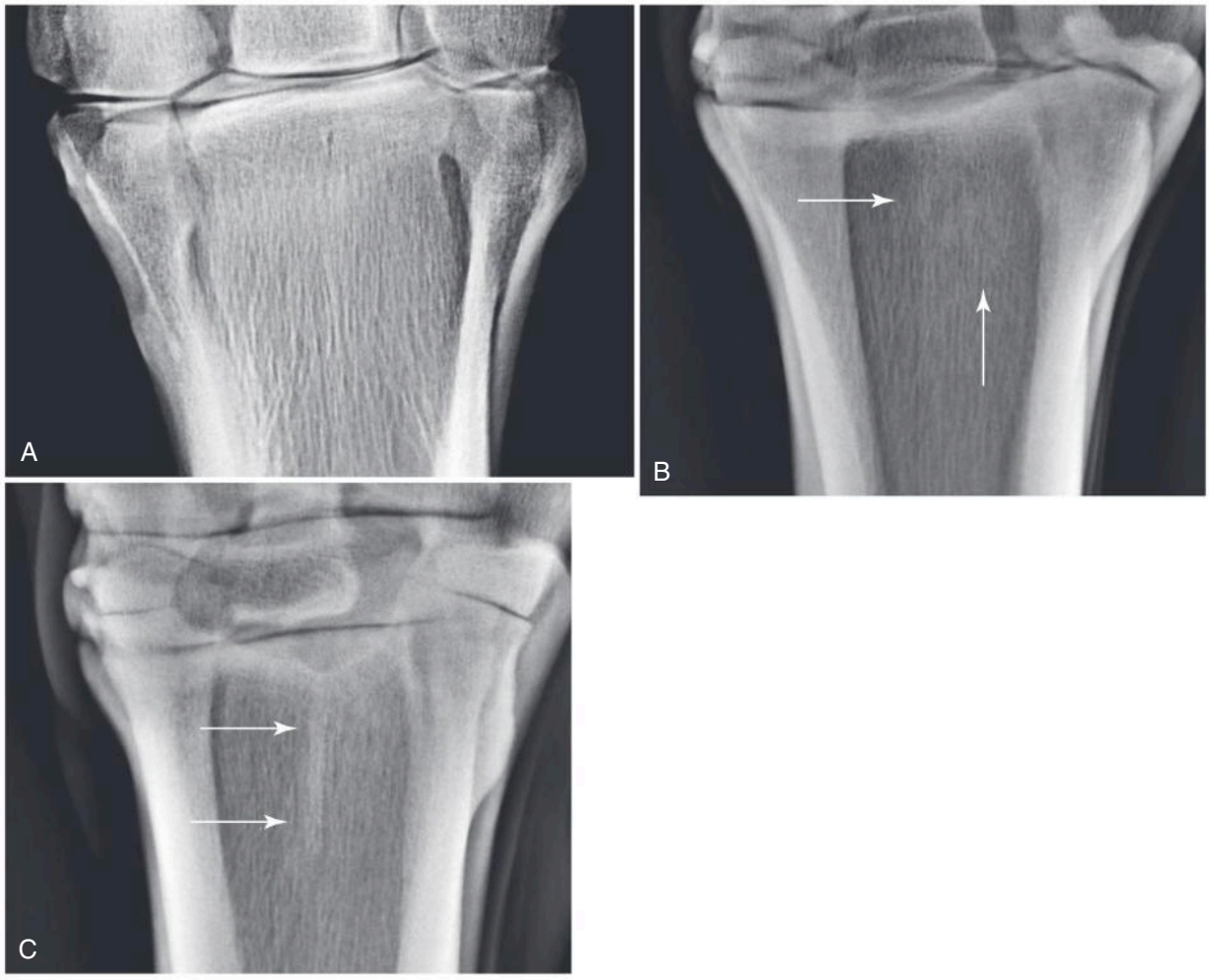


Fig. 24.13 **A,** Dorsopalmar radiograph of a normal proximal metacarpal region. Note the uniform but mildly course trabeculae in the third metacarpal bone. **B,** Dorsoplantar radiograph of a proximal metatarsal region. Lateral is to the *right.* There is mild diffuse increased mineral opacity in the proximolateral aspect of the third metatarsal bone (*white arrows*). This can be an incidental finding. **C,** Dorsoplantar radiograph of a proximal metatarsal region. Lateral is to the *right.* There is a linear axial region of increased opacity in the proximal aspect of the third metatarsal bone (*white arrows*). This can be an incidental finding.

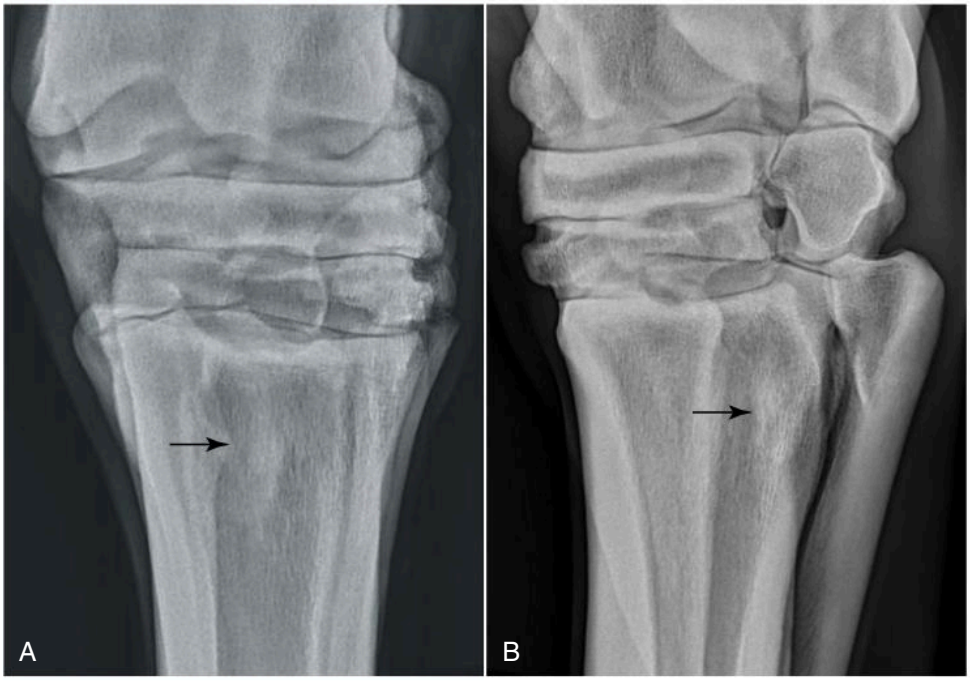


Fig. 24.14 Dorsoplantar **(A)** and dorsolateral-plantaromedial **(B)** projections of the right proximal metatarsus. Lateral is to the *left* on the dorsoplantar projection. There is moderate, ill-de fined and irregular sclerosis of the proximal plantarolateral aspect of the third metatarsal bone, representing chronic enthesopathy at the attachment of the proximal suspensory ligament (*arrow*). Mild to moderate proximal suspensory desmopathy and a small avulsion fracture were identified on concurrent ultrasound examination.

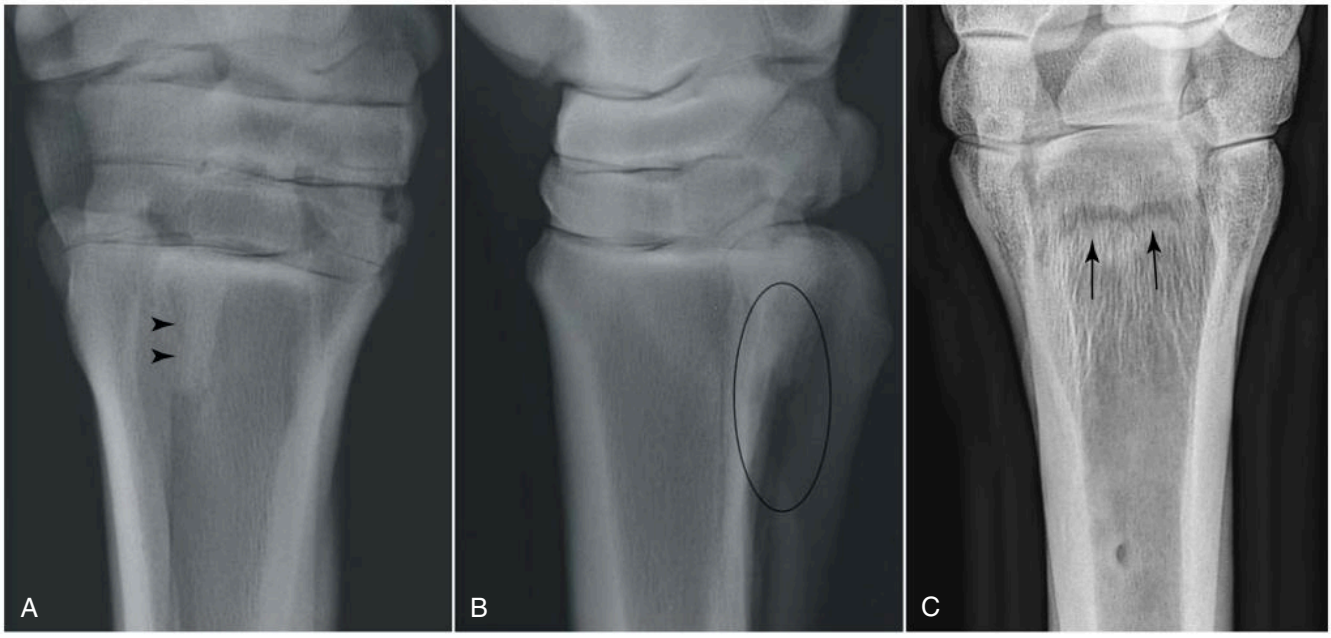


Fig. 24.15 Dorsoplantar (lateral is to the *left*) **(A)** and lateromedial **(B)** projections collimated on the proximal metatarsus. **A,** A sclerotic, ovoid mineral opacity is superimposed on the lateral aspect of the proximal third metatarsal bone (*arrowheads*), with decreased mineral opacity along the distal border. **B,** The lateromedial projection helps to elucidate the fracture margins, and confirms there is an avulsion fracture fragment separated from the plantar cortex of the third metatarsal bone (*circled*). **C,** Dorsopalmar radiograph of a proximal metacarpal region of an elite horse. Lateral is to the *right.* There are broad curved radiolucent lines (*black arrows*) in the proximal aspect of the third metacarpal bone representing avulsion fracture of the origin of the suspensory ligament from the palmar aspect of the third metacarpal bone.

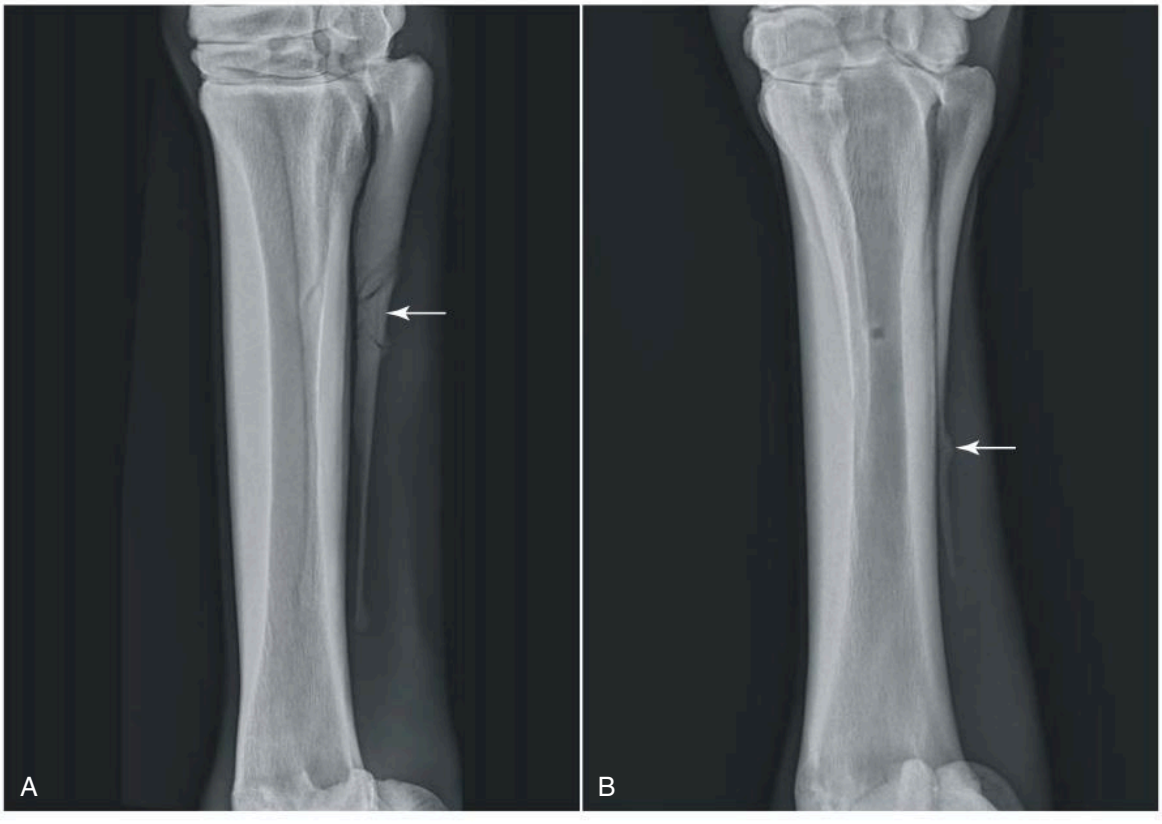


Fig. 24.16 **A,** Dorsolateral-plantaromedial oblique projection of the metatarsus, dorsal is to the *left.* There is a sharply margined, comminuted fracture of the fourth metatarsal bone mid body due to trauma (*arrow*). **B,** Dorsolateral-palmaromedial oblique projection of the right metacarpus of a Standardbred racehorse with a chronic fracture of the distal body of the fourth metacarpal bone (*arrow*) in association with severe, suspensory body and biaxial branch desmopathy. The most distal aspect of the second and fourth metacarpal bones had been previously excised.



Fig. 24.17 **A,** Dorsolateral-palmaromedial oblique projection of the metacarpus. At the proximal to mid fourth metacarpal bone, there is spiculated, osseous proliferation (*arrow*) and associated, moderate soft tissue thickening. **B,** Transverse plane ultrasound image of the lateral aspect of the suspensory ligament body at the level of the exostosis (*asterisk*), made with a linear transducer. Dorsal is to the *left.* There is focal enlargement of the lateral aspect of the suspensory ligament body, with hypoechogenicity and fiber pattern disruption (*arrow*). **C,** Transverse plane ultrasound image at the same level as **B** using an oblique angle of insonation. Dorsal is to the *left.* The ligament fibers are hypoechoic due to anisotropism and fiber pattern disruption can be seen (*arrow*). The exostosis was surgically removed and marked focal desmopathy of the suspensory ligament was noted intraoperatively.

fractures of the dorsal cortex (Fig. 24.18). Evidence of osseous remodeling may precede fracture formation and includes endosteal or trabecular bone sclerosis, osseous proliferation and/or lysis, and concurrent soft tissue thickening or joint effusion. Recognizing incomplete fractures as early as possible is imperative because they may progress to complete catastrophic fractures. Radiographic projections in which the primary x-ray beam is tangential to the fracture line will be most diagnostic; thus, special radiographic projections may be helpful in addition to the standard series. When evaluating for incomplete condylar fractures, more thorough evaluation includes a dorsopalmar projection of the joint in flexion or a dorsodistal-palmaroproximal oblique projection.[29,30] Even with ideal positioning, however, fractures may not be radiographically apparent for 10 to 14 days and, even then, may be subtle. For thorough evaluation of cases in which stress fractures are clinically suspected, but not identified radiographically, alternative imaging such as nuclear scintigraphy or positron emission tomography (PET) should be considered.

OTHER IMAGING TECHNIQUES

Alternative imaging modalities such as ultrasonography, computed tomography (CT), MRI, nuclear scintigraphy, and PET serve as a complement to radiography in the metacarpus, when clinically indicated and available.

Ultrasonography

Ultrasound is commonly performed of the palmar metacarpus and provides a widely accessible, portable, and practical approach for more thorough evaluation of soft tissues. The superficial nature of the palmar soft tissues of the metacarpus makes ultrasound ideal for evaluation of this region when performed by experienced ultrasonographers.

When preparing for transcutaneous ultrasonography, adequate preparation of the site is imperative and should include clipping the hair, thoroughly cleaning the skin, and applying acoustic coupling agents such as alcohol and/or ultrasound gel. Two techniques are commonly utilized for

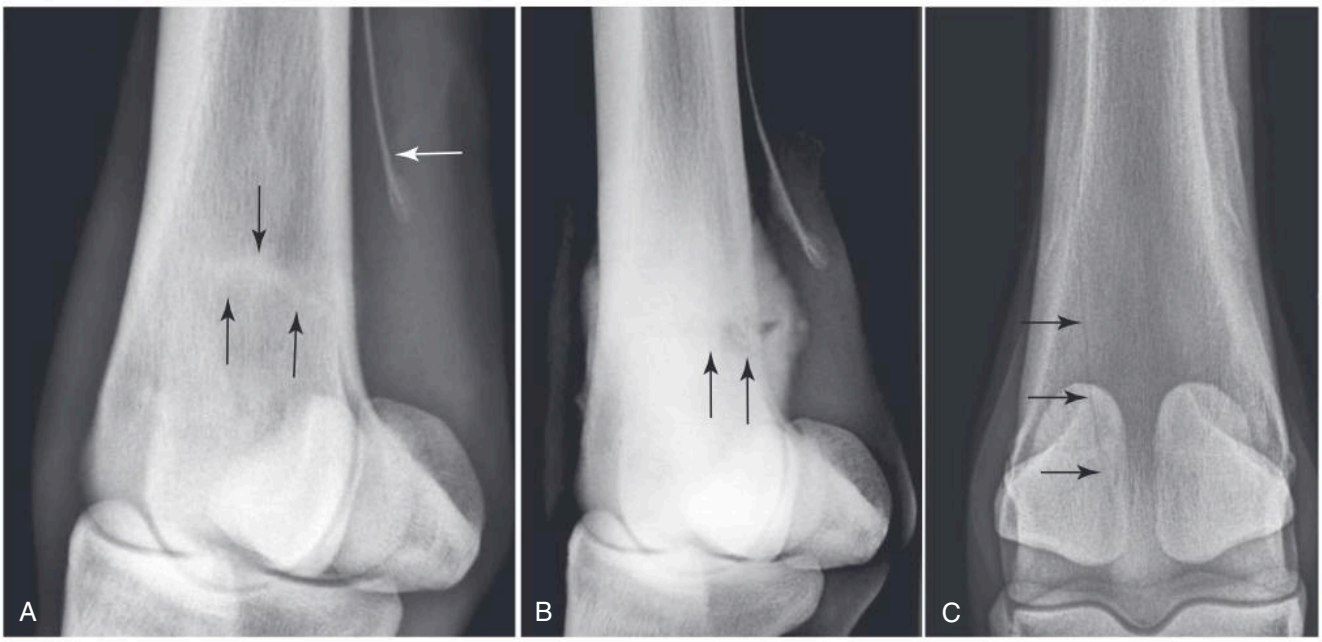


Fig. 24.18 **A,** Dorsolateral/palmaromedial oblique radiograph of a distal metacarpal region of a 3-year-old Thoroughbred flat racehorse, 3 days after the onset of acute severe lameness associated with soft tissue swelling and focal pain in the distal palmarolateral aspect of the metacarpal region. The distal aspect of the fourth metacarpal bone is distorted in shape (*white arrow*) because of the soft tissue swelling. There is an ill-defined transverse radiopaque line (*black arrows*) in the palmar aspect of the third metacarpal bone. This is a distal metaphyseal stress fracture. **B,** Dorsolateral/palmaromedial oblique radiograph of the distal metacarpal region of the same horse as in **A**, 30 days after the onset of acute severe lameness. There is increased bowing of the distal aspect of the fourth metacarpal bone because of extensive periosteal callus on the palmar aspect of the third metacarpal bone. There is also periosteal callus dorsomedially. There is diffuse increased radiopacity of the cancellous bone in the metaphyseal region of the third metacarpal bone and an ill-defined transverse radiolucent line (*black arrows*) toward the palmarolateral aspect of the third metacarpal bone. **C,** Dorsoplantar projection of the right distal metatarsus. Lateral is to the *left.* An ill-defined, incomplete lateral condylar stress fracture is present (*black arrows*). (Image courtesy Dr. Margret Thompson, Cornell University.)

evaluating different regions of the metacarpus and metatarsus, including measuring the distance from the point of the hock or accessory carpal bone to the area of interest or using defined anatomical regions or zones.[10,31] A systematic approach should be followed for each exam. Structures should be evaluated in both transverse (short axis) and longitudinal (long axis) planes, with consistent transducer orientation and comparison to the contralateral limb. For evaluation of the palmar metacarpus, a linear transducer with a frequency range of 8 to 15 megahertz is an ideal starting point; however, it is recommended to use the highest frequency possible while still achieving the depth penetration needed to image the entire area of interest. Use of an acoustic standoff pad is necessary to eliminate the effect of near-field artifact when evaluating more superficial structures. Frequency, focal zones, gain, and depth should be routinely adjusted as needed to maximize image quality. Recognizing ultrasound artifacts including, but not limited to, edge shadowing, distal acoustic enhancement, and distal acoustic shadowing is essential for accurate image interpretation. Anisotropism is a particularly important principle to understand with regard to musculoskeletal imaging. It explains the effect that the incident angle of the ultrasound beam has on the appearance of fibrillar structures such as tendons or ligaments.[31] When the ultrasound beam is perpendicular to such structures, the majority of sound is reflected and echogenicity is maximized, and when the angle of insonation is decreased, the echogenicity of that structure is decreased, and the tendon or ligament will appear hypoechoic (Fig. 24.19).[32] This artifact can be helpful in differentiating tissue types such as fat or fascia surrounding a tendon or ligament. Without a thorough understanding of this phenomenon, areas of hypoechogenicity due to decreased angles of insonation can be falsely interpreted as pathology.

Sonographic anatomy and technique for evaluation of the palmar metacarpus and metatarsus have been described.[8,10,33–36] In the palmar metacarpus, the superficial and deep digital flexor tendons, accessory ligament of the deep digital flexor tendon, and the suspensory ligament are easily identified, and synovial structures such as the digital sheath can be evaluated (Fig. 24.20). In order to optimize imaging parameters, it is ideal to evaluate the more superficial structures (superficial and deep digital flexor tendons) independently of the deeper structures (accessory ligament of the deep digital flexor tendon and suspensory ligament body), and the suspensory ligament branches should be evaluated from the bifurcation of the suspensory ligament to their insertion on the proximal sesamoid bones using a medial and lateral approach.[33] For the more superficial structures, such as the superficial digital flexor tendon and suspensory ligament branches, a standoff pad should be used.[31,33] The metacarpus should be carefully evaluated from a medial and lateral approach in addition to a palmar approach in order to include the peripheral margins of the soft tissue structures, and to evaluate for peritendinous or periligamentous tissue proliferation.

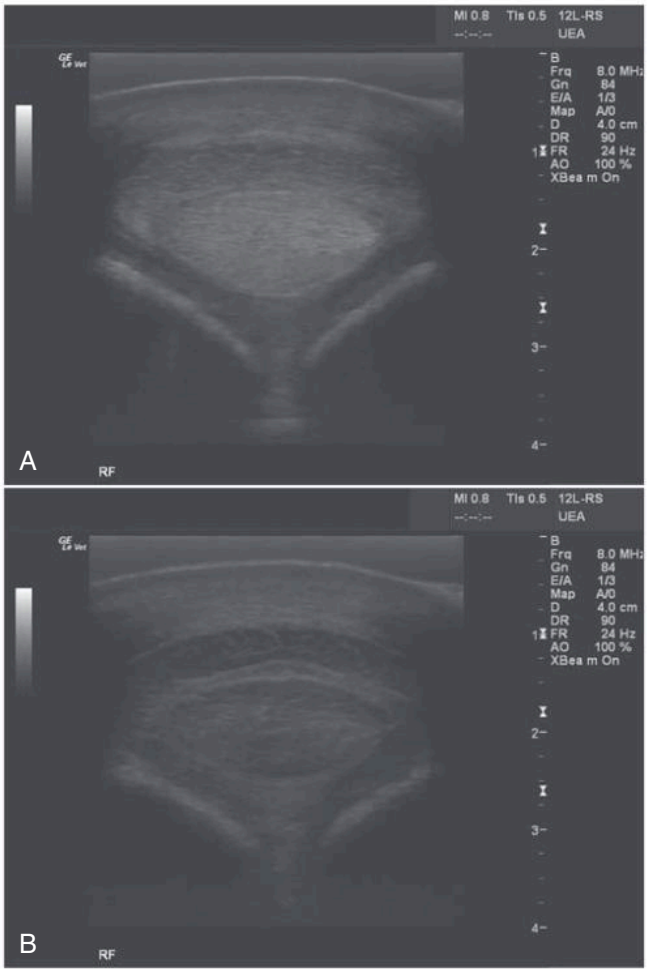


Fig. 24.19 Transverse plane ultrasound images of the distal metacarpus using a linear transducer at the level of the proximal sesamoid bones. Lateral is to the *right*. Images demonstrate the principal of anistropism. **A,** The ultrasound beam is oriented perpendicular to the superficial and deep digital flexor tendon fibers and echogenicity of the flexor tendons is maximized. **B,** The ultrasound beam is oriented obliquely to the long axis of the tendons and the echogenicity of the flexor tendons is decreased relative to **A**.

Abnormal sonographic findings in the equine metacarpus may include focal or diffuse ligament or tendon enlargement, margin irregularity/tearing, or changes in echogenicity. Cross-sectional area measurements can be obtained to objectively measure size and to compare these measurements over time, and normal measurements have been reported in the metacarpus/metatarsus.[37–39] Tendon or ligament hypoechogenicity, termed *core lesions* when they occur centrally, may result from areas of fiber pattern irregularity, edema, or hematoma formation and can be focal or diffuse. Focal regions of increased tendon or ligament echogenicity may result from scar tissue/fibrin formation or mineralization. The use of color and power Doppler interrogation has been described as a complement to B-mode ultrasound evaluation of tendons and ligaments in the metacarpus and may be helpful for assessment of healing[40–42] (Fig. 24.21).

Superficial digital flexor tendinopathy is the most common tendon injury in athletic horses and frequently involves tendon enlargement and palpable heat, pain, and swelling in the mid metacarpus. Sonographic findings often include focal areas of hypoechogenicity centrally or peripherally within the tendon; however, diffuse hypoechogenicity throughout a region of the tendon may also occur (Fig. 24.22). Although the mid metacarpal region is most commonly affected, superficial digital flexor tendinopathy can occur at the most proximal aspect of the tendon,[43] as well as in the carpal canal of middle-aged to older horses, where it is often characterized by focal, palmar hypoechogenicity.[44] Less commonly, lesions of the superficial digital flexor tendon may be seen at the level of the digital sheath.[45]

Deep digital flexor tendinopathy is often located at the level of the digital sheath, and may have concurrent digital sheath effusion and/or tenosynovitis.[46] Most commonly, lesions consist of marginal tears. Hypoechoic lesions, which may extend to the tendon periphery, tendon enlargement, and perilesional tissue proliferation, may be seen (Fig. 24.23).[47] The pathology of the manica flexoria may also be seen in the digital sheath and includes asymmetry, heterogeneous echogenicity, lack of margin definition, partial or complete tears, abnormal sliding of the deep and superficial digital flexor tendons, and displacement of the superficial digital flexor tendon on dynamic exam.[45,48] Complete evaluation of the tendons in the digital sheath is challenging. Evaluation from a medial and lateral approach in addition to a palmar approach is important for margin

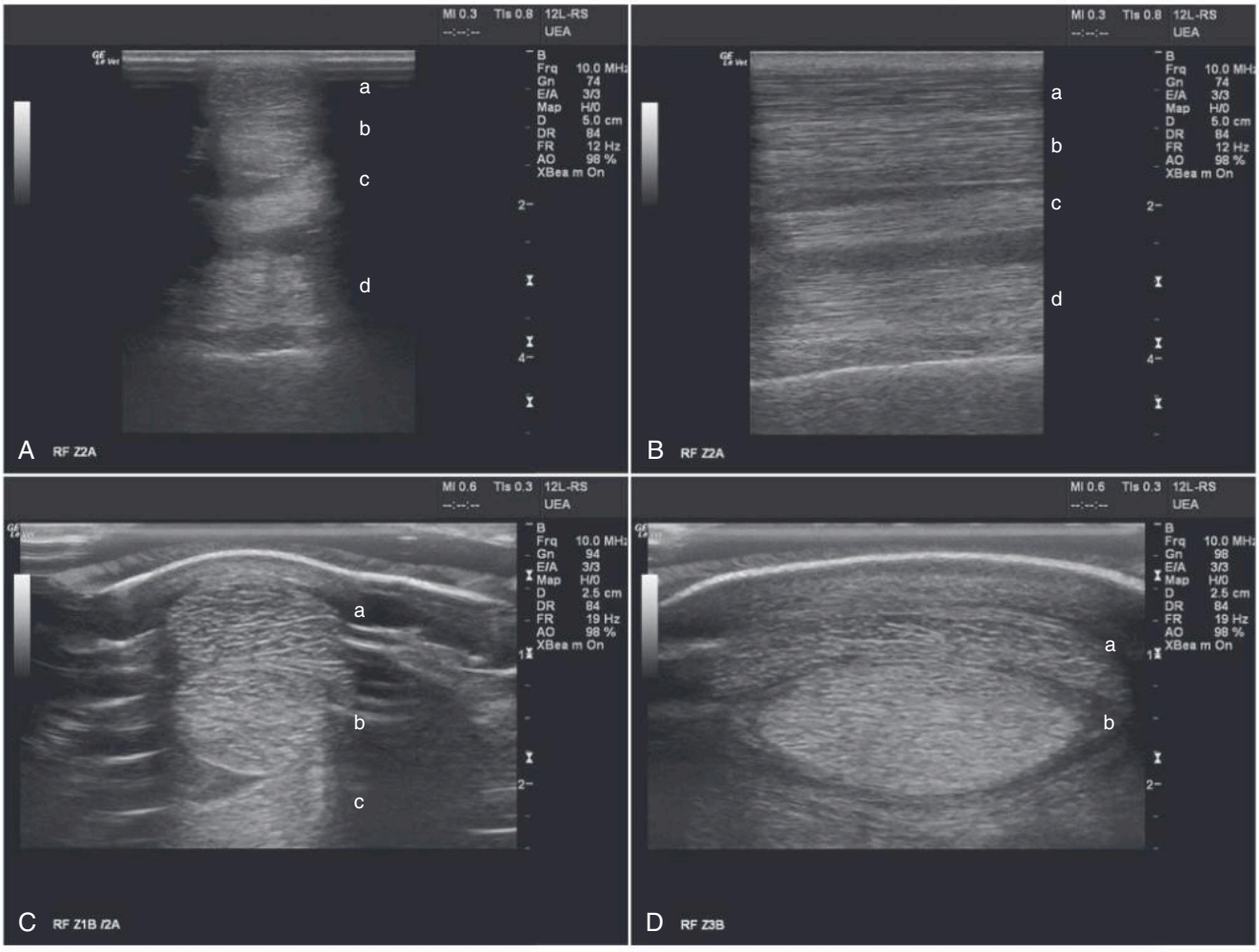


Fig. 24.20 **A—C,** Ultrasound images of the proximal metacarpus (zone 2A) obtained with a linear transducer. Transverse plane image (medial is to the *left*) **(A)** and longitudinal **(B)** plane image (proximal is to the *left*) optimized for the suspensory ligament and accessory ligament of the deep digital flexor tendon. **C,** Transverse plane image optimized for the superficial and deep digital flexor tendons. Note the change in position of the focal zones and decreased image depth when evaluating the more superficial structures. **D,** Transverse plane ultrasound image at the level of the distal metacarpus (zone 3B) obtained with a linear transducer. Anatomy for **A—D** is labeled as follows: *a,* superficial digital flexor tendon; *b,* deep digital flexor tendon; *c,* accessory ligament of the deep digital flexor tendon; *d,* suspensory ligament.

evaluation, scanning the limb in a non—weight-bearing position and dynamic evaluation is helpful.[45] Ultrasonography has been reported to have limited sensitivity and specificity for lesion identification in the digital sheath and some lesions may only be identified using tenoscopy.[47]

Desmopathy of the accessory ligament of the deep digital flexor tendon is relatively common in the forelimb,[49—51] and less commonly reported in the hindlimb.[8,10,33,35,36,38] Pathology can be focal or diffuse and often results in characteristic lateralized, mid metacarpal soft tissue swelling. However, pathology has been reported to be localized to the proximal aspect of the ligament at the level of the distal carpus and proximal metacarpus, without concurrent, palpable swelling.[52] Comprehensive evaluation of the accessory ligament of the deep digital flexor tendon should include both a palmar and lateral approach. Sonographic findings include diffuse or focal ligamentous enlargement, which may result in contact with the suspensory ligament and/or superficial digital flexor tendon, loss of margin definition, peripheral tears along the lateral border, or heterogeneous or hypoechoic regions (Fig. 24.24).

Desmopathy of the suspensory ligament may occur anywhere from the proximal attachment to the branches. The cortical surface of the third metacarpal or metatarsal bone at the proximal attachment and proximal sesamoid bones, at the insertion of the branches, should be carefully evaluated for evidence of enthesopathy or avulsion fractures.[17] Proximal suspensory desmopathy can present a diagnostic challenge as the close proximity to the distal tarsal joints reduces the specificity of diagnostic analgesia in this region and the complex anatomy of the ligament makes ultrasound evaluation particularly challenging. MRI is the gold standard for evaluation of the ligament; however, ultrasound has been shown to be reliable for detection of suspensory ligament pathology.[53] Comprehensive ultrasound evaluation of the proximal suspensory ligament should include the use of non—weight-bearing positioning and off angle insonation to help evaluate the ligament margins and distinguish the ligament fibers from the internal fat and muscle bundles and surrounding fascia (Fig. 24.25).[31] In the metatarsus, optimal evaluation of the proximal suspensory ligament is achieved from a

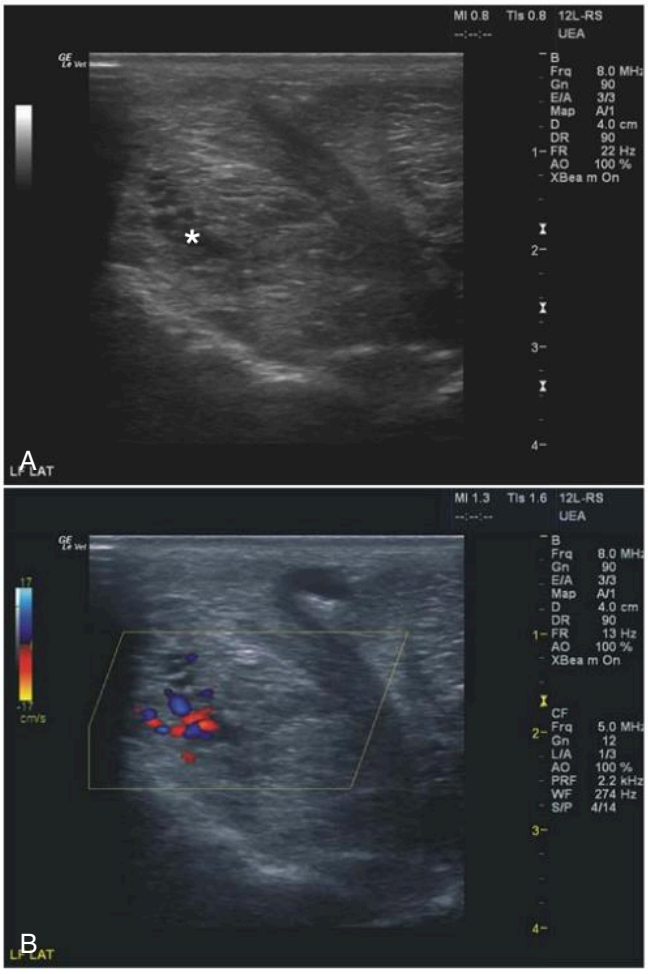


Fig. 24.21 **A,** Transverse plane ultrasound image of the suspensory ligament body in the mid metacarpus obtained with a linear transducer and dorsal is to the *left.* A focal region of decreased echogenicity and fiber disruption is present in the suspensory ligament body (*arrow*). **B,** Same ultrasound image as in **A** with the addition of color Doppler interrogation. Moderate Doppler signal is present at the level of the lesion, indicative of increased vascularity at this site.

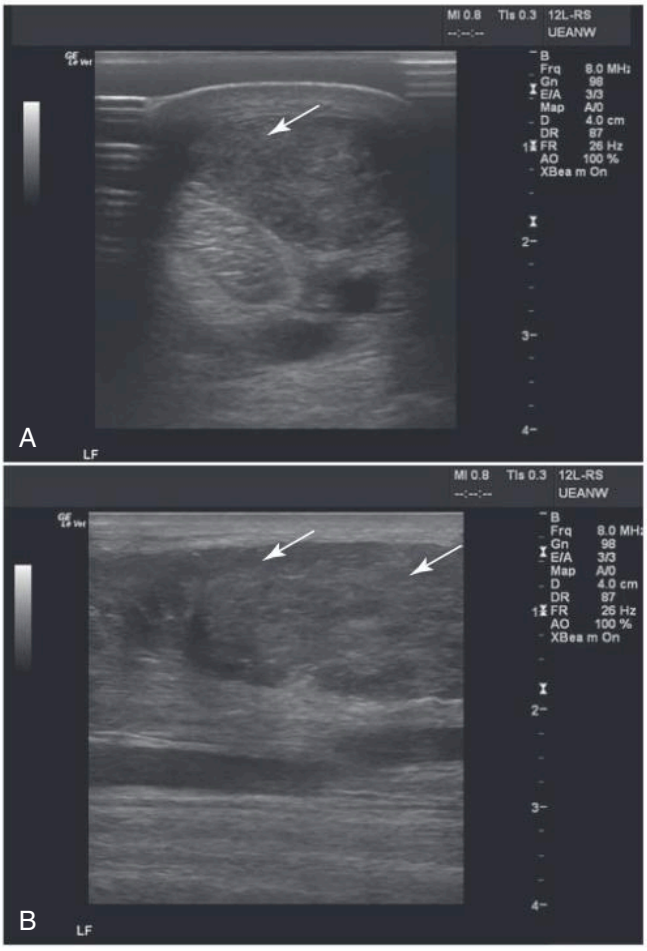


Fig. 24.22 **A,** Transverse plane ultrasound image of the left mid metacarpus acquired with a linear transducer. Lateral is to the *left.* **B,** Longitudinal plane ultrasound images of the left mid metacarpus acquired with a linear transducer. Proximal is to the *left.* In both images, severe, extensive fiber disruption and enlargement of the superficial digital flexor tendon is present (*arrows*).

plantaromedial approach, just distal to the chestnut rather than from a true plantar approach.[31,36] Common findings of pathology in the region of the suspensory ligament origin and body include enlargement, bulging of the palmar/plantar margin or an ill-defined dorsal margin and changes in echogenicity of the ligamentous fibers, and loss of the normal fat and muscle distribution (Fig. 24.26).[10] Dorsal margin irregularity and enlargement are often best seen in the non–weight-bearing position using off angle insonation.[10] Pathology of the suspensory ligament branches may include enlargement, margin irregularity or tears, areas of increased or decreased echogenicity, and periligamentous tissue proliferation (Fig. 24.27). Desmopathy may be biaxial. It is important to note that sonographic abnormalities of the suspensory branches can be seen in nonlame horses.[17] Due to the subsynovial location of a portion of the suspensory ligament branches, concurrent pathology of the metacarpophalangeal joint should be evaluated.[11]

Computed Tomography and Magnetic Resonance Imaging

Cross-sectional imaging, such as CT and MRI, often provide a valuable complement to radiography of the metacarpus. With increasing availability of these modalities, and ability to image the equine limb without general anesthesia, the utility of these modalities is becoming more apparent. MRI is generally considered the gold standard for soft tissue evaluation due to its superior contrast resolution, and allows for evaluation of increased osseous fluid content such as secondary to contusion, edema, or necrosis.[9,54,55] CT allows for rapid cross-sectional image acquisition and provides excellent contrast and spatial resolution. Because it eliminates the challenges of radiographic superimposition, CT allows for more complete evaluation of complex anatomical structures, and may be more sensitive for identification of subtle osseous pathology that may not be radiographically apparent (Fig. 24.28). Both CT and low-field-strength MRI can be performed in the standing horse; however, more complete MRI evaluation of the metacarpus and metatarsus requires general anesthesia to limit the motion artifact inherent in the standing horse.

Nuclear Scintigraphy and Positron Emission Tomography

Both nuclear scintigraphy (^{99m}Tc-diphosphonate) and PET (^{18}F-sodium fluoride) can be highly sensitive at identifying areas of rapid bone turnover by accumulating at sites where the hydroxyapatite matrix is exposed. The scintigraphic

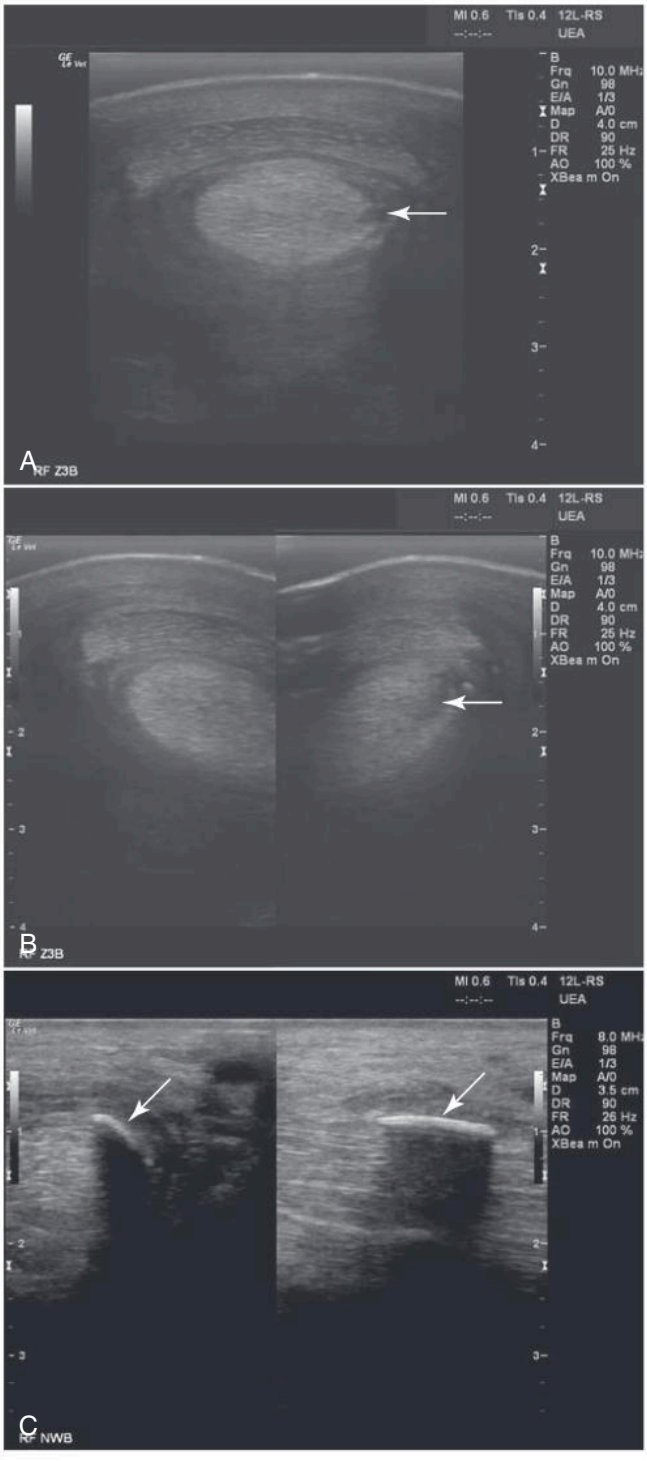


Fig. 24.23 **A,** Transverse plane ultrasound images of the right distal metacarpus at the level of the digital sheath, just proximal to the proximal sesamoid bones, acquired with a linear transducer. Lateral is to the *right.* **B,** Side by side images of the medial aspect (*left*) and lateral aspect (*right*) of the distal metacarpus, at the same level as **A**. The lateral aspect of the deep digital flexor tendon has focal moderate fiber abnormalities that extend to the lateral margin (*arrow*). The adjacent lateral aspect of the superficial digital flexor tendon is mildly to moderately enlarged with mild to moderate fiber abnormalities and focal dystrophic mineralization. **C,** Transverse plane (*left*) and longitudinal plane (*right*) non−weight-bearing images of the superficial and deep digital flexor tendons at the same level as **A** and **B**. A well-defined, hyperechoic linear region of mineralization with distal acoustic shadowing is seen in the lateral periphery of the superficial digital flexor tendon (*arrow*).

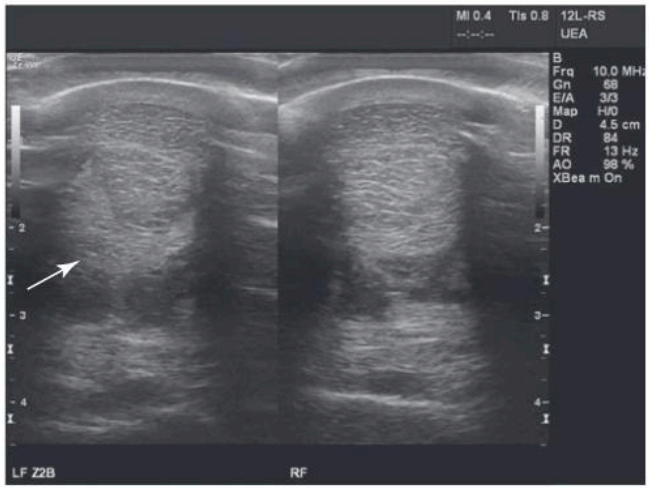


Fig. 24.24 Transverse plane, side-by-side ultrasound images of the left (lateral is to the *left*) and right (lateral is to the *right*) proximal metacarpus acquired with a linear transducer. The left fore accessory ligament of the deep digital flexor tendon is moderately and diffusely enlarged without distinct fiber abnormalities (*arrow*).

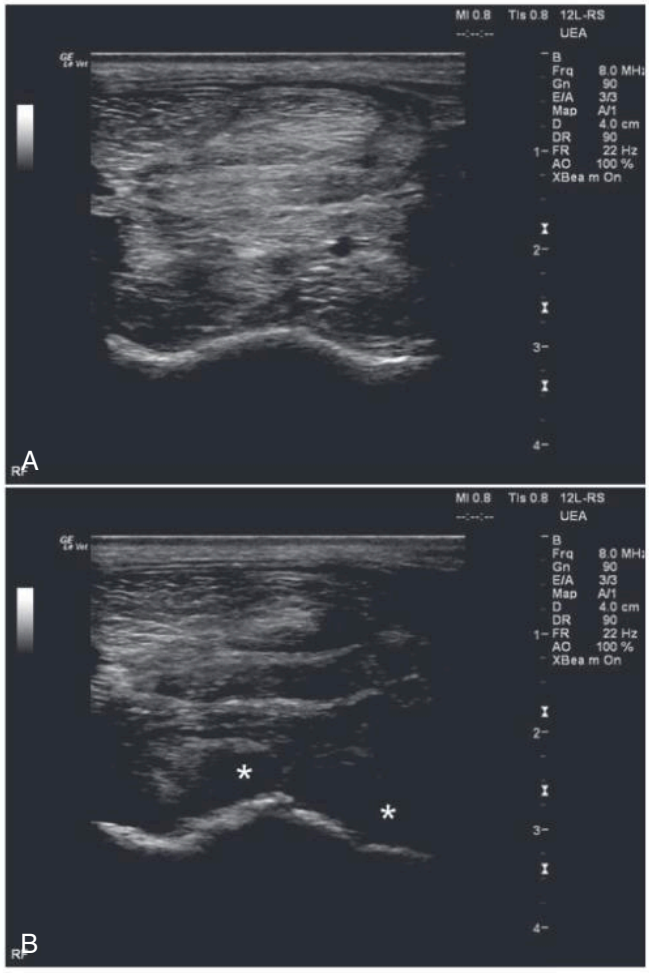


Fig. 24.25 **A and B,** Transverse plane ultrasound images of the proximal aspect of the right fore suspensory ligament with the limb non-weight-bearing. Lateral is to the *right.* **A,** The ultrasound beam is perpendicular to the long axis of the limb. **B,** Ultrasound beam is obliquely oriented relative to the long axis of the limb. Using this technique, the ligament fibers are hypoechoic (*asterisks*) and can be distinguished from the more hyperechoic, internal fat and muscle bundles, and surrounding fascia.

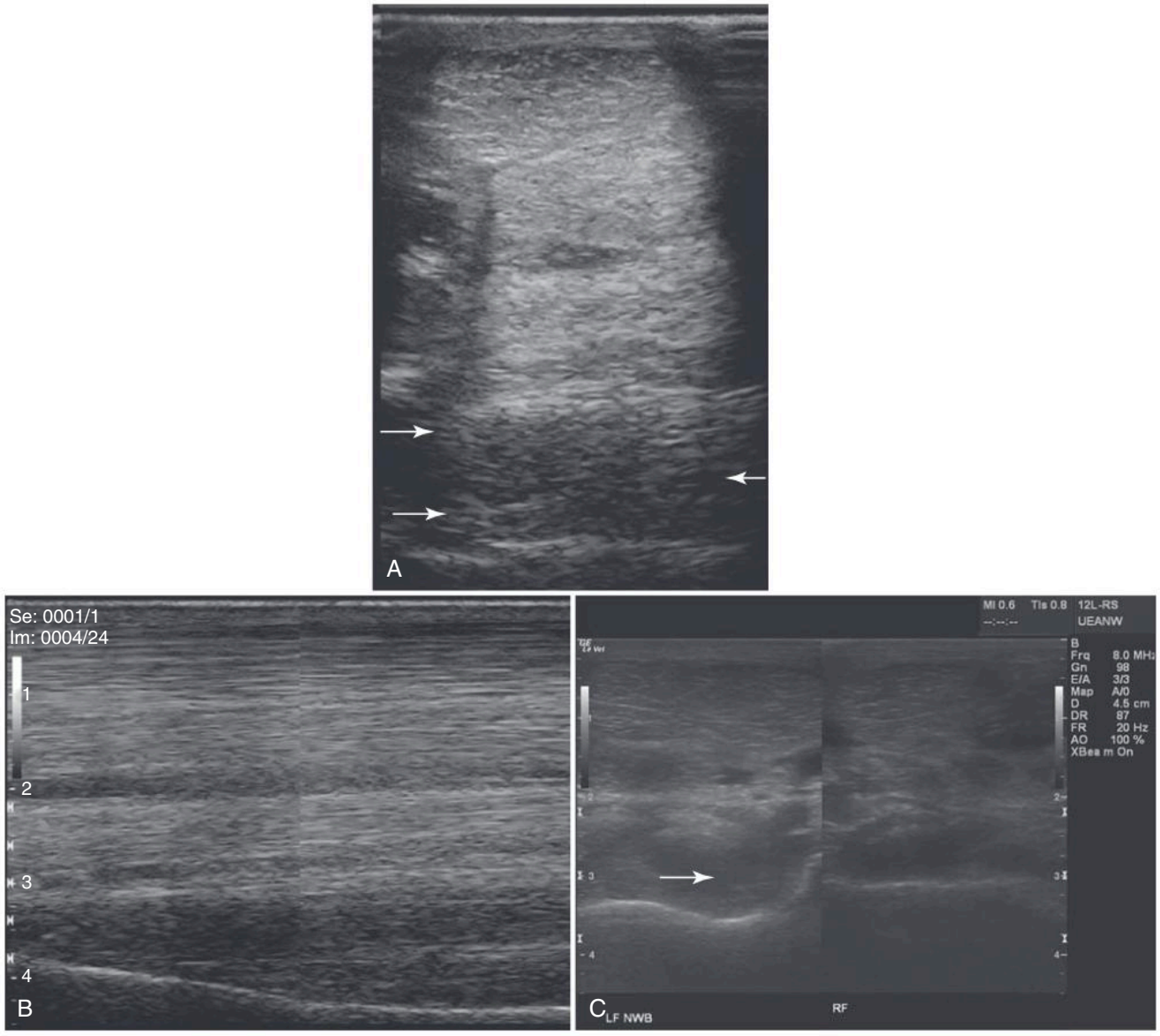


Fig. 24.26 **A,** Transverse ultrasonographic image of a proximal metatarsal region obtained using a virtual convex array transducer. Medial is to the *left*. The suspensory ligament is enlarged (*arrows*) and has a diffuse reduction in echogenicity dorsally. **B,** Longitudinal ultrasonographic image of the proximal metatarsal region of the same limb as in **A**. Proximal is to the *left*. There is marked loss of echogenicity and long parallel linear echos in the proximal aspect of the suspensory ligament. **C,** Transverse plane, comparative ultrasound images of the left and right fore proximal suspensory ligaments using a split screen. The left fore proximal suspensory ligament is to the *left* (medial is to the *right*) and the right fore proximal suspensory ligament is to the *right* (medial is to the *left*). The limbs are imaged non–weight-bearing using off-angle insonation. The medial lobe of the left fore proximal suspensory ligament is moderately enlarged with moderate fiber abnormalities in the dorsal portion of the ligament causing palmar displacement of the fat and muscle bundle (*arrow*). The normal right fore proximal suspensory ligament is included for comparison.

appearance of the third metacarpal and metatarsal bones and common pathology in this region have been described.[12,56–60] While nuclear scintigraphy is very sensitive for identifying regions of bone turnover, findings are rarely specific for pathology and may not indicate the source of pain or lameness (Fig. 24.29). Scintigraphic findings must be correlated with clinical signs, response to diagnostic analgesia, and other imaging findings.

Limited information is available regarding the utility of PET in equine musculoskeletal imaging; however, given its tomographic nature, high sensitivity for identifying bone turnover, and the ability to colocalize images with other modalities, it is likely to become increasingly more prevalent (Fig. 24.30). [61–64] Further, ^{18}F-fluorodeoxyglucose PET can provide functional information about soft tissue structures and has been used to identify metabolically active deep digital flexor tendon (DDFT) lesions in horses.[65] Both nuclear scintigraphy and PET are available in the standing horse, eliminating the risk of injury during recovery. Currently available equine PET scanners can only image the appendicular skeleton distal to the level of the antebrachium and distal tibia while whole body evaluation is possible with nuclear scintigraphy.

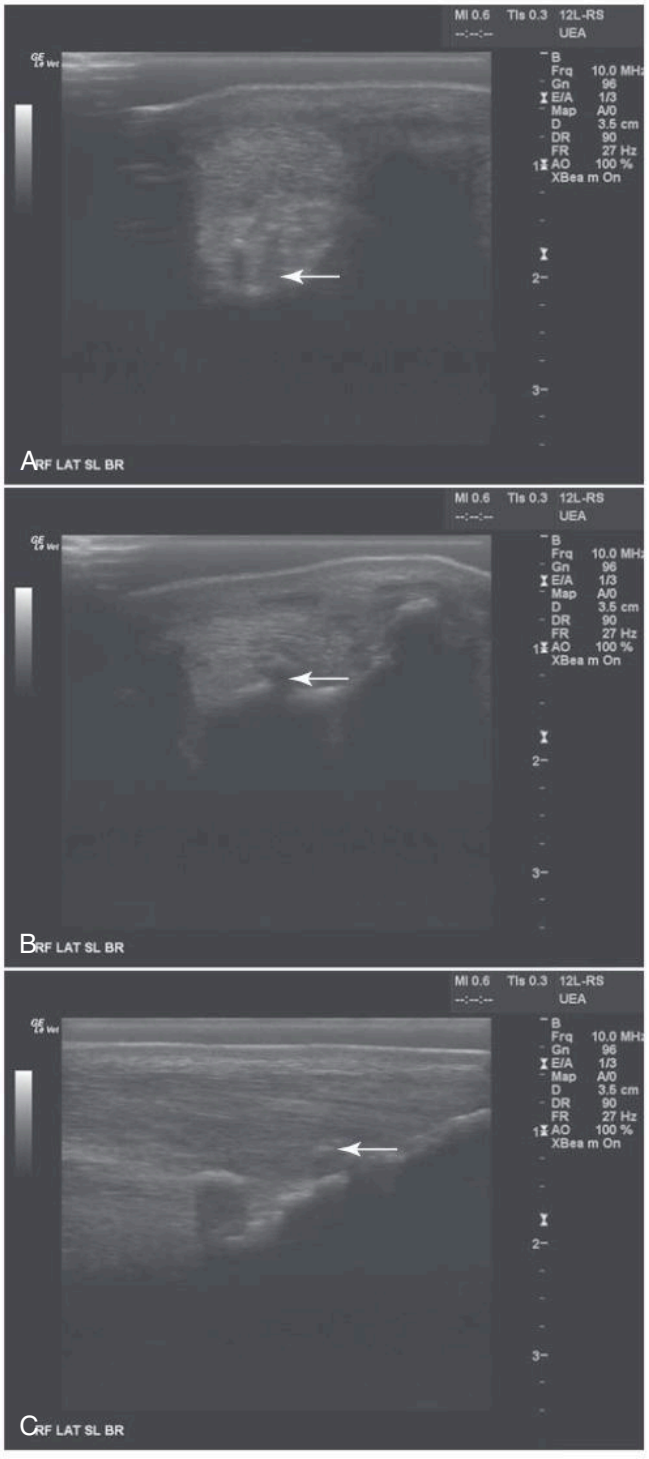


Fig. 24.27 **A and B,** Transverse plane ultrasound images of the lateral suspensory ligament branch made with a linear transducer. Dorsal is to the *left.* **A,** The mid aspect of the lateral suspensory ligament branch has multifocal, mild to moderate fiber abnormalities, hyperechoic foci with distal acoustic shadowing (*arrow*), moderate enlargement and mild to moderate periligamentous tissue proliferation. **B,** The distal aspect of the suspensory ligament branch near the insertion on the proximal sesamoid bone. Mild to moderate fiber abnormalities are present (*arrow*). **C,** Long axis image of the right fore lateral suspensory ligament branch insertion on the lateral, proximal sesamoid bone. Proximal is to the *left.* There is moderate to marked enthesopathy characterized by proliferation, avulsion fragments, and/or dystrophic mineralization (*arrow*) at the attachment to the sesamoid bone.

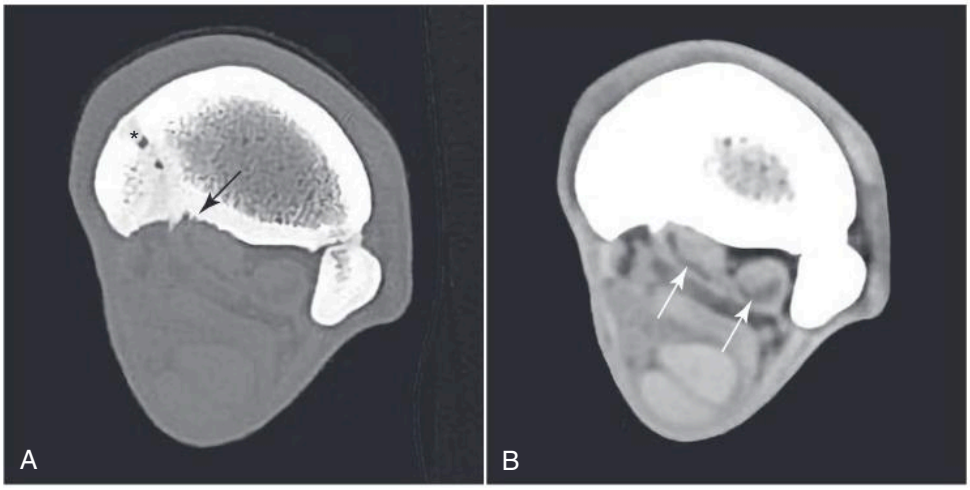


Fig. 24.28 Transverse plane computed tomography (CT) images of the proximal metacarpal region in bone (**A**) and soft tissue (**B**) algorithms. Lateral is to the *right.* **A,** Subtle osseous proliferation and resorption are present along the palmar medial aspect of the third metacarpal bone at the attachment of the medial lobe of the proximal suspensory ligament (*arrow*). Mineralization of the interosseous ligament between the second and third metacarpal bones is also noted (*asterisk*). **B,** Using a soft tissue algorithm, it is possible to differentiate between the ligamentous tissue and the hypoattenuating, fat/muscular portions of the proximal suspensory ligament (*arrows*).

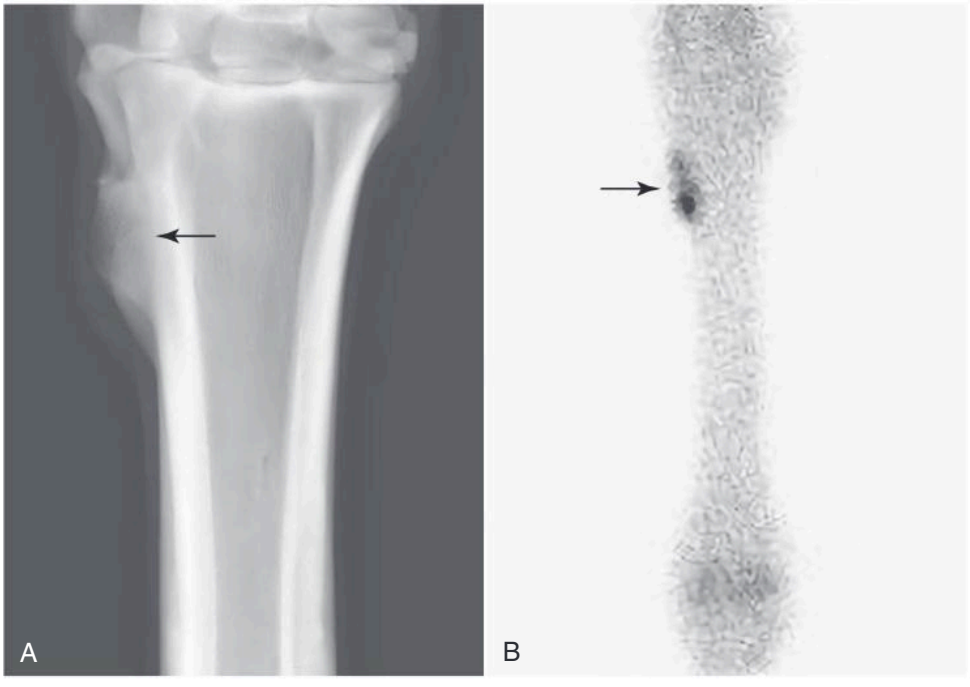


Fig. 24.29 **A**, Dorsoplantar radiograph of the left proximal metatarsus. Lateral is to the *left.* A smooth, well-defined exostosis is present along the proximal lateral aspect of the fourth metatarsal bone. **B,** Plantar nuclear scintigraphic image of the left metatarsus of the same horse. Lateral is to the left. Focal, moderate increased radiopharmaceutical uptake is identified in the region of the exostosis (*arrow*). This lesion was nonpainful on palpation, without associated lameness.

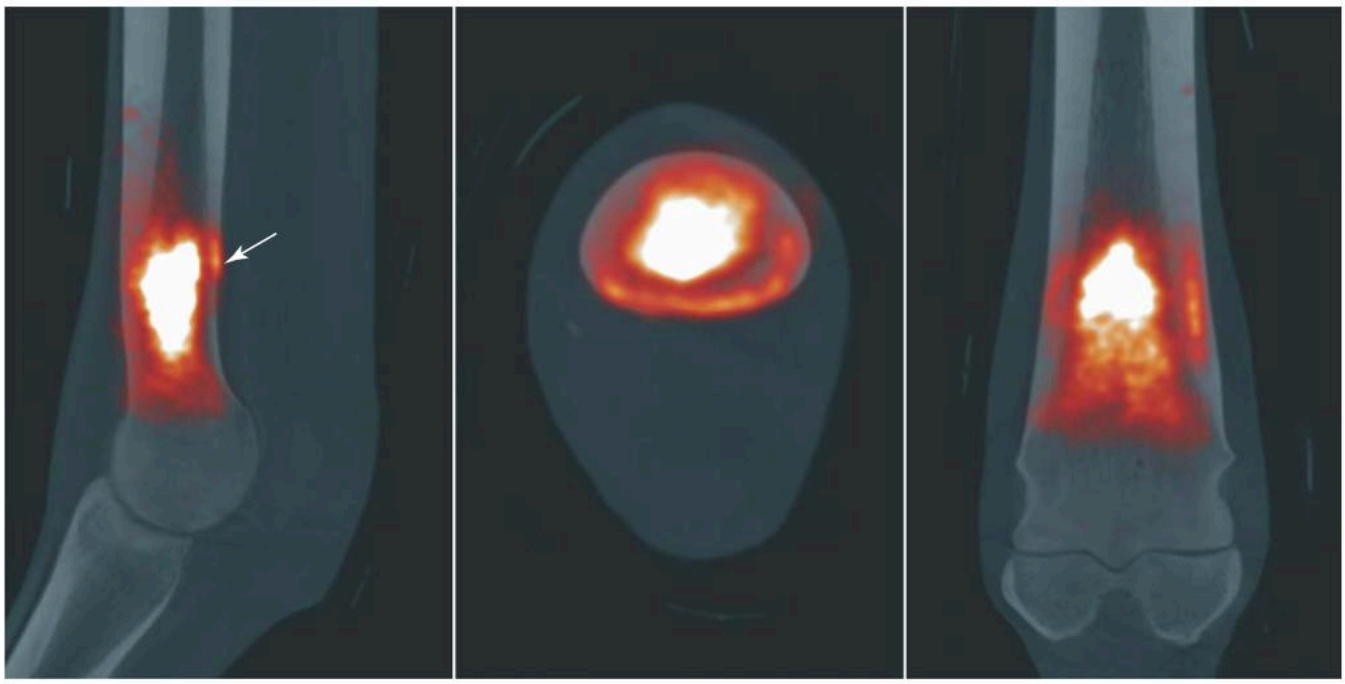


Fig. 24.30 Sagittal (*left*), transverse (*middle*), and dorsal (*right*) plane coregistered standing cone beam computed tomography (CT) and positron emission tomography (PET) images of the distal metacarpal region in a 3-year-old Thoroughbred. On CT images, an ill-defined stress fracture was identified in the palmar cortex of the distal diaphysis of the third metacarpal bone. This corresponds to focal, severe increase in radiopharmaceutical (F^{18}-NaF) uptake in this region on the PET scan (*arrow*). Additionally, there is an increase in radiopharmaceutical uptake within the medullary cavity of the third metacarpal bone at this site, confirming the stress fracture and associated trauma to the trabecular bone in the medullary cavity. (Image courtesy of Dr. Kate Bills, University of Pennsylvania, New Bolton Center.)

Acknowledgment

With special thanks to prior authors of this chapter for their contributions.

REFERENCES

1. Lane EJ, Proto AV, Phillips TW. Mach bands and density perception. *Radiology*. 1976. Published online October 1.
2. Fairburn A, Dyson S, Murray R. Clinical significance of osseous spurs on the dorsoproximal aspect of the third metatarsal bone. *Equine Vet J*. 2010;42(7):591–599.
3. Les CM, Stover SM, Willits NH. Necropsy survey of metacarpal fusion in the horse. *Am J Vet Res*. 1995;56(11):1421–1432.
4. Simon V, Dyson SJ. Radiologic anatomic variation of the carpus in horses with carpal lameness and control horses. *Vet Radiol Ultrasound Off J Am Coll Vet Radiol Int Vet Radiol Assoc*. 2010;51(6):601–606.
5. Nagy A, Dyson S. Anatomical, magnetic resonance imaging and histological findings in the accessory ligament of the deep digital flexor tendon of forelimbs in nonlame horses. *Equine Vet J*. 2011;43(3):309–316.
6. Muylle S, Vanderperren K, Saunders J, Simoens P. Morphometric data on the accessory ligament of the deep digital flexor tendon in the equine hindlimb. *Vet J*. 2010;184:298–302.
7. Nagy A, Dyson S. Magnetic resonance imaging and histological findings in the proximal aspect of the suspensory ligament of forelimbs in nonlame horses. *Equine Vet J*. 2012;44(1):43–50.
8. Bischofberger AS, Konar M, Ohlerth S, et al. Magnetic resonance imaging, ultrasonography and histology of the suspensory ligament origin: a comparative study of normal anatomy of Warmblood horses. *Equine Vet J*. 2006;38(6):508–516.
9. Nagy A, Dyson S. Magnetic resonance anatomy of the proximal metacarpal region of the horse described from images acquired from low- and high-field magnets. *Vet Radiol Ultrasound*. 2009;50(6):595–605.
10. Werpy NM, Denoix JM. Imaging of the equine proximal suspensory ligament. *Vet Clin North Am Equine Pract*. 2012;28(3):507–525.
11. Minshall GJ, Wright IM. Arthroscopic diagnosis and treatment of intra-articular insertional injuries of the suspensory ligament branches in 18 horses. *Equine Vet J*. 2006;38(1):10–14.
12. Dyson S. Musculoskeletal scintigraphy of the equine athlete. *Semin Nucl Med*. 2014;44(1):4–14.
13. Rooney J, Prickett M. Foreleg splints in horses. *Cornell Vet*. 1966;56(2):259–269.
14. Zubrod CJ, Schneider RK, Tucker RL. Use of magnetic resonance imaging identify suspensory desmitis and adhesions between exostoses of the second metacarpal bone and the suspensory ligament in four horses. *J Am Vet Med Assoc*. 2004;224(11):1815–1820, 1789.
15. Mair TS, Dyson SJ, Fraser JA, Edwards GB, Hillyer MH, Love S. Hypertrophic osteopathy (Marie's disease) in Equidae: a review of twenty-four cases. *Equine Vet J*. 1996;28(4):256–262.
16. Moens Y, Verschooten F, Moor D, Wouters L. Bone sequestration as a consequence of limb wounds in the horse. *Vet Radiol*. 1980;21(1):40–44.
17. Dyson SJ, Arthur RM, Palmer SE, Richardson D. Suspensory ligament desmitis. *Vet Clin North Am Equine Pract*. 1995;11(2):177–215.
18. Dyson S. Proximal suspensory desmitis in the hindlimb: 42 cases. *Br Vet J*. 1994;150(3):279–291.
19. Hinkle FE, Selberg KT, Frisbie DD, Barrett MF. Radiographic changes of the proximal third metatarsal bone do

not predict presence or severity of proximal suspensory desmopathy in a predominately Quarter Horse population. *Equine Vet J*. 2022;(n/a):1–9.
20. Bramlage LR, Gabel AA, Hackett RP. Avulsion fractures of the origin of the suspensory ligament of the horse. *J Am Vet Med Assoc*. 1980;176(10 pt 1):1004–1010.
21. Kidd J. Management of splint bone fractures in horses. *In Pract*. 2003;25(7):388–395.
22. Verschooten F, Gasthuys F, De MOOR A. Distal splint bone fractures in the horse: an experimental and clinical study. *Equine Vet J*. 1984;16(6):532–536.
23. Seabaugh KA, Hubert JD, Kawcak CE, et al. Effect of sequential removal of parts of the second metacarpal bone on the biomechanical stability of the equine carpus. *Vet Surg*. 2012;41(7):862–868.
24. Riggs CM, Whitehouse GH, Boyde A. Pathology of the distal condyles of the third metacarpal and third metatarsal bones of the horse. *Equine Vet J*. 1999;31(2):140–148.
25. Ross MW, Ford TS, Orsini PG. Incomplete longitudinal fracture of the proximal palmar cortex of the third metacarpal bone in horses. *Vet Surg*. 1988;17(2):82–86.
26. Shan R, Johnston AS, Rosanowski SM, O'Shea J, Riggs CM. Stress fracture of the palmar, distal cortex of the third metacarpal bone: a diagnostic challenge with a good prognosis. *Equine Vet J*. 2022;54(1):74–81.
27. Ross MW, Martin BB. Dorsomedial articular fracture of the proximal aspect of the third metacarpal bone in Standardbred racehorses: seven cases (1978–1990). *J Am Vet Med Assoc*. 1992;201(2):332–335.
28. Watt BC, Foerner JJ, Haines GR. Incomplete oblique sagittal fractures of the dorsal cortex of the third metacarpal bone in six horses. *Vet Surg*. 1998;27(4):337–341.
29. Kawcak CE, Bramlage LR, Embertson RM. Diagnosis and management of incomplete fracture of the distal palmar aspect of the third metacarpal bone in five horses. *J Am Vet Med Assoc*. 1995;206(3):335–337.
30. Pilsworth RC, Hopes R, Greet TR. A flexed dorso-palmar projection of the equine fetlock in demonstrating lesions of the distal third metacarpus. *Vet Rec*. 1988;122(14):332–333.
31. Werpy NM, Denoix JM, McIlwraith CW, Frisbie DD. Comparison between standard ultrasonography, angle contrast ultrasonography, and magnetic resonance imaging characteristics of the normal equine proximal suspensory ligament. *Vet Radiol Ultrasound*. 2013;54(5):536–547.
32. Fornage BD. The hypoechoic normal tendon. A pitfall. *J Ultrasound Med*. 1987;6(1):19–22.
33. Whitcomb MB. Ultrasonographic evaluation of the metacarpus, metatarsus, and pastern. *Clin Tech Equine Pract*. 2004;3(3):238–255.
34. Wood AK, Sehgal CM, Polansky M. Sonographic brightness of the flexor tendons and ligaments in the metacarpal region of horses. *Am J Vet Res*. 1993;54(12):1969–1974.
35. Denoix JM, Busoni V. Ultrasonographic anatomy of the accessory ligament of the superficial digital flexor tendon in horses. *Equine Vet J*. 1999;31(3):186–191.
36. Denoix JM, Farres D. Ultrasonographic Imaging of the proximal third interosseous muscle in the pelvic limb using a plantaromedial approach. *J Equine Vet Sci*. 1995;15(5):346–350.
37. Smith RKW, Jones R, Webbon PM. The cross-sectional areas of normal equine digital flexor tendons determined ultrasonographically. *Equine Vet J*. 1994;26(6):460–465.
38. Gillis C, Meagher DM, Cloninger A, Locatelli L, Willits N. Ultrasonographic cross-sectional area and mean echogenicity of the superficial and deep digital flexor tendons in 50 trained thoroughbred racehorses. *Am J Vet Res*. 1995;56(10):1265–1269.
39. Gillis C, Sharkey N, Stover SM, Pool RR, Meagher DM, Willits N. Ultrasonography as a method to determine tendon cross-sectional area. *Am J Vet Res*. 1995;56(10):1270–1274.
40. Rabba S, Grulke S, Verwilghen D, Evrard L, Busoni V. B-mode and power Doppler ultrasonography of the equine suspensory ligament branches: a descriptive study on 13 horses. *Vet Radiol Ultrasound*. 2018;59(4):453–460.
41. Lacitignola L, Rossella S, Pasquale DL, Crovace A. Power Doppler to investigate superficial digital flexor tendinopathy in the horse. *Open Vet J*. 2020;9(4):317.
42. Murata D, Misumi K, Fujiki M. A preliminary study of diagnostic color Doppler ultrasonography in equine superficial digital flexor tendonitis. *J Vet Med Sci*. 2012;74(12):1639–1642.
43. Chesen AB, Dabareiner RM, Chaffin MK, Carter GK. Tendinitis of the proximal aspect of the superficial digital flexor tendon in horses: 12 cases (2000–2006). *J Am Vet Med Assoc*. 2009;234(11):1432–1436.
44. Gates S, Hinnigan G, Rich A, Ricci E, Owen K. A case series of five horses with superficial digital flexor tendon lesions in the carpal canal. *J Equine Vet Sci*. 2021;103:103656.
45. Garcia da Fonseca RM, Evrard L, Rabba S, Salciccia A, Busoni V. Dynamic flexion/extension and non-weight bearing ultrasonography is helpful for identifying manica flexoria tears in horses. *Vet Radiol Ultrasound*. 2019;60(1):65–74.
46. Barr ARS, Dyson SJ, Barr FJ, O'Brien JK. Tendonitis of the deep digital flexor tendon in the distal metacarpal/metatarsal region associated with tenosynovitis of the digital sheath in the horse. *Equine Vet J*. 1995;27(5):348–355.
47. Smith MRW, Wright IM. Noninfected tenosynovitis of the digital flexor tendon sheath: a retrospective analysis of 76 cases. *Equine Vet J*. 2006;38(2):134–141.
48. Kent AV, Chesworth MJ, Wells G, et al. Improved diagnostic criteria for digital flexor tendon sheath pathology using contrast tenography. *Equine Vet J*. 2020;52(2):205–212.
49. McDiarmid AM. Eighteen cases of desmitis of the accessory ligament of the deep digital flexor tendon. *Equine Vet Educ*. 1994;6(1):49–56.
50. van den Belt AJ, Becker CK, Dik KJ. Desmitis of the accessory ligament of the deep digital flexor tendon in the horse: clinical and ultrasonographic features. A report of 24 cases. *Zentralbl Veterinarmed A*. 1993;40(7):492–500.
51. Dyson SJ. Desmitis of the accessory ligament of the deep digital flexor tendon: 27 cases (1986–1990). *Equine Vet J*. 1991;23(6):438–444.
52. Dyson S. Proximal injuries of the accessory ligament of the deep digital flexor tendon in forelimbs and hindlimbs: 12 horses (2006–2010). *Equine Vet Educ*. 2012;24(3):134–142.
53. Dyson S, Murray R, Pinilla MJ. Proximal suspensory desmopathy in hindlimbs: a correlative clinical, ultrasonographic, gross post mortem and histological study. *Equine Vet J*. 2017;49(1):65–72.
54. Brokken MT, Schneider RK, Sampson SN, Tucker RL, Gavin PR, Ho CP. Magnetic resonance imaging features of proximal metacarpal and metatarsal injuries in the horse. *Vet Radiol Ultrasound*. 2007;48(6):507–517.
55. Powell SE, Ramzan PHL, Head MJ, Shepherd MC, Baldwin GI, Steven WN. Standing magnetic resonance imaging detection of bone marrow oedema-type signal pattern associated with subcarpal pain in 8 racehorses: a prospective study. *Equine Vet J*. 2010;42(1):10–17.
56. Ehrlich PJ, Dohoo IR, O'Callaghan MW. Results of bone scintigraphy in racing Standardbred horses: 64 cases (1992–1994). *J Am Vet Med Assoc*. 1999;215(7):982–991.

57. Markel MD, Snyder JR, Hornof WJ, Meagher DM. Nuclear scintigraphic evaluation of third metacarpal and metatarsal bone fractures in three horses. *J Am Vet Med Assoc.* 1987;191(1):75–77.
58. Koblik PD, Hornof WJ, Seeherman HJ. Scintigraphic appearance of stress-induced trauma of the dorsal cortex of the third metacarpal bone in racing Thoroughbred horses: 121 cases (1978–1986). *J Am Vet Med Assoc.* 1988;192(3):390–395.
59. Weekes JS, Murray RC, Dyson SJ. Scintigraphic evaluation of the proximal metacarpal and metatarsal regions in clinically sound horses. *Vet Radiol Ultrasound.* 2006;47(4):409–416.
60. Dyson SJ, Weekes JS, Murray RC. Scintigraphic evaluation of the proximal metacarpal and metatarsal regions of horses with proximal suspensory desmitis. *Vet Radiol Ultrasound.* 2007;48(1):78–85.
61. Spriet M, Edwards L, Arndt S, et al. Validation of a dedicated positron emission tomography scanner for imaging of the distal limb of standing horses. *Vet Radiol Ultrasound Off J Am Coll Vet Radiol Int Vet Radiol Assoc.* 2022;63(4):469–477.
62. Spriet M. Positron emission tomography: a horse in the musculoskeletal imaging race. *Am J Vet Res.* 2022;83(7). ajvr.22.03.0051.
63. Spriet M, Espinosa P, Kyme AZ, et al. Positron emission tomography of the equine distal limb: exploratory study. *Vet Radiol Ultrasound.* 2016;57(6):630–638.
64. Spriet M, Espinosa-Mur P, Cissell DD, et al. 18 F-sodium fluoride positron emission tomography of the racing Thoroughbred fetlock: validation and comparison with other imaging modalities in nine horses. *Equine Vet J.* 2019;51(3):375–383.
65. Wilson S, Spriet M, Mur PE, et al. 18Fluorine-fluorodeoxyglucose positron emission tomography for assessment of deep digital flexor tendinopathy: an exploratory study in eight horses with comparison to CT and MRI. *Vet Radiol Ultrasound.* 2021;62(5):610–620.

ELECTRONIC RESOURCES

Additional information related to the content in Chapter 24 can be found online at eBooks.Health.Elsevier.com.

- Chapter Quiz

CHAPTER 25

Equine Fetlock Joint

Kathryn W. Bills

ANATOMY

The equine fetlock, or metacarpophalangeal (MCP) and metatarsophalangeal (MTP) articulations are high motion hinge joints, formed by the distal end of the metacarpal (or metatarsal) bone and the proximal end of the proximal phalanx. It is not possible to reliably differentiate the right from the left or the forelimb from the hindlimb on unlabeled radiographs. The articular surface of the proximal phalanx is concave and has a sagittal groove opposing the sagittal ridge at the distal end of the third metacarpal (MC III) or the third metatarsal (MT III) bone. This ridge and groove divide the weight-bearing surface into two unequal parts, the third metacarpal/metacarpal condyles and the proximal phalanx medial and lateral fovea. The largest surface is on the medial (or axial) side, where loading is greatest. The sagittal ridge of MC III or MT III is received into a depression at the palmar* surface that is created by the proximal sesamoid bones and the intersesamoidean ligament. The joint has two radii of articulation. The dorsal radius serves the weight-bearing portion, and the palmar radius conforms to the articulation with the proximal sesamoid bones.[1] The junction of these radii of articulation often appears flat in lateral radiographs and may be confused with a lesion of the articular surface and subchondral bone, which is complicated by the fact that pathology occurs in the same location.

The joint capsule attachments at the proximal end of the proximal phalanx are immediately periarticular, with a palmarodistal recess between the proximal phalanx and the distal sesamoidean ligaments. The capsule attaches to the distal end of MC III or MT III at the periarticular margins. Dorsally, a large recess extends proximally and forms a pouch. The palmar joint capsule extends proximal to the sesamoid bones between the suspensory ligament and MC III or MT III.[1] Ligaments associated with the MCP and MTP articulations are described elsewhere.[2]

RADIOGRAPHIC EXAMINATION

The examination of the fetlock joint should include the proximal interphalangeal joint and the distal third of the metacarpal or metatarsal bones. Identification markers are essential in radiographic examination of the MCP or MTP articulation; right versus left and front versus hind should be designated clearly. If oblique views are obtained, the direction of the x-ray beam designates the name of the projection from point-of-entrance to point-of-exit. Markers should be placed at the lateral aspect of the anatomic part of interest on all views, except for the lateromedial view for which markers should be placed dorsally.[3]

Survey radiographic examination of the joint should include a lateromedial, a dorsopalmar, and two oblique projections (dorsal 15-degree proximal 45-degree lateral-palmarodistomedial and dorsal 15-degree proximal 45-degree medial-palmarodistolateral), with the limb bearing weight if possible. In the author's opinion, using a horizontal oblique projection has less utility than the incorporation of 15-degree proximal to distal angle as palmar fragments are easily missed on the horizontal oblique projections. The survey examination should precede any special radiographic projections or contrast studies of the joint. The lateromedial projection should be made with the primary beam centered at the articulation and directed parallel to an imaginary line connecting the condylar fossae at the distal end of MC III or MT III. A true lateromedial projection is essential to properly assess the sagittal ridge of distal MC III or MT III.[4] For the dorsopalmar projection, because the plane of the joint is at an angle to the solar surface of the hoof, the primary beam is directed from dorsoproximal to palmarodistal at least 10 to 15 degrees (forelimb 10, hindlimb 15). This should result in the projection of the proximal sesamoid bones over the distal aspect of MC III or MT III and the joint space projected with maximal width.[5] The dorsal 15-degree proximal 45-degree lateral/palmarodistomedial and dorsal 15-degree proximal 45-degree medial/palmarodistolateral projections should be a routine part of the survey examination. These oblique views are necessary to view the abaxial aspects of the articular surfaces, the periarticular margins, and the proximal sesamoid bones. Oblique views made in a dorsal 60-degree lateral/palmaromedial or dorsal 60-degree medial/palmarolateral direction allow the best visibility of the dorsal eminence of the proximal phalanx, which is located near midline, and the axial aspect of the proximal sesamoid bones as well as the joint space between the dorsal margin of the proximal sesamoid bone and the palmar condyle. Some prefer using the 60-degree oblique view as the routine oblique view rather than the oblique views made at 45 degrees because of improved delineation of the axial margin of the proximal sesamoid bones (Fig. 25.1).[6]

Additional projections of the joint may be indicated according to the information gained from the routine survey radiographs or based on discipline-specific indications, such as the flexed dorsopalmar projection for the Thoroughbred racehorse.[4,7] The lateromedial projection during flexion is performed while the foot is held off the ground as if the sole of the hoof were being inspected visually. Alternate positions include variations in the degree of flexion and flexed oblique views. These projections may provide better visibility of subarticular surfaces at the dorsal aspect of distal MC III or MT III, the proximal part of the proximal phalanx, and the articular margins of the proximal sesamoid bones.[5]

A dorsal 30-degree proximal 70-degree lateral-palmarodistomedial oblique projection, or "elevated angle oblique," can be used to assist in the evaluation of the palmar

*"Palmar(o)" is used throughout this chapter with the understanding that "plantar(o)" should be substituted if reference is being made to the hindlimb.

condyle of the third metacarpal bone, the base of the proximal sesamoid bones, and the palmar processes of the proximal phalanx, particularly in cases of comminuted fracture of the latter.[4]

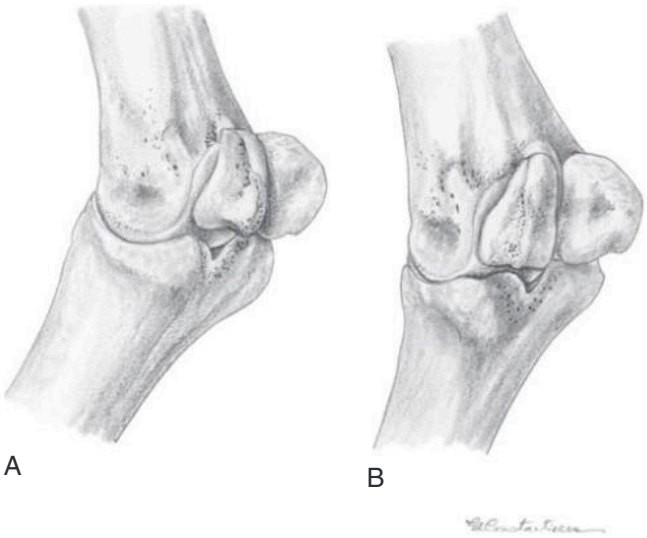


Fig. 25.1 The effect of angle of obliquity on the different aspects of the proximal sesamoid bones that will be projected. **A,** The dorsal 30-degree proximal, 45-degree medial (or lateral)/palmarodistolateral (or medial) view of the metacarpophalangeal (MCP) joint best demonstrates the abaxial aspect of the sesamoid bones where the branches of the suspensory ligament attach. **B,** Dorsal 30-degree proximal, 60-degree medial (or lateral)/palmarodistolateral (or medial) view of the joint maximizes the evaluation of the dorsal eminence of P1. (Drawing courtesy Gheorghe M. Constantinescu, DVM, University of Missouri, Columbia.)

The dorsodistal-palmaroproximal projection is made while the limb is extended and weight bearing. In this projection, a tangential view of the articular margin of the distal aspect of MC III or MT III is created. The foot is elevated on a block, and the limb is extended. The primary beam direction is approximately 125 degrees to the axis of the metacarpal or metatarsal bone.[8] The angle of the primary beam determines the tangent of the joint surface that is visible. In an ideally positioned radiograph, the distal third of the proximal sesamoid bones will be superimposed with the articular margin. This projection is particularly helpful for identifying incomplete condylar fractures and characterizing palmar comminution.

The palmaroproximal-palmarodistal projection is used to see the palmar articular surface of MC III or MT III and the proximal sesamoid bones. Positioning of the patient requires that the x-ray tube be placed close to the horse's body. The limb should be positioned as far caudal as possible, and the foot is placed on a supporting tunnel containing a cassette.[5] Inherent magnification results from the use of this projection because of the distance between the proximal sesamoid bones and the detector.

The abaxial surfaces of the proximal sesamoids may be examined further by placing the detector medial or lateral to the joint on the affected side. The x-ray beam is then directed in a dorsal 50-degree proximal, 45-degree lateral/distopalmaromedial or dorsal 50-degree proximal, 45-degree medial/distopalmarolateral direction, respectively, to create a tangential view of the proximal sesamoid bones.[9] This positioning results in the x-ray beam being directed downward at the sesamoid bones at an angle of 50 degrees from horizontal. This tangential projection is beneficial in assessing whether articular involvement is present with sesamoid lesions and to better characterize occult suspensory ligament avulsions or basilar sesamoid fractures. The results can affect the surgical approach (Fig. 25.2A,C).

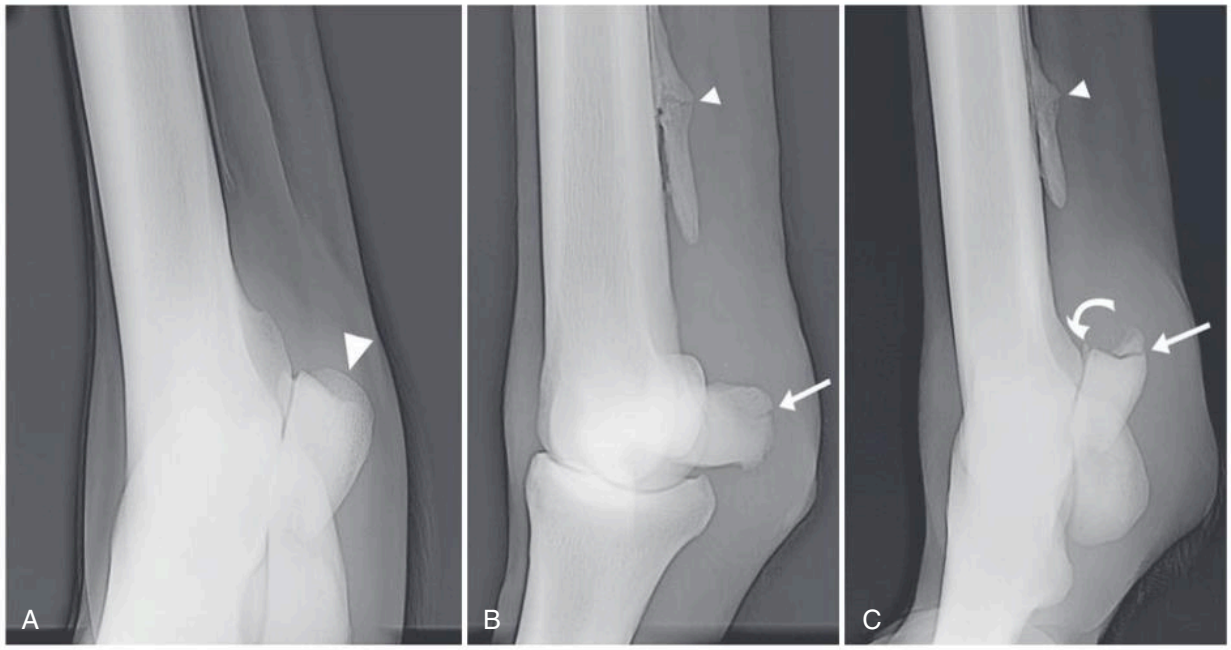


Fig. 25.2 **A,** A dorsal 50-degree proximal, 45-degree medial/distopalmarolateral view; note the normal appearance of the proximal abaxial aspect of the sesamoid bone on this tangential view (*white arrowhead*). **B and C,** Oblique views of an apical sesamoid fracture. **B,** A dorsal 30-degree proximal, 60-degree lateral/palmarodistomedial oblique view. A fracture of the lateral sesamoid bone is visible (*white arrow*) and the fracture appears incomplete. A chronic fracture of the distal MC IV is also present (*white arrowhead*). **C,** A dorsal 50-degree proximal, 45-degree medial/distopalmarolateral view of the same horse. From this projection it is apparent that the sesamoid fracture is both complete and articular (*straight white arrow*) with a small articular fragment (*curved white arrow*). The chronic distal MC IV fracture is also visible (*white arrowhead*). (Courtesy Scott E. Palmer, VMD, Dipl. ABVP-Equine, New Jersey Equine Clinic, Clarksburg, New Jersey.)

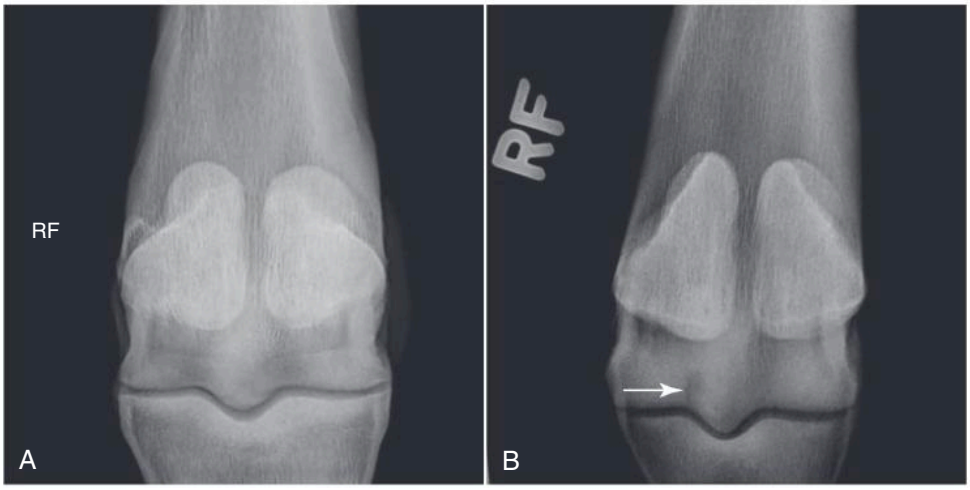


Fig. 25.3 Dorsopalmar **(A)** and flexed dorsopalmar **(B)** radiographs of the right metacarpophalangeal joint from the same horse. A lucent line (*white arrow*) is present in the lateral parasagittal groove and is only noted on the flexed projection. Also note the increased conspicuity of the marked surrounding lateral parasagittal groove sclerosis.

A flexed dorsopalmar projection is acquired by positioning the foot in a block (e.g., Hickman navicular block) to provide a more predictable degree of fetlock flexion. The primary beam is angled between 0 and 35 degrees depending on the tangential surface of the condyle attempting to be imaged.[10] The projection is particularly useful for identifying unicortical condylar fractures, palmar comminution of said condylar fractures, and axial sesamoid lesions (Fig. 25.3).[11]

The dorsoproximal-dorsodistal projection is used to improve visualization of the dorsal margin of the metacarpal/metatarsal condyles. With the metacarpus aligned perpendicular to the ground, the fetlock is held in a flexed position with the detector held horizontal to the ground under the joint. The beam is variably angled, between 45 and 70 degrees, to create a tangential image of the dorsodistal metacarpal condyle and helps to characterize the dorsal articular margin (Fig. 25.4). The ideal projection angle will depend upon where a particular lesion is located along the curvature of the condyle, most commonly in the dorsal to mid-thirds of the medial aspect.[12]

Contrast arthrography of the MCP or MTP joint and intrathecal injection of the digital flexor tendon sheath is sometimes useful but has largely been replaced by ultrasonographic assessment. For contrast arthrography, 5 to 10 mL of water-soluble contrast medium containing 300 mg/mL of iodine is injected using aseptic technique. Injection of contrast medium should follow arthrocentesis and withdrawal of an equal volume of synovial fluid. Injection is made into the lateral pouch of the joint, proximal to the lateral sesamoid bones and dorsal to the suspensory ligament or into the dorsal synovial recess. The joint should be flexed, extended, and massaged vigorously before radiography to distribute the contrast medium throughout the joint.

ALTERNATIVE IMAGING MODALITIES

Ultrasound offers detailed evaluation of soft tissues surrounding the MCP or MTP joint and is used frequently to complement the radiographic examination. Portable ultrasound machines can be used to image the extensor and flexor tendons, manica flexoria, the suspensory and distal sesamoidean ligaments, the intersesamoidean ligament, the synovial lining and joint recesses, collateral ligaments, cortical margins, and portions of the articular cartilage of standing horses at rest.[13] More recently, non–weight-bearing and dynamic ultrasound of the suspensory branches and digital flexor tendon sheath has been performed.[14,15] The normal sonographic features of the MCP and MTP joints have been described.[16]

Nuclear scintigraphy for evaluation of bone utilizing ^{99m}Tc-methylene diphosphonate (MDP) or ^{99m}Tc-hydroxymethylene disphosphonate (HDP) has been performed for decades. It is highly sensitive for detecting osseous fetlock pathology in many disciplines.[17,18] Pathologic changes and nonpathologic manifestations of adaptive remodeling of bone can be identified, so knowledge of discipline-specific patterns of uptake is imperative for correct interpretation.[19]

In addition to conventional radiography, computed tomography (CT) may be useful in selected patients to image the MCP or MTP joint.[20] CT excels in the evaluation of bone and is useful in imaging condylar and complex fractures, developmental orthopedic disease, and manifestations of early joint disease, such as small osteophytes, subchondral and trabecular sclerosis, osseous cyst-like lesions (OCLLs), subchondral bone injury secondary to repetitive trauma, and ill-defined lysis as found in joint sepsis and septic osteomyelitis[21,22] (Fig. 25.5). There is wider availability of standing fan- and cone-beam CT systems with similar performance in identification of osseous fetlock pathology in various disciplines.[23–25] The speed of image acquisition is also a benefit compared to other standing cross-sectional imaging modalities, such as low-field magnetic resonance imaging (MRI). Finally, similar to certain MRI sequences, CT volume data acquisition allows for multiplanar reconstruction and reformatting of images such that an infinite number of planes can be evaluated with a single scan of the region of interest.

MRI is commonly used to evaluate the equine distal limb, including the MCP or MTP joints.[21,26–31] A distinct advantage of MRI is the exceptional soft tissue contrast resolution and ability to evaluate articular cartilage (Figs. 25.6–25.8). Magnetic resonance (MR) examinations usually include several types of acquisition sequences to allow evaluation of different anatomic and pathologic features, based on the composition of each tissue. MR systems employing high-field magnets require that horses be under general anesthesia for imaging. Low-field MR



Fig. 25.4 **A,** Schematic drawing for positioning the limb and detector to acquire the flexed dorsoproximal-dorsodistal oblique projection (*top image*) of the fetlock and resultant well-positioned radiograph (*bottom image*). The tangential projection allows isolation of the dorsal margin of the metacarpal condyle to increase the detection of subchondral bone disease **(B)**, which manifests radiographically as regions of sclerosis with central demineralization/lucent regions (*white arrow*). (Images courtesy of Dr. Laura Faulkner, Watermark Equine, Ridgefield, CT, USA. Line drawing in (A) is contributed by Beth Mellor.)

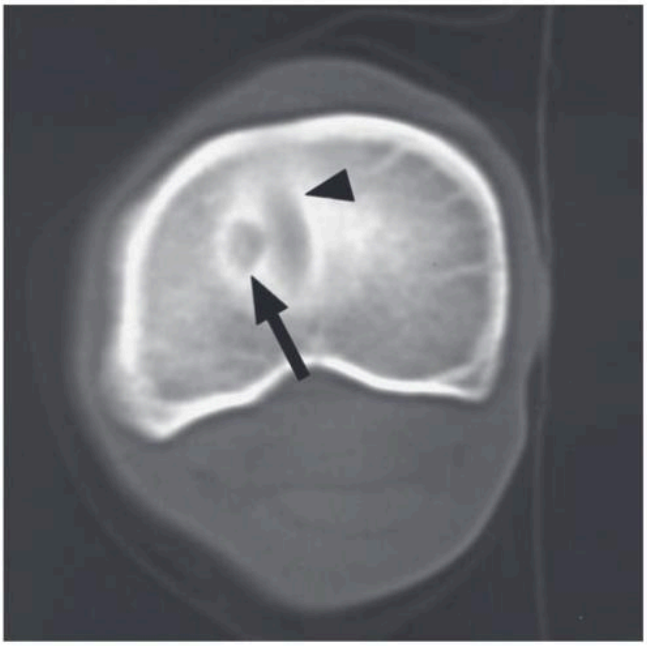


Fig. 25.5 A transverse 1.5-mm-thick computed tomography (CT) image of the proximal aspect of the proximal phalanx. A small, oval, hypoattenuating subchondral demineralization lesion (*black arrow*) is surrounded by hyperattenuating sclerotic bone just lateral parasagittal to the sagittal groove (*black arrowhead*).

systems are available for imaging the limbs of standing horses. However, volume averaging and motion artifact remain limitations of these, especially proximal to the distal phalanx, although motion correction techniques improve resolution.[32]

Finally, the most recently developed imaging modality for evaluating the equine fetlock is positron emission tomography (PET), utilizing both ^{18}F-NaF and ^{18}F-FDG tracers for bone and soft tissue imaging, respectively. As a cross-sectional imaging modality, PET combines the benefits of tomographic imaging with the high sensitivity and physiologic information from scintigraphy and has the highest lesion detection and agreement amongst specialty and general practitioners compared to other modalities.[33] PET has already demonstrated an ability to detect injuries at sites unable to be diagnosed by radiographs, such as the dorsal aspect of the proximal sesamoid bone (Fig. 25.9).

RADIOGRAPHIC INTERPRETATION OF DISEASES OF THE METACARPOPHALANGEAL/METATARSOPHALANGEAL ARTICULATION

Joint disease in many horses is often associated with training-associated repetitive trauma and the pathologic changes may be characteristic of the joint or function of the horse. A study of racetrack injuries has provided an overview of pathologic findings and pathogenesis of MCP or MTP joint disease.[34] Lameness and distension of a joint are the initial clinical signs that typically precede the request for radiographic examination following localization with diagnostic analgesia. The earliest signs of joint disease may remain obscure on radiographs, because wear lines in the articular cartilage or synovial hypertrophy are usually unrecognized. Radiographs of the contralateral joint are helpful for comparison. Although pathologic change is often bilateral, it is usually in different stages of development between limbs.

Joint Effusion

Joint effusion is usually a result of trauma and subsequent joint debris and not necessarily due to permanent degenerative



Fig. 25.6 Magnetic resonance (MR) images of right and left distal MC III. **A,** Sagittal proton density-weighted MR image of the metacarpophalangeal (MCP) joint. The deep digital flexor tendon courses along the palmar aspect (*white arrowhead*) and the distal sesamoidean ligaments originate on the distal margin of the proximal sesamoid bone (*short white arrow*). The synovial fluid in the palmar pouch can be visualized clearly (*long white arrow*). **B,** Sagittal proton density-weighted MR image of the contralateral MCP joint. Distal MC III medial condyle high fluid signal (*black arrow*) is consistent with subchondral injury, with an associated articular cartilage defect. **C,** Transverse spectral presaturation with inversion recovery weighted image of the affected area in **B** that removes signal derived from fat. This increases the visibility of the MC III medial condyle lesion (*white arrow*).

changes of the articular surfaces.[35] Radiographic signs include soft tissue swelling and joint distention. With chronic insults, dystrophic calcification of the periarticular soft tissues may also be present.[36]

Villonodular Synovitis

Villonodular synovitis leads to a firm, nonfluctuating swelling located primarily at the dorsoproximal aspect of the joint. Villonodular masses arise from enlargement of the synovial pad of the joint capsule and are associated with repetitive trauma. The condition is usually diagnosed by clinical signs, history, palpation, and ultrasound. With time, the radiographic signs will include mild to severe smooth erosion of distal MC III or MT III at the region just distal to the dorsal joint capsule attachment (Fig. 25.10). Periarticular bone proliferation may be present. With arthrography, radiolucent, space-occupying masses resulting from synovial villus hypertrophy can usually be identified in the dorsal recess of the joint (Fig. 25.11). Erosion occurring along the palmar/plantar surface of the distal MC III or MT III is termed *supracondylar lysis.*

Supracondylar Lysis

In MC III or MT III, the radiographic features of supracondylar lysis are similar to those in villonodular synovitis affecting the dorsoproximal aspect of the joint, except that supracondylar lysis occurs at the palmar (or plantar) surface of the bone. Changes are caused by chronic proliferative synovitis. Radiographic signs are joint distention and smooth osteolysis at the distal palmar cortex of MC III or MT III, distal to the joint capsule attachment (see Fig. 25.10B). Arthrography may be difficult to perform because of the presence of hypertrophied synovium and diminished synovial joint space. The erosive concavity formed in the bone is usually readily apparent (see Fig. 25.11).

Degenerative Joint Disease

Degenerative joint disease, also termed *osteoarthritis* or *osteoarthrosis*, is a nonspecific term describing the deterioration of articular and periarticular structures. It is a chronic disorder characterized by progressive deterioration of articular cartilage that results in a radiographic loss in joint space and proliferative changes in the joint margin and capsule.[34]

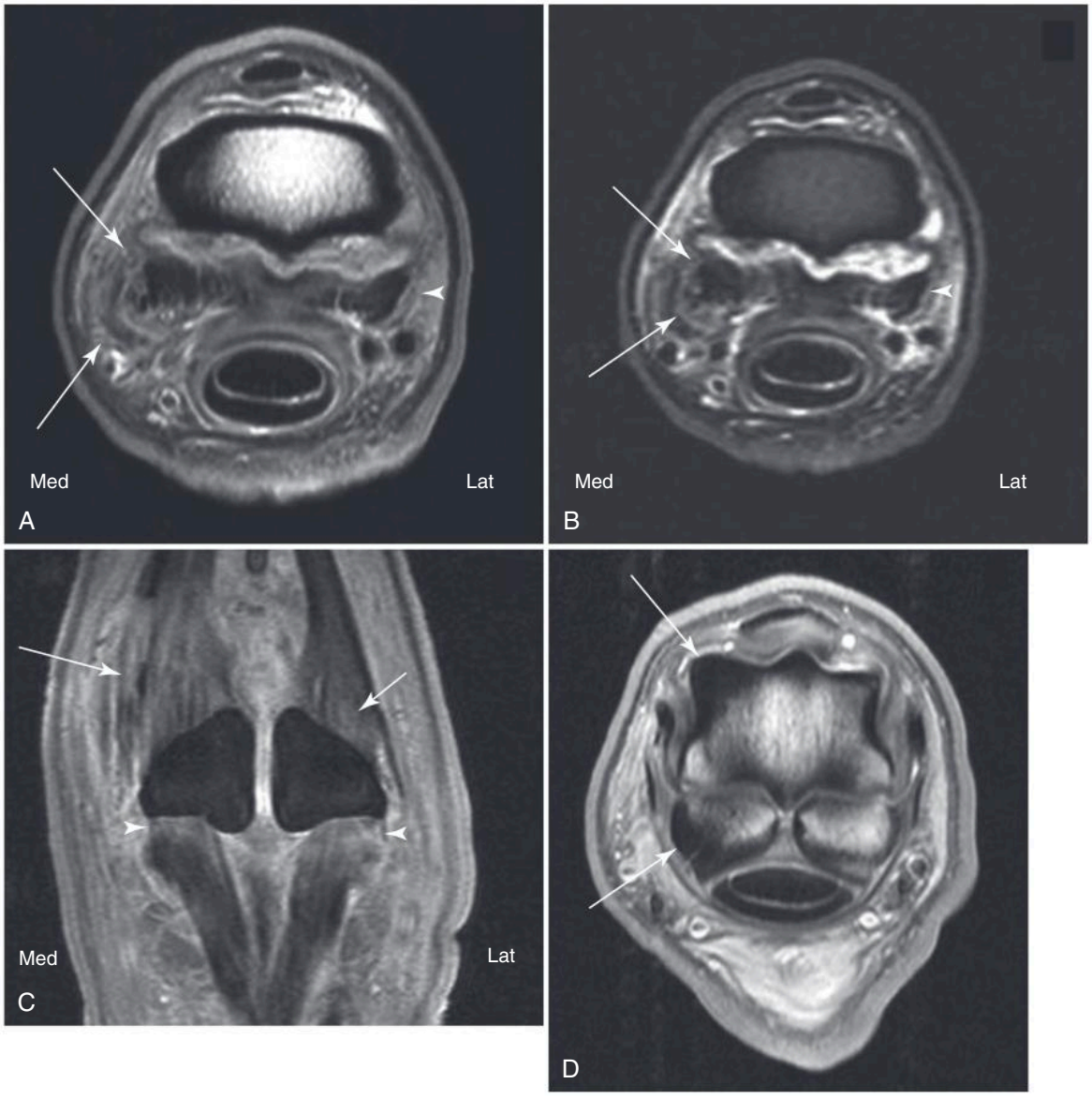


Fig. 25.7 Magnetic resonance (MR) images of a 12-year-old male Friesian with right metatarsophalangeal (MTP) joint swelling and lameness. Radiographically, there was marked periarticular soft tissue swelling, especially along the medial and plantar aspects, but no bone changes were present. Transverse proton density image **(A)** and transverse short time inversion recovery image **(B)** of the joint immediately proximal to the proximal sesamoid bones. There is marked enlargement and abnormal signal of the medial branch of the suspensory ligament (*white arrows*) with surrounding periligamentous fibrosis and soft tissue swelling. The abaxial margin of the lateral branch of the suspensory ligament has an abnormal hyperintensity (*white arrowhead*). **C,** Dorsal gradient recalled echo image of the proximal sesamoid bones. There is diffuse disruption and enlargement of the medial branch of the suspensory ligament (*large white arrow*) and focal disruption of the lateral branch of the suspensory ligament at the insertion to the sesamoid bone (*small white arrow*). In addition, there is abnormal signal and morphology of the proximal aspect of the oblique distal sesamoidean ligaments (*white arrowheads*). **D,** Transverse proton density image at the level of the mid-body of the proximal sesamoid bones. There is sclerosis in the dorsal medial condyle of the third metatarsal bone and along the abaxial margins of the medial proximal sesamoid bone (*white arrows*). *Lat,* Lateral; *Med,* medial.

The first stages include cartilage degeneration and formation of wear lines characteristic of hinge joints. The most common joint in the horse to develop spontaneous osteoarthritis is the metacarpo(tarso) phalangeal joint due to the relatively thin articular cartilage compared to other joints. The articular surfaces develop linear erosions that form grooves oriented parallel to the direction of joint motion.[37] Cartilaginous fibrillation and erosions form on the surface, and subsequent wear results in narrowing of the joint space. If reduction in the width of a joint space is confirmed on two radiographic views, cartilage thinning is likely. Progressive loss of joint width is a subjective finding and must be assessed in conjunction with clinical signs to determine its significance (Fig. 25.12).

Radiographic signs of degenerative joint disease are soft tissue swelling, narrowed joint space, and bone remodeling, including lysis and proliferation (e.g., osteophytes and

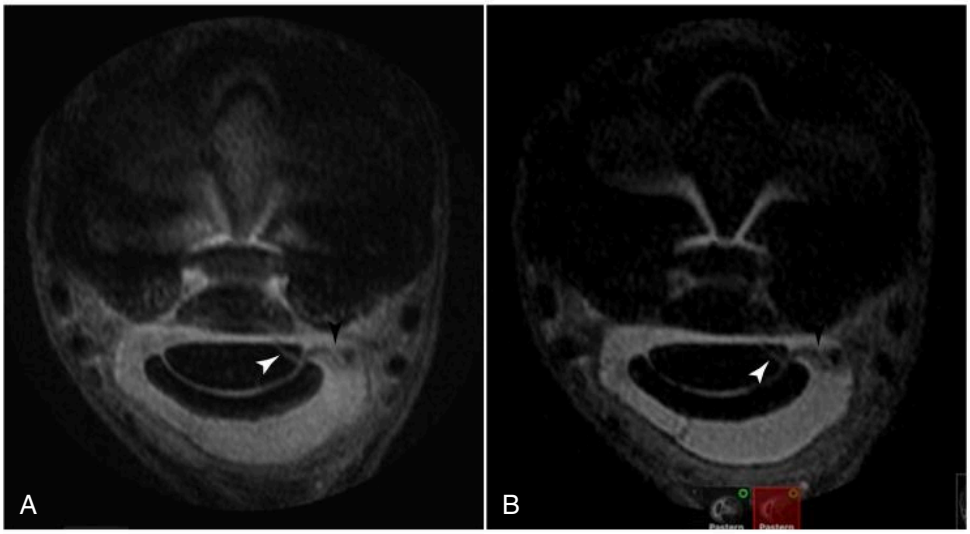


Fig. 25.8 A 9-year-old Arabian with acute digital flexor tendon sheath tenosynovitis: transverse proton density **(A)** and T2-weighted fast-spin echo (T2W FSE) **(B)** images. There is moderate to marked digital flexor tendon sheath effusion secondary to an oblique dorsolateral peripheral tear of the deep digital flexor tendon (DDFT) just distal to the metacarpophalangeal joint (*white arrowhead*). Also note the amorphous heterogeneous intermediate intensity tissue lateral to the tear, consistent with torn DDFT fibers (*black arrowhead*). This type of lesion is best visualized on the T2W images due to partial mitigation of magic angle artifact.

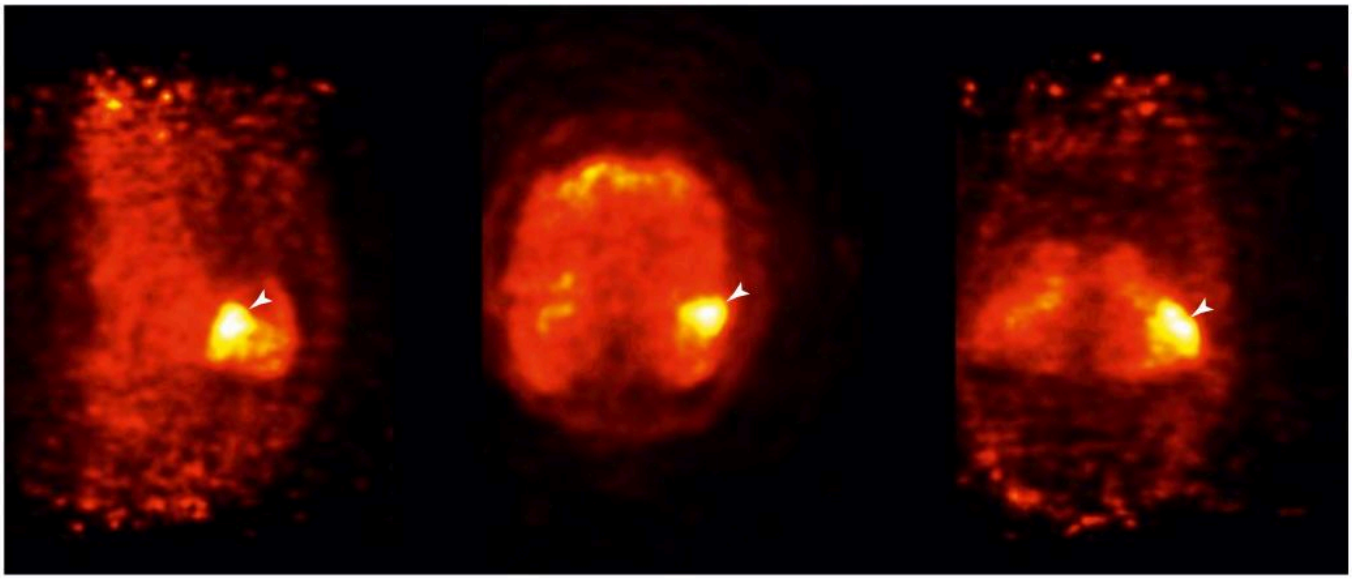


Fig. 25.9 Sagittal (*left*), transverse (*middle*), and dorsal (*right*) ^{18}F-NaF positron emission tomography of a Thoroughbred racehorse fetlock. Dorsal is to the left in the sagittal image. Medial is to the right in the transverse and dorsal plane images. Marked, focal radioavidity (*white arrowheads*) is present in the dorsal, abaxial midaspect of the medial proximal sesamoid bone, a known site of demineralization that acts as a stress riser to proximal sesamoid fracture in Thoroughbred racehorses. (Courtesy of Mathieu Spriet, DVM, MS, DACVR, DECVDI, DACVR-EDI, University of California at Davis, Davis, California, USA.)

enthesophytes) (see Fig. 25.12). These findings may occur in any combination. Joint capsule thickening may be suspected but is rarely visualized, even on high-detail radiographs. Soft tissue swelling results from synovial effusion, as well as hypertrophy and proliferation of other periarticular soft tissues.

Chronic osteoarthritis is characterized by sclerosis or eburnation of subchondral bone, with loss of trabecular architecture because of erosion of the overlying articular cartilage. Repetitive stress or trauma at the joint capsule attachments results in enthesophyte formation (see Fig. 25.10). Similar, but not identical, are periarticular osteophytes that form at the margin of narrowed joints in response to damage to the articular surface as the disease progresses (Fig. 25.13, eFig. 25.1). Of note, many joint disorders can progress to a common end point having the stereotypic features of chronic degenerative joint disease.[34] The initiating factors of degenerative joint disease may be difficult or impossible to determine in the late stages of the disease.



eFig. 25.1 Dorsolateral-palmaromedial radiograph of a horse with chronic degenerative joint disease and a subchondral bone defect. A focal ill-defined, irregularly margined subchondral radiolucency with surrounding sclerosis is seen at the dorsodistal aspect of the medial condyle of the third metacarpal bone. There is moderate osseous proliferation along the dorsomedial aspect of the distal metacarpus and proximal phalanx. Mild soft tissue thickening is present.

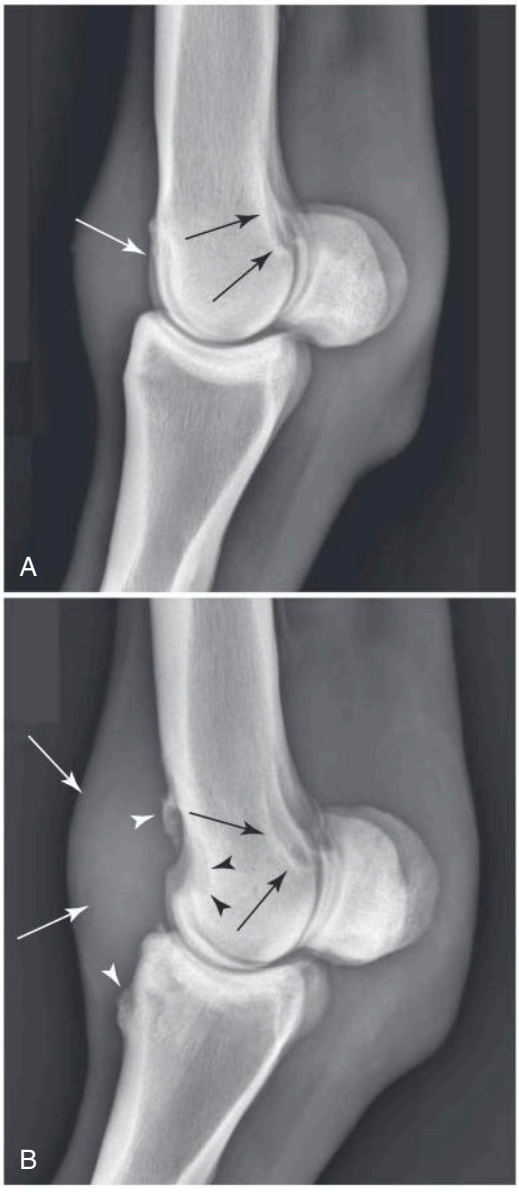


Fig. 25.10 Lateromedial radiograph of two metacarpophalangeal (MCP) joints with changes of mild **(A)** and severe **(B)** villonodular synovitis. **A,** Swelling dorsal to the joint, erosion of bone at the dorsoproximal joint capsule attachment (*white arrow*), and early evidence of supracondylar lysis at the palmar cortex (*black arrows*) are present. **B,** This joint has more chronic changes with severe swelling (*white arrows*), bone erosion at the dorsoproximal joint capsule attachment (*black arrowheads*), supracondylar lysis (*black arrows*), and periarticular enthesophytes (*white arrowheads*). Bone remodeling is also present at the proximodorsal aspect of the proximal phalanx, as well as along the palmar border of the sesamoid bones.

Cortisone Arthropathy

Cortisone arthropathy may involve articular and periarticular structures and may lead to variable degrees of degeneration and proliferation. Repeated steroid injections result in localized demineralization of bone and decreased trabecular detail. Long-term changes include mineralization in the periarticular soft tissues associated with deposition of steroid within those structures. A differential diagnosis of steroid-induced arthritis should be considered in the presence of degenerative change or collapse of subchondral bone with mineralization in periarticular soft tissue (Fig. 25.14).



Fig. 25.11 Positive-contrast arthrogram of a horse with moderate villonodular synovitis. A space-occupying mass is present in the dorsoproximal aspect of the joint space (*small black arrowheads*). A space-occupying mass at the palmar surface fills the area of supracondylar lysis (*thick black arrowheads*), secondary to synovial hypertrophy.

Osteochondrosis and Osteochondritis Dissecans

Osteochondral fragments of the dorsoproximal aspect of the proximal phalanx are common in young, untrained horses of all breeds but particularly in Warmblood populations. There is a similar distribution between the fore and hindlimbs; however, the medial aspect of the proximal phalanx is highly overrepresented. The fragments are typically smooth and histologically are not representative of any particular disease process, but given they are surrounded by smooth hyaline cartilage, a developmental orthopedic condition though juvenile trauma has also been suggested. Fragments are not typically associated with lameness in this population.[38]

Osteochondral fragments of the palmar aspect of the joint have been given three classifications.[39] Type I fragments occur at the proximal end of the proximal phalanx, just medial or lateral to the sagittal groove in the region of attachment of the short distal sesamoidean ligaments; type II fragments have an origin from the wing of the proximal phalanx (Figs. 25.15 and 25.16). Type III fragments originate from the basilar margin of the sesamoid bones and are discussed under the section on sesamoid basilar fractures (Fig. 25.17). Type I or II fragments have the highest incidence in Standardbreds and were originally reported as avulsion fractures.[40] Because of the anatomic origin, symmetry, and breed predilection, these fragments have been suggested by some to be the result of osteochondrosis. These fragments are the subject of much controversy. Studies have focused on radiography,[40–44] etiology,[45] heritability,[46] the effect of patient size,[47] epidemiology,[48] surgical treatment,[49] and prognosis.[42]

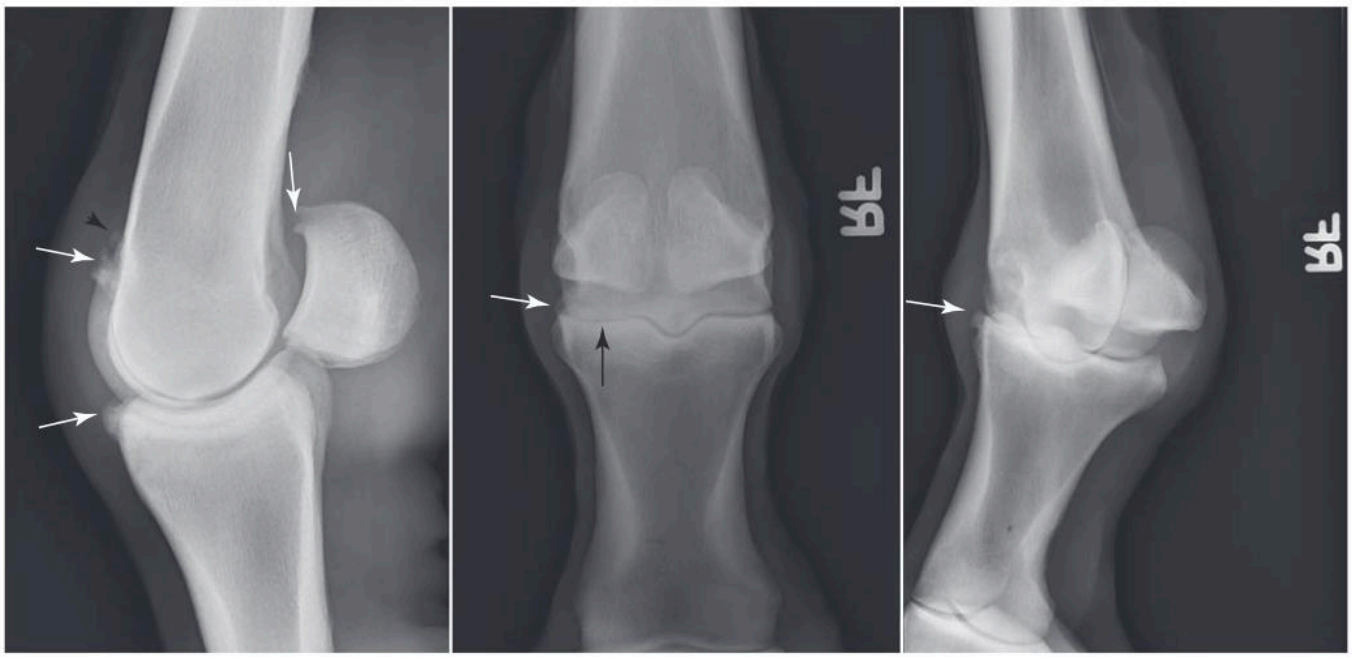


Fig. 25.12 Flexed lateromedial (*left*), dorsopalmar (*middle*), and dorsolateral-palmaromedial oblique (*right*) radiographs of a metacarpophalangeal joint with severe osteophytosis (*white arrows*, dorsoproximomedial proximal phalanx, dorsodistomedial metacarpal condyle, proximal sesamoid apices), osteochondral fragmentation (*black arrowhead*), medial joint space narrowing (*black arrow*), proximomedial proximal phalanx trabecular sclerosis. Periarticular soft tissue thickening is also present.

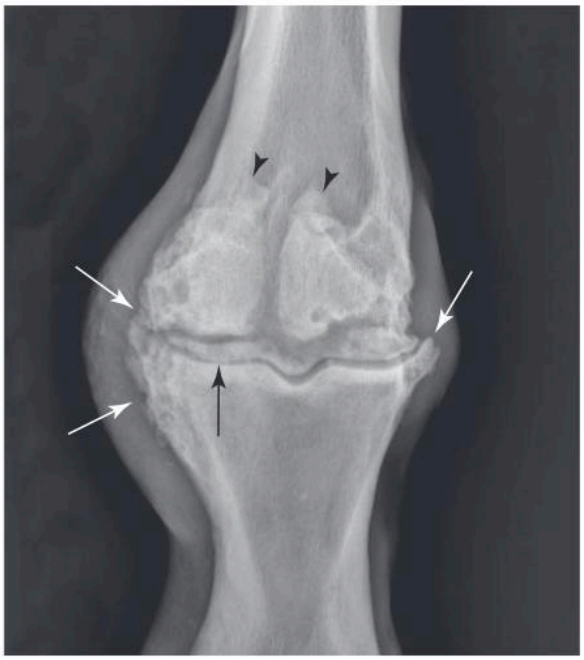


Fig. 25.13 Dorsopalmar radiograph with changes of chronic, severe degenerative joint disease. Narrowing of the joint space (*black arrow*) and formation of osteophytes at the joint margin (*white arrows*) and sesamoid bone remodeling (*black arrowheads*) are visible, in addition to multifocal small ovoid radiolucent regions along the joint articulation secondary to synovial invaginations from chronic degeneration.



Fig. 25.14 Lateromedial radiograph of a horse with cortisone arthropathy. There is narrowing of the joint space and severe periarticular bone proliferation of the dorsal and palmar aspects of the distal metacarpal bone, proximal aspect of the proximal phalanx, and the apical margins of the proximal sesamoid bones. Dystrophic synovial mineralization is present. Mineralization in periarticular soft tissues is typical of cortisone arthropathy. (Courtesy Stephanie Nykamp, DVM, DACVR, Ontario Veterinary College, Guelph, Ontario, Canada.)



Fig. 25.15 Dorsal 45-degree medial/palmarolateral radiograph of the metacarpophalangeal (MCP) joint with a large type II fragment (*black arrows*) originating from the medial palmar eminence of the proximal phalanx.

Osteochondrosis of the sagittal ridge of MC III or MT III is usually diagnosed in young horses and occurs with variable radiographic expression (Fig. 25.18, eFig. 25.2). Radiographic signs may vary from small areas of flattening to large excavations of subchondral bone of the sagittal ridge and free osseous fragmentation. Lesions are best seen on flexed lateral projections of the MCP or MTP joint and can also be seen on dorsopalmar projections. Detached osteochondral fragments may be found in close association to the bone defect or may be nestled in distant recesses of the joint.[50]

Osseous Cyst-Like Lesions

Ovoid lucent regions with thin rims of surrounding sclerosis can be found in the distal metacarpal condyle and proximal aspect of the proximal phalanx and variably can be a cause of lameness (Fig. 25.19, eFig. 25.3). The etiology is uncertain with both developmental and juvenile trauma etiologies proposed. Subchondral OCLLs can also occur at the proximal end of the proximal phalanx and are often difficult to see radiographically.

Septic Arthritis

Septic arthritis may be associated with hematogenous spread of microorganisms, such as occurs with omphalophlebitis, or by direct contamination because of trauma or nonsterile invasive techniques. Radiographic signs of early septic arthritis are periarticular soft tissue swelling and distention of the joint. Progression of the disease results in malalignment, subluxation, or collapse of the joint (Fig. 25.20) and subchondral bone lysis and periosteal proliferation at the joint margins (Fig. 25.21). The cartilage space may appear increased at areas of subchondral bone lysis. Diminished joint space is evidence of the loss of articular cartilage that typically precedes subchondral bone change.

The radiographic signs of increased apparent joint space must be analyzed critically. Incomplete ossification of the cartilage model is normally present in young, developing animals. The large soft tissue space at articular margins diminishes progressively with skeletal maturity. Furthermore, radiographs made in non–weight-bearing horses will cause joint spaces to be widened compared with weight-bearing projections. Whenever possible, the horse should bear normal weight on the joint at the time of radiography. Increased thickness of the articular cartilage has not been documented in animals. Excessive fluid or soft tissue in the joint space, as occurs with immune-mediated arthritis, results in a wider joint space. However, such diseases have not been documented in the horse.

Nonseptic inflammatory joint diseases have varied causes and may be difficult to classify. Radiographic signs are distension of the joint and displacement of periarticular soft tissues. If the condition is chronic, periarticular osteoproliferation may develop.

Subchondral Bone Disease

Historically erroneously referred to as *traumatic osteochondrosis*, a consensus term of "subchondral bone disease" has been recommended by experts to describe an osseous injury that occurs due to repetitive cyclic stress leading to marked trabecular sclerosis and variably shaped central demineralization.[51] The most common site of subchondral bone injury is found in the distal aspect of MC III or MT III of Thoroughbred racehorses.[34,39] The radiographic findings are an ill-defined or well-demarcated radiolucent region with variable thickness rim of surrounding sclerosis that may extend several centimeters deep to the articular margin. A lateromedial radiograph of the joint may best demonstrate the depth of the lesion in the condyle, although the lesions are typically best visible on the flexed dorsopalmar projection. The shape of the defect may be a linear defect, shallow concavity, a deep concavity, crescentic, oval, or circular. The ovoid/circular changes are typically at the junction of the radii of articulation between the MCP or the MTP joint and the metacarposesamoidean or metatarsosesamoidean articular surface while the linear lesions are most commonly identified in the parasagittal grooves (see Fig. 25.3). Cavitation of the joint surface may exist, although advanced degenerative subchondral bone changes can also be found with the overlying cartilage intact at the articular surface.

There is increasing recognition that nonracing sport horses are afflicted by subchondral bone disease in discipline-specific patterns, but the imaging manifestation of regions of sclerosis with central demineralization is conserved across breeds and disciplines. The sagittal groove, medial fovea of the proximal phalanx, and the dorsomedial MC III/MT III condyles are overrepresented in nonracing sport horses[17,52] (Fig. 25.22). Variable angle dorsopalmar projections can improve the conspicuity of sagittal groove lesions, while the dorsoproximal to dorsodistal oblique projection is best to characterize medial condylar injury (see Fig. 25.4). These lesions can sometimes be miscategorized as OCLLs, but from an etiologic standpoint, differ from OCLLs as described previously.[53]

Condylar Fractures

Fractures in the distal condyle of MC III or MT III occur most commonly in Thoroughbred racehorses due to acute exacerbation of underlying subchondral bone disease. The forelimbs are more affected than the hind. The palmar aspect of the lateral parasagittal groove is the most commonly affected site and lesions can be difficult to identify radiographically until more advanced disease is present. The flexed dorsopalmar projection and 125 dorsodistal-palmaroproximal projections are



eFig. 25.2 Flexed lateromedial radiograph of the metacarpophalangeal joint of a horse with osteochondrosis of the sagittal ridge of the third metatarsal bone. A concave defect is seen along the dorsal and proximal surface of the sagittal ridge of the third metatarsal bone.



eFig. 25.3 Flexed dorsopalmar radiograph of a horse with an osseous cyst-like lesion in the medial condyle of the third metacarpal bone. Moderate sclerosis surrounds the defect.

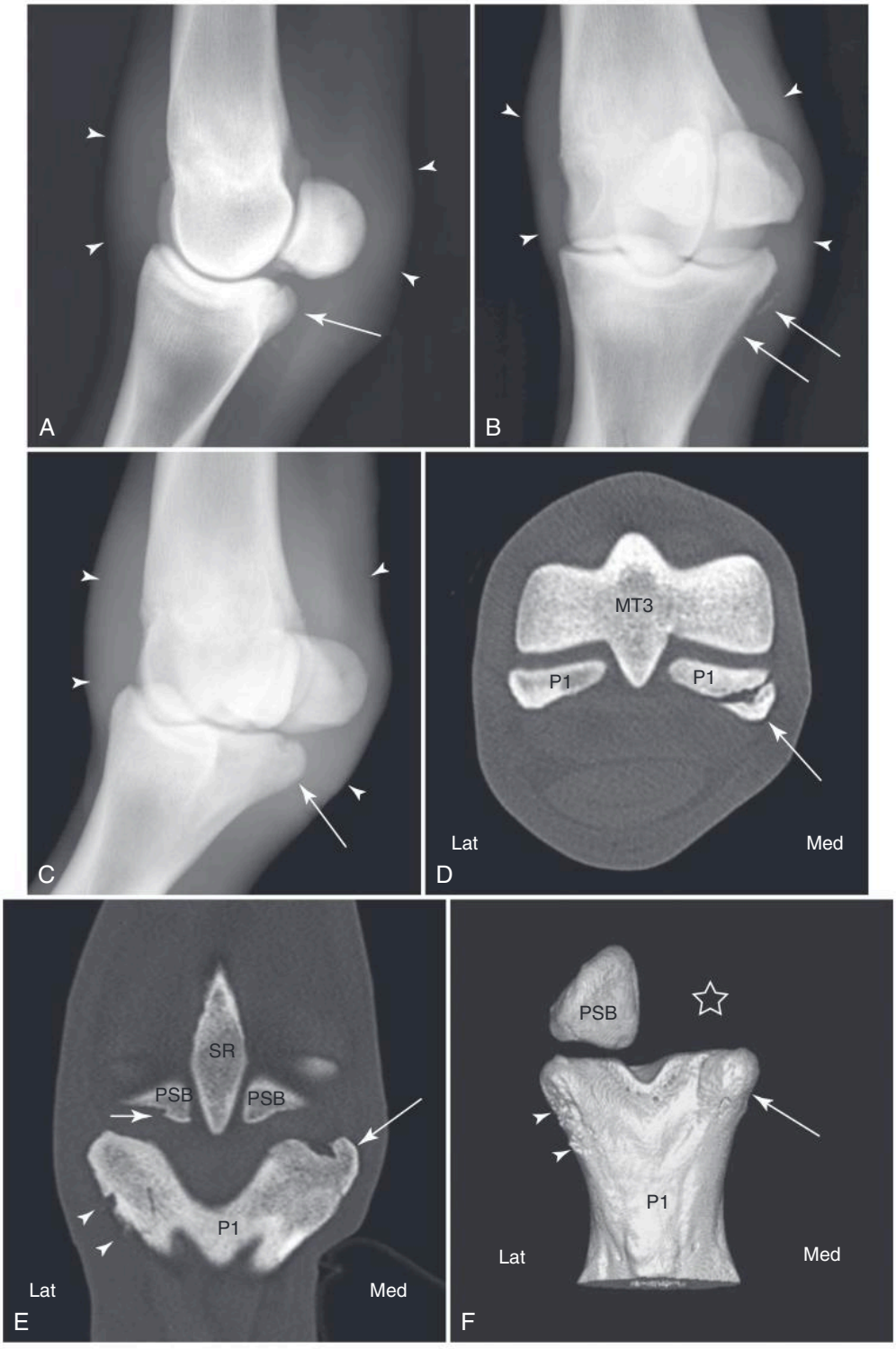


Fig. 25.16 Radiography and computed tomography (CT) images of a 1-year-old male Quarter horse. **A,** Lateral radiograph of the right metatarsophalangeal (MTP) joint. There is diffuse soft tissue swelling (*white arrowheads*) with osseous remodeling and fragments associated with the plantar process of the proximal phalanx (*large white arrow*). **B,** Dorsolateral/plantaromedial radiograph. Note the soft tissue swelling (*white arrowheads*) and periosteal proliferation and fragmentation associated with the proximal lateral first phalanx (*white arrows*). **C,** Dorsomedial/plantarolateral radiograph. Note the soft tissue swelling (*white arrowheads*) and slight defect of the medial plantar process of the first phalanx (*large white arrow*). **D,** Transverse CT image at the level of MTP joint. Note the slightly displaced fragment of the medial plantar process of the proximal phalanx (*white arrow*). **E,** Reconstructed dorsal CT image of the plantar aspect of the metacarpophalangeal (MCP) joint. Note the large osteophyte associated with the medial plantar process (*large white arrow*), the osseous proliferation immediately distal to the lateral plantar process (*white arrowheads*), and a small enthesophyte off the axial aspect of the distal margin of the lateral proximal sesamoid bone (*small white arrow*). **F,** Three-dimensional surface rendering of the plantar aspect of the MTP joint following digital elimination of the medial proximal sesamoid bone (*star*). Note the attached osseous fragment of the medial plantar process (*long white arrow*) and periosteal proliferation along the proximal lateral cortex of the proximal phalanx (*white arrowheads*). *MT3,* Third metatarsal bone; *P1,* first phalanx; *PSB,* proximal sesamoid bones; *SR,* sagittal ridge of third metatarsal bone.

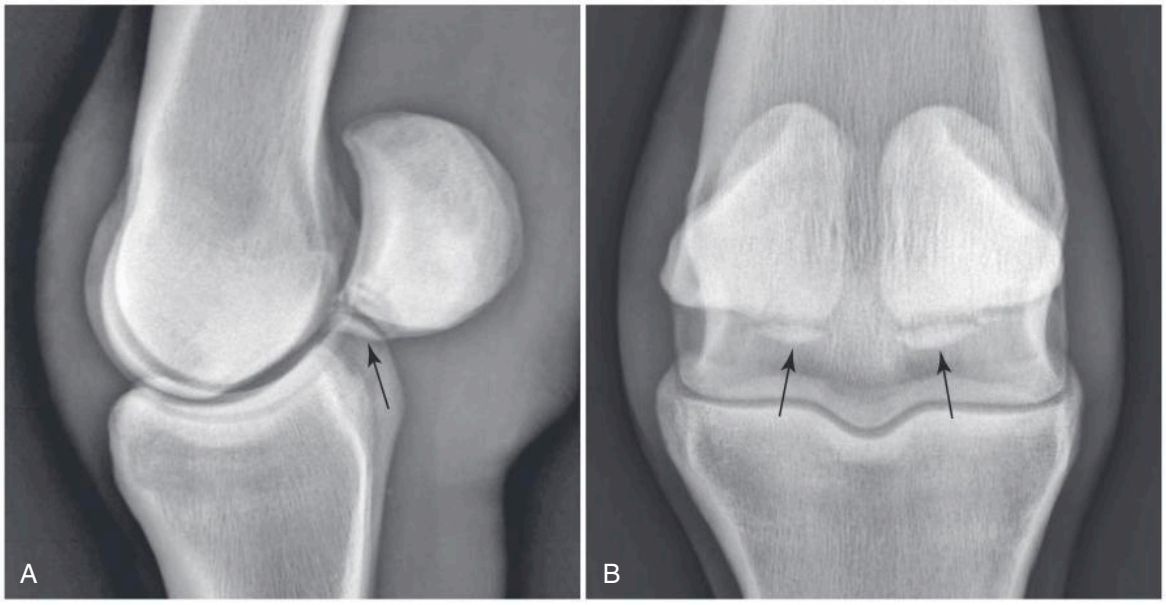


Fig. 25.17 Flexed lateromedial and dorsopalmar radiographs of a metacarpophalangeal (MCP) joint with bilateral type III fractures originating from the basilar margin of the proximal sesamoid bones. A crescent-shaped fragment **(A)** is present along the distal aspect of the proximal sesamoid bones; and on **B,** it is apparent that both proximal sesamoid bones are affected (*black arrows*).

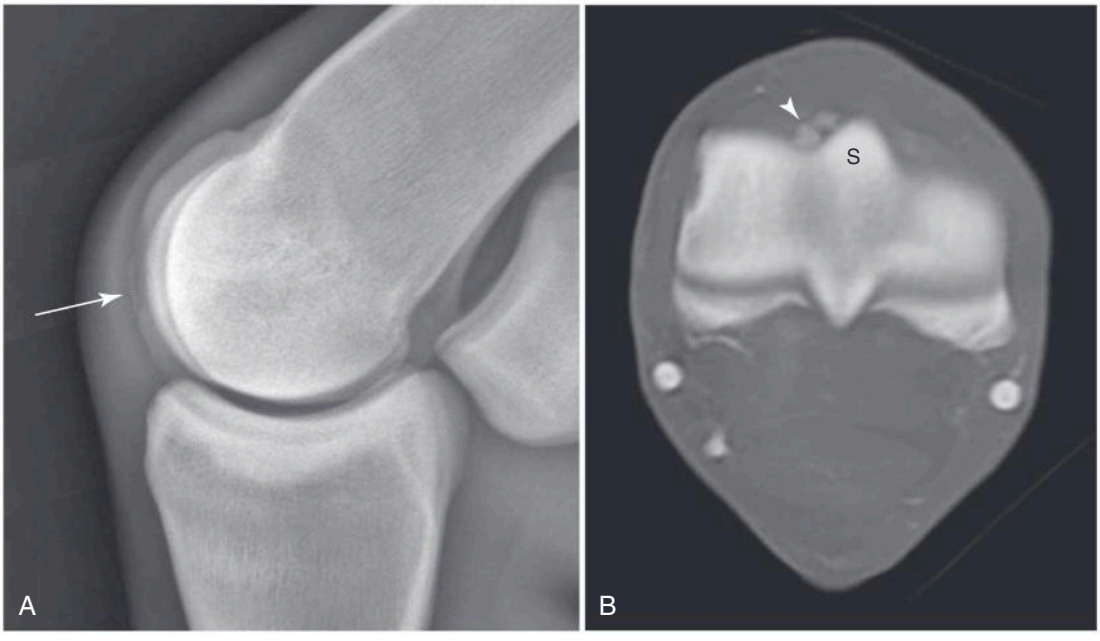


Fig. 25.18 **A,** Flexed metacarpophalangeal (MCP) joint with osteochondrosis of the sagittal ridge of MC III. There is excavation of subchondral bone (*white arrow*). **B,** Transverse computed tomography (CT) image at the distal edge of the sagittal ridge of the third metacarpal bone with two adjacent osteochondral fragments (*white arrowhead*). These fragments came from the proximal aspect of the proximal phalanx, and therefore, the sagittal ridge is smooth. *S,* Sagittal ridge of third metatarsal bone. (**A,** Courtesy John C. Janicek, DVM, MS, DACVS, Weems and Stephens Equine Hospital, Aubrey, Texas, USA.)

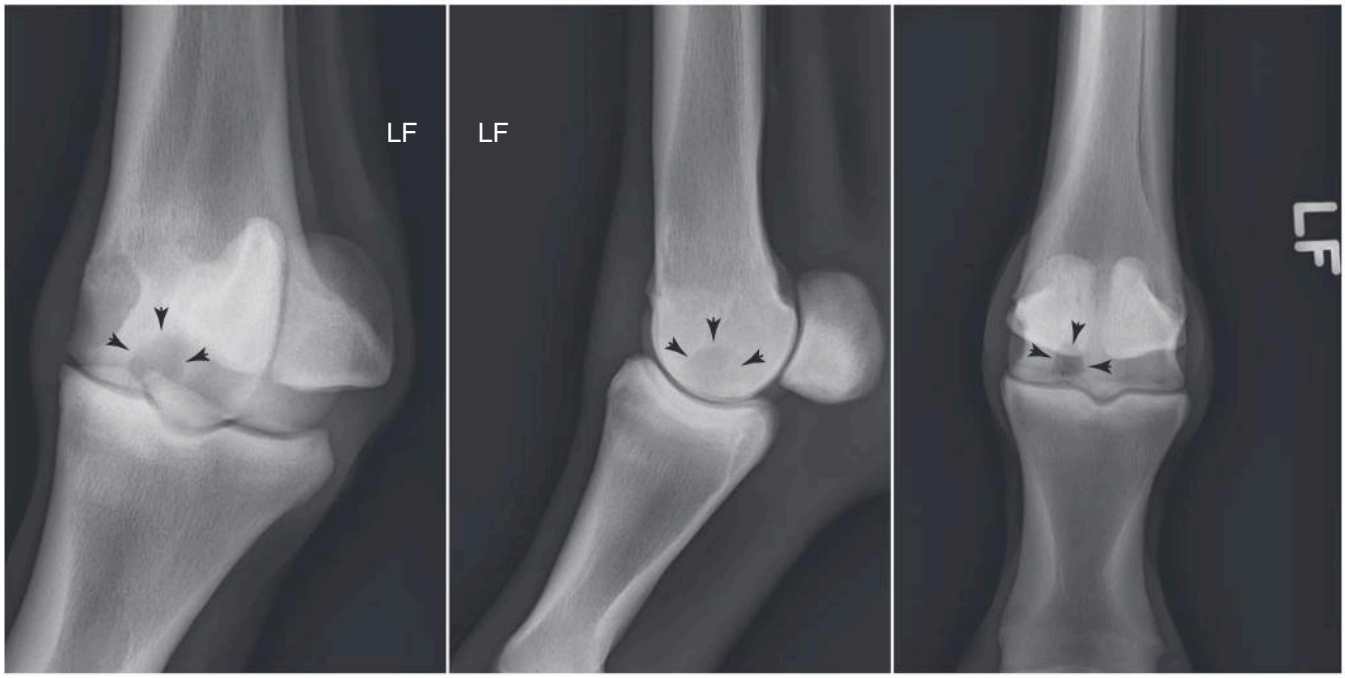


Fig. 25.19 Dorsolateral-palmaromedial oblique (*left*), lateromedial (*middle*), and dorsopalmar (*right*) radiographs of a horse with a distal third metacarpal osseous cyst-like lesion. An ovoid lucent structure with surrounding radiopaque sclerosis (*black arrowheads*) is visible on all three images, demonstrating that the lesion involves the medial condyle of the distal metacarpus. Periarticular remodeling is also seen on all three views.

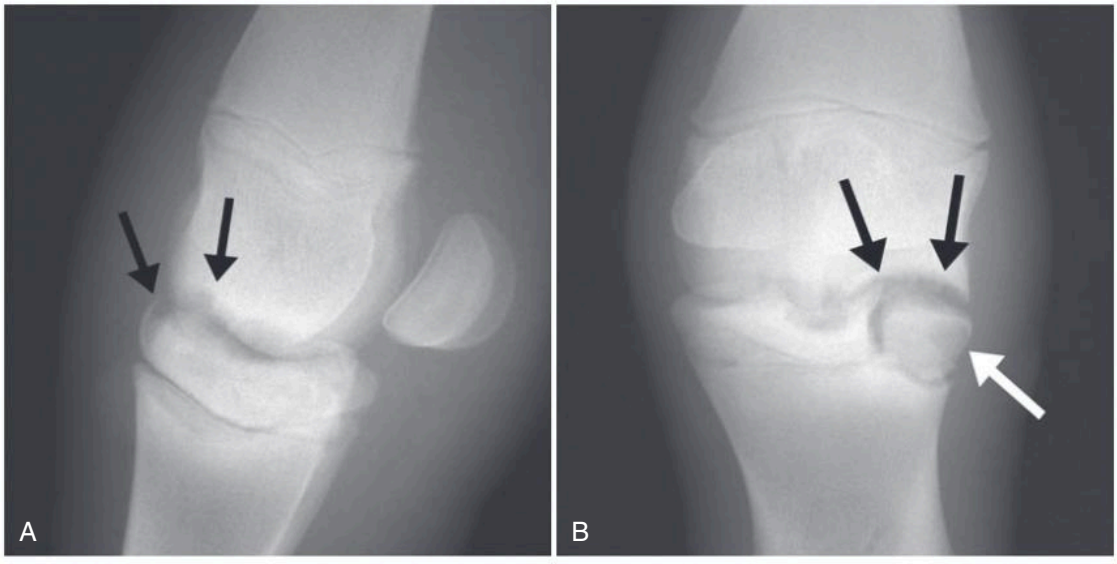


Fig. 25.20 Lateromedial and dorsopalmar views of a 1-month-old filly with soft tissue swelling, septic arthritis, and osteomyelitis. **A,** There is severe osteolysis of the subchondral bone of the distal aspect of the third metatarsal bone and the proximal epiphysis of the proximal phalanx (*black arrows*). **B,** There is severe erosion of the subchondral bone of the distal aspect of the third metatarsal bone (*black arrows*) and a large osteolytic fragment involving the medial side of the proximal epiphysis of the proximal phalanx (*white arrow*). These changes are consistent with advanced septic arthritis and septic epiphysitis with a pathologic Salter-Harris type III fracture of the epiphysis.

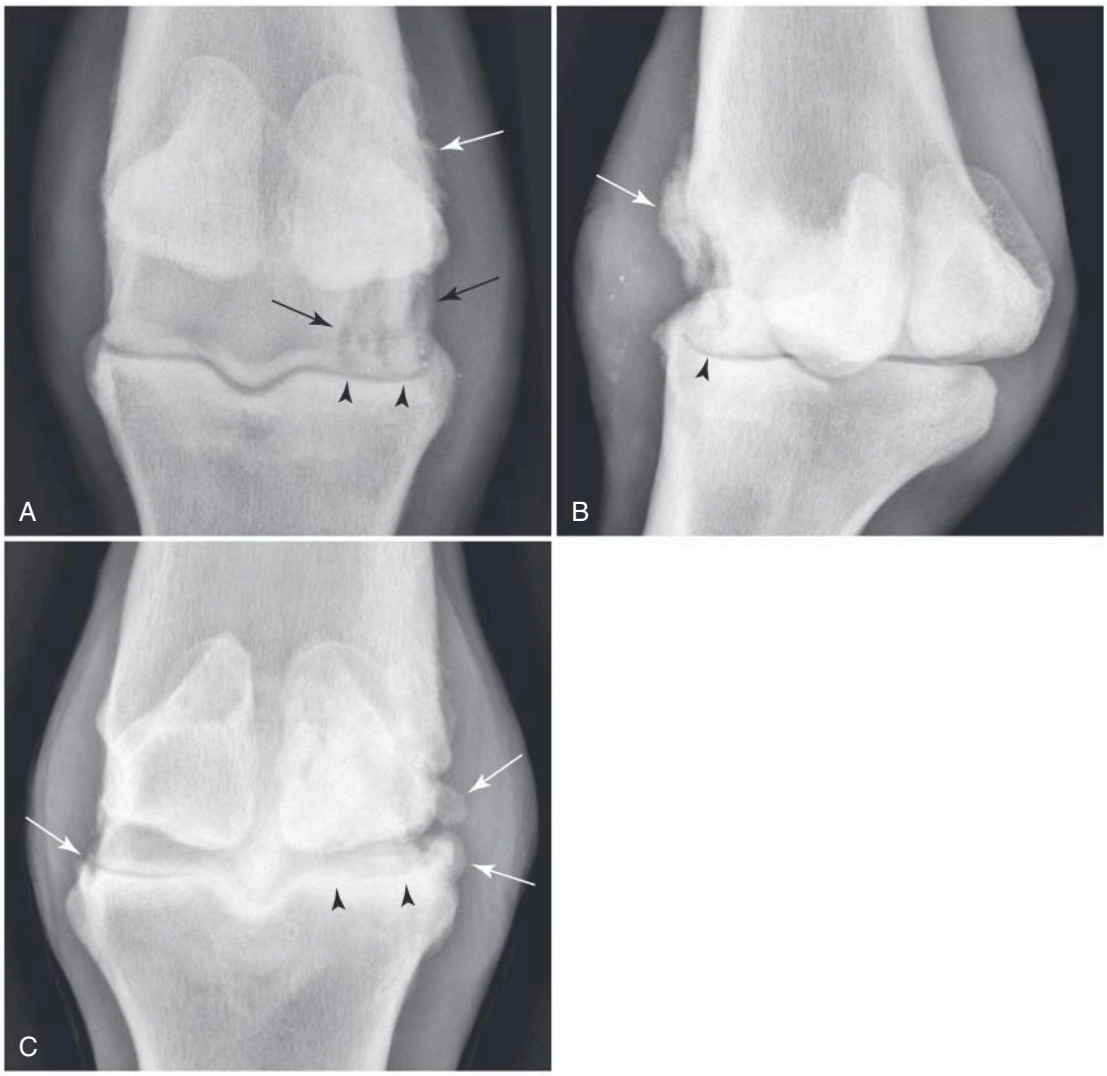


Fig. 25.21 Dorsopalmar **(A)** and dorsolateral/palmaromedial **(B)** radiographs of a horse with active septic arthritis. There is lysis of cortical and subchondral bone of the medial condyle of the third metacarpal bone (*black arrows*), irregular periosteal proliferation (*white arrows*), and mild joint space narrowing (*black arrowheads*). **C,** Dorsopalmar radiograph of a horse with chronic septic arthritis that is no longer active. There is severe erosion of subchondral bone of the opposing joint surfaces with resulting sclerosis and joint space collapse (*black arrowheads*). Smooth bone proliferation is evident on all periarticular surfaces (*white arrows*). Generalized soft tissue swelling is present surrounding the joint on all three radiographs.



Fig. 25.22 Dorsal plane (*left*) and sagittal plane (*right*) reformatted standing cone-beam computed tomography (CT) images of dorsomedial third metacarpal condylar subchondral bone disease (demineralization [*white arrowheads*]) in an aged Warmblood. For the dorsal image, medial is to the *left.* Note the somewhat ill-defined ovoid region of hypoattenuation with marked adjacent trabecular sclerosis that extends palmar and proximal to the lesion.

the most sensitive for incomplete fracture identification and characterization of palmar comminution that is not apparent on standard radiographic series[7,8,11] (see Fig. 25.3). Lateral condylar fractures most commonly propagate proximally and laterally toward the lateral cortex while medial fractures are more likely to spiral proximally; thus, radiographic evaluation of the latter requires radiograph acquisition of the entire metacarpus/metatarsus. With the exception of Standardbred racehorses, distal MC III or MT III condyle fractures in other breeds are typically the result of a single traumatic event. Radiographic signs include uneven joint surface, interruption of the metaphyseal cortex, and the presence of a radiolucent fracture line extending from the joint surface to the cortex. The fractures in Thoroughbred racehorses (Fig. 25.23) may be displaced, complete but nondisplaced, or incomplete and in a lower percentage of horses, associated with axial fracture of the ipsilateral sesamoid bone.[54,55] Prognosis after surgical treatment varies but is best for fractures without concurrent sesamoid fracture, palmar comminution, or intra-articular fragmentation.[55–57] A dorsal 20-degree medial-palmarolateral projection can improve the sensitivity of detection for this lesion.[58]

Sagittal or parasagittal fractures of the proximal phalanx in racehorses often result from prodromal accumulated microtrauma.[59] If there is distal extension of the fracture, this may extend to the proximal interphalangeal joint or obliquely through the lateral cortex of the proximal phalanx.[60] Highly comminuted proximal phalanx fractures resulting from rotational or torsional forces are not uncommon in nonracing sport and pleasure horses. Fracture location and severity must be considered relative to surgical repair and prognosis.[61]

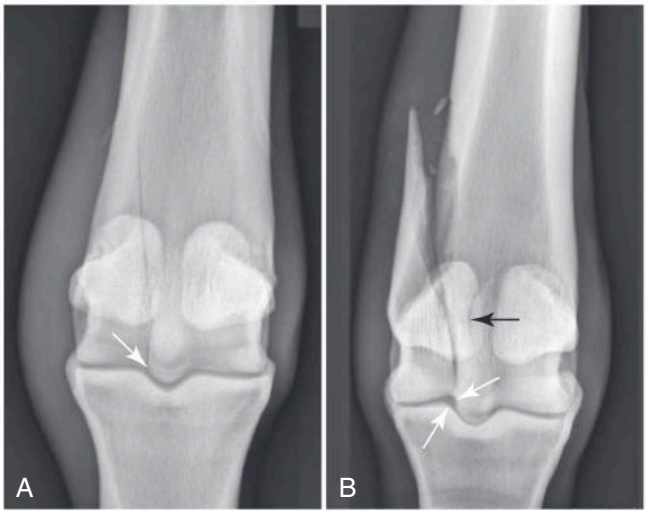


Fig. 25.23 Dorsopalmar radiographs of two horses with third metacarpal lateral condylar fractures. **A,** Incomplete, nondisplaced articular fracture (*white arrow*). **B,** Complete, displaced fracture resulting articular incongruity (*white arrows*). Concurrent axial fracture of the lateral proximal sesamoid is present (*black arrow*).

Traumatic Osteochondral Fragmentation, Chip Fractures

Traumatic osteochondral fragmentation is most common in racehorses, with the forelimbs and the medial periarticular eminence of the proximal phalanx highly overrepresented. This is the result of repetitive impact of the proximal phalanx with the dorsodistal metacarpus/tarsus in extension.[62–64] Acute chip fractures may have sharp borders and angular configurations. Chronic chip fractures undergo remodeling and have smooth, rounded borders. The latter are usually attached to the joint capsule or to the joint margin as an exostosis (Fig. 25.24, eFig. 25.4). Free joint bodies may displace or move about within the joint.

Osteochondral fragments arising from the palmarolateral/plantarolateral or palmaromedial/plantaromedial eminences of the proximal phalanx (Fig. 25.25, eFig. 25.5) have been reported as chronic or juvenile avulsion fractures[34,40,45,65] but are considered by some to be manifestations of osteochondrosis as described earlier.[41–49,66,67]

Fractures of the Proximal Sesamoids

Proximal sesamoid fractures are consistently of three types: apical, midbody, or basilar. Some may be found as osteochondral fragments separated from the sesamoid apex (apical

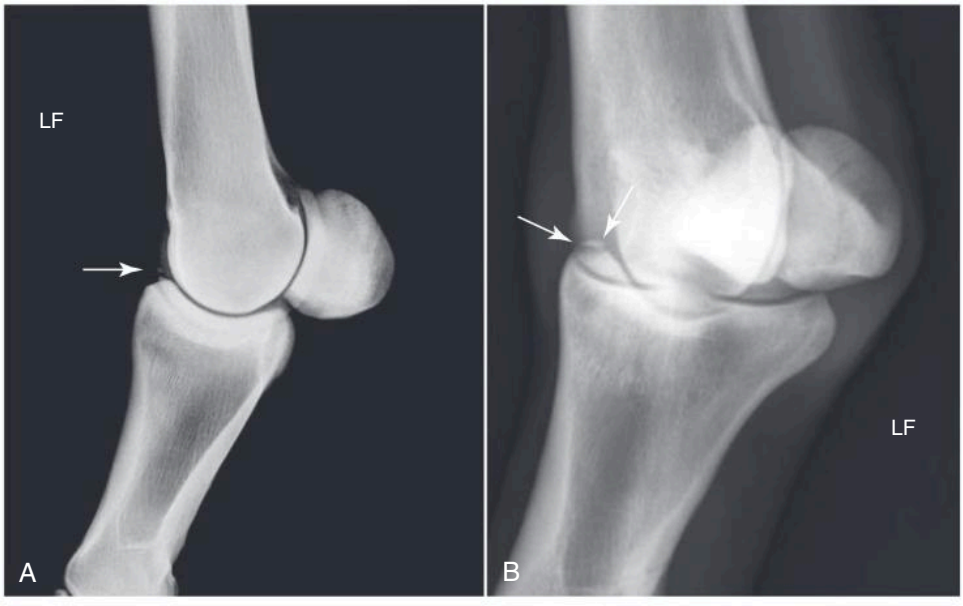
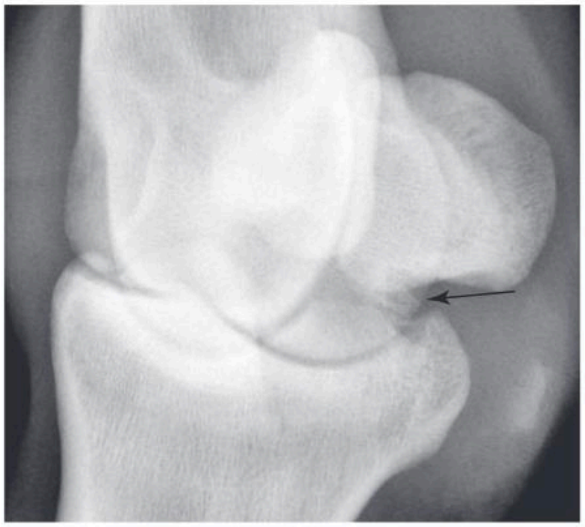


Fig. 25.24 Lateromedial **(A)** and dorsolateral-palmaromedial oblique **(B)** radiographs of a 3-year-old Thoroughbred racehorse. An osteochondral (chip) fracture (*white arrows*) is present at the dorsoproximomedial periarticular rim of the proximal phalanx with adjacent concave fragment bed within the parent bone.



eFig. 25.4 Flexed lateromedial radiograph of a horse with a dorsal metatarsophalangeal osteochondral (chip) fragment.



eFig. 25.5 Dorsolateral-plantaromedial radiograph of the metatarsophalangeal joint of a horse with an osteochondral fragment arising from the plantarolateral eminence of the proximal phalanx (*black arrow*).

fractures; see Fig. 25.2) or base (basilar fractures; see Fig. 25.17). Fractures through the body of a sesamoid may have a narrow cleavage line, indicating that the suspensory apparatus remains intact (Fig. 25.26A). Wide separation of sesamoid fragments usually indicates bilateral sesamoid fractures and disruption of the fibers of the suspensory ligament (see Fig. 25.26B). Hyperextension of the MCP or MTP joint is apparent if stress is applied to the joint or if the limb is bearing weight with disruption of the suspensory ligament.

Abaxial fractures are detected by using special radiographic projections. These fractures result from avulsion of bone by a portion of the attachment of the branches of the suspensory ligament on the medial or lateral abaxial aspects of the respective proximal sesamoid (Fig. 25.27, eFig. 25.6, see Fig. 25.2A,C).



Fig. 25.25 Dorsolateral/plantaromedial radiograph of the metatarsophalangeal (MTP) joint of a horse with an osteochondral fragment arising from the plantarolateral eminence of the proximal phalanx (*black arrow*). These fragments have features of chip fractures but are still often lumped with the osteochondrosis complex of lesions.

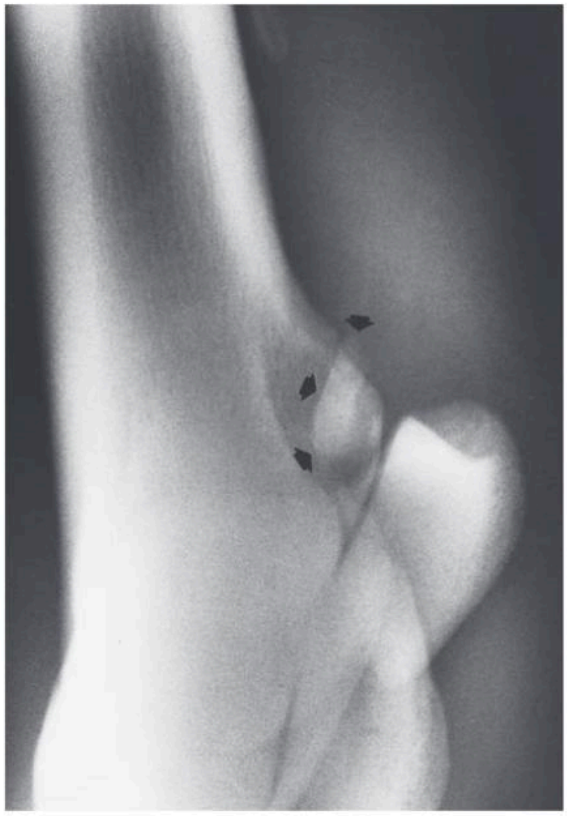


Fig. 25.27 Dorsal 50-degree proximal, 45-degree medial/palmarodistolateral radiograph of a horse with an apical, articular fracture of the medial proximal sesamoid bone (*black arrowheads*). The fracture originates at an articular surface and emerges at the abaxial surface of the sesamoid bone.

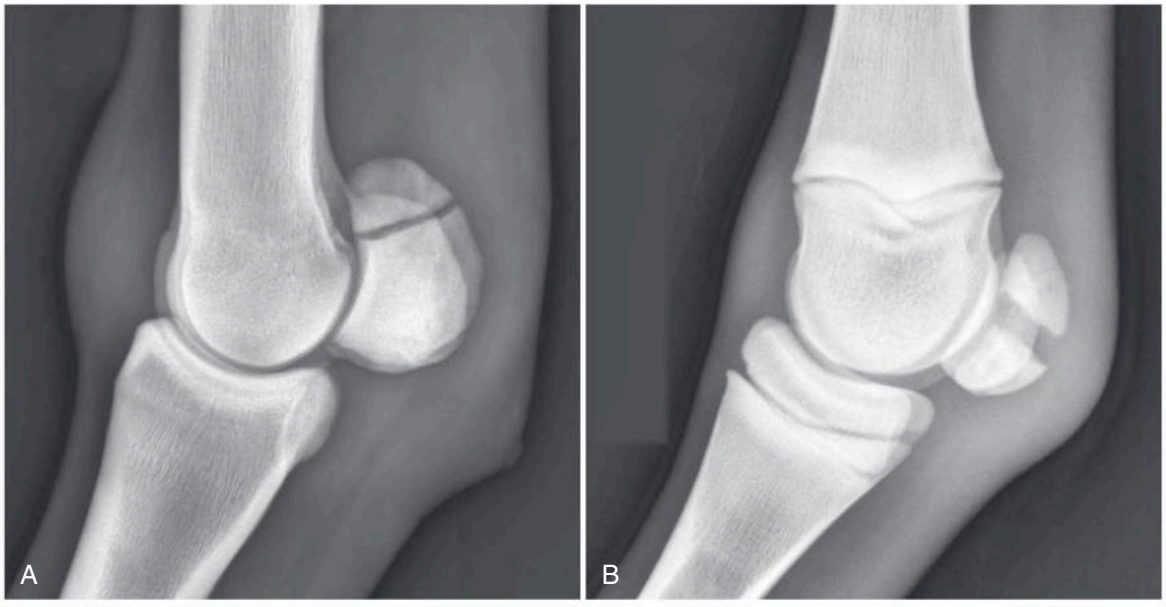


Fig. 25.26 **A,** Large apical fracture of one of the proximal sesamoid bones with mild displacement. **B,** Midbody fracture of a proximal sesamoid bone with displacement. (**A,** Courtesy John C. Janicek, DVM, MS, DACVS, Weems and Stephens Equine Hospital, Aubrey, Texas, USA.)



eFig. 25.6 Dorsolateral-plantaromedial radiograph of a horse with a chronic apical fracture of the medial sesamoid bone of the left metatarsophalangeal joint. The fragment has rounded margins and is mildly proximally displaced.

Recently, dorsal subchondral bone injury of the proximal sesamoid bones has been implicated as the underlying cause of midbody sesamoid fractures in racehorses.[68] However, these lesions are essentially impossible to detect radiographically and require cross-sectional imaging for diagnosis (i.e., CT, MRI, PET).

The prognosis of sesamoid fractures is correlated to the type of fracture and damage to the associated structures. Reviews of the clinical aspects of apical[69] and basilar[70] sesamoid fractures are available.

Sesamoiditis, Suspensory Enthesopathy

Sesamoiditis is characterized radiographically by bone proliferation on nonarticular surfaces of the proximal sesamoid bones.[71] Sesamoiditis is usually associated with degenerative change in the suspensory ligament and degenerative remodeling or fracture at the distal ends of MC II or MT IV. Linear or ovoid lysis may appear to penetrate the sesamoid from the abaxial surface. The linear lesions typically represent widened vascular channels while ovoid or cyst-like lesions represent suspensory branch enthesis resorption (Fig. 25.28, eFig. 25.7). Axial sesamoiditis is somewhat rare with numerous speculative etiologies, including infarction, infection, and trauma.[72] Axial and intersesamoidean sesamoid pathology is notoriously painful typically with a poor prognosis for athletic soundness regardless of the underlying etiology.

Disuse Atrophy of Bone

The earliest manifestation of disuse atrophy is typically in the proximal sesamoid bones but may also be recognized in the long bones as a reduction in medullary opacity and cortical thinning. Trabeculae within the bone become large and coarse. This change occurs because of altered stress or axial weight bearing and may not signify primary pathologic change in the joint (Fig. 25.29).

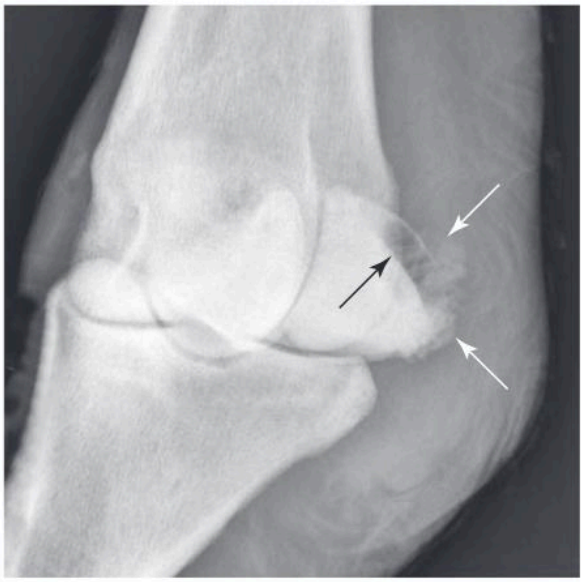


Fig. 25.28 Dorsal 45-degree medial/palmarolateral radiograph of a horse with sesamoiditis of the medial proximal sesamoid bone. Degenerative remodeling is present with increased size of vascular channels within the sesamoid bone and enthesis resorption (*black arrow*) and palmar enthesophytosis (*white arrows*). Soft tissue swelling surrounds the metacarpophalangeal (MCP) joint.



Fig. 25.29 Lateromedial **(A)** and dorsal 45-degree medial/palmarolateral **(B)** radiographs of the distal third metacarpal bone and the proximal phalanx of a horse recently having external support removed from the leg. Sclerosis surrounds the transverse pin tracts, but the remaining bone has advanced osteopenia. Generalized remodeling of bone has occurred, and the cortices are thin. Osseous trabeculae are coarse and irregular, with no organized pattern and linear radiolucent lines running the length of included portion of the third metacarpal bone. The sesamoid bones have a sponge-like appearance. There is generalized soft tissue swelling and periarticular remodeling along the dorsal aspect of the metacarpophalangeal (MCP) joint.



eFig. 25.7 Dorsomedial-palmarolateral radiograph of a horse with sesamoiditis of the medial proximal sesamoid bone. The vascular channels are widened and there is enthesophytosis near the attachment site of the annular and/or suspensory ligaments.

Acknowledgment

With special thanks to prior authors of this chapter for their contributions.

REFERENCES

1. Getty RS. *Grossman's the Anatomy of the Domestic Animals*. 5th ed. Philadelphia: Saunders; 1975:357–360.
2. Weaver JC, Stover SM, O'Brien TR. Radiographic anatomy of soft tissue attachments in the equine metacarpophalangeal and proximal phalangeal region. *Equine Vet J*. 1992;24(4):310–315.
3. Rendano VT. Equine radiology. The fetlock. *Mod Vet Pract*. 1977;58(10):871–875.
4. Butler JA, Colles CM, Dyson SJ, et al. *Clinical Radiology of the Horse*. London: Blackwell; 2017:175–215.
5. Morgan JP. *Techniques of Veterinary Radiography*. 5th ed. Ames: Iowa State University; 1993.
6. O'Brien T. *Radiography for the Ambulatory Equine Practitioner*. Jackson, WY: Teton; 2005.
7. Davis A, Fan X, Shen L, Robinson P, Riggs C. Improved radiological diagnosis of palmar osteochondral disease in the Thoroughbred racehorse. *Equine Vet J*. 2017;49(4): 454–460.
8. Hornof WJ, O'Brien TR. Radiographic evaluation of the palmar aspect of the equine metacarpal condyles: a new projection. *Vet Radiol*. 1980;21:161.
9. Palmer SE. Radiography of the abaxial surface of the proximal sesamoid bones of the horse. *J Am Vet Med Assoc*. 1982;181(3):264–265.
10. Pilsworth RC, Hopes R, Greet TR. A flexed dorso-palmar projection of the equine fetlock in demonstrating lesions of the distal third metacarpus. *Vet Rec*. 1988;122(14): 332–333.
11. Ramzan P, Palmer L, Powell S. Unicortical condylar fracture of the Thoroughbred fetlock; 45 cases (2006–2013). *Equine Vet J*. 2015;47(6):680–683.
12. De Guio C, Segard-Weisse E, Thomas-Cancian A, Schramme M. Bone marrow lesions of the distal condyles of the third metacarpal bone are common and not always related to lameness in sports and pleasure horses. *Vet Radiol Ultrasound*. 2018;60(2):167–175.
13. Seignour M, Coudry V, Norris R, et al. Ultrasound examination of the palmar/plantar aspect of the fetlock in the horse. Technique and normal images. *Equine Vet J*. 2012;24:18–29.
14. DiGiovanni DL, Radmacher N, Riggs LM, et al. Dynamic sonography of the equine metacarpo (tarso) phalangeal digital flexor tendon sheath. *Vet Radiol Ultrasound*. 2016;57(6):621–629.
15. Werpy N, Chapman K, Griffith L. Non-weight bearing ultrasonographic examination allows the diagnosis of longitudinal fiber disruption (split) in the equine suspensory ligament branches not visible on weight bearing examination. *Vet Radiol Ultrasound*. 2020;62(1):84–97.
16. Denoix JM, Jacot S, Bousseau B, et al. Ultrasonographic anatomy of the dorsal and abaxial aspects of the equine fetlock. *Equine Vet J*. 1996;28(1):54–62.
17. Trope GD, Anderson GA, Whitton RC. Patterns of scintigraphic uptake in the fetlock joint of Thoroughbred racehorses and the effect of increased radiopharmaceutical uptake in the distal metacarpal/tarsal condyle on performance. *Equine Vet J*. 2011;43(5):509–515.
18. Dyson S, Murray R. Osseous trauma in the fetlock region in mature sport horses. *AAEP Proceedings*. 2006;52:443–456.
19. Twardock AR. Equine bone scintigraphic uptake patterns related to age, breed, and occupation. *Vet Clin N Am-Equine*. 2001;17(1), 75-04.
20. Vanderperren K, Ghaye B, Snaps FR, et al. Evaluation of computed tomographic anatomy of the equine metacarpophalangeal joint. *Am J Vet Res*. 2008;69(5):631–638.
21. Olive J, D'Anjou MA, Alexander K, et al. Comparison of magnetic resonance imaging, computed tomography, and radiography for assessment of noncartilaginous changes in equine metacarpophalangeal osteoarthritis. *Vet Radiol Ultrasound*. 2010;51(3):267–279.
22. Morgan J, Santschi E, Zekas L, et al. Comparison of radiography and computed tomography to evaluate metacarpo/metatarsophalangeal joint pathology of paired limbs of thoroughbred racehorses with severe condylar fracture. *Vet Surg*. 2006;35(7):611–617.
23. Curtiss A, Ortved K, Dallap-Schaer B, et al. Validation of standing cone beam computed tomography for diagnosing subchondral fetlock pathology in the Thoroughbred racehorse. *Equine Vet J*. 2020;53(3):510–523.
24. Johnston GCA, Ahern BJ, Palmieri C, Young A. Imaging and gross pathologic appearance of changes in the parasagittal groove of Thoroughbred racehorses. *Animals*. 2021; 11(12):3366.
25. Brounts SH, Lund J, Whitton RC, Ergun D, Muir P. Use of a novel helical fan beam imaging system for computed tomography of the distal limb in sedated standing horses. 167 cases (2019–2020). *J Am Vet Med A*. 2022;260(11): 1351–1360.
26. Tucker RL, Sande RD. Magnetic resonance imaging and computed tomography: evaluation of equine musculoskeletal conditions. *Vet Clin North Am Equine Pract*. 2001;17:145.
27. Smith M, Dyson S. In: Murray R, Equine MRI, eds. *Normal Anatomy: The Fetlock Region*. West Sussex, UK: Wiley-Blackwell; 2011:173–189.
28. Powell S. In: Murray R, Equine MRI, eds. *The Fetlock Region*. West Sussex, UK: Wiley-Blackwell; 2011:315–360.
29. Dyson S, Murray R. Magnetic resonance imaging of the equine fetlock. In: Orsini J, ed. *Clinical Techniques in Equine Practice*. Philadelphia: Elsevier/Saunders; 2007: 62–78.
30. Brama PA, Tekoppele JM, Bank RA, et al. Topographical mapping of biochemical properties of articular cartilage in the equine fetlock joint. *Equine Vet J*. 2000;32(1):19–26.
31. Smith S, Dyson SJ, Murray RC. Magnetic resonance imaging of distal sesamoidean ligament injury. *Vet Radiol Ultrasound*. 2008;49(6):516–528.
32. McKnight AL, Manduca A, Felmlee JP, et al. Motion correction techniques for standing equine MRI. *Vet Radiol Ultrasound*. 2004;45(6):513–519.
33. Spriet M, Arndt S, Pige C, et al. Comparison of skeletal scintigraphy and standing 18F-NaF positron emission tomography for imaging the fetlock in 33 Thoroughbred racehorses. *Vet Radiol Ultrasound*. 2022;1–8 (published online).
34. Pool RR, Meagher DM. Pathologic findings and pathogenesis of racetrack injuries. *Vet Clin North Am Equine Pract*. 1990;6(1):1–30.
35. Bramlage L. Part 1. Operative orthopedics of the fetlock joint of the horse: traumatic and developmental diseases of the equine fetlock joint. *Milne Lecture AAEP Annual Convention*. 2009;55.
36. Gillette EL, Thrall DE, Lebel JL. *Carlson's Veterinary Radiology*. 3rd ed. Philadelphia: Lea & Febiger; 1977:435.
37. McIlwraith CW, Frisbie DD, Kawcak CE. The horse as a model of naturally occurring osteoarthritis. *Bone Joint Res*. 2012;1(11):297–309.
38. Declercq K, Martens A, Maes D, Boussauw B, Forsyth R, Boening KJ. Dorsoproximal proximal phalanx osteochondral fragmentation in 117 Warmblood horses. *Vet Comp Orthop Traumatol*. 2009;22(1):1–6.

39. O'Brien TR, Hornof WJ, Meagher DM. Radiographic detection and characterization of palmar lesions in the equine fetlock joint. *J Am Vet Med Assoc.* 1981;178(3): 231–237.
40. Petterson H, Ryden G. Avulsion fractures of the caudoproximal extremity of the first phalanx. *Equine Vet J.* 1982;14(4):333–335.
41. Carlsten J, Sandgren B, Dalin G. Development of osteochondrosis in the tarsocrural joint and osteochondral fragments in the fetlock joints of Standardbred trotters. I. A radiological survey. *Equine Vet J.* 1993;16:42. suppl.
42. Grøndahl AM, Engeland A. Influence of radiographically detectable orthopedic changes on racing performance in Standardbred trotters. *J Am Vet Med Assoc.* 1995;206(7):1013–1017.
43. Gaschen L, Burba DJ. Musculoskeletal injury in thoroughbred racehorses: correlation of findings using multiple imaging modalities. *Vet Clin North Am Equine Pract.* 2012;28(3):542–551.
44. Kawack CE, McIlwraith CW. Proximodorsal first phalanx osteochondral chip fragmentation in 336 horses. *Equine Vet J.* 1994;26(5):392–396.
45. Dalin G, Sandgren B, Carlsten J. Plantar osteochondral fragments in the fetlock joints of Standardbreds: result of osteochondrosis or trauma? *Equine Vet J.* 1993;suppl 16:62.
46. Philipsson J, Andréasson E, Sandgren B, et al. Osteochondrosis in the tarsocrural joint and osteochondral fragments in the fetlock joints in Standardbred trotters. II. Heritability. *Equine Vet J.* 1993;suppl 16:38.
47. Sandgren B, Dalin G, Carlsten J, et al. Development of osteochondrosis in the tarsocrural joint and osteochondral fragments in the fetlock joints of Standardbred trotters. II. Body measurements and clinical findings. *Equine Vet J.* 1993;suppl 16:48.
48. Sandgren B, Dalin G, Carlsten J. Osteochondrosis in the tarsocrural joint and osteochondral fragments in the fetlock joints in Standardbred trotters. I. Epidemiology. *Equine Vet J.* 1993;suppl 16:31.
49. Fortier LA, Foerner JJ, Nixon AJ. Arthroscopic removal of axial osteochondral fragments of the plantar/palmar proximal aspect of the proximal phalanx in horses: 119 cases (1988–1992). *J Am Vet Med Assoc.* 1995;206(1): 71–74.
50. Yovich JV, McIlwraith CW, Stashak TS. Osteochondritis dissecans of the sagittal ridge of the third metacarpal and metatarsal bones in horses. *J Am Vet Med Assoc.* 1985;186(11):1186–1191.
51. Smith MWR, Kawcak CE, McIlwraith CW. Science in brief: report on the Havermeyer Foundation workshop on subchondral bone problems in the equine athlete. *Equine Vet J.* 2016;48:6–8.
52. Gold S, Werpy N, Gutierrez-Nibeyro S. Injuries of the sagittal groove of the proximal phalanx in Warmblood horses detected with low-field magnetic resonance imaging: 19 cases (2007–2016). *Vet Radiol Ultrasound.* 2017;58(3):344–353.
53. Ammann L, Ohlerth S, Furst AE, Jackson MA. Differences of morphological attributes between 62 proximal and distal subchondral cystic lesions of the proximal phalanx as determined by radiography and computed tomography. *J Am Vet Med A.* 2022;83(12).
54. Zekas LJ, Bramlage LR, Embertson RM, et al. Characterization of the type and location of fractures of the third metacarpal/metatarsal condyles in 135 horses in central Kentucky (1986–1994). *Equine Vet J.* 1999;31(4): 304–308.
55. Rick MC, O'Brien TR, Pool RR, et al. Condylar fractures of the third metacarpal bone and third metatarsal bone in 75 horses. Radiographic features, treatments, and outcome. *J Am Vet Med Assoc.* 1983;183(3):287–296.
56. Zekas LJ, Bramlage LR, Embertson RM, et al. Results of treatment of 145 fractures of the third metacarpal/metatarsal condyles in 135 horses (1986–1994). *Equine Vet J.* 1999;31(4):309–313.
57. Cianci JM, Wulster KB, Richardson DW, Stefanovski D, Ortved KF. Computed tomographic assessment of fracture characteristics and subchondral bone injury in Thoroughbred racehorses with lateral condylar fractures and their relationship to outcome. *Vet Surg.* 2022;51(3):426–437.
58. Labbe K, Pigott JH. Radiographic technique to improve diagnosis of sagittal axial sesamoid fracture in racing Thoroughbreds with lateral condylar fracture. *Equine Vet Edu.* 2022;34(4):200–206.
59. Ramzan PHL, Powell SE. Clinical and imaging features of suspected prodromal fractures of the proximal phalanx in three Thoroughbred racehorses. *Equine Vet J.* 2010;42(2): 164–169.
60. Smith MRW, Corletto FC, Wright IM. Parasagittal fractures of the proximal phalanx in Thoroughbred racehorses in the UK: outcome of repaired fractures in 113 cases (2007–2011). *Equine Vet J.* 2017;49(6):784–788.
61. Holcombe SJ, Schneider RK, Bramlage LR, et al. Lag screw fixation of noncomminuted sagittal fractures of the proximal phalanx in racehorses: 59 cases (1973–1991). *J Am Vet Med Assoc.* 1995;206(8):1195–1199.
62. Yovich JV, McIlwraith CW. Arthroscopic surgery for osteochondral fractures of the proximal phalanx of the metacarpophalangeal and metatarsophalangeal (fetlock) joints in horses. *J Am Vet Med Assoc.* 1986;188(3):273–279.
63. Ramzan PHL, Wylie CE. Nonsurgical and surgical management of metacarpo/metatarsophalangeal joint dorsal chip fracture in the Thoroughbred racehorse. *Equine Vet J.* 2020;52:399–403.
64. Walsh R, Smith MRW, Wright IM. Frequency distribution of osteochondral fragmentation of the dorsoproximal articular surface of the proximal phalanx in racing Thoroughbreds in the UK. *Equine Vet J.* 2018;50(5):624–628.
65. Nixon AJ, Pool RR. Histologic appearance of axial osteochondral fragments from the proximoplantar/proximopalmar aspect of the proximal phalanx in horses. *J Am Vet Med Assoc.* 1995;207(8):1076–1080.
66. Barclay WP, Foerner JJ, Phillips TN. Lameness attributable to osteochondral fragmentation of the plantar aspect of the proximal phalanx in horses. 19 cases (1981–1985). *J Am Vet Med Assoc.* 1987;191(7):855–857.
67. Grøndhal AM. Incidence and development of ununited proximoplantar tuberosity of the proximal phalanx in Standardbred trotters. *Vet Radiol Ultrasound.* 1992;33:18.
68. Schaffer SK, To C, Garcia T, Fyhrie DP, Uzal FA, Stover SM. Subchondral focal osteopenia associated with proximal sesamoid bone fracture in Thoroughbred racehorses. *Equine Vet J.* 2021;53:294–305.
69. Spurlock GH, Gabel AA. Apical fractures of the proximal sesamoid bones in 109 Standardbred horses. *J Am Vet Med Assoc.* 1983;183(1):76–79.
70. Parente EJ, Richardson DW, Spencer P. Basal sesamoidean fractures in horses: 57 cases (1980–1991). *J Am Vet Med Assoc.* 1993;202(8):1293–1297.
71. Blevins WE, Widmer WR. Radiology in racetrack practice. *Vet Clin North Am Equine Pract.* 1990;6(1):31–61.
72. Le Roux C, Carstens A. Axial sesamoiditis in the horse: a review. *J S Afr Vet Assoc.* 2018;89:1544.

ELECTRONIC RESOURCES

Additional information related to the content in Chapter 25 can be found online at eBooks.Health.Elsevier.com.

- Chapter Quiz

CHAPTER 26

Equine Pastern

Elizabeth Biscoe • Dana A. Neelis

OVERVIEW

The proximal phalanx (P1) and middle phalanx (P2) are the osseous structures of the equine pastern region. In the horse, the proximal phalanx is the longest of the phalanges, with the middle phalanx being approximately half of the length of the proximal phalanx. The proximal interphalangeal (pastern) joint is a diarthrodial joint formed where the proximal and middle phalanges meet. The pastern region is supported by multiple soft tissue structures, including the medial and lateral collateral ligaments, straight and oblique distal sesamoidean ligaments, superficial and deep digital flexor tendons, collateral sesamoidean ligament (suspensory ligament of the navicular bone), abaxial and axial palmar (plantar) ligaments, proximal and distal digital annular ligaments, and the extensor tendons. The digital flexor tendon sheath is also located along the palmar/plantar aspect of the pastern region. No muscle is present in the pastern region and there is very little fat delineating these soft tissue structures on radiographs. Detailed radiographic anatomy of this region is illustrated in Chapter 16 and can be found in multiple published sources, including comparative images of the anatomy on multiple imaging modalities (i.e., ultrasound, magnetic resonance imaging [MRI]) for reference.[1–4]

INDICATIONS FOR RADIOGRAPHY

Radiographs of the pastern are often included on survey images of the foot and/or fetlock; however, radiographs centered on the proximal interphalangeal joint are necessary to minimize distortion and obtain a more detailed assessment of this joint and the middle phalanx if disease is localized to this region. Imaging of the pastern may be pursued when clinically indicated from the history, findings from physical or lameness examinations, or results of diagnostic analgesia (i.e., palmar digital, abaxial, or basi-sesamoid nerve blocks).

ALTERNATE IMAGING OF THE PASTERN

Alternate imaging modalities (i.e., standing low-field vs. high-field MRI, computed tomography [CT], ultrasound) are very often used to assess the pastern region, especially when there is concern for abnormalities of the soft tissue structures. These modalities will not be discussed in detail in this chapter but will be referenced when applicable.

TECHNICAL FACTORS

Patient Preparation

Preparation of the pastern region for radiographic examination is similar to preparation of the foot. Removal of any dirt, debris, or iodine-containing substances from the skin or haircoat of the pastern region is needed to avoid artifacts. Elevation of the foot with the use of positioning devices (i.e., wooden blocks) is helpful to center the radiographic beam on the proximal interphalangeal joint.

Recommended Views

Lateromedial, dorsopalmar,* dorsomedial-palmarolateral oblique, and dorsolateral-palmaromedial oblique views are routinely obtained for assessment of the pastern. Flexed lateromedial and/or oblique views may be used for assessment of the periarticular margins of the proximal interphalangeal joint.[3] Obtaining the dorsopalmar view with a 5- to 10-degree angle from proximal to distal, with corresponding mild angulation of the imaging plate, may also be helpful for assessing this joint.

NORMAL RADIOGRAPHIC ANATOMY AND ANATOMICAL VARIATIONS

A few normal anatomic and incidental variants are present in the pastern region and should be noted to avoid misinterpreting these areas as pathologic during radiographic assessment.[3,5,6] On the dorsopalmar view of the distal limb, the proximal interphalangeal joint space is normally mildly wider than the fetlock joint, but narrower when compared to the distal interphalangeal joint (Fig. 26.1). If the patient is properly positioned with even weight bearing on the foot, the proximal interphalangeal joint space should be symmetric in width from medial to lateral; however, if the patient is placing more weight on one side of the limb or the other, this may create the appearance of asymmetric joint space narrowing.[7]

An area devoid of trabeculae is present centrally within the proximal phalanx, and occasionally a similar, but smaller, region is present centrally within the middle phalanx. On radiographs, this area appears more radiolucent than the remainder of the medullary cavity and is most apparent on the dorsopalmar view (Fig. 26.2). This radiolucent area may appear circular or ovoid and is variable in size. On the dorsopalmar view of the proximal phalanx, thin radiopaque lines, extending from proximal to distal, are visible along the medial and lateral aspects of this radiolucent region in the medullary cavity. These are the sites of attachment of the oblique distal sesamoidean ligaments and should not be misinterpreted as a lesion. On the lateromedial view, the distal aspect of the insertion of the oblique distal sesamoidean ligaments is also commonly visible as a small area of irregular bone along the palmar cortex of the distal third of the proximal phalanx. This area may be more prominent in older and/or larger horses.[3]

*Palmar/dorsopalmar is used throughout this chapter with the understanding that plantar/dorsoplantar should be substituted if referencing the hindlimb.

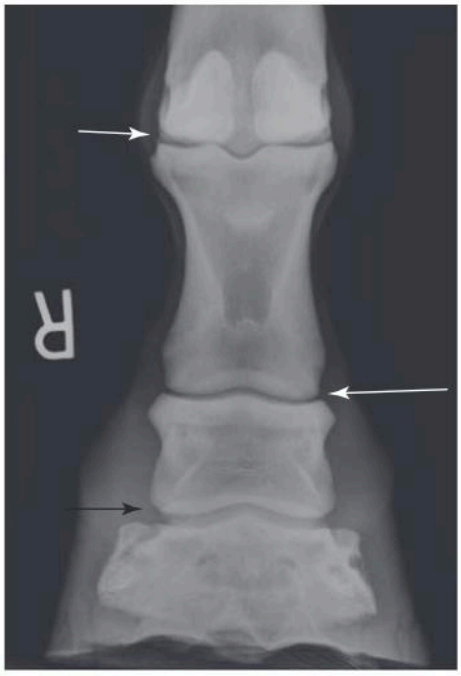


Fig. 26.1 Dorsopalmar view of the distal limb. On this view, the width of the joint spaces of the fetlock joint (*short white arrow*), proximal interphalangeal joint (*long white arrow*), and distal interphalangeal joint (*short black arrow*) can be compared. The distal interphalangeal joint space is typically the widest, followed by the proximal interphalangeal joint, with the fetlock joint being the narrowest.



Fig. 26.2 Dorsopalmar view of the distal limb. A small, round, mineral opacity that corresponds to the ergot is present summating with the proximal phalanx (*short white arrow*). A round radiolucency is present in the mid medullary cavity of the proximal phalanx (*long white arrow*), often where the cortices of the bone are thickest. A thin radiopaque rim may be seen around this central region of radiolucency. A small, round radiolucency is present along the distal aspect of the proximal phalanx, which is associated with the small concavity in the distal palmar aspect of the bone and should not be confused for a cyst (*between the short black arrows*). The nutrient foramen appears as a small linear lucency along the proximal aspect of the middle phalanx, near midline (*long black arrow*).

The ergot can be visible as a round soft tissue to mineral opacity superimposed with the proximal phalanx on the dorsopalmar view (see Fig. 26.2). On the corresponding lateromedial view, the ergot will be located along the palmar aspect of the skin.

A small palmar concavity is present between the medial and lateral condyles of the distal aspect of the proximal phalanx. This concavity may create another round radiolucent region near midline on dorsopalmar radiographs and should not be mistaken for a cyst in the distal aspect of the bone (see Fig. 26.2).

A nutrient foramen may be identified radiographically in the proximal phalanx but can be variable in position. The position of the nutrient foramen of the proximal phalanx on forelimb radiographs has been characterized in two studies.[8,9] A nutrient foramen was identified radiographically in the majority of forelimbs reviewed (77% of Thoroughbreds and 69.5% of Standardbreds) and was present either within the dorsal or palmar cortex. The appearance of the nutrient foramen can be bilaterally symmetrical in some horses but asymmetrical in others. A nutrient foramen was not found in both the dorsal and palmar cortex of the same limb; however, both were occasionally present in the proximal phalanx of foals (Fig. 26.3). In another review of dorsal foramina in the proximal phalanx, the nutrient foramen was found in the dorsal cortex of 27.5% of the forelimbs and hindlimbs evaluated.[10] In this study, three breeds of horses (Standardbreds, Warmbloods, and Friesians) were included, and in most of the horses the dorsal foramen was identified unilaterally.

The nutrient foramen in the dorsal aspect of the proximal phalanx is best seen on the lateromedial view and most commonly courses obliquely from proximal to distal at the level of the mid diaphysis (see Fig. 26.3, also see Fig. 26.6B). On the dorsopalmar view, the foramen in the dorsal cortex appears as a thin lucent line in the medullary region near midline (see Fig. 26.6A). When in the palmar cortex, the foramen is typically



Fig. 26.3 Lateromedial view of the proximal phalanx in a 2-month-old foal. Linear radiolucencies are present along the dorsal (*long white arrow*) and palmar (*short white arrow*) cortices of the diaphysis. These are normal nutrient foramina and were bilaterally symmetric in the forelimbs of this patient.

in the distal third of the bone and courses in a shorter oblique to transverse direction.

RADIOGRAPHIC ABNORMALITIES

Osseous Lesions

Osteochondrosis/Osteochondral Fragments

Developmental disease, such as osteochondrosis, does not occur as commonly in the proximal interphalangeal joint as in other joints of the horse. Osteochondral fragments, secondary to osteochondrosis, are occasionally found in the proximal interphalangeal joint. In one study assessing presale radiographs of Warmbloods, an osteochondral fragment was present in the proximal interphalangeal joint in 0.9% of horses.[11] Osteochondral fragments have been described along the dorsal/dorsomedial and palmar/plantar aspects of the proximal interphalangeal joint, originating from the distal aspect of the proximal phalanx (most common) or proximal aspect of the middle phalanx.[12–17] Dorsal fragments have been suggested to be developmental in origin, whereas palmar fragments have been proposed to be due to partial avulsion fractures of the soft tissue attachments along the proximal interphalangeal joint during hyperextension of the joint.[3,12,13,17] Osteochondral fragments in the proximal interphalangeal joint may be incidental findings but have also been associated with lameness. In these horses, removal of the fragments is often recommended and return to previous levels of athletic performance has been reported.[12,17,18]

Osseous Cyst-Like Lesions

Osteochondrosis can also manifest as subchondral cystic lesions along the proximal interphalangeal joint, especially in a juvenile patient with no history of trauma.[19,20] Osseous cyst-like lesions (also known as subchondral cystic lesions or cysts, osseous cysts, or subchondral cyst-like osteochondrosis) can occur in the pastern region and are typically found in the subchondral bone near, and often communicating with, the proximal interphalangeal joint[21] (Fig. 26.4, eFig. 26.1). These cysts are most commonly identified unilaterally in the distal condyle of the proximal phalanx, although bilateral lesions are possible.[15,19,22,23] These lesions are more common in the hindlimb. Radiographically, these lesions may initially appear as a small depression, flattening or concavity in the articular margin but can later progress to a round, ovoid, conical-shaped or multichambered radiolucency in the subchondral bone.[3,21] Single cysts or multiple cysts may be present, with varying degrees of surrounding sclerosis. In addition to osteochondrosis, these cystic lesions can develop secondary to osteoarthritis, infection, or trauma; however, the etiology of these cysts is still debated.[19–23]

Variable degrees of lameness have been reported in patients with osseous cyst-like lesions, likely associated with the extent of joint involvement. These lesions are typically more clinically significant when the cyst communicates with the joint; therefore, careful assessment of the radiographs for any involvement of the articular surface, such as a thin cloaca or a wider, broader area of radiolucency between the cyst and articular margin, is advised. Advanced imaging (i.e., MRI) may be needed in some horses to confirm the diagnosis of a cyst and/or to determine if the cyst is communicating with the joint. In young horses, small subchondral cysts can be identified incidentally on survey radiographs and may resolve or cause minimal clinical signs; however, others will progress with secondary osteoarthritis and be associated with clinically significant lameness.[22,24,25]



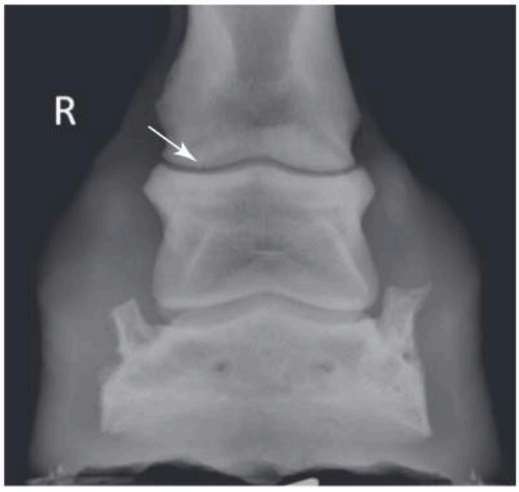
Fig. 26.4 Dorsopalmar view of the right front proximal interphalangeal joint. A round, mildly irregular radiolucency (*white arrow*) is present in the proximal subchondral bone of the middle phalanx with surrounding sclerosis, most consistent with an osseous cyst-like lesion.

Fractures

Fractures of the proximal and middle phalanges are relatively common, and radiography is often the initial imaging modality used for diagnosis. These fractures can be identified in all breeds/types of horses; however, fractures of the proximal phalanx occur most commonly in racehorses (i.e., Thoroughbreds, Standardbreds), while middle phalanx fractures are more common in Western performance horses (Quarter horses).[15,17,26] These fractures can be simple (noncomminuted) or comminuted, incomplete or complete, monoarticular or biarticular, and course primarily in a sagittal or dorsal plane relative to the long axis of the bone. Fig. 26.5 illustrates the various configurations of fractures in the proximal and middle phalanges. Lameness associated with an incomplete fracture may vary from minimal to severe, but horses with complete or comminuted fractures typically have an acute onset of severe lameness. Fractures may initially be nondisplaced and difficult to diagnose radiographically; therefore, if a fracture is suspected, several oblique views should be performed to identify the fracture and determine its complexity. Repeat radiographs 10 to 14 days after an injury will often allow better visualization of a nondisplaced fracture as the fracture line may be slightly wider due to resorption of the fracture margins. Periosteal new bone formation, suggestive of callus formation, can be present along the cortices of the phalanges, especially if the fracture is more chronic. Advanced imaging (i.e., CT or MRI) may be needed to identify the fracture (usually if the fracture is nondisplaced), determine the exact fracture configuration, and for surgical planning.[27,28] In one study comparing radiography and CT, CT was able to diagnose 4 of 20 fractures that were not identified radiographically.[29]

Proximal Phalanx. Fractures of the proximal phalanx at the level of the fetlock joint, such as osteochondral fragments, chip fractures, or palmar/plantar proximal tuberosity fractures, are common, especially in racehorses.[26] These fractures are described in detail in Chapter 25.

Sagittal (midsagittal or parasagittal) fractures of the proximal phalanx are frequently diagnosed and can have multiple configurations, most often originating from the midsagittal groove of the proximal articular surface.[26,30–32] These fractures can be (1) short or long incomplete fractures, (2) complete monoarticular or biarticular fractures, or (3) comminuted fractures. These fractures are typically best visible on the dorsopalmar



eFig. 26.1 Dorsopalmar view of the right front pastern in a Paint horse. There is a small concave radiolucent defect in the distolateral subchondral bone of the proximal phalanx (*arrow*) with mild surrounding sclerosis, consistent with an osseous cyst-like lesion.

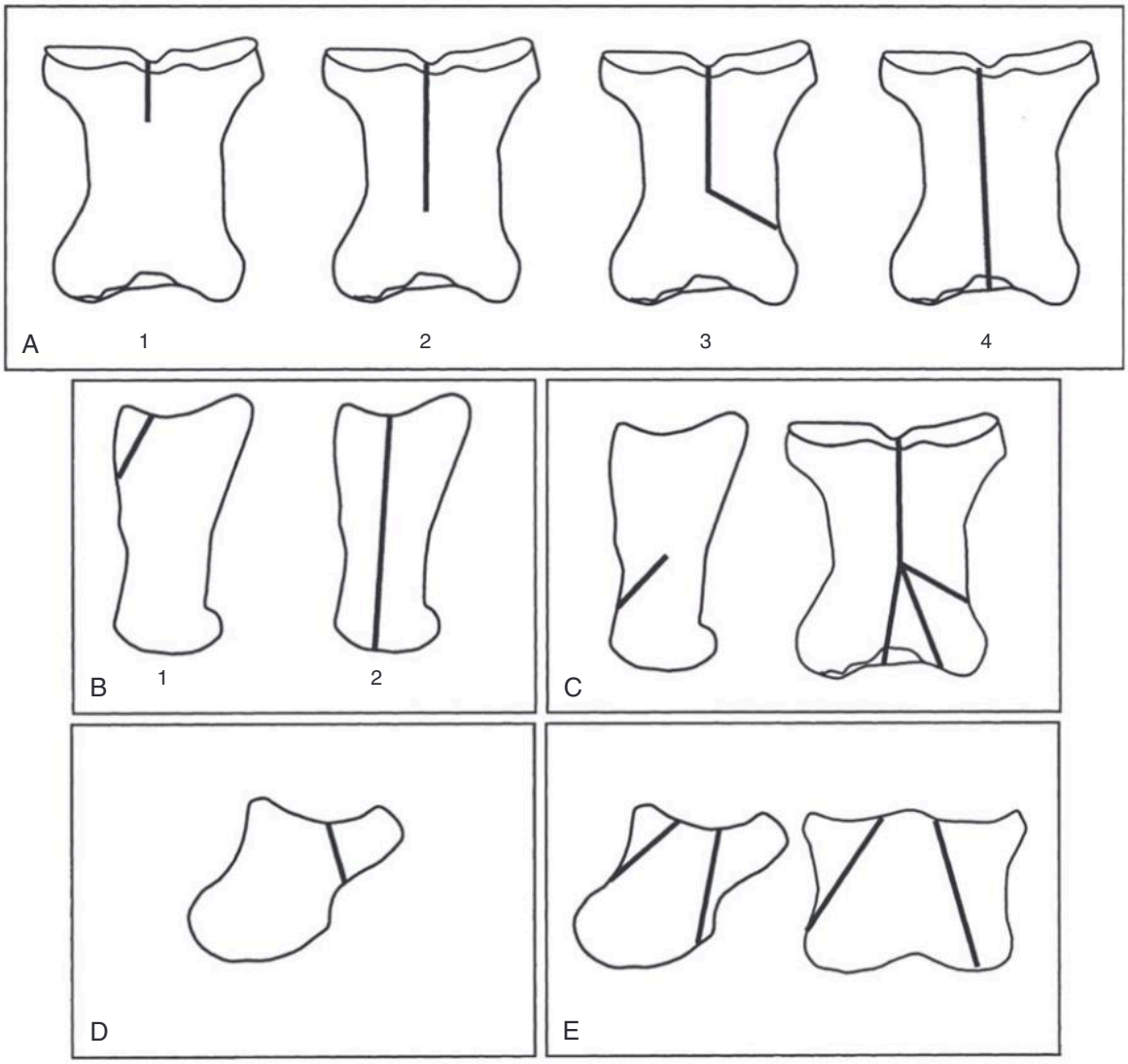


Fig. 26.5 **A–E,** Common fracture configurations of the proximal and middle phalanges. *Proximal phalanx:* **A,** Sagittal plane fractures, noncomminuted. *1,* Incomplete, monoarticular (short, <30 mm variation); *2,* incomplete, monoarticular (long, >30 mm variation); *3,* complete, monoarticular; *4,* complete, biarticular. **B,** Dorsal plane fractures, noncomminuted. *1,* Complete, monoarticular; *2,* complete, biarticular. **C,** Comminuted, complete, biarticular, dorsal, and/or sagittal plane. *Middle phalanx:* **D,** Palmar/plantar eminence (monoarticular, complete). **E,** Comminuted, complete, biarticular.

views; however, oblique views (i.e., 5–15 degrees medial or lateral to the midsagittal plane) may be needed for identification.

The incomplete, monoarticular sagittal fracture is the most common configuration[30,33] (Figs. 26.6 and 26.7). This fracture type is most often identified in young (2- to 3-year-old) racehorses, actively racing and/or training, although can also be seen in endurance or sporthorses.[15] These fractures are more common in the forelimbs of Thoroughbreds and hindlimbs of Standardbreds. The fracture typically originates at the level of the fetlock joint, near midline, within the sagittal groove of the proximal articular margin and then propagates distally.[26,30,31,34,35] Two variations of incomplete sagittal fractures have been reported, including a (1) short fracture (<30 mm extension into the diaphysis) and (2) long fracture (>30 mm extension in the diaphysis). These sagittal fractures may course in a slightly spiral or oblique manner and are often seen as parallel or offset radiolucent fracture lines on the dorsopalmar view due to the dorsal and palmar/plantar aspects of the fracture being in slightly different planes (see Fig. 26.7). Subchondral cystic lesions have been reported to occur with incomplete fractures, particularly the short variation.[34,35] Horses with incomplete fractures of the proximal phalanx may present with more subtle lameness but many have a severe, acute lameness. Most of these horses often have fetlock effusion as the fractures frequently involve the fetlock joint.

With increasing evidence to indicate that these fractures can be the result of repetitive stress and adaptive failure, careful radiographic assessment of the proximal articular margins of the proximal phalanx is recommended, especially in performance horses.[36] These subtle early changes, such as small subchondral fissures or changes in subchondral bone thickness, may represent increased risk for a development of a fracture in the future.[33,36–38]

Complete sagittal fractures, either biarticular or monoarticular, are less common than incomplete fractures. This type of fracture is most commonly reported in the Western



Fig. 26.6 Dorsopalmar **(A)** and lateromedial **(B)** views of the proximal phalanx in an adult horse. **A,** Incomplete short sagittal fracture (*short black arrow*) in the proximal phalanx, originating in the midsagittal groove, with surrounding sclerosis. The normal nutrient foramen is visible on this view and should not be misinterpreted as a fracture (*short white arrow*). **B,** The normal nutrient foramen is seen as a thin linear radiolucency coursing obliquely in a proximal to distal orientation (*black arrow*).



Fig. 26.7 Dorsopalmar view of the fetlock in the forelimb of a 2-year-old racehorse. Noncomminuted, incomplete, monoarticular long sagittal fracture of the proximal phalanx, originating from the midsagittal groove of the proximal articular margin. Two linear radiolucent fracture lines (*black arrows*) are identified on this view, corresponding to the slightly different location of the fracture in the dorsal and palmar cortices. (Image courtesy Dr. Samantha Morello, University of Wisconsin-Madison, WI.)

performance horse. Two variations of this fracture occur: (1) biarticular fracture involving the fetlock and proximal interphalangeal joints and (2) monoarticular fracture, often exiting through the lateral distal palmar/plantar cortex.

Comminuted fractures of the proximal phalanx are also relatively common. These fractures typically involve the fetlock and proximal interphalangeal joints (biarticular) and more frequently exit the lateral cortex. These fractures may involve the entire length of the proximal phalanx or only be found in the proximal or distal portion. Not surprisingly, these fractures have the most guarded prognosis for survival and poor prognosis for return to performance.[30,35,39]

Dorsal plane fractures of the proximal phalanx are less common and are best seen on lateromedial views. There are three different configurations for dorsal plane fractures: (1) incomplete proximal dorsal articular fractures, (2) complete proximal dorsal articular fractures, and (3) fractures that extend from the midportion of the proximal articulation into the proximal phalanx, toward the proximal interphalangeal joint.[15,40] Proximal dorsal fractures occur most commonly in the hindlimb of Standardbred and Thoroughbred racehorses.[15,26,41]

Other infrequently reported fractures of the proximal phalanx include physeal fractures (typically Salter-Harris type II) in foals and weanlings and incomplete distal articular fractures.[15] Avulsion fractures of the proximal annular ligament in the hindlimb have also been described.[42] These fractures are identified along the proximal plantar aspect of the proximal phalanx, at the proximal site of attachment of the proximal digital annular ligament, and are associated with variable degrees of lameness.

Middle Phalanx. Fractures of the middle phalanx are most common in Western performance or working horses, polo ponies, and jumpers during activity; however, fractures have also developed during light/leisure activity or paddock turnout.[17,27,43–45] Most middle phalanx fractures are thought to occur due to the extreme simultaneous compression and torsion forces placed on the middle phalanx while the foot is fixed to the ground, such as during tight turns and sudden stops.[44,45] These horses are typically lame with variable swelling of the

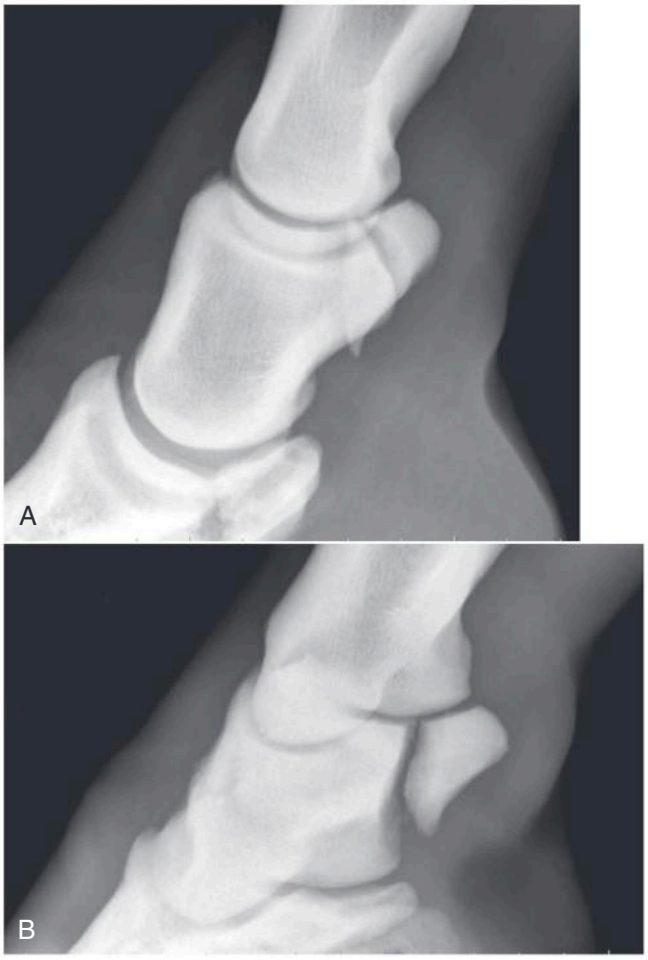


Fig. 26.8 **A–B,** Lateromedial and oblique views of the distal limb. Non-comminuted, complete, monoarticular fracture of the medial palmar eminence of the middle phalanx. The oblique view **(B)** aids in displaying the fracture plane and involvement of the proximal interphalangeal joint.

pastern region. Fractures of the middle phalanx more commonly affect the hindlimbs; however, forelimb fractures are more frequently comminuted.[15,17,43,45] Fractures of the middle phalanx can be: (1) comminuted (most common), (2) involving the palmar/plantar eminences (uni- or biaxial), and, less frequently, (3) osteochondral (chip) fractures. Physeal fractures have been reported in young horses but are rare.

Fractures of the palmar (plantar) eminences more commonly involve both eminences (biaxial).[17] When the distal palmar (plantar) eminences are fractured, without comminution, the fragments are displaced in a palmar or plantar direction (Fig. 26.8). This is most often identified in the hindlimb. Biaxial eminence fractures typically result in instability of the joint and, in severe cases, the proximal interphalangeal joint is luxated with proximal displacement and overriding of the middle phalanx relative to the proximal phalanx (Fig. 26.9, eFig. 26.2).

The comminuted fractures are typically biarticular, involving both the proximal and distal interphalangeal joints (Fig. 26.10, eFig. 26.3). Additionally, comminution of the fracture may only be present in the proximal aspect of the bone with one or more fracture lines extending distally to the distal interphalangeal joint.[17,43] Involvement of the distal interphalangeal joint significantly affects the prognosis, and treatment of this type of fracture and multiple radiographic views or advanced imaging



Fig. 26.9 Lateromedial view of the distal limb. Complete, monoarticular biaxial fracture of the middle phalanx in the hindlimb. The medial and lateral plantar eminences are both fractured with plantar displacement of the fracture fragments, resulting in instability and luxation of the proximal interphalangeal joint.

may be needed to identify involvement of this joint. Additional imaging (i.e., CT) may be needed to better determine the degree of comminution and joint involvement or to assist with surgical planning.[46]

Osteomyelitis

Infection of the pastern region is most common secondary to trauma, a complication of surgery, or less commonly, due to hematogenous dissemination. Penetrating trauma and lacerations can result in a secondary infection of the soft tissue and/or bone. Additionally, sequestrum formation can occur in the pastern region, often associated with a history of a draining wound. There is one report of osteomyelitis developing after proximal interphalangeal arthrodesis due to a fracture where osteolysis and osteoproliferation of the proximal and middle phalanges occurred with sequestrum formation.[47] Increased rates of infection have also been reported after surgical repair of highly comminuted fractures of the proximal phalanx.[35] Hematogenous osteomyelitis and septic physitis are much more common in foals (Fig. 26.11, eFig. 26.4). In a study of foals, hematogenous osteomyelitis was frequently identified in the distal limb but more commonly in the distal phalanx than the more proximal phalanges.[48] One case of fungal osteomyelitis caused by *Cryptococcus gattii* has been reported in the proximal phalanx of an adult horse.[49]

New Bone Formation

Enthesophyte formation can occur at the sites of ligament attachments along the pastern region. Bone proliferation is often identified along the palmar aspect of the mid to distal aspect of the proximal phalanx associated with the distal sesamoidean ligaments. These changes may be associated with desmopathy and should prompt further assessment of the soft tissue structures in this region.

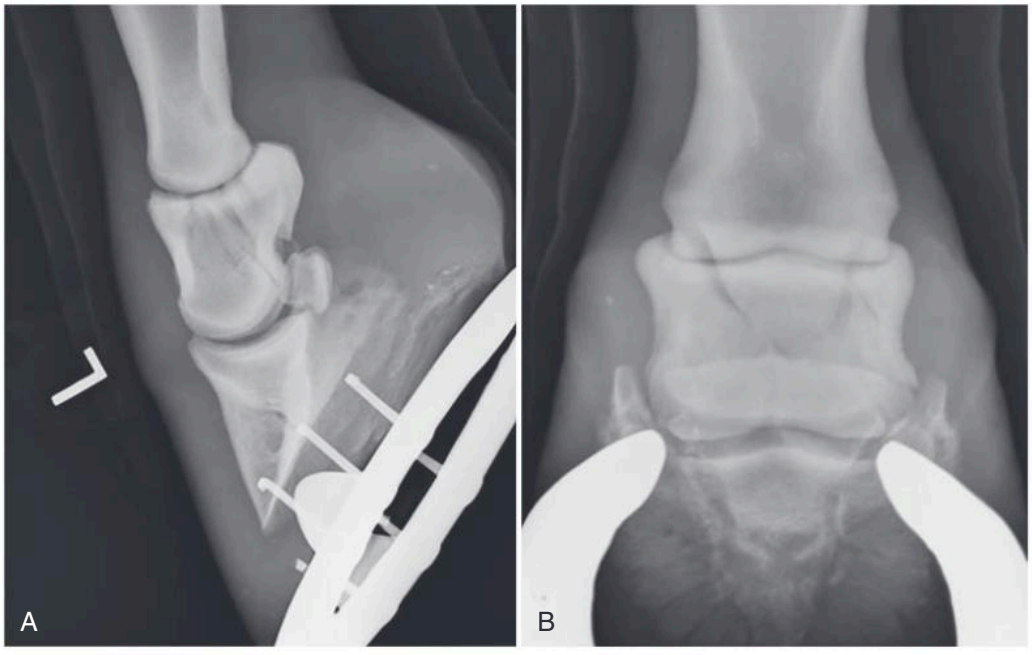
Focal periosteal new bone formation/periostitis and regional soft tissue swelling in the diaphyseal region of the proximal or middle phalanges not corresponding to ligament or capsular attachments are most likely secondary to trauma. The bone generally remodels with time, although periosteal new bone may persist after resolution of the soft tissue component and



eFig. 26.2 Lateromedial view of the distal limb. There is a closed, comminuted biarticular fracture of the middle phalanx of the hindlimb. Fracture of the medial and lateral plantar eminences results in subluxation of the proximal interphalangeal joint. Notice a thin radiolucent fissure line that extends distally into the plantar articular surface of the distal interphalangeal joint.



eFig. 26.4 Dorsopalmar view of the distal limb of a horse presented a week after laceration of the distal limb, which was initially treated conservatively. There is soft tissue swelling of the distal limb, most pronounced medially. There is irregular resorption of the distomedial aspect of the proximal phalanx covered by a thin rim of cortical bone. The diagnosis was osteomyelitis with sequestrum formation.



eFig. 26.3 Comminuted fracture of the middle phalanx. **A,** Lateromedial view of the distal limb. **B,** Dorsopalmar view of the distal limb. The horse was non−weight bearing for the radiographs. Multiple fracture lines are evident on both views involving the proximal and distal interphalangeal joints.

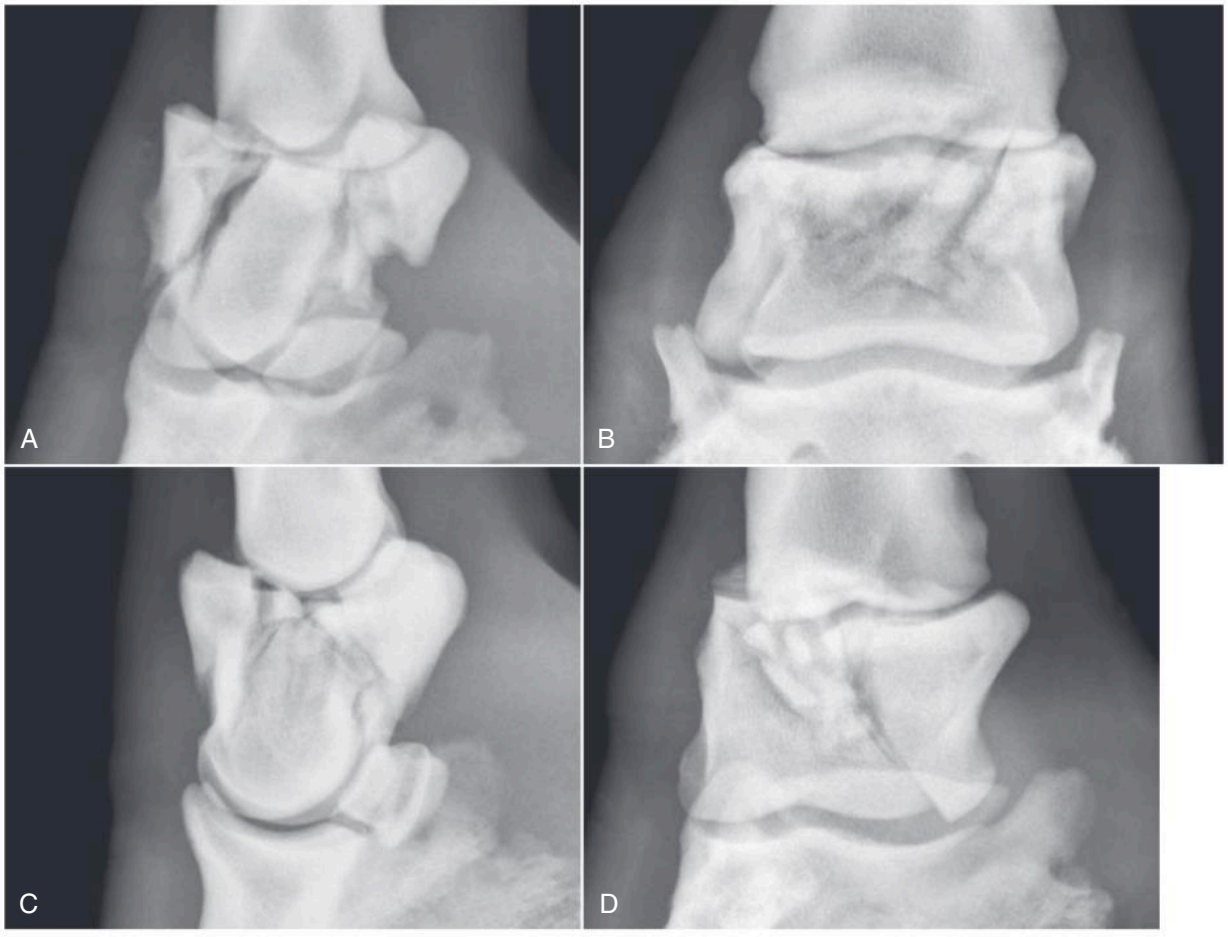


Fig. 26.10 **A–D,** Lateromedial, dorsopalmar, and oblique views of the distal limb. Comminuted, multiplane, biarticular middle phalanx fracture. The oblique views are helpful to confirm the involvement of both the proximal and distal interphalangeal joints. The horse was not bearing weight for the images. With weight bearing, the proximal interphalangeal joint would be luxated.

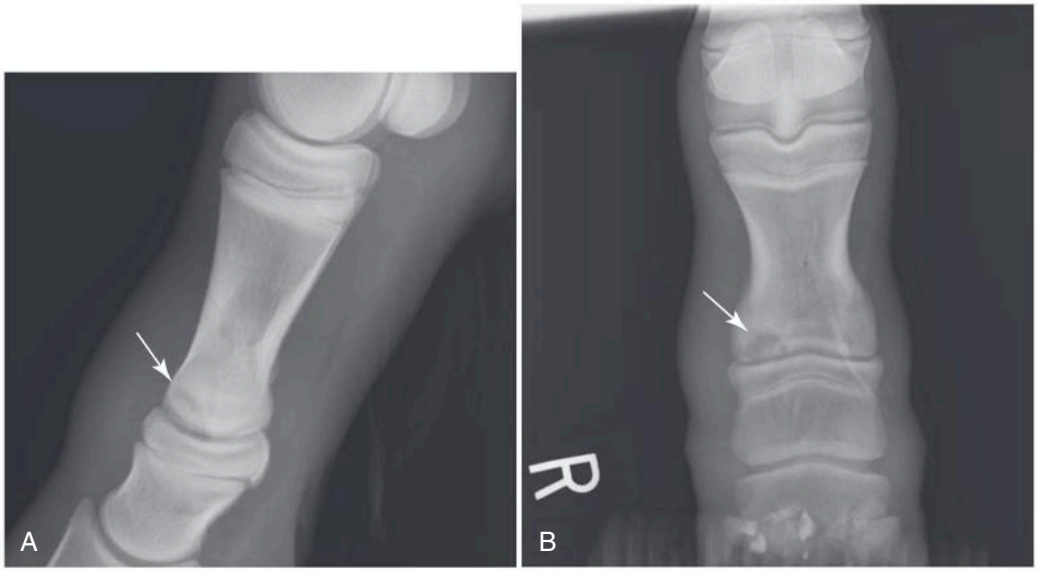


Fig. 26.11 Lateromedial **(A)** and dorsopalmar **(B)** views of the distal limb in a foal. A large radiolucency is present in the subchondral bone of the distodorsal lateral condyle of the proximal phalanx (*white arrows*) with adjacent soft tissue swelling. The diagnosis was osteomyelitis. (Images courtesy Dr. Tom Wilkinson Jr., Washington State University, WA.)

can enlarge with chronic repetitive trauma, such as continued focal impingement along the medial aspect of the pastern by the contralateral limb.

Bone Marrow Lesions

Horses with an acute onset of severe lameness localized to the pastern region may not have radiographic evidence of disease. In these horses, advanced imaging (i.e., MRI) is often pursued for further assessment. MRI is helpful to better exclude the possibility of a fracture and to look for evidence of a bone marrow lesion, which is a lesion characterized by increased fluid signal (high signal on fat- suppressed or inversion recovery sequences) and reduced T1 signal within the bone (Fig. 26.12).

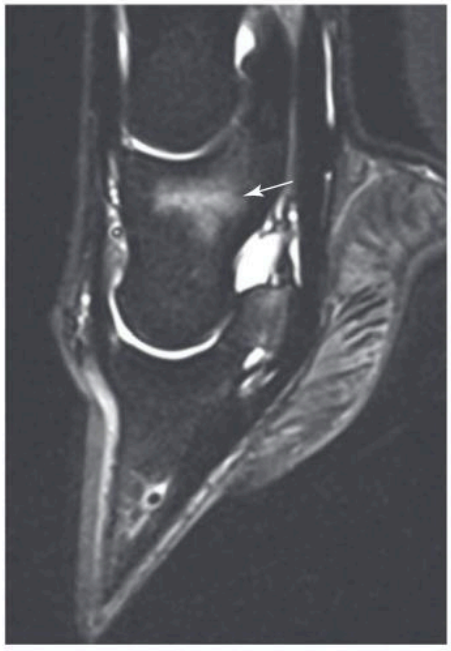


Fig. 26.12 Magnetic resonance imagery (MRI) of the distal forelimb, sagittal short tau inversion recovery (STIR) sequence. On this sequence, the normal fat in the bone marrow is nulled or black. Note the large area of increased signal in the proximal aspect of the middle phalanx (*white arrow*). This is consistent with a bone marrow lesion.

Bone marrow lesions, also known as bone edema or edema-like change, can be secondary to an osseous contusion (bone bruise), bone edema, fibrosis, or osteonecrosis, and often, these lesions are clinically significant. Many of these lesions will resolve with rest and time; however, some will be persistently lame due to development of osteonecrosis, subchondral and trabecular bone loss, and progressive joint pathology.[50–52]

Joint Pathology

Osteoarthritis

Osteoarthritis a chronic degenerative disorder of synovial joints that occurs when articular cartilage deteriorates, over time resulting in radiographically detectable changes including periarticular new bone formation, subchondral sclerosis and/or lucency, and changes in the width of the joint space. Regional soft tissue swelling may also be seen, associated with the adjacent ligaments/tendons, joint effusion, capsular and synovial thickening, or periarticular fibrosis. Periarticular new bone can present as osteophytes (new bone arising along the articular margins) and enthesophytes (new bone at the attachments of periarticular soft tissues, including ligaments, tendons, and the joint capsule). Causes of osteoarthritis include chronic age-related degeneration, acute or chronic repetitive trauma, infection/septic arthritis, abnormal limb conformation, or developmental joint disease. The inciting underlying cause of proximal interphalangeal osteoarthritis may not be evident radiographically, with limb deformity a notable exception.

The proximal interphalangeal joint is commonly affected by osteoarthritis. It is a low-motion joint which bears a high load, particularly in Western performance horses.[24] Since the proximal interphalangeal joint does not have a high range of motion during athletic activity, a smaller region of the joint surface has higher weight-bearing load for a longer time period. This results in articular cartilage and subchondral bone damage, and initiates the cascade of inflammation leading to osteoarthritis.[15,24] Small periarticular osteophytes along the dorsoproximal aspect of the middle phalanx are often the initial radiographic indicator of proximal interphalangeal degenerative joint disease (Fig. 26.13A). As disease progresses, subchondral bone modeling, sclerosis, and demineralization may become evident (see Fig. 26.13B). Late-stage changes include joint space narrowing, progressive lysis of the subchondral bone, advancing sclerosis, and more extensive periarticular osteophytosis (see Fig. 26.13C). Over time, ankylosis or partial ankylosis of the joint can develop (see Fig. 26.13D, eFig. 26.5).



Fig. 26.13 Lateromedial projections of the proximal interphalangeal joint, with progressive osteoarthritis: mild **(A)**, moderate **(B)**, moderate-severe **(C)**, and severe with near ankylosis **(D)**. Note progressive periarticular osteophyte and enthesophyte formation, sclerosis, subchondral lysis, and joint space narrowing **(D)**.



eFig. 26.5 Dorsopalmar view of the right front proximal interphalangeal joint of a 10-year-old Quarter horse with severe osteoarthritis. There is narrowing of the lateral aspect of the joint with associated subchondral sclerosis, and regional osteophytosis and enthesophytosis.

The early radiographic changes indicative of proximal interphalangeal osteoarthritis (small periarticular osteophytes and enthesophytes at ligamentous or capsular attachments) can be incidental in some cases, however these lesions could predict future or developing problems and should be considered in light of the clinical exam and response to regional anesthesia, as well as the onset of lameness (acute versus chronic).

Subchondral Bone Trauma

Severe acute-onset lameness can be seen with trauma and secondary articular cartilage and subchondral bone injury in the proximal interphalangeal joint. The radiographic manifestations can be subtle, and MRI is more sensitive in identifying and characterizing these injuries, particularly in the acute phase (Fig. 26.14A). These lesions also demonstrate marked focal radiopharmaceutical uptake on bone scintigraphy (see Fig. 26.14B). If visible radiographically, lesions can be seen as elongated horizontal or focal circular regions of subchondral lucency in the proximal aspect of the middle phalanx (see Fig. 26.14C, eFig. 26.6), which may become more evident over time and can extend into the trabecular bone.[3] Periosteal proliferation and periarticular osteophyte formation can be seen secondary to this articular cartilage and subchondral bone damage, representing developing degenerative joint disease. The prognosis is guarded in these cases.

Subchondral bone trauma also occurs focally in the distal dorsal aspect of the middle phalanx, either medially or laterally, and is only diagnosed with MRI as increased fluid signal (hyperintensity on fat-suppressed images and hypointensity on T1-weighted images). No radiographic abnormalities are identified in association with this syndrome.

Septic Arthritis

Joint infection arises from penetrating wounds, iatrogenic injections, or hematogenous spread (most commonly in foals). The proximal interphalangeal joint is uncommonly involved in septic polyarthritis in foals.[53–55] Sepsis of the proximal interphalangeal joint should be considered with any lacerations near the joint in conjunction with persistent substantial lameness. Initially, no radiographic changes may be evident with septic arthritis. Synovial proliferation and effusion may cause intracapsular soft tissue swelling although this is difficult to detect radiographically as the proximal interphalangeal joint pouch is relatively small. Positive contrast arthrography and/or contrast fistulography can be helpful to confirm communication between the joint and a wound/wound tract. Early osseous changes include proliferative bone at the joint capsular attachments and/or along the chondro-osseous junctions at the joint periphery. With progressive cartilage deterioration, joint space narrowing can be seen, although care should be taken to ensure even weight bearing when assessing joint space width radiographically.[7] Subchondral irregularity, lysis, and sclerosis can be identified as intra-articular infection progresses (Fig. 26.15A,B). Periosteal new bone also develops along the articular margins. The prognosis is always guarded.

Subluxation/Luxation

Dorsal displacement of the distal aspect of the proximal phalanx with increased flexion of the proximal interphalangeal joint is generally referred to as subluxation. This is most commonly seen in younger horses although it can occur in older horses, is more common in the hindlimbs, and may be unilateral or bilateral.[3] Potential causes include flexor deformities caused by contracture of the deep digital flexor tendon and straight distal sesamoidean ligament, injuries to the suspensory ligament and extensor branches, or injuries to the palmar/plantar ligaments of the proximal interphalangeal joint. Dorsal subluxation may be appreciated on physical examination as abnormal dorsal movement of the distal end of the proximal phalanx at a walk and can occasionally be appreciated at rest. An audible click is sometimes heard when the subluxation is reduced upon full weight bearing. In lateral radiographic projections there is mild dorsal displacement of the distal aspect of the proximal phalanx and increased flexion of the proximal interphalangeal joint. No additional radiographic changes are generally apparent. Palmar/plantar subluxation is typically associated with acute trauma and rupture of the distal sesamoidean ligaments or injury to the superficial digital flexor tendon branches or middle scutum, and there may be associated avulsion fragments or enthesophytes at ligament insertions.[15] Ultrasound examination of the soft tissues of the pastern is indicated in such horses for further evaluation. Degenerative joint disease may also develop with chronic subluxation.

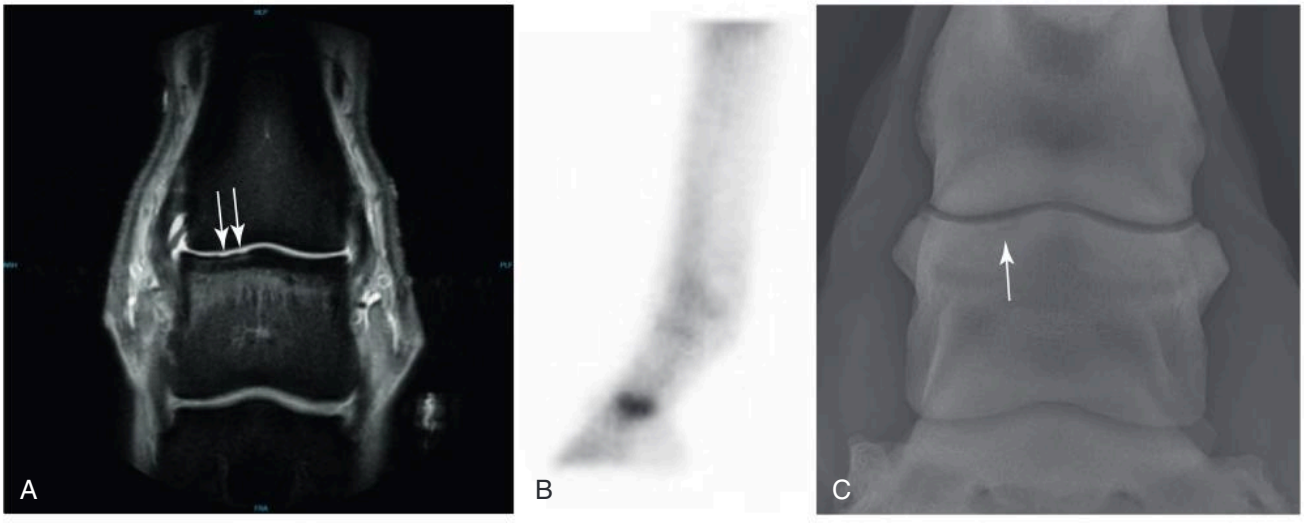
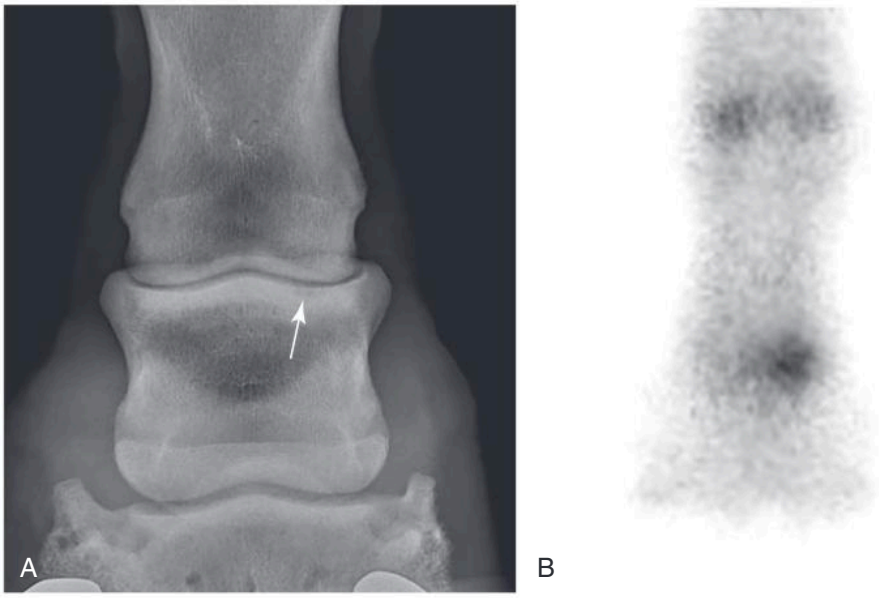


Fig. 26.14 **A–C,** Acute subchondral bone injury of the middle phalanx. **A,** Dorsal plane fat-suppressed magnetic resonance image (MRI) with extensive increased fluid signal in the proximal to mid portion of the middle phalanx and subchondral bone and cartilage defects (*white arrows*). **B,** Lateral nuclear scintigraphic image of the same patient with marked focal increased radiopharmaceutical uptake in the proximal aspect of the middle phalanx, corresponding to the region of subchondral bone injury. **C,** Dorsopalmar radiographic image of the same horse, with subtle subchondral lucency along the proximal aspect of the middle phalanx (*white arrow*).



eFig. 26.6 Subchondral bone injury of the middle phalanx. **A,** Dorsopalmar radiograph of the pastern: A subtle subchondral radiolucency with adjacent sclerosis (*arrow*) is visible in the proximal middle phalanx. **B,** Dorsal nuclear scintigraphic image of the distal forelimb with marked focal uptake in the proximal middle phalanx, corresponding to the lesion seen radiographically.



Fig. 26.15 Lateromedial **(A)** and dorsopalmar **(B)** images of the proximal interphalangeal joint of an adult horse with chronic proximal interphalangeal sepsis. There is extensive periarticular remodeling, subchondral sclerosis, subchondral lysis, and joint space narrowing. Mild soft tissue swelling is seen dorsally, primarily intracapsular. This horse also has mild dorsal subluxation of the proximal interphalangeal joint.

Luxation of the proximal interphalangeal joint is typically evident clinically and can be seen with significant trauma to the limb, such as large fractures of the proximal and middle phalanges and/or with avulsion fractures at supporting ligament attachments (see Fig. 26.9).

Hyperextension of The Proximal Interphalangeal Joint

Hyperextension of the proximal interphalangeal joint is uncommon although can be seen with rupture of both the straight distal sesamoidean ligament and the superficial digital flexor tendon. Hyperextension of the proximal interphalangeal joint can also be seen with concomitant hyperextension of the metacarpophalangeal and distal interphalangeal joints, either in foals as a congenital deformity or secondary to weak flexor tendons (resulting from poor nutrition, systemic disease, or after prolonged splinting or casting of the limb) or as an acquired deformity secondary to rupture or avulsion of the deep digital flexor tendon.

Soft Tissue Lesions

Soft tissue changes detectable radiographically can include thickening, altered shape/contour, or abnormal opacity. Increased soft tissue can be seen surrounding joints, either confined to the region of the joint capsule (intracapsular fluid and/or synovial thickening) or external to the joint capsule (extracapsular inflammation, fluid, fibrosis, or cellular infiltrates). Increased extracapsular soft tissue can obscure intracapsular soft tissue changes. Soft tissue thickening or abnormal contour away from the joint may indicate trauma, infection, tendon/ligament injury, acute or chronic wound, granulation tissue, or a soft tissue mass/neoplasm.

Injuries to the tendons and ligaments of the pastern region are common but cannot be accurately diagnosed radiographically. Ultrasound, MRI, and to some degree CT (particularly contrast-enhanced) are superior to radiographs for detecting soft tissue injuries. Regions of osseous proliferation can be seen in association with ligament injury, typically present at the attachment sites as enthesophytes. A thorough knowledge of the soft tissue attachments in the region is necessary for accurate radiographic interpretation; several detailed references for soft tissue attachments are available.[3,4,56] The most common sites for enthetic new bone in the pastern region include the attachments of the oblique distal sesamoidean ligaments (Fig. 26.16), the collateral ligaments of the proximal and distal interphalangeal joints, the proximal and distal digital annular ligaments, the ligaments between the proximal phalanx and the ungular cartilages, and the palmar/plantar ligaments of the proximal interphalangeal joint (Fig. 26.17). Enthesophytes may be of variable to no clinical significance, although indicate an area of potential active or historical injury. Enthetic bone production does not typically resolve following resolution of associated soft tissue injury. Occasionally, avulsion fragmentation can occur at tendinous/ligamentous insertions.

Dystrophic mineralization can develop within tendons or ligaments secondary to chronic injury or may be seen in pericapsular soft tissues associated with previous corticosteroid injections or focal necrosis associated with prior neurectomy. Intraligamentous mineralization is most commonly seen in the distal sesamoidean ligaments (see Fig. 26.16). This is of variable/equivocal significance and should be correlated with ultrasound and clinical examination.

Gas opacity in the regional soft tissues is also sometimes identified, most commonly secondary to regional anesthesia or open skin wounds (Fig. 26.18). Infection with gas-producing organisms is rare.

Miscellaneous Diseases of the Pastern

Hypertrophic osteopathy (Marie's disease) is uncommon but does occur.[57–60] This condition is characterized by soft tissue

swelling of the limbs and periosteal bone proliferation along the diaphyses and epiphyses of affected long bones.[58] Concurrent intrathoracic disease is typically the cause of hypertrophic osteopathy; however, occasionally the syndrome is idiopathic or associated with extrathoracic disease. If the underlying disease can be successfully treated, the signs associated with hypertrophic osteopathy can improve and even completely regress. However, in general, many horses with this condition have a poor prognosis as the underlying disease is often serious or fatal.

Cutaneous neoplasms occur in the pastern region, including mast cell tumors,[61–64] carcinomas,[65] and sarcoids (Fig. 26.19).[66] Mast cell tumors, also known as mastocytosis or mastocytomas, are uncommon neoplasm. In one series of mast cell tumors, Arabians were overrepresented.[61] These tumors are most commonly identified as a solid mass arising from the skin, similar to cutaneous mast cell tumors in other animals, and are typically benign, well-demarcated and slow growing. The mast cell tumors on the distal limbs tend to be nonpainful, firm and immobile, and in close proximity to a joint.[63] Additionally, these masses are often calcified.[62]



Fig. 26.16 Lateromedial view of the pastern region. Soft tissue mineralization is evident in the superficial digital flexor tendon and straight distal sesamoidean ligament. There is mild smooth enthesopathy at the insertion of the oblique distal sesamoidean ligament on the mid-aspect of the proximal phalanx (*arrow*). This horse also has a mild distal interphalangeal flexural deformity.

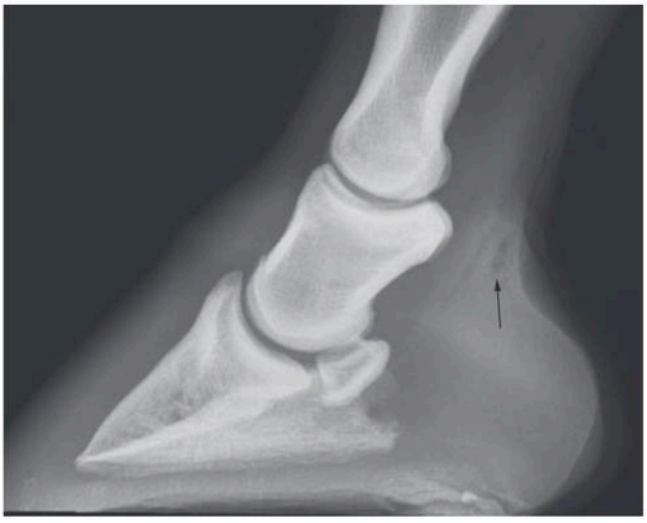


Fig. 26.18 Lateromedial view of the pastern region. Gas is present in the palmar soft tissues (*arrow*) secondary to diagnostic nerve block.



Fig. 26.17 Dorsomedial palmarolateral oblique projection with mild osseous proliferation (*arrow*) at the attachment of the medial abaxial palmar ligament of the proximal interphalangeal joint.



Fig. 26.19 Lateromedial view of the pastern region of a 26-year-old Arabian. A broad-based convex soft tissue opaque mass is present along the dorsal aspect of the mid diaphysis of the proximal phalanx. The adjacent bone is normal. A sarcoid was diagnosed histopathologically.

Osseous neoplasia is uncommon in the distal limb of horses but can include benign (i.e., osteoma, ossifying fibroma) and malignant (i.e., osteosarcoma) etiologies. An osteosarcoma has been reported in the middle phalanx of a horse.[67] In this horse, an aggressive bone lesion was identified radiographically throughout the middle phalanx, with a pathologic fracture. An ossifying fibroma has been described in the proximal phalanx of a horse.[68] Radiographically, multifocal areas of osteolysis with surrounding sclerosis were identified in the distomedial aspect of the proximal phalanx, involving the distal articular margin and subchondral bone. A traumatic osseous cyst-like lesion was the primary differential as many of these areas were well defined; however, an ossifying fibroma was diagnosed histopathologically.

Benign mineralization, such as dystrophic mineralization or osseous metaplasia, have also been described in the distal limb and typically occur secondary to previous trauma or soft tissue injury. One report of focal osseous metaplasia described a focal, well-circumscribed extraskeletal mineralized mass in the plantar pastern of the right hindlimb causing a chronic lameness.[69] This mass was suspected to be causing lameness due to compression on the adjacent plantar digital nerve.

REFERENCES

1. Schebitz H, Wilkens H. *Atlas of Radiographic Anatomy of the Horse*. Philadelphia: Saunders; 1978.
2. Smallwood JE, Holliday SD. Xeroradiographic anatomy of the equine digit and metacarpophalangeal region. *Vet Radiol*. 1987;28:166.
3. Butler JA, Colles CM, Dyson SJ, et al. *Clinical Radiology of the Horse*. 3rd ed. Oxford, UK: Blackwell; 2008.
4. Denoix JM. *The Equine Distal Limb Atlas of Clinical Anatomy and Comparative Imaging*. Ames: Iowa State University; 2002.
5. Becht JL, Park RD, Kraft SL, et al. Radiographic interpretation of normal skeletal variations and pseudolesions in the equine foot. *Vet Clin North Am Equine Pract*. 2001;17(1):1–18.
6. Hinkle FE, Johnson SA, Selberg KT, Barrett MF. A review of normal radiographical variants commonly mistaken for pathological findings in horses. *Equine Vet Educ*. 2020;12:664–672.
7. Contino EK, Barrett MF, Werpy NM. Effect of limb positioning on the radiographic appearance of the distal and proximal interphalageal joint spaces of the forelimbs of horses during evaluation of dorsopalmar radiographs. *J Am Vet Med Assoc*. 2014;244(10):1186–1190.
8. Losonsky JM, Kneller SK. Variable location of nutrient foramina of the proximal phalanx in the forelimbs of Standardbreds. *J Am Vet Med Assoc*. 1988;193(6):671–673.
9. Kneller SK, Losonsky JM. Variable locations of nutrient foramina of the proximal phalanx in the forelimbs of Thoroughbreds. *J Am Vet Med Assoc*. 1990;197(6):736–738.
10. Frietman S, van Proosdij R, ter Braake F, de Heer N. A detailed radiographic description of the nutrient foramen of the dorsal cortex of the proximal phalanx in horses. *Equine Vet Educ*. 2020;32(suppl 10):72–77.
11. Stock K, Hamann H, Distl O. Prevalence of osseous fragments in distal and proximal interphalangeal, metacarpo- and metatarsophalangeal and tarsocrural joints of Hanoverian Warmblood horses. *J Vet Med*. 2005;52:388–394.
12. Schneider RK, Ragle CA, Carter BG, et al. Arthroscopic removal of osteochondral fragments from the proximal interphalangeal joint of the pelvic limb in three horses. J Am Vet Med *Assoc*. 1994;205:79–82.
13. Fjordbakk CT, Strand E, Milde AK, et al. Osteochondral fragments involving the dorsomedial aspect of the proximal interphalangeal joint in young horses: 6 cases (1997–2006). *J Am Vet Med Assoc*. 2007;230:1498–1501.
14. Modransky PD, Grant BD, Rantanen NW, et al. Surgical treatment of a palmar midsagittal fracture of the proximal second phalanx in a horse. *Vet Surg*. 1982;4:129–131.
15. Ross MW, Dyson SJ. *Diagnosis and Management of Lameness in the Horse*. ed 2. St Louis: Saunders/Elsevier; 2011.
16. Welch RD, Watkins JP. Osteochondral fracture of the proximal palmar middle phalanx in a Thoroughbred. *Equine Vet J*. 1991;23:67–69.
17. Watkins JP. Fractures of the middle phalanx. In: Nixon AJ, ed. *Equine Fracture Repair*. Philadelphia: WB Saunders Co; 1996.
18. Radcliffe RM, Cheetham J, Bezuidenhout AJ, et al. Arthroscopic removal of palmar/plantar osteochondral fragments from the proximal interphalangeal joint in four horses. *Vet Surg*. 2008;37(3):733–740.
19. Trotter GW, McIlwraith CW, Norrdin RW, et al. Degenerative joint disease with osteochondrosis of the proximal interphalangeal joint in young horses. *J Am Vet Med Assoc*. 1982;180:1312–1318.
20. Nixon AJ. In: Auer JA, Stick JA, Surgery E, eds. *Phalanges and the Metacarpophalangeal and Metatarsophalangeal Joints*. 3rd ed. St Louis: Saunders Elsevier; 2006.
21. Sherlock C, Mair T. Osseous cyst-like lesions/subchondral bone cysts of the phalanges. *Equine Vet Educ*. 2011;23(4):191–204.
22. McIlwraith CW. Subchondral bone cysts in the horse: aetiology, diagnosis and treatment options. *Equine Vet Educ*. 1998;10(6):3131–3317.
23. Ammann L, Ohlerth S, Fürst AE, Jackson MA. Differences of morphological attributes between 62 proximal and distal subchondral cystic lesions of the proximal phalanx as determined by radiography and computed tomography. *Am J Vet Res*. 2023;83(12).
24. McIlwraith CW, Frisbie DD, Kawcak C, Van Weeren R, eds. *Joint Disease in the Horse*. St. Louis: Elsevier; 2016.
25. Kol'vek F, Krešáková L, Vdoviaková K, et al. Modified proximal interphalangeal joint arthrodesis in a yearling filly with an osseous cyst-like lesion in the proximal phalanx. *Animals (Basel)*. 2021;11(4):948.
26. Richardson DW. Fractures of the proximal phalanx. In: Nixon AJ, ed. *Equine Fracture Repair*. Philadelphia: WB Saunders Co; 1996.
27. Rose PL, Seeherman H, O'Callaghan MO. Computed tomographic evaluation of comminuted middle phalangeal fractures in the horse. *Vet Radiol Ultrasound*. 1997;38:424.
28. Brunishoz HP, Hagen R, Furst AE, et al. Radiographic and computed tomographic configuration of incomplete proximal fractures of the proximal phalanx in horses used for racing. *Vet Surg*. 2015;44(7):809–815.
29. Crijns CT, Martens A, Bergman HJ, et al. Intramodality and intermodality agreement in radiography and computed tomography of equine distal limb fractures. *Equine Vet J*. 2014;46(1):92–96.
30. Ellis DR, Simpson DJ, Greenwood RE, Crowhurst JS. Observations and management of fractures of the proximal phalanx in young Thoroughbreds. *Equine Vet J*. 1987;19(1):43–49.
31. Holcombe SJ, Schneider RK, Bramlage LR, et al. Lag screw fixation of noncomminuted sagittal fractures of the proximal phalanx in racehorses: 59 cases (1973–1991). *J Am Vet Med Assoc*. 1995;206:1195–1199.
32. Tetens J, Ross MW, Lloyd JW. Comparison of racing performance before and after treatment of incomplete, mid sagittal

fractures of the proximal phalanx in Standardbreds: 49 cases (1986–1992). *J Am Vet Med Assoc.* 1997;210:82–86.
33. Smith MRW, Wright IM. Radiographic configuration and healing of 121 fractures of the proximal phalanx in 120 Thoroughbred racehorses (2007–2011). *Equine Vet J.* 2014;46(1):81–87.
34. Kümmerle JM, Auer JA, Rademacher N, et al. Short incomplete sagittal fractures of the proximal phalanx in ten horses not used for racing. *Vet Surg.* 2008;37(2):193–200.
35. Markel MD, Richardson DW, Nunamaker DM. Comminuted first phalanx fractures in 30 horses: surgical vs nonsurgical treatments. *Vet Surg.* 1985;14(2):135–140.
36. Ramzan PHL, Powell SE. Clinical and imaging features of suspected prodromal fracture of the proximal phalanx in three Thoroughbred racehorses. *Equine Vet J.* 2010; 42:164.
37. Dyson S, Nagy A, Murray R. Clinical and diagnostic imaging findings in horses with subchondral bone trauma of the sagittal groove of the proximal phalanx. *Vet Radiol Ultrasound.* 2011;52(6):596–604.
38. Powell SE. Low-field standing magnetic resonance imaging findings of the metacarpo/metatarsophalangeal joint of racing Thoroughbreds with lameness localized to the region: a retrospective study of 131 horses. *Equine Vet J.* 2012;44(169):2–12.
39. Markel MD, Martin BB, Richardson DW. Dorsal frontal fractures of the first phalanx in the horse. *Vet Surg.* 1985;14:36–40.
40. Kraus BM, Richardson DW, Nunamaker DM, Ross MW. Management of comminuted fractures of the proximal phalanx in horses: 64 cases (1983–2001). *J Am Vet Med Assoc.* 2004;224:254–263.
41. Wright IM, Minshall GJ. Short frontal plane fractures involving the dorsoproximal articular surface of the proximal phalanx: description of the injury and a technique for repair. *Equine Vet J.* 2018;50:54–59.
42. O'Brien EJO, McAlpine JM, Schramme MC, et al. Avulsion of the proximal digital annular ligament in five hindlimbs. *Equine Vet Educ.* 2018;30(8):427–432.
43. Colahan PT, Wheat JD, Meagher DM. Treatment of middle phalangeal fractures in the horse. *J Am Vet Med Assoc.* 1981;178:1182–1185.
44. Rick MC. Fractures of the middle phalanx. In: White NA, Moore JN, eds. *Current Practice of Equine Surgery.* Philadelphia: Lippincott; 1990.
45. Stashak TS. *Adams' Lameness in Horses.* 5th ed. Philadelphia: Lippincott Williams & Wilkens; 2002.
46. Perrin RAR, Launois MT, Brogniez L, et al. The use of computed tomography to assist orthopaedic surgery in 86 horses (2002–2010). *Equine Vet Educ.* 2011;23:306.
47. Brasche SU, Rick MC, Herthel DJ. Treatment of a horse with osteomyelitis following repair of a middle phalangeal fracture via pastern arthrodesis. *Equine Vet Educ.* 2004;16(5): 262–266.
48. Neil KM, Axon JE, Begg AP, et al. Retrospective study of 108 foals with septic osteomyelitis. *Aust Vet J.* 2010;88(1–2):4–12.
49. Lenard ZM, Lester NV, O'Hara AJ, et al. Disseminated cryptococcosis including osteomyelitis in a horse. *Aust Vet J.* 2007;85(1–2):51–55.
50. Dyson SJ, Murray R, Schramme MC. Lameness associated with foot pain: results of magnetic resonance imaging in 199 horses (January 2001–December 200) and response to treatment. *Equine Vet J.* 2005;37:113–121.
51. Olive J, Mair TS, Charles B. Use of standing low-field magnetic resonance imaging to diagnose middle phalanx bone marrow lesions in horses. *Eq Vet Educ.* 2009;21:116–123.
52. Werpy N. Diagnosis of middle phalanx bone marrow lesions in horses using magnetic resonance imaging and identification of phase effect cancellation for proper image interpretation. *Equine Vet Educ.* 2009;21(3):125–130, 2009.
53. Steel CM, Hunt AR, Adams PL, et al. Factors associated with prognosis for survival and athletic use in foals with septic arthritis: 93 cases (1987–1994). *J Am Vet Med Assoc.* 1999;215(7):973–977.
54. Vos NJ, Ducharme NG. Analysis of factors influencing prognosis in foals with septic arthritis. *Ir Vet J.* 2008;61(2):102–106.
55. Wright L, Ekstrom CT, Kristoffersen M, et al. Haematogenous septic arthritis in foals: short- and long-term outcome and analysis of factors affecting prognosis. *Equine Vet Educ.* 2017;29(6):328–336.
56. Weaver JCB, Stover SM, O'Brien TR. Radiographic anatomy of soft tissue attachments in the equine metacarpophalangeal and proximal phalangeal region. *Equine Vet J.* 1992;24(4):310–315.
57. Levoie J, Carlson GP, George L. Hypertrophic osteopathy in three horses and a pony. *J Am Vet Med Assoc.* 1992;201: 1900–1904.
58. Mair TS, Dyson SJ, Frasser JA, et al. Hypertrophic osteopathy (Marie's disease) in Equidae: a review of twenty-four cases. *Equine Vet J.* 1996;28(4):256–262.
59. Schleining JA, Voss ED. Hypertorphic osteopathy secondary to gastric squamous cell carcinoma in a horse. *Equine Vet Educ.* 2004;16:304–307.
60. Tomlinson JE, Divers TJ, McDonough SP, et al. Hypertrophic osteopathy secondary to nodular pulmonary fibrosis in a horse. *J Vet Intern Med.* 2011;25(1):153–157.
61. McEntee MF. Equine cutaneous mastocytoma: morphology, biological behavior and evolution of the lesion. *J Comp Pathol.* 1991;104:171–178.
62. Samii VF, O'Brien TR, Stannard AA. Radiographic features of mastocytosis in the equine limb. *Equine Vet J.* 1997;29(1):63–66.
63. Scott DW, Miller WH. Mast cell tumor. In: Scott D, Miller W, eds. *Equine Dermatology.* 2nd ed. St. Louis Missouri: Elsevier; 2003.
64. Mair TS, Krudewig C. Mast cell tumours (mastocytosis) in the horse: a review of the literature and report of 11 cases. *Equine Vet Educ.* 2008;20(4):177–182.
65. Dörner CA, Castellón CH, Yañez D. Clinical presentation and treatment of multifocal epitrichial sweat gland carcinoma in a horse. *Austral J Vet Sci.* 52(3):109-112.
66. Sloet van Oldruitenborgh-Oosterbaan MM, Grinwis GCM. Equine sarcoidosis: clinical signs, diagnosis, treatment and outcome of 22 cases. *Vet Dermatol.* 2013;24(1): 218–224.e48.
67. Cillan-Garcia E, Kearns LJ, Hetzel U, et al. Osteosarcoma of the middle phalanx in a horse. *Equine Vet Educ.* 2010;22:535.
68. Balducci J, Selberg K, Pool R, Radue RP. Primary ossifying fibroma of the proximal phalanx in a horse. *Equine Vet Educ.* 2020;32(6):O41–O44.
69. Grabski M, Fews D, Busschers E. Hindlimb lameness associated with a focal osseous metaplasia in an 18-year-old Welsh Section D mare. *Eq Vet Educ.* 2017;29(3):121–124.

ELECTRONIC RESOURCES

Additional information related to the content in Chapter 26 can be found online at eBooks.Health.Elsevier.com.

- Chapter Quiz

CHAPTER 27

Equine Foot

Myra F. Barrett • Elizabeth Acutt • Federica Morandi

OVERVIEW

The equine digit is comprised of the three phalanges and associated proximal and distal interphalangeal joints; the podotrochlear (navicular) apparatus, including the navicular bone and navicular bursa; the distal termination of the flexor and extensor tendons; other supporting soft tissues; and the hoof capsule.[1–3] This chapter focuses specifically on the structures of the foot.

INDICATIONS FOR RADIOGRAPHY

Radiography is the primary imaging modality for evaluation of the foot. Indications for radiographs of the digit include pre-purchase examinations; lameness localized to the foot with regional analgesia (palmar digital and/or abaxial or basi-sesamoid nerve block) or intra-articular analgesia of the distal interphalangeal joint; assessment of osseous and/or synovial involvement in foot wounds or abscesses; suspected trauma; and monitoring the progression or resolution of known abnormalities.

TECHNICAL FACTORS

Patient Preparation

Pertinent information obtained from the patient's history and physical examination is crucial to determine the significance of many radiographic abnormalities of the equine foot. The results of diagnostic nerve blocks should also be considered, whilst noting the growing body of literature suggesting that these blocks may diffuse beyond previously described boundaries.[4,5] Dirt, skin lesions, specialized shoes, pads, and foot packing material can all produce artifactual opacities that complicate radiographic interpretation. All external material should be removed from the haircoat and hoof wall. Whenever possible, shoes and pads should be removed. The sole and sulci of the frog should be cleaned thoroughly. The sulci may then be filled uniformly with a material of soft tissue opacity (e.g., Play-Doh, Hasbro, Pawtucket, RI) to the level of the solar surface (Fig. 27.1). Packing the central and collateral sulci can help eliminate radiolucent linear regions created when the air-filled sulci are superimposed on the distal phalanx in the dorsal 65-degree proximal-palmarodistal (D65Pr-PaDiO)* or other views, which may imitate the appearance of fracture lines (see

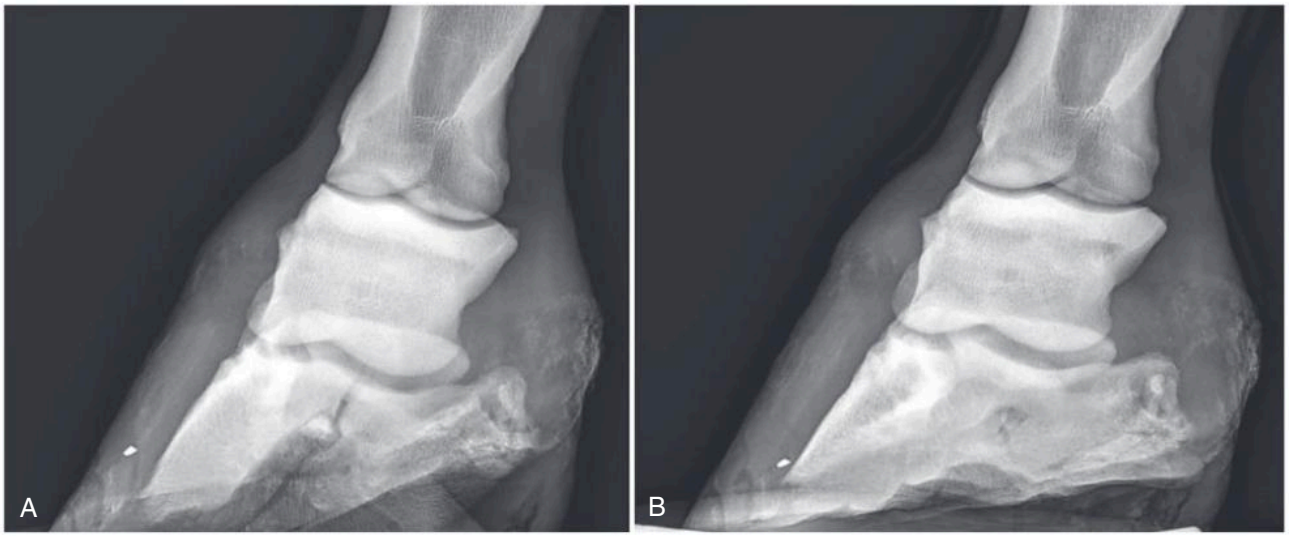


Fig. 27.1 **A**, Dorsolateral-palmaromedial oblique view of a normal foot without the sulci packed. Note the linear gas lucency in one of the sulci that can appear as a fracture line within the distal phalanx. **B,** The same foot as **A** with the sulci packed, resulting in resolution of the appearance of distal phalanx fracture.

*Palmar(o) is used throughout this chapter with the understanding that plantar(o) should be substituted if reference is being made to the hind digit.

Fig. 27.1). However, occasionally, packing can also increase the number of artifacts, especially if insufficient packing material is applied; therefore, in some cases, leaving the foot unpacked is preferred. The horse should be positioned with both feet on even wooden blocks so as to elevate the feet and facilitate the inclusion of the entire hoof capsule within the field of view. Additional positioning aids, such as a cassette tunnel or upright pedal block, should be used to assist in radiographic evaluation of the navicular bone (Fig. 27.2). When possible, an upright pedal block is preferred to a cassette tunnel for the D65Pr-PaDiO and dorsal 65-degree proximal 45-degree lateral(medial)-palmarodistomedial(lateral) oblique (D65Pr45L[M]-PaDiM[L]O) views since it allows for a tangential orientation of the x-ray beam to the plate, thereby limiting distortion and magnification artifacts. Not all patients are cooperative with placing their feet in the upright blocks, and in those cases a tunnel can suffice.

Recommended Views

The standard views included in a series for assessment of the foot and pastern are included in Table 27.1. Excellent descriptions of positioning are available for additional information.[6,7]



Fig. 27.2 Positioning of the foot for acquisition of dorsal 60–65-degree proximal to palmarodistal oblique radiograph using a Redden navicular block, NANRIC, Lawrenceburg KY.

Alternate Imaging of the Foot

Ultrasound, nuclear scintigraphy, magnetic resonance imaging (MRI), and computed tomography (CT) are used to enhance the assessment of foot lameness. Standing open and conventional open and closed magnets are being used with increasing frequency to assess the soft tissues and bone of the foot. Although these modalities are not discussed in detail in this chapter, specific notation will be made regarding important alternate imaging findings where applicable.

NORMAL RADIOGRAPHIC ANATOMY (INCLUDING VARIATIONS)

Osseous Structures

The appearance of the dorsal margin of the distal interphalangeal joint can vary in several ways, and this is a common area of radiographic misinterpretation. The shape of the extensor process of the distal phalanx (P3) and the dorsodistal margin of the middle phalanx (P2) may vary among individual animals from rounded to pointed (Fig. 27.3).[8] Pointed margins may be mistaken for periarticular osteophytes. Closely examining the joint for other signs of degenerative changes and comparing with the contralateral limb to assess for symmetry can help to distinguish between osteoarthritis changes and normal variation. The dorsal cortex of P2 should be smooth on a straight lateral view. If the lateromedial view is slightly oblique, the eminences for attachment of the collateral ligaments of the distal interphalangeal joint become more conspicuous and can be misinterpreted as abnormal (Fig. 27.4).

The radiographic appearance of the normal P3 in the D65Pr-PaDiO view varies in several respects.[7,9] The most obvious is the number and distribution of vascular channels (Fig. 27.5). The number of vascular channels is typically greater in rear P3 than in front P3.[8] All vascular channels radiate from the solar canal to the solar border.

A smoothly rounded concavity in the toe of the distal phalanx may be present in the normal horse (see Fig. 27.5). This notch is referred to as the *crena marginalis solaris* or, more commonly, the *crena*. In a radiographic study of the foredigit of the developing Quarter horse, a crena was identified in foals between 4 and 22 weeks of age in 83% of the distal phalanges evaluated.[10] The depth of this notch usually does not exceed 1.5 cm.[2] The crena is more conspicuous in front than in hind feet.[9] Ninety percent of sound racing Thoroughbreds have bilateral symmetry in the presence of the crena in the front feet,

Table • **27.1**

Views for Equine Foot Evaluation.

STRUCTURES EVALUATED	VIEWS
Distal phalanx	Dorsopalmar view with horizontal beam (0-degree) and foot on block to include soft tissues of the sole on the radiograph
	Lateromedial view with horizontal beam (0-degree) and foot on block to include soft tissues of the sole on the radiograph
	Dorsal 65-degree proximal-palmarodistal oblique
Distal interphalangeal joint	Dorsal 65-degree proximal-palmarodistal oblique
	Dorsopalmar view with horizontal beam (0-degree)
	Lateromedial view with horizontal beam (0-degree)
	Two oblique views: dorsal 65-degree proximal, 45-degree lateral-palmarodistomedial and dorsal 65-degree proximal, 45-degree medial-palmarodistolateral oblique
Navicular bone	Dorsal 65-degree proximal-palmarodistal oblique
	Palmar 45-degree proximal-palmarodistal oblique

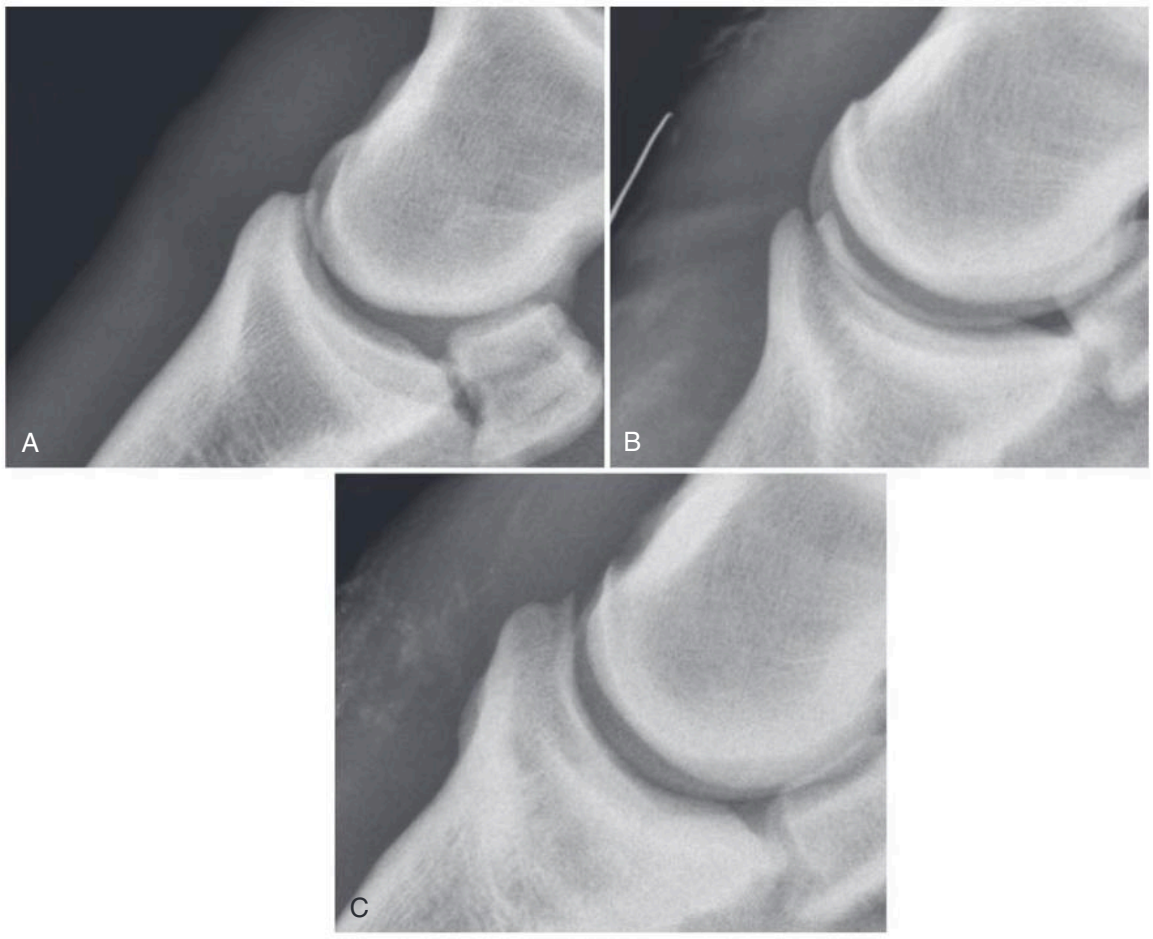


Fig. 27.3 **A–C,** Normal variations in the shape of the extensor process of the distal phalanx, as might be seen on the lateromedial view.



Fig. 27.4 Smooth eminences associated with the origins of the distal interphalangeal joint collateral ligaments on dorsal P2 (*arrow*) are highlighted by the slight dorsopalmar obliquity of this lateromedial radiograph. This is a normal finding that should not be confused with abnormal osseous proliferation.

5% asymmetry in the front feet, and 5% in neither front foot.[9] Heavier breed horses such as drafts and Friesians tend to have more prominent crena than light breed horses. Space occupying lesions within the hoof capsule, such as keratomas, discussed later in this chapter, may also give rise to regions of smooth concavity at the distal phalanx solar margin. However, these will be asymmetric between feet, may be present anywhere along the solar margin, and may be of variable depth. Comparing with the contralateral limb and correlating with clinical signs help to differentiate a normal crena from resorption due to a space occupying mass.

The palmar processes of the P3 become ossified more extensively with age (Fig. 27.6) and it is not uncommon to identify a separate osseous body of one or both palmar processes as an incidental radiographic variant (Fig. 27.7).

The flexor cortex of the navicular bone should be smooth with sharp definition between the cortex and spongiosa. The opacity of the flexor cortex should be uniform, aside from a small, well-defined crescent-shaped radiolucency that can be found in the central eminence (a.k.a. sagittal ridge). This lucent region is due to a normal area of decreased mineral density and/or a synovial fossa. This fossa is occasionally seen as a dimple on the flexor surface on the lateral view. A lucent crescent can also exist without a prominent synovial fossa due to a trabecular bone island interposed between two parallel cortical bone plates of the central eminence (Fig. 27.8).[11] This should not be confused with flexor cortical lysis, discussed later.

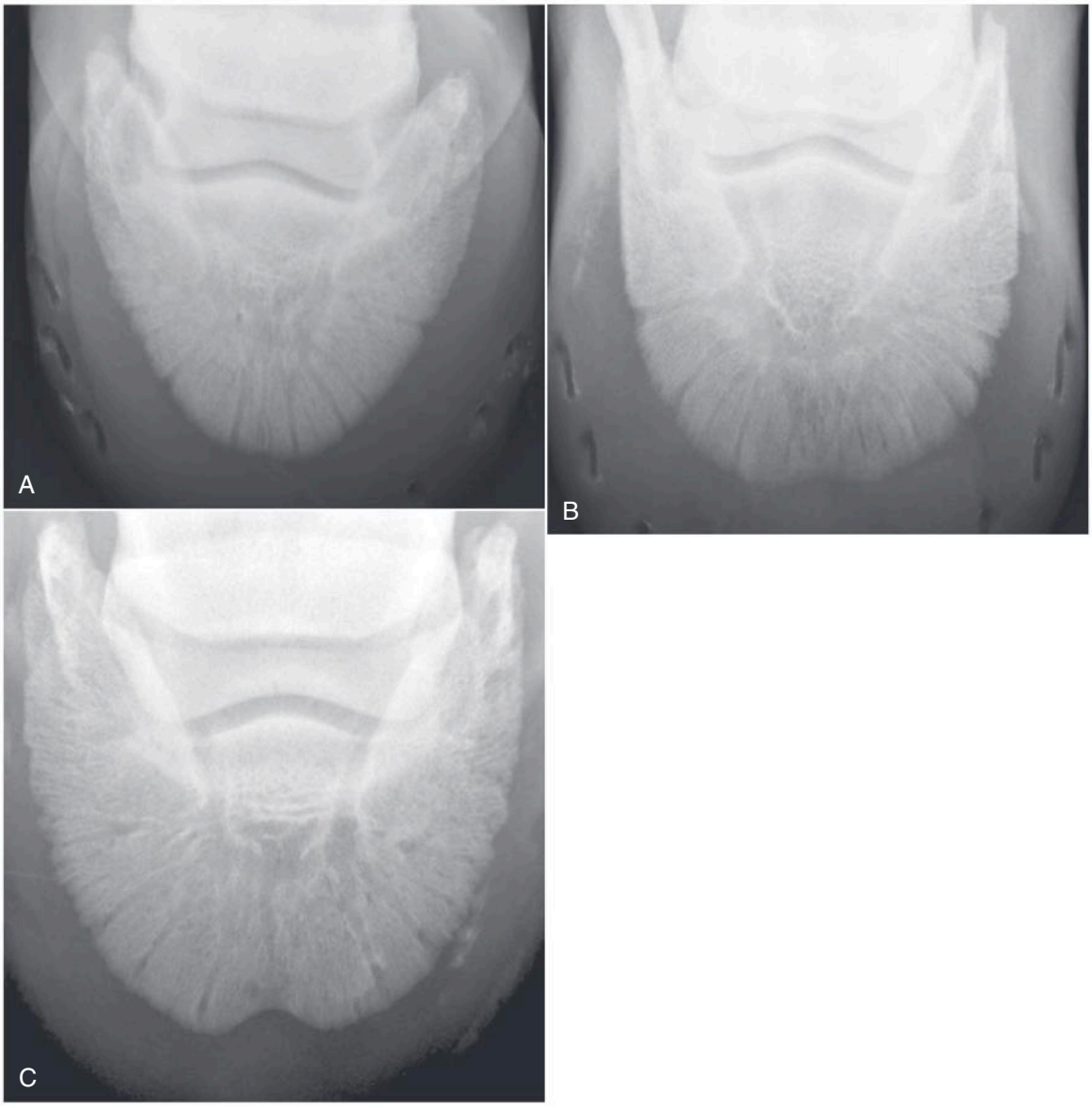


Fig. 27.5 Three horses with variation in the solar margin contour of the toe of the distal phalanx. **A,** A hind foot with a smooth convex contour; **B,** a front foot with a shallow concavity; and **C,** a front foot with a deeper concavity. The concavities in **B** and **C** are examples of the crena. These should not be misinterpreted as regions of lysis. However, current and resolved lesions can cause this same appearance and must be correlated with con firmatory evidence of foot disease. Note also the variation in the pattern of vascular channels.

Joints

The distal interphalangeal joint should have smooth margins and be symmetrical in width on the medial and lateral aspect of the joint. If the joint is narrower on one side, then the radiograph must be assessed for patient positioning, sole conformation, or articular cartilage damage. The distal interphalangeal joint should be wider than the proximal interphalangeal joint and this can be used as an internal reference when assessing the joint space.

Similarly, the articulation of the navicular bone with the middle phalanx should be smooth and well defined. Pathologic changes of this articulation are less common than palmar navicular bone damage and are part of distal interphalangeal joint degenerative changes.

Soft Tissue Structures

The equine digit is anatomically complex. The origins and insertions of the soft tissues in this region are well described and illustrated in other texts.[7,9] The flexor tendons run on the palmar aspect of the phalanges. The superficial digital flexor tendon (SDFT) terminates at the proximal aspect of the middle phalanx. The deep digital flexor tendon (DDFT) runs farther distally, passing over the flexor cortex of the navicular bone and inserting onto the flexor surface of the distal phalanx. The distal digital annular ligament originates on the proximal phalanx and forms a sheet palmar to the DDFT, extending to the level of the navicular bone. The navicular bone is suspended proximally by the collateral sesamoidean ligament, extending from the proximal cortex and dividing into medial and lateral

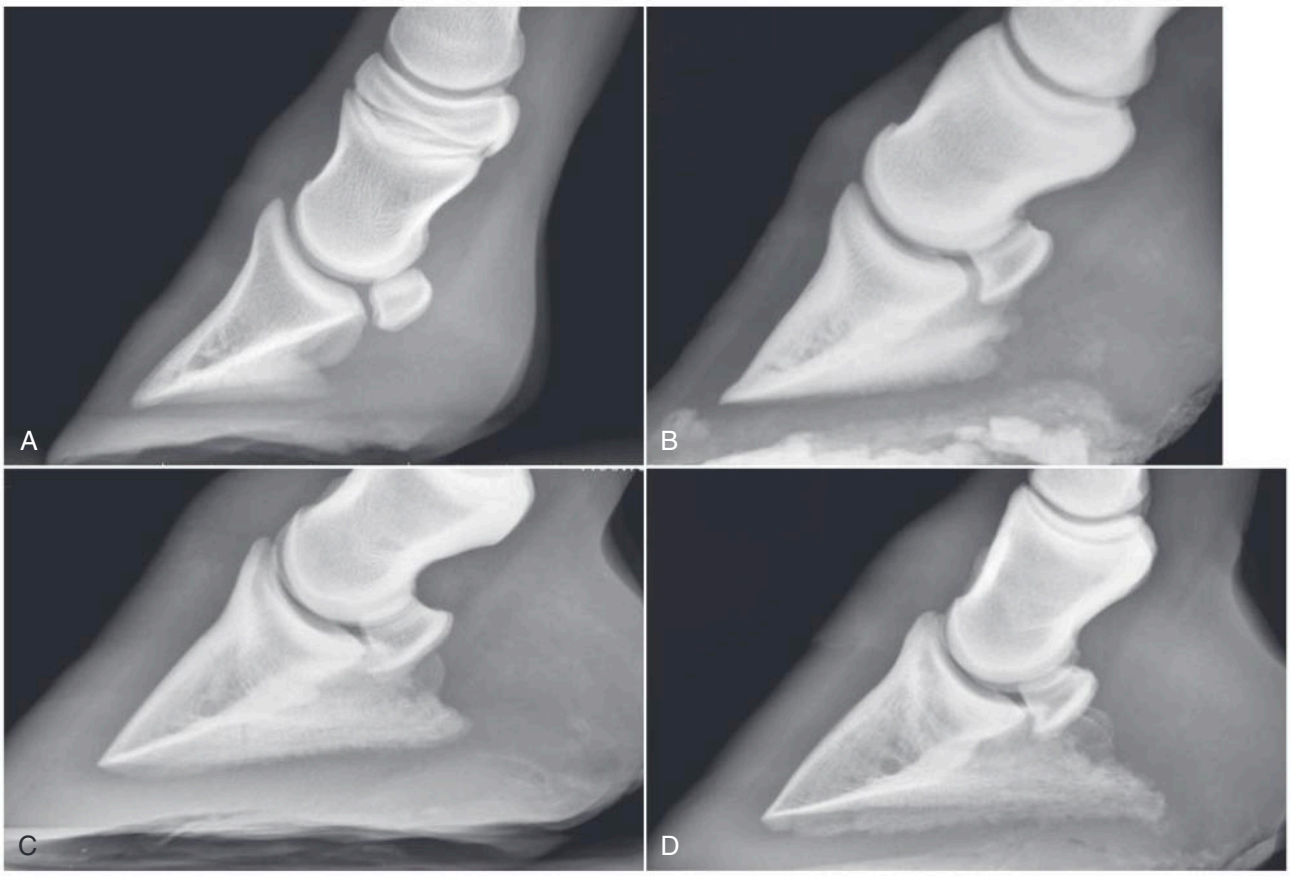


Fig. 27.6 Palmar processes of the normal distal phalanx in the horse become ossified more extensively with age. Lateromedial views of **(A)** a 3-month-old Saddlebred foal, **(B)** a 1-year-old Quarter horse, **(C)** a 6-year-old Paint, and **(D)** a 16-year-old Quarter horse. In all four images, the mildly more opaque soft tissue band of the deep digital flexor tendon (DDFT) can be seen along the palmar aspect. The distinctly less opaque corium of the hoof capsule is also visible along the dorsal border of the distal phalanx, extending around the toe and for a variable length along the solar border.

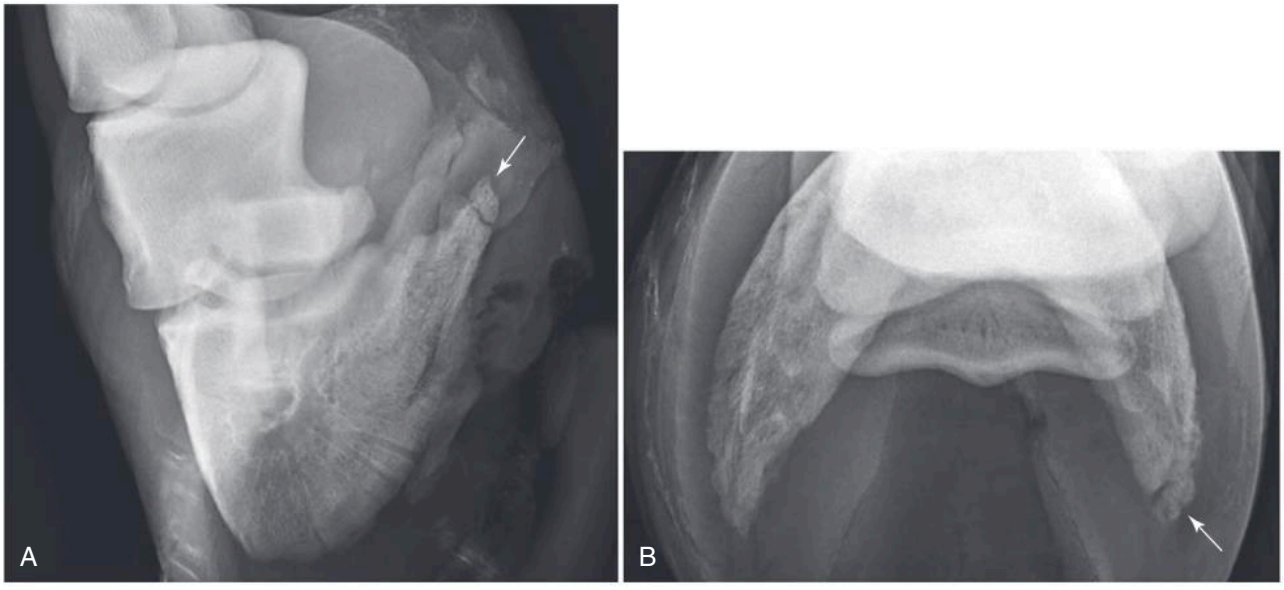


Fig. 27.7 Small separate center of ossification at the palmar aspect of the medial palmar process of P3 (*white arrows*) on D65Pr45M-PaDiLO **(A)** and PaPr-PaDiO **(B)** views.

portions that attach to the distal aspect of the proximal phalanx, in close association with the proximal interphalangeal joint collateral ligaments. The distal impar ligament runs from the distal cortex of the navicular bone to attach on the proximal flexor surface of the distal phalanx. The navicular bursa is located between the DDFT and navicular bone, collateral sesamoidean ligament, and impar ligament and normally maintains a low volume of synovial fluid. The collateral ligaments of the distal interphalangeal joint originate from small depressions on the middle phalanx and course in a palmar distal orientation to their respective fossae in the distal phalanx.

RADIOGRAPHIC CHANGES SECONDARY TO DISEASE WITHIN THE FOOT

Osseous Pathology

Osteochondrosis

Osteochondrosis lesions are not common in the distal interphalangeal joint. Fragmentation of the P3 extensor process is occasionally seen and may be considered developmental or traumatic dependent on clinical history and presentation, although often the etiology may not be definitively determined. Fragments are usually well identified radiographically on a lateromedial projection (Fig. 27.9). Arthroscopic removal is generally associated with a favorable prognosis, although development of distal interphalangeal joint osteoarthritis is a known sequela, particularly if there is extensive involvement of the articular surface.[12]

Fragmentation of the palmar articular surface of the distal phalanx has also been reported.[13] Histological evaluation suggested a traumatic origin in some horses but was consistent with a diagnosis of osteochondritis dissecans in one case. These fragments are best seen on the D65Pr-PaDiO and associated 65-degree medial and lateral oblique views (Fig. 27.10). MRI and CT revealed associated articular pathology that was underestimated on radiography. This report found that all of these fragments were associated with lameness and the majority had a poor prognosis despite conservative and/or surgical therapy.

Osseous Cyst-Like Lesions

Round to conical, variably sized, radiolucent lesions surrounded by a sclerotic rim occur in the phalanges. The phalanges are the second most common locations for such lesions, the stifle being the most common.[14] These have been called *subchondral cysts*, *osseous cysts*, or *subchondral cyst-like osteochondrosis*, with the current preferred term *osseous cyst-like lesions* (OCLLs). Because these lesions lack an epithelial lining and frequently communicate with the joint cavity, they are not true bone cysts. The etiology of these lesions is debated. In the young horse with no trauma history, the lesion is likely developmental. Subchondral bone ischemia and necrosis secondary to trauma, infection, and osteoarthritis have also been correlated with the presence of these OCLLs.[15] Clinical expression of

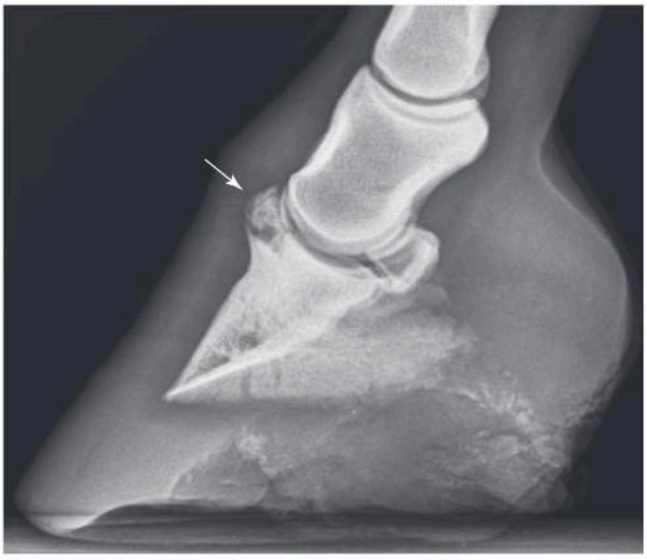


Fig. 27.9 P3 extensor process fragmentation (*white arrow*), seen on the lateromedial view.

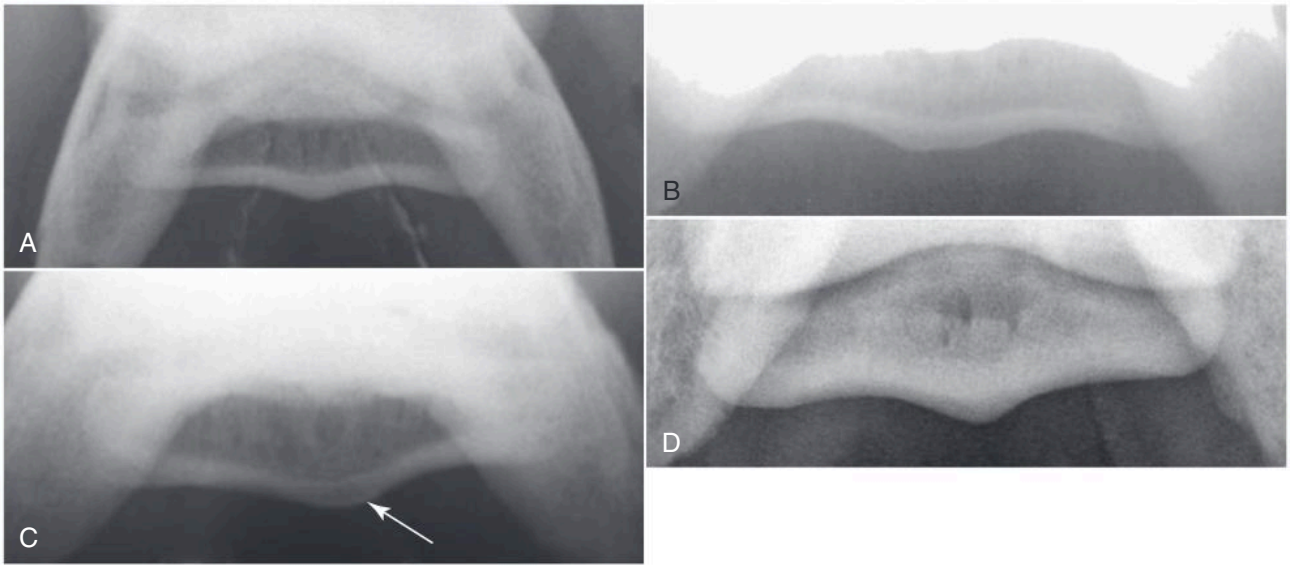


Fig. 27.8 Normal variations in the appearance of the navicular flexor cortex. The flexor cortex should be smoothly marginated and have an abrupt demarcation from the less-opaque medullary spongiosa. **A,** Prominent central eminence. **B,** Blunted central eminence. **C,** Crescent-shaped radiolucency in central eminence (*white arrow*). **D,** Either altered beam angulation or patient motion may result in indistinct interface between the cortex and the medullary spongiosa, falsely suggesting navicular sclerosis. The lateral view in this horse was normal, and a repeat palmaroproximal/palmarodistal projection with better beam angulation showed normal corticomedullary distinction.

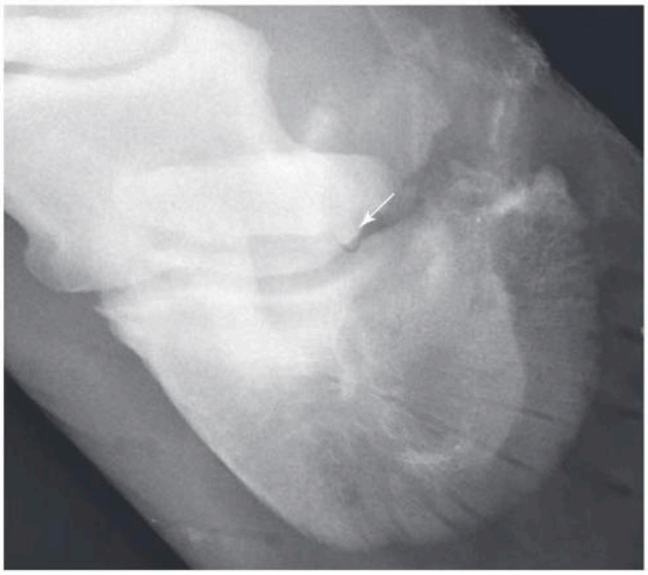


Fig. 27.10 Fragmentation of the palmar surface of P3 (*white arrow*), seen on the D65Pr45M-PaDiLO view.

lameness is suggested to relate to the extent of articular surface involvement. Some lesions have no visible connection to the articular cartilage or joint surface. Others have a thin neck or a broader base of connection to the articular margin.

OCLLs of the distal interphalangeal joint have a reported prevalence of 1.9%.[16] The majority of these are located in the central aspect of the distal phalanx, although OCLLs of distal P2 are also observed. In the distal phalanx, the lesion may be in the extensor process or, more likely, at the weight-bearing surface.[17] Indentations of the articular surface of the distal phalanx have been identified uncommonly (<3% prevalence) in horses of multiple breeds and disciplines, with a possible predilection in Friesian horses.[18] These may be, but are not always, associated with an underlying OCLL. These lesions are generally evident radiographically. Those of small diameter or shallow depth can be subtle. MRI (region of intermediate to high signal intensity on all sequences), scintigraphic (region of increased radionuclide uptake), and CT (low attenuating center surrounded by hyperattenuating rim) imaging can also be used to identify these lesions. MRI can be used to better characterize these lesions and identify associated articular cartilage defects. In one study, MRI was able to identify associated OCLLs not appreciated radiographically in 50% of cases. Some of these defects were identified on prepurchase radiographs of clinically sound horses. Many occurred in conjunction with additional pathology of the distal interphalangeal joint, including synovitis, osteophytosis, extensor process fragmentation, and distal phalanx fracture, which may have contributed to lameness in affected horses.[18] In another study, OCLLs were seen in contralateral limb in horses with bilateral defects but unilateral lameness.[16] The clinical significance of such lesions therefore remains uncertain. Successful outcomes have been reported following both surgical debridement and conservative treatment.[14,19,20] Pathological fracture secondary to a large osseous cyst of the distal phalanx has also been reported.[21]

OCLLs in the distal phalanx can be differentiated from other lesions producing an ovoid lucency within the bone by their proximity to, and frequent communication with, the articular surface. The most common of these other lesions is keratoma. *Keratoma* is an abnormal mass of hyperplastic squamous epithelial cells with abundant keratin and granulation tissue. These develop within the hoof wall arising from the stratum germinativum of the coronary band, from the inner dorsal wall, or in the sole. In most instances, they manifest as an aberrant, tubular proliferation of keratin that progress distally from the coronary band with normal hoof growth. Less commonly, a more spherical solitary growth of keratin is present within the hoof capsule. Keratomas are considered to be caused by traumatic or infectious insult to the hoof.[22] Lameness ranges from weeks to months and may be associated with unsuccessful resolution of presumed simple solar abscesses. Visible deformity at the coronary band, of the hoof wall, or sole is often clinically evident. The mass effect can cause localized resorption of an adjacent area of the distal phalanx, most commonly appearing as a semicircular defect along the solar margin. This is often best demonstrated on a D65Pr-PaDiO radiograph (Fig. 27.11, eFig. 27.1). Osseous resorption secondary to keratomas may be differentiated from septic pedal osteitis by its smooth and sometimes sclerotic margin. When a more rounded rather than cylindrical keratoma is present, resorption may be more prominent on the dorsal cortex or flexor surface, seen best on a lateromedial view (Fig. 27.11). Uncommonly, the mass may be partially mineralized.[23] Histologic evaluation of soft tissue masses of the sole and hoof is needed for definitive diagnosis. CT and MRI can be used to accurately localize and characterize keratomas, and may improve surgical planning, and lead to reduced hoof wall removal and postsurgical complications.[24–26]

Epidermoid cysts are rare pseudo-neoplastic lesions, also characterized by a focal accumulation of (laminated) keratin. In contrast to keratomas, these lesions do not contain granulation tissue and inflammatory cells, and do not arise from the hoof wall. Pathologic evaluation (gross and histopathology) is useful to facilitate diagnosis. Two reports of intraosseous epidermoid cysts in the equine distal phalanx exist.[27,28] These were characterized radiographically and on CT as large, well-circumscribed heterogeneously radiolucent/hypoattenuating regions within the distal phalanx. Epidermoid cysts have also been reported in other locations within the equine foot, including the distal interphalangeal joint and digital sheath.[29–31] Their characteristics on MRI were suggestive of a lesion containing proteinaceous material.

Neoplasia of the equine foot is rare but may also produce a lucent region within the distal phalanx. Squamous cell carcinoma, melanoma, anaplastic sarcoma, hemangioma, and mast cell tumor have all been reported.[32–36] Typically, these lesions cause large, irregular regions of osteolysis with poorly defined margins and an indistinct zone of transition on radiographs. Horses with aggressive neoplasia in the foot may present with severe lameness and deteriorate rapidly.[33] *Osteosarcoma* is extremely rarely reported in the appendicular bones of the horse, with only six cases reported.[32] The radiographic appearance of one horse resembled that in dogs with an aggressive mixed bone response. Pathologic fracture was present.

OCLLs are commonly misdiagnosed within the equine navicular bone. While true cyst-like lesions can occur, the most common cause of the appearance of a centrally located, rounded lucent region within this bone on a D65Pr-PaDiO radiographic projection is superimposition of a region of flexor cortical lysis (Fig. 27.12). Cystic dilation of one or more of the synovial invaginations at the distal aspect of this bone can also occur.



eFig. 27.1 Dorsolateral-palmaromedial oblique view of the distal phalanx. A well-de fined concave defect is seen in the lateral aspect of the distal phalanx consistent with a keratoma.

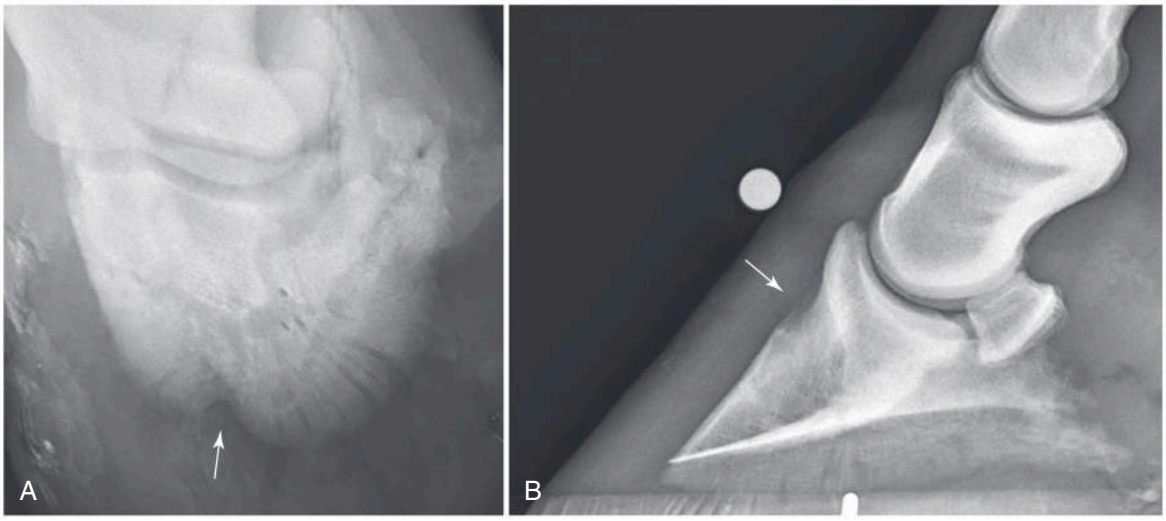


Fig. 27.11 **A,** Classic keratoma resulting in smooth concave osseous resorption at the solar margin of P3 (*arrow*). **B,** Atypical keratoma resulting in smooth concave osseous resorption at the dorsal cortex of P3 (*arrow*).

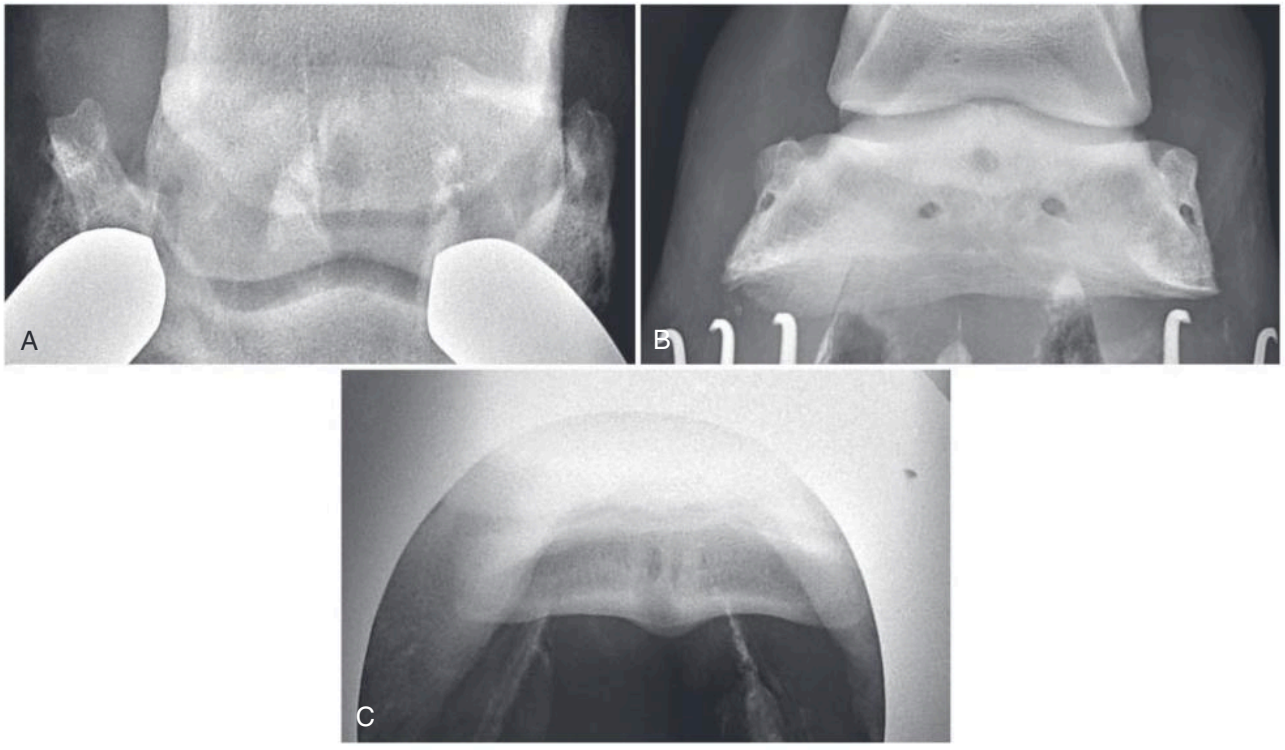


Fig. 27.12 Rounded lucent region within the mid aspect of the navicular bone on the D65Pr-PaDiO **(A)** and horizontal dorsopalmar (DP) **(B)** views, confirmed as flexor cortical erosion on the skyline view **(C)**.

Fractures

Phalangeal fractures occur in a wide variety of horse breeds and after varied activities. Radiography is the most often used mode of screening for identification. Knowing the common distribution of phalangeal fractures associated with breed and discipline can guide a thorough assessment of those areas in the lame horse.[37,38] It is now recognized that some diagnostic imaging changes are prodromal features of potential impending fractures, particularly in racing and sport horses. In a study comparing agreement in fracture evaluation between radiography and CT, CT identified 4 of 20 fractures that were not identified by radiography.[39] CT evaluation of fracture complexity is superior to that of radiography, particularly when planning surgical treatment. Intraoperative CT is being used in some facilities.[40,41]

Navicular Bone

True navicular fractures are uncommon.[42] The most frequently reported type is complete, minimally displaced parasagittal fractures, although other configurations, including comminuted fractures, can occur. Traumatic etiologies are considered most likely. It can be challenging to distinguish fractures from the developmentally abnormal bipartite (or even tripartite) navicular bones. Bi- or tripartite navicular bones are often found bilaterally (Fig. 27.13). These horses are frequently sound and

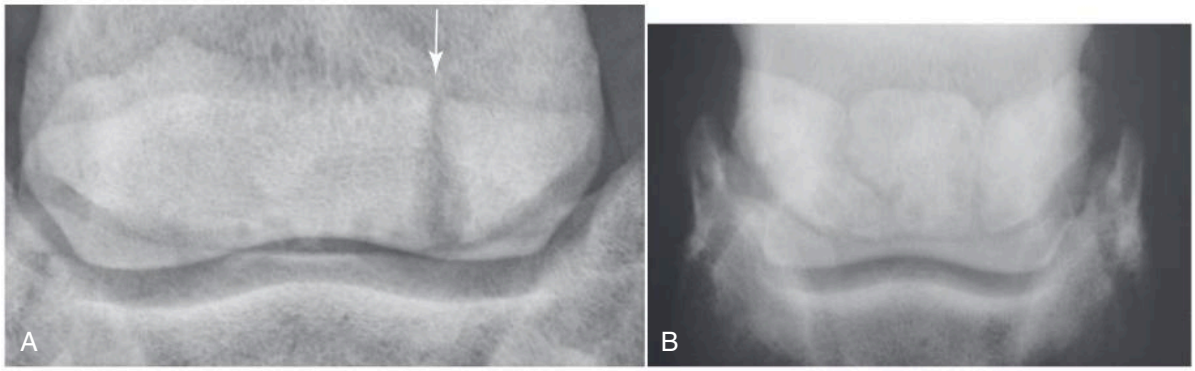


Fig. 27.13 **A,** Complete navicular bone fracture (*white arrow*). **B,** Tripartite navicular bone; notice the smooth margins of the navicular fragments. This was a mature horse with tripartite navicular bones in both front feet and minimal lameness. (Courtesy Dr. Robert J. Bahr, Oklahoma State University, Stillwater, OK.)

in athletic work, although the developmental abnormality can also lead to degenerative bone remodeling. Navicular bone fractures generally form a fibrous union resulting in radiographically persistent fracture lines, even in chronic cases.[43] Complete fractures are more commonly seen in the forelimb.[42] In the authors' experience, the athletic outcome from navicular bone fractures is variable and likely depends on other comorbidities sustained at the time of trauma or as a sequela to the fracture. An incidence of 1.5% was reported for "clinically silent" navicular fractures during radiographic screening of 200 Warmblood yearlings.[42]

Fragments of the distal border of the navicular bone are seen with relative frequency but are more likely to represent a developmental anomaly or feature of navicular syndrome (discussed later) than traumatic fractures (Fig. 27.14). They are commonly seen alongside other degenerative navicular changes and have been identified more commonly in lame than sound horses in some population studies.[42] However, their frequent presence in nonlame horses makes their clinical significance questionable in the absence of additional navicular changes.[44] These have been postulated to represent dystrophic mineralization or osseous metaplasia within the distal sesamoidean impar ligament, or separate centers of ossification. The accompanying concave defect in the distal border of the navicular bone suggests they may be avulsed fragments. Larger fragments are relatively well identified on radiographs, although the sensitivity of this modality for their identification is lower than cross-sectional modalities.

Distal Phalanx

A fracture classification system (types I through VII; illustrated in Fig. 27.15F) describes the fractures of the distal phalanx.[45] Fractures are classified based on region of the bone affected, articular or nonarticular involvement, and anatomic plane of the fracture, as follows:

I. Nonarticular fracture of palmar or plantar process
II. Articular fracture, extending from distal interphalangeal joint to solar margin (Fig. 27.16)
III. Articular fracture, midsagittal, divides distal phalanx into equal parts (Fig. 27.17)
IV. Articular fracture, extensor process (Fig. 27.18)
V. Articular fracture, comminuted body fracture (not of type II, III, or IV)
VI. Solar margin fracture (see Fig. 27.40B,C)
VII. Palmar process fracture in foals (Fig. 27.19)

Trauma is the most common cause of distal phalanx fractures; however, they also occur as pathologic fractures secondary to infective pedal osteitis and laminitis. Because the hoof wall restricts displacement of bone fragments, diagnosis of the distal phalanx fracture depends on visualization of the fracture line. If the plane of the primary x-ray beam is not parallel to the fracture plane, the superimposed parts of the bone obscure the fracture line. Therefore, a comprehensive series of foot radiographs, as outlined in Table 27.1, is recommended. A recent study found that radiographic identification of palmar/plantar process fractures (types I and II) was improved via the inclusion of oblique projections (palmaro 50-degree proximal 45-degree medial(lateral)-dorsodistolateral(medial) oblique (Pa50Pr45M[L]-DdiL[M]O views; Fig. 27.20) and therefore it may be helpful to include these views in cases with a suspicion of distal phalanx fracture.[46] Occasionally, the horizontal beam oblique views (dorsal 45-degree lateral[medial]-palmaromedial[lateral] (D45L[M]-PM[L]O)) typically used to assess the proximal interphalangeal joint may more effectively demonstrate the articular component of a fracture. Identification of type VI fractures requires careful assessment of the solar margin. Overexposure of the image makes this fracture difficult to see.

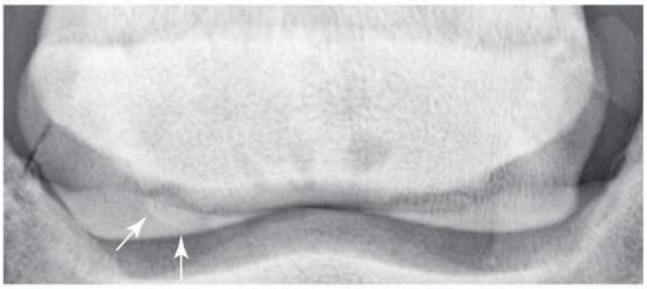


Fig. 27.14 Chip fracture at the distal navicular border. The small fragment (*white arrows*) and the underlying fracture bed can be seen. A medullary cyst-like lesion is also present.

Two large retrospective studies have reported the prevalence of distal phalanx fracture types. In a predominantly Warmblood population, type I fractures were most often seen, followed by type II. In contrast, in a population in which Quarter horses were the most common breed, type VI fractures predominated. In Thoroughbred racehorses, type II fractures appear to be the most frequently reported configuration.[41,45,47] Type II fractures are often distributed in accordance with the direction of racing; the forelimb that bears the most weight in turns is at greatest risk. In addition, since racehorses in North America race in a counterclockwise direction, fractures tend to involve the lateral aspect of the left front limb or the medial aspect of the right front limb.[6] Fractures of the extensor process (type IV) can result in small or quite large (>25% of the joint surface) fragments.[12,48,49] A question exists as to whether the smaller lesions are true fractures or a result of developmental defect. Larger fragments are more likely of traumatic

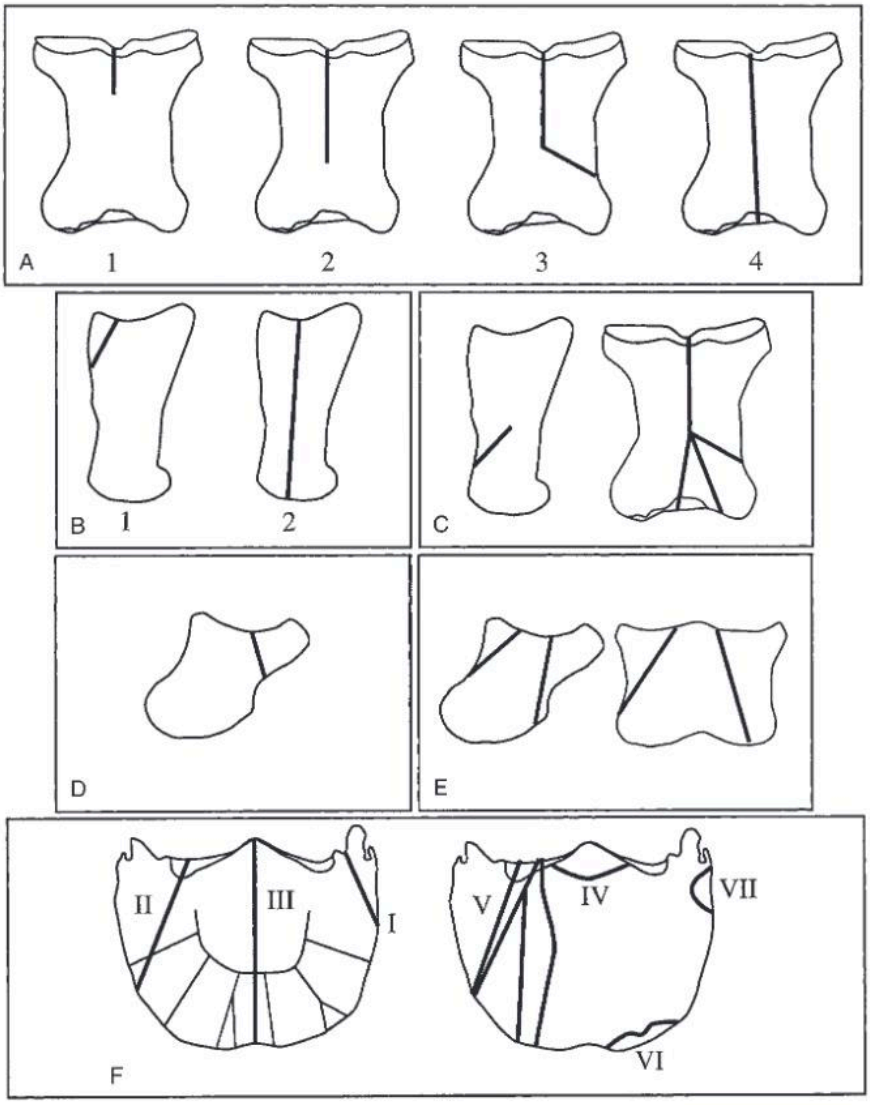


Fig. 27.15 Common fractures of the phalanges. *Proximal phalanx:* **A,** Sagittal plane fractures, noncomminuted. *1,* Incomplete, monoarticular (short, less than 30 mm variation); *2,* incomplete, monoarticular (long, more than 30 mm variation); *3,* complete, monoarticular; *4,* complete, biarticular. **B,** Dorsal plane fractures, noncomminuted. *1,* Complete, monoarticular; *2,* complete, biarticular. **C,** Comminuted, complete, biarticular, dorsal, and/or sagittal plane. *Middle phalanx:* **D,** Palmar/plantar eminence (monoarticular, complete). **E,** Comminuted, complete, biarticular. *Distal phalanx:* **F,** *I,* Nonarticular, palmar/plantar process; *II,* articular, extending from distal interphalangeal joint to solar margin; *III,* articular, midsagittal, divides into equal parts; *IV,* articular, extensor process; *V,* articular, comminuted body fracture

origin. Front limbs are more often affected than hindlimbs. Type V fractures require cross-sectional imaging to identify the various fracture planes. The type VI fracture is often found in association with radiographic signs of laminitis (32% of type VI fractures in one study) (see Fig. 27.40B,C).[45]

The progression of healing of a distal phalanx fracture is difficult to determine radiographically because of the minimal amount of external (periosteal) osseous callus produced by this bone. The periosteum of the distal phalanx is poorly developed and does not respond with abundant proliferation to the stimulation of direct trauma. From a multicenter study of 285 horses with distal phalanx fractures, those that had radiographic follow-up assessment showed evidence of healing of types I to III on average by 16 weeks with a range of 2 to 87 weeks from the start of their treatment.[50] Mean time of bone union was significantly shorter for horses 3 years old or younger. Bone union began at the solar margin and progressed to the articular surface in these horses; this is speculated to be due to improved blood supply in the periphery of the bone.[51] Because of the fibrous component of healing, radiographic bone union and clinical soundness do not correlate accurately.[50] Nonarticular type I fractures had the best prognosis for return to original or expected level of work or performance than type III followed by type II fractures. Surgical fixation has been advocated in articular fractures to maximize congruity of the joint surface and mitigate against the development of secondary osteoarthritic changes.[41]

Fractures of the extensor process generally produce more proliferative bone than other types of distal phalangeal fractures (see Fig. 27.18B). However, large extensor process fragments may not heal by bone union but by fibrous union, making them predisposed to loosening with additional trauma. In horses with

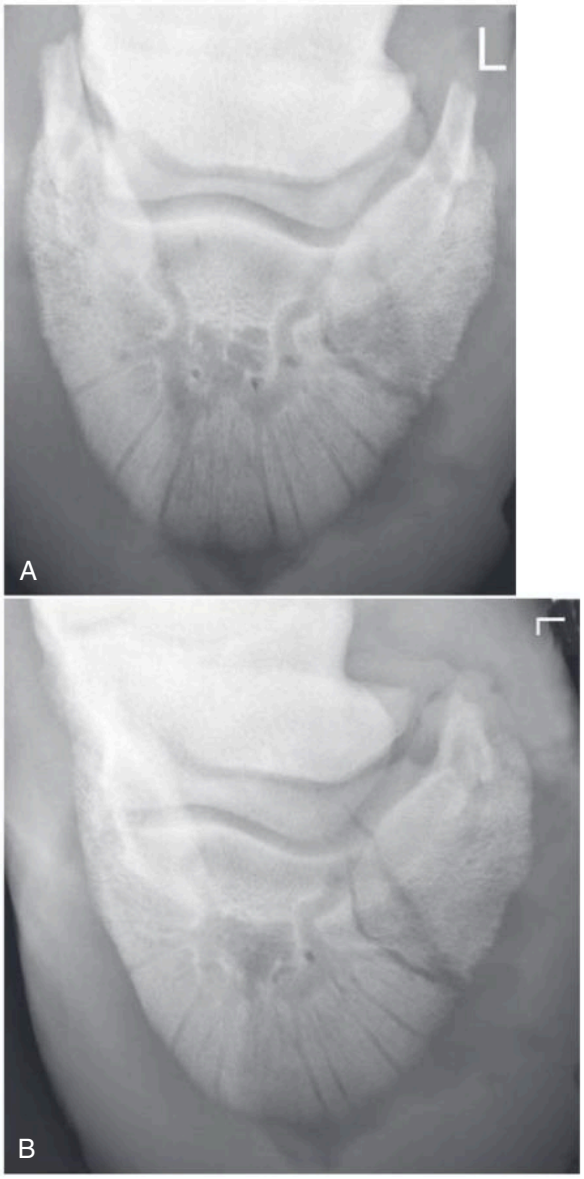


Fig. 27.16 Oblique fracture of the lateral wing of the distal phalanx. **A,** The fracture is subtle in the standard dorsal 65-degree proximal/palmarodistal view. Because there is minimal distraction, the x-ray beam must pass parallel through the fracture gap for optimal depiction. The curvature of the foot necessitates oblique projections to identify these fractures, particularly at the acute stage. **B,** This is a dorsal 65-degree proximal 45-degree lateral/palmarodistal view. The fracture is evident and approaches but does not disrupt the subchondral bone. However, the location along the joint contour makes this a type II fracture.



Fig. 27.17 **A,** Midsagittal, articular fracture (type III) of the distal phalanx. The fracture is seen easily in the dorsal 65-degree proximal/palmarodistal view, and a small offset is evident at the articular border. **B,** In the horizontal (0-degree) dorsopalmar view, the fracture may have been mistaken for air in the heel crevice or as an extension of the air in the central sulcus of the frog. The fracture line has been marked with a *white arrow* and *asterisks* placed in the sulci of the frog. This horse also has grade 5 ossification of the collateral cartilages. The lateral ossification is separated at the base.

chronic, recurrent lameness, surgical removal of the extensor process fragment has been recommended. In a study of 18 Friesian horses treated by surgical removal, the long-term outcome was good in 82% and was best in those horses used for pleasure riding and low-level dressage or driving competition.[12] In the radiographic follow-up evaluations, some horses had filling of the fragment defect with subchondral bone.

The type VII palmar process fracture of foals has been described in Arabian, Quarter horse, Thoroughbred, and Warmblood horses (see Figs. 27.15F and 27.19).[52,53] Fractures may be uni- or biaxial and may be seen in one or both forelimbs. Whilst the microradiographic and histologic appearance in most foals studied is consistent with fracture healing, rather than a separate center of ossification, affected foals are rarely lame and this finding is often incidental. Foals through 12 weeks old have a lucent line between the proximal and distal angles of the palmar process. This line is normal and should not be mistaken for a fracture (Fig. 27.21). In the horses studied from 1 week to 12 months, fracture identification is more evident after 3 months and most are healed without intervention at 12 months. The etiology is undetermined, with most recent theories related to effect of genetics, normal process of foot development, hoof conformation, and foot balance.[53] The long-term effects of these fractures have not been assessed.

Pedal Osteitis

The term *equine pedal osteitis* is typically used to refer to chronic remodeling and demineralization of the solar margin of the distal phalanx, generally seen in response to repetitive concussive trauma.[54] Radiographically, this may appear as

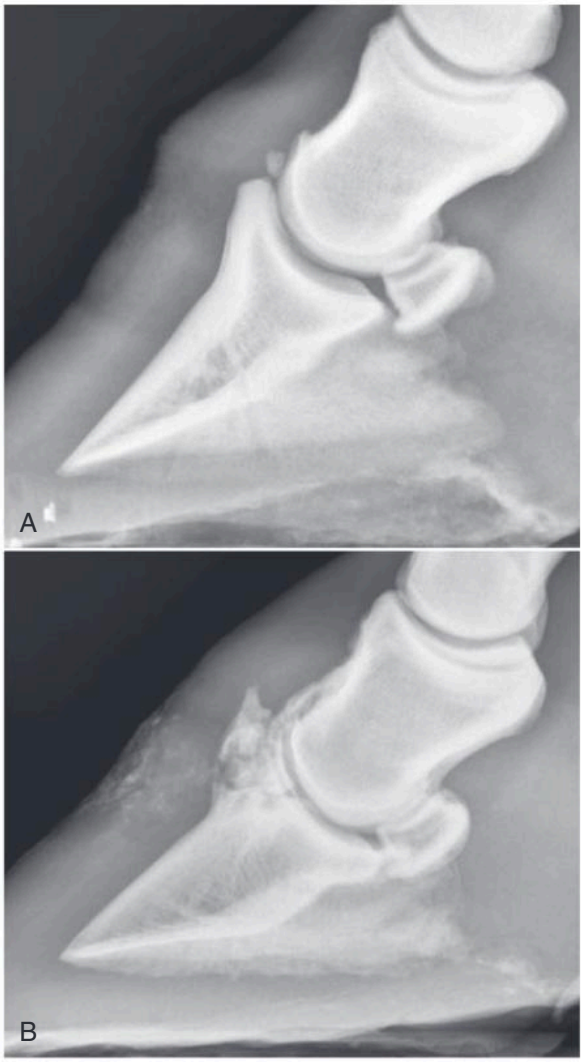


Fig. 27.18 Fractures of the extensor process in two horses. **A,** 2-year-old male Standardbred with a small rounded fragment separated from the extensor process of a front distal phalanx. There is enlargement of the soft tissue at the coronary band. There is no evident deficit in the contour of the extensor process, suggesting that this may have been of developmental origin. This horse developed fragmentation in the opposite front extensor process approximately 1 year later during race training. **B,** 20-year-old Quarter horse gelding with a large extensor process fracture. Circular lucencies in the distal phalanx at the distal palmar aspect of the fracture line, rounding of the fragment edges at the articular border, and the new bone on the dorsal surface of the middle phalanx are indicative of a chronic nonunion or fibrous union.

diffuse roughening of the solar border creating a ragged, lacy appearance when viewed on the lateromedial or D65Pr-PaDiO projection (Fig. 27.22). Once the primary insult and pedal osteitis become inactive, little change in the appearance of the roughened contour of the solar margin is seen. The normal appearance of the solar surface of the distal phalanx varies considerably, and a mild degree of incidental irregularity may be misinterpreted as disease. A positive response to hoof testers, positive response to softer footing or sole padding, an increased number and diameter of vascular channels seen concomitantly with demineralization of the bone, and thinning of the sole of the foot increase the probability of pedal osteitis being the cause of lameness. Thus, clinical signs must be considered in the determination of whether a radiographically irregular margin of the distal phalanx is an indicator of active remodeling. Whilst typically a diffuse change, pedal osteitis can be a localized change due to chronic medial-lateral imbalance or secondary to another lesion within the hoof capsule, such as a subsolar abscess. It is difficult to determine radiographically if such focal pedal osteitis is associated with localized infection. In these cases, MRI can provide additional information for differentiating disease processes and thereby help determine the appropriate management plan.

Infection

Osteomyelitis and Septic Osteitis

Septic pedal osteitis refers to infection of the distal phalanx. The most common cause is penetrating foreign objects through the sole. Common radiographic changes are discrete areas of lysis, irregular margin, and decreased opacity of the distal phalanx, typical of chronic inflammation (Fig. 27.23, eFig. 27.2). Gas may be present in the soft tissue adjacent to the surface of the distal phalanx. Separation of a piece of the distal phalanx may represent a pathologic fracture or sequestrum (see Fig. 27.23). Clinically, a draining tract at the sole or coronary band may be found. Contrast fistulography or images made with a radiopaque stylet in the tract can be helpful to assess if the tract includes involvement of bone, tendons, ligaments, or regional synovial structures (distal interphalangeal joint and/or navicular bursa), which necessitates aggressive treatment. If a metallic foreign body is evident at physical examination, radiographs should be made before removal to determine the depth of its penetration and its relation to the regional bone (Fig. 27.24). In one study of penetrating injuries to the frog, septic osteitis of the distal phalanx was cited as a reason for euthanasia.[55] These injuries are discussed in more detail at the end of this chapter.

Another possible cause of septic pedal osteitis is hematogenous spread. Of 108 Thoroughbred foals with 141 sites of hematogenous osteomyelitis, there were a significant number with phalangeal involvement.[56] This included 25 distal phalanx lesions in 21 foals. None of the foals with a solar margin lesion had visible evidence of sole bruising or a penetrating wound. Radiographic lysis was present in four foals with a sequestrum. The hindlimb was affected more commonly (62% of lesions). Three of four foals with extensor process lesions had concurrent septic arthritis. Although the proximal physis and epiphysis of the proximal and middle phalanges are common potential locations for hematogenous osteomyelitis, the distal phalanx has not typically been evaluated. Eighty-six percent of the foals with distal phalanx lesions were discharged from the hospital, and 50% of those that trained for racing had official race starts. Septic osteomyelitis of the navicular bone can also occur, with the majority of cases occurring secondary to penetrating injury to the foot.[55]

Bone Marrow Lesions

Bone marrow edema, edema-like signal, bone bruises, contusions, and bone marrow lesions (BMLs) are all terms used to refer to trabecular changes resulting in the increased presence of fluid within bone. These lesions cannot be identified radiographically, and diagnosis is almost always via MRI. Lesions may be visible on nuclear scintigraphy but cannot be differentiated from other lesions causing focal intraosseous increased radiopharmaceutical uptake. The appearance on MRI is that of a region of low signal on T1- and T2*-weighted sequences that has high signal on fat-suppressed sequences, such as the short tau inversion recovery (STIR). Multiples patterns of BML have been identified, including BML associated with joint pathology,



eFig. 27.2 Septic pedal osteitis with adjacent hoof wall defect. A concave radiolucent defect is present along the lateral solar margin of P3. The lateral solar margin is irregular. A wedge-shaped gas opacity defect in the hoof wall with a linear gas tract extends to the solar margin.

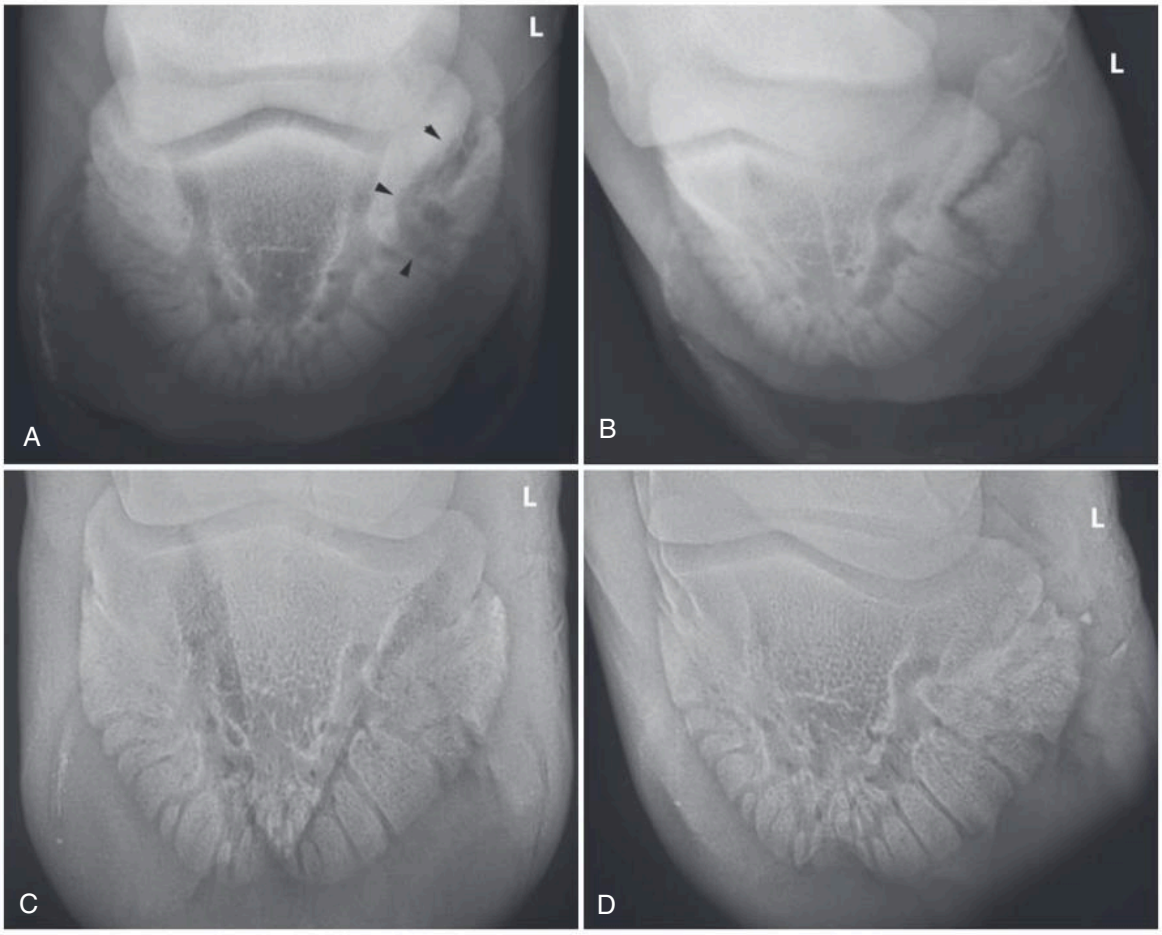


Fig. 27.19 A palmar process fracture in the distal phalanx of a foal (type VII in Fig. 27.15F). **A and B** were obtained at 3 months; **C and D** are at age 5 months. *Black arrowheads* in **A** indicate one edge of the fracture extending from the incisure of the palmar process to the solar margin. **B** is the dorsal 65-degree proximal, 45-degree medial/palmarodistolateral oblique projection that better demonstrates the fracture gap and separated triangular fragment. In **C and D,** (the oblique projection) the fracture is minimally visible and was considered clinically healed. *L* marks the lateral side of the foot.

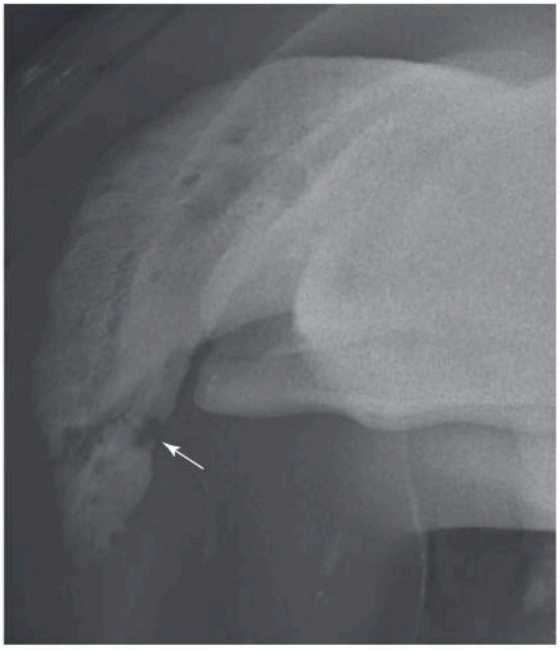


Fig. 27.20 PaPrM(L)-DDiL(M)O view of P3 palmar process fracture (*white arrow*).



Fig. 27.21 Dorsal 65-degree proximal/palmarodistal view of the distal phalanx of a normal foal. Note the normal radiolucent line in the palmar process (*white arrow*), which should not be confused with a fracture.

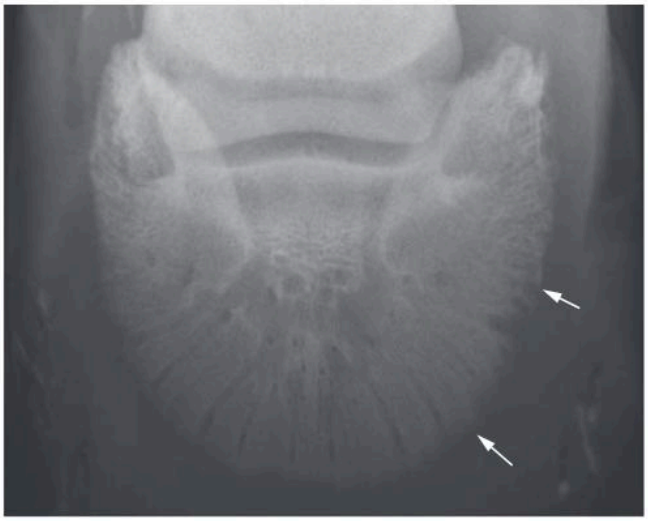


Fig. 27.22 Dorsal 65-degree proximal/palmarodistal view of the distal phalanx of a horse with pedal osteitis. The solar border between the *arrows* is irregular compared with the opposite margin. The horse was sensitive to hoof testers in this region, and no lesions were found in the sole. Gas lucencies in the peripheral soft tissues are the result of the recently pulled shoe and nails.

BML associated with soft tissue injury, BML associated with acute trauma, and BML that is unassociated with other injury in the absence of current lameness.[57] Whilst the clinical significance of this latter group of lesions in some horses has been debated, it is the authors' experience that the majority of BMLs have clinical relevance and, where extensive and/or associated with particularly pronounced signal abnormalities, can be a source of profound pain. In addition, if such a lesion is identified in a nonlame leg, such horses may subsequently develop lameness and progressive arthrosis in the proceeding months.[58] Although some BMLs can resolve quickly (within 3–4 months), with an accompanying rapid improvement in lameness, severe injury can result in the development of osteonecrosis of the trabecular and subchondral bone and progressive articular pathology. These horses remain lame during the rehabilitation period and have a poorer prognosis for return to athletic activity.[58] BM edema-type pattern seen at the entheses of the distal interphalangeal joint (DIPJ) collateral ligament without associated ligament desmopathy has a reportedly good to excellent prognosis for return to activity.[59]

It is worth noting that diffuse increased signal throughout the distal phalanx on fluid-sensitive sequences, particularly within the flexor surface, can also be seen with demineralization associated with disuse osteopenia. This is frequently found in horses with chronic lameness or those that have undergone extensive layup.

Palmar endosteal fluid signal is a common finding within the navicular bone on MRI. This fluid signal may indicate edema, inflammatory infiltrate, trabecular remodeling, fibrosis, hemorrhage, or necrosis. These various etiologies cannot technically be differentiated based upon the MRI appearance; however, these differential diagnoses can be ranked based upon severity and extent of fluid signal and when interpreted in light of clinical history (including lameness severity and chronicity), other changes of the navicular bone, and additional regional pathology (e.g., navicular bursitis, deep digital flexor tendinopathy etc.)

Navicular Syndrome

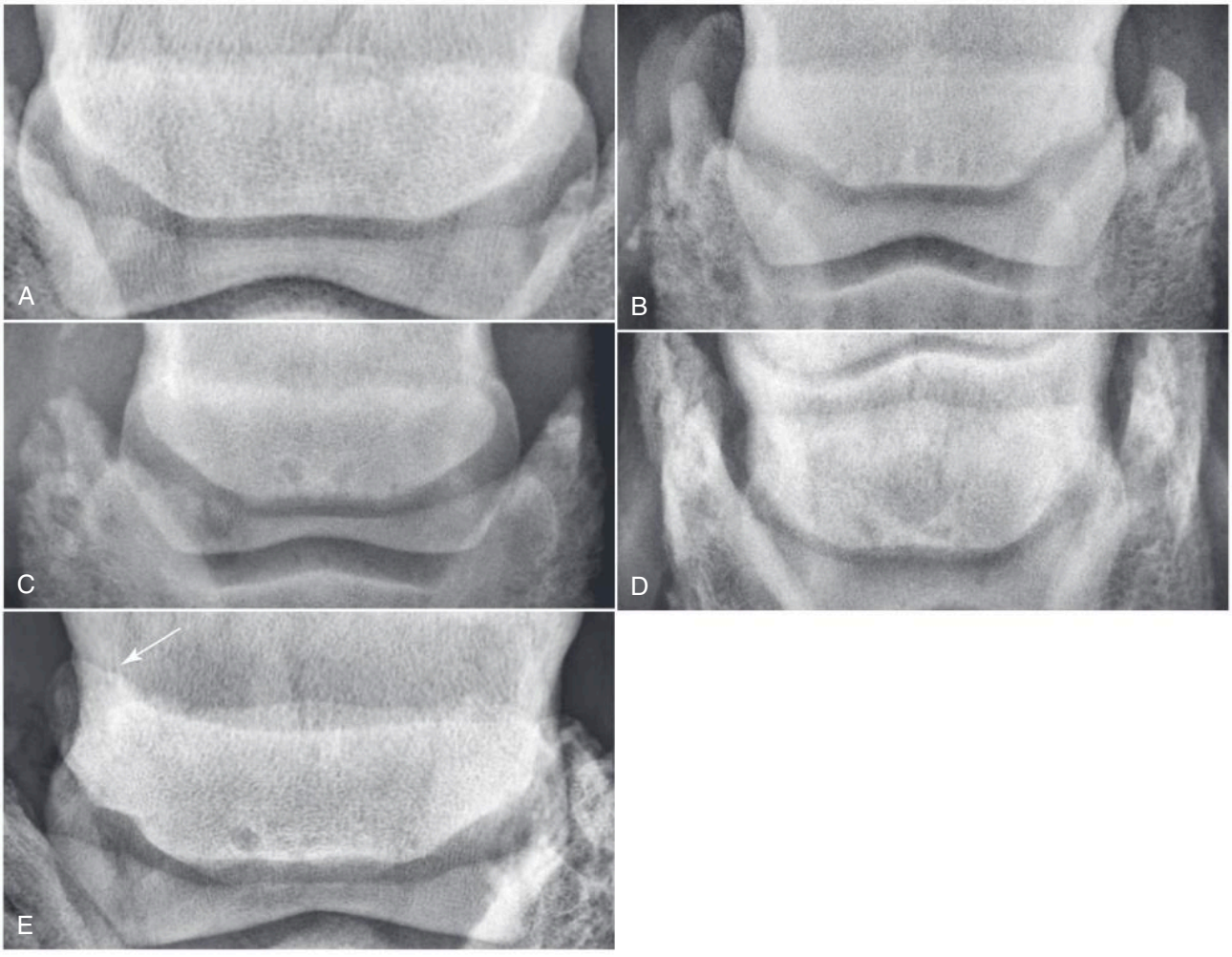
Navicular syndrome, also known as navicular disease, is a chronic, often progressive condition characterized by a spectrum of changes within the navicular bone and surrounding podotrochlear apparatus. Osseous navicular changes are described here, while the pathology of the soft tissues of the podotrochlear apparatus is discussed in more detail later in the chapter. Navicular syndrome primarily occurs in forelimbs and changes are frequently bilateral, even in cases presenting for unilateral lameness.[60] Breed predispositions are observed, although it is unknown whether a true genetic component of disease exists, or rather if it is a feature of the differences in foot conformation between breeds. The syndrome is seen most commonly in Quarter horses, which often have small, upright feet.[61]

Early or mild navicular bone changes that may be detected radiographically include characteristic dilation of the synovial invaginations present along the distal border (eFig. 27.3). These invaginations can vary in size, shape, and number. In a normal horse, these structures appear as a low number (in the region of 3–7) of small (less than a couple of millimeters), concave indentations of uniform or tapering width with a broad base. In navicular syndrome, several larger invaginations with a narrow base and bulbous proximal portion, a so-called "lollipop" shape, may be seen. It is important to note that there is a variation in size and number across different breeds. A greater number of larger synovial invaginations may be seen in Warmbloods without other evidence of navicular degeneration or lameness.[62] Enlarged synovial invaginations have been shown to be associated not only with primary remodeling of the navicular bone but can also result due to pathology of the distal interphalangeal joint.[63]

Medial and lateral triangular bone production of the proximal border of the navicular bone indicates enthesopathy of the collateral sesamoidean ligament (see eFig. 27.3). This change alone is often incidental but may be considered to fall within the spectrum of navicular syndrome. A more reliable indicator of navicular bone degenerative remodeling at the proximal cortex is dilation of the proximal vascular channels. This can be difficult to identify radiographically unless more advanced, but is easily appreciated with MRI.

Sclerosis of the navicular bone spongiosa rarely occurs as a form of adaptive remodeling and is an indication of degenerative change. A hallmark finding for this change is loss of distinction between the flexor cortex and sclerotic medullary bone. The loss of distinction can be focal or diffuse. A focal area of loss of distinction is often found in conjunction with an adjacent focal area flexor cortical erosion. Care should be taken when interpreting skyline views since superimposition of the most proximal and distal aspects of the curved flexor cortex of the navicular bone can give the false appearance of linear sclerosis of the palmar medullary cavity.

Flexor cortical lysis is found with more advanced cases of navicular syndrome and is often associated with greater lameness and a more guarded prognosis.[7,64,65] Flexor cortical lysis may be seen as ill-defined, often rounded to ovoid lucent regions within the bone on the D65Pr-PaDiO view. To confirm their location, erosions may also be seen as decreased mineral density within the flexor cortex on a skyline view (Fig. 27.25). These should be differentiated from the aforementioned normal, crescent-shaped lucency within the sagittal ridge. Skyline views obtained at multiple degrees of proximodistal obliquity may be required in order for the x-ray beam to be tangential to the region of lysis. Flexor cortical erosions most



eFig. 27.3 Dorsoproximal/palmarodistal views of the navicular bone. **A,** Normal navicular bone. **B,** Enlargement of synovial invaginations of the distal navicular border. **C,** Lollipop-shaped synovial invaginations of the distal navicular border. **D,** Cyst-like cavitation over the plane of the navicular medullary cavity. Remember that flexor cortical erosions often falsely mimic medullary cavity cysts on angled dorsoproximal/palmarodistal views. Thus, the palmaroproximal/palmarodistal and/or lateral view would be needed in this situation to determine the location of the lesion accurately. **E**, Large enthesophyte (*white arrow*) on the lateral margin of the navicular bone.

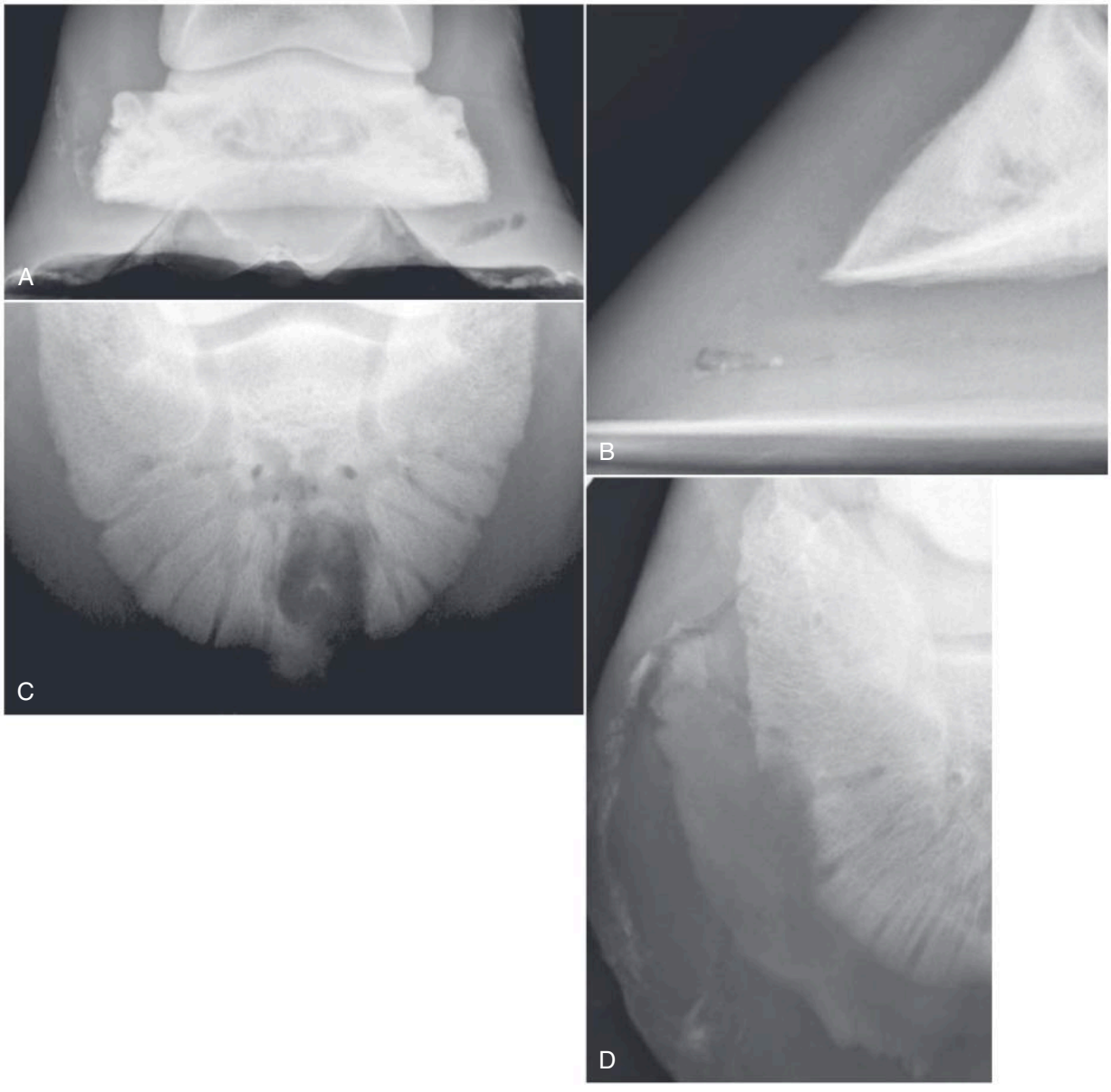


Fig. 27.23 Variations seen with infective pedal osteitis associated with foot abscesses in three horses. Horse 1 **(A)** has only gas in the subsolar soft tissues with no bone lesion. Images **B and C** are the second horse. In **B,** there is subsolar gas at the toe. The dorsal border of the distal phalanx from the toe to midbody is abnormally thin and has an irregular surface. In **C,** a large circular osteolytic area is present on the midline toe. A small mineralized opacity consistent with a sequestrum is present in the lytic area. In horse 3 **(D)**, there is a smoothly marginated concave defect in the solar border of the quarter region. This was associated with a resolving abscess.

commonly occur within the distal portion of this bone and therefore more shallow projections can help to highlight this region.[66] Flexor cortical erosions may also be seen as regions of decreased cortical bone density and associated loss of corticomedullary distinction on a well-positioned lateromedial foot radiograph.

The presence of fluid within the navicular bone is a common finding on MRI, both in horses with other evidence of navicular syndrome and as an isolated finding. When trabecular fluid signal is seen within an otherwise normal navicular bone, this likely represents mild trabecular bone remodeling, transient inflammation, edema, or, less likely, hemorrhage and is of variable clinical significance. This type of bone fluid signal often resolves with rest. Fluid signal of the navicular bone in conjunction with other degenerative changes is more likely to be associated with trabecular bone remodeling, osteofibrosis and potentially osteonecrosis. The only way to definitively differentiate between these varied causes of navicular bone fluid is to monitor its progression or resolution on sequential MRI scans (Fig. 27.26).

ARTICULAR PATHOLOGY

Disease of the proximal interphalangeal joint of the digit is discussed in Chapter 26; therefore, this section will focus on

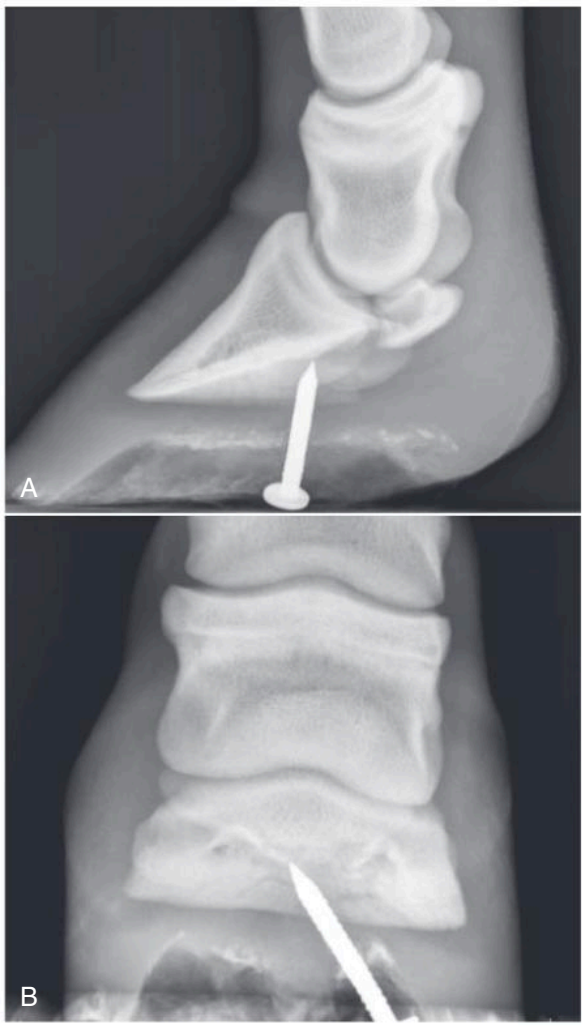


Fig. 27.24 **A and B,** A nail foreign body has penetrated the sole of the foot. The tip of the nail is near the palmar surface of the distal phalanx on the midline at the level of insertion of the deep digital flexor tendon (DDFT). Radiography, using orthogonal views, done with the foreign body present is more valuable in determining its relation to the bone, tendon, and ligament locations than radiographs made after the foreign body has been removed.

pathology of the distal interphalangeal joint. This joint is stabilized within the foot due to containment within hoof capsule and periarticular fibrous connective tissue attachments.

Osteoarthritis

Osteoarthritis is a chronic disorder of synovial joints characterized by progressive deterioration of articular cartilage and reactive changes in the joint margin, joint capsule, and synovium. Primary osteoarthritis is an age-related disease of slow onset, resulting in gradual degradation of normal joint structure and function as a result of the chronic repetitive trauma associated with intensive athletic activity. Secondary osteoarthritis may occur as a result of acute trauma, infection, poor limb conformation, and developmental orthopedic disease. The distal interphalangeal joints can be affected by any of these causes.

Radiographic findings characteristic of osteoarthritis are bone formation (osteophytes) at the periarticular margins, enthesophytes at the sites of supporting ligaments and joint capsule, sclerosis and lucencies in the subchondral bone, and changes in the joint space width. These features are demonstrated in Fig. 27.27 and Fig. 27.28, which utilizes the proximal interphalangeal joint to illustrate the various osteoarthritic changes. Focally increased soft tissue proximodorsal to the coronary band suggests intra-articular effusion and/or synovitis of the distal interphalangeal joint, which may accompany osteoarthritis of this joint. Degenerative changes within the articular cartilage are an important component of osteoarthritis but cannot be visualized on radiographs unless damage is extensive enough to cause joint space collapse. It is important to rule out uneven weight bearing as a cause of artifactual narrowing.[68] Abduction of the leg by 5 to 10 degrees results in significant narrowing of the medial aspect of the proximal and distal interphalangeal joint spaces compared to the lateral joint spaces. The effect is more evident in the distal interphalangeal joint space and with the larger degree of abduction. Conversely, a unipedal stance can result in compression of the lateral aspects and widening of the medial aspects of the joint.[67]

A wide spectrum of combination and degree of the previously mentioned changes is seen. Synovitis is an early sign of joint disease. Effusion, synovial proliferation, and joint capsule thickening can be best characterized on MRI. CT can also demonstrate these changes, particularly if positive contrast medium is used, either intravascularly or intra-articularly. Ultrasound is a more accessible modality for imaging these soft

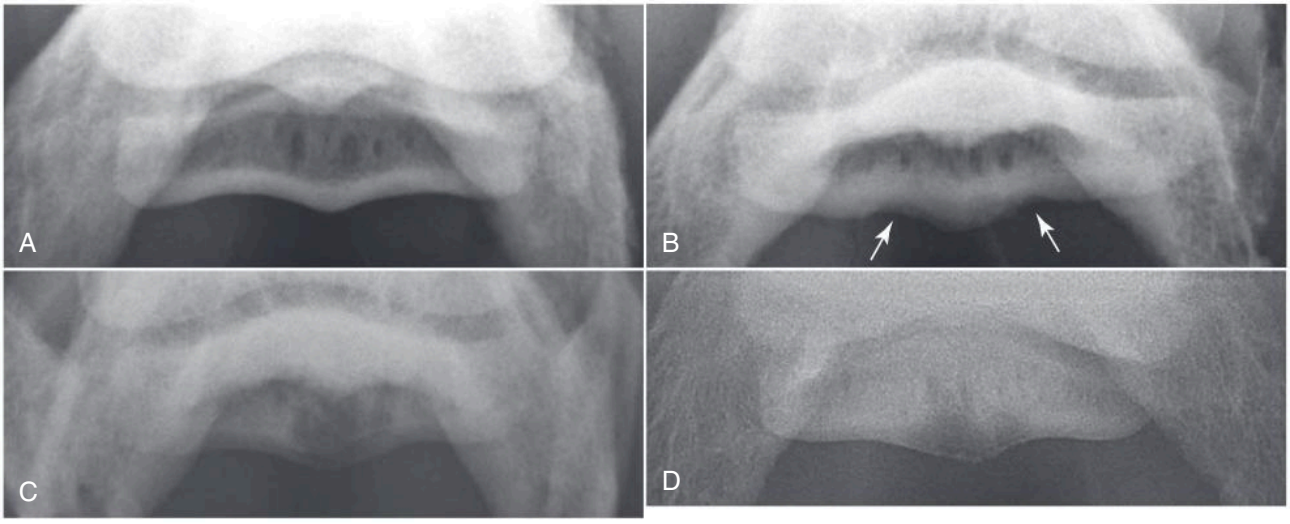


Fig. 27.25 Palmaroproximal/palmarodistal views of the navicular flexor cortex and medulla showing various abnormalities. **A,** En face view of enlarged distal border synovial invaginations. **B,** Flexor cortex erosions (*arrows*) result in a loss of the normal smooth flexor contour. **C,** Large focal cortical lysis causing disruption of the flexor cortex over the central eminence. **D,** Large area of cortical lysis of the flexor surface over the central eminence, with concurrent osteosclerosis in the central portion of the medullary cavity.

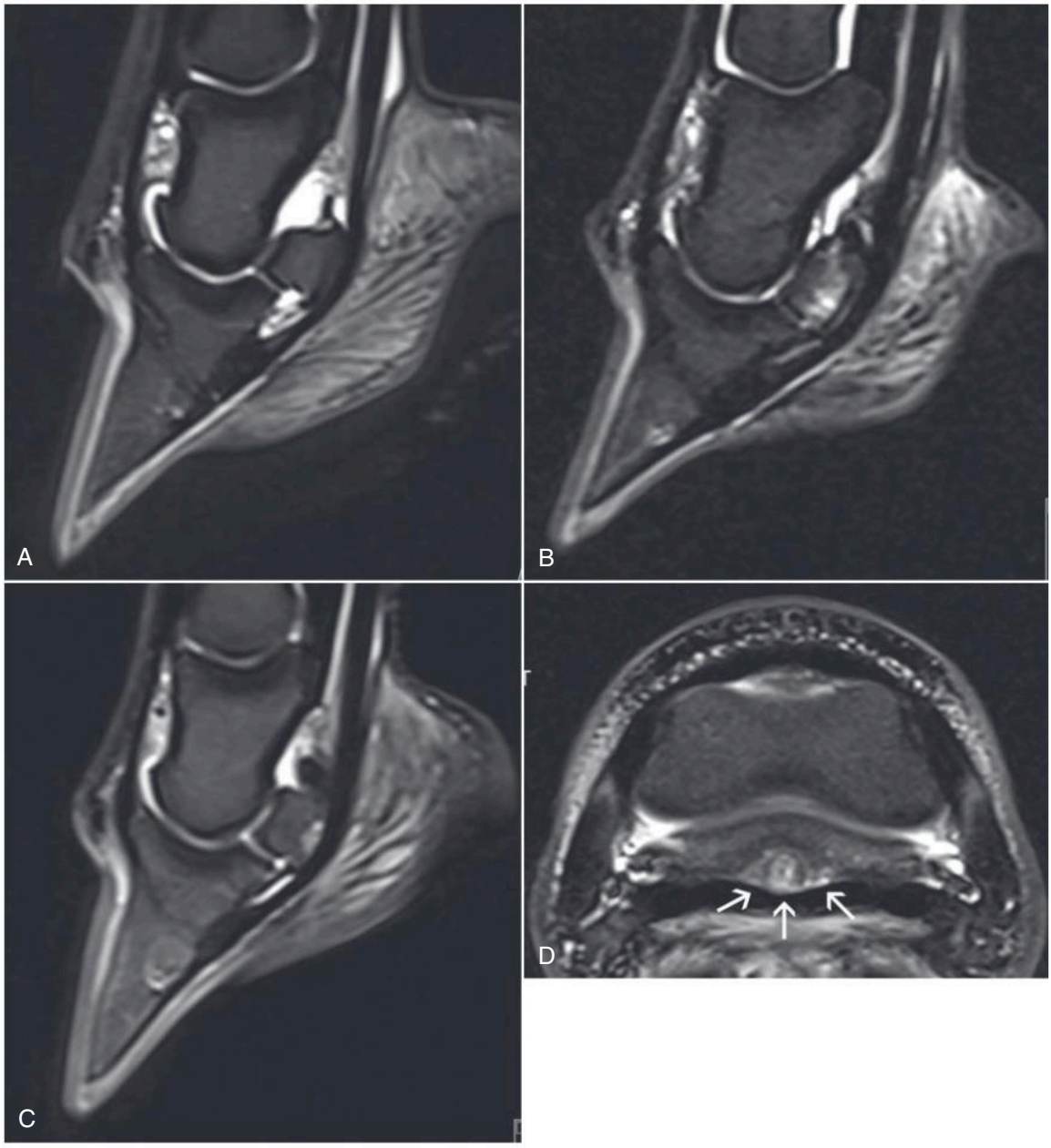


Fig. 27.26 Sagittal **(A—C)** and transverse **(D)** plane short T1 inversion recovery (STIR) images of the foot and navicular bone. **A,** Normal navicular bone. **B,** Increased fluid signal within the navicular bone, indicating marrow edema; notice the thickening of the collateral sesamoidean ligament. **C and D,** Focal hyperintense erosion extending from the flexor surface into the medulla of the navicular bone (*white arrows*), surrounded by mild sclerosis.

tissues, but access is limited by the hoof capsule and is confined to a few small windows of visualization.

Osteophytes at the periarticular margins of the distal phalanx are usually seen in conjunction with triangular osteophytes at the distodorsal aspect of the middle phalanx. Forty-five degree dorsolateral-palmaromedial and dorsomedial-palmarolateral oblique views with either a horizontal beam, or with a 65-degree proximodistal angle, can highlight these osteophytes. The distopalmar aspect of the middle phalanx and dorsoproximal margin of the navicular bone are other locations for osteophytes of the distal interphalangeal joint.

Enthesopathy of the distal interphalangeal joint capsule can be identified as a region of irregular osseous proliferation on the dorsal cortex of the mid-distal aspect of the middle phalanx on the lateromedial view. Care should be taken to distinguish this from the normal smooth protuberances either side of midline that represent the origins of the distal interphalangeal joint collateral ligaments (see Fig. 27.4). It is important to accurately identify distal interphalangeal joint capsule enthesopathy since this feature is often associated with other pathologic findings in the joint such as articular cartilage loss or collateral ligament injury.

Articular cartilage changes are best assessed on a high-field MRI system. Low-field MRI can provide some information but is not consistently reliable, particularly for the detection of partial thickness cartilage erosions.[69—71] Advanced articular cartilage loss in the distal interphalangeal joint may be accompanied by underlying subchondral bone abnormalities, with or



Fig. 27.27 **A and B,** These images depict the typical radiographic features of chronic proximal interphalangeal osteoarthritis. Osteophytes, enthesophytes, joint space narrowing (asymmetric in this example), subchondral sclerosis, and subchondral cysts are evident.

without associated trabecular bone changes.[72] In 11 lame horses evaluated with MRI, subchondral trabecular bone damage was found that was not evident radiographically.[73] These changes consisted of subchondral fluid signal with and without cyst formation. Subchondral remodeling is less commonly found in the distal interphalangeal joint than the proximal interphalangeal and fetlock joints. There can be extensive articular cartilage damage in the distal interphalangeal joint without identifiable subchondral bone changes.

Septic Arthritis

Infective agents are most commonly introduced into the distal interphalangeal joint by penetrating wounds or iatrogenic injections. Any laceration near a joint that is associated with significant and persistent lameness warrants concern for extension to the joint and infection. The joint pouches of the distal interphalangeal joint are large, extending proximal to the midplane of the middle phalanx.[3] One large retrospective study of heel bulb lacerations found that the distal interphalangeal joint was involved in 13% of these injuries.[74] During the initial stage of infection, no radiographic changes may be present. Inflammation of the synovium and effusion may create a focal enlargement at or just proximal to the coronary band (Fig. 27.29).

Options for assessing the likelihood of joint involvement secondary to an acute penetrating wound or laceration on radiographs include firstly assessing for soft tissue swelling and radiolucent gas foci within the region of the joint recesses. If none is identified or if the gas cannot be definitively localized to the joint, placement of a sterile metallic probe within the wound/tract and repeating radiographs may be valuable to assess the trajectory and depth of injury. Additionally, use of positive contrast techniques may assist in demonstrating or ruling out joint communication. A fistulogram may be performed in which contrast medium is instilled directly into the wound prior to radiographic assessment. Documenting the subsequent dispersal of contrast medium may demonstrate extension into the region of the joint. However, it can be difficult to generate sufficient pressure to distend the tract with contrast medium, particularly if the wound is not fresh. An alternative is positive-contrast arthrography. This was successful at identifying communication of the contrast medium from the joint to the external wound in one study of horses suspected to have joint infection but no bone changes.[64] This is the authors' preferred contrast technique in cases such as these.

In the nonacute stage, one of the earliest radiographic signs of septic arthritis is irregularity at the joint capsule insertion or chondro-osseous junction on the perimeter of the joint surfaces. As cartilage begins to deteriorate, thinning of the joint space is seen. As the infection invades the deeper regions of the cartilage and reaches the subchondral bone, the subchondral bone margin becomes irregular because of lysis (see Fig. 27.28). Lysis of the subchondral bone causes the joint to be widened unevenly. At this stage, periosteal new bone should be evident at the joint margins (Fig. 27.30). Septic arthritis always has a guarded prognosis. Ultrasound evaluation of the dorsal joint pouch can be used to identify severe septic distal interphalangeal synovitis and may also be used for ultrasound guided collection of fluid, which can be difficult in proliferative joints. Typically, septic effusion will be slightly more echogenic than the fluid seen with nonseptic inflammation and is often associated with a greater degree of synovial proliferation. MRI provides the ability to detect septic osteoarthritis at an early stage via the identification of features such as diffuse hyperintensity within the adjacent tissues, severe, contrast-enhancing synovial proliferation[75] and is also valuable for more rapid identification of secondary osteomyelitis via the detection of intraosseous fluid.

Deformity of the Distal Interphalangeal Joint

The clinical appearance of DIPJ flexural deformity varies with the degree of hyperflexion from mild to an almost vertical orientation of the hoof wall to the ground (Fig. 27.31). Flexural deformity may be either congenital or acquired in the foal. Older horses may develop a flexural deformity secondary to lesions of the accessory ligament of the DDFT or chronic damage resulting in contracture of the DDFT.[76] Radiography is used to assess changes in the distal phalanx and screen for possible concurrent bone or joint lesions. Changes in the distal phalanx range from none to widened vascular channels and bone resorption at the solar margin. If the deformity is corrected early, the bone changes can resolve.

Hyperextension of the distal interphalangeal joint may occur in newborn foals as a congenital abnormality affecting all three joints of the foot. Weakened flexor tendons may also be a result of poor nutrition, slow or incomplete recovery from a systemic disease, or after prolonged periods of external support (splinting or casting) of the leg. Acquired hyperextension to the point

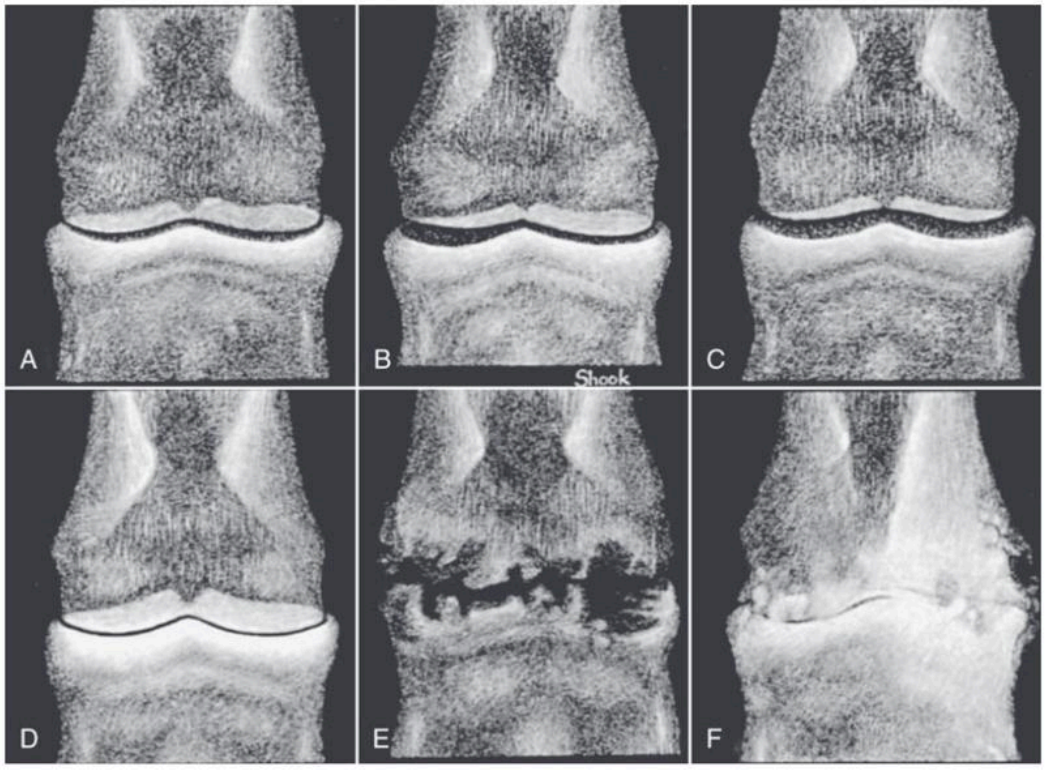


Fig. 27.28 Changes in joint space width, subchondral bone opacity, or both, as seen in the dorsopalmar view of the proximal interphalangeal joint, and likely causes. **A,** Normal joint space and subchondral bone. **B,** Widened joint space on the lateral or medial side, no subchondral bone changes. Artifact is caused by asymmetric weight distribution on the foot or unbalanced hoof trimming. **C,** Widened joint space, no subchondral bone changes; not weight bearing at time of radiography or increased intra-articular fluid volume. **D,** Uniformly narrowed joint space, no subchondral bone changes. Artifact caused by x-ray beam angulation, asymmetric foot placement, or uniform degenerative wearing and loss of articular cartilage. **E,** Widened joint space, lysis of the subchondral bone; active septic arthritis. **F,** Narrowed joint space, irregular opacity, and contour of subchondral bone; chronic low-grade septic arthritis or chronic osteoarthritis caused by trauma-related instability or poor conformation. (Illustration courtesy Richard A. Shook, DVM.)

of joint (sub)luxation is also caused by rupture of the DDFT or avulsion of its insertion (Fig. 27.32). Subluxation has also been reported following severe lacerations of the common digital extensor tendon and rupture of the distal interphalangeal joint collateral ligaments.[77–79] Stress views may be needed to detect subluxation. Secondary changes expected with subluxation are enthesophyte formation at the ligament insertion sites and osteoarthritis. The range of change will depend on the severity of the initial injury and the frequency of recurring subluxation, but severe osteoarthrosis and/or ankylosis is a sequela with an associated poor prognosis.

SOFT TISSUE PATHOLOGY

Soft Tissue Structures

Although the soft tissues of the equine foot are generally poorly visualized radiographically, indirect evidence of soft tissue injury can be gained by associated osseous changes. Therefore, knowledge of the attachment sites of the joint capsules, tendons, and ligaments is imperative. The DDFT can often be seen in the lateromedial view as a slightly more opaque soft tissue band as it passes between the level of the proximal aspect of the middle phalanx and the proximal margin of the navicular bone. The most common radiographic finding to provide direct evidence of damage to the DDFT in the foot is the presence of mineral within the tendon.

To adequately assess the soft tissues of the distal limb, imaging modalities other than radiography must be employed. Ultrasound and MRI are well recognized for their value in assessing soft tissue injuries, although the use of ultrasound for assessing injuries of the foot is limited by the hoof capsule. CT, particularly with the use of contrast medium, is also valuable for assessing soft tissue damage in the foot. Comparing the results of advanced imaging to radiographs improves the interpretation of radiographs. The radiographic signs of abnormal soft tissue include alteration of thickness, contour, or opacity. A diffuse increase in soft tissue thickness in the region of the foot and pastern may indicate edema and/or cellulitis, whilst more focal, localized swelling may indicate trauma or, depending on proximity to a synovial structures, intracapsular effusion or synovial proliferation. An irregular surface contour suggests acute laceration or chronic granulation tissue. Increased opacity within soft tissue is usually caused by dystrophic mineralization (Fig. 27.33). Decreased opacity within the soft tissues is caused by gas, which may be secondary to recent diagnostic nerve block, open skin wounds or abscessation due to a gas-producing organism (Fig. 27.34).

Soft Tissue Enthesopathy

Stress at the point of attachment of a tendon, ligament, joint capsule, or other soft tissue structure onto an osseous structure is termed *enthesopathy* and is often radiographically apparent. Changes may manifest as osseous proliferation, resorption, or a

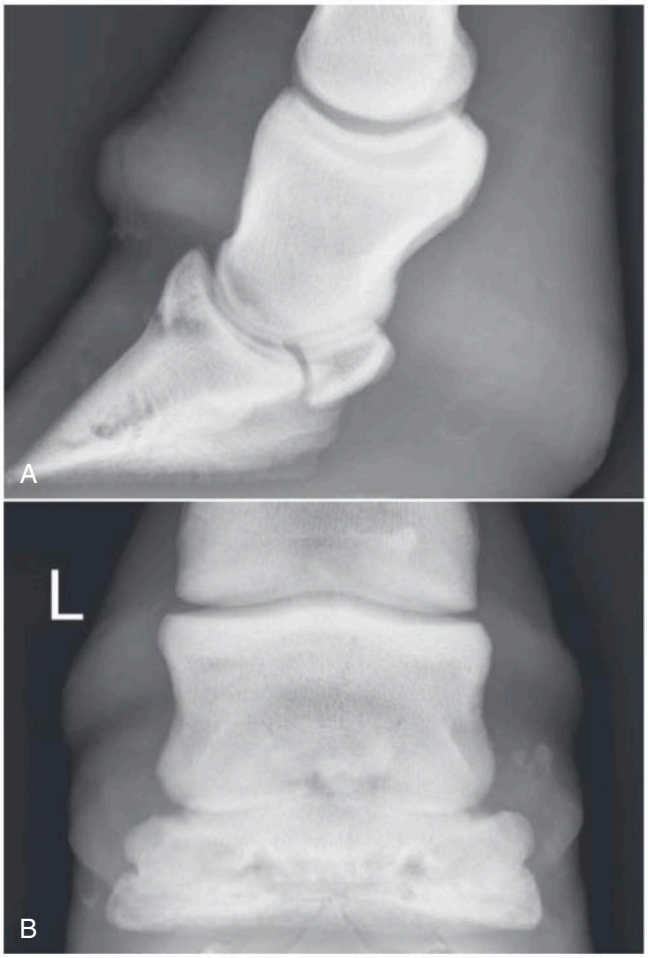


Fig. 27.29 **A and B,** This yearling sustained unknown trauma to the foot causing a significant lameness. The following day a draining tract developed at the dorsal coronary band. One and a half weeks later, the lameness persisted, and radiographs were acquired. There is evident swelling at the coronary band, as well as thinning of the distal interphalangeal joint space (narrower than the proximal interphalangeal joint space), subchondral lucency of distal dorsal half of the middle phalanx, and a separation of a large extensor process fragment from the distal phalanx. No new bone formation is evident. These changes are indicative of septic arthritis with osteomyelitis of the middle and distal phalanges with fracture and probable sequestrum formation of the extensor process.

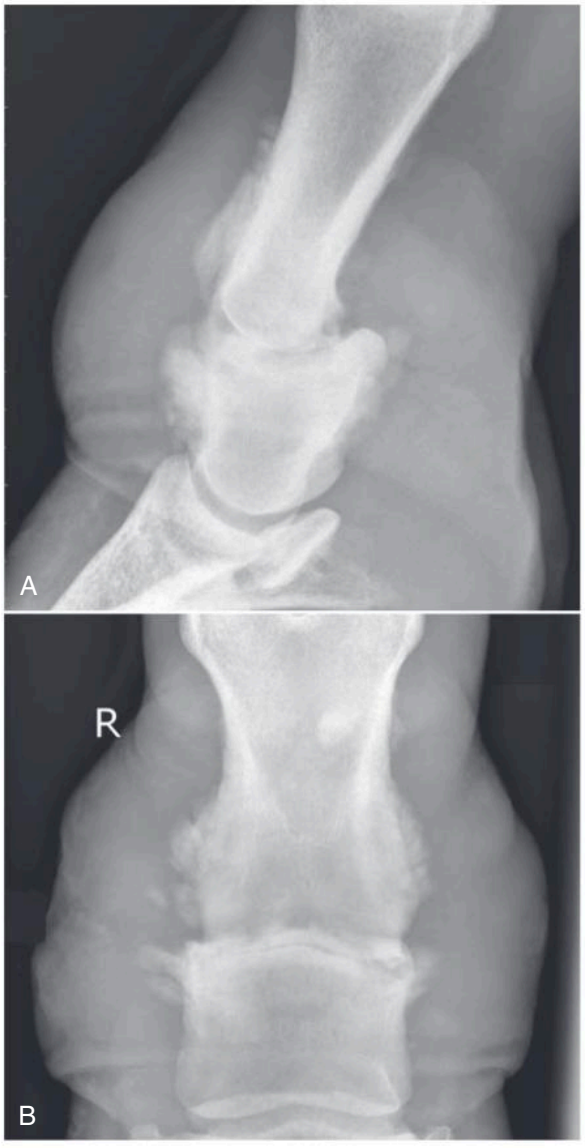


Fig. 27.30 **A and B,** The proximal interphalangeal joint is narrowed dramatically with mild palmar subluxation. Focal areas of subchondral lysis are evident in the proximal aspect of the middle phalanx. The periosteal new bone formation has a palisading appearance, and there is soft tissue swelling. These features are typical of chronic active infection and joint instability.

combination of the two. Avulsion fracture at soft tissue attachment sites occurs uncommonly and will be evident as a bone fragment displaced in the direction of traction of the tendon/ligament. Regions of new bone formation (enthesophytes) are commonly seen on the cortical surfaces of the phalanges. Early or mild enthesopathy manifests as often focal or smooth undulating bone production. With further progression, the enthesophyte may form a smooth, hook-like, or spur-like shape, projecting in the direction of tension or traction. The significance of enthesophytes varies depending upon location. Enthesophytosis of the distal interphalangeal joint capsule on the dorsal cortex of the middle phalanx is frequently an indicator of other significant joint pathology. Enthesopathy can also present as bone loss, which is often seen in the collateral fossae of the distal phalanx, although substantial bone loss can occur before it is identified radiographically. When visible, it presents as regions of rounded bone loss, seen best on D65Pr-PaDiO and D65Pr45L(M)-PaDiM(L)O views (Fig. 27.35, eFig. 27.4). Lesions at the site of insertion of the distal sesamoidean impar ligament on the flexor surface of the distal phalanx have been characterized histopathologically as a resorptive bone cavity containing cellular debris and chondroid metaplasia.[80] This lucency is best identified in the dorsal 60-degree proximal/palmarodistal oblique view, occurring most frequently in the central region of the distal phalanx just distal to the distal border of the navicular bone in this view (Fig. 27.36). If large, enough, these lesions can also be identified on lateromedial projections (see Fig. 27.36). However, similar to the resorptive lesions of the collateral fossae, bone loss at the distal sesamoidean impar ligament attachment is often not well seen radiographically when compared to CT and MRI.

Collateral Ligaments

Desmopathy of the collateral ligaments of the distal interphalangeal joint is a significant cause of foot lameness, which may present in the absence of the radiographic changes. Ultrasound in the region of the coronary band may detect changes in the proximal third of the ligament; however, damage is more



eFig. 27.4 Enthesopathy of the lateral collateral ligament of the distal interphalangeal joint. An ill-de fined radiolucency surrounded by a region of sclerosis is present in the dorsal aspect of the lateral palmar process of the distal phalanx at the insertion of the lateral collateral ligament.



Fig. 27.31 Flexural deformity of the distal interphalangeal joint in a 4-month-old foal. The dorsal surface of the distal phalanx remains parallel to the dorsal hoof wall; however, both structures assume an abnormally vertical position. There is mild modeling of the toe of the distal phalanx. The straight course of the deep digital flexor tendon (DDFT) is visible.

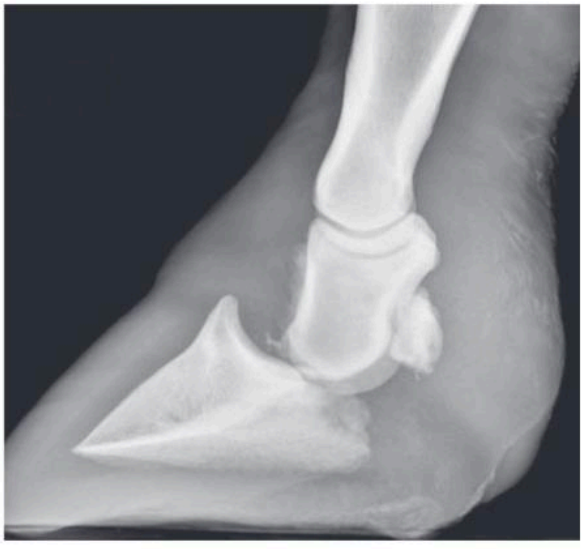


Fig. 27.32 Luxation of the distal interphalangeal joint because of severe trauma to the supporting soft tissue structures of the joint. Dorsal displacement of the distal phalanx is caused by avulsion of the deep digital flexor tendon (DDFT) insertion and the subsequent unreciprocated traction of the common digital extensor tendon. The distal sesamoidean impar ligament is also ruptured, allowing proximal displacement of the navicular bone.

frequently found in the distal portion. MRI is the most useful imaging modality to define the changes in these ligaments (eFig. 27.5).[77,81] Knowledge of the appearance of magic angle artifact in these ligaments, particularly on low-field MRI, will prevent overdiagnosis of collateral ligament injury.[82–84] Imaging may also be used to direct targeted treatment of collateral ligaments injuries, such as radiograph-guided injection of the collateral ligament fossae or MRI- or ultrasound-guided intralesional or periligamentous injection.[85–88]



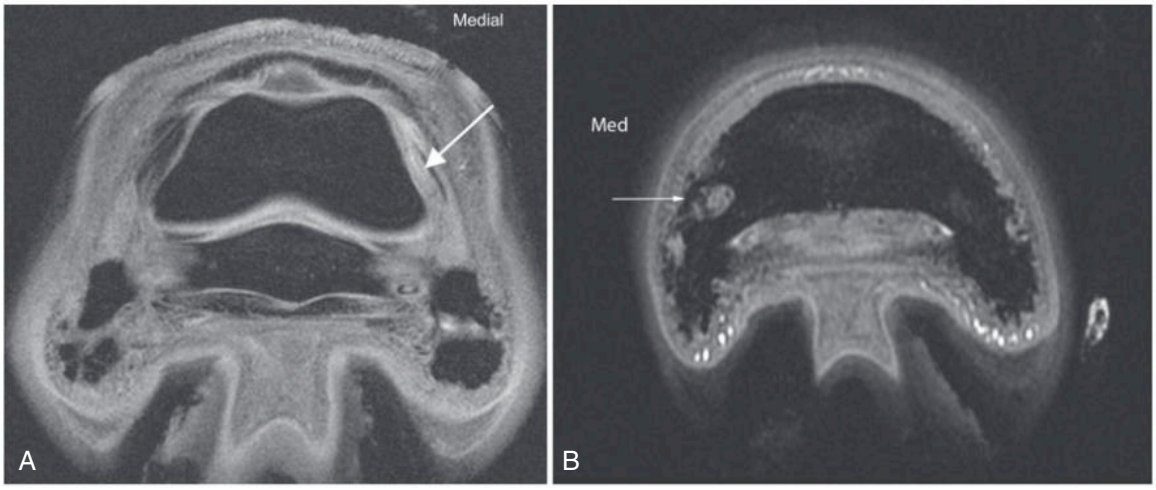
Fig. 27.33 Soft tissue mineralization is evident in the superficial digital flexor tendon and straight sesamoidean ligament. There is mild smooth enthesopathy at the insertion of the oblique sesamoidean ligament on the midaspect of the proximal phalanx (*arrow*). This horse also has a mild distal interphalangeal flexural deformity.



Fig. 27.34 Gas is present in the palmar soft tissues (*arrow*) secondary to diagnostic nerve block.

Tendinopathy and Desmopathy

Strain injury results from damage to ligaments or tendons induced by overuse or overstress. Radiographically, localized soft tissue swelling may be the only finding. Dystrophic mineralization can develop in a chronically inflamed tendon and may be visible on radiographs (see Fig. 27.33), although dystrophic mineral within several soft tissue structures has also been reported as an incidental finding and depends in part on the location of the mineralization.[89] Tendon and ligament injury can be best imaged by ultrasound, MRI, contrast-enhanced CT, and, less commonly, vascular and soft tissue pool phase scintigraphy.[64,90–92] Ultrasound is the most commonly available



eFig. 27.5 Two horses with lesions involving the collateral ligaments of the distal interphalangeal joint shown by gradient recalled echo images. **A** is a transverse image of a horse with collateral desmitis. Note the increased signal within and adjacent to the medial collateral ligament (*white arrow*) compared with the normal lateral side. **B** is from a horse with a cystic lesion (*arrow*) in the distal phalanx at the insertion of the medial collateral ligament that was also evident in the dorsal series (not shown).

modality for soft tissue assessment of the pastern but is limited in the foot region by poor access through the hoof and sole. The increasing availability of low-field standing magnetic resonance (MR) scanners has resulted in increased use of MRI in horses and thereby the identification of numerous tendon and ligament abnormalities. MRI has become the modality of choice when lameness is persistent and the other modalities have negative or equivocal findings. Injuries to specific soft tissues of the foot are discussed in more detail below.



Fig. 27.35 Region of irregular osseous resorption of the distal interphalangeal joint lateral collateral ligament fossa of P3 (*white arrow*), representing insertional resorptive enthesopathy of this ligament.

Injuries to the DDFT are common within the foot and are categorized in four forms: (1) dorsal border tears; (2) core lesions; (3) sagittal or parasagittal splits; or (4) tendinosis.[64,92] The distribution of these lesions varies by location (Fig. 27.37). Dorsal border fibrillations are most common at the level of the proximal recess of the navicular bursa (also referred to as *suprasesamoidean location*) and navicular bone. Core lesions are common in the pastern and suprasesamoidean regions, and distal to the navicular bone. Sagittal/parasagittal splits are common at the navicular bone level (region 2 in Fig. 27.37). Insertional tendinopathies occurring immediately proximal to the insertion of the tendon on P3 can have a variety of configurations.[93,94] DDF tendinopathy in the pastern is readily identified on ultrasound; more distal tendinopathy is limited by the hoof capsule. Transcuneal ultrasonography has been reported but is technically challenging and provides limited visualization.[95–97] Lesions of the DDFT have been identified by (contrast-enhanced) CT, but MRI is generally considered the superior modality for full characterization of tendinopathy and any additional changes within the foot.[91] It is worth noting that three-quarters of horses with DDFT injuries in the pastern were shown to have additional injuries to this tendon within the foot; therefore, if a lesion is detected on pastern ultrasound, MRI of the foot for assessment of further tearing is particularly warranted.[98]

Podotrochlear Apparatus

The term *podotrochlear apparatus* has been used to refer to the regional structures of the palmar/plantar foot, in particular

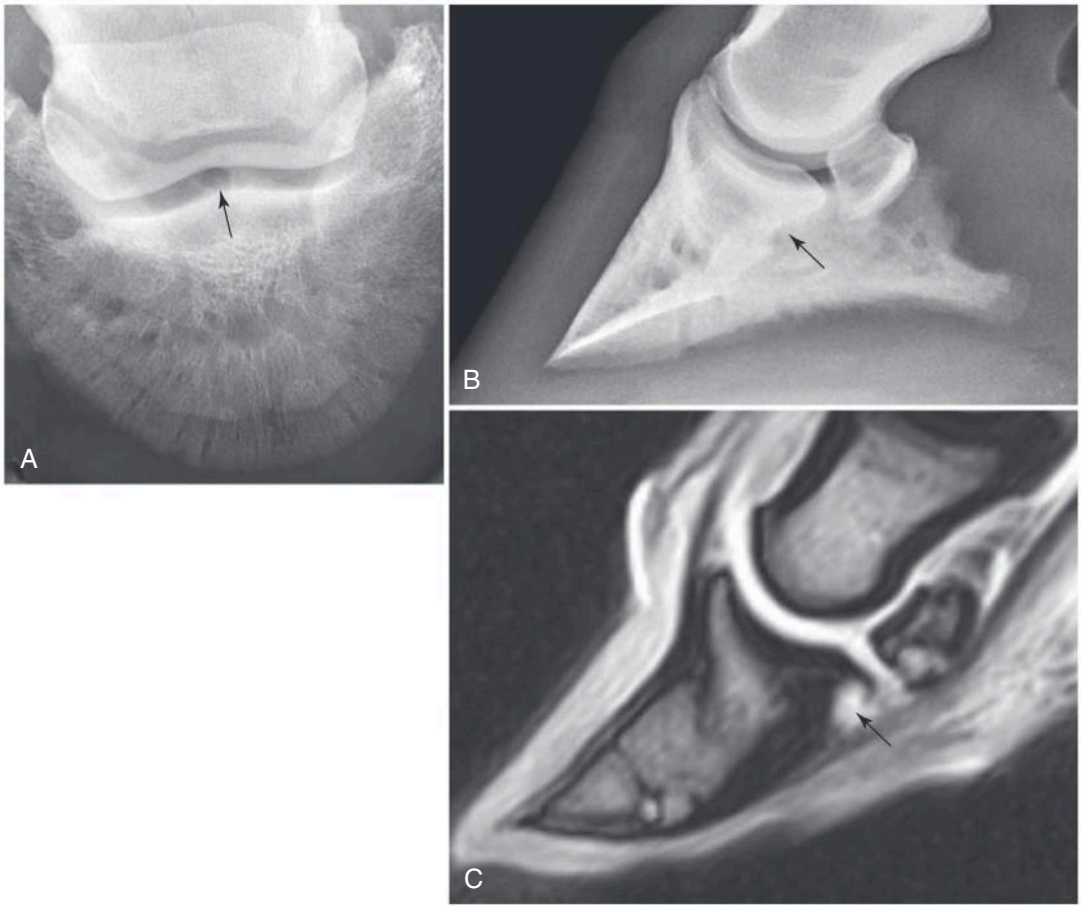


Fig. 27.36 Resorptive enthesopathy of the impar ligament (*black arrows*) on D65Pr-PaDiO **(A)** and lateromedial **(B)** radiographic views, and on a sagittal T2*-weighted magnetic resonance (MR) image **(C)**.

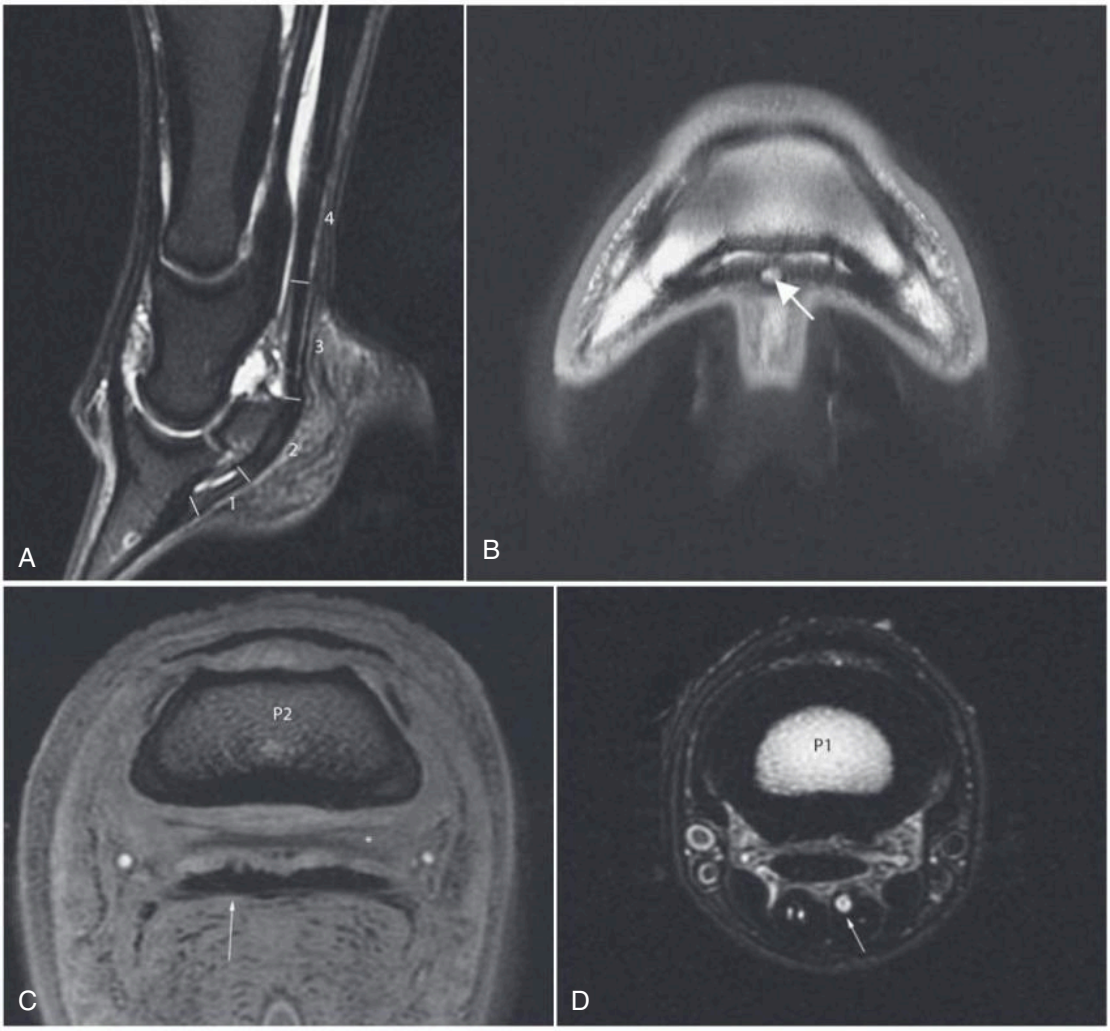


Fig. 27.37 This grouping shows common lesions of the deep digital flexor tendon (DDFT) in the foot region, as seen on magnetic resonance imagery (MRI). The sagittal **(A)** plane indicates the regions of the tendon as relates to where different types of tendon lesions are identified. **B through D** images are transverse planes with lateral on the left of the image. **B** is a proton density sequence that shows a core lesion (*white arrow*) in the insertional region 1. **C** is a T2-weighted gradient echo sequence that shows dorsal border fibrillations of the lateral lobe in the suprasesamoidean region 3 (*arrow* points to the palmar border of the tendon). In **C,** the *asterisk* is within the medial portion of the collateral distal sesamoidean ligament. **D** is a T2-weighted fast spin—echo sequence that shows bilobed core lesions (larger in the medial lobe [*arrow*]) within the pastern region 4.

those in close association with the navicular bone. These include the collateral sesamoidean ligament, distal sesamoidean (impar) ligament, distal digital annular ligament, navicular bursa, and the DDFT within the hoof capsule. Fiber disruption of the dorsal border of the DDFT at the level of the proximal recess of the navicular bursa is a relatively common finding on horses undergoing MRI of the foot. Mild fibrillation in this region may be considered to be of limited clinical significance since it has been seen in the sound limb of unilaterally lame horses. However, cleft-shaped tears are a clinically relevant finding and may often occur in combination with other changes to the podotrochlear apparatus, most notably, erosions of the navicular bone flexor cortex and/or inflammation of the navicular bursa. This association between flexor cortical lysis and DDFT dorsal border abrasions is a part of the reason as to why this is a particularly concerning radiographic finding.

Navicular bursitis can be generally categorized into two main types: proliferative bursitis, in which synovial proliferation predominates, and effusive bursitis, characterized primarily by an abundance of synovial fluid. Proliferative synovium can develop into intrabursal adhesions, most frequently in association with tearing of the dorsal border of the DDFT.

The ligaments of the podotrochlear apparatus are susceptible to the desmopathy changes previously described. One unique feature of the impar ligament is its fenestrated appearance in the absence of pathology. In horses with navicular syndrome, this ligament may lose these fenestrations and become thickened, and may contact the dorsal border of the DDFT at its insertion. This feature, along with the other described changes of the podotrochlear apparatus, is best identified on MRI.[80,99–101] Ultrasound performed between the heel bulbs with a microconvex probe can be used to visualize the suprasesamoidean DDFT, proximal recess of the navicular bursa, collateral sesamoidean ligament, and distal digital annular ligament.[98] However, because the ultrasound beam is not tangential to the structures of interest, assessment of echogenicity is limited. Transcuneal ultrasound, in which the structures of the foot are visualized via a window through the frog, may also be performed.[102,103]

THE HOOF

The hoof wall consists of the epidermis and the dermis (or corium), the latter bound to the parietal surface of the distal phalanx. The epidermal layers are the stratum externum (tectorium), the stratum medium, and the stratum internum (lamellatum and white line at the ground surface). The lamellae of the stratum internum interdigitate with the dermal lamellae. Between the dermal lamellae and the parietal surface of P3 is a dense network of fibers that includes vessels and nerves (stratum reticulare). Because of the composition of these layers, there is a distinct radiographic opacity difference visible at the junction of the stratum medium and stratum internum and the superficial more radiopaque layer and less radiopaque deep layer are readily differentiated (Fig. 27.38) and correlate with MRI depiction of the layers.[104] The complex anatomic connection between the stratum internum, the corium, and the ridges of the parietal surface of the distal phalanx forms a functional suspensory apparatus of the distal phalanx.[105] The junction of the coronary band and the most proximal extent of the hoof wall is not always clearly distinct in lateromedial and dorsopalmar views.

Hoof Balance

Unbalanced trimming and improper shoeing of the foot can result in lameness. Lateromedial and dorsopalmar radiographic views of the foot can be used to assess foot balance.[106,107] When radiographic views are used in this manner, particular attention must be paid to positioning of the foot, the center of the x-ray beam, and degree of weight bearing on the limb being assessed. The measurements used to assess foot balance radiographically are shown in Fig. 27.39. In the lateromedial view, the dorsal hoof wall should be parallel to the wall at the heel. The pastern axis, as seen in the lateromedial view, is a line that divides the middle phalanx into equal dorsal and palmar halves. Ideally, this line similarly bisects the proximal phalanx and is parallel to the dorsal cortex of the distal phalanx. When this line is carried through to intercept with a line on the bearing surface of the hoof wall, it should create an angle of 45 to 55 degrees (front foot) or 50 to 55 degrees (hind foot) with the bony solar margin.[106] Significant differences were induced in the angles of the interphalangeal joints when the hoof angle was altered.[106] The greatest difference in angle occurred in the distal interphalangeal joint. Clinically, such a change in the angle of the distal interphalangeal joint may influence the strain on the DDFT.[106] The angle of intercept of a line parallel to the solar margin of the distal phalanx and the line of the weight-bearing surface of the hoof wall should be 5 to 10 degrees.[7] The length of the toe region compared with the heel region of the bearing surface of the hoof wall is judged by comparison with the distal interphalangeal joint. A line from the center of the best-fit circle of curvature of the joint space, when drawn perpendicular to the weight-bearing surface, should be at the middle of the weight-bearing surface.[7,106] The lateral and medial portions of the hoof wall should be of equal length. An

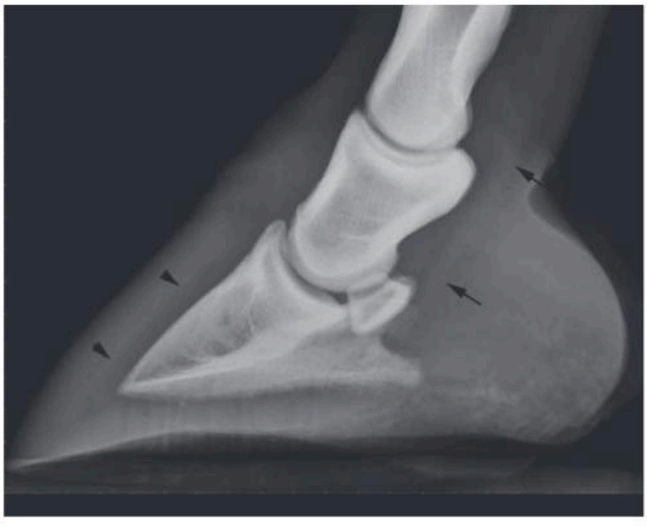


Fig. 27.38 Lateral view of the foot showing the delineation of the deep digital flexor tendon (DDFT; *arrows*). The distinct opacity difference in the dorsal hoof wall allowing identification of two layers is evident. The *arrowheads* mark the interface between the superficial stratum medium and deeper stratum internum.

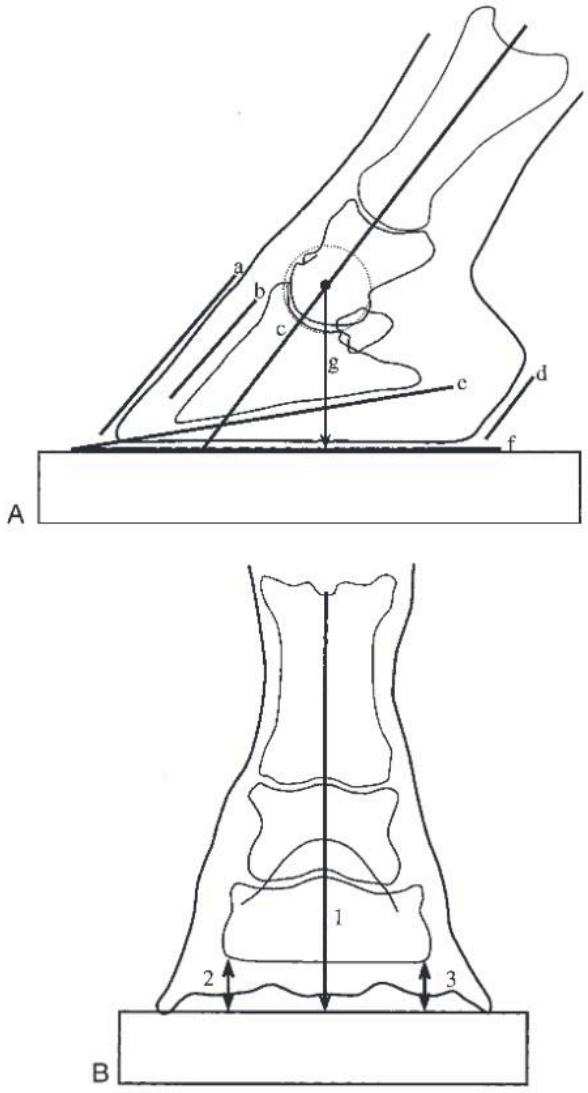


Fig. 27.39 Radiographic measurements for foot balance. **A,** Assessment from the lateromedial view of normal foot. *a,* Line parallel to dorsal hoof wall; *b,* line parallel to dorsal cortex of the distal phalanx; *c,* line that bisects the middle phalanx into equal dorsal and palmar halves; *d,* line drawn parallel to the bulbs of the heel; *e,* line drawn parallel to the solar surface of the distal phalanx; *f,* line drawn parallel to the bearing surface of the hoof wall; *g,* line from center of best-fit circle for the distal interphalangeal joint drawn perpendicular to the bearing surface of the hoof wall. Line *a* should be parallel to lines *b*, *c*, and *d*. Line *g* should intersect at the midpoint of the bearing surface of the hoof wall. Angle *af,* 45 to 55 degrees in a front foot; 50 to 55 degrees in a hind foot; angle *ef,* 5 to 10 degrees. **B,** Assessment from dorsopalmar view of the normal foot. *1,* Line bisecting the phalanges; *2 and 3,* lines from respective lateral and medial solar margins of the distal phalanx to bearing surface of the hoof wall. These lines should be parallel to line *1*. Distance *2 = 3*.

elaborate set of measurements has been made on the dorsopalmar view to assess the effects of uneven mediolateral hoof wall trimming.[106,107] This method was used to assess the effects of using the corrective full rolling shoe in horses that were lame because of interphalangeal degenerative joint disease.[108]

The distal border of the distal phalanx should be at an angle of 3 to 10 degrees relative to the sole of the hoof. A neutral or negative so-called "palmar angle" puts strain on the soft tissues supporting the palmar/plantar soft tissues on the limb and has been associated with scintigraphic evidence of subchondral bone injury in the palmar/plantar third metacarpal/tarsal condyles, in addition to hindlimb lameness originating from both the tarsi and stifles.[109,110]

Laminitis

The normal orientation of the distal phalanx to the hoof is maintained by the complex structure of the interplay between the epidermal, dermal, and parietal surface of P3 forming the suspensory apparatus of the distal phalanx as noted in the description of the normal soft tissues of the foot.[105] Insult to this unique anatomic structure can result in the loss of mechanical support of the distal phalanx within the hoof capsule. *Laminitis* is the general clinical term used to refer to the complex of signs expressed by the horse and its effects on the structural relations of the hoof wall, the distal phalanx, and sole from a variety of insults. Most horses that develop clinical laminitis do so because of a systemic illness, typically equine metabolic syndrome.[111] Horses with protracted, severe, unilateral limb lameness are at risk for developing supporting limb laminitis in the contralateral limb, particularly those in full limb or transfixation casts for a long duration.[112,113] The development of supporting limb laminitis often occurs as rapid, severe failure of the suspensory apparatus of the distal phalanx manifesting as full sinking of the distal phalanx within the hoof capsule and has associated high mortality.[114]

Although differences of opinion exist regarding the terminology and categorization of this complex condition, several clinical phases or stages of laminitis are recognized: developmental, acute, and chronic.[115] *Developmental laminitis* is defined as the period between the initial insult to the first expression of lameness. It may be as short as 24 hours or as long as 60 hours.[115] This is likely an imperceptible stage to the owner unless access to excessive grain or grass is known to have occurred or a systemic disease or other condition is present that warrants concern for initiation of laminitis. This period is a prevention phase for mechanical failure of the foot complex.[115] *Acute laminitis* represents the phase from the first expression of lameness through 72 hours without evidence of mechanical collapse or at any time that signs of mechanical collapse occur.[115] Radiographs in either the developmental or the acute phase will rarely show signs of laminar inflammation and instead serve as a baseline for future comparison. Horses may recover fully from either developmental or acute laminitis with no loss of mechanical support. If, however, radiographic or clinical signs of distal phalanx displacement are seen, the phase of chronic laminitis has begun.[115]

Radiographic Evaluation of Laminitis

Radiographic evaluation of any horse with a clinical impression of pain and lameness caused by laminitis is justified. The goals of radiography are to detect changes indicative of mechanical failure and observe changes that contribute to formulation of prognosis and therapy. Front feet are affected most commonly. Placement of radiopaque markers on the foot has been advocated, but variation in normal measurements across patient types, in addition to variability in marker positioning may decrease their utility.[116,117]

The earliest radiographically detectable signs of laminitis involve the dorsal laminae. Thickening of the more radiolucent, sensitive laminae such that this layer represents more than one-third to one-half of the width of the whole dorsal wall and loss of distinction between this layer and the overlying radiopaque, keratinized hoof wall are both early radiographic signs of laminar inflammation. Crucially, these changes are often irreversible, thus their presence on radiographs is merely evidence of a laminitic episode, which may be the cause of the current lameness, or a residual change from a prior insult.

In the normal foot, the dorsal cortex of the distal phalanx should be parallel to the dorsal margin of the hoof wall in the lateromedial view. Divergence of these surfaces, with the toe region of the distal phalanx deviating or rotating in a palmar direction, is an indication of mechanical separation of the dermal and epidermal laminae (Figs. 27.40 and 27.41). This is the easiest of the distal phalanx displacements to detect radiographically. The angle at the point of convergence can be measured and is referred to as the *degree of rotation* (see Fig. 27.41C). Phalangeal malalignment (broken forward hoof pastern axis) due to rotation of the distal phalanx may be exacerbated by contraction of the DDFT, or if the more rapid growth of the hoof wall at the heel is managed improperly. Vertical displacement or "sinking" of the distal phalanx can be difficult to detect, especially earlier in the progression of disease. In the normal foot, the proximal edge of the extensor process of the distal phalanx is positioned roughly at the same plane or just proximal to the junction of the hoof wall and coronary band. Subjective distal displacement of the extensor process in combination with a concave defect and/or radiolucent "halo" in the soft tissues at the level of the coronary band can be radiographic indicators of sinking. Uniaxial distal displacement of the distal phalanx can occur and is most frequently seen medially.[118] Serial radiographs are often used to monitor laminitic changes and comparison between time points can help to better identify vertical displacement.

Other radiographic changes that can be seen with chronic and progressive laminitis include a very thin sole. The change in the position of the toe of the distal phalanx may cause a convex bulge in the sole contour, or the toe may penetrate through the sole. Lateral foot radiographs that are centered at the sole rather than at the coronary band are better for assessing these changes. Separation of the dorsal laminae can be seen as a single lucent line between the layers of the hoof wall on the lateral view (see Fig. 27.40D) and as a series of vertically oriented, thin, parallel lucent lines in the D65Pr-PaDiO view. This may progress to laminar necrosis, with eventual dissection of gas between the laminae once necrosis erodes through to the coronary band or white zone of the sole. Larger regions of radiolucency are more likely to be associated with secondary soft tissue infection.

In addition to the laminar changes, the distal phalanx undergoes characteristic changes associated with laminitis. These changes include bone production along the dorsal cortex of the distal phalanx dome-shaped contour, lipping or ski-slope-shaped bone formation at the toe, enlargement of the vascular channels, solar margin lysis, resorption of the palmar cortex, and/or angular orientation of a solar margin fracture (type VI) (see Fig. 27.40).

Because of the severe morbidity and protracted treatment required for chronic laminitis, indicators of prognosis for success or failure of treatment are desired. Various radiographic measurements have been assessed retrospectively to define reliable predictors of outcome for horses with chronic laminitis. Fig. 27.41 and eFig. 27.6 illustrate several of these measurements. Sole thickness (sole depth), not included in these illustrations, is measured from the toe of the distal phalanx to the ground surface, or top of the shoe, or to the distal soft tissue border of the sole if the horse has a prominent cup-shaped bottom of the foot (see Fig. 27.40A). The normal sole thickness should be greater than 15 mm in normal horses and greater



eFig. 27.6 Rotational and sinking laminitis. There is plantar rotation and vertical displacement of the distal phalanx.

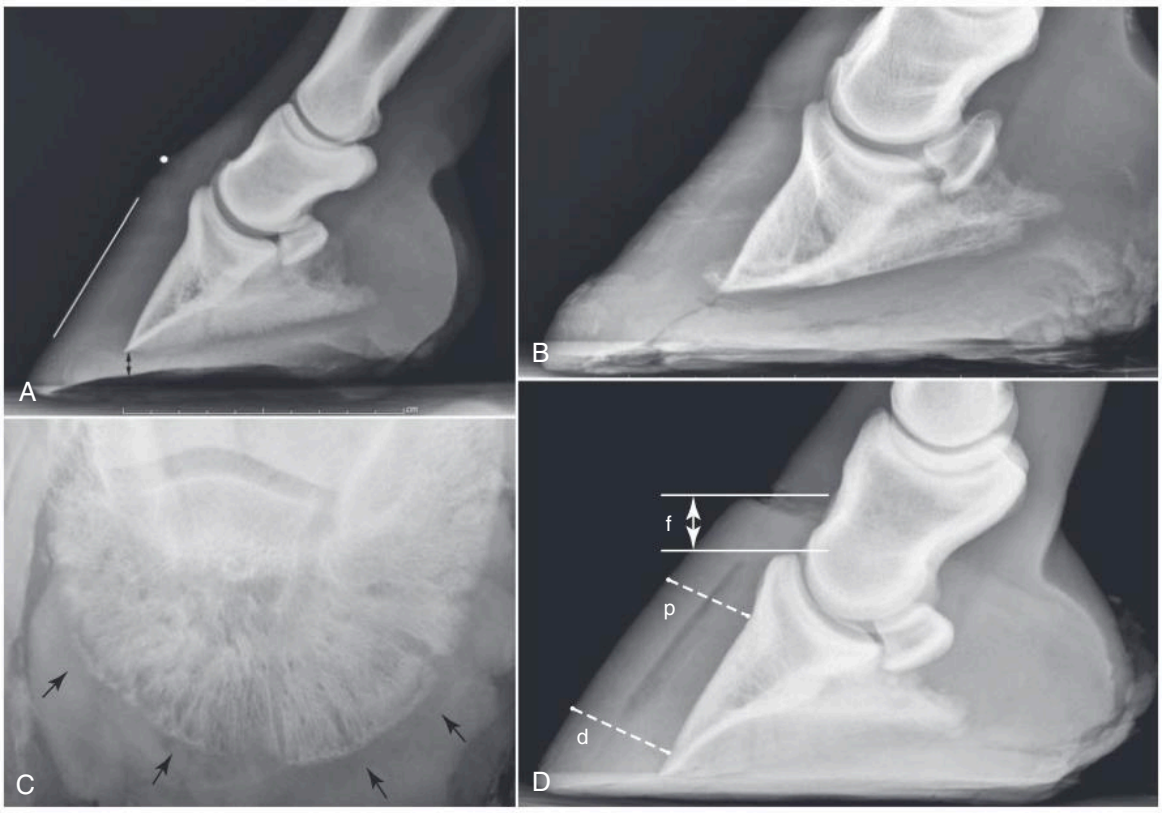


Fig. 27.40 Three variations of chronic laminitis. **A** is a horse with supporting limb laminitis with mild palmar rotation of the distal phalanx. The *white line* simulates the position for placement of a radiopaque marker on the dorsal hoof wall surface. The *white dot* simulates the location for placement of a marker at the coronary band. Palpation of the hoof wall and coronary band junction is important to achieve proper placement of this marker. The *double-headed arrow* shows the location for measuring sole depth or sole thickness. **B and C** are images of a horse with more chronic laminitis. In addition to rotation of the distal phalanx, there is a linear gas shadow extending from the sole to the toe. A bone fragment is present at the toe because of pathologic distal phalanx fractures along the medial and lateral solar margins (type VI) as seen in **C** (*arrows*). Punctate radiolucencies in the trabecular region are end-on vessels increased in number and diameter. **D** is a horse that developed plantar rotation and vertical displacement of the distal phalanx within 3 weeks of a severe injury to the contralateral limb. There is a marked indentation at the coronary band. The sole is extremely thin at the toe. Gas is also evident at the laminar junction. Measurements made on the images indicated a founder distance *(f)* of 18 mm, proximal dorsal hoof wall distance *(p)* of 28 mm, and distal dorsal hoof wall distance *(d)* of 33 mm.

than 10 mm in normal ponies and more thin-soled Thoroughbred racehorses.[119,120] Even though none has been completely reliable when used as the only indicator, trends have been identified. In general, the more deviant from normal, the more guarded the prognosis. The vertical distance between the proximal limit of the dorsal hoof wall and the proximal limit of the extensor process of the distal phalanx has been measured to generate a *founder distance* (Fig. 27.41B).[116] When corrected for magnification, this distance in 25 normal horses was an average of 4 mm (range, −2 to 11 mm) in the front feet and an average of 4.6 mm (range, −2 to 9 mm) in the hind feet.[116] The wide variation in these measurements reflects the spectrum of equine foot conformation and a single measurement alone is of limited value. Serial measurements in repeated radiographic studies may give more meaningful information about progression of laminitis in that individual patient. Evaluating a large number of horses for prognostic indicators of poor outcome, distal displacement of the distal phalanx was the only radiographic variable associated with an increased probability of death.[120] However, the severity of the lameness was the single best predictor of outcome. Others concur that radiographic assessment is important in establishing and monitoring bone stability within the hoof but should not be used as an isolated indicator of outcome.[121]

Digital venography can be used to evaluate several foot problems, most notably laminitis. This procedure is described in detail within the literature and involves the administration of positive contrast medium via a palmar digital vein followed by rapid acquisition of lateromedial and dorsopalmar radiographs of the foot.[7,122] In a normal horse, the contrast medium is maintained within the vasculature and the tip of the distal phalanx is located proximal to the circumflex vein. In horses with laminitis, there may be compression of vasculature, failure of adequate filling, rapid extravascular diffusion of contrast medium, and/or an altered (more distal) position of the tip of the distal phalanx relative to the circumflex vein.[7,123] This technique has been used to guide treatment recommendations and inform prognostication; however, imaging findings should be considered in the context of the clinical appearance when making decisions.[124]

MRI can be used to detect laminitis, even in the acute stages. A study of active phase laminitis was performed using a 4.7 T magnet, and it was possible to detect changes in laminar and corium structure and signal intensity that correlated strongly with the histologic diagnosis of acute laminitis.[124] In this study the sensitivity of MRI for detecting these changes was 95% to 100%, compared with just 48% to 58% for radiography. Changes such as laminar fibrillation and signal alterations within the

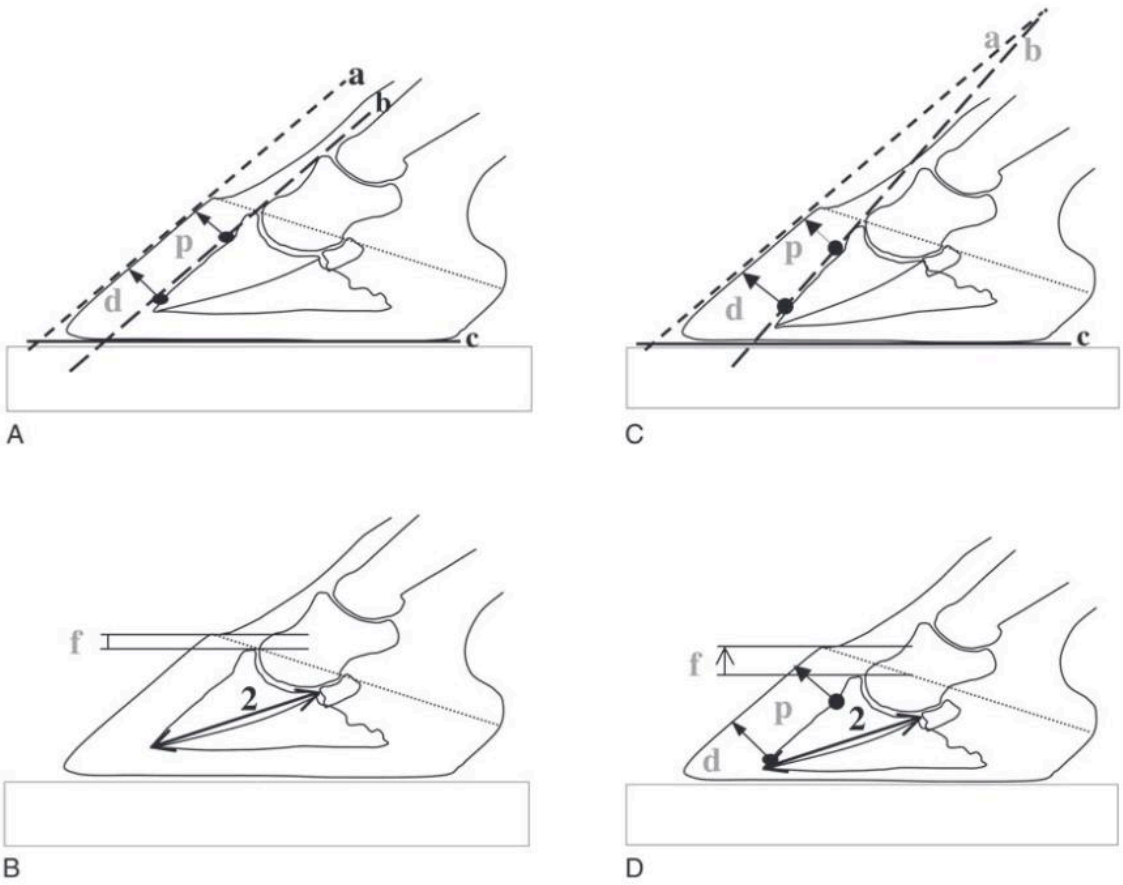


Fig. 27.41 **A and B,** Radiographic measurements of the normal foot. **A,** Line *a* is parallel to the hoof wall. Line *b* is parallel to the dorsal cortex of the distal phalanx. Line *c* is parallel to the weight-bearing surface of the hoof wall. Angle *ac* is the hoof axis. Angle *bc* is the foot axis. Distance *p* is the thickness of the dorsal soft tissues measured 5 mm distal to the junction of the extensor process with the dorsal cortex. Distance *d* is the thickness of the dorsal soft tissues measured 6 mm proximal to the most distal point of the dorsal cortex. **B,** Line *2* is the length of the palmar cortex measured from the solar margin at the distal toe to the palmar articular edge between the distal phalanx and the distal sesamoid bone. Distance *f* is the vertical distance or "founder" distance measured between coronary band and proximal edge of the extensor process. **C and D,** Radiographic measurements of the foot with chronic laminitis. **C,** Foot with chronic laminitis exhibiting displacement of the distal phalanx as rotation only. Lines *a* and *b* are no longer parallel and converge proximally, forming angle *ab* or the rotation angle. Distance *d* is greater than distance *p.* **D,** Foot with chronic laminitis exhibiting distal phalanx displacement as vertical displacement (sinking) only. Founder distance *f* is increased. Distance *p* equals *d,* but both are greater than normal. The percentage that *d* is of line *2* will be greater than normal. (See text for normal and abnormal values.) (Reproduced with permission from Lindford RL, O'Brien TR, Trout DR. Qualitative and morphometric radiographic findings in the distal phalanx and digital soft tissues of sound Thoroughbred racehorses. *Am J Vet Res.* 1993;54:38; and Cripps PJ, Eustace RA. Radiological measurements from the feet of normal horses with relevance to laminitis. *Equine Vet J.* 1999;31:427.)

corium are also detectable with other high-field systems in more common clinical use (1–3 T).

Ungual (Collateral) Cartilages

The ungual cartilages extend in a proximopalmar direction from the palmar processes of the distal phalanx. There are multiple ligaments associated with these cartilages which anchor them to adjacent osseous structures. These include the chondropedal (attach to the proximal phalanx), chondrocoronal (attach to the middle phalanx), chondrotendinous (attach to the extensor process of the distal phalanx), chondroungular (attach to the palmar processes of the distal phalanx), and chondrosesamoidean ligaments (attach to the navicular bone). In addition, fibers of the distal interphalangeal collateral ligaments connect to the dorsal aspect of these cartilages.[3,125]

Tears of the Ungual Cartilages

Tears of the unossified ungual cartilages can occur and are frequently associated with severe injury of the adjacent soft tissues, particularly the collateral ligaments of the distal interphalangeal joint. This diagnosis can only be made definitively on MRI or high-quality contrast-enhanced CT.

Ossification/Calcification (Sidebones)

This is a common finding in radiographs of the distal part of the digit, especially in draft-breed horses. Ascribing clinical significance of ossified cartilages can be difficult. Many consider this finding to be incidental or, if asymmetric within a foot, indicative of increased stress on the ossified portion.[126] A grading scheme has been used to grade the ossification as depicted in the weight-bearing horizontal dorsopalmar view (see Fig. 27.42).[56] Generally, ossification begins at the base of the

cartilage and advances proximally. Separate centers of ossification occur and can be located anywhere within the cartilage (Fig. 27.43). The radiolucent line that separates the center of ossification generally has smooth, rounded margins and should not be misinterpreted as a fracture. Moderate to extensive grades of ossification have been suggested to have an association with foot lameness, including injuries of the collateral ligaments of the distal interphalangeal joint and the distal phalanx.

Fracture of the ossified cartilage occurs most commonly at the base attachment to the palmar process. Fractures typically occur in an axial proximal to abaxial distal and palmar to dorsal direction. Fracture borders are sharp and irregular compared to the borders of the gap between a separate center of ossification that has not fused to the base region. These fractures may be visible radiographically, particularly when a comprehensive series of foot radiographs is acquired. In some instances, the fracture line itself may be indistinguishable radiographically; however, the osteosclerosis at the base of the cartilage and proximal aspect of the associated palmar process that often precedes such fractures may be visible. Detection of this change should prompt more careful interrogation of this region for evidence of fracture, possibly to include additional imaging modalities such as MRI and/or nuclear scintigraphy.[127] MRI may also reveal intraosseous fluid within the surrounding bone. Fractures frequently extend through the ipsilateral distal interphalangeal collateral ligament fossa and the majority are associated with enlargement and signal change within the collateral ligament itself.[128] In addition, the ligaments of the ungual cartilages are often injured in conjunction with the fracture. These associated soft tissue injuries likely contribute towards lameness in these patients.

Infection (Quittor)

Penetrating wounds or lacerations in the coronary band region can introduce infection into the ungual cartilages. Necrosis associated with infection of this cartilage is called *quittor*. In acute infections, radiography should be considered to assess for the presence of radiopaque foreign material or a deeper lesion in the adjacent bones. In chronic infections, a draining tract is typical. Fistulography may be used to determine the depth and direction of such tracts.[129] Extension to the distal interphalangeal joint is uncommon unless it occurs iatrogenically during aggressive establishment of drainage or debridement of the necrotic cartilage. Ultrasound may be used to evaluate the proximal extent of the cartilages that project above the coronary band. With infection, they may demonstrate increased echogenicity and irregular margins. It may also be possible to trace draining tracts to the margins of the cartilages. Preoperative MRI was used to evaluate five suspected cases of quittor that had been unresponsive to conservative management or had lameness greater than expected.[130] The low-field (0.27 T) standing MR studies showed abnormal signal in the cartilage and abnormalities in the chondrocoronal and chondrosesamoidean ligaments. Additional extension of involvement in three of the horses to either the distal or middle phalanges and involvement of the collateral ligament of the distal interphalangeal joint was identified and aided in the management of the patients.

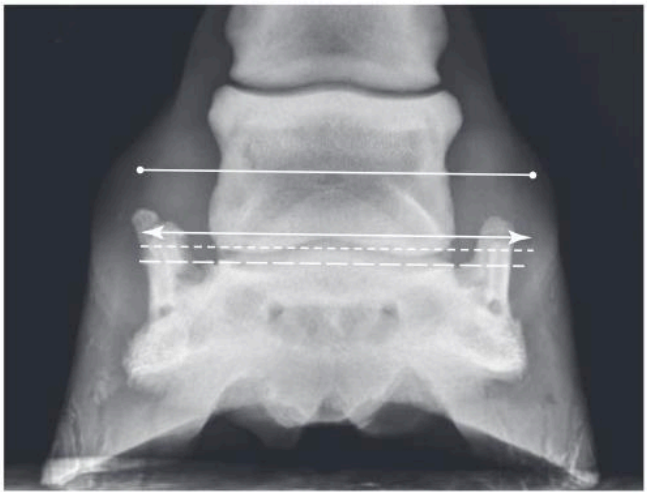


Fig. 27.42 This horse has ossification of the collateral cartilages. The *lines* demonstrate the levels used for the grading scheme to quantify ossification. Ossification to the level of the *dashed line* is grade 1; to the level of the *dotted line* is grade 2; to the level of the *line with arrows* is grade 3; to the level *between the line with arrows and line with dots* is grade 4; and to the level *proximal to the line with dots* is grade 5. This horse has grade 4 ossification of both cartilages.

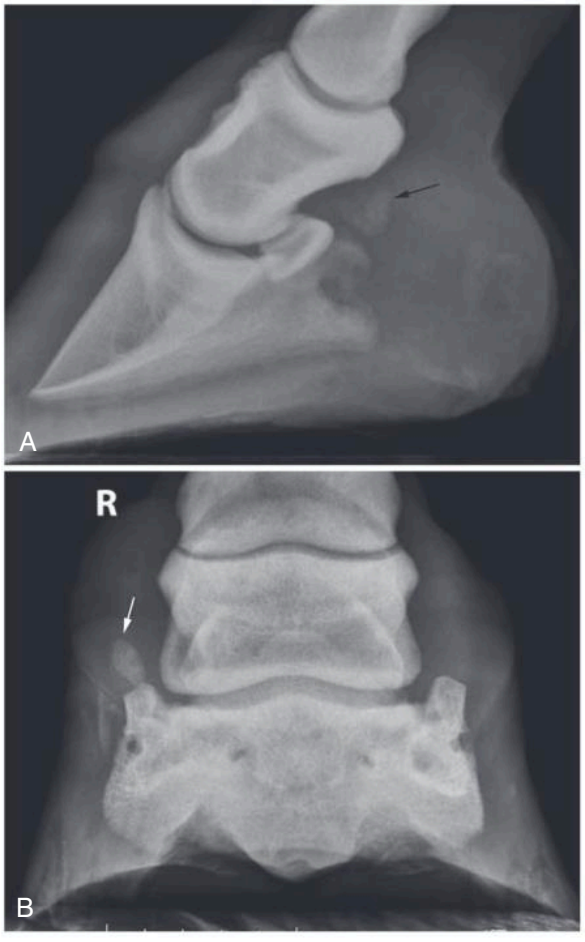


Fig. 27.43 **A and B,** Lateral-medial and dorsopalmar views of the foot. The lateral collateral cartilage has ossified from a separate center (*arrow* in each view), as well as from the base of attachment to the palmar process. This pattern of ossification is given a grade 3. The medial collateral cartilage has ossified uniformly from the base attachment and is also a grade 3. Additional abnormalities in this horse are mild distal interphalangeal flexion, mild new bone on the dorsal surface of the middle phalanx, and moderate, mildly irregular new bone on the proximal dorsal border of the middle phalanx. The enthesophyte formation on the middle phalanx is diagnostic of sprain injury and at the level of the proximal interphalangeal joint is most probably associated with arthritis. The flexion of the distal interphalangeal joint may be secondary to distal limb pain or an artifact of incomplete weight bearing at the time of image exposure and needs to be correlated with the clinical exam findings.

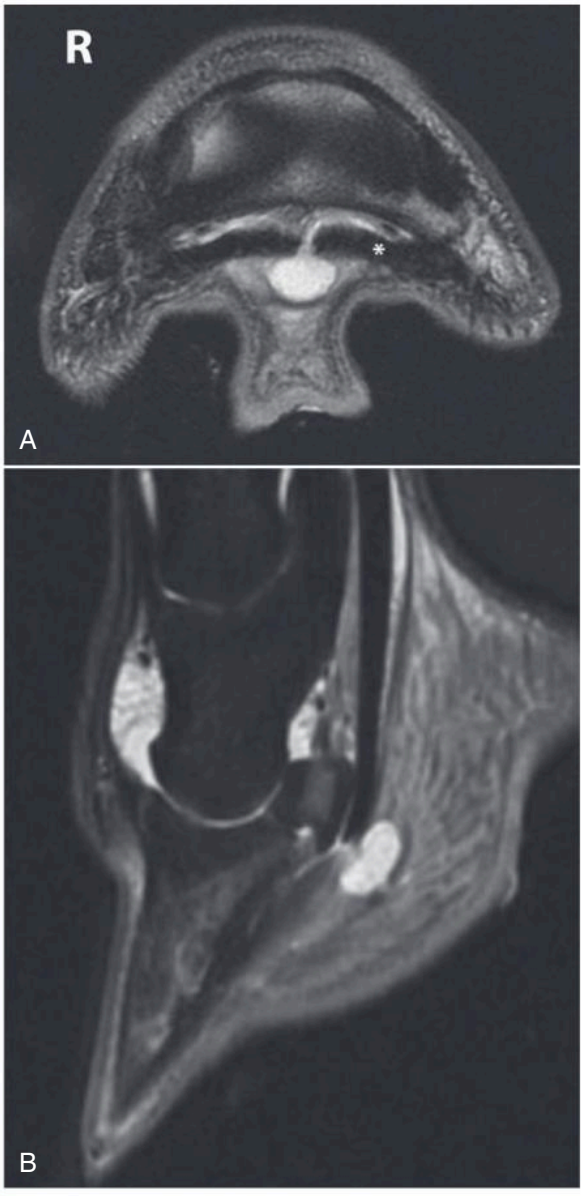


Fig. 27.44 This mare had a penetrating injury to the sole 3 weeks prior, was not responding to treatment, and her lameness was worsening. Transverse proton density weighted **(A)** and sagittal short tau inversion recovery **(B)** magnetic resonance (MR) images show a round region of hyperintensity palmar to the deep digital flexor tendon (*asterisk*) at the level of its curvature around the distal border of the navicular bone. In **A,** a communication with the podotrochlear bursa through the midpane of the tendon is evident. In **B,** there is hyperintense signal in the medullary cavity of the navicular bone and in the central region of the third phalanx. The changes in the third phalanx and navicular bone are consistent with bone edema and likely inflammation. Surgery confirmed the communication with the bursa. Aggressive lavage was done; the horse was discharged with a therapeutic shoe and lost to follow-up.

Penetrating Solar Injuries

Radiographic investigation of horses with solar penetration was briefly discussed in the previous section on septic arthritis. A key point worthy of mention is, where possible, to obtain radiographs with the penetrating object in situ so as to document its precise trajectory. However, radiography is often not able to detect the extent of soft tissue injury or early bone changes in these injuries and CT or MRI can yield important information. CT has improved accuracy for detecting foreign bodies compared to radiography or MRI, so it could be considered when there is suspicion of indwelling foreign material.[131,132] MRI may demonstrate the penetrating tract as a region of signal void with or without signal changes consistent with recent hemorrhage.[131,133] Determination of the structures involved, region of sole penetration, as well as time from sole penetration had a significant association with outcome (Fig. 27.44).[134] In one study in 55 horses with solar penetration injuries evaluated by low-field (0.3 T) MRI, synovial involvement had a guarded prognosis for survival to discharge and a poor prognosis for return to preinjury athletic performance.[133] Penetration of the central sulcus and involvement of P3, and delayed intensive treatment were associated with euthanasia. In this study, lesions of the DDFT were most commonly seen at the insertion on the distal phalanx, were often severe, and were the most common reason for euthanasia. However, a more recent MRI study of 11 cases of penetrating injury without synovial sepsis found that 60% of horses with insertional DDFT tendinopathy secondary to penetrating injury returned to full athletic function and the remaining 40% were sound.[135]

REFERENCES

1. Schebitz H, Wilkens H. *Atlas of Radiographic Anatomy of the Horse*. Philadelphia: Saunders; 1978.
2. Smallwood JE, Holliday SD. Xeroradiographic anatomy of the equine digit and metacarpophalangeal region. *Vet Radiol*. 1987;28:166.
3. Denoix JM. *The Equine Distal Limb Atlas of Clinical Anatomy and Comparative Imaging*. Ames: Iowa State University; 2002.
4. Nagy A, Bodo G, Dyson SJ, et al. Diffusion of contrast medium after four different techniques for analgesia of the proximal metacarpal region: an in vivo and in vitro study. *Equine Vet J*. 2012;44(6):668–673.
5. Contino EK, King MR, Valdés-Martinez A, et al. In vivo diffusion characteristics following perineural injection of the deep branch of the lateral plantar nerve with mepivacaine or iohexol in horses. *Equine Vet J*. 2015;47(2):230–234.
6. Barrett M, Acutt E, Redding WR, et al. Chapter 3: Diagnostic imaging radiography. In: *Adams and Stashak's Lameness in Horses*. 7th ed. Hoboken, NJ: Wiley-Blackwell; 2020.
7. Butler JA, Colles CM, Dyson SJ, et al. *Clinical Radiology of the Horse*. 4th ed. Chichester, West Sussex, UK: John Wiley & Sons Inc; 2017.
8. Hinkle FE, Johnson SA, Selberg KT, et al. A review of normal radiographical variants commonly mistaken for pathological findings in horses. *Equine Vet Educ*. 2020;32(12):664–672.
9. Linford RL, O'Brien TR, Trout DR. Qualitative and morphometric radiographic findings in the distal phalanx and digital soft tissues of sound Thoroughbred racehorses. *Am J Vet Res*. 1993;54(1):38–51.
10. Smallwood JE, Albright SM, Metcalf MR, et al. A xeroradiographic study of the developing equine forefdigit and metacarpophalangeal region from birth to six months of age. *Vet Radiol*. 1989;30(98).
11. Berry CR, Pool RR, Stover S, et al. Radiographic/morphologic investigation of a radiolucent crescent within the flexor central eminence of the navicular bone in thoroughbreds. *Am J Vet Res*. 1992;53(9):1604–1611.
12. Compagnie E, Ter Braake F, de Heer N, et al. Arthroscopic removal of large extensor process fragments in 18 Friesian horses: long-term clinical outcome and radiological follow-up of the distal interphalangeal joint. *Vet Surg*. 2016;45(4):536–541.
13. Lloyd KA, Smith MRW, Whitton RC, et al. Osteochondral fragmentation of the palmarolateral/plantarolateral aspect

of the distal phalanx in four horses: a novel location. *Equine Vet Educ.* 2022;34(4):e163–e168.
14. Barrett MF, Zubrod CJ. Use of magnetic resonance imaging to detect and direct therapy of osseous cystic lesions at the solar surface of the third phalanx of a horse. *Equine Vet Educ.* 2008;20(19).
15. Sherlock CE, Mair TS. Osseous cyst-like lesions/subchondral bone cysts of the phalanges. *Equine Vet Educ.* 2011;23:191.
16. Fairburn AJ, Sherlock CE, Partridge SM, et al. A case-control study of the morphological measurements of equine distal interphalangeal joints affected by osseous cyst-like lesions. *Equine Vet Educ.* 2021;34(9):473–479.
17. Mair TS, Sherlock CE. Osseous cyst-like lesions in the feet of lame horses: diagnosis by standing low-field magnetic resonance imaging. *Equine Vet Educ.* 2008;20(47).
18. Frietman SK, Van Aert CDM, ter Braake F, et al. A detailed radiographic description and correlated magnetic resonance imaging findings of an infrequently identified articular indentation of the articular margin of the distal phalanx. *Equine Vet Educ.* 2022;34(12):626–634.
19. Peter VG, O'Keeffe TA, Smith LCR, et al. Radiographic identification of osseous cyst-like lesions in the distal phalanx in 22 lame Thoroughbred horses managed conservatively and their racing performance. *Front Vet Sci.* 2018;5(286):1–7.
20. Story MR, Bramlage LR. Arthroscopic debridement of subchondral bone cysts in the distal phalanx of 11 horses (1994–2000). *Equine Vet J.* 2004;36(4):356–360.
21. Ball AN, Hoaglund EL, Pool R, et al. Multimodal imaging to identify and characterize a P3 cystic lesion and pathologic fracture. *J Equine Vet Sci.* 2020;86:1–6.
22. Valentine BA, Scott EA, Watrous BJ, et al. What is your diagnosis? Keratoma in a horse's hoof. *J Am Vet Med Assoc.* 2000;217(7):993–994.
23. Getman LM, Davidson EJ, Ross MW, et al. Computed tomography or magnetic resonance imaging-assisted partial hoof wall resection for keratoma removal. *Vet Surg.* 2011;40(6):708–714.
24. Mair TS, Linnenkohl W. Low-field magnetic resonance imaging of keratomas of the hoof wall. *Equine Vet Educ.* 2012;24:459–468.
25. Rowland AL, Goodrich LR, Bass LD, et al. Diagnosis and treatment of biaxial keratomas in the left fore foot of a 15-year-old Clydesdale mare. *Equine Vet Educ.* 2016;28:310.
26. Katzman SA, Spriet M, Galuppo LD, et al. Outcome following computed tomographic imaging and subsequent surgical removal of keratomas in equids: 32 cases (2005–2016). *J Am Vet Med Assoc.* 2019;254(2):266–274.
27. Headley SA, Kummala E, Saarinen H, et al. Diagnostic exercise: intraosseous epidermoid cysts in the third phalanx of a dressage mare. *Vet Pathol.* 2009;46(2):355–357.
28. Fraser B, Else RW, Jones E. Intraosseous epidermoid cyst of the third phalanx in a Thoroughbred gelding. 2006;159(11):360–362.
29. Mageed M, Elfadl A. Computed tomography and magnetic resonance imaging of an epidermoid cyst in a foot of a horse. *J Equine Vet Sci.* 2020;94:1–5.
30. Hibner-Szaltys M, Hann MJ, Woods SCC, et al. Diagnosis and arthroscopic removal of an intra-articular epidermoid cyst in the distal interphalangeal joint of a 15-year-old horse. *Equine Vet Educ.* 2022;00:1–6.
31. Joostens Z, Vanslambrouck L, De Cock H, et al. Epithelial inclusion cyst of the equine digital flexor tendon sheath: diagnosis by ultrasonography and magnetic resonance and successful treatment by tenoscopy. *Vlaams Diergeneeskundig Tijdschrift.* 2019;88(6):320–326.
32. Cillan-Garcia E, Kearns LJ, Hetzel U, et al. Osteosarcoma of the middle phalanx in a horse. *Equine Vet Educ.* 2010; 22:535.
33. Osborne C, Elce YA, Meehan L, et al. Neoplasia within the equine foot: a retrospective case series of four horses. *Equine Vet Educ.* 2021;34(10):e431–437.
34. Gelatt KJ, Neuwirth L, Hawkins DL, et al. Hemangioma of the distal phalanx in a colt. *Vet Radiol Ultrasound.* 1996;37(4):275–280.
35. Nagel H, Lang H, Guitart S, et al. Multi-modality imaging of aggressive submural neoplasia of the hoof in two horses. *Aus Vet J.* 2022;100(7):336–341.
36. Moulin N, Schramme M, François I, et al. Long-term outcome of treatment of a squamous cell carcinoma of the foot by amputation of the distal limb in a pony. *Equine Vet Educ.* 2018;32(3):137–143.
37. Clegg PD. Musculoskeletal disease and injury, now and in the future. Part 1: fractures and fatalities. *Equine Vet J.* 2011;43(6):643–649.
38. Sarrafian TL, Case JT, Kinde H, et al. Fatal musculoskeletal injuries of Quarter horse racehorses 314 cases (1990–2007). *J Am Vet Med Assoc.* 2012;241(7):935–942.
39. Crijns CP, Martens A, Bergman HJ, et al. Intramodality and intermodality agreement in radiography and computed tomography of equine distal limb fractures. *Equine Vet J.* 2014;46(1):92–96.
40. Perrin RAR, Launois MT, Brogniez L, et al. The use of computed tomography to assist orthopaedic surgery in 86 horses (2002–2010). *Equine Vet Educ.* 2011;23:306.
41. Smanik LE, Stefanovski D, Reilly PT, et al. Computed tomographic guidance for internal fixation of type II distal phalangeal fractures in 51 horses. *Equine Vet J.* 2021;54(4):679–692.
42. Nixon AJ. *Equine Fracture Repair.* 2nd ed. Chichester, West Sussex, UK: John Wiley & Sons Inc; 2020.
43. Rick MC. Navicular bone fractures. In: White NA, Moore JN, eds. *Current Practice of Equine Surgery.* Philadelphia: Lippincott; 1990:602–605.
44. Yorke EH, Judy CE, Saveraid TC, et al. Distal border fragments of the equine navicular bone: association between magnetic resonance imaging characteristics and clinical lameness. *Vet Radiol Ultrasound.* 2013;55(1):35–44.
45. Honnas CH, O'Brien TR, Linford RL. Distal phalanx fractures in horses: a survey of 274 horses with radiographic assessment of healing in 36 horses. *Vet Radiol.* 1989;29(98).
46. Fairburn AJ, Sherlock CE, Mair TS. Palmar/plantar oblique projections improve radiographic detection of fractures of the palmar/plantar processes of the equine distal phalanx. *Vet Radiol Ultrasound.* 2022;63(6):681–690.
47. Rijkenhuizen ABM, de Graaf K, Hak A, et al. Management and outcome of fractures of the distal phalanx: a retrospective study of 285 horses with a long term outcome in 223 cases. *Vet J.* 2012;192(2):176–182.
48. Dechant JE, Trotter GW, Stashak TS, et al. Removal of large fragments of the extensor process of the distal phalanx via arthrotomy in horses: 14 cases (1992–1998). *J Am Vet Med Assoc.* 2000;217(9):1351–1355.
49. Crowe OM, Hepburn RJ, Kold SE, et al. Long-term outcome after arthroscopic debridement of distal phalanx extensor process fragmentation in 13 horses. *Vet Surg.* 2010;39(1):107–114.
50. Bhatnagar AS, Pleasant RS, Dascanio JJ, et al. Hoof conformation and palmar process fractures of the distal phalanx in Warmblood foals. *J Equine Vet Sci.* 2010;30:349.
51. Schade SM, Arnoczky SP, Bowker RM. The microvasculature in the equine distal phalanx: implications for fracture healing. *Vet Comp Orthop Traumatol.* 2014;27(02):102–106.
52. Faramarzi B, McMicking H, Halland S, et al. Incidence of palmar process fractures of the distal phalanx and association with front hoof conformation in foals. *Equine Vet J.* 2015;47(6):675–679.

53. Faramarzi B, Dobson H. Palmar process fractures of the distal phalanx in foals: a review. *Equine Vet Educ.* November 2015;12. https://doi.org/10.1111/eve.12509.
54. Down SS, Dyson SJ, Murray RC. Ossification of the cartilages of the foot. *Equine Vet Educ.* 2007;19(51).
55. Kilcoyne I, Dechant JE, Kass PH, et al. Penetrating injuries to the frog (cuneus ungulae) and collateral sulci of the foot in equids: 63 cases (1998–2008). *J Am Vet Med Assoc.* 2011;239(8):1104–1109.
56. Neil KM, Axon JE, Begg AP, et al. Retrospective study of 108 foals with septic osteomyelitis. *Aust Vet J.* 2010; 88(1–2):4–12.
57. Olive J, Mair TS, Charles B, et al. Use of standing low-field magnetic resonance imaging to diagnose middle phalanx bone marrow lesions in horses. *Equine Vet Educ.* 2009;21(3):116–123.
58. Werpy N. Diagnosis of middle phalanx bone marrow lesions in horses using magnetic resonance imaging and identification of phase effect cancellation for proper image interpretation. *Equine Vet Educ.* 2009;21(3): 125–130.
59. Cantatore F, Cavallier F, Biggi M. Bone marrow oedema-type pattern at the enthesis of the collateral ligaments of the distal interphalangeal joint: magnetic resonance findings and long-term prognosis. *Equine Vet J.* 2021;53(S55):28.
60. Wright IM. A study of 118 cases of navicular disease: clinical features. *Equine Vet J.* 1993;25(6):488–492.
61. Ackerman N, Johnson JH, Dorn CR. Navicular disease in the horse: risk factors, radiographic changes, and response to therapy. *J Am Vet Med Assoc.* 1977;170(2):183–187.
62. van Hoogmoed LM, Snyder JR, Thomas HL, et al. Retrospective evaluation of equine prepurchase examinations performed 1991–2000. *Equine Vet J.* 2003;35(4): 375–381.
63. McParland TJ, Horne CR, Robertson JB, et al. Alterations to the synovial invaginations of the navicular bone are associated with pathology of both the navicular apparatus and distal interphalangeal joint when evaluated using high field MRI. *Vet Radiol Ultrasound.* 2022;1–9.
64. Lutter JD, Schneider RK, Sampson SN, et al. Medical treatment of horses with deep digital flexor tendon injuries diagnosed with high-field-strength magnetic resonance imaging: 118 cases (2000–2010). *J Am Vet Med Assoc.* 2015;247(11):1309–1318.
65. Sherlock C, Mair T, Blunden T. Deep erosions of the palmar aspect of the navicular bone diagnosed by standing magnetic resonance imaging. *Equine Vet Educ.* 2008; 40(7):684–692.
66. Johnson SA, Barrett MF, Frisbie DD. Additional palmaroproximal–palmarodistal oblique radiographic projections improve accuracy of detection and characterization of equine flexor cortical lysis. *Vet Radiol Ultrasound.* 2018;59(4):387–395.
67. Joostens Z, Evrard L, Busoni V. Unipodal stance influences radiographic evaluation of foot balance in horses. *Vet Radiol Ultrasound.* 2019;60(3):273–279.
68. Contino EK, Barrett MF, Werpy NM. Effect of limb positioning on the radiographic appearance of the distal and proximal interphalangeal joint spaces of the forelimbs of horses during evaluation of dorsopalmar radiographs. *J Am Vet Med Assoc.* 2014;244(10):1186–1190.
69. Murray RC, Mair TS, Sherlock CE, et al. Comparison of high-field and low-field magnetic resonance images of cadaver limbs of horses. *Vet Rec.* 2009;165(10):281–288.
70. Smith MA, Dyson SJ, Murray RC. Reliability of high- and low-field magnetic resonance imaging systems for detection of cartilage and bone lesions in the equine cadaver fetlock. *Equine Vet J.* 2012;44(6):684–691.
71. van Zadelhoff C, Schwarz T, Smith S, et al. Identification of naturally occurring cartilage damage in the equine distal interphalangeal joint using low-field magnetic resonance imaging and magnetic resonance arthrography. *Front Vet Sci.* 2020;6(508):1–10.
72. McIlwraith CW, Frisbie DD, Kawcak CE, et al. *Joint Disease in the Horse.* 2nd ed. St. Louis, Missouri, USA: Elsevier; 2016.
73. Olive J. Distal interphalangeal articular cartilage assessment using low-field magnetic resonance imaging. *Vet Radiol Ultrasound.* 2010;51(3):259–266.
74. Janicek JC, Dabareiner RM, Honnas CM, et al. Heel bulb lacerations in horses: 101 cases (1988–1994). *J Am Vet Med Assoc.* 2005;226(3):418–423.
75. Easley JT, Brokken MT, Zubrod CJ, et al. Magnetic resonance imaging findings in horses with septic arthritis. *Vet Rad Ultrasound.* 2011;52(4):402–408.
76. Yiannikoruis S, Schneider RK, Samson SN, et al. Desmotomy of the accessory ligament of the deep digital flexor tendon in the forelimb of 24 horses 2 years and older. *Vet Surg.* 2011;40(3):272–276.
77. Dakin SG, Dyson SJ, Murray RC, et al. Osseous abnormalities associated with collateral desmopathy of the distal interphalangeal joint: part 1. *Equine Vet J.* 2009;41(8):786–793.
78. Zubdrod CJ, Farnsworth KD, Tucker RL, et al. Injury of the collateral ligaments of the distal interphalangeal joint diagnosed by magnetic resonance. *Vet Radiol Ultrasound.* 2005;46(1):11–16.
79. Dyson SJ, Murray R, Schramme M, et al. Collateral desmitis of the distal interphalangeal joint in 18 horses (2001–2002). 2004;36(2):160–166.
80. Young AC, Dimock AN, Puchalski SM, et al. Magnetic resonance and radiographic diagnosis of osseous resorption of the flexor surface of the distal phalanx in the horse. *Equine Vet J Suppl.* 2012;43:3–7.
81. Dyson SJ, Murray P, Schramme MC. Lameness associated with foot pain: results of magnetic resonance imaging in 199 horses (January 2001–December 2003) and response to treatment. *Equine Vet J.* 2005;37:113.
82. Gutierrez-Nibeyro SD, Werpy NM, White NA, et al. Standing low-field magnetic resonance imaging appearance of normal collateral ligaments of the equine distal interphalangeal joint. *Vet Radiol Ultrasound.* 2011; 52(5):521–533.
83. Smith MA, Dyson SJ, Murray RC. Is a magic angle effect observed in the collateral ligaments of the distal interphalangeal joint or the oblique sesamoidean ligaments during standing magnetic resonance imaging? *Vet Radiol Ultrasound.* 2008;49(6):509–515.
84. Werpy NM, Ho CP, Kawcak CE. Magic angle effect in normal collateral ligaments of the distal interphalangeal joint in horses imaged with a high-field magnetic resonance imaging system. *Vet Radiol Ultrasound.* 2010;51(1):2–10.
85. White NA, Barrett JG. Magnetic resonance imaging-guided treatment of equine distal interphalangeal joint collateral ligaments: 2009–2014. *Front Vet Sci.* 2016;3(73):1–6.
86. Lamb MM, Barrett JG, White NA, et al. Accuracy of low-field magnetic resonance imaging versus radiography for guiding injection of equine distal interphalangeal joint collateral ligaments. *Vet Radiol Ultrasound.* 2013; 52(2):174–181.
87. Lewis D, Scott M, Fischer CD, et al. Feasibility for ultrasound-guided injection of the collateral ligaments of the distal interphalangeal joint in horses. *Vet Radiol Ultrasound.* 2016;57(3):299–305.
88. Kirkpatrick CJ, Ernst NS, Trumble TN. Palmar/plantar approach for radiographic-guided injection of the equine distal interphalangeal joint collateral ligament insertion. *Vet Rec.* 2019;184(17);527–527.

89. O'Brien EJ, Smith RWK. Mineralization can be an incidental ultrasonographic finding in equine tendons and ligaments. 2018;59(5):613–623.
90. Mair TS, Kinns J. Deep digital flexor tendonitis in the equine foot diagnosed by low-flied magnetic resonance imaging in the standing patient: 18 cases. *Vet Radiol Ultrasound*. 2005;46(6):458–466.
91. Vallance SA, Bell RJW, Spriet M, et al. Comparison of computed tomography, contrast-enhanced computed tomography and standing low-field magnetic resonance imaging in horses with lameness localized to the foot. Part 2: lesion identification. *Equine Vet J*. 2012;44(2):149–156.
92. Bolt DM, Dixon JJ. Deep digital flexor tendon lesions in the foot—a career-ending injury for the equine athlete? *Livestock*. 2016;21:196.
93. Dyson s, Murray R. Magnetic resonance imaging evaluation of 264 horses with foot pain: the podotrochlear apparatus, deep digital flexor tendon and collateral ligaments of the distal interphalangeal joint. *Equine Vet J*. 2007;39(4):340–343.
94. Sampson SN, Schneider RK, Gavin PR, et al. Magnetic resonance imaging findings in horses with recent onset navicular syndrome but without radiographic abnormalities. *Vet Radiol Ultrasound*. 2009;50(4):339–346.
95. Busoni V, Lahaye B, Denoix JM. Transcuneal ultrasonographic findings in the podotrochlear apparatus: comparison with postmortem in 14 equine digits. *J Equine Vet Sci*. 2006;26(3):113–119.
96. Jacquet S, Denoix JM. Ultrasonographic examination of the distal podotrochlear apparatus of the horse: a transcuneal approach. *Equine Vet Educ*. 2011;24(2):90–96.
97. Evrard L, Joostens Z, Vandersmissen M, et al. Comparison between ultrasonographic and standing magnetic resonance imaging findings in the podotrochlear apparatus of horses with foot pain. *Front Vet Sci*. 2021;8(675180):1–13.
98. Acutt EV, Contino EK, Frisbie DD, et al. Deep digital flexor tendon lesions in the pastern are associated with the presence of distal tendinopathy. *Equine Vet J*. 2021;54(3):502–512.
99. Biggi M, Dyson S. Comparison between radiological and magnetic resonance imaging lesions in the distal border of the navicular bone with particular reference to distal border fragments and osseous cyst-like lesions. *Equine Vet J*. 2010;42(8):707–712.
100. Dyson S, Pool R, Blunden T, et al. The distal sesamoidean impar ligament: comparison between its appearance on magnetic resonance imaging and histology of the axial third of the ligament. 2010;42(4), 332-229.
101. Barrett MF, Frisbie DD, King MR, et al. A review of how magnetic resonance imaging can aid in case management of common pathological conditions of the equine foot. 2017;29(12):683–693.
102. Whitcomb MB. Ultrasonographic appearance and distribution of deep digital flexor injuries in the pastern region. *AAEP Proc*. 2008;54:453–454.
103. Kidd JA, Lu KG, Frazer ML, eds. *Atlas of Equine Ultrasonography*. 2nd ed. Chichester, West Sussex, UK: John Wiley & Sons Inc; 2022.
104. Grundmann IN, Drost WT, Zeas LJ, et al. Quantitative assessment of the equine hoof using digital radiographs and magnetic resonance imaging. *Equine Vet J*. 2015;47(5):542–547.
105. Pollitt CC. Collins SN: the suspensory apparatus of the distal phalanx in normal horses. *Equine Vet J*. 2016;48(4):496–501.
106. Caudron I, Grulke S, Farnir F, et al. Radiographic assessment of equine interphalangeal joints asymmetry: articular impact of phalangeal rotations (part I). *J Vet Med*. 1998;45(6–7):319–325.
107. Caudron I, Grulke S, Farnir F, et al. Radiographic assessment of equine interphalangeal joints asymmetry: articular impact of asymmetric bearings (part II). *J Vet Med*. 1998;45(6–7):327–335.
108. Caudron I, Miesen M, Grulke S, et al. Radiological assessment of the effects of a full rolling motion shoe during asymmetrical bearing. *Equine Vet J Suppl*. 1997;23: 20–22.
109. Pezzanite L, Bass L, Kawcak C, et al. The relationship between sagittal hoof conformation and hindlimb lameness in the horse. *Equine Vet J*. 2018;51(4):464–469.
110. Walmsley EA, Jackson M, Wells-Smith L, et al. Solar angle of the distal phalanx is associated with scintigraphic evidence of subchondral bone injury in the palmar/plantar aspect of the third metacarpal/tarsal condyles in Thoroughbred racehorses. *Equine Vet J*. 2019;51(6):720–726.
111. Pollitt CC. Laminitis pathophysiology. In: Floyd AE, Mansmann RA, eds. *Equine Podiatry*. St Louis: Saunders/Elsevier; 2007:313.
112. Virgin JE, Goodrich LR, Baxter GM, et al. Incidence of support limb laminitis in horses treated with half limb, full limb or transfixation pin casts: a retrospective study of 113 horses (2000-2009). *Equine Vet J*. 2011;40:7–11.
113. van Eps A, Collins SN, Pollitt CC. Supporting limb laminitis. *Vet Clin North Am Equine Pract*. 2010;26(2): 287–302.
114. Hood DM. Laminitis in the horse. *Vet Clin North Am Equine Pract*. 1999;15(2):287–294.
115. Floyd AE, Mansmann RA, eds. *Equine Podiatry*. St Louis: Saunders/Elsevier; 2007.
116. Cripps PJ, Eustace RA. Radiological measurements from the feet of normal horses with relevance to laminitis. *Equine Vet J*. 1999;31(5):427–432.
117. Thieme K, Ehrle A, Lixcher C. Radiographic measurements of the hooves of normal ponies. *Vet J*. 2015;206(3):332–337.
118. Sherlock C, Parks A. Radiographic and radiological assessment of laminitis. *Equine Vet Educ*. 2013;25(10):524–535.
119. Kummer M, Geyer H, Imboden I, et al. The effect of hoof trimming on radiographic measurements of the front feet of normal Warmblood horses. *Vet J*. 2006;172(1):58–66.
120. Orsini JA, Parsons CS, Capewell L, et al. Prognostic indicators of poor outcome in horses with laminitis at a tertiary care hospital. *Can Vet J*. 2010;51(6):623–628.
121. Hunt RJ, Wharton RE. Clinical presentation, diagnosis, and prognosis of chronic laminitis in North America. *Vet Clin North Am Equine Pract*. 2010;26(1):141–153.
122. Rucker A. Equine venography and its clinical application in North America. *Vet Clin North Am Equine Pract*. 2010;26(1):167–177.
123. Kramer J, Rucker A, Leise B. Venographic evaluation of the circumflex vessels and lamellar circumflex junction in laminitic horses. *Equine Vet Educ*. 2018;32(7):386–392.
124. Arble JB, Mattoon JS, Drost WT, et al. Magnetic resonance imaging of the initial active stage of equine laminitis at 4.7 T. *Vet Radiol Ultrasound*. 2009;50(1):3–12.
125. Ruohoniemi M, Makela O, Eskonen T. Clinical significance of ossification of the cartilages of the front feet based on nuclear bone scintigraphy, radiography and lameness examinations in 21 Finnhorses. *Equine Vet J*. 2004; 36:143–148.
126. Ross MW, Dyson SJ. *Diagnosis and Management of Lameness in the Horse*. 2nd ed. St Louis: Saunders/Elsevier; 2011.
127. Dakin SG, Robson KE, Dyson SJ. Fractures of ossified cartilages of the foot: 10 cases. *Equine Vet Educ*. 2006;18:130.
128. Selberg K, Werpy N. Fractures of the distal phalanx and associated soft tissue and osseous abnormalities in 22 horses with ossified sclerotic ungual cartilages diagnosed

with magnetic resonance imaging. *Vet Radiol Ultrasound*. 2011;52(4):394–401.
129. Smith MRW. Infection of the cartilages of the foot. *Equine Vet Educ*. 2014;26(11):580–583.
130. Meehan LJ, Taylor SE, Labens R, et al. Magnetic resonance imaging assisted management in five cases of suspected quittor. *Vet Comp Orthop Traumatol*. 2016;29(1):75–82.
131. del Junco CI, Mair TS, Powell SE, et al. Magnetic resonance imaging findings of equine solar penetration wounds. *Vet Radiol Ultrasound*. 2012;53(1):71–75.
132. Ogden NKE, Milner PI, Stack JD, et al. CT more accurately detects foreign bodies within the equine foot than MRI or digital radiography. *Vet Radiol Ultrasound*. 2020;62(2):225–235.
133. Urraca del Junco CI, Mair TS, Powell SE, et al. Magnetic resonance imaging findings of equine solar penetration wounds. *Vet Radiol Ultrasound*. 2012;53(1):71–75.
134. Findley JA, Pinchbeck GL, Milner PI, et al. Outcome of horses with synovial structure involvement following solar foot penetrations in four UK veterinary hospitals: 95 cases. *Equine Vet J*. 2014;46(3):352–357.
135. Schiavo S, Cillán-García E, Elce Y, et al. Horses with solar foot penetration, deep digital flexor tendon injury, and absence of concurrent synovial sepsis can have a positive outcome. *Vet Radiol Ultrasound*. 2018;59(6):697–704.

ELECTRONIC RESOURCES

Additional information related to the content in Chapter 27 can be found online at eBooks.Health.Elsevier.com.

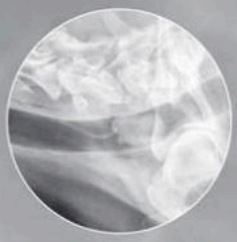
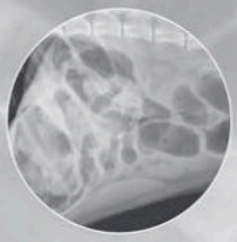
- Chapter Quiz

This page intentionally left blank

SECTION IV

The Thoracic Cavity Canine, Feline and Equine



28 **Principles of Radiographic Interpretation of the Thorax**
Donald E. Thrall

29 **Canine and Feline Larynx and Trachea**
Randi Drees

30 **Pharynx, Upper Esophageal Sphincter, and Esophagus**
Rachel E. Pollard

31 **Canine and Feline Thoracic Wall**
Gabriela S. Seiler

32 **Canine and Feline Diaphragm**
Elissa K. Randall

33 **Canine and Feline Mediastinum**
Federica Morandi • Donald E. Thrall

34 **Canine and Feline Pleural Space**
Gabriela S. Seiler

35 **Canine and Feline Cardiovascular System**
Elodie Huguet • Clifford Berry

36 **Canine and Feline Lung**
Isabelle Masseau

37 **Equine Thorax**
Stephanie G. Nykamp

CHAPTER 28

Principles of Radiographic Interpretation of the Thorax

Donald E. Thrall

Acquisition of thoracic radiographs is a common radiographic examination in small animal practice. Radiographs of at least part of the thorax can also be obtained in foals and in most adult horses.

NOMENCLATURE

In daily practice, the naming of conventional lateral thoracic radiographs made with the patient lying on their side and a vertically directed x-ray beam violates the point-of-entrance to point-of-exit nomenclature system described in Chapter 6. If the patient was on the left side, for example, the correct name for this view would be a *right-left* lateral because the x-ray beam enters on the right side and exits on the left. But in daily practice, the naming of such a view is abbreviated to designate the side the patient is lying on; in this case a *left lateral*. Similarly, a thoracic radiograph made with the patient lying on the right side would be a *right lateral* view.

In the adult horse, lateral thoracic radiographs are made with the patient standing and a horizontally directed x-ray beam. Therefore, the point-to-entrance to point-of-exit system should still be used, and lateral radiographs should be designated as either left-right or right-left laterals.

In all species, ventrodorsal (VD) and dorsoventral (DV) radiographs of the thorax are named according to the point-of-entrance to point-of-exit of the x-ray beam.

RADIOGRAPHIC TECHNIQUE: DOG AND CAT

A relatively low contrast image of the thorax is preferred. The air in the lung will provide the necessary level of contrast and there is not a need to enhance contrast using technical factors. With analog technology, a low-contrast image is obtained by using a high kilovoltage peak (kVp)—low milliampere-seconds (mAs), combination, and this approach can also be used with digital systems. However, in digital imaging the contrast of the image is controlled primarily by the processing algorithm that is applied to the raw image data. Therefore, it is important that the correct processing parameters are assigned to thorax studies when the digital image system is compiled. For patients thicker than 10 cm, a grid should be used to remove scattered x-rays from the beam.

Exposure time is critical when radiographing the thorax. Motion is the biggest enemy of image detail in veterinary radiology. Respiratory motion can induce blurring and lead to reduced detail. This reduces the ability to interpret the radiograph accurately. To minimize the effects of motion, the shortest exposure time and highest milliamperes (mA) setting possible should be used to produce the needed mAs.

Ideally, the respiratory pattern of the patient should be observed for a few seconds before the radiographic exposure is made so that the exposure can be coordinated with peak inspiration. The increased lung aeration at peak inspiration will optimize pulmonary contrast and reduce the false impression of pulmonary disease caused by poor aeration (Fig. 28.1).

RADIOGRAPHIC TECHNIQUE: HORSE

The same technical principles relating to radiography of the canine and feline thorax also apply to the horse. Radiographing the equine thorax does not require the massive exposure factors that might be expected based on the sheer size of the thorax because of the large volume of air present in the equine lungs. However, obtaining radiographs of all regions of the equine thorax when using a grid will require more output than typically available from a portable x-ray unit, such as those used commonly to radiograph equine extremities. It may be possible to obtain diagnostic-quality radiographs of the dorsocaudal portion of the equine thorax with a portable x-ray machine and without a grid, but obtaining suitable radiographs in other regions of the thorax with this type of equipment will not be possible because of the thickness of the horse, and the amount of scatter produced from intervening soft tissue.

POSITIONING: DOG AND CAT

The routine thoracic radiographic examination in the dog and cat should consist of left lateral, right lateral, and either VD or DV projections. The entire thoracic cavity should be included in the image. This seems obvious, but omitting the cranial or caudal part of the thorax from the field of view is a common error, which increases the chance of missing a lesion. The field of view should extend from just cranial to the thoracic inlet, to a few centimeters caudal to the last rib. The dorsocaudal tips of the caudal lobes extend further caudally than anticipated. Even in the largest dogs, including the entire thoracic cavity in one 14-inch by 17-inch image is usually possible. For the occasional huge dog where this is not possible, then each projection (left lateral, right lateral, VD or DV) should be divided into cranial and caudal portions.

For lateral and VD/DV views of the thorax, the forelimbs should be pulled cranially to remove the brachial muscles from being superimposed on the cranial aspect of the thorax. Failure to do this will cause an artificial increase in radiographic opacity and lead to errors in interpretation of the cranial mediastinum and cranial lung lobes. This is a common mistake. Poor attention to positioning and technique will result in incorrect assessments and potentially unnecessary emotional and financial stress for the animal owner (Fig. 28.2).

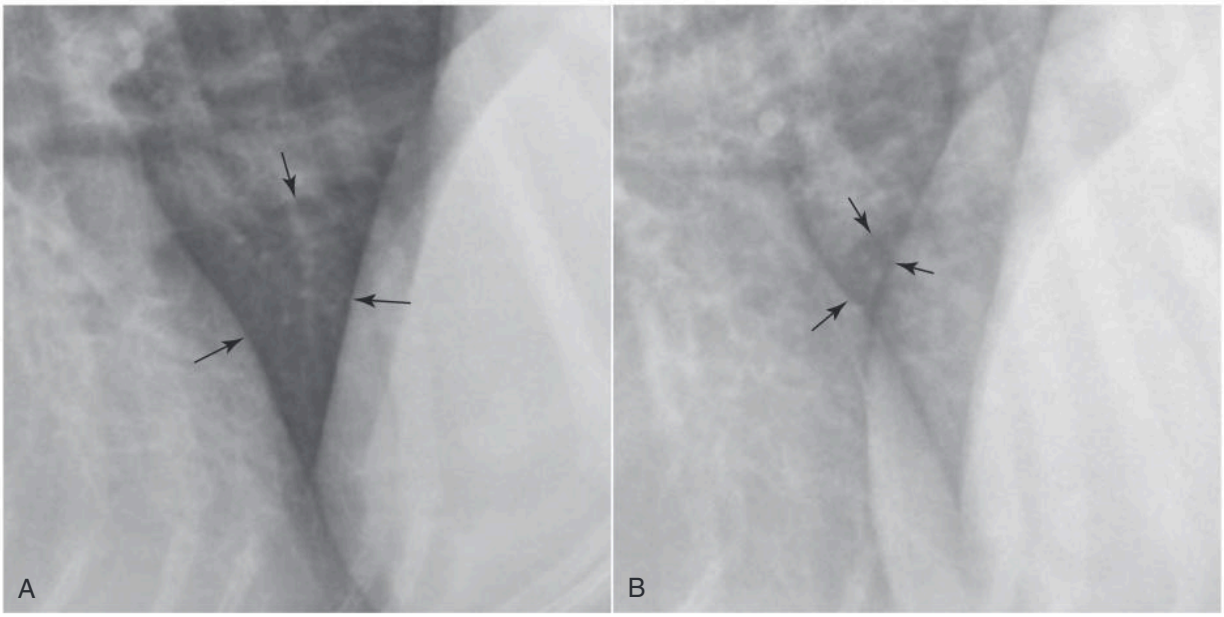


Fig. 28.1 Close-up view of the caudoventral aspect of the thorax in a dog at inspiration **(A)** and expiration **(B).** The size of the triangular region of lung between the caudal vena cava, heart, and diaphragm (*arrows*) can be used as an indicator of the degree of lung inflation that was present when the radiograph was acquired. Note the reduction in size of this region of lung and the overall increased lung opacity, in **B** versus **A**. Poor ventilation is a common cause of overdiagnosis of pulmonary disease.

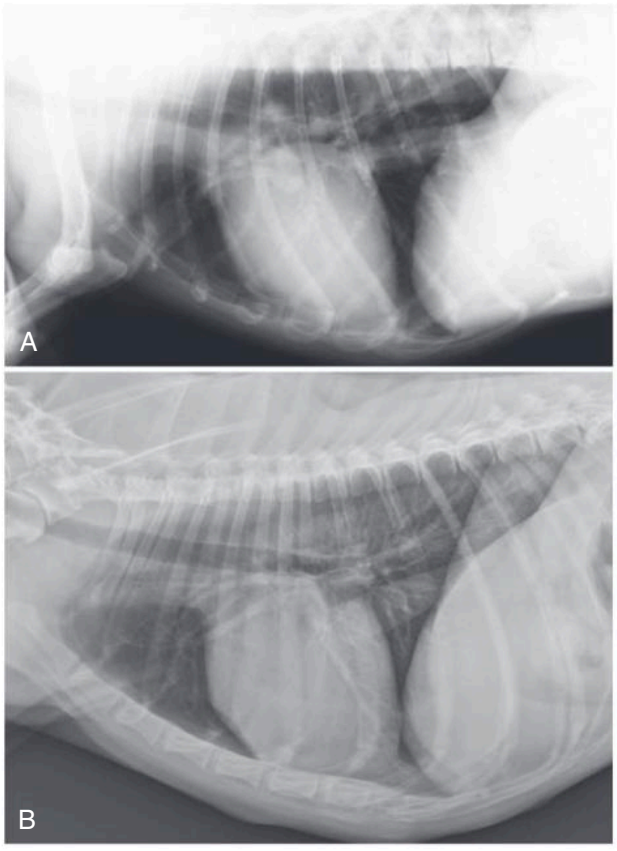


Fig. 28.2 **A,** Initial thoracic radiograph of a dog. A diagnosis of multiple pulmonary nodules was made. There are numerous technical problems with this radiograph. The patient is rotated, the image contrast is too high, and the thoracic limbs are superimposed on the cranial aspect of the thorax. The patient was referred to an oncologist. **B,** Repeat thoracic radiograph where the positioning and technique are excellent. The radiograph is normal. The poor technique used in the initial radiograph resulted in unnecessary financial burden and emotional stress for the owner.

POSITIONING: HORSE

In small foals or miniature horses, it may be possible to acquire lateral thoracic radiographs by restraining the subject on a small-animal x-ray table and using a vertically directed x-ray beam. However, obtaining conventional VD or DV thoracic radiographs in a horse can only be accomplished in the smallest and most compliant patients. If a VD view is able to be acquired, the cardiac silhouette will appear very large due to magnification (Fig. 28.3), and this is often misinterpreted as cardiac enlargement.

Most thoracic radiographs of horses are acquired with the horse standing. Lateral views are therefore acquired with a horizontally directed x-ray beam, and DV or VD views are not obtained. The plate should not be held by hand when radiographing the equine thorax. The light field that corresponds to the primary x-ray beam is visible only on the side of the horse closest to the x-ray tube, meaning that no part of the light field can be seen on the plate. Therefore, aligning the x-ray beam with the plate is impossible when the plate is held by hand. This invariably results in the primary x-ray beam striking the person holding the plate. A wall-mounted plate holder, as described in Chapter 9, or a floor-mounted mobile plate holder should be used for equine thoracic radiography. When using these devices, the x-ray beam can be aligned with the plate before the horse is brought into position next to the plate.

Given the large size, it is not possible to obtain a radiograph of the entire equine thoracic cavity in one image, except in young foals or miniature horses. For lateral radiographs of an adult horse, four images are usually acquired: (1) craniodorsal, (2) caudodorsal, (3) cranioventral, and (4) caudoventral. The approximate location for each of these views is illustrated in Fig. 28.4.

Radiographic magnification is an important consideration when interpreting equine thoracic radiographs. This has already been discussed relative to the appearance of the heart of a foal in a VD radiograph. But, also as a result of the large diameter of the

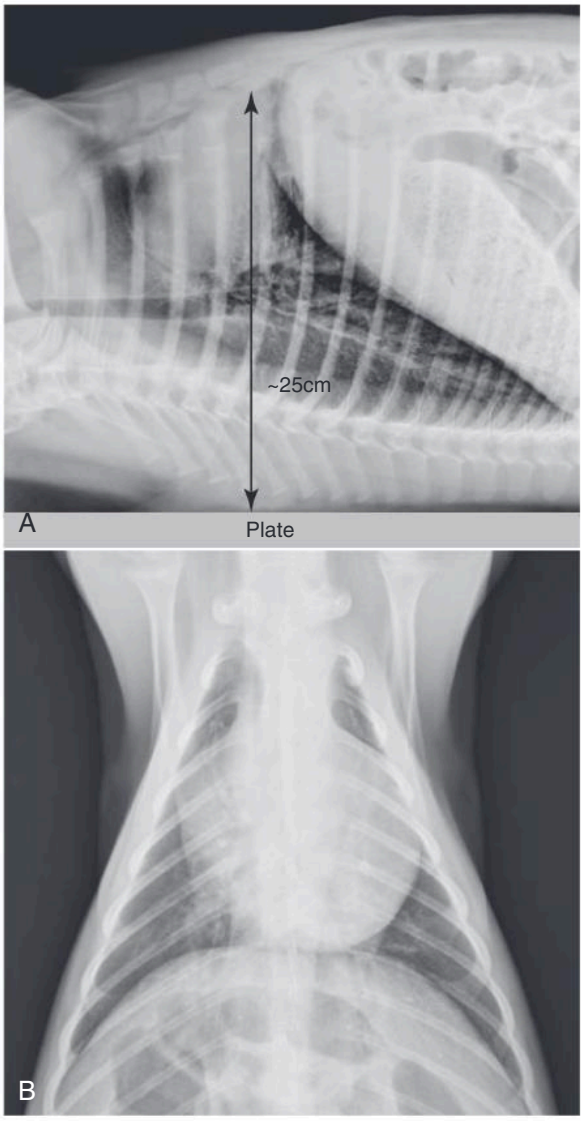


Fig. 28.3 **A,** Illustration of the geometry for obtaining a ventrodorsal (VD) view of the thorax in a foal. Due to the shape of the foal thorax, the cardiac apex may be approximately 25 cm from the plate, resulting in marked magnification of the heart. **B,** VD radiograph of a normal 4-week-old mule; the heart appears large for the reasons described in **A** of this illustration.

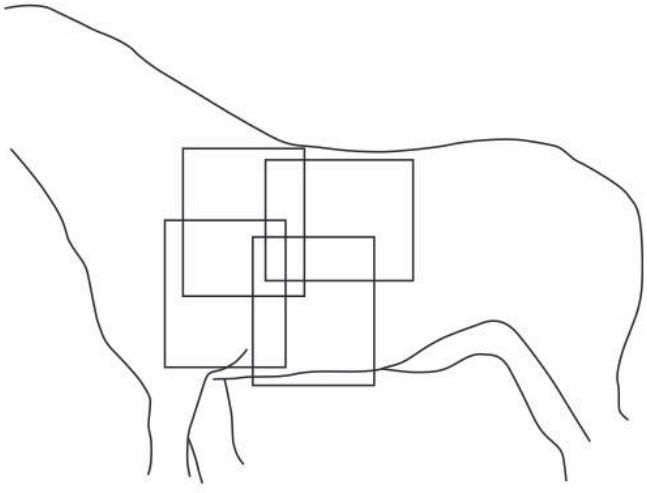


Fig. 28.4 Outline of a horse showing the approximate locations of the plate for a four-view radiographic examination that would include the entire thoracic cavity.

thorax of an adult horse, a lesion in the lung on the side closest to the x-ray tube could be approximately 35 cm from the plate. This would lead to the lesion being magnified by approximately 1.5 times. At this level of magnification, the resultant blurring could result in the lesion being inconspicuous, especially if the lesion is small. To rule out the presence of a small lesion, left-right *and* right-left thoracic radiographs should be obtained.* This means that eight exposures would be necessary for complete radiographic examination of the thorax. Alternatively, the x-ray tube can be moved further from the cassette to reduce geometric magnification, but this will require an increase in the mAs that is proportional to the square of the distance.[1] Whether this approach is feasible depends on the capacity of the x-ray equipment.

WHY ARE BOTH LEFT AND RIGHT LATERAL THORACIC VIEWS NEEDED ROUTINELY IN SMALL ANIMALS?

When an animal is in lateral recumbency, the dependent lung partially collapses due to the heart compressing the lung, and cranial excursion of the dependent side of the diaphragm. This pulmonary collapse, which causes the lung to have increased opacity, occurs rapidly in awake, sedated, and anesthetized dogs and cats after being placed in lateral recumbency. The extent of this lung collapse can be illustrated in a thoracic radiograph made with the dog in lateral recumbency and using a horizontally directed x-ray beam. This view is correctly termed a *right* (or *left*) *recumbent horizontal-beam VD* (Fig. 28.5). The amount of collapse of the down lung is pronounced but is not seen specifically in a conventional lateral radiograph because the aerated nondependent lung is superimposed on the collapsed dependent lung. Recumbency-associated atelectasis also occurs in the dorsocaudal aspect of the caudal lung lobes when the patient is placed in dorsal recumbency for the VD view (Fig. 28.6), but to a lesser extent than in lateral recumbency (compare with Fig. 28.5B).

The reduced aeration of the down, dependent, lung is problematic for two reasons. First, in lateral radiographs, the increased opacity of the partially collapsed dependent lung results in the overall opacity of the lung field being increased over that present in VD or DV radiographs where there is less or no atelectasis, respectively. Overinterpreting this increased opacity in lateral radiographs as lung disease is a common mistake (Fig. 28.7). If an increase in overall lung opacity is suspected from one or both lateral views, it is critical that this be confirmed in the VD view to rule out that the suspected lung disease is artifactual, caused by atelectasis. The use of sedation or anesthesia for the radiographic examination will exacerbate the amount of recumbency-associated atelectasis that is present. If thoracic radiographs are made of an anesthetized patient, positive pressure ventilation helps to reduce the amount of atelectasis that occurs.

Second, the increased opacity of the collapsed dependent lung will silhouette with any soft tissue lesion in that lung. This renders the lesion inconspicuous in the radiograph (Figs. 28.8–28.10).[2,3] If only one lateral view is acquired and there is a lesion that is not visible in the VD view, it could be missed depending on which lateral view is acquired. Clearly, three-view thoracic radiographic examinations are needed to prevent significant lesions from being missed.[3]

*For an example of how a lesion in a large patient can be missed due to magnification please see Fig. 38.5. This example is in the abdomen but the same principle applies to the thorax.

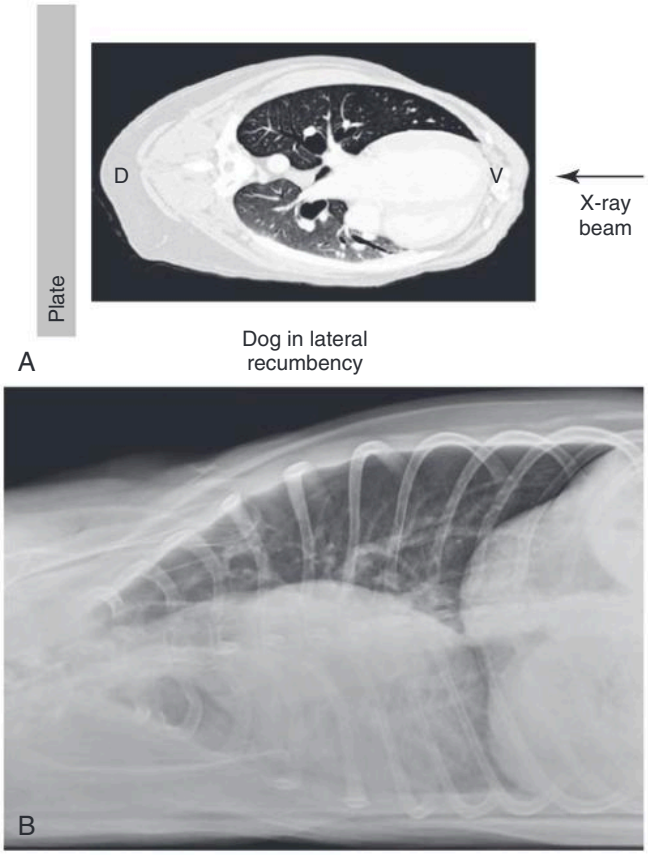


Fig. 28.5 **A,** Method of acquiring a horizontal-beam ventrodorsal (VD) radiograph of the thorax. The transverse computed tomography (CT) image of the thorax represents the dog being radiographed. This dog is in right recumbency. The x-ray beam is directed onto the ventral surface and the plate positioned dorsally. **B,** Radiograph resulting from the positioning illustrated in part **A**. This radiograph would be termed a right recumbent horizontal-beam VD view. Note the marked collapse of the dependent right lung. The heart is shifted into the dependent right hemithorax and is compressing the lung. The diaphragm is also displaced cranially, also compressing the lung. *D,* Dorsal; *V,* ventral.

SPECIFIC FEATURES OF CANINE AND FELINE THORACIC RADIOGRAPHS

Pulmonary Vessels

The pulmonary artery and vein in the right cranial lobe are used commonly as a basis for assessing the pulmonary circulation.[4] This is done by comparing the respective size of these vessels, which requires that other structures are not superimposed. These specific pulmonary vessels are isolated, and more conspicuous, in a left lateral than in a right lateral radiograph (Fig. 28.11). In right recumbency the right cranial lobe vessels are displaced dorsally and become superimposed on the left-sided vessels, whereas in left recumbency the left- and right-sided vessels are not superimposed.

The left cranial lobe pulmonary vessels cannot usually be assessed or compared accurately in either the left or right lateral view, because they are located more dorsally in the thorax and usually superimposed on other vessels or the thicker dorsal portion of the mediastinum.

Pulmonary arteries and veins can also be compared in the caudal lung lobes. This is best accomplished in a DV view. The caudal lobe pulmonary vessels are more conspicuous in DV compared to VD radiographs for two main reasons: (1) a perpendicular orientation with the primary x-ray beam and (2) less adjacent pulmonary atelectasis (Figs. 28.12 and 28.13).

Diaphragm

The diaphragm consists of a left crus and a right crus (collectively the crura) dorsally and a dome ventrally. The diaphragmatic hiatus for the caudal vena cava is located slightly to the right of midline and passes through the right diaphragmatic crus. In the left lateral view, the two dorsal crura of the diaphragm diverge from each other, whereas in the right lateral view they are more parallel (Fig. 28.14). In the right lateral view, the dependent right crus will be cranial to the left crus because of pressure from abdominal contents, and therefore the caudal vena cava will silhouette, or merge, with the more cranial right crus. In the left lateral view, the left crus will be cranial to the right crus, and the caudal vena cava will be superimposed on the left crus before silhouetting, or merging, with the more caudally located right crus that contains the caval hiatus (see Fig. 28.14). Therefore, the appearance of the junction of the caudal vena cava with the diaphragm can be used as a way to distinguish a left lateral from a right lateral radiograph if an external marking system has not been used. However, this principle is not 100% accurate, because occasionally, the left crus will be cranial to the right crus in the right lateral view, and vice versa.

Cardiac Silhouette

There is only a minor difference in the appearance of the cardiac silhouette in left vs. right lateral views. In general, the cardiac silhouette will appear slightly rounder and the apex may be slightly elevated from the sternum in the left lateral view compared with the right lateral view (Fig. 28.15). Comparatively, there is a major difference in the appearance of the cardiac silhouette in VD versus DV radiographs. In sternal recumbency for the DV radiograph, the ventral aspect of the diaphragm is displaced cranially where it contacts the heart and displaces it, typically to the left. The heart is also more upright in the thoracic cavity when the patient is in sternal recumbency, making it appear rounder (Fig. 28.16). The rounder appearance and displacement to the left that occur normally in DV radiographs are commonly misinterpreted as cardiomegaly. The extent of leftward cardiac displacement in DV radiographs is more pronounced in large dogs and will not be as obvious in small dogs or cats.[5–7]

Accessory Lung Lobe

The cranial excursion of the diaphragm that occurs in sternal recumbency also impinges on the territory of the accessory lung lobe. This diminishes the ability to evaluate the accessory lobe and caudal mediastinum, and significant disease in this area can be missed in DV radiographs because of this impingement (see Fig. 28.16). As with cardiac displacement, the amount of impingement on the accessory lobe and caudal mediastinal regions in DV radiographs caused by cranial excursion of the diaphragm is more noticeable in large dogs and is not as significant in small dogs or cats.

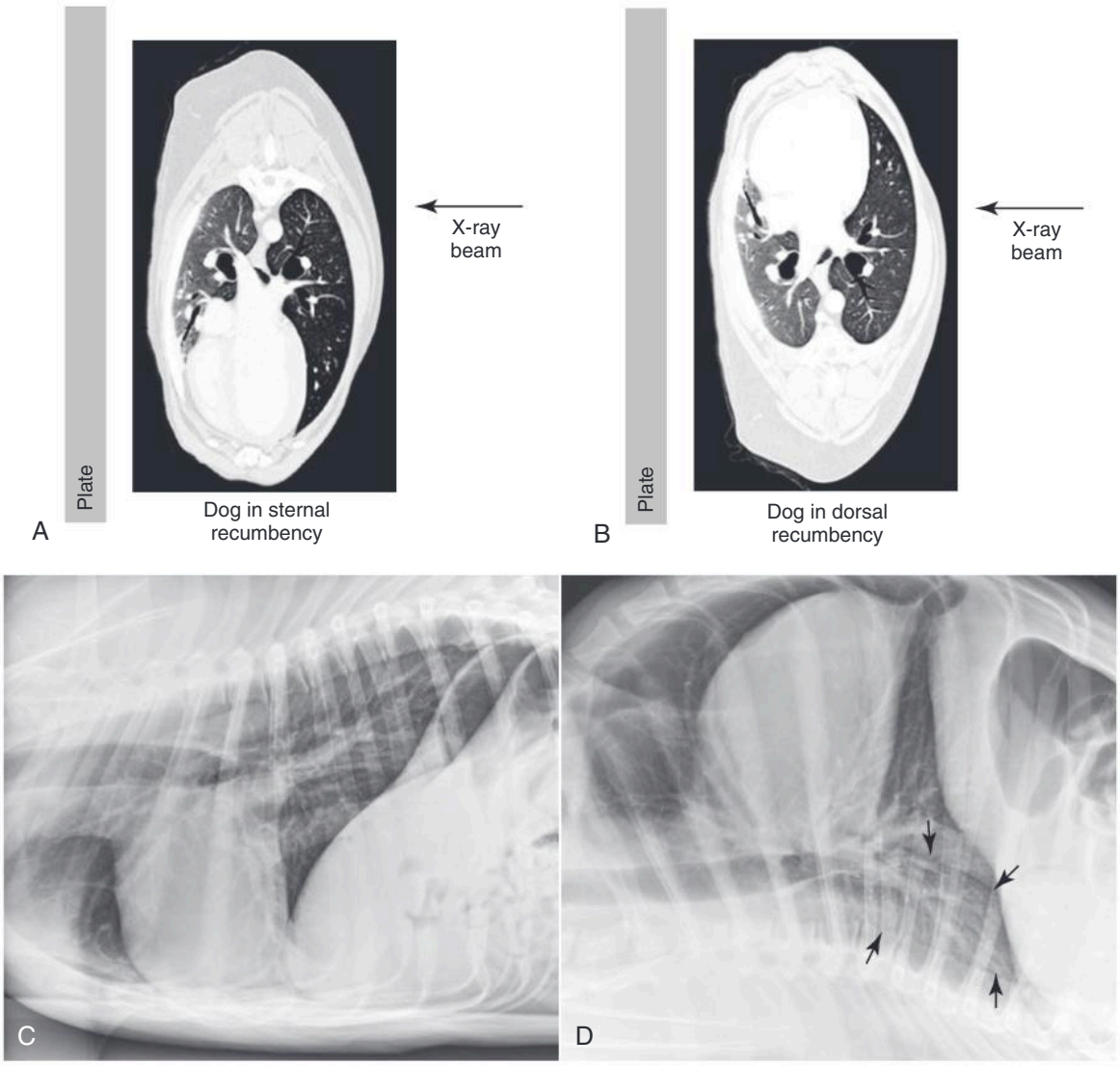


Fig. 28.6 Horizontal-beam lateral thoracic radiographs. **A,** Geometry for acquiring a horizontal-beam lateral thoracic radiograph with a dog in sternal recumbency. This is the body position used for a conventional dorsoventral (DV) radiograph, but the plate would be beneath the dog, with the x-ray beam striking the dorsal surface of the dog. **B,** Geometry for acquiring a horizontal-beam lateral thoracic radiograph with a dog in dorsal recumbency. This is the body position used for a conventional ventrodorsal (VD) radiograph, but the plate would be beneath the dog with the x-ray beam striking the ventral surface of the dog. **C,** Radiograph made with geometry illustrated in **A** with the dog in sternal recumbency. Note the absence of recumbency-associated atelectasis in the dependent ventral aspect of the lung. **D,** Radiograph made with geometry illustrated in **B** with the dog in dorsal recumbency. There is a small amount of atelectasis of the dependent caudal-dorsal aspect of the lung (*black arrows*) but not to the extent seen in the dependent lung in a dog in lateral recumbency (compare with Fig. 28.5B). In **D,** note that the caudal lobe pulmonary vessels are surrounded by atelectasis. This will cause silhouetting and render them more difficult to identify in the VD view compared with the DV view.

Ancillary Factors

The body habitus and presence of cutaneous lesions are ancillary factors that have a significant effect on the appearance of canine and feline thoracic radiographs.

Body Habitus

The volume of extrathoracic soft tissue will influence the overall radiographic opacity of the lung (Fig. 28.17), and can result in overdiagnosis of lung disease. The opacity created by excessive tissue in the body wall will be especially problematic with film-screen technology, because the contrast resolution of the film-screen system is not capable of compensating for the opacity created by this tissue (Fig. 28.18).

Intrathoracic fat accumulation can also be problematic. One common example is an accumulation of mediastinal fat being

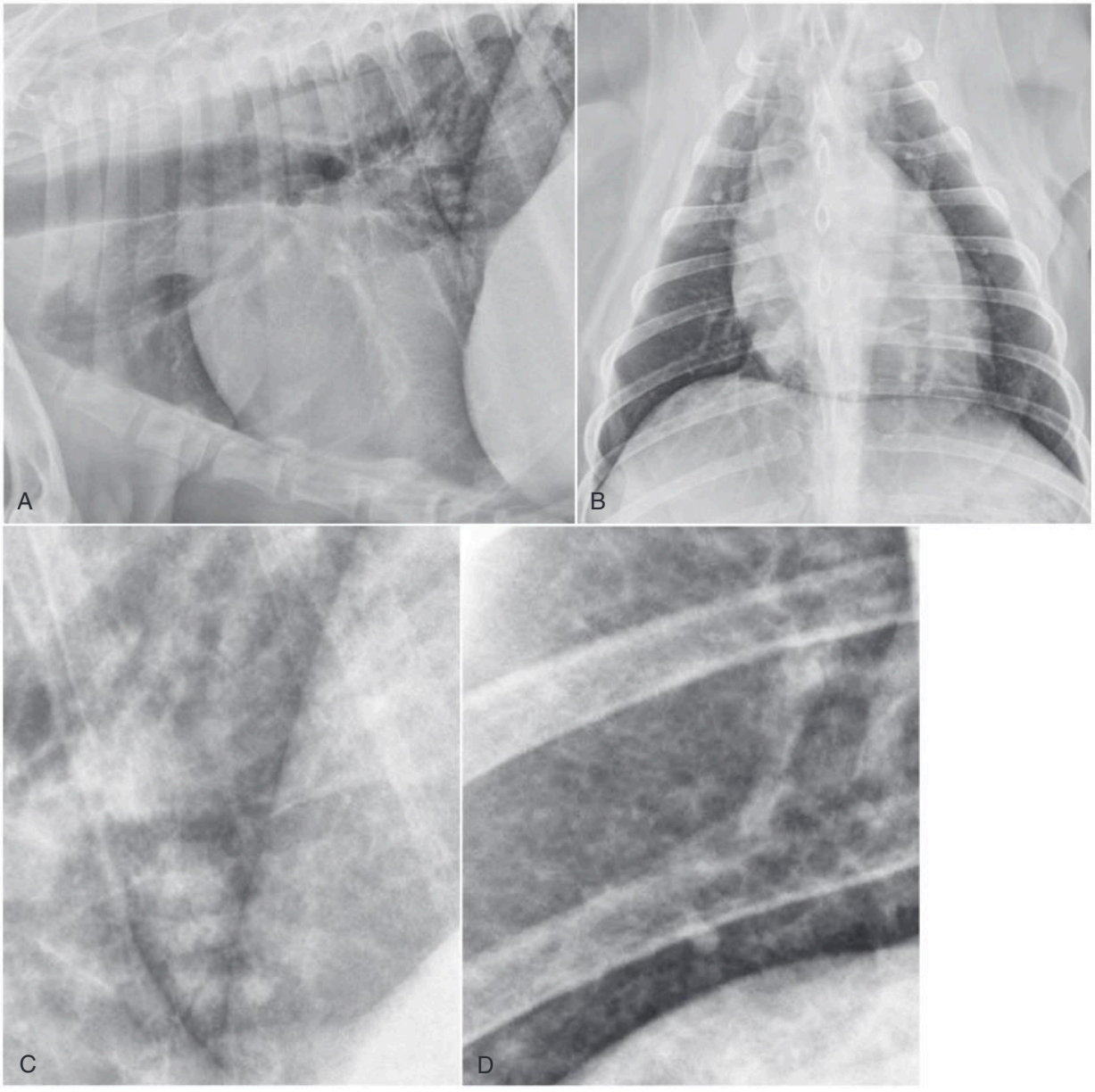


Fig. 28.7 Left lateral **(A)** and dorsoventral (DV) **(B)** thoracic radiographs of a dog, and close-up views of the dorsocaudal lung field from the lateral radiograph **(C)** and the right-caudal lung field from the DV radiograph **(D)**. The increased atelectasis that occurs in lateral views results in an overall increased opacity to the lungs **(A and C).** In the DV projection, where lungs are better aerated, they are more radiolucent **(B and D)**, confirming that the increased pulmonary opacity seen in the lateral view was an artifact of poor ventilation. The increased lung opacity commonly encountered in lateral views is often misinterpreted as lung disease.

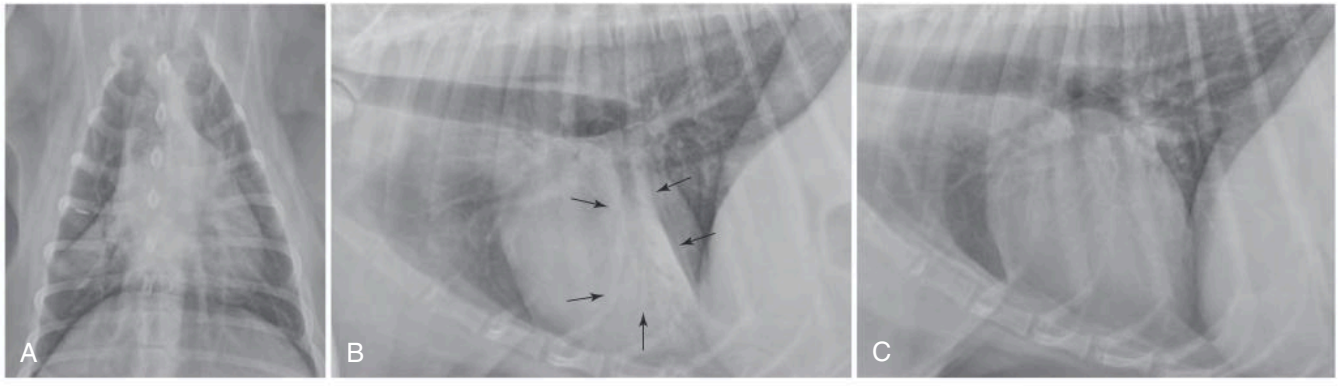


Fig. 28.8 **A,** Dorsoventral (DV) radiograph of a dog with pneumonia in the right middle lung lobe. **B,** Left lateral radiograph. Superimposed on the cardiac silhouette are multiple air bronchograms created by the alveolar nature of the disease in the right middle lung lobe (*black arrows*). The lung lesion is highly conspicuous in this view because the pneumonia is in the upper, nondependent, lung surrounded by aerated lung to provide contrast. **C,** Right lateral radiograph. The pneumonia is in the down, dependent, lung, which is atelectatic. The increased opacity of the atelectatic lung silhouettes with the pneumonia, and it is not visible.

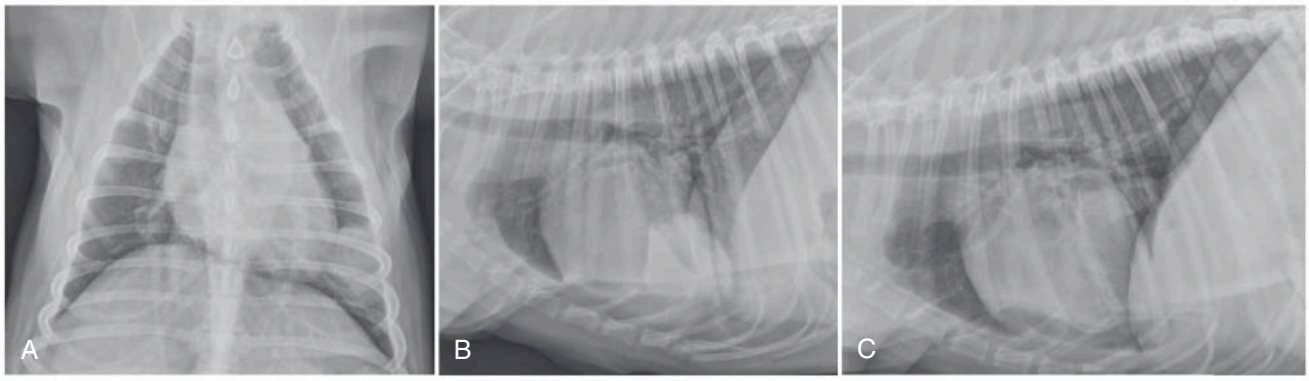


Fig. 28.9 **A,** Dorsoventral (DV) radiograph of a dog with a large mass in the left caudal lung lobe. **B,** Right lateral radiograph of the same dog. The mass is in the up, nondependent, lung and surrounded by aerated lung, making is highly visible. **C**, Left lateral radiograph of the same dog. The mass is now in the collapsed down, dependent, lung and is not visible because of silhouetting by the surrounding atelectatic lung.

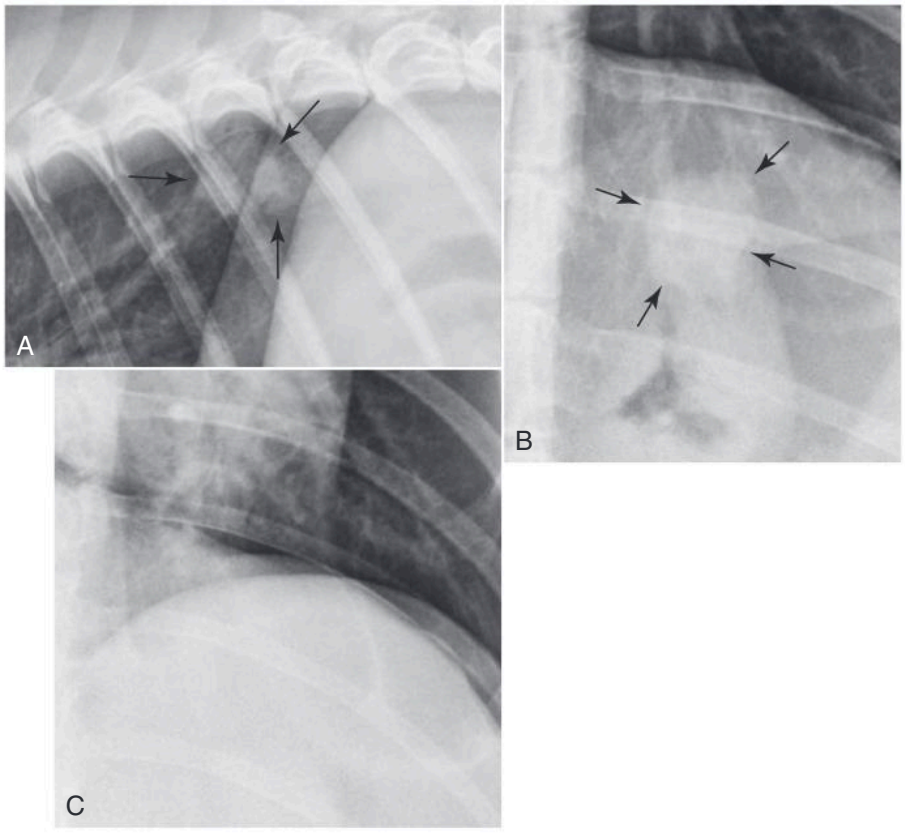


Fig. 28.10 Lateral radiograph of a dog with an ill-defined nodule in the dorsocaudal aspect of the lung (**A,** *black arrows*). This nodule is clearly seen in a dorsoventral (DV) view (**B,** *black arrows*), because it is surrounded by aerated lung. The nodule is not visible in the ventrodorsal (VD) view **(C)**, because it is surrounded by atelectatic lung in the dependent (dorsal) aspect of the thorax.

misinterpreted as a mediastinal mass in VD or DV radiographs (Fig. 28.19). This is particularly common in brachycephalic dogs. In contrast to a large mediastinal mass, mediastinal fat does not lead to tracheal deviation or lateral rounding of the mediastinal contour. Mediastinal fat can also give the false impression of cardiac enlargement, particularly right-sided cardiomegaly. Often, in this instance, the fat is not visible per se, and the distinction between cardiomegaly and adjacent fat may have to be made using echocardiography or with computed tomography (CT) (Fig. 28.20).

Cutaneous Lesions

Normal thoracic wall structures, or lesions superimposed on the thorax, can appear as a pulmonary lesion. Common

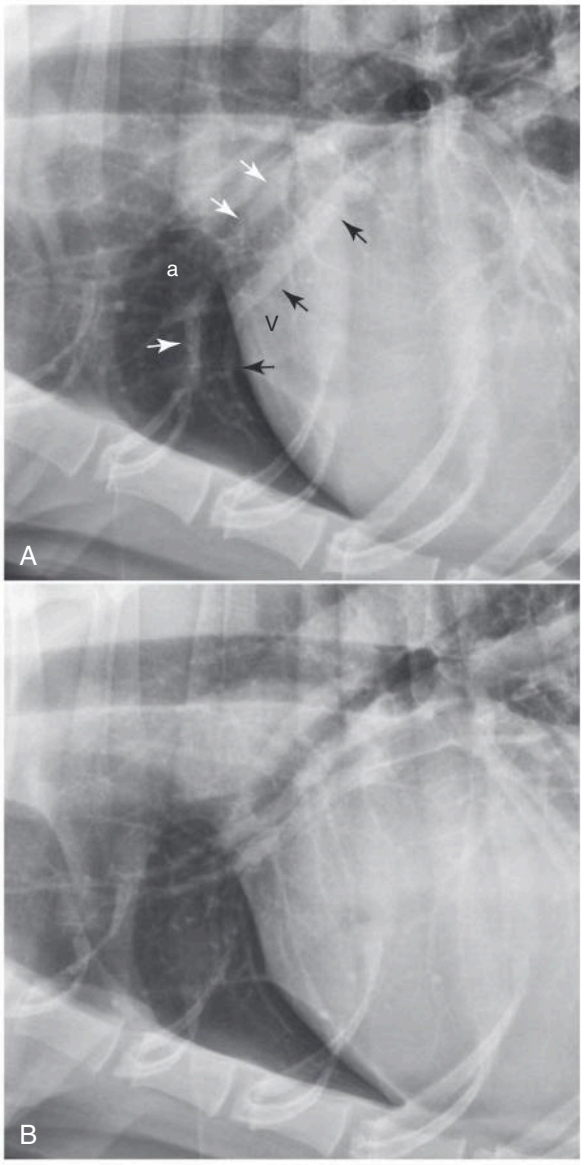


Fig. 28.11 Left **(A)** and right lateral **(B)** radiographs of the cranioventral aspect of the thorax of a dog. The right cranial lobe pulmonary artery (*a, white arrows*) and vein (*V, black arrows*) can be distinguished clearly in the left lateral view. In the right lateral view, these two vessels are superimposed with each other and with the vessels from the left cranial lobe and cannot be identified individually. In **A,** the pulmonary artery and vein in the left cranial lobe are dorsal to the right cranial lobe vessels.

examples include summation opacities created by nipples (Fig. 28.21), cutaneous lesions such as a pedunculated tumor or engorged tick (Fig. 28.22), and costochondral junctions (Fig. 28.23). All of these can be misinterpreted as a pulmonary nodule. The basis of cutaneous lesions creating such a conspicuous opacity was discussed in Chapter 6.

INTERPRETATION PARADIGM

Like in all body systems, an organized approach to radiographic interpretation of the thorax is needed. This begins with an overview of technique, according the following questions, followed by evaluation for abnormalities.

- Are the radiographic views adequate, and are all of the views that are needed present?
- Is the positioning adequate?
- Are the images overexposed or underexposed?
- Were the images acquired using an antiscatter grid? Should an antiscatter grid have been used?
- Was the patient sedated or anesthetized for the radiographic examination, and did this affect the appearance of the images?
- Were the images obtained at peak inspiration or during expiration, and did this affect pulmonary opacity?
- What is the breed and body habitus of the patient, and how is this going to affect the appearance of the images?
- Were the images acquired with a vertically directed x-ray beam with the cassette in an x-ray table, or was a horizontally directed x-ray beam used with the cassette in a mobile or a wall-mounted cassette holder?
- Are there morphologic aspects of the patient that are going to influence the appearance of the radiographs? These include things like a missing limb or cutaneous nodules or masses that will be superimposed on the thorax.

After these variables have been considered, the images can be scrutinized for abnormalities. The roentgen sign and DAMNITV (degenerative, anomalous, metabolic, neoplastic, infectious [inflammatory, immune], traumatic, vascular) methods described in Chapter 6 should be used. Inexperienced interpreters often begin by looking at the lungs, because a suspicion of pulmonary disease is a common reason that thoracic radiographs are acquired. This is a mistake and will lead to other lesions being overlooked. The search pattern is also important. A random search pattern may be appropriate for experienced radiologists, but beginning interpreters should develop an organized approach to searching radiographs.[8] Having a mental checklist to guide the order of interpretation will reduce the number of errors (Box 28.1).

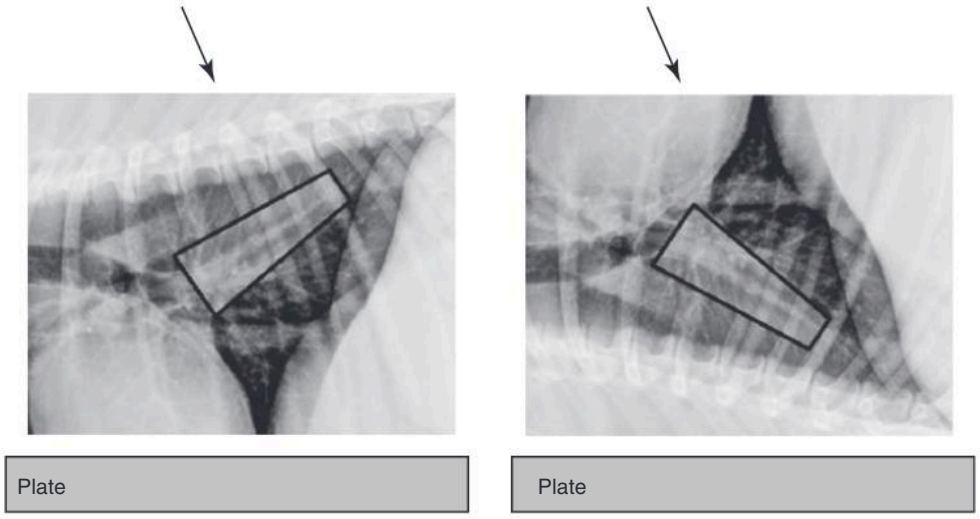


Fig. 28.12 Effect of dorsal versus sternal recumbency on the orientation of the caudal lobe pulmonary vessels with respect to the primary x-ray beam. As the center of the primary x-ray beam is approximately at the level of the cardiac silhouette, the beam (*arrows*) will be diverging at the level of the caudal lobe pulmonary vessels. In the *left panel*, the dog is positioned for a dorsoventral (DV) radiograph. In this view the caudal lobe vessels, shown *outlined,* are nearly perpendicular to the x-ray beam and will not be distorted. In the *right panel*, the dog is in position for a ventrodorsal (VD) radiograph. In this view, the caudal lobe vessels, shown *outlined*, are at an angle with respect to the primary x-ray beam and will be distorted. There is also more surrounding atelectasis in the VD view, which further reduces visibility of the caudal lobe vessels.

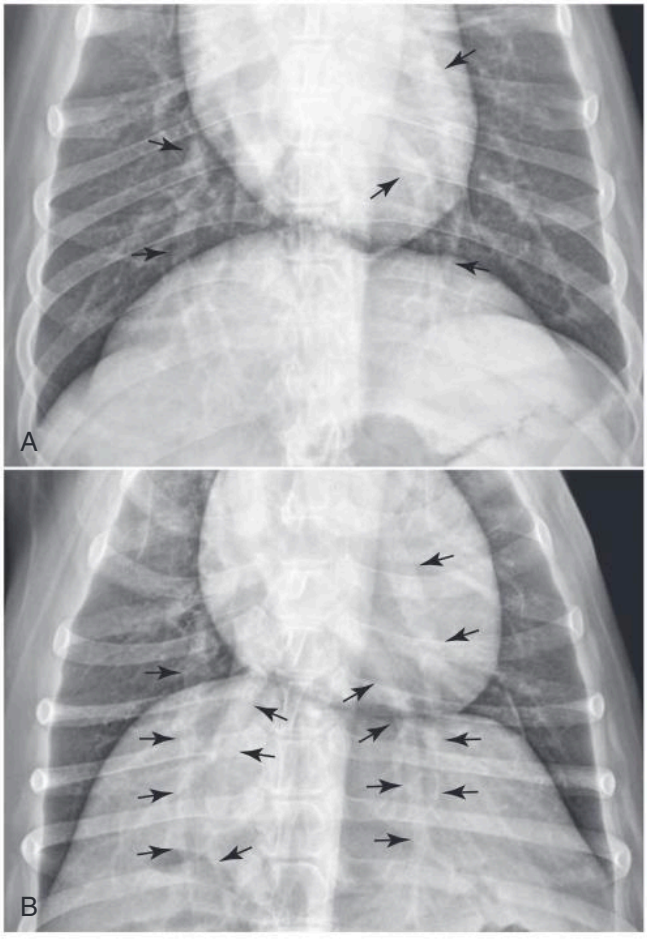


Fig. 28.13 Ventrodorsal (VD) **(A)** and dorsoventral (DV) **(B)** radiographs of the caudal aspect of the thorax of a dog. The caudal lobe pulmonary vessels (*black arrows*) are more conspicuous in the DV view than in the VD view for the reasons mentioned in the text and illustrated in Fig. 28.12.

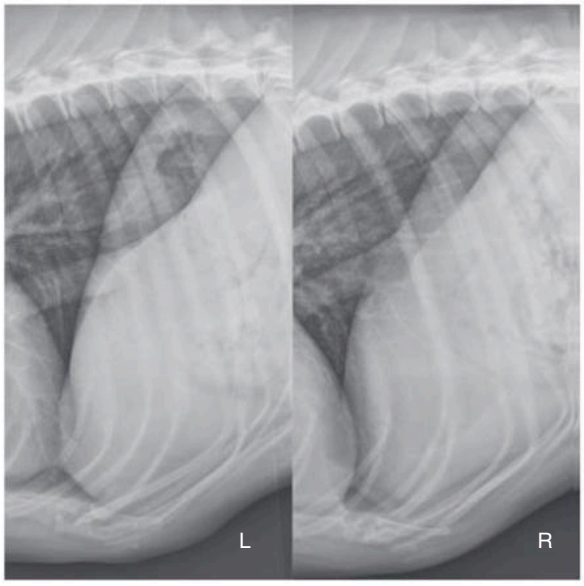


Fig. 28.14 Left (L) and right (R) lateral radiographs of the caudal thorax of a dog. In the left lateral view, the dorsally located diaphragmatic crura diverge more than in the right lateral view. Also, in the left lateral view, the left crus is more cranial, and the caudal vena cava is superimposed on it before joining the right crus that contains the caval hiatus. In the right lateral view, the right crus of the diaphragm that contains the caval hiatus is more cranial, and the caudal vena cava joins this more cranial crus.

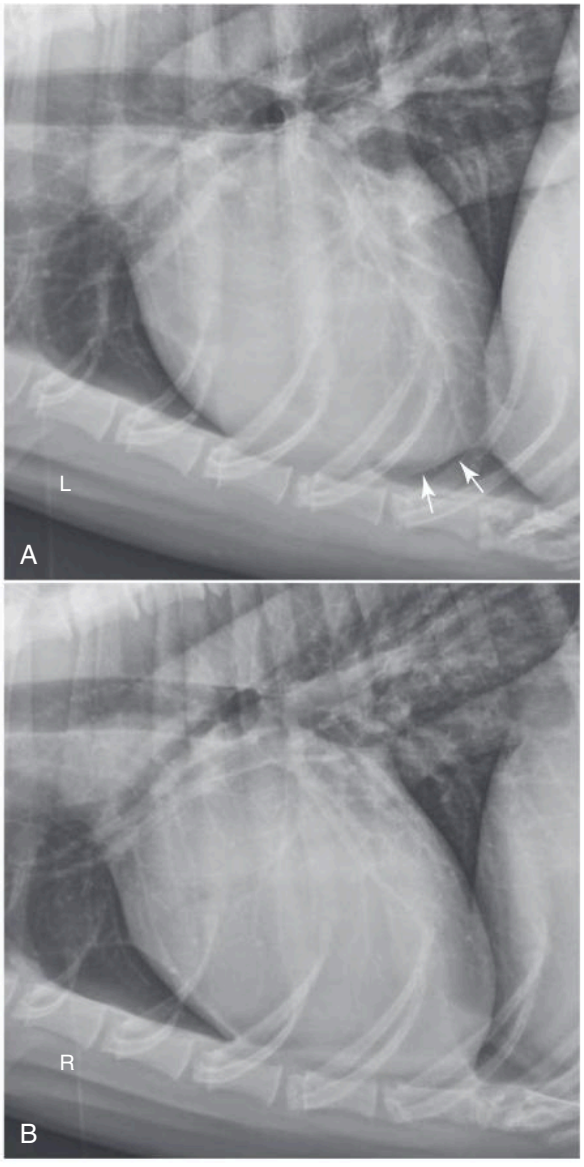


Fig. 28.15 Left lateral **(A)** and right lateral **(B)** thoracic radiographs of the cardiac silhouette in a dog. In the left lateral view, the cardiac silhouette will usually appear slightly rounder, and there will be some slight separation of the cardiac apex from the sternum (*white arrows* in **A**).



Fig. 28.16 Ventrodorsal (VD) **(A)** and dorsoventral (DV) **(B)** thoracic radiographs. In the DV radiograph, the diaphragm is displaced cranially where it contacts the heart and pushes it into the left hemithorax. The cardiac silhouette is also smaller and rounder, because it is more upright in the thoracic cavity. In a DV view, the cranial excursion of the diaphragm also impinges on the territory of the accessory lung lobe and interferes with the evaluation of that region.

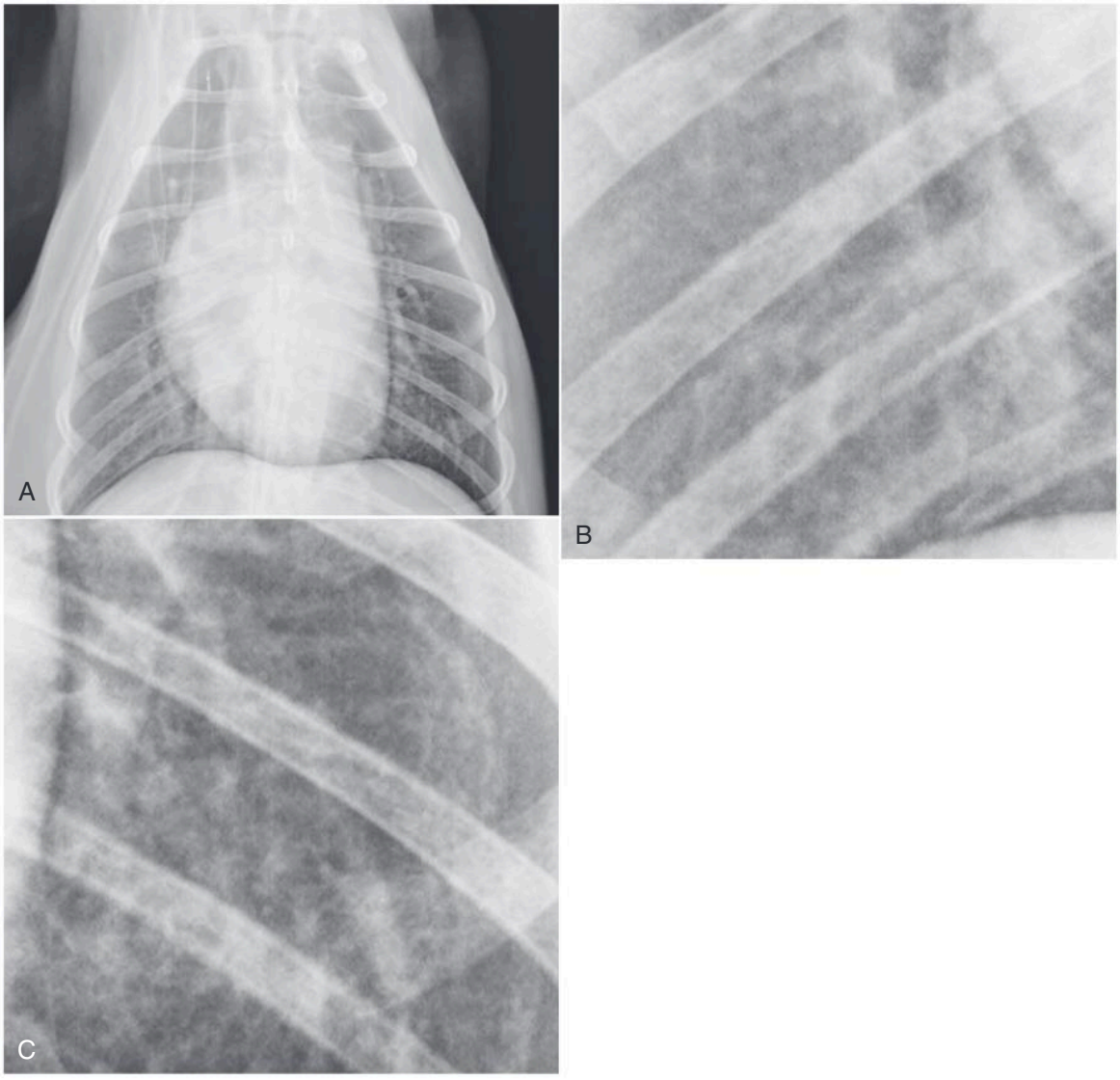


Fig. 28.17 **A,** Ventrodorsal (VD) thoracic radiograph of a dog having undergone a left forelimb amputation. The soft tissues of the left thoracic wall are thinner due to the missing limb and secondary disuse atrophy. This leads to a difference in opacity of the left vs. right hemithorax that can be misinterpreted as a difference in lung opacity. In close-up views from the right **(B)** and left **(C)** caudal lobes, the lung opacity appears increased on the right side. This illustrates how the amount of thoracic wall soft tissue can influence the radiographic opacity of the lung. The right lung could easily be misdiagnosed as having an increase in interstitial opacity.

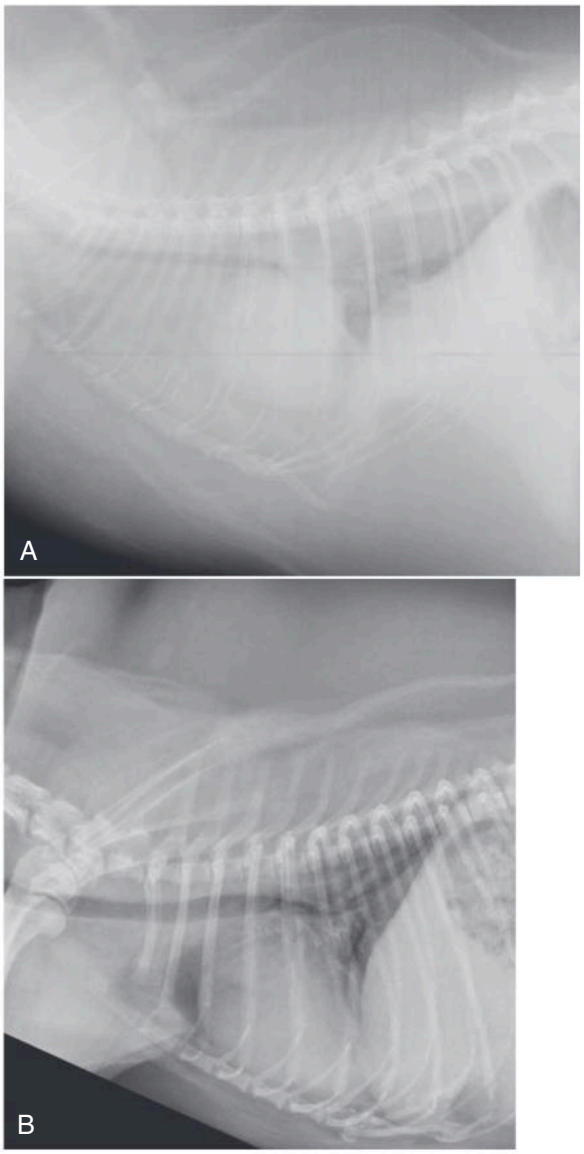


Fig. 28.18 Lateral thoracic radiographs of a morbidly obese cat made using a film-screen system **(A)** and of a morbidly obese dog made using a direct digital system **(B)**. The contrast resolution of the film-screen system cannot accommodate for the huge volume of fat, and the lungs cannot be assessed. With the digital system the lungs remain relatively radiolucent, but there will still be some background opacity created by the fat that could be misinterpreted as lung disease.

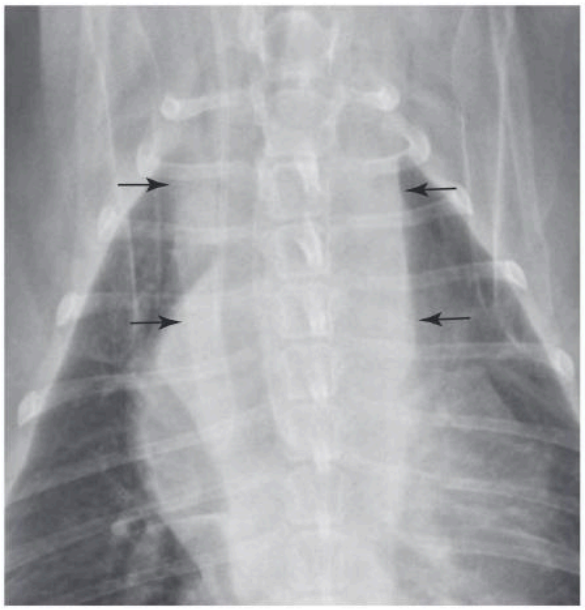


Fig. 28.19 Ventrodorsal (VD) radiograph of an obese dog. Fat deposition causes widening of the cranial mediastinum (*black arrows*), which could be misinterpreted as a mass. Notice, however, that the outlines of the cranial mediastinum are not rounded. There was no evidence of a cranial mediastinal mass in the lateral projections.

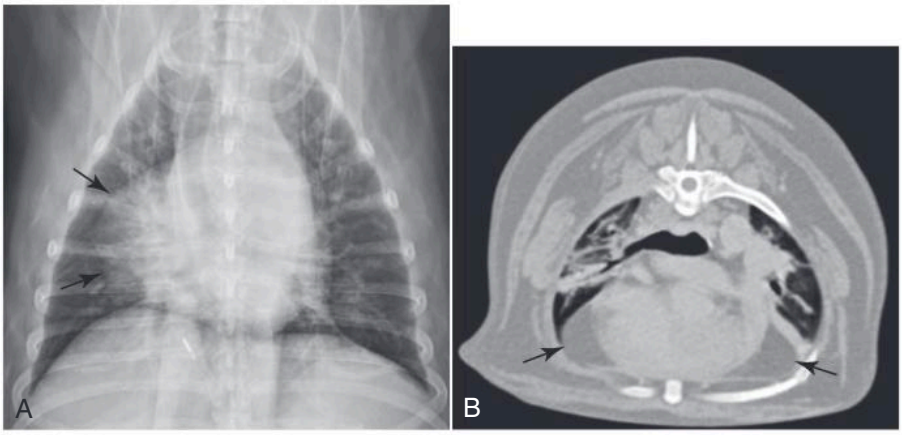


Fig. 28.20 **A,** Ventrodorsal (VD) thoracic radiograph. The cardiac silhouette is enlarged, especially on the right side (*black arrows*). **B,** Computed tomography (CT) image of the same patient. There is a large volume of mediastinal fat (*black arrows*) that is the cause of the enlargement of the cardiac silhouette in the radiograph.

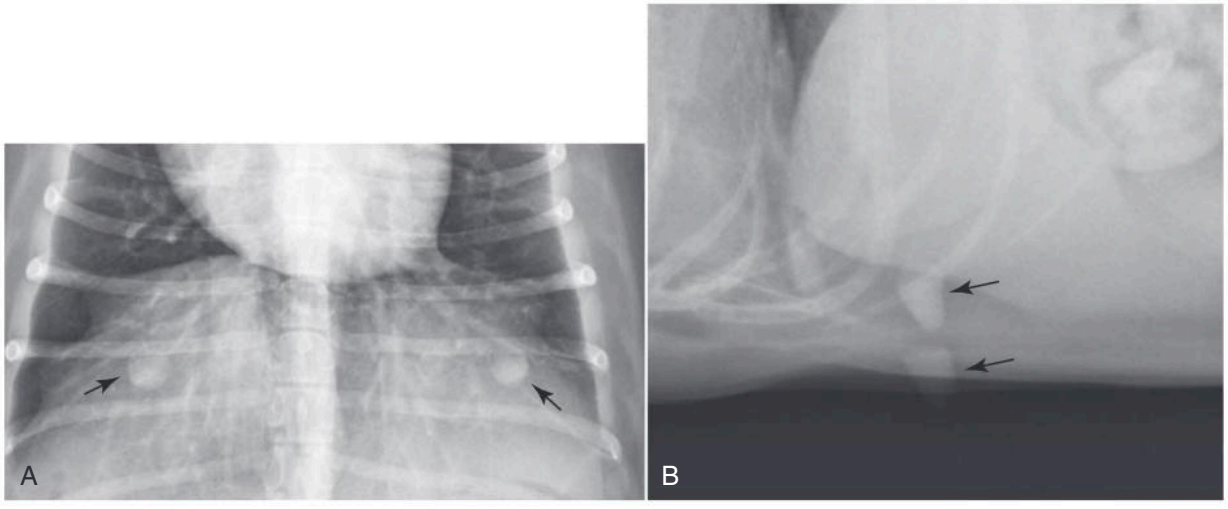


Fig. 28.21 **A,** Ventrodorsal (VD) radiograph of the caudal aspect of the thorax of a dog with two opacities that appear as pulmonary nodules (*black arrows*). These are caused by enlarged nipples on the cranial abdominal mammary glands. The bilaterally symmetric nature of these opacities would be unusual for pulmonary nodules, and enlarged nipples can be seen in the lateral view (*black arrows* in **B**). If the enlarged nipple is unilateral and cannot be seen in the lateral view, the body wall should be examined clinically. If necessary, a radiopaque marker can be applied to the nipples on the patient and the radiograph repeated to determine if the questionable lung opacity is caused by a nipple or by a pulmonary nodule.

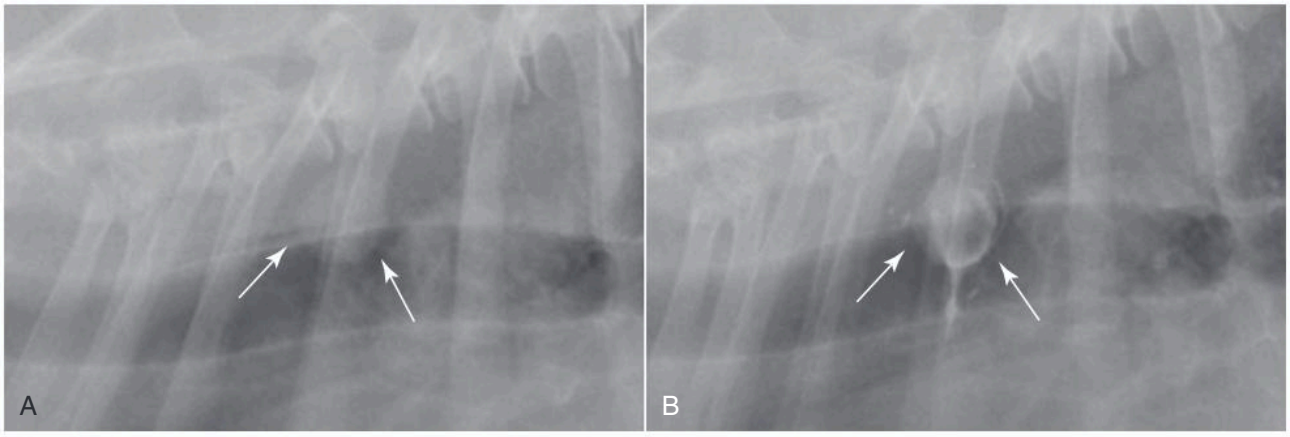


Fig. 28.22 **A,** Close-up from a right lateral thoracic radiograph of a dog where there is a nodular opacity that has the appearance of a pulmonary nodule (*white arrows*). A cutaneous nodule was discovered in a corresponding area on the thoracic wall and it was marked with a small amount of barium and the radiograph repeated. **B,** The barium is confined to the nodular opacity (*white arrows*), confirming that it is not a pulmonary nodule but a superimposition opacity from the cutaneous nodule.

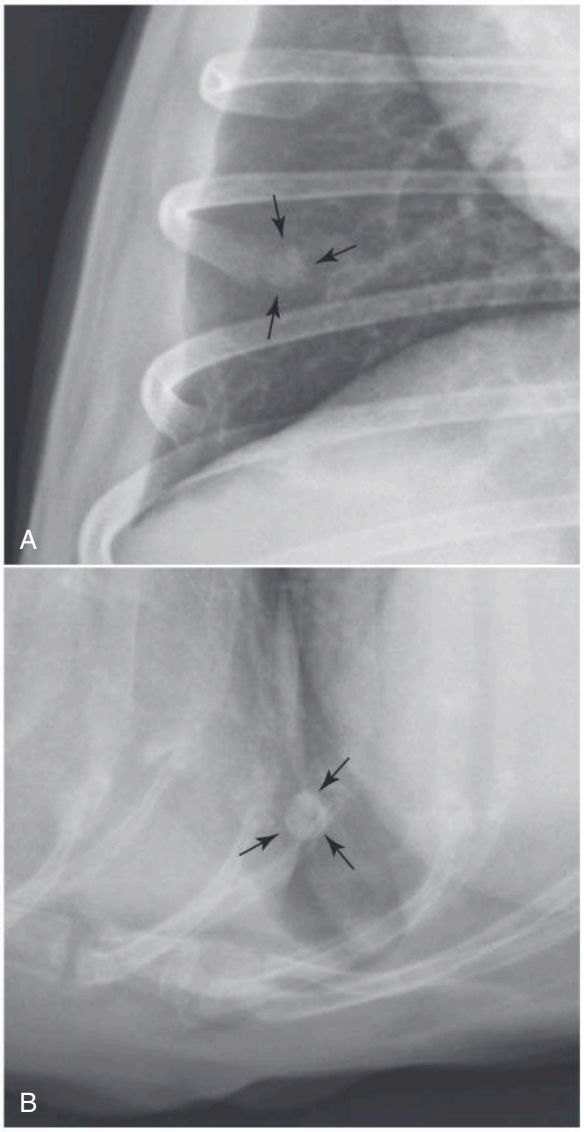


Fig. 28.23 Lateral **(A)** and ventrodorsal (VD) **(B)** radiographs of a dog with a nodular opacity (*black arrows*) that could be misinterpreted as a pulmonary nodule. In each radiograph, the suspicious opacity is located at the end of a rib and is caused by remodeling of the costochondral junction. This is a common change, especially in older dogs.

Box • **28.1**

Checklist for Interpretation of Thoracic Radiographs

Heart
Major vessels
Pulmonary vasculature
Lung parenchyma
Pleural space
Mediastinum
Esophagus
Diaphragm
Trachea
Thoracic wall and bones
Visible portion of neck
Cranial abdomen

REFERENCES

1. Feeney D, Gordon B, Johnston G, et al. A 200 centimeter focal spot-film distance (FFD) technique for equine thoracic radiography. *Vet Radiol Ultrasound.* 1982;23(13).
2. Spencer C, Ackerman N, Burt J. The canine lateral thoracic radiograph. *Vet Radiol Ultrasound.* 1981;22:262.
3. Ober CP, Barber D. Comparison of two- vs. three-view thoracic radiographic studies on conspicuity of structured interstitial patterns in dogs. *Vet Radiol Ultrasound.* 2006;47(6):542–545.
4. Thrall D, Losonsky J. A method for evaluating canine pulmonary circulatory dynamics from survey radiographs. *J Am Anim Hosp Assoc.* 1976;12:457.
5. Brinkman EL, Biller D, Armbrust L. The clinical usefulness of the ventrodorsal versus dorsoventral thoracic radiograph in dogs. *J Am Anim Hosp Assoc.* 2006;42(6):440–449.
6. Carlisle C, Thrall D. A comparison of normal feline thoracic radiographs made in dorsal versus ventral recumbency. *Vet Radiol Ultrasound.* 1982;23(3).
7. Ruehl W, Thrall D. The effect of dorsal versus ventral recumbency on the radiographic appearance of the canine thorax. *Vet Radiol Ultrasound.* 1981;22(10).
8. Halvorsen JG, Swanson D. Interpreting office radiographs. A guide to systematic evaluation. *J Fam Pract.* 1990;31(6):602–610.

ELECTRONIC RESOURCES

Additional information related to the content in Chapter 28 can be found online at eBooks.Health.Elsevier.com

- Chapter Quiz

CHAPTER 29

Canine and Feline Larynx and Trachea

Randi Drees

ANATOMIC CONSIDERATIONS: NORMAL ANATOMY

The upper respiratory system comprises the air-filled pharynx, the larynx, and trachea. Typically, the pharynx has the widest lumen, followed by the larynx and the trachea, which is slightly smaller in diameter.

Pharynx: The soft palate divides the pharynx into the dorsally located nasopharynx and ventrally located oropharynx. The caudally adjacent larger laryngopharynx is divided from the nasopharynx by the palatopharyngeal arches, which form the soft tissue line extending caudodorsally from the soft palate, and from the oropharynx by the epiglottis (Fig. 29.1).[1] The piriform recesses are caudodorsally oriented extensions of the laryngopharynx.

Larynx: The epiglottis is usually surrounded by gas and extends to just overlap the tip of the soft palate dorsally or ventrally.[2] In larger dogs, the cuneiform process, which is the rostral portion of the arytenoid cartilage, is occasionally visible. The other laryngeal cartilages are represented by an indistinct soft tissue opacity superimposed on the laryngeal lumen. Gas-filled ventricular saccules are seen occasionally.

In older dogs, and even younger large-breed dogs, laryngeal cartilages may become mineralized, the cricoid cartilage often being the most evident (Fig. 29.2).[3] In brachycephalic dog breeds, the larynx can be positioned slightly more caudally compared to mesaticephalic dogs.[4]

Anatomic structures of interest surrounding the pharyngolarynx with potential secondary effects on the upper respiratory tract are:

- Rostrally: base of the tongue and mandibular lymph nodes
- Laterally: hyoid bones, mandibular and parotid salivary glands
- Caudodorsally: medial retropharyngeal lymph nodes and esophagus
- Caudoventrally: thyroid glands

The hyoid apparatus is paired, except for the basihyoid bone, which facilitates identification of unilateral abnormalities. The normal cricopharyngeus muscle representing the cranial esophageal sphincter sometimes appears as a distinct soft tissue structure dorsal to the larynx and can be misinterpreted as a soft tissue mass.

Trachea: The tracheal lumen is normally gas filled and the luminal diameter is similar between the cervical and thoracic regions. In large-breed dogs, it sometimes widens in the caudal cervical region. The diameter of the normal trachea can also vary mildly between inspiration and expiration. The ratio between tracheal diameter and thoracic inlet height is proportionally larger in dogs with greater body weight and smaller in brachycephalic breeds.[5] The cranial thoracic trachea is approximately parallel to the vertebral column and slightly closer to the vertebral column at the level of the thoracic inlet. In the mid-thorax, the trachea deviates ventrally relative to the vertebral column in most patients (Fig. 29.3). Tracheal rings may mineralize with age and become visible.

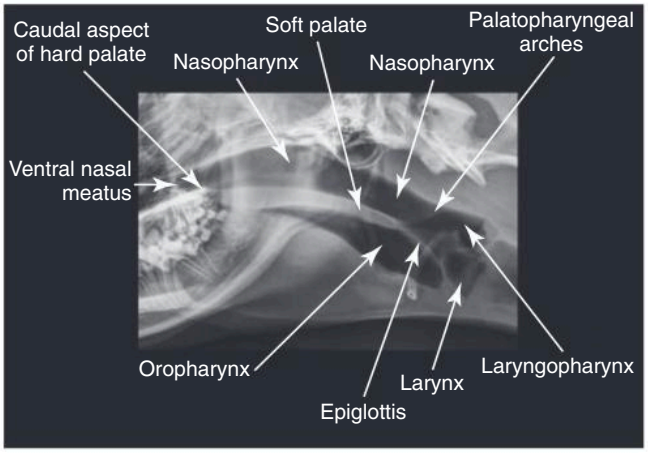


Fig. 29.1 Normal lateral canine pharyngeal/laryngeal region.

RADIOGRAPHIC TECHNIQUE

Pharyngolarynx

The lateral view with the head in neutral position and padding under the nose to avoid angulation is most useful.[6] Any degree

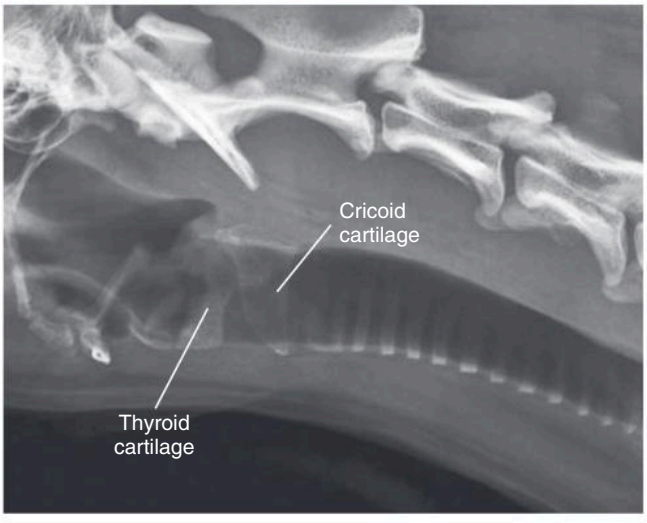


Fig. 29.2 Lateral radiograph of a 9-year-old dog. The laryngeal and tracheal cartilages are mineralized, which aids in their differentiation. This is a normal variant and not pathologic.

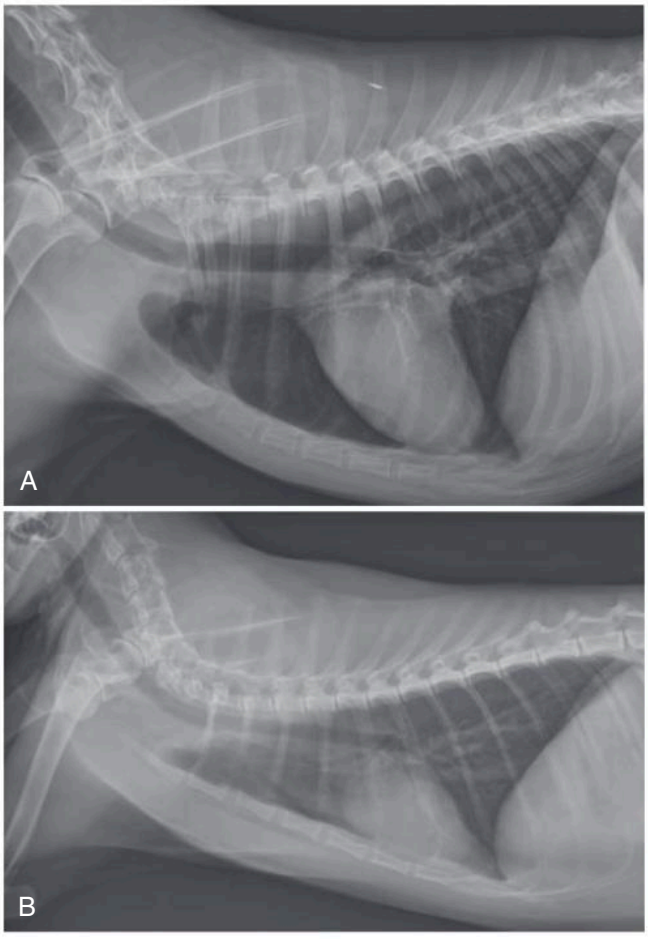


Fig. 29.3 Lateral radiographic view of the normal trachea of a dog **(A)** and a cat **(B)**. Note the similar tracheal luminal size in the cervical and thoracic region and ventral deviation of the trachea from the vertebral column in the thoracic region, in comparison to a relatively parallel position further cranially.

of obliquity results in underestimation of luminal diameter and overestimation of the surrounding soft tissue structures, such as the soft palate and laryngeal cartilages, which can mimic a mass. Superimposition of the ear cartilages with the pharyngolarynx should be avoided.

Ventrodorsal (VD) and oblique views are complementary to establish lesion laterality yet are limited by superimposition of the skull and cervical spine.

Technique parameters offering high-contrast images (relatively low kilovoltage peak [kVp] and high milliampere second [mAs] if using an analog system) selected according to the thickness of the ventral cervical soft tissues are recommended. If possible, the endotracheal tube should be withdrawn during radiography. Differentiation of the various structures is more difficult in obese patients because of narrowing of the air-filled compartments.

Trachea

The lateral view with the head mildly extended is most useful for evaluation of the trachea (see Fig. 29.3). The position of the thoracic portion of the trachea can vary with patient positioning: when the patient's head is ventroflexed, focal dorsal displacement of the trachea can mimic a cranial mediastinal mass (Fig. 29.4). Conversely, extreme extension of the neck can cause tracheal narrowing.

On a dorsoventral radiograph, the thoracic portion of the trachea is located on or curves mildly to the right of midline.[7] In brachycephalic breeds and obese dogs with mediastinal widening, the trachea curves more markedly to the right due to the larger amount of mediastinal fat, and this should not be confused with displacement from a mass, such as from a heart base tumor (Fig. 29.5).

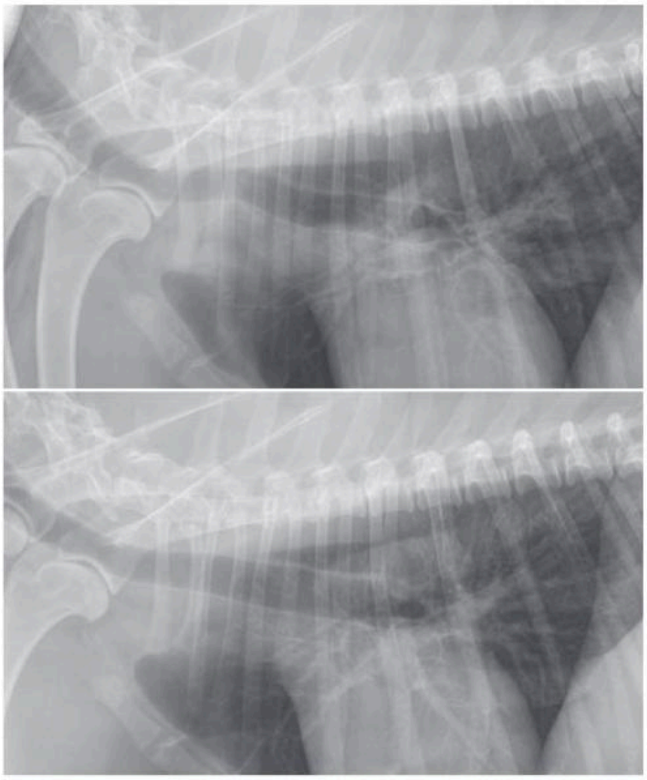


Fig. 29.4 Right lateral (*top*) thoracic radiograph with ventroflexion of the head: Patient positioning has affected the appearance of the trachea. There is focal dorsal elevation of the cranial aspect of the thoracic trachea that can be misinterpreted as being caused by a mediastinal mass. The trachea has a normal course in the left lateral (*bottom*) radiograph where the head is extended.

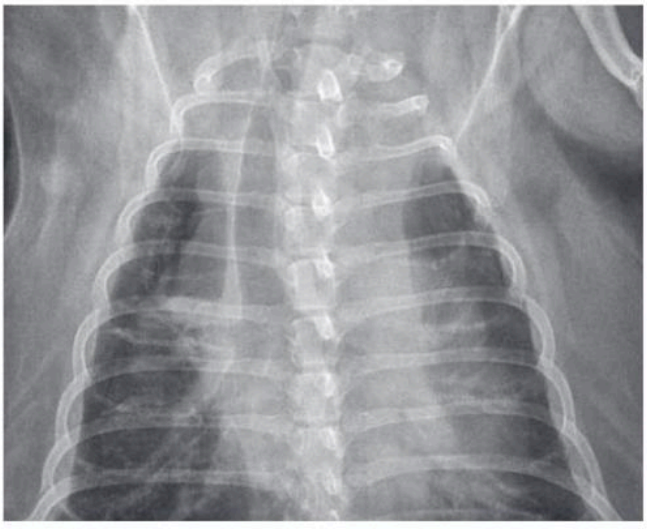


Fig. 29.5 Dorsoventral thoracic radiograph of an obese dog. There is rightward deviation of the thoracic trachea caused by the large amount of mediastinal fat. This is a normal variation and not significant.

RADIOGRAPHIC SIGNS OF DISEASE

Pharyngolarynx

Indications for radiography of the pharyngolarynx include respiratory difficulty and stertor caused by a suspected upper respiratory obstruction, ptyalism, gagging, dysphagia, dysphonia, a palpable mass or swelling, or a visible draining tract. Although ultrasound is useful for evaluating the soft tissues surrounding the upper respiratory tract, radiography is better suited for assessing their impact on the upper respiratory tract lumen. In addition, radiography can help screening for nonpalpable masses.[8] Ultimately, cross-sectional imaging such as computed tomography (CT) is often needed to assess the pharyngolarynx.

Masses

Pharyngolaryngeal masses may be extramural, mural, or intraluminal.

Extramural masses can originate from any of the structures surrounding the pharyngolarynx (Box 29.1) and may be neoplastic (Fig. 29.6, eFig. 29.1), infectious/inflammatory (Fig. 29.7, eFig. 29.2) traumatic, or hemorrhagic in nature. Radiographically, extramural masses usually present as soft tissue thickening which is poorly delineated from the surrounding soft tissues and may cause displacement and/or narrowing of the respiratory tract lumen. Their interface with the air-filled lumen is smoothly marginated and broad based. Their origin is determined based on their location relative to the pharyngolarynx.

Box • 29.1

Differential Diagnoses for Pharyngolaryngeal Masses

Extramural
- Lymph nodes: adenitis, neoplasia
- Salivary glands: sialocele, sialoadenitis, neoplasia
- Esophagus: neoplasia, granuloma
- Thyroid neoplasia (carcinoma) (including ectopic, base of the tongue)
- Malignant nerve sheath tumor
- Carotid body tumor
- Soft tissue trauma, penetrating wound and/or foreign body (hematoma, seroma, cellulitis, abscess)
- Coagulation disorder (hematoma)

Mural
- Neoplasia: adenocarcinoma, squamous cell carcinoma, lymphoma, plasmacytoma, rhabdomyoma, rhabdomyosarcoma, chondrosarcoma, granular cell tumor, mast cell tumor
- Tonsillitis, tonsillar neoplasia
- Granuloma/abscess: fungal (blastomycosis, cryptococcosis, pythiosis), granulomatous laryngitis (cats), lymphoplasmacytic inflammation (cats), chronic foreign body, *Cuterebra* migration
- Polyps: nasopharyngeal (cats), laryngeal
- Chondritis, laryngitis, viral papillomatosis
- Laryngeal cyst
- Brachycephalic syndrome: elongated, edematous soft palate

Intraluminal
- Foreign body (especially if soft tissue opacity)

Mural masses tend to be smaller when clinical signs appear, given that their impact on the respiratory lumen is more direct. Thus, they can be very difficult to identify radiographically, and endoscopy or direct pharyngolaryngoscopic examination as well as CT may be more useful.

- In cats, the two most common forms of pharyngolaryngeal mural neoplasia are lymphoma and squamous cell carcinoma, and in the larynx the arytenoid cartilage is most often involved.[9,10]
- In dogs, in the pharynx, squamous cell carcinoma (in particular tonsillar) is most common, with sarcoma, melanoma, and lymphoma also reported.[11–13] In the larynx, epithelial tumors and rhabdomyoma/rhabdomyosarcoma are most frequent, although mast cell tumor, various sarcomas, oncocytoma, plasma cell tumor, and melanoma are also seen.[10,14,15]

Superimposition of the normal laryngeal cartilage can make laryngeal masses difficult to detect. Laryngeal masses are



Fig. 29.6 Radiograph of a dog evaluated for a cervical mass. A mass located dorsal to the pharynx, larynx, and cervical portion of the trachea displaces these structures ventrally. There is effacement of the fascial planes in the cervical region. Carcinoma of salivary or sebaceous origin was diagnosed.



Fig. 29.7 Radiograph of an anesthetized cat with acute dyspnea and a submandibular mass. Ill-defined soft tissue thickening is present ventral and caudal to the mandibular and pharyngeal region, compatible with cellulitis. Complete reduction of the air-filled volume of the oropharynx and incomplete reduction in volume of the nasopharynx are present.



eFig. 29.1 Lateral cervical radiograph of a dog presented for neck pain. A soft tissue mass expands the retropharyngeal space and displaces the laryngopharynx ventrally. Carcinoma was diagnosed on cytology.



eFig. 29.2 Lateral cervical radiograph of a young cat with gagging and retching on pharyngeal palpation. The soft palate and laryngeal soft tissues are thickened without a distinct mass. Laryngitis was confirmed via endoscopy.

characterized primarily by an increase in soft tissue opacity with diffuse thickening, decreased margination of (pharyngo) laryngeal structures, and/or airway stenosis (Fig. 29.8).[9] They can also appear well defined (Fig. 29.9, eFig. 29.3) and/or lobulated if surrounded by air.[10] Horizontal epiglottic displacement can occur.[16]



Fig. 29.8 Radiograph of a cat with inspiratory difficulty and change in meow. There is a round increased soft tissue opacity in the midventral aspect of the laryngeal lumen (*white arrow*). A laryngeal squamous cell carcinoma was diagnosed.

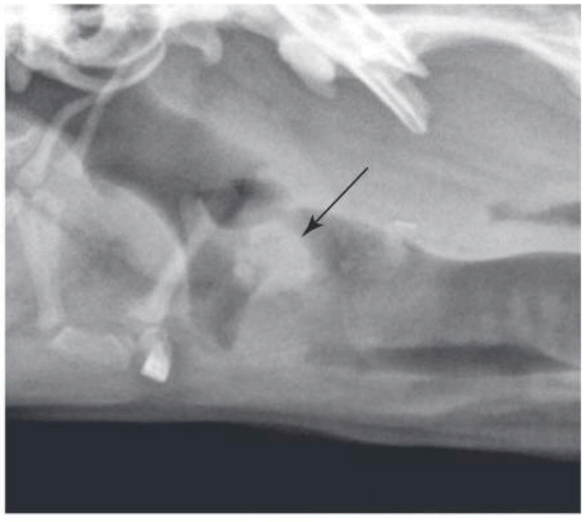


Fig. 29.9 Lateral radiograph of a dog with progressive inspiratory noise. There is a well-defined soft tissue mass (*black arrow*) at the dorsal aspect of the larynx. The diagnosis was benign hyperplastic fibroepithelial polyp.

Ectopic thyroid tissue can be found anywhere along the thyroglossal tract, from the base of the tongue to the base of the heart, and may undergo malignant transformation. Ectopic thyroid carcinoma resulting in effacement of the basihyoid bone and creating a ventral cervical mass has been recognized as a specific syndrome.[17] These tumors are strongly vascularized, heterogeneous masses with foci of mineralization and areas of colloid material accumulation. These tumors result in severe lysis of the basihyoid bone and infiltration of the laryngeal wall (Fig. 29.10, eFig. 29.4).

Trauma and Foreign Body

Pharyngolaryngeal trauma occurs most often because of a penetrating wound originating either internally from the upper respiratory tract or esophagus, due to a stick injury, or externally, such as a bite or gunshot wound, less commonly from blunt trauma. Soft tissue thickening representing swelling and/or a mass may be found with hematoma, cellulitis, granuloma, myositis, and/or abscess. Gas opacities in the subcutaneous tissues and between muscle and tissue planes represent emphysema if linear. Focal rounded gas accumulation may represent an abscess (Fig. 29.11). The sublingual area is reported as the most common entry site for stick injuries in dogs.[18] Emphysema has been reported in 83% of dogs with acute oropharyngeal stick injury and can extend to pneumomediastinum, pneumothorax, mediastinitis, and pleural effusion.[19] Pharyngeal diverticulum,[20] stenosis, cervical swelling, and draining sinus tracts[18] can be complications of trauma.

In addition to other surrounding bone structures, hyoid bone fracture and laryngeal cartilage fracture can occur, particularly when the region has been crushed.[21] These structures should be examined for symmetry and normal contour. Oblique projections may help evaluation of the hyoid apparatus. Hyoid bone fractures may be open to the upper respiratory tract and therefore contaminated.

Foreign bodies are visible when they are mineral or metallic, such as gunshot particles, needles, fishhooks, and bones. Plant material is usually only visible radiographically when large, containing (dry wood) or surrounded by gas (Fig. 29.12). CT[22] or magnetic resonance imaging (MRI)[23] can aid the localization of smaller plant material foreign bodies. In patients with a draining tract, fistulography with iodinated contrast medium can aid in foreign body detection.

Brachycephalic Syndrome

Brachycephalic syndrome comprises a complex of static and dynamic upper respiratory disorders in brachycephalic breeds

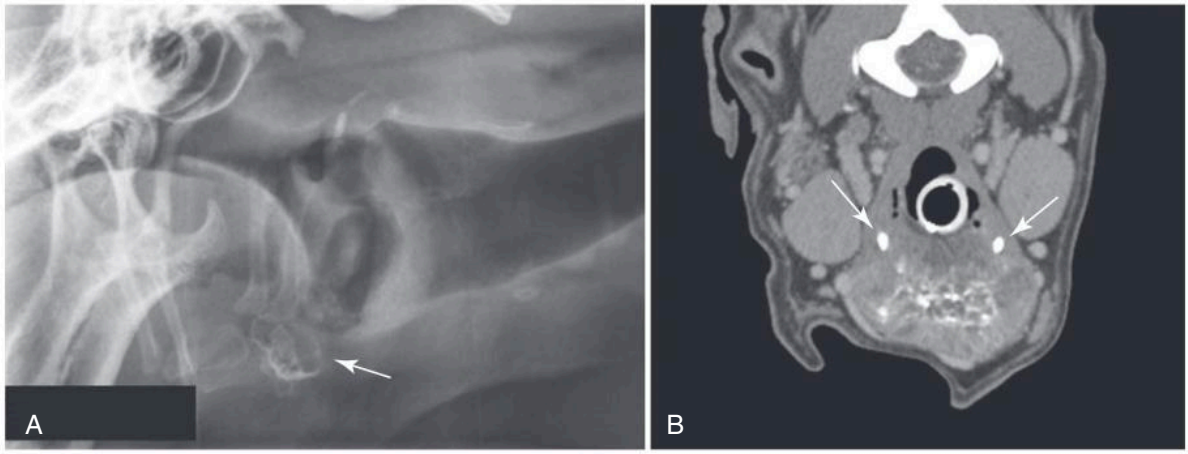


Fig. 29.10 **A,** Lateral cervical radiograph of a dog with an early ectopic basihyoid thyroid carcinoma. There is irregularity and expansion of the basihyoid bone. **B,** Transverse, precontrast, computed tomography (CT) image of the hyoid region of a dog with more advanced ectopic basihyoid thyroid carcinoma. There is a large mass with extensive mineralization that has caused effacement of the basihyoid bone. The normal paired thyrohyoid bones, just caudal to the location of the normal basihyoid bone, are visible and not involved (*white arrows*).



eFig. 29.3 Radiograph of an adult cat presented for respiratory distress. Ill-defined soft tissue opacity fills the nasopharynx and laryngopharynx, completely obliterating the air space, except for the piriform recess, and causing border effacement of the dorsal margin of the soft palate. The airway is maintained with an endotracheal tube. A nasopharyngeal mast cell tumor was diagnosed.



eFig. 29.4 Lateral cervical radiograph of a dog with ectopic basihyoid thyroid carcinoma. The basihyoid bone is expanded with multifocal radiolucencies within.



Fig. 29.11 Lateral radiograph of a cat with coughing, hemoptysis, and a history of dietary indiscretion. Multiple linear and round gas opacities are present throughout the submandibular and cervical soft tissues, and the submandibular soft tissues are thickened. There is a rectangular air-filled structure with opaque borders ventral to the epiglottis, superimposed on the oropharynx. A plastic cap was removed at surgery. There was a breach of the pharyngeal wall leading to soft tissue emphysema.

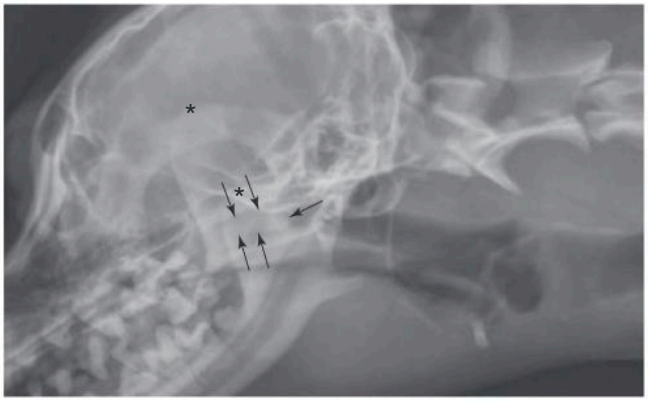


Fig. 29.12 Lateral radiograph of a Dachshund presenting with retching and sneezing. There is a triangular soft tissue opacity in the nasopharyngeal lumen (*black arrows*), best outlined along the ventral and caudal borders by gas in the nasopharynx. A piece of wood was retrieved endoscopically. Note that obliquity (*asterisks* showing coronoid processes of the mandible) causes artificial narrowing of the nasopharyngeal and oropharyngeal lumen.

of dogs and cats (Box 29.2). Diagnosis is typically made by clinical, radiographic, and laryngoscopic examination.[24] Radiographically, soft palate hyperplasia appears as elongation and thickening of the soft palate beyond the tip of the epiglottis, and subsequent narrowing of the nasopharyngeal and oropharyngeal diameters (Fig. 29.13). Relative macroglossia,[25] hypertrophy, and eversion of the tonsils and redundant mucosal folds[26] cause additional, often dynamic, narrowing of the pharyngeal lumen. Aberrant nasopharyngeal turbinates are typically diagnosed using CT examinations (Fig. 29.14).[27] Glottis and cricoid cartilage narrowing as well as dynamic laryngeal collapse occur in a laterolateral direction, and are typically diagnosed with a combination of laryngoscopy and CT examination; radiographic diagnosis using a VD view remains difficult unless severe (Fig. 29.15). Additional pharyngeal contraction and laryngospasm can occur and diagnosis relies on dynamic endoscopy, fluoroscopy, or CT examination.[28] An impression of increased laryngeal soft tissue is nonspecific for collapse and can represent mucosal edema in the larynx.[18] Diagnosing eversion of the laryngeal saccules relies on endoscopic evaluation.[29] Tracheal hypoplasia (see Trachea section) can be diagnosed radiographically.

Box • 29.2

Key Features of Brachycephalic Airway Syndrome

Primary Static Bone Factors
- Skull conformation anomalies
  - Shorter and wider skull: nasal passage narrowing and altered nasopharyngeal anatomy
  - Aberrant conchae and nasopharyngeal turbinates: upper airway narrowing

Primary Static Soft Tissue Factors
- Stenotic nares: upper airway narrowing
- Soft palate hyperplasia: nasopharyngeal lumen narrowing
- Macroglossia: pharyngeal lumen narrowing
- Tracheal hypoplasia

Secondary Dynamic Soft Tissue Factors
- Nasopharyngeal obstruction and collapse
- Tonsillar eversion and hypertrophy
- Laryngeal collapse, everted laryngeal saccules, laryngeal mucosal edema
- Tracheal and bronchial collapse

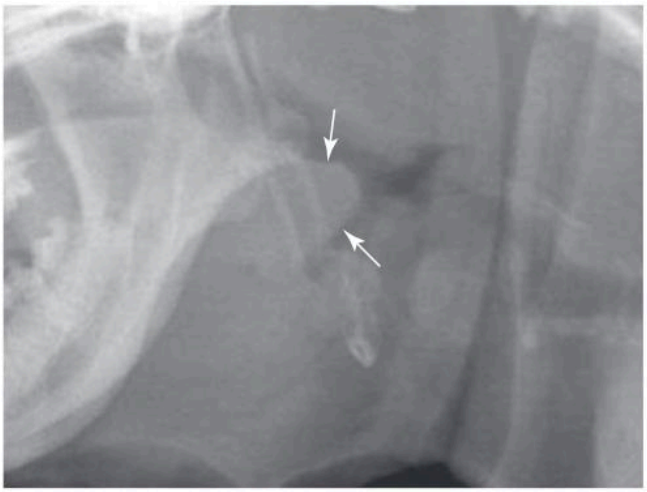


Fig. 29.13 Lateral radiograph of a French bulldog. There is soft palate elongation and thickening (*white arrows*) and increased soft tissue opacity in the laryngeal region, which is compatible with edema and upper airway narrowing found with brachycephalic syndrome.

An upper airway obstructive syndrome, different from the brachycephalic syndrome, has been described in Norwich terriers, presenting with redundant supra-arytenoid folds and multifactorial laryngeal narrowing. Associated laryngeal collapse may be suspected on radiographs and CT if there is diminished visibility of laryngeal margins, soft tissue thickening of the larynx, loss of the laryngeal gas column, and laterolateral narrowing of the laryngeal lumen at the ventral region of the thyroid cartilage. Laryngeal narrowing is best assessed on CT or laryngoscopy.[30]

Epiglottic Retroversion

Epiglottic retroversion occurs due to excessive caudal epiglottic retroflexion, causing intermittent obstruction of the rima glottidis.[31] The condition is rare, and most commonly seen in

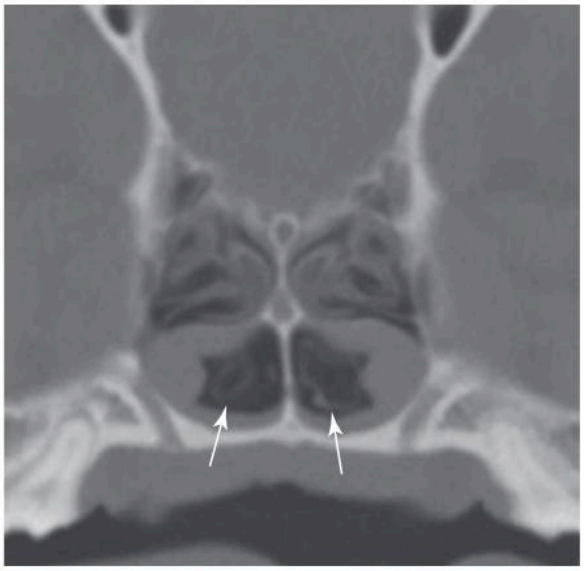


Fig. 29.14 Transverse plane computed tomography image of the head of a French bulldog with brachycephalic airway syndrome, featuring moderate (grade III) aberrant turbinates (*arrows*) extending into the region of the choanae.



Fig. 29.15 Ventrodorsal radiograph of a dog with laryngeal collapse. The laryngeal lumen is narrow (*black arrows*).

middle-aged to older, small-breed, spayed female dogs with overconditioned body habitus. Approximately 80% of cases are secondary to other upper airway diseases (such as tracheal collapse, brachycephalic syndrome, or laryngeal paralysis), and retroversion can be associated with epiglottic fracture, malacia, or peripheral neuropathy.[31] It appears radiographically or fluoroscopically as a more vertically positioned epiglottis that extends dorsally to the dorsal wall of the laryngopharynx (Fig. 29.16).[31,32]

Pharyngeal Collapse

Pharyngeal collapse results in complete or partial dorsal displacement of the soft palate/ventral displacement of the pharyngeal wall (Fig. 29.17, eFig. 29.5). It can be identified on radiographs in some patients, but fluoroscopy is particularly



Fig. 29.16 Lateral view of the laryngeal region of a dog, showing the epiglottis (*asterisk*) more vertically positioned than expected. During the fluoroscopic examination, further retroflexion of the epiglottis was seen, consistent with epiglottic retroversion. (Image courtesy Dr. Gabriela Seiler.)

helpful as the condition is commonly dynamic. It is usually associated with tracheal/bronchial collapse and/or brachycephalic syndrome.[33,34]

Dynamic upper airway collapse (laryngeal or pharyngeal) has been reported in cats secondary to respiratory distress caused by asthma or presumed inflammatory/infectious disorders, high-grade lymphoma infiltrates in the pharyngeal region, or possibly related to vigorous exercise.[35–37]

Nasopharyngeal Stenosis

Nasopharyngeal stenosis is a relatively rare pathological narrowing of the nasopharyngeal lumen and can present as a congenital abnormality with a septal structure in the lumen or acquired, secondary to an inflammatory/infectious condition, surgical manipulation, trauma, tumor, or polyp. In dogs, aspiration rhinitis related to an anesthetic event, and in cats, inflammatory or infectious causes are the most common causes of acquired stenoses.[38–40] Radiographically, a narrow band of soft tissue superimposed on the nasopharyngeal lumen and slight focal dorsal deviation of the soft palate may be seen.[41] Cross-sectional imaging (CT or MRI), including sagittal and dorsal reformatted images, provides enhanced identification of the disease features (Fig. 29.18, eFig. 29.6). A congenital form of nasopharyngeal stenosis has been proposed in Dachshunds, thought to be caused by a primary palatopharyngeal dysgenesis. Thickening of the palatopharyngeal muscles leads to a horizontal band of soft tissue that separates or even obliterates the nasopharynx from the rest of the pharynx and larynx.[42]

Pharyngitis and Laryngitis

Generalized swelling of the upper airway can be caused by edema due to respiratory distress, as seen in brachycephalic breeds, and/or inflammatory conditions. Other causes are upper respiratory infection, such as with infectious tracheobronchitis or viral rhinotracheitis, or oral cavity infection and ingestion of caustic or toxic substances, such as *Dieffenbachia* plant species.[43,44]

Trachea

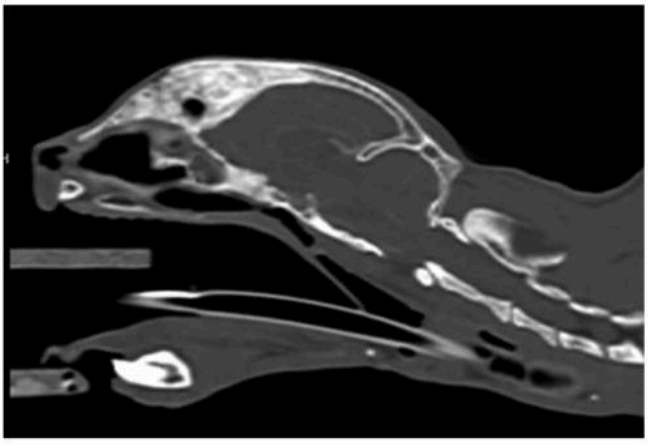
Specific indications for radiography of the trachea are coughing, particularly if induced by tracheal palpation, and respiratory distress caused by a suspected upper respiratory obstruction.

Masses

Extramural cervical, cranial mediastinal, and heart base masses can cause tracheal displacement, narrowing, and collapse. The most common mass lesions to cause tracheal displacement and



eFig. 29.5 Lateral radiograph of a Boston terrier with brachycephalic syndrome. The soft palate is thickened and elongated, resulting in narrowing of the nasopharynx and oropharynx. Note the shortened nasal cavities and absent frontal sinuses.



eFig. 29.6 Sagittal reformatted computed tomography (CT) image of a cat with nasopharyngeal stenosis. There is a focal soft tissue band that spans the lumen of the nasopharynx.

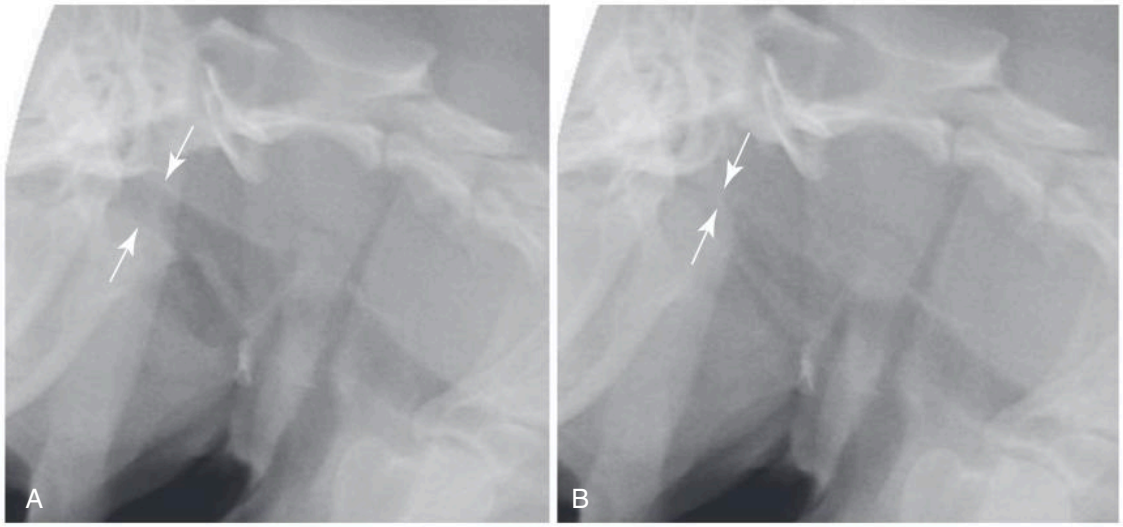


Fig. 29.17 Lateral dynamic digital radiographs of a pug with brachycephalic syndrome and dynamic pharyngeal collapse. In **A,** the nasopharynx is normally open, and the lumen is clearly visible (*white arrows*). In **B,** the lumen of the nasopharynx (*arrows*) is completely collapsed. Collapse was initiated at the beginning of inspiration and opening on the beginning of expiration.

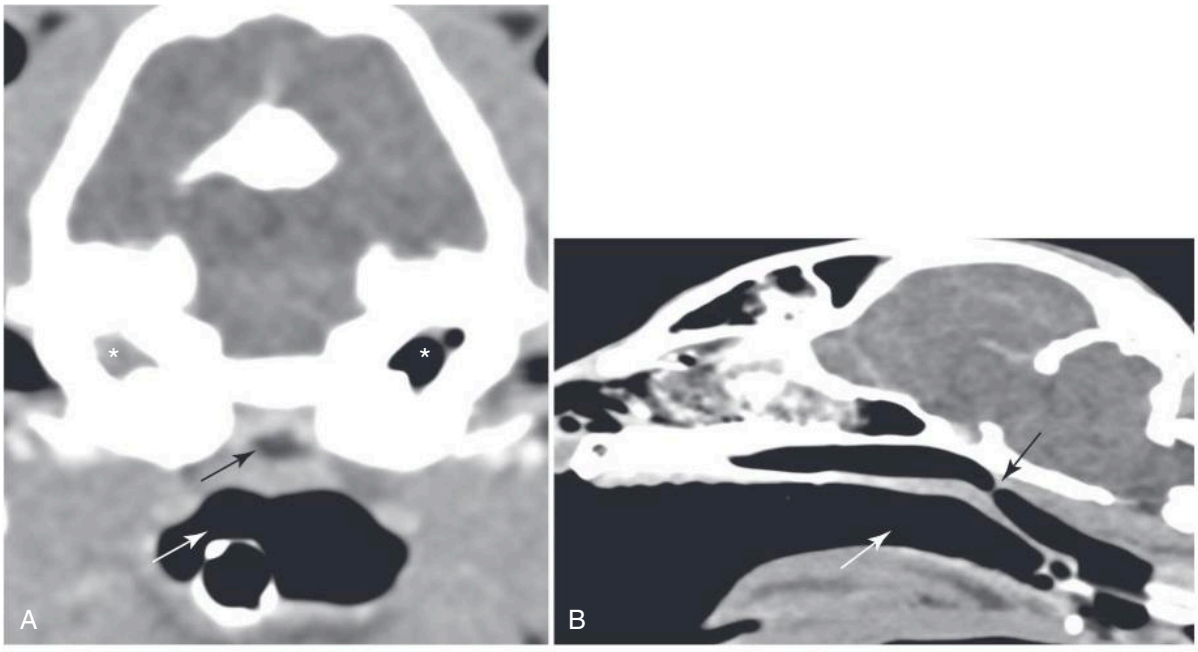


Fig. 29.18 Transverse plane **(A)** and sagittal reformatted **(B)** computed tomography (CT) image of a 9-month-old cat with intermittent and progressive episodes of reverse sneezing and increased respiratory effort. There is marked focal narrowing of the mid nasopharyngeal lumen (*black arrow*), consistent with nasopharyngeal stenosis. The oropharyngeal lumen is normal (*white arrow*). Endoscopy confirmed a most likely congenital soft tissue stricture in the region and additional inflammatory changes. The patient also had bilateral otitis media (*white asterisks*).

narrowing include thyroid carcinoma, cervical or thoracic lymphadenopathy, other mediastinal masses such as thymoma, heart base tumors, or, particularly in cats, mediastinal cysts. Heart base tumors tend to cause deviation of the trachea to the right.[45] Dorsal displacement of the caudal thoracic trachea and carina is seen with left-sided cardiomegaly and ventral displacement with tracheobronchial lymphadenomegaly (Table 29.1). Peritracheal or intramural hemorrhage from rodenticide toxicity[46] (Fig. 29.19) and a peripheral nerve sheath tumor[47] have been reported to cause tracheal luminal narrowing in the dog. Additionally, with persistent right fourth aortic arch, a mild-to-marked focal leftward displacement of the trachea is often seen on a dorsoventral radiograph.[7]

Mural tracheal masses are uncommon but when present are most often neoplastic. Benign tracheal tumors in dogs include osteochondroma, most commonly found in young dogs, followed by chondroma and leiomyoma.[10] Malignant tumors include lymphoma (cats particularly), sarcoma (fibrosarcoma, chondrosarcoma, histiocytic sarcoma), adenocarcinoma, squamous cell carcinoma, and plasmacytoma.[10,48] Other considerations are hematoma secondary to trauma or coagulation disorders including rodenticide toxicity, amyloidosis,[49]

Table • 29.1

Considerations for Radiographically Detectable Deviation of the Trachea in the Lateral Projection.

LOCATION OF DEVIATION	DIRECTION OF DEVIATION	CONSIDERATIONS
Cervical	Ventral	Thyroid mass Retropharyngeal lymphadenomegaly Vertebral/paravertebral mass
Cranial mediastinum	Dorsal	Cranial mediastinal mass (including cranial mediastinal lymphadenomegaly, thymoma, mediastinal cyst, etc.) For a complete list of mediastinal masses, please refer to Chapter 33. Neck position during radiography
Cranial mediastinum	Ventral	Neurogenic tumor Esophageal enlargement/mass
Heart base	Dorsal	Heart base mass Pulmonary artery enlargement Right atrial enlargement
Carina	Dorsal	Left atrial enlargement Tracheobronchial lymphadenomegaly (usually ventral but can be dorsal) Generalized cardiomegaly
Carina	Ventral	Tracheobronchial lymphadenomegaly

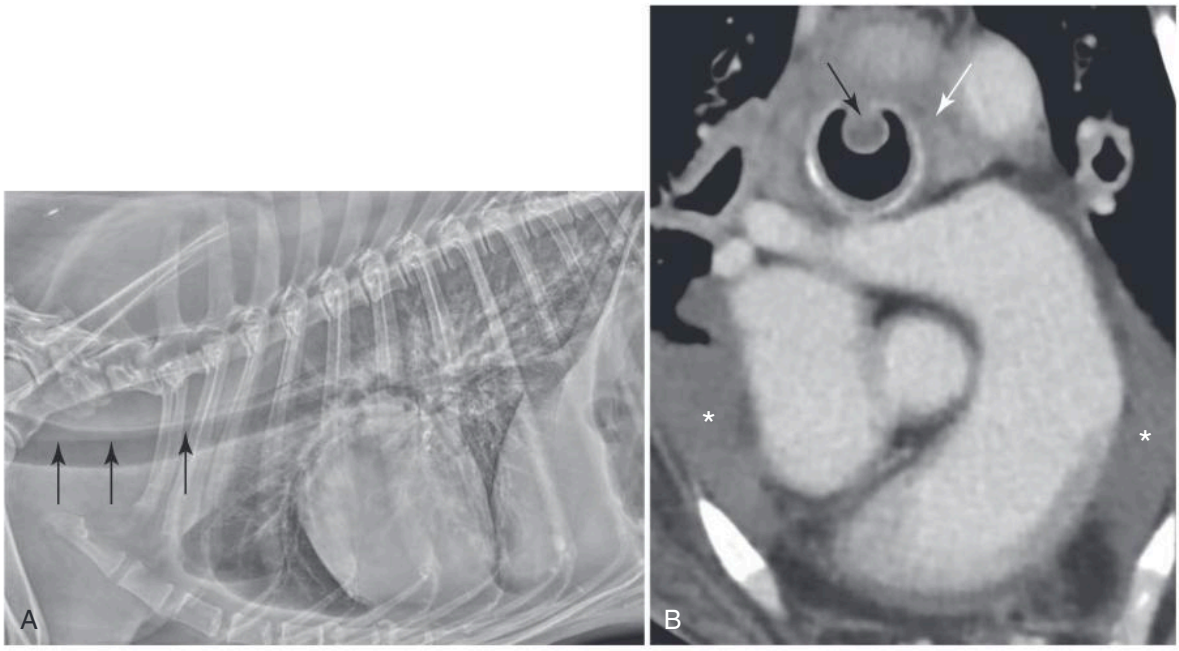


Fig. 29.19 Lateral radiograph **(A)** and transverse plane post contrast CT examination **(B)** of a dog presenting with productive frothy and hemorrhagic cough after rodenticide ingestion. There is a thin, soft tissue band superimposed over the dorsal aspect of the trachea (*black arrows*), which corresponded to submucosal hemorrhage in the dorsal tracheal membrane as seen on the CT examination as marked redundancy and thickening of the dorsal tracheal membrane. There is evidence of additional peritracheal hemorrhage (*white arrow*), mild pleural effusion (*asterisks*), and hemorrhagic pulmonary infiltrates.

inflammatory polyp,[50] and granuloma secondary to foreign body migration, mycobacterial infection, zygomycosis,[51] and parasitic disease. In particular, *Oslerus (Filaroides) osleri* granulomas can be seen near the carina in the dog, and aberrant tracheal *Cuterebra* migration has been reported in a cat.[52] Tracheal masses are usually solitary and distinct, protruding into the lumen, and are well seen because of the contrast provided by the surrounding air (Fig. 29.20).

Masses may be mineralized when they are of cartilage origin, such as osteochondromas.[10]

Foreign Bodies

Tracheal foreign bodies usually result from orotracheal aspiration, such as a tooth, kibble, stone (Fig. 29.21), bone, plant material, or a severed endotracheal tube. Rarely, foreign bodies can migrate from the surrounding soft tissues.[53–55] Young cats and hunting dogs are affected most commonly, possibly because of the small diameter of their trachea and the nature of their activity, respectively.[53,54] The negative contrast afforded by intraluminal tracheal air helps in the detection of both mineral and soft tissue opacity foreign bodies. Since inhaled

foreign bodies are most often lodged at the carina, particular attention should be paid to this area (eFig. 29.7). As an alternative to bronchoscopy, fluoroscopic guidance of forceps can be used for tracheal foreign body retrieval.[54,55]

Rupture/Avulsion and Stenosis

Tracheal rupture is a tear in the tracheal wall or the tissues lining the tracheal wall, and may be caused by endotracheal intubation, a penetrating wound (dog bites particularly), blunt trauma, or a foreign body.[56–58] Iatrogenic rupture can be caused by a tube stylet, inappropriately sized endotracheal tube, rotation of the anesthetized patient without disconnecting the tube, and/or excessive dilatation of the tube cuff.[59] Subcutaneous emphysema and pneumomediastinum can be severe and are more readily identified than the actual tracheal tear, which may not be visible radiographically (Fig. 29.22).[57,59] Intratracheal fluid, mural hematoma, and stenosis are seen occasionally.[57]

Tracheal avulsion is a complete severance of the trachea, most commonly in intrathoracic location in cats, following blunt trauma with severe hyperextension of the head and neck. Paradoxically, patients are often presented 1 to 3 weeks following the traumatic event, when signs of pneumomediastinum and soft tissue emphysema have resolved.[60] Most commonly, there is complete circumferential tracheal wall discontinuity 1 to 4 cm cranial to the carina, resulting in focal, well-defined, spherical dilation of the tracheal lumen outlined by a thin, soft tissue opacity margin representing either intact tracheal adventitia or surrounding mediastinal tissue and termed *pseudoairway* (Fig. 29.23).[60,61] This finding is usually associated with stenosis of the tracheal lumen at the margins of the avulsed trachea.[60] Mainstem bronchial avulsion has also been reported.[62]

Stenosis and tracheal diverticulum are complications of the same causes that predispose to tracheal rupture/avulsion, in addition to tracheal surgery.[63,64] A focal, static area of tracheal narrowing or widening is seen. Stenosis can also be seen with neoplasia causing annular tracheal narrowing.[10]

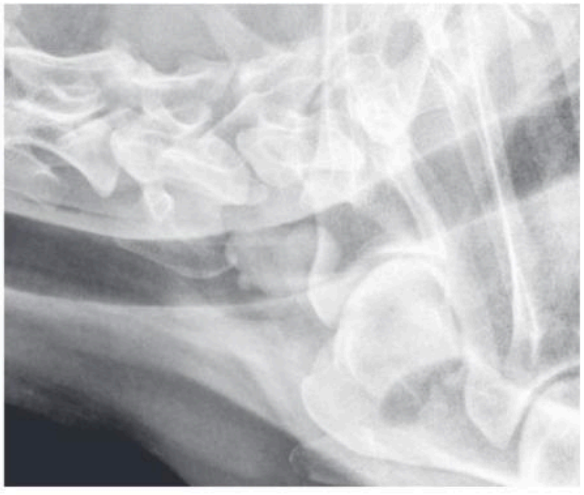


Fig. 29.20 Lateral radiograph of a dog with a small oval intratracheal mass at the thoracic inlet. Tracheal masses extending into the lumen will be sharply outlined by the contrast from surrounding air. This lesion was first thought to be a foreign body but was determined endoscopically to be a pedunculated mass. The diagnosis was B-cell tumor. As this radiograph is slightly oblique, one of the transverse processes of C6 is superimposed on the trachea, just cranial to the mass.

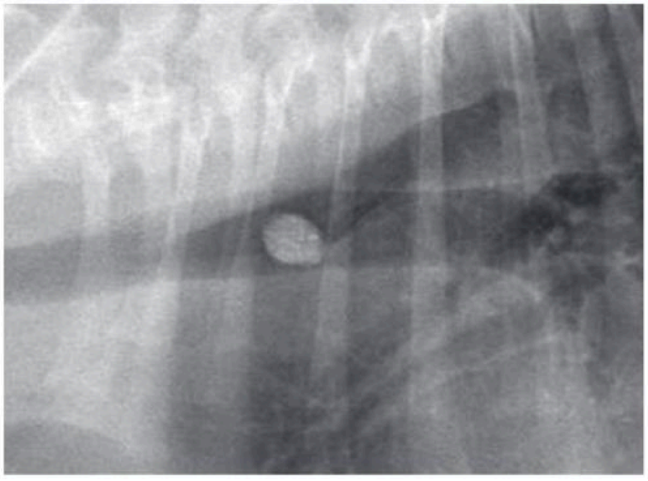


Fig. 29.21 Radiograph of a dog that developed a cough after being observed eating rocks. A well-defined granular mineral opacity structure is present in the caudal aspect of the trachea. A rock was removed endoscopically.



Fig. 29.22 Lateral radiograph of a cat presenting with extensive subcutaneous edema 3 days following a routine dental prophylaxis treatment. There is focal loss of the dorsal outline of the trachea (*white arrows*) and a fusiform soft tissue opacity (*white asterisk*) superimposed over the dorsal tracheal lumen, representing a markedly redundant (considered torn) tracheal membrane, indicating a tracheal tear. There is also extensive subcutaneous emphysema in the cervical and thoracic region, pneumomediastinum and partial atelectasis of the lungs.

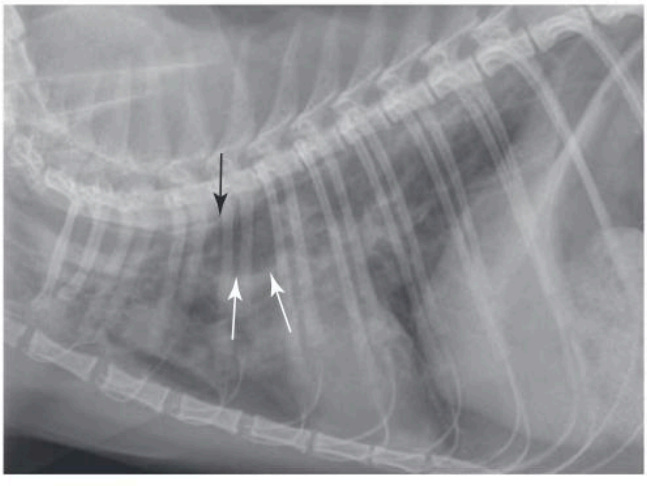
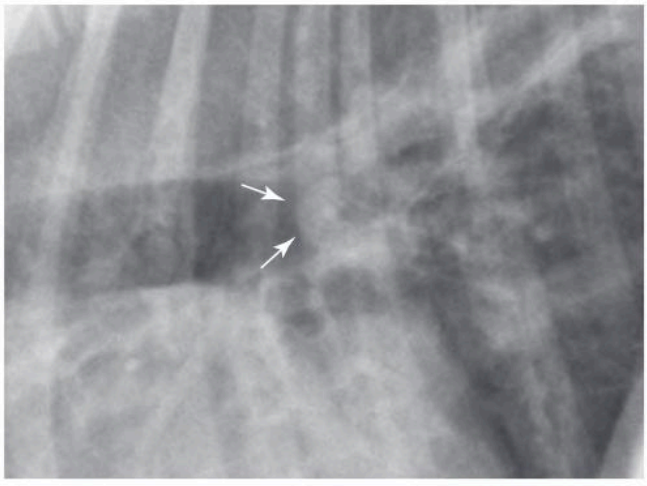


Fig. 29.23 Lateral radiograph of a cat 48 hours after being hit by car. There is a gas-filled saccular structure representing a pseudoairway (*white arrows* indicate ventral margin of sac). The caudal margins of the avulsed trachea can be seen (*black arrow*). There is also evidence of pneumomediastinum, pulmonary contusions, esophageal gas dilation, and aerophagia.



eFig. 29.7 Lateral radiograph of a dog with acute coughing and respiratory distress. There is a sharp, curving, air-tissue interface at the carina (*white arrows*). A pea was removed from the trachea endoscopically.

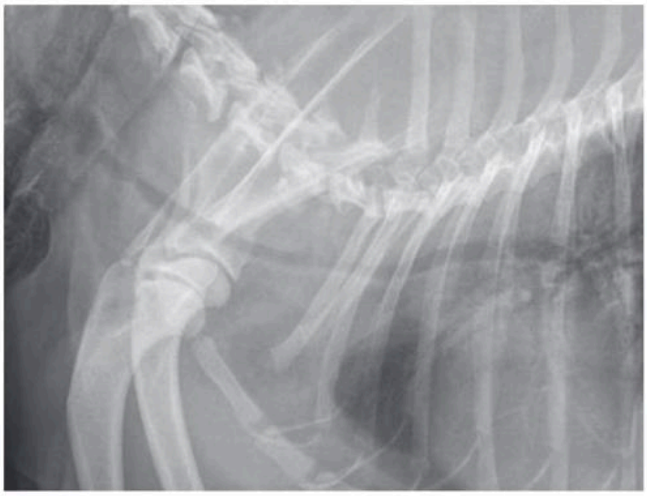


Fig. 29.24 Radiograph of a pug that presented for seizures and a cough. Generalized tracheal narrowing is present, measuring 8% of the height of the thoracic inlet, compatible with tracheal hypoplasia.

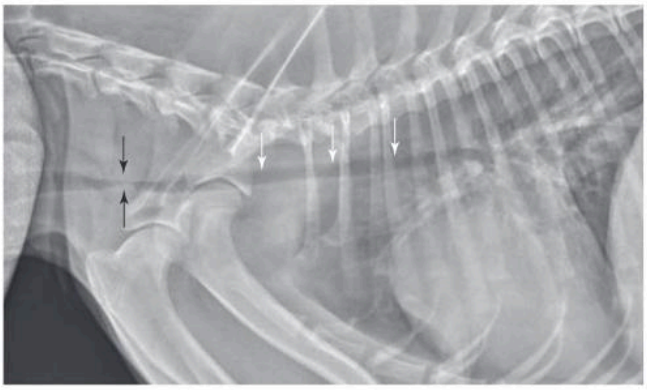


Fig. 29.25 Lateral radiograph of a dog with acute onset of cough following anesthesia for routine spay procedure. There is focal narrowing of the cranial cervical tracheal lumen due to luminal soft tissue thickening (*black arrows*) and an undulating soft tissue opacity superimposed on the dorsal tracheal lumen (*white arrows*) in the caudal cervical and thoracic trachea. Endoscopy confirmed marked inflammation and hemorrhage in the cranial cervical tracheal region, presumed due to trauma related to prior intubation, and associated moderate tracheal inflammation in the further caudal trachea.

Hypoplasia

Tracheal hypoplasia is characterized by generalized reduction in tracheal diameter (Fig. 29.24) due to apposed or overlapping tracheal cartilages and a shortened or absent dorsal tracheal membrane. Approximately 39% of brachycephalic dogs with signs of brachycephalic airway obstruction syndrome have tracheal hypoplasia,[65] and in 10% of dogs, the diagnosis of tracheal hypoplasia is incidental.[66] The diagnosis is made more difficult by the fact that non-bulldog brachycephalic breeds, both with and without respiratory signs, have a smaller average tracheal-diameter-to-thoracic-inlet-height ratio (16% ± 3%) than nonbrachycephalic dogs (20% ± 3%). English bulldogs have an even smaller ratio (13% ± 4%).[5] The smallest ratio in asymptomatic bulldogs was 9%. More recently, tracheal-diameter to thoracic-inlet–height ratio was measured in 32 asymptomatic/grade 1 English bulldogs and found to be 17% ± 3% on radiographs and 26% ± 3% on CT, which is greater than previous measurements.[67] The ratio between tracheal diameter and cricoid cartilage height is also smaller for brachycephalic breeds.[5]

Normal tracheal diameter:thoracic inlet height in cats is 18% in domestic short-haired cats and 20% in Persians.[68] Tracheal hypoplasia has been reported in a kitten with mucopolysaccharidosis VII.[69]

Tracheitis

Generalized tracheal narrowing may be caused by severe tracheitis that leads to thickening of the tracheal mucosa. Tracheitis can be difficult to differentiate from tracheal hypoplasia, and the conditions can occur concurrently. Common causes of tracheitis are inhalation of toxic or chemical irritants, trauma, and upper respiratory infection (Fig. 29.25).

Redundant Tracheal Membrane

The presence of a dorsal tracheal luminal soft tissue opacity in dogs between the midcervical and midthoracic portions of the trachea can be caused by the dorsal tracheal membrane, representing the trachealis muscle and connective tissue bridging the gap between the aspect of the tracheal cartilages.[70] The dorsal tracheal membrane can usually be differentiated from the slightly opaquer dorsal tracheal wall. Visibility of the tracheal membrane dorsally does not necessarily indicate abnormal redundancy, but it can be caused by contraction, or invagination, of the membrane.[70] The opacity caused by a visible dorsal tracheal membrane can be dynamic, depending on phase of respiration (Fig. 29.26, Video 29.1). Its prominence can also be influenced by patient obliquity, displacement of the esophagus

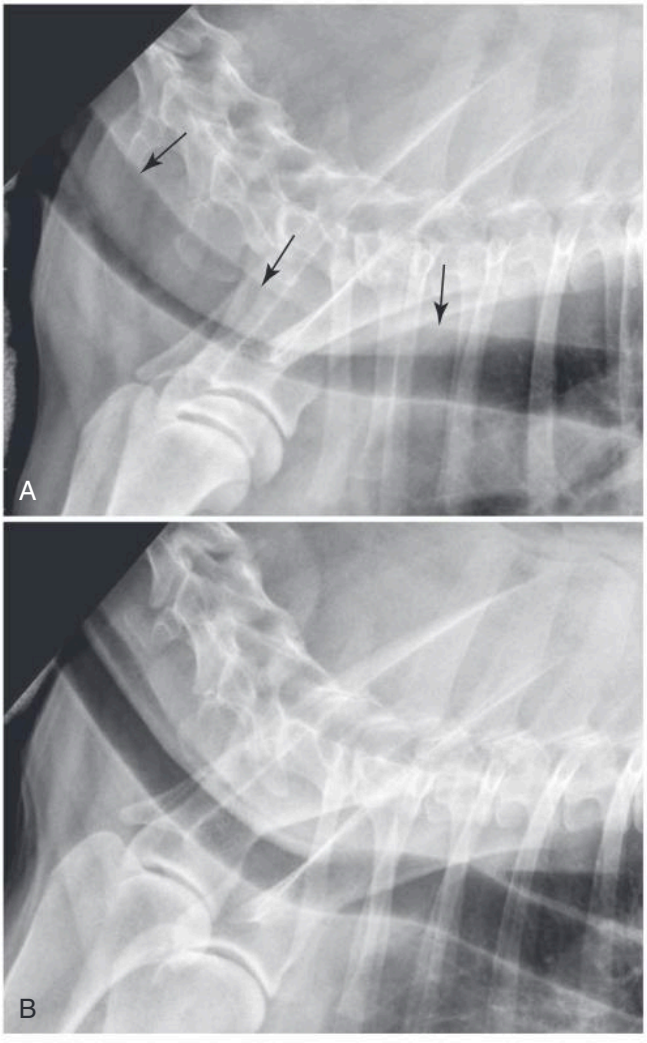


Fig. 29.26 **A,** Lateral view of the cervicothoracic region showing the tracheal lumen dorsally opacified by a visible dorsal tracheal membrane. The dorsal wall is the trachea is also visible (*black arrows*). In **B,** the gas column is wider as the membrane has moved dorsally. There is also a small amount of gas in the cranial cervical and caudal thoracic esophagus.



Fig. 29.27 Radiograph of a dog with neck pain. No respiratory signs were reported. Approximately 75% collapse of the cervical trachea is present. The tracheal collapse was presumed to be static.

onto the tracheal membrane, and tracheal rotation.[70] In large-breed and asymptomatic small-breed dogs, a visible dorsal tracheal membrane as the only tracheal abnormality is unlikely to be responsible for clinical signs. On the other hand, dogs with tracheal collapse showed a larger tracheal luminal height superimposed by the dorsal tracheal membrane, due to pathological stretching of the dorsal tracheal membrane, and this likely contributes to clinically relevant airway narrowing.[70] The greater the opacification superimposed on the tracheal lumen, the greater the chance that the patient has tracheal collapse.[70]

Tracheal and Bronchial Collapse

Tracheal collapse is commonly seen in middle-aged and older miniature- and toy-breed dogs. Affected dogs typically have chronic cough, although signs of upper respiratory obstruction can occur in severely affected patients. Collapse can be static (Fig. 29.27, Video 29.2) or dynamic (Fig. 29.28, eFig. 29.8); in the latter, severity depends on the phase of the respiratory cycle (Videos 29.3 through 29.5). Tracheal collapse is typically associated with tracheal chondromalacia or a weakened dorsal tracheal membrane.[71] Recently, tracheal malformation resulting in dorsal deviation of the ventral tracheal rings with a "W-shape" resulting in a static obstruction has been suggested as a different underlying cause.[72,73] Collapse can occur anywhere from the midcervical region to the entire thoracic trachea. Particular attention should be paid to the mainstem and lobar bronchi, which are often involved, either along with tracheal collapse or as the sole abnormality. Intrathoracic tracheal collapse is usually more pronounced on expiration, whereas collapse in the cervical and thoracic inlet regions is more pronounced on inspiration.[74–76] The sudden increase in intrathoracic pressure during coughing exacerbates intrathoracic tracheal collapse.[71] The chronic cough caused by tracheal collapse contributes to a cycle of chronic inflammation, which in turn worsens chondromalacia. Cervical tracheal collapse can lead to laryngeal collapse and upper respiratory edema through chronic inflammation and increased inspiratory pressure.[71] Pharyngeal collapse can also be associated with tracheal and bronchial collapse and can sometimes explain persistent increased respiratory effort following stenting.[33]

Static tracheal collapse can be seen on survey lateral radiographs of the thorax and cervical region as a persistent dorsoventral narrowing of the tracheal lumen. Tracheal collapse with axial rotation has been described in dogs, resulting in increased dorsoventral height of the trachea in the caudal cervical and cranial thoracic region, with an apparent intraluminal soft tissue opacity, corresponding to a redundant tracheal membrane (Fig. 29.29, eFig. 29.9).[77] Even when collapse is not identified,

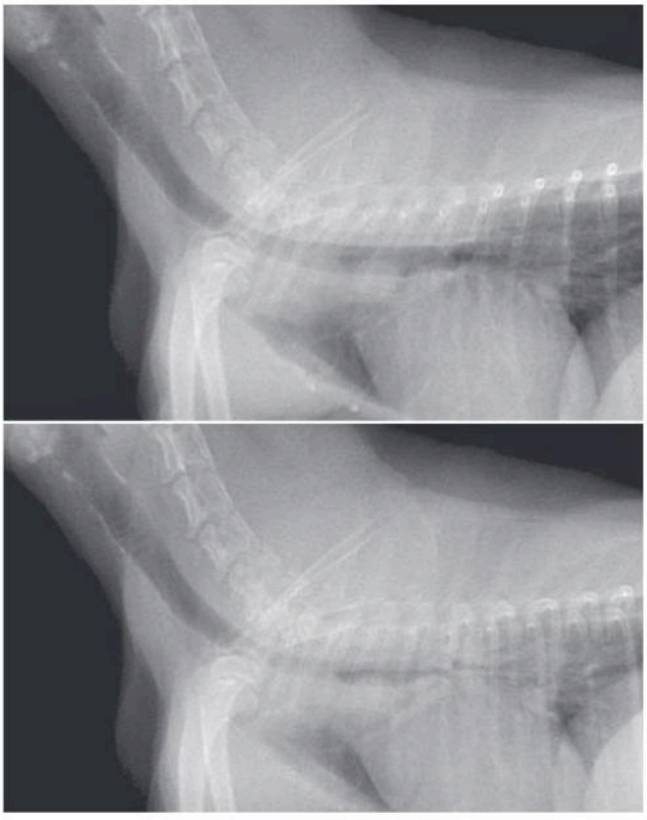


Fig. 29.28 Dynamic inspiratory (*top*) and expiratory (*bottom*) radiographic frames of a dog with chronic coughing. Approximately 50% dynamic collapse of the thoracic portion of the trachea and complete collapse of the caudal lobar mainstem bronchi occur on expiration (*bottom*).

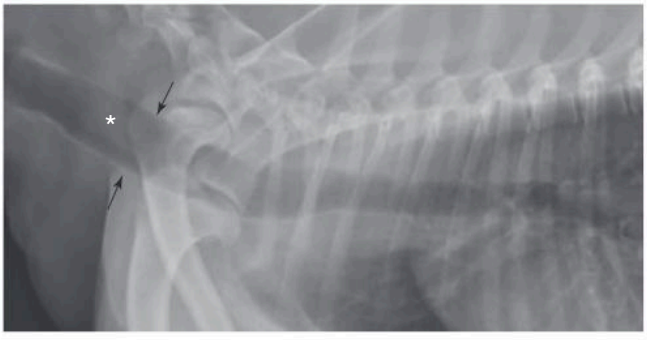
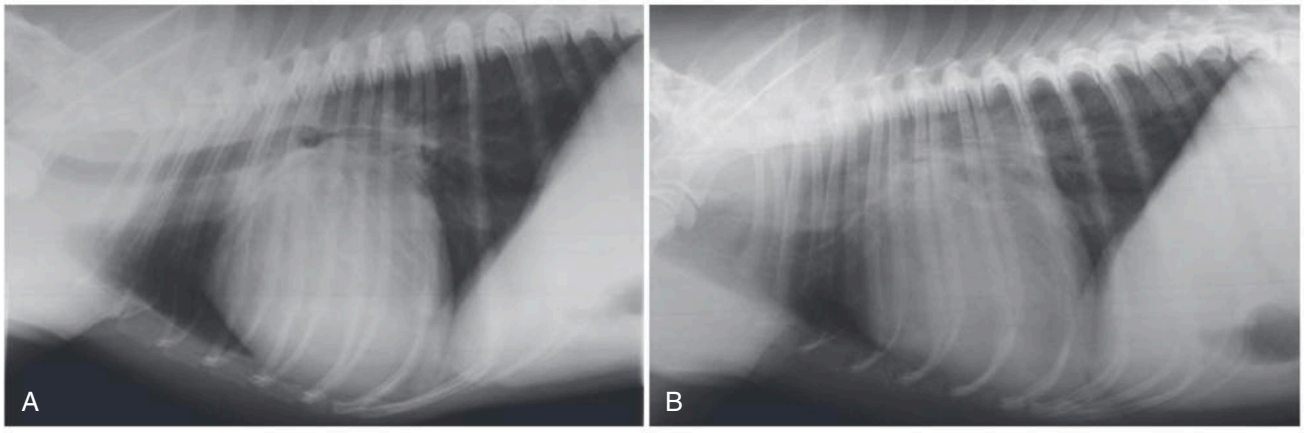


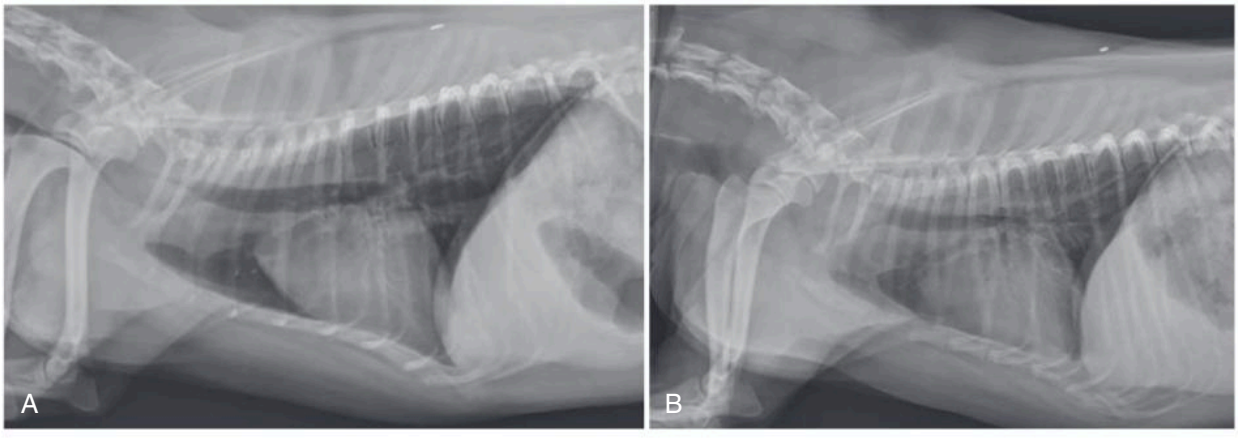
Fig. 29.29 Tracheal collapse with axial rotation shown in the lateral radiograph of a dog. There is increased dorsoventral height of the caudal cervical and cranial thoracic trachea (*black arrows*) and an intraluminal soft tissue opacity (*asterisk*), which represents the redundant tracheal membrane.

an undulating appearance of the tracheal wall and mild variation in luminal diameter are suggestive of chondromalacia. If fluoroscopy is not available, paired lateral radiographs made on peak inspiration and expiration can help characterize dynamic tracheal collapse, although agreement between radiographs and bronchoscopy is lower than between fluoroscopy and bronchoscopy.[78] A craniocaudal projection of the thoracic inlet with dorsal extension of the head and neck resulting in a transverse, or end-on, view of the trachea at the thoracic inlet has been described to complement the diagnosis of tracheal collapse,[63] but this rarely adds useful information.

Fluoroscopy remains the best imaging method to evaluate tracheal collapse, detecting a greater number and more severe grade of collapse than radiographs, particularly in the thoracic



eFig. 29.8 Lateral radiographs of the thorax of a dog with tracheal collapse. The tracheal lumen is normal in diameter during inspiration **(A)** and collapses completely during cough **(B)**.



eFig. 29.9 Lateral radiographs of a dog with tracheal collapse obtained during inspiration **(A)** and expiration **(B)**. The intrathoracic tracheal lumen is narrowed during expiration **(B)**. Note also the dorsoventral widening and increased opacity of the caudal cervical trachea caused by collapse and rotation of the trachea.

region.[75] A complete fluoroscopic examination includes evaluation of the tracheal diameter over several normal respiratory cycles, followed by evaluation during induced cough, which has the best agreement with bronchoscopy.[78] In some animals with tracheal collapse (26%), it can be difficult to induce a cough.[78] In this instance, inspiratory and expiratory effort mimicking cough can be increased by briefly obstructing the nares and mouth.

Bronchial collapse is difficult to diagnose accurately, with discrepancies between radiographs, fluoroscopy, and bronchoscopy, probably due to dynamic differences during the respiratory cycle and cough, patient positioning, and poor image resolution. It is seen most frequently during fluoroscopy with induction of cough.[78] Right middle and left cranial lobar bronchi are most commonly collapsed on bronchoscopy.[74]

In very small patients, or to better evaluate the mainstem bronchi, additional image detail can be obtained by making a rapid series of radiographic images (dynamic digital radiography) over a respiratory cycle as opposed to using fluoroscopy, while recognizing that this results in greater x-ray exposure. Performing fluoroscopy in both right and left lateral recumbency may improve detection of bronchial collapse and placing the patient in sternal recumbency may additionally help.[78] Complete radiographic evaluation of the thorax should be made in dogs suspected of tracheal collapse to evaluate for related conditions, such as bronchitis, bronchiectasis, and cardiac disease.[71,79]

Location and extent of maximal collapse are often evaluated using the following scale: 25%, 50%, 75%, and 90% to 100% reduction of tracheal diameter.[75] This scale is similar to the grading system used to evaluate tracheal collapse at bronchoscopy. A reduction in tracheal diameter of 25% or less is probably within normal limits of variation of the respiratory cycle.[75] Using CT, up to 24% change in cervical tracheal cross-sectional area and 19% variation in thoracic tracheal height are seen in healthy dogs under forced inspiration.[80]

Endotracheal stenting through fluoroscopic guidance has become commonplace for the treatment of tracheal collapse. Prior to placing a stent, complete fluoroscopic evaluation should be made to characterize the extent of collapse fully and determine the presence of mainstem bronchi involvement. Survival time of dogs with and without bronchial collapse is similar after tracheal stenting.[73] Also, images made during positive-pressure maximal tracheal dilation with a radio-opaque measurement device are required to determine appropriate stent size.[81] During follow-up radiographic evaluation, the stent should be evaluated for correct placement, fraying or fracture, and migration, and the trachea evaluated for inflammatory tissue ingrowth and progressive tracheal collapse (Fig. 29.30).[72,81,82] Subsequent tracheal collapse can develop in the unstented portion of the trachea.

Tracheal collapse in the cat is rare. Although usually secondary to an extratracheal mass effect or intratracheal pressure changes caused by upper airway obstruction,[83,84] primary collapse has been reported.[85]

Cranial Lung Lobe Herniation

Cranial lung lobe herniation is protrusion of the lung cranial to the cranial skeletal margin of the thoracic cavity and is best seen with fluoroscopy or occasionally on expiratory radiographs (Fig. 29.31).[86] Chronic or acute airway obstruction due to obstructive airway disease including tracheal and bronchial collapse during expiration creates increased intrathoracic pressure and can result in dynamic herniation of the cranial lung lobes through the thoracic inlet (see Fig. 29.31, see Video 29.3).[70,87,88] Associated radiographic findings can include kinking of the extrathoracic trachea (39%), collapse of the intrathoracic trachea, as well as bronchial collapse.[86]

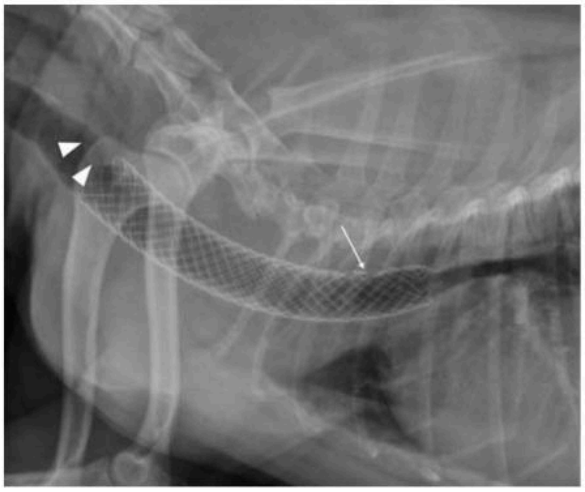


Fig. 29.30 Lateral radiograph of a dog with respiratory signs several weeks after tracheal stent placement. Focal soft tissue thickening of the dorsal tracheal wall at the cranial end of the stent (*arrowheads*) bulges into the tracheal lumen, compatible with inflammatory tissue ingrowth. The caudal aspect of the stent is fractured resulting in partial tracheal collapse (*arrow*).

Upper Airway Obstruction

Radiographic examination of animals with signs of upper respiratory obstruction should be performed with care and minimal restraint. Radiographs should be withheld until the animal is stable enough to undergo complete examination. Several indirect radiographic findings can be seen secondary to upper airway obstruction in both dogs and cats and can be useful if the primary cause of obstruction is not identified readily, such as with laryngeal paralysis. These findings are often more marked in cats, possibly because of the pliability of their tissues. Changes include:

- Pulmonary hyperinflation or underinflation
- Upper airway dilation or collapse
- Caudal displacement of the larynx and pharynx and straightening of the hyoid apparatus[30]
- Hiatal hernia[89]
- Gastrointestinal signs of aerophagia[63,90,91]
- Inward deviation of intercostal muscles in dogs and a dorsoventral flattening of the thorax in cats caused by increased negative intrathoracic pressure[91]
- Acquired pectus excavatum[92]
- Aspiration pneumonia and postobstruction pulmonary edema

ULTRASOUND

Because the upper respiratory tract is air-filled, ultrasound is of limited use for the evaluation of mural and intraluminal abnormalities. Nonetheless, the epiglottis, laryngeal and cricoid cartilages, and vocal folds can be identified and the transverse scan plane is most useful.[93] Ultrasound examinations can be helpful in the evaluation of laryngeal paralysis if reduced lateral motion of the cuneiform processes of the arytenoid cartilages can be

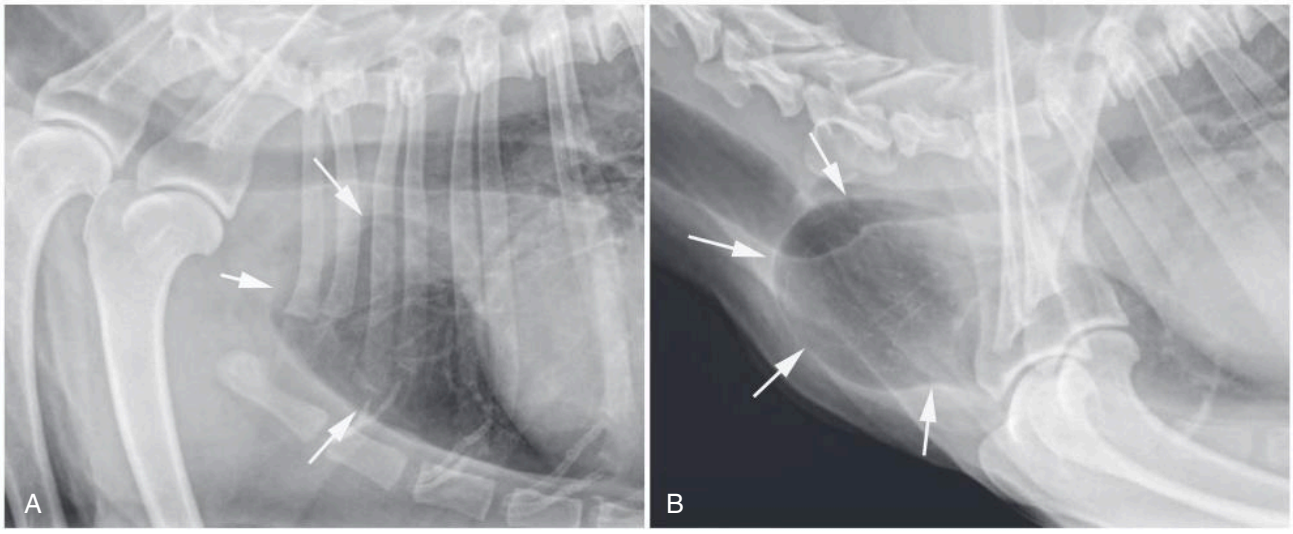


Fig. 29.31 Inspiratory **(A)** and expiratory **(B)** radiographs of a dog with marked collapse of the principal bronchi, which occurs on expiration. In **A,** the cranial lung lobes (*white arrows*) are within the thoracic cavity, extending only a very small distance cranial to the first rib. In **B,** the cranial lung lobes (*white arrows*) have herniated through the thoracic inlet and the cranial margin extends cranially to the level of the C5 to C6 disc space. The lung lobes herniate because the airway collapse that occurs on expiration prevents air from leaving the lungs and as the thoracic cavity becomes smaller the lungs do not reduce in volume as they normally would and are forced through the thoracic inlet. There is also kinking of the trachea superimposed on the herniated lung lobes.

identified.[94,95] Ultrasound may be beneficial for identification of extramural mass lesions and determination of their origin if not obscured by air in the pharyngolarynx, and allows for tissue sampling.[94]

COMPUTED TOMOGRAPHY AND MAGNETIC RESONANCE IMAGING

CT and MRI are both excellent for evaluating the soft tissues surrounding the upper respiratory tract. With faster multidetector units, many CT examinations can be done under sedation, thereby avoiding the need for anesthesia and interference with lesion detection through endotracheal intubation.[96] Examination with the mouth opened to approximately 30 to 45 degrees improves visualization of the pharyngeal structures and is particularly important when evaluating patients for nasopharyngeal stenosis.[97] Three-dimensional virtual endoscopic reformatting can be useful and is essential for CT evaluation of laryngeal collapse/paralysis.[29] Images should be acquired sufficiently caudally to include the medial retropharyngeal lymph nodes. Intraluminal air as well as typically the need for general intubation with placement of an endotracheal tube can limit the usefulness of MRI.[98]

Pharyngolaryngeal Masses

CT examination is well suited to evaluate extramural, mural, and intraluminal abnormalities. Lymph node involvement and osteolysis associated with aggressive pharyngolaryngeal neoplastic or infectious processes, such as squamous cell carcinoma and tonsillar neoplasia, can also be identified using CT.[12,13,99] The tonsillar fossa of the oropharynx is the most common location of pharyngeal neoplasia, specifically squamous cell carcinoma, which can also be bilateral. Tumor mineralization is reported in squamous cell carcinoma and pharyngeal osteosarcoma and can occur in both the mass and regional lymph nodes. Hyoid bone lysis can be a feature of tonsillar squamous cell carcinoma[12] and also as a result of ectopic basihyoid thyroid carcinoma, as described earlier.[17] Marked medial retropharyngeal lymph node enlargement, rounded shape, and heterogeneous enhancement have been reported in most cases of pharyngeal neoplasia, and isolated medial retropharyngeal lymphadenomegaly can be seen in tonsillar neoplasia without tonsillar enlargement.[12,13]

Trauma and Foreign Body

The layered linear appearance of oropharyngeal stick foreign bodies and their contrast-enhancing surrounding inflammatory reaction are well seen on CT.[100] Similarly, MRI readily identifies the inflammatory reaction and regional lymph node enlargement in addition to well-defined linear areas of low-signal intensity representing wooden foreign bodies.[101,102] Spatial understanding of the location of the foreign body is more intuitive using cross-sectional imaging in comparison to ultrasound, thereby helping subsequent surgical planning.[100,102] CT sinography can also be helpful.[103]

CT is also described for hyoid bone fractures and malformation, laryngeal cartilage fracture,[21] and tracheal rupture.[104] In tracheal and left mainstem bronchial avulsion, airway discontinuity and pseudoairway formation can be seen, and CT is useful for measuring the extent of the lesion for planning endotracheal intubation and surgical repair.[84]

Upper Airway Collapse and Tracheal Hypoplasia

CT has been reported in dogs with respiratory distress due to laryngeal paralysis, brachycephalic syndrome, including tracheal hypoplasia, laryngeal collapse and saccule eversion, tracheal/bronchial collapse, and tracheal stenosis. Multiple scans and three-dimensional virtual endoscopic rendering were necessary for detecting laryngeal collapse and laryngeal paralysis.[29]

CT has also been suggested as providing greater accuracy for stent measurement for tracheal collapse with less interobserver variability than fluoroscopy.[105] Tracheal measurements in normal dogs are on average 1 mm larger on CT than on radiographs under equivalent positive pressure manual ventilation.[106] CT can detect pharyngeal soft tissue thickening (mucosal proliferation), a smaller cross-sectional area of the nasopharynx, in addition to osseous abnormalities in feline acromegaly.[107] Everted saccules and diffuse tracheal narrowing can be seen with feline laryngotracheitis.[96,108]

Acknowledgment

With special thanks to prior authors of this chapter for their contributions.

REFERENCES

1. Gaskell CJ. The radiographic anatomy of the pharynx and larynx of the dog. *J Small Anim Pract*. 1974;15(2):89–100.
2. Aron DN, Crowe DT. Upper airway obstruction. General principles and selected conditions in the dog and cat. *Vet Clin North Am Small Anim Pract*. 1985;15(5):891–917.
3. O'Brien J, Harvey C, Tucker J. The larynx of the dog: its normal radiographic anatomy. *Vet Radiol*. 1969;10(38).
4. Plotsky K, Rendall D, Chase K, Riede TL. Cranio-facial remodeling in domestic dogs is associated with changes in larynx position. *J Anat*. 2016;228(6):975–983.
5. Harvey C, Fink E. Tracheal diameter: analysis of radiographic measurements in brachycephalic and non-brachycephalic dogs. *J Am Animal Hosp Assoc*. 1982; 18:570.
6. Ha Y, Kim J, Chung K, Yoon H, Eom K. Fluoroscopic evaluation of laryngopharyngeal anatomic variations attributable to head posture in dogs. *Am J Vet Res*. 2021;82(1):55–62.
7. Buchanan JW. Tracheal signs and associated vascular anomalies in dogs with persistent right aortic arch. *J Vet Intern Med*. 2004;18(4):510–514.
8. Holt D, Brockman D. Diagnosis and management of laryngeal disease in the dog and cat. *Vet Clin North Am Small Anim Pract*. 1994;24(5):855–871.
9. Jakubiak MJ, Siedlecki CT, Zenger E, et al. Laryngeal, laryngotracheal, and tracheal masses in cats: 27 cases (1998–2003). *J Am Anim Hosp Assoc*. 2005;41(5):310–316.
10. Carlisle C, Bierry D, Thrall D. Tracheal and laryngeal tumors in the dog and cat: literature review and 13 additional patients. *Vet Radiol*. 1991;32:229.
11. Todoroff RJ, Brodey RS. Oral and pharyngeal neoplasia in the dog: a retrospective survey of 361 cases. *J Am Vet Med Assoc*. 1979;175(6):567–571.
12. Carozzi G, Zotti A, Alberti M, et al. Computed tomographic features of pharyngeal neoplasia in 25 dogs. *Vet Radiol Ultrasound*. 2015;56(6):628–637.
13. Thierry F, Longo M, Peccu E, et al. Computed tomographic appearance of canine tonsillar neoplasia: 14 cases. *Vet Radiol Ultrasound*. 2018;59(1):54–63.
14. Venker-van Haagen AJ. Diseases of the larynx. *Vet Clin North Am Small Anim Pract*. 1992;22(5):1155–1172.
15. MacPhail C. Laryngeal disease in dogs and cats. *Vet Clin North Am Small Anim Pract*. 2014;44(1):19–31.
16. Wheeldon EB, Suter PF, Jenkins T. Neoplasia of the larynx in the dog. *J Am Vet Med Assoc*. 1982;180(6):642–647.
17. Rossi F, Caleri E, Bacci B, et al. Computed tomographic features of basihyoid ectopic thyroid carcinoma in dogs. *Vet Radiol Ultrasound*. 2013;54(6):575–581.
18. Griffith LG, Tiruneh R, Sullivan M, Reid SW. Oropharyngeal penetrating injuries in 50 dogs: a retrospective study. *Vet Surg*. 2000;29(5):383–388.
19. Doran IP, Wright CA, Moore AH. Acute oropharyngeal and esophageal stick injury in forty-one dogs. *Vet Surg*. 2008;37(8):781–785.
20. Ober CP, Spotswood TC, Hancock R. Fatal venous air embolism in a cat with a retropharyngeal diverticulum. *Vet Radiol Ultrasound*. 2006;47(2):153–158.
21. Francis KA, Goggin JM, Hoskinson JJ. Imaging diagnosis—laryngeal collapse due to cricoid cartilage fracture. *Vet Radiol Ultrasound*. 2008;49(4):360–361.
22. Lamb CR, Pope EHW, Lee KCL. Results of computed tomography in dogs with suspected wood foreign bodies. *Vet Radiol Ultrasound*. 2017;58(2):144–150.
23. Dobromylskyj MJ, Dennis F, Ladlow FJ, Adams VJ. The use of magnetic resonance imaging in the management of pharyngeal penetration injuries in dogs. *J Small Anim Pract*. 2008;49(2):74–79.
24. Krainer D, Dupré G. Brachycephalic obstructive airway syndrome. *Vet Clin North Am Small Anim Pract*. 2022;52(3):749–780.
25. Jones BA, Stanley BJ, Nelson NC. The impact of tongue dimension on air volume in brachycephalic dogs. *Vet Surg*. 2020;49(3):512–520.
26. Hobson HP. Brachycephalic syndrome. *Semin Vet Med Surg*. 1995;10(2):109–114.
27. Auger M, Alexander K, Beauchamp G, Dunn M. Use of CT to evaluate and compare intranasal features in brachycephalic and normocephalic dogs. *J Small Anim Pract*. 2016;57:529–536.
28. Hara Y, Teshima K, Seki M, Kazushi A, Yamaya Y. Pharyngeal contraction secondary to its collapse in dogs with brachycephalic airway syndrome. *J Vet Med Sci*. 2020;82(1):64–67.
29. Stadler K, Hartman S, Matheson J, et al. Computed tomographic imaging of dogs with primary laryngeal or tracheal airway obstruction. *Vet Radiol Ultrasound*. 2011;52(4): 377–384.
30. Johnson LR, Mayhew PD, Steffey MA, et al. Upper airway obstruction in Norwich terriers: 16 cases. *J Vet Intern Med*. 2013;27(6):1409–1415.
31. Skerrett SC, McClaran JK, Fox PR, et al. Clinical features and outcome of dogs with epiglottic retroversion with or without surgical treatment: 24 cases. *J Vet Intern Med*. 2015;29(6):1611–1618.
32. Flanders JA, Thompson MS. Dyspnea caused by epiglottic retroversion in two dogs. *J Am Vet Med Assoc*. 2009;235(11):1330–1335.
33. Rubin JA, Holt DE, Reetz JA, et al. Signalment, clinical presentation, concurrent diseases, and diagnostic findings in 28 dogs with dynamic pharyngeal collapse (2008–2013). *J Vet Intern Med*. 2015;29(3):815–821.
34. Pollard RE, Johnson LR, Marks SL. The prevalence of dynamic pharyngeal collapse is high in brachycephalic dogs undergoing videoflouroscopy. *Vet Radiol Ultrasound*. 2018;59:529–534.
35. Davis A, Khorzad R, Whelan M. Dynamic upper airway obstruction secondary to severe feline asthma. *J Am Anim Hosp Assoc*. 2013;49(2):142–147.
36. Fujiwara-Igarashi A, Yu Y, Hamamoto Y, Hasegawa D, Fujita M. Dynamic pharyngeal collapse in three cats with different pharyngeal pathology. *J Vet Med Sci*. 2019;81(7): 1012–1016.
37. Zaid MS, Prorat-Mosenco Y, Mosenco AS. Dynamic collapse of the common pharynx in a cat. *J Vet Intern Med*. 2011;25:1458–1460.
38. Coolman BR, Marretta SM, McKiernan BC, et al. Choanal atresia and secondary nasopharyngeal stenosis in a dog. *J Am Anim Hosp Assoc*. 1998;34(6):497–501.
39. Berent AC. Diagnosis and management of nasopharyngeal stenosis. *Vet Clin Small Anim*. 2016;(46):677–689.
40. Burdick S, Berent A, Weisse C, et al. Interventional treatment of benign nasopharyngeal stenosis and imperforate nasopharynx in dogs and cats: 46 cases (2005–2013). *J Am Vet Med Assoc*. 2018;253(10):1300–1308.
41. Boswood A, Lamb CR, Brockman DJ, et al. Balloon dilatation of nasopharyngeal stenosis in a cat. *Vet Radiol Ultrasound*. 2003;44(1):53–55.

42. Kirberger RM, Steenkamp G, Spotswood TC, et al. Stenotic nasopharyngeal dysgenesis in the dachshund: seven cases (2002–2004). *J Am Anim Hosp Assoc*. 2006;42(4):290–297.
43. Peterson K, Beymer J, Rudloff E, et al. Airway obstruction in a dog after *Dieffenbachia* ingestion. *J Vet Emerg Crit Care*. 2009;19(6):635–639.
44. Dixon A, Tivers MS, Packham L, Black V. Infiltrative laryngeal disease in dogs. *J Small Anim Pract*. 2020;61(9):568–575.
45. Zekas LJ, Adams WM. Cranial mediastinal cysts in nine cats. *Vet Radiol Ultrasound*. 2002;43(5):413–418.
46. Berry B, Gallaway A, Thrall D, et al. Thoracic radiographic features of anticoagulant rodenticide toxicity in fourteen dogs. *Vet Radiol Ultrasound*. 1993;34:391.
47. Essman SC, Hoover JP, Bahr RJ, et al. An intrathoracic malignant peripheral nerve sheath tumor in a dog. *Vet Radiol Ultrasound*. 2002;43(3):255–259.
48. Stann SE, Bauer TG. Respiratory tract tumors. *Vet Clin North Am Small Anim Pract*. 1985;15(3):535–556.
49. Besancon MF, Stacy BA, Kyles AE, et al. Nodular immunocyte-derived (AL) amyloidosis in the trachea of a dog. *J Am Vet Med Assoc*. 2004;224(8):1302–1306.
50. Sheaffer KA, Dillon AR. Obstructive tracheal mass due to an inflammatory polyp in a cat. *J Am Anim Hosp Assoc*. 1996;32(5):431–434.
51. Snyder KD, Spaulding K, Edwards J. Imaging diagnosis—tracheobronchial zygomycosis in a cat. *Vet Radiol Ultrasound*. 2010;51(6):617–620.
52. Fitzgerald SD, Johnson CA, Peck EJ. A fatal case of intrathoracic cuterebriasis in a cat. *J Am Anim Hosp Assoc*. 1996;32(4):353–357.
53. Volta A, Piccionello AP, Bonazzi M, et al. What is your diagnosis? Bronchial foreign body. *J Am Vet Med Assoc*. 2007;230(2):191–192.
54. Tivers MS, Moore AH. Tracheal foreign bodies in the cat and the use of fluoroscopy for removal: 12 cases. *J Small Anim Pract*. 2006;47(3):155–159.
55. Nutt LK, Webb JA, Prosser KJ, et al. Management of dogs and cats with endotracheal tube foreign bodies. *Can Vet J*. 2014;55(6):565–568.
56. Hardie EM, Spodnick GJ, Gilson SD, Benson JA, Hawkins EC. Tracheal rupture in cats: 16 cases (1983–1998). *J Am Vet Med Assoc*. 1999;214(4):508–512.
57. Basdani E, Papazoglou LG, Patsikas MN, et al. Upper airway injury in dogs secondary to trauma: 10 dogs (2000–2011). *J Am Anim Hosp Assoc*. 2016;52(5):291–296.
58. Lotti U, Niebauer G. Tracheobronchial foreign bodies of plant origin in 153 hunting dogs. *Compend Cont Educ Pract Vet*. 1992;14:900.
59. Mitchell SL, McCarthy R, Rudloff E, et al. Tracheal rupture associated with intubation in cats: 20 cases (1996–1998). *J Am Vet Med Assoc*. 2000;216(10):1592–1595.
60. White RN, Burton CA. Surgical management of intrathoracic tracheal avulsion in cats: long-term results in 9 consecutive cases. *Vet Surg*. 2000;29(5):430–435.
61. White RN, Milner HR. Intrathoracic tracheal avulsion in three cats. *J Small Anim Pract*. 1995;36(8):343–347.
62. Schmierer PA, Schwarz A, Bass DA, et al. Novel avulsion pattern of the left principal bronchus with involvement of the carina and caudal thoracic trachea in a cat. *J Feline Med Surg*. 2014;16(8):695–698.
63. Mattoon JS, Drost WT. Radiographing the trachea in small animals. *Vet Med*. 2004;72.
64. Griffiths LG, Sullivan M, Lerche P. Intrathoracic tracheal avulsion and pseudodiverticulum following pneumomediastinum in a cat. *Vet Rec*. 1998;142(25):693–696.
65. Fasanella FJ, Shivley JM, Wardlaw JL, et al. Brachycephalic airway obstructive syndrome in dogs: 90 cases (1991–2008). *J Am Vet Med Assoc*. 2010;237(9):1048–1051.
66. Coyne BE, Fingland RB. Hypoplasia of the trachea in dogs: 103 cases (1974–1990). *J Am Vet Med Assoc*. 1992;201(5):768–772.
67. Kaye BM, Boroffka SAEB, Haagsman AN, et al. Computed tomographic, radiographic, and endoscopic tracheal dimensions in English bulldogs with grade 1 clinical signs of brachycephalic airway syndrome. *Vet Radiol Ultrasound*. 2015;56(6):609–616.
68. Hammond G, Geary M, Coleman E, et al. Radiographic measurements of the trachea in domestic shorthair and Persian cats. *J Feline Med Surg*. 2011;13(12):881–884.
69. Schultheiss PC, Gardner SA, Owens JM, et al. Mucopolysaccharidosis VII in a cat. *Vet Pathol*. 2000;37(5):502–505.
70. Lindl-Bylicki BJ, Johnson LR, Pollard RE. Comparison of the radiographic and tracheoscopic appearance of the dorsal tracheal membrane in large and small breed dogs. *Vet Radiol Ultrasound*. 2015;56(6):602–608.
71. Johnson L. Tracheal collapse. Diagnosis and medical and surgical treatment. *Vet Clin North Am Small Anim Pract*. 2000;30(6):1253–1266.
72. Violette NP, Weisse C, Berent AC, Lamb KE. Correlations among tracheal dimensions, tracheal stent dimensions, and major complications after endoluminal stenting of tracheal collapse syndrome in dogs. *J Vet Intern Med*. 2019;33(5):2209–2216.
73. Weisse C, Berent AC, Violette NP, et al. Short-, intermediate-, and long-term results for endoluminal stent placement in dogs with tracheal collapse. *J Am Vet Med Assoc*. 2019;254(3):380–392.
74. Johnson LR, Pollard RE. Tracheal collapse and bronchomalacia in dogs: 58 cases (7/2001–1/2008). *J Vet Intern Med*. 2010;24(2):298–305.
75. Macready DM, Johnson LR, Pollard RE. Fluoroscopic and radiographic evaluation of tracheal collapse in dogs: 62 cases (2001–2006). *J Am Vet Med Assoc*. 2007;230(12):1870–1876.
76. Maggiore AD. An update on tracheal and airway collapse in dogs. *Vet Clin North Am Small Anim Pract*. 2020;50(2):419–430.
77. Heng HG, Lim CK, Gutierrez-Crespo B, Guptill LF. Radiographic and computed tomographic appearance of tracheal collapse with axial rotation in four dogs. *J Small Anim Pract*. 2018;59:53–58.
78. Johnson LR, Singh MK, Pollard RE. Agreement among radiographs, fluoroscopy and bronchoscopy in documentation of airway collapse in dogs. *J Vet Intern Med*. 2015;29(6):1619–1626.
79. Marolf A, Blaik M, Specht A. A retrospective study of the relationship between tracheal collapse and bronchiectasis in dogs. *Vet Radiol Ultrasound*. 2007;48(3):199–203.
80. Leonard CD, Johnson LR, Bonadio CM, et al. Changes in tracheal dimensions during inspiration and expiration in healthy dogs as detected via computed tomography. *Am J Vet Res*. 2009;70(8):986–991.
81. Sura PA, Krahwinkel DJ. Self-expanding nitinol stents for the treatment of tracheal collapse in dogs: 12 cases (2001–2004). *J Am Vet Med Assoc*. 2008;232(2):228–236.
82. Moritz A, Schneider M, Bauer N. Management of advanced tracheal collapse in dogs using intraluminal self-expanding biliary Wallstents. *J Vet Intern Med*. 2004;18(1):31–42.
83. Fujita M, Miura H, Yasuda D, et al. Tracheal narrowing secondary to airway obstruction in two cats. *J Small Anim Pract*. 2004;45(1):29–31.
84. Hendricks JC, O'Brien JA. Tracheal collapse in two cats. *J Am Vet Med Assoc*. 1985;187(4):418–419.
85. Mims HL, Hancock RB, Leib MS, et al. Primary tracheal collapse in a cat. *J Am Anim Hosp Assoc*. 2008;44:149.

86. Nafe LA, Robertson ID, Hawkins EC. Cervical lung lobe herniation in dogs identified by fluoroscopy. *Can Vet J*. 2013;54(10):955–959.
87. Guglielmini C, Simone AD, Valbonetti L, Dina A. Intermittent cranial lung herniation in two dogs. *Vet Radiol Ultrasound*. 2007;48(3):227–229.
88. Lee J, Yun S, Lee I, Choi M, Yoon J. Fluoroscopic characteristics of tracheal collapse and cervical lung herniation in dogs: 222 cases (2012-2015). *J Vet Sci*. 2017;18(4):499–505.
89. Arndt JW, Marks SL, Kneller SK. What is your diagnosis? Hiatal hernia due to laryngeal squamous cell carcinoma. *J Am Vet Med Assoc*. 2006;228(5):693–694.
90. Schachter S, Norris CR. Laryngeal paralysis in cats: 16 cases (1990–1999). *J Am Vet Med Assoc*. 2000;216(7):1100–1103.
91. Mattoon JS, Drost WT. Pharyngeal and laryngeal radiography in small animals. *Vet Med*. 2004;50.
92. Kurosawa TA, Ruth JD, Steurer J, et al. Imaging diagnosis—acquired pectus excavatum secondary to laryngeal paralysis in a dog. *Vet Radiol Ultrasound*. 2012;53(3):329–332.
93. Bray JP, Lipscombe VJ, White RA, Rudorf H. Ultrasonographic examination of the pharynx and larynx of the normal dog. *Vet Radiol Ultrasound*. 1998;39(6):566–571.
94. Rudorf H, Barr F. Echolaryngography in cats. *Vet Radiol Ultrasound*. 2002;43(4):353–357.
95. Rudorf H, Barr FJ, Lane JG. The role of ultrasound in the assessment of laryngeal paralysis in the dog. *Vet Radiol Ultrasound*. 2001;42(4):338–343.
96. Stadler K, O'Brien R. Computed tomography of nonanesthetized cats with upper airway obstruction. *Vet Radiol Ultrasound*. 2013;54:231–236.
97. Laurenson MP, Zwingenberger AL, Cissell DD, et al. Computed tomography of the pharynx in a closed vs. open mouth position. *Vet Radiol Ultrasound*. 2011;52(4):357–361.
98. Vázquez JM, Arencibia A, Gil F, et al. Magnetic resonance imaging of the normal canine larynx. *Anat Histol Embryol*. 1998;27(4):263–270.
99. Gendler A, Lewis JR, Reetz JA, et al. Computed tomographic features of oral squamous cell carcinoma in cats: 18 cases (2002–2008). *J Am Vet Med Assoc*. 2010;236(3):319–325.
100. Nicholson I, Halfacree Z, Whatmough C, et al. Computed tomography as an aid to management of chronic oropharyngeal stick injury in the dog. *J Small Anim Pract*. 2008;49(9):451–457.
101. Potanas CP, Armbrust LJ, Klocke EE, et al. Ultrasonographic and magnetic resonance imaging diagnosis of an oropharyngeal wood penetrating injury in a dog. *J Am Anim Hosp Assoc*. 2011;47(1):e1–e6.
102. Dobromylskyj MJ, Dennis R, Ladlow JF, et al. The use of magnetic resonance imaging in the management of pharyngeal penetration injuries in dogs. *J Small Anim Pract*. 2008;49(2):74–79.
103. Jones JC, Ober CP. Computed tomographic diagnosis of nongastrointestinal foreign bodies in dogs. *J Am Anim Hosp Assoc*. 2007;43(2):99–111.
104. Bhandal J, Kuzma A. Tracheal rupture in a cat: diagnosis by computed tomography. *Can Vet J*. 2008;49(6):595–597.
105. Williams JM, Krebs IA, Riedesel EA, et al. Comparison of fluoroscopy and computed tomography for tracheal lumen diameter measurement and determination of intraluminal stent size in healthy dogs. *Vet Radiol Ultrasound*. 2016;57(3):269–275.
106. Montgomery JE, Mathews KG, Marcellin-Little DJ, et al. Comparison of radiography and computed tomography for determining tracheal diameter and length in dogs. *Vet Surg*. 2015;44(1):114–118.
107. Fischetti AJ, Gisselman K, Peterson ME. CT and MRI evaluation of skull bones and soft tissues in six cats with presumed acromegaly versus 12 unaffected cats. *Vet Radiol Ultrasound*. 2012;53(5):535–539.
108. Lamb CR, Ciasca TC, Mantis P, et al. Computed tomographic signs of acromegaly in 68 diabetic cats with hypersomatotropism. *J Feline Med Surg*. 2014;16(2):99–108.

ELECTRONIC RESOURCES

Additional information related to the content in Chapter 29 can be found online at eBooks.Health.Elsevier.com

- Chapter Quiz
- Videos

CHAPTER 30

Pharynx, Upper Esophageal Sphincter, and Esophagus

Rachel E. Pollard

INTRODUCTION

Clinical signs related directly to pharyngeal, cricopharyngeal, and esophageal diseases include gagging, retching, regurgitation, painful swallowing, and dysphagia.[1] Signs developing secondary to esophageal disease include pharyngeal and upper airway inflammation, nasal discharge, weight loss, pneumomediastinum, pneumothorax, pleural effusion, and respiratory disease. Acute respiratory signs may develop secondary to compression of the trachea by an esophageal foreign body or as a result of aspiration of regurgitant material. A strong link between a variety of respiratory diseases and digestive disorders has recently been established.[2–4]

ANATOMIC AND PHYSIOLOGIC FEATURES

Swallowing is an essential and complex process that results in bolus delivery from the oral cavity to the stomach. The actions involving lapping of liquid and prehension and chewing of food are voluntary and require coordinated movements of the tongue and jaws. Once a bolus is propelled into the pharyngeal region, the swallowing reflex occurs involuntarily requiring input from the sensory and motor branches of the trigeminal, the hypoglossal, facial, and glossopharyngeal nerves.[5] The pharynx contracts caudally against the base of the tongue to push the bolus toward the upper esophageal sphincter (UES) (Fig. 30.1). To protect the larynx and airway, the epiglottis flips upward. In coordination with pharyngeal contraction, the paired cricopharyngeus and thyropharyngeus muscles that make up the UES relax to allow passage of the bolus into the proximal esophagus. Subsequently, the UES closes to prevent retrograde movement of the bolus back into the pharynx and the epiglottis returns to its relaxed position so that normal respiration may resume.

The esophagus is a distensible tube responsible for the transport of the bolus from the UES to the stomach. Similar to the rest of the gastrointestinal tract, the esophagus is a layered structure with the innermost surface being lined by mucosa. The submucosa, muscularis, and externally the adventitia are the remaining layers.[6] In the dog, the muscularis layer consists of striated muscle. In the cat, the muscularis layer consists of striated muscle cranially but changes to smooth muscle in the caudal third, resulting in the characteristic "herring bone" appearance on contrast esophagography (Fig. 30.2). A bolus may be transported from the proximal esophagus to the lower esophageal sphincter (LES) by primary or secondary peristaltic waves.[7] A primary peristaltic wave is a continuation of pharyngeal contraction that will propel the bolus directly to the stomach. If primary peristalsis fails, then the bolus is transported

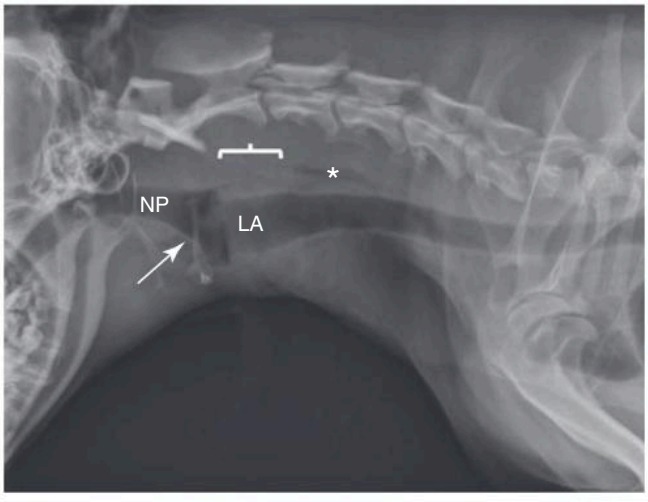


Fig. 30.1 Lateral radiograph of dog showing normal cervical anatomy. *White bracket* = upper esophageal sphincter; *white arrow* = epiglottis. *Asterisk* = air in the proximal esophagus. *LA,* Larynx; *NP,* nasopharynx.

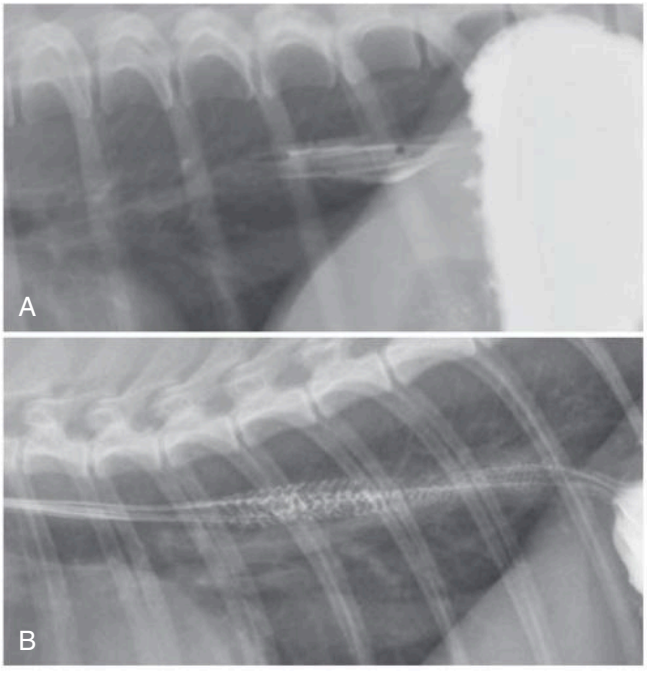


Fig. 30.2 **A,** Barium-contrast esophagram of the caudal esophagus in a normal dog. Note the linear arrangement of the mucosal folds. **B,** Barium-contrast esophagram of the caudal esophagus in a normal cat. Note the herringbone appearance to the mucosa in the caudal aspect of the esophagus that is created by the obliquely oriented smooth muscle in this region.

to the stomach either by secondary peristalsis or with the ensuing primary peristaltic wave generated by the next bolus.

In the cervical region, the esophagus is located slightly to the left of the trachea, gradually becoming completely left sided at the thoracic inlet (Fig. 30.3A).[7] The left common carotid artery, vagosympathetic trunk, internal jugular vein, and tracheal duct course through the angle between the esophagus and the longus capitis muscle. The right common carotid artery, vagosympathetic trunk, internal jugular vein, and tracheal duct are lateral to the trachea on the right side. The thoracic portion of the esophagus is in close proximity to the trachea. The esophagus is to the left of the trachea at the thoracic inlet (see Fig. 30.3B), but gradually courses dorsally over the point of bifurcation of the trachea at the level of the fifth and sixth thoracic vertebrae (see Fig. 30.3C). At its dorsal location, it lies to the right of the aortic arch and ventral to the longus colli muscles. Between the tracheal bifurcation and caudal esophageal sphincter, the esophagus lies in the median plane (see Fig. 30.3D). The vagal nerves run dorsocaudally across the sides of the esophagus and unite at the dorsal aspect of the esophagus a few centimeters cranial to the esophageal hiatus to form the vagal trunk, which passes through the hiatus with the esophagus.

The LES is a focal narrowing of the esophagus at the junction with the stomach that is toned at rest to prevent retrograde movement of gastric contents. The sphincter is made up of a focal thickening of the muscularis layer of the esophagus, a confluence of gastric rugae at the gastroesophageal junction oriented transversely to the sphincter, and a muscular sling created by the diaphragm.[6] A short segment of the esophagus

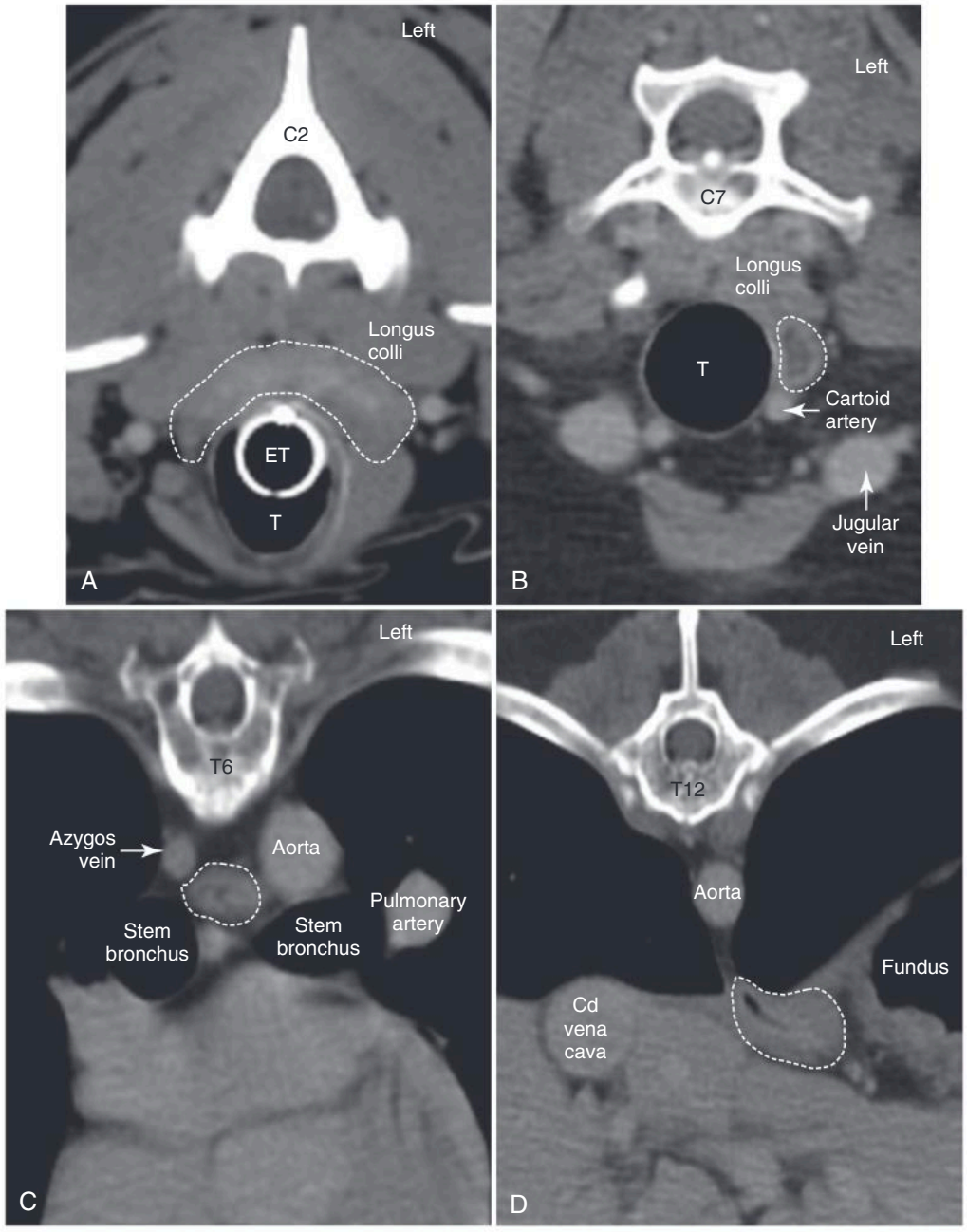


Fig. 30.3 Transverse computed tomography (CT) images of the thorax of a dog at the level of the cricopharyngeal sphincter **(A)**, the thoracic inlet **(B)**, the base of the heart **(C)**, and the level of caudal esophageal sphincter **(D)**, illustrating the relationship of the esophagus (outlined with *dotted line*) to surrounding structures. *C2,* Second cervical vertebra; *C7,* seventh cervical vertebra; *Cd,* caudal; *ET,* endotracheal tube; *T6,* sixth thoracic vertebra; *T12,* twelfth thoracic vertebra, *T,* trachea.

resides on the abdominal side of the diaphragm where the relatively positive intra-abdominal pressure compresses it. When a bolus is transported caudad by the esophagus, the LES relaxes to allow passage into the stomach.

Vascular supply to the esophagus is complicated and begins in the cervical region with branches of the thyroid arteries. The bronchoesophageal artery is the main source to the cranial two-thirds of the thoracic portion. Esophageal branches of the aorta and/or intercostal arteries supply the remainder of the esophagus, and the terminal portion is supplied by the left gastric artery. The azygous vein and left gastric vein drain the thoracic portion. Lymphatic drainage is through the medial retropharyngeal, deep cervical, cranial mediastinal, bronchial, portal, splenic, and gastric lymph nodes.

Innervation of the esophagus is complex and involves 25 paired spinal ganglia from C2 to L5. Neurologic control of swallowing is coordinated by cranial nerves V (trigeminal), VII (facial), IX (glossopharyngeal), X (vagus), and XII (hypoglossal), and their nuclei in the brainstem that, in turn, are controlled by areas of the reticular formation referred to as the swallowing center.[8]

RADIOGRAPHY

Survey radiography of the thorax and neck is often the first imaging step for the evaluation of an animal with suspected pharyngeal, UES, or esophageal disease. This should include three projections of the thorax (dorsoventral or ventrodorsal [VD], right, and left lateral) and at least one lateral projection of the neck. Care should be taken to ensure that the radiograph of the neck is adequately positioned. More specifically, the lateral cervical study must not be rotated and the head should be extended as poor positioning can distort anatomy and seriously compromise interpretation. The pharynx, larynx, and UES should be included.

The normal esophagus is usually empty and rarely visible on thoracic radiographs in cats and dogs because of its location within the mediastinum and silhouetting with adjacent muscles and mediastinal structures. On left lateral thoracic radiographs, the normal caudal thoracic esophagus sometimes contains a small amount of fluid and can be seen as a faint tubular soft tissue opacity between the descending aorta and caudal vena cava (Fig. 30.4A); this appearance is rare in right lateral radiographs. Gas can accumulate focally in the esophagus in animals that are excited, sedated or anesthetized, and dyspneic; this gas accumulation is usually minimal, and the most commonly located just cranial to the tracheal bifurcation (see Fig. 30.4B). The tissue band between the trachea and esophagus (*white arrows*) is termed the *tracheal stripe sign*, also called the *tracheoesophageal stripe sign* and *esophageal stripe sign.* This is created by summation of the ventral aspect of the esophageal wall with the dorsal aspect of the tracheal wall, each outlined by gas in their respective lumen. The tracheal stripe sign is a

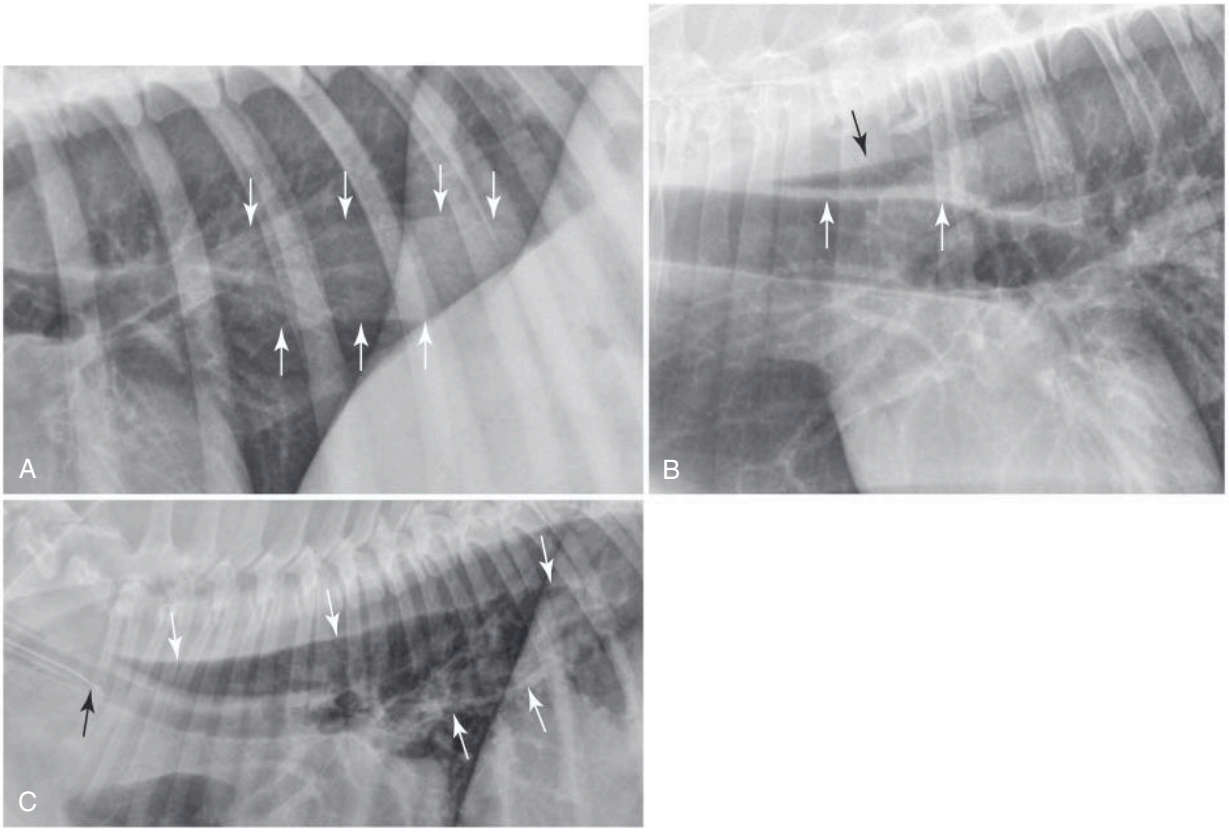


Fig. 30.4 Variations in the appearance of the normal esophagus. **A,** Left lateral radiograph of a normal adult dog. The caudal one-third of the esophagus is visible as a soft tissue band between the aorta and caudal vena cava (*white arrows*). This finding is usually not present on right lateral radiographs of normal dogs. **B,** Left lateral radiograph of a normal adult dog where there is a small amount of gas in the esophagus just cranial to the tracheal bifurcation (*black arrow*). This will not be visible in the ventrodorsal (VD) view. The tissue band between the trachea and esophagus (*white arrows*) is termed the *tracheal stripe sign,* also called the tracheoesophageal stripe sign and esophageal stripe sign. This is created by summation of the ventral aspect of the esophageal wall with the dorsal aspect of the tracheal wall, each outlined by gas in their respective lumen. The tracheal stripe sign is a reliable sign of esophageal gas. **C,** Left lateral radiograph of an anesthetized dog. The endotracheal tube is visible (*black arrow*). There is generalized megaesophagus (*white arrows*) because of the anesthesia. The enlarged esophagus is causing ventral displacement of the intrathoracic trachea. Radiographically, this cannot be distinguished from pathologic megaesophagus.

reliable sign of esophageal gas (see Fig. 30.4B). Focal esophageal gas collections are dynamic and may appear differently or be absent in other radiographs acquired during the same study. General anesthesia or aerophagia may lead to severe dilation of the esophagus, which can appear identical to pathologic megaesophagus (see Fig. 30.4C). Anesthesia-related megaesophagus will resolve spontaneously when the patient is awake again.

Survey radiographs will help define if aspiration pneumonia is present. Aspiration pneumonia is common in animals with swallowing disorders and typically involves the dependent aspect of the right and left cranial and right middle lung lobes. Since the right middle lung lobe is a common site for aspiration, the left lateral thoracic view is essential for complete assessment of the lung.[9] When megaesophagus is identified, the presence of aspiration pneumonia has a negative association with survival time.[10]

The absence of abnormal findings on survey radiographs of the esophagus does not eliminate the possibility of esophageal disease. In animals with appropriate clinical signs of esophageal disease, contrast studies of the esophagus should be considered. However, in cases where severe aspiration pneumonia is present, contrast studies should be delayed until such time as pneumonia is resolved as aspiration of barium during the imaging procedure will further compromise lung function.

CONTRAST RADIOGRAPHY

Survey radiographs of the thorax and cervical region are ideally performed immediately before a contrast esophagram. Box 30.1 contains a list of contrast study techniques used for examination of the esophagus. The type of contrast medium selected to perform contrast radiography depends on several factors.[11] Barium paste or cream is viscous and may adhere best to mucosal irregularities. However, due to the viscosity of these agents, barium paste and cream may not flow well around intraluminal lesions and are contraindicated in animals at increased risk for aspiration, because aspirated paste can cause airway obstruction.[6] Liquid barium (60% weight-volume) is the most common medium used for contrast radiography of the pharynx and esophagus.[12] Dosage is related to size so that cats should receive 5 to 7 mL boluses, small- to medium-sized dogs should receive 15 mL boluses, while larger dogs should receive 20 to 30 mL boluses of liquid barium orally.[12]

When endoscopy is likely to follow or if perforation of the pharynx, cricopharynx, or esophagus is suspected, nonionic iodinated contrast agents are preferable to barium so as to avoid the granulomatous reaction associated with leakage into the cervical soft tissues or mediastinum.[13] Ionic, iodinated contrast agents are specifically contraindicated due to the potential for life-threatening pulmonary edema that can result from aspiration into the lungs. Esophageal perforation should be suspected when survey radiographs identify gas in the cervical soft tissues or mediastinum but no external wounds are present. Soft tissue swelling in the cervical region with regional emphysema is suggestive of perforation. Opacification and widening of the mediastinum may accompany pneumomediastinum when perforation of the thoracic esophagus has resulted in mediastinitis.[14] In these instances, nonionic, iodinated contrast medium should be diluted 50:50 with sterile water and 10 to 15 mL boluses are administered orally.[15] Sedation should generally be avoided unless absolutely necessary since tranquilizers result in significant alterations in swallowing function.[15] However, should sedation be required, acepromazine may be administered but may increase esophageal transit times, particularly at higher doses.[16]

Regardless of the type of contrast medium used, the animal is restrained in right lateral recumbency and liquid contrast medium is administered orally using a catheter-tipped syringe.

Box • 30.1

Techniques for Esophageal Contrast Studies

Static Barium Esophagram

Special Considerations

No sedation

Contraindicated for esophageal perforation

Use barium paste instead of barium suspension for evaluating mucosa

Aspiration potential

Procedure

Survey lateral and ventrodorsal (VD) radiographs of the neck and thorax

Orally administer via syringe in lateral recumbency

- Small dog: 15 mL of 60% weight/volume preformulated barium sulfate suspension
- Large dog: 20–30 mL of 60% weight/volume preformulated barium sulfate suspension
- Cat: 5–7 mL of 60% weight/volume preformulated barium sulfate suspension

Lateral radiographs of the neck and thorax immediately after oral administration

VD radiographs of thorax immediately

Right and left oblique VD thoracic radiographs

Repeat entire procedure if amount of contrast medium in esophagus is insufficient

Static Barium Meal Esophagram

Special Considerations

Can identify small or incomplete obstructions that allow liquid to pass

Should be used if the esophagram with liquid barium is negative

Should be used if the patient can swallow liquids but not solid food clinically

Should not be performed if perforation is suspected

Procedure

Dogs: 1 cup dry kibble mixed with 20 mL barium sulfate suspension

Cats: 1/2 cup dry kibble or soft food mixed with 10 mL barium sulfate suspension

Perform following the swallowing study using liquid barium suspension

Provide the food mixture while in lateral recumbency or place in mouth

Perform same sequence of radiographs as for liquid barium

Static Iodinated Esophagram

Special Considerations

Can be used before endoscopy or if perforation is suspected

Do not use ionic contrast medium because it can cause pulmonary edema if aspirated

Procedure

Dog: 10–15 mL of a 50:50 mixture of nonionic iodinated contrast medium and water

Cat: 5–10 mL of a 50:50 mixture of nonionic iodinated contrast medium and water

Administer the liquid via syringe in lateral recumbency

Perform radiographic procedures as for liquid barium

From Wallack ST. Static barium esophagram. In: *The Handbook of Veterinary Contrast Radiography.* Solana Beach, CA: San Diego Veterinary Imaging; 2003:45–53.



Fig. 30.5 Right lateral radiograph of a cat where barium was injected into the trachea postmortem to demonstrate the appearance of barium accumulation in the airways and lung parenchyma.

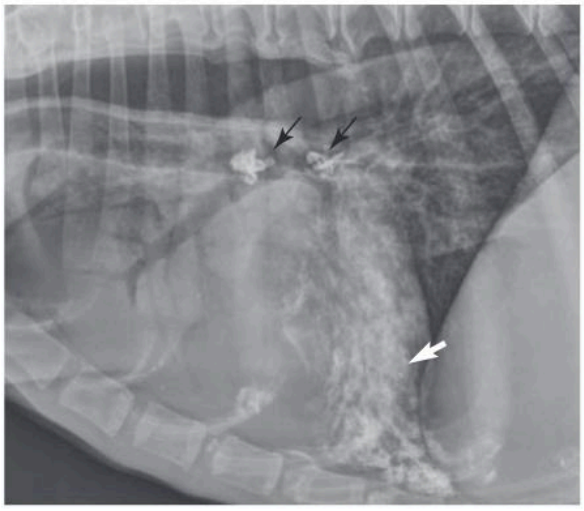


Fig. 30.6 Lateral thoracic radiograph of a 9-year-old standard poodle. Barium aspiration occurred in the right middle lung lobe 1 year prior (*white arrow*). The regional lymph nodes have an amorphous mineral opacity (*black arrows*) because of lymphatic transport of aspirated barium. Active pneumonia, unrelated to barium aspiration, is present in the right cranial lung lobe.

Lateral and dorsoventral radiographs of the neck and thorax should be obtained during swallowing or as soon after swallowing as possible. It is wise to obtain images of multiple swallows and to confirm the presence of a suspected lesion on multiple projections. When perforation is unlikely, kibble is then soaked in barium and administered orally.[12] Additional lateral and VD radiographs of the neck and thorax should be obtained. Barium-soaked kibble is particularly helpful when trying to identify esophageal strictures through which liquid barium may pass unimpeded. Mixing iodinated contrast agents with kibble is not advised since iodinated agents are typically used when perforation is suspected and esophageal leakage of kibble is undesirable.[15]

Barium or iodine aspiration is a potential complication of performing esophageal contrast studies. Aspiration of a small amount of liquid barium is usually insignificant. Pneumonia and lung granuloma formation are rare complications of barium aspiration. Aspirated barium is cleared from the airways by ciliary action, as well as coughing. If barium enters the alveolar space, it may remain there permanently (Fig. 30.5). Lymphatic uptake of aspirated barium will also be evident as amorphous mottled opacities in the region of the mediastinal and tracheobronchial lymph nodes, which may also be a permanent finding (Fig. 30.6).



Fig. 30.7 A radiolucent squeeze cage made of polycarbonate can be used to examine the swallowing phases in a dog in a standing position with reduced radiation exposure to personnel and mimic a normal swallowing posture.

CONTRAST VIDEOFLUOROSCOPIC SWALLOWING STUDIES

When a functional or transient disorder of swallowing is suspected and cannot be defined by survey or contrast radiography, contrast videofluoroscopic assessment of swallowing is indicated. When performing dynamic fluoroscopic swallowing studies, it is essential to protect personnel involved in the study from scattered radiation by establishing barriers of lead-impregnated rubber or other shielding between the primary beam and the attending personnel.[8]

In preparation for a videofluoroscopic swallowing study (VFSS), the animal is ideally fasted for 12 hours prior to the procedure. Liquid barium (60% weight-volume) is the most common contrast medium used but, similar to contrast radiography, nonionic iodinated medium diluted 50:50 with sterile water can be used in cases where perforation of the pharynx or esophagus is suspected. The animal is then positioned on the fluoroscopy table. The animal can either be restrained in lateral recumbency on the fluoroscopy table or imaged in sternal or standing position using a cross-table imaging orientation. The differences between sternal and lateral body positioning during VFSS have been reported in the dog and cervical esophageal transit times are significantly delayed in laterally recumbent dogs.[17] However, a specific positioning device is ideal to minimize patient motion during sternally positioned or standing studies (Fig. 30.7) and, in the authors' experience, head motion remains problematic during these examinations, particularly in dogs with dysphagia. As with contrast radiography, sedation should be avoided when performing contrast-enhanced videofluoroscopy due to the inherent alteration in swallowing function that results from tranquilization.

Standardization of videofluoroscopic contrast swallowing studies is essential for accurate interpretation, because bolus size and form (solid vs. liquid) can significantly alter many of the quantitative and qualitative features.[18] Measurements of pharyngeal constriction ratio (PCR), time to maximum pharyngeal contraction, time to cricopharyngeal sphincter opening, time to epiglottis reopening, and the percentage of secondary peristaltic waves do not differ with body position but

other esophageal transit times and frequency of peristaltic waves do.[17] Regardless of body position, liquid barium should be administered orally in small (5–10 mL) boluses using a catheter-tipped syringe. At least three complete swallows should be observed and at least one bolus should be followed all the way to the stomach. Barium-soaked soft food followed by barium-soaked kibble should also be given orally and bolus propulsion observed fluoroscopically to rule out abnormalities that allow liquid passage but affects passage of solid foods. Recording the study and performing frame-by-frame analysis can provide quantitative measures of swallowing function.

Many quantitative parameters have been reported as valuable assessments of pharyngeal and cricopharyngeal function.[17–21] These include the interswallow interval ([ISI]; time in seconds between two successive, uninterrupted swallows from the onset frame of swallow 1 to the onset frame of the subsequent swallow), swallow rate (the number of swallows per 3-second interval of uninterrupted prehension), jaw cycles per swallow ratio (the number of licks from maximum jaw excursion to the following maximum jaw excursion), time from swallow onset (Fig. 30.8A) to proximal esophageal sphincter/UES opening (Fig. 30.8B), time to maximum laryngeal excursion (Fig. 30.8C), time to maximum pharyngeal contraction (Fig. 30.8D), time to air column reopening/epiglottis reopening (Fig. 30.8E), and time to proximal esophageal sphincter/UES closure (Fig. 30.8F). When making quantitative measures, videos are viewed frame by frame where each frame represents 1/30th of a second. The frame in which the epiglottis is observed to close over the larynx is considered as the starting point for all time measurements. The swallow is considered completed when the epiglottis is observed to reopen. Once the number of frames to each point in the swallow is calculated, that number can be divided by 30 to obtain the number of seconds from the initiation of the swallow to each particular event within that swallow. The contraction of the pharynx can also be assessed using frame-by-frame analysis to facilitate calculation of the PCR.[19] From the digitized videofluoroscopic studies, a hold frame and a maximum contraction frame are selected. The hold frame is identified as a frame in which the larynx appeared at rest without rostral or caudal motion. The maximum contraction frame is identified as a frame in which the dorsal pharyngeal wall had reached its most

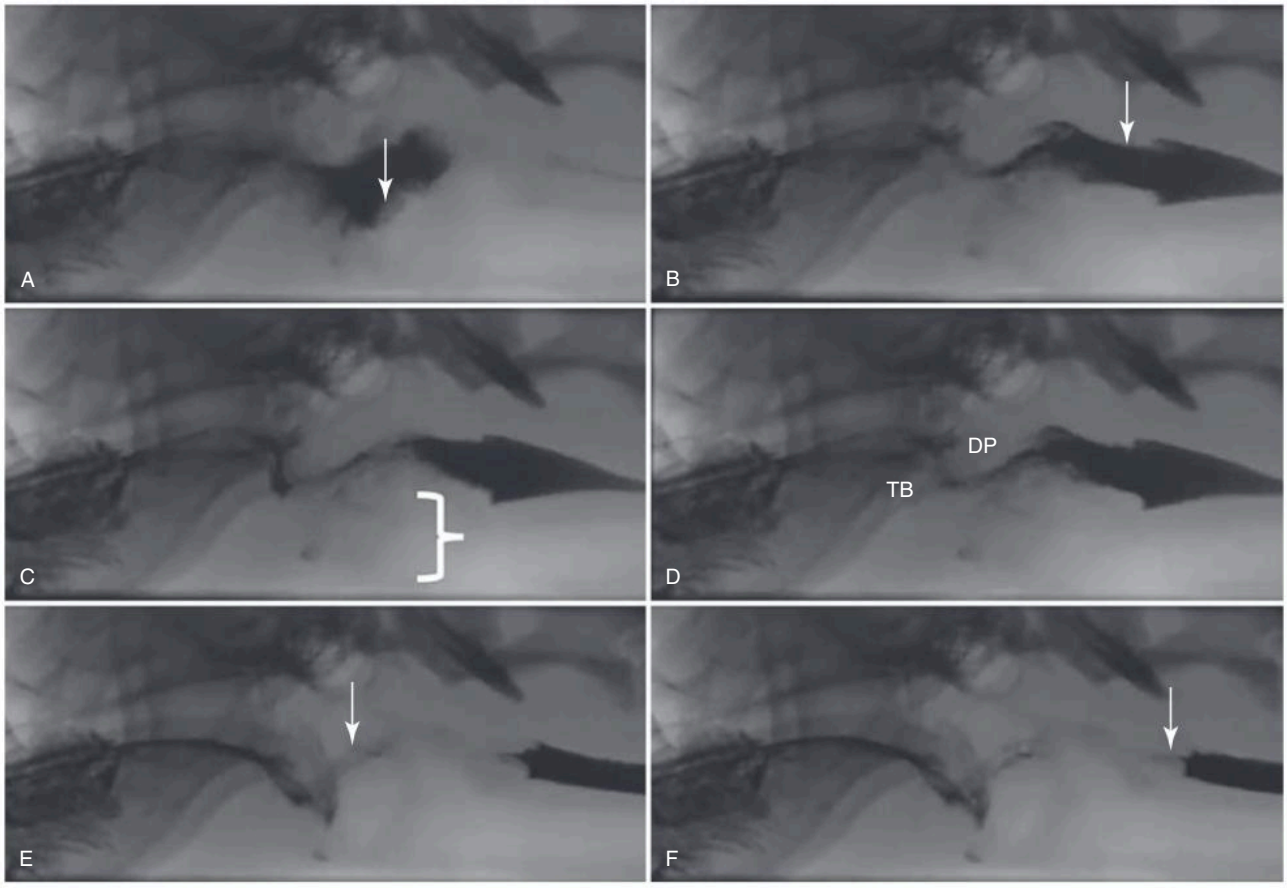


Fig. 30.8 Representative images are shown from a contrast videofluoroscopic evaluation of swallowing obtained from a healthy dog. Typically, the number of frames is counted from onset of swallowing to specified events and converted to seconds based on a 30-frame-per-second image acquisition. **A,** Swallow onset frame indicated by closure of the epiglottis (*white arrow*) and perpendicular movement of the bolus toward the pharynx. **B**, First frame in which the upper/proximal esophageal sphincter (*white arrow*) is open. **C,** Frame in which the larynx is in its most rostral position (*white bracket*). **D,** Frame obtained at maximal pharyngeal contraction where tongue base (*TB*) and dorsal pharyngeal wall (*DP*) are in contact and have their most ventral and caudal position. **E,** Frame in which the air column in the pharynx has reappeared (*white arrow*) due to opening of the epiglottis and relaxation of the pharynx. **F,** Frame in which the bolus has completely passed into the proximal esophagus and the upper/proximal esophageal sphincter is closed (*white arrow*). (Reproduced with permission from Pollard RE. Videofluoroscopic evaluation of the pharynx and upper esophageal sphincter in the dog: a systematic review of the literature. *Front Vet Sci.* 2019;6:117.)

ventral and caudal position. For the hold frame, a region of interest (ROI) is drawn around the airspace beginning dorsal to the soft palate then rostrally to the hyoid apparatus and tympanic bulla, dorsally to the dorsal aspect of the pharyngeal wall, caudally along the dorsal aspect of the pharyngeal wall to the UES, and ventrally around the corniculate process of the arytenoid cartilage to include the vallecula, finally connecting the epiglottis to the starting point (Fig. 30.9A). The UES is specifically defined as the region in the cranial esophagus that remained the narrowest through the study.[22] For the maximum contraction frame, an ROI is drawn around any residual barium or airspace identified within the pharyngeal area (see Fig. 30.9B). ROIs are expressed in pixel numbers and the PCR is calculated by dividing the number of pixels in the maximum contraction frame by the number of pixels in the hold frame. Normal reference ranges for quantitative measures are outlined in Table 30.1, including measurements made with animals in different body positions, consuming different bolus sizes and of various ages.

Techniques for VFSS in dogs with megaesophagus have been reported with the intent of defining LES function, assess for any evidence of peristalsis, and to determine the optimal dietary consistency for expedition of esophageal clearance.[23,24] Dogs are fasted for 12 hours prior to imaging and positioned in a size appropriate Bailey chair with the photon beam directed horizontally to yield a lateral projection of the cervical and thoracic esophagus to the level of the LES (Fig. 30.10A,B). Bolus consistencies are similar to above and include liquid barium, barium-soaked soft food/slurry and barium-soaked kibble. VFSS is performed along the entire length of the esophagus at baseline, for the first 20 seconds or until complete esophageal clearance, and then every 5 minutes for up to 15 minutes following liquid administration and 30 minutes after each food type. Fluoroscopic evaluation is discontinued if all material clears from the esophagus or after 15 minutes for liquid and 30 minutes for slurry and kibble, whichever comes first.

Regardless of the VFSS study performed, in normal animals, there should be no retention of barium in the oral or pharyngeal cavity during swallowing. Some coating of the mucosa is normal. No contrast medium should be present in the pharynx, larynx, or trachea after swallowing. Small volumes of contrast medium may accumulate in the proximal esophagus if bolus size is inadequate for stimulation of a primary peristaltic wave. However, larger boluses should trigger primary peristalsis, or secondary peristalsis should initiate once boluses accumulate to an adequate size.

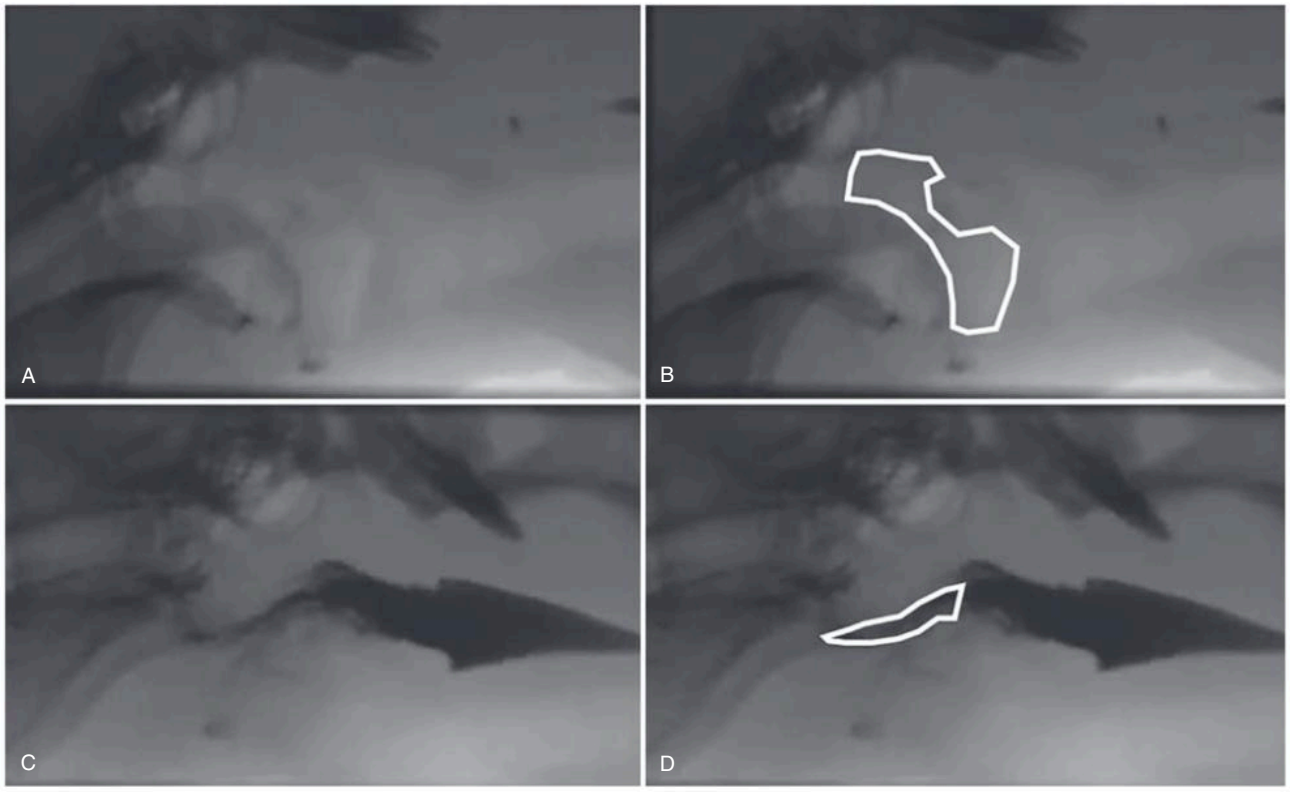


Fig. 30.9 The pharyngeal constriction ratio (PCR) is a metric of pharyngeal function and is calculated by measuring the area in the pharynx at maximal contraction (maximal contraction frame) and dividing that by the area of the pharynx at rest (hold frame). **A,** Hold frame from a contrast videofluoroscopic evaluation of swallowing obtained from a healthy dog. **B,** Same image as in **A** with the area of pharynx outlined including the airspace beginning dorsal to the soft palate then rostrally to the hyoid apparatus and tympanic bulla, dorsally to the dorsal aspect of the pharyngeal wall, caudally along the dorsal aspect of the pharyngeal wall to the cranial esophageal sphincter, ventrally around the corniculate process of the arytenoid cartilage to include the vallecula, and finally connecting the epiglottis to the starting point. **C,** Maximal contraction frame from the same dog as in **A** and **B**. **D,** Maximal contraction frame from the same dog as in **A** and **B** with the area of the pharynx defined. (Reproduced with permission from Pollard RE. Videofluoroscopic evaluation of the pharynx and upper esophageal sphincter in the dog: a systematic review of the literature. *Front Vet Sci.* 2019;6:117.)

Table • **30.1**

Summary of Quantitative Parameters Obtained From Videofluoroscopic Swallowing Studies.

	BONADIO ET AL.[17]		CHENEY ET AL.[18]			HARRIS ET AL.[21]		
PARAMETER	**LATERAL**	**STANDING**	**SMALL BOLUS**	**MEDIUM BOLUS**	**LARGE BOLUS**	**JUVENILE**	**ADULT**	**GERIATRIC**
UES open	0.10 ± 0.02	0.11 ± 0.02	0.09 ± 0.02	0.08 ± 0.02	0.08 ± 0.02	0.04 ± 0.02	0.05 ± 0.03	0.03 ± 0.02
Max LE	NA	NA	NA	NA	NA	0.07 ± 0.03	0.08 ± 0.04	0.10 ± 0.06
Max PC	0.11 ± 0.04	0.10 ± 0.03	0.15 ± 0.04	0.16 ± 0.04	0.17 ± 0.04	0.11 ± 0.06	0.12 ± 0.04	0.11 ± 0.02
Epi open	0.24 ± 0.04	0.25 ± 0.05	0.22 ± 0.05	0.23 ± 0.04	0.25 ± 0.04	0.28 ± 0.06	0.26 ± 0.06	0.30 ± 0.05
UES close	0.25 ± 0.04	0.27 ± 0.04	0.25 ± 0.06	0.26 ± 0.05	0.29 ± 0.05	0.33 ± 0.03	0.31 ± 0.06	0.35 ± 0.06
PCR	0.11 ± 0.35	0.14 ± 0.04	0.13 ± 0.03	0.13 ± 0.03	0.13 ± 0.04	NA	NA	NA
ISI	NA	NA	NA	NA	NA	1.51 ± 1.97	1.14 ± 0.53	1.19 ± 0.69
Swallow rate (per 3 seconds)	NA	NA	NA	NA	NA	1.65 ± 1.20	2.65 ± 0.70	2.35 ± 0.65
Jaw cycles per swallow ratio	NA	NA	NA	NA	NA	2.70 ± 2.68	2.85 ± 1.15	3.00 ± 1.25

Epi, epiglottis; *ISI,* interswallow interval; *LE,* laryngeal excursion; *Max,* maximum; *NA,* not assessed; *PC,* pharyngeal contraction; *PCR,* pharyngeal constriction ratio; *UES,* upper esophageal sphincter.
Modified from Pollard RE. Videofluoroscopic evaluation of the pharynx and upper esophageal sphincter in the dog: a systematic review of the literature. *Front Vet Sci*. 2019;6:117.

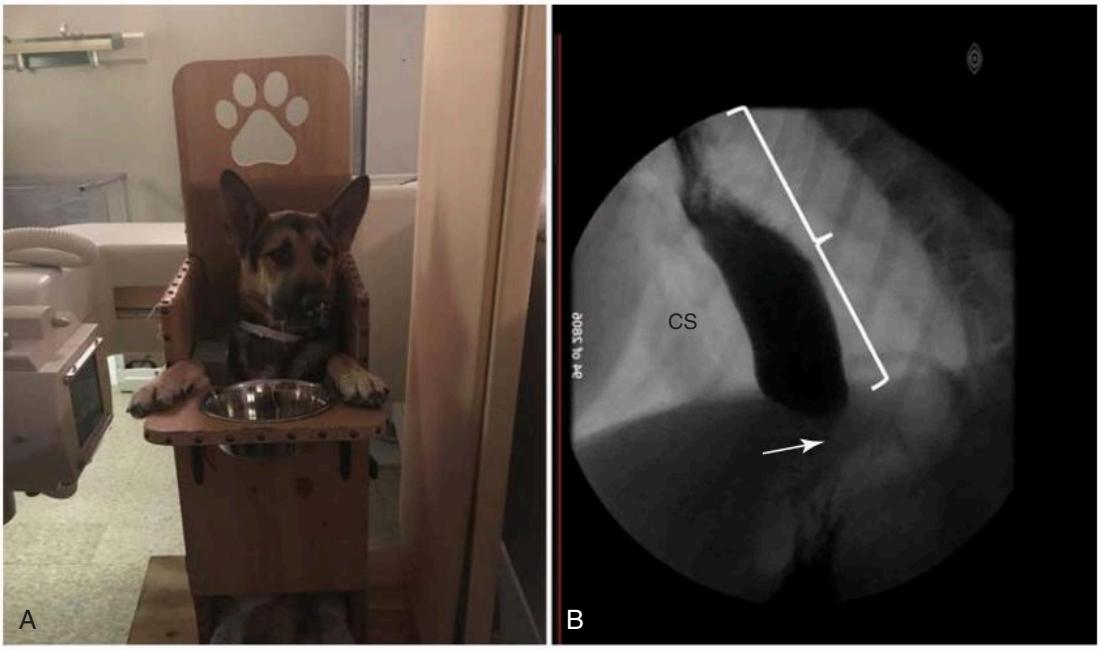


Fig. 30.10 **A,** Dog with megaesophagus positioned in a Bailey chair with the fluoroscopic unit oriented so as to image horizontally through the thorax. **B,** Lateral fluoroscopic image of the same dog as in **A** showing barium accumulation in the dilated caudal thoracic esophagus (*white bracket*) with the lower esophageal sphincter remaining closed (*white arrow*). *CR,* Cardiac silhouette.



Fig. 30.11 Lateral cervical radiograph of an adult dog. An ingested bone is lodged in the pharynx (*white arrow*).

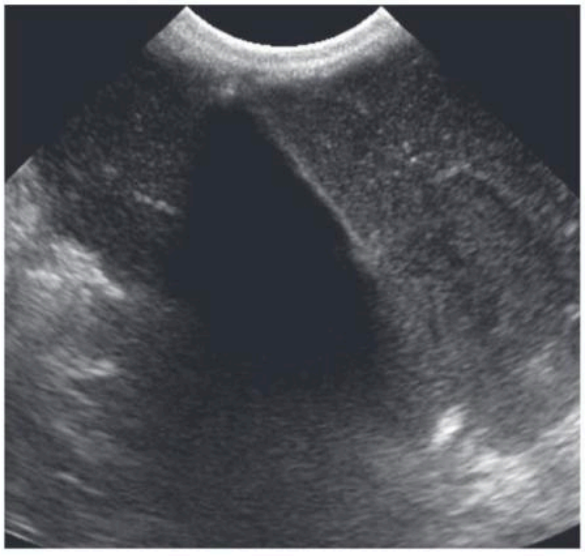


Fig. 30.12 Ultrasound image of the cervical region of a dog with nonspecific swelling of the cranioventral aspect of the neck. There is a large subcutaneous fluid accumulation and multiple, linear, hyperechoic shadowing structures that were determined to be splinters of wood.

PHARYNGEAL AND CRICOPHARYNGEAL DYSPHAGIA

Dysphagia can be morphologic or functional in origin. Morphologic causes include trauma, foreign body, an oral or pharyngeal mass, and regional lymphadenopathy. Lateral and VD survey radiographs of the pharyngeal and cervical region and thorax are indicated to screen for radiopaque foreign bodies, such as bones, needles, and fish hooks (Fig. 30.11). Soft tissue swelling and gas pockets can be seen with perforating pharyngeal trauma, abscesses, or nonradiopaque foreign bodies, such as wooden sticks. Ultrasonography can be useful to determine the source of nonspecific pharyngeal swelling and to identify nonradiopaque foreign bodies (Fig. 30.12).

When a morphologic cause for dysphagia cannot be found, VFSS is indicated to assess function (Table 30.2). Dogs with oral phase dysphagia have difficulty with prehension and bolus formation and with transport to the pharynx. Oral dysphagia is usually characterized by the animal dropping food or liquid from its mouth and drooling.[19] The oral phase of swallowing is the only voluntary portion of the swallowing process. In oral dysphagia, there is failure of aboral transport of liquid or food and lack of bolus formation to induce the swallowing reflex. These disorders are typically diagnosed by watching the animal eat and rarely require imaging. However, if VFSS is performed, liquid contrast medium pools in the dependent vestibule of the

Table • 30.2

Types of Dysphagia, Causes, and Fluoroscopy Findings.

TYPE	CAUSES	FLUOROSCOPIC FEATURES
Oral	Neuromuscular disease	Bolus not formed or delayed formation
	Inflammation	Bolus not propelled caudally to pharynx
	Oral foreign body	Weak plunger-like movement of tongue
	Tongue abscess	Weak pharyngeal contractions
		Subsequent stages are normal
Pharyngeal	Myositis and myopathy	Normal oral stage
	Post-cricopharyngeus myectomy	Remains synchronous with cricopharyngeal phase
		Retention of contrast medium in the pharynx
	Neuromuscular disease	No change in time to cricopharyngeal sphincter opening
	Inflammation	Inadequate pharyngeal contraction
	Trauma	Pharyngeal constriction ratio prolonged (0.6)
	Idiopathic	Misdirection of the bolus into larynx or nasopharynx
Cricopharyngeal chalasia	Cricopharyngeus myotomy	Relaxation or incompetence of the cricopharyngeal sphincter
	Radiation therapy	Cricopharyngeal sphincter may appear air-filled
	Myasthenia gravis	Prolonged time to cricopharyngeal sphincter opening (28 seconds)
		Weak pharyngeal contractions may also be present
		Aspiration into larynx or trachea possible
Cricopharyngeal achalasia	Idiopathic	Incomplete or lack of opening of cricopharyngeal sphincter
		Vigorous attempts to pass bolus to cricopharyngeal sphincter
		Synchrony of timing of the opening of the cricopharyngeal sphincter
		Delayed time to cricopharyngeal sphincter opening
		Barium retention in pharynx
		Aspiration into larynx or trachea possible
Esophageal dysmotility	Delayed maturation	Megaesophagus may be present in young dogs
	Esophagitis	Abnormal primary wave (bolus moves <5 cm aborally)
		Abnormal secondary wave (bolus retention after two or more subsequent swallows)
		Retrograde >10 cm
		Prolonged esophageal transit time >5 seconds

mouth or flows out of the mouth. The backward and forward movement of the tongue will be normal or reduced. The bolus will not be formed and propelled aborally, or its formation will be delayed. The onset of the pharyngeal phase of swallowing may also be delayed. If a swallow is achieved, the pharyngeal and esophageal phases of swallowing are usually normal.

Pharyngeal dysphagia is often characterized by nonspecific signs, such as gagging, retching, and the necessity for multiple swallowing attempts before movement of a bolus into the esophagus.[20] Pharyngeal dysphagia is diagnosed when the contraction of the dorsal pharyngeal wall against the tongue base is weak so that presentation of the bolus to the UES lacks vigorous momentum. The cricopharyngeal phase may or may not be normal. Pharyngeal dysphagia is often the result of neuromuscular disorders that result in weakness or as a result of pharyngeal inflammation. Videofluoroscopic abnormalities include (1) slow contraction of the pharynx, (2) incomplete enclosure of the bolus, (3) incomplete rostral and dorsal movement of the larynx, and (4) absence of forceful contraction of the pharynx to propel the bolus through the cricopharyngeal sphincter. The UES may not open or open to a reduced diameter because of the weakness of the pharyngeal contraction, and this could be misinterpreted as a cricopharyngeal disorder. The PCR was developed to identify dogs with weak pharyngeal contraction that would make them poor candidates for myotomy when cricopharyngeal dysphagia is diagnosed and to better differentiate them from those with cricopharyngeal dysphagia.[19] Dogs with decreased pharyngeal contraction have a significantly higher PCR compared with healthy dogs, but this can also be present in dogs with cricopharyngeal dysphagias. The discerning factor between pharyngeal dysphagia and cricopharyngeal dysphagia is the time to opening of the cricopharyngeal sphincter, which is significantly shorter in pharyngeal dysphagia.[19]

Cricopharyngeal dysphagia is a functional abnormality involving failure of the cricopharyngeal sphincter to open fully (cricopharyngeal achalasia) or at the appropriate time (cricopharyngeal dyssynchrony). The clinical signs of cricopharyngeal dysphagia are similar to those of pharyngeal dysphagia (Fig. 30.13).[19] Although specific breed predilections have not been reported, cricopharyngeal achalasia is often associated with toy breeds.[25] The exact etiology has not been determined, but most affected patients develop clinical signs soon after weaning, suggesting that cricopharyngeal achalasia is a congenital disorder.[26] Critical to the diagnosis is the documentation of delayed or nonopening of the UES and a lack of coordination between pharyngeal contraction and opening of the UES, which requires fluoroscopy (Fig. 30.14). Time from onset of swallowing to opening of the UES is delayed in dogs with cricopharyngeal achalasia compared with normal dogs (0.31 ± 0.14 vs. 09 ± 0.02 seconds for liquids and 0.37 ± 0.06 vs. 0.10 ± 0.03 seconds for kibble).[19] The same is true for UES

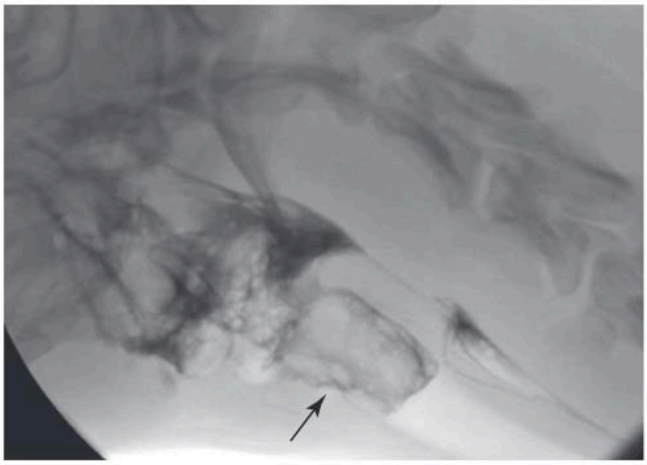


Fig. 30.13 Lateral digital fluoroscopic image of barium swallow in a 2-year-old Border collie with cricopharyngeal dysphagia. The timing of the pharyngeal and cricopharyngeal phases was abnormal, a tight bolus is not present, and barium has been aspirated into the laryngotrachea (*black arrow*). The cricopharyngeal phase was normal but delayed.

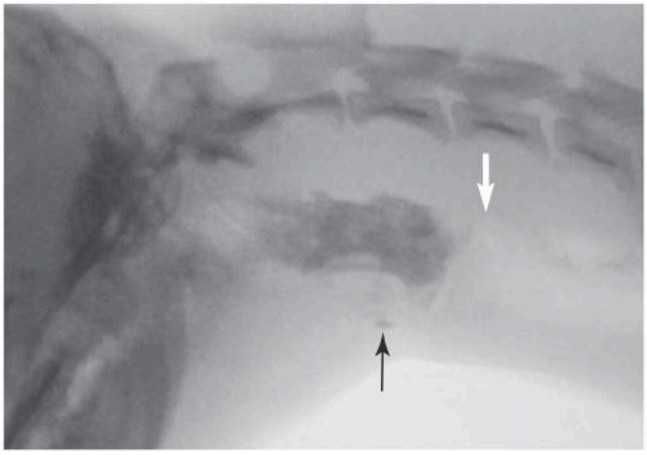


Fig. 30.14 Lateral videofluoroscopic image of a barium swallow in a 1.5-year-old Peekapoo that had severe cricopharyngeal dysphagia. A large bolus (*black arrow*) is present cranial to the closed cricopharyngeal sphincter (*white arrow*). The cricopharyngeal sphincter opened after many swallowing attempts.

closure times. No differences exist in time to maximal pharyngeal contraction and epiglottic reopening between normal dogs and those with cricopharyngeal achalasia with either liquid or kibble meals.

In cricopharyngeal chalasia, the UES does not maintain positive resting pressure between swallows. On survey radiographs, air will often be present in the UES (Fig. 30.15). Cricopharyngeal chalasia can be found in dogs with myasthenia gravis. Barium administration is contraindicated in the presence of a statically open UES because of the increased risk of aspiration.

Dysphagia in cats is less commonly reported than in dogs. Esophageal phase dysphagia is the most common type occurring in cats, with hiatal hernia, dysmotility, and stricture being the most common causes.[27] Quantitative evaluation of the PCR, time to maximal pharyngeal contraction, time to opening of the epiglottis, as well as proximal esophageal sphincter opening and closing times in cats with esophageal dysphagia are similar to that reported in healthy dogs.[27] However, studies in a healthy cat cohort are lacking.

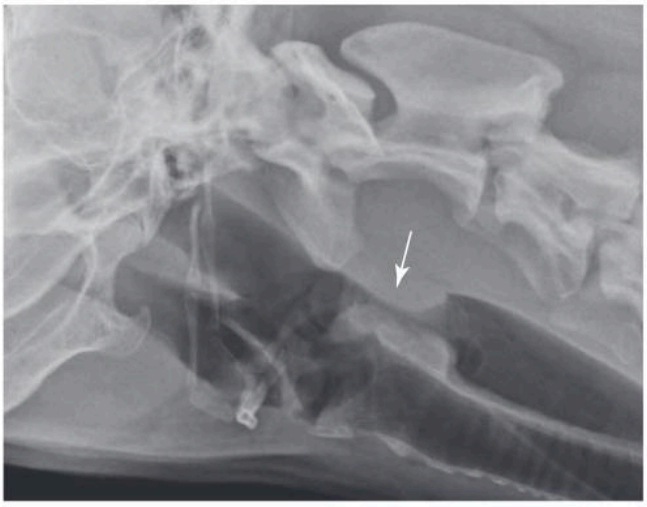


Fig. 30.15 Lateral cervical radiograph of a 5-year-old mastiff with cricopharyngeal chalasia. The cricopharyngeal sphincter is open and contains gas (*white arrow*), as does the cervical esophagus. Cricopharyngeal and cranial esophageal gas is often seen with cricopharyngeal chalasia. The administration of barium is contraindicated in this instance because of increased risk for aspiration.

ESOPHAGEAL DISORDERS

Esophageal motility disorders may result in abnormal peristalsis, transport, and motor function, and clinical signs of regurgitation are common. Survey radiographs can help detect structural abnormalities, such as segmental or generalized dilation of the esophagus, abnormal esophageal content because of lack of normal peristalsis, and the presence of aspiration pneumonia. If survey radiographs are negative in animals with regurgitation, contrast studies are necessary to rule out esophageal disease. Peristaltic abnormalities, hypomotility, strictures, or radiolucent foreign bodies causing obstruction can go undetected on survey radiographs. Mechanical obstruction because of foreign body or stricture can be diagnosed with a static barium esophagram, but accurate assessment of motility requires fluoroscopy. Following passage of a bolus through the UES, a primary peristaltic wave should propel the bolus to the stomach. If this process is interrupted, a secondary peristaltic wave may propel the bolus to the LES in normal animals. It is important to note that, when assessed with VFSS, cervical esophageal transit time is significantly shorter for dogs in sternal recumbency compared to lateral.[17] The percentage of primary waves is significantly greater in liquid and kibble studies when done in sternal recumbency compared with lateral recumbency. Also, the percentage of swallows that have no associated primary peristaltic waves is higher in lateral recumbency. The percentage of secondary waves, however, does not differ between the two positions.[17]

Primary peristalsis can be disrupted by hypomotile segments, and secondary peristalsis may be absent in disease. Dogs with laryngeal paralysis may also have esophageal dysfunction.[28] Esophageal dysmotility in young dogs in the absence of megaesophagus is characterized by abnormal primary waves that move the bolus less than 5 cm aborally, and abnormal secondary waves that allow bolus retention in the esophagus after two subsequent swallows.[29] Retrograde flow of more than 10 cm is another finding associated with hypomotility, as is prolonged esophageal transit time (>5 seconds).[29] Esophageal dysmotility can be caused by delayed maturation, and spontaneous improvement after 1 year of age can occur because of maturation of the neuromuscular system.[30] Esophagitis is

another cause of abnormal esophageal motility. Gastroesophageal reflux occurs when gastric and duodenal contents enter aborally into the esophagus, and this can lead to dysmotility secondary to resultant esophagitis.[30]

Esophageal Dilation

Esophageal dilatation can be segmental or generalized depending on the cause and location of disease, and the dilatation can be either functional or mechanical. Generalized dilatation is typically caused by functional disease, whereas segmental dilatation is usually caused by foreign body, infiltrative disease such as neoplasia or inflammation, hiatal diseases, segmental motor disease, stricture, vascular ring anomaly, or redundant esophagus (Fig. 30.16).

Megaesophagus

The term *megaesophagus* describes a dilated and hypomotile esophagus resulting from neuromuscular dysfunction; this type of esophageal dilation is often idiopathic in dogs.[31]



Fig. 30.16 Barium swallow in an 8-year-old Shar-Pei. There is a focal redundancy of the esophagus at the thoracic inlet. This redundancy may be insignificant, but in some dogs, there is diminished contractility with retention of ingesta in this region. A dynamic esophagram is needed to assess the significance of esophageal redundancy.

Megaesophagus in dogs can also result from LES achalasia-like syndrome (LES-AS).[32] Megaesophagus is the most common cause of regurgitation in dogs and the most frequently reported motility disorder affecting the canine esophagus.[33] Megaesophagus is not common in cats but has been described in instances of pylorospasm. Predominant clinical signs in esophageal neuromuscular dysfunction are effortless regurgitation of tubular-formed, undigested food. Megaesophagus can be segmental (cervical or thoracic) or generalized and occurs secondary to diseases of the neuromuscular junction (myasthenia gravis), striated muscle (myositis), peripheral nerves (polyneuropathy), or central nervous system (inflammatory, toxic, and neoplastic).[31]

Radiographic signs of megaesophagus include dilatation of the esophagus with gas, retention of food or fluid, tracheal stripe sign, visibility of the longus colli muscle, ventral displacement of the intrathoracic trachea, ventral displacement of the heart, and aspiration pneumonia (Fig. 30.17; see Figs. 30.4C and 30.5). A cranial mediastinal mass may be present in dogs with thymoma and paraneoplastic myasthenia gravis (eFig. 30.1). When generalized megaesophagus is present, the thoracic segment of the esophagus is usually more severely dilatated than the cervical portion because of surrounding negative intrathoracic pressure. When gas filled, the esophagus can be difficult to discern because of the lucency of the surrounding lung. On lateral thoracic radiographs, two thin soft tissue opaque, parallel bands coursing from cranial to caudal in the dorsal aspect of the thorax represent the wall of the gas-filled esophagus. A focal indentation of the dorsal esophageal wall is caused by the azygous vein crossing over on the right. In the VD radiograph, the wall of the gas-filled esophagus is most often identified as a thin, soft tissue band to the left of the vertebral column. If the dilation is severe enough, a second band can also be seen on the right, converging with the left one at the caudal esophageal sphincter (see Fig. 30.17). When imaged with VFSS in a Bailey chair, dogs with LES-AS can be distinguished from dogs with idiopathic megaesophagus due to the presence of a "bird-beak" appearance to the LES.[32]

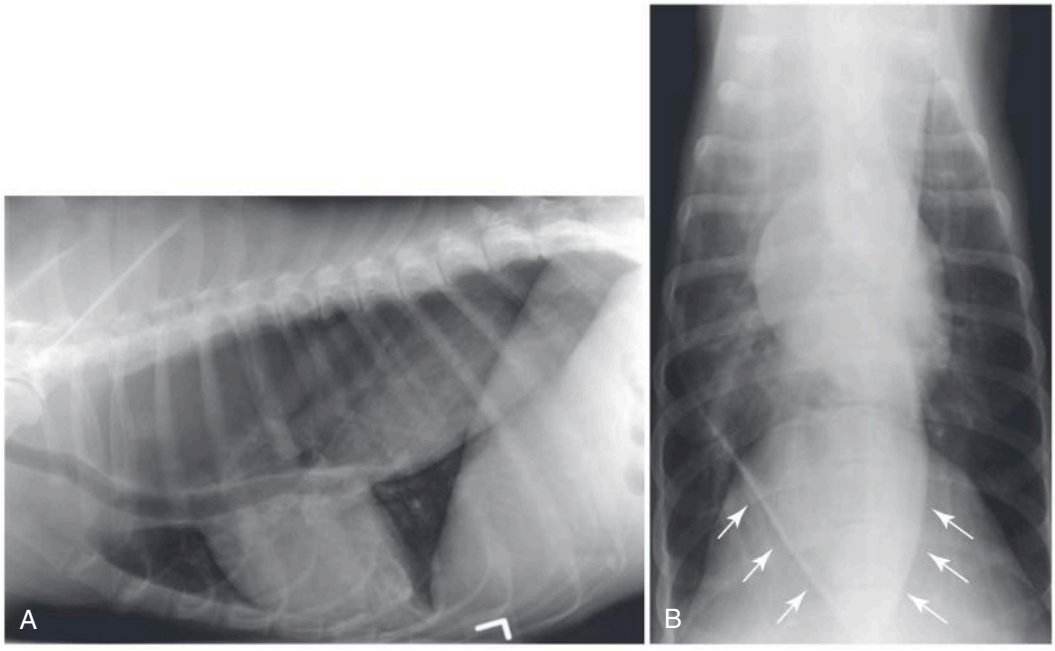
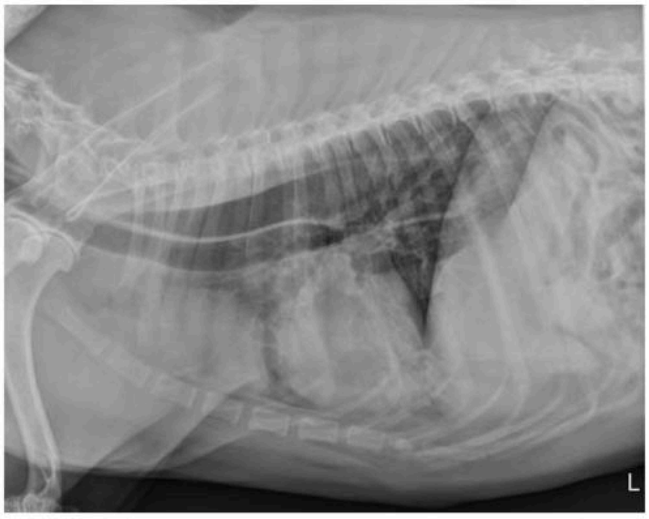


Fig. 30.17 **A,** Lateral radiograph of a 3-year-old German shepherd dog. The esophagus is severely dilated such that the trachea and heart are displaced ventrally. An alveolar pattern because of aspiration pneumonia is present in the periphery of the right middle lung lobe. **B,** Ventrodorsal (VD) radiograph of the same dog. The borders of the enlarged esophagus extend to the left and right side of the thorax and converge in a V shape near the caudal esophageal sphincter (*white arrows*).



eFig. 30.1 Left lateral thoracic radiograph of a Labrador retriever with megaesophagus, caused by paraneoplastic myasthenia gravis associated with thymoma. Note the gas distended esophagus. A soft tissue opacity mass is present cranioventral to the cardiac silhouette in the cranial mediastinum. A focal alveolar pulmonary pattern in the ventral aspect of the right middle lung lobe is consistent with aspiration pneumonia.

Hiatal Diseases

Esophageal hiatal diseases include dynamic esophageal and paraesophageal hernias, gastroesophageal intussusception, and gastroesophageal reflux. Clinical signs may be absent, or dogs may have recurrent gastrointestinal signs, such as regurgitation, retching, and possibly vomiting. Esophageal hernias can be congenital or acquired. The congenital form has been reported in shar-pei dogs.[34] In the acquired form, weakness of the diaphragm, elevated abdominal pressure, and upper airway obstruction are predisposing factors.

In dynamic hiatal hernias, the caudal esophageal sphincter and part of the gastric fundus move in and out of the caudal mediastinum through a weakened esophageal hiatus of the diaphragm. In most dogs and cats, this may happen intermittently and randomly making radiographic identification challenging. Brachycephalic breeds are prone to hiatal hernias in affiliation with brachycephalic upper airway obstruction due to excess negative thoracic pressure needed to respire against the obstructed upper airway.[35,36] In these breeds, hiatal herniation often accompanies inspiration and is more frequent, thereby making radiographic identification more likely.

If captured radiographically, there is a soft tissue, or mixed soft tissue and gas opacity between the aorta and caudal vena cava on lateral radiographs that silhouettes with the cranial diaphragmatic contour (Fig. 30.18, eFig. 30.2 and 30.3). If persistent on the VD view, the opacity has a midline location and is slightly on the left of the vertebral column. Dynamic esophageal hernia may be confirmed with static barium esophagraphy; however, VFSS is often necessary. If the fundus is herniated along with the esophagus, rugal folds outlined by barium may be visible. The caudal esophageal sphincter will also be located cranial to the diaphragm, and barium can be seen to reflux from the stomach into the caudal esophagus with VFSS.

Paraesophageal hernias are caused by the fundus being herniated into the mediastinum alongside of the esophagus with the caudal esophageal sphincter remaining in the abdomen (Fig. 30.19A). On VD radiographs, the herniated fundus is to the left of the esophagus, and hernia contents may move in and out with respiration (see Fig. 30.19B,C).

Gastroesophageal intussusception occurs when part of the stomach and possibly other abdominal organs, such as the spleen, evert into the esophageal lumen. The intussusceptum may be of homogeneous soft tissue opacity or may be a mixed soft tissue and gas opacity if there is gas trapped in the herniated portion of the stomach (Fig. 30.20). A feature that distinguishes gastroesophageal intussusception from a sliding or paraesophageal hernia is the sharply marginated cranial edge of the intussusceptum contrasted against a gas-filled esophageal lumen. Gastroesophageal intussusception is often acquired and secondary to esophageal dilatation or previous surgery at the caudal esophageal sphincter resulting in chalasia.

Gastroesophageal reflux occurs when gastric acid enters the esophagus; this usually results in esophagitis. Survey radiographs are usually normal, or there may be increased soft tissue opacity between the aorta and vena cava on both lateral projections. With increasing severity, the caudal esophagus may become enlarged and contain either air or fluid. Contrast esophagram studies are usually negative unless severe ulceration is present that leads to adherence of the contrast medium to the mucosa. Focal dilatation of the esophagus with contrast medium and/or obliteration of the linear folds normally outlined with barium can occur if the esophagitis is severe. Scarring and stricture can develop.

Redundant Esophagus

Redundant esophagus is often an incidental finding in brachycephalic breeds, such as bulldogs and Shar-Peis (see Fig. 30.16).

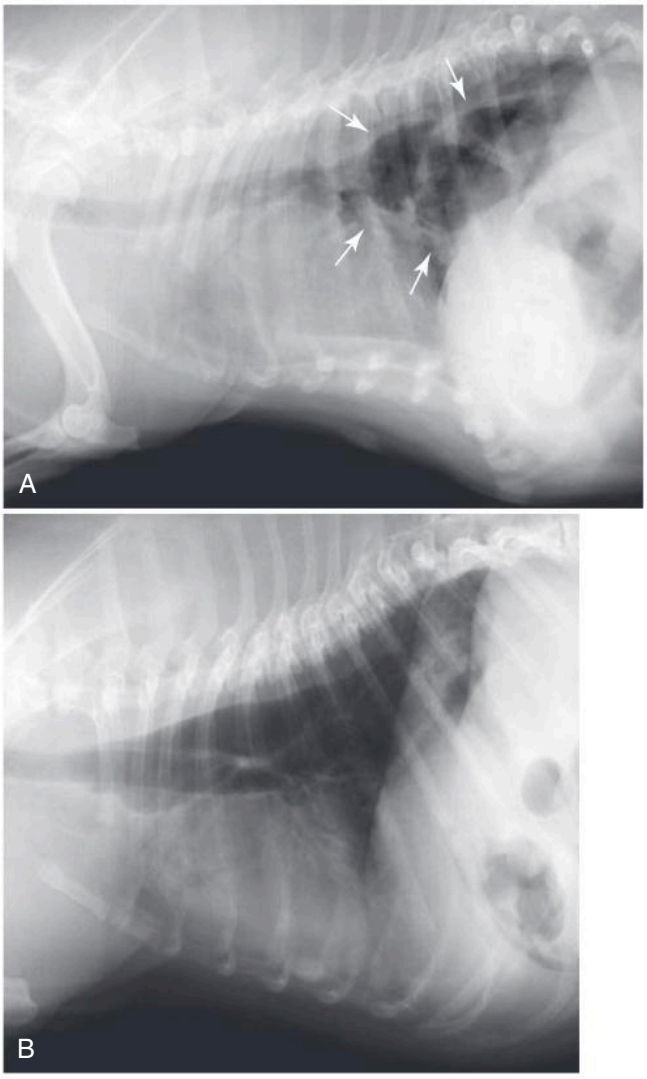


Fig. 30.18 **A,** Lateral thoracic radiograph of a 2-year-old bulldog with upper airway obstruction. There is cranial displacement of the stomach into the thorax (*white arrows*) and dorsal deviation of the sternum and ribs with a small lung volume. **B,** Same dog after endotracheal intubation and under anesthesia. The sternum resumes a normal position, the diaphragm is flatter and in a more caudal position, and the stomach is no longer displaced into the thorax. Residual gas dilatation of the esophagus could be caused by anesthesia or from previous aerophagia. The increase in intrathoracic pressure associated with alleviation of the airway obstruction allowed the stomach to reduce spontaneously into the abdomen.

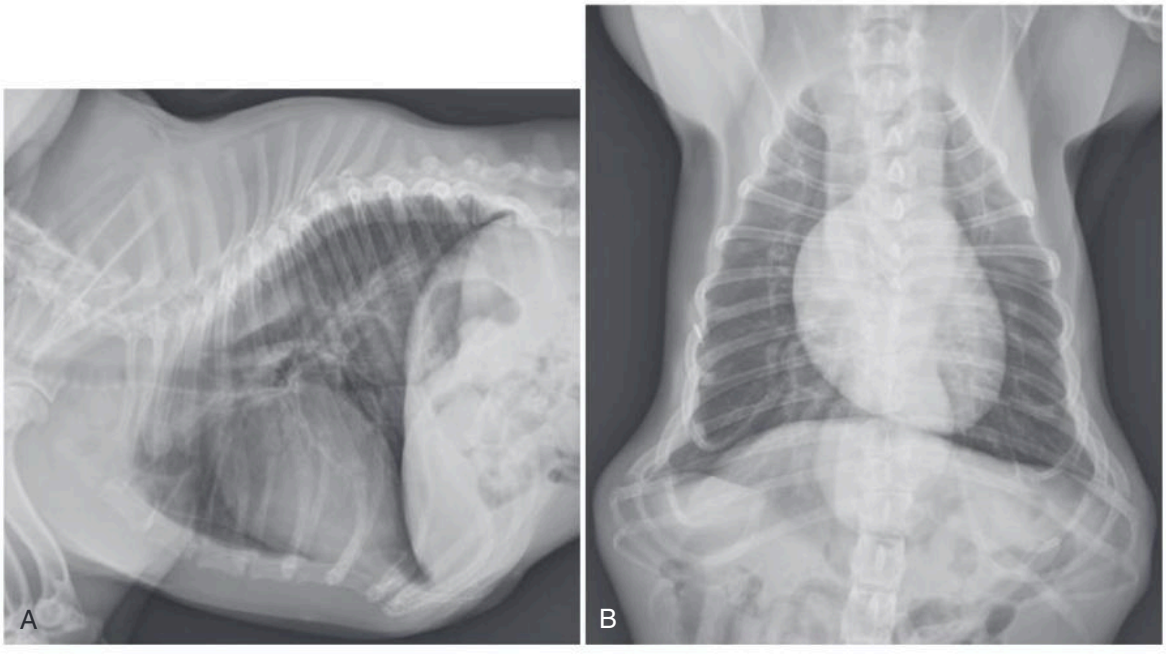
Survey radiographs may be normal, or focal dilatation of the esophagus with gas can be seen at the thoracic inlet. In static barium esophagrams, the esophagus has a tortuous course at the thoracic inlet that appears as a diverticulum ventral to the trachea. The accumulation of contrast medium in a redundant esophagus is usually only temporary, and the esophagus will appear normal on subsequent radiographs. With VFSS, the redundant segment typically has normal motility. Occasionally, there will be a clinically significant motility disorder associated with the redundant region of the esophagus.

FOREIGN BODIES

Esophageal foreign bodies are more common in dogs than cats, and some terrier breeds appear to be predisposed.[37] Survey radiography should include the region from the base of the



eFig. 30.2 Lateral thoracic radiographs of a cat with a sliding hiatal hernia. A soft tissue opaque convex structure is present at the craniodorsal aspect of the diaphragm. Gas within the gastric fundus can be followed into this structure, confirming its gastric origin. This was not present in other views consistent with a sliding hiatal hernia.



eFig. 30.3 **A**, Lateral thoracic radiograph of a French bulldog with brachycephalic syndrome. Note the ovoid soft tissue opacity in the region of the caudal esophagus. **B**, Ventrodorsal radiograph of the same dog. An ovoid soft tissue opacity is present in midline, extending from the region of the cardia to the esophagus, consistent with a hiatal hernia.

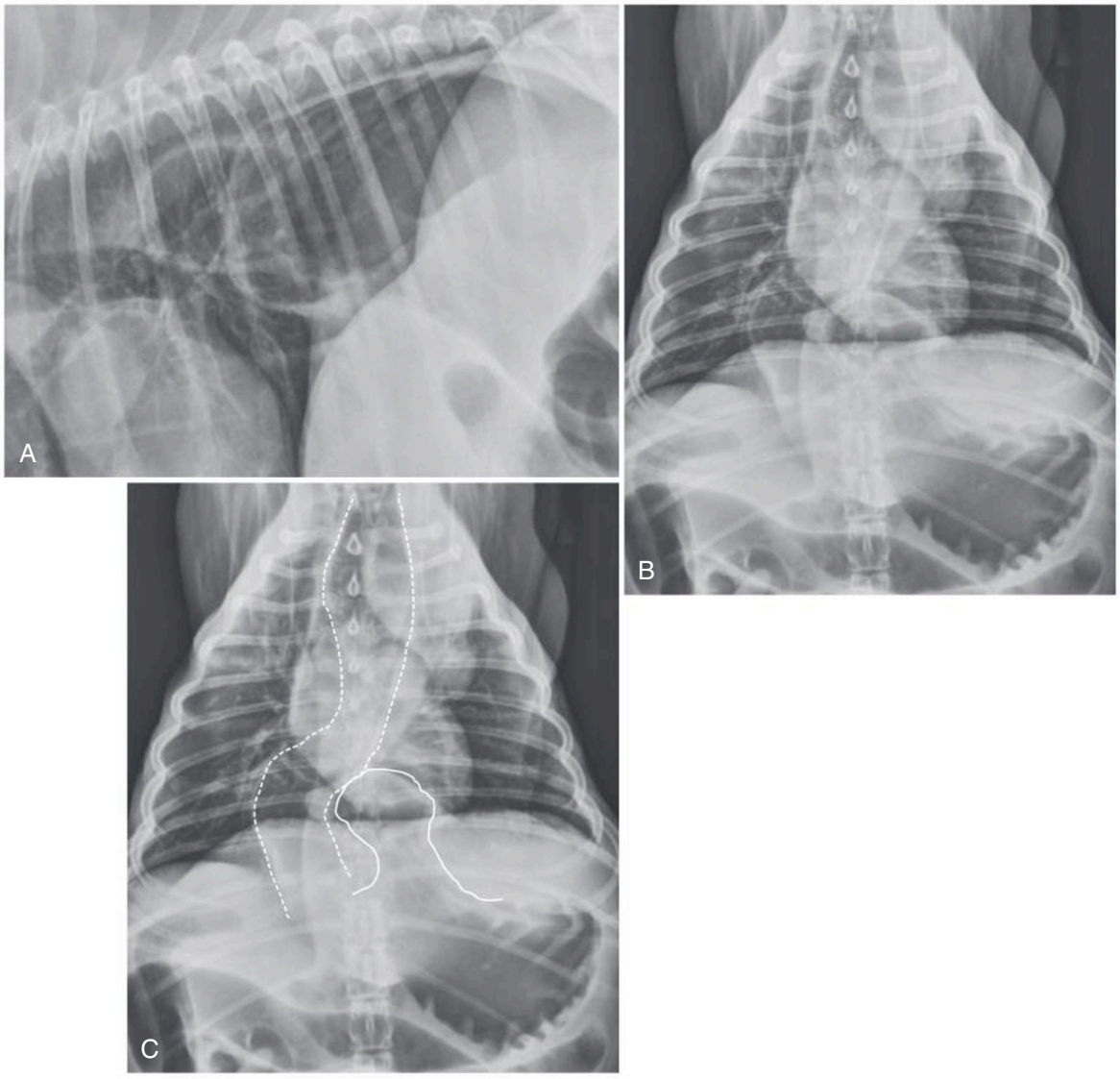


Fig. 30.19 **A,** Lateral thoracic radiograph of a 13-year-old miniature schnauzer. A compartmentalized, gas-filled structure is present in the caudodorsal thorax. This appearance could be caused by either a paraesophageal hernia or a sliding hiatal hernia. Ventrodorsal (VD) radiograph **(B)** and annotated VD radiograph **(C)** of the same dog. The gas-filled structure, which is the fundus (*solid line*), is to the left of midline and adjacent to the gas-filled and dilatated esophagus (*dotted line*), which takes on a tortuous course and is displaced to the right. The soft tissue mass in the left cranial thoracic quadrant is a thymoma.

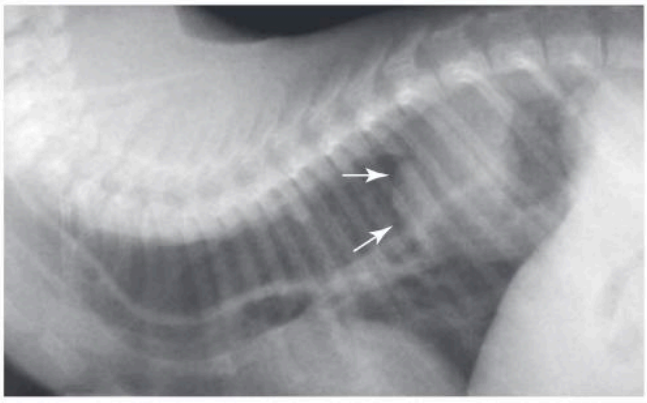


Fig. 30.20 Lateral thoracic radiograph of an 8-week-old Bengal kitten. The thoracic esophagus is gas dilatated with ventral displacement of the trachea and heart. A mixed soft tissue and gas mass with a sharply defined round cranial border (*white arrows*) is present in the dorsocaudal aspect of the thorax. This appearance of a gas-filled esophagus with a caudally located intraluminal mass having a sharply marginated cranial border is characteristic of gastroesophageal intussusception.

tongue to the diaphragm. Foreign bodies are most often located at the thoracic inlet, base of the heart, or just cranial to the diaphragm, sites where the esophagus is limited in its ability to distend. Common radiographic features are visibility of the distinct foreign material, gas in the esophagus contrasting with the foreign body, esophageal dilation orad to the obstruction, and signs of perforation (pleural or mediastinal effusion or pneumomediastinum).[38] Nonobstructive foreign bodies, such as fishhooks and other sharp objects, tend to lodge in the pharyngeal region (Fig. 30.21; see Fig. 30.11). Radiopaque foreign material, such as bones or metal, is recognized easily compared with nonradiopaque material, such as plastic and cartilage, which appears as focal soft tissue opacity in the region of the esophagus (Fig. 30.22, eFig. 30.4). A soft tissue opaque esophageal foreign body may appear similar to an esophageal neoplasm, an esophageal abscess, mediastinal mass, paraesophageal hernia, or lung mass (see Fig. 30.22). A static contrast esophagram can help to differentiate these conditions. Contraindications for a barium swallow include survey radiographic evidence of pneumothorax, pneumomediastinum, and mediastinal or pleural fluid, which are signs of potential esophageal perforation (Fig. 30.23).



eFig. 30.4 Lateral thoracic radiograph of a 5-month-old terrier with a dog treat lodged in the caudal thoracic esophagus. The cranial thoracic esophagus is mildly gas distended, whereas a large soft tissue opacity structure expands the caudal esophagus. An angular mineral opacity at the cranial aspect of the foreign body represents a swallowed deciduous tooth. There is no evidence of perforation.

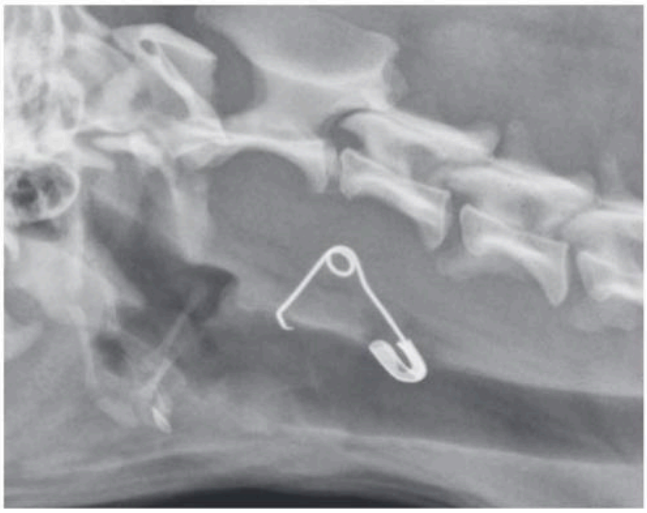


Fig. 30.21 Open safety pin obstructing the cervical esophagus caudal to the cricopharyngeal sphincter.

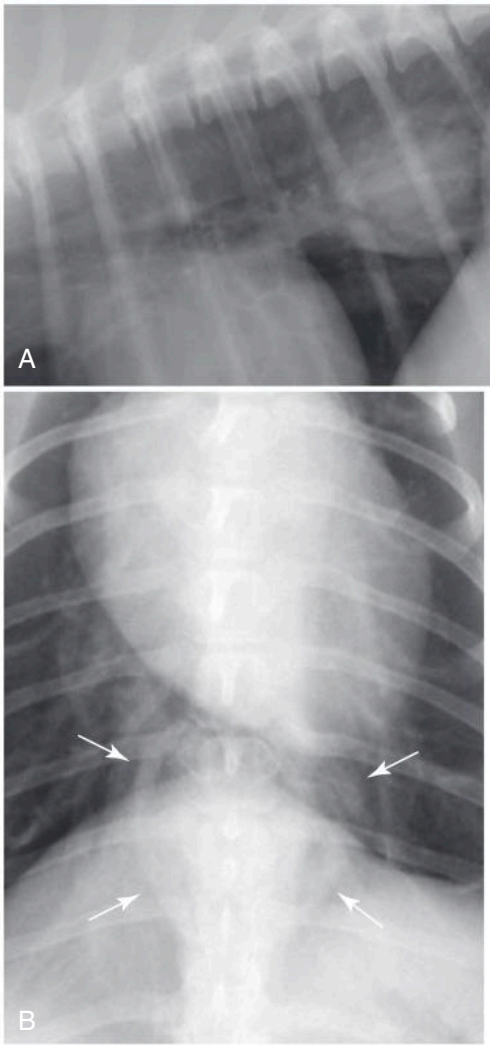


Fig. 30.22 **A,** Lateral thoracic radiograph of a 4-year-old Chihuahua. There is a soft tissue mass in the caudodorsal aspect of the thorax between the aorta and caudal vena cava with its caudal border superimposed with the diaphragm. Based on this appearance, the considerations are esophageal foreign body, esophageal mass, paraesophageal hernia, or pulmonary mass. **B,** Ventrodorsal (VD) radiograph of the same dog. The mass is on the midline (*white arrows*), making a pulmonary mass unlikely. Endoscopy was performed, and a hard, cartilaginous foreign body was removed.

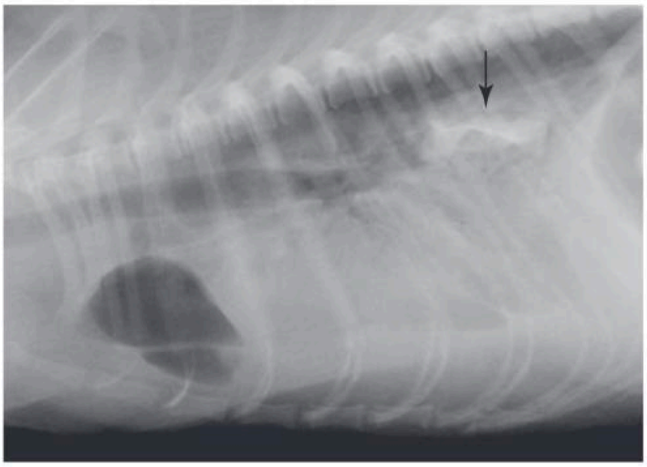


Fig. 30.23 Right lateral radiograph of a dog with a bone lodged in the caudal aspect of the esophagus (*black arrow*). There is also pleural fluid and pneumothorax. A barium esophagram should not be done in this situation because of the high likelihood of esophageal perforation. If an esophagram is necessary, water-soluble contrast medium should be used.

VASCULAR RING ANOMALIES

Regurgitation due to vascular ring anomalies presents at an early age in most instances; however, it can have late-onset occurrence in both cats and dogs.[39–41] Under normal conditions, the aorta is derived from the left fourth aortic arch while the right fourth aortic arch typically regresses. Anomalous development of the aortic arches can lead to secondary extrinsic esophageal compression. Esophageal compression secondary to a vascular malformation is termed *vascular ring anomaly*. Of the seven types of vascular ring anomalies that are described, types I through III have a persistent right aortic arch, type IV has a double aortic arch, and types V through VII have a left aortic arch with combinations of persistent right ligamentum arteriosum and right subclavian arteries, all of which cause entrapment of the esophagus.[42–44]

Development of the aortic arch from the right fourth aortic arch with regression of the left fourth aortic arch, termed *persistent right fourth aortic arch*, is the most common vascular ring anomaly that leads to entrapment of the esophagus. In the normal situation where the aorta is derived from the left fourth arch, the aorta, main pulmonary artery, and interconnecting ligamentum arteriosum are all on the left side of the trachea and esophagus.[42] When the aorta is derived from the right fourth aortic arch rather than the left, the aorta is on the right side of the trachea and esophagus, whereas the main pulmonary artery is on the left side. In this configuration, the ligamentum arteriosum compresses the esophagus against the trachea and base of the heart as it passes from right (aorta) to left (pulmonary artery) (Fig. 30.24). The compression results in esophageal dilation cranial to the base of the heart. Survey radiographs may be normal if the esophagus is not dilated, but this is unusual. The dilated portion of the esophagus cranial to the heart base creates a mass effect that contains air and/or ingesta and usually displaces the trachea ventrally (Figs. 30.25 and 30.26), although occasionally the enlarged esophagus will slide laterally and become positioned ventral to the trachea (Fig. 30.27). In some dogs, it is possible to see the trachea being deviated focally toward the left on VD projections (see Fig. 30.25), and the normal left lateral margin of the aorta may not be evident. In a static barium esophagram, the narrowing of the esophagus at the heart base can be confirmed (see Fig. 30.30). Keep in mind that a single narrowed area in the esophagus may represent a peristaltic wave and strictures or

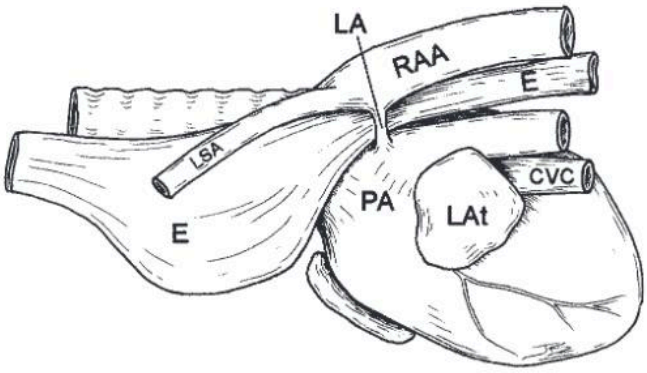


Fig. 30.24 Schematic of persistent right aortic arch. This view from the left shows the ligamentum arteriosus (*LA*) connecting the descending right aortic arch (*RAA*) to the main pulmonary artery (*PA*) causing constriction of the esophagus (*E*) between these structures and the heart base. *CVC,* Caudal vena cava; *LAt,* left atrium; *LSA,* left subclavian artery. (Figure courtesy Dr. Barbara Watrous, DACVR.)

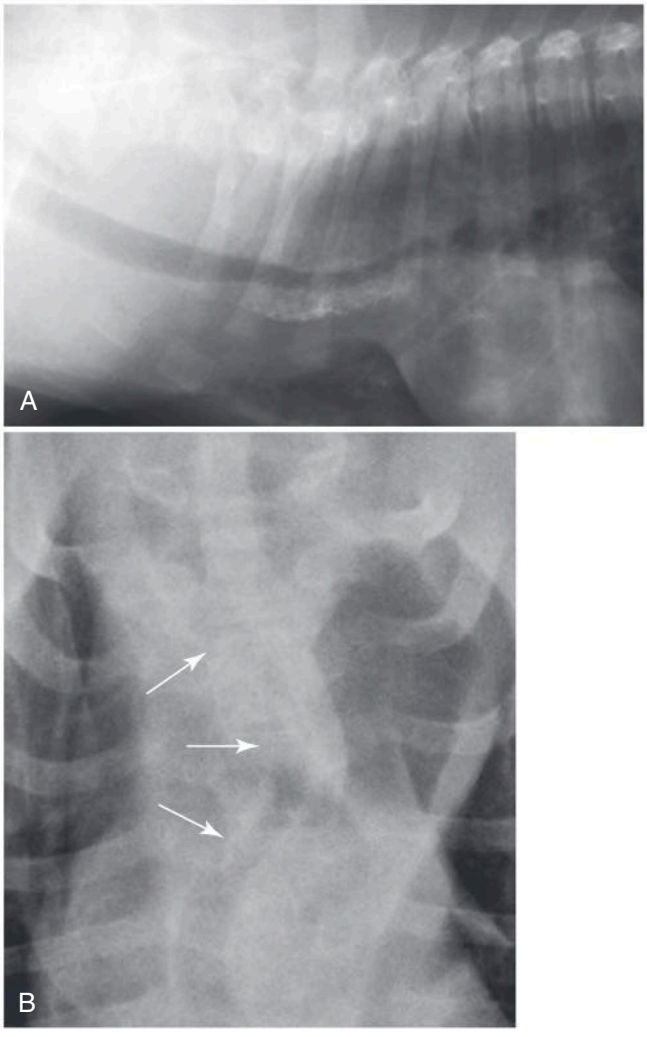


Fig. 30.25 **A,** Lateral thoracic radiograph of a 2-month-old German shepherd with a persistent right fourth aortic arch. The thoracic trachea is displaced ventrally, and there is a superimposed mottled mineral opacity because of foreign material in the enlarged esophageal segment cranial to the heart base. The caudal thoracic esophagus appeared normal. **B,** Ventrodorsal (VD) radiograph of the same dog. The trachea is displaced to the left (*white arrows*).

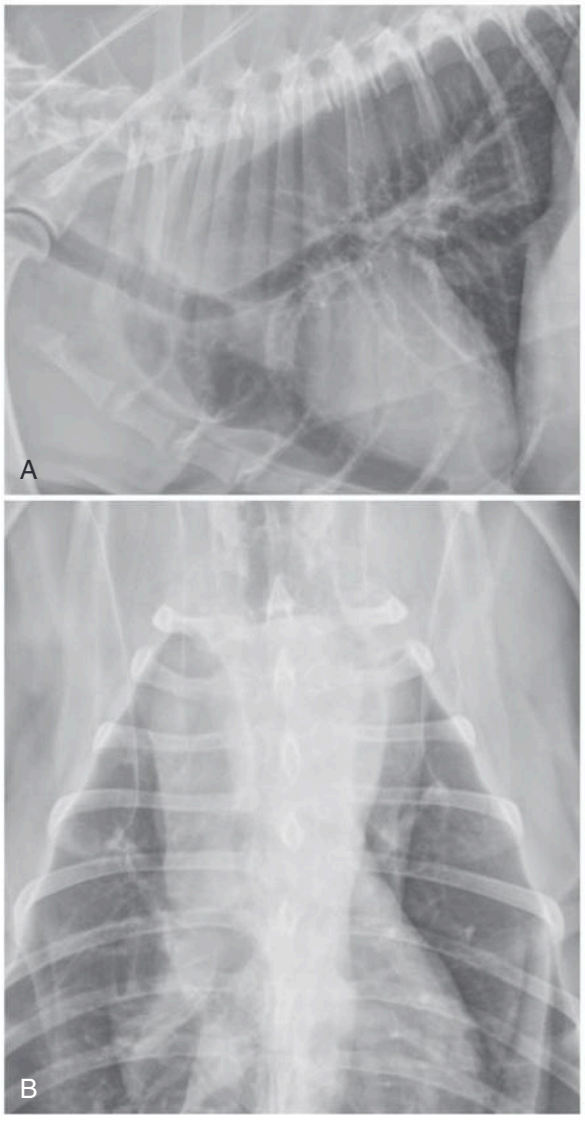


Fig. 30.26 Lateral **(A)** and dorsoventral (DV) **(B)** radiographs of a dog with a persistent right fourth aortic arch. There is dilatation of the cranial aspect of the thoracic esophagus that causes ventral displacement of the trachea. In the DV view, there is a mass effect in the cranial mediastinum. The caudal aspect of the thorax is normal.

vascular ring anomalies should only be diagnosed if persistent narrowing is present on several projections and abnormal dilation of the esophagus is present. VFSS can be useful to assess whether esophageal peristalsis orad to the vascular ring is present as this may influence likelihood of recovery. A persistent left cranial vena cava can accompany persistent right fourth aortic arch and is important that the abnormal left vena cava is recognized at the heart base when a left-thoracotomy is performed to correct the vascular ring constriction.[45]

An aberrant right subclavian artery can also lead to a vascular ring compression of the esophagus. Normally, the right subclavian artery branches from the brachiocephalic trunk but may instead arise directly from the aortic arch, distal to the origin of the left subclavian artery. The right subclavian artery then crosses over the dorsal aspect of the esophagus as it travels from the left side of the median plane, where the normal aortic arch resides, to supply the right forelimb (Figs. 30.28 and 30.29). The site of compression caused by an aberrant subclavian artery is usually slightly more cranial than that caused by a persistent right fourth aortic arch (see Fig. 30.29), and the

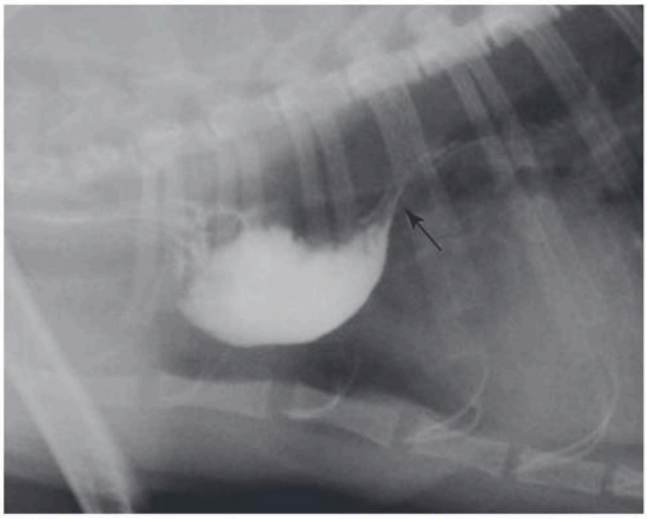


Fig. 30.27 Lateral radiograph of a barium esophagram in an 11-month-old cat with a persistent right fourth aortic arch. Focal dilatation and ventral displacement of the esophagus is present between the thoracic inlet and heart. The contrast column tapers off and narrows at the heart base (*black arrow*) because of the vascular ring constriction.

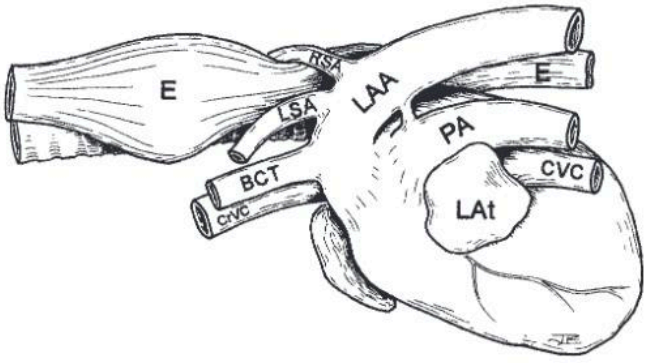


Fig. 30.28 Schematic of aberrant right subclavian artery. This view, from the left side, shows the right subclavian artery (*RSA*) arising from the left-sided aortic arch (*LAA*) and coursing over the top of the esophagus (*E*), causing compression of the esophagus. *BCT,* Brachiocephalic trunk; *CrVC,* cranial vena cava; *CVC,* caudal vena cava; *LAt,* left atrium; *LSA,* left subclavian artery; *PA,* pulmonary artery. (Figure courtesy Dr. Barbara Watrous, DACVR.)

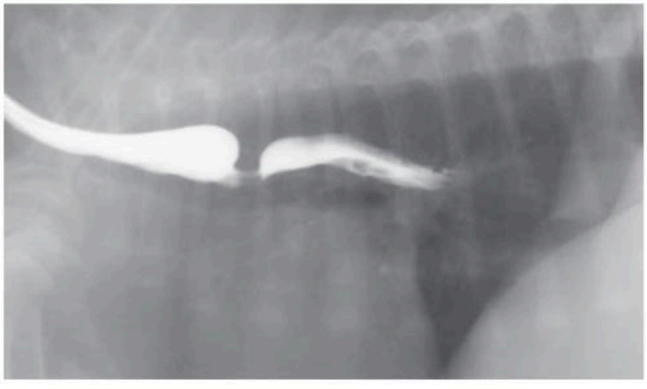


Fig. 30.29 Barium esophagram in a dog with esophageal compression caused by an aberrant right subclavian artery. The indentation in the dorsal aspect of the esophagus results from the compression created by the right subclavian artery passing dorsal to the esophagus as it courses from the left-sided aortic arch to the right forelimb.

compression may not be as severe because the esophagus is not trapped against a solid organ ventrally as it is with persistent right fourth aortic arch.

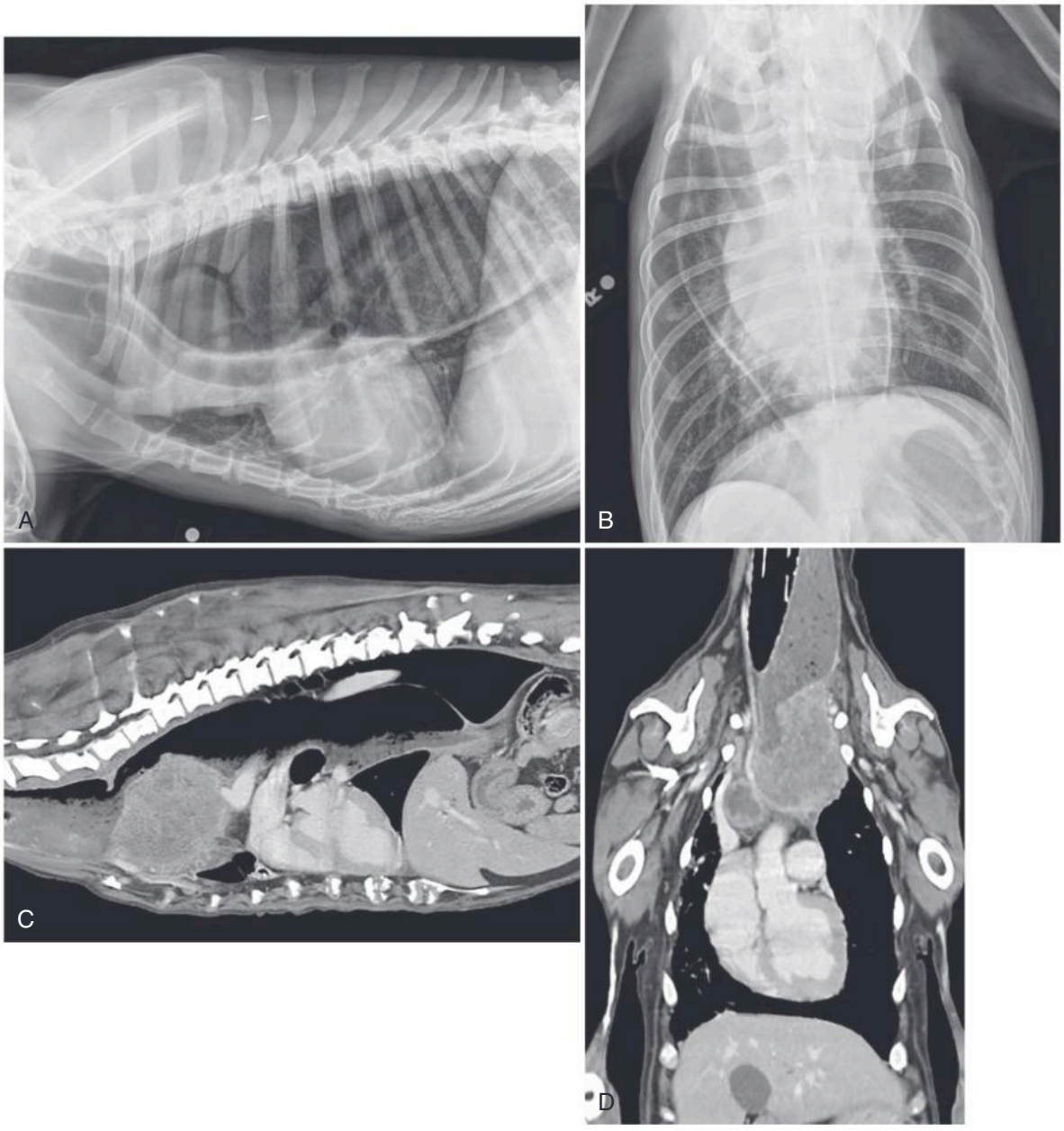
INFLAMMATORY DISEASES

Esophagitis

Esophagitis can result from infection, ingestion of hot or corrosive substances, vomiting, gastroesophageal reflux, megaesophagus, and foreign body obstructions. Survey radiography is usually unremarkable. Aspiration pneumonia can be identified, but the diagnosis of esophagitis usually requires endoscopy. The esophagus may have reduced motility and therefore be dilated with gas or fluid, but this is a nonspecific finding. Ulcerations, motility disorders, or mechanical obstruction secondary to inflammation requires contrast procedures to be characterized further. If severe esophagitis is present, then segmental narrowing, irregular mucosal contours, indistinct folds of the esophageal wall, and thickening of the wall may be present in static barium contrast studies. Fluoroscopic contrast studies may be characterized by segmental spasticity and minor dilation. Gastroesophageal reflux may be identified with VFSS.

Strictures

Esophageal strictures usually result from foreign body or gastroesophageal reflux. Esophageal strictures thought to be related to gastroesophageal reflux during anesthesia are usually located at the caudal portion of the thoracic esophagus, caudal to the base of the heart.[46] Strictures of the esophagus typically have a smoothly bordered, tapered appearance caudally (Fig. 30.30). Survey radiography may be unremarkable, or there may be segmental or generalized dilatation of the esophagus, depending on the site and extent of the stricture. Contrast esophagraphy is used to determine the location, size, and length of the stricture for treatment planning (see Fig. 30.30). Moreover, the contrast study helps to determine if the stricture is mural, extramural, or luminal. Smoothly bordered mucosal surfaces outlined with contrast medium and having a circumferential narrowing on lateral and VD projections are the typical appearance of a mural stenosis caused by chronic inflammation or scarring. An irregularly bordered mucosal surface can be seen with neoplastic infiltration of the wall or severe ulceration because of inflammation. Extramural compressions have a smoothly bordered contrast column that is convex and tapering toward the narrowing in one projection with the narrowed portion appearing widened in the orthogonal projection. Thyroid masses, enlarged lymph nodes, and cervical abscesses can impinge on or invade the cervical esophagus, causing obstruction. If liquid barium passes through the narrowed region or no abnormality is seen, then barium-soaked kibble can be used to identify a stricture that allows fluid but not solids to pass. Esophageal neoplasms are rare in dogs and cats. Osteosarcoma and fibrosarcoma of the esophagus are reported in areas endemic for *Spirocerca lupi*.[47] Squamous cell carcinoma, adenocarcinoma, branchioma, branchial cleft cysts, papilloma, angioleiomyosarcoma, and leiomyosarcoma have also been reported but are rare.[48–52] If the neoplasm is large enough, it may be recognized on survey radiographs as a soft tissue mass associated with the esophagus (Fig. 30.31, eFig. 30.5). The esophagus may be dilatated cranial to the mass, but this is not always present. Differentiation of esophageal masses from an esophageal foreign body or a nonesophageal mass may require esophagraphy, CT, or endoscopy (see Fig. 30.31). Dystrophic mineralization of esophageal masses is rare, but its presence can be associated with neoplasia, *Spirocerca* infection, or oral administration of radiopaque medication. Esophageal dilation cranial to an esophageal mass may also be present. Obstruction or stenosis at the tumor site, mucosal irregularity caused by



eFig. 30.5 Left lateral **(A)** and ventrodorsal **(B)** radiographs of a German shepherd dog with a mural esophageal squamous cell carcinoma in the cranial thorax. The esophagus is diffusely severely gas distended and causes ventral displacement of the trachea. A rounded soft tissue mass is visible at the ventral and left lateral aspect of the esophagus. A clear association with the esophageal wall cannot be con firmed radiographically. **C and D,** Sagittal and dorsal reformatted computed tomography images of the same dog after intravenous contrast medium administration. The mass is heterogeneously contrast enhancing and expands the left ventral esophageal wall.

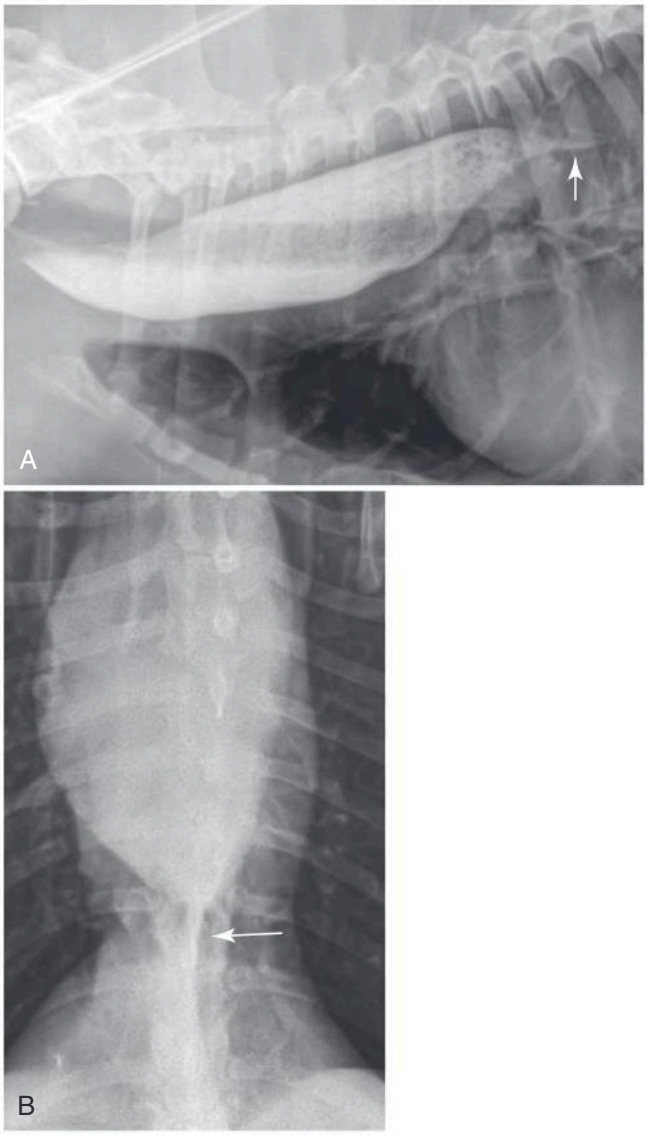


Fig. 30.30 **A,** Lateral radiograph of a barium swallow in a 3.5-year-old Siberian husky with an esophageal stricture. There is dilatation of the esophagus cranial to the carina that tapers smoothly caudally at the site of the stricture (*white arrow*). No contrast medium entered the caudal esophagus. **B,** Ventrodorsal (VD) radiograph of the same dog. The dilated, barium-filled esophagus tapers to a narrow point just caudal to the base of the heart (*white arrow*).

infiltration and ulceration, and/or the location and extent of the infiltration can be evaluated with static esophagraphy. Temporary or persistent retention of barium may occur because of lack of secondary peristalsis where the wall is stiffened because of tumor infiltration. Mural thickening, asymmetry of the lumen, absence of the mucosal folds, ulceration of the mucosa with barium retention, and a locally enlarged or dilated esophagus are suggestive of neoplasia. Infection of dogs and other carnivores with the nematode *S. lupi* occurs in tropical and subtropical regions throughout the world.[53] The parasite infects mainly the esophagus and aorta, leading to gastrointestinal, respiratory, and circulatory signs.[54] In survey radiographs, there may be a mediastinal mass in the region of the caudal thoracic esophagus because of granuloma formation (Fig. 30.32). The inflammatory esophageal mass can become neoplastic, with osteosarcoma and fibrosarcoma being reported. There may be new bone formation on the ventral aspect of thoracic vertebrae dorsal to the mass and also enlargement of the descending aorta.[55–57] *S. lupi* has also caused spinal cord chondrosarcoma.[58] Radiographic abnormalities of the aorta are rare, but dilatation of the proximal descending aorta and aortic mineralization have been reported.[59] In spirocercosis-endemic areas, dorsoventral and right lateral projections are recommended, because they also allow for better visualization of descending aortic aneurysms and prevent interpreting the potentially normally visible esophagus in left lateral images as a mass.[60] However, as noted in Chapter 28, obtaining both left and right lateral views of the thorax should be routine procedure. Contrast studies of the esophagus confirm the granuloma to be originating from the esophagus and are usually characterized by an irregular mucosal border with outpouchings and filling defects. Endoscopy provides similar information, and the parasite may be visualized directly in some dogs.[14] Computed tomography (CT) provides information in confirming nonesophageal or extraesophageal masses to be spirocercosis related because of earlier detection of aortic mineralization and spondylitis.[61] CT angiography perfusion analysis of esophageal nodules can be used to help differentiate nonneoplastic from neoplastic nodules associated with *S. lupi*. *S. lupi*–induced esophageal sarcomas are statistically significantly less perfused than nonneoplastic granulomatous nodules.[62]

DIVERTICULA, PERFORATION, AND FISTULA FORMATION

Esophageal diverticula are pouches of variable size that are either acquired or congenital. The acquired form is caused by a thinning of the esophageal wall that allows it to bulge. Causes include esophagitis, strictures, ulceration from a foreign body, vascular ring anomaly, hiatal hernia, parasites, and periesophageal inflammation. Esophageal diverticula can be classified as either pulsion or traction types. Increased intraluminal pressure from a foreign body or chronic functional obstruction can cause a pulsion diverticulum. Pulsion diverticula are located most commonly between the heart and diaphragm. Traction diverticula are formed because of adhesions on the esophageal wall and are often located in the cranial and midthoracic esophagus.

With an esophageal diverticulum, survey radiographs are characterized by a circumscribed soft tissue mass or outpouching of the esophagus, impacted ingesta, or a mixed gas and soft tissue content (Fig. 30.33). Following survey radiography, further imaging may include endoscopy, CT, or contrast esophagraphy. Contrast medium retention in the outpouching on serial radiographs helps to confirm the diagnosis. Endoscopy is indicated to fully assess the mucosal lining and the size of the opening into the diverticulum for surgical planning.

Perforation of the esophagus occurs either acutely because of a sharp foreign body or chronically because of slow pressure necrosis from a foreign body or neoplasia.[63,64] Perforations can communicate with the mediastinum and/or the pleural space. Bony foreign bodies, a bodyweight of less than 10 kg, and esophageal foreign body present for more than 3 days are considered significant risk factors for complications.[63] Complication rates of esophageal foreign bodies are reported to be

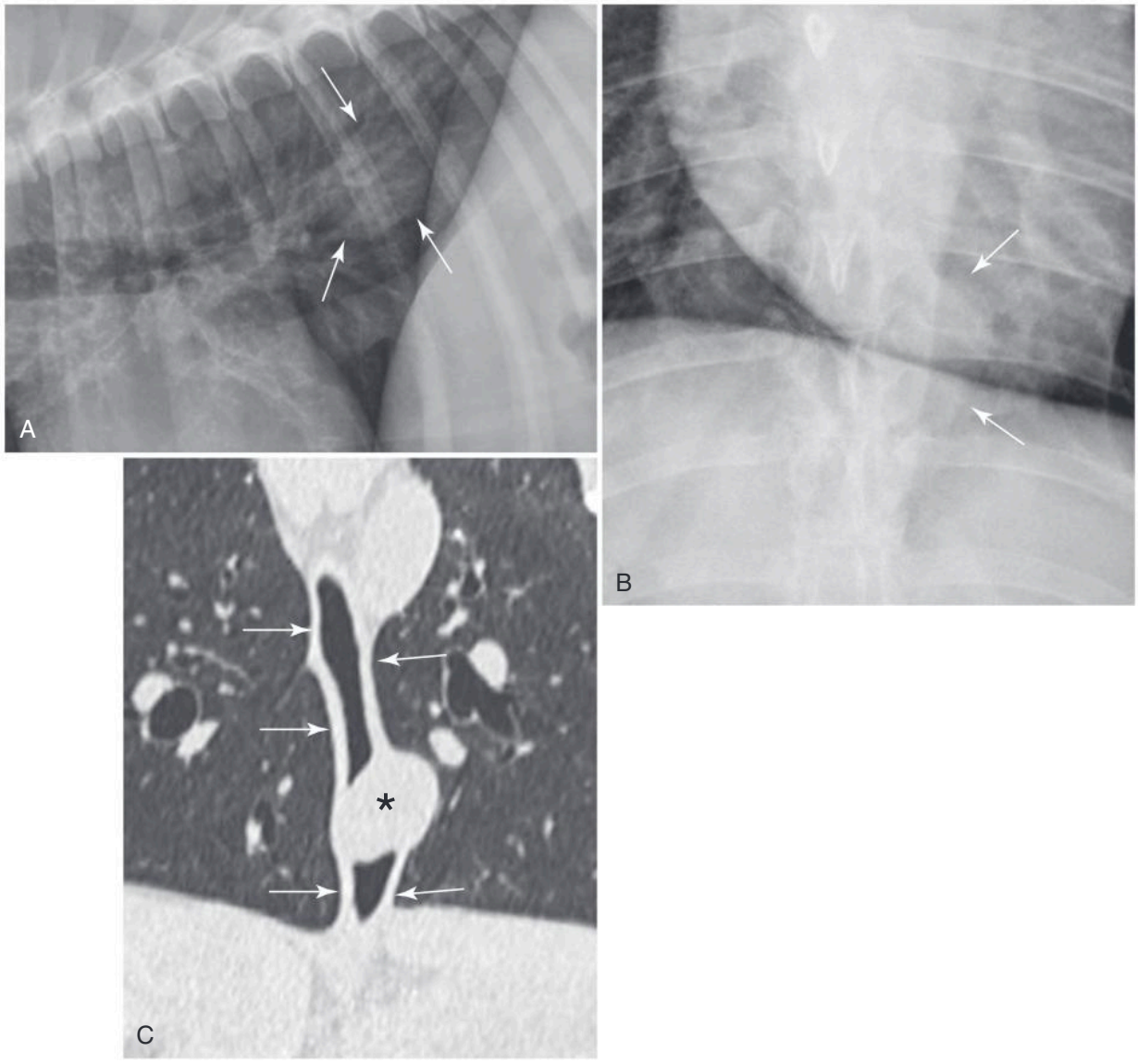


Fig. 30.31 Lateral **(A)** and ventrodorsal (VD) **(B)** radiographs of a dog with a small mass (*white arrows*) in the caudal aspect of the thorax. This mass is in a position consistent with esophagus but could also be a pulmonary or a nonesophageal mediastinal mass. A barium esophagram would be helpful in this patient, but a computed tomography (CT) was done instead. **C,** Dorsal plane reconstructed CT image of the caudal thorax in a plane through the esophagus. The esophagus is mildly dilated with gas (*white arrows*), and there is a mass arising from the left wall (*asterisk*). The mass appears benign because of its smooth margins. The histologic diagnosis of this mass is not known.

12.7% and include perforation, stricture, diverticula, periesophageal abscess, pneumothorax, pleural effusion, and respiratory arrest.[65] Cervical perforations have a better prognosis than thoracic perforations because of the development of septic mediastinitis, pleuritis, and pyothorax when there is perforation of the thoracic esophagus. Radiographically, mediastinal widening caused by inflammation or abscess formation, pneumomediastinum, and extension of gas along the fascial planes of the neck, pneumothorax, and pleural effusion may be present (Fig. 30.34; see Fig. 30.23, eFig. 30.6). A multimodality approach (radiography, contrast esophography, CT, esophagoscopy) to diagnosing esophageal perforations is often warranted.[64] Pleural fluid analysis, thoracic ultrasound, or thoracic CT may be helpful to confirm the presence of a perforation and determine the source of pleural fluid or pneumomediastinum and to best assess the mediastinal structures before performing a contrast esophagram or endoscopy. An esophageal contrast study with nonionic iodinated water-soluble contrast medium can be considered to confirm the perforation. However, water-soluble contrast medium may have poor adherence to devitalized tissue, may not coat the foreign material, and may even bypass an obstruction, giving a false-negative diagnosis.



eFig. 30.6 Lateral thoracic radiograph of a dog 3 days after endoscopic removal of a chronic esophageal foreign body. The esophagus remains mildly gas distended. There is gas and fluid in the ventral pleural space, consistent with esophageal rupture due to esophageal wall necrosis associated with the foreign body.

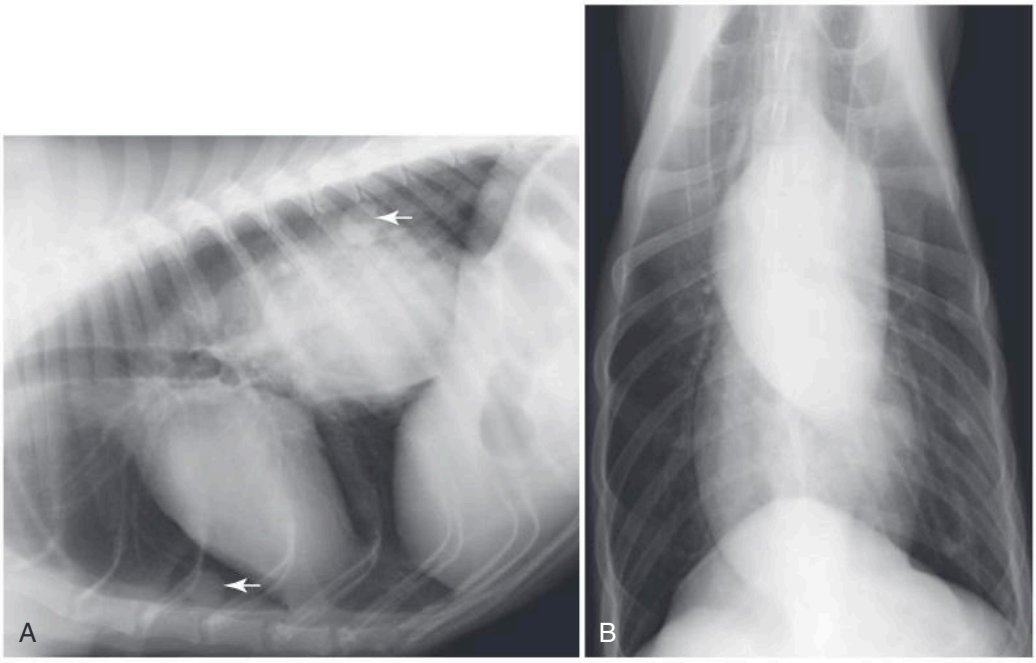


Fig. 30.32 **A,** Right lateral thoracic radiograph of a 2-year-old dog. There is a large mass caused by *Spirocerca lupi* infection in the region of the caudal esophagus. Several lung nodules are present (*white arrows*). The lung nodules suggest malignant transformation of the esophageal mass with secondary pulmonary metastasis. **B,** Ventrodorsal (VD) radiograph of same dog. The mass is midline, and the aorta is not visible. (Image courtesy the Department of Companion Animal Clinical Sciences, Faculty of Veterinary Science, University of Pretoria.)

Esophageal fistulas can be congenital or acquired.[65] Congenital forms are typically bronchoesophageal communications, but tracheoesophageal communications also occur.[66] Acquired forms are typically due to esophageal perforation resulting in communication with the airways of the trachea or lung.[67] Survey radiographs may be characterized by an ill-defined soft tissue or mixed pulmonary opacity. The diagnosis of an esophageal fistula relies upon demonstrating a communication between the esophagus and the airway with contrast medium or bronchoscopy. A swallow with liquid barium will usually show communication from the esophagus into the airway via a fistulous tract.

ESOPHAGEAL VARICES

Esophageal and paraesophageal varices may result from portal hypertension that generates reversal of portal blood flow, which diverts venous blood in a cranial direction through the left gastric vein to the venous plexus of the esophagus.[68,69] Obstructions of the cranial vena cava can also lead to the formation of esophageal and paraesophageal varices. The varices can drain into the azygous vein, the caudal vena cava, or into the portal system, depending on the site of the obstruction. Gallbladder and choledochal varices, omental varices, duodenal varices, phrenicoabdominal varices, colic varices, and abdominal wall varices drain into the caudal vena cava and result from portal hypertension. CT angiography is necessary for determining the origin, course, and termination of these vessels, and their underlying cause (Fig. 30.35). Of note is that bronchoesophageal artery hypertrophy should be included in the differential diagnosis of esophageal and paraesophageal varices in dogs as the two diseases appear similarly on CT angiography.[70] Both portal hypertension causing varices and bronchoesophageal artery hypertrophy secondary to chronic pulmonary or thromboembolic disease can occur concomitantly and can make imaging interpretation challenging. High-quality CT-angiography scans together with knowledge of the anatomy and possible physiopathology changes are essential for the diagnosis of these complex vascular anomalies.

AERODIGESTIVE DISORDERS

Aerodigestive disorders are a group of diseases which arise as a result of the close link between the digestive and respiratory tracts. Typically, animals with aerodigestive disease will present with symptoms of respiratory dysfunction (cough, recurring pneumonia) without typical gastrointestinal signs. However, with further exploration, gastrointestinal dysfunction such as pharyngeal weakness, esophageal dysmotility, or reflux emerges as the underlying pathology ultimately leading to laryngeal penetration-aspiration (P-A) and/or aspiration pneumonia.[4,71] As many as 81% of dogs with respiratory signs and with no evidence of gastrointestinal symptoms have been reported to have abnormalities on VFSS.[4] Therefore, VFSS is indicated in dogs with respiratory disease for which an underlying cause is nebulous. A grading scheme for laryngeal P-A of contrast material as visualized on VFSS has been developed so as to determine the prevalence and clinical significance of this process. Pathologic P-A has been defined as a score ≥ 3 which indicates contrast medium entering or surpassing the supraepiglottic space during VFSS. Some animals will have clinically silent P-A and dogs with pharyngeal disease and esophago-oropharyngeal reflux are prone to pathologic P-A.[72]

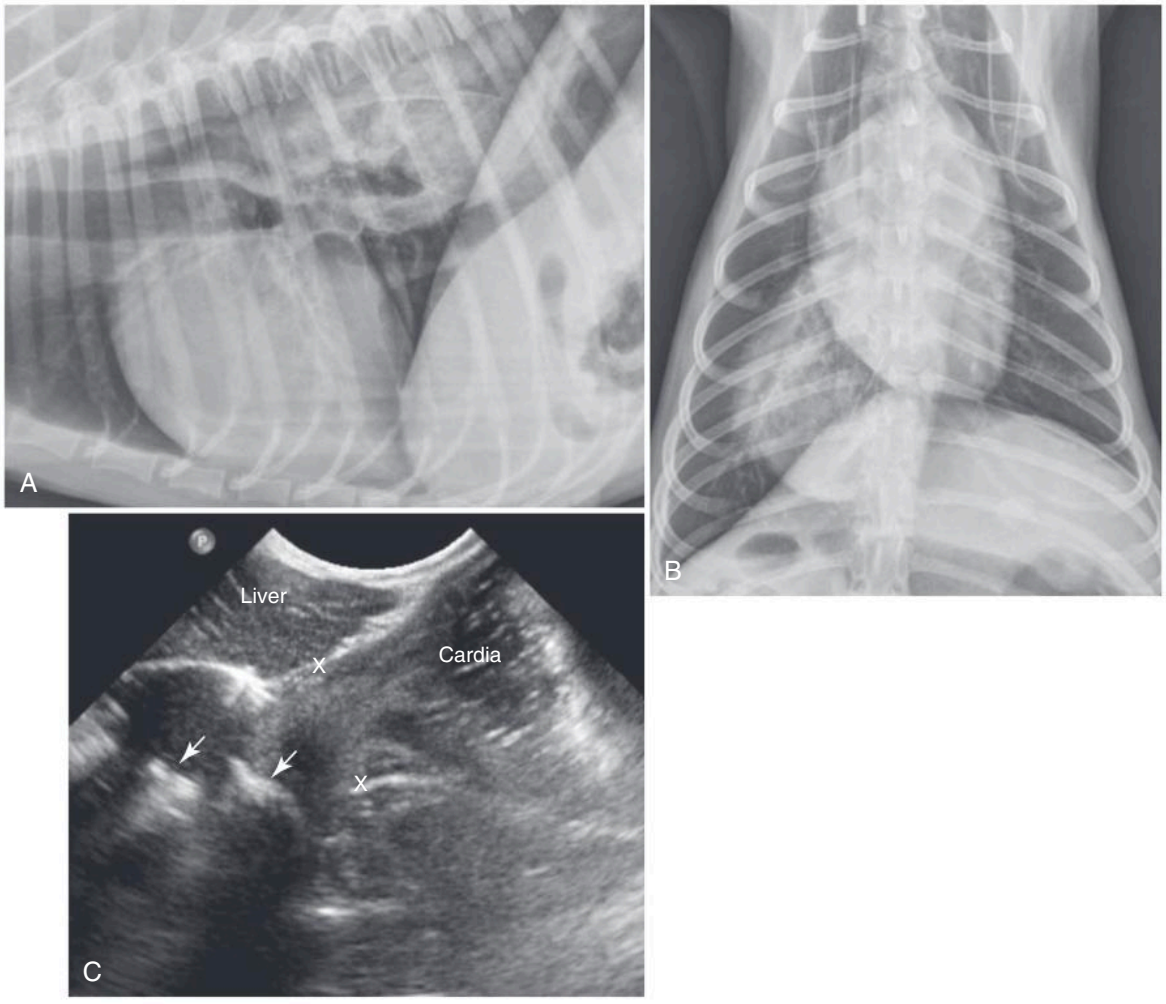


Fig. 30.33 **A,** Lateral radiograph of an 8-year-old Papillon. There is a mixed soft tissue and mineral opacity between the aorta and caudal vena cava in the caudodorsal aspect of the thorax. **B,** Ventrodorsal (VD) radiograph of the same dog. There is a large, right-sided mixed soft tissue and mineral opaque mass with a sharply de fined right lateral border at the midline and to the right of the spine. An esophageal diverticulum containing bony foreign material was suspected. **C,** Ultrasound image of the same dog. The probe is positioned at the ventral midline pointing cranially and to the left to visualize the diaphragm and esophageal hiatus (calipers). The esophagus is dilatated at the hiatus and multiple linear, hyperechoic shadowing structures (*white arrows*) and mixed echogenic fluid can be seen filling the caudal esophagus.

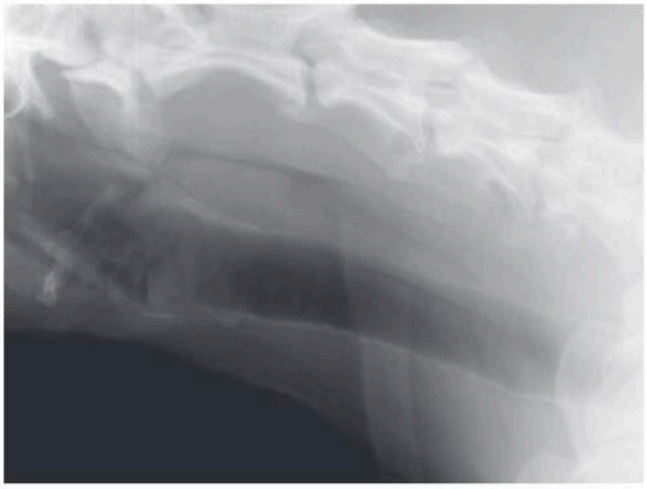


Fig. 30.34 Lateral cervical radiograph in a dog with acute ptyalism and vocalizing. Linear gas opacities are present dorsal to the cricopharyngeal sphincter and trachea. Perforating wood splinters were found on inspection of the mouth.

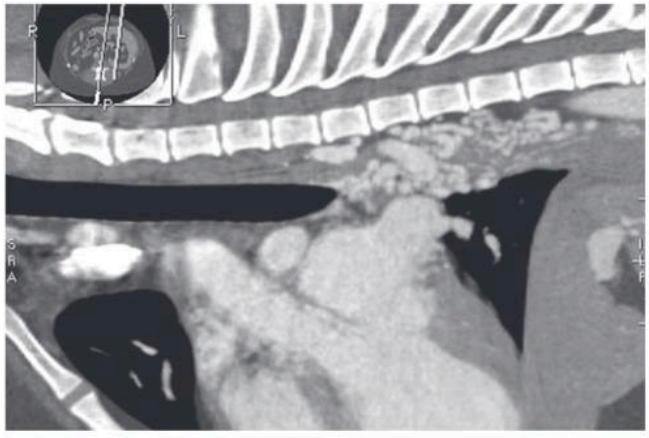


Fig. 30.35 Sagittal plane reconstruction of a computed tomography (CT) image of a dog with esophageal varices caused by portal hypertension. (Image courtesy Dr. Giovanna Bertolini, Clinica Veterinaria San Marco.)

Acknowledgment

With special thanks to prior authors of this chapter for their contributions.

REFERENCES

1. Suter PF. Swallowing problems and esophageal abnormalities. In: Suter PF, Lord PF, eds. *Thoracic Radiography: Thoracic Diseases of the Dog and Cat*. Wettswil, Switzerland; 1984:295–349.
2. Poncet CM, Dupre GP, Freiche VG, et al. Long-term results of upper respiratory syndrome 516 surgery and gastrointestinal tract medical treatment in 51 brachycephalic dogs. *J Small Anim Pract*. 2006;47:137–142.
3. Poncet CM, Dupre GP, Freiche VG, et al. Prevalence of gastrointestinal tract lesions in 73 519 brachycephalic dogs with upper respiratory syndrome. *J Small Anim Pract*. 2005;46:273–279.
4. Grobman ME, Masseau I, Reinero CR. Aerodigestive disorders in dogs evaluated for cough using respiratory fluoroscopy and videofluoroscopic swallow studies. *Vet J*. 2019;251:105344.
5. Gengler W. Gagging. In: Ettinger SJ, Feldman EC, eds. *The Textbook of Veterinary Internal Medicine*. St Louis, Mo, USA: Saunders Elsevier; 2010:189–191.
6. Watrous BJ. The esophagus. In: Thrall DE, ed. *Veterinary Diagnostic Radiology*. 5th ed. St. Louis, Mo, USA: Saunders Elsevier; 2007:495–511.
7. Jergens AE. Diseases of the esophagus. In: Ettinger SJ, Feldman EC, eds. *The Textbook of Veterinary Internal Medicine*. St Louis, Mo, USA: Saunders Elsevier; 2010:1487–1499.
8. Suter PF, Watrous BJ. Oropharyngeal dysphagia in the dog: a cinefluorographic analysis of experimentally induced and spontaneously occurring swallowing disorders; I. Oral stage and pharyngeal stage dysphagias. *Vet Radiol Ultrasound*. 1980;21:24–39.
9. Kogan DA, Johnson LR, Sturges BK, Jandrey KE, Pollard RE. Etiology and clinical outcome in dogs with aspiration pneumonia: 88 cases (2004–2006). *J Am Vet Med Assoc*. 2008;233(11):1748–1755.
10. McBrearty AR, Ramsey IK, Courcier EA, Mellor DJ, Bell R. Clinical factors associated with death before discharge and overall survival time in dogs with generalized megaesophagus. *J Am Vet Med Assoc*. 2011;238(12):1622–1628.
11. O'Brien TR. Esophagus. In: O'Brien TR, ed. *Radiographic Diagnosis of Abdominal Disorders in the Dog and Cat: Radiographic Interpretation, Clinical Signs, Pathophysiology*. Philadelphia, Pa, USA: WB Saunders; 1978:141.
12. Wallack ST. Introduction to barium sulfate. In: Wallack ST, ed. *The Handbook of Veterinary Contrast Radiography*. 2003:1–4. San Diego Veterinary Imaging, Solano Beach, Calif, USA.
13. Seiler G, Rytz U, Gaschen L. Radiographic diagnosis—cavitary mediastinal abscess. *Vet Radiol Ultrasound*. 2001;42(5):431–433.
14. Dvir E, Kirberger RM, Malleczek D. Radiographic and computed tomographic changes and clinical presentation of spirocercosis in the dog. *Vet Radiol Ultrasound*. 2001;42(2):119–129.
15. Wallack ST. Iodinated esophagram-dog. In: Wallack ST, ed. *The Handbook of Veterinary Contrast Radiography*. San Diego Veterinary Imaging. Solano Beach, Calif, USA; 2003:52.
16. Gaynor F, Hoffer RE, Nichols MF, et al. Physiologic features of the canine esophagus: effects of tranquilization on esophageal motility. *Am J Vet Res*. 1980;41(5):727–732.
17. Bonadio CM, Pollard RE, Dayton PA, Leonard CD, Marks SL. Effects of body positioning on swallowing and esophageal transit in healthy dogs. *J Vet Intern Med*. 2009;23(4):801–805.
18. Cheney DM, Marks SL, Pollard RE. Effect of bolus size on deglutition and esophageal transit in healthy dogs. *Vet Radiol Ultrasound*. 2016;57:359–365.
19. Pollard RE, Marks SL, Davidson A, Hornof WJ. Quantitative videofluoroscopic evaluation of pharyngeal function in the dog. *Vet Radiol Ultrasound*. 2000;41(5):409–412.
20. Pollard RE, Marks SL, Leonard R, Belafsky PC. Preliminary evaluation of the pharyngeal constriction ratio (PCR) for fluoroscopic determination of pharyngeal constriction in dysphagic dogs. *Vet Radiol Ultrasound*. 2007;48(3):221–226.
21. Harris RA, Grobman ME, Allen MJ, et al. Standardization of a videofluoroscopic swallow study protocol to investigate dysphagia in dogs. *J Vet Intern Med*. 2017;31:383–393.
22. Leonard R, Kendall K, McKenzie S. UES opening and cricopharyngeal bar in nondysphagic elderly and nonelderly adults. *Dysphagia*. 2004;19(3):182–191.
23. Haines JM, Khoo A, Brinkman E, Thomason JM, Mackin AJ. Technique for evaluation of gravity-assisted esophageal transit characteristics in dogs with megaesophagus. *J Am Anim Hosp Assoc*. 2019 Jul/Aug;55(4):167–177.
24. Lyngby JG, Haines JM, Guess SC. Use of a videofluoroscopic feeding evaluation to guide management of dogs with congenital idiopathic megaesophagus. *Vet Med Sci*. 2022 Jul;8(4):1434–1442.
25. Simpson KW. Disease of the esophagus. In: Ettinger SJ, Feldman EC, eds. *Textbook of Veterinary Internal Medicine: Diseases of the Dog and Cat*. 7th ed. Philadelphia: Saunders; 2023:1487–1500.
26. Watrous BJ. Clinical presentation and diagnosis of dysphagia. *Vet Clin North Am Small Anim Pract*. 1983;13(3):437–459.
27. Levine JS, Pollard RE, Marks SL. Contrast videofluoroscopic assessment of dysphagic cats. *Vet Radiol Ultrasound*. 2014;55(5):465–471.
28. Stanley BJ, Hauptman JG, Fritz MC, et al. Esophageal dysfunction in dogs with idiopathic laryngeal paralysis: a controlled cohort study. *Vet Surg*. 2010;39(2):139–149.
29. Bexfield NH, Watson PJ, Herrtage ME. Esophageal dysmotility in young dogs. *J Vet Intern Med*. 2006;20(6):1314–1318.
30. Diamant N, Szczepanski M, Mui H. Idiopathic megaesophagus in the dog: reasons for spontaneous improvement and a possible method of medical therapy. *Can Vet J*. 1974;15(3):66–71.
31. Kyles AE. Swallowing disorders. In: Bojrab MJ, ed. *Disease Mechanisms in Small Animal Surgery*. 3rd ed. Philadelphia: Lea & Febiger; 2010:205–209.
32. Grobman ME, Schachtel J, Gyawali CP, Lever TE, Reinero CR. Videofluoroscopic swallow study features of lower esophageal sphincter achalasia-like syndrome in dogs. *J Vet Intern Med*. 2019 Sep;33(5):1954–1963.
33. Guilford WG. Diseases of swallowing. In: Guilford G, Center SA, Strombeck DR, et al., eds. *Strombeck's Small Animal Gastroenterology*. 3rd ed. Philadelphia: Saunders; 1996:211–238.
34. Callan MB, Washabau RJ, Saunders HM, et al. Congenital esophageal hiatal hernia in the Chinese shar-pei dog. *J Vet Intern Med*. 1993;7(4):210–215.
35. Reeve EJ, Sutton D, Friend EJ, Warren-Smith CMR. Documenting the prevalence of hiatal hernia and oesophageal abnormalities in brachycephalic dogs using fluoroscopy. *J Small Anim Pract*. 2017;58(12):703–708.
36. Luciani E, Reinero C, Grobman M. Evaluation of aerodigestive disease and diagnosis of sliding hiatal hernia in

brachycephalic and nonbrachycephalic dogs. *J Vet Intern Med*. 2022 Jul;36(4):1229–1236.
37. Houlton JEF, Herrtage ME, Taylor PM, et al. Thoracic esophageal foreign bodies in the dog: a review of ninety cases. *J Small Anim Pract*. 1985;7:521–536.
38. Thompson HC, Cortes Y, Gannon K, et al. Esophageal foreign bodies in dogs: 34 cases (2004–2009). *J Vet Emerg Crit Care*. 2012;22(2):253–261.
39. Buchanan JW. Tracheal signs and associated vascular anomalies in dogs with persistent right aortic arch. *J Vet Intern Med*. 2004;18(4):510–514.
40. Yoon H, Kim J, Kwon GB, et al. Imaging diagnosis—computed tomographic angiography characteristics of multiple vascular anomalies in a senior dog with late-onset regurgitation. *Vet Radiol Ultrasound*. 2018;59(5):E44–E49.
41. Shannon D, Husnik R, Fletcher JM, et al. Persistent right aortic arch with an aberrant left subclavian artery, Kommerell's diverticulum and bicarotid trunk in a 3-year-old cat. *JFMS Open Rep*. 2015;1(2):2055116915614590.
42. Kyles AE. Vascular ring anomalies. In: Bojrab MJ, ed. *Disease Mechanisms in Small Animal Surgery*. 3rd ed. Philadelphia: Lea & Febiger; 2010:350–354.
43. Holt D, Heldmann E, Michel K, et al. Esophageal obstruction caused by a left aortic arch and an anomalous right patent ductus arteriosus in two German Shepherd littermates. *Vet Surg*. 2000;29(3):264–270.
44. Hurley K, Miller MW, Willard MD, et al. Left aortic arch and right ligamentum arteriosum causing esophageal obstruction in a dog. *J Am Vet Med Assoc*. 1993;203(3):410–412.
45. Larcher T, Abadie J, Roux FA, et al. Persistent left cranial vena cava causing oesophageal obstruction and consequent megaoesophagus in a dog. *J Comp Pathol*. 2006;135:150–152.
46. Adamama-Moraitou KK, Rallis TS, Prassinos NN, et al. Benign esophageal stricture in the dog and cat: a retrospective study of 20 cases. *Can J Vet Res*. 2002;66(1):55–59.
47. Dvir E, Clift SJ, Williams MC. Proposed histological progression of the *Spirocerca lupi*-induced oesophageal lesion in dogs. *Vet Parasitol*. 2010;168:71–77.
48. Gibson CJ, Parry NM, Jakowski RM, et al. Adenomatous polyp with intestinal metaplasia of the esophagus (Barrett esophagus) in a dog. *Vet Pathol*. 2010;47(1):116–119.
49. Wray JD, Blunden AS. Progressive dysphagia in a dog caused by a scirrhous, poorly differentiated peri-oesophageal carcinoma. *J Small Anim Pract*. 2006;47(1):27–30.
50. Ranen E, Shamir MH, Shahar R, et al. Partial esophagectomy with single layer closure for treatment of esophageal sarcomas in 6 dogs. *Vet Surg*. 2004;33(4):428–434.
51. Gualtieri M, Monzeglio MG, Di Giancamillo M. Oesophageal squamous cell carcinoma in two cats. *J Small Anim Pract*. 1999;40(2):79–83.
52. Teo LH, Cahalan SD, Benigni L, et al. Oesophageal angioleiomyosarcoma in a cat. *J Feline Med Surg*. 2014;16(10):846–852.
53. Fisher MM, Morgan JP, Krecek RC, et al. Radiography for the diagnosis of spirocercosis in apparently healthy dogs, St. Kitts, West Indies. *Vet Parasitol*. 2009;160:337–339.
54. Harrus S, Harmelin A, Markovics A, et al. *Spirocerca lupi* infection in the dog: aberrant migration. *J Am Anim Hosp Assoc*. 1996;32(2):125–130.
55. Gaschen L, Kircher P, Lang J. Endoscopic ultrasound instrumentation, applications in humans, and potential veterinary applications. *Vet Radiol Ultrasound*. 2003;44(6):665–680.
56. Berry WL. *Spirocerca lupi* esophageal granulomas in 7 dogs: resolution after treatment with doramectin. *J Vet Intern Med*. 2000;14(6):609–612.
57. Kirberger RM, Clift SJ, van Wilpe E, et al. *Spirocerca lupi* associated vertebral changes: a radiologic-pathologic study. *Vet Parasitol*. 2013;195:87–94.
58. Lindsay N, Kirberger R, Williams M. Imaging diagnosis—spinal cord chondrosarcoma associated with spirocercosis in a dog. *Vet Radiol Ultrasound*. 2010;51(6):614–616.
59. Kirberger RM, Stander N, Cassel N, et al. Computed tomographic and radiographic characteristics of aortic lesions in 42 dogs with spirocercosis. *Vet Radiol Ultrasound*. 2013;54(3):212–222.
60. Kirberger RM, Dvir E, van der Merwe LL. The effect of positioning on the radiographic appearance of caudodorsal mediastinal masses in the dog. *Vet Radiol Ultrasound*. 2009;50(6):630–634.
61. Kirberger RM, Cassel N, Stander N, et al. Triple phase dynamic computed tomographic perfusion characteristics of spirocercosis induced esophageal nodules in non-neoplastic versus neoplastic canine cases. *Vet Radiol Ultrasound*. 2015;56(3):257–263.
62. Doran IP, Wright CA, Moore AH. Acute oropharyngeal and esophageal stick injury in forty-one dogs. *Vet Surg*. 2008;37(8):781–785.
63. Paradise H, Mathews KG, Cohen EB. Imaging diagnosis—use of radiography, computed tomography, and endoscopy in the diagnosis of esophageal perforation by an extraluminal tracheal ring prosthesis in a golden retriever. *Vet Radiol Ultrasound*. 2017;58(4):E37–E41.
64. Gianella P, Pfammatter NS, Burgener IA. Oesophageal and gastric endoscopic foreign body removal: complications and follow-up of 102 dogs. *J Small Anim Pract*. 2009;50(12):649–654.
65. Basher AW, Hogan PM, Hanna PE, et al. Surgical treatment of a congenital bronchoesophageal fistula in a dog. *J Am Vet Med Assoc*. 1991;199(4):479–482.
66. Della Ripa MA, Gaschen F, Gaschen L, et al. Canine bronchoesophageal fistulas: case report and literature review. *Compend Contin Educ Vet*. 2010;32(4):E1.
67. Dodman NH, Baker GJ. Tracheo-oesophageal fistula as a complication of an oesophageal foreign body in the dog. *J Small Anim Pract*. 1978;19(5):290–296.
68. Bertolini G. Acquired portal collateral circulation in the dog and cat. *Vet Radiol Ultrasound*. 2010;51(1):25–33.
69. Ledda G, Caldin M, Mezzalira G, et al. Multidetector-row computed tomography patterns of bronchoesphageal artery hypertrophy and systemic-to-pulmonary fistula in dogs. *Vet Radiol Ultrasound*. 2015;56(4):347–358.
70. Wallack ST. Static barium esophagram. In: *The Handbook of Veterinary Contrast Radiography*. Solana Beach, CA: San Diego Veterinary Imaging; 2003:45–53.
71. Grobman M. Aerodigestive disease in dogs. *Vet Clin North Am Small Anim Pract*. 2021;51(1):17–32.
72. Grobman M, Carlue E, Reinero CR. Incidence, clinical signs and videofluoroscopic swallow study abnormalities associated with airway penetration and aspiration in 100 dogs. *J Vet Intern Med*. 2022;36(6):2149–2159.
73. Pollard RE. Videofluoroscopic evaluation of the pharynx and upper esophageal sphincter in the dog: a systematic review of the literature. *Front Vet Sci*. 2019;6:117.

ELECTRONIC RESOURCES

Additional information related to the content in Chapter 30 can be found online at eBooks.Health.Elsevier.com.

- Chapter Quiz

CHAPTER 31

Canine and Feline Thoracic Wall

Gabriela S. Seiler

The thoracic wall is composed of rigid structures such as the spine, sternum ribs, and costal cartilages as well as the interconnecting soft tissue structures including the skin, subcutaneous fat, subcutaneous and intercostal musculature, as well as the parietal pleura, blood vessels, nerves, and lymphatics. The thoracic wall plays an important role in protecting the thoracic soft tissue structures and is an integral part of pulmonary ventilation. Careful inspection of the thoracic wall structures is an important part of the interpretation of thoracic radiographs and other imaging modalities. Radiographs are typically indicated for initial evaluation of a thoracic wall lesion, and additional imaging methods are selected based on findings. Thoracic ultrasound is an excellent method to evaluate the layers of the thoracic wall, and investigate peripheral thoracic masses to determine if they are pulmonary or extrapleural in origin. Ultrasound-guided fine needle aspirates or biopsy of soft tissue or bone lesions may be obtained. Contrast-enhanced computed tomography (CT) is often used to get a more global assessment of the thoracic cavity and thoracic wall, and for surgical or radiation therapy planning.

THE NORMAL THORACIC WALL

Dogs and cats both have 13 thoracic vertebrae and paired ribs, although transitional vertebrae are common anomalies. The appearance and orientation of the ribs are somewhat dependent on breed and thoracic conformation in dogs, whereas it is more consistent in cats. Typically, the first few ribs are positioned vertically and perpendicular to the spine in the lateral and ventrodorsal (VD) projections, respectively. Towards the caudal thoracic spine, the ribs become progressively caudally oriented proximally with a more or less pronounced craniomedial curvature of the costal cartilages. The orientation of the ribs depends on the phase of respiration and the depth of inspiration. At full inspiration the ribs are in a more perpendicular orientation to the spine, whereas they are more caudally oriented during expiration (Fig. 31.1). In dogs, variations in thoracic wall conformation can be breed related. Costochondral conformation in chondrodystrophic breeds can lead to misdiagnosis of pneumothorax or pleural effusion as discussed in Chapter 34 (Fig. 31.2).

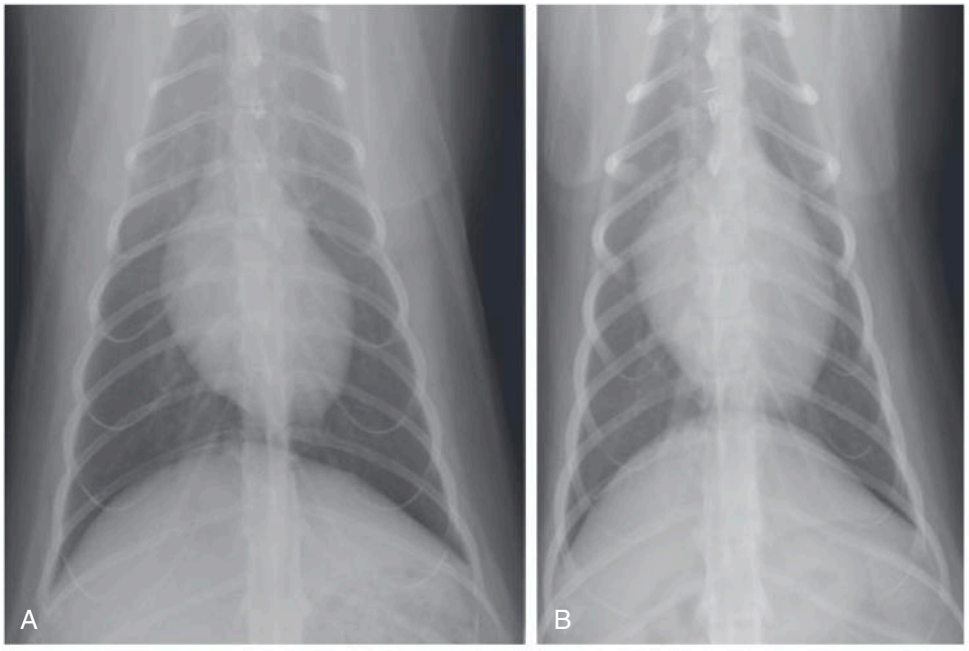


Fig. 31.1 Inspiratory **(A)** and expiratory **(B)** ventrodorsal (VD) thoracic radiographs of an adult cat. Notice the different more cranial orientation of the ribs and flattened shape of the diaphragm during inspiration compared with expiration.

When interpreting thoracic radiographs, it is important to follow each rib from its costovertebral to its costochondral junction as rib lesions such as fractures or lysis can be subtle and are easily overlooked. In general, it is helpful to look for symmetry of the left and right ribs and intercostal spaces in the VD or dorsoventral (DV) projections, and look for abrupt changes in direction of the ribs in a lateral view as well as loss of parallel orientation of the contralateral ribs (Fig. 31.3). The appearance of the costal cartilages depends on the age of the patient. In juvenile animals the cartilages are soft tissue opaque and poorly delineated from the rest of the thoracic structures. As animals progress in age, particularly dogs, costal cartilages often become mineralized and can exhibit exuberant, expansile areas of mineralization that can be confused with pathology such as lung nodules (Fig. 31.4). The sternocostal junction is a synovial joint for the first eight to nine ribs and the remaining ribs are fused to each other and to the sternum to form the costal arch. The last one or two rib pairs are not fused to the costal arch. The sternum is composed of three parts, the manubrium, body, and xiphoid. Degenerative changes of the sternum are common and are usually not clinically significant (Fig. 31.5).

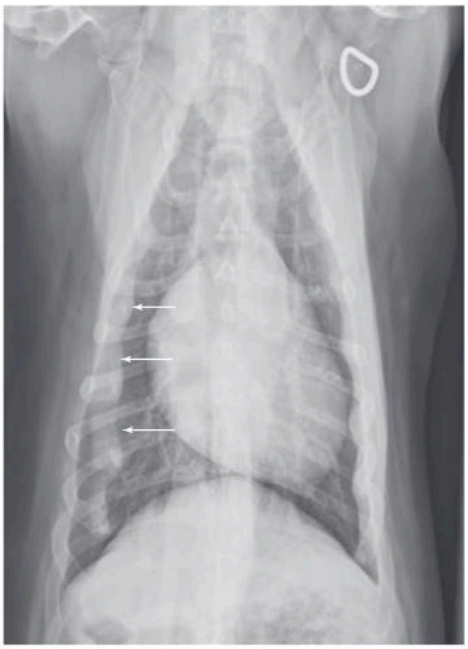


Fig. 31.2 Ventrodorsal (VD) thoracic radiograph of a normal adult Bassett hound. The curved shape of the ribs common in this breed creates a soft tissue opacity along the thoracic wall (*white arrows*) that could be misinterpreted as thoracic wall thickening or pleural effusion.

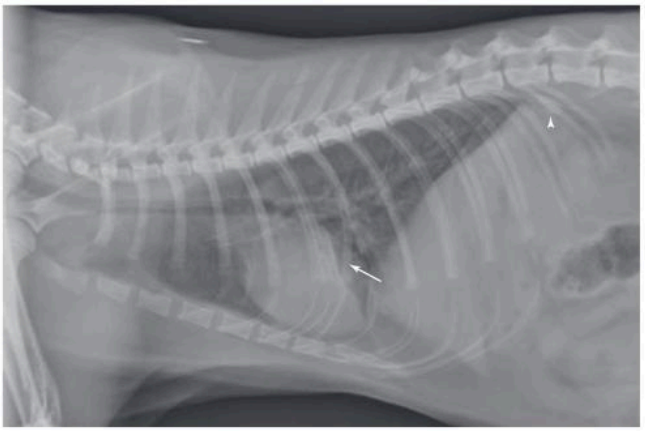


Fig. 31.3 Lateral thoracic radiograph of a cat with chronic healed rib fractures. Callus formation on a T13 rib (*arrowhead*) is identified as focal smoothly margined thickening. A prior T7 rib fracture (*white arrow*) is best identified based on its different orientation compared with adjacent ribs.

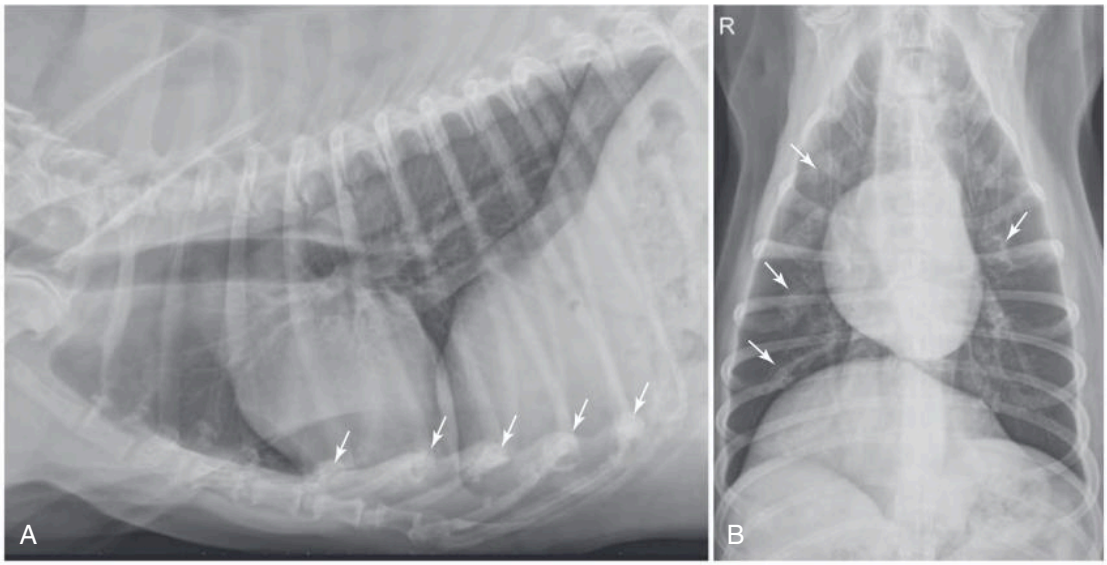


Fig. 31.4 Lateral **(A)** and ventrodorsal (VD) **(B)** thoracic radiographs of a 15-year-old Labrador retriever. The costochondral junctions are enlarged and irregularly mineralized with a nodular appearance (*white arrows*). Costochondral junctions superimposed over the lung parenchyma in the VD projection can mimic pulmonary lesions (*white arrows*).

The soft tissues of the thoracic wall should always be scrutinized for soft tissue nodules such as nipples, skin nodules (papillomas, lipomas), engorged ticks, etc., that could mimic the appearance of a pulmonary nodule in orthogonal projection due to summation artifact. Application of radiopaque markers such as barium paste on an identified thoracic wall nodule followed by repeat radiographs can be useful to localize a questionable opacity (Fig. 31.6). As mentioned earlier for the evaluation of rib lesions, the soft tissues of the thoracic wall should be evaluated for symmetry, focal thickening, disruptions, and changes in opacity in all projections. Common artifacts that need to be differentiated from pathology are overlying skin folds, and wet hair coat artifact.

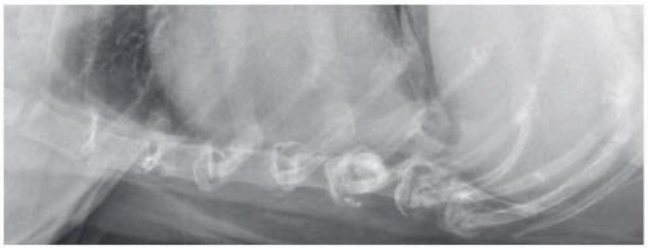


Fig. 31.5 Right lateral radiograph of a middle-aged German shepherd with extensive costal cartilage mineralization and sternebral and costochondral degeneration. The changes are not clinically significant.

CONGENITAL AND DEVELOPMENTAL ABNORMALITIES

Transitional vertebrae may be present at the cervicothoracic and thoracolumbar junction. The 13th vertebra is most commonly affected and can have unilateral or bilateral hypoplastic or aplastic ribs, or anomalous transverse vertebrae (Fig. 31.7). Anomalous rudimentary ribs are occasionally present on the seventh cervical vertebra. Fusion of the first ribs may also be observed (Fig. 31.8). These findings are usually not clinically relevant; however, they should be documented to avoid mistakes in vertebral counts when surgical procedures are planned. Congenital sternal anomalies are characterized by reduction or increasing number of segments, or fusion of adjacent segments. Anomalies of the xiphoid have been reported to be associated with peritoneopericardial diaphragmatic hernia.[1] An abnormal shape of the caudal portion of the

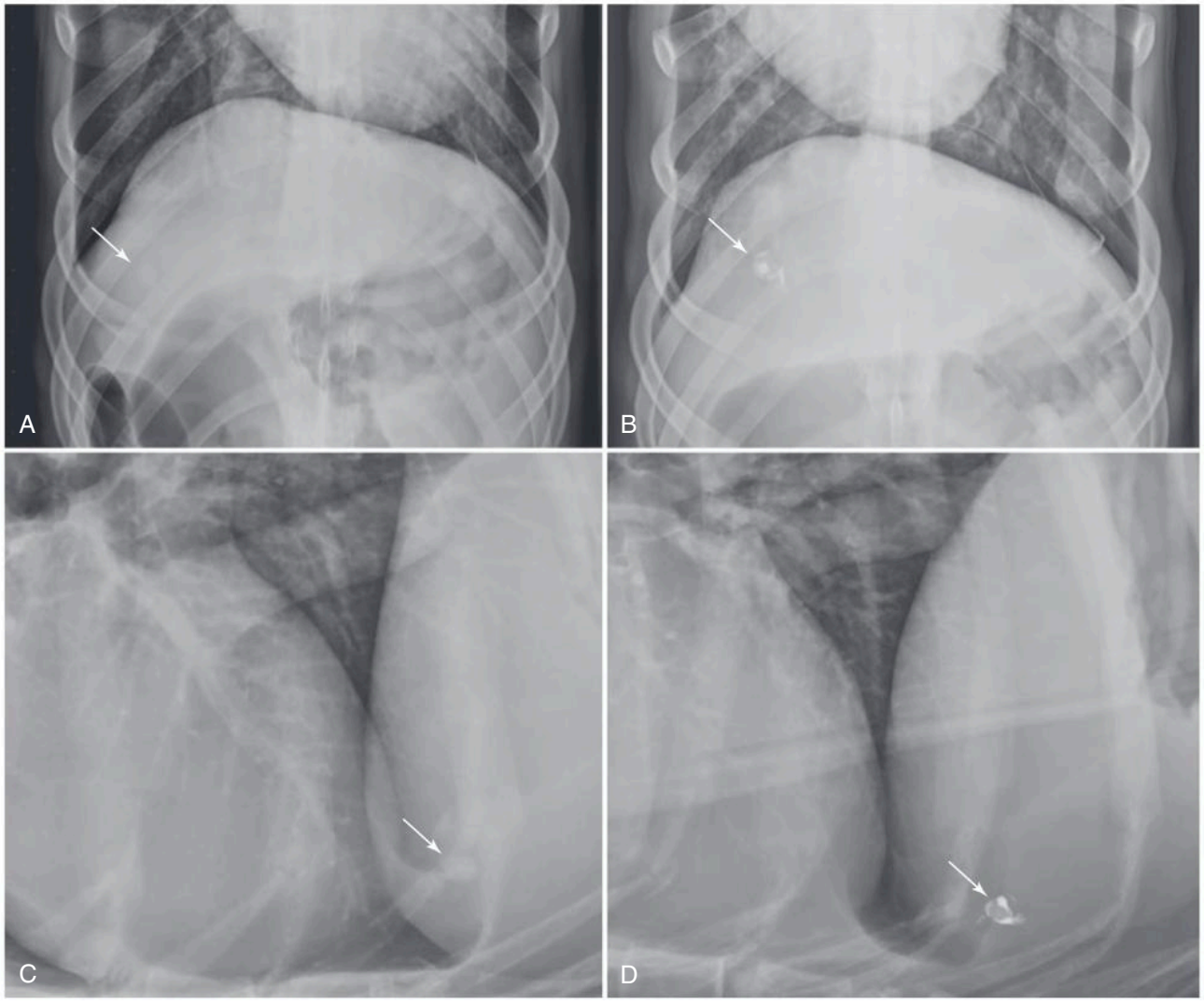


Fig. 31.6 **A,** Ventrodorsal (VD) radiograph of a dog with a soft tissue nodule identified in the right caudal thorax (*arrow*). **C,** On a lateral radiograph, the nodule is visible in the ventral thorax (*arrow*). After application of barium paste to a nipple, VD **(B)** and lateral **(D)** radiographs were repeated, confirming that the nodular opacity was created by the nipple (*arrows*).

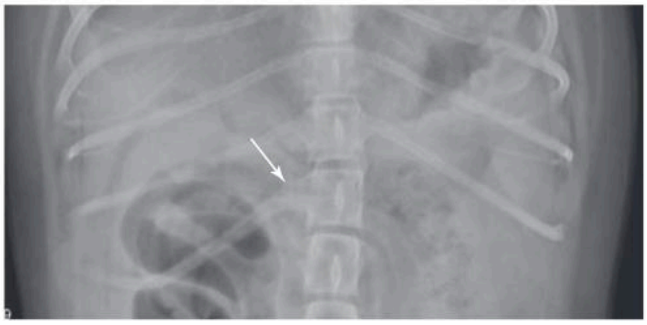


Fig. 31.7 Ventrodorsal (VD) radiograph of a dog with a transitional thoracolumbar vertebra. The right T13 rib (*arrow*) has a broadened attachment to the vertebra similar to a transverse process, whereas the left rib is absent.

sternum can manifest as dorsal displacement with resulting pectus excavatum (also called funnel chest) (Fig. 31.9) or ventral displacement or pectus carinatum (pigeon chest) (Fig. 31.10).[2] These abnormal conformations are typically congenital in origin in dogs and cats, but have to be differentiated from deformations of the thoracic cavity caused by chronic airway obstruction such as laryngeal paralysis which can cause the appearance of pectus excavatum.[3] Pectus excavatum can be associated with respiratory and cardiovascular anomalies and results in dorsal ventral narrowing of the thorax. In young puppies, it may have to be surgically corrected if there is respiratory or cardiovascular compromise (Fig. 31.11).[4] Pectus carinatum is caused by idiopathic overgrowth of the costal cartilages and may also be associated with congenital heart disease and/or sternal segment absence.

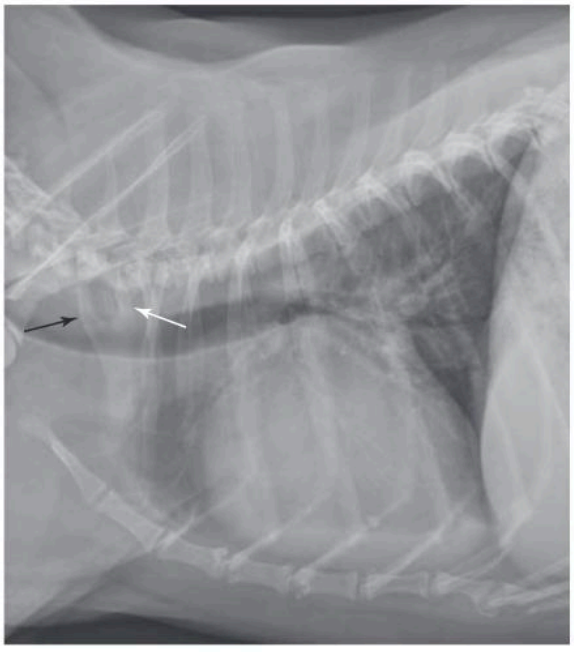


Fig. 31.8 Lateral thoracic radiograph of a dog with an anomalous rib on the seventh cervical vertebra (*black arrow*), fused with an abnormally broadened first rib (*white arrow*).



Fig. 31.10 Left lateral thoracic radiograph of an adult French bulldog with pectus carinatum. The caudal portion of the sternum is ventrally deviated resulting in a deep chest conformation. Multiple thoracic hemivertebrae are also present.

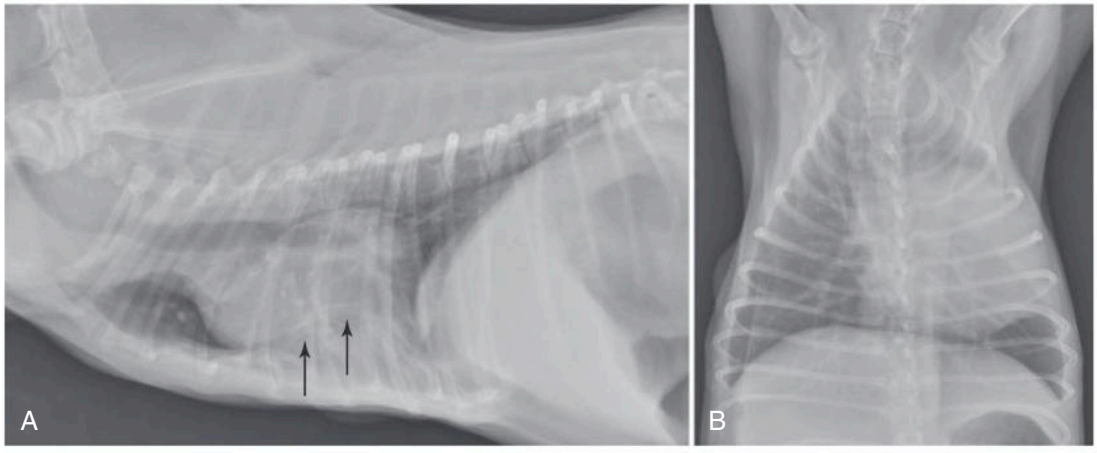


Fig. 31.9 Right lateral **(A)** and ventrodorsal (VD) **(B)** thoracic radiographs of an adult Shih Tzu with pectus excavatum. The caudal portion of the sternum is dorsally deviated (*black arrows*) causing ventrodorsal narrowing of the thorax, dorsal displacement, and shift of the cardiac silhouette into the left hemithorax.

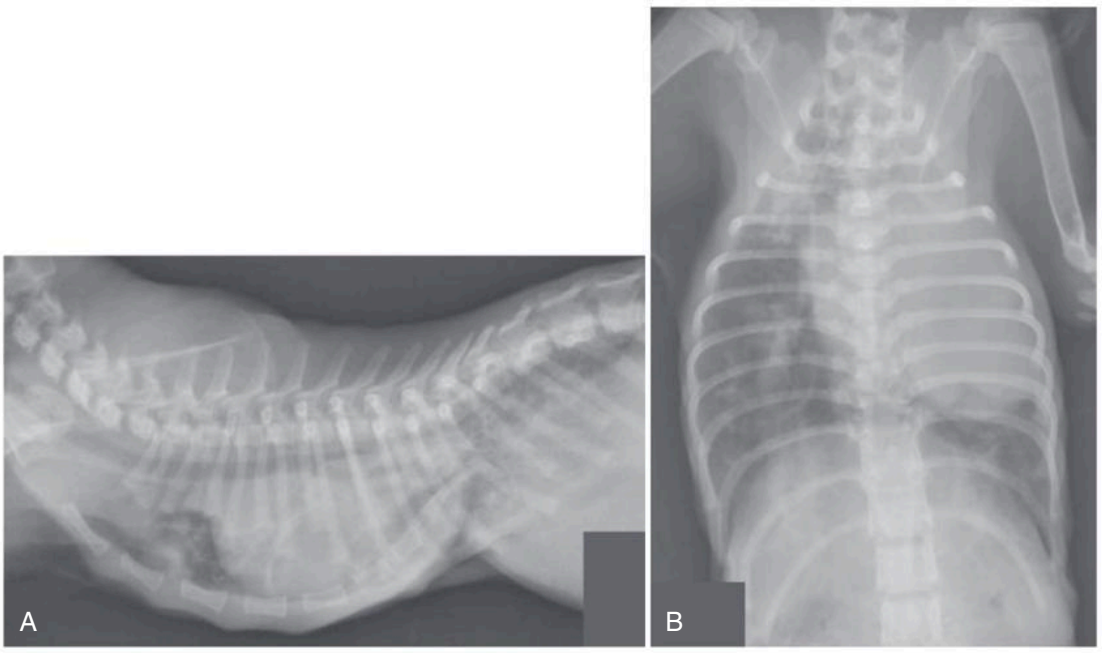


Fig. 31.11 Left lateral **(A)** and dorsoventral (DV) **(B)** thoracic radiographs of an 8-week-old Bengal cat with pectus excavatum that causes severe dorsoventral narrowing of the thorax, displacement of the cardiac silhouette into the left hemithorax, and collapse of the left cranial lung lobe resulting in increased respiratory rate. External splinting improved the kitten's respiratory pattern.

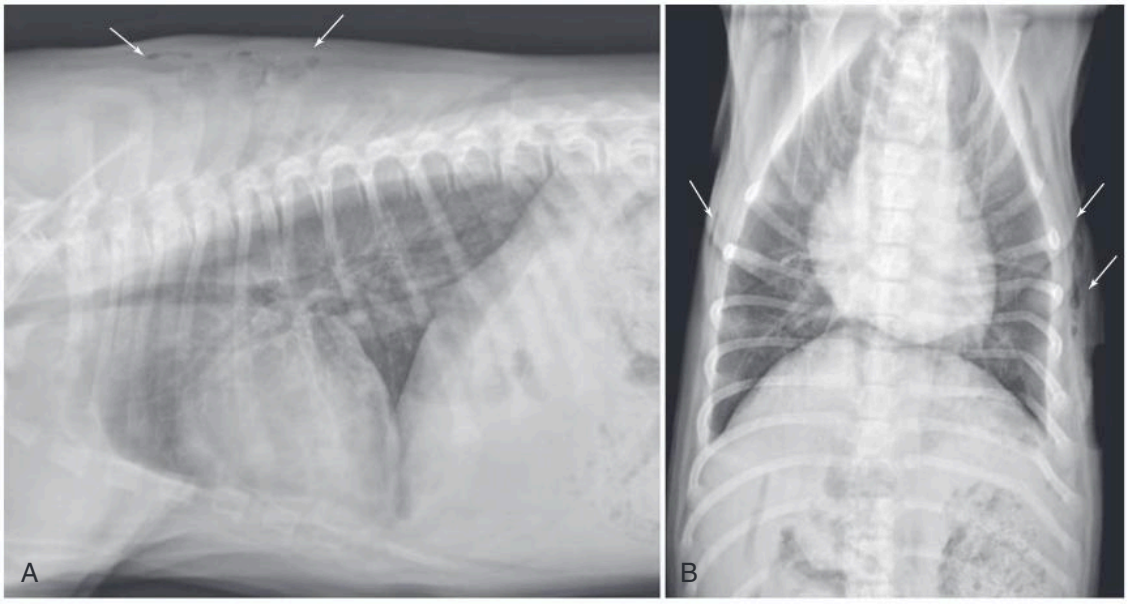
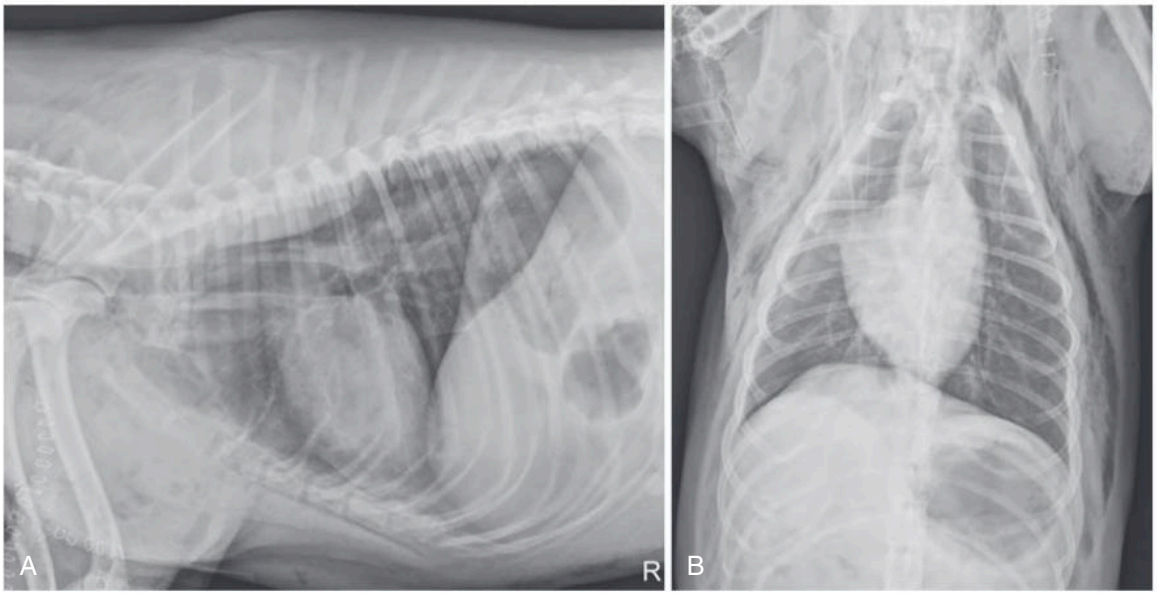


Fig. 31.12 Left lateral **(A)** and ventrodorsal (VD) **(B)** thoracic radiographs of a 1-year-old mixed-breed dog presented after being attacked by another dog. Multiple gas lucencies are seen in the dorsal soft tissues, the left and to a lesser extent the right thoracic wall (*white arrows*). Multiple left-sided rib fractures are also present.

THORACIC WALL TRAUMA

Thoracic wall trauma caused by impact or bite wounds is not uncommon in small animals.[5] Soft tissue swelling is often the first sign of thoracic wall trauma; however, it may be difficult to identify in lateral radiographs. Slight obliquity in VD projections causing inherent asymmetry of the thoracic wall may also be a hindrance. Trauma with disruption of the skin surface results in subcutaneous emphysema with gas accumulation within the soft tissues of the thoracic wall (Fig. 31.12, eFig. 31.1). Other causes for subcutaneous emphysema of the thoracic wall include trauma to the cervical soft tissues or large airways (Fig. 31.13). Subcutaneous fluid administration will result in subcutaneous emphysema associated with a focal soft tissue thickening. Deeper trauma to the thoracic wall with disruption of the intercostal muscles manifests as separation of the ribs and asymmetry of the rib spaces (Fig. 31.14). These changes are important to recognize as the mechanical function of ventilation may be impaired. If unilateral rib fractures are present, the resulting pain can cause the patient to take shallow breaths and minimize movement on this side and asymmetry of the left and right thoracic walls may be noticed. It has been advocated that



eFig. 31.1 Right lateral **(A)** and ventrodorsal (VD) **(B)** thoracic radiographs of a 7-year-old Boxer who was attacked by another dog. There are extensive skin lacerations and subcutaneous emphysema present. Multiple skin staples and drains are visible in the axillary regions bilaterally.

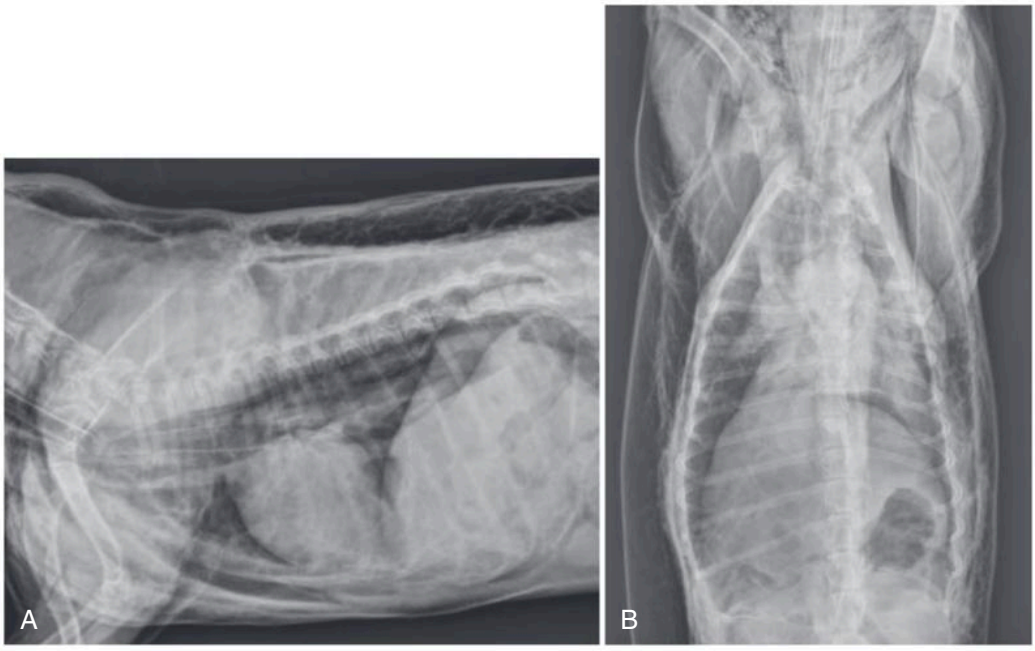


Fig. 31.13 Left lateral **(A)** and dorsoventral (DV) **(B)** thoracic radiographs of a 6-year-old Jack Russell terrier with severe subcutaneous emphysema pneumomediastinum and pneumothorax following anesthesia. Tracheal laceration was confirmed endoscopically.



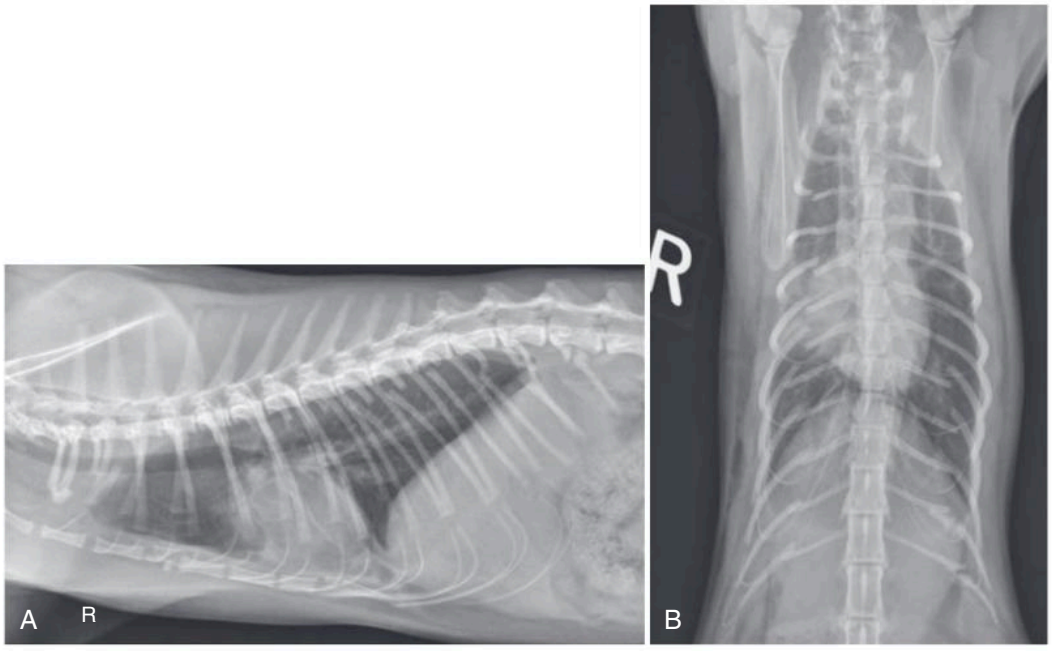
Fig. 31.14 Ventrodorsal (VD) radiograph of a 12-year-old Shih Tzu with tearing of the left cranial thoracic wall intercostal musculature, resulting in increased distance between the third and fourth ribs. Notice also the soft tissue swelling and subcutaneous emphysema of the thoracic wall at this level.

changing the hanging protocol of thoracic radiographs with 90- or 180-degree rotation will improve detection of rib fractures, but this is not recommended, as only a small improvement in accuracy of novice readers was shown with 90-degree rotation.[6] It is more important to include careful evaluation of the ribs in the standard search pattern of thoracic radiographic interpretation. Acute rib fractures are recognized by their sharp margins, whereas rounding and remodeling of the fracture margins and smooth new bone formation are indicative of the healing process (Fig. 31.15, eFigs. 31.2 and 31.3). Traumatic rib fractures have to be differentiated from pathologic fractures due to aggressive lesions. Aggressive rib lesions are discussed in more detail later. Ultrasound can be helpful in evaluating questionable rib fractures since soft tissue masses associated with aggressive lesions as well as irregular lysis can be easier to identify, and tissue sampling can be performed (Fig. 31.16). Spontaneous rib fractures, without external trauma, may occur in cats with chronic respiratory disease. This is presumed to be due to mechanical failure (a form of pathologic fracture), perhaps combined with age-related osteopenia[7] (Fig. 31.17). Typically, the midportion of the caudal ribs is affected. Flail chest is caused by segmental rib fractures of at least two adjacent ribs at two different levels or five or more sequential single rib fractures which results in separation of a thoracic wall segment from the normal respiratory bellows. The resulting destabilized thoracic wall segment moves paradoxically to the normal thoracic wall with inlet displacement during inspiration and outward displacement during expiration[8,9] (Fig. 31.18). Sternal trauma most commonly manifests as luxation rather than fracture and can be painful and associated with soft tissue swelling when acute (Fig. 31.19).

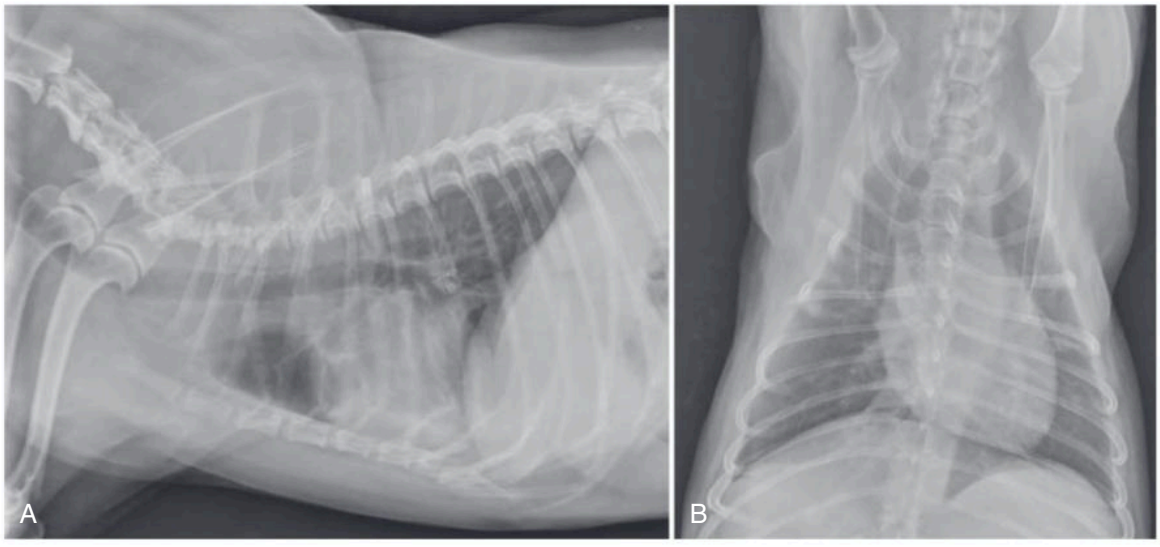
THORACIC WALL MASS LESIONS

The Extrapleural Sign

The extrapleural sign relates to any mass arising outside the parietal pleural, for example in the ribs or soft tissues of the thoracic wall. All extrapleural masses are characterized by growth into rather than expansion within the thoracic cavity. As long as the parietal pleura is intact, the smooth surface of the mass is preserved, and there is often a draping appearance at the junction of the mass with the thoracic wall. Loss of the sharp delineation of an extrapleural lesion can be a sign of



eFig. 31.2 Lateral **(A)** and ventrodorsal (VD) **(B)** radiographs of a cat with acute rib fractures. Right ribs 4 through 13 and left ribs 1, 2, and 9 through 12 are fractured, the result of being hit by a car. The fracture margins are sharp and distinct. Subcutaneous emphysema is present in the right thoracic wall. Ill-de fined opacities are present in the right middle lung lobe, likely secondary to pulmonary contusions. Also present are chronic, healing fractures of left ribs 12 and 13. There is rounding of the fracture margins with callus formation.



eFig. 31.3 Right lateral **(A)** and ventrodorsal (VD) **(B)** thoracic radiographs of a mixed-breed dog who was hit by a car. There are acute fractures of the right third, fourth, and fifth ribs.

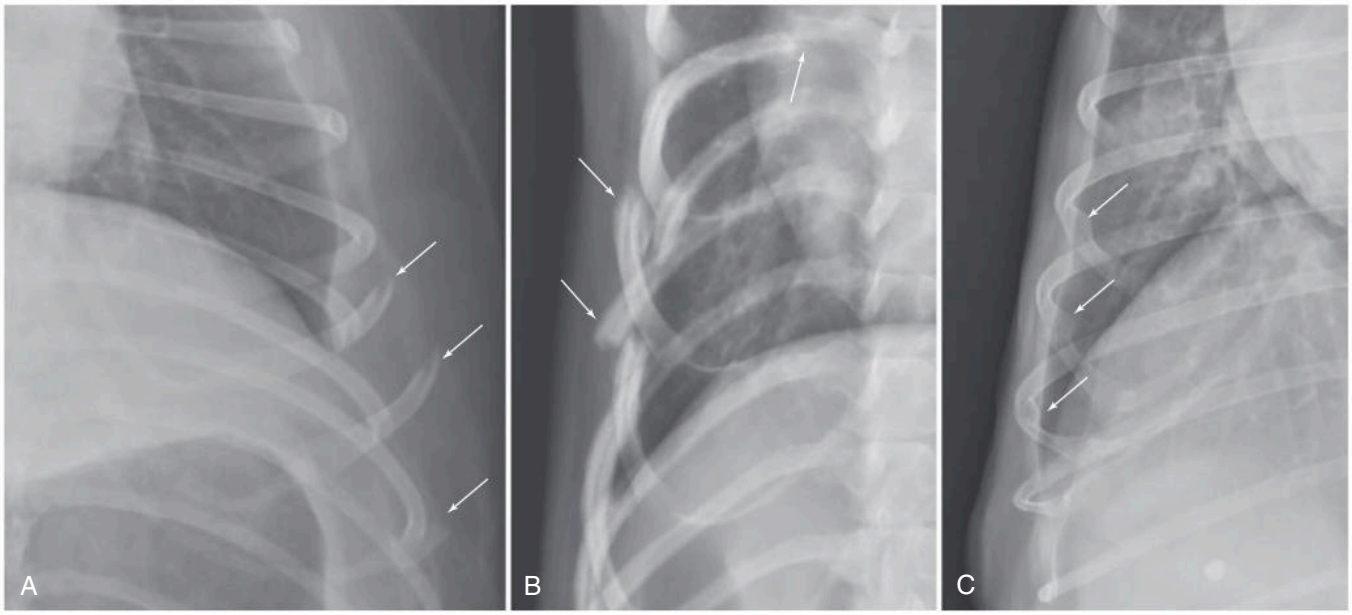


Fig. 31.15 Ventrodorsal (VD) thoracic radiographs of three different dogs with rib fractures in various stages of healing, indicated by *white arrows*. **A,** Acute rib fractures are characterized by sharp margins and regional soft tissue swelling. **B,** Healing rib fractures with remodeling and periosteal reaction along the fracture fragments. **C,** Healed rib fractures with smooth bridging callus causing focal widening of the ribs.

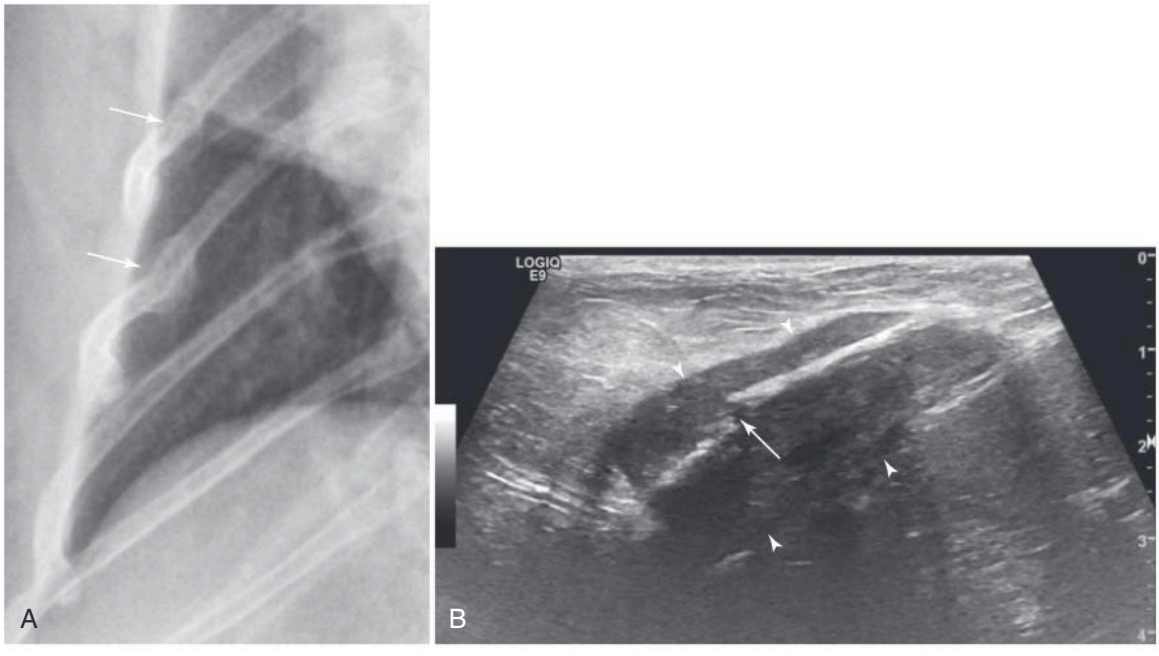


Fig. 31.16 Ventrodorsal (VD) radiograph (**A)** of an 8-year-old cat with a fracture of the right ninth rib with focal surrounding bone proliferation. A second focal osseous proliferation is seen on the eighth rib (*white arrows*). **B,** Ultrasound image of the right ninth rib in the same orientation as on the radiograph; dorsomedial is to the *right* of the image. The ultrasound image shows a hypoechoic mass lesion (*arrowheads*) surrounding the rib fracture (*arrow*). The distal fracture fragment has an irregular periosteal outline consistent with lysis. Fine needle aspirates confirmed metastatic fibrosarcoma.

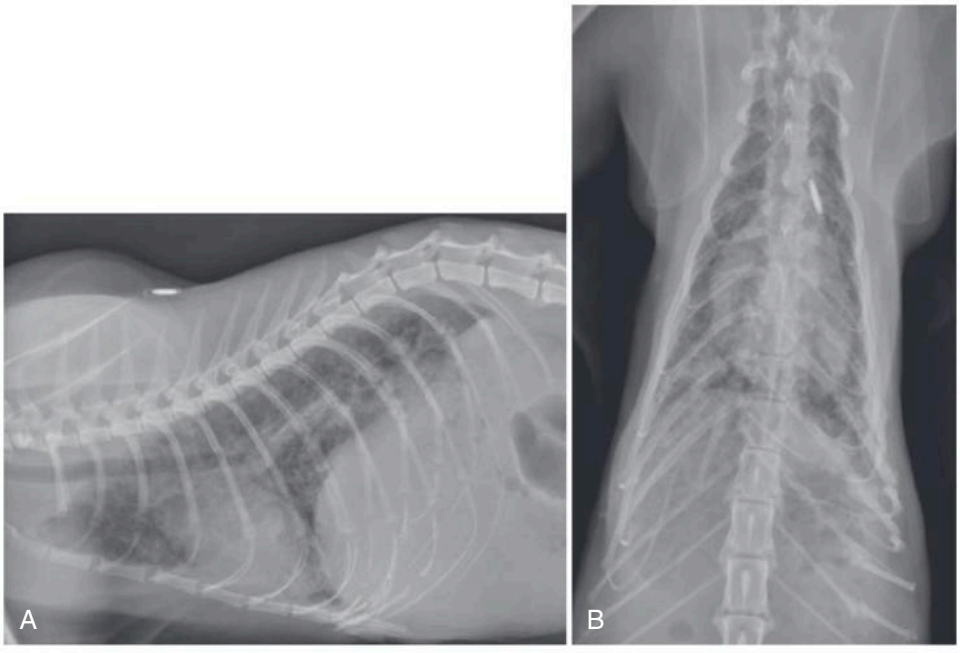


Fig. 31.17 Right lateral **(A)** and ventrodorsal (VD) **(B)** thoracic radiographs of an adult Siamese cat with severe inflammatory airway disease. There are multiple chronic, healing fractures of the left caudal ribs. No trauma was known and the fractures were thought to be caused by chronic increased respiratory effort.



Fig. 31.18 Ventrodorsal (VD) thoracic radiographs of a mixed-breed dog with bilateral multiple rib fractures. Several ribs are fractured at two levels (*white arrows*) and more than five ribs in a row are fractured, resulting in flail chest formation.

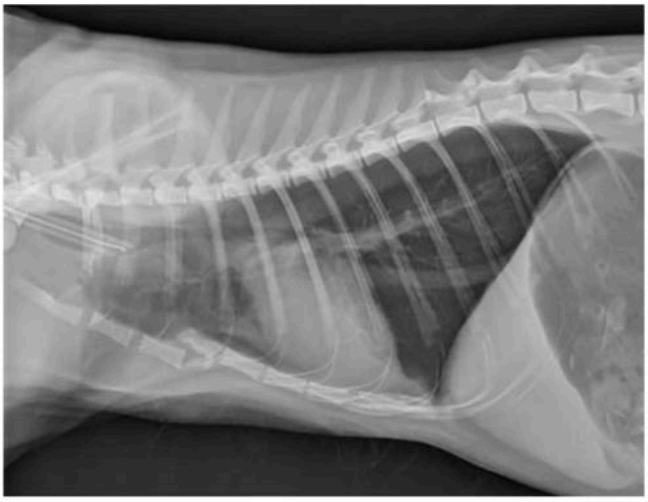


Fig. 31.19 Right lateral thoracic radiograph of an adult cat with sternal luxation after trauma. An endotracheal tube is present.

invasion through the parietal pleura and potentially into the lung (Fig. 31.20). An extrapleural sign is only visible if the x-ray beam encounters the lesion perpendicularly. Radiographic signs of extrapleural lesions are listed in Box 31.1. When using ultrasound to differentiate an extrapleural from a pulmonary mass lesion, it is important to observe respiratory motion. A pulmonary lesion will glide along the thoracic wall in synchrony with respiration, unless there are adhesions present, whereas a thoracic wall mass will remain static against the gliding lung surface.

Soft Tissue Lesions

Soft tissue masses of the thoracic wall are common in older patients. Lipomas are most commonly located subcutaneously and are characterized by fat opacity and smooth margins, although they may be infiltrative[10] (Fig. 31.21). Fibrosarcomas

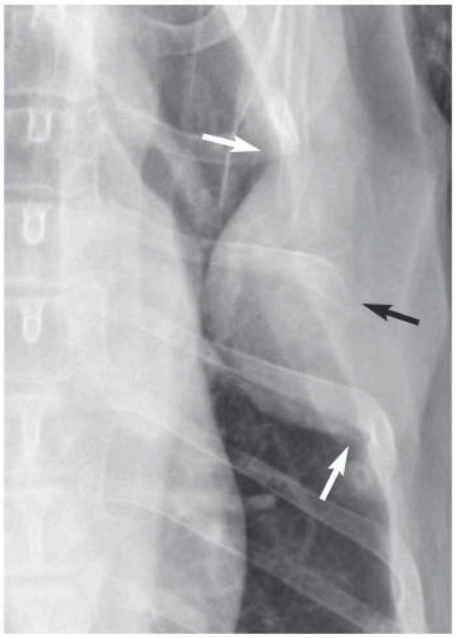


Fig. 31.20 Ventrodorsal (VD) thoracic radiograph of a dog. There is lysis of the distal aspect of the left fourth rib (*black arrow*) with a poorly defined extrathoracic mass and a well-defined intrathoracic mass. The intrathoracic component of the mass is broad based along the intrathoracic wall surface and has a convex margin. The cranial and caudal margins of the mass taper along the thoracic wall (*white arrows*). These radiographic findings are characteristic of an extrapleural sign.



Fig. 31.21 Dorsoventral (DV) thoracic radiograph of a dog with a right-sided thoracic wall lipoma. Notice the fat opacity of the mass lesion that expands the right thoracic wall.

Box • 31.1

Radiographic Signs of Extrapleural Lesions

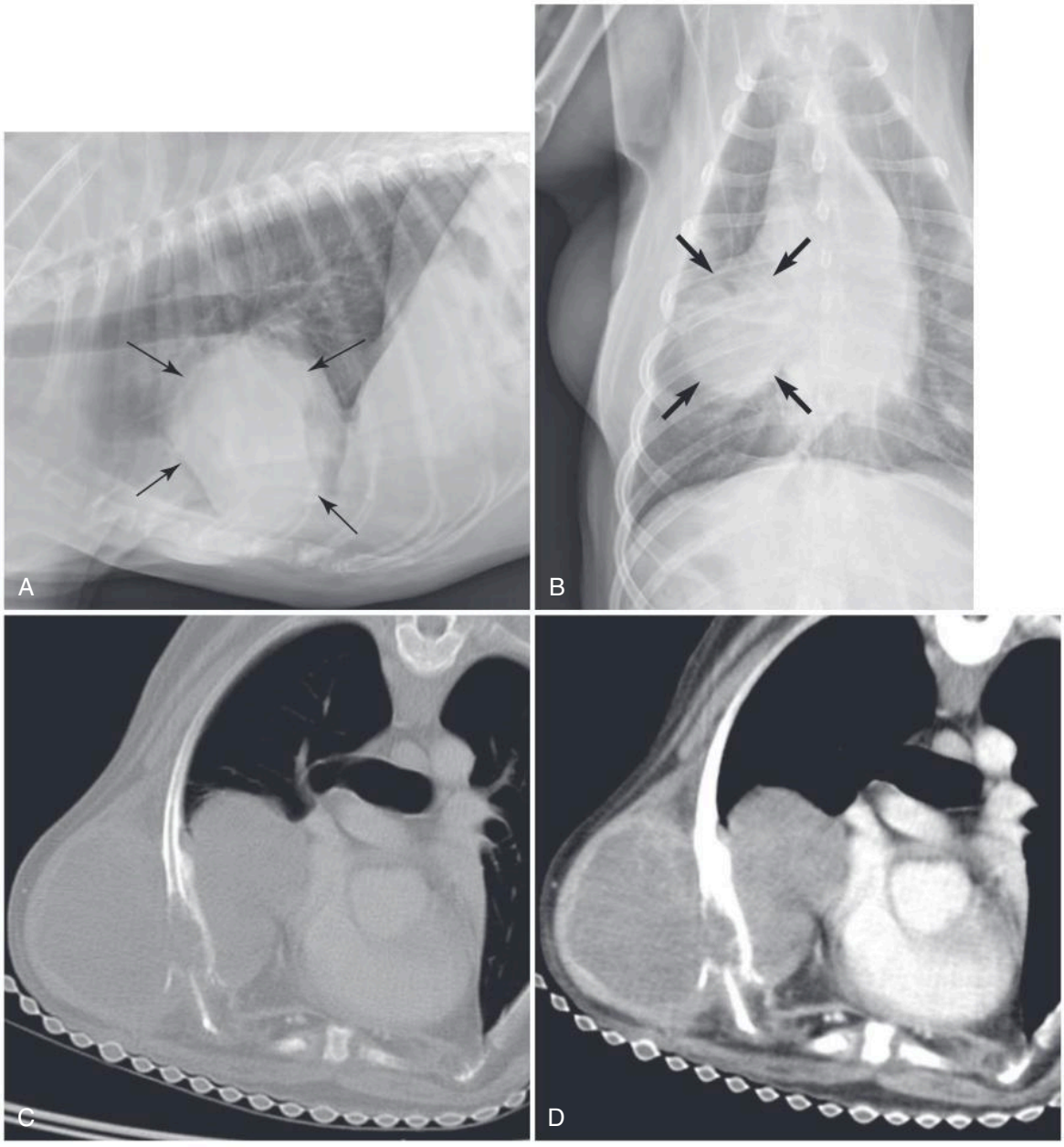
- Broad base along the thoracic wall
- Well-defined convex surface facing the lung parenchyma
- Tapered cranial and caudal edges of the lesion, merging with the pleural surface
- Widening of the intercostal space and splaying of the adjacent ribs
- Periosteal reaction and/or lysis of ribs or sternebrae
- Soft tissue thickening of the thoracic wall adjacent to and continuous with the extrapleural mass lesion
- Disruption of the fascial planes of the thoracic wall
- Abnormalities of the pleural space such as effusion occur late in the disease process

at sites of known vaccination, especially in the interscapular region, may be identified radiographically as convex soft tissue swelling dorsal to the thoracic spinous processes (Fig. 31.22). Soft tissue masses such as soft tissue sarcomas and adenocarcinomas are soft tissue opaque and often more irregular in outline, and may occur anywhere in the thoracic wall. Secondary bone invasion or destruction is possible. CT imaging is needed to evaluate the full extent of these lesions and determine the presence of bone lysis[11] (Fig. 31.23). Thoracic wall infection and cellulitis of the thoracic wall are most commonly caused by penetrating trauma and migrating foreign bodies such as grass awns. Fistulography, using either radiography or CT imaging, may be helpful to determine the extent of a superficial draining tract and the connection with intrathoracic structures[12] (Fig. 31.24).

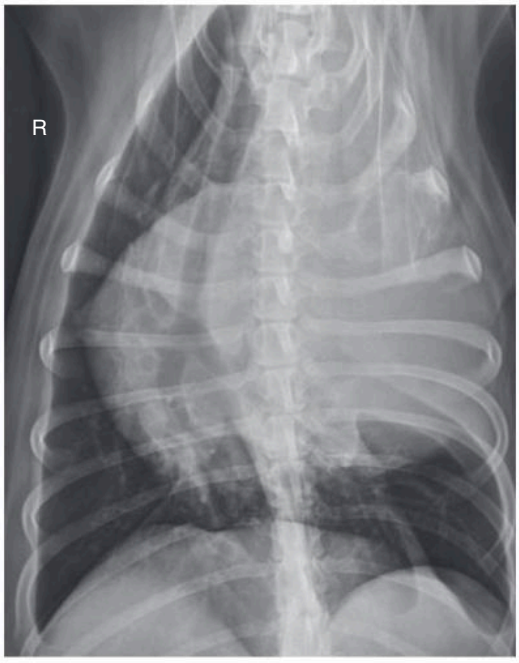
Lesions of the Ribs and Sternum

Mass lesions associated with the ribs or sternum can be benign or malignant in nature. The majority of primary rib tumors are osteosarcomas and chondrosarcomas with a smaller portion of other sarcomas (fibrosarcoma, hemangiosarcoma).[13,14] They usually arise near the costochondral junction, are aggressive in nature, and cause lysis and irregular periosteal reaction of the affected ribs. Amorphous mineralization of the associated soft tissue mass is common. The extent of the lesion is often underestimated radiographically and clinically, as most of the tumor mass is intrathoracic. CT gives a much more detailed assessment of the size and origin of a rib mass, effect on adjacent structures, and presence of metastatic lesions (Fig. 31.25, eFig. 31.4). The intrathoracic portion of a rib tumor may be misinterpreted as a pulmonary mass if the adjacent ribs are not examined for the presence of lysis or periosteal reactions (Fig. 31.26) Primary rib tumors typically affect a single rib, although the adjacent ribs can be affected by the mass and have signs of periostitis, compression atrophy, or invasion (eFigs. 31.5 and 31.6). Differential diagnoses for multiple aggressive rib lesions include metastatic neoplasia or marrow-associated tumors such as multiple myeloma (Fig. 31.27, eFig. 31.7). Metastatic neoplasia is often more lytic or expansile than proliferative with variable degree of periosteal reaction (eFig. 31.8).

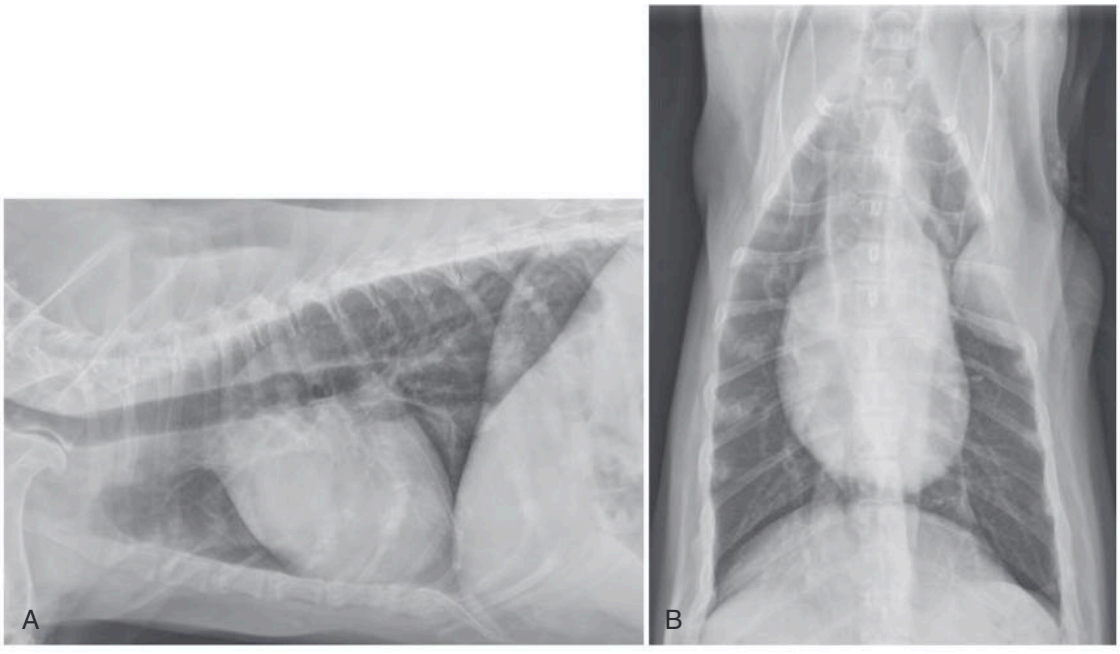
Cartilaginous exostoses or osteochondromas are benign bone perforations characterized by a cartilage cap and can be singular or multiple (multiple cartilaginous exostoses or osteochondromatosis) (Fig. 31.28). Single osteochondromas most commonly occur in growing dogs and growth of the mass stops with skeletal maturation. They appear as well-defined, thin-walled bony expansile lesions proliferating from the cortical



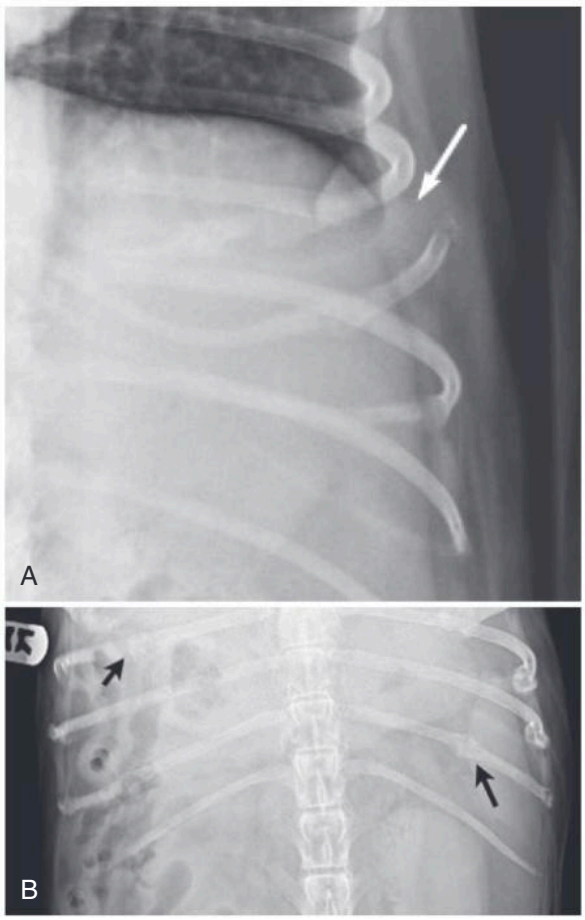
eFig. 31.4 Left lateral **(A)** and dorsoventral (DV) **(B)** thoracic radiographs of a dog. A poorly margined, soft tissue mass is present to the right of the cardiac silhouette on the DV view (*black arrows*) and summating with the cardiac silhouette on the lateral view (*black arrows*). On the DV radiograph, the mass could be mistaken for a pulmonary lesion. Transverse computed tomography (CT) images at the level of the fifth ribs in a bone window **(C)** and in a soft tissue window after **(D)** administration of iodinated intravenous contrast medium. The lesion originates from the distal right fifth rib. A soft tissue mass is associated with the rib lysis, and a large extrathoracic component is also present. After contrast medium administration **(D)**, slight rim enhancement of the soft tissue mass, as well as the heart, great vessels, and pulmonary vessels, is seen. The histopathologic diagnosis of the rib lesion was osteosarcoma.



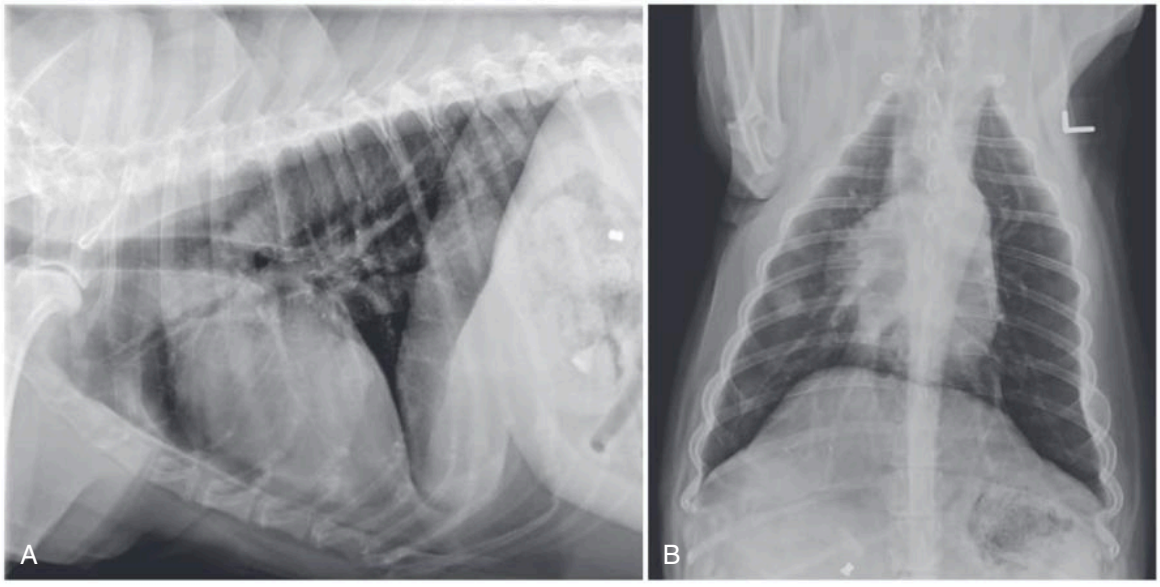
eFig. 31.5 Ventrodorsal (VD) thoracic radiograph of a dog with a primary tumor of the left fourth rib. There is minimal mass extrathoracically but a large mass intrathoracically has displaced the heart to the right. This discrepancy between the size of the extrathoracic and intrathoracic components of primary rib tumors is common and leads to a delay in diagnosis.



eFig. 31.6 Left lateral **(A)** and ventrodorsal (VD) **(B)** thoracic radiographs of a dog with a primary rib tumor of the left fourth rib. The rib is discontinuous and decreased in opacity at the center of the mass. The soft tissue component of the mass bulges into the left cranial thorax, creating an extrapleural sign in the VD projection.



eFig. 31.7 **A,** Ventrodorsal (VD) radiograph of a dog with lysis of the distal aspect of the left 10th rib (*white arrow*) caused by metastatic melanoma. **B,** VD radiograph of a dog with multiple metastatic rib lesions caused by metastatic prostatic carcinoma. There is both lytic and irregular productive bone pathology of the right 10th rib and the left 12th ribs (*black arrows*). Proliferative bone overlying the left 10th rib is associated with the 9th costochondral junction.



eFig. 31.8 Right lateral **(A)** and dorsoventral (DV) **(B)** radiograph of a dog with an expansile lesion of the left ninth rib, diagnosed as plasma cell tumor.

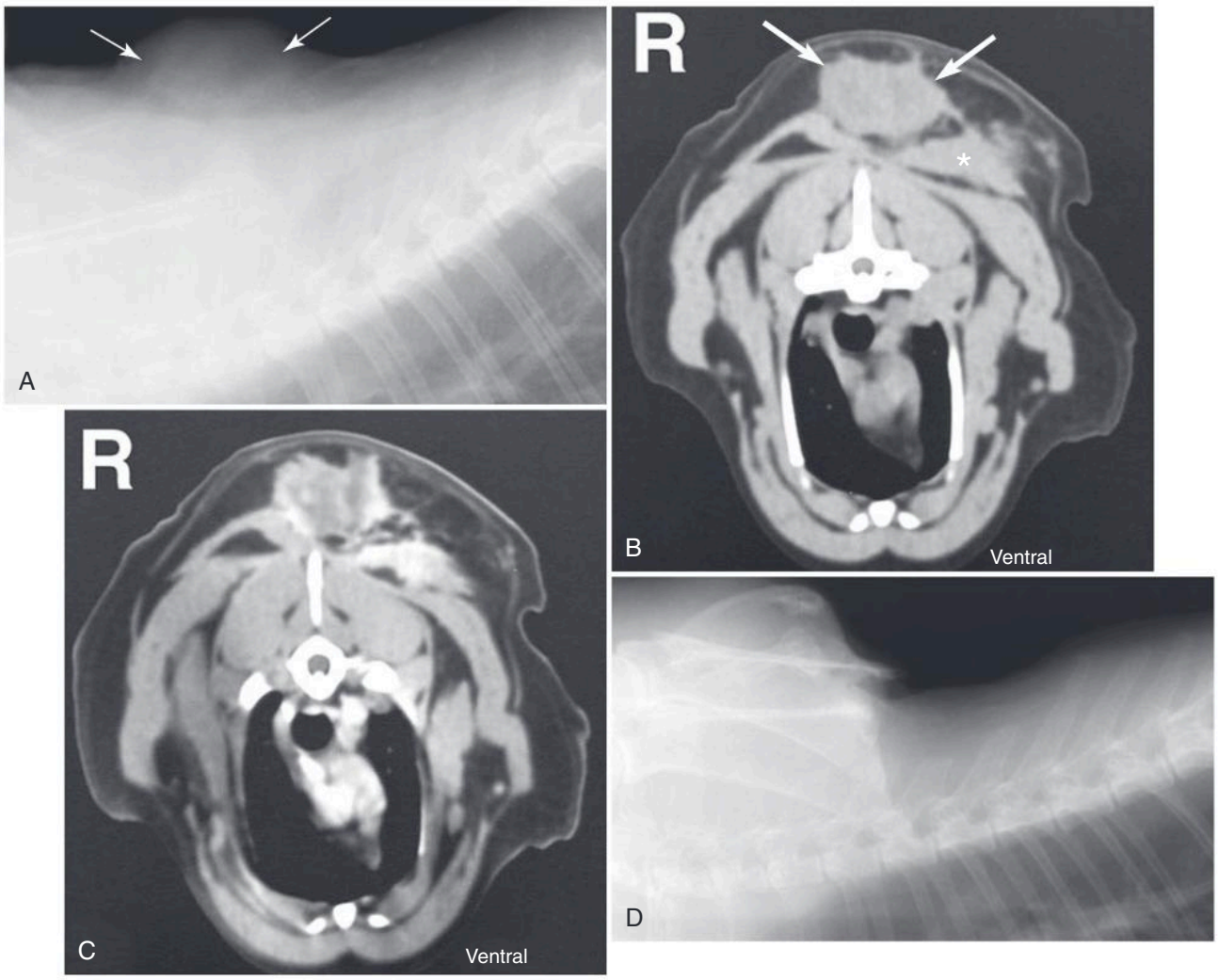
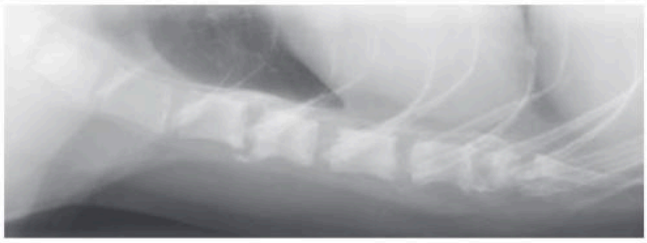


Fig. 31.22 Right lateral radiograph **(A)** and precontrast **(B)** and postcontrast **(C)** computed tomography (CT) images of a cat with a vaccine-associated interscapular fibrosarcoma. A soft tissue mass with a dorsal convex margin is present in the subcutaneous tissues dorsal to the proximal margin of the scapulae (*white arrows*) on the thoracic radiograph **(A)**. On the precontrast CT image **(B)** acquired just caudal to the scapulae, the irregularly margined mass is seen clearly in the fat just dorsal to a thoracic spinous process (*white arrows*). In addition, soft tissue opaque stranding is identified in the fat surrounding the mass and just lateral to the left trapezius muscle (*asterisk*), which is also thickened and irregular in contour. After intravenous administration of iodinated contrast medium, heterogeneous enhancement of the dorsal subcutaneous mass, left trapezius muscle, and soft tissue stranding within the regional fat are present, consistent with neoplastic infiltration and associated inflammation. Contrast-medium opacification of the great vessels cranial to the heart is also seen. Although lysis and remodeling of osseous structures were not identified, soft tissue contrast opacification was observed along the peripheral surfaces of the caudal scapulae and multiple spinous processes. In the interest of obtaining a complete surgical excision, large portions of the scapulae and thoracic spinous processes 2 through 6 were removed **(D)**.

surface of ribs or vertebrae and can cause regional mass effect and compression atrophy of adjacent structures. Multiple cartilaginous exostoses are more common in cats than in dogs. Malignant transformation is possible and then the radiographic appearance will be similar to a primary rib tumor.[15]

Primary or metastatic sternebral tumors are rare and usually of mesenchymal origin. Aggressive sternal neoplasia may be difficult to differentiate from destructive sternebral osteomyelitis and tissue sampling is needed to obtain a diagnosis (Fig. 31.29). Hematogenous infection may affect the sternebral space, and appear similar to discospondylitis in the spine. Sternal osteomyelitis can be a result of trauma or a migrating foreign body, prior trauma, or surgery[16,17] (Fig. 31.30, eFig. 31.9). It is important to closely evaluate the sternum for signs of an aggressive lesion as sternal degenerative changes are common and subtle irregular periosteal reactions or focal lysis may be dismissed. Rib infection is uncommon and most commonly the result of trauma with a penetrating wound. Severe pyothorax may result in rib periostitis which is characterized by periosteal reaction without a soft tissue mass. Hypertrophic osteopathy is a rare differential diagnosis for periosteal reactions along multiple ribs without lysis (Fig. 31.31). However, the differentiation between rib infection and neoplasia is difficult and often impossible.



eFig. 31.9 Right lateral radiograph of the ventral aspect of the thorax of a dog. Sternebral endplate lysis and subchondral sclerosis are present from the caudal endplate of segment 4 through the cranial aspect of segment 8. The intersternebral spaces appear wide in this region. The radiographic signs are consistent with sternal osteomyelitis. *Staphylococcus aureus* was isolated from the urine, and hematogenous spread to the sternum was suspected.

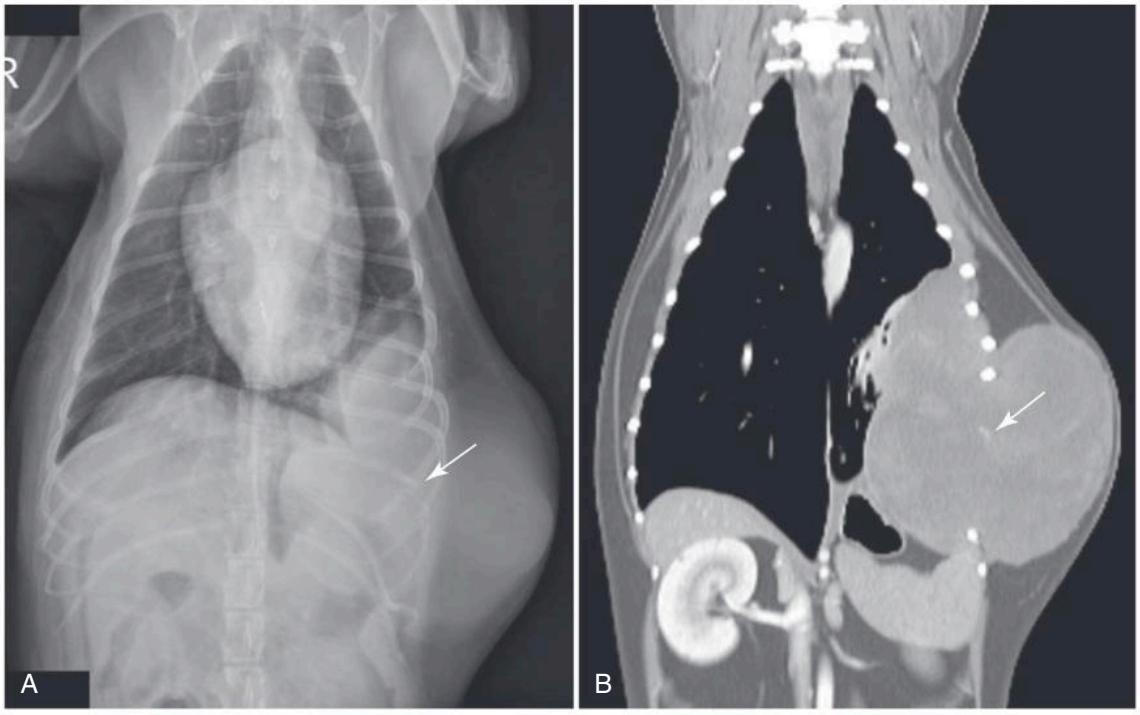


Fig. 31.23 Ventrodorsal (VD) thoracic radiograph **(A)** and corresponding computed tomography (CT) image reformatted in a dorsal plane (**B**) of a Cairn terrier with a thoracic wall mass. There is a large lobulated soft tissue mass in the left caudal thoracic wall that extends into the thorax causing displacement and compression of the adjacent lung. The rib spaces are widened at the level of the mass and there is focal lysis of the left 11th rib (*white arrows*).

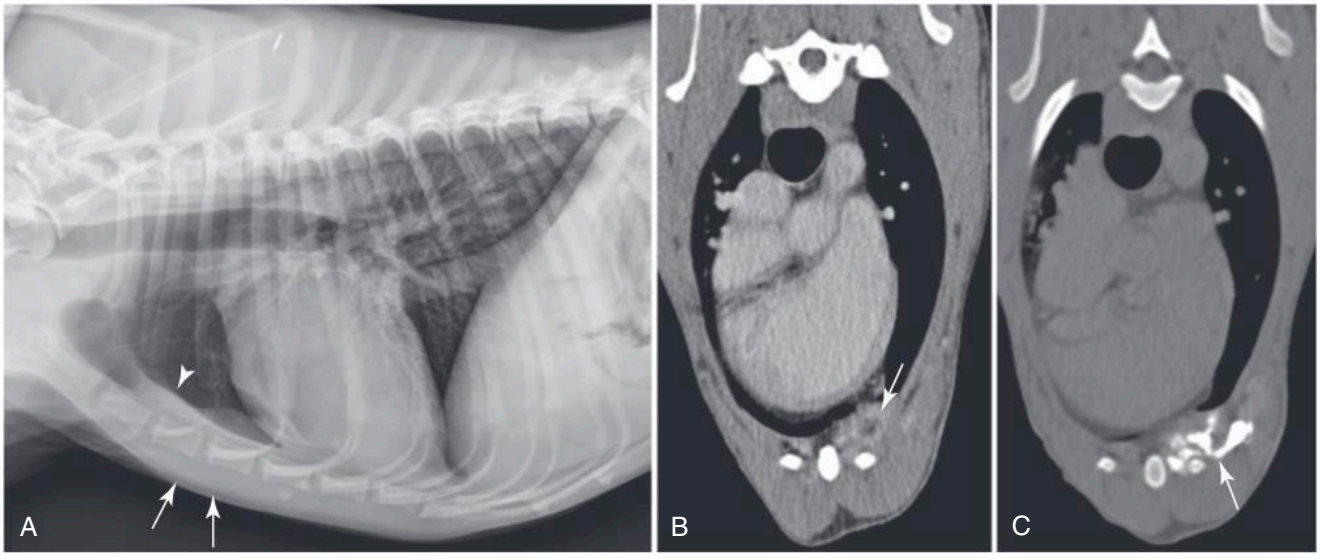


Fig. 31.24 Right lateral thoracic radiograph **(A)** of a 3-year-old Irish setter with a fistulous draining tract at the level of the third sternebral. Focal soft tissue thickening is noted at this level (*white arrows*) and there is focal retrosternal soft tissue thickening in the region of the sternal lymph nodes (*arrowhead*). **B,** Contrast-enhanced computed tomography (CT) image of the thorax. A peripherally contrast-enhancing round structure is seen subpleurally to the left of the sternum (*arrow*). **C,** CT-fistulogram, iodinated contrast medium was injected into the external fistulous tract. Contrast medium extends from the thoracic wall to the subpleural structure (*arrow*), confirming the connection of this structure with the external draining tract. A grass awn was removed surgically.

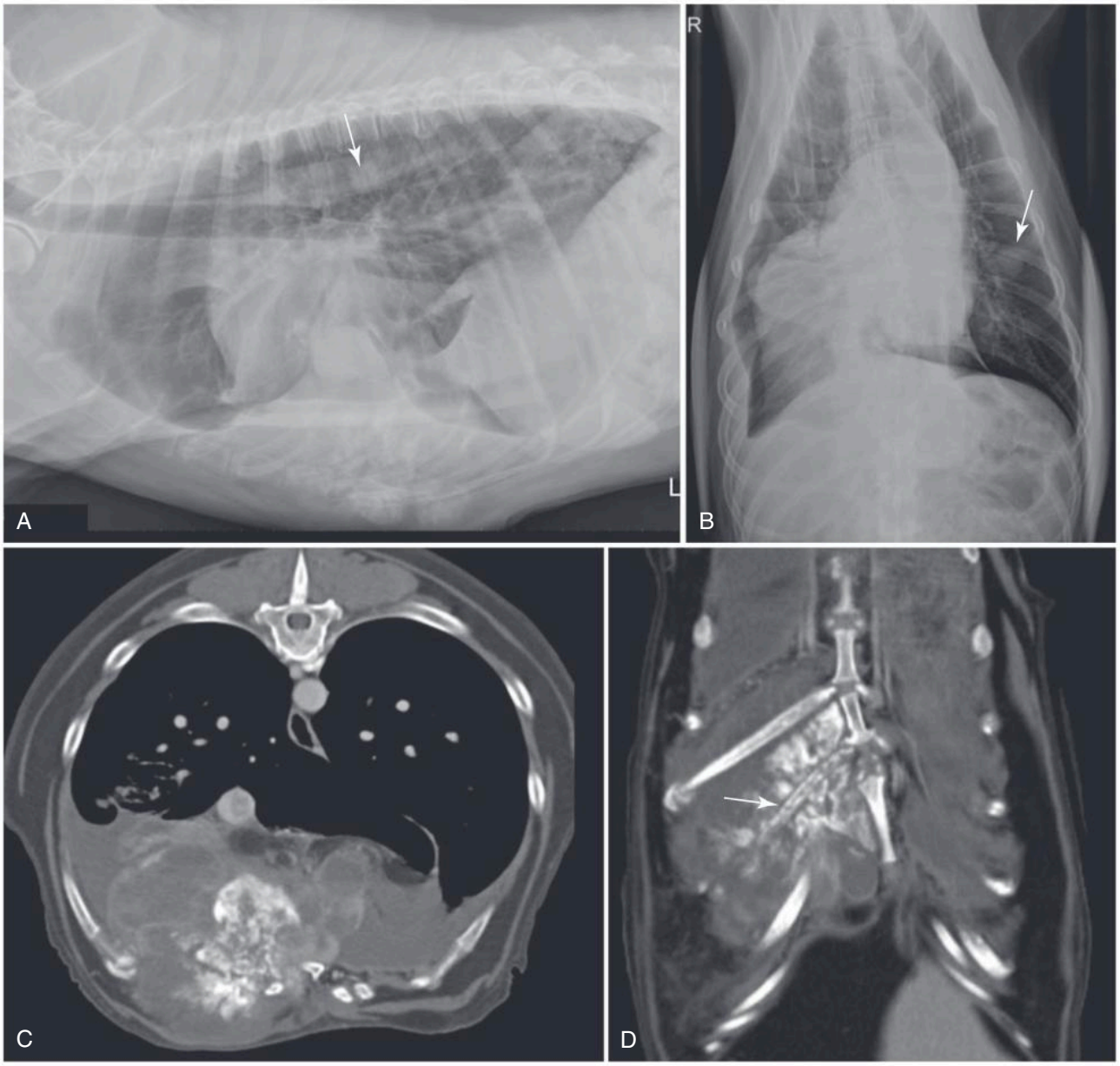


Fig. 31.25 Left lateral **(A)** and ventrodorsal (VD) **(B)** thoracic radiographs of a Labrador retriever with a ventral thoracic wall mass. Extensive amorphous mineralization is present at the level of the caudal sternum and costal cartilages. A soft tissue mass extends into the thorax and silhouettes with surrounding pleural effusion. Pulmonary soft tissue nodules are indicated with *white arrows*. Transverse **(C)** and dorsal reformatted **(D)** computed tomography (CT) images of the same dog. The intrathoracic portion of the mass is heterogeneously contrast enhancing and centrally mineralized. Adjacent pleural effusion is visible. In the dorsal reformatted image, moth-eaten lysis of the costal cartilage of the right eighth rib is identified (*white arrow*). Osteosarcoma of the right eighth rib was confirmed histopathologically.

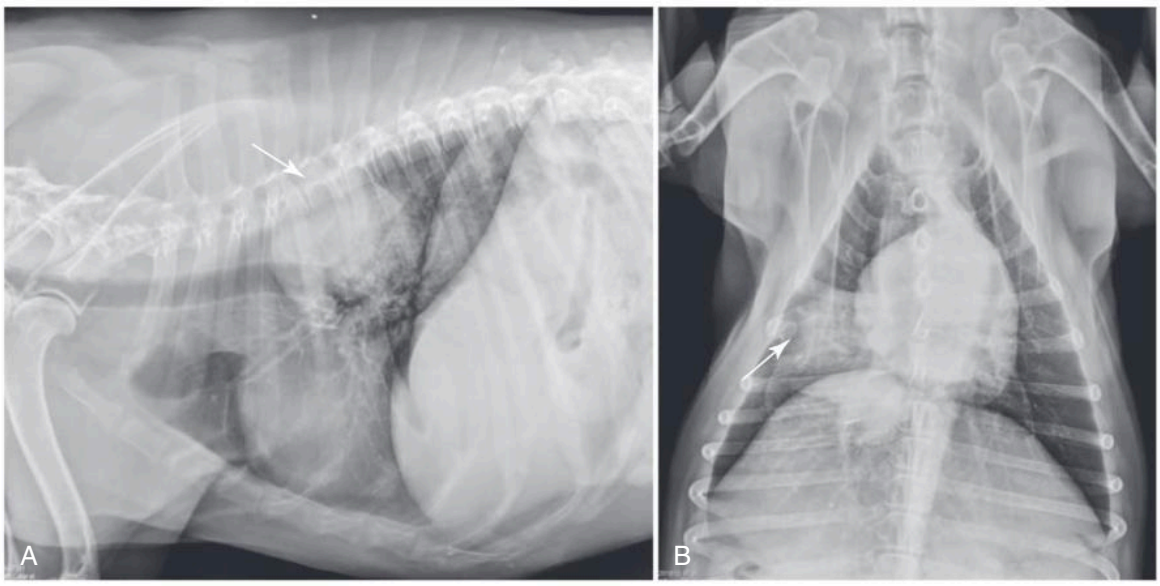


Fig. 31.26 Left lateral **(A)** and dorsoventral (DV) **(B)** thoracic radiographs of a dog with a right fifth rib chondrosarcoma. The mass could be mistaken as pulmonary in origin if the absence of the proximal portion of the right fifth rib (*arrows*) was not noticed.

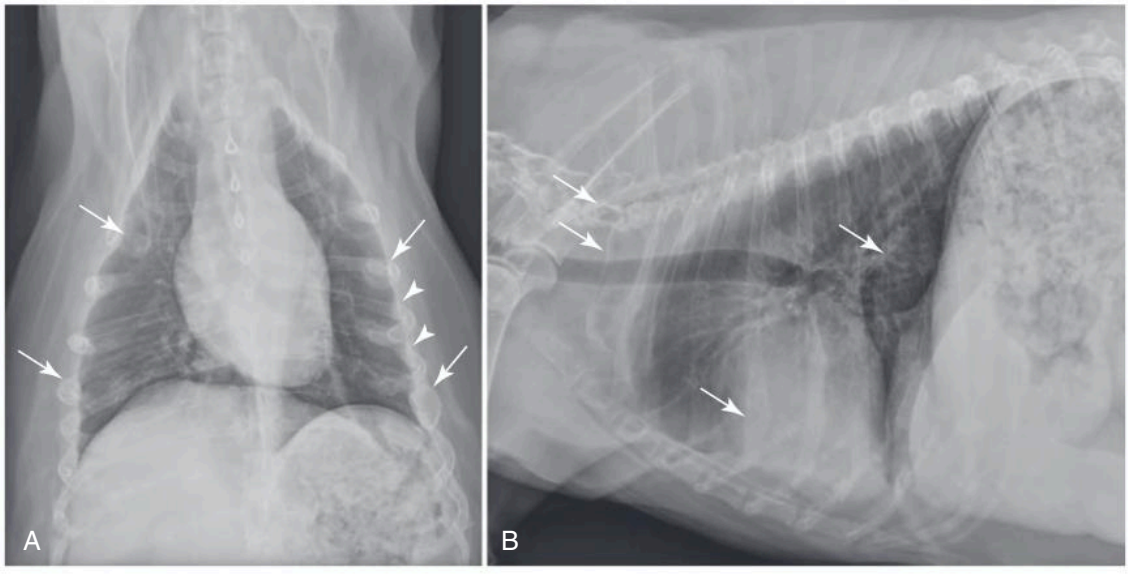


Fig. 31.27 Ventrodorsal (VD) **(A)** and right lateral **(B)** thoracic radiographs of a dog with multiple myeloma. There are numerous expansile rib and vertebral lesions; some of them are pointed out by *white arrows*. Pathologic rib fractures (*arrowheads*) are also present.

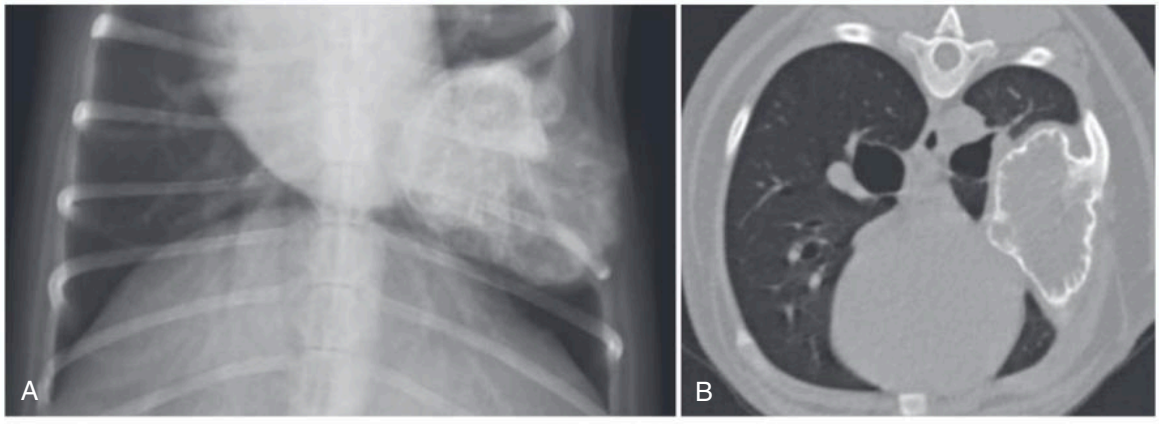


Fig. 31.28 Ventrodorsal (VD) radiograph of the caudal thorax **(A)** and transverse computed tomography (CT) image **(B)** of an 8-month-old Goldendoodle with an expansile rib mass, diagnosed as osteochondroma histopathologically. The lesion extends from the cortex of the left eighth rib, is peripherally mineralized, and causes displacement of the adjacent lungs.



Fig. 31.29 Left lateral **(A)** and ventrodorsal (VD) **(B)** thoracic radiograph of a dog with osteosarcoma of the third sternebra. The sternebra is decreased in radiopacity with an irregular periosteal reaction. A pathologic compression fracture has caused shortening of the sternebra. There is a large amount of soft tissue swelling ventral to the sternum.



Fig. 31.30 Osteomyelitis of the third and fourth sternebrae after a median sternotomy. The endplates are irregularly margined and sclerotic, and the intersternebral space is narrowed. There is increased radiolucency surrounding the cerclage wires within these sternebrae.

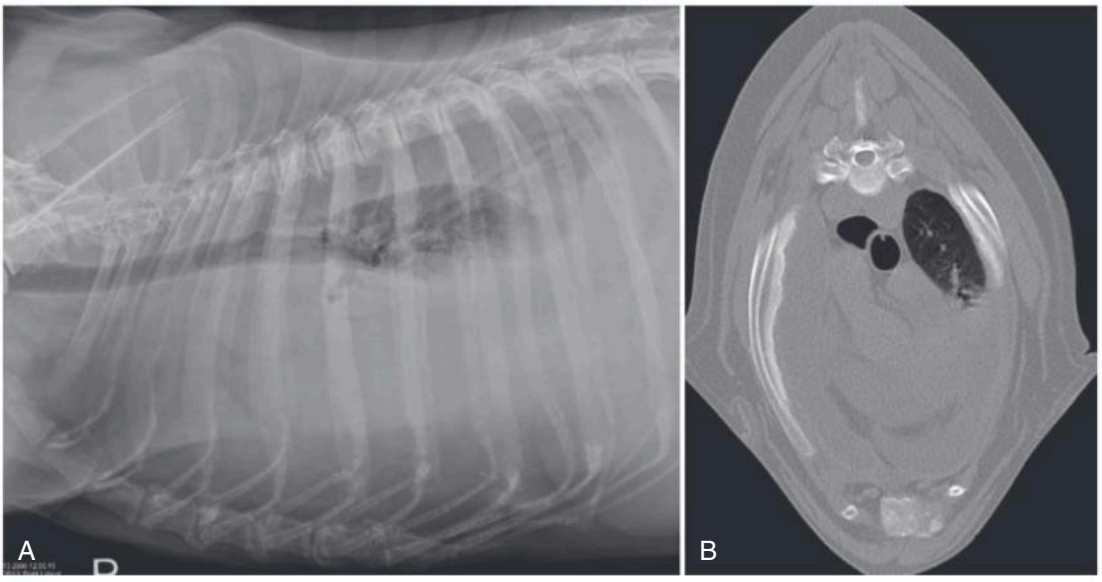


Fig. 31.31 Right lateral thoracic radiograph **(A)** and transverse computed tomography (CT) image **(B)** of a dog with chronic mesothelioma and bilateral pleural effusion. There are extensive, irregular periosteal reactions present along all ribs, predominantly along the medial cortical surface of the ribs. There is no evidence of cortical lysis. Hypertrophic osteopathy secondary to intrathoracic disease was suspected.

Acknowledgment

With special thanks to prior authors of this chapter for their contributions.

REFERENCES

1. Evans SM, Biery DN. Congenital peritoneopericardial diaphragmatic hernia in the dog and cat: a literature review and 17 additional case histories. *Vet Radiol.* 1980;21(3):108–116.
2. Bąkowska J, Proks P, Stehlik L, Irova K, Bugyiova K. Pectus excavatum in seven dogs. *J Comp Pathol.* 2017;156(1):87.
3. Kurosawa TA, Ruth JD, Steurer J, Austin B, Heng HG. Imaging diagnosis—acquired pectus excavatum secondary to laryngeal paralysis in a dog. *Vet Radiol Ultrasound.* 2012;53(3):329–332.
4. Nganvongpanit K, Yano T. Prevalence of swimming puppy syndrome in 2,443 puppies during the years 2006–2012 in Thailand. *Vet Med Int.* 2013;2013:617803.
5. Cabon Q, Deroy C, Ferrand FX, et al. Thoracic bite trauma in dogs and cats: a retrospective study of 65 cases. *Vet Comp Orthop Traumatol VCOT.* 2015;28(6):448–454.
6. Lamb CR, Parry AT, Baines EA, Chang YM. Does changing the orientation of a thoracic radiograph aid diagnosis of rib fractures? *Vet Radiol Ultrasound.* 2011;52(1):75–78.
7. Hardie EM, Ramirez IIIO, Clary EM, et al. Abnormalities of the thoracic bellows: stress fractures of the ribs and hiatal hernia. *J Vet Intern Med.* 1998;12(4):279–287.
8. Cappello M, De Troyer A. Actions of the inspiratory intercostal muscles in flail chest. *Am J Respir Crit Care Med.* 1997;155(3):1085–1089.
9. Olsen D, Renberg W, Perett J, Hauptman JG, et al. Clinical management of flail chest in dogs and cats: a retrospective study of 24 cases (1989–1999). *J Am Anim Hosp Assoc.* 2002;38(4):315–320.
10. McEntee MC, Thrall DE. Computed tomographic imaging of infiltrative lipoma in 22 dogs. *Vet Radiol Ultrasound.* 2001;42(3):221–225.
11. Saba CF. Vaccine-associated feline sarcoma: current perspectives. *Vet Med Res Rep.* 2017;8:13–20.
12. Lamb CR, Pope EHW, Lee KCL. Results of computed tomography in dogs with suspected wooden foreign bodies. *Vet Radiol Ultrasound.* 2017;58(2):144–150.
13. Baines SJ, Lewis S, White RAS. Primary thoracic wall tumours of mesenchymal origin in dogs: a retrospective study of 46 cases. *Vet Rec.* 2002;150(11):335.
14. Chun R. Common malignant musculoskeletal neoplasms of dogs and cats. *Vet Clin North Am Small Anim Pract.* 2005;35(5):1155–1167.
15. Czerwik A, Olszewska A, Starzomska B, et al. Multiple cartilaginous exostoses in a Swiss Mountain dog causing thoracolumbar compressive myelopathy. *Acta Vet Scand.* 2019;61(1):1–6.
16. Wainberg SH, Brisson BA, Hayes GM, Mackenzie S. Use of gentamicin sulfate-impregnated sponges as adjuvant therapy for the treatment of chronic foreign body associated sternal osteomyelitis in a dog. *Can Vet J.* 2015;56(11):1161–1165.
17. Gilding T, Guilliard MJ. What is your diagnosis? Osteomyelitis of the fourth sternebra. *J Small Anim Pract.* 2003;44(7):297–335.

ELECTRONIC RESOURCES

Additional information related to the content in Chapter 31 can be found online at eBooks.Health.Elsevier.com

- Chapter Quiz

CHAPTER 32

Canine and Feline Diaphragm

Elissa K. Randall

The diaphragm is the musculotendinous partition between the thoracic and abdominal cavities. Embryologically, the diaphragm is formed by the septum transversum ventrally and by the mesentery of the foregut and two pleuroperitoneal folds dorsally.

Movement of the diaphragm provides approximately 75% of the change in intrathoracic volume during quiet respiration, with the intercostal muscles providing the remainder.[1] The diaphragm also acts as a mechanical partition between the thorax and the abdomen. Lymph vessels from the abdomen penetrate the diaphragm and drain into the thoracic lymph nodes and vessels. Thus, inflammatory or neoplastic abdominal disease may spread to the mediastinum and pleural space. Lymph flow from the abdomen is primarily cranially with the final destination being the thoracic trunks, but there are lymphatic vessels in the thorax that drain to the abdomen.[2]

The diaphragm consists of a tendinous center and three thin peripheral muscles: (1) the pars lumbalis, (2) the pars costalis, and (3) the pars sternalis. The pars lumbalis consists of the right and left crura, which attach to the cranial ventral border of L4 and the body of L3. The attachment area on these vertebrae occasionally has a concave indistinct ventral margin that may be mistaken for bone lysis (Fig. 32.1). The pars costalis attaches in an oblique direction to the 13th through 8th ribs, and the pars sternalis attaches to the xiphoid cartilage.[3] The diaphragm is convex and extends into the thorax from its attachments, creating the phrenicocostalis and phrenicolumbalis recesses.

There are three openings through the diaphragm: (1) the dorsally located aortic hiatus encloses the aorta, azygos and hemiazygos veins, and the lumbar cistern of the thoracic duct; (2) the centrally located esophageal hiatus encloses the esophagus and vagus nerve trunks; and (3) the caudal vena cava foramen is located at the junction of the muscular and tendinous portions of the diaphragm.

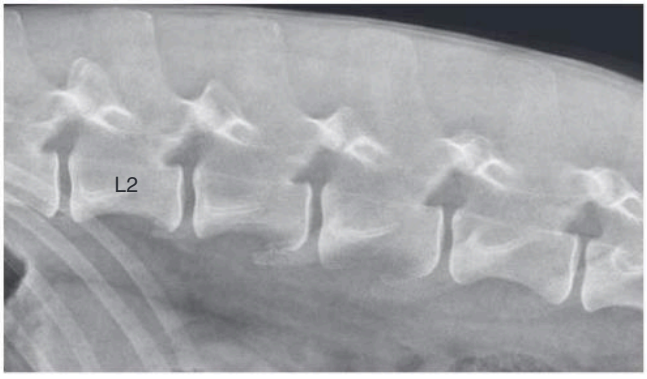


Fig. 32.1 Lateral view of the lumbar spine of a normal dog. Compared with L2 and L5, note the indistinct ventral cortex of L3 and L4 caused by the diaphragm attachment site. This can be misinterpreted as lysis if this normal appearance is not understood. *L2,* Second lumbar vertebra.

NORMAL RADIOGRAPHIC ANATOMY

Radiographically, only a portion of the diaphragm can be seen on any one view. Radiographic visualization of the diaphragm depends on adjacent structures being of different opacity. Most of the thoracic diaphragmatic surface is visible because of the adjacent gas-filled lungs. The phrenicocostalis and phrenicolumbalis recesses are not in contact with the lungs and therefore not outlined. A large portion of the abdominal diaphragmatic surface is not seen because it silhouettes the adjacent liver. The ventral abdominal diaphragmatic surface is visible on the lateral view when fat is present within the falciform ligament. The dorsal aspect of the left diaphragmatic crus and the gastric wall appear as one linear structure when gas is present in the gastric cardia.

Diaphragmatic structures that may be seen distinctly on a radiograph are the right and left crura and the cupula (body) (Figs. 32.2–32.5). Associated structures that may also be seen are the caudal vena cava and the caudal ventral mediastinum. On the lateral view, the caudal vena cava is confluent with the right crus, and the gastric fundus may be seen adjacent to the

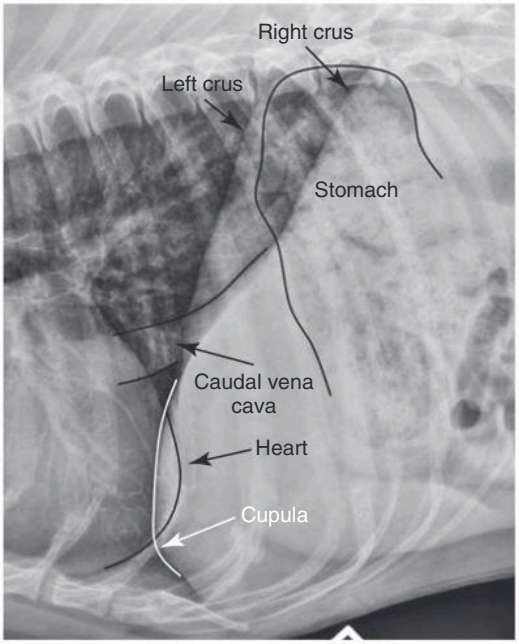


Fig. 32.2 Left lateral radiograph of the diaphragmatic region of a normal dog. In left recumbency, the dependent left crus is usually positioned cranial to the nondependent right crus. The right crus is identified by the confluence of the caudal vena cava, which bypasses the left crus before silhouetting with the right crus. These positional relationships are more consistent in large dogs and less consistent in small dogs and cats.

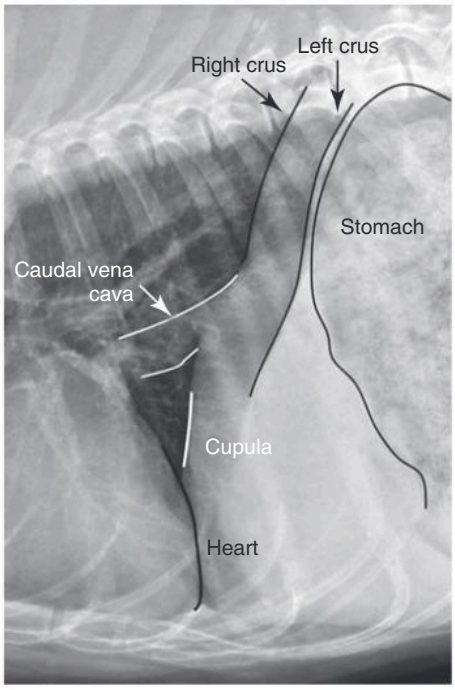


Fig. 32.3 Right lateral radiograph of the diaphragmatic region of a normal dog. In right recumbency, the dependent right crus is usually positioned cranial to the nondependent left crus. The cranially located right crus is identified by the confluence of the caudal vena cava. These positional relationships are more consistent in large dogs and less consistent in small dogs and cats.

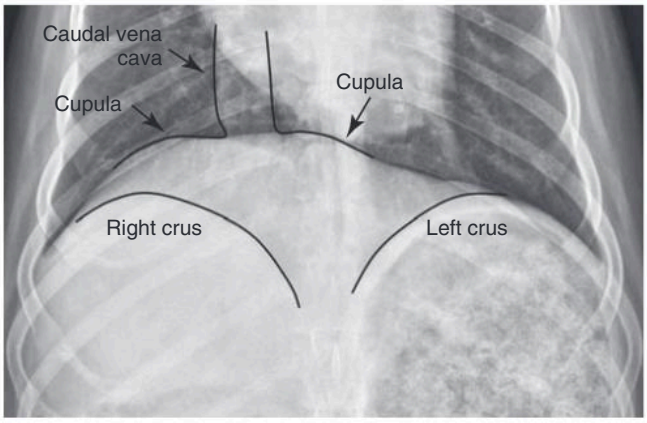


Fig. 32.4 Ventrodorsal (VD) radiograph of the diaphragmatic region of a normal dog with the cupula and both crura projecting into the thorax.

abdominal surface of the left crus (see Figs. 32.2 and 32.3). The cupula is the most cranial convex portion of the diaphragm on both the lateral and the dorsoventral (DV) or ventrodorsal (VD) views. The thoracic surface of the diaphragm may be visible as one, two, or three convex projections into the thoracic cavity (see Figs. 32.4 and 32.5).

Several normal variations of diaphragmatic position and shape may be seen radiographically. Factors that cause this variable appearance are both real and apparent. Real factors consist of breed, age, obesity, phase of respiration, and gravity. Apparent factors are x-ray beam centering and animal positioning during radiographic examination. Many combinations are possible when all permutations of these variables are considered.[4] Most of these variables are not radiographically significant; however, some must be recognized and understood

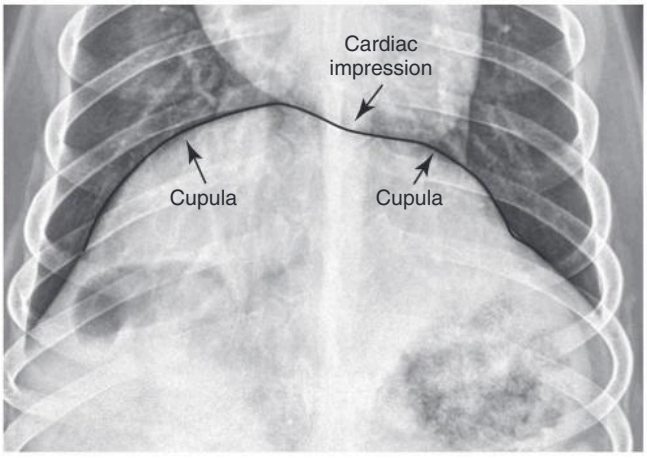


Fig. 32.5 Dorsoventral (DV) radiograph of the diaphragmatic region of a normal dog with only one convex shape projecting into the thorax.

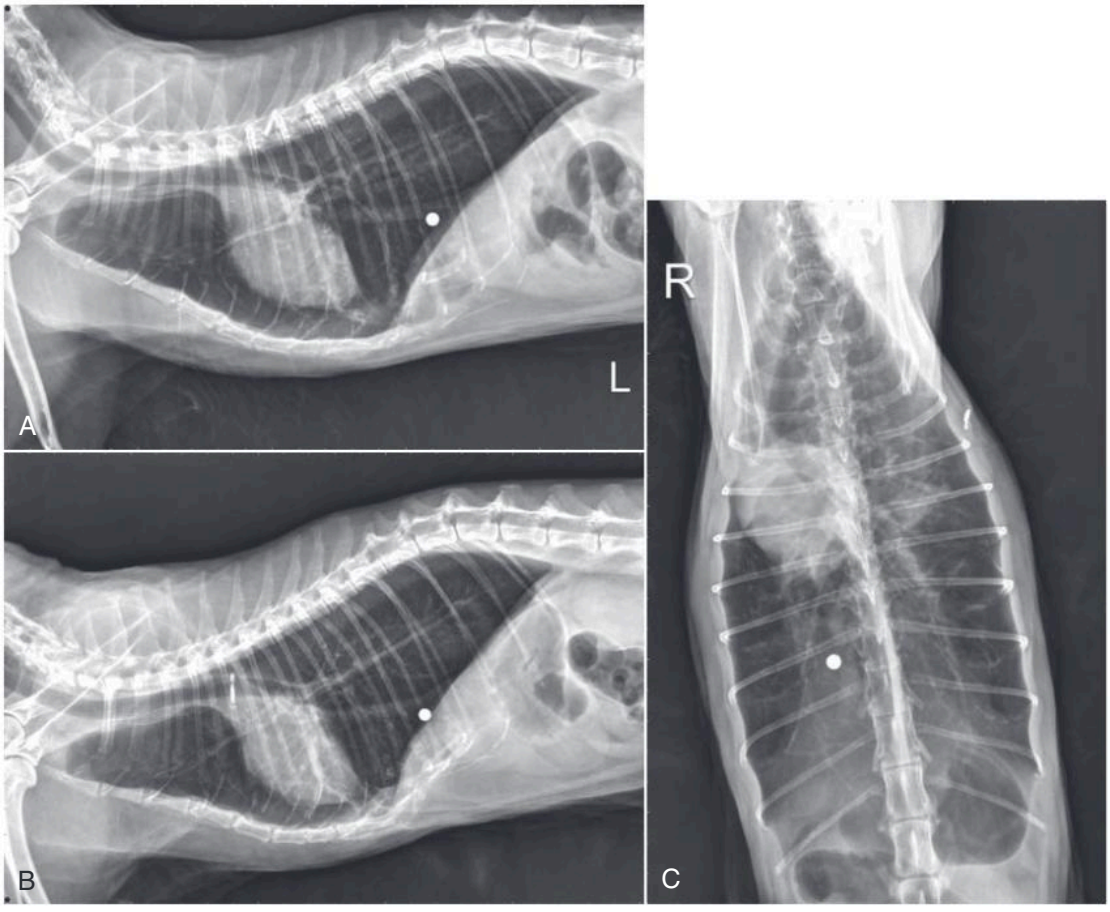
to avoid confusion. Changes most apparent radiographically are the position, shape, and appearance of the cupula and crura. The relative position of the crura depends mostly on the position and size of the animal and primary x-ray beam centering.

The diaphragm usually looks different in left versus right lateral thoracic radiographs. The most dependent crus is usually displaced cranially when an animal is in lateral recumbency since the dependent lung is less inflated and abdominal contents displace the dependent diaphragm cranially. In right lateral recumbency, the crura usually appear to be parallel (see Fig. 32.3); in left lateral recumbency, they sometimes appear to cross. The crura also appear to be more extensively separated, by up to 2.5 vertebral lengths, if the animal is rotated slightly or if the x-ray beam is centered over the mid or cranial thorax.[4] As already mentioned, the confluence of the caudal vena cava with the diaphragm can be used to distinguish the left from right crus.

The radiographic appearance of the diaphragm in VD or DV projections varies with x-ray beam centering. The diaphragm may appear as two or three separate dome-shaped structures (see Fig. 32.4) or as a single dome-shaped structure (see Fig. 32.5). The three structures represent the cupula and two crura. A single domed diaphragm may be seen on a VD view when the x-ray beam is centered on the mid-abdomen or on a DV view when the x-ray beam is centered mid-thorax. Two or three separate domed structures are seen on a VD view with the x-ray beam is centered mid-thorax or on a DV view with the x-ray beam centered mid-abdomen.[4]

Diaphragmatic position and shape vary with phase of respiration, and intra-abdominal pressure. The normal intersection point of the diaphragm and spine is between T11 and T13 but may vary between T9 and L1. The diaphragm changes position with normal respiration from one-half to two vertebral lengths. On a lateral thoracic view made in extreme inspiration, the diaphragm is oriented more vertically; the shape changes from convex to straight (Fig. 32.6). The diaphragm is displaced cranially by increased intra-abdominal pressure, which may be caused by obesity, ascites, gastric or intestinal distention, abdominal pain, or abdominal masses.

Separate diaphragmatic structures are not seen as distinctly in the cat, probably because of the relatively small thoracic size (Fig. 32.7). On extreme inspiration, particularly if the animal is in respiratory distress, of if there is a large volume of free pleural air as with a tension pneumothorax, small symmetric muscle projections are noted from the thoracic diaphragmatic surface in the VD or DV view (Fig. 32.8, eFig. 32.1). This has been referred to as *tenting* of the diaphragm and is discussed in Chapter 36 in reference to pulmonary hyperinflation.



eFig. 32.1 Left lateral **(A)**, right lateral **(B)**, and dorsoventral (DV) **(C)** radiographs of a cat who presented in respiratory distress. Note the flattening of the diaphragm and separation between the cardiac silhouette and the diaphragm, indicating hyperinflation. There is also tenting of the diaphragm on the DV. There is collapse of the right cranial and middle lung lobes with a rightward mediastinal shift and expansion of the left cranial lung lobe. These changes give the appearance of the heart being elevated from the sternum on the lateral views. This should not be mistakenly interpreted as pneumothorax, as pulmonary vessels can be seen extending beyond the ventral margin of the cardiac silhouette, indicating that there is inflated lung in that region. Note there is an incidental metallic ballistic foreign body in the right caudal thorax.

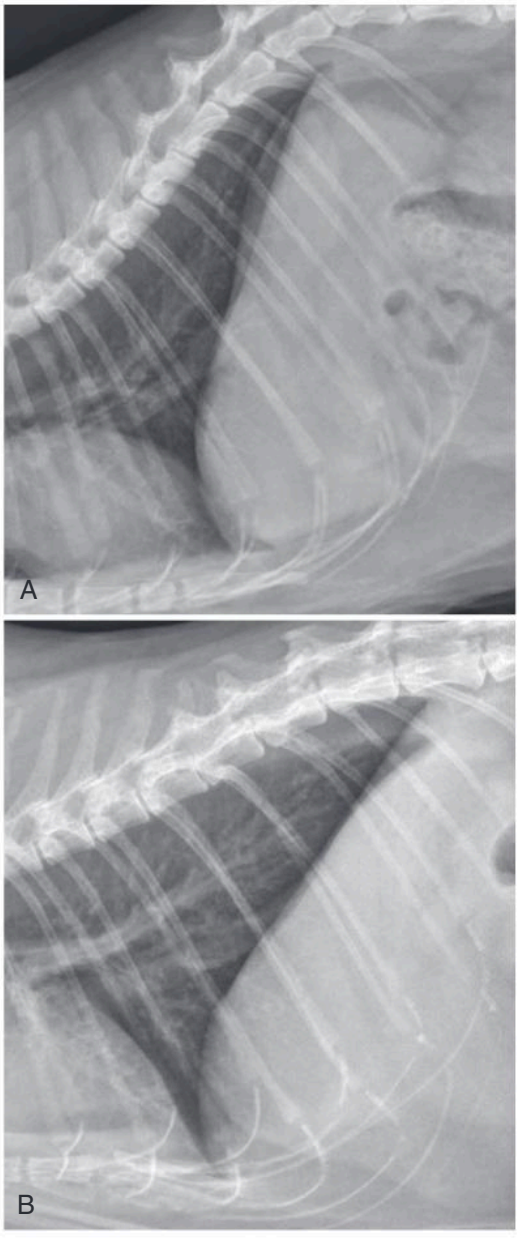


Fig. 32.6 Lateral views of the diaphragmatic region of two different normal cats on expiration **(A)** and on full inspiration **(B)**. The entire diaphragm is displaced caudally with inspiration and has a flatter contour compared with expiration.

RADIOGRAPHIC SIGNS OF DIAPHRAGMATIC DISEASE

The signs directly associated with the diaphragm are not as numerous and specific as those in many other organs. Radiographic changes observed most frequently with diaphragmatic disease include general or focal loss of the thoracic diaphragmatic surface outline and changes in diaphragmatic shape and position (Table 32.1).

The thoracic diaphragmatic surface will not be visible radiographically if soft tissue or fluid contacts the surface. Normal variations in diaphragm shape occur most frequently on the cupula often caused by contact with the heart (Fig. 32.9) or position of the animal during radiographic examination. The cupula may appear more convex and extending to a more cranial position in the thorax in some large-breed dogs. This may also be the result of a flaccid tendinous membrane, or it may be associated with a peritoneopleural hernia, which often produces no clinical signs.

Thoracic masses or lung disease silhouetting with the diaphragm, hiatal and small traumatic diaphragmatic hernias, masses originating from the diaphragm, and chronic pleural inflammatory reactions are the most frequent pathologic causes associated with diaphragmatic shape changes. An asymmetric diaphragmatic shape may occur with unilateral tension pneumothorax or hemiparalysis. Suspected hemiparalysis should be confirmed by observing diaphragmatic movement during fluoroscopy.

Positional changes consist of cranial and caudal displacement. Because the position of the diaphragm changes during the respiratory cycle, minor abnormalities in position are difficult to diagnose and in most instances are not clinically significant. Severe positional changes may be significant and indicative of thoracic or abdominal disease. Cranial diaphragmatic displacement is usually associated with abdominal disease (see Table 32.1) or generalized diaphragmatic paralysis, which should be confirmed by fluoroscopic observation. Less commonly, restrictive thoracic disease with reduced lung volume may cause cranial displacement. Caudal diaphragmatic displacement is usually associated with severe respiratory disease. The caudally positioned diaphragm is an attempt by the animal to increase the level of systemic oxygenation, which may be low because of ventilation or perfusion deficiencies in the lungs. Bilateral tension pneumothorax or large volume pleural effusion may also cause a caudally displaced diaphragm from increased pleural pressure.

Although many of the radiographic signs of diaphragmatic disease are not specific, their cause should be determined. In some instances, ultrasonography, computed tomography (CT), or additional radiographic studies, such as positional views with a horizontally directed x-ray beam and contrast medium studies, may be indicated to determine the cause of the radiographic signs.

DIAPHRAGMATIC DISEASES

The most frequently observed diaphragmatic diseases in the dog and cat are hernias, which may be traumatic or congenitally predisposed. Motor or innervation disturbances occur less frequently. Tumors associated with the diaphragm are rare.

Diaphragmatic Hernias

A diaphragmatic hernia is a protrusion of abdominal viscera through the diaphragm into the thorax. Diaphragmatic hernias that may be recognized radiographically include traumatic, peritoneopericardial, hiatal, peritoneopleural, and those secondary to congenital diaphragmatic defects.

Trauma is the most common cause of diaphragmatic hernia, which may be more accurately called traumatic diaphragmatic hernia or diaphragmatic rupture. A high momentary increase in abdominal pressure when the glottis is open produces a high pleuroperitoneal pressure gradient that may result in a diaphragmatic hernia. The high pleuroperitoneal gradient may produce a rent in the muscular portion of the diaphragm, or it may force abdominal viscera through congenitally weak or defective areas. Clinical signs that may be observed with diaphragmatic hernias include dyspnea, pain, vomiting, regurgitation, muffled heart sounds, and a weak femoral pulse.[5,6] Some diaphragmatic hernias may not cause clinical signs and are detected incidentally.

Radiography plays an important role in confirming a diagnosis of diaphragmatic hernia and may provide information about location, extent, contents, and secondary complications

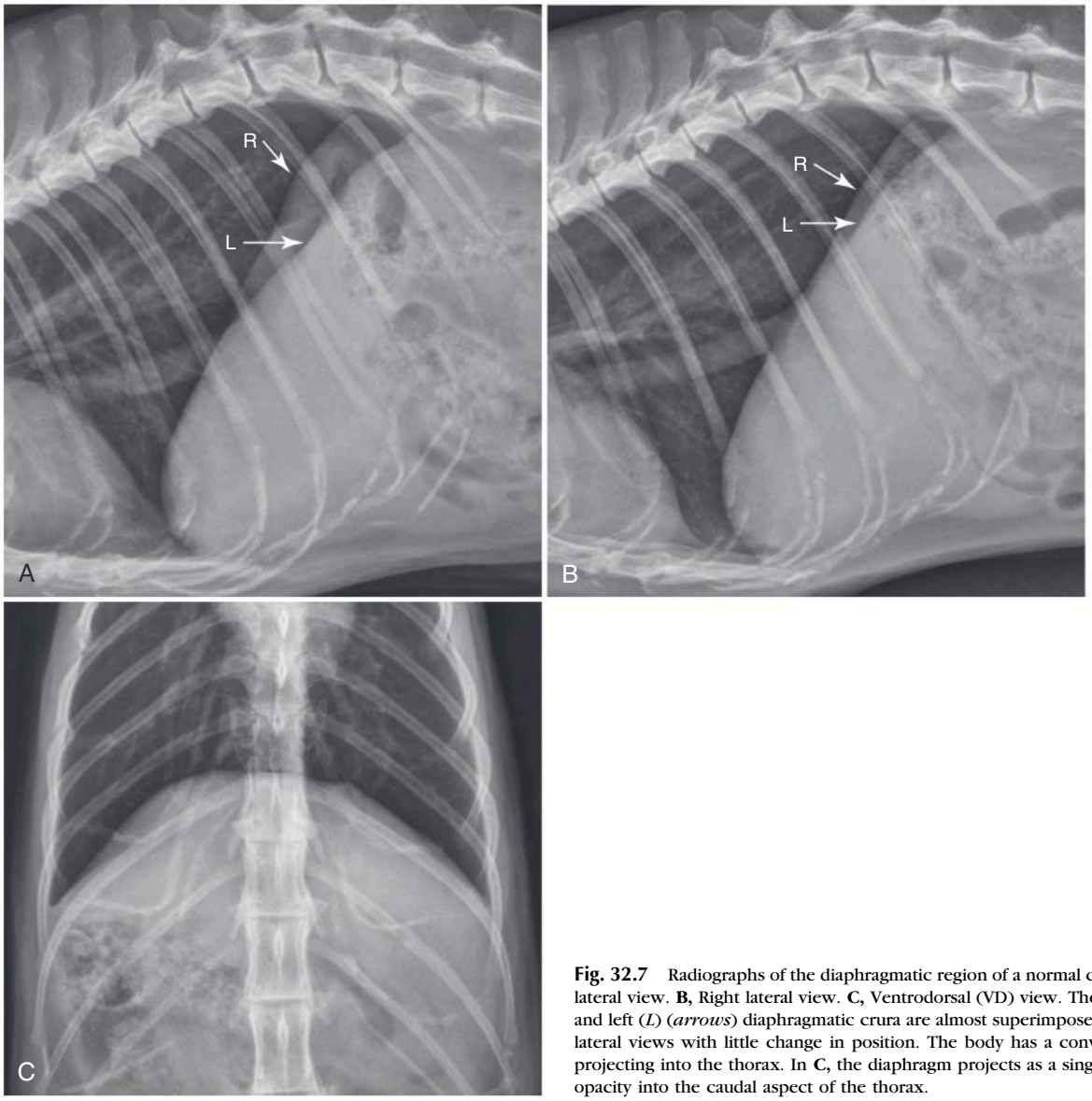


Fig. 32.7 Radiographs of the diaphragmatic region of a normal cat. **A,** Left lateral view. **B,** Right lateral view. **C,** Ventrodorsal (VD) view. The right (*R*) and left (*L*) (*arrows*) diaphragmatic crura are almost superimposed on both lateral views with little change in position. The body has a convex shape projecting into the thorax. In **C,** the diaphragm projects as a single convex opacity into the caudal aspect of the thorax.

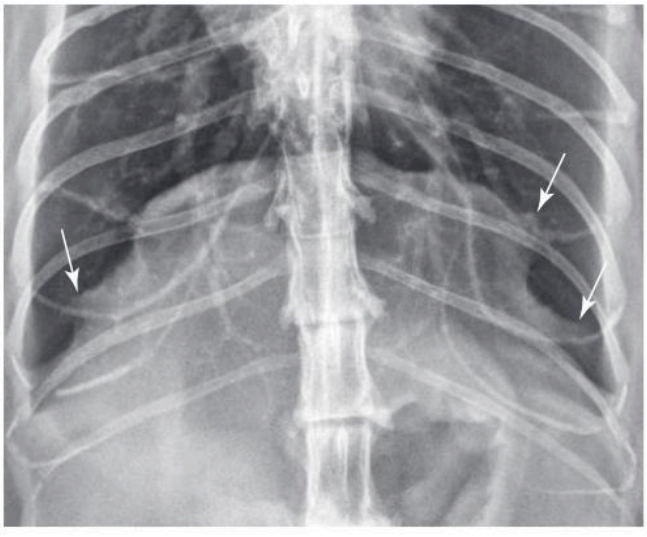


Fig. 32.8 Ventrodorsal (VD) view of the diaphragmatic region of a normal cat on deep inspiration. Small, regularly spaced projections (*white arrows*) are evident along the thoracic diaphragmatic surface. This so-called *tenting* reflects the pulling of the diaphragm against its costal attachments.

associated with the hernia.[7–11] If a diagnosis cannot be confirmed from survey radiographs (Box 32.1), ultrasonography, CT, and/or other imaging procedures may be performed to provide additional diagnostic information. Other radiographic procedures consist of administration of oral barium sulfate, positional radiographic views, and removal of pleural fluid and repeat radiography of the thorax.

To ascertain the position of the stomach and proximal small bowel, a small amount (1–2 mL/kg) of barium sulfate (30% w/v) can be given orally and radiographs obtained after 15 to 20 minutes. Radiographs made with a horizontal x-ray beam help differentiate solid abdominal organs in the thorax from pleural fluid (Fig. 32.10). Thoracocentesis and pleural fluid removal followed by another radiographic examination provide better radiographic delineation of structures within the thorax. Abdominal radiographs may be helpful to determine the absence or abnormal position of abdominal organs. Any or all of these procedures may be used, but the simplest should be used first.

Positive-contrast peritoneography or pleurography, portography, cholecystography, angiocardiography, angiography, and nonselective cardiography are potentially useful in diagnosing diaphragmatic hernias, but these are not commonly used

Table • 32.1

Radiographic Signs of Diaphragmatic Disease.

RADIOGRAPHIC SIGNS	CAUSES
General loss of diaphragmatic thoracic surface outline	Bilateral pleural fluid Generalized pulmonary disease in caudal lung lobes
Localized or partial loss of the thoracic surface outline	Thoracic masses adjacent to the diaphragm Diaphragmatic hernias Focal pulmonary disease in caudal lung lobes
Shape changes	Thoracic masses adjacent to the diaphragm Hiatal hernias Small diaphragmatic hernias Pleural reaction on the diaphragmatic surface Neoplasia arising from the diaphragm Hemiparalysis of the diaphragm Unilateral tension pneumothorax
Position Changes	
Cranial displacement	Obesity Peritoneal fluid Abdominal pain Abdominal masses or organ enlargement; liver enlargement and masses frequently cause cranial displacement Generalized diaphragmatic paralysis Cranial displacement of the cupula caused by a diaphragmatic defect with the peritoneum and pleura intact
Caudal displacement	Severe respiratory distress—ventilation or perfusion problems Tension pneumothorax Caudal displacement of the cupula caused by contact with the heart

currently or are more difficult and are therefore used rarely (Fig. 32.11).[12–15]

Ultrasonographic examination of the diaphragm may add diagnostic information, particularly for patients with pleural fluid that obliterates soft tissue. The examination is best done transhepatically.[16] Ultrasonographic signs of a diaphragmatic hernia include identification of abdominal structures within the thorax, particularly the liver, and an interruption in the diaphragmatic outline.[16–18] An interruption in the diaphragmatic outline may not be seen consistently with diaphragmatic hernia.[19]

CT examination of the thorax will add diagnostic information, although CT is usually not necessary for a diagnosis of a diaphragmatic hernia. Contrast-enhanced CT will better define which organs are herniated and the location of the hernia, and it can distinguish hernia from caudal thoracic or diaphragmatic masses (Fig. 32.12). CT may be more useful in more unusual cases, such as herniations through the aortic hiatus, esophageal hiatus, or caval foramen or peritoneopleural hernia.[20,21]

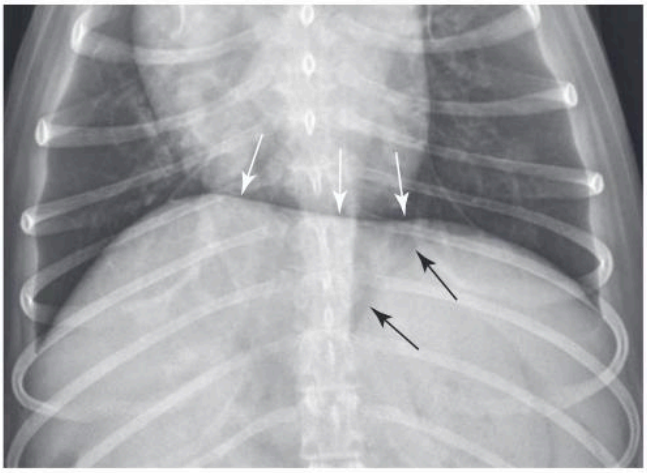


Fig. 32.9 Ventrodorsal (VD) view of the diaphragmatic region of a normal dog. A cardiac impression (*white arrows*) is present on the diaphragmatic body (cupula). The left diaphragmatic crus (*black arrows*) is visible. The right crus is not visible as a separate structure.

Box • 32.1

Radiographic Signs Associated With Traumatic Diaphragmatic Hernia

Abdominal Viscera Within the Thorax
- Gas- or ingesta-filled bowel
- Gas- or ingesta-filled stomach
- Identifiable parenchymal organs, such as the liver and spleen

Displacement of Abdominal Structures—Cranial
- Liver
- Small bowel
- Stomach
- Spleen

Displacement of Thoracic Structures—Generally Displaced Cranially and Laterally Away From an Abnormal Opaque Area in the Thorax
- Heart
- Mediastinum
- Lungs

Partial or Complete Loss of the Thoracic Diaphragmatic Surface Outline
- Pleural fluid or mass
- Lung fluid or mass

Divergence of Diaphragmatic Crura or Cranial Angulation of Diaphragm
- Pleural fluid

Traumatic Diaphragmatic Hernias

In one study, only half of the animals with a trauma-induced diaphragmatic hernia had a history of known trauma.[6] Traumatic diaphragmatic hernias usually involve the muscular portion of the diaphragm.[6,22] It has been suggested that right

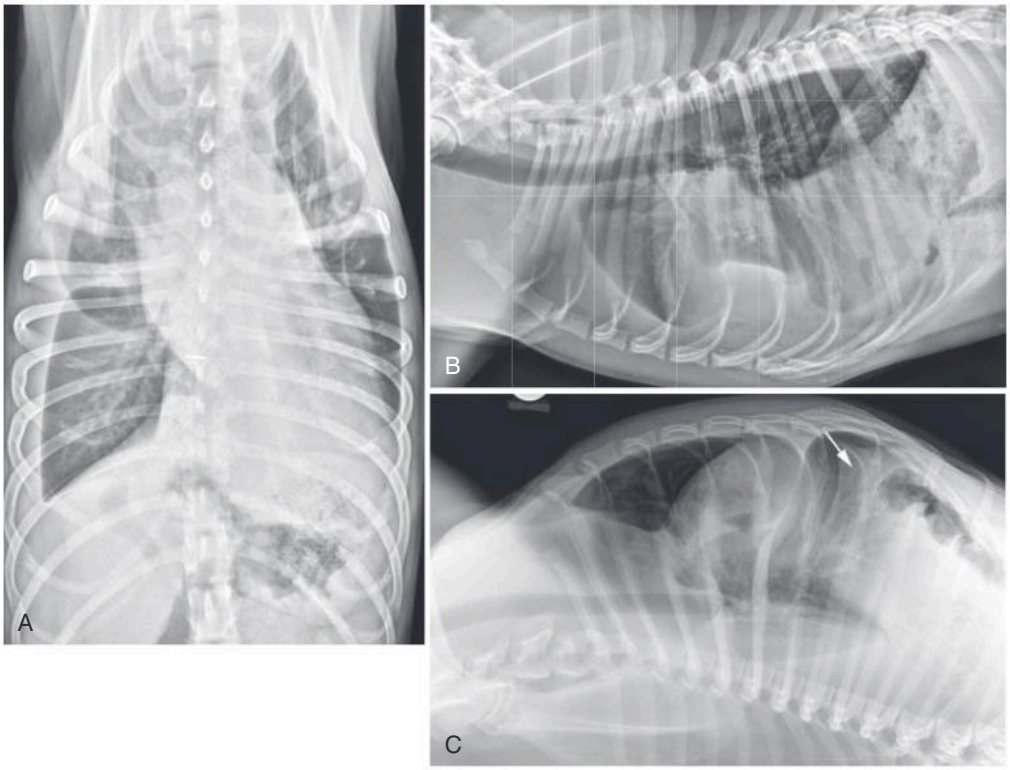


Fig. 32.10 Ventrodorsal (VD) **(A)**, lateral **(B)**, and horizontal beam lateral **(C)** views of a dog with a traumatic diaphragmatic hernia. **A,** An increased opacity in the left caudal thorax is apparent. There is loss of the thoracic diaphragmatic surface outline over the cupula and left crus and partial loss of the cardiac silhouette outline. Bilateral pleural effusion is present. **B,** The outline of the cardiac silhouette and ventral diaphragm are indistinct due to focal increased soft tissue opacity. There is ventral soft tissue opacity and rounded and retracted lung lobes, consistent with pleural effusion. **C,** There is increased soft tissue opacity dorsally, consistent with pleural effusion gravitating to the dependent portion of the thorax. However, an abnormal soft tissue opacity remains in the caudal ventral thorax and the ventral diaphragmatic outline is still not visible in its expected location (*white arrow*), consistent with a diaphragmatic hernia.



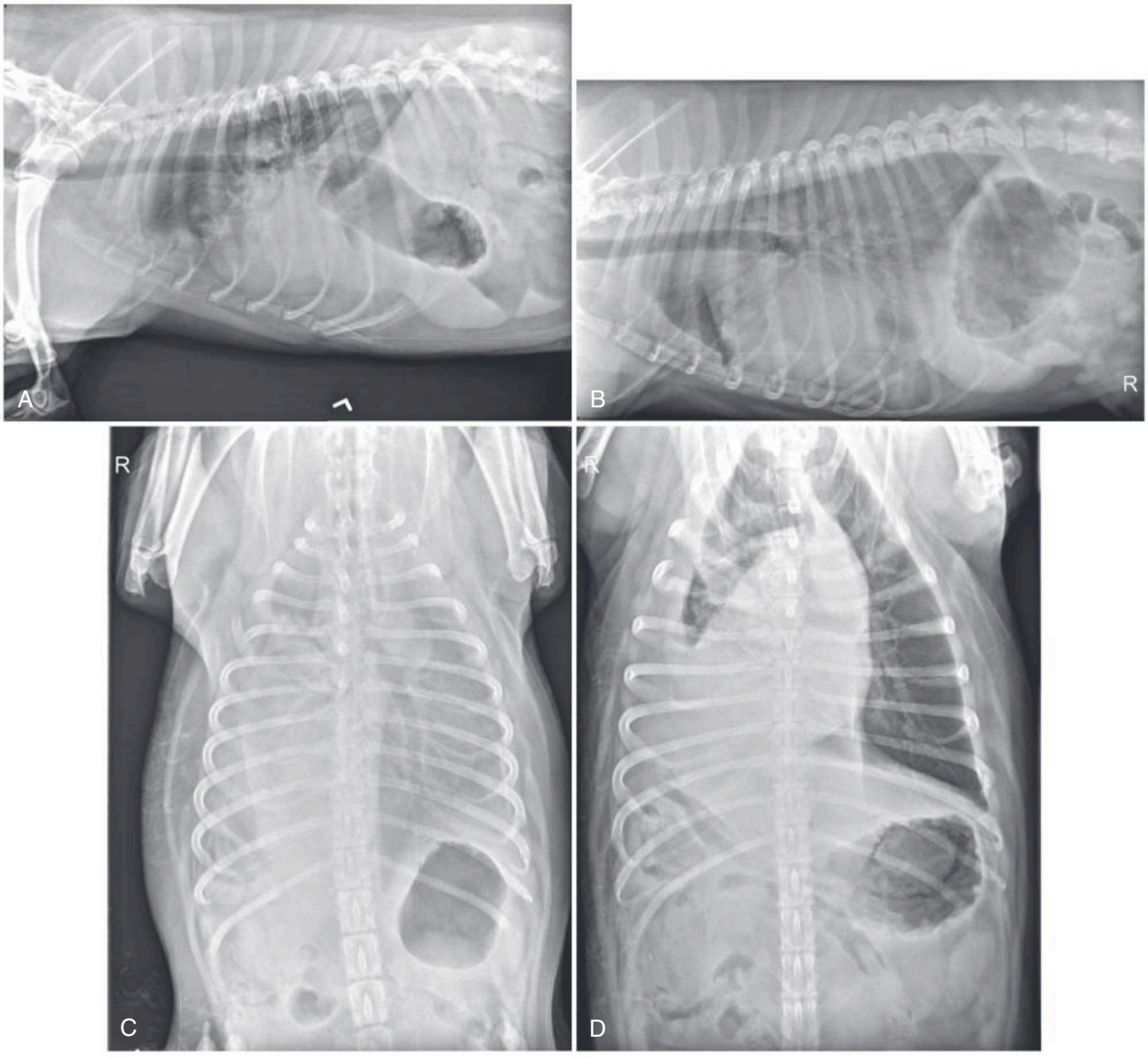
Fig. 32.11 A lateral abdominal radiograph of a positive-contrast peritoneogram. The abdominal surface of the diaphragm has an indistinct outline (*small black arrows*), with contrast medium visible in the pleural cavity (*large black arrows*). These are reliable radiographic signs of a diaphragmatic defect and a diaphragmatic hernia.

and left incidence distribution is equal,[16] but a higher incidence on the right side has been reported in the dog.[6] Most frequently herniated organs are, in order of prevalence, the liver, small bowel, stomach, spleen, and omentum.[6,9,22–24] In patients with a chronic diaphragmatic hernia, the liver and small intestine are the most frequently herniated, followed by omentum, spleen, stomach, colon, and pancreas. Strangulation of organs may be found at surgery.[25]

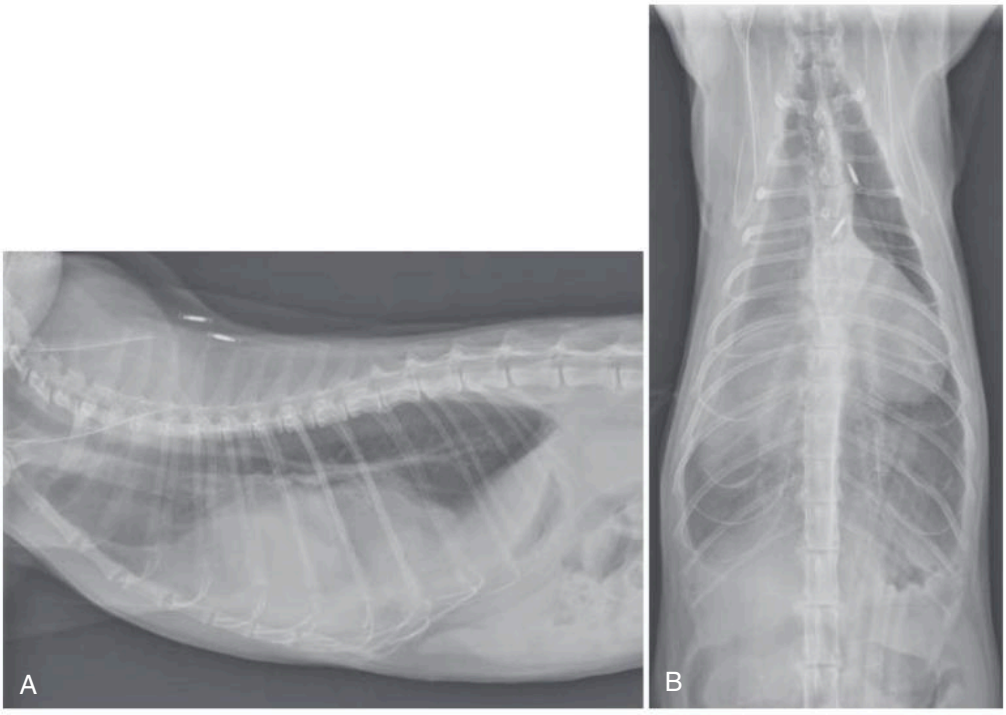
The most consistent radiographic signs of traumatic diaphragmatic hernia are:

- Abdominal viscera within the thorax
- Displacement of abdominal or thoracic organs, or both
- Partial or complete loss of the thoracic diaphragmatic surface outline
- Asymmetry or altered slope to the diaphragm on the lateral projection[11]
- Presence of pleural fluid (Fig. 32.13, eFigs. 32.2–32.4)

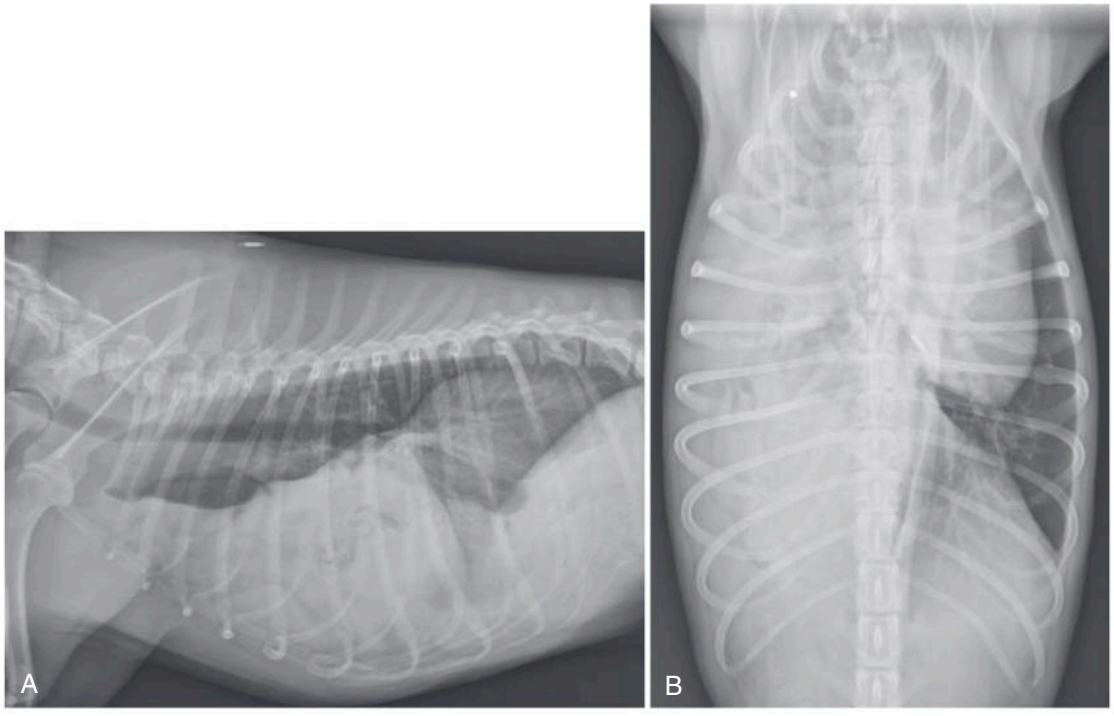
Identification of abdominal structures in the thorax is a conclusive sign of diaphragmatic hernia. Small bowel is easily identified when it is gas filled; when fluid filled, it appears as a tubular structure. The stomach may be filled with gas, fluid, or ingested material. In addition, gastric rugal folds may provide a marker for identifying the stomach within the thorax. A herniated, gas-distended stomach can be mistaken for a unilateral left pneumothorax, and the stomach should be decompressed and repositioned immediately by surgical intervention (Fig. 32.14).[6] Such instances are life-threatening because of potential or actual cardiovascular tamponade.



eFig. 32.2 Left lateral **(A)**, right lateral **(B)**, dorsoventral (DV) **(C)**, and ventrodorsal (VD) **(D)** radiographs of a dog who had been hit by a car and has a right-sided traumatic diaphragmatic hernia. The gas in the stomach and small intestines shifts on the different views, as does the pleural effusion. Having all four views available gives a more complete picture of which organs are herniated and where they are located.



eFig. 32.3 Lateral **(A)** and ventrodorsal **(B)** radiographs of a cat who was hit by a car. The cardiac silhouette and cranioventral diaphragmatic contour are poorly outlined and there is border effacement with multiple soft tissue opaque structures that are partly outlined by fat. The gastric axis is cranially displaced, and the triangular splenic silhouette is cranioventrally displaced into the region of the falciform fat immediately caudal to the costal arch. The cardiac silhouette is displaced to the left by a poorly defined soft tissue opacity structure in the right caudal thorax, representing herniated liver. There is retraction of the right lung consistent with pleural effusion.



eFig. 32.4 Lateral **(A)** and ventrodorsal **(B)** thoracic radiographs of a terrier with a traumatic diaphragmatic hernia. The diaphragmatic contour is not continuous, and abdominal viscera can be identified in the right side of the thorax, resulting in a mediastinal shift to the left. The right hemithorax is filled with soft tissue structures and some small tubular gas filled intestines. The abdominal volume is reduced and the normal hepatic silhouette is absent.

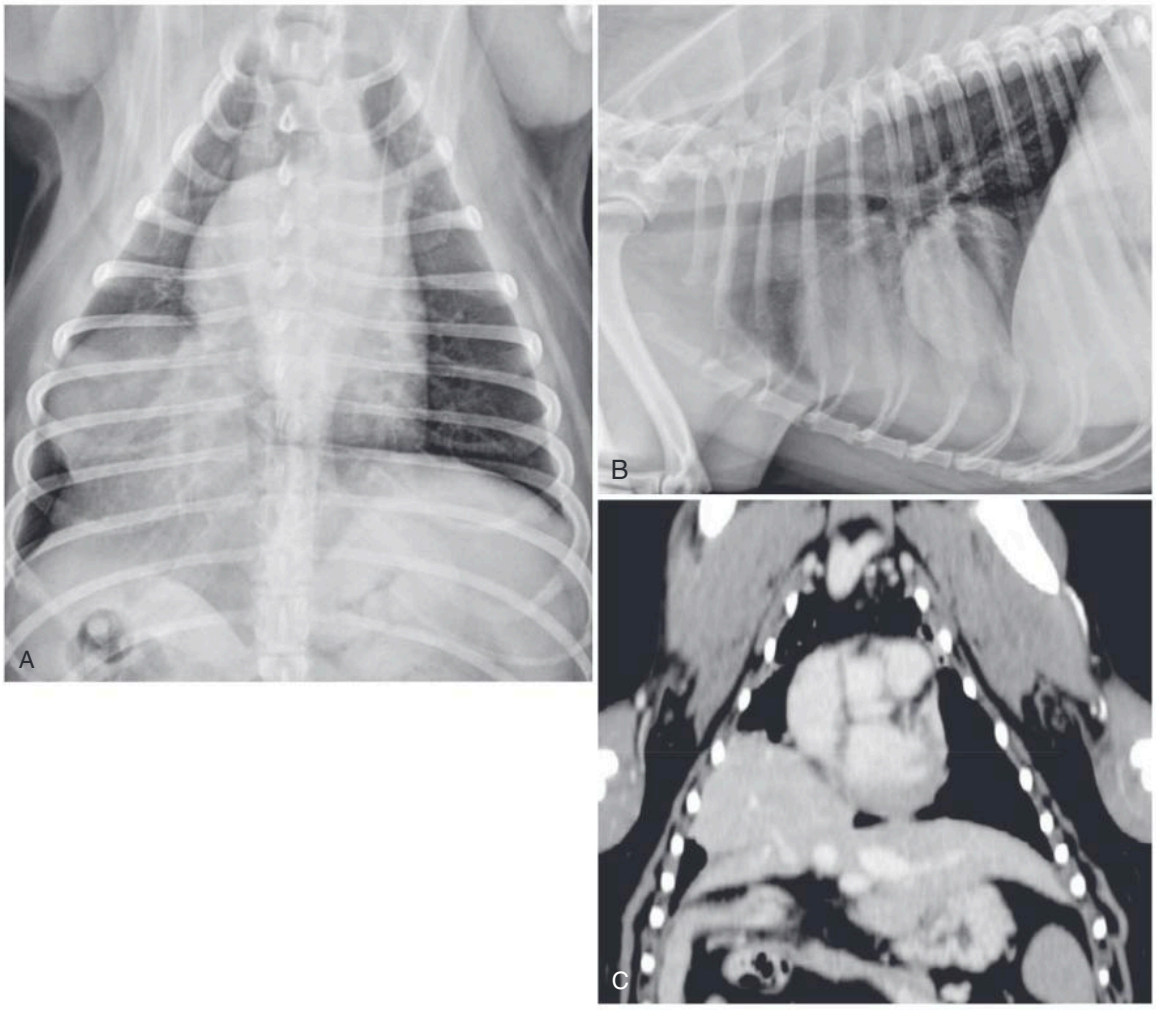


Fig. 32.12 Right lateral **(A)**, ventrodorsal (VD) **(B)** thoracic radiographs and a dorsally reformatted computed tomography (CT) image **(C)** of a dog with a diaphragmatic hernia. **A,** There is a rounded soft tissue mass in the mid-caudal thorax and focal loss of the outline of the ventral aspect of the cardiac silhouette and ventral diaphragm. **B,** The medial and caudal margins of the soft tissue mass in the right caudal thorax are less distinct, and there is loss of the outline of the right crus of the diaphragm. **C,** CT confirmed that the soft tissue opacity in the right caudal thorax was a liver lobe that had herniated through the caval foramen.

Herniated solid abdominal parenchymal organs are difficult to distinguish from localized pleural fluid, pulmonary opacity, or both. Omentum is the most difficult to detect unless it is herniated in association with other abdominal organs. In such instances, it helps outline abdominal visceral organs.

In the absence of finding abdominal organs in the thorax, cranial abdominal organ displacement or absence of abdominal organs from their normal location is an indirect sign of diaphragmatic hernia. The liver, spleen, small bowel, and stomach must be assessed closely for displacement. Barium sulfate may also be administered to identify the stomach and help detect mild to moderate gastric displacement not observed on survey radiographs.

The heart, mediastinum, and lungs may also be displaced, depending on the size and position of abdominal organs within the thorax. The heart and lungs are usually displaced cranially and either medially or laterally by herniated abdominal viscera, and the mediastinum is usually shifted from its midline position. A localized diaphragmatic surface outline loss usually indicates the area through which the hernia has occurred. Abdominal viscera and/or pleural fluid adjacent to the thoracic diaphragmatic surface cause the outline loss. This occurrence must be distinguished from the many other thoracic conditions that produce soft tissue opacity adjacent to the diaphragm. Pleural fluid is present consistently with chronic diaphragmatic hernias, or if a herniated abdominal organ, most usually the liver, is strangulated through a small diaphragmatic opening.[24] Pleural fluid is a nonspecific sign of diaphragmatic hernia and often masks other more important radiographic signs. Thoracocentesis and aspiration of the pleural fluid may be necessary before the hernia can be detected radiographically. The use of a small amount of barium can be highly specific and provide the diagnosis (Fig. 32.15).

Congenitally Predisposed Diaphragmatic Hernias

Approximately 15% of all diaphragmatic hernias are congenitally predisposed.[9] Included in this group are peritoneopericardial diaphragmatic hernias (PPDHs), hiatal hernias, and peritoneopleural hernias. Herniation in association with congenital diaphragmatic defects may occur in an animal of any age after abdominal trauma or transitory increase in intra-abdominal pressure. Defects in diaphragmatic development may be present and never result in a hernia.



Fig. 32.13 Lateral **(A)** and ventrodorsal (VD) **(B)** radiographs of the thorax of a dog with a traumatic diaphragmatic hernia. Radiographic signs of a diaphragmatic hernia in **A** are gas-filled stomach (*white arrow*) within the thorax, cranial displacement of abdominal structures, and a cranially displaced diaphragmatic segment. Radiographic signs in **B** are the mediastinal shift to the left, away from the herniated viscera; gas-filled stomach and bowel within the thorax (*white arrows*); cranially displaced abdominal structures; and loss of the right diaphragmatic surface outline.

Peritoneopericardial Diaphragmatic Hernias

A PPDH occurs when abdominal viscera herniate into the pericardial sac through a congenital hiatus formed between the tendinous portion of the diaphragm and the pericardial sac. This has been reported to occur in littermates,[26] and a predisposing trait may be carried on a simple autosomal recessive gene in cats, with a 1:500 to 1:1500 rate of incidence.[27] Domestic long-hair cats, Himalayans, and Maine Coon cats appear to be overrepresented, as do Weimaraner dogs.[28,29] The hernia may have been present from birth or is acquired. Mild increases in intra-abdominal pressure may cause abdominal organs to herniate through a congenital hiatus.

Peritoneopericardial hernias may produce clinical signs, but are often an incidental radiographic finding in old or young animals.[5,28–34] The liver is herniated most frequently; the stomach, omentum, and small bowel have a less frequent occurrence of herniation.[35] Hepatic cysts have also been reported to be associated with liver herniation into the pericardial sac.[36]

Radiographic signs associated with peritoneopericardial hernias are listed in Box 32.2. Herniated abdominal organs in the pericardial sac are usually caudal, or caudal and lateral, to the heart. Gas- or ingesta-filled hollow visceral organs are not difficult to identify within the pericardial sac, but the conspicuity of the gas-containing viscus may be a function of body position during radiography (Fig. 32.16, eFig. 32.5). Radiographically, gas within the bowel is in abrupt contrast to the adjacent structures of soft tissue opacity. Solid parenchymal organs, unless surrounded by omentum, are difficult to distinguish as separate structures within the pericardium. When abdominal organs are herniated into the pericardial sac, cranial and ventral organ displacement within the abdomen may be seen, but this displacement is usually not as pronounced as that noted with traumatic diaphragmatic hernias.

A large, round cardiac silhouette and a cardiac silhouette with an abnormal convex projection on the caudal border are signs consistent with PPDHs. These two signs depend on the amount of abdominal viscera within the pericardial sac. Large amounts of viscera produce a large, round cardiac silhouette, whereas smaller amounts, such as a portion of the liver, falciform fat, or stomach, may produce only an abnormal convex caudal cardiac border. A large, round silhouette must be differentiated from pericardial effusion, generalized heart enlargement, or both. An abnormally convex caudal cardiac border must be differentiated from neoplasia, pleural granulomas, or localized pleural fluid.

An indistinguishable outline to the ventral diaphragmatic surface and the caudal ventral cardiac silhouette is produced by the communication between the two structures. This finding must be differentiated from normal contact between the heart and diaphragm, pleural fluid, localized pleuritis, and pleural granulomas. On the lateral view, identification of the dorsal peritoneopericardial mesothelial remnant between the heart and diaphragm is a consistent radiographic sign of peritoneopericardial hernia in cats (Fig. 32.17, eFig. 32.6).[37] Sternal abnormalities may also be present.[34]

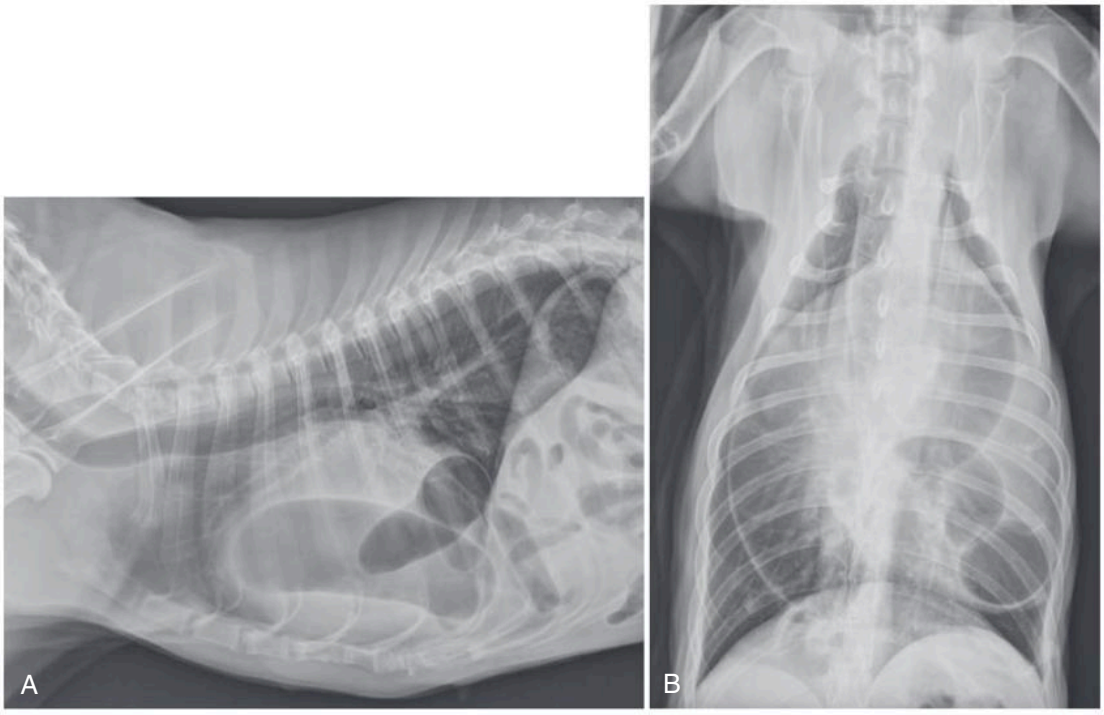
Additional radiographic studies that may be performed to confirm a diagnosis include oral administration of barium sulfate, nonselective angiography,[38] and peritoneography. Barium sulfate may be used to demonstrate gastrointestinal structures within the pericardial sac or cranial ventral displacement of abdominal structures (Fig. 32.18).

Ultrasonography has been successfully used to diagnose PPDHs.[16–19] Ultrasonography is a reliable imaging modality to use for documentation of a peritoneopericardial hernia in patients where soft tissue opaque abdominal structures are in the pericardial sac and difficult to differentiate from the heart on radiographs. If available, an ultrasound examination should be considered before contrast examinations are performed to assist in the diagnosis of PPDH.

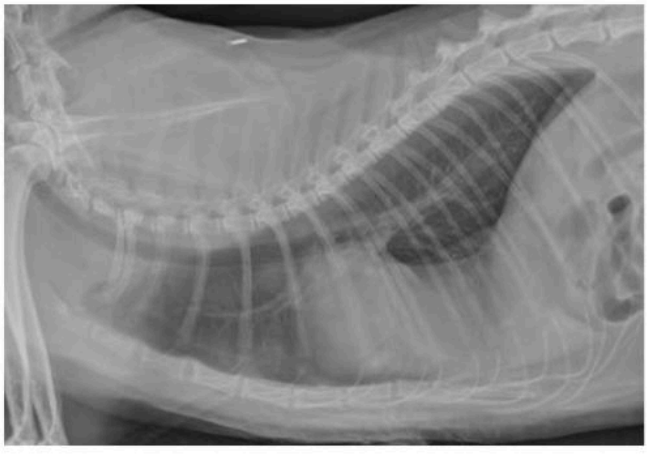
CT can assist in determining which structures are herniated, and it can confirm a PPDH in cases in which radiographs are not conclusive or when more information is desired prior to surgery.

Hiatal Hernias

Hiatal hernias occur when a portion of stomach enters the thorax through the esophageal hiatus and can be congenital or acquired. Two recognized types of hiatal hernias exist: sliding (or dynamic) and paraesophageal.[39–41] The gastroesophageal sphincter and a portion of the stomach, usually the cardia, are herniated into the thorax with sliding hiatal hernias.[42] Sliding hiatal hernias are usually congenital and found in younger animals.[41] They are often associated with esophagitis from gastroesophageal reflux. As the name implies, the caudal esophagus and the cardia slide intermittently from the abdomen into the thorax, causing temporary cranial displacement of the thoracic esophagus. Because the hernia is dynamic, it may not



eFig. 32.5 Lateral **(A)** and ventrodorsal **(B)** radiographs of a young German shepherd dog with peritoneopericardial diaphragmatic hernia. The cardiac silhouette is severely enlarged, and distended, tubular gas-filled intestines are present within the pericardium. The distension is consistent with strangulation.



eFig. 32.6 Lateral thoracic radiograph of a cat with peritoneopericardial diaphragmatic hernia. The cardiac silhouette is enlarged and poorly separated from the diaphragm. A soft tissue band extending between the cardiac silhouette and the diaphragm at the level of the caudal vena cava represents a mesothelial remnant. The falciform fat is reduced in volume in the abdomen and the majority is displaced into the pericardial sac.

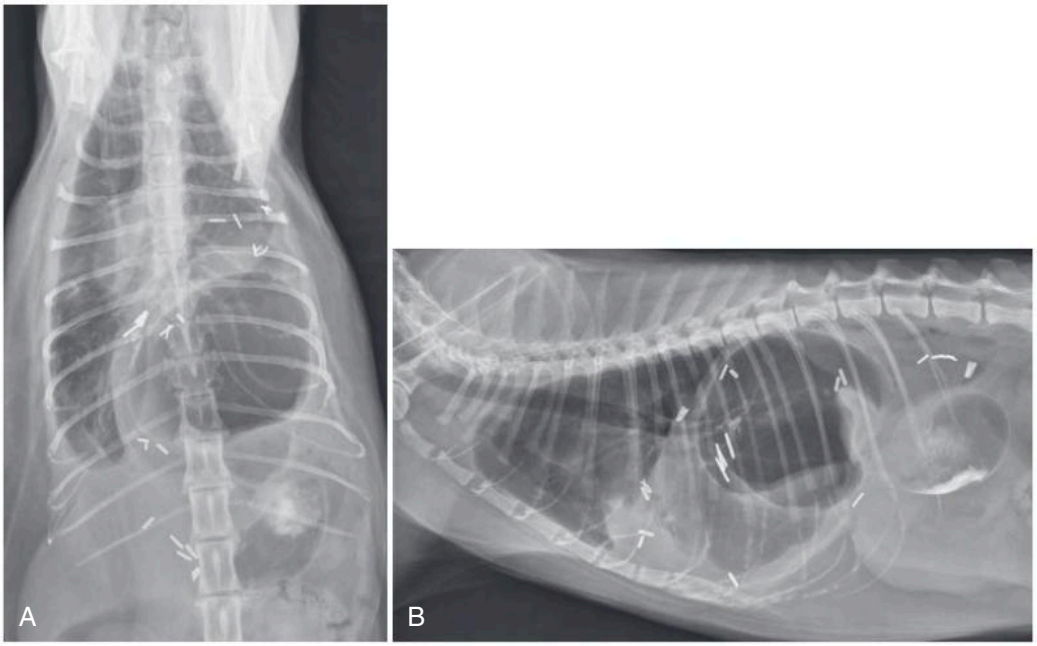


Fig. 32.14 Ventrodorsal (VD) **(A)** and lateral **(B)** views of the thorax of a cat with a traumatic diaphragmatic hernia of the stomach. Hemoclips are present from a previous surgery. **A,** The gas-filled stomach is herniated into the left hemithorax, displacing the heart and lungs to the *right*. The normal gastric and left diaphragmatic outlines are not present. **B,** The severely gas-distended stomach occupies the majority of the caudal thorax and obscures the cardiac silhouette.

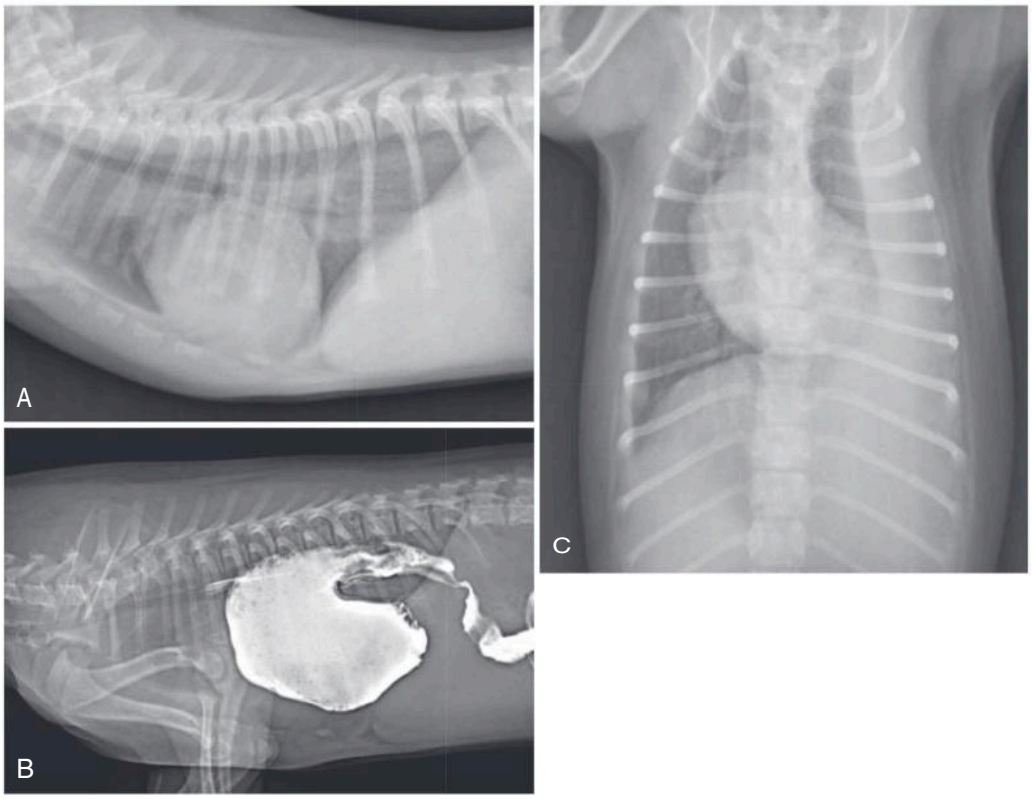


Fig. 32.15 Right lateral **(A)** and ventrodorsal (VD) **(B)** thoracic radiographs of an adult Yorkshire terrier that sustained a fall approximately 7 days previously. The patient was normal until today when dyspnea developed. There is only a mild nonspecific increase in thoracic radiographic opacity in the lateral view. In the VD view, there is a homogeneous increase in opacity along the left thoracic wall and border effacement of the diaphragm. This could be a hernia but a hematoma in the pleural space could also be considered. Following administration of a small amount of barium **(C)**, it is apparent that the stomach is herniated into the thorax, confirming a diaphragmatic hernia.

Box • **32.2**

Radiographic Signs Associated With Peritoneopericardial Diaphragmatic Hernias

- Abdominal organs identified in the pericardial sac; gas, ingested material, or structures of soft tissue opacity may be present
- Large, round cardiac silhouette
- Convex projection of the caudal cardiac silhouette
- Indistinguishable border of the ventral thoracic diaphragmatic surface and the caudal ventral cardiac silhouette
- Confluent silhouette between the diaphragm and the heart
- Dorsal peritoneopericardial mesothelial remnant between the heart and diaphragm on the lateral view in cats
- Sternal changes

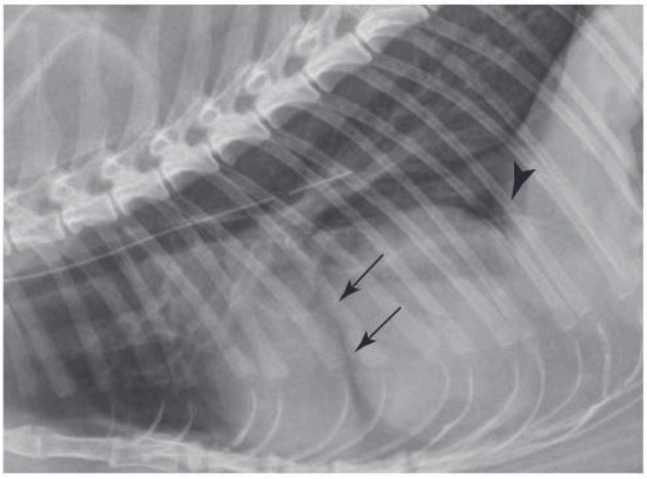


Fig. 32.17 Lateral view of a cat with a peritoneopericardial diaphragmatic hernia. The outline of a dorsal peritoneopericardial mesothelial remnant is visible cranial to the diaphragm (*black arrowhead*). The liver and omentum are herniated into the pericardial sac. The caudal border of the heart is visible (*black arrows*) because of fat in the adjacent omentum.

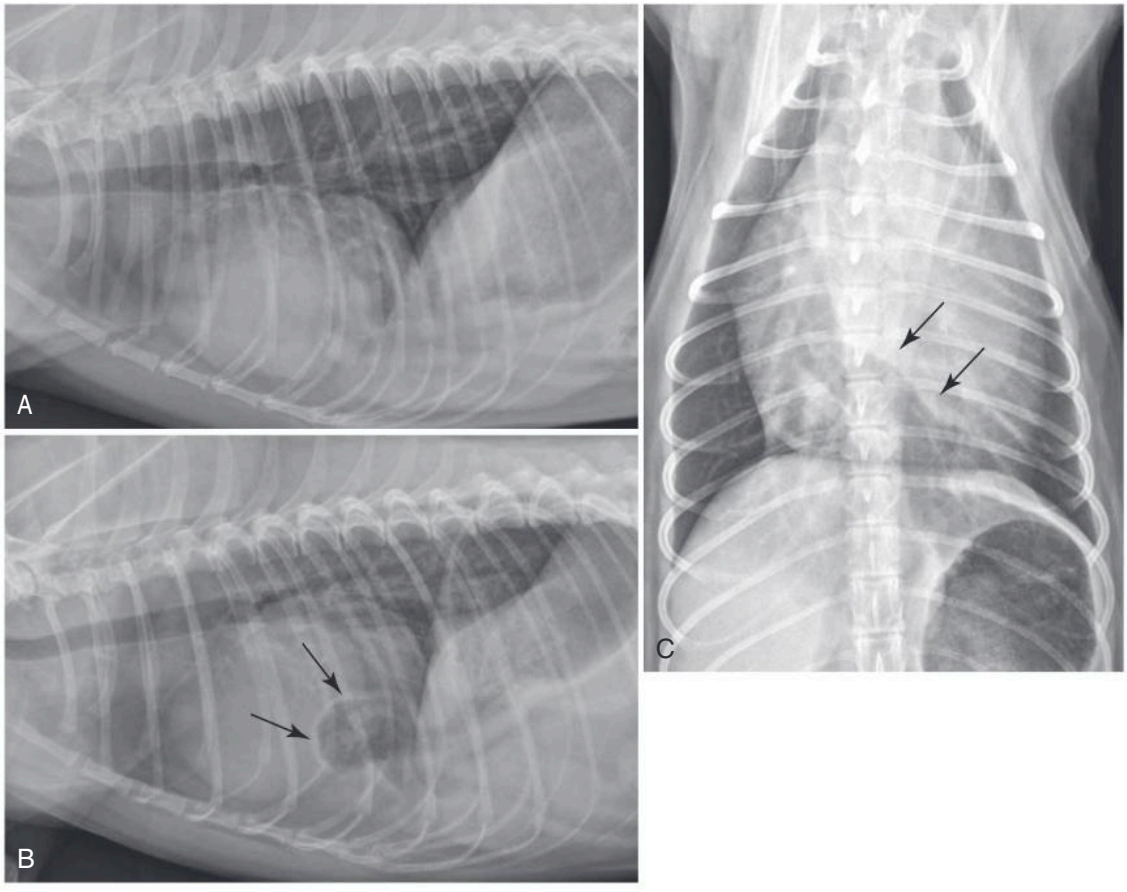


Fig. 32.16 Right lateral **(A)**, left lateral **(B)**, and ventrodorsal (VD) **(C)** radiographs of a dog with a peritoneopericardial diaphragmatic hernia. Various opacities are visualized in the pericardial sac, including gas, soft tissue, and fat. The gas filled herniated portion of the stomach is better visualized on the left lateral and VD views (*black arrows*). The amount of gas within organs in the pericardial sac will change depending on the position of the patient; no gas may be visible in some positions.

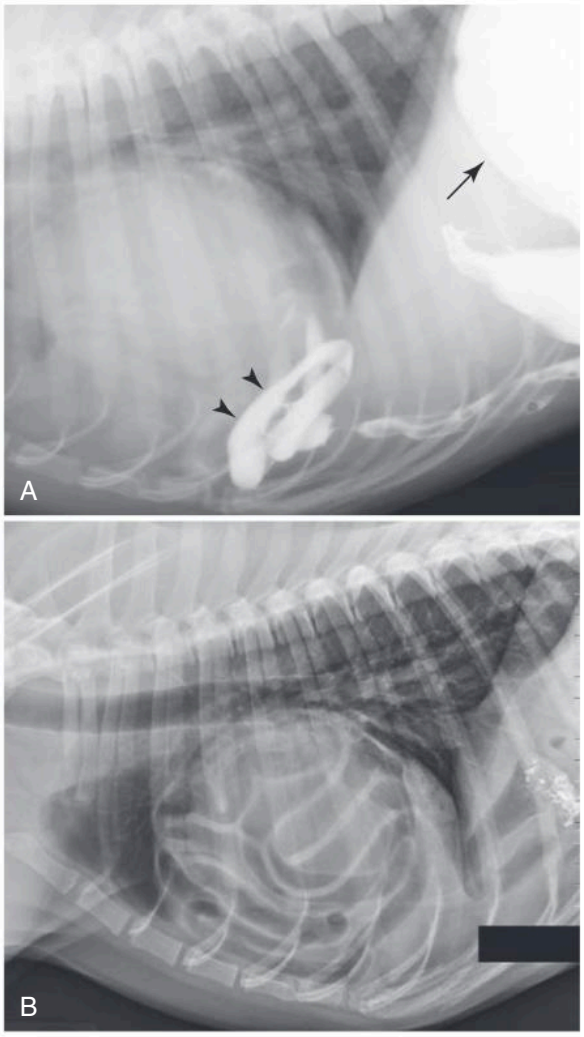


Fig. 32.18 Right lateral **(A)** and left lateral **(B)** views of the thorax of a dog with a peritoneopericardial diaphragmatic hernia. **A,** Barium is present in the normally positioned stomach (*black arrow*), as well as in small intestines (*black arrowheads*) that are herniated into the pericardial sac. **B,** Radiographs of the same patient made at a later time reveal diffuse gas filling of the small intestines, which provides negative contrast that allows easy identification of small intestines within the pericardial sac. (Courtesy Dr. Amy Habing, Ohio State University, Columbus, OH.)

be seen on any one radiograph; fluoroscopic examination is often necessary to make a diagnosis. Patients with nonsliding hiatal hernias have been reported, with the gastroesophageal sphincter and the gastric cardia displaced through the esophageal hiatus and fixed within the thorax.[42]

A paraesophageal hiatal hernia is produced when the cardia or cardia and fundus of the stomach or other soft tissue structures herniate through, or alongside, the esophageal hiatus and become positioned adjacent to the esophagus. They are usually static and do not slide between the thorax and abdomen, and the gastroesophageal sphincter is in a normal position.[40,42] The herniated stomach may cause esophageal obstruction from external pressure on the caudal esophagus.

Hiatal hernias have also been classified as types I through IV. Type I represents a sliding hiatal hernia, type II represents a paraesophageal hernia, and type III represents a combination of type I and type II. Type IV has been described two ways: (1) as a type III hernia combined with herniation of another organ rather than the stomach or (2) as a gastroesophageal intussusception. Other complicated hernias, such as a hernia through the esophageal hiatus combined with a second, separate gastric herniation through a defect in the diaphragm have been reported.[41]

Box • 32.3

Radiographic Signs Associated With Sliding Hiatal Hernias

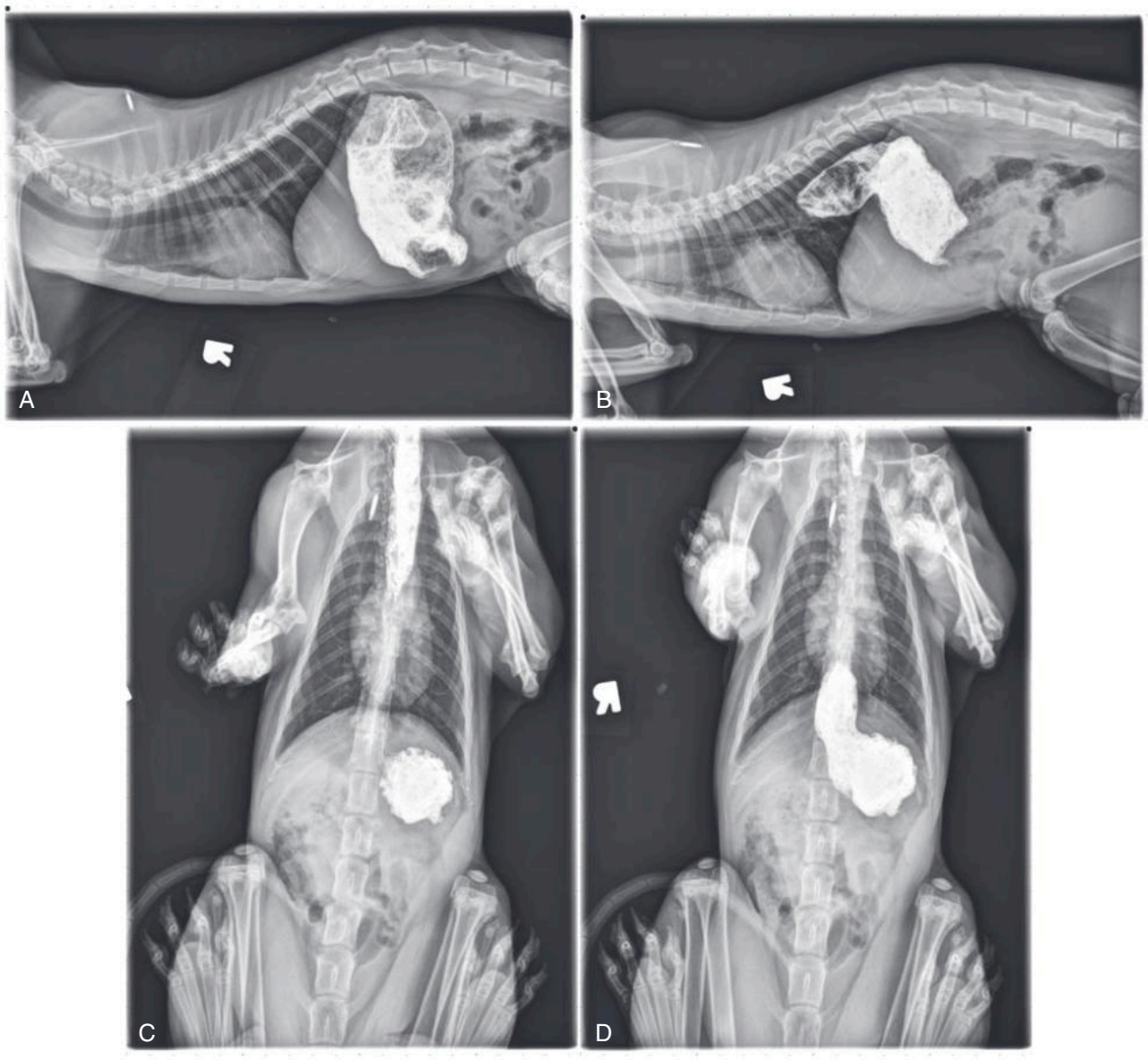
Survey Radiographs
- Soft tissue mass adjacent to the left diaphragmatic crus close to midline
- Loss of thoracic surface outline on the left diaphragmatic crus
- Cranial displacement of the gastric cardia producing an abnormal gastric shape
- Dilated esophagus
- Pneumonia

Esophagram
- Dilated esophagus
- Hypomotile esophagus
- Gastroesophageal sphincter within the thorax represented by a circumferentially narrowed area of the esophagus
- Gastric cardia within the thorax
- Gastroesophageal reflux

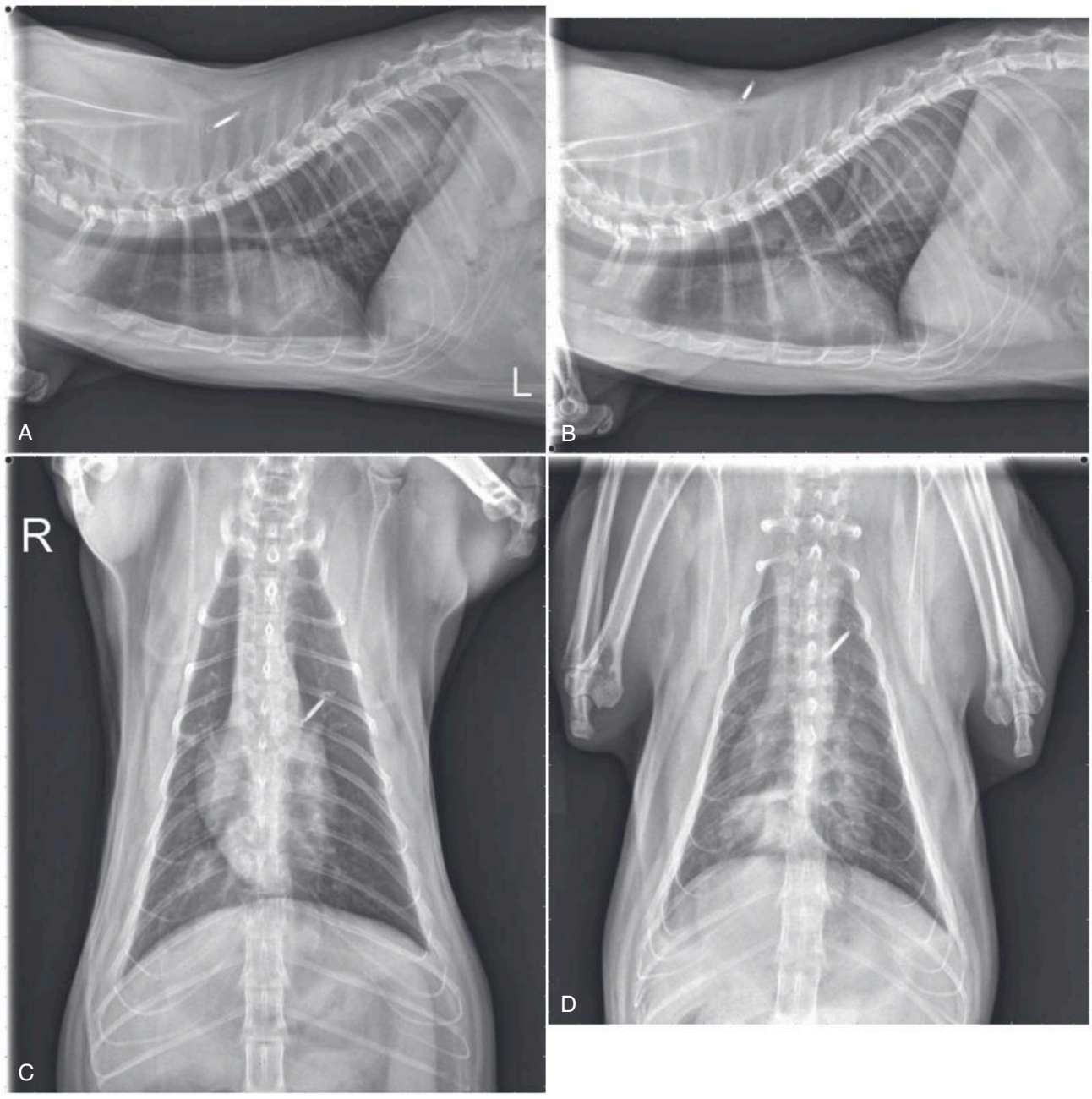
Hiatal hernias occur in both the dog and the cat.[43] They can be associated with other esophageal conditions in shar-pei dogs.[43] There may be no clinical signs, or vomiting, regurgitation, excessive salivation, dysphagia, and dyspnea may be observed.[43–45] Hiatal hernias can be associated with esophageal dysmotility and are seen more frequently in brachycephalic dogs, especially French bulldogs. Decreased intrathoracic pressure associated with increased respiratory effort may be the cause of these hernias in brachycephalic dogs.[46] Hiatal hernia may be suspected from the clinical signs and survey radiographic findings but must be confirmed by an esophagram.

Radiographic signs of a sliding hiatal hernia are listed in Box 32.3. The most consistent survey radiographic sign is stomach displacement. The cardia appears to be stretched toward the diaphragm or may extend into the thorax. This displacement produces an abnormal shape to the cardia and fundus remaining in the abdomen. The caudal esophagus may or may not be distended, and a soft tissue mass may be seen adjacent to the left diaphragmatic crus (Fig. 32.19, eFig. 32.7, Video 32.1). The size and visibility of this mass depend on the amount of stomach that has herniated into the thorax. The soft tissue mass associated with a hiatal hernia must be differentiated from pulmonary or diaphragmatic masses. Diaphragmatic tumors occur but are rare.[47]

A dilated caudal esophagus is usually best detected and evaluated with an esophagram. An esophagram is also helpful for differentiating the type of hiatal hernia. The caudal esophageal sphincter and a portion of the cardia are cranial to the diaphragm with a sliding hiatal hernia.[48] The caudal esophageal sphincter can be identified as a concentric, smooth, 1- to 2-cm narrowing in the caudal esophagus (Fig. 32.20). Displacement and narrowing of the caudal esophagus by the cardia and fundus can be seen with paraesophageal hiatal hernias. Barium outlining the caudal esophagus can also be seen superimposed over the herniated paraesophageal soft tissue (Fig. 32.21, eFig. 32.8, Video 32.2).



eFig. 32.7 Radiographs of a 7-month-old cat who presented for chronic vomiting. After survey images were acquired and were considered normal, the patient was fed barium-coated food and additional radiographs were obtained. Images **A** and **C** are lateral and dorsoventral (DV) images that show barium-coated food in the stomach. Images **B** and **D** are lateral and DV images that show herniation of the stomach and barium-coated food into the caudal thorax. This indicates a sliding hiatal hernia. In addition, there is barium-coated food in the caudal cervical and cranial thoracic esophagus on the DV views, which may be due to decreased esophageal transit or extensive gastroesophageal reflux.



eFig. 32.8 Left lateral **(A)**, right lateral **(B)**, ventrodorsal (VD) **(C)**, and dorsoventral (DV) **(D)** radiographs as well as an ultrasound video loop (Video 32.2) of a 1-year-old cat. The owners noticed wheezing and occasional vomiting. Radiographs show a soft tissue and fat opacity in the caudodorsal thorax, which were interpreted to be either a diaphragmatic hernia or paraesophageal hernia. Ultrasound showed fat and the stomach herniating through the diaphragm. Surgery confirmed a paraesophageal hernia including the stomach and fat.

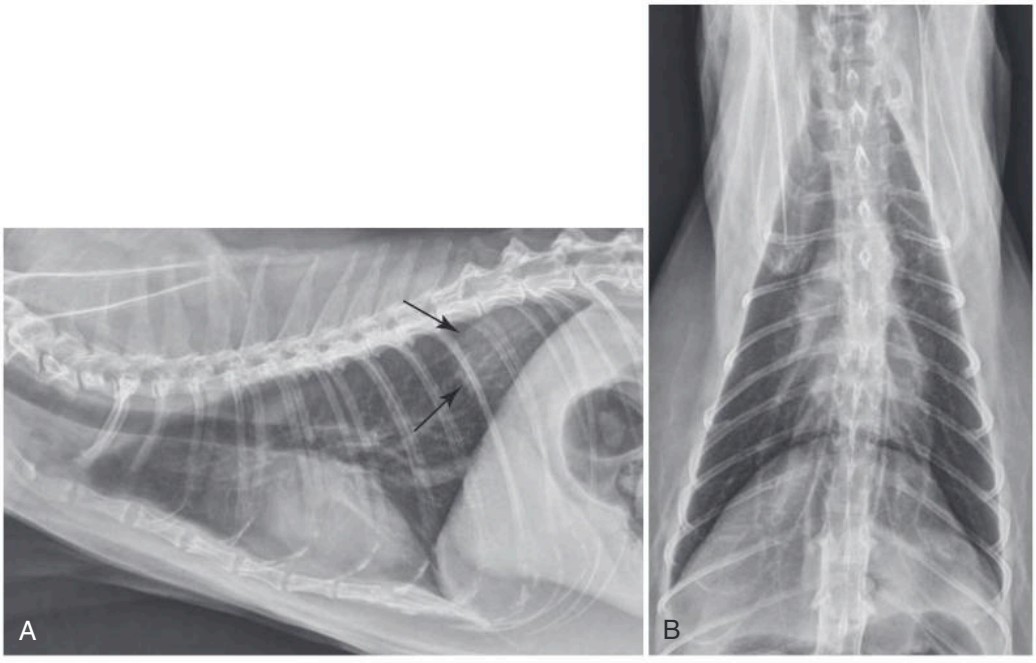


Fig. 32.19 **A,** Lateral thoracic view with a soft tissue opacity in the caudodorsal thorax (*black arrows*). The soft tissue opacity is suspect for a hiatal hernia. **B,** Ventrodorsal (VD) view at the same time is normal, which supports the diagnosis of sliding hiatal hernia.

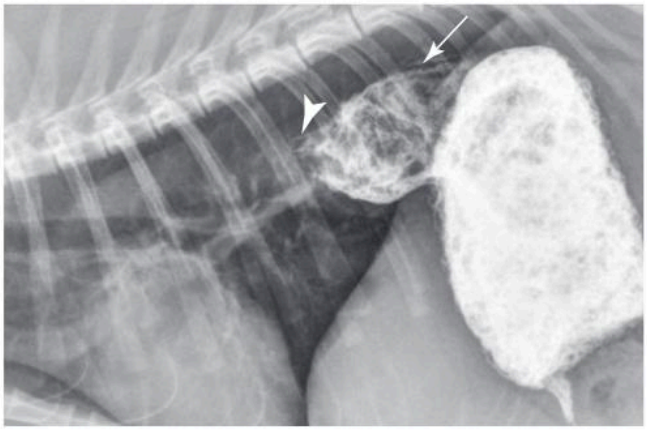


Fig. 32.20 Right lateral view of barium esophagram in a cat with a sliding hiatal hernia. Contrast medium is present in the stomach including the gastric cardia (*white arrow*), which tapers cranially (*white arrowhead*). The gastroesophageal sphincter and gastric cardia are displaced cranial to the diaphragm through the esophageal hiatus.

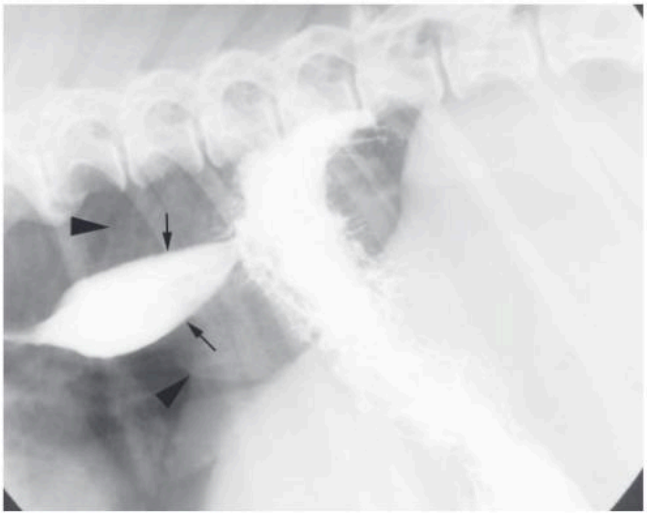


Fig. 32.21 Lateral view of the thorax. Barium is filling and outlining the caudal esophagus (*black arrows*). The barium-filled caudal esophagus is superimposed over a soft tissue organ (*black arrowheads*) cranial to the diaphragm and adjacent to one side of the esophagus. This is consistent with a paraesophageal hiatal hernia.

Gastroesophageal Intussusception

Gastroesophageal intussusception occurs when the stomach, with or without the spleen, duodenum, pancreas, and omentum, invaginates through the esophageal hiatus into the caudal esophagus.[40,42,49,50] They occur most frequently in male and German shepherd dogs and in animals with a pre-existing dilated esophagus.[50] Gastroesophageal intussusception usually produces an esophageal obstruction, which results in rapid deterioration of the animal's condition with a high mortality rate; a timely diagnosis is therefore essential.[50]

On survey radiographs, a large soft tissue mass is seen adjacent to the diaphragm, usually accompanied by a dilated esophagus. There is also usually a sharp air/soft tissue interface between the displaced stomach in the caudal esophagus and the gas in the distended cranial aspect of the esophagus (Fig. 32.22). With an esophagram, gastroesophageal intussusceptions produce a large intraluminal filling defect within the caudal esophagus, rugal folds may be outlined with barium, and barium does not usually enter the stomach (Box 32.4).

Peritoneopleural Hernias

Congenital diaphragmatic defects resulting in peritoneopleural hernias are rare in the dog and cat[51–55] and have been confused with pulmonary masses.[56] The defects are created when the septum transversum or the pleural peritoneal folds do not develop and fuse to form a complete diaphragm. The diaphragmatic defect allows abdominal viscera to enter the

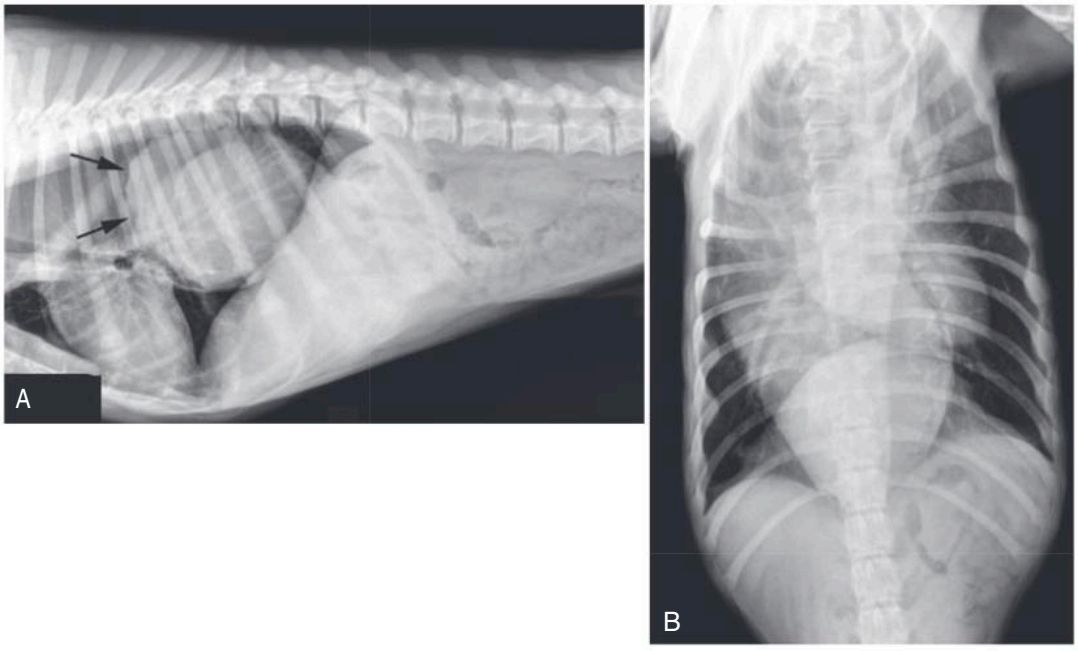


Fig. 32.22 Lateral **(A)** and ventrodorsal (VD) **(B)** views of a juvenile German shepherd with a gastroesophageal intussusception. There is a large soft tissue mass in the caudal thorax, centered on the midline. This represents the stomach herniated into the caudal aspect of the esophagus. The cranial aspect of the esophagus is dilated and there is a sharp air/gas interface in the lateral view (*black arrows*) outlining the cranial margin of the herniated stomach.

Box • 32.4

Radiographic Signs Associated With Gastroesophageal Intussusception

Survey Radiographs
- Soft tissue mass adjacent to the diaphragm
- Cranial displacement of the stomach with or without the spleen or duodenum
- Dilated esophagus
- Convex of tissue/air interface between herniated stomach and gas in cranial esophagus

Esophagram
- Intraluminal filling defect in the caudal esophagus
- Barium outline of rugal folds
- No barium within the stomach

thoracic cavity but they remain contained by serosa or pleura, producing a pleuroperitoneal hernia. These are also called true diaphragmatic hernias.[57]

In human beings, diaphragmatic defects have a familial incidence with a multifactorial mode of inheritance.[58] Congenital defects in dogs have been reported in the muscular diaphragm, dorsolateral in position at the site of the pleuroperitoneal canal,[55] and in the membranous diaphragm associated with umbilical hernias.[5,52] Bochdalek hernias are common peritoneopleural hernias in children, but are rarely reported in veterinary medicine. These are hernias at the dorsolateral margins of the diaphragm through the lumbocostal trigone, due to a failure of closure of the pleuroperitoneal canal in children. There is also a report of extension of a retroperitoneal lipoma through the lumbocostal trigone.[59]

The radiographic signs of peritoneopleural hernias associated with muscular diaphragmatic defects can be the same as for traumatic diaphragmatic hernias (Fig. 32.23, eFig. 32.9), although pleural effusion typically only occurs with traumatic hernias. With membranous defects, however, the liver (in dogs) or the falciform fat (in cats) is displaced cranially, while remaining in the caudal ventral thorax, and is often confined to the mediastinum because the peritoneal membrane and pleura are intact (Fig. 32.24).[60]

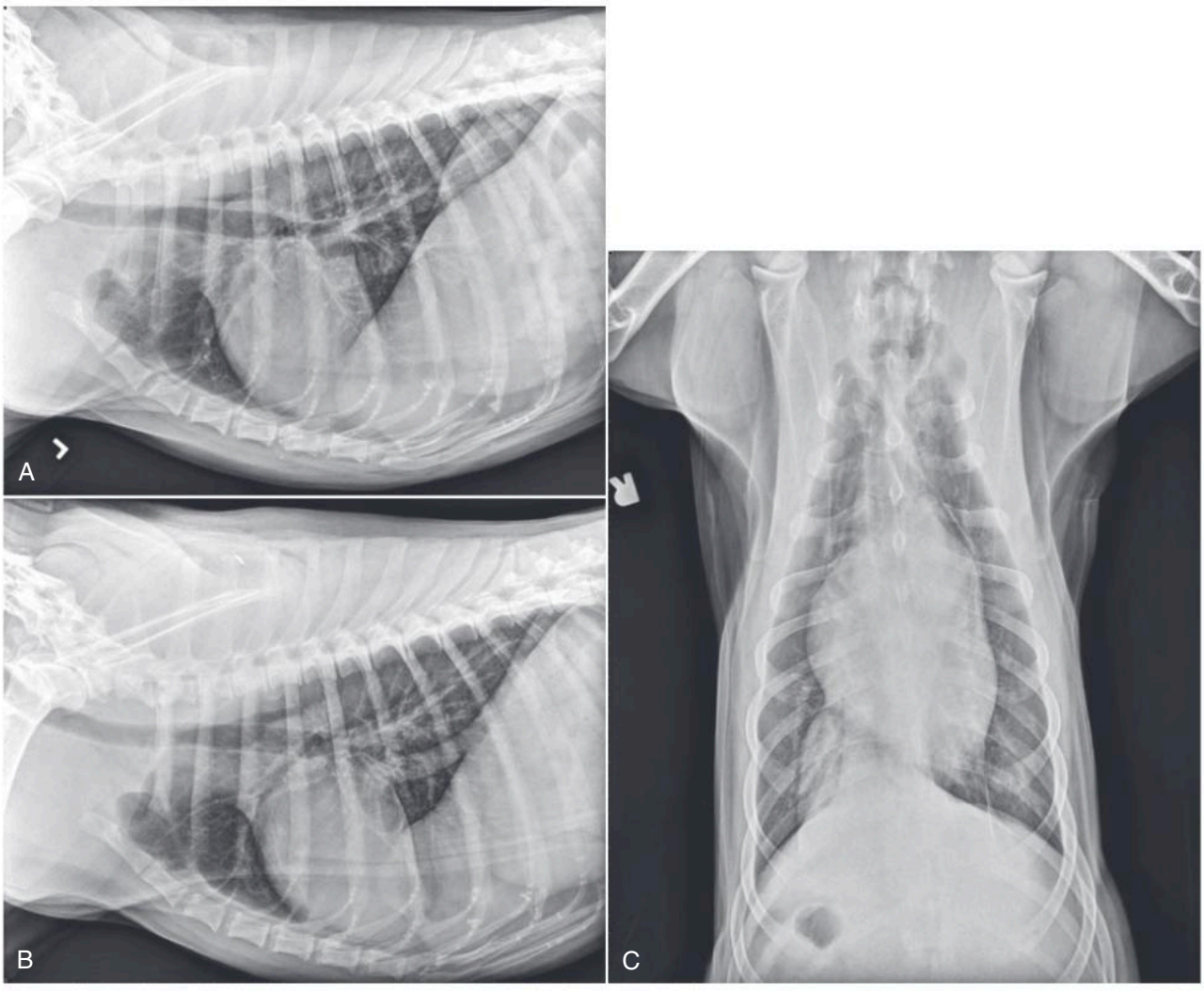
Foraminal Hernias

Herniations may occur through the aortic hiatus, esophageal hiatus, or caval foramen. These are rare in humans and veterinary patients. Caval foramen hernias can look like caudal pulmonary masses and may cause compression of the caudal vena cava. CT may be required for correct diagnosis.[20,21]

Motor Disturbances of the Diaphragm

The diaphragm is the principal muscle of respiration and is innervated by the phrenic nerve.

Motor disturbances of the diaphragm consist of unilateral paralysis, bilateral paralysis, and diaphragmatic flutter.[1] Diaphragmatic paralysis may result from pneumonia, trauma, myopathies, and neuropathies, or the cause may be unidentified.[1] Transient post-traumatic hemidiaphragmatic paralysis has been reported in cats.[61] Diaphragmatic paralysis should be suspected when one or both diaphragmatic crura are displaced cranially (Fig. 32.25). Confirmation of paralysis is best achieved with fluoroscopy. Unequal movement between the crura is seen with unilateral paralysis. With bilateral paralysis, minimal or no diaphragmatic movement or a paradoxic cranial displacement of the flaccid diaphragm may occur during inspiration.[62] Bilateral paralysis may be more difficult to confirm with fluoroscopy, because diaphragmatic movement is sometimes produced by compensatory abdominal muscle contraction during respiration. The term *diaphragmatic eventration* is sometimes used for focal weakening of the diaphragm with



eFig. 32.9 Left lateral **(A)**, right lateral **(B)**, and ventrodorsal (VD) **(C)** images of a 5-year-old Weimaraner who had an incidental finding of an abnormal diaphragm on images at the referring clinic. At the time he presented for further workup of the diaphragm, the only clinical abnormality was a left thoracic limb lameness. On all images, the right aspect of the cupula of the diaphragm is cranially displaced into the right ventral thorax. There is homogeneous soft tissue opacity contained in the extension of the diaphragm. Peritoneopleural hernia was suspected and confirmed on surgery.

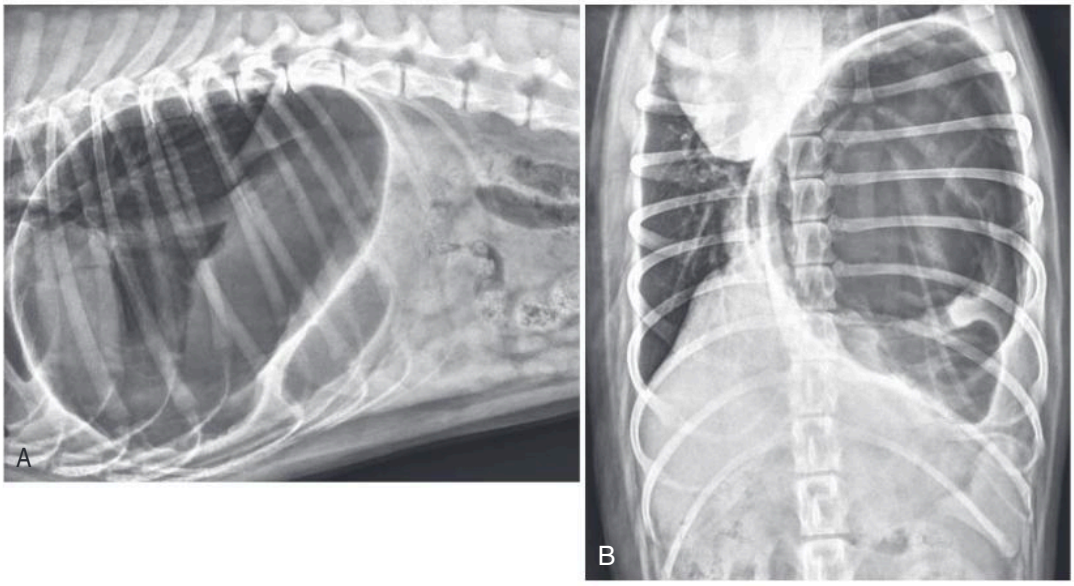


Fig. 32.23 Right lateral **(A)** and ventrodorsal (VD) **(B)** views of a dog. A defect in the left dorsolateral aspect of the muscular portion of the diaphragm resulted in a congenital diaphragmatic hernia. The gas-filled stomach is within the thorax.

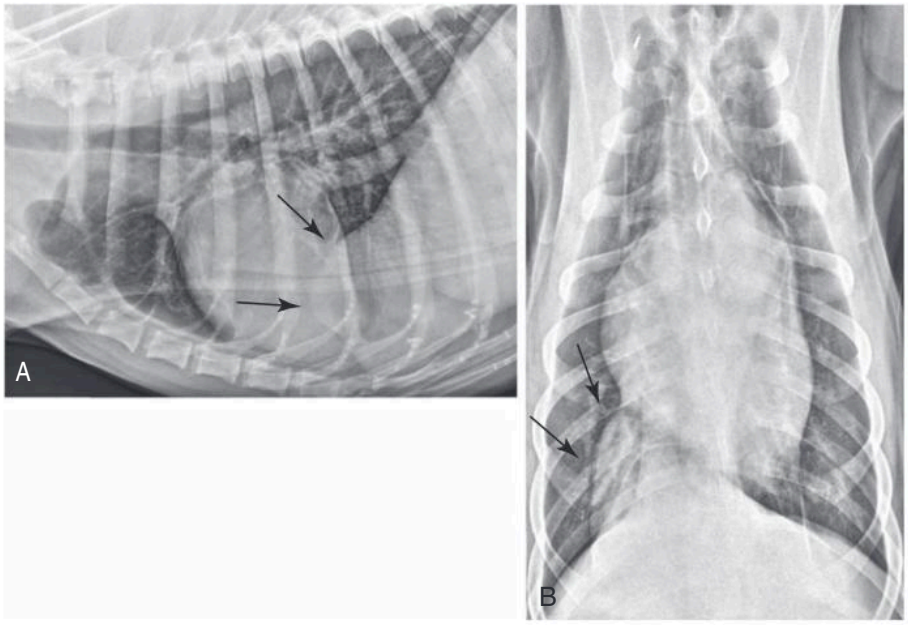


Fig. 32.24 Right lateral **(A)** and ventrodorsal (VD) **(B)** views of a dog thorax. A defect is present in the membranous portion of the diaphragm. A portion of liver is displaced cranially into the right ventral thorax (*arrows*) and surrounded with intact peritoneum and parietal pleura.

cranial displacement of the affected portion of the diaphragm. This condition is difficult to diagnose radiographically.

Diaphragmatic flutter is most often associated with contractions of the diaphragm synchronous with the heartbeat. It is usually transient in nature and can be easily diagnosed with fluoroscopy by observing contractions of the diaphragm in synchrony with the heartbeat.[63]

Muscular Dystrophy

Muscular dystrophy caused by dystrophin deficiency occurs rarely in dogs[64] and cats.[65,66] In dogs with muscular dystrophy, radiographic abnormalities include diaphragmatic asymmetry, diaphragmatic undulation, and gastroesophageal hiatal hernia.[67,68] In cats an irregular, scalloped appearance of the diaphragm, particularly along the ventral margin, was a consistent finding observed on radiographs after 7 months of age.[65] The scalloped margin, noted best on the lateral view, should not be confused with the normal scalloping observed on the VD view in cats on maximal inspiration (see Fig. 32.7). The scalloped appearance is caused by muscular hypertrophy, which can be confirmed by ultrasound.[65] Muscular hypertrophy produced with feline muscular dystrophy has also been reported to cause megaesophagus from extraluminal hiatal obstruction. Definitive laboratory tests, such as immunofluorescence or immunoblot tests, are necessary to establish the diagnosis of muscular dystrophy.

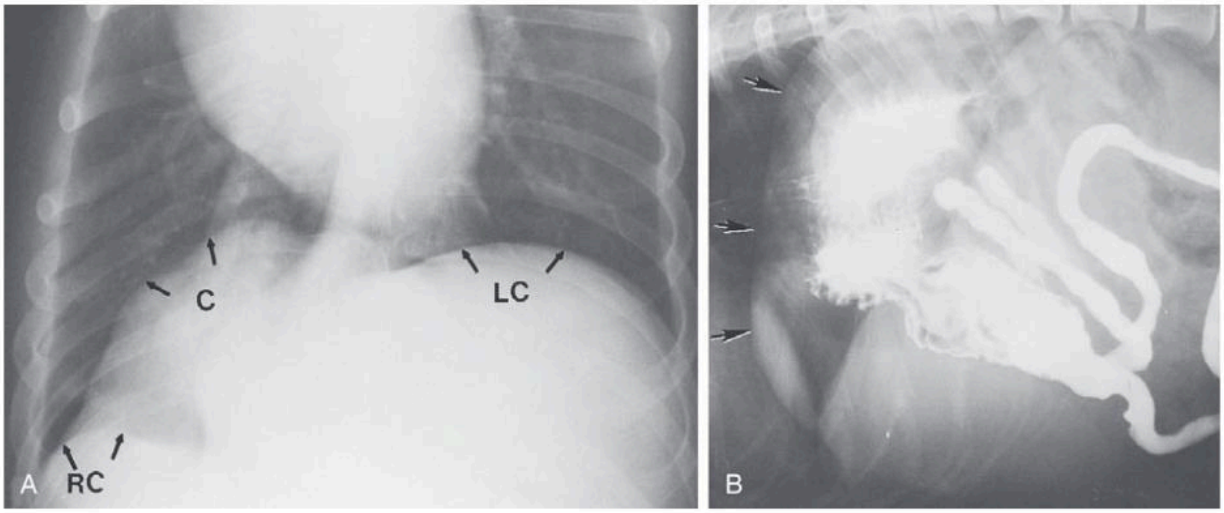


Fig. 32.25 Ventrodorsal (VD) **(A)** and lateral **(B)** radiographs of the cranial abdomen. Hemiparalysis of the left diaphragm is present. **A,** The left diaphragmatic crus (*LC*) is cranial to the right crus (*RC*). The cupula (*C*) and *RC* are in a normal inspiratory position. **B,** The cranial position of the left diaphragmatic crus (*black arrows*) causes the gastric cardia and fundus to be displaced cranially.

REFERENCES

1. Ganong W. *Review of Medical Physiology*. 22nd ed. New York: McGraw-Hill; 2005:652.
2. Baum H. The Lymphatic System of the Dog. Original German text translated by Mayer M, Bettin L, Bellamy K, Stamm I. USask Open Press; 2021. https://openpress.usask.ca/k9lymphaticsystem/.
3. Evans HE. *Miller's Anatomy of the Dog*. 4th ed. Philadelphia: Saunders; 2013:222.
4. Grandage J. The radiology of the dog's diaphragm. *J Small Anim Pract*. 1974;15(1):1–18.
5. Schulman J. Peritoneopericardial diaphragmatic hernia in a dog. *Mod Vet Pract*. 1979;60(4):306–308.
6. Garson HL, Dodman NH, Baker GJ. Diaphragmatic hernia: analysis of fifty-six cases in dogs and cats. *J Small Anim Pract*. 1980;21(9):469–481.
7. Farrow CS. Radiographic diagnosis of diaphragmatic hernia. *Mod Vet Pract*. 1983;64:979.
8. Silverman S, Ackerman N. Radiographic evaluation of abdominal hernias. *Mod Vet Pract*. 1977;58(9):781–785.
9. Wilson 3rd GP, Hayes Jr HM. Diaphragmatic hernia in the dog and cat: a 25-year overview. *Semin Vet Med Surg*. 1986;1(4):318–326.
10. Levine SH. Diaphragmatic hernia. *Vet Clin North Am Small Anim Pract*. 1987;17(2):411–430.
11. Stokhof AA, Wolvekamp WTC, Hellebrekers LJ, et al. Traumatic diaphragmatic hernia in the dog and cat. *Tijdschr Diergeneeskd*. 1986;111(Suppl 1):62S.
12. Rendano VT. Positive contrast peritoneography: an aid in the radiographic diagnosis of diaphragmatic hernia. *J Am Vet Radiol Soc*. 1979;20(67).
13. Stickle RL. Positive-contrast celiography (peritoneography) for the diagnosis of diaphragmatic hernia in dogs and cats. *J Am Vet Med Assoc*. 1984;185:325.
14. Williams J, Leveille R, Myer CW. Imaging modalities used to confirm diaphragmatic hernia in small animals. *Compend Small Anim*. 1998;20:1199.
15. Choi J, Kim H, Kim M, Yoon J. Imaging diagnosis – positive contrast peritoneographic features of true diaphragmatic hernia. *Vet Radiol Ultrasound*. 2009;50:185–187.
16. Lamb CR, Mason GD, Wallace MK. Ultrasonographic diagnosis of peritoneopericardial diaphragmatic hernia in a Persian cat. *Vet Record*. 1989;125(8):186.
17. Hay WH, Woodfield JA, Moon MA. Clinical, echocardiographic, and radiographic findings of peritoneopericardial diaphragmatic hernia in two dogs. *J Am Vet Med Assoc*. 1989;195(9):1245–1248.
18. Hashimoto A, Kudo T, Sawashima I. Diagnostic ultrasonography of noncardiac intrathoracic disorders in small animals. *Res Bull*. 1990;55:235.
19. Hodges RD, Tucker RL, Brace JJ. Radiographic diagnosis (peritoneopericardial diaphragmatic herniation in a dog). *Vet Radiol Ultrasound*. 1993;34:249.
20. Kim J, Kim S, Jo J, Lee S, Eom K. Radiographic and computed tomographic features of caval foramen hernias of the liver in 7 dogs: mimicking lung nodules. *J Vet Med Sci*. 2016;78(11):1693–1697.
21. Park J, Lee H, Jeong S. Caval foramen hernia in a dog: preoperative diagnosis and surgical treatment. *J. Vet Med Sci*. 2020;82(11):1602–1606.
22. Carb A. Symposium on surgical techniques in small animal practice. Diaphragmatic hernia in the dog and cat. *Vet Clin North Am*. 1975;5(3):477–494.
23. Wilson GP, Newton CD, Burt JK. A review of 116 diaphragmatic hernias in dogs and cats. *J Am Vet Med Assoc*. 1971;159(9):1142–1145.
24. Boudrieau RJ, Muir WW. Pathophysiology of traumatic diaphragmatic hernia in dogs. *Compend Contin Educ Pract Vet*. 1987;9:379.
25. Minihan AC, Berg J, Evans KL. Chronic diaphragmatic hernia in 34 dogs and 16 cats. *J Am Anim Hosp Assoc*. 2004;40(1):51–63.
26. Feldman DB, Bree MM, Cohen BJ. Congenital diaphragmatic hernia in neonatal dogs. *J Am Vet Med Assoc*. 1968;153(7):942–944.
27. Saperstein G, Harris S, Leipold HW. Congenital defects in domestic cats. *Feline Pract*. 1976;6(18).
28. Reimer SB, Kyles AE, Filipowisz DE, et al. Long-term outcome of cats treated conservatively or surgically for peritoneopericardial diaphragmatic hernia: 66 cases (1987–2002). *J Am Vet Med Assoc*. 2004;224(5):728–732.
29. Banz A, Gottfried S. Peritoneopericardial diaphragmatic hernia: a retrospective study of 31 cats and eight dogs. *J Am Anim Hosp Assoc*. 2010;46:398–404.
30. Björck GR, Tigerschiöld A. Peritoneo-pericardial diaphragmatic hernia in a dog. *J Small Anim Pract*. 1970;11(9):585–590.

31. Gourley IM, Popp JA, Park RD. Myelolipomas of the liver in a domestic cat. *J Am Vet Med Assoc.* 1971;158(12): 2053–2057.
32. Rendano VT, Parker RB. Polycystic kidneys and peritoneopericardial diaphragmatic hernia in the cat: a case report. *J Small Anim Pract.* 1976;17(7):479–485.
33. Weitz J, Tilley LP, Moldoff D. Pericardiodiaphragmatic hernia in a dog. *J Am Vet Med Assoc.* 1978;173(10): 1336–1338.
34. Evans SM, Biery DN. Congenital peritoneopericardial diaphragmatic hernia in the dog and cat. *Vet Radiol.* 1980;21:108.
35. Neiger R. Peritoneopericardial diaphragmatic hernia in cats. *Compend Contin Educ Pract Vet.* 1996;18:461.
36. Liptak JM, Bissett SA, Allan GS, et al. Hepatic cysts incarcerated in a peritoneopericardial diaphragmatic hernia. *J Feline Med Surg.* 2002;4(2):123–125.
37. Berry CR, Koblik PD, Ticer JW. Dorsal peritoneopericardial mesothelial remnant as an aid to the diagnosis of feline congenital peritoneopericardial diaphragmatic hernia. *Vet Radiol.* 1990;31:239.
38. Willard MD, Aronson E. Peritoneopericardial diaphragmatic hernia in a cat. *J Am Vet Med Assoc.* 1981;178(5):481–483.
39. Edwards MH. Selective vagotomy of the canine oesophagus: a model for the treatment of hiatal hernia. *Thorax.* 1976;31(2):185–189.
40. Teunissen GHB, Happ RP, Van Toorenburg J, et al. Esophageal hiatal hernia: case report of a dog and a cheetah. *Tijdschr Diergeneeskd.* 1978;103:742.
41. Ellison GW, Lewis DD, Phillips L, et al. Esophageal hiatal hernia in small animals: literature review. *J Am Anim Hosp Assoc.* 1984;20:783.
42. Ellis Jr FH. Controversies regarding the management of hiatus hernia. *Am J Surg.* 1980;139(6):782–788.
43. Stickle R, Sparschu G, Love N, et al. Radiographic evaluation of esophageal function in Chinese Shar Pei pups. *J Am Vet Med Assoc.* 1992;201(1):81–84.
44. Miles KG, Pope ER, Jergens AE. Paraesophageal hiatal hernia and pyloric obstruction in a dog. *J Am Vet Med Assoc.* 1988;193(11):1437–1439.
45. Gordon LC, Friend EJ, Hamilton MH. Hemorrhagic pleural effusion secondary to an unusual type III hiatal hernia in a 4-year-old Great Dane. *J Am Anim Hosp Assoc.* 2010;46(5):336–340.
46. Eivers C, Chicon Rueda R, Luiti T, Salavati Schmitz S. Retrospective analysis of esophageal imaging features in brachycephalic versus non-brachycephalic dogs based on videofluoroscopic swallowing studies. *J Vet Int Med.* 2019;33:1740–1746.
47. Anderson GM, Miller DA, Miller SW. Peripheral nerve sheath tumor of the diaphragm with osseous differentiation in a one-year-old dog. *J Am Anim Hosp Assoc.* 1999;35:319.
48. Steiner GM. Gastro-oesophageal reflux, hiatus hernia, and the radiologist with special reference to children. *Br J Radiol.* 1977;50(591):164–174.
49. Pollock S, Rhodes WH. Gastroesophageal intussusception in an Afghan hound. *J Am Vet Radiol Soc.* 1970;11(5).
50. Leib MS, Blass CE. Gastroesophageal intussusception in the dog: a review of the literature and a case report. *J Am Anim Hosp Assoc.* 1984;20:783.
51. Bath GF. Congenital diaphragmatic hiatus in a dog. *J S Afr Vet Assoc.* 1976;47(1):55–56.
52. Nicholson C. Defective diaphragm associated with umbilical hernia. *Vet Rec.* 1976;98(21):433–434.
53. Sawyer SL. Defective diaphragm associated with umbilical hernia. *Vet Rec.* 1976;98(24):490.
54. Swift BJ. Defective diaphragm associated with umbilical hernia. *Vet Rec.* 1976;98(25):511.
55. Valentine BA, Cooper BJ, Dietze AE, et al. Canine congenital diaphragmatic hernia. *J Vet Intern Med.* 1988;2(3): 109–112.
56. White JD, Tisdall PL, Norris JM, et al. Diaphragmatic hernia in a cat mimicking a pulmonary mass. *J Feline Med Surg.* 2003;5(3):197–201.
57. Cariou M, Shihab N, Kenny P, Baines S. Surgical management of an incidentally diagnosed true pleuroperitoneal hernia in a cat. *J Fel Med Surg.* 2009;11:873–877.
58. Wolff G. Familial congenital diaphragmatic defect: review and conclusions. *Hum Genet.* 1980;54(1):1–5.
59. Klosterman E, Heng H, Freeman L, Childress M. Transdiaphragmatic extension of a retroperitoneal lipoma into the intrathoracic extrapleural space via the lumbocostal trigone in a dog. *J Am Vet Med Assoc.* 2012;240:978–982.
60. Voges AK, Bertrand S, Hill RC, et al. True diaphragmatic hernia in a cat. *Vet Radiol Ultrasound.* 1997;38(2):116–119.
61. Vignoli AM, Toniato M, Rossi F, et al. Transient post-traumatic hemidiaphragmatic paralysis in two cats. *J Small Anim Pract.* 2002;43(7):312–316.
62. Greene CE, Basinger RR, Whitfield JB. Surgical management of bilateral diaphragmatic paralysis in a dog. *J Am Vet Med Assoc.* 1988;193(12):1542–1544.
63. Mainwaring CJ. Post-traumatic contraction of the diaphragm synchronous with the heartbeat in a dog. *J Small Anim Pract.* 1988;32:329.
64. Cooper BJ, Winand NJ, Stedman H, et al. The homologue of the Duchenne locus is defective in X-linked muscular dystrophy of dogs. *Nature.* 1988;334(6178):154–156.
65. Berry CR, Gaschen FP, Ackerman H. Radiographic and ultrasonographic features of hypertrophic feline muscular dystrophy in two cats. *Vet Radiol Ultrasound.* 1992;33:357.
66. Gaschen FP, Haugh PG, Swendrowske MA. Hypertrophic feline muscular dystrophy. A unique clinical expression of dystrophin deficiency. *Feline Pract.* 1994;22(23).
67. Brumitt JW, Essman SC, Kornegay JN, et al. Radiographic features of Golden Retriever muscular dystrophy. *Vet Radiol Ultrasound.* 2006;47(6):574–580.
68. Jones BR, Brennan S, Mooney CT, et al. Muscular dystrophy with truncated dystrophin in a family of Japanese Spitz dogs. *J Neurol Sci.* 2004;217(2):143–149.

ELECTRONIC RESOURCES

Additional information related to the content in Chapter 32 can be found online at eBooks.Health.Elsevier.com.

- Chapter Quiz
- Videos

Video 32.1 Video loop of a 3-year-old English bulldog with chronic regurgitation for 1 year. The video shows cranial herniation of the stomach into the caudal thorax after a food bolus passes into the stomach. This is consistent with a sliding hiatal hernia.

Video 32.2 Ultrasound video loop of a 1-year-old cat. The owners noticed wheezing and occasional vomiting. Radiographs (eFig. 32.8) show a soft tissue and fat opacity in the caudodorsal thorax, which were interpreted to be either a diaphragmatic hernia or paraesophageal hernia. Ultrasound showed fat and the stomach herniating through the diaphragm. Surgery confirmed a paraesophageal hernia including the stomach and fat.

CHAPTER 33

Canine and Feline Mediastinum

Federica Morandi • Donald E. Thrall

NORMAL ANATOMY

There is one pleural sac on each side of the thoracic cavity, and the mediastinum is the space between them (Table 33.1). The pleural layer bounding the mediastinum on each side is termed *mediastinal pleura.* Other components of the pleural sac are the *costal parietal pleura*, which is attached to the thoracic wall; the *diaphragmatic parietal pleura*, which is attached to the diaphragm; and the *visceral pleura*, which covers the lung. All of these pleural layers are contiguous. The connection between the mediastinal and visceral pleural layers occurs at the hilus of the lung, where the mediastinal pleura is reflected onto the surface of the lung as visceral pleura (Figs. 33.1 and 33.2).

The mediastinum extends from the thoracic inlet to the diaphragm and is located mainly in the midsagittal plane, thereby dividing the thoracic cavity into right and left halves (see Figs. 33.1 and 33.2). The mediastinum is arbitrarily subdivided into a cranial portion, cranial to the heart; a middle portion at the level of, and containing the heart; and a caudal portion, caudal to the heart. The mediastinum is also divided into dorsal and ventral portions by a dorsal plane coursing through the tracheal bifurcation. The mediastinum is not a closed space. It communicates cranially with the fascial planes of the neck by way of the mediastinal structures passing through the thoracic inlet, such as the esophagus and trachea and some major vessels. Caudally, the mediastinum communicates with the retroperitoneal space through the aortic hiatus. These communications enable the spread of mediastinal disease to the neck and retroperitoneal space, and vice versa. The mediastinum does not normally communicate with the peritoneal cavity.

In most dogs and cats, the mediastinal pleural layers do not form an anatomic barrier between the left and right pleural spaces, because normal mediastinal pleura contain fenestrations. Thus, unilateral pleural fluid or gas is not usually contained to one side by the mediastinum. For example, 22 of 24 dogs having air injected into one pleural space quickly developed bilateral pneumothorax.[1] Pleural fluid or gas may remain unilateral if the mediastinal pleura is not fenestrated; if the normal fenestrations become closed because of inflammation or plugging, such as with purulent or neoplastic effusion; or if the pleural fluid is too viscous to pass through a normal fenestration.

Of all of the structures in the mediastinum (see Table 33.1), only the heart, trachea, caudal vena cava, aorta, and, in young animals, the thymus are visible normally. Occasionally, a portion of the normal esophagus may be seen (see Chapter 30). The other mediastinal structures are not seen normally, because they are either too small or there is insufficient interposed fat to provide contrast, leading to border effacement.

The cranial mediastinum immediately ventral to the trachea normally is of homogeneous soft tissue opacity in a lateral radiograph. The structures in this portion of the mediastinum (left subclavian artery, brachiocephalic trunk, cranial vena cava mediastinal lymph nodes) are not visible individually because they are in contact with each other and there is insufficient interposed fat to provide contrast (Fig. 33.3). In lateral radiographs, the mediastinum just ventral to the trachea is thicker and thus more radiopaque than the mediastinum just dorsal to the sternum (Fig. 33.4).

In ventrodorsal (VD) or dorsoventral (DV) thoracic radiographs, most of the cranial mediastinum is superimposed on the spine in the midsagittal plane (Fig. 33.5). In obese patients, particularly brachycephalic patients, the cranial mediastinum is increased in width because of fat accumulation, and this can be misdiagnosed as a pathologic mass (Fig. 33.6). Contrary to a mediastinal mass, the borders of the mediastinum tend to remain straight with mediastinal fat only, whereas they tend to be laterally convex in the presence of a mediastinal mass. Other imaging modalities, such as ultrasound or computed tomography (CT), may be necessary to confirm that fat deposition is the cause of increased mediastinal width in obese patients.

The mediastinum normally deviates from the midline in three locations: (1) the cranioventral mediastinal reflection, (2) the caudoventral mediastinal reflection, and (3) the vena caval mediastinal reflection (*plica venae cavae*). The first two are visible in thoracic radiographs of many dogs and cats, although not universally. The plica venae cavae is not seen radiographically in normal dogs or cats.

The cranioventral mediastinal reflection appears in VD or DV radiographs as a curving radiopaque line, just to the left of midline, extending from approximately T1 or T2 to the region of the main pulmonary artery. The concave side of the line is to the right (see Figs. 33.4 and 33.5). The cranioventral mediastinal reflection is caused by extension of the apex of the right cranial lobe across midline, pushing the mediastinum to the left (see Fig. 33.4). The thickness of the cranioventral mediastinal reflection is affected by the amount of fat it contains (see Fig. 33.6). On the lateral view, the cranioventral mediastinal reflection is often identified approximately midway between the thoracic inlet and the heart (see Fig. 33.3). The thymus lies in the cranioventral mediastinal reflection and can sometimes be identified in VD or DV radiographs of young animals as a triangular soft tissue opacity (Fig. 33.7). The normal thymus is in close contact with the cranial contour of the cardiac silhouette and may lead to a false impression of cardiomegaly when visible in a lateral projection. The internal thoracic arteries and veins are also located in the cranioventral mediastinal reflection and are not visible radiographically.

The caudoventral mediastinal reflection is seen only on VD or DV radiographs, but not in lateral views. It is created by extension of the accessory lobe of the right lung across midline to the left, thereby pushing the mediastinum to the left

Table • 33.1

Mediastinal Organs.

ORGAN	CRANIAL MEDIASTINUM	MIDDLE MEDIASTINUM	CAUDAL MEDIASTINUM
Cranial vena cava	x		
Thymus	x		
Sternal lymph nodes	x		
Aortic arch	x		
Brachiocephalic artery	x		
Left subclavian artery	x		
Mediastinal lymph nodes	x		
Trachea	x	x	
Right and left vagosympathetic trunk	x	x	
Dorsal intercostal arteries and veins	x	x	x
Internal thoracic arteries and veins	x	x	x
Esophagus	x	x	x
Thoracic duct	x	x	x
Right and left sympathetic trunks	x	x	x
Right and left phrenic nerves	x	x	x
Descending aorta		x	x
Bronchoesophageal arteries and veins		x	x
Azygos vein		x	x
Heart		x	
Tracheobronchial lymph nodes		x	
Main pulmonary artery		x	
Main pulmonary veins		x	
Principal bronchi		x	
Caudal vena cava			x
Right and left vagus nerves			x

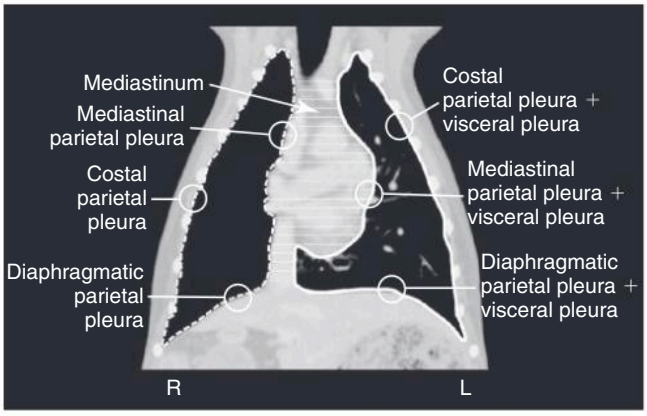


Fig. 33.1 Dorsal plane computed tomography (CT) image of a canine thorax at the level of the base of the heart. The right lung and thus the visceral component of the right pleural sac have been photographically removed from the image. Thus, the *dotted line* in the right hemithorax represents the parietal portion of the right pleural sac. The designation of mediastinal versus costal versus diaphragmatic parietal pleura is based on the location of the pleural layer, and these pleural layers are contiguous. The left lung has not been photographically removed from the image. As the left lung is covered in visceral pleura, the *solid line* designates contact between the visceral and parietal pleural layers of the left pleural sac. The pleural space is the potential space between the parietal and visceral pleural layers. Under normal circumstances the parietal and visceral pleural layers are in contact and the pleural space is only a potential space. The mediastinum, shown here with *horizontal white lines*, is a real space and is located between the two pleural sacs. *L*, Left; *R*, right.

(see Fig. 33.2). The caudoventral mediastinal reflection consists of four pleural layers, which are, from right to left: (1) the visceral pleura of the accessory lobe, (2) the mediastinal parietal pleura of the right pleural sac, (3) the mediastinal parietal pleura of the left pleural sac, and (4) the visceral pleura of the left caudal lobe (see Fig. 33.2). The caudoventral mediastinal reflection appears as a relatively straight radiopaque line in the caudal left hemithorax, extending from the region of the cardiac apex in a caudolateral direction toward the gastric fundus (Fig. 33.8). The caudoventral mediastinal reflection has been incorrectly termed the *phrenicopericardial ligament* (also called the *cardiophrenic* or *sternopericardiac ligament*); however, this ligament, which is a continuation of the apex of the fibrous pericardium and is contained within the caudoventral mediastinum, is not visible radiographically as an individual structure.[2] As for the cranioventral mediastinal reflection, the thickness of the caudoventral mediastinal reflection depends on the amount of fat it contains (Fig. 33.9).

PATHOLOGIC MEDIASTINAL CONDITIONS

Mediastinal abnormalities can be divided into three general classifications: (1) mediastinal shift, (2) mediastinal mass(es), and (3) pneumomediastinum.

Mediastinal Shift

The most common causes of an ipsilateral mediastinal shift are lung atelectasis caused by reduced ventilation or prolonged lateral recumbency. Therefore, mediastinal shift is often seen in

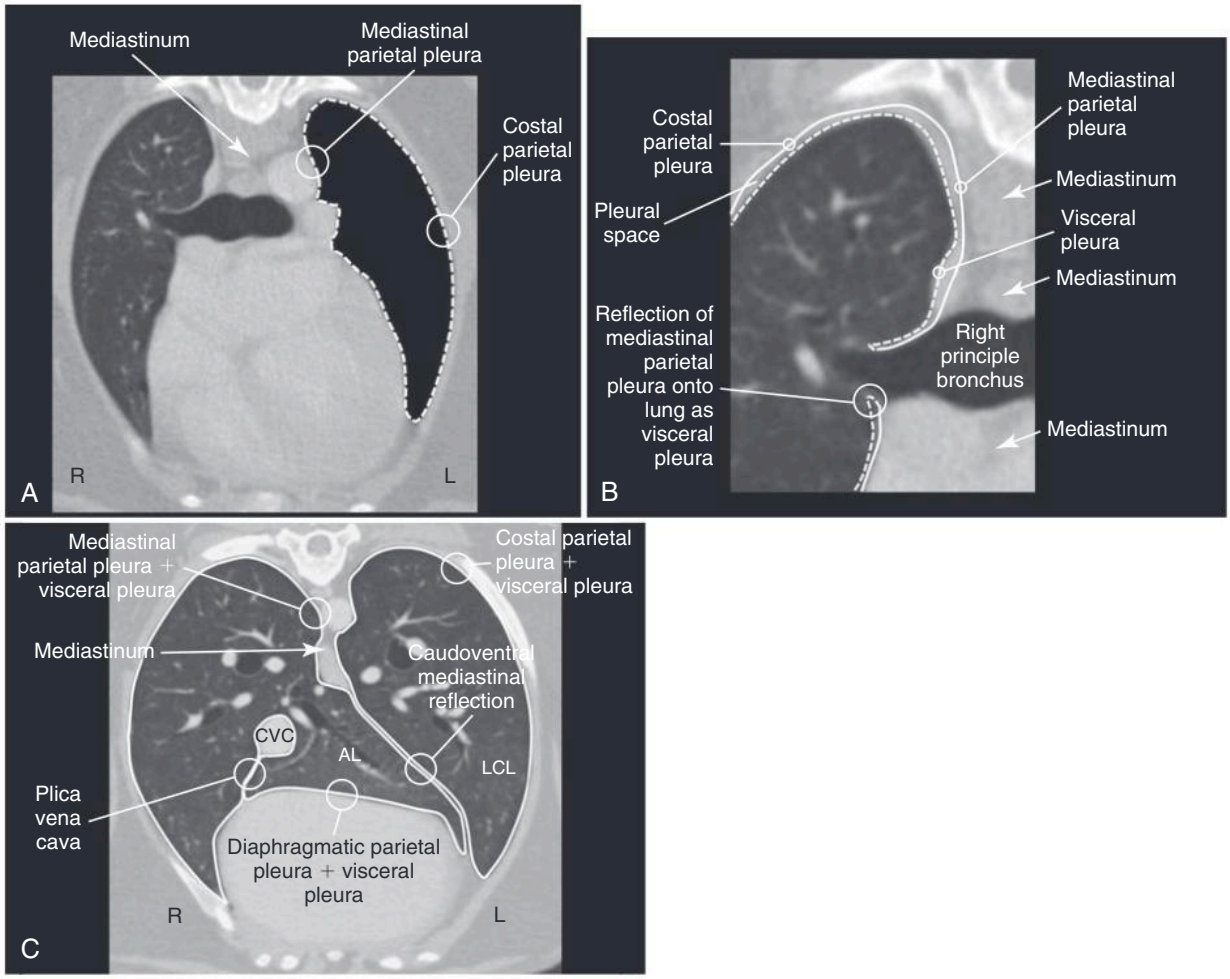


Fig. 33.2 Transverse plane computed tomography (CT) images of a canine thorax. **A,** Just caudal to the tracheal bifurcation. The left lung has been photographically removed from the image to show the relationship of the mediastinal and costal components of the parietal pleural sac (*dotted line*). The diaphragmatic parietal pleura is not visible in **A,** because the diaphragm is caudal to this slice. **B,** Close-up of the right hilus. At the hilus the mediastinal parietal pleura reflects onto the surface of the lung where it becomes visceral pleura. The space between the visceral and parietal pleural layers is the pleural space. The pleural space is only a potential space in normal animals; here a small space is shown for illustrative purposes but this does not exist normally in vivo. The mediastinum is the space between the left and right pleural sacs (*white arrows* in **B**). **C** is a transverse slice in the caudal thorax, caudal to the tracheal bifurcation. The *solid lines* designate contact between the visceral and parietal pleural layers. The pleural space is the potential space between the parietal and visceral pleural layers. The mediastinum is the space between the two pleural sacs. A fold of pleura, the plica vena cava, encircles the caudal vena cava (*CVC*). The plica vena cava is not seen radiographically. The accessory lobe (*AL*) pushes the mediastinal pleura to the left, forming the caudoventral mediastinal reflection. There are then four pleural layers making up the caudoventral mediastinal reflection; from right to left these are (1) visceral pleura from accessory lobe, (2) right mediastinal parietal pleura, (3) left mediastinal parietal pleura, and (4) visceral pleura from left caudal lobe (*LCL*). *L*, Left; *R*, right.

animals under general anesthesia. Atelectasis results in decreased lung volume and increased lung opacity, and the heart will be shifted toward the abnormally opaque lung. Distinguishing normal atelectatic from diseased atelectatic lung is usually not possible radiographically. A contralateral mediastinal shift occurs as a result of a unilateral increase in lung volume, the presence of an intrathoracic mass, or unilateral increased pleural pressure. A mediastinal shift is detected in VD or DV radiographs by noting a change in the position of visible mediastinal organs or the position of mediastinal reflections. Displacement of the heart to the left or right is the most reliable sign of a mediastinal shift (Fig. 33.10). Suboptimal patient positioning due to rotation causes deviation of the sternum to the right or left and the false impression of a mediastinal shift. Detection of a mediastinal shift is often the first clue of a thoracic abnormality (Fig. 33.11).

Mediastinal Masses

Mediastinal masses are common, and the specific etiology is rarely determined on radiographs alone; typically, the use of another imaging modality or an aspirate or biopsy is needed. However, the portion of the mediastinum where the mass resides can help to formulate and rank potential differential diagnoses (Table 33.2).

The VD or DV projection is usually more useful than the lateral view in deciding whether an intrathoracic mass is

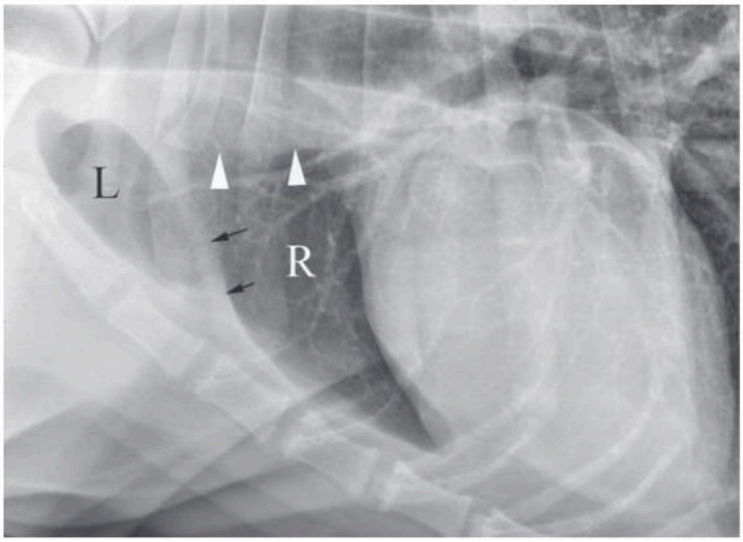


Fig. 33.3 Left lateral radiograph of the thorax of a normal dog. The homogeneous opacity ventral to the trachea (*white arrowheads* indicate ventral margin of opacity) is part of the cranial mediastinum. Although several different organs are in this part of the mediastinum (e.g., left subclavian artery, brachiocephalic trunk, and cranial vena cava), they cannot be discerned because they are in contact with each other, and there is not enough intervening fat to provide contrast. The mediastinum extends from the ventral aspect of the trachea to the sternum, but it is more radiopaque immediately ventral to the trachea because it is thickest at this location (see Fig. 33.4). Note also the cranioventral mediastinal reflection (*black arrows*) between the cranial portion of the left cranial lobe (*L*) and the right cranial lobe (*R*) (see Fig. 33.4).

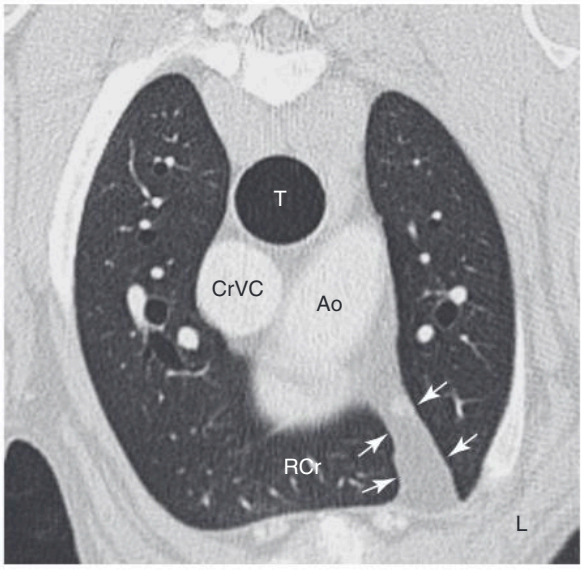


Fig. 33.4 Transverse computed tomography (CT) image of the canine thorax just cranial to the base of the heart. Note the greater thickness of the mediastinum just dorsal and ventral to the trachea compared to just dorsal to the sternum. The greater thickness of the dorsal mediastinum accounts for the homogeneous opacity seen ventral to the trachea in lateral thoracic radiographs (see Fig. 33.3). Note the cranial vena cava (*CrVC*) and aorta (*Ao*) ventral to the trachea (*T*). Insufficient fat is present for these vessels to be seen in radiographs, but the greater inherent contrast resolution of CT images allows them to be seen with this modality. Also note how the ventral aspect of the mediastinum is pushed to the left (*white arrows*) by the right cranial lung lobe (*RCr*). This is the *cranioventral mediastinal reflection*, which can often be seen radiographically, as in Figs. 33.3 and 33.5.

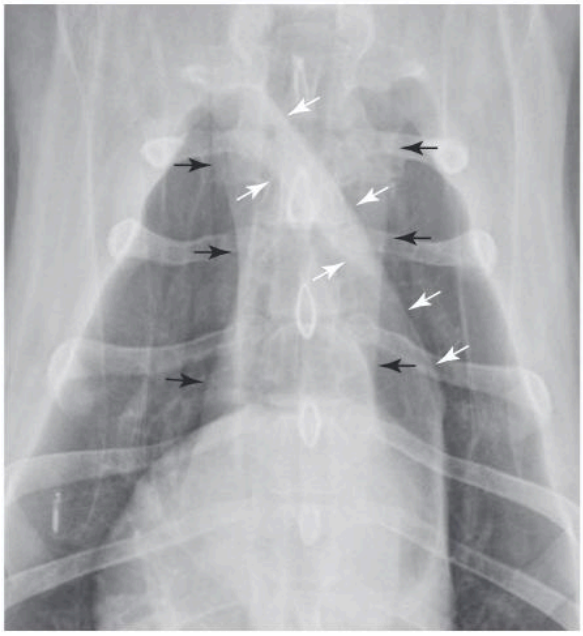


Fig. 33.5 Ventrodorsal (VD) radiograph of the cranial aspect of the thorax of a normal dog. The cranial mediastinum is superimposed on the cranial aspect of the thoracic spine; it is relatively indistinct, but the lateral margins of the thicker dorsal aspect of the mediastinum can be discerned (*black arrows*). Note the cranioventral mediastinal reflection between the right cranial lobe and the cranial part of the left cranial lobe (*white arrows*). See Fig. 33.3 for the appearance of this reflection in the lateral view and Fig. 33.4 for an illustration of the right lung pushing the mediastinum to the left to create the reflection.

located in the mediastinum versus the lung or the thoracic wall. Mediastinal origin of a thoracic mass should be considered if the mass lies on, or adjacent to, the midline; if the mass location is consistent with the cranioventral or caudoventral mediastinal reflections; or if the mass causes deviation of another mediastinal structure. Pulmonary masses can, at times, cause displacement of mediastinal structures, but this is not as common as with a mediastinal mass. Mediastinal masses are rarely completely outlined by gas, as a lung mass would be, because a mediastinal mass is in contact with other soft tissue structures within the mediastinum.

Cranioventral Mediastinal Masses

Masses in the cranioventral aspect of the mediastinum are common. Mild enlargement of the sternal lymphocenter is perhaps the smallest detectable cranioventral mediastinal mass; this relates to the isolated location of the sternal lymphocenter in the ventral aspect of the cranial mediastinum, dorsal to the second to third sternebra. The ventral mediastinum is thin in this region, and there are no other structures to silhouette with an enlarged sternal lymph node.

The sternal lymphocenter is usually represented by paired left and right cranial sternal lymph nodes in the dog, and by a

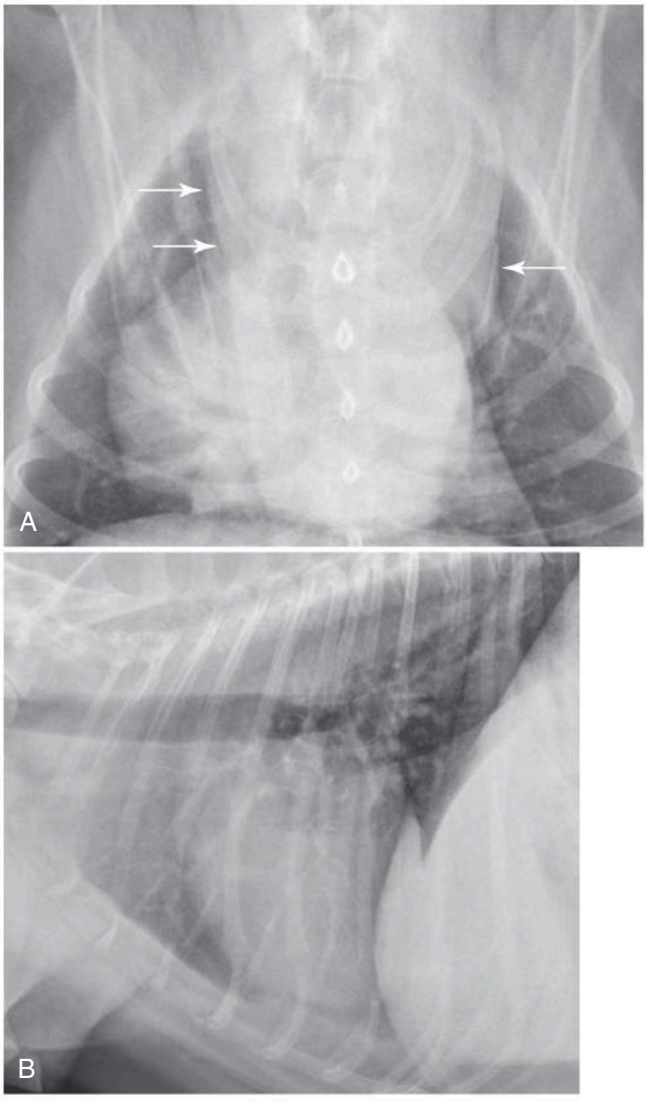


Fig. 33.6 **A,** Dorsoventral (DV) radiograph of the cranial aspect of the thorax of an obese dog. The cranial mediastinum contains a large amount of fat and as a result is widened (*white arrows*). Care must be taken to avoid misinterpreting a wide mediastinum in an obese animal as a mediastinal mass. Ultrasound or computed tomography (CT) imaging may be necessary to make a definitive assessment. **B,** Lateral radiograph of the same dog as in **A**. There is no evidence of a mediastinal mass. Had there been a mass in the mediastinum as large as suggested from the ventrodorsal (VD) view, dorsal displacement of the trachea would have been expected, which is not seen here. The large amount of fat in the cranial mediastinum has, however, increased the opacity of the cranioventral aspect of the thoracic cavity in the lateral view nonspecifically.

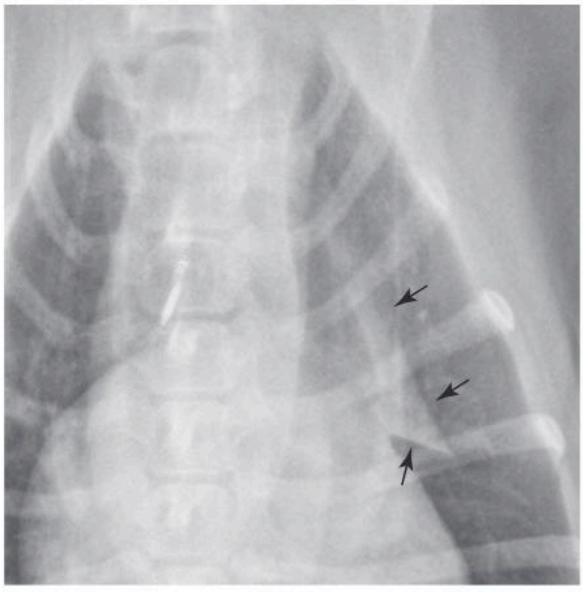


Fig. 33.7 Ventrodorsal (VD) radiograph of the thorax of a normal young dog. The thymus, located in the cranioventral mediastinal reflection, has not involuted completely and appears as a sail-shaped opacity cranial and to the left of the cardiac base (*black arrows*).

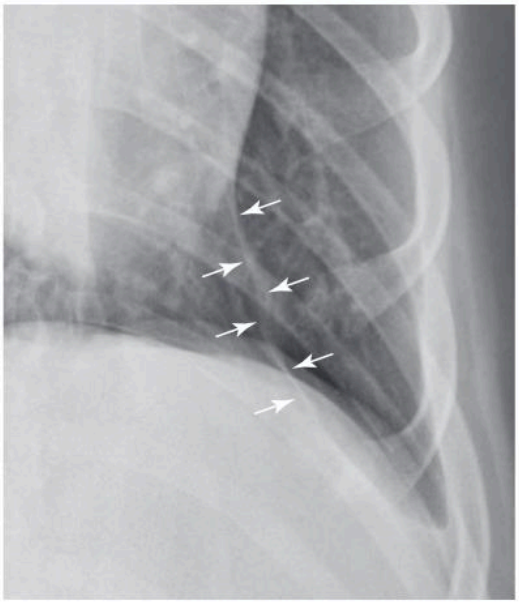


Fig. 33.8 Ventrodorsal (VD) radiograph of the caudal thorax of a dog with a normal body habitus. The caudoventral mediastinal reflection is a thin opacity extending from the region of the cardiac apex caudolaterally to the left (*white arrows*).

single lymph node in the cat. The dog occasionally has only a single median sternal lymph node; in rare instances, a double lymph node may be present on one side. Afferent lymphatics to the sternal lymph node arise in the abdominal wall and perforate the diaphragm near the middle of the costal arch, and run deep to the pleura in the costodiaphragmatic recess. The sternal lymphocenter receives tributaries from the ribs, sternum, serous membranes, thymus, adjacent muscles, peritoneal cavity, and mammary glands.[3,4] A fusiform opacity up to 3 cm in length, presumably representing a normal sternal lymph node, can be seen in the right lateral view of some normal dogs[5]; this is commonly misinterpreted as a mass.

Although sternal lymph node enlargement may be primary, as with lymphoma, more often it is a sign of abdominal disease, as with abdominal fluid, peritonitis, or peritoneal tumor seeding.[6] Thus, if sternal lymph node enlargement is seen, abdominal disease should be investigated. Sternal lymph node enlargement appears as an isolated small soft tissue mass dorsal to the second to third sternebra, and is best seen on a lateral projection (Fig. 33.12). The ventral margin of an enlarged sternal lymph node has a broad base of contact with the sternum on lateral views (see Fig. 33.12). A mildly enlarged sternal lymph node can appear slightly different in size and shape in the left versus right lateral view due to different orientations with respect to the primary x-ray beam (see Fig. 33.12). An enlarged sternal lymph node is not as conspicuous in VD or DV

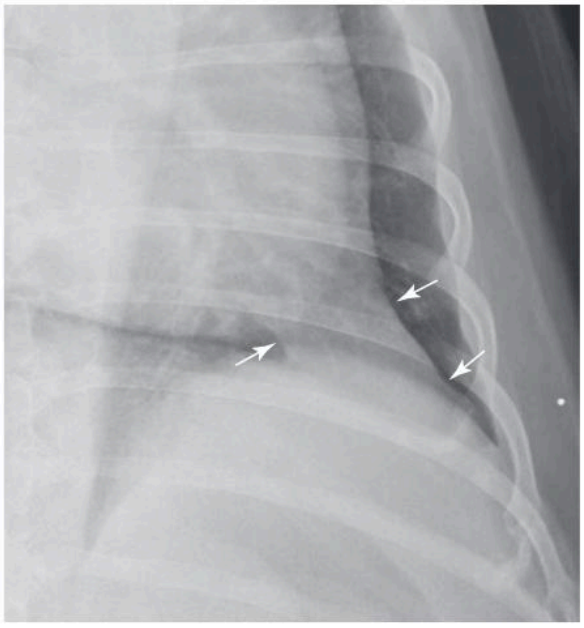


Fig. 33.9 Ventrodorsal (VD) radiograph of the caudal aspect of the thorax of an obese dog. The caudoventral mediastinal reflection is thick as a result of fat deposition (*white arrows*). Compare its thickness in this radiograph with that in Fig. 33.8.

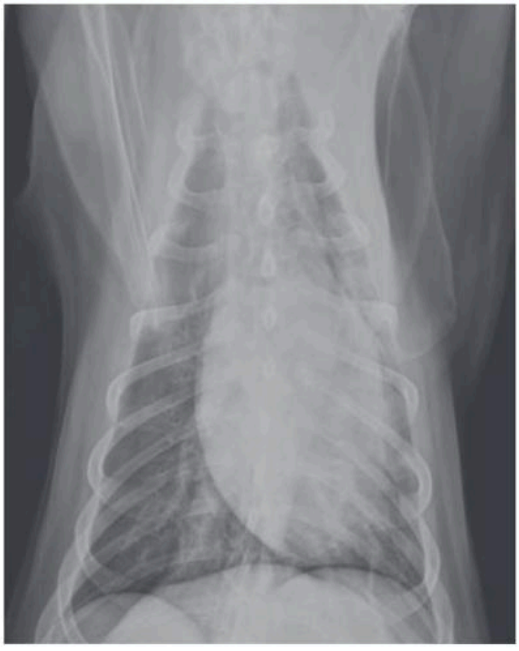


Fig. 33.10 Ventrodorsal (VD) thoracic radiograph of a dog. The heart and therefore the mediastinum are shifted to the left, and there is a generalized increase in opacity of the left lung. This dog is paralyzed, and continued left recumbency has resulted in atelectasis and a mediastinal shift toward that side. One cannot tell for certain that there is not disease in the left lung, but given the history and mediastinal shift, the lung opacity on the left is most likely due to atelectasis.

radiographs as it is in lateral radiographs, but can be sometimes seen as a focal widening of the cranial mediastinum just caudal to the thoracic inlet (Fig. 33.13, eFig. 33.1).

A mediastinal cyst, more common in cats than in dogs, is another cause of a relatively small cranioventral mediastinal

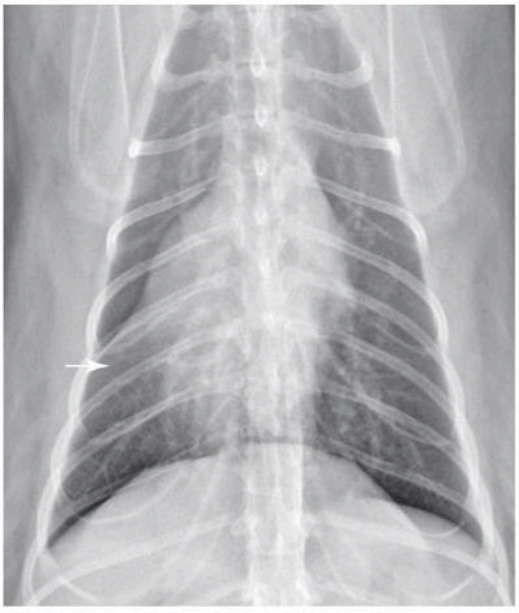
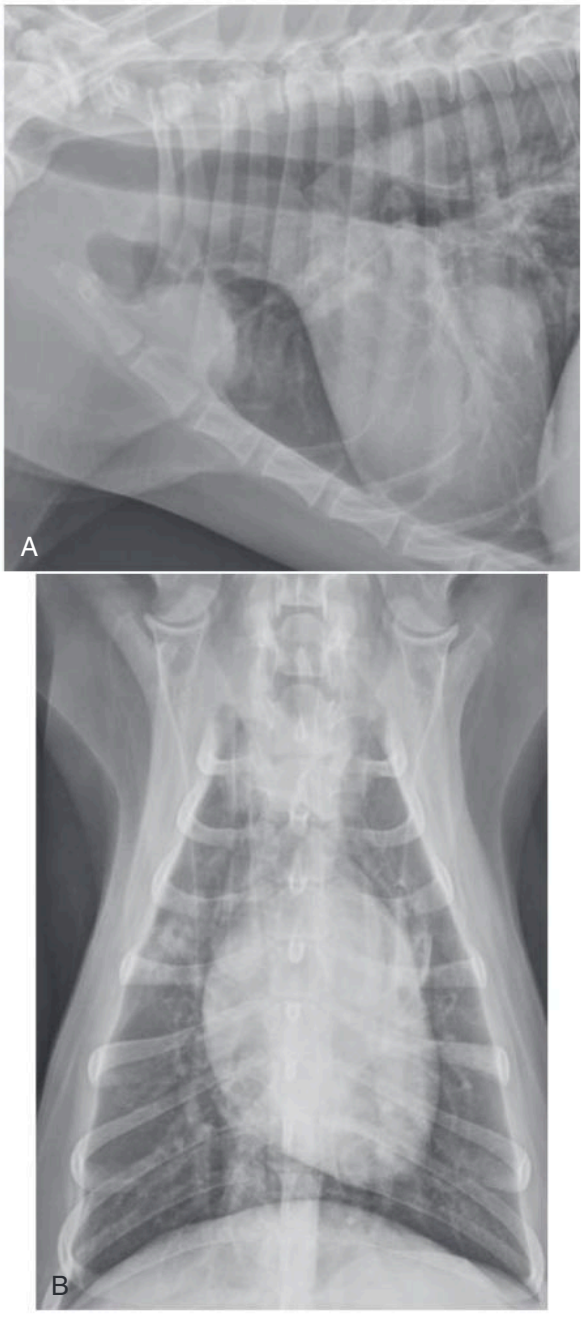


Fig. 33.11 Ventrodorsal (VD) radiograph of a cat with mediastinal shift, signified by malpositioning of the heart to the right. The cardiac malpositioning is the most conspicuous abnormality in the image. On close inspection, there is increased opacity of the right middle lung lobe (*white arrow*) with partial border effacement of the right aspect of the cardiac silhouette. This increased lung opacity is caused by partial collapse of the right middle lobe due to bronchial obstruction associated with feline asthma. Right lung atelectasis from prolonged recumbency or reduced ventilation caused by sedation would have this identical appearance. Cardiac displacement can be the first radiographic clue of intrathoracic disease.

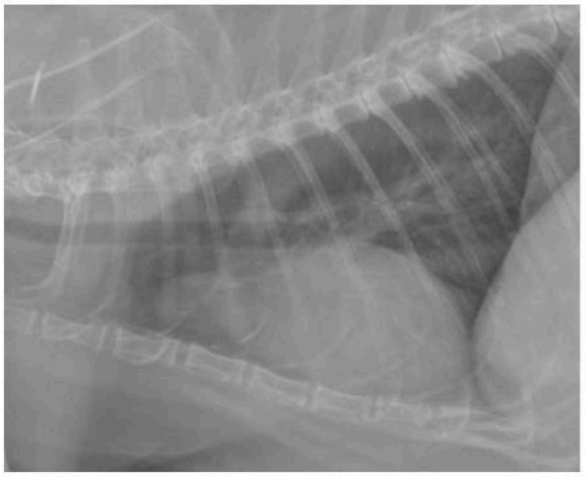
mass. Mediastinal cysts are typically located more caudally than the sternal lymphocenter, and more ventral than the cranial mediastinal lymph nodes (Fig. 33.14, eFig. 33.2). Mediastinal cysts are usually an insignificant incidental finding, but they may enlarge slowly and cause compression of neighboring structures, and require drainage or excision.[7] Ultrasound imaging is useful in establishing the cystic nature of the mass versus the solid nature of enlarged lymph nodes or thymoma (see Fig. 33.14).

With other cranioventral mediastinal masses, which are typically larger than sternal lymphadenomegaly or mediastinal cysts, opacification of the entire cranioventral mediastinum and border effacement of the cranial margin of the heart is commonly seen in lateral views. In VD or DV views, the cranial mediastinum appears wide, and there is border effacement of the cranial margin of the heart; the extent of these changes depends on the size of the mass. The trachea may be displaced dorsally, again depending on the size of the mass (Figs. 33.15 and 33.16, eFig. 33.3). The largest cranioventral mediastinal masses have the same features as moderately sized cranioventral masses, with the additional presence of more pronounced tracheal displacement, and outright cardiac displacement (Fig. 33.17, eFig. 33.4).

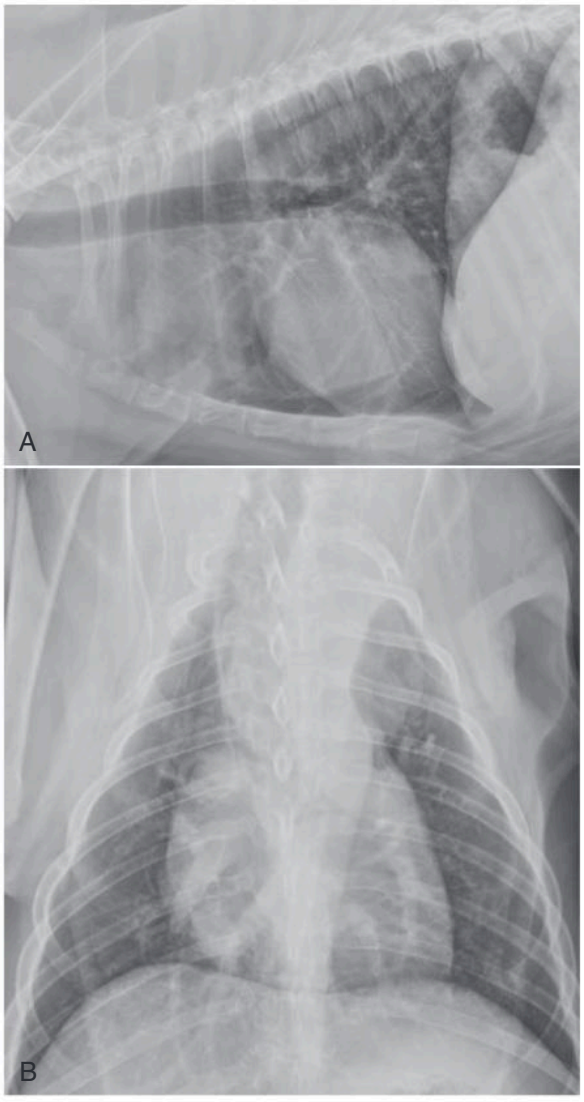
Because enlarged cranial mediastinal lymph nodes are a common cause of a cranioventral mediastinal mass, some understanding of their function is important. The cranial mediastinal lymph nodes vary in number, shape, and size, and most lie along the cranial vena cava and brachiocephalic, left subclavian, and costocervical arteries, just ventral to the trachea. Afferent lymphatics come from the muscles of the neck, thorax and abdomen, scapula, last six cervical vertebrae, thoracic vertebrae, ribs, trachea, esophagus, thyroid gland, thymus, mediastinum, costal pleura, heart, and aorta. The cranial mediastinal



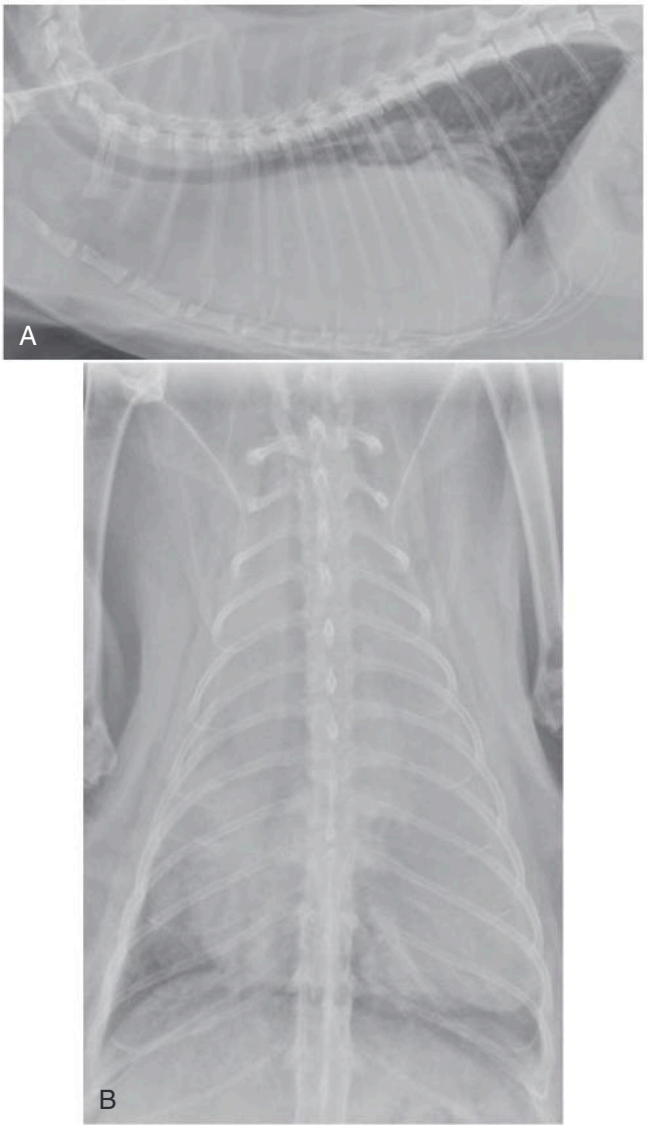
eFig. 33.1 Lateral **(A)** and ventrodorsal (VD; **B**) radiographs of the thorax of a dog with lymphoma and enlargement of the sternal lymph node. There is a broad-based soft tissue mass dorsal to the second sternebral in **A** and focal widening of the cranial mediastinum in **B**.



eFig. 33.2 Left lateral radiograph of a cat with a cranial mediastinal cyst. A well-delineated round soft tissue opacity is present cranial to the cardiac silhouette. Presence of a cyst was confirmed ultrasonographically.



eFig. 33.3 Left lateral **(A)** and dorsoventral (DV; **B**) radiographs of a dog with a mass in the cranioventral mediastinum. There is increased soft tissue opacity in the cranial mediastinum ventral to the trachea, with a lobulated appearance. In the DV projection the mediastinum is widened with a convex lateral contour.



eFig. 33.4 Lateral **(A)** and ventrodorsal (VD; **B**) radiographs of a cat with a large cranial mediastinal mass. The mass causes dorsal displacement of the trachea and caudodorsal displacement of the tracheal bifurcation and cardiac silhouette. The trachea is displaced to the right in the VD projection. The histologic diagnosis was thymoma.

Table • 33.2

Causes of Mediastinal Masses.

CAUSE OF MASS	MEDIASTINAL LOCATION
Vascular ring anomaly (segmental cranial esophagomegaly)	Craniodorsal*
Neurogenic tumor	Craniodorsal or dorsal
Hematoma	Variable, but may have a craniodorsal predilection
Mediastinal lymphadenopathy	Cranioventral
Sternal lymphadenopathy	Cranioventral
Thymoma	Cranioventral
Mediastinal cyst (branchial cyst)	Cranioventral
Ectopic thyroid or parathyroid tumor	Cranioventral, perihilar
Mediastinal abscess—usually caused by esophageal perforation	Cranioventral, caudoventral, caudal, dorsal
Hilar lymphadenopathy	Middle
Heart base mass†	Middle, cranioventral to tracheal bifurcation
Mid-esophageal foreign body	Middle, dorsal to tracheal bifurcation
Paraspinal tumor	Dorsal
Generalized megaesophagus	Dorsal
Spirocerca lupi	Caudodorsal
Caudal esophageal mass or foreign body	Caudodorsal
Mediastinal diaphragmatic hernia	Caudoventral
Hiatal hernia	Caudal to caudodorsal
Diaphragmatic eventration	Caudal, caudoventral, caudodorsal

*Marked segmental esophagomegaly may lead to a cranioventral mediastinal mass as the enlarged esophagus gravitates ventral to the trachea.
†Heart base mass as used here is nonspecific and could apply to a tumor of the base of the heart, a right atrial tumor, or enlargement of the main pulmonary artery.

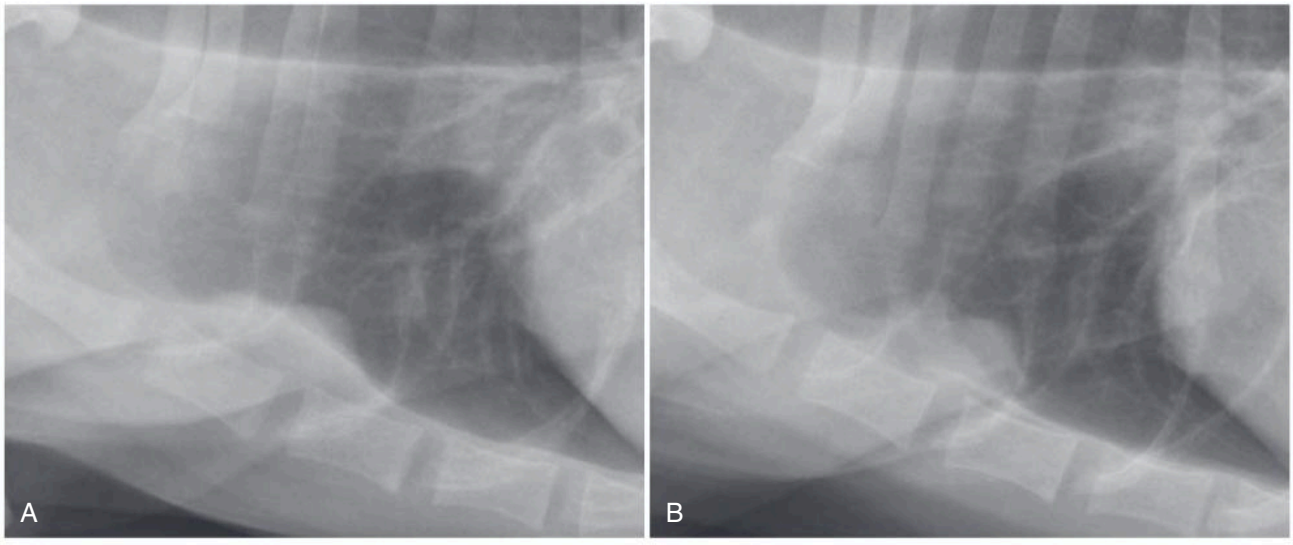


Fig. 33.12 Left **(A)** and right **(B)** lateral radiographs of a dog with mild enlargement of the sternal lymph node. The enlarged lymph node appears as a small mass dorsal to the second and third sternebra. Finding a slightly different size and shape of an enlarged sternal lymph in left versus right lateral views is common. Note the typical broad base of contact of the ventral margin of the sternal lymph node with the thoracic wall.

lymph nodes also receive efferent lymphatics from the intercostal, sternal, middle, and caudal deep cervical, tracheobronchial, and pulmonary lymph nodes.[3] The cranial mediastinal lymph nodes do not enlarge secondary to abdominal disorders.

The thymus is another common source of a cranioventral mediastinal mass. As previously noted, the normal thymus can be seen in young dogs as a triangular or sail-like opacity in the cranioventral mediastinal reflection in VD or DV views (see Fig. 33.7). The thymus undergoes involution as animals age, and should be radiographically inconspicuous in most dogs by approximately 1 year of age. Rebound thymic hyperplasia, in which the thymus atrophies during illness, and undergrows excessive regrowth in the recovery phase, results in thymic enlargement with normal shape, and has been occasionally

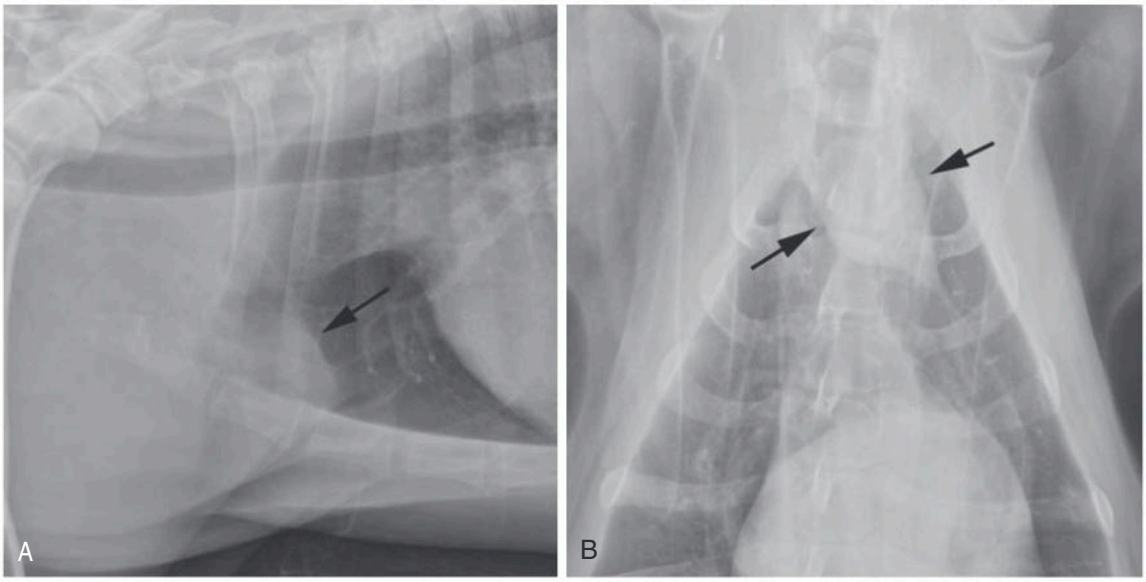


Fig. 33.13 Lateral **(A)** and ventrodorsal (VD; **B**) radiographs of the thorax of a dog with enlargement of the sternal lymph node. There is a soft tissue mass dorsal to the cranial aspect of the sternum in **A** (*black arrow*) and widening of the cranial mediastinum in **B** (*black arrows*). The diagnosis was histiocytic sarcoma. Note the broad ventral base of contact of the enlarged sternal lymph node with the thoracic wall in the lateral view.

described in animals.[8] A thymoma can reach enormous proportions in the cranioventral mediastinum and then extend caudolaterally, adjacent to the heart, as in Fig. 33.17 and eFig. 33.4.

Occasionally, cranioventral pulmonary masses located near midline can be difficult to differentiate from cranial mediastinal masses; in such cases, CT is needed to determine the exact origin of the mass.

Dorsal Mediastinal Masses

Dorsal mediastinal masses, whether in the cranial, middle, or caudal aspect of the mediastinum, cause widening of the mediastinum in the VD or DV view (Figs. 33.18 and 33.19). The caudal mediastinum can be evaluated more thoroughly in a VD view, compared with a DV view, because cranial excursion of the diaphragm in the DV view leads to compression of the caudal mediastinum.[9,10]

The most common cause of a dorsal mediastinal mass is enlargement of the esophagus, which can be generalized or segmental. Enlargement of the cranial aspect of the thoracic esophagus, such as from a vascular ring anomaly, typically causes a craniodorsal mediastinal mass with ventral displacement of the trachea in the lateral view, and widening of the cranial mediastinum in the VD or DV view. The presence of esophageal gas (see Fig. 33.18), or a heterogeneous opacity created by esophageal contents, differentiates esophageal enlargement from other dorsal mediastinal masses. If a dorsal mediastinal mass is homogeneous, it is usually impossible to determine the origin of the mass from survey radiographs alone (Fig. 33.20).

The presence of regurgitation is not necessarily helpful in establishing the origin of a dorsal mediastinal mass as esophagus, because any mass in this location can compress the esophagus and lead to regurgitation. Radiographic signs of esophageal enlargement are discussed more completely in Chapter 30. If the esophagus is suspected as the origin of a dorsal mediastinal mass, an esophagram can be helpful for positive identification.

Craniodorsal Mediastinal Masses

Craniodorsal mediastinal masses are rare (see Table 33.1). A craniodorsal mediastinal mass typically causes ventral and rightward displacement of the trachea (see Fig. 33.19).

Hilar-Region Mediastinal Masses

The main causes of a mediastinal mass in the hilar region are enlargement of the tracheobronchial lymph nodes or a mass arising from the base of the heart (see Table 33.2).

The tracheobronchial lymphocenter is subdivided into the right, left, and middle tracheobronchial lymph nodes. The right and left lymph nodes lie on the lateral side of their respective bronchus and are also in contact with the trachea. The right lymph node is ventral to the azygos vein, and the left lymph node is ventral to the aorta. The middle tracheobronchial lymph node is the largest of the group, and it has the form of a V with the point lying in the angle formed by the tracheal bifurcation. Afferent lymphatics to the tracheobronchial lymph nodes come primarily from the lungs and bronchi, but they also come from the thoracic parts of the aorta, esophagus, trachea, heart, mediastinum, and diaphragm.[3]

Enlargement of the tracheobronchial lymph nodes classically results in a soft tissue mass located dorsocaudal to the tracheal bifurcation on the lateral view, which usually causes cranioventral displacement of a principal bronchus or tracheal bifurcation. If the enlarged lymph nodes reside primarily ventral to the tracheal bifurcation, dorsal displacement of the bifurcation will result instead, which can be confused with left atrial dilation; however, this is very uncommon. Both tracheobronchial lymph node enlargement and left atrial dilation can cause lateral divergence or splaying of the principal bronchi on the VD or DV view (Fig. 33.21); therefore, a lateral view is required to differentiate lymphadenopathy from left atrial enlargement. The extent of the hilar mass effect and degree of splaying of the principal bronchi depend on the magnitude of enlargement of the tracheobronchial lymph nodes, or the extent of left atrial dilation. With mild tracheobronchial lymph node enlargement, displacement of a principal bronchus in a

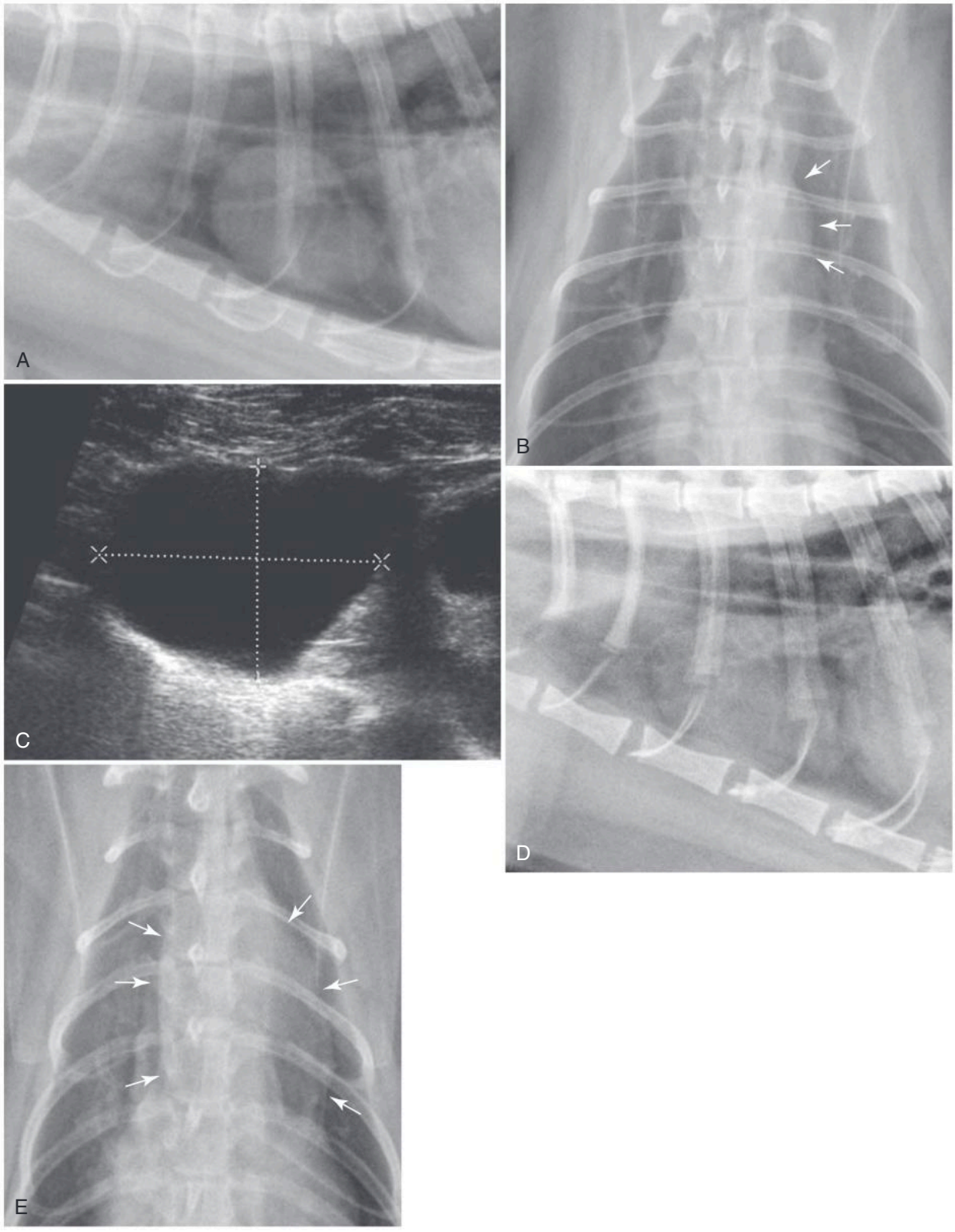


Fig. 33.14 Left lateral **(A)** and ventrodorsal (VD; **B**) thoracic radiographs of a cat. There is a well-defined mass in the cranioventral aspect of the mediastinum. The mass is very conspicuous in the lateral view and causes an ill-defined left mass effect in the VD view (*white arrows*). This cat has mild pneumomediastinum secondary to a tracheal puncture that occurred during blood draw from the jugular vein, and this may have increased the conspicuity of the mass slightly. The mass is more caudal than expected for a cranial mediastinal lymph node or a sternal lymph node and does not have the broad base of ventral contact with the sternum that is typical of sternal lymph node enlargement. Ultrasound imaging **(C)** allows identification of the hypoechoic cystic contents and establishes the diagnosis of mediastinal cyst. The *dotted lines* in **C** are the electronic calipers of the ultrasound machine being used to obtain measurements of the mass, which in this cat were 1.8 cm cranial/caudal and 2.5 cm dorsal/ventral. The cyst in this cat was not drained or removed; and in left lateral **(D)** and VD **(E)** radiographs made 18 months later, the cyst has enlarged (*white arrows*). This cyst is not large enough to require excision but should be monitored subsequently to avoid complications resulting from enlargement and organ compression.

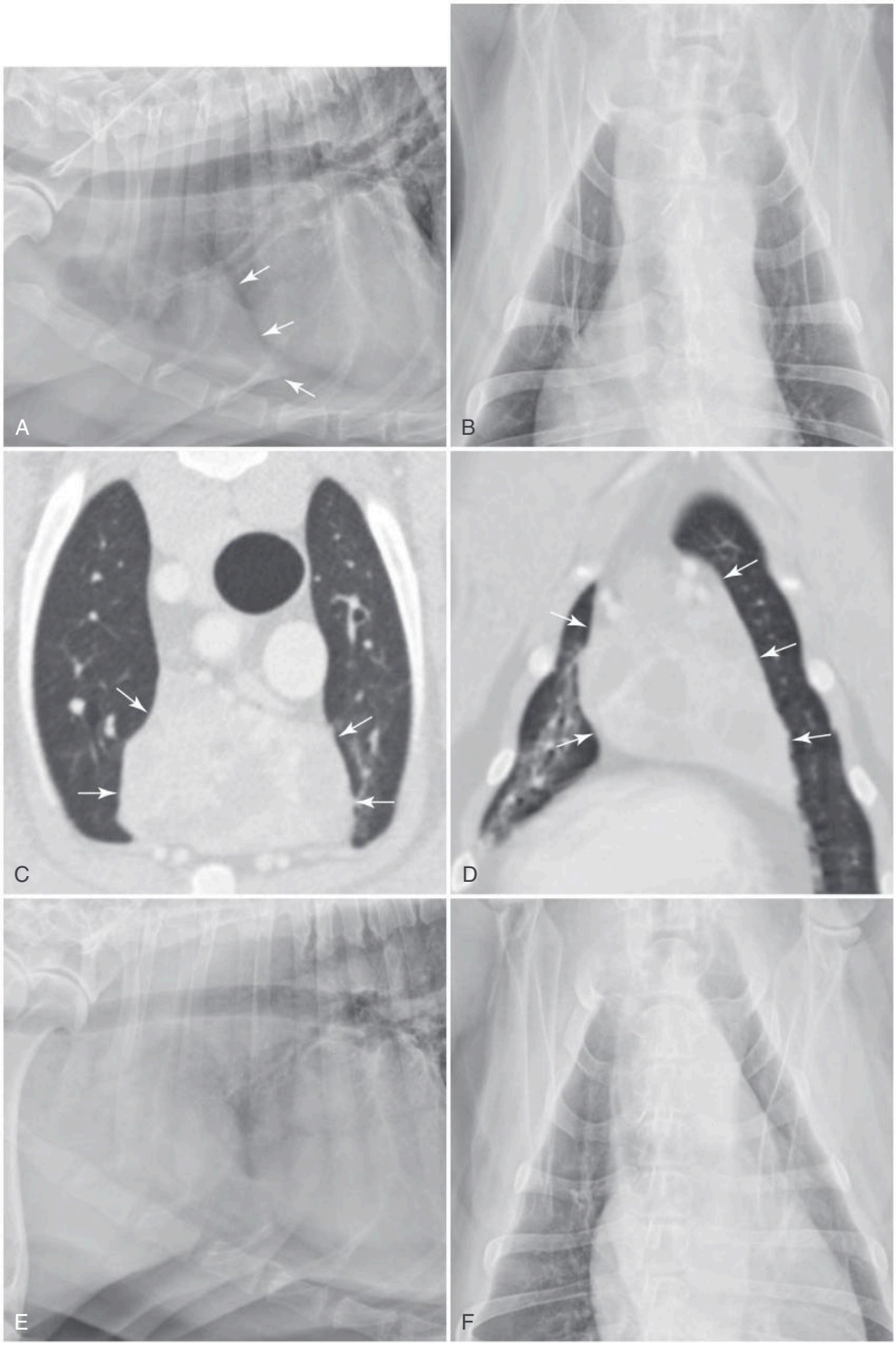


Fig. 33.15 Right lateral **(A)** and ventrodorsal (VD; **B**) radiographs of a dog with a mass in the cranioventral mediastinum. In **A,** the cranioventral mediastinum has overall increased opacity, and the edge of a mass is visible caudoventrally (*white arrows*), contrasted by lung. In **B,** the cranial mediastinum is wide. The trachea is not displaced in either **A** or **B**. This patient was not obese, and mediastinal fat would therefore not be a likely cause for this appearance. Transverse **(C)** and dorsal **(D)** contrast-enhanced computed tomography (CT) images of the thorax were acquired a few days after the images in **A** and **B**. The mass is clearly visible in the ventral aspect of the cranial mediastinum (*white arrows*). Right lateral **(E)** and VD **(F)** radiographs acquired 4 months after those in **A** and **B**. The mass is larger and more obvious, displacing the trachea dorsally and to the right. The mass was removed completely by transsternal thoracotomy, and the histologic diagnosis was thymoma.

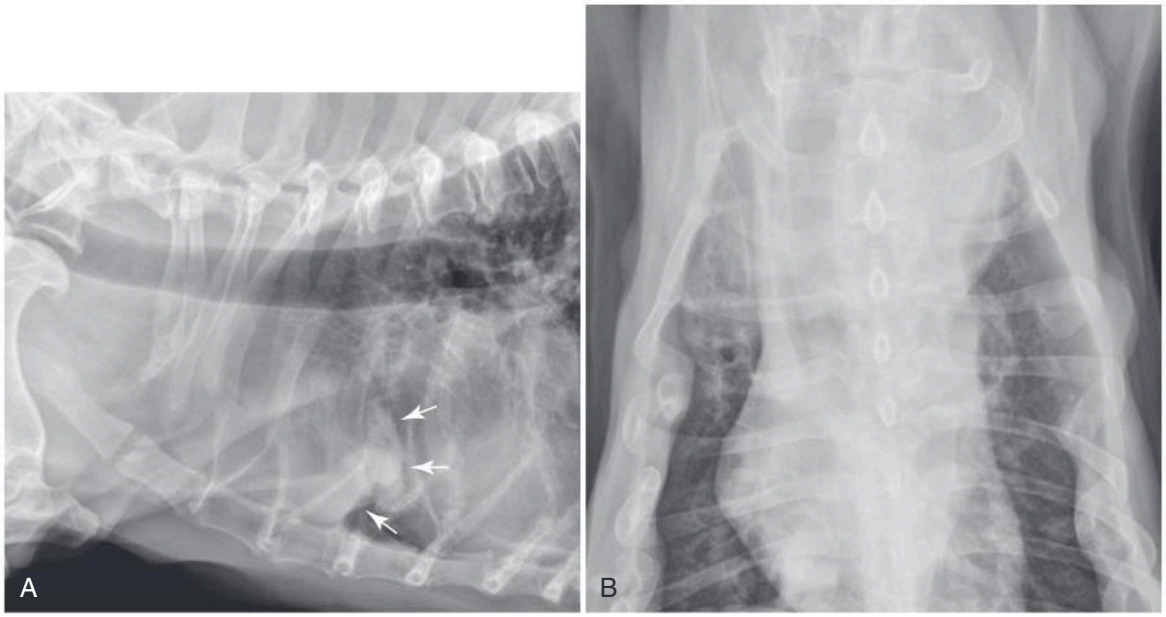


Fig. 33.16 Lateral **(A)** and ventrodorsal (VD; **B**) thoracic radiographs of a Basset hound with a moderately sized mediastinal mass. **A,** The mediastinum ventral to the trachea has increased opacity, and the edge of a mass is visible caudally (*white arrows*), contrasted by lung. The mass has caused mild dorsal displacement of the trachea, which is now parallel to the vertebrae. The mass also causes border effacement of the cranial aspect of the cardiac silhouette. **B,** The cranial mediastinum is wide, and there is border effacement of the cranial margin of the heart. The trachea is displaced slightly to the right. This patient is not obese; thus excessive mediastinal fat is an unlikely cause of this radiographic appearance, and a cranioventral mediastinal mass is the most likely diagnosis. Considerations for this mass are cranial mediastinal lymph node, thymus, and branchial cyst. Sonography or computed tomography (CT) could provide more information about the character of the mass, but an aspirate may be needed for de finitive diagnosis.

cranioventral direction in the lateral view may be the most conspicuous abnormality (Fig. 33.22). With progressive enlargement of the tracheobronchial lymph nodes, the mass effect becomes more pronounced and splaying of principal bronchi becomes evident in the VD or DV view (Fig. 33.23, eFig. 33.5).

Masses arising from the base of the heart tend to be relatively inconspicuous since much of the mass is surrounded by other soft tissue structures, resulting in border effacement. These lesions usually create an ill-defined mass effect, rather than a distinct mass, and may become very large before being detectable on survey radiographs. Heart base region masses typically cause rightward displacement of the trachea just cranial to the bifurcation, which may be the most conspicuous finding (Fig. 33.24, eFig. 33.6). As the heart base mass enlarges, the tracheal displacement becomes more pronounced, but the mass itself is still not likely to be seen (Fig. 33.25). A heart base mass may represent a heart base tumor, a right atrial tumor, a tumor arising from ectopic thyroid tissue, or an enlarged main pulmonary artery.

Caudoventral Mediastinal Masses

Caudoventral mediastinal masses are uncommon, and most are associated with the diaphragm, such as a diaphragmatic eventration, or a hernia (see Table 33.1; Fig. 33.26). Caval foramen hernia may also cause a caudoventral mediastinal mass effect. Caudoventral mediastinal masses may cause border effacement of the diaphragm and/or cardiac displacement. In VD or DV views, caudoventral mediastinal masses are often located to the left of midline because of the normal left-sided location of the caudoventral mediastinal reflection (see Fig. 33.26).

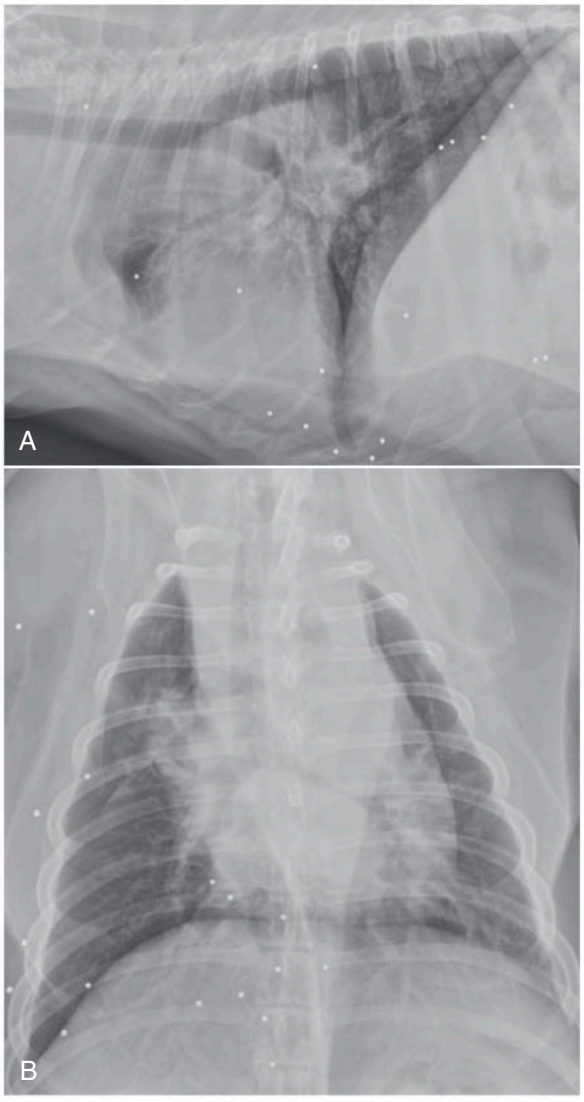
As the accessory lung lobe is located on midline, a mass arising from the accessory lobe can appear identical to a caudoventral mediastinal mass[11] (Fig. 33.27). Large accessory lobe masses will cause border effacement of the caudal vena cava, because the accessory lobe surrounds this structure (see Fig. 33.27). However, border effacement of the caudal vena cava can occur with any large caudoventral mediastinal mass; therefore, this sign cannot be used to differentiate accessory lobe masses from caudoventral mediastinal masses. Visibility of the caudal vena cava may be preserved with small caudoventral mediastinal masses, even if of accessory lobe origin (see Fig. 33.26). CT is usually needed to differentiate caudoventral mediastinal masses from accessory lobe masses.

Caudodorsal Mediastinal Masses

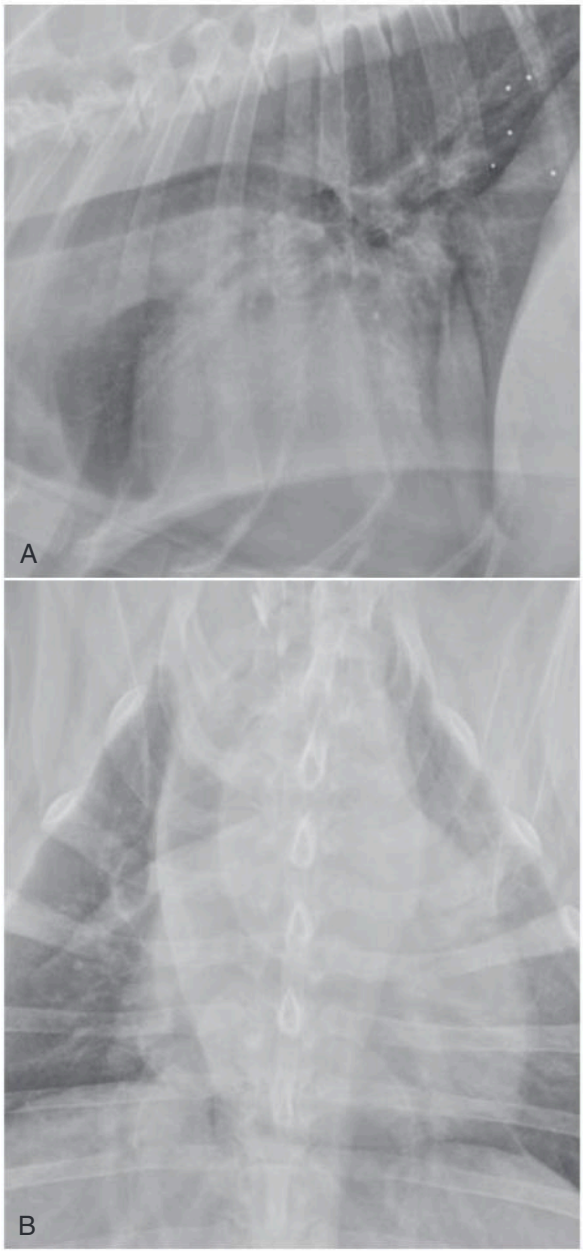
The mediastinal serous cavity is a normal, mesothelium-lined anatomic space in the caudodorsal mediastinum. It is located to the right of the esophagus and extends from the diaphragm to the heart base. Purulent material can accumulate in this cavity forming paraesophageal empyema, possibly due to foreign material migration or extension of infectious disease from the adjacent accessory lung lobe (Fig. 33.28).[12] Mediastinal serous cavity mesothelioma has also been reported in dogs.[13] Esophageal foreign bodies can have the appearance of a caudodorsal mediastinal mass but are typically associated with a degree of esophageal gas dilation cranial to the foreign material (see Fig. 33.20).

Some Facts About Mediastinal Lymph Nodes

The drainage patterns of mediastinal lymph nodes were defined in the section dealing with mediastinal masses. Mediastinal lymph node enlargement can be associated with a variety of diseases, but the most common causes are primary lymphoid neoplasia and mycotic infection. Spread of peritoneal disease to the sternal lymph node was discussed earlier.



eFig. 33.5 Right lateral **(A)** and ventrodorsal (VD; **B**) radiographs of a dog with lymphoma and enlargement of the tracheobronchial lymph nodes. In **A,** the tracheal bifurcation is displaced cranioventrally. In **B,** there is splaying of the main stem bronchi. The cranial mediastinum is widened due to sternal and cranial mediastinal lymphadenomegaly. Metallic gunshot pellets are present in the left hemithorax.



eFig. 33.6 Right lateral **(A)** and dorsoventral (DV; **B**) radiographs of a dog with a heart base tumor (chemodectoma). There is mild dorsal elevation of the trachea cranial to the bifurcation in **A**. In **B,** the trachea is deviated to the right with an increased soft tissue opacity in the region of the heart base.

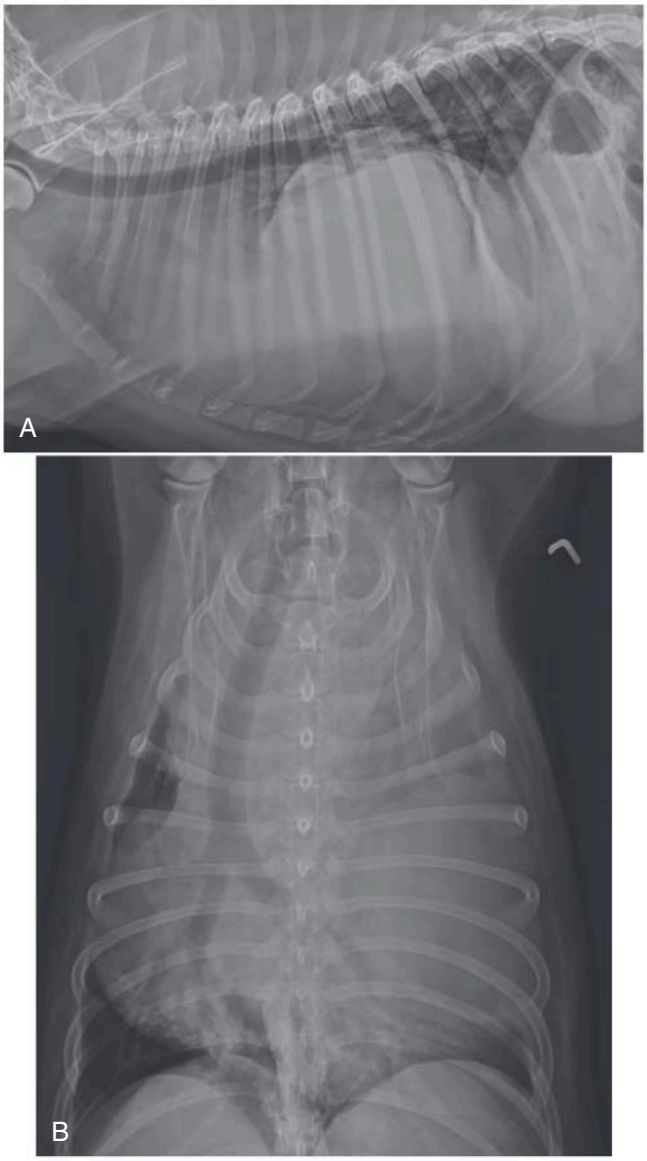


Fig. 33.17 Right lateral **(A)** and ventrodorsal (VD; **B**) radiographs of a dog with a massive, lobular mass arising from the left cranioventral mediastinum. The trachea is severely displaced dorsally and to the right, and the heart is displaced caudodorsally and to the right. There is marked border effacement of the cardiac silhouette in both **A** and **B**. In **B,** the mass extends caudally along the left margin of the heart, and contacts the diaphragm. This dog presented with minor exercise intolerance and muffled left-sided heart sounds; the paucity of clinical signs coupled with the extremely large mass is most consistent with a slow-growing thymoma.

In the cat, lymphoma is a common cause of enlargement of the cranial mediastinal lymph nodes. The thymus may also be affected. In the dog, lymphoma results in enlargement of the sternal lymph nodes in slightly over half of affected patients, but enlargement of cranial mediastinal or tracheobronchial lymph nodes is uncommon.[14] Other reticuloendothelial malignancies, such as pulmonary lymphomatoid granulomatosis[15,16] and disseminated histiocytic sarcoma,[17] are also characterized by a high frequency of lymph node enlargement, particularly the tracheobronchial lymph nodes. In pulmonary lymphomatoid granulomatosis and disseminated histiocytic sarcoma, there is usually accompanying pulmonary parenchymal disease, and isolated mediastinal lymph node enlargement is unusual. Pulmonary mycoses, especially blastomycosis and coccidioidomycosis, are associated with a high prevalence of mediastinal lymph node enlargement. Interestingly, there are a variety of diseases that one might expect to result in mediastinal lymph node enlargement but rarely do, at least to the extent that the enlarged lymph nodes are visible radiographically (Box 33.1).

Distinguishing a Mediastinal Mass From a Lung Mass

Radiographic differentiation of a lung mass from a mediastinal mass is not always possible. Many lung masses can be distinguished from mediastinal masses, because the lung mass is lateral to the mediastinum, surrounded by air-filled lung, and is therefore more sharply marginated (Fig. 33.29). Some mediastinal masses, however, may protrude laterally (Fig. 33.30), or be in a thin portion of the mediastinum (Fig. 33.31) and be surrounded by air making them sharply margined and easily mistaken for a lung mass. In addition, lung masses located in the more medial part of the lung can contact the margin of the mediastinum, particularly in the cranioventral thorax, and not be completely surrounded by gas. For these reasons, definitive localization of many intrathoracic masses is not always possible based on radiographs alone. If thoracotomy is being considered, and the location of the mass is not obvious from radiographs, a presurgical CT scan can assist in determining the origin, location, and extent of the mass and can guide the surgical approach (e.g., intercostal vs. median thoracotomy).

Confounding Effects of Pleural and Mediastinal Fluid

As previously noted, cranial mediastinal masses often cause elevation of the trachea. Elevation of the trachea may also result from a large amount of pleural fluid that results in lung displacement from buoyancy (Fig. 33.32).[18] A small volume of pleural fluid does not result in tracheal elevation unless a mediastinal mass is also present. If pleural fluid is present, definitive radiographic identification of a concurrent mediastinal mass is usually not possible. However, if the mass is large enough to compress the trachea and/or displace the tracheal bifurcation caudally, the presence of a mass can be inferred.

Mediastinal fluid can be difficult to differentiate from pleural effusion that has accumulated in the cranial thorax along the mediastinum. Mediastinal effusion is most commonly caused by hemorrhage, either secondary to trauma with rupture of thymic vessels in young dogs, or secondary to coagulopathies such as rodenticide toxicity.

If pleural fluid obscures the mediastinum, and a mediastinal mass is suspected, various interventions can be used. The easiest and often the most successful is to remove the pleural fluid and repeat the radiographs. Positioning the patient upright and using a horizontally directed x-ray beam to take advantage of gravity, which causes pleural fluid to move away from the area of the suspected mediastinal mass, is often not successful or informative. If available, ultrasound or CT can be used to evaluate for a mass in the mediastinum.[19,20] Pleural fluid provides an excellent acoustic window for sonographic examination, and ultrasound-guided aspiration or biopsy aid in achieving a definitive diagnosis.

Pneumomediastinum

Pneumomediastinum denotes free gas in the mediastinum. The radiographic findings of pneumomediastinum depend on the volume of gas present. Regardless of the amount of gas present, pneumomediastinum is rarely visible in VD or DV views because the overall size of the mediastinum is not increased, and the mediastinal gas is superimposed on the midline and obscured by other structures. Lateral views are typically the most useful for detecting pneumomediastinum. With a large volume of mediastinal gas, organs and structures not normally seen (such as the esophagus, brachiocephalic trunk, and left subclavian artery) become visible because of the contrast

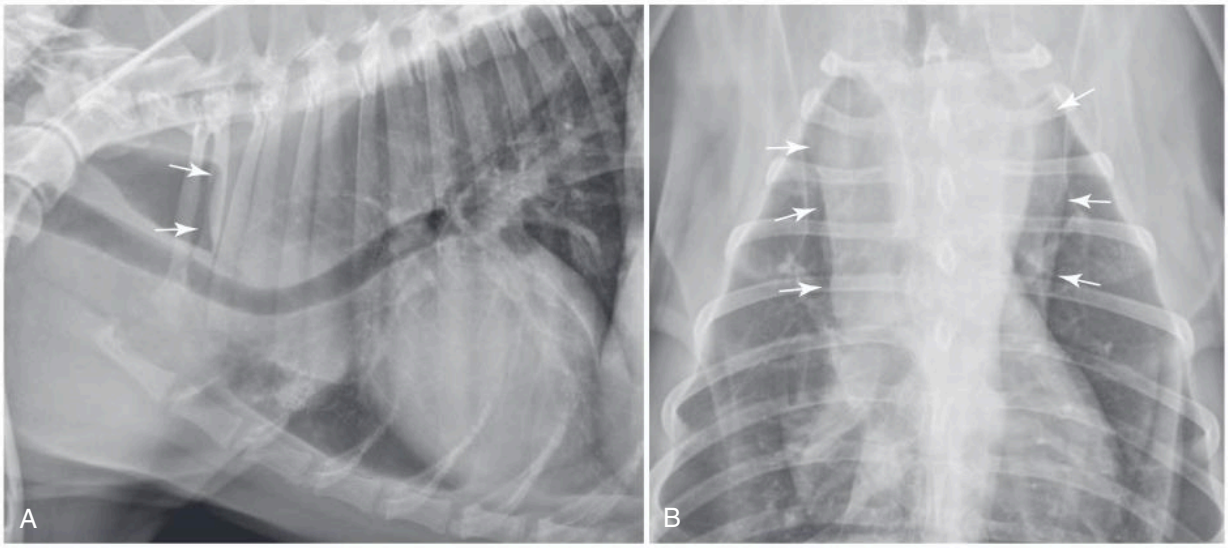


Fig. 33.18 Lateral **(A)** and dorsoventral (DV; **B**) radiographs of a dog with a craniodorsal mediastinal mass caused by a vascular ring anomaly leading to segmental megaesophagus. The enlarged esophagus displaces the trachea ventrally. In **A,** an interface between esophageal contents and gas trapped in the cranial esophagus (*white arrows*) lends support to the mass being of esophageal origin. In **B,** the mass causes widening of the cranial mediastinum (*white arrows*) as expected. From the DV view, the mass cannot be diagnosed as esophagus or localized to the dorsal versus ventral aspects of the mediastinum.

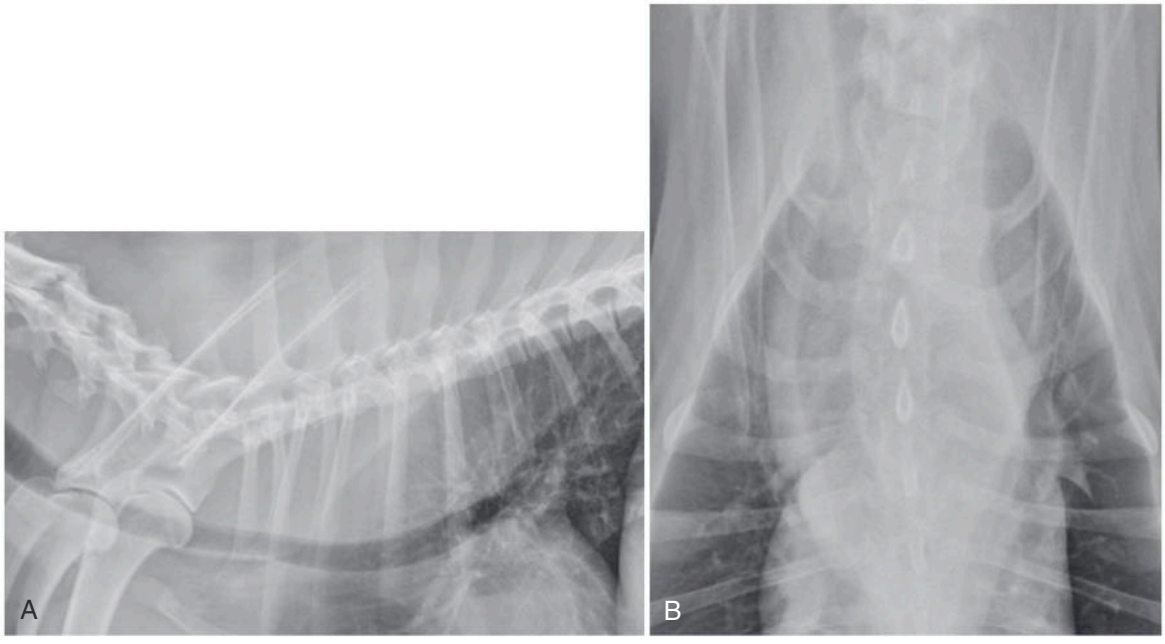


Fig. 33.19 Lateral **(A)** and ventrodorsal (VD; **B**) thoracic radiographs of a dog with a craniodorsal mediastinal abscess. In **A,** there is a homogeneously opaque mass in the craniodorsal aspect of the mediastinum that displaces the trachea ventrally. The mass extends into the cervical region, dorsal to the trachea. In **B,** the cranial mediastinum is wider than normal, and the trachea is displaced to the right. The origin of this mass cannot be determined from these radiographs; esophageal origin cannot be ruled out.

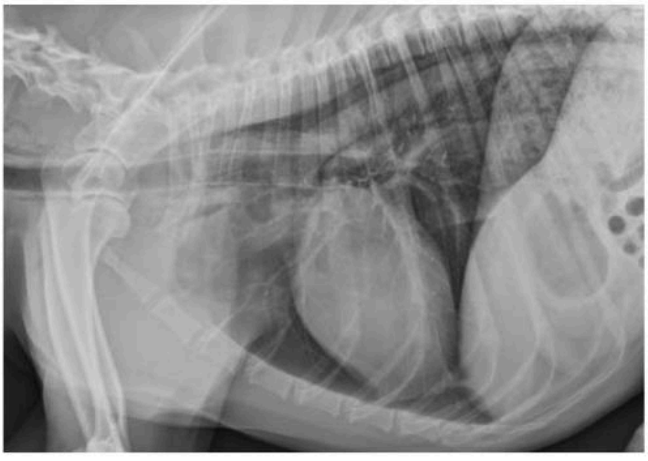
afforded by the adjacent gas (Fig. 33.33, eFig. 33.7). With smaller amounts of mediastinal gas, the changes are less dramatic; for example, the only abnormality may be visualization of the adventitial surface of the trachea (Fig. 33.34A), or a heterogeneous appearance to the cranioventral mediastinum due to gas pocketing (see Fig. 33.34B). If there are large amounts of subcutaneous gas in addition to pneumomediastinum, the superimposed subcutaneous gas creates a very heterogeneous opacity in lateral views, which can lead to overestimation of the volume of gas present in the mediastinum, or even a misdiagnosis of pneumomediastinum (Fig. 33.35).

Pneumomediastinum may progress to pneumothorax if mediastinal gas dissects through the mediastinal pleura into the pleural space. Conversely, pneumothorax does not progress to pneumomediastinum. Dyspnea is usually not seen with pneumomediastinum, unless it results in pneumothorax.

Because of the communication of the mediastinum with the neck and retroperitoneal space, pneumomediastinum may result in subcutaneous emphysema and/or pneumoretroperitoneum (Fig. 33.36, eFig. 33.8). Alternatively, gas in the retroperitoneal space or fascial planes of the neck may diffuse into the mediastinum.



eFig. 33.7 Lateral thoracic radiograph of a cat with pneumomediastinum. The cranial mediastinal vessels and ventral tracheal wall are outlined by gas. A gastroesophageal tube is present.



eFig. 33.8 Lateral radiograph of a dog with pneumomediastinum and pneumoretroperitoneum after esophageal rupture. Gas is outlining the tracheal wall and cranial mediastinal vessels. The aorta is sharply outlined by gas extending into the retroperitoneal space. Cervical subcutaneous emphysema is present as well.

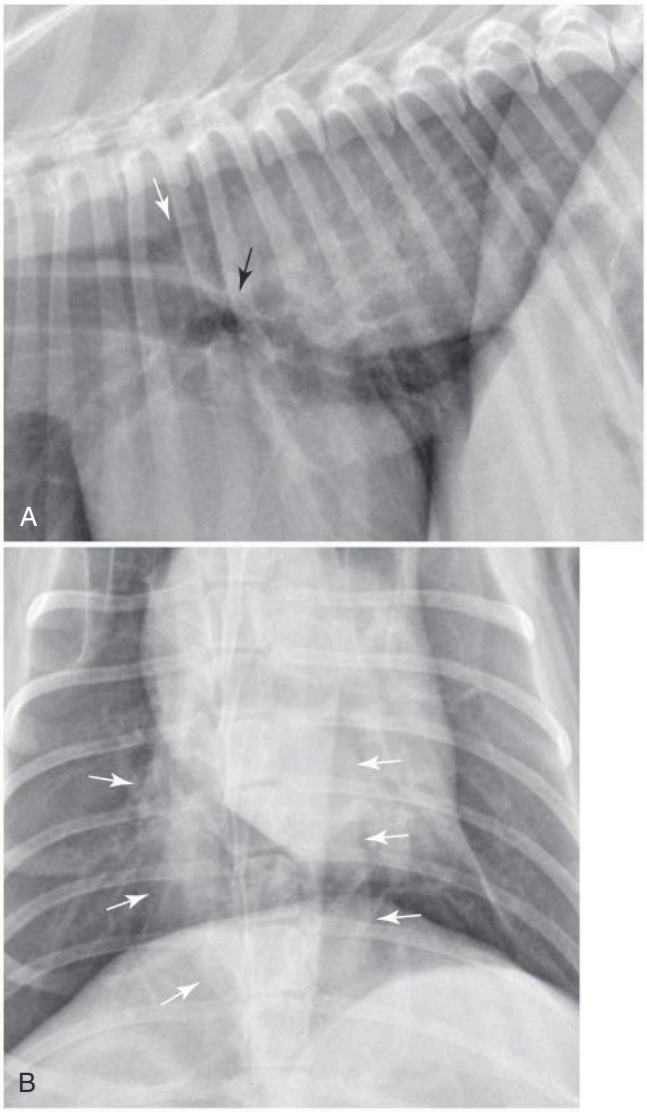


Fig. 33.20 Lateral **(A)** and ventrodorsal (VD; **B**) thoracic radiographs of a dog with a caudal esophageal foreign body. The foreign body is homogeneous and causes a caudodorsal mediastinal mass that in **A** displaces the tracheal bifurcation slightly in a cranioventral direction (*black arrow*). There is also a focal gas collection in the esophagus cranial to the mass (*white arrow* in **A**). In **B,** the mass has caused widening of the caudal mediastinum (*white arrows*). It is not possible to determine from these radiographs whether the mass is esophageal in origin. The small esophageal gas collection could be secondary to extrinsic compression of the esophagus by a soft tissue mass of another origin.

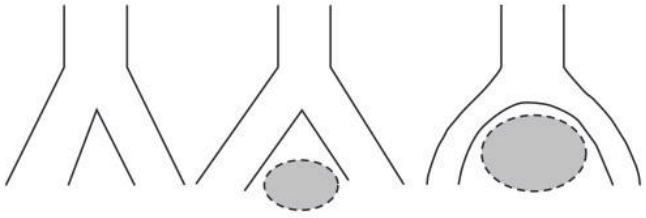


Fig. 33.21 The shape of the principal bronchi in a ventrodorsal (VD) radiograph in the normal state (*left*) and when a mass is present between them (*middle* and *right*). An enlarged left atrium or tracheobronchial lymph node between the principal bronchi may result in the principal bronchi being displaced laterally (*middle*) or, more commonly, assuming a curved appearance (*right*).

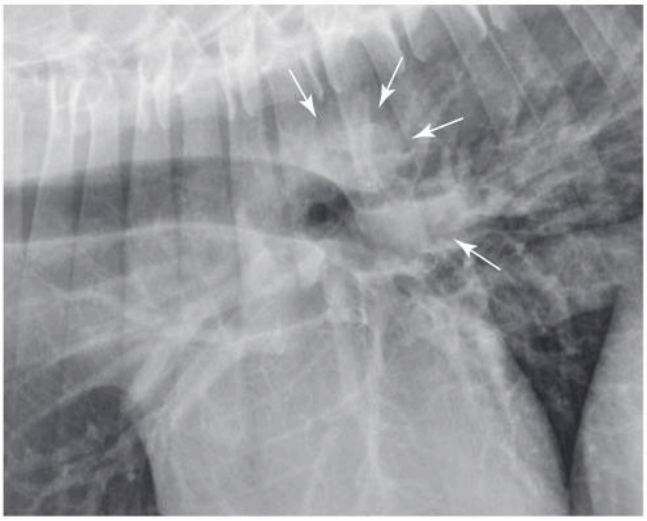


Fig. 33.22 Right lateral radiograph of a dog with mild enlargement of the tracheobronchial lymph nodes. There is a small mass effect caudodorsal to the tracheal bifurcation (*white arrows*) that has caused cranioventral displacement of the bifurcation. Splaying of the principal bronchi was not evident in the ventrodorsal (VD) view.

Pneumomediastinum can result from a variety of causes. It is common for air to escape into the pulmonary interstitium from sites of intrapulmonary alveolar rupture that do not involve the visceral pleural surface of the lung. These intrapulmonary ruptures can be microscopic, with air leaking into the mediastinum and tracking in a retrograde direction in the loose connective tissue adjacent to bronchi and vessels into the mediastinum.[21,22] This phenomenon, called the *Macklin effect*, is a relatively frequent occurrence following blunt thoracic trauma,[23,24] such as a motor vehicle accident, and also after iatrogenic pulmonary hyperinflation during anesthesia or resuscitation.[25] Pneumothorax is not present when pneumomediastinum results from the Macklin effect, unless the visceral pleura becomes torn, or the mediastinal air accumulation extends to the pleural space.

Another common cause of pneumomediastinum is dissection of gas from the fascial planes of the neck into the mediastinum. Gas in the neck commonly results from neck trauma, such as a bite wound. Intrafascial cervical gas can also result from a tracheal perforation. In cats, the trachea can easily be perforated inadvertently during jugular venipuncture, and this can lead to air leaks and pneumomediastinum, as gas tracks down the neck. If a tracheal tear is intrathoracic, air enters the mediastinum directly. Tracheal rupture in anesthetized cats associated with overdistention of the endotracheal tube cuff is a noteworthy cause of pneumomediastinum.[26,27] Cuff overdistention may cause rupture of the trachealis muscle at the point of attachment to the tracheal cartilages. Tracheal rupture may occur at a modest cuff volume and may not be immediately apparent to the anesthetist. Development of subcutaneous emphysema occurs quickly following tracheal rupture from cuff over distention, and the amount of subcutaneous gas is usually pronounced. If subcutaneous emphysema develops during a surgical procedure, the anesthetist must be aware of this potentially fatal complication.

Other less common causes of pneumomediastinum are esophageal perforation as a result of trauma, foreign body, neoplasia, inflammation, or malposition of a feeding tube[28]; extension of retroperitoneal gas into the mediastinum; and presence of gas-producing organism in the mediastinum.

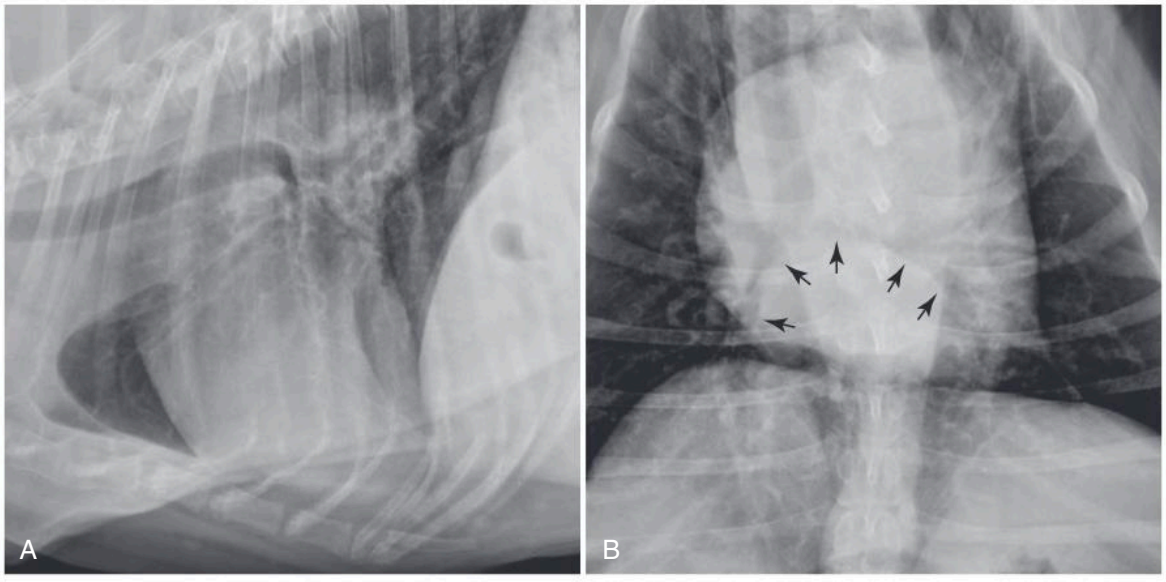


Fig. 33.23 Right lateral **(A)** and ventrodorsal (VD; **B**) radiographs of a dog with pronounced enlargement of the tracheobronchial lymph nodes. In **A,** there is a mass caudodorsal to the tracheal bifurcation that has displaced the bifurcation cranioventrally. In **B,** there is splaying of the principal bronchi (*black arrows*) because of the interposed enlarged tracheobronchial lymph nodes.

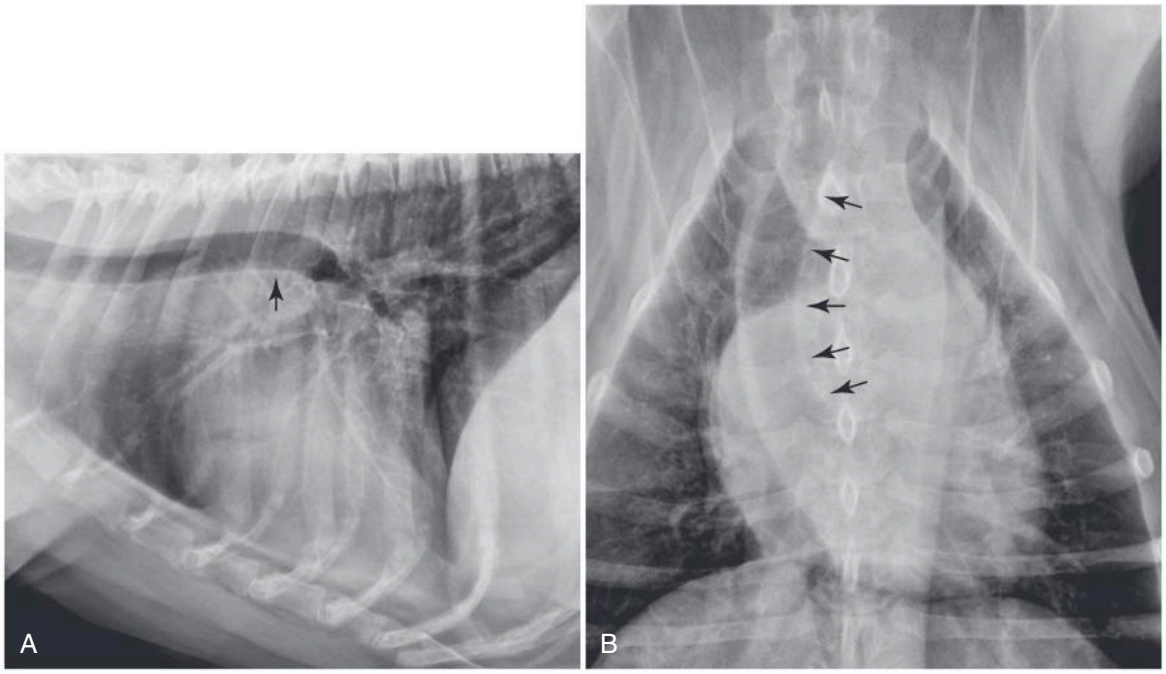


Fig. 33.24 Right lateral **(A)** and ventrodorsal (VD; **B**) radiographs of a dog with a heart base tumor (chemodectoma). In **A,** there is slight focal elevation of the trachea just cranial to the bifurcation (*black arrow*). Enlargement of the left and/or right tracheobronchial lymph nodes could also produce this appearance, but there is no evidence of enlargement of the middle tracheobronchial lymph node, which detracts from the tracheobronchial lymph nodes being the cause of the tracheal elevation seen here. Also, in **B,** there is sharp deviation of the intrathoracic trachea to the right (*black arrows*), which is not usually seen with tracheobronchial lymph node enlargement. The chemodectoma itself is not visible. These tracheal changes are often the only radiographic sign of the presence of a heart base mass.

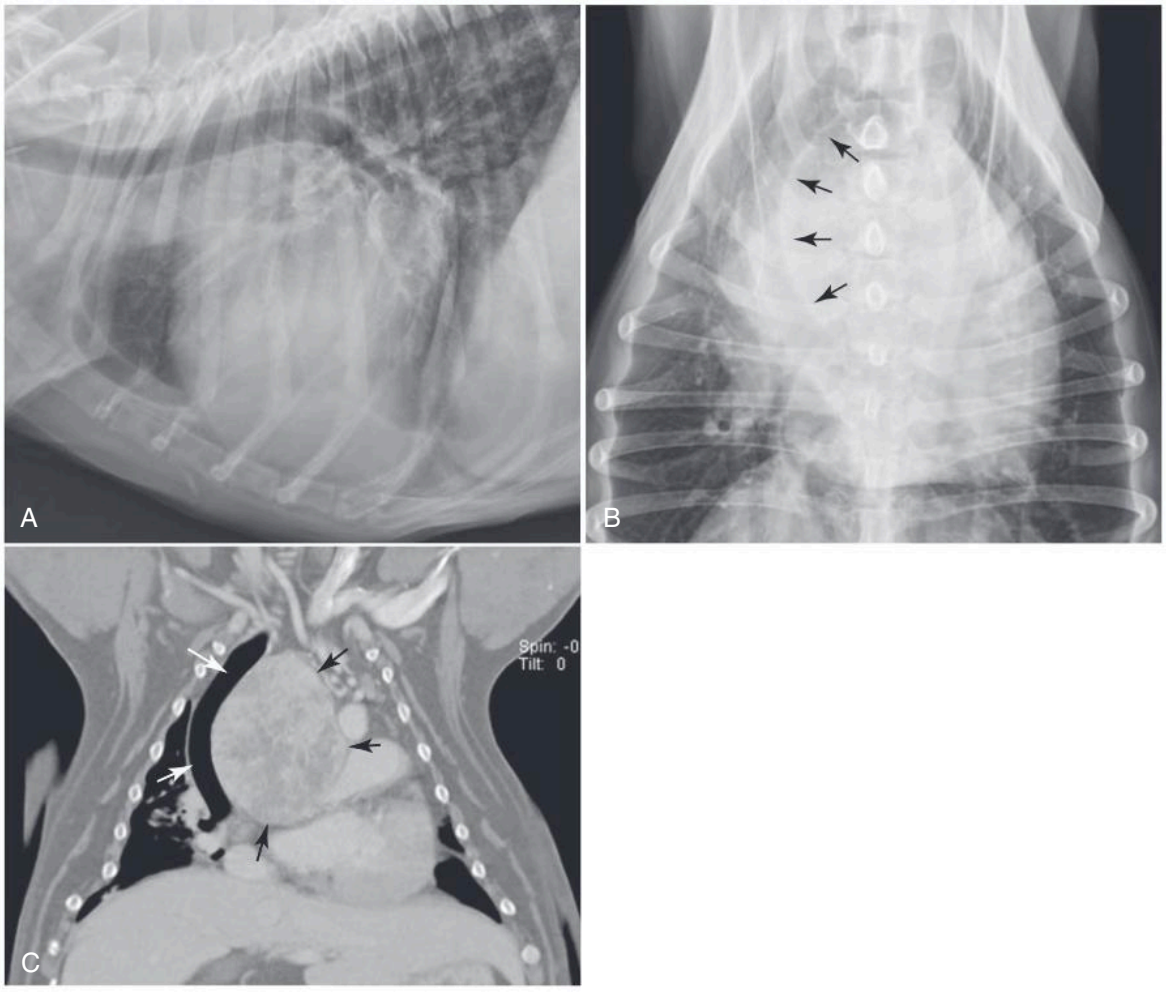


Fig. 33.25 Right lateral **(A)** and ventrodorsal (VD; **B**) radiographs of a dog with a chemodectoma that is larger than the one illustrated in Fig. 33.24. In **A,** there is elevation of the trachea over the base of the heart, and in **B,** there is rightward displacement of the majority of the intrathoracic trachea (*black arrows*). These findings are typical of a large heart base mass. In this dog, the mass itself, even though larger than the one illustrated in Fig. 33.24, is still not overtly conspicuous. **C,** Dorsal plane contrast-enhanced computed tomography (CT) image of another dog with a large chemodectoma (*black arrows*). The image plane is through the level of the heart base. The tumor displaces the trachea (*white arrows*) to the right. The mass is in the mediastinum and contacts the heart. This leads to border effacement, and this is the reason heart base tumors are so inconspicuous radiographically.

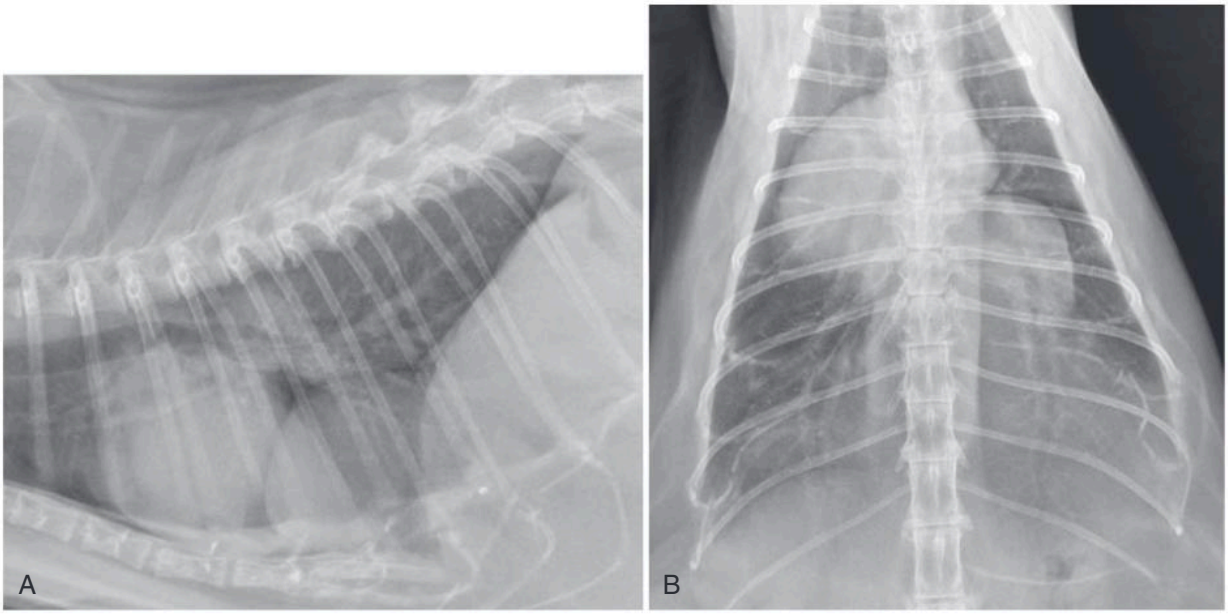


Fig. 33.26 Right lateral **(A)** and dorsoventral (DV; **B**) radiographs of a cat with a lipoma in the caudoventral mediastinum. In **B,** this mass causes border effacement of the diaphragm and is located to the left of midline because of the caudoventral mediastinal reflection being on the left. The heart is displaced to the right. In **A,** the opacity of the mass is slightly less than expected for soft tissue, but making the definitive diagnosis of lipoma from these radiographs is not possible and an aspirate would be required. Visualization of the caudal vena cava has been preserved in **A** due to the ventral location of the mass.

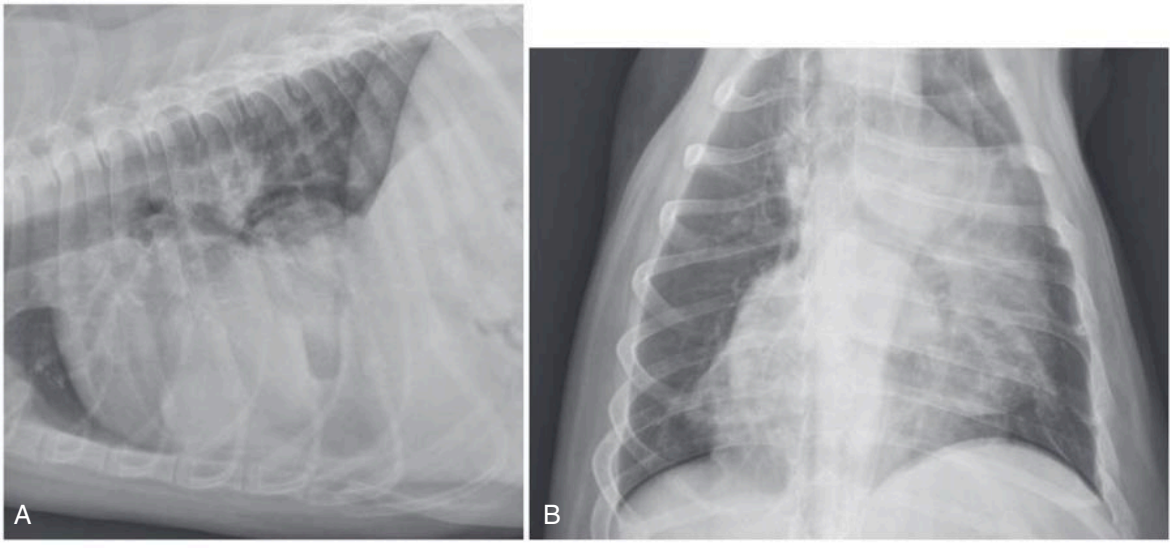


Fig. 33.27 Left lateral **(A)** and ventrodorsal (VD; **B**) radiographs of a dog with a primary tumor of the accessory lung lobe. Given the normal position of the accessory lung lobe, masses arising in the accessory lobe will be on the midline in VD or dorsoventral (DV) views and in the caudoventral aspect of the thorax in lateral view. As such, they are often confused with a mediastinal mass. Accessory lobe masses will usually cause border effacement of the caudal vena cava, as seen here due to the caudal vena cava running through the center of the accessory lung lobe. This mass is also causing border effacement of the diaphragm and displacement of the cardiac apex to the left.

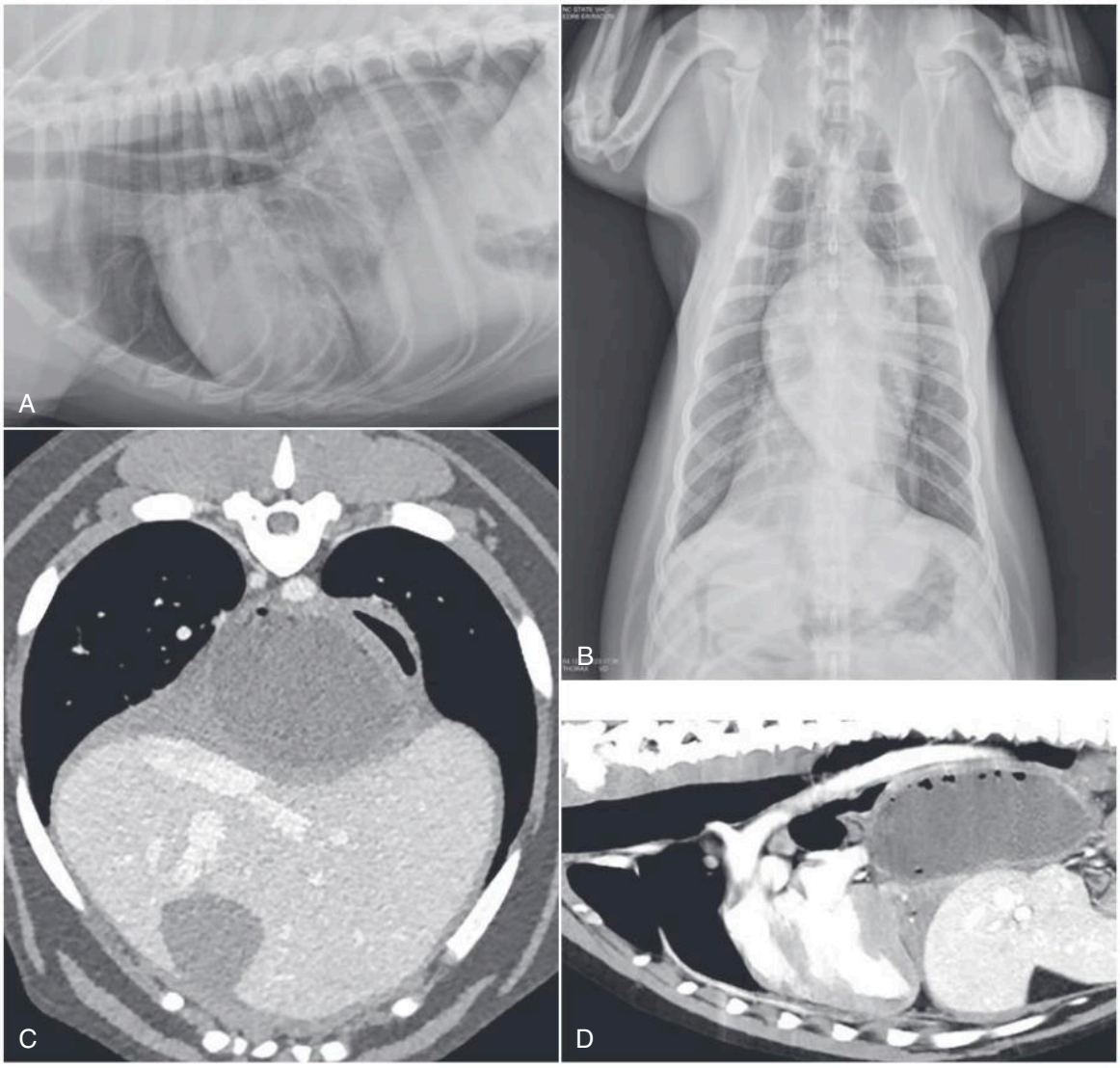


Fig. 33.28 Left lateral **(A)** and ventrodorsal (VD, **B**) radiographs of a dog with empyema of the mediastinal serous cavity. A large ovoid soft tissue opacity is present in the caudodorsal mediastinum at the level of the esophagus. A small amount of gas is present in the cranial thoracic esophagus. In **B**, the soft tissue mass lesion expands the caudal mediastinum to the right of midline. Transverse **(C)** and sagittal reformatted **(D)** contrast-enhanced computed tomography image of the same dog. A large fluid-filled centrally non-contrast-enhancing structure is present in the caudal mediastinum to the right of the mildly gas distended esophagus. Small gas bubbles are present in the dorsal aspect of the cavitary lesion.

Box • **33.1**

Diseases Not Typically Associated With Radiographically Detectable Mediastinal Lymph Node Enlargement

- Primary lung tumor
- Metastatic lung tumor
- Bacterial pneumonia
- Pyothorax
- Rib tumors

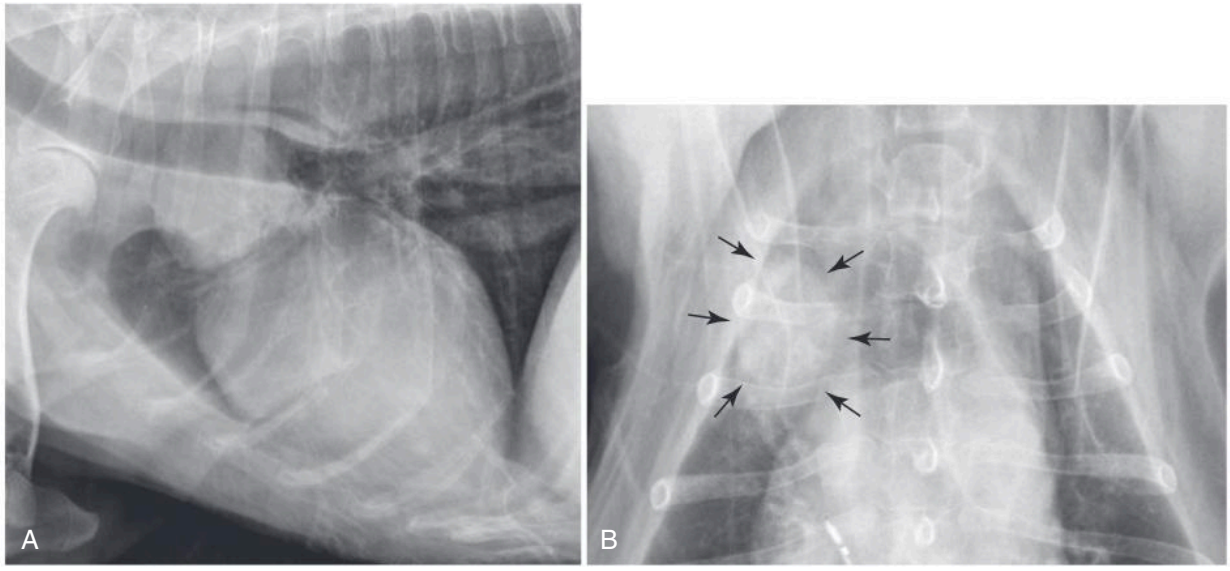


Fig. 33.29 Right lateral **(A)** and ventrodorsal (VD; **B**) radiographs of a dog. In **A,** there is a mass in the cranial aspect of the thorax, ventral to the trachea and just cranial to the tracheal bifurcation. This mass is well marginated ventrally but poorly marginated dorsally. The sharp margination ventrally suggests a pulmonary location for the mass, but a mediastinal mass extending laterally where it would be surrounded by lung cannot be ruled out. In **B,** the mass is located in the right cranial aspect of the thorax (*black arrows*). Because no part of the mediastinum is present normally in this region, the most likely diagnosis is pulmonary mass.

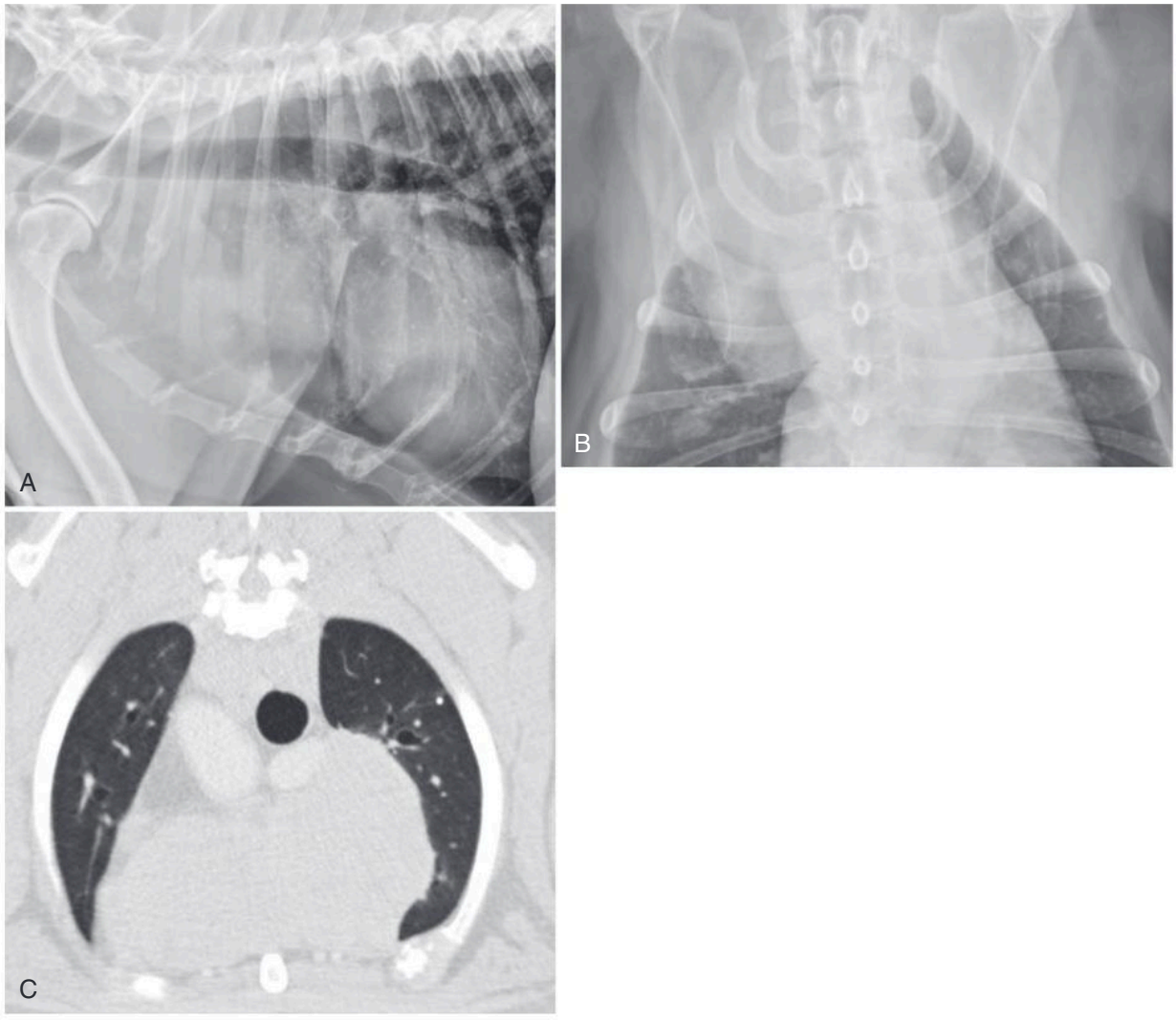


Fig. 33.30 Left lateral **(A)** and dorsoventral (DV; **B**) radiographs of a dog with a large mass in the cranial thorax. In **A,** there is a mass ventral to the trachea, but the trachea is not elevated. In **B,** the mass is to the right of midline, and the caudal border is sharply outlined by air. These findings are consistent with the mass being in the right cranial lung lobe. However, in a computed tomography (CT) image of the thorax **(C)**, it was clear that the mass was in the cranial mediastinum. Lobular mediastinal masses can be surrounded by more air than expected, providing for sharp margination leading to misdiagnosis of the mass as pulmonary rather than mediastinal.

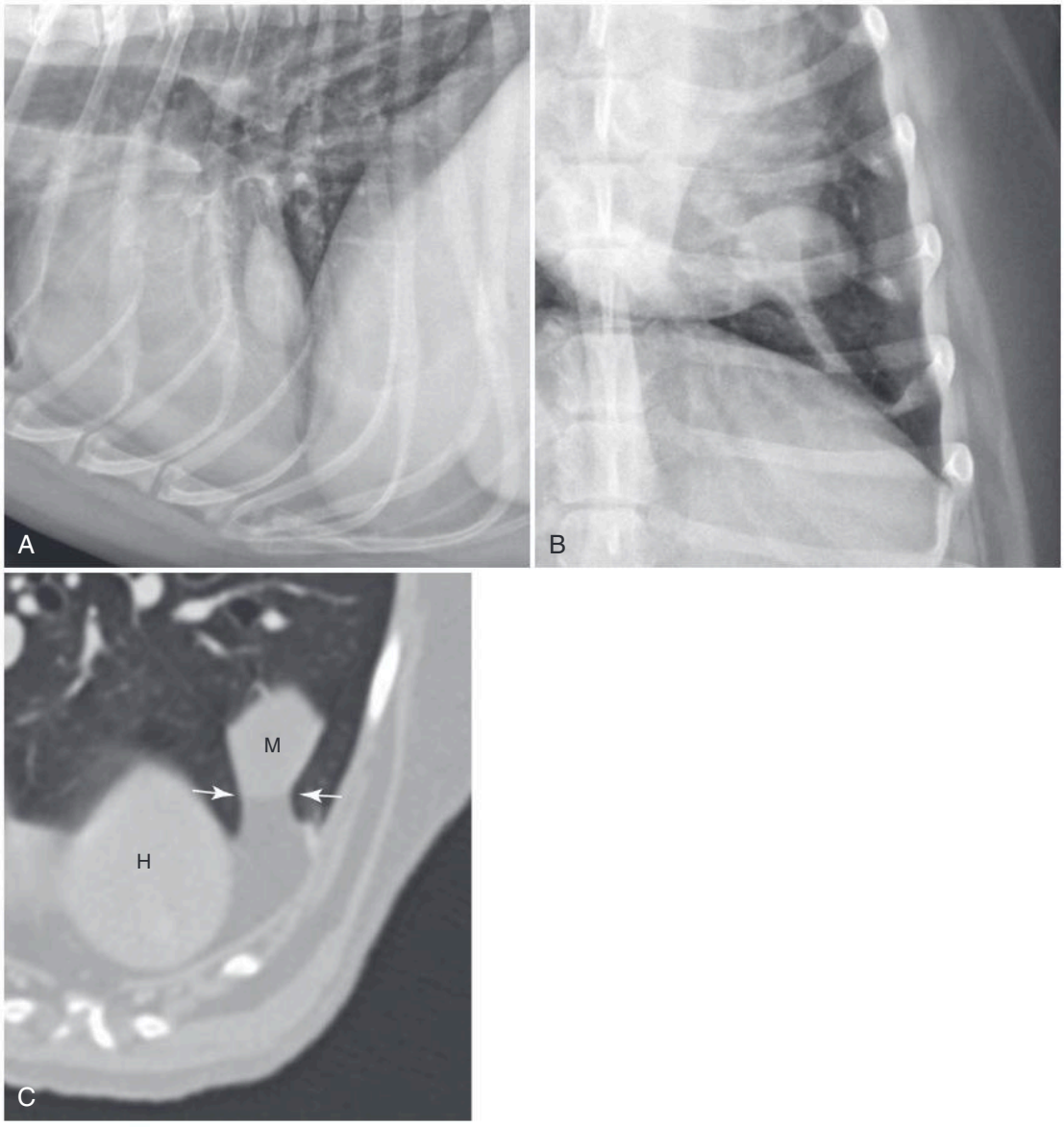


Fig. 33.31 Right lateral **(A)** and ventrodorsal (VD; **B**) radiographs of a dog with a mass in the left caudal thorax. The mass is sharply marginated, making it most consistent with a lung mass. In a computed tomography (CT) image **(C)** of the thorax, the mass (*M*) can be seen to be located in the mediastinum where the caudal mediastinal reflection (*arrows*) envelops the mass. *H*, Heart.

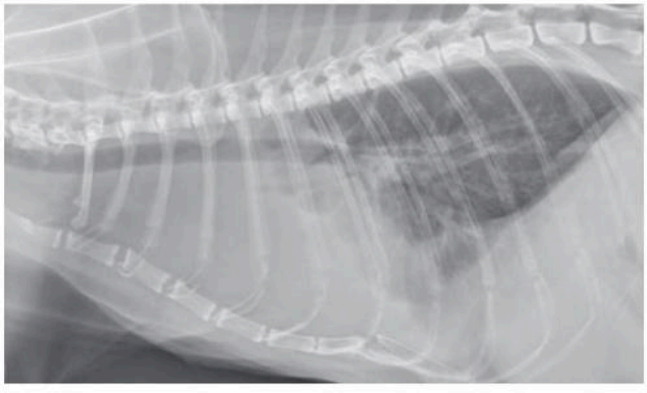


Fig. 33.32 Lateral radiograph of the thorax of a cat with pleural effusion. The trachea is displaced dorsally, but the presence of a mediastinal mass cannot be confirmed radiographically because pleural fluid may be accompanied by tracheal elevation when no mediastinal mass is present because of the lungs floating in the effusion. A thoracic mass cannot be seen, and the trachea is not compressed. Radiography after fluid removal, ultrasonography, or computed tomography (CT) would be more sensitive for determining whether a mediastinal mass was present in this cat.

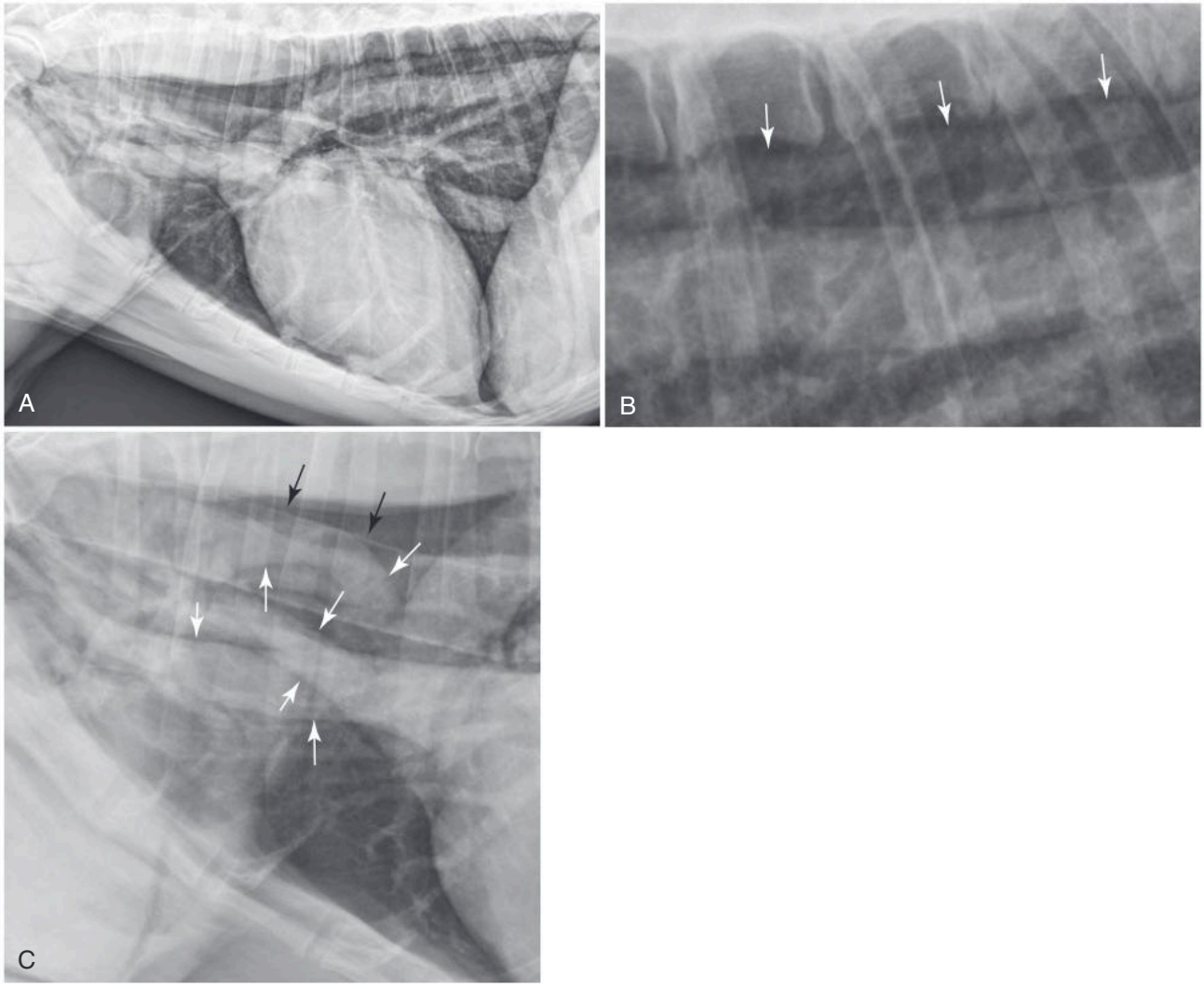


Fig. 33.33 Lateral **(A)** thoracic radiograph of a dog with pronounced pneumomediastinum. The undulating path of the aorta is an aging change and is an incidental finding not related to the pneumomediastinum. The mediastinal gas provides increased contrast that increases the conspicuity of mediastinal structures. **B** is a close-up view of the descending aorta. Mediastinal gas in this region provides contrast for visualization of the azygos vein, dorsal to the aorta (*white arrows*). The azygos vein is not normally seen in thoracic radiographs. **C** is a close-up view of the cranial mediastinum. The mediastinal gas in this region results in very sharp delineation of the adventitial surface of the trachea (*black arrows*). The mucosal and adventitial surfaces of the trachea each have adjacent gas, and therefore both surfaces are highly conspicuous. Also in **C,** the gas in the cranial mediastinum has created a heterogeneous appearance, and large mediastinal vessels can be seen (*white arrows*) as individual structures. Normally, this region has a homogeneous appearance (see Fig. 33.3).

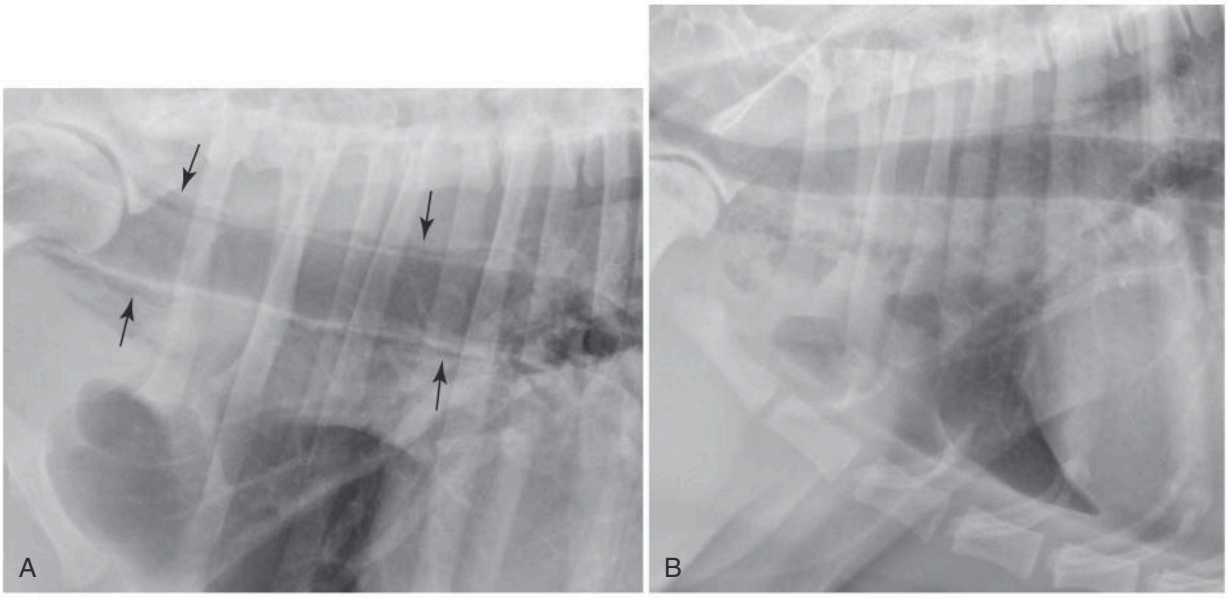


Fig. 33.34 Lateral radiographs of two dogs with a minimal pneumomediastinum. In **A,** the gas is localized around the trachea, leading to increased conspicuity of its adventitial surface (*black arrows*). In **B,** the gas has collected in pockets in the cranioventral aspect of the mediastinum, creating an unstructured mottled radiolucency. With regard to the appearance in **B,** the ventrodorsal (VD) view should be consulted to make sure that the mottling is not caused by superimposition of pockets of subcutaneous emphysema.

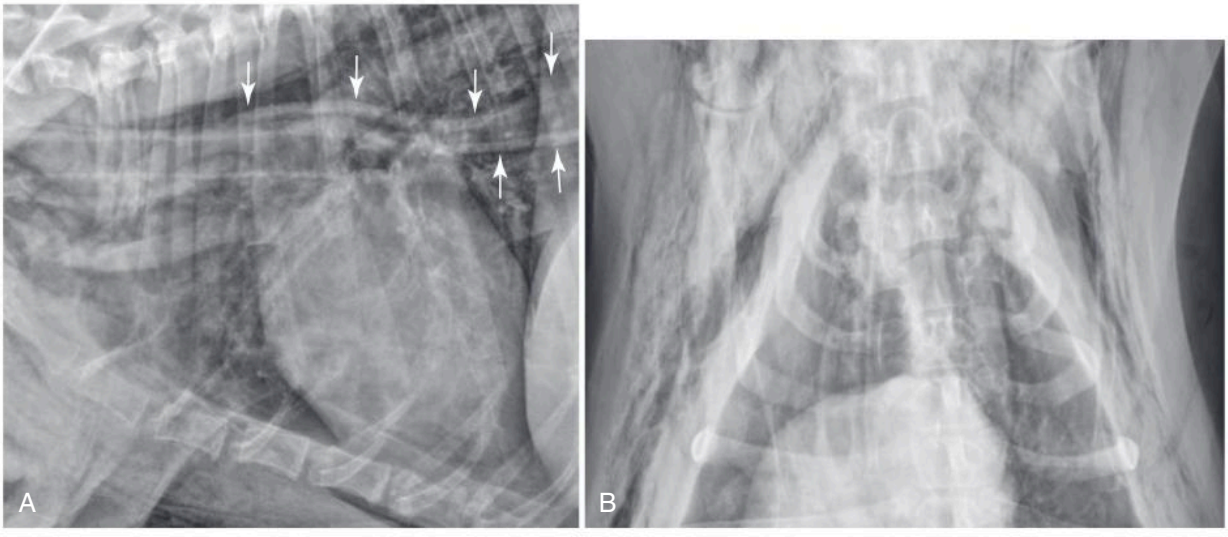


Fig. 33.35 Lateral **(A)** and ventrodorsal (VD; **B**) radiograph of a dog with pneumomediastinum and a large amount of coexisting subcutaneous emphysema. In **A,** the adventitial margin of the trachea and cranial mediastinal vessels are seen because of the contrast afforded by the mediastinal air. The adventitial surface of the esophagus is also visible (*white arrows*). In addition, the cranioventral mediastinum has a mottled appearance. This mottling can be caused by air pocketing in the mediastinum; but in this patient, much of it is caused by superimposition of the subcutaneous emphysema, as can be seen in **B**. In **A,** the mottling extends ventral to the thorax, which is also evidence of coexisting subcutaneous emphysema.

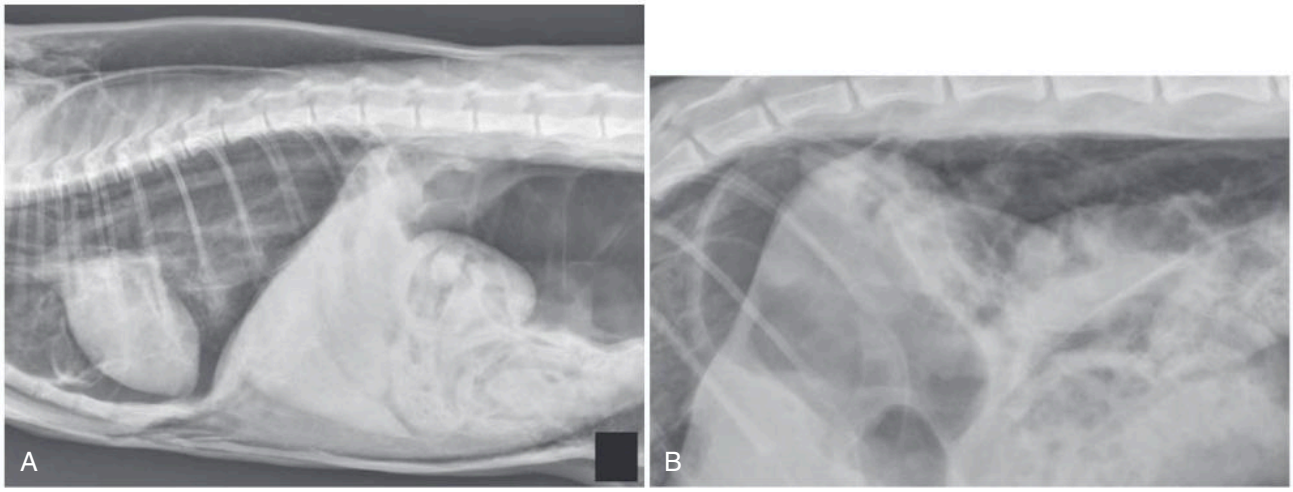


Fig. 33.36 **A,** Lateral radiograph of a cat with pneumomediastinum that has resulted in massive pneumoretroperitoneum. There is also subcutaneous emphysema. **B,** Lateral radiograph of a cat with pneumomediastinum where the extent of pneumoretroperitoneum is less.

REFERENCES

1. Kern D, Carrig C, Martin R. Radiographic evaluation of induced pneumothorax in the dog. *Vet Radiol Ultrasound*. 1994;35:411.
2. Burk R. Radiographic definition of the phrenicopericardiac ligament. *J Am Vet Radiol Soc*. 1976;17:216.
3. Bezuidenhout AJ. The lymphatic system. In: Evans H, ed. *Miller's Anatomy of the Dog*. 3rd ed. Philadelphia: Saunders; 1993:545–550.
4. Tompkins M. Lymphoid system. In: Hudson L, Hamilton W, eds. *Atlas of Feline Anatomy for Veterinarians*. Philadelphia: Saunders; 1993.
5. Kirberger RM, Avner A. The effect of positioning on the appearance of selected cranial thoracic structures in the dog. *Vet Radiol Ultrasound*. 2006;47(1):61–68.
6. Hopper B, Lester N, Irwin P, et al. Imaging diagnosis: pneumothorax and focal peritonitis in a dog due to migration of an inhaled grass awn. *Vet Radiol Ultrasound*. 2004;45(2):136–138.
7. Zekas LJ, Adams WM. Cranial mediastinal cysts in nine cats. *Vet Radiol Ultrasound*. 2002;43(5):413–418.
8. Cordella A, Saunders JS, Stock E. CT characteristics of the thymus in adult dogs with non-thymic neoplasia compared to young dogs. *Vet Sci*. 2023;10(3):192.
9. Ruehl Jr WW, Thrall D. The effect of dorsal versus ventral recumbency on the radiographic appearance of the canine thorax. *Vet Radiol*. 1981;22(10).
10. Brinkman EL, Biller D, Armbrust L. The clinical usefulness of the ventrodorsal versus dorsoventral thoracic radiograph in dogs. *J Am Anim Hosp Assoc*. 2006;42(6):440–449.
11. Lora-Michiels M, Biller DS, Olsen D, et al. The accessory lung lobe in thoracic disease: a case series and anatomical review. *J Am Anim Hosp Assoc*. 2003;39(5):452–458.
12. Gendron K, McDonough SP, Flanders JA, Tse M, Scrivani PV. The pathogenesis of paraesophageal empyema in dogs and constancy of radiographic and computed tomography signs are linked to involvement of the mediastinal serous cavity. *Vet Radiol Ultrasound*. 2018;59(2):169–179.
13. McDonough SP, Scrivani PB, Gendron K, Tse M. Mediastinal serous cavity mesothelioma in two dogs. *J Am Anim Hosp Associ*. 2022;58(4):194–202.
14. Ackerman N, Madewell BR. Thoracic and abdominal radiographic abnormalities in the multicentric form of lymphosarcoma in dogs. *J Am Vet Med Assoc*. 1980;176(1):36–40.
15. Berry CR, Moore PF, Thomas WP, et al. Pulmonary lymphomatoid granulomatosis in seven dogs (1976–1987). *J Vet Intern Med*. 1990;4(3):157–166.
16. Fitzgerald SD, Wolf DC, Carlton WW. Eight cases of canine lymphomatoid granulomatosis. *Vet Pathol*. 1991;28(3):241–245.
17. Fulmer AK, Mauldin GE. Canine histiocytic neoplasia: an overview. *Can Vet J*. 2007;48(10):1041–1043.
18. Snyder P, Sato T, Atkins C. The utility of thoracic radiographic measurement for the detection of cardiomegaly in cats with pleural effusion. *Vet Radiol*. 1990;31(89).
19. Reichle JK, Wisner ER. Non-cardiac thoracic ultrasound in 75 feline and canine patients. *Vet Radiol Ultrasound*. 2000;41(2):154–162.
20. Konde L, Spaulding K. Sonographic evaluation of the cranial mediastinum in small animals. *Vet Radiol*. 1991;32:178.
21. Macklin C. Transport of air along sheaths of pulmonic blood vessels from alveoli to mediastinum: clinical implications. *Arch Intern Med*. 1939;64:913.
22. Macklin M, Macklin C. Malignant interstitial emphysema of the lungs and mediastinum as an important occult complication in many respiratory diseases and other conditions: an interpretation of the clinical literature in the light of laboratory experiment. *Medicine (Baltimore)*. 1944;23:281.
23. Baharudin A, Sayuti RM, Shahid H. The Macklin effect—pneumomediastinum and pneumopericardium following blunt chest trauma. *Med J Malaysia*. 2006;61(3):371–373.
24. Wintermark M, Schnyder P. The Macklin effect: a frequent etiology for pneumomediastinum in severe blunt chest trauma. *Chest*. 2001;120(2):543–547.
25. Brown DC, Holt D. Subcutaneous emphysema, pneumothorax, pneumomediastinum and pneumopericardium associated with positive-pressure ventilation in a cat. *J Am Vet Med Assoc*. 1995;206(7):997–999.

26. Mitchell S, McCarthy R, Rudloff E, et al. Tracheal rupture associated with intubation in cats: 20 cases (1996–1998). *J Am Vet Med Assoc.* 2000;216(10):1592–1595.
27. Hardie EM, Spodnick GJ, Gilson SD, et al. Tracheal rupture in cats: 16 cases (1983–1998). *J Am Vet Med Assoc.* 1999;214(4):508–512.
28. Kelly S, Bandt C. Inadvertent placement of an esophagostomy tube into the mediastinum of a cat. *Can Vet J.* 2022;63(11):1124–1128.

ELECTRONIC RESOURCES

Additional information related to the content in Chapter 33 can be found online at eBooks.Health.Elsevier.com.

- Chapter Quiz

CHAPTER 34

Canine and Feline Pleural Space

Gabriela S. Seiler

PLEURAL ANATOMY AND PHYSIOLOGY

The pleural space is the space between two pleural layers, the visceral and parietal pleura. The visceral pleura covers the lung, whereas the parietal pleura covers the mediastinum, diaphragm, and thoracic wall. There are two distinct pleural sacs dividing the left and right thorax; however, mediastinal fenestrations allow fluid and air to travel between the pleural sacs in the majority of dogs and cats (Fig. 34.1) The pleural space normally contains a few milliliters of fluid which facilitates gliding of the lung surface against the thoracic wall during respiration and maintains negative pressure in the pleural space, which is thought to prevent or reduce atelectasis in normal animals. Pleural fluid is produced by the mesothelial cells of the pleural layer and is reabsorbed by the pleura and associated lymphatics.

NORMAL RADIOGRAPHIC APPEARANCE OF PLEURA AND PLEURAL THICKENING

Normal pleura is usually not visible radiographically. Pleura is very thin and also silhouettes with adjacent soft tissue everywhere except in interlobar fissures, where two layers of visceral pleura are in contact only with lung. Thin pleural lines between lobes are sometimes visible radiographically, particularly in the caudoventral thorax. These thin pleural lines may be because of the x-ray beam striking normal interlobar pleura exactly head-on, resulting in absorption of a sufficient number of x-rays for the pleura to be seen, or because of slightly thickened pleura or a trace pleural effusion (Fig. 34.2). Accessory pleural fissures are common in dogs and may result in atypical fissure lines being visible in addition to the interlobar fissure lines.[1] Radiographic determination of whether isolated,

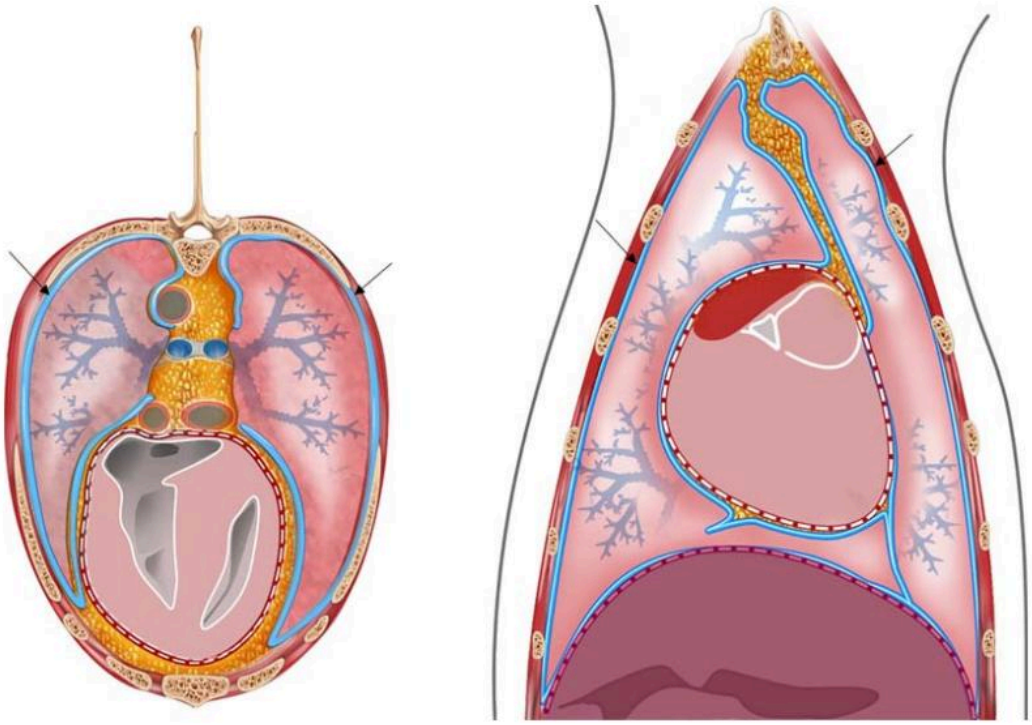


Fig. 34.1 The thorax in transverse **(A)** and dorsal **(B)** planes illustrating the relationship of the pleural layers. There are two distinct pleural sacs (*arrows*). **A,** Note how the mediastinal pleura is reflected onto the lung to become pulmonary pleura. **B,** Note the continuity of the costal, mediastinal, and diaphragmatic parts of each parietal sac. The heart is depicted by the *dotted line.* Also note that the pleural space is not continuous with the mediastinum. (Courtesy Harvey Medical Production.)

thin pleural lines are normal or are caused by mild thickening is impossible. In either instance, this finding is usually of no clinical significance. When pleural thickening is more advanced, wider pleural fissure lines between lung lobes may be seen (Fig. 34.3).

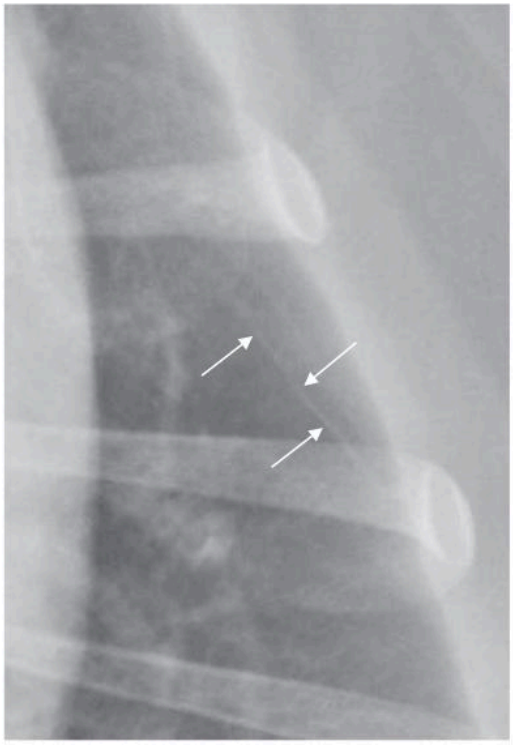


Fig. 34.2 Close-up view of a portion of the left hemithorax of a dog. A thin pleural fissure is visible (*white arrows*). Distinguishing radiographically whether this is caused by x-rays striking a normal fissure or by slight pleural thickening is impossible. This distinction is usually not clinically necessary.

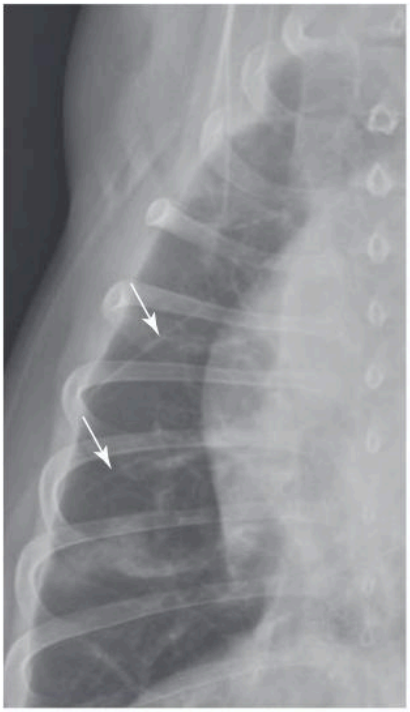


Fig. 34.3 Close-up view of the right hemithorax of a dog with multiple mildly widened pleural fissures (*white arrows*). The cranially located fissure line is thicker than normal (compare with Fig. 34.2) and may be caused by either pleural thickening or a small amount of pleural fluid.

PLEURAL FLUID

Causes of Pleural Fluid

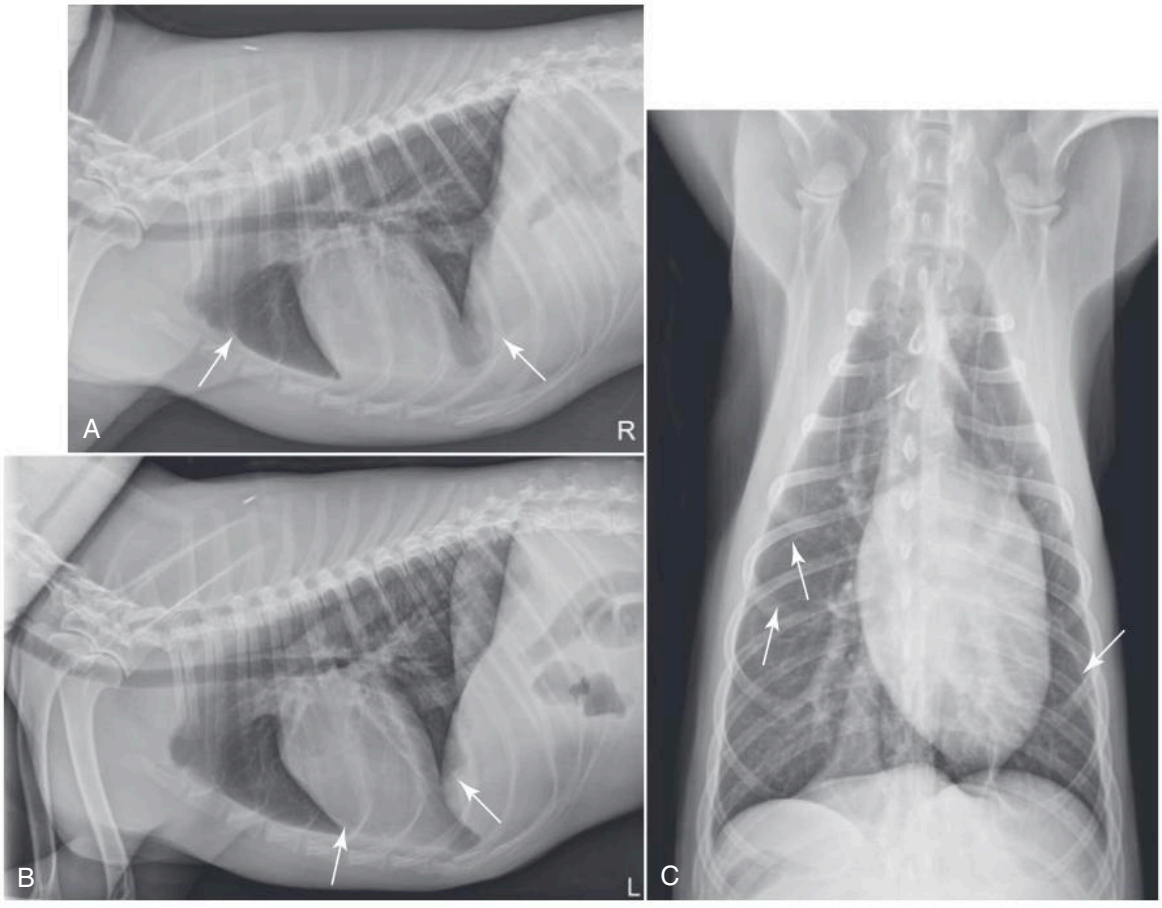
Normal homeostasis of pleural fluid is maintained by the difference of hydrostatic pressures between the systemic and pulmonary circulations and by drainage through the lymphatic vessels. Pleural effusion is therefore the result of either high production and/or increased vascular permeability, decreased reabsorption, decreased lymphatic drainage, or a combination of thereof. Fluid in the pleural space can be an exudate, transudate, or modified transudate, chyle, or hemorrhage and can result from many causes (Table 34.1). The radiographic changes associated with pleural fluid depend on the volume of fluid, the position of the animal in relation to the x-ray beam, the distribution of the fluid, and whether the fluid is free or trapped, so-called *loculated fluid.* There are no radiographic criteria that allow differentiation of an exudate from a transudate, although an exudate may be more asymmetrically distributed. Measurement of Hounsfield units in computed tomography (CT) has a limited ability to predict the characteristics of pleural fluid in dogs.[2] It is often not possible to determine the cause of pleural effusion radiographically, particularly since even large intrathoracic lesions can be obscured, but radiographs should always be evaluated for the presence of additional findings that may help in determining the most likely cause as outlined in Table 34.1. Making additional radiographs after removal of the fluid may provide important information. Any amount of pleural fluid is clinically significant, and attempts should be made to reach a definitive diagnosis. Thoracocentesis with appropriate fluid analysis should be considered if pleural fluid is identified. Ultrasound can be used to determine the presence of pleural effusion if radiographs are equivocal and to guide needle placement for diagnostic or therapeutic thoracocentesis. This is especially helpful in patients with chronic effusion that may be loculated with fibrin strands that tend to adhere to the needle. Ultrasound may also be able to identify mass lesions or cardiac changes which are obscured by the pleural effusion radiographically. The improved contrast resolution of CT imaging and lack of superimposition allow detection of concurrent or causative lesions including mass lesions, lung lobe torsions, and traumatic lesions.

Radiographic Appearance of Pleural Fluid

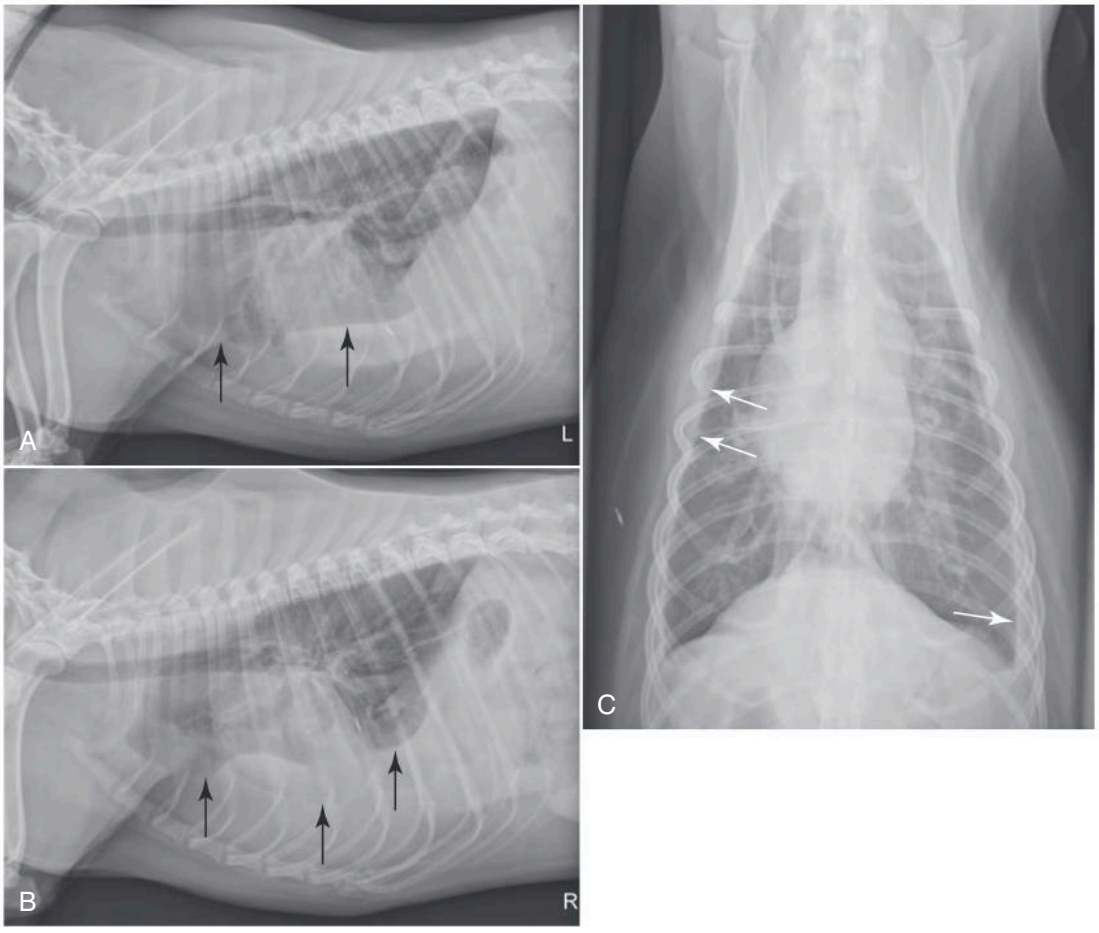
Regardless of the cause, if the negative pressure in the pleural space is not maintained, elastic recoil leads to retraction of the lung lobe margins and separation of the lobar margins from each other, which is the main radiographic finding associated with pleural space disease.[3] Pleural fluid distributes itself according to gravity and the ability of the lung to expand—that is, lung compliance.[4] It is important to realize that the radiographic appearance of pleural fluid in ventrodorsal (VD) versus dorsoventral (DV) radiographs is different. In DV radiographs, with the dog in sternal recumbency, fluid gravitates ventrally and causes border effacement of the heart. In VD radiographs, with the dog in dorsal recumbency, pleural fluid does not obscure the heart because the fluid gravitates to the dorsal aspect of the thorax, where it does not make contact with the heart and does not cause border effacement (Fig. 34.4). Also, the overall opacity of the thorax will be greater in DV radiographs in patients with pleural fluid because the fluid depth is greater (see Fig. 34.4). Radiographic signs of free pleural fluid are listed in Box 34.1.

Interlobar Fissures

The width and number of interlobar fissures seen with pleural fluid depend on the amount of fluid and the relative position of the patient and the x-ray beam (Fig. 34.5, eFigs. 34.1 and 34.2). Approximately 100 mL of fluid must be present in the pleural space of a medium-sized dog before widened interlobar fissures become visible radiographically.[4] Thus, any radiographic evidence of pleural fluid signifies a relatively large fluid volume,



eFig. 34.1 Right lateral **(A)**, left lateral **(B)**, and ventrodorsal **(C)** radiograph of a dog with a small volume of pleural fluid. Several thin pleural fissure lines are best seen in the lateral projections (*white arrows*). The ventral fissure lines widen slightly towards the periphery of the lung lobes (*white arrows*). Note also the mild rounding of the ventral lung lobe margins.



eFig. 34.2 Left lateral **(A)**, right lateral **(B)**, and ventrodorsal **(C)** radiograph of a dog with a moderate volume of pleural fluid. There is increased opacity of the ventral thorax with border effacement of the cardiac silhouette and diaphragm. The lung lobes are rounded (*black arrows*) and retracted from the thoracic wall in **C** (*white arrows*).

Table • 34.1

Causes of Pleural Fluid.

CAUSE	FLUID TYPE	POSSIBLE ADDITIONAL RADIOGRAPHIC FINDINGS
Congestive heart failure Dog: right-sided cardiac disease, pericardial effusion Cat: left-sided cardiac disease	T, M, CH	Dogs: right-sided or globoid cardiomegaly, dilated caudal vena cava Cats: left-sided cardiomegaly, sometimes dilated pulmonary veins
Pyothorax • Dog: Nocardia, actinomyces • Cat: Pasteurella, bacteroides, fusobacterium	E	Often unilateral or loculated effusion. Look for thoracic wall trauma, foreign material, esophageal rupture, pulmonary abscess
Feline infectious peritonitis	E	Abdominal effusion commonly present
Mediastinal neoplasia • Lymphoma • Thymoma	M, E, CH	Cranial mediastinal mass
Pulmonary Neoplasia • Pulmonary carcinoma • Metastatic carcinoma • Hemangiosarcoma	M, E, CH, H	Pulmonary mass or nodules
Pleural or thoracic wall neoplasia • Mesothelioma • Rib tumors	M, E	Extrapleural sign, pleural nodules, rib lysis, and/or periosteal reaction
Chylothorax • Idiopathic • Thoracic duct rupture	CH	Rounded lung lobes, effusion may be loculated
Trauma • Diaphragmatic hernia • Thoracic wall trauma • Surgical intervention	M, E, H	Thoracic wall defect, emphysema, or swelling Discontinuous diaphragm, cranial displacement of abdominal organs
Heartworm disease	M, CH	Enlarged pulmonary arteries, right heart enlargement
Pulmonary disease • Pneumonia, pulmonary abscess • Lung lobe torsion	E, H	Pneumonia: ventral alveolar pattern without mediastinal shift Abscess: cavitary lesion with surrounding consolidation Lung lobe torsion: vesicular gas pattern, enlarged lung lobe, discontinuous bronchus
Hypoalbuminemia	T	Concurrent abdominal effusion
Abdominal disease • Pancreatitis • Bile peritonitis	E	Peritoneal effusion, possible cranial abdominal mass effect
Mediastinitis, mediastinal abscess	E	Mediastinal mass effect, mediastinal effusion
Coagulopathies Von Willebrand Rodenticide toxicity	H	May have mediastinal or tracheal wall hemorrhage

CH, Chyle; *E,* exudate; *H*, hemorrhage; *M,* modified transudate; *T,* transudate.

and one that can be sampled by thoracocentesis. Visibility of fluid-containing interlobar fissures results when the x-ray beam strikes the fissure in a parallel fashion, or head-on. Some fluid-containing fissures may not be seen, because their relation to the x-ray beam is not head-on. Pleural fissure lines caused by fluid rather than pleural thickening or fortuitous alignment of the x-ray beam with the pleural space may widen towards the periphery of the thorax with a triangular appearance, caused by rounding of the lung margins. With a *small amount of fluid*, interlobar fissures are more likely to be seen on VD rather than DV radiographs, because when in dorsal recumbency for a VD radiograph, there is a tendency for fluid to enter interlobar fissures (see Fig. 34.3). This is opposed to sternal recumbency for a DV radiograph where the fluid collects dorsal to the sternum (see Fig. 34.4).[2,3] A small amount of pleural fluid usually results in visible interlobar fissures in lateral views as well, commonly superimposed on the cardiac silhouette.

Retraction of Lung Margins

With moderate or pronounced pleural fluid, the number and width of interlobar fissures increase, and fluid also collects between the thoracic wall and the lung, resulting in lung retraction (Figs. 34.6 and 34.7). Retraction of lung from the thoracic wall is characterized by a soft tissue opacity rim between the lung lobe margins and the thoracic wall, and mild rounding of the lung lobe margins. The pleural fluid surrounds the lung, but the fluid will be most apparent radiographically where the x-ray beam strikes the fluid/lung interface in a parallel fashion (see Fig. 34.5). Therefore, more pleural fluid is present than

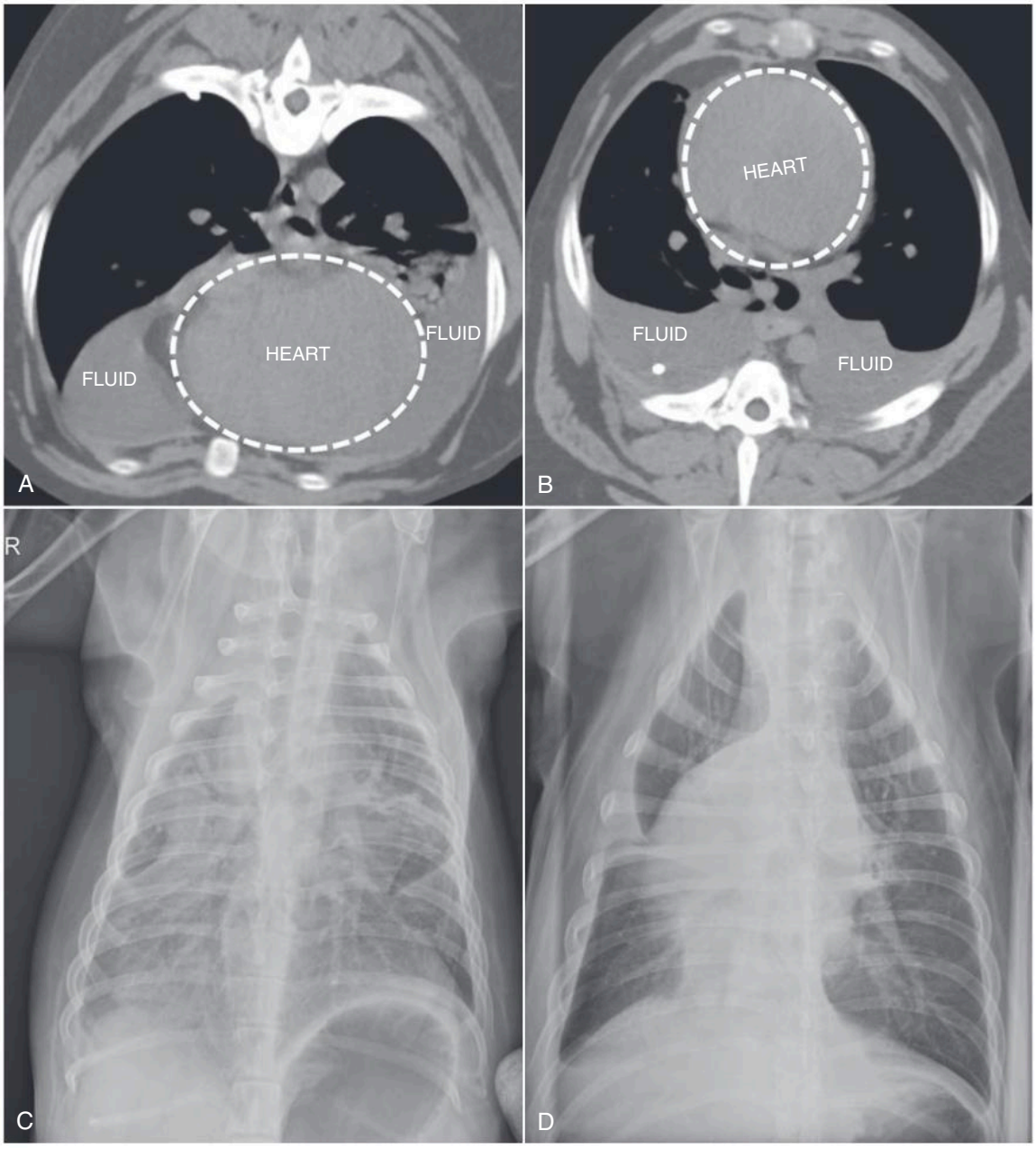


Fig. 34.4 Transverse computed tomography (CT) images of the thorax imaged in ventral **(A)** and dorsal **(B)** recumbency, and dorsoventral (DV) **(C)** and ventrodorsal (VD) **(D)** radiographs of the thorax of a dog with pleural fluid. **A and C,** The patient is in ventral recumbency and fluid gravitates ventrally. The fluid is in contact with the heart, thus obscuring the heart radiographically because of border effacement (i.e., the silhouette sign). When the patient is in dorsal recumbency for the VD radiograph **(B, D)**, the fluid gravitates dorsally and is not in contact with the heart; thus, the cardiac silhouette is visible because it is surrounded by air-filled lung that provides contrast. The overall thoracic opacity is greater because the absolute depth of the fluid is greater when the patient is in ventral recumbency **(A, C)** because the ventral part of the thoracic cavity is narrower, and the fluid rises to a higher level.

predicted based on the amount of lung retraction (Fig. 34.8). Pleural fluid may cause blunting of the costophrenic angle in VD radiographs if fluid is present between the dorsocaudal aspect of the lung and diaphragm. Rounding of the costophrenic angles will seldom be the only radiographic sign of pleural fluid.

Retrosternal Soft Tissue Opacity and Silhouette Sign

In lateral radiographs, pleural fluid can also result in a region of homogeneously increased opacity dorsal to the sternum (Fig. 34.9; also see Figs. 34.6C and 34.7B). This opacity results from fluid having collected in the ventral aspect of the thorax and layered against the mediastinum in the nondependent hemithorax. The margin of this retrosternal opacity often appears *scalloped* because of adjacent, partially collapsed lung that alters the configuration of the fluid. It is important to differentiate retrosternal pleural fluid from mediastinal fat. In presence of pleural fluid, the borders of the cardiac silhouette and diaphragm are effaced, whereas mediastinal fat will create contrast with the diaphragmatic and cardiac margins.

Box • 34.1

Roentgen Signs of Free Pleural Fluid

1) Widened interlobar fissures that are of soft tissue opacity
   a) Usually most conspicuous in ventrodorsal (VD) and lateral radiographs
2) Retraction of pleural surface of lung away from pleural surface of thoracic wall, with interposed soft tissue opacity
   a) Seen first in VD radiographs
3) Increased soft tissue opacity with scalloped margins dorsal to sternum
   a) Seen in lateral radiographs
4) Increased opacity of the pulmonary parenchyma
   i) Seen in all views, caused by atelectasis and superimposed fluid
5) Decreased cardiac silhouette visualization
   a) Usually seen in dorsoventral (DV) radiographs
6) Obscured diaphragmatic outline
   a) Seen in all views
7) Blunting of costophrenic sulci
   a) Seen rarely, only in VD radiographs
   b) Expansion of thoracic cavity, diaphragm is flattened
      i) Only with large volume of fluid, seen in all views

Asymmetric Distribution of Pleural Fluid

Pleural fluid is usually relatively equally distributed between the right and left pleural spaces. Some patients, however, have asymmetric fluid distribution. Causes of unilateral or asymmetric pleural fluid include a difference in compliance between lung lobes, the closing of mediastinal fenestrations from inflammation or a mass, and an anatomically complete mediastinum (eFig. 34.3). Pyothorax is a common cause of unilateral or asymmetric pleural fluid because of the viscous nature of the exudate (Fig. 34.10), but other types of fluid can also be asymmetric. Chronic pleural effusions, particularly with exudative, hemorrhagic, or chylous effusions, result in pleural thickening and entrapment of fluid in fibrous capsules. Pleuritis causes the lung lobe margins to be markedly rounded or scalloped (see Fig. 34.10B). Lung reexpansion can be reduced in presence of pleuritis, and this can result in lung rupture and pneumothorax if the pleural fluid is rapidly removed during thoracocentesis (eFig. 34.4). Parenchymal disease or bronchial obstruction of a single lung lobe can also result in focal unilateral accumulation of pleural fluid due to decreased fluid absorption and decreased pleural pressure.

Horizontal-Beam Radiography

Identification of a small amount of pleural fluid may not be possible on survey radiographs if the x-ray beam fails to strike a fluid/lung interface head-on (see Fig. 34.8). If identification of a small amount of pleural fluid is critical, a horizontally directed

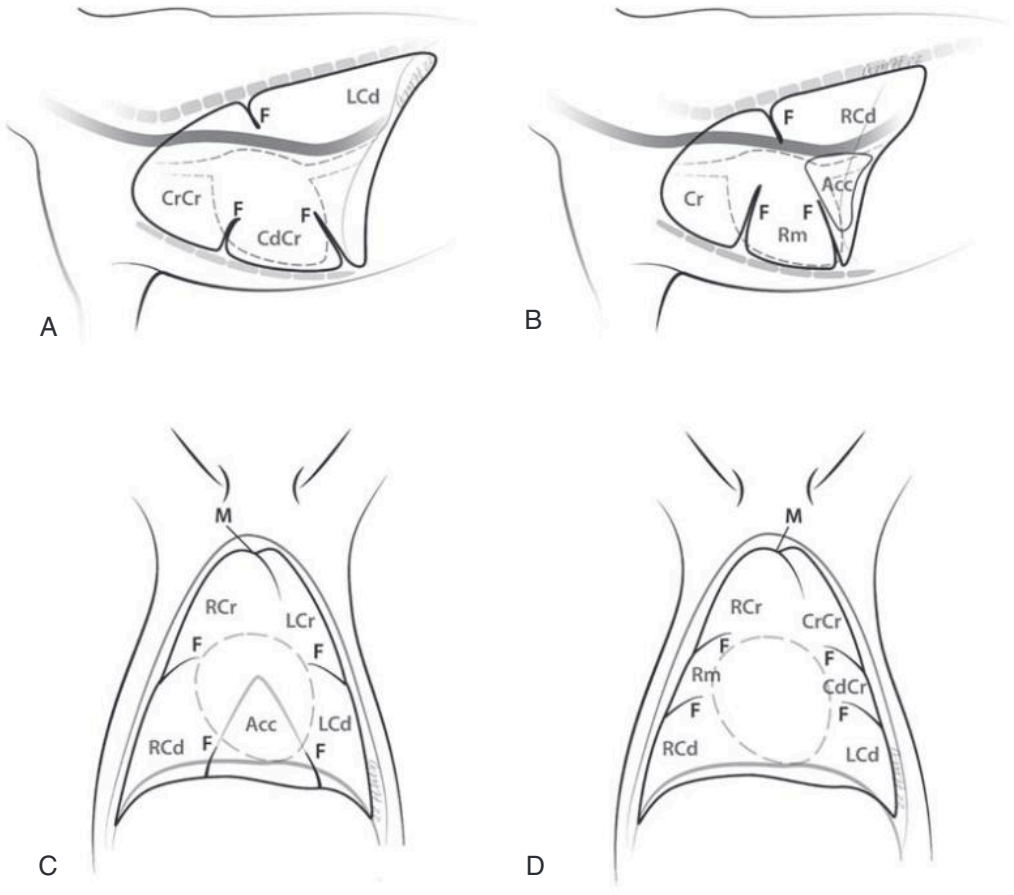
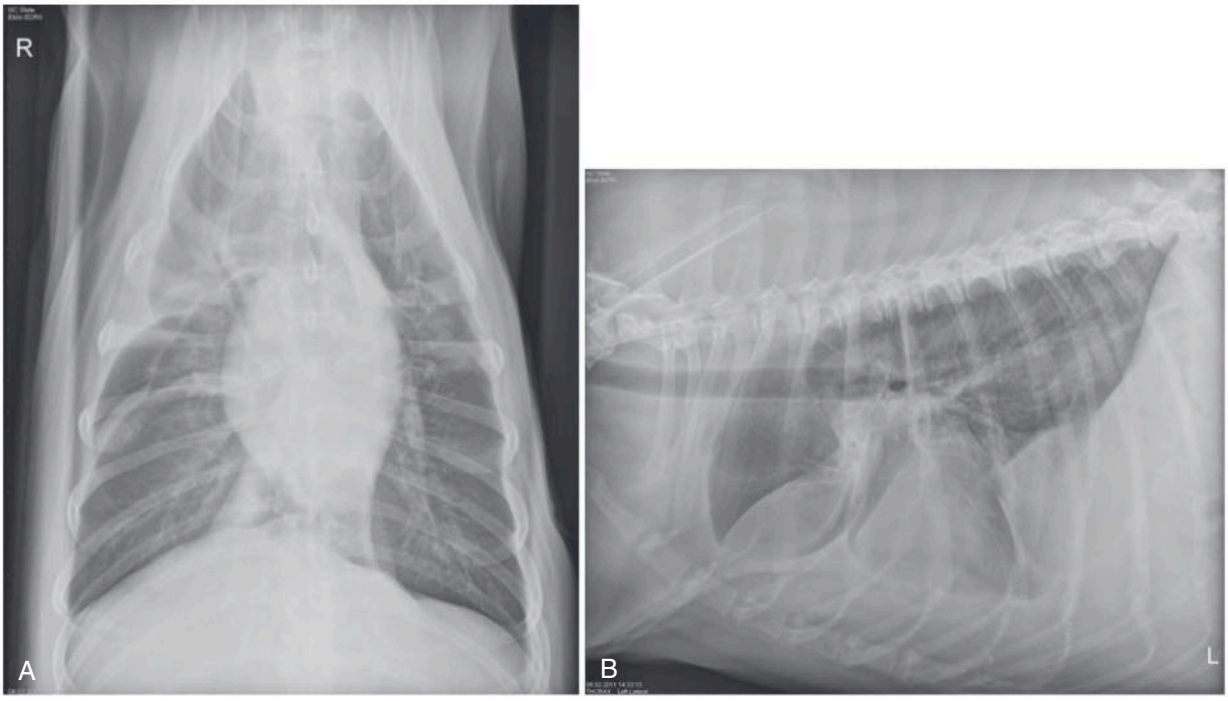
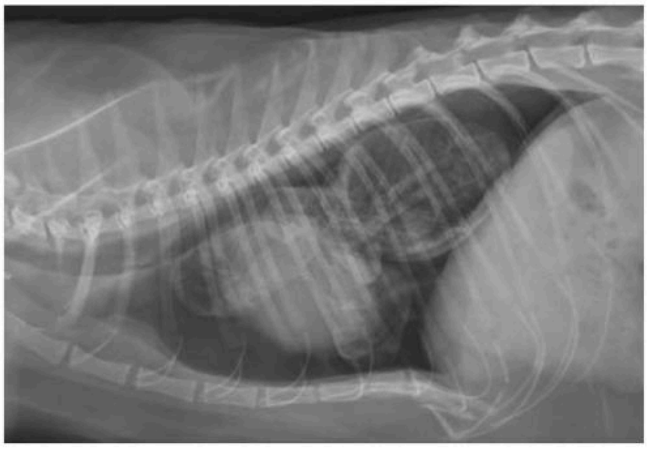


Fig. 34.5 The location of interlobar fissures. The exact fissures visible when pleural fluid is present depends on the position of the patient, the volume of fluid, and whether the x-ray beam strikes the fissure in a parallel orientation. Only fluid-filled fissures that are struck in a parallel fashion will be seen. **A,** Fissures of the lateral aspect of the left lung. These fissures are more likely to be seen when the patient is in left recumbency. **B,** Fissures of the lateral aspect of the right lung, best seen when the patient is in right recumbency. **C,** Fissures on the dorsal aspect of the lungs, best seen when the patient is in dorsal recumbency. The costophrenic sulcus may become rounded when patients with pleural fluid are in dorsal recumbency. **D,** Fissures on the ventral aspect of the lungs, best seen when the patient is in ventral recumbency. *Acc,* Accessory lobe; *Cd,* caudal lobe; *CdCr,* caudal part of left cranial lobe; *Cr,* right cranial lobe; *CrCr,* cranial part of left cranial lobe; *F,* interlobar fissure; *L,* left; *M,* mediastinal reflection; *R,* right; *Rm,* right middle lobe.



eFig. 34.3 **A,** Ventrodorsal radiograph of a dog with moderate pleural effusion on the *right* and mild pleural effusion on the *left*. The right hemithorax is more opaque and there is more pronounced lung lobe retraction from the thoracic wall whereas only a few fissure lines are visible in the left hemithorax. **B,** Left lateral radiograph of the same dog. There is increased opacity of the ventral thorax with border effacement of the cardiac silhouette and diaphragm and several widened pleural fissure lines are visible.



eFig. 34.4 Left lateral radiograph of a cat with bilateral pneumothorax after thoracocentesis to remove pleural effusion. Note the radiolucent space around the lungs without bronchovascular markings. The lung lobes are markedly rounded due to fibrosing pleuritis in this cat with chronic pleural effusion.

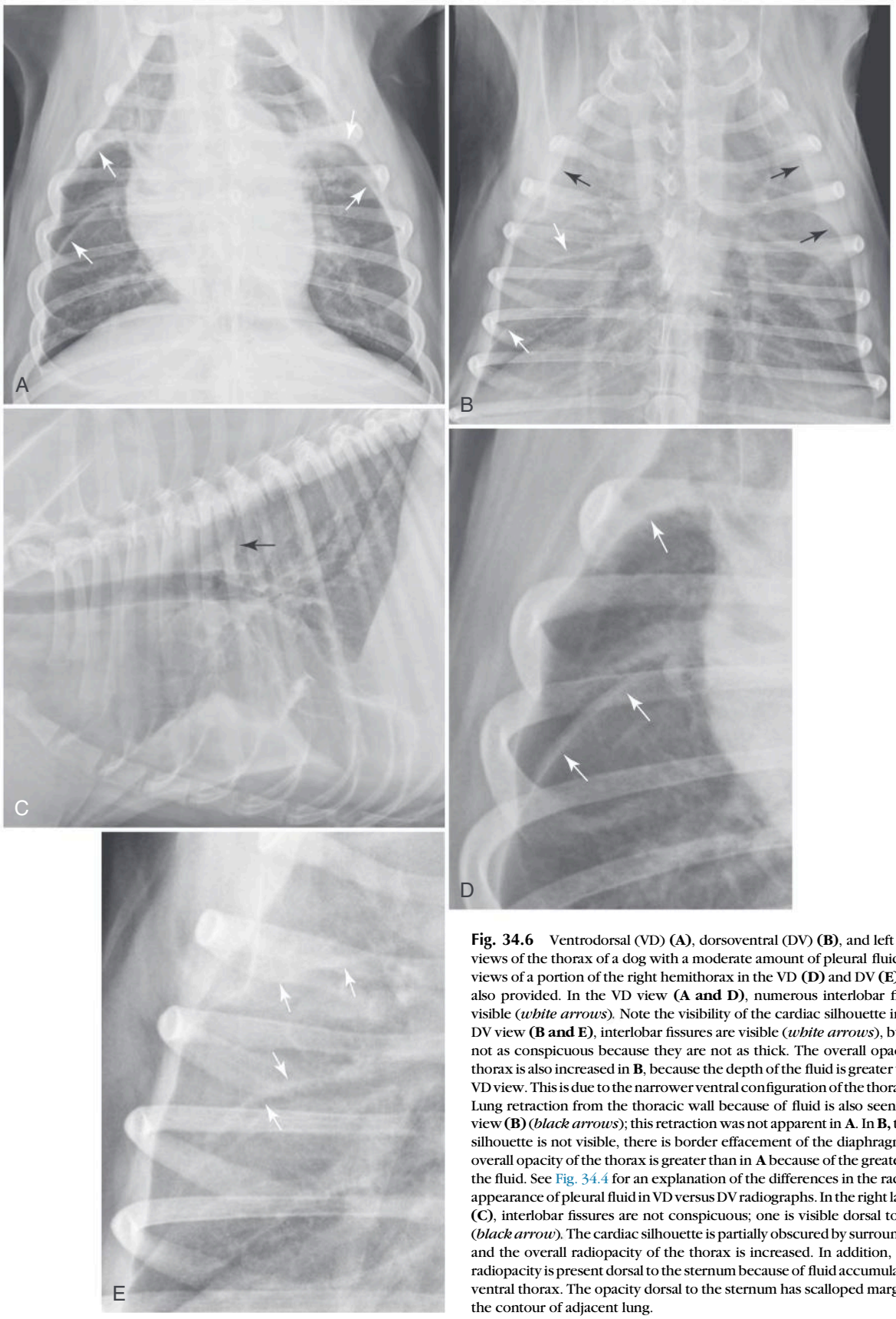


Fig. 34.6 Ventrodorsal (VD) **(A)**, dorsoventral (DV) **(B)**, and left lateral **(C)** views of the thorax of a dog with a moderate amount of pleural fluid. Close-up views of a portion of the right hemithorax in the VD **(D)** and DV **(E)** views are also provided. In the VD view **(A and D)**, numerous interlobar fissures are visible (*white arrows*). Note the visibility of the cardiac silhouette in **A**. In the DV view **(B and E)**, interlobar fissures are visible (*white arrows*), but they are not as conspicuous because they are not as thick. The overall opacity of the thorax is also increased in **B**, because the depth of the fluid is greater than in the VD view. This is due to the narrower ventral configuration of the thoracic cavity. Lung retraction from the thoracic wall because of fluid is also seen in the DV view **(B)** (*black arrows*); this retraction was not apparent in **A**. In **B,** the cardiac silhouette is not visible, there is border effacement of the diaphragm, and the overall opacity of the thorax is greater than in **A** because of the greater depth of the fluid. See Fig. 34.4 for an explanation of the differences in the radiographic appearance of pleural fluid in VD versus DV radiographs. In the right lateral view **(C)**, interlobar fissures are not conspicuous; one is visible dorsal to the heart (*black arrow*). The cardiac silhouette is partially obscured by surrounding fluid, and the overall radiopacity of the thorax is increased. In addition, an area of radiopacity is present dorsal to the sternum because of fluid accumulation in the ventral thorax. The opacity dorsal to the sternum has scalloped margins due to the contour of adjacent lung.

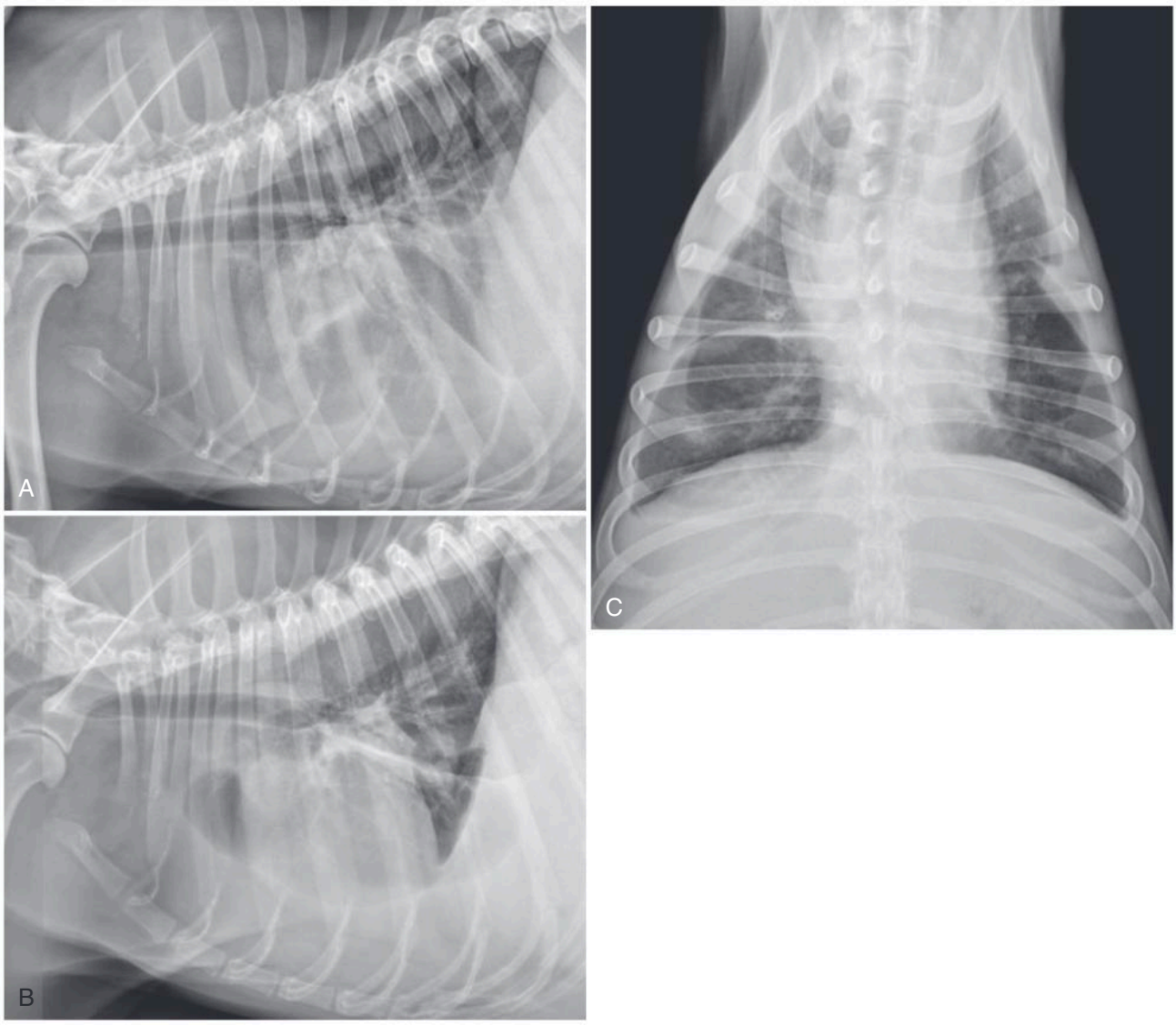


Fig. 34.7 Left lateral **(A)**, right lateral **(B)**, and ventrodorsal (VD) **(C)** radiographs of a dog with a large volume of pleural fluid. In the VD view **(C)**, the lungs are markedly retracted from the thoracic wall by the fluid. The heart is visible, as expected. In the lateral views, the fluid has obscured much of the normal thoracic detail. This volume of fluid could obscure significant lesions in the thoracic cavity. In **C,** note especially the inability to evaluate the cranial mediastinum because of the fluid. The ribs should always be scrutinized carefully in patients with pleural fluid to ensure that the fluid is not the result of a rib tumor. Thoracic ultrasonography or computed tomography (CT) may be helpful in deciding if an underlying mass is present in the thorax.

x-ray beam may be used to ensure a head-on relation between the x-ray beam and the fluid/lung interface. If free pleural fluid is present, it gravitates dependently where the x-ray beam strikes it in a parallel fashion (Fig. 34.11). A sharply demarcated, straight fluid line is only seen when there is a free fluid/free air interface, such as with coexisting pleural fluid and pneumothorax. Horizontal-beam radiographs may also be useful in distinguishing pleural fluid from an intrathoracic mass as the cause of an intrathoracic opacity, as discussed before (see Fig. 34.9).

Pitfalls in Pleural Fluid Diagnosis

Various normal structures can be misinterpreted as pleural fluid. Thickened pleura may have an appearance identical to pleural fluid (see Fig. 34.3). A distinction may be made by using a horizontally directed x-ray beam or with sonography.[4] A mineralized costal cartilage is sometimes confused with an interlobar fissure. The position of these two structures is similar, but their shape is different. Pleural fissure lines are distinctly curving, with the concave surface on the caudal aspect of the fissure line. Costal cartilages are more linear and can usually be seen to attach to the end of a rib (Fig. 34.12). Thoracic wall deformities, as found in chondrodystrophic breeds, such as the Basset hound, may result in increased radiopacity at the margin of the lung field. Without knowledge of this fact, the opacity may be misinterpreted as retraction of the lung from the thoracic wall because of pleural fluid (Fig. 34.13). Accumulation of pleural fluid along the cranial mediastinum can mimic presence of the mediastinal mass. Evaluation of tracheal shape and position of the carina is helpful for differentiating mediastinal masses from pleural effusion. While large volumes of pleural effusion can lead to dorsal

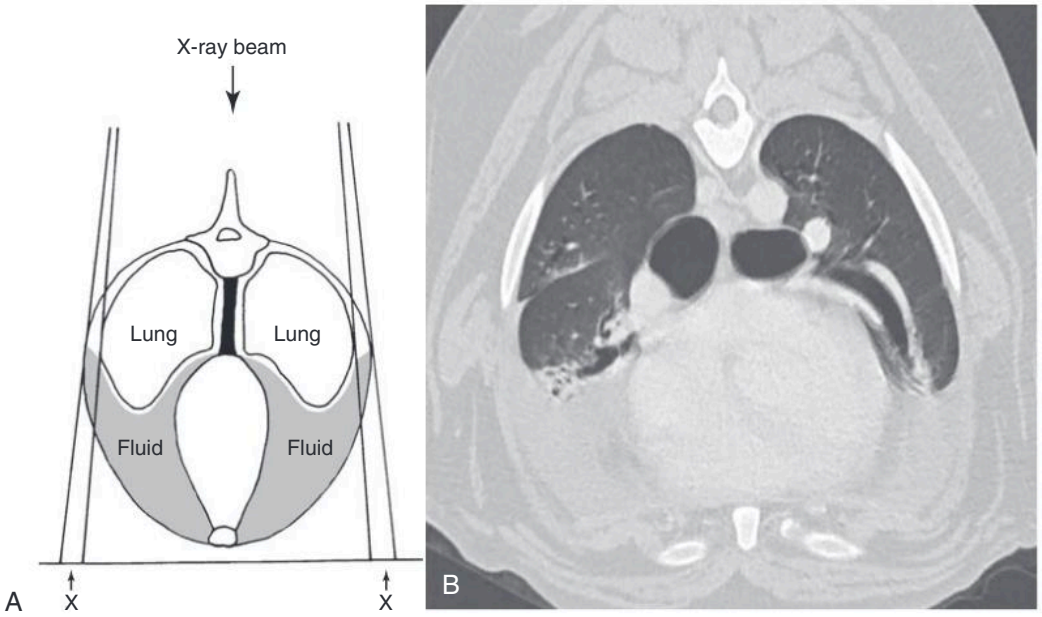


Fig. 34.8 Principle of lung retraction as a result of pleural fluid. **A,** Diagram of a patient with a large amount of pleural fluid being radiographed in ventral recumbency for a dorsoventral (DV) view. Fluid has gravitated ventrally, causing lung retraction. The full extent of the lung retraction is not apparent radiographically because the main fluid/lung interface, ventral to the lung, is not being struck in a parallel fashion by the x-ray beam. The only lung retraction that will be seen is in the regions indicated by (*X*) because here the fluid/lung interface is struck head-on by the x-ray beam. In the central portion of the thorax, the overall radiopacity will increase, and the heart will be obscured, but the lung retraction will not be apparent. **B,** Transverse computed tomography (CT) image of the thorax of a dog in sternal recumbency with pleural fluid. The fluid has pooled ventrally causing lung retraction from the ventral aspect of the thoracic cavity. However, the fluid is not dissecting between the lungs and the thoracic wall; thus, no part of the fluid/lung interface will be struck in a parallel fashion by the oncoming x-ray beam, and there will not be evidence of lung retraction in a DV radiograph of this patient even though there is a large amount of pleural fluid.

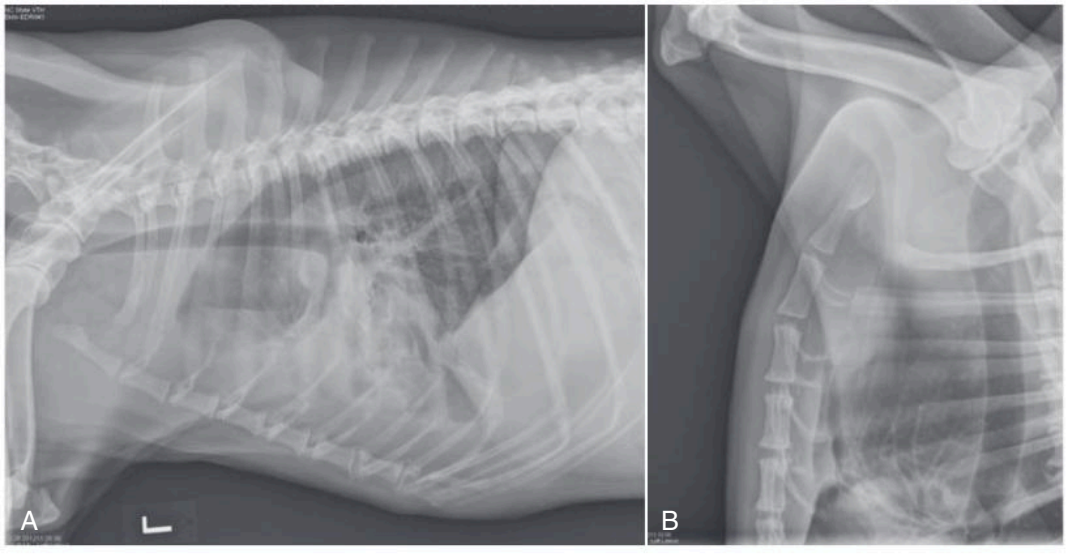


Fig. 34.9 **A,** Conventional lateral radiograph made with a vertically directed x-ray beam. **B,** Lateral radiograph made with a horizontally directed x-ray beam with the patient held in a sitting, upright position. In the conventional right lateral radiograph **(A)**, there is an opacity dorsal to the sternum and it is uncertain whether this opacity represents a mass or pleural fluid. In the radiograph made with a horizontal beam and the patient in upright position **(B)**, there is a rounded retrosternal soft tissue opacity mass visible consistent with an enlarged sternal lymph node. Note that a sharp horizontal fluid line is not present in the horizontal-beam radiograph **(B)** because sharp fluid lines are seen only when there is a free fluid/free air interface.

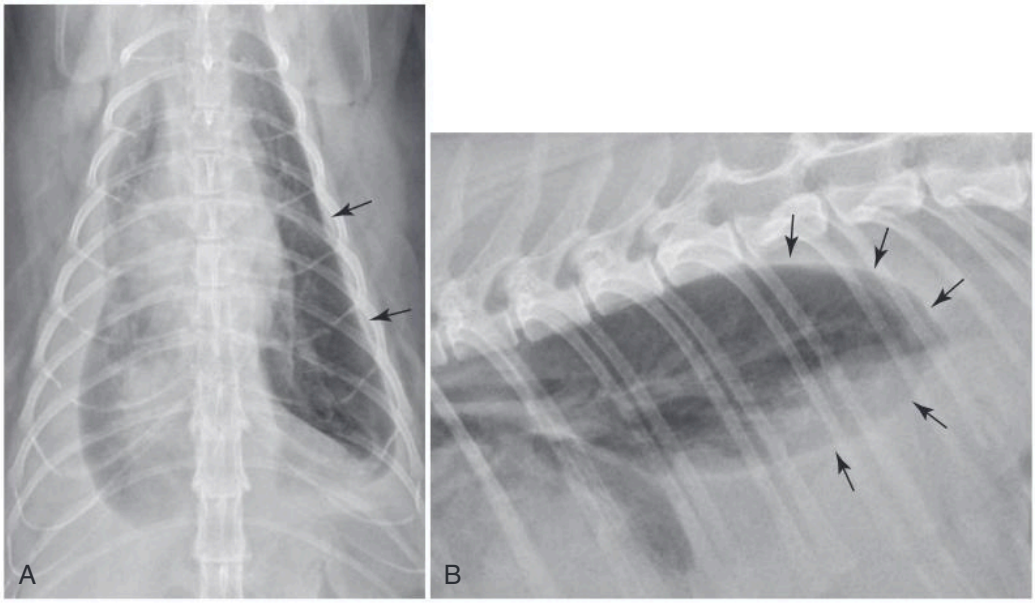


Fig. 34.10 **A,** Ventrodorsal (VD) thoracic radiograph of a cat with asymmetric pleural fluid. There is a small amount of pleural fluid on the left, evidenced by lung retraction (*black arrows*). On the right, there is extensive lung retraction. An asymmetric distribution of pleural fluid such as seen here occurs commonly with an exudate, but any fluid can be asymmetric if the inciting factor is unilateral and mediastinal fenestrations are closed. Ultrasound imaging or computed tomography (CT) would be useful in further characterizing the cause of the unilateral fluid in this patient. Thoracocentesis will also be valuable. **B,** Close-up view of the dorsocaudal aspect of the thorax of the same cat. The retracted lung margin is round rather than having a normal sharp triangular border, indicating pleural fibrosis (*black arrows*). Pleural fibrosis will develop with chronic pleural fluid and will limit the ability of the lung to expand following subsequent fluid removal.

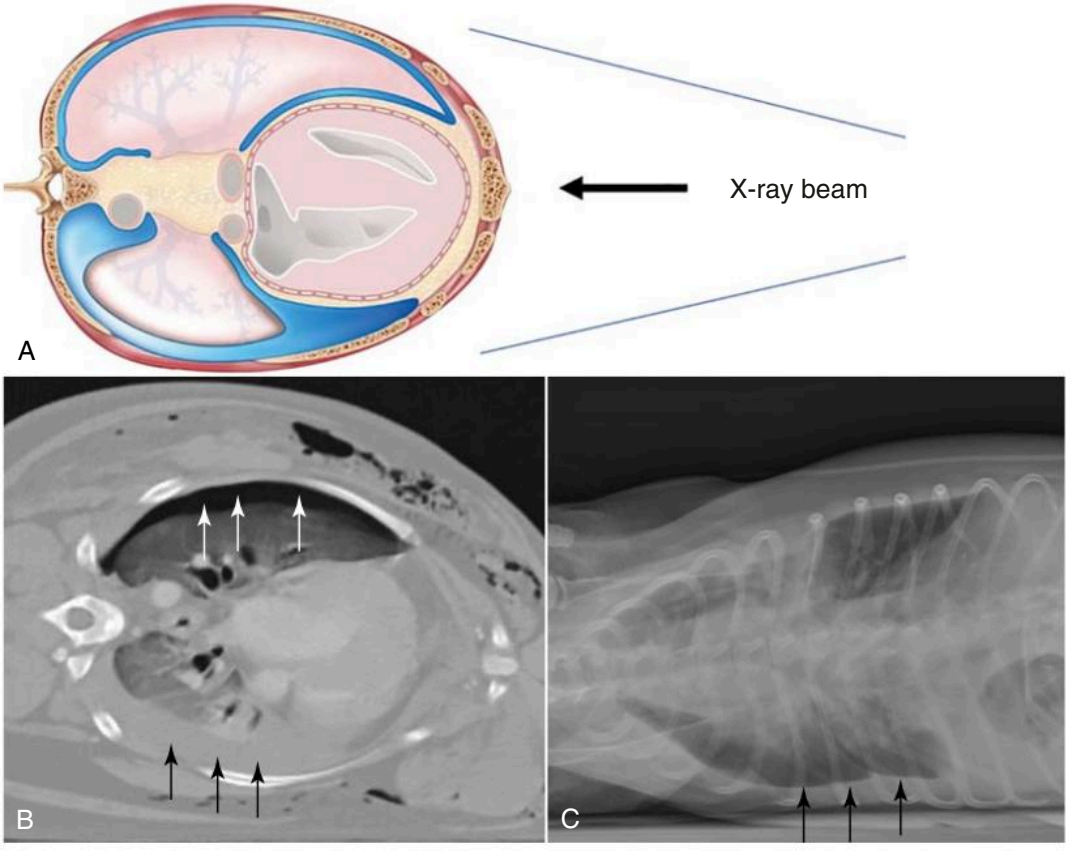


Fig. 34.11 **A,** Drawing illustrating the principle of using a horizontal-beam radiograph to detect pleural fluid. If the mediastinum is complete, fluid in the nondependent hemithorax layers against the mediastinum and is not detectable radiographically. Fluid in the dependent hemithorax, or fluid in the nondependent hemithorax that can move through the mediastinum, gravitates between the lung and the thoracic wall, where the horizontally directed x-ray beam strikes it in a parallel fashion. **B,** Computed tomography (CT) image of a patient with pleural effusion (*black arrows*) and a small amount of pneumothorax (*white arrows*) after trauma. The patient was imaged in lateral recumbency as illustrated in **A**. Pleural fluid accumulates in the dependent thorax whereas free pleural air accumulates in the nondependent thorax. Subcutaneous emphysema is also present. **C,** Horizontal-beam ventrodorsal (VD) thoracic radiograph of a different dog with pleural fluid. The dog was in left lateral recumbency and a horizontally oriented x-ray beam directed onto the sternum. Fluid has pooled against the left thoracic wall causing lung retraction (*black arrows*).

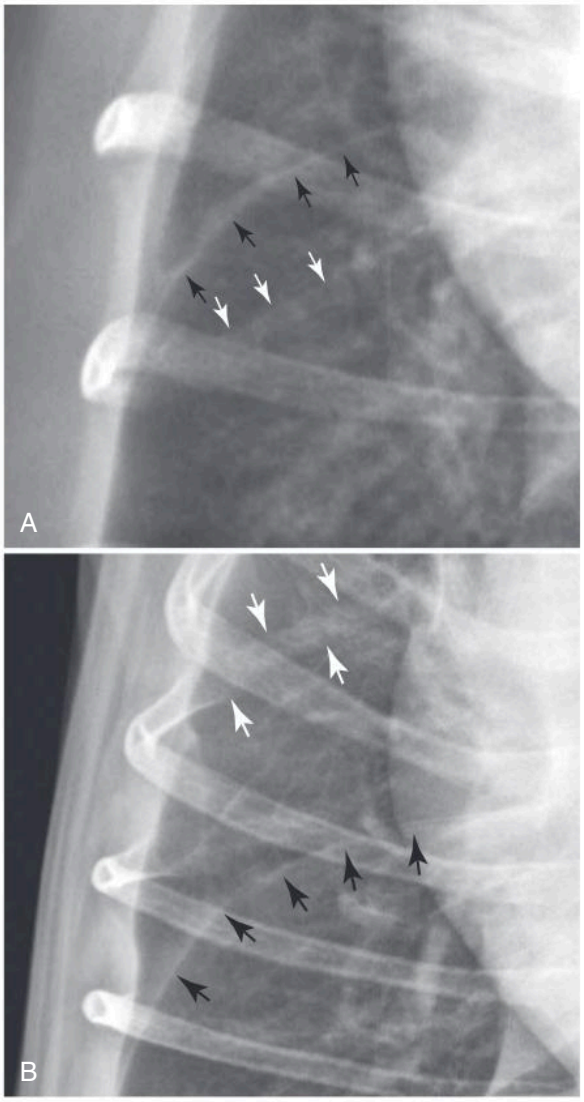


Fig. 34.12 **A and B,** Ventrodorsal (VD) radiographs of two dogs with mild pleural fluid. Interlobar fissures can be seen in each dog; the fissure lines are curving with the caudal aspect of the fissure being concave (*black arrows*). In these dogs, the costal cartilages (*white arrows*) are larger and more linear, and they can be followed laterally to attach to a rib.



Fig. 34.13 Ventrodorsal (VD) view of the left caudolateral aspect of the thorax of a normal Basset hound. An area of soft tissue opacity is present medial to the left thoracic wall; this is caused by the irregular thoracic wall conformation in this chondrodystrophic dog. The location and appearance of this opacity may result in it being confused with pleural fluid; however, interlobar fissures are not seen and this is a tip-off that this opacity is an artifact.

Box • 34.2

Causes of Pneumothorax

- Tear in lung involving visceral pleura
- Thoracic wall rent
- Extension of pneumomediastinum into pleural space
- Rupture of cavitary lung lesion

displacement of the trachea, it remains straight and parallel to the spine whereas mediastinal masses often cause a curved displacement of the trachea. Even large amounts of pleural effusion are not able to caudally displace the cardiac silhouette and carina. Horizontal-beam radiography with the patient in the upright position as well as ultrasonography are useful to differentiate between masses and effusions.

Simultaneous Pleural and Peritoneal Fluid

The detection of simultaneous pleural and peritoneal fluid is an important finding. Of 48 dogs with simultaneous peritoneal and pleural fluid, 32 had either neoplastic or cardiovascular disease. Simultaneous pleural and peritoneal fluid is an indicator of severe disease with poor prognosis.[5]

PNEUMOTHORAX

Causes of Pneumothorax

Air or gas in the pleural space is termed *pneumothorax*. Air can enter the pleural space through a thoracic wall defect or from the lung or mediastinum (Box 34.2). Radiographs should be evaluated for the presence of thoracic wall or mediastinal trauma, and for the presence of cavitary lung lesions. CT imaging is more sensitive for detecting cavitary lesions, and positive pressure ventilation during CT can improve detection of pulmonary bullae.[5,6] In most animals, pneumothorax is bilateral, and this relates either to a bilateral source of pleural air or to movement of air through the mediastinum. When unilateral pneumothorax was induced in 24 dogs, bilateral pneumothorax was observed immediately after air instillation in 22 dogs, indicating rapid movement of air through fenestrations in the mediastinum.[7] Unilateral pneumothorax, however, can occur for the same reasons as for unilateral pleural fluid.

Radiographic Appearance of Pneumothorax

The character of the radiographic changes resulting from air in the pleural space depends on the volume of air and the relative position of the patient and the x-ray beam. In general, lateral views are more sensitive for detection of pneumothorax than VD or DV views.[8] Roentgen signs of pneumothorax are listed in Box 34.3.

Box • 34.3

Radiographic Signs of Pneumothorax

1. Retraction of pleural surface of lung away from pleural surface of thoracic wall, with interposed radiolucency; lung markings do not extend to thoracic wall
   a. Seen first in lateral radiographs
2. Focal air collection around cardiac apex
3. Appearance of dorsal displacement of the heart
   a. Seen in lateral views

Lung Retraction From Pneumothorax

With a small volume of pleural air, separation of the lung from the thoracic wall is small and appears as a thin radiolucent line (Fig. 34.14). As in pleural fluid, air surrounds the lung but is most apparent radiographically when the air/lung interface is struck in a parallel fashion by the x-ray beam. The lack of pulmonary vascular markings within the pleural gas allows differentiation from normal air-filled pulmonary parenchyma in many but not all cases. Air-containing interlobar fissures are almost never seen with pneumothorax, because air does not dissect between lung lobes as fluid usually does. A mild pneumothorax may also result in air collection against the cardiac apex. This occurs when the air is trapped against the mediastinum, most often in the dependent hemithorax (Fig. 34.15). With increasing amounts of pleural air, these changes become more pronounced in lateral views, but the changes in the VD or DV view may remain inconspicuous or minimal (Fig. 34.16, eFigs. 34.5 and 34.6). With pronounced pneumothorax, lung collapse is visible in VD or DV radiographs as well, usually best seen in the caudal thorax (Fig. 34.17). The secondary lung collapse leads to the lung becoming more opaque than normal. The degree of increased lung opacity is directly related to the degree of collapse. This increased opacity resulting from atelectasis can interfere with radiographic evaluation of the lung parenchyma. If the pneumothorax is open (i.e., with no valve at the site of air entrance), air may continue to enter the pleural space until pleural pressure equals atmospheric pressure. At this point, the lung is maximally collapsed but still maintains roughly the shape of a normal lung because of its elasticity.

"Elevation" of the Heart From the Sternum

The appearance of dorsal displacement, or elevation, of the heart from the sternum is seen commonly in lateral radiographs of patients with pneumothorax (see Fig. 34.16). The heart is not actually elevated but displaced into the dependent hemithorax because of a lack of underlying inflated lung to support the heart in its normal midline position. As the heart falls into the dependent hemithorax, it slides dorsally, creating the appearance of elevation on a lateral radiograph (Fig. 34.18). Although pneumothorax is the most common cause of the appearance of elevation of the cardiac silhouette on the lateral view, this can also occur with decreased heart size, in normal dogs with an extremely deep thoracic cavity, in hypovolemic patients, and in patients with hyperinflated lungs (Fig. 34.19).

Tension Pneumothorax

Tension pneumothorax occurs when pleural space pressure exceeds atmospheric pressure during both phases of respiration. Tension pneumothorax results from a check-valve mechanism at the origin of pleural space air. Air enters the thorax with each breath but cannot escape. In tension pneumothorax, increased pleural pressure causes the lung to collapse to a greater degree than even its maximal collapse in an open pneumothorax. Thus, it may no longer maintain the shape of a lung but may assume the appearance of an amorphous opacity compressed against the midline (Fig. 34.20). With unilateral tension pneumothorax, the increased pleural space pressure will cause a contralateral mediastinal shift (Fig. 34.21, eFig. 34.7). Tension pneumothorax may also result in caudal displacement of the diaphragm to the degree that its

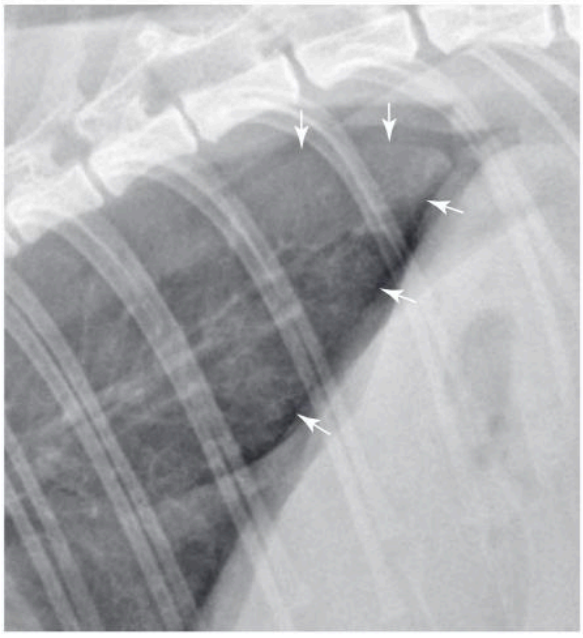
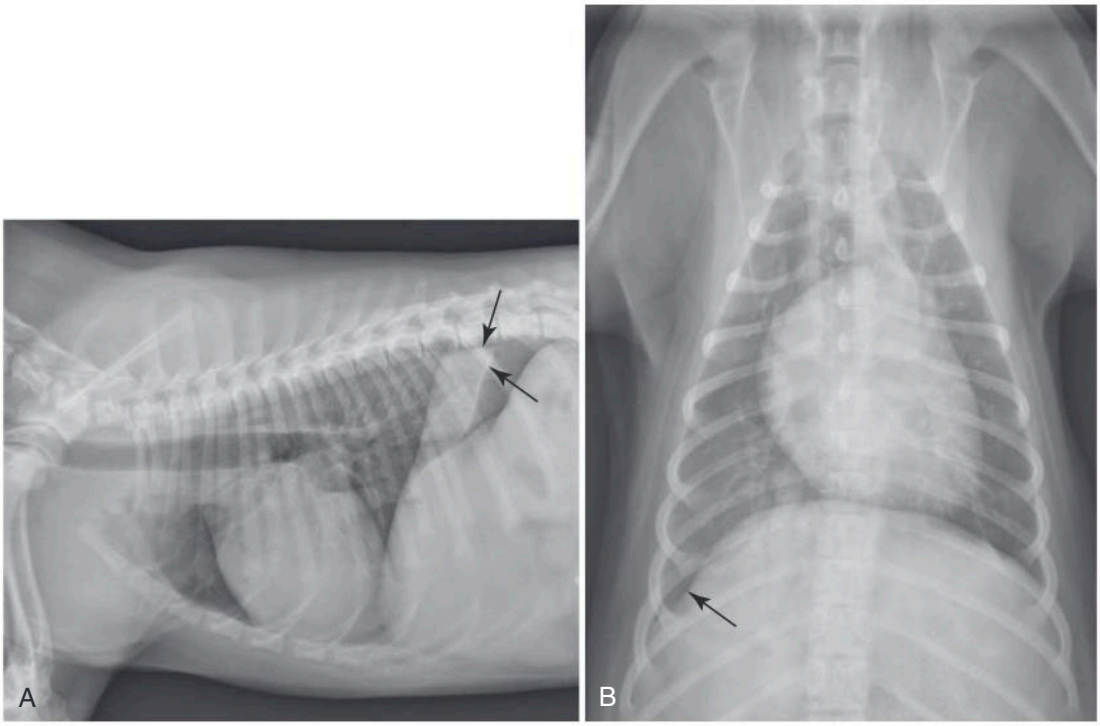


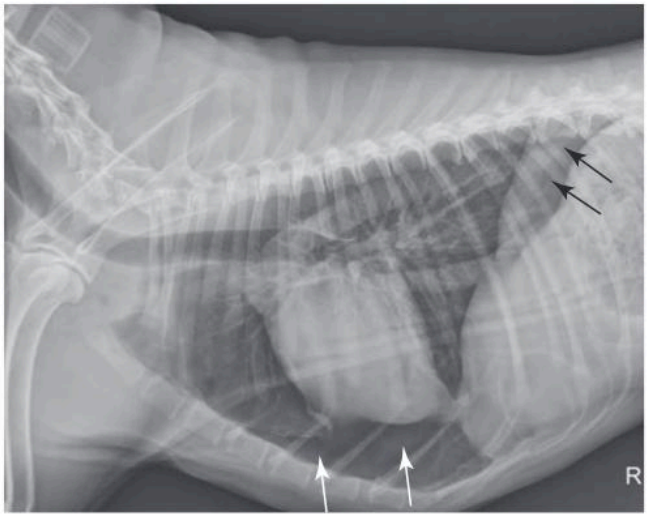
Fig. 34.14 Lateral radiograph of a cat with mild pneumothorax. The air in the nondependent hemithorax collects around the dorsocaudal aspect of the lung, causing the lung to collapse slightly (*white arrows*), creating a thin radiolucency between the lung and thoracic wall.



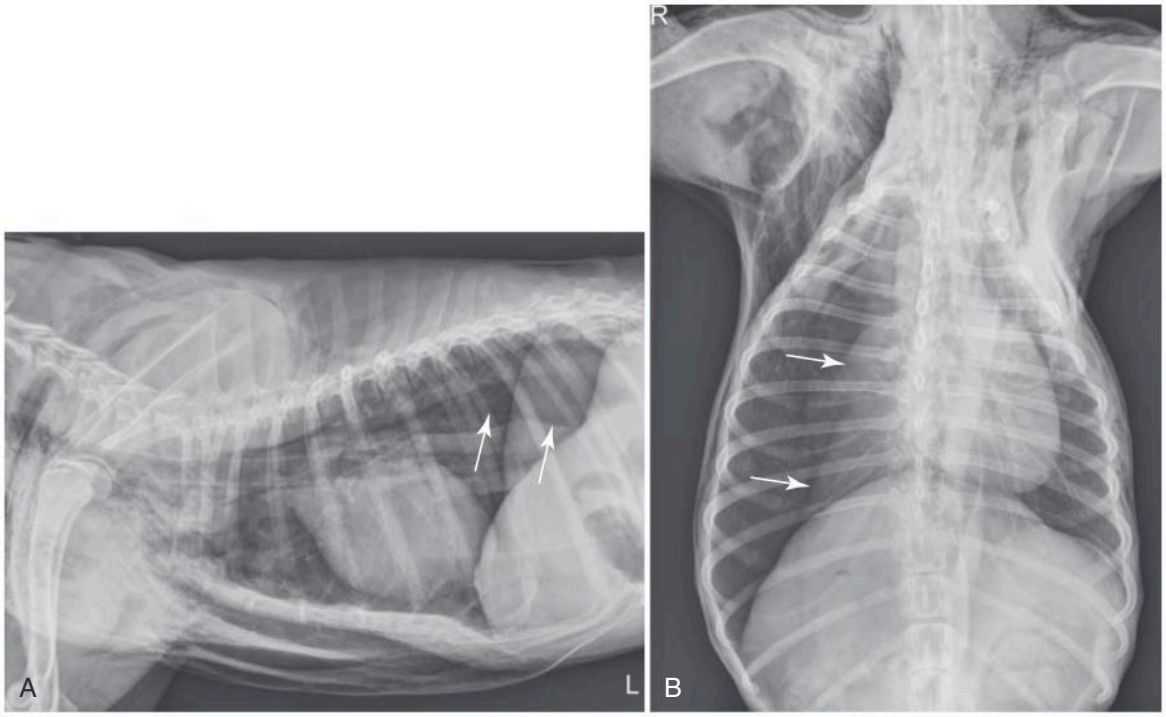
Fig. 34.15 Lateral radiograph of a dog with mild pneumothorax. In this patient, the air is trapped in the dependent hemithorax against the cardiac apex (*white arrow*). There were no regions of lung retraction at the periphery of the thorax in this dog, and this was the only radiographic evidence of pneumothorax.



eFig. 34.5 **A,** Left lateral radiograph of a dog with pneumothorax after being hit by a car. The caudal lung lobe is retracted from the thoracic wall (*black arrows*) and free air is visible in the lumbophrenic angle. **B,** Dorsoventral radiograph of the same dog. The pneumothorax is more difficult to see, but a radiolucent rim (*black arrow*) is visible along the caudal lung lobe margin. The increased opacity of the right caudal lung lobe is partly due to atelectasis but pulmonary contusions may be present as well.



eFig. 34.6 Right lateral radiograph of a dog with a moderate amount of spontaneous pneumothorax. There is radiolucent gas accumulated ventral to the cardiac silhouette and the caudodorsal lung lobes are retracted (*black arrows*). Thin-walled radiolucent structures (*white arrows*) were confirmed to be pulmonary bullae/blebs on computed tomography (CT) imaging.



eFig. 34.7 **A,** Left lateral thoracic radiograph of an American Staffordshire terrier after a dog fight. There is extensive subcutaneous emphysema and pneumomediastinum. The caudal lung lobe margins are retracted (*white arrows*) indicating the presence of free air in the caudal thorax. **B,** Dorsoventral radiograph of the same dog. There is a large amount of free air in the right hemithorax with severe lung lobe retraction (*white arrows*) and a mediastinal shift to the left consistent with tension pneumothorax.

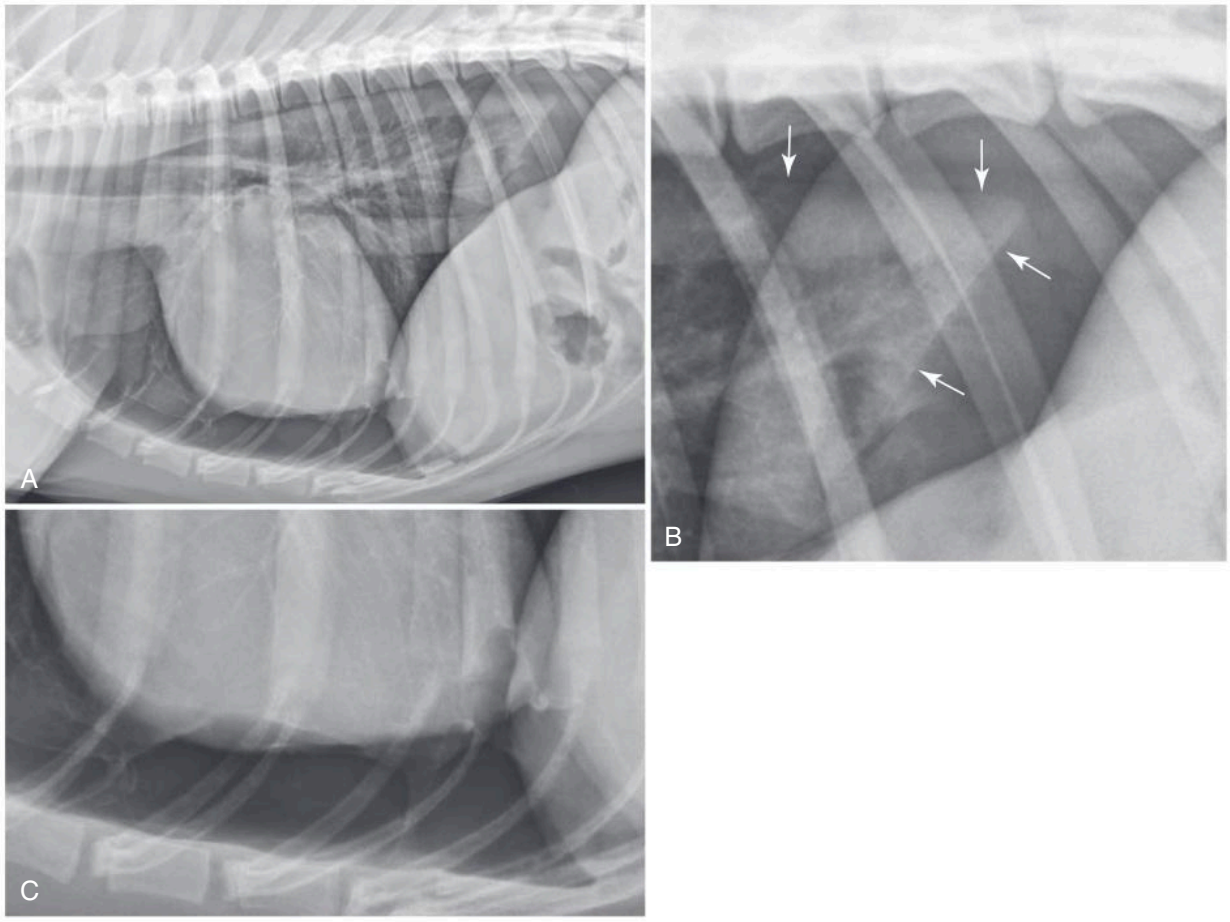


Fig. 34.16 **A,** Left lateral radiograph of a dog with moderate pneumothorax, with close-up views of the dorsocaudal **(B)** and ventral **(C)** aspects of the thorax. There was no evidence of pneumothorax in the ventrodorsal view. **B,** Air in the nondependent hemithorax has risen to the dorsocaudal aspect of the thorax, causing retraction of the caudal lobe from the thoracic wall and diaphragm (*white arrows*). **C,** Secondary atelectasis in the dependent lung allows the heart to slide into the dependent hemithorax, creating a space between the heart and sternum. The air in this region makes this space highly radiolucent.

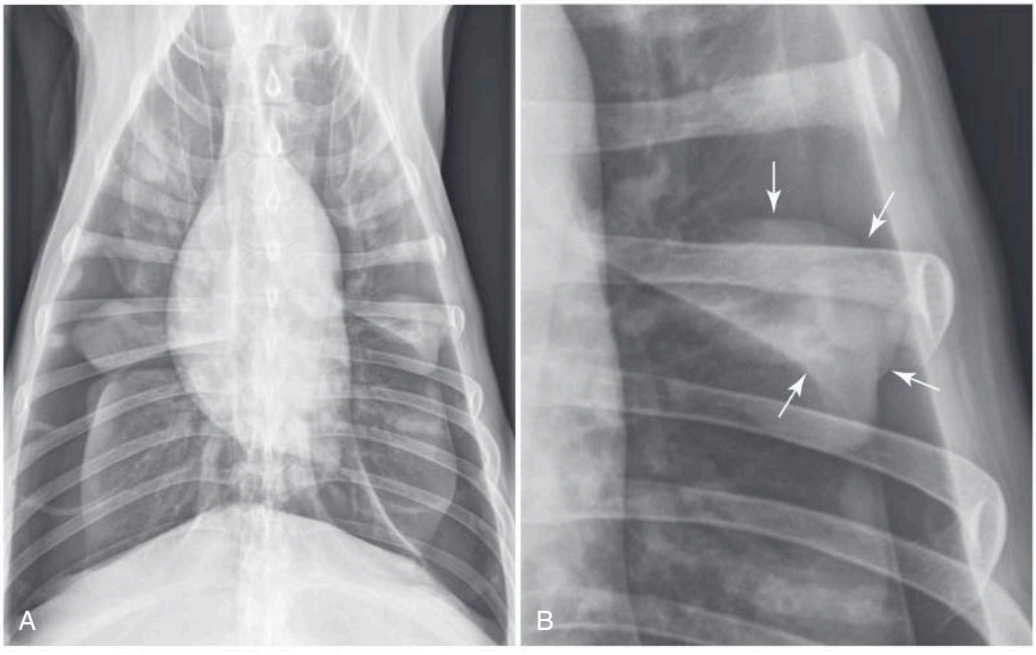


Fig. 34.17 **A,** Ventrodorsal (VD) thoracic radiograph of a dog with a large volume of air in the right and left pleural cavity. The lungs are partially collapsed and therefore of increased radiopacity. **B,** The caudal part of the left cranial lobe is very opaque (*white arrows*); it cannot be determined radiographically whether this is because of atelectasis or pulmonary disease.

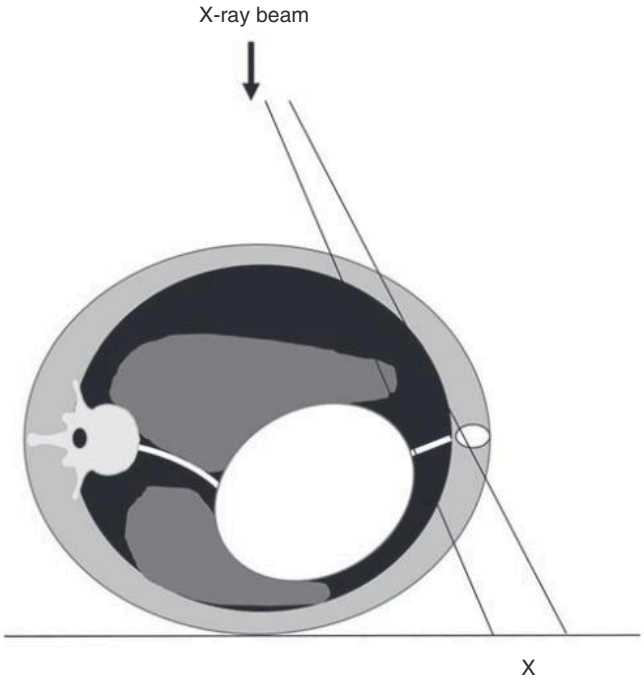


Fig. 34.18 Principle of dorsal displacement, or elevation, of the heart from the sternum in lateral radiographs of patients with pneumothorax. When the patient is in lateral recumbency, the collapse of the lung in the dependent hemithorax due to the pneumothorax allows the heart to slide into the dependent hemithorax. As it slides, it moves dorsally because of the shape of the thoracic wall, thus creating a space between the heart and the sternum. As x-rays pass through this space, the heart appears dorsally displaced, or elevated, from the sternum on the lateral view by the distance (*X*).

costal attachments become visible; this is termed *tenting* of the diaphragm (Fig. 34.22). In conventional pneumothorax, the cardiac silhouette is usually shifted toward the side of the thorax containing the most air, but in a tension pneumothorax, it is shifted to the opposite side because of the increased pleural space pressure. Tension pneumothorax is uncommon, but it is important to recognize because it is potentially fatal and requires immediate thoracocentesis.

Horizontal-Beam Radiography

As with a small amount of pleural fluid, a small amount of pleural air may not be apparent radiographically. The likelihood of diagnosing pneumothorax is increased by using a horizontally directed x-ray beam and placing the patient in lateral recumbency and directing the x-ray beam onto the sternum. By so doing, air will collect beneath the nondependent thoracic wall where the x-ray beam strikes it in a parallel fashion. Justification for using horizontal-beam radiography should be based on the suspected underlying cause. For example, pneumothorax resulting from lung disease is a potentially serious event, whereas a small pneumothorax occurring after trauma with no associated clinical signs may not be significant.

Pitfalls in Pneumothorax Diagnosis

The causes of elevation of the cardiac silhouette from the sternum in lateral views other than pneumothorax have already been discussed (see Fig. 34.19). In VD views, skin folds can result in a radiolucent area that is superimposed over the lateral aspect of the thorax. In many patients, it may not be possible to identify lung markings in the radiolucent area. In these instances, a correct diagnosis of skin-fold artifact can be made by noting that the opacity of the fold extends beyond the limits of the thorax (Fig. 34.23).

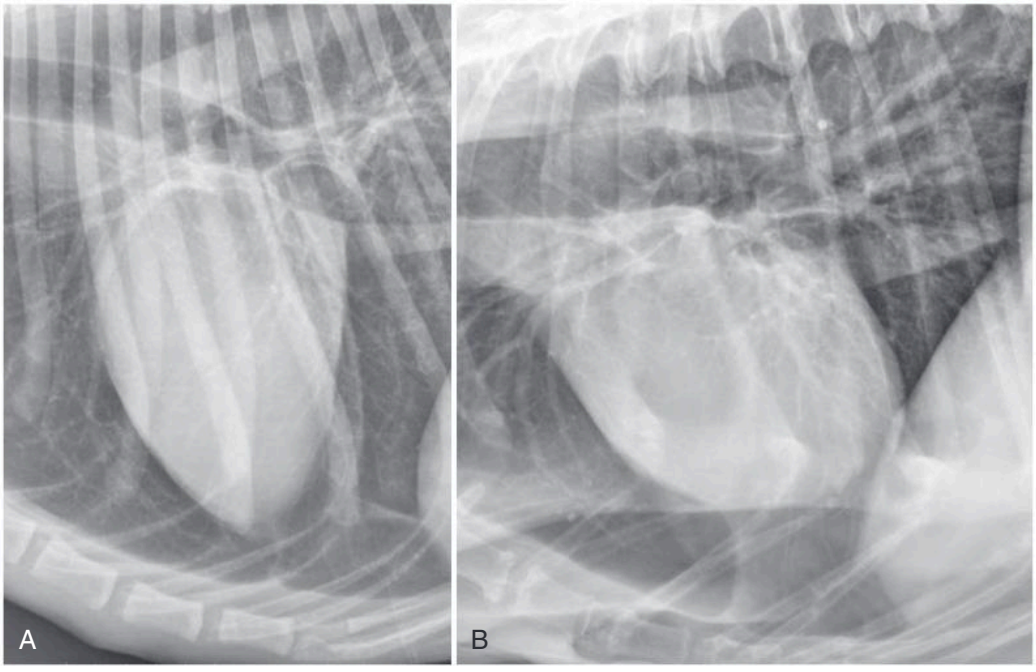


Fig. 34.19 **A,** Lateral radiograph of a dog with volume depletion secondary to Addison's disease. The cardiac silhouette is small and retracted from the sternum. **B,** Lateral radiograph of a dog with a very narrow ventral thoracic cavity. There is inadequate room for the cardiac silhouette to occupy the ventral aspect of the thorax. The position of the heart in each of these radiographs could lead to a misdiagnosis of pneumothorax. The correct assessment is based on the lack of any other signs of pneumothorax and the lack of a distinctly radiolucent region without vascular markings ventral to the heart.

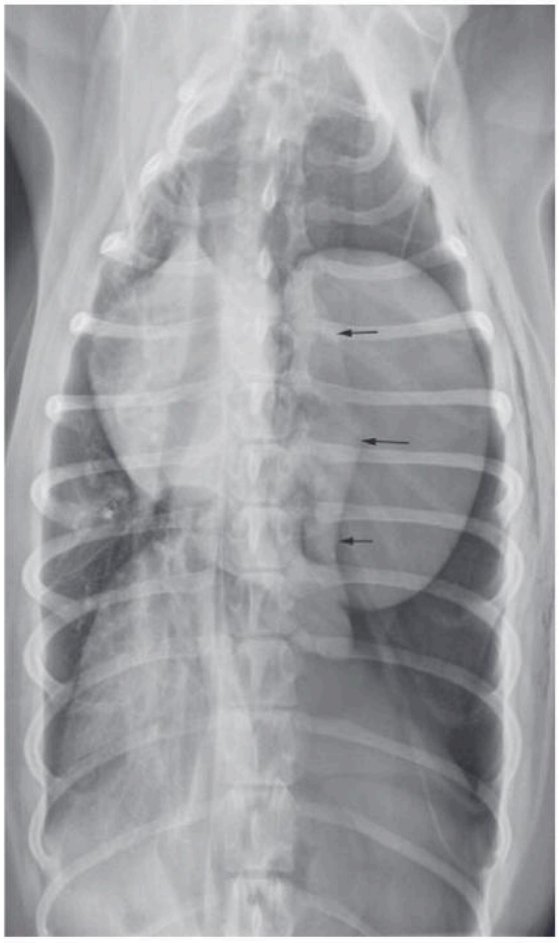


Fig. 34.20 Dorsoventral (DV) radiograph of a dog with a left-sided tension pneumothorax. Note the displacement of the cardiac silhouette to the right. The homogeneous mass on the left is a congenital lung cyst. This cyst is not touching the left thoracic wall and is not causing the cardiac displacement. There is a left-sided pneumothorax, and the left lung is collapsed as an amorphous opacity against the midline (*black arrows*). The left aspect of the diaphragm is displaced caudally. Note the relative radiolucency of the caudal aspect of the left pleural cavity because of the caudal displacement of the diaphragm on that side. The degree of lung collapse, the diaphragm displacement, and the contralateral mediastinal shift (heart shift) are all signs of tension pneumothorax.

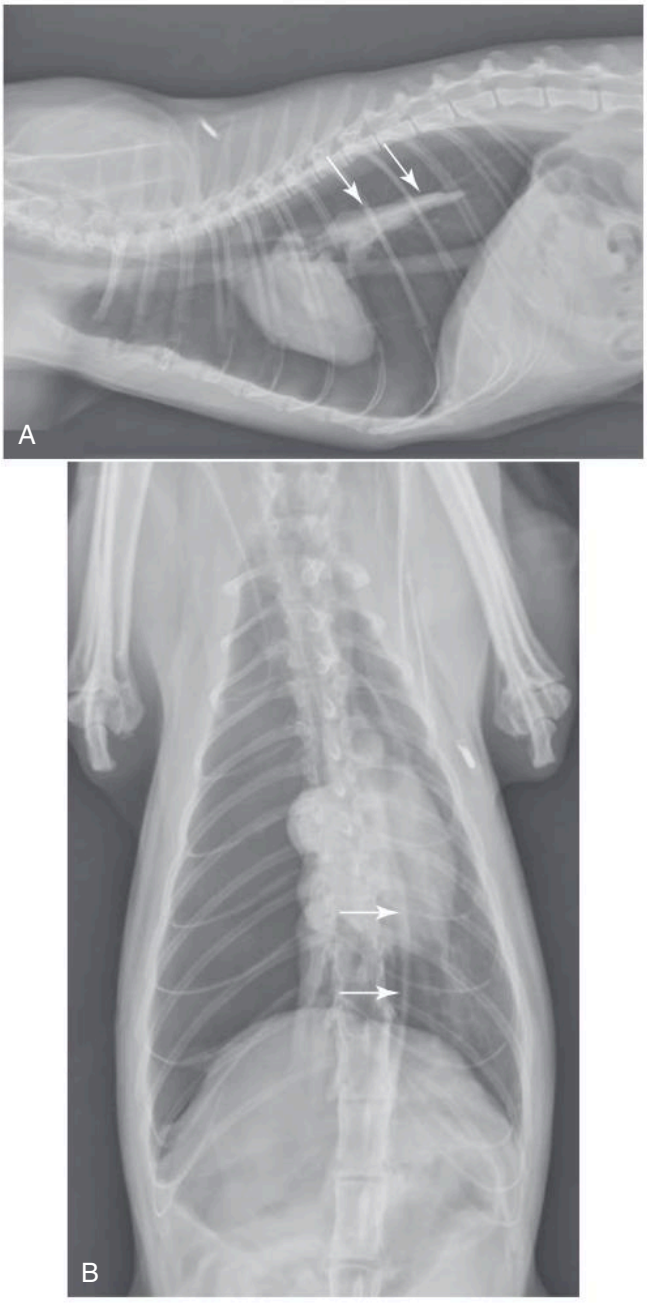


Fig. 34.21 **A,** Right lateral radiograph of a cat with a right-sided tension pneumothorax. The right lung is severely collapsed (*white arrows*). The thoracic cavity is expanded with flattening of the diaphragm and a large amount of free air is seen ventral to the cardiac silhouette. **B,** Dorsoventral (DV) radiograph of a cat with a right-sided tension pneumothorax. The right lung is collapsed and rounded, and the mediastinum (*white arrows*) is shifted to the *left*. Gas is obvious in the right pleural space. The diaphragm is displaced caudally and there is elevation of the ribs on the right side.

PLEURAL THICKENING, NODULES, AND MASSES

Disorders of the pleural lining such as thickening, nodules, and masses are difficult to recognize radiographically in the presence of pleural effusion. Pleuritis, as mentioned earlier, may be the result of chronic pleural effusion but can also be caused by inflammation of adjacent pulmonary parenchyma as with bronchopneumonia or pleuropneumonia as well as pulmonary neoplasia. The most common cause of infectious pleuritis in cats is feline infectious peritonitis. Pleural neoplasia is rare and includes mesothelioma and metastatic neoplasia, namely, metastatic pulmonary carcinoma (Fig. 34.24).[9] Radiographically, they are recognized by an extrapleural sign, described in Chapter 31. Pleural thickening and pleural masses are more readily identified using ultrasonography or contrast-enhanced CT.[10,11] Rounded atelectasis is an unusual form of atelectasis that can be seen in patients with inflammatory pleural effusion and pleuritis, and could be mistaken for a neoplastic lesion. The CT appearance of rounded atelectasis in dogs and cats has been described as nodular soft tissue attenuating lesions that abut the visceral pleura with an acute angle.[12–14]

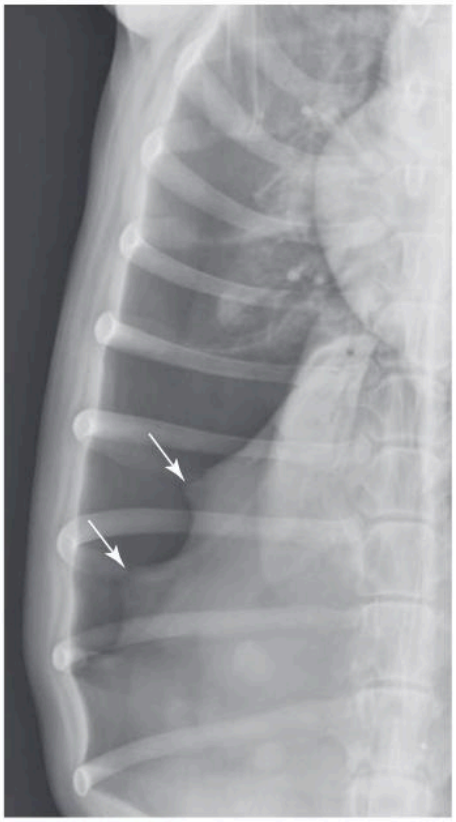


Fig. 34.22 Close-up view of the caudal aspect of the right hemithorax of a dog with tension pneumothorax. The increased pleural space pressure has displaced the right aspect of the diaphragm caudally, causing tension at the costal attachment sites and creating a tented appearance (*white arrows*). Tenting can also occur with pulmonary hyperinflation; but if seen with pneumothorax, it is a reliable sign of tension pneumothorax.



Fig. 34.23 Close-up ventrodorsal (VD) view of the right caudal aspect of the thorax of a dog in which a skin-fold artifact is visible. There is a very radiolucent region just beneath the right thoracic wall with a sharp delineation to a more radiopaque region of the lung that could have the appearance of pneumothorax (*white arrows*). However, faint vascular markings are visible within the more radiolucent region (*white arrows*) and the medial margin of this area is formed by an opaque line that extends caudally beyond the limits of the thoracic cavity (*black arrows*), confirming a skin-fold artifact.

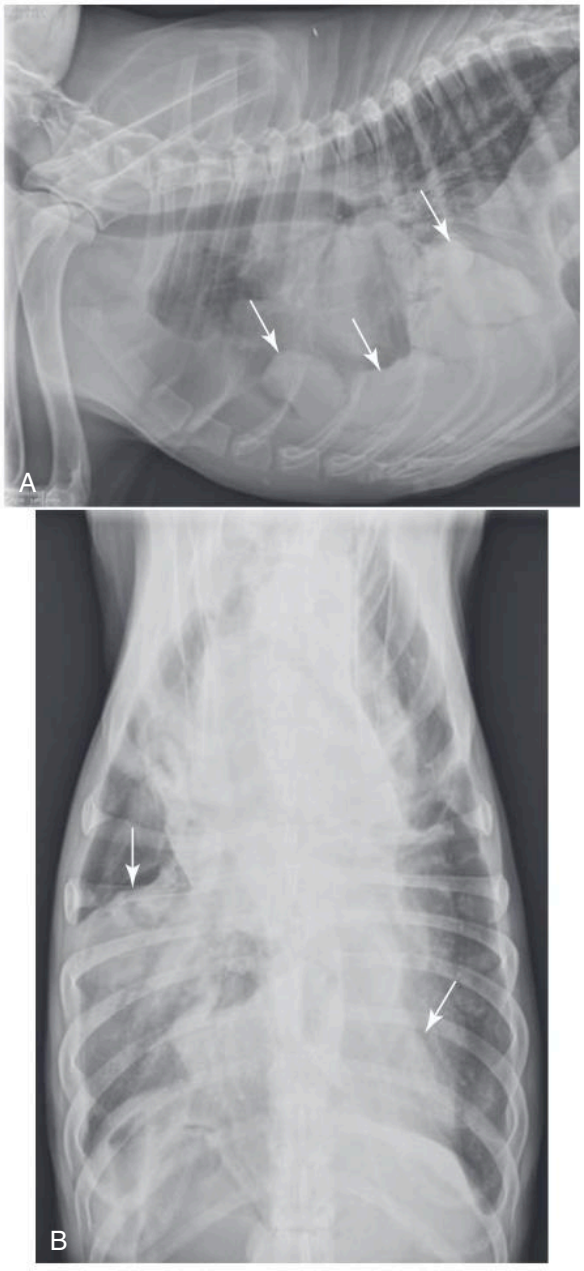


Fig. 34.24 **A,** Left lateral radiograph of a dog with pleural masses suspected to be mesothelioma cytologically. A large lobular soft tissue mass extends to the level of the 5th ribs and silhouettes with the diaphragm caudally (*white arrows*). The mass is outlined by a small amount of free gas in the pleural space. **B,** Dorsoventral radiograph of the same dog. A soft tissue opacity mass fills the right caudal thorax and crosses midline to the left (*white arrows*).

Acknowledgment

With special thanks to prior authors of this chapter for their contributions.

REFERENCES

1. Mendoza P, Giglio RF, Olmo C, Abbott JR, Johnson RD, Berry CR. Anatomic characterization of pulmonary accessory fissures in canine cadavers. *Anat Histol Embryol*. 2019;48(2):157–163. https://doi.org/10.1111/ahe.12424.
2. Woods SJ, Spriet M, Safra N, Cissell DD, Borjesson DL. Hounsfield units are a useful predictor of pleural effusion cytological type in dogs but not in cats. *Vet Radiol Ultrasound Off J Am Coll Vet Radiol Int Vet Radiol Assoc*. 2018;59(4):405–411. https://doi.org/10.1111/vru.12618.
3. Mitrouska I, Klimathianaki M, Siafakas N. Effects of pleural effusion on respiratory function. *Can Respir J*. 2004;11(7):499–503. https://doi.org/10.1155/2004/496901.
4. Groves T, Ticer J. Pleural fluid movement: its effect on appearance of ventrodorsal and dorsoventral radiographic projections. *Vet Radiol Ultrasound*. 1983;24:99.
5. Reetz JA, Caceres AV, Suran JN, Oura TJ, Zwingenberger AL, Mai W. Sensitivity, positive predictive value, and interobserver variability of computed tomography in the diagnosis of bullae associated with spontaneous pneumothorax in dogs: 19 cases (2003–2012). *J Am Vet Med Assoc*. 2013;243(2). https://doi.org/10.2460/javma.243.2.244.
6. Toshima A, Fulkerson CV, Kagawa Y, Murakami M. Positive pressure ventilation computed tomography in dogs with recurrent spontaneous pneumothorax. Abstract ACVR Annual Conference 2022, Reno NV.
7. Kern D, Carrig C, Martin R. Radiographic evaluation of induced pneumothorax in the dog. *Vet Radiol Ultrasound*. 1995;35:411.
8. Aronson E, Reed A. Radiology corner – pneumothorax: ventrodorsal or dorsoventral view. *Vet Radiol Ultrasound*. 36:109.
9. McDonough SP, Scrivani PV, Gendron K, Tse M. Mediastinal serous cavity mesothelioma in two dogs. *J Am Anim Hosp Assoc*. 2022;58(4):194–202. https://doi.org/10.5326/JAAHA-MS-7016.
10. Weston PJ, Baines SJ, Finotello R, Mortier JR. Clinical, CT, and ultrasonographic features of canine and feline pleural and peritoneal carcinomatosis and sarcomatosis. *Vet Radiol Ultrasound Off J Am Coll Vet Radiol Int Vet Radiol Assoc*. 2021;62(3):331–341. https://doi.org/10.1111/vru.12951.
11. Reetz JA, Buza EL, Krick EL. CT features of pleural masses and nodules. *Vet Radiol Ultrasound Off J Am Coll Vet Radiol Int Vet Radiol Assoc*. 2012;53(2):121–127. https://doi.org/10.1111/j.1740-8261.2011.01883.x.
12. Kakkar C, Koteshwara P, Kadavigere R. Round atelectasis. *Lung India*. 2015;32(6):646–647. https://doi.org/10.4103/0970-2113.168105.
13. Woodring JH. Pleural effusion is a cause of round atelectasis of the lung. *J Ky Med Assoc*. 2000;98(12):527–532.
14. Tran DT, Donovan TA, Le Roux A. Computed tomography features of rounded atelectasis in chronic inflammatory pleural effusions in cats and dogs. Abstract ACVR Annual Conference 2022, Reno NV.

ELECTRONIC RESOURCES

Additional information related to the content in Chapter 34 can be found online at eBooks.Health.Elsevier.com.

- Chapter Quiz

CHAPTER 35

Canine and Feline Cardiovascular System

Elodie Huguet • Clifford Berry

INTRODUCTION

High-quality thoracic radiographs are essential for the interpretation of the cardiovascular system. The cardiovascular system in the dog and cat is complex, and basic patterns of recognition are critical for correct radiographic evaluation. Computed tomography (CT) and magnetic resonance imaging (MRI) provide superior spatial and temporal resolution of cardiac structures but are less widely available and require anesthesia or sedation in patients who may be at risk of cardiovascular compromise. Echocardiography is the most practical, safe, and widely used imaging modality for evaluation of cardiovascular morphology and function. While echocardiography is best for assessing the heart, radiographs provide other information, such as vascular status and presence of heart failure. Hence, a comprehensive evaluation of the cardiovascular structures is best routinely achieved with the complementary use of thoracic radiographs and echocardiography.

RADIOGRAPHIC PROJECTIONS AND TECHNICAL CONSIDERATIONS

Three-view thoracic radiographs including right lateral, left lateral, and dorsoventral (DV) and/or ventrodorsal (VD) projections are the standard. For assessment of cardiovascular structures, a DV projection may be preferred to the VD to minimize cardiac magnification and optimize aeration of the caudal lung lobes and caudal lobar pulmonary vasculature. When possible, radiographs should be obtained before echocardiography to avoid atelectasis from prolonged lateral recumbency and wet-hair artefacts due to the presence of gel or alcohol. When positioning the patient for thoracic radiographs, the primary x-ray beam should be centered on the heart to avoid distortion of the cardiovascular structures, and radiographs should be acquired during peak inspiration to avoid atelectasis being misinterpreted as pulmonary disease. The effects of positioning on the appearance of the normal cardiac silhouette and associated vasculature are further discussed in Chapter 28.

INTERPRETATION PARADIGM FOR THE CARDIOVASCULAR STRUCTURES

A systematic evaluation for the thorax is essential. Initially, an interpretation paradigm for the cardiovascular system involves four basic questions related to the various roentgen signs (size, shape, margin, position, number, and opacity) to help formulate a differential diagnosis list, as depicted in Fig. 35.1. These

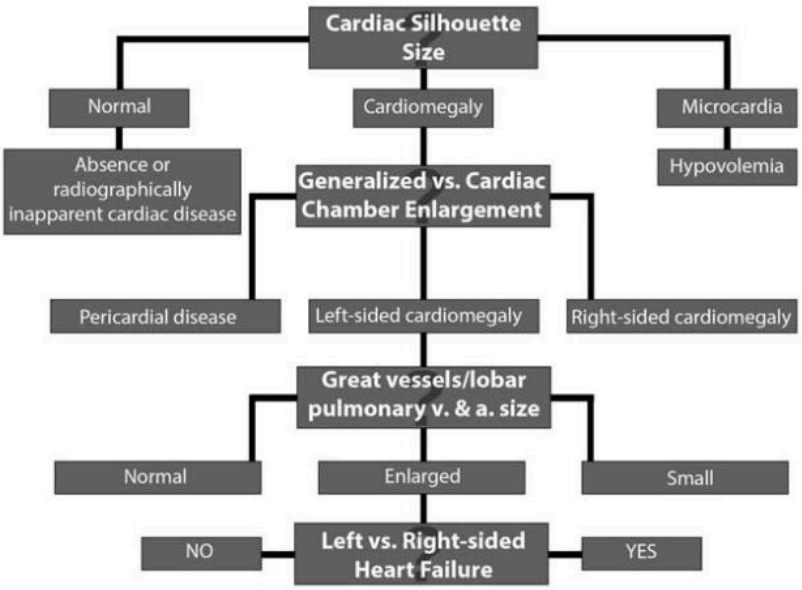


Fig. 35.1 Interpretation paradigm for the cardiovascular system.

questions should be answered in combination with each other to prioritize differential diagnoses. These questions are as follows:

1. Is there a size change of the cardiac silhouette?
2. Is enlargement pericardial disease or localized to the right and/or left cardiac chambers?
3. Are there any changes noted to the great vessels? This is particularly important for the evaluation of the aortic arch and descending thoracic aorta, main pulmonary artery, and the caudal vena cava. Also, are there changes associated with the lobar pulmonary vasculature? If so, is the lobar pulmonary vasculature small or enlarged? If enlarged, are both the pulmonary artery and vein enlarged or is one enlarged relative to the other?
4. Is there radiographic evidence of left- or right-sided congestive heart failure?

EVALUATION OF CARDIAC SILHOUETTE SIZE

Because fluid and soft tissue opacities are radiographically indistinguishable, the heart and pericardial sac are interpreted as a single unit, termed the *cardiac silhouette*. Vascular changes and pericardial disease may also affect cardiac silhouette size and margination. It is also important to keep in mind that absence of cardiomegaly does not exclude the presence of cardiac disease. When evaluating the cardiac silhouette for size, qualitative and quantitative methods are utilized. Comparisons of both methods did not find a significant increase in interpretation accuracy when the quantitative method was used in conjunction with qualitative means of evaluating heart size.[1] A higher confidence level and degree of accuracy may be expected with increased experience and severity of cardiomegaly.[1] In all instances, inherent variations in cardiac silhouette size should be considered between different breeds of dogs. For example, the cardiac silhouette in deep-chested dogs may appear abnormally small, whereas the cardiac silhouette in barrel-chested dogs may look abnormally large (Fig. 35.2A–F). Cats have a more uniform body conformation, which may facilitate the evaluation of feline cardiac silhouette size.[1] The cardiac silhouette in kittens may look enlarged in the absence of disease. Qualitative assessment of cardiac silhouette size is often facilitated by the recognition of specific cardiac chamber enlargement, described in the following section.

Multiple techniques are proposed for the evaluation of cardiac silhouette size. The most common of these is the vertebral heart scale (VHS), which was instituted to take into account the influence of body conformation on the size of the cardiac silhouette.[2] The VHS is obtained by measuring the length of the long and short axes of the heart on a high-quality right lateral radiograph and scaling these measurements against the length of the vertebral bodies starting at T4 to quantify heart size in terms of corresponding vertebral number. Based on 100 clinically normal dogs, the normal mean VHS ± 2 SD was 9.7 ± 1 vertebrae. To further reduce variation, VHS measurements specific to particular breeds of dogs have been established and are listed in eTable 35.1. The influence of respiration and the cardiac cycle can affect obtained VHS measurements by up to 1.0 vertebral body length and should be kept in mind when assessing the cardiac silhouette using this method (Video 35.1).[3] Normal VHS measurements (7.5 ± 0.3 vertebrae) are also available in cats.[4] While the VHS may be a useful adjunct method for the assessment of cardiac silhouette size, it is of particular use for the longitudinal assessment of cardiac disease progression and treatment within an individual patient.

An alternative and more efficient method of assessing the cardiac silhouette size using a heart to single vertebra ratio (HSVR) was recently proposed, taking into account the potential presence of vertebral anomalies, which may affect VHS measurements. Using a similar approach, the length and width of the cardiac silhouette are measured and added before subtracting from the length of a single morphologically normal vertebra at T4–T8, including the caudal intervertebral disc space.[5] Obtained measurements are comparable to reported normal VHS measurements, although a higher accuracy is reported with HSVR measurements calculated using T7 as a reference vertebra.[5] Other quantitative measurements of cardiac size are proposed and mostly anecdotal (Table 35.1); therefore, these methods should be applied with caution given the lack of research to support their accuracy and unclear effect of patient conformation on obtained measurements.

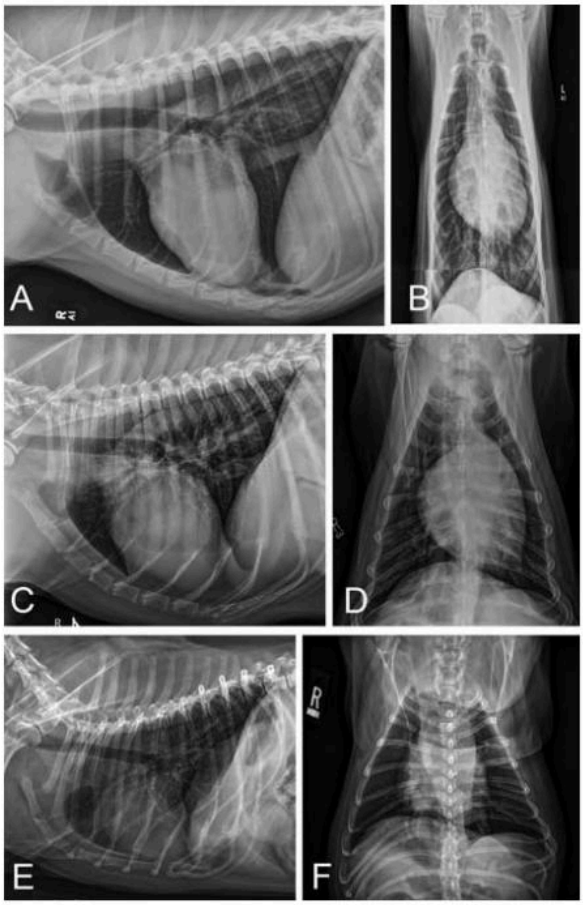


Fig. 35.2 Right lateral and ventrodorsal thoracic radiographs from a normal Borzoi **(A and B)**, a normal Labrador retriever **(C and D)**, and a normal pug **(E and F)**, illustrating the effect of body conformation on the appearance of the cardiac silhouette.

With advanced age, the long axis of the cardiac silhouette in cats may gradually rotate and be in a plane that is more horizontal to the sternum. Cats with such variation to the orientation of their cardiac silhouette are said to have a "lazy heart." When obtaining measurements of the cardiac silhouette in older cats, the orientation of the cardiac silhouette should be taken into consideration. Additionally, the aortic arch may be enlarged and redundant in older cats, as characterized by the presence of a bulge at the cranial aspect of the cardiac silhouette (e.g., aortic knob). While these findings commonly represent normal age variants, systemic hypertension and hyperthyroidism may also be contributing factors.[6]

Microcardia is sometimes identified on thoracic radiographs in dogs and cats, and is rarely associated with primary cardiac disease. Rather, microcardia is primarily indicative of hypovolemia with reduced circulating cardiovascular volume from dehydration, blood loss, or hypoadrenocorticism (Fig. 35.3A,B).[7] Radiographically, the cardiac silhouette becomes abnormally

eTable • 35.1

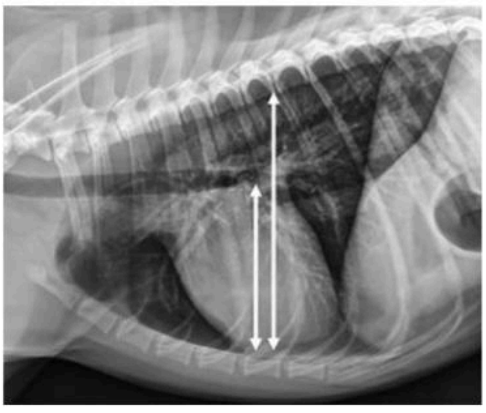
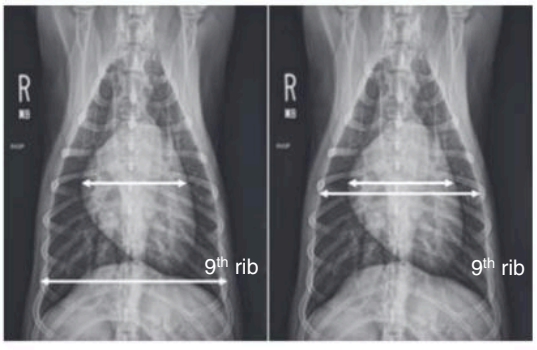
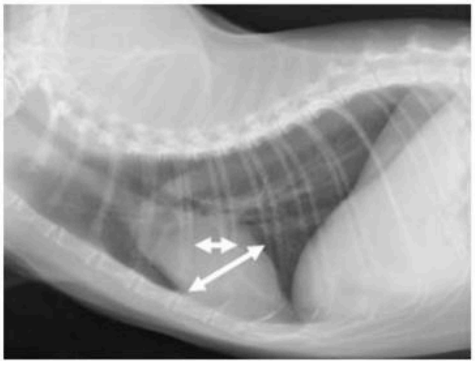
Breed-Specific VHSs in Dogs.[86–100]

BREED	RECUMBENCY	VHS	REFERENCES
Pug	Right	9.1 ± 2.7	Jepsen-Grant et al. (2013)
Pomeranian	Right	4.5 ± 2.4	Jepsen-Grant et al. (2013)
Yorkshire terrier	Right	3.2 ± 1.5	Jepsen-Grant et al. (2013)
Dachshund	Right	6.9 ± 2.8	Jepsen-Grant et al. (2013)
	Right	10.3 [range 9.25–11.55]	Birks et al. (2017)
	Left	10.1 [range 8.7–11.31]	Birks et al. (2017)
Bulldog	Right	26.7 ± 13.2	Jepsen-Grant et al. (2013)
Shih Tzu	Right	6.5 ± 2.0	Jepsen-Grant et al. (2013)
Lhasa Apso	Right	8.2 ± 3.2	Jepsen-Grant et al. (2013)
Boston terrier	Right	8.9 ± 2.6	Jepsen-Grant et al. (2013)
Chihuahua	Right	10.0 ± 0.6	Puccinelli et al. (2020)
Cavalier King Charles spaniel	Right	10.6 ± 0.5	Lamb et al. (2001)
German shepherd	Right	9.7 ± 0.8	Lamb et al. (2001)
Boxer	Right	11.6 ± 0.8	Lamb et al. (2001)
Doberman	Right	10.0 ± 0.6	Lamb et al. (2001)
Poodle	Right	10.12 ± 0.51	Fonsecapinto and Iwasaki (2004)
	Right	9.72 ± 0.73	Azevedo et al. (2016)
Turkish shepherd	Left	9.7 ± 0.67	Gulanber et al. (2005)
Whippet (show)	Left	10.5 ± 0.6	Bavegems et al. (2005)
	Right	10.8 ± 0.6	
Whippet (racing)	Left	11.1 ± 0.4	Bavegems et al. (2005)
	Right	11.4 ± 0.4	
Greyhound	Left/Right	10.5 ± 0.1	Marin et al. (2007)
Rottweiler	Left/Right	9.8 ± 0.1	Marin et al. (2007)
Beagle	Left	10.2 ± 0.4	Kraetschmer et al. (2008)
	Right	10.5 ± 0.4	
Iranian native dogs	Left	9.4 ± 0.55	Ghadiri et al. (2010)
	Right	9.4 ± 0.54	
American pit bull terrier	Right	10.9 ± 0.4	Lahm et al. (2011)
Indian mongrel dogs	Right	9.7 ± 0.67	Bodh et al. (2016)
Labrador retriever	Left	10.29 ± 0.04	Gugjoo et al. (2013)
	Right	10.39 ± 0.05	Bodh et al. (2016)
	Left	10.22 ± 0.20	
	Right	10.39 ± 0.19	
		10.39 ± 0.19	
Spitz	Left	10.03 ± 0.11	Bodh et al. (2016)
	Right	10.21 ± 0.1	
Belgian Malinois	Right	9.58 ± 0.53	Colina et al. (2015)

VHS, Vertebral heart scale.

Table • **35.1**

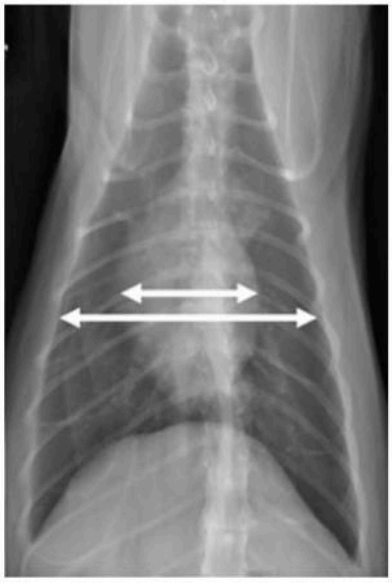
Additional Quantitative Methods for the Assessment of Cardiac Silhouette Size.

DOGS			
Lateral projections	Height of cardiac silhouette/dorsoventral height of thoracic cavity	<2/3 at the same level	
	Cardiac silhouette width to number of equivalent intercostal spaces*	2.5–3.5	
Ventrodorsal/ Dorsoventral projections	Maximal width of the cardiac silhouette/width of the thoracic cavity	<1/2 at ninth rib <2/3 at the same level	
CATS			
Lateral projections	Cardiac silhouette width to number of equivalent intercostal spaces*	2–3	

Continued

Table • 35.1

***Additional Quantitative Methods for the Assessment of Cardiac Silhouette Size.*—cont'd**

Ventrodorsal/ Dorsoventral projections	Maximal width of the cardiac silhouette/width of the thoracic cavity	<1/2	

*Width is the measurement obtained at the widest point perpendicular to the long axis of the cardiac silhouette.

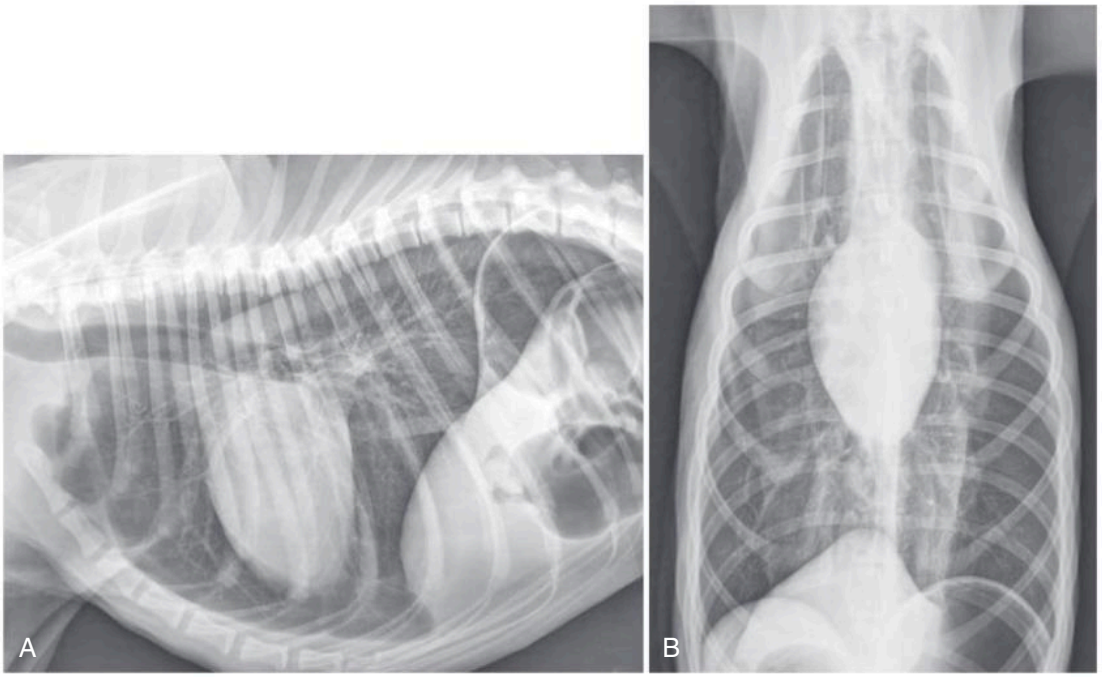


Fig. 35.3 Lateral **(A)** and ventrodorsal **(B)** radiographs of a dog with hypovolemia secondary to hypoadrenocorticism. The cardiac silhouette is small and subsequently elevated from the sternum. The lobar pulmonary vessels and the caudal vena cava are thinned. The lungs are hyperlucent with the false impression of increased lung volume secondary to the microcardia.

small in size with normal margins. The lobar pulmonary vasculature will often be concurrently thinned with subsequent diffuse hyperlucency of the lungs. The caudal vena cava may also be undercirculated with increased severity and will be persistently narrowed.

SPECIFIC PATTERNS OF CARDIAC CHAMBER ENLARGEMENT

Because individual cardiac chambers, sites of great vessel emergence/convergence, and the pericardium are radiographically indistinguishable, evaluation of the cardiac silhouette margins is essential to localize alterations to specific cardiac chambers or the great vessels in the dog based on their relative positioning. For this purpose, a "clock face" analogy is commonly used to correlate alterations to the cardiac silhouette at specific sites to corresponding anatomical cardiovascular structures on both lateral and VD/DV projections (Fig. 35.4A,B). The positioning of the feline heart and subtlety of specific cardiac chamber enlargement on thoracic radiographs limits the use of this approach in cats.

Left Atrium

Enlargement of the left atrium is the most frequently encountered cardiac enlargement in the dog due to the high prevalence of myxomatous mitral valve disease. On lateral projections, enlargement of the left atrium in the dog causes bulging of the dorsocaudal margin of the cardiac silhouette at the 12–2 o'clock position. The caudal border is subsequently flattened to mildly concave, resulting in a loss of the caudal "cardiac waist" (Fig. 35.5). On the VD/DV projection, this bulge corresponds to a rounded focal region of increased soft tissue opacity caudal to the tracheal bifurcation. Superimposition and summation of the enlarged left atrium over the cardiac silhouette can create the appearance of a double wall due to distinction of both the caudal border of the left atrium and cardiac silhouette (Fig. 35.6A,B).

With left atrial enlargement, splaying of the principal bronchi may be observed on the VD/DV projections (Figs. 35.7 and 35.8A,B). Similar splaying of the principal bronchi may occur secondary to tracheobronchial lymphadenopathy but this typically causes ventral displacement of the tracheal bifurcation in lateral views (see Chapter 33). In contrast, left atrial enlargement typically causes dorsal displacement of the tracheal bifurcation. Some dogs with a dorsally displaced

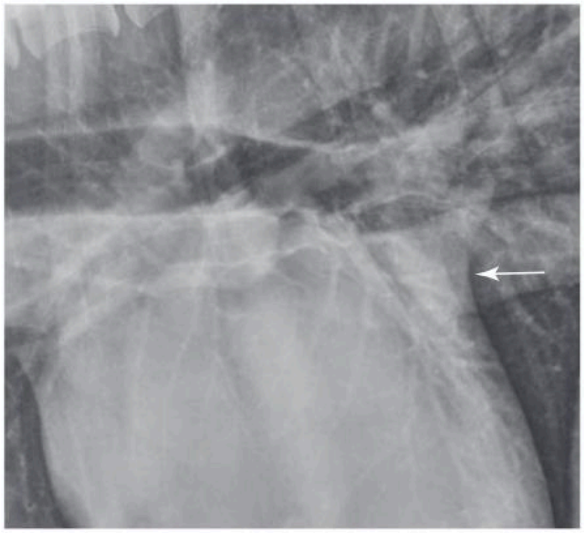


Fig. 35.5 Lateral radiograph of a dog with an enlarged left atrium. Along the caudodorsal aspect of the cardiac silhouette, in the region of the left atrium at the 12–2 o'clock position, a bulge is identified and is associated with concavity of cardiac silhouette margin caudally (*white arrow*).

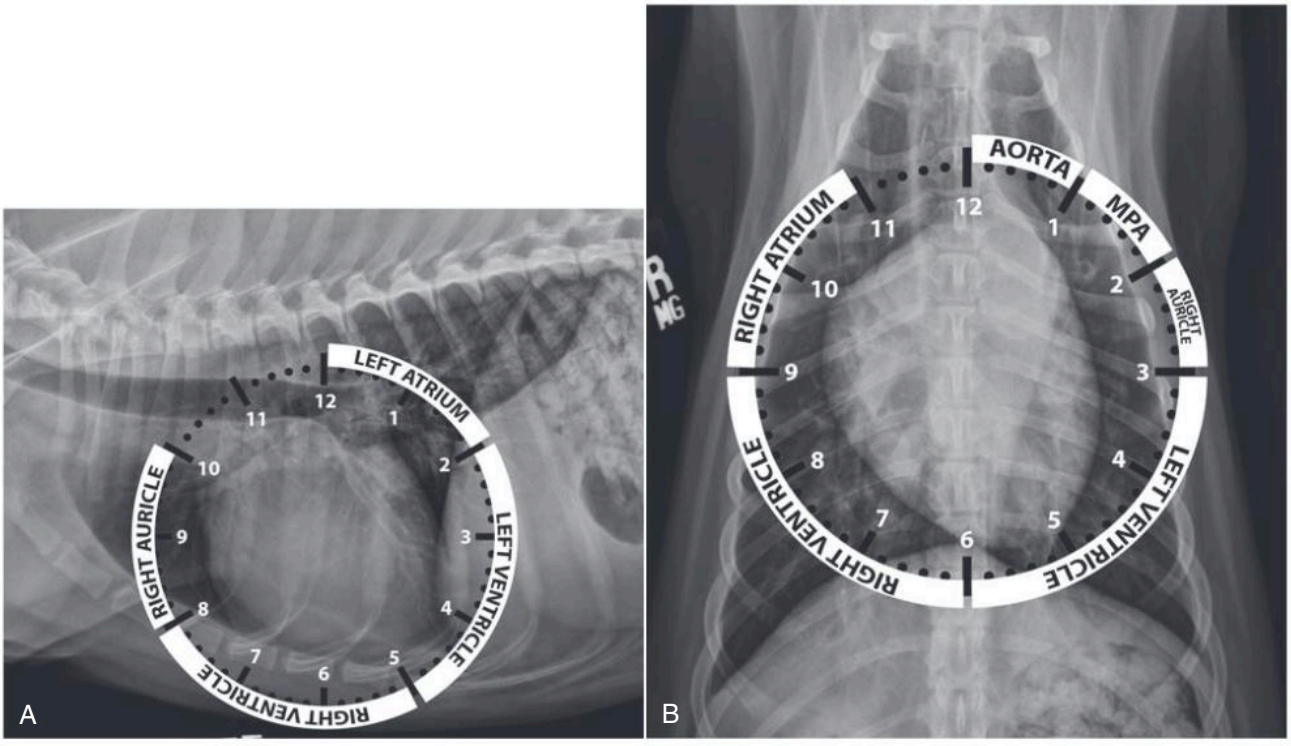


Fig. 35.4 Lateral **(A)** and ventrodorsal **(B)** projections centered on the cardiac silhouette illustrating the clockface analogy for the localization of individual cardiac chambers are sites of emergence or convergence of the great vessels.

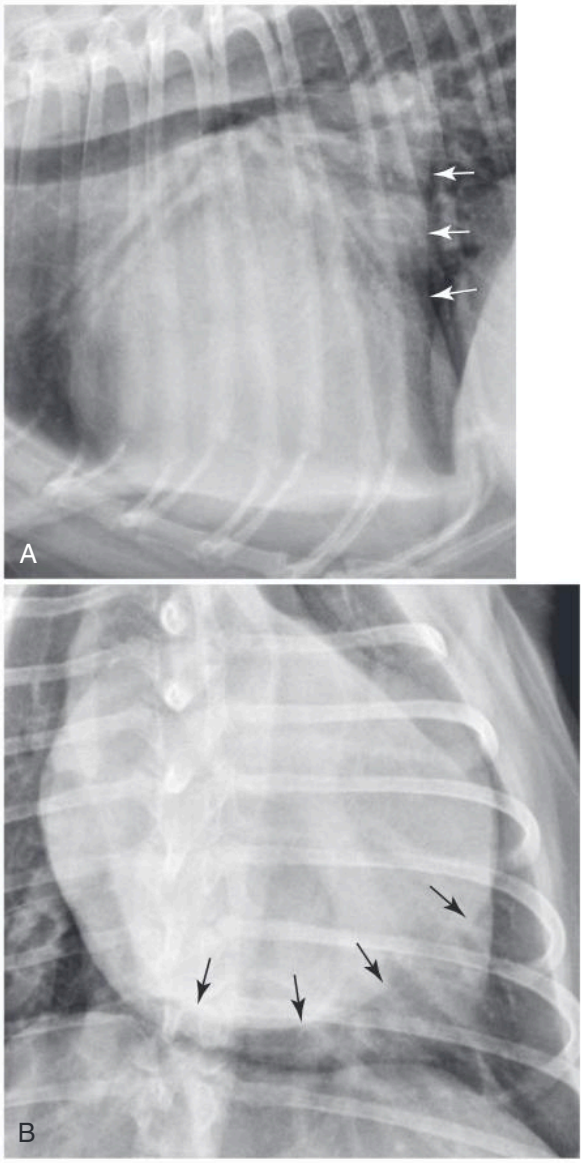


Fig. 35.6 Lateral **(A)** and dorsoventral **(B)** projections of a dog with severe left atrial enlargement. On the lateral projection **(A)**, a large bulge is seen along the caudodorsal aspect of the cardiac silhouette with associated concavity of the caudal cardiac silhouette margin (*white arrows*). On the dorsoventral projection **(B)**, the enlarged left atrium corresponds to a focal region of increased soft tissue opacity (*black arrows*) superimposed on the remainder of the heart with a caudal margin separate from the caudal margin of the cardiac silhouette, resulting in a double wall appearance.

tracheal bifurcation will also have narrowing of the left principal bronchus (see Fig. 35.8A,B). A compressive effect on the left and right principal bronchi has been described in the presence of left atrial enlargement due to the spatial relationship between the vertebral column, aorta, left principal bronchus, and left atrium.[8] While the bronchial narrowing may be attributed to direct impingement from the adjacent enlarged left atrium, coexisting bronchomalacia may facilitate this process as a result of altered bronchial wall integrity and/or cause bronchial collapse (Video 35.2).[9] Coughing in dogs with left atrial enlargement is common and can be attributed to tracheal narrowing versus pulmonary edema.[9,10] The absence of cough receptors within the alveoli and interstitium is a likely explanation; however, in dogs, coughing is to be expected in the

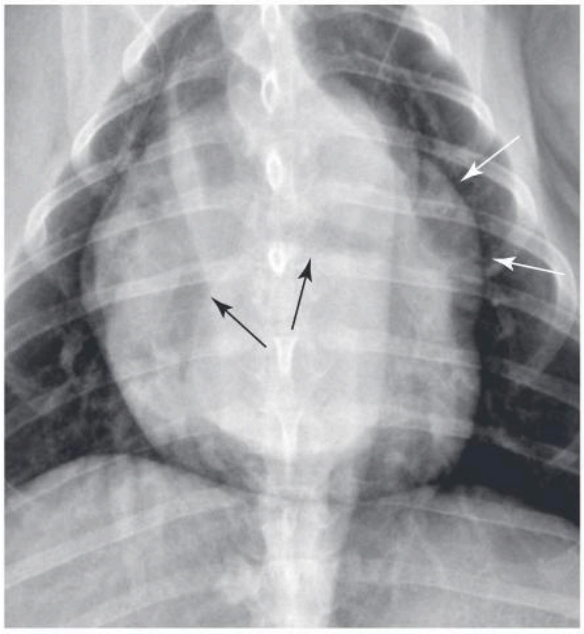


Fig. 35.7 Dorsoventral projection of a dog with pronounced left atrial dilation. The enlarged left atrium has caused abaxial displacement of the principal bronchi (*black arrows*). There is also a bulge on the left aspect of the cardiac silhouette that is consistent with left auricular enlargement (*white arrows*).

presence of large amounts of cardiogenic pulmonary edema infiltrating into the larger bronchial structures.[9] Therefore, causes of a cough other than heart failure should always be considered in dogs with a heart murmur. In cats, coughing due to pulmonary edema is very uncommon.

Enlargement of the left auricle is less readily identified than left atrial enlargement and is most prevalent when a higher degree of left atrial enlargement is present. On the VD/DV projection, enlargement of the left auricle may create a focal bulge along the left cardiac border in the 2–3 o'clock position (see Fig. 35.7).

While left atrial enlargement is most commonly evaluated subjectively, the vertebral left atrial size (VLAS) can be used to quantify left atrial enlargement in dogs with good repeatability.[11,12] On either a left or right lateral projection, VLAS indexes are obtained by measuring the distance from the mid ventral aspect of the carina to the most caudal margin of the left atrium at the intersection with the dorsal border of the caudal vena cava. This measurement is transposed to the vertebral column, starting at the cranial margin of T4, to count the equivalent vertebral body number.[13] In 80 healthy dogs, the normal medial VLAS was 1.9 with a reference interval of 1.4 to 2.2.[12] A cutoff value of $\geq$2.3 may support a diagnosis of left atrial enlargement in dogs.[12,13]

Left atrial enlargement in cats is much less conspicuous, and in many cats there are no radiographic changes. In some instances, a bulge may be observed along the caudodorsal margin of the cardiac silhouette and is associated with concavity of the caudal margin (Fig. 35.9). Left atrial enlargement in the cat is also associated with an increase in width of the cardiac silhouette in the region of the cardiac base on the VD/DV projections. In the presence of marked left atrial enlargement, the cardiac silhouette may be "valentine shaped" (Fig. 35.10). While a "valentine-shaped" cardiac silhouette may be associated with the presence of biatrial enlargement, it is most often observed with left atrial enlargement alone.[14]

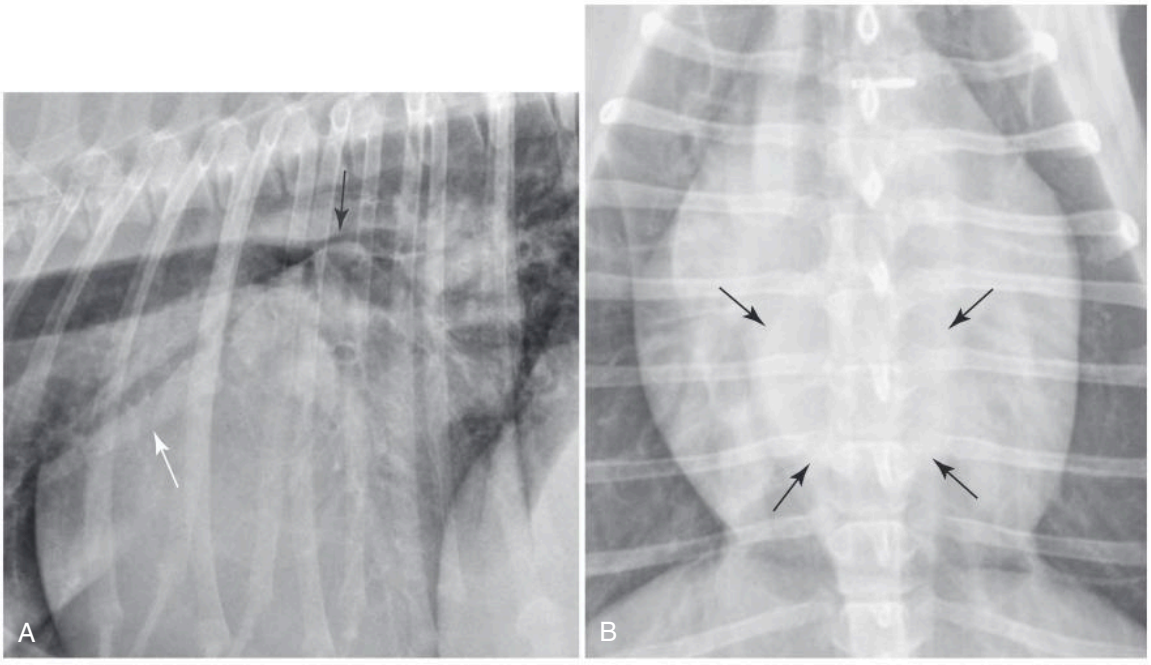


Fig. 35.8 Lateral **(A)** and dorsoventral **(B)** projections of a dog with marked left atrial enlargement. In **A,** there is dorsal displacement of the trachea and narrowing of the left principal bronchus (*black arrow*). The left cranial lobe pulmonary vein is also distended (*white arrow*) compared with the corresponding artery, consistent with pulmonary venous hypertension secondary to mitral insufficiency. In **B,** the dilated left atrium represents a region of increased soft tissue opacity caudal to the tracheal bifurcation (*black arrows*) causing splaying of the principal bronchi.

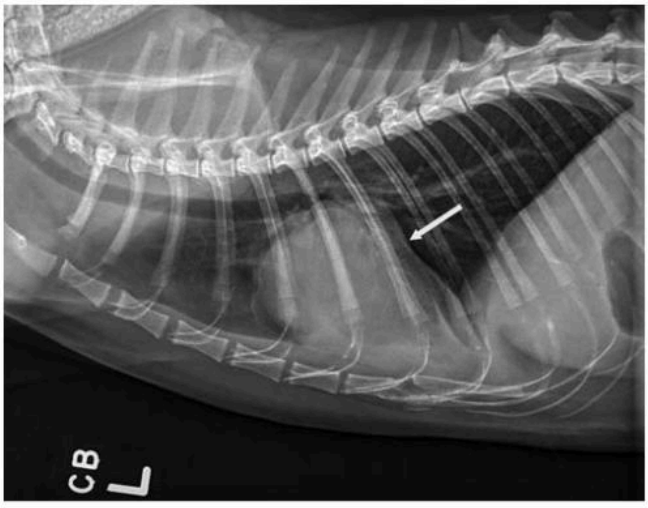


Fig. 35.9 Lateral projection of a cat with left atrial enlargement. A concave depression is present along the caudodorsal margin of the cardiac silhouette (*white arrow*), similar to that seen in many dogs. This is less commonly observed in cats with left atrial dilation than in dogs but is occasionally seen.

Left Ventricle

In both cats and dogs, concentric hypertrophy of the ventricular wall is most commonly seen as a response to pressure overload and mainly occurs at the expense of lumen volume. Therefore, the cardiac margins in the left ventricular region will often maintain a normal contour. In comparison, eccentric hypertrophy is mostly seen in compensation to volume overload and can result in radiographically detectable left



Fig. 35.10 Dorsoventral projection of a cat with marked enlargement of the left atrium. The cardiac silhouette is increased in width in the base region (*black arrows*) and is therefore referred to being "valentine shaped."

ventricular enlargement. In more severe cases of left ventricular enlargement, possibly exacerbated by the concurrent presence of left atrial enlargement, the cardiac silhouette may be increased in apical to basilar length with subsequent dorsal displacement of the trachea at the level of the carina. On VD/DV projections, the cardiac apex may have a rounded contour and may be displaced to the right.

Enlargement of the left ventricle is a likely response to chronically increased preload and may decompensate into left-sided congestive heart failure

Right Atrium

Right atrial enlargement is uncommonly isolated as an independent entity, especially in cats, but may be occasionally seen in dogs with tricuspid dysplasia. Interpretation of right atrial enlargement is supported by the concurrent presence of a bulge at the 9–11 o'clock position along the cardiac silhouette on the VD/DV projection (Fig. 35.11A,B). Enlargement of the right auricle may be associated with a soft tissue bulge along the cranial margin of the cardiac silhouette on the lateral projections. Nonspecific enlargement of the cardiac silhouette may be seen in cats with right atrial enlargement and is usually associated with other cardiac chamber changes.

Right Ventricle

Similar to the left ventricle, the right ventricle may enlarge as a result of both concentric and eccentric hypertrophy. Isolation of right ventricular enlargement in cats is very rare. The right ventricle undergoes concentric hypertrophy in response to pressure overload, as with pulmonic stenosis or pulmonary hypertension, as with heartworm disease. Hypertrophy mainly occurs at the expense of lumen volume and may lead to no or minimal change in the appearance of the cardiac silhouette. On lateral projections, rounding of the cardiac margin in the 5–8 o'clock position may be seen and associated with dorsal displacement or elevation of the cardiac apex from the sternum (Fig. 35.12B,C). On the VD/DV projections, this is further supported by rounding of the cardiac silhouette in the 6–9 o'clock position with an associated leftward apical shift, giving the cardiac silhouette a pronounced "reversed-D" shape (see Fig. 35.12A).

Care should be taken to not over-read the more rounded appearance of the cranial and right lateral margins of the cardiac silhouette as it may be artefactual on expiratory radiographs or may represent a normal variation in some breed of dogs, such as brachycephalic dogs. Additionally, the cranial and right lateral margins of the cardiac silhouette may be rounded in the presence of severe left-sided cardiomegaly due to morphological distortion of cardiac anatomy from the severe left atrial and ventricular enlargement.[15] A more rounded appearance of the right margin of the cardiac silhouette and leftward displacement of the cardiac silhouette may be seen on DV projections when compared to VD projections.

Generalized Cardiomegaly

A generalized enlargement of the cardiac silhouette without apparent cardiac chamber enlargement should raise concerns for pericardial disease in both dogs and cats. With generalized cardiomegaly, the heart occupies a larger portion of the thoracic cavity while maintaining smooth and rounded margins on all projections. The rounded shape of the cardiac silhouette is commonly referred to as being "globoid" in appearance. The cardiac margins may also be better defined due to separation of

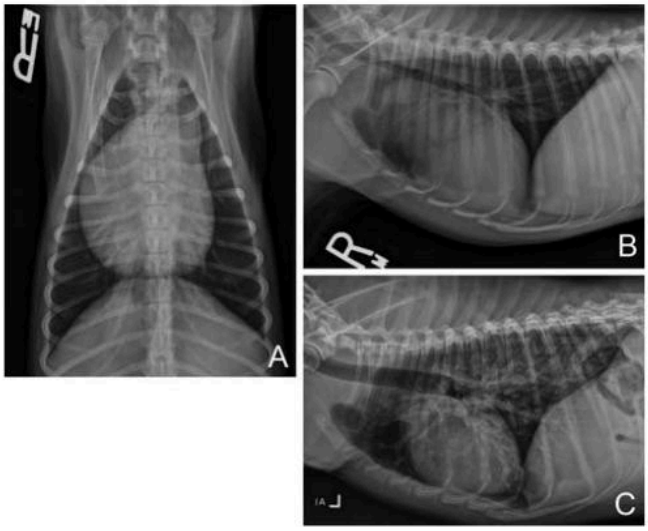


Fig. 35.12 Ventrodorsal **(A)** and right lateral **(B)** projections of a dog with pulmonic stenosis and right ventricular hypertrophy, and left lateral projection of a dog with heartworm disease **(C)**. In **A,** the right lateral margin of the cardiac silhouette is moderately rounded with leftward displacement of the cardiac apex and a reversed-D appearance of the cardiac silhouette. Enlargement of the main pulmonary artery is also visible and correlated with a bulge at the 1–2 o'clock position along the cardiac silhouette. In **B,** the right ventricle correlates to rounding of the cranioventral margin of the cardiac silhouette. Similar rounding of the cranioventral margin of the cardiac silhouette is seen in **C** and is associated with increased elevation of the cardiac apex from the sternum.

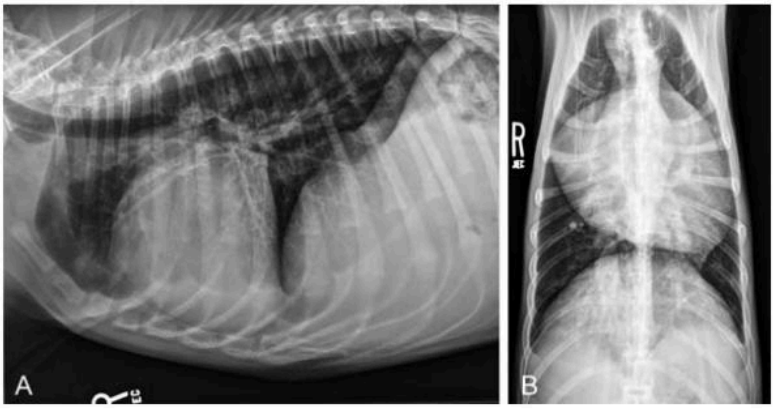


Fig. 35.11 Right lateral **(A)** and dorsoventral **(B)** projections of a Doberman pinscher with tricuspid dysplasia. A bulge is visible in the region of the right atrium consistent with right atrial enlargement.

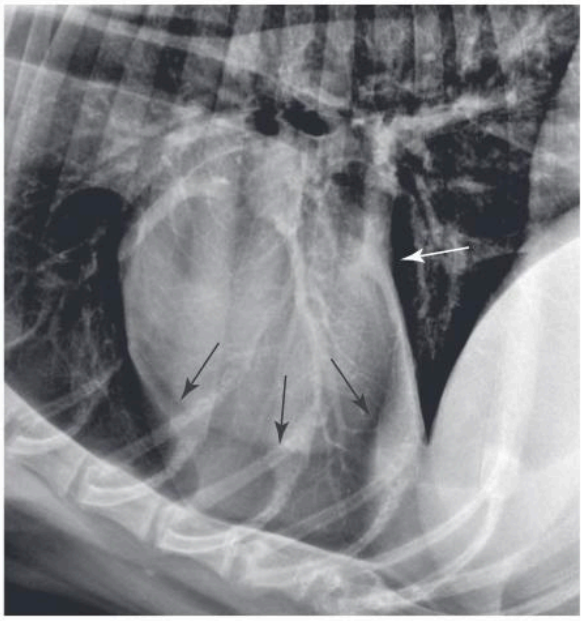


Fig. 35.13 Lateral projection of a Doberman pinscher. The presence of fat in the pericardium results in a generalized enlargement of the cardiac silhouette. The less opaque fat creates contrast for visualization of the actual margin of the heart (*black arrows*). This dog also has left atrial enlargement, as characterized by the presence of a bulge along the caudodorsal aspect of the cardiac silhouette associated with concavity of the cardiac silhouette margin caudodorsally (*white arrow*).

the pericardium from the cardiac margins and reduced motion artefacts. If the cardiac structures maintain a homogeneous soft tissue opacity, pericardial effusion should be considered, keeping in mind the heart may have an enlarged and rounded appearance due to the presence of increased pericardial fat in dogs and cats (Fig. 35.13). On the other hand, if the opacity of the cardiac silhouette is heterogeneous, especially with continuity of the cardiac silhouette and ventral aspect of the diaphragm, a peritoneopericardial diaphragmatic hernia should be considered.

Obtaining high-quality radiographs on peak inspiration is important for the assessment of cardiomegaly as a decrease in thoracic volume is observed with pulmonary underinflation and the cardiac silhouette may subsequently appear larger relative to the amount of aerated lung surrounding it (see Chapter 28).

SPECIFIC PATTERNS OF GREAT VESSEL ENLARGEMENT

Caudal Vena Cava

The caudal vena cava is variable in size depending on the phase of respiration and cardiac cycle. The caudal vena cava size is commonly assessed subjectively for size; however, the normal caudal vena cava should be less than 1.5 times the diameter of the descending aorta.[16,17] The caudal vena cava can enlarge in response to increased central venous pressure, but the size of the caudal vena cava is not an accurate way to evaluate central venous pressure. Valid inferences on cardiovascular disease cannot typically be made based on the size of the caudal vena cava only.

Kinking of the caudal vena cava is occasionally observed on lateral projections in dogs and may represent a recumbency-dependent change due to a positional shift of the cardiovascular structures, or an association with trauma, cardiovascular disease, or neoplasia (Fig. 35.14).[17,18] While kinking of the caudal vena cava may be a primary cause for postsinusoidal obstruction of venous flow (e.g., Budd-Chiari syndrome), it may also represent a secondary change seen in response to crowding of the caudal intrathoracic structures from cardiomegaly and/or an increase in intra-abdominal pressure, such as secondary to peritoneal effusion or organomegaly/presence of a mass.[17,18]

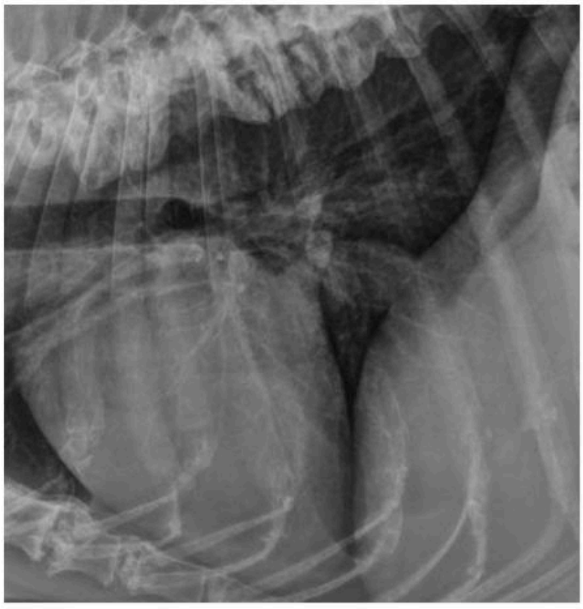


Fig. 35.14 Right lateral projection of a dog with kinking of the caudal vena cava, presumed to be recumbency dependent in the absence of apparent cardiovascular disease and neoplasia.

Narrowing of the caudal vena cava is primarily seen with hypovolemia and is commonly identified in conjunction with microcardia. The caudal vena cava may be intermittently narrowed with the phase of the cardiac cycle; therefore, a diagnosis is best supported by persistent narrowing of the caudal vena cava on both lateral projections (see Fig. 35.3A,B).

Aorta

Widening of the cranial and middle mediastinum in proximity to the heart base can indicate dilation of the aortic arch in both dogs and cats. On the VD/DV projections, a focal bulge in the descending aorta is suggestive of aortic dilation, as seen in patients with aortic stenosis and patent ductus arteriosus, and may correlate with an increase in soft tissue opacity at the cranial aspect of the cardiac silhouette on lateral projections (Fig. 35.15A,B). In older cats, redundancy of the aortic arch and tortuosity of the descending aorta are described to likely represent a normal age variant although systemic hypertension and hyperthyroidism may also contribute (Fig. 35.16A).[6] On the VD/DV projections, the aorta is occasionally projected end-on within the left side of the mediastinum and should not be misinterpreted as a pulmonary nodule (see Fig. 35.16B).[6]

Main Pulmonary Artery

Under normal conditions, the main pulmonary artery cannot be delineated on evaluation of the cardiac silhouette. In the presence of main pulmonary artery enlargement, a bulge at the 1–2 o'clock position in the region of the main pulmonary artery may be isolated on VD/DV projections (Fig. 35.17). With increased severity, the trachea may be displaced to the right at the level of the heart base. An increase in soft tissue opacity may also be

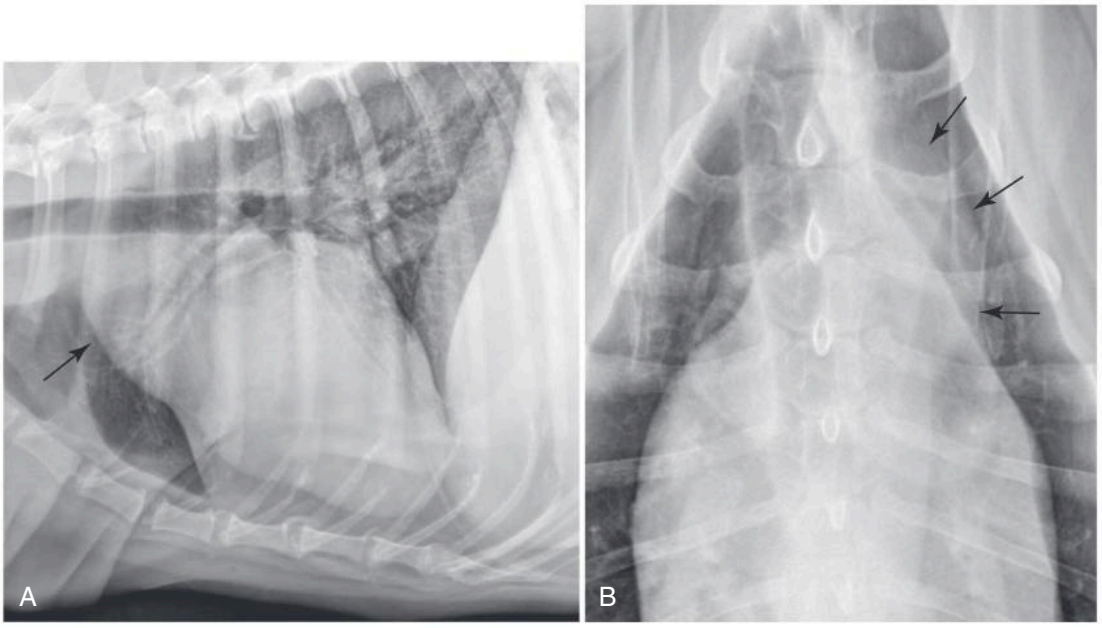


Fig. 35.15 Lateral **(A)** and dorsoventral **(B)** projections of a dog with aortic stenosis. In **A,** the dilated aortic arch represents a bulge on the craniodorsal aspect of the cardiac silhouette (*black arrow*). In **B,** the enlarged aortic arch is seen bulging at the cranial, and slightly left, aspect of the cardiac silhouette (*black arrows*).

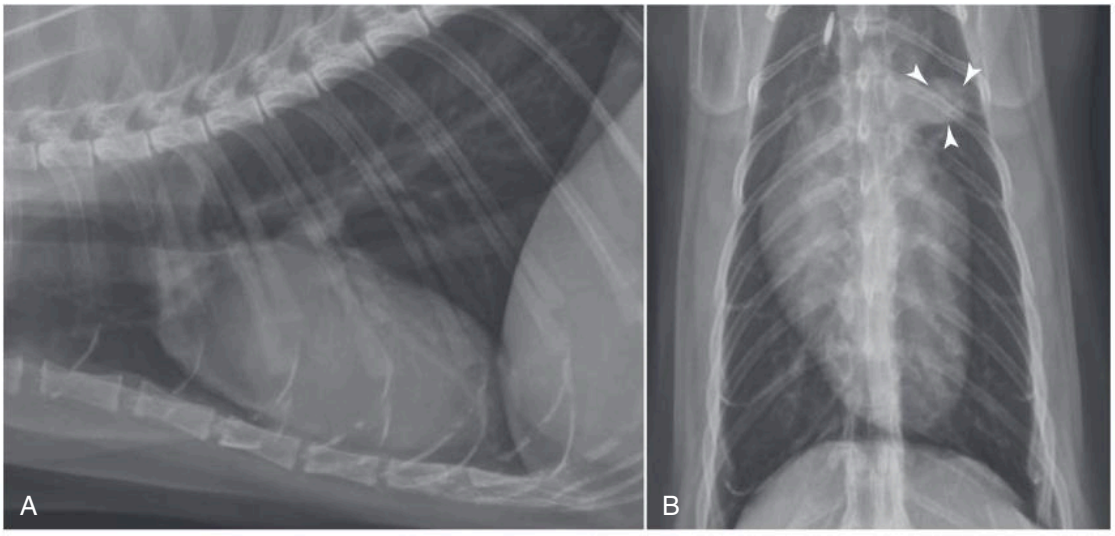


Fig. 35.16 Lateral **(A)** and ventrodorsal **(B)** projections of two different cats with age-associated redundancy and tortuosity of the aorta. In **A,** the aortic arch extends more cranial than normal, and the descending aorta is tortuous. In **B**, the aortic arch is projection end-on, representing a focal soft tissue opacity to the left of midline (*white arrowheads*), which should not be misinterpreted as a pulmonary mass.

seen on the lateral projections at the heart base where the left and right pulmonary arteries converge and are seen end-on. Enlargement of the main pulmonary artery is not recognized routinely on lateral projections. Identification of main pulmonary enlargement in cats may be more difficult due to a less pronounced elevation of the main pulmonary artery margin from the cardiac silhouette in cats and some variations in the orientation of the main pulmonary artery at the heart base in comparison to dogs. Considered causes for main pulmonary artery enlargement in dogs and cats include pulmonary hypertension, as from heartworm infection, and turbulence, as from pulmonic stenosis or patent ductus arteriosus.

SPECIFIC PATTERNS OF LOBAR PULMONARY VESSEL CHANGES

A thorough evaluation of the lobar pulmonary vasculature is integral to the assessment of the cardiovascular structures. The cranial lobar pulmonary arteries and veins are best visible on the lateral projections and most prominent in the nondependent lung lobe. Superimposition of the lobar pulmonary artery and veins on the VD/DV projections limits interpretation. Separation of the left and right cranial lobar pulmonary arteries and veins is greatest on the left lateral projection: therefore, evaluation of the right cranial lobar pulmonary vasculature in the

better inflated nondependent right cranial lung lobe is usually easiest (Fig. 35.18A,B). The caudal lobar pulmonary vasculature is best evaluated on VD/DV projections and optimized on the DV projection due to better inflation of the nondependent caudal lung lobes and increased magnification (Fig. 35.19A,B). Additionally, the caudal lobar pulmonary vessels are more perpendicular to the diverging x-ray beam, resulting in less distortion. The lobar pulmonary arteries and veins are located on opposite sides of their corresponding lobar bronchus. On lateral projections, the cranial lobar arteries are dorsal and the veins are ventral to the bronchus, whereas the caudal lobar pulmonary arteries are lateral and veins are medial to their corresponding bronchus on the VD/DV projections.[19] As a simplified means to recall the relative positioning of the lobar pulmonary arteries and veins to each other, the lobar pulmonary arteries may be expressed as being "up and away," while the veins are "ventral and central."



Fig. 35.17 Dorsoventral projection of a dog with dilation of the main pulmonary artery (*black arrows*).

Under normal conditions, the lobar pulmonary arteries and veins should be symmetrical in size.[19] Additionally, normal lobar pulmonary arteries and veins follow a generally straight path as they gradually taper in the periphery of the lung field. The size of the cranial lobar pulmonary vessels may be assessed by comparing vessel diameter to the width of the fourth rib just ventral to the vertebral column on lateral projections and the width of the ninth rib in the VD/DV projections.[19,20] Variable rib conformation and a wide range of normal values limit the clinical usefulness of these comparisons.

Certain diseases cause predictable changes in the size or shape of either pulmonary arteries alone or pulmonary veins alone, or both simultaneously, and are associated with the following conditions:

- *Enlarged lobar pulmonary arteries and veins:* Volume overload is the most common cause for lobar pulmonary vessel enlargement and may be iatrogenic, such as from overzealous intravenous fluid administration. Other causes may include left-to-right shunting congenital cardiovascular anomalies, peripheral arteriovenous fistula, and decreased cardiac output resulting in fluid retention (Fig. 35.20A,B). The concurrent presence of lobar pulmonary vein congestion and pulmonary hypertension can be a cause for simultaneous lobar pulmonary artery and vein enlargement.
- *Small lobar pulmonary arteries and veins*: Diffuse thinning of the lobar pulmonary vasculature results in a generalized hyperlucency of the pulmonary parenchyma due to pulmonary undercirculation. Causes may include dehydration, diuretic administration, or blood loss and are often associated with concurrent caval undercirculation and microcardia (see Fig. 35.3A,B). Pulmonary undercirculation with thinning of the lobar pulmonary arteries and veins is also seen in dogs and cats with right-to-left shunting congenital heart anomalies (Fig. 35.21A,B). Such changes are less conspicuous and uncommonly recognized in cats.

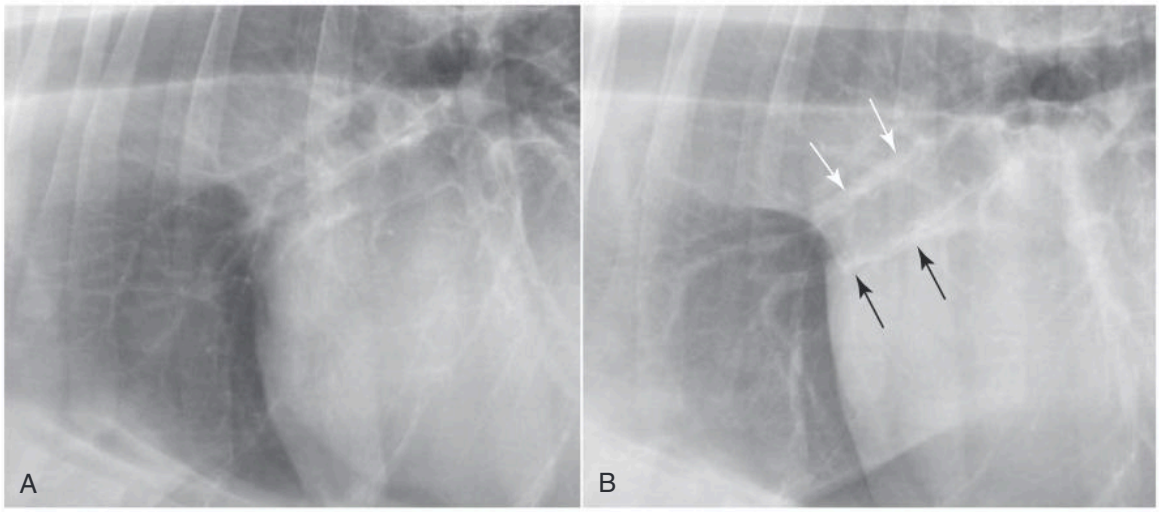


Fig. 35.18 Close-up from right **(A)** and left **(B)** lateral projections of a normal dog. On the right lateral projection **(A)**, the left and right cranial lobar pulmonary arteries and veins are superimposed and cannot be evaluated. On the left lateral projection **(B)**, the right cranial lobar pulmonary artery (*white arrows*) and right cranial lobar pulmonary vein (*black arrows*) are more clearly seen. The ability to distinguish the right cranial artery from the vein is typically easier on a left lateral projection. Note the similar size of the artery and vein in **B**.

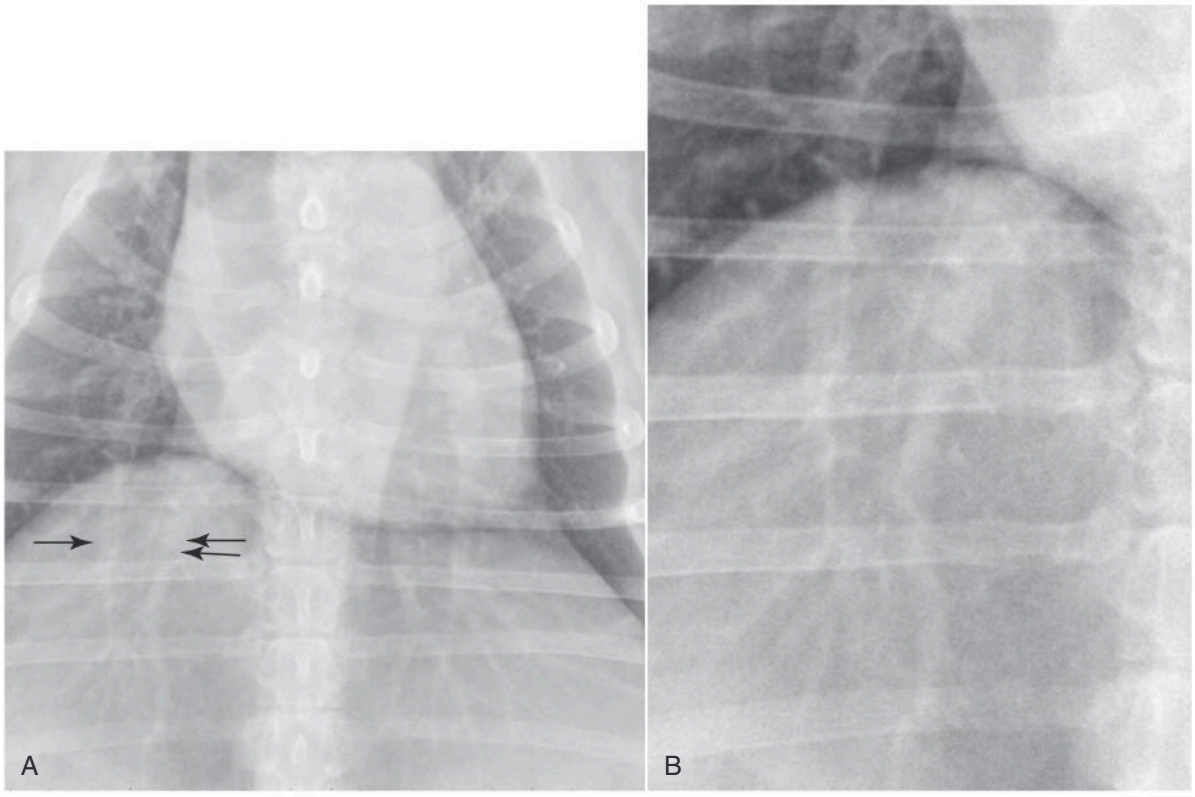


Fig. 35.19 Dorsoventral **(A)** projection of a normal dog with a close-up view **(B)** of the right caudal lobar pulmonary vessels. The right caudal lobe pulmonary artery (*single black arrow*) is lateral to the bronchus, whereas the right caudal lobe pulmonary vein is medial (*double black arrows*). On close inspection, the mineralized wall of the caudal lobe bronchus can be seen between the artery and vein. Note that in this dog, as in most, the bronchus does not occupy the entire space between the artery and vein. When the bronchus is not mineralized, inferring that it occupies the entire distance between its associated artery and vein is inaccurate.

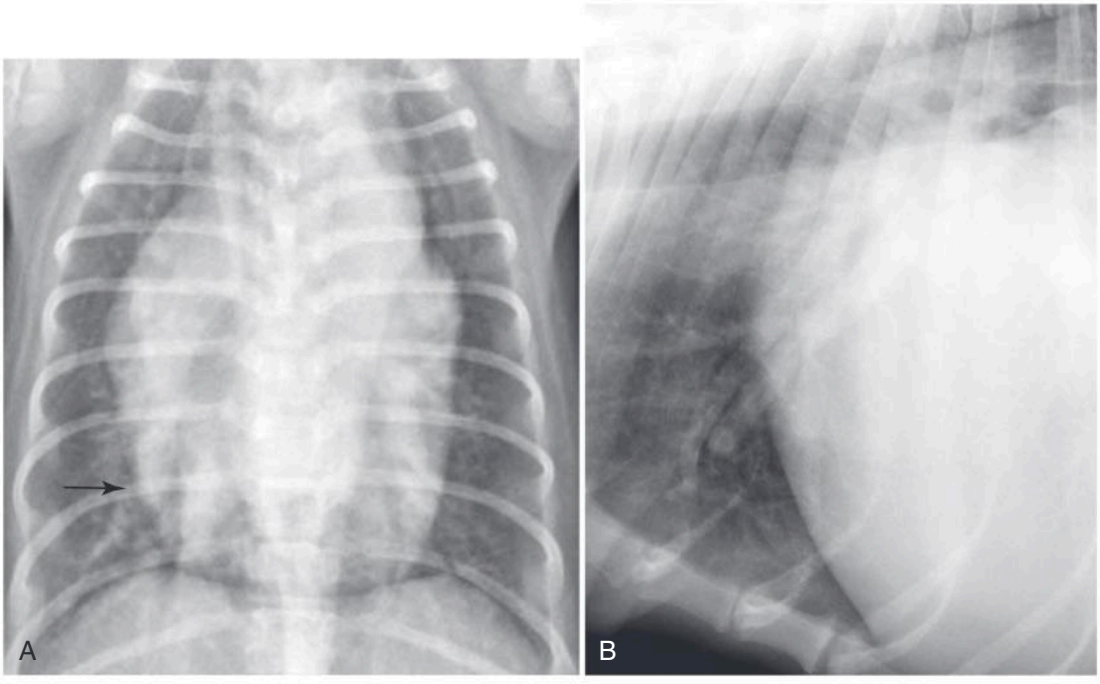


Fig. 35.20 Dorsoventral **(A)** and lateral **(B)** projections of two different dogs with a patent ductus arteriosus. The caudal lobar pulmonary arteries and veins are both enlarged as a result of overcirculation of the pulmonary vascular system. Note the size of the summation shadow where the vessels cross the right ninth rib (*black arrow*) in **A** and compare to Fig. 35.17. The shape of these summation shadows indicates that both the right caudal lobar pulmonary artery and vein are enlarged.

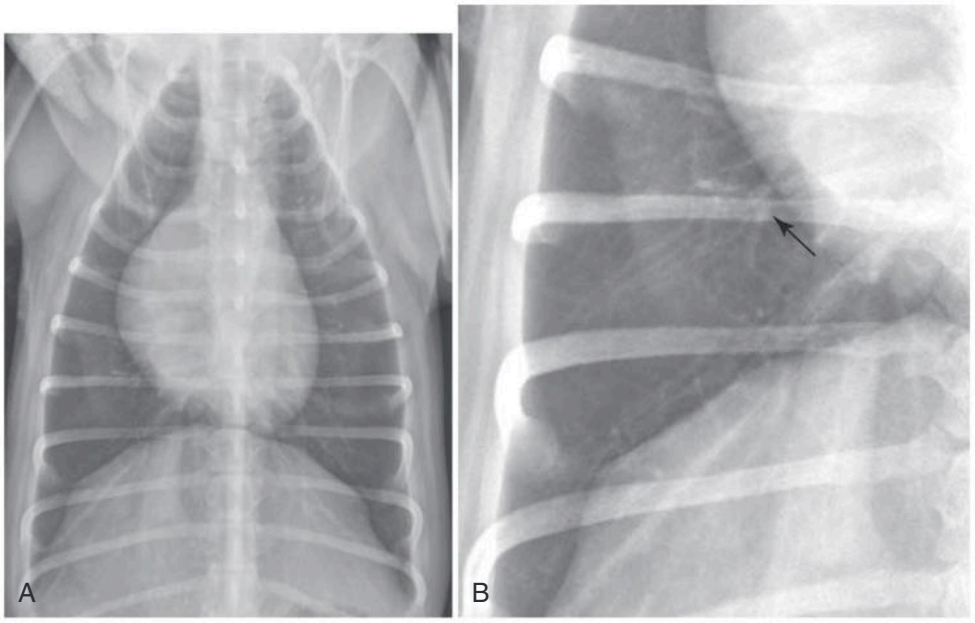


Fig. 35.21 Ventrodorsal **(A)** projection of a dog with pulmonary undercirculation from multiple congenital cardiac anomalies with close-up image of the right caudal lung lobe **(B)**. The pulmonary vessels are small and poorly defined. In **B,** note the small size of the right caudal lobe pulmonary vein where it crosses the right ninth rib (*black arrow*).

- *Enlarged lobar pulmonary arteries with normal veins*: The most common cause in the dog is pulmonary hypertension. Depending on the patient's demographic (e.g., southeastern states), heartworm disease may be the most likely etiology (eFigs. 35.1–35.3). In cats, feline asthma is most prevalent, although heartworm disease is also occasionally identified (see eFig. 35.2).
- *Enlarged lobar pulmonary veins with normal arteries*: Lobar pulmonary vein enlargement is most seen in dogs with mitral valve insufficiency resulting in left-sided volume overload and subsequent pulmonary venous hypertension. A similar finding is inconsistently observed in cats.
- Tortuous pulmonary vessels: Tortuosity of the pulmonary vessels is most commonly seen in dogs and cats with pulmonary hypertension. The most common causes are heartworm disease in dogs and shunting congenital cardiovascular abnormalities in cats (see eFig. 35.3D). Peripherally, the lobar pulmonary arteries may also be blunted (Fig. 35.22).

In some instances, perivascular disease in the adjacent lung parenchyma can partially or completely border efface and reduce the conspicuity of the pulmonary vasculature rendering interpretation difficult. This may be especially encountered in dogs and cats with left-sided congestive heart failure.

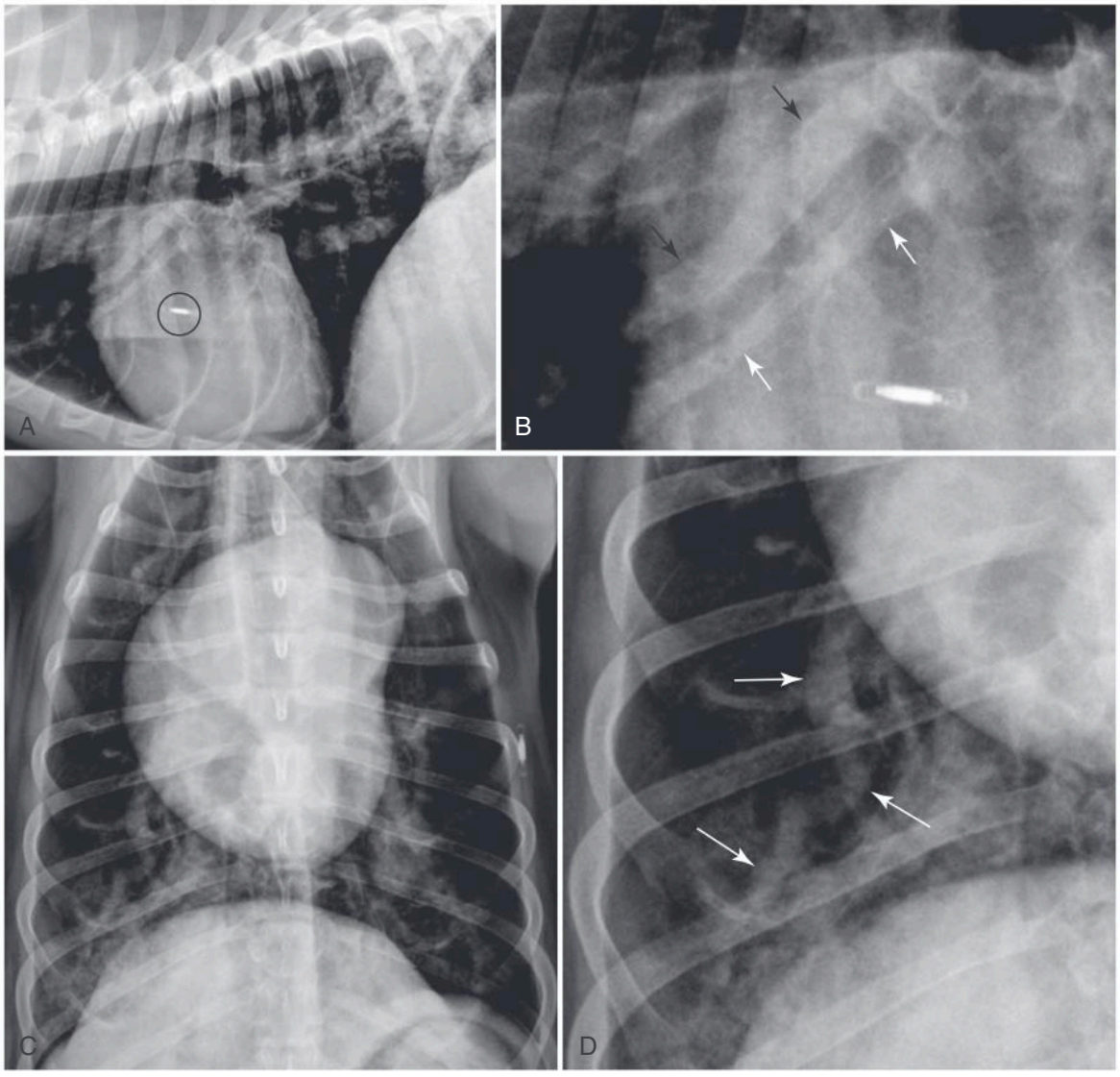


Fig. 35.22 Close-up view of the left caudal thorax of a dog with severe heartworm disease. The left caudal lobe pulmonary artery is severely dilated (*black arrows*). At the most caudal pair of arrows, the vessel ends abruptly, or is truncated. This is due to an intravascular thrombus completely obstructing the lumen at this level with marked reduction in vessel diameter distal to the obstruction.

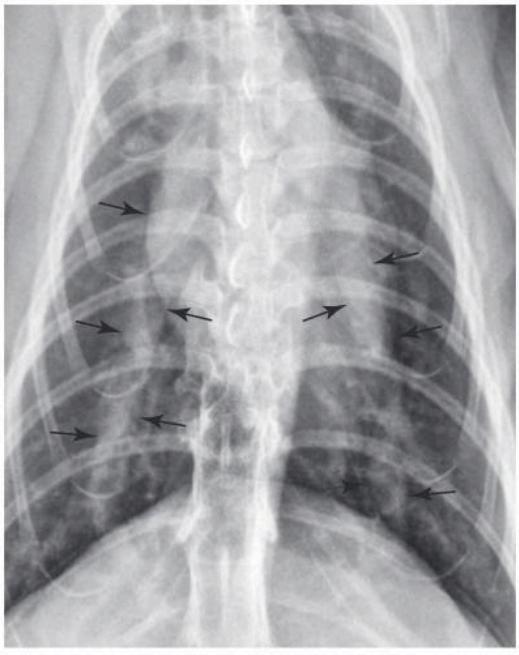
FEATURES OF CONGESTIVE HEART FAILURE

Left-Sided Congestive Heart Failure

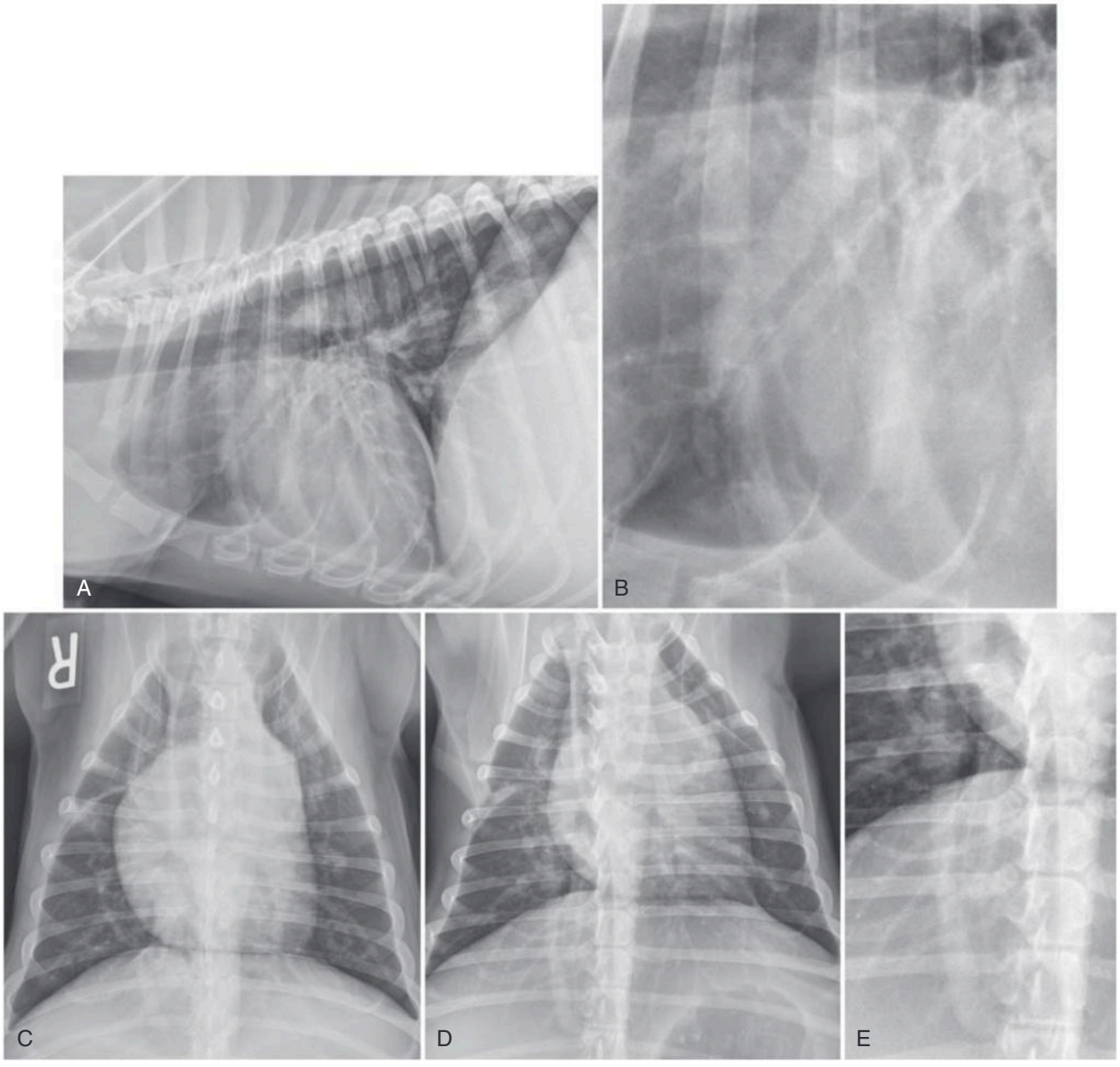
Volume and pressure overload of the left ventricle may result in backward congestion (hypertension) of the lobar pulmonary veins. Pulmonary venous hypertension may ultimately result in the development of cardiogenic pulmonary edema due to transudation of fluid from the pulmonary capillaries into the lung interstitium. In very early left-sided heart failure, poorly defined interstitial pulmonary edema may be observed, but



eFig. 35.1 Lateral **(A)**, close-up lateral **(B),** dorsoventral (DV; **C**), and close-up DV **(D)** radiographs of the thorax of a dog with heartworm disease. In **A,** the right cranial lobe pulmonary artery is larger than the right cranial lobe vein, and there is an intense alveolar pattern in the dorsocaudal aspect of the lung. The opacity encircled (*black circle*) is an identification microchip. In **B,** the enlarged right cranial lobe pulmonary artery (*black arrows*) compared to the right cranial lobe vein (*white arrows*) is very conspicuous. In **C,** the main pulmonary artery is dilated, the right ventricle appears enlarged, and there are patchy alveolar opacities in both caudal lung lobes, more intense on the right. In **D,** the right caudal lobe pulmonary artery is tortuous (*white arrows*). The vein cannot be seen because of the alveolar pattern in the right caudal lobe. The alveolar pattern in this dog is likely caused by thromboembolism given its patchy intense distribution. That it is caused by an allergic reaction cannot be ruled out.



eFig. 35.2 Dorsoventral (DV) radiograph of a cat infected with heartworms. Both caudal lobe pulmonary arteries are enlarged (*black arrows*). Looking closely, smaller (normal) caudal lobe pulmonary veins are present medial to each artery. Enlargement of the main pulmonary artery is not seen in cats with heartworm disease, although it is likely present.



eFig. 35.3 Left lateral **(A)**, close-up left lateral **(B)**, ventrodorsal (VD; **C**), dorsoventral (DV; **D**), and close-up DV **(E)** radiographs of a dog with heartworm disease. In **A** and **B,** note the enlargement of the right cranial lobe artery compared with the vein. In **C,** note the reversed-D appearance of the cardiac silhouette, consistent with right ventricular hypertrophy. In **D** and **E,** note the enlargement of the right caudal lobe artery compared with the vein. These findings are typical of canine heartworm disease.

more commonly an alveolar pattern develops. It is important to note that lobar pulmonary vein enlargement is not commonly present when there is cardiogenic pulmonary edema. Pulmonary arterial hypertension is also common in dogs with left-sided heart disease; this may or may not lead to pulmonary arterial enlargement (eFigs. 35.4–35.6).

Cardiogenic pulmonary edema in dogs is most commonly caudodorsally distributed. However, a perihilar, diffuse, or multifocal distribution is also possible but less prevalent. The pattern of pulmonary edema distribution in dogs with mitral valve insufficiency has been associated with the direction of the regurgitant jet. A symmetric distribution was associated predominantly with a central mitral regurgitant jet, whereas an asymmetric distribution was usually associated with an eccentric jet.[21] When asymmetric in distribution, more severe cardiogenic pulmonary edema is identified in the right caudal lung lobe in relation to the left caudal lung lobe. In dogs with cardiogenic pulmonary edema due to dilated cardiomyopathy (DCM), a diffuse unstructured to alveolar pulmonary pattern with a ventral distribution is observed at a higher frequency (Fig. 35.23). Cardiogenic pulmonary edema more often has a multifocal to diffuse distribution in cats. Many cats with left heart failure also have pleural effusion in addition to pulmonary edema.

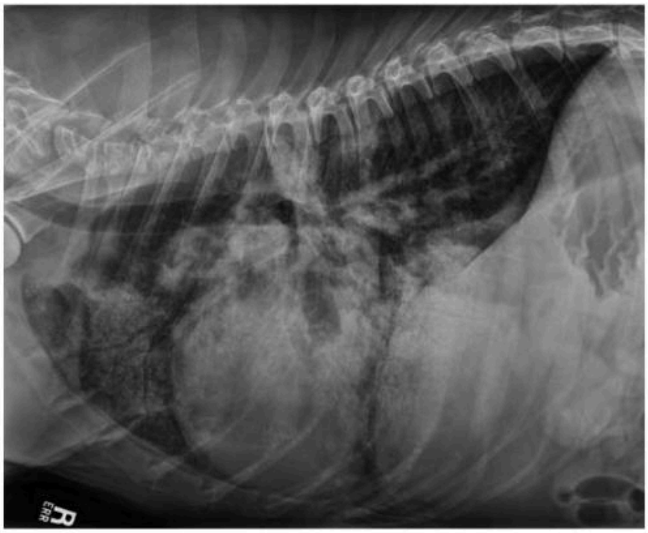


Fig. 35.23 Right lateral projection of a dog with dilated cardiomyopathy and left-sided congestive heart failure. The bulge along the caudodorsal aspect of the cardiac silhouette is indicative of left atrial enlargement and results in straightening of the caudal margin of the cardiac silhouette. The lobar pulmonary veins are enlarged due to left-sided volume overload from myocardial failure. A diffuse unstructured interstitial pulmonary pattern is seen throughout the pulmonary parenchyma and is greater in severity ventrally, where it coalesced into an alveolar pulmonary pattern. This distribution represents a more typical manifestation of cardiogenic pulmonary edema in dogs with dilated cardiomyopathy. (Image courtesy Rachel Lee, DVM.)

Right-Sided Congestive Heart Failure

Right-sided heart disease may result in right ventricular volume and pressure overload with subsequent caudal vena cava and hepatic enlargement. With progression, abdominal effusion, and sometimes pleural effusion, develops (Fig. 35.24A,B).

ABNORMAL OPACITY OF THE CARDIAC SILHOUETTE

In the absence of a peritoneopericardial diaphragmatic hernia, alterations to the normal homogeneous soft tissue opacity of the cardiac silhouette are rare and more commonly associated with the presence of aortic root mineralization and the presence of intraventricular gas. Aortic root mineralization is much more common in dogs than cats.[22] On lateral projections, a poorly to well-defined irregular to curvilinear region of mineralization is present at the level of the aortic root, superimposed over the craniodorsal aspect of the cardiac silhouette (Fig. 35.25). Aortic root mineralization may represent a normal age-associated change and is usually of no clinical significance.[22]

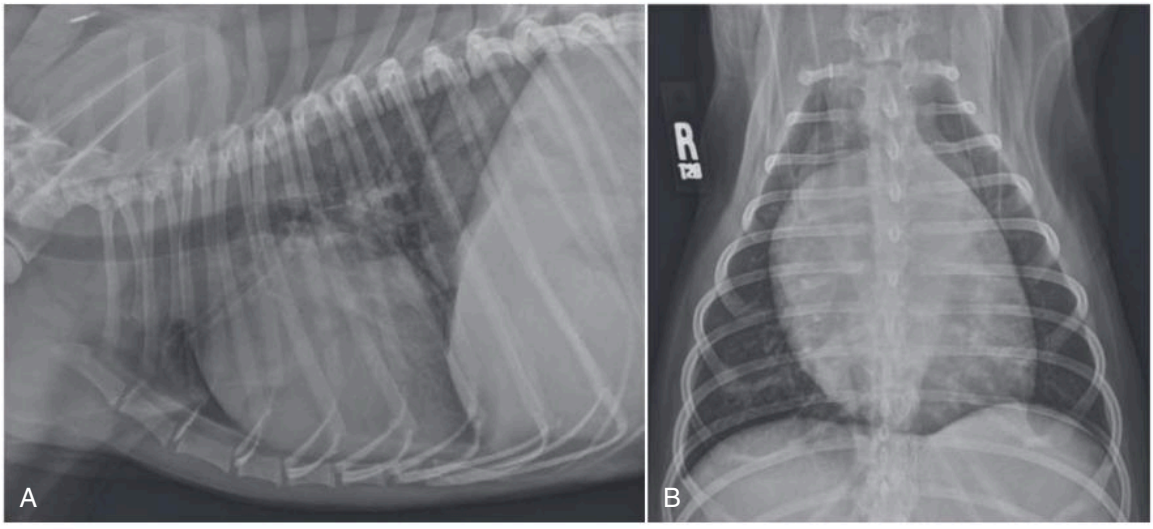
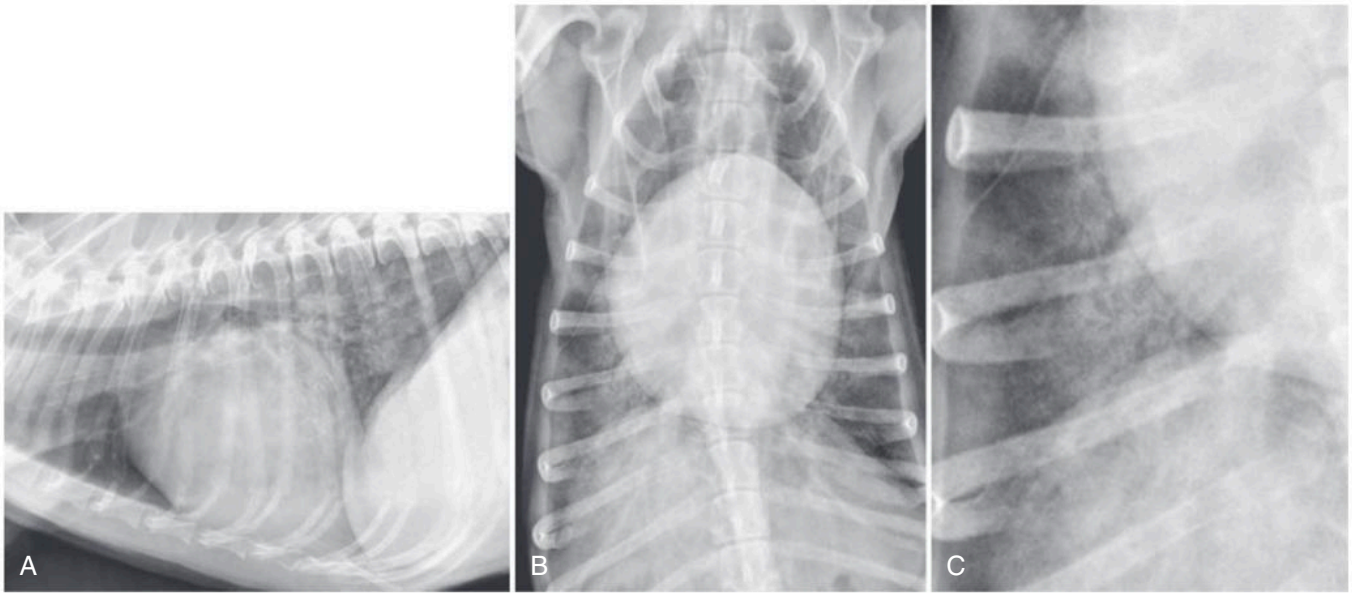
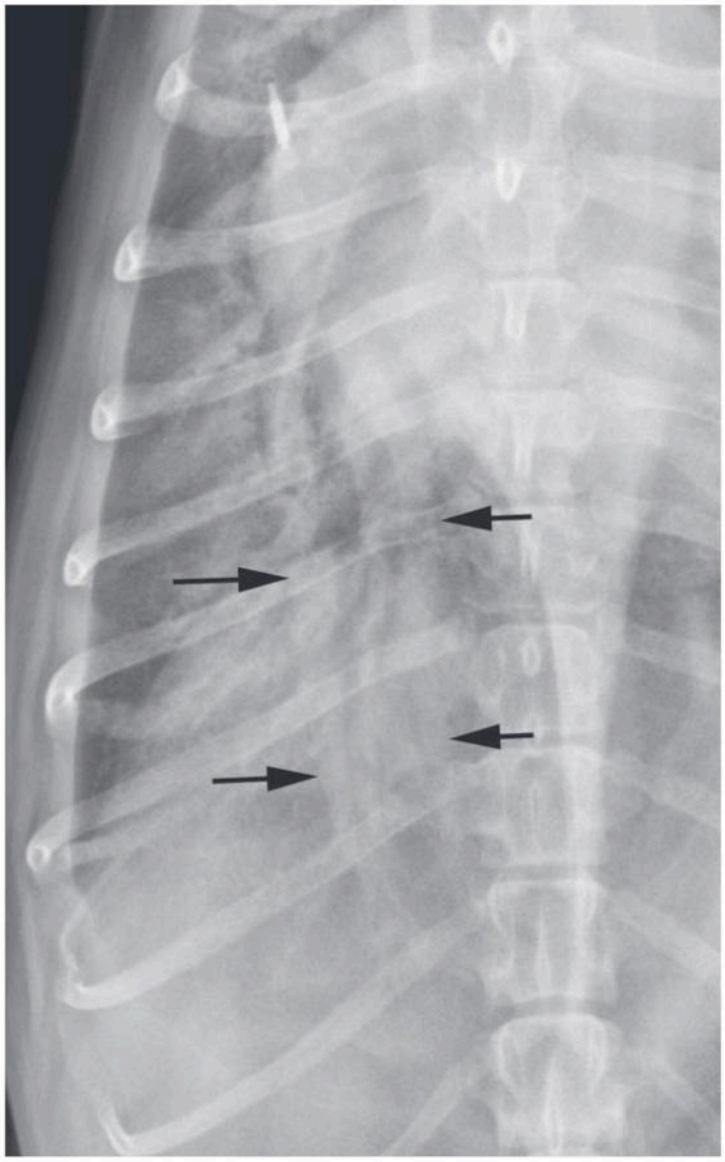


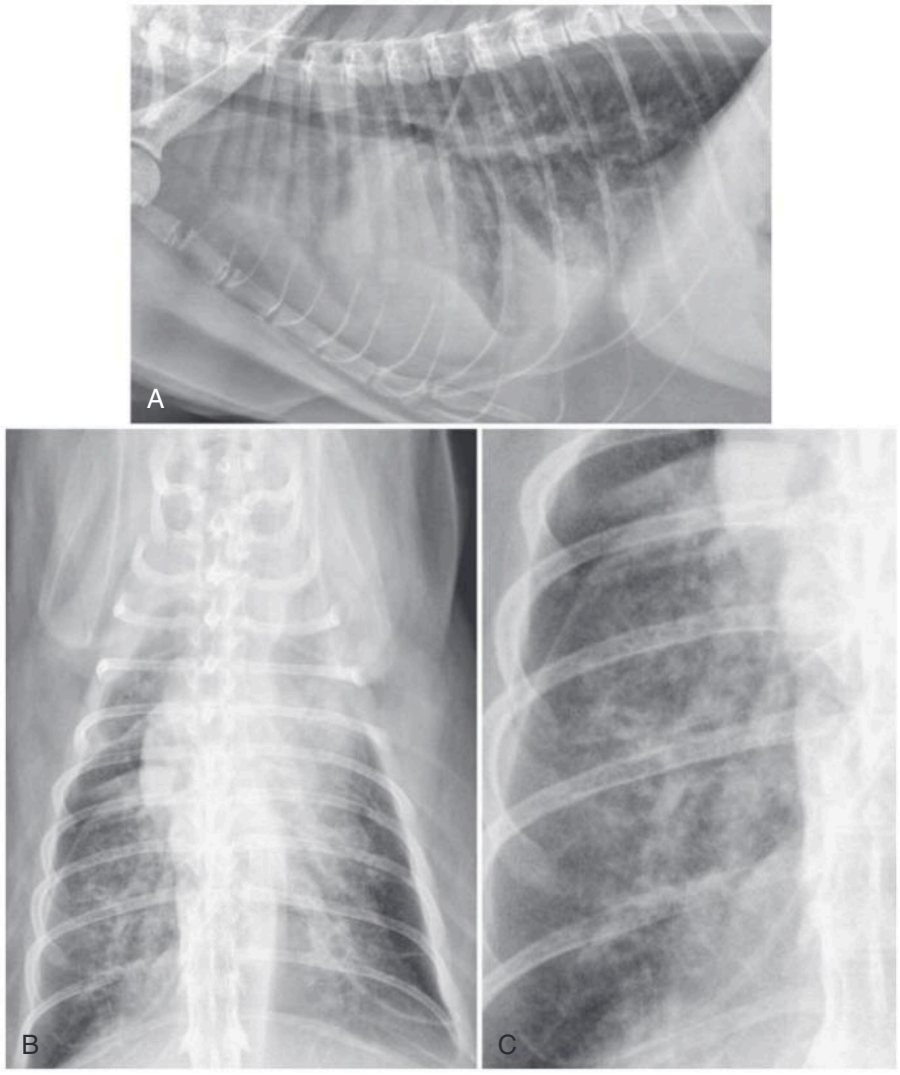
Fig. 35.24 Left lateral **(A)** and ventrodorsal **(B)** projections of a dog with right-sided cardiomegaly and right-sided congestive heart failure. The cranial and right lateral margins of the cardiac silhouette are rounded with leftward displacement of the cardiac apex and a "reversed-D" shape on the ventrodorsal projection. The caudal vena cava is distended and the liver is enlarged due to backward congestion. In combination with the presence of scant pleural effusion, the poor abdominal serosal detail is secondary to the presence of peritoneal effusion and indicative of right-sided congestive heart failure.



eFig. 35.4 Left lateral **(A)**, dorsoventral (DV; **B**), and close-up DV **(C)** radiographs of a dog with left-sided heart failure secondary to mitral insufficiency. In **A,** the heart and left atrium are enlarged. Pulmonary vessels are difficult to identify because of border effacement created by edema in adjacent lung. The caudal lung lobes appear abnormally opaque in this lateral view, but this may be caused by poor ventilation, and recumbency-associated atelectasis. Any suspicious lung opacity identified in the lateral view must be confirmed in the DV or ventrodorsal (VD) view. In **B,** there is an alveolar pattern in the right middle and caudal lobes. This can be seen in the close-up **(C)**. Note the poor visualization of pulmonary vessels in these lobes because of border effacement from the pulmonary edema. This patchy alveolar pattern, even without visualization of air bronchograms, is typical of cardiogenic pulmonary edema.



eFig. 35.5 Close-up of the right caudal thorax from a dog with mitral insufficiency and left heart failure. The pulmonary arteries and veins are both enlarged (*black arrows*). The *upper arrows* are at the level of the right ninth rib, and it is apparent that the summation shadow of both the right caudal lobar pulmonary artery and vein with the rib is larger in the horizontal direction, evidence of vascular enlargement. The enlargement of both pulmonary arteries and veins in this dog with left heart failure is due to a combination of pulmonary arterial and venous hypertension. Fluid retention would be another differential for this appearance.



eFig. 35.6 Left lateral **(A),** ventrodorsal (VD; **B**), and close-up VD **(C)** radiographs of a cat with left-sided heart failure caused by hypertrophic cardiomyopathy. Pleural effusion is obvious in **A.** The heart cannot be seen clearly in this patient. One expects the heart to be enlarged in cats with hypertrophic cardiomyopathy and heart failure, but it may be normal radiographically in some cats. Pleural effusion is also noted in the dorsoventral (DV) view **(B)**. Also, the caudal lobe pulmonary arteries and veins both appear enlarged. This is often seen in cats in heart failure and could be due to either coexisting pulmonary arterial and venous hypertension or fluid retention, or both. A heterogeneous, relatively unstructured pulmonary pattern is present in the caudal lobes that is consistent with pulmonary edema; see close-up in **C.** This heterogeneous pattern is typical of pulmonary edema in cats and is more common than more uniform homogenous lung opacification.

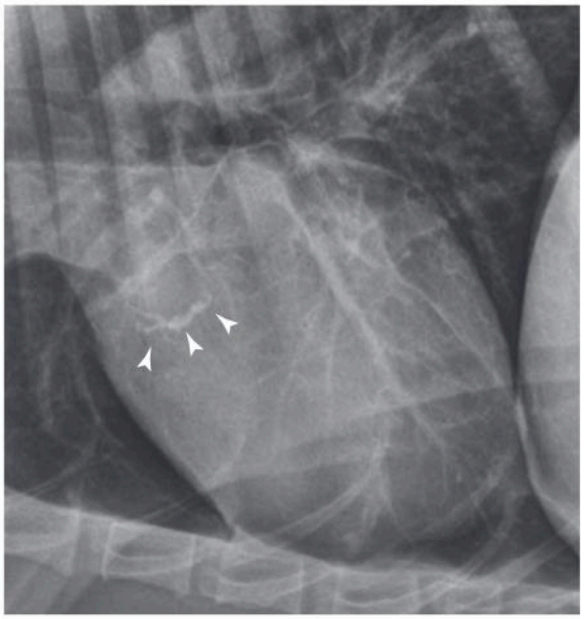


Fig. 35.25 Right lateral radiograph of a dog with aortic root mineralization (*white arrowheads*), representing an incidental age-associated change.

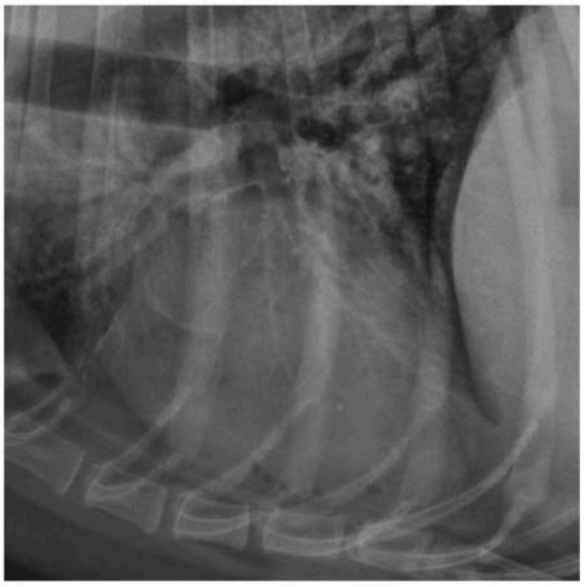


Fig. 35.26 Right lateral projection of a dog with a small amount of intraventricular gas due to recent cephalic vein injection.

A small amount of gas in the plane of the right atrium is occasionally identified on lateral projections (Fig. 35.26). This is usually iatrogenic. While small amounts of gas are unlikely to cause clinical signs, air embolization can be fatal.[23,24] Maintaining the patient in left lateral recumbency may be advantageous to prevent dissemination of gas into the lobar pulmonary arteries.

Acquired Cardiovascular Diseases

Acquired cardiovascular diseases are more prevalent than congenital heart diseases in dogs and cats, reported to represent up to 94.05% of all cardiac abnormalities.[25] Of these, valvular disease is most common in dogs, whereas cats more often have myocardial failure. Factors, such as age, breed, and diet, may increase the risk of acquired heart disease in both dogs and cats. Early diagnosis of acquired disease is important to avoid irreversible cardiac damage.

Myxomatous Mitral Valve Disease

Myxomatous mitral valve disease is the most common acquired heart disease in dogs, representing approximately 75% of all cardiac disease in small animal practice.[26] Myxomatous mitral valve disease is highly prevalent in older small breed dogs, reported in 85% of 13-year-old dogs at necropsy, and may be inherited in certain dog breeds, such as the Cavalier King Charles spaniel.[26,27]

Valve leaf degeneration often leads to left-sided cardiac decompensation and heart failure.[28] Rupture of chordae tendineae and atrial rupture may result in a rapid clinical decline.[28,29] Radiographic signs of myxomatous mitral valve disease include (eFigs. 35.7 and 35.8):

- Left atrial, and sometimes auricular enlargement, as described earlier.
- The sole or combined presence of left atrial and ventricular enlargement will result in an increase in apical to basilar length of the cardiac silhouette.
- Distention of lobar pulmonary veins can result from pulmonary venous hypertension.
- Cardiogenic pulmonary edema from left-sided heart failure. This usually develops in the absence of lobar pulmonary venous enlargement.
- Distention of the pulmonary arteries with an artery to vein ratio >1.1 has been described as supportive of pulmonary hypertension in patients with myxomatous mitral valve disease.[30]

Myxomatous Tricuspid Valve Disease

Approximately 54% of patients with myxomatous mitral valve degeneration have concurrent myxomatous tricuspid valve degeneration.[31] Minor tricuspid valve regurgitation may be negligible; however, severe tricuspid valve degeneration can result in valvular insufficiency and right-sided volume overload. The right atrium and ventricle will become enlarged with associated eccentric hypertrophy. Backward congestion may decompensate into right-sided heart failure with pleural and abdominal effusion developing from the increased hydrostatic pressure.

Radiographic signs of myxomatous tricuspid valve disease include (Fig. 35.27A,B):

- Right atrial and ventricular enlargement is more likely to be radiographically recognized in the presence of at least moderate cardiac chamber enlargement.
- Distention of the caudal vena cava and generalized hepatomegaly are indicative of systemic venous hypertension.
- Peritoneal and/or pleural effusion will develop due to right-sided cardiac decompensation.

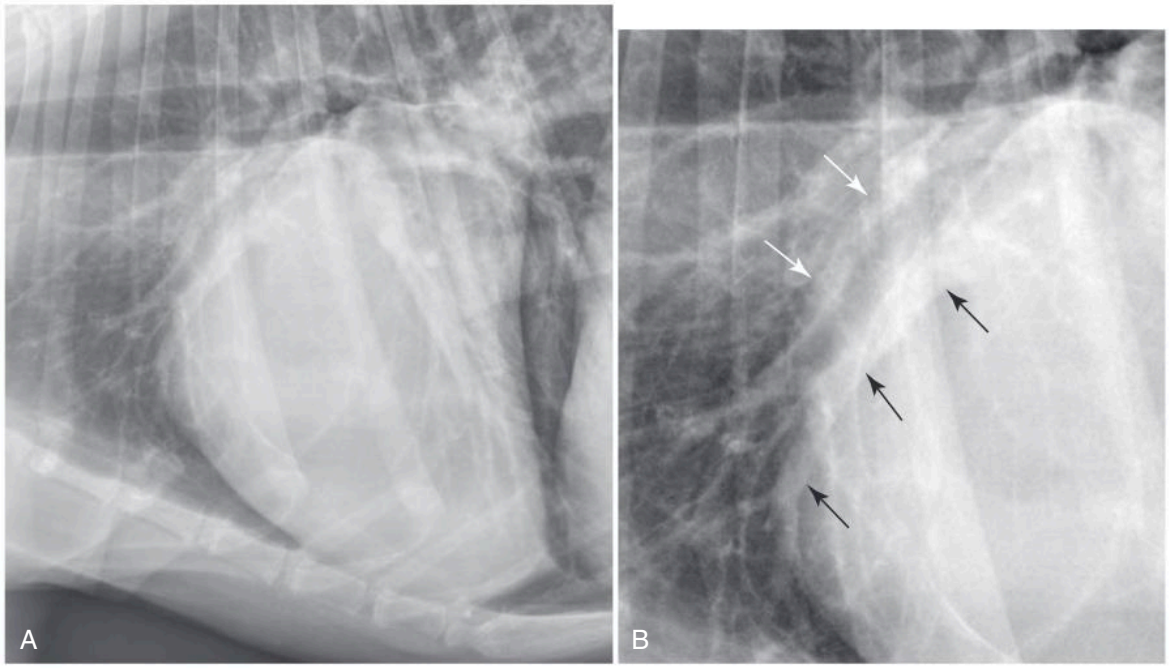
Cardiomyopathies

Cardiomyopathies are diseases of the heart muscle and have variable etiologies and presentation in both dogs and cats.

Dilated cardiomyopathy (DCM) is most prevalent in large breed male dogs and is also seen in cats. Canine breeds predisposed to DCM include the Doberman Pinscher, Great Dane, Irish Wolfhound, and Boxer. Although the cause for myocardial failure is not fully understood, genetic mutation, systemic disease, toxins, and nutritional deficiencies (including a more recent correlation between DCM and grain-free diets) are possible etiologies.[32] Failure of the myocardium results in progressive concentric dilation of the left ± right cardiac chambers. The heart becomes volume overloaded, and mitral valve dysfunction may result from a change in shape of the mitral annulus because of cardiac dilation. Enlargement of the pulmonary arteries and veins is commonly seen due to intravascular fluid retention, and may be followed by the development



eFig. 35.7 Lateral **(A)**, dorsoventral (DV; **B**), and close-up DV **(C)** views of a dog with compensated mitral insufficiency. In **A,** the heart is enlarged, and the left atrium is dilated. In **B,** the heart is also enlarged, and the right caudal lobar pulmonary vein is enlarged compared with the artery. This can also be seen in a close-up **(C)** where the right caudal lobar vein (*black arrows*) is considerably larger than the artery (*white arrows*). This is an example of compensated mitral insufficiency. Pulmonary venous hypertension transmitted from the increased left atrial pressure causes the pulmonary vein enlargement, but there is no evidence of pulmonary edema to signify left-sided heart failure.



eFig. 35.8 Lateral radiograph **(A)** and close-up lateral radiograph **(B)** of a dog with compensated mitral insufficiency. The left atrium and the right cranial lobe vein are enlarged, a sign consistent with pulmonary venous hypertension. The venous enlargement (*black arrows*) compared to the normal artery (*white arrows*) is clearly seen in **B.**

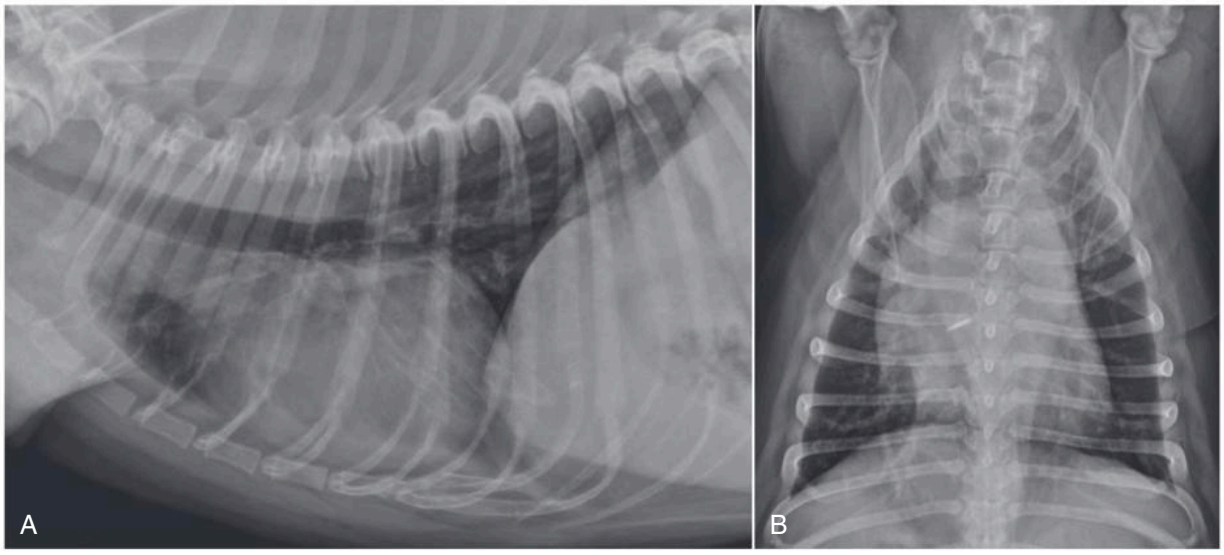


Fig. 35.27 Left lateral **(A)** and ventrodorsal **(B)** projections of a dog diagnosed with myxomatous tricuspid valve disease. The cranial and right lateral margins of the cardiac silhouette are rounded and the cardiac apex is displaced to the left with a "reversed-D" shape of the cardiac silhouette due to right atrial and ventricular enlargements. No evidence of right-sided congestive failure is seen.

of cardiogenic pulmonary edema. Dilation of the pulmonary arteries may also be associated with the development of pulmonary hypertension from activation of the renin-angiotensin system in response to decreased renal perfusion and/or the presence of chronic heart failure.[33]

Radiographic features of DCM include (see Fig. 35.23, Fig. 35.28, eFig. 35.9):

- Left atrial and ventricular enlargement. Cardiomegaly is the most common radiographic abnormality in dogs with DCM and is reported in up to 80% of dogs.[34] However, given the large size and variable thoracic conformation of dogs typically affected with DCM, breed variations need to be taken into account when evaluating the cardiac silhouette for cardiomegaly. The cardiac silhouette may be normal in some dogs. A mean VHS of 11.8 (range 11.0—12.6) may be suggestive of cardiomegaly in dogs with DCM.[33] In cats, the cardiac silhouette may be "valentine shaped."
- Concurrent enlargement of the right heart is observed in more advanced cases and may not be apparent on thoracic radiographs if mild in severity.
- Cardiogenic pulmonary edema due to left-sided heart failure is identified in the majority of dogs (74%) at the time of radiographic evaluation.[34] Most dogs in heart failure from DCM will have a bronchointerstitial pattern, rather than the typical dorsocaudal alveolar pattern seen in dogs with left heart failure from mitral valve disease. A ventral distribution of an interstitial, coalescing into alveolar pattern can be seen in a subset of dogs with DCM, possibly attributed to chronicity.[32,33]
- The presence of pleural effusion, caval distention, hepatomegaly, and/or peritoneal effusion from right-sided heart failure is often seen.

Arrhythmogenic right ventricular cardiomyopathy, also known as ARVC or Boxer cardiomyopathy, is a familial myocardial disease in Boxer dogs but can also affect other breeds of dogs and cats. The myocardium of the right ventricle is affected primarily; however, involvement of the left ventricle and atria is also possible. The myocardium becomes inflamed (e.g., myocarditis) and replaced by fat ± fibrosis, leading to the development of potentially fatal ventricular arrhythmias.[35] With disease progression and not necessarily before the emergence of arrhythmias, the cardiac chambers may undergo eccentric hypertrophy and become volume overloaded. When in excess, the heart will decompensate into right-sided congestive heart failure.[36]

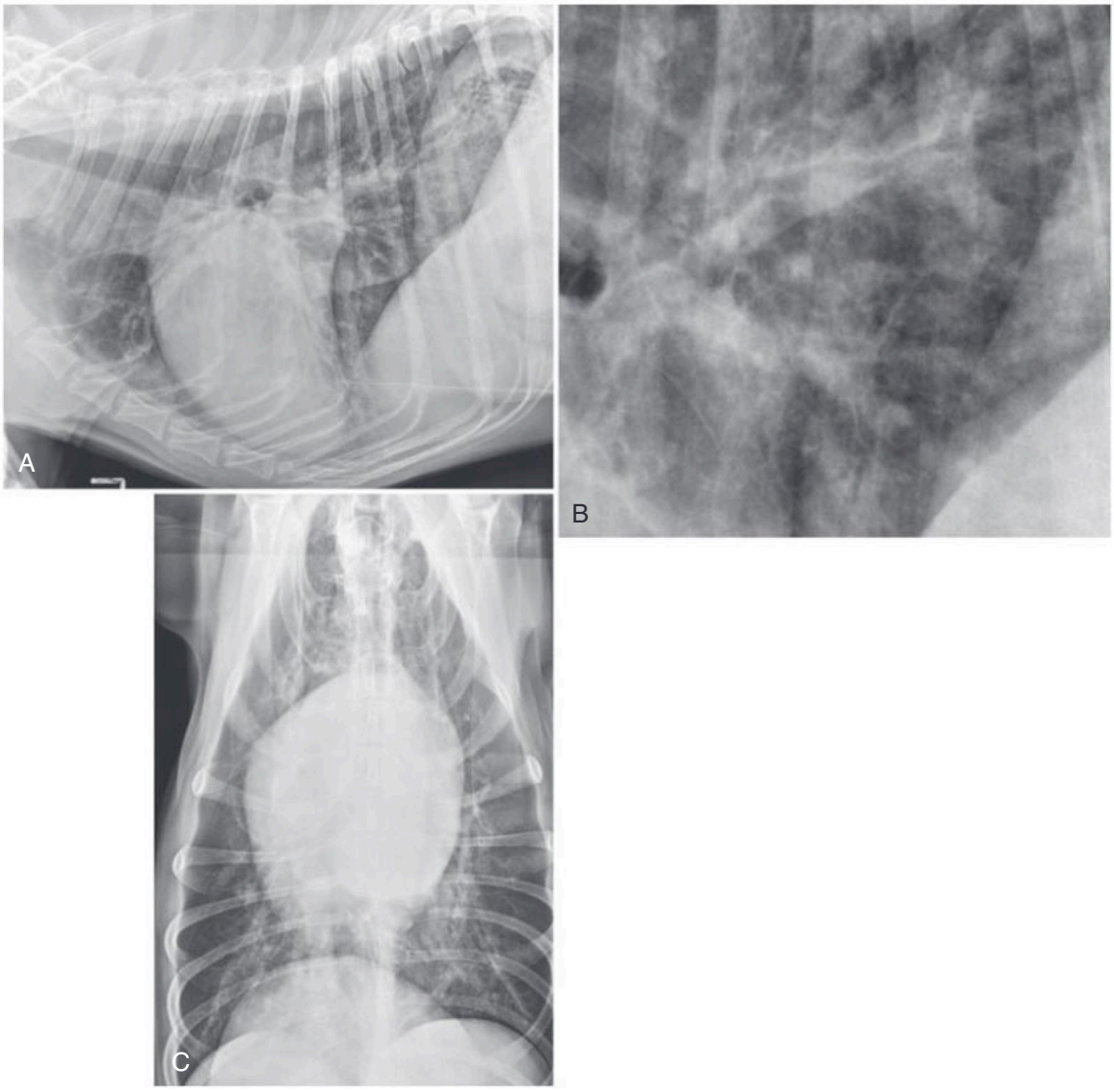
Radiographic features of ARVC include:

- Commonly, there are no thoracic radiographic abnormalities.
- Right-sided cardiomegaly is seen with more advanced systolic dysfunction and congestion.
- Right-sided congestive heart failure is occasionally observed.

Hypertrophic cardiomyopathy (HCM) is the most common acquired heart disease in cats and is familial in some breeds, such as the Maine Coon and Norwegian Forest cat.[37] HCM is seen occasionally in dogs with a much lower prevalence than in cats. Concentric hypertrophy of the left ventricle causes a decrease in ventricular volume capacity and increase in left ventricular filling pressure.[38] The decrease in stroke volume is counteracted by tachycardia, which in turn further limits filling of the left ventricle. Therefore, the left atrium becomes overloaded with further backward hypertension of the lobar pulmonary veins as the disease progresses. In some instances, the papillary muscles may become thickened and result in mitral valve insufficiency, further exacerbating dilation and hypertension of the left atrium. The mitral valve may have altered motion and deviate toward the left ventricular outflow tract, causing dynamic outflow obstruction of the left ventricle during systole.[39] Other diseases, such as systemic arterial hypertension, hyperthyroidism, and aortic stenosis, should be ruled out as a cause for ventricular hypertrophy.

Radiographic features of feline HCM include the following (Fig. 35.29A,B):

- Left atrial dilation is characterized by increased length and width of the cardiac silhouette. The dorsocaudal margin of the cardiac silhouette may be rounded with concavity of the caudal margin. In the presence of moderate to severe left atrial enlargement, the cardiac silhouette may have a "valentine-shaped" heart on VD/DV projections. This is enhanced by the absence of left ventricular enlargement, because the hypertrophy is constrictive (concentric), or



eFig. 35.9 Lateral **(A)**, close-up lateral **(B)**, and ventrodorsal (VD; **C**) radiographs of a dog with dilated cardiomyopathy and left-sided heart failure. The heart in some patients with dilated cardiomyopathy may appear normal. In this dog, there is enlargement of the left atrium and the right cranial lobe pulmonary vein **(A)**, likely resulting from mitral valve dysfunction with secondary pulmonary venous hypertension. **A** and **C** have the appearance of increased lung opacity. In **B,** this opacity can be seen to have a bronchial and unstructured interstitial pattern. This lung pattern is more typical of an inflammatory etiology than cardiogenic pulmonary edema, except in dogs with dilated cardiomyopathy, where it is a typical manifestation of cardiogenic pulmonary edema due to a peribronchial accumulation of the edema fluid.

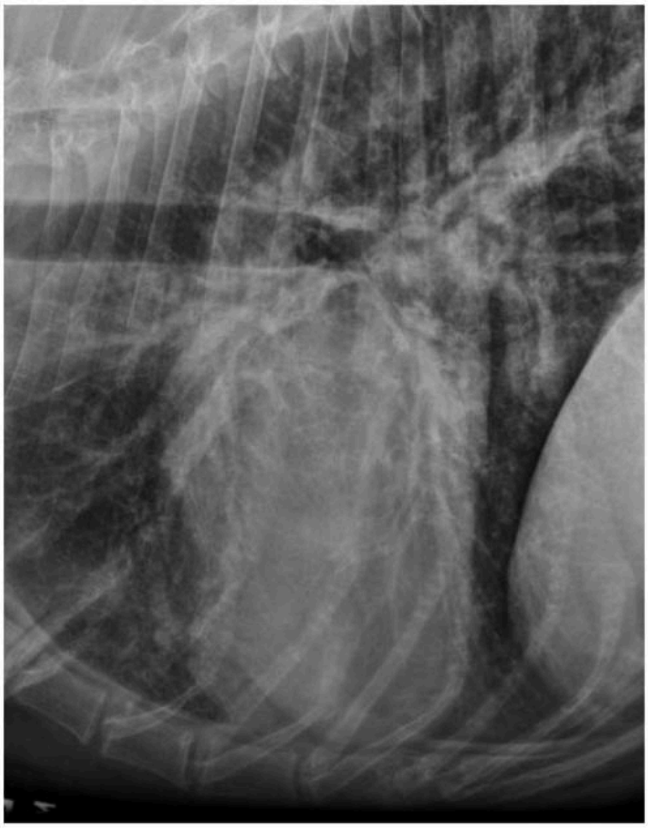


Fig. 35.28 Left lateral projection of a dog with dilated cardiomyopathy and left-sided congestive heart failure. The body conformation of the patient needs to be taken into consideration on evaluation of the cardiac silhouette. While the heart does not appear to occupy a large portion of the thoracic cavity due to the deep-chested conformation of the dog, a distinct soft tissue bulge is seen along the caudodorsal aspect of the cardiac silhouette and there is straightening of the caudal cardiac silhouette margin, suggestive of left atrial enlargement. The pulmonary veins are markedly larger that their corresponding arteries due to backward hypertension. A diffuse unstructured interstitial pulmonary pattern with a more pronounced ventral distribution is seen diffusely within the pulmonary parenchyma. This represents a prevalent distribution of cardiogenic pulmonary edema in dogs with dilated cardiomyopathy and should not be misinterpreted as pneumonia or allergic airway disease. Additionally, linear soft tissue opacities are seen extending within the periphery of the lung lobes due to either vascular enlargement, peribronchial cuffing and/or bronchial thickening.

inward, so the myocardium thickens at the expense of the left ventricular chamber size but does not increase its exterior dimensions.

- Distention of the pulmonary veins is occasionally seen but is less common in feline patients with left-sided cardiac decompensation when compared to dogs.
- Development of pulmonary edema indicates left-sided heart failure. A variable appearance and distribution are common in cats, including unstructured interstitial and alveolar patterns with a diffuse or multifocal distribution.[40]
- Pleural effusion is identified in approximately half of cats in left-sided heart failure.[39] Anatomical variations in the feline pleural venous and capillary vasculature may explain this difference. A greater degree of left atrial dysfunction may also contribute to this finding.[40]

Restrictive and unclassified cardiomyopathies also occur in cats and share similar radiographic features to HCM. These cannot be differentiated on thoracic radiographs. The cause of restrictive cardiomyopathies is not known. The left ventricular wall is restricted by the presence of fibrosis in lieu of hypertrophy, resulting in similar systolic dysfunction and congestion of the left atrium.[41,42] Cats with myocardial abnormalities which are not typical for hypertrophic or restrictive cardiomyopathies are considered "unclassified."[42]

Pulmonary Hypertension

Pulmonary hypertension results in reduced blood flow and oxygen delivery to the lungs, as well as a backward increase in pressure within the right cardiac chambers. The right ventricle and atrium enlarge due to pressure overload, and concentric thickening of the cardiac chamber walls develops with chronicity from the increased cardiac workload. When in excess, the caudal vena cava and liver may also become enlarged, and the emergence of peritoneal ± pleural effusion indicates right-sided cardiac decompensation.[43] While a diagnosis of pulmonary hypertension is best made with echocardiography, changes to the cardiovascular structures on thoracic radiographs can support a diagnosis and direct the need of further diagnostic imaging to confirm a diagnosis.[43,44] Thoracic radiographs may also help identify an underlying cause, which may vary from pulmonary cardiovascular disease, or primary pulmonary or systemic disease.[44] The American College of Veterinary Internal Medicine (ACVIM) recently published a consensus statement classifying the etiologies of pulmonary hypertension in dogs as follows:[43]

1. Pulmonary arterial hypertension (idiopathic, heritable, drug and toxin induced, congenital cardiac shunts, pulmonary vasculitis, pulmonary veno-occlusive disease or pulmonary capillary hemangiomatosis)
2. Pulmonary hypertension due to left heart disease (left ventricular dysfunction, canine DCM, myocarditis, and acquired/congenital valvular disease)
3. Pulmonary hypertension secondary to respiratory disease, hypoxia, or both (chronic obstructive airway disorders, tracheal or mainstem bronchial collapse, primary pulmonary parenchymal disease, obstructive sleep apnea/sleep disordered breathing, chronic exposure to high altitudes, and developmental lung disease)
4. Pulmonary emboli/thrombi/thromboemboli
5. Parasitic disease (*Dirofilaria* or *Angiostrongylus* infection)
6. Pulmonary hypertension with multifactorial or unclear mechanisms

Pulmonary hypertension is less prevalent in cats and possibly underdiagnosed. It may be associated with similar etiologies as dogs but predominant with diseases of higher prevalence in cats, such as chronic lower airway disease (e.g., feline asthma), left-sided heart failure, or upper respiratory obstructions (e.g., nasopharyngeal polyp).[45] Depending on the underlying etiology and severity, pulmonary hypertension may be reversible in both dogs and cats. Therefore, an early diagnosis and prompt medical management are important to prevent irreversible changes and progression, which may ultimately carry a poor prognosis.[43,45]

Radiographic features of pulmonary hypertension include the following (Fig. 35.30A,B):

1. Right-sided cardiomegaly is seen in response to pressure overload and associated concentric ventricular hypertrophy. Mild right-sided cardiomegaly may not be radiographically apparent.
2. Dilation of the main pulmonary artery is recognized by the presence of a bulge at the 1−2 o'clock position on the VD/DV projections. The main pulmonary artery becomes enlarged from turbulence of blood flow and increased pressure. In dogs and cats with heartworm disease, enlargement of the main pulmonary artery may be due to the physical presence of heartworms and/or thrombi within the main pulmonary artery. The degree of this

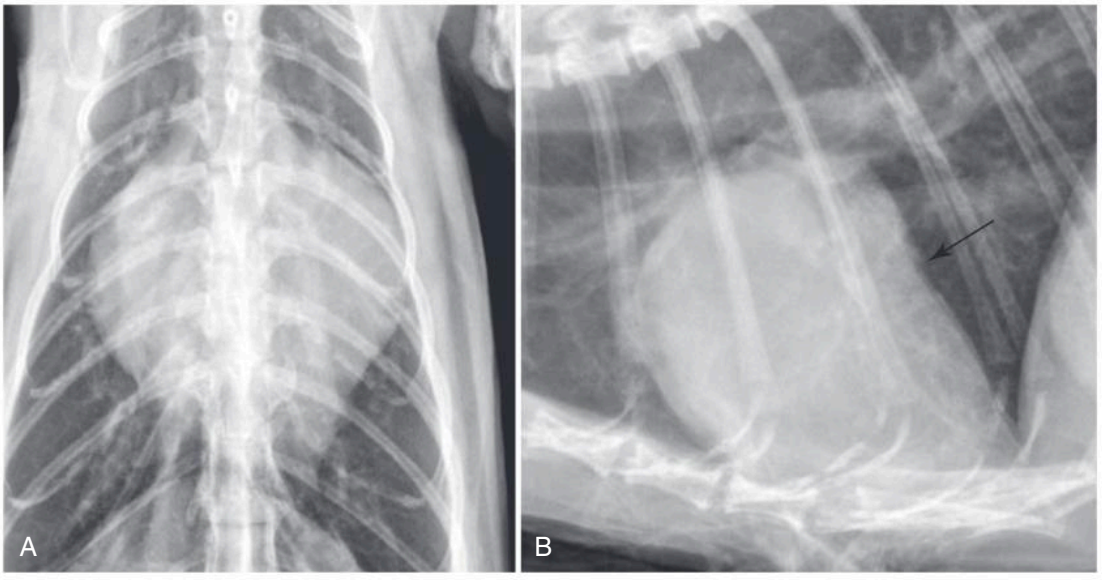


Fig. 35.29 Lateral **(A)** and ventrodorsal **(B)** projections of a cat with hypertrophic cardiomyopathy without evidence of heart failure. In **A**, the presence of marked left atrial enlargement is associated with elongation and widening of the cardiac silhouette, giving the cardiac silhouette a "valentine heart" shape. This extent of left atrial enlargement is sometimes misdiagnosed as biatrial enlargement. Although one cannot be sure whether only the left atrium is dilated without echocardiography, a very large left atrium alone can create the valentine appearance. In **B,** the enlarged left atrium is not as obvious, because it is superimposed on the cardiac silhouette; this is dissimilar to the dog, in which an enlarged left atrium causes a mass effect in the region of the tracheal bifurcation. The enlarged left atrium in this cat does create a focal concave defect in the shape of the cardiac silhouette (*black arrow* in **B**).

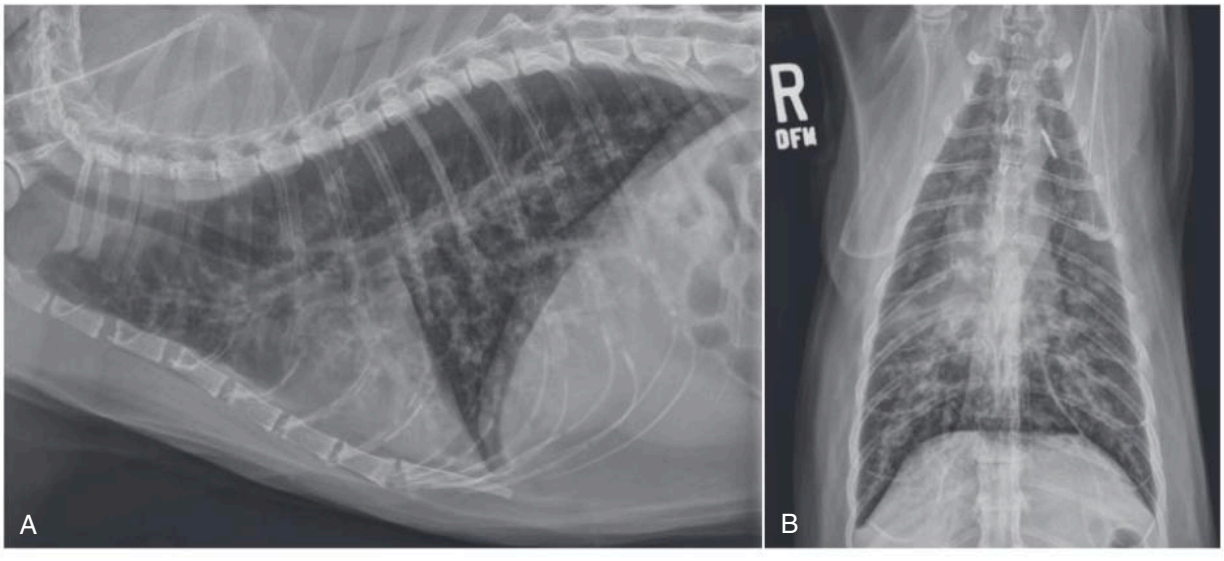


Fig. 35.30 Left lateral **(A)** and dorsoventral **(B)** projections of a cat with severe feline allergic airway disease and moderate cardiomegaly with pulmonary artery and variable mild venous enlargement. Pulmonary hypertension was confirmed with echocardiography. Enlargement of the main pulmonary artery is not discernible and is rarely seen in cats.

change and other radiographic abnormalities seen with heartworm disease vary depending on the duration of the infection and worm burden.

3. Enlargement and tortuosity of the lobar pulmonary arteries are uncommonly seen in response to pulmonary hypertension.
4. Mineralization of the lobar pulmonary arteries may be observed in dogs with chronic heartworm disease, likely secondary to chronic vasculitis or mineralized thrombi.
5. Peripheral blunting of the lobar pulmonary arteries is occasionally seen with pulmonary thromboembolization. Thromboemboli may represent coagulated blood, bacterial conglomerates, neoplasia, or dead adult worm fragments in dogs and cats with heartworm disease.
6. Distention of the caudal vena cava and hepatomegaly are indicative of increased central venous pressure, and the subsequent development of peritoneal ± pleural effusion is seen with right-sided heart failure.

Pericardial Effusion

Pericardial effusion is the collection of fluid within the pericardial space. This fluid can reduce contractility (tamponade)

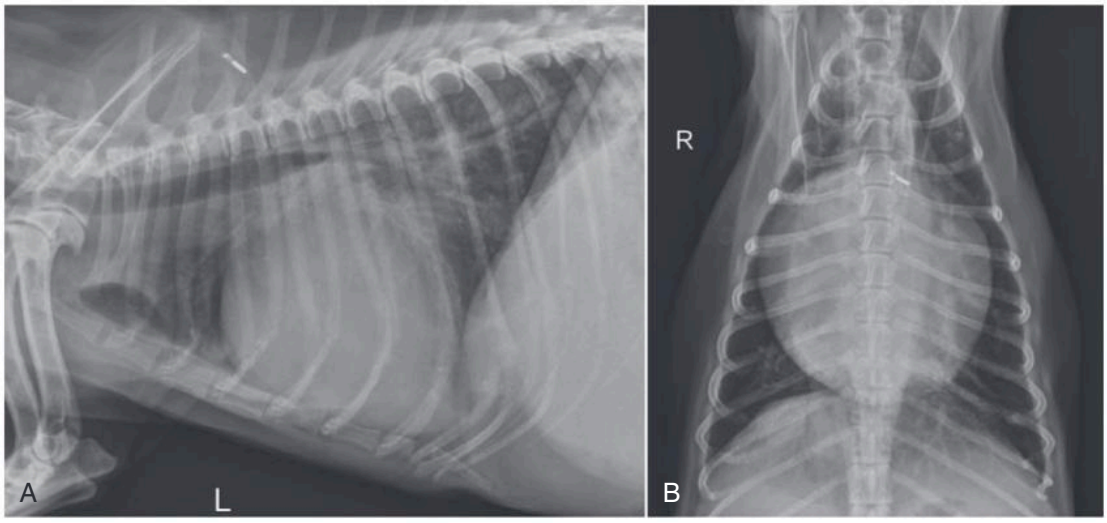


Fig. 35.31 Left lateral **(A)** and dorsoventral **(B)** projections of a dog with cardiomegaly and a globoid cardiac silhouette. This appearance is consistent with pericardial effusion, but based on the radiographs, a peritoneal-pericardial hernia or generalized cardiomegaly cannot be eliminated. This dog had pericardial effusion, along with hepatomegaly, peritoneal and scant pleural effusion due to right-sided heart failure from cardiac tamponade.

and can be life-threatening.[46,47] Pericardial effusion is diagnosed more frequently in dogs than cats and is most often neoplastic in etiology or due to idiopathic pericarditis. Less common causes include cardiac chamber rupture from volume overload or trauma, or infectious processes.[46] Congestive heart failure is reported to be the most cause of pericardial effusion in cats.[48] Regardless of the cause, diastolic function is altered by tamponade. Jugular vein distention is seen in response to the increased pressure, and caudal vena cava and hepatic enlargement may also be observed and followed by the development of peritoneal and pleural effusion due to cardiac decompensation into right-sided heart failure.[46,47]

Radiographic features of pericardial effusion include the following (Fig. 35.31A,B, eFig. 35.10):

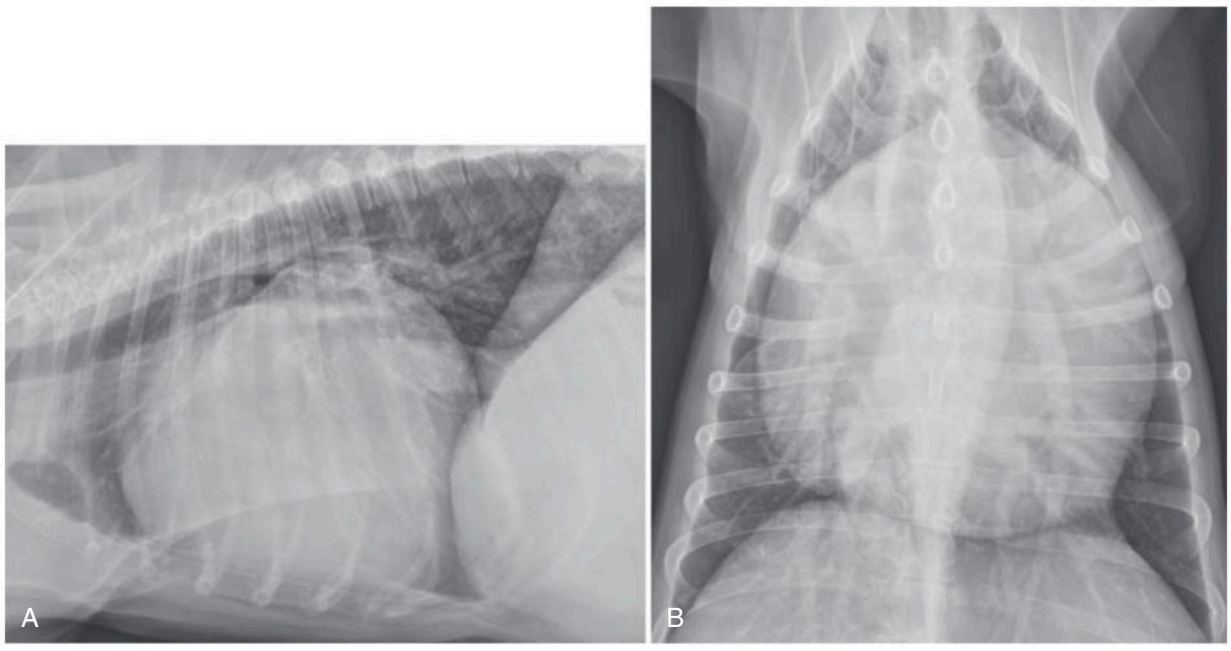
- Enlargement and rounding of the cardiac silhouette are seen with larger amounts of pericardial effusion, creating a globoid contour. This finding has been reported in up to 80% of dogs with pericardial effusion.[47] With smaller amounts of pericardial effusion, the cardiac silhouette may maintain a normal contour. Cardiomegaly and rounding of the cardiac silhouette on thoracic radiographs are poorly sensitive and specific for the presence of cardiac tamponade.[49]
- Distention of the caudal vena cava and hepatomegaly are signs of increased central venous pressure if pericardial tamponade is severe enough to prevent diastolic filling of the right atrium and ventricle. The concurrent presence of peritoneal ± pleural effusion is suggestive of right-sided congestive heart failure.

Neoplasia

Cardiac tumors have a low incidence in dogs, representing 0.121% and 4.33% of all tumor types, and an even lower incidence is reported in cats.[50] The most common cardiac tumor reported in dogs is hemangiosarcoma (69% prevalence), followed by aortic body tumors (chemodectoma and paraganglioma) and lymphoma. Lymphoma is the most common neoplastic disease of the feline heart. Both dogs and cats can have metastatic lesions to the heart from tumors of other tissue origin.[50,51] While most cardiac tumors are diagnosed in middle-aged to older patients, lymphoma can affect dogs and cats of any age.[50] Hemangiosarcoma most commonly originates from the right atrium/auricle and is highly metastatic. On the other hand, heart base tumors are less aggressive and are primarily identified at the aortic root.[50,51] Brachycephalic dogs are predisposed to heart base tumors, and it is speculated that chronic hypoxia may be an inciting etiology.[50] Hemangiosarcoma may also be identified at the aortic root, and lymphoma may affect any part of the heart. When larger in size, right atrial/auricular and heart base masses can obstruct the right cardiac chambers and cause vena caval and hepatic hypertension with risks of right-sided cardiac decompensation. Pericardial effusion may develop in some cases and result in cardiac tamponade. Cardiac tumors may be difficult to identify on thoracic radiographs, and echocardiography and advanced imaging (CT or MRI) are superior for the diagnosis and characterization of cardiac neoplasms in dogs and cats.[50,51] However, radiographs remain a good screening tool and should be scrutinized for the presence of a mass even in asymptomatic cases as they may often be found incidentally.

Radiographic features of cardiac neoplasia include the following (Fig. 35.32A,B):

- Heart base and right atrial/auricular tumors cannot be differentiated on thoracic radiographs. When larger in size, a soft tissue opaque mass may be seen at the base of the cardiac silhouette, causing dorsal and rightward displacement of the trachea.
- Cardiomegaly with rounding (globoid appearance) is indicative of pericardial effusion.
- Distention of the caudal vena cava and hepatomegaly are seen secondary to obstruction of venous return to the right heart.
- Peritoneal ± pleural effusion is suggestive of right-sided heart failure.



eFig. 35.10 Left lateral **(A)** and dorsoventral (DV; **B**) radiographs of a dog with a globoid-appearing cardiac silhouette. This appearance is consistent with pericardial effusion, but based on the radiographs, a peritoneal-pericardial hernia or generalized cardiomegaly cannot be eliminated. This dog had pericardial effusion.

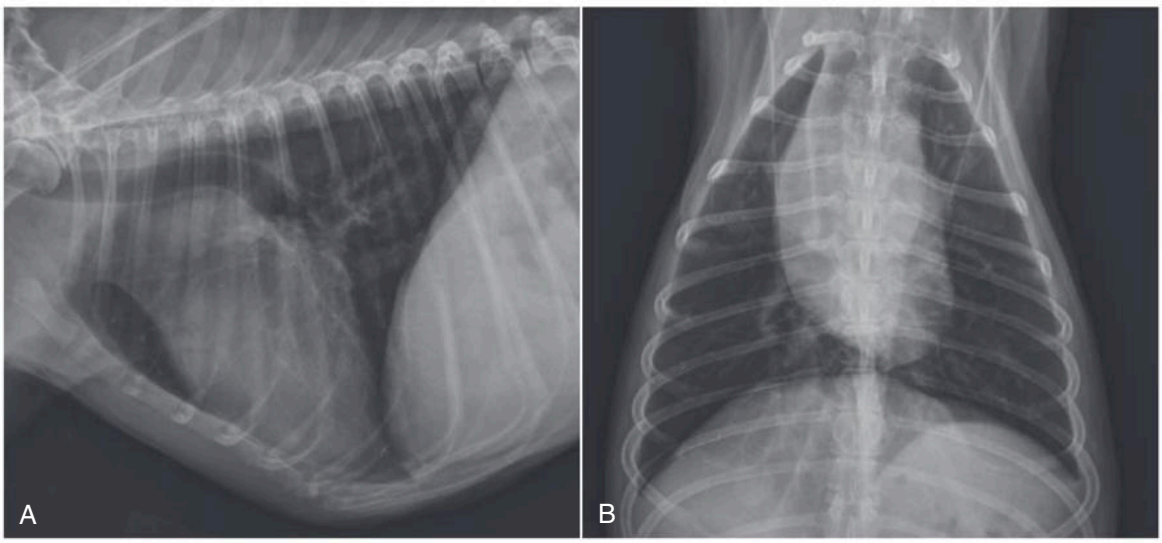


Fig. 35.32 Left lateral **(A)** and dorsoventral **(B)** projections of a dog with a heart base mass. In the region of the heart base, an ill-defined, homogeneously soft tissue opaque mass causes moderate to severe, focal and dorsal displacement of the intrathoracic trachea and moderate widening of the cranial mediastinum. This mass border effaces the cranial margin of the cardiac silhouette, widens the cranial mediastinum, and causes caudal displacement of the proximal descending aorta.

Acknowledgment

With special thanks to prior authors of this chapter for their contributions.

REFERENCES

1. Lamb CR, Tyler M, Boswood A, et al. Assessment of the value of the vertebral heart scale in the radiographic diagnosis of cardiac disease in dogs. *Vet Rec.* 2000;146(24):687–690.
2. Buchanan JW, Bucheler J. Vertebral scale system to measure canine heart size in radiographs. *J Am Vet Med Assoc.* 1995;206(2):194–199.
3. Olive J, Javard R, Specci S, et al. Effect of cardiac and respiratory cycles on vertebral heart score measured on fluoroscopic images of healthy dogs. *J Am Vet Med Assoc.* 2015;246:1091.
4. Litster AL, Buchanan JW. Vertebral scale system to measure heart size in radiographs of cats. *J Am Vet Med Assoc.* 2000;216(2):210–214.
5. Costanza D, Greco A, Piantedosi D, et al. The heart to single vertebra ratio: a new objective method for radiographic assessment of cardiac silhouette size in dogs. *Vet Radiol Ultrasound.* 2022.
6. Moon ML, Keene BW, Lessard P, et al. Age related changes in the feline cardiac silhouette. *Vet Radiol Ultrasound.* 1993;34:315.
7. Melian C, Stefanacci J, Peterson ME, Kintzer PP. Radiographic findings in dogs with naturally-occurring primary hypoadrenocorticism. *J Am Anim Hosp Assoc.* 1999;35(3):208–212.
8. Côté E, Weisse C, Lamb K, Tozier E. Computed tomographic assessment of principal bronchial anatomy in dogs of various thoracic conformations: 93 cases (2012–2017). *J Am Vet Med Assoc.* 2022;1:1–10.
9. Lebastard M, Le Boedec K, Howes M, et al. Evaluation of bronchial narrowing in coughing dogs with heart murmurs using computed tomography. *J Vet Intern Med.* 2021;35(3):1509–1518.
10. Ferasin L, Crews L, Biller DS, Lamb KE, Borgarelli M. Risk factors for coughing in dogs with naturally acquired myxomatous mitral valve disease. *J Vet Intern Med.* 2013;27(2):286–292.
11. Keene BW, Atkins CE, Bonagura JD, et al. ACVIM consensus guidelines for the diagnosis and treatment of myxomatous mitral valve disease in dogs. *J. Vet. Intern. Med.* 2019;33(3):1127–1140.
12. Vezzosi T, Puccinelli C, Tognetti R, Pelligra T, Citi S. Radiographic vertebral left atrial size: a reference interval study in healthy adult dogs. *Vet Radiol Ultrasound.* 2020;61(5):507–511.



Congenital Cardiovascular Diseases (Described in the Online Version Only)

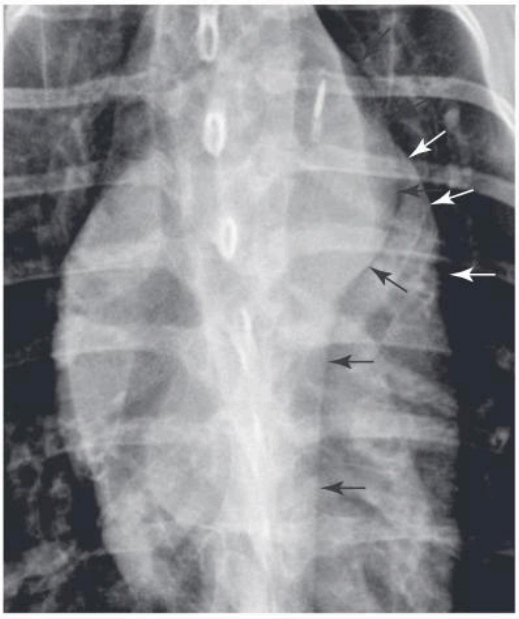
Congenital cardiovascular conditions are rare, representing a small percentage of all cardiovascular diseases diagnosed in dogs and cats.[52,53] Alterations during embryogenesis result in cardiovascular anomalies at birth which can impair cardiovascular function depending on their type, location, and size.[53,54] While these congenital cardiovascular conditions are most often diagnosed at a young age, they are also occasionally identified in older patients.[47] The prognosis is variable depending on the type and features of the cardiovascular anomaly. In most cases, early recognition is important to improve outcome and prevent the development of irreversible cardiovascular changes and complications.[53]

PATENT DUCTUS ARTERIOSUS

Patent ductus arteriosus occurs when the fetal ductus arteriosus, which shunts blood from the pulmonary artery into the systemic circulation, fails to close after birth. Under normal conditions, the ductus arteriosus closes in response to a decrease in resistance within the pulmonary arterial vasculature, an increase in oxygen partial pressure, and declining prostaglandin levels.[55,56] When the ductus arteriosus fails to close, a permanent communication is formed between the aorta and the main pulmonary artery. Pressure differences between these two vessels result in continuous shunting of blood from the aorta into the main pulmonary artery (left-to-right shunting). A backward increase in pressure within the left cardiac chambers causes concentric hypertrophy of the left ventricle and left atrium with subsequent reduced systolic function.[55–57] The lobar pulmonary veins may become enlarged and left-sided congestive heart failure is identified on rare occasions.[56] A gradual increase in pulmonary arterial pressure is seen in response to chronic pulmonary overcirculation and the development of congestive heart failure. As a result, a reversal in blood flow direction occurs through the shunt in more advanced cases (right-to-left shunting).[55] Factors leading to this change in hemodynamics are known as Eisenmenger syndrome and are a poor prognostic indicator. While patent ductus arteriosus is the most common congenital cardiac defect in dogs, a high incidence is also reported in cats.[55,58–60]

Radiographic features of left-to-right patent ductus arteriosus include (eFigs. 35.11, 35.12A,B, and 35.13):

- Dilation of the descending aorta at the level of the aortic arch is caused by turbulent blood flow. At the heart base, the aorta is enlarged and is occasionally associated with a bulge at the 12–1 o'clock position along the cardiac on the VD/DV projections in both dogs and cats.
- Dilation of the main pulmonary artery is indicative of increased arterial pressure and flow.
- Enlargement of the left auricle is seen in more advanced cases.
- A "three knuckles" sign is seen with the combined identification of an aortic, main pulmonary artery, and left auricular bulge along the cardiac silhouette on the VD/DV projections in dogs and is commonly associated with a patent ductus arteriosus. The absence of a "three knuckles" sign does not exclude a diagnosis as it has been reported to be present in only 26% of dogs with a patent ductus arteriosus.[56]
- Enlargement of the left atrium ± ventricle is seen in response to pressure overload. The left ventricle is dilated in the earlier phase of the disease and may be normal in size with hypertrophy. Cardiomegaly is commonly recognized on thoracic radiographs in cats with patent ductus arteriosus.[55]



eFig. 35.11 Dorsoventral (DV) projection of a dog with a patent ductus arteriosus. The descending portion of the aortic arch is focally dilated, resulting in a bulge at the 1–2 o'clock position along the cardiac silhouette (*black arrows*). The main pulmonary artery is also mildly dilated, as characterized by the presence of a bulge at the 2–3 o'clock position along the cardiac silhouette (*white arrows*).

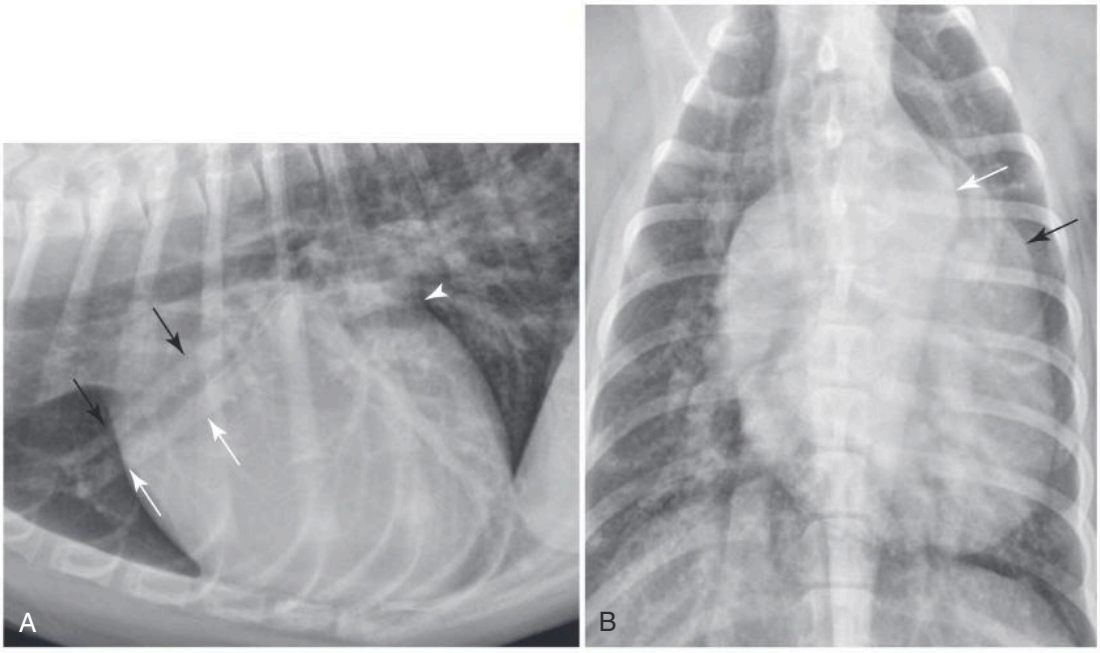
- Dilation of the lobar pulmonary arteries and veins is indicative of overcirculation and is reported to be more commonly seen on the VD/DV projections.[56]
- Cardiogenic pulmonary edema from left-sided congestive heart failure correlates with an unstructured interstitial to alveolar pulmonary pattern, which is prevalently caudodorsally distributed in dogs. A diffuse or multifocal distribution ± pleural effusion is seen most commonly in cats.

Radiographic features of right-to-left patent ductus arteriosus include:

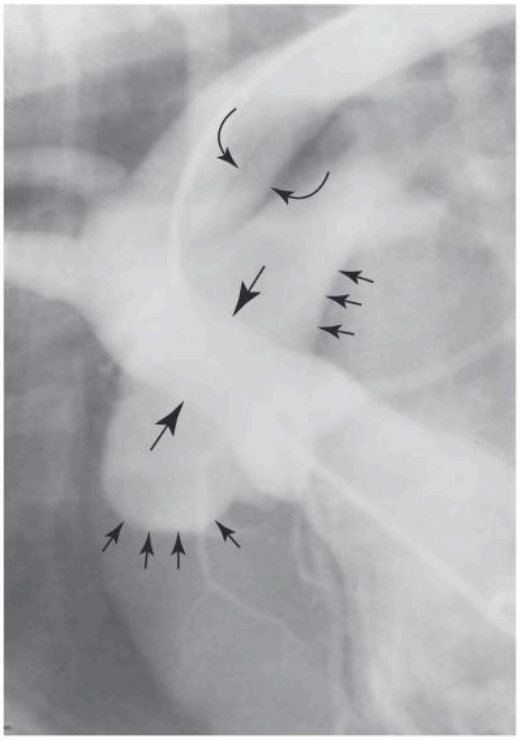
- Right-sided cardiomegaly is frequently identified due to pressure overload. In cats, isolation of the right atrium and ventricle on radiographs is limited, and a generalized increase in cardiac size is most often seen.
- Cardiogenic pulmonary edema is present in the majority of dogs and cats with right-to-left patent ductus arteriosus.[61]
- Enlargement of the main pulmonary artery due to pulmonary hypertension is reported in 50% of the dogs and cats with patent ductus arteriosus.[61]

VENTRICULAR SEPTAL DEFECT

Ventricular septal defects represent the most common congenital heart anomalies in cats and are also prevalent in dogs.[59,62,63] A hereditary predisposition is reported in some dogs, such as Keeshond dogs.[64] Ventricular septal defects are openings within the interventricular septum associated with misalignment and malformation of the ventricular septum during embryogenesis.[62,63] Failure of septation most commonly occurs at the junction between the membranous and muscular parts of the septum and are therefore referred to be perimembranous. These defects are located just ventral to the aortic valve and in the subvalvular region of the tricuspid valve. Associated cardiovascular changes depend on the size of the defect.[62,63] Ventricular septal defects are classified as being either resistive or nonresistive. Small defects are commonly resistive and able to maintain pressure differences between the



eFig. 35.12 Lateral **(A)** and dorsoventral **(B)** projections of a dog with a patent ductus arteriosus. The heart is enlarged due to left ventricular hypertrophy, although the diagnosis of hypertrophy cannot be made from these radiographs. A focal aortic arch dilation is visible in the dorsoventral projection (*white arrow*), and the conspicuity of the left auricle *(black arrow)* is also increased and associated with a bulge at the 2–3 o'clock position along the cardiac silhouette. In **A,** the right cranial pulmonary lobar artery (*black arrows*) and vein (*white arrows*) are dilated. Left atrial dilation has created a concave shape change in the lateral view (*white arrowhead*). The lungs have an unstructured increase in opacity because of overcirculation within small pulmonary vessels.

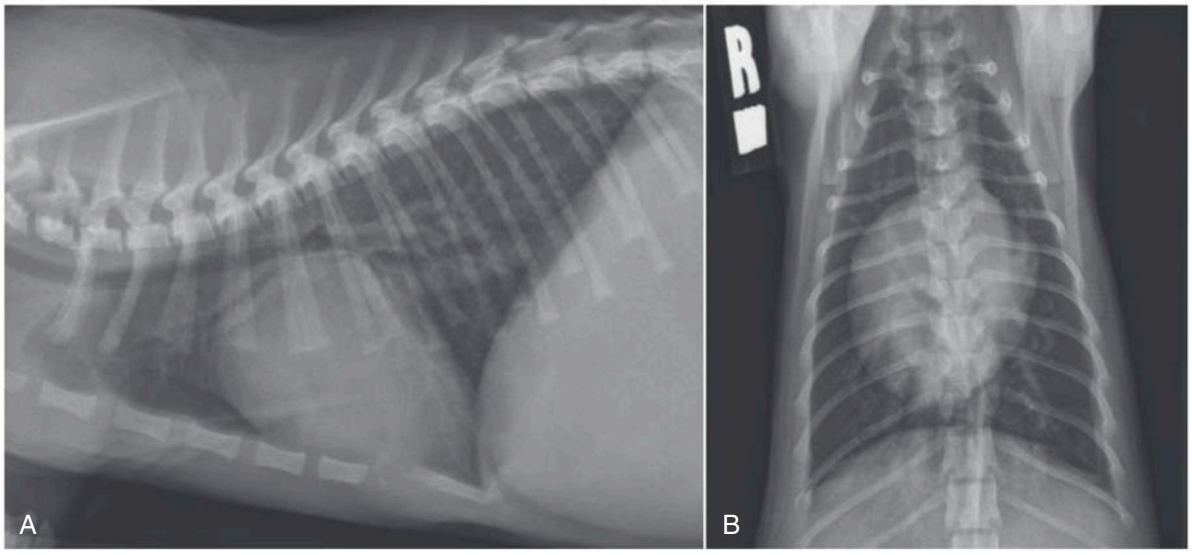


eFig. 35.13 Selective left ventricular angiocardiogram of a dog with a patent ductus arteriosus. The dilated main pulmonary artery segment (*small thin arrows*) and the ascending aorta (*solid arrowheads*) are accentuated by positive-contrast medium, and the patent ductus arteriosus (*curved arrows*) lies between the descending aorta and the main pulmonary artery segment and is opacified because of the left-to-right shunting of blood.

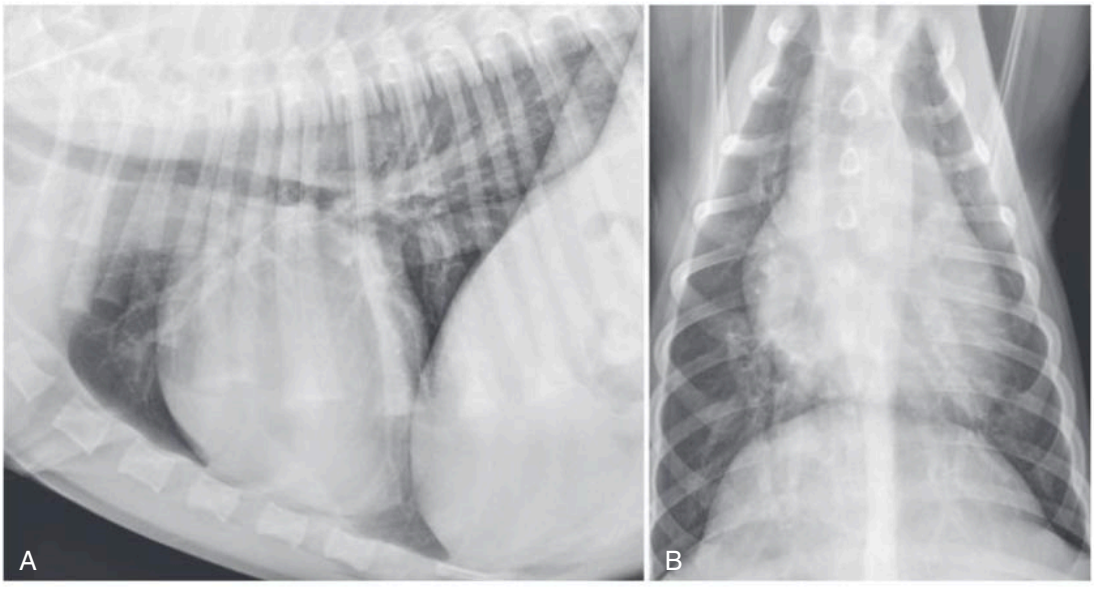
left and right ventricles during systole. In comparison, blood follows the path of least resistance with larger cardiac defects and is shunted from the left ventricle into the lower pressure right ventricle during systole; therefore, these defects are characterized as being nonresistive. Blood is commonly shunted directly into the right outflow tract; hence, right-sided cardiomegaly is usually not seen with these lesions. Overcirculation of the pulmonary vasculature will result in backward overloading of the left heart. Left-sided cardiomegaly with eccentric hypertrophy may be observed in more advanced cases. When in excess, cardiogenic edema associated with left-sided congestive heart failure will ensue. The persistent shunting of blood into the pulmonary arterial vasculature results in a progressive increase in pulmonary arterial pressure, which may be exacerbated by the development of cardiogenic pulmonary edema. A subsequent increased pressure overload on the right cardiac chambers predisposes to shunt reversal (right-to-left shunting), consistent with Eisenmenger syndrome. While small ventricular septal defects may have a good prognosis, larger defects have a poorer prognosis which is guarded once shunt reversal is observed.[62]

Radiographic features of ventricular septal defects include (eFigs. 35.14A,B,E and 35.15):

- No abnormalities may be radiographically apparent in the presence of a small defect.
- Enlargement of the left atrium and ventricle is seen in response to pulmonary overcirculation. A nonspecific increase in cardiac silhouette size may be identified in cats.
- Varying degrees of main pulmonary artery enlargement are also possible, depending on the level and size of the defect.
- Enlargement of the right ventricle may be observed and raises concerns for shunt reversal (right-to-left).
- Pulmonary edema is seen in cases with left-sided congestive heart.



eFig. 35.14 Lateral **(A)** and dorsoventral **(B)** projections of a cat with a ventricular septal defect. The cardiac silhouette is enlarged with an elongated and widened contour, resulting in dorsal displacement of the carina. The pulmonary lobar arteries and veins are mildly enlarged.



eFig. 35.15 Lateral **(A)** and dorsoventral (DV; **B**) radiographs of a dog with a ventricular septal defect. In **A,** there is excessive elevation of the cardiac apex from the sternum consistent with right ventricular hypertrophy, mild dilation of the left atrium, and slight enlargement of the left cranial lobe pulmonary artery and vein, consistent with mild pulmonary overcirculation. In **B,** the apex is displaced to the left as a result of the dog being in sternal recumbency, and the appearance of excessive cardiac mass on the left is deceptive. Slight enlargement of the caudal lobe pulmonary arteries and veins is present, consistent with mild overcirculation. These findings are typical of, but not conclusive proof of, a ventricular septal defect

- The concurrent presence of pleural and peritoneal effusion with caval and hepatic enlargement are indicative of biventricular failure.
- Hypoperfusion of the lung may be observed in the presence of pulmonary hypertension or pulmonic stenosis and shunt reversal.

ATRIAL SEPTAL DEFECT

Atrial septal defects are embryological anomalies resulting in an abnormal communication between the atria.[65] Such defects are rare in dogs and cats, representing 0.7% to 3.7% and up to 10% of canine and feline congenital heart diseases, respectively.[58,65] However, the prevalence may be higher than previously reported, with access to higher-quality Doppler technology allowing for the recognition of smaller defects.[65] Boxers may be overrepresented.[65,66] Atrial septal defects can be divided into three categories, ostium secundum, ostium primum, and sinus venosus defects, based on their location.[65] Ostium secundum defects are most prevalent in dogs and are located at the level of the foramen ovale, dorsal to the atrioventricular valves. In contrast, cats commonly have ostium primum defects located in closer proximity to the atrioventricular valves, which are often

identified in combination with other congenital heart anomalies, such as dysplasia of the atrioventricular valve.[57,63] Sinus venosus defects are infrequently encountered in both dogs and cats. Similar to ventricular septal defects, small communications within the septal wall may not alter cardiovascular hemodynamics and remain clinically silent.[57] With larger defects, shunting of blood from the higher pressure left atrium to the right atrium results in volume overload and eccentric hypertrophy of the right cardiac chambers. With progression, the caudal vena cava and liver become enlarged, and the subsequent development of peritoneal ± pleural effusion indicate right-sided congestive heart failure.[67] The increased pressure within the right cardiac chambers, possibly exacerbated by concurrent pulmonic valve insufficiency and pulmonary hypertension, can result in reversed direction of blood flow through the atrial septal defect (left-to-right shunting) when in excess to the left atrial pressure.[67]

Radiographic features of ventricular septal defects include (see eFig. 35.15A,B):

- No abnormalities may be radiographically apparent in the presence of a small defect.
- Right-sided cardiomegaly is the most common abnormality identified with larger septal defects due to volume overload with left-to-right shunting.[67]
- Enlargement of the main and lobar pulmonary arteries is suggestive of pulmonary hypertension.
- Enlargement of the caudal vena cava and liver may be followed by the emergence of pleural and peritoneal effusion in patients with right-sided heart failure.

PULMONIC STENOSIS

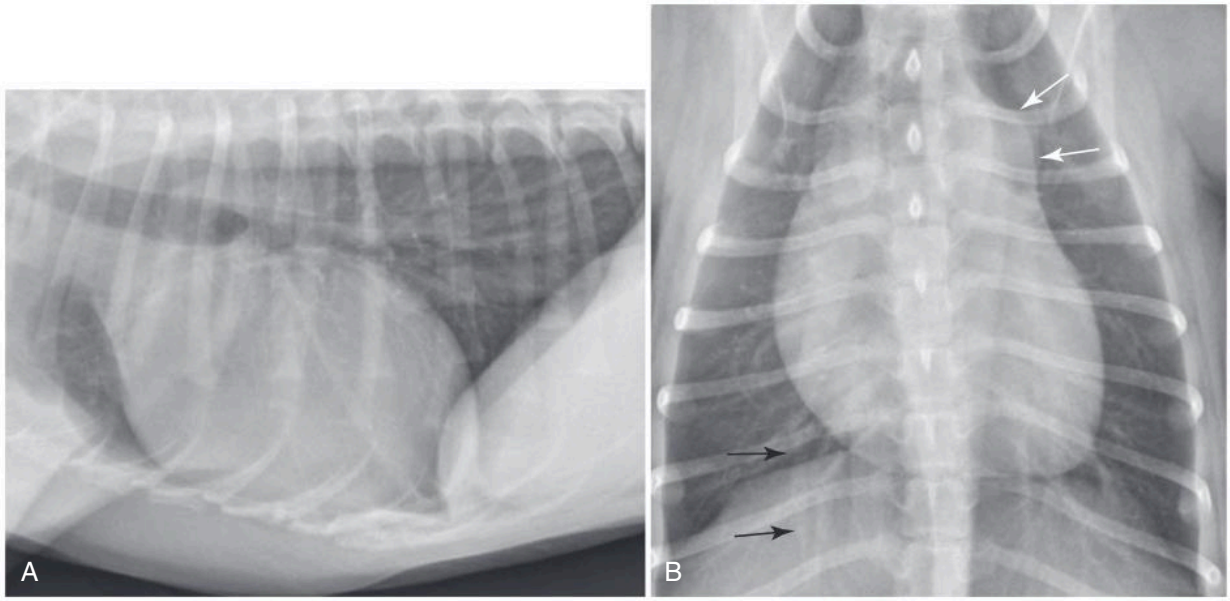
Pulmonic stenosis has a higher prevalence in dogs than cats. Depending on the location of the stenosis, supravalvular, valvular, or subvalvular morphologies have been described, with valvular stenosis being most common in dogs.[68,69] Pulmonic stenosis is defined as a narrowing of the pulmonic valve due to an abnormal development of the valve leaflets.[68–70] Blood flow through the right ventricular outflow tract is subsequently obstructed, resulting in right ventricular pressure overload and concentric hypertrophy of the right ventricle.[68,69] While there is an overall decrease in blood flow through the right ventricular outflow tract, ejection of a high-velocity jet through the stenosis and poststenotic turbulence of blood flow result in focal dilation of the main pulmonary artery.[69] Pressure overload of the right cardiac chambers may result in enlargement of the caudal vena cava and liver with progressive emergence of peritoneal ± pleural effusion from right-sided congestive heart failure.[68–70] In brachycephalic dogs, pulmonic stenosis can be associated with aberrant coronary artery, which may affect treatment options.[71]

Radiographic features of pulmonic stenosis include (eFig. 35.16):

- Dilation of the main pulmonary artery. While mild pulmonic stenosis may not cause any radiographically detectable abnormalities, the main pulmonary artery may be so markedly enlarged in more severe cases that concurrent focal right-sided deviation of the trachea is occasionally seen and may be difficult to differentiate from a heart base or right atrial/auricular mass.
- Normal to decreased size of the lobar pulmonary vasculature is associated with pulmonary undercirculation.
- Enlargement of the right ventricle is seen in response to pressure overload and ventricular hypertrophy may not be radiographically apparent if mild in severity.
- Enlargement of the caudal vena cava and liver may be followed by the emergence of pleural and peritoneal effusion in patients with right-sided heart failure.

AORTIC STENOSIS

Stenosis of the aorta at the level of the left outflow tract is commonly identified in dogs and is rarely described in cats.[72–75] Stenotic lesions are classified as being subvalvular,

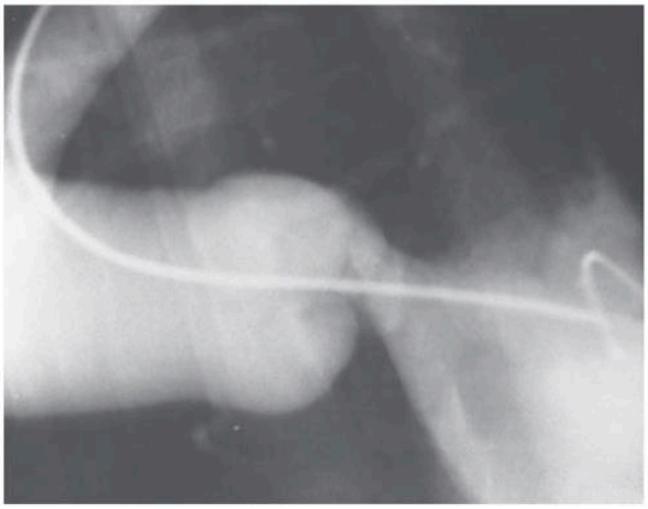


eFig. 35.16 Lateral **(A)** and dorsoventral **(B)** projections of a dog with pulmonic stenosis. The cranial and right lateral margins of the cardiac silhouette are rounded with elevation of the cardiac apex from the sternum, indicative of right ventricular enlargement, likely hypertrophy. The main pulmonary artery is enlarged in the dorsoventral projection, as characterized by the presence of a bulge at the 2–3 o'clock position along the cardiac silhouette (*white arrows*). The lobar pulmonary arteries are normal (*black arrows* in **B**).

valvular, or supravalvular based on their location with subvalvular lesions being most prevalent in dogs.[72,75] On the other hand, a larger number of valvular lesions are reported in cats.[72,74] Obstruction of the left ventricular outflow tract results in left-sided pressure overload and concentric hypertrophy of the left ventricular wall. Pulmonary venous hypertension with left-sided heart failure may be seen with increased severity and chronicity. In some cases, the coronary vasculature is undercirculated, putting patients at risks of developing fatal arrhythmias due to myocardial ischemia.[72–74]

Radiographic features of aortic stenosis include (eFigs. 35.17 and 35.18):

- No radiographic abnormalities may be apparent in mild cases.
- Bulging of the aortic arch correlates to the presence of poststenotic aortic dilation in more severe cases.
- Enlargement of the left atrium and ventricle is seen in response to pressure overload.
- Dilation of the lobar pulmonary veins is indicative of pulmonary venous hypertension.
- Cardiogenic pulmonary edema is indicative of left-sided congestive heart failure.



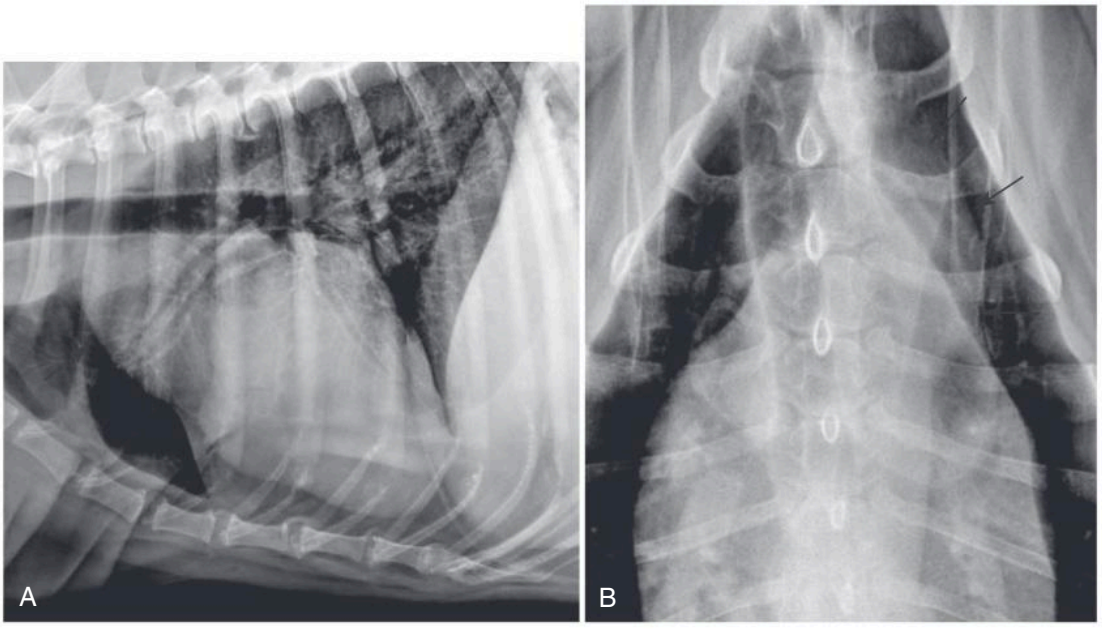
eFig. 35.17 Left ventricular angiocardiogram in a dog with subvalvular aortic stenosis. Note the narrow subvalvular region and dilation of the aorta distal to the aortic sinus. The aorta should be no wider than the sinus; enlargement of the aorta distal to the sinus is caused by turbulent flow.

TRICUSPID VALVE DYSPLASIA

Tricuspid valve dysplasia is most prevalent in large dog breeds and represents the second most common congenital heart disease in cats.[59,60,65,76] Congenital malformation and thickening of the tricuspid valve result in tricuspid valve insufficiency and systolic dysfunction. Shortening of the chordae tendineae may further restrict closure of the tricuspid valve and exacerbate valvular dysfunction.[76,77] Although rare in dogs and cats, an Ebstein anomaly represents a form of tricuspid valve dysplasia, in which there is abnormal ventral positioning of the tricuspid valve into the right ventricle, often also associated with systolic dysfunction.[76,77] In all instances, the right atrium becomes volume overloaded due to the presence of tricuspid valve regurgitation. Eccentric hypertrophy of the right ventricle is also seen in more severe cases. With excessive volume overload of the right ventricle, increased pressure within the caudal vena and liver may be observed. The emergence of peritoneal ± pleural effusion supports a diagnosis of right-sided congestive heart failure.[76,77]

Radiographic features of tricuspid valve dysplasia include:

- Right-sided cardiomegaly may be radiographically apparent in more severe cases of tricuspid valve insufficiency, volume overload, and right atrial and ventricular enlargement. In cats, a nonspecific generalized enlargement of the cardiac silhouette is more commonly observed.
- Enlargement of the caudal vena cava and hepatomegaly may precede right-sided congestive heart failure, as evidenced by the development of peritoneal and/or pleural effusion.



eFig. 35.18 Lateral **(A)** and dorsoventral (DV; **B**) radiographs of a dog with aortic stenosis. In **A,** the dilated aortic arch appears as a bulge on the craniodorsal aspect of the cardiac silhouette (*black arrow*). In **B,** the enlarged aortic arch appears as an opacity at the cranial, and slightly left, aspect of the cardiac silhouette (*black arrows*).

MITRAL VALVE DYSPLASIA

Mitral valve dysplasia is defined as a congenital malformation and thickening of the mitral valve leaflets, which is infrequently identified in dogs and cats.[59,78] Mitral valve function may be further impaired by thickening and/or shortening of the chordae tendineae. Mitral valve insufficiency during systole results in regurgitation of blood into the left atrium and volume overload. Eccentric hypertrophy of the left ventricle is seen with increased chronicity and severity. With excessive left-sided volume overload, backward pulmonary venous hypertension and left-sided congestive heart failure may ensue.[78] Although rarely reported in both dogs and cats, mitral valve dysplasia may be associated with stenosis of the mitral valve annulus.[59,78]

Radiographic features of mitral valve dysplasia include:

- Left-sided cardiomegaly is commonly identified.
- Pulmonary venous distention may be observed in some cases due to pulmonary venous hypertension.
- Cardiogenic pulmonary edema is indicative of left-sided congestive heart failure.

MITRAL VALVE STENOSIS

Mitral valve stenosis may represent a form of mitral valve dysplasia and is defined as a reduced size of the mitral valve annulus due to embryological malformation (e.g., thickening and fusion) of the mitral valve leaflets. Subsequent obstruction of the mitral valve results in an increase in left atrial pressure. Pulmonary venous hypertension and left-sided congestive heart failure are seen in more severe cases. Although uncommon, both dogs and cats may be affected.

Radiographic features of mitral valve stenosis include:

- Left atrial enlargement due to an increase in transmitral resistance is the main radiographic feature reported.[79] In cats, cardiomegaly with convexity of the caudal cardiac margin may be suggestive of left atrial enlargement.[80]
- Development of cardiogenic pulmonary edema with or without lobar pulmonary vein enlargement due to left-sided heart failure represents a frequent sequela in dogs within 1 year of diagnosis and is also commonly identified in cats.[79,80]

TETRALOGY OF FALLOT

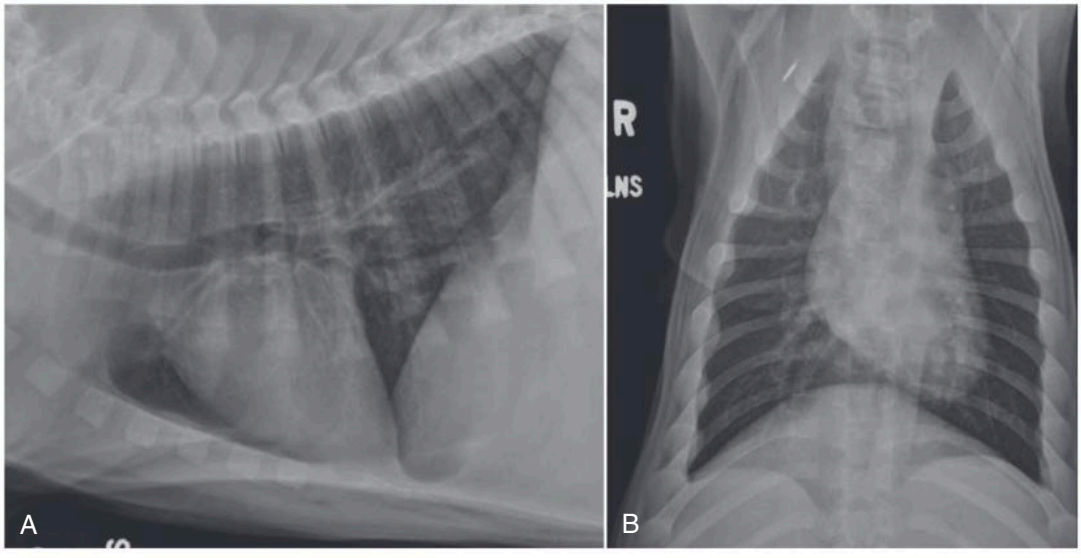
Tetralogy of Fallot is an uncommon but highly fatal complex of cardiac abnormalities in dogs and cats. It is a result of abnormal ventricular septation during embryogenesis and is comprised of a combination of four congenital anomalies, consisting of a ventricular septal defect, overriding aorta, obstruction of the right ventricular outflow tract, and right ventricular hypertrophy.[81,82] Cardiac function is most affected by the size of the ventricular septal defect and severity of the pulmonic stenosis. With mild pulmonic stenosis, blood is shunted through the ventricular septal defect from the higher pressure left ventricle to the right ventricle (left-to-right shunting). However, the pulmonic stenosis is often so severe that there is pressure overload of the right ventricle in excess to the systolic pressure of the left ventricle, resulting in shunt reversal (right-to-left).[81,82] Bidirectional shunting is reported in half of dogs and cats with tetralogy of Fallot at the time of diagnosis.[81] With shunt reversal, the pulmonary vasculature is subsequently undercirculated. Right-sided congestive heart failure represents a rare complication.[81,82]

Radiographic features of tetralogy of Fallot include (eFig. 35.19A,B):

- Right-sided cardiomegaly is most commonly observed due to the high prevalence of right-to-left shunting. In dogs, the cardiac silhouette will have rounded cranial and right lateral margins with leftward displacement of the cardiac apex and a "reversed-D" appearance. In milder cases, left-sided cardiomegaly may predominate. In cats, nonspecific generalized cardiomegaly may be seen.
- Decreased size of the lobar pulmonary vasculature is seen with right-to-left shunting of blood through the ventricular septal defect due to arterial and venous undercirculation. The main pulmonary artery may be reduced in size, resulting in a focal concavity of the cardiac silhouette in the VD/DV projection.

COR TRIATRIATUM SINISTRUM/COR TRIATRIATUM DEXTRUM

Cor triatriatum is a rare congenital heart disease in dogs and cats in which the left atrium (cor triatriatum sinistrum) or right

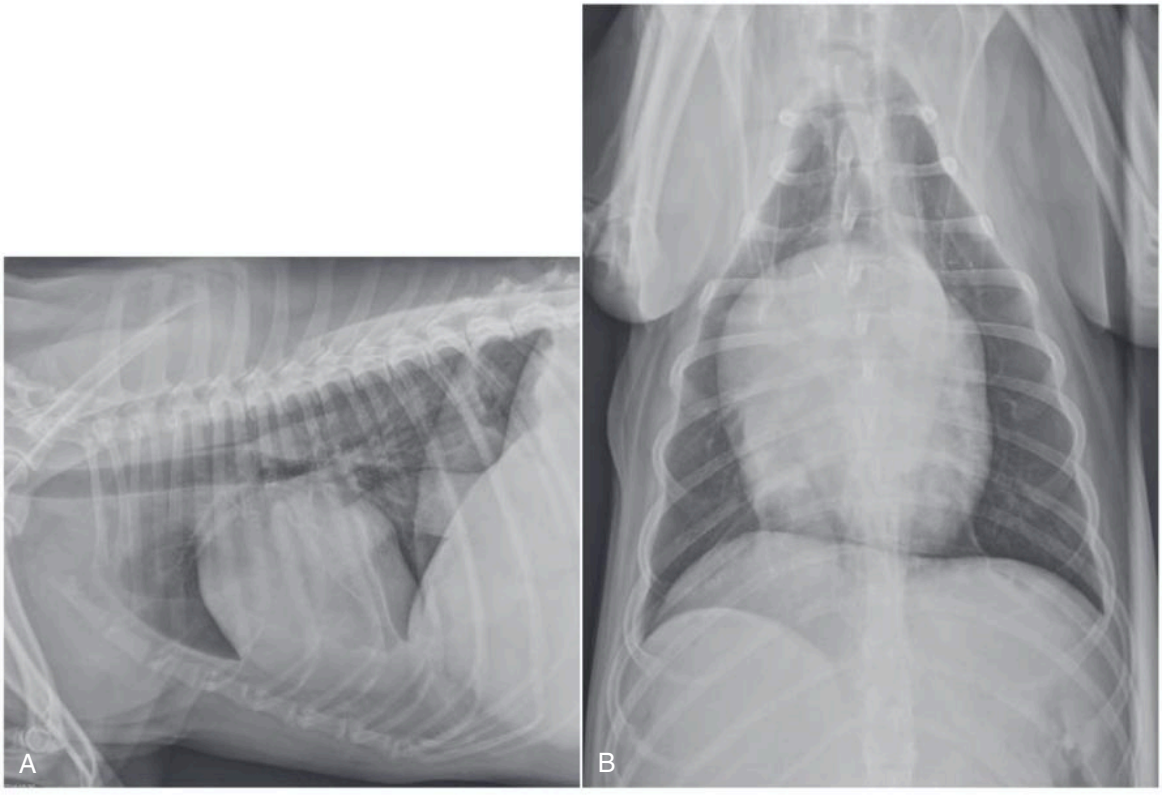


eFig. 35.19 Left lateral **(A)** and dorsoventral **(B)** projections of a dog with tetralogy of Fallot. The right heart is enlarged and rounded. The cardiac apex is elevated from the sternum and is shifted to the left. The pulmonary vasculature is reduced in diameter consistent with a right-to-left shunt.

atrium (cor triatriatum dextrum) is separated by a membranous remnant, resulting in a three atrial chambers.[83–85] This membrane varies in size and shape and may be intact or fenestrated.[83,84] In some instances, other congenital cardiovascular anomalies may be present. Manifestation of cardiac decompensation in dogs and cats with cor triatriatum sinistrum and dextrum depends on the presence and degree of obstruction of venous return into the left and right atrium, respectively.[83,84] Cor triatriatum sinistrum may result in left-sided volume overload and subsequent pulmonary venous hypertension and cardiac decompensation.[83,85] Alternatively, cor triatriatum dextrum may result in caudal vena cava and hepatic enlargement with subsequent right-sided congestive heart failure.[83] Some dogs and cats without hemodynamic alterations may remain asymptomatic and undiagnosed.[83–85]

Radiographic features of cor triatriatum sinistrum/dextrum include (eFig. 35.20):

- Variable degree of left or right atrial enlargement may be seen with cor triatriatum sinistrum or dextrum, respectively.
- Enlargement of the lobar pulmonary veins may predominate in patients with cor triatriatum sinistrum. Cardiogenic pulmonary edema due to left-sided congestive heart failure may be present.
- Enlargement of the caudal vena cava and hepatomegaly may also predominate in dogs and cats with cor triatriatum dextrum. The emergence of peritoneal and/or pleural effusion supports a diagnosis of right-sided congestive heart failure.



eFig. 35.20 Left lateral **(A)** and ventrodorsal **(B)** projections of a dog with cor triatriatum dexter. The cardiac silhouette is enlarged resulting in dorsal displacement of the trachea. The caudal vena cava is enlarged and dorsally convex. A convex soft tissue margin superimposed with the right heart and caudal vena cava in the ventrodorsal (VD) projection may represent the caudal chamber of the right atrium. Peritoneal serosal detail is reduced due to peritoneal effusion consistent with right heart failure.

13. Malcolm EL, Visser LC, Phillips KL, Johnson LR. Diagnostic value of vertebral left atrial size as determined from thoracic radiographs for assessment of left atrial size in dogs with myxomatous mitral valve disease. *J Am Vet Med Assoc*. 2018;253(8):1038–1054.
14. Oura TJ, Young AN, Keene BW, et al. A valentine-shaped cardiac silhouette in feline thoracic radiographs is primarily due to left atrial enlargement. *Vet Radiol Ultrasound*. 2015;56(3):245–250.
15. Huguet EE, Vilaplana Grosso F, Lamb WR, et al. Interpretation of cardiac chamber size on canine thoracic radiographs is limited and may result in the false identification of right-sided cardiomegaly in the presence of severe left-sided cardiomegaly. *Vet Radiol Ultrasound*. 2021;62(6):637–646.
16. Lehmukhl LB, Bonagura JD, Biller DS, Hartman WM. Radiographic evaluation of caudal vena cava size in dogs. *Vet Radiol Ultrasound*. 1997;38(2):94–100.
17. Cornelius L, Mahaffey M. Kinking of the intrathoracic caudal vena cava in five dogs. *J Small Anim Pract*. 1985;26(2):67–80.
18. Pelosi A, Prinsen JK, Eyster GE, Schall W, Olivier NB. Caudal vena cava kinking in dogs with ascites. *Vet Radiol Ultrasound*. 2012;53(3):233–235.
19. Thrall DE, Losonsky JM. A method for evaluating canine pulmonary circulatory dynamics from survey radiographs. *J Am Anim Hosp Assoc*. 1976;12:457.
20. Oui H, Oh J, Keh S, et al. Measurements of the pulmonary vasculature on thoracic radiographs in healthy dogs compared to dogs with mitral regurgitation. *Vet Radiol Ultrasound*. 2015;56(3):251–256.
21. Diana A, Guglielmini C, Pivetta M, et al. Radiographic features of cardiogenic pulmonary edema in dogs with mitral regurgitation: 61 cases (1998–2007). *J Am Vet Med Assoc*. 2009;235(9):1058–1063.
22. Schwarz T, Sullivan M, Störk CK, Willis R, Harley R, Mellor DJ. Aortic and cardiac mineralization in the dog. *Vet Radiol Ultrasound*. 2002;43(5):419–427.
23. Josephson S, Ovenfors CO. Experimental pulmonary air embolism: angiographic study in dogs. *Invest Radiol*. 1970;5(4):220–231.
24. Verstappen FTJ, Bernards JA, Kreuzer F. Effects of pulmonary gas embolism on circulation and respiration in the dog. *Pflügers Archiv*. 1970;368(1):89–96.
25. Baisan RA, Condurachi E, Turcu CA, Vu V. Prevalence of cardiac diseases in small animals: a five-year single-centre retrospective study. *Rev Rom Med Vet*. 2021;31(2):35–40.
26. Atkins C, Bonagura J, Ettinger S, et al. Guidelines for the diagnosis and treatment of canine chronic valvular heart disease. *J Vet Intern Med*. 2009;23(6):1142–1150.
27. Bionda A, Cortellari M, Bagardi M, et al. A genomic study of myxomatous mitral valve disease in Cavalier King Charles Spaniels. *Animals*. 2020;10(10):1895.
28. Fox PP. Pathology of myxomatous mitral valve disease in the dog. *J Vet Cardiol*. 2012;14(1):103–126.
29. Serres F, Chetboul V, Tissier R, et al. Chordae tendineae rupture in dogs with degenerative mitral valve disease: prevalence, survival, and prognostic factors (114 cases, 2001–2006). *J Vet Intern Med*. 2007;21(2):258–264.
30. Lee SK, Choi J. Caudal pulmonary artery to vein ratio on radiography can predict pulmonary hypertension in dogs with mitral regurgitation. *Vet Radiol Ultrasound*. 2022.
31. Borgarelli M, Buchanan JW. Historical review, epidemiology and natural history of degenerative mitral valve disease. *J Vet Cardiol*. 2012;14(1):93–101.
32. Lee RP, Huguet EH, Adin DB, Hernandez JA, Vilaplana Grosso FR. Radiographic features of cardiogenic pulmonary edema in dogs with dilated cardiomyopathy [abstract]. In: *ACVR Annual Meeting*. NV: Reno; 2022.
33. Ames MK, Atkins CE, Pitt B. The renin-angiotensin-aldosterone system and its suppression. *J Vet Intern Med*. 2019;33(2):363–382.
34. Martin MWS, Stafford Johnson MJ, Celona B. Canine dilated cardiomyopathy: a retrospective study of signalment, presentation and clinical findings in 369 cases. *Journal of Small Animal Practice*. 2009;50(1):23–29.
35. Cunningham SM, Dos Santos L. Arrhythmogenic right ventricular cardiomyopathy in dogs. *J Vet Cardiol*. 2022;40:156–169.
36. Schober KE, Wetli E, Drost WT. Radiographic and echocardiographic assessment of left atrial size in 100 cats with acute left-sided congestive heart failure. *Vet Radiol Ultrasound*. 2014;55(4):359–367.
37. Häggström J, Fuentes VL, Wess G. Screening for hypertrophic cardiomyopathy in cats. *J Vet Cardiol*. 2015;17:S134–S149.
38. Rohrbaugh MN, Schober KE, Rhinehart JD, Bonagura JD, Habing A, Yildiz V. Detection of congestive heart failure by Doppler echocardiography in cats with hypertrophic cardiomyopathy. *J Vet Intern Med*. 2020;34(3):1091–1101.
39. Abbott JA. Feline hypertrophic cardiomyopathy: an update. *Vet Clin North Am Small Anim Pract*. 2010;40(4):685–700.
40. Guglielmini C, Diana A. Thoracic radiography in the cat: identification of cardiomegaly and congestive heart failure. *J Vet Cardiol*. 2015;17:S87–S101.
41. Chetboul V, Passavin P, Trehiou-Sechi E, et al. Clinical, epidemiological and echocardiographic features and prognostic factors in cats with restrictive cardiomyopathy: a retrospective study of 92 cases (2001–2015). *J Vet Intern Med*. 2019;33(3):1222–1231.
42. Ferasin L, Sturgess CP, Cannon MJ, Caney SM, Gruffydd-Jones TJ, Wotton PR. Feline idiopathic cardiomyopathy: a retrospective study of 106 cats (1994–2001). *J Feline Med Surg*. 2003;5(3):151–159.
43. Reinero C, Visser LC, Kellihan HB, et al. ACVIM consensus statement guidelines for the diagnosis, classification, treatment, and monitoring of pulmonary hypertension in dogs. *J Vet Intern Med*. 2020;34(2):549–573.
44. Adams DS, Marolf AJ, Valdés-Martínez A, Randall EK, Bachand AM. Associations between thoracic radiographic changes and severity of pulmonary arterial hypertension diagnosed in 60 dogs via Doppler echocardiography: a retrospective study. *Vet Radiol Ultrasound*. 2017;58(4):454–462.
45. Rolph KE, Cavanaugh SM. Feline pulmonary hypertension: are we overlooking an important comorbidity? *J Feline Med Surg*. 2022;24(12):e636–e646.
46. Scollan KF, Bottorff B, Stieger-Vanegas S, Nemanic S, Sisson D. Use of multidetector computed tomography in the assessment of dogs with pericardial effusion. *J Vet Intern Med*. 2015;29(1):79–87.
47. Johnson MS, Martin M, Binns S, Day MJ. A retrospective study of clinical findings, treatment and outcome in 143 dogs with pericardial effusion. *J Small Anim Pract*. 2004;45(11):546–552.
48. Hall DJ, Shofer F, Meier CK, Sleeper MM. Pericardial effusion in cats: a retrospective study of clinical findings and outcome in 146 cats. *J Vet Intern Med*. 2007;21(5):1002–1007.

49. Côté E, Schwarz LA, Sithole F. Thoracic radiographic findings for dogs with cardiac tamponade attributable to pericardial effusion. *J Am Vet Med Assoc.* 2013;243(2):232–235.
50. Treggiari E, Pedro B, Dukes-McEwan J, Gelzer AR, Blackwood L. A descriptive review of cardiac tumours in dogs and cats. *Vet Comp Oncol.* 2017;15(2):273–288.
51. Aupperle H, März I, Ellenberger C, Buschatz S, Reischauer A, Schoon HA. Primary and secondary heart tumours in dogs and cats. *J Comp Pathol.* 2007;136(1):18–26.

ELECTRONIC RESOURCES

Additional information related to the content in Chapter 35 can be found online at eBooks.Health.Elsevier.com

- Chapter Quiz
- Videos
- References



ONLINE ONLY REFERENCES

52. Schrope DP. Prevalence of congenital heart disease in 76,301 mixed-breed dogs and 57,025 mixed-breed cats. *J Vet Cardiol*. 2015;17(3):192–202.
53. Saunders AB. Key considerations in the approach to congenital heart disease in dogs and cats. *J Small Anim Pract*. 2021;62(8):613–623.
54. Oliveira P, Domenech O, Silva J, Vannini S, Bussadori R, Bussadori C. Retrospective review of congenital heart disease in 976 dogs. *J Vet Intern Med*. 2011;25(3):477–483.
55. Bascuñán A, Mankin KT, Saunders AB, et al. Patent ductus arteriosus in cats (*Felis catus*): 50 cases (2000–2015). *J Vet Cardiol*. 2017;19(1):35–43.
56. Van Israel N, French AT, Dukes-McEwan J, Corcoran BM. Review of left-to-right shunting patent ductus arteriosus and short term outcome in 98 dogs. *J Small Anim Pract*. 2002;43(9):395–400.
57. Saunders AB, Gordon SG, Boggess MM, Miller MW. Long-term outcome in dogs with patent ductus arteriosus: 520 cases (1994–2009). *J Vet Intern Med*. 2014;28(2):401–410.
58. Tidholm A. Retrospective study of congenital heart defects in 151 dogs. *J Small Anim Pract*. 1997;38(3):94–98.
59. Tidholm A, Ljungvall I, Michal J, Häggström J, Höglund K. Congenital heart defects in cats: a retrospective study of 162 cats (1996–2013). *J Vet Cardiol*. 2015;17:S215–S219.
60. Scansen BA, Schneider M, Bonagura JD. Sequential segmental classification of feline congenital heart disease. *J Vet Cardiol*. 2015;17:S10–S52.
61. Greet V, Bode EF, Dukes-McEwan J, Oliveira P, Connolly DJ, Sargent J. Clinical features and outcome of dogs and cats with bidirectional and continuous right-to-left shunting patent ductus arteriosus. *J Vet Intern Med*. 2021;35(2):780–788.
62. Bomassi E, Misbach C, Tissier R, et al. Signalment, clinical features, echocardiographic findings, and outcome of dogs and cats with ventricular septal defects: 109 cases (1992–2013). *J Am Vet Med Assoc*. 2015;247(2):166–175.
63. Schrope DP. Atrioventricular septal defects: natural history, echocardiographic, electrocardiographic, and radiographic findings in 26 cats. *J Vet Cardiol*. 2013;15(4):233–242.
64. Van Mierop LH, Patterson DF, Schnarr WR. Hereditary conotruncal septal defects in Keeshond dogs: embryologic studies. *Am J Cardiol*. 1977;40(6):936–950.
65. Chetboul V, Charles V, Nicolle A, et al. Retrospective study of 156 atrial septal defects in dogs and cats (2001–2005). *J Vet Med A*. 2006;53(4):179–184.
66. Buchanan JW. Prevalence of cardiovascular disorders. Congenital heart disease. In: Fox PR, Sisson D, Moïse NS, eds. *Textbook of Canine and Feline Cardiology: Principles and Clinical Practice*. 2nd ed. Philadelphia: Saunders; 1999.
67. Guglielmini C, Diana A, Pietra M, Cipone M. Atrial septal defect in five dogs. *J Small Anim Pract*. 2002;43(7):317–322.
68. Locatelli C, Spalla I, Domenech O, Sala E, Brambilla PG, Bussadori C. Pulmonic stenosis in dogs: survival and risk factors in a retrospective cohort of patients. *J Small Anim Pract*. 2013;54(9):445–452.
69. Ristic JM, Marin CJ, Baines EA, Herrtage ME. Congenital pulmonic stenosis a retrospective study of 24 cases seen between 1990–1999. *J Vet Cardiol*. 2001;3(2):13–19.
70. Francis AJ, Johnson MJS, Culshaw GC, Corcoran BM, Martin MWS, French AT. Outcome in 55 dogs with pulmonic stenosis that did not undergo balloon valvuloplasty or surgery. *J Small Anim Pract*. 2011;52(6):282–288.
71. Buchanan JW. Pathogenesis of single right coronary artery and pulmonic stenosis in English bulldogs. *J Vet Intern Med*. 2001;15:101–104.
72. Petrič AD, Perovič A, Švara T, Dovč P. Aortic Stenosis in Dogs and Cats: Past, Present and Future. In: *Aortic Stenosis—Current Perspectives*. IntechOpen; 2019.
73. Watson CE, Payne JR, Borgeat K. Valvular aortic stenosis in three cats. *J Vet Cardiol*. 2019;25:1–6.
74. Eason BD, Fine-Ferreira DM, Leeder D, Stauthammer C, Lamb K, Tobias A. Natural history of subaortic stenosis in 166 dogs (1999–2011). *J Vet Cardiol*. 2021;37:71–80.
75. Mishra A, Shahi A, Das B, Dwivedi PK, Jawre S, Singh R. Aortic stenosis in dogs: a brief review. *J Pharm Innov*. 2021;10(11):2161–2168.
76. Pasławska U, Noszczyk-Nowak A, Janiszewski A, Nicpoń J. Tricuspid dysplasia in dogs. *J Vet Res*. 2013;57(1):123–126.
77. Navarro-Cubas X, Palermo V, French A, Sanchis-Mora S, Culshaw G. Tricuspid valve dysplasia: a retrospective study of clinical features and outcome in dogs in the UK. *Open Vet J*. 2017;7(4):349–359.
78. Sudunagunta S, Hamilton-Elliott J, Dukes-McEwan J. Mitral valve dysplasia in eight English Springer Spaniels. *J Vet Cardiol*. 2021;33:52–60.
79. Lehmkuhl LB, Ware WA, Bonagura JD. Mitral stenosis in 15 dogs. *J Vet Intern Med*. 1994;8(1):2–17.
80. Campbell FE, Thomas WP. Congenital supravalvular mitral stenosis in 14 cats. *J Vet Cardiol*. 2022;14(1):281–292.
81. Chetboul V, Pitsch I, Tissier R, et al. Epidemiological, clinical, and echocardiographic features and survival times of dogs and cats with tetralogy of Fallot: 31 cases (2003–2014). *J Am Vet Med Assoc*. 2016;249(8):909–917.
82. Orton EC, Mama K, Hellyer P, Hackett TB. Open surgical repair of tetralogy of Fallot in dogs. *J Am Vet Med Assoc*. 2001;219(8):1089–1093.
83. Castagna P, Romito G, Toaldo MB. Cor triatriatum sinister in a dog. *J Vet Cardiol*. 2019;25:25–31.
84. Nadolny KE, Kellihan HB, Scansen BA, et al. Cor triatriatum dexter in 17 dogs. *J Vet Cardiol*. 2019;23:129–141.
85. Koie H, Sato T, Nakagawa H, Sakai T. Cor triatriatum sinister in a cat. *J Small Anim Pract*. 2000;41(3):128–131.
86. Jepsen-Grant K, Pollard RE, Johnson LR. Vertebral heart scores in eight dog breeds. *Vet Radiol Ultrasound*. 2013;54(1):3–8.
87. Puccinelli C, Citi S, Vezzosi T, Garibaldi S, Tognetti R. A radiographic study of breed-specific vertebral heart score and vertebral left atrial size in Chihuahuas. *Vet Radiol Ultrasound*. 2021;62(1):20–26.
88. Lamb CR, Wikeley H, Boswood A, Pfeiffer DU. Use of breed-specific ranges for the vertebral heart scale as an aid to the radiographic diagnosis of cardiac disease in dogs. *Vet Rec*. 2007;148(23):707–711.
89. Pinto ACB de CF, Iwasaki M. Radiographic methods in the cardiac evaluation dogs. *Veterinaria Noticias*. 2002;8(1):67–75.
90. Gülanber EG, Gönenci R, Kaya Ü, Aksoy Ö, Biricik HS. Vertebral scale system to measure heart size in thoracic radiographs of Turkish Shepherd (Kangal) dogs. *Turk J Vet Anim Sci*. 2005;29(3):723–726.
91. Bavegems V, Van Caelenberg A, Duchateau L, Sys SU, Van Bree H, De Rick A. Vertebral heart size ranges specific for whippets. *Vet Radiol Ultrasound*. 2005;46(5):400–403.
92. Marin LM, Brown J, McBrien C, Baumwart R, Samii VF, Couto CG. Vertebral heart size in retired racing Greyhounds. *Vet Radiol Ultrasound*. 2007;48(4):332–334.
93. Kraetschmer S, Ludwig K, Meneses F, Nolte I, Simon D. Vertebral heart scale in the beagle dog. *J Small Anim Pract*. 2008;49(5):240–243.
94. Birks R, Fine DM, Leach SB, et al. Breed-specific vertebral heart scale for the dachshund. *J Am Anim Hosp Assoc*. 2017;53(2):73–79.
95. Azevedo GM, Pessoa GT, da Silva Moura L, et al. Comparative study of the vertebral heart scale (VHS) and the

cardiothoracic ratio (CTR) in healthy poodle breed dogs. *Acta Sci Vet*. 2016;44(1):7.
96. Bodh D, Hoque M, Saxena AC, Gugjoo MB, Bist D, Chaudhary JK. Vertebral scale system to measure heart size in thoracic radiographs of Indian Spitz, Labrador retriever and Mongrel dogs. *Vet World*. 2016;9(4):371.
97. Ghadiri AR, Avizeh R, Fazli GH. Vertebral heart scale of common large breeds of dogs in Iran. *Iran J Vet Med*. 2010;4(2):107–111.
98. Cardoso MJL, Caludino JL, Melussi M. Measurement of heart size by VHS (vertebral heart size) method in healthy American pit bull terrier. *Ciência Rural*. 2011;41(1):127–131.
99. Gugjoo MB, Hoque M, Saxena AC, Zama MMS, Amarpal A. Vertebral scale system to measure heart size in dogs in thoracic radiographs. *Adv Anim Vet Sci*. 2013;1:1–4.
100. Colina CV, do Imperador BDG. Vertebral heart size in healthy Belgian Malinois dogs. *J Vet Adv*. 2015;5(12):1176–1180.

CHAPTER 36

Canine and Feline Lung

Isabelle Masseau

LUNG ANATOMY AND RADIOGRAPHIC APPEARANCE

To fulfill its role as the sole oxygen provider, the lungs contain a large amount of air, which provides contrast to the soft tissue opaque heart, major vessels (e.g., aorta, caudal vena cava), and pulmonary vasculature (Fig. 36.1). Additional opacity is provided by the musculoskeletal structures of the thorax, summating with the lungs (eFig. 36.1). The location of lung lobes is fairly constant among dogs and cats and their expected location can be extrapolated on standard three-view thoracic radiography, keeping in mind that lung lobes overlap considerably. The left lung is separated into cranial and caudal lung lobes (Fig. 36.2A). The left cranial lung lobe is further subdivided in cranial and caudal segments, connected to each other dorsally. The right lung is separated into cranial, middle, caudal, and accessory lung lobes (see Fig. 36.2B, inset, and C). The accessory lung lobe occupies a midline position, caudal to the heart, as seen on a ventrodorsal (VD) image of the thorax (see Fig. 36.2C, right bottom panel) and overlaps with the right caudal lung lobe on the left lateral view (see Fig. 36.2B).

Airways

A flowchart indicates the travel of air through the conduit airways up to the pulmonary parenchyma, where gas exchange occurs (Fig. 36.3). In general, the bronchial walls are too thin to be seen on radiography, unless they are mineralized or abnormally thick (Fig. 36.4).[1] Dogs >10 years old are more likely to have bronchial cartilage calcification, which may not be of clinical significance.[1] When the thickness allows their detection, the bronchial walls tend to taper as the bronchus courses away from its origin.

Parenchyma

The acinus constitutes the terminal respiratory unit where gas exchange occurs. This unit includes everything beyond the terminal bronchiole, that is, in the order of the incoming air flow, respiratory bronchioles, alveolar ducts, alveolar sacs, and alveoli (see Fig. 36.3). Alveoli are surrounded by a thin alveolar wall composed of epithelial cells, some of which produce surfactant, preventing collapse of alveoli during exhalation. A thin layer of connective tissue composed of collagen and elastic reticular fibers and occasional fibroblasts constitutes the supporting tissue (i.e., the interstitial space) of the pulmonary parenchyma. The sum of all terminal respiratory units with associated vessels and lymphatics and supporting connective tissue constitutes the pulmonary parenchyma. In many species (e.g., humans, pigs, cattle, and to a lesser extent horses, sheep, and goats), the lungs are further subdivided into pulmonary lobules, surrounded by connective tissue, known as interlobular septa, and disserved by a tertiary bronchus and its paired pulmonary artery.[2] Dogs and cats lack interlobular septa and thus do not share an organization into secondary pulmonary lobules.

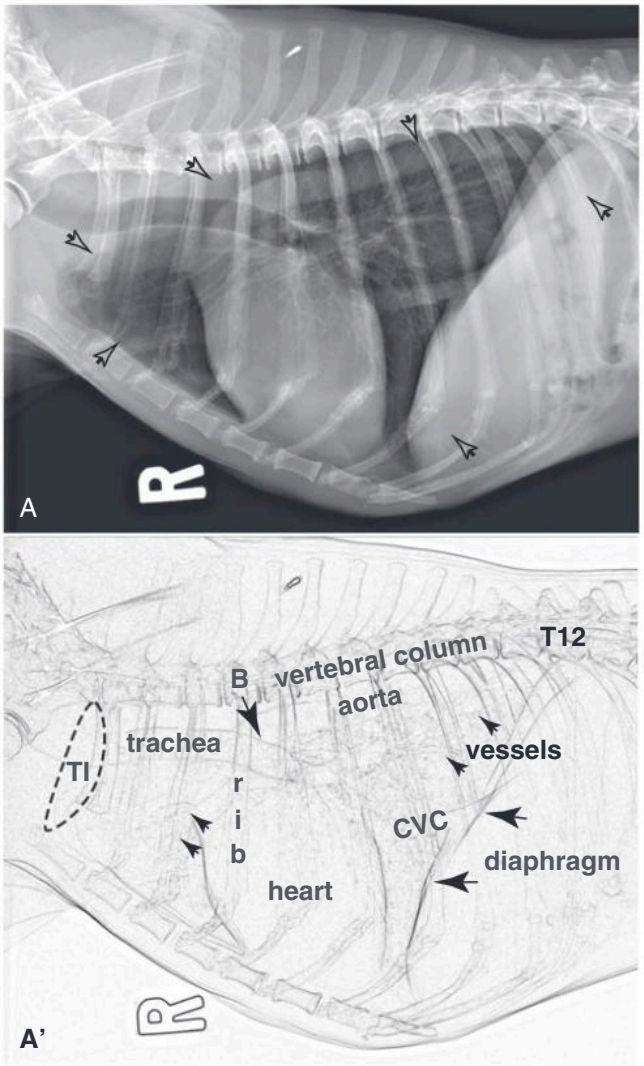
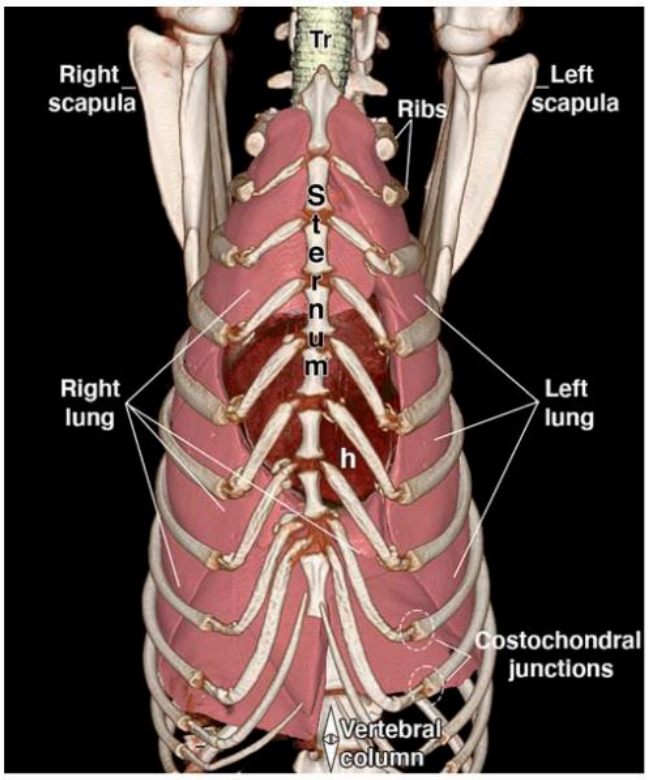


Fig. 36.1 The canine lungs on a right lateral radiographic image **(A)**, with contour tracings **(A')** of the structures. **A,** The pulmonary vasculature, the cardiac silhouette and major vessels, of soft tissue opacity, contrast with the lungs' predominantly air opacity. **A',** The lungs extend cranially to the thoracic inlet (*TI*) and caudally to the diaphragm (*large arrows*). Caudodorsally, the lungs are easily seen up to the 12th thoracic vertebra (*T12*). The aorta and caudal vena cava (*CVC*) travel through the mediastinum, flanked on either side by lungs. The transport of deoxygenated and oxygenated blood, from and to the heart, respectively, is carried out by a network of pulmonary arteries and veins (*small arrows*), located upstream and downstream of the pulmonary capillaries. The relative linear/reticular orientation of the summating pulmonary vasculature has led to the description of canine and feline lungs appearing on radiography as "a network of radiopacities" or "normal pulmonary markings."



eFig. 36.1 Ventral three-dimensional computed tomography (3D CT) image illustrating the canine lung's osseous boundaries of the thoracic cavity. The lungs are located in the thoracic cavity, on either side of the heart (*h*), hence their designation of right and left lungs. The right and left lungs are protected by an axial skeleton composed of the spine dorsally, the sternebrae (sternum) ventrally, and the ribs laterally. The scapulae offer some protection to the first thoracic vertebrae and proximal part of the first ribs. The trachea (*Tr*) connects the upper and lower respiratory tract.



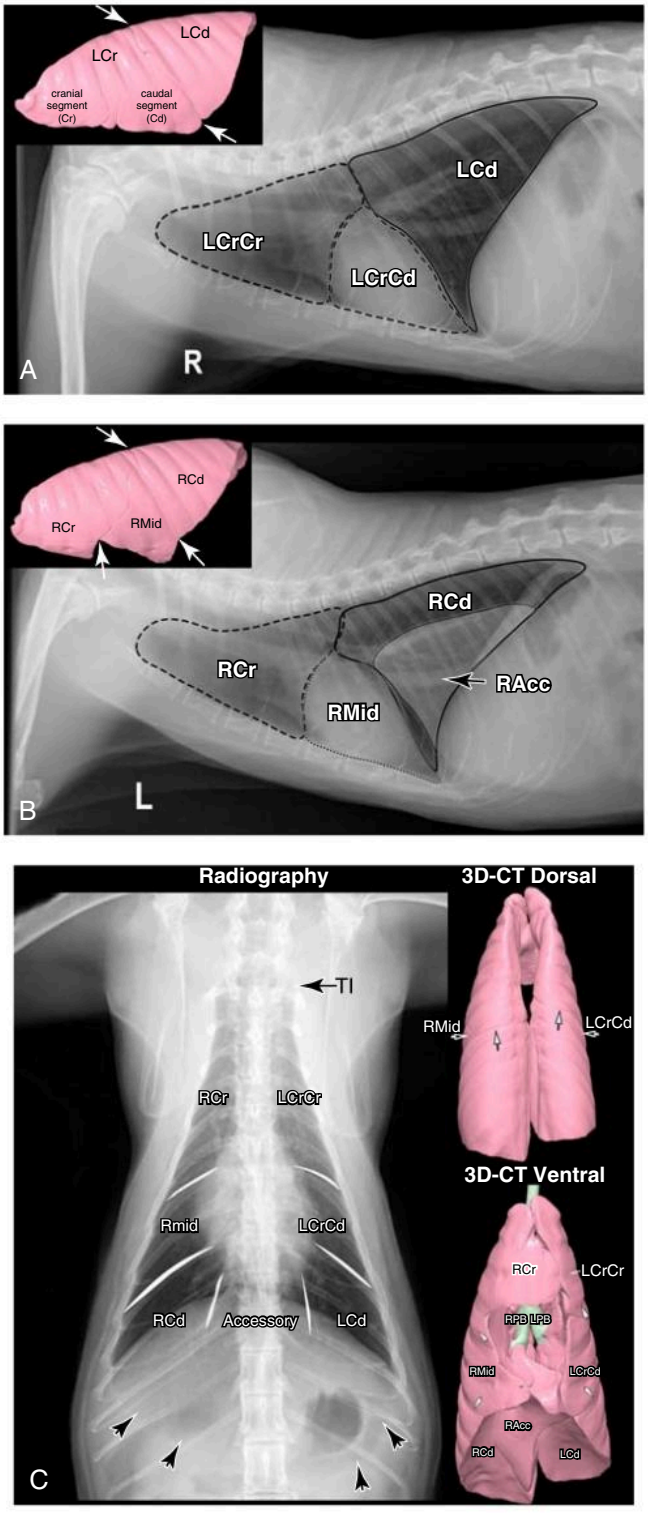


Fig. 36.2 Three-view recumbent thoracic radiography and three-dimensional (3D) computed tomography (CT) images of the lungs. Approximate location of the lung lobes or segments is indicated on the radiographic images. **A,** The left lung is divided into cranial *(LCr)* and caudal *(LCd)* lobes by deep fissures *(arrows)*. The cranial lung lobe is further subdivided into left cranial lobe cranial (*LCrCr*) and left cranial lobe caudal (*LCrCd*) subsegments, united dorsally. On a right lateral recumbent view, the caudal segment of the *LCrCd* summates with the cardiac silhouette. **B,** The right lung is separated by fissures (*inset, white arrows*) into four lobes: the right cranial (*RCr*), the right middle (*RMid*), the right caudal (*RCd*), and the accessory (*RAcc*) lung lobes. On a left lateral view, superimposed over the cardiac silhouette, is the right middle lung lobe. **C,** Dorsoventral view showing the lung lobation. The caudal lungs extend caudodorsally (*arrows*) to the attachment of the left and right diaphragmatic crura. *Right panels,* Dorsal (*top*) and ventral (*bottom*) 3D CT images of the lungs showing the fissures between the different lung lobes (*arrows*). The ventral image shows the midline position occupied by the accessory (*RAcc*) lung lobe. It is flanked on either side by the right caudal and left caudal lung lobes. *LPB,* Left principal bronchus; *RPB,* right principal bronchus.

Pulmonary Vasculature

At the hilum, each principal bronchus is accompanied by a pulmonary artery, arising from the pulmonary trunk. The right and left pulmonary arteries will branch out, in a pattern similar to the airways, coursing dorsal and lateral to the lobar bronchus. The pulmonary vein occupies a medial/ventral position to the bronchus. The smaller, individually indistinguishable vessels and bronchi contribute to the normal background opacity of the lung.

THE BREATHING CYCLE APPLIED TO THORACIC RADIOGRAPHY

Exposure factors tailored to the lungs will favor a wide range of shades of gray (low mAs, high kVp) to maximize detection of lung lesions. A short exposure time (e.g., 1/60 seconds or 1/120 seconds) minimizes motion artifact associated with respiration. Full inflation of the lungs promotes the visibility of the bronchial and vascular structures, and is more likely to depict lung lesions (Fig. 36.5).[3] Overinflation results in more radiolucency than normally expected.

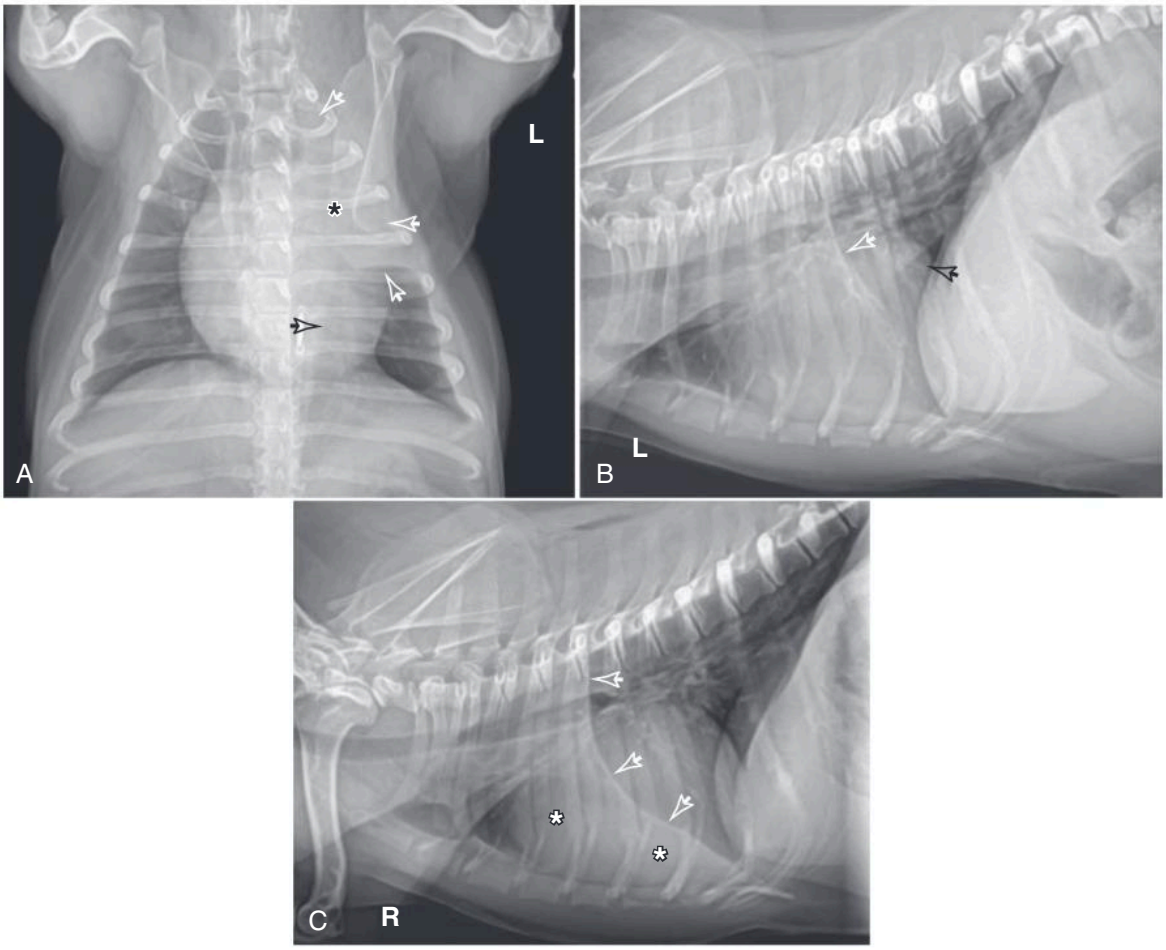
Exhalation is passive during quiet breathing. Relaxing muscles and diaphragm return to their normal position, allowing carbon dioxide containing air to be exhaled, and thus, generating increased pulmonary opacity and decreased contrast between bronchial and vascular structures and pulmonary parenchyma, and pulmonary lesions (see Fig. 36.5).[3]

Factors Affecting Lung Volume

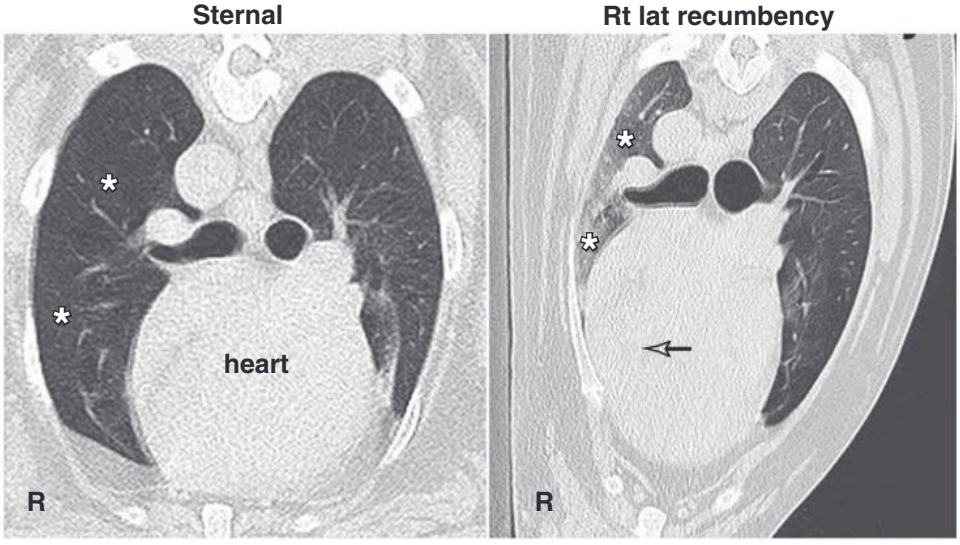
A dog's or cat's ability to inflate and then deflate their lungs depends on many factors, some of which are discussed in further detail later.

- Sedated dogs and cats with shallow breathing may not achieve maximal lung inflation.
- Placing healthy, conscious dogs in left or right lateral recumbency for 10 minutes leads to lung volume loss, even faster if sedated or anesthetized (Fig. 36.6, eFig. 36.2).[4–6] Keeping patients in lateral recumbency for as little time as possible prior to and during radiography acquisition best limits the effects of recumbency on lung volume (eFig. 36.3). Mechanical ventilation and adequate species-specific airway pressure during breath-hold technique and positive end-expiratory pressure may also help maintain better lung aeration while the animal is under general anesthesia.[7–11]
- Impaired caudal displacement of the diaphragm by, for example, excess abdominal content reduces the size of the thoracic cavity and is often compensated by increasing the width and depth leading to a barrel-chested appearance.[12]
- Any mechanism preventing ventilation of the alveoli, whether as a result of airway occlusion by tissue, fluid, or solid material, or as a result of compression by an extrapulmonary mass, will result in a reduction in volume.

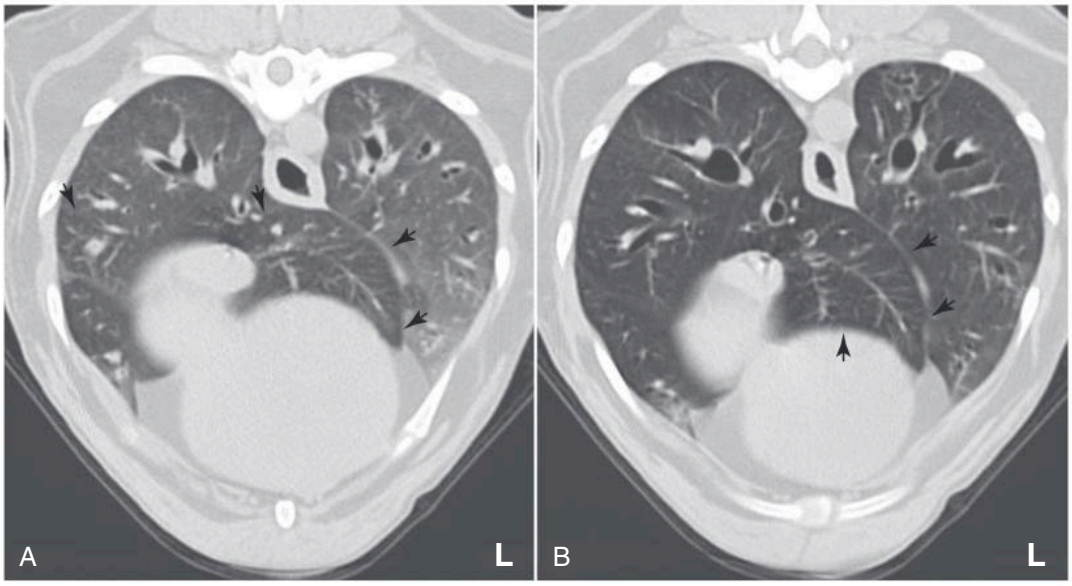
Airways have to remain open during exhalation to expel air out of the lung parenchyma. Abnormal closure of the airways on exhalation traps air. On imaging, abnormal air retention (i.e., dynamic air trapping) beyond the closed airway manifests as a region, segment, or lobe of the lung that fails to decrease in volume at expiration (eFig. 36.4).[13]



eFig. 36.2 Effect of 10 minutes of left lateral recumbency on a canine radiographic thoracic study. **A,** The ventrodorsal view shows an increase in opacity (*asterisk*) of the left cranial lung lobe region *(white arrows)* associated with a decreased in lung volume as indicated by the leftward mediastinal shift *(black arrow)*. **B,** Subsequently, a left lateral view was taken. Reduced inflation of the lungs is indicated by the small triangular region between the cardiac silhouette and the diaphragm *(black arrow)*. A radiopaque line (*white arrow*) is seen between the left cranial and left caudal lung lobes, consistent with a clear demarcation between the poorly inflated left cranial lung lobe compared to the left caudal lung lobe. **C,** On the right lateral view, taken immediately after the left, the left cranial lung lobe, especially the caudal segment, is markedly increased in opacity (*asterisks*), which is better seen than on the previous lateral recumbent view. This is probably attributed to the marked difference between aeration of the left cranial and left caudal lung lobes, as manifested by the lobar sign (*arrows*). The cranial displacement of this lobar sign is consistent with decreased lung volume of the left cranial lung lobe.



eFig. 36.3 Effect of recumbency on a transverse computed tomographic image. The dog was first imaged while in a sternal position. The right lung is of normal attenuation, as reflected by the blackness of the lung parenchyma (*asterisks*), and it is similar to that of the left lung. The heart occupies a midline position. The dog was then placed in right lateral (*Rt lat*) recumbency, leading a decrease in the volume of the right lung and its increase in attenuation (*asterisks*) as denoted by decreased blackness of the lung parenchyma. The heart is shifted to the side the dog was lying on (*arrow*), which corresponds to the right.



eFig. 36.4 Dynamic air trapping on paired breath-hold inspiratory:expiratory computed tomographic (CT) images. **A,** Expiratory CT image showing accentuation of lung regions, especially the accessory lung lobe, and to a lesser extent the ventral aspect of the right caudal lung lobe (*arrows*). These regions of dynamic air trapping create an inhomogeneous lung parenchyma on exhalation. These regions fail to show an increase in lung attenuation and decrease in lung volume as expected after exhaling. **B,** Inspiratory CT image at the same level, showing a fairly homogeneous and well aerated lung parenchyma. The *arrows* indicate the region of the accessory lung lobe.

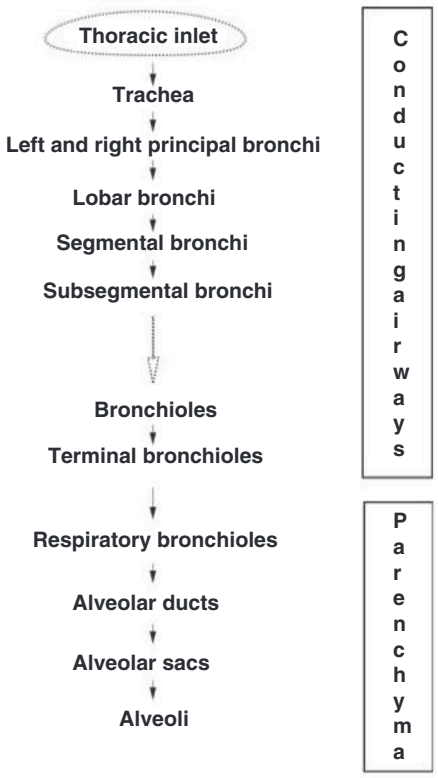


Fig. 36.3 Flowchart indicating the different structures traversed by air following its entry into the thoracic cavity. Air will flow from the nostrils through a series of upper and then lower conduits until the terminal respiratory units of the lungs are reached, where gas exchange occurs. Dogs and cats ventilate each lung through the left and right principal bronchi, also referred to as the mainstem bronchi, partitioning from the trachea. After a short course in the mediastinum, each principal bronchus, constituting the first generation of airways, enters the hilum of the right or left lungs and divides almost immediately into lobar bronchi, named after the lobe they ventilate. The lobar bronchi represent the second generation of airways and their branching pattern is fairly conserved among dogs and cats. Within each lung lobe, the lobar bronchus gives rise to segmental bronchi, also called tertiary bronchi (third generation) arising dorsally and ventrally for most lung lobes except for the right middle lung lobe, from which they emerge cranially and caudally. Segmental bronchi divide into subsegmental bronchi (fourth generation) which further subdivide into smaller subsegmental bronchi to 9 or 10 divisions. At the end, air will reach the smallest airway, the bronchiole. In contrast to bronchi, bronchioles lack cartilage in their walls. The terminal bronchioles are interposed between the conducting airways and the pulmonary parenchyma. No gas exchange occurs at this level. Air will then diffuse through the respiratory bronchioles, alveolar ducts, and alveolar sacs until they reach the pulmonary alveoli where exchange of oxygen or carbon dioxide will occur. The pulmonary parenchyma also includes small vessels <20–25 μm in diameter, predominantly capillaries, and represents the major component of lungs.

Standard Examination: Three Recumbent View Study (R, L, and VD/DV)

Lung assessment is best performed on thoracic radiographs captured during the inspiratory phase of respiration. Acquiring additional expiratory views can be useful for highlighting dynamic airway collapse.[14–17]

Right and left lateral recumbent views are mandatory for radiographic assessment of lung disease to mitigate the negative effect of recumbency on lung volume and aeration (Fig. 36.7). Omission of one (left or right) of the lateral recumbent views may result in misdiagnosis.[18] A VD view is usually best for assessment of the accessory lung lobe, whereas a dorsoventral (DV) view may be indicated for dorsally located lesions or to evaluate the caudodorsal pulmonary vasculature.

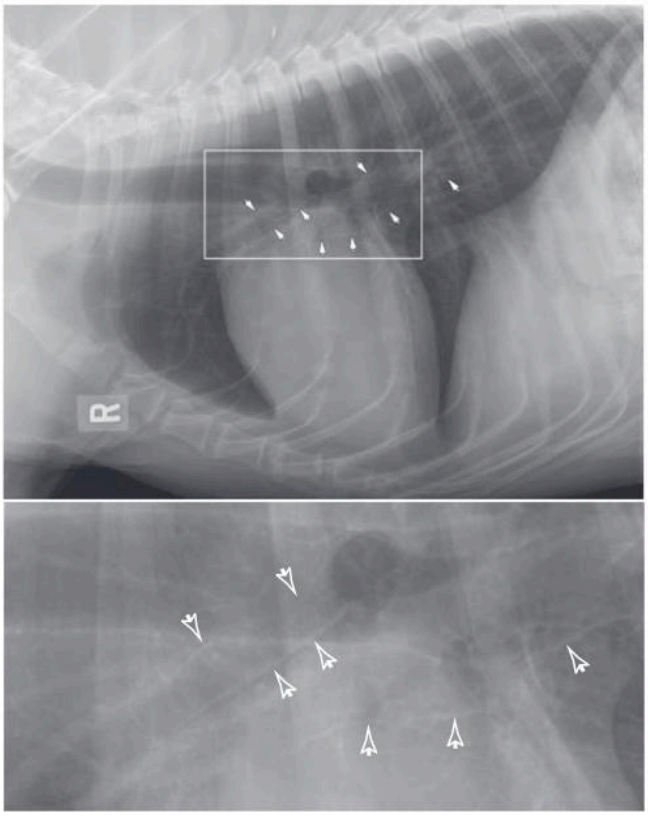


Fig. 36.4 Mineralization of the airway walls. Right lateral radiographic view showing mineralization of the bronchial walls (*arrows*) in an 8-year-old male castrated German shepherd dog without any respiratory clinical signs. *Inset,* the walls are sharply demarcated, thin, and of regular thickness. They are only detected near the hilum of the lungs.

Description of Lung Lesions

Interpretation of lung disease on thoracic radiography is challenging and there are several reasons for this.

1. The lungs are surrounded by numerous soft tissue and osseous structures that become superimposed over the lungs and add opacity on radiographs.
2. The different conformations of dog breeds challenge what is considered normal for one breed while abnormal for another.
3. The degree of lung expansion influences its radiographic appearance. Subtle lung lesions may be missed in expiratory radiographs.
4. Very few diseases, if any, have a pathognomonic radiographic appearance. It is common for diseases to share a few or even many radiographic findings.
5. A given disease may present with a wide spectrum of radiographic manifestations

RADIOGRAPHIC ASSESSMENT OF PULMONARY DISEASE

The pulmonary pattern recognition paradigm is widely used to assess the radiographic appearance of the lungs, with the intent to focus on the compartment of the lung that is abnormal (i.e., the pattern) as an organized approach to image evaluation. Certain patterns are associated with certain diseases, which can

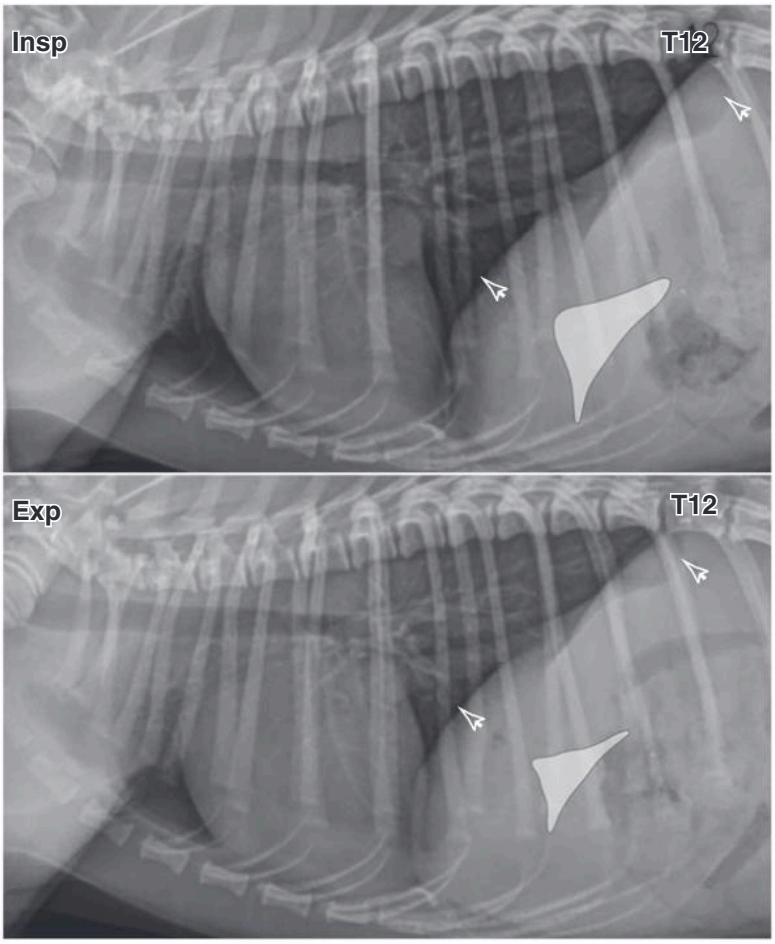


Fig. 36.5 Inspiratory and expiratory left lateral radiographic views. The lateral inspiratory view (*top, Insp*) is characterized by a slight elevation of the cranial border of the cardiac silhouette from the sternum due to in flation of the cranial lung lobes, caudal excursion of the lumbodiaphragmatic angles (*arrows*) caudal to T12, decreased diaphragmatic contact with the caudal border of the cardiac silhouette, and enlargement of the caudoventral lungs. These changes may not be visible in panting or tachypneic dogs.[4] Passive exhalation (*bottom, Exp*) is characterized by the cranial location of the diaphragmatic cupula, often superimposed the caudal border of the cardiac silhouette. A triangle-shape region (*white overlay*) outlining the borders of the cardiac silhouette, diaphragm, and caudal vena cava, represent a quick method to assess the phase of respiration. This region is larger on a view taken in inspiration compared to expiration.

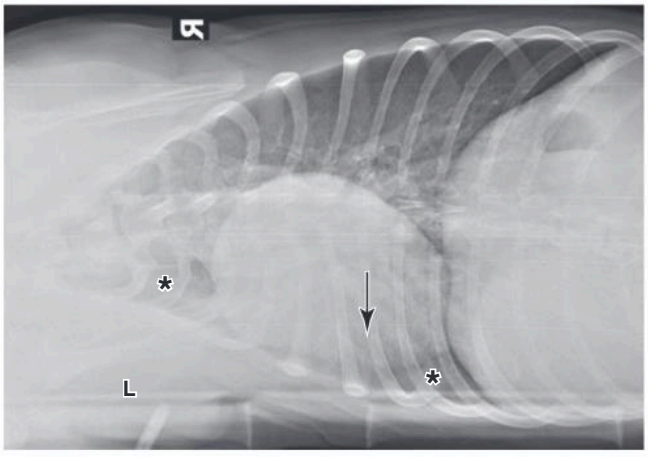


Fig. 36.6 Effect of body position on lung aeration using a horizontal x-ray beam. The patient was placed in left lateral recumbency and a horizontal x-ray beam oriented towards the sternum of the dog was used. The left lung ("bottom lung") is decreased in size (i.e., decreased lung volume) and increased in opacity (*asterisks*). The cardiac silhouette is shifted to the left (*arrow*). The nondependent lung ("top" lung), in this case the right lung, is well aerated and of normal opacity.

help in formulating differential diagnoses for a particular radiographic presentation. It is critical to understand, however, that the pulmonary patterns are not specific to any particular lung disease, with most conditions presenting at least two different pulmonary patterns or different combinations of patterns. It is therefore important to use roentgen signs (i.e., number, location/position, size, shape, opacity, contour, severity) in concert with pulmonary patterns to formulate a comprehensive description of pulmonary pathology.

The Use of Roentgen Signs

Number

A single lesion is called *focal* or *solitary*. When two or more lesions are visible surrounded by unaffected areas in the lung, the term *multifocal* is used. Multifocal lesions can be found in different lung lobes or in a single lung lobe.

Lesions involving the majority of a lung lobe/segment, with no evidence of unaffected areas, or with very little unremarkable lung, are ultimately *diffuse*. Although diffuse lesions often involve two or more lung lobes or segments, they can apply to lesions involving a single lung lobe or segment. Lesions targeting a specific anatomy, such as all intrathoracic airways, may also be termed diffuse.

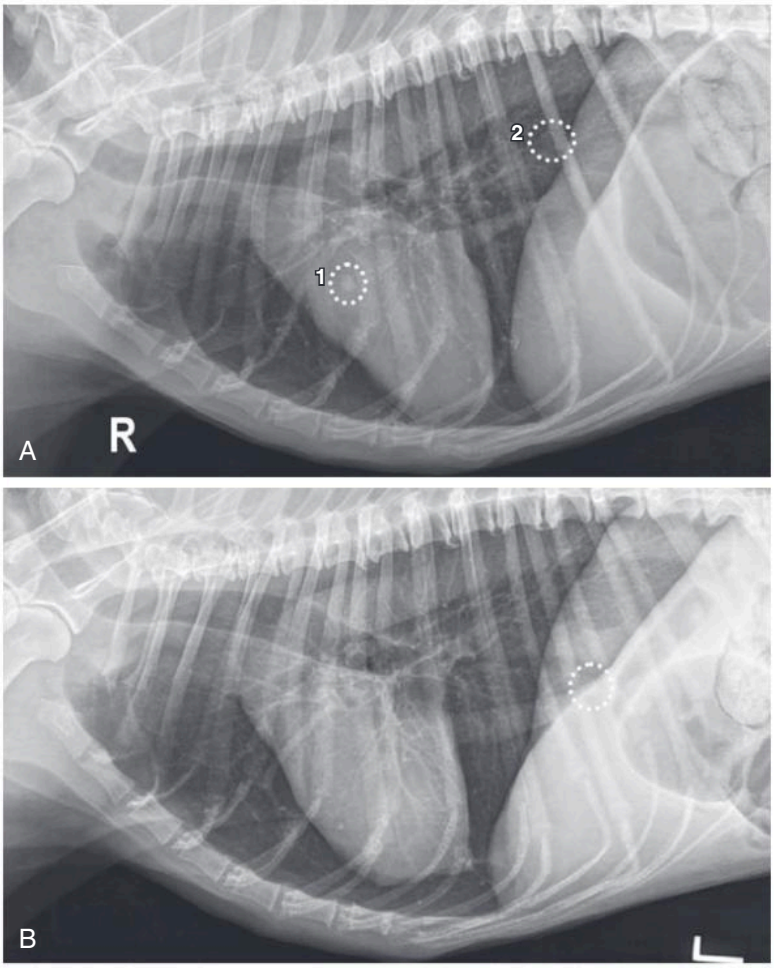


Fig. 36.7 The effect of recumbency on the detection of pulmonary nodules on radiography. **A,** Right lateral view showing an oval, well-demarcated, soft tissue opacity nodule superimposed over the cardiac silhouette (*1, dotted circle*). A second less defined soft tissue opaque nodule, is seen in the eighth intercostal space, partially superimposed over the ninth rib (*2, dotted circle*). **B,** When the dog is placed in left lateral recumbency, the nodules are no longer seen, instead a different nodule is visible superimposed over the caudal vena cava. The in flation of the dependent lung is reduced while the nondependent lung (i.e., the top lung) has better in flation. Because of this effect, small lesions in the left lung can only be seen in the right lateral view, and vice versa. The pulmonary nodules corresponded to pulmonary metastases from a transitional cell carcinoma of the urinary bladder.

Location/Position

The position of a lesion should be described based on lung lobation. Anatomical landmarks such as the heart base, caudal vena cava, and trachea can also be used to describe the position of a lesion relative to another structure. The location of lesions has also been categorized according to three concentric zones relative to the hilum of each lung, the central or perihilar, middle and peripheral regions.

There are a few diseases that tend to be more often associated with specific lung lobes or a location. Pulmonary edema of cardiogenic or noncardiogenic origin tends to have a bilateral symmetrical or asymmetrical appearance localizing first to the hilar region, and more pronounced in the caudal lung lobes, although other locations and distributions, especially in cats, are possible (Fig. 36.8).[19] Bronchopneumonia or aspiration pneumonia often localizes to the cranial or right middle lung lobes (Fig. 36.9). The caudal lung lobes are a common site for primary lung tumors (Fig. 36.10), while histiocytic sarcoma most commonly occurs in the left cranial and right middle lung lobes (Fig. 36.11).[20,21]

Size

Circular or oval lesions are commonly reported according to their diameter. Circular or oval lesions with a diameter of <3 cm are called *nodules*, while a lesion of or exceeding 3 cm is termed a *mass* (Fig. 36.12).[13,20,22] The presence of numerous small punctate soft tissue nodules throughout the lungs has been described as *miliary* nodules (Fig. 36.13).[23]

Mineral opacity lesions and metallic objects can be detected even if they are very small (~1 mm). Digital radiography can today reliably depict soft tissue nodules of 2 to 3 mm in diameter.[24–26] However, some nodules may be difficult to identify or completely missed on radiography compared to computed tomography (CT), even if their size exceeds the minimum detection threshold.[24–26] Pulmonary vessels can sometimes be confused with pulmonary nodules when viewed in cross-section or, in other words, end on (Fig. 36.14A). End-on vessels are superimposed over a parent vessel, usually linearly oriented, of the same or greater diameter, and located next to an end-on bronchus. End-on vessels are larger near the hilar region and smaller as they move away towards the periphery. When in doubt, oblique views can help to compensate for a possible overlap with a vascular shadow and to confirm the identification of a nodule.

Shape

Lung lesions can vary considerably in shape depending on their anatomical location and this topic is discussed further later.

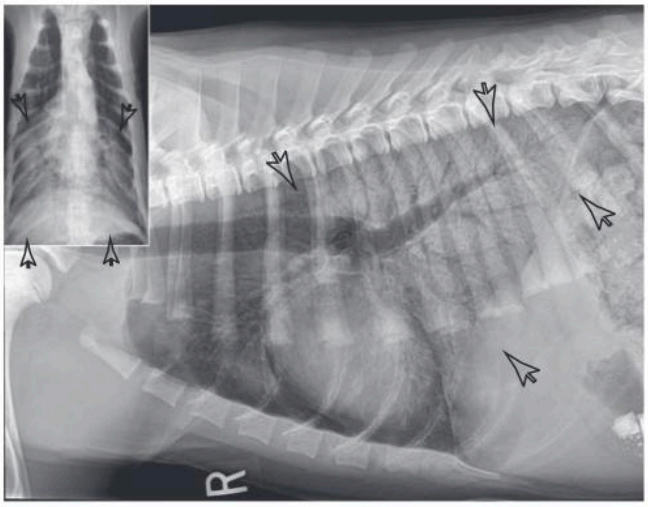


Fig. 36.8 Noncardiogenic pulmonary edema and its predominant caudal and bilateral lung distribution of lesions in 4-month-old Irish Wolfhound puppy after near-drowning. Right lateral view showing more profound lesions in the caudal lungs (*arrows*) in comparison to the cranial lungs. The marked increase in opacity associated with a loss of distinction of the pulmonary vessels, revealing only the air contained in the bronchi, corresponds to an alveolar pattern. *Inset,* Ventrodorsal view of the same dog showing lesions preferentially distributed to the left caudal, right caudal, and accessory lung lobes (*arrows*). A full-size ventrodorsal view is available on the online version (see eFig. 36.5).

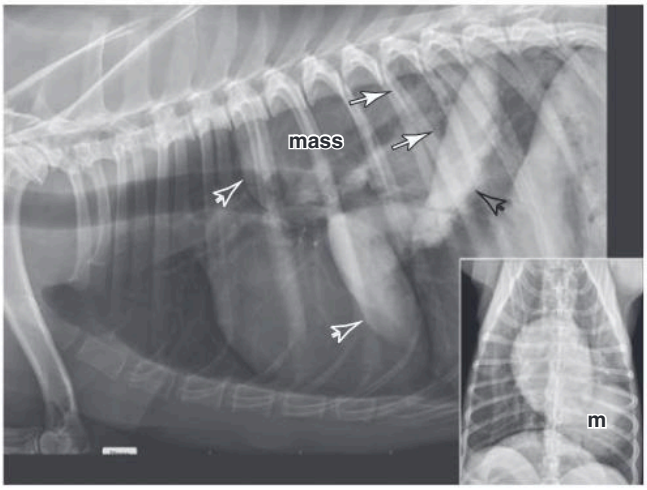


Fig. 36.10 A solitary soft tissue opaque pulmonary mass in a 12-year-old female spayed Labrador retriever. A large well-defined irregularly shaped solitary mass is seen in the left caudal lung lobe on the right lateral view. The soft tissue opaque mass has smooth margins cranially (*open white arrows*) and irregular margins caudally (*open black arrow*). Several small irregularly marginated gas bubbles are seen within the mass (*solid arrows*). No pulmonary nodules are seen in the reminder of the lung. *Inset*, The pulmonary mass (*m*) occupies the left caudal lung lobe. A full-size ventrodorsal view is available on the online version (eFig. 36.6). The dog underwent a left caudal lobectomy and recovered uneventfully. The mass was diagnosed as a grade II (moderately differentiated) pulmonary carcinoma on histopathology.

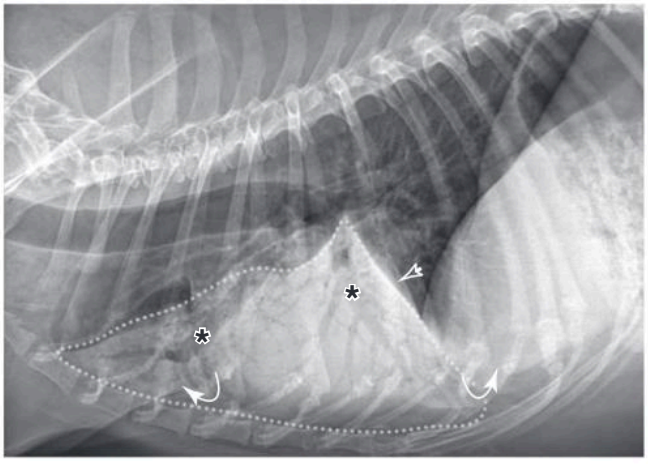


Fig. 36.9 Aspiration pneumonia in a 13-year-old female spayed mixed-breed canine. Left lateral view showing a severe increase in opacity in the region of the right cranial and right middle lung lobes (*dotted outline*) with air bronchograms (*asterisks*). There is border effacement (*curved arrows*) between the affected lung and the cardiac silhouette, and the diaphragm/liver. A lobar sign (*straight arrow*) is also noted between the affected right middle and spared right caudal lung lobes. These radiographic changes are characteristic of an alveolar pattern.

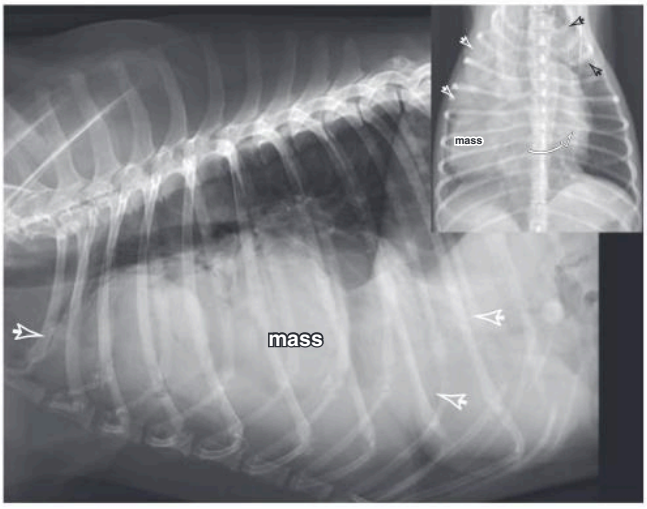
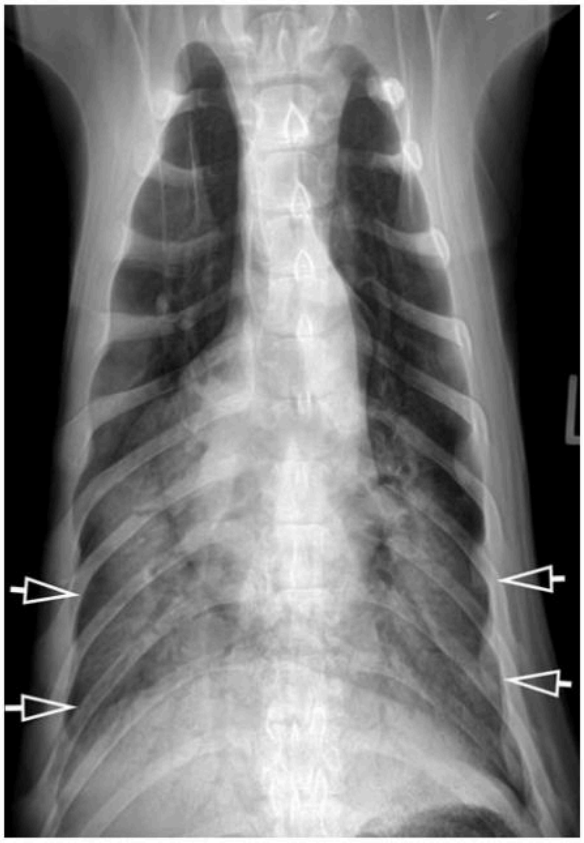


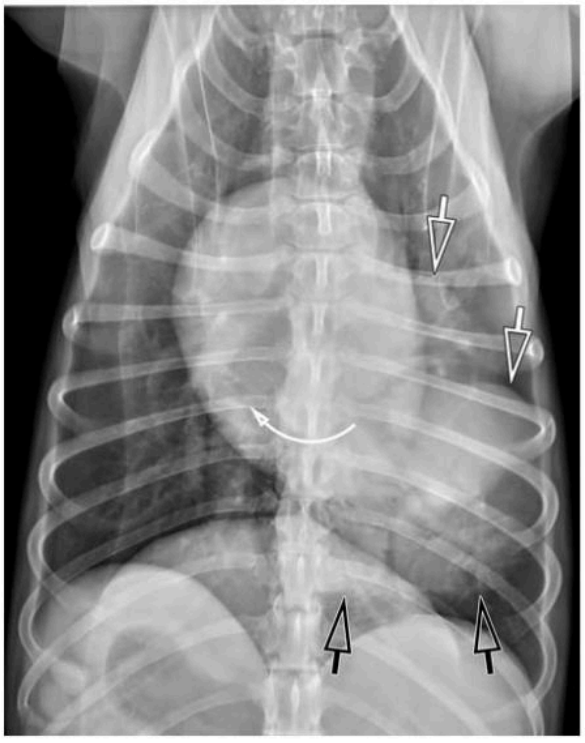
Fig. 36.11 Primary pulmonary histiocytic sarcoma in a 9-year-old female spayed miniature schnauzer. Left lateral view showing a large irregularly shaped and lobulated mass (*arrows*) occupying the entire cranioventral thorax extending caudally to silhouette with the diaphragm, and liver (*caudal arrows*). The soft tissue opaque mass also creates border effacement with the cranial mediastinum and cardiac silhouette. *Inset,* On the ventrodorsal view, the lung mass is distinguished in the region of the right middle and right caudal lung lobes with air surrounding its lateral aspect. The right cranial thorax is entirely soft tissue opaque with no distinction between the mass and the thoracic wall, cardiac silhouette, and mediastinum (*white arrows*). The left cranial thorax is occupied by an irregularly-shaped soft tissue opaque mass (*black arrows*), corresponding to enlarged mediastinal lymph nodes based on a following computed tomography (CT) study. The cardiac silhouette is slightly shifted to the left (*curved arrow*). A full-size ventrodorsal view (eFig. 36.7) and an inspiratory CT image (eFig. 36.8) are available on the online version.

Opacity

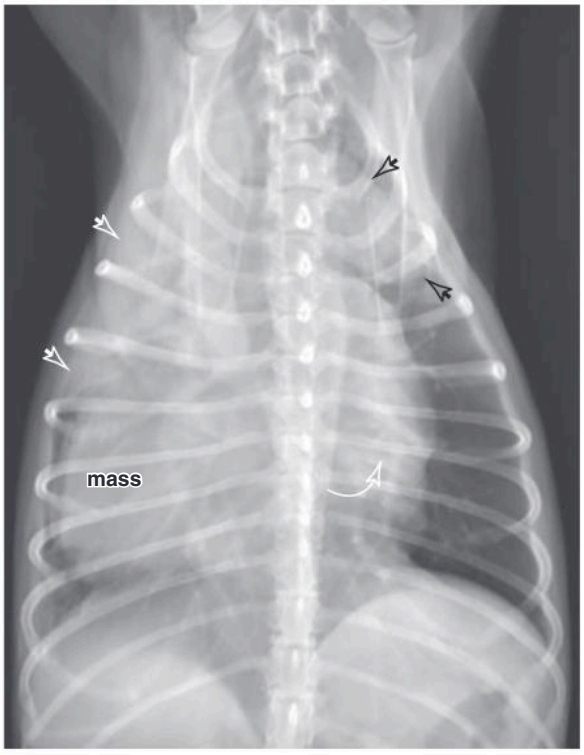
The lung opacity is intrinsically linked to lung volume. Lung underinflation results in an overall increase in opacity with crowded pulmonary vasculature, and crowded air bronchograms. In severe cases the pulmonary vasculature may be completely obscured by the lack of aeration of a lung segment or lobe(s) belonging to the side of which the animal was lying on (see eFig. 36.2). A mediastinal shift towards the dependent lung is an indirect sign of underinflation and atelectasis associated with recumbency.



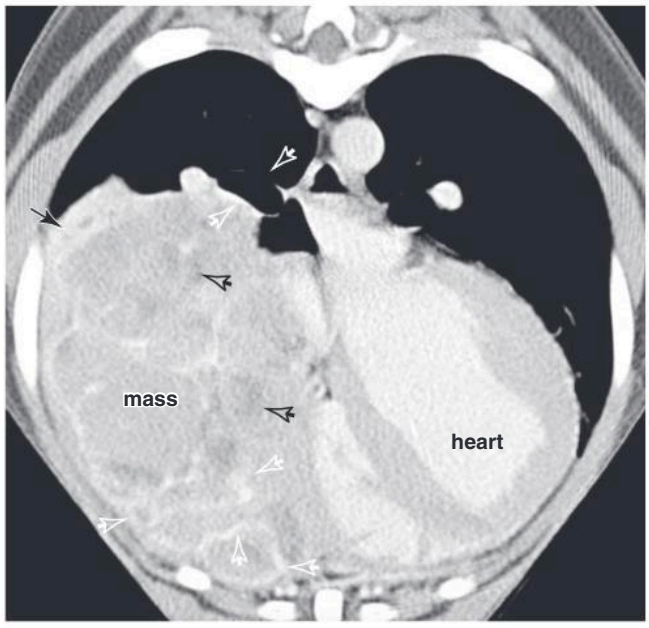
eFig. 36.5 Full-size ventrodorsal radiographic image of a 4-month-old Irish Wolfhound puppy after near-drowning. The lesions are bilateral, relatively symmetric, and more severe in the caudal and accessory lung lobes (*arrows*). In these regions, the pulmonary vasculature is indistinct.



eFig. 36.6 Full-size ventrodorsal radiographic image of a 12-year-old female spayed Labrador retriever with a grade II (moderately differentiated) pulmonary carcinoma. The pulmonary mass occupies the left caudal lung lobe, has a lobulated appearance cranially (*opened white arrows*) and irregular margins caudally (*opened black arrows*). The mass slightly displaces the cardiac silhouette to the right (*curved arrow*). Considering the large size of the mass, compression of the left cranial and accessory lung lobes is presumed, which was later confirmed on computed tomography.



eFig. 36.7 Ventrodorsal view of the same dog in Fig. 36.11. A pulmonary mass (primary pulmonary histiocytic sarcoma) is distinguished in the region of the right middle and right caudal lung lobes with air surrounding its lateral (costal) aspect. The right cranial lung field is entirely soft tissue opaque with no distinction between the mass and the thoracic wall, cardiac silhouette, and mediastinum. The left cranial lung field is occupied by an irregularly-shaped soft tissue opaque mass, which is surrounded by air cranially and caudally (*black arrows*), and corresponding to enlarged mediastinal lymph node based on the following computed tomography study (eFig. 36.8).



eFig. 36.8 Inspiratory computed tomography image of the same dog in Fig. 36.11. The image exhibits a heterogeneously contrast enhancing pulmonary mass lesion infiltrating the right lung, representing a primary pulmonary histiocytic sarcoma. The absence of a clear line of demarcation between the right cranial and right caudal lung lobes, hampered the determination of infiltrated lung lobes, as to whether the right caudal lung lobe was also involved with the right cranial lung lobe. The right middle lung lobe (*solid black arrow*) was also involved with the right cranial lung lobe. The right middle lung lobe (*solid black arrow*) was collapsed with absence of visualization of a portion of the right middle lobar bronchus. The right caudal lobar bronchus was compressed by the pulmonary mass (*in between straight white arrows*). The pulmonary mass had hypoattenuating areas on precontrast images that are accentuated postcontrast (*curved black arrows*). Markedly contrast enhancing linear regions (*white curved arrows*) are also seen at the periphery and within the mass, resulting in a lobulated appearance. The cardiac silhouette is shifted to the contralateral side.

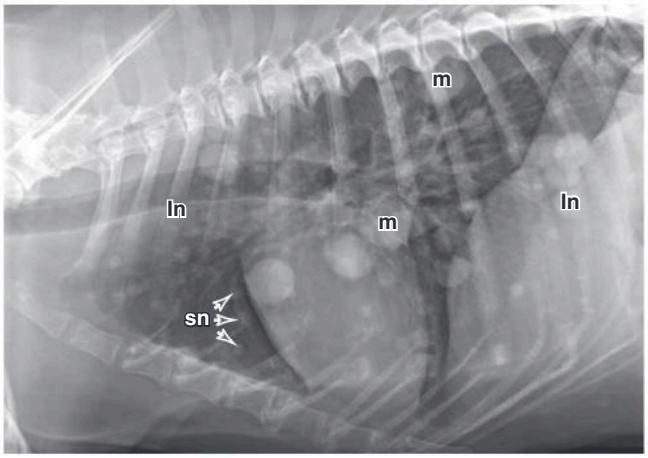


Fig. 36.12 Soft tissue pulmonary nodules and masses. Right lateral view of an 11-year-old female spayed German shepherd dog with multiple well-circumscribed soft tissue opaque small (*sn*; <1 cm) and large pulmonary nodules (*ln*; 1 < x < 3 cm), and a few pulmonary masses (> 3 cm), some of which are labeled. These nodules and masses are characteristic of a structured interstitial pattern. The pulmonary nodules and masses were presumed to represent pulmonary metastases from a previously diagnosed mammary adenocarcinoma.

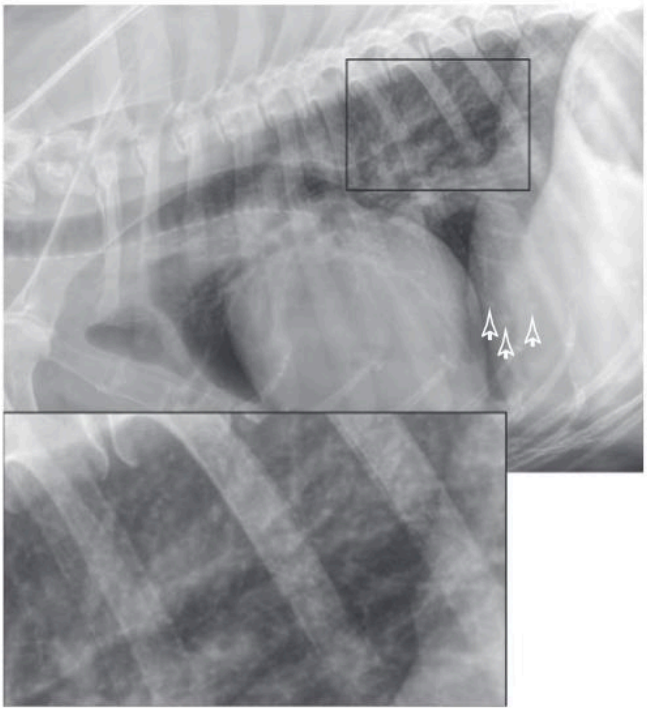


Fig. 36.13 Miliary structured interstitial pulmonary pattern in a 14-year-old male castrated Labrador retriever. The right lateral view shows diffuse miliary-sized nodules, of soft tissue opacity, throughout the lungs, resulting in a granular appearance (*inset*). A few small pulmonary nodules are also seen (*arrows*). Metastatic hemangiosarcoma was suspected based on findings of pericardial effusion and hemoabdomen.

Cellular infiltration, connective tissue deposition, and fluid collection in the lungs will generally result in increased soft tissue opacity. Mineral or metallic opacity can be caused by deposition of mineral concretions, dystrophic or metastatic mineralization of lung tissue, or inhalation of foreign material of metallic or mineral. Differential diagnoses for mineralization of the airways or pulmonary parenchyma are listed in Table 36.1. It is not uncommon to see small (~1–2 mm), circular to oval, well-circumscribed, mineralized nodules in the lungs of dogs, especially the cranial lung lobes (see Fig. 36.14B).[1] These opacities reflect osseous metaplasia (synonyms: heterotopic bone formation, pulmonary osteomas) and, in this instance, are not clinically significant.

Broncholithiasis (Fig. 36.15) and pulmonary alveolar microlithiasis represent additional conditions in which small mineral opacities are seen in the lungs. These rare disorders occur when calcium phosphate microliths collect in the airways or alveoli, respectively. The aggregates of micronodular calcifications in the alveoli may be more pronounced in the cranial lung lobes.[27,28]

Mineralization of the bronchial walls, bronchial lumen (i.e., *broncholithiasis*), pulmonary vasculature, or of unspecified location has also been found in cats with mycobacterial infections, at diagnosis or during treatment follow-up.[29] Prior infection (i.e., inactive) associated with *Histoplasma* spp may result in pulmonary nodule(s) with mineralized foci and should not be mistaken for pulmonary metastases.[30]

Rarely, metastatic neoplasia can result in mineralized lung lesions.[31] Differentiating osseous metaplasia nodules from metastatic nodules is of major clinical importance. In doubt, follow-up radiographs or CT examination are recommended.

A metallic opacity found within the airways or in the pulmonary parenchyma is in all instances foreign. Aspiration of liquid barium sulfate or iodine-based contrast agents has the potential to flow along the trachea and move downstream in the bronchial tree, after which it can collect in the parenchyma, if the amount is adequate. Serious complications associated with aspiration of large amounts of barium sulfate have been reported in dogs.[32] Metallic clips from prior lobectomy may also result in a small cluster of metallic opacities.

Contour

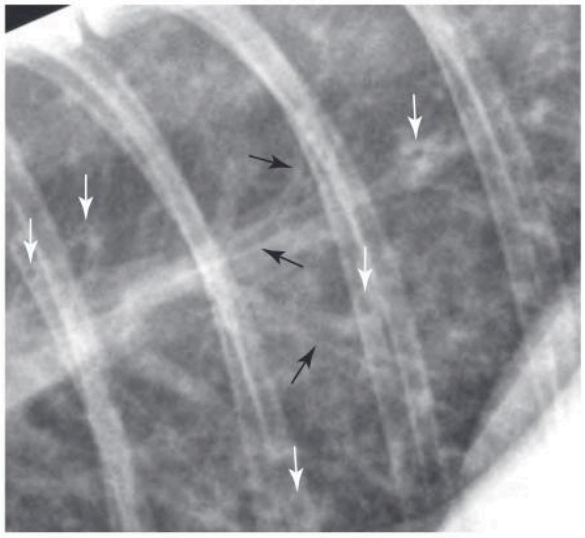
A lesion whose edges are sharp allowing easy distinction between unremarkable and affected lung is said to be well circumscribed with well-defined edges or clear margins. When it is difficult to outline a lesion, the edges of this lesion are poorly or ill-defined or blurred.[21] Distinction between benign and malignant lesions or between various types of lung tumors cannot be solely based on margin definition.[21]

Lesions Localized to the Airways

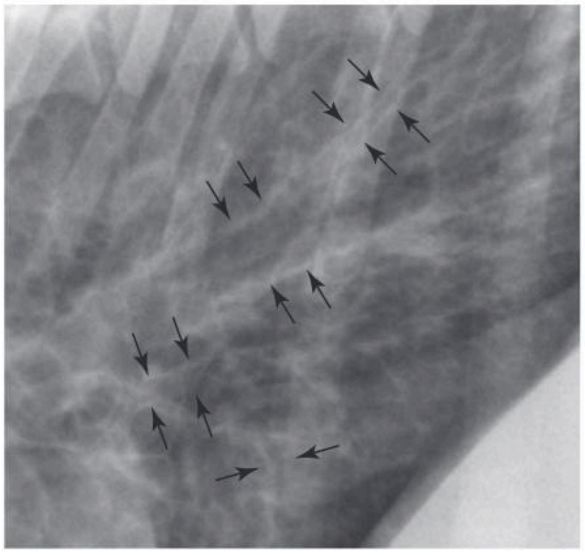
Involvement of large and medium-sized airways usually results in *bronchial wall thickening*, bronchial plugging, or bronchial dilation (i.e., *bronchiectasis)*.

Bronchial Pattern

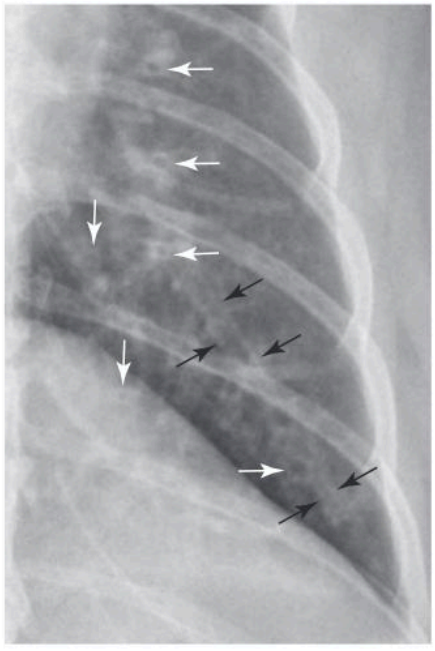
Bronchial wall thickening occurs as a result of edema, epithelial hypertrophy, glandular hyperplasia, smooth muscle hypertrophy and hyperplasia, adventitial thickening, mucus coating the surface of the airway lumen, or cellular invasion by inflammatory or neoplastic cells, or a combination of thereof. When viewed in a longitudinal plane, airway wall thickening may appear as tramlines or train tracks (Fig. 36.16, bottom left). When viewed end on, bronchial wall thickening will result in a "ring-like" appearance, or more commonly referred to as "doughnut-like" appearance (see Fig. 36.16, bottom right). A clear demarcation of the bronchial wall is only possible if air surrounds both the external and internal wall outlines, providing contrast with the soft tissue component of the wall. Recognition of many thick-walled bronchi, whether located on one or more lung lobes/segments, is termed *bronchial pattern* (Fig. 36.17, eFigs. 36.9–36.12).



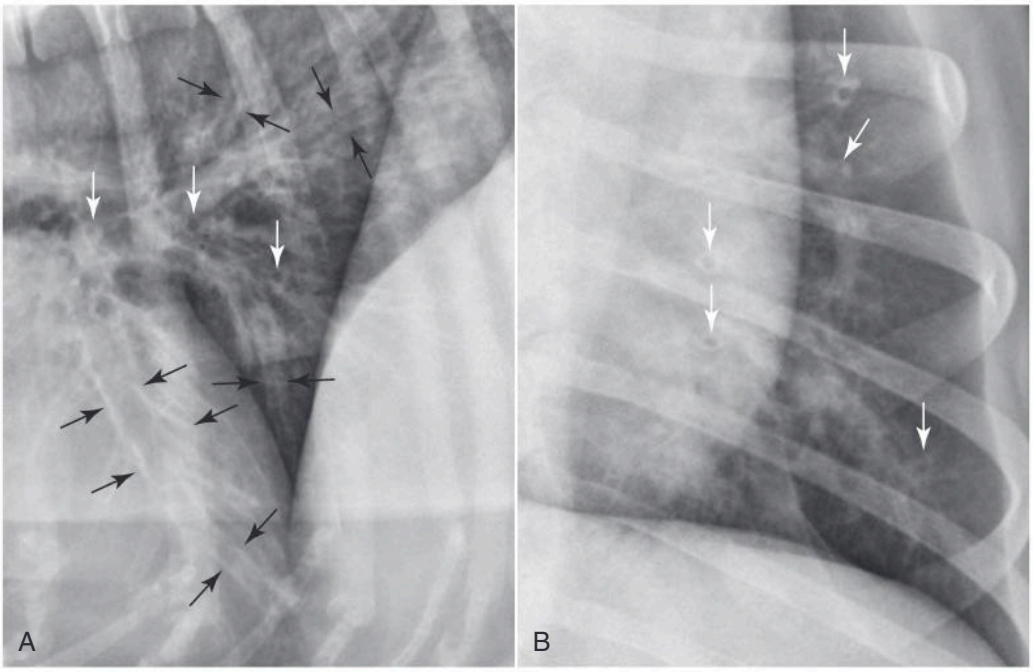
eFig. 36.9 Lateral radiograph of a cat with a mild to moderate bronchial pattern. There are numerous ring shadows (*white arrows*) and tram lines (*black arrows*). The entire lung field is abnormal, and only the most obvious ring shadows and tram lines have been pointed out.



eFig. 36.11 Lateral radiograph of a dog with a mild to moderate bronchial pattern. In this dog, the most conspicuous evidence of a bronchial pattern relates to the large number of tram lines (*black arrows*).



eFig. 36.10 Ventrodorsal (VD) radiograph of a cat with a moderate to pronounced bronchial pattern. There are numerous ring shadows (*white arrows*) and tram lines (*black arrows*). The entire lung field is abnormal, and only the most obvious ring shadows and tram lines have been pointed out.



eFig. 36.12 Lateral **(A)** and ventrodorsal (VD; **B**) radiographic images of a dog with a pronounced bronchial pattern. The numerous ring shadows (*white arrows*) and tram lines (*black arrows*) are evidence for a bronchial pattern.

Vetacademy.ir
مجموعه آموزشی پژوهشی
وت آکادمی
تلاش
#برای_دنیای_بهتر_حیوانات
تیم وت آکادمی
برای دسترسی به تازه ترین آموزش ها و
مطالب علمی دامپزشکی؛ وت آکادمی رو فالو کن
سایت مجموعه بزرگ آموزشی پژوهشی وت آکادمی
www Vet-academy.ir
صفحه ی اینستاگرام وت آکادمی
@Vetacademy.ir
دسترسی به آرشیو صد گیگ کتاب آموزش دامپزشکی به صورت رایگان
و جزوه های آموزشی در کانال تلگرامی
@Vetfiles
گروه بزرگ تلگرامی، پرسش و پاسخ و آموزش
@VetAcademyGp
صفحه رسمی آپارات وت آکادمی
aparat.com/vetacademy.ir

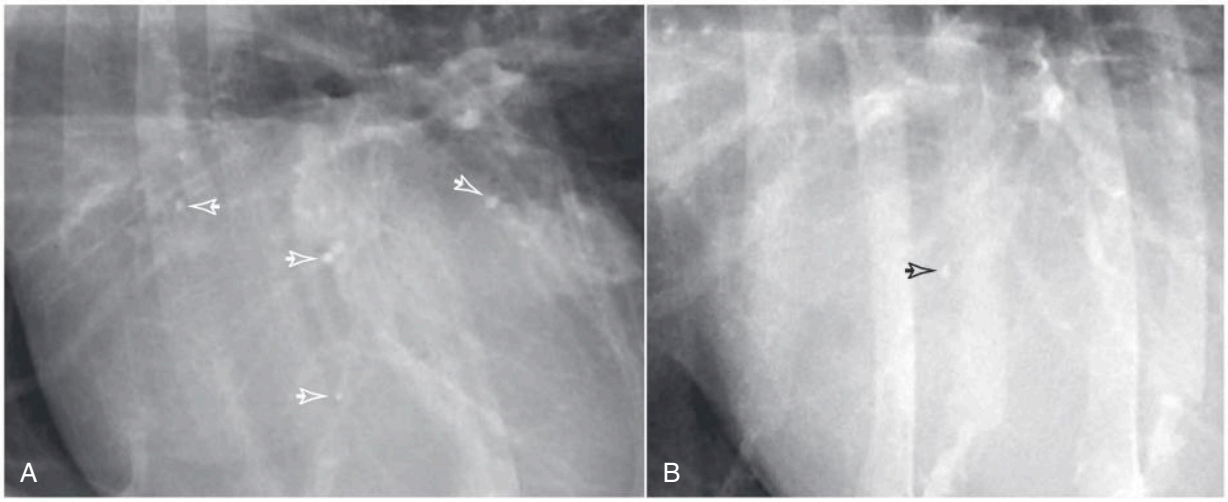


Fig. 36.14 Differentiating end-on vessels from pulmonary osteomas. **A,** End-on pulmonary vessels (*arrows*) are recognized by the degree of opacity for their small size, superimposition over a parent vessel of greater or similar size, and placement adjacent to a bronchus. **B,** A small, well-demarcated mineralized pulmonary nodule is shown (*arrow*), corresponding to a pulmonary osteoma. It is located in the ventral aspect of the cranial lung on this lateral view, which is a common location. In contrast to an end vessel, it is not superimposed over a parent vessel.

Table • **36.1**

Differential Diagnoses for Mineralization in the Lung.

ANATOMIC REGION	DIFFERENTIAL
Airways	Bronchial wall mineralization (e.g., incidental finding, with concurrent broncholithiasis, mycobacterial infections)
	Foreign material with mineral content
	Broncholithiasis (definition: deposition of mineral concretions in the lumen of bronchi or bronchioles)
	Reported with various diseases including airway disease, mycobacterial infections, pulmonary fibrosarcoma, pulmonary abscessation and pyothorax, and aspiration of mineral oil
Parenchyma	Pulmonary osteomas (synonyms: osseous metaplasia, heterotopic bone formation)
	Dystrophic or metastatic mineralization (e.g., end-stage pulmonary fibrosis, chronic renal disease, uremic pneumopathy, vitamin D toxicosis, hyperadrenocorticism, accidental ingestion of Tacalcitol ointment)
	Inactive histoplasmosis (i.e., well-circumscribed pulmonary nodules with mineralization)
	Metastatic neoplasia
	Exogenous corticosteroids
	Mycobacterial infections
	Associated with pleural effusion: mesothelioma/carcinomatosis
	Pulmonary alveolar microlithiasis (i.e., deposition of mineral concretions in the lumen of alveoli) with no familial basis identified in dogs or cats
	Reported with various diseases such as bronchopneumonia, chronic corticosteroid therapy, metastatic neoplasia

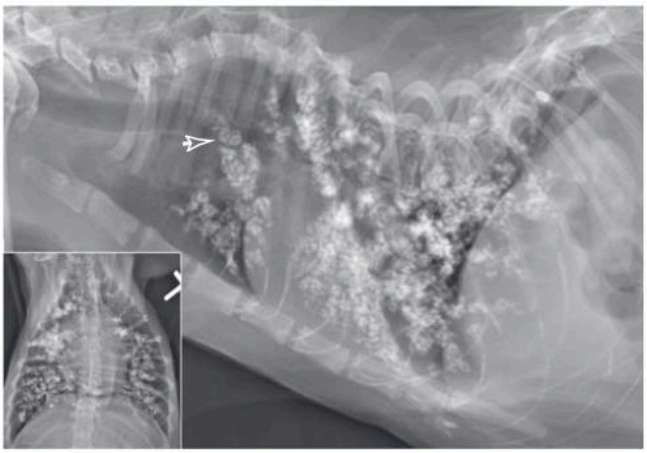


Fig. 36.15 Feline broncholithiasis. Right lateral view of an 11-year-old male castrated Birman cat showing multiple small clusters of mineralized opacities resulting in a "rosette-like" appearance (*arrow*). *Inset,* Ventrodorsal view demonstrating involvement of all lung lobes, with minimal asymmetry in the distribution of lesions between the left and right lungs. The rosette-like appearance on radiography is presumably from intraluminal mineralized concretions occupying nearby ectatic airways (i.e., bronchi and bronchioles).

When the thick-walled bronchus is no longer surrounded by air, it can lead to an irregular appearance of the wall or an inability to distinguish it from the surrounding parenchyma, resulting in peribronchial opacification, sometimes described as a bronchointerstitial pattern. With the increase in thickness of its walls, a bronchus of lower generation (>3) may become visible.

Inhaled foreign material that has passed the larynx or aspirated foreign material may reach intrathoracic airways and often reach the caudal or accessory lung lobes (Fig. 36.18). Foreign material of soft tissue opacity may go undetected on radiography, unless it is surrounded by air. Suspicion of inhaled foreign material not recognized on radiography may warrant advanced imaging such as bronchoscopy and/or CT.

Accumulation of fluid (i.e., pus, blood, saline/water, chyme) or soft tissue (i.e., cellular debris, solid gastric content) in the lumen of bronchi may appear tubular in shape in a longitudinal



Fig. 36.16 Schematic illustration of bronchial wall thickening. The *top panel* shows a normal bronchus in longitudinal and cross-section (end-on) with its paired pulmonary artery. Normal airways should have thin walls that are not usually perceived on radiography. *Bottom panel,* thickening of the bronchial wall may result in tramlines-like appearing structures when the bronchus is cut in a longitudinal plane or in a ring-like or doughnut-shape like appearance when cut in cross-section. The thickened bronchial wall, in close proximity with the paired pulmonary artery, may become effaced, due to a silhouette sign.

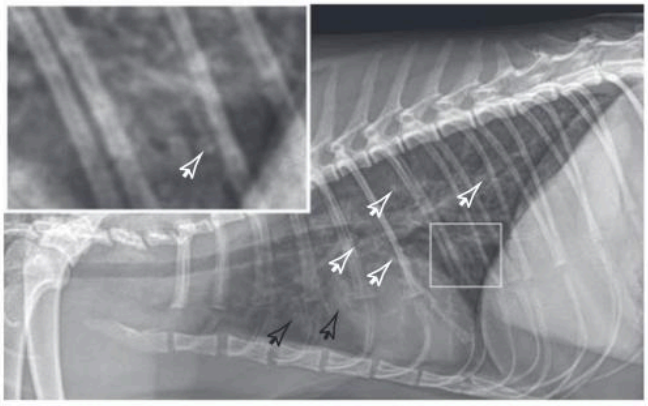


Fig. 36.17 Bronchial pattern in a 2-year-old female spayed Ocicat with allergic asthma. A large number of ring-like or doughnut-shape like (*white arrows*) and tramlines (*black arrows*) lesions are seen diffusely throughout the lung. *Inset,* Close-up on thickened airway walls viewed end on (*arrow*).

plane (Fig. 36.19) and circular when viewed in cross-section, independently of the nature of the content. This is more easily seen if the proximal aspect of the bronchus still contains air, providing contrast at the interface with the distal content. Purulent material/cellular debris/fluid/mucus may collect in bronchi in cases of infectious bronchopneumonia or eosinophilic disease,[33] more so in dilated bronchi.[34]

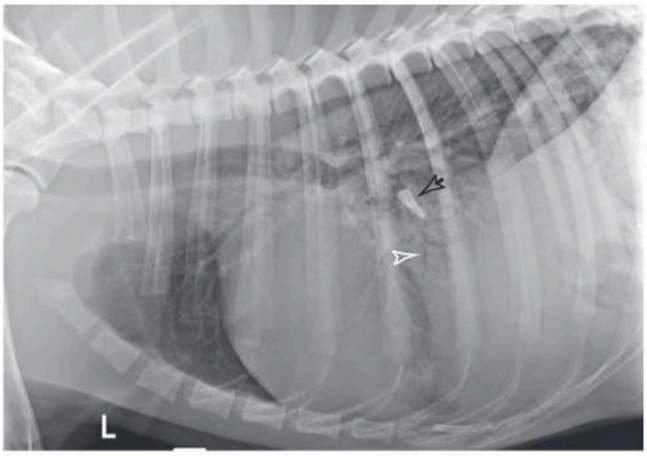


Fig. 36.18 Mineralized foreign object (a canine tooth) in the accessory lung lobe of a 2-year-old intact male German Shepherd dog. The dog was recently diagnosed with a fracture of the right maxillary canine tooth (#104). On the left lateral view, the fractured fragment of canine tooth (*black arrow*) is present in the accessory lung lobe. This lung lobe is also increased in opacity, with air bronchograms (*white triangle*) causing border effacement with the diaphragm and caudal border of the cardiac silhouette. On bronchoscopy, there was purulent exudate collected in the accessory lung lobe and the tip of the tooth could be seen in the lobar bronchus. Multiple attempts to remove the tooth with a basket retrieval device and biopsy forceps were unsuccessful. Upon recovery, the dog coughed the tooth up which was subsequently swallowed and visible in the gastrointestinal tract. The tooth was passed uneventfully. The dog was prescribed antimicrobials for bacterial pneumonia following aerobic and anaerobic bacterial growth on direct culture of isolates from collected bronchoalveolar lavage fluid.

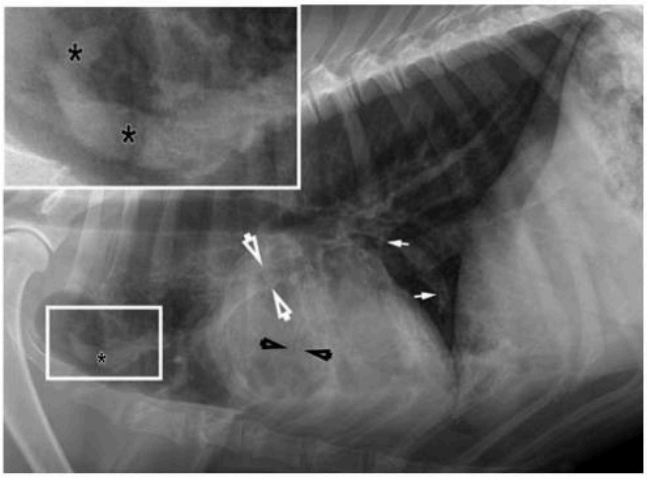


Fig. 36.19 Bronchial luminal filling in a 10-year-old female spayed Labrador retriever with bacterial pneumonia. Right lateral view showing a dilated bronchus (*large white arrows*) with intraluminal soft tissue material at its distal aspect (*asterisks*). Bronchial wall thickening is also visible in the ventral lungs as revealed by tramlines (*open black arrows*) and ring-like lesions (*solid white arrows*). *Inset,* Close-up image of the bronchial intraluminal soft tissue filling (*asterisk*).

Bronchial plugging refers to the collection of mucoid material in the lumen of a dilated bronchus. It has been reported in asthmatic cats with hyperplasia of the submucosal glands and proliferation of goblet cells. In this instance, resorptive atelectasis may occur in the nonventilated alveoli and airspaces beyond the occlusion (Fig. 36.20).

Bronchiectasis refers to the irreversible dilation of medium- and large-sized bronchus, a consequence of the destruction of the muscular elements of the bronchial walls. The imaging

result is a dilated bronchus that fails to taper as it extends away from its origin (referring to the parent bronchus from which it branches).[22] Bronchiectasis should not be confused with an air bronchogram, which consists in an air-filled bronchus surrounded by collapsed (nonventilated) or soft tissue-filled alveoli. Unlike an air bronchogram, an ectatic bronchus will remain dilated on serial radiography, even in the absence of active infection. Dogs with primary ciliary dyskinesia have defective respiratory cilia that impair mucociliary clearance and predispose to recurrent infection, often resulting in bronchiectasis.[35]

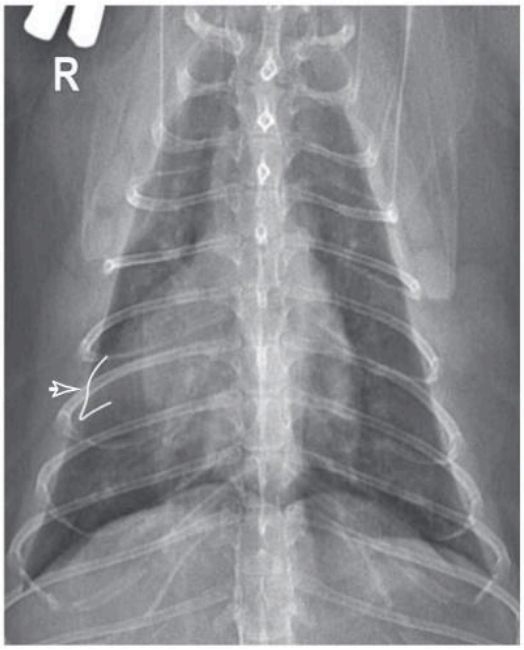


Fig. 36.20 Resorptive atelectasis of the right middle lung lobe in a 6-year-old female spayed Ocicat with allergic asthma. This is the same cat as in Fig. 36.17, but 4 years later. The right middle lung lobe (*arrow*) is collapsed, resulting in a triangular-shaped soft tissue opacity (*white outline*). A rightward mediastinal shift is visible. The right middle lobar bronchus was presumably plugged with mucus, the production of which is abnormally increased in asthma, causing a resorptive atelectasis of the right middle lung lobe.

Ectatic airways can take a cylindrical (or tubular; Fig. 36.21), saccular (sometimes also called cystic), or varicose shape, with some authors classifying saccular and cystic as two distinct forms[34] (see Fig. 36.21, eFigs. 36.13 and 36.14).[36] Bronchiectasis is often accompanied by bronchial wall thickening, which may explain accentuation of a bronchial pattern on radiography.

Lesions Localized to the Pulmonary Parenchyma

Parenchymal lesions include abnormalities of the terminal respiratory units including the alveoli (specifically the lumen of the alveoli), the interstitium (the septa bordering the alveolus), and the small vessels. Lesions affecting the pulmonary parenchyma may share a similar radiographic appearance regardless of etiology, chronicity, or anatomic structure affected. Several hypotheses can be put forward to explain this finding:

1. Radiography cannot distinguish between different types of cellular infiltration, fluid collection, fibrin and collagen deposits, formation of small thrombi, or emboli.
2. There is a close spatial relationship between the alveolar lumen and the septa.
3. Many diseases affect all three components of the parenchyma to varying degrees.

Despite their names, interstitial and alveolar patterns may not always correlate to the same histopathological location of disease.[37] Diseases affecting small airways, small pulmonary veins (e.g., pulmonary veno-occlusive disease), or pulmonary capillaries may lead to recognition of a structured or unstructured interstitial pattern on radiography.[38,39] As a precaution, it is therefore desirable to use the alveolar and interstitial patterns for descriptive terminology of lesions affecting the lung parenchyma, rather than true histological correlates.

Interstitial Pattern

Two major distinct forms characterize the *interstitial pattern* on radiography, the *structured (nodular) interstitial pattern* or the *unstructured interstitial pattern*, both of which can occur concurrently or accompanying another pattern. The nodular or structured interstitial pattern is characterized by the presence of nodules or masses in the lungs. A nonexhaustive list of differential diagnoses is provided for a structured interstitial pattern (Table 36.2). The number, size, location, and contour of nodules or masses can vary considerably within a group of diseases (e.g., neoplasia) or between diseases of different etiologies (e.g., histoplasmosis vs. neoplasia). Nodules are commonly seen with pulmonary metastatic disease

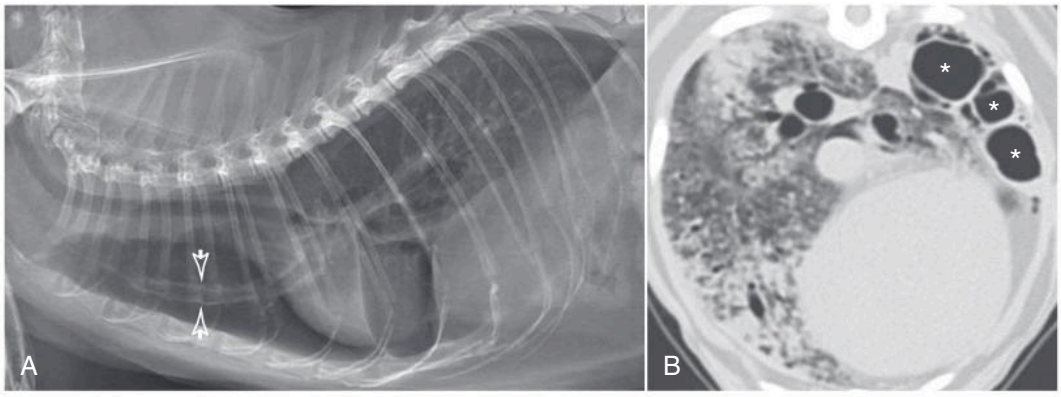
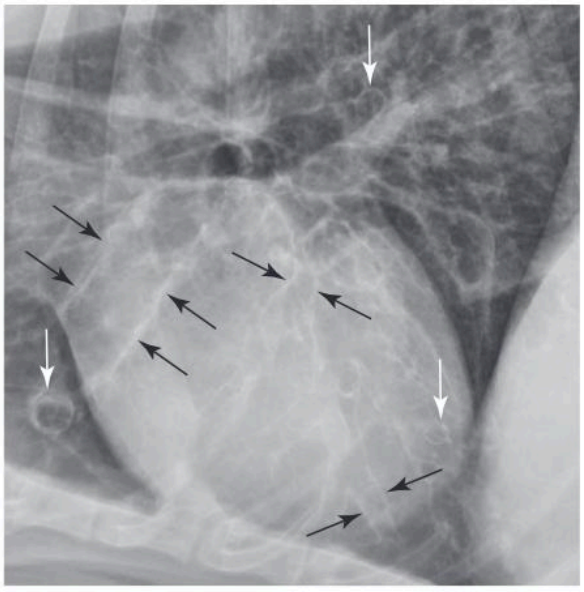
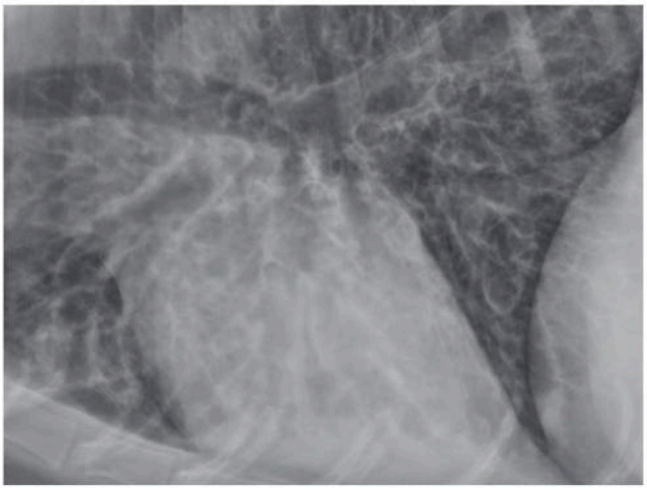


Fig. 36.21 Cylindrical and cystic bronchiectasis. **A,** Cylindrical bronchiectasis characterized by dilation of a cranial lobar bronchus *(between arrows)* in a 10-year-old male castrated Egyptian Mau cat. The bronchial walls are thickened and do not taper as they course away from their origin. On postmortem histopathologic examination, the cat was diagnosed with acute suppurative bronchopneumonia with chronic allergic asthma. **B,** Cystic bronchiectasis of the left caudal lobar bronchus (*asterisks*) on a transverse computed tomography image of an 8-year-old intact male miniature poodle canine with post-infectious bronchiolitis obliterans.



eFig. 36.13 Lateral radiographic image of a dog with bronchiectasis. There are numerous dilated ring shadows (*white arrows*) and wide tram lines (*black arrows*). The bronchial walls do not taper as they normally would and are thus still visible in the periphery of the lungs. Bronchial wall dilation (i.e., bronchiectasis) is irreversible and usually remains static on longitudinal studies.



eFig. 36.14 Lateral thoracic radiographic image of a dog with severe diffuse bronchiectasis and pneumonia. The opacity of the lung is increased in the ventral aspect of the thorax, superimposed on the heart, and there are multiple air bronchograms. The lumina of visible bronchi are dilated and somewhat saccular. In the dorsocaudal aspect of the lung, there is no alveolar disease, but the lumina of multiple bronchi are markedly dilated, which is indicative of bronchiectasis.

Table • 36.2

Differential Diagnoses for a Structured Interstitial Pattern (Nodule <3 cm in Diameter; Mass ≥3 cm in Diameter).

Pulmonary osteomas (synonyms: heterotopic bone formation, osseous metaplasia)*
Metastatic neoplasia
Pulmonary blastomycosis
Lymphoma
Hematogenous pneumonia
Primary lung tumor
Epithelial lung tumors (malignant > benign) such as adenocarcinoma (papillary, acinar), bronchioloalveolar carcinoma, bronchial gland carcinoma, or squamous cell carcinoma
Histiocytic sarcoma
Heartworm disease
Pulmonary histoplasmosis (active form; inactive is often associated with mineralization of the pulmonary nodules)
Eosinophilic lung disease not associated with *Dirofilaria immitis*
Hematoma
Paragonimiasis
Pulmonary coccidioidomycosis
Paenibacillus amylolyticus osteomyelitis with pulmonary granulomatous inflammation
Leptospirosis pulmonary hemorrhage syndrome
Pulmonary alveolar microlithiasis and pulmonary interstitial mineralization
Pulmonary meningotheliomatosis
Pulmonary veno-occlusive disease and pulmonary capillary hemangiomatosis
Bronchiolar disorders (CT only)

*Usually small mineralized nodules of 1–2 mm in diameter.

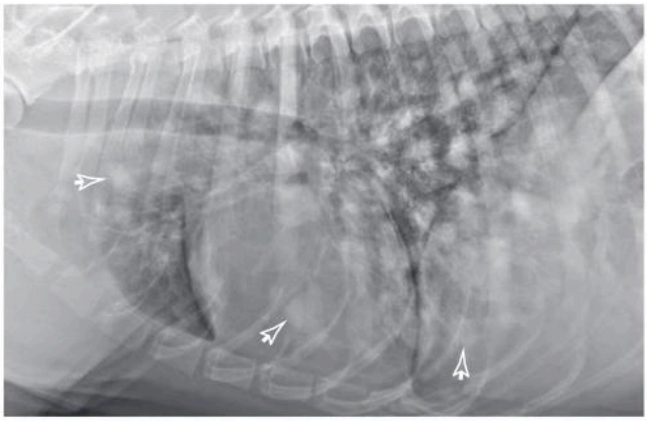


Fig. 36.22 Ill-defined nodular-shaped pulmonary lesions associated with eosinophilic lung disease in a 2-year-old male intact Rottweiler. There are numerous ill-defined soft tissue pulmonary nodules throughout the lung (*arrows*), in addition to bronchial wall thickening, an airway-centered unstructured interstitial pattern transitioning to multifocal areas of consolidation (or alveolar pattern). The dog had greatly improved after treatment with almost complete resolution of the nodular and consolidated parenchymal lesions.

(see Fig. 36.12).[25] However, pulmonary nodules may be radiographically detected with other conditions, such as eosinophilic diseases (Fig. 36.22),[39,40] fungal diseases (Fig. 36.23),[41] and embolic bacterial pneumonia (Fig. 36.24).[42] Although pulmonary metastatic disease is primarily associated with a structured or nodular interstitial pattern, it may also give rise to a bronchial, alveolar, or mixed pattern due to infiltration of alveoli by tumor cells or following alveolar collapse.[23] Pulmonary masses have been associated with primary and secondary lung tumors, eosinophilic lung diseases, and parasitic and fungal infections.[20,40]

The second type, called the *unstructured interstitial pattern*, is associated with a diffuse hazy increase in lung opacity, with a consequent reduction in the distinction of the smallest pulmonary vessels, without obscuring them entirely.

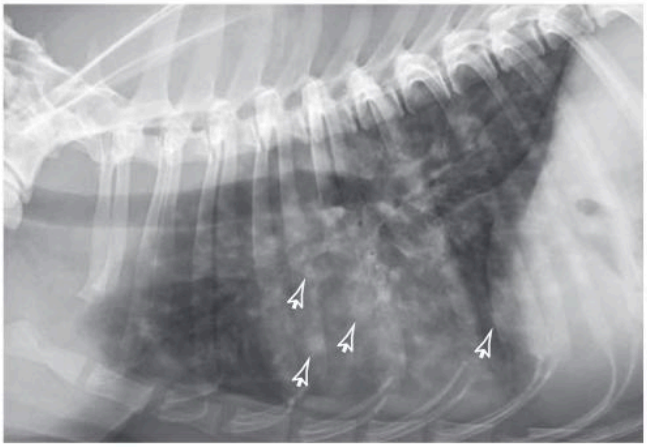


Fig. 36.23 Ill-defined nodular-shaped pulmonary lesions associated with blastomycosis in an 8-year-old female spayed mixed-breed dog. Numerous soft tissue pulmonary nodules, of varying size, and with ill-defined margins, are visible throughout the lung, some of which are indicated by *arrows*. The pulmonary vasculature is difficult to distinguish, especially in the caudal lung, referring to as an unstructured interstitial pattern. Multiple soft tissue pulmonary nodules were seen on computed tomography, performed later that day, with parenchymal lesions of ground-glass opacity and consolidation. The dog was positive for *Blastomyces* antigen on quantitative sandwich enzyme immunoassay (EIA).

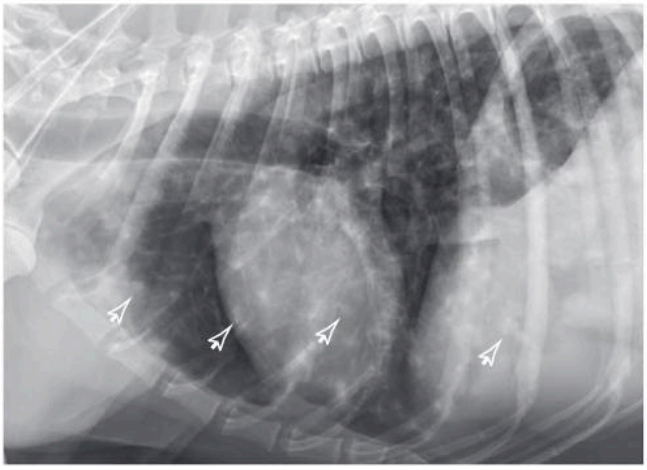


Fig. 36.24 Pulmonary nodules associated with embolic bacterial pneumonia in a 4-year-old neutered male Australian Poodle mix dog. There are multiple small soft tissue opaque pulmonary nodules (*arrows*), distributed multifocally in the entire lung. Lesions were distributed in all lung lobes based on the three thoracic views. On postmortem examination, the lung lesions were consistent with an embolic pneumonia, likely from a paraspinal abscess with extension into the epidural space.

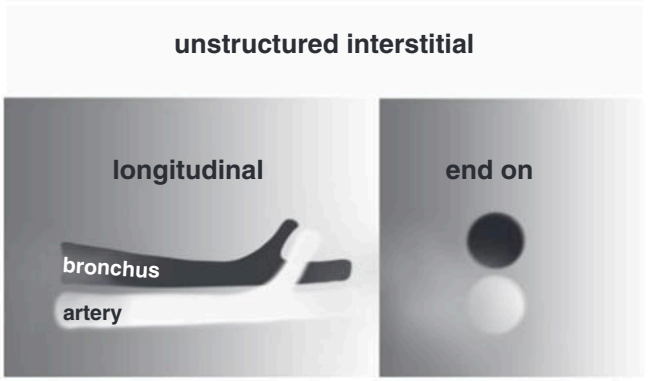


Fig. 36.25 Schematic representation of an unstructured interstitial pattern. When the opacity of the lung is increased focally, multifocally or diffusely, the affected region will show a reduction in the sharpness of the pulmonary artery margination on both longitudinal or cross-sectional planes.

It may also exhibit multiple, short indistinct nonvascular linear or reticular opacities in one or more lung lobe or segment (Fig. 36.25).[23] Overall increase in opacity associated with under inflated lungs, obesity, or motion artifact can have the appearance of an unstructured interstitial pattern and should be taken into account when interpreting lung patterns. The unstructured interstitial pattern can be detected with a variety of lung diseases such as infection, inflammation, neoplasia, edema, trauma, or toxicity (Table 36.3; Fig. 36.26, eFigs. 36.15 and 36.16).

The Paradox of Aging Lungs

Increased nonvascular linear markings in the lungs in association with pleural thickening and bronchial cartilage calcification in dogs has previously been attributed to aging.[1] At the time, the authors attributed these markings to increased connective tissue, mainly focal alveolar fibrosis, in lungs of old dogs associated with prior inflammation.[1] Two recent studies found no differences in pulmonary lesions scores between young and old dogs on radiography or CT, although older dogs were shown to have increased bronchial mucosal irregularity, prominent vessels, and bronchiectasis on bronchoscopy.[43] It remains unclear whether these discordant findings are associated with different environmental contexts, digitization of radiographic systems, or with the modality. It appears reasonable to suspect that as dogs live longer, they have a higher likelihood of accumulating structural lesions over time, possibly resulting in a subtle increase in nonvascular pulmonary markings. It may then become difficult to differentiate these structural lesions from clinically relevant active lesions. In these instances, advanced imaging (i.e., CT, bronchoscopy, positron emission tomography [PET]) and ancillary tests may be beneficial.

Alveolar Pattern

The *alveolar pattern* is characterized by increased pulmonary opacity with effacement of vascular markings, air-bronchograms, and a lobar sign. Increased opacity is of no particular shape, showing ill-defined or wispy margins in comparison to the surrounding parenchyma, rendering the pulmonary vessels within the affected area indistinct (Fig. 36.27). These areas do not appear as discrete circular or oval shaped lesions, as these would often be categorized as belonging to a structured interstitial pattern. Affected parenchymal areas silhouette (i.e., border effacement) with adjacent soft tissue lesions or structures (i.e., cardiac silhouette, diaphragm, cranial mediastinum, pleural fluid). The affected area may or may not

Table • 36.3

Differential Diagnoses for an Unstructured Interstitial Pattern (Often Seen in Combination With Other Patterns).

Lymphoma
Chronic bronchitis
Cardiogenic or noncardiogenic pulmonary edema
Bacterial pneumonia
Aspiration pneumonia
Interstitial lung disease including eosinophilic lung disease
Pulmonary contusions or hemorrhage
Pulmonary fibrosis
Fungal pneumonia
Metastatic neoplasia
Bronchiolar disorder
Parasitic lung disease (e.g., aelurostrongylosis, paragonimiasis, associated with *Crenosoma vulpis*)
Heartworm disease (*Dirofilaria immitis*, *Angiostrongylus vasorum*)
Respiratory viral infection
Pulmonary veno-occlusive disease and pulmonary capillary hemangiomatosis
Pulmonary alveolar proteinosis
Confounding factors that may mimic this pattern on radiography:
Decreased lung volume (e.g., associated with panting, exhalation, sedation, general anesthesia, prolonged recumbency, severe abdominal distension)
Obesity
Motion artifact
Superimposition with subcutaneous emphysema

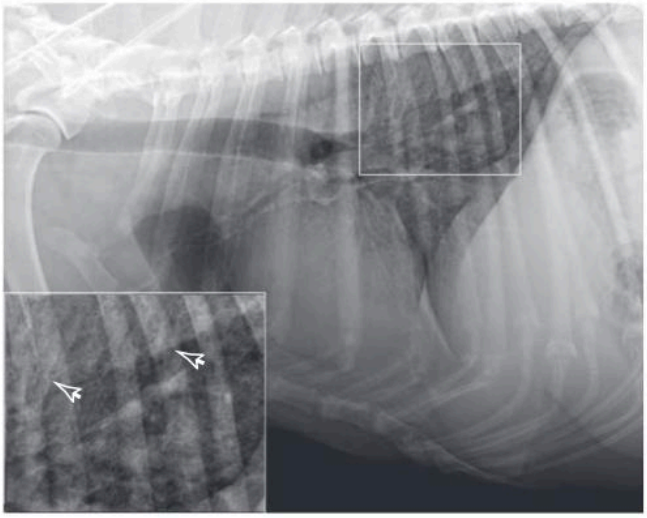


Fig. 36.26 Unstructured interstitial pattern in an 8-year-old male castrated Golden retriever with B-cell lymphoma. Right lateral view showing a diffuse unstructured interstitial pattern, more severe in the caudal lung. *Inset,* Close-up view of the caudodorsal portion of the lung exhibiting a marked decrease in black shadows (i.e., decrease in lung aeration). The heavy background of increased opacity makes it difficult to distinguish individual pulmonary vessels (*arrows*).



eFig. 36.15 Ventrodorsal (VD) radiographic image of a dog with a severe unstructured interstitial pattern associated with metastatic hemangiosarcoma. The lung field is increased in opacity and small pulmonary vessels are less distinct. There is no air bronchogram or silhouette sign with the diaphragm or cardiac silhouette and therefore, no alveolar pattern. One might misinterpret the pattern as being bronchial following an abnormal number of small ring shadows although no tram lines are appreciated.



eFig. 36.16 Ventrodorsal (VD) radiographic image of a dog with confirmed blastomycosis infection. The pulmonary pattern is an unstructured interstitial pattern.

be associated with the recognition of an *air-bronchogram(s)* or *lobar sign*. An air-bronchogram consists of a bronchus containing air that contrasts with the soft tissue opacity generated by the surrounding alveolar filling or alveolar collapse, making it visible (see Figs. 36.8 and 36.9). A *lobar sign* is seen when the borders of two lung lobe(s)/segment(s) become distinct from one another due to increased opacity in one lobe/segment while the other is relatively spared (Fig. 36.28, eFigs. 36.17–36.19). Diseases associated with an alveolar pattern can be of various origins (e.g., infectious, inflammatory, neoplastic, traumatic, toxic, foreign, or associated with fluid overload/congestive heart failure, fibrosis) and acute or chronic (Table 36.4).[42] Obstruction of an airway with subsequent resorptive atelectasis of the nonventilated alveoli may also result in an alveolar pattern.[23]

An alveolar pattern does not necessarily reflect an alveolar filling disorder, and alveolar filling disorders may result in different patterns than an alveolar pattern on radiography (Table 36.5).[2]

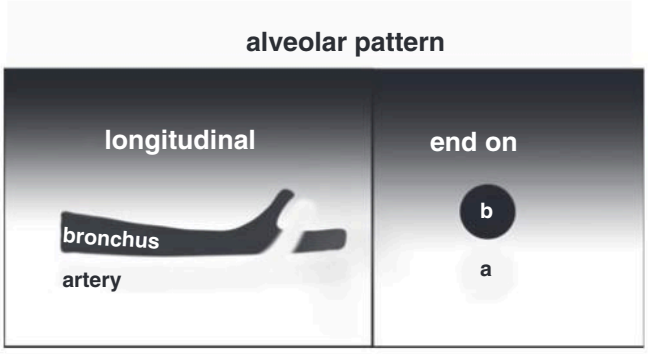


Fig. 36.27 Schematic representation of an alveolar pattern. The opacity of the lung is increased to the point where the pulmonary artery (*a*) becomes indistinct, silhouetting with the abnormal lung parenchyma. When air remains in the bronchus (*b*), an air bronchogram is visible, resulting from the contrast between the air black shadow and the surrounding alveolar filling or alveolar collapse.

Vascular Pattern

Enlargement of the pulmonary vasculature may disrupt the regular linear background markings of the lung, making it stand out more than normal. A vascular pattern could therefore be included in a comprehensive discussion of pulmonary patterns, but the vascular pattern is covered in Chapter 35 and not included here.

Focal, Multifocal, or Diffuse Areas of Decreased Radiographic Opacity

Cystic Air-Filled Lesions

Cystic air-filled lesions (synonym: pneumatocyst) can occur as the result of a congenital or acquired process.[44,45] Their content is typically air which is not limited by septa, airways, and capillaries, resulting in a focal radiolucency. They are usually well circumscribed, relatively circular in shape, and surrounded by a thin wall (<3 mm).[46] Malignant transformation of air-filled cystic lesions has been shown in two dogs.[47] In human medicine, cystic air-filled lesions comprise bulla, pneumatoceles, blebs, cavity or cavitating or cavitary nodule/mass/consolidation, and lung cysts. In veterinary medicine, several of these terms have been used interchangeably, the most often all-encompassing term being *bullae* for any thin-walled, relatively circular, air-filled structure, regardless of its size or presence or absence of concurrent lung diseases (Fig. 36.29).

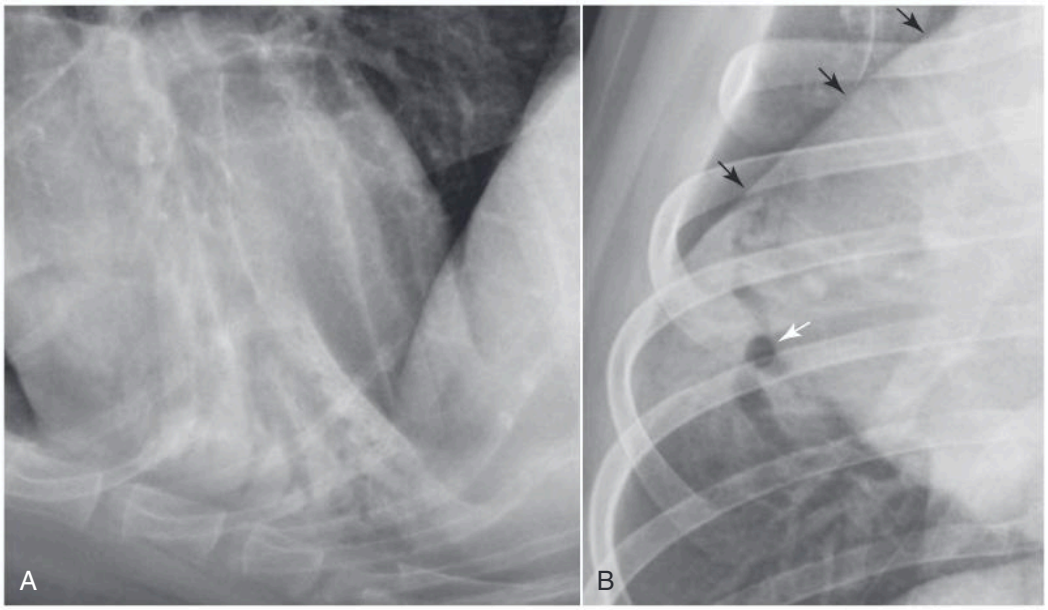
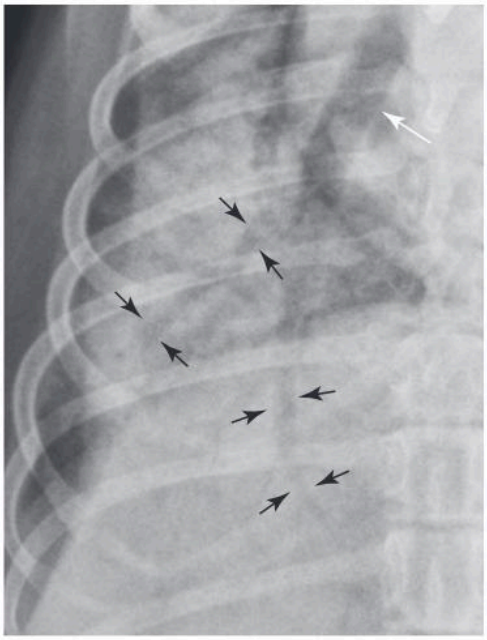
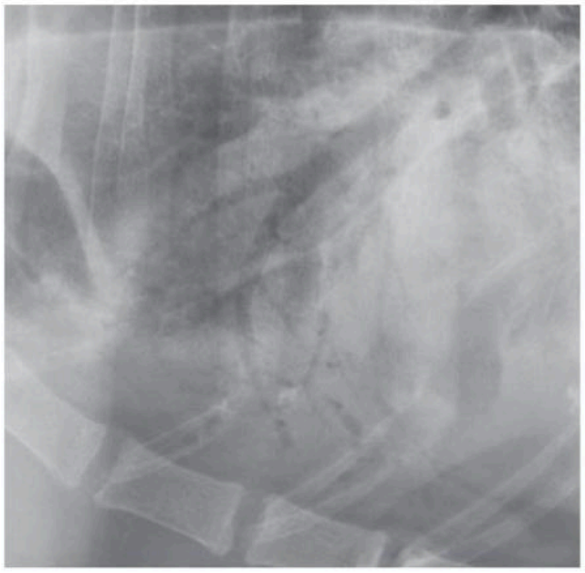


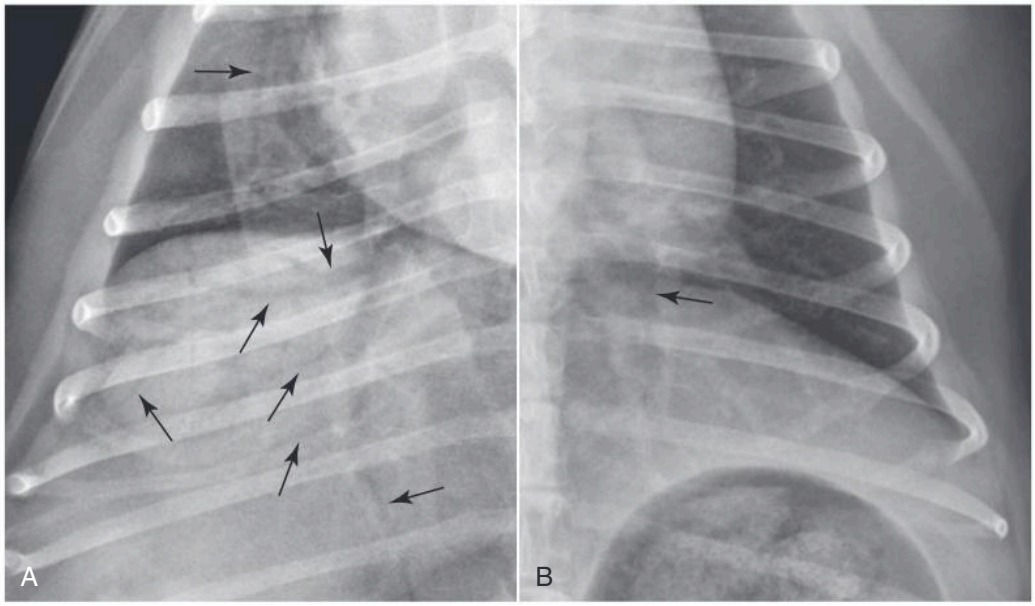
Fig. 36.28 Ventral **(A)** and right middle **(B)** regions of the thorax of a dog with an alveolar pattern. Numerous air bronchograms are seen throughout the increased lung opacity. In **A,** the branches of the air bronchogram are more crowded than normal because the lobe is also partially collapsed. In **B,** note how the increased opacity of the lung has caused border effacement, or silhouetting, of the right aspect of the cardiac silhouette. Border effacement of the heart is a common finding with an alveolar pattern when the abnormal lung and heart are in contact. The junction between the opacified right middle lobe and the normally aerated right cranial lobe creates a distinct transition, termed a *lobar sign* (*black arrows*). Also in **B,** an air bronchogram is struck end-on by the x-ray beam, creating a conspicuous circular radiolucency (*white arrow*).



eFig. 36.17 Right caudal aspect of the thorax of a dog with an alveolar pattern. Numerous air bronchograms are visible in the right caudal lung lobe (*black arrows*); not all air bronchograms have been designated with *arrows*. Care must be exercised in interpreting *normal* large bronchi as air bronchograms, especially when they are superimposed over the heart (*white arrow*). The wall of these large bronchi may be sufficiently thick to contrast against an opaque structure, such as the heart.



eFig. 36.18 Cranioventral aspect of the thorax of a dog with an alveolar pattern. Numerous air bronchograms are visible throughout the region of increased lung opacity.



eFig. 36.19 Close-up views of the right **(A)** and left **(B)** caudal aspect of the thorax of a dog with a mild alveolar pattern in the right caudal lung lobe. This is a minor change, and the slight increase in lung opacity is subtle. However, numerous air bronchograms are visible in the right caudal lung field (*black arrows* in **A**), and these are the key to making the diagnosis of an alveolar pattern. Air bronchograms are not seen in the left caudal lung field **(B)**. It is not uncommon to confuse the normal opacity between two large vessels (here the pulmonary artery and vein) as an air bronchogram as discussed in the text.

Table • 36.4

Differential Diagnoses for an Alveolar Pattern on Radiography.

Aspiration pneumonia
Bacterial pneumonia (i.e., community acquired, nosocomial, or secondary infection)
Cardiogenic or noncardiogenic pulmonary edema
Pulmonary contusions or hemorrhage
Obstructive (resorptive) or nonobstructive atelectasis
Severe lung underinflation associated with exhalation
Pulmonary thromboembolic disease
Eosinophilic lung disease
Heartworm disease (*Dirofilaria immitis*, *Angiostrongylus vasorum*)
End-stage pulmonary fibrosis
Fungal pneumonia
Bronchiolar disorder
Parasitic lung disease (e.g., aelurostrongylosis, paragonimiasis, parasitic disease associated with *Crenosoma vulpis*)
Pulmonary veno-occlusive disease and pulmonary capillary hemangiomatosis
Pulmonary alveolar proteinosis

Table • 36.5

Differential Diagnoses for Alveolar Filling Disorders.

SUBSTANCE FILLING THE ALVEOLI	DISEASE
Serous fluid	Cardiogenic or noncardiogenic pulmonary edema
Pus	Pneumonia
Blood	Pulmonary hemorrhage
Malignant cells	Bronchioloalveolar carcinoma
Concretions (calcium)	Pulmonary alveolar microlithiasis
Proteins	Pulmonary alveolar proteinosis, amyloidosis

Hypoperfusion

Occlusion of a pulmonary artery by a thrombus, embolus, or both can result in perfusion deficits of the terminal respiratory units beyond the blockage. Radiographic findings include an area of decreased opacity, or hypovascular pattern, in a peripheral, middle, or central region, relative to the rest of the lung (Fig. 36.30).[48,49] Abrupt truncation of a pulmonary artery may occasionally be detected.[48] Other radiographic parenchymal manifestations include interstitial pattern, mixed interstitial-alveolar pattern, and an alveolar pattern, with the right lung being more affected than the left, and the caudal lung lobes being more commonly favored. Cardiomegaly, pleural effusion, and pneumothorax can also be seen.[50]

Emphysema

The term *emphysema* implies a destruction of alveolar septa with air freely escaping from alveoli, and dilated airspaces distal to the terminal bronchiole as a consequence of inflammation.[22] It has been reported histologically in lungs of dogs with interstitial fibrosis,[1] pulmonary alveolar microlithiasis,[27] and broncholithiasis. The amount of emphysema necessary for its radiographic detection is unknown. It is rarely observed in canines and felines, but more frequent in cattle and humans.[1]

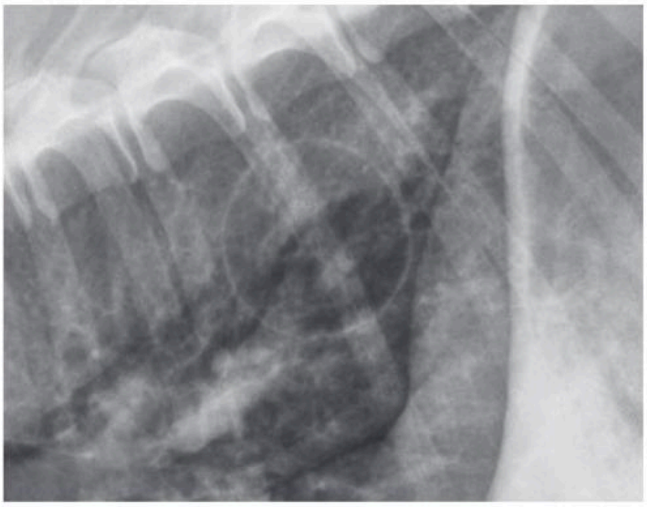


Fig. 36.29 Lateral radiograph of a dog with a bulla in the right caudal lung lobe. The lesion appears to only contain air and has a thin wall. This lesion could be congenital or secondary to previous lung trauma.

Hyperinflation and Air Trapping

Hyperinflation refers to an increase in lung volume exceeding that of a normal inspiration. In a conscious animal, it may be a fear response. In an animal under general anesthesia, increased lung volume may be a sequela of overinflation. In both instances, the opacity of the lungs is associated with a homogeneous decrease in radiopacity. Extension of the caudal boundaries of the lungs, flattening of the diaphragm, and cranial expansion of the rib cage may also be seen with hyperinflation. Hyperinflation may also occur as a compensatory mechanism when the ventilation of a lung lobe or segment is compromised or as a sequela of lobectomy.

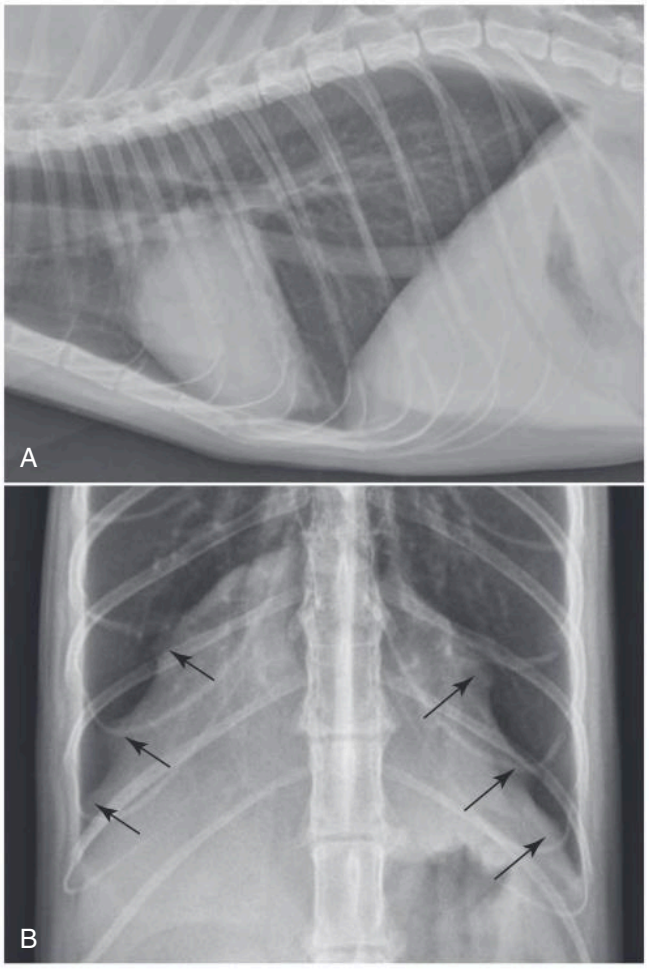
Air trapping refers to an excessive retention of air in the airspaces (i.e., respiratory bronchioles, alveolar ducts, alveolar sacs) and alveoli without destruction of the alveolar septa (see eFig. 36.4).[13] Severe lung hyperinflation on radiography captured in inspiration and expiration in an animal showing expiratory efforts may be suggestive of air trapping (Fig. 36.31, eFig. 36.20).

DIAGNOSTIC IMAGING OF SPECIFIC LUNG DISEASES

A wide variety of airway and parenchymal diseases can affect dogs and cats. Only a limited number of conditions will be presented here.

Aspiration Pneumonia

Aspiration of fluid, food, or acidic gastric content is common in dogs with pharyngeal and esophageal dysphagia, regurgitation, or vomiting. Dogs repetitively aspirating may have an impaired cough reflex. In brachycephalic dogs, recurrent aspiration pneumonia frequently underlies a comorbid condition such as hiatal hernia. In dogs having recently been under general anesthesia, aspiration pneumonia may be the result of a single episode. Dogs with aspiration pneumonia have similar radiographic changes to those seen with nonhematogenous bacterial



eFig. 36.20 Lateral **(A)** and ventrodorsal (VD; **B**) radiographs of a cat with pulmonary hyperinflation. In **A,** the distance between the heart and diaphragm is increased, and the diaphragm is flatter than normal. Note also the increase in size of the triangular lung region bounded by the ventral aspect of the caudal vena cava, cranioventral aspect of the diaphragm, and the caudal margin of the heart. In **B,** there are multiple, relatively sharp projections from the diaphragm (*black arrows*) that represent the costal attachment sites. The attachment sites are visible because the hyperinflated lung is pushing the diaphragm caudally, leading to tension at the point where the diaphragm attaches to the ribs.

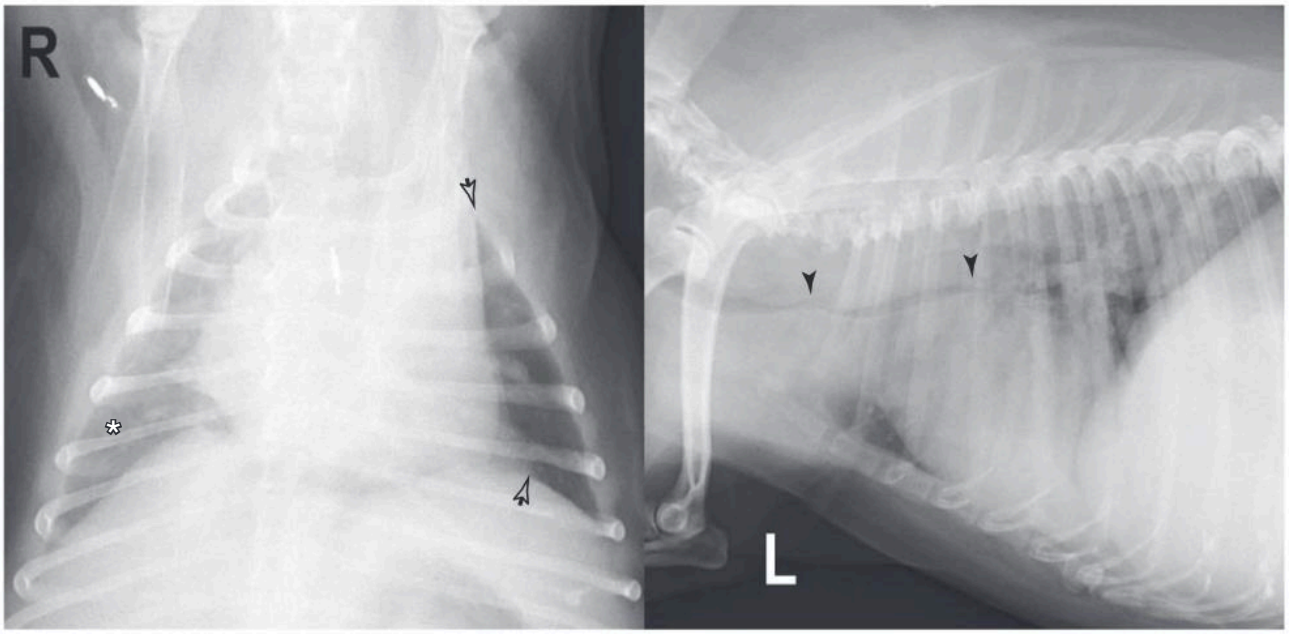


Fig. 36.30 Asymmetric lung opacity attributed to suspected pulmonary thromboembolic disease in a dog with a protein-losing nephropathy. The ventrodorsal view (*left panel*) shows the left lung (*arrows*) being less opaque than the right (*asterisk*). *Right panel,* Final diagnoses included tracheal and mainstem bronchial collapse (*black triangles*), suspect pulmonary thromboembolism secondary to a protein-losing nephropathy, and suspect mitral valve degenerative disease.

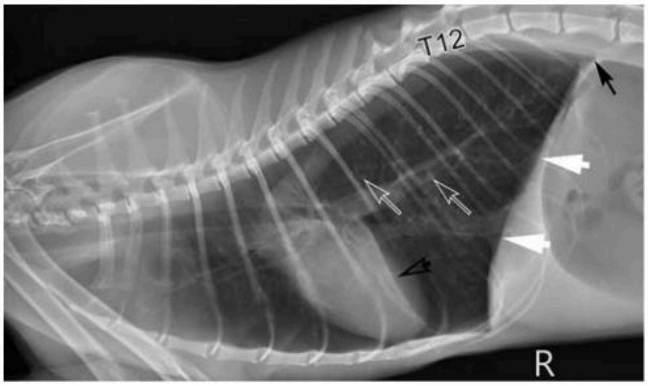


Fig. 36.31 Lung hyperinflation on a lateral radiographic view in an 8-year-old female spayed domestic shorthair cat with allergic asthma. Hyperin flation was diagnosed based on the marked caudal extension of the caudal lung beyond T12 with the lumbodiaphragmatic angles reaching the second lumbar vertebra (*solid black arrow*). Additional findings consistent with hyperinflation included flattening of the diaphragm (*solid white arrows*), marked cranial extension of the lungs cranial to the first ribs, and increased distance between the cardiac silhouette and the diaphragm. In this cat, hyperinflation was presumably attributed to air trapping secondary to allergic asthma. Additionally, a few thickened end-on bronchi are also noted (*open white arrows*). A lobar sign is seen between the atelectatic right middle (*open black arrow*) and right caudal lung lobes. The marked gas filled dilated stomach suggest aerophagia secondary to respiratory distress.

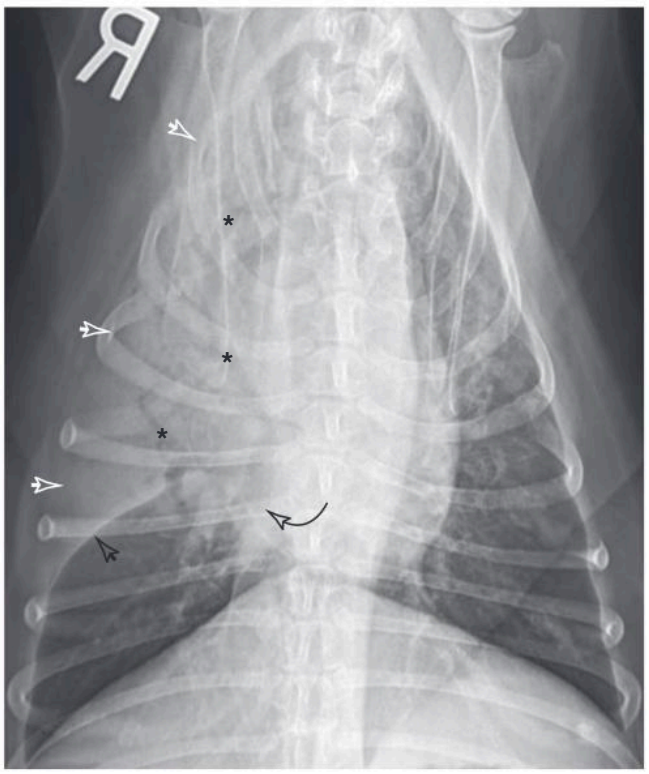
pneumonia, with the right middle and cranial lung lobes being more commonly affected. Dogs who have aspirated in other positions than standing or sternal may have a different distribution of lung lesions. An alveolar pattern with air bronchograms, a mixed interstitial-alveolar pattern, an interstitial pattern, or a mixed bronchial-interstitial-alveolar pattern is often seen with aspiration pneumonia (see Fig. 36.9, eFigs. 36.21 and 36.22). The number of lobes or segments affected is often limited, preferentially involving one or two lung lobes or segments. Aspiration pneumonia may be complicated by secondary bacterial pneumonia.

Bacterial Pneumonia

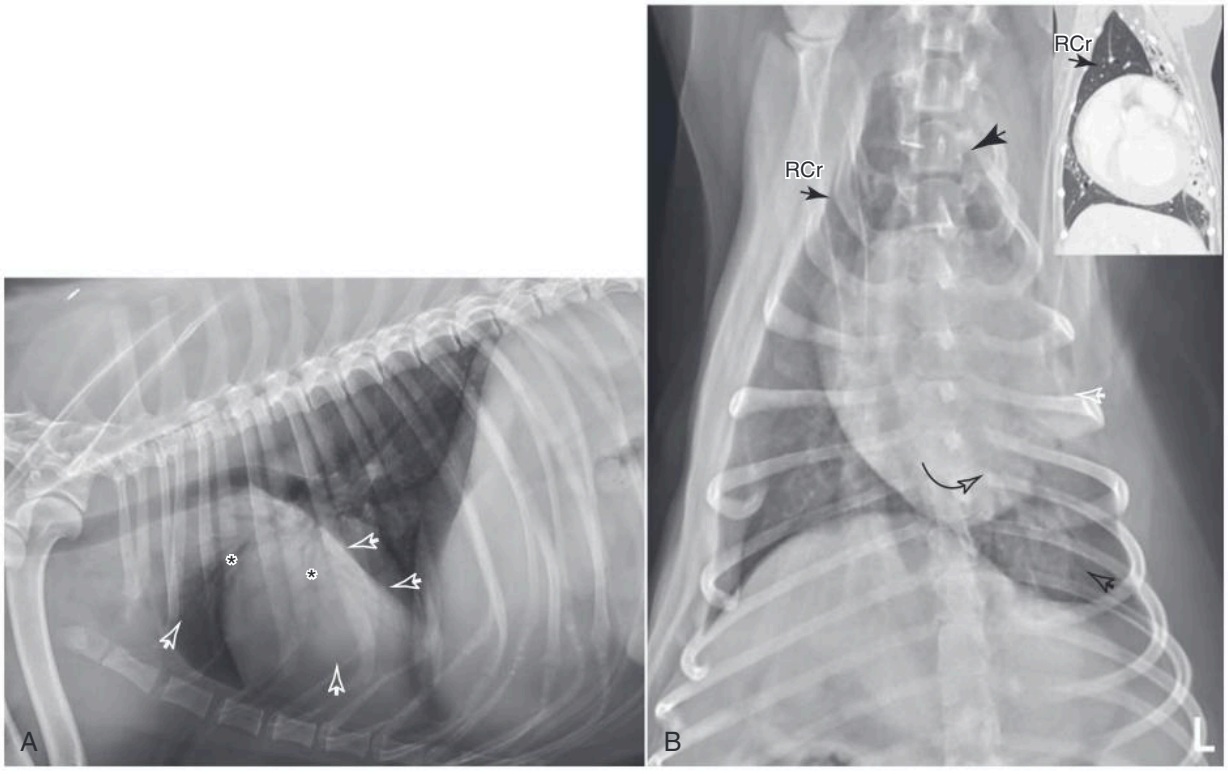
Bacterial pneumonia may occur secondary to impaired respiratory defenses, secondary to aspiration, respiratory viral infections, comorbid diseases, environmental stresses, and drug-induced immunosuppression or neutropenia. Bacterial pathogens responsible for community-acquired pneumonia in dogs are often opportunistic, whereas nosocomial pneumonia commonly involves multidrug-resistant and pathogenic bacteria. Bacterial pneumonia may be the result of canine infectious respiratory disease complex, in which multiple factors play a role. Lesions of bacterial pneumonia are often found in the cranioventral regions of the lungs, similar to aspiration pneumonia, and characterized by a multifocal or focal alveolar pattern, or less commonly a mixed patchy unstructured interstitial and bronchial pattern (Fig. 36.32). Of note, radiographic lesions may lag behind clinical and hematologic resolution of disease. Colonization of lungs by bacteria spreading from the blood circulation may have a different distribution of lesions with multifocal alveolar pattern or multifocal areas of consolidation or nodules that are not limited to the cranioventral regions of the lungs (see Fig. 36.24).

Feline Asthma

Hallmark features of asthma in cats include airway inflammation, excessive mucus production, intermittent reversible airway obstruction, nonspecific airway hyperreactivity, and airway remodeling. The lack of airway or lung parenchymal radiographic changes does not rule out asthma. Cats with asthma may show a bronchial pattern (see Fig. 36.17). Excessive mucus production can lead to bronchial luminal plugging, which can lead to lung collapse and resorptive atelectasis (see Fig. 36.20). Airway inflammation and remodeling result more commonly in an unstructured interstitial pattern on



eFig. 36.21 Alveolar pattern associated with aspiration pneumonia in a 13-year-old female spayed mixed breed canine. The right cranial and right middle lung lobes (*white arrows*) are severely increased in opacity, preventing distinction of pulmonary vasculature and consistent with an alveolar pattern. Several air bronchograms (*asterisk*) are seen within the affected lung lobes. A lobar sign (*straight black arrow*) is present between the right middle and right caudal lung lobes. The cardiac silhouette is slightly shifted to the right (*curved black arrow*), likely from an overall decrease in volume of the affected lung lobes.



eFig. 36.22 Asymmetrical cranial distribution of an alveolar pattern associated with aspiration pneumonia in an 8-year-old male castrated Brittany Spaniel dog. **A,** Right lateral view showing lesions in the cranial and caudal segments of the left cranial lung lobe (*arrows*). Several air bronchograms (*asterisks*) are seen in the affected region, consistent with persistent bronchial intraluminal air contrasting with surrounding soft tissue filled or collapsed alveoli. A lobar sign is seen between the left cranial and left caudal lung lobes (caudal arrows). These findings were consistent with an alveolar pattern in the left cranial lung lobe. **B,** Ventrodorsal (VD) view showing involvement of the cranial and caudal segments of the left cranial lung lobe (*open white arrow*) with hyperinflation of the right cranial lung lobe (*RCr*) as better seen on the dorsal computed tomography (CT) image (*inset, filled black arrow*). A mild mediastinal shift to the left (*curved arrow*) is also seen, with decrease in lung volume of the left cranial lung lobe. The left caudal lung is also increased in opacity (*open black arrowhead*) possibly from overlapping caudal segment of the left cranial lung lobe and mild decrease in lung volume.

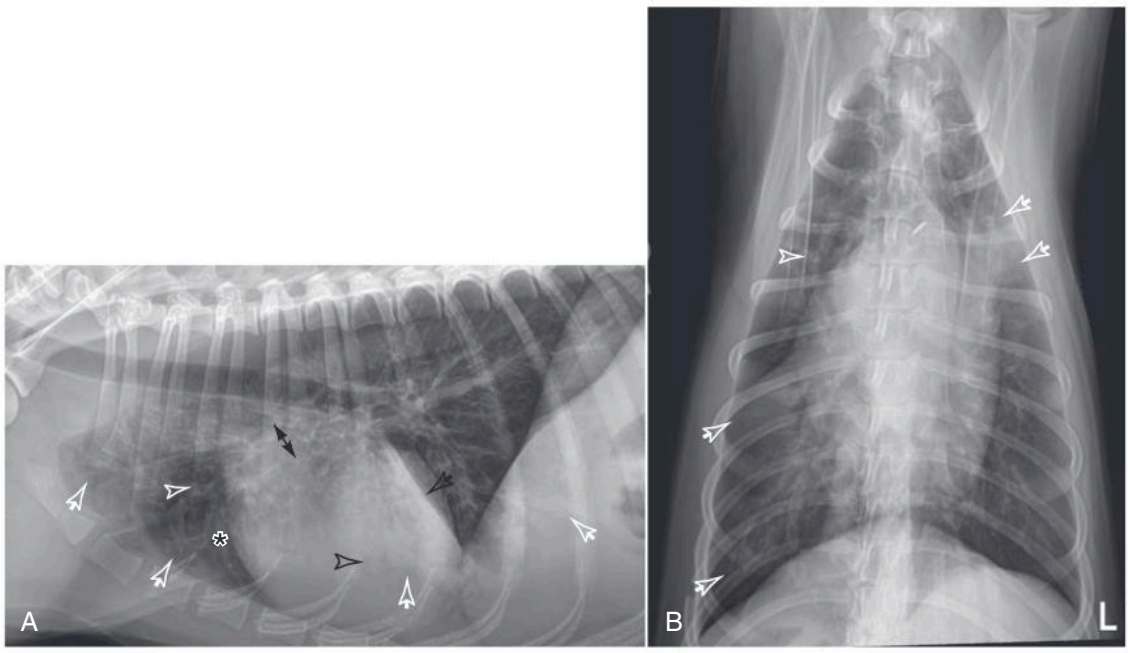


Fig. 36.32 Necrotizing bronchiolitis and bacterial bronchopneumonia in a 1.5-year-old female spayed giant schnauzer mixed-breed canine. **A,** Thoracic radiography showed pulmonary lesions in the cranial and caudoventral lungs (*white arrows*) characterized by an increase in soft tissue opacity, bronchial luminal dilation (*double arrowheads*), intraluminal filling of airways (*asterisk*), thickened bronchial wall as reflected by numerous doughnut-like lesions (*triangle*), and a few air bronchograms (*black triangle*) in the section of lungs superimposed over the cardiac silhouette, consistent with an alveolar pattern. A lobar sign (*black arrow*) between the right middle and right caudal lung lobe was also seen although the latter exhibited mild lesions. **B,** The ventrodorsal view showed multifocal lesions (*arrows*) involving the cranial segment of the left cranial, right middle, and to a lesser extent the right cranial and right caudal lung lobes. Computed tomography (CT) confirmed involvement of these lung lobes in addition to the accessory and left caudal lung lobes with consolidation preferentially located in their dependent regions, with the left caudal lung lobe being the least affected. CT also showed diffuse tree-in-bud lesions in the nonconsolidated parenchyma. The definitive diagnosis was marked multifocal necrotizing bronchiolitis and acute neutrophilic bronchopneumonia with intralesional bacterial cocci on histopathologic examination. Considering a negative polymerase chain reaction (PCR) result for canine influenza or canine distemper, a primary acute bacterial bronchopneumonia was suspected.

radiography, although an alveolar pattern may reflect severe parenchymal changes. Airway hyperreactivity may result in bronchoconstriction. As a result, air is trapped in the downstream airspaces and alveoli, which manifests as lung hyperinflation and secondary diaphragmatic flattening on radiography (see Fig. 36.31). It is important to remember that although asthma is an important differential in cats with cough and/or respiratory distress, it is not the only one. If the cat does not respond to steroids, it is probably because the cat does not have asthma but another type of chronic airway disorder affecting the large and/or small airways such as chronic bronchitis, parasitic bronchitis, bronchiectasis, or a primary or secondary bronchiolar disorder.

Chronic Bronchitis

Chronic bronchitis is a common noninfectious inflammatory disorder of middle-aged to older dogs of various breeds associated with a chronic cough (>2 months of duration), neutrophilic and/or eosinophilic airway inflammation, mucus hypersecretion, and loss of ciliated epithelial cells. It is not uncommon for the underlying cause not to be identified. Thoracic radiography and CT may be unremarkable in dogs with chronic bronchitis. When detected, lesions may include mild to severe thickening of the large and medium-sized airway walls, with or without bronchiectasis, resulting in a bronchial pattern (Fig. 36.33A). Additionally, CT can occasionally show patchy ground-glass opacity to consolidation and luminal plugging with mucus (see Fig. 36.33B).[51]

Lung Lobe Torsion

Lung lobe torsion is the rotation of a lobe or segment on its pedicle, partial or complete, often close to its emergence from the left or right principal bronchus, although mid lobar torsion has been reported.[52] Partial or complete torsion interferes with ventilation and venous drainage of the affected lobe or segment. Arterial supply may be reduced but not entirely absent initially. The affected lung becomes congested and consolidated and may undergo necrosis. Although any lobe can be affected, the right middle and left cranial lung lobes are more commonly involved, followed by the right cranial lung lobe (Fig. 36.34). Lung lobe torsion can be associated with pleural effusion, neoplasia, trauma, diaphragmatic hernia, or following a lobectomy.

Lung lobe torsion may manifest as an increased opacity and volume of the involved lung lobe(s) or segment(s), midline shift to the contralateral side, abrupt termination or narrowing of the lobar bronchial lumen, abnormal positioning of the bronchus and the vasculature, gas trapped within the lung lobe or segment (also described as vesicular gas pattern, vesicular emphysema, or emphysema), and peripheral hyperattenuating band, some of these signs being only seen on CT (Fig. 36.35, eFigs. 36.23 and 36.24).[53] The affected lung lobe or segment may have a hepatized appearance on ultrasound with a peripheral hypoechoic band.[54]

Primary Lung Tumors

Tumors arising from lung tissue are designated primary lung tumors, with epithelial tumors being considered the most



eFig. 36.23 Ventrodorsal (VD) radiograph of a dog with torsion of the right middle lung lobe. The right middle lobe has an alveolar pattern, and air bronchograms are visible. The shape of the right middle lung lobe is abnormal, being wider peripherally than at the hilus. There is bilateral pleural fluid. The radiographic findings in the lateral views were nonspecific; pleural fluid and the air bronchograms in the right middle lobe were visible, but the abnormal shape of the right middle lobe was not apparent.



eFig. 36.24 Ventrodorsal (VD) radiograph of a dog with torsion of the right middle lung lobe. This lobe has developed multifocal regions of trapped air, termed *vesicular gas pattern* or *vesicular emphysema.* This appearance is highly supportive of a lung lobe torsion but not pathognomonic.

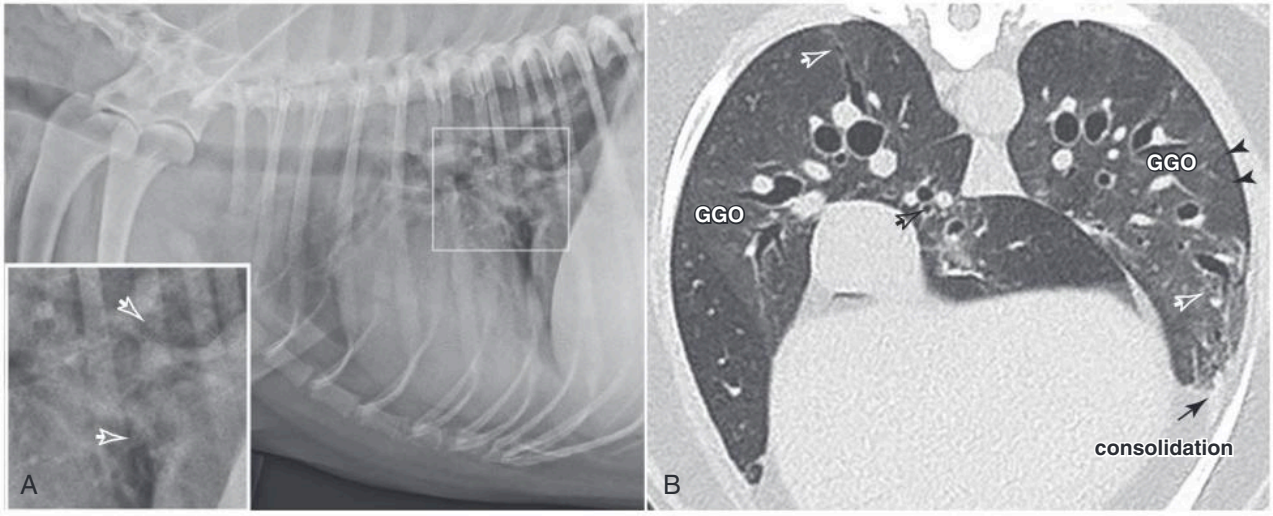


Fig. 36.33 Airway changes associated with chronic bronchitis in a 9-year-old intact male Shetland sheepdog. The dog was presented for a cough of approximately 6-month duration, which was exacerbated by exercise. **A,** A few thickened end-on bronchi (*inset, white arrows*) are seen in the caudal lung. The margins of the end-on bronchi are difficult to distinguish from the surrounding parenchyma due to poor lung inflation hampering assessment of the lung opacity. **B,** A transverse precontrast inspiratory computed tomography image acquired at the caudal aspect of the thorax is shown. Mosaic attenuation is seen with areas of ground-glass opacity (*GGO*) and consolidation interspersed with normal lung parenchymal attenuation. Bronchial wall thickening (*open black arrow*), peribronchial thickening (*white arrows*), and mild dilation of the small-sized airways (*triangles*) is exhibited.

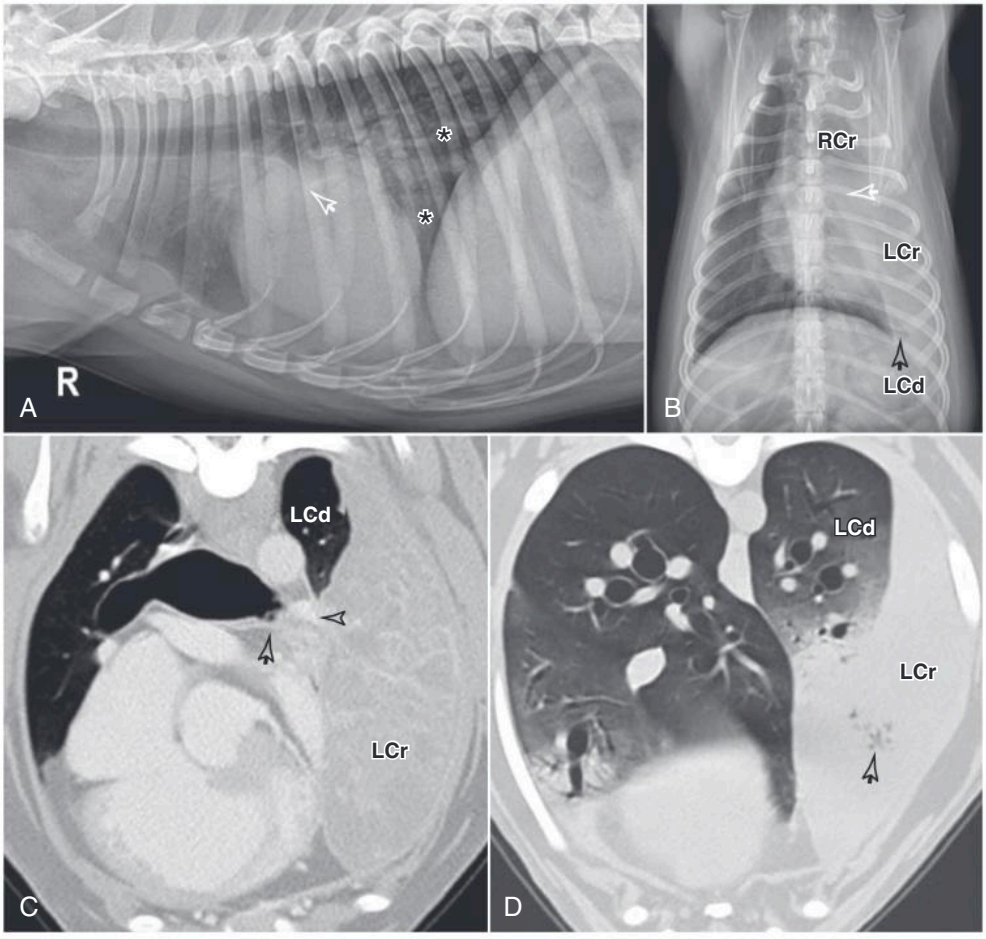


Fig. 36.34 Left cranial lung lobe torsion in a 2-year-old male castrated Shiba Inu canine. **A,** Right lateral view showing an axial rotation of the tracheal bifurcation and left principal bronchus leading to the left cranial lobar bronchus, which appears to be immediately blunted at its emergence (*arrow*). This presumably corresponds to the location of the torsion of the left cranial lung lobe. The increased opacity created by the enlarged left cranial lung lobe is difficult to perceive on the lateral view. A mixed pulmonary pattern (interstitial-alveolar) is noted in the caudal lung, more severe caudoventrally (*asterisks*). **B,** Ventrodorsal view demonstrating a marked increase in opacity of the left cranial lung lobe (*LCr*) which is slightly displaced caudally, and the absence of visualization of its emergence at its expected location (*white arrow*). The left caudal lung lobe is displaced caudally and medially (*LCd*). The mediastinum is mildly shifted to the left. The right cranial lung lobe is mildly hyperinflated and extends to the left, occupying a greater proportion of the left cranial lung than normally expected. **C,** Transverse postcontrast computed tomography (CT) image of the same dog showing the location of the twisted left cranial lung lobe at its emergence from the left principal bronchus (*open black arrow*) and the abrupt termination of the left lobar pulmonary artery (*triangle*). The left cranial lung lobe is enlarged and heterogeneously contrast enhancing. The *LCd* lung lobe is displaced caudally and reduced in volume. **D,** Postcontrast transverse CT image exhibiting a small number of persistent gas bubbles in the twisted left cranial lung lobe. The left caudal lung lobe is compressed by the enlarged left cranial lung lobe with secondary nonobstructive atelectasis. Of note, pleural effusion, which often accompany a lung lobe torsion, was not observed in this dog. *RCr,* Right cranial.

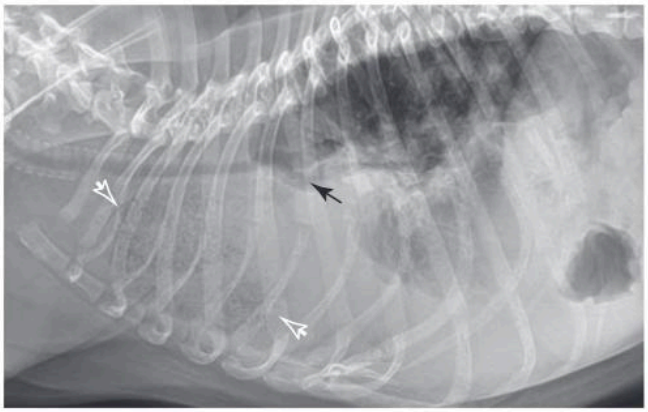


Fig. 36.35 Right cranial lung lobe torsion in a 3-year-old male intact bulldog. There is pleural effusion and trapped gas (also called vesicular gas pattern, vesicular emphysema, or emphysema) in the cranial lungs *(white arrows)*. The course of the lobar bronchus was seemingly interrupted *(black arrow)* with an abnormal appearance to the tracheal bifurcation. Collapse of the cranial segment of the left cranial lung lobe was also seen on the ventrodorsal view (not shown). Due to concerns of multi-organ failure and consideration of the dog's quality of life, the owners elected for euthanasia and consented to a necropsy. A right cranial lung lobe torsion with local extensive hemorrhage and necrosis of the lung parenchyma were confirmed at postmortem examination. The left cranial lung lobe was collapsed.

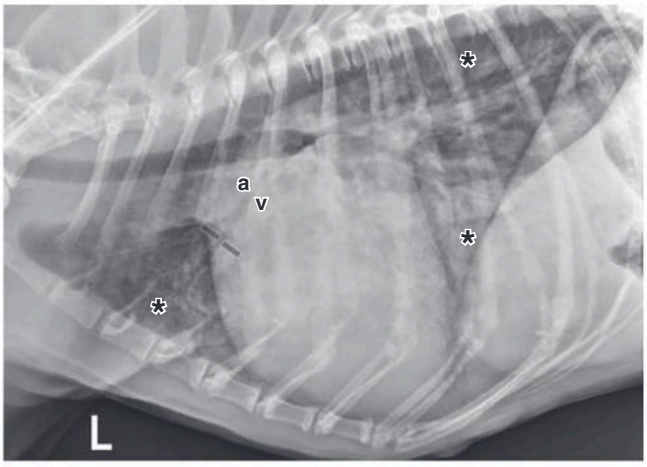


Fig. 36.36 Pulmonary arterial and venous enlargement in a 12-year-old female spayed mixed-breed dog with cardiogenic pulmonary edema secondary to congestive heart failure. Left lateral view showing an enlarged (*lines*) cranial lobar pulmonary artery (*a*) and vein (*v*). An unstructured interstitial to alveolar pattern is seen consistent with cardiogenic pulmonary edema (*asterisks*). Left-sided cardiomegaly attributed to mitral regurgitation secondary to myxomatous mitral valve disease. A ventrodorsal view of this dog is available on the online version (eFig. 36.26).

common. Epithelial lung tumors can be benign (papilloma and adenoma) or malignant. Various types of carcinomas (e.g., bronchial gland carcinoma, squamous cell carcinoma, adenocarcinoma, etc.) have been described in the canine and feline lung, leading to a wide range of appearances on imaging. A single soft tissue opaque mass with or without smaller nodules or masses representing metastases are often identified. Primary lung tumors in cats are often cavitated with a radiolucent center. Although any lung lobe can be affected, the larger pulmonary masses tend to occupy the caudal lung lobes (see Fig. 36.10). Central or perihilar masses are often of bronchial origin, whereas peripheral masses tend to arise from distal bronchiolar or alveolar epithelium.[2] Tracheobronchial lymphadenomegaly may also be present concurrently.[55] Primary pulmonary histiocytic sarcoma (see Fig. 36.11) and neuroendocrine tumors among other types can also be encountered. Histiocytic sarcoma tends to be more ventrally located than pulmonary carcinoma.

In cats, pulmonary adenocarcinomas may spread to the digits, causing lameness, and leading to the so-called feline "lung-digit syndrome." Osteolysis of the distal phalanx with potential extension to the distal interphalangeal joint and middle phalanx with osteolysis and/or periosteal proliferation and soft tissue thickening are often seen.

Pulmonary Edema

Pulmonary edema consists in the abnormal accumulation of transudate fluid in the alveoli and interstitium as a consequence of elevated hydrostatic pressure, increased permeability of the alveolar wall, impaired lymphatic drainage, or other miscellaneous causes. It impedes lung function, obstructing gas exchange at the alveolar level, among other processes.

Left-sided heart disease and excessive intravenous fluid administration are common causes of pulmonary edema from elevated hydrostatic pressure and are described in Chapter 35 (Fig. 36.36, eFig. 36.25).

Pulmonary edema can occur secondarily to noncardiac causes, including anaphylactoid reactions, endotoxemia, diffuse alveolar damage, and within bacterial pneumonia lesions. Acute upper-airway obstruction (e.g., strangulation, foreign objects, airway collapse, laryngeal pathology), increased intracranial pressure from central nervous system–derived trauma (e.g., cranial trauma, electric shock, seizures), hypoproteinemia, impaired lymphatic drainage, and high altitudes can also cause pulmonary edema.[2] Bilateral symmetric or asymmetric interstitial, alveolar, or mixed interstitial-alveolar patterns, without increases in the caliber of the pulmonary vasculature, are commonly found with noncardiogenic pulmonary edema (see Fig. 36.8).[56] Lesions can be focal, multifocal, or diffuse, the latter less common, and the peripheral region of the lungs superseding the central lung region in terms of common distribution.[56] Radiographic changes do not appear to be correlated with survival.[56]

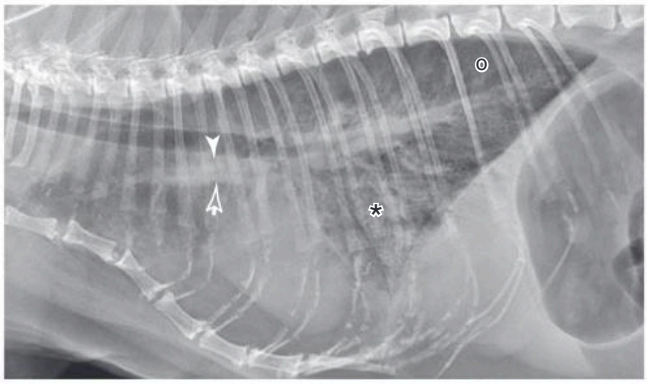
Eosinophilic Lung Diseases

Eosinophilic lung diseases represent a vast group of diseases of known (e.g., heartworm, fungal, bacterial, viral, drug reaction) and unknown (i.e., idiopathic) etiologies, affecting airways, parenchyma, or both. [2] In dogs, disease can be confined to the airways ("eosinophilic bronchitis"), to the parenchyma ("eosinophilic pneumonia"), or a combination of both ("eosinophilic bronchopneumopathy"). Eosinophilic lung diseases may have a wide spectrum of manifestations on radiography or CT, including the lack of detectable pulmonary lesions on radiography (Fig. 36.37). Involvement of airways often leads to a bronchial pattern. Bronchial plugging with soft tissue opacities may also be seen.[34,57]

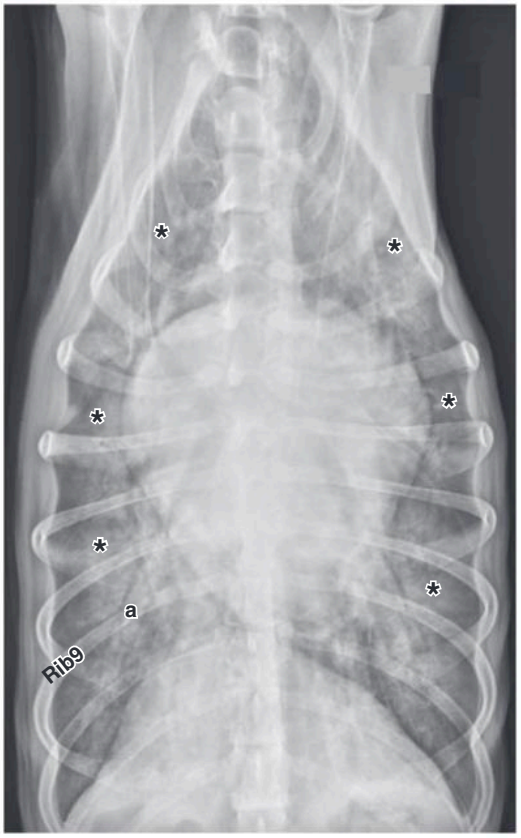
Parenchymal involvement may manifest as pulmonary nodules and/or pulmonary masses, of various sizes and locations, with preference to the caudal lung lobes, and can cause displacement, or partial or complete compression of nearby bronchi.[58] Solitary pulmonary masses with idiopathic eosinophilic lung disease have been described. Other manifestations of eosinophilic lung disease include an interstitial pattern, often mixed with a bronchial pattern, and an alveolar pattern on radiography.[33,57–59] Tracheobronchial and cranial mediastinal lymphadenopathy may accompany eosinophilic lung diseases.

Pulmonary Contusions and Hemorrhage

Pulmonary contusions occur as a sequela of sustained blunt force trauma. They manifest within hours of injury ranging



eFig. 36.25 Cardiogenic pulmonary edema secondary with intravenous fluid overload in a 10-year-old intact male domestic shorthair cat after treatment for diabetic ketoacidosis. On the right lateral view, the cranial lobar pulmonary artery (*filled triangle*) and vein (*open arrow*) are with ill-defined borders. The lungs are diffusely increased in opacity, more severe surrounding the lobar pulmonary vasculature and caudal and ventral to the cardiac silhouette (*asterisks*). An unstructured interstitial pattern is visible at the periphery of the caudal lung (*circle*). Echocardiography showed mild left atrium and ventricle chamber enlargement with ventricular wall thickness within the normal reference range, supportive of a diagnosis of congestive heart failure secondary to intravenous fluid administration



eFig. 36.26 Ventrodorsal view of the same dog in Fig. 36.36. Cardiogenic pulmonary edema secondary to congestive heart failure. The right and left lung fields are markedly increased in opacity with mild asymmetry. The severity of the pulmonary pattern hampers the visibility of the caudal lobar pulmonary vessels (*small asterisk*) at the 9th rib (*Rib9*). The left-sided cardiomegaly was attributed to myxomatous mitral valve disease.

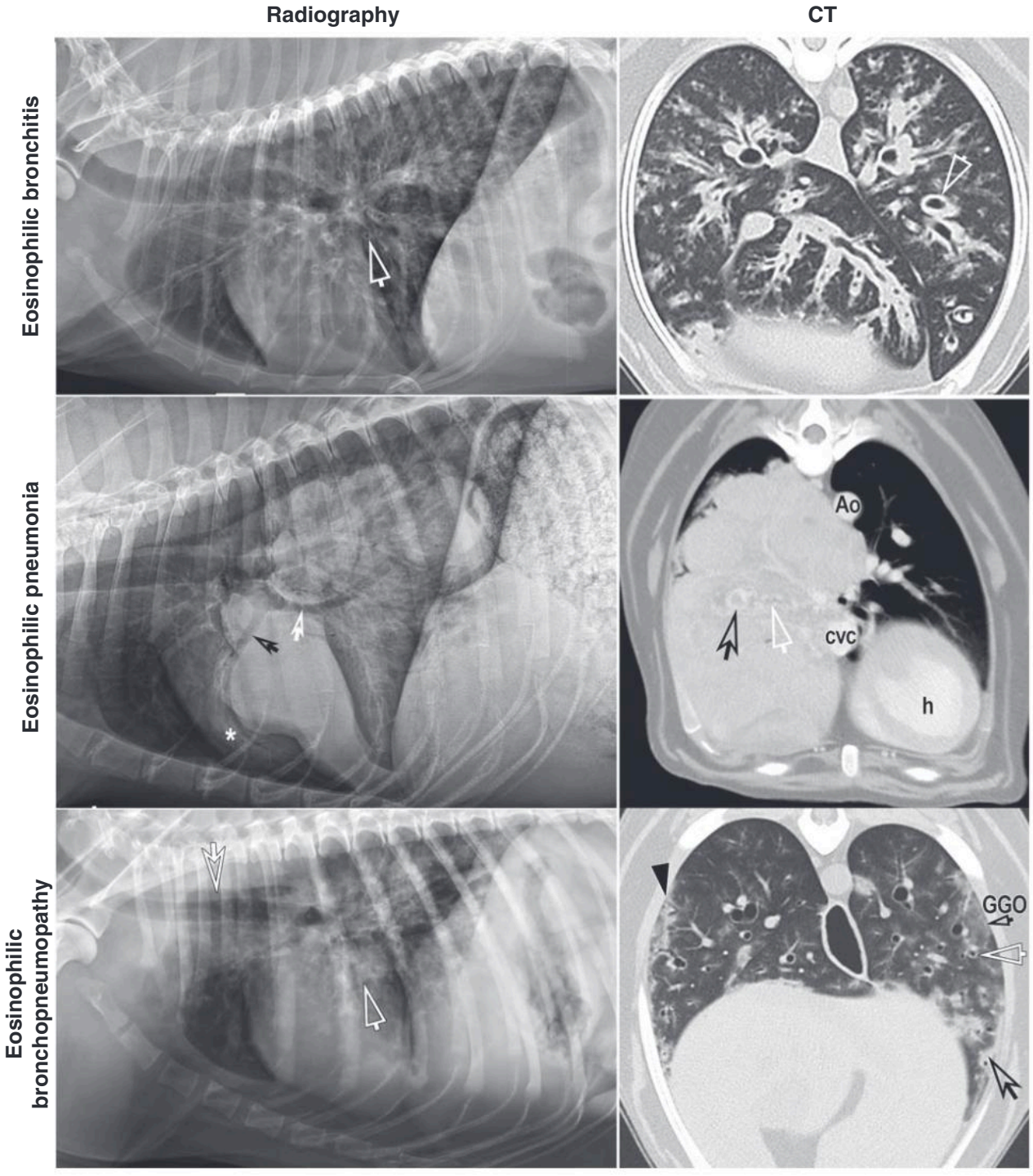


Fig. 36.37 Eosinophilic bronchitis, eosinophilic pneumonia, and eosinophilic bronchopneumopathy in the dog on radiography and computed tomography (CT). *Top panel,* Eosinophilic bronchitis in a 7-year-old female spayed Cavalier King Charles spaniel with respiratory distress. A severe diffuse bronchial pattern with bronchiectasis is seen on radiography. The *arrow* points to a thickened end-on airway. Inspiratory computed tomography (CT) revealed severe peribronchial thickening and mild to moderate bronchiectasis (*arrow*). *Middle panel,* Two-year-old female spayed German shepherd dog with a hypereosinophilic syndrome, a severe form of eosinophilic pneumonia. On radiography, an irregularly shaped soft tissue mass occupies the caudal thorax and causes an axial rotation of the tracheal bifurcation. The right caudal *(white arrow)* and right middle *(black arrow)* lobar bronchi are displaced ventrally and cranially, respectively. The right middle lung lobe is collapsed (*asterisk*). On CT, the large soft tissue attenuating pulmonary mass is irregularly marginated dorsally, and smooth elsewhere. A thrombus is seen in the right caudal lobar pulmonary artery (*open black arrow*). The mass is markedly contrast enhancing, with slightly less enhancement centrally, surrounding the compressed right caudal lobar bronchus (*open white arrow*). The mass also displaces the mediastinal structures including the aorta (*Ao*), caudal vena cava (*CVC*), and heart (*h*) to the contralateral side. *Bottom panel,* Eosinophilic bronchopneumopathy in a 7-year-old male castrated mixed breed. There is a diffuse mixed pulmonary pattern with numerous thickened end-on bronchi (*arrow*) and airway-centered unstructured interstitial pattern. A small amount of gas is noted in the esophagus (*curved white arrow*). Peribronchial thickening (*open arrow*), bronchiolectasis (*triangle*), occasional consolidation (*curved black arrow*), and ground-glass opacity (*GGO*), the latter more severe surrounding the airways and in the subpleural region are evident on CT. It is not possible to entirely rule out concurrent subpleural interstitial thickening in areas where GGO is present. Bronchiectasis of the medium- and large-caliber airways was also present diffusely.

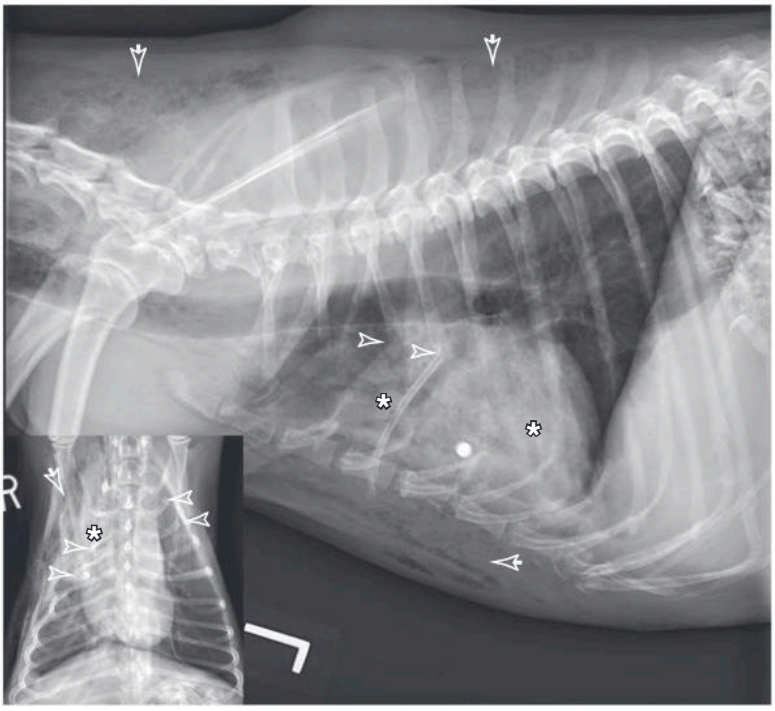


Fig. 36.38 Pulmonary contusions in a 10-year-old male castrated mixed-breed dog following a presumed encounter with a circulating motorized vehicle the evening prior to presentation. There is subcutaneous emphysema, predominantly right-sided (*open arrows*), rib fractures bilaterally (*triangles*) with intercostal tear, and increase in the opacity of the right cranial and right middle lung (*asterisks*), consistent with pulmonary contusions, although their visibility was impeded by superimposition with subcutaneous emphysema and edema/cellulitis associated with thoracic muscle injury. A circular metallic object visible in the right fourth intercostal space was believed to be incidental.

from focal, multifocal, or diffuse, ill-defined areas of interstitial to alveolar pattern on radiography (Fig. 36.38). The absence of pulmonary contusions on radiographs taken immediately after trauma or progression of pulmonary dysfunction despite mild radiographic changes on the initial study may require repeating radiography as detectable imaging changes can be delayed. Cavities which can contain gas and/or fluid can also be seen (Fig. 36.39). Radiography has a tendency to overestimate the severity of pulmonary contusions, and may not accurately reflect the severity of pulmonary dysfunction.[60] Radiographs should also be carefully examined for concurrent traumatic injuries such as pneumothorax, hemothorax, fractures, luxation and subluxation, and hemoperitoneum.

Pulmonary hemorrhage may also occur following non-traumatic causes such as bleeding disorders, rodenticide poisoning or other intoxication (e.g., copper sulfate powder), infection (e.g., leptospirosis, plague caused by *Yersinia pestis, Angiostrongylus vasorum*), drugs including anticoagulants, thrombosis, acute respiratory distress syndrome, pulmonary capillary hemangiomatosis, pulmonary veno-occlusive disease, or neoplasia. Unstructured interstitial, alveolar, and mixed interstitial-alveolar lung patterns have been described, with subtle differences in distribution according to the cause of pulmonary hemorrhage (Fig. 36.40).[61–63] Concurrent pleural effusion may occasionally be seen with pulmonary hemorrhage of various etiologies.

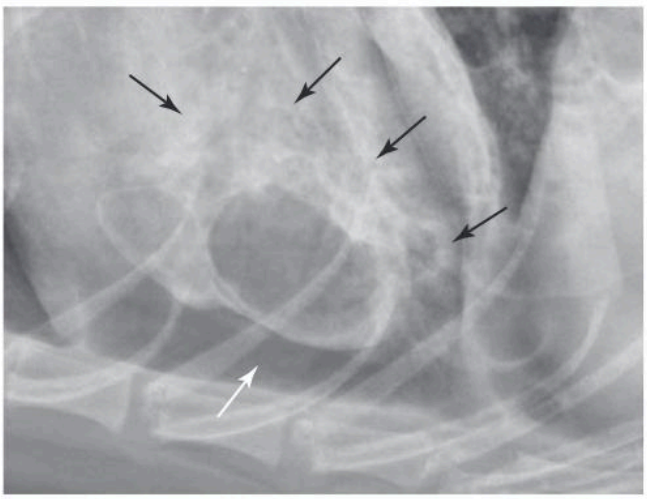


Fig. 36.39 Lateral radiograph of a dog recently hit by a car. There are multiple traumatic lacerations forming cavities filled with air in the periphery of the lung. Traumatic laceration cavities can collect air (pneumatocele), blood (hematocele), or both air and blood (hematopneumatocele). The wall of these lesions is slightly thicker and more irregular than encountered in a congenital bulla. However, the history of recent trauma and the finding of pneumothorax (*white arrow*) and an alveolar pattern consistent with hemorrhage (*black arrows*), support the occurrence of traumatic lesions.

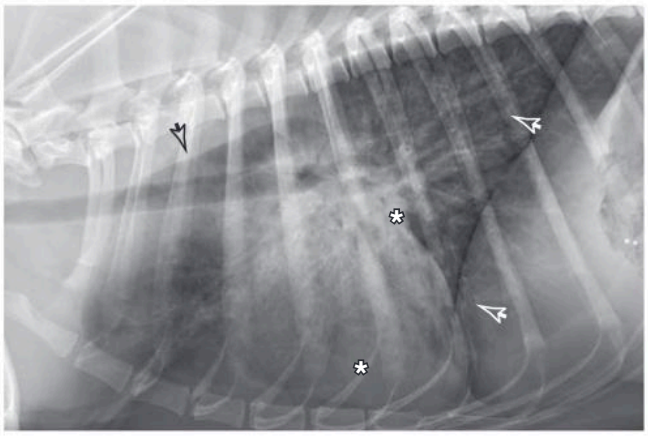


Fig. 36.40 Pulmonary hemorrhage secondary to suspected anticoagulant rodenticide exposure in a 17-month-old female spayed Labrador retriever. There is a diffuse mixed pulmonary pattern, with predominance of an unstructured interstitial pattern. Several irregularly marginated thickened end-on airways are seen (*white arrows*), although it is difficult to determine if this is the sole result of an airway-centered parenchymal infiltration or whether concurrent thickened bronchial walls also accompany the former. In the perihilar region and peripheral ventral areas, the severe unstructured interstitial pattern transitions to an alveolar pattern (*asterisks*). The cranial thoracic portion of the esophagus is gas filled (*black arrow*).

Acknowledgment

With special thanks to prior authors of this chapter for their contributions.

REFERENCES

1. Reif JS, Rhodes WH. The lungs of aged dogs: a radiographic-morphologic correlation. *Vet Radiol*. 1966;7:5–11.
2. Caswell JL, Williams KJ. Chapter 5 – respiratory system. In: Maxie MG, ed. *Jubb, Kennedy & Palmer's Pathology of Domestic Animals*. 6th ed. vol. 2. W.B. Saunders; 2016: 465–591.e464.
3. Silverman S, Suter PF. Influence of inspiration and expiration on canine thoracic radiographs. *J Am Vet Med Assoc*. 1975;166:502–510.
4. Lee SK, Park S, Cheon B, et al. Effect of position and time held in that position on ground-glass opacity in computed tomography images of dogs. *Am J Vet Res*. 2017;78: 279–288.
5. Foo TS, Pilton JL, Hall EJ, et al. Effect of body position and time on quantitative computed tomographic measurements of lung volume and attenuation in healthy anesthetized cats. *Am J Vet Res*. 2018;79:874–883.
6. Rozanski EA, Bedenice D, Lofgren J, et al. The effect of body position, sedation, and thoracic bandaging on functional residual capacity in healthy deep-chested dogs. *Can J Vet Res*. 2010;74:34–39.
7. Guarracino A, Lacitignola L, Auriemma E, et al. Which airway pressure should be applied during breath-hold in dogs undergoing thoracic computed tomography? *Vet Radiol Ultrasound*. 2016;57:475–481.
8. Allison A, Huizing X, Jolliffe C, et al. Effect of fixed value positive end expiratory pressure valves on canine thoracic volume and atelectasis. *J Small Anim Pract*. 2017;58:645–651.
9. Bernhard C, Masseau I, Dodam J, et al. Effects of positive end-expiratory pressure and 30% inspired oxygen on pulmonary mechanics and atelectasis in cats undergoing non-bronchoscopic bronchoalveolar lavage. *J Feline Med Surg*. 2017;19:665–671.
10. Martins ARC, Ambrósio AM, Fantoni DT, et al. Computed tomography assessment of tidal lung overinflation in domestic cats undergoing pressure-controlled mechanical ventilation during general anesthesia. *Front Vet Sci*. 2022;9:842528.
11. Henao-Guerrero N, Ricco C, Jones JC, et al. Comparison of four ventilatory protocols for computed tomography of the thorax in healthy cats. *Am J Vet Res*. 2012;73:646–653.
12. Morooka T, Niiyama M, Kougo A, et al. Radiographic evaluation of obesity-caused oppression of the thoracic cavity in beagles. *J Vet Med Sci*. 2004;66:489–494.
13. Masseau I, Reinero CR. Thoracic computed tomographic interpretation for clinicians to aid in the diagnosis of dogs and cats with respiratory disease. *Vet J*. 2019;253:105388.
14. Johnson LR, Singh MK, Pollard RE. Agreement among radiographs, fluoroscopy and bronchoscopy in documentation of airway collapse in dogs. *J Vet Intern Med*. 2015;29:1619–1626.
15. Lebastard M, Le Boedec K, Howes M, et al. Evaluation of bronchial narrowing in coughing dogs with heart murmurs using computed tomography. *J Vet Intern Med*. 2021;35(3):1509–1518.
16. Yoon H, Yu J, An G, et al. CT and radiographic evaluation of bronchial collapsibility at forced expiration in asymptomatic brachycephalic dogs. *Vet Radiol Ultrasound*. 2020;61:167–180.
17. Macready DM, Johnson LR, Pollard RE. Fluoroscopic and radiographic evaluation of tracheal collapse in dogs: 62 cases (2001–2006). *J Am Vet Med Assoc*. 2007;230:1870–1876.
18. Ober CP, Barber D. Comparison of two- vs. three-view thoracic radiographic studies on conspicuity of structured interstitial patterns in dogs. *Vet Radiol Ultrasound*. 2006;47:542–545.
19. Wilkins PA, Otto CM, Baumgardner JE, et al. Acute lung injury and acute respiratory distress syndromes in veterinary medicine: consensus definitions: the Dorothy Russell Havemeyer Working Group on ALI and ARDS in Veterinary Medicine. *J Vet Emerg Crit Care*. 2007;17:333–339.
20. Tsai S, Sutherland-Smith J, Burgess K, et al. Imaging characteristics of intrathoracic histiocytic sarcoma in dogs. *Vet Radiol Ultrasound*. 2012;53:21–27.
21. Barrett LE, Pollard RE, Zwingenberger A, et al. Radiographic characterization of primary lung tumors in 74 dogs. *Vet Radiol Ultrasound*. 2014;55:480–487.
22. Hansell DM, Bankier AA, MacMahon H, et al. Fleischner Society: glossary of terms for thoracic imaging. *Radiology*. 2008;246:697–722.
23. Suter PF, Chan KF. Disseminated pulmonary diseases in small animals: a radiographic approach to diagnosis. *Vet Radiol*. 1968;9:67–79.
24. Nemanic S, London CA, Wisner ER. Comparison of thoracic radiographs and single breath-hold helical CT for detection of pulmonary nodules in dogs with metastatic neoplasia. *J Vet Intern Med*. 2006;20:508–515.
25. Armbrust LJ, Biller DS, Bamford A, et al. Comparison of three-view thoracic radiography and computed tomography for detection of pulmonary nodules in dogs with neoplasia. *J Am Vet Med Assoc*. 2012;240:1088–1094.
26. Alexander K, Joly H, Blond L, et al. A comparison of computed tomography, computed radiography, and film-screen radiography for the detection of canine pulmonary nodules. *Vet Radiol Ultrasound*. 2012;53:258–265.
27. Sousa AC, Santos JC, Landolt C, et al. Clinicopathological and imaging features of pulmonary alveolar microlithiasis in a dog – a case report. *BMC Vet Res*. 2020;16:376.

28. Kubba MAG. Pulmonary ossification and microlithiasis in a bitch with multicentric mammary tumors. *Open Vet J*. 2017;7:273–276.
29. Bennett AD, Lalor S, Schwarz T, et al. Radiographic findings in cats with mycobacterial infections. *J Feline Med Surg*. 2011;13:718–724.
30. Ackerman N, Spencer CP. Radiologic aspects of mycotic diseases. *Vet Clin North Am Small Anim Pract*. 1982;12:175–189.
31. Jackson K, Boger L, Goldschmidt M, et al. Malignant pilomatricoma in a soft-coated wheaten terrier. *Vet Clin Pathol*. 2010;39:236–240.
32. Meola SD, Mazzaferro EM, Wheeler JL, et al. Medical and surgical management of severe barium aspiration in a dog. *J Vet Emerg Crit Care*. 2008;18:639–645.
33. Mesquita L, Lam R, Lamb CR, et al. Computed tomographic findings in 15 dogs with eosinophilic bronchopneumopathy. *Vet Radiol Ultrasound*. 2015;56:33–39.
34. Meler E, Pressler BM, Heng HG, et al. Diffuse cylindrical bronchiectasis due to eosinophilic bronchopneumopathy in a dog. *Can Vet J*. 2010;51:753–756.
35. Beck JA, Ard M, Howerth EW. Pathology in practice. Primary ciliary dyskinesia (PCD) with associated bronchopneumonia, bronchiectasis, and hydrocephalus in a dog. *J Am Vet Med Assoc*. 2014;244:421–423.
36. Hawkins EC, Basseches J, Berry CR, et al. Demographic, clinical, and radiographic features of bronchiectasis in dogs: 316 cases (1988–2000). *J Am Vet Med Assoc*. 2003;223:1628–1635.
37. Reinero CR, Jutkowitz LA, Nelson N, et al. Clinical features of canine pulmonary veno-occlusive disease and pulmonary capillary hemangiomatosis. *J Vet Intern Med*. 2019;33:114–123.
38. Jaffey JA, Williams KJ, Masseau I, et al. Vasoproliferative process resembling pulmonary capillary hemangiomatosis in a cat. *BMC Vet Res*. 2017;13(72).
39. Katajavuori P, Melamies M, Rajamaki MM. Eosinophilic pulmonary granulomatosis in a young dog with prolonged remission after treatment. *J Small Anim Pract*. 2013;54:40–43.
40. Confer AW, Qualls Jr CW, MacWilliams PS, et al. Four cases of pulmonary nodular eosinophilic granulomatosis in dogs. *Cornell Vet*. 1983;73:41–51.
41. Wolf AM, Green RW. The radiographic appearance of pulmonary histoplasmosis in the cat. *Vet Radiol*. 1987;28:34–37.
42. Rampacci E, Sforna M, Dentini A, et al. *Paenibacillus amylolyticus* osteomyelitis in a Poodle dog: case report and literature review. *J Vet Diagn Invest*. 2022;34:703–708.
43. Hornby NL, Lamb CR. Does the computed tomographic appearance of the lung differ between young and old dogs? *Vet Radiol Ultrasound*. 2017;58:647–652.
44. Dahl K, Rørvik AM, Lanageland M. Bronchogenic cyst in a German shepherd dog. *J Small Anim Pract*. 2002;43:456–458.
45. Pechman RD. The radiographic features of pulmonary paragonimiasis in the dog and cat. *Vet Radiol*. 1976;17:182–191.
46. Johnson VS, Corcoran BM, Wotton PR, et al. Thoracic high-resolution computed tomographic findings in dogs with canine idiopathic pulmonary fibrosis. *J Small Anim Pract*. 2005;46:381–388.
47. Bello AM, Anselmi C, Frau M, et al. Pulmonary carcinoma associated with cystic airspaces in two dogs. *J Small Anim Pract*. 2022;63:486–491.
48. Venco L, Genchi C, Genchi M, et al. Clinical evolution and radiographic findings of feline heartworm infection in asymptomatic cats. *Vet Parasitol*. 2008;158:232–237.
49. Flückiger MA, Gomez JA. Radiographic findings in dogs with spontaneous pulmonary thrombosis or embolism. *Vet Radiol*. 1984;25:124–131.
50. Johnson LR, Lappin MR, Baker DC. Pulmonary thromboembolism in 29 dogs: 1985–1995. *J Vet Intern Med*. 1999;13:338–345.
51. Mortier JR, Mesquita L, Ferrandis I, et al. Accuracy of and interobserver agreement regarding thoracic computed tomography for the diagnosis of chronic bronchitis in dogs. *J Am Vet Med Assoc*. 2018;253:757–762.
52. Hofeling AD, Jackson AH, Alsup JC, et al. Spontaneous midlobar lung lobe torsion in a 2-year-old Newfoundland. *J Am Anim Hosp Assoc*. 2004;40:220–223.
53. Seiler G, Schwarz T, Vignoli M, et al. Computed tomographic features of lung lobe torsion. *Vet Radiol Ultrasound*. 2008;49:504–508.
54. Belmudes A, Gory G, Cauvin E, et al. Lung lobe torsion in 15 dogs: peripheral band sign on ultrasound. *Vet Radiol Ultrasound*. 2021;62:116–125.
55. Ballegeer EA, Forrest LJ, Stepien RL. Radiographic appearance of bronchoalveolar carcinoma in nine cats. *Vet Radiol Ultrasound*. 2002;43:267–271.
56. Bouyssou S, Specchi S, Desquilbet L, et al. Radiographic appearance of presumed noncardiogenic pulmonary edema and correlation with the underlying cause in dogs and cats. *Vet Radiol Ultrasound*. 2017;58:259–265.
57. Johnson LR, Johnson EG, Hulsebosch SE, et al. Eosinophilic bronchitis, eosinophilic granuloma, and eosinophilic bronchopneumopathy in 75 dogs (2006–2016). *J Vet Intern Med*. 2019;33:2217–2226.
58. Fina C, Vignoli M, Terragni R, et al. Computed tomographic characteristics of eosinophilic pulmonary granulomatosis in five dogs. *Vet Radiol Ultrasound*. 2014;55:16–22.
59. Clercx C, Peeters D, Snaps F, et al. Eosinophilic bronchopneumopathy in dogs. *J Vet Intern Med*. 2000;14:282–291.
60. Campbell VL, King LG. Pulmonary function, ventilator management, and outcome of dogs with thoracic trauma and pulmonary contusions: 10 cases (1994–1998). *J Am Vet Med Assoc*. 2000;217:1505–1509.
61. Lippi I, Puccinelli C, Perondi F, et al. Predictors of fatal pulmonary haemorrhage in dogs affected by leptospirosis approaching haemodialysis. *Vet Sci*. 2021;8.
62. Schaffer PA, Hershkowitz CS, Dowers KL, et al. Delayed diagnosis of fatal pneumonic canine plague: clinical and pathologic features in two naturally infected Colorado dogs. *BMC Vet Res*. 2020;16:160.
63. Chapman PS, Boag AK, Guitian J, et al. *Angiostrongylus vasorum* infection in 23 dogs (1999–2002). *J Small Anim Pract*. 2004;45:435–440.

ELECTRONIC RESOURCES

Additional information related to the content in Chapter 36 can be found online at eBooks.Health.Elsevier.com.

- Chapter Quiz

CHAPTER 37

Equine Thorax

Stephanie G. Nykamp

RADIOGRAPHIC TECHNIQUE

Technical aspects of radiographing the equine thorax are covered in Chapter 28, but important principles are reiterated here. Radiographing the entire thorax of an adult horse requires a grid and large stationary x-ray tubes that are generally available only at referral centers. Portable radiographic tubes require an excessively long exposure time to penetrate the adult thorax; this usually results in motion artifact, rendering the images nondiagnostic. The advantages of digital imaging are covered in Chapter 2. The improved contrast of digital imaging is advantageous but the various processing algorithms from different systems can also increase the conspicuity of normal lung markings resulting in overinterpretation of the images. Digital images can have scatter correction in the processing algorithm but an antiscatter grid is still recommended for adult horses.[1]

Four overlapping 14-inch × 17-inch views are usually required to image the entire thorax of an adult horse. They are acquired in the craniodorsal, caudodorsal, caudoventral, and cranioventral aspects of the thorax (Fig. 37.1). In addition to these standard views, radiographs centered over any identified lesions may also be useful.

Lateral radiographs of the foal thorax may be made with a single 14-inch × 17-inch cassette and some portable x-ray tubes. Dorsoventral (DV) or ventrodorsal (VD) radiographs should also be acquired on foals whenever possible.

The horse should be positioned with the thoracic limbs slightly forward to reduce the amount of muscle mass superimposed on the cranial aspect of the thorax. Radiographs should be obtained during peak inspiration. In some instances, radiographs should also be obtained during expiration because a comparison of the degree of lung inflation between inspiratory and expiratory radiographs may be helpful in the diagnosis of air trapping from chronic pulmonary disease.

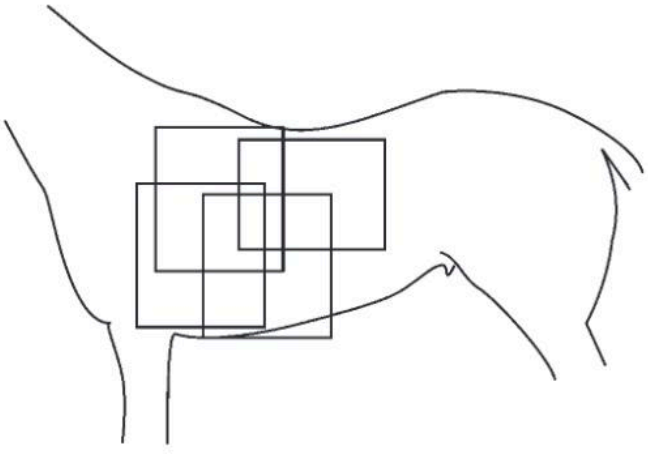


Fig. 37.1 Placement of cassettes or imaging plates for the four standard radiographic views of the equine thorax.

When thoracic radiographs are obtained in a standing horse, the lung closest to the cassette is seen most clearly. This occurs because the large width of the equine thorax results in the lung farthest from the cassette being magnified and blurred to the extent that even large lesions can be obscured. This is opposite to the situation in lateral radiographs of dogs and cats where lesions in the nondependent lung (i.e., farthest from the cassette) are seen most clearly because of the atelectasis that occurs in the dependent lung. In the horse, therefore, left-right and right-left radiographs are necessary to assess both the left and right lungs adequately in patients with pneumonia or neoplasia. Bilateral radiographs are less likely to impact the diagnosis in patients with diffuse or inflammatory disease but as this is not known prior to imaging bilateral radiographs are recommended.[2]

Radiographic exposure and degree of inspiration play an important role in the interpretation of thoracic radiographs and must be considered both for initial and serial radiographic examinations. As the quality of the radiograph improves, the amount of perceived interstitial lung pattern decreases.[3] If a radiograph is underexposed or obtained during expiration, the lungs will appear diffusely more opaque than normal, mimicking a mild diffuse interstitial lung pattern often mistaken for disease. If the radiographs are overexposed, small or mild lung lesions may be obscured.

Craniodorsal Projection

The dorsal portion of the heart, descending aorta, caudal vena cava, hilar pulmonary arteries and veins, trachea, and carina are visible (Fig. 37.2). The hilar portions of the lungs are visible but are difficult to evaluate because of the superimposition of the heart and blood vessels.

Caudodorsal Projection

This view provides the largest unobstructed view of the lungs (Fig. 37.3). The normal equine lung has a mild diffuse bronchointerstitial lung pattern when compared with canine and feline lungs. The pulmonary blood vessels should be seen clearly, tapering toward the periphery of the lung field.

Caudoventral Projection

The caudal borders of the heart, left atrium, caudal vena cava, pulmonary veins, and pulmonary arteries are evident on this view (Fig. 37.4). A small triangle of lung bounded by the caudal vena cava, caudal border of the heart, and cranioventral aspect of the diaphragm is evident. Because of the cardiac notch, no pulmonary markings are present over the central portion of the heart. The absence of pulmonary blood vessels in this region should not be mistaken for lung consolidation. The diaphragmatic reflection of the pleura follows the costochondral junctions to approximately the ninth rib and then travels dorsally,

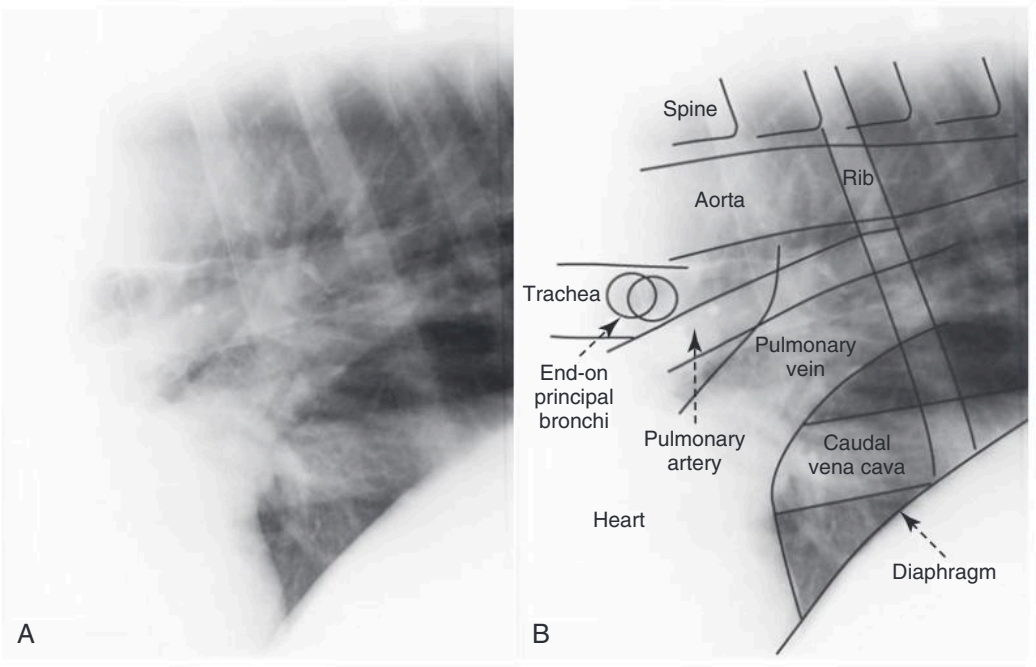


Fig. 37.2 Normal adult thoracic radiograph **(A)**, craniodorsal projection, and accompanying line drawing **(B)**.

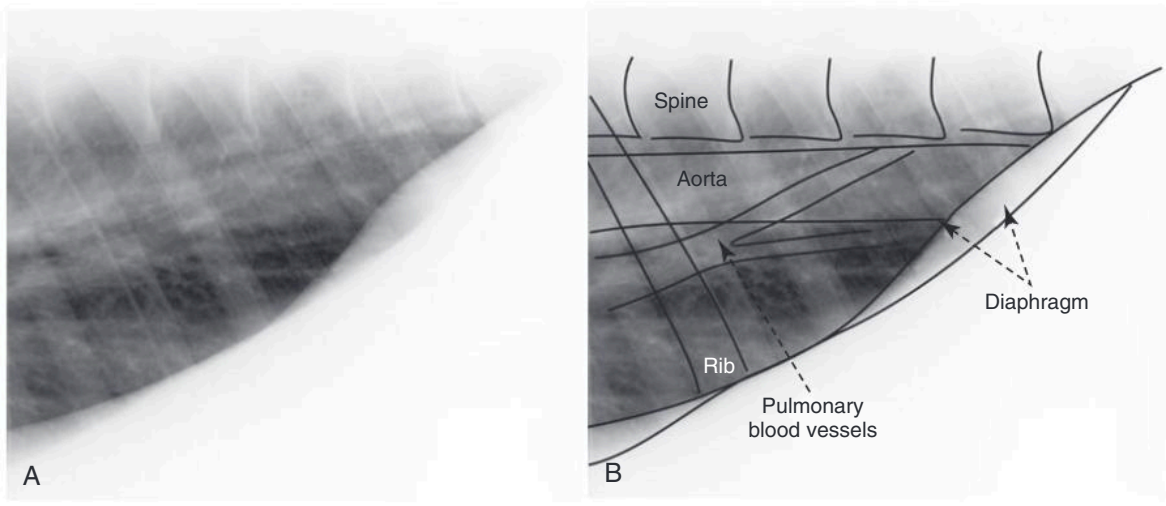


Fig. 37.3 Normal adult thoracic radiograph **(A)**, caudodorsal projection, and accompanying line drawing **(B)**.

paralleling the costal arch to the middle of the last rib. This means that the normal lung does not extend ventral to the costochondral junction and, in fact, usually ends approximately 4 inches above the costochondral junction in adult horses at rest.[4] Ventral to the costochondral junction is mediastinal fat that provides contrast between the caudal border of the heart and the diaphragm. This fat opacity should not be mistaken for pleural or pulmonary disease.

Cranioventral Projection

The cranial portions of the lung, cranial mediastinum, aortic arch, and trachea are evident on this projection (Fig. 37.5). The lung is difficult to evaluate in this region because of the superimposition of the thoracic limbs. Except for evaluating for a mediastinal mass, this is typically the least helpful of all projections.

NORMAL ANATOMY

The right and left lungs are not clearly divided by interlobar fissures. The left lung is divided into a cranial and caudal component. The right lung is divided into a cranial and caudal component and the accessory lobe. A prominent cardiac notch is present in the left and right lungs at the level of the third to the sixth ribs overlying the midventral aspect of the heart. The ventral aspect of the caudal lung lobes is visible as a triangle of lung bordered by the caudal aspect of the heart, diaphragm, and caudal vena cava. The appearance of the lungs is also influenced by the phase of respiration, age, and body condition.

Adults

Many adult horses with normal respiratory function and no clinical signs of respiratory disease have a mild, diffuse

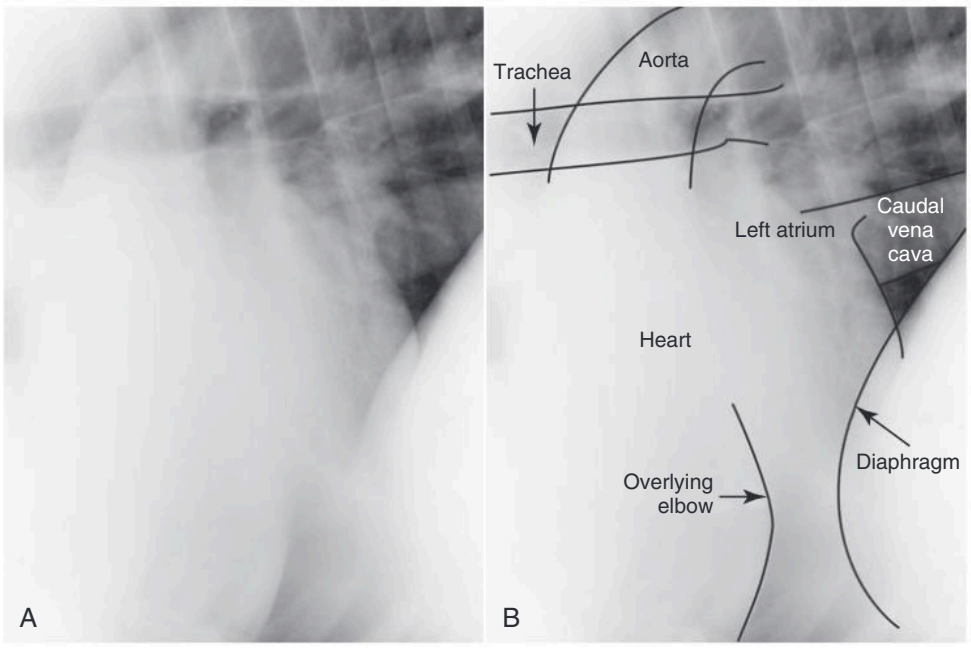


Fig. 37.4 Normal adult thoracic radiograph **(A)**, caudoventral projection, and accompanying line drawing **(B)**.

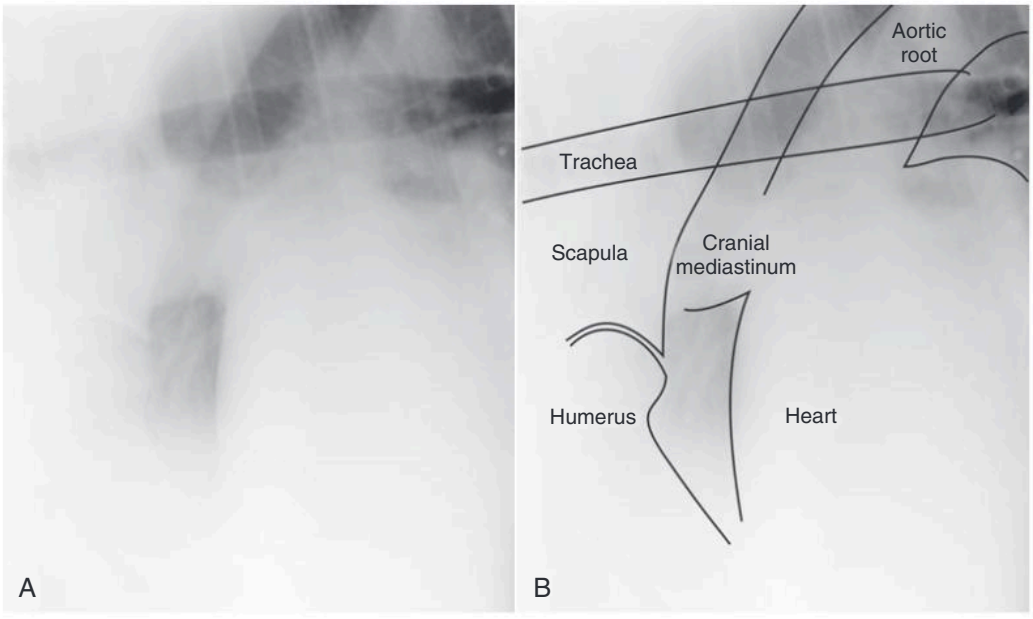


Fig. 37.5 Normal adult thoracic radiograph **(A)**, cranioventral projection, and accompanying line drawing **(B)**.

bronchointerstitial lung pattern as a normal variation which is even more prominent with digital imaging.[3,5] This opacity may be caused by the slightly more abundant lobulation and connective tissue that is present in horses or by subclinical peribronchial fibrosis.[3] The presence of this mild bronchointerstitial lung pattern means that the correlation between radiographic changes and clinical disease is often poor. Therefore, mild radiographic changes should be interpreted with caution (Fig. 37.6).[3,6,7]

Foals

When radiographed immediately after parturition, foals have a mild diffuse interstitial lung pattern because of incomplete expansion of the lungs, fluid in the small airways, and the uptake of fetal alveolar fluid in the interstitium (Fig. 37.7). This opacity should resolve within 6 hours of birth.[8–10] The thymus is large in foals and can sometimes be seen as a soft tissue opacity cranial to the heart. The thymus is largest at approximately 2 months of age and should regress as the foal ages.[9] Atelectasis occurs rapidly when foals are placed in lateral recumbency. This will result in the lungs of recumbent foals appearing more opaque than those of standing foals.[9]

Heart

Objective criteria for assessing heart size have not been established in horses.[11] The caudal border of the heart should be

straight and should parallel the angle of the ribs. Elevation of the trachea and increased sternal or diaphragmatic contact are indicative of cardiomegaly.[11] Assessment of cardiac size is easiest if the entire cardiac silhouette is visible in one image acquired with the x-ray beam centered over the heart. In foals, the cardiac silhouette occupies a larger volume of the thoracic cavity than it does in adults.[9] Based on objective measurements of cardiac size in foals, the height should be 6.6 to 7.8 times the length of a midthoracic vertebral body, and the width should be 5.6 to 6.3 times the width of a midthoracic vertebral body.[8] Echocardiography is superior to radiography in assessing cardiac size and function.

ALTERNATIVE IMAGING MODALITIES

Fluoroscopy is useful to evaluate esophageal disease, tracheal collapse, and the motion of thoracic masses. Unfortunately, fluoroscopy for equine evaluation is not available readily.[12]



Fig. 37.6 Right lateral radiograph of the caudodorsal thorax in an adult horse with no clinical signs. Note the mild diffuse bronchial lung pattern seen in normal horses.

The use of ultrasound is common in equine practice. Air prevents the transmission of ultrasound waves, so the ultrasound appearance of the normal lung is a bright interface with reverberation artifact characterized by equally spaced lines that parallel the surface of the lung (Fig. 37.8). In real time, the normal lung slides along the body wall during respiration. Ultrasound is more sensitive than radiographs in the detection of small pulmonary lesions as long as they extend to the pleural surface.[13] Ultrasound is the diagnostic test of choice for evaluating pleural disease in the horse because it is more sensitive to the detection of small amounts of fluid and provides information on the character of the fluid. [12,14] Ultrasound can also be used to assess the surface of the lung. A few areas of rough pulmonary surfaces that create a comet tail artifact can be seen in the ventral portions of the normal lung, but more extensive lesions will be present in horses with viral pneumonia and chronic pleural fibrosis (Fig. 37.9).[15,16] Ultrasound correlates well with radiographs and postmortem in cases of diffuse pulmonary disease such as acute interstitial pneumonia in foals.[17] Ultrasound is an inexpensive and accessible diagnostic test for serial monitoring for resolution or progression of disease. Point of care ultrasound as part of the routine physical examination is valuable in horses to detect pleural, pericardial, and peripheral pulmonary disease and is more readily available than radiographs.

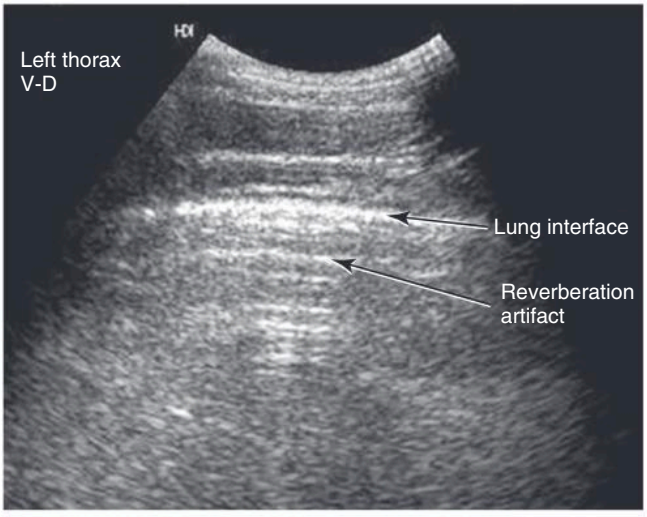


Fig. 37.8 Transverse ultrasound image of the normal left lung (ventrodorsal orientation). Note the equally spaced white lines (reverberation artifact) caused by the sound reflected at the air interface.

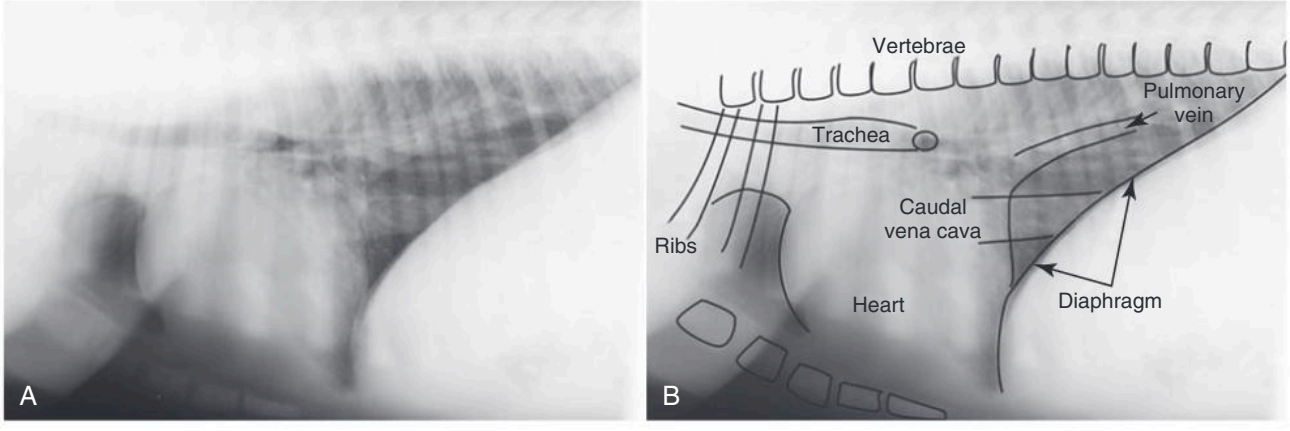


Fig. 37.7 Normal foal thoracic radiograph **(A)** and accompanying line drawing **(B)**.

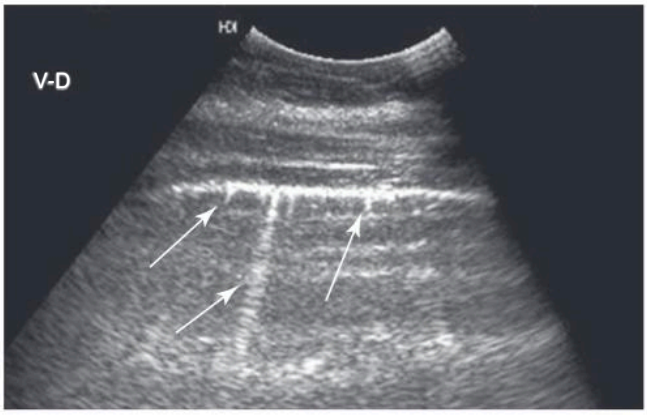


Fig. 37.9 Transverse ultrasound image of the lung. The pleural surface of the lung is rough, which results in a reverberation artifact, otherwise referred to as *comet tail artifact* (*arrows*). A few comet tails can be seen in normal horses.

Nuclear scintigraphy can provide physiologic information about perfusion and ventilation of the lungs. Ventilation studies can be useful in assessing chronic obstructive pulmonary disease and exercise-induced pulmonary hemorrhage.[18] The images are characterized by a patchy distribution with hot spots centrally caused by deposition of the injected isotope in the larger airways and cold spots peripherally from lack of ventilation. Additionally, radiopharmaceutical is cleared more rapidly from the lung of horses with chronic obstructive pulmonary disease than in normal horses.[19] Perfusion studies are used to evaluate for pulmonary thromboembolic disease, chronic obstructive pulmonary disease, and other diffuse diseases. In combination with ventilation studies, the patient can be evaluated for ventilation and perfusion mismatches. Because of the expensive equipment and the need to isolate the patient for approximately 24 hours after the study to allow for radioactive decay, these imaging studies are usually limited to referral hospitals.

Computed tomography (CT) is an excellent imaging modality for assessment of the thorax, but, because of equipment size, its use is restricted to smaller foals.[20] CT is more sensitive to the detection of pulmonary pathology and interpretation is less subjective than radiographs but is subject to positional atelectasis that occurs secondary to sedation or anesthesia (Fig. 37.10).[21] Compared to ultrasound, CT more accurately evaluates rib fractures in foals which assists in treatment planning.[22]

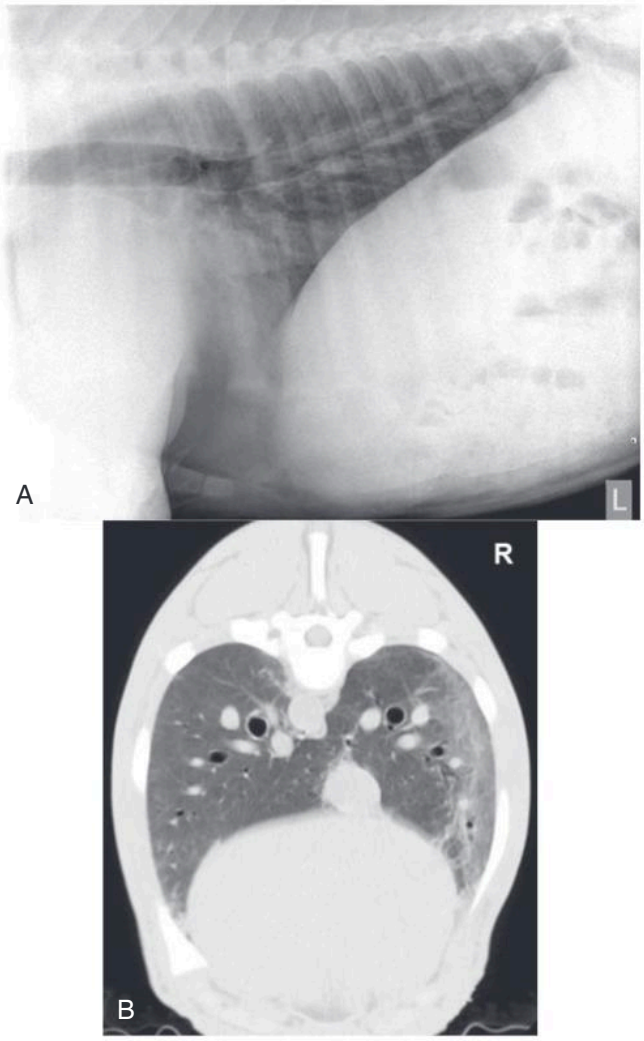


Fig. 37.10 Right-left lateral standing radiograph **(A)** and computed tomography (CT) image **(B)** of a foal that has been in right lateral recumbency. No abnormalities are noted on the radiograph. Increased attenuation is evident in the periphery of the right lung on the CT. This is due to positional atelectasis.

PULMONARY DISEASE

Radiographs complement a physical examination; they do not replace it. Physical examination can be unremarkable, and yet substantial radiographic abnormality can be present. Additionally, the radiographic resolution of disease often lags behind the clinical resolution. This should be considered when evaluating serial studies.[23] Bronchoalveolar lavage, a common diagnostic procedure in horses with respiratory disease, can cause an interstitial pulmonary pattern in the lungs and should be done following radiographs to avoid interpretation errors.[24]

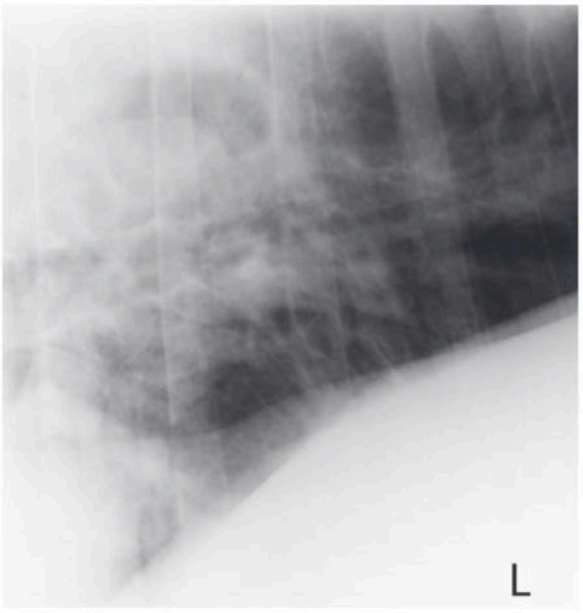
The patterns of pulmonary disease have been discussed in Chapter 36. As in the dog and cat, the radiographic pulmonary pattern correlates poorly with the histologic location of the disease. For example, in equine parasitic pneumonia, the most common pulmonary pattern is interstitial, but grossly, the disease is predominantly alveolar, and horses with a diffuse interstitial lung pattern have peribronchial disease on histologic examination.[3,25] But radiographic patterns can reflect the severity of the disease, with bronchial and interstitial patterns suggesting less severe disease than an alveolar pattern.[23] The distribution of the pulmonary disease may be more useful with regard to the cause of the pulmonary disease than the pattern itself.[9,26] For example, bronchopneumonia and aspiration pneumonia tend to have a cranioventral and caudoventral distribution, whereas pulmonary edema and interstitial pneumonia are more caudodorsal to diffuse in their distribution.

Pneumonia

In adults, bronchopneumonia is usually a result of transportation or stress, whereas in foals it is usually caused by sepsis or aspiration.[27,28] In adults and foals, bronchopneumonia can occur secondary to viral pneumonia.[28] Bacterial pneumonia and aspiration pneumonia usually occur in the cranioventral and caudoventral portions of the lung. The cranial portion of the lung is difficult to evaluate radiographically, so the disease is most conspicuous when superimposed on the caudal border of the heart (Fig. 37.11, eFig. 37.1). Bacterial pneumonia can result in an interstitial or alveolar lung pattern depending on the severity (Fig. 37.12). Abscess formation presents as solid or cavitated nodules that may be poorly or well defined (eFig. 37.2).



eFig. 37.1 Lateral caudoventral thoracic radiograph of a pony after an episode of choke. There is an interstitial, coalescing to alveolar pulmonary pattern present in the caudoventral lungs, caused by aspiration pneumonia.



eFig. 37.2 Right-left lateral caudodorsal radiograph in an adult horse with a focal pulmonary abscess. There is a circular soft tissue rim with a central gas opacity located dorsal to the tracheal bifurcation. In the pattern recognition scheme, this is a structured interstitial pattern.

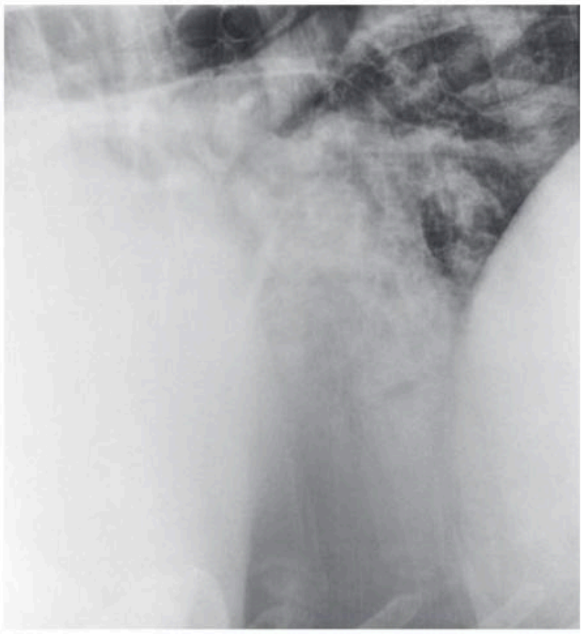


Fig. 37.11 Lateral caudoventral thoracic radiograph. A fairly intense soft tissue opacity is superimposed on the caudal aspect of the heart that partially silhouettes pulmonary blood vessels, making their margins appear indistinct. This lesion is caused by bronchopneumonia. In the pattern recognition scheme, this lesion is consistent with an interstitial pattern. The small irregular gas opacities overlying the heart are caused by small abscesses.

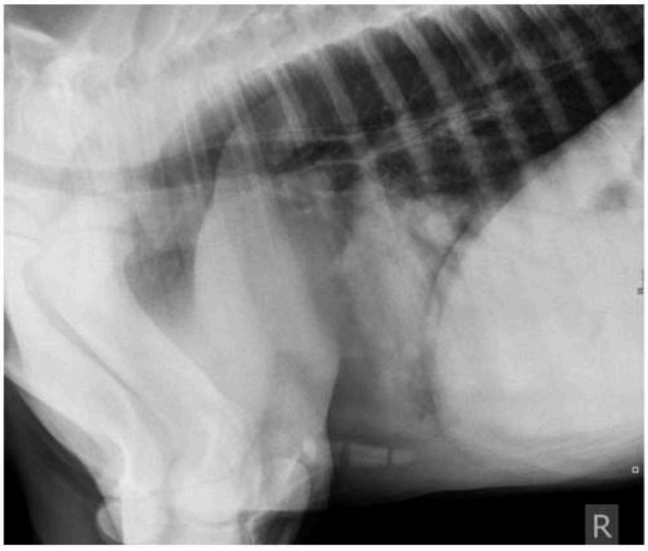


Fig. 37.12 Lateral thoracic radiograph of a foal. A soft tissue opacity that obscures the pulmonary blood vessels and faint air bronchograms is superimposed on the caudal aspect of the heart. In this foal, pneumonia developed as a result of aspiration of milk. In the pattern recognition scheme, this lesion is consistent with an alveolar pattern. A tube with a linear radiopaque marker is present in the esophagus.

The ultrasonographic appearance of pneumonic lung is a uniform echogenicity that resembles the appearance of liver (Fig. 37.13). Air-filled bronchi appear as hyperechoic, linear, branching structures that have a reverberation artifact. Fluid-filled bronchi appear as anechoic branching tubes (Fig. 37.14). Fluid-filled bronchi can be differentiated from blood vessels with Doppler interrogation.

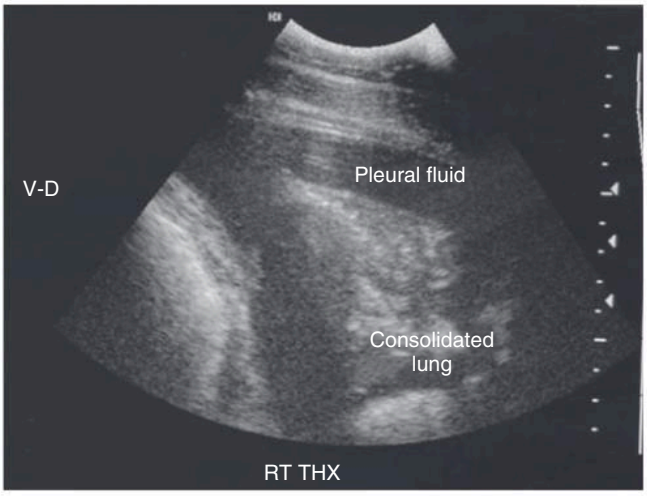


Fig. 37.13 This transverse ultrasound image is characterized by pleural fluid and consolidated lung. The lack of the normal reverberation artifact seen with aerated lung is evidence that the lung is abnormal. The lung has a relatively uniform soft tissue echogenicity similar to the appearance of normal liver and is triangular in shape. The pleural fluid is present between the lung and the body wall.

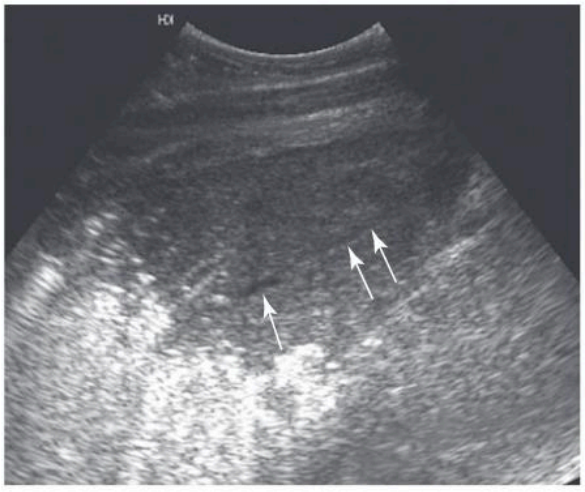


Fig. 37.14 This transverse ultrasound image shows consolidation of the lung and a fluid bronchogram (*arrows*). The deep aerated portion of the lung is the irregular hyperechoic interface.

Interstitial Pneumonia

Interstitial pneumonia occurs in foals and adults and can be acute or chronic.[29,30] The causative agent is usually not identified but may include infectious agents, toxins, systemic inflammatory response syndrome, or allergic factors.[23,27,29–31]

Interstitial pneumonia in foals is usually acute, and affected foals are typically 6 weeks to 6 months of age.[29,32] Chronic interstitial pneumonia has a more favorable prognosis, whereas acute interstitial pneumonia has a high mortality rate.[30,33] Whether the disease is acute or chronic, the radiographic changes are the same, a diffuse interstitial lung pattern.[29,32] A mild to moderate bronchial lung pattern may also be present.[30] The disease can result in increased vascular permeability and secondary pulmonary edema.[33] The severity of the changes on the initial radiographs and progression of the changes on subsequent radiographs are negative prognostic indicators.[23]

Interstitial pneumonia is rare in adults, and because the lung has a limited range of responses to injury, it usually presents as a chronic problem with secondary fibrosis, and affected horses

usually respond poorly to treatment.[28,33–36] The most common radiographic appearance is a patchy to diffuse alveolar lung pattern and the appearance can overlap with equine multinodular fibrosis with histopathology being the only way to determine the underlying cause.[29,36] Interstitial fibrosis can occur secondary to a variety of diseases.

Pulmonary Abscess

Pulmonary abscesses can form as a result of pleuropneumonia or develop independently and predominantly affect foals younger than 6 months of age.[37] They can occur anywhere in the lung, but unlike bronchopneumonia, abscesses are most commonly detected in the caudodorsal lungs.[38] This may be because of the excellent contrast provided by air-filled lung in this region. Abscesses are discrete, focal, soft tissue nodules or masses that may be sharply or poorly margined. If the abscess communicates with a bronchus or contains gas-forming bacteria, a discrete gas–fluid interface will be seen on horizontal-beam radiographs (Fig. 37.15, see eFig. 37.2) Well-margined pulmonary consolidation can mimic the appearance of a pulmonary abscess.

By obtaining left-right and right-left radiographs centered over the lesion, the abscess can be localized to one lung. When the abscess is located in the lung closest to the cassette or imaging plate, it will be smaller and more sharply marginated (Fig. 37.16). If the lesion is located close to midline, it will appear approximately the same on left-right and right-left radiographs.[39]

Ultrasound can be used to diagnose pleural-based pulmonary abscesses as well as abscesses that are within consolidated lung and that would not be evident on radiographs. Abscesses are usually hypoechoic to the surrounding pulmonary parenchyma and are defined by the absence of normal blood vessels and bronchi (Fig. 37.17).

Rhodococcus equi

Pneumonia caused by *Rhodococcus equi* in foals is a specific disease entity that frequently has a different radiographic



Fig. 37.15 Lateral radiograph of the craniodorsal thorax. A focal, cavitated pulmonary abscess is present. The dorsal portion of this abscess has a thick rim, and a distinct gas/fluid interface is seen.

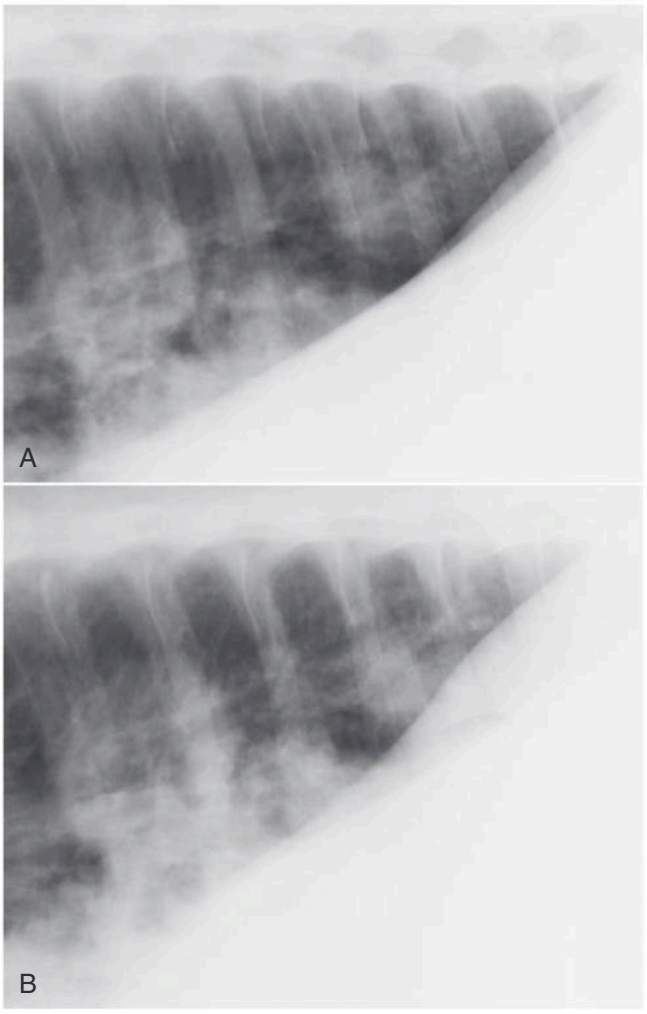


Fig. 37.16 Right-left **(A)** and left-right **(B)** radiographs of the caudal aspect of the thorax. The pulmonary nodule is smaller on the right-left radiograph, which means that it is in the left lung.

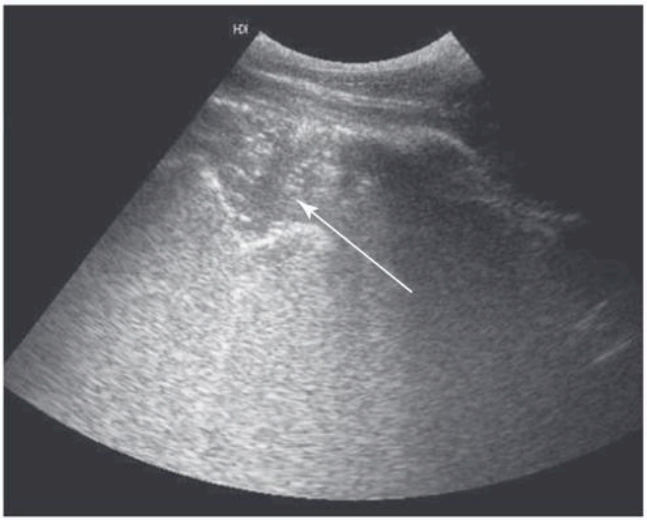


Fig. 37.17 Transverse ultrasound image of the left thorax. There is a focal hypoechoic nodule surrounded by air (*arrow*). This lesion was a pulmonary abscess.

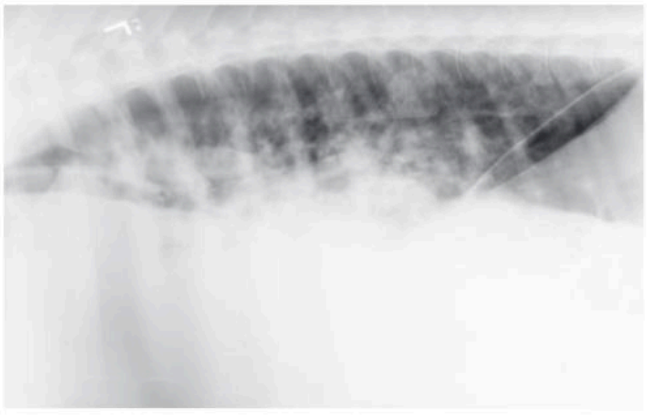


Fig. 37.18 Right-left lateral radiograph of a 3-month-old foal with pneumonia caused by *Rhodococcus equi* infection. An alveolar lung pattern is present in the ventral portion of the lung. Multiple soft tissue nodules are present dorsocaudally, the largest of which is cavitated. The nodules are caused by abscess formation.

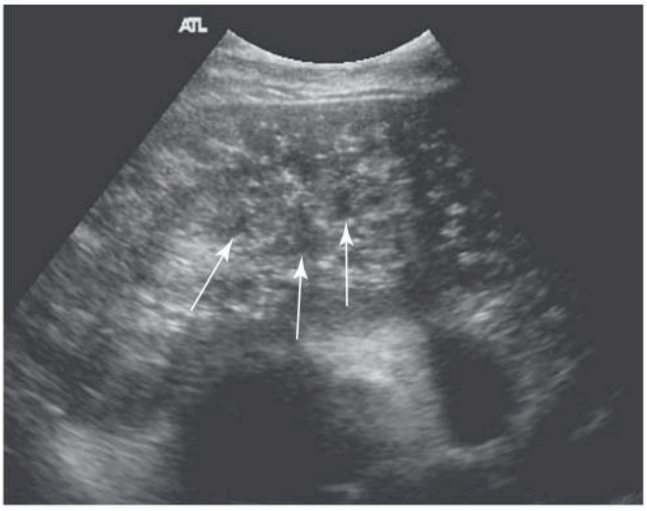


Fig. 37.19 Transverse ultrasound image of the left aspect of the thorax of a foal with *Rhodococcus equi* infection. The lung is consolidated completely with a heterogeneous echogenicity. Multiple small, hypoechoic nodules are evident (*arrows*). These are small abscesses within the consolidated lung.

appearance than bronchopneumonia or interstitial pneumonia. *R. equi* pneumonia typically has a patchy to diffuse alveolar lung pattern and/or discrete pulmonary nodules (abscesses) (Fig. 37.18, eFig. 37.3).[6,27] It can also result in consolidation of one lung lobe. Radiographic changes are most apparent at approximately 3 weeks after infection. The severity of the radiographic changes, including the severity of the alveolar pulmonary pattern and the number of cavitary lesions, has been negatively associated with prognosis.[40,41] Foals with an extensive alveolar lung pattern or pulmonary nodules (abscesses) were more likely to die.[42] Tracheobronchial and cranial mediastinal lymphadenopathy can also be detected. In most foals, the radiographic signs resolve completely within 3 months of appropriate therapy.[6] Ultrasonographic evidence of pneumonia has been highly associated with radiographic abnormalities making it a useful diagnostic field test and may allow for detection of abscesses within consolidated lung lobes that are not evident radiographically (Fig. 37.19).[43]

Fungal Pneumonia

Fungal pneumonia is rare in horses. It has a wide range of radiographic appearances. Although it cannot be differentiated reliably from bacterial pneumonia on the basis of radiographic appearance, the distribution of fungal pneumonia is usually more diffuse than bacterial pneumonia and typically has an interstitial to indistinct nodular appearance.[44–47] Tracheobronchial lymphadenopathy and pleural effusion may also be present.[44,46]

Viral Pneumonia

Viral pneumonia itself does not usually result in radiographic changes, but radiographs can still be indicated to evaluate for concurrent bacterial pneumonia, which is common and results in more severe clinical disease.[15,48] Ultrasonographically, there may be roughening of the pleural surface with production of comet tail artifacts and consolidation of the cranioventral aspect of the lung within 5 to 10 days of infection.[15]

Multinodular Pulmonary Fibrosis

Multinodular pulmonary fibrosis is a subset of pulmonary fibrosis associated with equine herpesvirus type 5 (EHV-5) and characterized by a severe diffuse nodular interstitial pulmonary pattern.[49–51] Clinical signs include weight loss, fever, tachypnea, tachycardia, neutrophilic lymphocytosis, and hyperfibrinogenemia, and increased respiratory effort.[37] The imaging findings are varied with a combination of bronchial, interstitial, and alveolar patterns but the majority of cases have multifocal nodules that are evident radiographically and with thoracic ultrasound.[50–52] Tracheobronchial lymphadenopathy can also be present[51] (Fig. 37.20).

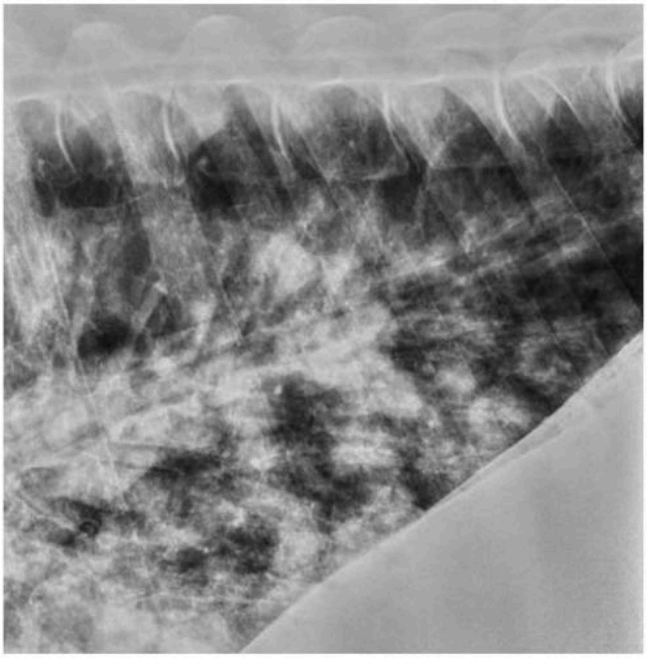
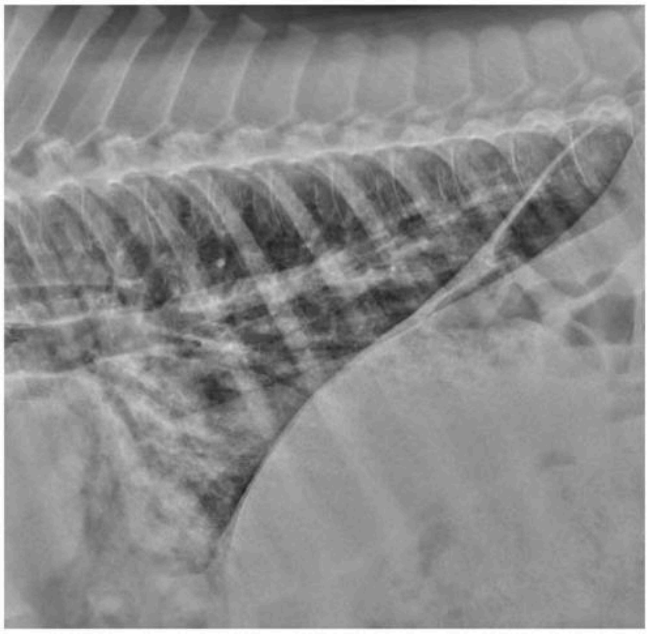


Fig. 37.20 Left lateral radiograph of the caudodorsal thorax of a horse with equine herpesvirus-5 (EHV-5) infection and multinodular pulmonary fibrosis. Note the multiple pulmonary nodules. There is a generalized unstructured interstitial pulmonary pattern present as well.

Other causes of a diffuse interstitial to nodular lung pattern are the eosinophilic pneumopathy, including multisystemic eosinophilic epitheliotropic disease (systemic disease), idiopathic chronic eosinophilic pneumonia (localized pulmonary disease), fungal pneumonia, pulmonary silicosis, and metastatic neoplasia.[53–56]

Inflammatory Airway Disease and Recurrent Airway Obstruction

Inflammatory airway disease and recurrent airway obstruction are two distinct clinical entities that are indistinguishable



eFig. 37.3 Left-right lateral radiograph of a foal with pneumonia caused by *Rhodococcus equi* infection. An alveolar lung pattern is present in the ventral portion of the lung with an adjacent interstitial pattern. Round soft tissue nodules in the ventral thorax represent abscess formation.

radiographically. The pathogenesis of inflammatory airway disease is unclear and may be caused by environmental or infectious causes. Horses of any age can be affected, but it is most commonly seen in young performance horses.[57,58] The clinical signs at rest are subtle, but exercise intolerance or poor performance are often noted.[59] Recurrent airway obstruction, known previously as *chronic obstructive pulmonary disease*, is a major cause of chronic respiratory disease in mature horses and results from inhalation of aerosolized allergens and endotoxin. The lack of labored breathing and severe exercise intolerance distinguish inflammatory airway disease from recurrent airway obstruction.[59] The clinical signs are attributed to bronchitis and bronchoconstriction.[59] As such, the majority of horses with inflammatory airway disease and recurrent airway obstruction have normal thoracic radiographs and radiographs are most helpful in ruling out the presence of other diseases.[3,60] If changes are present, they appear as a diffuse bronchointerstitial lung pattern caused by long-term remodeling of the bronchi. Only the most severe forms of inflammatory airway disease, fibrosis, and bronchiolitis result in radiographic changes.[25,61] Thickening of the bronchi enhances their radiographic visibility, resulting in a pronounced bronchial lung pattern with ring shadows and tram lines (Fig. 37.21, eFig. 37.4). Radiographic scoring systems have been used in an attempt to improve the detection of inflammatory airway disease, but there is no correlation between the score and presence of disease.[60] In recurrent airway obstruction, pulmonary hyperinflation may be present.[62] Hyperinflation is characterized by flattening of the diaphragm and no change in lung volume between inspiratory and expiratory radiographs because of air trapping. Although radiographs are not particularly useful for diagnosing these diseases, they are useful to rule out concurrent bronchopneumonia. Unlike in other species, recurrent airway obstruction generally does not result in chronic pulmonary arterial hypertension and secondary cardiomegaly. This is most likely because the disease is intermittent.[63,64] In end-stage bronchitis, tubular to saccular bronchiectasis can occur.[39]

Exercise-Induced Pulmonary Hemorrhage

Exercise-induced pulmonary hemorrhage is common in racing horses and is characterized by localized or diffuse parenchymal hemorrhage. It is caused by mechanical failure of the walls of the pulmonary capillaries when the internal pressure rises to high levels.[65] Horses with clinical signs of exercise-induced pulmonary hemorrhage often have no or mild radiographic abnormalities which are not distinguishable from airway disease.[66] Additionally, horses with no clinical signs may have severe radiographic changes.[66] Repeated episodes of hemorrhage may be necessary for the lesions to become evident radiographically.[67] If a radiographic lesion is present, it is always located in the caudodorsal lung field, superimposed on the diaphragm, and is usually characterized as a focal area of increased opacity of variable size with indistinct, oval to round cranial margins (Fig. 37.22, eFig. 37.5).[67,68] The radiopacity is usually either interstitial or alveolar in nature, leading to partial or complete silhouetting with the pulmonary blood vessels. An underlying bronchial pattern indicates a chronic lesion. Resolution of the lesion is common in serial radiographs. If the lesions appear cavitary with a distinct gas/fluid interface, a concurrent infection caused by the hemorrhage is suspected. Pleural fluid is also noted in some horses with exercise-induced pulmonary hemorrhage. The presence of comet tail artifacts in the caudodorsal lung on thoracic ultrasound has a high sensitivity (85.8%) and a low specificity (25.7%) for exercise-induced pulmonary hemorrhage.[69,70]

Pulmonary Contusions

Pulmonary contusions can occur as a result of trauma or penetrating wounds. These lesions are seen as poorly marginated areas of increased soft tissue opacity in the lung. The distribution of these lesions corresponds to the location of the trauma.

Pulmonary Edema

Pulmonary edema can result from many causes, including vasculitis, heart failure, and upper airway obstruction.[27,71,72] The distribution is caudodorsal to diffuse, and the pattern can be interstitial or alveolar (Fig. 37.23).[73] Ultrasonographically, diffuse rough pleural surfaces with comet tail artifacts caused by focal areas of consolidation can be seen.[28]

Neoplasia

Primary and metastatic lung tumors are rare in horses. Lung tumors appear as focal or multifocal discrete soft tissue nodules in the lungs.[74–78] The presence of pleural fluid is also common with neoplasia.[76,79] The differential diagnoses for these radiographic signs include abscessation and fungal pneumonia. Pulmonary abscesses and multinodular fibrosis are the most common cause of multifocal pulmonary nodules and should be

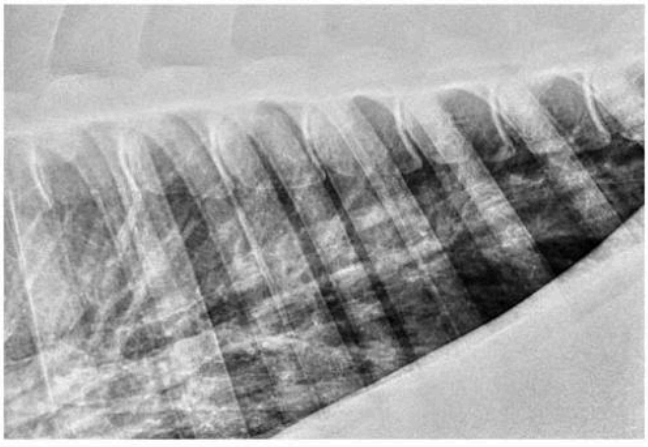


Fig. 37.21 Right lateral radiograph of an adult horse with chronic bronchitis and a bronchial pattern. Note the increased opacity that follows the airways, creating parallel lines and rings.

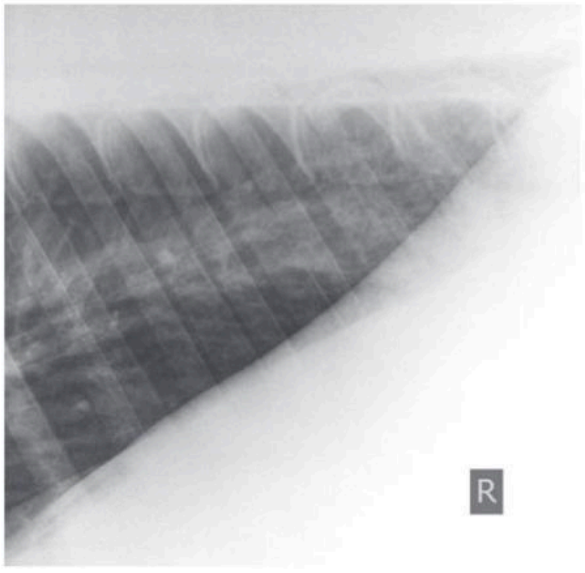
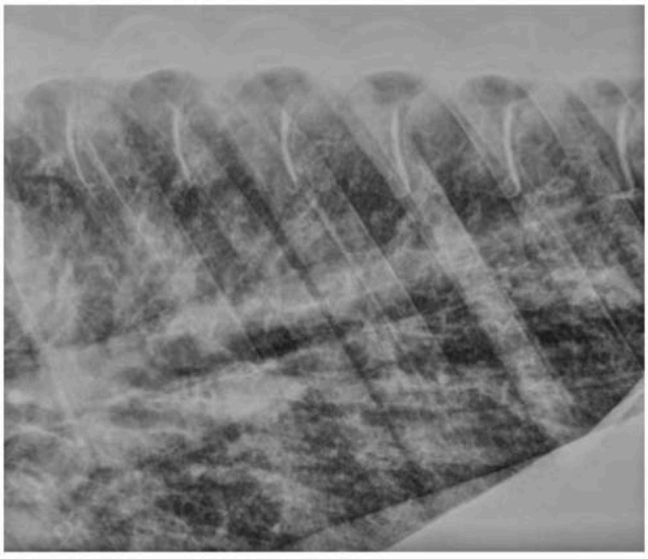
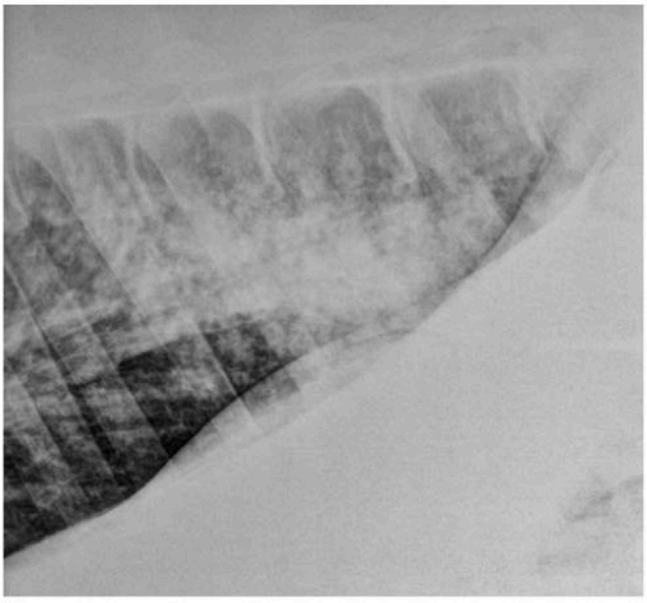


Fig. 37.22 Lateral radiograph of the caudal thorax. A patchy interstitial pattern is superimposed on the dorsal aspect of the diaphragm. This is a common location and appearance of exercise-induced pulmonary hemorrhage.



eFig. 37.4 Left lateral radiograph of an adult horse with chronic bronchitis. The bronchial markings are severely increased with a background of diffuse interstitial pattern.



eFig. 37.5 Lateral radiograph of the caudodorsal thorax of an adult horse with exercise-induced pulmonary hemorrhage. There is a poorly delineated dense interstitial to alveolar pulmonary pattern in the caudodorsal lungs.

considered more likely than neoplasia. If the lesions are pleural based, they can be examined by ultrasound and ultrasound-guided needle aspiration can be performed.[79] Tracheobronchial lymphadenopathy may also be present with primary lung tumors, metastatic tumors, and lymphoma.

Alterations in Pulmonary Vasculature

Assessment of pulmonary vasculature is based on a subjective assessment of the size and number of vessels. The pulmonary veins and arteries generally cannot be distinguished from each other. Diseases that cause overcirculation of the lungs, such as right-to-left shunts, will cause an increase in the size and number of all visible pulmonary blood vessels. Undercirculation of the lungs can be caused by shock or right-to-left shunts.[11]

Pulmonary Disease in Foals

A caudodorsal and caudoventral interstitial pattern is a common radiographic finding in foals.[23] This is nonspecific and can be caused by atelectasis, bacterial pneumonia, viral pneumonia, interstitial pneumonia, prematurity, dysmaturity, or failure of passive transfer, and the causes cannot be differentiated on the basis of radiographs alone (Fig. 37.24).[8,9,30,33,39] Foals with a diffuse distribution of pulmonary disease or a caudodorsal alveolar pattern have a significantly higher mortality rate.[23] Radiographs obtained immediately after parturition often have a diffuse interstitial lung pattern as a result of incomplete expansion of the lungs, fluid in the small airways, and the uptake of fetal alveolar fluid in the interstitium. This complicates the interpretation of these radiographs because it can mask pulmonary disease such as sepsis and acute respiratory distress because of a lack of surfactant. If the opacity does not resolve within 6 hours, it is more likely to be caused by underlying disease.[10]

Concurrent rib fractures may be present with severe respiratory disease in foals (Fig. 37.25).[8,9,30,33,39] Multiple ribs are usually fractured, and these can cause myocardial puncture, hemothorax, or pneumothorax.[74,80] Careful evaluation of the ribs is important, because rib fractures have been associated with increased morbidity and mortality.[81] Osteomyelitis of the costochondral junction is reported only rarely.[82] Ultrasound is superior to radiographs in detecting rib fractures but CT is superior to guide surgical repair (eFig. 37.6).[22,80]

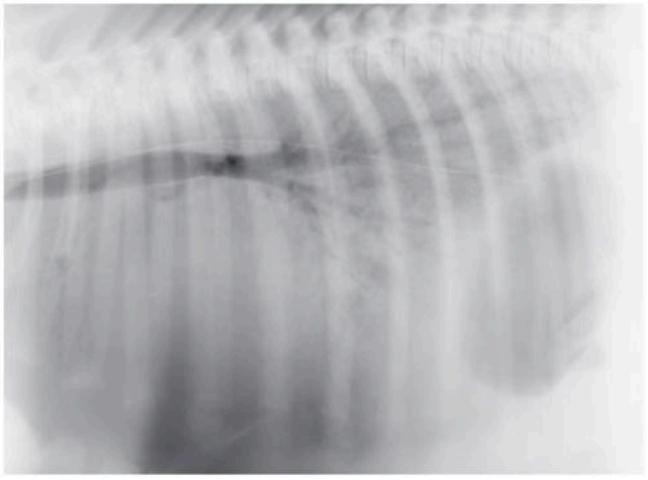


Fig. 37.23 Lateral radiograph of a premature foal with severe pulmonary edema. The lungs are diffusely increased in opacity, and multiple air bronchograms are present.

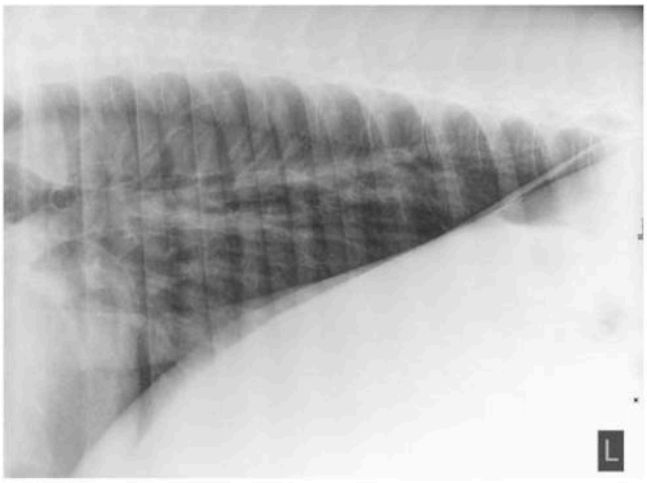


Fig. 37.24 Right-left lateral radiograph of a premature foal. A diffuse increased soft tissue opacity partially silhouettes the pulmonary blood vessels (interstitial pattern). This diffuse interstitial lung pattern was caused by prematurity and resolved with no treatment.

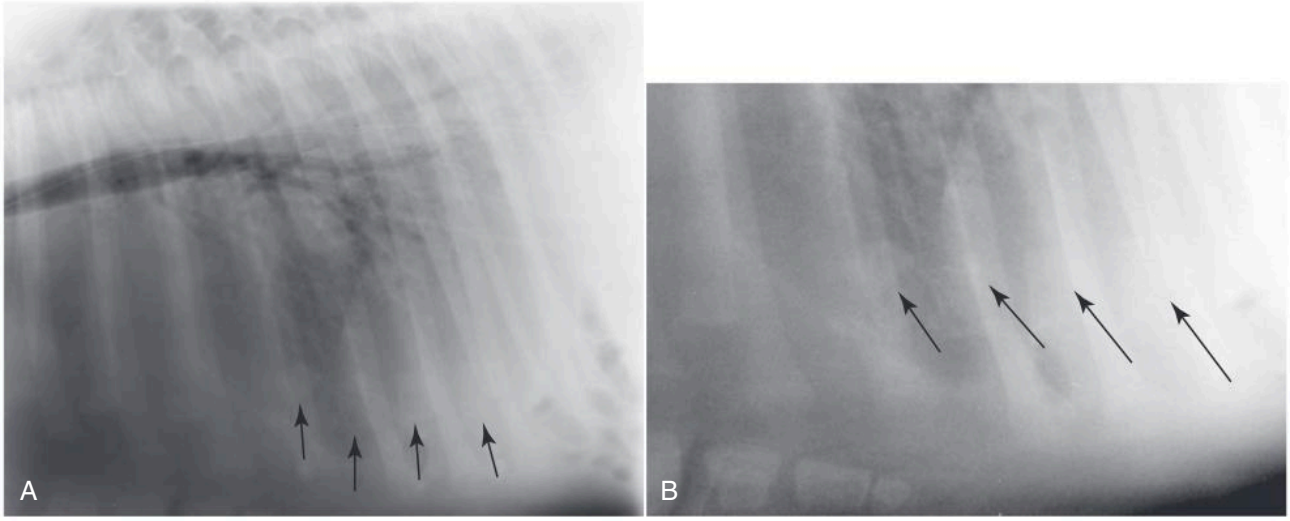
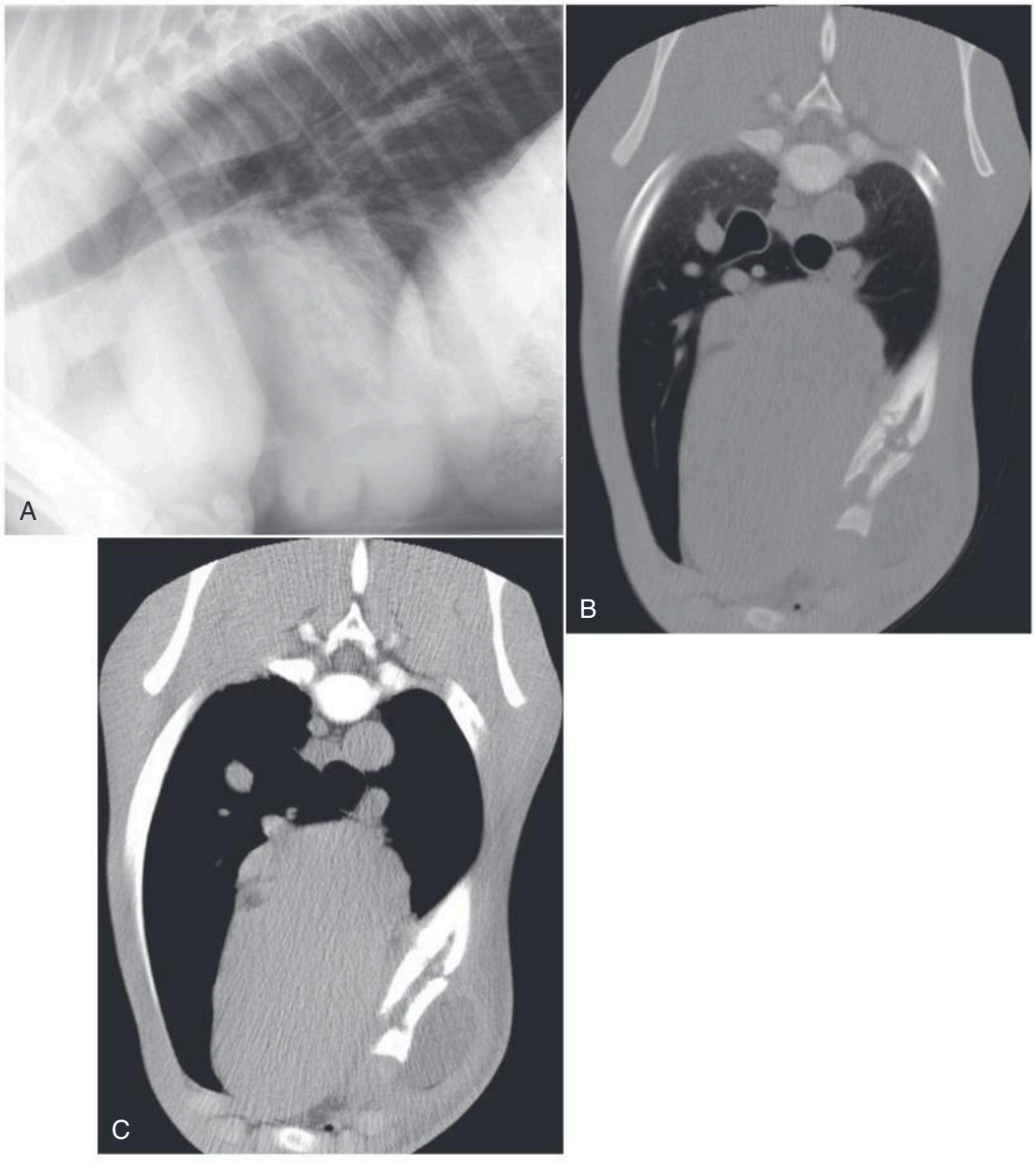


Fig. 37.25 **A,** Right-left lateral radiograph of a foal with severe respiratory distress. A diffuse alveolar pattern is present throughout the lungs and silhouettes with pulmonary blood vessels. Transverse fractures of the ventral portions of multiple ribs are present. **B,** Close-up of the ventral aspect of the thorax centered on the rib fractures (*arrows*).



eFig. 37.6 Left-right radiograph of the thorax **(A)** and transverse computed tomography (CT) in a bone **(B)** and soft tissue window **(C)** of a foal with increased respiratory effort. Radiographically, there is a soft tissue mass with focal gas opacities superimposed on the apex of the heart. In the CT images the fluid-filled mass and lysis and periosteal new bone formation of an adjacent rib are apparent. The rib lesion was not evident radiographically.

Acute interstitial pneumonia is a multifactorial syndrome that is also known as *acute lung injury* and *acute respiratory distress syndrome* in the most severe forms.[83] It is unclear whether these represent distinct clinical entities or severe manifestations of well-recognized pulmonary disease and a wide range of agents have been detected in foals with this syndrome including bacterial or viral infections as well as *Pneumocystis carinii* and coccidiomycosis, and toxic substances.[7,32,33,45,83] The severest presentation is associated with a high mortality rate.[84,85] These are syndromes and not a final diagnosis. Diffuse pulmonary inflammation results in increased vascular permeability and pulmonary edema, resulting in a diffuse, mixed interstitial to alveolar lung pattern that cannot be differentiated from other diffuse diseases.[28,86] Rapid resolution of the pulmonary edema has been associated with improved survival.[84] The presence of persistent radiographic changes after 24 months has been associated with reduced performance but many foals fully recover with no long-term effects.[83,87]

PLEURAL DISEASE

Pleural Fluid

The most common cause of pleural fluid in the horse is extension of bacterial pneumonia into the pleural space, resulting in pleuropneumonia.[48,88] Other causes of pleural fluid include neoplasia (lymphoma, mesothelioma, metastatic disease, and primary lung tumors), foreign bodies, and trauma (hemorrhage).[89,90] Pleural fluid is uncommon in foals except as a result of uroperitoneum.[9]

Pleural fluid gravitates to the dependent portion of the thorax and results in a homogeneous soft tissue opacity in the ventral aspect of the thorax (Fig. 37.26, eFig. 37.7). Because horses do not have prominent interlobular fissures, pleural fissure lines are rarely seen. Approximately 1 to 2 L of pleural fluid must be present to be detected radiographically. Therefore, normal thoracic radiographs do not eliminate the possibility of pleural fluid and thoracic ultrasound is complimentary to radiographs.[91] The fluid will initially silhouette the heart and diaphragm, resulting in loss of definition of these structures. As more fluid accumulates, normal lungs will be displaced dorsally. Because of surface tension, a discrete, horizontal fluid line is present only if free gas is also present in the pleural space (Fig. 37.27).

When pleural fluid is present, assessment of the lungs for concurrent disease is difficult to impossible.[25] Consolidated lung lobes are not displaced dorsally by the pleural fluid, so they are obscured. This makes the differentiation of pleural fluid from pneumonia difficult. Fibrin accumulation and inflammation can result in compartmentalization of pleural fluid with a unilateral distribution, even though the normal mediastinum is not complete. Repeating the radiographs after thoracocentesis provides more information on the presence and extent of any pulmonary disease.

Ultrasound is superior for evaluating the amount and character of pleural fluid, guiding thoracocentesis, and evaluating for resolution or progression (Fig. 37.28). It also allows the identification of consolidation of the lung and other

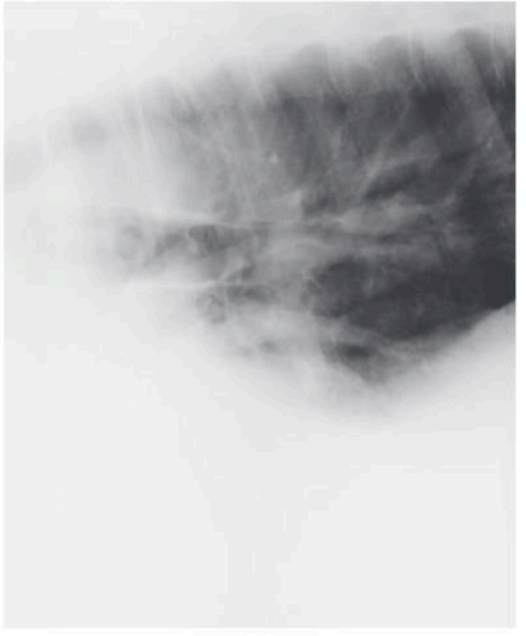


Fig. 37.26 Lateral radiograph of the caudodorsal aspect of the thorax of a horse with moderate pleural fluid. A uniform soft tissue opacity that silhouettes the heart and diaphragm is present in the ventral aspect of the thorax. A distinct fluid line is not visible because pneumothorax is not present. Differentiation of pleural fluid from consolidated lung can be difficult radiographically and often requires ultrasound examination.

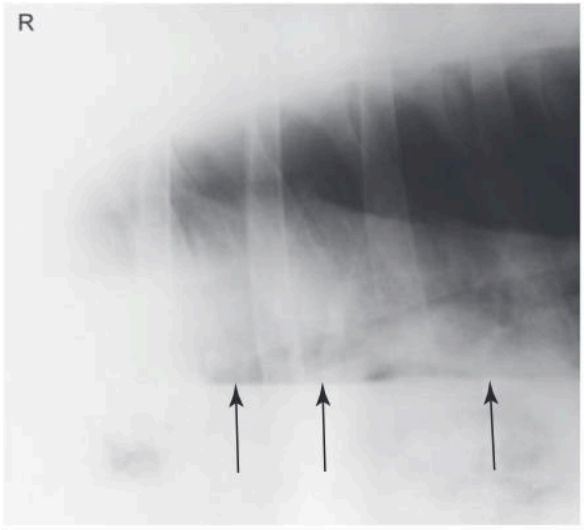


Fig. 37.27 Lateral radiograph of the thorax. A soft tissue opacity that silhouettes the diaphragm is present in the ventral thorax. This is caused by pleural fluid. A distinct, horizontal fluid line is evident (*arrows*) because of concurrent pneumothorax. A sharp pleural fluid line is seen only when concurrent pneumothorax is present.

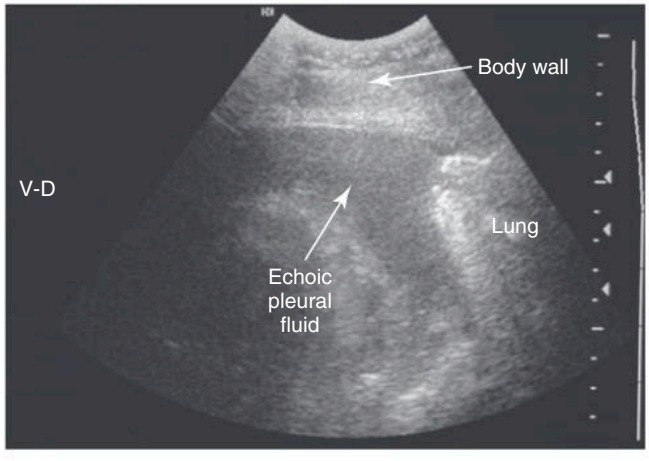


Fig. 37.28 Pleural fluid is present between the body wall and the lung; the fluid is highly echogenic. The lung is retracted away from the body wall and displaced dorsally.



eFig. 37.7 Lateral radiograph of the cranioventral thorax of a horse who experienced a perforating wound to the thorax a few days ago. There is increased soft tissue opacity of the cranioventral thorax. Multiple gas lucencies are present, some with a fluid level and gas cap. Pleural effusion was consistent with a pneumothorax with abscessation.

pleural-based lesions such as abscesses that may be masked radiographically by the pleural fluid. The volume of pleural fluid can be estimated with ultrasound based on the level of the fluid relative to various anatomic points. If only a small amount of fluid is present in the ventral thorax, the volume is approximately 0.5 L. If the dorsal extent of the pleural fluid is at the point of the shoulder, the volume is approximately 1.0 to 2.5 L. If the dorsal extent of the pleural fluid is 5 to 7 cm dorsal to the point of the shoulder, the volume is approximately 5 L. The character of the pleural fluid can be inferred by the ultrasound appearance, with more echoic fluids being more cellular, but thoracocentesis is required to diagnose the type of fluid definitively. Ultrasound is also helpful to identify the presence of fibrinous adhesions between the pleural surface of the lung and the body wall (Fig. 37.29). Neither of these changes can be identified radiographically.

Pneumothorax

Pneumothorax is rare in the horse and occurs most commonly as a result of trauma, as a sequela of pleuropneumonia, or from the tearing of pleural adhesions.[92] Iatrogenic causes of pneumothorax include complications from thoracocentesis and surgical procedures.

The presence of air in the pleural space results in retraction of the lungs from the body wall, permitting visualization of the dorsal margin of the lung because the air will rise to the dorsal aspect of the thorax. The free gas between the lung and the body wall contrasts with the edge of the lung, making it appear as an opaque line running roughly parallel to the vertebral column (Fig. 37.30). If pneumothorax is present concurrently with pleural fluid, a distinct horizontal gas/fluid interface will be present.

Radiography and ultrasound can both be used to diagnose pneumothorax, although radiography may be slightly more sensitive and is less operator dependent.[92] The ultrasonographic appearance of air (i.e., a bright interface with reverberation artifact) is the same whether it is free in the thorax or within the lung. The ultrasound diagnosis of pneumothorax requires the operator to identify that the air does not move with respiration. Additionally, if the dorsal portions of the thorax are not evaluated, free air can go undetected. Pneumothorax is easier to detect with ultrasound when pleural fluid is present concurrently.[92]

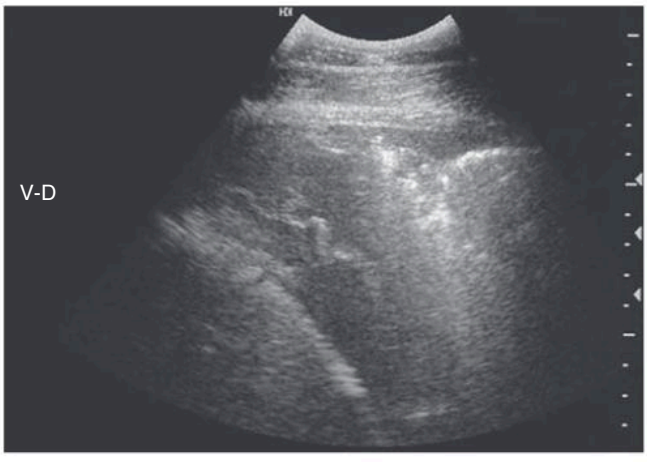


Fig. 37.29 Fibrin tags (adhesions) appear as echoic strands in the pleural effusion in this transverse ultrasound image.

Diaphragmatic Hernia

Diaphragmatic hernias can occur as a result of trauma, dystocia, strenuous exercise, or laparoscopic surgery. Radiographic identification of a diaphragmatic hernia requires detection of abdominal contents in the thoracic cavity. Most often, gas-filled bowel loops are detected in the caudodorsal portion of the thorax (Fig. 37.31, eFig. 37.8).[93] Pleural fluid may also be present.[94] Ultrasound can also be used to diagnose diaphragmatic hernias, particularly when pleural fluid is present. Not all of the diaphragm can be visualized with ultrasound, so the site of actual diaphragmatic disruption may not be apparent.[95]

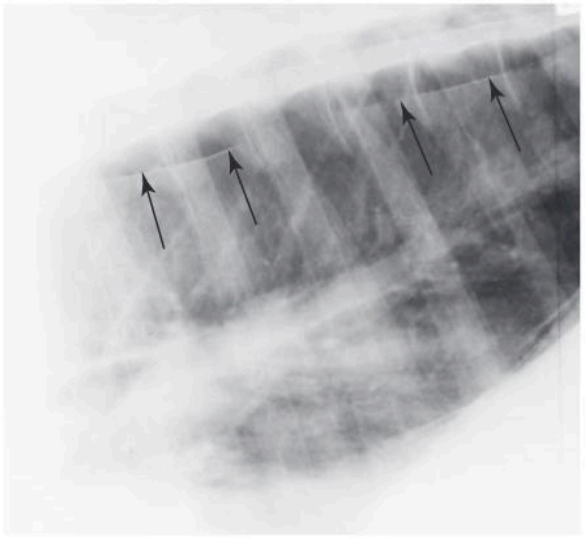


Fig. 37.30 Lateral radiograph of the caudal aspect of the thorax. Pneumothorax results in the lungs being retracted from the dorsal body wall; the edge of the lung appears as an opaque white line paralleling the vertebral column (*black arrows*).

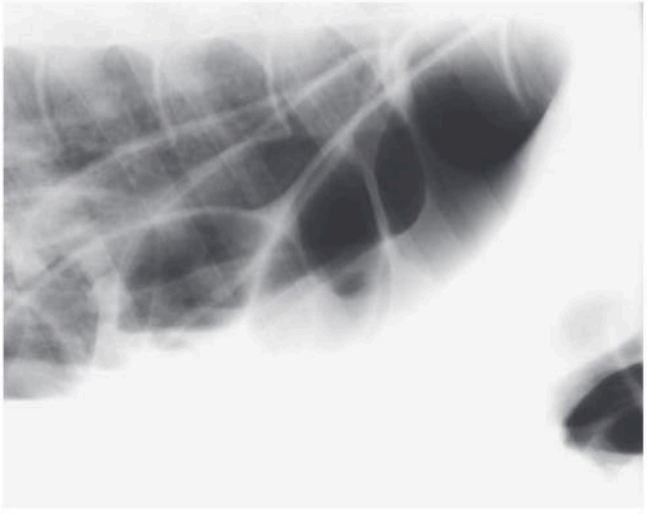
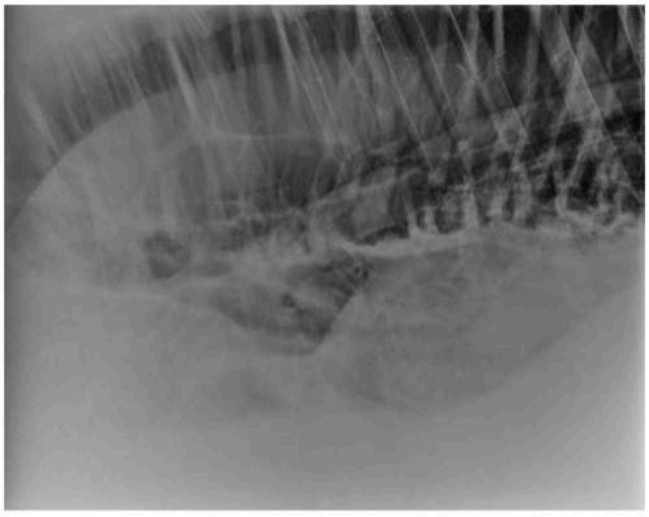


Fig. 37.31 Lateral radiograph of the caudal aspect of the thorax in an adult horse. Multiple gas-filled bowel loops are present in the thorax as a result of a diaphragmatic hernia.



eFig. 37.8 Lateral radiograph of the thorax of an adult horse. A large gas-filled sacculated structure is present in the caudodorsal thorax representing cecum or colon due to diaphragmatic hernia.

MEDIASTINAL DISEASE

Lymphadenopathy

The most common thoracic tumor in horses is lymphoma.[96] Lymphoma results commonly in a cranial mediastinal mass. Radiographically, this appears as a soft tissue mass cranial to the heart (Fig. 37.32).[97] With moderate cranial mediastinal lymphadenopathy, the mediastinum is wide, and the ventral border is irregular. More severe involvement causes loss of visualization of the normal aerated lung cranial to the heart as a result of atelectasis. Pleural fluid is also a common finding in lymphoma, which inhibits the radiographic detection of mediastinal masses.[98] Ultrasound is useful in these instances to characterize the quantity and quality of the fluid, as well as the presence of a mass, and to guide biopsy of the mass.[99] Most masses are multilobular and uniformly hypoechoic and frequently displace the heart caudally (Fig. 37.33).[97]

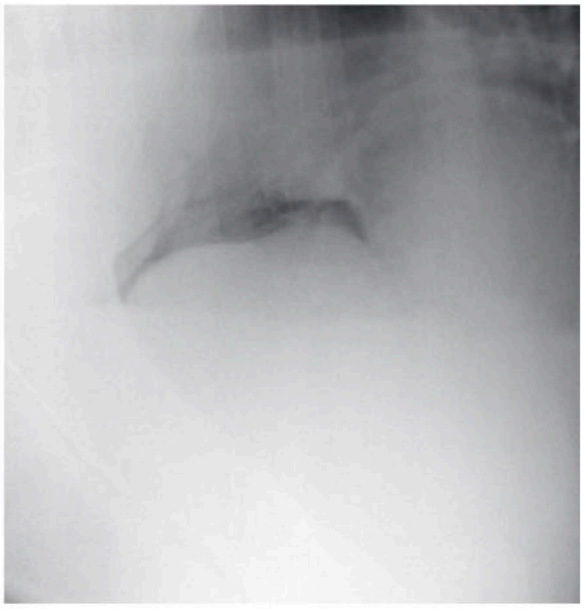


Fig. 37.32 Lateral radiograph of the cranial aspect of the thorax. A focal soft tissue mass is present cranial to the heart. The dorsal aspect of the mass is convex. Opposite lateral radiographs of the cranial aspect of the thorax had a similar appearance, indicating the structure was on the midline. This mass was confirmed to be mediastinal lymphoma.

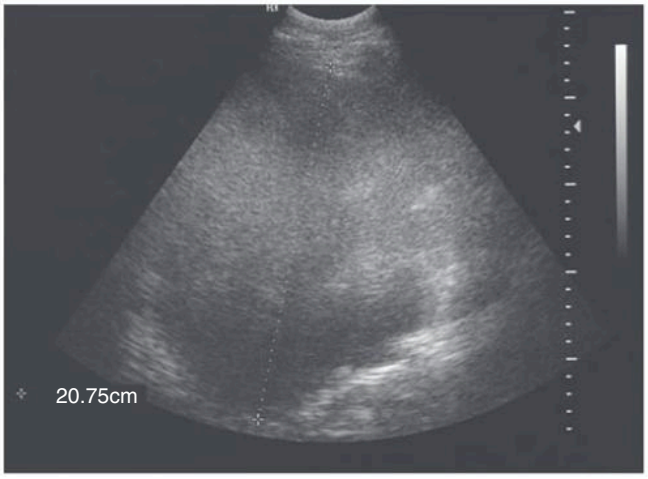


Fig. 37.33 A uniformly echoic mass can be seen in a transverse ultrasound image of the cranial aspect of the thorax of the horse in Fig. 37.32.

A poorly defined soft tissue opacity dorsal to the carina that displaces the trachea dorsally or ventrally and silhouettes the ventral border of the aorta is indicative of tracheobronchial lymphadenopathy.[20,97] Tracheobronchial lymphadenopathy may be difficult to differentiate from a pulmonary mass. Opposite lateral radiographs are helpful because the lymph nodes are midline structures and therefore should have the same appearance on both lateral radiographs. CT can also be used in foals to differentiate tracheobronchial lymphadenopathy from a pulmonary mass.[20]

Pneumomediastinum

Pneumomediastinum can occur as a result of punctures to the neck, rupture of the trachea, rupture of the esophagus, or a transtracheal wash. Spontaneous pneumomediastinum is also reported in horses with pre-existing pulmonary disease with no macroscopic evidence of a breach in the respiratory tract. Pulmonary disease can result in air escaping into the pulmonary interstitium and tracking along the bronchi and vessels into the mediastinum.[100] Linear gas opacities are seen tracking along the facial planes of the neck and mediastinum. This results in gas contrasting the trachea, esophagus, cranial vena cava, and aorta (Fig. 37.34). Pneumomediastinum can lead to pneumothorax if there is tearing of the mediastinal pleura.

TRACHEAL DISEASE

Tracheal collapse has been rarely reported in horses. DV flattening of the trachea is seen on the thoracic radiographs. Comparing radiographs obtained during inspiration and expiration may demonstrate a change in tracheal diameter associated with collapse. In normal adult Thoroughbred horses, the tracheal diameter does not change with the phase of respiration.[101] There may be an increased prevalence in American miniature horses, occurring in 6%–14% of all American miniature horses and can be subclinical.[102–104] Tracheal collapse can result in aspiration pneumonia, so radiographs of the entire thorax are indicated.[102]

Fluid can pool in the ventral aspect of the trachea at the thoracic inlet in horses that have aspirated. In severe tracheitis the tracheal wall may appear thick and irregular (Fig. 37.35).

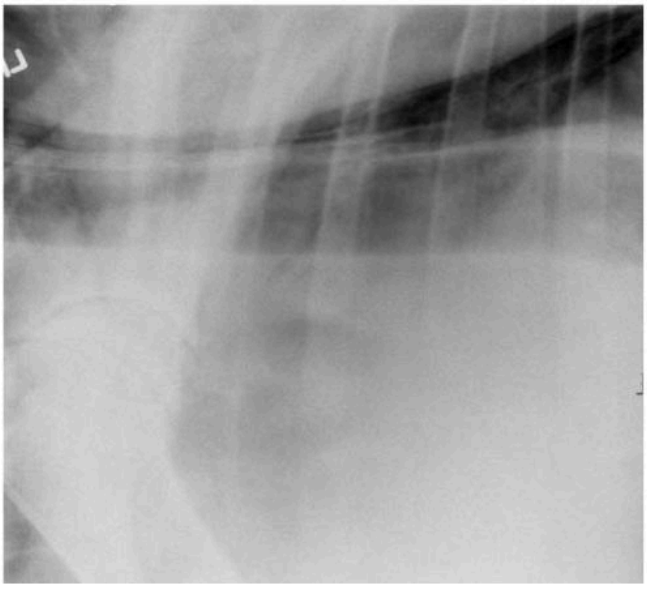


Fig. 37.34 Lateral radiograph of the craniodorsal aspect of the thorax. Gas is present in the cranial mediastinum. Linear gas opacities track through the mediastinum at the thoracic inlet accentuating the dorsal wall of the esophagus and trachea.



Fig. 37.35 Lateral radiograph of the cranial aspect of the thorax. The trachea is focally narrowed at the thoracic inlet, and the dorsal aspect of the lumen of the trachea has an irregular contour. This lesion was attributable to tracheal thickening from chronic tracheitis.

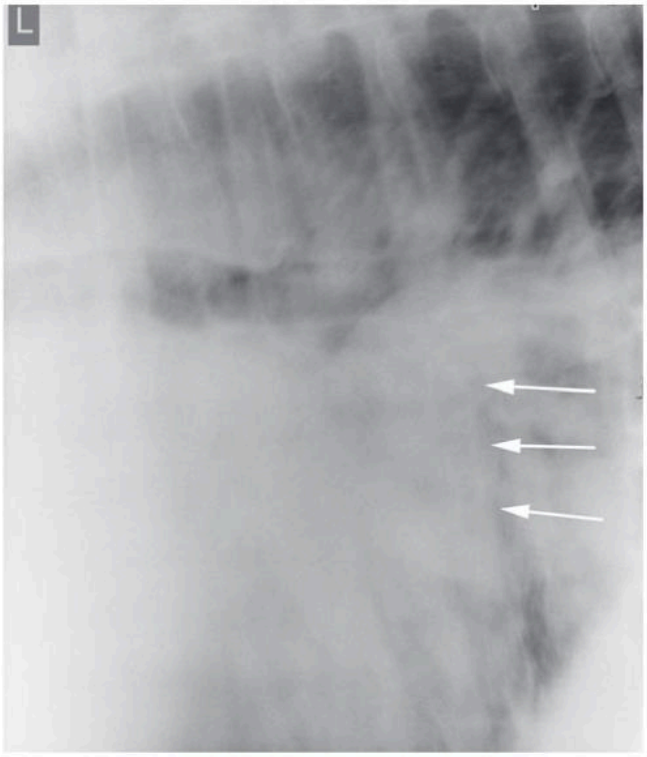


Fig. 37.36 Lateral radiograph of the thorax centered over the caudal heart. There is loss of the caudal cardiac waist (*arrows*) and dorsal displacement of the trachea, indicative of cardiomegaly. In the caudoventral and caudodorsal lung field, there is a moderate to severe soft tissue opacity. In the pattern recognition scheme this is an interstitial to alveolar lung pattern. This change is attributed to pulmonary edema.

ESOPHAGEAL DISEASE

The most common esophageal disease of horses is idiopathic obstruction caused by impaction of ingesta (choke).[105] Reported esophageal disease in horses includes congenital or acquired strictures, esophageal duplication cyst, esophageal atresia, vascular ring anomalies, space-occupying lesions (abscess, tumor), megaesophagus, esophageal ectasia, muscular hypertrophy, diverticuli, hiatal hernia, and esophagitis.[105–109] Regardless of the cause, most esophageal disease results in impaction of food within the esophagus.[105]

The normal esophagus is not visible in survey radiographs. In most horses, esophagoscopy has replaced the need for contrast studies of the esophagus because of its ease and availability. However, for adequate assessment of esophageal motility and swallowing, esophagraphy is still required. Esophagraphy can be performed with liquid or paste forms of barium as well as with barium-coated food administered orally. Barium paste coats the esophagus better, allowing the detection of mucosal abnormalities. If the oropharyngeal phase of swallowing is not of interest, then the contrast medium can be administered directly into the cranial aspect of the esophagus with an esophageal tube. The use of certain sedatives and the placement of an esophageal tube, however, can result in dilation of the esophagus in normal horses.[110] The use of fluoroscopy to observe swallowing is best because it allows a dynamic assessment of the esophagus, but obtaining static radiographs after the administration of contrast medium can be diagnostic because most esophageal diseases result in delayed transit time.[110] Minimal contrast medium should be retained in the esophagus, outlining the esophageal folds after normal swallowing.[110]

With the exception of esophageal impactions in which focal enlargement of the esophagus with a granular radiopacity is seen, most esophageal diseases are not evident on survey radiographs. In recurrent choke, esophagraphy is indicated to evaluate for underlying primary esophageal disease.[105] Focal narrowing of the esophagus is indicative of a stricture or extraluminal mass causing compression of the esophagus. Filling the esophagus with a large amount of contrast medium (up to 500 mL) through a cuffed nasoesophageal tube may be necessary to distend the esophagus adequately to detect some strictures. Esophagitis results in thickening of the esophageal wall, and accumulation of contrast medium may occur as a result of hypomotility. Focal esophageal ulcerations may be noted as the contrast medium adheres to the mucosa and creates irregular filling defects.

CARDIAC DISEASE

Radiographic assessment of heart size is difficult in adult horses because of a lack of objective criteria and the inability to obtain orthogonal radiographs.[11] Therefore, echocardiography is the most common diagnostic test for cardiac disease in horses. The radiographic signs of cardiomegaly are the same as in small animals. Straightening of the caudal aspect of the heart, increased sternal and diaphragmatic contact, and dorsal displacement of the trachea are indications of heart enlargement (Fig. 37.36).[11]

The radiographic signs of congestive heart failure are also the same as those seen in small animals. Pulmonary edema results in a diffuse to caudodorsal interstitial to alveolar lung pattern.[11,73] Pulmonary venous enlargement may also be seen.[73] Pleural fluid may be evident if biventricular heart failure is present.[11,73] For the diagnosis of pericardial fluid and pericarditis, ultrasound is preferred.[111]

REFERENCES

1. Lo WY, Hornof WJ, Zwingenberger AL, Robertson ID. Multislice imaging processing and antiscatter grids in digital radiographs. *Vet Radiol Ultrasound*. 2009;50:569–576.
2. Malek G, Leclere M, Masseau I, Linden A zur, Beauchamp G, Finck C. Bilateral thoracic radiographs increase lesion detection in horses with pneumonia or pulmonary neoplasia but do not bring any additional benefit for inflammatory or diffuse pulmonary disease. *Vet Radiol Ultrasound*. 2022.
3. Wisner ER, O'Brien TR, Lakritz J, Pascoe JR, Wilson DW, Tyler WS. Radiographic and microscopic correlation of diffuse interstitial and bronchointerstitial pulmonary patterns in the caudodorsal lung of adult thoroughbred horses in race training. *Equine Vet J*. 1993;25:293–298.
4. Singh B, Dyce KM (Keith M). *Dyce, Sack, and Wensing's Textbook of Veterinary Anatomy*. 5th ed. St. Louis, Missouri: Elsevier; n.d.
5. Sanderson GN, O'Callaghan MW. Radiographic anatomy of the equine thorax as a basis for radiological interpretation. *N Z Vet J*. 2011;31:127–130.
6. Ainsworth DM, Beck KA, Boatwright CE, Snedden KA, Rebhun WC. Lack of residual lung damage in horses in which *Rhodococcus equi*-induced pneumonia had been diagnosed. *Am J Vet Res*. 1993;54:2115–2120.
7. Lepage MFP, Gerber V, Suter MM. A case of interstitial pneumonia associated with *Pneumocystis carinii* in a foal. *Vet Pathol*. 1999;36:621–624.
8. Lamb CR, O'Callaghan MW, Paradis MR. Thoracic radiography in the neonatal foal: a preliminary report. *Vet Radiol*. 1990;31:11–16.
9. Lester GD, Lester NV. Abdominal and thoracic radiography in the neonate. *Vet Clin North Am Equine Pract*. 2001;17:19–46.
10. Kutasi O, Horvath A, Harnos A, Szenci O. Radiographic assessment of pulmonary fluid clearance in healthy neonatal foals. *Vet Radiol Ultrasound*. 2009;50:584–588.
11. Koblik PD, Hornof WJ. Diagnostic radiology and nuclear cardiology. Their use in assessment of equine cardiovascular disease. *Vet Clin North Am Equine Pract*. 1985;1:289–309.
12. Hoskinson JJ, Tucker RL, Lillich J, Bertone JJ. Advanced diagnostic imaging modalities available at the referral center. *Vet Clin North Am Equine Pract*. 1997;13:601–612.
13. Reef VB, Boy MG, Reid CF, Elser A. Comparison between diagnostic ultrasonography and radiography in the evaluation of horses and cattle with thoracic disease: 56 cases (1984–1985). *J Am Vet Med Assoc*. 1991;198:2112–2118.
14. Hinchcliff KW, Byrne BA. Clinical examination of the respiratory system. *Vet Clin North Am Equine Pract*. 1991;7:1–26.
15. Gross DK, Morley PS, Hinchcliff KW, Reichle JK, Slemons RD. Pulmonary ultrasonographic abnormalities associated with naturally occurring equine influenza virus infection in Standardbred racehorses. *J Vet Intern Med/American College of Veterinary Internal Medicine*. 2004;18:718–727.
16. Rantanen NW. The diagnosis of lung consolidation in horses using linear array diagnostic ultrasound. *J Equine Vet Sci*. 1994;14:79–80.
17. Punsmann S, Hellige M, Hoppe J, Freise F, Venner M. Diagnostic imaging in acute interstitial pneumonia in foals: high variability of interpretation of chest radiographs and good conformity between ultrasonographic and postmortem findings. *Vet Radiol Ultrasound*. 2021.
18. Rush BR, Hoskinson JJ, Davis EG, Matson CJ, Hakala JE. Pulmonary distribution of aerosolized technetium Tc 99m pentetate after administration of a single dose of aerosolized albuterol sulfate in horses with recurrent airway obstruction. *Am J Vet Res*. 1999;60:764–769.
19. Votion DM, Vandenput SN, Duvivier DH, et al. Alveolar clearance in horses with chronic obstructive pulmonary disease. *Am J Vet Res*. 1999;60:495–500.
20. Wion L, Perkins G, Ainsworth DM, Dykes NL, Divers TJ. Use of computerised tomography to diagnose a *Rhodococcus equi* mediastinal abscess causing severe respiratory distress in a foal. *Equine Vet J*. 2001;33:523–526.
21. Schliewert E-C, Lascola KM, O'Brien RT, et al. Comparison of radiographic and computed tomographic images of the lungs in healthy neonatal foals. *Am J Vet Res*. 2015;76:42–52.
22. Garrett KS, Embertson RM, Hopper SA, Woodie JB, McQuerry KJ. Preoperative computed tomographic evaluation of neonatal foals with rib fractures. *Vet Surg*. 2022:1–11.
23. Bedenice D, Heuwieser W, Brawer R, Solano M, Rand W, Paradis MR. Clinical and prognostic significance of radiographic pattern, distribution, and severity of thoracic radiographic changes in neonatal foals. *J Vet Intern Med/American College of Veterinary Internal Medicine*. 2003;17:876–886.
24. Barton AK, Schulze T, Doherr MG, Gehlen H. Influence of bronchoalveolar lavage on thoracic radiography in the horse. *J Vet Sci*. 2018;19:563–569.
25. Farrow CS. Radiographic aspects of inflammatory lung disease in the horse. *Vet Radiol*. 1981;22:107–114.
26. Nykamp SG, Scrivani P, Dykes NL. Radiographic signs of pulmonary disease: an alternative approach. *Compend Contin Educ*. 2002;24:25–36.
27. Wilkins PA. Lower respiratory problems of the neonate. *Vet Clin North Am Equine Pract*. 2003;19:19–33.
28. Wilkins PA. Lower airway diseases of the adult horse. *Vet Clin North Am Equine Pract*. 2003;19:101–121.
29. Buergelt CD. Interstitial pneumonia in the horse: a fledgling morphological entity with mysterious causes. *Equine Vet J*. 1995;27:4–5.
30. Nout YS, Hinchcliff KW, Samii VF, Kohn CW, Jose-Cunilleras E, Reed SM. Chronic pulmonary disease with radiographic interstitial opacity (interstitial pneumonia) in foals. *Equine Vet J*. 2002;34:542–548.
31. Buergelt CD, Hines SA, Cantor G, Stirk A, Wilson JH. A retrospective study of proliferative interstitial lung disease of horses in Florida. *Vet Pathol*. 1986;23:750–756.
32. Peek SF, Landolt G, Karasin AI, et al. Acute respiratory distress syndrome and fatal interstitial pneumonia associated with equine influenza in a neonatal foal. *J Vet Intern Med*. 2004;18:132–134.
33. Lakritz J, Wilson WD, Berry CR, Schrenzel MD, Carlson GP, Madigan JE. Bronchointerstitial pneumonia and respiratory distress in young horses: clinical, clinicopathologic, radiographic, and pathological findings in 23 cases (1984–1989). *J Vet Intern Med*. 1993;7:277–288.
34. Donaldson MT, Beech J, Ennulat D, Hamir AN. Interstitial pneumonia and pulmonary fibrosis in a horse. *Equine Vet J*. 1998;30:173–175.
35. Wong DM, Belgrave RL, Williams KJ, et al. Multinodular pulmonary fibrosis in five horses. *J Am Vet Med Assoc*. 2008;232:898–905.
36. Carrillo MF, Kemper D, Woods LW, Carvallo FR. Chronic interstitial pneumonia with features of organizing pneumonia in an adult horse. *J Vet Diagn Invest*. 2020;32:621–625.
37. Lavoie JP, Fiset L, Laverty S. Review of 40 cases of lung abscesses in foals and adult horses. *Equine Vet J*. 1994;26:348–352.

38. Ainsworth DM, Erb HN, Eicker SW, et al. Effects of pulmonary abscesses on racing performance of horses treated at referral veterinary medical teaching hospitals: 45 cases (1985–1997). *J Am Vet Med Assoc.* 2000;216:1282–1287.
39. Lavoie J-P, Dalle S, Breton L, Hélie P. Bronchiectasis in three adult horses with heaves. *J Vet Intern Med/American College of Veterinary Internal Medicine.* 2004;18:757–760.
40. Ainsworth DM, Eicker SW, Yeagar AE, et al. Associations between physical examination, laboratory, and radiographic findings and outcome and subsequent racing performance of foals with *Rhodococcus equi* infection: 115 cases (1984–1992). *J Am Vet Med Assoc.* 1998;213:510–515.
41. Giguère S, Roberts GD. Association between radiographic pattern and outcome in foals with pneumonia caused by *Rhodococcus equi*. *Vet Radiol Ultrasound.* 2012;53:601–604.
42. Falcon J, Smith BP, O'Brien TR, Carlson GP, Biberstein E. Clinical and radiographic findings in *Corynebacterium equi* pneumonia of foals. *J Am Vet Med Assoc.* 1985;186:593–599.
43. Ramirez S, Lester GD, Roberts GR. Diagnostic contribution of thoracic ultrasonography in 17 foals with *Rhodococcus equi* pneumonia. *Vet Radiol Ultrasound.* 2004;45:172–176.
44. Green SL, Hager DA, Mays MBC, Merritt AM. Acute diffuse mycotic pneumonia in a 7-month-old colt. *Vet Radiology.* 2005;28:216–219.
45. Maleski K, Magdesian KG, LaFranco-Scheuch L, Pappagianis D, Carlson GP. Pulmonary coccidioidomycosis in a neonatal foal. *Vet Rec.* 2002;151:505–508.
46. Ziemer EL, Pappagianis D, Madigan JE, Mansmann RA, Hoffman KD. Coccidioidomycosis in horses: 15 cases (1975–1984). *J Am Vet Med Assoc.* 1992;201:910–916.
47. Toribio RE, Kohn CW, Lawrence AE, Hardy J, Hutt JA. Thoracic and abdominal blastomycosis in a horse. *J Am Vet Med Assoc.* 1999;214, 1357-60–1335.
48. Mair TS, Lane JG. Pneumonia, lung abscesses and pleuritis in adult horses: a review of 51 cases. *Equine Vet J.* 1989;21:175–180.
49. Singh K, Holbrook TC, Gilliam LL, Cruz RJ, Duffy J, Confer AW. Severe pulmonary disease due to multisystemic eosinophilic epitheliotropic disease in a horse. *Vet Pathol.* 2006;43:189–193.
50. Wilkins PA. Equine multinodular pulmonary fibrosis: diagnosis and treatment. *Equine Vet Educ.* 2013;25. n/a-n/a.
51. Easton-Jones CA, Cissell DD, Mohr FC, Chigerwe M, Pusterla N. Prognostic indicators and long-term survival in 14 horses with equine multinodular pulmonary fibrosis. *Equine Vet Educ.* 2020;32:41–46.
52. Bell SA, Drew CP, Wilson WD, Pusterla N. Idiopathic chronic eosinophilic pneumonia in 7 horses. *J Vet Intern Med.* 2008;22:648–653.
53. Arens AM, Barr B, Puchalski SM, et al. Osteoporosis associated with pulmonary silicosis in an equine bone fragility syndrome. *Vet Pathol.* 2011;48:593–615.
54. Berry CR, O'Brien TR, Madigan JE, Hager DA. Thoracic radiographic features of silicosis in 19 horses. *J Vet Intern Med.* 1991;5:248–256.
55. Williams KJ, Maes R, Piero FD, et al. Equine multinodular pulmonary fibrosis: a newly recognized herpesvirus-associated fibrotic lung disease. *Vet Pathol.* 2007;44:849–862.
56. Niedermaier G, Poth T, Gehlen H. Clinical aspects of multinodular pulmonary fibrosis in two warmblood horses. *Vet Rec.* 2010;166:426–430.
57. Couëtil LL, Hoffman AM, Hodgson J, et al. *Inflammatory Airway Disease of Horses.* vol. 21. 2007:356–361.
58. Couëtil LL, Cardwell JM, Gerber V, Lavoie J-P, Léguillette R, Richard EA. Inflammatory airway disease of horses—revised consensus statement. *J Vet Intern Med.* 2016;30:503–515.
59. Léguillette R. Recurrent airway obstruction—heaves. *Vet Clin North Am Equine Pract.* 2003;19:63–86.
60. Mazan MR, Vin R, Hoffman AM. Radiographic scoring lacks predictive value in inflammatory airway disease. *Equine Vet J.* 2005;37:541–545.
61. Niedźwiedź A. Equine recurrent airway obstruction. *Macedonian Veterinary Review.* 2014.
62. Seahorn TL, Beadle RE. Summer pasture-associated obstructive pulmonary disease in horses: 21 cases (1983–1991). *J Am Vet Med Assoc.* 1993;202:779–782.
63. Sage AM, Valberg S, Hayden DW, Firshman AM, Jacob K. Echocardiography in a horse with cor pulmonale from recurrent airway obstruction. *J Vet Intern Med/American College of Veterinary Internal Medicine.* 2006;20:694.
64. Johansson AM, Gardner SY, Atkins CE, LaFevers DH, Breuhaus BA. Cardiovascular effects of acute pulmonary obstruction in horses with recurrent airway obstruction. *J Vet Intern Med/American College of Veterinary Internal Medicine.* 2007;21:302–307.
65. West JB, Mathieu-Costello O. Stress failure of pulmonary capillaries as a mechanism for exercise induced pulmonary haemorrhage in the horse. *Equine Vet Journal.* 1994;26:441–447.
66. Hinchcliff KW, Couëtil LL, Knight PK, et al. Exercise induced pulmonary hemorrhage in horses: American College of Veterinary Internal Medicine consensus statement. *J Vet Intern Med.* 2015;29:743–758.
67. Sweeney CR. Exercise-induced pulmonary hemorrhage. *Vet Clin North Am Equine Pract.* 1991;7:93–104.
68. Birks EK, Durando MM, McBride S. Exercise-induced pulmonary hemorrhage. *Vet Clin North Am Equine Pract.* 2003;19:87–100.
69. Ferrucci F, Stancari G, Zucca E, Ayalon S, Falcone C, Ferro E. Specificity and sensitivity of ultrasonography and endoscopy for the diagnosis of exercise-induced pulmonary haemorrhage (EIPH) in 157 race horses. *Vet Res Commun.* 2009;33:185–188.
70. Feudo CML, Stucchi L, Alberti E, et al. The role of thoracic ultrasonography and airway endoscopy in the diagnosis of equine asthma and exercise-induced pulmonary hemorrhage. *Vet Sci.* 2021;8:276.
71. Kollias-Baker CA, Pipers FS, Heard D, Seeherman H. Pulmonary edema associated with transient airway obstruction in three horses. *J Am Vet Med Assoc.* 1993;202:1116–1118.
72. Kaartinen MJ, Pang DSJ, Cuvelliez SG. Post-anesthetic pulmonary edema in two horses. *Veterinary Anaesthesia and Analgesia.* 2010;37:136–143.
73. Davis JL, Gardner SY, Schwabenton B, Breuhaus BA. Congestive heart failure in horses: 14 cases (1984–2001). *J Am Vet Med Assoc.* 2002;220:1512–1515.
74. Jean D, Lavoie JP, Nunez L, Lagacé A, Laverty S. Cutaneous hemangiosarcoma with pulmonary metastasis in a horse. *J Am Vet Med Assoc.* 1994;204:776–778.
75. Jorgensen JS, Geoly FJ, Berry CR, Breuhaus BA. Lameness and pleural effusion associated with an aggressive fibrosarcoma in a horse. *J Am Vet Med Assoc.* 1997;210:1328–1331.
76. Cook G, Divers TJ, Rowland PH. Hypercalcaemia and erythrocytosis in a mare associated with a metastatic carcinoma. *Equine Vet J.* 1995;27:316–318.
77. Facemire PR, Chilcoat CD, Sojka JE, et al. Treatment of granular cell tumor via complete right lung resection in a horse. *J Am Vet Med Assoc.* 2000;217:1522–1525.

78. Danton CA, Peacock PJ, May SA, Kelly DF. Anaplastic sarcoma in the caudal thigh of a horse. *Vet Rec*. 1992;131:188–190.
79. Anderson JD, Leonard JM, Zeliff JA, Garman RH. Primary pulmonary neoplasm in a horse. *J Am Vet Med Assoc*. 1992;201:1399–1401.
80. Jean D, Picandet V, Macieira S, Beauregard G, D'Anjou MA, Beauchamp G. Detection of rib trauma in newborn foals in an equine critical care unit: a comparison of ultrasonography, radiography and physical examination. *Equine Vet J*. 2007;39:158–163.
81. Schambourg MA, Laverty S, Mullim S, Fogarty UM, Halley J. Thoracic trauma in foals: post mortem findings. *Equine Vet J*. 2003;35:78–81.
82. Neil KM, Charman RE, Vasey JR. Rib osteomyelitis in three foals. *Australian Veterinary Journal*. 2010;88:96–100.
83. Punsmann S, Hoppe J, Klopfleisch R, Venner M. Acute interstitial pneumonia in foals: a severe, multifactorial syndrome with lung tissue recovery in surviving foals. *Equine Vet J*. 2021;53:718–726.
84. Dunkel B, Dolente B, Boston RC. Acute lung injury/acute respiratory distress syndrome in 15 foals. *Equine Vet J*. 2005;37:435–440.
85. Jose-Cunilleras E, Sibbons PD. Acute lung injury and acute respiratory distress syndrome: fashionable names for old conditions or new clinical entities in their own right? *Equine Vet J*. 2005;37:390–392.
86. Gough SL, Carrick J, Raidal SL, et al. *Chlamydia psittaci* infection as a cause of respiratory disease in neonatal foals. *Equine Vet J*. 2020;52:244–249.
87. Dunkel B. Acute lung injury and acute respiratory distress syndrome in foals. *Clin Techniques Equine Pract*. 2006;5:127–133.
88. Raphel CF, Beech J. Pleuritis secondary to pneumonia or lung abscessation in 90 horses. *J Am Vet Med Assoc*. 1982;181:808–810.
89. May J, Fews D, Tennant K, Mair T. Diagnostic dichotomy: a question of thoracic mesothelioma. *Equine Veterinary Education*. 2016. n/a-n/a.
90. Johns I, Marr C, DURHAM A, Mair T, McParland T. Causes of pleural effusions in horses resident in the UK. *Equine Veterinary Education*. 2016;29:144–148.
91. Prater PE, Patton CS, Held JP. Pleural effusion resulting from malignant hepatoblastoma in a horse. *J Am Vet Med Assoc*. 1989;194:383–385.
92. Boy MG, Sweeney CR. Pneumothorax in horses: 40 cases (1980–1997). *J Am Vet Med Assoc*. 2000;216:1955–1959.
93. Izing S, Kelemen Z, Bohák Z, Tóth P, Bodó G. Successful repair of diaphragmatic hernia with simultaneously performed thoracotomy and median laparotomy in a horse. *Vet Rec Case Reports*. 2021;9.
94. Everett KA, Chaffin MK, Brinsko SP. Diaphragmatic herniation as a cause of lethargy and exercise intolerance in a mare. *The Cornell Veterinarian*. 1992;82:217–223.
95. Hartzband LE, InterScience W, Kerr DV, Morris EA. Ultrasonographic diagnosis of diaphragmatic rupture in a horse. *Veterinary Radiology*. 1990:42–44.
96. Sweeney CR, Gillette DM. Thoracic neoplasia in equids: 35 cases (1967–1987). *J Am Vet Med Assoc*. 1989;195:374–377.
97. Garber JL, Reef VB, Reimer JM. Sonographic findings in horses with mediastinal lymphosarcoma: 13 cases (1985–1992). *J Am Vet Med Assoc*. 1994;205:1432–1436.
98. Camacho-Luna P, Andrews FM, Dehghanpir SD, et al. Bicavitary effusion in a horse with multicentric lymphoma. *Equine Vet Educ*. 2021;33:e224–e230.
99. Clercq DD, Loon G van, Lefère L, Deprez P. Ultrasound-guided biopsy as a diagnostic aid in three horses with a cranial mediastinal lymphosarcoma. *Vet Rec*. 2004;154:722–726.
100. Macklin CC. Transport of air along sheaths of pulmonic blood vessels from alveoli to mediastinum: clinical implications. *Arch Intern Med*. 1939;64:913–926.
101. Carstens A, Kirberger RM, Grimbeek RJ, Donnellan CMB, Saulez MN. Radiographic quantification of tracheal dimensions of the normal thoroughbred horse. *Vet Radiol Ultrasound*. 2009;50:492–501.
102. Aleman M, Nieto JE, Benak J, Johnson LR. Tracheal collapse in American miniature horses: 13 cases (1985–2007). *J Am Vet Med Assoc*. 2008;233:1302–1306.
103. Peyrecave-Capo X, Munoz-Diaz J, Ferrer GR, Watrelot D, Desjardins I. Acute tracheal trauma and chronic tracheal collapse in an asthmatic mature pony. *Equine Vet Educ*. 2022.
104. Every LJ, Hostnik ET, Hostnik LD, et al. Radiographic tracheal lumen to vertebral ratios in the normal American Miniature Horse. *Equine Vet J*. 2020;52:428–434.
105. Feige K, Schwarzwald C, Fürst A, Hotz BK. Esophageal obstruction in horses: a retrospective study of 34 cases. *Can Vet J La Revue Vétérinaire Canadienne*. 2000;41:207–210.
106. Clabough DL, Roberts MC, Robertson I. Probable congenital esophageal stenosis in a thoroughbred foal. *J Am Vet Med Assoc*. 1991;199:483–485.
107. Baker SJ, Johnson PJ, David A, Cook CR. Idiopathic gastroesophageal reflux disease in an adult horse. *J Am Vet Med Assoc*. 2004;224, 1967-70–1931.
108. Beaulieu A, Zakia LS, Ludwig L, Kenney D, Rätsep E, Nykamp S. Oesophageal muscular hypertrophy and pulsion diverticulum in a Friesian horse. *Veterinary Record Case Reports*. 2020;8:e001093-4.
109. Wong DM, Ruby RE, Eerde EV, Miles KG. Oesophageal ectasia as a cause of dysphagia and milk regurgitation in a neonatal foal. *Equine Vet Educ*. 2020;32:O45–O49.
110. King JN, Davies JV, Gerring EL. Contrast radiography of the equine oesophagus: effect of spasmolytic agents and passage of a nasogastric tube. *Equine Vet J*. 1990;22:133–135.
111. Worth LT, Reef VB. Pericarditis in horses: 18 cases (1986–1995). *J Am Vet Med Assoc*. 1998;212:248–253.

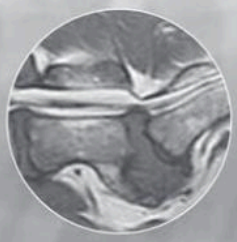
ELECTRONIC RESOURCES

Additional information related to the content in Chapter 37 can be found online at eBooks.Health.Elsevier.com.

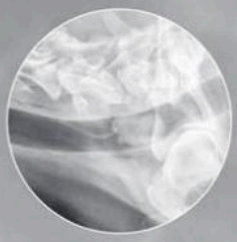
- Chapter Quiz

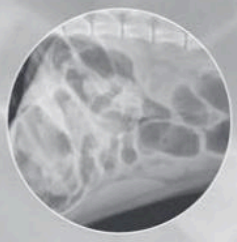
SECTION V











Abdominal Cavity: Canine and Feline

38 **Principles of Radiographic Interpretation of the Abdomen**
Donald E. Thrall

39 **Peritoneal Space**
Susanne M. Stieger-Vanegas

40 **Liver and Spleen**
Martha Moon Larson

41 **Kidneys and Ureters**
Gabriela S. Seiler • Ryan Appleby

42 **Urinary Bladder and Urethra**
Angela Marolf

43 **Prostate Gland**
Jimmy C. Lattimer • Melanie Anderson

44 **Uterus, Ovaries, Vagina, and Testes**
Federica Rossi

45 **Stomach**
Susanne M. Stieger-Vanegas

46 **Small Bowel**
Lorrie Gaschen • Elizabeth A. Riedesel

47 **Large Bowel**
Christine L. Gremillion

CHAPTER 38

Principles of Radiographic Interpretation of the Abdomen

Donald E. Thrall

Acquiring abdominal radiographs is common in small animal practice. Abdominal radiography is rarely performed in the adult horse, except for assessment of the cranioventral and/or ventral aspects of the abdomen for sand collections or enteroliths. The entire abdomen can be radiographed successfully in foals and miniature horses, but the conspicuity of abdominal organs is less than in dogs or cats because of the reduced abdominal fat and the larger volume of the equine gastrointestinal tract.

Sonography has many applications to assess the canine and feline abdomen but it should not be used for initial screening. Sonography is not a replacement for abdominal radiography. Sonography provides for real-time assessment of organ texture and vascular anatomy and perfusion that cannot be obtained with radiography, but sonography does not provide for a global assessment of the abdomen. Sonography is also useful for examining abdominal organs that are usually not visible radiographically, for example, gallbladder, adrenal glands, ureters, uterus, mesenteric lymph nodes, retroperitoneal lymph nodes, and the prostate gland. Because of the limited ability of radiology to examine the equine abdomen, sonography has assumed a more primary role than in small animals.

NOMENCLATURE

In daily practice, the naming of conventional lateral abdominal radiographs made with the patient lying on their side and a vertically directed x-ray beam violates the point-of-entrance to point-of-exit nomenclature system described in Chapter 6. If the patient was on the left side, for example, the correct name for this view would be a *right-left* lateral because the x-ray beam enters on the right side and exits on the left. But, in daily practice the naming of this view is abbreviated to designate the side the patient is lying on, in this case a *left lateral*. Similarly, an abdominal radiograph made with the patient lying on the right side would be a *right lateral* view. Since lateral equine abdominal radiographs are usually made with the patient standing and a horizontally directed x-ray beam, the point-to-entrance to point-of-exit system should be used. Thus, lateral radiographs should be described as either left-right or right-left views. In all species, ventrodorsal (VD) and dorsoventral (DV) radiographs of the abdomen are named according to the point-to-entrance to point-of-exit system.

PREPARATION

In the dog and cat, fasting or enema administration is not needed prior to abdominal radiography unless one is preparing the patient for a contrast study. If a bowel obstruction is being considered, enema administration is contraindicated because it will alter the native pattern of gas and fluid in the intestine, which is diagnostically important. There are no specific circumstances in the horse where fasting or enema administration is recommended before abdominal radiography.

RADIOGRAPHIC TECHNIQUE—DOG AND CAT

A relatively high-contrast image of the abdomen is preferred. This differs from the thorax where there is a large volume of air in the lung to provide contrast, making a low-contrast thoracic radiographic technique preferable. In the abdomen, it is only the interposed fat between the abdominal structures that provides contrast. Bowel gas provides contrast for assessing the lumen of the bowel, but bowel gas is not helpful for comparing parenchymal organs or for assessing the peritoneum or serosal surface of the intestines; it is the abdominal fat located in the mesentery and omentum that provides contrast between organs. As there is minimal difference in inherent radiographic opacity of fat vs. soft tissue, the contrast of an abdominal radiograph should be enhanced using radiographic technique. With analog technology, a high-contrast image is obtained using a low kilovoltage peak (kVp)—high milliampere seconds (mAs) technique, and this approach can also be used with digital systems. However, in digital imaging the contrast of the image is controlled primarily by the processing algorithm that is applied to the raw image data. Therefore, it is important that the correct processing parameters are assigned when the digital image system is set up initially. For patients thicker than 10 cm, a grid should be used to remove scattered x-rays from the beam. Exposure time is not as critical when radiographing the abdomen as when radiographing the thorax.

The respiratory pattern of the patient should be observed for a few seconds before the radiographic exposure is made so that the exposure can be coordinated with peak expiration. At expiration the diaphragm is further cranial, and there is less crowding of the abdomen. Timing the radiographic exposure to phase of respiration is not as important as in the thorax, but timing the exposure to peak expiration is a small adjustment that can be made that will add to the quality of abdominal radiographs.

RADIOGRAPHIC TECHNIQUE—HORSE

Radiographing the abdomen of all but the smallest horse requires massive exposure factors because of the sheer mass of the part. This is a major limiting factor. Also, there is relatively less fat in the equine abdomen to provide contrast, and the gastrointestinal content occupies a much greater volume of the abdomen, resulting in most organs being obscured. In adult horses, it will be difficult to assess anything but the position of large gas-containing structures or to identify large collections of

radiopaque material or objects, such as ingested sand[1] or a large enterolith. A portable x-ray unit such as those used commonly to radiograph equine extremities will not be adequate for equine abdominal radiography.

POSITIONING—DOG AND CAT

The routine abdominal radiographic examination in the dog and cat should consist of left lateral, right lateral, and VD projections. DV radiographs of the abdomen should not be made routinely because the abdomen will be more crowded, organ visibility will be reduced, and portions of the pelvic limbs are often superimposed on the abdomen (Fig. 38.1). A DV view may have to suffice when a patient cannot be positioned in dorsal recumbency for a VD view.

It is important that the entire abdominal cavity be included in the image. This seems obvious, but omitting the pelvic canal and perineum from the field of view is a common error, which increases the chance of missing a lesion. The field of view should extend from just cranial to the diaphragm to the level of the anus/perineum. For lateral views, the pelvic limbs should not be pulled caudally but should be kept perpendicular to the spine. This relaxes the caudoventral aspect of the abdominal wall and reduces crowding. Likewise, in the VD view, the pelvic limbs should ideally be flexed into a so-called *frog-leg position* rather than being pulled caudally, as is usually done. If the pelvic limbs are pulled caudally for the VD view, crowding will be increased, and skin folds will be created in the lateral thigh and/or caudal abdomen region. These skin folds create noticeable opacities that interfere with assessment of the caudal aspect of the abdomen (Fig. 38.2).

Even in the largest dog, it is usually possible to include the entire abdominal cavity in one 14-inch × 17-inch image. For the occasional huge dog where this is not possible, then each projection (left lateral, right lateral, VD) should be divided into cranial and caudal portions.



Fig. 38.1 A dorsoventral (DV) view of the abdomen. The pelvic limbs are superimposed on the caudal aspect of the abdomen and the caudal abdominal cavity is compressed and structures in this area cannot be evaluated. A DV view should not be a routine view for these reasons. This patient is also crooked, which adds to the reduced quality of this specific image.

POSITIONING—HORSE

In foals and miniature horses, it may be possible to obtain lateral abdominal radiographs by restraining a compliant animal on a conventional x-ray table and using a vertically directed x-ray beam, as in dogs and cats, but this is rarely done. Even in small horses, abdominal radiographs are usually obtained in a standing animal and using a horizontally directed x-ray beam (Fig. 38.3).

The plate should not be held by hand when radiographing the equine abdomen. The light field that corresponds to the primary x-ray beam is visible only on the side of the horse closest to the x-ray tube, meaning that no part of the light field can be seen on the plate. Therefore, aligning the x-ray beam with the plate is impossible when the plate is held by hand. This invariably results in the primary x-ray beam striking the person holding the plate. A wall-mounted plate holder, as described in Chapter 9, or a floor-mounted mobile plate holder should be used for equine abdominal radiography. When using these devices, the x-ray beam can be aligned with the plate before the horse is brought into position next to the plate.

As noted before, the overall conspicuity of abdominal organs in the horse is less than in the dog or cat because of the increased volume of the gastrointestinal tract and relatively reduced amount of abdominal fat. Some questions addressed by abdominal radiography in small horses or foals pertain to the presence of gastrointestinal foreign material, such as an enterolith or sand, or the presence of mechanical bowel obstruction, which will often be accompanied by increased bowel diameter and increased intraluminal fluid and gas.

The radiographic detail in the abdomen will be better in foals or miniature horses than in adult horses but meaningful information can sometimes be obtained in adult horses (Fig. 38.4). VD abdominal radiographs in small horses are rarely useful, or even possible to obtain, and most questions being addressed radiographically can be answered from lateral views.

Radiographic magnification has to be considered when radiographing the equine abdomen. As a result of the large diameter of the abdominal cavity of an adult horse, a lesion on the side closest to the x-ray tube could be 35 cm or more from the plate. This leads to the lesion being magnified by approximately 1.5 times. At this degree of magnification, the resultant blurring could result in the lesion being missed, especially if the lesion is small (Fig. 38.5). If a small lesion is a clinical concern, then left-right *and* right-left abdominal radiographs should be obtained.

WHY ARE BOTH LEFT AND RIGHT LATERAL ABDOMINAL VIEWS NEEDED ROUTINELY IN SMALL ANIMALS?

As in the thorax, obtaining both left lateral and right lateral views in addition to a VD view is recommended routinely but for a different reason, which is the use of bowel gas as an inherent contrast medium. The redistribution of bowel gas between the various views, and particularly between the left vs. right lateral view, can provide important information that allows the diagnosis to be made.

Of particular importance with regard to the redistribution of gastrointestinal gas as a function of position is the change in the appearance of the stomach. The stomach is an asymmetric structure with the larger fundus located in the left dorsal aspect of the abdomen, and the smaller pylorus located in the right ventral aspect of the abdomen (Fig. 38.6).[2,3] When the patient is in right recumbency, the pylorus will usually contain fluid or ingesta, and if there is gas in the

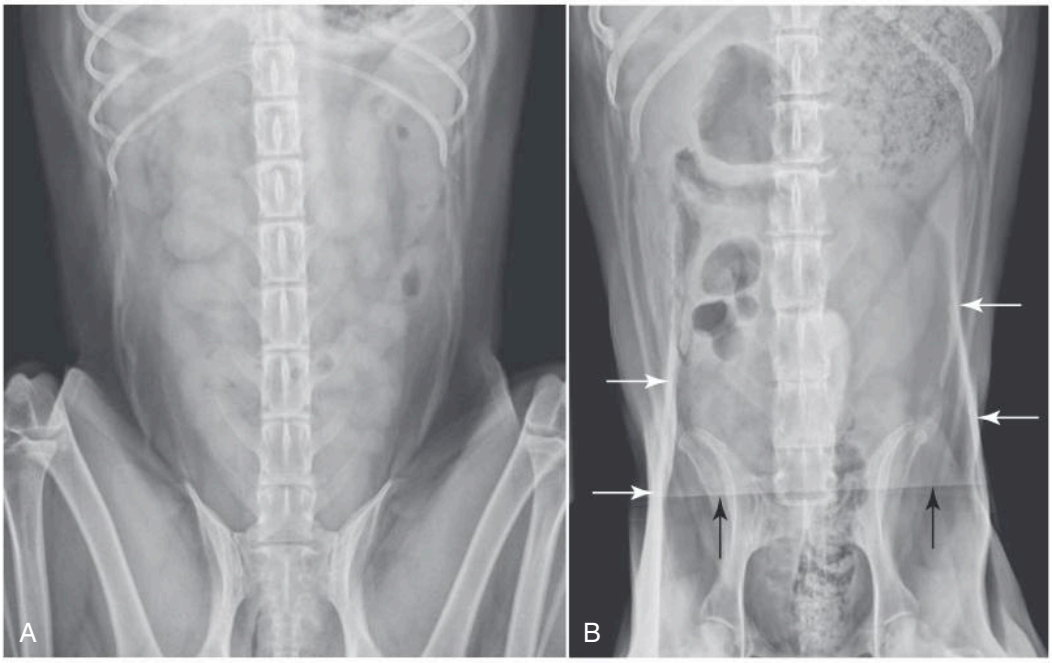


Fig. 38.2 Ventrodorsal (VD) abdominal radiographs from two dogs. In **A,** the pelvic limbs are flexed, allowing relaxation of the caudal abdominal muscles and expansion of the caudal aspect of the abdomen. In **B,** the pelvic limbs are pulled caudally, creating skin folds (*white arrows*) that can interfere with interpretation, and the caudal aspect of the abdomen is narrower and more crowded. Also in **B,** the edge of the positioning trough has created a linear opacity (*black arrows*) that can also interfere with interpretation. (Reproduced with permission from Thrall DE, Robertson IR. *Atlas of Radiographic Anatomy and Normal Anatomic Variants in the Dog and Cat.* 3rd ed. St. Louis: Elsevier/Saunders; 2023.)

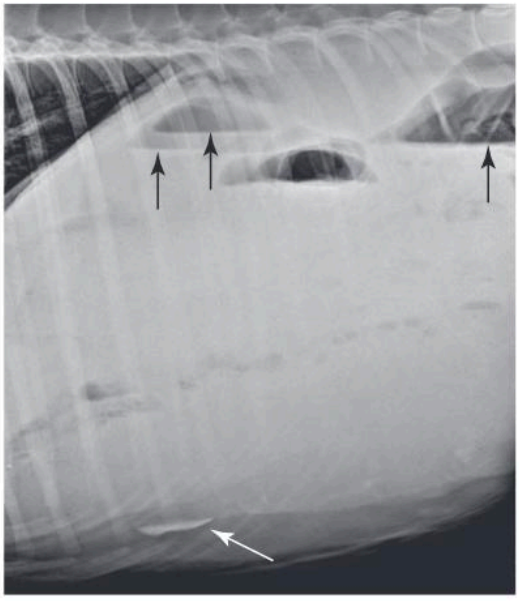


Fig. 38.3 Lateral radiograph of the cranial aspect of the abdomen of an adult American miniature horse. The small size of this horse allows for reasonable radiographic quality, but the conspicuity of organs is less than in a dog or cat because of the reduced amount of abdominal fat and the larger volume of the abdomen occupied by the gastrointestinal tract. There is a small amount of sand in the ventral aspect of the large bowel (*white arrow*); this is not significant. Horizontal gas/fluid interfaces (*black arrows*) in the bowel are seen because the radiograph was made with a horizontally directed x-ray beam. Visualization of gas/fluid interfaces to this extent is normal in the horse.

stomach, the gas will rise and collect in the body and fundus of the stomach. Alternatively, when the patient is in left recumbency, the fluid will usually gravitate to the fundus, and gas will rise and fill the pylorus. Therefore, the pylorus will be of soft tissue opacity in the right lateral view and contain gas in the left lateral view (Fig. 38.7). The difference in appearance of the stomach in left versus right lateral radiographs in an individual patient depends on the character of the gastric content and the relative amount of liquid versus solids. If there is mostly gas or mostly fluid or ingesta in the stomach, the stomach will commonly appear similar in left vs. right recumbency. The greatest difference in appearance of the stomach in the left vs. right lateral view occurs when the stomach is moderately distended and contains both gas and fluid (see Fig. 38.7).

Of particular importance is the realization that in right lateral views, especially in dogs, the pylorus can take on the appearance of a mass or foreign object because of the dependent fluid collection (see Fig. 38.7B). Also important is that ingested foreign material often becomes anchored in the pylorus. This emphasizes the importance of a left lateral radiograph to increase the chances of gas being in the pyloric antrum to provide contrast for the foreign material (Fig. 38.8). There is some evidence that it can be beneficial in dogs to obtain the left lateral projection first as it maximizes the likelihood of the duodenum being gas filled.[4]

As noted earlier, DV views of the abdomen are made rarely. Occasionally, a DV abdominal radiograph will be necessary when a VD view cannot be made (Fig. 38.9). The gravitational dependence of gas is one aspect of DV radiographs that may be useful, as illustrated in Fig. 38.9.

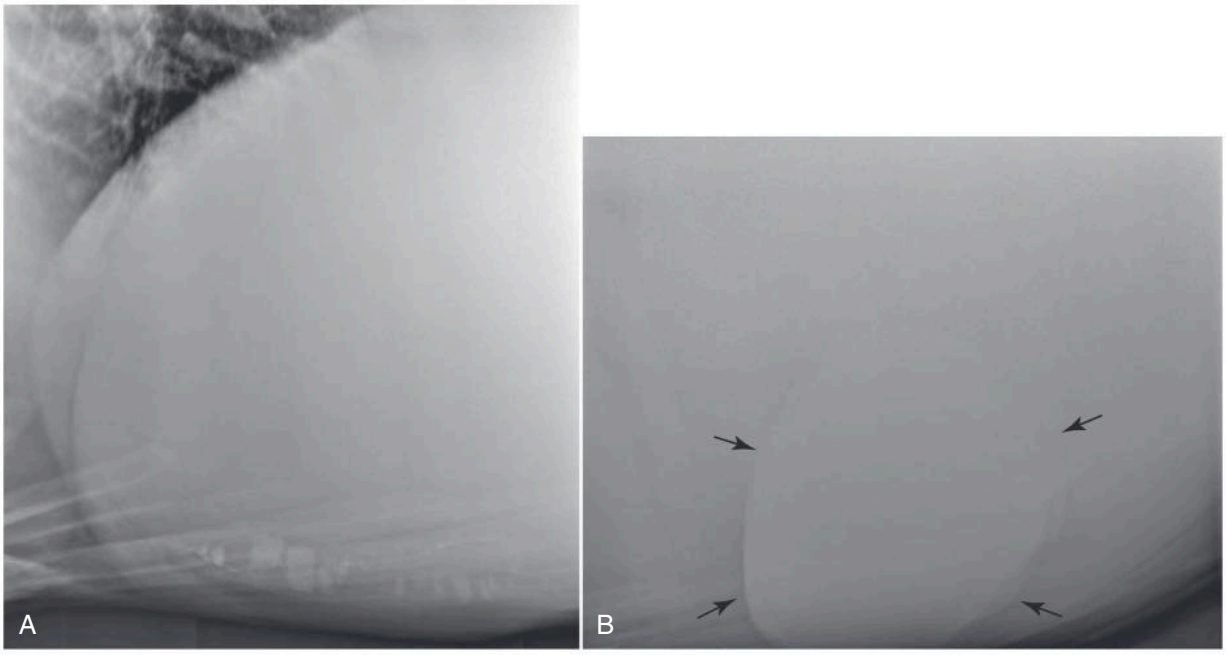


Fig. 38.4 Lateral radiographs of the cranioventral **(A)** and midventral **(B)** aspects of the abdomen of an adult Standardbred horse. The cranioventral aspect of the abdomen in **A** is devoid of any detail because of the extreme thickness of this region and the relatively homogeneous contents of the bowel; this is a normal appearance. However, this is a common location for sand to accumulate, and clinically insignificant sand accumulations are seen here. In **B,** there is a large circular radiopaque structure in the ventral aspect of the abdomen that represents an enterolith (*black arrows*).

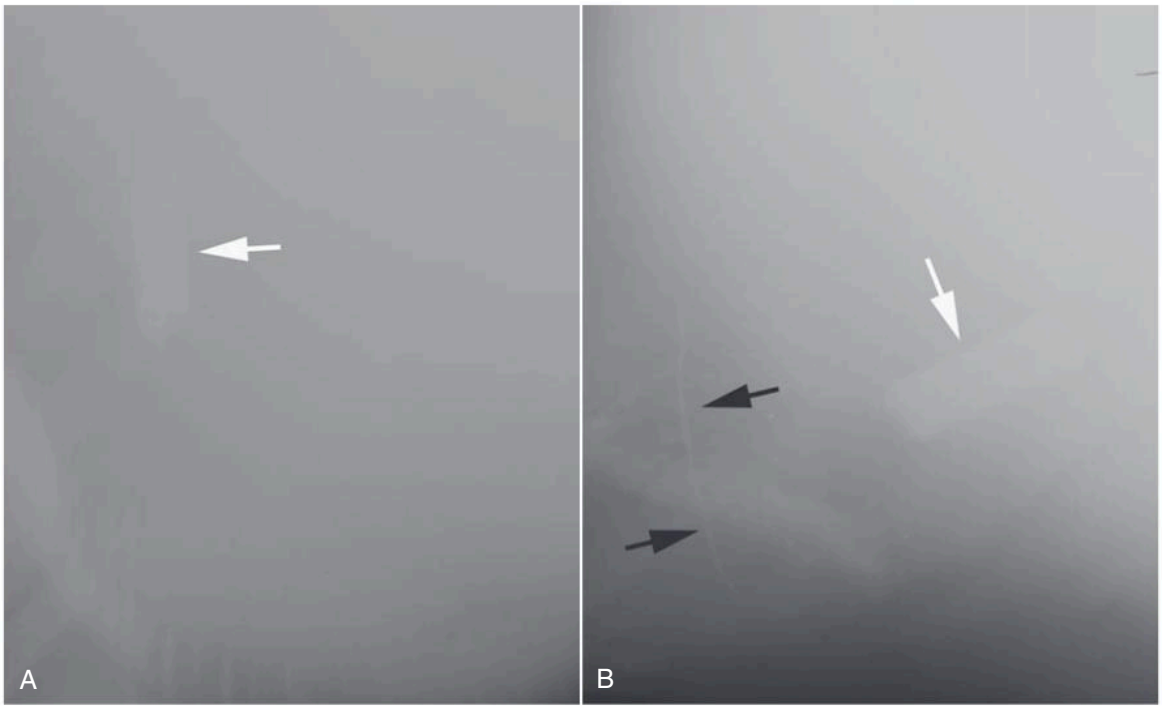


Fig. 38.5 Right-left lateral radiograph of the cranioventral aspect of the abdomen of an adult Holstein cow suspected of having traumatic reticuloperitonitis. Although this example is not in a horse, it illustrates the effect of magnification in a large patient. **(A)** There is a magnet in the reticulum (*white arrow*) but no evidence of metallic foreign material. When the opposite left-right lateral **(B)** was made, a wire (*black arrows*) is visible cranial to the reticulum confirming a penetrating foreign body from the reticulum. The magnet is also visible in **B (*white arrow*)**. The wire was not visible in the right-left radiograph because of magnification related to the large distance of the wire from the plate. When radiographed from the opposite side, the wire was much closer to the plate and was not blurred by magnification.

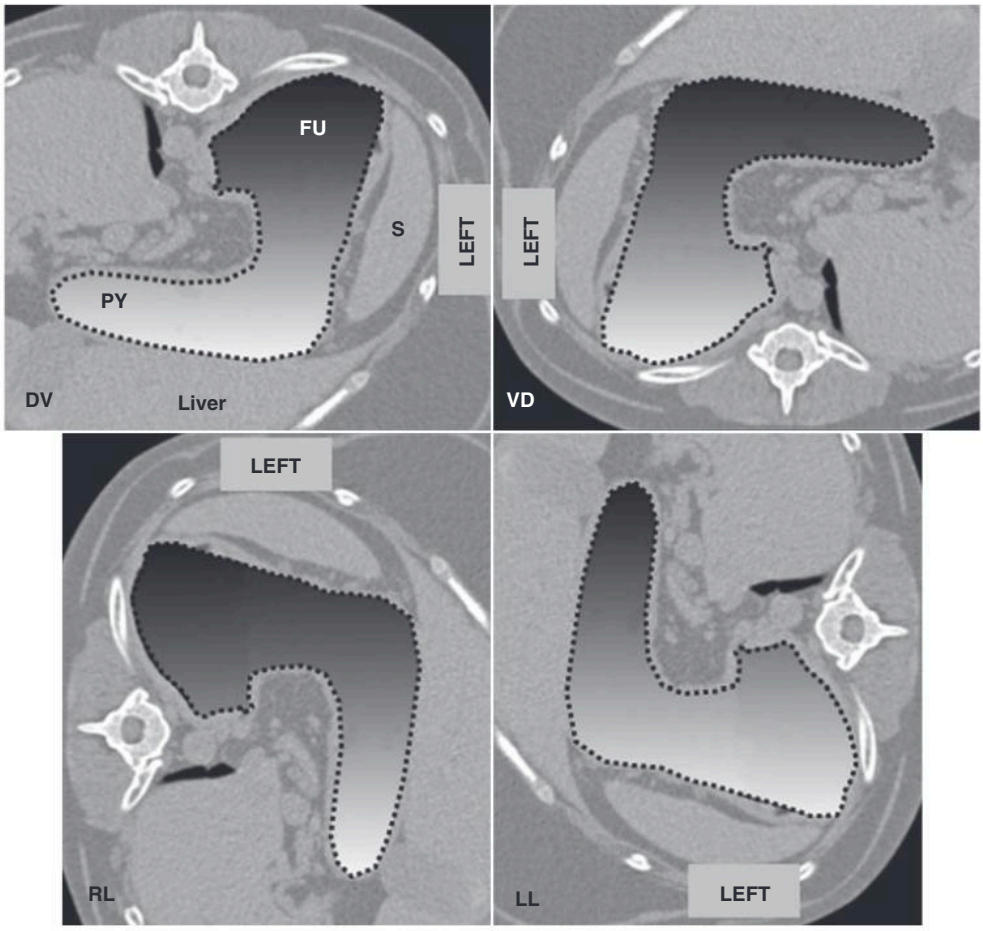


Fig. 38.6 Images depicting the normal distribution of gas vs. fluid in the stomach as a function of body position. The images are the same transverse computed tomography image of a dog rotated at 90-degree increments to illustrate sternal (*DV*), dorsal (*VD*), right (*R*), and left (*L*) recumbency. The stomach is outlined by a *dotted line.* The lumen of the stomach is shaded to illustrate the effect of gravity on redistribution of fluid (*white*) and gas (*black*) as a function of body position. The presence of gas in the pylorus in left recumbency is important clinically as the gas provides contrast for identification of foreign material that is trapped in the pylorus. *FU,* Fundus, *PY*, pylorus, *S,* spleen. (Reproduced with permission from Thrall DE, Robertson IR. *Atlas of Radiographic Anatomy and Normal Anatomic Variants in the Dog and Cat*. 3rd ed. St. Louis: Elsevier/Saunders; 2023.)

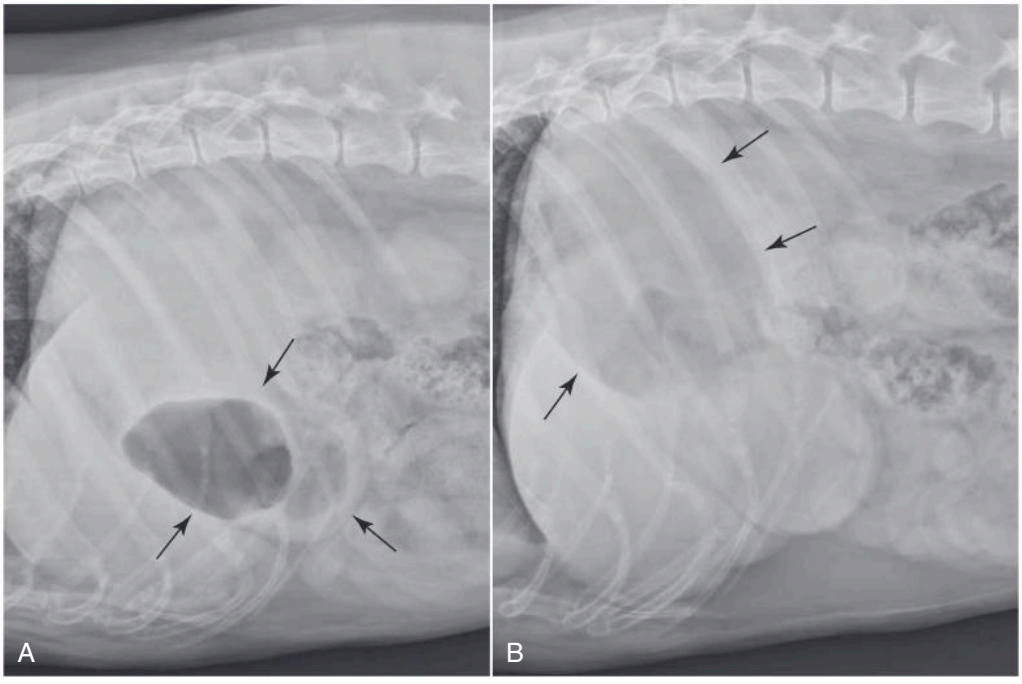


Fig. 38.7 Left **(A)** and right **(B)** lateral radiographs of the cranial aspect of the abdomen of a normal dog. In the left lateral view **(A)**, gas is present in the pylorus (*black arrows*). In right lateral recumbency, all of the gas is in the fundus (*black arrows*) and the pylorus is filled with fluid and appears as a round mass ventral to the fundus.

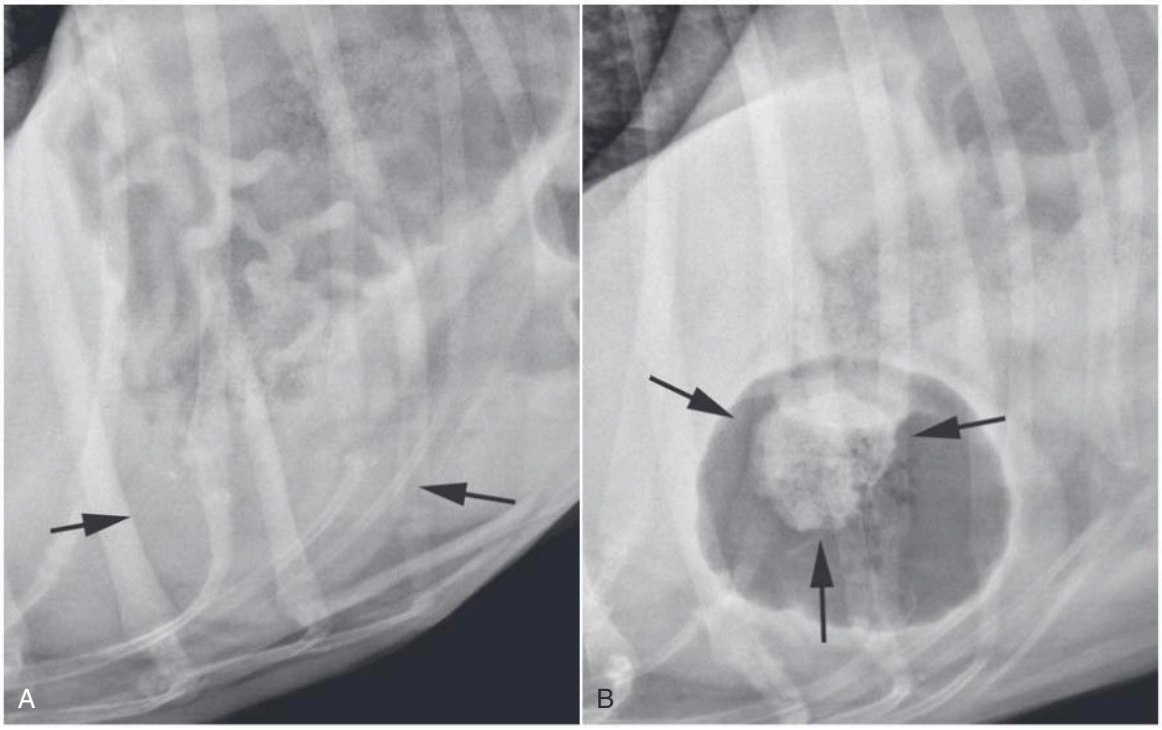


Fig. 38.8 Right lateral **(A)** radiograph of the abdomen of a dog suspected of having ingested foreign material. There is fluid in the pyloric antrum (*black arrows*) and the pylorus cannot be assessed for nonmineral foreign material due to silhouetting by the surrounding fluid. In a left lateral view **(B)**, gas in the pyloric antrum provides contrast for the foreign material anchored in the pyloric antrum (*black arrows*).

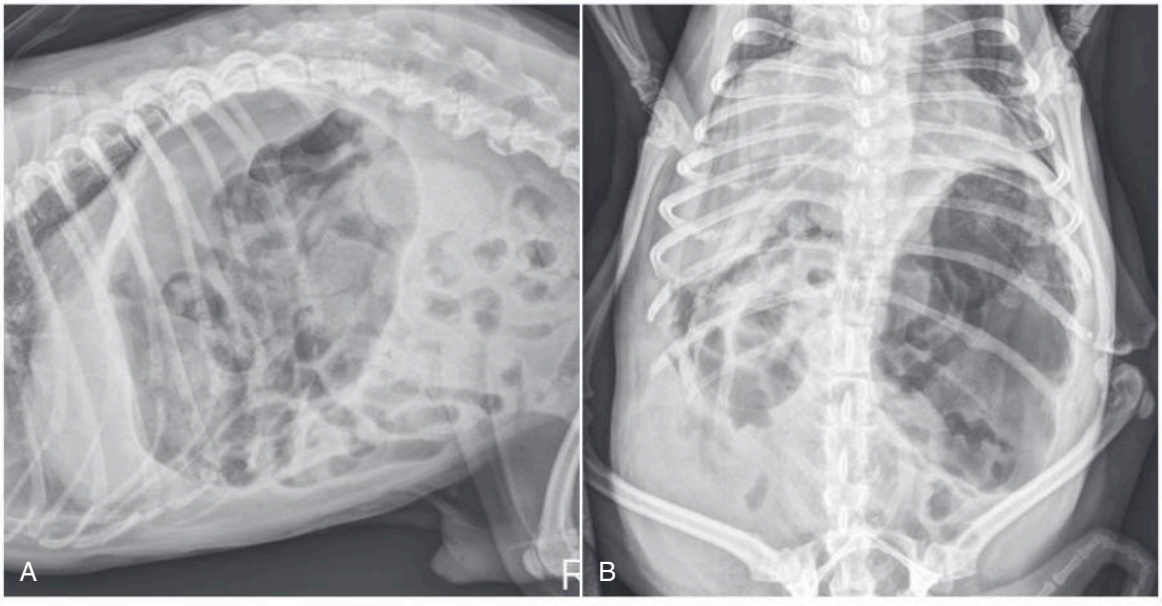


Fig. 38.9 Lateral **(A)** and dorsoventral (DV) **(B)** radiographs of the abdomen of a dog with acute abdominal distention and thoracic pain from rib fractures. In the lateral view **(A)**, there was concern whether the dilated stomach was in a normal position. Pain prevented obtaining a ventrodorsal (VD) radiograph so a DV was obtained instead. In the DV view **(B)**, gas has risen to the fundus because this part of the stomach is nondependent. There is no evidence of gastric malpositioning. This illustrates one of the few indications for obtaining a DV view of the abdomen versus a VD view. In **B,** note the increased crowding of the abdomen and superimposition of the pelvic limbs on the caudal abdomen, which are common problems with DV compared to VD abdominal radiographs.

ANCILLARY VIEWS

Right lateral, left lateral, and VD views of the abdomen will suffice for almost all canine and feline patients. If the status of the urethra in male dogs is of concern, as for assessment of urethral calculi, the right and left lateral views should be supplemented with a third lateral view made with the pelvic limbs pulled cranially. This provides an unobstructed view of the ischial arch and os penis, allowing for assessment of urethral calculi without superimposition of the pelvic limbs (Fig. 38.10).

A compression radiograph can be used to clarify a suspicious finding that cannot be confirmed because of superimposition.[5] The theory is to apply mild compression to displace superimposed organs from the field of view, leaving an unobstructed view of the region of interest. This technique can be applied in a lateral view to assess structures such as the uterine body or urinary bladder. Specialized inflatable compression paddles are available, but a wooden spatula or wooden spoon can also be used. Of course, care should be taken not to place compression on organs that are obviously diseased, and the amount of pressure placed should always be gentle (Fig. 38.11). The increased use of ultrasound for abdominal assessment has reduced the need for compression radiographs, but they remain a convenient method to increase the accuracy of radiographic interpretation in some patients where ultrasonography is not possible.

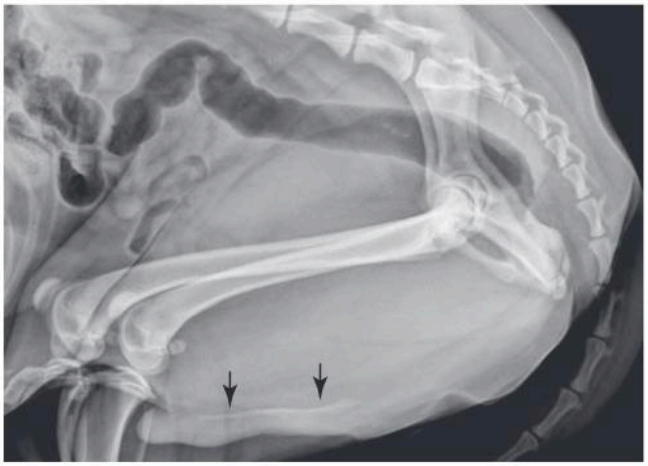


Fig. 38.10 Lateral radiograph of the caudal aspect of the abdomen with the pelvic limbs pulled cranially. This provides an unobstructed view of the urethral region and of the os penis (*black arrows*). This view is useful for assessing for urethral calculi or lesions of the os penis.

ANCILLARY FACTORS

There are no ancillary factors that affect the radiographic appearance of the equine abdomen other than body mass. However, for the dog and cat, the body habitus and presence of cutaneous structures or lesions are ancillary factors that have a significant effect on the appearance of the radiograph.

The volume of abdominal fat contained in the mesentery and omentum is directly related to the conspicuity of parenchymal organs and serosal margins in the abdomen because it is this fat that provides contrast between organs. It is absolutely critical for fat to be present if organs are going to be distinguished from one another in abdominal radiographs (Fig. 38.12). In emaciated (Fig. 38.13) or young (Fig. 38.14) animals, there is reduced fat that results in loss of conspicuity of the serosal margins.

Cutaneous lesions or superimposed superficial structures are not misinterpreted as a lesion as often in abdominal radiographs as they are in thoracic radiographs. One specific example of a superficial structure that is often misinterpreted as an abnormality in abdominal radiographs is superimposition of the prepuce and os penis on the caudal aspect of the abdomen in VD radiographs of male dogs (Fig. 38.15). The reason that cutaneous lesions create such a conspicuous opacity was discussed in Chapter 6.

SPECIFIC DIFFERENCES BETWEEN CANINE AND FELINE ABDOMINAL RADIOGRAPHS

There are several specific differences between canine and feline abdominal radiographs that are important to know to reduce the chance for an error in interpretation. These differences will all be covered in their respective section in the text, but a brief summary is also presented here.

Overconditioning results in increased intra-abdominal fat but this is disproportionate in cats compared to dogs (Fig. 38.16). The tendency for overweight cats to accumulate fat in the

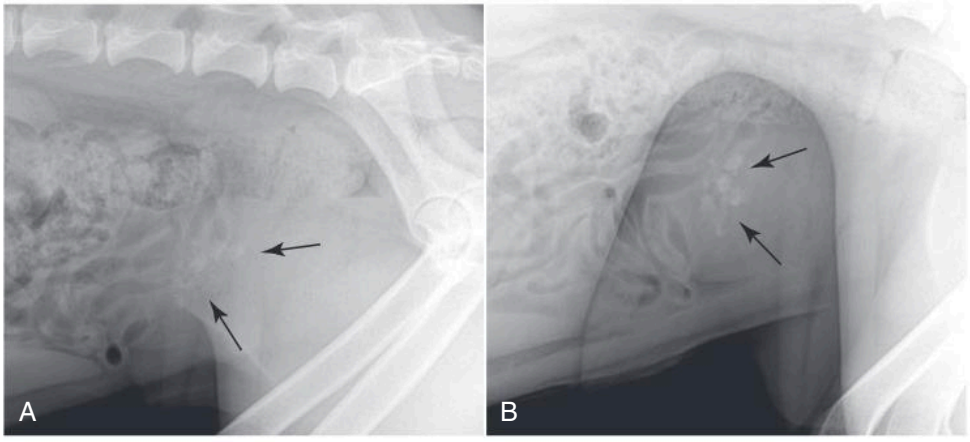


Fig. 38.11 Lateral radiograph of caudal aspect of the abdomen of a dog **(A)**. There are multiple small mineral opacities (*black arrows*) superimposed on the plane of the urinary bladder. These opacities could represent cystic calculi, but they could also represent superimposed bowel content. The caudal abdomen was compressed with a wooden spatula in a subsequent lateral radiograph **(B)** to displace the bowel, and the opacities (*black arrow*) are now clearly seen separate from the bowel, proving they are cystic calculi. The outline of the spatula is visible.

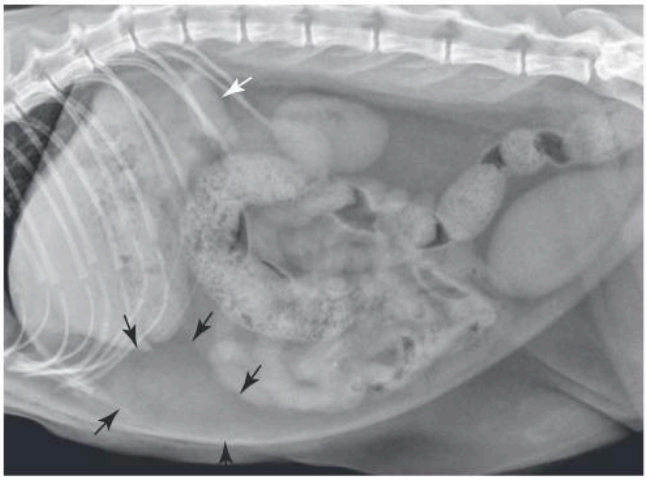


Fig. 38.12 Lateral radiograph of a cat with abundant abdominal fat. The fat provides contrast, and there is excellent discrimination between parenchymal organs. The kidneys, proximal aspect of the spleen (*white arrow*), jejunal segments, and the urinary bladder are all highly conspicuous because of the peritoneal fat. Note the large collection of falciform fat (*black arrows*).

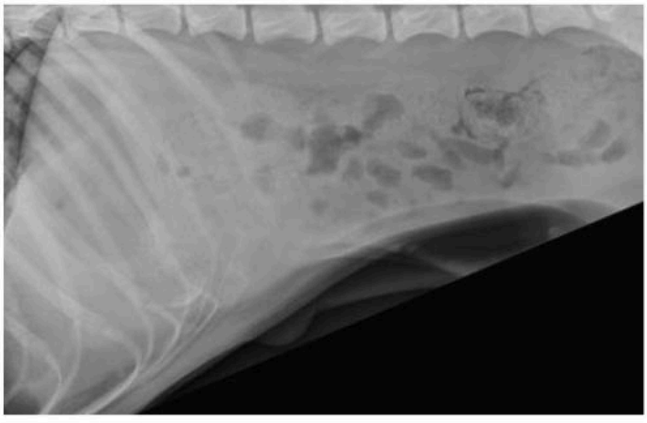


Fig. 38.13 Lateral radiograph of the abdomen of an emaciated dog. The conspicuity of the margin of abdominal organs is poor because of the lack of abdominal fat to provide contrast. With this appearance, radiographic assessment of the abdomen is compromised.

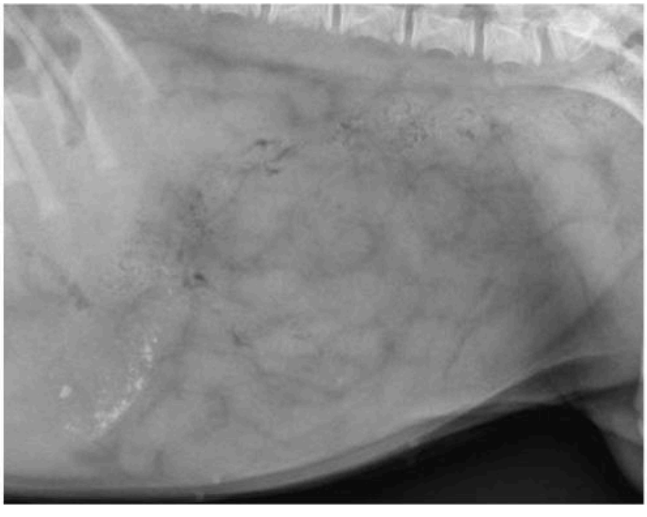


Fig. 38.14 Lateral radiograph of an 11-week-old dog. Intra-abdominal contrast is diminished because of the relative lack of abdominal fat. This is a common finding in young animals. Margin visualization is, however, better than in patients that are undernourished and emaciated (compare with Fig. 38.13).

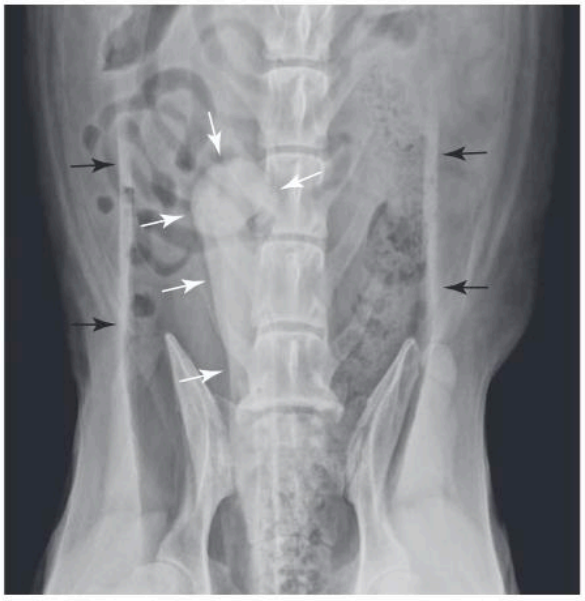


Fig. 38.15 Ventrodorsal (VD) view of the caudal aspect of the abdomen in a male dog. The superimposition opacity created by the prepuce (*white arrows*) can be misinterpreted as a mass. Note also the skin folds created by pulling the pelvic limbs caudally (*black arrows*) rather than having them flexed during radiography.

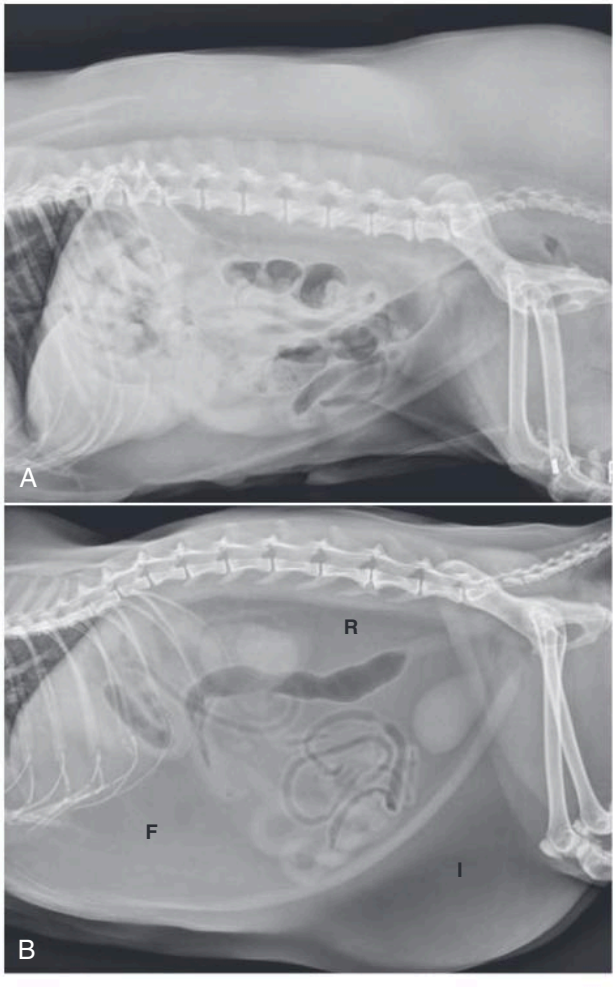


Fig. 38.16 Lateral abdominal radiographs of an overweight dog **(A)** and cat **(B)**. In the dog, there is massive subcutaneous fat accumulation. There is also marked fat deposition in the abdomen but not to the same extent as subcutaneously. In the cat, there is less subcutaneous fat deposition, but massive amounts of fat have accumulated in the abdominal cavity, retroperitoneal space (*R*), falciform region (*F*), and in the inguinal region (*I*).



Fig. 37.17 Contrast-enhanced transverse maximum intensity projection (MIP)[a] computed tomography image of the cranial abdomen of a normal cat. The left limb of the pancreas (*white arrows*) is located between the gastric fundus (*F*) and spleen (*S*) and is surrounded by fat, which provides radiographic contrast. The lateral aspect of the left limb of the pancreas often has a nodular appearance. The right limb of the pancreas is not included in this image. The hyperattenuating tubular structures medial to the pancreas are normal splenic veins. *L*, Left. (Reproduced with permission from Thrall DE, Robertson IR. *Atlas of Radiographic Anatomy and Normal Anatomic Variants in the Dog and Cat*. 3rd ed. St. Louis: Elsevier/Saunders; 2023.)

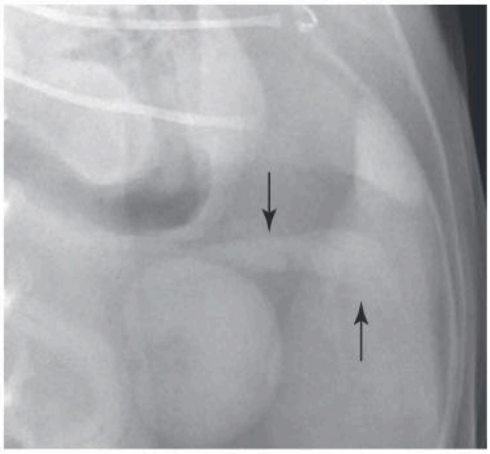


Fig. 38.18 Ventrodorsal radiograph of a 12-year-old domestic cat. The left limb of the normal pancreas is visible medial to the spleen (*black arrows*). The most lateral margin has a mildly lobular appearance. (Reproduced with permission from Thrall DE, Robertson IR. *Atlas of Radiographic Anatomy and Normal Anatomic Variants in the Dog and Cat*. 3rd ed. St. Louis: Elsevier/Saunders; 2023.)

falciform region is often misinterpreted as peritoneal fluid. Using the basic principles of radiographic opacities and the silhouette sign discussed in Chapter 6, this cannot be fluid, or the absolute opacity of the region would be greater, and there would also be silhouetting with the adjacent liver and jejunum.

In the dog, the pancreas is closely associated with the stomach, transverse colon, and descending duodenum, and as a result the normal canine pancreas is never visible radiographically. In the cat, however, the left limb of the pancreas extends lateral to the colon and resides just medial to the spleen and is surrounded by fat (Fig. 38.17). Therefore, the left limb of the pancreas can be evaluated specifically in radiographs (Fig. 38.18), and the adjacent fat can also be assessed for secondary changes as might occur with pancreatitis.

The proximal aspect of the spleen is usually visible in VD radiographs of normal dogs and normal cats, located just caudolateral to the gastric fundus. The distal aspect of the spleen is also commonly visible in dogs (Fig. 38.19A), but rarely in cats (Fig. 38.19B). This relates to the slightly different orientation of the spleen in the abdomen in dogs vs. cats. Visibility of the distal aspect of the spleen in the ventral abdomen in cats does not always mean that the spleen is enlarged, but this should be considered.

A unique feature of the feline stomach compared to the canine stomach is the presence of greater amounts of submucosal fat.[6] As fat is more radiolucent than soft tissue, the presence of fat in the gastric wall in some cats results in linear regions of decreased opacity extending radially from the lumen through the gastric wall when the stomach is empty and contracted (Fig. 38.20). This is a type of normal variation and is only found in a small fraction of cats.

Another unique feature of the feline stomach compared to the canine stomach is the relative position of the pylorus in the abdomen. In the dog, the pylorus is located to the right of midline, approximately midway between the spine and abdominal wall (Fig. 38.21A). In the cat, the pylorus is a more midline structure, being located directly on the midline, or just slightly to the right of the spine (see Fig. 38.21B). This difference is important as medial displacement of the pylorus is a sign of liver enlargement or a liver mass in dogs, whereas a medial location of the pylorus is normal in cats.

There is a marked difference in the morphology of the cecum in the dog vs. cat. In the dog, the cecum is a coiled structure that has a separate communication with the colon (Fig. 38.22). Thus, there are separate cecocolic and ileocolic valves in the dog. In the cat, the cecum is not a separate structure but is more of a small outpouching from the ascending colon and there is no unique cecocolic valve (Fig. 38.23). As a result, the cecum is a reliable landmark in the canine abdomen but not in the cat.

In many obese feline patients, the entire small intestine is lateralized into the right hemiabdomen (Fig. 38.24). It is important to recognize that this appearance is not the result of a pathologic abdominal mass.

ABDOMINAL MASS/MASS EFFECT

The location of an abdominal mass depends on its origin and the effects of gravity. Sometimes, an abdominal mass is suspected but not clearly seen. In this case, the abnormality is commonly described using the term *mass effect*. With a mass effect, displacement of multiple abdominal organs, such as the intestines, can be the only sign of the presence of a mass.

There are two anatomic compartments in the abdomen, the peritoneal and retroperitoneal spaces, and a mass can arise within either. The retroperitoneal space is in the dorsal abdomen; therefore, retroperitoneal masses are dorsal.

[a]An MIP image is a summation of several adjacent CT slices to obtain a volumetric image. The thickness of the volume depends on the number of CT images that are summed, and the thickness of each image.

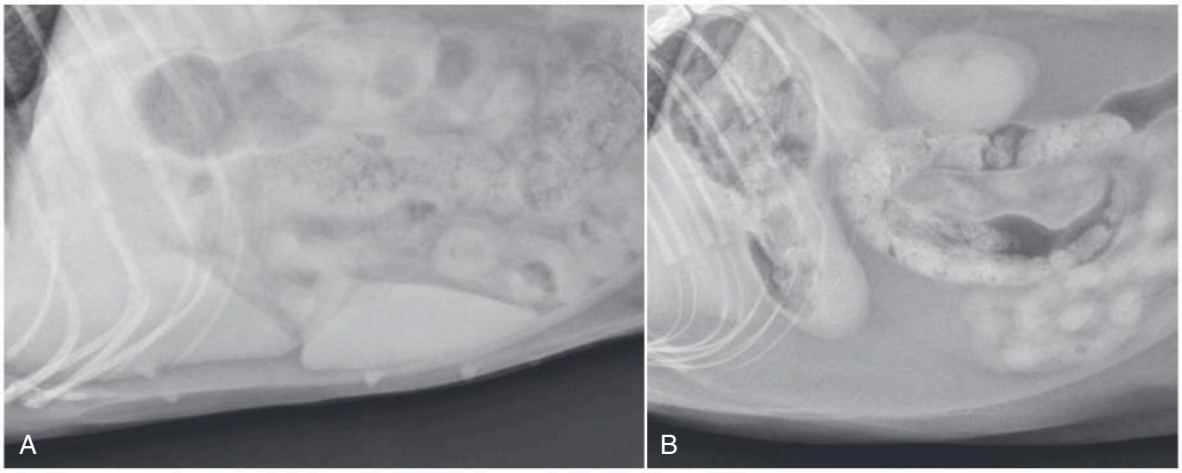


Fig. 38.19 Cranioventral aspect of the abdomen of a dog **(A)** and a cat **(B)**. In canine lateral radiographs, the distal extremity of the spleen is commonly visible, as seen here. In feline lateral radiographs, the distal aspect of the spleen is usually not seen in normal subjects, and is not present in this image.

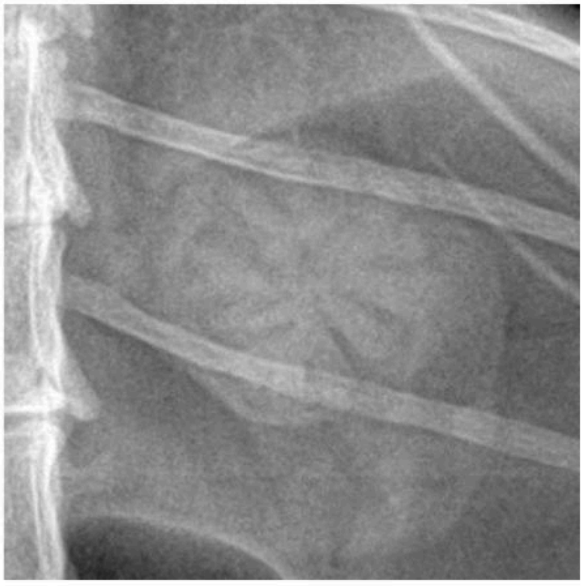


Fig. 38.20 Left cranial aspect of the abdomen of a cat having excessive fat in the gastric wall. The fat creates a striated appearance to the stomach, which is contracted. This is normal variation and is found in only a small fraction of cats.

An abdominal mass often causes displacement of the adjacent abdominal structures and the characteristics of the displacement are useful in estimating the origin of the mass; for example, cranial displacement of urinary bladder due to prostate gland enlargement, ventral displacement of colon due to renal mass, caudal displacement of stomach due to liver mass, to mention just a few (Table 38.1).

Also, the regional location of the mass within the abdomen is important in considering its origin. The origin of a mass is usually estimated in lateral views as superimposition of organs is less than in the VD view. By dividing the lateral view of the abdominal cavity into regions, the most likely origin of a mass can be estimated (Fig. 38.25, Table 38.1).

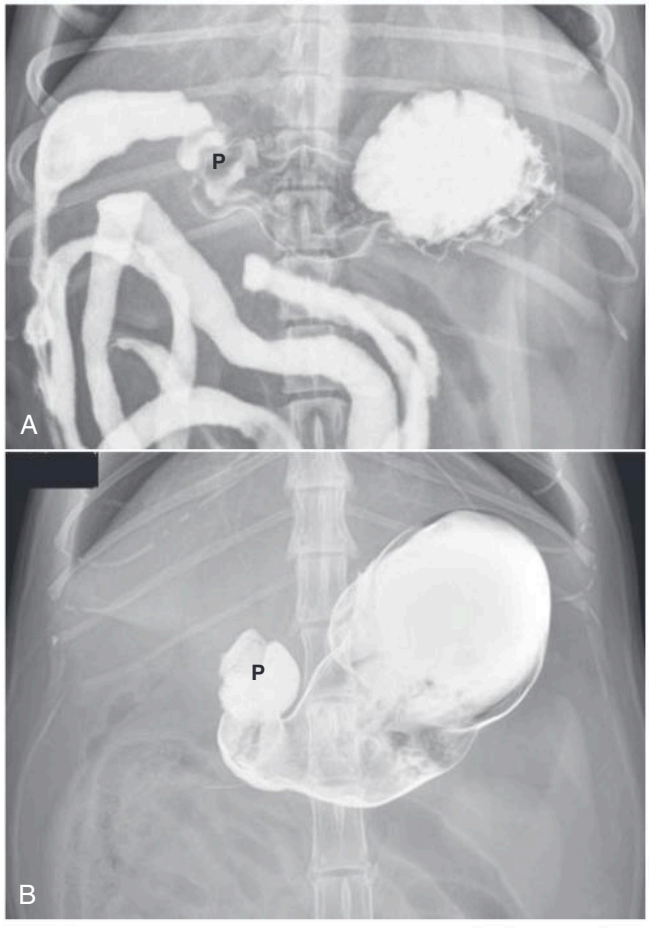


Fig. 38.21 Ventrodorsal radiographs of a 7-year-old Miniature Schnauzer **(A)** and a 12-year-old domestic cat **(B)**. In each animal, barium is present in the stomach. Note the more medial location of the pylorus (*P*) in the cat. The undulations in the pyloric antrum in **A** and **B** are due to normal peristalsis. (Reproduced with permission from Thrall DE, Robertson IR. *Atlas of Radiographic Anatomy and Normal Anatomic Variants in the Dog and Cat*. 3rd ed. St. Louis: Elsevier/Saunders; 2023.)

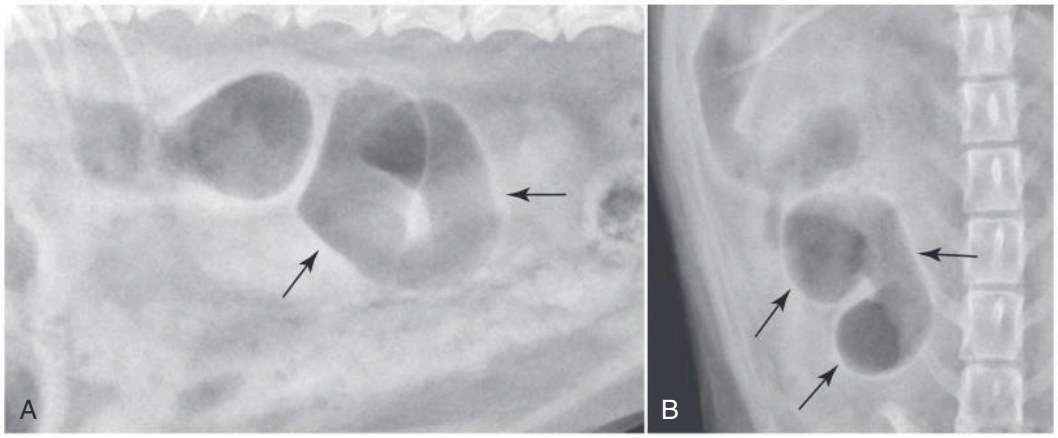


Fig. 38.22 Lateral **(A)** and ventrodorsal **(B)** radiographs of a 4-year-old Yorkshire terrier. The cecum is a gas-filled coiled structure and is visible in the central portion of the right abdomen (*black arrows*). (Reproduced with permission from Thrall DE, Robertson IR. *Atlas of Radiographic Anatomy and Normal Anatomic Variants in the Dog and Cat*. 3rd ed. St. Louis: Elsevier/Saunders; 2023.)

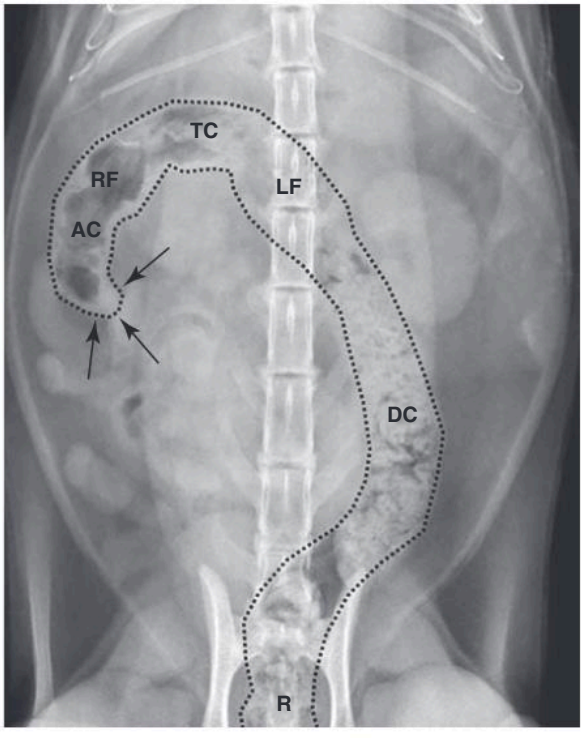


Fig. 38.23 Ventrodorsal radiograph of a 1-year-old domestic cat. The colon is outlined and various regions labeled. The feline cecum is not a distinct structure as it is in the dog, being designated as a proximal outpouching of the ascending colon (*black arrows*). *AC*, Ascending colon; *DC,* descending colon; *LF,* left colic flexure; *R,* rectum; *RF,* right colic flexure; *TC,* transverse colon. (Reproduced with permission from Thrall DE, Robertson IR. *Atlas of Radiographic Anatomy and Normal Anatomic Variants in the Dog and Cat.* 3rd ed. St. Louis: Elsevier/Saunders; 2023.)



Fig. 38.24 Ventrodorsal radiograph of an overconditioned cat. The entirety of the jejunum is located in the right hemiabdomen. This is a common normal variation in overconditioned cats; there is not a pathologic mass accounting for this.

Table • 38.1

Organ Displacements Occurring as a Result of Various Abdominal Masses.

ORIGIN	COMMON SECONDARY DISPLACEMENTS
Liver	Caudal displacement of the gastric axis
Gallbladder	Caudal displacement of the pyloric antrum
Hepatic lymph nodes	Caudal displacement of the body of the stomach and/or pyloric antrum
Gastric	Often characterized by abnormal shape and gas pattern rather than a mass effect
Spleen	Location of the mass variable depending on location within the spleen
Pancreas	Widening of the gastroduodenal angle, caudal displacement of the transverse colon
Mesenteric lymph nodes	Centrally located within the intestinal convolute, peripheral displacement of intestines
Small intestines	Location varies, typically associated with abnormal gas patterns
Mesenteric mass	Peripheral enteric displacement
Urinary bladder	Naturally variable in size, a mass may be recognized by distorted shape rather than size
Prostate	Cranial displacement of the urinary bladder and dorsal displacement of the rectum
Paraprostatic cysts	May be located cranial to the prostate to intrapelvic
Uterus	Craniodorsal displacement of small intestines, medial displacement of small intestines in the VD projection
Retained testicle	Location can range from the cranial aspect of the bladder to the inguinal canal
Kidneys	Left—ventral displacement of the descending colon Right—ventral displacement of ascending colon and cecum
Adrenal glands	Caudal and lateral displacement of the kidneys if large enough
Retroperitoneal hematoma or urinoma	Diffuse mass effect, may efface contours of kidneys
Ovaries	Can cause ventral displacement of the caudal pole of the ipsilateral kidney
Sublumbar lymph center	Ventral displacement of descending colon and rectum

VD, Ventrodorsal.

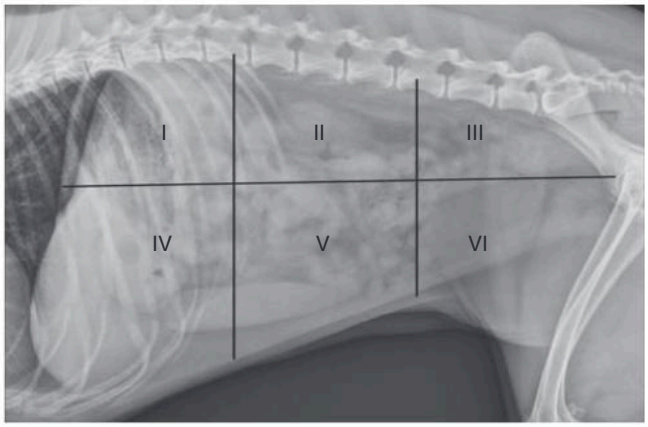
Masses in the dorsal abdomen can be either peritoneal (covered on all surfaces by visceral peritoneum) or retroperitoneal (covered only ventrally by visceral peritoneum). Peritoneal masses are usually more mobile than retroperitoneal masses.

INTERPRETATION PARADIGM

Like in all body systems, an organized approach to radiographic interpretation of the abdomen is needed. This begins with an overview of technique, according to the following questions, followed by evaluation for abnormalities.

- Are the radiographic views adequate, and are all of the views needed present?
- Is the positioning adequate?
- Are the images overexposed or underexposed?
- Are the images acquired with an antiscatter grid?
- What is the body habitus of the patient, and how is this going to affect the appearance of the abdomen?
- Were the images acquired with a vertically directed x-ray beam with the cassette in an x-ray table, or was a horizontally directed x-ray beam used with the cassette in a mobile or a wall-mounted cassette holder?
- Are there morphologic aspects of the patient that are going to influence the appearance of the radiographs? These include things such as cutaneous nodules or masses.

After these variables have been considered, the images can be scrutinized for abnormalities. The roentgen sign and DAMNITV (degenerative, anomalous, metabolic, neoplastic, infectious [inflammatory, immune], traumatic, vascular) methods described in Chapter 6 should be used. Inexperienced interpreters often begin by looking at the intestine, because a suspicion of an intestinal obstruction is a common reason that abdominal radiographs are acquired. This is a mistake and will lead to other lesions being overlooked. The search pattern is also important. A random search pattern may be appropriate for experienced radiologists but beginning interpreters should develop an organized approach to searching radiographs.[6,7] Having a mental checklist to guide the order of interpretation will reduce the number of errors (Table 38.2).



REGION	ORIGIN OF MASS WITHIN REGION
I: Masses in this region can be peritoneal or retroperitoneal	Cranial pole of right kidney Proximal extremity (head) of spleen Gastric fundus Gastric body Adrenal glands Proximal liver
II. Masses in this region are usually retroperitoneal	Caudal pole of right kidney Left kidney Ovaries Ureters Lymph nodes A dorsal jejunal mass will likely migrate ventrally into Zone V
III. Masses in this region can be peritoneal or retroperitoneal	Rectum Descending colon Sublumbar lymph nodes Ureters Cranial extension of pelvic mass
IV. Masses in this region are peritoneal	Ventral liver Pylorus Gallbladder Pancreas Proximal duodenum
V. Masses in this region are peritoneal	Pedunculated liver mass Ventral extremity (tail) of spleen Jejunum Cecum Descending colon Omentum Mesenteric lymph nodes Enlarge uterine horns
VI. Masses in this region are peritoneal	Prostate gland Urinary bladder Uterine body

Fig. 38.25 Schematic showing the abdominal cavity divided into six regions. Organs located in each region, and thus the most likely source of a mass in that region, are as shown in the following table.

Table • 38.2

Checklist for Interpretation of Abdominal Radiographs.

Stomach
Small intestine
Colon
Liver
Spleen
Kidneys/ureters
Prostate gland/uterus
Urinary bladder
Peritoneal space
Retroperitoneal space
Sublumbar lymph nodes
Bones
Penis
Abdominal wall
Included portion of the thorax

REFERENCES

1. Kendall A, Ley C, Egenvall A, et al. Radiographic parameters for diagnosing sand colic in horses. *Acta Vet Scand.* 2008;50(17).
2. Grandage J. The radiological appearance of stomach gas in the dog. *Aust Vet J.* 1974;50(12):529–532.
3. Love N. The appearance of the canine pyloric region in right versus left lateral recumbent radiographs. *Vet Radiol Ultrasound.* 1993;34:169.
4. Vander Hart D, Berry CR. Initial influence of right versus left lateral recumbency on the radiographic finding of duodenal gas on subsequent survey ventrodorsal projections of the canine abdomen. *Vet Radiol Ultrasound.* 2015;56:12–17.
5. Carrig C. The use of compression in abdominal radiography of the dog and cat. *J Am Vet Radiol Society.* 1976;17:178.
6. Heng HG, Wrigley RH, Kraft SL, Powers BE. Fat is responsible for an intramural radiolucent band in the feline stomach wall. *Vet Radiol Ultrasound.* 2005;46:54–56.
7. Halvorsen JG, Swanson D. Interpreting office radiographs. A guide to systematic evaluation. *J Fam Pract.* 1990;31(6):602–610.

ELECTRONIC RESOURCES

Additional information related to the content in Chapter 38 can be found online at eBooks.Health.Elsevier.com

- Chapter Quiz

CHAPTER 39

Peritoneal Space

Susanne M. Stieger-Vanegas

Peritoneal disease, especially peritonitis, occurs commonly and can be life-threatening, which requires a rapid accurate diagnosis and treatment. Peritoneal disease can be primary or secondary. Imaging examinations are helpful to identify and characterize peritoneal disease. The normal peritoneal folds and ligaments are difficult to identify, regardless of the imaging modality. However, knowledge of the peritoneum and peritoneal folds is important when evaluating the presence or spread of disease processes involving the peritoneum.

NORMAL ANATOMY AND IMAGING PROCEDURES

Anatomy of the Peritoneum

The abdomen is part of the trunk extending from the diaphragm to the pelvic canal. The abdominal and pelvic cavities, in addition to the scrotum in male animals, are lined by the peritoneum. The peritoneal structure is similar to the pleura, and comprises of a single layer of mesothelium on a basement membrane. The peritoneum is a thin, serous membrane, which is divided into parietal, visceral, and connecting layers, which are all continuous.[1–3] The parietal peritoneum covers the inner surface of the abdominal, pelvic, and scrotal cavities and is closely adhered to the abdominal musculature (Fig. 39.1). The visceral peritoneum is a reflection of the parietal peritoneum onto the organs of the abdominal, pelvic, and scrotal cavities, either in whole or in part. Organs in the abdominal cavity covered by visceral peritoneum are considered intraperitoneal. This includes the liver, gallbladder, spleen, pancreas, stomach, small and large intestines, as well as the ovaries in female animals. Most of the rectum in companion animals is in the peritoneal cavity; however, a short caudal segment is retroperitoneal before it ends at the anal canal. In female animals, the cranial aspect of the vagina is covered by peritoneum, which reflects dorsal to the colon and ventral to the urinary bladder.[1] The peritoneal space or peritoneal cavity is the space between the parietal and visceral peritoneal layers, and normally contains only a small amount of fluid for lubrication. Therefore, in strict anatomic terminology, the term *intraperitoneal*, with regard to organs, does not mean within the peritoneal space but is used for organs covered by the visceral peritoneum (see Fig. 39.1). Also, in common usage, the terms *peritoneal cavity* and *abdominal cavity* are often used interchangeably, but this is incorrect because the abdominal cavity includes the intraperitoneal and retroperitoneal organs.

The connecting peritoneum includes mesenteries, omenta, and intra-abdominal ligaments. Understanding the relationship of the connecting peritoneum and especially the ligamentous structures is a crucially important aspect of image interpretation, because it helps to understand the anatomic location and relationship of organs. The liver is attached to the diaphragm craniodorsally at the level of the caudal vena cava via the coronary, triangular, and falciform ligaments. The stomach is fixed to the diaphragm and pylorus through the omentum. Additionally, the stomach and spleen are connected by the gastrosplenic ligament. Furthermore, the descending colon is connected to the spleen and therefore to the stomach. The descending duodenum, pancreas, cecum, and ascending colon are fixed in relationship to each other. Moreover, the proximal aspect of the ascending duodenum is connected to the descending colon by the duodenocolic ligament.[3] The mesenteric root is the site of the attachment of the mesentery to the dorsal abdominal wall, which commonly is located ventral to the second lumbar vertebra. The mesentery is the double layer of the visceral peritoneum suspending the intestines from the parietal peritoneum. The jejunum and ileum are not connected via ligaments to other structures in the abdomen and are therefore relatively mobile in the abdomen.

The space between the dorsal margin of the parietal peritoneum and the abdominal wall is the retroperitoneal space. The retroperitoneal space extends from the diaphragm to the

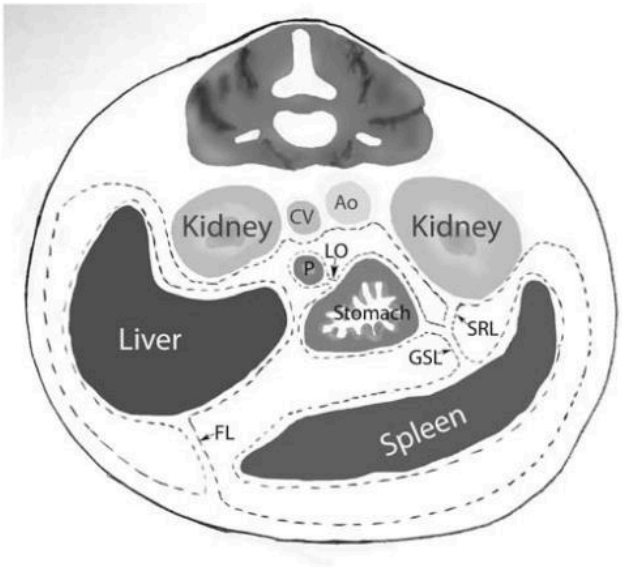


Fig. 39.1 Illustration of the anatomy of the peritoneum. The peritoneum (*dashed line*) lines the abdominal and pelvic cavities. The connecting peritoneum forms intra-abdominal ligaments including the splenorenal ligament (*SRL*), the gastrosplenic ligament (*GSL*), and falciform ligament (*FL*). The lesser omentum (*LO*) connects from the liver and diaphragm to the lesser curvature of the stomach including pylorus (*P*) and proximal aspect of the duodenum. Abdominal organs covered by the peritoneum (visceral) are considered intraperitoneal. The kidneys, aorta (*Ao*), and caudal vena (*CV*) cava are retroperitoneal. The space between parietal and visceral peritoneal layers is the peritoneal space.

anus and is outside the peritoneal cavity. Organs in part covered by visceral peritoneum and near the wall of the abdominal cavity are termed *retroperitoneal.*[4] These organs are usually covered on the ventral aspect by the peritoneum and include adrenal glands, kidneys, ureters, major blood vessels, and regional lymph nodes. Additionally, the ventral aspect of the prostate gland in male dogs is retroperitoneal. The retroperitoneal space communicates cranially with the mediastinum through the aortic hiatus and caudally with the extraperitoneal aspect of the pelvic canal.[5] The peritoneal cavity is completely closed in the male animal; in the female, it connects via the cranial aspect of the uterine horns with the exterior of the body.

Radiography of the Peritoneum

The peritoneum is typically not seen on survey radiographs, but its evaluation is an essential aspect in interpreting abdominal radiographs. It is evaluated indirectly by analyzing anatomic organ relationships and radiographic opacity variations in the abdomen.[3] Identifying the origin of peritoneal disease is based on evaluating the shape, size, location, radiopacity, and margination of organs and the radiopacity throughout the abdominal cavity. In the diseased state, connecting organs can be displaced and altered in shape and radiopacity, which can help in identifying the disease origin and the ranking of differential diagnoses.[3]

Fat is typically present throughout the abdomen, primarily in the falciform ligament, the greater omentum, the mesentery, and the retroperitoneal space. The presence of abdominal fat is important for visceral organ delineation because fat is of lesser radiographic opacity and provides contrast between the organs (Fig. 39.2). The greater omentum, which is located mainly ventral in the abdomen and is very movable, contains variable amounts of fat and therefore contributes to the areas of decreased radiopacity noted ventrally on abdominal radiographs.[3]

The amount and character of intra-abdominal fat depend on the age of the animal and the body habitus. In emaciated patients, the abdomen is often tucked up (see Fig. 39.2C); however, the possibility of coexisting small volumes of peritoneal fluid or peritonitis cannot be excluded. Larger volumes of peritoneal fluid will lead to a distended abdomen. Normal dogs and cats younger than a few months of age (approximately 2–3 months) lack sufficient fat to provide intra-abdominal contrast; thus, the abdomen appears to be of relatively uniform soft tissue opacity (see Fig. 39.2D). Another factor is that young patients have a relatively higher proportion of brown (multilocular) fat than adults. Brown fat has an opacity closer to that of soft tissue because of its higher water content. As young animals mature, the water content of the brown fat decreases.[6] As brown fat is replaced by white fat, the contrast between intra-abdominal soft tissues (organs) increases.

Ultrasound of the Peritoneum

Ultrasound is often the method of choice to evaluate the peritoneum and abdominal cavity, especially when increased peritoneal or retroperitoneal fluid is suspected. However, limited

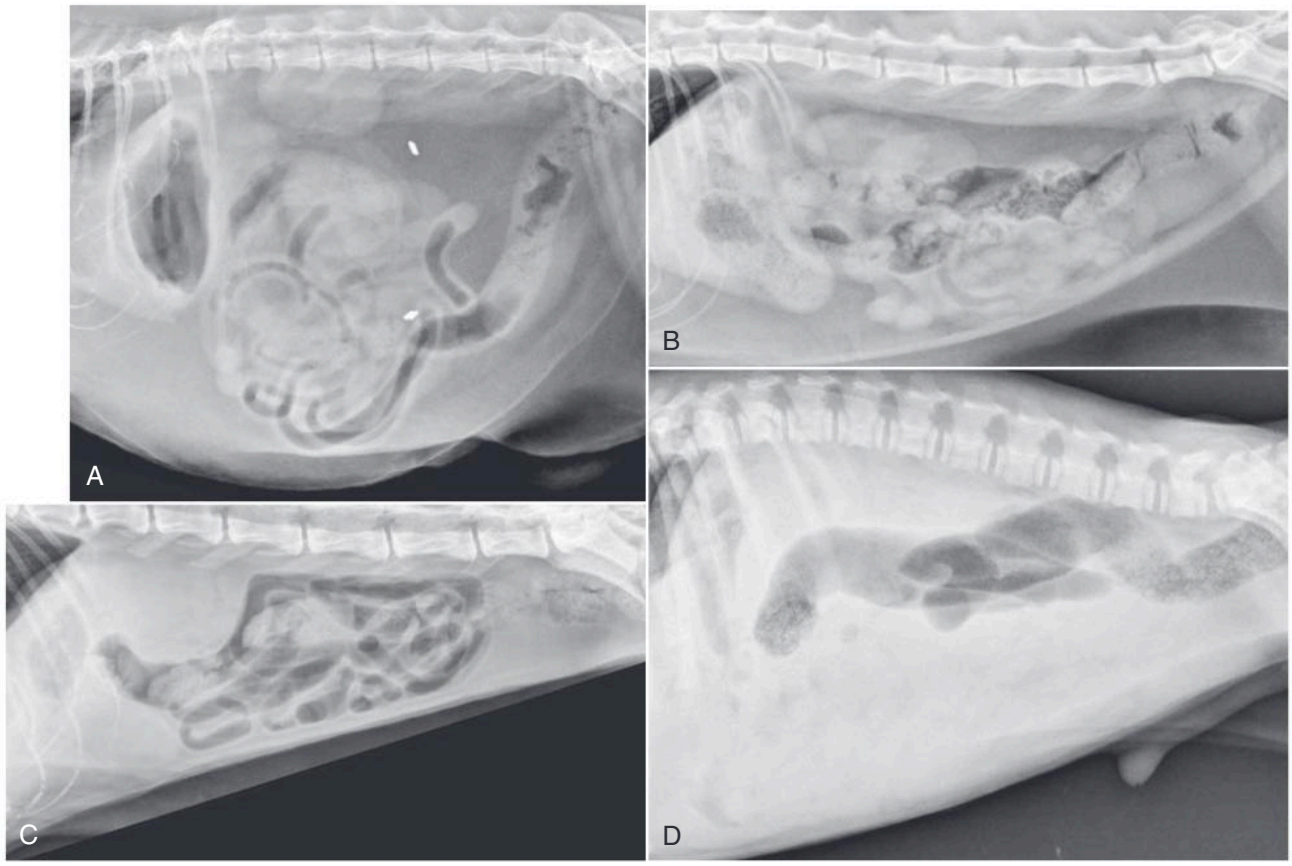


Fig. 39.2 Lateral views of the abdomen illustrating the effect of different amounts of abdominal fat. **A,** Obese cat. Extensive fat depositions in the falciform, omental, mesenteric, and retroperitoneal areas provide contrast between viscera. Metallic objects represent vascular clips from a previous ovariohysterectomy. **B,** Normal cat. Fat deposition is less than that in **A,** but it is adequate to allow visualization of viscera. **C,** Emaciated cat. Without interposed fat, border effacement of viscera is present, producing a uniform, homogeneous abdomen devoid of contrast except for gas in the bowel loops. **D,** Normal 2-month-old Golden retriever. Reduced visualization of abdominal organs and poor contrast are caused by a relative lack of fat in this young dog; this is a normal finding.

information is available regarding the ultrasound evaluation of peritoneal disease in animals, compared to the vast amount of information available regarding sonography of solid organs. In the initial ultrasound examination, an overview of the abdomen is obtained, using a medium- to high-frequency ultrasound probe. For peritoneal disease, greater attention is given to the near field and along the diaphragmatic border to evaluate for the presence of small lesions involving the peritoneum. The normal peritoneum is a smooth, thin, echogenic line in the deepest aspect of the abdominal wall. Usually, the intestinal loops can move smoothly through the abdominal cavity and motion is noted between the intestines and abdominal wall. Not only does ultrasound provide the option to assess the peritoneal surfaces, but if peritoneal disease is present, ultrasound-guided fine-needle aspiration can be performed relatively safely and can help in differentiating between normal, inflammatory, and neoplastic conditions.

Computed Tomography of the Peritoneum

Computed tomography (CT) and especially multidetector CT is suitable for the evaluation of disease of the abdominal cavity and peritoneum.[7] CT is an excellent technique to evaluate the complex anatomy of the peritoneum. Especially, the ability to perform isotropic voxel CT imaging with sagittal and dorsal reformatting provides excellent anatomic information, which is key to the understanding of peritoneal disease. Traditionally, radiography often combined with abdominal ultrasound has been the modality of choice to evaluate for peritoneal disease; however, in recent years, CT has been shown to be valuable for evaluation of the abdomen and peritoneal structures particularly in larger dogs.

PERITONEAL AND RETROPERITONEAL DISEASE

Decreased Abdominal Surface Visualization

Peritoneal Effusion

Fluid in the intraperitoneal space is termed *peritoneal fluid*, and fluid in the retroperitoneal space, *retroperitoneal fluid.* The term *abdominal fluid* should be avoided because it is nonspecific and would include peritoneal and/or retroperitoneal fluid. A small amount of peritoneal fluid is normal in the abdominal cavity of dogs and cats. Effusion is the abnormal or increased accumulation of fluid in any cavity lined by mesothelial cells. The type of fluid varies dependent on the underlying cause and can range from being acellular with low protein content (i.e., transudate) to fluid with an increased cell or protein content or fluid containing abnormal cells or substances (i.e., modified transudate or exudate). No imaging modality can provide a definitive diagnosis about the fluid characteristics, and fluid analysis is highly valuable and necessary to characterize the type of effusion.

Radiographically, increased fluid within the peritoneal cavity or retroperitoneal space causes a loss of the differential opacity interface between soft tissue and fat and therefore a loss of contrast between organs. In animals with intraperitoneal fluid, there is overall more soft tissue opacity in the peritoneal cavity. The presence of peritoneal fat normally allows us to see the serosal margins of organs. When fluid is present between abdominal viscera, this causes border effacement of viscera and results in added overall soft tissue opacity. In practice, all peritoneal fluids are of soft tissue opacity, comparable to the visceral organs. In many instances, the fluid is limited to the peritoneal space, and contrast between the kidneys and adjacent retroperitoneal fat is preserved. Causes for loss of peritoneal contrast include not only the lack of fat and peritoneal effusion, but also peritonitis, and peritoneal neoplasia. A wet hair coat, or hair coated with ultrasound gel, may create the appearance of altered peritoneal space opacity, and this should not be confused with a true loss of peritoneal detail caused by the aforementioned reasons. See Box 39.1 for causes of decreased serosal surface definition.

The idea that any volume of fluid results in complete obliteration of serosal margins on radiographs is incorrect. The degree to which serosal margin detail is obscured by fluid is determined by the relative amounts of fat versus fluid. The more fat that is present, the more fluid is needed to cause complete obliteration of serosal margins. Thus, organ margins may still be visible when free intraperitoneal fluid is present.

A large volume of peritoneal fluid appears as homogeneous soft tissue opacity uniformly distributed throughout the abdominal cavity (Fig. 39.3, eFig. 39.1). A large volume of fluid will also cause abdominal distention with outward protrusion of the contour of the abdominal wall (rounded abdomen) and may displace the diaphragm cranially. The abdomen may also be somewhat pendulous in normal immature patients. If relatively mobile segments of bowel contain gas, they often float to the highest or uppermost area within the abdominal cavity. These segments will be in the central portion of the abdomen on a lateral radiograph made with a vertical x-ray beam. Gas-filled bowel loops in a noncentral location in patients with a large amount of peritoneal fluid suggest the presence of an abdominal mass or adhesions that prevent free movement of intestinal segments (Fig. 39.4). However, this finding should be interpreted with caution, as the presence of a large amount of peritoneal fat may also cause asymmetric bowel location,

Box • 39.1

Differential Diagnoses for Decreased Serosal Surface Visualization

Lack of intra-abdominal fat
Young patient (brown fat)
Peritoneal effusion (transudate, modified transudate, exudate)
Peritonitis
Peritoneal neoplasia (primary or metastatic)
Mass effect caused by crowding of viscera
Superimposed external material (wet hair, ultrasound gel, etc.)
Underexposure

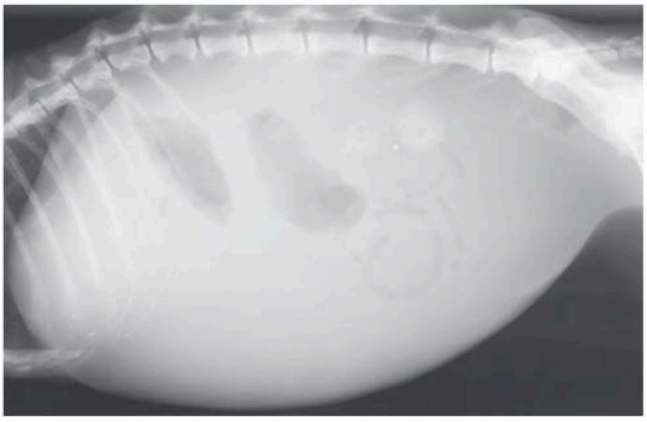
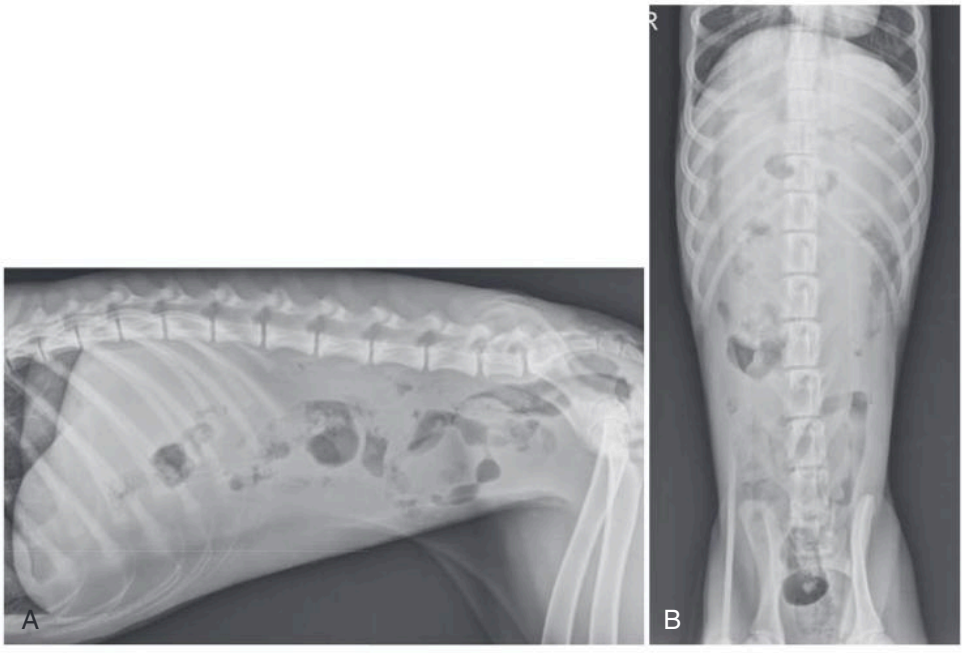


Fig. 39.3 Lateral view of the abdomen of a cat with a large volume of peritoneal fluid. Homogeneous soft tissue opacity is distributed uniformly throughout the distended abdomen, and there is a loss of contrast. No fluid is noted in the retroperitoneal space, but fascial planes and organs in the retroperitoneal space are not visible because of superimposition of the peritoneal fluid.



eFig. 39.1 Lateral **(A)** and ventrodorsal **(B)** radiographs of a dog with peritoneal effusion. There is a loss of peritoneal serosal detail. The serosal surfaces of the intestinal loops are not outlined anymore, whereas the gas content is still visible.

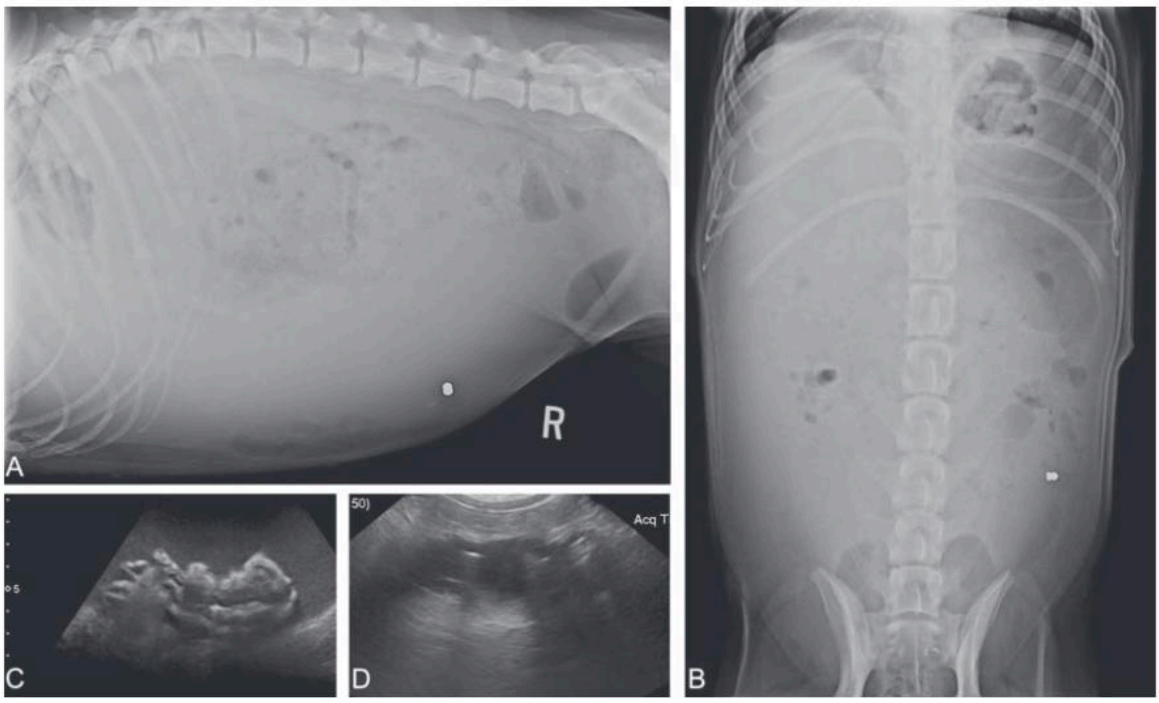


Fig. 39.4 Lateral radiograph **(A)** and ventrodorsal radiograph **(B)** of the abdomen of a 13-month-old Labrador retriever. Peritoneal fluid and gas are present. The peritoneal gas is in an unusual location for bowel gas, ventral to the urinary bladder in the lateral view, and on both views the peritoneal gas bubbles have a nonspherical shape suggesting adhesions. On transverse ultrasound images of the abdomen, multiple segments of jejunum are adhered **(C)**. Extensive echogenic peritoneal fluid is present. **D,** Additionally, peritoneal gas is present in a hypoechoic area adjacent to a segment of jejunum with severely altered wall layering suggestive of intestinal perforation.

especially in cats. Sclerosing encapsulating peritonitis, which is a rare form of chronic peritonitis, may cause soft tissue attenuating material to be asymmetrically positioned in the abdomen obscuring organ visualization and abdominal organs may be abnormally positioned. On ultrasound, large quantities of peritoneal fluid can be seen in addition to small bands of tissue covering organ surfaces.[8] The presence or absence of coexistent peritonitis cannot be ascertained in patients with a large amount of peritoneal fluid and fluid analysis is necessary for further evaluation.

Smaller amounts of peritoneal fluid, peritonitis, or carcinomatosis may produce a mottled, hazy, or irregular loss of contrast on survey radiographs (Fig. 39.5). Individual viscera may be visible, but the margins of soft tissue structures are indistinct or blurred. With small amounts of peritoneal fluid, this appearance can be the result of interdigitation of fluid within folds in the greater omentum and small bowel but without total border effacement.[3] Peritonitis may produce a similar effect. Smaller amounts of peritoneal effusion may be caused by early fluid accumulation of a generalized process or by more localized disease. Localized disease may lead to focally abnormal serosal margin detail with normal serosal margins visible elsewhere in the peritoneal space.

One method of assessing the abdominal cavity for fluid accumulation or peritoneal disease (peritonitis, carcinomatosis, steatitis) is to compare the contrast of the peritoneal versus retroperitoneal spaces. Normally, detail and contrast in the peritoneal and retroperitoneal spaces should be the same. However, because many diseases resulting in peritoneal fluid do not affect the retroperitoneal space, retroperitoneal detail is often preserved when peritoneal fluid has altered the serosal margin of bowel and other intraperitoneal organs (Fig. 39.6). It is important to remember, however, that a large volume of peritoneal fluid can obscure the retroperitoneal space because of superimposition. Loss of contrast and detail can also occur

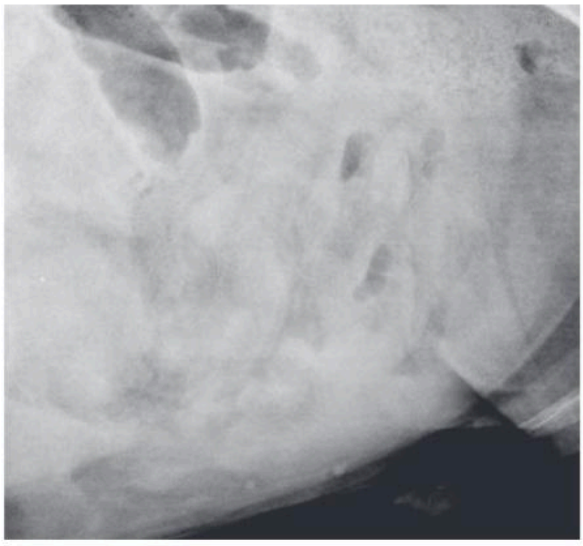


Fig. 39.5 Lateral radiograph of the midabdomen of a dog with peritoneal fluid. There is a mottled, hazy, irregular fluid opacity in the abdomen leading to blurring of the margins of soft tissue structures and a loss of contrast. This radiographic appearance could be caused by the presence of an exudate or hemorrhage; but in this dog, it was caused by hypoproteinemia.

specifically in the retroperitoneal space, and is an indication of fluid or, less commonly, inflammation (Fig. 39.7).

Peritoneal fluid absorption is dependent on the properties of the fluid, as well as the peritoneal membrane.[9] Manipulation of viscera during laparotomy produces changes that may appear similar radiographically to peritonitis, and these changes may be modified by the amount of tissue trauma.[3] Solutions containing water, electrolytes, and relatively low-molecular-weight



Fig. 39.6 Lateral view of the abdomen of a cat with peritoneal fluid. Serosal contrast in the peritoneal space is markedly reduced, but there is good contrast with visualization of fascial planes and fat in the retroperitoneal space. The falciform fat in the cranioventral aspect of the abdomen, which is extraperitoneal, is also normal. Comparison of the appearance of the fat in the peritoneal versus retroperitoneal spaces can assist in the radiographic detection of either retroperitoneal or peritoneal disease. There is also renal mineralization and a large calcified peritoneal body.



Fig. 39.7 Lateral view of the abdomen of a dog with rodenticide toxicity. There is fluid opacity in the retroperitoneal space with blurring of the margin of the lumbar musculature and a streaky appearance to the retroperitoneal fat. Note the normal sharp serosal margin detail and contrast in the peritoneal space.

components are absorbed normally by the peritoneal membrane within 24 hours. Proteinaceous fluids (such as serum, blood, and lymph) are absorbed more slowly and may be present for 1 to 2 weeks. These changes can be visible radiographically after laparotomy and should not be mistaken for complications. Static or increasing fluid accumulation in the postoperative period is abnormal. If complications are suspected, cytologic evaluation of the fluid will be necessary to differentiate between normal postsurgical fluid and fluid caused by septic peritonitis or other conditions.

Small amounts of intraperitoneal fluid may not be detected using radiography but are detected readily using ultrasound. Ultrasound guidance can be used to collect fluid samples. Using

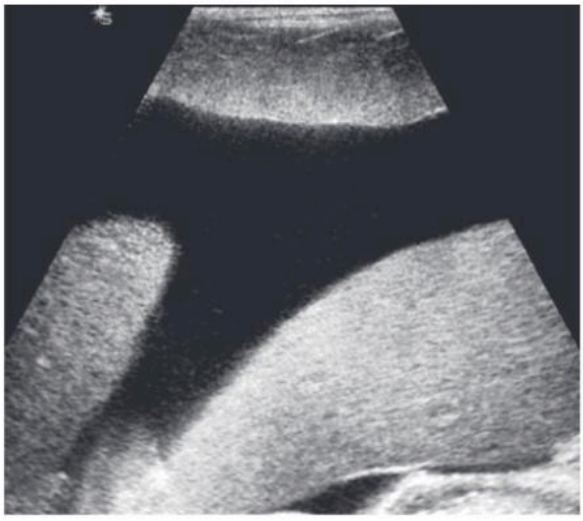


Fig. 39.8 Longitudinal ultrasound image of a dog with ascites. Anechoic fluid is present between and surrounding liver lobes. The lack of echoes in the fluid is consistent with the fluid being of low cellular content.

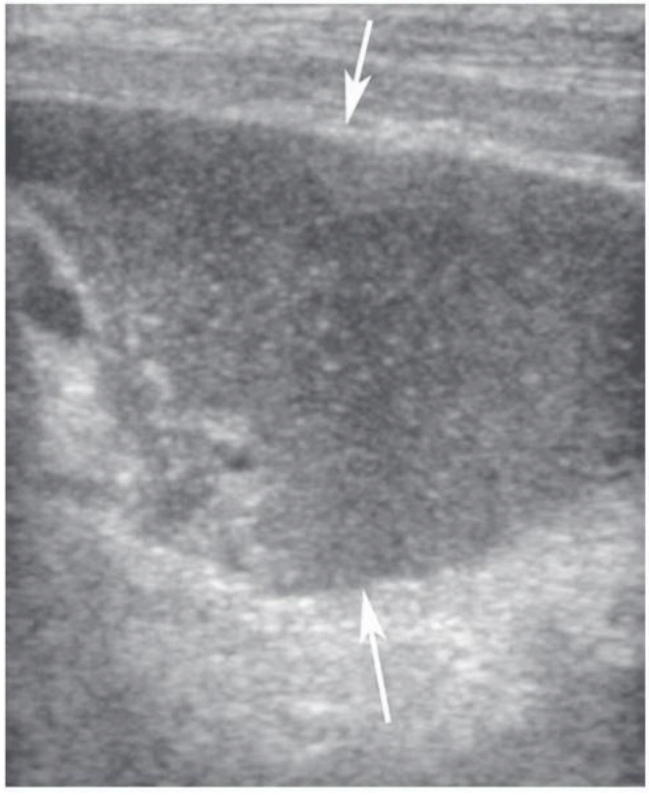


Fig. 39.9 Longitudinal ultrasound image of a 6-year-old dog with an abdominal mass and peritoneal effusion. Free peritoneal fluid (*white arrows*) with low-level echoes is compatible with highly cellular fluid.

focused assessment of the abdomen with sonography for trauma (FAST) in nontraumatized patients, it was determined that unstable patients had a higher likelihood of peritoneal fluid than stable patients.[10] Fluid can also be characterized by its echogenicity. Fluid with low cellular content, such as urine or a transudate, is anechoic (Fig. 39.8); fluid with moderate to high cellular content, such as exudate, blood, and chyle, is more echoic (Fig. 39.9; see Fig. 39.4C,D).

Peritoneal Metastasis and Steatitis

An ill-defined nodular, miliary, or granular pattern to the abdomen (Fig. 39.10, eFig. 39.2) may be caused by seeding of the peritoneum with multiple, metastatic foci, or steatitis. Examples of tumors associated with metastatic spread include hemangiosarcoma of the spleen and carcinoma of various abdominal organs. The term *carcinomatosis* in strict terms should only be used for epithelial cancers or carcinomas disseminated throughout the body. In the past, or in colloquial terms, the term *carcinomatosis* has been used to describe the spread of any cancer; however, that is not correct. Carcinoma of the liver, pancreas, and intestinal tract commonly has peritoneal metastatic seeding in dogs and cats. In cats, parietal and visceral peritoneal masses have been described with carcinomatosis, but not with other diseases, and might therefore be a strong indicator for neoplastic disease.[11] Small miliary peritoneal masses might not be seen on radiographs and can easily be missed on ultrasound (Figs. 39.11 and 39.12).

Steatitis is the inflammation of fat, commonly yellow fat, causing saponification and fat necrosis. Steatitis commonly occurs secondary to an inflammatory process (e.g., pancreas or gastrointestinal tract), abdominal neoplasia,[12] or trauma[13] or can be idiopathic.[14] Steatitis caused by pancreatitis or pancreatic neoplasia in dogs and cats can result from the escape of proteolytic enzymes causing saponification of omental and mesenteric fat.[15] Additionally, in cats, steatitis can result from vitamin E deficiency and/or an excessive amount of polyunsaturated fatty acids in their diet. Rarely steatitis is a result of

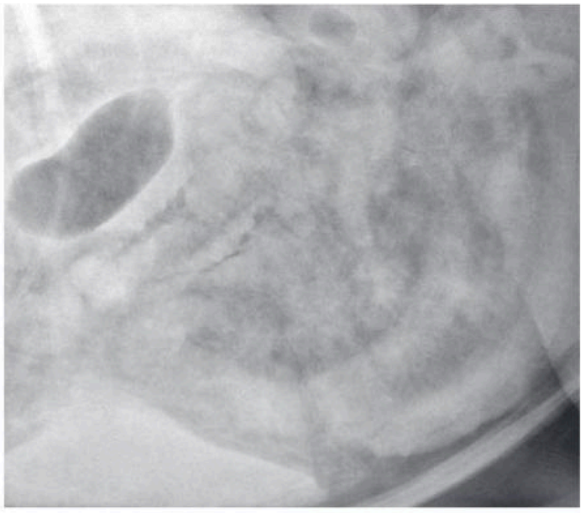


Fig. 39.10 Close-up of the cranioventral aspect of the abdomen of a dog with a ruptured splenic hemangiosarcoma leading to peritoneal metastasis. The mesenteric fat has a mottled appearance.

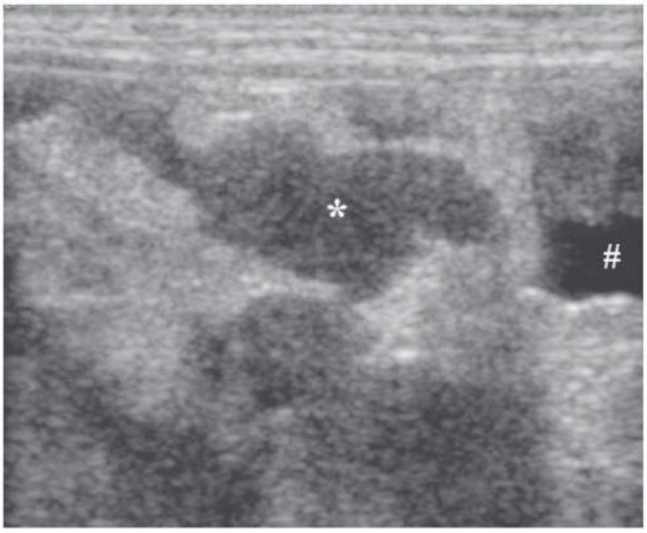


Fig. 39.12 Longitudinal ultrasound image of a 9-year-old dog with peritoneal metastasis, which is hypoechoic, irregularly shaped material (*asterisk*) interspersed through the more echogenic mesenteric fat. A small amount of anechoic peritoneal fluid is present on the right edge of the image (*number sign*).

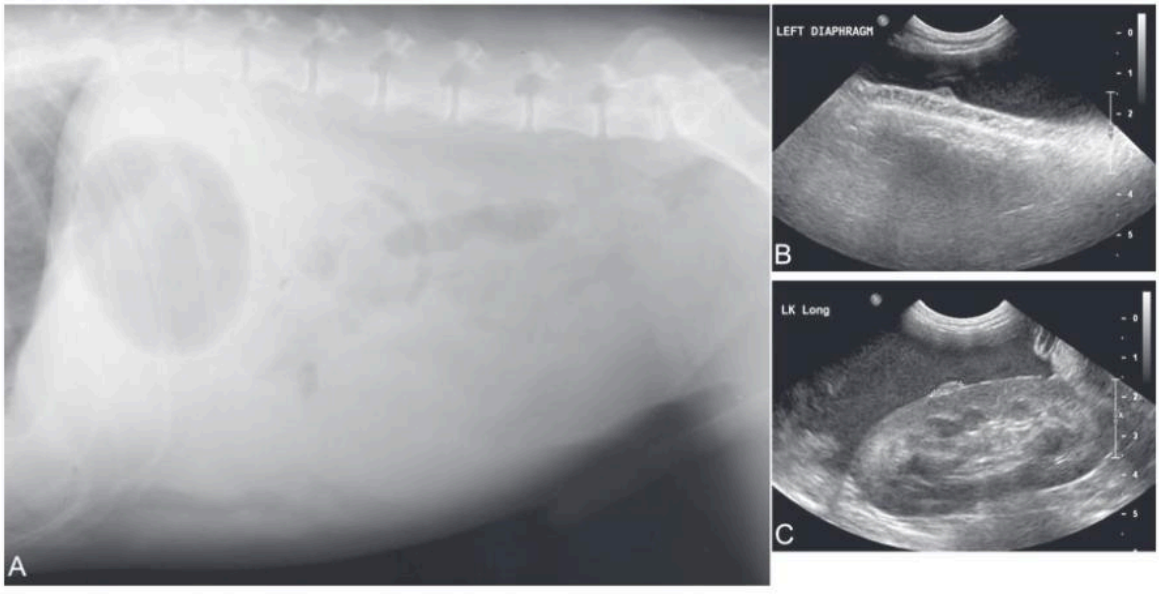
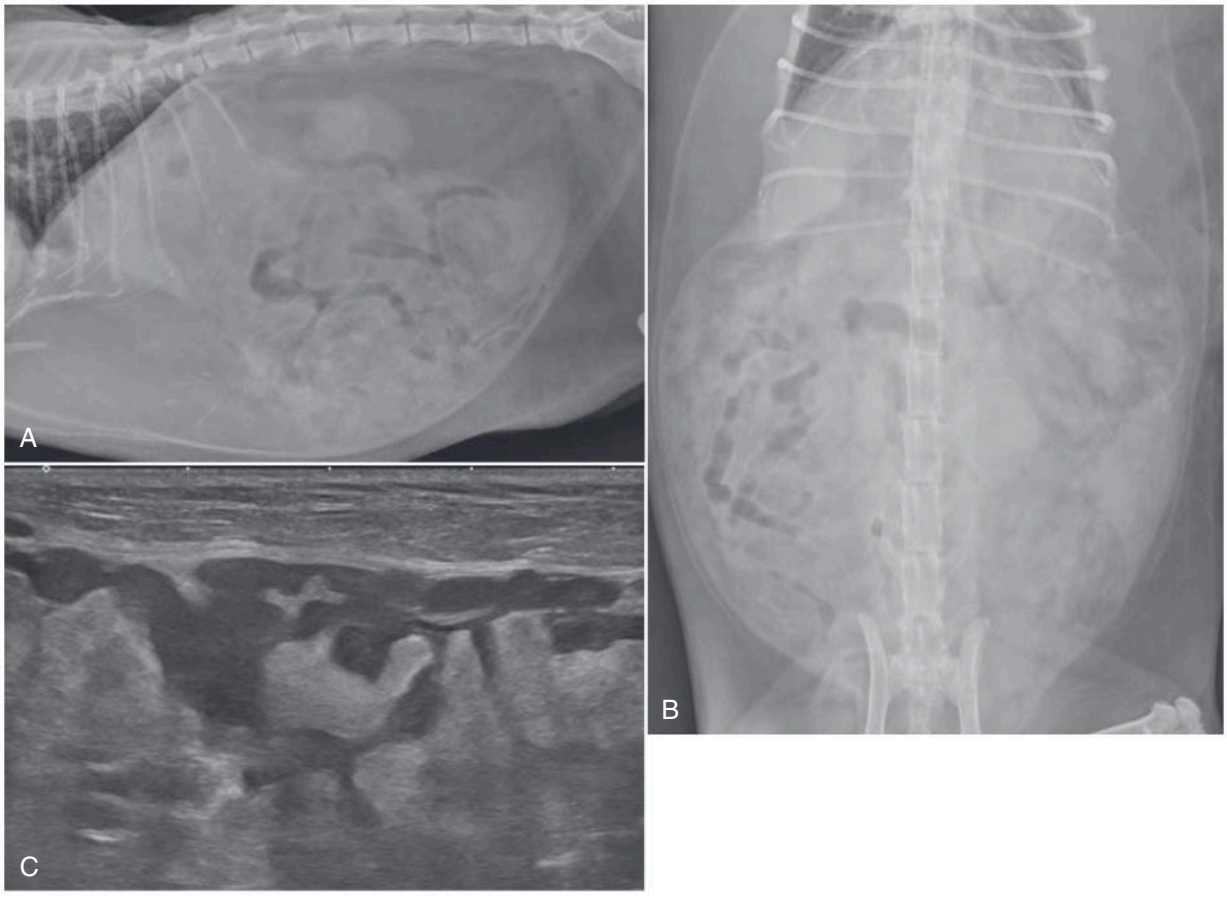


Fig. 39.11 **A,** Lateral radiograph of a dog with peritoneal fluid and lack of definition of the ventral aspect of the liver with the spleen. The gastric axis is in normal position, suggesting that the liver is of normal size. On ultrasound, a splenic tumor with rupture and echogenic peritoneal fluid, as well as multiple, small, round to ovoid, hypoechoic nodules along the peritoneal surface **(B, C)** were noted. On image **C,** no fluid is present in the retroperitoneal space, which is consistent with the lateral radiograph and the good definition of the fascial planes in the retroperitoneal area. Fine-needle aspiration confirmed peritoneal metastatic disease secondary to splenic hemangiosarcoma.



eFig. 39.2 Lateral **(A)** and ventrodorsal **(B)** radiographs of a cat with carcinomatosis. Peritoneal serosal detail is severely reduced in the midventral abdomen and has a mottled appearance. Notice that both kidneys are reduced in size and irregular in shape, as with chronic kidney disease. Longitudinal ultrasound image acquired with a linear transducer **(C)** of the peritoneal space of the same cat. Hypoechoic nodular tissue extends along the body wall and into the hyperechoic peritoneal fat. A small amount of effusion is also present.

severe hypocalcemia.[16] Sonographically, hyperechoic masses, which are not part of an organ might be noted in the abdominal cavity.

Peritoneal Masses

Primary de novo peritoneal neoplasia is uncommon in companion animals. Primary peritoneal neoplasia includes mesothelioma, leiomyoma, or carcinoma where the primary origin is not identified. Other differentials for peritoneal masses include cyst, hematoma, abscess, and granuloma. In the northwestern portion of the United States and Canada, as well as portions of Europe, peritoneal infection by *Mesocestoides* species tapeworms may manifest as varying-sized, cavitary, septated structures with echogenic particles within the fluid.[17] Peritoneal masses can be solid or cavitary, and samples can be obtained for cytologic evaluation. Ultrasound sampling yielded diagnostic information in about 70% of small animal patients with peritoneal, mesenteric, and omental disease in one study. However, ultrasound criteria alone are not reliable in differentiating neoplastic from inflammatory peritoneal disease, nor for exclusion of peritoneal disease in every patient.

Retroperitoneal Fluid

Fluid in the retroperitoneal space can lead to alternating fat and soft tissue opacities, or streaking, as the fluid dissects between fascial planes in the retroperitoneal area. The most common causes of isolated retroperitoneal fluid are hemorrhage (Fig. 39.13, eFig. 39.3), as with rodenticide toxicity, trauma or neoplasia (adrenal mass, hemangiosarcoma), and urine leakage. Retroperitoneal inflammation with increased fluid can also result from a migrating grass awn, a penetrating wound, ligatures from ovariohysterectomy, and perforation of the urethra during catheterization.

Retroperitoneal Masses

Neoplastic and inflammatory masses can occur in the retroperitoneal space, and radiographically, a soft tissue mass effect may be noted. Retroperitoneal disease can result in decreased delineation of the kidneys and retroperitoneal fat. Ultrasound is often helpful for further evaluating the retroperitoneal space; however, when complex disease affecting the retroperitoneal space is suspected, contrast-enhanced CT with reformatted images in various planes likely provides the most accurate information.

Lipoma is the most common primary tumor occurring in the retroperitoneal space and is usually noted as a fat attenuating area on radiographs or CT images. Nonparenchymal hemangiosarcoma may also occur in the retroperitoneal space. Some metastatic tumors can involve the retroperitoneal space, including lymphosarcoma and neoplasia originating from the kidneys, ureters, prostate gland, anal sacs, perineum, and mammary glands. Nonneoplastic masses most commonly occur secondary to migrating foreign bodies or trauma.

Increased Abdominal Surface Visualization

Peritoneal Gas (Pneumoperitoneum)

Pneumoperitoneum is free gas or air in the peritoneal cavity. The two most common causes of pneumoperitoneum in companion animals are penetration of the abdominal wall, either during surgery or by penetrating wounds, and disruption of the wall of a hollow viscus, which most commonly involves the gastrointestinal tract.[18] It is important to realize that not all intestinal perforations lead to free peritoneal gas; in some instances, adhesions between the omentum and intestines form and seal the defect, thereby resulting in only a small volume of intestinal content leaking into the peritoneal space. After laparotomy, a moderate amount of gas may persist for days to weeks. The duration of surgically induced pneumoperitoneum depends on the amount of gas present, as well as the size and body condition of the patient. Larger quantities of gas take longer to resolve than smaller quantities. After injection of air into the peritoneal cavity, a pneumoperitoneum was noted for up to 25 days in dogs.[19] Penetrating abdominal wounds are usually diagnosed by physical findings. In patients with a penetrating wound, differentiating whether free peritoneal gas is caused solely by penetration of the abdomen or is the result of concurrent organ rupture is impossible from radiographs. However, if the penetrating wound is very small and large

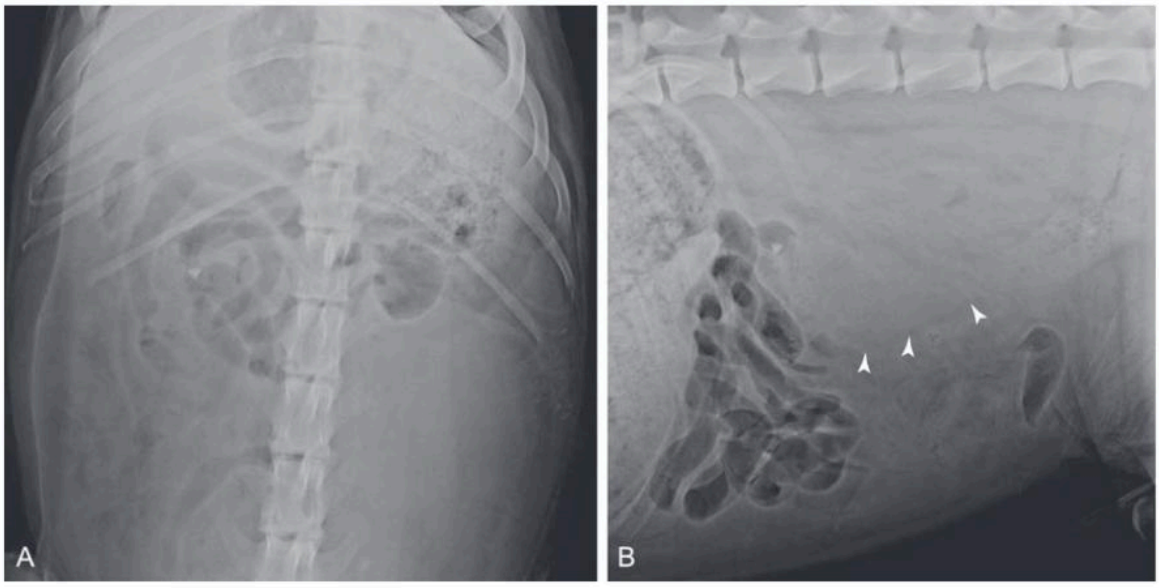
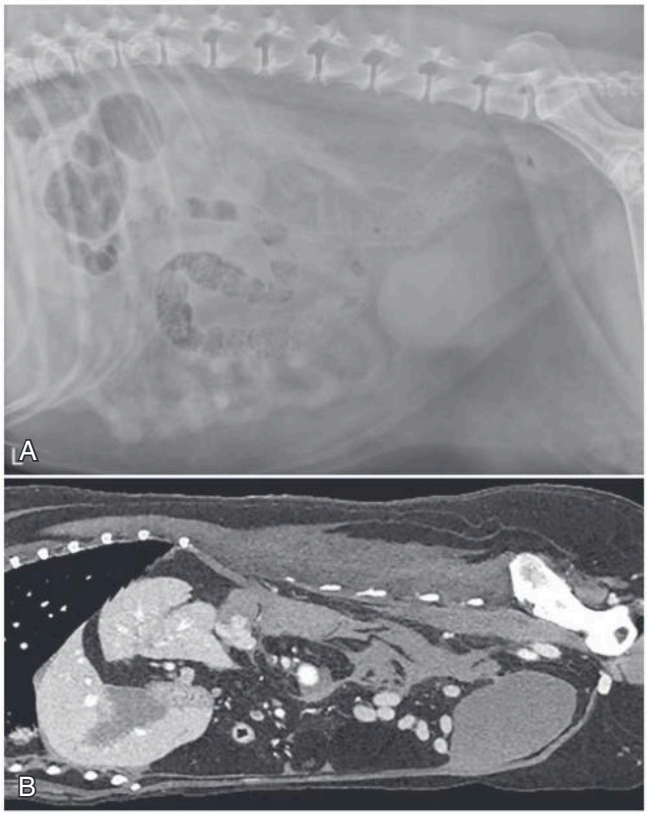


Fig. 39.13 **A,** Ventrodorsal survey radiograph of a dog with retroperitoneal hemorrhage post vehicular trauma. An area of increased soft tissue attenuation is noted in the location of the left kidney. The left kidney cannot be de fined. This was caused by retroperitoneal hemorrhage due to partial rupture of the cortex of the left kidney. The ureters were intact. **B,** Lateral radiograph. A diffuse soft tissue attenuating, streaky area is noted in the retroperitoneal space (*arrowheads*), ventrally displacing the descending colon. The peritoneal serosal detail is normal.



eFig. 39.3 **A,** Lateral radiograph of a dog with a ruptured adrenal mass causing retroperitoneal effusion. The colon is ventrally displaced and there are streaks of soft tissue opacity that extend through the retroperitoneal space. An ill-defined mass effect is seen dorsal to and surrounding the left kidney. Wet hair artifact causes some streaking of the ventral abdominal fat and inguinal area. **B,** Sagittal reformatted computed tomography image of the same dog. The retroperitoneal space is predominantly filled with soft tissue attenuating material consistent with hemorrhage, whereas the peritoneal fat is hypoattenuating.

amounts of free peritoneal gas are present, a perforation of a hollow organ secondary to injury should be highly suspected. If subcutaneous emphysema is superimposed over the abdominal cavity (such as, caused by trauma), it may be difficult to discern whether there is concurrent peritoneal gas or not.

Radiography is currently the most common technique to evaluate for the presence of free peritoneal gas. A small volume of free peritoneal gas can be difficult to recognize on conventional radiographs made with a vertically directed x-ray beam, because the gas bubbles are small and irregular in shape and may be misinterpreted as bowel gas unless they reside in a region where bowel is not found normally (Fig. 39.14, eFig. 39.4).[3] Larger gas volumes may coalesce into a larger bubble. This larger bubble may still be difficult to recognize on a radiograph made with a vertical x-ray beam, because it is superimposed over other viscera. In addition, this larger bubble may simulate a gas-containing organ, such as the stomach. Free peritoneal gas usually floats to the highest point within the abdomen. In lateral recumbency, this is usually under the caudal aspect of the ribs or in the midabdomen. The concurrent presence of peritoneal effusion may make recognition of the gas bubble easier because the fluid provides more uniform, homogeneous soft tissue background opacity (Fig. 39.15A). However, if a combination of a small volume of peritoneal gas and fluid is present, the attenuation of gas might be higher than expected as it is summating with fluid and may look more similar to peritoneal fat and might therefore be missed. Occasionally, the amount of gas will be large enough to outline serosal surfaces of viscera, such as bowel loops, the stomach, and the diaphragm (see Fig. 39.15B).

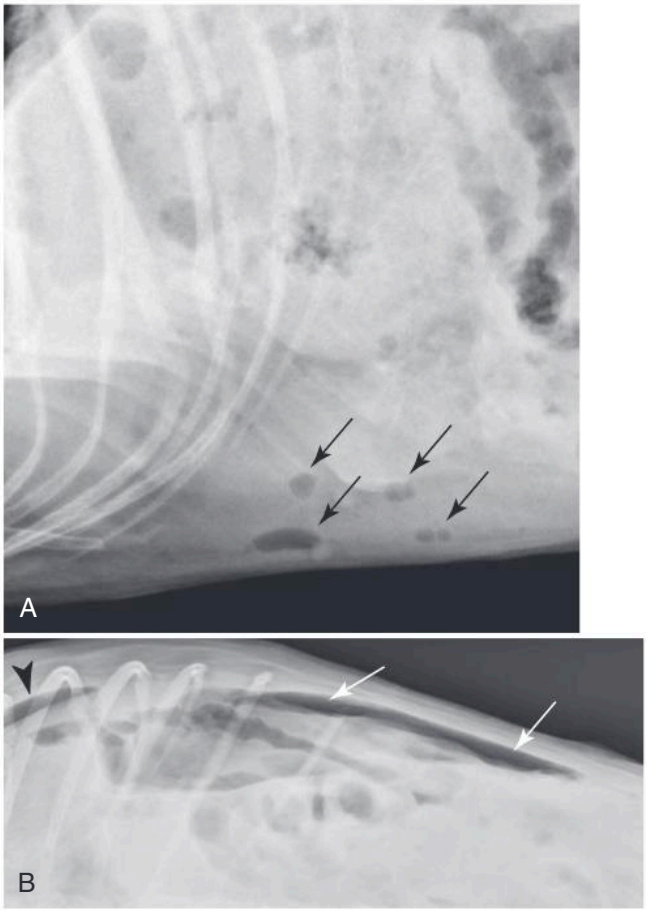


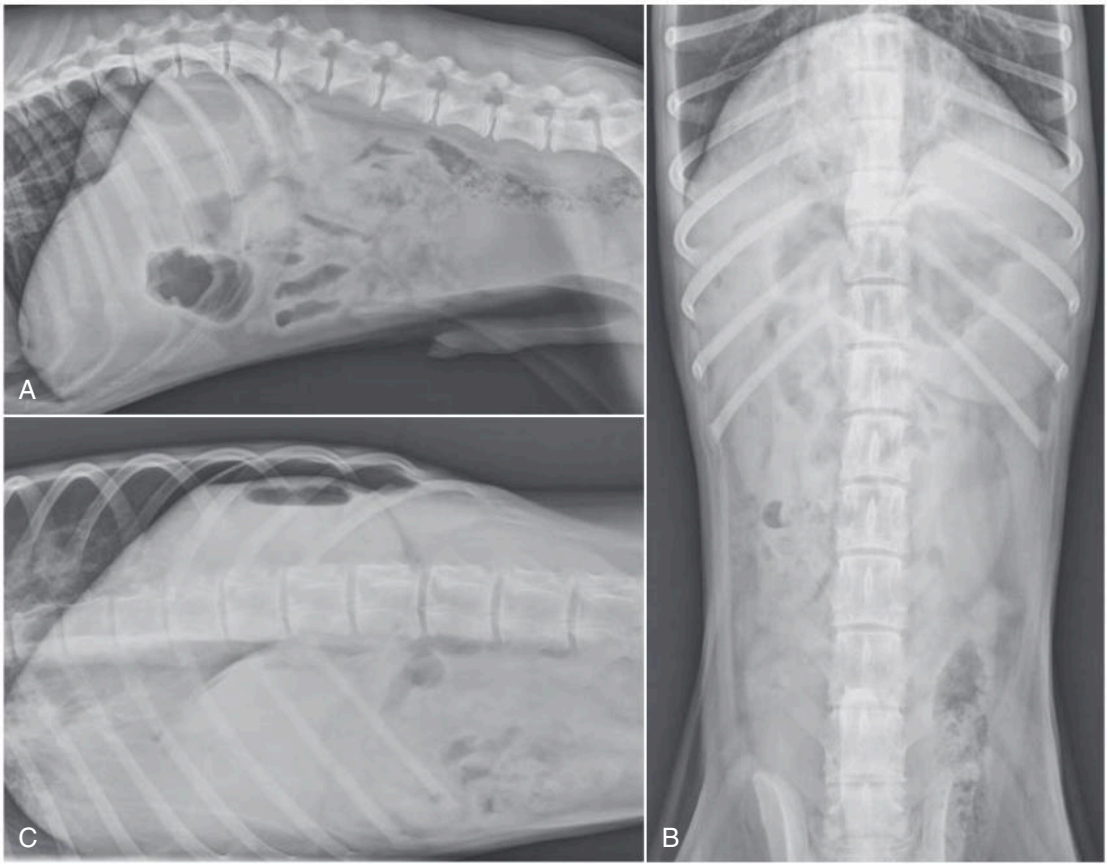
Fig. 39.14 **A,** Lateral radiograph of the cranioventral aspect of the abdomen of a dog with a ruptured bowel that has led to pneumoperitoneum. Extraluminal gas in this patient appears as small gas bubbles in a location not expected for bowel (*black arrows*). The location of this gas is a good indicator that it is extraluminal. Had these gas collections been in the mid aspect of the abdomen, they might not have been recognized as abnormal. **B,** Horizontal-beam abdominal radiograph of the same dog as in **A**. The dog was placed in left lateral recumbency and a horizontally directed x-ray beam was used to make the radiograph. The free gas has collected beneath the right abdominal wall (*white arrows*). The more cranially located gas is in the lung (*black arrowhead*). There is more free peritoneal gas than would be estimated from the conventional lateral projection in part **A**.

Because free gas rises to the highest point within the abdomen, it may be isolated visually from superimposed structures by a horizontally directed x-ray beam. With a small volume of gas, putting the patient in position for 10 minutes before radiographic exposure may be helpful to allow most of the gas to migrate and coalesce at the uppermost portion of the abdomen. The most sensitive projection for detecting a small volume of peritoneal gas is a lateral view, made with a horizontally directed x-ray beam with the patient in dorsal recumbency and with the cranial portion of the abdomen elevated slightly so small amounts of gas accumulate between the liver, diaphragm, and ventral aspect of the abdominal wall (Fig. 39.16).[20] Another projection used for documenting free peritoneal gas is a ventrodorsal (VD) view obtained with the patient in left recumbency with the use of a horizontally directed x-ray beam. Gas will usually collect under the highest portion of the right abdominal wall (see Fig. 39.14B), which is usually under the caudal aspect of the ribs. Raising or lowering either end of the animal shifts the point of gas accumulation. With film radiography, exposure factors should be lowered to intentionally underexpose the abdomen, making the gas more conspicuous. With digital images, the brightness should be increased to address the same goal. A horizontal-beam view with the animal in right recumbency is not recommended, because the gas bubble rises to the left side and gas within the fundus of the stomach may be misinterpreted as free peritoneal gas.

Horizontal-beam radiography is a useful tool for diagnosing free peritoneal gas quickly, cheaply, and with confidence; however, making radiographs with a horizontally directed x-ray beam can be technically challenging if the unit does not allow manipulation of the x-ray tube head or the imaging plate is fixed in position. The ease of performing horizontal-beam radiography should be one factor considered when purchasing a new x-ray system.

Ultrasound is a sensitive method for detection of free peritoneal gas but is dependent on the experience of the operator.[21] Additionally, it may allow the cause of pneumoperitoneum to be identified (see Fig. 39.4D). Reverberation artifacts, or dirty shadowing, are commonly noted at the soft tissue to air interface, which typically results in a high-amplitude linear echo with distal shadowing (enhanced peritoneal stripe sign/increased echogenicity of peritoneal stripe) originating at nondependent portion of the peritoneal lining (Fig. 39.17).[22] Small volumes of free peritoneal gas can also be seen as reverberation artifacts between abdominal structures, including the mesentery and omentum. Small volumes of gas may not interfere with sonographic evaluation, but large volumes of gas hinder complete evaluation of the peritoneal space. In dogs, as little as 0.4 mL air in the peritoneal space could be detected using ultrasound.[23] Additionally, movement of the free air can be noted when shifting the position of the patient.

Gas bubbles within peritoneal fluid are a strong indication for gastrointestinal perforation, especially when no prior peritoneal fluid sampling was performed.[24] As would be expected, pneumoperitoneum in conjunction with gastric dilatation or volvulus is predictive for gastric necrosis. Prior percutaneous trocarization can confound the situation by leading to pneumoperitoneum and/or pneumatosis mimicking gastric necrosis.[25]



eFig. 39.4 Lateral **(A)**, ventrodorsal **(B)**, and horizontal beam radiograph **(C)** with the dog in right lateral recumbency. Small gas bubbles superimposed over the gastric fundus and the ventral aspect of the liver are suspicious for extraluminal gas, but the findings are subtle. In the horizontal view **(C)**, free peritoneal gas is accumulated under the rib cage, outlining the wall of the gastric fundus and the diaphragm.

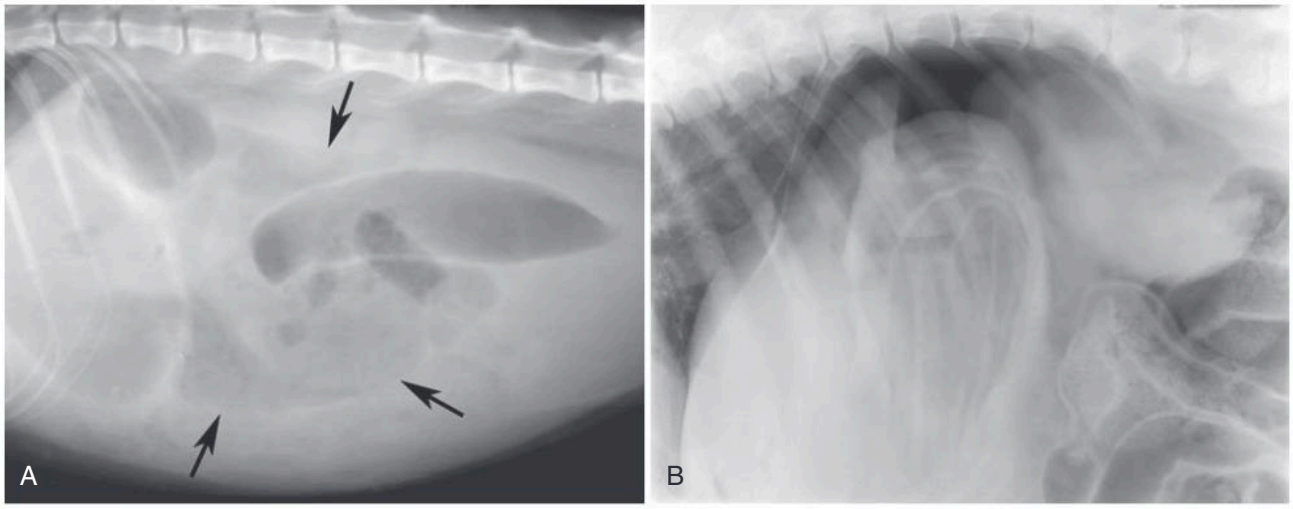


Fig. 39.15 **A,** Lateral survey radiograph of a cat with peritoneal effusion and a large amount of free peritoneal gas with margins of the gas pocket indicated by *black arrows*. **B,** Lateral survey radiograph of the abdomen of a dog immediately after laparotomy. A large volume of free peritoneal gas outlines the caudal surface of the right crus of the diaphragm, the cranial pole of the right kidney, the caudal surface of part of the liver, and the serosal surfaces of some bowel loops.

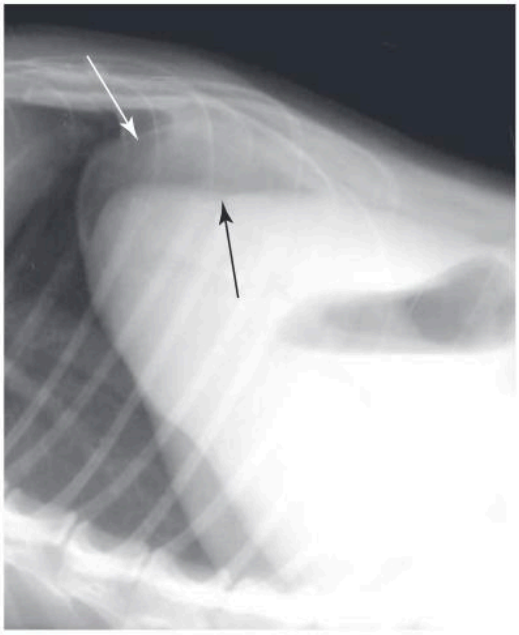


Fig. 39.16 Lateral view of the abdomen made with the patient in dorsal recumbency with the cranial abdomen slightly elevated, and the use of a horizontally directed x-ray beam. Free peritoneal gas has accumulated between the diaphragm (*white arrow*), the liver (*black arrow*), and the ventral abdominal wall. The diagnosis was ruptured stomach.

Retroperitoneal Gas (Pneumoretroperitoneum)

The term *pneumoretroperitoneum* indicates the presence of gas within the retroperitoneal space. Retroperitoneal gas is uncommon and can be caused by a perforation injury or migrating foreign body or surgical access to the retroperitoneal space, including secondary to laparoscopy or secondary to spinal surgery, perforation, or rupture of a hollow viscus, such as the rectum or the vagina in female animals. Furthermore, retroperitoneal gas can occur as a result of extension of a pneumomediastinum (see Chapter 33). Retroperitoneal gas is confined to the retroperitoneal space in the dorsal abdomen and is best seen on a lateral radiograph (Fig. 39.18).

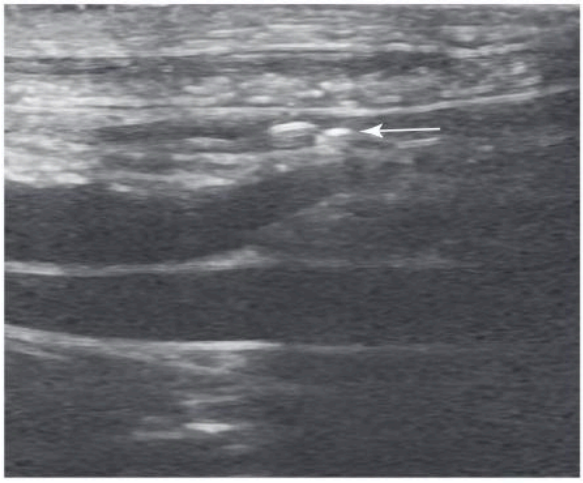
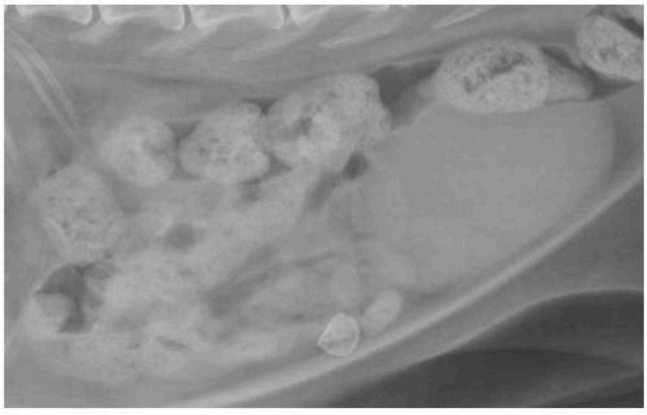


Fig. 39.17 Abdominal sonogram of a dog with a small amount of peritoneal gas. Even small gas collections create strong reflective artifacts (*white arrow*).

Intra-Abdominal Mineral Opacity

Increased mineral opacity not associated with the gastrointestinal tract is relatively uncommon in companion animals. Focal calcified bodies, usually with an opaque periphery, may be found in the peritoneal space (Fig. 39.19, eFig. 39.5; see Fig. 39.6). These are thought to be the result of dystrophic calcification of necrotic mesenteric fat and are not considered clinically significant.[26] Although not common, they are seen more often in cats than dogs. These have been referred to as *Bates bodies*.[27]

Calcification of soft tissue is divided into a metastatic and dystrophic type, and both have a wide range of causes. Metastatic calcification occurs secondary to the deposition of calcium salts in previously normal tissue secondary to abnormal calcium and phosphorus metabolism, primarily in animals with chronic renal disease,[26] hyperparathyroidism, vitamin D and possibly vitamin A intoxication, hypothyroidism, or due to paraneoplastic hypercalcemia. Metastatic calcification can occur anywhere but often involves the blood vessels, kidneys, and gastric mucosa (Fig. 39.20). It is important to remember



eFig. 39.5 Lateral radiograph of the caudoventral abdomen of a cat with focal mineralized fat necrosis (Bates body). A rounded, slightly angular nodule with a mineral opaque peripheral shell is visible at the cranioventral aspect of the urinary bladder.

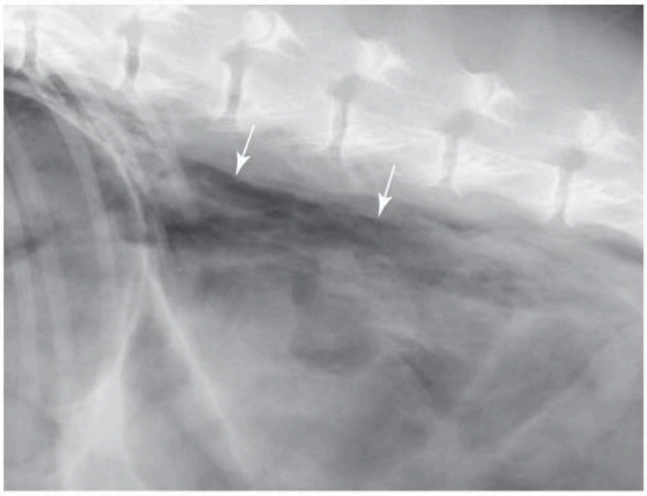


Fig. 39.18 Lateral view of a dog with pneumomediastinum. The pneumomediastinum is not visible in this image. Some of the mediastinal gas dissected along the fascial planes through the aortic hiatus into the retroperitoneal space (*white arrows*).

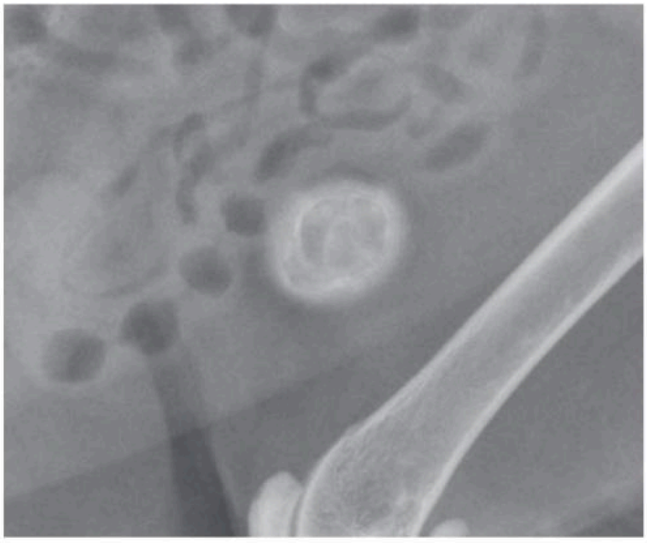


Fig. 39.19 Lateral radiograph of a cat with a focal calcified body in the peritoneal space. The calcified body was an incidental finding and thought to be a result of dystrophic calcification of necrotic fat.

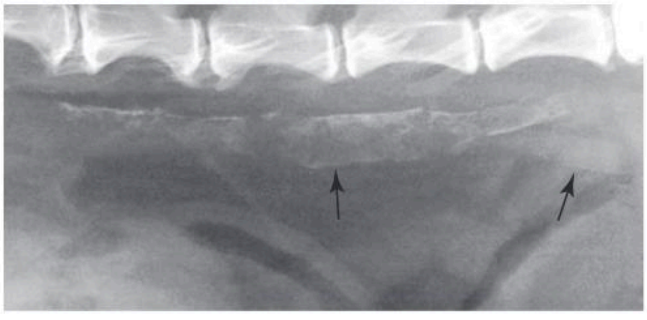


Fig. 39.20 Lateral view of the caudal abdomen of a 13-year-old Shetland sheepdog in chronic renal failure. The aorta and external iliac arteries (*black arrows*) are visible because of metastatic calcification.

that the term *metastatic* in regards to calcification does not indicate neoplasia, but indicates mineralization of normal tissue secondary to hypercalcemia. Dystrophic calcification is the deposition of calcium salts in abnormal tissue, which is injured, degenerated, or dead and causes include inflammation or infection and can in addition to the reported Bates bodies also be seen with hyperadrenocorticism or atherosclerosis.[28]

Rarely, peritoneal mineralization might be noted surrounding foreign material, such as a sponge left behind during previous surgery,[29] or a mineralized fetus may be seen in the peritoneal space with ectopic pregnancy. Clinical signs may be caused by necrosis or mechanical interference, or the condition may be an incidental finding.

NORMAL ANATOMY AND IMAGING OF THE ABDOMINAL WALL

Normal Anatomy and Imaging Techniques

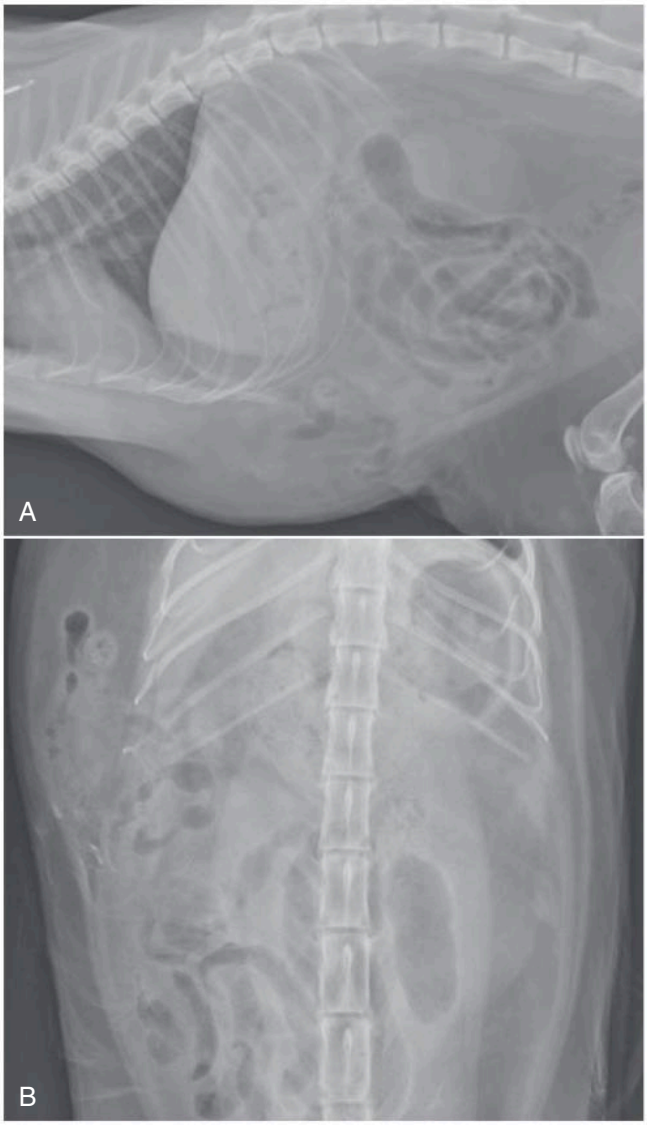
The normal abdominal wall consists of the external and internal oblique abdominis and the transverse abdominis muscles. On radiographs, the external oblique muscles can be identified due to the presence of fat on either side. The internal oblique and transverse abdominis muscles are visible radiographically, because they are continuous with the rib cage. On dorsoventral (DV) or VD radiographs, the lateral abdominal wall is best visualized. On lateral radiographs, the ventral portion of the abdominal wall is best evaluated. The cranial ventral abdominal wall thins, and ventral to the liver is often difficult to evaluate. Caudally, the abdominal wall is approximately the same width as the ventral aspect of the pelvis. The internal surface of the abdominal wall should be smooth and continuous.[3] The abdominal wall muscles and lesions thereof are often best visualized when struck tangentially by the x-ray beam. Ultrasound, especially when using a high-frequency probe, allows differentiation and evaluation of the different abdominal wall layers.

Abdominal Wall Abnormalities

Primary abdominal wall lesions can be classified as nonneoplastic and neoplastic. Nonneoplastic lesions include congenital abdominal wall hernia, trauma to the abdominal wall (Fig. 39.21, eFig. 39.6), postsurgical dehiscence, inflammation, and infection (e.g., secondary to a migrating foreign body), edema, subcutaneous emphysema, or mineralization. Abdominal wall disruption may be noted on radiographs. However, the extent of abdominal wall involvement may be better evaluated using ultrasound or CT with reformatted images in various planes. Additionally, displacement of abdominal organs into the abdominal wall defect can be identified using radiography, ultrasound, and CT. Common organs displaced into abdominal wall defects include the small intestine and urinary bladder; however, any other organ can be displaced. Tubular or round gas pockets summating with the abdominal wall can indicate herniated bowel loops (Fig. 39.22, eFig. 39.7). This is important to recognize, because herniated intestinal loops can get incarcerated and necrotic due to constriction by the abdominal wall defect.

Gas from a variety of causes may be present in the soft tissues surrounding the abdomen. Abrasions with lacerations secondary to trauma often produce a mottled, irregular gas pattern.

Mineralization is occasionally present in the soft tissues surrounding the abdomen. For example, calcinosis cutis associated with Cushing syndrome may produce nodular or linear calcification of soft tissues, most often dorsally along the skin or subcutaneous tissues and sometimes in the ventral abdominal wall. Lipomas are considered one of the most common benign primary tumors of the abdominal wall, and usually appear as a fat attenuating mass in the abdominal wall on radiographs or CT images. Rarely, mineralization of lipomas occurs in animals. Diffuse amorphous mineralization may be noted summating with the abdominal cavity in an abdominal wall extra-abdominal



eFig. 39.6 Lateral **(A)** and ventrodorsal **(B)** radiographs of a cat that was attacked by a dog. There is disruption of the outline of the cranioventral **(A)** and right craniolateral **(B)** abdominal wall with extension of small intestines into the subcutaneous tissues lateral to the rib cage.



eFig. 39.7 Lateral abdominal radiograph of a dog with ventral abdominal wall (umbilical) hernia. A small intestinal loop can be seen traversing the normal outline of the ventral abdominal wall and extending into the hernia.



Fig. 39.21 Ventrodorsal radiograph of a cat post vehicular trauma. Extensive avulsion of the right abdominal wall is noted. The left abdominal wall is intact (*white arrows*).

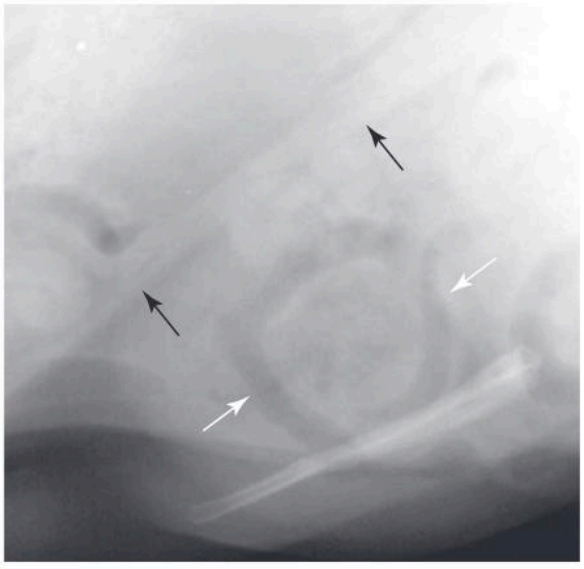


Fig. 39.22 Lateral view of the abdomen of a dog with tubular gas opacities (*white arrows*) ventral to the abdominal wall from an inguinal hernia with entrapped small intestine within the hernia. The level of the abdominal wall is indicated by the *black arrows*.

chondrolipoma, and this might be misinterpreted as a mineralized abdominal mass.[30]

Soft tissue attenuating masses of the abdominal wall such as fibrosarcoma can occur in the abdominal wall of cats, and commonly CT imaging is performed to evaluate the extent of the lesion. Transitional cell carcinoma might spread to the abdominal wall secondary to percutaneous tissue sampling or surgery and it is recommended to avoid percutaneous sampling of transitional cell carcinoma.[31]

ABDOMINAL LYMPH NODES

Normal Anatomy and Imaging Techniques

Anatomy

Abdominal lymph nodes are divided into two groups: parietal and visceral. The parietal group includes the lymph centers of the abdominal and pelvic walls, including the lumbar, iliosacral, and iliofemoral lymph centers. All parietal lymph nodes, except the iliofemoral lymph nodes, are in the retroperitoneal space and receive afferent lymphatics from the spine, adrenal glands, kidneys, genital organs, excluding part of the mammary glands, caudodorsal abdomen, pelvis, and pelvic limbs. The iliofemoral lymph center consists of only one distal femoral lymph node, which is in the deep medial femoral fascia at the distal part of the femoral triangle and only present in about 10% of dogs.[1] Efferent vessels from the parietal lymph nodes drain into the lumbar trunk, which in turn empties into the cisterna chyli. The more cranially located parietal lymph nodes may bypass the lumbar trunk and drain directly into the cisterna chyli. Many of the parietal lymph nodes are developed inconsistently and may be absent. However, the medial iliac lymph nodes, the largest lymph nodes of the iliosacral lymph center, are always present. The medial iliac lymph nodes, previously known as the *external iliac lymph nodes*,[1] are located ventral to the caudal lumbar spine between the deep circumflex iliac and external iliac arteries (aortic trifurcation). One lymph node is usually present on each side, but occasionally two lymph nodes are noted on one or both sides. The medial iliac lymph nodes are reported to lie ventral to L5 and L6[1]; however, these lymph nodes often are located ventral to L6 and L7.[3] The medial iliac lymph nodes receive afferent lymphatics from the urogenital tract, as well as from other structures in the caudal abdomen, pelvis, and pelvic limbs.

The visceral group of abdominal lymph nodes is divided into subgroups that are associated with specific organs.[1] The visceral lymph group drains the liver, spleen, pancreas, stomach, and intestine. The lymph centers of the abdominal viscera can be divided into the celiac, cranial mesenteric, and caudal mesenteric lymph centers. The celiac lymph center consists of all lymph nodes serving organs that are supplied by the celiac artery, which includes the hepatic, splenic, gastric, and pancreaticoduodenal lymph nodes. The cranial mesenteric lymph center consists of the jejunal and colic lymph nodes. The jejunal lymph nodes, which were previously called the *cranial mesenteric lymph nodes*, are the largest of the visceral lymph nodes and receive afferent lymphatics from the jejunum, ileum, and pancreas.[1] The colic lymph nodes generally are located in proximity to the ascending and transverse colon and in the dog close to the descending colon.[32] The caudal mesenteric lymph center consists of the caudal mesenteric lymph nodes and serves the caudal aspect of the descending colon to rectum.[32] The caudal mesenteric lymph nodes send lymph in part to the medial iliac lymph nodes or the lumbar trunk or like the other abdominal visceral lymph nodes to the intestinal trunk, which then empties into the cisterna chyli.[1]

Radiography of Lymph Nodes

Normal lymph nodes are usually not visible radiographically.

Ultrasound of Lymph Nodes

Ultrasound is likely the most widely used technique to assess abdominal and retroperitoneal lymph nodes in dogs and cats. Various ultrasound characteristics of normal and abnormal lymph nodes have been described. It is important to remember that normal lymph nodes can be quite variable in size, and therefore size measurements need to be treated with caution when deciding on diseased versus normal lymph nodes. When evaluating the size of lymph nodes, the maximal thickness or width of lymph nodes is more reliable than the length of lymph nodes.[33] For the medial iliac lymph nodes and other lymph nodes as well, lymph node size is directly proportional to body size. Furthermore, abdominal lymph nodes, specifically the jejunal lymph nodes, might be slightly larger in younger animals

compared to older animals. Lymph nodes are often hypoechoic to isoechoic to surrounding tissue with a distinct cortex and medulla or homogeneous echotexture. Their surface is usually smooth and often clearly defined.

The medial iliac and jejunal lymph nodes are the largest and most consistent in the abdominal cavity, and can be found sonographically more often than other lymph nodes when normal.[33,34] Normal lymph nodes have an echogenicity similar to surrounding mesentery and adjacent musculature,[34] but knowledge of their location and careful identification of elongated structures of uniform echotexture and thin echogenic capsules can permit detection (Fig. 39.23). High-frequency transducers are necessary to obtain resolution adequate for imaging normal lymph nodes.

The medial iliac lymph nodes are found by following the terminal portion of the aorta and caudal vena cava carefully in long axis and transverse image planes. In some instances, finding the lymph nodes by scanning in a transverse plane and looking for subtle round structures with thin echogenic borders on either side of the aorta is easier (see Fig. 39.23B). Alternatively, the medial iliac lymph nodes may be easier to find in the dorsal plane.[35] In the sagittal plane, the lymph nodes appear fusiform (see Fig. 39.23A). The visceral lymph nodes are seen more often when abnormal and are encountered as hypoechoic nodules detected during routine scanning. They are identified as lymph nodes based on their location usually along the vascular supply of a specific organ.

Computed Tomography of Lymph Nodes

CT is an excellent technique to evaluate abdominal lymph nodes, because it allows delineation of peritoneal anatomy. Isotropic voxel scanning with reformation in sagittal, dorsal, or oblique planes helps to evaluate the size, shape, location, and contrast enhancement behavior of these lymph nodes.

The jejunal and medial iliac lymph nodes are most commonly identified in dogs[36] and cats. Colic lymph nodes are generally not identified in dogs but often seen in cats. Most abdominal lymph nodes have a homogeneous attenuation pattern before and after intravenous iodinated contrast medium injection. Some lymph nodes are peripherally hyperattenuating relative to the center.[36] Considering that the sacral lymph nodes are not routinely accessible with ultrasound, CT (or magnetic resonance imaging [MRI]) should be considered when staging dogs with apocrine gland tumors.[37]

Abnormalities of Abdominal Lymph Nodes

Imaging Findings

Abdominal lymph nodes are seen radiographically only if they are enlarged or mineralized. Abundant retroperitoneal or peritoneal fat helps provide contrast between enlarged lymph nodes and surrounding soft tissue structures. Of the parietal lymph nodes, the medial iliac nodes are most commonly the only lymph nodes that enlarge to the degree that they are seen radiographically. Care should be taken not to confuse the deep circumflex arteries and veins that are projected end-on in lateral radiographs with enlarged medial iliac lymph nodes (Fig. 39.24). Enlarged medial iliac lymph nodes appear as a soft tissue mass in the retroperitoneal space ventral to L6 and L7 (Fig. 39.25). If node enlargement is severe, the lymph nodes are



Fig. 39.24 Lateral view of the abdomen of a normal dog. Note the fat opacity within the retroperitoneal space. Ill-defined nodular soft tissue opacities in the caudal retroperitoneal space seen ventral to L6 (*black arrows*) represent end-on projections of the deep circumflex iliac arteries and veins, not lymph nodes.

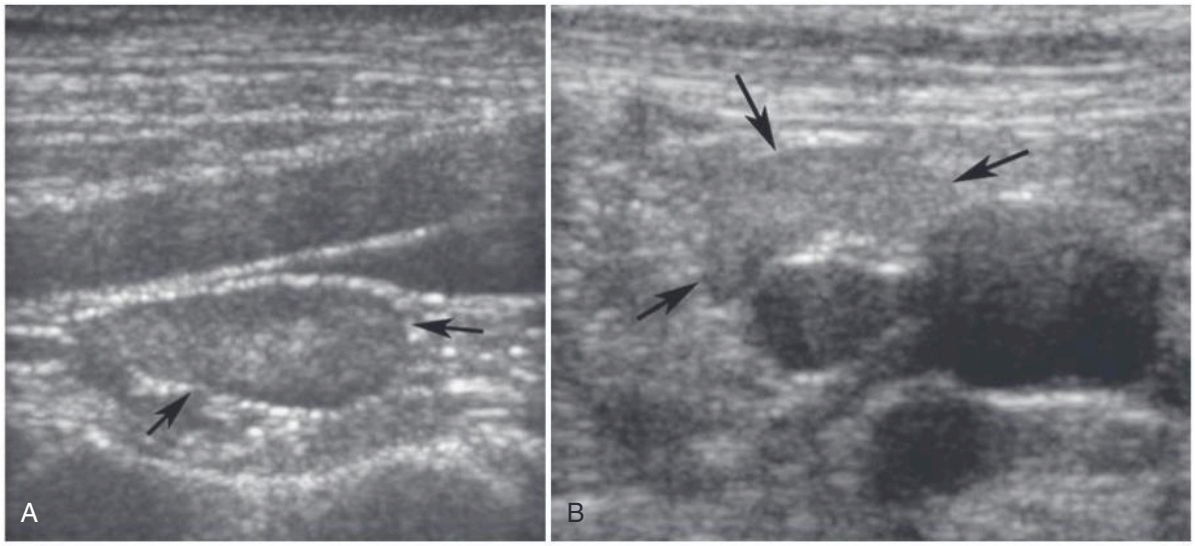


Fig. 39.23 Longitudinal **(A)** and transverse **(B)** ultrasound images of a normal medial iliac lymph node. On the longitudinal view, the lymph node (*black arrows*) is elongated and just ventral to the aorta near the aortic bifurcation. The lymph node is nearly isoechoic to surrounding structures and has a thin echogenic capsule. On the transverse image, the lymph node (*black arrows*) is a curved structure just ventrolateral to the aorta. Ventral is to the *top* **(A** and **B)**, and cranial is to the *left* **(A)**.

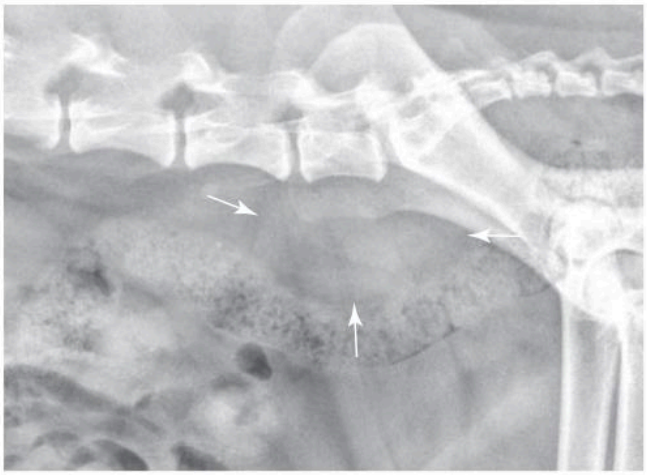


Fig. 39.25 Lateral view of the abdomen of a dog with anal gland adenocarcinoma. The medial iliac lymph nodes are mildly enlarged and appear as an ill-defined soft tissue mass (*white arrows*) in the retroperitoneal space ventral to L7. The colon is displaced ventrally.

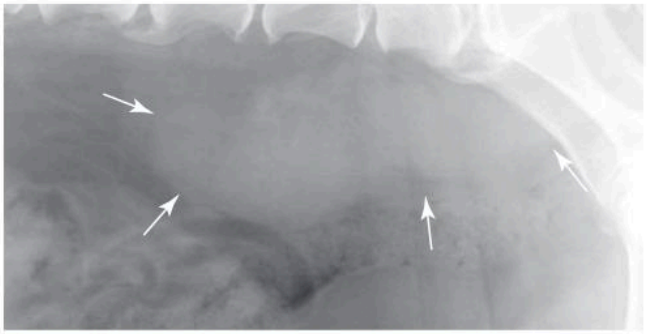


Fig. 39.26 Lateral view of the abdomen of a dog with lymphosarcoma. Medial iliac lymph node enlargement is severe and appears as a soft tissue mass in the retroperitoneal space extending caudally from L4-L5 into the pelvic canal (*white arrows*).

more conspicuous and extend more cranially (Fig. 39.26). Enlarged sublumbar lymph nodes frequently displace the descending colon and rectum ventrally (eFig. 39.8). However, a ventral course of the colon can be normal and is not an indication of medial iliac lymph node enlargement unless a soft tissue mass is present in the expected location of the lymph nodes. The most common cause of medial iliac lymphadenopathy is neoplasia. Neoplastic lymph node involvement may be primary (e.g., lymphoma) or metastatic (e.g., from caudal abdominal or pelvic neoplasms).[37] Inflammatory disease may also cause enlargement of the medial iliac lymph nodes, but this is less common. Inflammatory causes include migrating foreign bodies in the iliopsoas musculature, urogenital infection, and less commonly gastrointestinal or skeletal inflammation.

Visceral abdominal lymph nodes rarely enlarge enough to be seen radiographically, and tend to silhouette with surrounding organs. Jejunal lymph nodes may occasionally enlarge sufficiently and appear as an ill-defined central abdominal mass displacing the intestine peripherally.

Ultrasonographically, abnormal lymph nodes enlarge and become rounder and more hypoechoic (Fig. 39.27).[33,38] Neoplastic lymph nodes generally have a short-to-long axis ratio of more than 1:2, narrow or absent hilus, hypoechogenicity, sharp borders, a resistive index (RI) greater than 0.65, a pulsatility index (PI) greater than 1.45, and often distal acoustic enhancement. These findings tend to not be present in reactive lymph nodes.[38,39] Heterogeneity of enlarged lymph nodes is associated with malignancy in the dog, but lymph node heterogeneity is not predictive of malignancy in the cat.[40] Fine-needle aspirates obtained with ultrasound guidance are helpful for determining the cause of lymph node enlargement.

CT and MRI allow evaluation of abdominal and retroperitoneal lymph nodes for disease, and they may be more sensitive for detecting enlarged lymph nodes than abdominal ultrasound. Additionally, lymph nodes in the pelvic canal are not accessible with ultrasound and can easily be assessed using CT and MRI. However, similarly to ultrasound, enlargement of lymph nodes noted on CT or MRI is not an indication for metastatic disease. Currently, there are no pathognomonic imaging findings for metastatic lymphadenopathy; enlarged lymph nodes should be sampled when tumor staging is performed.[41]

PANCREAS

Normal Anatomy and Imaging Techniques

Anatomy

The body of the pancreas lies between the pylorus and the proximal descending duodenum. The right lobe of the pancreas extends caudally from the body and lies adjacent to the medial aspect of the descending duodenum. The left lobe of the pancreas lies between the stomach and transverse colon, extending from the pancreatic body toward the left kidney on the medial aspect of the spleen.[42] As opposed to dogs, the left lobe is larger than the right lobe in cats.

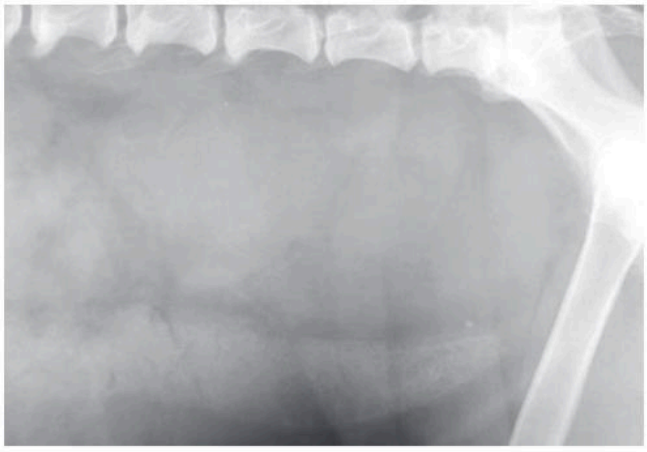
Radiography of the Pancreas

The normal pancreas is not visible on abdominal radiographs of dogs because of silhouetting with the adjacent tissues. Occasionally, the left limb of the pancreas can be seen on VD views in obese cats as an area of soft tissue opacity between the fundus of the stomach, the spleen, and the left kidney (Fig. 39.28).

Ultrasound of the Pancreas

Sonographic evaluation of the pancreas is standard practice for evaluating patients suspected of having pancreatitis or pancreatic masses, because the pancreas is better evaluated sonographically than radiographically. Endoscopic ultrasound shows promise evaluating the pancreas[43]; however, it is not commonly available and requires anesthesia, whereas transabdominal ultrasound can be performed in awake and sedated patients. Fasting of the patient is recommended, to reduce artifacts caused by ingesta and gas which can obscure the pancreas.[44] The normal pancreas can be difficult to identify sonographically because of its small size, usually having an echogenicity similar to surrounding fat, and absence of a well-defined capsule. Therefore, identifiable landmarks are used to scan the pancreatic area and are described in a recent consensus statement on abdominal ultrasound.[45,46]

When visible, the pancreas has a subtle echogenic capsule (Fig. 39.29), and it is somewhat hypoechoic, being less echogenic than the spleen but more echogenic than the liver.[45] Occasionally, the pancreaticoduodenal vein, which lies within the pancreas and runs parallel to the duodenum, can be identified in dogs (see Fig. 39.29).[33] The pancreas is more likely to be identified in puppies, thin dogs, and dogs with peritoneal fluid. A hyperechoic pancreas can be noted in healthy dogs and can be associated with endocrinopathies such as hyperadrenocorticism.[47] In cats, the normal pancreas is isoechoic to the liver and hypoechoic to the surrounding mesentery, findings that do not appear to change with age, sex, body weight, or body condition.[45,48] The normal width (ventral to dorsal dimension) of the left lobe and body of the pancreas is approximately 0.25 to 1.0 cm, and the right lobe is commonly reported slightly smaller at between approximately 0.3 and



eFig. 39.8 Lateral view of the abdomen of a dog with metastatic mast cell tumor. A large soft tissue mass caused by enlargement of the medial iliac lymph nodes extends from L3-L4 into the pelvic canal, displacing the colon and rectum ventrally.

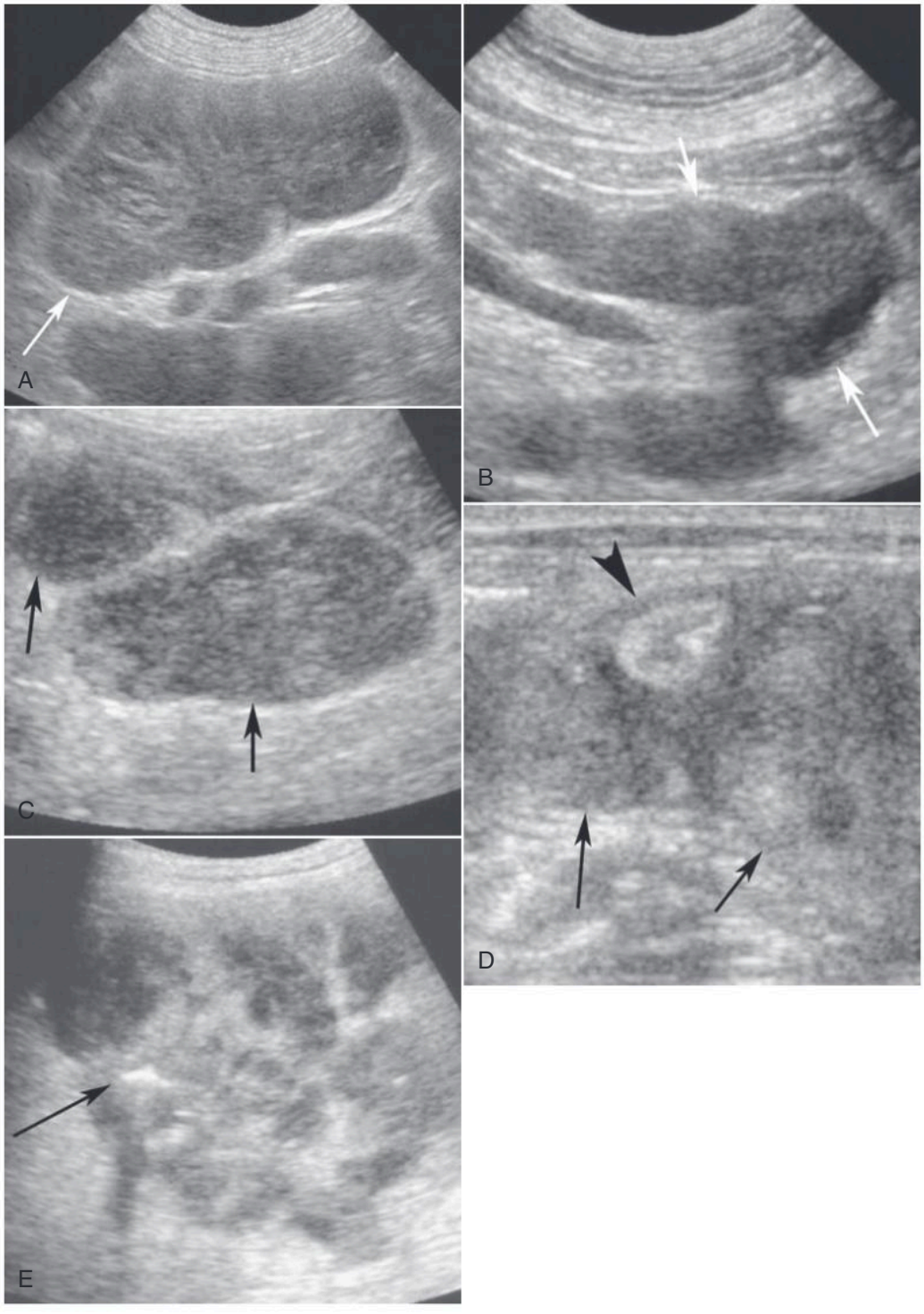


Fig. 39.27 Sonographic appearance of abnormal lymph nodes. **A,** Enlarged, hypoechoic medial iliac lymph node (*white arrow*) surrounding the aorta in a dog with lymphoma. **B,** Enlarged jejunal lymph node (*white arrows*) in a dog with lymphoma. This lymph node is hypoechoic to surrounding tissues and is irregular in shape. **C,** Enlarged jejunal lymph nodes (*black arrows*) in a dog with inflammatory bowel disease. Lymphoid hyperplasia was found on evaluation of lymph node aspirates. Both lymph nodes are hypoechoic and appear like those seen in the dog with lymphoma **(B)**. **D,** Enlarged ileocolic lymph nodes in a cat with lymphoma. The ileum (*black arrowhead*) is seen in cross-section surrounded by enlarged hypoechoic lymph nodes (*black arrows*). **E,** A large mixed echogenic mass in the mid abdomen of a dog. The mass incorporated intestinal segments. Gas (*black arrow*) within one bowel segment is seen as an echogenic focus producing acoustic shadowing. The hypoechoic to nearly anechoic areas were presumed to be enlarged mesenteric lymph nodes as lymphoma was diagnosed from aspirates of these structures.

0.6 cm.[49] The maximum dimension of the right lobe of the pancreas in healthy dogs was reported to range between 0.9 to 2.1 cm; however, it is unclear if the measurement corresponded to the VD maximum dimension reported in other studies.[50] The feline pancreatic duct width should normally be less than approximately 0.25 cm but can enlarge with age.[49,51,52]

Ultrasound of the pancreas using intravenous microbubble contrast medium improves visibility of the pancreas, allows for evaluation of pancreatic tissue perfusion, and therefore helps to detect lesions with an altered vascular pattern.[53] Contrast-enhanced ultrasound of the pancreas shows promise in dogs and cats in differentiating a diseased versus normal pancreas.[54,55] Transabdominal or endoscopic ultrasound-guided fine-needle aspirates can be obtained relatively safely to further evaluate the pancreas.[56,57]



Fig. 39.28 Ventrodorsal radiograph of a normal cat. The left lobe of the pancreas is visible (*black arrow*).

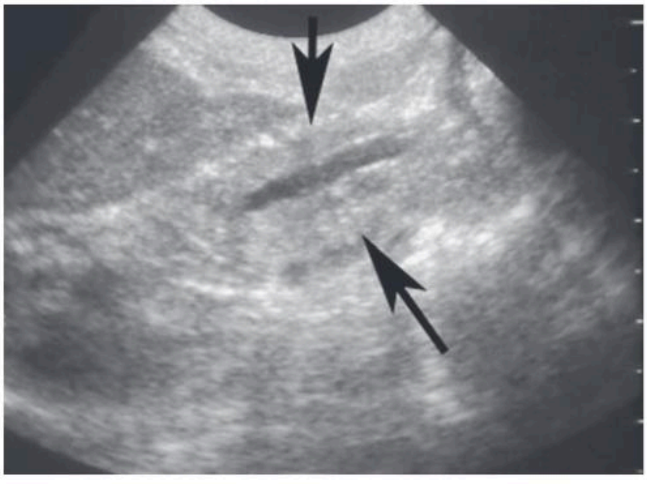


Fig. 39.29 Sagittal ultrasound image of the pancreas of a normal dog. The pancreas (*black arrows*) is the poorly defined structure adjacent to the liver, having approximately the same echogenicity as the mesentery. The hypoechoic structure in the middle of the pancreas is the pancreaticoduodenal vein.

Computed Tomography and Magnetic Resonance Tomography of the Pancreas

CT and MRI are used increasingly to evaluate the pancreas. They allow evaluation of the pancreas without summation of other organs, and intravenous injection of contrast medium allows assessment of perfusion of the organ. MRI further allows for cholangiography without the need for retrograde contrast medium injection into the bile duct.

The normal pancreas on CT imaging is a thin organ that is triangular in cross-section and hypoattenuating to the spleen and liver and uniformly contrast enhancing.[58,59] Using MRI, the normal pancreas is a thin, flat structure that is homogeneously hyperintense relative to the liver on precontrast T1-weighted images and isointense to hypointense on T2-fat-saturated images.[60,61]

Scintigraphy of the Pancreas

With the availability of abdominal ultrasound and cross-sectional imaging techniques, scintigraphy is rarely used to evaluate the pancreas; however, scintigraphy has shown promise in patients for insulinoma identification when no abnormality was noted sonograpically.[62]

Disease of the Pancreas

Inflammation of the Pancreas (Pancreatitis)

Pancreatitis is the most common exocrine pancreatic disorder in dogs and cats.[63] Diagnosing pancreatitis can be challenging, especially in cats.[64] Acute pancreatitis is a common cause of localized peritonitis. The frequency and appearance of radiographic changes caused by acute pancreatitis are variable (Box 39.2).[65,66] Changes are usually localized to the right cranial abdomen, where the right lobe of the pancreas is closely associated with the proximal duodenum and pyloric antrum, or to the midline just caudal to the stomach, where the body and left lobe of the pancreas are located. The major radiographic abnormality is usually an increased, irregular soft tissue opacity in the right mid to cranial abdomen, indicating localized peritonitis (Fig. 39.30A, eFig. 39.9). On the VD view, the cranial right abdomen is normally more opaque than the left side, and the normal appearance is commonly misdiagnosed as pancreatitis.[3]

The proximal descending duodenum may be displaced ventrally or toward the right to produce a broad curvature, and the pylorus of the stomach may be displaced toward the left. Less frequently, the transverse colon may be displaced caudally. Bowel loops adjacent to the pancreas (such as, the proximal descending duodenum) may contain gas; they may also have loss of tone and be dilated or spastic.

Combined with history and clinical findings, ultrasound has become a useful diagnostic aid for patients with pancreatitis (Box 39.3).[33,63,64,67] In patients with mild pancreatitis, the pancreas may be uniformly hypoechoic surrounded by more echogenic fat (Fig. 39.31).[64,68] Dilation of the pancreatic duct may be more sensitive as an initial sign of pancreatitis in cats.[69] However, the feline pancreatic duct does tend to increase in

Box • 39.2

Radiographic Signs of Pancreatitis

Increased soft tissue opacity, cranial right abdomen
Soft tissue mass effect caudal to stomach
Focal decrease in serosal detail, cranial right abdomen
Gas-distended descending duodenum (sentinel loop sign)
Displacement of adjacent intestinal structures
Radiographs may be normal



eFig. 39.9 Lateral **(A)** and ventrodorsal **(B)** abdominal radiographs of a dog with pancreatitis. Peritoneal serosal detail is reduced in the midcranial abdomen. An ill-defined soft tissue opacity mass effect is seen caudal to the stomach in the lateral projection. There is widening of the gastroduodenal angle in the VD projection with caudal displacement of the transverse colon.

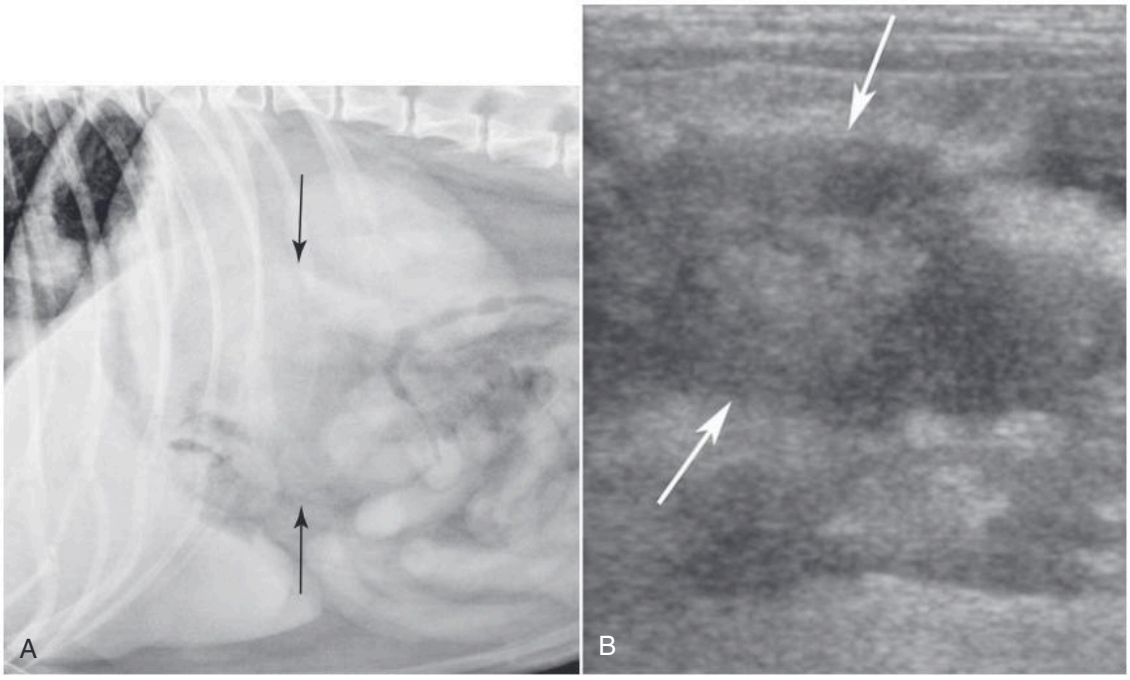


Fig. 39.30 **A,** Lateral survey radiograph of a dog with increased irregular soft tissue opacity in the mid cranial to cranial abdomen because of localized peritonitis (*between black arrows*). This is a difficult assessment to make; recognizing this change requires high-contrast radiographs and a patient with adequate peritoneal fat. **B,** Transverse ultrasonographic view of the right limb of the pancreas in the same dog. Note the pancreas (*white arrows*) is enlarged, hypoechoic, and irregular in shape, and the surrounding mesentery is hyperechoic. The diagnosis was pancreatitis.

Box • 39.3

Ultrasonographic Signs of Pancreatitis

Enlarged pancreas
Hypoechoic pancreas
Hyperechogenicity of the surrounding mesentery and fat
Possible cavitary lesions
Possible dilation of biliary or pancreatic ducts
Possible peritoneal fluid
May be normal

width with increasing age; thus, dilation of the pancreatic duct should not be used as the only marker of pancreatitis in older cats.[49,51] In more severe inflammation and pancreatic necrosis, the pancreas may be enlarged and contain irregularly shaped hypoechoic and hyperechoic areas (Fig. 39.32).[57,65,70] Other findings may include cavitary lesions, duodenal thickening, biliary obstruction, localized peritoneal fluid, and dilation of the pancreatic duct.[71] Hypoechoic areas within the pancreas are likely caused by inflammation, hemorrhage, necrosis, and edema.[71] Hyperechoic areas may be from fibrosis.[71] The surrounding tissue may be increased in echogenicity as a result of acoustic enhancement through hypoechoic areas in the pancreas or saponification of mesenteric fat. In spite of these criteria, pancreatitis remains difficult to diagnose, especially in cats.[71] Also, false-negative results may be seen in dogs.[72] Differentiation of acute versus chronic pancreatitis is also difficult,[73] and chronic pancreatitis may be more common in dogs than previously thought.[74]

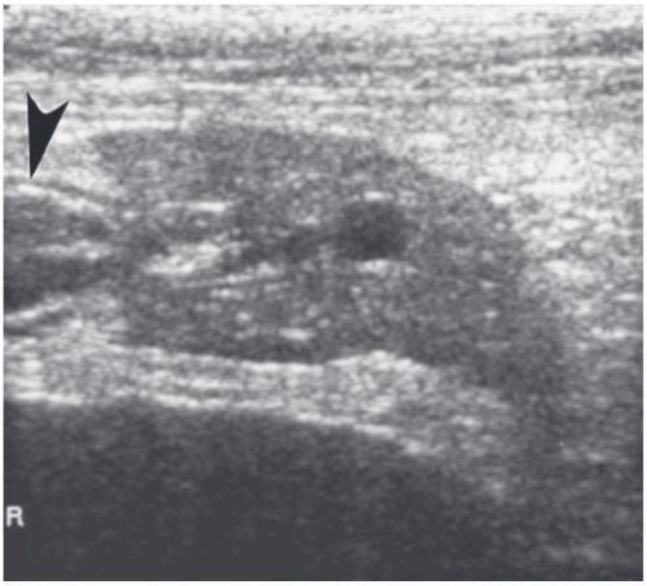


Fig. 39.31 Transverse ultrasound image of the right lobe of the pancreas of a dog with mild pancreatitis. The pancreas is less echogenic than normal, is hypoechoic to surrounding fat, and lies just ventral to the liver and medial to the duodenum (*black arrowhead*). The pancreaticoduodenal vein is the round anechoic structure within the pancreas.

Pancreatic pseudocysts, cysts and abscesses may occur as a result of pancreatitis (see Box 39.3).[75–77] They appear as large, mostly anechoic masses in the pancreatic area with distal acoustic enhancement and low-level internal echoes (Fig. 39.33A). Abscesses may be difficult to differentiate ultrasonographically from a pseudocyst; ultrasound-guided aspirates

are helpful differentiating the two.[75] If a pancreatic mass lies near the opening of the common bile duct, biliary obstruction may result. True pancreatic cysts are rare but have been reported in at least two cats. Clinical signs (vomiting) resolved after surgical removal of the cyst in one patient,[78] and multiple recurring cysts were identified in another patient associated with pancreatic inflammation, atrophy, and diabetes mellitus.[79] Another rare finding is a calculus within the pancreatic duct.[80]



Fig. 39.32 Longitudinal ultrasound image of the right lobe of the pancreas in a dog with pancreatitis. The pancreas is enlarged and hypoechoic, and the surrounding mesentery is hyperechoic. This is a common appearance in dogs with moderate to severe pancreatitis.

CT is the modality of choice in human patients for diagnosing pancreatitis; however, in animals, limited information is available about the clinical utility of CT for diagnosing pancreatitis. Results from the use of CT for diagnosing pancreatitis in cats are disappointing as the diagnosis was made in only 2 out of 10 cats.[81] Ultrasound may be more sensitive than CT for detecting pancreatitis in cats.[82] However, in dogs, a three-phase contrast-enhanced CT protocol showed promise, because in all dogs with suspected pancreatitis, the pancreas was enlarged, homogeneously or heterogeneously contrast enhancing and had ill-defined borders. Dogs with heterogeneous contrast enhancement of the pancreas had an overall poorer clinical outcome than dogs with a homogeneous contrast enhancement of the pancreas.[83] Additional complications of pancreatitis (such as, thrombus formation) may be noted on CT studies.[83–85]

Limited information about the use of MRI for diagnosing pancreatitis is available. However, in cats, MRI had promise with the abnormal pancreas being T1 precontrast hypointense and T2 hyperintense, with a dilated pancreatic duct.[60]

Neoplasia of the Pancreas

Pancreatic tumors are uncommon and are not detected radiographically before they are large, but they may be detected sonographically. The most common primary tumors of the pancreas include islet cell carcinoma compatible with insulinoma, followed by pancreatic adenocarcinoma. Invasion of the pancreas by tumors of the stomach or duodenum or secondary to lymphoma have been described.[86] Exocrine pancreatic carcinomas tend to invade the duodenum and often metastasize to regional lymph nodes, liver, and the peritoneum.[87] Functional islet cell tumors may be benign or malignant and should be

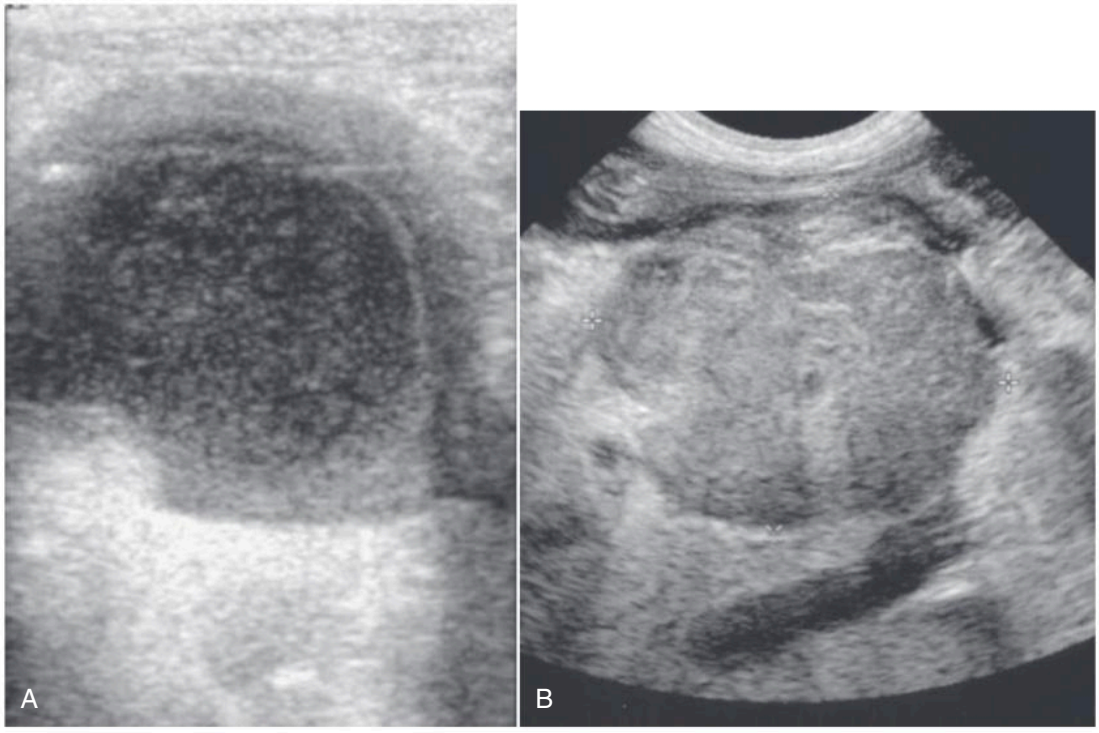


Fig. 39.33 **A,** Longitudinal ultrasound image of the right lobe of the pancreas in a dog. A large pancreatic abscess is present with a thick hyperechoic capsule and less echogenic internal contents. **B,** Longitudinal ultrasound image of the right limb of the pancreas in a dog. A solid, midlevel echogenic pancreatic tumor is present adjacent to the duodenum (*top right*).

suspected in dogs with persistent hypoglycemia. The sensitivity of ultrasound for detecting pancreatic tumors varies and ranges from 28% to 75%.[86,88,89] Both types of primary tumors may appear as discrete hypoechoic nodules or masses.[86] Similarly, in nodular hyperplasia, hypoechoic lesions can be detected; however, often there is more than one hypoechoic lesion and the nodules commonly are smaller than 1 cm.[90] The only definitive difference in cats between nodular hyperplasia and pancreatic neoplasia was the presence of a single nodule measuring larger than 2 cm in one dimension.[90] Additionally, ectopic splenic tissue in the pancreas, which is rare, might be confused with a pancreatic tumor.[91] Another potential source of error is misinterpretation of enlarged hypoechoic lymph nodes as a pancreatic mass.[86] Islet cell tumors can be small and difficult to detect sonographically; therefore, a negative examination does not rule out neoplasia. Only approximately 30% of insulinomas can be detected with ultrasound.[92]

Contrast-enhanced ultrasonography of the pancreas may improve the ability to detect pancreatic tumors and further improve the ability to differentiate between exocrine and endocrine pancreatic tumors in dogs. Pancreatic adenocarcinoma, an exocrine pancreatic tumor, was hypoechoic in precontrast images and hypovascular following microbubble contrast medium injection, whereas insulinomas were hypervascular after contrast medium injection.[93] CT has promise in evaluation of pancreatic masses, including insulinomas,[88,94,95] but surgical evaluation remains the gold standard. Both pancreatitis and pancreatic neoplasms may cause biliary dilation, lymphadenopathy, and peritoneal fluid. Hyperechoic or heterogeneous masses are found more often in pancreatitis, and discrete hypoechoic nodules are more characteristic of neoplasia. The main sonographic features that may help distinguish between inflammation and neoplasia are a diffusely hypoechoic pancreas in dogs with pancreatitis and hypoechoic nodules in dogs with neoplasms.[96] Others suggest that abnormalities of the liver and pancreas, combined with a lack of pain, are suggestive of neoplasia (see Fig. 39.33B).[70] In cats, there was overlap in the radiographic and sonographic appearance of neoplasia and nodular hyperplasia; however, if a solitary pancreatic nodule 2 cm in diameter or larger was present, neoplasia was more likely.[90]

Correlation with history, clinical signs, and other diagnostic findings may negate the need for tissue sampling. However, if a definitive diagnosis is needed, tissue sampling is necessary.[70] Needle aspiration and surgical biopsy of the pancreas have been associated with increased serum trypsin-like immunoreactivity and mild pancreatic inflammation and/or necrosis, but not an increase in canine-specific pancreatic lipase.[97] A single biopsy may not be sufficient because pancreatic diseases tend to be focal and randomly distributed.[98] However, ultrasound-guided fine-needle aspiration of the pancreas may provide valuable diagnostic information while having a low rate of clinical complications in dogs. Again, a normal sonographic examination of the pancreas does not rule out pancreatic disease, especially infiltrative or inflammatory disease. This is particularly true for cats.

Cystic Lesions of the Pancreas

Cystic lesions of the pancreas are infrequently reported in dogs and cats and mainly include pseudocysts[99,100] and cysts[101]; cystic neoplastic lesions are rarely reported. Pancreatic pseudocysts, which lack a lining surrounding the fluid accumulation, are more commonly reported and are the result of a pancreatitis, whereas true pancreatic cysts have an epithelial lining surrounding the fluid accumulation are less frequently reported. On radiographs, dependent on the size of the cystic lesion, a mass effect in the cranial abdomen may be noted (Fig. 39.34), and on abdominal ultrasound, anechoic fluid accumulations can be seen in the pancreas.

ADRENAL GLANDS

Normal Anatomy and Imaging Techniques

Anatomy

Each adrenal gland has a distinct cortex and medulla, which are anatomically distinct and functionally independent from each other. The cortex secretes steroid hormones, including cortisol, aldosterone, androgens, and estrogen. The medulla produces catecholamine. Both adrenal glands are in the retroperitoneal space. The right adrenal gland is bordered dorsally by the psoas minor muscle and the crus of the diaphragm, medially by the caudal vena cava, ventrolaterally by the right kidney, and cranioventrally by the right lateral liver lobe. The left adrenal gland is bordered dorsally by the psoas minor muscle, ventrally by the spleen, laterally by the left kidney, and medially by the aorta.[1]

Radiography of the Adrenal Glands

Normal adrenal glands are not seen radiographically and can only be seen when enlarged and/or mineralized. In dogs, an adrenal tumor had to be larger than 2 cm to be noted on survey radiographs.[102] In cats, mineralization of the adrenal glands can occur normally and is generally dystrophic in nature and rarely due to adrenalitis. [103] It usually involves the cortex and rarely the medulla. Mineralization of the adrenal glands in cats has only shown a weak to moderate correlation with age and has been noted in normal kittens and cats younger than 6 months of age.[103]

Ultrasound of the Adrenal Glands

Ultrasound is the most widely used imaging technique to evaluate the adrenal glands in dogs and cats and is a powerful diagnostic tool when combined with appropriate clinical and biochemical tests. Ultrasound has been used to evaluate normal canine adrenal glands,[104] normal feline adrenal glands,[105] and dogs with hyperadrenocorticism,[106,107] hypoadrenocorticism,[108] and adrenal masses.[109] However, the ability to image the adrenal glands accurately depends on the quality of the equipment, operator experience, and size of the patient. The adrenal glands are imaged more easily in smaller patients where higher-resolution probes can be used to obtain quality images with adequate penetration. Sedation may be helpful in some patients who resist abdominal compression by the transducer. An intercostal approach may be necessary to image the right adrenal gland.

To find the left adrenal gland, the cranial pole of the left kidney is scanned in a sagittal plane, and then the transducer is slid medially towards the aorta. The left adrenal gland lies just ventrolateral to the aorta between the cranial mesenteric and renal arteries.[46] Occasionally, the left adrenal gland may be located slightly cranial to the celiac and cranial mesenteric arteries. To obtain a full longitudinal view of the left adrenal gland, the probe may need to be rotated so the aorta is imaged obliquely. The normal canine left adrenal gland is usually shaped like a peanut shell or dumbbell[110] (Fig. 39.35A).

Care should be taken not to confuse the adrenal gland with a lymph node. Both adrenal glands of dogs and cats are hypoechoic to the surrounding fat and hypoechoic or isoechoic when compared with the renal cortex. Occasionally, the adrenal gland has a layered appearance, with the medulla being more echogenic than the cortex. This layered appearance has

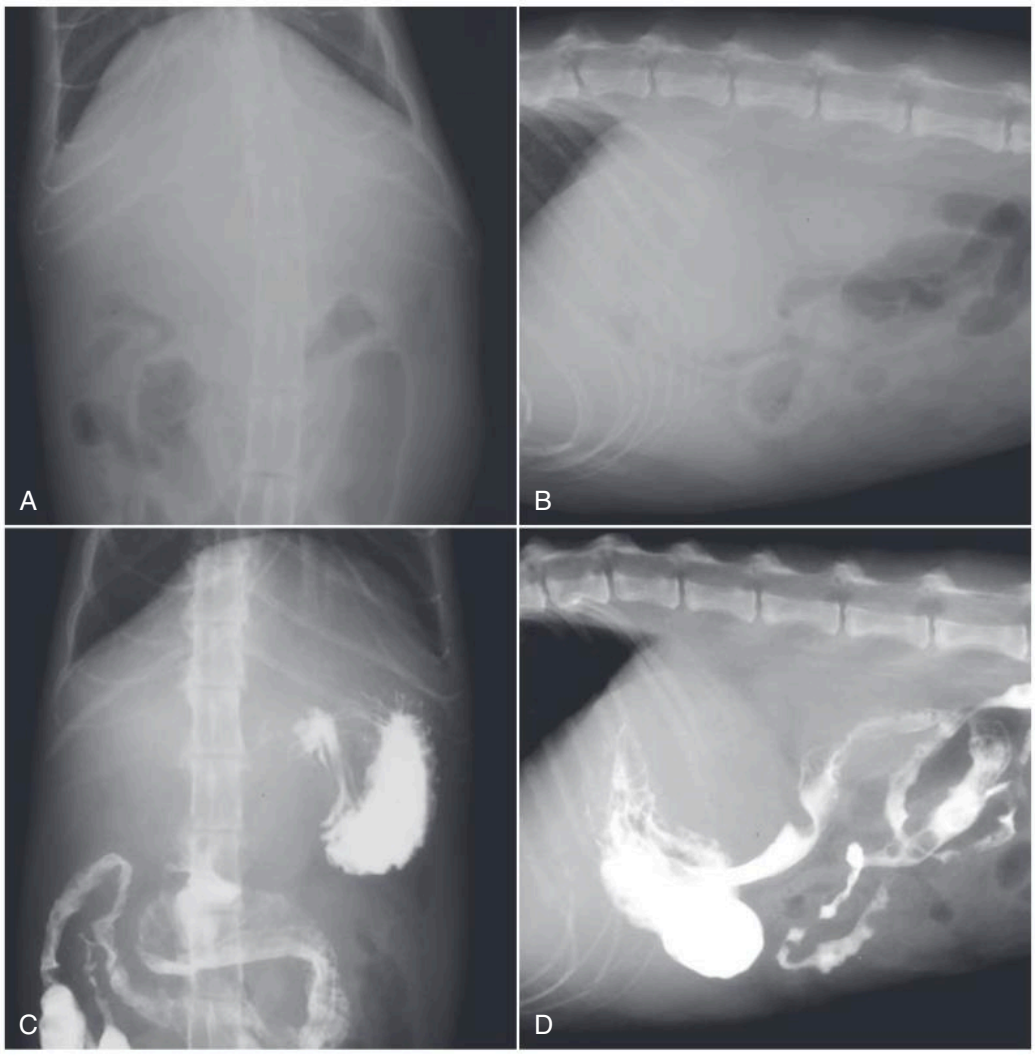


Fig. 39.34 Ventrodorsal **(A)** and lateral **(B)** survey radiographs and ventrodorsal **(C)** and lateral **(D)** radiographs post oral barium administration of the abdomen of a cat with a large pancreatic cyst. A large soft tissue attenuating mass is present in the right to central aspect of the abdomen **(A, B)**. In the survey radiographs, the stomach is fluid filled and incompletely defined, and on the contrast study, left lateral **(C)** and ventral displacement of the stomach **(D)**, and on **D,** also of the duodenum is noted.

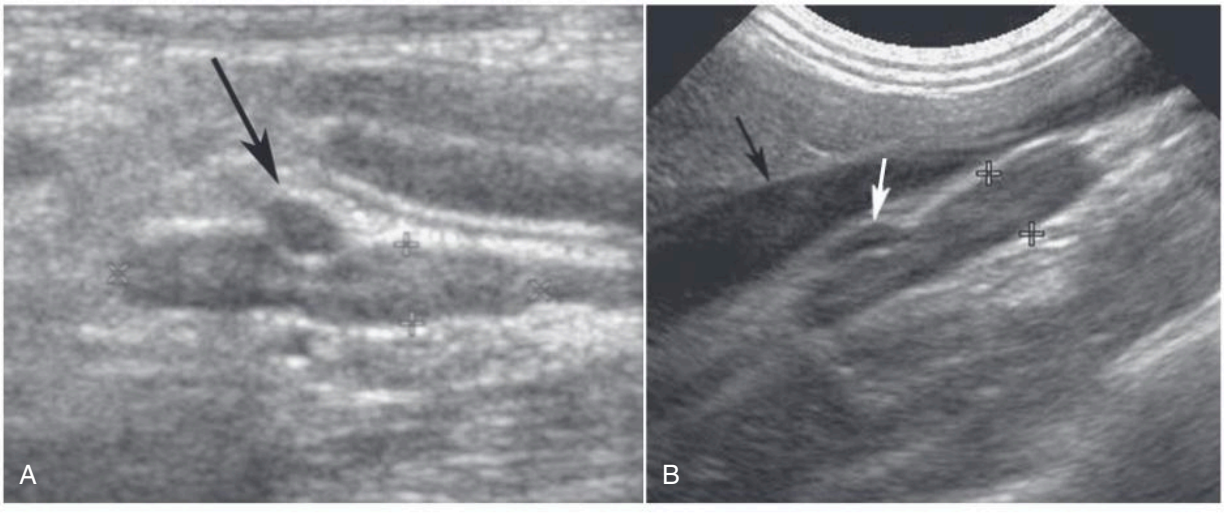


Fig. 39.35 Longitudinal ultrasound images of a normal left **(A)** and right **(B)** canine adrenal gland. **A,** The left adrenal gland has a dumbbell shape and lies just ventral to the phrenicoabdominal vein (*black arrow*). It is less echogenic than surrounding fat. **B,** The right adrenal gland is an elongated hypoechoic structure just dorsal to the caudal vena cava (*black arrow*). The right adrenal gland in this dog is surrounded by a hyperechoic capsule. The phrenicoabdominal vein (*white arrow*) is less often visualized on the right side. The head is to the *left* and ventral to the *top*.

been ascribed to both normal[33,110] and hyperplastic glands.[33,110] A hyperechoic capsule can often be identified (see Fig. 39.35B). In cats, both adrenal glands are oblong and oval to bean shaped.[105]

The right adrenal gland is more difficult to image than the left, especially in larger dogs. After the cranial pole of the right kidney is scanned in a sagittal plane, the transducer is moved medially to find the caudal vena cava. The right adrenal gland lies dorsolateral to the caudal vena cava and cranial to the renal vein.[46] The phrenicoabdominal veins cross the ventral surfaces of both adrenal glands and can occasionally be identified with high-resolution transducers or by using color Doppler. The shape of the right adrenal gland of the dog is different from that of the left. The right has been described as having a comma-shaped or bent-arrow conformation.[110] Many large-breed dogs have adrenal glands with an elongated, thin shape. This is suspected to be a normal variant.

Ultrasonographic determination of adrenal gland size has been used as an aid for evaluating dogs suspected of having hyperadrenocorticism and hypoadrenocorticism. A wide range of values (length, width, and thickness) have been reported in regards to normal adrenal gland size. The normal adrenal gland has been reported from 0.91 to 5.02 cm in length, from 0.19 to 1.74 cm in width, and from 0.17 to 1.07 cm in thickness.[33,111–114] Adrenal gland length is proportional to body weight, but the diameter (thickness or width) is not.[112,113] Therefore cross-sectional measurements are more valuable than length in the assessment of adrenal gland size. Adrenal gland thickness greater than 0.6 cm in small-breed and 0.74 cm on the left side and 0.81 cm on the right side in middle-aged to older large-breed dogs has been used as the criterion for maximum normal adrenal gland size.[104,115] However, adrenal gland measurements should not be used alone to diagnose abnormalities, because there is considerable overlap of adrenal size between normal versus abnormal dogs and variability of obtaining the measurements by observers.[116] The shape of the adrenal glands, the response of the patient to pituitary/adrenal axis testing, and the clinical signs must be correlated with the size of the adrenal glands when making a diagnosis.

Computed Tomography of the Adrenal Glands

CT is the most commonly used technique to evaluate the adrenal glands in human patients. In dogs and cats, ultrasound is the most commonly used technique. In one study, incidental adrenal gland masses were identified in 9.3% of dogs undergoing an abdominal CT examination, and these masses were more commonly noted in dogs older than 8 years of age.[117] The normal adrenal gland shape and size in CT images is similar to what has been reported in ultrasound studies. Normal adrenal glands have a homogeneous attenuation, which is similar in attenuation to the kidneys and similar in both adrenal glands.[118,119] The peak attenuation of adrenal glands in dogs after intravenous iodinated contrast medium injection is dependent on dose and timing.[119] The size and shape of the adrenal glands vary on CT images due to the position of the adrenal glands relative to the scan plane.

Magnetic Resonance Imaging of the Adrenal Glands

The adrenal gland size and shape on magnetic resonance (MR) images are like that seen in ultrasound and CT images. The signal on fast-spin echo (FSE) sequences, including T2-weighted, T1-weighted, and T1-weighted after administration of a paramagnetic contrast medium, was homogeneous and hypointense to surrounding tissue or a corticomedullary type pattern with a hyperintense central area surrounded by a hypointense peripheral rim of tissue. The left adrenal gland was often easier to define and more distinct. The demarcation of the right adrenal gland was more variable, especially if it was in contact with the liver or the caudal vena cava.[120]

Abnormalities of the Adrenal Glands

In cats and dogs, primary adrenal gland neoplasia causing clinical signs occurs rarely. Adrenal gland tumors comprise less than 1% to 2% of all canine tumors. Adrenal adenomas, adenocarcinomas, and pheochromocytomas are the most common lesions affecting the adrenal glands.[117] Hemangioma and myelolipomas have been described in the adrenal glands of dogs, but they occur rarely.[121–123] Malignant pheochromocytomas are the most aggressive adrenal gland tumors, with invasion of the adjacent vasculature noted in 20% to 93% of dogs and metastasis in up to 40% of dogs.[124,125]

With the advancement of imaging techniques, adrenal masses are more commonly diagnosed incidentally, which can be a dilemma.[126] No current imaging modality can reliably differentiate benign from malignant adrenal gland lesions, and further evaluation of these patients for hypokalemia, hypertension, and loss of the hypothalamic-pituitary-adrenal response to a low-dose dexamethasone stimulation test is recommended.[126,127]

Increase in Size

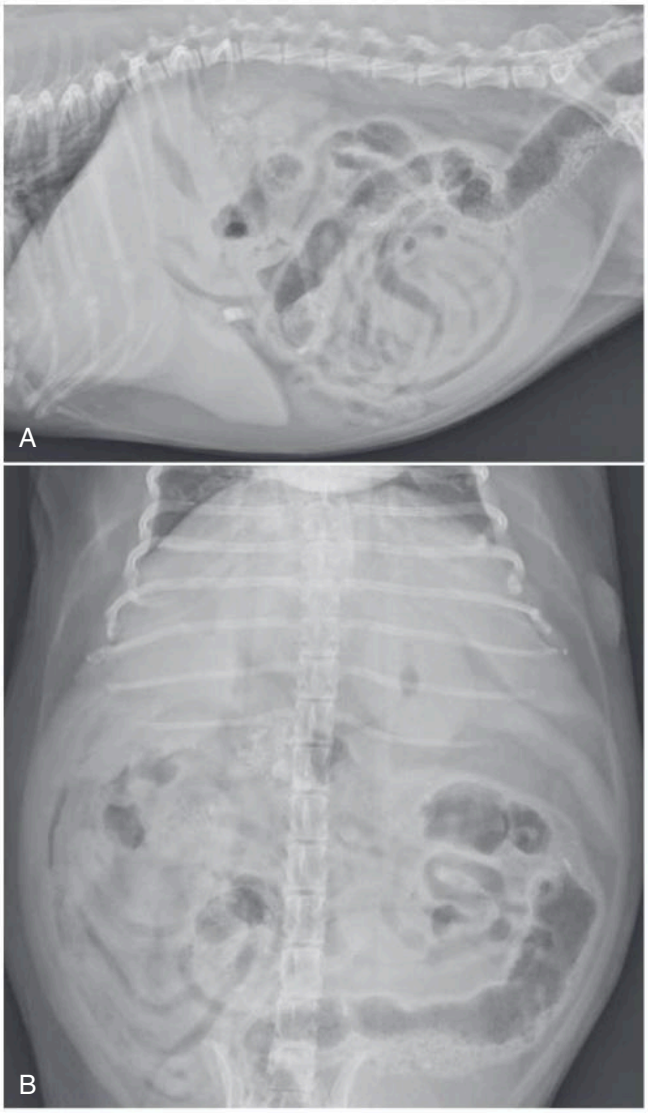
Radiography. Radiographically detectable adrenal gland enlargement may be caused by pheochromocytoma, cortical carcinoma, or adenoma.[128] An adrenal mass should be suspected when a soft tissue or partially mineralized mass is present craniomedial to a kidney (eFig. 39.10). The kidney may be displaced caudolaterally by the mass. Large left adrenal masses may displace the fundus of the stomach cranially, the transverse colon caudoventrally, and the left kidney caudally (eFig. 39.11). Masses of the right adrenal gland may be more difficult to detect radiographically than those of the left because of the position of the right adrenal gland near the liver. Functional adrenal carcinomas and adenomas occur with equal frequency in the right and left adrenal glands; adrenal tumors occasionally occur bilaterally.[109] Functional adrenocortical carcinomas or adenomas are found in 10% to 20% of dogs with Cushing syndrome.[129,130]

Dystrophic mineralization of adrenal tumors may occur (Fig. 39.36, see eFig. 39.10).[40,126,131,132] Radiographically visible adrenal calcification in dogs with Cushing syndrome is highly suggestive of neoplasia. In dogs with functional adrenal tumors, 92% and 54% of radiographically visible carcinomas and adenomas, respectively, were calcified.[109] In another study, adrenal calcification was found in 54% and 60% of carcinomas and adenomas, respectively. Carcinomas and pheochromocytomas may invade local tissues, including the caudal vena cava, and metastasize to the liver, lymph nodes, lungs, and kidneys.[130] When adrenal carcinomas are advanced, it may not be possible to determine the origin of the primary mass lesion radiographically. In such an instance, the metastases may be the major radiographic finding, although an ill-defined soft tissue mass may be present in the craniodorsal abdomen.

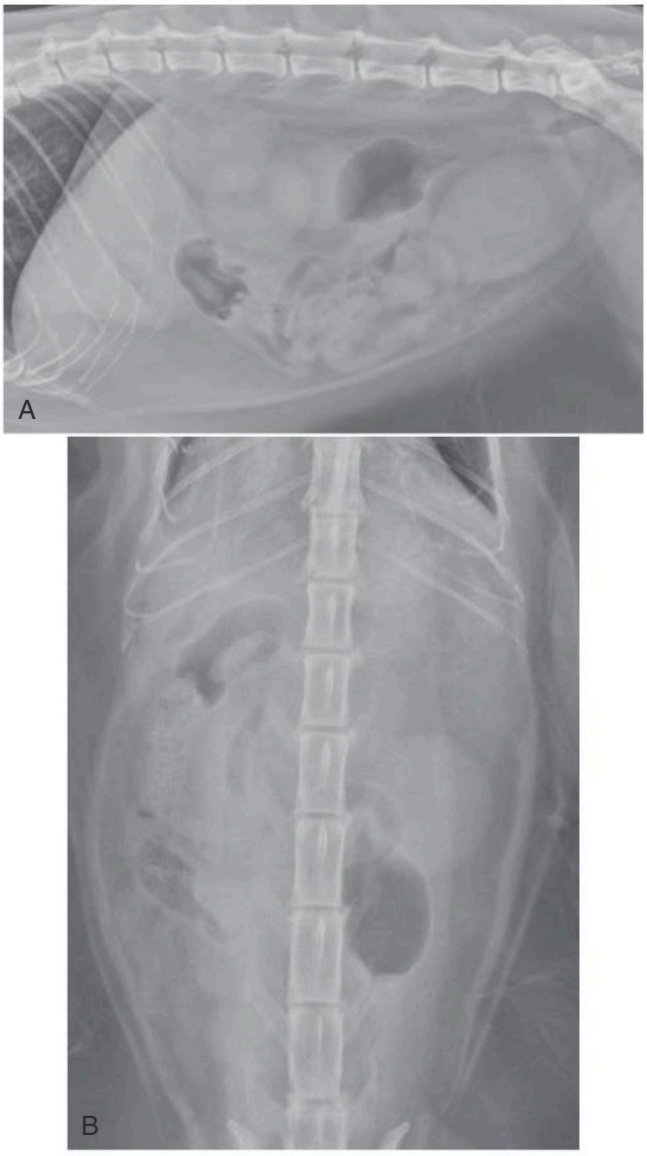
Mineralization may occur in nonneoplastic adrenal glands (Fig. 39.37), especially in cats.

Adrenal gland dysfunction usually causes radiographically detectable changes. In patients with Cushing syndrome, this includes hepatomegaly, bronchopulmonary mineralization, dystrophic mineralization of the skin and other soft tissues, and adrenal gland enlargement with mineralization when functional tumors are present. Pulmonary arterial thrombosis also occurs in dogs with Cushing syndrome, but this is difficult to detect radiographically.[133]

Ultrasound. The use of ultrasound is not recommended as a screening test for hyperadrenocorticism,[134] although ultrasound is useful in differentiating pituitary-dependent hyperadrenocorticism (PDH) and functional adrenocortical neoplasia.[114,135] In dogs with PDH, the adrenal glands have a plump appearance; they are bilaterally enlarged, uniformly hypoechoic, and normally shaped (Fig. 39.38).[104,112,136]



eFig. 39.10 Lateral **(A)** and ventrodorsal **(B)** radiographs of a dog with a mineralized adrenal carcinoma. An amorphous mineralization is seen in the craniodorsal abdomen at the cranial aspect of the kidneys in the lateral view **(A)**. The mineralization is seen to the right of midline at the level of T13-L1 in the ventrodorsal projection **(B)**. Hepatomegaly and a pendulous abdomen are consistent with signs of hyperadrenocorticism.



eFig. 39.11 Lateral **(A)** and ventrodorsal **(B)** radiographs of a cat with an aldosterone producing left adrenal carcinoma (aldosteronoma). Three rounded soft tissue opacities are visible in the cranial retroperitoneal space. The two more caudoventrally positioned structures are consistent with the renal silhouettes, evidenced by a faint fat opacity in the region of the renal pelvis. The more craniodorsally located structure is irregularly shaped. The structure is seen slightly to the left of midline at the level of L2. A left adrenal mass was confirmed with ultrasound.

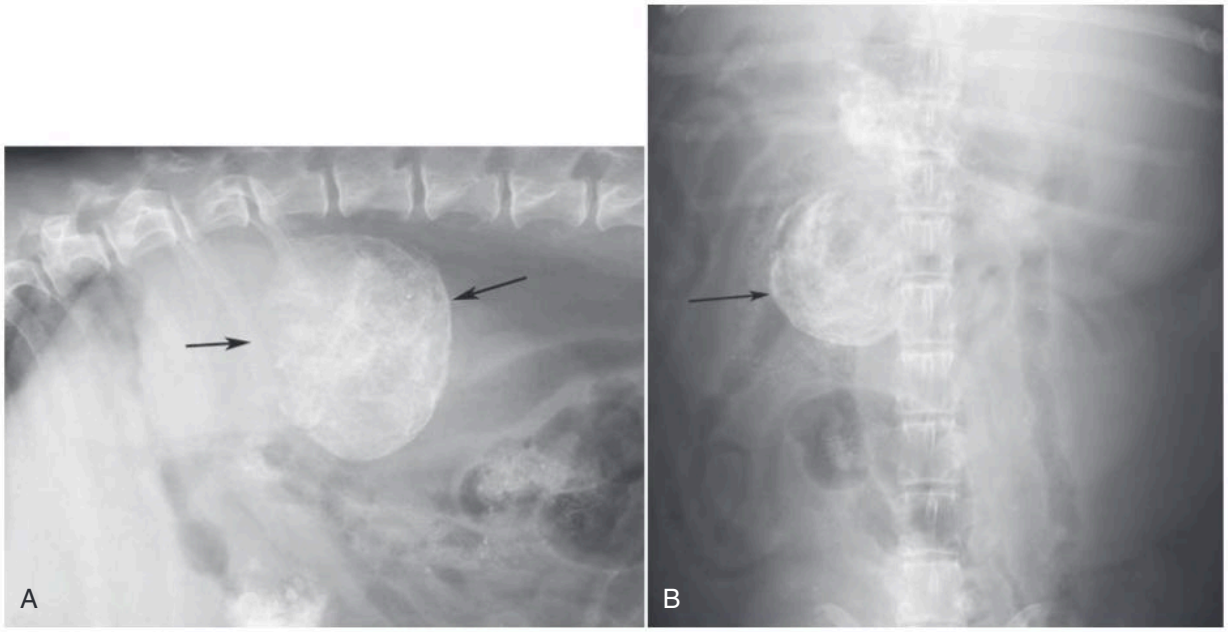


Fig. 39.36 Lateral **(A)** and ventrodorsal **(B)** radiographs of a 14-year-old dog. A large mineralized mass is present caudal to the stomach and just to the right of midline (*black arrows*). The mass is a malignant functional adrenocortical tumor causing hyperadrenocorticism. A small amount of mineralized ingesta is present within the pyloric region of the stomach.

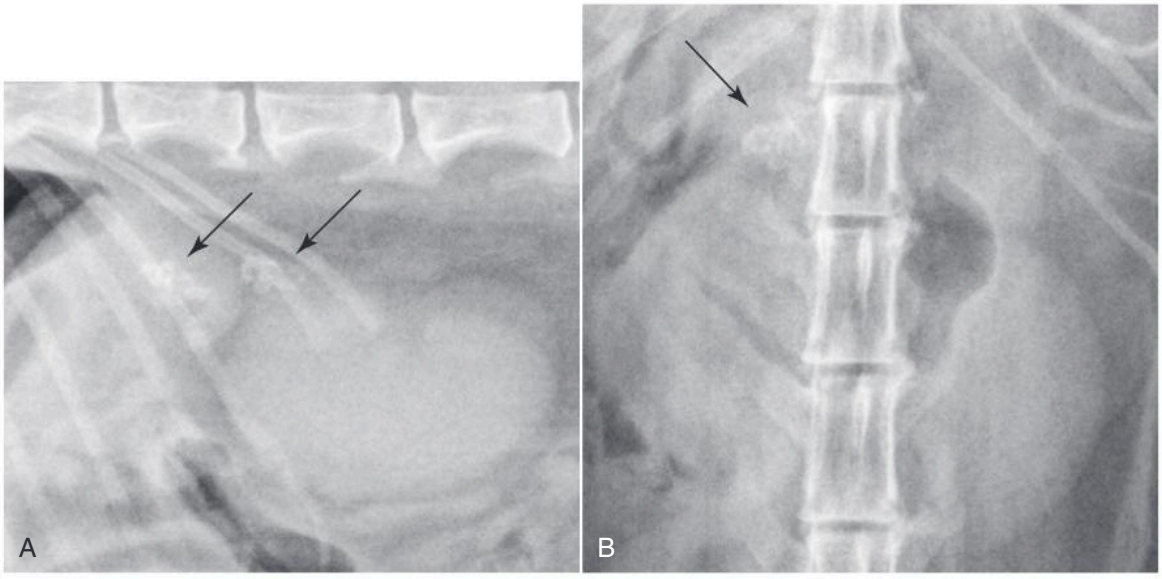


Fig. 39.37 Lateral **(A)** and ventrodorsal **(B)** radiographs of an 8-year-old domestic cat. The adrenal glands are mineralized (*black arrows*). The left adrenal gland is not visible in the ventrodorsal image because it is superimposed on the spine. This finding is clinically insignificant.

Normal adrenal gland size does not rule out PDH.[104] Adrenal gland tumors cause gland enlargement with loss of normal shape and a change in echotexture (Figs. 39.39–39.41). Adrenal tumors are most often unilateral but may occur bilaterally.[107,109] In dogs with functional adrenocortical tumors, there is some disagreement regarding atrophy of the contralateral gland, with some studies suggesting that atrophy occurs,[122] whereas others suggest that the contralateral adrenal gland is often of normal size.[107,109] One study in dogs suggests that in instances of asymmetric adrenal gland size, if the thickness of the smaller gland is less than 0.5 cm, it is most likely caused by adrenal-dependent hyperadrenocorticism (vs. PDH) with atrophy of the contralateral gland.[122]

Ultrasound is not useful in differentiating benign and malignant lesions (Box 39.4).[109] Mineralization may be seen in both benign and malignant neoplasms, as well as in adrenocortical hyperplasia.[108,109] In one report, pheochromocytomas and adenocarcinomas tended to be round masses, whereas adenomas, hyperplasia, and adrenal metastasis tended to appear as nodules.[109] Because PDH-induced nodular cortical hyperplasia may appear similar to small functional adrenocortical tumors, ultrasound is not useful in differentiating the two.[108]



Fig. 39.38 Longitudinal ultrasound image of the left adrenal gland *(cursors)* of a Dachshund with pituitary-dependent hyperadrenocorticism (PDH). The adrenal gland has a plump appearance but is normally shaped. The gland is enlarged, measuring 2.6 cm in length and 1.0 cm in thickness. The hypoechoic cortex can be differentiated from the more echogenic medulla. This layered appearance has been described in normal dogs and in dogs with hyperadrenocorticism. The *white arrow* points to the aorta.

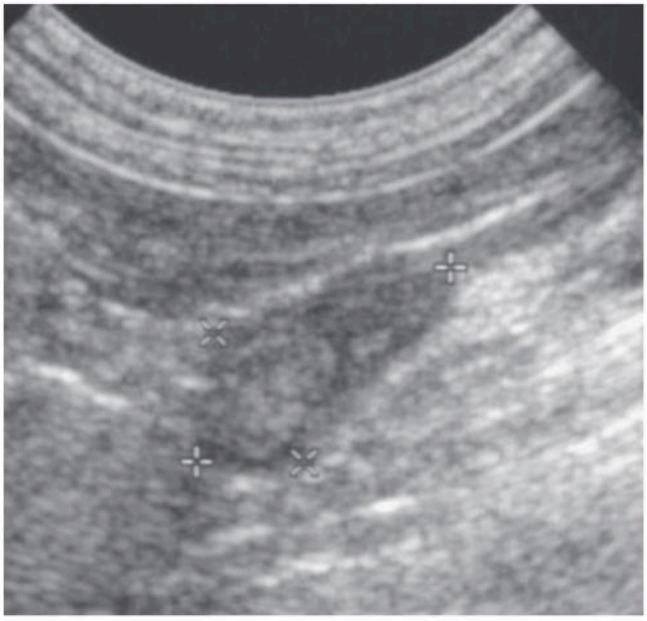


Fig. 39.39 Longitudinal ultrasound image of the left adrenal gland of a 12-year-old mixed-breed dog. A hyperechoic nodule is present in the cranial pole of the adrenal gland. The ultrasonographic appearance of this nodule is not specific and could be caused by neoplasia (varying types), granuloma, or nodular hyperplasia.

Screening for hyperadrenocorticism by imaging of the adrenal glands with CT or MRI is also not recommended, although these modalities are useful for imaging the pituitary gland.[134]

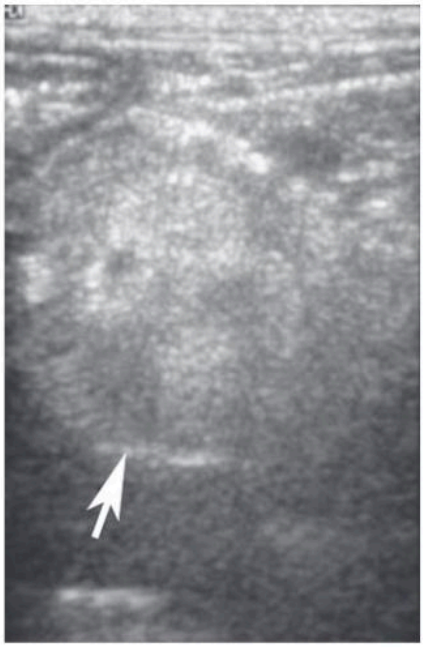


Fig. 39.40 Transverse ultrasound image of the right adrenal gland (*white arrow*) of a 13-year-old Shih Tzu with hyperadrenocorticism. The adrenal gland is enlarged, round, and of mixed echogenicity, containing hyperechoic nodules. Histopathologically, the adrenal gland contained myelolipomas and adenomas.



Fig. 39.41 Longitudinal ultrasound image of the left adrenal gland of the same dog as in Fig. 39.36. The adrenal gland is a large, curvilinear hyperechoic line (*black arrow*) with distal acoustic shadowing, consistent with the appearance of mineral. The diagnosis was adrenocortical tumor.

Ultrasound is helpful in evaluating extension of tumors into surrounding tissues, especially the caudal vena cava. An adrenal mass invading the caudal vena cava may extend as far cranially as the right atrium.[131,137] Adrenal gland lymphoma has been described to appear as hypoechoic adrenal glands in one cat and as a mass involving the adrenal glands and midline structures in another.[138] Adrenal gland tumors in cats can cause

Box • 39.4

Differential Diagnosis for Adrenal Masses

Adenoma
Nodular hyperplasia
Adrenocortical carcinoma
May be:
- Metabolically inactive
- Cortisol secreting
- Aldosterone secreting

Granuloma
Myelolipoma
Metastatic neoplasia
Pheochromocytoma

primary hyperaldosteronism.[132] Ultrasound-guided biopsy and fine-needle aspiration of the adrenal gland are not commonly performed in animals due to risk of potentially fatal catecholamine release in the presence of a pheochromocytoma, but they have been reported without complication in a small number of patients.[109,132,139,140] Adrenal gland tumors have also been reported to hemorrhage spontaneously, leading to retroperitoneal hemorrhage[141] or a sonographically complex adrenal mass (see Box 39.4).[109]

Treatment of patients with hyperadrenocorticism with mitotane or trilostane is common. Trilostane causes an increase in adrenal gland size,[142,143] with the maximum size seen at 6 weeks after initiation of therapy.[142] The differentiation of the layers within the adrenal glands is increased with the outer hypoechoic zone being increased in echogenicity and the inner hyperechoic zone being decreased in echogenicity. After 6 months to 1 year of treatment, the size of the adrenal glands is unchanged, but the shape may become irregular and the parenchyma inhomogeneous with an inability to discern the layers of the gland.[142,143] These changes may be caused by coagulative necrosis.[144] Mitotane causes adrenal gland heterogeneity, presumably from necrosis. Mitotane may also cause the adrenal glands to become smaller, in contrast to the effects of trilostane.[145]

Both adrenocorticotropic hormone and ultrasound have a sensitivity of 100% and a specificity of 95% in differentiating PDH from adrenal-dependent hyperadrenocorticism in dogs.[136] Although uncommonly reported, enlarged adrenal glands can be found in patients with oversecretion of sex hormones.[135]

Computed Tomography. The attenuation values of the adrenal glands in normal dogs and dogs with PDH are similar.[119] In human patients, precontrast hypoattenuating nodular lesions were more likely to be adenomas, but the difference in attenuation was less apparent in postcontrast images. Furthermore, CT may allow differentiation between the different tumor types in human patients but that has not been confirmed in animals. However, a peripheral rim enhancement in delayed postcontrast phase images correlated well with fibrous encapsulation of the tumor and a heterogeneous pattern of contrast enhancement of the adrenal gland was associated with adrenal hemorrhage or infarction.[146] Additionally, CT is an excellent modality to evaluate the extent of vascular invasion by an adrenal tumor.[146,147]

Decrease in Size

In six dogs with hypoadrenocorticism, the adrenal glands were measurably smaller than the adrenal glands of normal dogs using ultrasound.[108] It has also been suggested that an adrenal gland width of less than 0.32 cm is highly suggestive of hypoadrenocorticism.[114]

Acknowledgment

With special thanks to prior authors of this chapter for their contributions.

REFERENCES

1. Evans H, De Lahunta A. *Miller's Anatomy of the Dog*. ed 4. St Louis: Saunders; 2013.
2. Nickel R, Schummer A, Seiferle E. *The Viscera of the Domestic Mammals*. Berlin, Heidelberg: Springer; 1979.
3. O'Brien TR. *Radiographic diagnosis of abdominal disorders in the dog and cat. Radiographic Interpretation, Clinical Signs, Pathophysiology*. Philadelphia: WB Saunders; 1978.
4. Thrall DE, Roberston ID. *Normal Radiographic Anatomy and Anatomic Variants in the Dog and Cat*. ed 2. St Louis: Elsevier; 2016.
5. Johnston DE, Christie BA. The retroperitoneum in dogs: anatomy and clinical significance. *Compend Contin Educ Pract Vet USA*. 1990;1027.
6. Johnson PR, Greenwood MRC. The adipose tissue. In: Weiss L, ed. *Cell and Tissue Biology: A Textbook of Histology*. ed 6. Baltimore: Urban and Schwarzenberg; 1988.
7. Zwingenberger AL, Wisner ER. *Atlas of Small Animal CT and MRI*. Oxford, UK: Wiley Blackwell; 2015.
8. Veiga-Parga T, Hecht S, Craig L. Imaging diagnosis—sclerosing encapsulating peritonitis in a dog. *Vet Radiol Ultrasound*. 2015;56(6):E65–E69.
9. Luttwak EM, Fabian RP, Mordochovich D. Role of peritoneal absorption in ascites. *Surg Gynecol Obstet*. 1975;141(5):693–698.
10. McMurray J, Boysen S, Chalhoub S. Focused assessment with sonography in nontraumatized dogs and cats in the emergency and critical care setting. *J Vet Emerg Crit Care (San Antonio)*. 2016;26(1):64–73.
11. Monteiro CB, O'Brien RT. A retrospective study on the sonographic findings of abdominal carcinomatosis in 14 cats. *Vet Radiol Ultrasound*. 2004;45(6):559–564.
12. Root CR, Lord PF. Peritoneal carcinomatosis in the dog and cat: its radiographic appearance. *Vet Radiol Ultrasound*. 1971;12(1):54–59.
13. Aydin Y, Temizsoylu D, Toplu N, et al. Diffuse mesenteric lipodystrophy (massive fat necrosis) in a cat. *Aust Vet J*. 2002;80(6):346–348.
14. Komori S, Nakagaki K, Koyama H, et al. Idiopathic mesenteric and omental steatitis in a dog. *J Am Vet Med Assoc*. 2002;221(11):1591–1593, 1574.
15. Fabbrini F, Anfray P, Viacava P, et al. Feline cutaneous and visceral necrotizing panniculitis and steatitis associated with a pancreatic tumour. *Vet Dermatol*. 2005;16(6):413–419.
16. Zini E, Hauser B, Ossent P, et al. Pansteatitis and severe hypocalcaemia in a cat. *J Feline Med Surg*. 2007;9(2):168–171.
17. Caruso KJ, James MP, Fisher D, et al. Cytologic diagnosis of peritoneal cestodiasis in dogs caused by *Mesocestoides* sp. *Vet Clin Pathol*. 2003;32(2):50–60.
18. Smelstoys JA, Davis GJ, Learn AE, et al. Outcome of and prognostic indicators for dogs and cats with pneumoperitoneum and no history of penetrating trauma: 54 cases (1988–2002). *J Am Vet Med Assoc*. 2004;225:251–255.
19. Probst CW, Stickle RL, Bartlett PC. Duration of pneumoperitoneum in the dog. *Am J Vet Res*. 1986;47:176–178.
20. Guffy M. *A Radiological Study of Hydroperitoneum and Pneumoperitoneum in the Dog*. Fort Collins: Colorado State University; 1966.
21. Klibanov AL, Rasche PT, Hughes MS, et al. Detection of individual microbubbles of ultrasound contrast agents: imaging of free-floating and targeted bubbles. *Invest Radiol*. 2004;39:187–195.

22. Hefny AF, Abu-Zidan FM. Sonographic diagnosis of intraperitoneal free air. *J Emerg Trauma Shock*. 2011;4(4):511–513.
23. Choi H, Lee Y, Park K, et al. Sonographic detection of small amounts of free peritoneal gas in beagle dogs. *J Vet Med Sci*. 2012;74(4):491–494.
24. Boysen SR, Tidwell AS, Penninck DG. Ultrasonographic findings in dogs and cats with gastrointestinal perforation. *Vet Radiol Ultrasound*. 2003;44(5):556–564.
25. Fischetti AJ, Saunders HM, Drobatz KJ. Pneumatosis in canine gastric dilatation-volvulus syndrome. *Vet Radiol Ultrasound*. 2004;45(3):205–209.
26. Lamb CR, Kleine LJ, McMillan MC. Diagnosis of calcification on abdominal radiographs. *Vet Radiol*. 1991;32:211–220.
27. Schwarz T, Morandi F, Gnudi G, et al. Nodular fat necrosis in the feline and canine abdomen. *Vet Radiol Ultrasound*. 2000;41:335–339.
28. Lee E, Kim HW, Bae H, Yu D, Choi J. Radiography and CT features of atherosclerosis in two miniature schnauzer dogs. *J Vet Sci*. 2020;21(6):e89.
29. Haddad JL, Goldschmidt MH, Patel RT. Fibrosarcoma arising at the site of a retained surgical sponge in a cat. *Vet Clin Pathol*. 2010;39:241–246.
30. Tanabe S, Yamada K, Kobayashi Y, et al. Extra-abdominal chondrolipoma in a dog. *Vet Radiol Ultrasound*. 2005;46:306–308.
31. Higuchi T, Burcham GN, Childress MO, et al. Characterization and treatment of transitional cell carcinoma of the abdominal wall in dogs: 24 cases (1985–2010). *J Am Vet Med Assoc*. 2013;242:499–506.
32. Nickel R, Schummer A, Seiferle E. *Lehrbuch der Anatomie der Haustiere*. ed 2. Berlin: Parey; 1984.
33. Penninck D, D'Anjou MA. *Small Animal Ultrasonography*. Oxford: Wiley; 2015.
34. Mayer MN, Lawson JA, Silver TI. Sonographic characteristics of presumptively normal canine medial iliac and superficial inguinal lymph nodes. *Vet Radiol Ultrasound*. 2010;51(6):638–641.
35. Llabres-Diaz FJ. Ultrasonography of the medial iliac lymph nodes in the dog. *Vet Radiol Ultrasound*. 2004;45:156–165.
36. Beukers M, Grosso FV, Voorhout G. Computed tomographic characteristics of presumed normal canine abdominal lymph nodes. *Vet Radiol Ultrasound*. 2013;54:610–617.
37. Anderson CL, MacKay CS, Roberts GD, et al. Comparison of abdominal ultrasound and magnetic resonance imaging for detection of abdominal lymphadenopathy in dogs with metastatic apocrine gland adenocarcinoma of the anal sac. *Vet Comp Oncol*. 2015;13:98–105.
38. Nyman HT, Kristensen AT, Flagstad A, et al. A review of the sonographic assessment of tumor metastases in liver and superficial lymph nodes. *Vet Radiol Ultrasound*. 2004;45:438–448.
39. Prieto S, Gomez-Ochoa P, De Blas I, et al. Pathologic correlation of resistive and pulsatility indices in canine abdominal lymph nodes. *Vet Radiol Ultrasound*. 2009;50:525–529.
40. Kinns J, Mai W. Association between malignancy and sonographic heterogeneity in canine and feline abdominal lymph nodes. *Vet Radiol Ultrasound*. 2007;48:565–569.
41. Palladino S, Keyerleber MA, King RG, et al. Utility of computed tomography versus abdominal ultrasound examination to identify iliosacral lymphadenomegaly in dogs with apocrine gland adenocarcinoma of the anal sac. *J Vet Intern Med*. 2016;30(6):1858–1863.
42. Probst A, Kneissl S. Computed tomographic anatomy of the canine pancreas. *Vet Radiol Ultrasound*. 2001;42:226–230.
43. Morita Y, Takiguchi M, Yasuda J, et al. Endoscopic ultrasonography of the pancreas in the dog. *Vet Radiol Ultrasound*. 1998;39:552–556.
44. Garcia DA, Froes TR. Importance of fasting in preparing dogs for abdominal ultrasound examination of specific organs. *J Small Anim Pract*. 2014;55:630–634.
45. Etue SM, Penninck DG, Labato MA, et al. Ultrasonography of the normal feline pancreas and associated anatomic landmarks: a prospective study of 20 cats. *Vet Radiol Ultrasound*. 2001;42:330–336.
46. Seiler GS, Cohen EB, D'Anjou MA, et al. ACVR and ECVDI consensus statement for the standardization of the abdominal ultrasound examination. *Vet Radiol Ultrasound*. 2022;63(6):661–674.
47. Granger LA, Hilferty M, Francis T, et al. Variability in the ultrasonographic appearance of the pancreas in healthy dogs compared to dogs with hyperadrenocorticism. *Vet Radiol Ultrasound*. 2015;56(5):540–548.
48. Larson MM, Panciera DL, Ward DL, et al. Age-related changes in the ultrasound appearance of the normal feline pancreas. *Vet Radiol Ultrasound*. 2005;46(3):238–242.
49. Hecht S, Penninck DG, Mahony OM, et al. Relationship of pancreatic duct dilation to age and clinical findings in cats. *Vet Radiol Ultrasound*. 2006;47(3):287–294.
50. Wickramasekara Rajapakshage BK, Ellearaewe Garuhamilage JP, De Silva DD, et al. Dimensional ultrasonographic relationship of the right lobe of pancreas with associated anatomic landmarks in clinically normal dogs. *J Vet Med Sci*. 2016;78(1):1–5.
51. Brinkman-Ferguson EL, Biller DS. Ultrasound of the right lateral intercostal space. *Vet Clin North Am Small Anim Pract*. 2009;39:761–781.
52. Penninck DG, Zeyen U, Taeymans ON, et al. Ultrasonographic measurement of the pancreas and pancreatic duct in clinically normal dogs. *Am J Vet Res*. 2013;74:433–437.
53. Lim SY, Nakamura K, Morishita K, et al. Qualitative and quantitative contrast enhanced ultrasonography of the pancreas using bolus injection and continuous infusion methods in normal dogs. *J Vet Med Sci*. 2013;75(12):1601–1607.
54. Rademacher N, Ohlerth S, Scharf G, et al. Contrast-enhanced power and color Doppler ultrasonography of the pancreas in healthy and diseased cats. *J Vet Intern Med*. 2008;22:1310–1316.
55. Rademacher N, Schur D, Gaschen F, et al. Contrast-enhanced ultrasonography of the pancreas in healthy dogs and in dogs with acute pancreatitis. *Vet Radiol Ultrasound*. 2016;57:58–64.
56. Kook PH, Baloi P, Ruetten M, et al. Feasibility and safety of endoscopic ultrasound-guided fine needle aspiration of the pancreas in dogs. *J Vet Intern Med*. 2012;26:513–517.
57. Cordner AP, Sharkey LC, Armstrong PJ, et al. Cytologic findings and diagnostic yield in 92 dogs undergoing fine-needle aspiration of the pancreas. *J Vet Diagn Invest*. 2015;27(2):236–240.
58. Choi SY, Choi HJ, Lee KJ, et al. Establishment of optimal scan delay for multi-phase computed tomography using bolus-tracking technique in canine pancreas. *J Vet Med Sci*. 2015;77:1049–1054.
59. Caceres AV, Zwingenberger AL, Hardam E, et al. Helical computed tomographic angiography of the normal canine pancreas. *Vet Radiol Ultrasound*. 2006;47:270–278.
60. Marolf AJ, Kraft SL, Dunphy TR, et al. Magnetic resonance (MR) imaging and MR cholangiopancreatography findings in cats with cholangitis and pancreatitis. *J Feline Med Surg*. 2013;15:285–294.

61. Marolf AJ, Stewart JA, Dunphy TR, et al. Hepatic and pancreaticobiliary MRI and MR cholangiopancreatography with and without secretin stimulation in normal cats. *Vet Radiol Ultrasound*. 2011;52:415–421.
62. Lester NV, Newell SM, Hill RC, et al. Scintigraphic diagnosis of insulinoma in a dog. *Vet Radiol Ultrasound*. 1999;40:174–178.
63. Steiner JM, Williams DA. Feline exocrine pancreatic disorders, Vet Clin North Am small. *Anim Pract*. 1999;29:551–575.
64. Williams JM, Panciera DL, Larson MM, et al. Ultrasonographic findings of the pancreas in cats with elevated serum pancreatic lipase immunoreactivity. *J Vet Intern Med*. 2013;27:913–918.
65. Gibbs C, Denny HR, Minter HM, et al. Radiological features of inflammatory conditions of the canine pancreas. *J Small Anim Pract*. 1972;13:531–544.
66. Kleine LJ, Hornbuckle WE. Acute pancreatitis: the radiographic findings in 182 dogs. *Vet Radiol*. 1978;19: 102–106.
67. Mattoon JS, Nyland TG. *Small Animal Diagnostic Ultrasound*. ed 3. St Louis: Elsevier; 2015.
68. Hecht S, Henry G. Sonographic evaluation of the normal and abnormal pancreas. *Clin Tech Small Anim Pract*. 2007;22(3):115–121.
69. Wall M, Biller DS, Schoning P, et al. Pancreatitis in a cat demonstrating pancreatic duct dilatation ultrasonographically. *J Am Anim Hosp Assoc*. 2001;37(1):49–53.
70. Bennett PF, Hahn KA, Toal RL, et al. Ultrasonographic and cytopathological diagnosis of exocrine pancreatic carcinoma in the dog and cat. *J Am Anim Hosp Assoc*. 2001;37:466–473.
71. Saunders HM, VanWinkle TJ, Drobatz K, et al. Ultrasonographic findings in cats with clinical, gross pathologic, and histologic evidence of acute pancreatic necrosis: 20 cases (1994–2001). *J Am Vet Med Assoc*. 2002;221:1724–1730.
72. Ruaux CG. Diagnostic approaches to acute pancreatitis. *Clin Tech Small Anim Pract*. 2003;18:245–249.
73. Ferreri JA, Hardam E, Kimmel SE, et al. Clinical differentiation of acute necrotizing from chronic nonsuppurative pancreatitis in cats: 63 cases (1996–2001). *J Am Vet Med Assoc*. 2003;223:469–474.
74. Watson PJ, Archer J, Roulois AJ, et al. Observational study of 14 cases of chronic pancreatitis in dogs. *Vet Rec*. 2010;167(25):968–976.
75. VanEnkevort BA, O'Brien RT, Young KM. Pancreatic pseudocysts in 4 dogs and 2 cats: ultrasonographic and clinicopathologic findings. *J Vet Intern Med*. 1999;13: 309–313.
76. Marchevsky AM, Yovich JC, Wyatt KM. Pancreatic pseudocyst causing extrahepatic biliary obstruction in a dog. *Aust Vet J*. 2000;78(2):99–101.
77. Rutgers C, Herring DS, Orton C. Pancreatic pseudocyst associated with acute pancreatitis in a dog: ultrasonographic diagnosis. *J Am Anim Hosp Assoc*. 1985;21: 411–416.
78. Coleman MG, Robson MC, Harvey C. Pancreatic cyst in a cat, N Z. *Vet J*. 2005;53(2):157–159.
79. Branter EM, Viviano KR. Multiple recurrent pancreatic cysts with associated pancreatic inflammation and atrophy in a cat. *J Feline Med Surg*. 2010;12(10):822–827.
80. Bailiff NL, Norris CR, Seguin B, et al. Pancreatolithiasis and pancreatic pseudobladder associated with pancreatitis in a cat. *J Am Anim Hosp Assoc*. 2004;40:69–74.
81. Gerhardt A, Steiner JM, Williams DA, et al. Comparison of the sensitivity of different diagnostic tests for pancreatitis in cats. *J Vet Intern Med*. 2001;15:329–333.
82. Forman MA, Marks SL, De Cock HE, et al. Evaluation of serum feline pancreatic lipase immunoreactivity and helical computed tomography versus conventional testing for the diagnosis of feline pancreatitis. *J Vet Intern Med*. 2004;18(6):807–815.
83. Adrian AM, Twedt DC, Kraft SL, et al. Computed tomographic angiography under sedation in the diagnosis of suspected canine pancreatitis: a pilot study. *J Vet Intern Med*. 2015;29:97–103.
84. Jaeger JQ, Mattoon JS, Bateman SW, et al. Combined use of ultrasonography and contrast enhanced computed tomography to evaluate acute necrotizing pancreatitis in two dogs. *Vet Radiol Ultrasound*. 2003;44:72–79.
85. Spillmann T, Litzlbauer H, Moritz A, et al. Computed tomography and laparoscopy for the diagnosis of pancreatic diseases in dogs. In: *Proceedings of the American College of Veterinary Internal Medicine*. 2000:485–487.
86. Lamb CR, Simpson KW, Boswood A, et al. Ultrasonography of pancreatic neoplasia in the dog: a retrospective review of 16 cases. *Vet Rec*. 1995;137(3):65–68.
87. Jubb KVF, Kennedy PC, Palmer N. The pancreas. In: *Pathology of Domestic Animals*. ed 4. St Louis: Elsevier; 1985:313–327.
88. Robben JH, Pollak YWEA, Kirpensteijn J, et al. Comparison of ultrasonography, computed tomography, and single-photon emission computed tomography for the detection and localization of canine insulinoma. *J Vet Intern Med*. 2005;19(15).
89. Goutal CM, Brugmann BL, Ryan KA. Insulinoma in dogs: a review. *J Am Anim Hosp Assoc*. 2012;48:151–163.
90. Hecht S, Penninck DG, Keating JH. Imaging findings in pancreatic neoplasia and nodular hyperplasia in 19 cats. *Vet Radiol Ultrasound*. 2007;48:45–50.
91. Ramírez GA, Altimira J, García-González B, et al. Intrapancreatic ectopic splenic tissue in dogs and cats. *J Comp Pathol*. 2013;148(4):361–364.
92. Feldman EC, Nelson RW, Reusch C, et al. *Canine and Feline Endocrinology*. ed 4. St Louis: Elsevier; 2015.
93. Vanderperren K, Haers H, Van der Vekens E, et al. Description of the use of contrast-enhanced ultrasonography in four dogs with pancreatic tumours. *J Small Anim Pract*. 2014;55(3):164–169.
94. Head LL, Daniel GB, Becker TJ, et al. Use of computed tomography and radiolabeled leukocytes in a cat with pancreatitis. *Vet Radiol Ultrasound*. 2005;46:263–266.
95. Iseri T, Yamada K, Chijiwa K, et al. Dynamic computed tomography of the pancreas in normal dogs and in a dog with pancreatic insulinoma. *Vet Radiol Ultrasound*. 2007;48:328–331.
96. Lamb CR, McEvoy FJ. Comparison of ultrasonographic findings in canine pancreatitis and pancreatic neoplasia [abstract]. *Vet Radiol Ultrasound*. 1995;36.
97. Cordner AP, Armstrong PJ, Newman SJ, et al. Effect of pancreatic tissue sampling on serum pancreatic enzyme levels in clinically healthy dogs. *J Vet Diagn Invest*. 2010;22(5):702–707.
98. Newman S, Steiner J, Woosley K, et al. Localization of pancreatic inflammation and necrosis in dogs. *J Vet Intern Med*. 2004;18(4):488–493.
99. Hines BL, Salisbury SK, Jakovljevic S, et al. Pancreatic pseudocyst associated with chronic-active necrotizing pancreatitis in a cat. *J Am Anim Hosp Assoc*. 1996;32(2): 147–152.
100. VanEnkevort BA, O'Brien RT, Young KM. Pancreatic pseudocysts in 4 dogs and 2 cats: ultrasonographic and clinicopathologic findings. *J Vet Intern Med*. 1999;13: 309–313.

101. Healy DM, Cassidy JP, Martin SA. A true congenital pancreatic cyst in a dog. *BMC Vet Res*. 2022;18:304.
102. Voorhout G, Stolp R, Rijnberk A, et al. Assessment of survey radiography and comparison with x-ray computed tomography for detection of hyperfunctioning adrenocortical tumors in dogs. *J Am Vet Med Assoc*. 1990;196: 1799–1803.
103. Herbach N, Wiele K, Konietschke U, et al. Pathologic alterations of canine and feline adrenal glands. *Open J Pathol*. 2016;6:140–153.
104. Soulsby SN, Holland M, Hudson JA, et al. Ultrasonographic evaluation of adrenal gland size compared to body weight in normal dogs. *Vet Radiol Ultrasound*. 2015;56: 317–326.
105. Zimmer C, Hörauf A, Reusch C. Ultrasonographic examination of the adrenal gland and evaluation of the hypophyseal-adrenal axis in 20 cats. *J Small Anim Pract*. 2000;41:156–160.
106. Besso JG, Penninck DG, Gliatto JM. Retrospective ultrasonographic evaluation of adrenal lesions in 26 dogs. *Vet Radiol Ultrasound*. 1997;38:448–455.
107. Tidwell AS, Penninck DG, Besso JG. Imaging of adrenal gland disorders. *Vet Clin North Am Small Anim Pract*. 1997;27:237–254.
108. Hoerauf A, Reusch C. Ultrasonographic evaluation of the adrenal glands in six dogs with hypoadrenocorticism. *J Am Anim Hosp Assoc*. 1999;35:214–218.
109. Hoerauf A, Reusch C. Ultrasonographic characteristics of both adrenal glands in 15 dogs with functional adrenocortical tumors. *J Am Anim Hosp Assoc*. 1999;35:193–199.
110. Nyland TG, Mattoon JS, Herrgesell EJ, et al. Adrenal glands. In: Nyland TG, Mattoon JS, eds. *Small Animal Diagnostic Ultrasound*. St Louis: Elsevier; 2002:196.
111. de Chalus T, Combes A, Bedu AS, et al. Ultrasonographic adrenal gland measurements in healthy Yorkshire terriers and Labrador retrievers. *Anat Histol Embryol*. 2013;42: 57–64.
112. Barthez PY, Nyland TG, Feldman EC. Ultrasonographic evaluation of the adrenal glands in dogs. *J Am Vet Med Assoc*. 1995;207:1180–1183.
113. Mogicato G, Layssol-Lamour C, Conchou F, et al. Ultrasonographic evaluation of the adrenal glands in healthy dogs: repeatability, reproducibility, observer-dependent variability, and the effect of bodyweight, age and sex. *Vet Rec*. 2011;168(5):130.
114. Wenger M, Mueller C, Kook PH, et al. Ultrasonographic evaluation of adrenal glands in dogs with primary hypoadrenocorticism or mimicking diseases. *Vet Rec*. 2010;167:207–210.
115. Choi J, Kim H, Yoon J. Ultrasonographic adrenal gland measurements in clinically normal small breed dogs and comparison with pituitary-dependent hyperadrenocorticism. *J Vet Med Sci*. 2011;73:985–989.
116. Barberet V, Pey P, Duchateau L, et al. Intra- and interobserver variability of ultrasonographic measurements of the adrenal glands in healthy Beagles. *Vet Radiol Ultrasound*. 2010;51:656–660.
117. Blaser A, Dennler M, Mosing M, et al. Effects of contrast medium injection technique on attenuation values of adrenal glands in healthy dogs during contrast-enhanced computed tomography. *Am J Vet Res*. 2016;77:144–150.
118. Bertolini G, Furlanello T, De Lorenzi D, et al. Computed tomographic quantification of canine adrenal gland volume and attenuation. *Vet Radiol Ultrasound*. 2006;47: 444–448.
119. Morandi F. Adrenal glands. In: Schwarz T, Saunders J, eds. *Veterinary Computed Tomography*. Ames, IA: Wiley-Blackwell; 2011:351–355.
120. Llabres-Diaz FJ, Dennis R. Magnetic resonance imaging of the presumed normal canine adrenal glands. *Vet Radiol Ultrasound*. 2003;44:5–19.
121. Morandi F, Mays JL, Newman SJ, et al. Imaging diagnosis—bilateral adrenal adenomas and myelolipomas in a dog. *Vet Radiol Ultrasound*. 2007;48(3):246–249.
122. Tursi M, Iussich S, Prunotto M, et al. Adrenal myelolipoma in a dog. *Vet Pathol*. 2005;42(2):232–235.
123. Lee HC, Jung DI, Moon JH, et al. Clinical characteristics and outcomes of primary adrenal hemangioma in a dog. *Res Vet Sci*. 2013;95(2):572–575.
124. Barthez PY, Marks SL, Woo J, et al. Pheochromocytoma in dogs: 61 cases (1984–1995). *J Vet Intern Med*. 1997;11: 272–278.
125. Barrera JS, Bernard F, Ehrhart EJ, et al. Evaluation of risk factors for outcome associated with adrenal gland tumors with or without invasion of the caudal vena cava and treated via adrenalectomy in dogs: 86 cases (1993–2009). *J Am Vet Med Assoc*. 2013;242(12):1715–1721.
126. Myers NC. Adrenal incidentalomas. Diagnostic workup of the incidentally discovered adrenal mass. *Vet Clin North Am Small Anim Pract*. 1997;27(2):381–399.
127. Baum JI, Boston SE, Case JB. Prevalence of adrenal gland masses as incidental findings during abdominal computed tomography in dogs: 270 cases (2013–2014). *J Am Vet Med Assoc*. 2016;249:1165–1169.
128. Schaer M. Pheochromocytoma in a dog: a case report. *J Am Anim Hosp Assoc*. 1980;79:583.
129. Owens JM, Drucker WD. Hyperadrenocorticism in the dog: canine Cushing's syndrome. *Vet Clin North Am*. 1977;7(3):583–602.
130. Labelle P, Kyles AE, Farver TB, et al. Indicators of malignancy of canine adrenocortical tumors: histopathology and proliferation index. *Vet Pathol*. 2004;41:490–497.
131. Pradelli D, Quintavalla C, Domenech O, et al. Tumour thrombus: direct endoluminal 'caudal caval vein-right atrium' extension in a dog affected by adrenal neoplasia. *Vet Res Commun*. 2003;27(Suppl 1):787–789.
132. Moore LE, Biller DS, Smith TA. Use of abdominal ultrasonography in the diagnosis of primary hyperaldosteronism in a cat. *J Am Vet Med Assoc*. 2000;217:213–215.
133. Burns MG, Kelly AB, Hornof WJ, et al. Pulmonary artery thrombosis in three dogs with hyperadrenocorticism. *J Am Vet Med Assoc*. 1981;178:388–393.
134. Behrend EN, Kemppainen RJ. Diagnosis of canine hyperadrenocorticism. *Vet Clin North Am Small Anim Pract*. 2001;31:985–1003.
135. Boag AK, Neiger R, Church DB. Trilostane treatment of bilateral adrenal enlargement and excessive sex steroid hormone production in a cat. *J Small Anim Pract*. 2004;45:263–266.
136. Gould SM, Baines EA, Mannion PA, et al. Use of endogenous ACTH concentration and adrenal ultrasonography to distinguish the cause of canine hyperadrenocorticism. *J Small Anim Pract*. 2001;42(3):113–121.
137. Benchekroun G, de Fornel-Thibaud P, Rodriguez Pineiro MI, et al. Ultrasonography criteria for differentiating ACTH dependency from ACTH independency in 47 dogs with hyperadrenocorticism and equivocal adrenal asymmetry. *J Vet Intern Med*. 2010;24:1077–1085.
138. Parnell NK, Powell LL, Hohenhaus AE, et al. Hypoadrenocorticism as the primary manifestation of lymphoma in two cats. *J Am Vet Med Assoc*. 1999;214(8):1208–1211.
139. Rosenstein DS. Diagnostic imaging in canine pheochromocytoma. *Vet Radiol Ultrasound*. 2000;41:499–506.
140. Chun R, Jakovljevic S, Morrison WB, et al. Apocrine gland adenocarcinoma and pheochromocytoma in a cat. *J Am Anim Hosp Assoc*. 1997;33:33–36.

141. Whittemore JC, Preston CA, Kyles AE, et al. Nontraumatic rupture of an adrenal gland tumor causing intra-abdominal or retroperitoneal hemorrhage in four dogs. *J Am Vet Med Assoc*. 2001;219:329–333.
142. Ruckstuhl NS, Nett CS, Reusch CE. Results of clinical examinations, laboratory tests, and ultrasonography in dogs with pituitary-dependent hyperadrenocorticism treated with trilostane. *Am J Vet Res*. 2002;63:506–512.
143. Mantis P, Lamb CR, Witt AL, et al. Changes in ultrasonographic appearance of adrenal glands in dogs with pituitary-dependent hyperadrenocorticism treated with trilostane. *Vet Radiol Ultrasound*. 2003;44:682–685.
144. Chapman PS, Kelly DF, Archer J, et al. Adrenal necrosis in a dog receiving trilostane for the treatment of hyperadrenocorticism. *J Small Anim Pract*. 2004;45:307–310.
145. Horauf A, Reusch C. [Effects of mitotane therapy in dogs with pituitary dependent Cushing syndrome on the adrenal gland size—an ultrasonographic study]. *Schweiz Arch Tierheilkd*. 1999;141:239–245.
146. Gregori T, Mantis P, Benigni L, et al. Comparison of computed tomographic and pathologic findings in 17 dogs with primary adrenal neoplasia. *Vet Radiol Ultrasound*. 2015;56:153–159.
147. Schultz RM, Wisner ER, Johnson EG, et al. Contrast-enhanced computed tomography as a preoperative indicator of vascular invasion from adrenal masses in dogs. *Vet Radiol Ultrasound*. 2009;50:625–629.

ELECTRONIC RESOURCES

Additional information related to the content in Chapter 39 can be found online at eBooks.Health.Elsevier.com

Chapter Quiz

CHAPTER 40

Liver and Spleen

Martha Moon Larson

RADIOLOGY OF THE LIVER

The liver is the largest solid organ in the abdomen. Changes in hepatic size, shape, location, and opacity are used to assess the liver for possible abnormality.[1–5]

The liver is in the cranial aspect of the abdomen between the diaphragm, which delineates its cranial border, and the stomach, right kidney, and cranial portion of the duodenum, which define the caudal extent. The liver is nearly entirely within the costal arch, with the caudal ventral border, composed of the left lateral liver lobe in the dog, extending just slightly beyond the costal arch. In dogs with a deep thoracic cavity, the liver lies more completely within the costal arch, whereas greater caudal hepatic extension is present in dogs with shallow, wide thoracic conformation. Abundant falciform fat, especially in cats, can result in dorsal displacement of the ventral aspect of the liver on lateral views (Fig. 40.1). On ventrodorsal (VD) views, the liver is distributed symmetrically in dogs, but a larger portion is often right sided in cats (Fig. 40.2).

Hepatic shape may not be visible without sufficient surrounding omental and falciform fat. The caudoventral hepatic margin protruding slightly from the costal arch should be relatively sharply marginated and triangular. It may protrude farther caudally in right lateral recumbent views, where it may merge with the spleen, blurring exact definition. If lateral views are slightly oblique, the liver can appear to have round margins, which should not be confused with hepatic enlargement.

The gallbladder is located just to the right of midline, in the cranioventral portion of the liver, but is not visible normally because of silhouetting with the soft tissue of the liver (Fig. 40.3). In some cats, the gallbladder can be seen on lateral abdominal radiographs as a curved structure protruding from the ventral liver margin (see Fig. 40.3C).

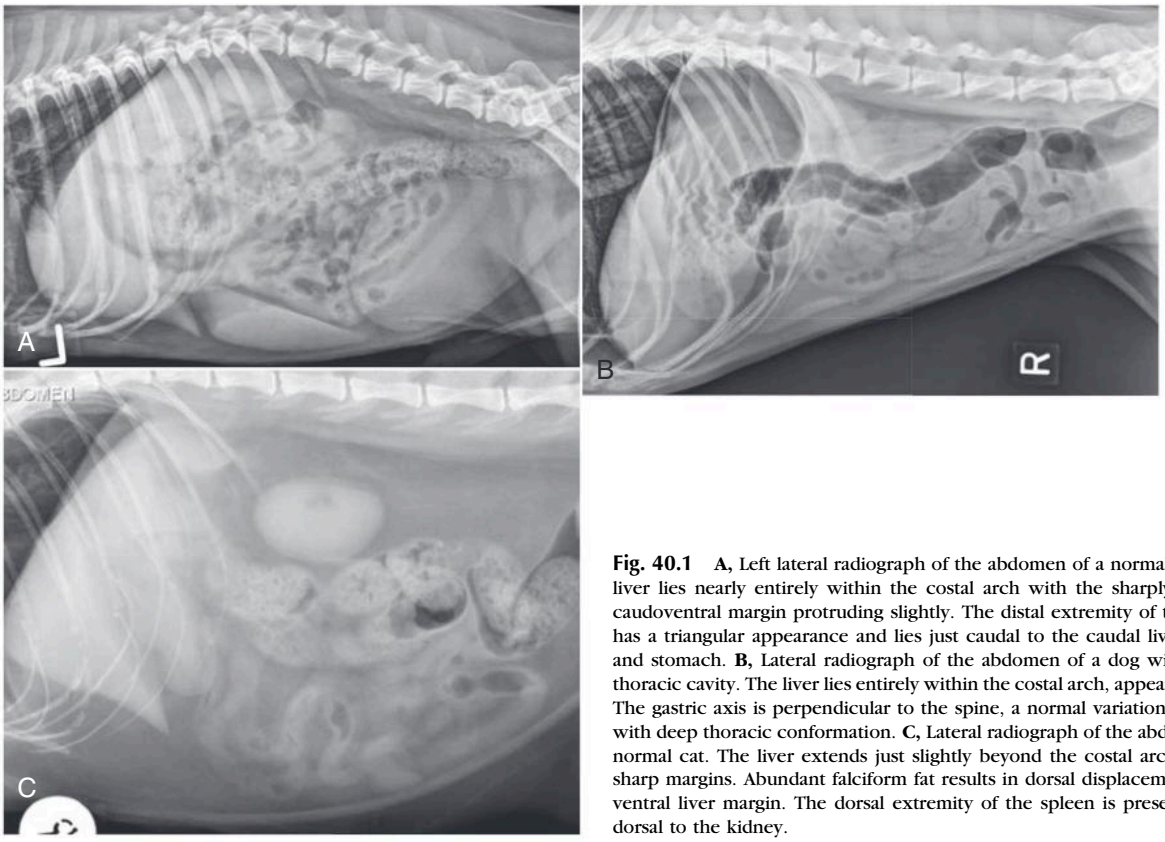


Fig. 40.1 **A,** Left lateral radiograph of the abdomen of a normal dog. The liver lies nearly entirely within the costal arch with the sharply outlined caudoventral margin protruding slightly. The distal extremity of the spleen has a triangular appearance and lies just caudal to the caudal liver margin and stomach. **B,** Lateral radiograph of the abdomen of a dog with a deep thoracic cavity. The liver lies entirely within the costal arch, appearing small. The gastric axis is perpendicular to the spine, a normal variation for a dog with deep thoracic conformation. **C,** Lateral radiograph of the abdomen of a normal cat. The liver extends just slightly beyond the costal arch and has sharp margins. Abundant falciform fat results in dorsal displacement of the ventral liver margin. The dorsal extremity of the spleen is present craniodorsal to the kidney.

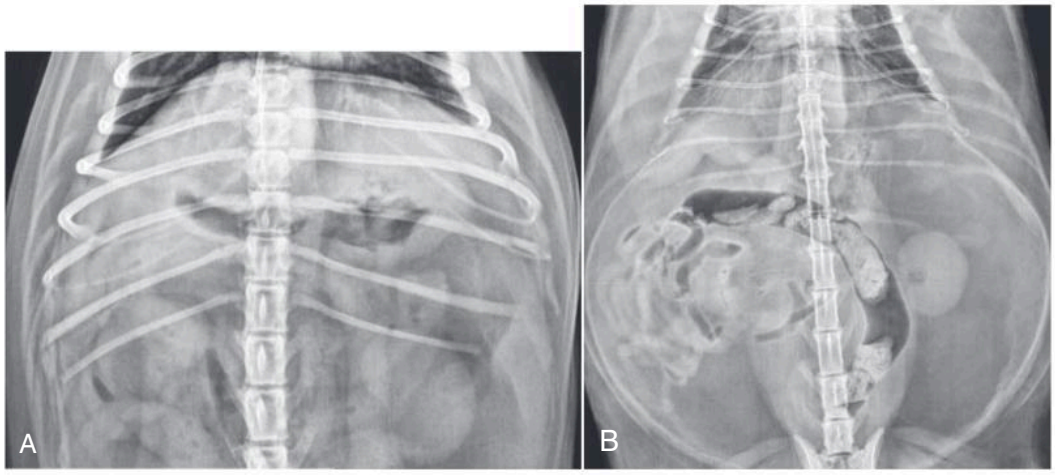


Fig. 40.2 **A,** Ventrodorsal (VD) radiograph of the cranial aspect of the abdomen of a normal dog. The liver lies cranial to and silhouettes the gastric shadow. **B,** VD radiograph of the abdomen of a normal cat. The liver is more to the right side than in a dog and is better visualized in this cat because of surrounding abundant fat.

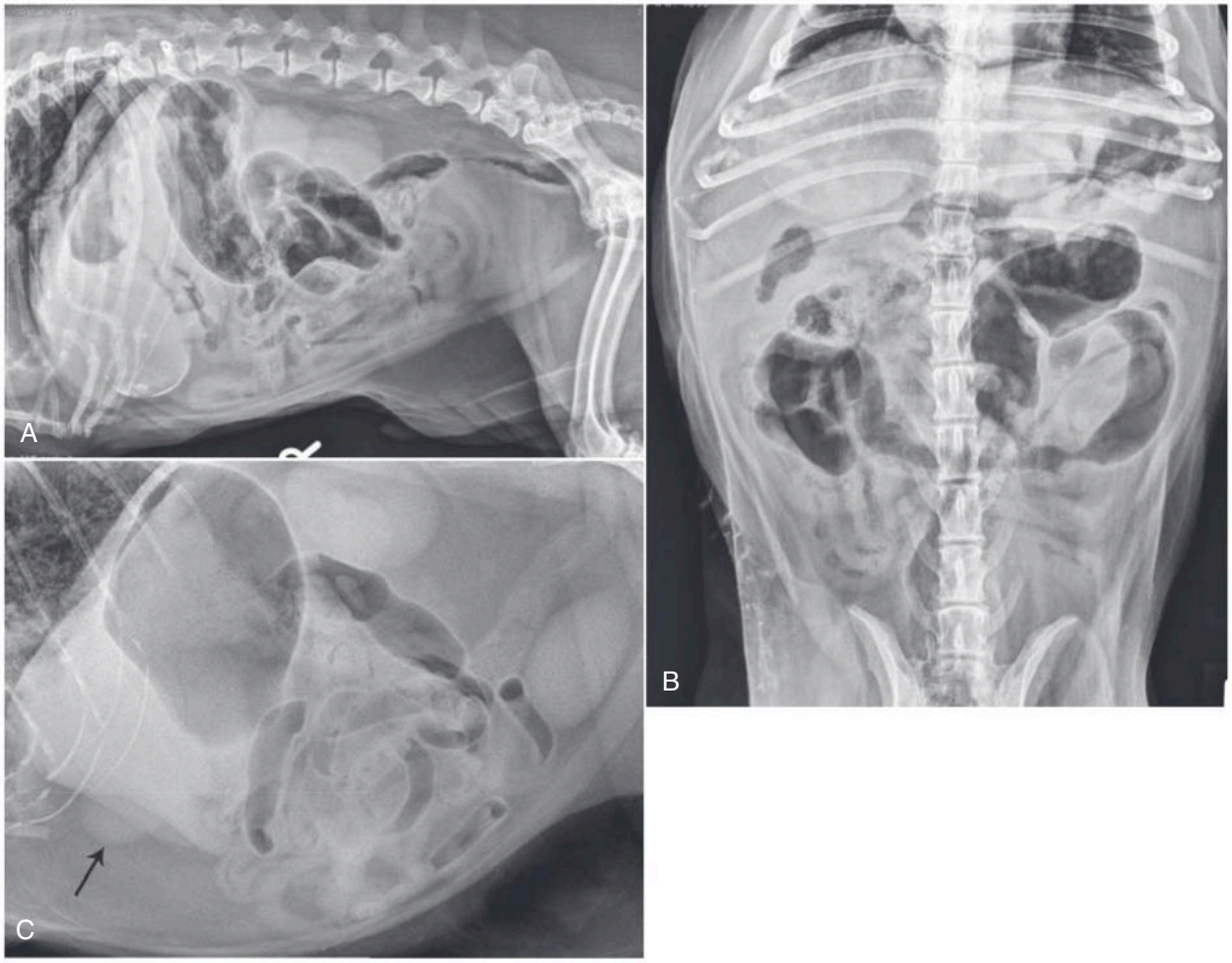


Fig. 40.3 Right lateral **(A)** and ventrodorsal (VD; **B**) radiographs of the abdomen in a dog with a history of elevated liver enzymes. The gallbladder is mineralized and is therefore conspicuous in the right cranial portion of the liver. **C,** Lateral abdomen radiograph of a cat presented for respiratory distress secondary to cardiogenic edema. The gallbladder can be seen protruding from the ventral aspect of the liver (*arrow*). This is a normal finding.

Hepatomegaly

Hepatic enlargement can be detected radiographically, although mild size changes cannot be assessed accurately. The classic radiographic signs of generalized hepatomegaly are rounding or blunting of the caudoventral liver margins, along with extension beyond the costal arch, and caudal, and perhaps medial, displacement of the gastric axis (Figs. 40.4 and 40.5).[5–7]

Several nonpathologic conditions can result in extension of hepatic margins beyond the costal arch, including overexpansion of the thorax or deep inspiration (Fig. 40.6). Older dogs and cats can have stretching or elongation of the triangular ligaments attaching the liver to the diaphragm, resulting in sagging and caudal extension of the liver. The same phenomenon can occur in obese dogs with a pendulous abdomen. In the obese dog, the liver does not extend as far dorsally. Some brachycephalic and chondrodystrophic dogs have caudal extension of the liver because of it being aligned more horizontally compared with deep-chested breeds. In addition, neonatal and young dogs and cats have a larger liver size compared with body size, creating the appearance of hepatomegaly without a true hepatic abnormality (Fig. 40.7).[1,8] Because of the numerous normal variations that can cause hepatic lobe extension beyond the costal arch, rounding or blunting of these lobes should also be present before hepatomegaly is concluded.

With generalized hepatomegaly, caudal displacement of the stomach, right kidney, transverse colon, and cranial duodenal flexure may occur, along with dorsal displacement of the

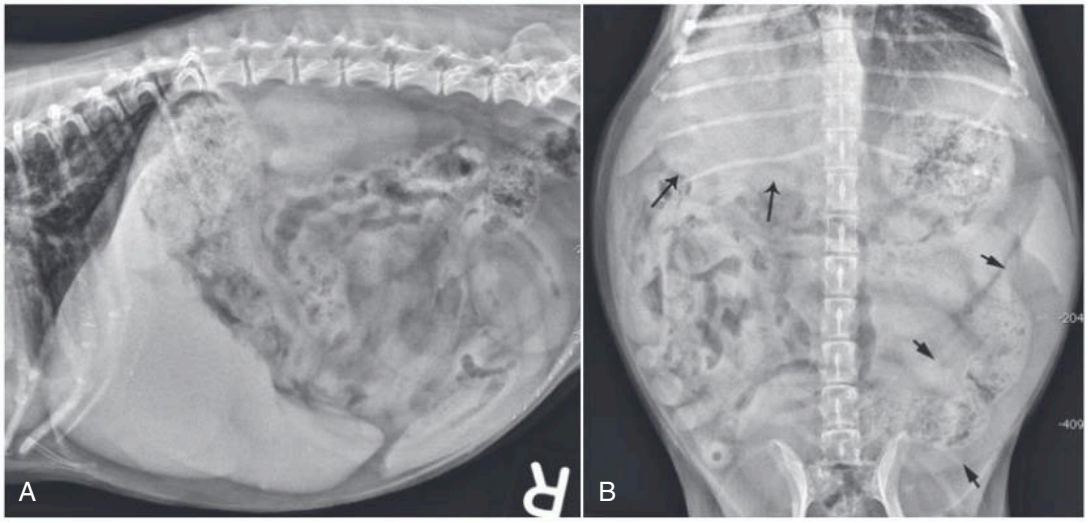


Fig. 40.4 Lateral **(A)** and ventrodorsal (VD; **B**) radiographs of a dog with generalized hepatomegaly secondary to steroid hepatopathy. The liver has rounded, blunt margins and extends well beyond the costal arch resulting in caudal displacement of adjacent viscera (*long black arrows* on VD view). On the VD view, the normal spleen is noted along the left lateral wall (*short black arrows*).

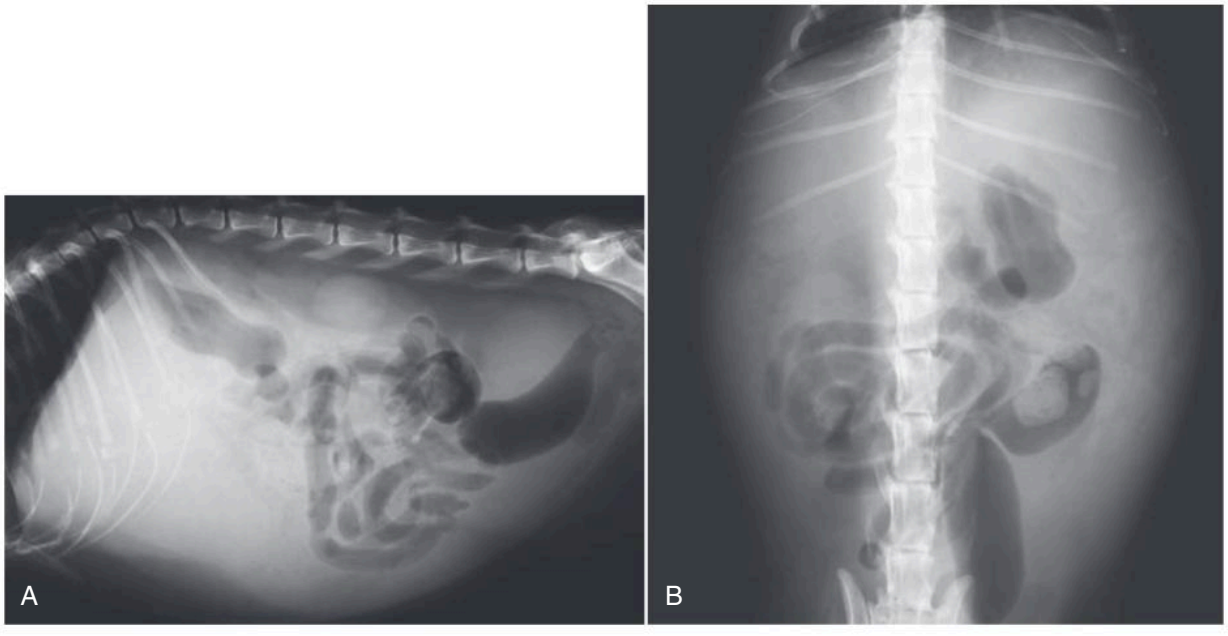


Fig. 40.5 Lateral **(A)** and ventrodorsal (VD; **B**) radiographs of the abdomen of a cat with lymphosarcoma. Although peritoneal fluid obscures abdominal detail, the marked caudal, dorsal, and left-sided gastric displacement is consistent with severe hepatomegaly.

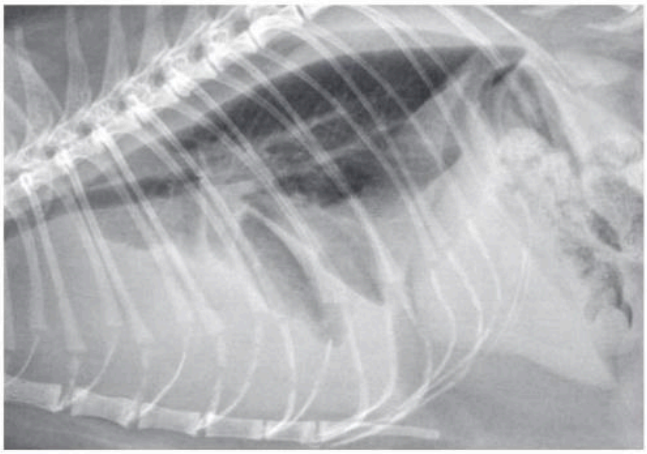


Fig. 40.6 Lateral radiograph of the thorax of a cat with pleural effusion. The overexpanded thorax results in caudal displacement of the diaphragm and liver margins with subsequent apparent hepatomegaly. The liver margins remain relatively sharp.

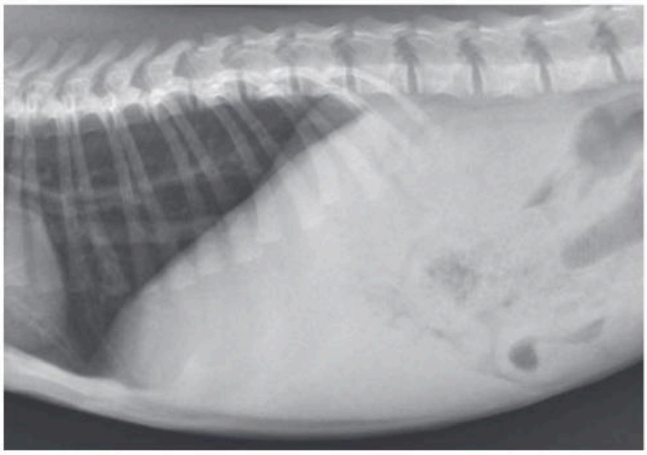


Fig. 40.7 Lateral radiograph of the abdomen of a normal puppy. The liver is large compared with overall abdominal size, which is a normal finding in young dogs and cats.

pylorus. On VD views, the enlarged liver will cause displacement of the body and pyloric portion of the stomach caudally, and to the left (see Fig. 40.4). Both lateral and VD abdominal views should be examined to evaluate liver size because hepatomegaly is sometimes obvious only on one view.

Causes of generalized hepatomegaly are numerous, and radiographs alone are insufficient in most instances to narrow the list. Hepatic congestion, vacuolar hepatopathy, inflammatory and infiltrative disease, and storage disease are all possibilities. Hepatic ultrasound can be used to determine internal architecture and is better suited than radiography for narrowing the list of considerations for hepatomegaly.

Visualization of focal hepatomegaly depends on the degree of enlargement and the lobe affected. Focal hepatic masses usually result in distortion of the hepatic outline and are continuous with the liver in at least one projection.[5–7] Left hepatic masses result in displacement of the stomach and spleen dorsally and to the right. Right-sided hepatic masses displace the stomach and duodenum to the left and dorsally and the small bowel caudally (Figs. 40.8 and 40.9, eFig. 40.1). The right kidney and distal extremity of the spleen may also be displaced caudally by a right-sided hepatic mass.

With few exceptions, masses located cranial to the ventral aspect of the stomach are hepatic in origin.[6] Although hepatic masses classically result in caudal displacement of the stomach, a focal mass can extend caudal to the stomach (Fig. 40.10, eFig. 40.2).[7] Differentiation of a caudally located, pedunculated hepatic mass from a splenic mass based on radiographs alone is difficult. Differentials for focal hepatic masses include primary and metastatic neoplasia, abscess, granuloma, and hepatic cyst.

Microhepatia

As with subtle hepatomegaly, slight decreases in hepatic size are not identified accurately radiographically. Marked microhepatia results in cranial displacement of the stomach and decreased distance between the diaphragm and gastric lumen (Fig. 40.11). Hepatic atrophy due to a congenital portosystemic shunt and chronic hepatopathy such as fibrosis or cirrhosis are the two most common causes of microhepatia. Diaphragmatic hernia with displacement of the liver cranial to the diaphragm can give the appearance of a small liver, but there will be intrathoracic abnormalities in this instance.

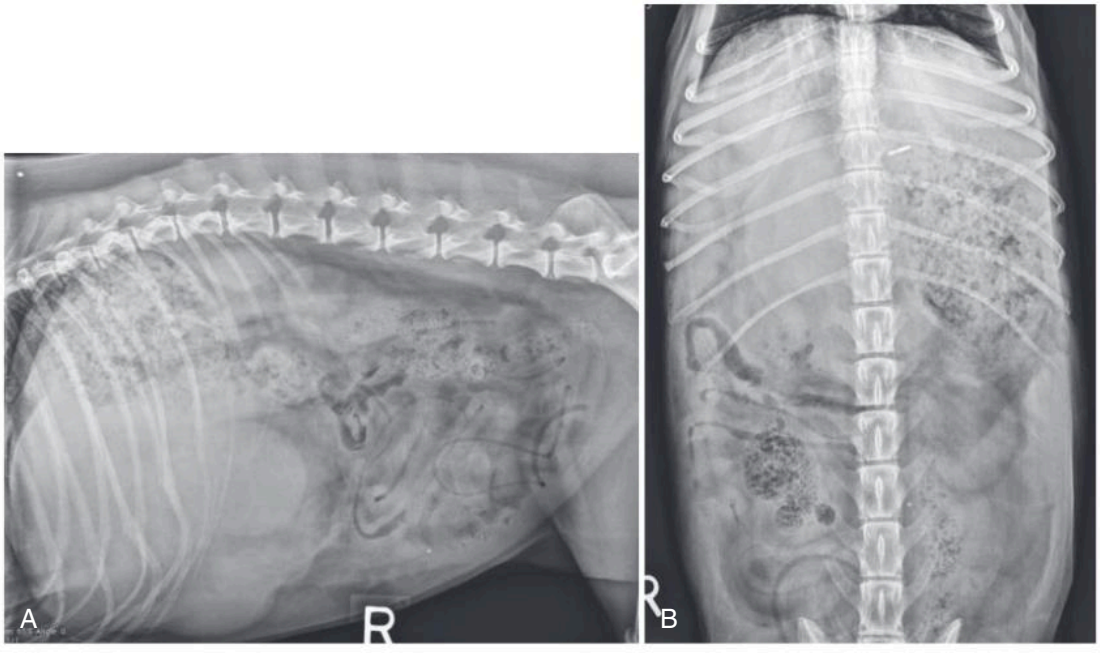
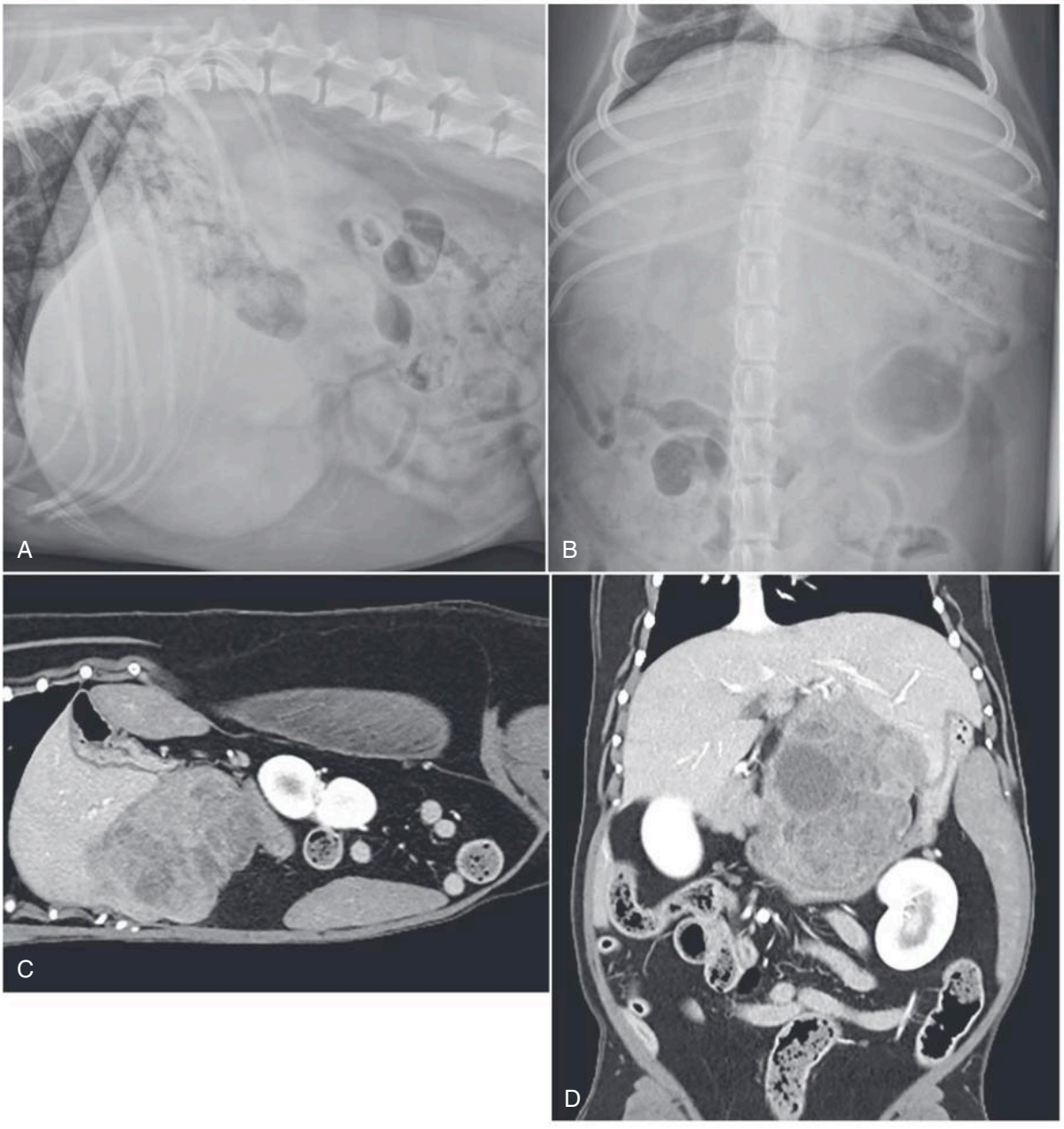
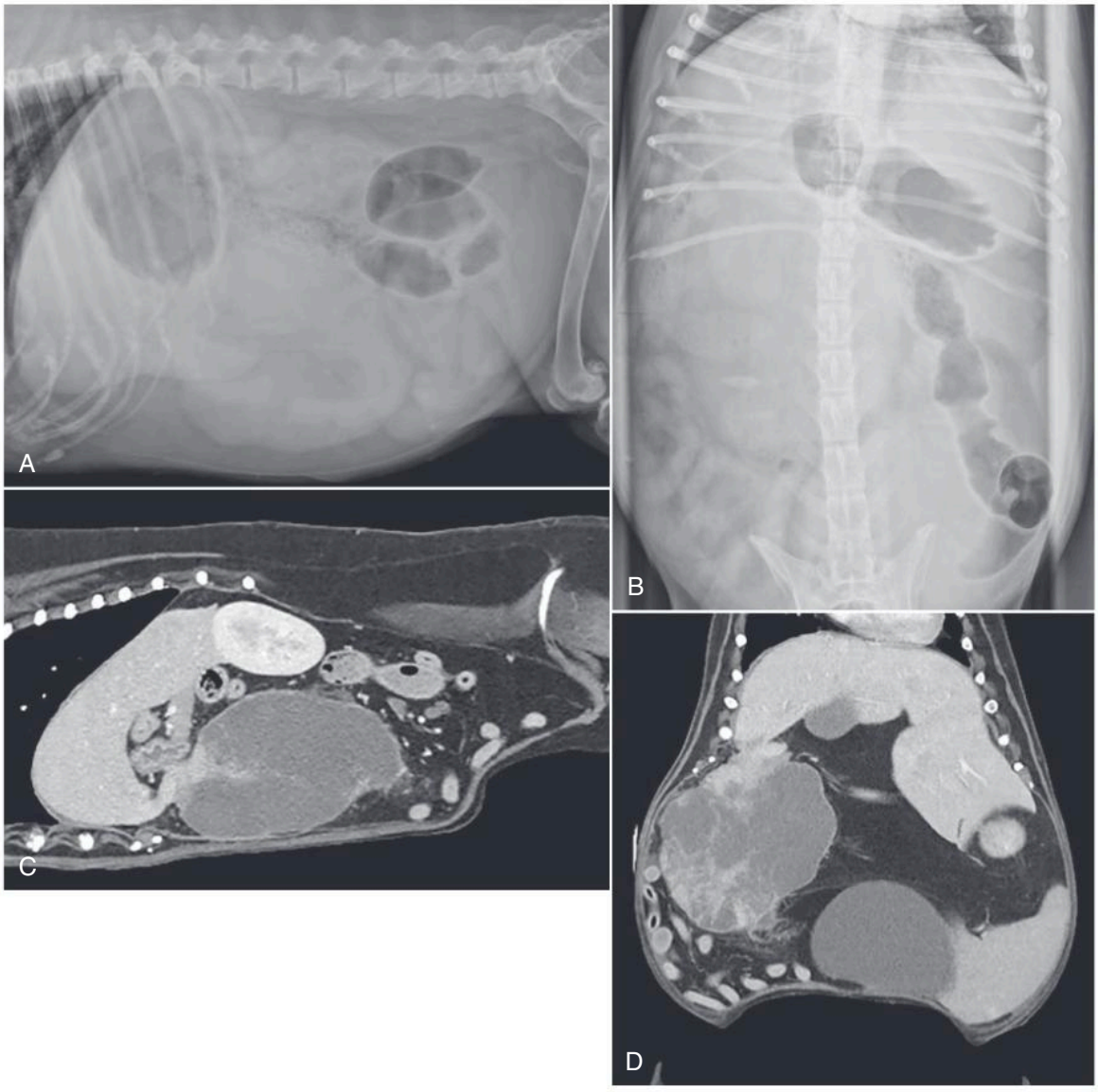


Fig. 40.8 Lateral **(A)** and ventrodorsal (VD; **B**) radiographs of the abdomen of a dog with hepatocellular carcinoma. The liver is focally enlarged with rounded margins.



eFig. 40.1 Right lateral **(A)** and ventrodorsal (VD; **B**) radiographs and sagittal **(C)** and dorsal **(D)** reformatted contrast-enhanced CT images of the cranial abdomen of a dog with a liver mass. The hepatic silhouette is enlarged resulting in caudal displacement of the gastric axis and marked rounding of the caudal hepatic margin. A mass effect is present centrally in the cranial abdomen on the VD projection with caudal displacement of the stomach. Presence of a heterogeneously contrast-enhancing mass originating from the left medial liver lobe could be con firmed with CT imaging. Hepatocellular carcinoma was the histopathologic diagnosis.



eFig. 40.2 Right lateral **(A)** and ventrodorsal **(B)** radiographs and sagittal **(C)** and dorsal **(D)** reformatted contrast-enhanced computed tomography (CT) images of a dog with a pedunculated liver mass. A rounded, slightly lobulated mass is present in the mid ventral abdomen in **A,** caudal to the stomach and a caudoventrally located liver lobe. The mass is visible in the mid abdomen, extending to the right of midline in **(B)**. The mass could be identified as hepatic in origin on CT images **(C, D)**.

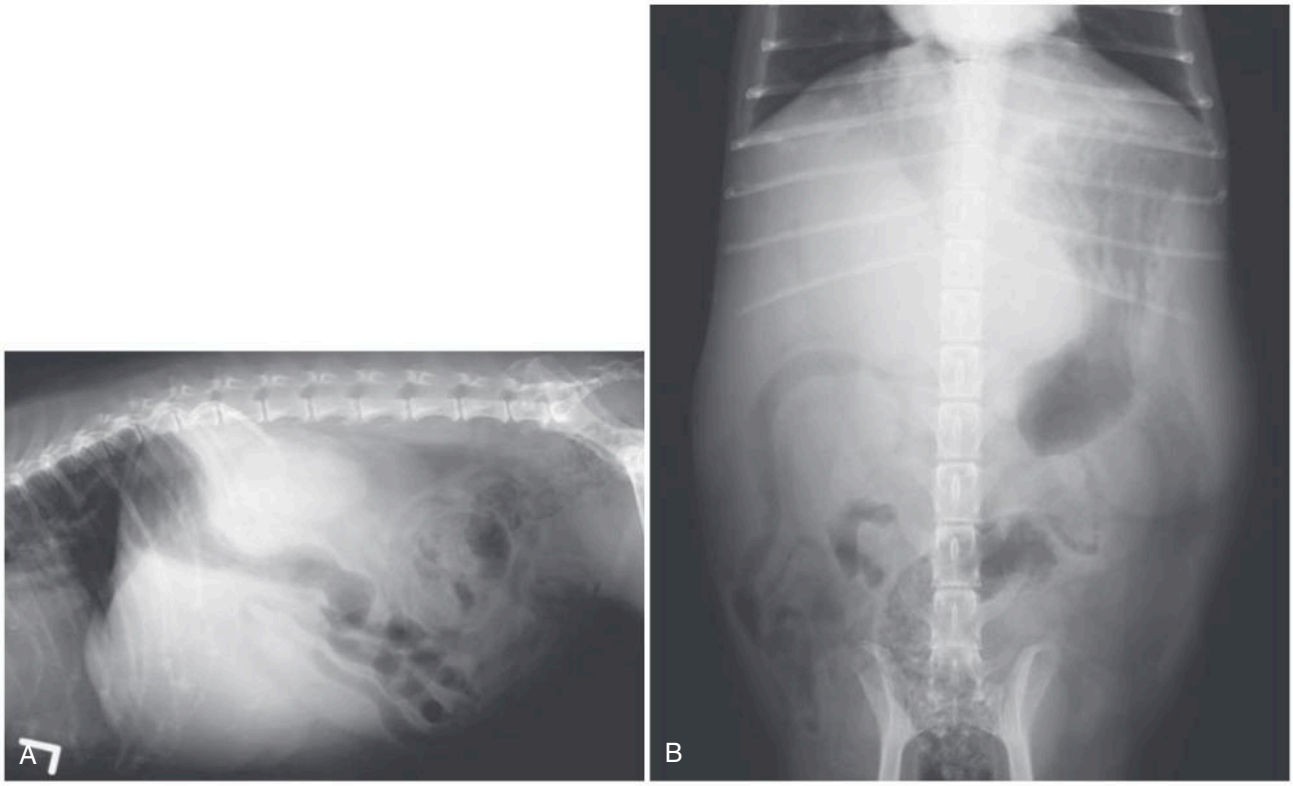


Fig. 40.9 Lateral **(A)** and ventrodorsal (VD; **B**) radiographs of the abdomen of a dog with hepatocellular carcinoma. The right side of the liver is enlarged, resulting in caudal, dorsal, and left-sided displacement of the stomach. The small bowel is displaced caudally. Faint mineralization is present in the ventral portion of the liver on the lateral view.

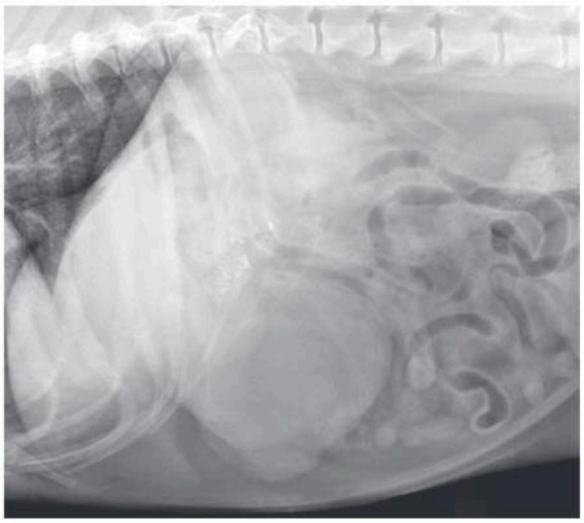


Fig. 40.10 Lateral radiograph of the abdomen of a dog with hepatic carcinoma. The hepatic mass extends caudal to the stomach, mimicking a splenic mass.

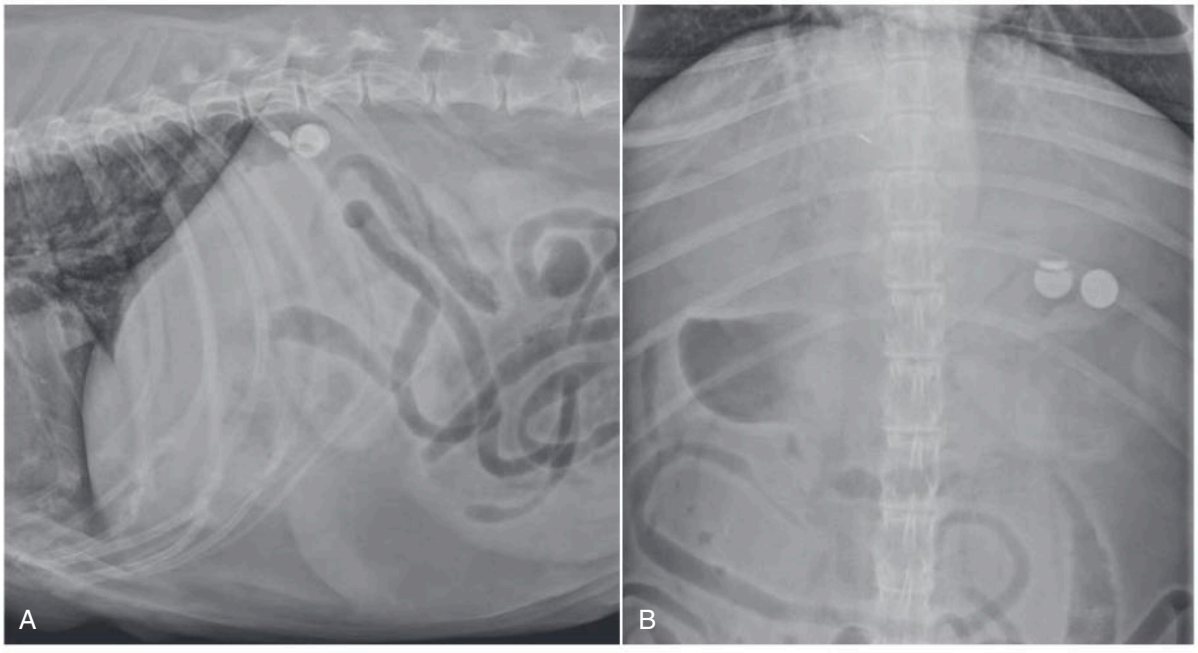
Hepatic Opacity

The normal liver is of soft tissue opacity. Mineral opacities can occur in the hepatic parenchyma or biliary system.[9] Choleliths should be considered when focal mineral opacities are visible in the area of the gallbladder (Fig. 40.12). Linear trails of mineralized opacities extending peripherally within the hepatic parenchyma are indicative of choledocholiths, or calculi within the bile ducts.[9] Biliary calculi are uncommon in dogs and cats but are visible radiographically if they contain sufficient calcium (see Fig. 40.12).[10–13] These are often incidental findings, but choledocholiths can cause biliary obstruction, especially in the cat. Mineralization of the biliary tree is seen occasionally in dogs with bile duct carcinoma.[14] Mineralization of the gallbladder wall has been associated with gallbladder carcinoma, as well as cholecystitis or cystic mucinous hyperplasia (see Fig. 40.3A,B).[13]

Dystrophic calcification of hepatic granulomas, abscesses, hematomas, neoplastic masses, or areas of hepatic necrosis have been documented (see Fig. 40.9). Echinococcosis infection can result in large hepatic soft tissue masses with mineralization of varying patterns and should be considered in endemic areas.[15]

Radiolucent areas within the liver are indicative of intrahepatic gas, either in the biliary system, portal venous system, or hepatic parenchyma. Gas within portal vessels may occur because of severe necrotizing gastritis or enteritis, which is often associated with gastric dilation and volvulus complex. Gastrointestinal ulceration, distention, trauma, or interventional procedures may allow gas to ascend into the portovenous circulation (Fig. 40.13A, eFig. 40.3).[16–18] A linear, branching radiolucent appearance, similar to air bronchograms, may be visible.

Gas in or around the gallbladder occurs with emphysematous cholecystitis, and this can be found in both diabetic and nondiabetic dogs.[19,20] Gas is seen initially in the gallbladder wall, followed by more complete filling of the lumen (see Fig. 40.13B,C). The gas eventually extends to the pericholecystic tissues. Gas bubbles conforming to the shape of the distended gallbladder can be seen within 24 to 48 hours of onset of disease. Obstruction of the cystic duct may be a common predisposing factor for emphysematous cholecystitis. Gas lucencies within the biliary system can also be seen after surgery of the duodenum or biliary system. Incidental reflux of



eFig. 40.3 Left lateral **(A)** and ventrodorsal **(B)** radiographs of a dog with emphysematous cholecystitis. Note the septated gas accumulation cranial to the pyloric antrum in both views. Peritoneal serosal contrast is reduced. The radiopaque round structures in the gastric fundus represent radiopaque medication (bismuth tablets).

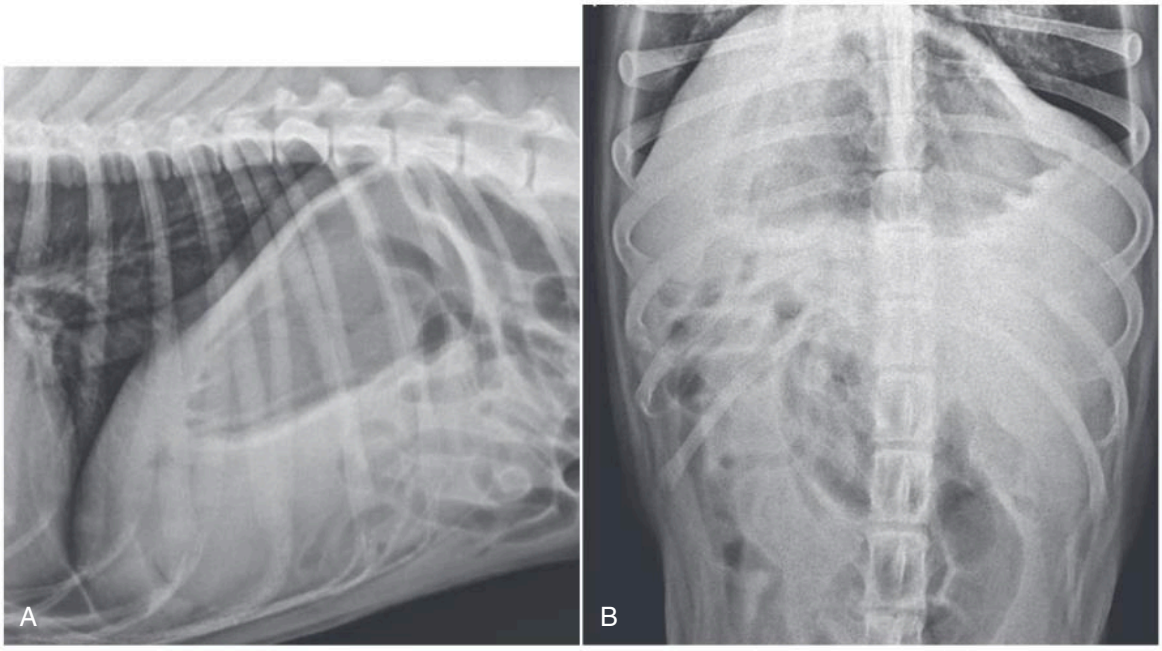


Fig. 40.11 Lateral **(A)** and ventrodorsal (VD; **B**) radiographs of the abdomen of a dog with chronic hepatitis that led to microhepatia. There is marked cranial displacement of the stomach.

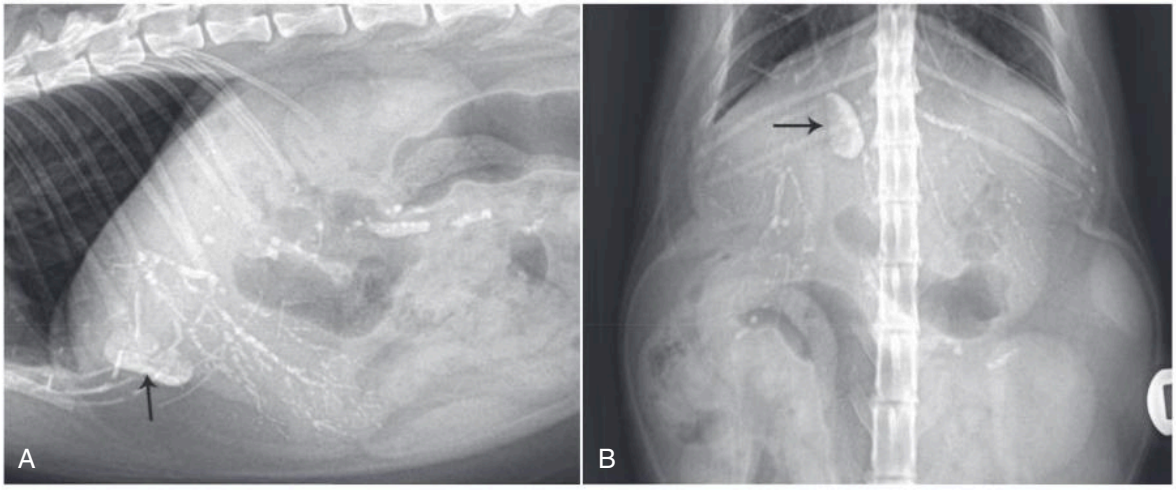


Fig. 40.12 Lateral **(A)** and ventrodorsal (VD; **B**) radiographs of a cat with a large radiopaque cholelith (*arrow*) and trails of mineralized choledocholiths and pancreatoliths.

gas into the bile duct from the duodenum is occasionally seen in cats. This may be because of incompetence of the sphincter of Oddi.[2]

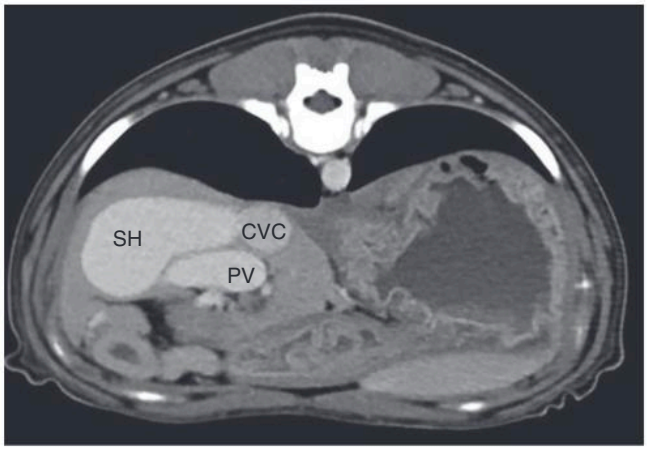
Hepatic abscess with gas-forming organisms may result in gas opacities within the hepatic parenchyma.[21,22] These abscesses appear as irregularly stippled or mottled gas patterns, usually in a localized area (Fig. 40.14). Hepatomegaly or a hepatic mass is typically present with hepatic abscess with or without gas formation. Abscesses may be secondary to necrotic tumors, ascending portal infection, adjacent infection (pancreatitis), or penetrating wounds.

COMPUTED TOMOGRAPHY OF THE LIVER

Most common indications for computed tomography (CT) of the liver currently are vascular malformations and hepatic masses.

Vascular Malformations

Portosystemic shunts are congenital or acquired anomalies of the portal vasculature in which blood bypasses the liver and enters the systemic circulation directly. In the past, radiographic techniques have been used to identify and characterize the anomalous vessels, including cranial mesenteric portography, percutaneous splenoportography, and operative mesenteric portography.[23–26] CT angiography has largely replaced radiographic portography in the evaluation of portosystemic shunts.[27–32] CT is minimally invasive and provides delineation of the portal vein and portal tributaries following intravenous injection of contrast medium (Fig. 40.15, eFig. 40.4). Reformatted images in different planes or 3D renderings can be created to provide detailed evaluation of the vascular malformation, and aid in surgical planning. With dual-phase CT angiography, postcontrast images are acquired during calculated peak hepatic arterial and portal venous phases. In a survey of CT angiography studies, the most common



eFig. 40.4 Transverse contrast-enhanced computed tomography image of a dog with a right divisional intrahepatic portosystemic shunt. An anomalous shunt vessel (*SH*) is seen originating from the portal vein (*PV*), looping to the right and dorsally where it eventually enters the caudal vena cava (*CVC*).

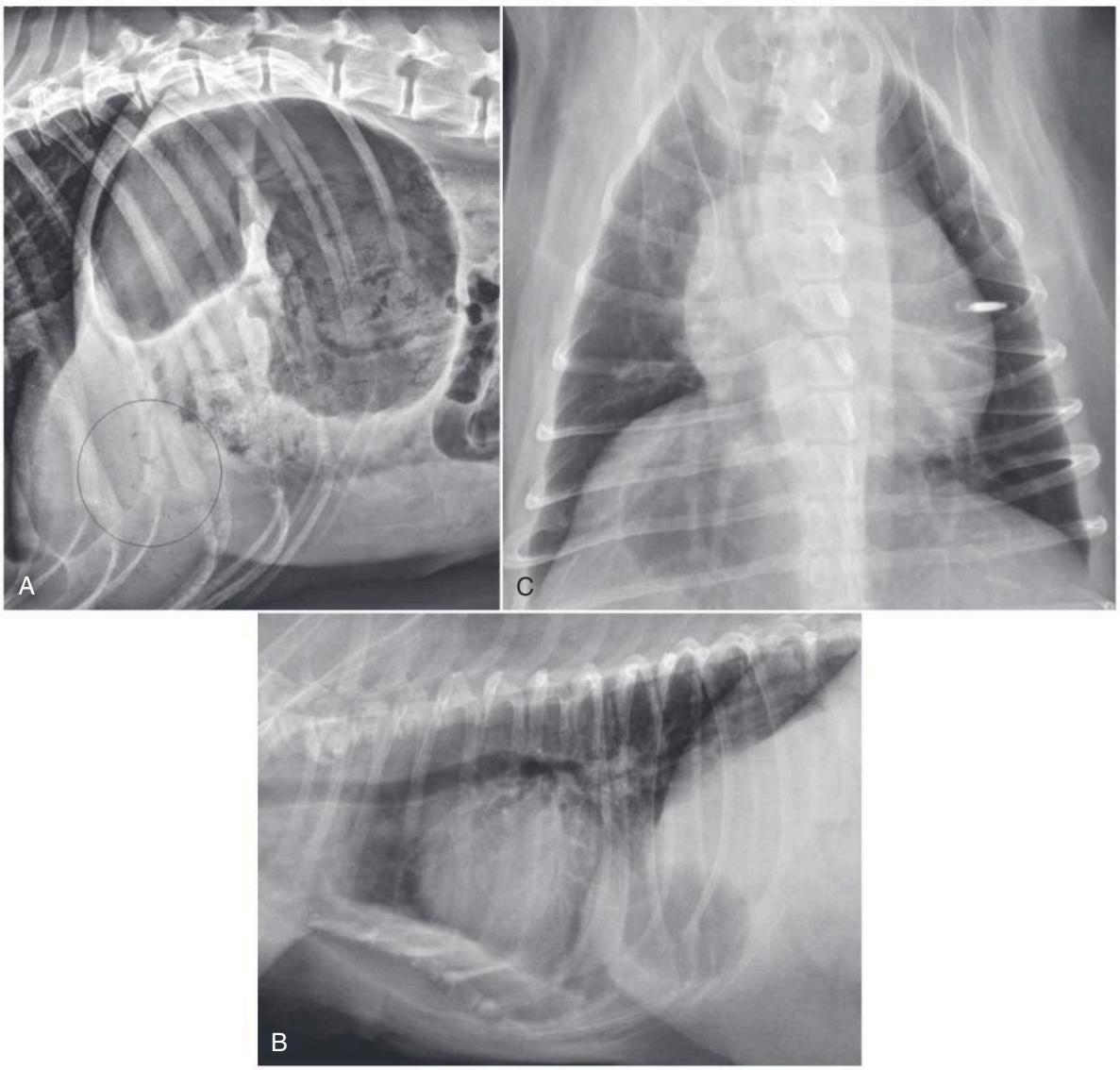
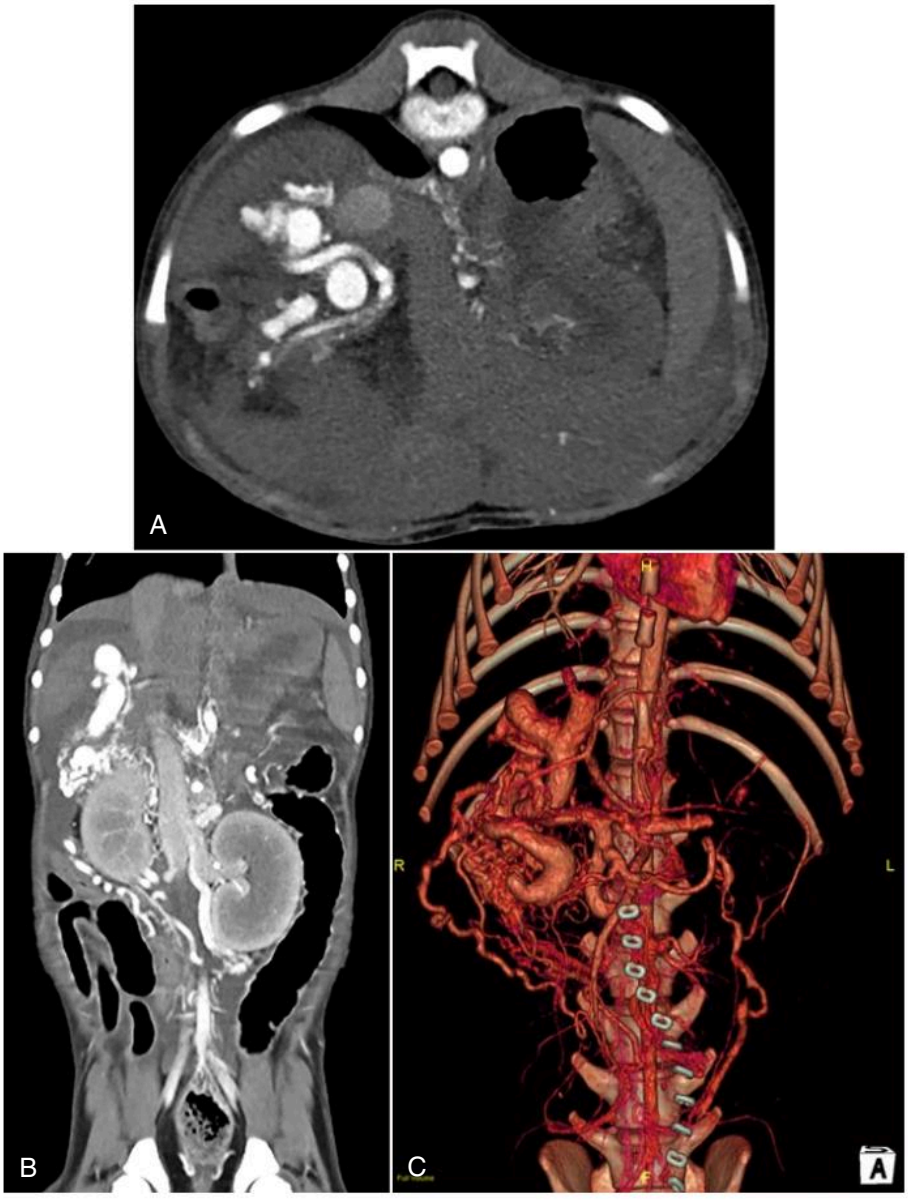


Fig. 40.13 Radiolucencies in liver. **A,** Lateral cranial abdominal radiograph of a dog with gastric dilatation and volvulus. Gas is visible in the portal vasculature of the liver (within *circle*) **(B)** lateral and **(C)** ventrodorsal thoracic radiographs of a dog with emphysematous cholecystitis. Gas completely fills the gallbladder lumen.

extrahepatic shunts identified were (named from origin to insertion) spleno-phrenic, spleno-azygous, spleno-caval, left or right gastric-caval, and right gastric-caval with caudal loop.[31,32] Arterioportal communications are rare congenital disorders where an abnormal connection between the hepatic arterial and the portal venous system is formed. CT findings include early contrast enhancement of the portal venous system in the arterial phase and typically a cluster of enlarged, tortuous vessels in a portion of the liver (eFig. 40.5).[33–35]

Hepatic Masses

CT is commonly used for evaluation of hepatic masses, helping to determine exact location in terms of lobe or lobes involved, vascular involvement, and extent of disease for surgical planning. Multiphase contrast-enhanced CT protocols have been used to evaluate patterns of contrast uptake of hepatic masses to help differentiate benign from malignant disease.[36–38] In triple-phase studies, postcontrast images are acquired at 13 to 20 seconds (hepatic arterial phase), 30 to 40 seconds (early portal venous phase), and 120 seconds (equilibrium or delayed phase) after injection.[36,37] In these studies, most hepatocellular carcinomas had heterogeneous enhancement in all phases, and were hypoattenuating compared to normal liver parenchyma in the portal and delayed phase (Fig. 40.16). Metastatic lesions within the liver were homogeneous, with hypoattenuation compared to normal liver in all postcontrast phases. Benign hepatic adenomas had more diffuse enhancement in the hepatic arterial phase, with persistent enhancement in the portal venous phase. Finally, nodular hyperplastic lesions were homogeneous, often with marked contrast enhancement in the hepatic arterial and portal venous phases, with isoattenuation compared to normal hepatic parenchyma in the delayed phase. In a similar study using dual-phase contrast imaging, with images acquired within 30 seconds and at least 60 seconds post initiation of contrast administration, no CT features were significantly associated with benign or malignant hepatic lesions.[38] There appears to be enough overlap in the contrast enhancement pattern of benign and malignant lesions, that CT findings alone are not sufficient to accurately predict the type of disease. Histopathology remains the gold standard.[38]



eFig. 40.5 Transverse **(A)**, dorsal reformatted **(B)**, and 3D reconstructed **(C)** computed tomography images of a dog with an arterioportal malformation. Images were acquired in the arterial phase of contrast enhancement. There is enhancement of the portal venous system compared to the caudal vena cava, and a cluster of dilated tortuous vessels is seen in the right liver and surrounding the cranial aspect of the right kidney. Anomalous vessels at the caudal pole of the left kidney represent acquired shunt vessels.



Fig. 40.14 Lateral abdominal radiograph of a dog with hepatic abscessation. Stippled radiolucencies in the cranial margin of the liver represent gas within the abscess. *A,* Abscess; *S,* stomach.

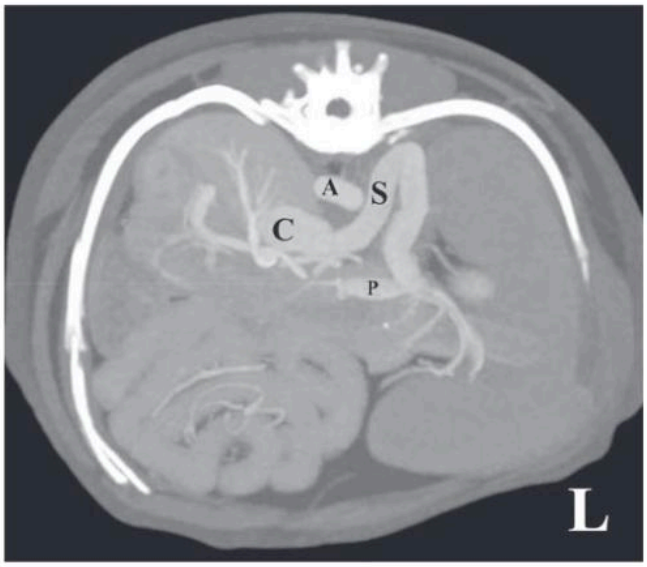


Fig. 40.15 Maximum intensity projection (MIP) reformatted transverse computed tomography angiogram of the cranial abdomen. A large tortuous extrahepatic shunting vessel (*S*) extends from the portal vein (*P*) into the caudal vena cava (*C*). *A,* Aorta; *L,* left.

ULTRASOUND OF THE LIVER

Ultrasound examination of the liver allows detailed evaluation of hepatic internal architecture, including the hepatic vasculature and biliary system. Ultrasound is also useful in guiding aspirates and biopsies for nonsurgical, less invasive diagnoses.

The liver can be imaged through a combination of subcostal, subxiphoid, and right and left intercostal windows. Intercostal windows may be the best way to evaluate the liver in a deep-chested dog, patients with gas-distended stomach, or in dogs with microhepatia. The right dorsal intercostal window allows excellent visibility of the porta hepatis, the caudate liver lobe, and the right kidney in many dogs. This window can also be used in cats but is not as often needed. Transducer frequencies ranging from 5 to 10MHz will accommodate most small animal patients. Transducers with smaller footprints are best for intercostal windows.

Based on the individual scatter pattern, each abdominal organ has a characteristic texture and appearance. The liver has a moderately coarse texture and is usually hypoechoic to the spleen and, in cats, the falciform fat (Fig. 40.17).[39–41] When using the right renal cortex for comparison to the caudate liver lobe, the liver may be isoechoic, or slightly hypoechoic or hyperechoic. The use of the renal cortex for comparison is therefore limited. The renal cortex of many normal cats is hyperechoic due to lipid deposition, and this should be considered before interpreting the liver as hypoechoic.[42] Assessment of echogenicity in any organ is subjective and any change should be correlated with the overall clinical picture.

Hepatic margins should be smooth and sharp but are better delineated ultrasonographically if adjacent peritoneal fluid is present (Fig. 40.18). The liver is bordered cranially and dorsally by an echogenic line representing the interface between the diaphragm and lung/pleura. A mirror-image artifact is frequently noted deep to the diaphragmatic interface, giving the false impression of liver on both sides of the diaphragm (see Chapter 3).

As with assessing echogenicity, the ultrasound assessment of liver size is subjective and based on operator experience, patient conformation, and adjacent organs. A small liver is difficult to evaluate sonographically, because gas from a more cranial located stomach can obscure it. The gallbladder may appear large relative to overall hepatic size (Fig. 40.19). Liver size may appear decreased in dogs with a deep thoracic cavity where liver location is more completely within the costal arch. Intercostal ultrasound windows may be needed in these patients. The enlarged liver can be examined relatively easily with ultrasound, because it extends well beyond the xiphoid cartilage and covers the right kidney more completely (Fig. 40.20). Liver margins may appear rounded and may extend beyond the left lateral margin of the stomach.

Hepatic and portal veins are visible routinely within hepatic parenchyma. Portal veins are smoothly tapering vessels characterized by bright, echogenic borders (see Fig. 40.17E).[39,40] The larger left and smaller right branches originate from the main portal vein near the porta hepatis, although they branch in different imaging planes. Portal blood flow courses normally from the hepatic hilus toward the periphery. Hepatic veins are anechoic linear structures extending through the parenchyma. Hepatic vein borders are not echogenic except at their confluence with the caudal vena cava, immediately adjacent to the diaphragm. Hepatic venous flow courses normally toward the hepatic hilus, into the caudal vena cava. In many dogs, the right lateral dorsal intercostal window provides an excellent window to the aorta, caudal vena cava, and main portal vein (Fig. 40.21). Normal hepatic arteries are not visible without Doppler examination. The caudal vena cava courses through the liver in the right lateral abdominal quadrant. The hepatic artery is located between the caudal vena cava and portal vein, coursing cranially from the celiac artery. It may not be consistently identified without Doppler ultrasound.

The gallbladder is an oval, anechoic structure in the right cranioventral portion of the liver (see Fig. 40.17A). Gallbladder size varies widely, and distention is normal in fasted or anorexic patients. Normal gallbladder volume in the dog is 1 mL/kg or less body weight, and it can be measured with the ellipsoid formula (length × width × height × 0.52).[43,44] Cats may have a more uniform gallbladder volume of 2.4 mL, with no apparent association with body weight.[43,45] Intraluminal gallbladder contents are typically anechoic, although gallbladder sludge, which is dependent echogenic material without acoustic

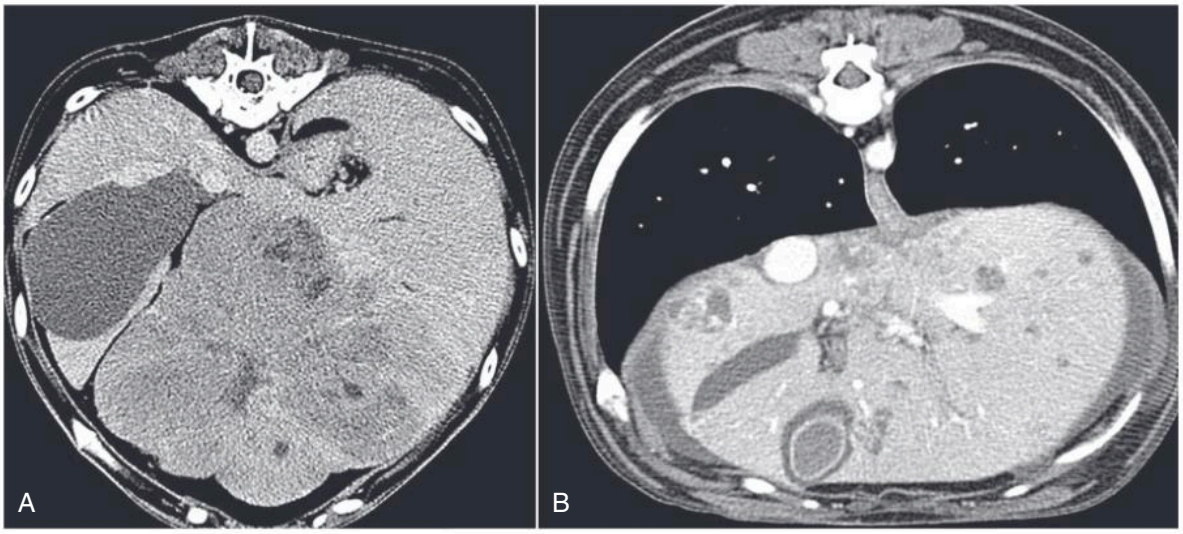


Fig. 40.16 Transverse postcontrast computed tomography images of dogs with hepatic neoplasia. In **A,** a large, hypoattenuating, lobular mass is present in the left lateral liver lobe. Hepatocellular carcinoma was diagnosed on histopathology post liver lobe resection. In **B,** multiple hypoattenuating nodules are noted throughout the hepatic parenchyma. The gallbladder wall is thickened, with a double-layered appearance. Hepatic metastasis secondary to a jejunal carcinoma was diagnosed on necropsy. Gallbladder wall edema was of undetermined etiology.

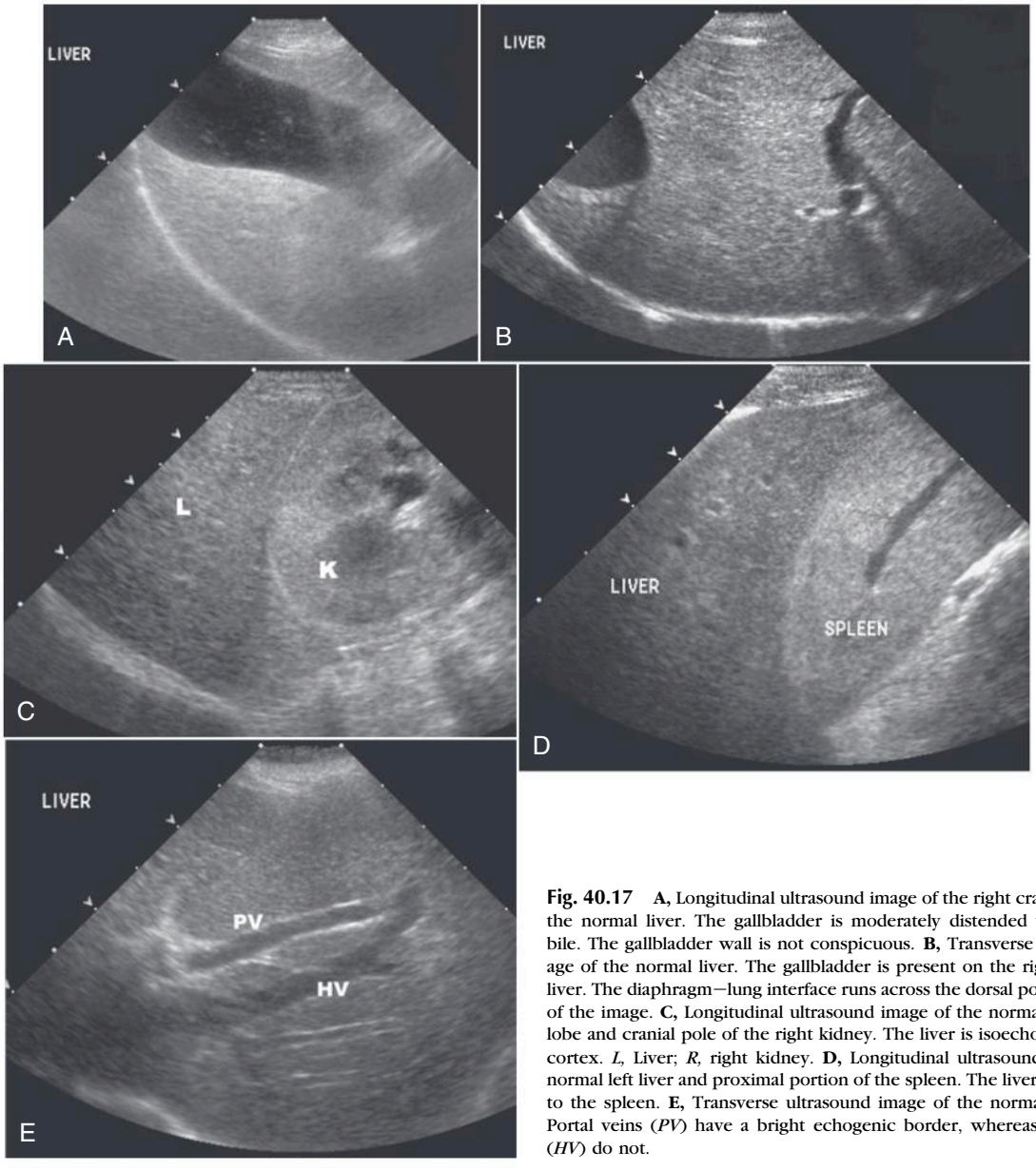


Fig. 40.17 **A,** Longitudinal ultrasound image of the right cranial portion of the normal liver. The gallbladder is moderately distended with anechoic bile. The gallbladder wall is not conspicuous. **B,** Transverse ultrasound image of the normal liver. The gallbladder is present on the right side of the liver. The diaphragm—lung interface runs across the dorsal portion (*bottom*) of the image. **C,** Longitudinal ultrasound image of the normal caudate liver lobe and cranial pole of the right kidney. The liver is isoechoic to the renal cortex. *L,* Liver; *R,* right kidney. **D,** Longitudinal ultrasound image of the normal left liver and proximal portion of the spleen. The liver is hypoechoic to the spleen. **E,** Transverse ultrasound image of the normal canine liver. Portal veins (*PV*) have a bright echogenic border, whereas hepatic veins (*HV*) do not.

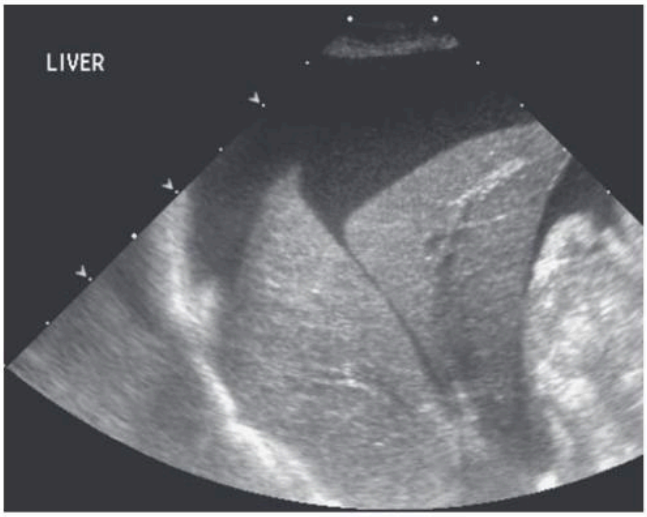


Fig. 40.18 Longitudinal ultrasound image of a dog with ascites. The normal liver lobes have a well-defined sharp, linear margin.

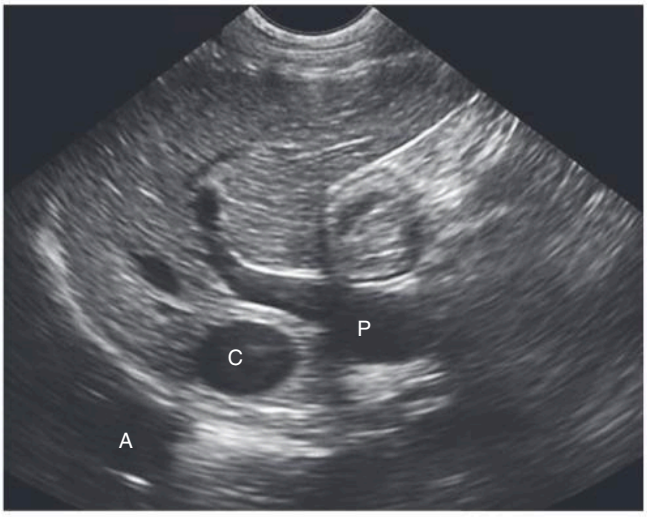


Fig. 40.21 Right lateral intercostal ultrasound image of a normal dog. Dorsal is at left and ventral is at right of the image. The top of the image represents the right abdominal wall with the left abdominal wall being at the bottom of the image. *A,* Aorta; *C,* caudal vena cava; *P,* portal vein.

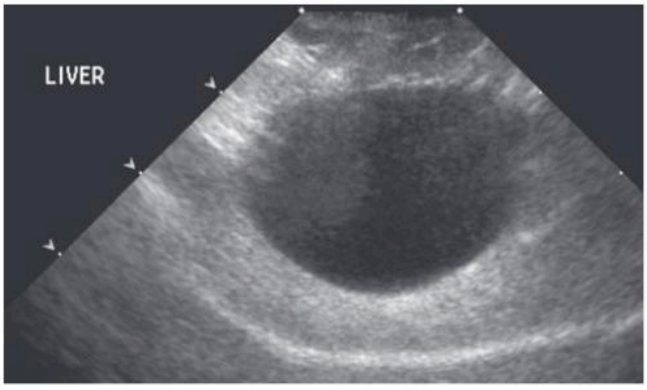


Fig. 40.19 Transverse ultrasound image of the liver in a dog with a small liver secondary to a portosystemic shunt. The liver is subjectively small with the gallbladder occupying a large portion.

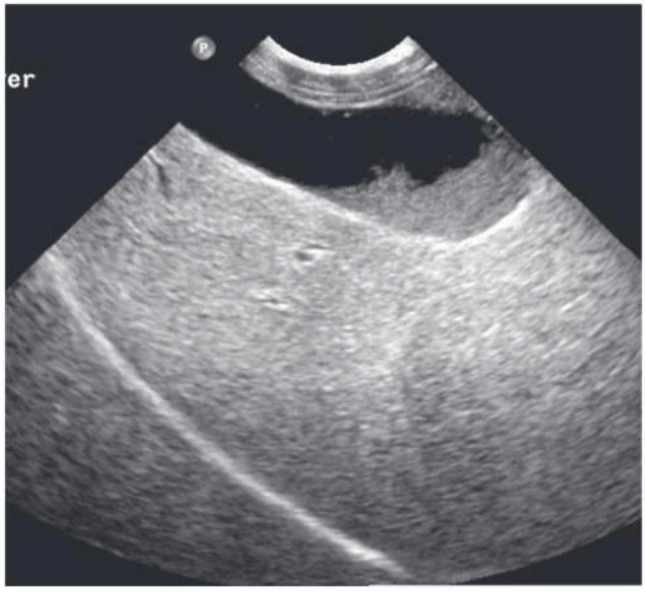


Fig. 40.22 Longitudinal ultrasound image of the liver and gallbladder of a normal dog. Echogenic biliary sludge is present in the dependent portion of the gallbladder.

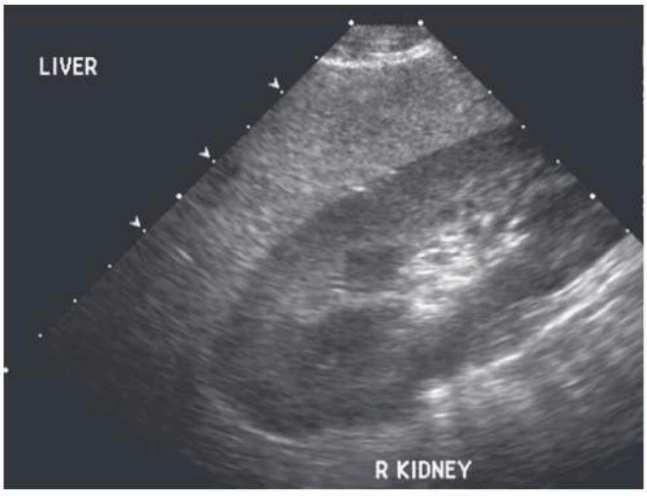


Fig. 40.20 Longitudinal ultrasound image of the caudate liver lobe and right kidney of a dog with hepatic lipidosis. The caudate lobe surrounds the right kidney completely, consistent with hepatomegaly. The liver is markedly hyperechoic to the renal cortex.

shadowing, is seen frequently[46] (Fig. 40.22). Although sludge is common in dogs with no indication of biliary disease, one study suggests that it could be an indication of gallbladder dysmotility.[46–48] The normal gallbladder wall is thin and indistinct. In the cat, gallbladder wall thickness should be less than 1 mm or not visible at all.[49] The normal canine gallbladder wall typically measures 1 to 2 mm, but normal ranges have not been established.[48,50] A study of 74 normal dogs noted median gallbladder wall thickness of 1 mm.[48] A duplicate or septate gallbladder is seen occasionally as a normal variation in cats and is caused by abnormal embryonic development.[51] The common bile duct is immediately ventral to the portal vein but is visible more consistently in the cat, where it can usually be followed to the duodenal papilla (Fig. 40.23). Normal common bile duct diameter in the cat is 4 mm or less.[52] If visible, the canine bile duct should be 3 mm or less.[53] Normal intrahepatic bile ducts are not visible.

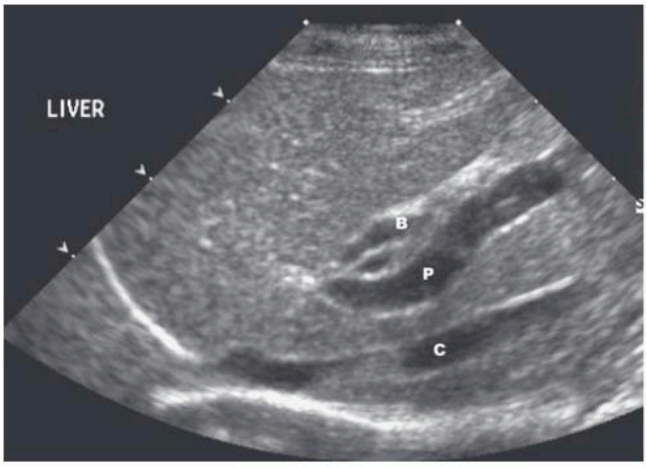


Fig. 40.23 Longitudinal ultrasound image of the liver in a normal cat. *B,* Bile duct; *C,* caudal vena cava; *P,* portal vein.

Abnormal Ultrasonographic Appearance of the Liver

Ultrasound is helpful in differentiating between diffuse and focal hepatic disease in patients with hepatomegaly and/or elevated liver enzymes. Diffuse hepatic disease may cause no change in the ultrasound appearance of the liver. However, changes in hepatic echogenicity, increase or decrease in size, and irregular or rounded margins point to diffuse hepatopathy.[39,40,54–56] A *hyperechoic* liver is identified by comparison with the echogenicity of an adjacent organ, such as being isoechoic or hyperechoic to spleen, or the in cats, the falciform fat. Loss or decreased conspicuity of the periportal echoes and abnormally increased attenuation of sound as it passes through the liver are indications of hyperechoic hepatic parenchyma (Fig. 40.24). Several diffuse hepatopathies can potentially result in either a diffusely hyperechoic liver, or a mottled appearance (i.e., hyperechoic parenchymal background with poorly defined hypoechoic nodules).[39,40,54–56] Vacuolar hepatopathies, including lipidosis and steroid hepatopathy, are likely the most frequent diagnosis when this appearance is seen (Fig. 40.25). Hepatic lipidosis in cats is a

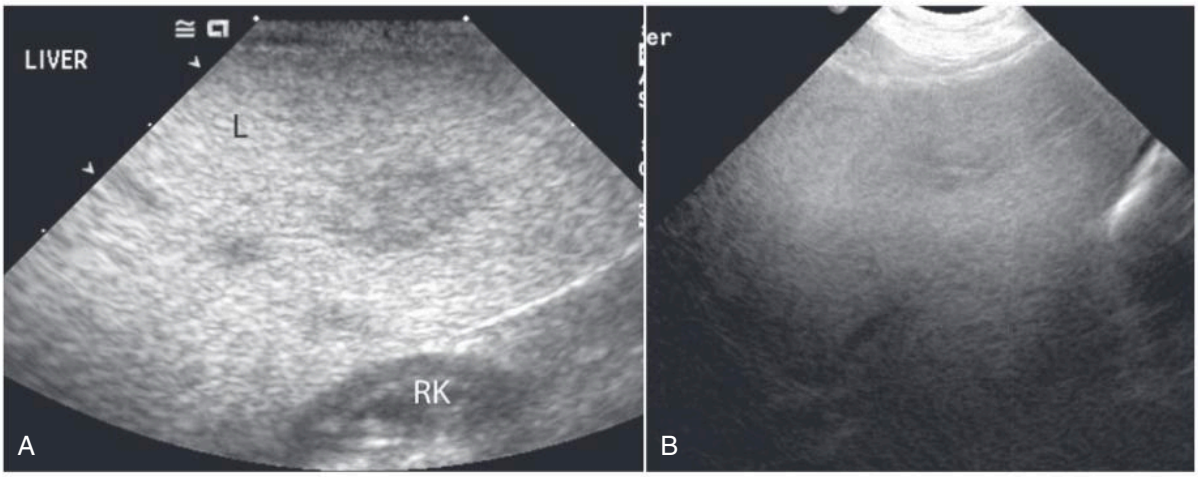


Fig. 40.24 **A,** Longitudinal ultrasound image of the caudate liver lobe and a portion of the right kidney (*RK*). The liver parenchyma is diffusely hyperechoic compared to the renal cortex, secondary to steroid hepatopathy. A few hypoechoic nodules (likely nodular hyperplasia) are present. *L,* Left. **B,** Transverse image of the liver from a dog with steroid hepatopathy. The liver is diffusely hyperechoic, with a dense texture resembling the spleen. Deeper portions of the liver are incompletely visualized due to exaggerated attenuation of the sound beam.

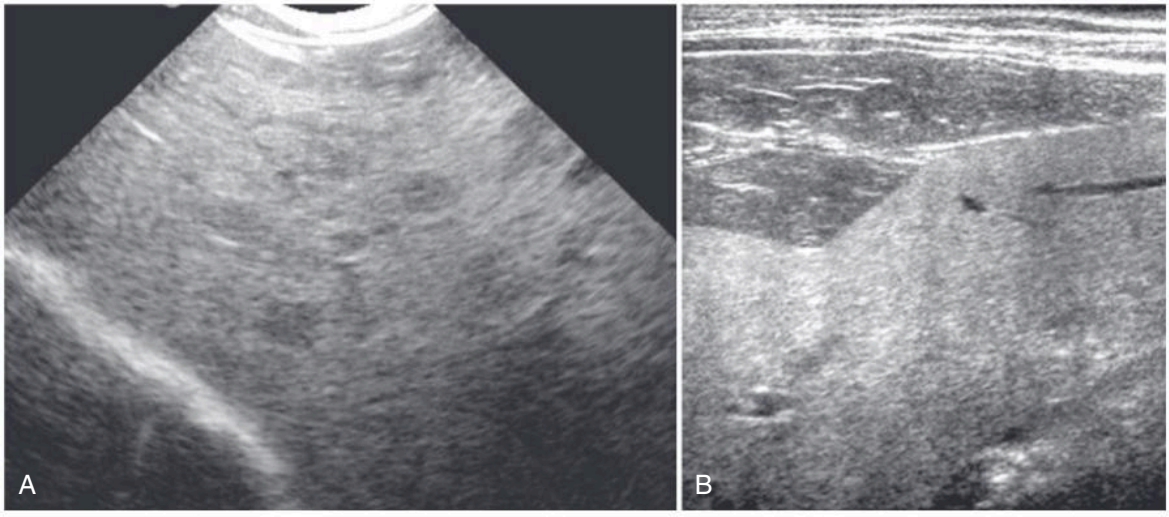


Fig. 40.25 **A,** Longitudinal ultrasound image of the liver with a mottled parenchyma (hyperechoic background with poorly defined hypoechoic nodules). Vacuolar hepatopathy was diagnosed on a fine needle aspirate. **B,** Transverse image of the liver in a cat with elevated liver enzymes. The liver parenchyma is markedly hyperechoic to adjacent falciform fat. Although this can be normal in some obese cats, hepatic lipidosis was diagnosed on cytology from a fine needle aspirate.

common diffuse feline hepatopathy, and it results in a liver parenchyma that is hyperechoic to adjacent falciform fat. However, a nonpathologic hyperechoic liver can be present in some obese cats, and ultrasound alone is likely insufficient for the diagnosis.[55,57] Chronic hepatitis with parenchymal fibrosis can also cause increased echogenicity, although liver size is variable and may be normal, increased, or decreased. Hepatic cirrhosis typically results in a small, irregular, hyperechoic liver, often with numerous hypoechoic nodules (Fig. 40.26). Ascites often accompanies cirrhosis secondary to portal hypertension. Other hepatic diseases that may result in increased/mottled parenchymal echogenicity include chronic hepatitis, lymphosarcoma, amyloidosis, and cholangiohepatitis. In cats with cholangitis/cholangiohepatitis complex, the liver can appear normal, or hyperechoic, secondary to lipidosis; hypoechoic liver may also occur.[55,57] Mast cell infiltration in the liver results in a variable appearance, from normal to increased echogenicity and size. Hypoechoic nodules may be present[58,59] (Fig. 40.27). However, the sonographic appearance of the liver (and spleen) may be a poor predictor of cytologic mast cell infiltration.[59–61]

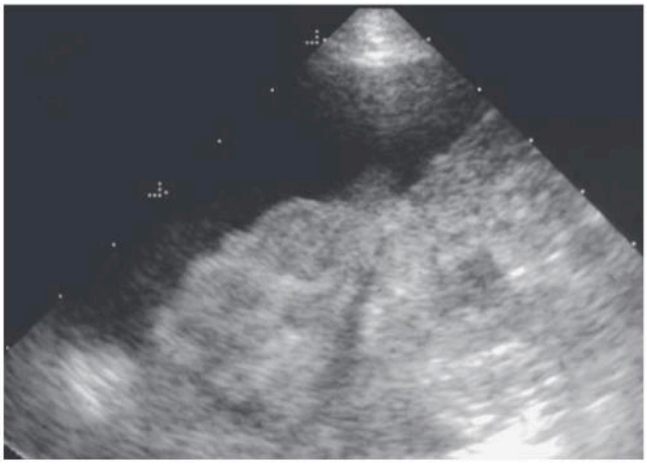


Fig. 40.26 Longitudinal ultrasound image of the liver in a dog with cirrhosis and ascites. The liver margins are irregular and rounded, and hypoechoic nodules are present within the parenchyma.

A decrease in hepatic echogenicity results in increased periportal echoes which is a somewhat subjective assessment. Decreased hepatic echogenicity may occur with hepatic congestion, lymphosarcoma, leukemia, amyloidosis, and cholangitis/cholangiohepatitis. A dilated caudal vena cava and hepatic veins will accompany hepatic congestion. Acute suppurative hepatitis such as leptospirosis can cause hypoechogenicity from inflammation and edema. However, this may be uncommon, even with severe disease.[54,62,71,83]

As noted previously, diffuse, even severe hepatic disease can appear normal ultrasonographically. Acoustic impedance of normal versus diseased tissue may simply be insufficient to permit visible change.[76,84,85] Any suspected hepatopathy should be compared with clinical signs and laboratory data, and a biopsy is necessary for definitive diagnosis.[63–66] Prebiopsy coagulation screening is a useful precaution when liver disease is suspected.

Focal hepatic disease appears as a nodule or mass that differs in texture and echogenicity from surrounding normal liver parenchyma. They may interrupt the hepatic margin, resulting in change of shape or contour. Relatively small nodules can be detected, especially when using high-frequency transducers. Although ultrasound is sensitive for detecting hepatic nodules, it is not specific, and numerous considerations are possible for focal disease. Cysts, abscesses, primary or metastatic neoplasia, hematomas, granulomas, nodular hyperplasia, and focal extramedullary hematopoiesis can all produce focal hepatic disease and may be difficult to differentiate on the basis of ultrasound appearance alone.[39,40,56,67] However, ultrasound is extremely useful in differentiating cystic versus solid masses; focal, multifocal, or diffuse distribution of masses; and the relation of the mass to adjacent structures, such as large blood vessels, diaphragm, or gallbladder.

Hepatic neoplastic masses are variable in appearance, and they can be hyperechoic, hypoechoic, or of mixed echogenicity, solid, cystic, or cavitated (Fig. 40.28).[68–80] The ultrasound appearance is not specific for a particular tumor, and as in diffuse disease, there appears to be poor correlation to cytologic and histopathologic diagnosis.[39,40,55,56,58,60,67,81–83] A positive cytological diagnosis of neoplasia is often accurate, but a negative cytologic evaluation does not rule out neoplasia.[83] Primary hepatic tumors are classified as massive (e.g., with a solitary mass affecting a single lobe), multifocal

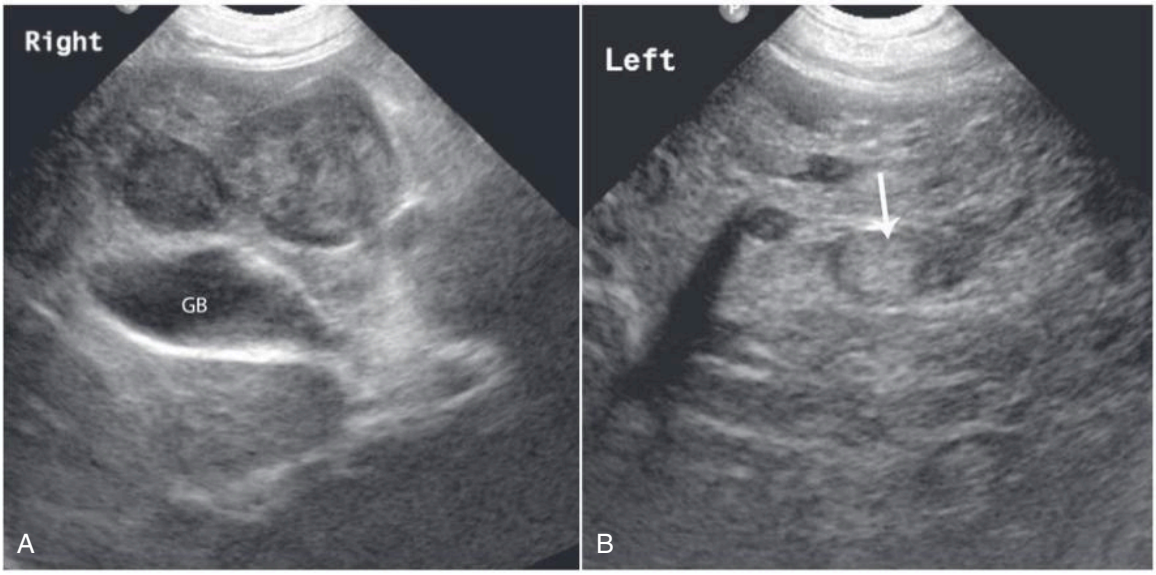


Fig. 40.27 Mast cell tumor in the liver. **A,** An ovoid, mixed echogenic mass is noted just ventral to the gallbladder (*GB*). Mast cell tumor was diagnosed on cytology from a fine-needle aspirate. **B,** Multiple variably sized hypoechoic and target-like (*arrow*) nodules are present throughout the liver parenchyma. Mast cell tumor was diagnosed in multiple organs (liver, spleen, kidneys, lymph nodes) on necropsy exam.

(e.g., with nodular disease in multiple lobes), and diffuse (e.g., multifocal coalescing nodules in all lobes).[70,73] Hepatocellular carcinoma is the most common primary tumor in the dog, and it is most often massive in classification (see Fig. 40.28A). Other primary hepatic tumors include cholangiocarcinoma, which is the second most common primary hepatic neoplasia in the dog, neuroendocrine tumor, hemangiosarcoma, and histiocytic sarcoma (see Fig. 40.28B).[70–75] Hepatic lymphosarcoma may result in a normal-appearing liver, or a diffuse increase or decrease in echogenicity; more focal changes include hypoechoic nodules/areas (see Fig. 40.28C).[64,83] Metastatic disease in the liver is the most common hepatic malignancy in the dog at 2.5 times the frequency of primary hepatic neoplasia, and most often originates from the spleen, gastrointestinal tract, and pancreas.[72] Like primary hepatic neoplasia, metastatic disease may be hyperechoic or hypoechoic, but more often it has a multifocal nodular or mass-like appearance (see Fig. 40.28D).[68,69,82] Metastatic disease cannot be differentiated from primary hepatic malignancy based solely on the ultrasound appearance.[68,69,82] Target lesions, which are focal masses with a hyperechoic center and hypoechoic periphery, are most commonly associated with malignancy, but they have been reported with benign disease processes (see Fig. 40.27B).[41,67,84] Biliary cystadenoma (bile duct adenoma) is the most common primary hepatic neoplasia in the cat, and it may be focal or multifocal.[75–80] Although variable in appearance, the presence of a cystic component somewhere in the mass is a consistent finding (Fig. 40.29). Biliary cystadenomas may appear multilocular, containing thin-walled cysts, or as hyperechoic masses with a cystic component. Most cystic portions of these masses will be characterized by acoustic enhancement. Cholangiocarcinoma is the most common feline primary hepatic malignancy.[75–80]

Hepatic nodular hyperplasia, a common benign lesion in older dogs, is usually silent clinically but may result in elevations in serum alkaline phosphatase.[71,85,86] It has a variety of sonographic appearances and cannot be differentiated from neoplasia without biopsy (Fig. 40.30). Hyperechoic,

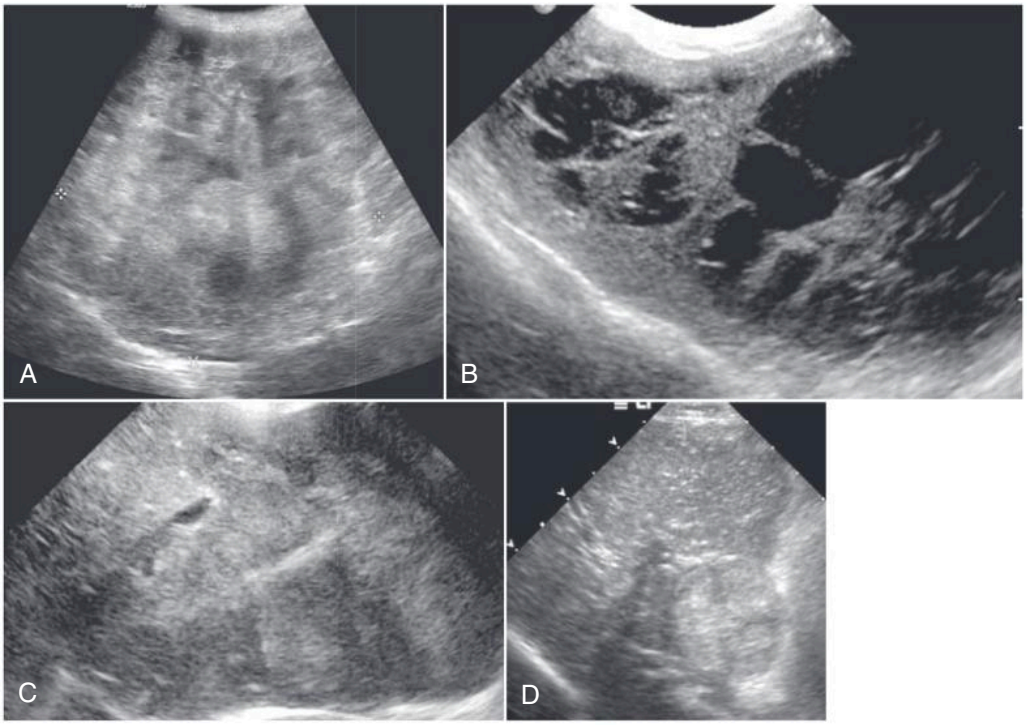


Fig. 40.28 Hepatic neoplasia. **A,** A large (approximately 10 cm) hyperechoic and hypoechoic mass (same dog as Fig. 40.8). Hepatocellular carcinoma was diagnosed on histopathology of the lobe. **B,** Multiple anechoic cavitations are present throughout the liver parenchyma. Hemangiosarcoma was diagnosed at necropsy. **C,** Longitudinal image of the left liver in a dog with lymphosarcoma. The liver is enlarged with rounded margins and a heterogeneous parenchyma. **D,** A focal hyperechoic nodule is noted distorting the liver capsule. Metastatic hemangiosarcoma was diagnosed at necropsy exam.

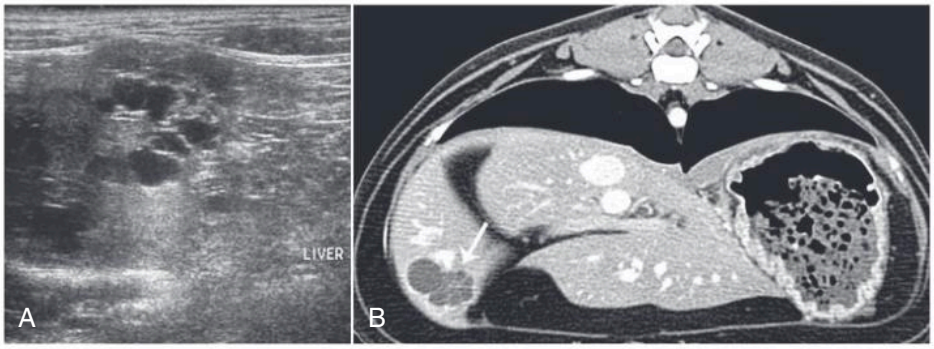


Fig. 40.29 **A,** Longitudinal ultrasound image of the liver from a cat with cystadenoma. A mass with anechoic cystic components, some with acoustic enhancement, is present. **B,** Transverse computed tomography image of a cat with cystadenoma (*arrow*). The mass is cystic in appearance and non−contrast enhancing.

hypoechoic, isoechoic, and mixed echogenicity nodules, some with cavitation, are all possible.[86]

Contrast-enhanced ultrasonography is used with some success to improve visualization of hepatic nodules and aid in differentiating benign and malignant hepatic nodular disease.[87–89] After injection of an ultrasound contrast agent, benign regenerative nodules were isoechoic to surrounding normal liver during peak normal liver perfusion, whereas malignant nodules were hypoechoic at peak normal liver perfusion. Identification of tumor type was not possible.

Chronic hepatitis may also result in a diffuse nodular appearance (Fig. 40.31). Hyperechoic hepatic parenchyma surrounds multifocal hypoechoic nodules (nodular hyperplasia).[39,40,56] Liver size may be normal or decreased. Hepatocutaneous syndrome (superficial necrolytic dermatitis) should be suspected when the liver parenchyma has a honeycomb appearance with hyperechoic hepatic parenchyma surrounding hypoechoic focal nodular areas (Fig. 40.32).[90–93] These patients have concurrent dermal lesions in the footpads and mucocutaneous junctions. A biopsy is critical in making the diagnosis.

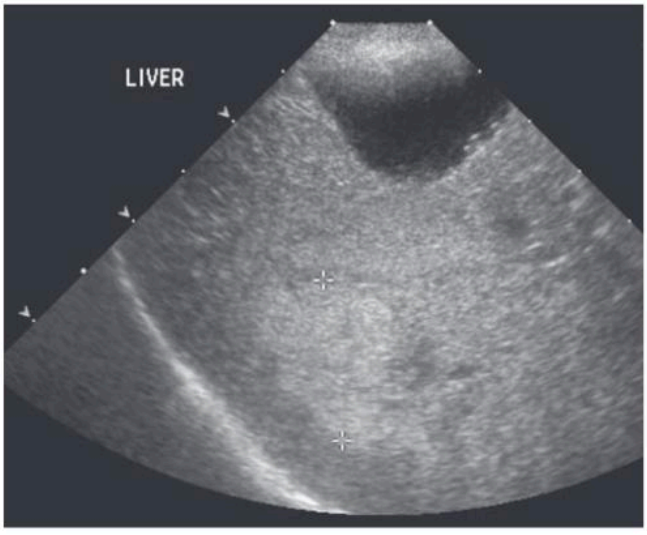


Fig. 40.30 Longitudinal ultrasound image of the liver from a dog with a hyperechoic nodule dorsal to the gallbladder (between calipers). Nodular hyperplasia was diagnosed histopathologically.

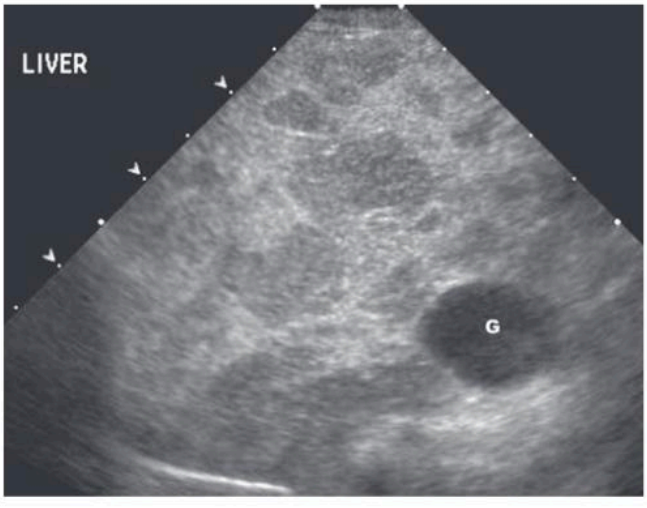


Fig. 40.31 Transverse ultrasound image of the liver from a dog with chronic hepatitis. Multiple hypoechoic nodules are present within a hyperechoic liver parenchyma. *G,* Gallbladder.

Hepatic abscesses and hematomas have a variable appearance depending on duration. Abscesses often have an echogenic rim with a central anechoic or hypoechoic area.[21,22,94–96] They may contain gas, resulting in an echogenic interface with deep acoustic shadowing (Fig. 40.33). Hepatic abscesses may appear as a simple hypoechoic mass resembling nodular hyperplasia or neoplasia. Hematomas may be hyperechoic initially because of gas or red blood cell aggregates and then progress to hypoechoic or anechoic and finally back to hyperechoic because of reorganization or possible mineralization.[38,97] Hepatic cysts have a more consistent appearance, as a fluid-filled, anechoic structure with a well-defined, thin wall and acoustic enhancement. Usually an incidental finding, hepatic cysts have the potential to produce clinical signs if large enough or numerous enough to replace liver parenchyma. They can be associated with polycystic kidney disease, so the kidneys should be evaluated carefully if hepatic cysts are noted.

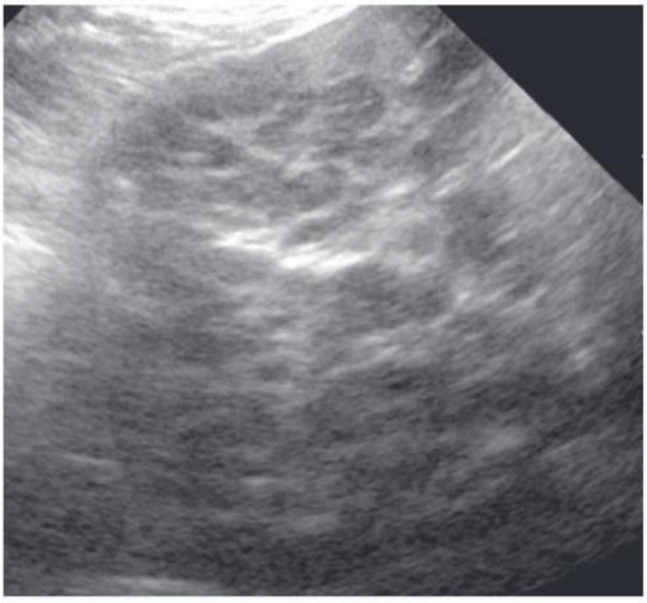


Fig. 40.32 Longitudinal ultrasound image of the liver from a dog with hepatocutaneous syndrome. Multiple hypoechoic nodules within the liver result in a honeycomb appearance.

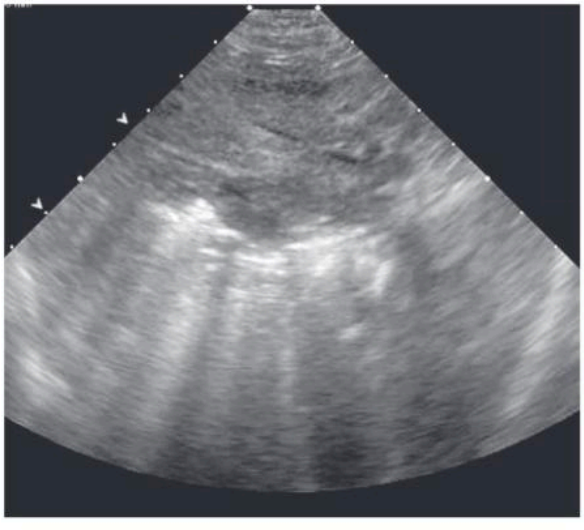


Fig. 40.33 Longitudinal ultrasound image of the liver from the dog in Fig. 40.14. Echogenic shadows and reverberation artifacts are noted deep to gas pockets within the liver. This dog had hepatic abscessation secondary to hepatic carcinoma.

Liver lobe torsion is variable in appearance.[97,98] The abnormally positioned lobe may be hypoechoic or mixed in echogenicity. Doppler evidence of blood flow is reduced or absent in the abnormally positioned lobe (Fig. 40.34).

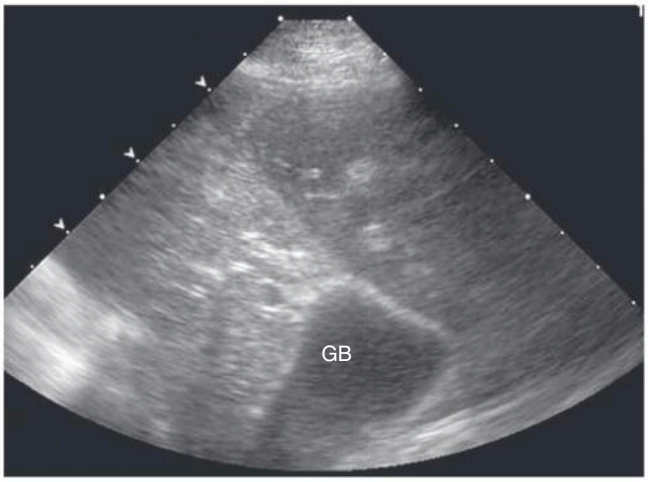


Fig. 40.34 Transverse image of the liver from a dog with torsion of the right medial liver lobe. The left portion of the liver is hypoechoic and is sharply demarcated from the normal right side of liver. Doppler signal was not present in the abnormal liver lobe. *GB,* Gallbladder.

Disease of the Biliary System

Ultrasound is an important component in the diagnosis of gallbladder and bile duct disease, and in determining the cause of icterus. Abnormal wall thickness, luminal contents, obstruction, and mass lesions may be diagnosed on ultrasound examination.

Thickening of the gallbladder wall is a nonspecific sign found with primary gallbladder inflammation or neoplasia, or nonbiliary diseases that have a secondary effect on the gallbladder wall.[99–106] Wall thickening can appear double layered with a central hypoechoic layer between hyperechoic layers, or it may be diffusely thickened, irregular, and hyperechoic (Fig. 40.35). Cholecystitis (inflammation of the gallbladder) can be acute or chronic, and has nonspecific ultrasound changes, ranging from normal (no change) to hyperechoic, irregular thickening of the wall (see Fig. 40.35B).[105–107] Sludge, both mobile and nonmobile, is often present. In one study, the finding of immobile gallbladder sludge had a 70% sensitivity and 100% specificity for the diagnosis of bactibilia and bacterial cholecystitis.[107] In a population of cats suspected to have hepatobiliary disease, cats with either/or a thickened gallbladder wall or intraluminal sludge were 21 times more likely to have positive results of bacterial culture in bile.[108]

Emphysematous cholecystitis, usually associated with a septic process and gas-forming bacteria, results in intraluminal echogenic foci and reverberation artifact. Cystic mucinous hyperplasia is noted as an incidental finding at necropsy, but it may be a predisposing factor in gallbladder mucocele formation.[110] Hyperplastic gallbladder wall epithelium, cystic

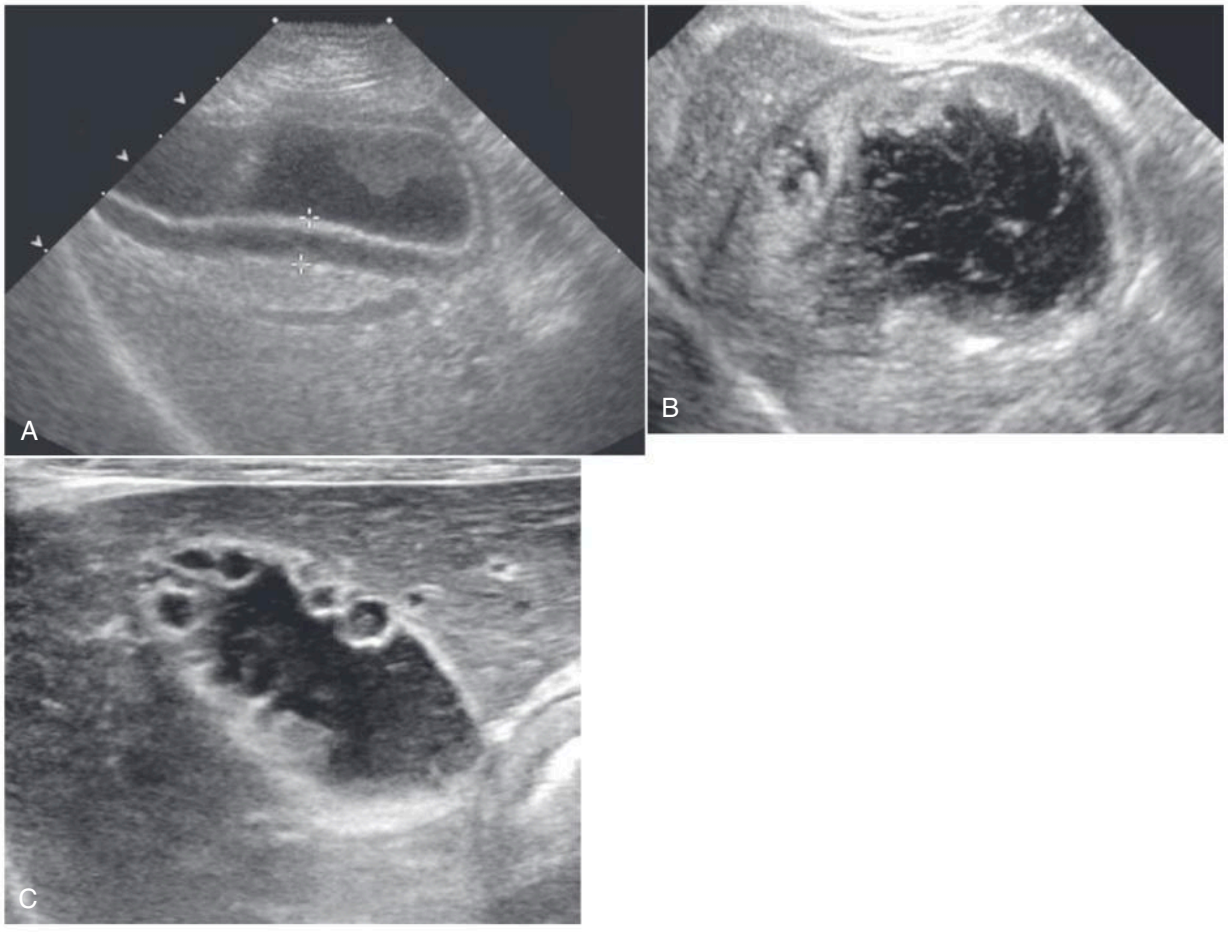


Fig. 40.35 Gallbladder wall thickening. **A,** Longitudinal ultrasound image of the liver and gallbladder from a dog with right-sided congestive heart failure. The gallbladder wall (between calipers) is thickened and has a layered appearance secondary to edema. **B,** Ultrasound image of the gallbladder in a dog presented for elevated liver enzymes. The wall is thickened and irregular secondary to cholecystitis. **C,** Cystic thickening of the gallbladder wall in a dog with no clinical signs consistent with cystic mucinous hyperplasia.

accumulations of mucus, and papillary projections create the appearance of sessile or polypoid masses along an irregularly thickened gallbladder wall (see Fig. 40.35C). Edema of the gallbladder wall, with a characteristic double-layered appearance, can be present secondary to acute cholecystitis, right-sided congestive heart failure, portal hypertension, hypoproteinemia, sepsis, blood transfusions, sedation with dexmedetomidine, and anaphylaxis (see Fig. 40.35A).[40,51,97,99,101–104] Peritoneal fluid surrounding the gallbladder can result in a false impression of wall thickening. Percutaneous cholecystocentesis for culture and cytology of the intraluminal bile can be performed with care, although complications appear to be uncommon.[108,109] Gallbladder wall thickening may be permanent because of inflammation and fibrosis despite resolution of the underlying disease process.[39]

Cholecystoliths, or calculi within the gallbladder, are echogenic focal structures, often with acoustic shadowing, and they may be single or multiple.[10,12,110,111] They are typically mobile, falling to the dependent portion of the gallbladder (Fig. 40.36).

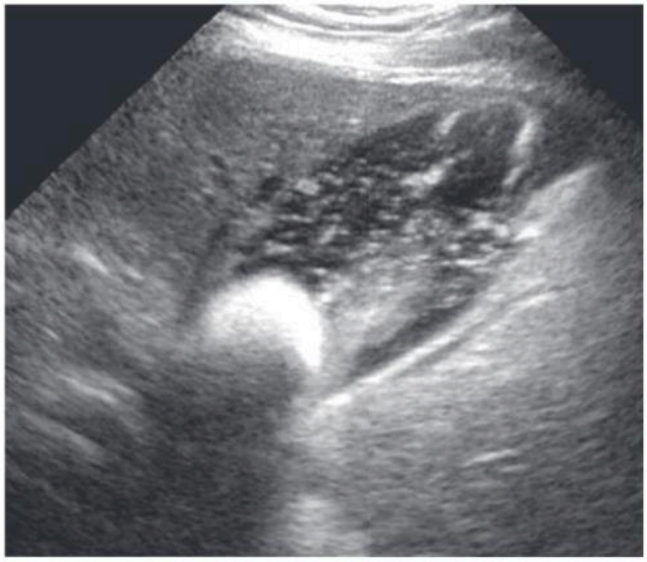


Fig. 40.36 A large, hyperechoic cholelith with acoustic shadowing is present in the dependent portion of the gallbladder lumen.

Choledocholiths are stones within the bile duct, hepatic ducts, and interlobar ducts.[9] Although cholecystoliths and choledocholiths are frequently incidental, they have the potential to cause biliary obstruction. Choledocholiths located in the distal bile duct, in or around the duodenal papilla, are one of the more common causes of biliary obstruction in cats, and they are often associated with cholangitis/cholangiohepatitis as a comorbidity.[111,112] In one study, a high prevalence of bacterial infection was noted in cats with cholelithiasis.[112]

As noted earlier, intraluminal echogenic, nonshadowing, dependent, mobile biliary sludge is present in up to 66% of dogs undergoing routine ultrasound exam, and 35% to 48% of all dogs regardless of health status.[46,48,113–115] Canine dependent biliary sludge does not appear to change significantly over time based on one study that followed asymptomatic canine patients for a 1-year period.[48] Another study noted that dogs with biliary sludge may have decreased gallbladder emptying compared to dogs without sludge.[47] It is hypothesized that decreased emptying may predispose to gallbladder mucocele formation secondary to biliary stasis, bile inspissation, and increased mucus accumulation.[47,48] Despite a high prevalence in asymptomatic dogs, biliary sludge may not be a completely benign process.[48,105–107,116] Nondependent biliary sludge may represent a risk factor for development of a biliary mucocele, particularly in predisposed breeds.[117] Prevalence of biliary sludge in cats undergoing abdominal ultrasound ranges from 14% to 44%.[118,119] While one study indicated sludge was predictive of increased liver enzymes and total bilirubin, a second study showed no increase, although gallbladder wall thickening was significantly associated with gallbladder sludge.[118,119]

Gallbladder emptying can be determined by measuring gallbladder volume pre and post feeding. After a 12-hour fast, volume is determined using the previously noted ellipsoid formula. At 60- and 120-minutes post meal or prokinetic agent, such as erythromycin, gallbladder volume is reassessed. In normal dogs, gallbladder volume post feeding should be less than 1 mL/kg, or it should be reduced by at least 25%.[44,120] Mean pre- and postprandial (2 hours post feeding) volumes of 2.47 ± 1.16 mL and 0.88 ± 0.13 mL, respectively, have been reported in normal cats.[121]

Gallbladder mucocele is an accumulation of nondependent sludge, semisolid mucin, and inspissated bile, creating an intraluminal centralized echogenicity with peripheral striations, often with a striated or stellate appearance (Fig. 40.37).[122–130]

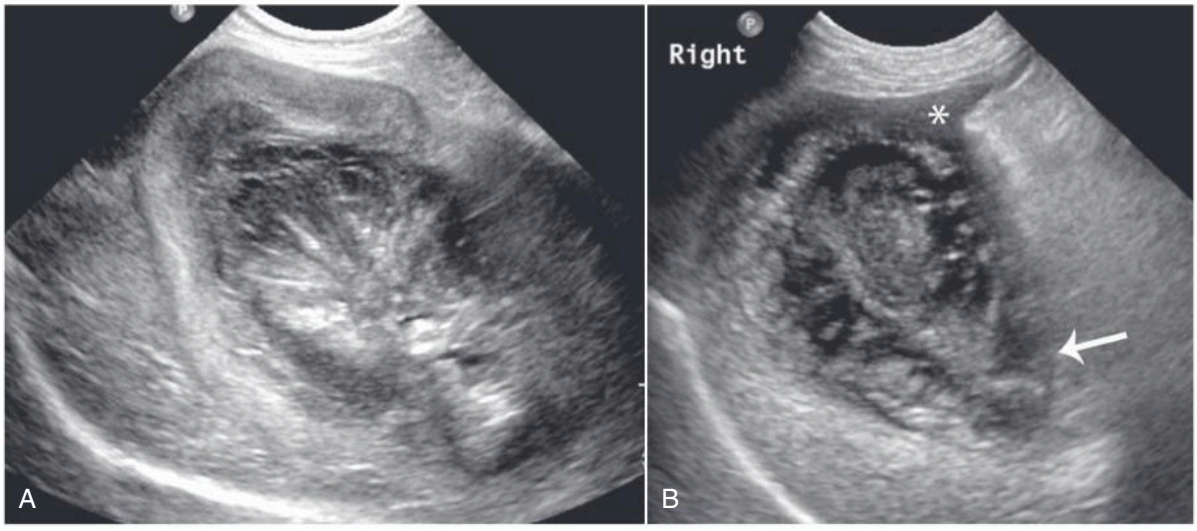


Fig. 40.37 **A,** Longitudinal ultrasound image of a gallbladder mucocele. Echogenic biliary sludge fills the gallbladder lumen, creating a striated appearance along the periphery. The gallbladder wall is markedly thickened. **B,** A gallbladder mucocele is present, with centralized, echogenic sludge and peripheral striations. The gallbladder wall is poorly defined caudally (*arrow*), and hyperechoic fat surrounds the gallbladder. Focal fluid accumulation (*asterisk*) is present. These are all consistent with gallbladder rupture.

Mucocele formation is caused by excess secretion of a gel-forming mucin by the gallbladder epithelium. Mucus granules become tethered to each other and the epithelium, resulting in abnormal physical and functional properties and inspissation of the bile.[131] Biliary obstruction by mucinous plugs within the cystic and bile duct may occur and lead to distention of the intrahepatic and/or extrahepatic biliary system. Ischemic necrosis of the gallbladder wall can lead to rupture. Gallbladder mucoceles have been associated with a 50% incidence of loss of gallbladder wall integrity and/or acute rupture.[122] The presence of discontinuity of gallbladder wall, pericholecystic hyperechoic fat, and/or pericholecystic fluid is strongly suggestive of gallbladder rupture (see Fig. 40.37B).[126] Sensitivity of ultrasound for detection of gallbladder rupture is low (56.1%), with a high specificity (91.7%) in one study.[132] Contrast-enhanced ultrasound evaluation of the gallbladder allows identification of ischemic necrosis or rupture of the gallbladder wall with a higher sensitivity and specificity than conventional sonography.[133] Predisposing factors to gallbladder mucocele include breed (Cocker Spaniel, Sheltie, Miniature Schnauzer, Border Terrier) and some endocrinopathies including hyperadrenocorticism, hypothyroidism, hyperlipidemia, and diabetes mellitus.[134–136] A biliary mucocele is identified occasionally as an incidental finding in patients without clinical signs or serum biochemical changes. Feline gallbladder mucoceles are uncommon, because cats have fewer mucus-secreting glands in the gallbladder compared to dogs.[137]

Extrahepatic biliary obstruction (EHBO) results in a retrograde dilation of the biliary system.[138] With complete obstruction, the gallbladder and cystic duct distend within 24 hours with progressive dilation of the common bile duct within 48 hours (Fig. 40.38). Gallbladder distention may be minimal in the face of chronic inflammation and fibrosis. Progressive dilation of the common bile duct and hepatic ducts occurs during the next 3 to 4 days with dilation of lobar and interlobar ducts by 7 days. This results in multiple tortuous, irregularly branching anechoic linear tracks within the liver. These can be differentiated from hepatic vessels with Doppler interrogation (see Fig. 40.38B). Pancreatitis is one of the most common causes of EHBO in the dog, with choledocholithiasis or neoplasia of the liver, bile duct, pancreas, or duodenum also capable of causing obstruction (Fig. 40.39).[139] Tumors and inflammation of the bile duct, pancreas, and duodenum, along with choledocholithiasis, are more commonly noted in the cat (see Fig. 40.39A,B,D).[111] In 30 cats with EHBO, gallbladder distension was present in only 43%, and it was not considered a reliable indicator of biliary obstruction. More reliable was dilation of the bile duct, present in 97% obstructed cats.[111] Focal sludge accumulation within the feline bile duct cannot easily be differentiated from a neoplastic mass. Incomplete or early obstruction may not cause visible biliary dilation. Bile duct dilation may be prolonged, persisting after relief of the obstruction.[39]

Cholangitis/cholangiohepatitis (inflammatory infiltrate confined to the portal region of the liver with or without involvement of the hepatic parenchyma) complex is an important biliary disease in cats. Ultrasound changes with this disease include thickened gallbladder wall, often with a palisade type irregular mucosa, intraluminal gallbladder or bile duct sludge, choleliths/choledocholiths, and thickened, tortuous, and sometimes dilated bile ducts (see Fig. 40.39A).[140,141] No ultrasound changes are present in some cats with cholangitis/cholangiohepatitis. Comorbidities include EHBO, cholecystitis, cholelithiasis, ductal plate malformations, inflammatory bowel disease, and pancreatitis.[142–144] Microcholelithiasis accumulation at the duodenal papilla may be related to pancreatitis in cats.[143] Cholangitis is now also recognized in dogs, and can be present concurrently with cholecystitis and biliary mucocele.[145,146] Ultrasound findings are variable and nonspecific, and include gallbladder wall thickening, distension of the common bile duct, cholelithiasis, and mucoceles.[145]

Vascular Disease

Venous congestion occurs with right-sided congestive heart failure or obstructive lesions in the posthepatic caudal vena cava. The hepatic caudal vena cava and hepatic veins both dilate in response to the elevated pressure (Fig. 40.40). The liver may also enlarge and become hypoechoic, although echogenicity changes may not be consistent. Dilation of the caudal vena cava and hepatic veins, along with ascites, suggests the possibility of disease cranial to the diaphragm.

Ultrasonography can be used to identify most portosystemic shunts reliably, although detection of these vascular anomalies requires a good knowledge of vascular anatomy. An abnormal shunting vessel is the most reliable indication of portosystemic shunt, but other changes, including a small liver that is uniform

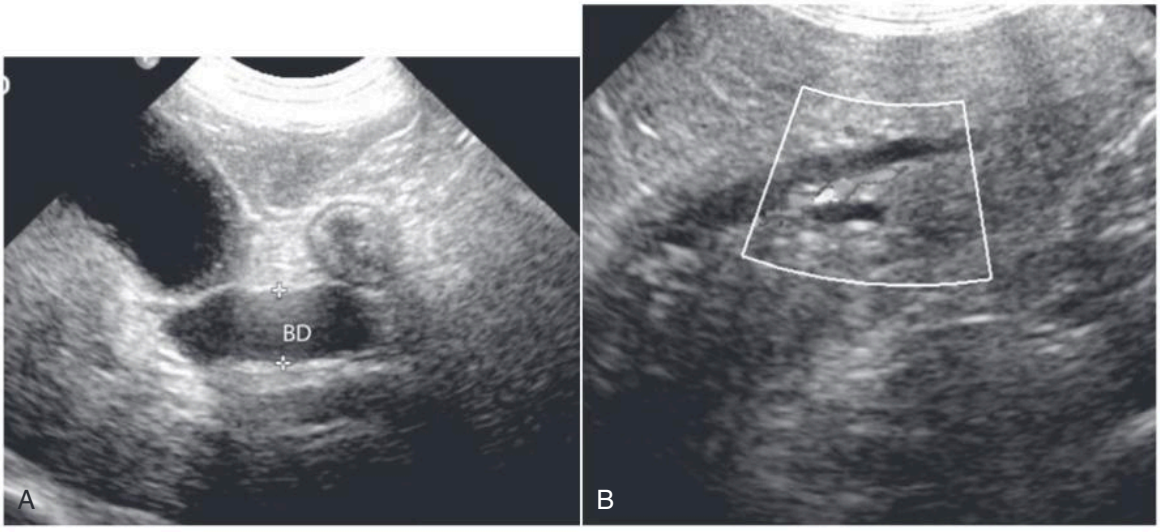


Fig. 40.38 Extrahepatic biliary obstruction. **A,** Longitudinal ultrasound image of a dog with extrahepatic biliary obstruction as a result of pancreatitis. The gallbladder and bile duct (*BD*) are moderately distended. **B,** Ultrasound image of a portion of liver in a cat with chronic biliary obstruction. Dilated intrahepatic bile ducts (with no color Doppler signal) are present.

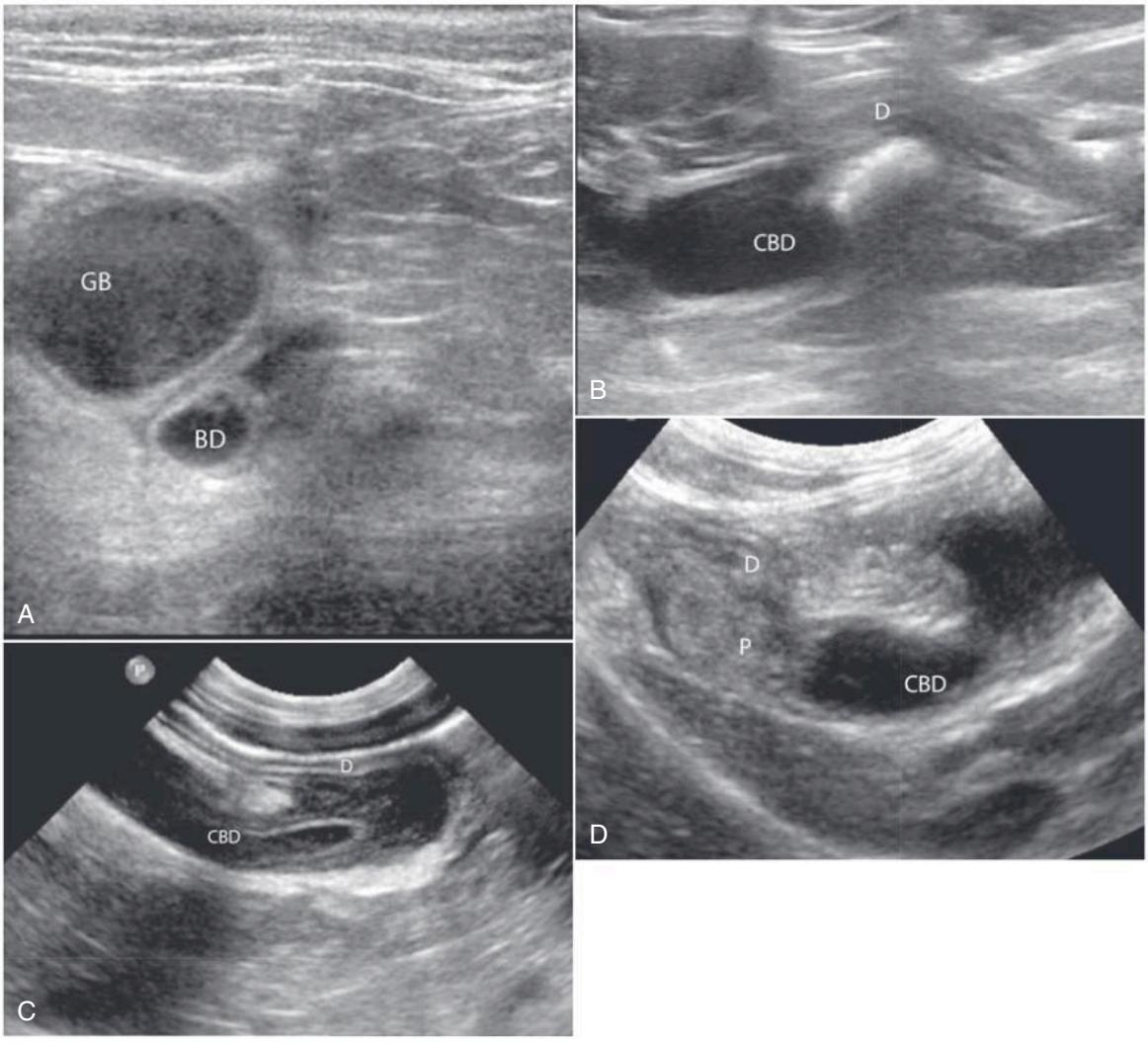


Fig. 40.39 Extrahepatic biliary obstruction. **A,** Ultrasound image of the gallbladder (*GB*) and bile duct (*BD*) in a cat with cholangitis and biliary obstruction. The bile duct is thickened and dilated. The gallbladder wall is thickened. **B,** Dilated bile duct (*CBD*) secondary to obstruction by a choledocholith at the duodenal papilla (*D*) in a cat with cholangitis. **C,** CBD secondary to obstruction by a mass at the level of the duodenal papilla (*D*) in a dog presented for elevated liver enzymes. Lymphoma was diagnosed on cytology from a fine needle aspirate of the mass. **D,** CBD secondary to a plug of inspissated bile (*P*) at the level of the duodenal papilla (*D*) in a cat with cholangitis.

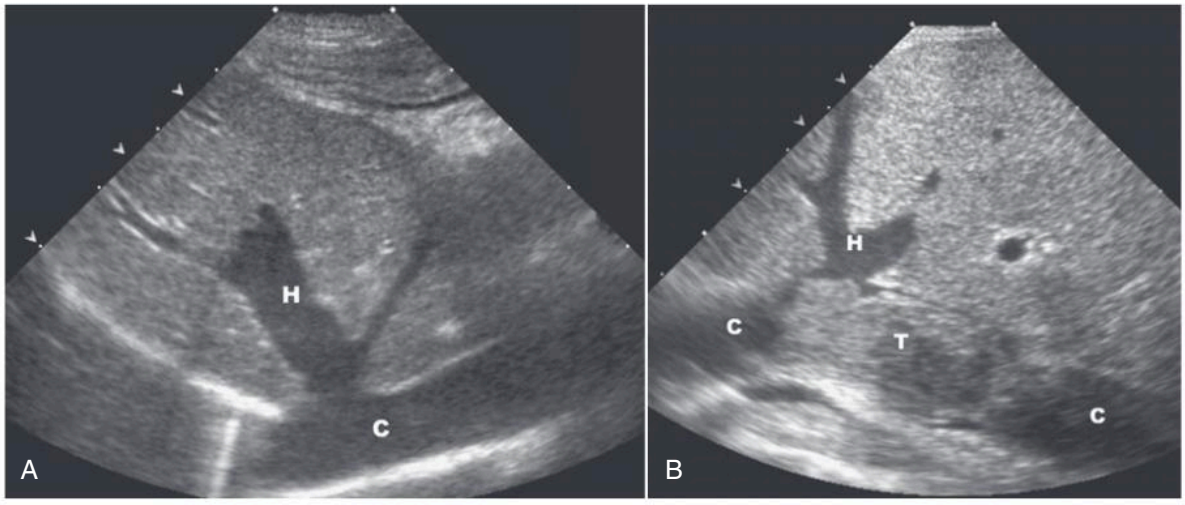


Fig. 40.40 Venous congestion. **A,** Right lateral oblique ultrasound image of the liver. The caudal vena cava (*C*) and hepatic veins (*H*) are distended as a result of right-sided congestive heart failure. **B,** An intraluminal tumor thrombus (*T*) obstructs the caudal vena cava (*C*) and hepatic veins (*H*) resulting in venous congestion.

and normal in echogenicity, decreased or absent intrahepatic portal vasculature, decreased size of extrahepatic portal veins, enlarged kidneys, and renal/ureteral/cystic and/or urethral calculi (urate calculi), are often present (Fig. 40.41; see Fig. 40.19).[147,148]

Extrahepatic shunts affect cats and small-breed dogs primarily, and the most common finding is a single shunt vessel connecting the portal vein, or more likely a major tributary of the portal vein, such as splenic, left gastric, or right gastric vein, to the caudal vena cava between the right renal vein and hepatic veins (see Fig. 40.41B,C,D).[147,148] Extrahepatic shunt vessels may be difficult to identify because of poor acoustic windows associated with the small liver or the presence of bowel gas. A right dorsal intercostal window, in addition to routine views, is helpful in detecting the anomalous shunt vessel. In this window, the portal vein and caudal vena cava are visible as they enter the porta hepatis, and abnormal shunting vessels may be identified. The portion of the portal vein cranial to the origin of the shunt is often decreased in size, with a portal vein:aortic ratio of less than 0.65, whereas the normal ratio is 0.7 to 1.25. Dogs with shunt ratio of >0.8 did not have an extrahepatic shunt.[147] Pulsed-wave or color Doppler interrogation of the caudal vena cava is helpful in assessing for abnormal turbulence where a shunting vessel enters.[147,148] Shunt vessels terminating in the azygous vein may be more difficult to follow, but they might be seen terminating in an enlarged azygous vein adjacent to the aorta or esophagus. Acquired extrahepatic shunt vessels attributable to hepatic disease and portal hypertension may appear as a grouping of multiple variably sized, tortuous vessels, often medial to the spleen and left kidney. Color Doppler imaging may be needed to find these abnormal vessels.[148]

Intrahepatic shunts affect primarily large-breed dogs. Left divisional shunts, such as a patent ductus venosus, right divisional shunts, and central-divisional shunts can be identified. A right lateral intercostal window, in addition to the standard ventral abdominal approach, is helpful in identifying the right divisional intrahepatic shunting vessel between the main portal vein and caudal vena cava (see Fig. 40.41A).[147,148,149]

Arterioportal communications are rare malformations in dogs and cats. Typically, an abnormally dilated and tortuous cluster of vessels is visible within or adjacent to the liver. Upon Doppler interrogation, hepatofugal flow and an arterial spectral Doppler signal in the portal vein confirm the presence of an arterioportal communication.[33–35] An uncommon form of splenosystemic shunt has been described in cats.[150] These splenosystemic shunts were identified as an anomalous vessel arising from the splenic vein, coursing caudal to the left kidney assuming a generally tortuous path, and continuing to the left renal vein, caudal vena cava adjacent to the renal vein, or medial to the left kidney. Neutered female cats were overrepresented. It could not be determined whether these shunts

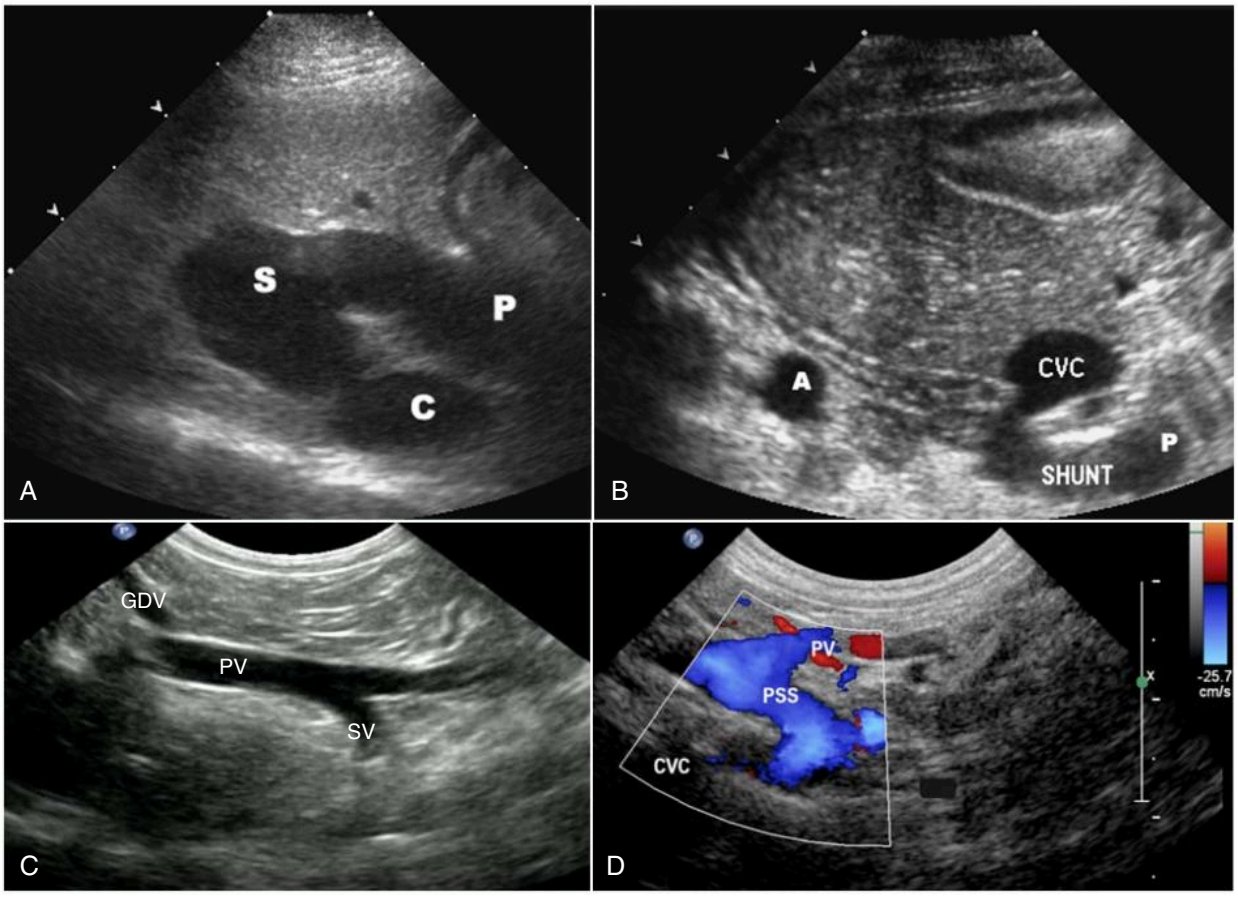


Fig. 40.41 Portosystemic shunts. **A,** Right lateral intercostal ultrasound image of a young dog with a right divisional intrahepatic portosystemic shunt. Dorsal is to the *left* of the image and right is at the *top* of the image. *C,* Caudal vena cava; *P,* portal vein; *S,* shunt. **B,** Right lateral intercostal ultrasound image of a young dog with an extrahepatic portosystemic shunt. Dorsal is to the *left* of the image, and right is at the *top* of the image. *A,* Aorta; *CVC,* caudal vena cava; *P,* portal vein. **C,** Sagittal image of the normal portal vein and tributaries. *GDV,* Gastroduodenal vein; *PV,* portal vein; *SV,* splenic vein. **D,** Same window as **C,** with color Doppler evaluation of a splenocaval shunt. Abnormal flow through the shunting vessel is blue, indicating flow away from the portal vein and towards the caudal vena cava. *CVC,* Caudal vena cava; *PSS,* portosystemic shunting vessel.

were congenital or acquired in origin. However, these shunts do not appear to share similar clinical or anatomic features with previously described congenital portosystemic shunts in cats. This type of shunt can occasionally be visible in survey abdominal radiographs as a tortuous vessel caudal to the spleen in VD radiographs (Fig. 40.42).

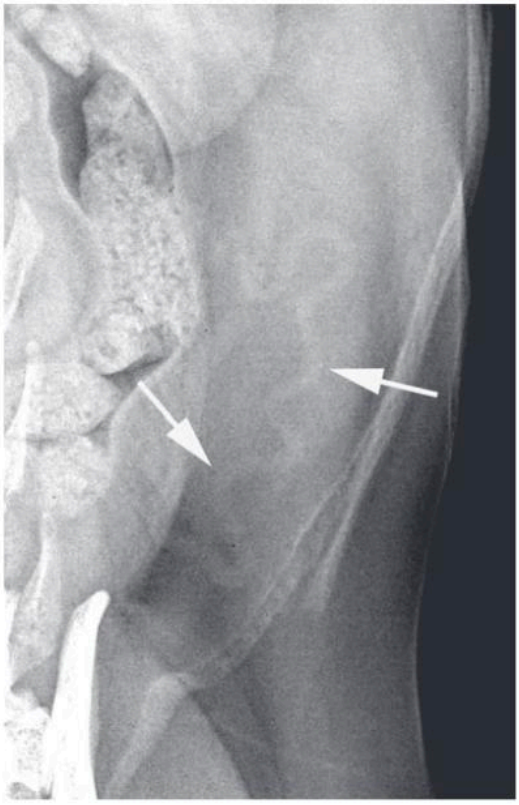


Fig. 40.42 Ventrodorsal (VD) radiograph of the abdomen of a cat in the region caudal to the spleen. A tortuous vessel, representative of a splenocaval shunt, is visible (*white arrows*).

RADIOLOGY OF THE SPLEEN

The spleen is a dynamic organ; and in the dog, the size and location of the spleen can vary widely. There are numerous variations on the radiographic appearance of the normal spleen in dogs and to a lesser extent in cats.[1–3] The spleen is divided into a dorsal extremity, termed the *head* of the spleen; a body; and a ventral extremity, termed the *tail* of the spleen. The dorsal extremity is relatively fixed in the left craniodorsal aspect of the abdomen. The ventral extremity is not fixed, and in the dog, the position of this portion of the spleen can vary considerably. On VD views of the canine abdomen, the dorsal extremity of the spleen is seen typically as a triangular soft tissue opacity caudolateral to the gastric fundus and craniolateral to the left kidney (Fig. 40.43A). The remainder of the spleen may extend caudally, adjacent to the left lateral abdominal wall, or more medially across the midline. When the spleen extends medially, the full length of the spleen is not visualized completely.

On lateral views, the triangular soft tissue opacity of the dorsal extremity of the spleen is located dorsally, caudal to the stomach. The ventral extremity typically is a triangular soft tissue opacity immediately caudal and slightly ventral to the pylorus or liver (see Fig. 40.1A). The ventral extremity of the spleen is often more conspicuous on right lateral views of the abdomen but may silhouette the caudal margin of the liver and be poorly delineated.

The feline spleen is thinner and smaller compared with the canine spleen and less variable in size and position (see Fig. 40.43B; also see Fig. 40.1C). Like the dog, the dorsal extremity of the spleen is seen on VD views in the left cranial abdomen, caudolateral to the stomach and craniolateral to the left kidney. On VD views, the ventral extremity usually extends caudally along the left lateral abdominal wall, but the amount of visible spleen varies with body fat, positioning, gastric contents, and splenic position.[151]

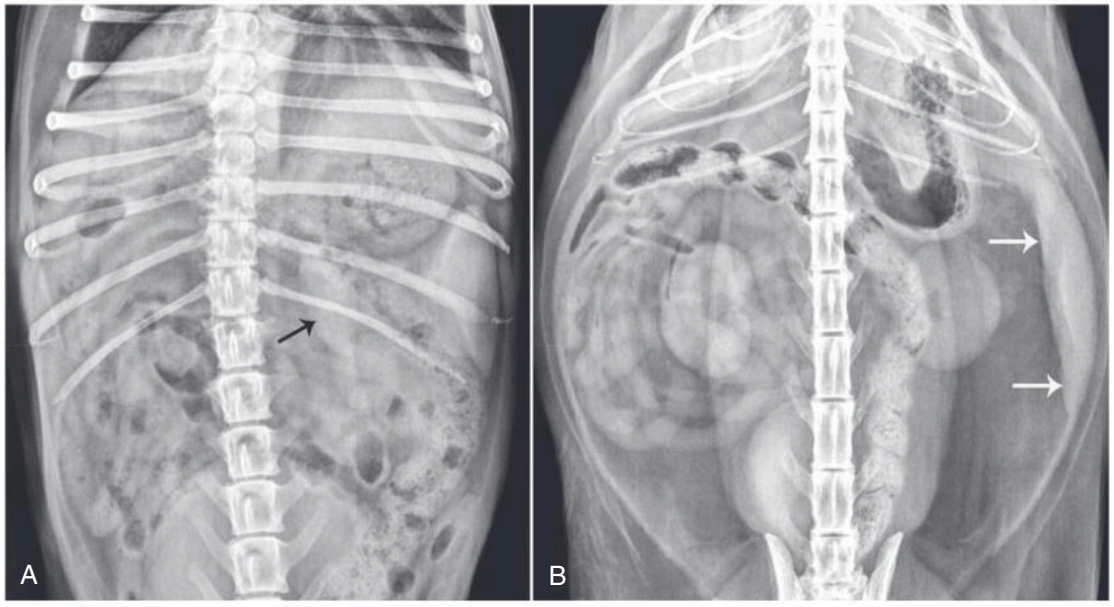


Fig. 40.43 Normal spleen. **A,** Ventrodorsal (VD) radiograph of the abdomen of a normal dog. The dorsal portion of the spleen is visible in the left cranial abdomen, caudolateral to the gastric fundus and craniolateral to the left kidney. The more ventral portion is noted by the *black arrow*. **B,** VD radiograph of the abdomen of a normal cat. The entire spleen can be visualized extending caudally along the left lateral abdomen (*white arrows*).

On lateral abdominal views in the cat, the dorsal extremity may be visible caudal and dorsal to the gastric fundus. The ventral extremity of a normal spleen is rarely visible in the cat. In 100 cats with a presumably normal spleen, the ventral extremity was visible on a lateral radiograph in only one cat.[151]

In both dogs and cats, it is important to realize that the entire spleen is rarely visible on a single radiographic projection.

Splenic Size

Radiographic assessment of splenic size in the dog is very subjective, because normal size varies widely. Feline splenic size appears to be more consistent. Splenomegaly in the cat should be considered if the ventral extremity is visible on the lateral projection of the abdomen.[151] In the dog, and to a lesser extent in the cat, generalized splenomegaly results in thickened, rounded, blunted margins, and dorsal and caudal displacement of the jejunum on lateral views (Fig. 40.44). Organ displacement on the VD view as a result of the enlarged spleen depends on the portion of the spleen that is enlarged and the degree of enlargement. The jejunum may be displaced to the right or left, whereas an enlarged dorsal extremity results in cranial displacement of the stomach.

Considerations for diffuse splenomegaly are numerous and include inflammation caused by infection with toxoplasmosis, fungal organisms, *Mycoplasma haemofelis,* ehrlichiosis, hyperplasia (e.g., hemolytic disorders), systemic lupus erythematosus, chronic bacteremic disorders, congestion (e.g., from impaired venous drainage), portal hypertension, splenic torsion/infarction, anesthetic drugs, infiltrative disease (e.g., primary and metastatic neoplasia), and extramedullary hematopoiesis.[152–155] Lymphosarcoma, leukemia, systemic mastocytosis, multiple myeloma, and malignant histiocytosis can all result in diffuse neoplastic splenic enlargement. Splenomegaly in the cat is less likely to be benign, because the feline spleen is considered nonsinusoidal and less capable of storing large amounts of blood.[155–157] Compared with the dog, generalized splenomegaly in the cat is most commonly caused by neoplastic infiltration, primarily lymphosarcoma, and mast cell tumor (see Fig. 40.44B).[157,158]

Sedation with acepromazine resulted in significantly increased radiographic splenic size, while sedation with midazolam/butorphanol combination, and dexmedetomidine/butorphanol/ketamine combinations resulted in a trend towards increased splenic size in the cat.[159]

Splenic torsion occurs when the spleen rotates around its mesenteric axis, resulting in complete occlusion of venous drainage and eventual arterial occlusion. This results in marked splenomegaly, as well as an atypical splenic location.[160,161] The spleen may undergo torsion on its own or in association with gastric volvulus. It may acquire a reverse C-shape on the lateral view or may simply appear as a mass in the ventral abdomen

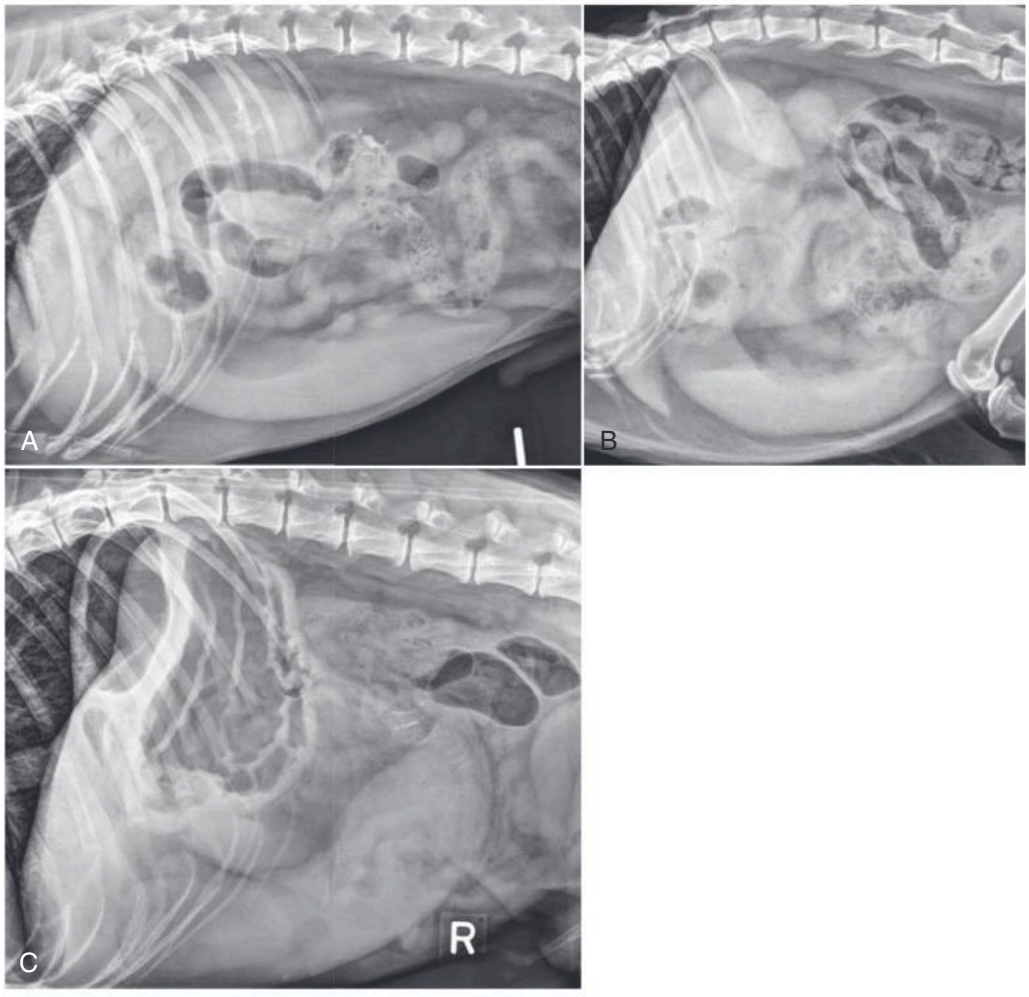


Fig. 40.44 Splenomegaly. **A**, Lateral abdominal radiograph of a sedated dog. The spleen is elongated, with rounded margins secondary to congestion. **B,** Lateral abdominal radiograph of a cat with splenic lymphosarcoma. The spleen is visible on lateral images appearing markedly elongated with rounded margins secondary to neoplastic infiltration. **C,** Lateral abdominal radiograph of a dog with gastric volvulus. The spleen is markedly enlarged, with elongation and rounding of margins secondary to splenic torsion.

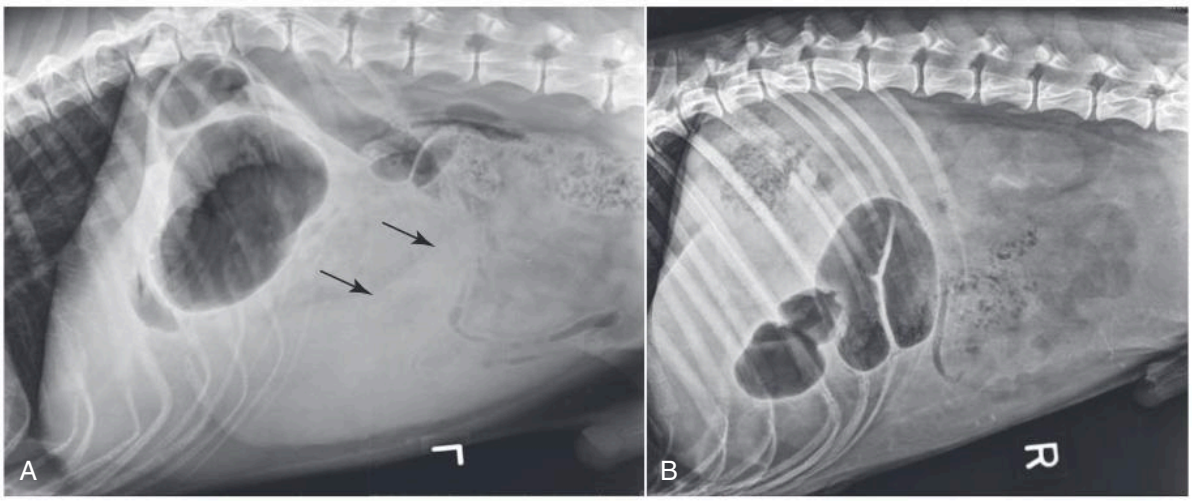


Fig. 40.45 **A,** Lateral radiograph of the abdomen of a dog with splenic torsion. The spleen is enlarged and displaced caudally and dorsally (*black arrows*). **B,** Lateral radiograph of the abdomen of a dog with a large splenic abscess. A stippled gas pattern is present within both the head and tail of the spleen.

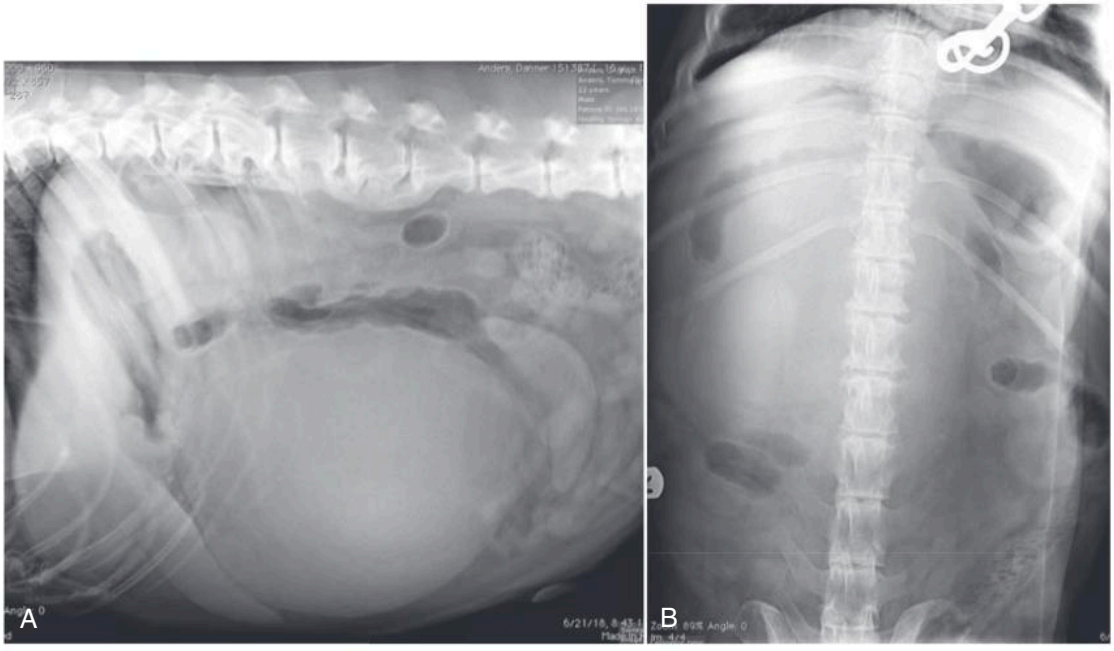


Fig. 40.46 Lateral **(A)** and ventrodorsal (VD; **B**) radiographs of the abdomen of a dog with splenic hemangiosarcoma in the ventral extremity of the spleen, seen along the ventral abdomen on the lateral view, and to the *right* of midline on the VD view.

(Fig. 40.45 and eFig. 40.6). The dorsal extremity of the spleen may not be visible in the normal left craniodorsal location because of the malposition or accompanying peritoneal fluid. If gas-producing bacteria proliferate within the ischemic parenchyma, emphysematous changes may occur and result in a mottled or foamy radiographic appearance (see Fig. 40.45B).[161] CT has been used in the diagnosis of splenic torsion, and the findings include splenomegaly, a corkscrew-like soft tissue mass representing the rotated splenic pedicle, and lack of contrast enhancement.[162]

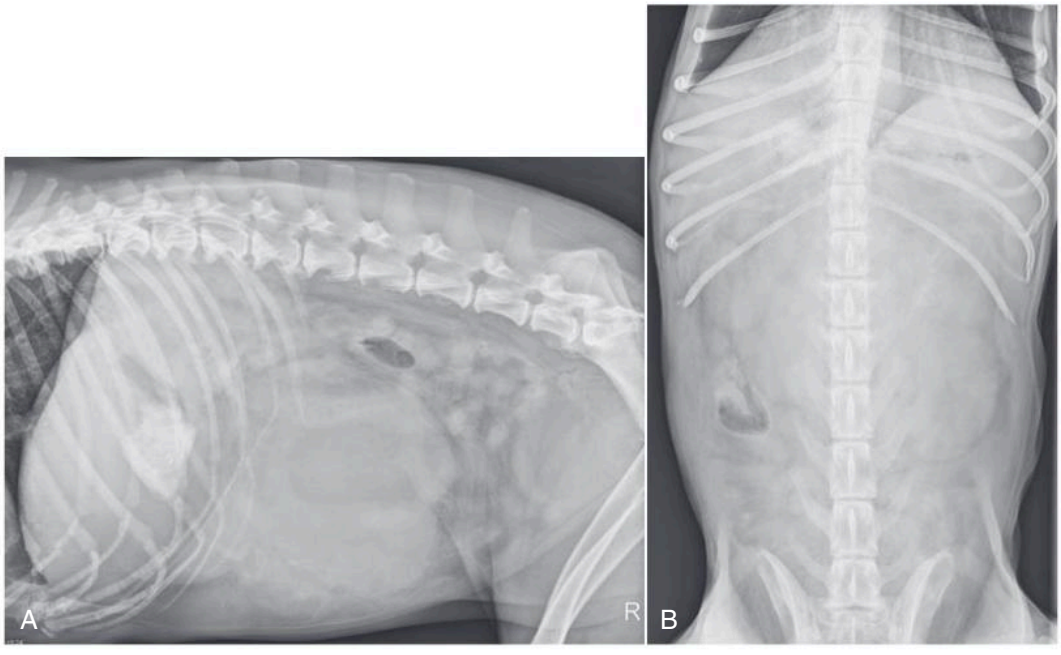
A splenic mass results in local displacement of adjacent viscera according to the location of the mass in the spleen (Figs. 40.46 and 40.47, eFig. 40.7). Although often sharply marginated, the splenic mass may be obscured partially or completely by secondary peritoneal hemorrhage. A mass in the body or ventral extremity of the spleen is a very common cause of a ventral abdominal mass, and on the lateral view results in dorsal and caudal displacement of the jejunum. On VD views, ventral splenic masses may be midline or to the right or left of midline.

Masses of the dorsal extremity of the spleen are less common and may displace the stomach cranially with caudal, medial, and ventral displacement of the jejunum and descending colon. The left kidney may be displaced caudally as well.

Differentials for a splenic mass include benign and neoplastic conditions. Primary and metastatic neoplasia, hematoma, nodular hyperplasia, extramedullary hematopoiesis, and abscess are all considerations.[158,164–166] Hemangiosarcoma is the most common neoplasm of the canine spleen, but splenic hematoma and hyperplastic nodules are the most common



eFig. 40.6 Left lateral **(A)** and ventrodorsal (VD; **B**) radiographs of a dog with splenic torsion. The spleen is severely enlarged, occupying the majority of the mid ventral abdomen. The normally triangular dorsal extremity is not visible in the left cranial abdomen in the VD view. Splenic torsion was con firmed surgically.



eFig. 40.7 Left lateral **(A)** and ventrodorsal (VD; **B**) radiographs of a dog with a splenic mass. A ventral abdominal mass is seen on the lateral view, causing dorsal and caudal displacement of the small intestines. The mass is visible in the mid abdomen in the VD projection. There is reduced serosal peritoneal detail with soft tissue streaks throughout the ventral abdominal fat, consistent with peritoneal effusion. A small amount of mineral material is present in the gastric pyloric antrum. Hemangiosarcoma was diagnosed histopathologically.

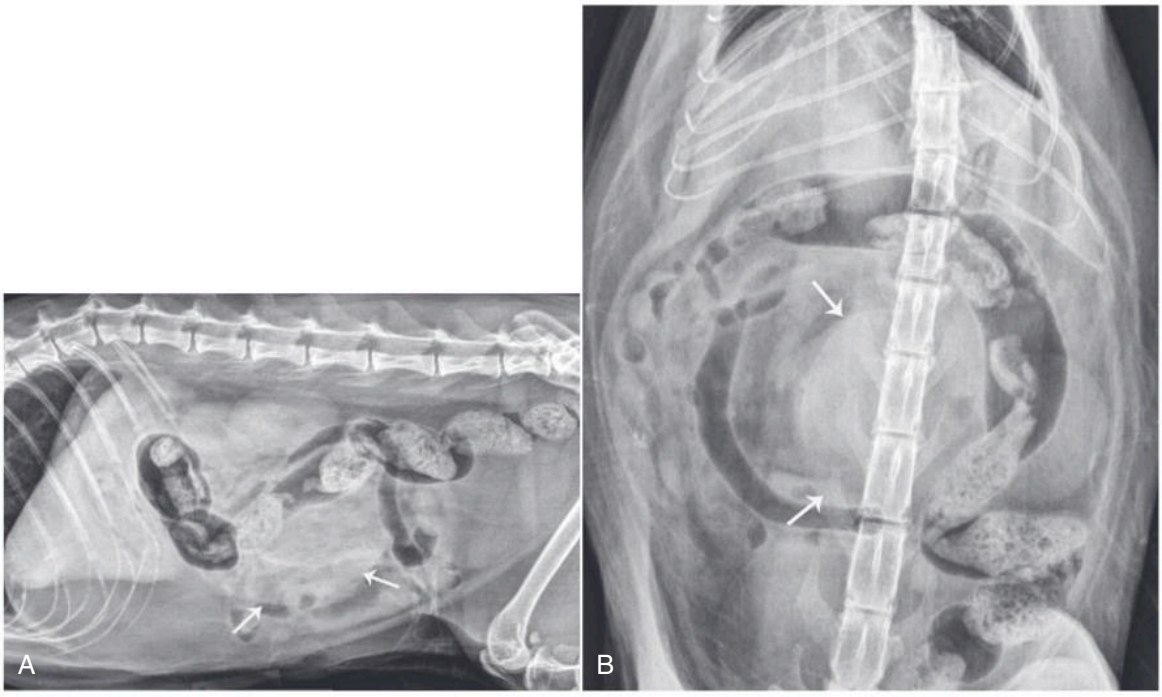


Fig. 40.47 Lateral **(A)** and ventrodorsal (VD; **B**) radiographs of the abdomen of a cat with a splenic hemangiosarcoma in the ventral extremity of the spleen, creating a poorly defined mass effect caudal to the stomach on the lateral view, and on the midline on the VD view (*arrows*). Abdominal effusion results in a partial loss of contrast and detail in the mid abdomen.

causes of splenic lesions.[166] Peritoneal effusion may accompany both benign and neoplastic diseases.

Splenic Opacity

Normal splenic opacity is that of soft tissue. Mineralization of the spleen may be the result of dystrophic calcification of abscesses, hematomas, fungal granulomas, or neoplastic masses, and can be associated with endocrine disease. Gas within the spleen may result from splenic torsion. As noted in the liver, gas may ascend into the portovenous circulation and affect the spleen.[16,17] Gas-forming organisms in splenic abscesses can create focal radiolucencies. Spontaneous emphysematous splenitis has been reported in Golden Retrievers resulting in a mass effect with coalescing vesicular-like gas pattern in the splenic region[166] (see Fig. 40.45B).

ULTRASOUND OF THE SPLEEN

The spleen is well suited to ultrasound examination because of the superficial location and lack of intervening gas-containing structures. Higher-frequency transducers may be used because of the superficial location.

Splenic location varies. The dorsal extremity of the spleen is in the left craniolateral abdominal quadrant and may be beneath the costal arch. Intercostal windows are sometimes necessary in deep-chested dogs. The canine splenic body and ventral extremity may extend caudally along the left lateral abdomen or move medially across the ventral midline. It often appears folded on itself. The feline spleen is more consistent in location, along the left lateral abdominal wall, and rarely folds on itself unless enlarged.

The splenic parenchyma has a uniform echotexture with a fine, dense pattern.[167,168] Echogenicity of the canine spleen is slightly greater than the liver (Fig. 40.48). Splenic margins are linear and smooth, with mild indentations noted along the mesenteric border where splenic veins exit. Splenic arteries are not usually seen without Doppler interrogation. Tissue surrounding splenic veins at the hilus may be highly echogenic normally because of capsular invagination and fat.[167]

When enlarged, the spleen may extend caudally or more completely cover the ventral abdomen. Splenic borders become rounded or blunted, or appear to bulge from the capsule, compared with the normal sharp, linear appearance (Fig. 40.49). The spleen has no absolute size limits in the dog. The normal feline spleen is less variable in size than the dog, and objective measurements have been determined. Mean splenic height, measured in the transverse plane, in the proximal third of the spleen, adjacent to a splenic vein, is 7.1 mm, with a range from 5.1 to 9.1 mm (see Fig. 40.48C).[169] Similar splenic measurements were determined in a second study, where normal feline splenic height was 8.2 ± 1.4 mm (range: 5.3–11.1 mm).[170]

Abnormal Splenic Ultrasonographic Findings

Diffuse Disease

As in the liver, diffuse splenic disease potentially causes changes in size, shape, or echogenicity. Splenomegaly with either normal or decreased echogenicity has numerous causes, including congestion, neoplasia, infarction, inflammation, immune-mediated disease, chronic hemolytic anemia, parasitic infection, extramedullary hematopoiesis, and bacterial or fungal infection.[157,167,168,170,175]

Extramedullary hematopoiesis often results in generalized splenomegaly, with normal echogenicity, or a coarse or mottled appearance. Lymphoid hyperplasia can also have a diffuse mottled appearance.

Splenic congestion as a result of a phenothiazine and pentobarbital drug group results in splenomegaly with no associated change in echogenicity in the dog.[170] Acepromazine has a similar appearance in the cat.[159] Congestion from portal hypertension appears similar, but dilated splenic veins may also be present. Splenic torsion, a form of splenic congestion, has a variety of appearances.[160,172] Splenomegaly may be the only

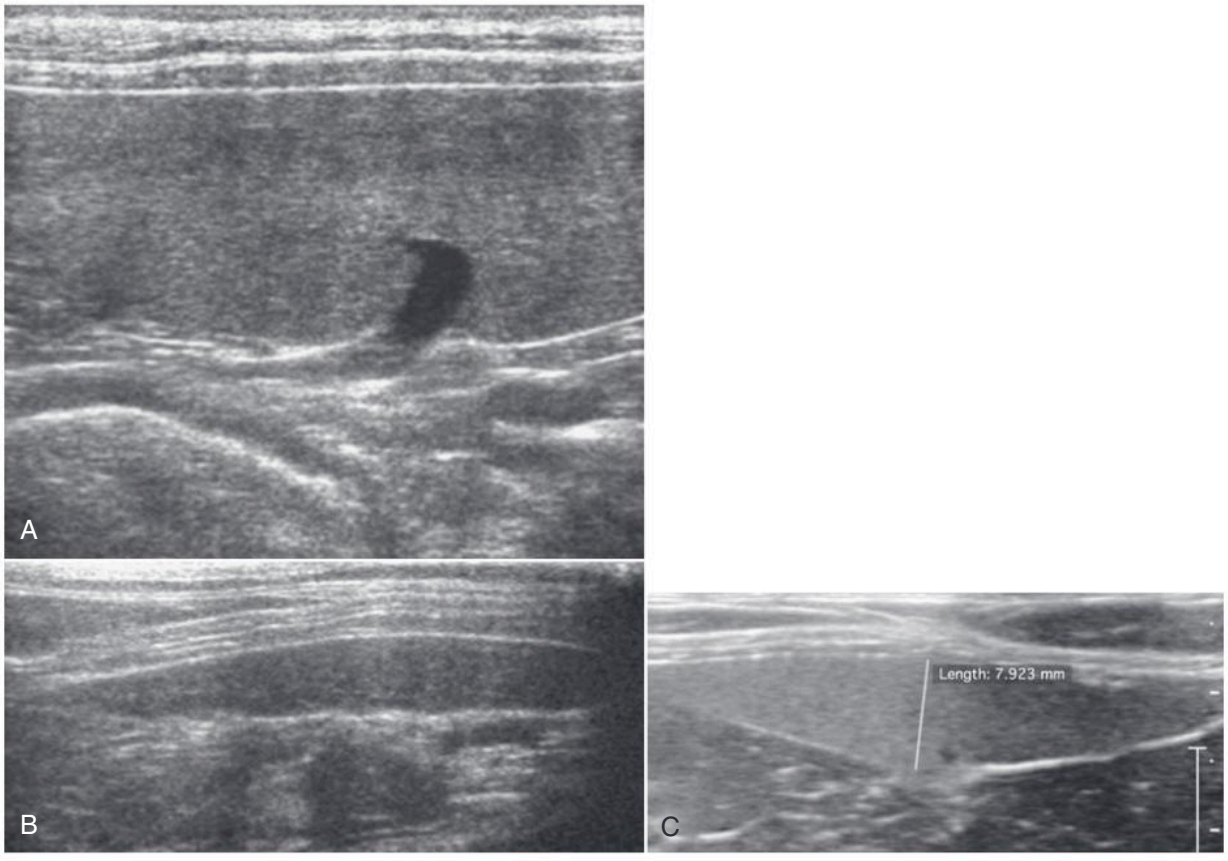


Fig. 40.48 Normal ultrasound appearance of the spleen. **A,** Longitudinal ultrasound image of the normal canine spleen. A splenic vein is visible leaving the splenic hilus. **B,** Longitudinal ultrasound image of the normal feline spleen. The feline spleen is typically a linear, thin structure, and smaller than in the dog. **C,** Transverse image of a feline spleen illustrating measurement of splenic height.

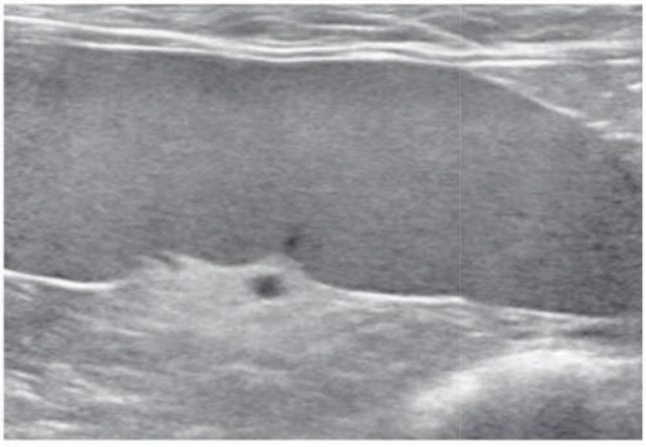


Fig. 40.49 Longitudinal ultrasound image of an enlarged feline spleen caused by lymphoma (cat from Fig. 40.43B). The spleen is rounded and thickened with undulating margins (compare with Fig. 40.48B).

finding. However, splenomegaly with a diffuse hypoechoic parenchyma, separated by linear echogenicities that represent dilated hyperechoic vessels, is highly suggestive of torsion (Fig. 40.50). Splenic veins may be dilated with visible intravascular echogenicities representing formed thrombi or static echogenic blood. Complete absence of flow at the splenic hilus is also common, as is accompanying peritoneal fluid. A hyperechoic triangular area surrounding the splenic veins has been associated with splenic torsion.[171] Gas within the parenchyma may indicate the presence of necrosis and gas-forming organisms. Diffuse splenic infarction as a result of other disease processes can have an identical appearance.[172]

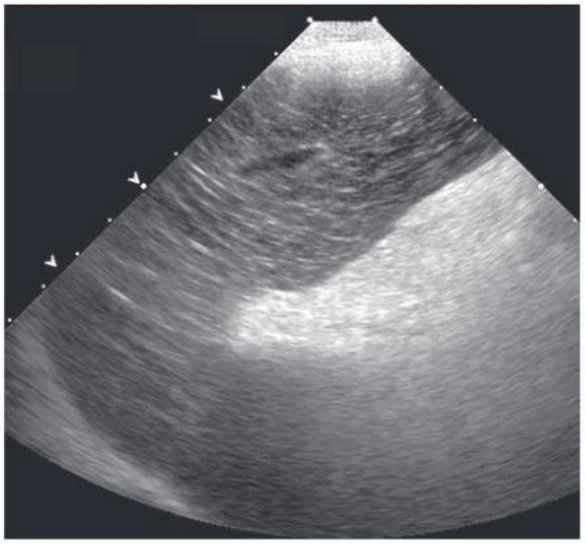


Fig. 40.50 Longitudinal ultrasound image of the spleen in a dog with splenic torsion (dog from Fig. 40.45A). The spleen is enlarged and hypoechoic with linear echogenicities representing dilated vessels.

Diffuse neoplastic infiltration of the spleen has a variety of appearances, and tumor type cannot be determined from the ultrasound appearance.[58,64,157,167,168,173,174]

Lymphosarcoma, mast cell tumor, malignant histiocytosis, leukemic infiltration, and multiple myeloma can all result in splenomegaly with normal or decreased echogenicity. The parenchyma may appear uneven or coarse. Focal or multifocal nodules of varying sizes that are usually hypoechoic may also be

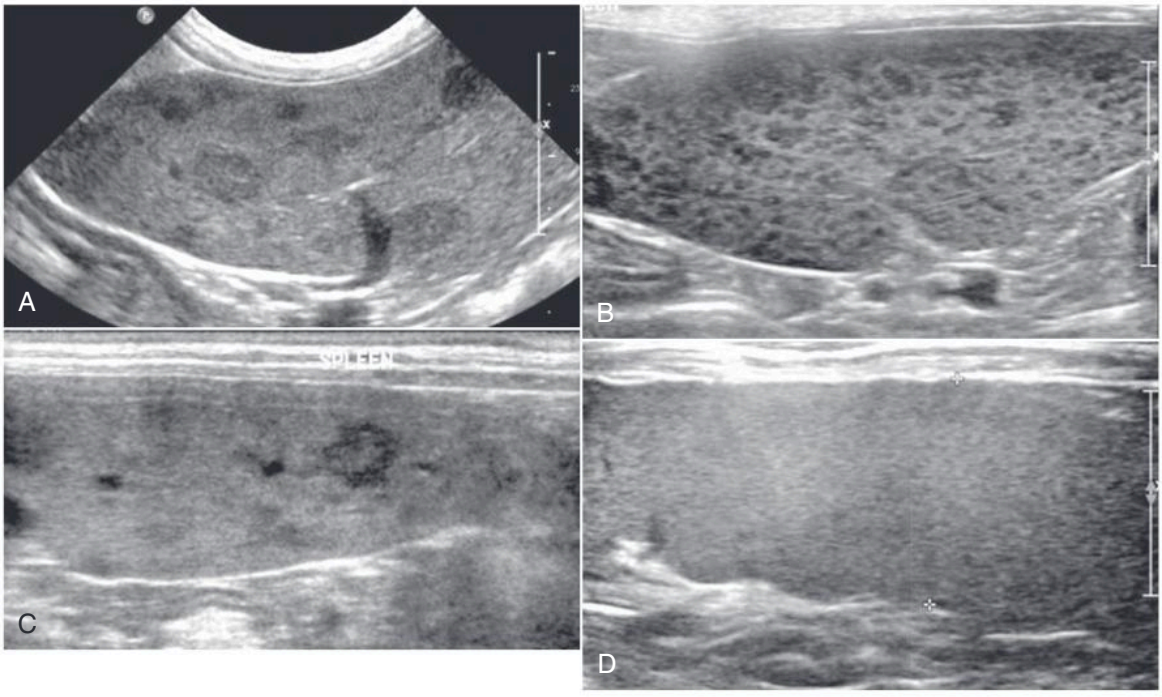


Fig. 40.51 Splenic neoplasia. **A,** Longitudinal image of the spleen in a dog with histiocytic sarcoma. Multiple variably sized hypoechoic nodules are present. **B,** Longitudinal image of the spleen in a dog with lymphoma. Multiple hypoechoic nodules create a "Swiss cheese" appearance. **C,** Longitudinal image of a dog with jejunal carcinoma. Multiple hypoechoic splenic nodules were diagnosed as metastatic carcinoma at necropsy. **D,** Longitudinal image of the spleen in a cat diagnosed with mast cell tumor. The spleen is enlarged, with rounded undulating margins.

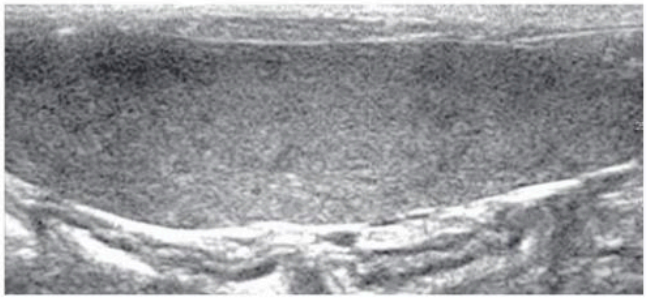


Fig. 40.52 Longitudinal image of the spleen in a cat with histoplasmosis. The spleen is mildly enlarged with a coarse and heterogeneous parenchyma.

present (Fig. 40.51; see Fig. 40.49). A diffuse nodular pattern of small hypoechoic nodules, termed a *Swiss cheese appearance*, is suggestive of lymphosarcoma, but other tumors (e.g., malignant histiocytosis and mast cell tumor) must also be considered. This appearance is normal in juvenile animals.

Splenitis due to fungal infection, such as histoplasmosis in cats, can result in irregular splenomegaly with a hypoechoic to subtle mottled or, rarely, discrete nodular appearance when imaged with a high frequency transducer (Fig. 40.52).[175]

Diffusely increased splenic echogenicity is less common but may be seen with chronic vascular compromise, peritonitis, infection, or diffuse nonneoplastic infiltrative disease, such as extramedullary hematopoiesis.[167,168]

Focal Disease

As in the liver, numerous considerations exist for focal disease, including primary and secondary neoplasia, nodular hyperplasia, hematoma, focal extramedullary hematopoiesis, abscess, cyst, and infarction (Figs. 40.53 and 40.54; see Figs. 40.51 and 40.52). Lymphosarcoma, one of the most common splenic tumors, has a variety of appearances. In addition to the diffuse changes described previously, lymphosarcoma may also produce focal hypoechoic or anechoic nodules or a single complex or cavitated mass.[64,173] Histiocytic sarcoma also creates focal hypoechoic splenic nodules/masses. Splenic masses attributable to hemangiosarcoma are typically complex with hypoechoic, hyperechoic, and anechoic areas caused by

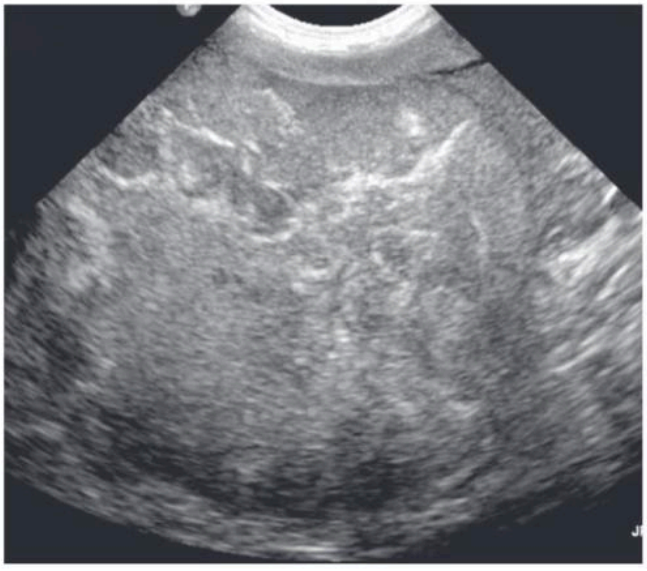


Fig. 40.53 Longitudinal image of a large, well-defined, slightly hyperechoic (to normal spleen) splenic mass with hyperechoic striations in a dog. Extramedullary hematopoiesis was diagnosed on cytology from a fine needle aspirate.

hemorrhage, necrosis, and fibrotic or calcified tissue (see Fig. 40.54).[167,168] Peritoneal fluid often accompanies hemangiosarcoma, and the liver and kidneys should be evaluated carefully for metastasis. Splenic hematomas are similar in appearance to those described in the liver and may be associated with acute or previous trauma or develop from lymphoid hyperplasia or neoplastic disease (Fig. 40.55).[163,167,168,176] Splenic hematomas are indistinguishable sonographically from splenic hemangiosarcoma, and both may enlarge over time.[177]

Metastatic carcinoma can result in variably sized hypoechoic nodules; target-like nodular lesions can also occur (see Fig. 40.51C).

Splenic abscesses are uncommon, but they can have a complex appearance similar to hemangiosarcoma or hematoma.[167,168,178] Splenic abscesses can vary from a simple hypoechoic, poorly defined area to a complex, cavitated mass. Echogenic areas with shadowing within the mass may indicate gas formation (Fig. 40.56). Myelolipomas are fatty, hyperechoic nodules occasionally seen in the normal spleen, especially along the peripheral margin or adjacent to vessels (Fig. 40.57).[179,180] Splenic myelolipomas are benign incidental findings but can be quite large. Rarely, mast cell tumors have been reported to cause hyperechoic nodules in the spleen.[157]

The echogenicity of focal splenic infarction changes over time. Initially, infarcts are hypoechoic and may appear as a well-demarcated round or bulging mass or simple focal enlargement of the spleen (Fig. 40.58).[162] With age, infarcts become increasingly echogenic and often are demarcated sharply from the normal splenic parenchyma. With color Doppler interrogation, there is a lack of blood flow in the infarcted area.

Nodular lymphoid hyperplasia in the spleen has a similar appearance to that in the liver, and it is likely the most common abnormality of the spleen identified on ultrasound.[39] The splenic border may simply be smoothly irregular or isoechoic; hypoechoic or hyperechoic nodules may be present. Hyperplastic nodules can be quite large and complex. Extramedullary hematopoiesis can appear as hypoechoic, hyperechoic, or mixed echogenicity nodules and/or masses (see Fig. 40.52).

As in the liver, splenic ultrasound is sensitive but not specific for both diffuse and focal splenic disease, with a large amount of overlap between normal and diseased spleen and between various splenic diseases. A normal ultrasound appearance does not rule out disease. Splenic nodules/masses are commonly encountered incidentally, and they are frequently benign.[181] Larger nodule size (1−2 cm), multiple nodules, the presence of

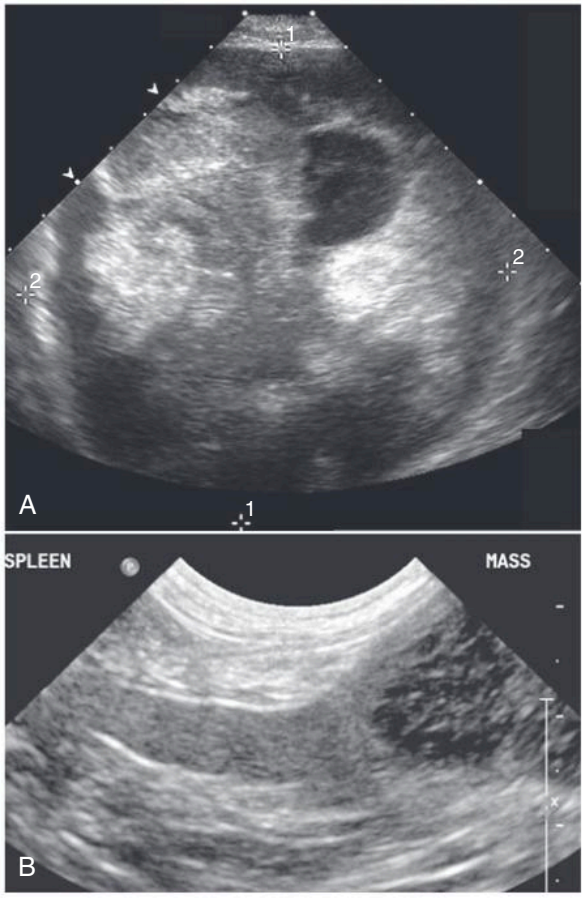


Fig. 40.54 **A,** Longitudinal image of a splenic hemangiosarcoma in a dog. Areas of hyperechogenicity, hypoechogenicity, and anechogenicity likely represent hemorrhage and necrosis. **B,** Longitudinal image of the spleen in a cat (from Fig. 40.46) with hemangiosarcoma. A focal hypoechoic cavitated mass is present on the ventral extremity of the spleen.

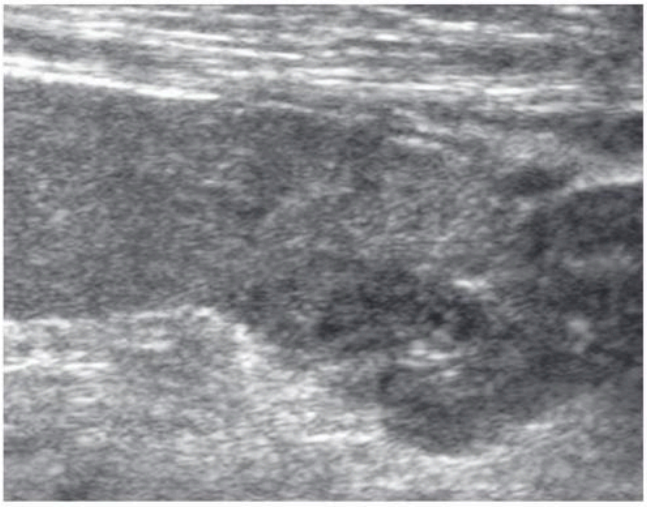


Fig. 40.55 Longitudinal ultrasound image of the ventral extremity of the spleen in a dog with a splenic hematoma after being hit by car. Multiple poorly defined, coalescing hypoechoic nodules are present as a result of hematoma formation.

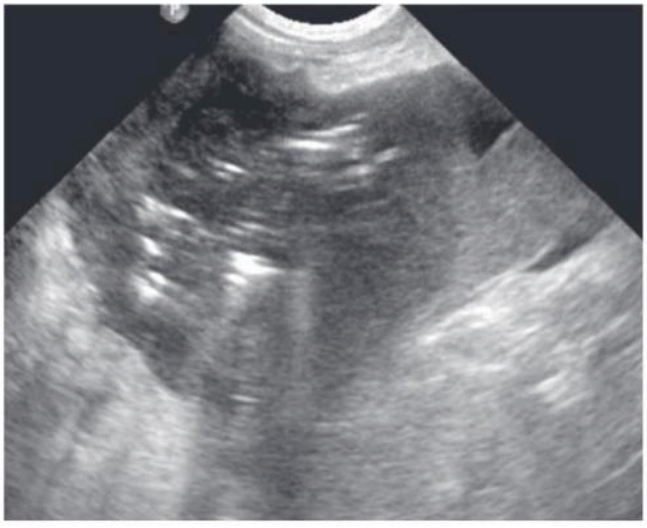


Fig. 40.56 Longitudinal image of the spleen in a dog presented for lethargy and fever. A focal, slightly hypoechoic (to normal spleen) mass protrudes from the splenic capsule, and it contains multiple hyperechoic interfaces with reverberation artifact consistent with gas. A splenic abscess was confirmed at necropsy.

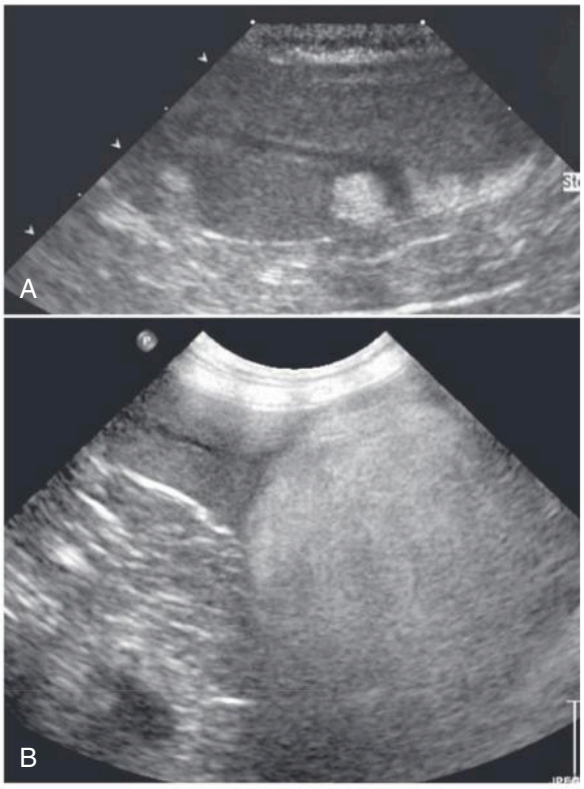


Fig. 40.57 **A,** Longitudinal ultrasound image of the spleen in a dog. Myelolipomas, seen as focal hyperechoic nodules, some with acoustic shadowing, are present along the dorsal border. **B,** A large, focal hyperechoic mass is noted in the splenic body. Myelolipoma was diagnosed on cytology from a fine needle aspirate.

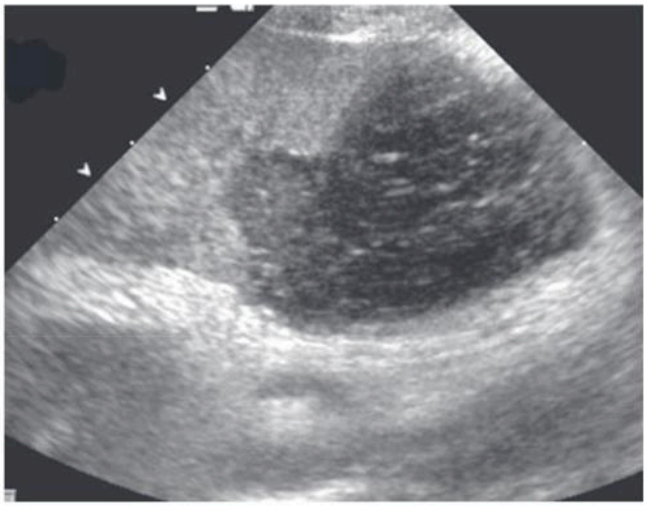


Fig. 40.58 Longitudinal ultrasound image of the spleen in a dog. The dorsal extremity of the spleen is hypoechoic with well-demarcated margins. No perfusion was present in the hypoechoic portion, which is consistent with an acute infarct.

multiple targetoid lesions, and presence of peritoneal fluid increase the likelihood of clinically important disease.[182] Tissue samples are necessary for a more definitive diagnosis. Although diagnosis of diffuse splenic disease (e.g., lymphosarcoma or extramedullary hematopoiesis) may be achieved with needle aspiration, cavitated mass lesions (e.g., hemangiosarcoma or hematoma) may be diagnosed more accurately by splenectomy and histopathologic evaluation.[183] Tru-Cut biopsies of the spleen using 18 g needles have been reported with minimal complications.[184]

REFERENCES

1. Farrow CF. The abdomen. In: Farrow CF, ed. *Radiology of the Cat*. St Louis: Mosby—Year Book; 1996:139—218.
2. Schwarz T. The liver and gall bladder. In: O'Brien R, Barr F, eds. *BSAVA Manual of Canine and Feline Abdominal Imaging*. Gloucester: British Small Animal Veterinary Association; 2009:144—156.
3. Kealy JK. The abdomen. In: Kealy JK, McCallister H, eds. *Diagnostic Radiology and Ultrasonography of the Dog and Cat*. 4th ed. St Louis: Elsevier/Saunders; 2005:35—48.
4. Suter PF. Radiographic diagnosis of liver disease in dogs and cats. *Vet Clin North Am*. 1982;12(2):153—173.
5. Biller DS, Partington BP. Hepatic imaging with radiology and ultrasound. *Vet Clin North Am Small Anim Pract*. 1995;25(2):305—335.
6. Root CR. Abdominal masses: the radiographic differential diagnosis. *Vet Radiol*. 1974;15(26).
7. Liptak JM, Cernell WS, Withrow SJ. Liver Tumors in cats and dogs. *Compend Cont Educ Small Pract January*. 2004:50—57.
8. Nickel R, Schummer A, Seiferle E, et al. *The Viscera of the Domestic Mammals*. Berlin: Verlag Paul Parey; 1973.
9. Genain MA, Barbosa A, Herrtage M, et al. Clinical relevance of radiographic linear branching mineral opacities in the canine liver. *J Small Anim Pract*. 2018;59:432—437.
10. Kirpenstein J, Fingland RB, Ulrich T, et al. Cholelithiasis in dogs: 29 cases (1980—1990). *J Am Vet Med Assoc*. 1993; 202(7):1137—1142.
11. Brömel C, Léveillé R, Scrivani PV, et al. Gallbladder perforation associated with cholelithiasis and cholecystitis in a dog. *J Small Anim Pract*. 1998;39(11):541—544.
12. Eich CS, Ludwig LL. The surgical treatment of cholelithiasis in cats: a study of nine cases. *J Am Anim Hosp Assoc*. 2002;38(3):290—296.
13. Thamm DH. Hepatobiliary tumors. In: Withrow SJ, MacEwen EG, eds. *Small Animal Clinical Oncology*. Philadelphia: Saunders; 2001:327—334.
14. Brömel C, Smeak DD, Léveillé R. Porcelain gallbladder associated with primary biliary adenocarcinoma in a dog. *J Am Vet Med Assoc*. 1998;213(8):1137—1139.
15. Scharf G, Deplazes P, Kaser-Hotz B, et al. Radiographic, ultrasonographic, and computed tomographic appearance of alveolar echinococcosis in dogs. *Vet Radiol Ultrasound*. 2004;45(5):411—418.
16. Gaschen L, Kircher P, Venzin C, et al. Imaging diagnosis: the abdominal air-vasculogram in a dog with splenic torsion and clostridial infection. *Vet Radiol Ultrasound*. 2003;44(5):553—555.
17. Sebastiá C, Quiroga S, Espin E, et al. Portomesenteric vein gas: pathologic mechanisms, CT findings, and prognosis. *Radiographics*. 2000;20(5):1213—1224.
18. Cordella A, Bertolini G. Multidetector-row CT reveals different patterns of hepatic portal venous gas and pneumobilia. *Vet Radiol Ultrasound*. 2021;62:68—75.
19. Burk RL, Johnson GR. Emphysematous cholecystitis in the nondiabetic dog: three case histories. *Vet Radiol*. 1980;21:242.
20. Armstrong JA, Taylor SM, Tryon KA, et al. Emphysematous cholecystitis in a Siberian husky. *Can Vet J*. 2000;41(1): 60—62.
21. Manfredi S, Fabbi M, Bonazzi M, et al. Ultrasonographic differentiation between portal venous and parenchymal gas may be important for the prognosis of canine and

feline Hepatic emphysema: 37 cases. *Vet Radiol Ultrasound*. 2019;60:734–744.
22. Grooters AM, Sherding RG, Johnson SE. Hepatic abscesses in dogs. *Compend Cont Educ*. 1995;17:833.
23. Moon ML. Diagnostic imaging of portosystemic shunts. *Semin Vet Med Surg (Small Anim)*. 1990;5(2):120–126.
24. Hergessell EJ, Hornof WJ, Koblik PD. Percutaneous ultrasound-guided trans-splenic catheterization of the portal vein in the dog. *Vet Radiol Ultrasound*. 1999;40:509.
25. Scrivani PV, Yeager AE, Dykes NL, et al. Influence of patient positioning on sensitivity of mesenteric portography for detecting an anomalous portosystemic blood vessel in dogs: 34 cases (1997–2000). *J Am Vet Med Assoc*. 2001;219(9):1251–1253.
26. White RN, Macdonald NJ, Burton CA. Use of intraoperative mesenteric portovenography in congenital portosystemic shunt surgery. *Vet Radiol Ultrasound*. 2003;44(5): 514–521.
27. Zwingenberger AL, Schwarz T. Dual-phase angiography of the normal canine portal and hepatic vasculature. *Vet Radiol Ultrasound*. 2004;45(2):117–124.
28. Winter MK, Kinney LM, Kleine LJ. Three-dimensional helical computed tomographic angiography of the liver in five dogs. *Vet Radiol Ultrasound*. 2005;46:494.
29. Zwingenberger AL, Schwarz T, Saunders HM. Helical computed tomographic angiography of canine portosystemic shunts. *Vet Radiol Ultrasound*. 2005;46(1):27–32.
30. Bertolini G, Rolla EC, Zotti A, et al. Three-dimensional multislice helical computed tomography techniques for canine extra-hepatic portosystemic shunt assessment. *Vet Radiol Ultrasound*. 2006;47(5):439–443.
31. Nelson NC, Nelson LL. Anatomy of extrahepatic portosystemic shunts in dogs as determined by computed tomography angiography. *Vet Radiol Ultrasound*. 2011;52(5):498–506.
32. Fukushima K, Kanemoto H, Ohno K, et al. Computed tomographic morphology and clinical features of extrahepatic portosystemic shunts in 172 dogs in Japan. *The Veterinary Journal*. 2014;199:376.
33. Specchi S, Rossi F, Weisse C, et al. Canine and feline abdominal arterioportal communications can be classified based on branching patterns in computed tomographic angiography. *Vet Radiol Ultrasound*. 2018; 59(6):687–696.
34. Zwingenberger AL, McLear R, Weisse C. Diagnosis of arterioportal fistulae in four dogs using computed tomographic angiography. *Vet Radiol Ultrasound*. 2005;46(6): 472–477.
35. Bertolini G. Anomalies of the portal venous system in dogs and cats as seen on multidetector-row computed tomography: an overview and systematization proposal.
36. Fukushima K, Kanemoto H, Ohno K, et al. CT characteristics of primary hepatic mass lesions in dogs. *Vet Radiol Ultrasound*. 2012;53:252.
37. Kutara K, Seki M, Ishikawa C, et al. Triple-phase helical computed tomography in dogs with hepatic masses. *Vet Radiol Ultrasound*. 2014;55(1):7–15.
38. Jones ID, Lamb CR, Drees R, et al. Associations between dual-phase computed tomography features and histopathologic diagnoses in 52 dogs with hepatic or splenic masses. *Vet Radiol Ultrasound*. 2016;57(2):144–153.
39. Moon Larson M, Mattoon J, Lawrence Y, et al. Liver. In: Mattoon JS, Sellon RK, Berry C, eds. *Small Animal Diagnostic Ultrasound*. 4th ed. St. Louis; 2021:355–421.
40. d'Anjou MA. Liver. In: Penninck D, d'Anjou MA, eds. *Atlas of Small Animal Ultrasonography*. 2nd ed. Ames, IA: Blackwell; 2015.
41. Ivancic M, Mai W. Qualitative and quantitative comparison of renal vs. hepatic ultrasonographic intensity in healthy dogs. *Vet Radiol Ultrasound*. 2008;49(4):368–373.
42. Yabuki A, Endo Y, Sakamoto H, et al. Quantitative assessment of renal cortical echogenicity in clinically normal cats. *Anat Histol Embryol*. 2008;37(5):383–386.
43. Center SA. Diseases of the gallbladder and biliary tree. *Vet Clin North Am Small Anim Pract*. 2009;39(3):543–598.
44. Ramstedt KL, Center SA, Randolph JF, et al. Changes in gallbladder volume in healthy dogs after food was withheld for 12 hours followed by ingestion of a meal or a meal containing erythromycin. *Am J Vet Res*. 2008;69(5): 647–651.
45. Penninck DG, Brisson JO, Webster CR. Sonographic assessment of gallbladder volume in normal cats. *Vet Radiol Ultrasound*. 2010;51(6):665–666.
46. Brömel C, Barthez PY, Léveillé R, et al. Prevalence of gallbladder sludge in dogs as assessed by ultrasonography. *Vet Radiol Ultrasound*. 1998;39(3):206–210.
47. Tsukagoshi T, Ohno K, Tsukamoto A, et al. Decreased gallbladder emptying in dogs with biliary sludge or gallbladder mucocele. *Vet Radiol Ultrasound*. 2012;53(1):84–91.
48. DeMonaco SM, Grant DC, Larson MM, et al. Spontaneous course of biliary sludge over 12 months in dogs with ultrasonographically identified biliary sludge. *J Vet Intern Med*. 2016;30:771–778.
49. Hittmair KM, Vielgrader HD, Loupal G. Ultrasonographic evaluation of gallbladder wall thickness in cats. *Vet Radiol Ultrasound*. 2001;42(2):149–155.
50. Spaulding KA. Ultrasound corner: gallbladder wall thickness. *Vet Radiol Ultrasound*. 1993;34:270.
51. Moentk J, Biller DS. Bilobed gallbladder in a cat: ultrasonographic appearance. *Vet Radiol Ultrasound*. 1993;34:354.
52. Léveillé R, Biller DS, Shiroma JT. Sonographic evaluation of the common bile duct in cats. *J Vet Intern Med*. 1996;10(5):296–299.
53. Zeman RK, Taylor KJ, Rosenfield AT, et al. Acute experimental biliary obstruction in the dog. Sonographic findings and clinical implications. *Am J Roentgenol*. 1981;136(5):965–967.
54. Biller DS, Kantrowitz B, Miyabayashi T. Ultrasonography of diffuse liver disease: a review. *J Vet Intern Med*. 1992;6(2):71–76.
55. Newell SM, Selcer BA, Girard E, et al. Correlation between ultrasonographic findings and specific hepatic diseases in cats: 72 cases (1985–1997). *J Am Vet Med Assoc*. 1998;213(1):94–98.
56. Feeney DA, Anderson KL, Ziegler LE, et al. Statistical relevance of ultrasonographic criteria in the assessment of diffuse liver disease in dogs and cats. *Am J Vet Res*. 2008;69(2):212–221.
57. Marolf AJ, Leach L, Gibbons DS, et al. Ultrasonographic findings of feline cholangitis. *J Am Anim Hosp Assoc*. 2012;48(1):36–42.
58. Sato AF, Solano M. Ultrasonographic findings in abdominal mast cell disease: a retrospective study of 19 patients. *Vet Radiol Ultrasound*. 2004;45(1):51–57.
59. Finora K, Leibman NF, Fettman MJ, et al. Cytological comparison of fine-needle aspirates of liver and spleen of normal dogs and of dogs with cutaneous mast cell tumours and an ultrasonographically normal appearing liver and spleen. *Vet Comp Oncol*. 2006;4(3):178–183.
60. Stefanello D, Valenti P, Faverzani S, et al. Ultrasound-guided cytology of spleen and liver: a prognostic tool in canine cutaneous mast cell tumor. *J Vet Intern Med*. 2009;23(5):1051–1057.

61. Book AP, Fidel J, Wills T, et al. Correlation of ultrasound findings, liver and spleen cytology, and prognosis in the clinical staging of high metastatic risk canine mast cell tumors. *Vet Radiol Ultrasound*. 2011;52(5):548–554.
62. Sonet J, Barthelemy A, Goy-Thollot I. Prospective evaluation of abdominal ultrasound findings in 35 dogs with leptospirosis. *Vet Radiol Ultrasound*. 2017;59:98–106.
63. Tchelepi H, Ralls PW, Radin R, et al. Sonography of diffuse liver disease. *J Ultrasound Med*. 2002;21(9):1023–1032.
64. Lamb CR, Hartzband LE, Tidwell AS, et al. Ultrasonographic findings in hepatic and splenic lymphosarcoma in dogs and cats. *Vet Radiol*. 1991;32:117.
65. Léveillé R, Partington BP, Biller DS, et al. Complications after ultrasound-guided biopsy of abdominal structures in dogs and cats: 246 cases (1984–1991). *J Am Vet Med Assoc*. 1993;203(3):413–415.
66. de Rycke LM, van Bree HJ, Simoens PJ. Ultrasound-guided soft tissue core biopsy of liver, spleen and kidney in normal dogs. *Vet Radiol Ultrasound*. 1999;40(3):294–299.
67. Warren-Smith CM, Andrew S, Mantis P, et al. Lack of associations between ultrasonographic appearance of parenchymal lesions of the canine liver and histological diagnosis. *J Small Anim Pract*. 2012;53(3):168–173.
68. Whiteley MB, Feeney DA, Whiteley LO, et al. Ultrasonographic appearance of primary and metastatic canine hepatic tumors. *J Ultrasound Med*. 1989;8(11):621–630.
69. Nyman HT, Kristensen AT, Flagstad A, et al. A review of the sonographic assessment of tumor metastases in liver and superficial lymph nodes. *Vet Radiol Ultrasound*. 2004;45(5):438–448.
70. Liptak JM, Dernell WS, Monnet E, et al. Massive hepatocellular carcinoma in dogs: 48 cases (1992–2002). *J Am Vet Med Assoc*. 2004;225(8):1225–1230.
71. Liptak J. Hepatobiliary tumors. In: Withrow SJ, Vail DM, Page RL, eds. *Withrow and MacEwan's Small Animal Clinical Oncology*. 5th ed. St Louis: Elsevier/Saunders; 2013.
72. Cullen JM, Popp JA. Tumors of the liver and gallbladder. In: Meuten DJ, ed. *Tumors in Domestic Animals*. 4th ed. Ames, IA: Iowa State Press; 2002.
73. Patnaik AK, Hurvitz AI, Lieberman PH. Canine hepatic neoplasms: a clinicopathological study. *Vet Pathol*. 1980;17(5):553–564.
74. Affolter VK, Moore PF. Localized and disseminated histiocytic sarcoma of dendritic cell origin in dogs. *Vet Pathol*. 2002;39(1):74–83.
75. Balkman C. Hepatobiliary neoplasia in dogs and cats, vet clinic small. *Anim*. 2009;39(3):617–625.
76. Patnaik AK. A morphologic and immunohistochemical study of hepatic neoplasms in cats. *Vet Pathol*. 1992;29(5):405–415.
77. Post G, Patnaik AK. Nonhematopoietic hepatic neoplasms in cats: 21 cases (1983–1988). *J Am Vet Med Assoc*. 1992;201(7):1080–1082.
78. Lawrence HJ, Erb HN, Harvey HJ. Nonlymphomatous hepatobiliary masses in cats: 41 cases (1972 to 1991). *Vet Surg*. 1994;23(5):365–368.
79. van Sprundel R, van den Ingh T, Guscetti F, et al. Classification of primary hepatic tumours in the cat. *Vet J*. 2014;202(2):255–266.
80. Nyland TG, Koblik PD, Tellyer SE. Ultrasonographic evaluation of biliary cystadenomas in cats. *Vet Radiol Ultrasound*. 1999;40(3):300–306.
81. Bahr KL, Sharkey LC, Murakami T, et al. Accuracy of US-guided FNA of focal liver lesions in dogs: 140 cases (2005–2008). *J Am Anim Hosp Assoc*. 2013;49(3):190–196.
82. Murakami T, Feeney DA, Bahr KL. Analysis of clinical and ultrasonographic data by use of logistic regression models for prediction of malignant versus benign causes of ultrasonographically detected focal liver lesions in dogs. *Am J Vet Res*. 2012;73(6):821–829.
83. Crabtree AC, Spangler E, Beard D, et al. Diagnostic accuracy of gray-scale ultrasonography for the detection of hepatic and splenic lymphoma in dogs. *Vet Radiol Ultrasound*. 2010;51(6):661–664.
84. Cuccouillo A, Lamb CR. Cellular features of sonographic target lesions of the liver and spleen in 21 dogs and a cat. *Vet Radiol Ultrasound*. 2002;43(3):275–278.
85. Prause LC, Twedt DC. Hepatic nodular hyperplasia. In: Bonagura JD, ed. *Current Veterinary Therapy XIII: Small Animal Practice*. Philadelphia: Saunders/Elsevier; 2000:675–676.
86. Stowater JL, Lamb CR, Schelling SH. Ultrasonographic features of canine hepatic nodular hyperplasia. *Vet Radiol Ultrasound*. 1990;31:268.
87. Ziegler LE, O'Brien RT, Waller KR, et al. Quantitative contrast harmonic ultrasound imaging of the normal canine liver. *Vet Radiol Ultrasound*. 2003;44(4):451–454.
88. O'Brien RT, Iani M, Matheson J, et al. Contrast harmonic ultrasound of spontaneous liver nodules in 32 dogs. *Vet Radiol Ultrasound*. 2004;45(6):547–553.
89. Ohlerth S, O'Brien RT. Contrast ultrasound: general principles and veterinary clinical applications. *Vet J*. 2007;174(3):501–512.
90. Nyland TG, Barthez PY, Ortega TM, et al. Hepatic ultrasonography and pathologic findings in dogs with canine superficial necrolytic dermatitis. *Vet Radiol Ultrasound*. 1996;37:200.
91. Kimmel SE, Christiansen W, Byrne KP. Clinicopathological, ultrasonographic, and histopathological findings of superficial necrolytic dermatitis with hepatopathy in a cat. *J Am Anim Hosp Assoc*. 2003;39(1):23–27.
92. March PA, Hiller A, Weisbrode SE, et al. Superficial necrolytic dermatitis in 11 dogs with a history of phenobarbital administration (1995–2002). *J Vet Intern Med*. 2004;18:65.
93. Hall-Fonte DL, Center SA, McDonough SP, et al. Hepatocutaeous syndrome in Shih Tzus: 31 cases (1996–2014). *J Am Vet Med Assoc*. 2016;248(7):802–813.
94. Schwarz LA, Penninck DG, Léveillé-Webster C. Hepatic abscesses in 13 dogs: a review of the ultrasonographic findings, clinical data and therapeutic options. *Vet Radiol Ultrasound*. 1998;39(4):357–365.
95. Zatelli A, Bonfanti U, Zini E, et al. Percutaneous drainage and alcoholization of hepatic abscesses in five dogs and a cat. *J Am Anim Hosp Assoc*. 2005;41(1):34–38.
96. Sergeeff JSJ, Armstrong PJ, Bunch SE. Hepatic abscesses in cats: 14 cases (1985–2002). *J Vet Intern Med*. 2004;18(3):295–300.
97. Sonnenfield JM, Armbrust LJ, Radlinsky MA, et al. Radiographic and ultrasonographic findings of liver lobe torsion in a dog. *Vet Radiol Ultrasound*. 2001;42(4):344–346.
98. Schwartz SG, Mitchell SL, Keating JH, et al. Liver lobe torsion in dogs: 13 cases (1995–2004). *J Am Vet Med Assoc*. 2006;228(2):242–247.
99. Quantz JE, Miles MS, Reed AL, et al. Elevation of alanine transaminase and gallbladder wall abnormalities as biomarkers of anaphylaxis in canine hypersensitivity patients. *J Vet Emerg Crit Care*. 2009;19(6):536–544.
100. Gaschen L. Update on hepatobiliary imaging. *Vet Clin North Am Small Anim Pract*. 2009;39(3):439–467.
101. Van Breda Vriesman AC, Engelbrecht MR, Smithuis RH, et al. Diffuse gallbladder wall thickening: differential diagnosis. *Amer J Radiol*. 2007;188:495–501.
102. Lisciandro GR, Gambino JM, Lisciandro SC. Thirteen dogs and a cat with ultrasonographically detected gallbladder

wall edema associated with cardiac disease. *J Vet Int Med*. 2021;35:1342–1346.
103. Seitz MA, Lee AM, Woodruff KA, et al. Sedation with dexmedetomidine is associated with transient gallbladder wall thickening and peritoneal effusion in some dogs undergoing abdominal ultrasonography. *J Vet Intern Med*. 2021;35:2743–2751.
104. Bini G, Cohen EB, Chiavaccini L, et al. Intravenous dexmedetomidine, morphine, or a combination can result in gallbladder wall thickening with no significant association with plasma histamine concentrations. *Vet Radiol Ultrasound*. 2022;63:319–327.
105. O'Neill EJ, Day MJ, Hall EJ, et al. Bacterial cholangitis/cholangiohepatitis with or without concurrent cholecystitis in four dogs. *J Small Anim Pract*. 2006;47(6):325–335.
106. Mitsui I, Ohtsuki S, Uchida K. Chronic cholecystitis of dogs: clinicopathologic features and relationship with liver. *Animals*. 2021;11. https://doi.org/10.3390/ani11113324.
107. Lawrence YA, Ruaux CG, Nemanic S, et al. Characterization, treatment, and outcome of bacterial cholecystitis and bactibilia in dogs. *J Am Vet Med Assoc*. 2015;246(9):982–989.
108. Policelli Smith R, Gookin JL, Smolski W, et al. Association between gallbladder ultrasound findings and bacterial culture of bile in 70 cats and 202 dogs. *J Vet Intern Med*. 2017;31:1451–1458.
109. Schiborra F, McConnell JF, Maddox TW. Percutaneous ultrasound-guided cholecystocentesis: complications and association of ultrasonographic findings with bile culture results. *J Small Anim Pract*. 2017;58(7):389–394.
110. Aguirre A. Diseases of the gallbladder and extrahepatic biliary system. In: Ettinger S, Feldman E, eds. *Textbook of Veterinary Internal Medicine*. St Louis: Elsevier; 2010.
111. Gaillot HA, Penninck DG, Webster CR, et al. Ultrasonographic features of extrahepatic biliary obstruction in 30 cats. *Vet Radiol Ultrasound*. 2007;48(5):439–447.
112. Center SA, Randolph JF, Warner KL, et al. Bacterial culture and immunohistochemical detection of bacteria and endotoxin in cats with suppurative cholangitis-cholangiohepatitis syndrome. *JAVMA*. 2022;260(2):194–211.
113. Secchi P, Poppl AG, Ilha A, et al. Prevalence, risk factors, and biochemical markers in dogs with ultrasound-diagnosed biliary sludge. *Res Vet Sci*. 2012;93(3):1185–1189.
114. Bandyopadhyay S, Varshney JP, Hoque M, et al. Prevalence of cholecystic disease in dogs: an ultrasonographic evaluation. *Asian J Anim Vet Adv*. 2007;2(4):234–238.
115. Cook AK, Jambhekar A, Dylewski AM. Gallbladder sludge in dogs: ultrasonographic and clinical findings in 200 patients. *J Am Anim Hosp Assoc*. 2016;52:125–131.
116. Butler T, Bexfield N, Dor C. A multicenter retrospective study assessing progression of biliary sludge in dogs using ultrasonography. *J Vet Intern Med*. 2022;36(3):976–985.
117. Mizutani S, Torisu S, Kaneko Y, et al. Retrospective analysis of canine gallbladder contents in biliary sludge and gallbladder mucoceles. *J Vet Med Sci*. 2017;79(2):366–374.
118. Harran N, d'Anjou MA, Dunn M, et al. Gallbladder sludge on ultrasound is predictive of increased liver enzymes and total bilirubin in cats. *Can Vet J*. 2011;52(9):999–1003.
119. Villm J, DeMonaco S, Larson M. Prevalence of gallbladder sludge and associated abnormalities in cats undergoing abdominal ultrasound. *Vet Radiol Ultrasound*. 2022;63:601–608.
120. Viljoen AD, Tamborini A, Bexfield NH. Gall bladder ejection fractions in dogs investigated for chronic altered appetite: 14 cases (2015–2017). *J Sm Anim Pract*. 2021;62:1101–1107.
121. Diana A, Guglielmini C, Specchi S, et al. Ultrasonographic evaluation of preprandial and postprandial gallbladder volume in healthy cats. *Am J Vet Res*. 2012;73:1583–1588.
122. Besso JG, Wrigley RH, Gliatto JM, et al. Ultrasonographic appearance and clinical findings in 14 dogs with gallbladder mucocele. *Vet Radiol Ultrasound*. 2000;41(3):261–271.
123. Pike FS, Berg J, King NW, et al. Gallbladder mucocele in dogs: 30 cases (2000–2003). *J Am Vet Med Assoc*. 2004;224(10):1615–1622.
124. Worley DR, Hottinger HA, Lawrence HJ. Surgical management of gallbladder mucoceles in dogs: 22 cases (1999–2003). *J Am Vet Med Assoc*. 2004;225(9):1418–1422.
125. Walter R, Dunn ME, d'Anjou MA, et al. Nonsurgical resolution of gallbladder mucocele in two dogs. *J Am Vet Med Assoc*. 2008;232(11):1688–1693.
126. Crews LJ, Feeney DA, Jessen CR, et al. Clinical, ultrasonographic, and laboratory findings associated with gallbladder disease and rupture in dogs: 45 cases (1997–2007). *J Am Vet Med Assoc*. 2009;234(3):359–366.
127. Aguirre AL, Center SA, Randolph JF, et al. Gallbladder disease in Shetland Sheepdogs: 38 cases (1995–2005). *J Am Vet Med Assoc*. 2007;231(1):79–88.
128. Uno T, Okamoto K, Onaka T, et al. Correlation between ultrasonographic imaging of the gallbladder and gallbladder content in eleven cholecystectomised dogs and their prognoses. *J Vet Med Sci*. 2009;71(10):1295–1300.
129. Choi J, Kim A, Keh S, et al. Comparison between ultrasonographic and clinical findings in 43 dogs with gallbladder mucoceles. *Vet Radiol Ultrasound*. 2014;55(2):202–207.
130. Jaffey JA, Kreisler R, Shumway K, et al. Ultrasonographic patterns, clinical findings, and prognostic variables in dogs from Asia with gallbladder mucocele. *J Vet Intern Med*. 2022;36:566–575.
131. Gookin JL, Mathews KG, Cullen J, Seiler G. Qualitative metabolomics profiling of serum and bile from dogs with gallbladder mucocele formation. *PloS One*. 2018;13(1):e0191076.
132. Jaffey JA, Graham A, VanEerde E, et al. Gallbladder mucocele: variables associated with outcome and the utility of ultrasonography to identify gallbladder rupture in 219 dogs (2007–2016). *J Vet Intern Med*. 2018;32:195–200.
133. Bargellini P, Orlandi R, Paloni C, et al. Evaluation of contrast-enhancing ultrasonography as a method for detecting gallbladder necrosis or rupture in dogs. *Vet Radiol Ultrasound*. 2016;57(6):611–620.
134. Mesich ML, Mayhew PD, Paek M, et al. Gall bladder mucoceles and their association with endocrinopathies in dogs: a retrospective case-control study. *J Small Anim Pract*. 2009;50(12):630–635.
135. Gookin JL, Correa MT, Peters A, et al. Association of gallbladder mucocele histologic diagnosis with selected drug use in dogs: a matched case-control study. *J Vet Intern Med*. 2015;29(6):1464–1472.
136. Jaffey JA, Pavlick M, Webster CR, et al. Effect of clinical signs, endocrinopathies, timing of surgery, hyperlipidemia, and hyperbilirubinemia on outcome in dogs with gallbladder mucocele. *The Vet Journal*. 2019;251. https://doi.org/10.1016/j.tvjl.2019.105350.
137. Bennett SL, Milne M, Slocombe RF, et al. Gallbladder mucocele and concurrent hepatic lipidosis in a cat. *Aust Vet J*. 2007;85(10):397–400.

138. Nyland TG, Gillett NA. Sonographic evaluation of experimental bile duct ligation in the dog. *Vet Radiol.* 1982;23:252.
139. Wilkinson AR, DeMonaco SM, Panciera DL, et al. Bile duct obstruction associated with pancreatitis in 46 dogs. *J Vet Intern Med.* 2020;34:1794–1800.
140. Callahan JE, Haddad JL, Brown DC, et al. Feline cholangitis: a necropsy study of 44 cats (1986–2008). *J Feline Med Surg.* 2011;13(8):570–576.
141. Brain PH, Barrs VR, Martin P, et al. Feline cholecystitis and acute neutrophilic cholangitis: clinical findings, bacterial isolates, and response to treatment in six cases. *J Feline Med Surg.* 2006;8(2):91–103.
142. Jaffey JA. Feline cholangitis/cholangiohepatitis complex. *J Small Anim Pract.* 2022;63:573–589.
143. Center SA, Randolph JF, Warner KL, et al. Clinical features, concurrent disorders, and survival time in cats with suppurative cholangitis-cholangiohepatitis syndrome. *JAVMA.* 2022;260:212–227.
144. Fragkou FC, Adamamma-Moraitou K, Poutahidis T, et al. Prevalence and clinicopathological features of triaditis in a prospective case series of symptomatic and asymptomatic cats. *J Vet Intern Med.* 2016;30:1031–1045.
145. Harrison JL, Turek BJ, Brown DC, et al. Cholangitis and cholangiohepatitis in dogs: a descriptive study of 54 cases based on histopathologic diagnosis (2004–2014). *J Vet Intern Med.* 2018;32:172–180.
146. Tamborini A, Jahns H, McAllister H, et al. Bacterial cholangitis, cholecystitis, or both in dogs. *J Vet Intern Med.* 2016;30:1046–1055.
147. Anjou MA, Penninck D, Cornejo L, et al. Ultrasonographic diagnosis of portosystemic shunting in dogs and cats. *Vet Radiol Ultrasound.* 2004;45(5):424–437.
148. d'Anjou MA. The sonographic search for portosystemic shunts. *Clin Tech Small Anim Pract.* 2007;22(3):104–114.
149. Salwei RM, O'Brien RT, Mathieson JS. Use of contrast harmonic ultrasound for the diagnosis of congenital portosystemic shunts in three dogs. *Vet Radiol Ultrasound.* 2003;44:301.
150. Palerme JS, Brown JC, Marks SL, et al. Splenosystemic shunts in cats: a retrospective of 33 cases (2004–2011). *J Vet Int Med.* 2013;27:1347.
151. Johnson KL, Porter EG, Berry CB. Analysis of feline splenic radiographic measurements and their correlation to ultrasonographic measurements. *J Fel Med Surg.* 2016;1.
152. Neer TM. Clinical approach to splenomegaly in dogs and cats. *Compend Contin Educ Pract Vet Small Anim.* 1996;18(35).
153. Wilson DV, Carpenter RE, Evans AT. The effect of four anesthetic protocols on splenic size in dogs. *Vet Anaesth Analg.* 2003;30(2):100–101.
154. Baldo CF, Garcia-Pereira FL, Nelson NC, et al. Effects of anesthetic drugs on canine splenic volume determined via computed tomography. *Am J Vet Res.* 2012;73(11):1715–1719.
155. Reese SL, Zekas LJ, Iazbik C, et al. Effect of sevoflurane anesthesia and blood donation on the sonographic appearance of the spleen in 60 healthy cats. *Vet Radiol Ultrasound.* 2013;54(2):168–175.
156. Kealy JK, McAllister H, Graham JP. *Diagnostic Radiology and Ultrasonography of the Dog and Cat.* 5th ed. Philadelphia: Saunders/Elsevier; 2011.
157. Hanson JA, Papageorges M, Girard E, et al. Ultrasonographic appearance of splenic disease in 101 cats. *Vet Radiol Ultrasound.* 2001;42(5):441–445.
158. Spangler WL, Culbertson MR. Prevalence and type of splenic disease in cats: 455 cases (1985–1991). *J Am Vet Med Assoc.* 1992;201(5):773–776.
159. Auger M, Fazio C, de Swarte M, et al. Administration of certain sedative drugs is associated with variation in sonographic and radiographic splenic size in healthy cats. *Vet Radiol Ultrasound.* 2019;60(6):717–728.
160. DeGroot W, Giuffrida MA, Rubin J, et al. Primary splenic torsion in dogs: 102 cases (1992–2014). *J Am Vet Med Assoc.* 2016;248(6):661–668.
161. Stickle RL. Radiographic signs of isolated splenic torsion in dogs: eight cases (1980–1987). *J Am Vet Med Assoc.* 1989;194(1):103–106.
162. Patsikas MN, Rallis T, Kladakis SE, et al. Computed tomography diagnosis of isolated splenic torsion in a dog. *Vet Radiol Ultrasound.* 2001;42(3):235–237.
163. Wrigley RH, Konde LJ, Park RD, et al. Clinical features and diagnosis of splenic hematomas in dogs: 10 cases (1980–1987). *J Am Anim Hosp Assoc.* 1989;25:371.
164. Weinstein MJ, Carpenter JL, Schunk CJ. Nonangiogenic and nonlymphomatous sarcomas of the canine spleen: 57 cases (1975–1987). *J Am Vet Med Assoc.* 1989;195(6):784–788.
165. Spangler WL, Culbertson MR. Prevalence, type, and importance of splenic diseases in dogs: 1,480 cases (1985–1989). *J Am Vet Med Assoc.* 1992;200(6):829–834.
166. Battiato P, Fernandez Y, Salguüero R, et al. Spontaneous emphysematous splenitis: radiographic and ultrasonographic findings in three Golden Retriever dogs. *Vet Radiol Ultrasound.* 2021;62:309–315.
167. Mattoon JS, Duffy M. Spleen. In: Mattoon JS, Sellon RK, Berry CR, eds. *Small Animal Diagnostic Ultrasound.* 4th ed. St. Louis: Elsevier; 2021.
168. Hecht S. Spleen. In: Penninck D, d'Anjou MA, eds. *Atlas of Small Animal Ultrasonography.* 2nd ed. Ames, IA: Blackwell; 2015.
169. Sayre RS, Spaulding KA. Formulation of a standardized protocol and determination of the size and appearance of the spleen in healthy cats. *J Feline Med Surg.* 2014;16(4):326–332.
170. O'Brien RT, Waller KR, Osgood TL. Sonographic features of drug-induced splenic congestion. *Vet Radiol Ultrasound.* 2004;45(3):225–227.
171. Mai W. The hilar perivenous hyperechoic triangle as a sign of acute splenic torsion in dogs. *Vet Radiol Ultrasound.* 2006;47(5):487–491.
172. Hardie EM, Vaden SL, Spaulding K, et al. Splenic infarction in 16 dogs: a retrospective study. *J Vet Intern Med.* 1995;9(3):141–148.
173. Cruz-Arámbulo R, Wrigley R, Powers B. Sonographic features of histiocytic neoplasms in the canine abdomen. *Vet Radiol Ultrasound.* 2004;45(6):554–558.
174. Ramirez S, Douglass JP, Robertson ID. Ultrasonographic features of canine abdominal malignant histiocytosis. *Vet Radiol Ultrasound.* 2002;43(2):167–170.
175. Atiee G, Kvitko-White H, Spaulding K, et al. Ultrasonographic appearance of histoplasmosis identified in the spleen in 15 cats. *Vet Radiol Ultrasound.* 2014;55(3):310–314.
176. Hanson JA, Penninck DG. Ultrasonographic evaluation of a traumatic splenic hematoma and literature review. *Vet Radiol Ultrasound.* 1994;35:463.
177. Wrigley RH, Park RD, Konde LJ, et al. Ultrasonographic features of splenic hemangiosarcoma in dogs: 18 cases (1980–1986). *J Am Vet Med Assoc.* 1988;192(8):1113–1117.
178. Konde LJ, Lebel JL, Park RD, et al. Sonographic application in the diagnosis of intraabdominal abscess in the dog. *Vet Radiol.* 1986;27:151.
179. Walzer C, Hittmair K, Walzer-Wagner C. Ultrasonographic identification and characterization of splenic nodular lipomatosis or myelolipomas in cheetahs *(Acinonyx jubatus). Vet Radiol Ultrasound.* 1996;37:289.

180. Schwarz LA, Penninck DG, Gliatto J. Ultrasound corner: canine splenic myelolipomas. *Vet Radiol Ultrasound*. 2001;42(4):347–348.
181. Cleveland MJ, Casale S. Incidence of malignancy and outcomes for dogs undergoing splenectomy for incidentally detected nonruptured splenic nodules or masses: 105 cases (2009–2013). *J Am Vet Med Assoc*. 2016;248(11):1267–1273.
182. Yankin I, Nemanic S, Funes S, et al. Clinical relevance of splenic nodules or heterogeneous splenic parenchyma assessed by cytologic evaluation of fine-needle samples in 125 dogs (2011–2015). *J Vet Intern Med*. 2020;34:125–131.
183. Ballegeer EA, Forrest LJ, Dickinson RM, et al. Correlation of ultrasonographic appearance of lesions and cytologic and histologic diagnoses in splenic aspirates from dogs and cats: 32 cases (2002–2005). *J Am Vet Med Assoc*. 2007;230(5):690–696.
184. Watson AT, Penninck D, Knoll JS, et al: Safety and correlation of test results of combined ultrasound-guided fine-needle aspiration and needle core biopsy of the canine spleen, *Vet Radiol Ultrasound* 52(3):317–322.

ELECTRONIC RESOURCES

Additional information related to the content in Chapter 40 can be found online at eBooks.Health.Elsevier.com

- Chapter Quiz

CHAPTER 41

Kidneys and Ureters

Gabriela S. Seiler • Ryan Appleby

Renal disease is common in dogs and cats, and imaging is an integral part of the diagnostic workup of these patients. Multiple imaging modalities are available to evaluate the kidneys and ureters, and the modality to select depends on the type of information desired. In this chapter, the indications, technique, and normal imaging findings, as well as the imaging appearance of diseases of the upper urinary tract, are reviewed.

NORMAL ANATOMY AND IMAGING PROCEDURES

Radiography

Indications

Radiographs are often obtained in the diagnostic workup of patients with abdominal disease, and interpretation of the radiographic appearance of the kidneys is an important skill. Radiographs are useful to identify broad changes in the roentgen signs (size, number, shape, opacity, location, margination) associated with the kidneys and ureters as well as to detect associated retroperitoneal or bone disease. Survey radiographs are indicated if there is a history of trauma to the abdomen or pelvis with possible involvement of the urinary tract or if a dorsal abdominal mass is suspected. Survey radiographs are an essential part of any abdominal radiographic procedure involving contrast medium.

Technique

A diagnostic radiographic study of the abdomen and kidneys should always include both left and right lateral as well as ventrodorsal (VD) views of the abdomen. Patient rotation should be minimized as even mild rotation may dorsally or medially displace one kidney and superimposition with the spine reduces visibility. Right lateral radiographs provide more longitudinal separation between the right and left kidney.[1] Suspected ureteral calculi can be separated from gastrointestinal content by use of oblique projections or compression techniques. Feces may have to be eliminated, by means of fasting or an enema, prior to a radiographic study to evaluate the distal ureters.

Normal Radiographic Findings

The kidneys are located in the retroperitoneal space and outlined by surrounding fat.

Canine kidneys are oval (Fig. 41.1). The cranial pole of the right kidney is often poorly visible, because it abuts and silhouettes with the caudate lobe of the liver. The left kidney is more mobile than the right, and it can be located relatively ventrally in animals with a large amount of retroperitoneal fat. In the VD projection, the right kidney is located at the level of the 13th rib but is often obscured by liver and other superimposed abdominal organs, whereas the left kidney is normally visible caudal to the gastric fundus and caudomedial to the proximal extremity of the spleen at the level of L1-L3.

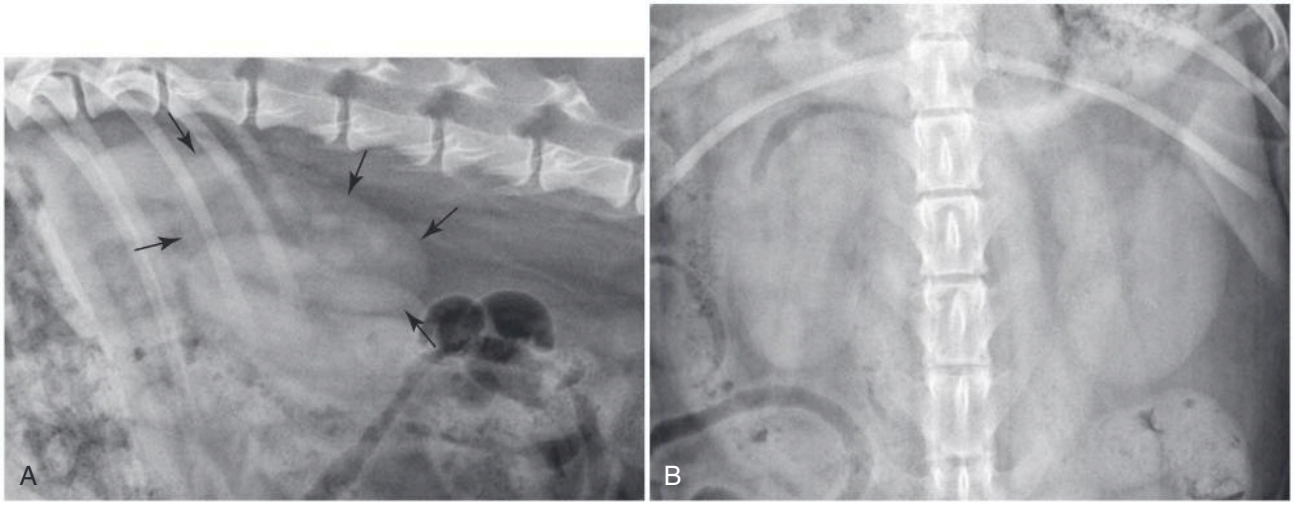


Fig. 41.1 Lateral **(A)** and ventrodorsal (VD; **B**) radiographs of the abdomen of a normal dog. The kidneys are oval and outlined by retroperitoneal fat. The right kidney (*black arrows*) is more cranial and, in this dog, slightly more dorsal to the left kidney.

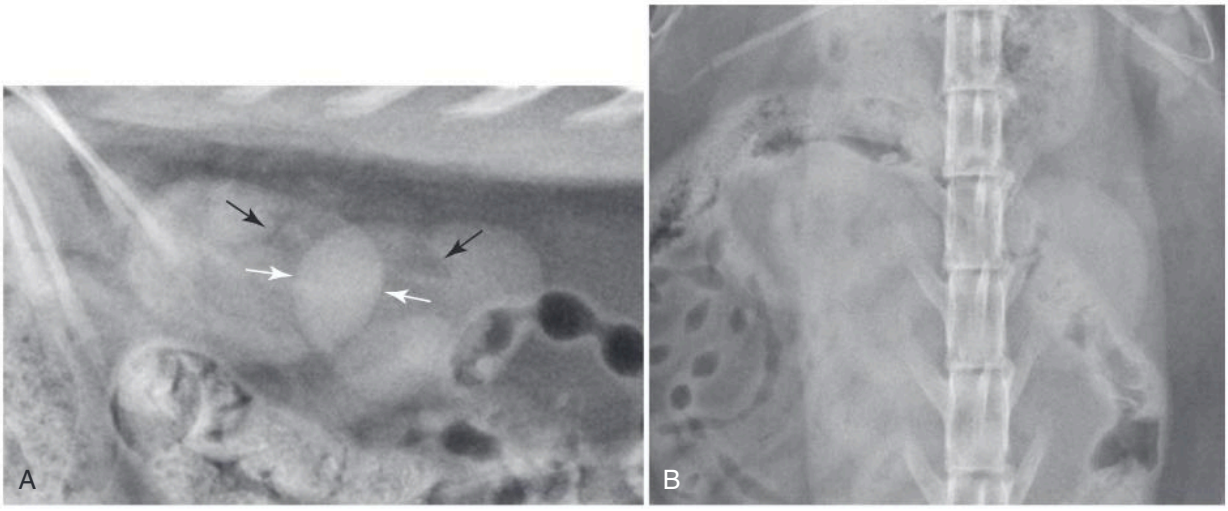


Fig. 41.2 Lateral **(A)** and ventrodorsal (VD; **B**) radiographs of the abdomen of a normal cat. Both kidneys are relatively round with a smooth surface. Fat opacity is visible at the renal hilus in the lateral view (*black arrows*); this is a normal finding in many cats. Note the summation opacity in the lateral view (*white arrows*) where the kidneys overlap. The right kidney is not readily perceptible in the VD view because of superimposed bowel.

Feline kidneys are more rounded and are located typically between L1 and L4, either at the same level or with the right kidney in a more cranial position (Fig. 41.2). In lateral radiographs, the caudal pole of the right kidney may overlap the cranial pole of the left kidney and the summation of the two poles can give the false impression of a small rounded kidney or a retroperitoneal mass (see Fig. 41.2A).

An ectopic kidney or kidneys in a very caudal location occur sporadically.[2] Normal ureters are not visible radiographically.

Small kidneys are indicative of chronic disease, whereas large kidneys are associated with more acute processes. In general, assessment of renal length is more reliable on VD projections because there is no overlap of the kidneys, and magnification of both kidneys is equal. Renal length in normal dogs ranges between 2.5 and 3.5 times the length of L2.[3] In cats, the normal renal length has been measured to be 2.4 to 3.0 times the length of L2.[4] Older cats without signs of renal disease can have smaller kidneys (1.9–2.6 times the length of L2); however, it is difficult to know whether subclinical renal disease may have been present in these cats.[4] Hormonal influence depending on reproductive status alters renal length in cats, both in males and females. Intact cats tend to have larger kidneys (range 2.1–3.2 times the length of L2) than neutered cats (1.9–2.6 times the length of L2).[5] It is important to realize that these normal relationships were determined from a relatively small number of cats and are only intended as guidelines.

Normal kidneys are of uniform soft tissue opacity and smoothly marginated, although fat deposition in the renal pelvis in cats can lead to focal central radiolucency (see Fig. 41.2A). Mineralization associated with the kidneys or ureters is always abnormal, although it may not necessarily be the cause of clinical signs.

Ultrasonography

Indications

Ultrasonographic evaluation of the renal parenchyma is indicated if there is evidence of renal dysfunction. Specific indications include clinicopathologic abnormalities (azotemia, elevated symmetric dimethylarginine [SDMA], change in urine specific gravity), abnormal renal palpation or abdominal radiographic findings, and clinical signs such as hematuria, polyuria, oliguria, or anuria. Renal ultrasound may serve as a screening tool for congenital renal diseases such as aplasia, hypoplasia, dysplasia, and polycystic kidney disease.[2,6,7]

Although ultrasound findings are usually not disease specific, they allow differentiating acute and chronic renal changes, mass lesions, cysts, mineralizations, and alterations of the collecting system and ureters. Needle aspirates or biopsies can be obtained under ultrasound guidance.[8,9] Doppler ultrasound is a useful addition to the grayscale ultrasound examination to evaluate for abnormal renal perfusion caused by infarction, transplant rejection, or mass lesions.[10] Contrast-enhanced ultrasound allows more detailed and more sensitive assessment of renal vasculature and perfusion, and normal perfusion parameters have been described in dogs and cats.[11,12] Contrast-enhanced ultrasound of the canine and feline kidney has potential for delineation of renal parenchymal lesions such as masses or infarcts.[13,14]

Technique

Renal ultrasound should be performed with the highest frequency transducer that enables adequate penetration. In most dogs and cats, 7.5 to 15 MHz is appropriate; 5 MHz or lower frequency transducers should only be used in large dogs. Subcostal or intercostal windows with the patient in lateral or dorsal recumbency allow access to the kidneys, depending on patient size and thoracic conformation. Standard image planes include dorsal (Fig. 41.3A), sagittal (see Fig. 41.3B), and transverse (see Fig. 41.3C) planes, always followed by fanning the transducer through the entire kidney. Renal length should be measured along its maximal pole-to-pole length in a sagittal or dorsal plane image, while avoiding obliquity which would result in artificial shortening of the kidney. The renal pelvis is best evaluated in dorsal and transverse planes. The ureters can be followed caudally from the renal pelvis if dilated. To verify patency and normal location of the ureterovesical junction, the bladder should be evaluated for presence of two urine jets from the dorsolateral bladder wall. If not seen with conventional grayscale imaging, Doppler ultrasound can be used to better delineate the jet. Addition of a diuretic markedly improves frequency and visibility of ureteral jets by increasing urine production and altering the specific gravity of the urine exiting the ureterovesicular junction compared with the urine already present in the bladder.[15]

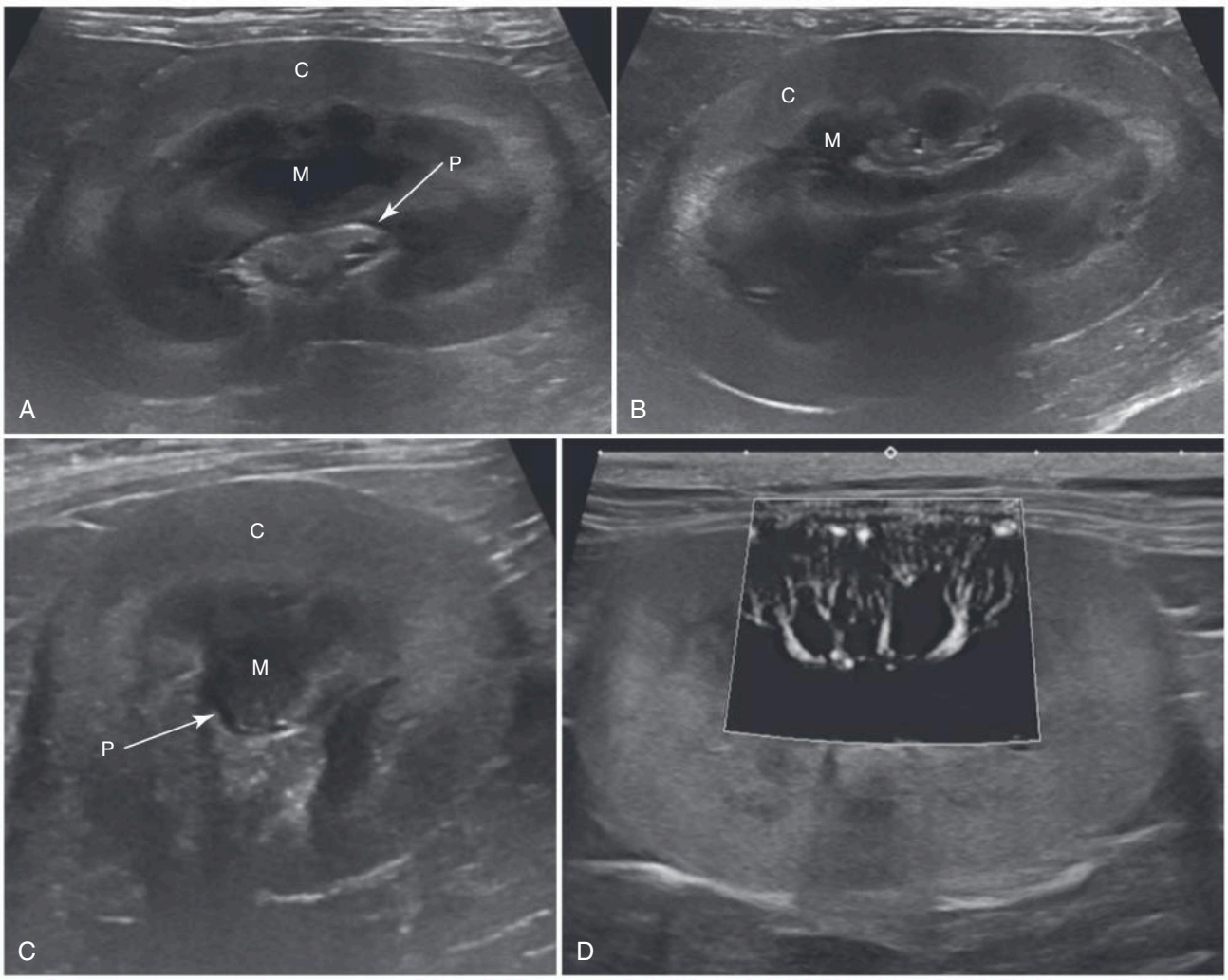


Fig. 41.3 Ultrasound images of a normal canine kidney in dorsal **(A)**, sagittal **(B)**, and transverse **(C)** planes. The renal vasculature is shown with microvascular Doppler **(D)**. The medulla (*M*) is hypoechoic relative to the cortex (*C*) and is divided by the hyperechoic interlobar vessels and pelvic diverticula. The renal pelvis (*P*) is mildly distended and is best seen in transverse and dorsal planes (*white arrows*).

Normal Ultrasonographic Findings

Normal canine and feline kidneys are outlined by a thin, smooth hyperechoic capsule and have a clear distinction between cortex and medulla (see Fig. 41.3). The renal cortex in most patients is hypoechoic to isoechoic to the liver and spleen, although dogs and cats without evidence of renal disease may have a renal cortex that is hyperechoic to liver.[16] In cats, cortical hyperechogenicity can occur with fat deposition.[17]

The normal medulla is hypoechoic, creating a well-defined transition to the cortex. The interlobar vessels and pelvic diverticula give the renal medulla a lobulated appearance. The arcuate vessels are seen at the corticomedullary junction as short, hyperechoic parallel lines that may produce a distal shadow, not to be confused with renal mineralization. The renal pelvis is normally collapsed, but a smoothly margined, thin rim of fluid of up to 2 mm in diameter can be seen in normal animals, especially when using high-resolution transducers.[18] Increased diuresis, caused by exogenous fluid administration or polyuria/polydipsia, results in mild pyelectasia.[18] The pelvic diverticula are not visible normally. The renal pelvis is surrounded by the hyperechoic sinus, which contains dense fibrous tissue and fat, particularly in overweight cats.

Normal kidney size in cats ranges between 3.0 and 4.3 cm.[19] In dogs, size is much more variable depending on body weight and conformation. As a rule of thumb, 10 mm per 10 pounds of body weight can be added within the normal range of 3 to 10 cm.[20] A ratio of 5.5 to 9.1 of the maximal renal length to the luminal diameter of the aorta at the level of the kidney is proposed to take patient size into account.[21] Even using this method, the large range of normal values makes detection of subtle size changes challenging. Renal length, therefore, is not very helpful as an isolated criterion, unless markedly abnormal, and all other ultrasonographic findings have to be taken into account to determine if a kidney is normal or not.

With Doppler ultrasound, the renal artery and vein, interlobar, arcuate, and interlobular vessels can be identified (see Fig. 41.3D). The resistive index should be less than 0.72 in dogs and 0.70 in cats, and the pulsatility index less than 1.52 in dogs and 1.29 in cats.[22] Normal ureters are visible only with high-resolution ultrasound systems and ideal patient-related conditions. Ureters are best followed from a transverse view of the renal pelvis, because they turn medially and can be tortuous until they extend caudally, lateral to the aorta and caudal vena cava. Thin hyperechoic walls and occasional waves of peristalsis with a small bolus of fluid passing through can be seen in a normal ureter.

Excretory Urography and Contrast-Enhanced Computed Tomography

Indications

Intravenous administration of iodinated contrast medium, followed by imaging either with radiography (excretory urography [EU] or intravenous pyelography) or computed tomography (CT) allows assessment of renal structure and vascularity, patency of the collecting system, and to some degree, renal function. The use of EU has decreased but it can still provide useful information. CT has the advantage of imaging the urinary tract without superimposition of other soft tissue or osseous structures, with the option of multiplanar and three-dimensional reconstructions. Indications for EU or CT include urinary tract trauma, hematuria, suspected ureteral ectopia, assessment of retroperitoneal masses, and in some instances, ureteral obstruction. Dual-phase renal angiography can be performed to assess the arterial and venous blood supply of the kidneys separately. This is used mainly for presurgical assessment of feline kidney donors.[23,24] While both methods allow a crude estimation of renal functionality, it is possible to calculate glomerular filtration rate in dogs and cats using contrast-enhanced CT imaging.[25–27]

This has to be weighed against the fact that administration of contrast medium itself poses a risk in the presence of renal disease. Adverse reactions to the intravenous administration of iodinated contrast media include nausea, vomiting, hives, hypotension, and importantly, contrast medium–induced renal failure. Renal insufficiency is a risk factor for development of contrast medium–induced nephropathy, together with the presence of hypovolemia.[10,11,28,29] Contraindications therefore include anuric renal failure, dehydration, hypotension, and known hypersensitivity to iodinated contrast media.

Technique

Patient preparation is a key to obtaining a diagnostic study. Food, but not water, should be withheld for at least 12 to 24 hours before the study. A cleansing enema can be used to evacuate the colon, preferably several hours before the study to allow fecal material and gas to pass. This is more important for EU where superimposition with a full colon may render the study nondiagnostic. The patient should be hydrated and have adequate renal function. Because iodinated contrast medium leads to increased urine-specific gravity and may also inhibit bacterial growth for at least 24 hours, urinalysis should be performed before contrast medium is administered.[30]

Sedation or general anesthesia is recommended for both studies, and an intravenous catheter should be in place throughout the study to provide venous access if complications arise. Survey radiographs or CT images prior to contrast medium administration are an essential part of both studies as small urinary calculi and parenchymal mineralizations may be obscured by the contrast medium.

Excretory urography: Iodinated contrast medium is administered intravenously as a bolus injection at a dose of 600 to 700 mg iodine (I) per kg body weight.[13,14] VD and right lateral abdominal radiographs are acquired immediately after injection and are repeated typically after 5, 20, and 40 minutes or until a diagnosis is reached. Oblique projections for better visualization of the ureters can be added at 5 minutes and later time points. To evaluate the renal arteries, a VD radiograph should be acquired 5 to 7 seconds after bolus injection of contrast medium.

Computed tomography: Iodinated contrast medium is administered intravenously as a bolus at a dose of 400 to 800 mg I/kg body weight. Image series are acquired to evaluate the different phases of contrast medium excretion as outlined later. Optimal ureteral opacification occurs 3 minutes post injection and can persist for about 1 hour.[31] Image series may have to be repeated several times to visualize the entire course of both ureters because of ureteral peristalsis. Positioning the patient in sternal recumbency with the pelvis elevated is helpful in outlining the ureterovesical junctions, because the contrast medium will accumulate in the bladder apex away from the neck, facilitating the distinction between the contrast medium–filled ureters and the bladder neck.

Normal Imaging Findings

For iodinated contrast medium to be excreted normally by the kidneys, normal arterial and venous flow, an anatomically normal kidney, functioning nephrons, and unobstructed flow of urine away from the kidneys into the urinary bladder are necessary. There are three phases of contrast medium excretion. The vascular phase starts approximately 5 to 7 seconds after intravenous bolus injection. In the nephrogram phase, contrast medium is present in the renal parenchyma through glomerular filtration into the nephrons. The nephrogram phase begins after approximately 10 seconds and lasts up to 2 minutes until the pyelogram phase starts and the nephrogram begins to fade (Fig. 41.4). Nephrogram opacity/attenuation should continue to decrease progressively; only approximately 25% of normal dogs still have a detectable nephrogram 2 hours after contrast medium injection.[32] In the pyelogram phase, contrast medium is filtered into the collecting system without tubular reabsorption or secretion.

Normal renal imaging on CT has been reported in dogs where the normal renal length–to–L2 vertebral body ratio in CT imaging was determined to be 2.7 (95% confidence interval [CI], 2.5–2.9), and the renal length–to–aortic ratio was 7.4 (95% CI, 7.07–7.74).[33,42] If renal function is normal, the collecting system is consistently more opaque/attenuating than the renal parenchyma. The normal renal pelvis is curvilinear and less than 2 mm in width. The pelvic diverticula may be seen in some dogs and most cats and appear as thin (1 mm) spikes radiating from the pelvis toward the periphery. Neither the renal pelvis nor the diverticula should have blunted, rounded edges. The ureters tend not to be filled with contrast medium uniformly throughout their length because of ureteral peristalsis. Imaging, therefore, may have to be repeated to assess the entire length of the ureters. Normal ureters are not more than 2 to 3 mm in width. They terminate at the dorsal aspect of the bladder neck, where they curve cranially for a short distance before entering the wall. The duration and intensity of the opacification of the kidney during an excretory urogram depend on the dose of contrast medium administered; renal perfusion; glomerular filtration; tubular reabsorption of water; the patient's hydration status, which is important to maintain adequate renal perfusion; and patency of the renal outflow tract.

Antegrade Ultrasound-Guided Pyelography

Indications

Ultrasound-guided injection of contrast medium into the renal pelvis leads to excellent opacification of the collecting system because the contrast medium is not diluted, and its concentration in the collecting system is not dependent on renal function. This procedure can be performed in azotemic patients without loss of image quality. In addition, each renal pelvis and ureter can be assessed individually. Other advantages include the lack of systemic contrast medium reactions and collection of urine directly from the renal pelvis for urinalysis and microbiologic testing. The main indication for this procedure is suspected ureteral obstruction. Contraindications include coagulopathies, because some hemorrhage may occur. Adverse effects may be significant and include hemorrhage, focal damage of renal tissue, and spread of infection in the presence of pyelonephritis or pyonephrosis with perirenal sepsis and abscessation. Contrast medium may also leak into the retroperitoneal space.[34] Loss of renal function secondary to the

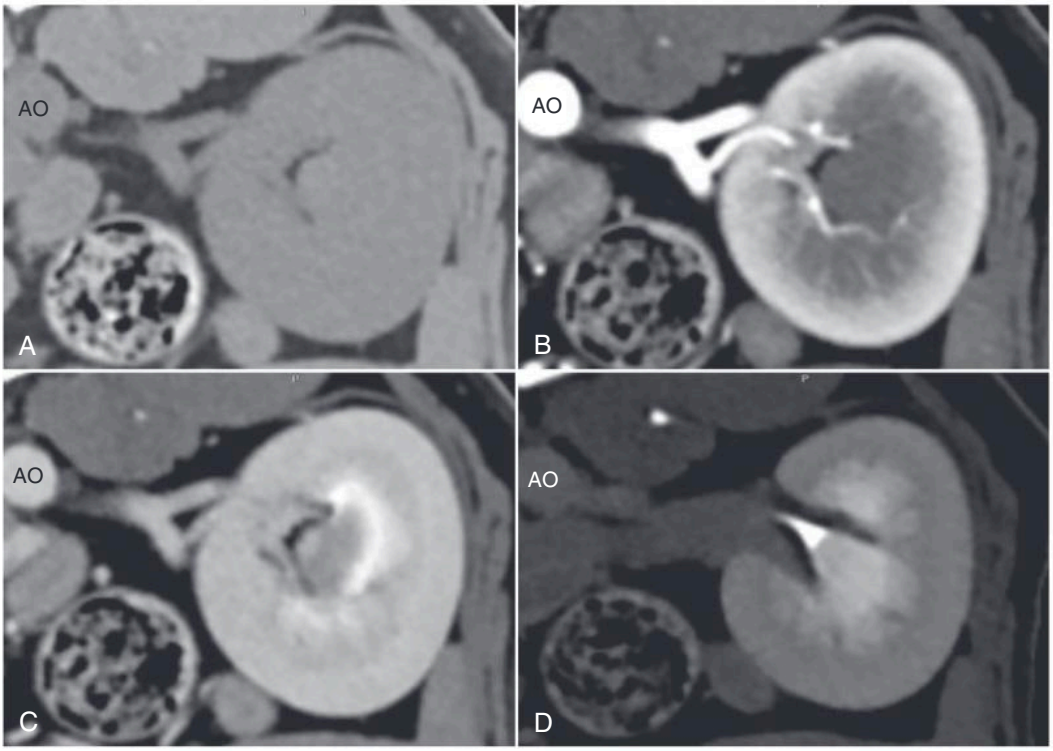


Fig. 41.4 Transverse contrast-enhanced computed tomography images of a dog with no signs of renal disease. The left kidney is shown before contrast medium administration **(A)**, during the vascular phase **(B)**, venous phase **(C)**, and pyelogram phase **(D)** after intravenous administration of iodinated contrast medium. The aorta is labeled (*AO*). In **B,** the renal vessels are enhanced; in **C,** the renal parenchyma is enhanced; and in **D,** contrast medium has reached the renal pelvis and proximal ureter.

procedure is minimal but should be a consideration in patients with already severely compromised renal function.

Technique

Heavy sedation or general anesthesia is necessary. The skin is prepared aseptically, and a 22- to 25-gauge needle connected with an extension set and three-way stopcock is introduced into the renal pelvis under ultrasound or fluoroscopic guidance. Depending on the size of the renal pelvis, 1 to 2 mL of urine is removed for laboratory testing. Nonionic iodinated contrast medium equivalent to half of the volume of urine removed is then introduced slowly, and the size of the renal pelvis is monitored with ultrasound or fluoroscopy.[34] Overdistention of the renal pelvis should be avoided, because rupture may occur. Immediately after contrast medium injection, VD, oblique, and lateral abdominal radiographs are acquired. If bilateral abnormalities are suspected, the procedure can be repeated on the contralateral side.

Normal Imaging Findings

The renal pelvis becomes distended with mild blunting of the pelvic diverticula, as contrast medium is introduced under mild pressure. If the ureter is patent, contrast medium should appear in the urinary bladder almost immediately (Fig. 41.5). Narrowing of the ureter may be observed because of peristalsis; repeat images will be needed to differentiate between peristalsis and stricture.

Magnetic Resonance Imaging

Magnetic resonance imaging (MRI) is used in people to assess renal diseases, perfusion, and function, but little work has been performed in small animals. Advantages and indications are similar to those described for CT, but use is limited by cost, availability, and duration of the imaging studies. Protocols for magnetic resonance angiography of the renal vasculature in renal transplant donors are available.[35]

Scintigraphy

Compared with other nonimaging renal function testing, renal scintigraphy using technetium-99m diethylenetriamine pentaacetic acid has the advantage of being able to determine the relative contribution of each kidney to total renal function. This is especially important in patients with impaired renal function before planned nephrectomy. Describing the technique of renal scintigraphy is beyond the scope of this chapter, and readers are referred to another source.[36]

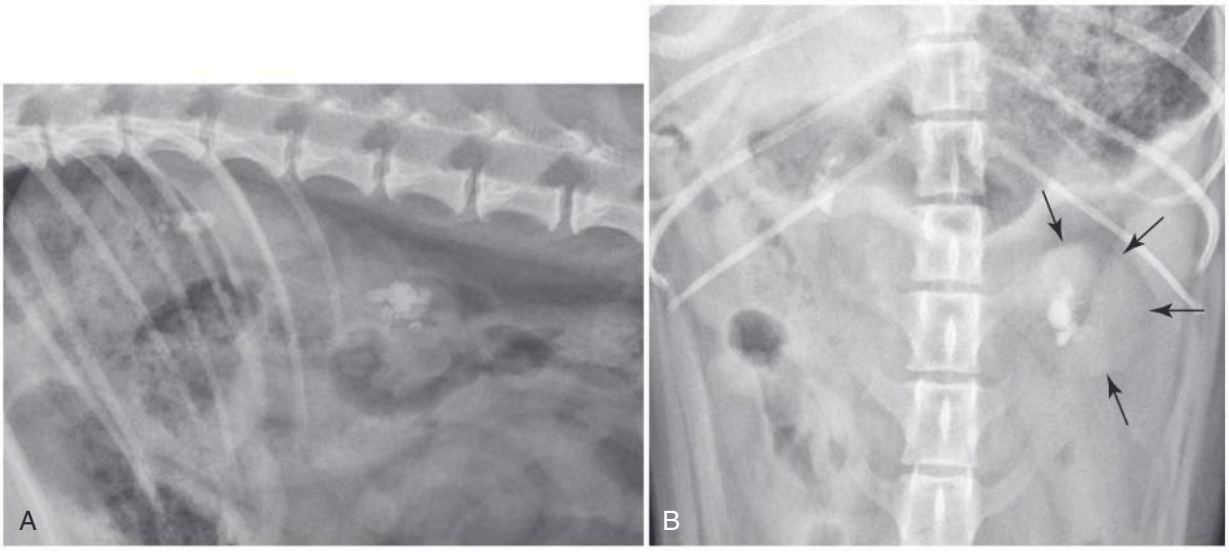
RENAL DISEASES

Abnormal Renal Size

It is important to keep in mind that renal size and shape may be normal in the presence of renal disease. In particular, early chronic, acute toxic, inflammatory, or infectious nephropathies, as well as amyloidosis, do not always lead to alteration of renal size or shape.[37]

Small Kidneys

Reduced renal size is most commonly caused by chronic nephropathy. Chronic renal disease is also associated with other radiographic findings that may include abnormal, irregular shape due to cortical infarcts, and renal mineralizations (Fig. 41.6, eFig. 41.1). Other differentials of bilaterally reduced renal size include congenital anomalies such as dysplasia or hypoplasia.[7] Renal atrophy is seen with chronic, longstanding ureteral obstruction and is thus usually associated with hydronephrosis; the affected kidney (typically only one) can thus be reduced or relatively normal in size.



eFig. 41.1 Left lateral **(A)** and ventrodorsal (VD; **B**) radiographs of a dog with chronic renal disease. Both kidneys are very small, rounded, and irregular and contain multiple nephroliths. *Black arrows,* Left kidney.

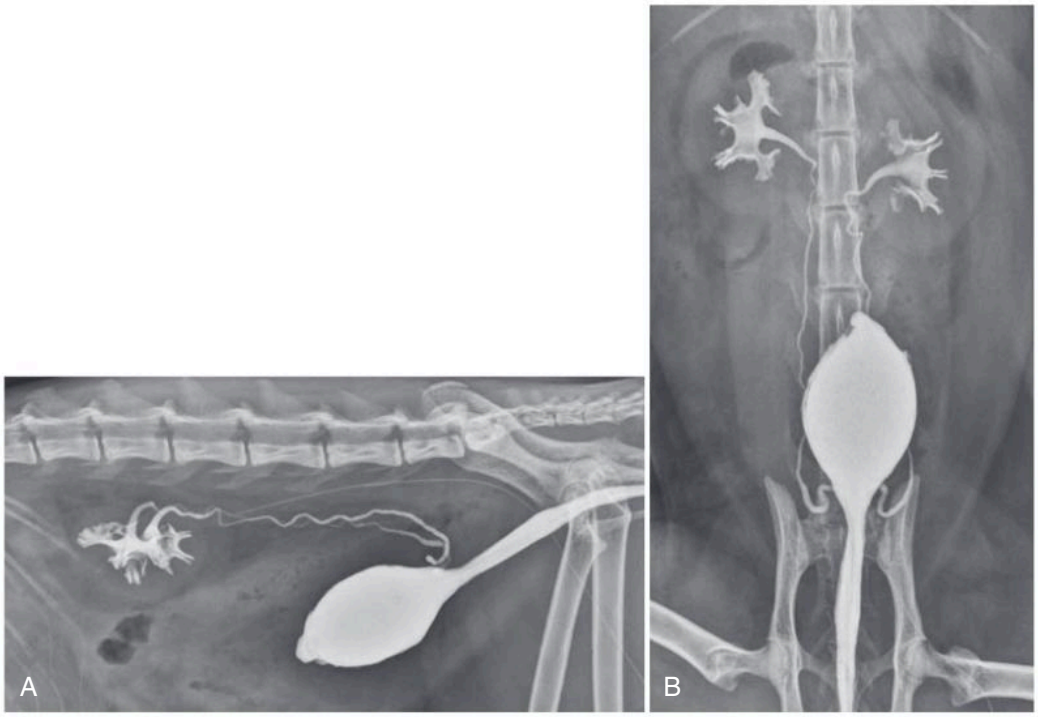


Fig. 41.5 Lateral **(A)** and ventrodorsal (VD; **B**) radiographs of a cat after an ultrasound-guided antegrade pyelogram was performed in both kidneys. The renal pelvis is mildly dilated in both kidneys because of injection pressure. Both ureters are filled with contrast medium and terminate in the dorsal aspect of the bladder neck. Ureteral obstruction is not present. Note the curved appearance of the normal distal ureter. The apex of the urinary bladder is irregular because of polypoid cystitis. A central venous catheter is present in the caudal vena cava.

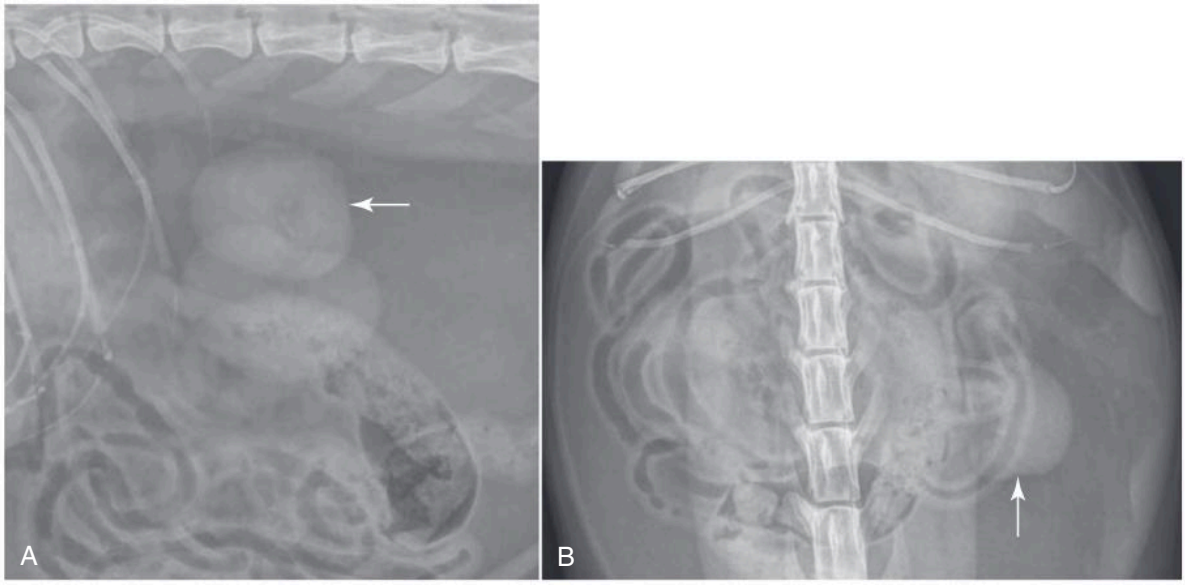
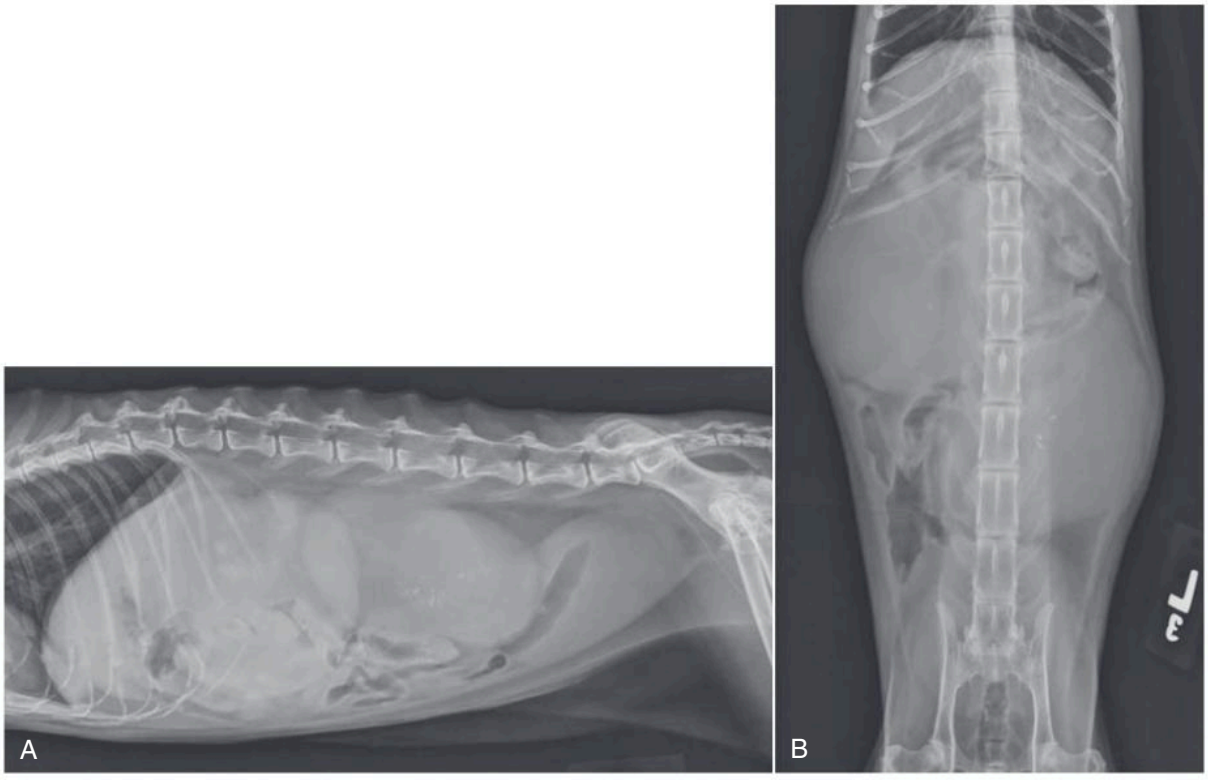


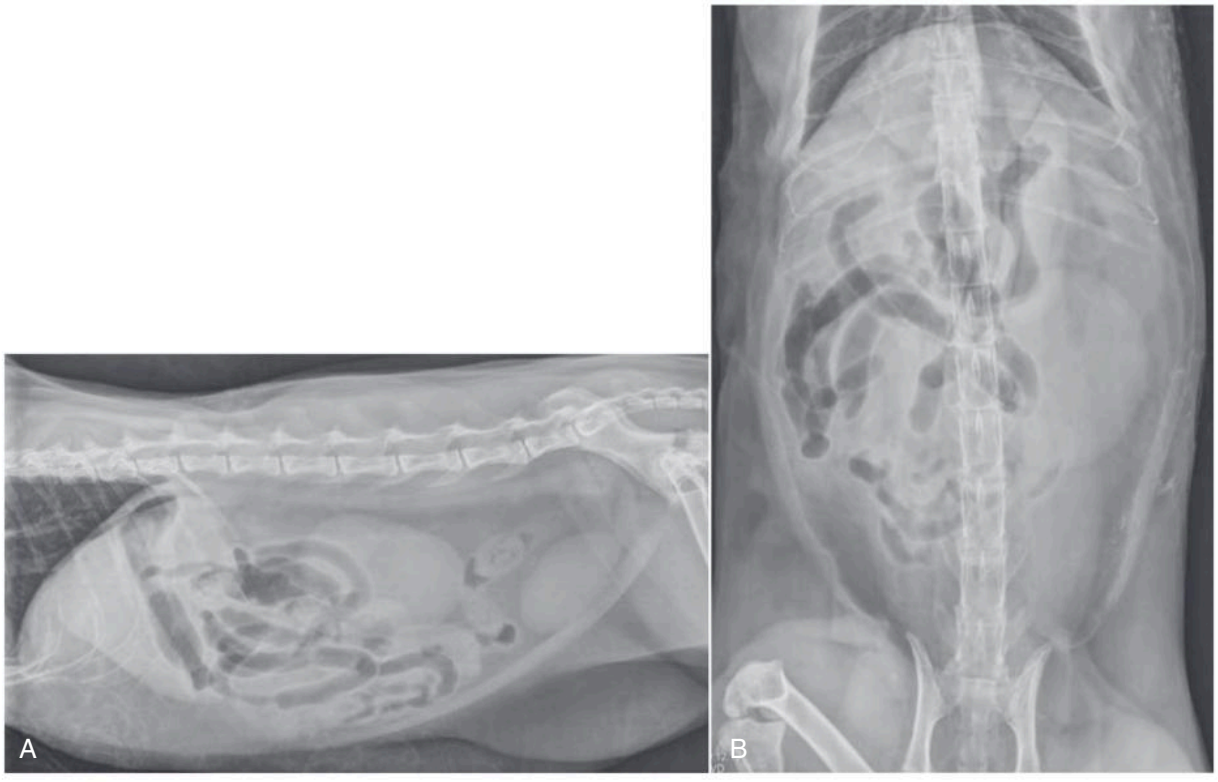
Fig. 41.6 Left lateral **(A)** and ventrodorsal **(B)** radiographs of a cat with chronic kidney disease. The left kidney is reduced in size and has a flattened caudal pole (*arrows*) due to cortical infarction.

Large Kidneys

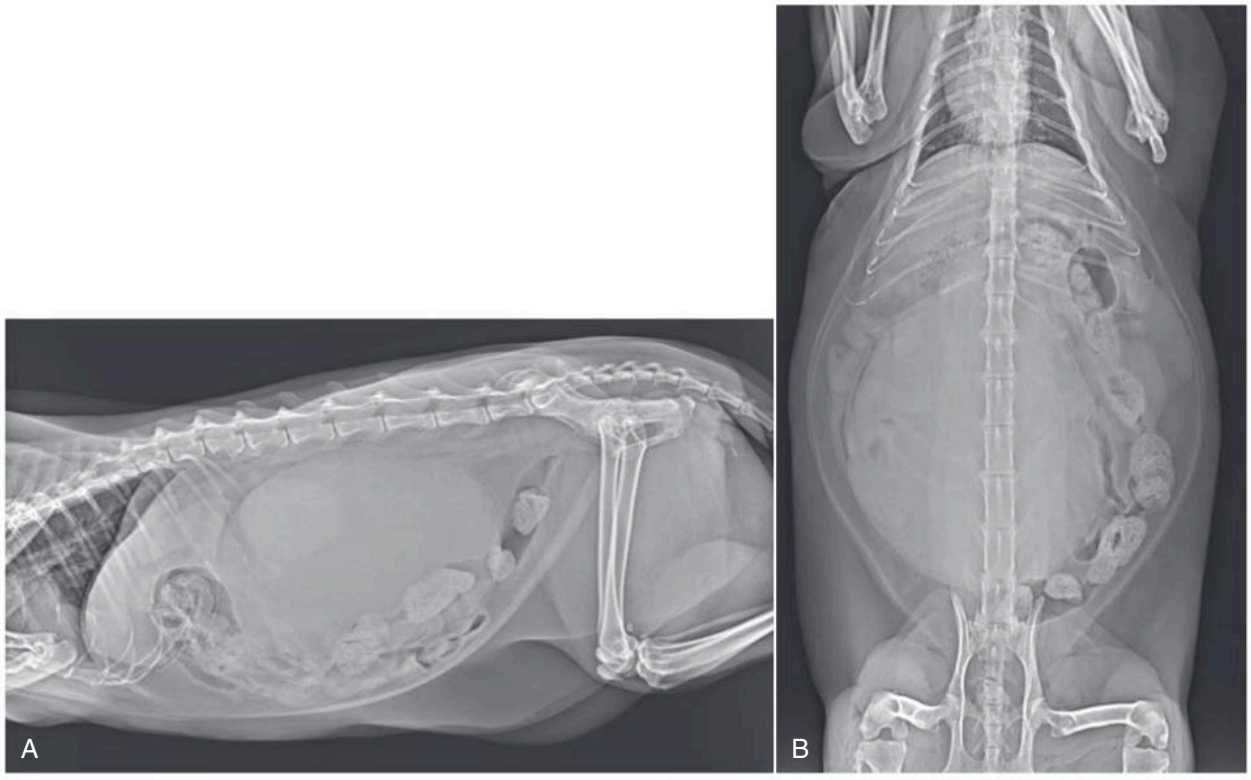
Renomegaly causes a mass effect in the retroperitoneal space, evidenced by ventral displacement of the gastrointestinal tract and other organs (Fig. 41.7, eFig. 41.2). Left renal enlargement leads to ventral or lateral displacement of the descending colon and small intestines (Fig. 41.8, eFig. 41.3), whereas right renomegaly is associated with ventral displacement of the ascending colon and duodenum (Fig. 41.9, eFig. 41.4). Differential diagnoses for renomegaly are subdivided based on the presence of unilateral versus bilateral enlargement and alterations in margination and are listed in Table 41.1. Bilateral mild renomegaly may be seen with acute kidney injury, pyelonephritis, amyloidosis, with congenital portosystemic shunts as well as acromegaly in cats. Bilateral renomegaly in portosystemic shunts is thought to be due to hypertrophy in an attempt remove and metabolize ammonia and some gluconeogenesis.[38] Acromegalic cats have measurably larger kidneys, adrenal glands, and pancreas as well as a subjectively larger liver than



eFig. 41.2 Left lateral **(A)** and ventrodorsal **(B)** radiographs of a cat with bilateral polycystic renal disease. The kidneys are severely enlarged and have undulant margins caused by the cysts. Linear mineralizations are visible along the renal pelvic recesses.



eFig. 41.3 Left lateral **(A)** and ventrodorsal **(B)** radiographs of a cat with right renal agenesis and enlargement of the left kidney due to compensatory hypertrophy. Linear soft tissue opacity lines along the ventral and lateral body wall are caused by wet hair artifact.



eFig. 41.4 Left lateral **(A)** and ventrodorsal **(B)** radiographs of a cat with severe right renomegaly. Notice how the gastrointestinal tract is displaced ventrally and to the *left*. The left kidney has irregular margins.

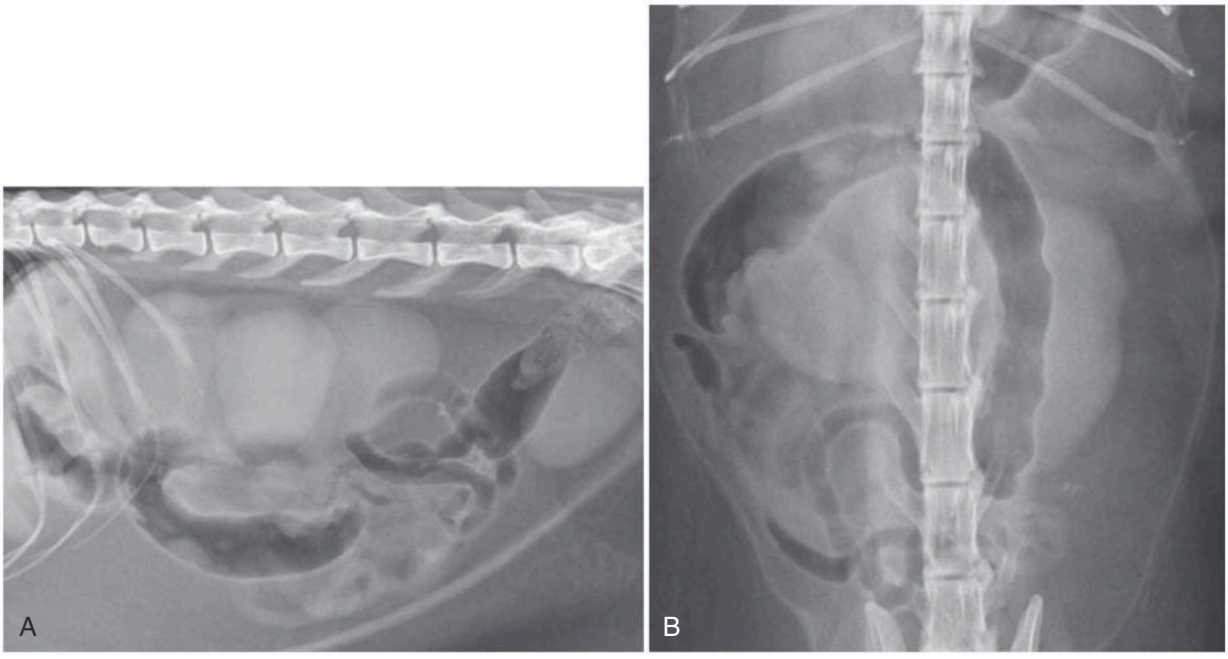


Fig. 41.7 Left lateral **(A)** and ventrodorsal (VD; **B**) radiographs of the abdomen of a cat with bilateral renomegaly caused by renal lymphoma. Both kidneys are large and have undulating margins. The gastrointestinal tract is displaced ventrally.

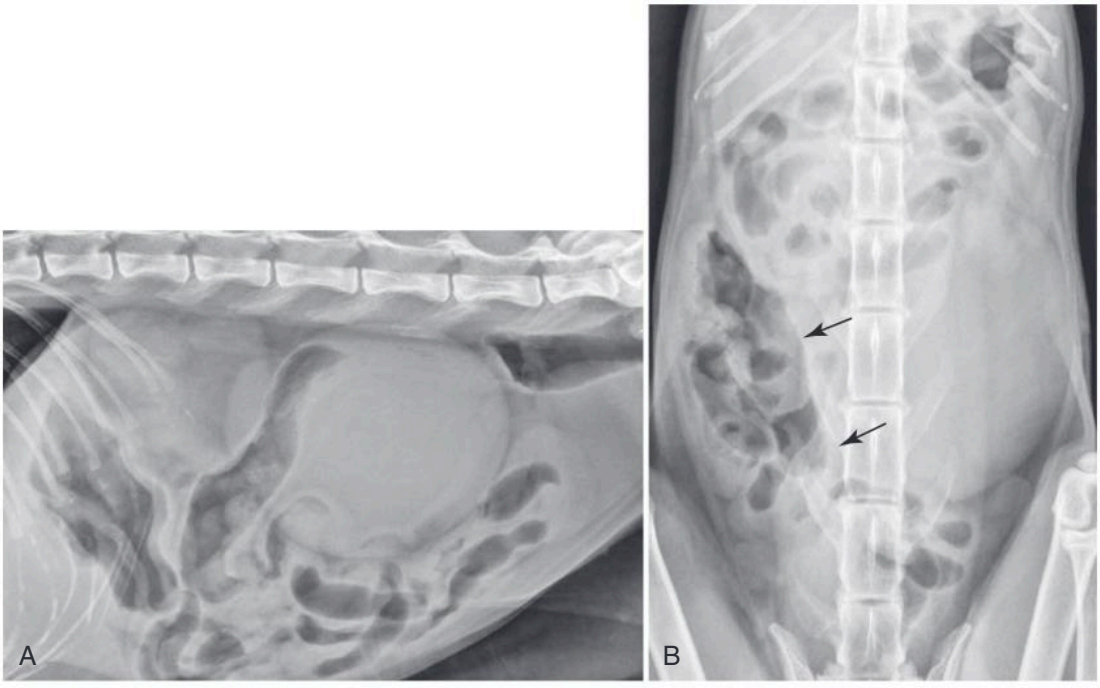


Fig. 41.8 Lateral **(A)** and ventrodorsal (VD; **B**) abdominal radiographs of a cat with left renal enlargement. The enlarged kidney displaces the small intestines ventrally and the descending colon (*black arrows*) to the right **(B)**.

nonacromegalic cats, caused by the anabolic effects of insulin-like growth factor 1 (IGF-1).[39] Unilateral mild renomegaly with a normal shape and smooth outline is most commonly seen with compensatory hypertrophy caused by contralateral chronic degenerative or obstructive disease, occasionally also due to subcapsular fluid accumulation (urine, hemorrhage or pus) or renal neoplasia, although with renal neoplasia or subcapsular changes, a change in shape is often appreciated.

Bilateral markedly enlarged kidneys with a smooth outline are seen with renal lymphoma (see Fig. 41.7), feline infectious peritonitis (FIP), bilateral hydronephrosis, or bilateral perinephric pseudocysts. Hydronephrosis and perinephric pseudocysts are often unilateral, or at least asymmetrical in appearance. Unilateral severe renomegaly with a smooth outline is most commonly seen with hydronephrosis, renal tumors and subcapsular fluid, or unilateral perinephric

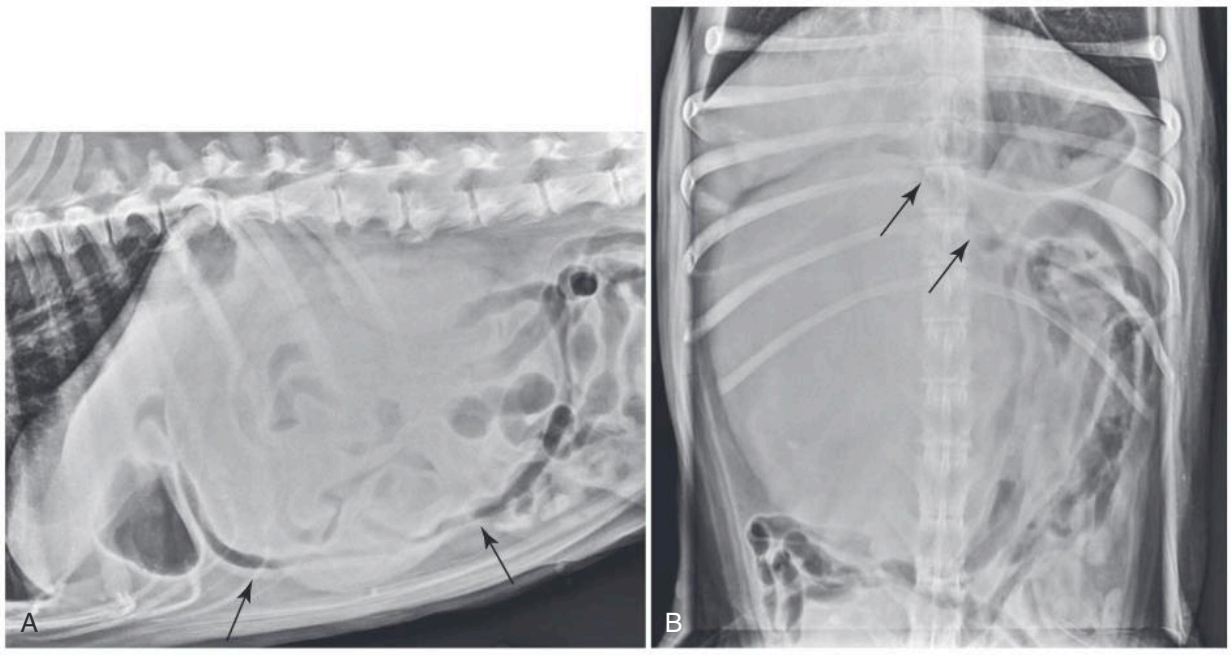


Fig. 41.9 Lateral **(A)** and ventrodorsal (VD; **B**) abdominal radiographs of a dog with right renal carcinoma. The right kidney is severely enlarged, and displaces the duodenum (*black arrows*) ventrally **(A)** and to the left **(B)**.

Table • 41.1

Differential Diagnoses for Changes in Renal Size and Shape.

BILATERAL	UNILATERAL
Mildly Enlarged Kidney, Smooth Outline	
• Acute kidney injury	• Compensatory hypertrophy
• Acute pyelonephritis	• Renal neoplasia (except lymphoma)
• Congenital portosystemic shunts	• Subcapsular abscess or hemorrhage
• Amyloidosis	
• Acromegaly	
Markedly Enlarged Kidney, Smooth Outline	
• Hydronephrosis	• Hydronephrosis
• Renal lymphoma	• Renal tumor
• Feline infectious peritonitis	• Subcapsular hematoma or abscess
• Feline perinephric pseudocysts	• Feline perinephric pseudocyst
Enlarged Kidney, Irregular Outline	
• Metastatic neoplasia	• Primary renal tumor
• Polycystic kidney disease	• Metastatic neoplasia
• Feline infectious peritonitis	• Renal abscess
	• Renal hematoma
	• Renal granuloma
	• Renal cysts
Small Kidney, Smooth or Irregular in Outline	
• Chronic renal disease	• Chronic renal disease
• Developmental hypoplasia or dysplasia	• Atrophy secondary to obstruction

pseudocyst. Enlarged kidneys with an abnormal shape and irregular outline increase the concern for a more severe disease process such as neoplasia, abscessation, granuloma, or hemorrhage. Renal cysts, however, can result in markedly irregular and enlarged kidneys. Bilateral enlargement is typically present with polycystic kidney disease, whereas an idiopathic renal cyst may be unilateral. Bilateral renal neoplasia is most commonly due to metastatic or multicentric disease (hemangiosarcoma, histiocytic sarcoma). Primary renal tumors such as adenocarcinoma are typically unilateral in occurrence, although they can metastasize to the contralateral side. Irregular renomegaly in a juvenile patient may be seen with nephroblastoma, which can manifest in the kidney or the spine. Presence of renomegaly should always prompt further workup of the patient to determine the source of the abnormal size, either within or outside the urinary system.

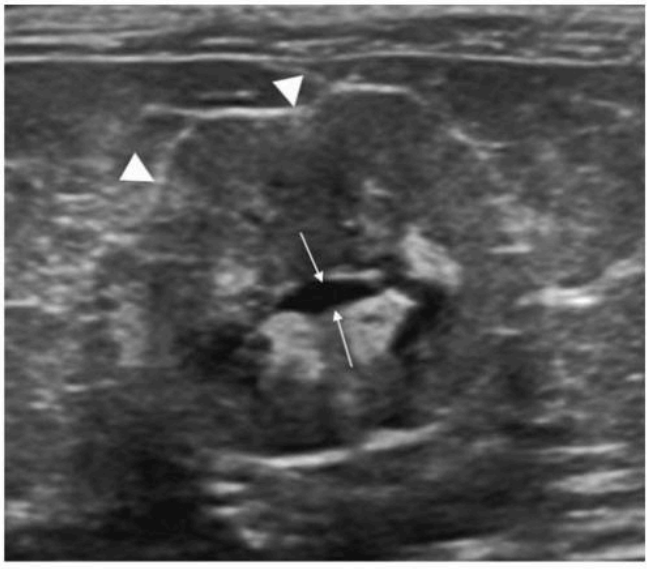
Contrast procedures (EU or CT), or ultrasound, have to be used to determine if the renal enlargement is caused by parenchymal disease or by dilation of the collecting system or renal capsule.

Abnormal Renal Structure

Diffuse Parenchymal Abnormalities

Renal structure is evaluated best with ultrasound. Because of the large variability in normal renal size, architecture, and echogenicity, subtle changes in renal structure are not always detected. In fact, it is common for patients with acute kidney injury and glomerulonephritis to have normal appearing kidneys on ultrasound.[40]

Chronic Nephropathies. Chronic tubulointerstitial inflammation and fibrosis are the predominant histopathologic findings in chronic kidney disease, regardless of the underlying cause. This results in poor corticomedullary definition caused by cortical and medullary hyperechogenicity, which is one of the most common changes associated with chronic renal disease, together with small renal size, small cortical cysts, and parenchymal mineralization (Fig. 41.10, eFig. 41.5). Renal fibrosis



eFig. 41.5 Ultrasound image of chronic renal disease in a cat. The kidney is small, rounded, and irregular with multiple wedge-shaped hyperechoic cortical indentations consistent with chronic infarction (*white arrowheads*) and mild pyelectasia (*arrows*). The cortex and medulla cannot be distinguished from each other.

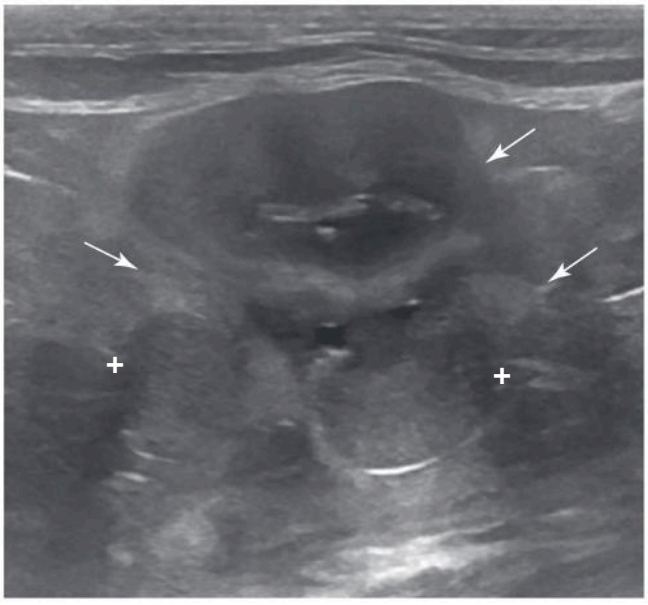


Fig. 41.10 Ultrasound image of chronic renal disease in a cat in a longitudinal plane, the length of the kidney is indicated with *cursors*. The kidney is small, rounded, and irregular with multiple wedge-shaped hyperechoic cortical indentations consistent with chronic infarction (*arrows*). The cortex and medulla are poorly delineated from each other.

may disrupt close interaction of peritubular capillaries with renal tubules resulting in ischemia and cortical infarction, which are visible as linear or triangular hyperechoic lesions in the cortex. On ultrasound, infarcts appear as wedge-shaped, hyperechoic areas in the cortex with an associated cortical defect. The appearance of infarcts has also been described on CT where they appear as a hypoattenuating region following contrast enhancement. They are often wedge shaped and are sometimes associated with flattening or depression of the adjacent cortical margin.[41] Parenchymal atrophy, infarction, and fibrosis can result in distortion of the shape of the renal pelvis. Reduced cortical thickness has been associated with reduced renal function in cats.[42] The type of underlying renal disease cannot usually be determined at this stage. Renal dysplasia is usually diagnosed late in the disease process and changes in the kidneys resemble those from any other chronic renal disease.[43,61]

Acute Nephropathies. Ultrasonographic findings associated with acute kidney injury leading to acute tubular necrosis, interstitial nephritis, or glomerulonephritis include renal enlargement, subcapsular or perirenal effusion, and cortical hyperechogenicity. In severe or advanced disease, the medullary echogenicity increases as well, leading to reduced corticomedullary distinction. Acute kidney injury in dogs and cats has many causes, including toxins (e.g., ethylene glycol, lily in cats, and grapes in dogs), bacterial, protozoal, and rickettsial infections (e.g., leptospirosis, babesiosis, Lyme disease, pyelonephritis), drugs, hypercalcemia, sepsis, ischemia, multiple organ dysfunction syndrome, pancreatitis, and hyperviscosity.[44] It is usually not possible to determine the cause of acute kidney injury by ultrasound, and biopsy may be needed. The Doppler examination of renal vasculature with calculation of the resistive index may add some information. For example, elevation of the renal resistive index is seen with active tubulointerstitial or vascular disease; however, it remains a nonspecific parameter.[45] Ethylene glycol toxicity leads to the most dramatic increase in cortical and medullary echogenicity with a hypoechoic rim at the corticomedullary junction and hypoechoic central medullary regions (Fig. 41.11).[46] The increased



Fig. 41.11 Ultrasound image of the right kidney of a dog that ingested ethylene glycol the night before. The renal cortex and medulla are extremely hyperechoic; a thin hypoechoic rim delineates the corticomedullary junction.

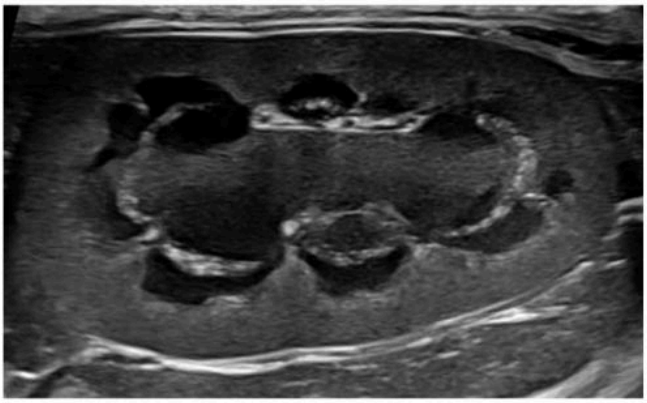


Fig. 41.12 Longitudinal ultrasound image of the left kidney of a 2-year-old cat with normal renal values and urine concentration. A thin hyperechoic medullary rim can be a normal variant.

echogenicity is attributed to deposition of calcium oxalate crystals in the kidneys.[47]

A hyperechoic medullary rim parallel to the corticomedullary junction is observed commonly and may be seen in clinically normal dogs and cats[47] (Fig. 41.12). A wide medullary band is more commonly associated with renal pathology than a thin rim.[48,49] It can be seen with mineralization, necrosis, and hemorrhage associated with many different disease processes, including acute tubular necrosis, leptospirosis, pyogranulomatous vasculitis in cats with FIP (Fig. 41.13), and in hypercalcemic nephropathy.[47–51] Hypercalcemic nephropathy is characterized by variable degrees of calcification and necrosis of renal tubules and collecting ducts. The corticomedullary rim corresponds to increased calcium deposits at this site.[52] Ring- or band-like structures with an echogenic wall in the corticomedullary region may be seen in kidneys of dogs infected with giant kidney worms *(Dioctophyme renale)* in endemic regions.[53]

Focal or Multifocal Abnormalities

Renal Mineralization. Renal mineralization, because of nephrolithiasis or dystrophic mineralization, is common, especially in older patients. All types of nephroliths are detectable ultrasonographically and are characterized by a hyperechoic

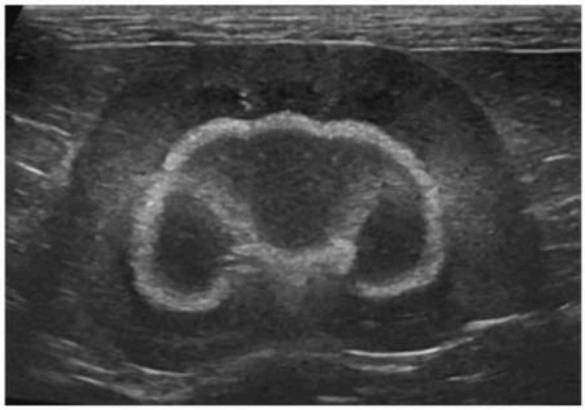


Fig. 41.13 Ultrasound image of a 7-month-old cat with feline infectious peritonitis. The kidney is overall hypoechoic, but a pronounced hyperechoic band is present parallel to the corticomedullary junction.

surface and a distal acoustic shadow. Calculi in the renal pelvis may lead to obstruction either directly in the renal pelvis or if they move into the ureter. However, it is not always possible to differentiate dystrophic mineralization from small nephroliths in the pelvic diverticula. Dystrophic mineralization tends to occur along the pelvic diverticula to form linear hyperechoic striations with a distal acoustic shadow and is usually accompanied by other chronic renal changes (Fig. 41.14). Diffuse cortical or medullary foci of mineralizations are often not detected radiographically but appear as punctate hyperechogenicities on ultrasound.

Renal Cysts. Radiographic changes due to cyst formation are seen only if cysts lead to kidney enlargement or distortion of the renal capsule (Fig. 41.15). Round filling defects may be seen in the nephrogram phase of an EU or CT, although nodules or masses could have the same appearance. Ultrasonographically, renal cysts are readily identified as anechoic round structures with distal acoustic enhancement and a thin edge artifact (Fig. 41.15, eFig. 41.6).[6,21] Internal echoes caused by hemorrhage or cellular debris may be observed. Inherited polycystic kidney disease is seen in long-haired cats (autosomal dominant), sometimes associated with hepatic and pancreatic cysts, and Cairn terriers (recessive mode of inheritance) and can be identified at a young age.[6,21,54,62] In severe instances where the renal parenchyma is almost completely obliterated by the cysts, renal function may be impaired (see Fig. 41.15). Cysts are usually located at the corticomedullary junction.[6,21] Solitary cysts can occur in any feline and canine breed and are not clinically significant if the renal architecture is otherwise normal. Small cortical cysts are observed commonly in conjunction with chronic degenerative renal disease. Nodular dermatofibrosis in German shepherd dogs is associated with renal cystadenocarcinoma. Although predominantly cystic, these lesions have a mass-like tissue component that infiltrates the renal parenchyma and may protrude into the cysts[55,63] (Fig. 41.16). Other differential diagnoses for cystic lesions with a thick wall or a solid component include renal abscess or a cavitated, necrotic tumor.

Perirenal Fluid. Perirenal or subcapsular fluid may be the result of acute renal failure, urine leakage, ureteral obstruction, hemorrhage, abscessation, perirenal pseudocysts, and neoplasia. If the fluid is subcapsular, renomegaly is seen on radiographs. EU, ultrasound, or contrast-enhanced CT is necessary to differentiate subcapsular fluid from renal parenchymal disease. Radiographically, fluid buildup outside the renal capsule leads to an increased opacity of the retroperitoneal space with a mottled or streaked appearance and loss of the outline of the kidneys or enlargement of the

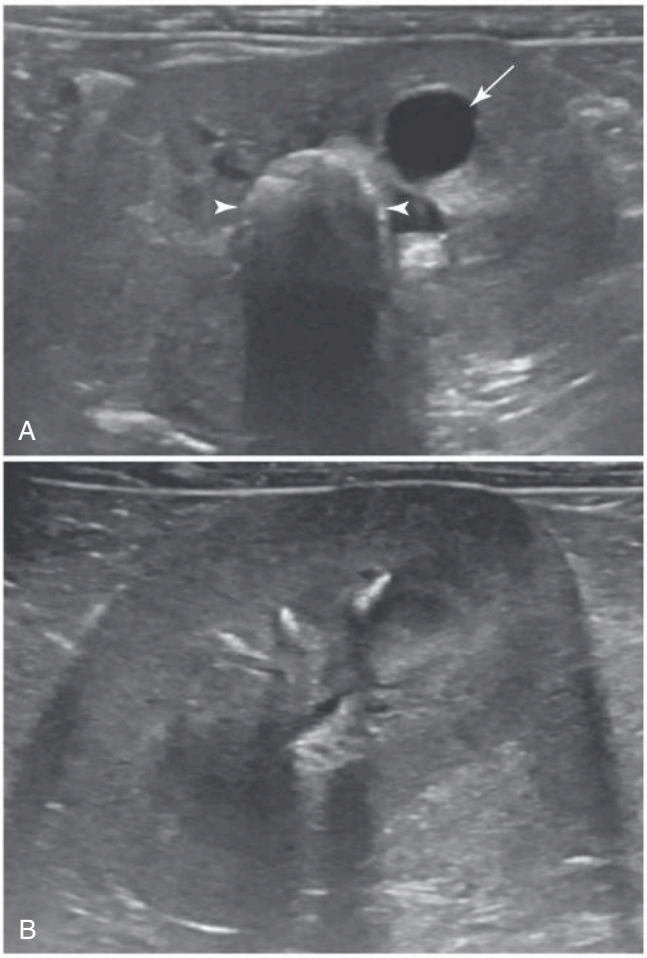
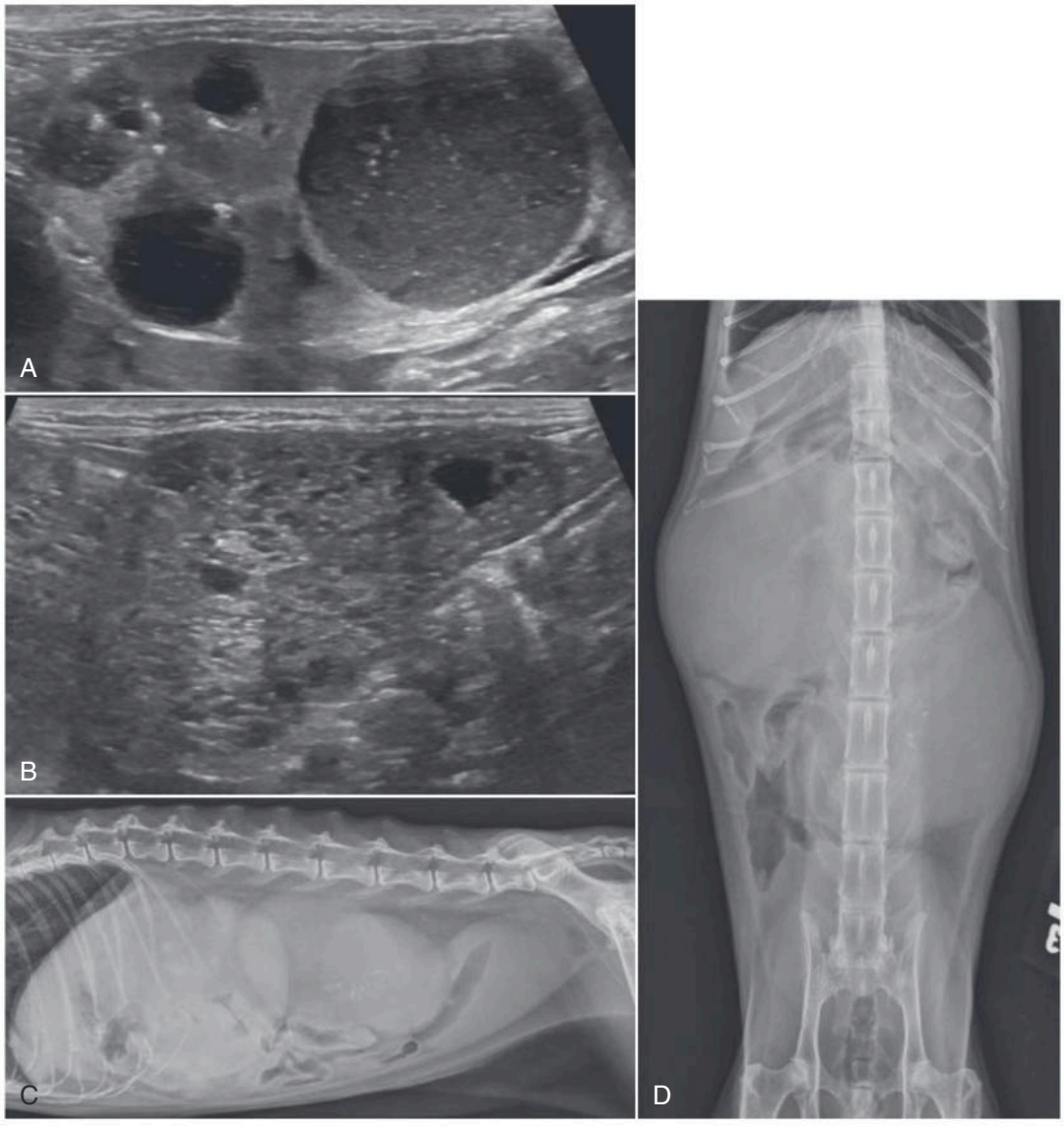


Fig. 41.14 Long-axis ultrasound images of two canine kidneys with mineralization. In image **A,** a curvilinear nephrolith is present in the renal pelvis, creating a distal shadow (*arrowheads*). A large renal cyst is seen at the corticomedullary junction of the caudal renal pole (*arrow*). In image **B,** the mineralization is dystrophic in nature and extends along the pelvic diverticula, creating a hyperechoic striated appearance.

retroperitoneal space. Extracapsular fluid is characterized sonographically by triangular fluid accumulations adjacent to the kidney, predominantly on the dorsal aspect. Common causes include urinary tract rupture and acute renal failure (Fig. 41.17).[56,64] Proposed mechanisms for the fluid accumulation in the absence of rupture include tubular backleak of an ultrafiltrate into the renal interstitial space in excess of what the lymphatics can drain, either because of increased tubular permeability or obstructive disease.[56] Focal inflammation of the retroperitoneal fat resulting in an increased echogenicity may be seen with renal abscessation and pyelonephritis. Pseudocyst formation is caused by a transudate and has been associated with underlying renal parenchymal disease, such as interstitial nephritis. The affected kidneys are often reduced in size and have signs of chronic renal disease (Fig. 41.18).[57]

Renal Mass Lesions. Renal mass lesions can be caused by hematoma, abscess, neoplasia, and granuloma. Primary renal tumors are usually unilateral and include renal cell carcinoma, squamous cell carcinoma, papillary carcinoma, and nephroblastoma.[58] Other tumors that may affect the kidneys are histiocytic sarcoma, plasma cell tumor, metastatic carcinoma, hemangiosarcoma, and lymphosarcoma.[59] Larger masses can be identified radiographically as asymmetric renal enlargement.



eFig. 41.6 Ultrasound image of the left kidney **(A)** and liver **(B)** of a cat with polycystic disease. The renal parenchyma **(A)** is largely replaced by small and large cysts—some with echogenic contents. Numerous cysts are disseminated through the liver parenchyma **(B)**. Left lateral **(C)** and ventrodorsal (VD; **D**) radiographs of the abdomen of a cat with polycystic disease. Both kidneys are severely enlarged with undulating margins. Linear mineralizations are present along the pelvic recesses of both kidneys.

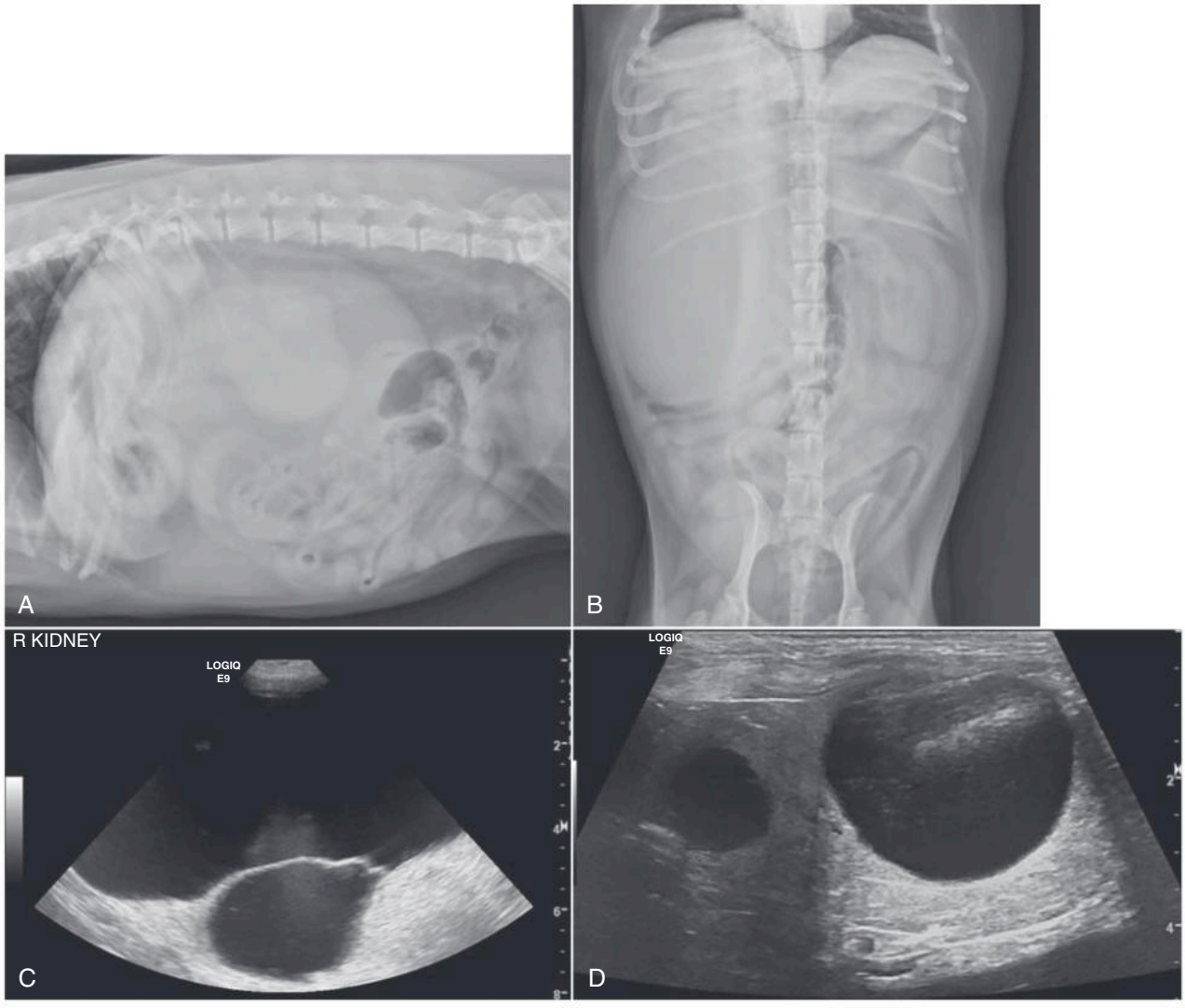


Fig. 41.15 Lateral **(A)** and ventrodorsal **(B)** radiographs and longitudinal ultrasound images of the right **(C)** and left **(D)** kidneys of a Chihuahua with polycystic kidney disease. The right renal parenchyma is almost completely effaced by large cysts **(C)** causing severe renomegaly on radiographs. Multiple cysts in the left kidney **(D)** distort the normal shape of the kidney seen both ultrasonographically and radiographically.



Fig. 41.16 Longitudinal ultrasound image of the left kidney of a 9-year-old German shepherd dog with nodular dermatofibrosis and renal cystadenocarcinoma. The renal parenchyma is distorted by multiple complex cystic masses.

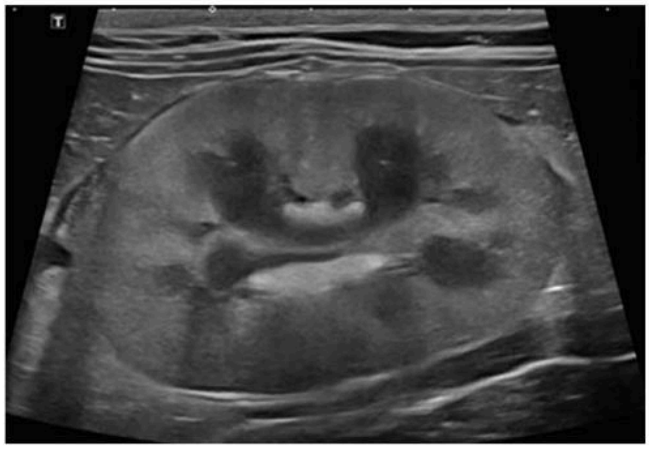


Fig. 41.17 Long-axis ultrasound image of the left kidney of a dog diagnosed with acute kidney injury due to leptospirosis infection. Anechoic fluid surrounds the renal capsule. The kidney is overall hyperechoic with mild pyelectasia.



Fig. 41.18 Long-axis ultrasound image of the right kidney of a cat with a perinephric pseudocyst. The kidney is reduced in size, irregular in shape, and has poor corticomedullary distinction, parenchymal mineralizations, and pyelectasia. There is a large amount of encapsulated anechoic perirenal fluid.

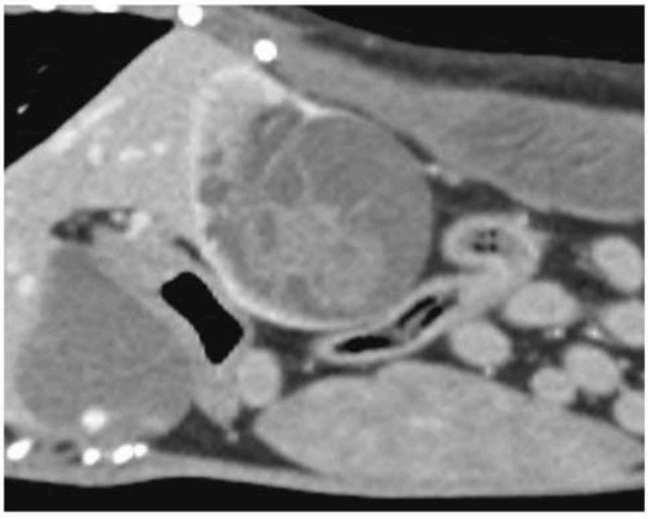


Fig. 41.19 Postcontrast sagittal computed tomography image of the right kidney of a dog with a nephroblastoma. A small portion of the cranial pole of the kidney becomes opacified with contrast medium and still resembles the original kidney, but the caudal portion is replaced by a large, heterogeneously contrast-enhancing mass.

Renal masses have less contrast medium uptake on EU or CT compared to the surrounding or contralateral renal parenchyma, because of lack of filtration and concentration of the contrast medium. Heterogeneous contrast enhancement within the mass may be seen if the mass is necrotic or cavitated (Fig. 41.19). There is a wide variability in the ultrasound appearance of renal tumors. Most primary renal tumors appear as complex or homogeneous, well-perfused masses obliterating the normal renal architecture (Fig. 41.20, eFig. 41.7). Cavitated masses are seen with renal hemangiosarcoma. Round cell tumors, such as histiocytic sarcoma, tend to be very hypoechoic.[60] Renal lymphoma occurs bilaterally and causes enlarged, irregularly shaped kidneys with a hyperechoic cortex.[61,62] Focal or multifocal nodules and masses have also been reported. A subcapsular, hypoechoic rim is associated with renal lymphoma in cats, with a positive predictive value of 80.9% and a negative predictive value or 66.7%. The subcapsular thickening is thought to represent regional subcapsular infiltrate with lymphoma rather than fluid (Fig. 41.21, eFig. 41.8).[61] Subcapsular hypoechoic rims can also be found, more rarely, with other neoplasms or with FIP. Contrast-enhanced CT may be helpful in complex renal

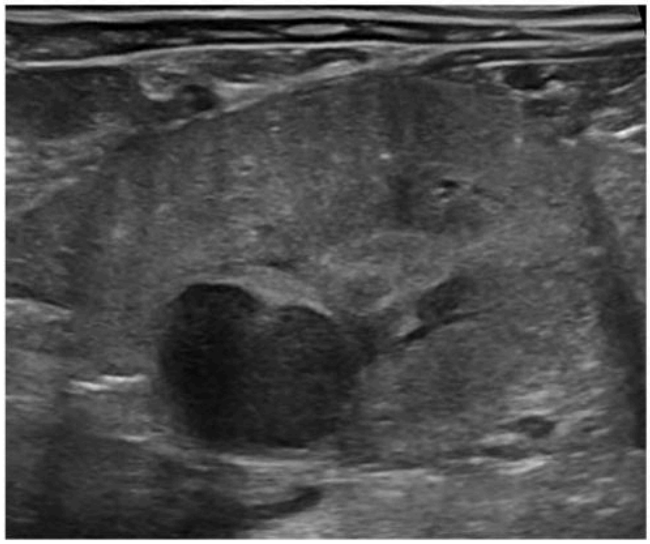


Fig. 41.20 Longitudinal ultrasound image of the right kidney of a 13-year-old Dachshund with renal carcinoma. A lobulated hypoechoic nodule is present in the cranial pole of the kidney. The renal parenchyma otherwise has signs of chronic nephropathy with poor corticomedullary definition and punctate cortical mineralizations.

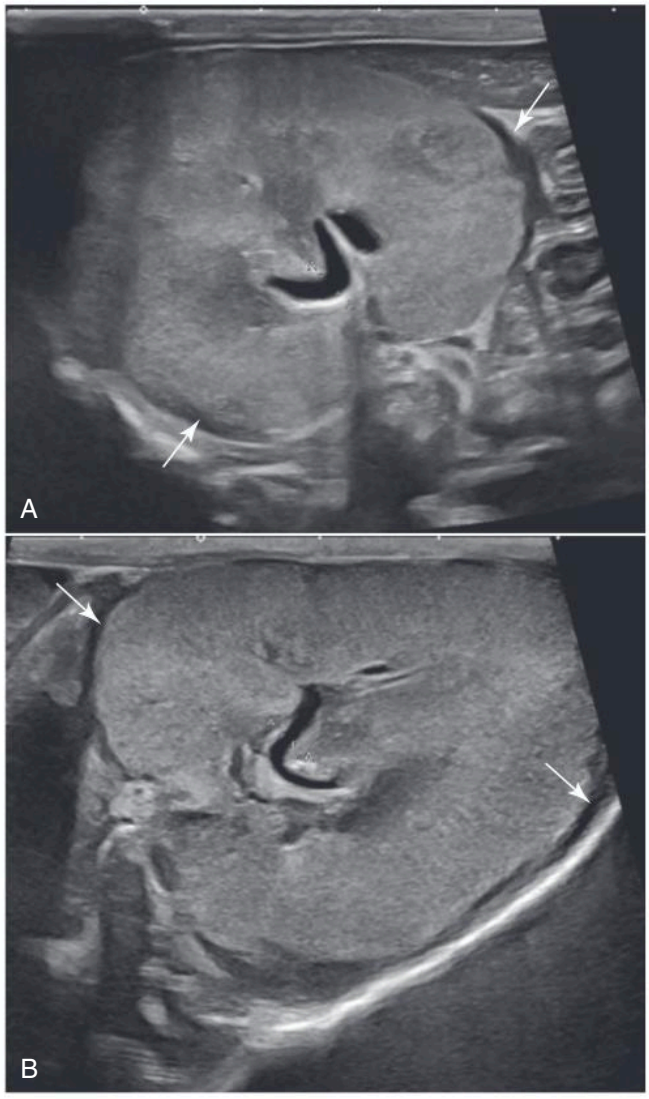
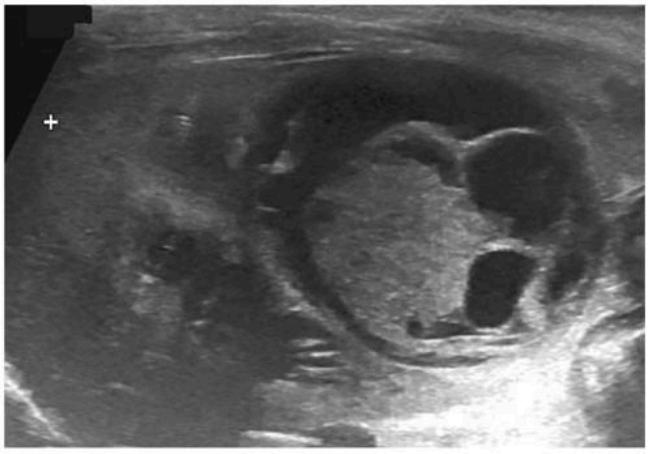
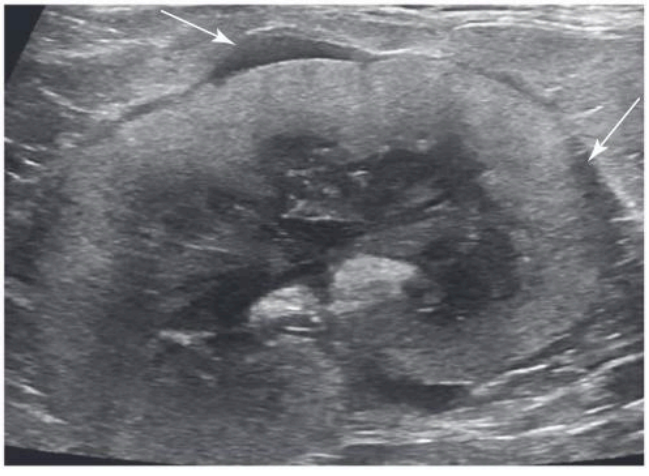


Fig. 41.21 Transverse ultrasound images of the left **(A)** and right **(B)** kidney of a cat with renal lymphoma. Both kidneys are enlarged, hyperechoic, and have a hypoechoic subcapsular rim (*arrows*). Mild pyelectasia is indicated by calipers.



eFig. 41.7 Long-axis ultrasound image of the kidney of a dog with nephroblastoma. A complex, partially cavitated mass occupies the caudal pole of the kidney distorting the normal architecture. A small portion of residual renal tissue remains in the cranial pole (the *cursor* marks the cranial aspect of the cranial pole).



eFig. 41.8 Long-axis ultrasound image of the kidney of a cat with renal lymphoma. The kidney is enlarged, irregular in shape, and has a hyperechoic cortex. A hypoechoic subcapsular thickening is seen surrounding the kidney (*white arrows*).

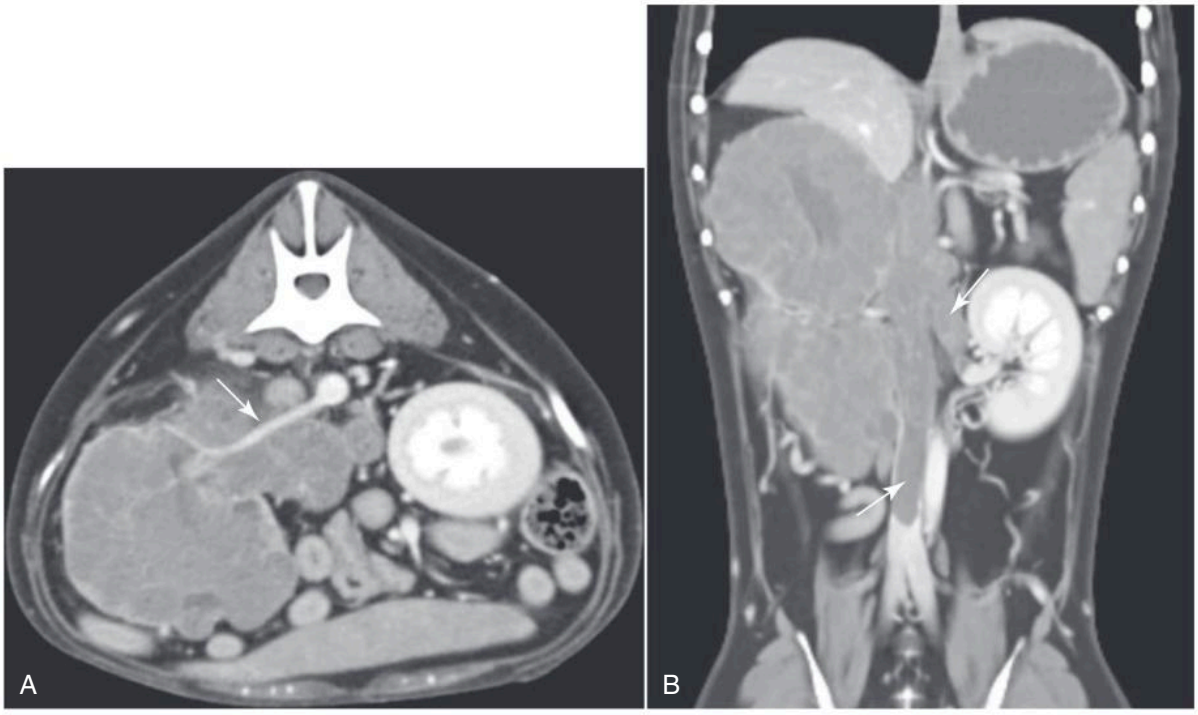


Fig. 41.22 Transverse **(A)** and dorsal **(B)** computed tomography images of a dog with a right dorsal abdominal mass. The mass is identified as right kidney by the right renal artery entering the mass (**A,** *arrow*). The mass is invading the left renal vein and caudal vena cava (**B,** *arrows*).

masses where local invasiveness and surgical resectability have to be established (Fig. 41.22).

An abscess typically has a liquid content surrounded by a thick capsule; occasionally, hyperechoic comet-tail speckles may be seen if gas is produced within the abscess (Fig. 41.23). The fluid is often very echogenic, and the cellular component tends to settle in the dependent portion.[63] Hematomas secondary to trauma or renal biopsy led to disruption of the normal kidney structure with hypoechoic or hyperechoic areas within the parenchyma and/or subcapsular fluid accumulation. However, many inflammatory lesions (such as, solid abscesses, fungal granulomas, or pyogranulomas associated with FIP) can look very similar to neoplastic masses. Needle aspirates or biopsy is required for a definitive diagnosis.

Diseases of the Collecting System

Distention of the renal pelvis can be observed in dogs and cats with increased urine production caused by diuretic therapy or renal insufficiency, or it can be associated with congenital malformations of the ureters, such as ectopic ureter or ureterocele, infection, or lower urinary tract obstruction.[18]

Pyelonephritis and Pyonephrosis

Acute pyelonephritis can lead to mild renal enlargement, whereas renal size is reduced in chronic pyelonephritis. Typically, there is mild to moderate pyelectasia.[64] The mean diameter of the renal pelvis with pyelonephritis is reported to be 3.6 mm in dogs and 4.0 mm in cats. However, this range is quite wide, with overlap with other nonobstructive or obstructive renal diseases, and even with normal animals.[18] More important, the shape of the renal pelvis is usually distorted with infection, resulting in blunted and asymmetric pelvic diverticula, seen both on EU and ultrasound (Figs. 41.24 and 41.25). Additionally, on ultrasound imaging, echogenic debris may be observed in the renal pelvis and proximal ureter rather than anechoic urine, and the renal pelvis may be surrounded by an echogenic rim caused by fibrotic change.[64–66] The echogenicity of the renal cortex may be uniformly or heterogeneously

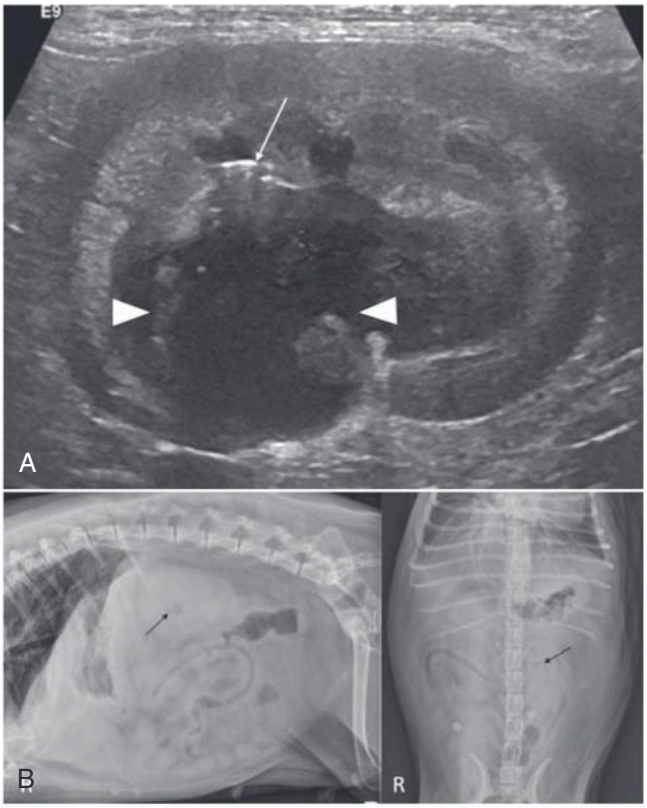


Fig. 41.23 Long-axis ultrasound image **(A)** and right lateral and ventrodorsal (VD) radiographs **(B)** of the left kidney of a dog presented for diabetic ketoacidosis and urinary tract infection that developed a renal abscess. The cranial pole of the kidney is enlarged and contains a poorly delineated hypoechoic cavity (*arrowheads*). A focus of hyperintensity with reverberation artifact, consistent with gas, is present in the dorsal portion of the cavity (*arrow*). Gas bubbles are superimposed over the cranial pole of the left renal silhouette in both radiographic projections (*arrows*).

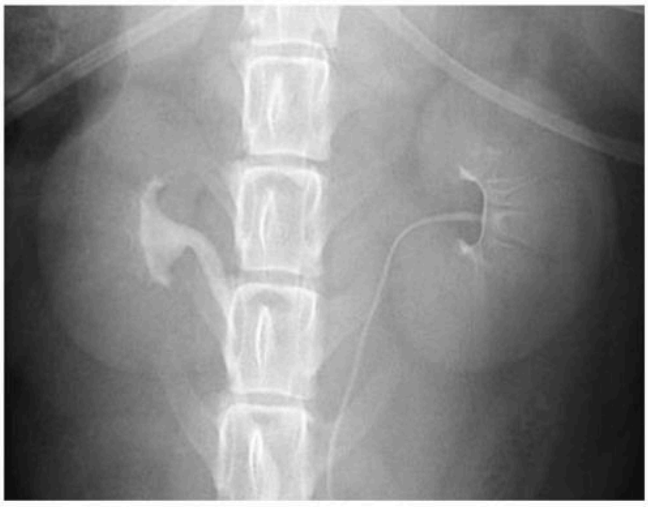


Fig. 41.24 Ventrodorsal (VD) image obtained 20 minutes after intravenous administration of iodinated contrast medium in a dog with pyelonephritis of the right kidney. The renal pelvis and proximal ureter are dilated on the right. The renal pelvis is distorted, and the pelvic diverticula are short and blunt compared with the contralateral normal left kidney.

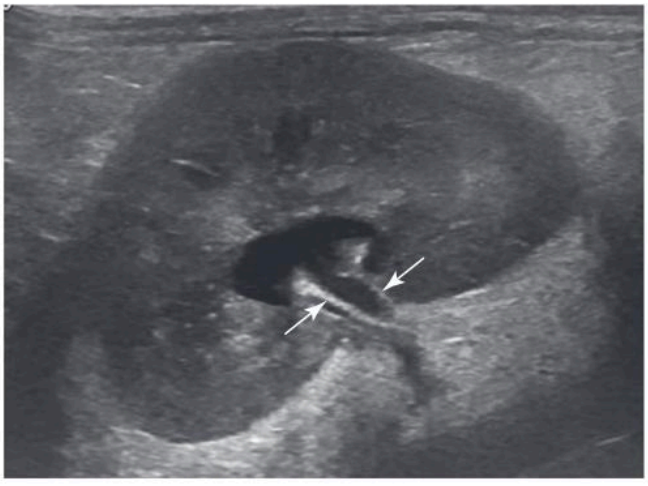


Fig. 41.25 Long-axis ultrasound image of the left kidney of a dog with acute pyelonephritis. The renal pelvis is dilated and distorted, and the pelvic diverticula are blunted. Note the hyperechoic lining of the proximal ureter (*white arrows*), which is consistent with fibrotic change. The renal medulla is hyperechoic, resulting in poor corticomedullary definition. The retroperitoneal fat surrounding the kidney is very hyperechoic and inflamed.

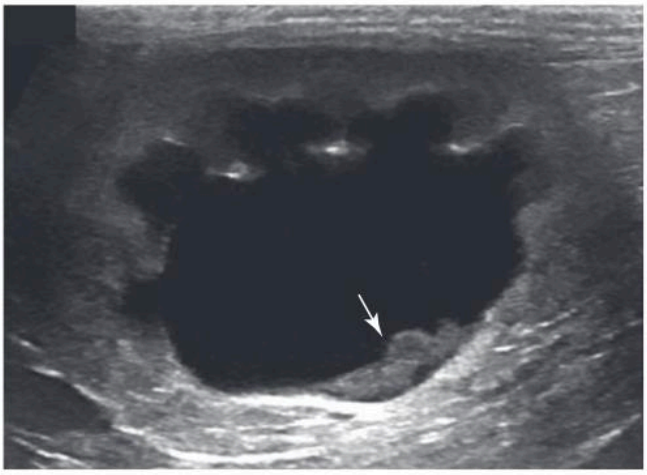


Fig. 41.26 Ultrasound image of a dog with severe hydronephrosis because of ureteral obstruction by a urinary bladder mass. The renal pelvis and pelvic diverticula are distended, and the renal cortex is thin. A small amount of cellular debris is accumulated in the dependent portion of the renal pelvis (*white arrow*).

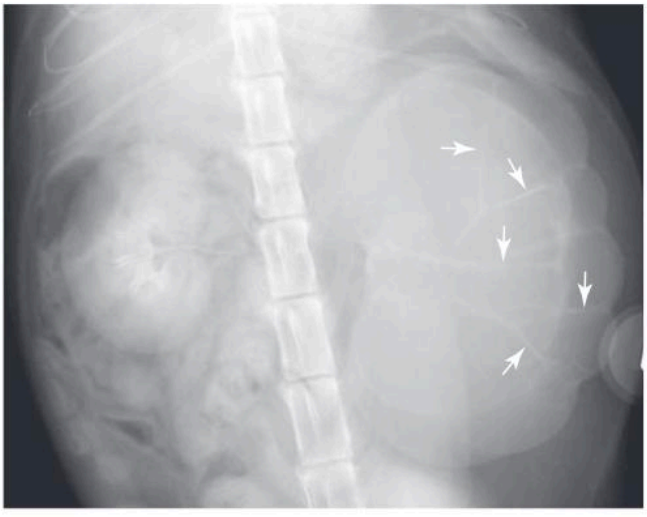


Fig. 41.27 Excretory urogram of a cat with severe left hydronephrosis. Contrast enhancement is seen only in the left kidney along the elongated renal vasculature (*white arrows*) and has not accumulated in the renal pelvis.

increased. In severe acute pyelonephritis, regional inflammation of the perirenal fat results in a hyperechoic rim around the kidney and proximal ureter (see Fig. 41.25), often with a small amount of retroperitoneal effusion. Thickening of the proximal ureteral wall and mild ureteral dilation without evidence of intraluminal obstruction are common. Chronic pyelonephritis is difficult to distinguish from other chronic renal diseases, because it is characterized by small, irregularly shaped kidneys with mild pyelectasia.[64] Pyonephrosis is characterized by echogenic fluid in the renal pelvis with sediment settling to the dependent portion (Fig. 41.26).[65]

Hydronephrosis

Hydronephrosis is defined as distention of the renal pelvis and pelvic diverticula, most commonly caused by urinary tract obstruction.[18] In severe hydronephrosis, the renal parenchyma is obliterated almost completely, and only a thin rim of cortex remains. Because renal vessels must still reach the cortex, elongated thin interlobar vessels may be seen forming radial streaks in the fluid-filled cavity in the nephrogram phase of an excretory urogram (Fig. 41.27). If the remaining renal parenchyma is functional, contrast medium will outline the dilated renal pelvis in the pyelogram phase. Anechoic fluid distention of the renal pelvis and diverticula is seen on ultrasound, until the kidney essentially becomes one cystic structure with a thin cortical rim (see Fig. 41.26). Ureteral obstruction or aberrant termination of the ureters is a primary concern if hydronephrosis is present, and a detailed investigation of the ureters should be performed (discussed later).

Abnormal Renal Function

Abnormal renal function cannot be determined radiographically or ultrasonographically. However, secondary signs of renal failure may be apparent. Acute renal failure is often associated with perirenal effusion, which is best seen with ultrasound imaging. Renal secondary hyperparathyroidism leads to

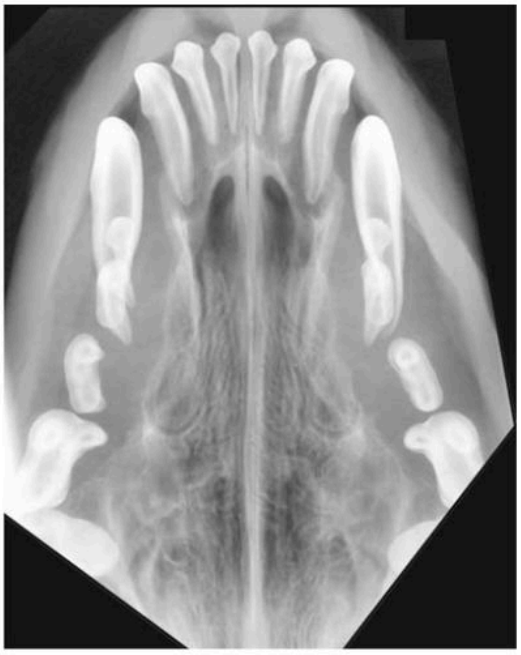


Fig. 41.28 Dorsoventral radiograph of the maxilla of a dog with renal failure and secondary hyperparathyroidism. The lamina dura and adjacent maxillary bone surrounding the teeth have been resorbed and replaced by fibrous tissue, resulting in markedly reduced opacity around the teeth.

generalized osteopenia evidenced by thinning of the bone cortex with a double cortical line. The skull is usually affected first. Bone resorption of the maxilla and mandible with fibrous replacement results in thickening with reduced radiopacity. The normally opaque lamina dura disappears, resulting in dramatically increased contrast to the teeth (Fig. 41.28).[67] Metastatic mineralization of stomach wall, blood vessels, and parenchymal organs (such as, liver and spleen) may be observed with chronic renal failure if the calcium-to-phosphate ratio is increased. Mild hyperplasia of the parathyroid glands can be detected ultrasonographically in animals with chronic, but not with acute, renal failure.[68]

Renal function can only be estimated crudely using EU or contrast-enhanced CT. However, there are instances where an estimation of renal function, such as determining whether there is any function at all in a kidney, may be adequate for surgical planning. The degree and change of renal opacification over time after contrast medium injection, as well as the relationship between nephrogram and pyelogram phase, can be used to determine problems with renal function (Fig. 41.29, eFig. 41.9).[69] The findings and their possible interpretation are listed in Box 41.1. Observation of abnormal opacification patterns after intravenous contrast medium administration is essential to recognize and treat contrast medium—associated renal dysfunction. If more precise measurement of renal function is needed, renal scintigraphy using technetium-99m diethylenetriamine pentaacetic acid can be used to calculate individual and global renal function.[36] A protocol for measurement of glomerular filtration rate using CT is also available.[26,27]

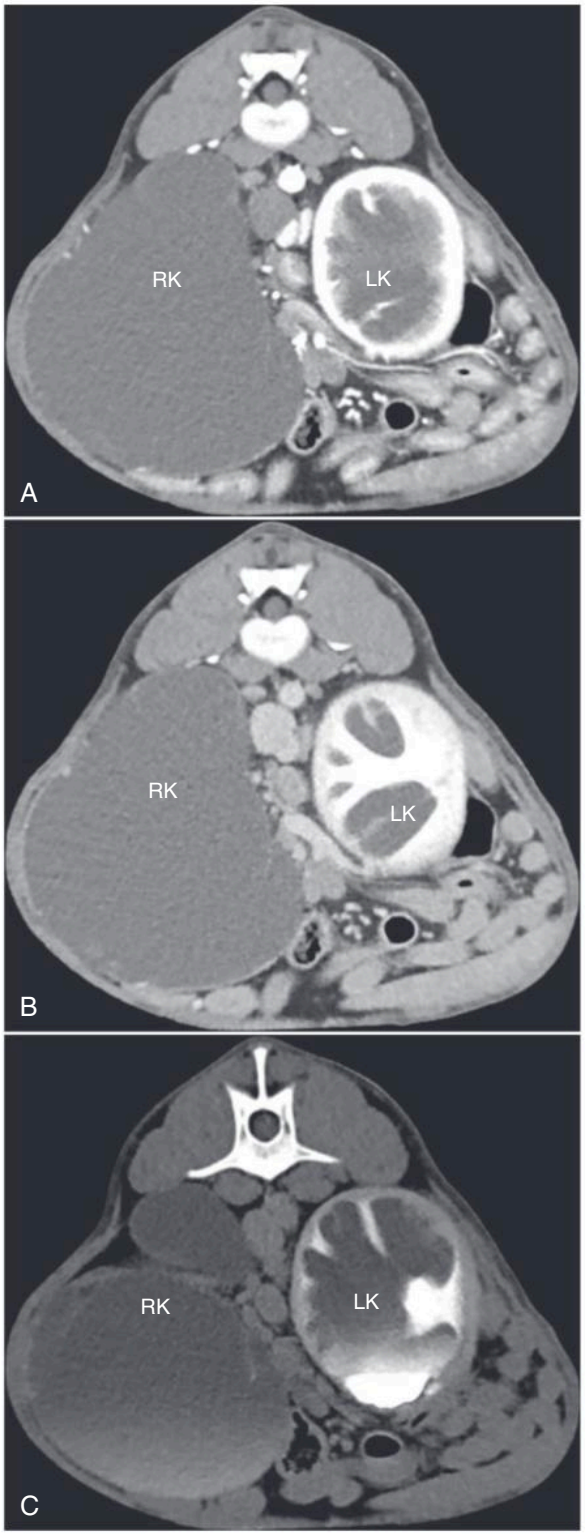
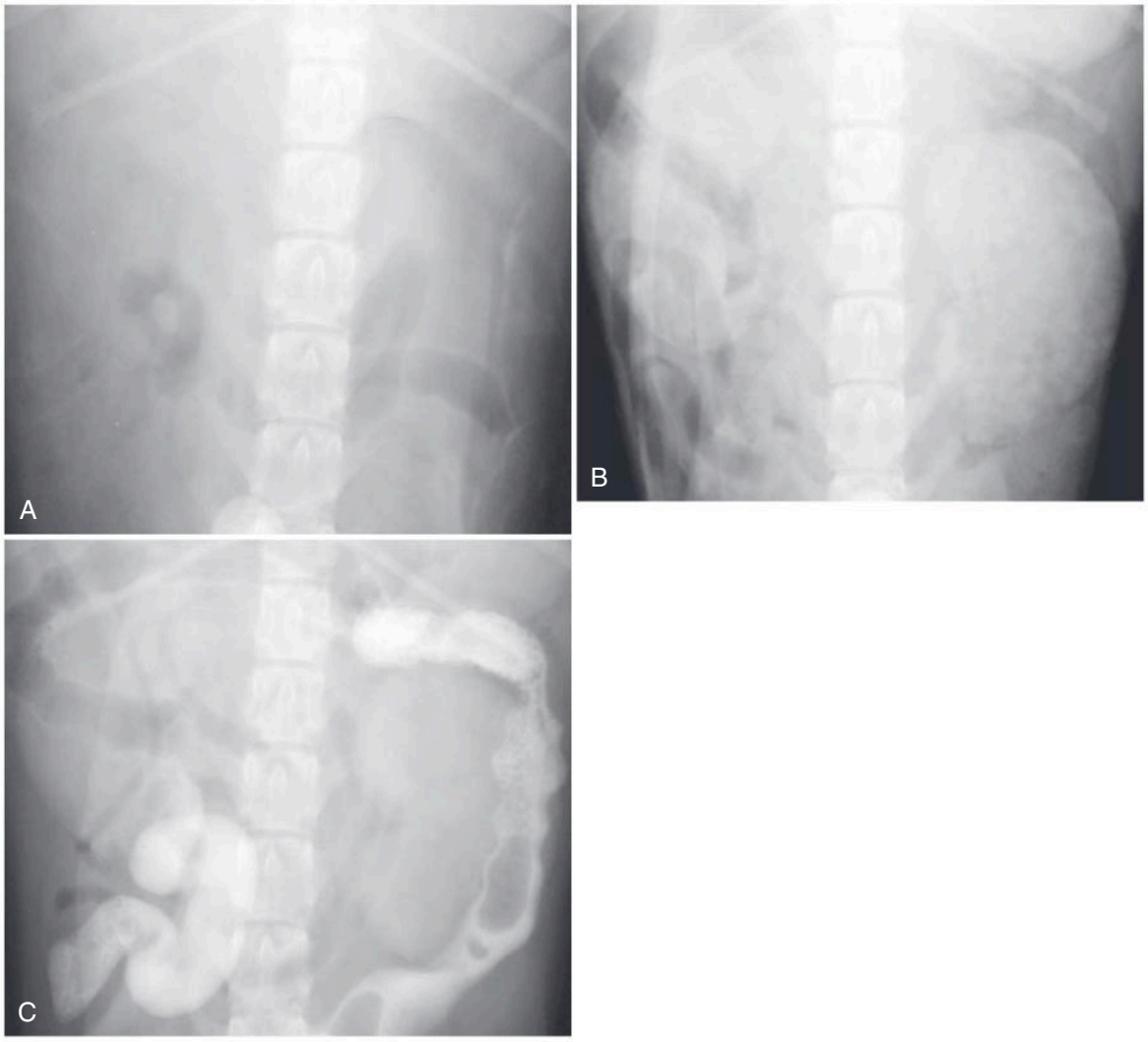


Fig. 41.29 Transverse computed tomography images of a dog with bilateral hydronephrosis, acquired immediately (**A**, vascular phase), 1 minute (**B**, nephrogram phase), and 5 minutes (**C**, pyelogram phase) after intravenous contrast medium injection. The right kidney (*RK*) is more severely affected and has almost no discernible renal tissue left and the nephrogram is almost completely absent. A small amount of contrast medium is seen in the ventral portion of the dilated renal pelvis in the pyelogram phase indicating minimal residual renal function. The left (*LK*) renal pelvis is also severely distended but there is appropriate contrast enhancement in all phases.

DISEASES OF THE URETERS

Most ureteral diseases result in dilatation of some or all of the ureter. Differential diagnoses for ureteral dilatation include obstruction (e.g., calculi, clots, strictures, masses), ectopic



eFig. 41.9 Ventrodorsal (VD) radiographs of the kidneys of a dog with congenital polycystic kidney disease before **(A)**, 5 minutes after **(B)**, and 18 hours after **(C)** intravenous injection of iodinated contrast medium. There is opacification of the kidneys during the nephrogram phase **(B)** with multiple small filling defects corresponding to the cystic lesions. The pyelogram phase, however, is delayed, and the nephrogram persists over a long period of time **(C)**. Contrast medium has been excreted through the biliary system and had accumulated in the colon **(C)**. Contrast medium–induced renal failure was suspected.

Box • 41.1

Functional Aspects of the Excretory Urogram

Good initial nephrogram followed by gradual decrease over 1–3 minutes, simultaneous with the appearance of the pyelogram
- Normal

Poor initial nephrogram that fades quickly
- Insufficient dose of contrast medium
- Primary polyuric renal failure

Poor initial nephrogram followed by persistent opacification
- Severe generalized renal disease (primary glomerular dysfunction or severe generalized acute or chronic renal disease)

Poor initial nephrogram followed by progressive increase in opacification
- Acute extrarenal obstruction
- Systemic hypotension before contrast medium administration
- Poor renal blood flow

Good initial nephrogram followed by persistent or increasing opacity
- Systemic hypotension (may be contrast medium induced)
- Contrast medium–induced renal failure
- Acute tubular necrosis
- Acute tubular obstruction

Poor opacification of the pyelogram phase
- Renal failure—decreased concentrating ability

ureter, inflammation (e.g., ureteritis, pyelonephritis), atony, and ureteral tears. Differentiation of these conditions is essential for best treatment selection.

Ureteral Obstruction

Ureteral calculi, ureteral strictures, and masses associated with the urinary bladder neck are the most common causes of ureteral obstruction. Preureteral vena cava (circumcaval ureter) is a common vascular anomaly in cats (prevalence of 22.4%) where the ureter courses dorsal to the caudal vena cava and displaces the vena cava ventrally. This anomaly has been associated with ureteral strictures in people and may predispose cats for urinary tract signs.[70,79] Ureteral dilation and varying degrees of hydronephrosis are consequences of ureteral obstruction that are apparent with most imaging modalities. A severely dilated ureter may be seen on survey radiographs as a tubular, tortuous structure in the retroperitoneal space extending from the kidneys to the dorsal aspect of the urinary bladder trigone, and ureteral calculi may be radiopaque and visible in the course of the ureter (Fig. 41.30, eFig. 41.10). The presence, location, and degree of obstruction have to be verified using additional imaging modalities, such as ultrasound, antegrade pyelography, EU, or CT. On an EU or CT study with contrast medium, a filling defect and lack of contrast medium distal to the filling defect confirm ureteral obstruction. Ultrasonographically, a dilated ureter can usually be followed from the renal pelvis to an intraluminal obstruction, such as a calculus. Ureteral calculi appear as round or irregularly-shaped intraluminal hyperechoic structures with distal shadowing (Fig. 41.31). A ureteral stricture can be recognized as focal narrowing surrounded by hyperechoic tissue, which is most commonly seen in the proximal ureter.[71] However, it should be noted that in some patients, the ureter is not dilated all the way to the obstruction, and in those instances, a small calculus or ureteral stricture may be missed.[72] Obstructions caused by soft tissue structures, such as hypoechoic mucous plugs and hematomas, as well as strictures, can be difficult to identify ultrasonographically, because they are often not distinct from the retroperitoneal fat and ureteral wall. If in doubt, the ultrasound examination can be repeated the next day to assess progression of ureteral or renal pelvic dilation, or contrast procedures (such as antegrade pyelography or CT) could be considered (Fig. 41.32). Obstruction warrants decompression by stent or subcutaneous ureteral bypass placement. Degree of renal pelvic distension, although not useful as a prognostic indicator, can help in determining the presence of ureteral obstruction. Renal pelvis dilation greater than 13 mm has a high specificity for ureteral obstruction.[18] The resistive index is expected to increase in an obstructed kidney after administration of a diuretic.[73,81] EU is the least valuable method for detecting



Fig. 41.30 Lateral abdominal radiograph of a small-breed dog with cystic and ureteral calculi. The ureteral calculi are visible as rows of mineral opacities extending along the path of the ureters in the retroperitoneal space. Note that the round soft tissue opacities ventral to the L6–7 disc space are not ureteral calculi but represent normal end-on views of the circumflex iliac vessels (*arrowhead*). A mineral opacity, as well as a gas bubble (from prior catheterization), is visible in the urinary bladder.

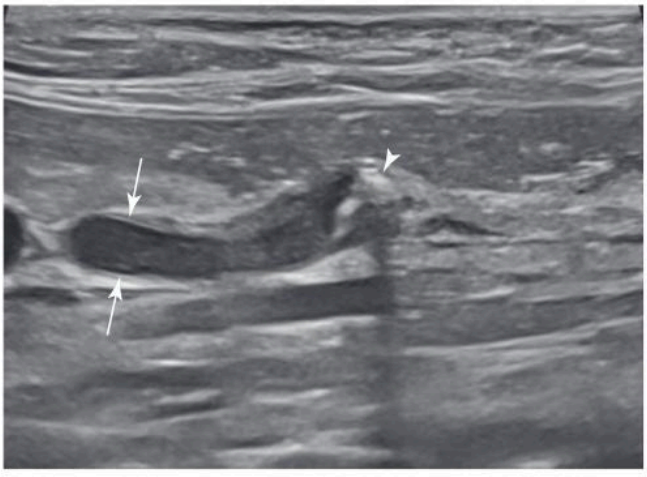
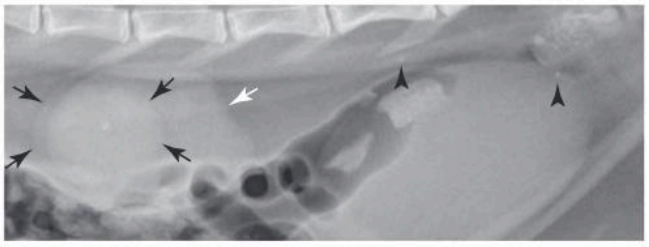


Fig. 41.31 Longitudinal ultrasound image of the proximal left ureter. The ureter is dilated and fluid filled proximally (*arrows*). The dilation abruptly ends at an intraluminal, irregularly margined hyperechoic ureteral calculus with distal acoustic shadowing (*arrowhead*), causing obstruction.



eFig. 41.10 Lateral radiograph of a cat with ureteral calculi leading to obstruction of the left ureter. The right kidney *(black arrows)* is small and round, consistent with chronic disease, and there is a small urolith in the right renal pelvis. The left kidney is larger but has a cortical defect (*white arrow*) in the caudal pole indicating infarction. Two small, round calculi (*black arrowheads*) are present along the path of the ureter. These were confirmed to be calculi with ultrasound.

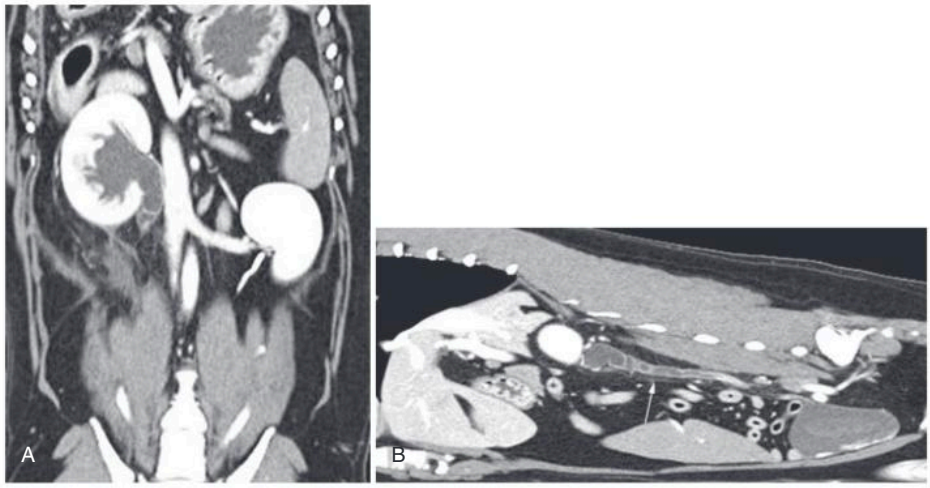


Fig. 41.32 Dorsal **(A)** and sagittal **(B)** reformatted postcontrast computed tomography images of the right kidney and ureter of a dog with suspected ureteral obstruction. Ultrasonographically, the ureter was dilated and filled with anechoic material, presumed to be fluid. On the dorsal image **(A)**, the renal pelvis is distended but not filled with contrast medium; instead there is a large filling defect. This filling defect extends into a dilated, tortuous proximal ureter, obstructing it (**B**, *arrow*). The kidney and ureter were removed surgically after unsuccessful attempts to flush out the obstructive ureteral material. Histopathologically, severe pyelonephritis and ureteritis with hemorrhage and fibrin deposition were diagnosed.

the site of ureteral obstruction, because ureteral opacification is often poor owing to increased interstitial pressure in the kidney and decreased renal function and subsequent poor contrast medium excretion. In addition, it is more difficult to clearly identify and follow each ureter with this technique.

Ureteroliths

Ureteral calculi are often radiopaque and therefore visible on survey abdominal radiographs; they are best seen on lateral radiographic views (see Fig. 41.30). In cats, struvite calculi are more common than calcium oxalate calculi, whereas in dogs, both struvite and calcium oxalates are common.[74] Radiographic identification of ureteral calculi can be hindered by superimposition of mineralized particles in the gastrointestinal tract, especially the colon. Compression views are a simple radiographic technique that allows displacement of overlying gastrointestinal structures. The round opacity created by the end-on view of the deep circumflex iliac vessels seen on lateral radiographs should not be confused with ureteral calculi (see Fig. 41.29). The sensitivity for detection of ureteroliths when combining radiographs and ultrasound is approximately 90%.[72] Ultrasonographically, ureteral calculi appear as round to slightly irregular, hyperechoic structures with a strong distal acoustic shadow (see Fig. 41.31). A twinkling artifact may be seen when using color Doppler ultrasound.[75]

Ectopic Ureters

Ectopic ureters are congenital abnormalities of the ureteral junction with the bladder. One or both ureters may be affected. Ectopic ureters may terminate in the bladder neck, urethra (Fig. 41.33), and in rare instances in the vagina. In the majority of cases, the distal portion of the abnormal ureter tunnels in the wall of the bladder neck and proximal urethra before opening into the urethral lumen (intramural ectopic ureter). In these instances, the ureter appears to terminate normally at the bladder neck but continues to tunnel caudally below the mucosa.[76] Extramural ectopic ureters insert directly in a caudal location. The differentiation can be difficult as both types of ectopic ureters tend to run parallel to the bladder trigone and urethra as they reach the pelvic inlet. Ectopic ureters can be normal in size but are often dilated and tortuous with associated hydronephrosis. The intrapelvic location of the terminal ureter in these patients creates difficulties for evaluation with both EU and ultrasonography. Careful patient preparation (sedation, empty colon, and rectum) is important. Urethrography may have to be added to an excretory urogram if it is inconclusive. Vaginourethrography has been described as a diagnostic method; however, it should be avoided if possible due to complications such as vaginal rupture (Fig. 41.34). Fluoroscopy may also be helpful to identify the ureteral opening and is often used in conjunction with cystoscopy during interventional procedures to address ureteral ectopia.[76] Administration of a diuretic is very helpful to enhance the ureteral jets during ultrasound evaluation.[15] CT is increasingly used for diagnosis of ectopic ureter.[77,78] Lack of superimposition of skeletal and gastrointestinal structures is a major advantage of the use of CT for this purpose (Fig. 41.35).

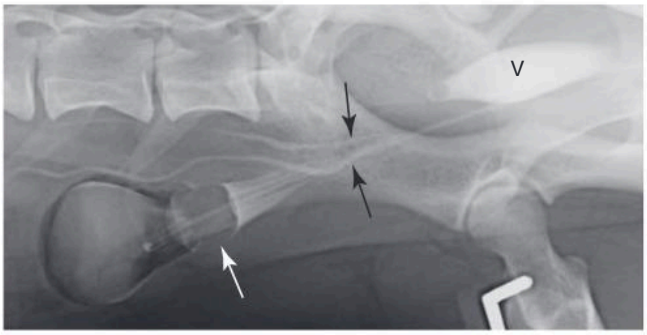


Fig. 41.33 Ventrodorsal (VD) oblique radiograph from an excretory urogram of a dog with bilateral ectopic ureter. A catheter was inserted into the urinary bladder, which was insufflated with gas to provide negative contrast for the ureterovesical junctions. The bulb of the catheter (*white arrow*) is in the bladder neck. The ureters (*black arrows*) extend beyond the bladder neck and enter the proximal urethra. Contrast medium is also present in the vagina (*V*).

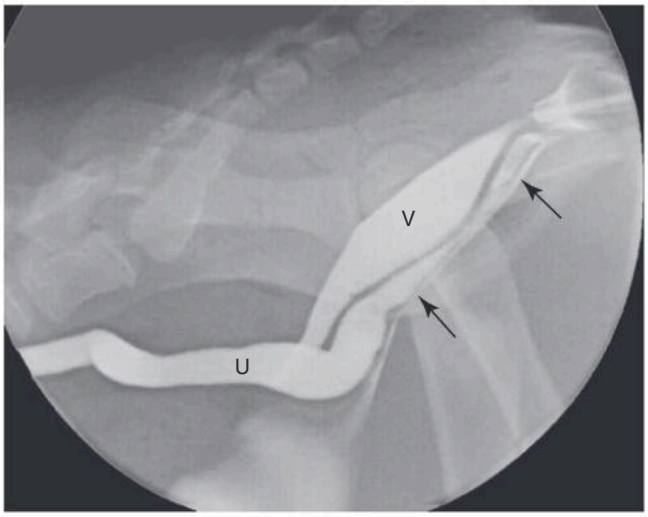


Fig. 41.34 Vaginourethrogram of a female dog with a single ectopic ureter. Contrast medium was injected into the vestibule of the vagina. The ureter (*U*) is dilated and tortuous. It extends caudally between the vagina (*V*) and urethra (*black arrows*) and enters the distal urethra.

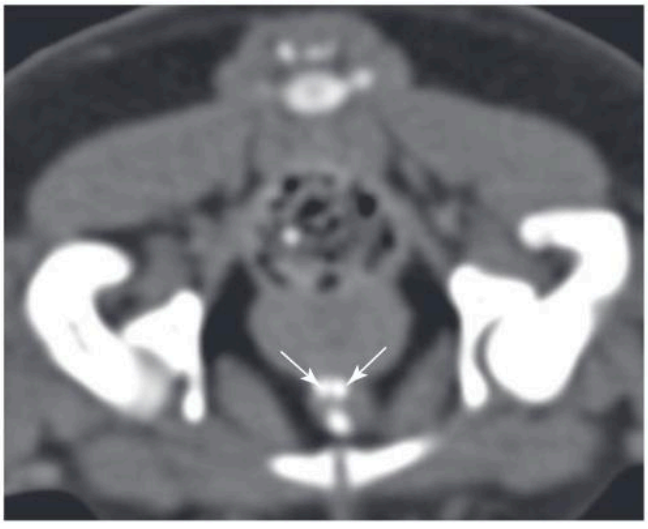


Fig. 41.35 Transverse computed tomography image of the urethra and distal ureters in a dog with bilateral ectopic ureters. The two ureters (*white arrows*) course dorsal to the urethra. They inserted into the urethra just caudal to this image plane.

Ureteroceles

Ureteroceles are cystic dilations of the terminal ureter and are classified as orthotopic or ectopic. Orthotopic ureteroceles are also called intravesicular ureteroceles and are dilatations of the submucosal portion of the distal ureter. Orthotopic ureteroceles extend into the lumen of the urinary bladder and communicate with the urinary bladder lumen through an opening. Ectopic ureteroceles on the other hand are associated with ectopic ureters and located in the bladder neck or urethra (Fig. 41.36). Ureteroceles may cause obstruction and secondary hydroureter and hydronephrosis which can be unilateral (grade 2) or bilateral (grade 3) if the ureterocele is large enough to affect the ureterovesicular junction on the contralateral side.[79,80] The appearance of ureteroceles on CT or EU depends on the timing. The ureterocele may fill with contrast medium before the urinary bladder and present as radiopaque round structure but later in the study or in a cystogram it may present as filling defect if the remainder of the urinary bladder is completely opacified. Similarly, a round, anechoic cystic structure at the ureterovesical junction, usually within the bladder lumen, is visible ultrasonographically.[79,81]

Ureteroceles are often associated with narrowing of the ureteral orifice and therefore have to be treated either surgically or with laser ablation.

Ureteral Tumors

Ureteral tumors are rare. Reported types include leiomyoma, leiomyosarcoma, and urothelial carcinoma. Extension of a transitional cell carcinoma of the urinary bladder neck into the distal ureter is common. Fibroepithelial polyps in the proximal aspect of the ureter have been described in dogs.[82] The etiology is unclear; they may be inflammatory in origin, similar to polypoid cystitis, or hamartomatous or neoplastic, but they have a good prognosis when removed.

TRAUMA TO THE URETERS AND KIDNEY

Abdominal or pelvic canal trauma may affect the kidneys and/or ureters. Renal hemorrhage, renal rupture, renal artery or vein avulsion, or ureteral or renal pelvis tears are possible consequences. Survey radiographs are always indicated if retroperitoneal trauma is suspected, and the visible portion of the retroperitoneal space should always be examined in patients with pelvic trauma. Either urine or hemorrhage in the retroperitoneal space results in decreased retroperitoneal detail as the normal fat opacity surrounding the kidneys and large vessels is replaced by heterogeneous soft tissue opacity with a streaked appearance caused by fluid traveling along fascial planes. If a

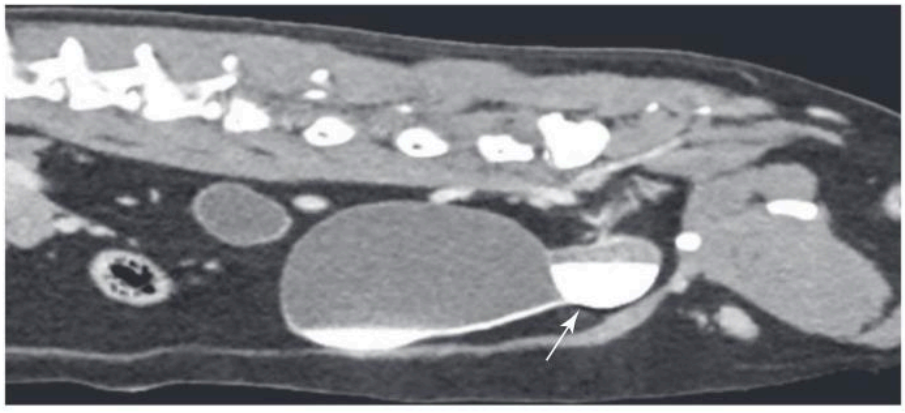


Fig. 41.36 Sagittal reconstructed computed tomography image of a dog with ectopic ureter and an ectopic ureterocele which is partially filled with contrast medium (*arrow*). A small amount of contrast medium is present in the ventral portion of the urinary bladder as well.

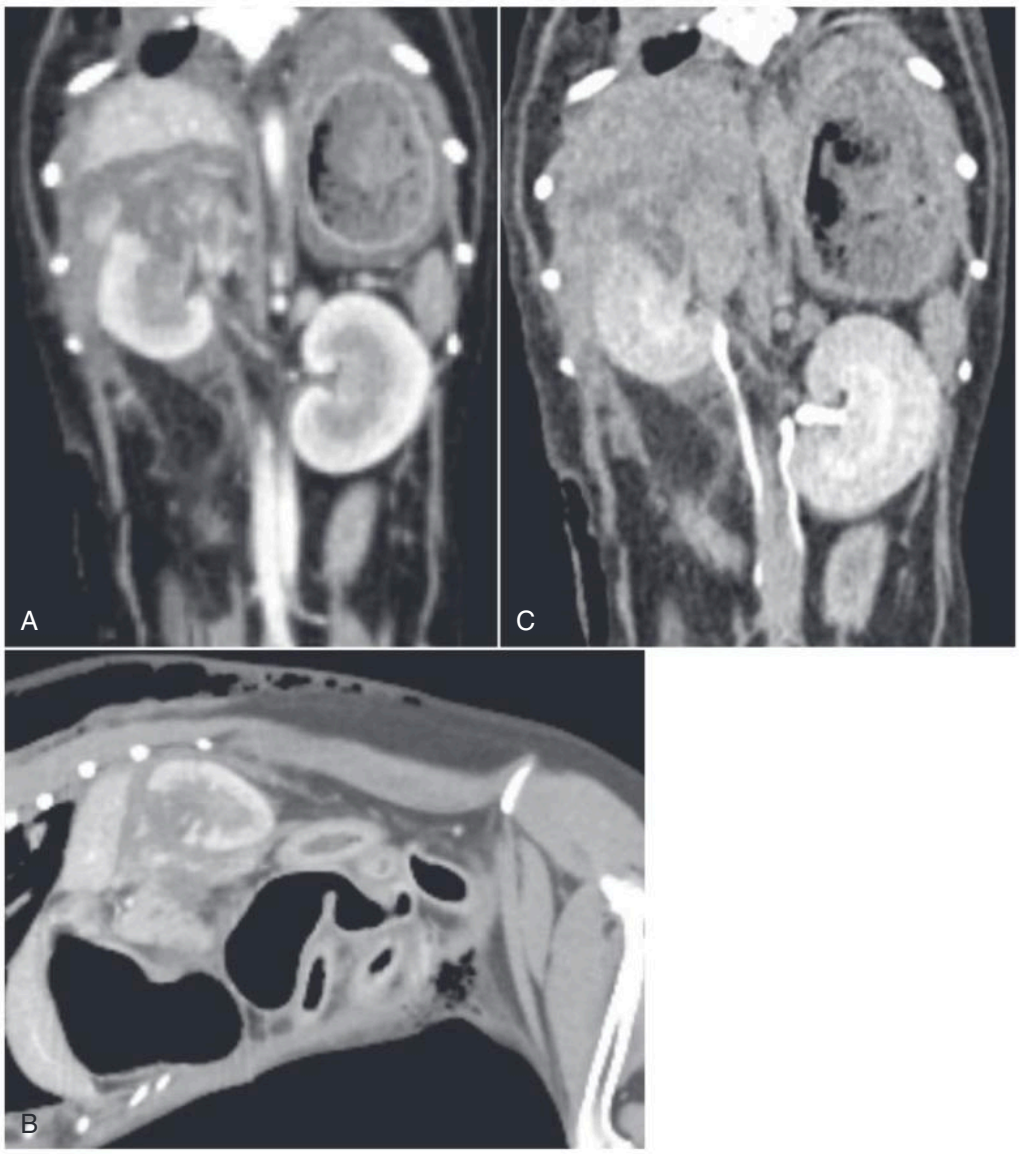


Fig. 41.37 Dorsal **(A)** and sagittal **(B)** plane reconstructed computed tomography images of the nephrogram and dorsal **(C)** plane reconstructed CT image of the pyelogram of a dog with kidney rupture after trauma (dog bite). The cranial pole of the right kidney is poorly delineated and the structure is disrupted. Contrast enhancement is reduced in the cranial pole of the right kidney. The right ureter appropriately fills with contrast medium which indicates that the remaining renal parenchyma is functional **(C)**. The surrounding retroperitoneal space is soft tissue attenuating consistent with hemorrhage and inflammation.

large volume of fluid is present, widening of the retroperitoneal space with secondary ventral displacement of large and small bowel results. Renal displacement is associated with vascular avulsion, and body wall or diaphragmatic hernias. Renal enlargement can be the result of subcapsular hemorrhage or encapsulated urine accumulation (urinoma). Urinoma formation can also be associated with ureteral injury and urine leakage.[83] All these radiographic findings need to be evaluated further with additional imaging methods. CT provides the most complete evaluation of suspected renal trauma.[84] CT allows simultaneous assessment of trauma to soft tissue and bones, as well as blood supply of injured organs (Fig. 41.37). If urinary tract rupture is suspected, a contrast study using either EU or contrast-enhanced CT is indicated unless there are contraindications to using iodinated contrast media. The site of urinary tract rupture is apparent as leakage of contrast medium (Fig. 41.38).

In clinical practice, ultrasound is often the first advanced imaging method used when urinary tract trauma is suspected and survey radiographs are not conclusive, because it is noninvasive and can be performed in the awake patient. However, information gained with regard to urinary tract trauma is often limited, except in patients with complete disruption of the renal architecture or blood supply. More subtle urinary tract tears are difficult to detect with certainty, and the use of ultrasound is limited to guide sampling of retroperitoneal fluid pockets. Complete ureteral tears of some duration can be suspected if focal dilatation of the proximal ureter is seen, in addition to retroperitoneal effusion, because the site of rupture often contracts and adhesions form, essentially leading to ureteral obstruction. Doppler ultrasound can be used to verify both arterial supply and venous drainage of the kidney.

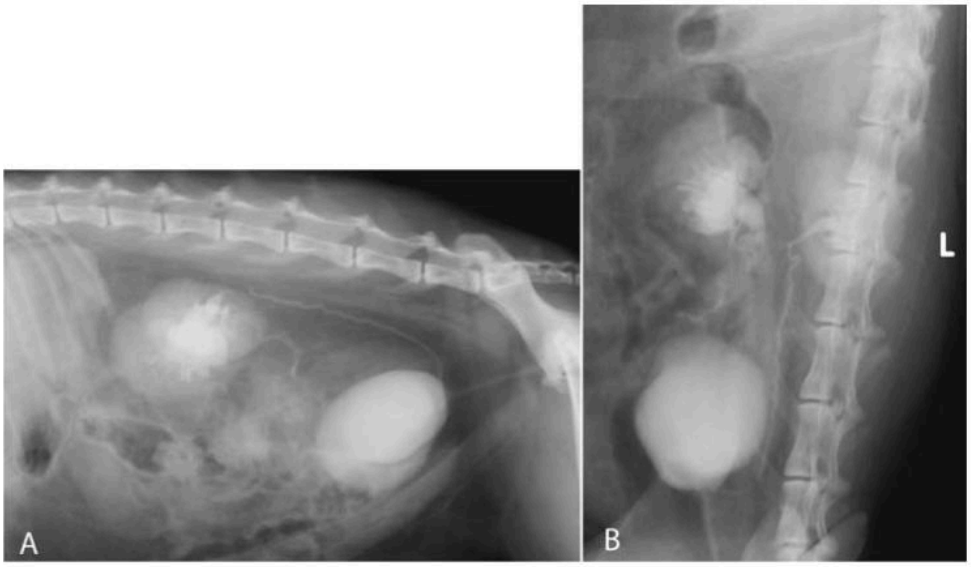


Fig. 41.38 Lateral **(A)** and oblique ventrodorsal (VD; **B**) radiographs acquired in the pyelogram phase of an excretory urogram in a cat 2 days after a ureteral calculus had been removed surgically. The left ureter is continuously filled with contrast medium and contrast medium reaches the bladder. The right ureter is dilated and tortuous and does not extend to the urinary bladder. Contrast medium has accumulated in the peritoneal space. Right ureteral rupture was confirmed surgically.

REFERENCES

1. Allen G. Radiology in the diagnosis of kidney disease. *Aust Vet Pr*. 1982;12:97.
2. Greco DS. Congenital and inherited renal disease of small animals. *Vet Clin North Am Small Anim Pract*. 2001;31(2):393–399. https://doi.org/10.1016/s0195-5616(01)50211-9. viii.
3. Finco D, Stiles N, Kneller S, Lewis R, Barrett R. Radiologic estimation of kidney size of the dog. *J Am Vet Med Assoc*. 1971;159(8):995–1002.
4. Kneller S, Barrett R. Feline kidney mensuration. *Acta Radiol*. 1972;suppl(319):279–280.
5. Shiroma JT, Gabriel JK, Carter RL, Scruggs SL, Stubbs PW. Effect of reproductive status on feline renal size. *Vet Radiol Ultrasound Off J Am Coll Vet Radiol Int Vet Radiol Assoc*. 1999;40(3):242–245. https://doi.org/10.1111/j.1740-8261.1999.tb00355.x.
6. Reichle JK, DiBartola SP, Léveillé R. Renal ultrasonographic and computed tomographic appearance, volume, and function of cats with autosomal dominant polycystic kidney disease. *Vet Radiol Ultrasound Off J Am Coll Vet Radiol Int Vet Radiol Assoc*. 2002;43(4):368–373. https://doi.org/10.1111/j.1740-8261.2002.tb01020.x.
7. Seiler GS, Rhodes J, Cianciolo R, Casal ML. Ultrasonographic findings in Cairn Terriers with preclinical renal dysplasia. *Vet Radiol Ultrasound Off J Am Coll Vet Radiol Int Vet Radiol Assoc*. 2010;51(4):453–457. https://doi.org/10.1111/j.1740-8261.2010.01674.x.
8. Vaden SL. Renal biopsy of dogs and cats. *Clin Tech Small Anim Pract*. 2005;20(1):11–22. https://doi.org/10.1053/j.ctsap.2004.12.003.
9. Vaden SL, Levine JF, Lees GE, Groman RP, Grauer GF, Forrester SD. Renal biopsy: a retrospective study of methods and complications in 283 dogs and 65 cats. *J Vet Intern Med*. 2005;19(6):794–801. https://doi.org/10.1892/0891-6640(2005)19[794:rbarso]2.0.co;2.
10. Schmiedt CW, Delaney FA, McAnulty JF. Ultrasonographic determination of resistive index and graft size for evaluating clinical feline renal allografts. *Vet Radiol Ultrasound Off J Am Coll Vet Radiol Int Vet Radiol Assoc*. 2008;49(1):73–80. https://doi.org/10.1111/j.1740-8261.2007.00321.x.
11. Choi SY, Jeong WC, Lee YW, Choi HJ. Contrast enhanced ultrasonography of kidney in conscious and anesthetized beagle dogs. *J Vet Med Sci*. 2016;78(2):239–244. https://doi.org/10.1292/jvms.15-0199.
12. Schweiger H, Ohlerth S, Gerber B. Contrast-enhanced ultrasound of both kidneys in healthy, non-anaesthetized cats. *Acta Vet Scand*. 2015;57:80. https://doi.org/10.1186/s13028-015-0172-5.
13. Haers H, Vignoli M, Paes G, et al. Contrast harmonic ultrasonographic appearance of focal space-occupying renal lesions. *Vet Radiol Ultrasound Off J Am Coll Vet Radiol Int Vet Radiol Assoc*. 2010;51(5):516–522. https://doi.org/10.1111/j.1740-8261.2010.01690.x.
14. Kinns J, Aronson L, Hauptman J, Seiler G. Contrast-enhanced ultrasound of the feline kidney. *Vet Radiol Ultrasound Off J Am Coll Vet Radiol Int Vet Radiol Assoc*. 2010;51(2):168–172. https://doi.org/10.1111/j.1740-8261.2009.01646.x.
15. Gremillion C, Cohen EB, Vaden S, Seiler G. Optimization of ultrasonographic ureteral jet detection and normal ureteral jet morphology in dogs. *Vet Radiol Ultrasound Off J Am Coll Vet Radiol Int Vet Radiol Assoc*. 2021;62(5):583–590. https://doi.org/10.1111/vru.13000.
16. Ivancić M, Mai W. Qualitative and quantitative comparison of renal vs. hepatic ultrasonographic intensity in healthy dogs. *Vet Radiol Ultrasound Off J Am Coll Vet Radiol Int Vet Radiol Assoc*. 2008;49(4):368–373. https://doi.org/10.1111/j.1740-8261.2008.00383.x.
17. Yeager AE, Anderson WI. Study of association between histologic features and echogenicity of architecturally normal cat kidneys. *Am J Vet Res*. 1989;50(6):860–863.
18. D'Anjou MA, Bédard A, Dunn ME. Clinical significance of renal pelvic dilatation on ultrasound in dogs and cats. *Vet Radiol Ultrasound Off J Am Coll Vet Radiol Int Vet Radiol Assoc*. 2011;52(1):88–94.
19. Walter PA, Feeney DA, Johnston GR, Fletcher TF. Feline renal ultrasonography: quantitative analyses of imaged anatomy. *Am J Vet Res*. 1987;48(4):596–599.

20. Barr F, Holt P, Gibbs C. Ultrasonographic measurement of normal renal parameters. *J Small Anim Pract*. 1990;31:180.
21. Mareschal A, d'Anjou MA, Moreau M, Alexander K, Beauregard G. Ultrasonographic measurement of kidney-to-aorta ratio as a method of estimating renal size in dogs. *Vet Radiol Ultrasound Off J Am Coll Vet Radiol Int Vet Radiol Assoc*. 2007;48(5):434–438. https://doi.org/10.1111/j.1740-8261.2007.00274.x.
22. Novellas R, Espada Y, Ruiz de Gopegui R. Doppler ultrasonographic estimation of renal and ocular resistive and pulsatility indices in normal dogs and cats. *Vet Radiol Ultrasound Off J Am Coll Vet Radiol Int Vet Radiol Assoc*. 2007;48(1):69–73. https://doi.org/10.1111/j.1740-8261.2007.00206.x.
23. Bouma JL, Aronson LR, Keith DG, Saunders HM. Use of computed tomography renal angiography for screening feline renal transplant donors. *Vet Radiol Ultrasound Off J Am Coll Vet Radiol Int Vet Radiol Assoc*. 2003;44(6):636–641. https://doi.org/10.1111/j.1740-8261.2003.tb00522.x.
24. Cáceres AV, Zwingenberger AL, Aronson LR, Mai W. Characterization of normal feline renal vascular anatomy with dual-phase CT angiography. *Vet Radiol Ultrasound Off J Am Coll Vet Radiol Int Vet Radiol Assoc*. 2008;49(4):350–356. https://doi.org/10.1111/j.1740-8261.2008.00378.x.
25. Alexander K, Dunn M, Carmel EN, Lavoie JP, Del Castillo JRE. Clinical application of Patlak plot CT-GFR in animals with upper urinary tract disease. *Vet Radiol Ultrasound Off J Am Coll Vet Radiol Int Vet Radiol Assoc*. 2010;51(4):421–427. https://doi.org/10.1111/j.1740-8261.2010.01670.x.
26. Granger LA, Armbrust LJ, Rankin DC, Ghering R, Bello NM, Alexander K. Estimation of glomerular filtration rate in healthy cats using single-slice dynamic CT and Patlak plot analysis. *Vet Radiol Ultrasound Off J Am Coll Vet Radiol Int Vet Radiol Assoc*. 2012;53(2):181–188. https://doi.org/10.1111/j.1740-8261.2011.01899.x.
27. O'Dell-Anderson KJ, Twardock R, Grimm JB, Grimm KA, Constable PD. Determination of glomerular filtration rate in dogs using contrast-enhanced computed tomography. *Vet Radiol Ultrasound Off J Am Coll Vet Radiol Int Vet Radiol Assoc*. 2006;47(2):127–135. https://doi.org/10.1111/j.1740-8261.2006.00118.x.
28. Rao QA, Newhouse JH. Risk of nephropathy after intravenous administration of contrast material: a critical literature analysis. *Radiology*. 2006;239(2):392–397. https://doi.org/10.1148/radiol.2392050413.
29. Thomsen HS. European Society of Urogenital Radiology (ESUR) guidelines on the safe use of iodinated contrast media. *Eur J Radiol*. 2006;60(3):307–313. https://doi.org/10.1016/j.ejrad.2006.06.020.
30. Feeney DA, Osborne CA, Jessen CR. Effect of multiple excretory urograms on glomerular filtration of normal dogs: a preliminary report. *Am J Vet Res*. 1980;41(6):960–963.
31. Barthez PY, Begon D, Delisle F. Effect of contrast medium dose and image acquisition timing on ureteral opacification in the normal dog as assessed by computed tomography. *Vet Radiol Ultrasound Off J Am Coll Vet Radiol Int Vet Radiol Assoc*. 1998;39(6):524–527. https://doi.org/10.1111/j.1740-8261.1998.tb01643.x.
32. Feeney DA, Barber DL, Culver DH, Prasse KW, Thrall DE, Lewis RE. Canine excretory urogram: correlation with baseline measurements. *Am J Vet Res*. 1980;41(2):279–283.
33. Hoey SE, Heder BL, Hetzel SJ, Waller KR. Use of computed tomography for measurement of kidneys in dogs without renal disease. *J Am Vet Med Assoc*. 2016;248(3):282–287. https://doi.org/10.2460/javma.248.3.282.
34. Adin CA, Herrgesell EJ, Nyland TG, et al. Antegrade pyelography for suspected ureteral obstruction in cats: 11 cases (1995-2001). *J Am Vet Med Assoc*. 2003;222(11):1576–1581. https://doi.org/10.2460/javma.2003.222.1576.
35. Cavrenne R, Mai W. Time-resolved renal contrast-enhanced MRA in normal dogs. *Vet Radiol Ultrasound Off J Am Coll Vet Radiol Int Vet Radiol Assoc*. 2009;50(1):58–64. https://doi.org/10.1111/j.1740-8261.2008.01490.x.
36. Daniel GB, Mitchell SK, Mawby D, Sackman JE, Schmidt D. Renal nuclear medicine: a review. *Vet Radiol Ultrasound Off J Am Coll Vet Radiol Int Vet Radiol Assoc*. 1999;40(6):572–587. https://doi.org/10.1111/j.1740-8261.1999.tb00883.x.
37. Stokes JE, Forrester SD. New and unusual causes of acute renal failure in dogs and cats. *Vet Clin North Am Small Anim Pract*. 2004;34(4):909–922. https://doi.org/10.1016/j.cvsm.2004.03.006. vi.
38. D'Anjou MA, Penninck D, Cornejo L, Pibarot P. Ultrasonographic diagnosis of portosystemic shunting in dogs and cats. *Vet Radiol Ultrasound*. 2004;45(5):424–437. https://doi.org/10.1111/j.1740-8261.2004.04076.x.
39. Lourenço BN, Randall E, Seiler G, Lunn KF. Abdominal ultrasonographic findings in acromegalic cats. *J Feline Med Surg*. 2015;17(8):698–703. https://doi.org/10.1177/1098612X14556847.
40. Rivers BJ, Johnston GR. Diagnostic imaging strategies in small animal nephrology. *Vet Clin North Am Small Anim Pract*. 1996;26(6):1505–1517. https://doi.org/10.1016/s0195-5616(96)50138-5.
41. Sutthigran S, Saisawart P, Klaengkaew A, et al. Use of contrast-enhanced computed tomography to detect kidney infarction in dogs. *J Vet Intern Med*. 2022;36(1):164–170. https://doi.org/10.1111/jvim.16343.
42. Yan GY, Chen KY, Wang HC, Ma TY, Chen KS. Relationship between ultrasonographically determined renal dimensions and International Renal Interest Society stages in cats with chronic kidney disease. *J Vet Intern Med*. 2020;34(4):1464–1475. https://doi.org/10.1111/jvim.15814.
43. Felkai C, Vörös K, Vrabély T, Vetési F, Karsai F, Papp L. Ultrasonographic findings of renal dysplasia in cocker spaniels: eight cases. *Acta Vet Hung*. 1997;45(4):397–408.
44. Ross L. Acute kidney injury in dogs and cats. *Vet Clin North Am Small Anim Pract*. 2022;52(3):659–672. https://doi.org/10.1016/j.cvsm.2022.01.005.
45. Morrow KL, Salman MD, Lappin MR, Wrigley R. Comparison of the resistive index to clinical parameters in dogs with renal disease. *Vet Radiol Ultrasound*. 1996;37(3):193–199.
46. Adams WH, Toal RL, Breider MA. Ultrasonographic findings in dogs and cats with oxalate nephrosis attributed to ethylene glycol intoxication: 15 cases (1984–1988). *J Am Vet Med Assoc*. 1991;199(4):492–496.
47. Mantis P, Lamb CR. Most dogs with medullary rim sign on ultrasonography have no demonstrable renal dysfunction. *Vet Radiol Ultrasound Off J Am Coll Vet Radiol Int Vet Radiol Assoc*. 2000;41(2):164–166. https://doi.org/10.1111/j.1740-8261.2000.tb01471.x.
48. Cordella A, Pey P, Dondi F, et al. The ultrasonographic medullary "rim sign" versus medullary "band sign" in cats and their association with renal disease. *J Vet Intern Med*. 2020;34(5):1932–1939. https://doi.org/10.1111/jvim.15878.
49. Ferreira A, Marwood R, Batchelor D, Maddox T, Mortier JR. Prevalence and clinical significance of the medullary rim sign identified on ultrasound of feline kidneys. *Vet Rec*. 2020;186(16):533. https://doi.org/10.1136/vr.105619.

50. Forrest LJ, O'Brien RT, Tremelling MS, Steinberg H, Cooley AJ, Kerlin RL. Sonographic renal findings in 20 dogs with leptospirosis. *Vet Radiol Ultrasound Off J Am Coll Vet Radiol Int Vet Radiol Assoc*. 1998;39(4):337–340. https://doi.org/10.1111/j.1740-8261.1998.tb01617.x.
51. Lewis KM, O'Brien RT. Abdominal ultrasonographic findings associated with feline infectious peritonitis: a retrospective review of 16 cases. *J Am Anim Hosp Assoc*. 2010;46(3):152–160. https://doi.org/10.5326/0460152.
52. Barr FJ. Hypercalcemic nephropathy in three dogs: sonographic appearance. *Veterinary Radiology*. 1989;30:169–173. https://onlinelibrary.wiley.com/doi/abs/10.1111/j.1740-8261.1989.tb00770.x. Accessed July 13, 2022. Accessed.
53. Rahal SC, Mamprim MJ, Oliveira HS, et al. Ultrasonographic, computed tomographic, and operative findings in dogs infested with giant kidney worms (*Dioctophyme renale*). *J Am Vet Med Assoc*. 2014;244(5):555–558. https://doi.org/10.2460/javma.244.5.555.
54. McKenna SC, Carpenter JL. Polycystic disease of the kidney and liver in the Cairn Terrier. *Vet Pathol*. 1980;17(4):436–442. https://doi.org/10.1177/030098588001700405.
55. Moe L, Lium B. Computed tomography of hereditary multifocal renal cystadenocarcinomas in German shepherd dogs. *Vet Radiol Ultrasound Off J Am Coll Vet Radiol Int Vet Radiol Assoc*. 1997;38(5):335–343. https://doi.org/10.1111/j.1740-8261.1997.tb02094.x.
56. Holloway A, O'Brien R. Perirenal effusion in dogs and cats with acute renal failure. *Vet Radiol Ultrasound Off J Am Coll Vet Radiol Int Vet Radiol Assoc*. 2007;48(6):574–579. https://doi.org/10.1111/j.1740-8261.2007.00300.x.
57. Beck JA, Bellenger CR, Lamb WA, et al. Perirenal pseudocysts in 26 cats. *Aust Vet J*. 2000;78(3):166–171. https://doi.org/10.1111/j.1751-0813.2000.tb10585.x.
58. Bryan JN, Henry CJ, Turnquist SE, et al. Primary renal neoplasia of dogs. *J Vet Intern Med*. 2006;20(5):1155–1160. https://doi.org/10.1892/0891-6640(2006)20[1155:prnod]2.0.co;2.
59. Borjesson DL. Renal cytology. *Vet Clin North Am Small Anim Pract*. 2003;33(1):119–134. https://doi.org/10.1016/s0195-5616(02)00086-4.
60. Cruz-Arámbulo R, Wrigley R, Powers B. Sonographic features of histiocytic neoplasms in the canine abdomen. *Vet Radiol Ultrasound Off J Am Coll Vet Radiol Int Vet Radiol Assoc*. 2004;45(6):554–558. https://doi.org/10.1111/j.1740-8261.2004.04095.x.
61. Valdés-Martínez A, Cianciolo R, Mai W. Association between renal hypoechoic subcapsular thickening and lymphosarcoma in cats. *Vet Radiol Ultrasound Off J Am Coll Vet Radiol Int Vet Radiol Assoc*. 2007;48(4):357–360. https://doi.org/10.1111/j.1740-8261.2007.00256.x.
62. Williams AG, Hohenhaus AE, Lamb KE. Incidence and treatment of feline renal lymphoma: 27 cases. *J Feline Med Surg*. 2021;23(10):936–944. https://doi.org/10.1177/1098612X20984363.
63. Hylands R. Veterinary diagnostic imaging. Retroperitoneal abscess and regional cellulitis secondary to a pyelonephritis within the left kidney. *Can Vet J Rev Veterinaire Can*. 2006;47(10):1033–1035.
64. Neuwirth L, Mahaffey M, Crowell W, et al. Comparison of excretory urography and ultrasonography for detection of experimentally induced pyelonephritis in dogs. *Am J Vet Res*. 1993;54(5):660–669.
65. Choi J, Jang J, Choi H, Kim H, Yoon J. Ultrasonographic features of pyonephrosis in dogs. *Vet Radiol Ultrasound Off J Am Coll Vet Radiol Int Vet Radiol Assoc*. 2010;51(5):548–553. https://doi.org/10.1111/j.1740-8261.2010.01702.x.
66. Vourganti S, Agarwal PK, Bodner DR, Dogra VS. Ultrasonographic evaluation of renal infections. *Radiol Clin North Am*. 2006;44(6):763–775. https://doi.org/10.1016/j.rcl.2006.10.001.
67. Sarkiala EM, Dambach D, Harvey CE. Jaw lesions resulting from renal hyperparathyroidism in a young dog—a case report. *J Vet Dent*. 1994;11(4):121–124.
68. Reusch CE, Tomsa K, Zimmer C, et al. Ultrasonography of the parathyroid glands as an aid in differentiation of acute and chronic renal failure in dogs. *J Am Vet Med Assoc*. 2000;217(12):1849–1852. https://doi.org/10.2460/javma.2000.217.1849.
69. Feeney DA, Barber DL, Osborne CA. Functional aspects of the nephrogram in excretory urography: a review. *Vet Radiol*. 1982;23:43.
70. Pey P, Marcon O, Drigo M, Specchi S, Bertolini G. Multidetector-row computed tomographic characteristics of presumed preureteral vena cava in cats. *Vet Radiol Ultrasound Off J Am Coll Vet Radiol Int Vet Radiol Assoc*. 2015;56(4):359–366. https://doi.org/10.1111/vru.12251.
71. Zaid MS, Berent AC, Weisse C, Caceres A. Feline ureteral strictures: 10 cases (2007–2009). *J Vet Intern Med*. 2011;25(2):222–229. https://doi.org/10.1111/j.1939-1676.2011.0679.x.
72. Kyles AE, Hardie EM, Wooden BG, et al. Clinical, clinicopathologic, radiographic, and ultrasonographic abnormalities in cats with ureteral calculi: 163 cases (1984–2002). *J Am Vet Med Assoc*. 2005;226(6):932–936. https://doi.org/10.2460/javma.2005.226.932.
73. Choi H, Won S, Chung W, et al. Effect of intravenous mannitol upon the resistive index in complete unilateral renal obstruction in dogs. *J Vet Intern Med*. 2003;17(2):158–162. https://doi.org/10.1111/j.1939-1676.2003.tb02427.x.
74. Lulich JP, Osborne CA, Albasan H, Koehler LA, Ulrich LM, Lekcharoensuk C. Recent shifts in the global proportions of canine uroliths. *Vet Rec*. 2013;172(14):363. https://doi.org/10.1136/vr.101056.
75. Shabana W, Bude RO, Rubin JM. Comparison between color Doppler twinkling artifact and acoustic shadowing for renal calculus detection: an in vitro study. *Ultrasound Med Biol*. 2009;35(2):339–350. https://doi.org/10.1016/j.ultrasmedbio.2008.09.023.
76. Berent AC, Mayhew PD, Porat-Mosenco Y. Use of cystoscopic-guided laser ablation for treatment of intramural ureteral ectopia in male dogs: four cases (2006–2007). *J Am Vet Med Assoc*. 2008;232(7):1026–1034. https://doi.org/10.2460/javma.232.7.1026.
77. Samii VF, McLoughlin MA, Mattoon JS, et al. Digital fluoroscopic excretory urography, digital fluoroscopic urethrography, helical computed tomography, and cystoscopy in 24 dogs with suspected ureteral ectopia. *J Vet Intern Med*. 2004;18(3):271–281. https://doi.org/10.1892/0891-6640(2004)18<271:dfeudf>2.0.co;2.
78. Yoon HY, Mann FA, Punke JP, Jeong SW. Bilateral ureteral ectopia with renal dysplasia and urolithiasis in a dog. *J Am Anim Hosp Assoc*. 2010;46(3):209–214. https://doi.org/10.5326/0460209.
79. Lautzenhiser SJ, Bjorling DE. Urinary incontinence in a dog with an ectopic ureterocele. *J Am Anim Hosp Assoc*. 2002;38(1):29–32. https://doi.org/10.5326/0380029.
80. Stiffler KS, Stevenson MAM, Mahaffey MB, Howerth EW, Barsanti JA. Intravesical ureterocele with concurrent renal dysfunction in a dog: a case report and proposed

classification system. *J Am Anim Hosp Assoc.* 2002;38(1):33–39. https://doi.org/10.5326/0380033.
81. Eisele JG, Jackson J, Hager D. Ectopic ureterocele in a cat. *J Am Anim Hosp Assoc.* 2005;41(5):332–335. https://doi.org/10.5326/0410332.
82. Reichle JK, Peterson RA, Mahaffey MB, Schelling CG, Barthez PY. Ureteral fibroepithelial polyps in four dogs. *Vet Radiol Ultrasound Off J Am Coll Vet Radiol Int Vet Radiol Assoc.* 2003;44(4):433–437. https://doi.org/10.1111/j.1740-8261.2003.tb00481.x.
83. Tidwell AS, Ullman L, Schelling SH. Urinoma (para-ureteral pseudocyst) in a dog. *Vet Radiol Ultrasound.* 2005;31(4):203–206.
84. Kawashima A, Sandler CM, Corl FM, et al. Imaging of renal trauma: a comprehensive review. *Radiogr Rev Publ Radiol Soc N Am Inc.* 2001;21(3):557–574. https://doi.org/10.1148/radiographics.21.3.g01ma11557.

ELECTRONIC RESOURCES

Additional information related to the content in Chapter 41 can be found online at eBooks.Health.Elsevier.com

- Chapter Quiz

Vetacademy.ir
مجموعه آموزشی پژوهشی وت آکادمی
تلاش #برای_دنیای_بهتر_حیوانات
تیم وت آکادمی
برای دسترسی به تازه ترین آموزش ها و مطالب علمی دامپزشکی؛ وت آکادمی رو فالو کن
سایت مجموعه بزرگ آموزشی پژوهشی وت آکادمی
Vet-academy.ir
صفحه ی اینستاگرام وت آکادمی
@Vetacademy.ir
دسترسی به آرشیو صد گیگ کتاب آموزش دامپزشکی به صورت رایگان
و جزوه های آموزشی در کانال تلگرامی
@Vetfiles
گروه بزرگ تلگرامی، پرسش و پاسخ و آموزش
@VetAcademyGp
صفحه رسمی آپارات وت آکادمی
aparat.com/vetacademy.ir

CHAPTER 42

Urinary Bladder and Urethra

Angela Marolf

ANATOMY

The urinary bladder is divided grossly into three parts: the cranially located apex, the body in the middle, and the neck or trigone caudally (Fig. 42.1).[1,2] Three ligaments formed from peritoneal reflections hold the urinary bladder loosely in position.[2] The middle urinary bladder ligament extends along the ventral surface of the urinary bladder and two lateral ligaments extend along the lateral urinary bladder surfaces. These ligaments often contain large fat deposits, facilitating radiographic visualization of the urinary bladder neck and body. The cranial and dorsal surfaces of the urinary bladder are visible radiographically because of adjacent fat within the omentum and mesentery (Fig. 42.2).

The urinary bladder is located cranial to the pubis, dorsal to the rectus abdominis muscle, caudal to the small bowel and omentum, and ventral to the large bowel. In females, the body of the uterus lies between the urinary bladder and colon/rectum. The caudal portion of the normal urinary bladder may be cranial to the pubis or within the pelvic canal.[3,4] When distended, the caudal part of the urinary bladder is usually cranial to the pubis.[3,4] The normal urinary bladder in the cat is always intra-abdominal, being located 2 to 3 cm cranial to the pubis because of the long urinary bladder neck in this species (Fig. 42.3).[5]

Urinary bladder size varies with the amount of urine. After voiding, the urinary bladder may not be visible radiographically. With extreme distention, the apex may extend to the umbilicus. Severe distention may occur normally owing to lack of opportunity to void or because of a strange or unfamiliar environment. The urinary bladder in the dog is usually oval, but with distention, it becomes more ellipsoid. The feline urinary bladder is almost always ellipsoid (Fig. 42.4).

The normal urinary bladder has a soft tissue radiographic opacity. Any opacity greater or less than soft tissue within the urinary bladder on survey radiographs is abnormal. The musculomembranous urinary bladder wall consists of mucosal, submucosal, and muscular layers. The peritoneum is adherent to the serosal surface, providing a separate fourth layer. The thickness of the urinary bladder wall or characteristics of the mucosa cannot be evaluated on survey radiographs because of border effacement by urine in the lumen.

Radiographic visualization of the urinary bladder is reduced if there is insufficient abdominal fat, inadequate distention, and superimposed opacities. Intestinal content, pelvic limb musculature, and adjacent osseous structures may obscure all or part of the urinary bladder. Focal superimposition may be created by fluid-filled small bowel, nipples, the prepuce, and cutaneous masses. If necessary, some of these superimposition opacities can be eliminated or minimized by withholding food for 24 hours preceding the study, giving cleansing enemas, or using compression radiography, although these interventions are usually not necessary.

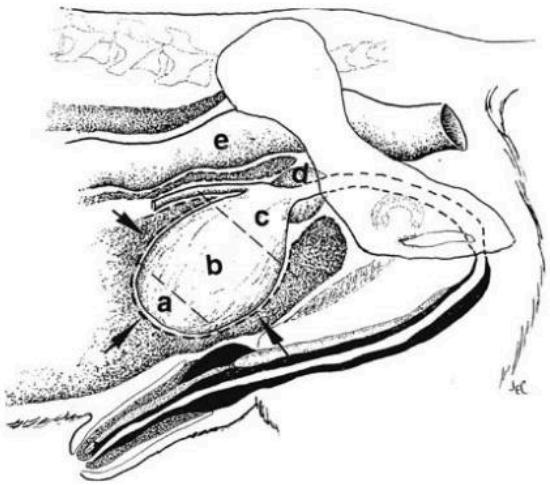


Fig. 42.1 Lateral view of the abdomen in a normal male dog. *a,* Apex of the urinary bladder; *b,* body of the urinary bladder; *c,* neck of the urinary bladder; *d,* prostate gland; *e,* descending colon. The *broken line* around the urinary bladder (*black arrows*) represents the surrounding adherent peritoneal reflection.

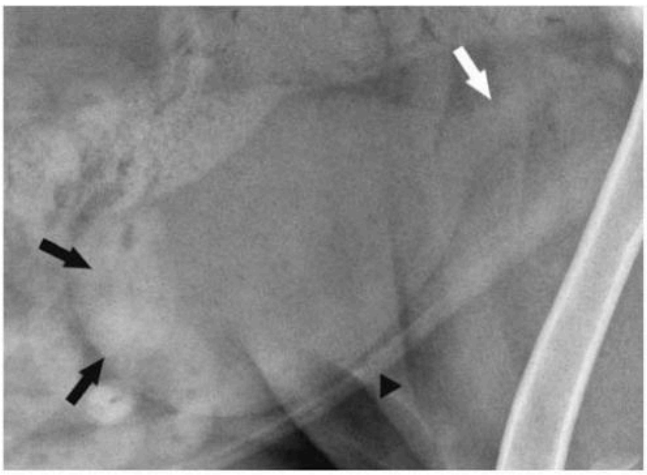


Fig. 42.2 Lateral radiograph of the caudal abdomen in a normal dog. The urinary bladder neck (*white arrow*) is well visualized because of fat within the urinary bladder ligaments. The rectus abdominis muscle (*black arrowhead*) is ventral to the urinary bladder. Bowel segments (*black arrows*) are superimposed over the apex of the urinary bladder.

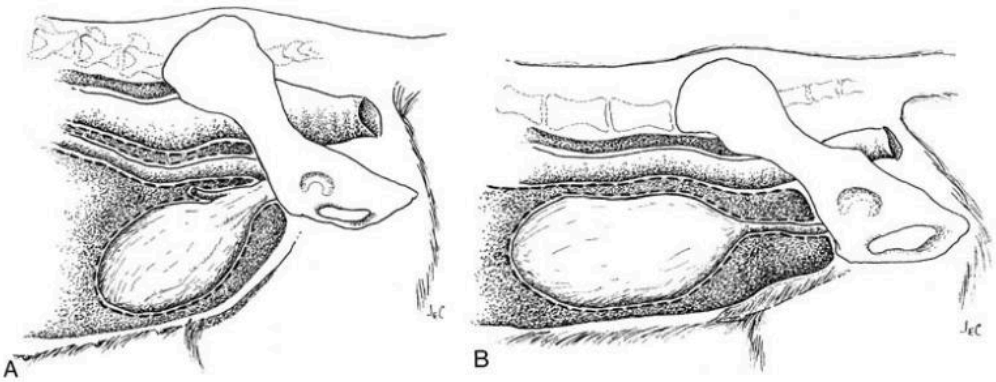


Fig. 42.3 **A,** Urinary bladder in a normal female dog. The canine urinary bladder is adjacent to the pubis and is oval. **B,** Urinary bladder in a normal cat. The feline urinary bladder is ellipsoid and has a long neck, which makes the urinary bladder appear displaced cranially from the pubis. The *broken line* around the urinary bladder in **A** and **B** denotes the peritoneal reflection. From Park RD. Radiology of the urinary bladder and urethra. In: O'Brien TR, ed. *Radiographic Diagnosis of Abdominal Disorders in the Dog and Cat.* Davis, CA: Covell Park Veterinary; 1981.

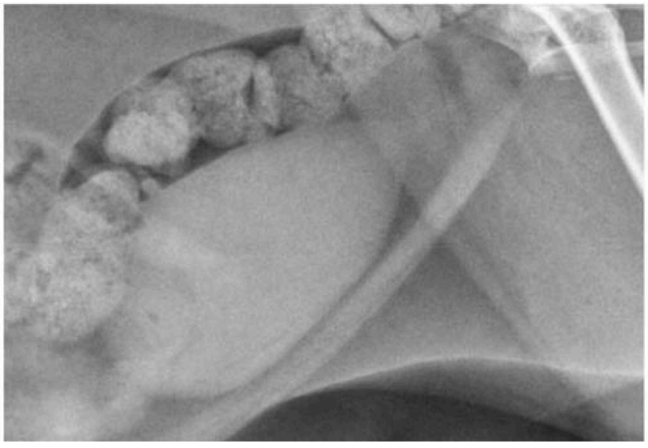


Fig. 42.4 Lateral radiograph of the caudal abdomen in a normal cat. The feline urinary bladder is ellipsoid and is located more cranially than in the dog because of a longer urinary bladder neck. Bowel segments are superimposed over the apex of the urinary bladder.

RADIOGRAPHIC SIGNS OF URINARY BLADDER DISEASE

There are few survey-radiographic signs of urinary bladder disease. Poor or nonexistent urinary bladder visualization and abnormal urinary bladder position, shape, size, and opacity indicate disease of the urinary bladder or, in many instances, disease of adjacent structures (Table 42.1).

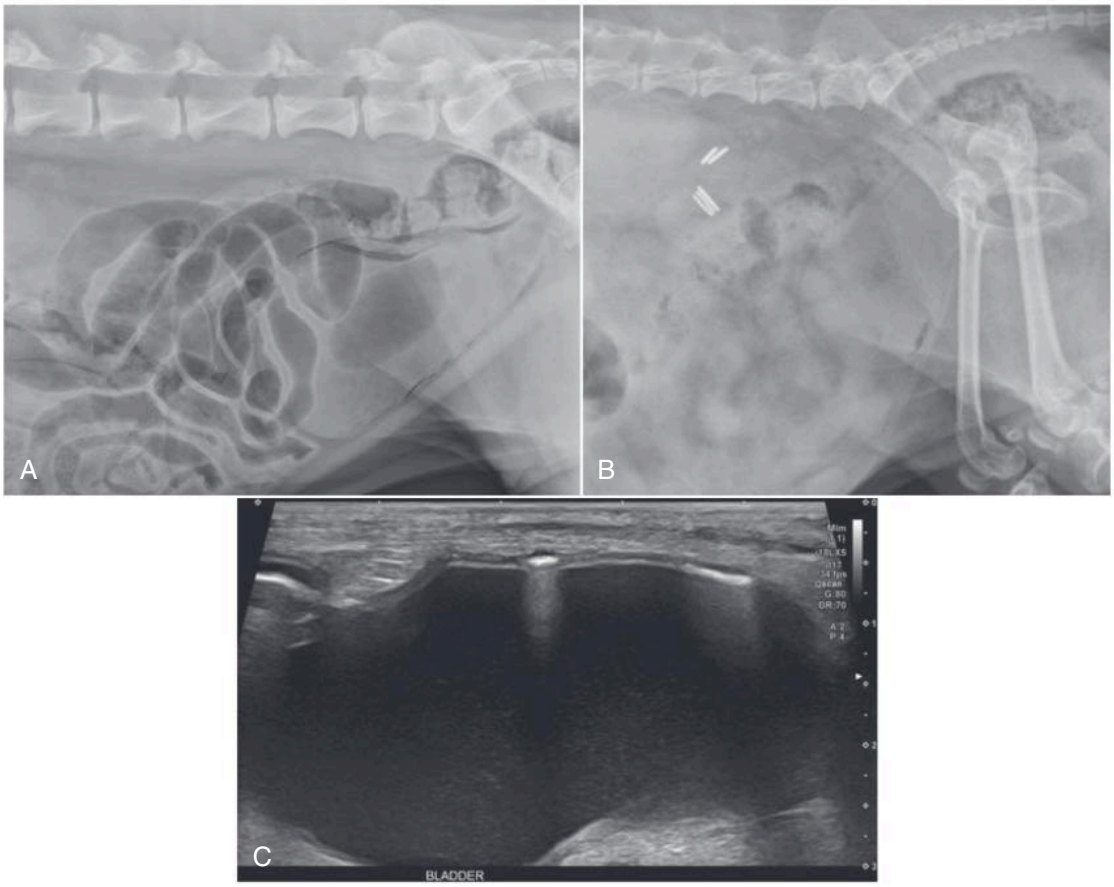
Poor radiographic delineation of the urinary bladder may occur regardless of whether serosal contrast in the caudal abdomen is good or decreased. If serosal contrast is good and the urinary bladder is not seen, the urinary bladder is empty or has been displaced caudally or ventrally. If serosal contrast is decreased and the urinary bladder surface is not seen distinctly, free peritoneal fluid or inadequate peritoneal fat may be the cause (Fig. 42.5).

The urinary bladder may be displaced abnormally in various directions.[6] The cause of urinary bladder displacement may sometimes be determined by observation of surrounding structures or organs (Fig. 42.6). With severe urinary bladder displacement, as with a hernia, cystography or ultrasonography may be needed for its identification. Urinary bladder retroflexion was observed in 24% (10/41) of dogs with a perineal hernia.[7] A urinary bladder partially within the pelvic canal (Fig. 42.7) may be associated with congenital urinary tract anomalies.[8] A pelvic urinary bladder has also been reported as a normal variation, and this finding should be correlated with clinical signs to determine its significance.[4,9] Incontinent female dogs with a pelvic urinary bladder usually have a shorter urethra than continent dogs.[10,11]

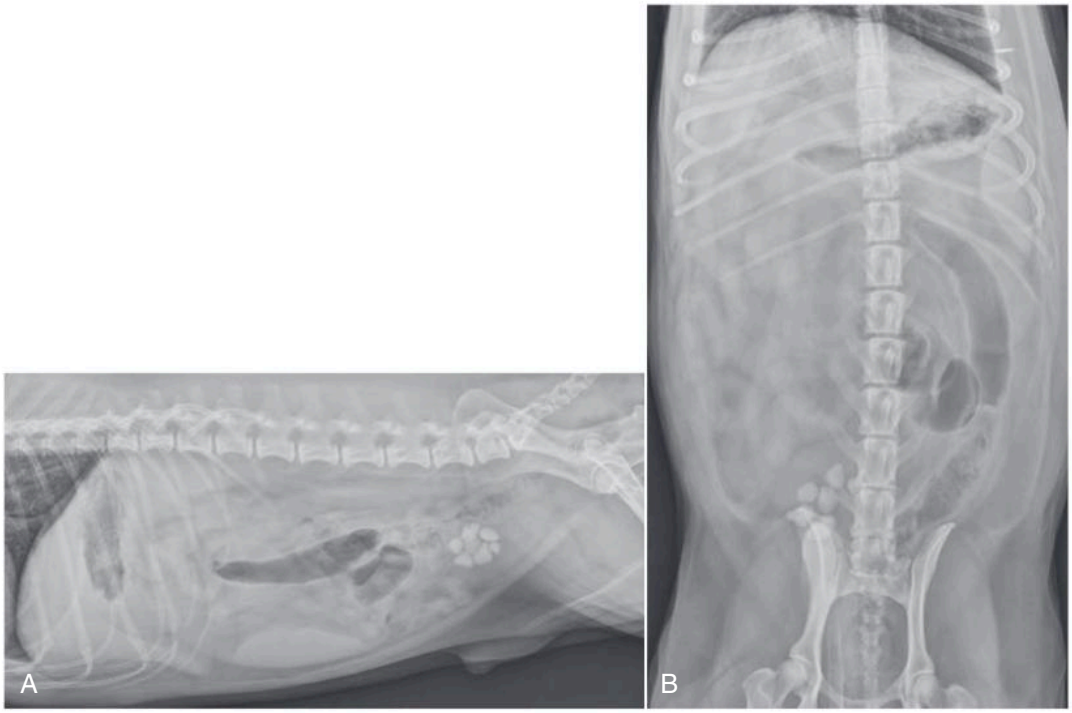
A change in shape of the urinary bladder is not common. Abdominal masses adjacent to the serosal surface of the urinary bladder may distort its shape. Tumors originating from the urinary bladder wall occasionally protrude from the serosal surface or cause thickening of the bladder trigone to produce a discernible change in shape of the urinary bladder but this is uncommon (Fig. 42.8).[12] A pointed apex with an elongated urinary bladder may occur with a persistent urachal ligament.[13] An abnormally small or large urinary bladder is difficult to diagnose radiographically because of the wide variation in normal size. In most instances, a consistently small or large urinary bladder with associated clinical signs is an indication that a contrast study or ultrasound examination should be performed to determine the cause of the suspected size change.

Any change in radiographic opacity in the urinary bladder is abnormal and usually easy to detect. Gas in the urinary bladder may be introduced iatrogenically from catheterization or cystocentesis. Small luminal gas bubbles are usually located in the center of the urinary bladder on a recumbent lateral view (Fig. 42.9). Gas in the urinary bladder lumen, urinary bladder wall, and occasionally the urinary bladder ligaments occurs with emphysematous cystitis (Fig. 42.10, eFig. 42.1). Emphysematous cystitis is produced by glucose-fermenting organisms and may be seen in association with diabetes mellitus.[14] Emphysematous cystitis without diabetes mellitus can also occur.[15,16]

Most increased opacities associated with the urinary bladder are calculi (see Fig. 42.6B, Fig. 42.11, eFigs. 42.2 and 42.3). Opacities need to be confirmed to be in the urinary bladder based on orthogonal radiographs. If doubt exists regarding the location or presence of cystic calculi, a compression view to displace adjacent structures overlapping or surrounding the urinary bladder (Fig. 42.12) and ultrasonography are ways to confirm the presence of calculi. The entire urinary tract from the kidneys to the terminus of the urethra should be examined for additional calculi. Not all calculi are radiopaque; thus, the absence of radiopacities within the urinary bladder does not rule out the presence of cystic calculi (Table 42.2). In cats with suspected feline idiopathic cystitis, survey radiographs, cystography, or ultrasonography can be used to evaluate the urinary bladder. Often, mild urinary bladder wall thickening may be observed with cystography.[17] Additionally, a horizontal-beam radiograph can be used to diagnose sand-like material



eFig. 42.1 **A, B,** Lateral radiographs of the caudal abdomen of two different dogs with emphysematous cystitis. Notice the rim of gas within the outline of the bladder wall. A cluster of gas bubbles is also present in the center of the urinary bladder. **C,** Sagittal ultrasound image of the urinary bladder of the dog depicted in **B**. Hyperechoic material with distal reverberation artifact can be seen in the ventral bladder wall in the near field, representing intramural gas.



eFig. 42.2 Lateral **(A)** and ventrodorsal **(B)** abdominal radiographs of a dog with urinary bladder calculi. Radiopaque irregularly rounded structures are present in the center of the urinary bladder



eFig. 42.3 Lateral abdominal radiograph of a dog with urinary bladder calculi. Small, round radiopaque structures are present in the center of the urinary bladder. Notice a single mineralized calculus in the region of the bladder trigone. This may represent a calculus in the ureterovesical junction or proximal urethra.

Table • 42.1

Urinary Bladder: Survey Radiographic Signs.

RADIOGRAPHIC SIGN	GAMUT OF CONDITION(S) OR DISEASE(S)
Visualization	
Urinary bladder not seen; abdominal serosal outlines are clear	Post voiding
	Displaced urinary bladder
	Perineal hernia
	Inguinal hernia
	Pelvic urinary bladder
	Normal
	Short urethra
	Ectopic ureter(s)
	Congenital urethrorectal fistula
Urinary bladder not seen; abdominal serosal outlines are not clearly seen	Peritoneal fluid
	Urine secondary to urinary bladder tear/rupture
	Transudate
	Exudate
	Hemorrhage
	Lack of peritoneal fat
	Emaciation
	Young animal (<4 months of age)
Abnormal Position	
Ventral displacement	Abdominal wall hernia
Cranial displacement	Prostate gland disease
	Neoplasia
	Prostatitis
	Prostatic or paraprostatic cyst
	Benign hypertrophy
	Large intrapelvic mass
Cranioventral displacement	Enlarged uterus
	Pyometra
	Pregnancy
	Sublumbar mass
	Large bowel distention
	Uterine stump granuloma or abscess
	Persistent patent urachus or urachal ligament
	Inguinal hernia
Caudal displacement	Perineal hernia
	Large abdominal mass
Dorsal displacement	Abdominal mass
Abnormal shape	Adjacent abdominal mass
	Neoplasia
	Abscesses/granulomas
	Persistent urachal ligament
Abnormal Size	
Increased	Urethral obstruction
	Urinary bladder neck obstruction
	Neurologic deficiencies
Decreased	Congenital anomalies
	Ectopic ureters
	Fistulas
	Cystitis
	Neoplasia
Mineral opacity	Calculi
	Urinary bladder wall mineralization
Lucent areas	Gas
	Iatrogenic
	Emphysematous cystitis

that will collect within the dependent portion of the urinary bladder. This additional view may be helpful in cats with feline idiopathic cystitis (feline lower urinary tract disease).[18] Radiopacities in the urinary bladder can also be produced by mineralization of the urinary bladder wall associated with neoplasia, chronic or encrusted cystitis, but this is unusual.[19]

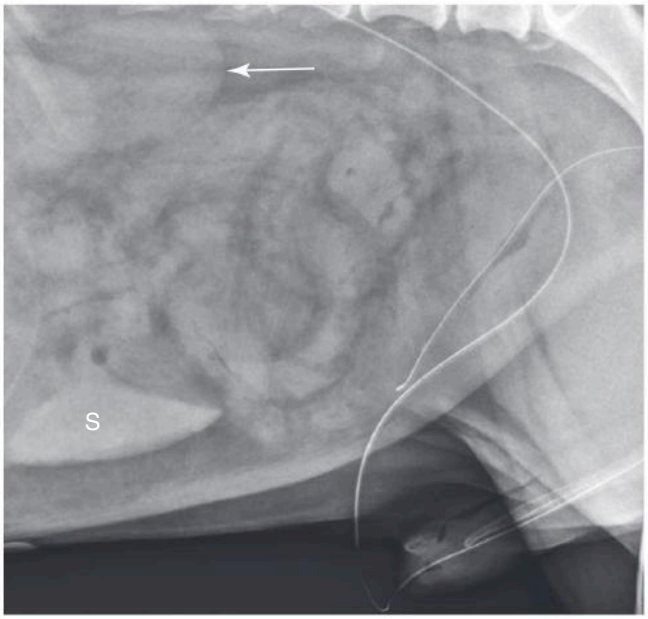


Fig. 42.5 Lateral radiograph of the abdomen of a dog. The left kidney (*white arrow*) is visible because of surrounding retroperitoneal fat. The serosal surfaces of the bowel and urinary bladder in the caudal aspect of the abdomen are indistinct because of free peritoneal fluid. The spleen (*S*) can be seen because of the focal nature of the free fluid in the caudal abdomen. A catheter is in the urinary bladder and looping over the caudal part of the abdomen.

CONTRAST CYSTOGRAPHY

Retrograde contrast cystography has largely been replaced by ultrasound but is a fast, simple, and inexpensive technique that may provide valuable diagnostic and prognostic information. Clinical indications for cystography include dysuria, pollakiuria,

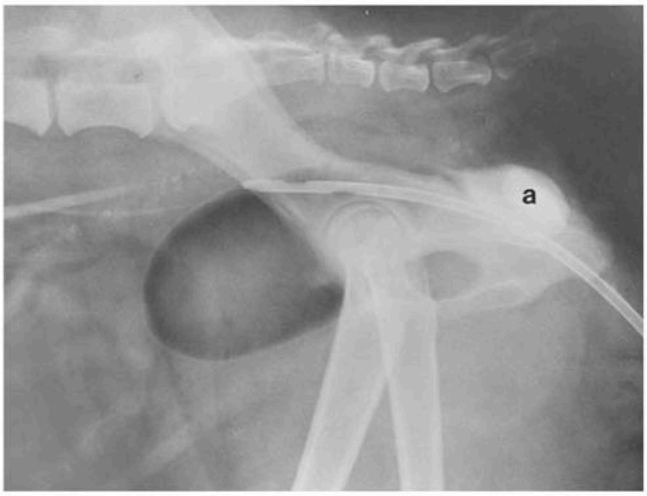


Fig. 42.7 Lateral radiograph of the caudal abdomen and pelvis after intravenous urography and double-contrast cystography. A radiopaque catheter is present in the urinary bladder, and the caudal aspect of the urinary bladder is within the pelvic canal. Contrast medium has accumulated in the vagina (*a*) because of an ectopic ureter.

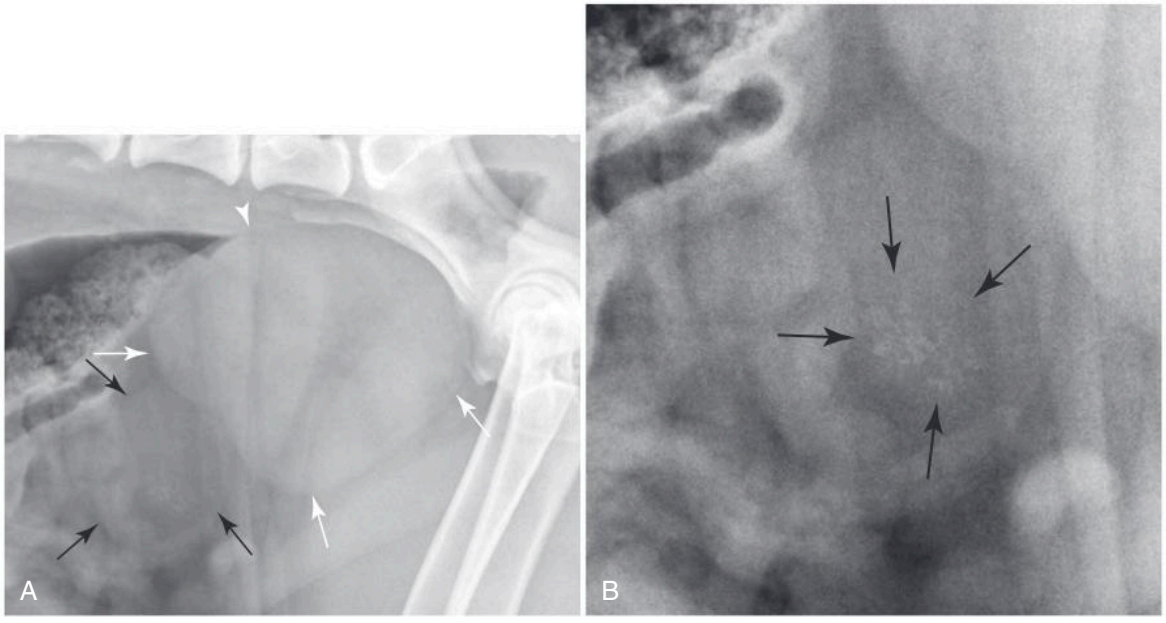


Fig. 42.6 **A,** Lateral radiograph of a dog with a large prostatic carcinoma (*white arrows*). The enlarged prostate gland displaces the urinary bladder (*black arrows*) cranially and compresses the terminal portion of the descending colon (*white arrowhead*). The prostate gland is more opaque than the urinary bladder because of its increased thickness. The enlarged prostate gland could be misinterpreted as the urinary bladder, except for the atypical shape. If there is a question whether a caudal abdominal mass is of urinary bladder origin, a positive-contrast cystogram or sonography would provide more information. **B,** Close-up of the urinary bladder from the same dog. There are numerous small radiopaque calculi in the lumen (*black arrows*).



Fig. 42.8 Oblique view of the abdomen after double-contrast cystography. A mass (*small black arrows*) is present on the cranioventral aspect of the gas-filled urinary bladder (*large black arrows*). The mass is a leiomyosarcoma originating from the urinary bladder; it gave the urinary bladder a bilobed appearance on the survey radiograph. This is an unusual manifestation of tumors of the urinary bladder.

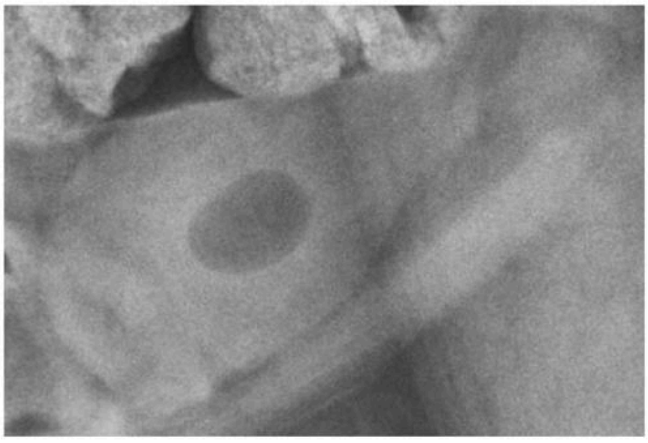


Fig. 42.9 Lateral view of the caudal abdomen of a cat. A central oblong air bubble introduced during cystocentesis is present in the urinary bladder. This radiolucency should not be misinterpreted as a calculus because positive-contrast medium has not been administered. So-called radiolucent calculi are really of soft tissue opacity and are not visible on survey radiographs. However, nonopaque calculi will appear relatively radiolucent when surrounded by positive-contrast medium is in the urinary bladder, creating a filling defect.

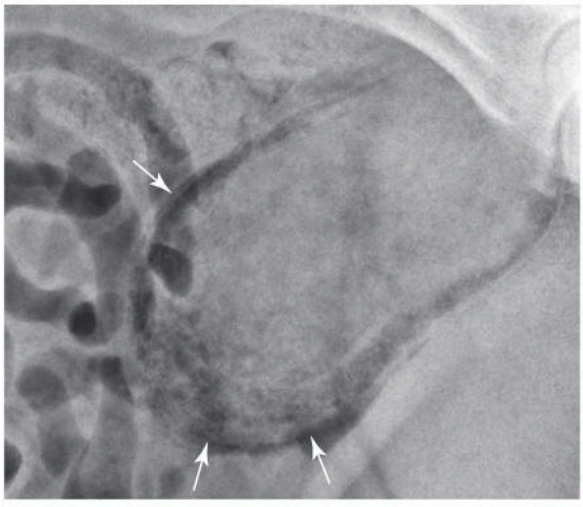


Fig. 42.10 Lateral view of the abdomen of a dog with gas (*white arrows*) in the urinary bladder wall and lumen. This appearance is typical of emphysematous cystitis, which in this dog was secondary to diabetes mellitus.

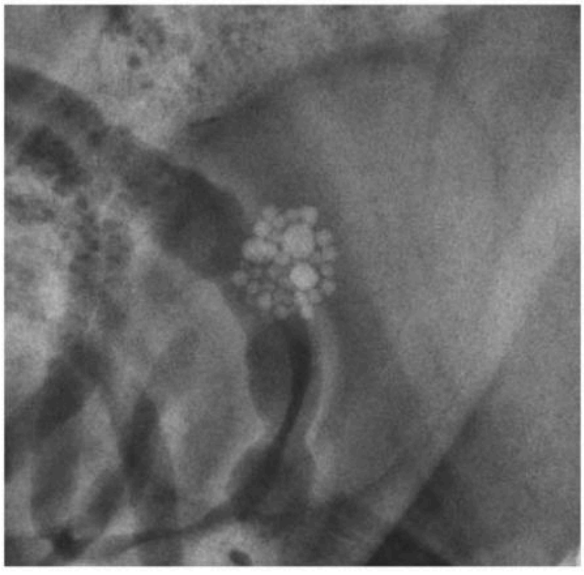


Fig. 42.11 Lateral radiograph of a dog with multiple, variably sized mineralized cystic calculi. Gas-filled bowl loops are superimposed over the apex of the urinary bladder

and intermittent or persistent chronic hematuria. Radiographic signs that suggest a need for cystography include identification of increased or decreased opacity in the urinary bladder, evaluation of caudal abdominal masses that may be associated with the urinary bladder, nonvisualization of the urinary bladder after abdominal trauma, and an abnormal shape or location of the urinary bladder. Cystography can be performed as negative-, positive-, or double-contrast procedure. Retrograde positive- and double-contrast procedures are often more useful to evaluate the urinary bladder than is negative-contrast cystography alone. Positive-contrast cystography is the method of choice for identifying urinary bladder location, tears, hernias, and abnormal communication with adjacent structures. Double-contrast cystography is better than positive-contrast cystography for assessing urinary bladder wall lesions and intraluminal filling defects. The selection of positive- or double-contrast cystography is based on clinical history, clinical signs, radiographic signs, and urinalysis findings (Table 42.3).

Cystography Technique

If possible, food should be withheld for 12 to 24 hours and an enema may need to be given preceding cystography because fecal material superimposed over the urinary bladder may mask important information.

All catheters and equipment should be sterilized, and the genitalia should be cleaned before the urinary bladder is catheterized. The equipment necessary for urinary bladder catheterization is illustrated in Fig. 42.13. Various other types of catheters are available.

Complications resulting from catheterization and cystography occur infrequently and are usually not detrimental. Iatrogenic trauma, bacterial contamination, or kinked and knotted urethral catheters may occur from improper catheterization.

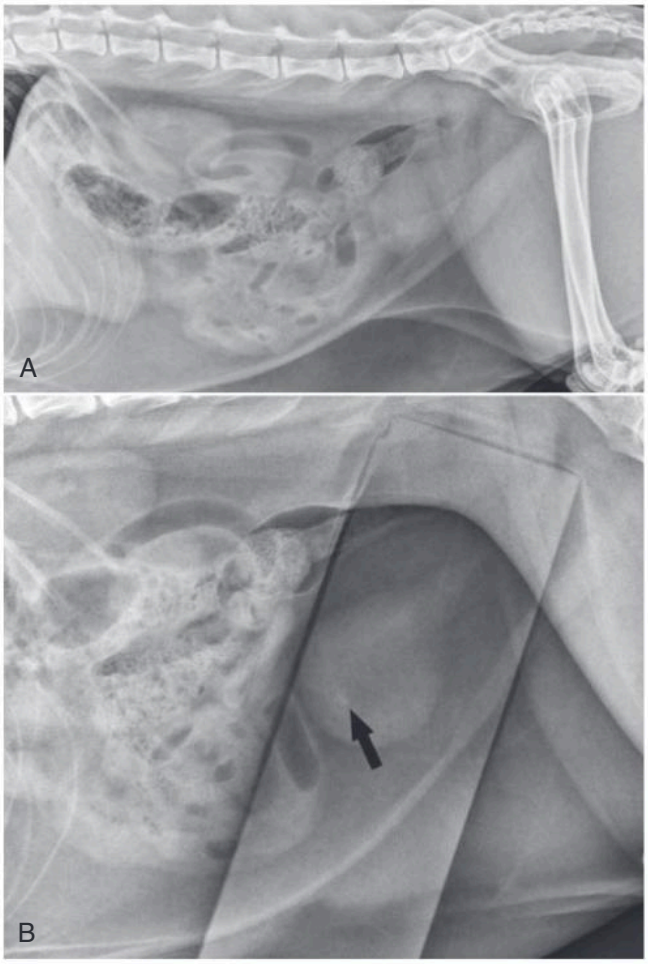


Fig. 42.12 **A,** Lateral radiograph of a cat with clinical signs of lower urinary tract disease. Note the superimposition of soft tissue structures and bowel over the urinary bladder. The ill-defined mineral opacity superimposed on the apex of the urinary bladder may be within the urinary bladder or in superimposed bowel. **B,** Compression view of the same animal after applying pressure with a nonradiopaque paddle. Note the displacement of bowel and radiopaque calculus in urinary bladder (*black arrow*).

Intramural and subserosal accumulation of contrast medium has occurred after maximal urinary bladder distention with a Foley catheter (Fig. 42.14).[20–22] This complication occurs more frequently in cats, often with a nondistended urinary bladder and minimal intravesicular pressure. It usually does not result in a clinical problem. Mucosal ulceration, inflammation, and granulomatous reactions may occur, but the changes are usually transitory and produce no serious clinical problems.[9] The most serious complication from negative-contrast cystography is gas embolization into the circulatory system, which may result in death.[23,24] Fortunately, such complications occur rarely. Death from gas embolism may be prevented by using more soluble nitrous oxide or carbon dioxide instead of room air.

Both negative- and positive-contrast media can be used for cystography. Negative-contrast media include room air, carbon dioxide, and nitrous oxide. Positive-contrast media are water-soluble organic iodides that should be used in an approximate 20% iodine solution. Barium should never be used for cystography.[20,24] The urinary bladder should be empty prior to administration of contrast medium. The volume of positive-contrast medium varies with body weight, the species, and the pathologic process present in the urinary bladder. An approximation of 10 mL per kilogram may be used.[24,25] The injection should be terminated before the estimated volume has

Table • 42.2

Radiopacity of Cystic Calculi on Survey Abdominal Radiographs.

CALCULUS COMPOSITION	OPACITY	SURFACE CHARACTERISTICS
Calcium oxalate	Moderately to markedly radiopaque	Sharp projections or smooth
Calcium phosphate	Moderately to markedly radiopaque	Smooth
Struvite (ammonium phosphate)	Moderately to markedly radiopaque	Usually smooth; can be spiculated
Silica	Moderately radiopaque	Jackstone appearance
Urate	Nonradiopaque to faintly radiopaque	Smooth
Cystine	Nonradiopaque to faintly radiopaque	Smooth

Table • 42.3

Indications for Type of Cystographic Procedure.

CONTRAST STUDY	INDICATIONS
Double-contrast cystogram	Suspect urinary bladder wall lesion(s), filling defects (calculi, blood clots, masses)
Positive-contrast cystogram	Suspect ruptured or abnormal urinary bladder location
Negative-contrast cystogram	Not frequently performed; can determine urinary bladder location or be used concurrently with other studies, such as CT excretory urography

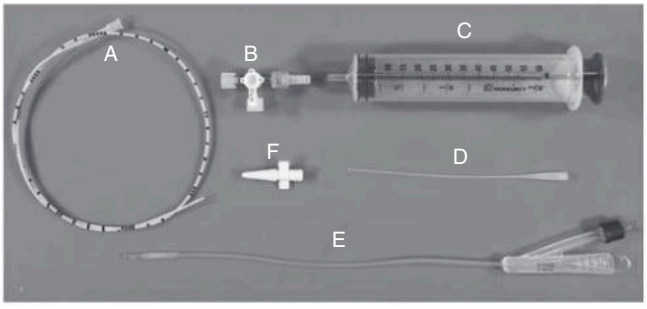


Fig. 42.13 Equipment for urinary bladder catheterization and cystography. *A,* Male urethral catheter; *B,* three-way valve; *C,* large syringe; *D,* Tomcat catheter; *E,* Foley (balloon-type) catheter; *F,* catheter connector for use with the male urethral catheter.

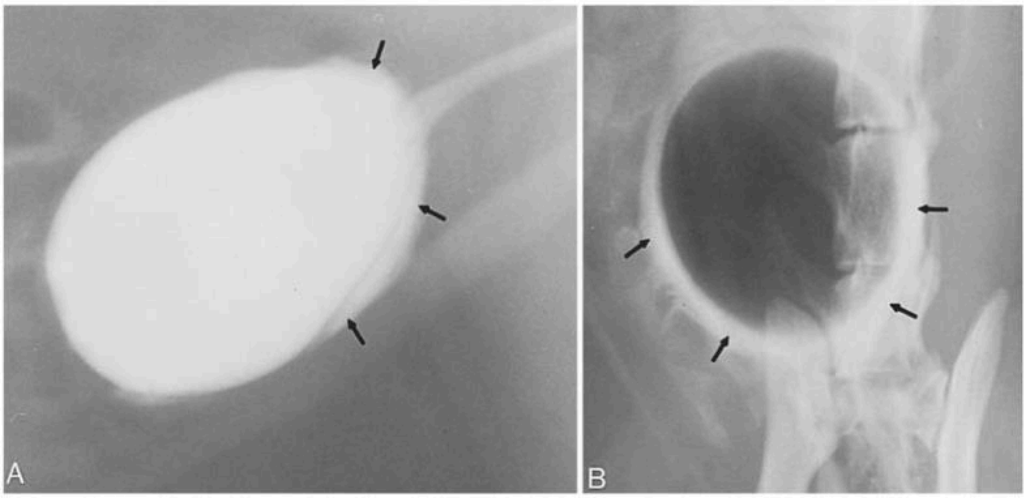


Fig. 42.14 Positive- **(A)** and double-contrast **(B)** cystogram where there has been subserosal accumulation of contrast medium (*black arrows*). This usually produces no severe or long-lasting complications. It is produced by a high intraluminal urinary bladder pressure and is predisposed by urinary bladder disease, particularly cystitis.

been administered if the urinary bladder feels adequately distended by external palpation, if reflux occurs around the catheter, or if back pressure is felt on the syringe plunger. Only moderate urinary bladder distention is recommended because maximal distention may obliterate subtle mucosal and urinary bladder wall changes and bears the risk of bladder rupture in case of chronic cystitis with reduced compliance of the bladder wall.[26] Lateral, ventrodorsal, ventral left–dorsal right, and ventral right–dorsal left radiographic views of the caudal abdomen should be made to examine the contrast medium–filled urinary bladder adequately. A double-contrast cystogram is performed by injecting a small volume of undiluted positive-contrast medium into the urinary bladder. The recommended dose of positive-contrast medium is 0.5 to 1 mL for a cat, 1 to 3 mL for a dog weighing less than 25 lb, and 3 to 6 mL for animals weighing more than 25 lb. Positive-contrast medium injection is followed by urinary bladder distention with negative-contrast medium (Fig. 42.15).

Radiographic Signs With Contrast Cystography

Radiographic signs observed with urinary bladder disease include intramural thickening, an irregular mucosal border, filling defects, and leakage (Table 42.4).[27] These radiographic changes must be differentiated from artifacts such as air bubbles and inadequate urinary bladder distention.

Intramural Changes (Urinary Bladder Wall Thickening)

The normal urinary bladder wall is approximately 1 mm thick regardless of the degree of distention.[9] Intramural changes are best demonstrated with double-contrast cystography and include focal or diffuse increased urinary bladder wall thickness (Fig. 42.16, eFig. 42.4). Mild urinary bladder wall thickening may be missed if the urinary bladder is distended completely.[26] Urinary bladder wall thickening may be caused by fibrous tissue proliferation or cellular infiltration from inflammation (cystitis), hemorrhage, or neoplasia. With chronic cystitis, subserosal leakage can occur due to necrosis of the urinary bladder mucosa (see Fig. 42.14). Intramural urinary bladder thickening causes decreased urinary bladder distensibility, which may be symmetric with diffuse intramural urinary bladder disease or asymmetric with focal intramural urinary bladder disease.

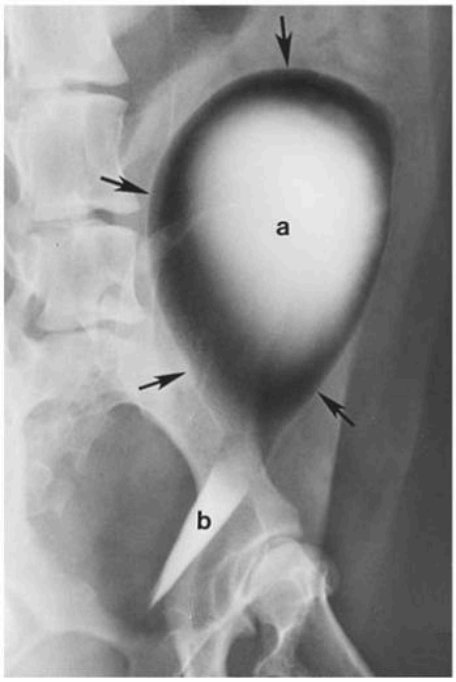
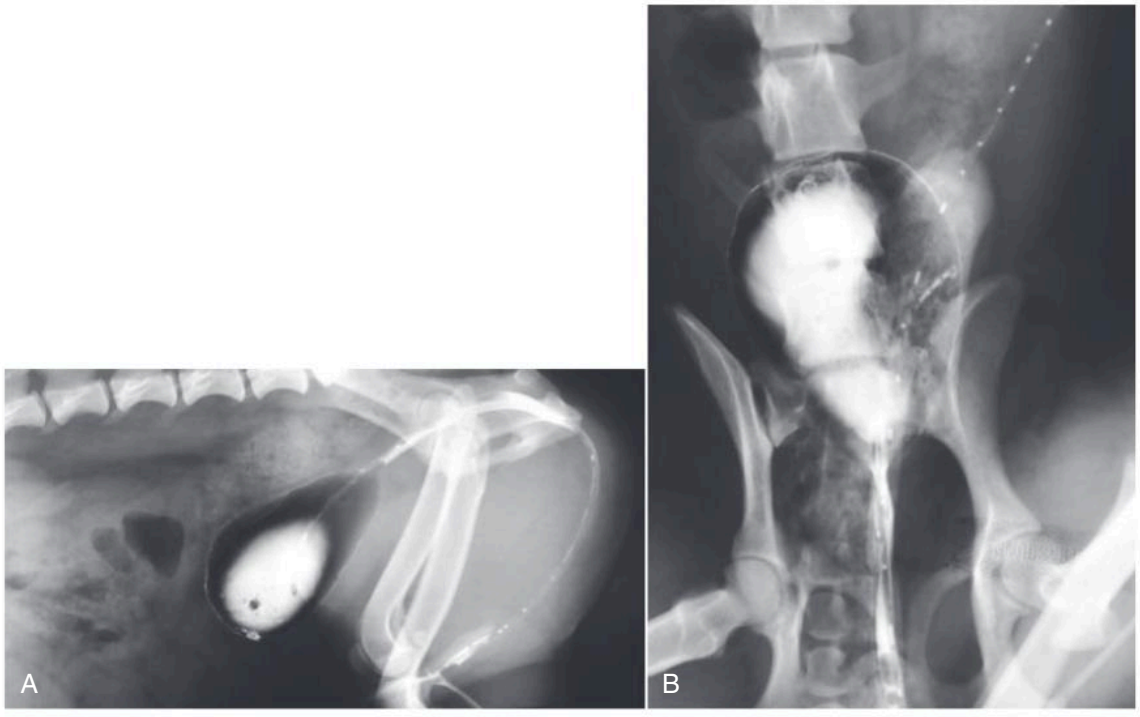


Fig. 42.15 Ventral left–dorsal right radiograph of a normal double-contrast cystogram. The urinary bladder wall (*black arrows*) is seen clearly. The contrast puddle in the dependent portion of the urinary bladder (*a*) and the contrast medium–filled urethra (*b*) are easily identified.

Mucosal Changes

The urinary bladder has a transitional epithelium, which appears smooth on a normal cystogram. Mucosal proliferation appears as an irregular outline along the inside urinary bladder surface and may be accentuated with inadequate urinary bladder distention, and can be obliterated if the urinary bladder is maximally distended.[26] The irregular mucosa is usually focally distributed but may be diffuse; it may vary in severity from a slightly irregular brush-type surface to a severe cobblestone appearance (Fig. 42.17). Ulcers may be present with mucosal



eFig. 42.4 Lateral and ventrodorsal double-contrast cystogram of a dog with urinary bladder calculi. The calculi are seen as filling defects in the center of the contrast medium pool in the middle of the bladder. The craniodorsal bladder wall is irregular. Focally adhered contrast medium may represent mucosal ulceration.

Table • 42.4

Cystographic Signs of Common Conditions of the Urinary Bladder.

	MUCOSAL CHANGES		INTRAMURAL THICKENING		FILLING DEFECT	
DISEASE	**FOCAL**	**DIFFUSE**	**FOCAL**	**DIFFUSE**	**ATTACHED**	**FREE**
Chronic cystitis	Cranioventral	Occasional	Cranioventral	Occasional (Cytoxan-induced cystitis)	Blood clots	Blood clots, calculi
Acute cystitis	—	—	—	—	—	Occasional blood clots
Cystic calculi	Cranioventral from cystitis	—	Cranioventral from cystitis	—	—	Calculi and occasional blood clots
Neoplasia	Any location within urinary bladder	Occasional	Any location within urinary bladder	Occasional	Sessile, occasionally pedunculated	Blood clots
Urinary bladder rupture or perforation	Contrast leakage into peritoneum at site of wall tear	—	—	—	—	Blood clots

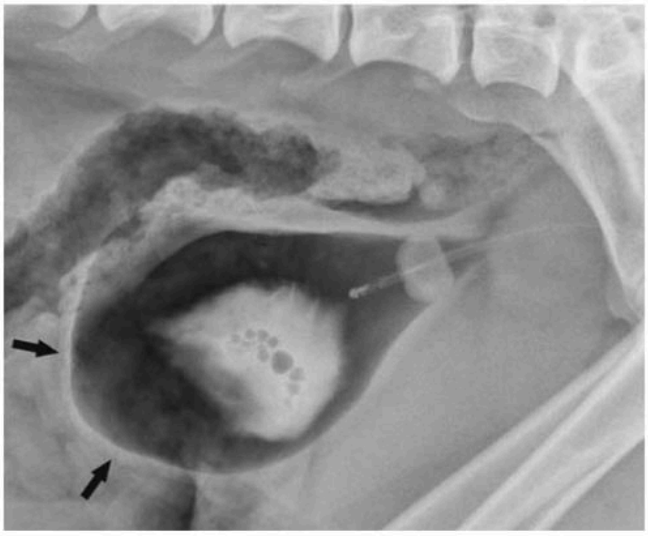


Fig. 42.16 Lateral radiograph of double-contrast cystogram. Mild diffuse urinary bladder wall thickening is present (*black arrows*). Multiple variably sized calculi appear as filling defects outlined by the contrast medium in the dependent portion of the urinary bladder.

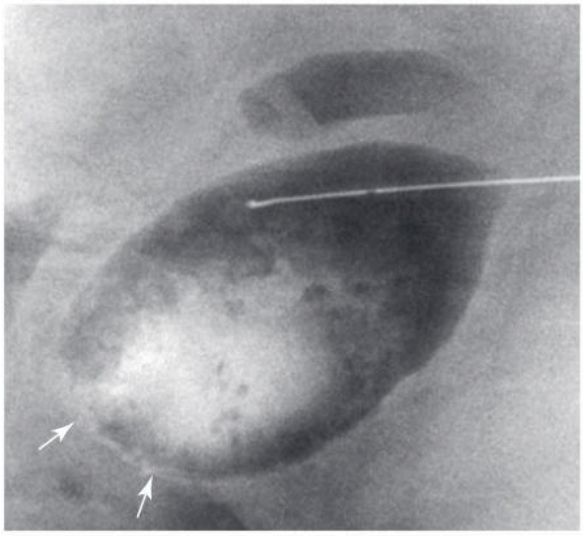


Fig. 42.17 Lateral radiograph of the urinary bladder during double-contrast cystography. Mild mucosal irregularity is present along the apex of the urinary bladder (*white arrows*) as a result of mild chronic cystitis.

proliferation and can be identified where contrast medium adheres to the mucosal surface.

Filling Defects

A urinary bladder filling defect results from anything occupying space within the urinary bladder lumen that displaces contrast medium. All filling defects appear radiolucent when surrounded with positive-contrast medium even though the opacity of the defect may not be inherently radiolucent. The size, shape, number, border contour, position within the lumen, and attachment to the urinary bladder wall help determine the nature of the filling defect (Table 42.5).

Filling defects may be *free* or *attached*. Common causes of free luminal filling defects are air bubbles, calculi, and blood clots[27] (Fig. 42.18, see eFig. 42.3). Abnormalities causing a free luminal filling defect are best demonstrated with double-contrast cystography and are located in the center of the urinary bladder on a recumbent lateral view. The concentration of the contrast medium and depth of the contrast puddle have an effect on visibility of cystic calculi.[28,29] Combining patient signalment and double-contrast cystographic findings can improve prediction of type of mineral calculus non-invasively.[30] Attached filling defects may be caused by neoplasia, inflammatory polyps, adherent calculi or blood clots, and ureteroceles.[31–33] Ureteroceles may communicate

Table • 42.5

Urinary Bladder Filling Defects.

LESION	SHAPE	ATTACHMENT	BORDER/CONTOUR	URINARY BLADDER WALL INFILTRATION (THICKENING)
Calculi	Round to slightly irregular	Free in lumen; center of contrast puddle	Indistinct	Variable; usually cranioventral if associated with cystitis
Sebaceous or mucous plug	Round or irregular	Free in lumen; center of contrast puddle	Smooth or irregular, distinct or indistinct	Variable; associated with cystitis
Polyp	Pedunculated or convex	Stalk or sessile	Smooth or irregular, often with ulceration	Variable; urinary bladder wall may be thick at attachment site
Epithelial neoplasia	Irregular or convex	Sessile	Irregular, often with ulceration	Urinary bladder wall often thick or infiltrated at base of attachment
Mesenchymal neoplasia	Convex	Sessile	Usually smooth	Originates within the urinary bladder wall
Blood clots	Irregular	Variable; may be free luminal	Irregular and indistinct	Thickened urinary bladder wall from primary disease process
Urinary bladder wall hematoma	Convex	Sessile	Smooth to slightly irregular	Originates within urinary bladder wall
Ureterocele	Convex to round	Sessile	Smooth	Originates within trigone region of the urinary bladder wall

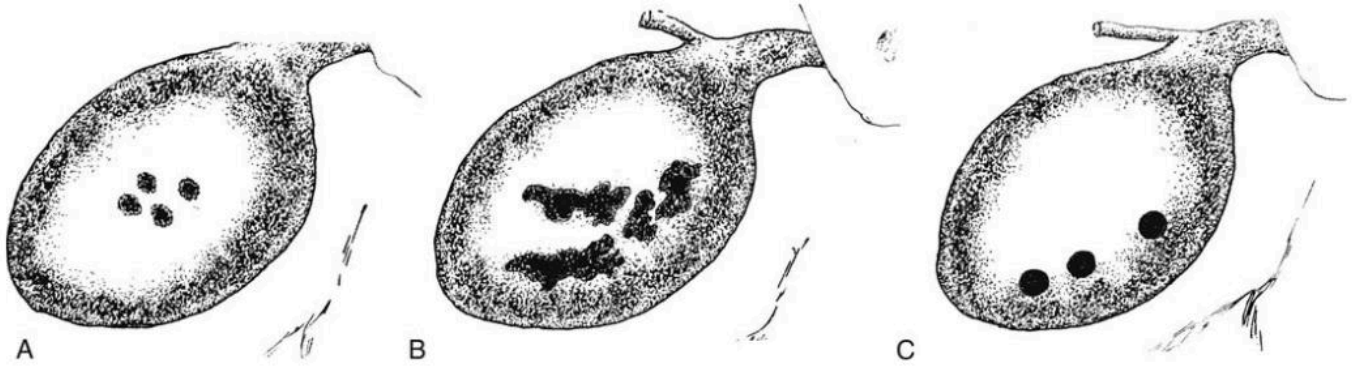


Fig. 42.18 Radiolucent luminal filling defects as might be seen in a double-contrast cystogram. **A,** Cystic calculi, in the center of the contrast puddle, are round with an indistinct border. **B,** Blood clots are irregularly shaped with irregular, indistinct borders; they may be located anywhere in the urinary bladder. **C,** Air bubbles are round with smooth, distinct borders; they are shown here at the periphery of the contrast puddle but are more often located centrally. (From Park RD. Radiology of the urinary bladder and urethra. In: O'Brien TR, ed. *Radiographic Diagnosis of Abdominal Disorders in the Dog and Cat.* Davis, CA: Covell Park Veterinary; 1981.)

partially with the urinary bladder and fill with positive-contrast medium and create what is known as the *cobra-head sign*, or they may not communicate and be a negative filling defect (see Fig. 42.19).[34] With double-contrast cystography, mural masses may be seen only when the x-ray beam is parallel to the interface between the mass and contrast medium.[35] Urinary bladder wall infiltration may be diagnosed as a thickened urinary bladder wall adjacent to the filling defect.[35] Often, a specific diagnosis of an attached filling defect cannot be made and histologic/cytologic evaluation is needed.

Contrast Leakage and Retention Patterns

Retrograde positive-contrast cystography is the best technique to assess leakage of urine from the urinary bladder. Urine leakage may occur into the urinary tract, adjacent visceral soft tissue structures, or the peritoneal cavity.

Vesicoureteral reflux can lead to contrast medium filling the ureters. Retention of urine contrast medium may occur in urachal anomalies (see Fig. 42.20), and traumatic urinary bladder diverticula (Fig. 42.21). Urachal anomalies include congenital or acquired diverticula, cysts, and persistent patent urachus or urachal ligament.[36–39] Congenital urachal anomalies are characterized by smooth contrast medium margins; they may be identified as an extension from the urinary bladder.

Contrast medium leakage from the urinary bladder to adjacent visceral structures may be seen with a congenital or acquired fistula. The organs most commonly involved are the rectum and the vagina. Such fistulas can usually be diagnosed dynamically with fluoroscopy or statically from a positive-contrast cystogram by noting contrast medium in the rectum or vagina simultaneously with or shortly after contrast medium is injected into the urinary bladder.[40]

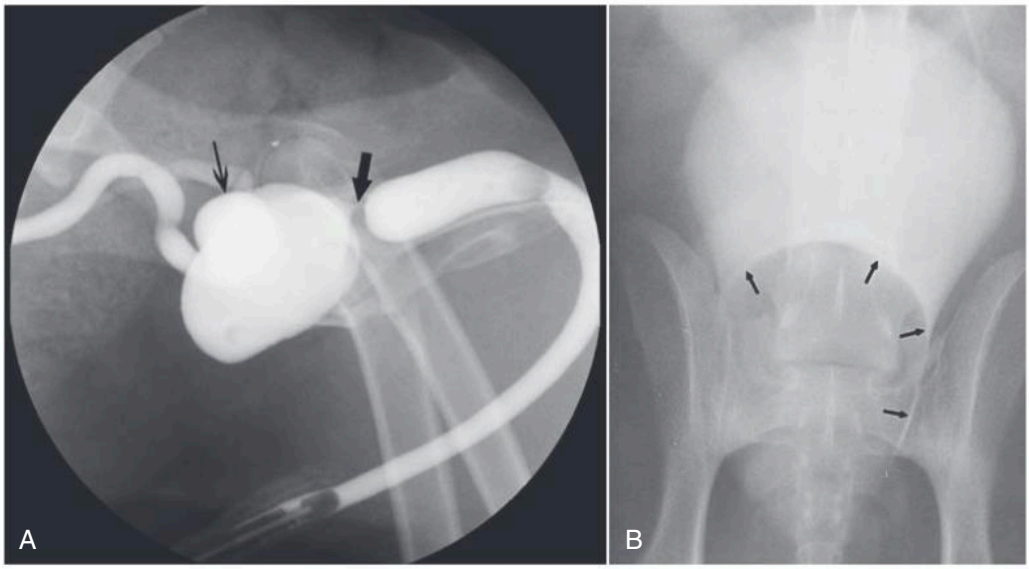


Fig. 42.19 **A,** Positive-contrast cystourethrogram. Lateral radiograph of urinary bladder and urethra. The round contrast medium–filled ureteral termination partially superimposed over the urinary bladder is a ureterocele (*thin black arrow*). Note the dilated ureter proximal to the ureterocele. A stricture of the prostatic urethra is also present (*thick black arrow*). **B,** Ventrodorsal radiograph of the urinary bladder filled with contrast medium during intravenous urography. The smooth luminal filling defect *(black arrows)* that projects into the urinary bladder neck is a ureterocele. In this patient the ureterocele is radiolucent because it does not contain contrast medium but is surrounded by contrast medium in the urinary bladder.

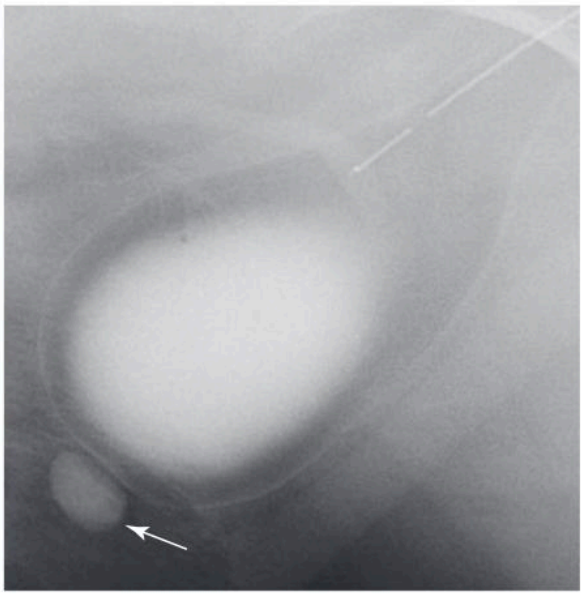


Fig. 42.20 Appearance of the cranioventral aspect of the urinary bladder during double-contrast cystography in a dog. A small oblong urachal diverticulum fills with contrast medium (*white arrow*). Contrast medium persisted in the diverticulum, evidence of urine retention that may predispose to a urinary tract infection.



Fig. 42.21 A traumatic urinary bladder diverticulum is present (*black arrows*). Immediately after trauma, traumatic diverticula must be differentiated from a urinary bladder contusion. Contusions usually heal within 48 hours, and the urinary bladder then distends symmetrically.

Contrast medium leakage into the peritoneal cavity and surrounding soft tissues has an irregular outline and usually occurs simultaneously with injection of contrast medium into the urinary bladder (Fig. 42.22, eFig. 42.5). With small urinary bladder neck tears, leakage of contrast medium may be slow with only a small volume appearing outside the urinary bladder.[5] In these instances, a second radiograph may be required 5 to 10 minutes after injection to identify delayed leakage from the urinary bladder into the peritoneal cavity.

Pitfalls with Cystographic Interpretation

Interpretation pitfalls seen commonly with contrast cystography are air bubble artifacts and pseudofilling defects. Three types of air bubble artifacts have been recognized: small air bubbles simulating calculi or other small luminal filling defects, a large air bubble simulating urinary bladder wall thickening, and multiple air bubbles creating a honeycomb appearance (Fig. 42.23). Air bubbles are radiolucent and have smooth, distinct borders.

Pseudofilling defects may be mistaken for urinary bladder neoplasia or other attached filling defects. These defects are



eFig. 42.5 Positive-contrast cystogram of a dog with bladder rupture after trauma. The bladder is small and contrast is leaking into the peritoneal cavity at the bladder apex. A round radiolucent filling defect in the bladder neck superimposed with the catheter represents the air-filled balloon of the Foley catheter.

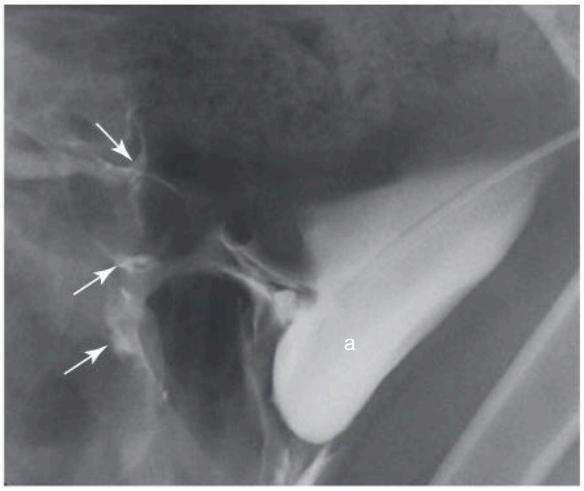


Fig. 42.22 Positive-contrast cystogram in a dog. Contrast medium fills the urinary bladder (*a*) but has also leaked into the peritoneal cavity (*white arrows*) from a dorsal urinary bladder wall tear.

created by inadequate urinary bladder distention combined with external pressure from adjacent abdominal structures. Pseudofilling defects have a smooth surface and taper on both borders; they can be obliterated with further urinary bladder distention (Fig. 42.24).

ULTRASONOGRAPHY

The fluid-filled urinary bladder is easily evaluated ultrasonographically. The superficial location of the urinary bladder enables high-resolution imaging, and urine provides high sonographic contrast, which results in good visibility of the urinary bladder wall and intraluminal abnormalities. Urolithiasis, neoplasia, cystitis, urachal, and vesicoureteral junction abnormalities can be identified by using ultrasonography.[41–43]

High-frequency transducers (7–15 MHz) are best for examination of the urinary bladder. A 5-MHz transducer may be necessary to penetrate to the far wall of a distended urinary bladder in large dogs. Linear and curved wide-aperture format transducers are particularly useful. Acoustic power and near gain should be decreased to suppress reverberation echoes generated between the transducer, the skin, and abdominal wall structures.

The ultrasonographic examination is best performed when the urinary bladder is moderately full. If a nearly empty urinary bladder is encountered, it should be reexamined when it is moderately distended after some hours of inside confinement, after administration of a diuretic, or after catheterization and sterile saline injection. The wall of a flaccid urinary bladder can be deviated inward by a distended colon, and the acoustic shadow artifacts generated by colonic contents can appear like the shadows generated by calculi.[44] A fully distended urinary bladder is also less desirable because subtle mural abnormalities may be more difficult to see. Normal urinary bladder wall thickness varies depending on the degree of urinary bladder distention and body weight, being 2.3 mm thick with minimal distention and 1.4 mm thick with moderate distention.[45] In normal adult cats, the mean urinary bladder wall thickness should not exceed 1.7 mm ± 0.6 mm.[46]

Urinary bladder ultrasonography can be performed with the patient in either dorsal or lateral recumbency. The urinary bladder should be evaluated in a transverse plane and orthogonally in either a sagittal or dorsal plane. Accurate assessment of urinary bladder wall thickness requires a perpendicular orientation of the ultrasound beam with the urinary bladder wall. Assessment of the cranial aspect of the urinary bladder wall is challenging because of the suboptimal beam alignment and the adjacent gas-filled bowel.[47] Side and grating lobe artifacts generated by the adjacent colon can give rise to an erroneous display of echogenic material in the urinary bladder lumen, and the curved urinary bladder wall can create additional echoes adjacent to the dorsal urinary bladder wall (Fig. 42.25).[48] Transducer rotation of 90 degrees over such suspicious areas is often helpful to enable recognition of the proximity of the colon and determination of the nature of the artifact. Free intraluminal abnormalities such as calculi, sediment, and blood clots gravitate to the most dependent aspect of the urinary bladder. In lateral recumbency, careful examination of the most dependent area of the urinary bladder is required so that small calculi are not overlooked. Additional imaging after the animal has been positioned in the opposite lateral recumbent or standing position allows detection of sediment swirling or gravitation of free intraluminal objects to a dependent position within the urinary bladder.

The normal urinary bladder is ovoid in shape with a slight elongation caudally at the neck. The ureters and urethra are not typically visible unless they become distended with urine. With high-resolution transducers, three distinct layers of the urinary bladder wall can be seen. The mucosa is a thin hyperechoic surface outlined against the urine, the middle muscle layer is hypoechoic, and the outer serosal layer is hyperechoic.[46] The cranioventral aspect of the wall may be slightly thinner than in other regions. Typically, normal urine is anechoic. However, suspended clumped hyperechoic foci can be identified in the urine of clinically normal cats with urine lipid.[49] The turbulence created by discharge of urine through the ureteral openings may generate transient echo jets in the urinary bladder lumen adjacent to the trigone.[50]

Intraluminal Changes

Urinary calculi, cellular and crystalline debris, gas, hemorrhage, and blood clots are detected readily by ultrasonography (Fig. 42.26A). Calculi and blood clots gravitate dependently whereas gas bubbles rise. The location of cellular and crystalline debris and fresh hemorrhage is more variable. Severe acute hemorrhage can fill the urinary bladder and give rise to a lacy hyperechoic pattern, which may change little with ballottement or animal repositioning (see Fig. 42.26B). A similar appearance can be observed with severe proteinuria and fat droplets.[51] Crystalline and cellular sediments generate a variably echogenic pattern in more dependent urine. In cats, the crystalline deposits may become thick enough to form a hyperechoic layer confluent with the urinary bladder wall that creates acoustic shadowing. Ballottement or changing patient position can differentiate the swirling sediment from calculi.

Calculi

The urine/calculus interface is intensely hyperechoic and usually appears convex. Multiple calculi often aggregate together and give rise to an irregular, somewhat continuous surface, which makes distinguishing and measuring individual calculi difficult. Distinct acoustic shadows may be observed deep to calculi (Fig. 42.27). Shadowing is related to size (height) of the calculus and transducer frequency, with increasing height of the calculus and increasing transducer frequency more likely to produce acoustic shadows.[52] The application of color Doppler to distinguish calculi based on the twinkling artifact occurring deep to the calculus can be used to discriminate mineralized from nonmineralized structures.[53] Smaller calculi may not generate the characteristic shadows if the focal zone is not optimized at the depth of the calculi. Echogenicity and acoustic shadow generation are independent of chemical composition, so radiopaque and nonradiopaque calculi can be detected by

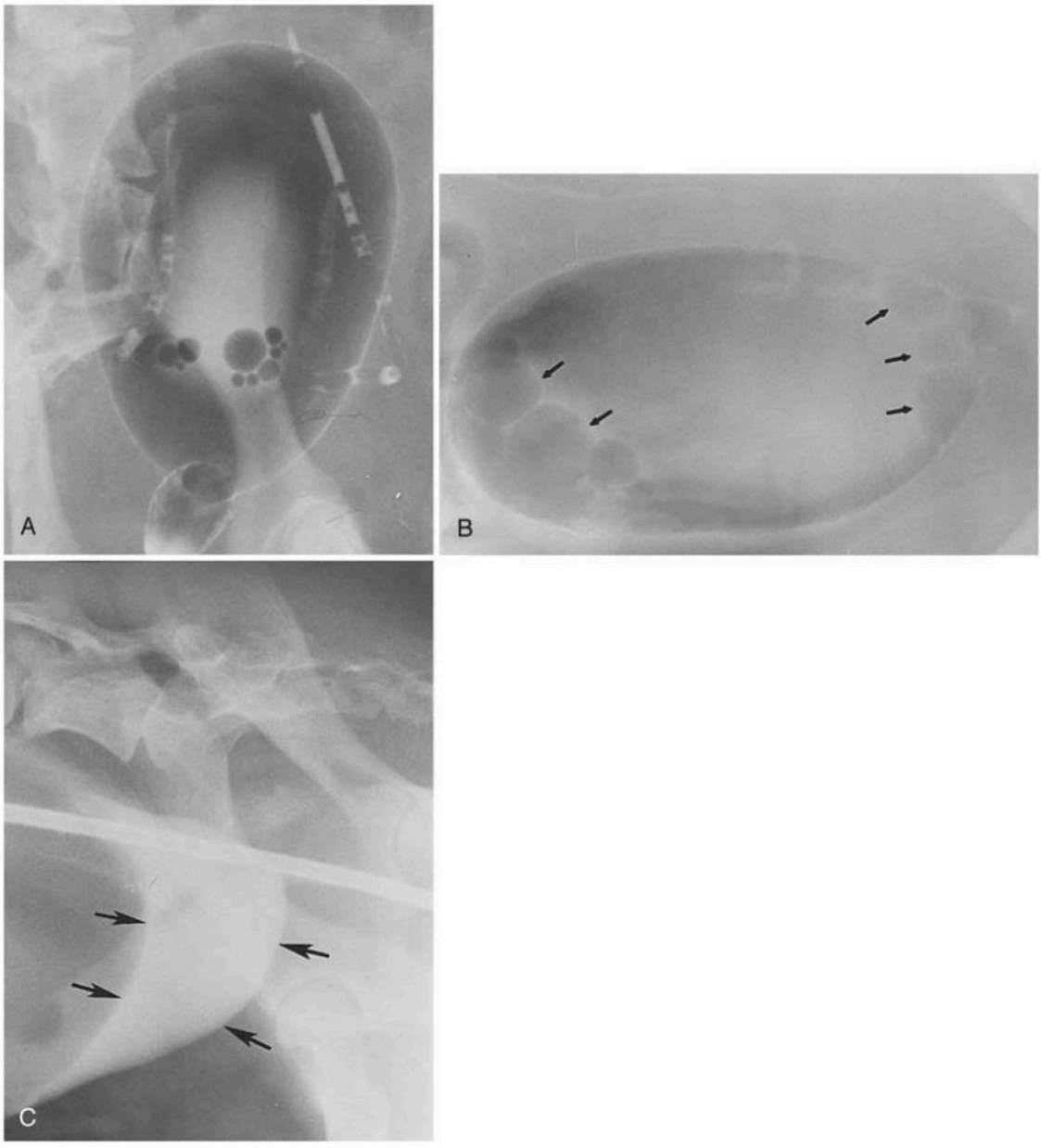


Fig. 42.23 Air bubble artifacts. **A,** Small air bubbles that cause free luminal filling defects in the urinary bladder during double-contrast cystography. Bubbles are also present in both ureters. **B,** A honeycomb appearance (*black arrows*) created by several adjacent air bubbles. **C,** A large air bubble in a mostly fluid-filled urinary bladder may produce the appearance of a thick urinary bladder wall. Here, the pseudothick wall (*black arrows*) is created by the interface between positive-contrast medium and gas. In this dog, the region between the *arrows* is more opaque than normal soft tissue because of the presence of contrast medium, and therefore this would not be confused with urinary bladder wall thickening.

sonography. Ballottement usually does not cause calculi to move, but placing the animal in a standing position allows detection of the relocated calculi into the cranioventral aspect of the urinary bladder. This action helps differentiate calculi from an adjacent colonic acoustic shadow and dystrophic mineralization in the urinary bladder wall.

Gas bubbles introduced accidentally by urinary bladder catheterization or cystocentesis are hyperechoic and can generate reverberation artifacts. Differentiation from calculi is easy because the bubble floats on top of the urine.

Blood Clots

Blood clots tend to be associated with the clinical observation of severe hematuria. Relative to normal urine, a blood clot commonly appears as a hyperechoic, nonshadowing, often layered, mobile mass.[54] Sometimes the clot may be attached to the wall, covering, or adjacent to a traumatic injury or a neoplastic mass.

Foreign Bodies

Urinary bladder foreign bodies, such as grass awns, have been reported and appear as linear to V-shaped hyperechoic structures with or without distal acoustic shadows.[55]

Mural Changes

Ultrasonography is especially useful for detecting changes from chronic cystitis and neoplasia. Contrast radiographic techniques are superior to sonography in diagnosing congenital

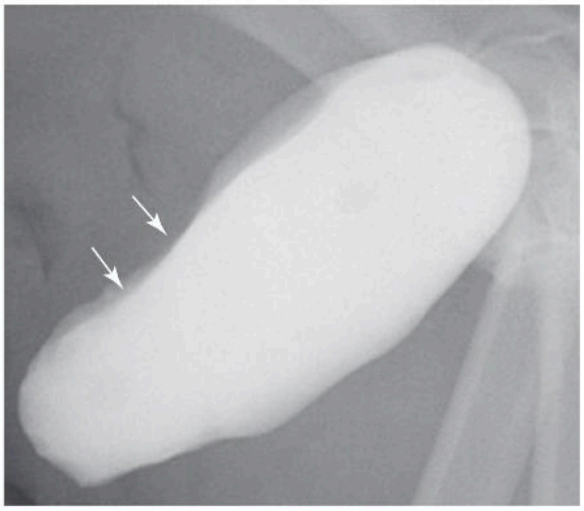


Fig. 42.24 Lateral radiograph of a positive-contrast cystogram. Pseudofilling defects or a false impression of irregularity of the urinary bladder wall (*white arrows*) can be created by pressure from adjacent abdominal structures on a partially distended urinary bladder.

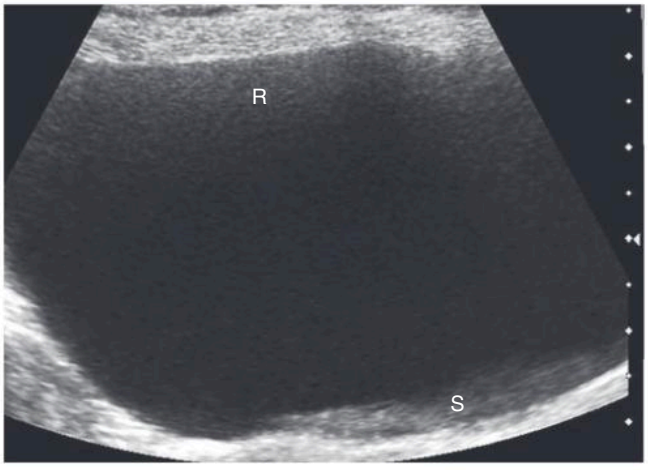


Fig. 42.25 Sonographic artifacts. Spurious echoes (*R*) are present in the ventral aspect of the lumen of the urinary bladder from reverberation artifact. Slice thickness and/or side (grating) lobe artifact (*S*) is present in the dorsal aspect of the urinary bladder, creating pseudoechogenic debris in the urine.

abnormalities of the urachus and ureters as well as urinary bladder rupture. However, infusion of microbubbled saline into the urinary bladder during a sonographic examination has been effective for diagnosing urine leakage in some patients.[56]

Cystitis

Chronic cystitis results in focal or diffuse thickening of the urinary bladder wall and is readily detected by sonography. The urinary bladder wall becomes abnormally hypoechoic, and the normal layering becomes less parallel. The urinary bladder wall measures abnormally thick (see Fig. 42.27), and hyperechoic cellular debris frequently accumulates in the urinary bladder lumen.[57] A normal sonographic appearance of the urinary bladder does not rule out mild or acute cystitis or idiopathic lower urinary tract disease in cats. Small polypoid mucosal masses or abscesses are also occasionally observed with chronic cystitis.[58] Polypoid cystitis is uncommon in dogs and can vary in sonographic appearance ranging from pedunculated, ovoid, or nodular urinary bladder wall changes (Fig. 42.28) and can be difficult to differentiate from neoplastic proliferations.[59] Polypoid cystitis is often located in the

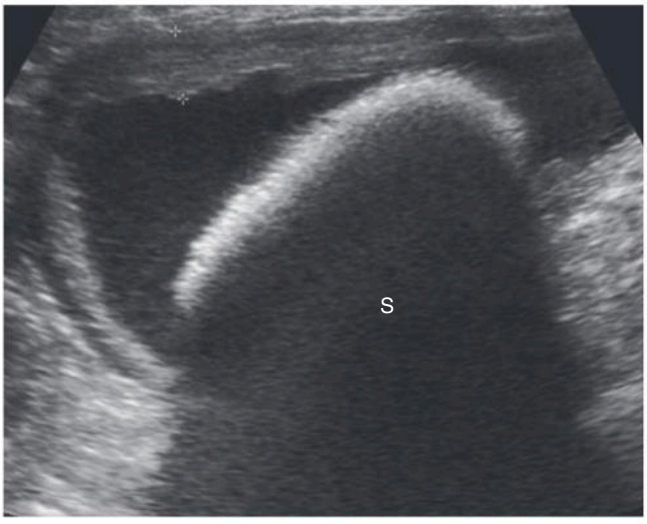


Fig. 42.27 Sagittal ultrasound image of the urinary bladder. A solitary, large calculus creates characteristic acoustic shadows (*S*) and irregular thickening of the cranioventral urinary bladder wall (calipers in image) secondary to cystitis.

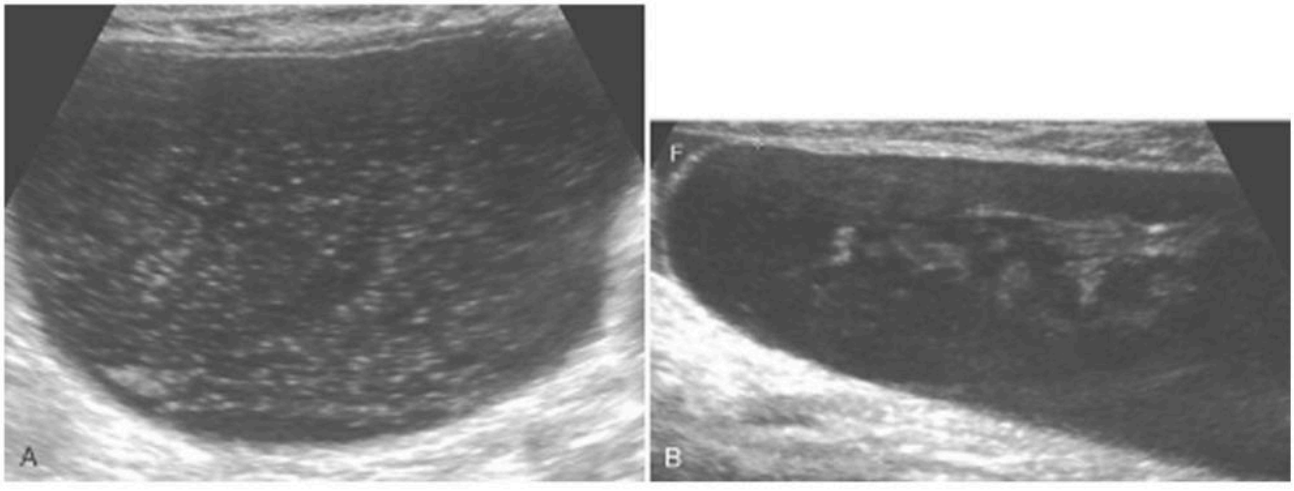


Fig. 42.26 **A,** Sagittal ultrasound image of the urinary bladder. Intraluminal, hyperechoic foci representing crystals (crystalluria) are present in the dependent portion of urinary bladder. **B,** Sagittal ultrasound image of the urinary bladder. Intraluminal, hyperechoic, lacy material is acute hemorrhage located in the mid and ventral aspects of the urinary bladder. A small amount of echogenic fluid representing free abdominal hemorrhage (*F*) is present adjacent to the cranioventral aspect of the urinary bladder.

cranioventral and craniodorsal portions of the urinary bladder.[59,60] Follow-up ultrasonographic evaluations should be made after treatment of polypoid cystitis to reevaluate the masses. Biopsy is needed for definitive diagnosis. Muscular hypertrophy resulting from chronic partial lower urinary tract obstruction can also cause urinary bladder wall thickening and may simulate the ultrasonographic appearance of cystitis. Encrusted cystitis is caused by *Corynebacterium urealyticum* infection and is characterized by a thickened urinary bladder wall with mineralized mucosal plaques.[61]

Emphysematous cystitis creates a confusing sonographic appearance because the gas artifacts can alter the normal appearance of the urinary bladder (Fig. 42.29). Linear hyperechogenicities with or without reverberation artifact, trapped in the urinary bladder wall and free in the urinary bladder lumen, can be seen.[16]

Associated Conditions

Urethral obstruction commonly occurs in cats. Echogenic urine sediment, urinary bladder wall thickening, pericystic effusion, hyperechoic pericystic fat, and increased urinary bladder echoes may be present. Upper urinary tract sonographic changes can be seen as well.[62]

A rare condition called uterus masculinus can be associated with chronic cystitis and an enlarged prostate gland in male dogs.[63] The sonographic changes describing this condition include identification of hypoechoic tubular or cylindrical structures originating from the craniodorsal aspect of the prostate gland, adjacent to the urinary bladder.[63]

Mural Hemorrhage

Mural hemorrhage can occur in patients with trauma or a bleeding disorder. This is associated with diffuse thickening of the urinary bladder wall that can resolve quickly after treatment is initiated.[64]

Neoplasia

Several kinds of urinary bladder tumors have been documented, with urothelial carcinoma (also referred to as transitional cell carcinoma) being the most common.[42] Urothelial carcinoma of the urinary bladder is characterized most frequently by an irregularly shaped, broad-based, complex to hypoechoic mass protruding into the urinary bladder lumen.[42] This tumor has similar features between dogs and cats; however, location can differ between species with it typically being located in the midbody in cats compared to trigonal locations in dogs.[65] Single or multiple masses may be present (Fig. 42.30). The echo pattern can vary if internal fibrosis, mineralization, and necrosis have developed. Adjacent blood clots can occur and can

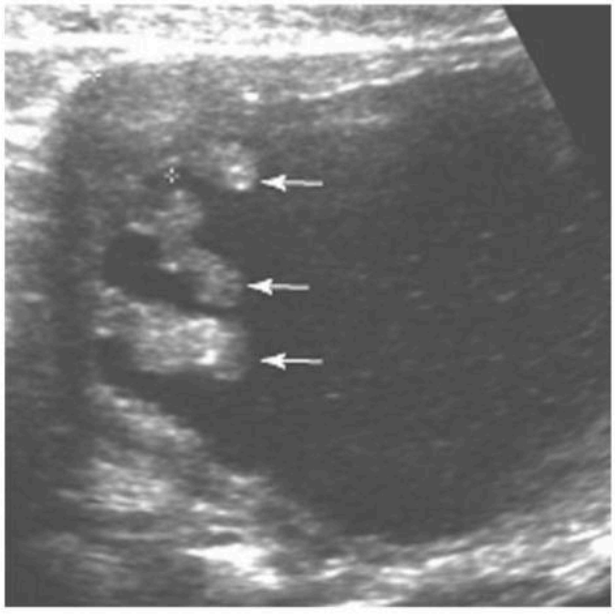


Fig. 42.28 Sagittal ultrasound image of the urinary bladder. There is focal urinary bladder wall thickening (calipers in image) with associated pedunculated, hyperechoic polyps (*white arrows*) secondary to polypoid cystitis. Echogenic intraluminal debris is present within the urine.

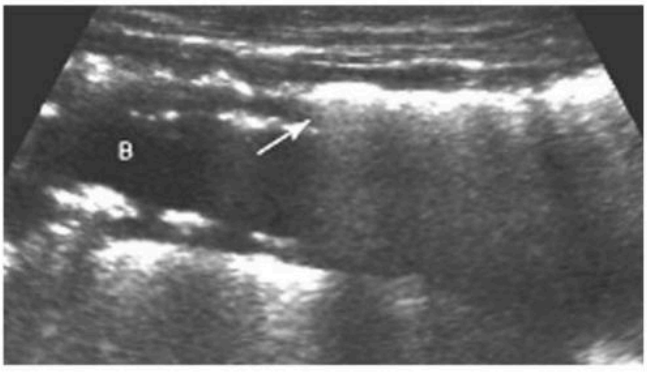


Fig. 42.29 Sagittal ultrasound image of the urinary bladder. Note the linear hyperechogenicities with and without reverberation (*white arrow*) artifact, trapped within the urinary bladder wall secondary to emphysematous cystitis. Anechoic urine is within the urinary bladder (*B*).

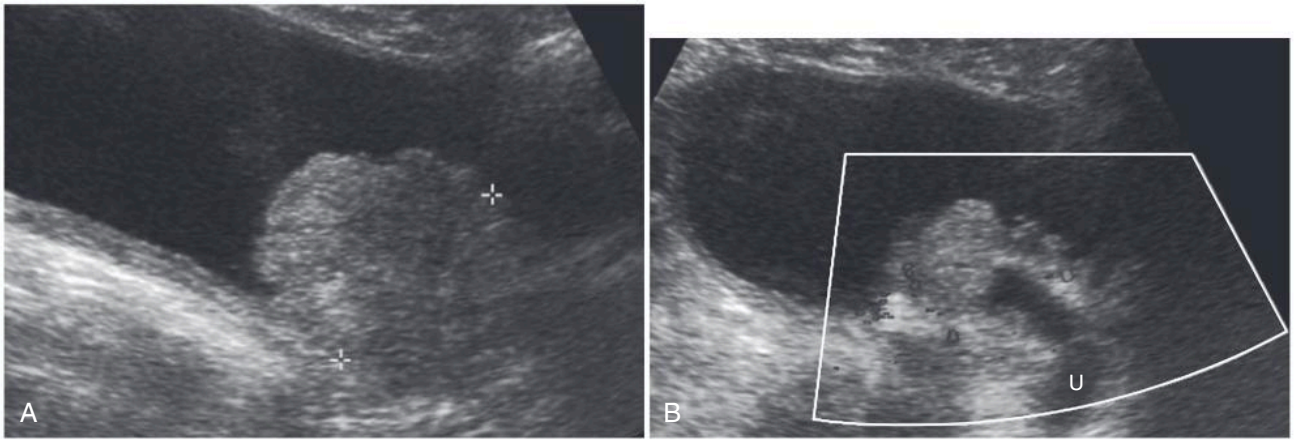


Fig. 42.30 **A,** Sagittal ultrasound image of the urinary bladder. There is a hyperechoic, broad-based mass in the urinary bladder neck from transitional cell carcinoma. **B,** This mass obstructed the adjacent ureter, causing hydroureter (*U*). Note the color Doppler box over the mass and ureter confirming no blood flow within the ureter.

contribute falsely to the size and echogenic texture of the mass. Contrast-enhanced ultrasound has been utilized to characterize transitional cell carcinoma. Features include avid enhancement of tumor tissue with a heterogeneous or homogeneous pattern with a loss of planes between the tumor and the muscular layer.[66] Regional lymph nodes can be assessed for changes in size, echogenicity, and shape which may be suspicious for metastasis. Several sonographic changes associated with canine urothelial carcinoma have been linked to a poorer prognosis; these include evidence of wall involvement by the tumor, trigone location, and heterogeneous echotexture.[42] Volume measurements of transitional cell carcinoma have been used to assess treatment response. Two-dimensional and three-dimensional ultrasound has been compared to computed tomography (CT) in assessing tumor volume in dogs with transitional cell carcinoma.[67] In this study, three-dimensional ultrasound was more accurate in assessing urinary bladder tumor volume than two-dimensional ultrasound when compared to CT.[67] A different study comparing volume measurements between ultrasound and CT utilizing different measuring techniques found that tumor volume measurements varied based on method and modality used.[68]

Smooth muscle neoplasia, such as leiomyoma or leiomyosarcoma, can appear as a single, round, well-defined intraluminal mass.[69] Urinary bladder fibrosarcomas and rhabdomyosarcomas are often located in the neck of the urinary bladder and are typically found in young dogs (eFig. 42.6).[70,71] Lymphoma has a similar sonographic appearance to other urinary bladder tumors but will usually be accompanied by lesions in other abdominal organs and lymph nodes[72] (eFig. 42.7).[71] Smooth isoechoic apex nodules have been described in Scottish terriers and were not associated with neoplasia.[73] Some highly aggressive carcinomas and mesenchymal tumors can spread through the urinary bladder wall. If a small intraluminal mass occurs, the urinary bladder can take on the appearance of severe cystitis. Unfortunately, the sonographic appearance of polypoid cystitis, adherent blood clots, and mural hematomas is similar to that of urinary bladder neoplasia. The observation of ureter dilation adjacent to the urinary bladder wall mass (see Fig. 42.30) and focal medial iliac lymphadenopathy tends to support the diagnosis of neoplasia. An aspirate, biopsy, or both are necessary to confirm the presence of urinary bladder neoplasia. The information gained from percutaneous aspiration of a urinary bladder mass must be weighed against the possibility of seeding the needle tract with tumor cells.[74]

Ureterovesicular Junction

The ureterovesicular junctions are small convex structures on the dorsal part of the urinary bladder.[50,76] However, they may not be identified if the urinary bladder is caudally located. Identifying a ureteral jet in the urinary bladder confirms a normal ureterovesicular junction.[50,76] Orthotopic and ectopic ureteroceles can be identified with ultrasound.[41,43] Ureteroceles are smooth, thin-walled cystic structures within the urinary bladder lumen, urinary bladder wall, or proximal urethra.[75,76] Ureteroceles have been described sonographically as a cyst within a cyst (Fig. 42.31).[77]

Computed Tomography and Magnetic Resonance Imaging of the Urinary Bladder

CT imaging is useful to diagnose abnormalities of the urinary bladder wall and ureterovesicular junction.[78] CT-excretory urography has also been used to definitively diagnose orthotopic ureteroceles in a dog.[79] CT imaging has been used to diagnose urinary bladder torsion noting the classic "whirl sign" often noted as a feature of torsion in other abdominal organs.[80]

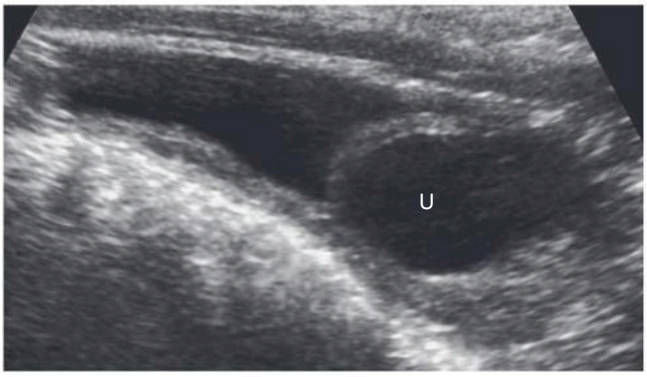


Fig. 42.31 Sagittal ultrasound image of the urinary bladder. Note the "cyst-within-a-cyst" appearance to the ureterocele (*U*) with the urinary bladder neck.

Advanced imaging of urinary bladder neoplasia in dogs and cats is more limited due to cost and decreased availability compared to ultrasound. Both modalities are excellent at evaluation of the primary lesion, ureters, adjacent lymph nodes, and other organs[81] (Fig. 42.32). Urothelial carcinoma of the urinary bladder can be evaluated with CT to determine extent of tumor size for pretreatment staging and to assess tumor response to treatment via volumetric comparison measurements (Fig. 42.33).[68,82]

URETHRA

Anatomy

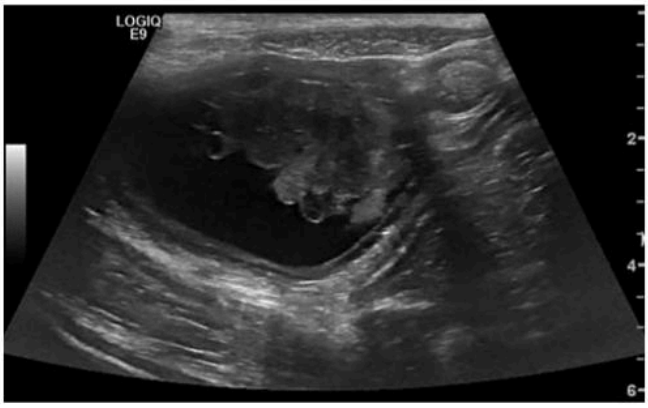
The male urethra comprises three major areas: the prostatic urethra, membranous urethra, and penile urethra (Fig. 42.34).[83] Combined, the prostatic and membranous portions make up the pelvic part of the urethra.[84] The prostatic urethra is surrounded completely by the prostate gland in the dog, whereas only dorsolaterally in the cat.[85] The membranous urethra is enveloped by cavernous tissue and the urethralis muscle.[85] The penile urethra extends from the ischial arch to the tip of the penis. This part of the urethra is also known as the cavernous urethra because the majority of it is encased by erectile tissues of the penis.[84] The most distal part of the penile urethra is inserted in and protected by the ventral urethral groove of the os penis in the dog. The arrangement of urethral muscle and surrounding spongy tissues confers a diffuse sphincter mechanism to the urethra in male dogs.

The female urethra is shorter and wider than in males and entirely pelvic in location. The external urethral orifice lies caudal to the vestibulovaginal junction, where a muscular urethral sphincter is present.[84]

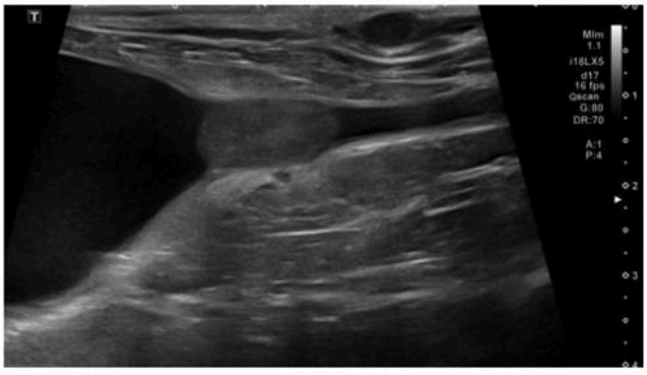
In the cat, the urinary bladder is typically intra-abdominal in position, and a relatively long prepelvic part of the urethra extends between the neck of the urinary bladder and the pelvic urethra.[85]

RADIOGRAPHY AND URETHROGRAPHY

Radiography of the urethra must include orthogonal caudal abdominal and/or pelvic images to ensure that the urethra is fully included in the field of view. In male dogs, lateral pelvic radiographs with the pelvic limbs both hip-extended (pulled caudally) and hip-flexed (pulled cranially) are also recommended to avoid missing lesions of the penile urethra caused by superimposition of the pelvic limbs. In a normal dog, the



eFig. 42.6 Sagittal plane ultrasound image of the bladder of a young dog with botryoid rhabdomyosarcoma of the urinary bladder. A heterogeneous, irregularly margined mass protrudes into the bladder lumen at the trigone. Several hypoechoic rounded lesions are seen along the surface of the mass which has given this tumor its name "botryoid" or "grape-like."



eFig. 42.7 Sagittal plane ultrasound image of the bladder of a cat with a mass in the bladder trigone and proximal urethra. Lymphoma was confirmed cytologically.



Fig. 42.32 **A,** Computed tomographic post−intravenous contrast of the urinary bladder. Note the irregularly contrast-enhancing thickened urinary bladder wall from infiltrative tumor (*white arrows*). The gas and oval hyperattenuating structure within the urinary bladder lumen is the inflated Foley bulb catheter (*white arrowhead*). **B,** Same study at level of ureterovesicular junction. Note the hydroureter (*U*) secondary to obstruction from the plaque-like mass.

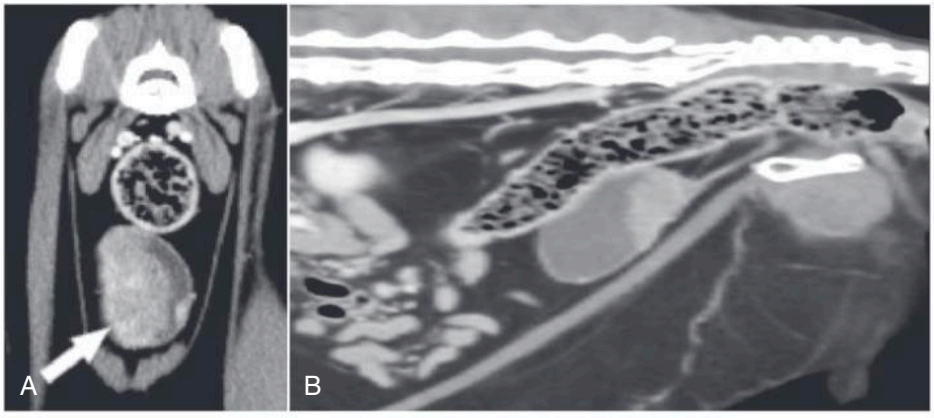


Fig. 42.33 **A,** Computed tomographic post−intravenous contrast of the urinary bladder for pretreatment radiation planning. In this transverse image there is a large contrast-enhancing mass arising from the right aspect of the urinary bladder trigone (*white arrow*). **B,** Reformatted sagittal plane image of the urinary bladder in which the contrast-enhancing mass at the trigone can be seen.

urethra is not visible on radiographs. Because of the more cranial position of the urinary bladder in cats, the prepelvic urethra may be visible if there is adequate surrounding fat to provide contrast.

Retrograde urethrography is a special radiographic technique to examine the urethra using positive-contrast medium. Only water-soluble, iodinated contrast medium should be used. The contrast medium can be diluted with sterile saline to a final concentration of approximately 150 mg iodine [I]/mL.[83,86] Patients generally require sedation, and evacuation of the colon and rectum through defecation or cleansing enemas is recommended to prevent superimposition of feces on the urethra. A fully distended urinary bladder provides counterpressure to contrast medium injection to allow maximal distention of the urethra.[87] Often cystography is performed first, and distention of the bladder with contrast medium should be maintained for urethrography. If necessary, sterile saline can be infused into an inadequately distended bladder. In addition to lateral and ventrodorsal projections, right ventral-left dorsal and left ventral-right dorsal oblique views should be included because the standard ventrodorsal projection may be less informative owing to superimposition of the pelvic and penile urethra.

In male dogs and cats, the procedure is performed by inserting a catheter into the distal penile urethra. A balloon-tipped (Foley) catheter is preferred in dogs, although a red rubber catheter may also be used.[88,86] The bulb of the Foley catheter is carefully inflated to a pressure that will not damage the urethra and left inflated no more than 15 minutes because excessive and prolonged pressure will damage the urethra.[89] In male cats, a red rubber or Tomcat catheter may be used

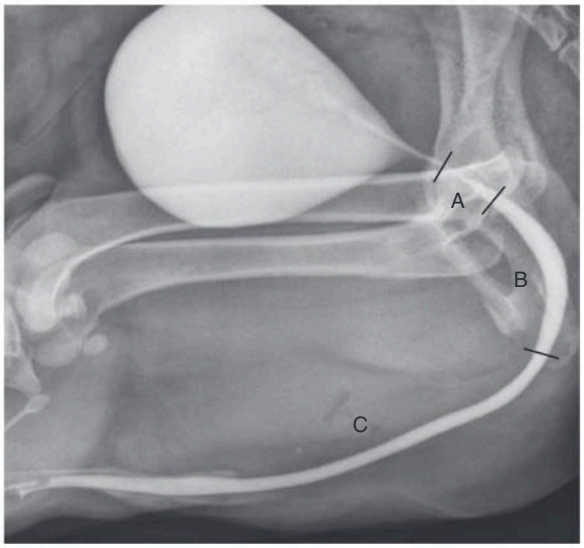


Fig. 42.34 Retrograde urethrography in a normal male dog. A Foley catheter is present in the distal penile urethra, and iodinated contrast medium was injected. The urethra comprises **(A)** the prostatic urethra, **(B)** the membranous urethra, and **(C)** the penile urethra. The normal urethra is smooth and distinctly margined with normal variation in diameter seen in the prostatic and membranous urethra.

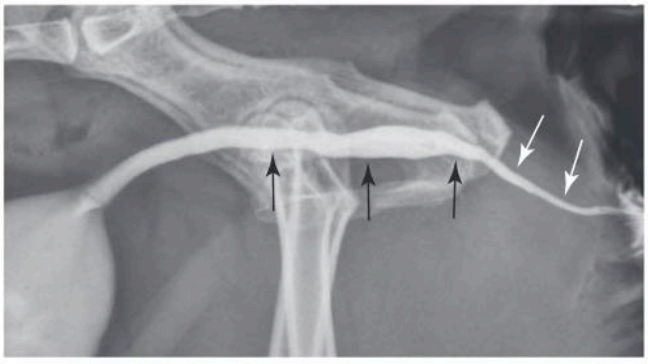


Fig. 42.35 Retrograde urethrography in a normal male cat. A Tomcat catheter is present in the distal penile urethra, and iodinated contrast medium is injected. The pelvic urethra (*black arrows*) is wide and smoothly margined. The penile urethra (*white arrows*) has a smaller diameter and does not distend as much.

(Fig. 42.35). Depending on patient size, 5 to 20 mL of contrast medium is injected and radiographs acquired during the delivery of the final 1 to 2 mL of the injection.[88] The normal urethra should be smoothly margined along its entire length. The prostatic urethra may be wider than the membranous urethra, although each can be variable in diameter depending on the degree of distention.[90] The penile urethra has a generally uniform diameter in dogs; in cats, it is relatively narrow.[91] Luminal narrowing with tapered margins may be seen normally at the ischial arch in dogs.[88]

Retrograde urethrography is challenging in female dogs and female cats because of the relatively shorter urethra. A Foley catheter is inserted into the distal urethra and inflated gently. Five to 10 mL of contrast medium is injected to distend the urethra and radiographs made at the end of injection (Fig. 42.36).[88] Vaginocystourethrography is an alternate

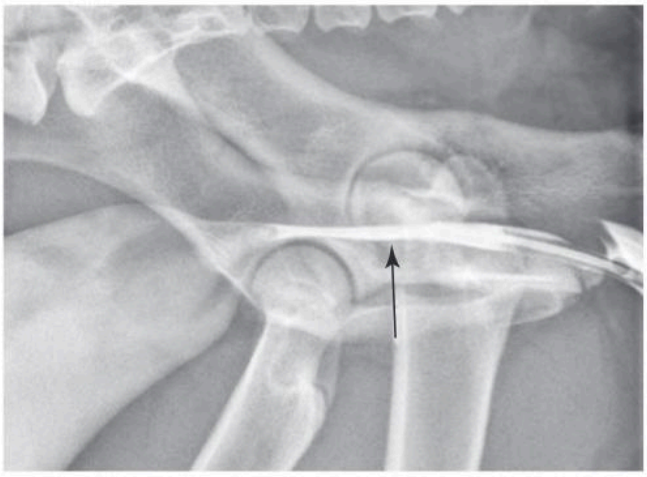


Fig. 42.36 Retrograde urethrography in a normal female dog. A Foley catheter is inserted 1 cm cranial to the external urethral sphincter and iodinated contrast medium is injected. The urethra (*black arrow*) has a smooth and distinct mucosal margin.

technique for evaluation of the female urethra and may be performed in dogs and cats (Fig. 42.37) (Video 42.1). The procedure is described in detail in Chapter 44. The normal urethra should be smoothly margined, and longitudinal striations attributable to mucosal folding may be seen depending on the degree of distention.[88]

The most significant potential complications of urethrography are iatrogenic rupture and urinary tract infection. These and other complications are uncommon when the procedure is performed correctly.[89]

ULTRASONOGRAPHY

Ultrasound examination of the urethra is generally limited to the most cranial portion of the pelvic urethra as interrogated from a ventral abdominal window.[91] Full distention of the urinary bladder promotes a more cranial position within the abdomen to allow examination of a greater length of pelvic urethra. In some patients, limited evaluation of the caudal aspect of the pelvic urethra can be performed using a sagittal perineal window. In males, the penile urethra can be traced along the penis best by using a high-frequency, linear array transducer with or without a standoff pad. Ultrasound is a complement to urethrography with the advantage of not requiring patient sedation.

The normal urethra is a smoothly margined, thin-walled, tubular structure of uniform diameter traced from the neck of the urinary bladder. Total urethral thickness is approximately 3 mm and is slightly greater in male dogs than in females.[92] The layers of the urethra usually cannot be resolved, and the normal lumen is not distended (Fig. 42.38).

Computed Tomography and CT Urethrography

CT can be used to evaluate the urethra and surrounding structures. Unlike ultrasonography, CT imaging can evaluate the portion of the urethra passing through the pelvis. The method for CT urethrography has been established in male and female dogs.[93,94] Qualitative and quantitative assessments of the urethra can be made. Urethral size differences have been noted between empty and distended urinary bladders in both male and female dogs.[93,94] Female dogs can have a normally narrowed urethra due to flexure related to an intrapelvic bladder

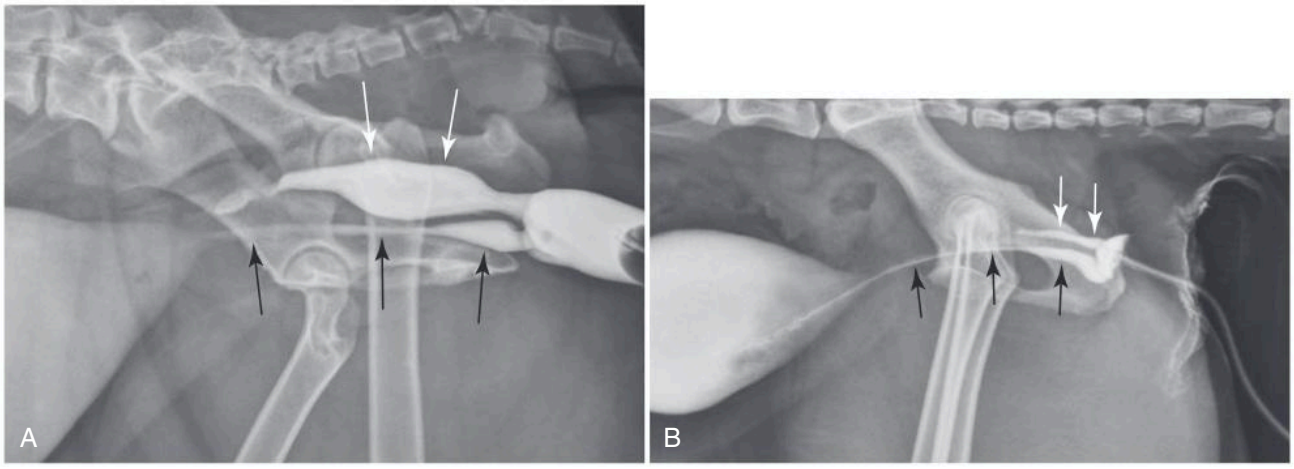


Fig. 42.37 Vaginocystourethrography in **(A)** a normal female dog and **(B)** a normal female cat. An insufflated Foley catheter is in the vestibule. As contrast medium is injected, the more cranial aspect of the vagina (*white arrows*) fills, followed by filling of the urethra (*black arrows*). Smooth, distinct mucosal margins of the urethra are seen.

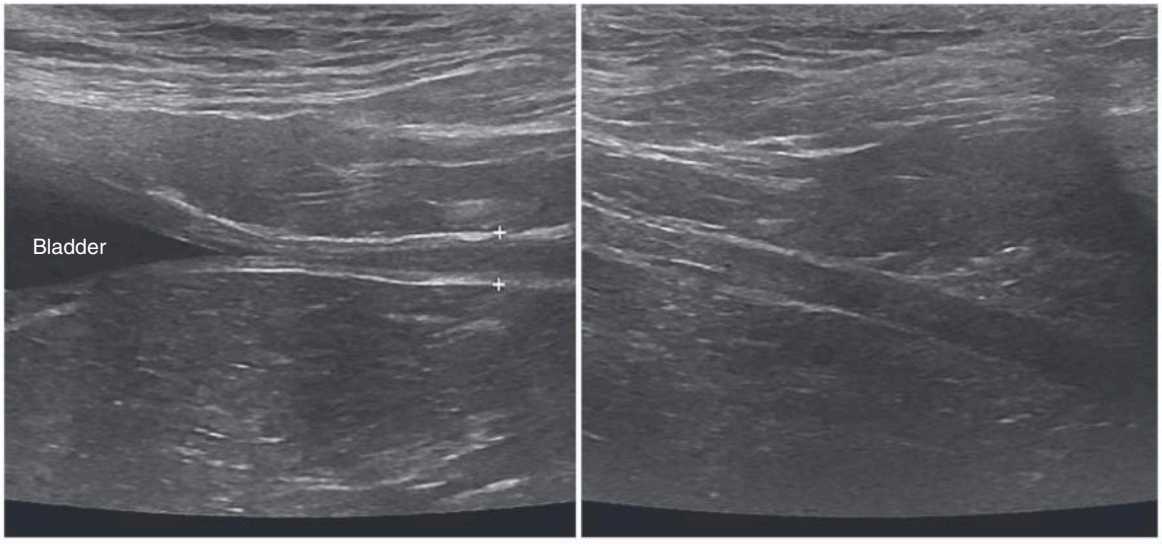


Fig. 42.38 Ultrasound image of the urethra in a normal female dog, sagittal views. The urethra (*white calipers*) is traced from the urinary bladder neck caudally in the image on the left. The more caudal aspect of the urethra is seen in the right image and is a uniform tubular structure. Visualization of the urethra becomes more difficult caudally because of the pubic bone.

location.[94] Advantages of CT urethrography over conventional radiography include lack of superimposition of pelvis and other structures and good visualization of the entire urethra.

DISEASES OF THE URETHRA

Urethral Calculi

Radiopaque urethral calculi may be seen on survey radiographs. In male dogs, calculi commonly occur at regions of luminal narrowing or restriction: the ischial arch and base of the os penis. In male cats with urethral obstruction secondary to sandy mineral calculi, a mineral plug may be seen in the penile urethra (Fig. 42.39). Because the urethra is not visible on survey radiographs, urethrography is required to confirm urethral calculi. Calculi appear as persistent, large focal or multifocal filling defects that distend the lumen of the urethra (Fig. 42.40). They are typically irregularly shaped and indistinctly margined. Air bubbles introduced into the urethra during contrast medium injection can generally be distinguished from calculi by their smoothly rounded shape, which does not distend the urethra, and inconsistent presence with subsequent injections of contrast medium (Fig. 42.41). Blood clots may be similar in appearance to calculi but may also be present inconsistently.[95,96]

On ultrasound, urethral calculi appear as focal or multifocal hyperechoic and intensely distally shadowing foci within the lumen, which may be distended proximal to the obstruction (Video 42.2) The associated urethral wall may be increased in thickness.[43,91]

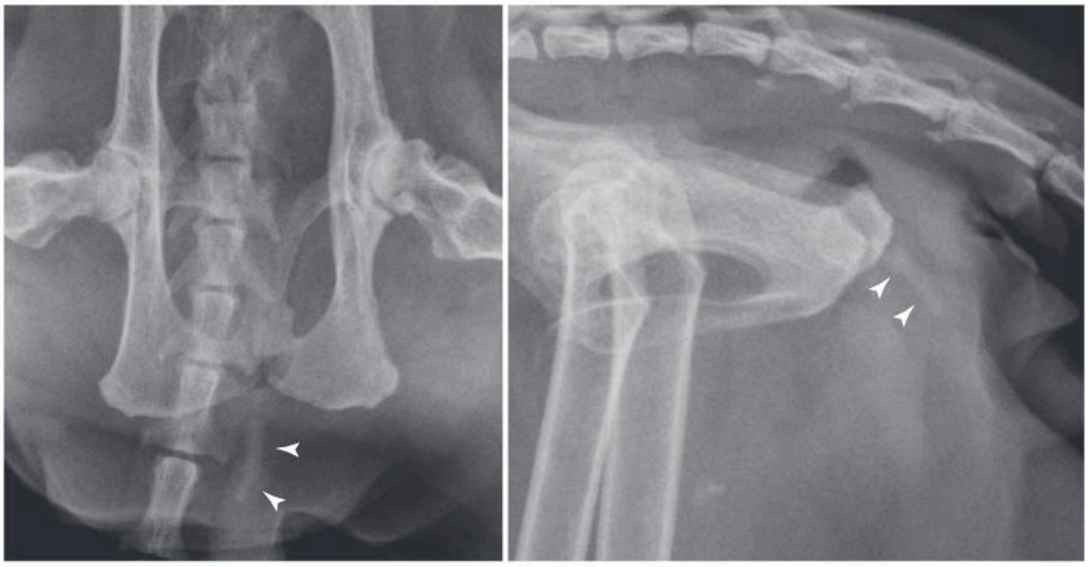


Fig. 42.39 Survey radiographs of a male cat with urinary obstruction. A faint, cone-shaped mineral opacity is seen in the region of the penile urethra (*white arrowheads*), consistent with urethral obstruction by sandy mineral calculi. (Courtesy Wm. Tod Drost, DVM, Ohio State University, Columbus, OH.)



Fig. 42.40 Retrograde urethrogram in a male dog with hematuria. An irregularly margined focal filling defect distends the lumen of the membranous urethra proximal to the ischial arch, consistent with a urethrolith.

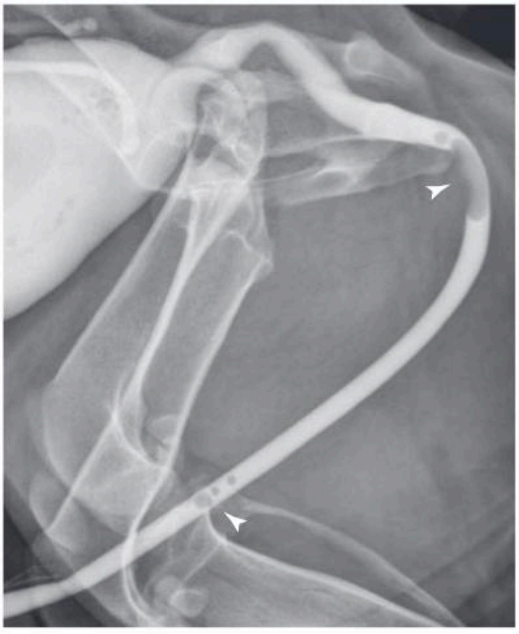


Fig. 42.41 Retrograde urethrogram in a male dog. Several gas bubbles are present in the penile urethra (*white arrowheads*). They are smoothly rounded and distinctly margined and do not distend the urethral lumen. These artifacts were not present on subsequent images following repeat injection of contrast medium.

There are several potential pitfalls in imaging of the urethra that can result in misdiagnosis of urethral calculi (Fig. 42.42). In male dogs, nipples may be superimposed upon the penis on lateral views. This can be differentiated from a calculus first by inspection of the patient for the presence of nipples adjacent to the prepuce. Coating the nipple with barium paste or another type of metallic marker and repeating the radiograph can be performed for definitive assessment. Some male dogs have a separate center of ossification of the os penis that results in a mineral body separate from the cranial tip of the os penis. This should be recognized as a normal anatomic variation and would be an unexpected location for a calculus. In some male cats, a small and faintly mineralized os penis is visible on radiographs and may be mistaken for urethrolithiasis.[97]

Urethral Neoplasia and Inflammation

Urethral mass lesions caused by neoplasia or inflammation are generally indistinguishable. Neoplasia is more common and may originate from the urethra or extend into the urethra from the urinary bladder or prostate gland, as with urothelial carcinoma and prostatic carcinoma.[91,98,99] Granulomatous urethritis is a less common infiltrative inflammatory disease reported in female dogs.[99] Fibroepithelial polyps of the urethra have also been reported.[100] With urethrography, the mucosal margin of the urethra is markedly irregular, and filling defects may be seen in the lumen (Fig. 42.43).[101] Narrowing of the lumen with intramural disease is expected, but widening may be seen with mass extension into the lumen. Extravasation of contrast

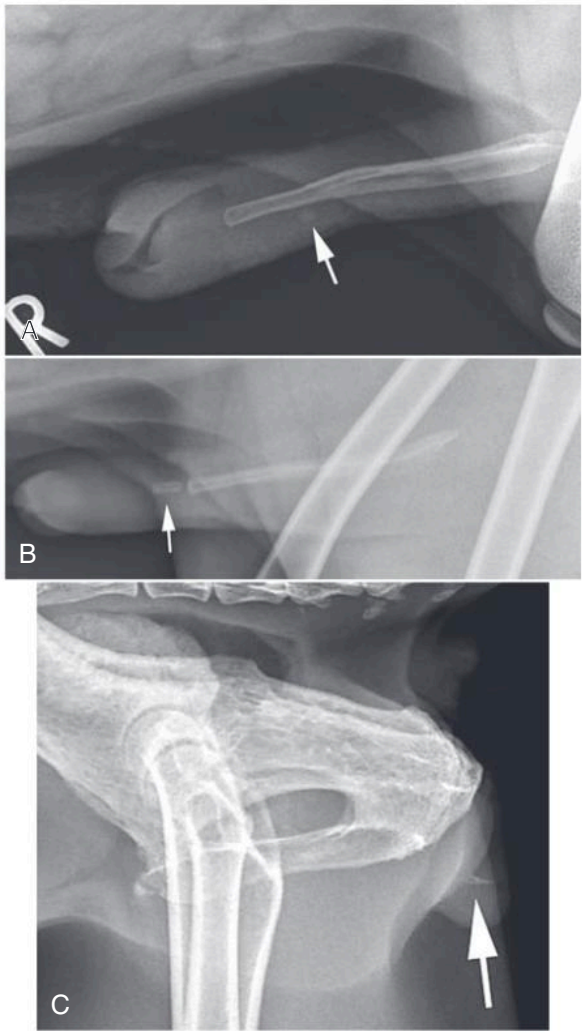


Fig. 42.42 Lateral radiographs of the canine and feline penis. **A,** A nipple is superimposed on the penile urethra (*white arrow*). **B,** Separate center of ossification at the tip of the os penis (*white arrow*). **C,** Os penis (*white arrow*) in a male cat.



Fig. 42.43 Retrograde urethrogram in a male dog with straining and pollakiuria. The mucosal margin of the prostatic urethra is markedly irregular and filled incompletely, and there is attenuation of the lumen diameter of the proximal membranous urethra. This patient had a prostatic carcinoma that had invaded the urethra.

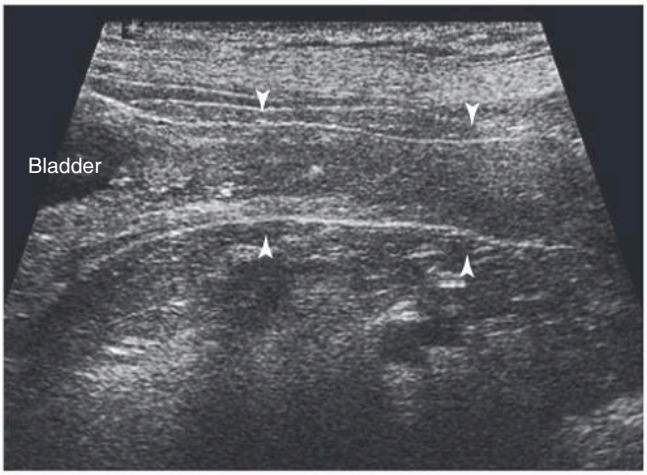


Fig. 42.44 Ultrasonography of the urethra in a female dog with chronic hematuria and straining. The urethra (*white arrowheads*) is markedly thickened and heteroechoic with extension of disease into the neck of the urinary bladder. Transitional cell carcinoma was diagnosed with biopsy. Granulomatous urethritis may have a similar appearance.

medium may also be seen with neoplasia, indicating mucosal erosion.

Ultrasonographic features of these lesions are variable but most often appear as a hypoechoic increase in thickness of the urethral wall, which may be uniform and circumferential or asymmetric (Fig. 42.44)[91,98] (Video 42.3). Advanced imaging of the urethra and pelvis can be performed; urethral neoplasia can be evaluated with CT to characterize tumor extent and lymph node abnormalities can indicate metastatic spread for pretreatment staging and to assess tumor response to treatment (Fig. 42.45).

Urethral Rupture

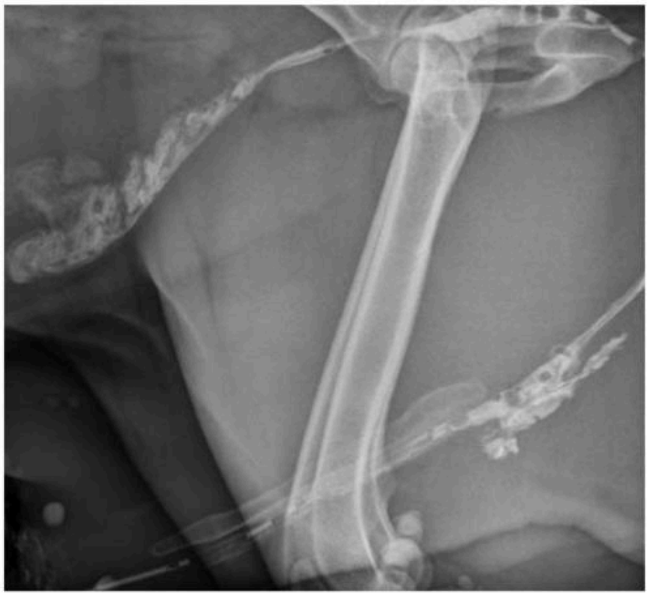
Rupture of the urethra is most commonly the result of pelvic trauma and is diagnosed by urethrography with extraluminal extension of contrast medium (Fig. 42.46, eFig. 42.8). Depending on the level of compromise, extravasation of contrast medium may extend into the peritoneal space, cavernous tissues of the penis, or soft tissues adjacent to the urethra.[88,95]

Other Diseases

Urethral stricture may occur secondary to urethral trauma or obstruction and is seen as an abrupt, focal luminal narrowing on urethrography. To differentiate a stricture from inadequate urethral distention or urethral spasm, the lesion should be persistent on multiple images made during injection of contrast medium into the urethra. A stricture may be accompanied by irregular margination and luminal dilation proximal to the lesion.[88] Fluoroscopy can provide real-time evaluation of the urethra during contrast medium injection to help confirm the diagnosis of stricture (Video 42.4).

Extraluminal masses arising from tissues adjacent to the urethra may cause broadly tapering narrowing of the lumen and displacement of the urethra.[95]

Urethral fistulas can be demonstrated as extraluminal extension of contrast medium to another hollow organ (e.g., the colon or vagina) (Fig. 42.47). In young patients, they are most often congenital anomalies but may also be acquired as a sequel to urethral trauma.[88,102]



eFig. 42.8 Retrograde urethrogram of a dog with urethral rupture. Contrast medium extravasation is seen just caudal to the os penis.

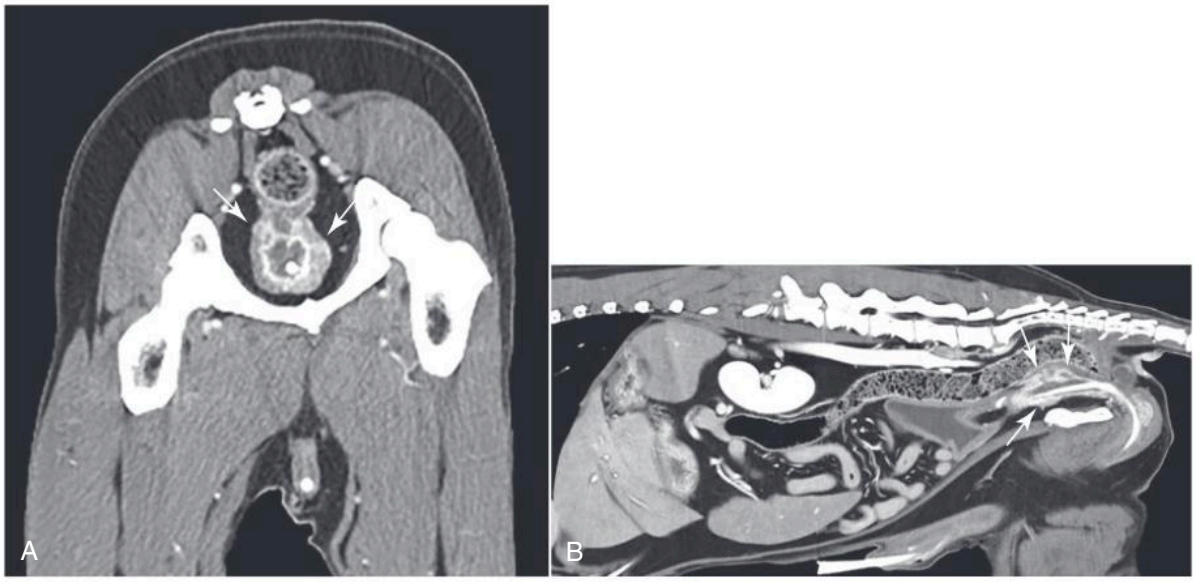


Fig. 42.45 Contrast-enhanced computed tomography images of a male dog with urethral obstruction due to prostatic carcinoma. **A,** Transverse plane image at the prostatic urethra. A hyperattenuating catheter is present in the lumen. Note the thickened urethral wall with heterogenous contrast enhancement (*white arrows*). **B,** Sagittal plane image of the prostatic urethra. Note the thickened urethral wall with heterogeneous contrast enhancement (*white arrows*).

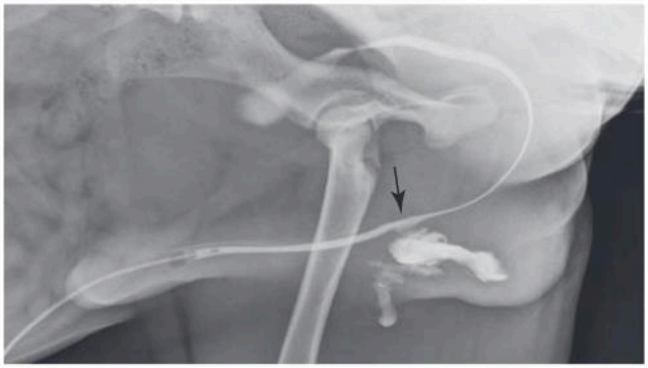


Fig. 42.46 Retrograde urethrogram in a male dog with a history of bite wounds in the region of the penile urethra. A large region of contrast medium extravasation is seen proximal to the os penis (*black arrow*) and extends through a cutaneous wound cranially, consistent with rupture of the penile urethra following puncture.



Fig. 42.47 Retrograde urethrogram in a young male English bulldog with a history of chronic urinary tract infections and urine leakage from the anus. Contrast medium extends dorsally from the membranous urethra (*white arrowheads*) to outline fecal material in the rectum. This urethrorectal fistula is likely congenital.

REFERENCES

1. International Committee on Veterinary Gross Anatomical Nomenclature (ICVGAN). *Nomina Anatomica Veterinaria*. ed 7. Hannover, Germany: Editorial Committee; 2017.
2. Hermanson JW, de Lahunta A, Evans HE. *Miller and Evan's Anatomy of the Dog*. 5th ed. Philadelphia: Saunders; 2020.
3. Mahaffey MB, Barsanti JA, Barder DL, Crowell DL. Pelvic bladder in dogs without urinary incontinence. *J Am Vet Med Assoc*. 1984;184(12):1477–1479.
4. Johnston GR, Osborne CA, Jessen CR, Feeney DA. Effects of urinary bladder distention on location of the urinary bladder and urethra of healthy dogs and cats. *Am J Vet Res*. 1986;47(2):404–415.
5. Nickel R, Schummer A, Seiferle E, et al. *The Viscera of the Domestic Mammals, (vol 184)*. 2nd ed. Berlin: Paul Parey/Springer-Verlag; 1973.
6. Neville-Towle J, Sakals S. Urinary bladder herniation through a caudoventral abdominal wall defect in a mature cat. *Can Vet J*. 2015;56(9):934–936.
7. Grand JG, Bureau S, Monnet E. Effects of urinary bladder retorflexion and surgical technique on postoperative complication rates and long-term outcome in dogs with perineal hernia: 41 cases (2002-2009). *J Am Vet Med Assoc*. 2013;243(10):1442–1447.
8. Adams WM, DiBartola SP. Radiographic and clinical features of pelvic bladder in the dog. *J Am Vet Med Assoc*. 1983;182(11):1212–1217.
9. Mahaffey M, Barber D, Basanti J. Simultaneous double-contrast cystography and cystometry in dogs. *Vet Radiol*. 1984;25:254–259.
10. Massat BJ, Gregory CR, Ling GV, Cardinet GH, Lewis EL. Cystourethropexy to correct refractory urinary incontinence due to urethral sphincter mechanism incompetence. Preliminary results in ten bitches. *Vet Surg*. 1993;22(4):260–268.
11. Applegate R, Olie S, Sabatino B. Urethral sphincter mechanism incompetence in dogs: an update. *J Am Anim Hosp Assoc*. 2018;54(1):22–29.
12. Patnaik AK, Greene RW. Intravenous leiomyoma of the bladder in a cat. *J Am Vet Med Assoc*. 1979;175(4):381–383.
13. Hansen JS. Persistent urachal ligament in the cat (report of two cases). *Vet Med Small Anim Clin*. 1972;67(10):1090.

14. Merkel LK, Lulich J, Polzin D, et al. Clinicopathologic and microbiologic findings associated with emphysematous cystitis in 27 dogs. *J Am Anim Hosp Assoc.* 2017;53(6): 313–320.
15. Lippi I, Mannucci T, Della Santa D, et al. Emphysematous cystitis: retrospective evaluation of predisposing factors and ultrasound features in 36 dogs and 2 cats. *Can Vet J.* 2019;60(5):514–518.
16. Petite A, Busoni V, Heinen MP, Billen F, Snaps F. Radiographic and ultrasonographic findings of emphysematous cystitis in four nondiabetic female dogs. *Vet Radiol Ultrasound.* 2006;47(1):90–93.
17. Buffington CA, Chew DJ, Kendall MS, et al. Clinical evaluation of cats with nonobstructive urinary tract diseases. *J Am Vet Med Assoc.* 1997;210(1):46–50.
18. Steyn P, Lowry J. Positional radiographic as an aid to diagnose sand-like uroliths in the urinary bladder of feline urologic syndrome in cats. *Feline Pract.* 1991;19:21–23.
19. Zotti A, Fant P, De Zan G, Mollo A, Busetto R. Chronic cystitis with ossification of the bladder wall in a 6-month-old German shepherd dog. *Can Vet J.* 2007;48(9):935–938.
20. Feeney DA, Johnston GR, Tomlinson MJ, Osborne CA. Effects of sterilized micropulverized barium sulfate suspension and meglumine iothalamate solution on the genitourinary tract of healthy male dogs after retrograde urethrocystography. *Am J Vet Res.* 1984;45(4):730–738.
21. Johnston GR, Stevens JB, Jessen CR, Osborne CA. Complications of retrograde contrast urethrography in dogs and cats. *Am J Vet Res.* 1983;44(7):1248–1256.
22. Barsanti JA, Crowell W, Losonsky J, Talkington FD. Complications of bladder distension during retrograde urethrography. *Am J Vet Res.* 1981;42(5):819–821.
23. Ackerman N, Wingfield WE, Corley EA. Fatal air embolism associated with pneumourethrography and pneumocystography in a dog. *J Am Vet Med Assoc.* 1972;160(12): 1616–1618.
24. Zontine W, Andrews L. Fatal air embolization as a complication of pneumocystography in two cats. *J Am Vet Med Assoc.* 1978;19:8–11.
25. Essman SC. Contrast cystography. *Clin Tech Small Anim Pract.* 2005;20:46–51.
26. Mahaffey M, Barsanti J, Browell W. Cystography: effect of technique on diagnosis of cystitis in dogs. *Vet Radiol.* 1989;30(261).
27. Johnston G, Feeney D. Radiographic evaluation of the urinary tract in dogs and cats: contemporary issues in small animal practice. *Nephrol Urol.* 1989;4:203.
28. Weichselbaum RC, Feeney DA, Jessen CR, Osborne CA, Dreytser V, Holte J. Urocystolith detection: comparison of survey, contrast radiographic and ultrasonographic techniques in an in vitro bladder phantom. *Vet Radiol Ultrasound.* 1999;40(4):386–400.
29. Weichselbaum RC, Feeney DA, Jessen CR, Osborne CA, Dunphy ED, Bartges JW. In vitro evaluation of contrast medium concentration and depth effects on the radiographic appearance of specific canine urolith mineral types. *Vet Radiol Ultrasound.* 1998;39(5):396–411.
30. Weichselbaum RC, Feeney DA, Jessen CR, Osborne CA, Holte J. An integrated epidemiologic and radiographic algorithm for canine urocystolith mineral type prediction. *Vet Radiol Ultrasound.* 2001;42(4):311–319.
31. Johnston GR, Walter PA, Feeney DA. Radiographic and ultrasonographic features of uroliths and other urinary tract filling defects. *Vet Clin North Am Small Anim Pract.* 1986;16(2):261–293.
32. Stiffler KS, McCrackin Stevenson MA, Mahaffey MB, Howerth EW, Barsanti JA. Intravesical ureterocele with concurrent renal dysfunction in a dog: a case report and proposed classification system. *J Am Anim Hosp Assoc.* 2002;38(1):33–39.
33. Colopy SA, Dennison SE, Kerwin-Lucchi LJ, Danielson KC. What is your diagnosis? Ectopic ureterocele. *J Am Vet Med Assoc.* 2011;238(3):293–294.
34. Sutherland-Smith J, Jerram RM, Walker AM, Warman CG. Ectopic ureters and ureteroceles in dogs: presentation, cause, and diagnosis. *Compend Contin Educ Pract Vet.* 2004:303–316.
35. Scrivani PV, Leveille R, Collins RL. The effect of patient positioning on mural filling defects during double contrast cystography. *Vet Radiol Ultrasound.* 1997;38(5): 355–359.
36. Remedios AM, Middleton DM, Myers SL, Outerbridge CA, Arnold PM. Diverticula of the urinary bladder in a juvenile dog. *Can Vet J.* 1994;35(10):648–650.
37. Scheepens ET. L'Eplattenier H: acquired urinary bladder diverticulum in a dog. *J Small Anim Pract.* 2005;46(12): 578–581.
38. Rahal SC, Mamprim MJ, Torelli SR. What is your diagnosis? Patent urachus. *J Am Vet Med Assoc.* 2004;225(7): 1041–1042.
39. Bartges J, Callens A. Congenital diseases of the lower urinary tract. *Vet Clin North Am Small Anim Pract.* 2015;45:703–719.
40. Osuna D, Stone E, Metcalf M. A urethrorectal fistula with concurrent urolithiasis in a dog. *J Am Anim Hosp Assoc.* 1989;25:35–39.
41. Hecht S. Diagnostic imaging of lower urinary tract disease. *Vet Clin North Am Small Anim Pract.* 2015;45(4): 639–663.
42. Hanazono K, Fukumoto S, Endo Y, et al. Ultrasonographic findings related to prognosis in canine transitional cell carcinoma. *Vet Radiol Ultrasound.* 2014;55(1):79–84.
43. Sutherland-Smith J, Penninck D. Bladder and urethra. In: *Atlas of Small Animal Ultrasonography.* 2nd ed. Ames, Iowa: Wiley & Sons Inc.; 2015.
44. Berry C. Differentiating cystic calculi from colon. *Vet Radiol.* 1992;33:283–285.
45. Geisse AL, Lowry JE, Schaeffer DJ, Smith CW. Sonographic evaluation of urinary bladder wall thickness in normal dogs. *Vet Radiol Ultrasound.* 1997;38(2):132–137.
46. Finn-Bodner S, Carter R, Gray B. *Sonographic Architecture and Morphometric Evaluation of the normal Feline Urinary Bladder wall.* Am Coll Vet Radiol; 1992.
47. Douglass J, Kremkan F. Ultrasound corner: the urinary bladder wall hypoechoic pseudolesion. *Vet Radiol Ultrasound.* 1993;34:45–46.
48. Barthez PY, Leveille R, Scrivani PV. Side lobes and grating lobes artifacts in ultrasound imaging. *Vet Radiol Ultrasound.* 1997;38(5):387–393.
49. Sislak M, Spaulding K, Zoran D, et al. Ultrasonographic characteristics of lipiduria in clinically normal cats. *Vet Radiol Ultrasound.* 2014;55(2):195–201.
50. Gremillion C, Cohen EB, Vaden S, Seiler GS. Optimization of ultrasonographic ureteral jet detection and normal ureteral jet morphology in dogs. *Vet Radiol Ultrasound.* 2021;62(5):583–590.
51. Finn-Bodem ST. The urinary bladder. In: Cartee RE, ed. *P.V. Practical Veterinary Ultrasound.* Philadelphia: Lea & Febiger; 1995:219.
52. Weichselbaum RC, Feeney DA, Jessen DA, Osborne CA, Dreytser V, Holte J. Relevance of sonographic artifacts observed during in vitro characterization of urocystolith mineral composition. *Vet Radiol Ultrasound.* 2000;41(5):438–446.
53. Louvet A. Twinkling artifact in small animal color-Doppler sonography. *Vet Radiol Ultrasound.* 2006;47(4):384–390.
54. Choi M, Kim Y. Ultrasonographic and contrast-enhanced CT imaging diagnosis of idiopathic renal hematuria with bilateral hydronephrosis and hydroureter in a dog. *Vet Radiol Ultrasound.* 2022;63(6):E21–E25.

55. Cherbinsky O, Westropp J, Tinga S, Jones B, Pollard R. Ultrasonographic features of grass awns in the urinary bladder. *Vet Radiol Ultrasound*. 2010;51(4):462–465.
56. Cote E, Carroll MC, Beck KA, Good L, Gannon K. Diagnosis of urinary bladder rupture using ultrasound contrast cystography: in vitro model and two case-history reports. *Vet Radiol Ultrasound*. 2002;43(3):281–286.
57. Finn-Bodner S, Hudson J, Brewer WG. Transabdominal sonographic evaluation of experimentally induced cystitis of the feline urinary bladder. In: *Scientific Proceedings of the ACVR*. 1993.
58. Carneiro RK, Pereira T, Brun MV, et al. Excretory urographic, ultrasonographic, and cystoscopic characteristics of urinary bladder abscesses in a dog. *Vet Radiol and Ultrasound*. 2022. https://doi.org/10.1111/vru.13095:1-4.
59. Takiguchi M, Inaba M. Diagnostic ultrasound of polypoid cystitis in dogs. *J Vet Med Sci*. 2005;67(1):57–61.
60. Martinez I, Matton JS, Easton KA, Chew DJ, DiBartola SP. Polypoid cystitis in 17 dogs (1978–2001). *J Vet Intern Med*. 2003;17(4):499–509.
61. Maurey C, Boulous HJ, Cannone-Guibert M, Benchekroun G. Clinical description of Corynebacterium urealyticum urinary tract infections in 11 dogs and 10 cats. *J Small Anim Pract*. 2019;60(4):239–246.
62. Nevins J, Mai W, Thomas E. Associations between ultrasound and clinical findings in 87 cats with urethral obstruction. *Vet Radiol Ultrasound*. 2015;56(4):439–447.
63. Lim C, Heng H, Hui T, et al. Ultrasonographic features of uterus masculinus in six dogs. *Vet Radiol Ultrasound*. 2015;56(1):77–83.
64. O'Brien RT, Wood EF. Urinary bladder mural hemorrhage associated with systemic bleeding disorders in three dogs. *Vet Radiol Ultrasound*. 1998;39(4):354–356.
65. Hamlin AN, Chadwick LE, Fox-Alvarez SA, et al. Ultrasound characteristics of feline urinary bladder transitional cell carcinoma are similar to canine urinary bladder transitional cell carcinoma. *Vet Radiol Ultrasound*. 2019;60:552–559.
66. Macri F, Di Pietro S, Mangano C, et al. Quantitative evaluation of canine urinary bladder transitional cell carcinoma using contrast-enhanced ultrasonography. *BMC Vet Res*. 2018;14(84).
67. Naughton J, Widner W, Constable P, et al. Accuracy of three-dimensional and two-dimensional ultrasonography for measurement of tumor volume in dogs with transitional cell carcinoma of the urinary bladder. *Am J Vet Res*. 2012;73(12):1919–1924.
68. Leffler AJ, Hostnik ET, Warry EE, et al. Canine urinary bladder transitional cell carcinoma tumor volume is dependent on imaging modality and measurement technique. *Vet Radiol Ultrasound*. 2018;59:767–776.
69. Heng JG, Lowry JE, Boston S, Gabel C, Ehrhart N, Gulden SM. Smooth muscle neoplasia of the urinary bladder wall in three dogs. *Vet Radiol Ultrasound*. 2006;47(1):83–86.
70. Takiguchi M, Watanabe T, Okada H, Kudo T, Yamada K, Yasuda J, Hashimoto A. Rhabdomyosarcoma (botryoid sarcoma) of the urinary bladder in a Maltese. *J Small Anim Pract*. 2002;43(6):269–271.
71. Olausson A, Stieger SM, Loefgren S, Gillingstam M. A urinary bladder fibrosarcoma in a young dog. *Vet Radiol Ultrasound*. 2005;46(2):135–138.
72. Benigni L, Lamb CR, Corzo-Menendez N, Holloway A, Eastwood JM. Lymphoma affecting the urinary bladder in three dogs and a cat. *Vet Radiol Ultrasound*. 2006;47(6):592–596.
73. Heng JG, Ramos-Vara JA, Fulkerson CM, et al. Ultrasonographic detection of apex nodules in the urinary bladder of Scottish Terriers. *Vet Radiol Ultrasound*. 2022;63:234–239.
74. Nyland TG, Wallack ST, Wisner ER. Needle-tract implantation following US-guided fine-needle aspiration biopsy of transitional cell carcinoma of the bladder, urethra, and prostate. *Vet Radiol Ultrasound*. 2002;43(1):50–53.
75. Lamb CR, Gregory SP. Ultrasonographic findings in 14 dogs with ectopic ureter. *Vet Radiol Ultrasound*. 1998;39(3):218–223.
76. Lamb CR. Ultrasonography of the ureters. *Vet Clin North Am Small Anim Pract*. 1998;28(4):823–848.
77. Takiguchi M, Yasuda J, Ochiai K, Morita Y, Hashimoto A. Ultrasonographic appearance of orthotopic ureterocele in a dog. *Vet Radiol Ultrasound*. 1997;38(5):398–399.
78. Rozear L, Tidwell A. Evaluation of the ureter and ureterovesicular junction using helical computed tomographic excretory urography in healthy dogs. *Vet Radiol Ultrasound*. 2003;44(2):155–164.
79. Secrest S, Britt L, Cook C. Imaging diagnosis—bilateral orthotopic ureteroceles in a dog. *Vet Radiol Ultrasound*. 2011;52(4):448–450.
80. Ricciardi M, Campanella A, Martino R. Computed tomographic features of urinary bladder torsion in two dogs. *J Sm Anim Pract*. 2018;59:188–195.
81. MacLeod A, Wisner E. Computed tomography and magnetic resonance imaging of the urinary tract. In: Bartges J, Polzin D, eds. *Nephrology and Urology of Small Animals*. Ames, IA: Blackwell Publishing; 2011.
82. Murphy S, Gutierrez A, Lawrence J, Bjorlin D, Mackie T, Forrest L. Laparoscopically implanted tissue expander radiotherapy in canine transitional cell carcinoma. *Vet Radiol Ultrasound*. 2008;49(4):400–405.
83. Park RD. Radiology of the urinary bladder and urethra. In: O'Brien TR, ed. *Radiographic Diagnosis of Abdominal Disorders in the Dog and Cat: Radiographic Interpretation, Clinical Signs, Pathophysiology*. Philadelphia: Saunders; 1978:605–609.
84. Evans HE, Chistensen GE. The urogenital system. In: Evans HE, Miller ME, eds. *Miller's Anatomy of the Dog*. 3rd ed. Philadelphia: Saunders; 1993:529–546.
85. Dyce KM, Sack WO, Wensing CJG. The pelvis and reproductive organs of the carnivores. In: *Textbook of Veterinary Anatomy*. 2nd ed. Philadelphia: Saunders; 1996:438–446.
86. Johnston GR, Feeney DA, Osborne CA. Urethrography and cystography in cats. 1. Techniques, normal radiographic anatomy, and artifacts. *Compend Contin Educ Pract Vet*. 1982;4:823.
87. Johnston GR, Jessen CR, Osborne CA. Effects of bladder distension on canine and feline retrograde urethrography. *Vet Radiol Ultrasound*. 1983;24:271.
88. Ticer JW, Spencer CP, Ackerman N. Positive contrast retrograde urethrography—a useful procedure for evaluating urethral disorders in the dog. *Vet Radiol Ultrasound*. 1980;21(2).
89. Johnston GR, Stevens JB, Jessen CR, et al. Complications of retrograde contrast urethrography in dogs and cats. *Am J Vet Res*. 1983;44:1248.
90. Feeney DA, Johnston GR, Osborne CA, et al. Dimensions of the prostatic and membranous urethra in normal-male dogs during maximum distension retrograde urethrocystography. *Vet Radiol Ultrasound*. 1984;25:249.
91. Nyland TG, Mattoon JS, Herrgesell EJ, et al. Urinary tract. In: Nyland TG, Mattoon JS, eds. *Small Animal Diagnostic Ultrasound*. 2nd ed. Philadelphia: Saunders; 2002:181–191.
92. Kim G, Ji Y, Choo D, et al. Evaluation of urethral thickness using ultrasonography in healthy small-breed dogs. *Front Vet Sci*. 2022:1051898. https://doi.org/10.3389/fvets.2022.

93. Kang K, Kim K, Oh D, et al. Retrograde CT urethrography using a power injector quantitatively reveals effects of bladder distension on urethral size in healthy male Beagle dogs. *Vet Radiol Ultrasound*. 2020;61:302–311.
94. Kang K, Kim K, So J, et al. The urethra of healthy female dogs can be normally narrowed due to the urethral flexure in retrograde CT urethrography. *Vet Radiol Ultrasound*. 2021;62:61–67.
95. Pugh CR, Rhodes WH, Biery DN. Contrast studies of the urogenital system. *Vet Clin North Am Small Anim Pract*. 1993;23:281.
96. Johnston GR, Feeney DA. Comparative organ imaging—lower urinary-tract. *Vet Radiol Ultrasound*. 1984;25:146.
97. Piola V, Posch B, Aghte P, et al. Radiographic characterization of the os penis in the cat. *Vet Radiol Ultrasound*. 2011;52:270.
98. Hanson JA, Tidwell AS. Ultrasonographic appearance of urethral transitional cell carcinoma in ten dogs. *Vet Radiol Ultrasound*. 1996;37:293.
99. Moroff SD, Brown BA, Matthiesen DT, et al. Infiltrative urethral disease in female dogs—41 cases (1980–1987). *J Am Vet Med Assoc*. 1991;199:247.
100. Grant DC, Troy CG. Recurrent urethral fibroepithelial polyps in a golden retriever. *J Am Anim Hosp Assoc*. 2014;50:361–365.
101. Ticer JW, Spencer CP, Ackerman N. Transitional cell-carcinoma of the urethra in 4 female dogs—its urethrographic appearance. *Vet Radiol Ultrasound*. 1980;21(12).
102. Chandler JC, MacPhail CM. Congenital urethrorectal fistulas. *Compend Contin Educ Pract Vet*. 2001;23:995.

ELECTRONIC RESOURCES

Additional information related to the content in Chapter 42 can be found online at eBooks.Health.Elsevier.com

- Chapter Quiz
- Videos

CHAPTER 43

Prostate Gland

Jimmy C. Lattimer • Melanie Anderson

NORMAL ANATOMY AND RADIOGRAPHIC APPEARANCE

The normal prostate gland (hereafter referred to as prostate) surrounds the most proximal aspect of the male canine urethra and lies ventral to the rectum and caudal to the urinary bladder, typically within the pelvic canal. The absolute normal size of the prostate is variable in the dog and is dependent on the age, size, and neuter status.[1] In many neutered dogs, the normal prostate is small (<2 cm) and not radiographically visible (Fig. 43.1A). When visible, the prostate is recognized radiographically by its round shape, soft tissue opacity, and its relation to adjacent organs. Delineation of an enlarged prostate from the urinary bladder is evident from a triangular fat opacity ventral to and between them (see Fig. 43.1B). The normal prostate in an intact dog should not be more than 70% of the height of the pelvic inlet on lateral views, measured as the distance between the ventral aspect of S1 and the cranial border of the dorsal pubis.[2] If seen on the ventrodorsal (VD) view, the normal prostate should not be more than 80% of the width of the pelvic canal. A full rectum may obscure the prostate on the VD view. If the shape or position of the prostate is altered, the gland may not be recognizable other than as an indistinct opacity between the bladder, rectum, and pelvis.

The normal prostate gland is not visible in the cat because of its location on the dorsal lateral surfaces of the mid pelvic urethra and small size. The normal feline prostate measures up to 10 mm in diameter.[3] Prostatic diseases causing clinical signs in cats are very rare and will not be considered further in this chapter.

DISEASES OF THE PROSTATE GLAND

Intrinsic disease of the prostate usually results in enlargement. Enlargement may also occur in response to extraprostatic influences, such as an androgen-producing testicular tumor and orchitis.[1] Because of the close functional association of the prostate and testes, any animal with prostatic disease should also be examined, preferably ultrasonographically, for testicular disease.

The most common prostatic disorder is benign prostatic hyperplasia (BPH), in which the prostate enlarges as a result of increased cell number as well as enlargement of the intercellular

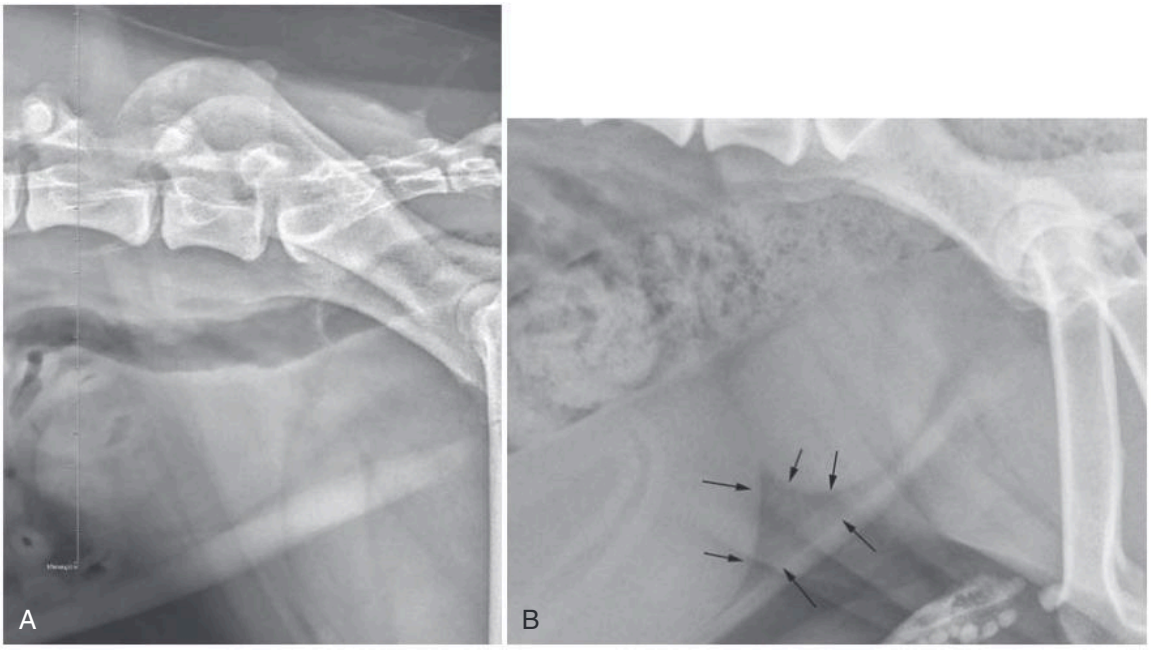


Fig. 43.1 **A,** Normal prostate in a dog neutered at a young age. The prostate is virtually indistinguishable from the urethra and the fat triangle is lost. **B,** Abdominal radiograph of a dog with benign prostatic hyperplasia. Note the cranial displacement of the urinary bladder and the triangular region of fat between the caudoventral aspect of the urinary bladder, the cranioventral aspect of the prostate gland, and the ventral abdominal wall (*black arrows*). This sign is a reliable indicator of prostate gland enlargement. There are also multiple calculi in the penile urethra.

and ductal spaces. BPH can occur in dogs are young as 2 to 3 years and affects more than 95% of intact dogs over 9 years of age.[4] This condition is considered normal in most intact dogs and may include both hyperplastic and hypertrophic processes.[1] Progressive enlargement often leads to development of dilated cystic spaces. Solid and cystic enlargements are therefore different stages of the same disease, with the latter being the advanced form.[4,5] The size of the cystic spaces varies from microscopic to large; these spaces may become so large that they distort the shape of the entire gland. Large cystic spaces predispose the gland to infection.[5]

Prostatitis is the second most common cause of prostatic enlargement and is usually bacterial in origin. The most common organisms isolated include *Escherichia coli*, *Staphylococcus* spp, *Streptococcus* spp, *Pseudomonas*, *Brucella canis*, *Proteus*, and *Mycoplasma*, among others. Usually, a mixed bacterial population is present.[6] The infection may arise within the prostate, or it may extend from other sources such as the urinary bladder or testicles. A normal prostate gland is more resistant to infection than is an enlarged or inflamed gland. Because many antibiotics do not penetrate the prostate readily, the gland may also be a reservoir for reinfection or extension to other organs.[4] There is improved penetration of antibiotics into an inflamed prostate due to disruption of the blood-prostate barrier.[6] Prostatic inflammation may vary from a mild transient process that causes minimal or no clinical signs to a fulminating hemorrhagic or emphysematous process that destroys the entire gland rapidly, resulting in severe systemic signs.[7–9] The latter may result in rupture of the capsule with secondary peritonitis and sepsis.

Chronic, recurrent prostatitis may result in a scarred, fibrotic gland that is typically normal in size or small. Chronic scarring may result in stricture of the urethra.[1,4] Such a stricture is difficult to recognize radiographically unless a urethrogram is performed.

Prostatic abscesses may form as a sequela of prostatitis or primary cystic disease. Large abscesses distort the shape of the prostate gland and may also rupture, causing peritonitis and sepsis.[10,11]

As previously stated, cysts form in advanced BPH and are usually contained within the gland. Squamous metaplasia can cause obstruction of the prostatic ducts, leading to retention cysts. Cysts protruding from the surface of the prostate or separate from the prostate are also referred to as *paraprostatic cysts* because they are no longer confined within the gland. They have been associated with cystic enlargement of the Müllerian ducts or remnants of the uterus masculinus.[12–14] Enlargement of the Müllerian ducts results in a bilateral tubular mass that resembles uterine enlargement.[15,16] These cysts may be sterile but often become infected, which may be the inciting cause for presentation to a veterinarian.[17,18] Cysts occasionally result from neoplasia, but this is rare. Formation of functional neoplastic secretory cells without an accompanying ductal system results in a cystic structure lined with neoplastic epithelium.

Prostatic tumors are rare in dogs and very rare in cats. The majority of prostatic tumors are carcinomas (adenocarcinoma, urothelial carcinomas, squamous cell carcinomas, undifferentiated carcinomas). Very rarely, mesenchymal cell tumors are identified.[19,20] Lymphoma may arise within the prostate but is more often involved secondarily and may serve as a sanctuary site for disease during treatment.[21] The incidence of all prostatic tumors is very low (0.35%).[22] Neutered male dogs have an odds ratio of approximately 2.84 in comparison to intact males.[23] Prostatic carcinoma is often advanced at presentation with metastasis to regional lymph nodes, the pelvis, lumbosacral spine, and distant sites such as the liver and lungs.[22–25] Patients may present with urinary signs as the tumor can invade or compress the urethra. Small in situ prostatic carcinomas are unusual but do occur; they are usually discovered as a result of metastasis rather than from their local effects. Large prostatic neoplasms are often infected or necrotic, and affected dogs may therefore have clinical signs of prostatitis. These tumors are often slow to be diagnosed, unless signs of metastasis are present, because of the tendency of clinical sign of cystitis or prostatitis to overshadow those of neoplasia.

Clinical Signs

The clinical signs of prostatic disease are usually localized to urinary or gastrointestinal signs. Stranguria, hematuria, and pyuria are seen commonly in cases of prostatitis and neoplasia.[1,4,5,24] In cases of marked prostatomegaly, patients may present with dyschezia and small or ribbon-like stools as the enlarged prostate gland displaces the colon and/or rectum dorsally, compressing the rectum (Fig. 43.2). Patients are often systemically ill in cases of acute prostatitis and may present with anorexia, fever, vomiting, abdominal pain, and preputial discharge, whereas patients with chronic prostatitis are often asymptomatic or display mild clinical signs. Most commonly, patients with chronic prostatitis will have a history of recurrent urinary tract infections and bloody urethral discharge. The prostate is typically normal in size and nonpainful on rectal palpation.[1,5]

A less common sign of prostatic disease is a pelvic limb gait abnormality manifesting as pelvic limb weakness and lumbar pain or myelopathy due to spinal metastasis or direct tumor extension into the vertebral canal. The animal may refuse to climb stairs and jump or may have a stiff gait. Owners often believe the animal has developed osteoarthritis, but such animals may have severe, active septic prostatitis or metastatic disease. The pain caused by the prostatic infection is exacerbated by walking, climbing, and jumping. Both pelvic limbs are usually affected. These animals are also usually sensitive to palpation of the caudal abdomen. Gait abnormalities are seen rarely in uncomplicated BPH.[22–25]

Radiographic Changes

Most common prostatic diseases cause enlargement. The enlargement may be symmetric (diffuse) or asymmetric (focal). Prostatic symmetry is usually judged by the shape of the prostate and the relative mass of the prostate gland with respect to the neck of the bladder and the pelvic inlet. Hyperplasia and

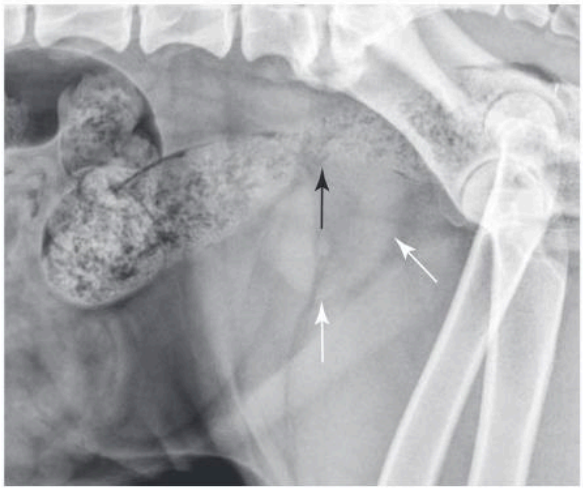


Fig. 43.2 Prostate gland enlargement in an intact dog with benign prostatic hyperplasia. The prostate gland (*white arrows*) is enlarged, and the urinary bladder is displaced cranially. The enlarged prostate is displacing the colon dorsally resulting in focal colonic narrowing (*black arrow*). The enlargement of the prostate gland is relatively symmetric in relation to the neck of the bladder.

prostatitis are examples that usually cause symmetric enlargement, whereas neoplasia and large cysts are examples that usually cause asymmetric enlargement.

Identification of prostatomegaly depends on identification of a soft tissue mass in the caudal aspect of the abdomen and on the relation of that mass to surrounding structures, principally the bladder, colon, and body wall. Prostatomegaly typically displaces the urinary bladder cranially. If prostatomegaly is uniform, bladder displacement is cranial along the floor of the abdomen. If prostatomegaly is eccentric, as often occurs with large cysts and abscesses and occasionally with tumors, the direction of bladder displacement may be variable. A cyst or abscess occasionally may extend dorsal to the bladder (Fig. 43.3). Alternatively, with ventral prostatomegaly, the bladder neck may be elevated.[1,5] Severe and irregular enlargement may also result in obliteration of the normal triangle of fat formed by junction of the caudal ventral bladder and the prostate gland.[26]

The other major radiographic sign of prostatomegaly is dorsal displacement of the colon (see Fig. 43.2). Prostatic enlargement, particularly if intrapelvic, may also cause narrowing of the lumen of the rectum and possible impaction of feces cranial to the site of rectal narrowing. This compression may be visible radiographically, or the colon may simply become confluent with the prostate mass at the pelvic inlet.

Very large prostatic lesions usually lie on the floor of the abdomen, so some dorsal displacement of the caudal abdominal contents can occur. Prostatic and paraprostatic cysts may become so large that they reach almost to the costal arch. Masses of this magnitude cause organ displacement so severe that the actual source of the mass may be difficult to determine without using special radiographic procedures, sonography, or advanced imaging such as computed tomography (CT). Prostatic disease that results in urethral stricture or urethral invasion, as in the case of neoplasia, may result in severe urinary bladder distention from obstruction, which is then secondarily responsible for the displacement of the abdominal structures cranial and dorsal to it.

A prostate that exceeds 90% of the distance from the pubis to the sacral promontory in an intact dog is considered pathologic.[2] Any enlargement (>2 cm) in a dog neutered more than a few months prior to imaging should be considered abnormal.[1,2] However, when a dog is neutered for treatment of prostatic disease, enlargement can persist for several months.[27] The actual degree of prostatic enlargement varies widely, however. For example, prostatic size may vary from slight enlargement to 10 times normal size for BPH, and the gland may actually decrease in size in chronic prostatitis due to fibrosis.[1,5] Acute prostatitis and neoplasia alone do not usually cause severe enlargement, as seen with BPH. However, a combination of pathologies may be present resulting in enlargement. Prostatic pathology may be discovered incidentally during abdominal imaging with ultrasound, CT, or magnetic resonance imaging (MRI), or on postmortem examination.

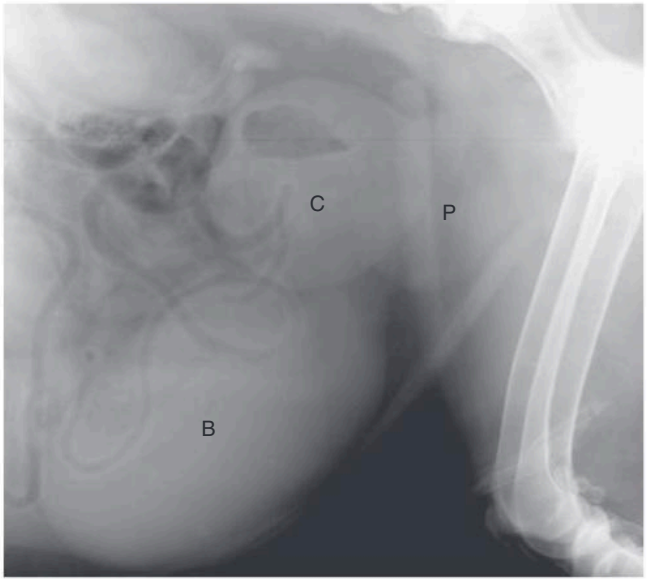


Fig. 43.3 A large, dorsally located paraprostatic cyst (*C*) arising from a prostate gland with benign prostatic hyperplasia. The cyst is seen dorsal and cranial to the enlarged prostate (*P*) and dorsal to the urinary bladder (*B*).

Paraprostatic cysts and abscesses usually have well-defined, sometimes mineralized margins that are easily seen (see Fig. 43.3, eFigs. 43.1 and 43.2).[14] Abscesses are typically poorly marginated and are often surrounded by edema or fluid, resulting poor delineation of the prostate, reduced periprostatic serosal detail, and a heterogeneous appearance of the caudal abdominal fat. A cyst or abscess may occasionally extend caudally into the pelvic canal; such lesions may not be readily visible on survey radiographs and may not produce the usual displacement of the bladder.[18] These lesions do, however, often produce marked displacement and compression of the rectum and are therefore recognized as an intrapelvic mass and on occasion can even be within the contents of a perineal hernia. Definitely distinguishing a cyst from an abscess on the basis of radiographic examination alone is impossible; however, if the margins are smooth, the structure is uniform in soft tissue opacity, and there is no evidence of regional inflammation (fluid/edema), a cyst is more likely.

Evaluation of prostatic margination is important. In the presence of emaciation, pelvic trauma, or abdominal effusion, the prostatic margins may be inconspicuous. If the prostate gland has smooth margins that are easily seen, the disease involving the gland is likely to be benign or is slowly progressing, such as BPH or low-grade or chronic prostatitis. An irregular or indistinct margin in the presence of adequate abdominal fat is more likely to be caused by an acute or aggressive process such as neoplasia or acute prostatitis.[8,9,11] Most patients with aggressive prostatic disease have some evidence of secondary inflammation affecting the surrounding tissues (Fig. 43.4, eFig. 43.3).

A change in the opacity of the prostate from its normal soft tissue opacity indicates severe or chronic disease. Areas of calcification within the gland are a sign either of longstanding prostatitis or of neoplasia. Wispy or indistinct calcification within the prostatic parenchyma has a strong positive predictive value (100%) for carcinoma in neutered dogs, whereas intact dogs are unlikely to have prostatic neoplasia if no mineralization is present (Fig. 43.5, eFig. 43.4).[28] Therefore, although unusual, indistinct calcification in the prostate gland is a serious finding that warrants biopsy. Prostate gland calcification may be more easily seen with ultrasonography or CT because of improved soft tissue contrast resolution and elimination of superimposed structures in comparison to standard radiography.

The prostate does not normally communicate with any air-containing organ, so it should not contain gas. Intraprostatic gas is evidence of gas-forming bacterial prostatitis. This is extremely rare.[9] Severe prostatitis results in hemorrhagic necrosis of the gland, potentially causing a generalized peritonitis and septic shock. Because of the rapidly fatal course of these infections, identification of noniatrogenic gas within the prostate carries an unfavorable prognosis. Rarely, the prostate may contain air because of reflux from the bladder during a negative- or double-contrast cystogram. Simple filling of the ducts with air does not necessarily indicate prostatic disease, but the



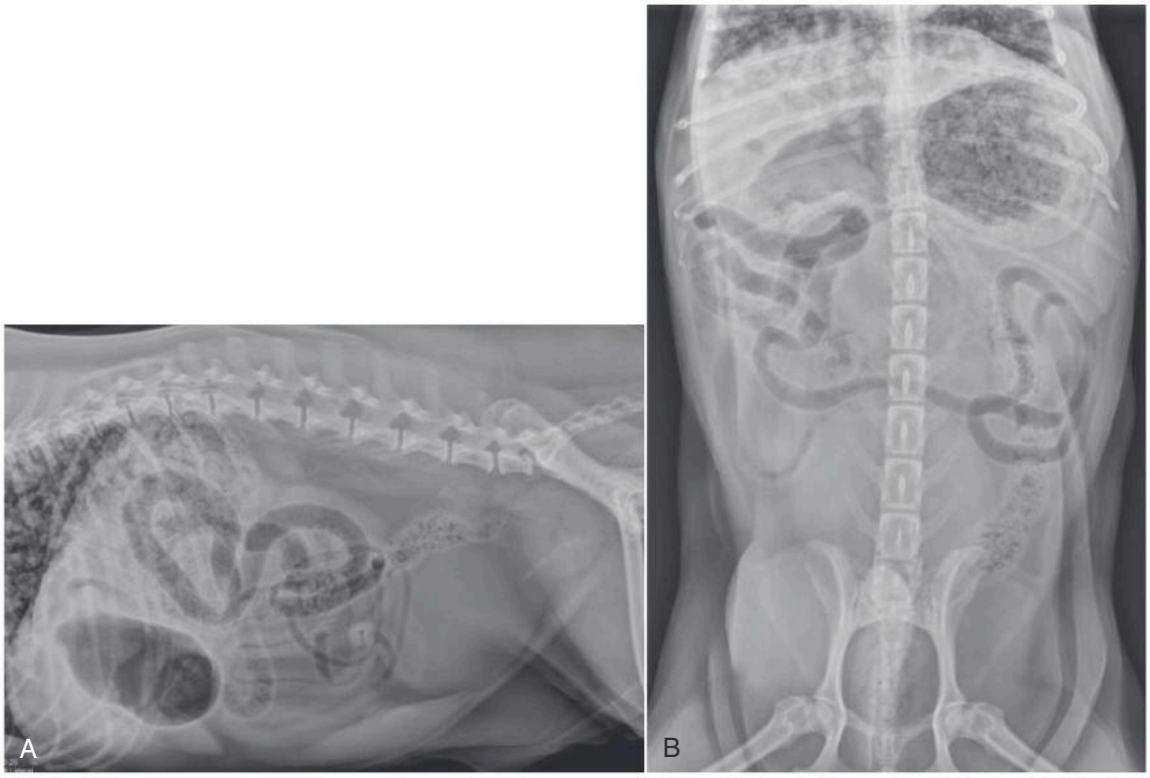
eFig. 43.1 Lateral radiograph of the caudal abdomen of a dog with a paraprostatic cyst. A large soft tissue opacity mass lesion is present dorsal to the urinary bladder, causing cranioventral displacement of the bladder, and dorsal displacement and compression of the caudal descending colon and rectum.



eFig. 43.2 Lateral radiograph of the caudal abdomen of a dog with a paraprostatic cyst. An ovoid, peripherally mineralized structure with a thinner stalk entering the pelvic canal is present dorsal to the urinary bladder and prostate.



eFig. 43.3 Lateral radiograph of the caudal abdomen of a dog with bacterial prostatitis. The prostate is severely enlarged, causing dorsal displacement and compression of the colon. The caudal abdominal fat surrounding the prostate is heterogeneous resulting in poor delineation of the margins of the prostate.



eFig. 43.4 Lateral **(A)** and ventrodorsal **(B)** abdominal radiographs of a dog with metastatic prostatic carcinoma. The prostate is enlarged with central areas of mineralization. Increased soft tissue opacity ventral to L6 and L7 may be indicative of enlarged medial iliac lymph nodes. There are numerous soft tissue opacity pulmonary nodules consistent with metastatic pulmonary disease.



Fig. 43.4 An enlarged prostate due to bacterial prostatitis. The markedly enlarged prostate is displacing the bladder cranially and impinging on the colon causing it to narrow slightly as it passes through the pelvic inlet. Note the wispy fluid opacity along the cranioventral aspect of the prostate in the caudoventral abdomen, consistent with effusion and/or edema, commonly seen with inflammation.



Fig. 43.5 Dense and wispy calcification in the enlarged prostate of a neutered dog. Diagnostic catheterization confirmed the radiographic diagnosis of prostatic carcinoma.

finding of air in pockets within the prostate gland following contrast administration is abnormal and most often associated with cyst formation.

Periosteal proliferation is sometimes seen on the ventral aspect of the caudal lumbar and/or sacral vertebrae (Fig. 43.6, eFig. 43.5) and pelvis because of regional metastasis from prostatic neoplasia. While this is the most common location, osseous metastasis is not limited to these regions and may also be found in the extremities and ribs.[22,24,26]

Special Radiographic Procedures for Evaluating the Prostate Gland

Although ultrasonography has enhanced the imaging of the prostatic parenchyma, retrograde urethrography is still a useful imaging procedure that should be considered in patients with suspected prostatic disease if ultrasound or other advanced imaging modalities are not available.[29]

The only special radiographic procedure that has been found to be uniformly useful in the evaluation of the prostate is the positive-contrast urethrogram. This procedure allows evaluation of the urethra itself and the position of the urethra in relation to suspected prostatic disease. Asymmetric positioning of the urethra within the prostate indicates an asymmetric disease process within the prostate such as a tumor or abscess, with abscesses being more common (Fig. 43.7). Invasion or stricture of the urethra in association with a prostatic mass, indicated by disruption of the smooth urethral margin, is a poor prognostic finding because of the danger that a urinary

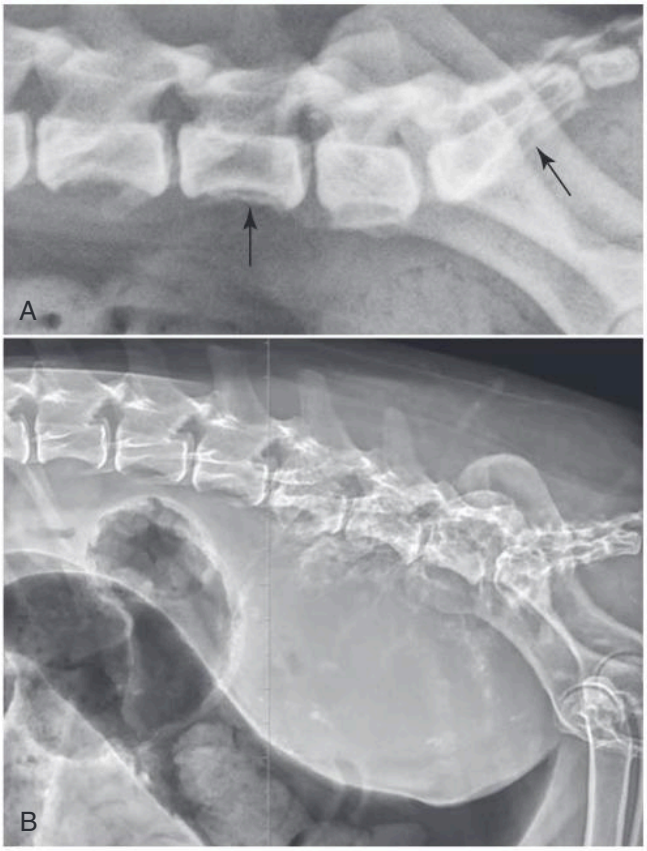


Fig. 43.6 **A,** Lateral lumbar radiographs of two dogs with metastatic prostate adenocarcinoma (early **A** and advanced **B**) to the lumbar vertebrae and the sacrum (*black arrows* in **A**). The prostate gland was not abnormal radiographically because of the small size of the tumor in both cases. A mass effect is present ventral to the lumbar spine in **B** due to the presence of metastatic lymphadenopathy.



eFig. 43.5 Lateral abdominal radiograph of a dog with metastatic prostatic carcinoma. The prostate is enlarged and poorly delineated from the urinary bladder. There is increased soft tissue opacity ventral to the caudal lumbar spine and a faint irregular periosteal reaction is seen along the ventral aspect of L6, L7, and the sacrum, and along the cranial contour of the ilium consistent with metastatic disease.

obstruction could occur. It is also a sign that aggressive disease is present.[29,30] Evidence of either asymmetric prostatic enlargement or urethral abnormalities is an indication for prostatic cytology, which is best acquired by diagnostic urethral catheterization.

Urethrography can be performed easily in the male dog, and several methods may be used. Urethrography provides indirect evidence of prostatic disease. If the urethra is deviated around a large mass or does not pass directly through the center of the prostate gland, the disease within the prostate is asymmetric, such as a cyst, abscess, or tumor. If the urethra passes directly through the middle of an enlarged prostate, the disease is more likely to be diffuse, such as hyperplasia or prostatitis (see Fig. 43.7A).

In addition, a urethrocystogram identifies the true location of the urinary bladder. In some instances, abdominal masses, such as an omental tumor, a paraprostatic cyst, or an enlarged retained testicle, lie next to the bladder and the mass can be misinterpreted as the urinary bladder. Knowing the identity of each mass is important, and urethrocystography is useful for this, especially if ultrasound is not available.

Signs of urethral disease of prostatic origin include urethral stricture, ulceration of the mucosa, and filling defects within the urethra. Ulceration or stricture of the prostatic urethra should be regarded as highly suggestive of neoplasia.[29]

Extravasation of contrast medium into the prostate should not be interpreted as abnormal as long as only the prostatic ducts fill with contrast medium (see Fig. 43.7B).[30] This appearance is often seen in animals with a normal prostate. However, pooling of the contrast medium within the prostate is abnormal. Large cavities with irregular walls that communicate with the urethra or cavitary smooth-walled lesions containing intraluminal masses are suggestive of neoplasia; aspiration may be indicated in these instances.[13,29] Conversely, if extravasation does not occur, the prostate gland is not necessarily normal or solid. Large cavitary lesions, such as cysts and abscesses, often attain their size because they do not communicate with the urethra.[1,18] If these lesions do fill with contrast medium, they are usually ovoid with smooth walls.

The normal prostatic urethra as seen on the urethrogram has a smooth mucosal border. The urethra is usually slightly greater in diameter near the center of the prostate and tapers slightly at the cranial and caudal borders. The degree of the central dilation depends somewhat on the size of the prostate, the disease present, the degree of bladder distention, and the amount of pressure applied during injection.[31] A small, smooth filling defect in the dorsal wall of the urethra near the center of the prostate gland represents the colliculus seminalis and is a normal finding (Fig. 43.8).[30]

The point at which the prostatic urethra joins the neck of the bladder should be evaluated carefully. Small filling defects or mucosal ulcers that may be early lesions of urothelial carcinoma may be detected. These small lesions may not be detected on a cystogram or even ultrasonography because they are obscured by the internal urethral sphincter, which is actually encircled by the prostate.

Percutaneous biopsy of presumed or suspected prostatic carcinoma or any urogenital neoplasm is controversial due to risk

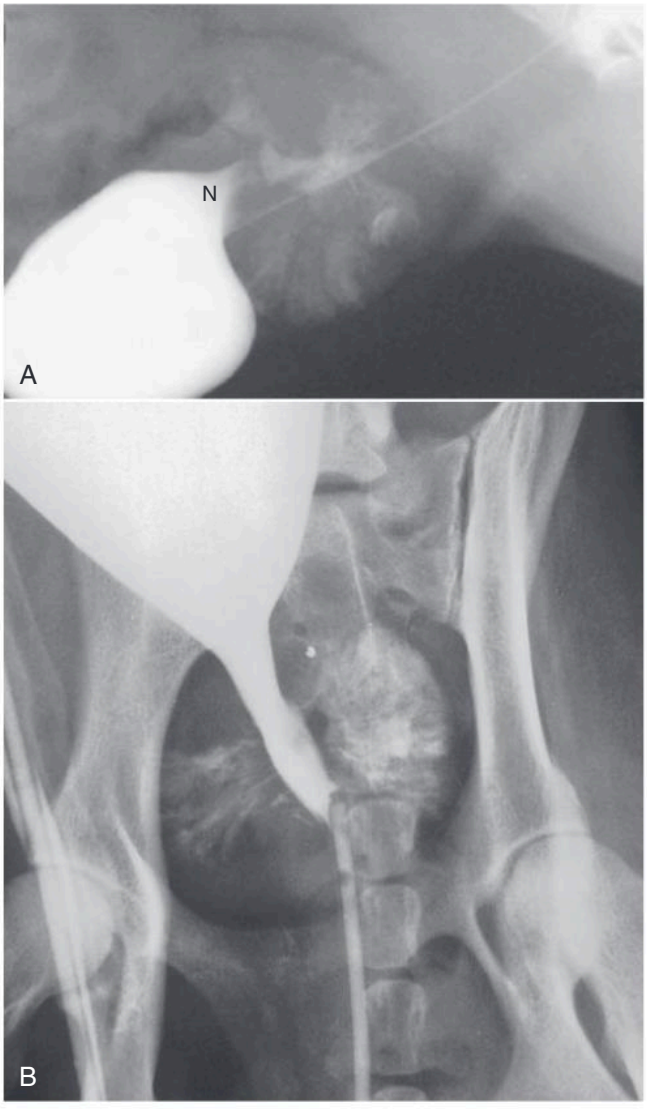


Fig. 43.7 **A,** Marked prostatic enlargement with dorsal elevation of the neck of the bladder (*N*). Note the reflux of contrast medium into the prostate gland. A catheter is present in the urethra. **B,** Filling of the prostatic ducts with contrast medium. No cavities are present. Although the prostate gland in this dog is enlarged, the filling of the prostatic ducts with contrast medium has no clinical significance.

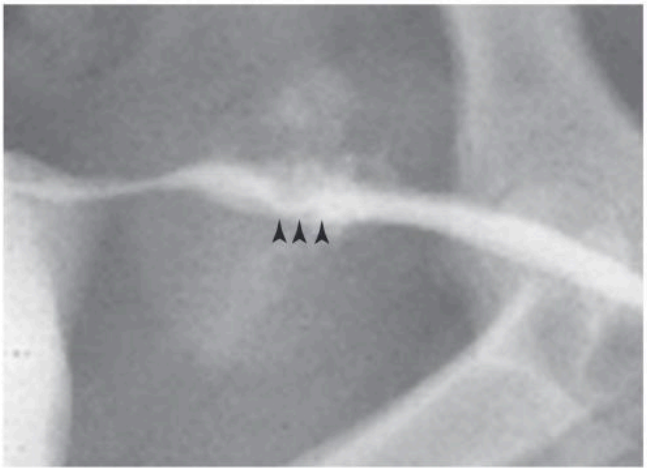


Fig. 43.8 The small filling defect (*black arrowheads*) in the dorsal wall of the prostatic urethra is a normal structure, the colliculus seminalis. It should not be mistaken for a lesion caused by prostatic or urethral disease.

of seeding the tumor cells into the peritoneum, pelvic cavity, and subcutaneous tissues. This has been seen in prostatic neoplasms as well as urinary bladder urothelial carcinoma.[32] Cytologic examination of urine sediment acquired during a urethral catheterization with flushing of the prostatic urethra should be performed before biopsy is considered as this procedure frequently is successful in confirming the presence of neoplasia.[33]

Ultrasonography for Evaluating the Prostate Gland

Diagnostic ultrasonography has largely supplanted radiography for the diagnosis of prostatic disease as it allows for evaluation of overall architecture and symmetry as well as subtle parenchymal abnormalities which are often not detected radiographically.[34]

Ultrasonographic examination of the prostate should also include the bladder and testicles, and regional lymph nodes. These associated structures may be affected secondarily in prostatic disease, or they may be the site of the primary disorder resulting in secondary prostatic changes. A very small normal gland, such as seen in a neutered dog, may not be seen if pelvic in location, but an abnormal prostate is usually visible cranial to the pubis. Images should be acquired in the transverse, sagittal, and parasagittal planes. Alternatively, a cine loop capture can be made while scanning slowly through the gland in the transverse plane. This will ensure that the entire prostate is adequately represented in captured images.[35] The prostate is typically imaged most easily from the right side of the os penis with the dog in dorsal recumbency by tracing the trigone of the urinary bladder caudally. In some dogs, angling the probe caudally is necessary to see the caudal pole of the prostate gland where it lies just dorsal to the pubic brim. Sedation is sometimes required for thorough assessment in uncooperative patients. Ultrasonographic measurement of the prostate and its lesions is performed easily with ultrasonography and has been found to be accurate.[2]

The normal prostate in a neutered male is uniformly relatively hypoechoic with a homogeneous, medium to fine echotexture relative to surrounding fat which has a coarser echotexture. The urethra is usually seen as a small hypoechoic region in the center of the gland surrounded by a narrow band of slightly hyperechoic tissue representing the urethral wall (Fig. 43.9).

BPH usually results in a uniformly enlarged gland that is hyperechoic and has smooth margins. The dorsal portion of the gland may be enlarged to a greater degree than the ventral portion, or vice versa, but the changes are generally symmetric from right to left (Fig. 43.10). This symmetry may be lost as the hyperplasia increases in severity and cysts develop. As cysts form, some invariably become larger than others and distort the shape of the prostate but typically do not extend beyond the capsule. Commonly, small anechoic cystic regions are seen within the parenchyma of dogs with BPH (Fig. 43.11).

The ultrasonographic changes seen in prostatitis vary from mild hyperechogenicity of the parenchyma with variable enlargement to severe prostatic enlargement with a mottled hyperechoic to hypoechoic pattern (Fig. 43.12). The shape of the prostate may be normal or markedly distorted. Distortion of the shape and margin is common when abscess formation is present in the gland. Some dogs may have a hypoechoic band of edema in the capsule outlining the prostate gland. Edema may also extend into the surrounding tissues, resulting in hyperechoic fat with hypoechoic striations adjacent to the prostate. In severe necrotizing prostatitis, delineation of the gland from the surrounding fat may be lost, and the prostate may appear as a dark structure with an irregular and indistinct margin. Generally speaking, the more acute and severe the inflammation is, the more hypoechoic the prostatic parenchyma becomes. In cases of chronic inflammation, the prostate is typically more hyperechoic due to fibrosis.

Cysts and abscesses within and attached to the prostate appear as thin-walled structures with variably hypoechoic centers. They vary widely in size from a couple of millimeters to several centimeters. Their contents may be anechoic, or they may have variable amounts of cellular debris within the lumen.[18] The presence of septation or large amounts of debris within the lumen is typically more indicative of abscess, whereas anechoic contents are suggestive of a cyst; however, this is not a universally accurate distinction. The presence of through transmission deep to a highly echogenic structure is indicative of a fluid-filled rather than a solid cellular mass. Color Doppler can be helpful for confirming vascularization within a prostatic lesion. Both cysts and abscesses occasionally occur in conjunction with neoplasia. Cavitary lesions with irregular internal margins or solid tissue masses within them are highly suggestive of neoplasia, whereas smooth margins are more indicative of cysts (Fig. 43.13).

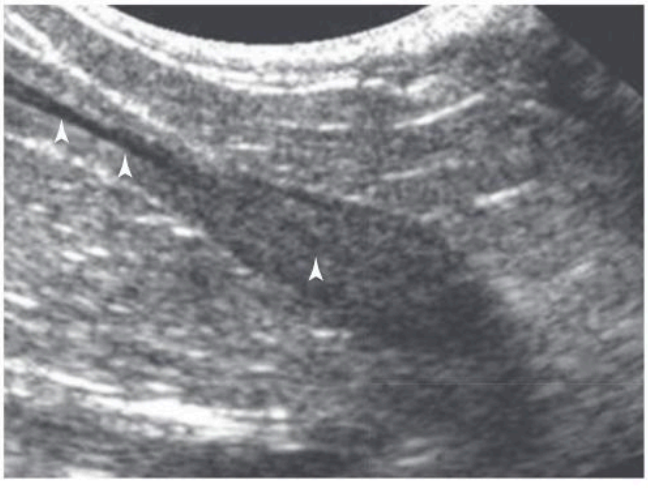


Fig. 43.9 Longitudinal ultrasonographic image of a normal prostate gland in a neutered dog. The prostate gland is small and the echogenicity is relatively homogeneous and mildly hypoechoic relative to surrounding fat. The urethra is identified a small hypoechogenicity in the center of the prostate gland (*white arrowheads*).

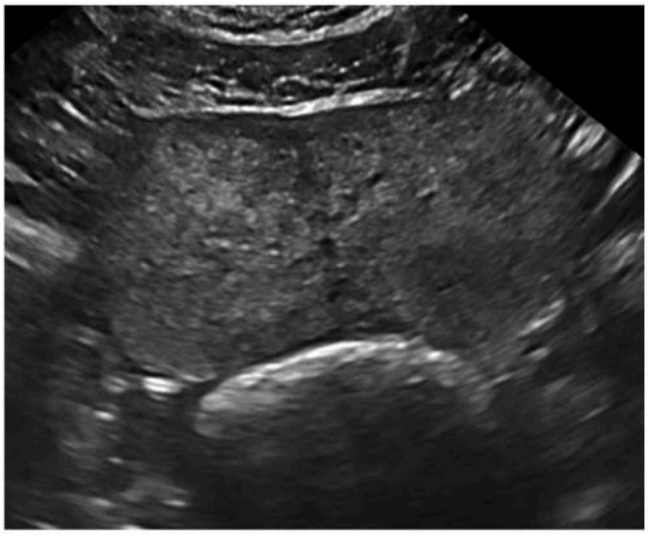


Fig. 43.10 Transverse ultrasound image of symmetric enlargement of a prostate gland in an intact male with benign prostatic hyperplasia.

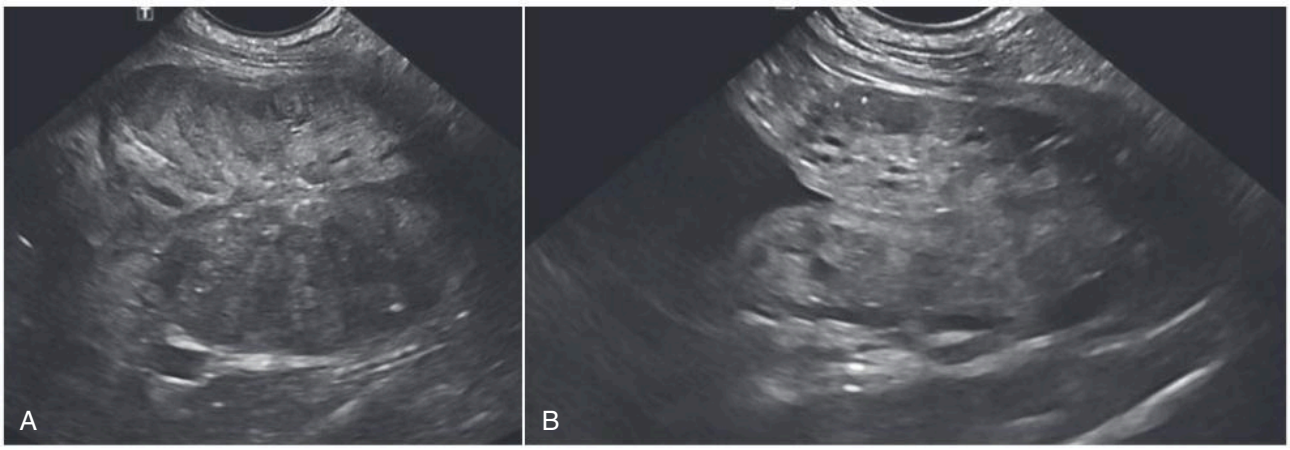


Fig. 43.11 Transverse **(A)** and sagittal **(B)** ultrasound images of an intact male dog with cystic benign prostatic hyperplasia. The prostate gland is enlarged, heterogeneous, and hyperechoic with numerous small, ovoid, thin-walled anechoic structures which display faint distal acoustic enhancement, consistent with cysts.

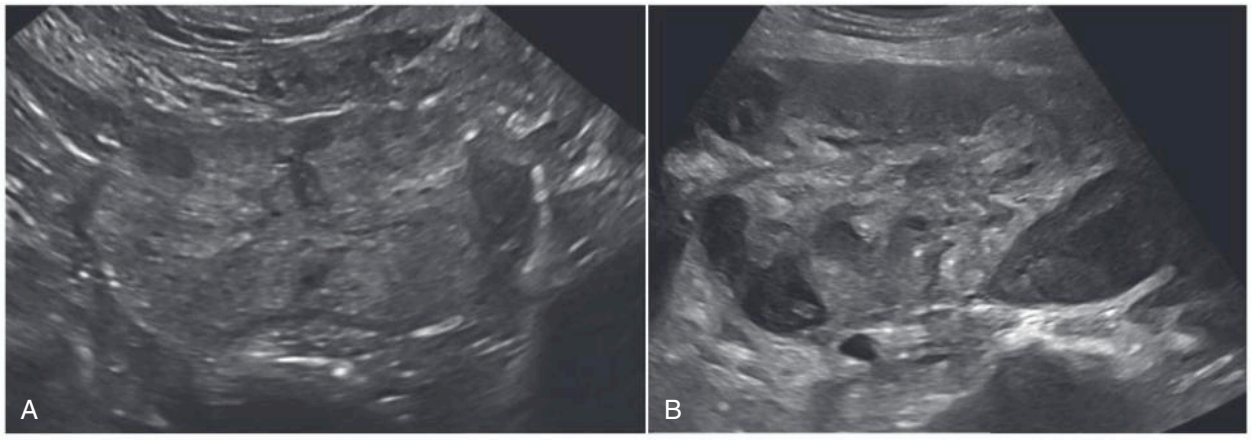


Fig. 43.12 **A,** An intact male with bacterial prostatitis. The prostate is enlarged with heterogeneous parenchyma and multifocal hypoechoic regions indicating possible edema and necrosis. **B,** Bacterial prostatitis with multiple abscesses. Note the echogenic fluid pockets which are filled with mobile cellular debris. The capsule is distorted and indistinct and the surrounding fat is hyperechoic. This patient presented in septic shock with a septic tarsal joint secondary to bacterial prostatitis.

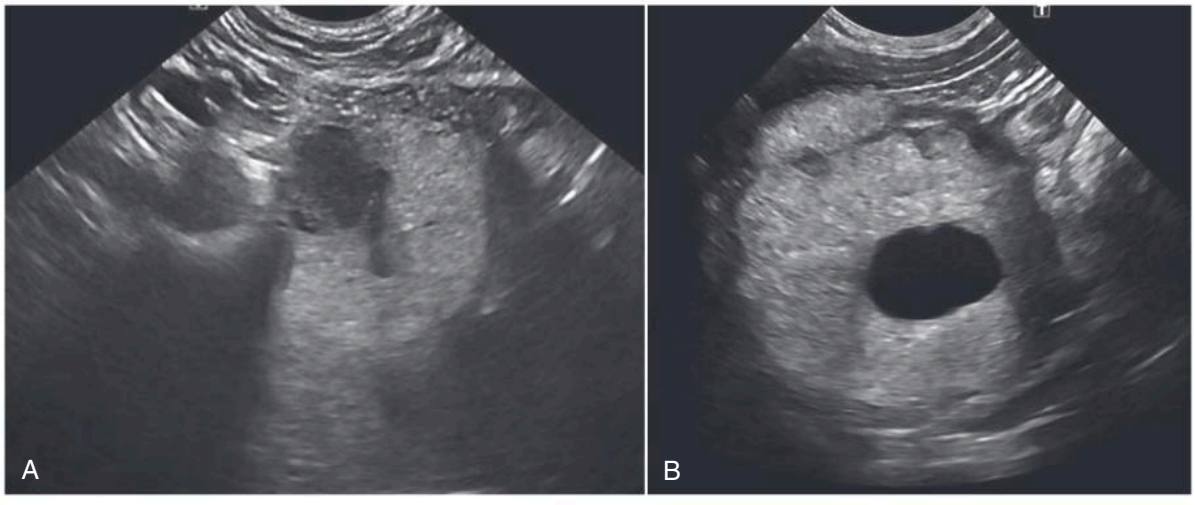


Fig. 43.13 Cavitation of the prostate gland is easily detected ultrasonographically. Such cavities may represent cysts or abscesses, but are also sometimes seen with neoplasia. Such findings warrant obtaining an ultrasound-guided prostatic wash for cytology and culture. Early cavitation is seen in **A** and more advanced cavitation is seen in **B**.

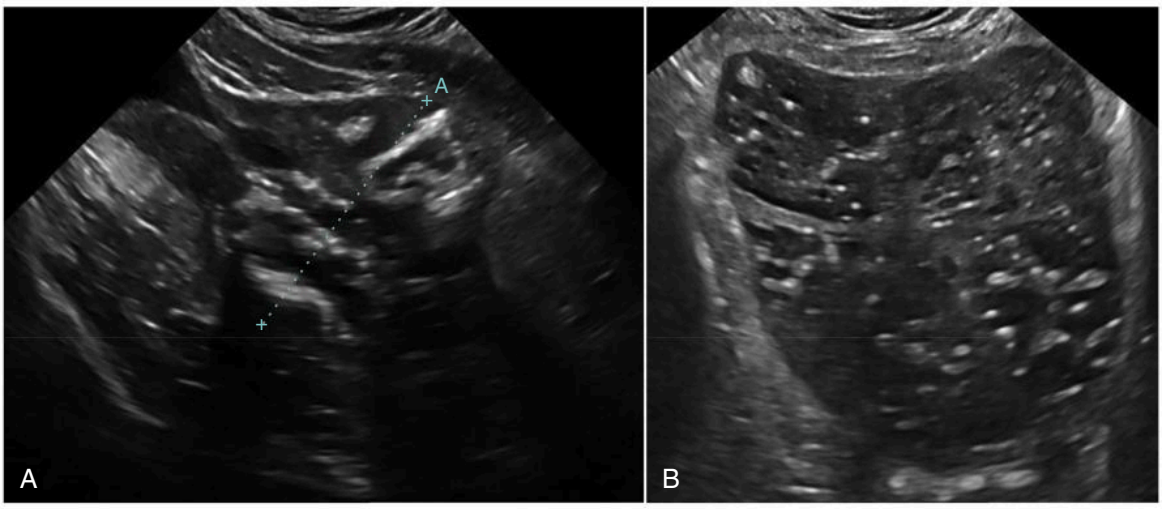


Fig. 43.14 Sagittal sonographic image of a prostate in a neutered male, displaying stippled and linear hyperechoic structures with distal shadowing consistent with calcification. Diagnosis was confirmed to be prostatic carcinoma **(A)**. Transverse ultrasonographic images of a symmetrically enlarged prostate with numerous tiny hyperechoic foci with minimal acoustic shadowing, diagnosis chronic prostatitis with dystrophic calcification in an intact male **(B)**.

Calcification within the prostate gland is recognized as bright echoes that cast shadows. Mineralization is generally considered a sign of malignancy, particularly in neutered males (Fig. 43.14). However, in some instances, chronic prostatitis in intact males can cause slight calcification of the prostate,[26] which is detectable with ultrasonography, and, anecdotally, small urinary calculi have been observed to become displaced into prostatic ducts. Thus, a diagnosis of malignancy should not be made on the basis of ultrasonographic evidence of calcification alone, but calcification is a strong justification for obtaining prostatic cytology or histopathology.

Malignant tumors of the prostate in the dog are usually advanced at the time of detection. These are highly aggressive and may destroy the architecture of the gland, resulting in a mixed echogenic pattern, and often causes asymmetric enlargement.

Contrast ultrasonography can be performed. In normal dogs, there is diffuse and uniform enhancement of the prostate.[36,37] Peak enhancement of the normal prostate occurs approximately 30 seconds after intravenous injection of the contrast agent. Prostatitis and BPH exhibit no difference in enhancement whereas prostatic carcinoma exhibited a significantly shorter time to enhancement and a greater level of enhancement than either normal dogs or dogs with benign disease.[37]

A definitive diagnosis of the type of prostatic disease cannot be made on the basis of ultrasonographic findings alone.[38] An ultrasound-guided biopsy (preferably via diagnostic catheterization) should be performed to support the ultrasonographic diagnosis. In dogs with suspected neoplasia, aspirates should be obtained of the primary lesion of interest as well as the other quadrants of the gland if the diagnosis cannot be made from diagnostic catheterization.

Computed Tomography and Magnetic Resonance Imaging

CT is rapidly becoming a mainstay of abdominal imaging in veterinary medicine and contrast enhanced CT provides superior evaluation of the prostate.[38] While not routinely used for evaluation of the prostate, MRI also provides superior images of the prostate and is especially useful for defining the internal architecture of the prostate gland.[39]

CT is more sensitive to changes in shape and opacity/attenuation of the prostate than is standard radiography. Contrast medium administration increases the conspicuity of the wall of cystic structures and perfused areas of neoplastic lesions. BPH and prostatitis cause uniform enlargement. Contrast enhancement is typically uniform with BPH with anechoic cystic lesions, whereas it is heterogeneous with prostatitis. Regional peritoneal fluid and fat stranding is often seen with prostatitis. In cases of prostatic neoplasia, asymmetric contrast enhancement and/or parenchymal mineralization are often appreciated (Fig. 43.15). CT may also be used to guide aspirates of small intraglandular sites with minimal special equipment needed.

Several different scanning sequences can be used with MRI to evaluate the prostate, with T2 and T1 (pre- and postcontrast) sequences being the most useful to clearly delineate the extent and character of the disease.[40] Cystic lesions can be detected easily without the use of contrast media, but small neoplastic lesions may not be. MRI and CT are also helpful for early detection of extension of disease beyond the prostate including metastasis to lymph nodes and osseous structures of the pelvis and spine. The greatest advantage of MRI is the excellent tissue contrast resolution and elimination of superimposition of structures, which allows better lesion characterization and localization (Fig. 43.16).

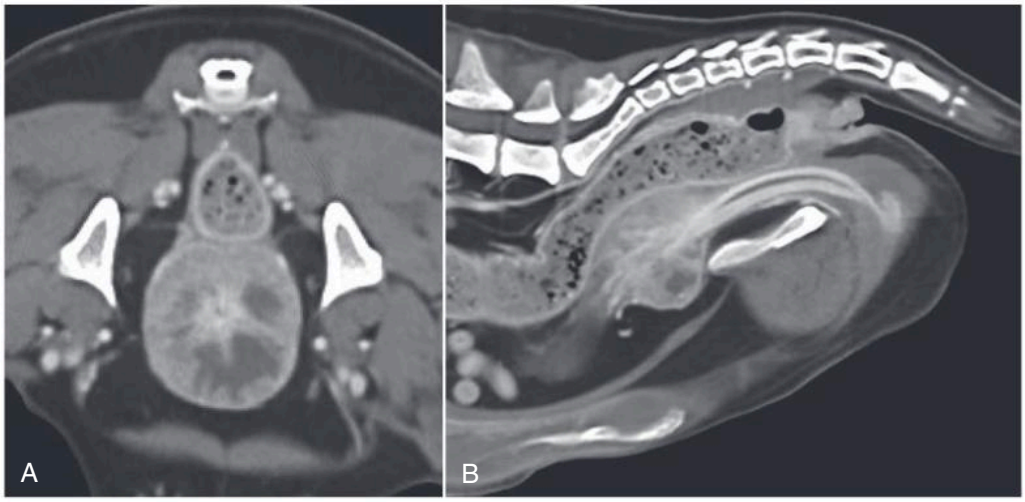


Fig. 43.15 **A,** Transverse, contrast-enhanced computed tomography (CT) image of a neutered male dog with prostatic carcinoma. The prostate gland is enlarged with asymmetrical and heterogeneous contrast enhancement. Note the faint mineral attenuating foci along the dorsal periphery of the gland bilaterally, a common feature of prostatic carcinoma. **B,** Sagittal, contrast-enhanced CT image of the same dog in image **A** with prostatic carcinoma. Note the asymmetric enlargement and heterogeneous contrast enhancement of the prostate gland. The margins of the urethra are indistinct and irregular indicating infiltration of neoplasia. Small mineral attenuating foci are seen cranially and ventrally.

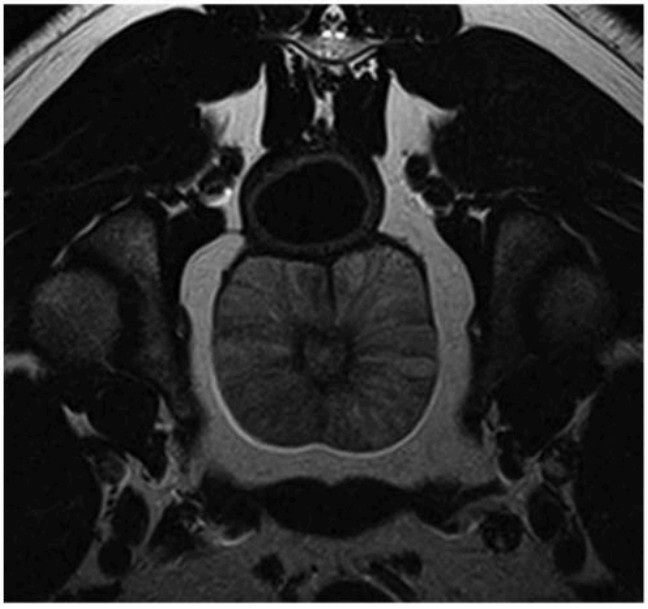


Fig. 43.16 Transverse, T2-weighted magnetic resonance image of the prostate in an intact male dog with benign prostatic hyperplasia. The prostate is symmetrically enlarged and diffusely hyperintense.

Acknowledgment

With special thanks to prior authors of this chapter for their contributions.

REFERENCES

1. Smith J. Canine prostatic disease: a review of anatomy, pathology, diagnosis, and treatment. *Theriogenology*. 2008;70:375–383.
2. Atalan G, Barr FJ, Holt PE. Comparison of ultrasonographic and radiographic measurements of canine prostate dimensions. *Vet Radiol Ultrasound*. 40(4):408-412.
3. Constantinescu GM. *Clinical Anatomy for Small Animal Practitioners*. Iowa State Press; 2002:294–295, 1999.
4. Korodi G, Igna V, Cernescu H, Mircu C, Frunză I, Knop R. Canine prostate pathology. Lucrari Stiintifice-Universitatea de Stiinte Agricole a Banatului Timisoara. *Medicina Veterinara*. 2008;41:187–194.
5. Barsanti JA, Finco DR. Canine prostatic diseases. *Vet Clin North Am Small Anim Pract*. 1986;16:587–599.
6. Ling GV, Ruby AL. Aerobic bacterial flora of the prepuce, urethra, and vagina of normal adult dogs. *Am J Vet Res*. 1987;39(4):695–698.
7. Zolton GM, Gricner TP. Prostatic abscess: surgical approach. *J Am Anim Hosp Assoc*. 1978;14:698.
8. Barsanti JA, Finco DR. Canine bacterial prostatitis. *Vet Clin North Am*. 1979;9:679.
9. Rohleder JJ, Jones JC. Emphysematous prostatitis and carcinoma in a dog. *J Am Anim Hosp Assoc*. 2002;38(5): 478–481.
10. Naouar S, Ati N, Braiek S, Kamel RE. Spontaneous rupture into the peritoneal cavity: unusual presentation of prostatic abscess. *Int J Surg Case Rep*. 2017;32:73–75.
11. Lea C, Walker D, Blazquez CA, Zaghloul O, Tappin S, Kelly D. Prostatitis and prostatic abscessation in dogs: retrospective study of 82 cases. *Australian Veterinary Journal*. 2022;100(6):223–229.
12. Palmieri C, Fonseca-Alves CE, Laufer-Amorim R. A review of canine and feline prostate pathology. *Front Vet Sci*. 2022;9:881232.
13. Smith J. Canine prostatic disease: a review of anatomy, pathology, diagnosis and treatment. *Theriogenology*. 2008;70(3):375–383.
14. Renfrew H, Barrett E, Bradley KJ, Barr FJ. Radiographic and ultrasonographic features of canine paraprostatic cysts. *Vet Radiol Ultrasound*. 2008;49(5):444–448.
15. Lim CK, Heng HG, Hui TY, Thompson CA, Childress MO, Adams LG. Ultrasonographic features of uterus masculinus in six dogs. *Vet Radiol Ultrasound*. 2015;56(1):77–83.
16. Atilola MAO, Pennock PW. Cystic uterus masculinus in the dog. *Vet Radiol*. 1986;27:8–14.
17. Polisca A, Troisi A, Fontaine E, Menchetti L, Fontbonne A. A retrospective study of canine prostatic diseases from 2002 to 2009 at the Alfort Veterinary College in France. *Theriogenology*. 2016;85(5):835–840.

18. Boland LE, Hardie RJ, Gregory SP, Lamb CR. Ultrasound-guided percutaneous drainage as the primary treatment for prostatic abscesses and cysts in dogs. *J Am Anim Hosp Assoc*. 2003;39(2):151–159.
19. Trovatelli M, Bassi J, Giudice C, Ferrari R, Longo M, Brizzola S. Prostatic leiomyosarcoma in a dog treated using a multimodal approach. *J Vet Intern Med*. 2021;35:1105–1110.
20. Holdsworth A, Bléhaut T, Reeve L, et al. An incidental prostatic leiomyoma in a dog. *Vet Rec Case Rep*. 2015;3:1–5.
21. Di Donato P, Zweifel R, Koehler K, et al. Predominance of hypoechoic tissue changes in nine dogs with malignant prostatic lymphoma. *Vet Radiol Ultrasound*. 2019;60:75–80.
22. Weaver AD. Fifteen cases of prostatic carcinoma in the dog. *Vet Rec*. 1991;109:71.
23. Bryan JN, Keeler MR, Henry CJ, et al. A population study of neutering as a risk factor for canine prostate cancer. *Prostate*. 2007;67:1174–1181.
24. LeRoy BE, Northrup N. Prostate cancer in dogs: comparative and clinical aspects. *Vet J*. 2009;180:149–162.
25. Bell FW, Klausner JS, Hayden DW, et al. Clinical and pathologic features of prostatic adenocarcinoma in sexually intact and castrated dogs: 31 cases (1970–1987). *J Am Vet Med Assoc*. 1991;199(11):1623–1630.
26. Feeney DA, Johnston GR, Klausner JS, Perman V, Leininger JR, Tomlinson MJ. Canine prostatic disease—comparison of radiographic appearance with morphologic and microbiologic findings: 30 cases (1981-1985). *J Am Vet Med Assoc*. 1987;190(8):1018–1026.
27. Cazzuli G, Damián JP, Molina E, Pessina P. Post-castration prostatic involution: a morphometric and endocrine study of healthy canines and those with benign prostatic hyperplasia. *Reprod Domest Anim*. 2022;57(2):157–164.
28. Bradbury CA, Westropp JL. Pollard RE Relationship between prostatomegaly, prostatic mineralization, and cytologic diagnosis. *Vet Radiol Ultrasound*. 2009;50(2):167–171.
29. Pugh CR, Rhodes WH, Biery DN. Contrast studies of the urogenital system, veterinary clinics of North America. *Small Animal Practice*. 1993;23(2):281–306.
30. Ackerman N. Prostatic reflux during positive contrast retrograde urethrography in the dog. *Vet Radiol*. 1983;24:251–259.
31. Johnston GR, Feeney DA, Osborne CA, et al. Effects of intravesical hydrostatic pressure and volume on the distensibility of the canine prostatic portion of the urethra. *Am J Vet Res*. 1985;46:509.
32. Vignoli M, Rossi F, Chierici C, et al. Needle tract implantation after fine needle aspiration biopsy (FNAB) of transitional cell carcinoma of the urinary bladder and adenocarcinoma of the lung. *Schweiz Arch Tierheilkd*. 2007;149(7):314–318.
33. Powe JR, Canfield PJ, Martin PA. Evaluation of the cytologic diagnosis of canine prostatic disorders. *Veterinary Clinical Pathology*. 2004;33:150–154.
34. Feeney DA, Johnston GR, Klausner JS. Two-dimensional, gray-scale ultrasonography. Applications in canine prostatic disease. *Vet Clin North Am Small Anim Pract*. 1985;15(6):1159–1176.
35. Seiler GS, Cohen EB, D'Anjou MA, et al. ACVR and ECVDI consensus statement for the standardization of the abdominal ultrasound examination. *Vet Radiol Ultrasound*. 2022;63(6):661–674.
36. Russo M, Vignoli M, Catone G, et al. Prostatic perfusion in the dog using contrast-enhanced Doppler ultrasound. *Reprod Domest Anim*. 2009;44(suppl 2):334.
37. Vignoli M, Russo M, Catone G, et al. Assessment of vascular perfusion kinetics using contrast-enhanced ultrasound for the diagnosis of prostatic disease in dogs. *Reprod Domest Anim*. 2011;46:209.
38. Lee KJ, Shimizu J, Kishimoto M, et al. Computed tomography of the prostate gland in apparently healthy entire dogs. *J Small Anim Pract*. 2011;52(3):146–151.
39. Pasikowska J, Hebel M, Niżański W, Nowak M. Computed tomography of the prostate gland in healthy intact dogs and dogs with benign prostatic hyperplasia. *Reprod Domest Anim*. 2015;50(5):776–783.
40. Yang NS, Johnson EG, Palm CA, et al. MRI characteristics of canine prostatic neoplasia. *Vet Radiol Ultrasound*. 2023;64:105–112.

ELECTRONIC RESOURCES

Additional information related to the content in Chapter 43 can be found online at eBooks.Health.Elsevier.com

- Chapter Quiz

CHAPTER 44

Uterus, Ovaries, Vagina, and Testes

Federica Rossi

Intact dogs and cats are commonly affected by diseases of the genital tract, especially infections and neoplasia. In spayed females, complications like ovarian/uterine stump infections or ovarian remnant syndrome may occur, and in cryptorchid males, retained testicles can be affected by torsion or neoplasia. All these are clinical situations where imaging is used as diagnostic workup and radiology and ultrasound are often combined. Radiographs are particularly helpful if there is significant enlargement of the genital organs and if gas and mineralization are present. Ultrasound is essential to evaluate small structures like the ovary or to define uterine content and wall structure. Cross-sectional imaging such as computed tomography (CT) is indicated to investigate challenging cases or to complete presurgical staging or radiation treatment planning in cases of genital neoplasia.

IMAGING PROCEDURES AND NORMAL ANATOMY OF THE FEMALE GENITAL TRACT

Radiography

Technique

A standard radiographic study includes three projections (left and right lateral and ventrodorsal) of the abdomen and the pelvis. A compression radiograph with the animal in lateral recumbency, as described in Chapter 38, may be added to decrease the superimposition between the colon, uterus, and urinary bladder in the caudal abdomen[1] (Fig. 44.1). However, this technique is usually replaced by ultrasonography.

Retrograde Vaginography

Positive contrast vaginography can be performed in dogs and cats under general anesthesia as part of the workup in case of vaginal diseases.[2,3] Because of technical challenges and reported high risks of vagina rupture if the tip of the catheter is placed too cranially in the vagina, this technique should be replaced by other diagnostic modalities (vaginoscopy or advanced cross-sectional imaging) whenever possible. If correctly performed (Fig. 44.2), it can be successfully used in special circumstances, especially with diseases which impair a complete direct examination of the vagina lumen.[4] To avoid misinterpretation due to fecal content in the descending colon and rectum, an enema is necessary before the procedure. A Foley catheter prefilled with contrast medium is placed at the vaginal vestibulum, caudal to the urethral orifice, and gently inflated with saline. A tissue forceps is positioned at the vulva to prevent contrast medium leakage and the expulsion of the catheter. Under fluoroscopic guidance, approximately 1 mL/kg of diluted iodinated contrast medium (150–200 mg I/mL concentration) is infused until moderate distention of the vagina and vestibulum is reached and the urethra is opacified. A slight narrowing is normally visible between the vagina and the vestibulum in the lateral view. If the procedure is performed in estrus and the cervix is open, contrast medium can enter the uterus. Incomplete distention of the vestibulum and vagina produces mucosal irregularity mimicking vaginal diseases. Air bubbles can be confused with filling defects caused by vaginal masses.

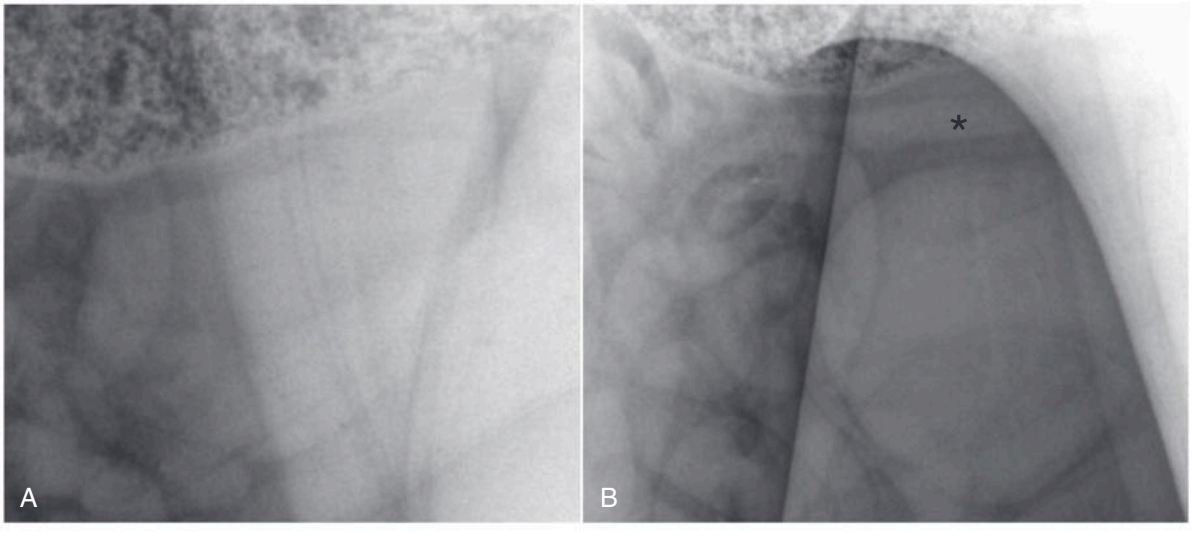


Fig. 44.1 Lateral standard and compression radiographs of the ventro-caudal abdomen of a normal female dog. The uterus (*asterisk*) is visible between the colon and the urinary bladder only in the compression view.

Anatomy and Normal Imaging Findings

The normal female genital tract is not usually visible on radiographs in the nonpregnant dog. The uterus can sometimes be identified in digital radiographs as a linear soft tissue opacity located between the descending colon and the urinary bladder on the lateral projection. However, the reported sensitivity of radiology is low (28%), even if caudal abdominal compression is used (58%) (see Fig. 44.1).[2] It is important to know the normal anatomic location of these structures in order to interpret abnormal findings (Fig. 44.3).[5,6] The small oval ovaries (approximately 1 × 2 cm in a medium-sized dog and 0.5 × 1 cm in the cat) lie caudolateral to each kidney, in contact with the parietal peritoneum of the abdominal wall, surrounded by the fat of the ovarian bursa. In the dog, the distance between the caudal pole of the kidney and the ovary is greater on the right side (2–3 cm versus 1 cm on the left). After multiple pregnancies, the ovaries assume a more caudoventral position.[5,6]

The uterine horns have variable length and uniform diameter in a nulliparous animal (0.5–1 cm in the bitch and 3–4 mm in the cat). In the proximal half, they assume a lateral position, in contact with the lumbar abdominal wall. Distally, they become more ventral and axially located, with variable contact with the descending colon and the small intestinal loops. In the caudal abdomen, the uterine horns converge dorsal to the urinary bladder. When enlarged because of pregnancy or fluid collection, the uterine horns bend upon themselves and displace ventrally. The short uterine body and neck (*cervix uteri*) lie dorsal to the urinary bladder and ventral to the descending colon to enter the pelvic inlet. The cervix is characterized by a thicker muscular layer; its lumen opens during estrus just before the luteinizing hormone (LH) peak. The vagina is a long tubular structure (12–15 cm in the dog and 2–3 in the cat), highly dilatable due to the presence of longitudinal folds. The cranial part of the vagina is covered by peritoneal reflection; the caudal part lies in the retroperitoneum. The most caudal portions of the female genital tract are the vestibulum and vulva. At the cranial vestibulum, the urethra opens ventrally with an elevated tubercle.

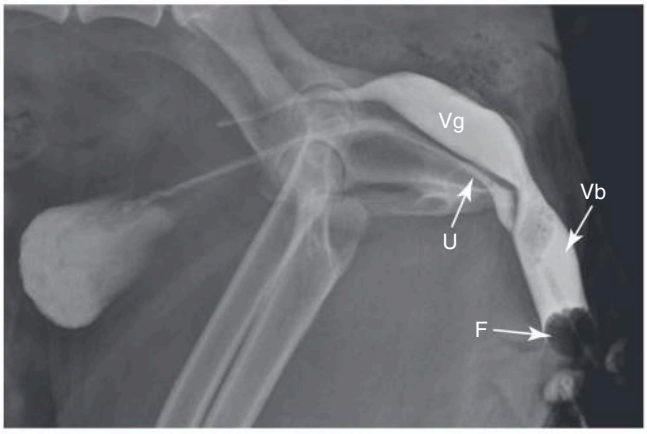


Fig. 44.2 Lateral view of a normal vaginogram. The balloon of the Foley catheter (*F*) is visible in the caudal aspect of the vestibule (*Vb*). To avoid overdistention or rupture of the vagina (*Vg*), it is important to make sure the tip of the catheter is within the vestibule, and not the vagina, when contrast medium is injected. As an added margin of safety, the tip of the Foley catheter can be removed before insertion. When the vestibule and vagina are distended maximally, further contrast medium injection usually results in filling of the urethra (*U*).

ULTRASOUND

Technique

Ultrasound provides information about size, shape, structure, and contents of the genital tract.[7,8]

The first general approach is usually performed with a medium-/high-frequency microconvex probe (5–7.5 MHz, depending on the animal size); however, a complete and detailed exam of the small uterine horns and superficial ovaries requires a linear high-frequency probe (10–18 MHz) especially in small-/medium-sized dogs and cats. To identify the ovaries, the caudal pole of the kidney is first imaged in longitudinal plane and the probe is translated caudally and slightly fanned laterally to scan the adipose area caudal to the kidney. The

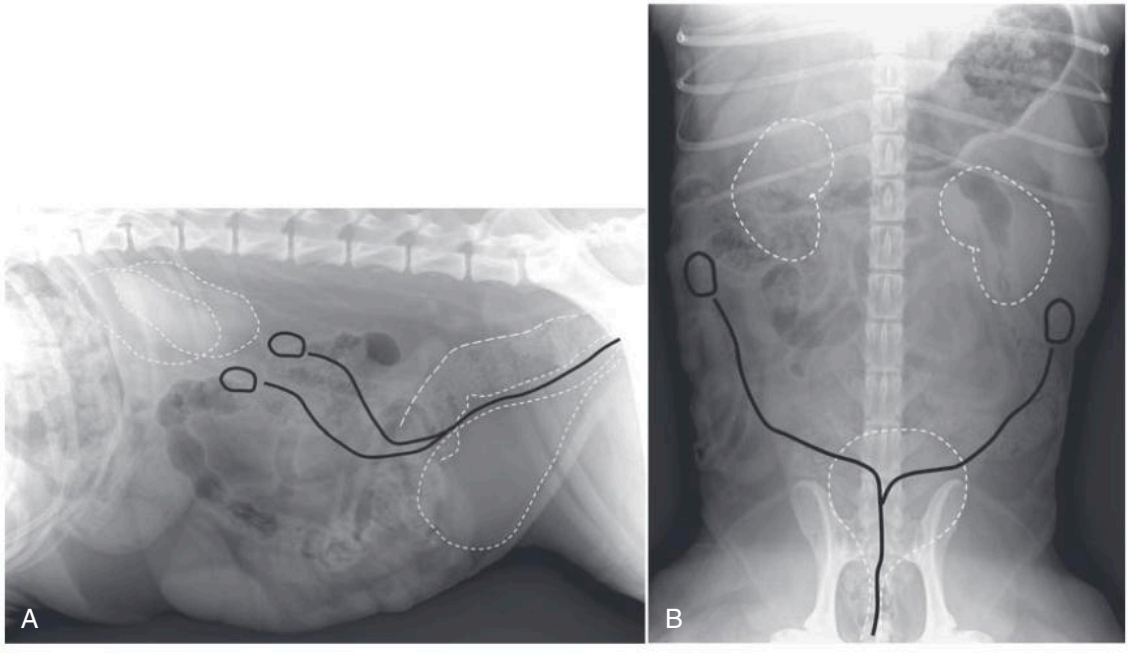


Fig. 44.3 Schematic representation of the position of the normal canine female genital tract in a lateral **(A)** and ventrodorsal **(B)** radiograph. The ovaries and uterus are indicated by *black lines*. The *white dotted lines* outline the kidneys, descending colon, and urinary bladder.

easiest way to localize the uterus is to start from the body and cervix in transverse plane. With the animal in dorsal or lateral recumbency, the colon and the urinary bladder are identified cranial to the pubis, and the uterus appears as a round/oval hypoechoic structure located between the two organs, often slightly displaced to the left or right. Moving the probe cranially, the bifurcation of the body into the two uterine horns is visible.

The normal vagina is difficult to see through the abdominal approach because of the intrapelvic location. The perineal window might be useful to identify the vulva and the caudal vagina especially if enlarged by diseases like masses or if distended by fluid.

Normal Imaging Finding

Table 44.1 and associated figures summarize the ultrasound features of the normal genital tract in the different phases of the cycle.[9–12]

During anestrus, the normal ovaries are oval hypoechoic structures compared to the hyperechoic fat of the ovarian bursa. Often, they are associated with edge shadowing, which helps in their identification. The uterine horns are hypoechoic with a diameter similar to the jejunal loops but without the wall layering and peristalsis typical for intestines.

Ovaries are easier to identify in the periovulatory period because they are larger and contain small cyst-like structures representing follicles or newly formed corpora lutea. Follicles have anechoic content and a thin wall (less than 1 mm). The number and size of follicles increase during proestrus until ovulation, when they become corpora lutea with a progressively more echogenic appearance and thicker wall. Corpora lutea identification can be challenging or impossible when they become isoechoic with the surrounding ovary.[11] Since follicles and newly formed corpora lutea may have a similar appearance, B-mode ultrasound alone cannot be used to accurately determine the ovulation time but must be interpreted in combination with clinical findings and laboratory results.[9,10] Sequential (daily) scanning of the ovary during proestrus using color Doppler can accurately predict ovulation in the dog, by detecting increases of the blood flow that correlate with LH peak.[11]

Under hormonal influence during proestrus/estrus and diestrus, the uterine wall mildly thickens, and this can improve its visibility. A minimal amount of anechoic to hypoechoic fluid can be observed in the lumen in proestrus/estrus or immediately after mating. The persistence of some fluid 5 to 14 days after ovulation suggests lack of pregnancy.[13]

COMPUTED TOMOGRAPHY

Technique

Standard CT examination is performed with the animal in sternal recumbency under general anesthesia. Pre- and post-contrast series are obtained after injection of iodinated contrast medium at the dose of 400 to 700 mg I/kg body weight. Delayed sequences (3 minutes or later) may be useful to better outline the caudal ureters or the urinary bladder neck which can be affected by uterine or vaginal diseases (e.g., stump granuloma/abscess).

Similar to retrograde vaginography, CT vagino-urethrogram can be performed using the same technique as previously described, with the only difference that the contrast medium concentration can be lowered to 100 mg I/mL. This technique can be useful in the diagnosis of vaginal masses and genitourinary congenital and acquires abnormalities like clefts, fistulae, stenoses, or strictures.[14,15]

Normal Imaging Findings

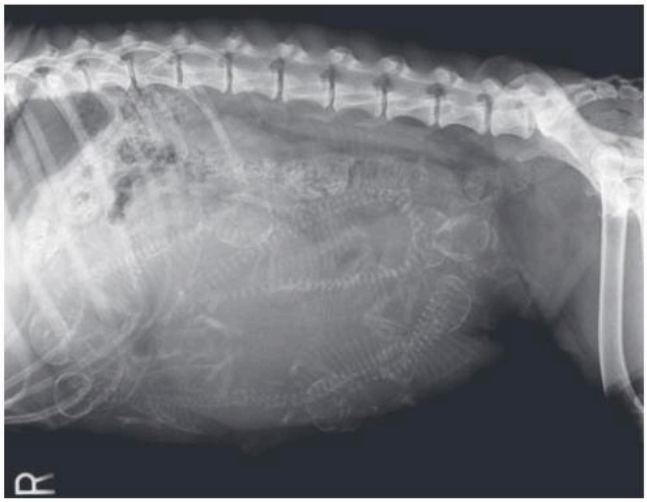
In anestrus, the ovaries are small, oval, and with homogeneous soft tissue attenuation (Fig. 44.4A). Follicles and corpora lutea are visible as small round hypoattenuating structures, often protruding from the ovarian surface. The uterus is a tubular organ, the uterine horns mix with the intestinal loops as they extend into the caudal abdomen to reach the dorsal aspect of the urinary bladder.[16] The uterine horns can be distinguished from the small bowel by its smaller diameter, different wall structure, and contrast enhancement (see Fig. 44.4B).[17] The uterine body and cervix are recognized between the colon and the urinary bladder; the cervix may be thickened during estrus (see Fig. 44.4C). The vagina is located in the pelvis. In post-contrast images, the urethral wall strongly enhances; this enables its identification caudally to the bladder neck (see Fig. 44.4D). The vestibulum is oriented caudoventrally and ends caudally with the vulva.

NORMAL PREGNANCY

Radiology and ultrasonography play an essential role in the pregnancy diagnosis and follow-up. Ultrasound can be used, together with the determination of the progesterone level, to establish the gestational age and the prediction of delivery timing. Both imaging techniques allow to determine litter size; however, radiology is more accurate compared to ultrasound.

The enlargement of the uterus during pregnancy can be detected with radiology by day 33 to 41.[18] The enlarged uterus initially is soft tissue opaque as with any other uterine fluid collection. Between 30 and 40 days after ovulation, the identification of multiple ovoid bulging areas of similar size might suggest the presence of gestational sacs (Fig. 44.5). Later, the uterus becomes more tubular.[3] Fetal mineralization starts 20 to 22 days before parturition (DBP) in dogs and 25 to 29 DBP in cats. The first structures that can be identified are the spine and the skull from day 43 in the dog and day 38 in the cat.[18,19] Progression of mineralization can be followed until the parturition, when the distal extremities of the fetus and the teeth are recognized (Fig. 44.6, eFig. 44.1). Table 44.2 summarizes the mineralization timing of some fetal structures in dogs and cats, which could be useful to predict parturition. A radiographic study taken with at least two orthogonal projections at the end of pregnancy can be used to determine fetal number and position, to compare their size with the pelvic diameter, and to exclude pelvic abnormalities which could cause mechanical dystocia. Both anterior and posterior presentation with extended limbs is normal. However, radiographs are not adequate to predict fetal maturity and establish the time of Cesarean section.[20] Radiographic or CT pelvimetry has been evaluated as a tool to assess pelvic conformation in some brachycephalic breeds and correlates with dystocia.[21,22]

Early pregnancy diagnosis with ultrasound relies on the visualization of the chorionic cavity/gestational sacs, which are reported to occur on day 18 after ovulation (defined as the day when the plasma progesterone level is first >4.0 ng/mL) in the bitch and as early as 10 days after breeding in the queen.[20] In clinical practice, scanning between the 25th and 30th days in the bitch and the 20th and 25th days after breeding in the queen allows to confirm the pregnancy and obtain fetal biometry measurements. Especially in the bitch, the exact conception time is usually not known and there is a risk of a false-negative result if the ultrasound examination is performed too early. The development of the fetal organs can be followed, and the detection time of specific structures is another reliable indicator

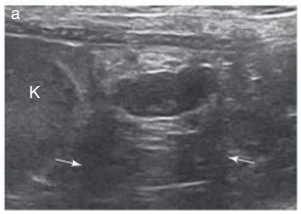
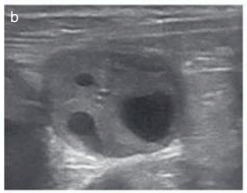
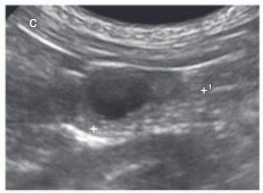
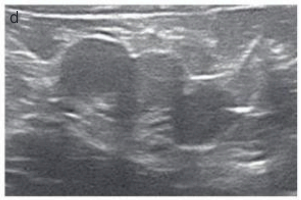


eFig. 44.1 Radiograph of a dog with a normal gravid uterus. Note the direction of displacement of other organs resulting from the enlarged uterus.

Vetacademy.ir
مجموعه آموزشی پژوهشی
وت آکادمی
تلاش
#برای_دنیای_بهتر_حیوانات
تیم وت آکادمی
برای دسترسی به تازه ترین آموزش ها و
مطالب علمی دامپزشکی؛ وت آکادمی رو فالو کن
سایت مجموعه بزرگ آموزشی پژوهشی وت آکادمی
Vet-academy.ir
صفحه ی اینستاگرام وت آکادمی
@Vetacademy.ir
دسترسی به آرشیو صد گیگ کتاب آموزش دامپزشکی به صورت رایگان
و جزوه های آموزشی در کانال تلگرامی
@Vetfiles
گروه بزرگ تلگرامی، پرسش و پاسخ و آموزش
@VetAcademyGp
صفحه رسمی آپارات وت آکادمی
aparat.com/vetacademy.ir

Table • **44.1**

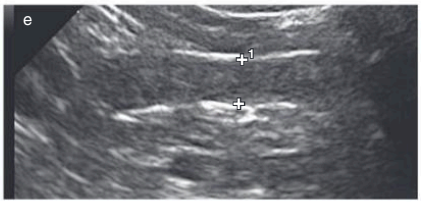
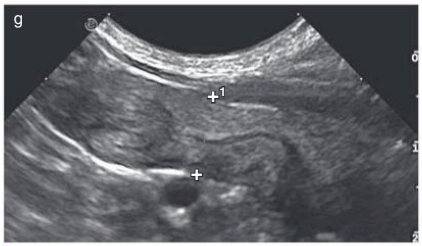
Ultrasonographic Features of the Normal Ovary and Uterus in the Different Cyclus Phases.[9–13]

OVARY	ANESTRUS	PROESTRUS/ESTRUS	DIESTRUS
	 **Table Fig. 44.1a** Ovary in anestrus. *K*, Kidney	  **Table Fig. 44.1b** Ovary with follicles. **Table Fig. 44.2c** Ovary (*between calipers*) with early corpus luteum	 **Table Fig. 44.1d** Ovary with multiple corpora lutea.
Shape	Oval to round	Round or lumpy due to protruding follicles	Round or lumpy due to protruding corpora lutea
Size	1–2 cm of length (dog) 7.1–13.9 mm of length (cat)	Enlarges due to follicles	Enlarges due to corpora lutea
Margins	Smooth	Smooth to irregular	Smooth to irregular
Echostructure/ echogenicity	Homogeneous, hypoechoic to the surrounding fat Iso- to hypoechoic to the renal cortex Associated with edge shadowing (*arrows*)	Heterogeneous **Follicles/early corpora lutea:** - Up to 10, follicles number decreases after ovulation - 4–11 mm (dog), 1–2.3 mm (cat) in diameter - Cystic-like structures with anechoic content - **Follicula**, thin hyperechoic wall (1 mm) - **Newly formed corpora lutea**, may have thicker wall and gradual increase in echogenicity	Homogeneous Corpora lutea appear solid, hypoechoic homogeneous
Relationship with other organs	**Dorsolateral:** abdominal wall **Medial:** large vessels (aorta, caudal vena cava) **Cranial:** kidney **Caudo-ventral:** small intestinal loops and colon		
Vessels	**Ovarian arteries**—origin directly from the aorta **Ovarian veins**—drain into the caudal vena cava (*right*) or left renal vein (*left*)	A significant increase of Doppler signal of the ovary is observed after the LH peak	
Regional lymph nodes	Lumbar aortic lymph nodes		

Continued

Table • **44.1**

Ultrasonographic Features of the Normal Ovary and Uterus in the Different Cyclus Phases.[9–13]

UTERUS	UTERINE HORNS	UTERINE BODY	UTERINE CERVIX
	 **Table Fig. 44.1e** Uterine horn in anestrus.	 **Table Fig. 44.1f** Uterine body (*between arrows*) in anestrus.	 **Table Fig. 44.1g** Uterine cervix (*between calipers*) during estrus.
Shape	Tubular (longitudinal), round/oval (transverse)		
Size	Varies depending on the dog size, previous pregnancies, and cyclus Dog: 0.5–1 cm; cat: 1–5.8 mm	Dog: 0.8–1 cm; cat: 1.5–5.3 mm	Identified as a thicker area caudal to the uterine body especially in estrus Dog: 0.8–1 cm
Margins		Smooth	
Echogenicity/ echostructure	Usually homogeneous hypoechoic Outer thin hyperechoic interface between the serosa and surrounding tissue Wall layering visible with high-resolution probe (hypoechoic endometrium and hyperechoic myometrium) Central hyperechoic lumen or small fluid accumulation often visible in proestrus and estrus	Homogeneous hypoechoic Minimal intraluminal fluid accumulation often visible in proestrus and estrus	Minimal intraluminal fluid accumulation often visible in proestrus and estrus
Relationship with other organs	Cranial: ovary Dorsolateral: abdominal wall Ventral and caudal: small intestinal loops and colon, urinary bladder	Cranial: uterine horns Caudal: cervix Dorsal: colon Ventral: urinary bladder	Cranial: uterine body Caudal: vagina Dorsal: colon Ventral: urinary bladder neck
Vessels	**Ovarian arteries**—origin directly from the aorta **Ovarian veins**—drain into the caudal vena cava (right) or left renal vein (left). They supply the cranial part of the uterus and anastomize with the **uterine arteries and veins**	**Uterine arteries and veins**—arise from the vaginal arteries/veins **Vaginal arteries and veins**—branch of the iliac internal arteries/veins	**Uterine arteries and veins**—arise from the vaginal arteries/veins **Vaginal arteries and veins**—branch of the iliac internal arteries/veins
Regional lymph nodes	**Cranial half:** lumbar aortic and medial iliac **Caudal half:** Internal, medial iliac, sacral	Internal, medial iliac, sacral	Internal, medial iliac, sacral

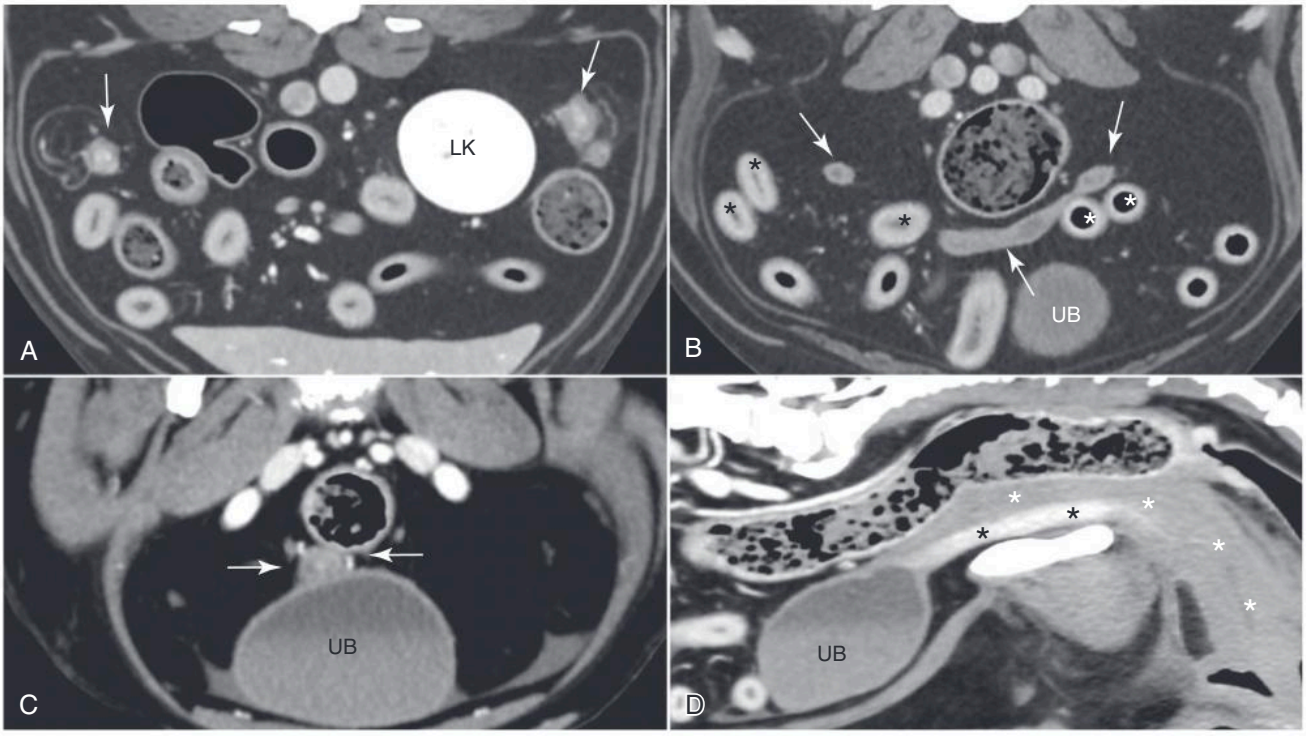


Fig. 44.4 Transverse **(A—C)** and sagittal reformatted **(D)** postcontrast computed tomography images of the normal canine female genital tract. **A**, Midabdomen. The ovaries (*white arrows)* appear as small structure with a soft tissue attenuation surrounded by the fat of the ovarian bursa. **B,** Mid-caudal abdomen. The uterine horns (*white arrows*) have a smaller diameter and different wall compared to small intestinal loops (*white asterisks*); they converge caudally dorsal to the UB and are minimally distended by fluid in this dog. **C,** Caudal abdomen. The uterine cervix (*between arrows*) is visible dorsal to the UB. **D,** The vagina (*white asterisks*) is located between the colon and the urethra (*black asterisks*). Note the strong urethra enhancement in the postcontrast study. *LK,* Left kidney; *UB,* urinary bladder.

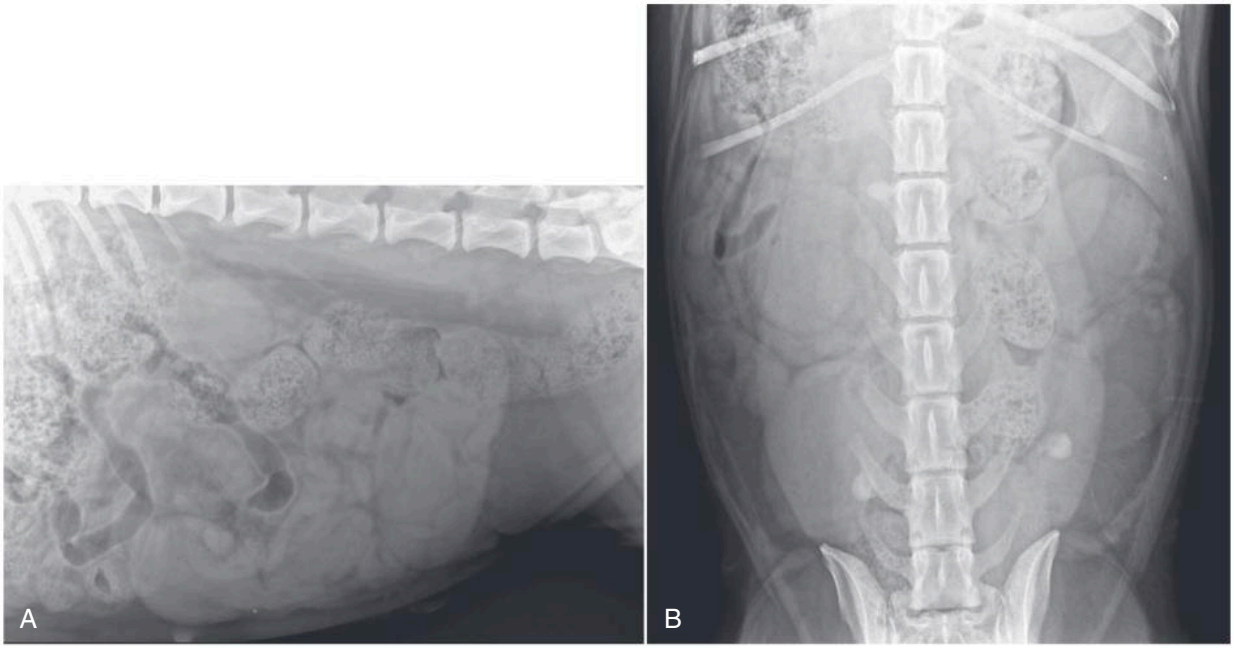


Fig. 44.5 Uterus enlargement in a pregnant bitch (35th day); the gestational chambers are seen as multiple oval soft tissue opacities located in the caudoventral abdomen in the lateral view **(A)** and close to the abdominal wall in the ventrodorsal view **(B)**.

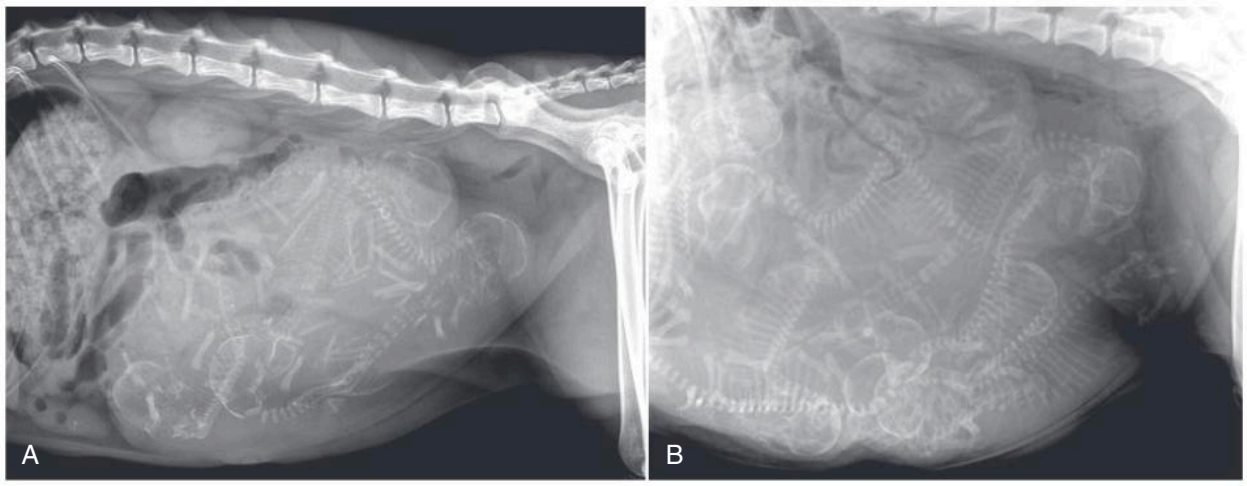


Fig. 44.6 Lateral abdominal radiograph during normal late pregnancy in a cat **(A)** and in a dog **(B)**.

Table • 44.2

Approximate Timing of Mineralization of Fetal Structures in Dogs and Cats.

	TIMING IN DAYS BEFORE PARTURITION[A]	
FETAL STRUCTURE	FELINE[21]	CANINE[20]
Uterus first seen	—	33–41
Spine	22–27	20–22
Skull	21–27	20–22
Ribs	20–25	20–22
Femur	19–23	15–18
Humerus	20–24	15–18
Radius	15–22	9–13
Tibia	15–21	9–13
Pelvis	8–20	9–13
Metacarpals/metatarsals	3–14	2–9
Phalanges	0–11	2–9
Calcaneus	0–10	2–9
Teeth	1–6	3–8

[a]The timings are given as the number of days before parturition.

of fetal age.[20,23] Table 44.3, with associated figures and videos, summarizes the timing and ultrasound features of the embryo/fetal structures during pregnancy.[23–25]

Estimation of parturition date can be performed by ultrasound. Multiple methods and formulas have been proposed with some limitations due to variation in breed and size (especially in dogs), litter size (only for cats), gestational period in which the measurement is performed, and measuring technique.[20,26–28] These formulas allow to calculate the DBP. In small- and medium-sized dogs, the internal diameter of the chorionic cavity (ICC) measured in the first half of pregnancy and the transverse biparietal skull diameter (BD) in the second half seem to be the most useful parameters, with 85% to 95% of reported accuracy in predicting DBP with an error of ±1–2 days. Accuracy is higher at week 5 of gestation and decreases after week 8. In large and giant dogs, the reported accuracy of measuring ICC is greater compared to the BD.[27]

Table 44.4 summarizes reported formulas that can be used in dogs and cats to calculate the number of DBP.

Establishing **litter size** by ultrasound is more challenging compared to radiography; this is due to technical difficulties (amount of fecal and intestinal gas content, overlapping of fetuses), limited field of view, and operator experience.[29] Embryonic or fetal resorption has an estimated incidence between 5% and 13% in bitches; this is a potential cause of litter overestimation. Reported accuracy of ultrasonography in determining litter size is 65%, increasing to 89.5% if an error of ±1 is considered.[29] To increase the success of the evaluation, scanning in transverse plane from caudal to cranial following the two uterine horns at around 30 days of gestation is recommended.[7]

ABNORMAL RADIOGRAPHIC AND ULTRASONOGRAPHIC FINDINGS DURING PREGNANCY

Combining ultrasound and radiology can be useful to detect uterine or fetal abnormalities during pregnancy.[30,31]

Early resorption of underdeveloped or malformed embryos can be documented ultrasonographically, the features depending upon the timing of the resorption. Early during pregnancy, a characteristic appearance of echogenic particles within the yolk sac, progressive loss of fluid volume, and hypoechogenicity of the adjacent uterus are observed. Gestational sacs are more irregular in shape and smaller compared to normal ones (Fig. 44.7A). Later cases are characterized by loss of the fetal heartbeat and fetal movements, blurring of the fetal margins, and more echogenic allantoic fluid.[31] Accumulation of gas in the fetal stomach or in the uterus can also be observed. Some fetal malformations can be diagnosed during pregnancy, for example, hydrocephalus and hydrops fetalis, where subcutaneous thickening due to edema, pleural, and pericardial fluid is reported.[30]

Radiographic signs of fetal death may be observed approximately 24 hours after death and are less reliable than sonographic indicators. The presence of gas within or around the fetus, overlapping or misalignment of the bones of the cranium, a tightly curled fetus, and collapse of the fetal skeleton may be evident (Fig. 44.8A,B). Care must be taken to differentiate these findings from gastrointestinal gas and projection obliquity especially in early phases. The presence of delayed development of a fetus relative to litter mates is also an indication of demise (Fig. 44.9A).

Table • **44.3**

US Findings in Normal Pregnancy.[25–27]

STRUCTURE	TIME, DAYS AFTER OVULATION (PROGESTERONE RAISE)	US FEATURES
Gestational sac **Chorionic cavity**	18th (dog) 10th (cat)	Anechoic round, thin walled
Early embryo	21st–23rd (dog) 17th (cat)	**Elongated** (dog), structure in contact with the uterine wall **Hyperechoic spot** protruding into the gestational chamber **Heartbeat** appears as hyperechoic flick

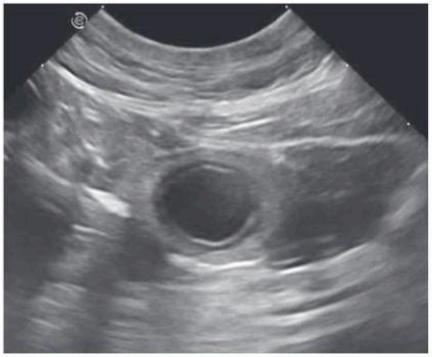


Table Fig. 44.3a Chorionic cavity—day 18.

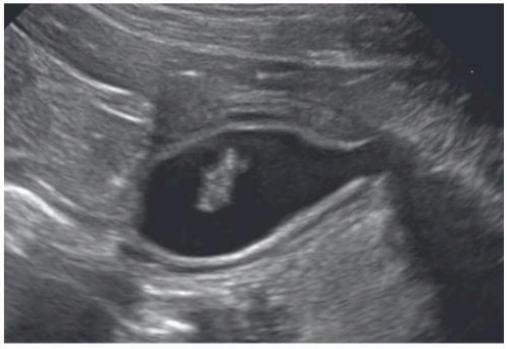


Table Fig. 44.3b Gestational sac with early embryo—day 21. Video 44.1 (heart flick)

Continued

Table • 44.3

US Findings in Normal Pregnancy.[25–27]*—cont'd*

STRUCTURE	TIME, DAYS AFTER OVULATION (PROGESTERONE RAISE)	US FEATURES
Late embryo	27th–31st (dog) 18th–20th (cat)	**Bipolar** (head and trunk) with limb buds (dog) **C-shape** with head, trunk, and thoracic limb buds; moves to the center of the sac (cat) Measurement of the internal diameter of the chorionic cavity **(ICC)**



Table Fig. 44.3c Chorionic cavity with bipolar fetus, day 28. Measurement of the internal diameter of the chorionic cavity (ICC).

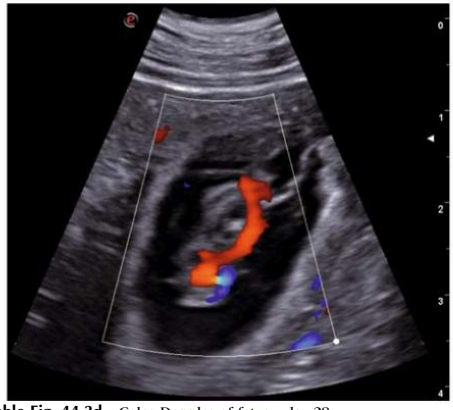


Table Fig. 44.3d Color Doppler of fetus—day 28.

Fetus—first organs	29th–33rd (dog) 39th (cat) 31st–35th (dog), 30th (cat) 35th–38th (dog) 40th–50th (cat) 41st–43rd (dog) 50th (cat) 50th 57th–63rd (dog), 40th (cat)	Stomach (anechoic) and skeleton (hyperechoic nonmineralized) Urinary bladder (anechoic) Lung (hyperechoic) and liver (hypoechoic) Kidneys Heart chambers and major vessels Mineralized skeleton (shadowing) Bowel—in dogs, peristalsis starts at the end Measurement of the transverse biparietal skull diameter **(BD)**
Fetal movements	32nd–24th (dog) 30th (cat)	

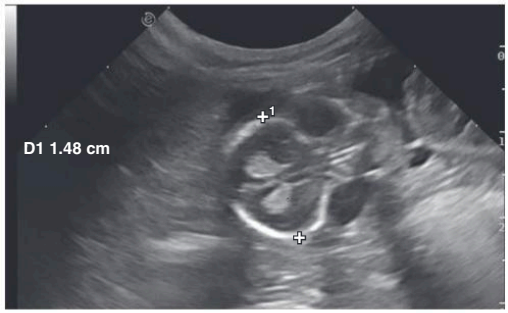


Table Fig. 44.3e Measurement of biparietal diameter (BD)—day 45.



Table Fig. 44.3f Sagittal fetus with visible heart, lung, aorta, liver, stomach—day 45.

Video 44.2 - fetal movements - day 45

Continued

Table • 44.3

US Findings in Normal Pregnancy.[25–27]*—cont'd*

STRUCTURE	TIME, DAYS AFTER OVULATION (PROGESTERONE RAISE)	US FEATURES
Placenta	25th–27th (dog)	Circumferential, focal thickening of the chorionic cavity wall, protruding toward the lumen, hyperechoic, at the periphery two areas of thickening (marginal hematomas)
Fetal membranes	18th–23rd 23rd–25th 29th–32nd 25th–29th	Anechoic content surrounds the early embryo Echogenic yolk sac membranes, folded around the embryo Collapsing yolk sac Thin hyperechoic allantoic membranes surrounding the embryo

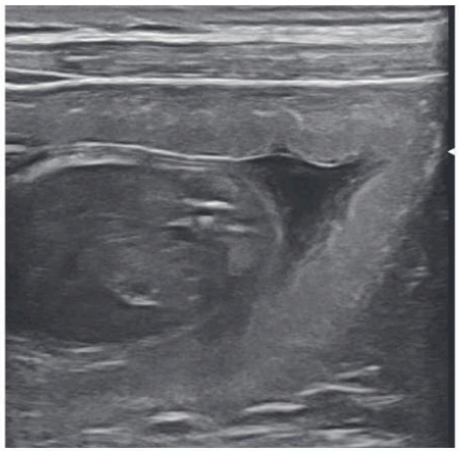


Table Fig. 44.3g Placenta—day 45.



Table Fig. 44.3h Fetal membranes—day 33.

Uterine vessels	Early pregnancy	Utero-placental arteries seen between gestational sacs Umbilical cord arteries and veins can be distinguished with Doppler after the fourth week. Arterial resistivity index (RI) and pulsatility index (PI) decrease during pregnancy



Table Fig. 44.3i Utero-placental vessels—day 38.



Table Fig. 44.3j Umbilical vessels—day 38

Table • 44.4

Ultrasonographic Calculation of Gestational Age (Days Before Parturition).

	DBP = ICC (MM)	DBP = BD (MM)	ACCURACY (%) ±2 DAYS (5−8 WEEKS OF GESTATION)
Dog—small size bitches[22]	−68.68/1.53	−25.11/0.61	85−95
Dog—medium size bitches[22]	−82.13/1.8	−29.18/0.7	85−95
Dog—large size bitches[29]	−105.1/2.5	−30/0.8	83.1 (ICC); 88.3 (BD)
Dog—giant size bitches[29]	−88.1/1.9	−29/0.7	100 (ICC); 84.6 (BD)
Cat[30]	−62.03/1.1	−23.39/0.47	61.5 (ICC)—85.7 (BD)

BD, Transverse biparietal diameter; *ICC*, internal diameter of the chorionic cavity.

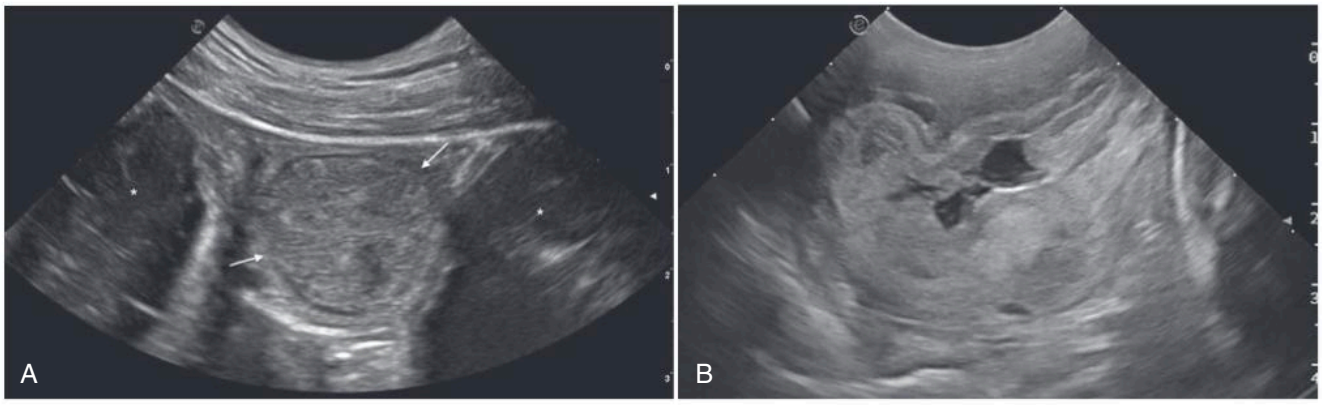


Fig. 44.7 Ultrasound images of two pregnant dogs. **A,** Early embryonic resorption; a small gestational chamber with hyperechoic content (*arrows*) is visible between two normal embryos (*asterisks*). **B,** Uterus after abortion of one of the two fetuses; the uterine wall is focally thickened with some intraluminal fluid. The viable fetus is not shown in this image.

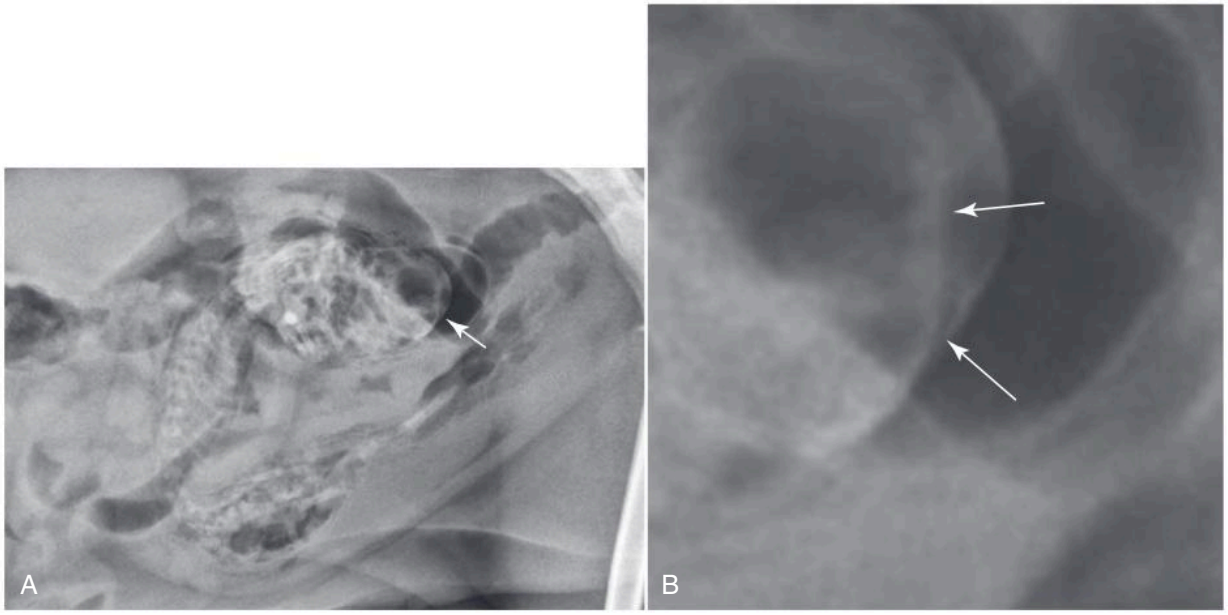


Fig. 44.8 Fetal demise in a cat. **A,** There is gas around the fetus and overlap of the skull bones (*white arrow*). **B,** Close-up of the skull and area of bone overlap (*white arrows*).

Mummification and ectopic pregnancy are rarely reported in dogs and occasionally in cats. Ectopic pregnancy can be primary (migration of the fertilized ova into the peritoneal cavity) or secondary to trauma or uterine rupture.[30] The residual parts of the mineralized fetuses are easily recognized radiographically (see Fig. 44.9 A,B).

Fetal distress at parturition can be monitored by ultrasound using M-mode or pulsed-wave Doppler. Bradycardia is the

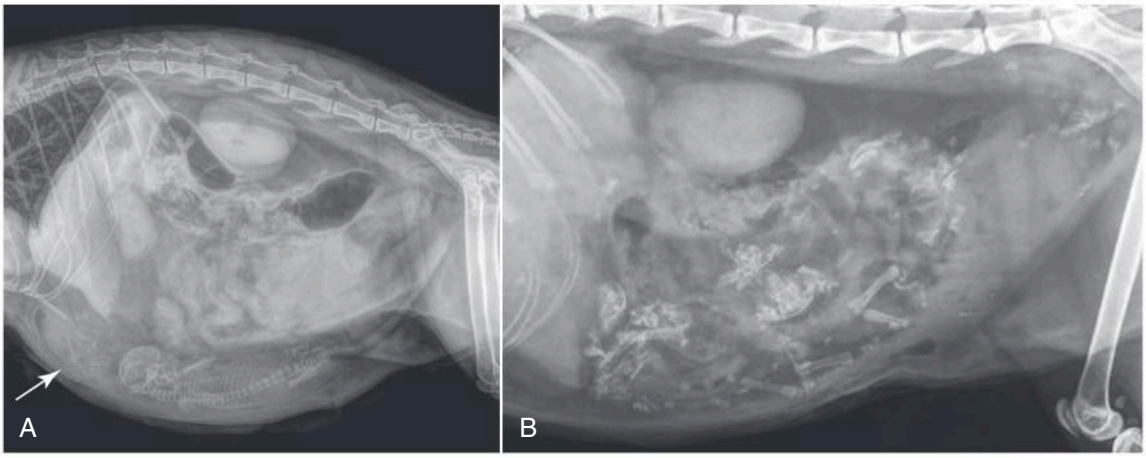


Fig. 44.9 Examples of uterine rupture, fetal death, and mummification at different stages in two cats. **A,** One well-developed fetus and a second smaller skeleton (*arrow*) are visible in the ventral abdomen; these were found outside the uterus in surgery. There is increased diffuse radiopacity and loss of serosal detail in the central abdomen consistent with peritonitis. **B,** Multiple fetal skulls and long bones are dispersed in the mid/central peritoneum. (Images courtesy Dr. Manuel Mastrelli and Dr. Barbara Sernani.)

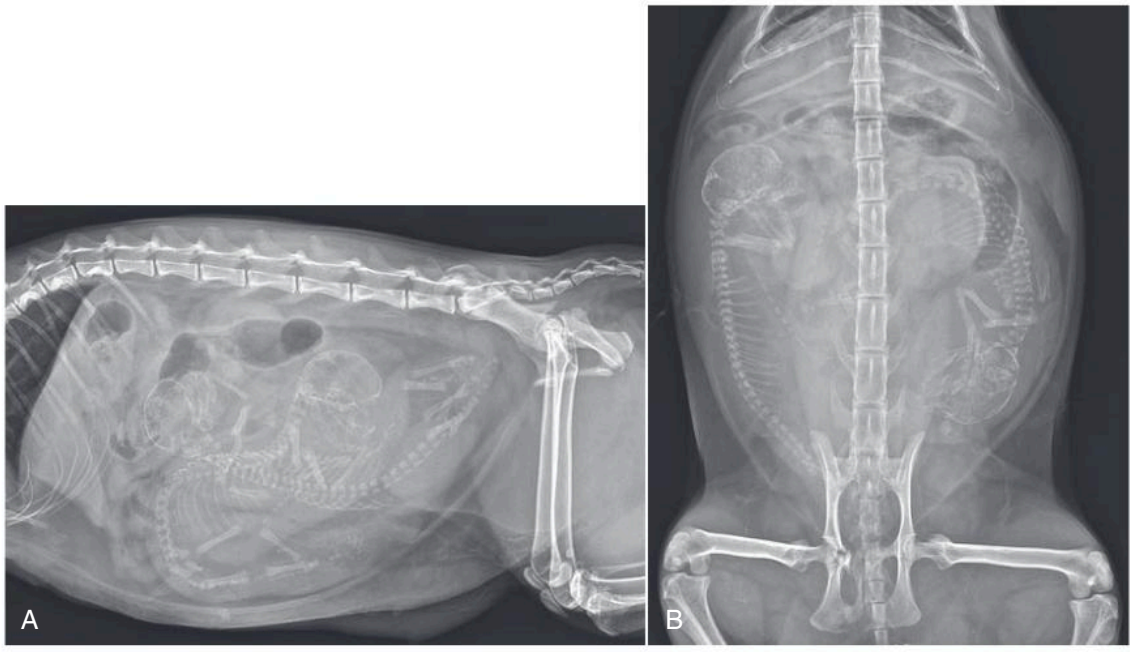


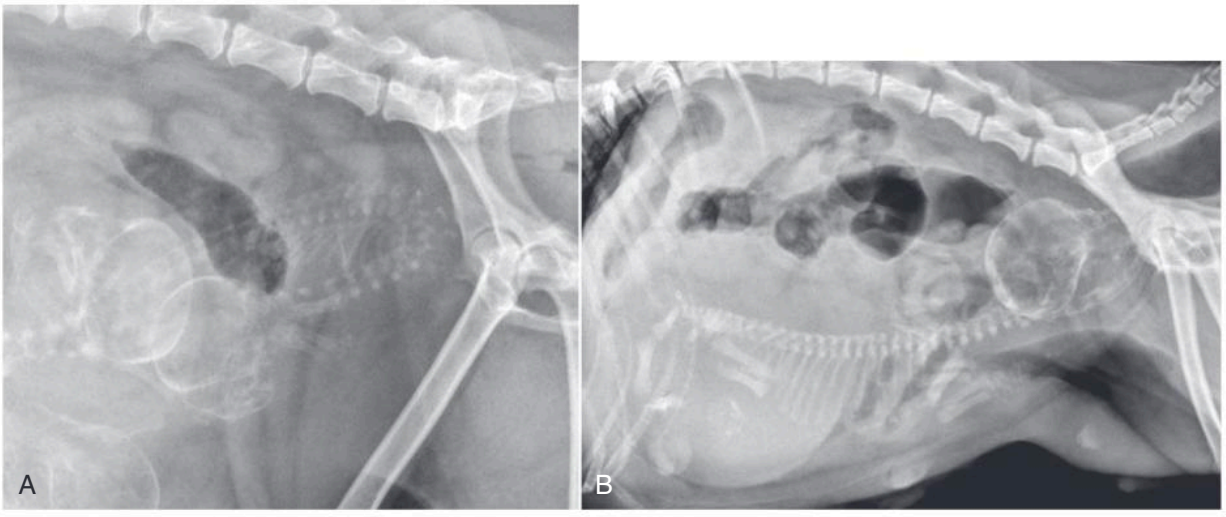
Fig. 44.10 Lateral **(A)** and ventrodorsal **(B)** radiographs of a cat traumatized at the end of pregnancy. The acetabular fracture and consequent narrowing of the pelvic canal were the causes of delayed delivery and dystocia.

normal response of the fetus to hypoxia; fetal bradycardia less than twice the maternal heart rate is considered an indication for a poor prognosis for survival.[30]

Dystocia (the difficulty in passing the fetus through the pelvic canal) can occur through maternal or fetal causes. Several of these, for example, uterine inertia, are undetectable radiographically. However, dystocia caused by fetal malposition, feto-maternal disproportion, or anatomic abnormalities of the pelvic canal can be detected radiographically. If the skull or shoulders are wider on the ventrodorsal view than the pelvic canal, disproportion is the likely cause of dystocia. Healed fractures can lead to pelvic canal narrowing in both canine and feline patients, preventing normal delivery (Fig. 44.10, eFig. 44.2). In breeding animals with a known history of trauma, prebreeding radiographs may be indicated to determine the likelihood of complications. Radiographs can also be used after whelping if there is clinical concern that a retained fetus may be present.

PUERPERIUM

After parturition, the uterus is expected to return to normal size after 4 to 6 weeks. A mildly enlarged uterus can be observed radiographically only for a few days.[32] By ultrasound, some changes can be found until the 15th week in dogs.[33] The uterine wall is thickened with visible layering. In the first week postpartum, placental sites are seen as focal areas of thickening with hypoechoic heterogeneous appearance, and a small quantity of luminal fluid can be observed. Involution of the



eFig. 44.2 Lateral radiograph of dogs with dystocia. In **A,** the fetus is presenting transversely. In **B,** there is a single fetus that has grown to a size that cannot pass through the pelvic canal.

Vetacademy.ir
مجموعه آموزشی پژوهشی
وت آکادمی
تلاش
#برای_دنیای_بهتر_حیوانات
تیم وت آکادمی
برای دسترسی به تازه ترین آموزش ها و
مطالب علمی دامپزشکی؛ وت آکادمی رو فالو کن
سایت مجموعه بزرگ آموزشی پژوهشی وت آکادمی
www Vet-academy.ir
صفحه ی اینستاگرام وت آکادمی
@Vetacademy.ir
دسترسی به آرشیو صد گیگ کتاب آموزش دامپزشکی به صورت رایگان
و جزوه های آموزشی در کانال تلگرامی
@Vetfiles
گروه بزرگ تلگرامی، پرسش و پاسخ و آموزش
@VetAcademyGp
صفحه رسمی آپارات وت آکادمی
آپارات aparat.com/vetacademy.ir

feline uterus occurs faster than in dogs and is complete by 24 days postpartum. After 14 days, the uterus diameter is less than 1 cm and distinct uterine layering is not visible by ultrasound.[34]

ABNORMAL RADIOGRAPHIC AND ULTRASONOGRAPHIC FINDINGS IN OVARIAN DISEASES

Ovarian Remnant Syndrome

This results from hormone production by ovarian remnant tissue, usually secondary to incomplete surgery. The right ovary is more frequently involved. Presurgical ultrasound is effective to identify the residual ovary especially during estrus; however, false-negative or false-positive studies are possible. The remnant presents as a hypoechoic structure often with cystic component located caudal to one of the kidneys.[35]

Ovarian Cysts

Functional (follicular or luteal) and nonfunctional ovarian cysts occur as solitary or multiple fluid-filled structures of variable size that are unilateral or bilateral in the bitch.[36] Larger cysts can be recognized radiographically and should be considered as a differential diagnosis for ovarian masses (Fig. 44.11A).[3] Ultrasonographically, regardless of their origin, they appear as anechoic, well-defined structures with thin wall and distal acoustic enhancement that may deform the outer margin of the ovary (see Fig. 44.11B). The size of the cyst does not correlate with the hormonal production, and follicular and luteal cysts often coexist in the same ovary.[36] Ovarian cysts may not be distinguishable from normal folliculi or corpora lutea during estrus; however, if the diameter is larger than 1 cm, a cyst is suspected. Correlation with clinical data (prolonged heat or anestrus, persistent diestrus, signs of hyperestrogenism) and hormonal status (increased estradiol or progesterone level) is needed to differentiate the two situations. Alternatively, ultrasound can be used to monitor the cystic structure over time. Normal follicles and corpora lutea should not persist longer than 30 and 60 days, respectively. Functional ovarian cysts predispose the bitch to the development of cystic endometrial hyperplasia (CEH)—pyometra complex.

Ovarian Masses

Ovarian tumors are classified, based on their histological type, into four categories: epithelial, sex cord-gonadal stromal, germ cell tumors, and mesenchymal neoplasia. Benign papillary adenomas and adenocarcinomas account for 40% to 50% of canine ovarian tumors; granulosa cell tumors represent the second most common ovarian tumor type in dogs and the most frequent feline ovarian neoplasia. Germ cell tumors (dysgerminoma and benign and malignant teratoma) are less common and benign and malignant mesenchymal neoplasia are considered rare.[37] In dogs, the metastatic potential is higher (48%) for adenocarcinoma compared to the other isotypes, with peritoneal cavity, omentum, lymph nodes, and liver being the most common sites of metastatic spread. In cats, ovarian involvement with lymphoma has been documented and approximately 50% of granulosa cell tumors are malignant.[38] Any of these tumor types may develop without clinical signs, and granulosa cell tumors and cystadenomas may secrete sex hormones. Ovarian neoplasia may be unilateral or bilateral, with epithelial tumors most likely to occur bilaterally.

Most ovarian masses that are large enough to be seen radiographically are neoplastic, although large ovarian cysts can be also visible (see Fig. 44.11A). Ovarian tumors appear as peritoneal soft tissue masses located in the mid central to ventral abdomen (Fig. 44.12A,B). Because of the peritoneal location and the presence of the elastic ovarian ligament, the enlarged ovary gravitates ventrally along the adjacent body wall; this is a useful criterion to differentiate these masses from retroperitoneal conditions. Ovarian masses result in medial but not ventral displacement of adjacent organs on radiographs. Right ovarian masses displace the descending duodenum and ascending colon medially, and left ovarian masses displace the

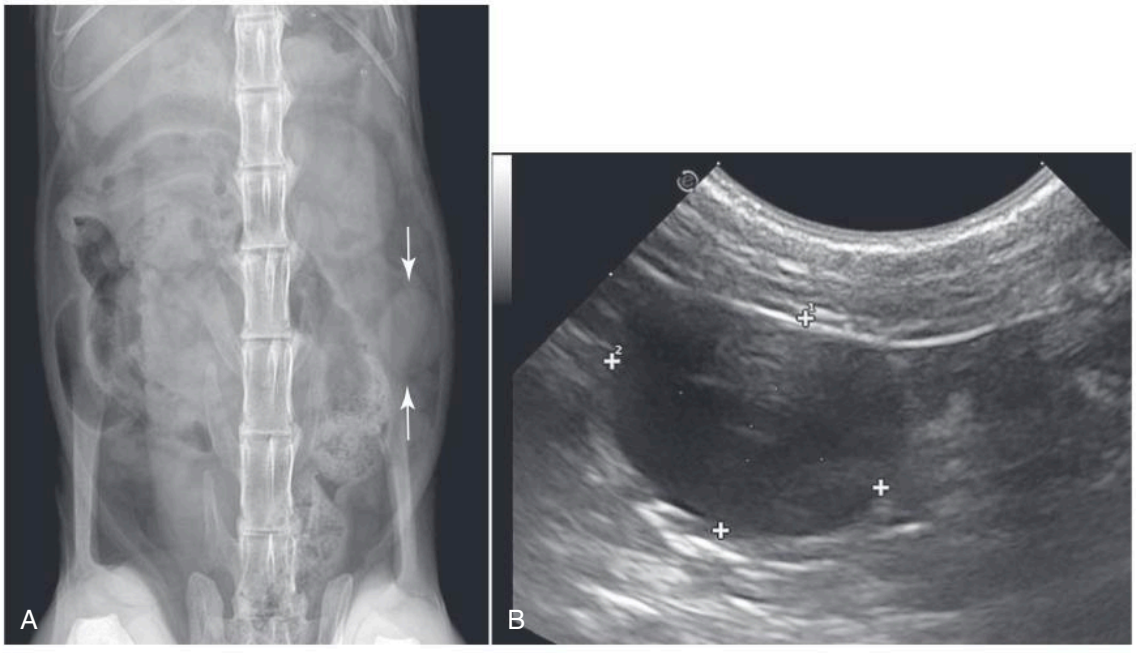


Fig. 44.11 Ventrodorsal (VD) radiograph **(A)** and ultrasonographic image **(B)** of a left ovarian cyst in a 4-year-old Main Coon cat. There is a well-defined, soft tissue round structure (*between arrows*) located caudal to the kidney in contact with the abdominal wall **(A)**, presenting with a thin wall and anechoic, homogeneous content in ultrasound (*between calipers*) **(B)**.

descending colon medially.[3] They may also result in ventral deviation of the caudal pole of the ipsilateral kidney. Mineralization is a common finding in teratomas and may be seen occasionally in teratocarcinomas.[39,40]

In spayed females, masses in the ovarian region can be a consequence of inflammation/infection of the ovarian stump and can appear similar to ovarian masses. The presence of adhesions with the peritoneum/retroperitoneum may fix the mass dorsally, preventing its ventral displacement and mimicking a retroperitoneal structure (Fig. 44.13A).

Ultrasonography provides detailed images of the mass architecture (see Figs. 44.11B, 44.12C,D, and 44.13B). Tumors may be small or large, solid or cystic in appearance. Mineralization or bone within teratomas and teratocarcinomas causes hyperechoic shadowing areas within the tumor.[39] The ultrasonographic appearance of ovarian tumors overlaps; therefore, cytology or histopathology is required for definitive diagnosis. Determination of a mass as ovarian in origin is based on its location and association with an adjacent uterine horn. This can be challenging with unilateral large ovarian neoplasia, which can be difficult to differentiate from other peritoneal masses.[39] In these cases, CT is indicated (see Fig. 44.12E).

Peritoneal fluid is common in animals with ovarian tumors and is often seen with carcinomatosis or compression of lymphatics by the mass itself. Ultrasound can be useful to evaluate the peritoneum and to search for nodules compatible with metastases. Hypoechoic nodules located in the connecting, visceral, or parietal peritoneum are detected especially if surrounded by fluid. Pyometra or CEH may be concurrent and is related to hormonal disturbances.

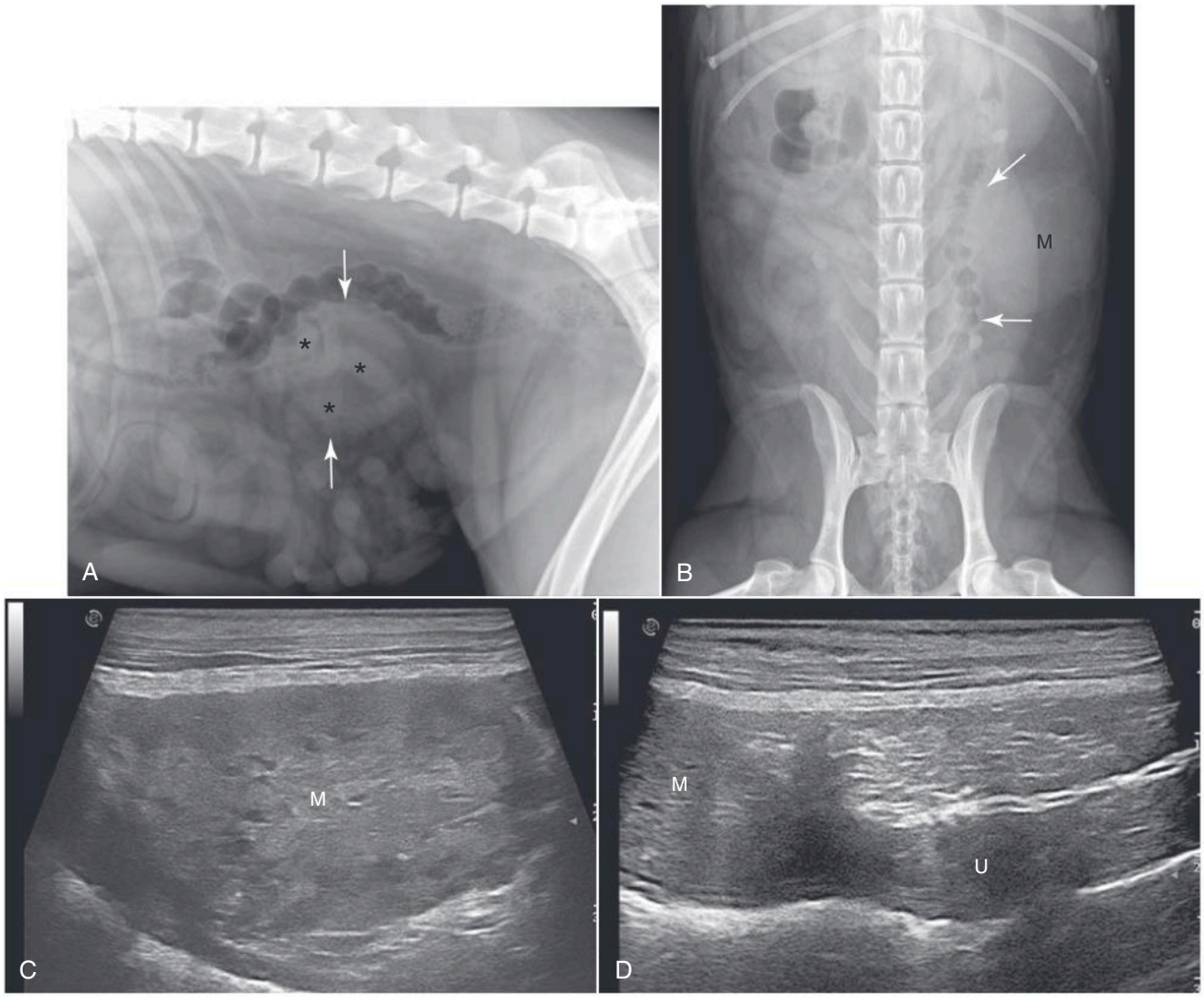


Fig. 44.12 Left ovarian adenocarcinoma in a dog evaluated by radiographs **(A, B)**, ultrasound (US) **(C, D)**, and computed tomography (CT) images in the transverse, sagittal, and dorsal plane, in the arterial and venous phase **(E)**. **A, B,** The mass (*white arrows*) is located caudoventral to the left kidney, surrounded by small intestinal loops (*asterisks*) **(A)**, and displaces the descending colon medially (*white arrows*) **(B)**. With US, the mass has a heterogeneous appearance with small hypoechoic cavities **(C)**. The connection with the uterine horn is demonstrated by US **(D)** and CT **(E)**. In CT, the mass shows a heterogeneous enhancement and is supplied by the ovarian vessels (*arrows*). The ovarian artery arises directly from the aorta and the ovarian vein ends in the left renal vein. * = small bowel loops. *A,* Aorta; *K,* kidney; *M,* mass; *U,* uterine horn.

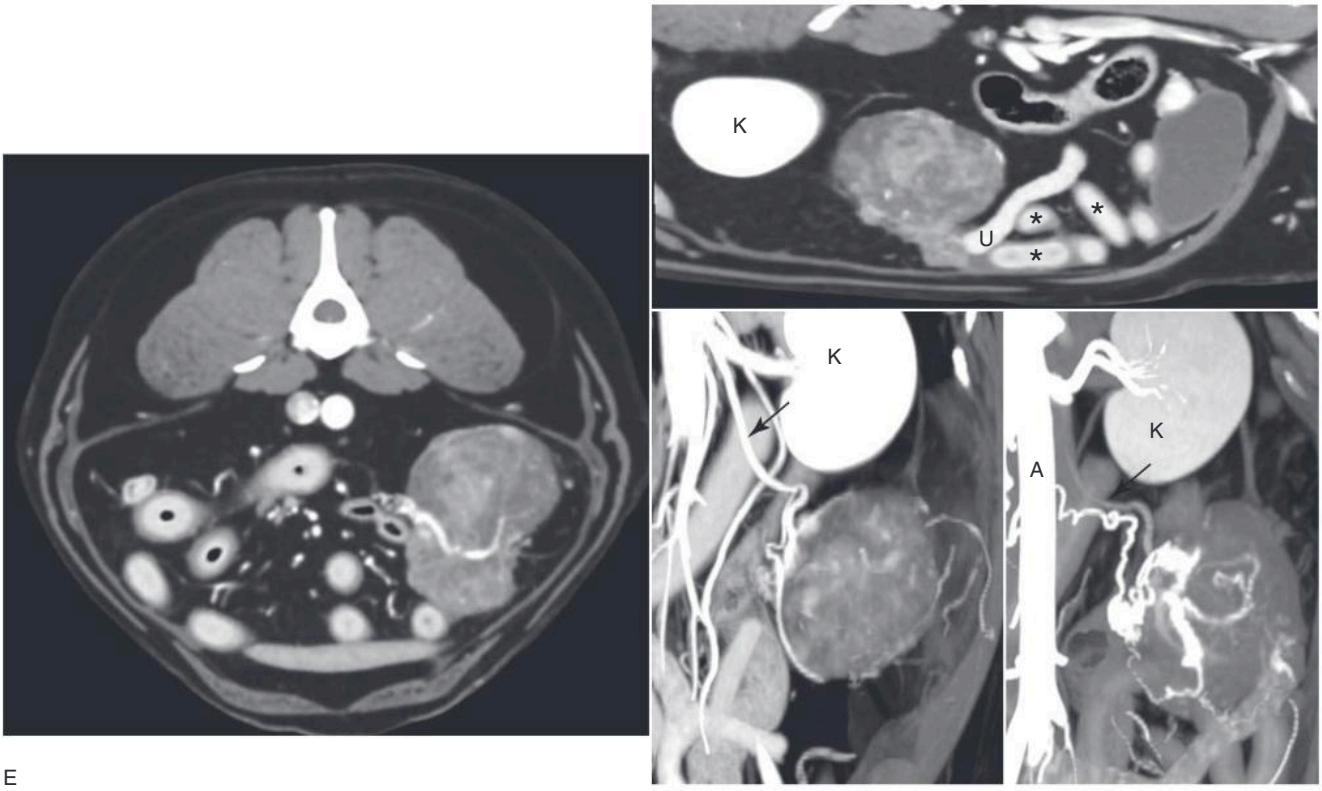


Fig. 44.12 cont'd

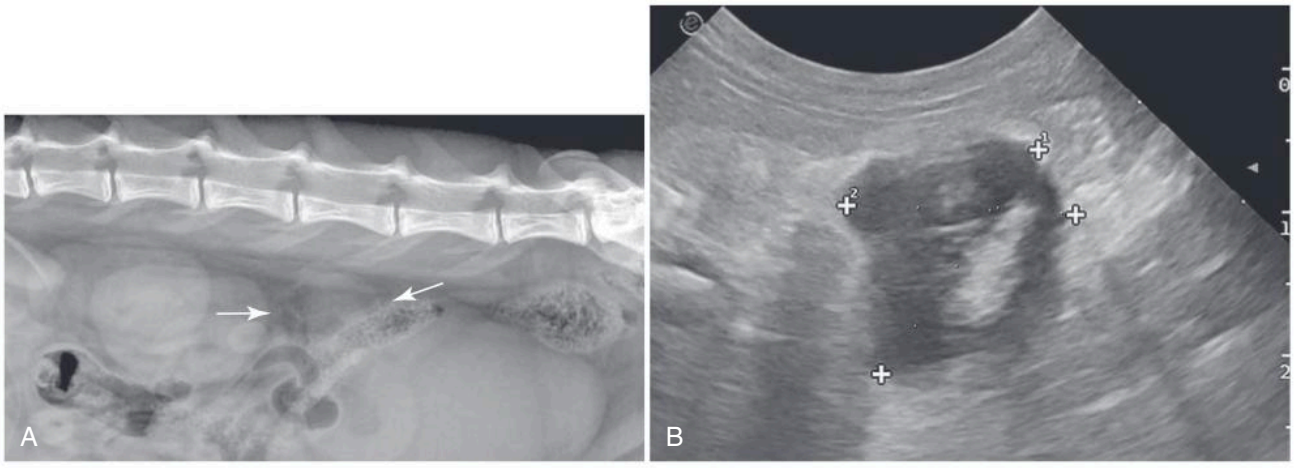


Fig. 44.13 Lateral radiographs **(A)** and sonographic (US) image **(B)** of an ovarian stump granuloma in a spayed cat (*between arrows*). The lesion (*between calipers*) is hypoechoic with hyperechoic center in ultrasound, surrounded by hyperechoic fat.

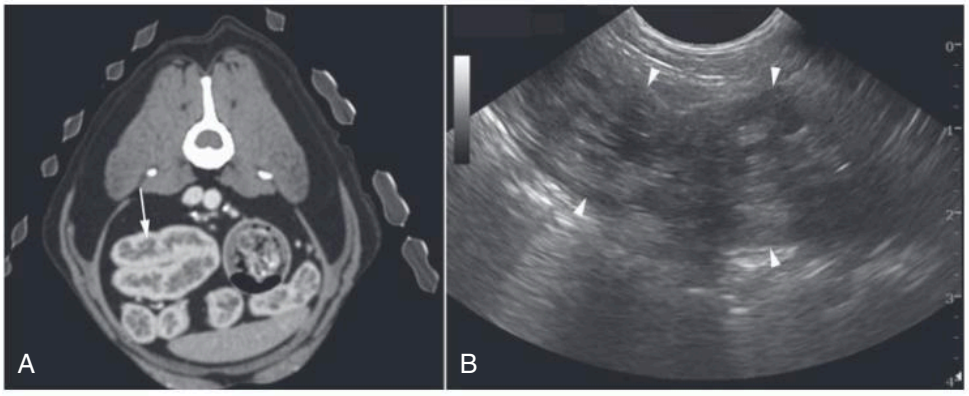
ABNORMAL RADIOGRAPHIC AND ULTRASONOGRAPHIC FINDINGS IN UTERINE DISEASES

Generalized Uterine Diseases

The most common cause of generalized uterine enlargement is uterine fluid collection. The type of accumulated fluid correlates with the systemic effects. Pyometra, particularly closed-cervix pyometra, can be a life-threatening condition that must be recognized and treated rapidly. Mucometra is an accumulation of sterile intraluminal mucoid fluid, hematometra is an accumulation of sterile, bloody fluid, and hydrometra is an accumulation of sterile, watery fluid.

CEH frequently develops in old bitches under the effect of pregestational stimulation during the luteal phase and often evolves to luminal fluid collection. Even in the early phase of the disease, diffuse or focal thickening of the uterine wall can be detected with ultrasound, associated with intramural focal anechoic structures representing dilated glands or ducts and accumulation of a small amount of intraluminal fluid (Fig. 44.14A,B, eFig. 44.3).[7]

Accumulation of sterile or infected material produces uterine horn enlargement. The echogenicity of the accumulated fluid cannot be used as definitive diagnosis. Anechoic content can be observed both with pyometra and hydrometra. The luminal fluid can be hypoechoic with echogenic swirling



eFig. 44.3 **A,** Postcontrast transverse computed tomography image of a uterus with severe cystic endometrial hyperplasia. The *arrow* indicates one of the large fluid-filled regions within the uterine horns. **B,** Longitudinal image of uterus with severe cystic endometrial hyperplasia (*between arrowheads*). Note the large anechoic, fluid-filled regions in the horn.

particles in case of pyometra, whereas mucometra and hematometra tend to have more homogeneously distributed echogenic fluid.[41] The degree of wall thickening is another nonspecific sign and varies with luminal distention and presence of intramural cysts (see Fig. 44.14).

Radiographically, the typical appearance of uterine enlargement is of a soft tissue tubular structure within the caudal and ventral aspects of the abdomen (Figs. 44.15 and 44.16, eFigs. 44.4–44.6). On lateral views, the enlargement of the uterine body is seen between the bladder and colon. However, this is not always easy to identify; a lateral compression radiograph may facilitate the identification of the uterine body distention. Enlargement of the uterine horns leads to tubular structures of soft tissue homogeneous opacity in the caudal and ventral aspects of the abdomen. In early enlargement, it may not be possible to differentiate the enlarged uterine horns from jejunum. On the ventrodorsal view, the enlarged uterus will appear as a soft tissue tubular structure lateral to the descending colon on the left and along the peripheral abdominal wall on the right.

Emphysematous pyometra is rarely reported in dogs.[42] In radiographs, one or both uterine horns can be affected; especially with unilateral involvement, the gas-filled uterus can be difficult to distinguish from the small or large intestine. In these cases, a positive-contrast study of the gastrointestinal tract can be indicated.

Peritonitis secondary to infection or uterine rupture may occasionally occur. Radiographic signs include loss of peritoneal detail with blurred serosal margins or complete border effacement of the abdominal viscera, and homogeneous or mottled increased soft tissue opacity depending on the fluid amount. Pneumoperitoneum may develop secondary to rupture of emphysematous pyometra (Fig. 44.17, eFig. 44.7). Small pockets of gas along the abdominal wall are more easily identified by ultrasound compared to radiology.

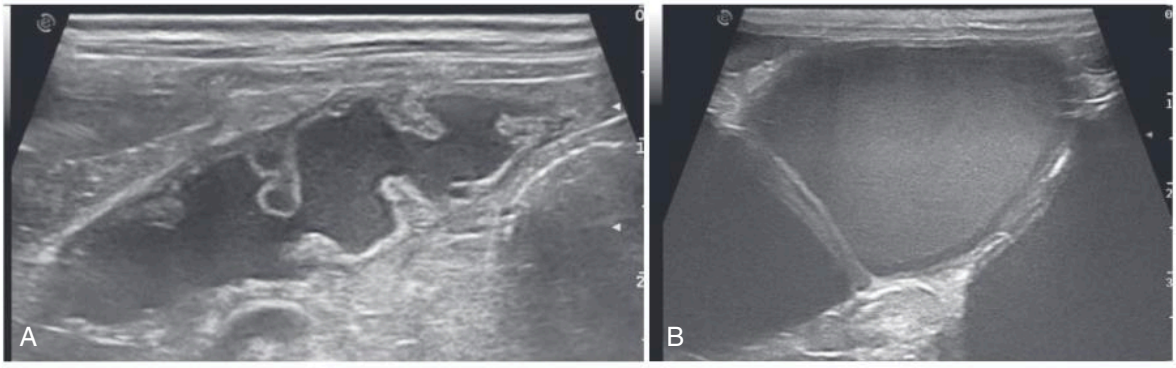


Fig. 44.14 Sonographic appearance of the cystic endometrial hyperplasia (CEH)—pyometra complex. **A,** Thickened, cystic uterine wall; the lumen is moderately dilated with echogenic fluid. **B,** Large amount of particulate material with severe distention of the uterus; the uterine wall is thin and smooth.

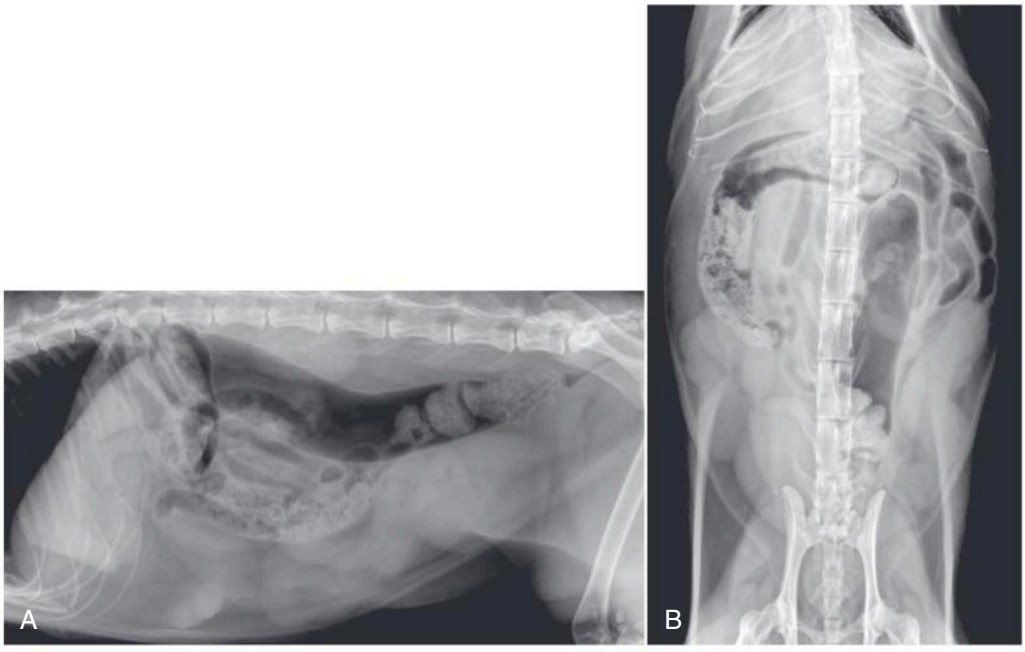
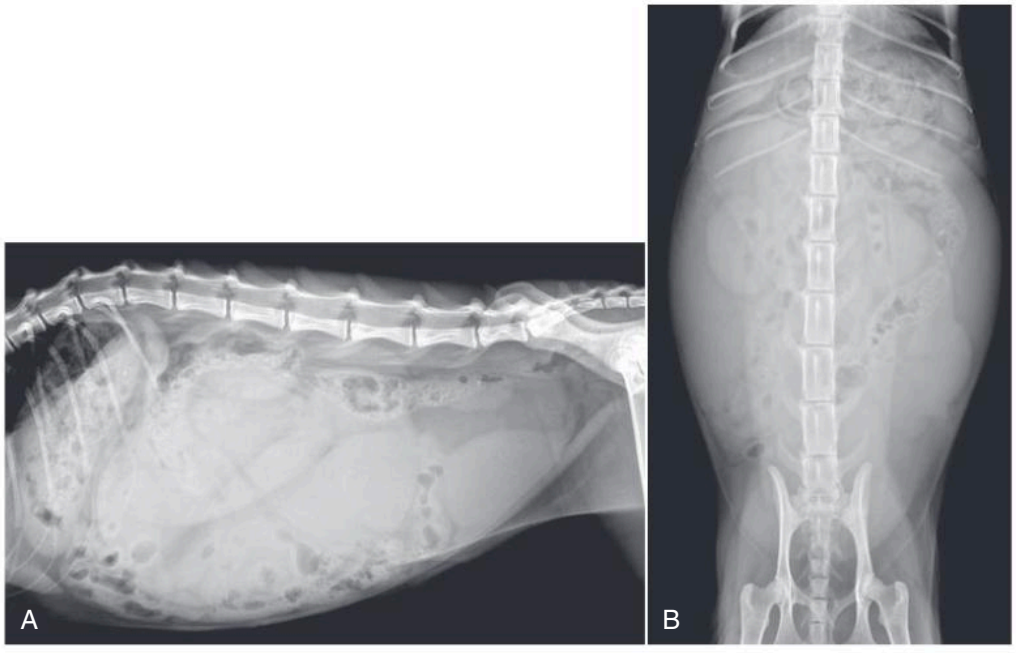
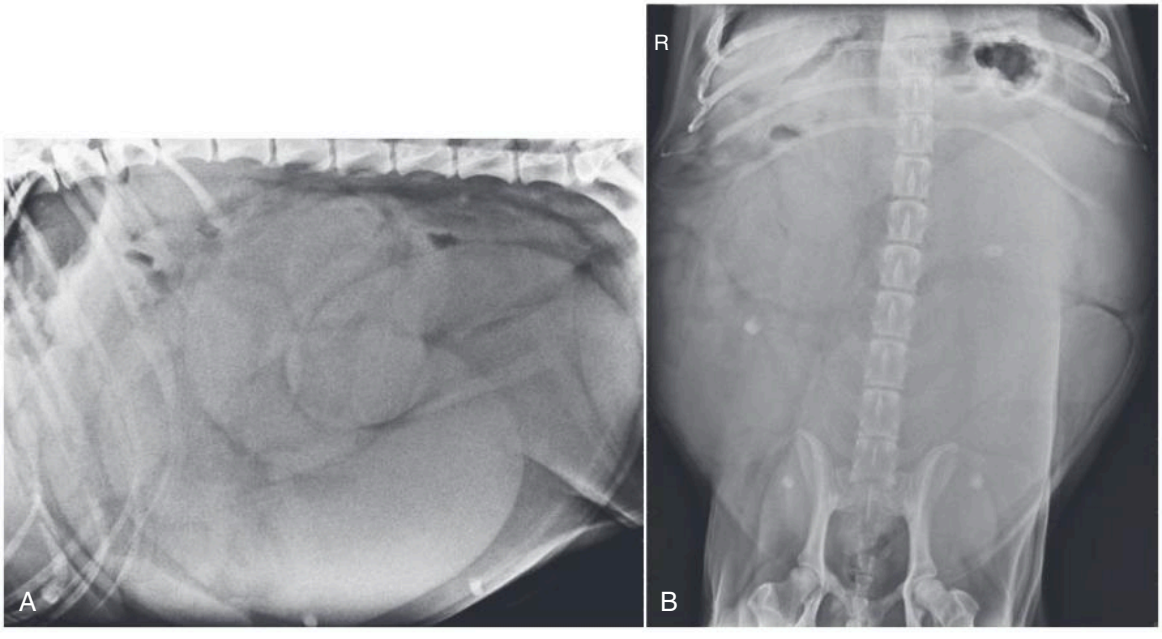


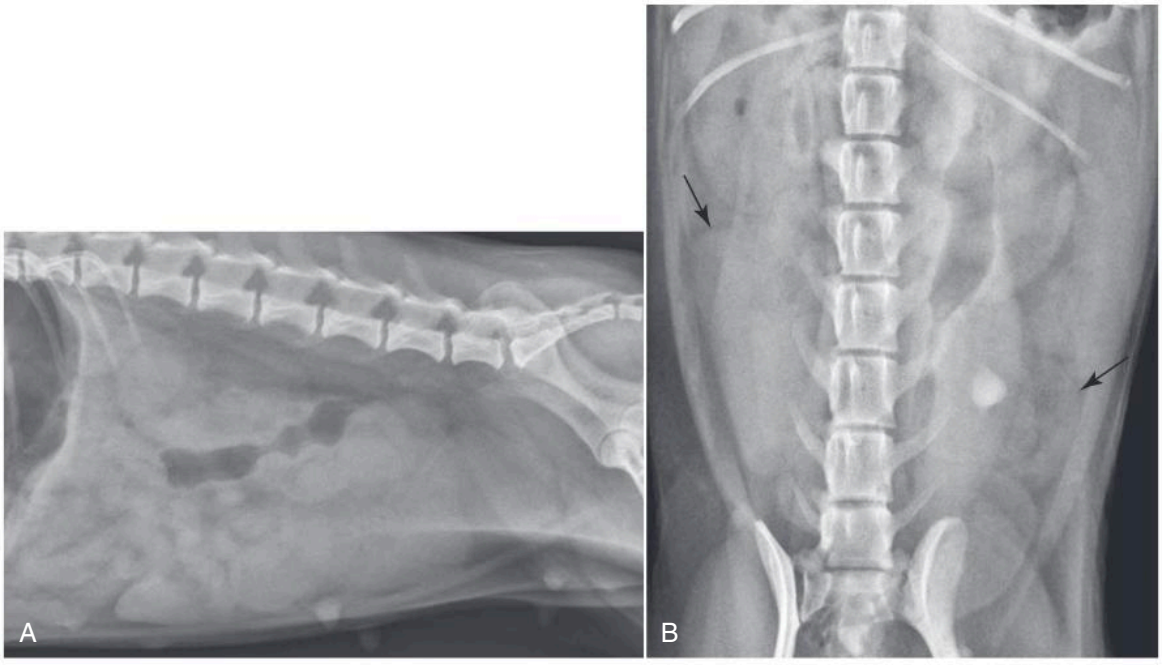
Fig. 44.15 Lateral **(A)** and ventrodorsal (VD) **(B)** radiographs of a cat with pyometra. The distended, tubular-shape uterus occupies the ventral abdomen, displacing the small intestine cranially and the caudal colon dorsally. The VD view shows enlargement of both uterine horns, which are in contact with the lateral abdominal wall.



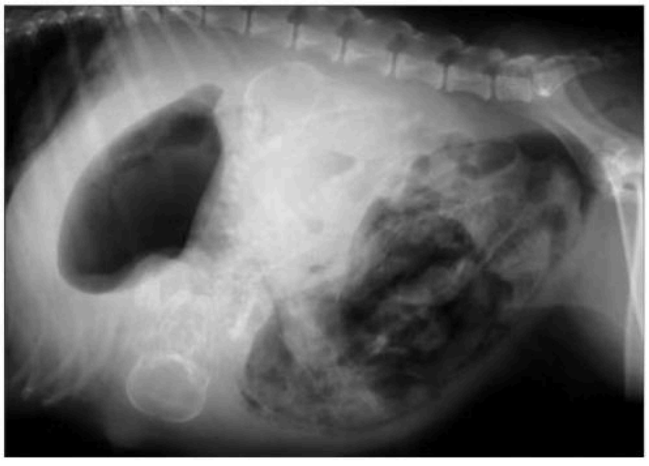
eFig. 44.4 Lateral **(A)** and ventrodorsal **(B)** radiographs showing a severely distended uterus associated with pyometra in a cat. The folded uterine horns fill most of the abdominal cavity with evident mass effect.



eFig. 44.5 **A and B,** Massive uterine distention associated with pyometra in a dog. There is a very large distended tubular soft tissue structure within the caudal and ventral aspects of the abdomen causing a marked associated mass effect.



eFig. 44.6 **A and B,** Moderate diffuse uterine enlargement associated with pyometra. Note the evidence of uterine enlargement bilaterally (*black arrows*) on the ventrodorsal view.



eFig. 44.7 Uterine emphysema and fetal death in a dog. One of the uterine horns is distended with gas content and disrupted skeletal fetal structures.

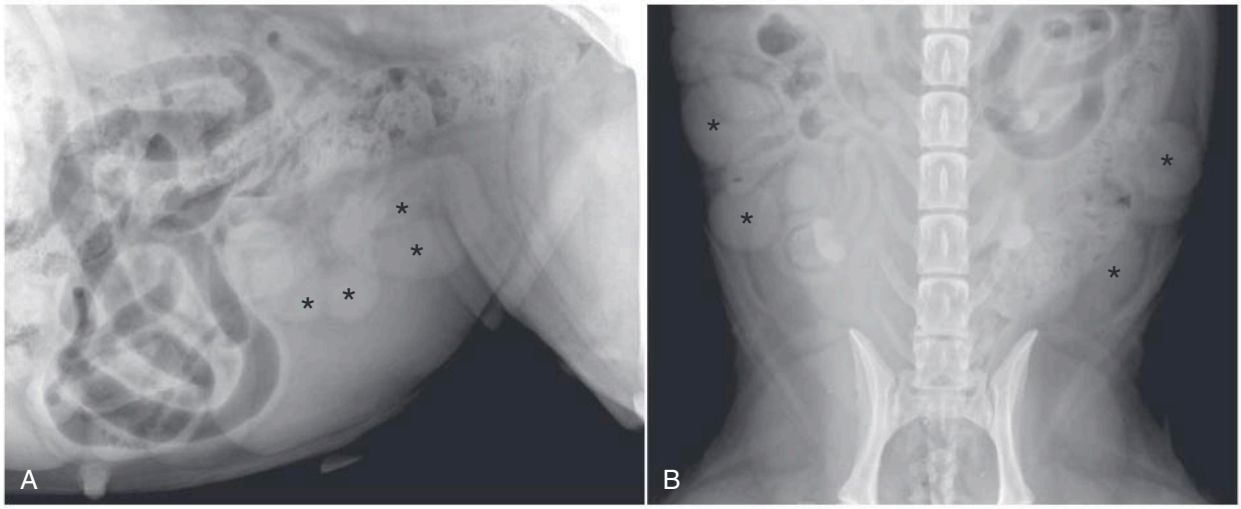


Fig. 44.16 Lateral **(A)** and ventrodorsal (VD) **(B)** radiographs of a dog with mild uterine distension. Note that the diameter of the uterine horns is similar to the jejunal loops. They can be identified because of the position (caudoventral in the lateral view and lateral in the VD view) and the homogeneous soft tissue opacity (*asterisks*).

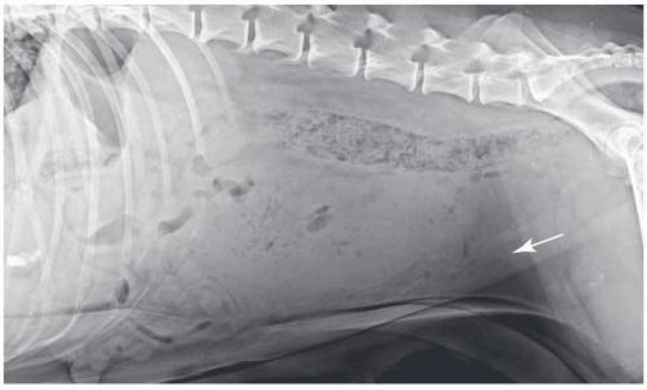


Fig. 44.17 Lateral radiograph of a dog with ruptured pyometra. There is an ill-defined mass located in the midventral abdomen with mixed soft tissue/gas opacity consistent with the enlarged uterus and associated peritoneal thickening/fluid. Small pockets of gas are visible also along the ventral abdominal wall and indicate pneumoperitoneum (*white arrow*). Differential diagnoses include rupture of an intestinal mass or abdominal abscess.

Mineralization of the endometrial wall associated with other uterine pathology has been reported in dogs and zoo animals and correlated with long-term administration of medroxyprogesterone acetate.[43]

Focal Uterine Diseases

Uterine torsion usually involves one of the two uterine horns. It is a rare complication of pregnancy and may occur in association with pyometra, hematometra, and endometrial polyps.[44,45] It is associated with a high mortality rate because of peritonitis and endotoxemia. The radiographic and sonographic appearance is not specific (Fig. 44.18). Asymmetric uterine involvement and presence of hyperechoic tissue between the distended horn and the uterine body in ultrasound might suggest uterine torsion. In most instances, the diagnosis will be made surgically.

Uterine stump disease may occur after ovariohysterectomy due to early postsurgical bleeding or late infection/granulomatous inflammation of the caudal uterine stump. Stump pyometra is associated with residual functional ovarian tissue. Abscesses or granulomas can develop as reaction to surgical material, whereas severe bleeding may be secondary to coagulopathy. In radiographs, a focal area of increased radiopacity may be observed between the colon and urinary bladder in the lateral view. This cannot be differentiated from neoplasia arising from the uterine stump. With ultrasound, thickening of the uterine stump of variable echogenicity is observed, often with a complex mass appearance.[7] One or multiple pockets of echogenic fluid may be present in case of recent bleeding or pus accumulation. Sometimes, surgical material in the granuloma can be present as hyperechoic foci associated with shadowing. Complications in case of site infection include involvement of adjacent bladder neck or vesico-urethral junction and peritonitis with fistulous tracts.

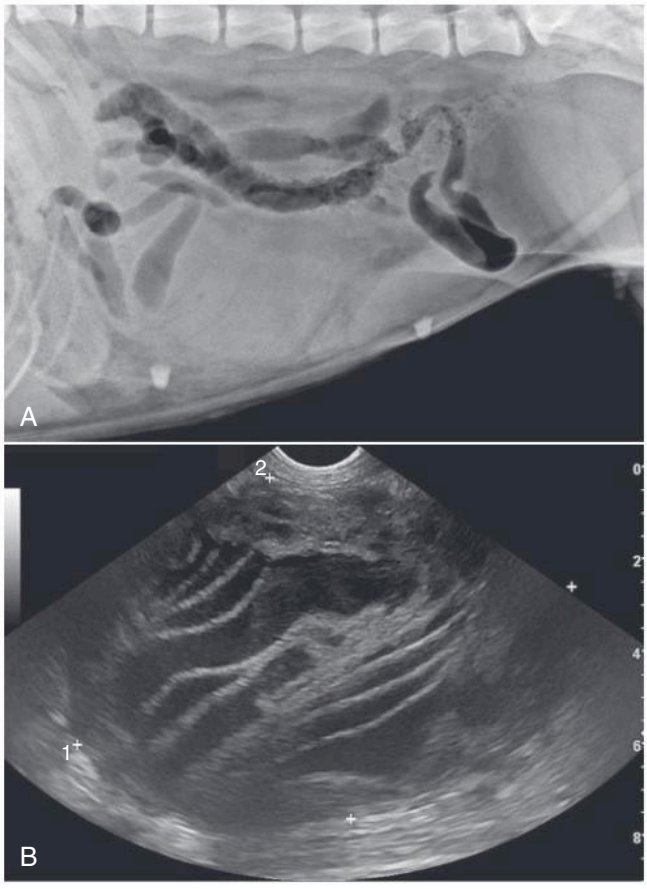
Rarely, plant **foreign bodies** may migrate from the vagina to the uterine body and horns. They usually appear as linear, hyperechoic, spindle-shaped structures of variable length, possibly associated with shadowing (Fig. 44.19, eFig. 44.8). Fluid accumulation, thickening of the uterine wall, and changes of the surrounding peritoneum can be observed.

Uterine Neoplastic and Nonneoplastic Nodules and Masses

Uterine neoplasia is considered rare in small animals, usually occurring in middle-aged to older animals; however, uterine adenocarcinoma has been reported in dogs and cats younger than 1 year of age. Leiomyoma is the most common tumor in dogs; this is a benign, slow-growing, noninvasive, and nonmetastasizing neoplasia, often incidentally diagnosed. Malignant aggressive adenocarcinoma is more frequently observed in cats. Other types of benign and malignant neoplasia can be rarely found in both species.[37]

Uterine nonneoplastic nodules and masses include granulomas, polyps, and focal or multifocal uterine wall hyperplasia. Polyps are focal growths of the uterine wall projecting into the lumen. They are variable in number and size, pedunculated or sessile, often associated with luminal fluid accumulation and rarely with torsion.[44]

Masses arising from the uterus can be identified radiographically depending on their size; however, even if large, they cannot be distinguished from segmental fluid. They present as soft tissue opacity, rarely mineralized. They are located in the midventral abdomen if originating from the uterine horns or in a more caudal position, between the colon and urinary bladder, if growing from the uterine body or cervix.[3,46] Dorsal displacement of the descending colon and cranial compression of the urinary bladder can be observed with large caudal masses. Differential diagnoses include extrauterine masses arising from the vagina, ovary, or mesentery.



eFig. 44.8 **A,** Uterine abscess associated with a retained surgical sponge after Cesarean section. The radiographic appearance is of a midabdominal mass with loss of serosal margin contrast, and it is not possible to con firm the mass as uterine. **B,** Sonographic appearance of the uterine abscess. Ultrasound evaluation con firmed a uterine origin, although the diagnosis of foreign body—associated abscess was made surgically.

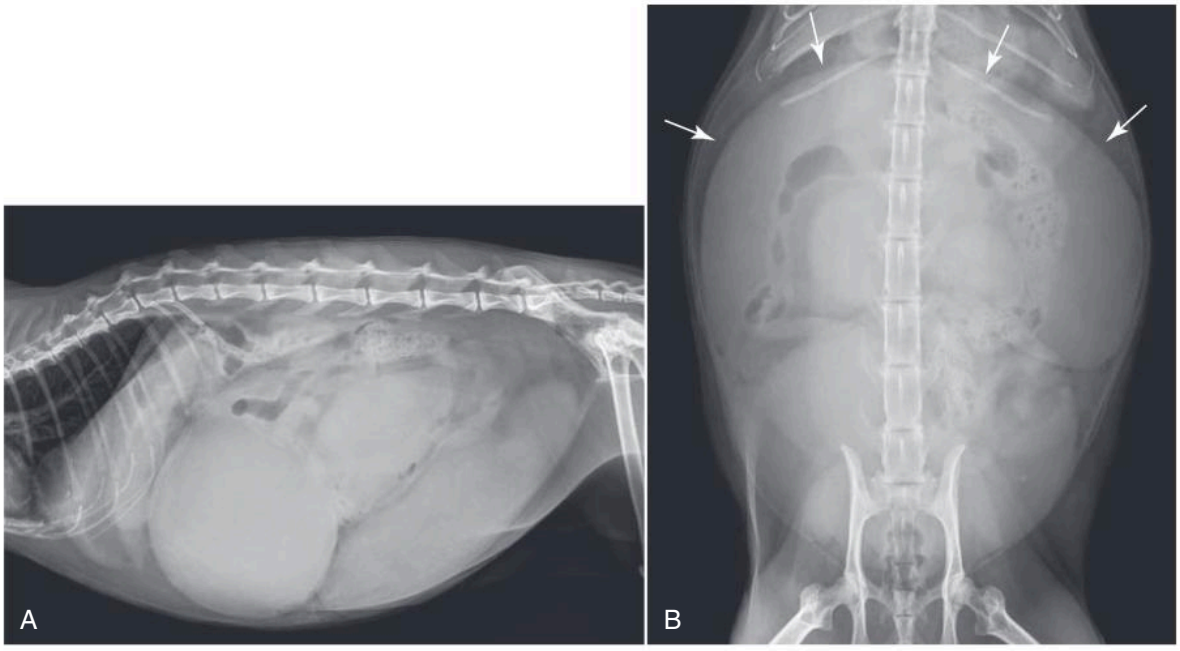


Fig. 44.18 Lateral **(A)** and ventrodorsal **(B)** radiographs of a cat with uterine torsion. There is a large, soft tissue tubular structure consistent with severely enlarged uterus. Cranially, this is bordered by a well-de fined, continuous convex surface, which crosses the abdomen from the left to the right (*white arrows*). Torsion of the left uterine horn was confirmed in surgery. (Courtesy of Antech Imaging Services.)

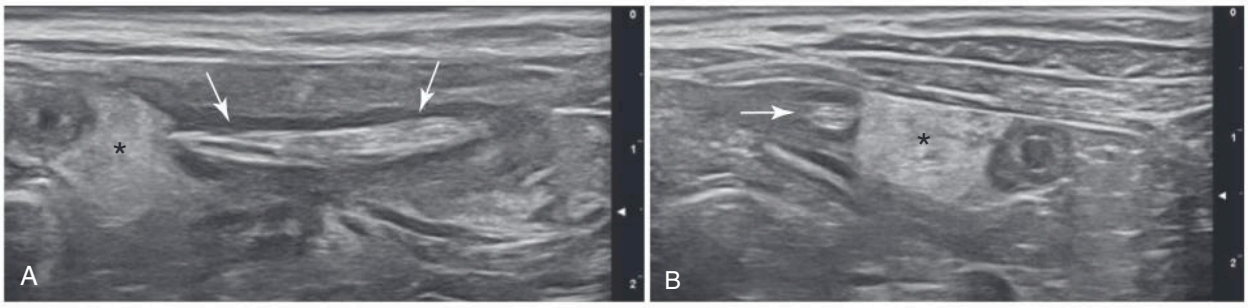


Fig. 44.19 Sonographic images of an ovariectomized Dachshund with a foreign body (plant awn) in the left uterine horn, migrated from the vulva. The dog was presented because of bloody vaginal discharge. There is a long, hyperechoic, striated structure in the lumen of the left uterine horn, without clear shadowing (*white arrows*). The right uterine horn is mildly distended by fluid. The adjacent tissue is marked hyperechoic due to focal inflammation (*asterisk*).

Uterine origin of a mass can be confirmed by ultrasound by tracing the connection with the surrounding normal uterus. This seems to be easier for body/cervical masses and more challenging with large masses arising from uterine horns. The presence of uterine luminal fluid may improve the visualization of the horn and its connection with the mass.[46] Ultrasound allows further characterization as solid or cystic mass, intramural or endoluminal location and to detect concomitant mineralization. Aggressive adenocarcinomas, most frequently encountered in cats, are often associated with peritoneal fluid and metastases (Fig. 44.20, eFig. 44.9).[37] Single or multiple intramural nodules have been described in young nonpregnant bitches affected by pseudoplacentational endometrial hyperplasia.[47] This proliferative condition is a variant of the more common CEH where the hyperplastic area appears as a more well-organized intramural pedunculated solid lesion. Ultrasonographically, they appear as hyperechoic nodules with possible striations, resembling placental remnants. Despite some characteristic features, the final diagnosis of a uterine mass requires histopathology.

ABNORMAL RADIOGRAPHIC AND ULTRASONOGRAPHIC FINDINGS IN VAGINAL DISEASES

Vaginoscopy is the method of choice to investigate vaginal diseases; however, radiology and ultrasound can sometimes be useful especially with large vaginal intramural masses. These are most frequently caused by benign vaginal neoplasia (fibroma and leiomyoma) and are recognized as soft tissue opacities in the pelvis causing dorsal displacement and compression of the rectum and cranioventral displacement of the urinary bladder neck. Vaginography can show a filling defect of the vaginal lumen, helping to evaluate the mass extent and its relationship with the vaginal wall and urethra. Care must be taken not to inject air accidentally during the procedure, because this can mimic a vaginal mass. Transabdominal ultrasound can be used to evaluate the cranial portion of the lesion with the ultrasound beam pointing caudally; however, the evaluation is limited by the pelvis. A perineal approach can be considered in case of caudal vaginal masses or abscesses caused by migrating foreign body, or to guide biopsy.



eFig. 44.9 Sonographic image of a uterine leiomyoma in a dog. The mass was an incidental finding during evaluation for an unrelated problem.

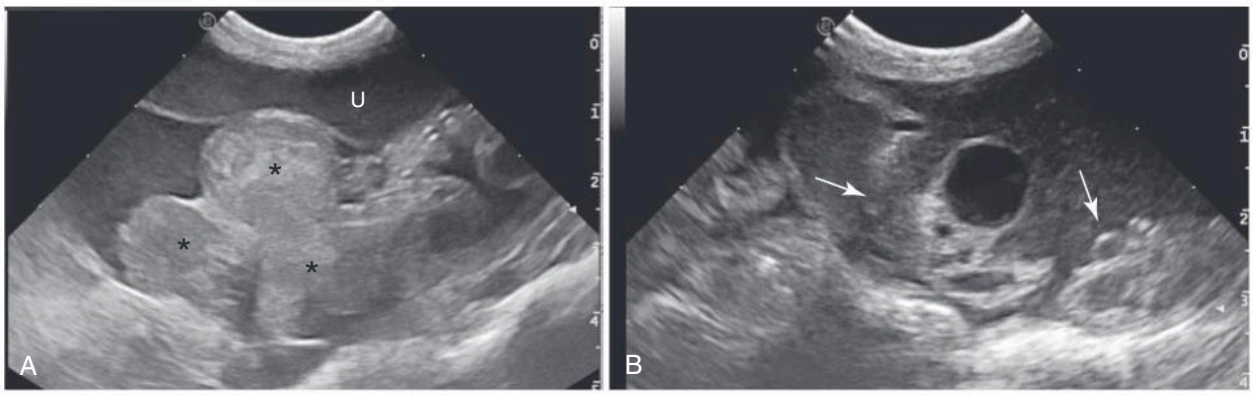


Fig. 44.20 Sonographic images of a cat with a diffuse uterine adenosquamous carcinoma, metastatic to the peritoneum. **A,** The right uterine horn (*U*) is distally distended with echogenic content, proximally multiple hyperechoic nodules are visible (*asterisks*). **B,** Free fluid, serosal thickening (*white arrows*) and cysts are visible in the adjacent peritoneum.

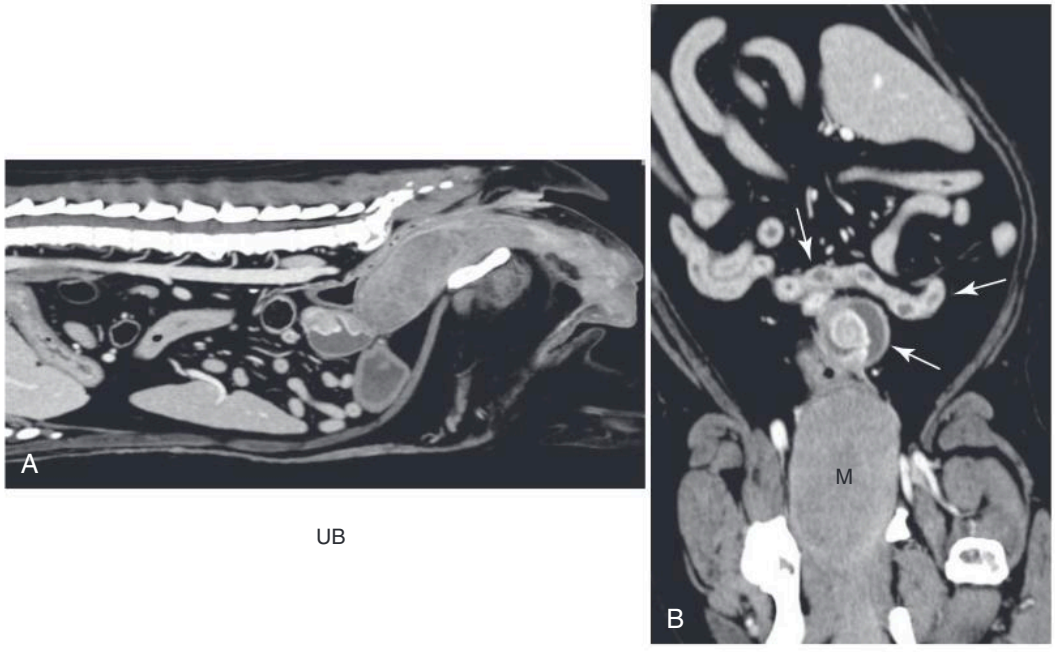


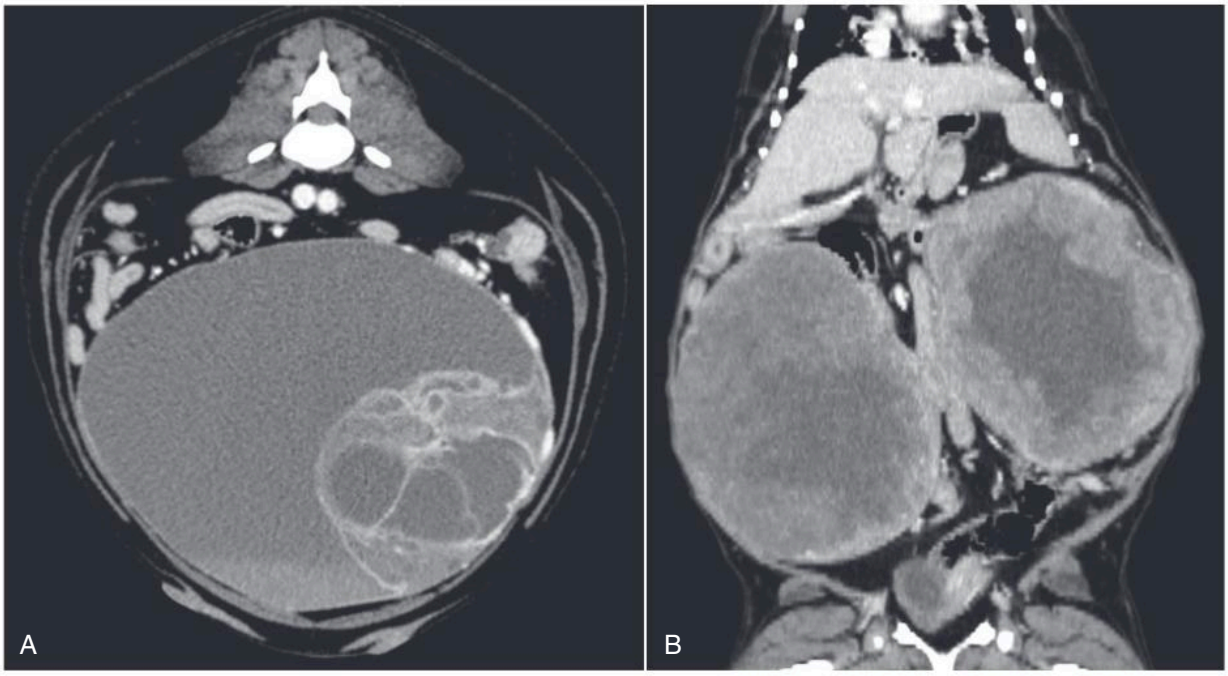
Fig. 44.21 Computed tomography images, reformatted in the sagittal **(A)** and dorsal **(B)** plane, of a dog with vaginal leiomyoma. The mass (*M*) arises from the vaginal wall and is cranially connected with the uterus. The uterine body and horns (*white arrows*) are distended with fluid-filled regions caused by concomitant endometrial cystic hyperplasia. The urinary bladder (*UB*) is compressed ventrally.

Other differential diagnoses for vaginal masses include other tumors like the transmissible venereal tumor (TVT) and some benign conditions like vaginal hyperplasia/prolapse. The clinical presentation helps the diagnosis and rarely imaging is required in these cases.

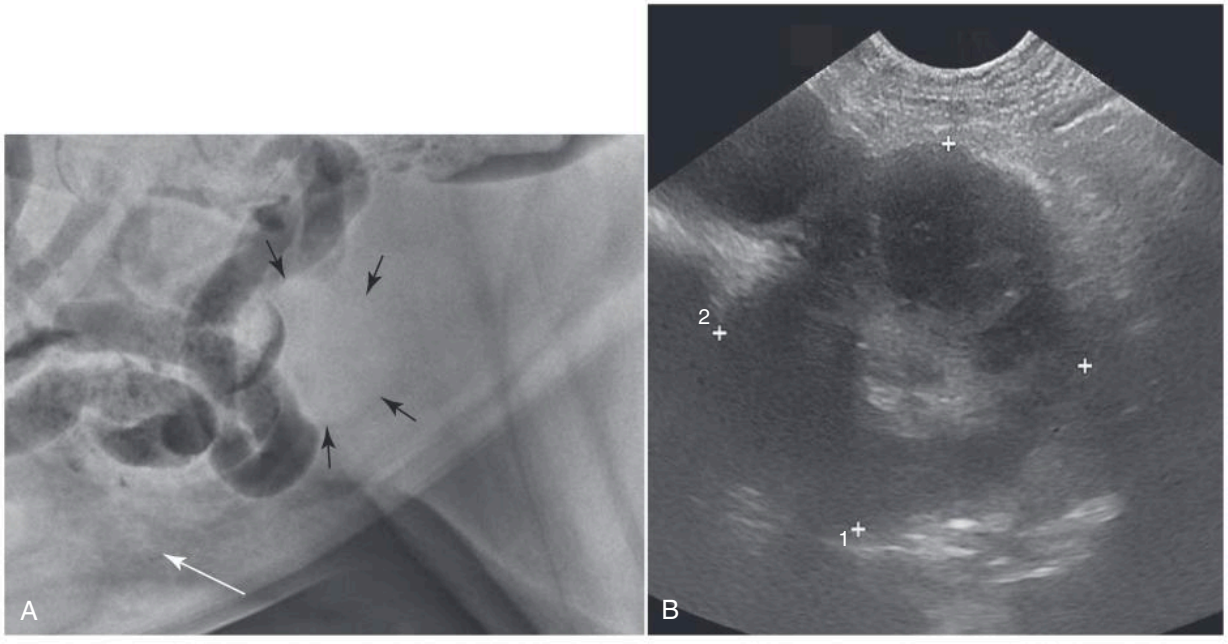
Positive urethro-vaginography may be helpful to investigate animals with genitourinary causes of dysuria. Vaginal fistula can be congenital or acquired due to trauma, surgery, or foreign bodies and can be highlighted by the passage of the contrast medium from the vagina to the urethra or to the surrounding peritoneum.

ABNORMAL CT FINDINGS IN FEMALE GENITAL TRACT DISEASES

Indications for CT include the diagnosis and staging of ovarian, uterine, and vaginal masses and challenging cases of genital tract infection or torsion. CT helps to assess the origin of genital masses and the relationship with surrounding organs and to establish surgical resectability (Fig. 44.21, eFig. 44.10).[48–50] Identification of the mass connection with an ovary or with a portion of the uterus or vagina is best performed using multiplanar reformatted images. Identifying vascular supply from an ovarian, uterine, or vaginal vessel can be used to confirm the genital origin of the mass.[51] For this reason, dual-phase CT scan, acquiring arterial and venous phases separately, can be useful (see Fig. 44.12). The vesicoureteral junction is frequently involved with uterine stump granulomas, with consequent hydroureter and/or hydronephrosis; this can be best demonstrated by scanning the animal in the delayed pyelographic/ureterographic phase (Fig. 44.22, eFig. 44.11). Placing a urinary catheter can be useful in case of large masses to assess the position and involvement of the urethra.[52] The enhancement evaluated in the postcontrast series provides information about the vascularization of the lesion. However, reliable CT criteria



eFig. 44.10 Two examples of large uterine masses investigated by computed tomography (CT). **A,** Transverse CT image of a dog affected by a large polyp of the left uterine horn. **B,** Dorsal reformatted image of a dog with bilateral uterine masses histologically diagnosed as fibroleiomyoma on the right and cystic endometrial hyperplasia and adenomyosis on the left. In both cases, CT was essential to confirm the uterine origin of the masses before surgery.



eFig. 44.11 **A,** Stump pyometra in a dog. There is a soft tissue mass in the caudal abdomen (*black arrows*), superimposed on the cranial margin of the urinary bladder. A focal loss of serosal detail is present adjacent to the cranial margin of the lesion (*white arrow*). This dog had the ovaries in situ, and also had a granulosa cell tumor. There was severe inflammation of the omental fat. **B,** Sonographic image of uterine stump pyometra.

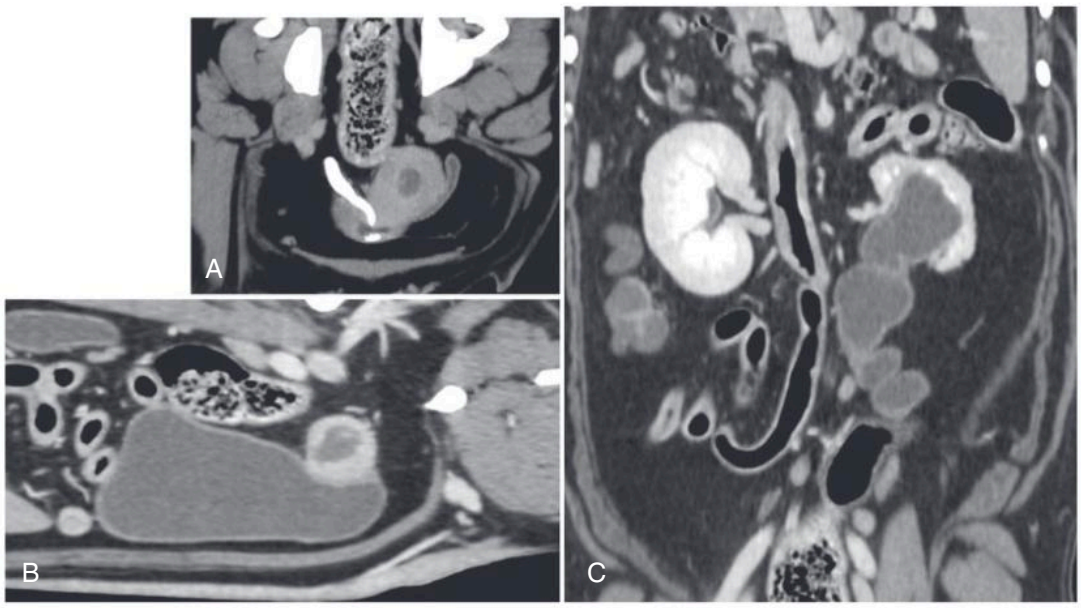


Fig. 44.22 Computed tomography images reformatted in the oblique **(A)**, sagittal **(B)**, and dorsal **(C)** plane of a dog with uterine stump granuloma, chronic hydroureter/nephrosis, and right kidney atrophy. **A, B,** The stump granuloma shows a fluid center surrounded by irregular thick wall; it compresses ventrally the bladder trigone and involves the vesicoureteral junction. Only the left ureter is functional. **C,** The right kidney is small and irregular in shape; the right ureter is severely dilated and nonfunctional.

to differentiate between benign and malignant neoplasia are not established. It has been suggested that benign mesenchymal neoplasia is associated with smaller size, homogeneous enhancement, and lack of bone involvement.[49,52] The presence of lymphadenopathy or other lesions compatible with metastatic spread indicates malignancy.

CT is an excellent image modality to diagnose complex urogenital conditions such as ureteral ectopia or urethrovaginal fistulas.[53]

IMAGING PROCEDURES AND NORMAL ANATOMY OF THE TESTICLES

Radiography is rarely used to investigate testicular diseases, with the exception of abdominal masses or torsion associated with retained testicles. Ultrasound on the other hand provides detailed information about the abnormalities of the testicular parenchyma and of the adnexa (scrotum, epididymis, distal part of the spermatic cord with the ductus deferens, vessels, and nerves).[54] Due to their superficial location, scrotal or inguinal testicles are best imaged with a high-frequency (8–13 MHz) linear probe. Longitudinal and transverse views of both testes are acquired and compared. Color, power, and pulsed-wave Doppler can be used to assess the arterial and venous flow and to investigate parenchymal vascularization.[55,56] For the search of retained abdominal testicles, which are more deeply located, a convex probe with mid to high frequency is often necessary especially in large dogs.

Color and power Doppler examination might be supportive to investigate dogs with infertility conditions.[57] CT of the normal male genital tract has been described.[58] The normal ultrasonographic anatomy of the testis and associated structures is summarized and illustrated in Table 44.5.

ABNORMAL RADIOGRAPHIC AND ULTRASONOGRAPHIC FINDINGS IN SCROTAL AND TESTICLE DISEASES

Extratesticular Diseases

Ultrasound is an accurate and rapid method to distinguish between testicular and nontesticular causes for scrotal swelling.[59,60] In case of severe scrotal skin diseases like severe edema, infection, or neoplasia, ultrasound can be used to evaluate concomitant involvement of the testicle or epididymis. Hydrocele is the most common cause of extratesticular fluid collection, and can result from trauma, neoplasia, infarction, torsion, or infection or can be idiopathic. Hydrocele may also develop secondary to peritoneal effusion, when fluid passes through the inguinal canal, and this may be associated with jejunal herniation. Hematoceles may occur with trauma, neoplasia, or diabetes mellitus. Pyoceles result from abscess rupture often within a pre-existing hydrocele. Extratesticular fluid collection is easily visualized as an anechoic to echogenic band surrounding the testicle, depending on the cellular content. Other indications for ultrasound include tunica vaginalis diseases like malformations, infections, trauma, or neoplasia.

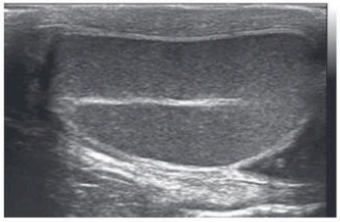
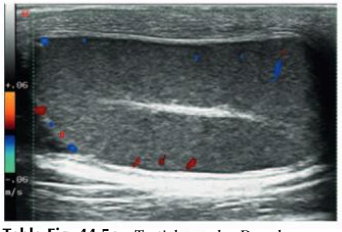
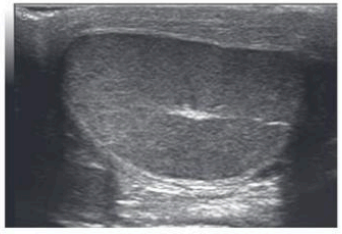
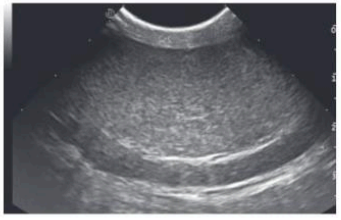
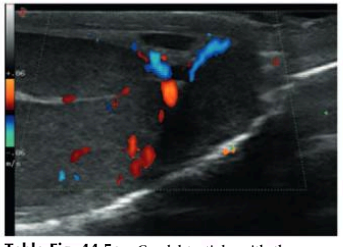
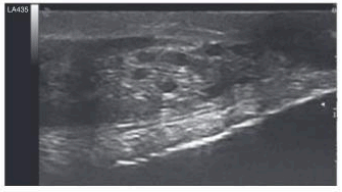
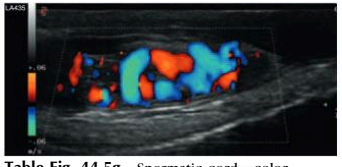
Inflammation

Epididymitis and orchitis can occur separately or concurrently, often secondary to retrograde prostatic or urinary bacterial infections. Penetrating wounds, migrating foreign bodies, and infections caused by *Brucella canis*, Rickettsia, fungal diseases, and feline coronavirus are other rare causes of infection.[61,62] Lymphoplasmacytic/immune-mediated orchitis is also reported; unilateral or bilateral involvement is possible.[63]

Ultrasonographic findings include enlarged testicle and/or epididymis, with patchy hypoechoic appearance, eventually focal changes due to abscesses, granulomas, or necrotic/

Table • **44.5**

US Feature of the Normal Testicles.

	SCROTUM/TESTICLE TUNICS (SKIN), TUNICA DARTOS (SMOOTH MUSCLE), AND ALBUGINEA (CONNECTIVE TISSUE)	TESTIS	EPIDIDYMIS	SPERMATIC CORD (DUCTUS DEFERENS AND ASSOCIATED VESSELS)
US images	 **Table Fig. 44.5a** Testicle longitudinal image.  **Table Fig. 44.5c** Testicle—color Doppler.	 **Table Fig. 44.5b** Testicle transverse image.	 **Table Fig. 44.5d** Testicle with body of the epididymis.  **Table Fig. 44.5e** Caudal testicle with the tail of the epididymis.	 **Table Fig. 44.5f** Spermatic cord—longitudinal image.  **Table Fig. 44.5g** Spermatic cord—color Doppler. *US*, Ultrasonography.
Location/ spatial orientation	Superficial, circumferential cover of the testicle	Oriented longitudinally	**Head:** at the cranial testicle pole **Body:** along the dorsolateral aspect of the testicle **Tail:** at the caudal testicle pole, continue cranially with the ductus deferens	Along the dorsomedial aspect of the testicle directed cranially to the inguinal canal, visible adjacent to the head of the epididymis

Size	Thin (few mm)	Variable depending on body weight, age, and health status Volume increases until the sixth year of age, then decreases Volume calculation (L × W × H × 0.71) accurate to predict true testicular volume	**Tail:** larger, more consistently displayed compared to the head and body	Very thin ductus deference, difficult to follow
Shape	Elongated	Oval	**Head and tail:** triangular **Body:** longitudinally elongated	
Echostructure/ echogenicity	Hyperechoic striated structure	Homogeneous, fine echotexture; echoic parenchyma interrupted by hyperechoic flecks (radiating connective septa from the albuginea) **Mediastinum testis:** central hyperechoic linear structure, longitudinally oriented	Homogeneous, hypoechoic to the testicle, might be anechoic	
Doppler examination[52,53]		Small marginal arteries can be detected at the testicular membranes (low resistance flow) Parenchyma low flow detected with power Doppler	Usually, no flow detected	Arterial and venous structures visualized with color Doppler. Cranial testicular artery with high resistance flow, becomes low resistance in the distal looping part



hemorrhagic areas and extratesticular fluid collection. Abscesses may appear as focal areas of anechoic/hypoechoic content surrounded by hyperechoic wall; granulomas have a more solid appearance. In chronic cases, the testicle may be reduced in size with more irregular margins. Differential diagnoses include neoplasia and torsion. Epididymal involvement and fluid accumulation orient to the diagnosis of orchitis (Fig. 44.23). Doppler ultrasound can be useful to differentiate between acute diffuse inflammation and torsion; diffuse hypervascularity is usually present with inflammation, whereas Doppler signal is lacking with torsion.[59,60] Contrast ultrasound is another excellent method to investigate testicular perfusion and may have a role in differentiating benign and malignant testicular diseases.[61,62]

Torsion

Scrotal testicles uncommonly undergo torsion; these are usually nonneoplastic. Ultrasonographic changes are visible already between 15 and 60 minutes after torsion and include enlargement of the spermatic cord, epididymis, and testicle associated with decreased diffuse echogenicity and loss of Doppler signal of the spermatic cord.[64] Other findings are scrotal thickening and hydrocele.

Torsion of abdominal retained testicles in dogs most often occurs secondary to testicular neoplasia; however, nonneoplastic testicles can be affected.[65,66] It is thought that the increased weight of pendulous, neoplastic abdominal testes may predispose to torsion. Clinical signs are severe and acute and mimic other acute abdominal emergencies. If severely enlarged, the testicle might be identified radiographically as a soft tissue opaque mass located caudal to the kidney or cranial to the urinary bladder with or without associated abdominal fluid. Inconsistent and reduced flow with color Doppler is the only differentiation from neoplasia only in ultrasound, making the final diagnosis challenging. In these cases, the different clinical presentation may support the diagnosis. Torsion of nonneoplastic cryptorchid testicle has been reported in few cases: the testicle and epididymis are enlarged, rounded with abnormal echogenicity (Fig. 44.24). Interestingly, hyperechoic appearance of the twisted testicle has been reported.[66] Adjacent effusion and/or peritoneal hyperechogenicity can be present due to focal peritonitis. The lack of testicular blood flow can be easily demonstrated by contrast-enhanced ultrasound.[67]

Cryptorchidism

Cryptorchidism is suspected if one or both testicles are not located within the scrotum in a dog after 6 to 8 weeks and in a newborn cat. However, in puppies and kittens until 6 months of age, the small and soft testes can move from the scrotum to the inguinal canal. In dogs, a genetic basis is suspected, with a reported incidence range from 1% to 15%, higher in small-size breed, most frequently unilateral and right sided.[68] Feline cryptorchidism is less frequent compared to dogs.

Ultrasound has a high predictive value for the final, surgical location of a retained testicle.[69] The ultrasonographic search of the cryptorchid testicle is best performed with the animal in dorsal recumbency. First, the affected side is identified by palpation of the scrotal testicle; this restricts the search to 50%. The scan starts in the subcutaneous inguinal region from the scrotum to the inguinal ring, then it continues in the abdomen just lateral to the urinary bladder neck cranially to the caudal pole of the ipsilateral kidney (Fig. 44.25). The testicle must be differentiated from the inguinal or colic/jejunal lymph nodes based on the shape (oval for the testicle and more elongated for the lymph nodes), the absence of the hilus, and the presence of the testicle mediastinum. The retained testicle is usually smaller compared to the scrotal one but similar in echogenicity and structure. Even subtle changes in echogenicity or structure should be considered suspect for neoplastic transformation. Testicle agenesis is rare however possible. If a suspected testicle is not identified, CT or MRI can be useful as further diagnostic methods.

Neoplasia

Canine testicular neoplasia is common in old intact dogs, with a reported prevalence between 9% and 27%, and is mainly represented by three types of tumors: interstitial cell (Leydig cell), Sertoli cell, and seminomas. Up to 20% of dogs diagnosed with testicular cancer have more than one primary testicular tumor; most of them are characterized by local invasion but rarely metastasize, with the highest metastatic rate (less than 15%) reported for Sertoli cell tumors and seminomas.[37] The risk of developing testicular neoplasia increases with a retained testis. Hyperestrogenism and femininization syndrome are commonly associated with Sertoli cell tumors. The main clinical signs include bilateral symmetric alopecia and hyperpigmentation, pendulous prepuce, gynecomastia, galactorrhea, atrophy of the penis, and squamous metaplasia of the prostate. Severe pancytopenia can also develop. Independent of the tumor type, atrophy of the contralateral testicle is common. As in ovarian neoplasia, the mass can be located between the caudal pole of the kidney and the inguinal canal. With large or mineralized masses, abdominal radiographs can show the lesion located in the mid to caudoventral abdomen (Fig. 44.26, eFigs. 44.12 and 44.13). If caudally located, the enlarged testicle can be confused with the urinary bladder or with a large para-prostatic cyst. Positive-contrast cystogram or ultrasound is indicated for

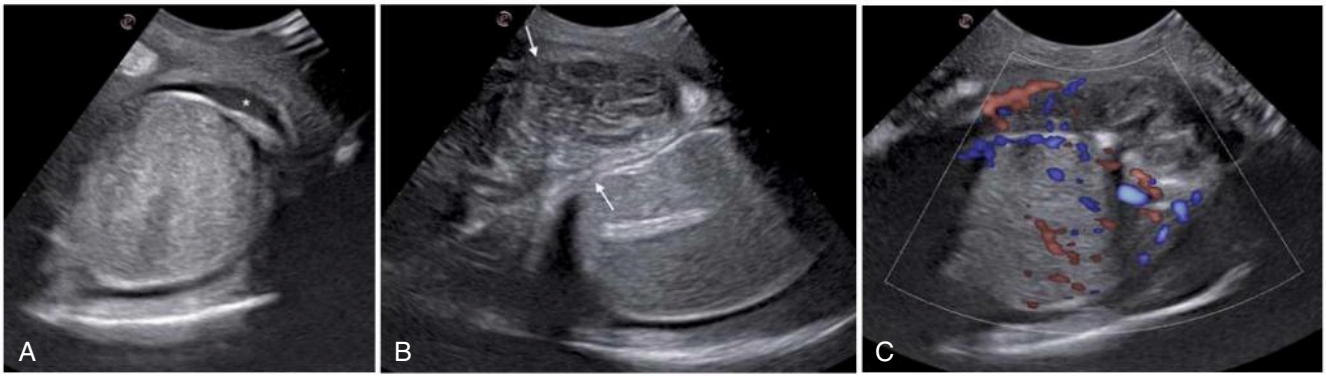
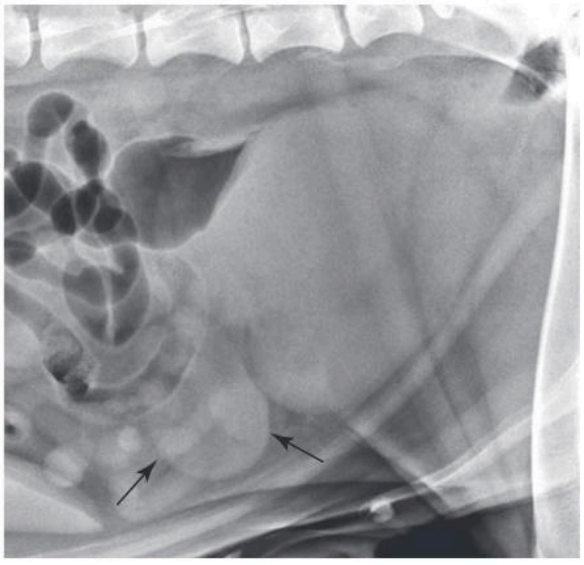
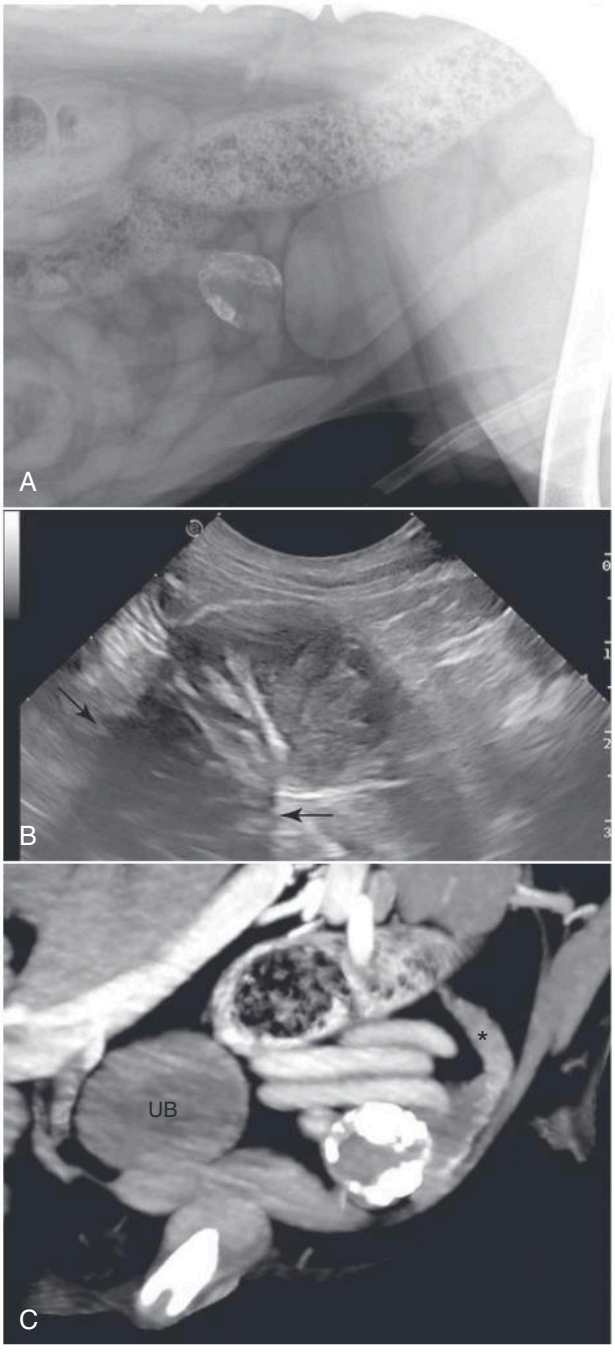


Fig. 44.23 Bacterial orchitis and epididymitis in a dog, longitudinal grey scale **(A, B)** and color Doppler **(C)** ultrasound images. **A,** The testicle is enlarged, mildly heterogeneous and surrounded by effusion (*asterisk*). **B, C,** The epididymis is severely enlarged (*between arrows*) and with increased Doppler signal.



eFig. 44.12 Lateral radiograph of a dog with a retained testicular Sertoli cell tumor (*black arrows*). There are also two oval masses in the caudal abdomen, representing two lobes of a severely enlarged cystic prostate gland, which often accompanies Sertoli cell tumors. The urinary bladder is empty and not visible.



eFig. 44.13 Mineralized seminoma in a dog. The neoplasia is located cranial to the urinary bladder **(A)** and appears heterogeneous with shadowing in US **(B,** *arrows*). With computed tomography (CT) **(C),** the identification of the spermatic cord (*asterisk*) confirms the testicle origin. *UB,* Urinary bladder.

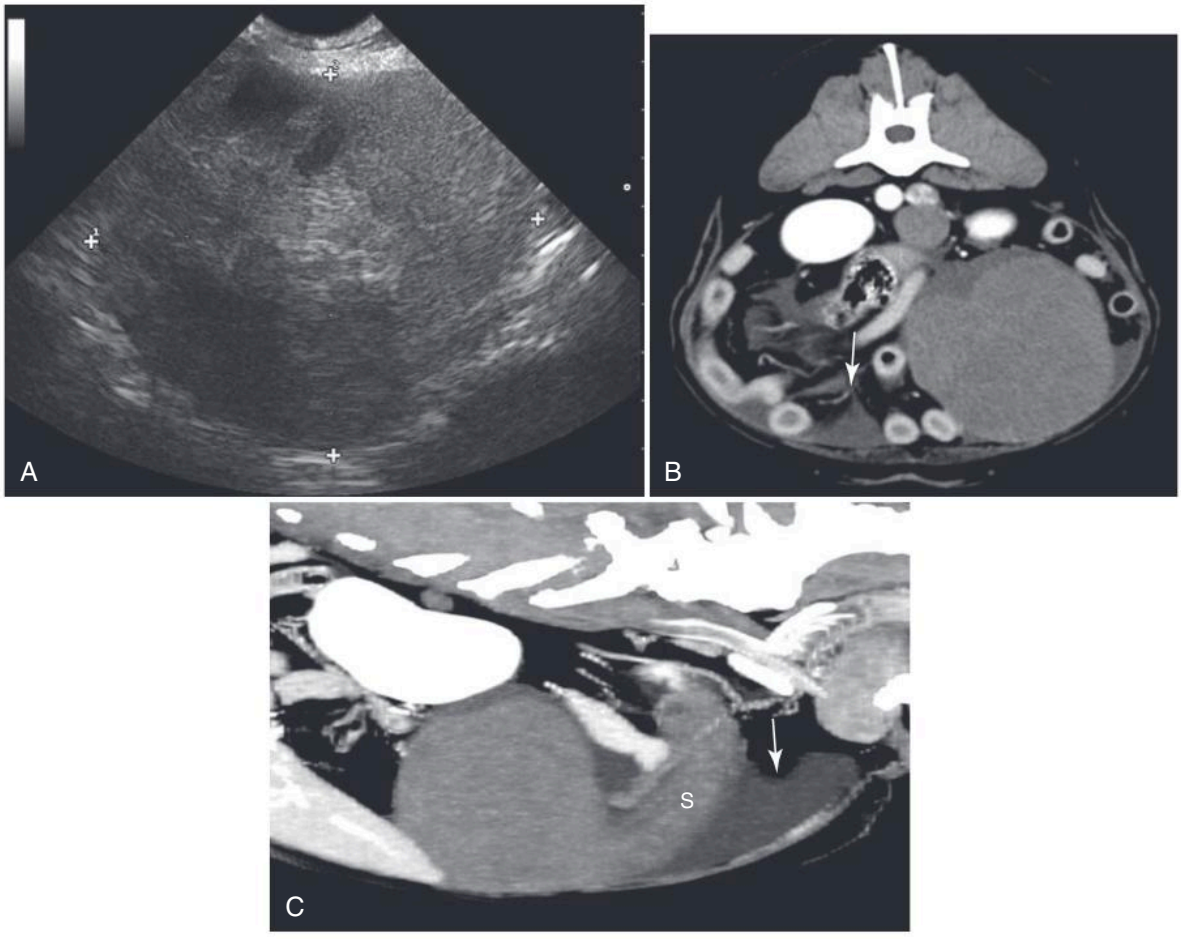


Fig. 44.24 Sonographic image **(A)**, transverse **(B)**, and oblique **(C)** reformatted computed tomography images of a dog with torsion of an abdominal testicle. The enlarged testicle (*between calipers*) has a complex echostructure in ultrasound **(A)** and appears as a nonenhancing mass in CT **(B)**. Note the enlarged spermatic cord (*S*) and some peritoneal free fluid (*white arrow*). In this case, the "whirl sign" was not detected.

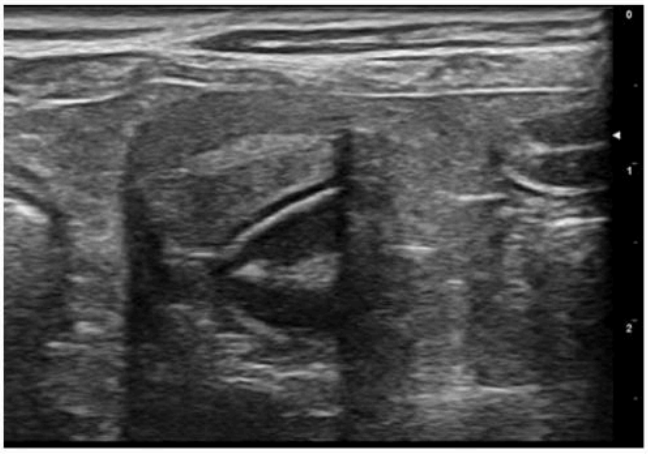


Fig. 44.25 Longitudinal sonographic image of a retained testicle. The testicle is located lateral to the urinary bladder, between a jejunal loop and the abdominal wall, and presents a normal structure, with a well-visible hyperechoic mediastinum.

identification. Thoracic radiographs complete the staging of these patients. Hypertrophic nipples can be obvious in case of Sertoli cell tumors and these must not be confused with pulmonary nodular lesions.

Ultrasound is the method of choice to image testicle nodules or masses.[70] They present with variable size, echogenicity, and structure; unfortunately, B-mode findings are not specific for the different tumor types[55,56] (see Fig. 44.26). If large, they alter the testicle architecture and may have a complex appearance with cystic, necrotic, or hemorrhagic areas and mineralization. Contralateral testicle atrophy and prostatic hyperplasia can be associated with functional neoplasia (Fig. 44.27). Color and power Doppler ultrasound can assess tumor vascularization. To improve tumor characterization, multiparameter evaluation including pulsed-wave Doppler, B-flow, and contrast ultrasound has been investigated, with some more specific pattern for Leydig cell tumors.[71,72]

ABNORMAL CT FINDINGS IN TESTICLES DISEASES

CT could be beneficial with challenging cases of retained testicles before surgery if abdominal ultrasound is not conclusive. Identification of the testicular artery and vein supplying a structure or a mass demonstrates a testicular origin. Visualization of a cord-like vascular pedicle composed by a venous plexus and tortuous arteries, consistent with the spermatic cord, is another useful CT finding.[48,73]

Testicular torsion can be also diagnosed with CT (see Fig. 44.24). The testicle is enlarged with reduced enhancement after contrast administration. Other CT findings include the

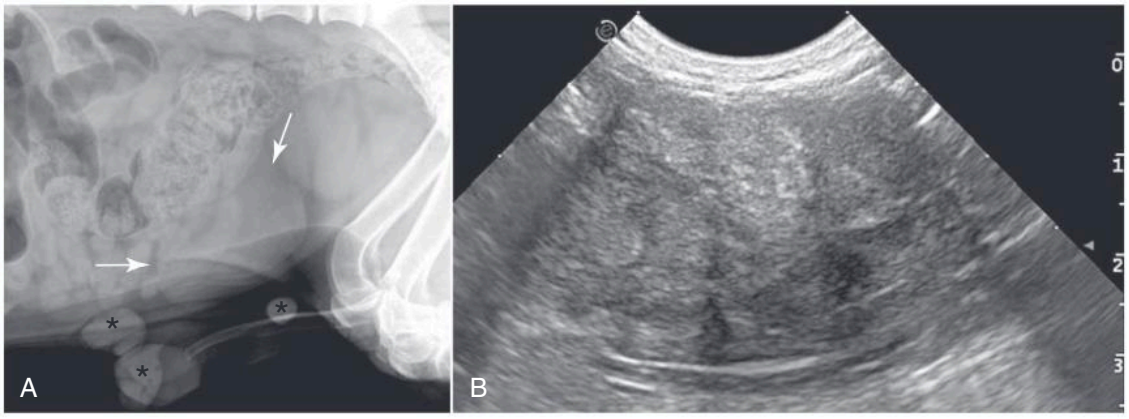


Fig. 44.26 Lateral radiograph **(A)** and sonographic image **(B)** of a Sertoli cell tumor (*arrows*) arising from a retained testicle. Note the enlarged nipples due to feminization syndrome (*asterisks*).

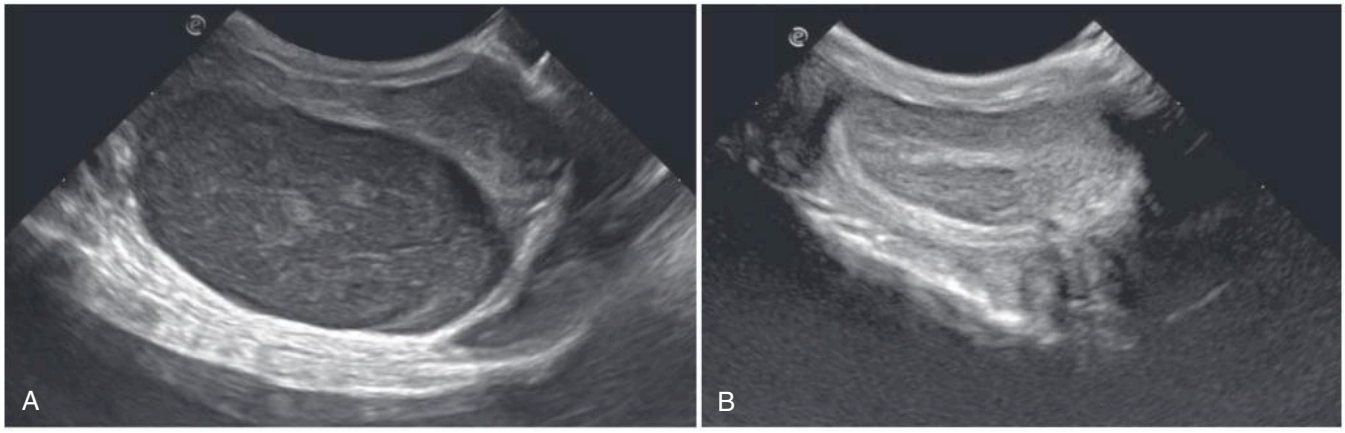


Fig. 44.27 Testicular seminoma appearing as a hypoechoic nodule **(A)** and associated contralateral testicle atrophy **(B)** in a dog.

"whirl sign," corresponding to the spermatic cord arranged in a whirl of fat and soft tissue striations, and a central testicular/spermatic cord crescentic to triangular fat pattern, described with nonneoplastic torsion.[73,74] These findings are similar to what is usually observed with splenic torsion.

Acknowledgment

With special thanks to prior authors of this chapter for their contributions.

REFERENCES

1. Armbrust LJ, Biller DS, Hoskinson JJ. Compression radiography: an old technique revisited. *J Am Anim Hosp Assoc.* 2000;36(6):537–541.
2. Woodland M, Pack L, Rist P, et al. Comparison of digital radiography, ultrasonography, and positive contrast vaginourethrography for determining reproductive status of female cats. *Vet Radiol Ultrasound.* 2014;55(4):368–373.
3. Rivers B, Johnston GR. Diagnostic imaging of the reproductive organs of the bitch. Methods and limitations. *Vet Clin North Am Small Anim Pract.* 1991;21(3):437–466.
4. Holt PE, Gibbs C, Latham J. An evaluation of positive contrast vaginourethrography as a diagnostic aid in the bitch. *J Small Anim Practice.* 1984;25:531–549.
5. Evans HE. *Miller's Anatomy of the Dog.* 3rd ed. Philadelphia: Saunders; 1993.
6. Barone R. *Anatomie Comparee des Mammiferes Domestiques.* 3rd ed. Tome 4, Splanchnologie: Baronne Edition; 2020.
7. Davidson AP, Baker TW. Reproductive ultrasound of the bitch and queen. *Top Companion Anim Med.* 2009;24(2):55–63.
8. Fulton RM. Focused ultrasound of the fetus, female and male, reproductive tracts, pregnancy and dystocia in dogs and cats. *Vet Clin Small Anim.* 2021;51(6):1249–1265.
9. Wallace SS, Mahaffey MB, Miller DM, et al. Ultrasonographic appearance of the ovaries of dogs during the follicular and luteal phases of the estrous cycle. *Am J Vet Res.* 1992;53(2):209–215.
10. England GC, Yeager AE. Ultrasonographic appearance of the ovary and uterus of the bitch during oestrus, ovulation and early pregnancy. *J Reprod Fertil Suppl.* 1993;47:107–117.
11. Bergeron LH, Nykamp SG, Brisson BA, et al. An evaluation of B-mode and color Doppler ultrasonography for detecting periovulatory events in the bitch. *Theriogenol.* 2013;79(2):274–283.
12. Gatel L, Rault DN, Chalvet-Monfray K, et al. Ultrasonography of the normal reproductive tract of the female domestic cat. *Theriogenology.* 2020;142:328–337.

13. Freeman SL, Green MJ, England GC. Prevalence and effect of uterine luminal free fluid on pregnancy and litter size in bitches. *Theriogenology*. 2013;80(2):73–76.
14. Weissmann A, Jimenez D, Torres B. Canine vaginal leiomyoma diagnosed by CT vaginourethrography. *J Am Anim Hosp Assoc*. 2013;49:394–397.
15. Agut A, Carrillo DJ, Anson A. Imaging diagnosis—urethrovaginal fistula caused by a migrating grass awn in the vagina. *Vet Radiol Ultrasound*. 2016;57(3):E30–E33.
16. Teixeira M, Francisco Gil F b, Vazquez JM, et al. Helical computed tomographic anatomy of the canine abdomen. *Veterinary J*. 2007;174:133–138.
17. Lee SK, Yoon S, Kim C, et al. Triple-phased mesenteric CT angiography using a test bolus technique for evaluation of the mesenteric vasculature and small intestinal wall contrast enhancement in dogs. *Vet Radiol Ultrasound*. 2019;60(5):493–501.
18. Rendano VT, Lein MSDH, Concannon PW. Radiographic evaluation of prenatal development in the beagle. *Vet Radiol*. 1984;25:132–141.
19. Haney DR, Levy JK, Newell SM, et al. Use of fetal skeletal mineralization for prediction of parturition date in cats. *J Am Vet Med Assoc*. 2003;223(11):1614–1616.
20. Beccaglia M, Alonge S, Trovo C, et al. Determination of gestational time and prediction of parturition in dogs and cats: an update. *Reprod Domest Anim*. 2016;51(suppl 1):12–17.
21. Eneroth A, Linde-Forsberg C, Uhlhorn M, et al. Radiographic pelvimetry for assessment of dystocia in bitches: a clinical study in two terrier breeds. *J Small Anim Pract*. 1999;40(6):257–264.
22. Dobak TP, Voorhout G, Vernooij CM, et al. Computed tomographic pelvimetry in English bulldogs. *Theriogenology*. 2018;15(118):144–149.
23. Siena G, Milani C. Usefulness of maternal and fetal parameters for the prediction of parturition date in dogs. *Animals Basel*. 2021;11(3):878.
24. Zambelli D, Prati F. Ultrasonography for pregnancy diagnosis and evaluation in queens. *Theriogenology*. 2006;66:135–144.
25. Concannon PW. Canine pregnancy: predicting parturition and timing events of gestation. In: Concannon PW, England G, Verstegen IIIJ, Linde Forsberg C, eds. *Recent Advances in Small Animal Reproduction*. United States: International Veterinary Informative Service; 2019:1–9.
26. Gatel L, Rault D, Chalvet-Monfray K, et al. Prediction of parturition time in queens using radiography and ultrasonography. *Anatomia Histologia and Embryologia*. 2015;44:241–246.
27. Alonge S, Beccaglia M, Melandri M, et al. Prediction of whelping date in large and giant canine breeds by ultrasonography foetal biometry. *J Small Anim Pract*. 2016;57(9):479–483.
28. Beccaglia M, Anastasi P, Grimaldi E, et al. Accuracy of the prediction of parturition date through ultrasonographic measurement of fetal parameters in the queen. *Vet Res Commun*. 2008;32:S99–101.
29. Lenard ZM, Hopper BJ, Lester NV, et al. Accuracy of prediction of canine litter size and gestational age with ultrasound. *Aust Vet J*. 2007;85(6):222–225.
30. England GCW. US assessment of abnormal pregnancy. *Am Vet Clin North Am Small Anim Pract*. 1998;28(4):849–868.
31. England GC, Russo M. Ultrasonographic characteristics of early pregnancy failure in bitches. *Theriogenology*. 2006;66(6–7):1694–1698.
32. Pharr W. Ultrasonography and radiography of the canine postpartum uterus. *Vet Radiol Ultrasound*. 1992;33:35–40.
33. Yeager AE, Concannon PW. Serial ultrasonographic appearance of postpartum uterine involution in beagle dogs. *Theriogenology*. 1990;34(3):523–535.
34. Ferretti LM, Newell SM, Graham JP, et al. Radiographic and ultrasonographic evaluation of the normal post-partum uterus. *Vet Radiol Ultrasound*. 2000;41:287–291.
35. Ball RL, Birchard SJ, May LR. Ovarian remnant syndrome in dogs and cats: 21 cases (2000–2007). *J Am Vet Med Assoc*. 2010;236(5):548–553.
36. Knauf Y, Bostedt H, Failing K, et al. Gross pathology and endocrinology of ovarian cysts in bitches. *Reprod Domest Anim*. 2014;49(3):463–468.
37. Vail DM, Thamm DH, Liptak JM. *Withrow & MacEven's Small Animal Clinical Oncology*. 6th ed. St Louis: Saunders; 2020.
38. Stein BS. Tumors of the feline genital tract. *J Am Anim Hosp Assoc*. 1981;17:1022–1025.
39. Diez-Bru N, Garcia-Real I, Martinez EM, et al. Ultrasonographic appearance of ovarian tumors in 10 dogs. *Vet Radiol Ultrasound*. 1998;39(3):226–233.
40. Greenlee PG, Patnaik AK. Canine ovarian tumors of germ cell origin. *Vet Pathol*. 1985;22(2):117–122.
41. Pretzer SD. Clinical presentation of canine pyometra and mucometra: a review. *Theriogenology*. 2008;70:359–363.
42. Mattei C, Fabbi M, Hansson K. Radiographic and ultrasonographic findings in a dog with emphysematous pyometra. *Acta Vet Scand*. 2018;60:67.
43. Jjeong E, Tan RM, Oh H, et al. Imaging diagnosis—endometrial mineralization in a dog. *Vet Radiol Ultrasound*. 2016;57(6):E67–E70.
44. Chambers B, Laksito M, Long F, et al. Unilateral uterine torsion secondary to an inflammatory endometrial polyp in the bitch. *Aust Vet J*. 2011;89(10):380–384.
45. Misumi K, Fujiki M, Miura N, et al. Uterine horn torsion in two non-gravid bitches. *J Small Anim Pract*. 2000;41(10):468–471.
46. Patsikas M, Papazoglou LS, Jakovljevic S, et al. Radiographic and ultrasonographic findings of uterine neoplasms in nine dogs. *J Am Anim Hosp Assoc*. 2014;50(5):330–337.
47. Ma LY, Heng HG, Chia MY, et al. Ultrasonographic appearance of pseudo-placentational endometrial hyperplasia in a dog. *Vet Radiol Ultrasound*. 2021;62(6):e58–e62.
48. Russo M, England GCW, Catone G, et al. Imaging of canine neoplastic reproductive disorders. *Animals Basel*. 2021;11(5):1213.
49. Spector DI, Fischetti AJ, Kovak-McClaran JR. Computed tomographic characteristics of intrapelvic masses in dogs. *Vet Radiol Ultrasound*. 2011;52(1):71–74.
50. Percival A, Singh A, zur Linden RA, et al. Massive uterine lipoleiomyoma and leiomyoma in a miniature poodle bitch. *Can Vet J*. 2018;59:845–850.
51. Rowan C, Cuddy L, Bryan J. Imaging diagnosis – computed tomography findings in a case of metastatic ovarian adenocarcinoma in a dog. *Vet Radiol Ultrasound*. 2017;58(6):E60–E63.
52. Barozzi MCM, Saba CF, Gendron KP. CT characteristics of uterine and vaginal mesenchymal tumours in dogs. *J Small Anim Pract*. 2021;62:293–299.
53. Schwarz T, Bommer N, Parys M, et al. Four-dimensional CT excretory urography is an accurate technique for diagnosis of canine ureteral ectopia. *Vet Radiol Ultrasound*. 2021;62(2):190–198.
54. Pugh CR, Konde LJ, Park RD. Testicular ultrasound in the normal dog. *Vet Radiol*. 1990;31(4):195–199.
55. Carrillo JD, Soler M, Lucas X, et al. Colour and pulsed Doppler ultrasonographic study of the canine testis. *Reprod Domest Anim*. 2012;47(4):655–659.

56. Gumbsch P, Gabler C, Holzmann A. Colour-coded duplex sonography of the testes of dogs. *Vet Rec*. 2002;151(5):140–144.
57. Lemos H, Dorado J, Hidalgo M, et al. Assessment of dog testis perfusion by colour and pulsed-Doppler ultrasonography and correlation with sperm oxidative DNA damage. *Top Companion Anim Med*. 2020;41:100452.
58. Dirrig H, Drees R, Lam R. Use of dual-phase contrast computed tomography for evaluation of the normal canine male genital tract. *J Small Animal Practice*. 2016.
59. Pugh CR, Konde LJ. Sonographic evaluation of canine testicular and scrotal abnormalities: a review of 26 case histories. *Vet Radiol Ultrasound*. 1991;32(5):243–250.
60. Davidson AP, Baker TW. Reproductive ultrasound of the dog and tom. *Top Companion Anim Med*. 2009;24(2):64–70.
61. Egloff S, Schneeberger M, Gobeli S, et al. *Brucella canis* infection in a young dog with epididymitis and orchitis. *Schweiz Arch Tierheilkd*. 2018;160(12):743–748.
62. Ober CP, Spaulding K, Breitschwerdt EB, et al. Orchitis in two dogs with Rocky Mountain spotted fever. *Vet Radiol Ultrasound*. 20004; 45(5):458–465.
63. Davidson AP, von Dehn BJ, Schlafer DH, et al. Adult-onset lymphoplasmacytic orchitis in a Labrador retriever stud dog. *Top Companion Anim Med*. 2015;30(1):31–34.
64. Hricak H, Lue T, Filly RA, et al. Experimental study of the sonographic diagnosis of testicular torsion. *J Ultrasound Med*. 1983;2(8):349–356.
65. Pearson H, Kelly DF. Testicular torsion in the dog: a review of 13 cases. *Vet Rec*. 1975;97(11):200–204.
66. Hecht S, King R, Tidwell AS, et al. Ultrasound diagnosis: intra-abdominal torsion of a non-neoplastic testicle in a cryptorchid dog. *Vet Radiol Ultrasound*. 2004;45(1):58–61.
67. Brown JM, Taylor KJ, Alderman JL, et al. Contrast-enhanced ultrasonographic visualization of gonadal torsion. *J Ultrasound Med*. 1997;16:309–316.
68. Khan FA, Gartley CJ, Khanam A. Canine cryptorchidism: an update. *Reprod Domest Anim*. 2018;53(6):1263–1270.
69. Felumlee AE, Reichle JK, Hecht S, et al. Use of ultrasound to locate retained testes in dogs and cats. *Vet Radiol Ultrasound*. 2012;53(5):581–585.
70. Johnston GR, Feeney DA, Johnston SD, et al. Ultrasonographic features of testicular neoplasia in dogs: 16 cases (1980-1988). *J Am Vet Med Assoc*. 1991;198(10):1779–1784.
71. Volta A, Manfredi S, Vignoli M, et al. Use of contrast-enhanced ultrasonography in chronic pathologic canine testes. *Reprod Domest Anim*. 2014;49(2):202–209.
72. Orlandi R, Vallesi E, Boiti C, et al. Characterization of testicular tumor lesions in dogs by different ultrasound techniques. *Animals (Basel)*. 2022;12(2):210.
73. Stokowski S, Ruth J, Lanz O, et al. Computed tomographic features in a case of bilateral neoplastic cryptorchidism with suspected torsion in a dog. *Front Vet Sci*. 2016;27;3:33.
74. Slaughter SA, Eitzer AD, Tolliver SA, et al. Computed tomography of testicular torsion in a juvenile dog with unilateral cryptorchidism. *Can Vet J*. 2022;63(5):515–520.

ELECTRONIC RESOURCES

Additional information related to the content in Chapter 44 can be found online at eBooks.Health.Elsevier.com

- Chapter Quiz
- Videos



CHAPTER 45

Stomach

Susanne M. Stieger-Vanegas

Diagnostic imaging is an important component in the clinical evaluation of animals with gastrointestinal disease. Survey radiographs are usually the first imaging modality, often followed or sometimes replaced by an ultrasound examination. Contrast radiographic studies remain in use but they are laborious and time consuming and are often replaced by ultrasound. Nevertheless, contrast radiography remains important for evaluation of functional disorders of the stomach and obstructive processes. Computed tomography (CT) is used increasingly for evaluation of the gastrointestinal tract, especially when disease staging is required. While magnetic resonance (MR) imaging is regularly used in human patients, it is rarely used for the evaluation of the gastrointestinal tract in animals.

NORMAL ANATOMY

The stomach is the relatively large muscular, hollow aspect of the digestive system, which fulfills an important function in the transient storage and digestion of food. The stomach is caudal to the liver, and when empty normally lies cranial to the last pair of ribs or slightly caudal to the costal arch.[1,2] The empty stomach has a U shape, which disappears with filling. In the filled state, the position of the caudal aspect of the stomach is variable and can be located as far caudal as the third to fourth lumbar vertebrae. Independent of filling stage, the stomach lies primarily to the left of midline in both the dog and cat.[2]

The stomach is arbitrarily subdivided into the cardia, fundus, body, and pylorus (Fig. 45.1).[1] The cardia is a small area at the esophagogastric junction immediately caudal to the diaphragm.

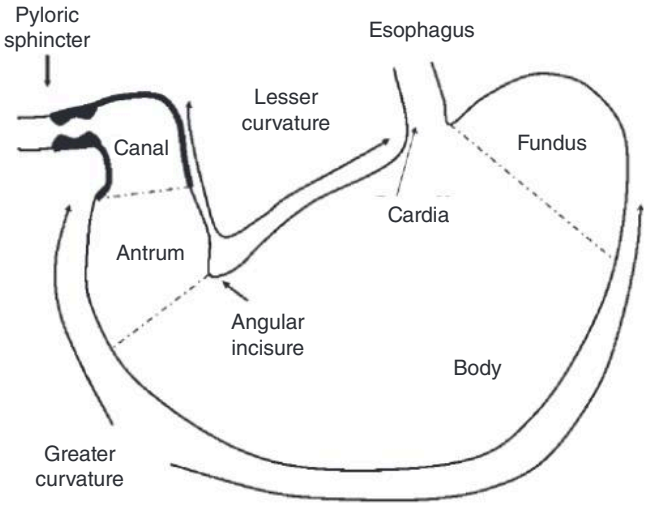


Fig. 45.1 The divisions of the stomach.

The fundus is the dome-shaped outpouching of the left dorsal aspect of the stomach. The fundus is the only portion of the stomach that normally can be in direct contact with the diaphragm. The body is the middle aspect of the stomach extending from the fundus to the pylorus and is the largest portion of the stomach. A large aspect of the body of the stomach is located to the left of midline. The distal third of the stomach is the pylorus, which is further subdivided into the pyloric antrum and the pyloric canal. The pyloric antrum includes the orad (proximal) two-thirds of the pylorus and is relatively thin walled and slightly expanded. The pyloric canal, which is the most aborad (distal) third of the pylorus, is more muscular and contains a double sphincter. The pyloric antrum is ventral to the fundus and in the dog is on or to the right of the midline, whereas in the cat, the pyloric antrum tends to be on midline. When the stomach is maximally distended, mainly the body and pyloric antrum of the stomach increase in width, whereas the pyloric canal does not change in size.[2]

Additional landmarks of the stomach include the greater and lesser curvatures and the angular incisure, or notch.[1] The greater curvature is the convex surface of the stomach extending from the cardia caudoventrally to the pylorus. The lesser curvature is the concave surface originating from the right lateral aspect of the cardia and extending cranioventrally to the pylorus. It is the shortest distance between the cardia and pylorus. The angular notch is the point of acute angulation of the lesser curvature, located approximately at the junction of the body and pyloric antrum.

The mucosal surface of the stomach is characterized by numerous folds or ridges called *rugal folds* or *rugae*, which are more distinct when the stomach is empty as they become flat when the stomach is expanded. The rugal folds are most prominent in the gastric body and fundus and flatten towards the pyloric antrum.

The greater omentum, which is a large, lacy, fat-containing double folded structure, attaches to the stomach and extends caudally to the urinary bladder, covering the intestines ventrally and laterally. The superficial aspect of the greater omentum originates from the greater curvature of the stomach and continues to the proximal part of the duodenum in alignment with the attachment of the lesser omentum to the duodenum.[1,3] The gastrosplenic ligament is part of the greater omentum and connects the hilus of the spleen to the greater curvature of the fundus and body of the stomach.[1] The lesser omentum is small and extends from the liver to lesser curvature of the stomach and the cranial part of the duodenum.[1,3] The largest aspect of the lesser omentum is the hepatogastric ligament connecting the liver with the lesser curvature of the stomach.[1]

IMAGING PROCEDURES

Radiography

Indications

Radiography is used commonly to evaluate the stomach. Survey radiographs allow evaluation of the position and content of the

stomach. Sometimes, gastric wall thickening or gas within the gastric wall, called gastric pneumatosis, can be detected. Gastric dilation and volvulus (GDV), a frequently occurring life-threatening disease in dogs, can usually be diagnosed radiographically. Furthermore, mineral or metal attenuating foreign bodies are easily detected on survey radiographs. Additionally, survey radiographs are highly sensitive for evaluating the presence of peritoneal gas, if a gastric perforation is suspected. Survey radiographs are also an important baseline if a contrast radiographic study is planned.

Radiographic Technique

Three, or preferably four, views of the abdomen are required for a thorough evaluation.[4] Performing left lateral, right lateral, ventrodorsal (VD), and dorsoventral (DV) views of the abdomen is especially valuable for the evaluation of the stomach as the position of the patient affects the position of the luminal gas and fluid within the stomach.[5] Due to gravity, fluid settles dependently, and gas rises to the highest part of the lumen of the stomach. This was discussed in detail in Chapter 38. These changes in appearance of the stomach help to evaluate all aspects of the stomach. Oblique views may occasionally be of value to isolate or project certain areas of the stomach, such as the pylorus, especially when a foreign body or pyloric wall mass is suspected.

Radiographic examination of the stomach in an animal that has fasted for 12 to 24 hours may be more informative than when the stomach is in the ambient state, as ingesta within the stomach may obscure some lesions or simulate other lesions.[6–8] However, this is not done routinely due to time constraints, and in some patients fasting may be contraindicated. Also, many drugs used for treatment of gastrointestinal disorders or for sedation to facilitate radiographic positioning, alter gastric motility and may cause gas distention of the stomach.

Normal Radiographic Findings

The stomach is usually easily recognized by its location, shape, and the content of gas, ingesta, or both. The entire stomach may not be discernible on survey radiographs if it is empty or if gastric fluid silhouettes with the liver or other abdominal structures.

As a general guide, the axis of the stomach from the fundus through the body and pylorus on the lateral view is either perpendicular to the spine, parallel to the ribs, or somewhere between these angles (Figs. 45.2A,B and 45.3A). On the lateral view, the pylorus may be superimposed over the body of the

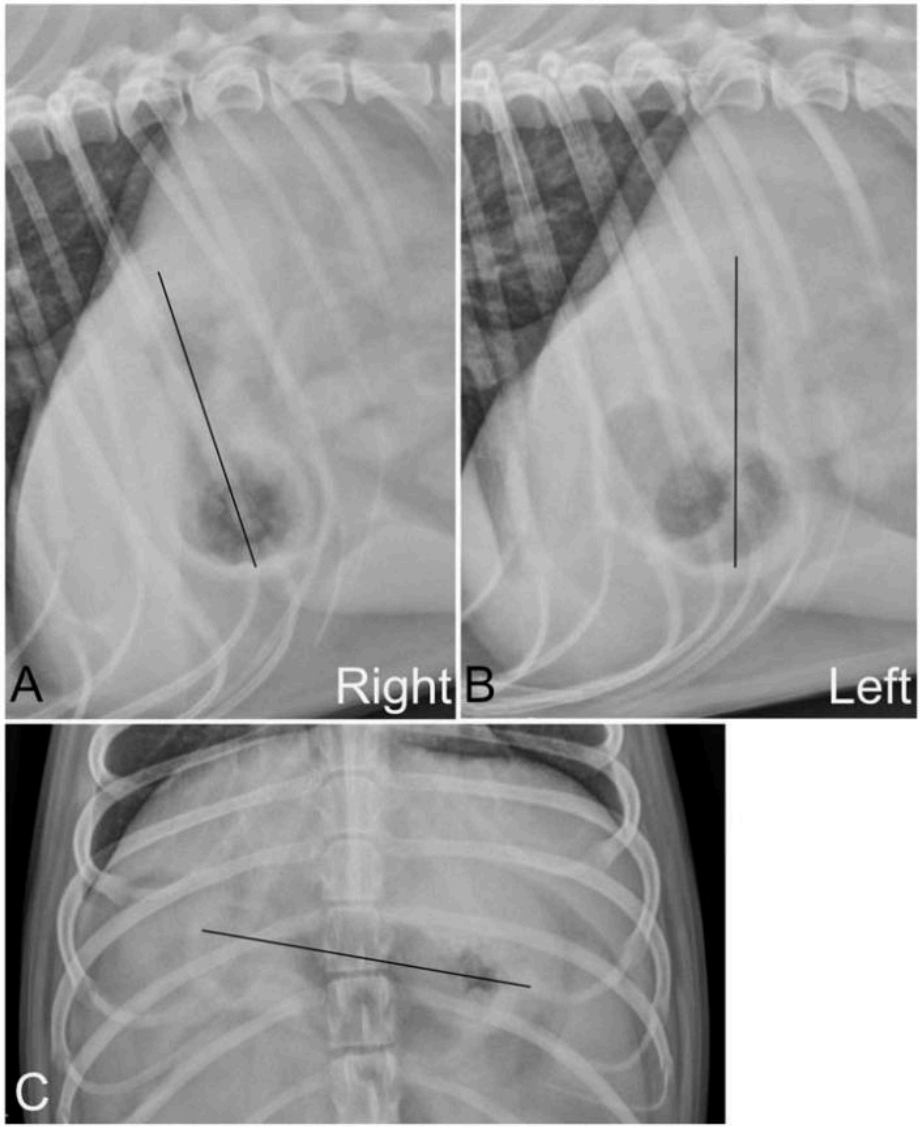


Fig. 45.2 Normal position of the gastric axis in different patient positions. **A,** Right lateral view of the abdomen of the dog. The gastric axis is parallel with the ribs. **B,** Left lateral view of the same dog. The gastric axis is perpendicular to the spine. **C,** Ventrodorsal view of the same dog. The gastric axis is mildly angled and nearly perpendicular to the spine.

stomach (see Fig. 45.2A) or located slightly cranial to the body of the stomach (see Fig. 45.2B). In VD radiographs, the long axis of the stomach is generally perpendicular to the spine with the stomach running transversely across the abdomen, making the angular notch difficult to identify (see Fig. 45.2C). On the VD view of the dog, the cardia, fundus, and body of the stomach are located to the left of midline, and the pyloric portions are located to the right of midline (Fig. 45.4A). The pyloric sphincter in the dog usually is located in the right cranial abdominal quadrant at approximately the level of the 10th or 11th rib and is usually cranial to the pyloric canal.[9] In immature dogs the pylorus may be located closer to midline than in adults.[10] Variations in the appearance of the stomach in the dog based on breed conformation have been described.[9] On the VD view of the cat, the stomach is more acutely angled compared to the dog, with the pylorus located at or near the midline (see Figs. 45.3B and 45.4B).

To understand the radiographic appearance of the stomach and movement of the gastric content when the position of the patient is altered, the stomach should be visualized as lying in a transverse plane with the fundus positioned dorsally on the left, and the pylorus ventrally on the right (eFig. 45.1). Thus, with a patient in ventral recumbency for a DV view, gas rises to the fundus, and fluid settles dependently to fill the pyloric portions and part of the gastric body (Fig. 45.5A, see eFig. 45.1A,B), whereas with a patient in dorsal recumbency for a VD view, fluid within the lumen follows gravity and settles dependently to the fundus and body of the stomach. Gas rises to the uppermost portion, which will be the pyloric antrum and the gastric body near midline (see Fig. 45.5B, eFig. 45.1C). On the left recumbent (right-left) lateral view (Figs. 45.5C and 45.6A), gas rises to the pyloric portion of the stomach, and fluid settles dependently in the fundus and body. A gas pocket may be trapped occasionally in the fundus in a left lateral view. The fundus and/or body may be difficult to see in a left lateral view because of the intraluminal fluid silhouetting with adjacent structures (see Fig. 45.6A). On the right recumbent (left-right) lateral view (see Figs. 45.5D and 45.6B), gas rises to the fundus and body, and fluid settles dependently to fill the pyloric portions and part of the body of the stomach. The fluid in the gastric body/antrum can create a round, circular, soft tissue attenuating area in the cranial abdomen (see Fig. 45.6B), which

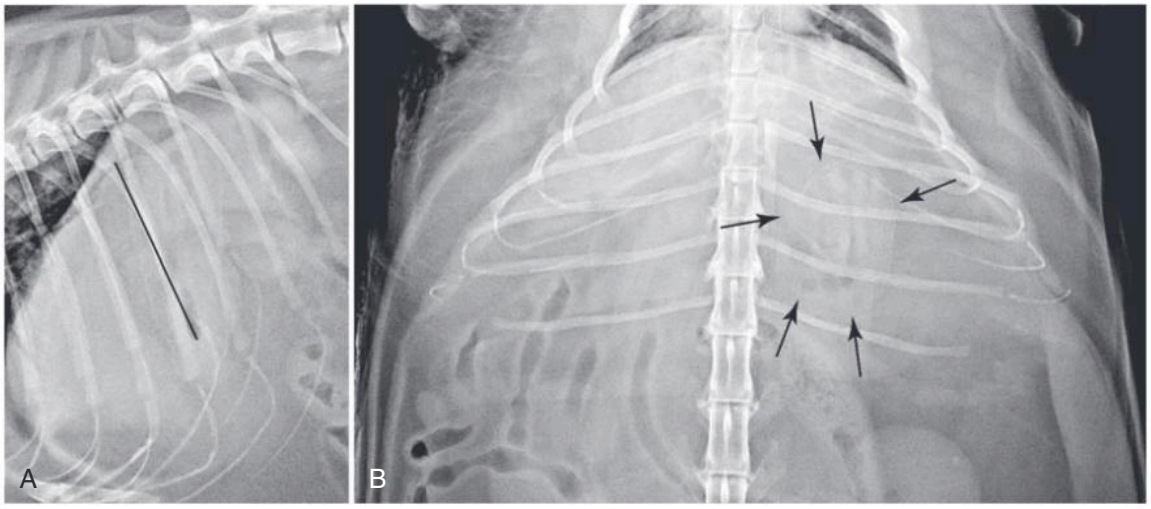


Fig. 45.3 Normal position of the stomach in a cat. **A,** Right lateral view of the abdomen of the cat. The gastric axis is parallel with the ribs. **B,** Ventrodorsal view of the same cat. The stomach (*arrows*) is acutely angled with the pylorus located on midline to slightly to the left of midline.

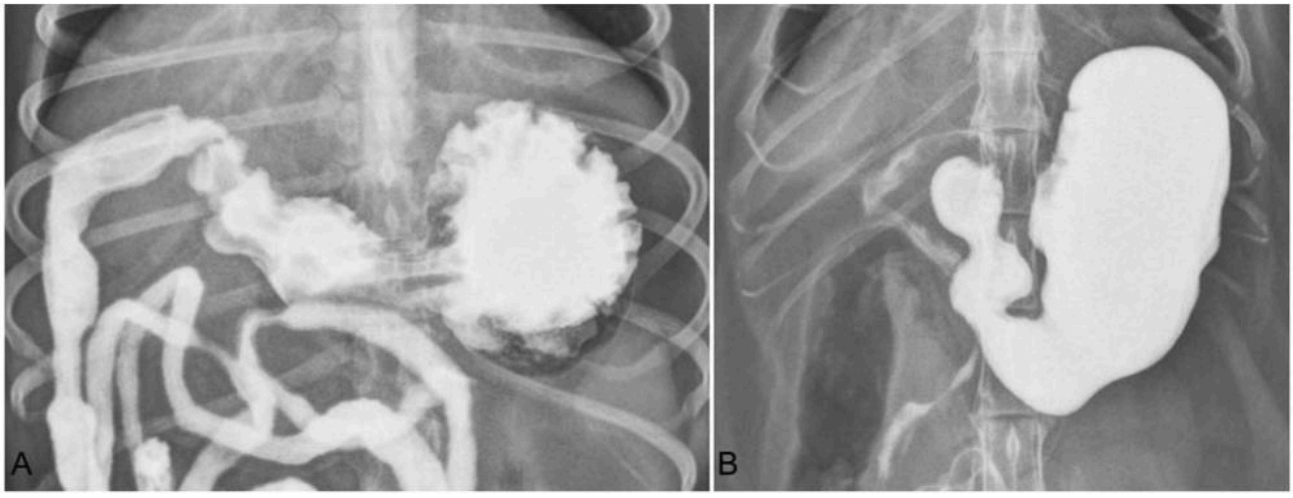
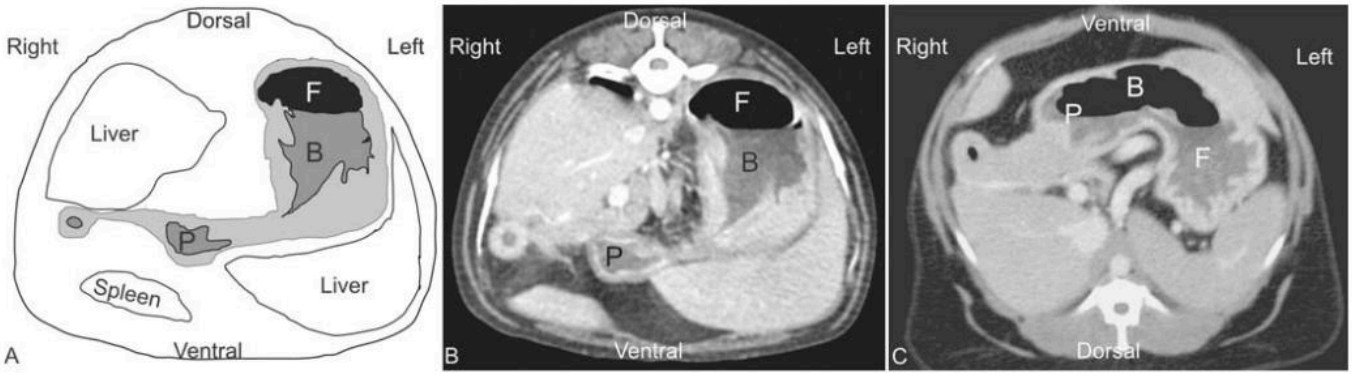


Fig. 45.4 Gastrograms illustrating the normal positions of the stomach with the patient in dorsal recumbency. **A,** Ventrodorsal view of a dog. The gastric axis of this dog is approximately perpendicular to the spine. **B,** Ventrodorsal view of a cat. The stomach is acutely angled with the pylorus located closer to midline than in the dog; this is a consistent species difference.



eFig. 45.1 **A,** Illustration of the anatomy of the stomach in a transverse plane through the stomach. The fundus (*F*) is located dorsally and on the left, whereas the pylorus (*P*) is located ventrally and on the right. **B,** Computed tomographic image of a normal dog in ventral recumbency at the level of the stomach. Fluid fills the pylorus (*P*) and body (*B*) of the stomach. The fundus (*F*) is gas filled. **C,** Computed tomographic image of a normal dog in dorsal recumbency at the level of the stomach. Fluid fills most of the fundus (*F*) and part of the pylorus (*P*), and the gas bubble floats near the midline in the body of the stomach (*B*).

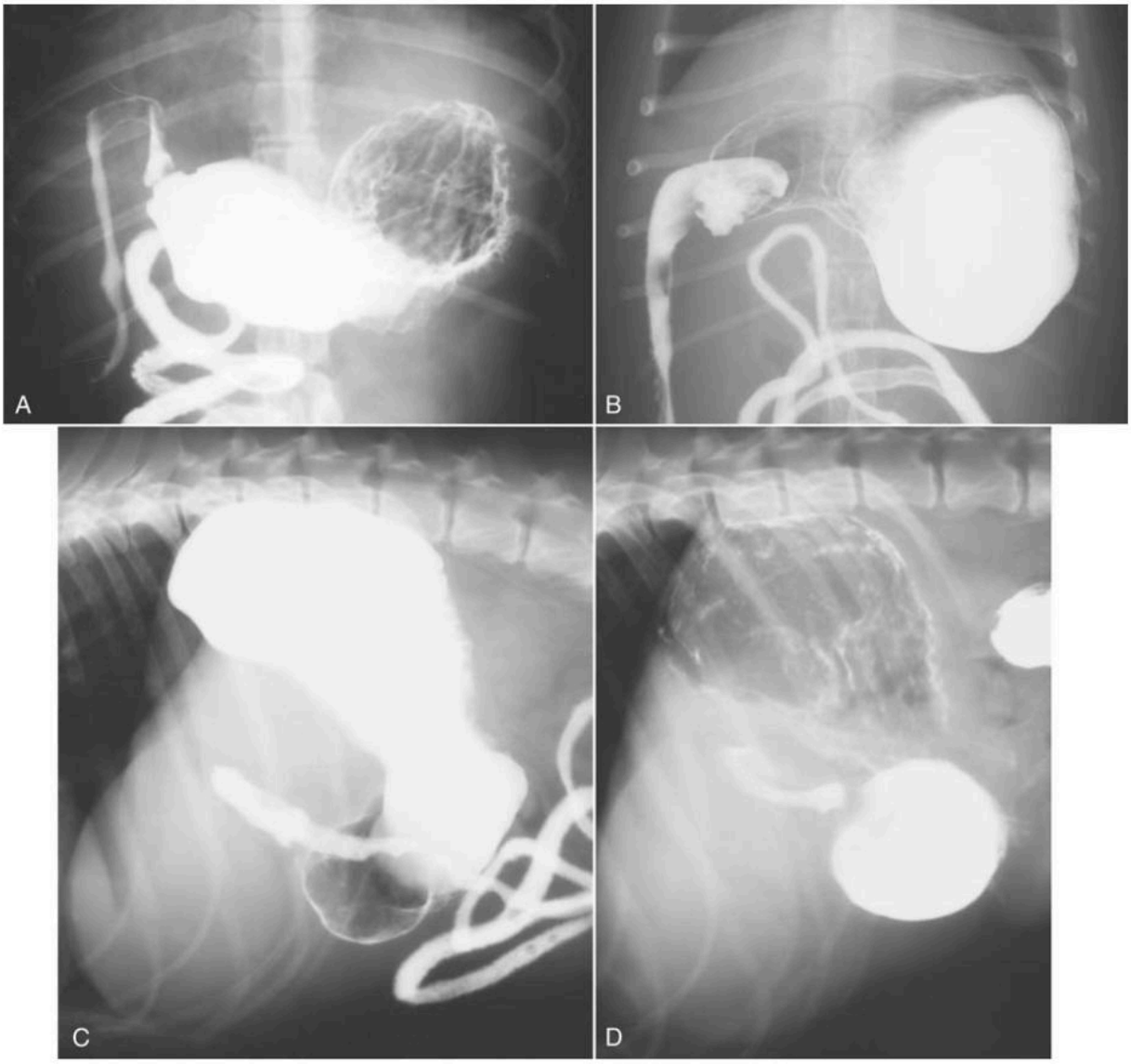


Fig. 45.5 Normal variations in fluid (barium) and gas distribution in the stomach with different patient positions. **A,** Dorsoventral view, in ventral recumbency. Gas rises to the fundus and fluid settles dependently to fill pyloric portions and part of the body. **B,** Ventrodorsal view, in dorsal recumbency. Gas is located in the body and pyloric antrum. Fluid settles dependently to fill the fundus and body. In this dog, there is a small amount of barium trapped in the pyloric antrum. **C,** Left lateral view. Gas rises to the pyloric portion, and fluid settles dependently to fill the fundus and body. **D,** Right lateral view. Gas rises to the fundus and body, when there is some barium adherent to the mucosa. Fluid settles dependently to fill the pyloric portion.

can be mistaken for a gastric foreign body or pathologic mass.[9,11] If a pyloric mass or foreign body is suspected on a right lateral view, a left lateral view should then be made to relocate gas to the pylorus to provide contrast.

Recognizing the variation in appearance of the normal stomach due to patient position and the volume and ratio of fluid to gas within the stomach is essential. The ability to take advantage of fluid and gas shifts within the stomach to highlight certain portions of the stomach more clearly is also important. Table 45.1 is a simplified summary of the expected changes in gas and fluid within the stomach due to change in patient position.

Rugal folds are seen inconsistently on survey radiographs. Radiographic assessment of rugal folds is subjective because they vary in size and number, and their appearance depends on the region of the stomach and degree of gastric distention.[8,12] Rugal folds are more tortuous in the nondistended stomach and become more uniform and parallel to the gastric curvature with increasing distention. Rugal folds may not be visible if the stomach is overdistended. Rugal folds are smaller and more spiral in the pyloric antrum.[8,13] A reference range for normal rugal fold thickness in dogs weighing 2 to 50 kg has been reported to be between 1 to 8 mm.[12] Rugal folds are smaller and fewer in number in cats than in dogs.[14] Additionally, a radiolucent line due to submucosal fat can often be seen normally in the gastric wall of the cat.[15]

Gastrography

Gastrography is often replaced by an abdominal ultrasound examination. However, due to gas in the stomach, the partial or complete intercostal location, or its large size, an ultrasound examination of the stomach might be limited and a contrast radiographic study may be needed to further evaluate the content and wall of the stomach. Furthermore, the evaluation

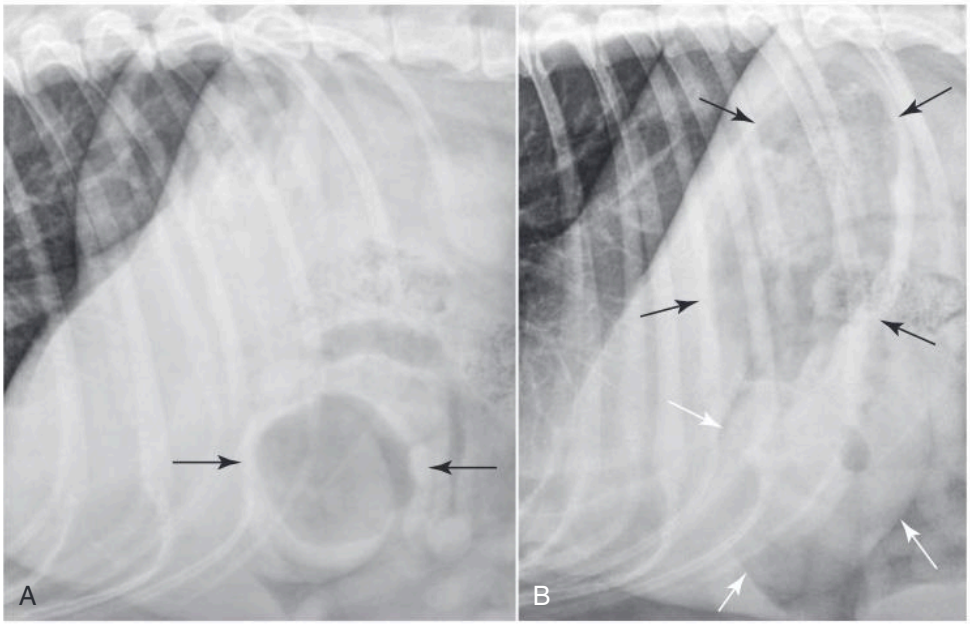


Fig. 45.6 Normal variation in fluid and gas distribution in the stomach as function of left versus right recumbency. **A,** Left lateral view. Gas rises to the pyloric portion (*black arrows*). In this dog, there is also some gas trapped in the fundus. Fluid settles dependently to the body, which is difficult to see. **B,** Right lateral view. Gas rises to fill the fundus and body (*black arrows*). Fluid settles dependently to the pyloric portion, which appears as a soft tissue mass (*white arrows*).

Table • 45.1

Distribution of Stomach Gas and Fluid as a Function of Radiographic Projection Using a Vertical X-Ray Beam.

RADIOGRAPHIC VIEW	LOCATION OF FLUID	LOCATION OF GAS
Dorsoventral	Body/pylorus	Fundus
Ventrodorsal	Fundus	Body (± pylorus)
Left recumbent lateral	Fundus	Pylorus (± body)
Right recumbent lateral	Pylorus	Fundus

of functional abnormalities of the stomach is typically performed with contrast radiography.

Survey radiographs should always be performed prior to a gastrogram. If possible, medications affecting gastric motility should be avoided or discontinued for an appropriate interval before any gastrointestinal contrast study is undertaken.[16–20] Contrast radiography of the stomach can be performed with negative- or positive-contrast media or a combination thereof. Positive-contrast radiography should not be performed or should be carried out with caution if the patient has unmanageable vomiting, suspected perforation of the gastrointestinal tract, or an evident need for surgery already noticeable on survey radiographs (Box 45.1).

Negative-Contrast Study of the Stomach (Pneumogastrography)

Negative-contrast studies of the stomach are rarely performed and are mainly used to assess for the presence of a gastric foreign body or to evaluate the position of the stomach. The benefit of negative-contrast gastrography is that endoscopy can follow immediately. However, if gastric ultrasound is planned, a pneumogastrogram is contraindicated as the air reduces the ability to evaluate the gastric wall and content.[21]

Technique for Pneumogastrography

A negative-contrast study of the stomach is performed by administering 6 to 12 mL of room air/kg body weight using an orogastric tube or by allowing the patient to drink carbonated liquid or orally administer a carbonated drink using a syringe. The stomach should palpate as moderately distended after the administration of air. The disadvantage of oral administration of carbonated liquid is that the stomach is often less distended and the additional fluid might conceal gastric lesions. Immediately after administering the gas, left lateral and VD views of the stomach should be obtained as these are usually the most diagnostic views to evaluate for pyloric outflow obstruction. These views should be followed by the other radiographic views.[21]

Positive-Contrast Gastrography

Various special contrast procedures using positive-contrast media or combinations of positive- with negative-contrast media are available to assess the stomach. They include conventional barium sulfate gastrography, low-volume gastrography, double-contrast gastrography, gastrography with iodinated contrast media, and gastric-emptying studies with barium/food or radiopaque marker/food mixtures.[6,9,10,13,14,17,22–30]

Technique for Positive-Contrast Gastrography

Patient preparation is extremely important when performing a diagnostic contrast study of the stomach. As mentioned before, food can mimic a gastric lesion and therefore the patient should be fasted for 12 to 24 hours. Orogastric intubation is recommended for all contrast studies of the stomach to reduce the risk of aspiration. Alternatively, the contrast medium can be placed in the buccal fold using a syringe or the patient can be given the opportunity to drink the contrast medium voluntarily,

Box • **45.1**

Positive-Contrast Gastrogram With Barium Sulfate Suspension

- Fast for 12 to 24 hours without or with cleansing enemas.
  - Food in the stomach will interfere with interpretation of gastric emptying time.
  - Ingesta may also obscure foreign bodies or small gastric lesions.
  - Gastrograms performed with food in the stomach are difficult to interpret.
- If possible, perform radiography without the use of sedatives.
  - Motility-altering drugs such as antiemetics may interfere with interpretation.
  - If sedatives are required because of the fractious nature of the patient, use the lowest dose possible, and interpret gastric emptying times with caution.
- Perform survey radiographs to assess patient preparation, establish radiographic technique, and possibly identify the problem without gastrography.
  - If an evident need for surgery is evident on survey radiographs, do not pursue a positive-contrast study.
- Administer barium sulfate suspension by an orogastric tube with the patient on the x-ray table ready for radiography (cassette in position, technique set, etc.).
  - Barium powder mixed with water is not recommended.
  - If patient has unmanageable vomiting, do not administer barium as it causes risk of aspiration.
- If a perforation of the gastrointestinal tract is suspected, use nonionic iodinated contrast medium or discuss surgical avenues.
- The dosage of barium used for a gastrogram depends on why the study is being performed. The recommended dosage is 8—12 mL barium/kg body weight for small and medium-sized dogs and 5—7 mL barium/kg body weight for large-sized dogs and 12—20 mL barium/kg body weight for cats. For simple location of the stomach, a very low dosage of 1—2 mL/kg can be used. If gastric emptying is of interest, the full dosage used for an upper gastrointestinal examination should be administered.
  - Feeding barium orally (i.e., without an orogastric tube) results in suboptimal distention of the stomach from emptying of the initial portions of barium before administration of the last portion.
  - Not administering enough barium is a common mistake.
  - Use caution to ensure that the orogastric tube is located in the esophagus, not the trachea.
    - Verify tube position by using fluoroscopy, survey radiograph, or palpation.
  - Before removing the tube, instill a small volume of air to clear the tube, then kink the tube before removal to prevent leakage of barium into the trachea.
- After removing the tube, immediately take radiographs centered over the stomach. All four views are recommended (right lateral, left lateral, dorsoventral, and ventrodorsal) and should be made as rapidly as possible.
- Additional radiographs (with or without obliques) should be made pending the results of the initial radiographs. If available, fluoroscopy is extremely helpful in the evaluation of gastrograms.
- Continue making radiographs (usually right lateral and ventrodorsal) until the majority of the barium is no longer seen within the stomach.
  - A small amount of residual barium coating the mucosa diffusely for several hours may be normal. Focal barium retention is suggestive of ulceration.
- The gastrogram may be combined with contrast evaluation of the small intestine.

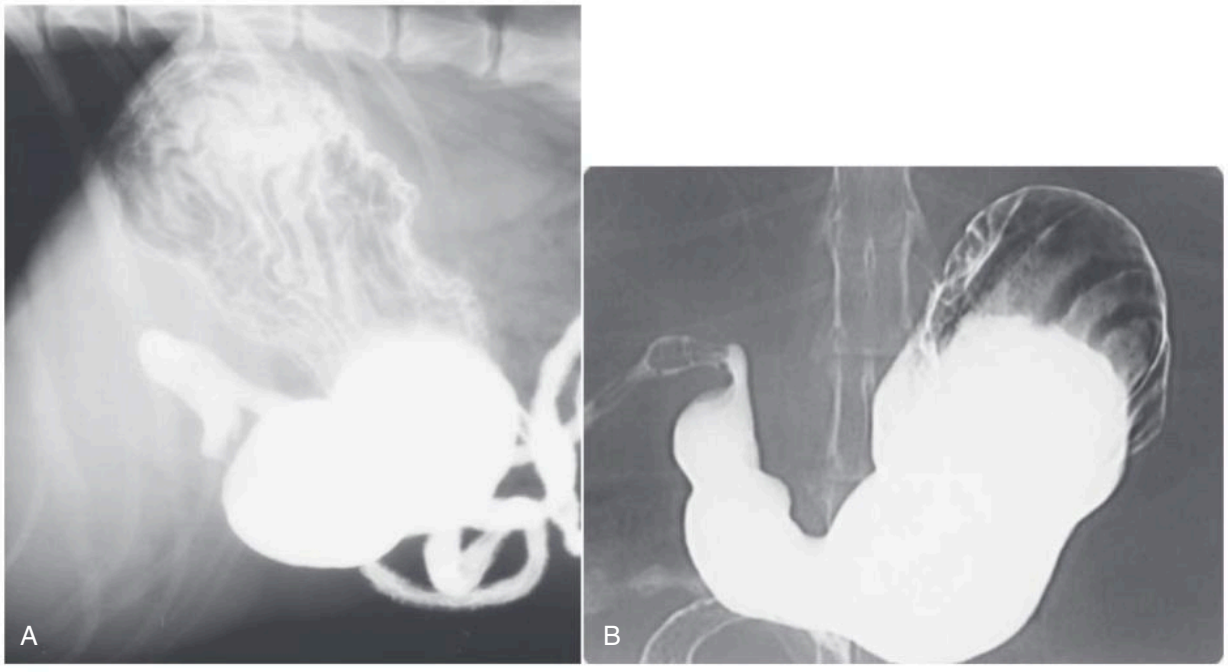
which is easier when iodinated contrast media are used. After contrast medium administration, it has been recommended to gently turn the patient to achieve uniform coating of the gastric mucosa. Immediately after contrast medium administration, left lateral, right lateral, VD, and DV views of the stomach should be made, which are then usually followed by left recumbent lateral and VD views of the abdomen after 15 minutes, 30 minutes, 45 minutes, and 1 hour, 2 hours, 3 hours, 4 hours, or until complete emptying of the stomach content is present (Fig. 45.7A—L). See Box 45.1 for one method of performing a positive-contrast gastrogram. If an iodinated, water-soluble contrast medium is used to perform a gastrogram, it should always be remembered that these contrast media can be hyperosmolar and cause an influx of water, introducing potential for patient dehydration or, if aspirated, pulmonary edema. Therefore, when iodinated contrast media are used, an orogastric intubation should always be performed, if the patient does not voluntarily drink the iodinated contrast medium. Iodinated contrast media are used in a dose of 2 to 3 mL/kg body weight to achieve approximately 600 to 700 mg iodine (I) per kilogram body weight. If the contrast medium is diluted (1:4), the dose should be increased to 6 to 12 mL/kg body weight.[31]

Normal Positive-Contrast Gastrographic Findings

With positive-contrast gastrography, normal rugal folds are best seen at the peripheral portions of the stomach (see Fig. 45.7), where they may appear end-on as regular small filling defects at the mucosal surface. If projected en face, rugal folds are not visible with positive-contrast gastrography unless the barium is well penetrated by the x-ray beam, or there is only a small amount of barium in the stomach. Rugal folds then appear as relatively radiolucent, linear filling defects separated by barium in the interrugal spaces (eFig. 45.2).

After administration of barium, gastric emptying should start within 15 minutes in most normal patients.[9,32,33] During gastrography with barium sulfate, the stomach generally empties within 1 to 4 hours in dogs (see Fig. 45.7I—L).[12,17] Rapid emptying of the stomach has no clinical significance, whereas delayed emptying is potentially of much greater significance.

The rate of gastric emptying is a complex phenomenon that is affected by the volume of gastric content, the chemical and physical properties of chyme entering the duodenum, various reflex mechanisms, certain medications, and the type of contrast medium used. Thus, a standard approach must be used to evaluate the rate of gastric emptying radiographically. Because the stomach starts to empty faster with an increased



eFig. 45.2 **A,** Right lateral barium gastrogram. Note the multiple curvilinear filling defects in the fundus region of the stomach. These filling defects are the rugae. **B,** Dorsoventral barium gastrogram. Radiolucent linear filling defects are from rugal folds projected en face.

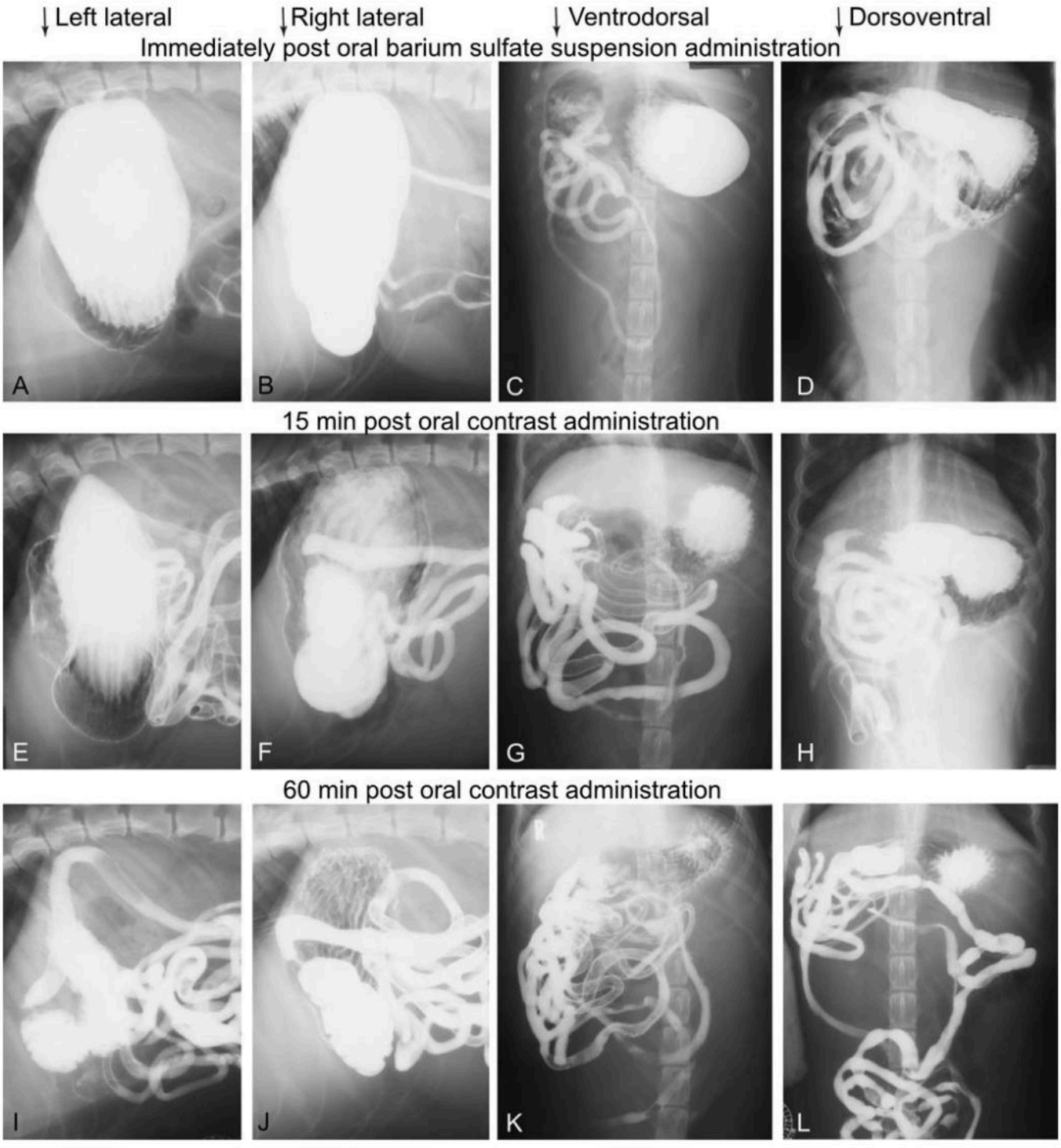


Fig. 45.7 Positive-contrast barium gastrography in a dog in different positions and with various time delays after contrast medium administration. Immediately **(A–D)**, 15 minutes **(E–H)**, and 60 minutes **(I–L)** after contrast medium administration. Continuous emptying of the stomach is noted with increasing time after contrast medium administration. **A, E, I,** Left lateral views. Most of the contrast medium is initially present in the gastric body and fundus. A small amount of gas is noted in the pylorus in the initial images, which is increasing 15 minutes after contrast medium administration and decreasing at 60 minutes with continuous emptying of the stomach. The pylorus is in part located cranial to the body of the stomach. **B, F, J,** Right lateral views. In the immediate image, the entire stomach is filled with contrast medium. In later images, gas is present in the fundus of the stomach and fluid is predominately present in the pylorus. The pylorus is summating ventrally with the body of the stomach. **C, G, F,** Ventrodorsal views. Most of the contrast medium in the stomach is in the fundus. A gas bubble is present in the body of the stomach. **D, H, L,** Dorsoventral views. Most of the contrast medium is in the body to pylorus of the stomach. Gas is present in the fundus of the stomach.

intraluminal volume, the dosage of contrast medium for a barium study must be standardized.[28] Low dosages may result in delayed gastric emptying, which leads to a false impression of pyloric obstruction or poor motility. If a standard technique has been used, and no medications that affect gastric emptying were administered, then delays in gastric emptying are likely related to psychological influences or disease at the pylorus. Emotional stress and noise may inhibit gastric movement.[34] Anxiety, fear, rage, or pain induced by physical manipulation of the patient, gastric intubation, and physical restraint may contribute to temporary delayed gastric emptying. Thus, patients with delayed gastric emptying must be allowed to calm down in a quiet environment before diagnostic significance is placed on this finding. For these reasons, minimal significance is usually placed on minor delays in gastric emptying if the stomach proceeds to empty normally after an initial delay.

Barium-food mixtures have been used to evaluate gastric function.[25,27] Emptying times for individual dogs were repeatable; however, the range of normal gastric emptying was so wide (7–15 hours) that this procedure is not useful for evaluation of gastric emptying unless gross abnormalities are present.[25] Gastric emptying times for dogs and cats can vary from 4 hours for high-moisture food to 16 hours for dry food.[8] An alternative technique for evaluating gastric emptying of solids in dogs and cats has been developed by using radiopaque barium-impregnated polyethylene spheres (BIPSs; Chemstock Animal Health Ltd., Christchurch, New Zealand) mixed with food.[23,26,30,35] The number and size of radiopaque spheres, type and amount of food, and fasting period must be standardized. An advantage of the BIPS technique is that it can be performed in most veterinary practices; however, it may require up to 10 hours to complete the study. Some controversy exists about the usefulness of BIPS for gastric emptying analysis, and these studies should be interpreted by a specialist.

Gastric peristalsis and gastric emptying may be observed directly during fluoroscopy with the use of a positive-contrast medium. Although a peristaltic contraction may be seen on a conventional radiograph during gastrography, this is a chance event depending on when the radiograph was made. A peristaltic contraction appears as an indentation of the wall of the stomach with slight dilation of the lumen immediately preceding the contraction. Peristaltic contractions are stronger and most obvious in the pyloric portion of the stomach.

Gastric Ultrasound

Indications

Ultrasound is a useful addition to radiography for evaluation of the gastrointestinal tract. It may eliminate the need for barium studies because gastric motility, wall thickness and architecture, and luminal contents may be evaluated sonographically.[36,37] In addition, ultrasound examination is quicker than an upper gastrointestinal series, not associated with electromagnetic radiation and may be equally sensitive and specific for detection of gastric disease. Ultrasound has been used to help diagnose gastric neoplasms,[38–44] inflammation or infection,[45,46] edema,[47] ulcers,[48] foreign bodies,[49,50] pyloric hypertrophy,[51] gastric mineralization,[52] gastroduodenal and gastrogastric intussusceptions,[53,54] gastric wall healing post surgery, and to evaluate gastropexy sites.[55–57] Additionally, fine needle aspirates and biopsies of the stomach can be obtained using ultrasound guidance.[42,58] Furthermore, new ultrasound techniques such as three-dimensional and endoscopic ultrasound are developing but limited in availability.[59] Endoscopic ultrasound combines the features of endoscopy with ultrasound to provide information about the gastroesophageal junction, gastric wall layers, and adjacent abdominal organs. The ability to perform the ultrasound in direct contact with the gastric wall using a high-frequency ultrasound probe allows the acquisition of high detail images.[60]

Ultrasound Technique

As a guideline for abdominal ultrasound, the highest frequency probe available and able to penetrate the area of interest should be chosen. For evaluating the stomach wall layers, 7.5 megahertz (MHz) or higher frequency transducers are preferred, but 5 MHz transducers may be needed to evaluate deeper portions of the stomach. Ideally, ultrasonography should be performed after a 12-hour fast and before barium is administered. If needed, intraluminal gas can be removed by an orogastric tube and the stomach distended with fluid to act as an acoustic window.[36,61] Technique and approaches to the stomach vary somewhat with patient conformation, position, and preference of the operator. Often, a dorsal or lateral recumbent position is chosen as a starting point. The stomach should be scanned in longitudinal and transverse planes and all aspects of the stomach from the cardia to the pylorus should be evaluated.[62] Most commonly, the ultrasound probe is positioned caudal the xiphoid and moved along the caudal aspect of ribs along the right and left abdominal wall to assess all aspects of the stomach. However, if the stomach is empty or cranially positioned, an intercostal approach to the stomach may be preferable. For the cardia a left craniodorsal and for the pylorus a right lateral intercostal approach may be chosen.[63] Gas and ingesta within the stomach may obscure the far wall and luminal content, but the lumen and far wall can be evaluated in patients in which the stomach contains fluid and little gas (Fig. 45.8A). Repositioning of the patient usually results in redistribution of luminal fluid and gas, allowing to evaluate most aspects of the stomach wall.[3,61]

Normal Ultrasonographic Findings

The appearance of the stomach varies with the amount of distention and the extent of luminal contents. When empty, the stomach may have a wagon-wheel appearance because of folding of the rugal folds (see Fig. 45.8B). This is especially noticeable in the cat. With increasing distention, rugal folds become less conspicuous. Under optimal ultrasound conditions, the five layers of the gastric wall are visible.[36] The innermost aspect of the gastric wall is hyperechoic and corresponds to the luminal surface of the mucosa, followed by the hypoechoic mucosa, the hyperechoic, thin submucosa, the hypoechoic muscularis, and the outermost hyperechoic subserosa/serosa (see Fig. 45.8). In the stomach, the mucosa and muscularis are often of similar thickness, which is different to the small intestine, where the mucosa is usually the thickest layer.[61] Sonographically, the cardia appears as a thick, tubular area at the border of the thoracic esophagus and fundus in the most left craniodorsal abdomen. All five wall layers of the cardia can be identified, with the muscularis being more prominent than the other layers.[38,64] The stomach wall thickness in dogs is 3 to 5 mm depending on the location and size of the dog, with larger dogs having a thicker stomach wall.[36] In cats, the rugal fold thickness has been reported as 2 to 5 mm, including the pylorus,[65,66] which is relatively similar to the dog. Sometimes, gastric wall thickness cannot be evaluated when the stomach is completely empty and the individual walls cannot be separated from each other. However, usually ingesta, fluid, and/or gas are present in the lumen of the stomach. Food can be difficult to differentiate from a foreign body and reevaluation of the patient may be necessary to see if the material in the stomach has changed over time. The mean number of peristaltic contractions observed in the stomach and proximal duodenum in dogs has been reported to be 4 to 5 per minute; however, with fasting of the patient (6 and 12 hours post prandial), lower mean contraction rates were observed.[36,37]

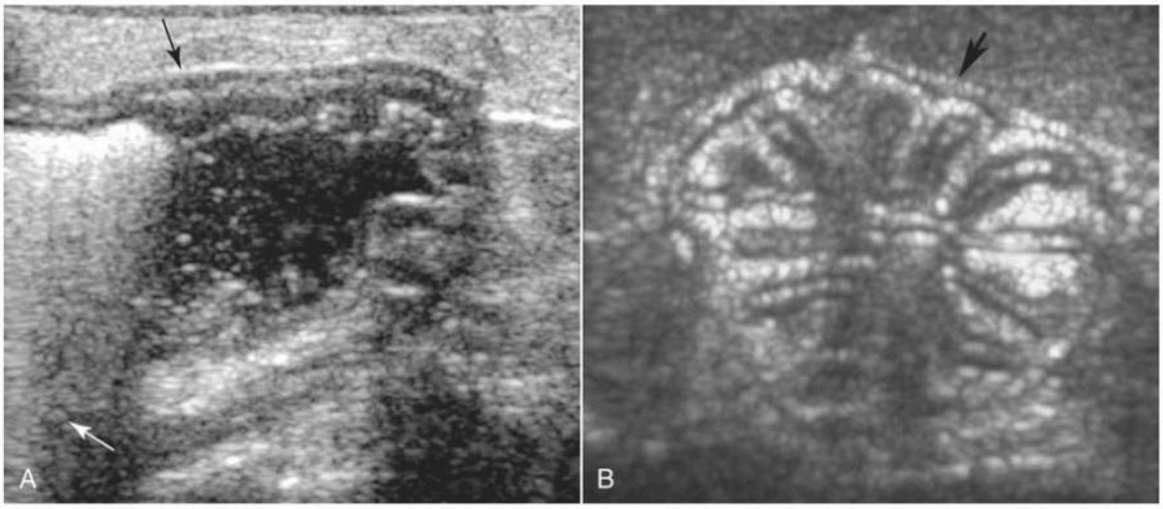


Fig. 45.8 Longitudinal ultrasound image of the stomach in a normal dog **(A)** and a normal cat **(B)**. **A,** The stomach is distended partially with gas and fluid. Gas in the lumen appears as a bright echo against the mucosal surface, producing reverberation artifact that prevents visualization of a portion of the far wall (region of *white arrow*). Fluid within the caudal half of the stomach provides a window for identification of the far wall. The five normal layers of the stomach wall can be identified as well as several rugal folds. The *black arrow* identifies the bright serosal layer. **B,** The stomach is empty and contracted, giving it a wagon-wheel appearance. The normal layered appearance of the stomach can be seen. The *black arrow* identifies the bright serosal surface. Caudal is to the *right,* and ventral is to the *top.*

Computed Tomography of the Stomach

CT is used commonly in people with gastrointestinal disease. In animals, CT is extensively used to evaluate the abdomen, but rarely used to evaluate the gastrointestinal tract. This difference is likely in part due to the difference in gas content of the gastrointestinal tract as well as the ease of intraluminal contrast medium administration in humans compared to companion animals, as well as the reduced access to CT compared with ultrasound in veterinary medicine. One of the benefits of CT is that intraluminal and extraluminal lesions of the stomach or gastrointestinal tract can be evaluated in the same procedure (Fig. 45.9A–D).

CT without intraluminal contrast medium administration has been used successfully in dogs and cats to evaluate the anatomy of the gastrointestinal tract,[67] to assess the gastrointestinal tract for the presence of wall lesions,[68,69] foreign bodies, or intestinal obstruction. However, if the stomach is collapsed or hyperattenuating intraluminal content is present, the gastric wall can appear artificially thickened or can only be incompletely evaluated. In human patients, the addition of intraluminal positive-contrast medium is considered a critical aspect of gastrointestinal CT scanning to distend the stomach and cause separation of the walls, allowing each wall to be evaluated individually. Conventional positive-contrast media such as barium sulfate and iodinated contrast medium formulations as well as neutral contrast media including water, milk, polyethylene glycol, etc., are commonly used in human patients to evaluate the gastrointestinal tract in CT studies. Hydro-CT, after orogastric tube administration of water and combining it with an intravenous iodinated contrast medium provided adequate distension of the stomach and allowed evaluation of the gastric wall in healthy dogs as well as in dogs and cats with suspected or diagnosed gastric neoplasia.[70]

Gastric Scintigraphy

Scintigraphy of the stomach is one of the least used imaging modalities in animals with gastrointestinal disease. Although nuclear medicine studies provide very limited or no information about gastric motility, they may be considered the gold standard for evaluating gastric emptying. Scintigraphy can be completed in 4 to 6 hours. However, even when using scintigraphy, there is high variability in gastric emptying or gastrointestinal transit times and this limits its clinical use.[19,71,72] Gastric emptying time is different in cats versus dogs as measured by BIPS compared with scintigraphy. Emptying times measured by BIPSs were also significantly longer relative to scintigraphy.[73,74] However, scintigraphy is of value when gastrointestinal bleeding is suspected.[75] The use of scintigraphy is limited by lack of access to scintigraphy equipment and the need for using radiopharmaceuticals, which require radiation safety precautions.[19,71,72]

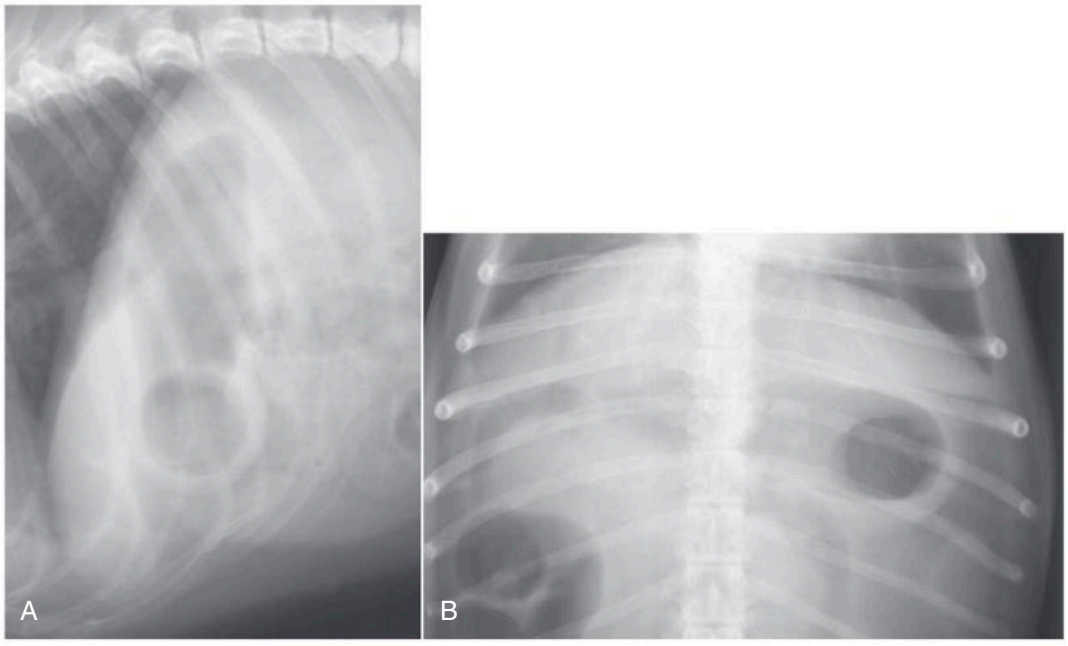
GASTRIC DISEASES

Displacement

Displacement With Intact Diaphragm

The stomach is a valuable landmark in the cranial abdomen for identifying space-occupying lesions of surrounding structures such as the liver cranially, the spleen left laterally, and the pancreas caudally. If the diaphragm is intact, cranial displacement of the stomach relative to the diaphragm can occur only with a decrease in the size of the liver (Table 45.2, eFig. 45.3). It is important to realize that axial patient rotation can create the artefactual impression of microhepatia.

Because the stomach is in close apposition with the liver, changes in size or position of the liver usually cause a change in position of the stomach. Generalized hepatomegaly often produces caudal and dorsal displacement of the stomach.[76] This displacement may be asymmetric if caused by a mass.[76] However, because the cardia is relatively fixed, even generalized hepatomegaly produces a nonuniform displacement of the stomach. Thus, on the lateral view, generalized hepatomegaly often produces caudal and dorsal displacement of the pylorus and body of the stomach, but not the fundus. This displacement changes the axis of the stomach so that the axis



eFig. 45.3 Cranial gastric displacement from a small liver secondary to a portosystemic shunt. The pylorus and body are displaced cranially on lateral **(A)** and ventrodorsal **(B)** views. In **B,** the fundus-pylorus angle is abnormal, with the pylorus being located more cranially than normal.

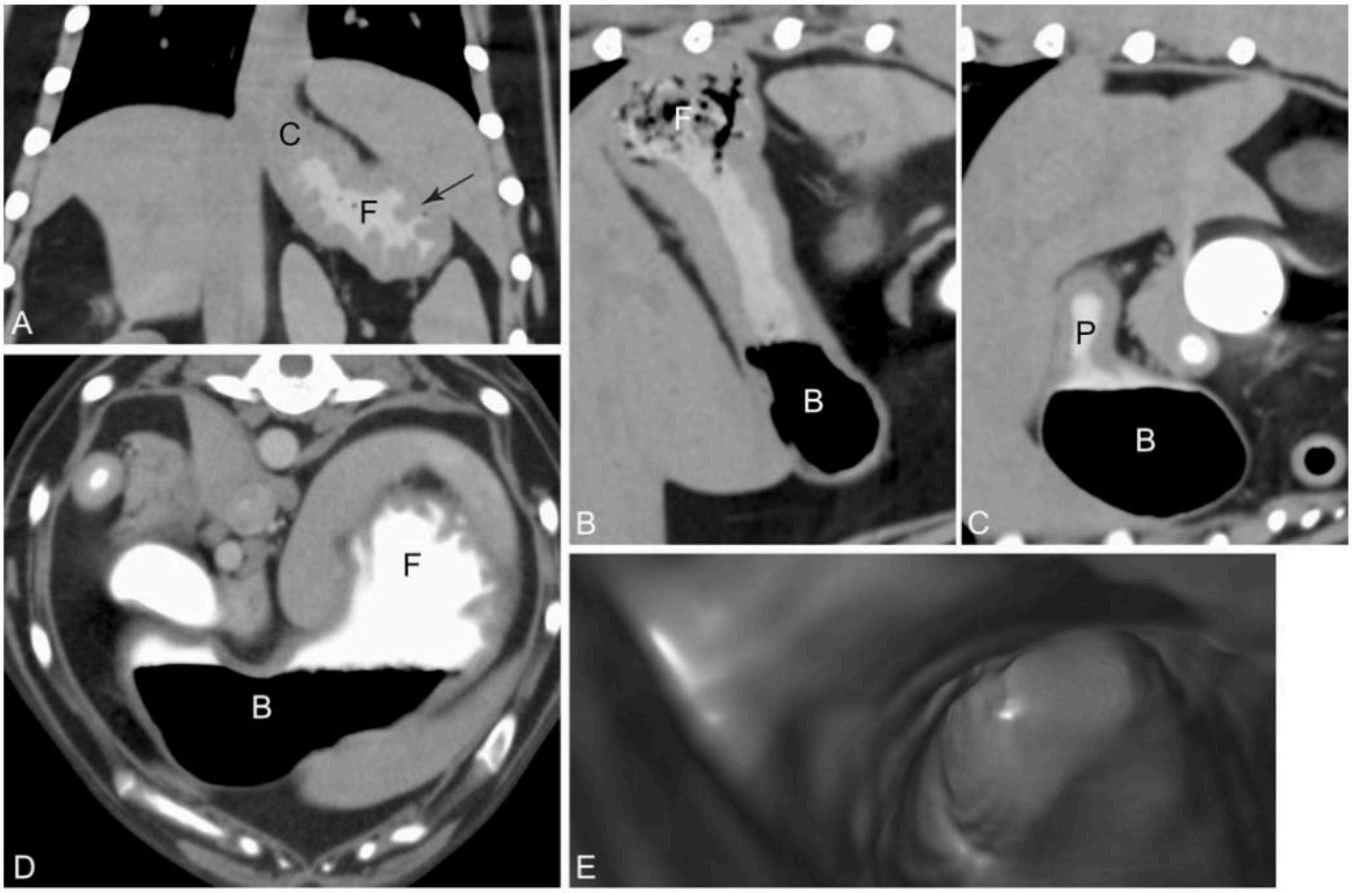


Fig. 45.9 Computed tomography (CT) images of the normal stomach of a dog after administration of iodinated contrast medium. The dog was in dorsal recumbency. **A,** Dorsally reformatted CT image of the stomach at the level of the cardia (*C*) to fundus (*F*). Normal rugal folds (*arrow*) are visible. **B,** Sagittally reformatted CT image of the stomach. The fundus (*F*) contains a small amount of contrast medium and gas. The body of the stomach (*B*) is gas filled. **C,** Sagittally reformatted CT image showing the smooth transition between the gas-filled body of the stomach and the contrast medium–filled pylorus (*P*). The gastric wall is thin and smooth, which is most noticeable in the mildly distended and gas-filled body of the stomach. **D,** Transverse CT image of the stomach. The fundus is contrast medium filled. The body of the stomach, which is the upper most aspect of the stomach with the dog in dorsal recumbency, contains a gas bubble. **E,** Virtual endoscopic image of the body of the stomach reconstructed from CT images. The wall of the body of the stomach is mildly folded and smooth outlined, similar to the CT images.

is no longer parallel with the ribs (Fig. 45.10A). On the VD or DV view, generalized hepatomegaly often causes displacement of the gastric body and pylorus caudally and toward the left (see Fig. 45.10B). This displacement changes the axis of the stomach so that it is no longer transverse. The assessment of gastric displacement as an indicator of liver size becomes especially valuable when the liver is not visible because of emaciation or abdominal effusion. In such patients, air in the stomach can often be used to define the axis of the stomach. A small volume of room air or barium may also be given to clarify the gastric axis if it cannot be assessed from the survey radiographs.

Abdominal masses that originate caudal to the stomach do not displace the stomach cranially because of the presence of the liver. Instead, such masses may distort the shape of the stomach as they press against and indent the stomach, or they may displace the stomach to the right or left. The relation of an abdominal mass to the stomach is often of value in helping define whether the mass originates in the liver, spleen, or pancreas (Fig. 45.11).

Displacement With Rupture or Hernia of the Diaphragm

Cranial displacement of the stomach may occur secondary to traumatic rupture of the diaphragm, that is, an acquired diaphragmatic hernia (Fig. 45.12), or secondary to a congenital hernia of the diaphragm and/or an abnormality of the gastroesophageal junction. These abnormalities can result in herniation of the liver, part of the liver, or the stomach into the thorax. Even if the stomach may not pass through a diaphragmatic hernia, the position of the stomach is an important consideration in patients suspected of having an acquired or congenital diaphragmatic hernia. A cranial shift of the axis of the stomach may help define whether the liver has herniated cranially through the diaphragm. Diseases of the diaphragm are discussed in more detail in Chapter 32.

Acquired Traumatic Hernia (Traumatic Diaphragmatic Rupture). Traumatic injuries to the diaphragm are commonly seen after vehicular trauma or high-rise injury in companion animals.[77] Dependent on the extent of injury to the diaphragm, gastric displacement may occur.[78] Rarely, a

Table • 45.2

Differential Diagnosis for Changes in Position of the Stomach.

NORMAL POSITION OF THE STOMACH	CRANIAL POSITION OF THE STOMACH			CAUDAL POSITION OF THE STOMACH	
Diaphragm intact	Diaphragm intact	Diaphragmatic hernia or rupture	Abnormal gastroesophageal junction	Caudal displacement of the diaphragm	Diaphragm intact, enlarged liver
Dependent on • Conformation of the patient • Gastric content • Gastric filling stage	Small liver (portosystemic shunt, cirrhosis)	Cranial displacement of the liver and/or gastrointestinal tract into the thorax • PPDH (peritoneopericardial diaphragmatic hernia) • Diaphragmatic rupture (acquired)	• Hiatal hernia	• Pneumothorax • Pleural fluid • Hyperinflation • Thoracic masses	• Generalized liver enlargement • Caudal displacement of the stomach, often asymmetric displacement
	Empty stomach	Cranial displacement of the stomach into the thorax	• Gastroesophageal intussusception		• Right liver lobe enlargement • Caudal and dorsal displacement of pylorus • Left liver lobe enlargement • Medial displacement of the fundus and body of the stomach

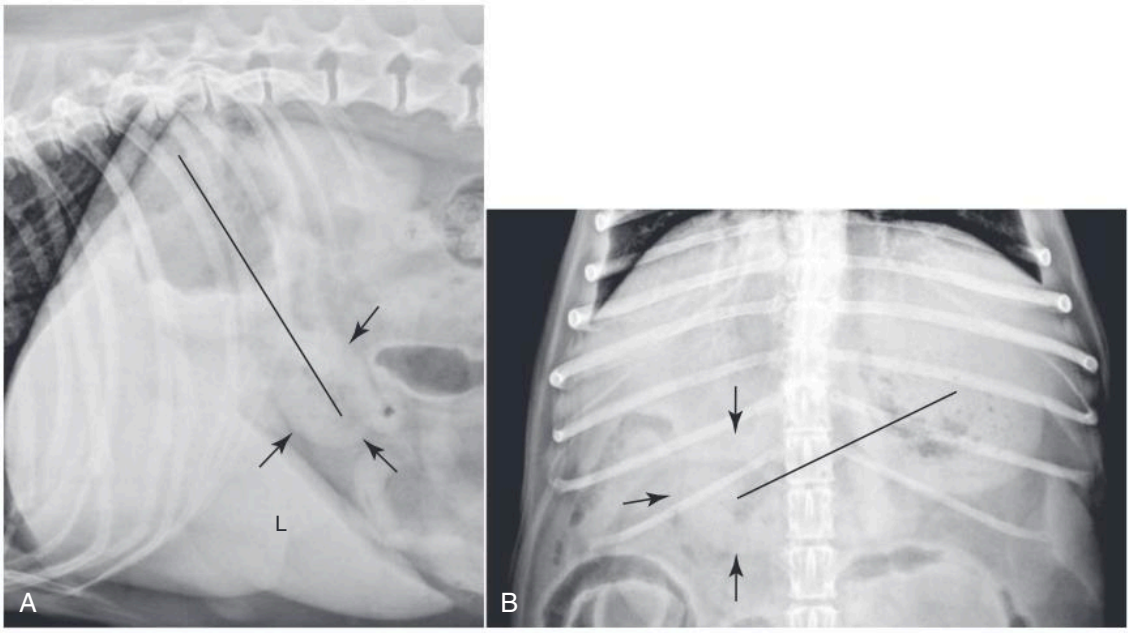


Fig. 45.10 Gastric displacement caused by hepatomegaly. **A,** Lateral view. The pylorus (*black arrows*) is displaced caudally by an enlarged liver (*L*), and the fundus-pylorus axis (*black line*) is no longer parallel with the ribs. **B,** Ventrodorsal view. The pylorus (*black arrows*) is displaced caudally and to the left, and the fundus-pylorus axis (*black line*) is no longer transverse.



Fig. 45.11 Ventrodorsal radiograph of a dog with a large pancreatic abscess. Barium has been administered. The pylorus is displaced to the left and cranially. The cranial duodenal flexure and proximal part of the descending duodenum have a broad arc around the cranial surface of the mass, which itself is not visible.



Fig. 45.12 Ventrodorsal radiograph of a dog with an acquired left-sided diaphragmatic hernia (rupture) that has allowed the fundus to shift cranially. Although there are no gas-containing bowel segments in the pleural space, the cranial position of the stomach is diagnostic for a diaphragmatic rupture.

"gastrothorax" may occur, where the stomach is displaced into the thorax and becomes markedly gas distended leading to increased pressure similar to a tension pneumothorax (Fig. 45.13). Radiography can help to differentiate between these two entities. In gastrothorax a large air-filled structure with or without an air–fluid interface is present in the thorax causing peripheral compression of the adjacent lung, obliterating the diaphragm and causing mediastinal shift. A curvilinear cranial outline is often visible. Similar radiographic features may also be noted in tension pneumothorax, but in tension pneumothorax, often the diaphragm can be outlined, while in gastrothorax, usually a left-sided loss of visualization of the diaphragm may be noted.[79] If it is unclear if the stomach is displaced cranially, a small amount of positive-contrast medium can be given to identify the location of the stomach or horizontal beam views may demonstrate a fluid–air interface in the lumen of the stomach. Alternatively, a gastric tube can be placed to release the air in the stomach and repeat radiographs should demonstrate decreased air filling of the displaced stomach.[79] It is important to remember that patients with an acquired traumatic hernia often suffer from significant other additional trauma to vital structures and stabilization of the patient before performing imaging studies is critical.

Hiatal or Peritoneopericardial Diaphragmatic Hernia. Hiatal hernia is common and results in cranial displacement of abdominal organs due to a defect in the esophageal hiatus.[80] Hiatal herniation depends on the size and location of the defect and results in cranial displacement of the gastroesophageal junction (sliding hernia or type 1 hiatal hernia) or cranial displacement of part of the stomach, usually the fundus, lateral to the esophagus with the gastroesophageal junction usually in a normal location (paraesophageal hernia or type 2 hiatal hernia) or a combination of the type 1 and 2 hiatal hernia (type 3 hiatal hernia).[81] Sliding hernias are the most common hiatal hernia in dogs and cats.[80] In patients with hiatal hernia, a cranial position of the stomach might be noted radiographically. Additionally, a soft tissue mass effect might be present in the caudodorsal thorax (Fig. 45.14). Sliding hernias can be a challenge radiographically as the stomach might not be displaced cranially at all times (see Fig. 45.14A). Obtaining radiographs after placing pressure on the abdomen or stimulating coughing to increase the abdominal pressure might help to identify the cranial position of the stomach or abdominal viscera (see Fig. 45.14C). If the stomach cannot be distinctively outlined, a low volume barium gastrogram can be performed to localize the position of the stomach.

Peritoneopericardial diaphragmatic hernia (PPDH) is an uncommon congenital malformation. A ventral communication between the abdomen and pericardial sac is present, which can result in cranial displacement of the stomach and/or other abdominal organs into the pericardial sac (Fig. 45.15).[82]

Gastroesophageal Intussusception. Gastroesophageal intussusception is uncommon and results from invagination of the stomach, with or without other abdominal organs, into the esophagus. This is only possible if a predisposing condition such as megaesophagus, dilation of the esophageal sphincter, or chronic vomiting is present. This is a surgical emergency as obstruction of vascular flow to the stomach leads to rapid decline of the patient. On radiographs a large well-defined soft tissue mass is usually present in the caudal esophagus with gas in a dilated esophagus cranial to the mass. Additionally, rugal folds might be visible at the cranial margin of the soft tissue mass due to the eversion of the gastric mucosa into the esophagus. The stomach or part of stomach is absent on abdominal radiographs.

Displacement Within the Stomach

Pylorogastric Intussusception. Pylorogastric intussusception is rarely seen in dogs and has so far not been reported in the cat. Other terms used for pylorogastric intussusception include gastrogastric or duodenogastric intussusception. Dogs with pylorogastric intussusception have ranged in age from 3 months to 15 years and there was no breed or size predilection. Radiographically, distension of the stomach and a large mass effect extending luminally into the pylorus to fundus area may be noted (Fig. 45.16). On ultrasound examination, displacement of the pylorus and duodenum into the pyloric antrum and fundus can be noted. Additionally, multiple concentric rings of hyperechogenicity and hypoechogenicity, resembling the intussuscepted gastric wall layers, thickening of

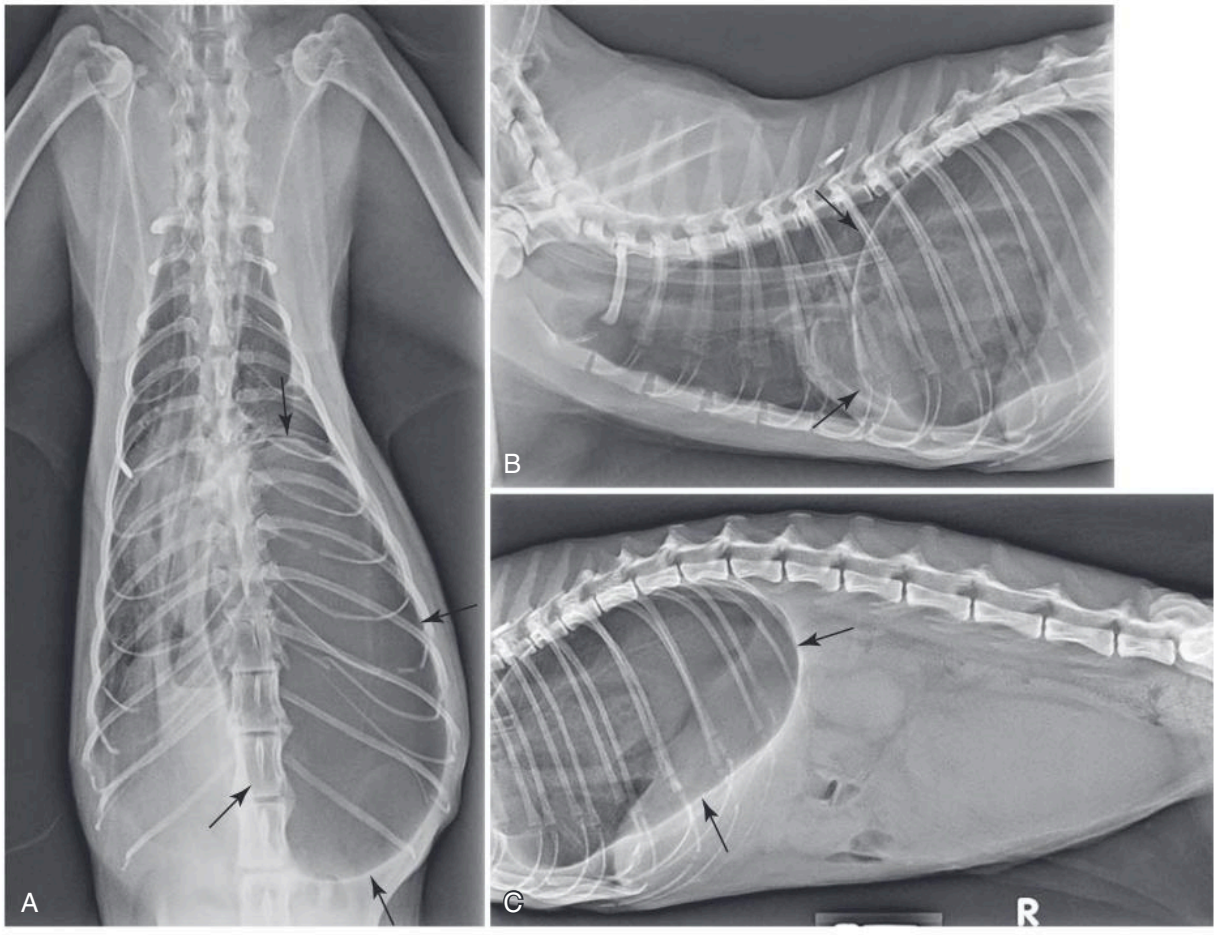


Fig. 45.13 Gastrothorax in 12-year-old cat secondary to a diaphragmatic rent which likely occurred when the cat was approximately 1-year-old and had a vehicular accident. Multiple prior thorax radiographs showed the stomach in normal position and size. Dorsoventral **(A)**, right lateral radiograph of the thorax **(B)**, and right lateral radiograph of the abdomen **(C)**. **A—C,** The stomach (*black arrows*) is severely gas distended and displaced cranially into the left hemithorax causing cranial and medial displacement of the left lung lobes. A normal left crus of the diaphragm is in the current study not seen. An esophageal feeding tube is present in thoracic esophagus. **C,** The stomach (*black arrows*) is not identified in the abdomen.

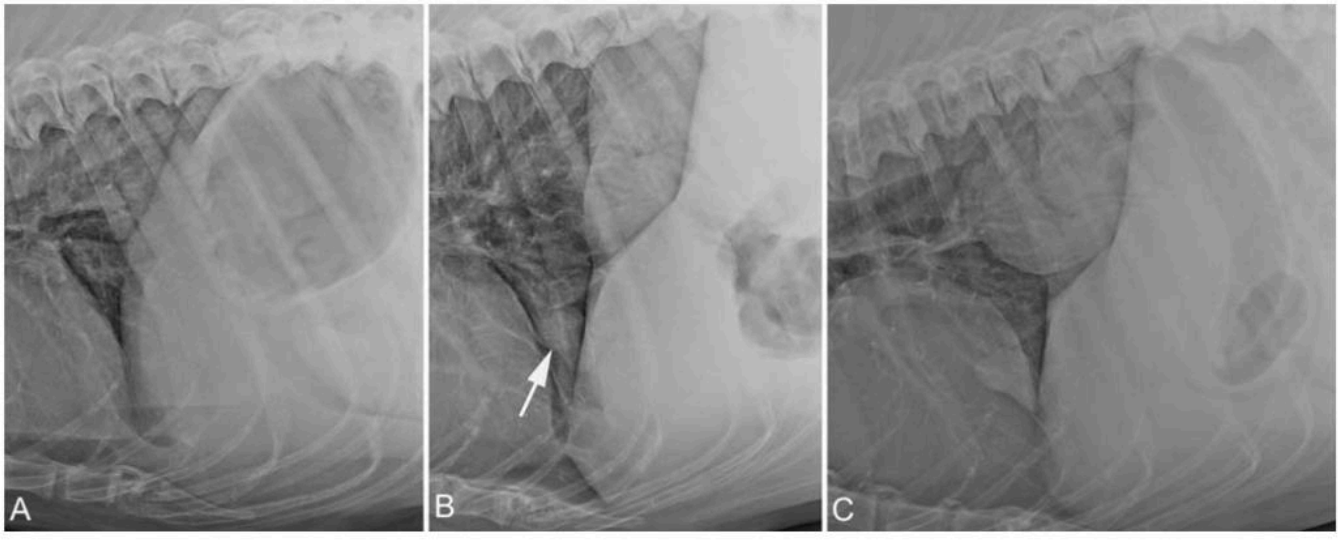


Fig. 45.14 Sliding hiatal hernia (type 1 hiatal hernia) in dog, which was presented for further evaluation of a previously detected right caudal lung mass. **A,** Right lateral radiograph. The stomach is in a normal position. **B,** Left lateral radiograph. The stomach is cranially positioned, but persistently summating mostly with the left crus of the diaphragm. The rugal folds are well visualized helping to identify the soft tissue structure as the stomach. A lung mass is noted in the ventral aspect of the right caudal lung lobe (*white arrow*). **C,** Left lateral radiograph after the dog coughed. The fundus and part of the body of the stomach are displaced cranially into dorsocaudal thorax. The esophagus and descending duodenum are dilated and gas filled.

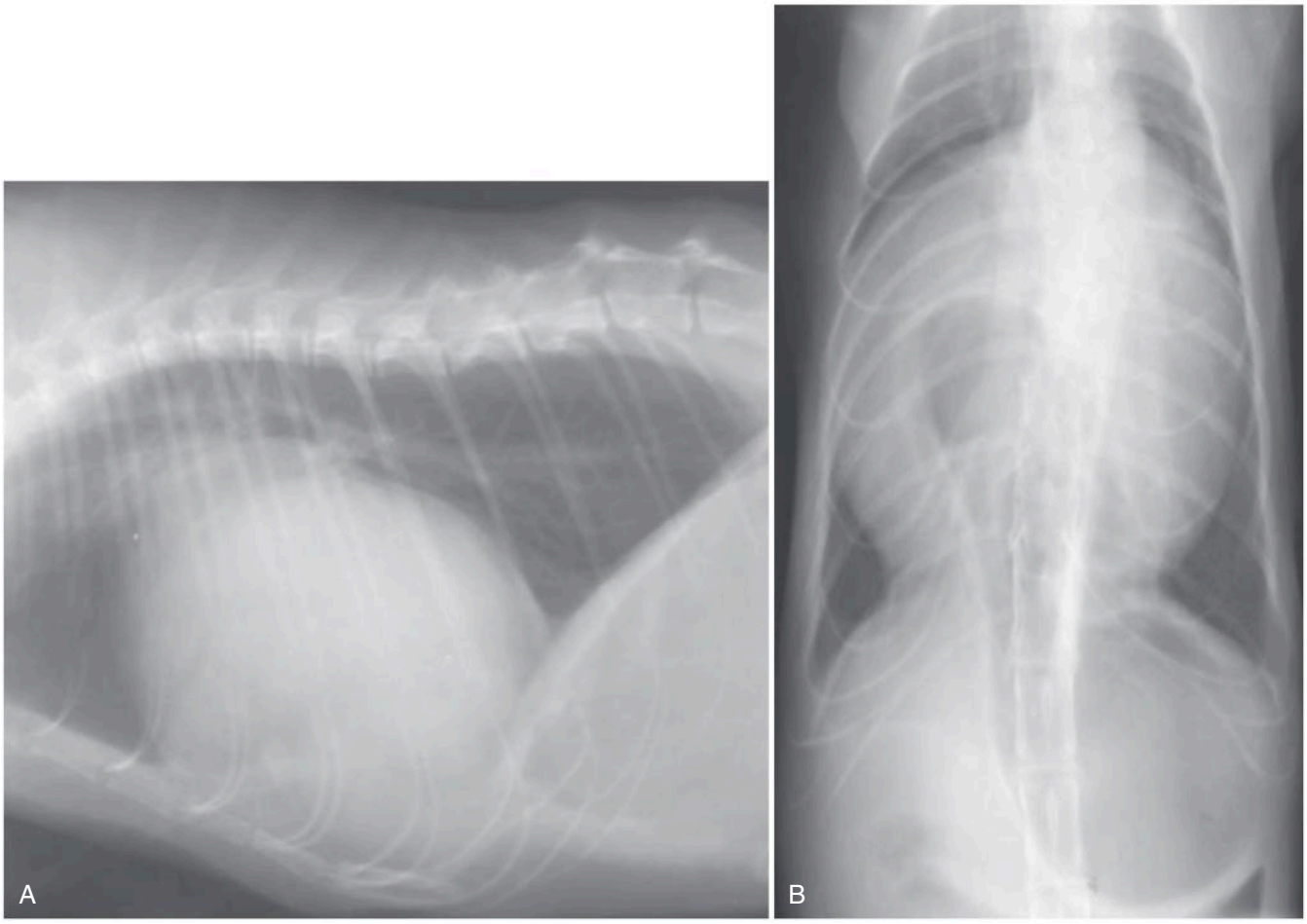


Fig. 45.15 Peritoneopericardial hernia in a cat. **A,** Right lateral radiograph. The cardiac silhouette is enlarged and has an irregular shape. Irregular gas opacities are summating with the cardiac silhouette. Effacement of the ventral diaphragmatic border is present. A large region of gas is superimposed on the liver. The thoracic spine has an undulating shape. **B,** Dorsoventral radiograph. The pylorus and part of the body of the stomach are displaced cranially and located within the pericardium.

the gastric wall with or without loss of wall layering, or a mass effect extending into the lumen of the fundus may be present.[53,83,84]

CHANGES IN GASTRIC SHAPE AND SIZE

Acute Gastric Dilation

Acute gastric dilation and gastric volvulus produce gaseous distention of the stomach. Although both fluid and gas are present in the stomach, gaseous distention is the predominant abnormality in these conditions.

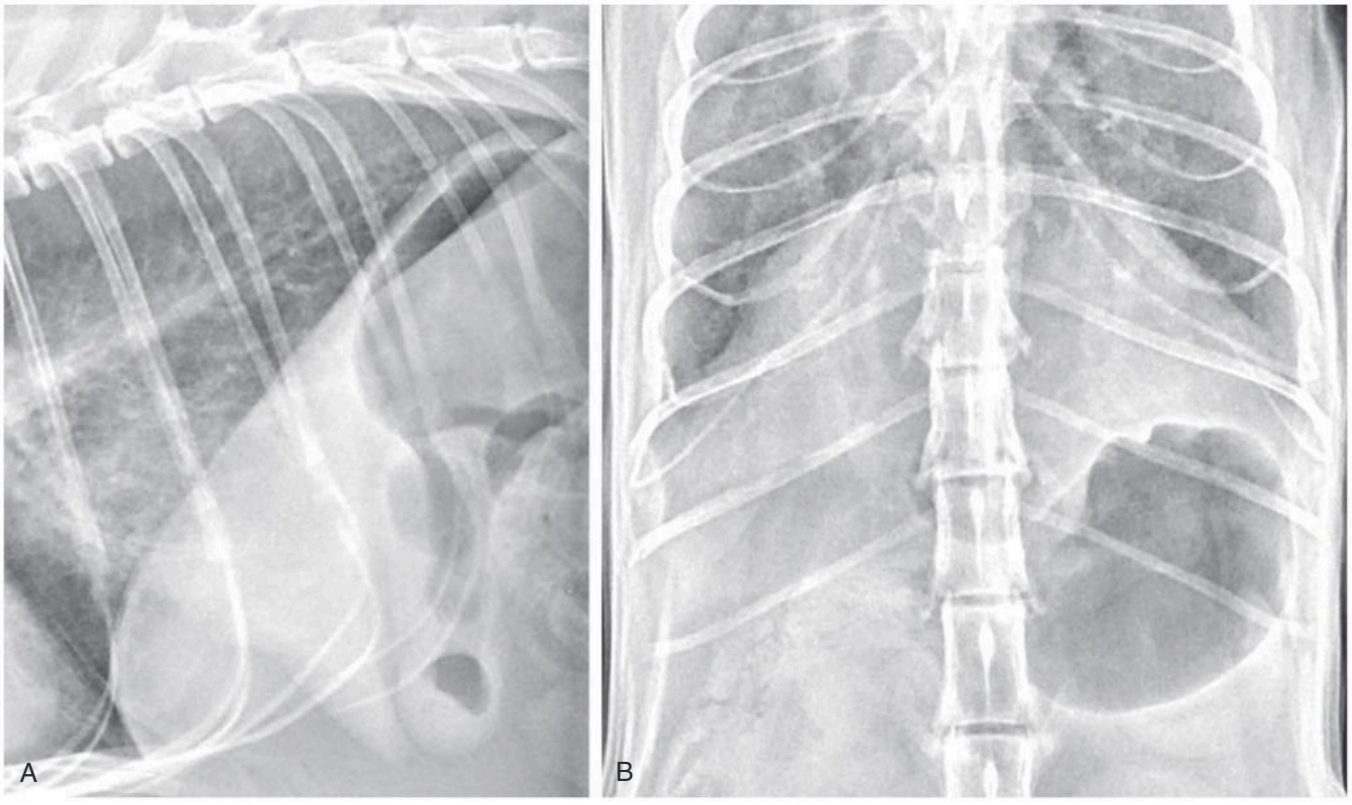
Acute gaseous distention of the stomach may be attributable to a variety of causes and can be caused by aerophagia as a result of severe dyspnea (eFig. 45.4) or pain. With acute gastric dilation, the stomach is enlarged and is filled primarily with gas but retains its normal position and anatomic relations (Fig. 45.17, eFig. 45.5). Thus, the pylorus is still located ventrally on the right and the fundus dorsally on the left. The normal position of the stomach can usually be verified by comparing right vs. left lateral views, evaluating the position of the stomach in a VD view. Recognition of the pylorus of a distended stomach is usually easier on lateral views than on the VD or DV view. Contrast gastrography may help in this localization but is usually not necessary.

Large quantities of free peritoneal gas tend to accumulate in the cranial abdomen in a lateral view, which can leave the impression of a gas-filled, round structure (Fig. 45.18). This abdominal gas bubble should not be confused with a gas dilated stomach or gastric volvulus and close attention should be paid to identify the correct position of the stomach and for the presence of abdominal gas. Positional radiographs can further help to identify the presence of gas in the abdomen and help to outline the correct position of the stomach.

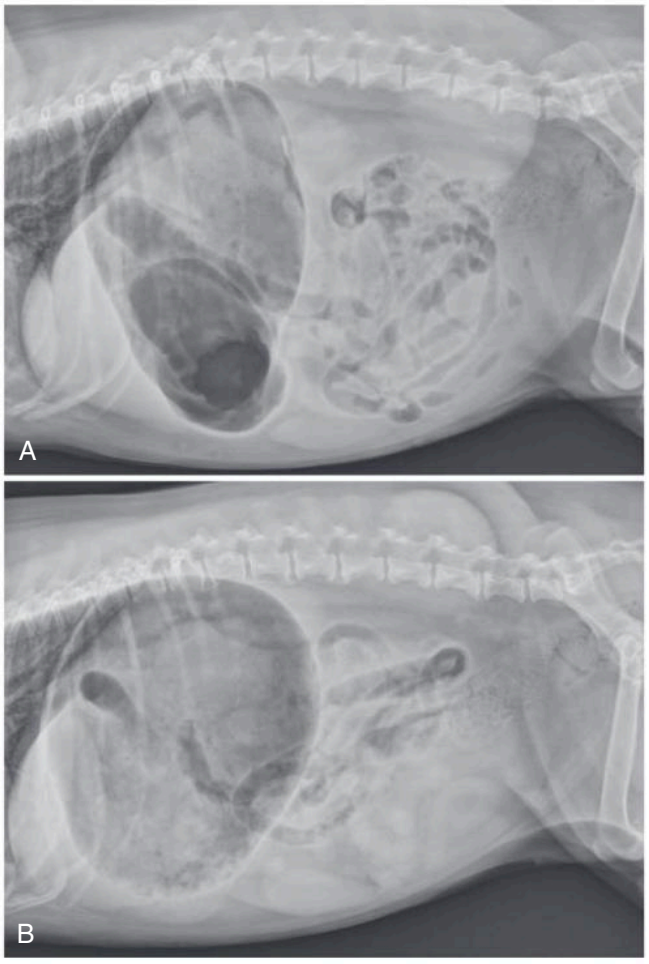
Gastric Dilation Volvulus

Gastric dilation volvulus (GDV) is a life-threatening condition and is differentiated from acute gaseous gastric dilation by the presence of gastric malpositioning in addition to pathologic gas distension. The cause of GDV is not completely understood; however, a variety of predisposing factors have been identified, including large-breed dog, increasing age, increased thoracic depth—to—height ratio, thin body condition, food volume, gastric foreign body, and splenectomy.[85–90] GDV has been reported in a dog as young as 5 weeks of age.[91] Although rare, a similar condition has been reported in the cat.[92] In the cat and small brachiocephalic dogs, a diaphragmatic hernia may be present as a predisposing factor.[93,94]

The radiographic appearance of the stomach varies depending on the type and degree of rotation and the amount



eFig. 45.4 Acute gastric gaseous dilation in a cat with severe respiratory distress due to cardiogenic pulmonary edema secondary to hypertrophic cardiomyopathy and left-sided heart failure. Right lateral **(A)** and dorsoventral **(B)** radiograph. The stomach is predominately gas filled and mildly to moderately dilated due to aerophagia. A diffuse unstructured interstitial lung pattern is noted in the caudal lung lobes.



eFig. 45.5 Left lateral **(A)** and right lateral **(B)** radiographs of a dog with gastric dilatation without volvulus. The pyloric antrum is gas filled and in a normal ventral position in the left lateral view. The fundus is gas filled in the right lateral view. The duodenum is seen exiting the stomach in a normal position.

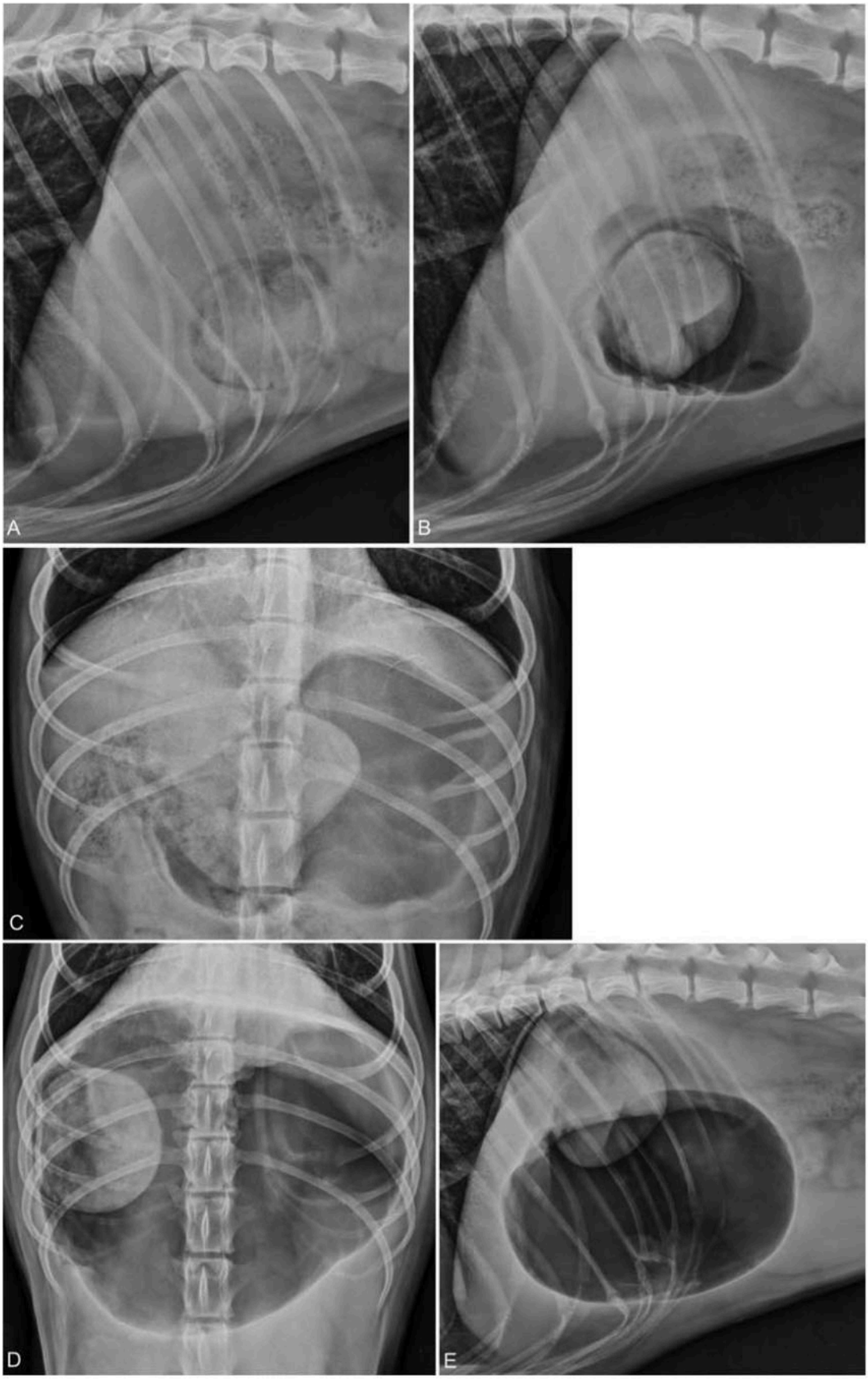


Fig. 45.16 Gastrogastric intussusception in a 4-year-old mixed-breed dog with acute vomiting. Right lateral **(A)**, left lateral **(B)**, and dorsoventral **(C)** radiograph of the abdomen. A large soft tissue opacity extends from the pylorus to the body of the stomach. In the most left lateral and central aspect of this soft tissue mass a small indentation is noted. Ventrodorsal **(D)** and right lateral **(E)** radiograph of the abdomen post negative gastrography. The luminal soft tissue mass extending from the pylorus area is unchanged and partially surrounded by a small rim of gas. In the pylorus, the mass cannot be differentiated from the gastric wall. In the body of the stomach, the mass is well differentiated from the gastric wall. Surgery confirmed a gastrogastric intussusception, in which the antrum of the stomach extended into the body of the stomach. The duodenum was not involved in the intussusception. (Courtesy DoveLewis Emergency Animal Hospital, Portland, Oregon.)

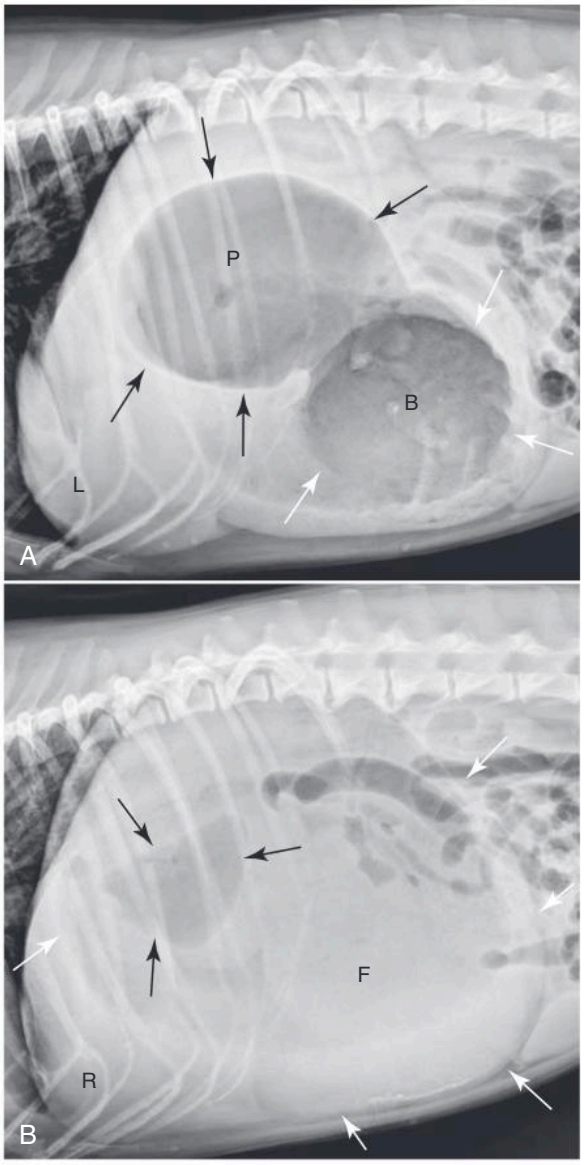


Fig. 45.17 Gastric dilation without volvulus. **A,** Left lateral view. Gas is present in the pyloric antrum (*P, black arrows*) and body (*B, white arrows*) of the stomach as expected. The narrowing between the body and pyloric antrum is a peristaltic contraction. **B,** Right lateral view. The fundus (*F, white arrows*) is extremely distended. There is a small amount of gas trapped in the pyloric antrum (*black arrows*). The distribution of gas as a function of left versus right recumbency is as expected in a normal subject, indicating that the stomach is not rotated, unless the rotation is 360 degrees, which is unusual.

of distention.[95,96] As the stomach dilates, the fundus and greater curvature rotate clockwise, when viewed from caudal to cranial, to lie along the ventral abdominal wall. The pylorus therefore shifts dorsally, cranially, and to the left, and the body of the stomach shifts toward the right. Because of the attachments of the proximal extremity of the spleen to the stomach, the spleen often follows the greater curvature toward the right.

The main radiographic features of GDV are:

- Gas and fluid distension of the stomach (more gas than fluid).
- The pylorus is displaced dorsally and to the left (unless a 360-degree torsion is present).
- With the patient in left lateral recumbency, fluid in the stomach fills the pylorus and gas fills the rest of the stomach.

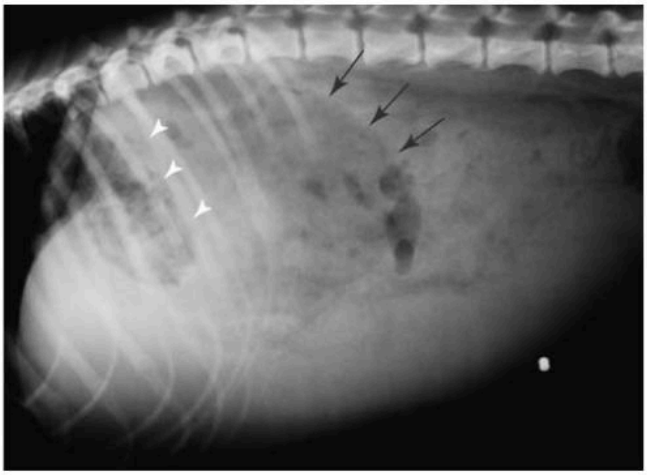
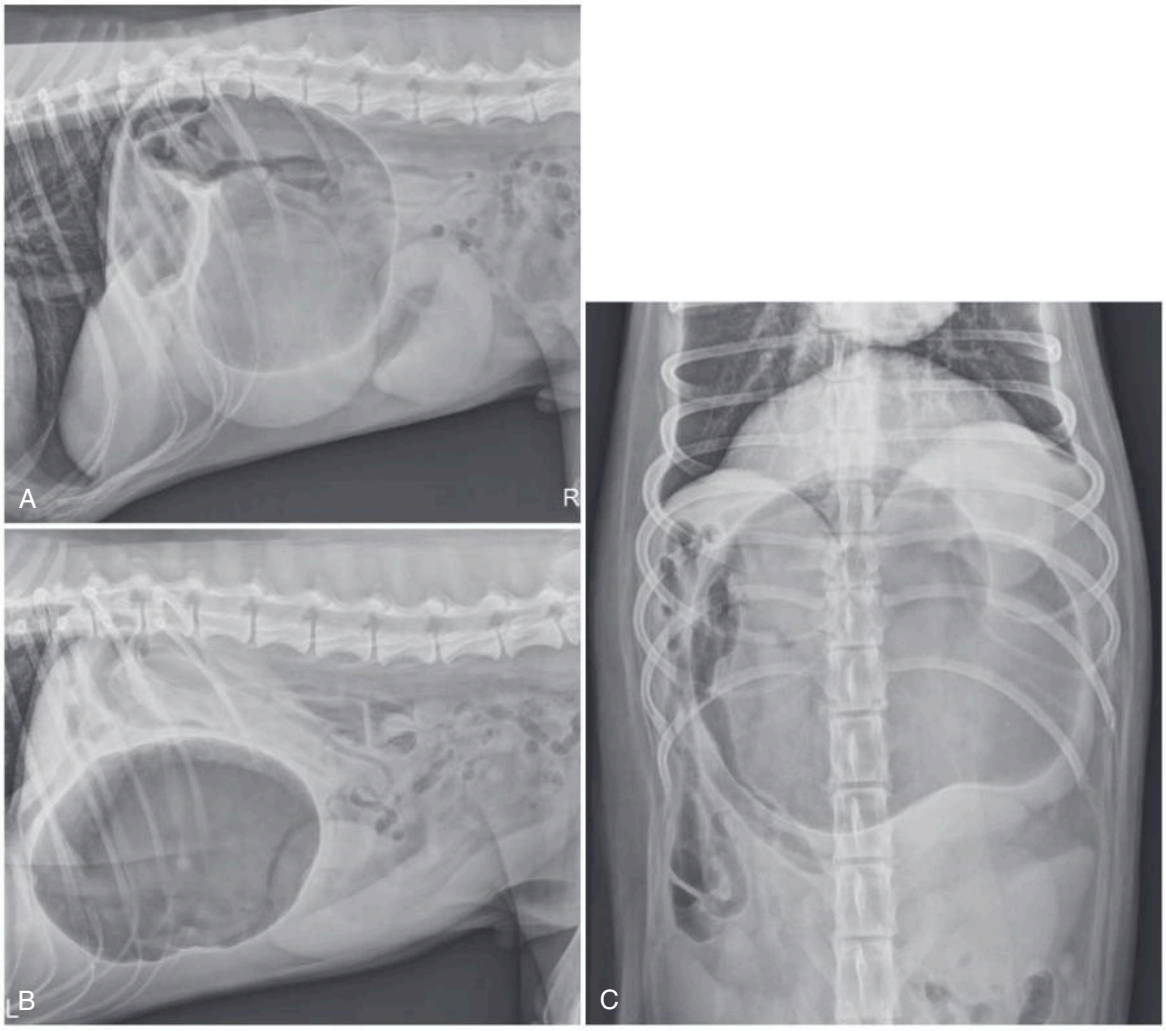
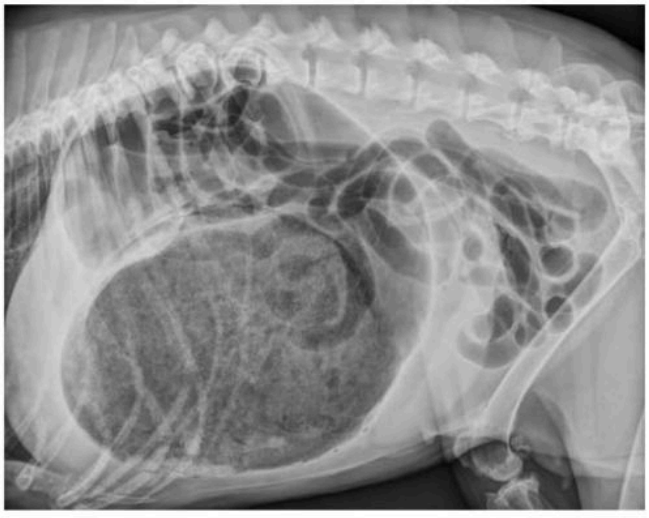


Fig. 45.18 Severe pneumoperitoneum secondary to intestinal perforations due to ballistic trauma. Left lateral radiograph. A large, round ovoid gas opacity is present in the cranial abdomen (*black arrows*). This should not be confused with acute dilation or volvulus of the stomach. The stomach is located in correct position in the cranial abdomen (*white arrowheads*), easily identified by the presence of rugal folds. The lack of serosal detail is secondary to the presence of peritoneal fluid due to severe chronic peritonitis.

- With the patient in right lateral recumbency, gas fills the pyloric portion and fluid shifts to the fundus or body of the stomach (Fig. 45.19, eFig. 45.6).
- The pylorus and duodenum are displaced to the left in the VD/DV projections.
- Compartmentalization is a term that refers to the radiographic appearance of soft tissue bands that project into or across the gas-filled lumen of the rotated stomach. These soft tissue bands result from folding of the stomach on itself as the folded wall projects into the lumen and is outlined by gas within the lumen. These bands may become more obvious with greater degrees of distention and are best seen in the right lateral view (see Fig. 45.19).
- The spleen is also often malpositioned in patients with GDV, and may be compromised because of impaired circulation (see Fig. 45.19). Outright torsion of the spleen may also occur; this further compromises the patient. The greater the gastric distention, the less likely the spleen is to be visualized radiographically because of crowding.
- Paralytic ileus of the small intestine, esophageal dilation, a reduced size of the caudal vena cava, and microcardia and small pulmonary vessels associated with shock may be present to variable degrees.
- The pylorus and fundus may be in a normal position in a 360-degree volvulus. Secondary signs of GDV as outlined earlier as well as inability to pass a tube are suggestive of a 360-degree rotation (Fig. 45.20).
- Gas within the gastric wall, termed *pneumatosis*, can occur but is infrequent (Fig. 45.21, eFig. 45.7).[9] Gastric pneumatosis in combination with GDV has a high specificity but a low sensitivity for predicting gastric wall necrosis.[97] Spontaneous pneumoperitoneum should also raise concern for the possibility of gastric necrosis. Prior trocharization of the stomach will complicate assessing the significance of pneumatosis or pneumoperitoneum. Overall, radiographs are a poor predictor of gastric wall necrosis in patients with gastric volvulus.
- Gastric volvulus may also be present without severe gastric distention. This situation may often exist for days or weeks after previous gastric decompression[98] or may be present at the time of initial presentation.[32]



eFig. 45.6 Right lateral **(A)**, left lateral **(B)**, and ventrodorsal (VD) **(C)** radiographs of a dog with gastric dilatation volvulus. The pyloric antrum is displaced dorsally and to the *left*, resulting in compartmentalization and a fold through the cranial aspect of the stomach in the right lateral view. The gas distended fundus is seen ventrally displaced in the left lateral view. The different portions of the stomach are more difficult to identify in the VD projection. Notice that the spleen is also abnormally positioned.



eFig. 45.7 Right lateral radiographs of a dog with gastric dilatation volvulus. The stomach is gas distended and compartmentalized. The pylorus is dorsally displaced. There is a thin rim of gas within the stomach wall, best seen ventrally. The small intestines and esophagus are mildly gas distended as well.

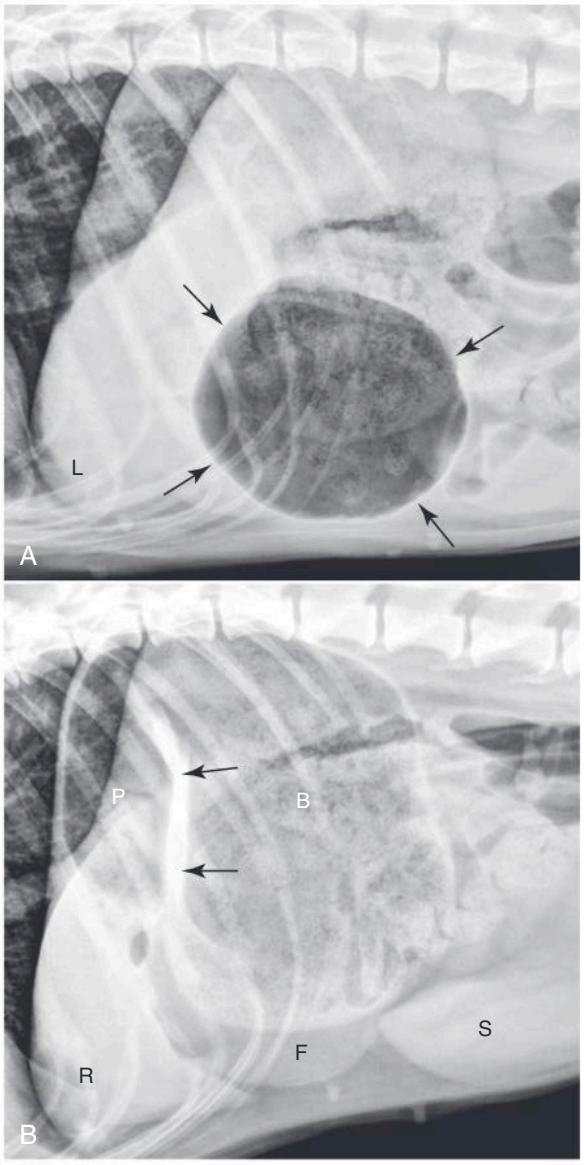


Fig. 45.19 Gastric volvulus. **A,** Left lateral view. The stomach is moderately distended with gas in the fundus (*black arrows*). This is easily misinterpreted as gas in the pylorus, as expected in the left lateral view. **B,** Right lateral view. The fluid shifts into the fundus (*F*), and gas outlines the pyloric portion (*P*) as well as the body (*B*). The compartmentalization (*black arrows*) between the pylorus and body, and the characteristic appearance of the pylorus in the dorsocranial aspect of the abdomen, indicate that the pylorus is on the *left* and the fundus is on the *right* and that there is a gastric volvulus. Note the malpositioned and slightly enlarged spleen (*S*). The spleen will follow the fundus because of anatomic connections.

The right lateral view is the most valuable radiographic projection to detect GDV as the displaced pylorus is gas-filled and compartmentalization is best visible. However, both lateral views should be acquired initially to increase the chance that the pylorus fills with gas and can be recognized. The goal is to make the diagnosis as quickly as possible because mortality is decreased if time between presentation and surgical intervention is decreased.[99] Recognizing the pyloric shift is more difficult in VD or DV radiographs; however, in unclear cases, they can be valuable. Positive-contrast gastrography may be performed to confirm the position of the stomach but usually is not needed.

Chronic Pyloric Obstruction

Pyloric outflow obstruction may be acute or chronic. Examples of causes for acute obstruction include gastric volvulus and foreign bodies. Obstructive pyloric diseases can be divided into those that encircle the pylorus, and are thus restrictive, and those that obstruct the pylorus by blocking its orifice. Restrictive diseases of the pylorus include hypertrophic pyloric stenosis, pylorospasm, inflammation or scarring, and neoplasia. Rarely, severe adhesions as caused by sclerosing encapsulating peritonitis can cause restrictive pyloric disease, where the gastric outflow tract is decreased in size and lacks normal functionality.[100] Pyloric obstructive diseases include gastric foreign bodies, mucosal inflammation or hypertrophy, and some mural lesions of the pyloric antrum.

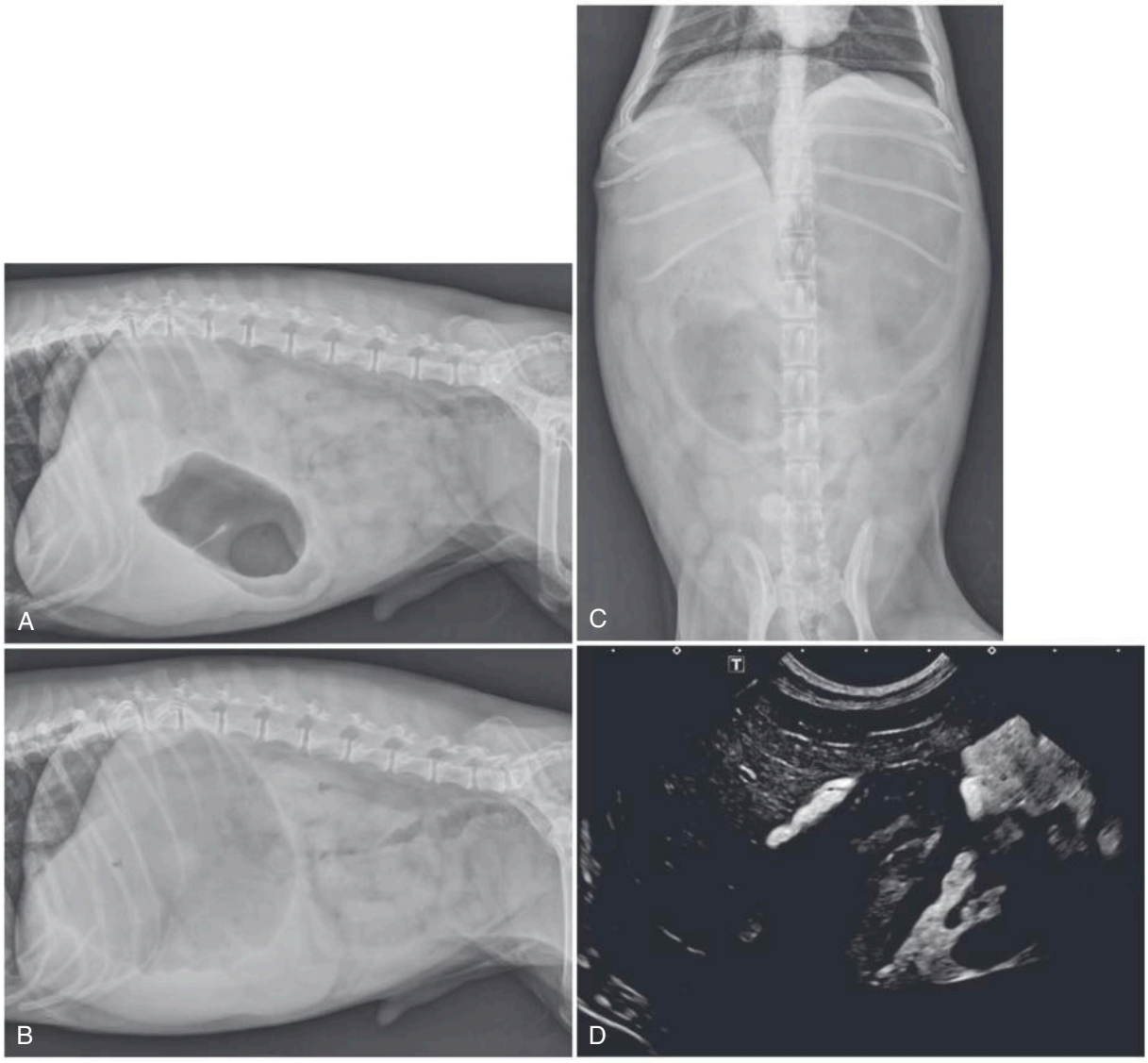
It should also be remembered that disease of the pancreas or proximal duodenum can lead to an outflow obstruction of the stomach, which might present similar to disease occurring at the pylorus itself.

Chronic partial pyloric obstruction often manifests on survey radiographs as fluid-filled gastric distention as opposed to the acute gaseous distention of GDV (Fig. 45.22, eFig. 45.8). The stomach is commonly quite large with chronic partial pyloric obstruction. However, the enlarged stomach may be more difficult to identify on survey radiographs when it is filled with fluid. Even when distended with fluid, the stomach usually still contains some gas. In these instances, however, the gas does not totally outline or fill the entire stomach. Instead, the smaller amount of gas floats as a bubble on top of the fluid and should not be mistaken as the limits of the stomach or gastric wall thickening. Caudal displacement of the transverse colon can also be used as an indicator of gastric distension.

The major effect of pyloric obstructive diseases is to restrict gastric emptying. Survey radiographic findings may vary from normal gastric size to enlargement depending on the severity and duration of the obstruction. However, differentiation of the pyloric obstructive diseases is difficult radiographically, especially without fluoroscopy. The stomach is a dynamic organ that changes appearance rapidly because of peristaltic waves, and a radiograph is simply a snapshot of the morphologic features of the stomach. The advantage of fluoroscopy is that sequential changes of the shape of the stomach can be observed. Even with fluoroscopy, however, differentiating some pyloric obstructive diseases is not possible. For example, hypertrophic pyloric stenosis, neoplasia, and mural scarring all may produce an annular type of stricture of the pylorus that prevents the pylorus from opening adequately.

Usually, contrast radiography or ultrasound is needed to establish the cause and site of the pyloric obstruction. With contrast studies, the major radiographic abnormality is delayed gastric emptying. However, an initial delay in gastric emptying may be of no clinical significance, because of the influence of various psychogenic factors discussed previously. This point is especially important if the stomach starts to empty normally after an initial delay or after the animal is allowed to calm down. Of more significance is a pronounced delay in gastric emptying when only a small amount of contrast medium passes from the stomach in a few hours. Because the normal stomach should be empty 1 to 4 hours after administration of contrast medium, retention of most of the barium within the stomach 3 or 4 hours after administration usually indicates pyloric obstructive disease (Fig. 45.23).

An annular type of stricture narrowing the pyloric sphincter may result in characteristic radiographic abnormalities. If



eFig. 45.8 Left lateral **(A)**, right lateral **(B)**, and ventrodorsal **(C)** radiographs of a dog with chronic pyloric outflow obstruction due to lymphoma. The stomach is normally positioned but severely distended with fluid and a small amount of gas. A rounded soft tissue opacity with a mass-like appearance is seen in the region of the pylorus in the left lateral view. The liver is moderately enlarged, resulting in caudal displacement of the stomach and has undulant margins. **D,** Ultrasound image of the pyloric canal of the same dog. The walls of the pyloric canal are thickened with poorly defined wall layers. Lymphoma was diagnosed cytologically.

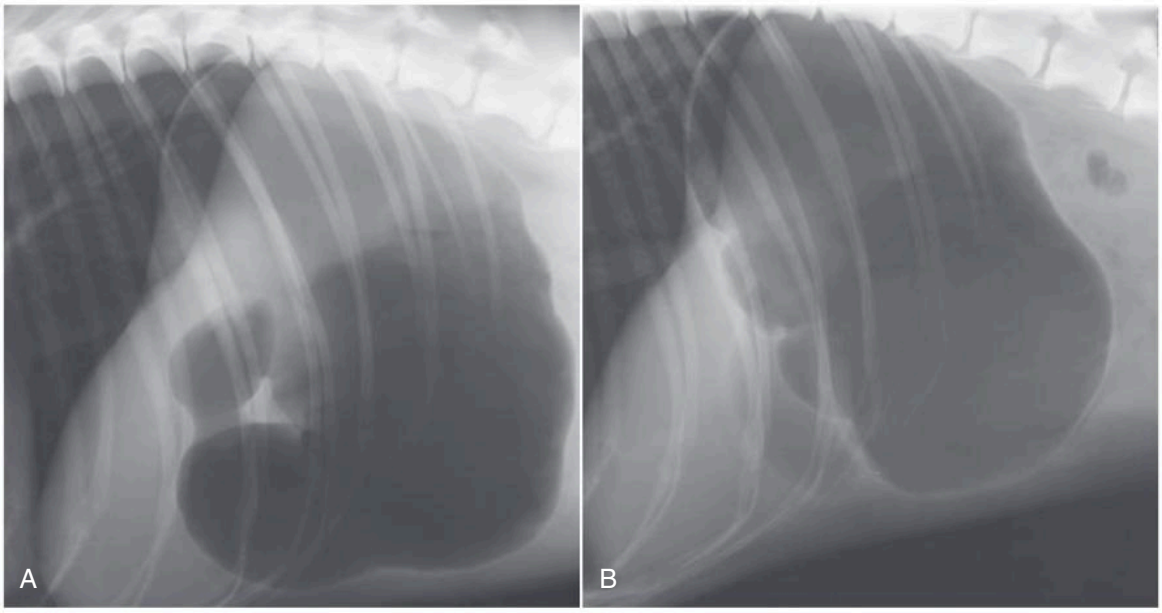


Fig. 45.20 Left **(A)** and right **(B)** lateral views of a dog with acute gastric dilatation. On the basis of these radiographic findings, the pylorus and the fundus are positioned normally. A gastric tube could not be passed into the stomach. Final diagnosis was 360-degree gastric volvulus.

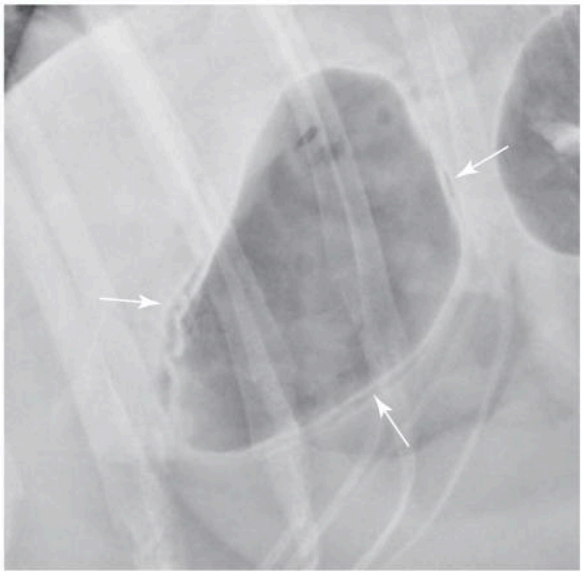


Fig. 45.21 Lateral radiograph of a dog with gas in the wall of the pyloric antrum (*white arrows*).

barium fills only the entrance of the lumen at the pyloric sphincter, the resultant radiographic appearance is referred to as the *beak sign*.[101] If barium fills the length of the narrowed lumen through the pyloric sphincter, the resultant radiographic appearance is referred to as the *string sign.*[101] A tit sign has been described as a relatively sharp, pointed outpouching of the pyloric antrum along the lesser curvature as a peristaltic wave pushes contrast medium in a peristaltic pouch up against the mass-type lesion around the pylorus[101] (Fig. 45.24, eFig. 45.9).

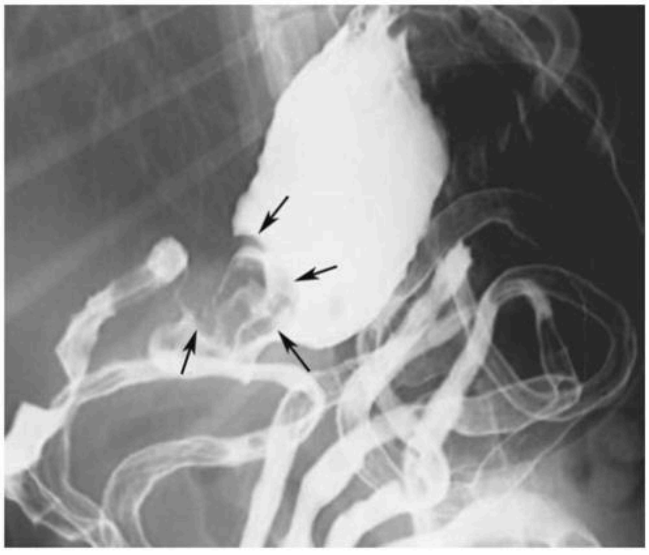
Sonographic thickening of the mucosa or muscular layer of the stomach wall can be noted and may help to differentiate between the various causes of pyloric obstruction. In dogs with chronic pyloric hypertrophy, the hypertrophic muscularis layer may be detected sonographically as a thick hypoechoic layer (Fig. 45.25). The thickness of the muscularis layer is greater than 3 mm in mild to moderate hypertrophy and greater than 8 mm in severely affected dogs. Vigorous, but ineffective, peristaltic contractions that fail to propel contents into the duodenum are seen in some patients.[51]

Pyloric obstructive diseases include gastric foreign bodies, mucosal inflammation or hypertrophy, and some mural lesions of the pyloric antrum. These types of lesions are more likely to produce filling defects within the lumen that occlude the orifice of the pyloric sphincter (see Fig. 45.24). Again, radiographic recognition of such a lesion is usually adequate diagnostically, and differentiation of the underlying cause may not be possible on radiographs. Ultrasound might provide additional information, including outlining of a foreign body.

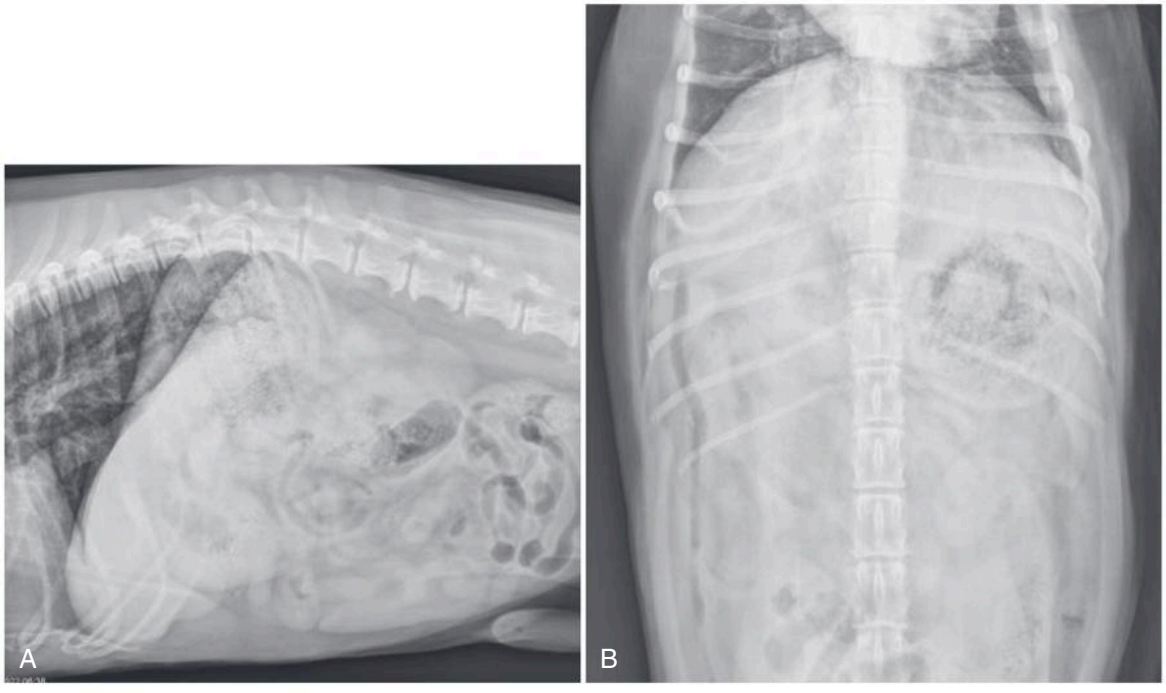
ABNORMAL GASTRIC CONTENT

Gastric Foreign Bodies

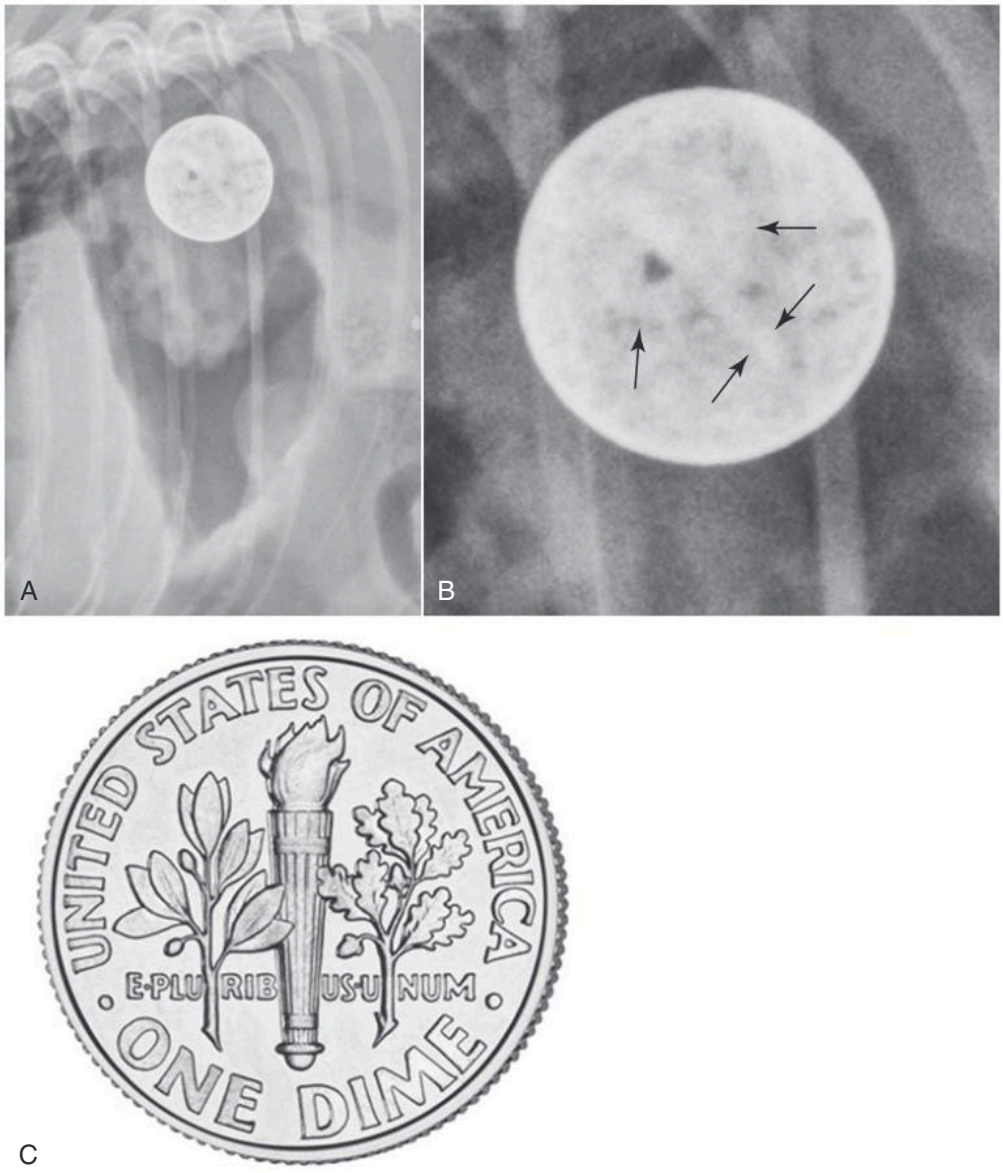
Radiopaque material within the stomach is commonly identified on survey radiographs (Fig. 45.26, eFig. 45.10). These opacities are most often the result of ingested food or bone fragments and may have no clinical significance if they are small and cause no obstructive pattern. More clinically significant foreign bodies, such as fishhooks and needles, are also readily visible and present no diagnostic dilemma. The finding of discoid metallic foreign bodies is significant, because certain zinc-containing coins (U.S. pennies minted after 1982 and Euro cents) can induce intravascular hemolysis and hemolytic anemia.[102–104] Radiographs of the abdomen are indicated in the evaluation of patients with intravascular hemolysis for this reason. Other types of metallic objects may also contain zinc. Determining the denomination of suspected coins may be possible radiographically (eFig. 45.11). If projected en face, the diameter can be measured and corrected for magnification and compared to the known diameter of coins. Ingested magnets may readily be seen on survey radiographs and this can cause



eFig. 45.9 Ventrodorsal oblique radiograph of the pylorus of a dog with obstructive disease of the pylorus. A hemispheric filling defect is at the pylorus that projects into the lumen (*black arrows*). Pronounced delay in gastric emptying was present.



eFig. 45.10 Left lateral **(A)** and ventrodorsal **(B)** radiographs of the stomach of a dog with a gastric foreign body. A rectangular structure with stippled gas lucencies is visible in the gastric fundus in the lateral view, whereas the foreign body is round in the ventrodorsal view with peripheral stippled gas lucencies. The appearance is consistent with corn cob ingestion.



eFig. 45.11 Lateral radiograph **(A)** of a dog with a discoid metallic gastric foreign body. Determining the type of coin is important based on the association of zinc toxicity with some coin types. This object is likely a U.S. dime, based on the markings **(B)** that resemble the engraving present on that particular coin (*arrows*) **(C)**. The magnification-corrected diameter of the coin was also identical to that expected for a U.S. dime.

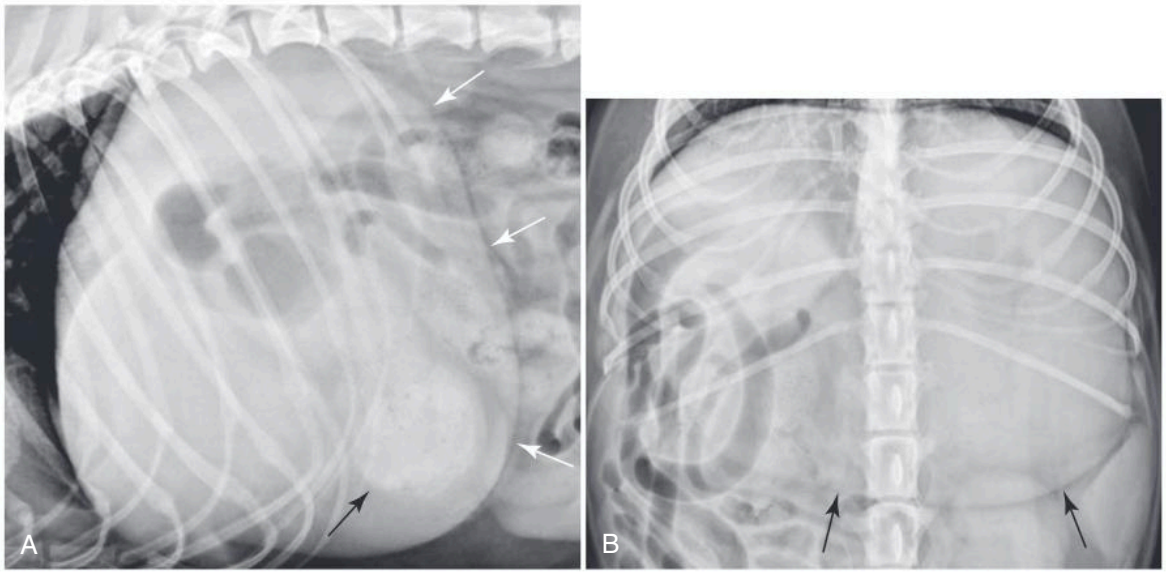


Fig. 45.22 Lateral **(A)** and dorsoventral **(B)** radiographs of a dog with fluid-filled gastric distention caused by chronic pyloric obstruction. The stomach is more difficult to identify when filled with fluid instead of gas. The caudal margin of the stomach is indicated in **A** by the *white arrows* and in **B** by the *black arrows.* In **A,** some opaque gastric contents have settled into the dependent pyloric region of the stomach (*black arrow*).

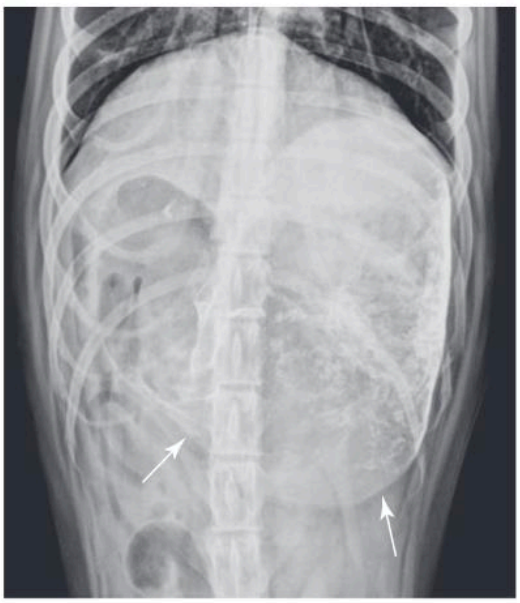


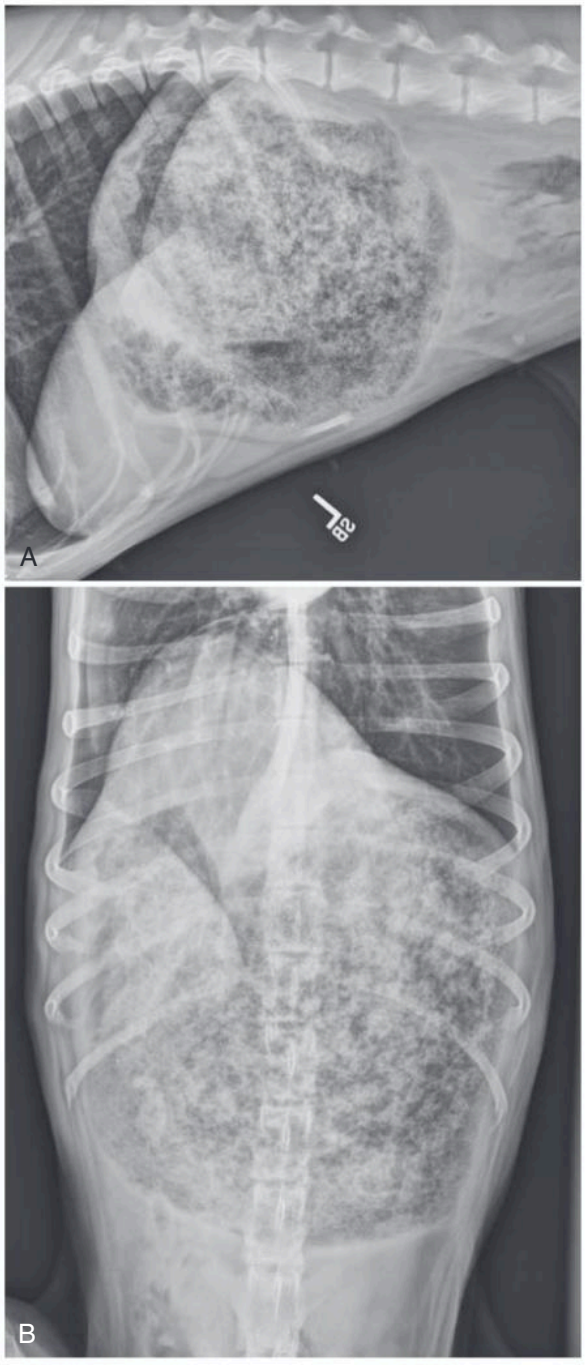
Fig. 45.23 Ventrodorsal radiograph 10 hours after barium was given. The stomach is distended (*white arrows*) with intraluminal gas and fluid and some of the barium. There should be no residual barium after 10 hours and this, along with the distention, is indicative of gastric outflow obstruction.

gastric ulceration, obstruction, and perforation secondary to pressure necrosis when more than one magnet is ingested. Early surgical intervention might help to alleviate the risk of gastric perforation or obstruction secondary to ingested magnets.[105,106] It is important to remember that certain metallic foreign bodies are not metal attenuating on radiographs; for example, aluminum is relatively radiolucent and is therefore difficult to detect on survey radiographs. It is also important to remember that dogs may swallow glue containing diphenylmethane diisocyanate, which expands extensively when exposed to moisture in the stomach filling the gastric lumen and thereby resulting in a severe outflow obstruction (eFig. 45.12).[107]

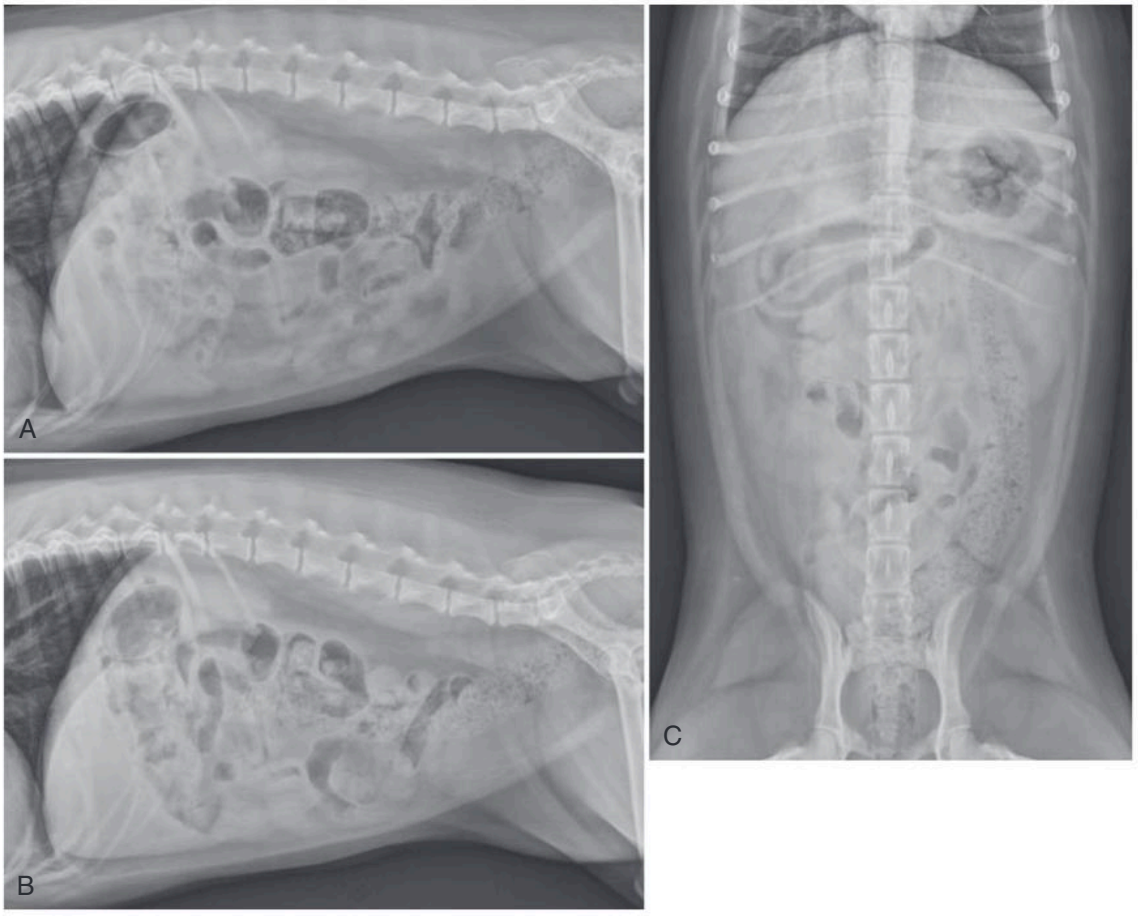
The stomach may occasionally contain nondescript radiopaque material of questionable significance (Fig. 45.27). The persistence of the abnormality is important. If the patient is stable and endoscopy is not used, repeat radiographs made after fasting for 12 to 24 hours may provide valuable information about the digestibility or potential transit of the suspicious material.

A greater problem exists with radiographic detection of nonopaque gastric foreign bodies. Such objects are usually difficult to see on survey radiographs. Several approaches exist to help in the radiographic identification of nonopaque gastric foreign bodies. The simplest is to use different patient positions. If the foreign body does not shift dependently with gastric fluid, then a different view may help outline the foreign body with gas. If a foreign body ingestion is suspected and endoscopy is not available, a contrast radiographic study, ultrasound, or CT study of the abdomen may be necessary for diagnosis. Giving a small amount of barium or gas (Fig. 45.28) may make such foreign bodies easier to see than with a standard gastrogram using a large volume of barium because the large volume may obscure the foreign body. Pneumogastrography is simple, easy to perform, cheap, and quick and requires no special equipment and can help outline gastric foreign bodies.[21]

The appearance of a foreign body on a gastrogram varies depending on the type of foreign body present. An object such as a solid ball creates a round, discrete filling defect within the barium. If the object has a nonabsorbent surface, it may not be visible after the stomach has emptied. Conversely, a rag or sock may not create an initial filling defect because the contrast medium may permeate the object. Because of absorption and retention of contrast medium, however, the foreign body may be better visible after the stomach has emptied. Gas containing radiolucent foreign bodies may be difficult to identify. Noticing a focal radiolucency with a consistent shape and often a thin peripheral soft tissue opaque rim is important to identify these foreign bodies (eFig. 45.13).



eFig. 45.12 Left lateral **(A)** and ventrodorsal **(B)** radiographs of the stomach of a dog after ingestion of glue containing diphenylmethane diisocyanate. The stomach is severely distended and completely filled with heterogeneous foreign material with a foamy appearance. The hardened material had to be removed via gastrostomy.



eFig. 45.13 Left lateral **(A)**, right lateral **(B)**, and ventrodorsal (VD) **(C)** radiographs of a dog who ingested a dog toy squeaker. The foreign body is gas filled and is visible in the lateral projections as oval radiolucency in the dorsal aspect of the fundus. In the VD projection, the foreign body is round and represents as a round radiolucency in the fundus

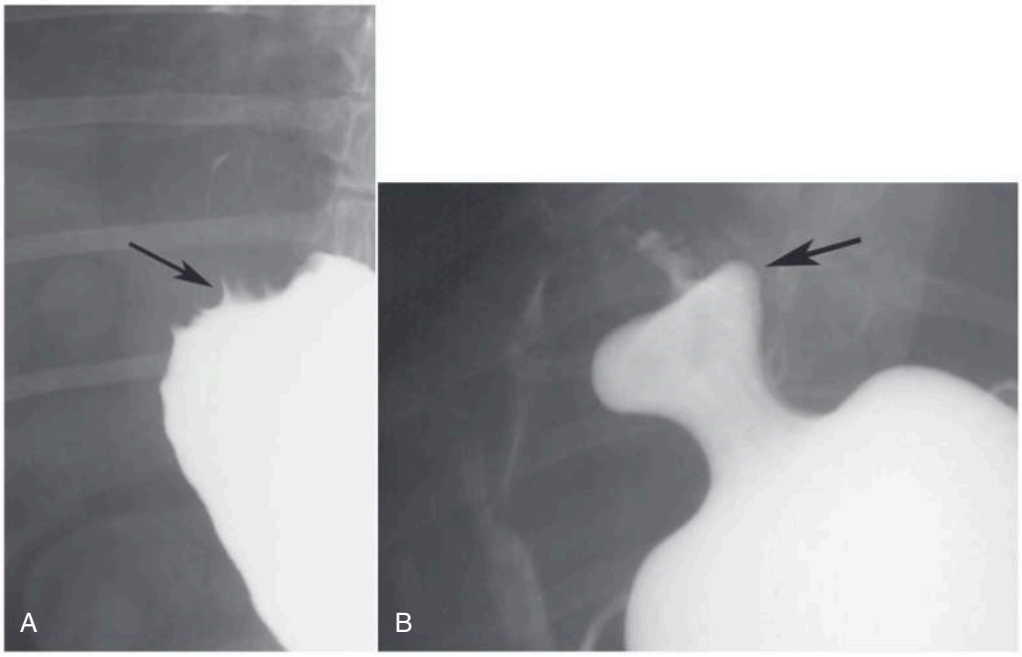


Fig. 45.24 **A,** Ventrodorsal radiograph of the pyloric region of a dog with restrictive disease of the pylorus. The string sign (*black arrow*) is caused by barium that fills the length of the lumen of the narrowed pyloric sphincter because of an annular type of stricture. **B,** Ventrodorsal radiograph of the pyloric region of another dog with restrictive disease of the pylorus. The peristaltic pouch (*black arrow*) is the outpouching of the pyloric antrum along the lesser curvature as a peristaltic wave pushes contrast medium up against the mass-type lesion encircling the pylorus. A pronounced delay in gastric emptying was also present.

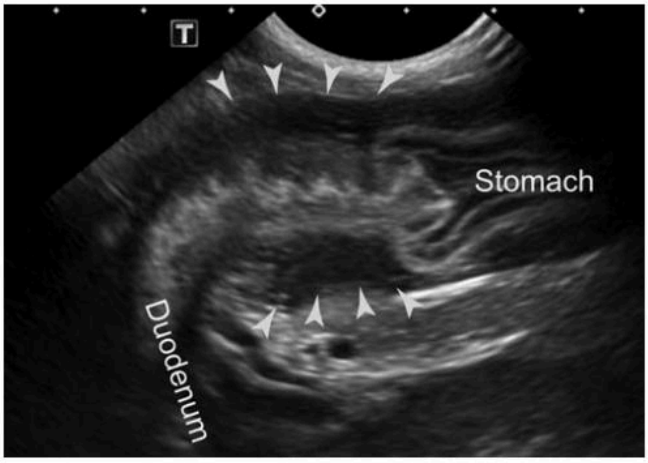


Fig. 45.25 Longitudinal ultrasound image of pyloric stenosis. The pylorus wall is moderately thickened (*white arrowheads*). The layered appearance of the pylorus wall is still present; the muscularis is markedly thickened and the luminal aspect of the pylorus wall is irregular. Caudal is to the *right*, and ventral is to the *top*.

Gastric foreign bodies may be identified ultrasonographically.[50] The ability to detect these objects depends on the presence of other gastric contents (e.g., gas, fluid, and food), the position of the object relative to the sound beam, and the object composition. Strong acoustic shadows with or without an echogenic acoustic interface are strongly suggestive of a foreign body. Linear foreign bodies are often hyperechoic, and cause plication of the stomach (Fig. 45.29); in cats the linear foreign body is often anchored around the base of the tongue; however, in dogs, they often originate from a foreign object lodged in the pylorus. Intraluminal fluid surrounding a foreign object facilitates its detection and the ability to distinguish reflective foreign body surfaces from intraluminal gas; therefore, adding water to the stomach may be beneficial in some patients. Objects that transmit sound may be seen more completely than those producing strong acoustic shadows. Repositioning of the patient while scanning might demonstrate mobility of the object in the stomach. However, like radiography, large foreign objects might not move or have only minimal movement as they might be lodged in the lumen of the stomach.

Gastric foreign bodies rarely cause perforation of the gastric wall, but when sharp objects such as wooden sticks, skewers, or metal brush bristles are swallowed, perforation may occur. Gastric perforation can result in peritoneal gas, which can be detected radiographically, sonographically, or by using CT. Sonographically, peritoneal gas as well as hyperechogenicity of the mesenteric fat and/or peritoneal fluid can be present.[108] CT may have a similar sensitivity as radiography and ultrasound in detecting peritoneal gas and may have the added benefit compared to ultrasound that no pressure to the abdomen is applied during the exam, which might be favorable in patients with acute abdominal signs.[109]

GASTRIC WALL CHANGES

Gastric Ulcers

Gastric ulceration is a multifactorial disease. Gastric ulcers may be benign or malignant. Benign gastric ulcers are also termed *peptic gastric ulcers* and result from a variety of causes.[110–112] Use of nonsteroidal anti-inflammatory drugs is a common cause of benign gastric ulcers.[113–115] Dachshunds with disc prolapse have a high prevalence of gastroduodenal ulceration.[116] This is thought to be from ulcerogenic drug administration as well as

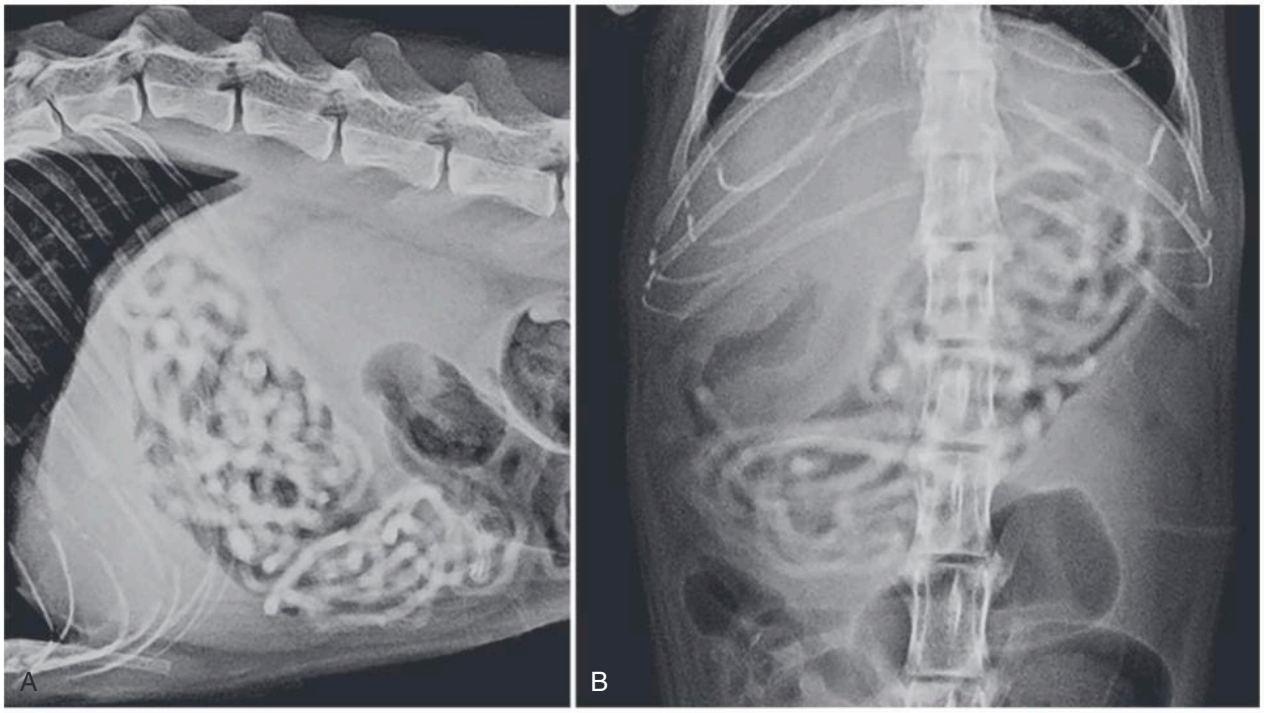


Fig. 45.26 Lateral **(A)** and ventrodorsal **(B)** radiographs of a cat with multiple linear to C-shaped foreign bodies consistent with hair ties. The hair ties are easily identified due to their attenuation and characteristic imaging appearance.

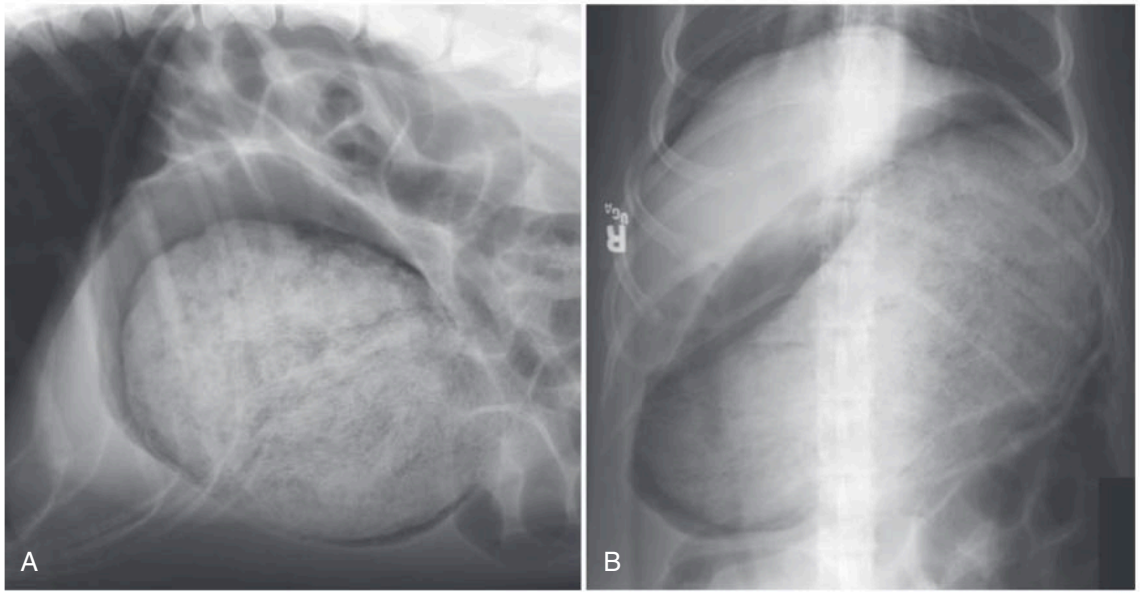


Fig. 45.27 Lateral **(A)** and ventrodorsal **(B)** radiographs of a dog with a large gastric foreign body. This radiopaque material is easy to visualize because of the large amount of gas surrounding the foreign body, which was aggregated leaves and plant material. Expansion of ingested polyurethane glue can also lead to a similar appearance.

autonomic disturbances, stress, hypovolemia, and other factors.[116] Gastric ulceration in combination with gastritis occurs frequently in working and sled dogs and its cause is not entirely understood, but might be in part caused by increased secretion of gastrin, exercise-induced hyperthermia, and damage to the gastric mucosa.[117] Malignant gastric ulcers occur in association with gastric neoplasia and may be caused by tumor necrosis.[110] The greatest risk factor for malignant ulcers in the dog is gastric adenocarcinoma.[115]

Gastric ulcers are difficult to identify on conventional radiographs. Ulcers are more conspicuous in barium studies, in which they are usually round to ovoid collections of barium. They produce craters in the wall of the stomach that appear as outpouchings from the lumen (Fig. 45.30). The contrast

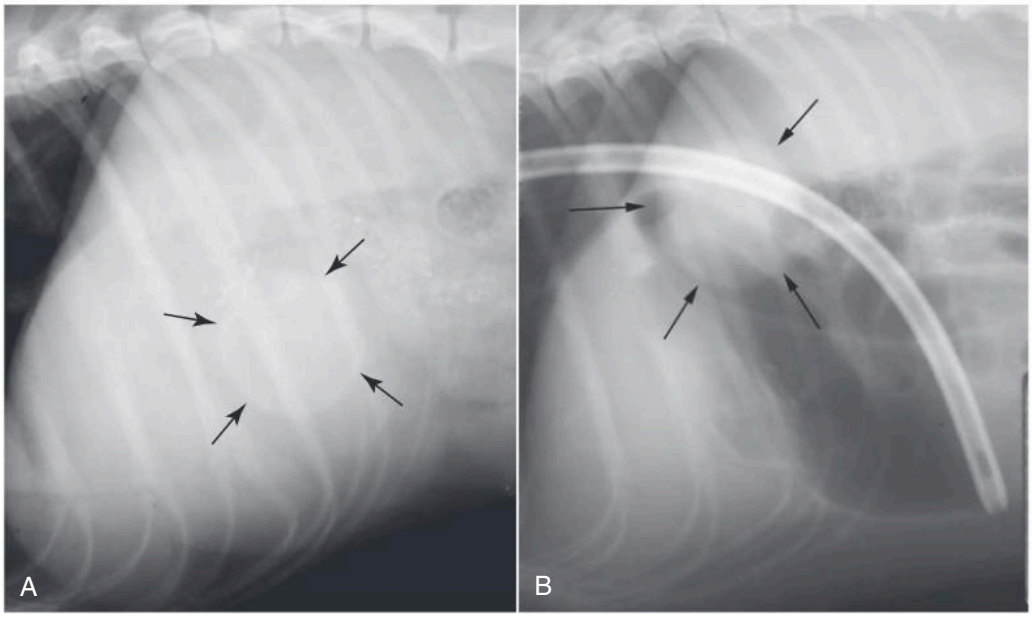


Fig. 45.28 A ball in the pyloric portion of the stomach (*black arrows*) is difficult to see on the right lateral view **(A)** because of fluid in the pylorus. In **B,** gas has been administered by a gastric tube, the ball (*black arrows*) is easier to see. Note the ball has moved to the fundus.

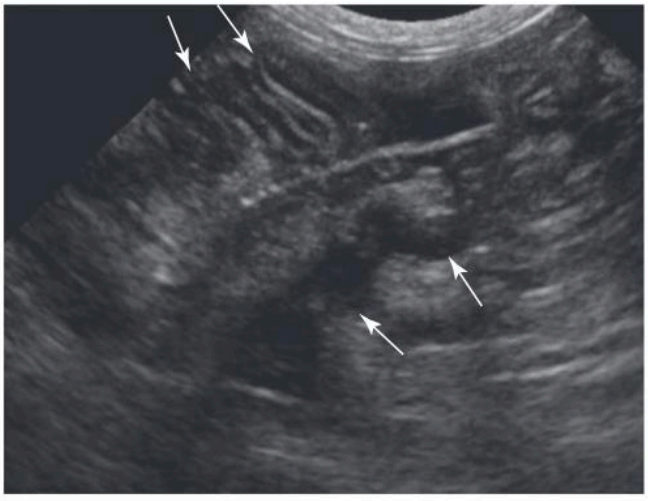


Fig. 45.29 Sagittal sonogram of the stomach of a cat with a luminal hyperechoic linear foreign object causing severe plication of the gastric wall (*white arrows*).

radiographic appearance of a gastric ulcer may vary depending on whether the ulcer is projected in profile, *en face*, or obliquely. The appearance of the ulcer may be altered further by gastric peristalsis. Manipulation of the patient during fluoroscopy allows a more complete and continuous evaluation of the margin and contour of the stomach. Double-contrast gastrography may also be of value because ulcers that are projected en face may be visible with double-contrast radiographic studies but are obscured with positive-contrast gastrography.[9]

Criteria have been established in human patients for the radiographic differentiation of benign and malignant gastric ulcers.[118–120] Thus, although contrast radiography may provide an excellent method for the recognition of gastric ulcers, infrequent use of single- and double-contrast gastrography, lack of fluoroscopy, and insufficient views all combine to limit the recognition of gastric ulcers in dogs and cats. In addition, experience is limited in differentiating benign and malignant gastric ulcers radiographically in dogs and cats. Ulceration is often associated with gastric carcinoma,[121,122] and gastric ulcers in dogs that are recognized on radiographs are often the result of neoplasia.[123] Thus, the radiographic recognition of a gastric ulcer should lead to strong consideration of neoplasia and further evaluation of the stomach with endoscopy and biopsy or by surgical exploration.

Some gastric ulcers may be detected sonographically (Fig. 45.30B) but many are not found.[48,124] Ultrasonographic features include the presence of a wall defect (crater) usually within the center of a locally thickened area of stomach wall. The thickened area may have loss of the normal layered appearance. Gastric fluid accumulation and decreased motility may also be noted. Additionally, central within the defect small hyperechogenicities with distal reverberation artifacts suggestive of gas may be noted in the gastric wall (pneumatosis) during an ultrasound examination.[125]

Gastric Bleeding

Gastrointestinal bleeding is a multifactorial disease and is suspected when the patient is vomiting blood-containing ingesta or fluid, or when digested blood is present in the feces. Survey radiographs may not demonstrate the cause of bleeding. Ultrasound or contrast radiography may demonstrate a thickening of the gastric wall[126] or a gastric ulcer as the site of the origin of bleeding; however, if no thickening or mass effect of the gastric wall is present, radiography and ultrasound may not be able to identify the precise site of bleeding and further imaging may be necessary. Gastrointestinal bleeding can be evaluated by scintigraphy using either intravenously administered ^{99m}technetium (^{99m}Tc)-labeled sulfur colloid or red blood cells. Scintigraphic studies using ^{99m}Tc-labeled red blood might be more sensitive than sulfur colloid studies as the labeled red blood cells circulate longer in the vascular system and therefore allow identification of sites of intermittent as well as acute bleeding.[127] The

downside of ^{99m}Tc sulfur colloid is that it is most sensitive in patients where active bleeding occurs as the sulfur colloid is rapidly taken up by the reticuloendothelial system and therefore does not allow detection of intermittent and chronic bleeding and in addition the uptake of the colloid by the reticuloendothelial system might hinder imaging of bleeding of gastrointestinal structures at the level of the liver and spleen.[75]

Gastric Neoplasia

Primary gastric neoplasia is rare in the dog and cat and no definitive underlying etiologies have been defined. Several types of benign and malignant gastric neoplasms occur and any region of the stomach may be involved. Polyps, also called glandular hyperplasia, hyperplastic or adenomatous polyp, adenomatous hyperplasia, or adenoma, may be clinically silent and most are found incidentally.[128,129] A variety of malignant gastric tumors have been described including carcinoma, adenocarcinoma, leiomyosarcoma, histiocytic sarcoma, fibrosarcoma lymphoma, mast cell, and gastric stromal tumor.[68,130,131] Gastric stromal tumors range in classification from benign to malignant. Adenocarcinoma is the most common malignant gastric tumor in dogs.[121,132] This tumor may occur in any region of the stomach but is found most often in the pyloric portion.[132,133] Gastric neoplasia occurs less frequently in the cat than in the dog,[134] and lymphosarcoma is the most common type of feline gastric neoplasm.[135]

The imaging appearance of gastric neoplasia varies and primarily depends on the size, shape, and location of the tumor. Inflammatory lesions can also result in thickening of the gastric wall[136] and have similar imaging findings as neoplastic lesions.[137,138] Furthermore, it is important to remember that the varying types of gastric tumors are difficult to differentiate based on imaging findings and therefore cytology or more commonly histopathology is required to differentiate inflammatory from neoplastic conditions and to categorize the tumor type.

The major radiographic feature of gastric neoplasia is that of a mass lesion that projects into the gastric lumen, creating a filling defect within the contrast medium. The more nodular and pedunculated the lesion, the easier it is to recognize it as a distinct mass (see Fig. 45.31). Larger masses may also lead to outflow obstruction.[139] Smaller mass lesions may be obscured completely by a relatively large volume of barium. Oblique projections, the conformation of the stomach, and peristaltic contractions may all contribute to obscuring some mass lesions of the stomach.

Tumors that are diffuse are more difficult to identify. Diffuse infiltrative lesions of the stomach wall may not produce distinct filling defects. Instead, they may alter the shape of the stomach and produce decreased motility of the involved area. If such diffuse lesions encircle a portion of the stomach, the radiographic appearance may be that of an annular narrowing or one in which the stomach has decreased distensibility in the affected area (see Fig. 45.31B, eFig. 45.14). Because of variations in appearance of the stomach created by peristalsis, persistence of a suspected abnormality on sequential radiographs is important. As stated earlier, the recognition of a gastric ulcer should also suggest the possibility of gastric neoplasia.

Gastric masses can be found on ultrasound examination of the stomach, thus often eliminating the need for radiographic contrast studies. However, it is important to remember that patients need to be repositioned to move the ingesta, fluid, and gas in the stomach to access all aspects of the gastric wall sonographically, and that gastric wall lesions might be missed if the stomach is filled with large amounts of gas or ingesta. Common ultrasound features include thickening of the stomach wall, loss or distortion of the normal layered appearance of the wall, and altered echogenicity and motility in the affected area (Fig. 45.32).[39–42,45,122,140,142] Although such lesions are most often associated with gastric neoplasia, similar changes have

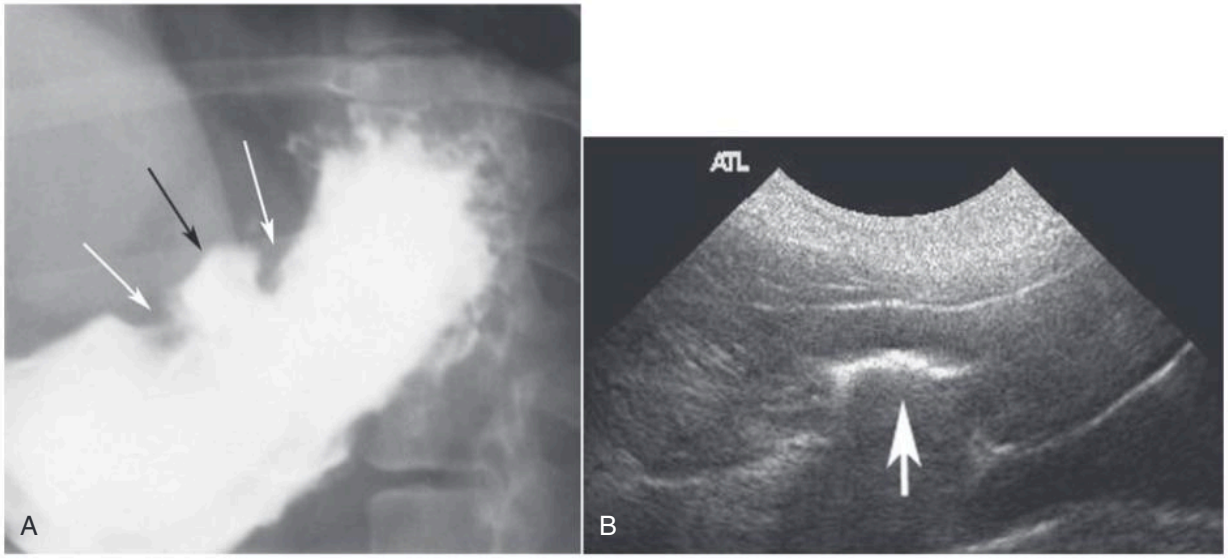
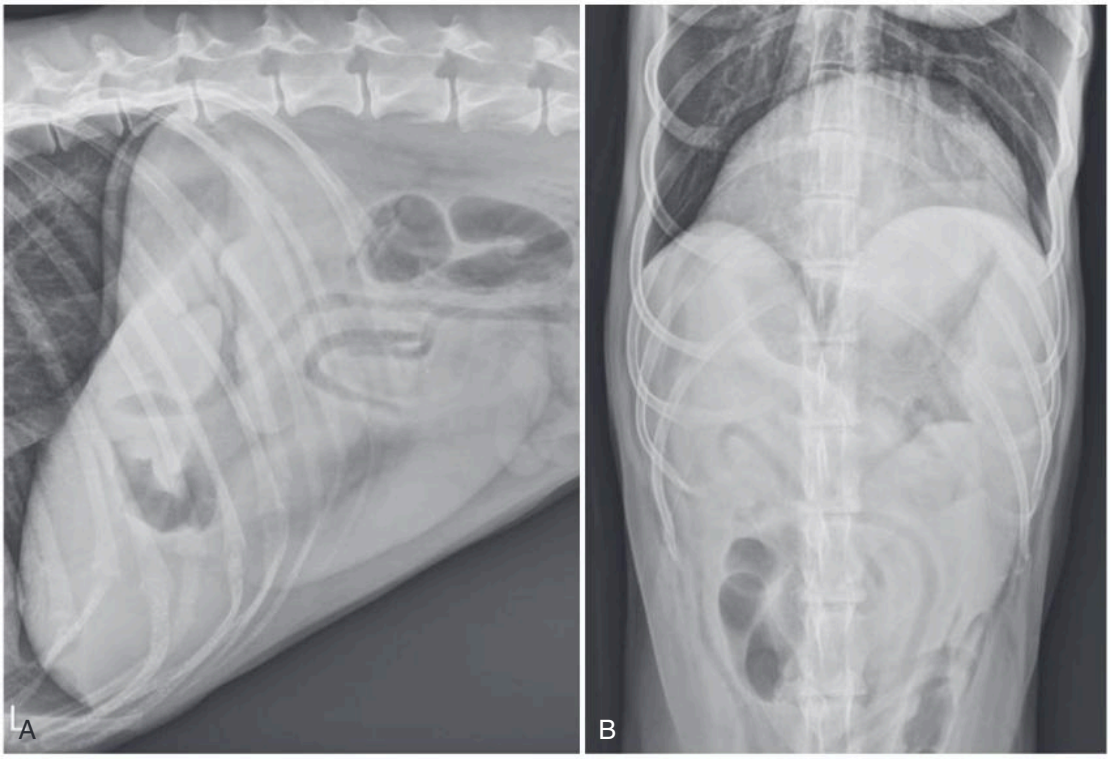


Fig. 45.30 **A,** Ventrodorsal oblique radiograph of the stomach of a dog with a gastric ulcer (*black arrow*). The filling defects protruding into the stomach (*white arrows*) represent the collar of the ulcer. **B,** Sagittal ultrasound image of the stomach of another dog. The pyloric region of the stomach is thickened, and layers are not identi fiable. The *white arrow* indicates a portion of the stomach wall that is focally thinner than the remainder. The mucosal surface of this area is hyperechoic. A large ulcer was found in this area at necropsy; the diagnosis was adenocarcinoma.



eFig. 45.14 Left lateral **(A)** and ventrodorsal **(B)** radiographs of the stomach of a dog with gastric lymphoma. The gastric wall is thickened with an angular appearance of the luminal gas which would be unusual for a luminal gas–fluid interface.

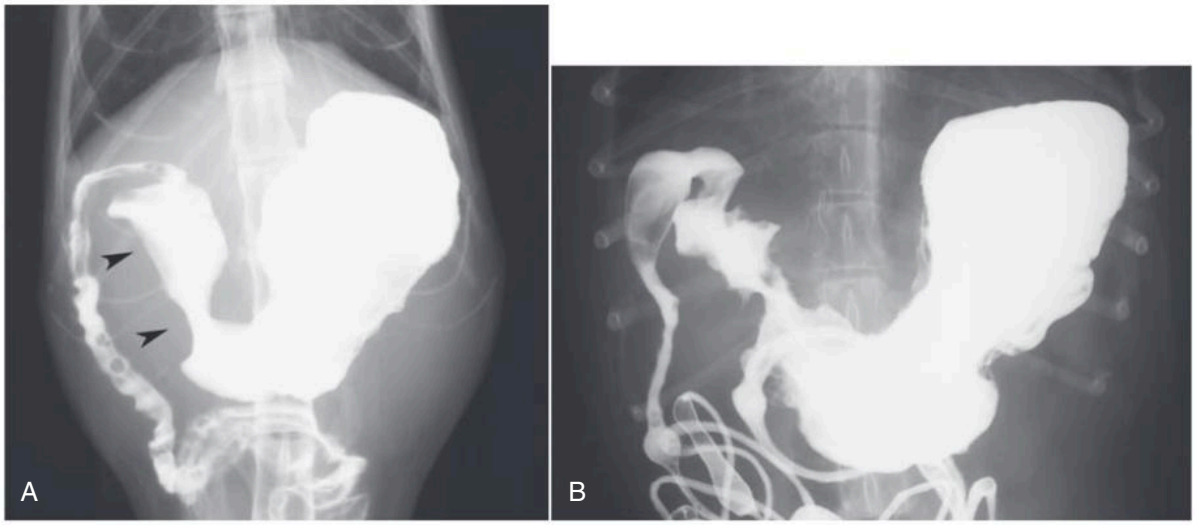


Fig. 45.31 **A,** Ventrodorsal barium gastrogram of a cat. A smooth filling defect is present from a mass along the greater curvature (*black arrowheads*). **B,** Ventrodorsal barium gastrogram of a dog. An annular mass encircles the pyloric portion and part of the body. This area failed to distend, and the abnormality persisted throughout the study. Final diagnosis was gastric adenocarcinoma.

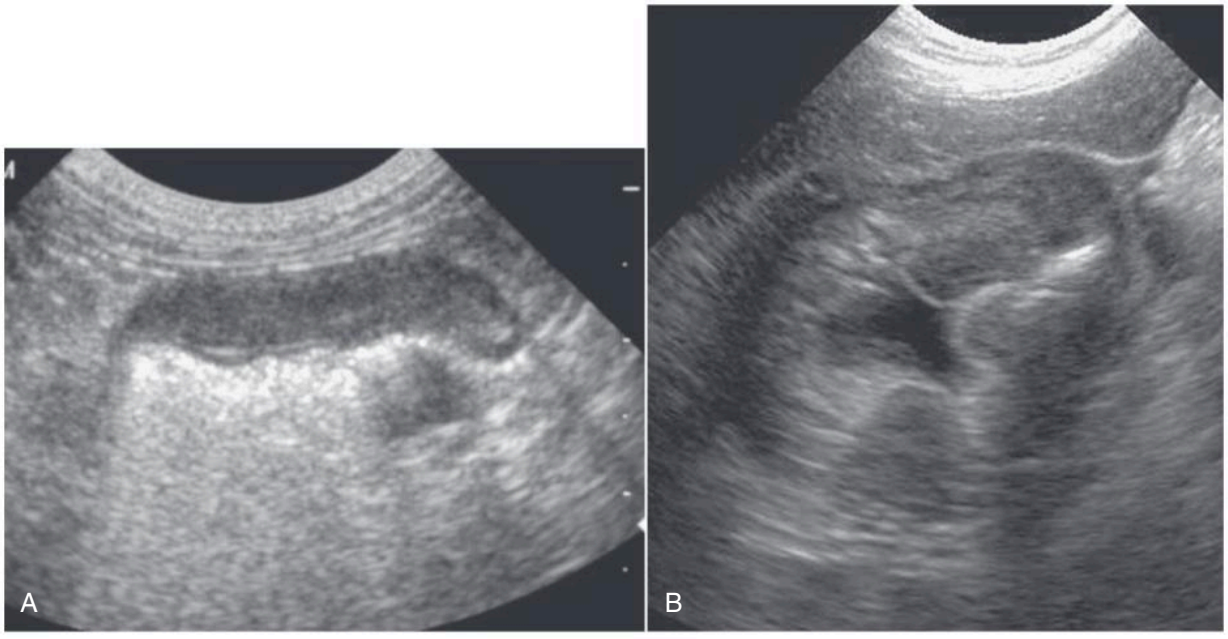


Fig. 45.32 Longitudinal ultrasound images of gastric neoplasia. **A,** Lymphosarcoma in the stomach wall of a cat. The stomach wall is thickened and hypoechoic and has lost the normal layered appearance. **B,** Suspected adenocarcinoma in the stomach wall of a dog. The wall is thickened uniformly and decreased in echogenicity. The normal layered appearance is disrupted. Caudal is to the *right,* and ventral is to the *top.*

been reported in dogs with pythiosis,[46] zygomycosis[142] and cats with eosinophilic gastritis[138] and gastritis secondary to actinomycosis.[137] Wall layering is usually preserved in gastric polyps but may have the appearance of a large sessile mass with the loss of wall layering.[143] Extension of the lesion through the serosal surface of the stomach has been reported in dogs with gastric carcinoma.[41] Another reported sonographic feature of gastric carcinoma is *pseudolayering* of the stomach wall, which is thought to be associated with uneven distribution of tumor in the layers of the stomach wall.[42,43] Instead of the five layers seen normally, a central, moderately echogenic zone between two lesser echogenic lines is seen.[43]

In dogs and cats with gastric neoplasia, maximal gastric wall thickness has been reported to range from 10 to 27 mm[40,43,52] and 8 to 25 mm, respectively,[39,44] whereas the reported normal gastric wall thickness is 3 to 5 mm in dogs and 2 to 5 mm in cats. Gastric wall measurements greater than 6 to 7 mm have been proposed as abnormal.[36] Although gastric wall thickening is an important abnormal finding, caution must be exercised when assessing wall thickness in a contracted, empty stomach

because a false-positive diagnosis of gastric mass can be made.[144] Distending the stomach with water may help distinguish true- and false-positive lesions, but real-time observation of gastric motility may be an easier way to distinguish the two because a lack of motility usually is seen in an abnormal wall segment.

Ultrasound also allows the evaluation of other organs including regional lymph nodes and the remainder of the small intestinal tract. Concurrent regional lymph node enlargement and ulceration of the affected area have been reported in both gastric carcinoma and lymphosarcoma.[40] Adenocarcinoma may spread to the liver in addition to regional lymph nodes. Sonographic lesions in the small intestine in combination with the gastric wall have a high likelihood to be secondary to lymphoma.[140] Cytologic or histopathologic evaluation is necessary for a definitive diagnosis of gastric wall lesions. Specimens can be obtained by ultrasound-guided fine-needle aspiration or tissue-core biopsy.[58,145]

Diffuse Diseases of the Stomach Wall

The stomach may be involved diffusely in a variety of nonneoplastic diseases that produce inflammation, edema, hypertrophy, atrophy, or mineralization. Acute gastritis may result from a variety of causes and is rarely associated with radiographic abnormalities. One of the forms of acute gastritis called *exercise-induced gastritis* is an important condition to remember as it is associated with a high morbidity and mortality in working dogs and sled dogs.[117] Chronic gastritis is diagnosed infrequently clinically and may also result from a variety of causes. Examples include chronic atrophic gastritis, chronic hypertrophic gastritis,[146,147] eosinophilic gastritis and pythiosis,[46] and zygomycosis.[142] Gastric wall edema can cause focal or diffuse thickening of the gastric wall and can be caused by a wide range of disease including inflammation of the stomach and pancreas, peritonitis, hypoalbuminemia, or neoplasia. It is important to differentiate gastric wall edema, which is primarily considered a benign disease process from gastric wall thickening caused by neoplasia.[47]

Imaging diagnosis of diffuse gastric disease is difficult and often no definitive answer can be given based on imaging findings (Fig. 45.33). Radiographically absent or diminished rugal folds, thickened rugal folds, nodules, or a thickened gastric wall may be seen with these diseases (see Fig. 45.33). Care must be taken when evaluating stomach wall thickness on survey radiographs. Fluid within the stomach may cause border effacement with the stomach wall, creating the illusion of increased thickness (Fig. 45.34). On contrast radiography, a relatively empty or mildly distended stomach, absence of a normal gastric rugal fold pattern, and multifocal filling defects can be noted. If a contrast radiographic study is performed,

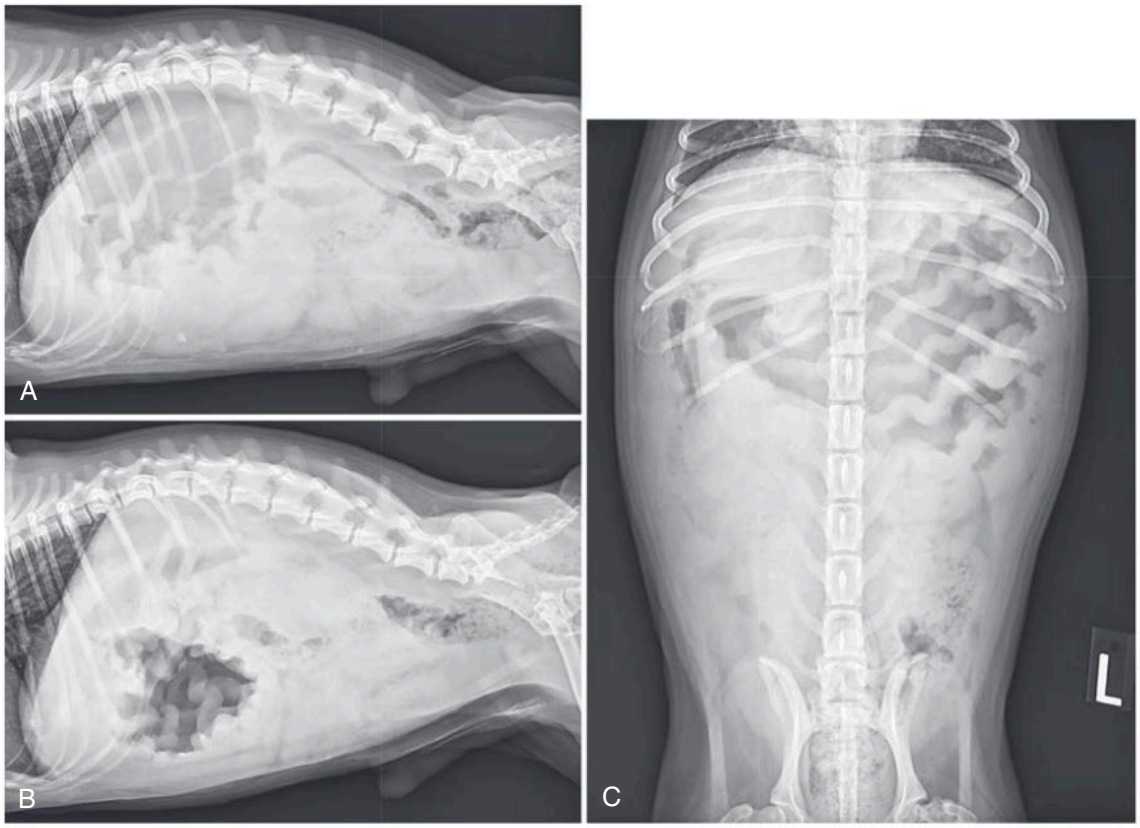


Fig. 45.33 Right and left lateral and ventrodorsal radiographs of the abdomen of a 2-year-old pug with an acute history of vomiting. The pug had previously been diagnosed with an extrahepatic shunt, portal hypoplasia, and microvascular dysplasia in all liver lobes. **A–C,** Diffuse thickening of the rugal folds is noted, which is suspected in part to be due to gastritis and gastric edema. A mildly reduced peritoneal detail is present secondary to a small volume of abdominal transudate. **C,** The rugal folds are larger in the body of the stomach and diminish in height towards the pyloric antrum, which would also be seen in normal rugal folds.



Fig. 45.34 Lateral survey radiograph of the abdomen of a cat with a thick gastric wall. The thickened wall is best visualized in the ventral midabdomen and is associated with a narrow, tubular, gas-filled lumen. Care should be taken when evaluating the stomach wall on survey radiographs because fluid in the lumen can silhouette with the wall, creating a false impression of wall thickening.

double-contrast radiography of the stomach is preferred as distension of the stomach allows to better assess the thickness of the gastric wall and rugal folds. Recent CT and ultrasound studies have described the appearance of gastric wall edema.[47,148] On ultrasound, thickening of the gastric wall, loss of wall layering, and a thickened medium echogenicity submucosal layer can be seen. On CT, a three-layer appearance of the gastric wall can be seen which is more apparent in the postcontrast images as the inner and outer layers are enhancing adjacent to the nonenhancing middle layer but can already be seen on precontrast studies (Fig. 45.35).

Gastric wall gas (pneumatosis) can sometimes be seen on radiography as well as ultrasound. A recent study suggests that similar to human patients, gastric pneumatosis can either occur secondary to life-threatening emphysematous gastritis or secondary to benign gastric emphysema. Both conditions have similar imaging features but have vastly different clinical presentations. All animals reported to have emphysematous gastritis had severe clinical signs including anorexia, hematemesis, lethargy, and leukocytosis and all animals had a poor outcome and were euthanized. All cases of gastric emphysema, which in human patients occurs secondary to mucosal rupture, had no or only mild gastrointestinal signs and resolved quickly on medical management (Fig. 45.36) without antibiotic treatment. In emphysematous gastritis and gastric emphysema, more than half of the gastric wall had gas present, which may help to differentiate these conditions from gastric ulceration.[149]

Ultrasonographic findings of inflammatory disease of the gastric wall are similar to those reported for gastric tumors and can range from increased gastric wall thickening with normal wall layering or loss of wall layer definition to altered echogenicity of the gastric wall.[39,137,138,150] Additionally, enlargement of regional lymph nodes has been noted with inflammatory disease of the stomach. As with most mass lesions discovered with ultrasound, biopsy is usually necessary for a definitive diagnosis.[151]

Soft tissue calcification may occur in association with chronic renal failure[52,150,152] or secondary to parasitic disease such as canine schistosomiasis due to *Heterobilharzia americana*.[153] In renal failure patients, mineralization of the gastric wall may be visible radiographically as thin, linear, mineralized opacities (Fig. 45.37).[150] Rugal mineralization is often more easily identified when the stomach is empty, and the mineralized mucosal fold pattern is more tightly grouped. Ultrasonographic findings of dogs with uremic gastropathy include thickened gastric wall and rugal folds and a hyperechoic zone at the mucosal/luminal interface caused by mucosal mineralization.[52] Ultrasound is likely more sensitive than radiography for detection of gastric lesions associated with uremia. *H. americana* is primarily found in the area of the Gulf Coast and south Atlantic states. Radiographically diffuse linear mineralizations can be noted throughout the small intestinal tract. On ultrasound, a thick, hyperechoic area of mineralization can be noted circumferentially through the submucosa and muscularis of the small intestinal tract.[153]

Although in many patients endoscopy is the method of choice for the diagnosis of gastric diseases, in some patients the mucosal surface of the stomach may be normal, leading to false-negative results by endoscopy.[151] Ultrasound demonstrates the morphologic features of the entire gastric wall unless the wall is hidden by gas or echogenic ingesta. In some patients, ultrasound may be more informative than endoscopy.[154]

Postoperative Stomach

Companion animals undergoing gastric surgery can have changes on postoperative imaging studies that mimic disease. It is often crucial when evaluating an imaging study to be familiar with the anatomic and physiologic changes that occur postoperatively as well as to be familiar with appropriate surgical techniques. One of the most common reasons for imaging the abdomen postoperatively include the evaluation of placed feeding tubes (gastric, gastrojejunal, etc.) or if the patient is not improving post gastric surgery as anticipated. Imaging procedures postoperatively can also be used to define a baseline appearance, allowing detection of early or late postoperative complications.

Radiography is often used as an initial technique to assess the extent of fluid and gas in the peritoneal cavity, position of the stomach, and presence and configuration of surgical clips, staples, drains, and tubes. Postoperative functional disturbances of motility of the stomach and intestinal tract, paralytic ileus, and vomiting are not uncommon.

If a subtotal gastrectomy is performed, no displacement of the stomach or stricture may be noted.[155] Similarly, if surgical gastric biopsies were performed, no displacement of the stomach would be expected. If a gastropexy was performed, which is a common procedure in dogs to prohibit GDV in the future by internally, permanently fixating the stomach to the abdominal wall in a way that gastric function is not affected, it is expected that the pylorus will be in close proximity to the right lateroventral abdominal wall. Radiographically, a caudoventral displacement of the pyloric antrum caudal to the last rib might be noted. If metallic staples were used for the gastropexy, they should be intact and the pyloric antrum should be near the staple line. The position of the stomach should remain

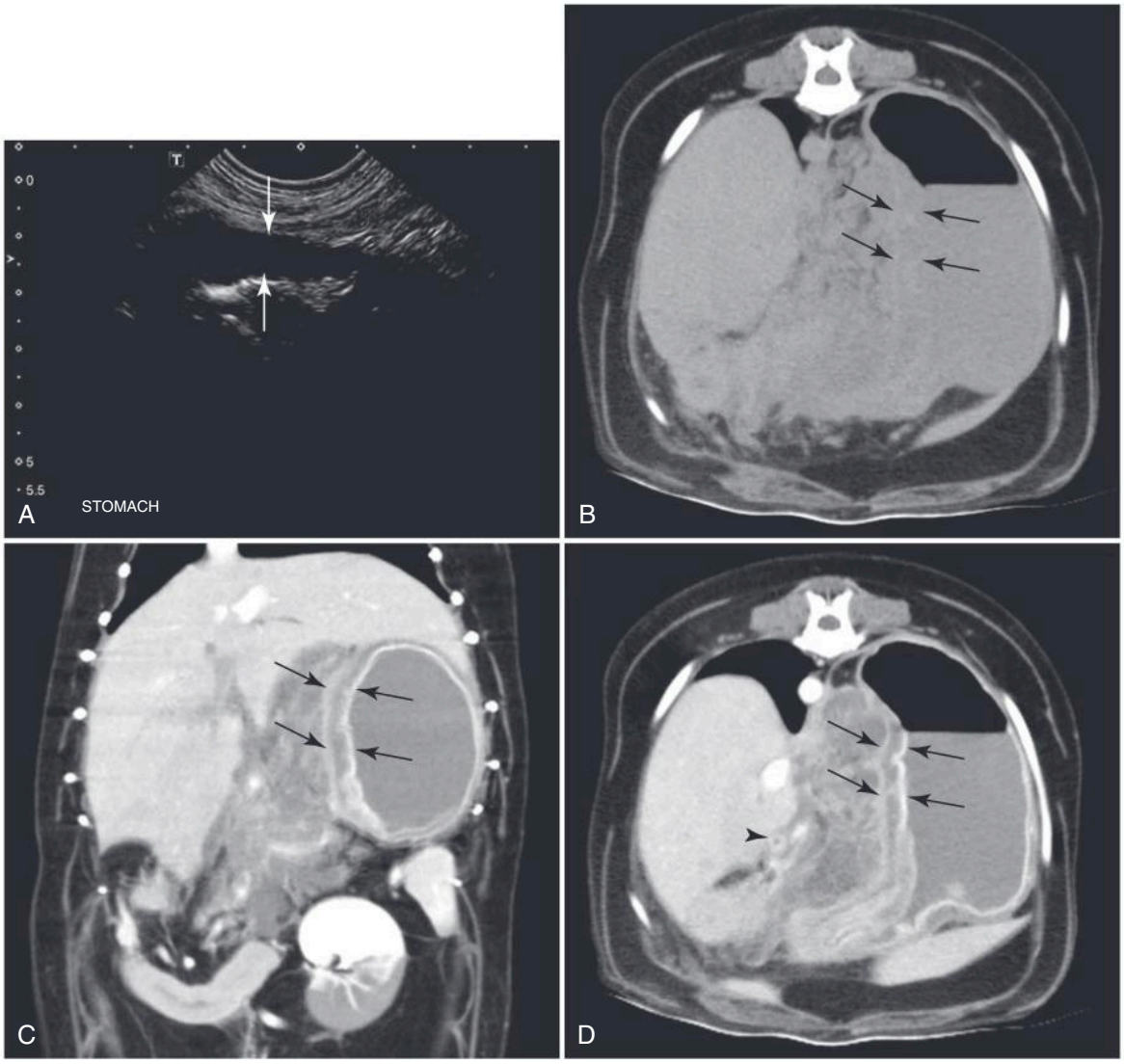


Fig. 45.35 Gastric wall edema in a dog with severe pancreatitis and portal vein thrombosis. **A,** Longitudinal ultrasonogram of the thickened hypoechoic gastric wall with loss of wall layering (*white arrows*). Computed tomography images with the dog in sternal recumbency illustrate **(B)** on precontrast administration, and **C—D,** post intravenous iodinated contrast agent injection images, the classic three-layered appearance of the gastric wall (*black arrows*). On **C—D,** the inner layer remains hypoattenuating, whereas the inner and outer layers are moderately contrast enhancing. On **B—D,** the far adjacent to the pancreas and lesser curvature of the stomach has a striated soft tissue attenuation secondary to peritonitis. **D,** A filling defect indicating thromboembolic disease is noted in the extrahepatic portal vein (*black arrowhead*) and similar lesions were seen in the intrahepatic portal veins.

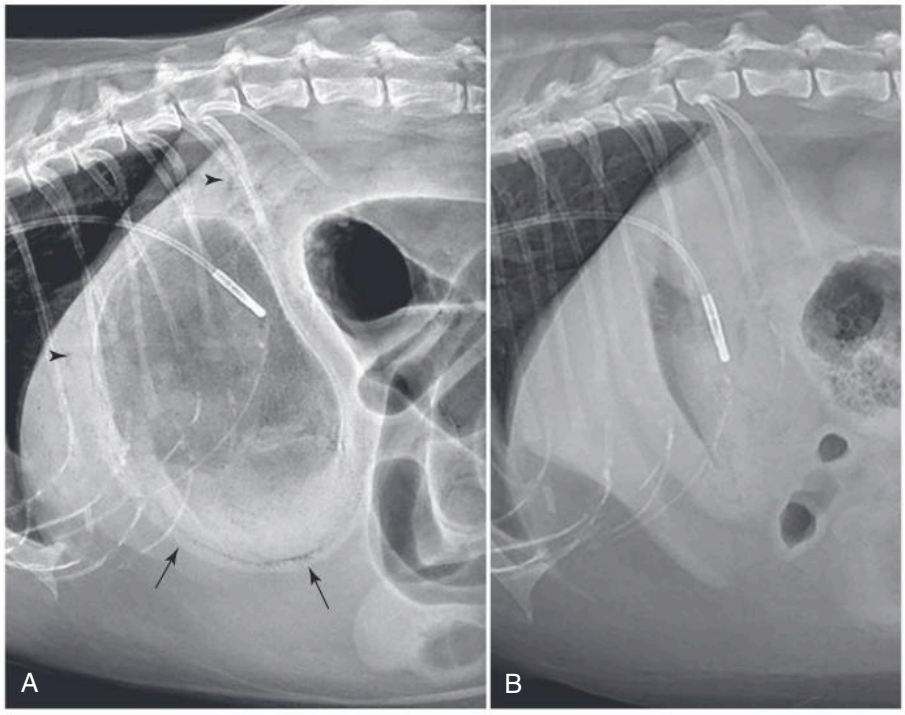


Fig. 45.36 Close-up lateral radiographs of the stomach of an 11-year-old cat, 3 days **(A)** and 4 days **(B)** after nasogastric feeding tube placement. **A,** Gas is diffusely summating with the gastric wall (*black arrows*), and as linear, branching structures with liver (*black arrowheads*). The gas in the liver was suspected to be in the portal vein branches. **B,** One day later, most of the gas in the liver and gastric wall has resolved with supportive medical management.



Fig. 45.37 Close-up ventrodorsal radiographs of a dog with gastric mineralization secondary to chronic renal failure. Thin, curvilinear, mineralized opacities that parallel the rugal folds of the stomach are caused by gastric calcification.

unchanged with distension of the stomach.[156] On ultrasound, gastropexy sites are easily identified, and most commonly a lack of sliding motion between the pyloric wall and the abdominal wall at the site of the gastropexy is suspected.[55,56,156]

It is also common to place gastric tubes using endoscopy and often no imaging procedures are required. However, the most common reason additional imaging might be performed is to evaluate whether the tube is misplaced submucosally, whether there is leakage at the tube site, or if inflammation at the skin surface is present and concern about extension into the peritoneal cavity exists. Submucosal placement or movement of the gastropexy tube may be noted using ultrasound. However, other imaging techniques might be chosen to further evaluate the site of the gastric tube placement. Radiography is often chosen as it provides a great overview and allows evaluation of the position of the stomach and tube relative to each other (Fig. 45.38). Additionally, iodinated contrast medium may be used to assess the patency and presence of leakage of the gastric tube (Fig. 45.39). Similarly, ultrasound might be used while a sterile saline solution is administered through the gastric tube. If leakage is present, contrast medium leakage may be noted on radiographs (see Fig. 45.39) or fluid extension outside the tube might be noted during the ultrasound examination.

Ultrasound is often chosen initially if fluid sampling is required, especially when a concern about septic peritonitis is present. If peritonitis is suspected post gastric surgery, the fat and mesentery adjacent to the stomach might be hyperechoic and additionally small to large quantities of fluid containing echogenic particles can be noted.

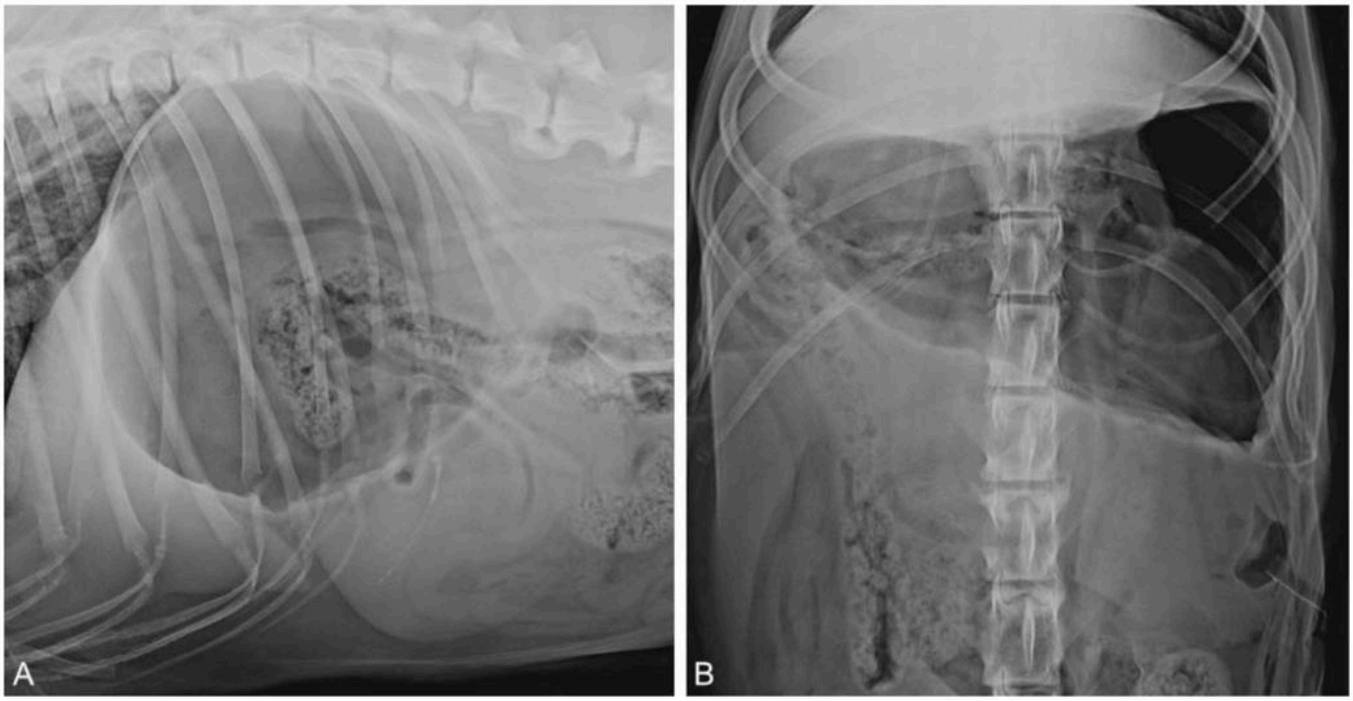


Fig. 45.38 Radiographs post gastrostomy tube placement in a dog. The dog presented with inflammation on the skin surface at the site of the tube placement and was evaluated for signs of tube leakage. **A,** Right lateral radiograph. The stomach has a pointed angle caudally toward the site of the gas-filled balloon of the gastric feeding tube. No free peritoneal gas or fluid is noted. **B,** Ventrodorsal radiograph. The stomach is altered in shape and extends along the left lateral abdominal wall further caudal and has a pointed angle. The gas-filled balloon of the gastric feeding tube is summating with the left lateral abdomen caudal of the gas dilated stomach.



Fig. 45.39 Right lateral radiograph of a dog with leakage at the site of the placement of the percutaneous endoscopic gastrostomy (PEG) tube. The PEG tube was placed to support adequate nutrition as the patient was not gaining weight and had recurrent pneumonia due to severe megaesophagus. Iodinated contrast medium was administered through the tube and leakage of contrast medium at the level of the gastric wall was present (*arrows*). The stomach has an abnormal shape, which is commonly seen post gastric tube placement or gastropexy.

Acknowledgment

With special thanks to prior authors of this chapter for their contributions.

REFERENCES

1. Evans H, De Lahunta A. *Miller's Anatomy of the Dog*. 4th ed. St. Louis: Saunders; 2013.
2. Nickel R, Schummer A, Seiferle E. *The Viscera of the Domestic Mammals*. Berlin, Heidelberg: Springer; 1979.
3. Doom M, de Rooster H, van Bergen T, et al. Morphology of the canine omentum part 2: the omental bursa and its compartments materialized and explored by a novel technique. *Anat Histol Embryol*. 2016;45:28–36.
4. Armbrust LJ, Biller DS, Hoskinson JJ. Case examples demonstrating the clinical utility of obtaining both right and left lateral abdominal radiographs in small animals. *J Am Anim Hosp Assoc*. 2000;36:531–536.
5. Grandage J. The radiological appearance of stomach gas in the dog. *Aust Vet J*. 1974;50:529–532.
6. Brawner Jr WR, Bartels JE. Contrast radiography of the digestive tract. Indications, techniques, and complications. *Vet Clin North Am Small Anim Pract*. 1983;13:599–626.
7. Root CR. Interpretation of abdominal survey radiographs. *Vet Clin North Am*. 1974;4:763–803.
8. Arnbjerg J. Gastric emptying time in the dog and cat. *J Am Anim Hosp Assoc*. 1992;28:77–81.
9. O'Brien TR. *Radiographic Diagnosis of Abdominal Disorders in the Dog and Cat: Radiographic Interpretation, Clinical Signs, Pathophysiology*. WB Saunders; 1978.
10. Miyabayashi T, Morgan JP. Upper gastrointestinal examinations: a radiographic study of clinically normal beagle puppies. *J Small Anim Pract*. 1991;32:83–88.
11. Love NE. The appearance of the canine pyloric region in right versus left lateral recumbent radiographs. *Vet Radiol Ultrasound*. 1993;34:169–170.

12. Jakovljevic S, Gibbs C. Radiographic assessment of gastric mucosal fold thickness in dogs. *Am J Vet Res*. 1993;54: 1827–1830.
13. Evans SM, Laufer I. Double contrast gastrography in the normal dog. *Veterinary Radiology*. 1981;22:2–9.
14. Evans SM, Biery DN. Double contrast gastrography in the cat. *Veterinary Radiology*. 1983;24:3–5.
15. Heng HG, Wrigley RH, Kraft SL, et al. Fat is responsible for an intramural radiolucent band in the feline stomach wall. *Vet Radiol Ultrasound*. 2005;46:54–56.
16. Bargai U. The effect of xylazine hydrochloride on the radiographic appearance of the stomach and intestine in the dog. *Veterinary Radiology*. 1982;23:60–63.
17. Gomez JA. The gastrointestinal contrast study. Methods and interpretation. *Vet Clin North Am*. 1974;4:805–842.
18. Hogan PM, Aronson E. Effect of sedation on transit time of feline gastrointestinal contrast studies. *Veterinary Radiology*. 1988;29:85–88.
19. Steyn PF, Twedt D, Toombs W. The effect of intravenous diazepam on solid phase gastric emptying in normal cats. *Vet Radiol Ultrasound*. 1997;38:469–473.
20. Scrivani PV, Bednarski RM, Myer CW. Effects of acepromazine and butorphanol on positive-contrast upper gastrointestinal tract examination in dogs. *Am J Vet Res*. 1998;59:1227–1233.
21. Bowlus RA, Biller DS, Armbrust LJ, et al. Clinical utility of pneumogastrography in dogs. *J Am Anim Hosp Assoc*. 2005;41:171–178.
22. Agut A, Sanchez-Valverde MA, Torrecillas FE, et al. Iohexol as a gastrointestinal contrast medium in the cat. *Vet Radiol Ultrasound*. 1994;35:164–168.
23. Allan FJ, Guilford WG, Robertson ID, et al. Gastric emptying of solid radiopaque markers in healthy dogs. *Vet Radiol Ultrasound*. 1996;37:336–344.
24. Allan GS, Rendano VT, Quick CB, et al. Gastrografin as a gastrointestinal contrast medium in the cat. *Veterinary Radiology*. 1979;20:110–116.
25. Burns J, Fox SM. The use of a barium meal to evaluate total gastric emptying time in the dog. *Veterinary Radiology*. 1986;27:169–172.
26. Chandler ML, Guilford G, Lawoko CR. Radiopaque markers to evaluate gastric emptying and small intestinal transit time in healthy cats. *J Vet Intern Med*. 1997;11:361–364.
27. Miyabayashi T, Morgan JP. Gastric emptying in the normal dog: a contrast radiographic technique. *Veterinary Radiology*. 1984;25:187–191.
28. Root CR, Morgan JP. Contrast radiography of the upper gastrointestinal tract in the dog. A comparison of micropulverized barium sulfate and U.S.P. barium sulfate suspensions in clinically normal dogs. *J Small Anim Pract*. 1969;10:279–286.
29. Williams J, Biller DS, Miyabayashi T, et al. Evaluation of iohexol as a gastrointestinal contrast medium in normal cats. *Vet Radiol Ultrasound*. 1993;34:310–314.
30. Guilford WG, Lawoko CR, Allan FJ. Accuracy of localizing radiopaque markers by abdominal radiography and correlation between their gastric emptying rate and that of a canned food in dogs. *Am J Vet Res*. 1997;58: 1359–1363.
31. Wallack ST. *The Handbook of Veterinary Contrast Radiography*. Solana Beach, CA: San Diego Veterinary Imaging, Inc.; 2003.
32. Funkquist B, Garmer L. Pathogenetic and therapeutic aspects of torsion of the canine stomach. *J Small Anim Pract*. 1967;8:523–532.
33. Gibbs C, Pearson H. The radiological diagnosis of gastrointestinal obstruction in the dog. *J Small Anim Pract*. 1973;14:61–82.
34. Gue M, Fioramonti J, Frexinos J, et al. Influence of acoustic stress by noise on gastrointestinal motility in dogs. *Dig Dis Sci*. 1987;32:1411–1417.
35. Hall JA, Willer RL, Seim 3rd HB, et al. Gastric emptying of nondigestible radiopaque markers after circumcostal gastropexy in clinically normal dogs and dogs with gastric dilatation-volvulus. *Am J Vet Res*. 1992;53:1961–1965.
36. Penninck DG, Nyland TG, Fisher PE, et al. Ultrasonography of the normal canine gastrointestinal tract. *Veterinary Radiology*. 1989;30:272–276.
37. Sanderson JJ, Boysen SR, McMurray JM, et al. The effect of fasting on gastrointestinal motility in healthy dogs as assessed by sonography. *JVECC*. 2017;27:645–650.
38. Gory G, Rault DN, Gatel L, et al. Ultrasonographic characteristics of the abdominal esophagus and cardia in dogs. *Vet Radiol Ultrasound*. 2014;55:552–560.
39. Grooters AM, Biller DS, Ward H, et al. Ultrasonographic appearance of feline alimentary lymphoma. *Vet Radiol Ultrasound*. 1994;35:468–472.
40. Kaser-Hotz B, Hauser B, Arnold P. Ultrasonographic findings in canine gastric neoplasia in 13 patients. *Vet Radiol Ultrasound*. 1996;37:51–56.
41. Lamb CR, Grierson J. Ultrasonographic appearance of primary gastric neoplasia in 21 dogs. *J Small Anim Pract*. 1996;40:211–215.
42. Penninck DG. Characterization of gastrointestinal tumors. *Vet Clin North Am Small Anim Pract*. 1998;28:777–797.
43. Penninck DG, Moore AS, Gliatto J. Ultrasonography of canine gastric epithelial neoplasia. *Vet Radiol Ultrasound*. 1998;39:342–348.
44. Penninck DG, Moore AS, Tidwell AS, et al. Ultrasonography of alimentary lymphosarcoma in the cat. *Vet Radiol Ultrasound*. 1994;35:299–306.
45. Rivers BJ, Walter PA, Johnston GR, et al. Canine gastric neoplasia: utility of ultrasonography in diagnosis. *J Am Anim Hosp Assoc*. 1997;33:144–155.
46. Graham JP, Newell SM, Roberts GD, et al. Ultrasonographic features of canine gastrointestinal pythiosis. *Vet Radiol Ultrasound*. 2000;41:273–277.
47. Murakami M, Heng HG, Lim CK, et al. Ultrasonographic features of presumed gastric wall edema in 14 dogs with pancreatitis. *J Vet Intern Med*. 2019;33:1260–1265.
48. Pennick D, Matz M, Tidwell A. Ultrasonography of gastric ulceration in the dog. *Vet Radiol Ultrasound*. 1997;38: 308–312.
49. Penninck DG, Nyland TG, Kerr LY, et al. Ultrasonographic evaluation of gastrointestinal diseases in small animals. *Veterinary Radiology*. 1990;31:134–141.
50. Tidwell AS, Penninck DG. Ultrasonography of gastrointestinal foreign bodies. *Vet Radiol Ultrasound*. 1992;33:160–169.
51. Biller DS, Partington BP, Miyabayashi T, et al. Ultrasonographic appearance of chronic hypertrophic pyloric gastropathy in the dog. *Vet Radiol Ultrasound*. 1994;35: 30–33.
52. Grooters AM, Miyabayashi T, Biller DS, et al. Sonographic appearance of uremic gastropathy in four dogs. *Vet Radiol Ultrasound*. 1994;35:35–40.
53. Huml RA, Konde LJ, Sellon RK, et al. Gastrogastric intussusception in a dog. *Vet Radiol Ultrasound*. 1992;33:150–153.
54. Watson PJ. Gastroduodenal intussusception in a young dog. *J Small Anim Pract*. 1997;38:163–167.
55. Tanno F, Weber U, Wacker C, et al. Ultrasonographic comparison of adhesions induced by two different methods of gastropexy in the dog. *J Small Anim Pract*. 1998;39:432–436.
56. Wacker CA, Weber UT, Tanno F, et al. Ultrasonographic evaluation of adhesions induced by incisional gastropexy in 16 dogs. *J Small Anim Pract*. 1998;39:379–384.

57. Mack RM, Staiger B, Langlois DK, et al. Development and characterization of a technique for percutaneous radiologic gastrojejunostomy tube placement in the dog. *J Vet Emerg Crit Care (San Antonio)*. 2016;26:646–653.
58. Penninck DG, Crystal MA, Matz ME, et al. The technique of percutaneous ultrasound guided fine-needle aspiration biopsy and automated microcore biopsy in small animal gastrointestinal diseases. *Vet Radiol Ultrasound*. 1993;34:433–436.
59. Pal M, Singh P, Tayal R, et al. A comparative study of two-dimensional and three-dimensional ultrasonography in evaluation of gastric affections in dogs. *Vet World*. 2015;8:707–712.
60. Gaschen L, Kircher P, Wolfram K. Endoscopic ultrasound of the canine abdomen. *Vet Radiol Ultrasound*. 2007;48:338–349.
61. Lamb CR. Abdominal ultrasonography in small animals: intestinal tract and mesentery, kidneys, adrenal glands, uterus and prostate. *J Small Anim Pract*. 1990;31:295–304.
62. Seiler GS, Cohen EB, d'Anjou MA, et al. ACVR and ECVDI consensus statement for the standardization of the abdominal ultrasound examination. *Vet Radiol Ultrasound*. 2022;63(6):661–674.
63. Larson MM, Biller DS. Ultrasound of the gastrointestinal tract. *Vet Clin North Am Small Anim Pract*. 2009;39:747–759.
64. Couturier L, Rault D, Gatel L, et al. Ultrasonographic characterization of the feline cardia and pylorus in 34 healthy cats and three abnormal cats. *Vet Radiol Ultrasound*. 2012;53:342–347.
65. Newell SM, Graham JP, Roberts GD, et al. Sonography of the normal feline gastrointestinal tract. *Vet Radiol Ultrasound*. 1999;40:40–43.
66. Goggin JM, Biller DS, Debey BM, et al. Ultrasonographic measurement of gastrointestinal wall thickness and the ultrasonographic appearance of the ileocolic region in healthy cats. *J Am Anim Hosp Assoc*. 2000;36:224–228.
67. Hoey S, Drees R, Hetzel S. Evaluation of the gastrointestinal tract in dogs using computed tomography. *Vet Radiol Ultrasound*. 2013;54:25–30.
68. von Babo V, Eberle N, Mischke R, et al. Canine non-hematopoietic gastric neoplasia. Epidemiologic and diagnostic characteristics in 38 dogs with post-surgical outcome of five cases. *Tierarztl Prax Ausg K Kleintiere Heimtiere*. 2012;40:243–249.
69. Murakami M, Heng HG, Sola M. CT features of confirmed and presumed gastric wall edema in dogs. *Vet Radiol Ultrasound*. 2022;63:711–718.
70. Terragni R, Vignoli M, Rossi F, et al. Stomach wall evaluation using helical hydro-computed tomography. *Vet Radiol Ultrasound*. 2012;53:402–405.
71. Hornof WJ, Koblik PD, Strombeck DR, et al. Scintigraphic evaluation of solid-phase gastric emptying in the dog. *Veterinary Radiology*. 1989;30:242–248.
72. Kunze CP, Hoskinson JJ, Butine MD, et al. Evaluation of solid phase radiolabels of dog food for gastric emptying. *Vet Radiol Ultrasound*. 1999;40:169–173.
73. Goggin JM, Hoskinson JJ, Kirk CA, et al. Comparison of gastric emptying times in healthy cats simultaneously evaluated with radiopaque markers and nuclear scintigraphy. *Vet Radiol Ultrasound*. 1999;40:89–95.
74. Lester NV, Roberts GD, Newell SM, et al. Assessment of barium impregnated polyethylene spheres (Bipsr) as a measure of solid-phase gastric emptying in normal dogs—comparison to scintigraphy. *Vet Radiol Ultrasound*. 1999;40:465–471.
75. Metcalf MR. Scintigraphic gastrointestinal bleeding localization with 99mTc-labeled red blood cells. *Veterinary Radiology*. 1987;28:96–100.
76. Suter PF. Radiographic diagnosis of liver disease in dogs and cats. *Vet Clin North Am Small Anim Pract*. 1982;12:153–173.
77. Worth AJ, Machon RG. Traumatic diaphragmatic herniation: pathophysiology and management, Compendium on Continuing Education for the Practicing Veterinarian. *Compend Contin Educ Pract Vet*. 2005;27(3):178–180.
78. Hoddinott K. Traumatic diaphragmatic hernia in a 5-month-old boxer dog. *Can Vet J*. 2013;54:507–509.
79. Zarelli M, Carrillo JD, Soler M, et al. What is your diagnosis? Tension gastrothorax. *J Am Vet Med Assoc*. 2010;236:733–734.
80. Ellison GW, Lewis DD, Phillips L, et al. Esophageal hiatal hernia in small animals: literature review and a modified surgical technique. *JAAHA*. 1987;391.
81. Miles KG, Pope ER, Jergens AE. Paraesophageal hiatal hernia and pyloric obstruction in a dog. *J Am Vet Med Assoc*. 1988;193:1437–1439.
82. Burns CG, Bergh MS, McLoughlin MA. Surgical and nonsurgical treatment of peritoneopericardial diaphragmatic hernia in dogs and cats: 58 cases (1999–2008). *J Am Vet Med Assoc*. 2013;242:643–650.
83. Lee H, Yeon S, Lee H, et al. Ultrasonographic diagnosis—pylorogastric intussusception in a dog. *Vet Radiol Ultrasound*. 2005;46:317–318.
84. Choi J, Keh S, Kim T, et al. Ultrasonographic findings of pylorogastric intussusceptions in two dogs. *J Vet Sci*. 2012;13:215–217.
85. de Battisti A, Toscano MJ, Formaggini L. Gastric foreign body as a risk factor for gastric dilatation and volvulus in dogs. *J Am Vet Med Assoc*. 2012;241:1190–1193.
86. Glickman LT, Glickman NW, Schellenberg DB, et al. Non-dietary risk factors for gastric dilatation-volvulus in large and giant breed dogs. *J Am Vet Med Assoc*. 2000;217:1492–1499.
87. Glickman LT, Glickman NW, Schellenberg DB, et al. Incidence of and breed-related risk factors for gastric dilatation-volvulus in dogs. *J Am Vet Med Assoc*. 2000;216:40–45.
88. Grange AM, Clough W, Casale SA. Evaluation of splenectomy as a risk factor for gastric dilatation-volvulus. *J Am Vet Med Assoc*. 2012;241:461–466.
89. Raghavan M, Glickman N, McCabe G, et al. Diet-related risk factors for gastric dilatation-volvulus in dogs of high-risk breeds. *J Am Anim Hosp Assoc*. 2004;40:192–203.
90. Schellenberg D, Yi Q, Glickman NW, et al. Influence of thoracic conformation and genetics on the risk of gastric dilatation-volvulus in Irish setters. *J Am Anim Hosp Assoc*. 1998;34:64–73.
91. Mazin RM, Christman A, Pasek A. Veterinary medicine today what is your diagnosis? *J Am Vet Med Assoc*. 2002;221:489–490.
92. Bredal WP, Eggertsdottir AV, Austefjord O. Acute gastric dilatation in cats: a case series. *Acta Vet Scand*. 1996;37:445–451.
93. Formaggini L, Schmidt K, De Lorenzi D. Gastric dilatation-volvulus associated with diaphragmatic hernia in three cats: clinical presentation, surgical treatment and presumptive aetiology. *J Feline Med Surg*. 2008;10:198–201.
94. Aslanian ME, Sharp CR, Garneau MS. Gastric dilatation and volvulus in a brachycephalic dog with hiatal hernia. *J Small Anim Pract*. 2014;55:535–537.
95. Funkquist B. Gastric torsion in the dog-I. Radiological picture during nonsurgical treatment related to the pathological anatomy and to the further clinical course. *J Small Anim Pract*. 1979;20:73–91.

96. Kneller SK. Radiographic interpretation of the gastric dilatation-volvulus complex in the dog. *JAAHA*. 1976;12: 154–157.
97. Mackenzie G, Barnhart M, Kennedy S, et al. A retrospective study of factors influencing survival following surgery for gastric dilatation-volvulus syndrome in 306 dogs. *J Am Anim Hosp Assoc*. 2010;46:97–102.
98. Frendin J, Funkquist B, Stavenborn M. Gastric displacement in dogs without clinical signs of acute dilatation. *J Small Anim Pract*. 1988;29:775–779.
99. Fischetti AJ, Saunders HM, Drobatz KJ. Pneumatosis in canine gastric dilatation-volvulus syndrome. *Vet Radiol Ultrasound*. 2004;45:205–209.
100. Carroll K, Wallace M, Hill T, et al. Pyloric outflow obstruction secondary to sclerosing encapsulating peritonitis in a dog. *Aust Vet J*. 2020;98:11–16.
101. Rhodes WH, Rad MMSV, Brodey RS. The differential diagnosis of pyloric obstructions in the dog. *Veterinary Radiology*. 1965;6:65–74.
102. Weingart C, Kohn B. [Zinc intoxication in a Yorkshire Terrier due to Euro cent ingestion]. *Schweiz Arch Tierheilkd*. 2009;151:75–81.
103. Meurs KM, Breitschwerdt EB, Baty CJ, et al. Postsurgical mortality secondary to zinc toxicity in dogs. *Vet Hum Toxicol*. 1991;33:579–583.
104. Torrance AG, Fulton Jr RB. Zinc-induced hemolytic anemia in a dog. *J Am Vet Med Assoc*. 1987;191:443–444.
105. Rossmeissl EM, Palmer KG, Hoelzler MG, et al. Multiple magnet ingestion as a cause of septic peritonitis in a dog. *J Am Anim Hosp Assoc*. 2011;47:56–59.
106. Hickey MC, Magee A. Gastrointestinal tract perforations caused by ingestion of multiple magnets in a dog. *J Vet Emerg Crit Care*. 2011;21:369–374.
107. Friday S, Murphy C, Lopez D, et al. Gorilla glue ingestion in dogs: 22 cases (2005–2019). *J Am Anim Hosp Assoc*. 2021;57(3):121–127.
108. Tyrrell D, Beck C. Survey of the use of radiography vs. ultrasonography in the investigation of gastrointestinal foreign bodies in small animals. *Vet Radiol Ultrasound*. 2006;47:404–408.
109. Shanaman MM, Schwarz T, Gal A, et al. Comparison between survey radiography, B-mode ultrasonography, contrast-enhanced ultrasonography and contrast-enhanced multi-detector computed tomography findings in dogs with acute abdominal signs. *Vet Radiol Ultrasound*. 2013;54:591–604.
110. Cotran RS, Robbins SL, Kumar V, et al. *Robbins Pathologic Basis of Disease*. 5th ed. Philadelphia: Saunders; 1994.
111. Howard EB, Sawa TR, Nielsen SW, et al. Mastocytoma and gastroduodenal ulceration. Gastric and duodenal ulcers in dogs with mastocytoma. *Pathol Vet*. 1969;6:146–158.
112. van der Gaag I, van Niel MH, Belshaw BE, et al. Gastric granulomatous cryptococcosis mimicking gastric carcinoma in a dog. *Vet Q*. 1991;13:185–190.
113. Stanton ME, Bright RM. Gastroduodenal ulceration in dogs. Retrospective study of 43 cases and literature review. *J Vet Intern Med*. 1989;3:238–244.
114. Jones RD, Baynes RE, Nimitz CT. Nonsteroidal anti-inflammatory drug toxicosis in dogs and cats: 240 cases (1989–1990). *J Am Vet Med Assoc*. 1992;201:475–477.
115. Jankowski M, Spużak J, Kubiak K, et al. Risk factors of gastric ulcers in dogs. *Pakistan Veterinary J*. 2015;35:93–97.
116. Dowdle SM, Joubert KE, Lambrechts NE, et al. The prevalence of subclinical gastroduodenal ulceration in Dachshunds with intervertebral disc prolapse. *J S Afr Vet Assoc*. 2003;74:77–81.
117. Davis MS, Williamson KK. Gastritis and gastric ulcers in working dogs. *Front Vet Sci*. 2016;3:30.
118. Nelson SW. The discovery of gastric ulcers and the differential diagnosis between benignancy and malignancy. *Radiol Clin North Am*. 1969;7:5–25.
119. Zboralske FF. Gastric ulcer. In: Margulis AR, Burhenne HJ, eds. *Alimentary Tract Roentgenology*. St Louis: CV Mosby; 1967:475–487.
120. Porcher P, Buffard P. Malignancy of the stomach. In: Margulis AR, Burhenne HJ, eds. *Alimentary Tract Roentgenology*. St Louis: CV Mosby; 1967:488–521.
121. Sautter JH, Hanlon GF. Gastric neoplasms in the dog: a report of 20 cases. *J Am Vet Med Assoc*. 1975;166:691–696.
122. Hayden DW, Nielsen SW. Canine alimentary neoplasia. *Zentralblatt für Veterinärmedizin Reihe A*. 2010;20: 1–22.
123. Barber DL. Radiographic aspects of gastric ulcers in dogs. *Veterinary Radiology*. 1982;23:109–116.
124. Liptak JM, Hunt GB, Barrs VR, et al. Gastroduodenal ulceration in cats: eight cases and a review of the literature. *J Feline Med Surg*. 2002;4:27–42.
125. Lang LG, Greatting HH, Spaulding KA. Imaging diagnosis—gastric pneumatosis in a cat. *Vet Radiol Ultrasound*. 2011;52:658–660.
126. Londono LA, Specht AJ, VanderHart DJ, et al. What is your diagnosis? Gastric wall hemorrhage secondary to anticoagulant rodenticide intoxication. *J Am Vet Med Assoc*. 2015;247:243–245.
127. Alavi A, Dann RW, Baum S, et al. Scintigraphic detection of acute gastrointestinal bleeding. *Radiology*. 1977;124: 753–756.
128. Gualtieri M, Monzeglio M. Gastrointestinal polyps in small animals. *European Journal of Comparative Gastroenterology*. 1996;1:1–11.
129. van der Gaag I. The histological appearance of peroral gastric biopsies in clinically healthy and vomiting dogs. *Can J Vet Res*. 1988;52:67–74.
130. Gualtieri M, Monzeglio MG, Scanziani E. Gastric neoplasia. *Vet Clin North Am Small Anim Pract*. 1999;29:415–440.
131. Willard MD. Alimentary neoplasia in geriatric dogs and cats. *Vet Clin North Am Small Anim Pract*. 2012;42:693–706.
132. Murray M, Robinson PB, McKeating FJ, et al. Primary gastric neoplasia in the dog: a clinico-pathological study. *Vet Rec*. 1972;91:474–479.
133. Patnaik AK, Hurvitz AI, Johnson GF. Canine gastric adenocarcinoma. *Vet Pathol*. 1978;15:600–607.
134. Brodey RS. Alimentary tract neoplasms in the cat: a clinicopathologic survey of 46 cases. *Zahnarztl Prax*. 1966;17:74–80.
135. Gieger T. Alimentary lymphoma in cats and dogs. *Vet Clin North Am Small Anim Pract*. 2011;41:419–432.
136. Hayden DW, Fleischman RW. Scirrhous eosinophilic gastritis in dogs with gastric arteritis. *Vet Pathol*. 1977;14: 441–448.
137. Pietra M, Zanoni RG, Peli A, et al. Gastric inflammatory pseudotumour secondary to *Actinomyces hordeovulneris* infection in a cat. *Ir Vet J*. 2015;69:12.
138. McConnell JF, Sparkes AH, Blunden AS, et al. Eosinophilic fibrosing gastritis and toxoplasmosis in a cat. *J Feline Med Surg*. 2007;9:82–88.
139. Teshima T, Matsumoto H, Michishita M, et al. Multiple inflammatory gastric polyps treated by endoscopic polypectomy with argon plasma coagulation in a dog. *J Small Anim Pract*. 2013;54:265–268.
140. Marolf AJ, Bachand AM, Sharber J, et al. Comparison of endoscopy and sonography findings in dogs and cats with histologically confirmed gastric neoplasia. *J Small Anim Pract*. 2015;56:339–344.

141. Hobbs J, Sutherland-Smith J, Penninck D, et al. Ultrasonographic features of canine gastrointestinal stromal tumors compared to other gastrointestinal spindle cell tumors. *Vet Radiol Ultrasound*. 2015;56:432–438.
142. Burke RL, Ackerman N. The abdomen. In: Burke RL, Ackerman N, eds. *Small Animal Radiology and Ultrasonography: A Diagnostic Atlas and Text*. 2nd ed. Philadelphia: Saunders; 1996:250–477.
143. Diana A, Penninck DG, Keating JH. Ultrasonographic appearance of canine gastric polyps. *Vet Radiol Ultrasound*. 2009;50:201–204.
144. Lamb CR, Forster-van Hijfte M. Ultrasound corner beware the gastric pseudomass. *Vet Radiol Ultrasound*. 1994;4;35:398–399.
145. Crystal MA, Penninck DG, Matz ME, et al. Use of ultrasound-guided fine-needle aspiration biopsy and automated core biopsy for the diagnosis of gastrointestinal diseases in small animals. *Vet Radiol Ultrasound*. 1993;34:438–444.
146. van der Gaag I, Happe RP, Wolvekamp WT. A boxer dog with chronic hypertrophic gastritis resembling Menetrier's disease in man. *Vet Pathol*. 1976;13:172–185.
147. Vaughn DP, Syrcle J, Cooley J. Canine giant hypertrophic gastritis treated successfully with partial gastrectomy. *J Am Anim Hosp Assoc*. 2014;50:62–66.
148. Murakami M, Heng HG, Sola M. CT features of confirmed and presumed gastric wall edema in dogs. *Vet Radiol Ultrasound*. 2022;63(6):711–718. https://doi.org/10.1111/vru.13123. Epub 2022 Jun 8. PMID: 35674240; PMCID: PMC9796106.
149. Thierry F, Ferreira MF, Paterson GK, et al. Canine and feline emphysematous gastritis may be differentiated from gastric emphysema based on clinical and imaging characteristics: five cases. *Vet Radiol Ultrasound*. 2019;60:136–144.
150. Barber DL, Rowland GN. Radiographically detectable soft tissue calcification in chronic renal failure. *Veterinary Radiology*. 1979;20:117–123.
151. Lidbury JA, Suchodolski JS, Steiner JM. Gastric histopathologic abnormalities in dogs: 67 cases (2002-2007). *J Am Vet Med Assoc*. 2009;234:1147–1153.
152. Parfitt AM. Soft-tissue calcification in uremia. *Arch Intern Med*. 1969;124:544–556.
153. Corapi WV, Ajithdoss DK, Snowden KF, et al. Multi-organ involvement of *Heterobilharzia americana* infection in a dog presented for systemic mineralization. *J Vet Diagn Invest*. 2011;23:826–831.
154. Beck C, O'Neill T, Holloway SA, et al. The use of ultrasound in the investigation of gastric carcinoma in a dog. *Aust Vet J*. 2001;79:332–334.
155. Bakhtiari J, Abdi M, Khalaj AR, et al. Comparative evaluation of two reconstructive methods following laparoscopic assisted subtotal gastrectomy in dogs. *BMC Res Notes*. 2012;5:1–6.
156. Belandria GA, Pavletic MM, Boulay JP, et al. Gastropexy with an automatic stapling instrument for the treatment of gastric dilatation and volvulus in 20 dogs. *Can Vet J*. 2009;50:733–740.

ELECTRONIC RESOURCES

Additional information related to the content in Chapter 45 can be found online at eBooks.Health.Elsevier.com

- Chapter Quiz

CHAPTER 46

Small Bowel

Lorrie Gaschen • Elizabeth A. Riedesel

Abdominal imaging can assist in making a definitive diagnosis or in deciding between medical or surgical treatment in patients with clinical signs that implicate involvement of the small bowel. However, imaging findings must be interpreted in context with the signalment and history, and results from a thorough physical examination, and pertinent laboratory tests. Survey radiographs and ultrasound evaluation have become the primary imaging modalities for assessment of the small intestinal tract and surrounding structures. Intestinal contrast studies are very useful in select situations. The role of advanced imaging—mainly computed tomography (CT) and contrast-enhanced ultrasound (CEUS)—in the diagnosis of intestinal disease is beginning to be understood. This chapter will focus on radiographic and ultrasonographic imaging interpretation of the small bowel and how CT and CEUS are being used diagnostically.

THE NORMAL SMALL BOWEL

Radiography

Three-view abdominal radiography including both right lateral and left lateral in addition to the ventrodorsal (VD) view is the new standard for survey abdominal radiography and is discussed in Chapter 38.[1] The major rationale for the routine acquisition of all three views is to take advantage of the redistribution of intraluminal gas, leading to a more complete examination. In the left lateral view, gastric gas, if present, can redistribute to the pyloric region, and usually also enter the duodenum and possibly the jejunum. If the VD is acquired after the left lateral view, gas will likely remain in the duodenum. Gas is more likely to be present in the duodenum in both the left lateral and VD views when the order of image acquisition is left lateral followed by VD followed by right lateral.[2] Other procedures, such as compression radiographs, may also be useful in the assessment of the intestinal tract[3] (Fig. 46.1).

Withholding food for 24 hours and administering a cleansing enema 2 to 4 hours before radiography will optimize radiographic interpretation of the small bowel as well as the stomach. This is not always possible in practice, and for the patient with acute abdominal pain, acute persistent vomiting, or palpable, enlarged fluid-filled or gas-filled bowel, no preparation is indicated as the native pattern of gas and fluid can be helpful diagnostically. If necessary, radiographs can be repeated after fasting and/or an enema. The roentgen sign assessment for the small intestine is summarized in Box 46.1. Abnormal margination, size, position, shape, and radiopacity can be assessed in survey radiographs, but mucosal irregularities, wall thickness and structure, and abnormal peristalsis or transit time are best determined from ultrasound or contrast studies.

A moderate amount of intraperitoneal fat provides good contrast for definition of the intestinal serosal surfaces (Fig. 46.2). Animals younger than 6 months or emaciated animals have poor serosal definition because of a lack of intra-abdominal fat. Serosal surfaces should be smooth and are seen most easily in regions where superimposition of multiple small and large bowel segments is minimal. A false interpretation of decreased serosal contrast often results when small bowel loops are overlapping in the central abdomen, when segments are crowded together by an abdominal mass, very distended urinary bladder, or when little or no gas is present in the bowel lumen (Fig. 46.3). Ultrasound is a more sensitive method to identify low-volume peritoneal effusion.

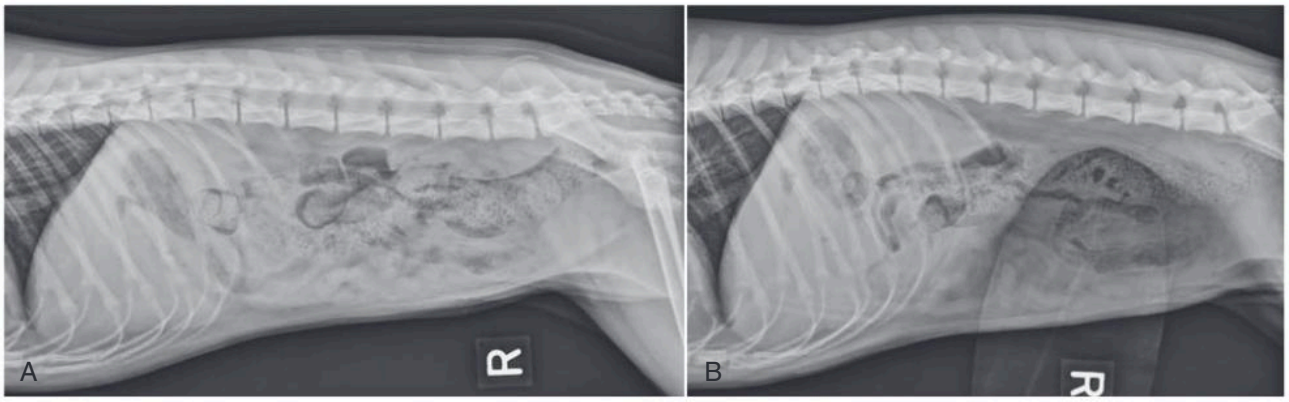


Fig. 46.1 **A,** Radiograph of a 2-year-old Labrador retriever with vomiting for 48 hours. There are segments of bowel with heterogeneous soft tissue content that are superimposed with one another and including the colon. Differentiating fecal material in the colon from that in the jejunum is challenging. In **B,** a wooden spoon is used to apply compression to the caudal abdomen and the heterogeneous content can now be clearly localized to a small intestinal segment. A sock was removed surgically.

Box • 46.1

Roentgen Signs in the Small Intestine

Margination: serosal surface definition
Size: diameter of lumen and/or serosa-to-serosa
Position: location within abdominal cavity
Shape: contour of bowel loops
Radiopacity: lumen contents and bowel wall
Architecture: mucosa/bowel wall smoothness
Motility: intermittent narrowing of contractions

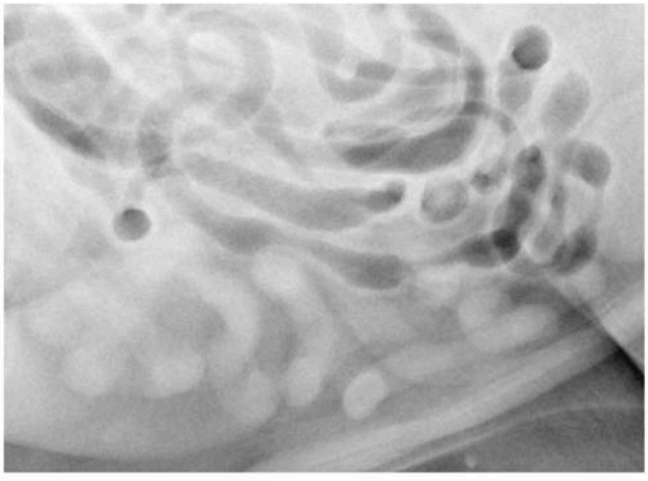


Fig. 46.2 Serosal edges of small intestine are seen easily in this dog with ample intraperitoneal fat. Bowel segments projected end-on appear as rings if the lumen contains air or as round nodules if the lumen is collapsed or contains fluid. Longitudinal sections are straight or curved with intermittent narrowing caused by peristalsis.

Generally, the small intestines are a uniform population of very similar diameter in the normal dog and cat, only seeming to vary due to contractions or variations in content. Because of the variation in canine body size and the magnification effects of radiography, no accurate, specific measurement for normal diameter of the small bowel exists. Table 46.1 summarizes guidelines for determining normal canine and feline relative bowel diameter based on the size of reference structures such as the ribs or vertebral bodies.[4–7] For measurements and calculated ratios to be most accurate, optimally positioned radiographs and positive identification that it is the small bowel being measured needs to be ensured. Although the duodenum may be slightly wider, the jejunum and ileum should have approximately the same diameter.[8] Reported measurements, however, are mostly guidelines, and for most observers, qualitative assessment of bowel size will be just as accurate as measurement techniques.

Judgment of the thickness of the intestinal wall on survey radiographs is unreliable. A normal-diameter bowel segment with a small volume of intraluminal air can be misinterpreted as a pathologically thickened segment. However, there will be patients in which the bowel wall is unquestionably too thick

Table • 46.1

Canine and Feline Small Bowel Normal Radiographic Measurements.

	CANINE	FELINE
Bowel diameter Serosa to serosa	≤2 times width of rib Ratio of maximal small bowel diameter to narrowest height of L5 body <1.6	≤12 mm* Ratio of maximum small bowel diameter to endplate height of L2 < 2.0

*Mucosa to mucosa based on gas or barium filled.

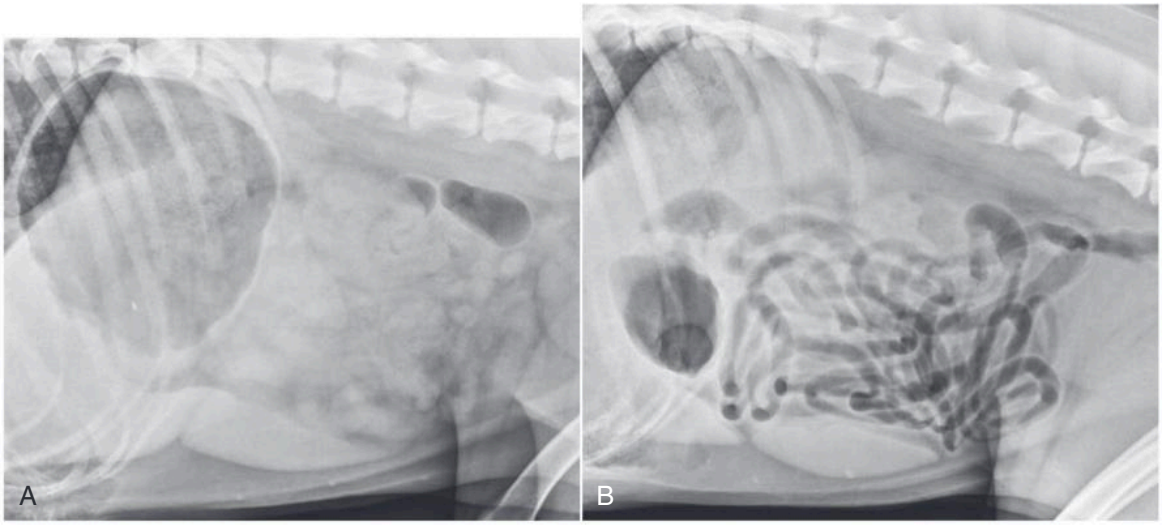


Fig. 46.3 Right and left lateral views illustrate the effect of lack of gas within the bowel. This effect can lead to the perception of poor serosal contrast and a misinterpretation of abdominal fluid. Images **A** and **B** are from the same dog obtained only minutes apart. In the right lateral view **(A)**, there is very little to no gas in many of the small bowel segments. There is also moderate distention of the stomach and the urinary bladder, crowding the bowel into the center of the abdomen and simulating a loss of serosal contrast. However, the serosal borders of the liver, spleen, and urinary bladder are clearly defined. In the left lateral view **(B)**, the gastric gas is redistributed throughout the small bowel, and serosal contrast seems improved because of the addition of the gas to the bowel lumen making it overall easier to identify individual segments of bowel.

(Fig. 46.4). In most instances, true thickening of the intestinal wall is better judged by ultrasound, contrast study, or palpation.

The small bowel has fixed and moveable segments. In the dog, the cranial duodenal flexure is fixed along the caudal surface of the right side of the liver by the hepatoduodenal ligament. The descending duodenum lies along the right abdominal wall. The caudal duodenal flexure is located at a transverse plane through the tuber coxae with the ascending duodenum continuing cranially from this point on the left side of the root of the mesentery. The initial portion of the ascending duodenum is attached by the duodenocolic ligament. The jejunum should be distributed uniformly throughout the peritoneal cavity, occupying space not taken up by distensible organs (stomach or urinary bladder), solid organs (liver, spleen, or kidneys), or fat. The ileum crosses from the left to the right midabdomen to terminate at the ileocolic junction.

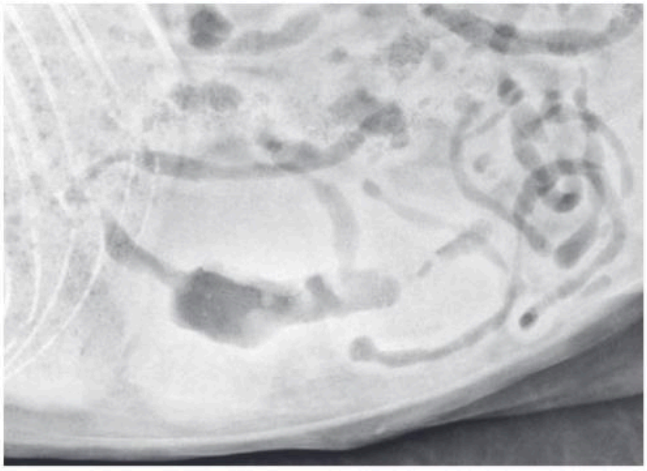


Fig. 46.4 Despite the general lack of accuracy in radiographic measurement of intestinal wall thickness, it is obvious that the wall of the bowel loop in the ventral aspect of the abdomen is abnormally thickened. The lumen is not uniformly distended. There is mottled soft tissue and fluid opacity between the thickened segment and the ventral abdominal wall consistent with focal fluid or deposition of cells on the serosa or mesentery and omentum. Ultrasound assessment is warranted to further characterize the bowel wall changes, to direct an aspirate or core biopsy, and to obtain a peritoneal fluid sample for analysis. See Fig. 46.35 for the ultrasound findings.

The cat differs from the dog in the position of the cranial duodenal flexure. In the cat, the cranial flexure usually creates a sharper angle with the pylorus and is located closer to the midline. The descending duodenum courses in a gently curved loop, positioning the caudal duodenal flexure at approximately midabdomen. The position of the remainder of the small bowel is the same as the dog.

Common positional variations of small bowel seen in normal dogs and cats include (1) a full stomach displacing the bowel caudally; (2) a distended urinary bladder displacing the bowel cranially; (3) intraperitoneal fat in obese cats causing the small bowel to be located centrally and/or on the right side; (4) in very obese cats, fat displacing the bowel into the central region of the abdominal cavity; and (5) in obese dogs, the bowel occupying the ventral portion of the pendulous abdominal cavity. Positional changes in the small intestine may also be indicative of disease in adjacent organs.

The normal small bowel appears in survey radiographs as smooth, continuously curving tubes or as solid end-on circles or rings (see Fig. 46.1). Bowel shape is dependent on the projection angle of the x-ray beam relative to the long or short axes of the loops and to the contractile activity of the smooth muscle. Segmental contractions give rise to spherical shapes; this is often described as *string-of-pearls* appearance in cats. Peristaltic contractions cause long tubular shapes. Occasionally, concave depressions in the antimesenteric mucosal border of the duodenum, referred to as *pseudoulcers*, can be seen at the gas-mucosal surface in dogs (Fig. 46.5A).[2]

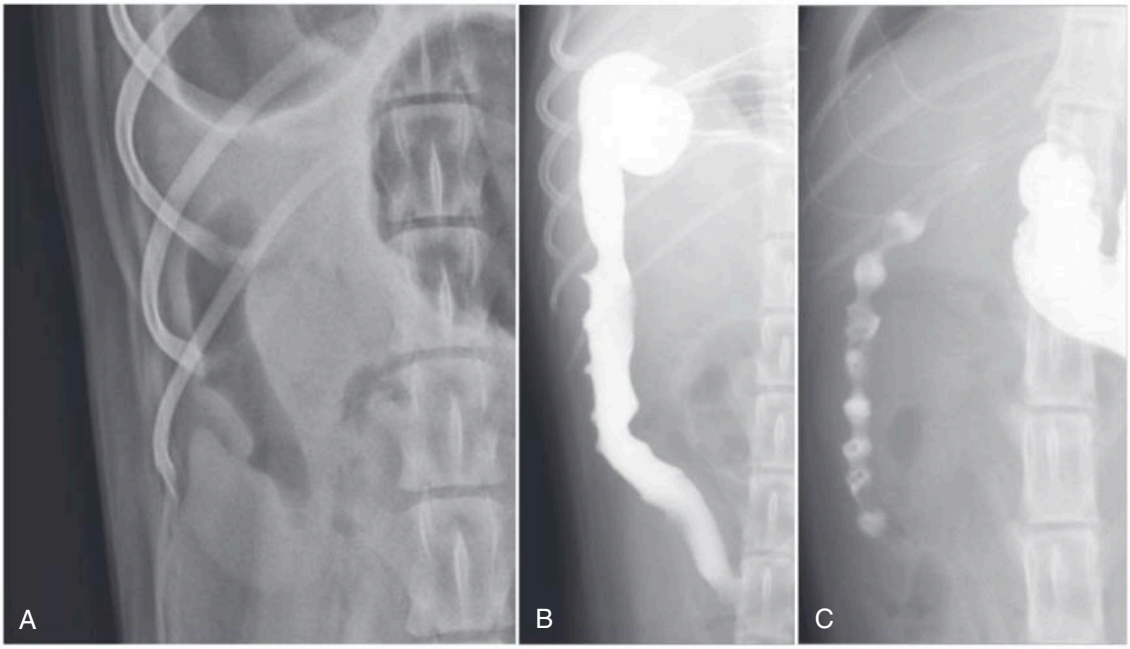


Fig. 46.5 Normal duodenal contours and mucosal surface shapes. Pseudoulcers of the dog are occasionally evident in a survey radiograph **(A)** when the duodenum is distended with gas or more commonly in barium contrast images **(B)**. Pseudoulcers are located on the antimesenteric wall and are caused by depression in the mucosa at sites of submucosal lymphoid follicles. One or more may be present. Normal *string-of-pearls* effect of the cat **(C)** can be seen in barium contrast images. The *string-of-pearls* effect is caused by circular muscle contractions that almost completely obliterate the lumen. These features are rarely seen in noncontrast images and in ultrasound studies.

The radiopacity of the normal small intestine is variable because of differing opacities of material within the lumen. In a nonfasted animal, any of the following may be seen in the lumen: gas, grainy-appearing mottled ingesta, which may include mineral (dirt, sand, bone) or metal, or fluid of homogeneous soft tissue opacity. The nondiscretionary eating habits or diet type of some dogs and cats may result in mineral or metallic opacities of small size being present in the small bowel. Clay-based cat litter and small gravel from dog runs are common examples. Gastrointestinal medications that contain calcium, magnesium, aluminum, bismuth, or silicate can impart significant radiopacity to the intestinal content.[9] Some pet vitamin and mineral supplements contain sufficient mineral to be visible radiographically. In general, tablets or capsules containing minerals are more likely to be visible than liquids containing these minerals.[9] In a fasted animal, the lumen may contain a small amount of ingested air, or it may be of homogeneous fluid, or soft tissue opacity if it is collapsed.

The amount of bowel that contains gas in the normal cat and dog is variable. Cats without gastrointestinal disease that are not fasted before radiography may have gas throughout the bowel.[7] In the fasted cat, gas is rarely present in the small intestine, but in fasted dogs, 30% to 60% of the small bowel content may be gas.[6,10] Animals stressed by handling or dyspneic animals frequently have a large amount of air in the small intestine due to aerophagia. The gas pattern is variable although most cats and dogs have a tubular pattern with gas in a continuous column except where interrupted by contraction. The bowel wall should be of uniform soft tissue opacity. This uniformity is most easily assessed in segments that contain air.

There are many small intestinal diseases that result in no survey radiographic changes. Regardless, survey radiographs are a valuable baseline prior to additional imaging studies such as ultrasound or contrast radiography. Some indications for these procedures are:

- Acute, persistent vomiting with negative findings on survey radiographs
- Recurrent vomiting, especially in animals refractory to symptomatic therapy and without other organ disease to explain the vomiting
- Palpable abdominal mass without obstructive bowel signs on survey radiographs
- Acute abdominal pain with an unusual or unexplained abnormality seen in the survey radiographs
- Weight loss with intermittent or recurrent diarrhea
- Melena or hematemesis

Ultrasound

The American College of Veterinary Radiology has provided a consensus statement on recommendations for performing an ultrasound examination of the gastrointestinal tract.[11] Observations that can be made from intestinal ultrasonography include assessment of wall thickness, wall layer pattern, type of content, and motility. Transducer frequencies of 7.5 MHz and higher enable the best identification of individual layers of the intestinal wall. Ultrasound imaging also allows assessment of structures adjacent to the intestine. The character of the mesentery and regional lymph nodes and presence of abdominal fluid should be assessed. Evaluation of the small bowel should be part of a complete systematic evaluation including solid organs, particularly the pancreas and liver, and the gallbladder and common bile duct. Ultrasound-guided fine-needle aspiration sampling for cytology and culture evaluation is useful in many patients.

The major obstacle for optimal ultrasound imaging is the presence of gas in the bowel. The current recommendation is an 8- to 12-hour fast when the focus of the examination is the gastrointestinal tract in nonurgent patients. When gas is present, the far wall cannot be assessed. Repositioning the patient, using gravity-based transducer placement, or repeating the examination later may overcome the artifacts induced by gas.

Each intestinal segment should be examined in the longitudinal and transverse plane (Fig. 46.6).[11] As many representative segments as possible of the jejunum and the ileocecocolic junction should be included. Both still and when possible, video clips of representative segments should be documented in the examination.

The normal small intestinal wall consists of alternating hyperechoic and hypoechoic layers. When no fluid or gas is present, a thin, hyperechoic line represents the lumen. From the lumen to the serosa, the tissue layers and echogenicities are as follows: hypoechoic mucosa, hyperechoic submucosa, hypoechoic muscularis, and hyperechoic serosa (see Fig. 46.6). The hypoechoic mucosal layer is the thickest of the individual layers and thus is dominant visually.[12] When fluid is in the lumen, the mucosal surface is normally hyperechoic (eFig. 46.1). If gas is in the lumen, a prominent *ring-down* reverberation artifact occurs as a stationary artifact in a relatively long length of bowel and as a moving reverberation artifact in peristaltic contraction. This artifact inhibits the assessment of the deeper wall. However, the presence of gas helps to identify the lumen in some abnormal segments. Acoustic shadowing artifact can occur with dense particles of

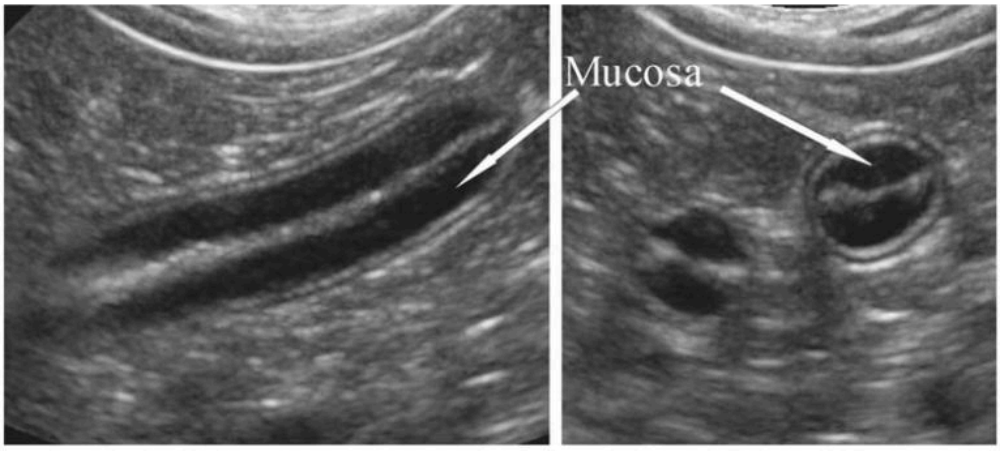
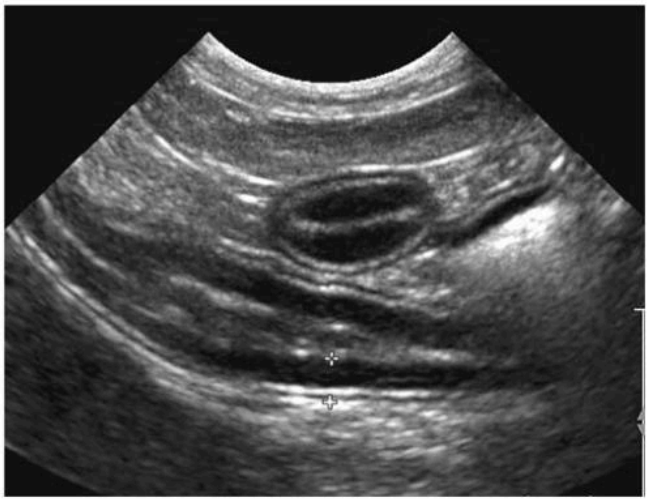


Fig. 46.6 Ultrasound images of a normal canine jejunum. The long axis is depicted on the *left* and transverse on the *right*. A four-layer alternating tissue echogenicity pattern can be identified. The mucosal layer is indicated by *arrows*. The central hyperechoic *line* represents the empty lumen.



eFig. 46.1 Three small bowel loops with different content. The oval section is empty and collapsed, the longitudinal section contains a small amount of mucoid fluid, and the section in the far right of the image contains gas. The ring-down artifact of the gas interferes with evaluation of the deep wall of this segment.

ingesta or foreign material. A short linear or focal hyperechogenicity occurs frequently at the equatorial tangents of transverse sections of empty bowel. This occurs because of widening of the intervillous space when the bowel folds.[13] With higher-frequency transducers (13–18 MHz), additional hyperechoic features are visible in the hypoechoic bowel layers; these are of questionable clinical significance. Ultrasonographic features of normal mid-duodenum, mid-jejunum, and mid-ileum using 13- and 15-MHz transducers were compared to histopathologic features in an ex vivo study.[14] The mucosa in all segments had a dual layer appearance with a hyperechoic band in the luminal, or inner, portion of the mucosa. This correlated with the intestinal villi, whereas the deeper portion of the mucosa corresponded to the lamina propria. The degree of hyperechogenicity of the villus portion was increased with the presence of lacteal dilation in the villi tips and fluid in the lumen (Fig. 46.7). A small proportion of ileal segments had an additional hyperechoic thin line in the deepest part of the mucosal layer that paralleled the submucosal layer. Histologically, these ileal segments had enlarged submucosal lymphoid follicles whereas those ileal segments without this hyperechoic line had no enlargement of the lymphoid follicles. Lastly, all segments had a hyperechoic thin line in the muscularis layer that paralleled the submucosal and serosal layers. Histologically, this was correlated with fibrous tissue in the myenteric plexus located between the inner circular and outer longitudinal components of the muscularis propria.

In 20 healthy intact male cats aged 6 to 18 months, an additional asymmetric hypoechoic layer was present in the ileum in all cats and more proximally in the jejunum in half of the cats.[15] In another cat of similar age, this was determined histologically to be due to lymphoid follicles. This extra hypoechoic submucosal layer has been observed occasionally in older cats but is more common in younger cats. The clinical relevance of this finding in any cat is unknown.

Diet and timing of ultrasound examination relative to food ingestion can affect the echogenicity of the mucosa. Hyperechoic mucosal speckles may be observed after a meal, most pronounced at 60 minutes postprandial[16] (Fig. 46.8). The effect at 60 minutes postprandial likely reflected physiologic lacteal dilation. Immediately postprandial, there would not be adequate time to stimulate physiologic lacteal dilation and thus the speculation is that the mucosal echogenicities are more likely an artifact of reflections and/or mixture of the mucus and food in the lumen at the mucosal surface (eFig. 46.2). This effect should be considered in patients being evaluated ultrasonographically for possible inflammatory bowel disease (IBD) and repeat scanning in the fasted state should be performed.

Wall thickness reference ranges for the dog and cat are summarized in Tables 46.2 and 46.3, respectively.[17,18] The American College of Veterinary Radiology consensus statement has recommended using the longitudinal plane for measuring wall thickness to avoid measurement error due to obliquity.[11] Using higher-frequency transducers and measures of wall thickness obtained in a longitudinal segment, there was a correlation between the duodenal and jejunal thickness and dog weight.[17] The ileum is the thickest segment in the cat.[18] Most recently, the thickness of individual bowel layers has been measured in normal cats (Table 46.3).[19] Correlation with histopathology in a larger number of cats will be needed to determine the clinical utility of these measurements.

The normal duodenum can be identified distinctly by its superficial right-side location and can be traced cranially into the stomach and caudally to the descending loop, which courses to the left. The duodenum can be scanned either from a subcostal or intercostal window depending on the chest conformation of the dog. The right dorsal intercostal window is helpful in deep-chested dogs to identify and trace the duodenum. In cats, the subcostal window is adequate due to its more midline location. With high-resolution transducers, the duodenal papilla can be seen in many cats and dogs (Fig. 46.9). The major duodenal papilla is immediately adjacent to the right limb of the pancreas. The feline duodenal papilla ranges from 2.9 to 5.5 mm wide and averages 4.0 mm in height when imaged in the transverse plane.[20] In 40 dogs of various breeds without gastrointestinal, hepatobiliary, or pancreatic disease, the major duodenal papilla had mean dimensions of 15.2 ± 3.5 mm length, 6.3 ± 1.6 mm width, and 4.3 ± 1.0 mm height.[21] There was an insufficient number of dogs to

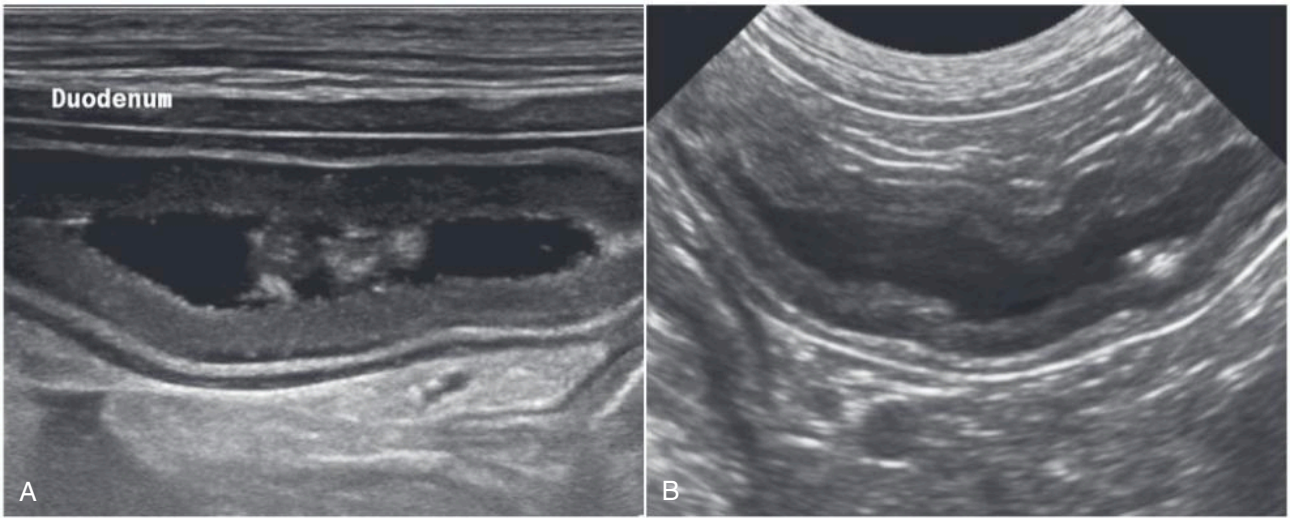
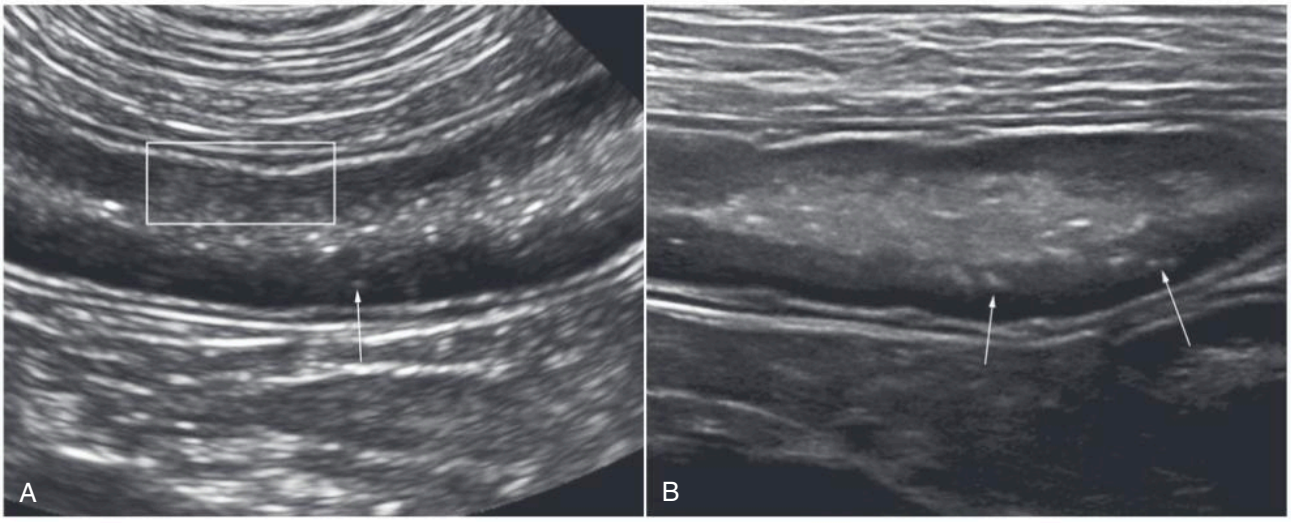


Fig. 46.7 Ultrasound images of canine duodenum and jejunum showing a double layer effect in the mucosal layer. **A** is the duodenum imaged with an 18-5 MHz linear transducer. There is fluid in the lumen and the inner band of the mucosal layer is thicker than the hypoechoic deeper portion. **B** is the jejunum of the same dog imaged with an 8-5 MHz curvilinear transducer. The dual band effect in the mucosal layer is visible. These features are nonspeci fic and can be found in both normal and abnormal patients. The signi ficance must be correlated with clinical signs, other tests of gastrointestinal function, and histopathologic assessment. Endoscopically obtained duodenal samples from this dog had evidence of mild lymphoplasmacytic in flammation.



eFig. 46.2 Long axis ultrasound views of the duodenum of a dog that was not fasted prior to imaging and had a mild to moderate volume of chyme in the bowel lumen. Echoes within the mucosal layer (*arrows and boxed area*) may represent reflections from the luminal content or physiologic lacteal dilation. **A** was acquired with an 8-5 MHz curvilinear transducer and **B** with an 18-5 MHz linear transducer.

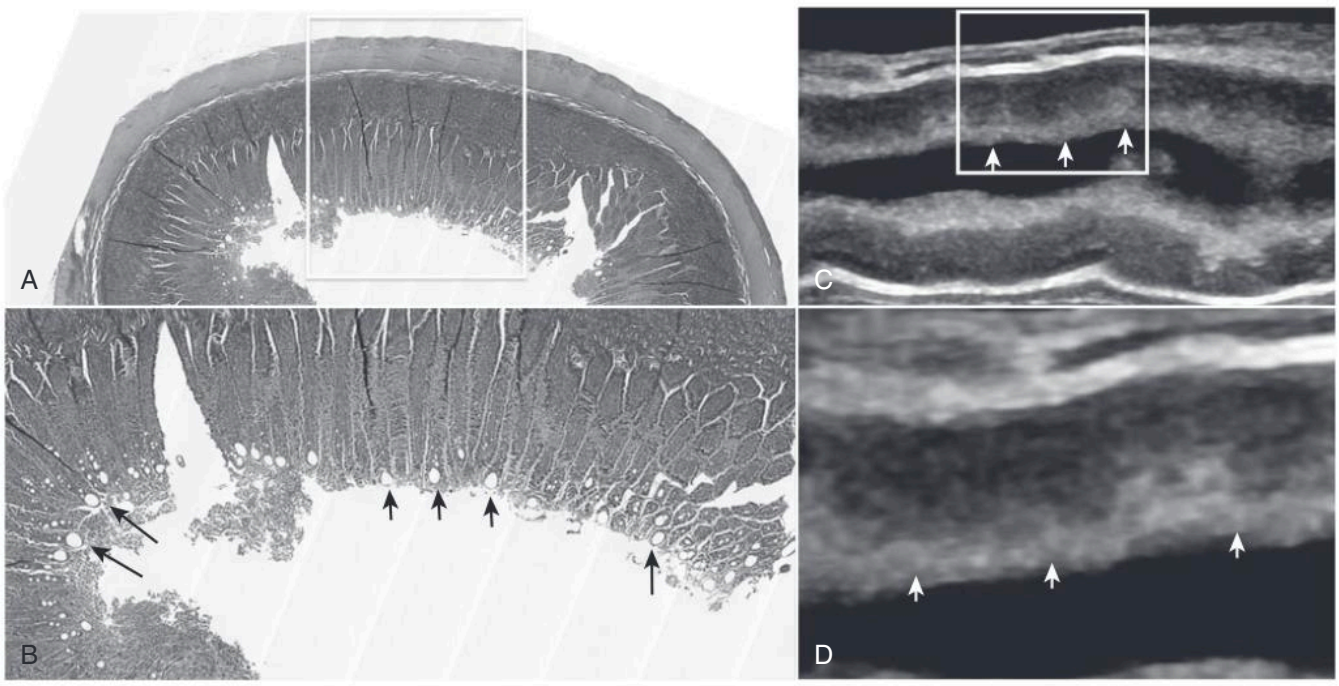


Fig. 46.8 Postprandial images of the jejunum. **A** and **B** are histopathologic full-thickness images from a cadaver that had been euthanized for reasons unrelated to the gastrointestinal tract and after a meal. **B** is the magnified area in the white box. The *black arrows* show lipid accumulation at the tips of the villi. **C,** Longitudinal ultrasound image of a section of jejunum in a water bath. *Arrows* show where the luminal surface of the mucosa is diffusely hyperechoic and in **D** how this region correlates to the lipid accumulation at the mucosal surface. This is a normal postprandial finding in dogs that should not be confused with pathology.

Table • 46.2

Canine Normal Small Bowel Wall Thickness Ultrasound Measurements.

	DUODENUM*	JEJUNUM*
Up to 20 kg	≤5.1	≤4.1
20–29.9 kg	≤5.3	≤4.4
>30 kg	≤6.0	≤4.7
Puppies†	3.8 ± 0.5 (3.2–4.8)	2.5 ± 0.5 (1.2–3.4)

*Wall thickness—mucosa to serosa, millimeters.
†Beagles 7–12 weeks of age with weight range 2.3–5 kg.

Table • 46.3

Feline Small Bowel Normal Ultrasound Measurements.

	WALL THICKNESS (mm)* MUCOSA TO SEROSA	WALL LAYER THICKNESS (mm)† (PERCENT OF WALL THICKNESS)
Duodenum	1.78–2.51	M—1.05–1.56 (57.7) Sm—0.29–0.43 (16.3) Mus—0.30–0.35 (12.7) S—0.23–0.36 (13.3)
Jejunum	1.96–2.67	M—1.04–1.55 (55.2) Sm—0.29–0.44 (16.0) Mus—0.25–0.45 (14.4) S—0.23–0.39 (14.4)
Ileum	2.5–3.59	M-If—0.31–0.62 (15.5) M-I—0.33–0.69 (24.0) Sm-If—0.95–2.12 (49.8) Sm-I—0.40–0.68 (25.7) Mus-If—0.44–0.95 (22.0) Mus-I—0.39–0.83 (31.6) S-If—0.26–0.57 (12.7) S-I—0.28–0.52 (16.7)

*Varies between authors dependent on frequency of transducer used.
†Individual layer thickness measured using 13 MHz.
D, Duodenum; *J,* jejunum; *I,* ileum between folds; *If,* ileum fold; *M,* mucosal; *Mus,* muscularis; *S,* serosa; *Sm,* submucosal.

determine differences between breeds but there was a significant increase in all values with increasing body weight. Pseudoulcers can be seen occasionally in the canine duodenum.

The jejunum and most of the ileum appear as nondescript bowel segments. The terminal 1 to 2 cm of the ileum, or the ileocolic junction, in the cat has the appearance of a wagon wheel in the transverse plane because of projection of the mucosa into the lumen.[18] An effective means of identifying the ileum is to observe its transition into the colon and then retrace it in an orad direction. Peristaltic contractions can be seen and vary from less than 1 to 3 per minute in the small intestine depending on the fasted state or amount of time after being fed.[22]

Regional lymph nodes should be evaluated in any ultrasound assessment of the small bowel. The duodenum is drained by hepatic and pancreaticoduodenal lymph nodes. These lymph

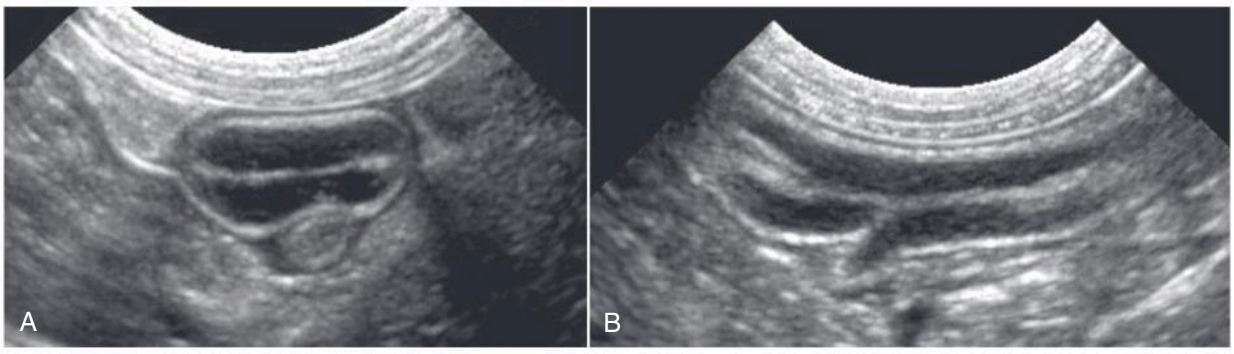


Fig. 46.9 Transverse **(A)** and oblique long axis **(B)** views of the major duodenal papilla. With dynamic imaging, the common bile duct can be followed into the lumen.

nodes are not seen consistently in normal patients. The jejunum and ileum are drained by the jejunal and colic lymph nodes, respectively, in the dog. In the cat, an ileocecal lymph node is also present. Normal lymph nodes are typically isoechoic to adjacent fat, with a more uniform echogenicity than fat, and may not be differentiated readily.

Microbubble CEUS has been explored for evaluation of perfusion patterns in abdominal organs including the small bowel.[23–25] Small intestinal perfusion abnormalities may be identified with this method, but it has not been shown to be able to differentiate IBD from normal intestines or intestinal.[26–28] The potential use of real-time shear wave elastography of small intestines has also been recently reported and reference values in healthy dogs have been established.[29]

Computed Tomography

The appearance of the small intestine in CT images was evaluated in 19 presumably normal dogs of various breeds and ages.[30] Individual bowel wall layers were not visible; however, a small percentage of segments had mild contrast enhancement of the mucosal and serosal layers. Bowel wall thickness and bowel diameter correlated well with reported normal radiographic and ultrasonographic reference ranges. No association was evident between patient age and wall thickness or bowel diameter. However, there were significant associations between body weight and wall thickness and between body weight and bowel diameter (eTable 46.1). A CT protocol designed to test injection timing for the assessment of the gastrointestinal wall showed that a 10- to 15-second delay was ideal for assessing jejunal wall enhancement in dogs.[31] However, inner wall layering was still not possible with this technique.

CT has recently been used to diagnose small intestinal obstructions in dogs and cats and found to be accurate in differentiating obstructive from nonobstructive intestinal content.[32] CT is proposed as an alternative to radiography due to the lack of superimposition of intestinal structures and also provides a full abdominal assessment in vomiting animals.

Contrast Examinations

Indications

Radiographic contrast studies of the small bowel can be used to identify the location of the bowel, patency of the lumen, perforation, wall irregularities in the contrast medium/mucosal interface, and assessment of transit time. Typically, gastrointestinal contrast studies involve orally administered positive-contrast media. The addition of the opposite lateral view and less frequently the dorsoventral view may shift natural luminal gas sufficiently to confirm an initial finding (Fig. 46.10) or discover a new finding (Fig. 46.11).[1]

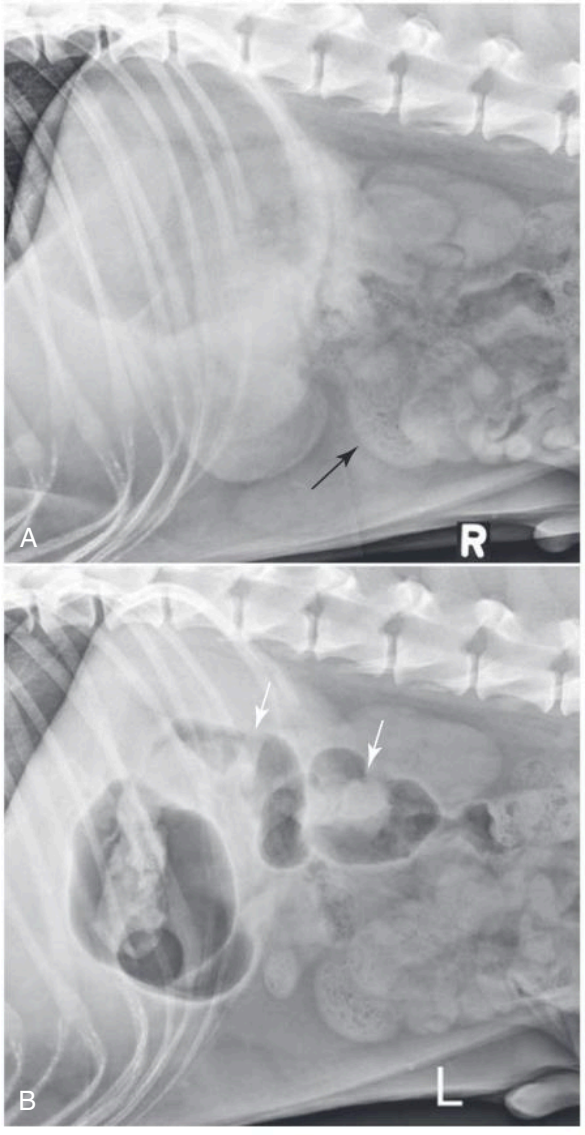


Fig. 46.10 The images show the use of the inherent gas as a contrast medium to confirm a gastrointestinal foreign body. In the right lateral view **(A)**, there is mottled gas and soft tissue opacity in a moderately focally dilated small intestinal loop (*black arrow*) in the cranial ventral region. Moderate gas and fluid distention of the stomach is also evident. In the left lateral view **(B)**, the redistribution of gastric gas provides contrast for identification of a soft tissue foreign body in the pylorus and mild plication of the proximal duodenum (*white arrows*). These findings confirm a fabric-type foreign body in the stomach with a linear component extending into the duodenum and proximal jejunum.

eTable • 46.1

Canine Small Bowel Normal CT Measurements.

CT wall thickness*	Up to 9 kg, 3.22 (2.59–3.30)†
Ascending duodenum	>9 kg, 4.84 (4.61–5.26)
CT wall thickness	Up to 9 kg, 2.58 (2.00–2.93)
Jejunum	>9 kg, 3.62 (3.31–3.87)
CT segment diameter‡	Duodenal cranial flexure:
Duodenum	Up to 9 kg, 9.23 (8.40–9.83)
	>9 kg, 13.20 (11.58–16.47)
	Descending duodenum:
	Up to 9 kg, 10.04 (8.79–10.46)
	>9 kg, 11.75 (11.60–16.33)
	Transverse duodenum:
	Up to 9 kg, 8.57 (7.35–9.31)
	>9 kg, 11.10 (10.70–13.28)
	Ascending duodenum:
	Up to 9 kg, 9.10 (8.43–9.98)
	>9 kg, 14.00 (12.00–15.37)
CT segment diameter	Up to 9 kg, 7.60 (6.95–8.21)
Jejunum	>9 kg, 10.10 (9.00–12.53)

*Mucosa to serosa—dimension in mm.
†Median and interquartile range.
‡Serosa to serosa.

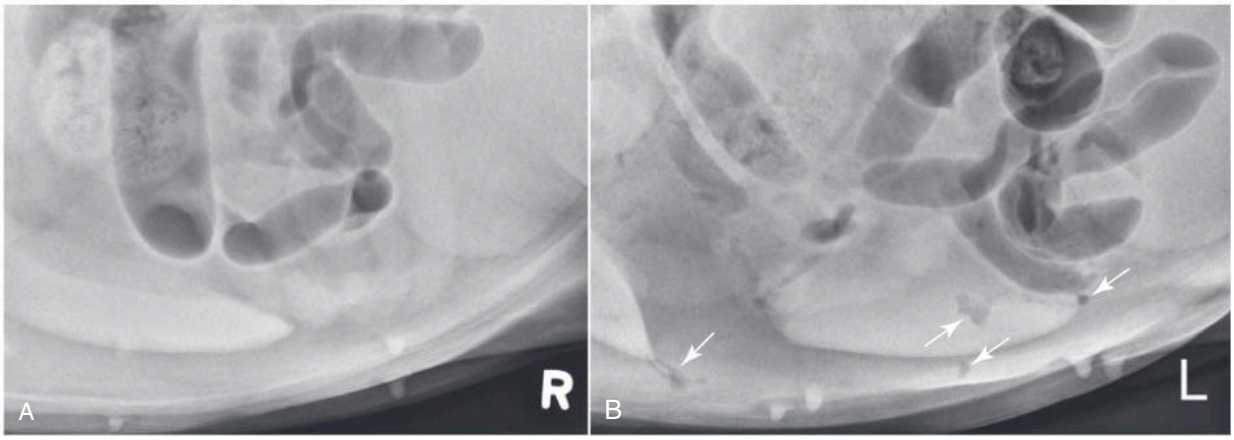


Fig. 46.11 In a close-up right lateral view **(A)**, there is normal serosal contrast. Bowel segments immediately cranial to the urinary bladder are of normal diameter and empty; however, one gas-filled segment is dilated. In the left lateral view **(B)**, there are four gas bubbles (*white arrows*) not within a bowel lumen, indicative of free peritoneal gas, most likely secondary to bowel perforation. A perforation in the distal duodenum caused by a linear foreign body was found at surgery.

Positive-contrast evaluation is not indicated when there is conclusive survey radiographic evidence of bowel obstruction. In most such patients, insufficient additional information will be gained because of the slow passage of contrast medium through atonic bowel proximal to the obstruction, especially in a weakened or debilitated animal, and the contrast study may delay or complicate a surgical procedure. If the clinical and survey radiographic findings are strongly suggestive of mechanical obstruction, an exploratory laparotomy can be justified.

Contrast studies are also not indicated in patients with survey radiographic evidence of free peritoneal gas that is not residual from recent laparotomy, penetrating trauma, or abdominocentesis as the gas is most likely from gastrointestinal perforation.[33] The combination of barium and intestinal contents within the peritoneal cavity causes more severe peritonitis, foreign body granulomas, or serosal adhesions.[34] However, if treated promptly and aggressively, patient outcome can be good.[35] Attempting to identify the location of the perforation is not as important as providing aggressive medical and surgical intervention. Ultrasound can also be used to detect free peritoneal gas associated with gastrointestinal perforation and prevents the additional contamination associated with barium leakage. Water-soluble organic iodine contrast media are either ionic or nonionic.[36] Ionic iodinated contrast media are not recommended for oral administration in young and debilitated patients and especially dehydrated patients, because the resultant fluid shift can worsen any hypovolemic state.[37]

Dual contrast radiography and ultrasonography can also be performed to assess the small intestine and is reported in healthy dogs.[38] Carboxymethylcellulose (0.5% solution) combined with iohexol (300 mg I/mL) and a dosage of 8.5 mL of carboxymethylcellulose/kg body weight and 1.5 mL of iohexol/kg body weight as a mixture can be used to assess the small intestine both radiographically and ultrasonographically. The dual contrast medium served to improve the ultrasonographic assessment of the small intestine by mitigating reverberation artifact from intraluminal gas.

Technique and General Interpretation

A brief description of the techniques and interpretation of intestinal contrast studies follows. More detailed descriptions are available elsewhere and discussed in Chapter 45.[39] Contrast studies can be divided into two categories based on the radiographic opacity imparted by the contrast medium. Positive-contrast studies increase the opacity of the bowel lumen and are done with barium sulfate suspensions or iodinated products. These contrast media are given orally or by orogastric intubation. Because the stomach is also opacified by these agents, the phrase *upper gastrointestinal contrast study* is used.

The volume of contrast medium in the intestinal lumen is critical for accurate interpretation. The intestine should be distended to its reasonable physiologic maximum. Failure to administer an adequate volume of contrast medium is one of the most frequent causes for a nondiagnostic barium study. Some recommended dosages for contrast medium are given in Table 46.4. A summary of the portions of the gastrointestinal tract seen at specific intervals after positive-contrast medium administration is presented in Table 46.5 and in Chapter 45.

Normal anatomic features of the duodenum made visible by positive-contrast medium should not be misinterpreted as lesions. Dogs often have multiple square-shaped outpocketings on the antimesenteric side of the descending duodenum. One or several may be present. These are termed *pseudoulcers* and are normal and caused by mucosal depressions over submucosal lymphoid accumulations (see Fig. 46.5B). Pseudoulcers are not found in the cat. Approximately 30% of normal cats have strong segmental contractions throughout the length of the duodenum that produce a *string-of-pearls* effect during the contrast study (see Fig. 46.5C).[6] Throughout the remainder of the small bowel, concentric narrowing of short lengths of bowel should be seen and are caused by peristalsis (eFig. 46.3). The location of such narrowing should vary during the time of study in the normal animal.

In a normal upper gastrointestinal study, luminal barium and gas may be present simultaneously. A double-contrast effect is present when the distention by gas is greater than that caused by the barium. The barium/mucosa interface appears typically as a thin opaque line. In other segments, gas may be present only as small bubbles. Findings on the barium contrast images that most strongly correlate with abnormalities are changes in the diameter of the bowel, extensive changes in the barium/mucosa interface, and changes in the rate of passage of barium. The intestinal tract is normally characterized by dynamic changes; thus, documenting a suspicious finding on multiple radiographs over time increases the significance of the finding.

Barium-impregnated polyethylene spheres (BIPSs) can be administered to assess for motility disorders and gastrointestinal obstructions. The spheres are formulated in two diameters:



eFig. 46.3 Variations of normal in cats and dogs that can be seen during the progression of small bowel transit. Several segments contain gas and barium providing a double-contrast effect. One segment has several adjacent contractions.

Table • 46.4

Recommended Dose Rate for Contrast Medium.

CONTRAST MEDIUM	DOG	CAT
Barium sulfate suspension*	6–12 mL/kg 20% (w/w)[14] or 6–10 mL/kg 60% (w/w)	12–16 mL/kg[6]
Organic iodine preparation (full strength)	2–3 mL/kg[8,14,15]	2 mL/kg[15]
Organic iodine, nonionic (240–300 mg iodine/mL)	10 mL/kg (1:2 dilution)[28]	10 mL/kg (1:2 dilution)[28,30]
Radiopaque markers (BIPSs)†	10 5-mm and 30 1.5-mm spheres	10 5-mm and 30 1.5-mm spheres

For references listed in this table, refer to Thrall DR. *Thrall Textbook of Veterinary Diagnostic Radiology*. 5th ed. St. Louis, MO: Saunders; 2007 [chapter 46]. ISBN 9781-4160-2615-0.
*A large volume of relatively dilute contrast medium is preferred by some to distend the intestinal lumen but not to obscure radiolucent luminal filling defects. The author prefers a full-strength barium suspension for its superior mucosal pattern definition.
†Follow manufacturer's specific directions for administration with or without food.
BIPSs, Barium-impregnated polyethylene spheres.

Table • 46.5

Upper Gastrointestinal Tract Film Sequence.

	BARIUM	IONIC AND NONIONIC ORGANIC IODINE	STRUCTURES USUALLY OPACIFIED IN NORMAL ANIMALS*
Dog	Immediate	Immediate	Stomach
	15 minutes	15 minutes	Stomach, duodenum
	30 minutes	30 minutes	Stomach, duodenum, jejunum
	1 hour	1 hour	
	2 hours		Stomach, duodenum, jejunum
	4 hours		
			Stomach, all parts of small bowel
			Small bowel, colon
Cat	Immediate	Immediate	Stomach
	5 minutes	5 minutes	Stomach, duodenum
	30 minutes	30 minutes	All parts of small bowel
	1 hour	1 hour	
			Small bowel, colon

*Because of the extreme variability of individual transit times, this list is only an approximation of the parts of the gastrointestinal tract seen at these times.

1.5 mm and 5 mm. The larger spheres are designed to become trapped at the oral aspect of an obstructing lesion, making them suitable for evaluation of partial and complete obstruction (Fig. 46.12).[40] BIPSs are typically administered with a meal. The type of meal influences the rate of gastric emptying. Thus, strict adherence to the manufacturer's recommendations must be maintained when the product is used for calculation of gastric emptying time and assessment of transit time.

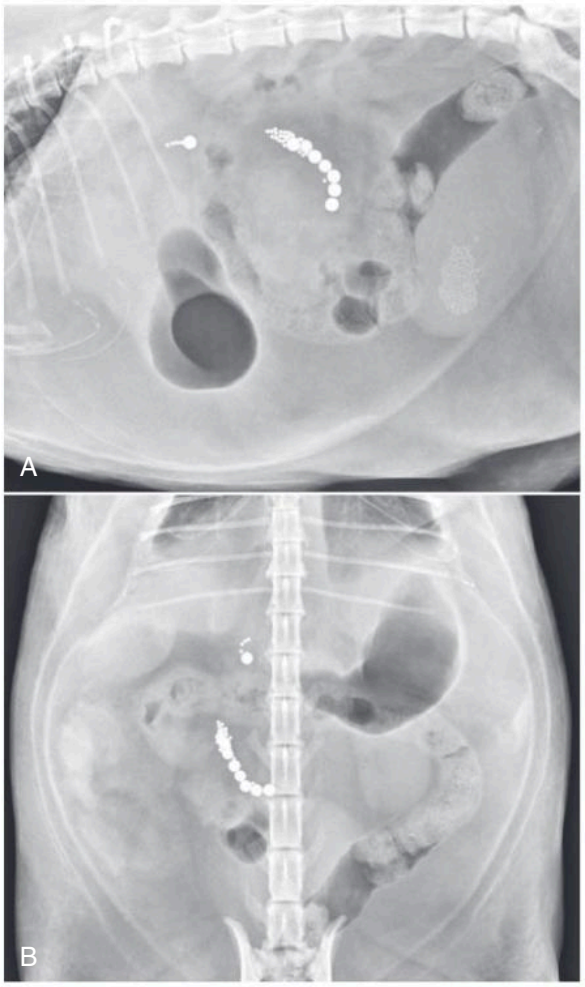


Fig. 46.12 Left lateral **(A)** and ventrodorsal (VD) **(B)** views of a cat given barium-impregnated polyethylene spheres (BIPSs) 12 hours before these radiographs were made. There is retention and clustering of the BIPSs in the duodenum. This is highly indicative of an obstruction. There is reduced serosal contrast in the mid-right abdomen. Ultrasonographically, there was plication of the jejunum. At surgical exploration, several perforations had been caused by fishing line foreign material.

ABNORMAL SMALL BOWEL

Nonobstructing Foreign Bodies

Radiopaque foreign objects can cause intestinal dilation or may be trapped proximal to a region of luminal narrowing due to mural thickening or extramural compression such as with adhesions from prior bowel surgery. However, some opaque foreign objects that are not associated with mechanical ileus may also be significant. For example, individual small rare earth magnets are likely to pass without complication. However, pressure necrosis can occur when there is transmural attraction of magnets in adjacent gastrointestinal segments, leading to bowel perforation (Fig. 46.13).[41–45] If magnet ingestion was not witnessed, and signs of peritonitis are not present, serial radiography can be used to monitor progression of transit. If these objects are not passing, surgical treatment could be considered.

U.S. pennies minted after 1982 and some non-U.S. coins have a major zinc composition and can cause hemolytic anemia

from acute zinc toxicity.[46] Hemolytic anemia from zinc toxicity is characterized by the formation of Heinz bodies. Zinc-containing game playing dye can also be problematic.[47] An acid pH is necessary for release of free zinc to cause toxicosis, which can occur over a period of just a few days. Importantly, by the time of radiography, the foreign objects may have moved into the small bowel, which decreases the suspicion for zinc toxicity. Signs of corrosion can be detected in many pennies that have been exposed to gastric acid, and any disk-shaped metallic foreign object should be checked closely for corrosion.

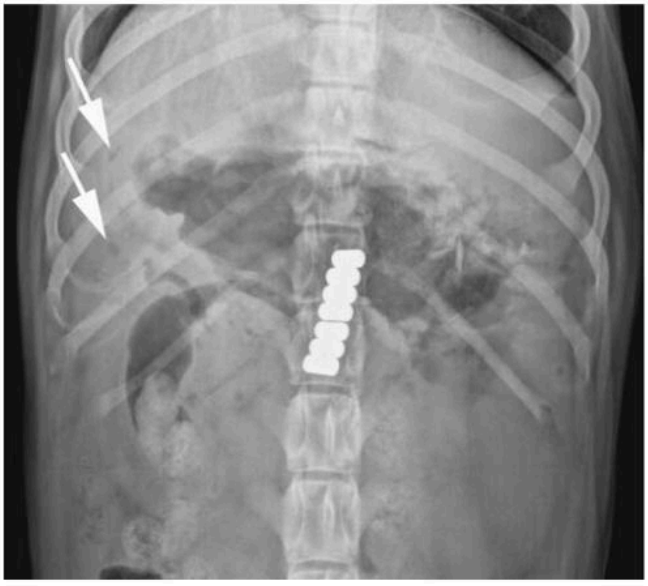


Fig. 46.13 Ventrodorsal radiograph of a dog that ingested seven rare earth magnets that have aligned. There are several foci of free abdominal gas (*white arrows*). At surgery, there was a gastric perforation and the magnets were free in the abdominal cavity. The magnets had pinched a segment of the gastric wall and caused pressure necrosis allowing the magnets to enter the abdominal cavity.

Sharply pointed radiopaque objects in the small bowel, such as a sewing needle, can potentially cause perforation and peritonitis but sewing needles with or without attached thread can pass through the gastrointestinal tract without complication. Clinical monitoring for signs of perforation and daily radiographic monitoring are justified, and if the sharp object has not passed within 3 days, surgical removal is warranted.[48]

Disease Resulting in Bowel Dilation

Failure of intestinal contents to pass through the intestinal tract is termed *ileus*. Ileus can be mechanical, caused by physical obstruction of the bowel, or functional (paralytic), in which peristaltic contractions of the bowel cease because of vascular or neuromuscular abnormalities. In functional ileus, the bowel remains patent.

The important imaging decision is whether the bowel dilation is indicative of a mechanical obstruction, and justifies a laparotomy, or if additional diagnostic tests are needed. In all instances, imaging decisions should not be made in isolation of all other patient information. In general, the appearance of mechanically obstructed bowel differs from functionally obstructed bowel by the following parameters:

1. Mechanically obstructed bowel is usually of larger diameter than functionally obstructed bowel.
2. Patients with mechanical obstruction usually have a mixed population of dilated and normal-diameter bowel segments, whereas patients with functional obstruction tend to have generalized mild dilation of the bowel.
3. Both gas and fluid are typically in the lumen of mechanically obstructed bowel, whereas functionally obstructed bowel tends to be completely gas filled or contain generalized fluid.

These parameters, however, are only guidelines and some overlap exists between mechanical and functional ileus, making the radiographic distinction impossible in some patients.

Table 46.6 lists diagnostic considerations for the more common patterns of bowel dilation. Patterns of dilation include (1) focal/mild: one to three loops are involved, and luminal distention is 1.5 to 2 times normal; (2) focal/severe: one to three loops are involved, and luminal distention is greater than twice normal (Fig. 46.14); (3) generalized/mild: all loops are involved, and luminal distention is 1.5 to 2 times normal

Table • 46.6

Pathologic Conditions by Length and Relative Distention of Affected Bowel.

FOCAL/MILD	FOCAL/SEVERE	GENERALIZED/MILD	GENERALIZED/SEVERE
Regional enteritis	Mechanical ileus	Functional ileus	Mechanical ileus
Regional peritonitis	Foreign object	Enteritis	Complete obstruction, distal bowel
Mechanical ileus, partial obstruction	Intussusception	Anticholinergic drugs	Intussusception
Early functional ileus	Bowel wall neoplasia	Electrolyte imbalance	Foreign object
Vascular compromise	Granulomatous wall infiltrate	Malabsorption	Bowel wall neoplasia
	Bowel stricture	Abdominal pain	Functional ileus
	Stenosis/atresia	Mechanical	Recent abdominal surgery
	Postsurgical adhesion	Partial obstructions at ileocolic junction (usually cats)	Spinal trauma (neurologic injury)
	Herniation		Intestinal volvulus (rare)
	Functional ileus		
	Parvovirus enteritis		
	Dysautonomia		

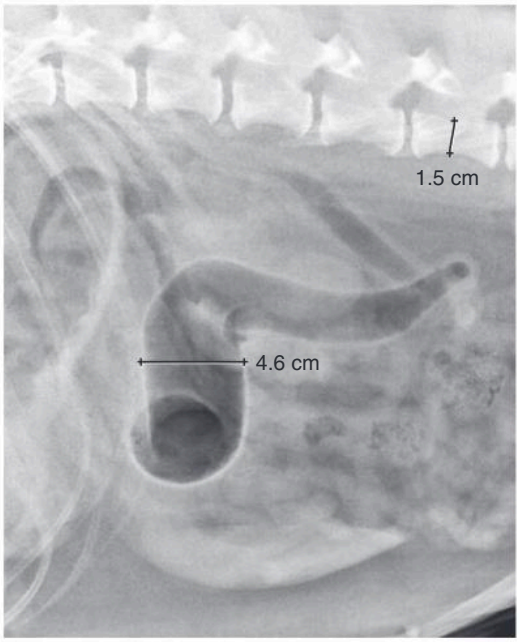


Fig. 46.14 A single severely dilated small bowel segment is present in this dog. The diameter is three times the central height of the L5 vertebral body. Several small bowel segments are seen caudal to the spleen and ventral to the fecal material in the colon. A segment of corncob, not visible, in the proximal jejunum was the cause of obstruction.



Fig. 46.15 This dog has mild generalized dilation of the small bowel. Most segments are gas filled with variable amounts of luminal gas. The bowel wall appears thick but this is likely due to silhouetting of luminal fluid with the wall. This dog had a history of mixed bowel diarrhea. The radiographic changes are supportive of but not diagnostic for enteritis.

(Fig. 46.15, eFig. 46.4); and (4) generalized/severe: all loops are involved, and luminal distention is greater than twice normal.

Mechanical Obstruction

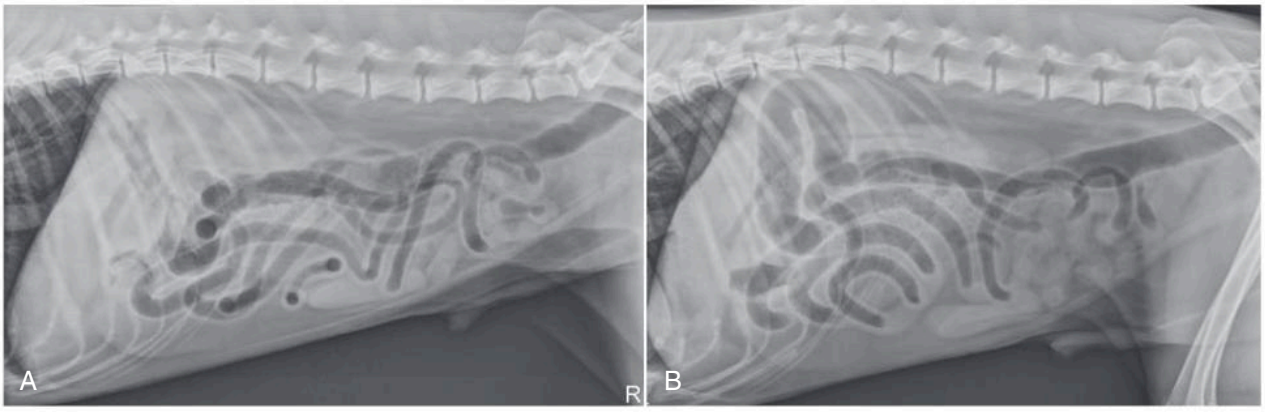
The small intestine can be occluded by foreign objects, intussusception, mural mass, or extrinsic lesions. The radiographic features of small bowel obstruction depend on three factors: the completeness of the obstruction, the location of the obstruction in the gastrointestinal tract, and the duration. The most consistent radiographic sign of mechanical obstruction is a variable degree of dilation of bowel segments orad to the site of obstruction (Fig. 46.16, eFig. 46.5). Subjective determination that bowel is significantly dilated can be made accurately even by interpreters with a beginning level of interpretation experience.[49] However, using ratios of small intestinal diameter to vertebral measurements may increase confidence that obstructive bowel disease is present. In dogs, determining the ratio of the small intestinal diameter relative to the L5 vertebral body height can be used, but it must be remembered that this ratio is only a guideline.[5] A ratio less than 1.4 to 1.6 usually rules out mechanical obstruction. Ratios of 1.95 were associated with a 77% to 80% probability of obstruction and a ratio of 2.07 was associated with an 86% to 90% probability of obstruction (see Fig. 46.18, eFig. 46.6).[49,50] In a series of cats, when the maximum small intestinal diameter to L2 vertebral endplate height was >2.0, gastrointestinal disease was present, and at a ratio of >2.5, the most likely abnormality was intestinal obstruction.[7]

A more distal obstruction leads to a greater number of distended segments. Obstructed bowel typically contains both fluid and gas unless the obstruction is quite proximal, allowing gas and fluid to reflux into the stomach. Depending on the location of a complete obstruction, there may be two distinctly different sizes of bowel with the smaller and normal diameter bowel distal or aboral to the dilated bowel. More complete and longer duration obstruction results in greater bowel distention. As intestines become progressively more distended, the segments become crowded into a relatively smaller space, often assuming a *stacked* appearance (Fig. 46.17).

Acute duodenal obstruction is challenging to diagnose because the stomach acts as a reservoir for gas and fluid that might collect. Also, if vomiting is frequent, the accumulated fluid and gas are expelled from the stomach and duodenum. With chronic duodenal obstruction, however, gastric distention develops (Fig. 46.18) and can be pronounced. A moderate to large volume of fluid and gas in the stomach, with an otherwise empty small intestinal tract, in a vomiting patient should raise suspicion of duodenal obstruction or pyloric outflow obstruction.

Partial obstructions may also be difficult to detect. This is particularly true when the partial obstruction is of short duration and in the proximal duodenum. Longstanding partial distal obstructions result in accumulation of opaque granular material proximal to the site of obstruction. This is caused by desiccation of ingesta that becomes trapped proximal to the obstruction. The desiccated material often has the appearance of feces, and the identification of this fecal-like material in the small rather than large bowel is a reliable sign of partial distal small bowel obstruction. This appearance has been referred to as the *gravel sign*. One scenario in which chronic partial obstruction occurs is elderly cats that develop an ileal adenocarcinoma causing partial bowel obstruction (Fig. 46.19, eFig. 46.7). If a bowel obstruction is complete, the intestine distal to the obstruction is likely to be empty.

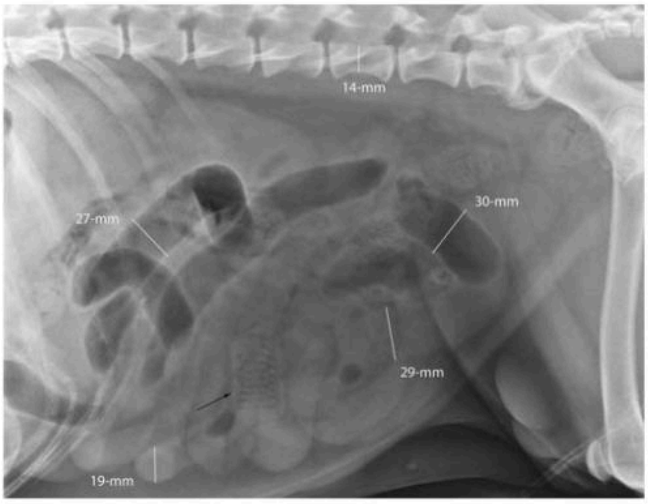
Foreign objects are a common cause of obstruction. Foreign bodies composed of mineral or metal are easily recognized. Small-sized rocks, clay litter, hard-shelled seeds, or other debris are ingested frequently by dogs and cats and opaque medicinal tablets may be administered by owners.[51] These small mineral opacities are usually incidental and pass without causing obstruction. Nonmineralized, nonmetallic foreign objects are much more difficult to identify. Fruit pits, corncobs, and other nonopaque objects may be recognized by their geometrically shaped radiolucencies on survey radiographs (see eFig. 46.6).[52] A nonopaque foreign object with irregular surfaces, especially with grooves or pockets, can entrap small, mineralized ingested debris and gas and may become more visible (Fig. 46.20, eFigs. 46.8, 46.9). Careful application of abdominal compression may enhance the conspicuity of these foreign objects (see Fig. 46.20B).



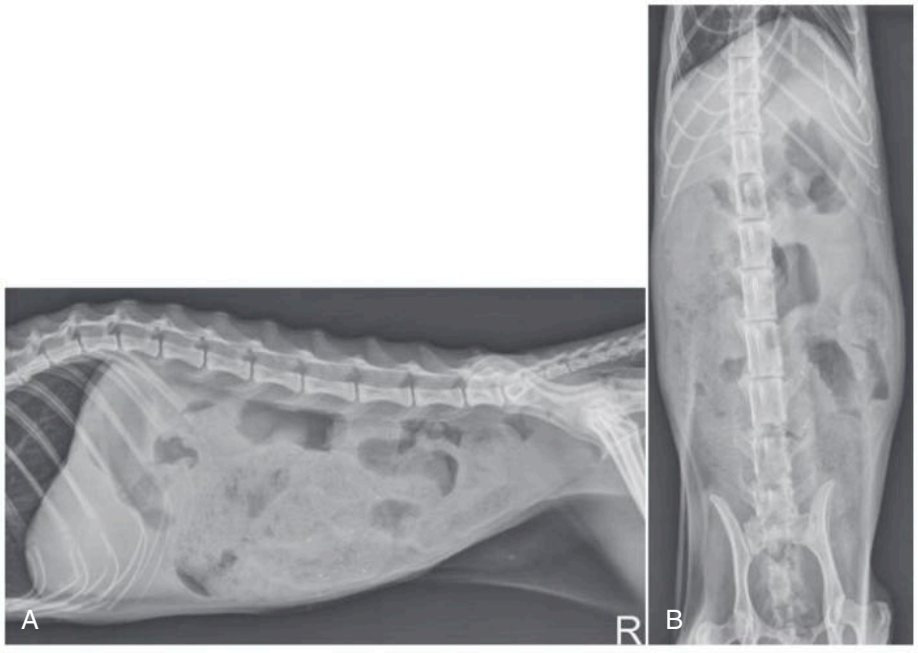
eFig. 46.4 Right lateral **(A)** and left lateral **(B)** radiographs of a dog with enteritis and functional ileus. All small intestines are uniformly mildly distended with gas.



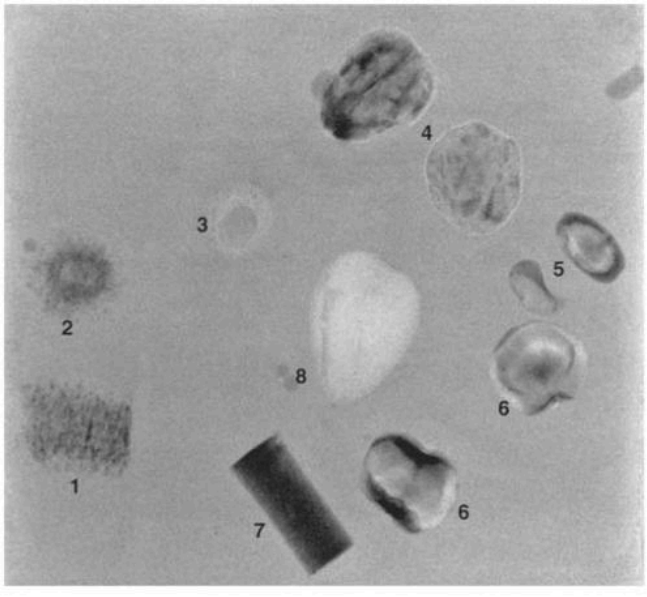
eFig. 46.5 Lateral radiograph of a dog with a cloth foreign body in the jejunum. Striated foreign material extends through the midabdomen and connects craniodorsally with a gas distended intestinal segment. Most of the small intestines are normal in diameter. The colon is visible at the pelvic inlet and is almost completely empty.



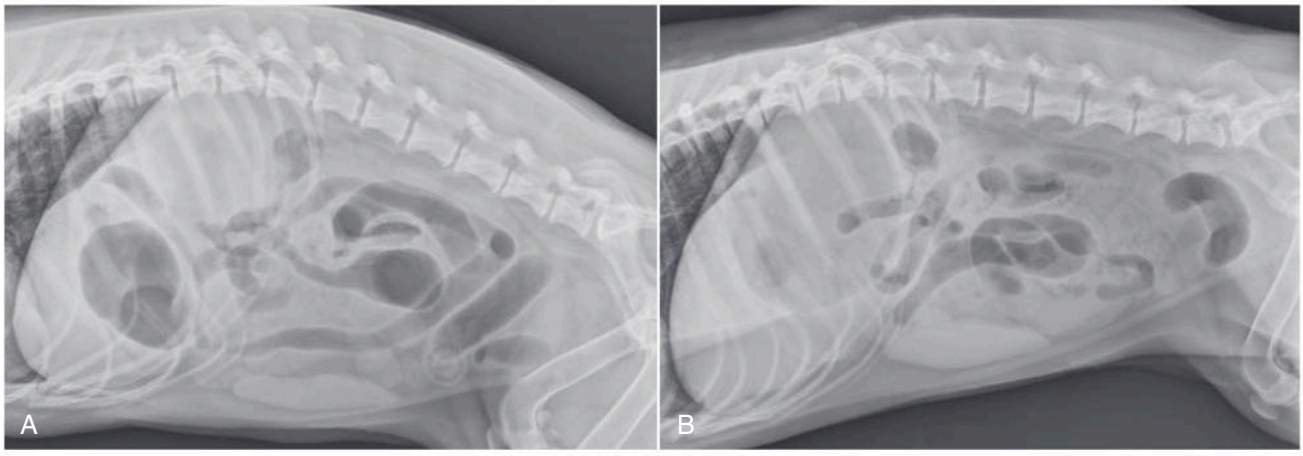
eFig. 46.6 Lateral radiograph of a dog with mechanical small bowel obstruction. The ratio of small intestinal diameter to the height of L5 ranges from 1.35 to 2.14 and is consistent with a moderately high probability of intestinal obstruction, up to 86% based on published values. Subjectively, there are two populations of small intestinal diameter and multiple segments are abnormally dilated, also supporting an obstruction. In this dog the diagnosis of obstruction is made obvious by the finding of a reticular gas pattern in one segment (*arrow*) that is characteristic of a corncob foreign body. This dog had been vomiting for 3 days. A corncob was removed from the ileum.



eFig. 46.7 Right lateral **(A)** and ventrodorsal **(B)** radiographs of a cat with chronic partial small intestinal obstruction secondary to an adenocarcinoma at the ileocecocolic junction. Multiple small intestinal segments are severely distended and filled with mixed soft tissue, gas, and mineral opacity material with a stippled appearance, resembling fecal material.



eFig. 46.8 Various nonopaque foreign bodies radiographed in a water bath. *1*, Section of corncob viewed side on; *2*, section of corncob viewed end-on; *3*, peach pit; *4*, walnuts; *5*, acorns; *6*, chestnuts; *7*, wine cork; *8*, avocado pit. (From Lamb CR, Hanson K. Radiological identification of nonopaque intestinal foreign bodies. *Vet Radiol Ultrasound.* 1994;35:87.)



eFig. 46.9 Left lateral **(A)** and right lateral **(B)** radiographs of a dog with small intestinal mechanical obstruction secondary to a corncob foreign body. There are multiple gas-distended small intestinal segments as well as segments with a normal diameter. The corncob foreign body is visible end-on in the caudoventral abdomen in the left lateral view **(A)** as a round intraluminal structure. In the right lateral view **(B)**, it is also visible caudoventrally but has a more rectangular, striated appearance.

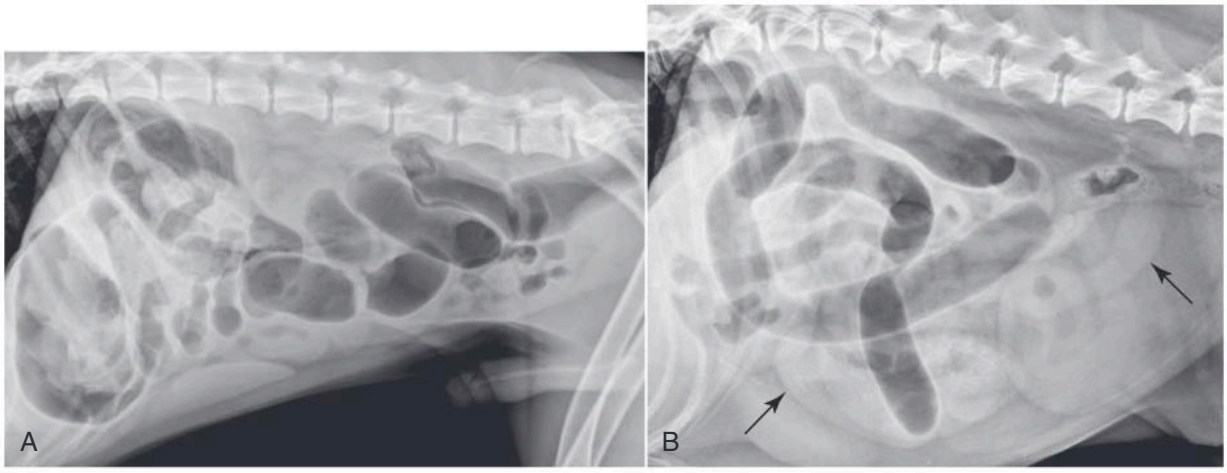


Fig. 46.16 **A,** Lateral radiograph of a dog with mechanical jejunal obstruction caused by a cloth foreign body. There are multiple small intestinal segments that are abnormally dilated. The configuration of the dilated segments indicates that they cannot all be colon. There are two populations of small bowel: large segments and normal segments. Having multiple populations of small bowel size is common in dogs with mechanical obstruction. This dog has less intraluminal fluid than most dogs with mechanical obstruction. **B,** Lateral radiograph of a dog with mechanical obstruction caused by a peach pit. There are a few gas-distended segments of jejunum, and some distended segments also contain fluid (*black arrows*).



Fig. 46.17 Lateral view of a dog with a distal small bowel obstruction. The bowel is not severely dilated, and there are several segments of normal diameter. However, those segments that are gas dilated are aligned vertically and horizontally in a *stacked* pattern. Metallic abdominal wall sutures are present from a surgery 7 years prior for removal of a foreign body.

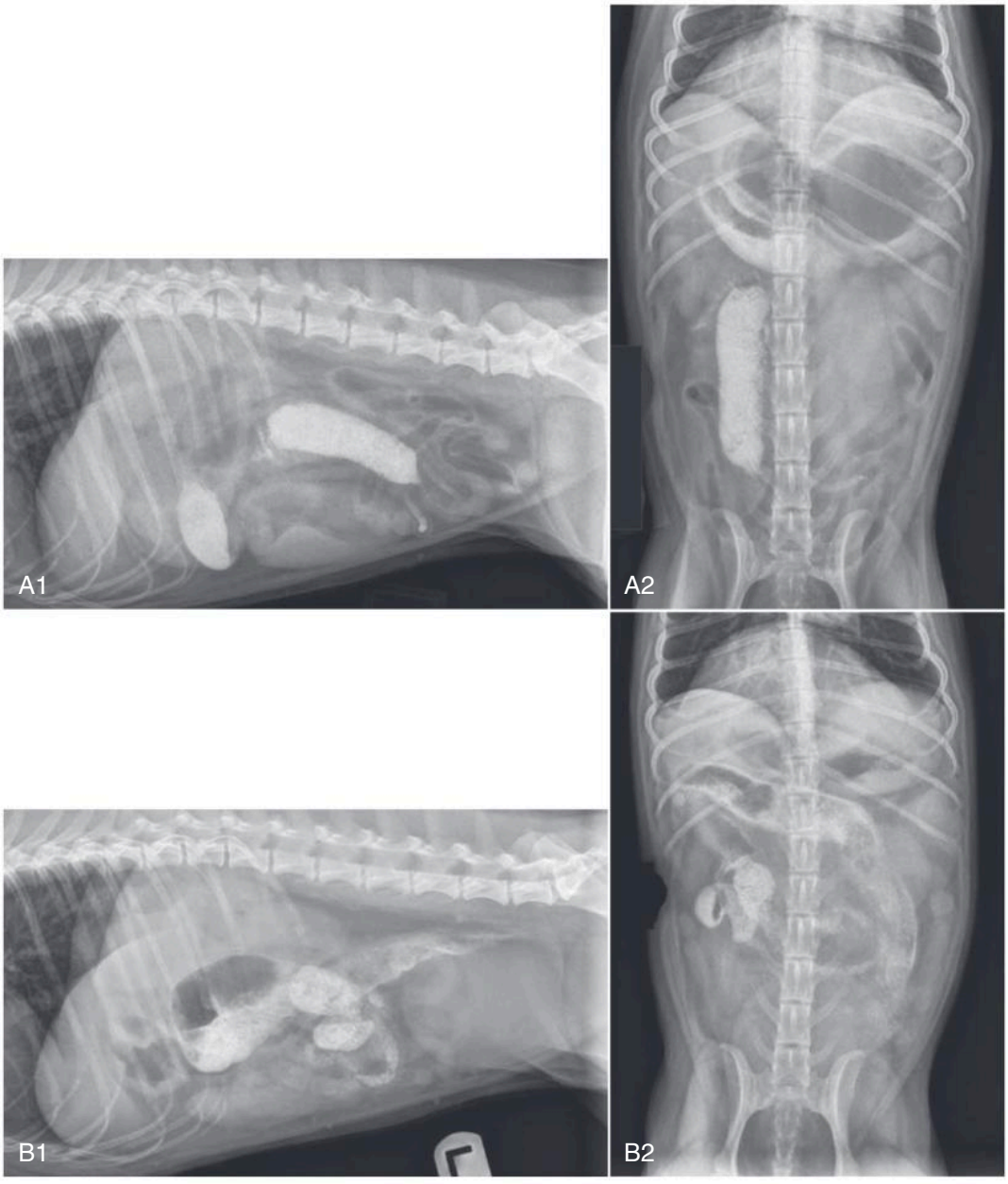
Sand impaction can also cause intestinal obstruction, and this tends to be in the distal small intestine (Fig. 46.21, eFig. 46.10).[53] Radiographically, there is segmental dilation of the bowel that contains mineral opaque material. Although sand particles are small, it is proposed that the sand coalesces and dehydrates to form the obstruction. Sequential radiographs can be used to monitor progression of the sand but if no progress is observed, a laparotomy should be considered.[53]

A pneumocolon can be used to differentiate the source of dilated bowel as small intestine versus colon and can assist in defining the location of obvious foreign material or mottled mineralized material to be in the small versus large bowel (Fig. 46.22, eFig. 46.11). The use of 24-hour serial survey radiographs, ultrasound evaluation, or a contrast study may be necessary to confirm the diagnosis of partial obstruction suggested by abnormal luminal contents. Persistence of small opaque foreign objects in the same intestinal location in serial radiographs over a 24- to 48-hour period should increase the suspicion of partial obstruction.

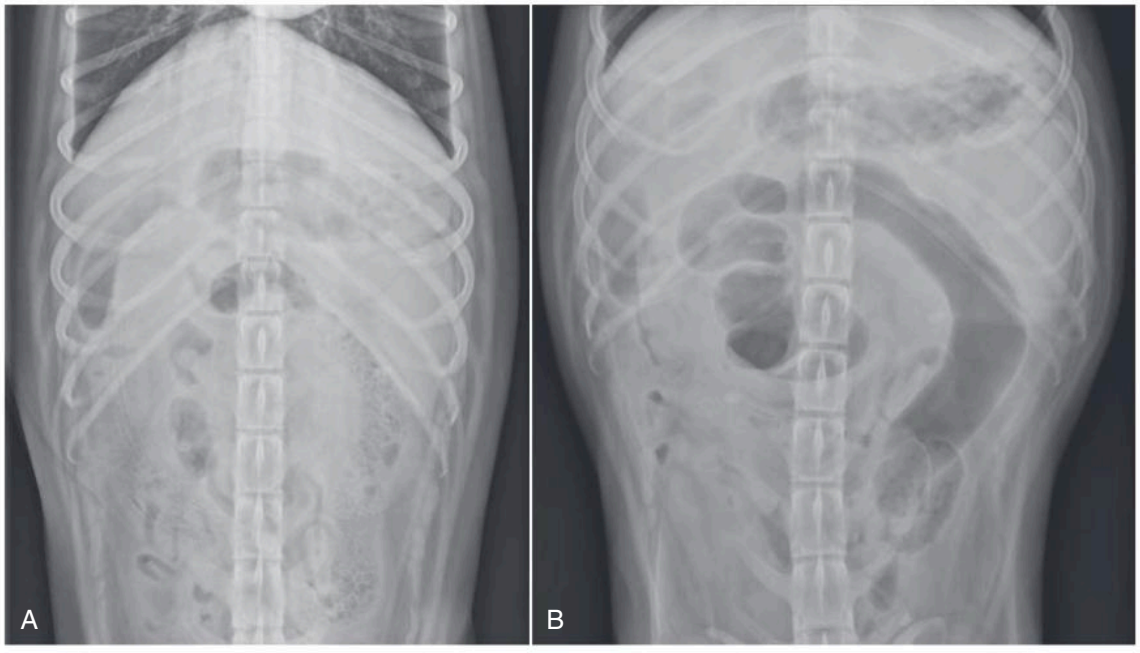
Two recent studies looked at the use of serial radiographs relative to mechanical bowel obstruction. One assessed the diagnostic accuracy of mechanical obstruction between initial and one follow-up radiograph between 7 and 28 hours. These dogs and cats ultimately had nonopaque foreign bodies causing partial or complete obstruction. Accuracy did not significantly increase after the follow-up radiograph, and when the repeat radiograph is inclusive, alternate diagnostic studies such as ultrasound should be considered.[54] The second study evaluated the incidence of resolution of mechanical obstruction and resolution of gastrointestinal foreign bodies as assessed by repeat radiographs after 36-hour intervals of medical management. Approximately 17% of patients with only small intestine affected and 11% of patients with gastric plus small intestinal foreign bodies and mechanical obstruction resolved after medical management.[55]

The ultrasonographic appearance of ingested foreign material varies according to the composition of the material (Fig. 46.23).[56] The acoustic pattern caused by the rigid foreign object may have a shape that can be recognized specifically. Objects that transmit the beam, such as some types of rubber balls, are more readily identified. Those that create a strong reflection with marked acoustic shadowing can be more difficult to define initially. When these objects cause incomplete obstruction, they are frequently associated with increased intestinal motility resulting from irritation. With more complete obstruction, the foreign object may be associated with accumulation of fluid in the bowel cranial to the obstruction. In vomiting dogs, ultrasound findings of a jejunal serosa-to-serosa measurement of more than 1.5 cm, with normal wall layering, and a fluid-filled or gas-filled lumen should prompt careful interrogation of the bowel for an obstructive lesion.[57] A wide range of motility, from reduced to increased, was observed in dogs with mechanical obstruction and was not found to be a useful discriminatory feature relative to nonobstructive causes of vomiting.[57]

Both dogs and cats can ingest linear foreign material. Linear types of foreign bodies accounted for 35% of foreign bodies in



eFig. 46.10 Lateral **(A1)** and ventrodorsal **(A2)** radiographs of a 3-year-old female spayed Shih Tzu with acute vomiting and lethargy. Mineral opaque jejunal content in multiple segments has a grainy structure. Lateral **(B1)** and ventrodorsal **(B2)** radiographs 24 hours later with fasting and fluid therapy, the content moved into the colon. This is an example of sand impaction resolved with medical therapy.



eFig. 46.11 Ventrodorsal radiographs of the cranial abdomen of a dog before **(A)** and after **(B)** performing a pneumocolon. Striated foreign material is visible in the right cranial abdomen medial to the duodenum. Particulate material is visible in the descending colon on the left side of the abdomen, but the ascending colon is not de finitively identified. The entirety of the colon and cecum is gas filled in **B** and the striated material is located in the small intestine.

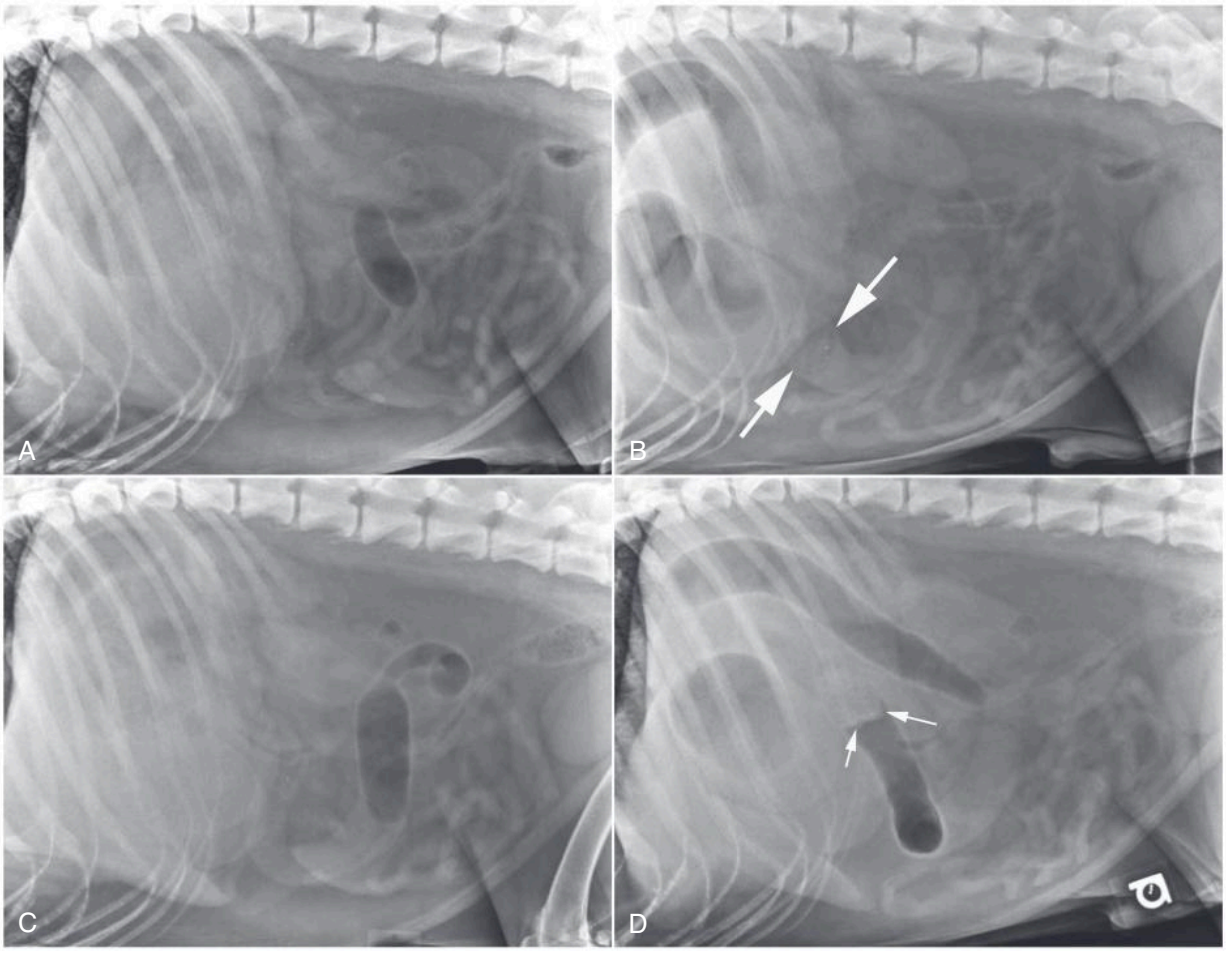


Fig. 46.18 Right and left lateral serial radiographs of a dog with acute onset of vomiting 2 days prior. Right lateral **(A)** and left lateral **(B)** views were obtained at presentation. In **A** the size of the stomach was judged to be at the upper limit of normal, containing both gas and fluid. There is also a single vertically oriented short segment of small bowel that is distended with gas, and there is a small amount of gas and granular material in the descending colon. The remainder of the bowel is gasless and of small diameter. In **B,** there is gas in the proximal duodenum, evidence that the pylorus is patent, and the duodenum is abnormally dilated. Immediately caudal and ventral to the fluid-filled pylorus is a round mottled opacity in a fluid-filled dilated segment (*white arrows*). Right **(C)** and left **(D)** lateral views were obtained several hours later. They are relatively unchanged from the earlier radiographs. However, in **D,** there is now gas in the distal duodenum outlining a soft tissue foreign body (*white arrows*). A focal mineral opacity is present in all views in the caudal ventral aspect of this foreign body that was subsequently identi fied as a corncob.

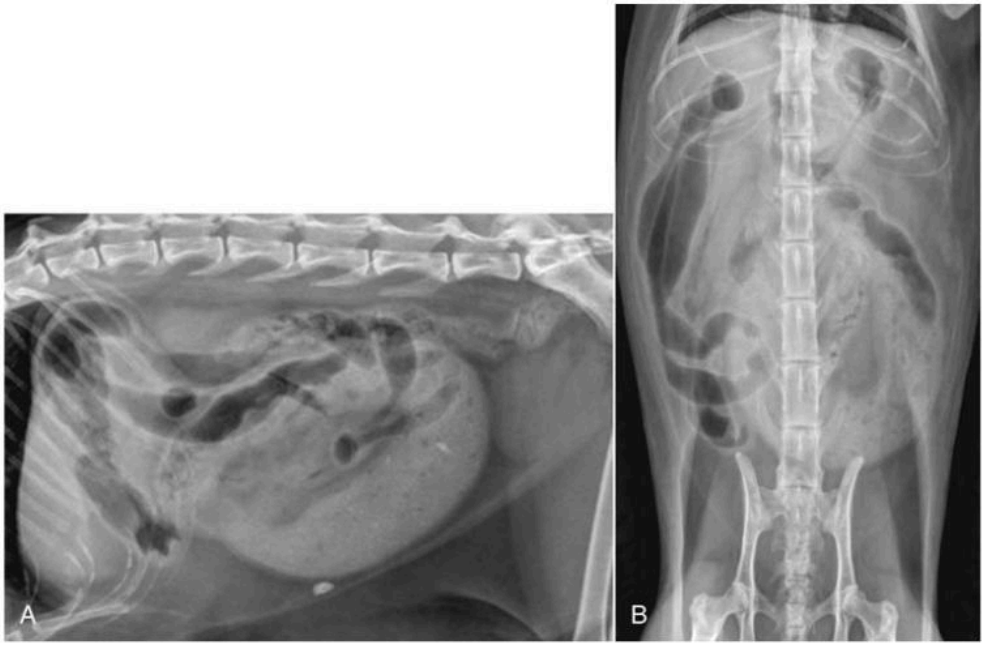


Fig. 46.19 Lateral **(A)** and ventrodorsal (VD) **(B)** radiographs of a cat with chronic partial ileal obstruction from an adenocarcinoma. The ileum is markedly distended with fecal-like material. This segment is differentiated from large bowel by its position ventral to the colon in **A** and its caudal flexure in **B**; the colon does not have a caudal flexure as seen in **B**. The opacity of the material in the bowel is caused by continued desiccation because of its inability to pass the obstruction. More proximal bowel segments may continue to remain normal.

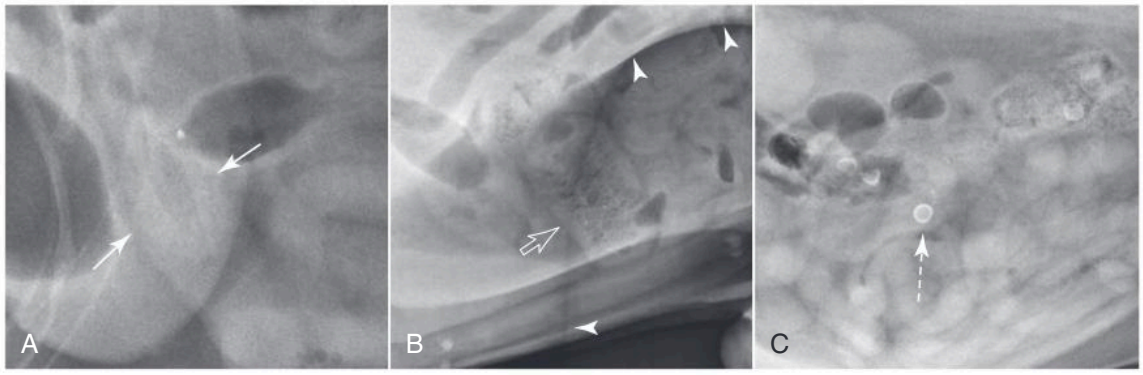


Fig. 46.20 Radiolucent and opaque foreign bodies. **A** is an obstructive peach pit (between the *white arrows*). Its subtle shape is defined best by the radiolucent oval center. A small focus of opaque debris is trapped in one of the crevasses of the outer surface. **B** is an obstructing corncob (*open arrow*). A compression paddle (border indicated by *white arrowheads*) was used to displace bowel, making the corncob more easily seen. Note the gas as well as mineral debris trapped in the kernel pockets. **C** is a dog with ingested Hackberry tree seeds (*dashed arrow*). Based on their size, they would not be expected to cause obstruction, and several are present in the colon.

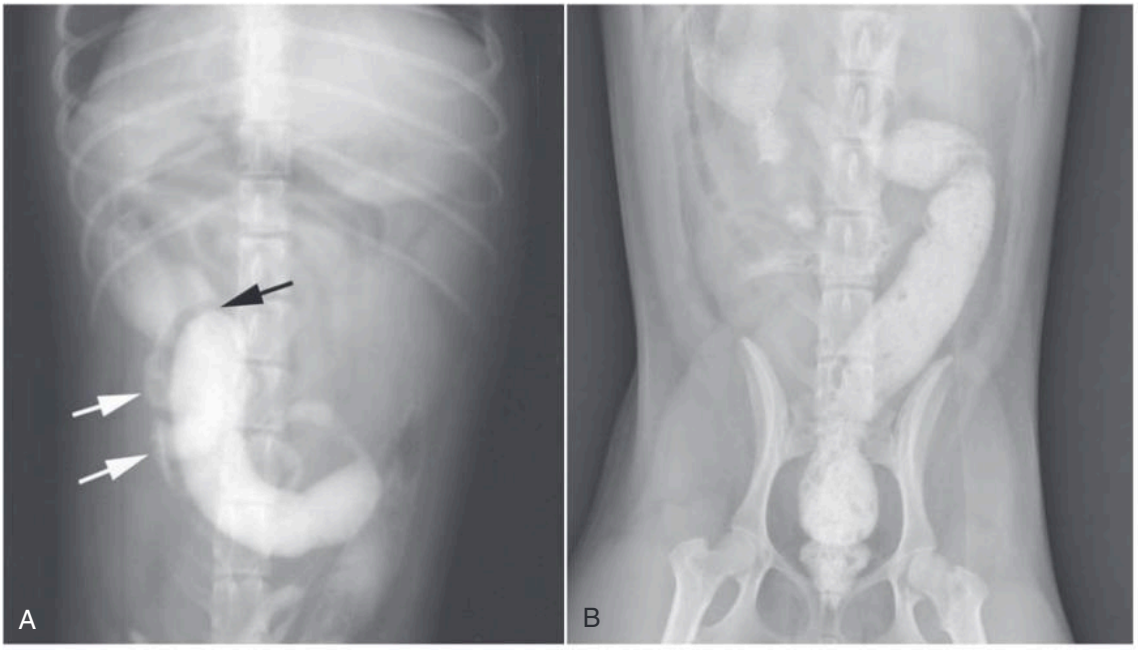
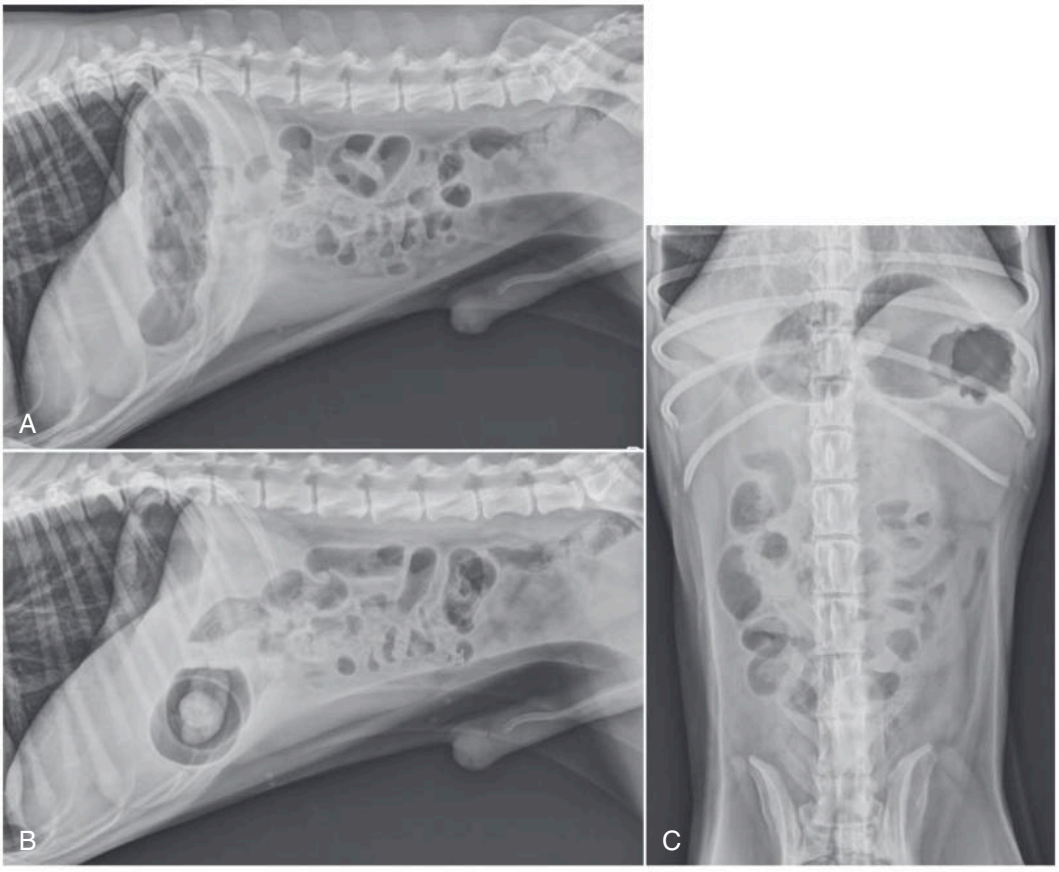
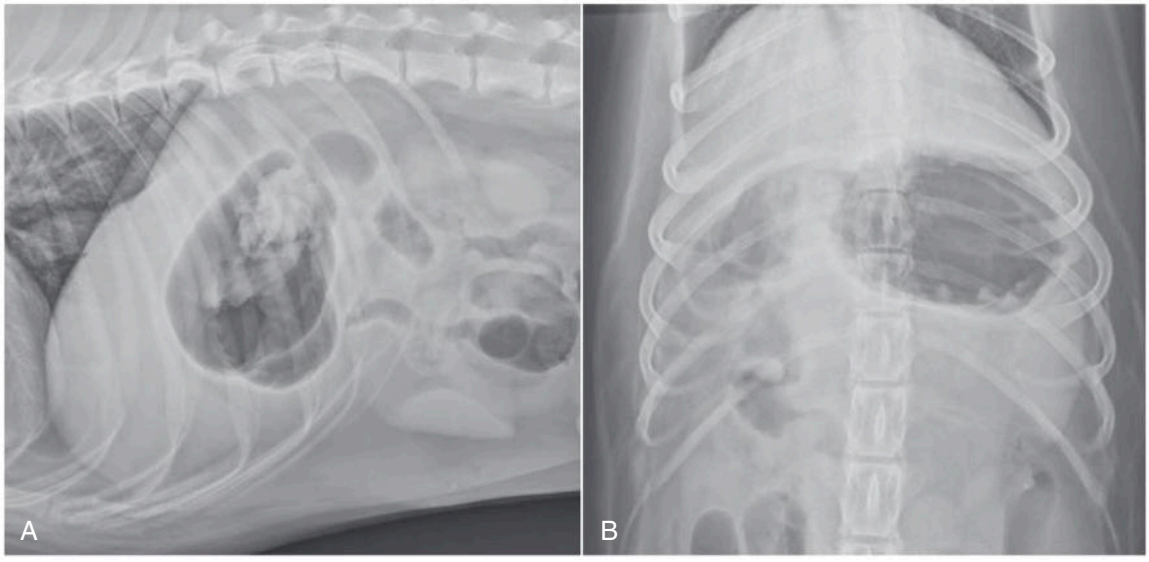


Fig. 46.21 **A,** Ventrodorsal (VD) radiograph of the abdomen of a dog with sand impaction of the ileum. The area of the ileocolic valve is indicated by the *black arrow*. There is a small amount of sand in the cecum (*white arrows*) and ascending colon. **B,** Follow-up radiograph in which the sand has moved spontaneously from the ileum into the colon, negating the need for a laparotomy. Follow-up radiographs are valuable to monitor the progression of intestinal foreign material; the clinical condition of the patient must be considered if follow-up radiographs are planned as acutely ill patients may be candidates for immediate laparotomy rather than a delay for additional images.

one population of dogs.[58] Linear foreign material that becomes trapped in the intestine usually causes both an abnormal shape and contour of the loops and an abnormal gas pattern (see Fig. 46.10).[7] Some portion of the linear material typically becomes fixed at an orad location, most commonly in the pylorus in dogs and under the tongue in cats.[58–60] The remainder of the length passes into the small intestine. The peristaltic action of the bowel causes it to climb along the linear foreign body, which results in a pleated, plicated, or bunched appearance of the affected loops. With a linear foreign body, the intestinal segments may not become markedly distended but gas commonly becomes trapped in pockets formed by the pleats. The result is an abnormal pattern of round, tapered, short-tubular, and sometimes crescent- or comma-shaped gas shapes (Fig. 46.24, eFig. 46.12). Gas bubbles of these shapes can be referred to as having a geometric shape. This pattern may be accentuated in the left lateral view as gastric gas moves into the duodenum from the stomach. The left lateral also often allows identification of foreign material anchored in the pylorus, surrounded by gas (Fig. 46.25, eFig. 46.13). The abnormal contour and plication pattern are usually obvious in a positive-contrast study (Fig. 46.26). Although barium can be used for positive-contrast studies in patients suspected of having a linear foreign body, if there is any concern for perforation of the bowel, consideration should be given to the use of low-osmolar water-soluble contrast medium to avoid barium contamination



eFig. 46.12 Right lateral **(A)**, left lateral **(B)**, and ventrodorsal **(C)** radiographs of a dog with linear foreign body obstruction. The small intestines are plicated with abnormal triangular and teardrop-shaped gas patterns. A foreign body is outlined by gas in the pyloric antrum in the left lateral projection **(B)**. The duodenum has a curved appearance as it connects to the pylorus.



eFig. 46.13 Left lateral **(A)** and ventrodorsal (VD) **(B)** radiographs of the cranial abdomen of a dog with linear foreign body obstruction. A foreign body is outlined by gas in the pyloric antrum in the left lateral projection **(B)**. The duodenum has a curved appearance as it connects to the pylorus. The normally straight course of the duodenum in the VD projection is not visible, instead the duodenum has a serpentine course.

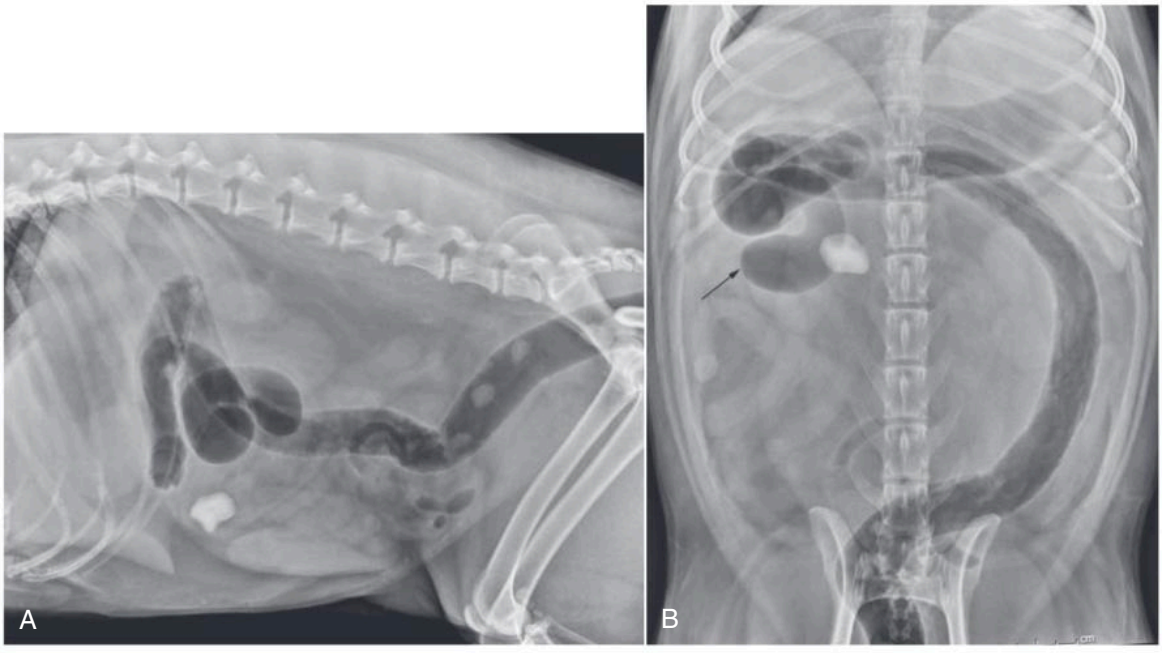


Fig. 46.22 Left lateral **(A)** and ventrodorsal (VD) **(B)** views following introduction of air into the colon (tubing evident in the distal descending colon). The pneumocolon defines that the obvious rock foreign body is not in the colon. A rock was removed from the duodenal-jejunal junction. The gas filled cecum is indicated by the *arrow*.

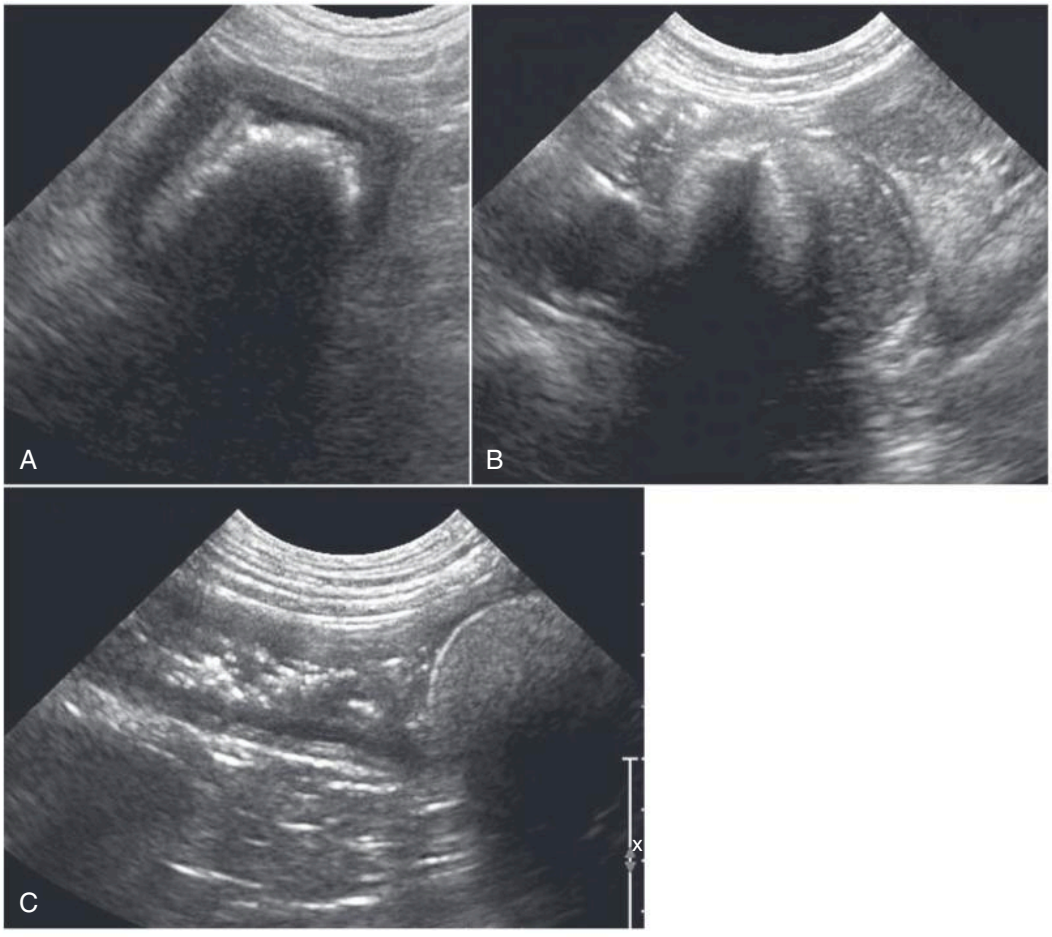


Fig. 46.23 Three ultrasound images of intestinal foreign bodies each with a different shape. All of these foreign bodies have strong acoustic shadowing. The object in **A** was undetermined, **B** was several pieces of hoof material, and **C** was a portion of a rubber ball. In **C,** there is a longitudinal section of the bowel orad to the foreign body that is filled with mucoid fluid.

of the abdomen. If the linear material is absorptive in nature, such as fabric, it can absorb fluid incompletely and have a mottled to linear, streaked gas pattern. In the cat, the plication of the bowel can cause a *clumped* or *bunched* positioning of the bowel. The displacement of the small bowel into the middle or right side of the abdomen in the obese cat should not be misinterpreted as plication caused by a linear foreign body (Fig. 46.27).

The ultrasound appearance of linear material depends on the amount of gas and fluid accumulated around the foreign material. Plication of the bowel around an echogenic line has been described most frequently (Fig. 46.28, eFig. 46.14).[56] This differs from the smooth, straight mucosa normally seen on either side of the bright linear stripe of an empty normal bowel lumen. If the linear foreign material is in the duodenum, it may be traceable into the stomach.[61]

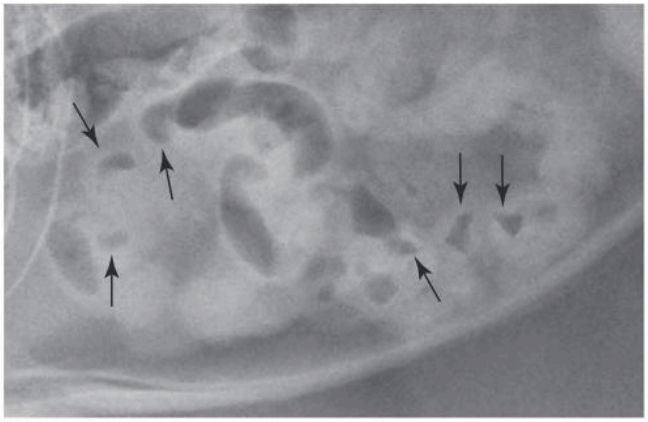


Fig. 46.24 Lateral view of a cat with a linear foreign body. The jejunum is bunched in the ventral abdomen, and gas has become trapped in the plications, creating small, irregularly shaped bubbles (*black arrows*), a pattern that is not typically present in normal bowel.

A serious complication of a chronic linear foreign body is laceration of the intestinal wall. If the laceration is small, serosal adhesion to an adjacent loop can occur, resulting in a fixed position of two or more loops. If the laceration is large, peritonitis occurs with possible free abdominal gas.

There are some differences between dogs and cats with regard to linear foreign objects: (1) affected dogs are usually older and have less irregularity in the gas pattern; (2) dogs are more prone to secondary intussusception; (3) dogs have more evidence of bowel trauma or bowel laceration and peritonitis, both radiographically and surgically; and (4) the probability of death as a result of linear foreign body is nearly twice as high in dogs as in cats.[60,61] Intestinal perforation caused by linear foreign material or other diseases should be suspected ultrasonographically when a combination of focal hyperechoic mesenteric fat, echogenic peritoneal effusion, and fluid in the bowel is identified.

Intussusception, the invagination of one portion (intussusceptum) of the gastrointestinal tract into the lumen (intussuscipiens) of an adjacent segment, can be initiated by many events, including motility disorders, inflammatory wall lesions, neoplasia, foreign bodies, or idiopathic causes.[62,63] Although an intussusception can occur anywhere along the digestive tract, the majority occur at the ileocolic or cecocolic junction. The radiographic appearance of an intussusception is influenced by the completeness of the obstruction.[8] Distal intussusceptions can result in generalized severe dilation of the small bowel, creating the typical appearance of mechanical obstruction, although many patients with an intussusception have a partial rather than a complete obstruction. The intussusceptum will occasionally create a visible soft tissue mass effect in the colon if sufficient gas is present in the intussuscipiens to provide contrast (Fig. 46.29). In most patients, however, differentiating intussusception from other causes of mechanical obstruction based solely on survey radiographs is not possible. Ultrasound

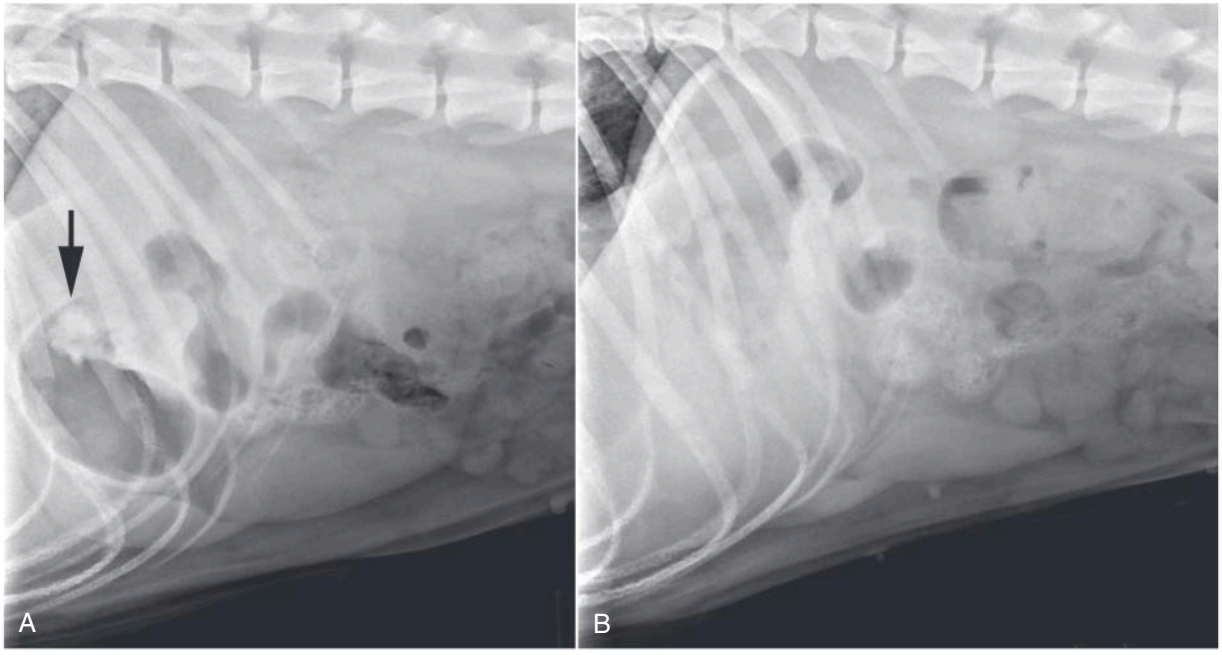
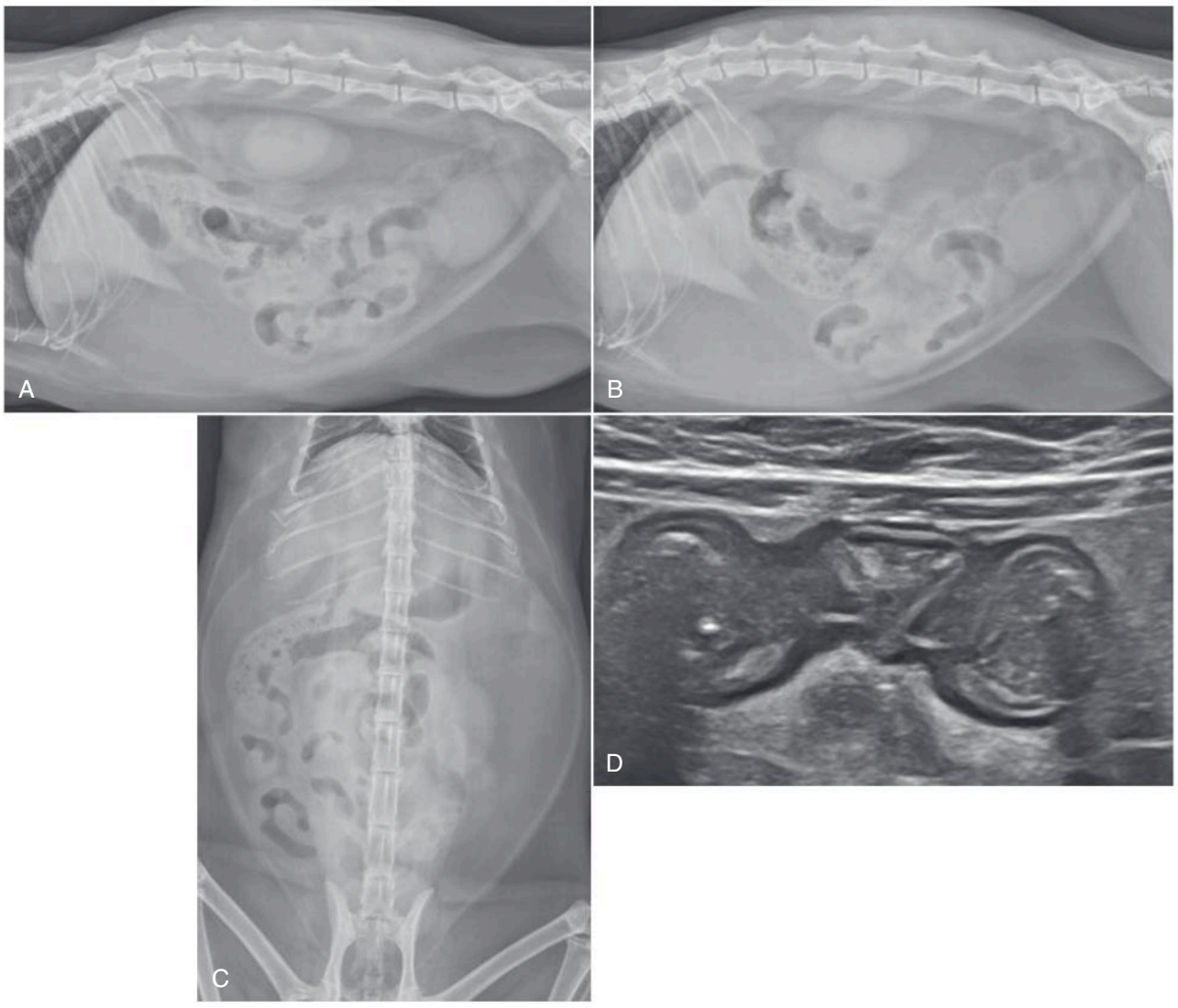


Fig. 46.25 Left **(A)** and right **(B)** lateral radiographs of a dog with a linear foreign body. The anchoring of the foreign material in the pylorus is obvious in the left lateral view (*black arrow*) due to gas being present in the pylorus. Some gas has also left the stomach in the left lateral view to enter the duodenum, and the pleated appearance of this segment of intestine is more obvious as a result compared to the right lateral.



eFig. 46.14 Left lateral **(A)**, right lateral **(B)**, and ventrodorsal **(C)** radiographs of a cat with linear foreign body obstruction. The small intestines are clumped together in the ventral abdomen. The outline of the small intestine is undulant, and there is an abnormal gas pattern with numerous comma-shaped or triangular gas opacities. **D,** Ultrasound image of a jejunal segment in the same cat. A thin hyperechoic line extends through the lumen, whereas the intestinal walls are folded around it. The central portion of the lumen has a triangular appearance, which corresponds to the triangular shape gas opacities seen radiographically.

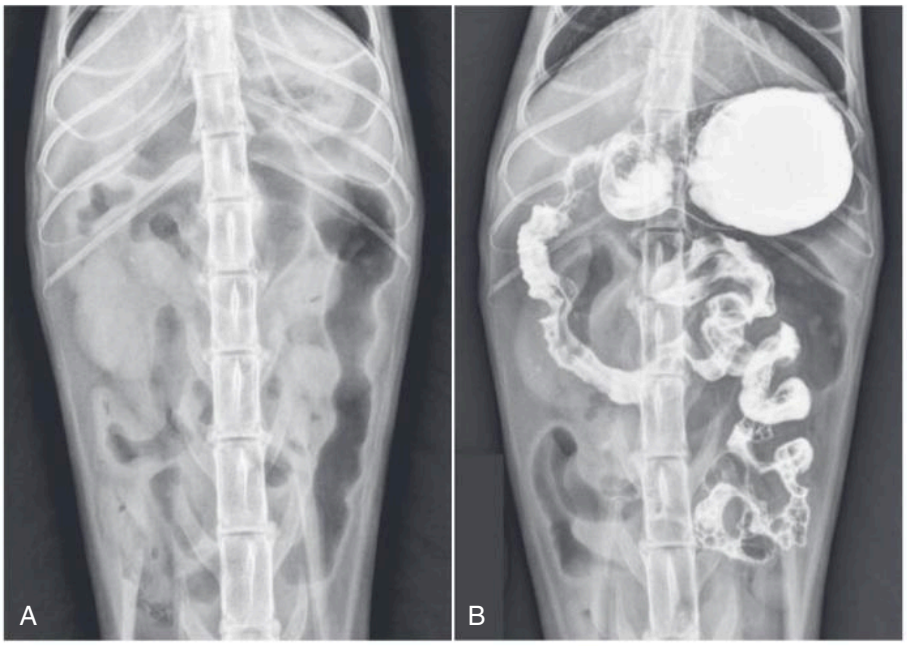


Fig. 46.26 Survey ventrodorsal (VD) and barium-contrast study of linear foreign body in a cat. In the survey image, there is an abnormally shaped gas accumulation in the right 12th intercostal space. The classic plication pattern of the bowel is visible in the barium image.

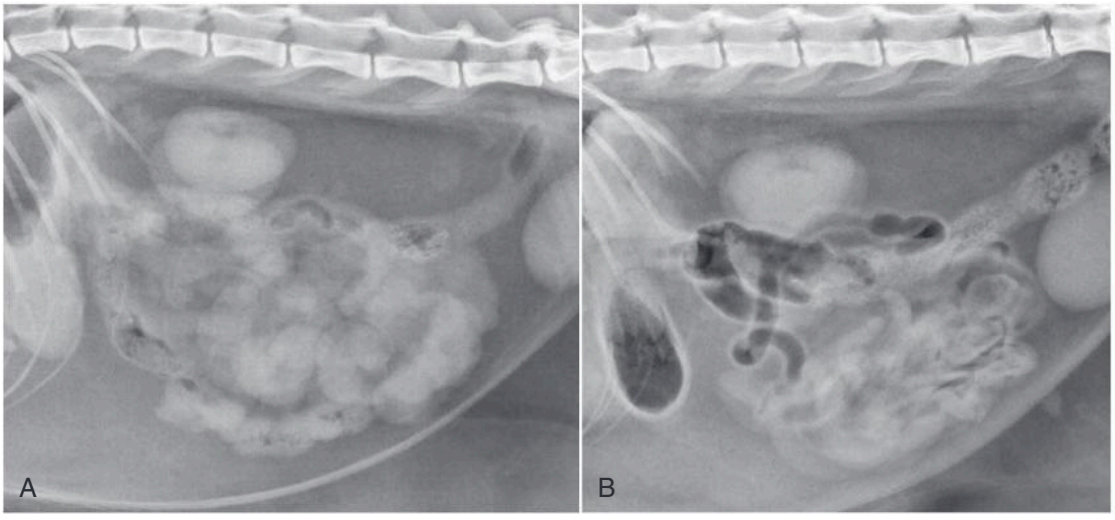


Fig. 46.27 Image **A** is an obese cat with an extensive jejunal linear foreign body. Image **B** is an obese cat without linear foreign body. Both have a relative *clumping* of the small intestine in the central abdomen. The effect of the intra-abdominal fat on the positioning of the small intestine makes differentiation of true plication difficult in the obese cat, particularly where there is minimal gas in the bowel to cause the formation of geometrically shaped gas bubbles. There is more pronounced serosal border undulation in cat **A** compared with **B** to increase suspicion of plication. Ultrasound or a contrast study can be used in such patients to confirm the linear foreign body.

evaluation is preferred to positive-contrast studies for substantiating the diagnosis.

Intussusceptions have a characteristic ultrasonographic appearance (Fig. 46.30). The telescoping effect results in a concentric ring appearance when viewed in the transverse plane and a multilinear pattern when viewed in the longitudinal plane.[64,65] A hyperechoic region is typically noted mildly eccentrically positioned within the concentric or linear pattern, caused by mesenteric fat pulled into the intussuscipiens. The shape of this hyperechoic material may be round or semilunar. If an anechoic feature is evident centrally, it most likely represents a small volume of fluid within the lumen of the intussusceptum; if evident eccentrically, it likely represents fluid between the intussusceptum and intussuscipiens. When viewed in the long axis, fluid distention is often seen in the bowel proximal to the lesion. Multiplane imaging of the suspected intussusception is important to confirm its features. Bowel loops situated immediately adjacent to each other may be misinterpreted as an intussusception.[66] Dogs with Doppler evidence of blood flow in the mesentery of the intussuscepted bowel were more likely to have successful reduction compared with those with no evidence of flow.[67]

Proliferating tissue masses originating within the intestinal wall include tumors, polyps, granulomatous infiltrates, and

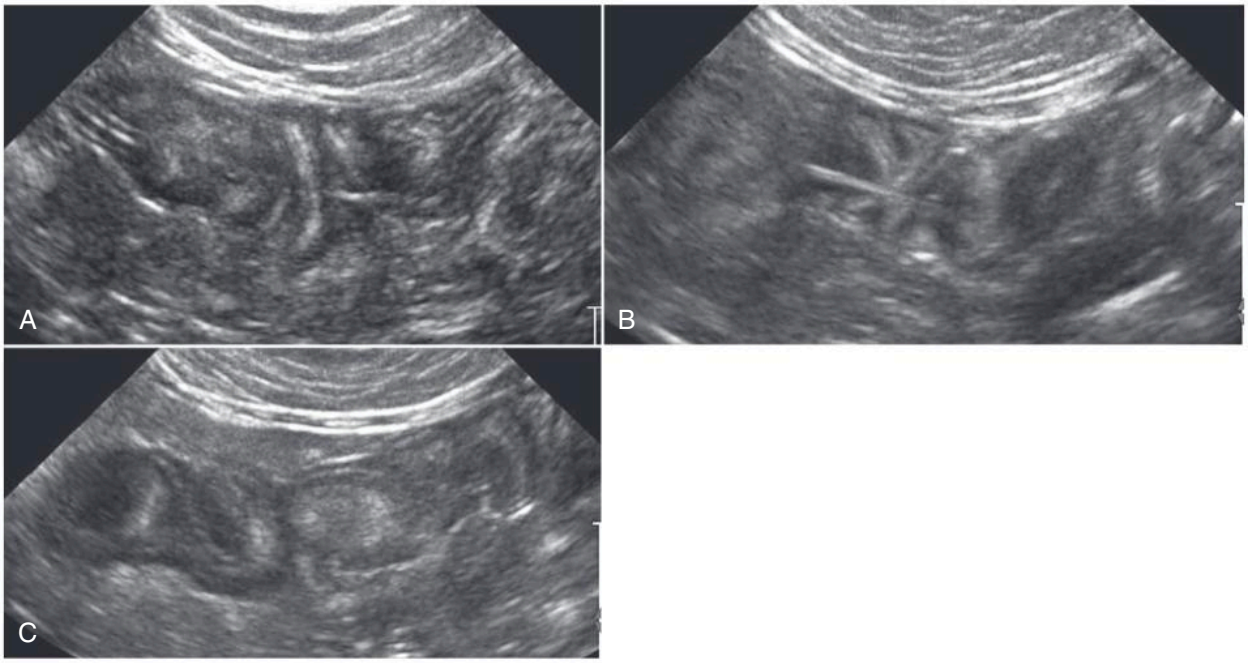


Fig. 46.28 Three ultrasound frames from a cat with a linear foreign body. The plication of the bowel is evident by the tightly undulating contour of the bowel wall and minimal distention of the lumen in all images. The linear hyperechoic streak in the central image represents the foreign material.

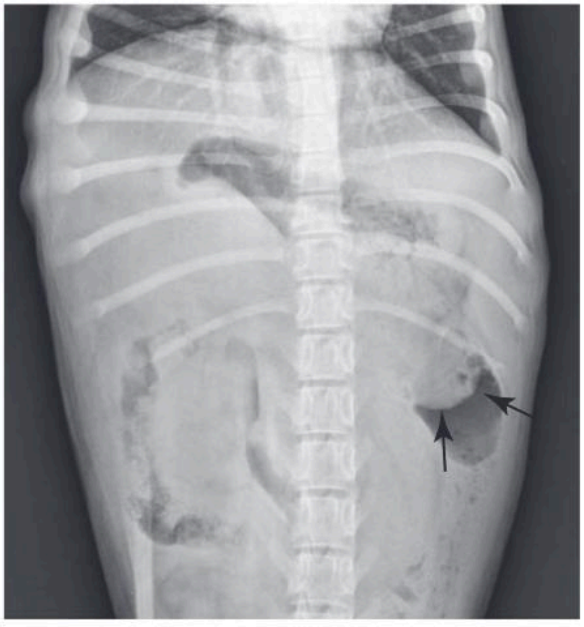


Fig. 46.29 Ventrodorsal radiograph of a dog with an ileocolic intussusception. This intussusception has not caused jejunal dilation, probably because the obstruction is not complete. The leading edge of the intussusceptum (*black arrows*) is visible in this patient as a round mass contrasted by colon gas. This appearance could be caused by a colonic foreign body but is more typical of an intussusception, and ultrasound should be performed for confirmation.

benign strictures. The development of an obstructive bowel pattern from these lesions depends on the size of the lesion and whether growth of the lesion is directed toward or away from the lumen. Progressive infiltration increases the probability of an obstruction if luminal narrowing occurs. Most patients present clinically during the phase of partial obstruction with focal mild to severe distention. Additional features of these masses are discussed later. Benign strictures in cats can occur in the duodenum, jejunum, or ileum and sonographic findings include gastric and generalized or segmental jejunal dilation consistent with mechanical obstruction. During the sonographic examination, ingesta does not propagate past the site of stricture and helps to make the diagnosis. Wall layering is typically disrupted and hypoechoic along a very short length of bowel, and wall thickening is mild to moderate (3–6 mm). Histopathology has shown fibrosis and inflammation at the stricture site.[68]

Lesions originating outside the intestinal wall can cause compression on a loop and result in partial or complete obstruction. Lesions in this category include adhesions from prior surgery, abdominal boundary hernias (congenital or traumatic), and occasionally masses originating from other abdominal organs (Fig. 46.31).

In some situations, CT may have applicability for evaluation of the patient with a clinical suspicion of mechanical bowel obstruction. Advantages include the tomographic nature of the images that eliminates superimposition of other organs on the intestinal tract, and the possibility of using reformatted images to provide a global view of the abdomen. In people, CT is used for identification of the location and level of the bowel lesion and in most instances allows the cause of obstruction to be determined. In dogs, a ratio of small intestinal diameter to L5 vertebral height of 2.5 as determined from CT images gave a sensitivity of 79% and a specificity of 72%.[69]

Functional Ileus

When peristaltic contractions of bowel cease because of vascular or neuromuscular abnormalities, the lumen dilates and remains patent. Many patients have no specific survey radiographic changes to allow discrimination between functional and mechanical ileus. As previously noted, the length of bowel affected may provide some differentiation, with localized

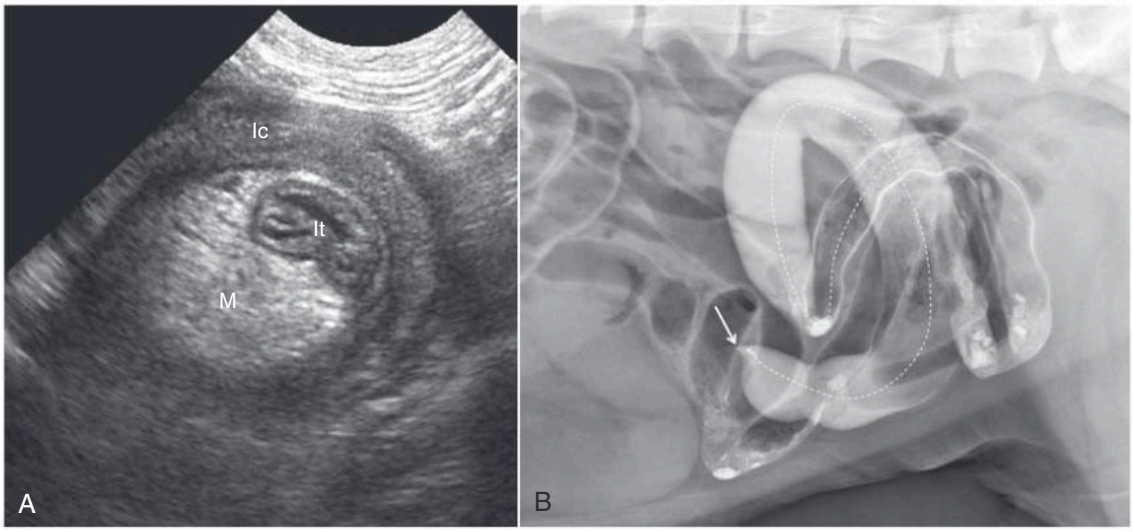


Fig. 46.30 **A,** A transverse ultrasound image of an intussusception. The wall layering pattern of the intussuscipiens in this patient is not clearly defined because of mucosal edema and dilation of mucosal lymphatics. *Ic,* Intussuscipiens; *It,* intussusceptum; *M,* hyperechoic mesenteric fat pulled in with the intussusceptum. In the radiographic study **(B)**, the narrowed lumen (*white arrow*) of the orad aspect of the intussusceptum is visible. The edema in the wall of the intussuscipiens in this patient has resulted in a stricture of the lumen, with resulting proximal dilation of small bowel. The *dashed white line* was added graphically and follows the course of the dilated bowel as it approaches the orad end of the intussusceptum. The increased opacity of the lumen of the dilated bowel was thought to be caused by medications that increased the opacity of the fluid.

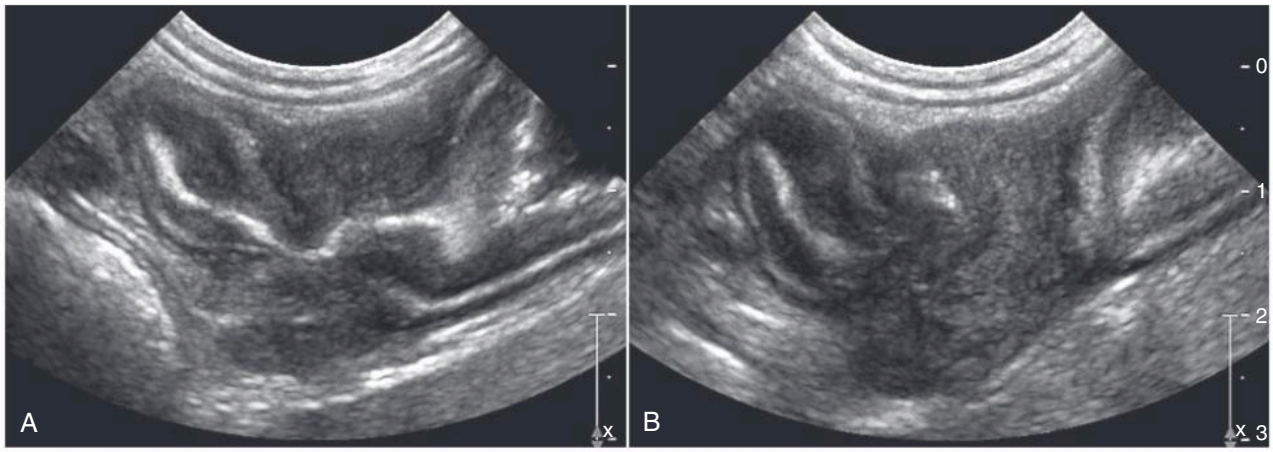


Fig. 46.31 Ultrasound images of partial bowel obstruction from an extrinsic granuloma caused by *Cryptococcus neoformans* infection. The constricting tissue does not originate from the bowel wall but focally encircles this loop. There is dilation of the orad segment on the *right* side of each image and a normal empty lumen on the aboral (*left*) side of each image.

dilation more likely from a mechanical cause and diffuse dilation more likely from functional ileus (see Fig. 46.15). However, overlap between functional and mechanical ileus occurs. Furthermore, chronic mechanical obstruction can eventually lead to functional ileus as the bowel becomes fatigued. The degree of dilation is not a specific differentiating feature.

There are no specific ultrasound or positive-contrast study features to differentiate chronic mechanical obstruction from functional ileus. The finding of peristalsis suggests exclusion of functional ileus. A thorough search of the bowel should be done to look for obvious obstructive causes such as a foreign body. The more common diseases that cause functional ileus include viral enteritis (canine parvovirus type 2 in particular), feline panleukopenia, chronic mechanical obstruction, and peritonitis.[70,71] Other less common diseases with a primary radiographic change of dilated intestinal loops include strangulation of the intestine through a hernia (vascular compromise), mesenteric volvulus (vascular compromise), spinal trauma (neurologic injury), segmental jejunal arterial thrombosis (vascular compromise), dysautonomia (autonomic nervous system disease), and intestinal pseudo-obstruction (tunica muscularis atrophy). Small intestinal segments can slip through traumatic tears or developmental hernias of the peritoneal cavity boundaries. The identification of such segments in an extra-abdominal location is usually easy because of gas within their lumen. Bowel dilation occurs if the rent becomes constrictive or if the loop twists, effectively occluding its outflow.

Mesenteric volvulus results in occlusion of the cranial mesenteric artery. The reduced blood supply leads to ischemic necrosis, gastrointestinal toxin release, shock, and subsequent paralytic ileus.[72,73] The initiating event for volvulus typically is



Fig. 46.32 Lateral radiograph of a dog with a jejunal volvulus. The extensive dilation of nearly all bowel segments is typical of jejunal volvulus. The metallic foreign body was incidental in this dog. A distal small bowel obstruction could cause this appearance, but more intraluminal fluid would be expected with a foreign body.

not known. Most dogs with mesenteric volvulus are large, have no distant or immediate prior history of gastrointestinal signs, and are presented for peracute or acute abdominal distention, abdominal pain, and shock. However, mesenteric volvulus has occurred after prior treatment for acute gastric dilation/volvulus and for intussusception. One group of dogs with mesenteric volvulus had a previous clinical diagnosis of pancreatic insufficiency and clinical signs of vomiting.[74] The radiographic signs are moderate to severe dilation of the small intestine with fluid and gas (Fig. 46.32, eFig. 46.15). Peritoneal effusion may be concurrent. Mesenteric volvulus has been diagnosed using CT imaging in two dogs.[75,76] A supporting feature was the "whirl sign" due to bowel loops, blood vessels, and fat twisting around the mesenteric attachment.

Ischemic injury can also occur segmentally. A cat with jejunal thrombosis resulting in segmental bowel infarction had radiographic evidence of segmental bowel dilation and delayed gastric emptying and intestinal transit. Sonographically, over the course of 72 hours, this bowel segment underwent progressive wall thickening, loss of wall layering, and finally a generalized hypoechoic wall. Peri-enteric hyperechoic mesenteric fat also developed.[77] Intestinal leiomyositis is a cause of chronic intestinal pseudo-obstruction (CIPO) in dogs that can lead to severe generalized gastrointestinal dilation due to mononuclear inflammation, myofiber degeneration, necrosis, and fibrosis of the intestinal walls centered at the muscularis propria layer. This disease is associated with a poor prognosis and requires full-thickness biopsies to be diagnosed.[78] Pseudo-obstruction is a severe form of motility disorders and can be idiopathic or due to infectious, inflammatory, paraneoplastic, metabolic, endocrine, or toxic etiologies. Abdominal radiographs can show gastric and segmental or generalized small intestinal dilation, similar to the findings of mechanical obstruction. Ultrasonographically, there is absent peristalsis of the affected segments with segmental or generalized small intestinal dilation. Distinct wall lesions were not evident. CT findings are reported as having generalized gastrointestinal dilation similar to functional ileus.[79–82]

Dysautonomia is an autonomic nervous system disease that can include vomiting, diarrhea, and inappetence. Radiographs of the abdomen are often characterized by focal or diffuse gastrointestinal dilation. Transit of intraluminal contrast medium is markedly delayed. The most unique feature of these patients is their geographic origin, the first being reported from the United Kingdom. Both dogs and cats can be affected. Additional patients have been reported in Europe and in the United States, mainly in Missouri and Kansas.[83,84] The vaccination history (parvovirus) and geographic region of origin (Missouri, Kansas, United Kingdom, and Europe) of a patient with concomitant signs of other autonomic nervous system dysfunction (dysautonomia), history of thromboembolic disease, and a thorough current history and physical examination are the most useful factors in ranking these causes of functional ileus higher than the causes of mechanical obstruction.

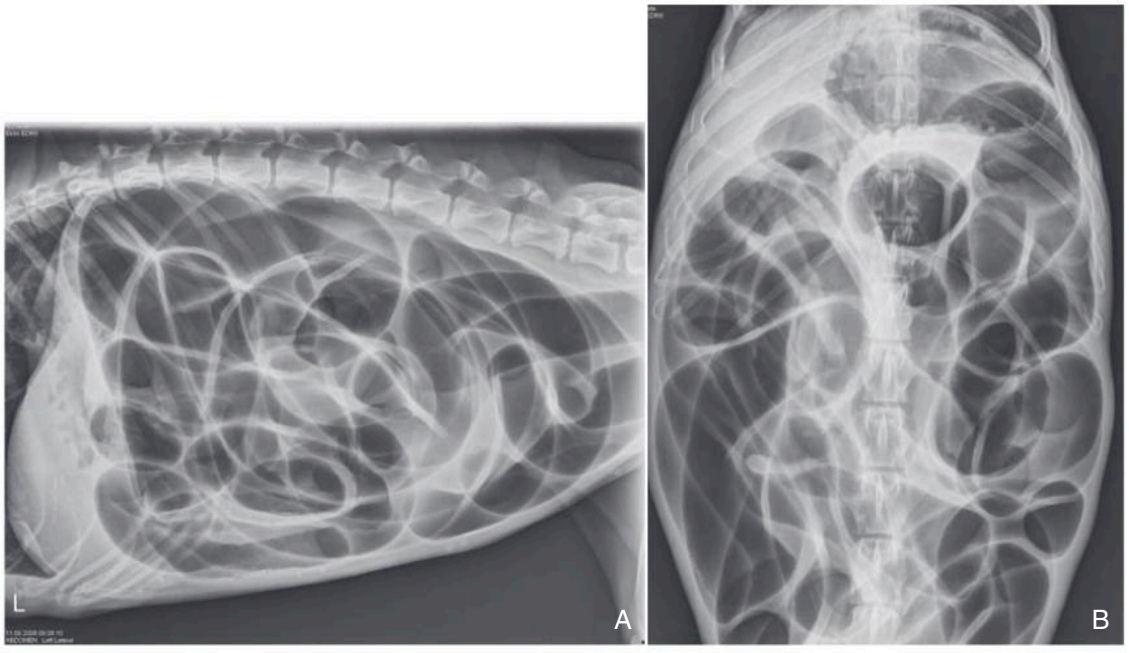
Ultrasound features of parvovirus enteritis were assessed in a cohort of dogs younger than 6 months of age.[86] More than 50% exhibited fluid-filled small bowel, absent peristalsis, decreased duodenal and jejunal mucosal layer thickness despite normal total wall thickness, indistinct jejunal wall layers, hyperechoic jejunal mucosa, and normal jejunal lymph nodes. Duodenal wall corrugation, a hyperechoic duodenal mucosal layer, and an irregular duodenal mucosal border were found less frequently. The bowel diameter was not measured; however, puppies with intussusception were excluded, thus attributing the fluid distention and atony to nonobstructive ileus. Feline panleukopenia has similar intestinal wall findings as in dogs with parvovirus with thinning of the mucosal layer but also associated with a thickened muscularis layer, hyperechoic mucosa, and a hyperechoic mucosal band.[71]

Infiltrative Bowel Disease

Infiltrative bowel disease indicates generalized or segmental infiltration of the bowel wall because of nonseptic inflammation, infection, or neoplasia. The effects are a change in wall thickness and alterations in the tissue character of individual layers. Secondarily, bowel motility may be altered, resulting in a change in bowel diameter. For example, inflammation of the proximal duodenum because of pancreatitis can cause the duodenum to take on a fixed or rigid appearance demonstrated radiographically by mild gas dilation.[87] A corrugated mucosal and submucosal contour pattern has been observed to be associated with pancreatitis.[88] However, this corrugated pattern is not specific to pancreatitis and can be seen with other causes of peritonitis as well as enteritis, neoplasia, and bowel wall ischemia.[36,88] Ultrasound is the only readily available imaging modality that can differentiate bowel wall layers.

Common primary neoplasms of the small intestine include adenocarcinoma, lymphosarcoma, mastocytoma, gastrointestinal stromal tumor (GIST), leiomyoma, and leiomyosarcoma. With immunohistochemistry, many previously diagnosed leiomyomas and leiomyosarcomas have been reclassified as GIST or GIST-like tumors.[89,90] Atypical primary tumors are osteosarcoma, fibrosarcoma, carcinoid, neurilemmoma, and hemangiosarcoma.[91–96] Benign adenomatous polyps of the duodenum occur in cats, with increased frequency among Asian breeds.[97] One polypoid Brunner's gland adenoma has been described in a dog.[98] There are no unique survey radiographic findings for any of these tumors. They may create no changes, create a soft tissue mass of variable size, or cause partial to complete obstruction resulting in bowel dilation. Accumulation of radiopaque foreign material (gravel sign) may be a consequence of partial obstruction. Identification of the mural infiltration causing the partial obstruction is best diagnosed with either ultrasound, oral positive-contrast evaluation, or contrast-enhanced CT.[30]

Masses associated with intestinal wall typically cause smoothly rounded protrusions toward the lumen but may be evident as a mass deforming the serosal contour (Fig. 46.33). If the mural mass surrounds the lumen, the lumen often becomes enlarged and irregularly shaped (see Fig. 46.3). Distinguishing radiographically between a large emphysematous mural tumor and a bowel-associated abscess is not possible in most patients.



eFig. 46.15 Left lateral **(A)** and ventrodorsal **(B)** radiographs of a dog with mesenteric volvulus. All small intestines are severely gas dilated and the abdomen is distended. The stomach is cranially displaced and there is a hiatal hernia present likely due to increased intra-abdominal pressure

Ultrasonographically, intestinal neoplasia usually results in more extensive obliteration of the intestinal wall layering and greater wall thickness and is more likely to be focal than are inflammatory infiltrates.[10,98–106] In 150 dogs, loss of wall layering was the most predictive feature for differentiating between enteritis and neoplasia.[107] No ultrasonographic pattern is 100% specific for differentiating the type of small intestinal neoplasia.

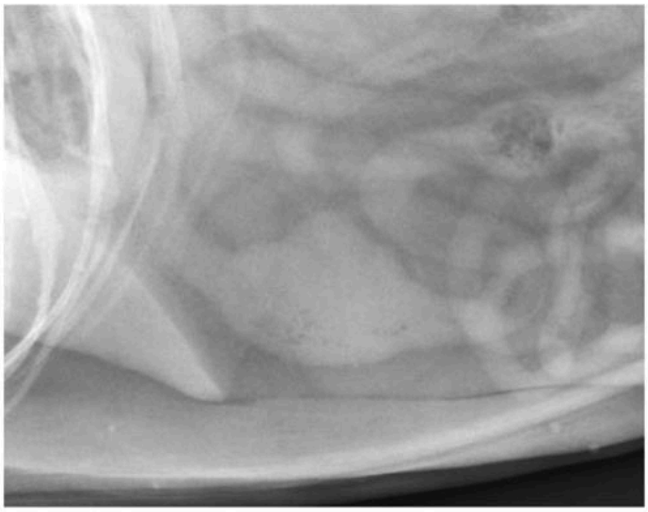


Fig. 46.33 There are bulges deforming the contour of a focal segment of small bowel. The loops entering and exiting the abnormal segment are visible. Differentials are neoplasia, granuloma, and abscess. Ultrasound imaging can further characterize the lesion and guide fine-needle aspirates and core biopsy.

Feline chronic enteropathy is common, and recognition of its causes has increased in recent years. Differentiating feline chronic inflammatory enteropathy (lymphocytic, plasmacytic, eosinophilic infiltration) from feline low-grade lymphoma poses diagnostic challenges that rely on a combination of physical examination findings, laboratory data, diagnostic imaging findings, and histopathologic, immunohistochemistry, and clonality features, which unfortunately all have overlapping findings between the two diseases.

The current nomenclature for diffuse T-cell lymphoma of the small intestines is feline low-grade intestinal T-cell lymphoma (LGITL, formerly enteropathy associated T-cell lymphoma [EATL type I or II]) due to T-cell lymphoproliferative disorder.[108]

Feline alimentary lymphoma is characterized by one of two patterns: a segmental mass or more diffuse thickening of the muscular layer (Fig. 46.34). The mass form, found in 75% of cats with alimentary lymphoma, is expressed as transmural circumferential thickening in the transverse plane (4–22 mm) with the wall layers replaced by hypoechoic or mixed echogenicity tissue and is due to high-grade alimentary lymphoma (HGAL) of small or large lymphocytes of B- or T-cell type (Fig. 46.35). About half of cats have associated enlargement of the mesenteric lymph nodes.[109,110]

The second pattern is that of LGITL that has preserved wall layers but exhibits thickening of the muscular layer

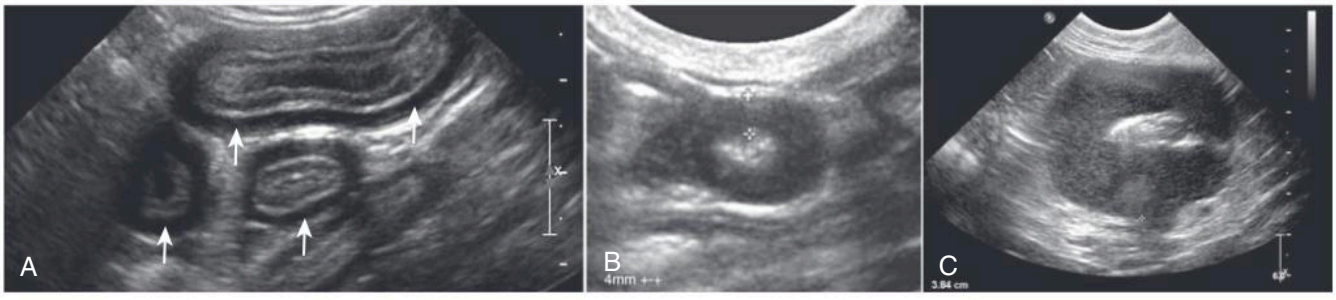


Fig. 46.34 Three examples of intestinal lymphoma in the cat. **A,** Generalized thickened muscularis due to low-grade intestinal T-cell lymphoma. **B,** Focal intestinal segment with transmural hypoechoic loss of layering. **C,** A large focal concentric wall mass with transmural hypoechoic loss of layering due to intestinal B-cell lymphoma.

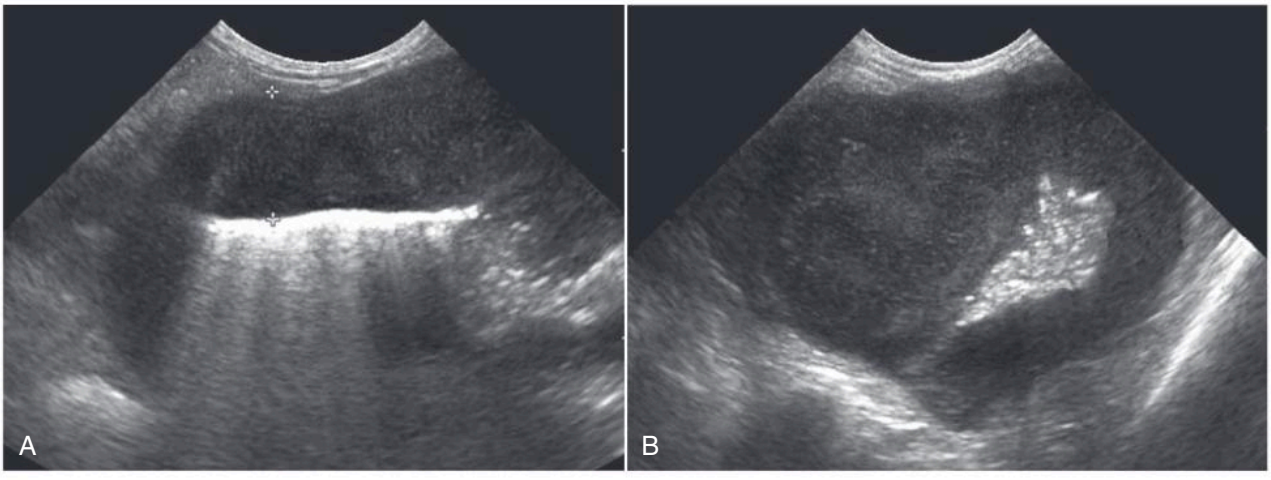


Fig. 46.35 Same cat as in Fig. 46.4. The abnormal bowel wall has transmural thickening and a loss of wall layering. The lesion is circumferential but asymmetric, and the lumen is patent, evident by gas and mucoid fluid. Although not pathognomonic, this is very characteristic of feline alimentary lymphoma.

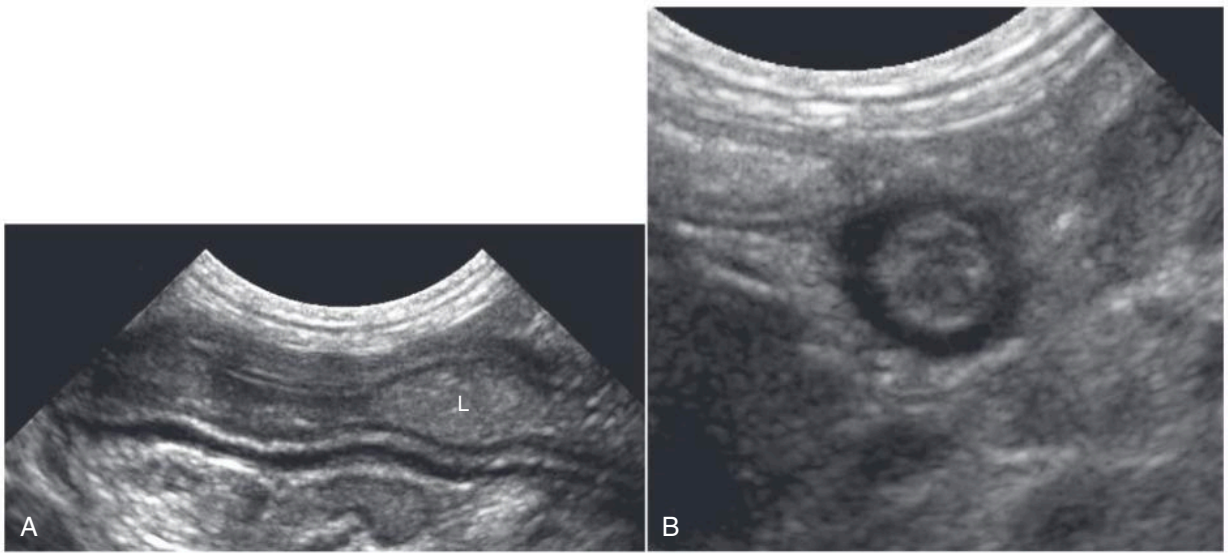


Fig. 46.36 Longitudinal section of the duodenum **(A)** and transverse section of the ileum **(B)** in a cat with muscular layer thickening associated with lymphoma. In the duodenum, the thickness of the muscular layer is best detected through the region where there is content in the lumen (*L*). At necropsy, there was extension of neoplastic cells into the submucosa and muscularis and occasionally outside of the serosa into the adjacent mesentery.

(Fig. 46.36).[108–110] Thickening of the muscular layer is characterized by it having a thickness equal to or greater than the mucosal layer. Ultrasound wall layering changes have been documented in cats with both LGITL and inflammatory enteropathy to differentiate from healthy individuals.[111]

Thickening of the muscular layer in the cat has been attributed to compensatory hypertrophy in response to a distal obstruction and idiopathic hypertrophy in the absence of obstruction.[112,113] The idiopathic form has also been associated with chronic enteritis.[113] The thickness of the muscularis of the duodenal and jejunal segments of 14 cats with small cell T-cell lymphoma and IBD and 19 healthy cats was compared. Increased (two times as thick) thickness of the muscularis propria was found in both affected groups compared to healthy cats.[109] Colic lymph nodes in this population in cats with lymphoma were increased compared to healthy cats. These findings are similar to that in a study of 300 cats with full-thickness biopsy confirmed inflammatory enteropathy (150 cats) or LGITL (124) and it was determined that the two etiologies cannot be differentiated based on wall layering and thickness.[110] In this study, it was also established that 86% of cats with a total wall thickness $\geq$2.8 mm had infiltrative disease of one or the other etiologies and suggested that segmental thickening could indicate more diffuse disease.

Fewer sonographic characteristics have been described for specific intestinal neoplasms in the dog. Differentiation of leiomyosarcoma from leiomyoma has been proposed based on leiomyosarcoma being larger (2–8 cm thick), eccentric, and having mixed echogenicity.[107] However, these patients were evaluated prior to the reclassification of many smooth muscle intestinal tumors as GISTs. In a more recent comparison of GIST and spindle cell tumors of the gastrointestinal tract, there were no specific ultrasound features that were distinguishing. Biopsy with immunohistochemical staining was needed to differentiate these tumors. The larger a bowel mass becomes, the more likely it is to have necrosis, which will appear as intralesional hypoechoic foci. Tumors that enlarge by exophytic growth can become quite large before clinical signs develop since they do not narrow the intestinal lumen. Other tumors of the canine small intestine are reported insufficiently to enable any conclusions about trends in their sonographic appearance (Fig. 46.37). Ultrasound evaluation of the intestine combined with ultrasound-guided fine-needle aspiration and microcore biopsy is an accurate method of minimally invasive diagnosis (Fig. 46.38).[109] However, depending on the sampling site, different outcomes in the same animal with both inflammatory and neoplastic infiltrative disease are possible.[30]

Metastatic bowel tumors are uncommon. Metastasis of mammary carcinoma to the jejunal muscular layer has been identified in a dog, and appeared as focal hypoechoic nodules.[114]

Infectious enteritis may be caused by viruses, bacterial, rickettsial, fungal (and fungal-like), or more rarely parasitic organisms (Fig. 46.39). Changes associated with parvovirus (canine parvovirus type 2) have been discussed earlier regarding abnormal bowel dilation. If parvoviral enteritis is suspected, imaging should be delayed until clinical testing can be performed. Other viral diseases that infect the small intestinal tract do not cause any specific radiographic or sonographic changes and thus are not discussed here. Bacterial overgrowth in the small intestine has also not been related to specific radiographic or sonographic changes.

Heterobilharzia americana (HA) or canine schistosomiasis can cause infection of the small intestines in addition to affecting other body organs.[115] Pathologically the trematode infiltrates the submucosa with oocytes and causes a granulomatous response. Radiographically, dogs with chronic enteropathy can show mineralization of the small intestinal wall. The mineralization is not consistently associated with hypercalcemia. In one report the mineralization was associated with a large number of calcified eggs in the bowel and other organs.[116] Ultrasonographically, the submucosa can be recognized as ill-defined thickening or contain variable degrees of pinpoint hyperechoic foci.[117–119] Hyperechoic foci can also be seen in the liver and mesenteric lymph nodes. In an assessment of HA-positive dogs compared to control dogs, thickening of the submucosa layer concurrent with the presence of hyperechoic foci in the liver, small intestine, and mesenteric lymph nodes provided differentiation of the infected dogs. The endemic range of HA is along the Atlantic and Gulf Coast of North America. Canine cases have also been diagnosed in Kansas, Oklahoma, Arkansas, Indiana, and Utah[120–122] (Fig. 46.40).

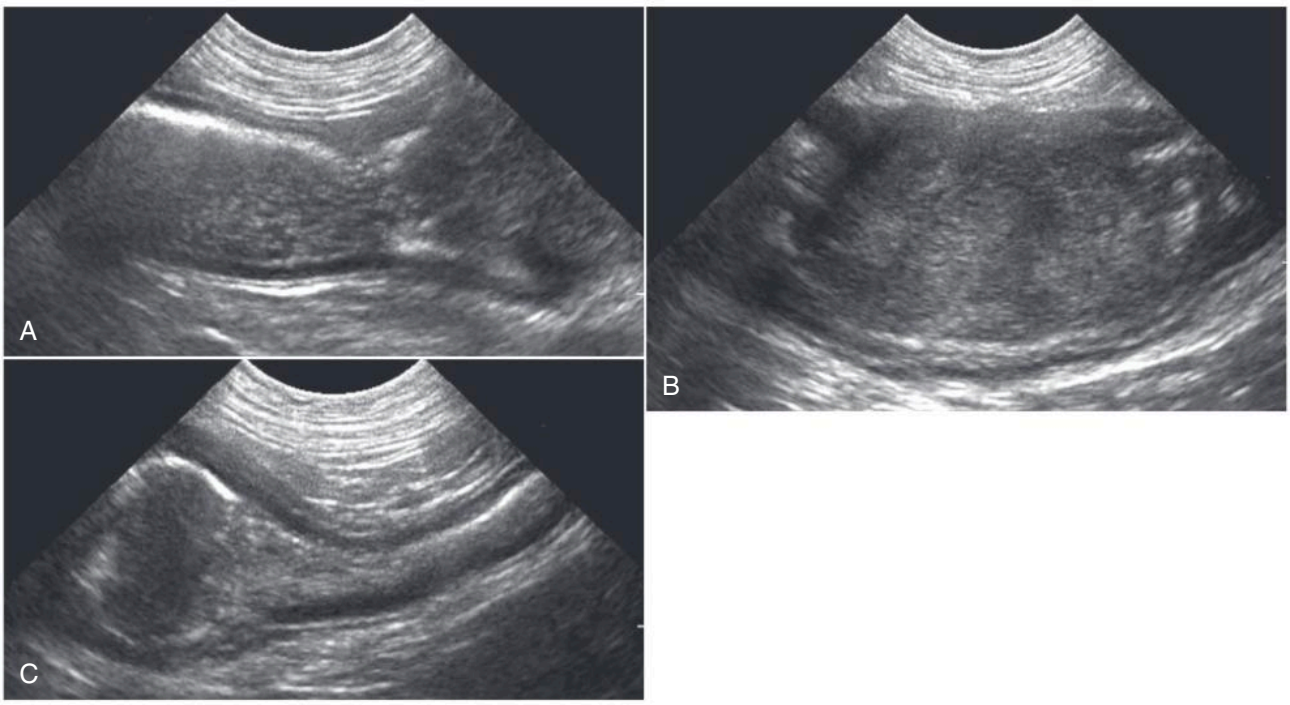


Fig. 46.37 Ultrasound images in sequence through the length of a segment of bowel with histopathologically confirmed hemangiosarcoma. **A** is orad to the mass, and there is mild dilation of the lumen filled with mucoid fluid. The mass is just evident to the *right* of the frame. **B** is at the level of the mass. The deep wall retains some evidence of wall layer pattern and the mass bulges into the lumen. **C** is aboral, and the bowel returns to normal.

When neoplasia, infection, and food-responsive disease are excluded from the broad category of infiltrative bowel disease, the general term *idiopathic IBD* is used. In both the canine and the feline patient, *IBD* refers to a group of disorders of undetermined etiology that cause chronic (>3 weeks) vomiting and/or diarrhea and have various populations of inflammatory cells in the bowel wall layers.[123–125] The most common of these is a lymphocytic-plasmacytic enteritis. Some breed-associated forms of IBD have been described—immunoproliferative enteropathy of Basenjis, familial protein-losing enteropathy (PLE) and protein-losing nephropathy in soft-coated Wheaten terriers, and gluten-sensitive enteropathy in Irish setters.[123] None of these breed-specific disorders have unique radiographic or ultrasonographic diagnostic findings. Equivocal radiographic and sonographic findings suggest additional diagnostic tests are necessary.

Inflammatory infiltrates are expected to increase bowel wall thickness or alter the character of the tissue. However, bowel wall thickness cannot be used to differentiate normal from affected dogs, although some dogs have mild thickening.[123–126] The finding of normal wall thickness may lead to a significant rate of false-negative diagnoses in animals with inflammatory infiltrates (Fig. 46.41).

Distinction of PLE from IBD and food-responsive disease in dogs is based on finding increased mucosal layer echogenicity with PLE, because of varying severity of hyperechoic vertical striations in the duodenum and jejunum (Fig. 46.42). Histologically, the vertical striations are associated with lymphangiectasia.[124,127,128] Dogs with IBD and food-responsive disease can also have increased echogenicity in the mucosal layer described as hyperechoic speckles, being oriented in a horizontal or focal dot pattern compared to the striation pattern. Total bowel wall thickening is inconsistent in PLE and, when present, is mild. Secondary findings in dogs with PLE included peritoneal effusion, edema of the pancreas, and distended bowel segments; however, these findings can also be present in dogs with IBD. Dogs with food-responsive disease do not typically have these secondary findings. Intestinal biopsy remains the definitive diagnostic test for infiltrative bowel disease.

Focal lipogranulomatous lymphangitis is a rare and severe form of canine IBD.[129,130] The etiology is undetermined, and diagnosis is made by histopathologic changes. Of the 17 dogs reported, most lesions occurred in the distal ileum and had sonographic changes of thickened wall (6–14 mm), retained layers, but with predominantly thickened muscular layer. Regional lymph nodes were enlarged but of normal echogenicity. Three dogs had an associated mass up to 4 cm in size extending from the serosa or in the adjacent mesentery. Inflammation, fibrosis, and necrosis mixed with dilated lacteals and lymphatic vessels are identified at histopathology.

Bowel-Associated Masses

Bowel-associated masses can be due to abscesses, hematomas, fungal granulomas, eosinophilic inflammation, and neoplasms. Bacterial abscesses can occur as focal lesions associated with the intestinal wall. A bowel-associated abscess can be a consequence of partial or complete intestinal perforation by foreign material with subsequent adhesions and abscess formation. The mass may result in regional loss of serosal detail or may displace adjacent bowel (Fig. 46.43). A mottled appearance may be seen in bowel-associated abscesses when exudate from the abscess drains into the lumen and is replaced by gas (see Fig. 46.43). Abscesses associated with the small intestine may originate from a source extrinsic to the wall. This may occur because of retained surgical sponges (gossypiboma) or be caused by a pancreatic abscess. Small intestinal wall hematoma has been reported with intestinal wire foreign body perforation.[131]

Although uncommon, mycotic infections of the intestinal tract include histoplasmosis, cryptococcosis,[132] and pythiosis.

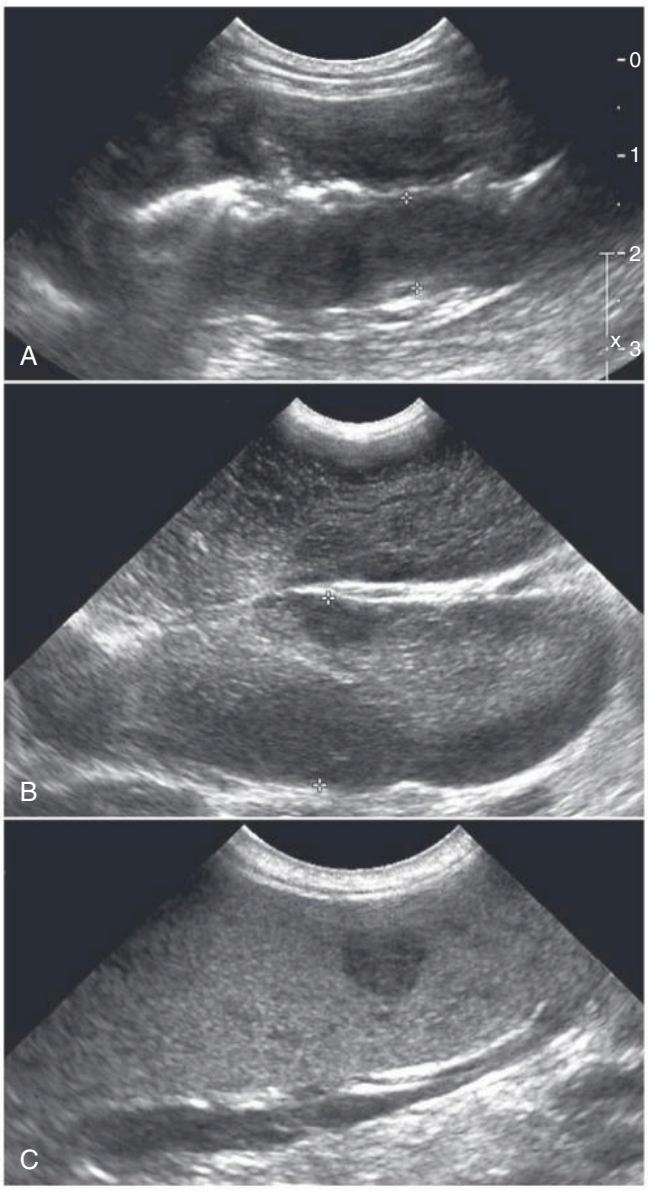


Fig. 46.38 Images of the small bowel **(A)**, mesenteric lymph node **(B)**, and spleen **(C)** in a dog with stage V lymphoma. Bowel wall layering is absent, and there is transmural thickening. The mesenteric lymph node is markedly enlarged and predominantly hypoechoic. Other abdominal lymph nodes were also abnormal. The spleen exhibits multifocal hypoechoic foci.

Pythiosis, an opportunistic water-borne oomycete, has been diagnosed in dogs in Oklahoma, including the northern region, in addition to its more common endemic locale along the Gulf Coast of North America.[133,134] Pathologic changes are often advanced by the time of clinical presentation. Pyogranulomatous lesions cause localized thickening of the intestinal wall that frequently extends through the serosa, along the mesentery, and into the mesenteric lymph nodes. This combination results in a palpable abdominal mass. Ultrasound features in dogs with pythiosis include thickening of the intestinal wall associated with loss of the layer pattern[135] (Fig. 46.44). The sonographic features are overlapping with intestinal neoplasia. Diagnosis and differentiation from neoplasia can be performed with tissue sampling, culture, and serology.[136] Noninfectious granulomas are rare in the dog and cat. Foreign material imbedded in the bowel wall is theorized to have incited a pyogranulomatous response leading to the development of a wall mass that



Fig. 46.39 Same dog as Fig. 46.33 at the time of initial presentation. There is echogenic peritoneal fluid (*white arrows*). A segment of jejunum was abnormal, characterized by transmural thickening (0.89 cm) with relative hyperechogenicity and no evidence of wall layering. Lymph nodes were enlarged. A diagnosis of *Cryptococcus neoformans* was made from mesenteric lymph node aspirates and confirmed when this segment of the jejunum was removed. Histopathologically, there were inflammatory cells and multiple granulomas with numerous yeasts in all layers.

became obstructive. In three dogs with intestinal pyogranuloma, radiographically, there was mild to moderate focal bowel dilation and a bowel wall mass was apparent sonographically.[137] Feline gastrointestinal eosinophilic sclerosing fibroplasia (FGESF) causes a mass in the small intestine with transmural hypoechoic loss of wall layering that ultrasonographically cannot be differentiated from neoplasia[138] (Fig. 46.45). FGESF lesions are characterized by eosinophilic infiltration with reactive fibroblasts and dense collagen and affect the pyloroduodenal and ileocecocolic junctions and the small intestine. Some cats have regional lymphadenopathy.

Miscellaneous Small Intestinal Diseases

Opacity changes in the intestinal wall are rare. Diffuse mineralization of the wall can occur by metastatic calcification because of hypercalcemia. Dogs and cats poisoned by cholecalciferol-based rodenticides and having ingested human antipsoriasis ointment containing calcitriol analogues can develop vomiting, which may lead to radiography and/or ultrasonography of the abdomen.[139–142] Diffuse calcification of the gastrointestinal tract may be found in these patients. Radiographically, the degree of calcification typically creates a thin line of opacity, imparting an enhanced contrast effect. Differential diagnosis for this type of diffuse mineralization should include other causes of hypercalcemia, including severe primary renal disease. Schistosomiasis has more recently been reported as a cause for small bowel wall calcification and should be included in the differential in geographic appropriate locations.[117]

Pneumatosis intestinalis and pneumatosis coli both refer to the presence of gas in the intestinal wall and pneumotosis coli is the more common of the two and discussed in Chapter 47. Numerous underlying causes can lead to this gas accumulation, including necrotizing enterocolitis, ischemic necrosis caused by volvulus, trauma, and bacterial origin in immunocompromised patients. Pneumatosis intestinalis has been reported in a dog following trauma and was detected by ultrasound evaluation.[143]

Two rare types of congenital gastrointestinal anomalies can involve the small intestine: a duplication cyst and diverticulum. A duplication cyst requires three features: an intimate association with the gastrointestinal tract, a well-developed muscular

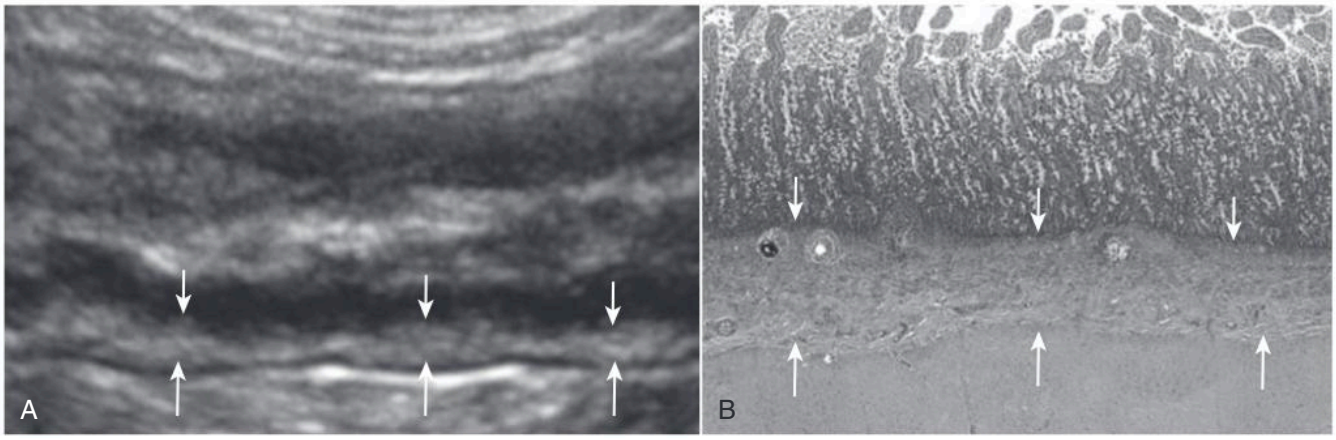


Fig. 46.40 A 4-year-old male Labrador retriever with chronic weight loss. **A,** Sagittal ultrasound image of the duodenum showing generalized disruption of the wall layering mainly due to ill-defined thickening of the submucosal layer (*white arrows*). **B,** Histologic image of the duodenum showing inflammatory infiltration and oocytes within the submucosal layer (*white arrows*) correlating to the thick submucosa in the ultrasound image. The diagnosis was *Heterobilharzia americanum* infection.

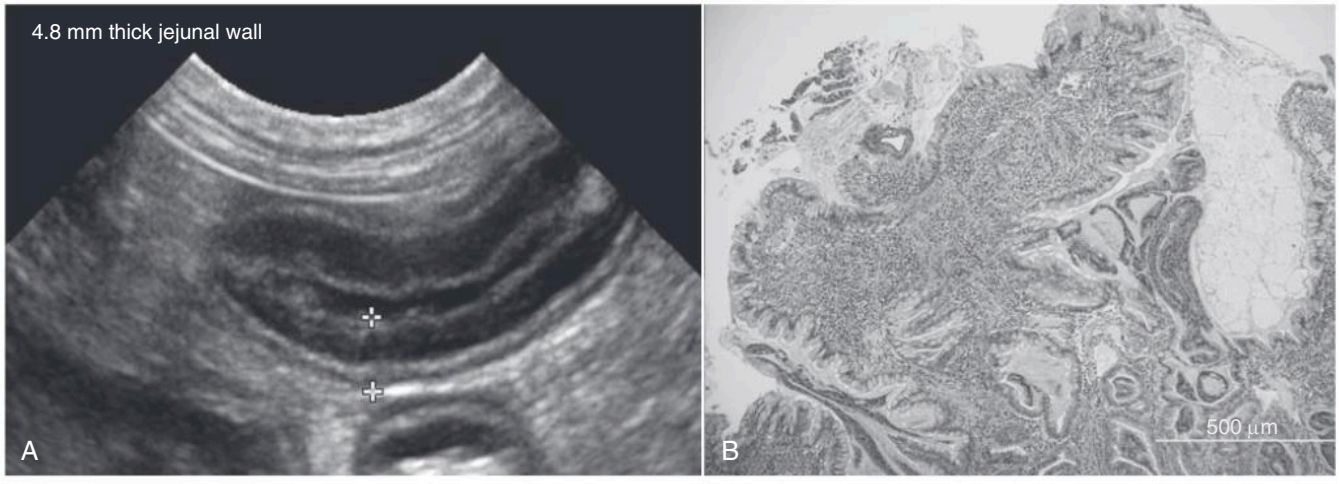


Fig. 46.41 Severe, chronic lymphocytic, plasmacytic enteritis in a 4-year-old Weimaraner with chronic small bowel diarrhea and weight loss. **A,** The intestinal wall is 4.8 mm thick (x—x), within normal limits for a large breed dog. **B,** The histopathology of mucosal biopsies shows severe chronic lymphocytic, plasmacytic enteritis which did not lead to overall wall thickening or altered wall layering. This case demonstrates that ultrasound can underestimate the presence of inflammatory bowel disease in affected dogs.

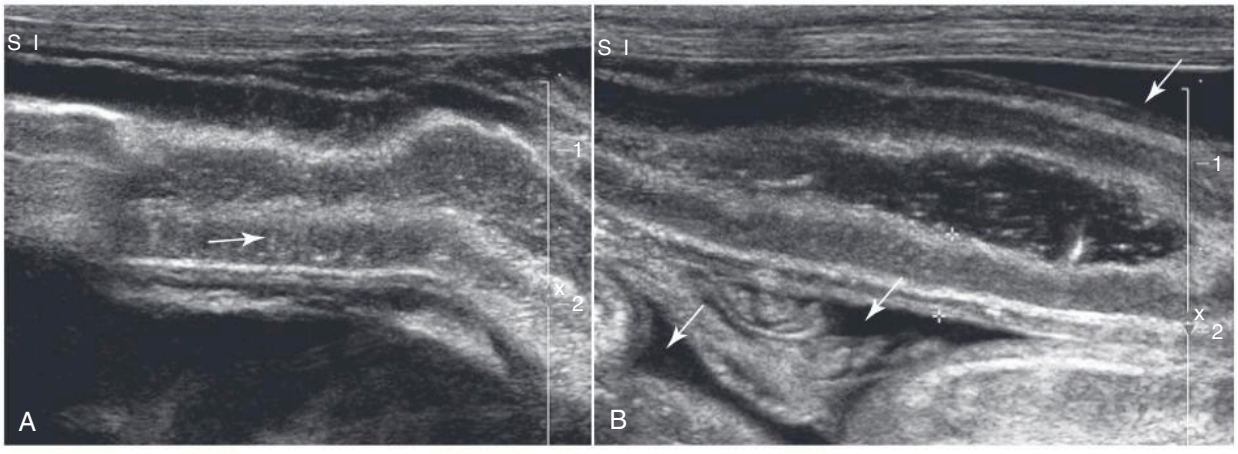


Fig. 46.42 **A,** Increased echogenicity of the mucosal layer and vertically oriented hyperechoic (*white arrow*) streaks are consistent with dilated lacteals in a patient with protein-losing enteropathy. In **B,** another patient with anechoic peritoneal fluid (*white arrows*) has a hyperechoic mucosal layer but with less evident streaking pattern. Biopsy would be needed for confirmation and identification of additional histologic abnormalities.

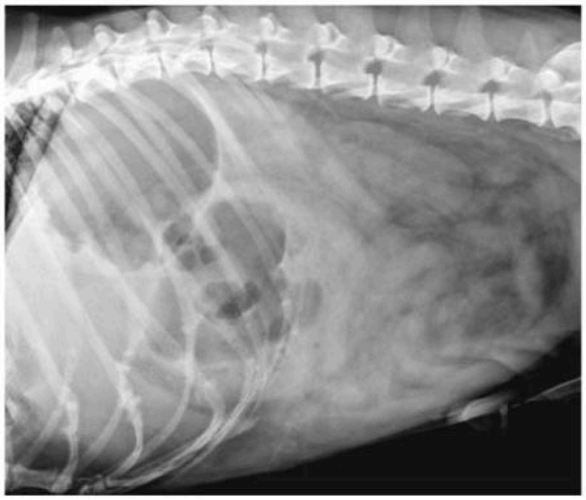


Fig. 46.43 Lateral radiograph of a dog with a large emphysematous mass caused by a jejunal abscess. The intraluminal gas arises when liquid contents of the mass drain into the bowel and the resulting cavity is filled with bowel gas. There is also a loss of serosal detail around the mass. A jejunal tumor could also have this appearance.

layer, and an epithelial lining.[145–150] They are characterized histologically by the presence of smooth muscle in their wall with an internal lining of intestinal epithelium. There may be goblet cells in the lining, which can produce mucin and fill the luminal cavity. The muscular layer of the cyst is continuous with the muscular layer of the associated bowel segment. In four dogs and three cats with a duplication cyst, the lumen of the cyst did not communicate with the lumen of the bowel. Radiographically, the cyst may be evident as an abdominal mass but may not have an obvious association with the small intestine. Sonographically, the cyst is frequently filled with fluid but may not easily be defined to be originating from the bowel. A three-layer wall character has been described with the inner and outer most layers being hyperechoic and the central layer hypoechoic.

A diverticulum is an outpouching from the wall of the gastrointestinal tract resulting in the formation of a sac.[151–153] Typically, the wall of the diverticulum contains the expected wall layering and the lumen of the diverticulum communicates with the bowel. Because of this communication, an oral positive-contrast study could be useful for demonstrating the communication. Three of the four affected dogs were young Boxers with two being littermates, and in all, the diverticulum

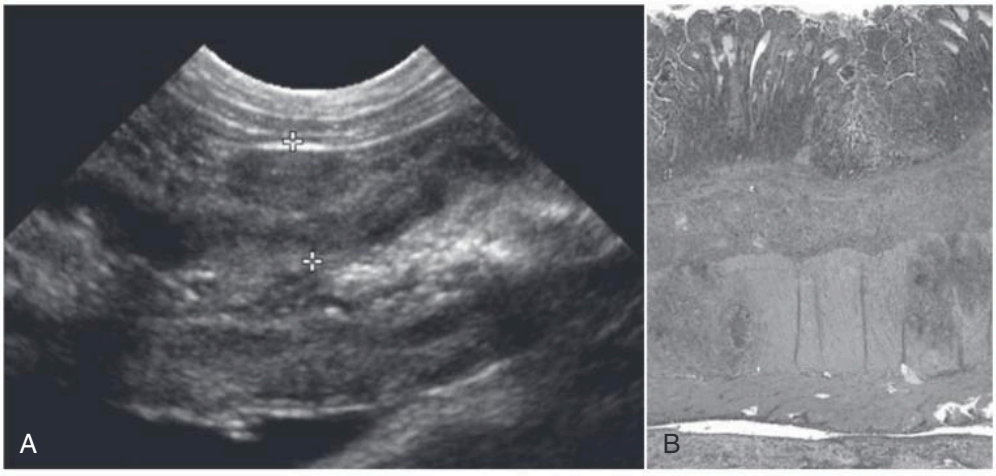


Fig. 46.44 A 1.5-year-old male neutered Labrador retriever with chronic weight loss. **A**, Sagittal ultrasound image of the duodenum showing generalized ill-defined loss of wall layering with alternating hyper- and hypoechoic bands of tissue. **B,** Histopathology image showing the diffuse inflammatory infiltration with alternating ill-defined thickened layers correlating to those identified in the ultrasound image. The diagnosis was pythiosis.

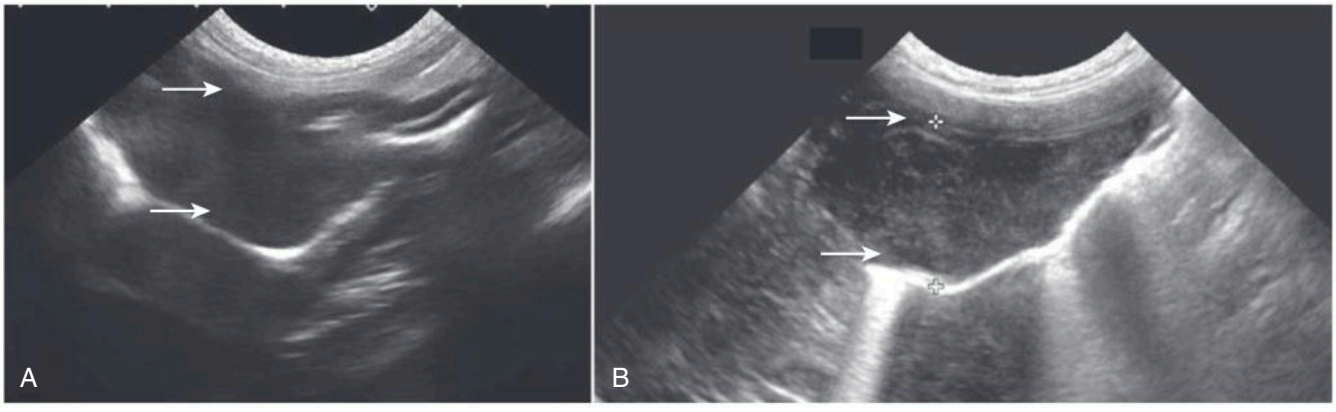


Fig. 46.45 **A,** Sagittal ultrasound image of the duodenum in a 4-year-old male neutered cat with chronic vomiting. An eccentric infiltrative wall mass is present (*white arrows*) that effaces the wall layering and displaces and distorts the hyperechoic luminal interface. **B,** A 6-year-old male neutered cat with a similar eccentric jejunal transmural hypoechoic wall mass with loss of wall layering and distortion of the hyperechoic luminal interface. Cat **A** was diagnosed with feline gastrointestinal eosinophilic sclerosing fibroplasia and cat **B** had intestinal lymphoma.

was at the distal flexure of the duodenum. Another difference between a duplication cyst and a diverticulum is that the former is more typically found on the mesenteric side of the bowel and the latter on the antimesenteric side. It is possible for the lining of the duplication cyst to be composed of heterotopic gastric mucosa.

REFERENCES

1. Armbrust LJ, Biller DS, Hoskinson JJ. Case examples demonstrating the clinical utility of obtaining both right and left lateral abdominal radiographs in small animals. *J Am Anim Hosp Assoc.* 2000;36:531.
2. Vander Hart D, Berry CR. Initial influence of right versus left lateral recumbency on the radiographic finding of duodenal gas on subsequent survey ventrodorsal projections of the canine abdomen. *Vet Radiol Ultrasound.* 2015;56(12).
3. Armbrust LJ, Biller DS, Hoskinson JJ. Compression radiography: an old technique revisited. *J Am Anim Hosp Assoc.* 2000;36:537.
4. Owens JM, Biery DN. *Radiographic interpretation for the small animal clinician.* 2nd ed. Baltimore: Williams & Wilkins; 1999.
5. Graham JP, Lord PF, Harrison JM. Quantitative estimation of intestinal dilation as a predictor of obstruction in the dog. *J Small Anim Pract.* 1998;39:521.
6. Morgan JP. The upper gastrointestinal examination in the cat: normal radiographic appearance using positive-contrast medium. *Vet Radiol.* 1981;22:159.
7. Adams WM, Sisterman LA, et al. Association of intestinal disorders in cats with findings of abdominal radiography. *J Am Vet Med Assoc.* 2010;236:880.
8. O'Brien TR. Small intestine. In: O'Brien TR, ed. *Radiographic Diagnosis of Abdominal Disorders in the Dog and Cat*. Philadelphia: Saunders; 1978:279–352.
9. Hall JA, Watrous BA. Effect of pharmaceuticals on radiographic appearance of selected examinations of the abdomen and thorax. *Vet Clin North Am Small Anim Pract.* 2000;30:349.
10. Weichselbaum RC, Feeney DA, Hayden DW. Comparison of upper gastrointestinal radiographic findings to histopathologic observations: a retrospective study of 41 dogs and cats with suspected small bowel infiltrative disease. *Vet Radiol Ultrasound.* 1994;35:418.
11. Seiler GS, Cohen EB, d'Anjou MA, et al. ACVR and ECVDI consensus statement for the standardization of the abdominal ultrasound examination. *Vet Radiol Ultrasound.* 2022;63:661–674.
12. Lamb CR. Recent developments in diagnostic imaging of the gastrointestinal tract of the dog and cat. *Vet Clin North Am Small Anim Pract.* 1999;29:307.
13. Rault DN, Besso JG, Boulouha L, et al. Significance of a common extended mucosal interface observed in transverse small intestine sonograms. *Vet Radiol Ultrasound.* 2004;45:177.
14. Le Roux AB, Granger LA, Wakamatsu N, , et alGaschen L. Ex vivo correlation of ultrasonographic small intestinal wall layering with histology in dogs. *Vet Radiol Ultrasound.* 2016;57:534.
15. Nielsen T, Lindstrom L, Ingman J, et al. High-frequency ultrasound of Peyer's patches in the small intestine of young cats. *J Feline Med Surg.* 2016;18:303.
16. Gaschen L, Granger LA, Oubre O, et al. The effects of food intake and its fat composition on intestinal echogenicity in healthy dogs. *Vet Radiol Ultrasound.* 2016;57:546.
17. Delaney F, O'Brien RT, Waller K. Ultrasound evaluation of small bowel thickness compared to weight in normal dogs. *Vet Radiol Ultrasound.* 2003;44:577.
18. Goggin JM, Biller DS, Debey BM, et al. Ultrasonographic measurement of gastrointestinal wall thickness and the ultrasonographic appearance of the ileocolic region in healthy cats. *J Am Anim Hosp Assoc.* 2000;36:224.
19. Di Donato P, Penninck D, Pieetra M, et al. Ultrasonographic measurement of the relative thickness of intestinal wall layers in clinically healthy cats. *J Feline Med Surg.* 2014;16:333.
20. Etue SM, Pennick DG, Labatto MA, et al. Ultrasonography of the normal feline pancreas and associated anatomic landmarks: a prospective study of 20 cats. *Vet Radiol Ultrasound.* 2001;42:330.
21. Mortier JR, Maddox TW, White GM, et al. Ultrasonographic appearance of the major duodenal papilla in dogs without evidence of hepatobiliary, pancreatic, or gastrointestinal tract disease. *Am J Vet Res.* 2016;77:597.
22. An Y, Lee H, Chang D, et al. Application of pulsed Doppler ultrasound for the evaluation of small intestinal motility in dogs. *J Vet Sci.* 2001;1:71.
23. Jimenez DA, O'Brien RT, Wallace JD, et al. Intraoperative contrast-enhanced ultrasonography of normal canine jejunum. *Vet Radiol Ultrasound.* 2011;52:196.
24. Diana A, Specchi S, Toaldo MB, et al. Contrast-enhanced ultrasonography of the small bowel in healthy cats. *Vet Radiol Ultrasound.* 2011;52:555.
25. Johnson-Neitman JL, O'Brien RT, Wallace J. Quantitative perfusion analysis of the pancreas and duodenum in healthy dogs by use of contrast-enhanced ultrasonography. *Am J Vet Res.* 2012;73:385.
26. Goodall EFP: Comparative imaging of surgical small intestinal disease in dogs: evaluation of pre-operative contrast-enhanced ultrasound, intra-operative contrast enhanced ultrasound, and triple-phase contrast-enhanced computed tomography. M.S. Thesis Abstract. Dept Veterinary Clinical Sciences, University of Illinois at Urbana-Champaign. http://hdl.handle.net/2142/90791.
27. Linta N, Pey P, Toaldo MB, et al. Contrast-enhanced ultrasonography in dogs with inflammatory bowel disease. *J Vet Intern Med.* 2021;35:2167–2176.
28. Nisa K, Lim SY, Shinohara M, et al. Evaluation of duodenal perfusion by contrast-enhanced ultrasonography in dogs with chronic inflammatory enteropathy and intestinal lymphoma. *J Vet Intern Med.* 2019;33:559–568.
29. Spużak J, Kubiak K, Glińska-Suchocka K, Jankowski M, Borusewicz P, Kubiak-Nowak D. Accuracy of real-time shear wave elastography in the assessment of normal small intestine mucosa in dogs. *Pol J Vet Sci.* 2019;22(3):457–461.
30. Hoey S, Drees R, Hetzel S. Evaluation of the gastrointestinal tract in dogs using computed tomography. *Vet Radiol Ultrasound.* 2013;554:25.
31. Siow JW, Chau J, Podadera JM, et al. Investigation of scan delays for CT evaluation of inner wall layering and peak enhancement of the canine stomach and small intestine using a 20 second fixed-injection-duration and bolus tracking technique. *Vet Radiol Ultrasound.* 2022:1–11.
32. Miniter BM, Arruda AG, Zuckerman J, et al. Use of computed tomography (CT) for the diagnosis of mechanical gastrointestinal obstruction in canines and felines. *PLoS One.* 2019. https://doi.org/10.1371/journal.pone.0219748.
33. Smelstoys JA, Davis GJ, Learn AE, et al. Outcome of and prognostic indicators for dogs and cats with pneumoperitoneum and no history of penetration trauma: 54 cases (1988–2002). *J Am Vet Med Assoc.* 2004;225:251.

34. Ko JJ, Mann FA. Barium peritonitis in small animals. *J Vet Med Sci*. 2014;76:621.
35. Renschler J, Tarigo J. What is your diagnosis? Particulate material in peritoneal fluid from a dog. *Vet Clin Pathol*. 2008;37:129.
36. Boysen SF, Tidwell AS, Pennick DG. Ultrasonographic findings in dogs and cats with gastrointestinal perforation. *Vet Radiol Ultrasound*. 2003;44:556.
37. Allan GS, Rendano VT, Quick CB, et al. Gastrografin as a gastrointestinal contrast medium in the cat. *Vet Radiol*. 1979;20(3).
38. Kang J, Oh D, Kim K, et al. Evaluation of a dual-purpose contrast medium for radiography and ultrasonography of the small intestine in dogs. *AJVR*. 2020;81(12).
39. Riedesel EA. Small bowel. In: Thrall DE, ed. *Textbook of Veterinary Diagnostic Radiology*. 5th ed. St. Louis: Elsevier-Saunders; 2007.
40. Robertson ID, Burbridge HM. Pros and cons of barium-impregnated polyethylene spheres in gastrointestinal disease. *Vet Clin North Am Small Anim Pract*. 2000;30:449.
41. Garneau MS, McCarthy RJ. Multiple magnetic gastrointestinal foreign bodies in a dog. *J Am Vet Med Assoc*. 2015;246:537.
42. Hickey MC, Magee A. Gastrointestinal tract perforations caused by ingestion of multiple magnets in a dog. *J Vet Emerg Crit Care (San Antonio)*. 2011;21:369.
43. Rossmeissl EM, Palmer KG, Hoelzler MG, et al. Multiple magnet ingestion as a cause of septic peritonitis in a dog. *J Am Anim Hosp Assoc*. 2011;47:56.
44. Creedy N, Bates N. Ingestion of multiple magnets by a dog. *Vet Rec*. 2011;169:504.
45. Kiefer K, Hottinger H, Kahn T, et al. Magnet ingestion in dogs: two cases. *J Am Anim Hosp Assoc*. 2010;46:181.
46. Luttgen PJ, Whitney MS, Wolf AM, et al. Heinz body hemolytic anemia associated with high plasma zinc concentration in a dog. *J Am Vet Med Assoc*. 1990;197:1347.
47. Clancey NP, Murphy MC. Zinc-induced hemolytic anemia in a dog caused by ingestion of a game-playing die. *Can Vet J*. 2012;53:383.
48. Pratt CL, Reineke EL, Dobratz KJ. Sewing needle foreign body ingestion in dogs and cats: 65 cases (2000–2012). *J Am Vet Med Assoc*. 2014;245:303.
49. Ciasca TC, David FH, Lamb CR. Does measurement of small intestinal diameter increase diagnostic accuracy of radiography in dogs with suspected intestinal obstruction? *Vet Radiol Ultrasound*. 2013;54:207.
50. Finck C, D'Anjou MA, Alexander K, et al. Radiographic diagnosis of mechanical obstruction in dogs based on relative small intestinal external diameters. *Vet Radiol Ultrasound*. 2014;55:472.
51. Lux DN, Hunt GB, Carr AH, et al. What is your diagnosis? An amoxicillin tablet. *J Am Vet Med Assoc*. 2013;243(45).
52. Lamb DR, Hansson K. Radiological identification on non-opaque intestinal foreign bodies. *Vet Radiol Ultrasound*. 1994;35:87.
53. Moles AD, McGhie JA, Schaaf OR, et al. Sand impaction of the small intestine in eight dogs. *J Small Anim Pract*. 2010;51(29).
54. Elser EB, Mai W, Reetz JA, et al. Serial abdominal radiographs do not significantly increase accuracy of diagnosis of gastrointestinal mechanical obstruction due to occult foreign bodies in dogs and cats. *Vet Radiol Ultrasound*. 2020;61(4):399–408.
55. Miles S, Gaschen L, Presley T, Lio C, Granger LA. Influences of repeat abdominal radiographs on the resolution of mechanical obstruction and gastrointestinal foreign material in dogs and cats. *Vet Radiol Ultrasound*. 2021;62(3):282–288.
56. Tidwell AS, Penninck DG. Ultrasonography of gastrointestinal foreign bodies. *Vet Radiol Ultrasound*. 1992;33:160.
57. Sharma A, Thompson MS, Scrivani PV, et al. Comparison of radiography and ultrasonography for diagnosing small-intestinal mechanical obstruction in vomiting dogs. *Vet Radiol Ultrasound*. 2011;52:248.
58. Hobday MM, Pachtinger GE, Drobatz KJ, et al. Linear versus non-linear gastrointestinal foreign bodies in 499 dogs: clinical presentation, management, and short-term outcome. *J Small Anim Pract*. 2014;55:560.
59. Evans KL, Smeak DD, Biller DS. Gastrointestinal linear foreign bodies in 32 dogs: a retrospective evaluation and feline comparison. *J Am Anim Hosp Assoc*. 1994;30:445.
60. Felts JF, Fox PR, Burk RL. Thread and sewing needles as gastrointestinal foreign bodies in the cat: a review of 64 cases. *J Am Vet Med Assoc*. 1984;184(56).
61. Hoffmann KL. Sonographic signs of gastroduodenal linear Foreign Body in 3 Dogs. *Vet Radiol Ultrasound*. 2003;44:466.
62. Lewis DD, Ellison GW. Intussusception in dogs and cats. *Compend Contin Educ Pract Vet*. 1987;9:523.
63. Burkitt JM, Drobatz KJ, Saunders HM, Washabau RK. Signalment, history, and outcome of cats with gastrointestinal tract intussusception: 20 cases (1986–2000). *J Am Vet Med Assoc*. 2009;234:771.
64. Lamb CR, Mantis P. Ultrasonographic features of intestinal intussusception in 10 dogs. *J Small Anim Pract*. 1998;39:437.
65. Patsikas MN, Jakovljevic S, Moustardas N, et al. Ultrasonographic signs of intestinal intussusception associated with acute enteritis or gastroenteritis in 19 young dogs. *J Am Anim Hosp Assoc*. 2003;39(57).
66. Patsikas MN, Papazoglou LG, Papaioannou NG, Dessiris AK. Normal and abnormal ultrasonographic findings that mimic small intestinal intussusception in the dog. *J Am Anim Hosp Assoc*. 2004;40:147.
67. Patsikas MN, Papazoglou LG, Jakovljevic S, Dessiris AK. Color Doppler ultrasonography in prediction of the reducibility of intussuscepted bowel in 15 young dogs. *Vet Radiol Ultrasound*. 2005;46:313.
68. Holloway A, Pivetta M, Rasotto R. Ultrasonographic and histopathological features in 8 cats with fibrotic small intestinal stricture. *Vet Radiol Ultrasound*. 2019;60:423–431.
69. Drost WT, Green EM, Zekas LJ, et al. Comparison of computed tomography and abdominal radiography for detection of canine mechanical intestinal obstruction. *Vet Radiol Ultrasound*. 2016;57:366.
70. Farrow CS. Radiographic appearance of canine parvovirus enteritis. *J Am Vet Med Assoc*. 1982;180(43).
71. Isaya R, Ciccarelli S, Enache D, et al. Gastrointestinal ultrasonographic findings in cats with feline panleukopenia: a case series. *BMC Veterinary Research*. 2021;17:20.
72. Nemzek JA, Walshaw R, Hauptman JG. Mesenteric volvulus in the dog: a retrospective study. *J Am Anim Hosp Assoc*. 1993;29:357.
73. Junius G, Appeldoorn AM, Schrauwen E. Mesenteric volvulus in the dog: a retrospective study of 12 cases. *J Small Anim Pract*. 2004;45:104.
74. Westermarck E, Rinaila-Parnanen E. Mesenteric torsion in dogs with chronic pancreatic insufficiency: 21 cases (1978–1987). *J Am Vet Med Assoc*. 1989;195:1404.
75. Chow K, Stent AW, Mile M. Imaging diagnosis – use of multiphasic contrast-enhanced computed tomography for diagnosis of mesenteric volvulus in a dog. *Vet Radiol Ultrasound*. 2014;55:74.
76. Javard R, Specchi S, Benamou J, et al. Ileocecocolic volvulus in a German shepherd dog. *Can Vet J*. 2014;55:1096.

77. Wallack ST, Hornof WJ, Herrgesell EJ. Ultrasonographic diagnosis-small bowel infarction in a cat. *Vet Radiol Ultrasound*. 2003;44:81.
78. Zacuto AC, Pesavento PA, Hill S, et al. Intestinal leiomyositis: a cause of chronic intestinal pseudo-obstruction in 6 dogs. *J Vet Intern Med*. 2016;30:132.
79. Harvey AM, Hall EJ, Day MJ, et al. Chronic intestinal pseudo-obstruction in a cat caused by visceral myopathy. *J Vet Intern Med*. 2005;19:111.
80. Couraud L, Jermyn K, Yam PS, Philbey AW. Intestinal pseudo-obstruction, lymphocytic leiomyositis and atrophy of the muscularis externa in a dog. *Vet Rec*. 2006;159(86).
81. Johnson CS, Fales-Williams AJ, Reimer SB, Lotsikas PJ, Haynes JS. Fibrosing gastrointestinal leiomyositis as a cause of chronic intestinal pseudo-obstruction in an 8-month old dog. *Vet Pathol*. 2007;44:106.
82. Eastwood JM, McInnes EF, White RN, et al. Cecal impaction and chronic intestinal pseudo-obstruction in dog. *J Vet Med A Physiol Pathol Clin Med*. 2005;52(43).
83. Detweiler DA, Biller DS, Hoskinson JJ, et al. Radiographic findings of canine dysautonomia in twenty-four dogs. *Vet Radiol Ultrasound*. 2001;42:108.
84. O'Brien DP, Johnson GC. Dysautonomia and autonomic neuropathies. *Vet Clin North Am Small Anim Pract*. 2002;32:251.
85. Novellas R, Simpson KE, Gunn-Moore DA, et al. Imaging findings in 11 cats with feline dysautonomia. *J Feline Med Surg*. 2010;12:584.
86. Stander N, Wagner WM, Goddard A, Kirberger RM. Ultrasonographic appearance of canine parvoviral enteritis in puppies. *Vet Radiol Ultrasound*. 2010;51:69.
87. O'Brien TR. Liver, spleen and pancreas. In: O'Brien TR, ed. *Radiographic Diagnosis of Abdominal Disorders in the Dog and Cat*. Philadelphia: Saunders; 1978:460–480.
88. Moon ML, Billar DS, Armbrust LJ. Ultrasonographic appearance and etiology of corrugated small intestine. *Vet Radiol Ultrasound*. 2003;44:199.
89. Maas CPHJ, Haar GT, VanDerGaag I, et al. Reclassification of small intestinal and cecal smooth muscle tumors in 72 dogs: clinical, histologic, and immunohistochemical evaluation. *Vet Surg*. 2007;36:302.
90. Hobbs J, Sutherand-Smith J, Penninck D, et al. Ultrasonographic features of canine gastrointestinal stromal tumors compared to other gastrointestinal spindle cell tumors. *Vet Radiol Ultrasound*. 2015;56:432.
91. Patniak AK, Hurvitz AI, Johnson GF. Canine gastrointestinal neoplasms. *Vet Pathol*. 1977;14:547.
92. Gibbs C, Pearson H. Localized tumors of the canine small intestine: a report of twenty cases. *J Small Anim Pract*. 1986;27:506.
93. Bruecker KA, Withrow SJ. Intestinal leiomyosarcomas in six dogs. *J Am Anim Hosp Assoc*. 1988;24:281.
94. Pardo AD, Adams WH, McCracken MD, et al. Primary jejunal osteosarcoma associated with a surgical sponge in a dog. *J Am Vet Med Assoc*. 1990;196:935.
95. Crawshaw J, Berg J, Sardinas JC, et al. Prognosis for dogs with nonlymphomatous, small intestinal tumors treated by surgical excision. *J Am Anim Hosp Assoc*. 1998;34:451.
96. Takahashi T, Kadosawa T, Nagase M, et al. Visceral mast cell tumors in dogs: 10 cases (1982–1997). *J Am Vet Med Assoc*. 2000;216:222.
97. MacDonald JM, Mullen HS, Moroff SD. Adenomatous polyps of the duodenum in cats: 18 cases (1985–1990). *J Am Vet Med Assoc*. 1993;202:647.
98. Bowen EJ, Mundy P, Tivers MS, et al. Duodenal Brunner's gland adenoma causing chronic small intestinal obstruction in a dog. *J Small Anim Pract*. 2012;53:136.
99. Hayden DW, Van Kruiningen HJ. Lymphocytic-plasmacytic enteritis in German shepherd dogs. *J Am Anim Hosp Assoc*. 1982;18(89).
100. Vest B, Margulis AR. Experimental infarction of small bowel in dogs. *AJR Am J Roentgenol*. 1964;92:1080.
101. Hendirk M. A spectrum of hypereosinophilic syndromes exemplified by six cats with eosinophilic enteritis. *Vet Pathol*. 1981;18:1888.
102. Tams TR. Chronic feline inflammatory bowel disorders: II. Feline eosinophilic enteritis and lymphosarcoma. *Compend Contin Educ Vet Pract*. 1986;8:464.
103. Rivers BJ, Walter PA, Feeney DA, et al. Ultrasonographic features of intestinal adenocarcinoma in five cats. *Vet Radiol Ultrasound*. 1997;38:300.
104. Myers NC, Penninck DG. Ultrasonographic diagnosis of gastrointestinal smooth muscle tumors in the dog. *Vet Radiol Ultrasound*. 1994;35:391.
105. Paoloni MC, Pennick DG, Moore AS. Ultrasonographic and clinicopathologic findings in 21 dogs with intestinal adenocarcinoma. *Vet Radiol Ultrasound*. 2002;43:562.
106. Crystal MA, Penninck DG, Matz ME, et al. Use of ultrasound-guided fine-needle aspiration biopsy and automated core biopsy for the diagnosis for gastrointestinal disease in small animals. *Vet Radiol Ultrasound*. 1993;34:438.
107. Penninck D, Smyers B, Webster CRL, et al. Diagnostic value of ultrasonography in differentiating enteritis from intestinal neoplasia in dogs. *Vet Radiol Ultrasound*. 2003;44:570.
108. Freiche V, Fages J, Paulin MV, et al. Clinical, laboratory and ultrasonographic findings differentiating low-grade intestinal T-cell lymphoma from lymphoplasmacytic enteritis in cats. *J Vet Intern Med*. 2021;35:2685–2696.
109. Daniaux LA, Laurenson MP, Marks SL, et al. Ultrasonographic thickening of the muscularis propria in feline small intestinal small cell T-cell lymphoma and inflammatory bowel disease. *J Feline Med Surg*. 2014;16(2):89–98.
110. Norsworthy GD. Results of histopathology, immunohistochemistry, and molecular clonality testing of small intestinal biopsy specimens from clinically healthy client-owned cats. *J Vet Intern Med*. 2019;33(4):1567–1568.
111. Chang J, Porter IR, Forman MA, Shcherban N, Basran PS. Intra- and interobserver assessments of intestinal wall thickness and segmentations from transverse sections of feline abdominal ultrasound images. *Vet Radiol Ultrasound*. 2023;64(1):131–139.
112. Bettini G, Maracchini M, Dell Salda L, et al. Hypertrophy of intestinal smooth muscle in cats. *Res Vet Sci*. 2003;75(43).
113. Diana A, Pietra M, Guglielmini C, et al. Ultrasonographic and pathologic features of intestinal smooth muscle hypertrophy in four cats. *Vet Radiol Ultrasound*. 2003;44:566.
114. Dominquez E, Anadon E, Espada E, et al. Imaging diagnosis-ultrasonographic appearance of small bowel metastasis from canine mammary carcinoma. *Vet Radiol Ultrasound*. 2014;55:208.
115. Cook AK. Schistosomiasis in the United States. *Vet Clin North Am Small Anim Pract*. 2022;52(6):1283–1303.
116. Corapi WV, Ajithdoss DK, Snowden KF, Spaulding KA. Multi-organ involvement of *Heterobilharzia americana* infection in a dog presented for systemic mineralization. *J Vet Diagn Invest*. 2011;23(4):826–831.
117. Moshnikova VS, Gilmour LJ, Cook AK, Fabiani M. Sonographic findings of pinpoint hyperechoic foci in the small intestine, liver, and mesenteric lymph nodes are indicative of canine *Heterobilharzia americana* infection. *Vet Radiol Ultrasound*. 2020;61:583–591.

118. Kvitko-White HL, Sayre RS, Corapi WV, Spaulding KA. Imaging diagnosis—*Heterobilharzia americana* infection in a dog. *Veterinary Radiology & Ultrasound*. 2011;52(5):538–541.
119. Le Roux A. What is your diagnosis? Heterobilharzia infection. *J Am Vet Med Assoc*. 2015;246(4):411–413.
120. Loker ES, Dolginow SZ, Pape S, et al. An outbreak of canine schistosomiasis in Utah: Acquisition of a new snail host (*Galba humilis*) by *Heterobilharzia americana*, a pathogenic parasite on the move. *One Health*. 17:13,
121. Rodriguez JY, Camp JW, Lenz SD, Kazacos KR, Snowden KF. Identification of *Heterobilharzia americana* infection in a dog residing in Indiana with no history of travel. *J Am Vet Med Assoc*. 2016;248(7):827–830.
122. German AJ, Hall EJ, Day MJ. Chronic intestinal inflammation and intestinal disease in dogs. *J Vet Intern Med*. 2003;17(8).
123. Gaschen L, Kircher P, Stuessi A, et al. Comparison of ultrasonographic findings with clinical activity index (CIBDAI) and diagnosis in dogs with chronic enteropathies. *Vet Radiol Ultrasound*. 2008;49(56).
124. Trepanier L. Idiopathic inflammatory bowel disease in cats—rational treatment selection. *J Feline Med Surg*. 2009;11(32).
125. Rudorf H, van Schaik G, O'Brien RT, et al. Ultrasonographic evaluation of the thickness of the small intestinal wall in dogs with inflammatory bowel disease. *J Small Anim Pract*. 2005;46:322.
126. Kull PA, Hess RS, Craig LE, et al. Clinical, clinicopathologic, radiographic and ultrasonographic characteristics of intestinal lymphangiectasia in dogs: 17 cases (1996–1998). *J Am Vet Med Assoc*. 2001;219:197.
127. Sutherland-Smith J, Penninck DG, et al. Ultrasonographic intestinal hyperechoic mucosal striations in dogs and associated lacteal dilation. *Vet Radiol Ultrasound*. 2007;48:51.
128. Watson VE, Hobday MM, Durham AC. Focal intestinal lipogranulomatous lymphangitis in 6 dogs (2008–2011). *J Vet Intern Med*. 2014;28(48).
129. Lecoindre A, Ledoindre P, Cadore JL, et al. Focal intestinal lipogranulomatous lymphangitis in 10 dogs. *J Small Anim Pract*. 2016;57:465.
130. Padalkar M, Savage M, Cohen EB. Small intestinal intramural hematoma secondary to a migrating wire foreign body in a dog. *Vet Radiol Ultrasound*. 2018;59(6): E61–E65.
131. Malik R, Hunt GB, Bellenger CR, et al. Intra-abdominal cryptococcosis in two dogs. *J Small Anim Pract*. 1999;40:387.
132. Helman RG, Oliver III J. Pythiosis of the digestive tract in dogs from Oklahoma. *J Am Anim Hosp Assoc*. 1999;35:111.
133. Miller RI. Gastrointestinal phycomycosis. *J Am Vet Med Assoc*. 1985;186:473.
134. Graham JP, Newell SM, Roberts GD, et al. Ultrasonographic features of canine gastrointestinal pythiosis. *Vet Radiol Ultrasound*. 2000;41:273.
135. Parker M, Rasche B, Mozzachio K, et al. Pathology in Practice. *J Am Vet Med Assoc*. 2022;259(S2):1–5.
136. Papazoglou LG, Tontis D, Loukopoulos P, et al. Foreign body-associated intestinal pyogranuloma resulting in intestinal obstruction in four dogs. *Vet Rec*. 2010;166:494.
137. Craig LE, Hardam EE, Hertzke DM, et al. Feline gastrointestinal eosinophilic sclerosing fibroplasia. *Vet Pathol*. 2009;46(1):63–70.
138. Gunther R, Felice LJ, Nelson RK, et al. Toxicity of a vitamin D_3 rodenticide to dogs. *J Am Vet Med Assoc*. 1988;193:211.
139. Morita T, Awakura T, Shimada A, et al. Vitamin D toxicosis in cats: natural outbreak and experimental study. *J Vet Med Sci*. 1995;57:831.
140. Fan TM, Simpson KW, Trasti S, et al. Calcipotriol toxicity in a dog. *J Small Anim Pract*. 1998;39:581.
141. Hare WR, Dobbs CE, Slaymen SA, et al. Calcipotriene poisoning in dogs. *Vet Med*. 2000;95:770.
142. Song YM, Lee JY, Lee JW, et al. Ultrasound findings of pneumatosis intestinalis in a dog. *J Vet Clin*. 2013;30:138.
143. Navas de Solis C, Palmer JE, Boston RC, et al. The importance of ultrasonographic pneumatosis intestinalis in equine neonatal gastrointestinal disease. *Equine Vet J*. 2012;44(suppl 41):64.
144. Spaulding KA, Cohn LA, Miller RT, et al. Enteric duplication in two dogs. *Vet Radiol*. 1990;31:83.
145. Radlinsky MAG, Biller DS, Nietfield J, et al. Subclinical intestinal duplication in a cat. *J Feline Med Surg*. 2005;7:223.
146. Kershaw O, Deppenmeier S, Gruber AD. Multiple cystic intestinal duplications in a cat. *Vet Pathol*. 2008;45:188.
147. Bernarde A, Forget J, Bernard F. Multiple level enteric duplication cysts in a cat. *Revue Vet Clin*. 2014;49(31).
148. Oui H, Lamm C, Stiver S, et al. Congenital lymphangiomatosis and an enteric duplication cyst in a young dog. *J Small Anim Pract*. 2014;55:379.
149. Walling BE, Arndt TM. Pathology in Practice. *J Am Vet Med Assoc*. 2015;246:1297.
150. Ablin LW, Moore FM, Shields Henney LH, et al. Intestinal diverticular malformation in dogs and cats. *Compend*. 1991;13:426.
151. van Kalveren NJ, Grinwis GCM, Brocks BAW, et al. Collapse following gastrointestinal bleeding secondary to a congenital duodenal diverticulum in two littermate boxer puppies. *J Small Anim Pract*. 2008;49:103.
152. Polf H, Poteet B. Imaging diagnosis – duodenal diverticulum in a dog. *Vet Radiol Ultrasound*. 2010;51(61).

ELECTRONIC RESOURCES

Additional information related to the content in Chapter 46 can be found online at eBooks.Health.Elsevier.com

- Chapter Quiz

CHAPTER 47

Large Bowel

Christine L. Gremillion

ANATOMY

The large intestine consists of the cecum, colon, rectum, and anal canal (Fig. 47.1). The cecum is a diverticulum arising from the proximal colon, located in the right midabdomen, at approximately the level of L3 and L4.[1] The cecum can be quite variable in shape and size depending on its luminal contents. In dogs, the cecum tends to be larger and sigmoid or c-shaped, whereas in cats the cecum is shorter in length and more cone-shaped (Fig. 47.2).[1,2] The mesentery of the colon (mesocolon) is present along its entire length, and is shorter than the mesentery of the small intestine. The mesocolon is also attached to the mesoduodenum via the duodenocolic ligament. These factors combine to make the large intestine overall less mobile than the small intestine, and thus, its normal position within the abdomen is more consistent.[1] The colon is divided into three parts: the ascending, transverse, and descending colon. The ascending colon is the most proximal portion of the colon, located in the cranial abdomen to the right of midline. The ascending colon is located near the descending duodenum, right lobe of the pancreas, and right kidney. The right colic flexure connects the ascending colon to the transverse colon. The transverse colon lives in the cranial abdomen, coursing from the right to left side, and is located adjacent to the greater curvature of the stomach and left lobe of the pancreas. The transverse colon communicates with the descending colon at the left colic flexure. The descending colon then courses caudally, parallel to the body wall, to the level of the pelvic inlet, where it transitions into the rectum without demarcation. The terminal portion of the descending colon and rectum are located dorsal to the urinary bladder, urethra, and prostate/uterus. The rectum then continues caudally to the level of the second or third caudal vertebrae, where it communicates with the anal canal.[1]

IMAGING PROCEDURES

Radiography

Normal Radiographic Findings

The colon is often readily visible on plain radiographs due to normal intraluminal gas and/or fecal contents, although areas devoid of contents may be indistinct. Fecal material often has a granular appearance with mixed soft tissue and gas opacity. The normal colon is shaped like a question mark or shepherd's crook, coursing from the ileocolic junction in the right midabdomen cranially, across midline, and then caudally along the left abdomen in the ventrodorsal view. Occasionally, the distal portion of the descending colon may partially extend to the right of midline in animals that have longer, redundant colons

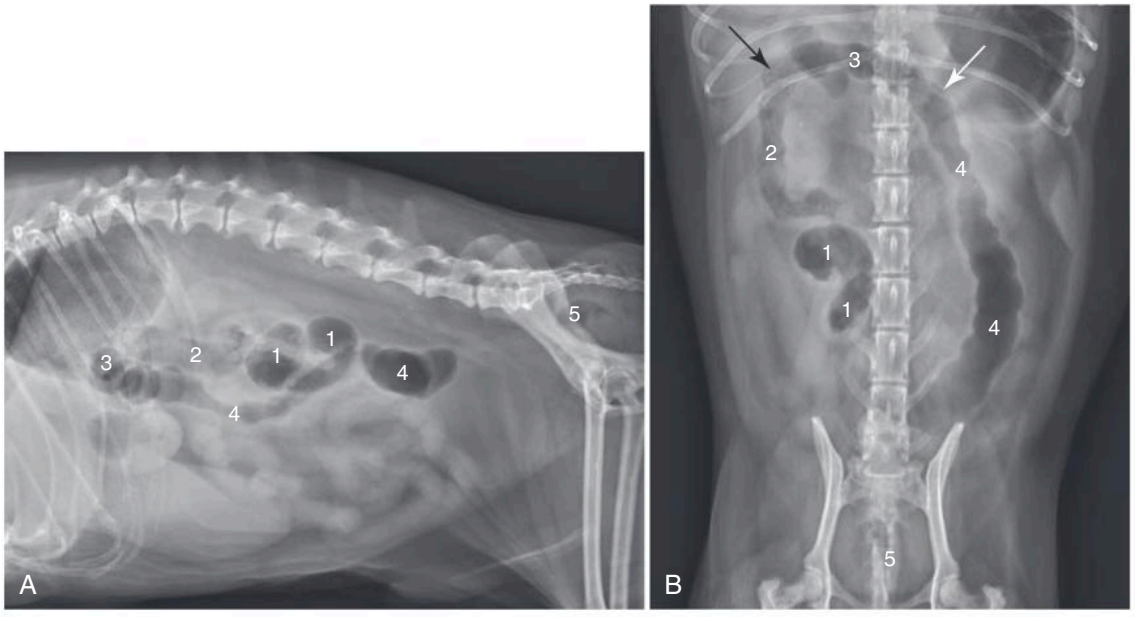


Fig. 47.1 Survey lateral **(A)** and ventrodorsal **(B)** radiographs of demonstrating normal large intestine anatomy. The large intestine is divided into the cecum *(1)*, ascending colon *(2)*, transverse colon *(3)*, descending colon *(4)*, rectum *(5)*, and anal canal. The right and left colic flexures are denoted by the *black* and *white arrows*, respectively.

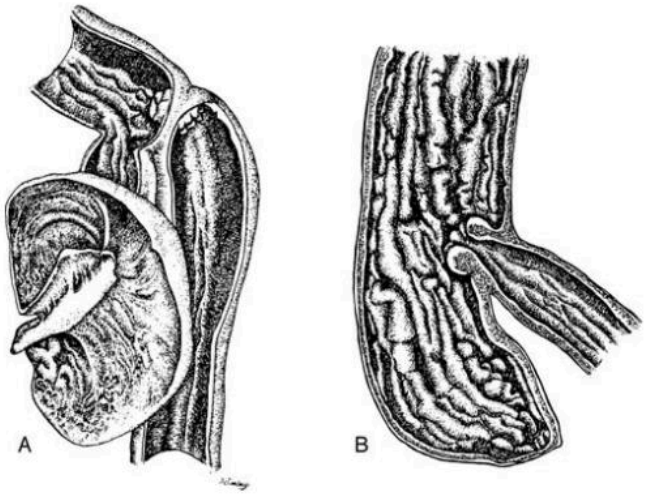


Fig. 47.2 The cecum of the dog **(A)** and cat **(B)** are anatomically and radiographically different. The canine cecum is semicircular and compartmentalized and normally contains some gas. The feline cecum is a short, cone-like structure with no compartmentalization and it rarely contains adequate gas or feces to be visualized radiographically. (Reproduced with permission from O'Brien TR. *Radiographic Diagnosis of Abdominal Disorders in the Dog and Cat.* Davis, CA: Covell Park Veterinary; 1981.)



Fig. 47.3 Ventrodorsal radiograph of a dog with a distended urinary bladder that resulted in displacement of the descending colon to the right of midline (*arrow*). This is a common change in the position of the descending colon and is not clinically significant.

or distention of the urinary bladder (Fig. 47.3).[3] In the lateral views, the entirety of the colon is typically located in the dorsal third of the abdomen, running approximately parallel to the vertebral column.[3] The diameter of the normal colon can be variable depending on the luminal contents, but in dogs, a general rule of thumb is that the colon diameter should be less than the length of the L7 vertebral body.[4] In cats, normal colon diameter should be less than 1.28 times the length of the L5 vertebral body.[5] The cecum is variably visible in dogs depending on the degree of distention. Due to the smaller size of the cecum in cats, it is often not seen radiographically. Gas is occasionally present in the anal sacs, which can appear as either unilateral or bilateral well-circumscribed lucencies summating with the ischia in the ventrodorsal view (Fig. 47.4). It is important not to confuse this finding with geographic bone lysis.

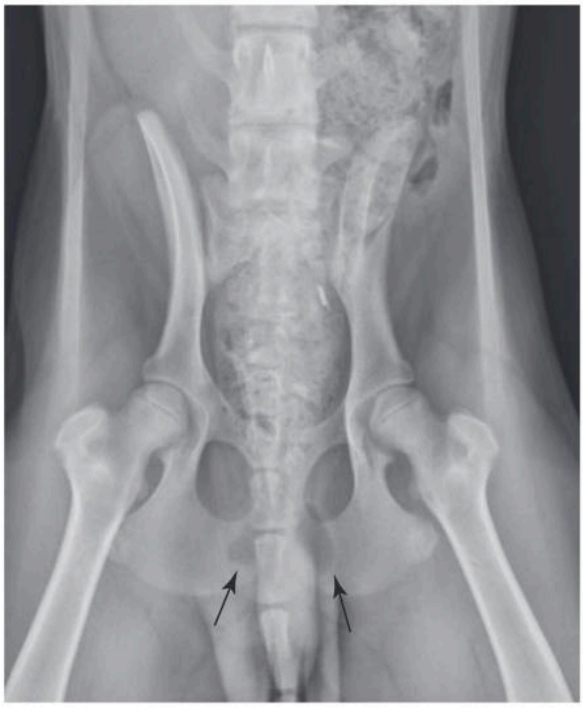


Fig. 47.4 Ventrodorsal radiograph of the pelvis. Gas is present in the anal sacs resulting in asymmetric, well-circumscribed gas opacities summating with the ischia (*arrows*). This should not be confused with bone lysis.

Contrast Radiography

Contrast radiography of the large intestine may be utilized when the diagnosis or appropriate treatment for a patient cannot be determined by survey radiographs and other imaging modalities are not available or desirable. The use of ultrasound and direct inspection of the large intestine via endoscopy have largely replaced many radiographic contrast studies of the colon[2]; however, contrast studies are still helpful for specific indications.

Pneumocolonography

Pneumocolonography, or negative contrast studies of the colon, are typically performed in patients to determine the position of the colon on radiographs and to differentiate it from distended small intestines.[3,6] Pneumocolonography has also been described in aiding the diagnosis of colonic torsion.[7] Survey radiographs should always be acquired first. With the patient positioned in lateral recumbency, approximately 1 to 3 mL/kg of air is introduced into a red-rubber catheter that is placed in the rectum and then lateral and ventrodorsal projections are obtained.[6] The final volume of air required to sufficiently fill the entirety of the colon is patient dependent, and often small increments of air are introduced, radiographs are acquired, and if there is an insufficient volume, the process is repeated. In most patients, it is desirable to fill the entirety of the colon with air to the level of the cecum.

Positive Contrast Enema

Positive contrast enemas with barium used to be the principal imaging technique for evaluation of the colon.[3,8,9] With the advancement of ultrasound and colonoscopy, barium enemas

are used less frequently; however, it is still a useful, minimally invasive, and quick procedure, particularly if there is a concern for colonic torsion and survey radiographs are equivocal.[10] Barium enema can also aid in the diagnosis of intussusception and colonic strictures if ultrasound and/or endoscopy are not readily available.

Survey radiographs should always be obtained prior to initiation of the study. Unless performed as an emergency procedure, preparation including a 12- to 24-hour fast, laxatives, and cleansing enemas is preferred.[9] The volume of contrast medium utilized depends on the indication for the study. A dose of approximately 10 to 15 mL/kg of body weight of barium suspension can be expected to fill the entirety of the colon[3,9]; however, this full volume is not required for diagnosis of all disease processes. A diagnosis of colonic torsion has been made using dosages of as little as 3 mL/kg of body weight.[10] Barium is usually administered via an inflatable Foley catheter placed in the distal rectum.[4,8,9] To minimize risk of perforation, the colon should either be filled slowly by gravity or infused in small increments until the desired effect is seen radiographically. Both lateral and ventrodorsal projections should be acquired following introduction of barium. If back pressure is present on the syringe, infusion of barium should be discontinued. If colonic perforation is suspected prior to initiation of the study, iodinated contrast medium should be used instead of barium due to the risk of granulomatous peritonitis with extravasation of barium.[9]

Ultrasound of the Large Bowel

Ultrasound allows assessment of large intestinal wall thickness, layering, and evidence of mass lesions, and also provides the ability to assess the surrounding mesentery and regional lymph nodes. Ultrasound-guided tissue sampling (fine needle aspirate or biopsy) can also be performed.[11] The primary limitation of ultrasound of the large bowel is the presence of feces and gas with distal acoustic shadowing and reverberation artifacts, respectively, which result in limited visibility of the bowel wall in the far-field of the image.

The wall of the large intestine is thinner than that of the small intestine, measuring only 1 to 2 mm in thickness on ultrasound.[12] Similar to the stomach and small intestine, distinct wall layers of the large intestine are visible: a hyperechoic luminal surface, hypoechoic mucosa, hyperechoic submucosa, hypoechoic muscularis, and hyperechoic outer serosa (Fig. 47.5). When the colon is empty, the wall can have an irregular appearance due to infolding and should not be confused with wall thickening. Occasionally, a thin hyperechoic line can be seen in the muscularis layer of the colon that parallels the serosal surface. Histologically, this correlates with fibrous tissue in the myenteric plexus. As this is seen in dogs without a history of diarrhea, this finding is considered a normal variant.[13] The descending colon can be easily recognized when imaging in a transverse plane in the caudal abdomen, where it lies dorsal to the urinary bladder at the pelvic inlet. The typical appearance of the colon is a thin-walled tubular structure with a curved hyperechoic luminal interface. When identified near the urinary bladder, the descending colon can then be traced cranially through the remainder of the large bowel. The ileocolic junction (Fig. 47.6), cecum, and ascending colon are located medial to the right kidney, which can serve as a landmark as well if unable to trace the entirety of the colon from distal to proximal.

Computed Tomography of the Large Bowel

Computed tomography (CT) provides a three-dimensional view of the large bowel and surrounding structures and is particularly helpful for assessing abnormalities within the pelvic canal compared to radiographs and ultrasound (Fig. 47.7).[14] When nonionic iodinated contrast medium is administered intravenously, the colonic mucosa strongly enhances, but discrete wall layers are not visible on CT.[15] Water, barium, and air have been described as luminal contrast agents.[16,17] Bowel preparation protocols may be utilized for bowel cleansing to optimize image quality and aid in interpretation.[18]

LARGE BOWEL DISEASES

Large Intestinal Displacement From Mass Effect

Abnormalities of the organs adjacent to the large intestine can result in displacement, and sometimes compression, of the colon and rectum depending on the severity (Figs. 47.8 and 47.9). Moderate to severe enlargement of the iliosacral lymph center will result in ventral displacement of the colon and/or rectum on lateral radiographs (Fig. 47.10A). Ventral displacement of the colon will also occur secondary to renomegaly and other causes of mass effects from the retroperitoneal space such as retroperitoneal effusion. Dorsal displacement of the colon and/or rectum commonly occurs secondary to enlargement of the prostate gland, uterus, vagina, or urinary bladder (see Fig. 47.10B).

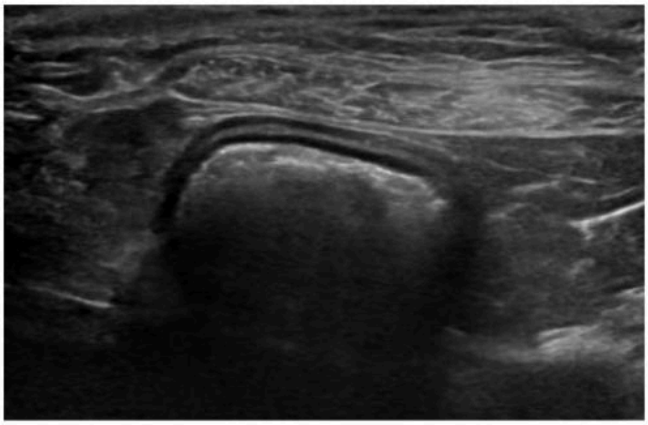


Fig. 47.5 Transverse ultrasound image of the normal descending colon of a dog. In contrast to the small intestine, the wall of the colon is thinner, with each layer contributing approximately equally to the overall wall thickness. The far wall of the colon is not visible in this image secondary to intraluminal feces and gas with associated distal shadowing and reverberation artifact.

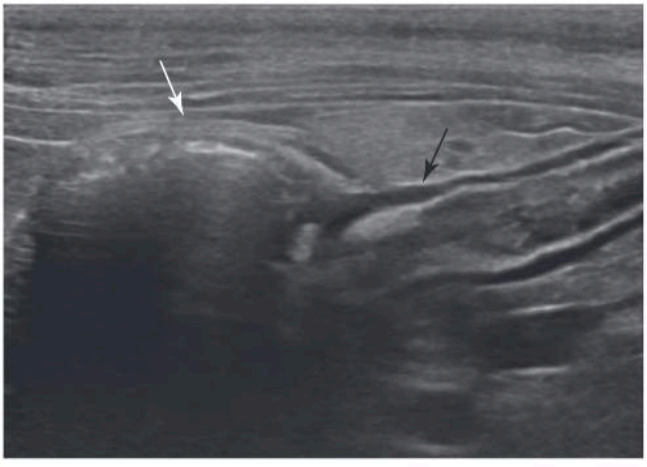


Fig. 47.6 Ultrasound image of the normal ileocolic junction in a cat. The ileum (*black arrow*), in longitudinal section, has prominent muscularis and submucosal layers. The ascending colon (*white arrow*) has a characteristic thin wall and contains internal fecal material with distal acoustic shadowing.

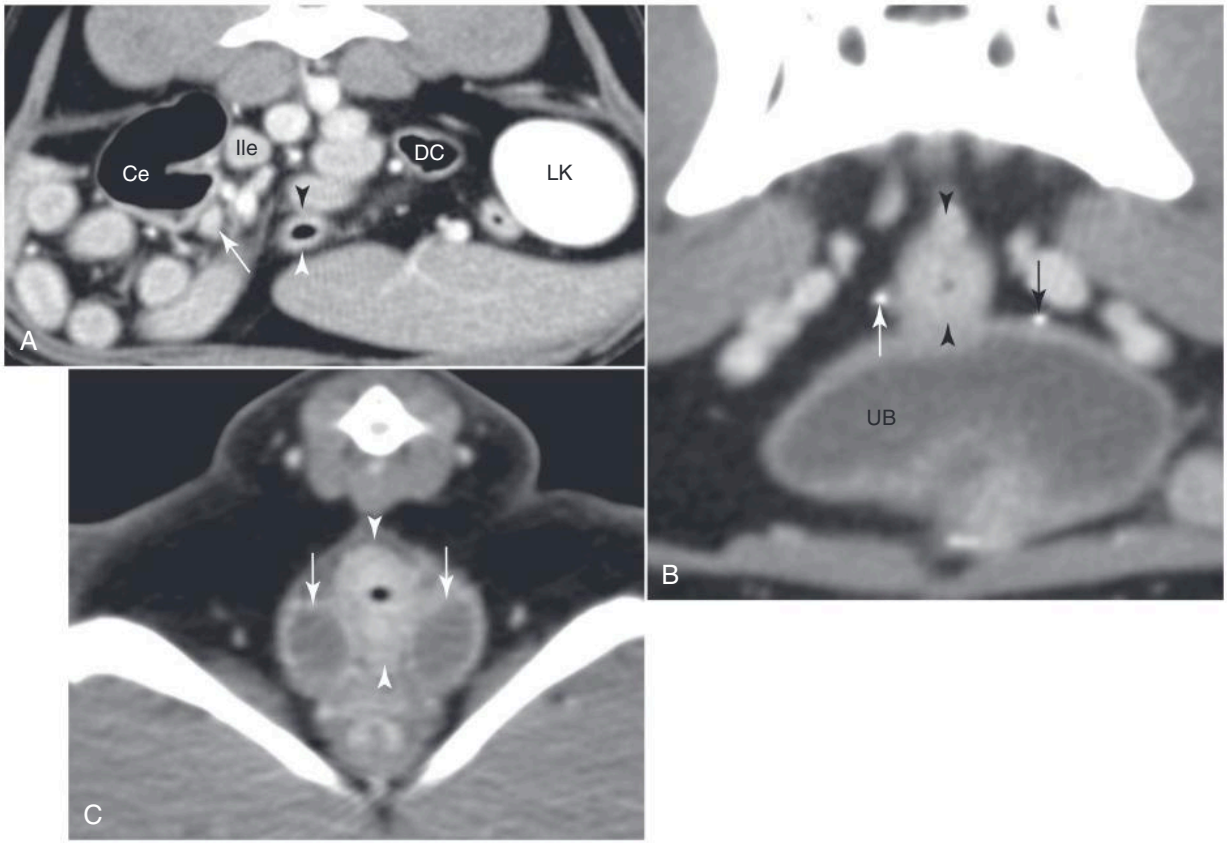


Fig. 47.7 Transverse, contrast-enhanced computed tomography images of the large intestine and adjacent organs in a normal dog. **A,** Cranial abdomen with a gas filled cecum (*Ce*), terminal ileum (*Ile*), right colic lymph node (*arrow*), transverse colon (*between arrowheads*) and descending colon (*DC*); *LK,* Left kidney. **B,** Pelvic inlet with the descending colon (*between arrowheads*), ureters (*arrows*), and urinary bladder (*UB*). The right ureter (*arrow*) is traveling toward the bladder neck in the right mesocolon directly adjacent to the colon wall. **C,** Caudal pelvis with rectum (*between arrowheads*) and adjacent anal gland sacs (*arrows*).

Displacement Within the Large Bowel

Intussusception

Intussusception occurs when a segment of intestine (the intussusceptum) telescopes or invaginates into an adjoining segment (the intussuscipiens). Intussusception is relatively common in young patients and frequently involves the ileocolic junction, although cecocolic (also referred to as "cecal inversion"; Fig. 47.11, eFig. 47.1), colocolic, and colorectal intussusceptions have also been reported.[19–22] Enteritis, parasitic infection, linear foreign bodies, and intestinal masses have been implicated as causes of intussusception, although occasionally it can be idiopathic. Radiographs in patients with intussusception can demonstrate small intestinal dilation secondary to partial or complete obstruction of the ileocolic junction, if present. Occasionally, if the lumen of the intussuscipiens contains gas, a convex soft tissue margin, representing the leading margin of the intussusceptum, can be seen (Fig. 47.12, eFig. 47.1). This is termed a *meniscus sign* and is suggestive of intussusception.[19] When the intussusceptum is outlined by barium from a positive contrast enema or gas, sometimes a "coiled-spring sign" can also be appreciated (Fig. 47.13, eFig. 47.2). On ultrasound, intussusceptions of the large intestine are similar to that seen in the small bowel, characterized by a target-like or "bullseye" appearance, consisting of multiple hyperechoic and hypoechoic concentric rings, caused by juxtaposition of the affected bowel walls, around a hyperechoic center of entrapped mesentery (Fig. 47.14).[19] Color Doppler can be helpful in assessing viability of the involved intestinal segments.[23]

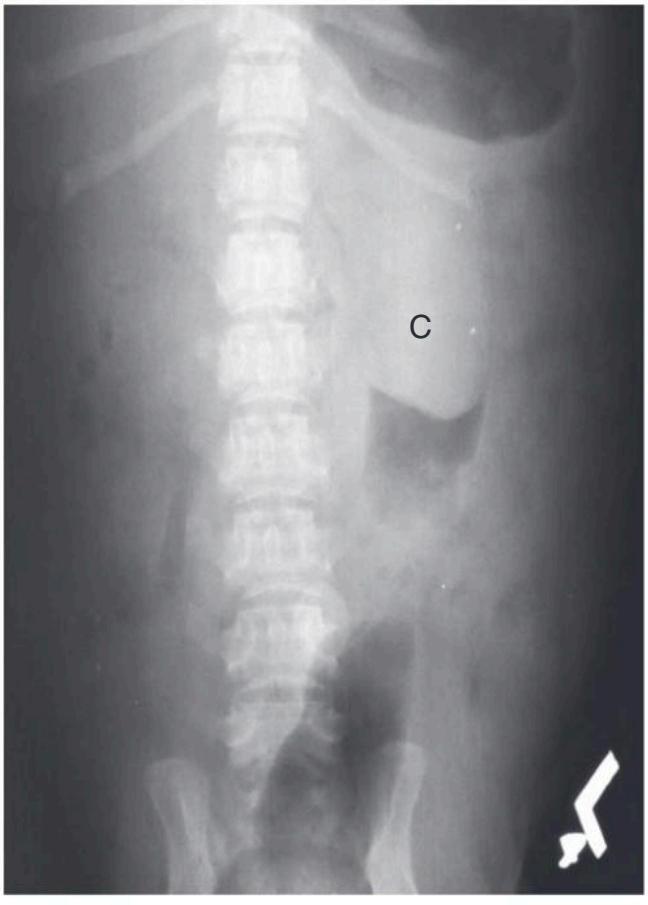
Displacement Within the Abdominal Cavity

Colonic Torsion/Volvulus

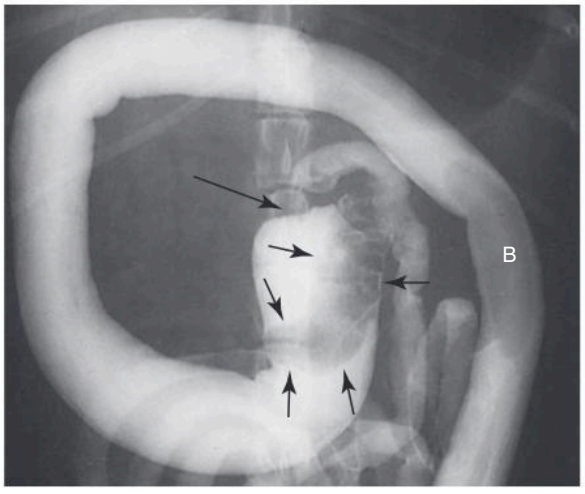
Both torsion and volvulus of the colon have been described in small animals, and these terms appear to be used interchangeably in the literature. Colonic torsion/volvulus occurs primarily in young to middle-aged medium and large breed dogs, although a single case of colonic volvulus has been reported in a domestic shorthair cat.[7,10,24–26] Clinical signs of shock may or may not be present upon evaluation; when absent, this can occasionally result in treatment delays, making rapid diagnosis imperative.[10] Radiographic findings of colonic torsion include segmental dilation of the colon, focal narrowing of the descending colon, displacement of the cecum to the left of midline, and displacement of the proximal descending colon to the right of midline (Fig. 47.15).[10] Barium enema is helpful in obtaining a definitive diagnosis, with characteristic longitudinal and helical striations visible in conjunction with focal narrowing at the site of torsion (Fig. 47.16, eFigs. 47.3 and 47.4). Additional findings of colonic torsion seen with CT include presence of the "whirl sign," distention of mesenteric vasculature, peritoneal effusion, and pneumatosis coli in a subset of patients.[27]

Large Intestinal Entrapment and Strangulation

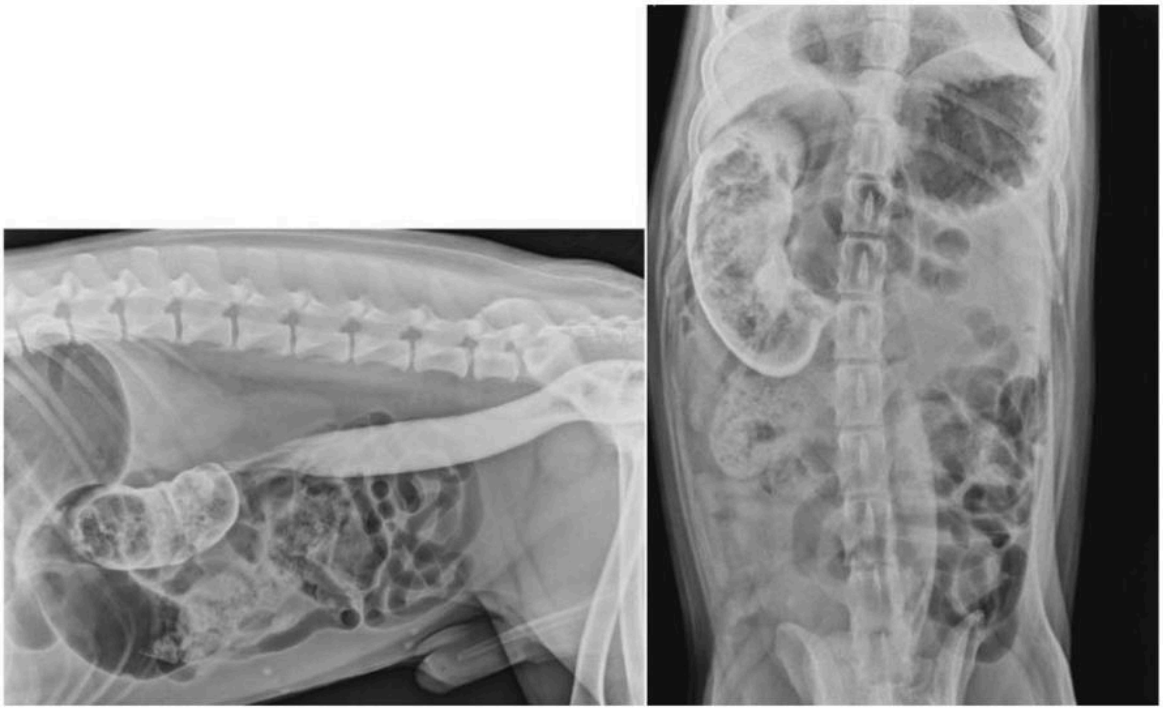
Colonic entrapment and strangulation are uncommon conditions but have been reported in dogs secondary to rupture of the duodenocolic ligament with secondary colonic entrapment, entrapment in gastropexy sites, and entrapment in omental rents and adhesions.[10,26,28,29]



eFig. 47.1 Survey ventrodorsal abdominal radiograph of a young dog with an ileocecocolic intussusception. The proximal descending colon (*C*) is distended by a homogeneous soft-tissue mass with a curved gas interface caudally. This mass is the leading edge of the intussusceptum and this sign, sometimes called the meniscus sign, is highly suggestive of intussusception.

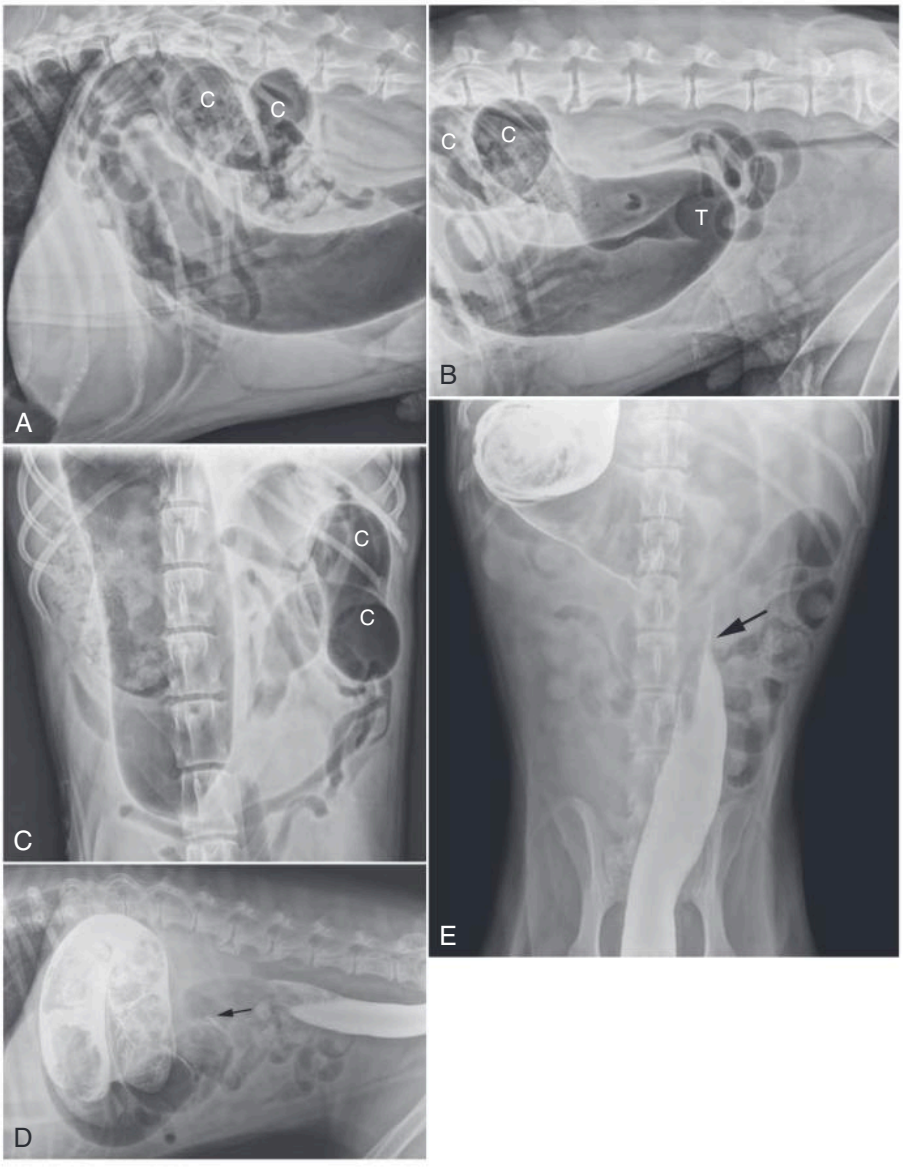


eFig. 47.2 Ventrodorsal radiograph of a barium enema of a young dog with a cecocolic intussusception. The intussusceptum appears as a radiolucent filling defect (*short arrows*) in the proximal aspect of the ascending colon. Note that the ileocolic junction (*long arrow*), and distal ileum are normal, ruling out ileocolic intussusception. The radiolucent region in the descending colon (*B*) is a gas bubble.



eFig. 47.3 Lateral and ventrodorsal views of a Great Dane with colonic torsion. A barium enema was performed. There is segmental dilation and displacement of the proximal descending colon resulting in a C-shaped distended bowel segment in the cranial abdomen. The distal descending colon is nondistended and cannot be traced in its entirety. In the ventrodorsal view, the cecum is displaced in the left abdomen and is located caudal to the body and fundus of the stomach.





eFig. 47.4 **A–E,** Lateral views of the cranial **(A)** and caudal **(B)** abdomen and a ventrodorsal **(C)** view of the cranial abdomen of a dog with a colonic volvulus. The large comma-shaped or C-shaped distended bowel segment in the cranial abdomen is typical of a colon torsion. Also, the cecum (*C*) is located dorsally and on the *left*, and the transverse colon (*T*) is in the midabdomen. **D and E,** Barium enema in another dog with a colon torsion showing the twist in the descending colon

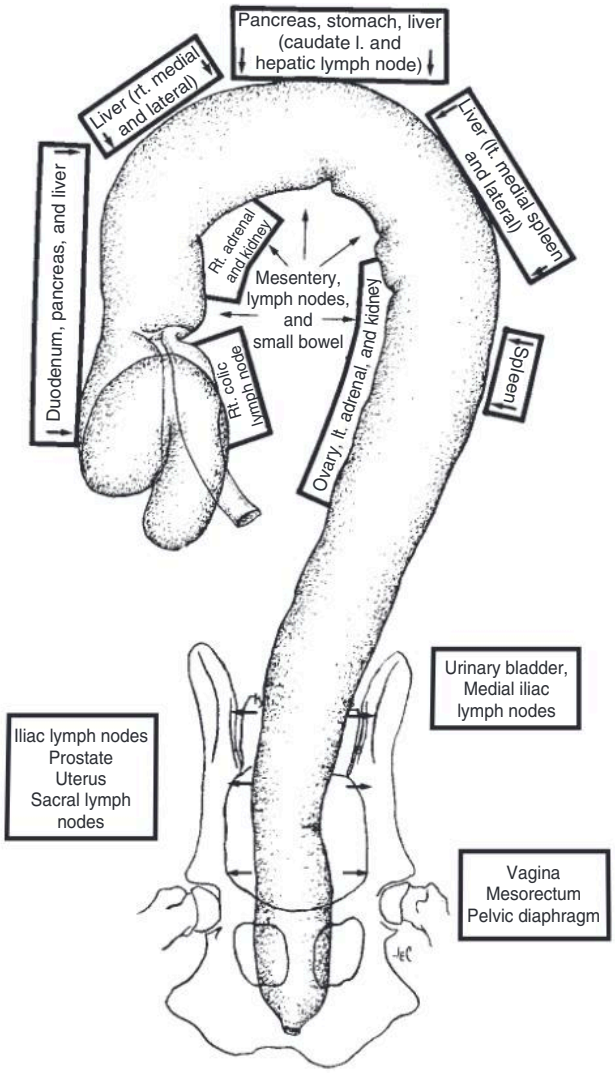


Fig. 47.8 Viscera adjacent to the large bowel may cause a change in position of a portion of the colon. This change in position may be indicative of disease or a variant of normal, depending on the cause of the deviation. The *arrows* indicate the direction of displacement of the colon that can occur when an adjacent organ enlarges. (Reproduced with permission from O'Brien TR. *Radiographic Diagnosis of Abdominal Disorders in the Dog and Cat*. Davis, CA: Covell Park Veterinary; 1981)

Displacement From Herniation

Perineal Hernia

In addition to herniation of the bladder and/or prostate into the perineal region, perineal hernias also frequently result in displacement of the rectum and/or descending colon into the perineal region (Fig. 47.17).

Alterations in Large Bowel Diameter

Constipation/Obstipation/Megacolon

Constipation is defined as reversible, infrequent, or difficult defecation with associated retention of fecal material.[2] Recurrent constipation that is refractory to treatment is termed *obstipation*, and implies a permanent loss of function.[2] Megacolon is a descriptive term, used when there is irreversible dilation of the colon, and represents end-stage colonic dysfunction in patients with obstipation.[2,5] (Fig. 47.18; eFig. 47.5A,B) Differentials for patients with chronic constipation, obstipation, and megacolon can be split into functional and mechanical causes. Functional causes include neuromuscular dysfunction; spinal cord diseases, including lumbosacral, cauda equina, and sacral spinal cord deformities (such as that seen in the Manx cat); hypogastric or pelvic nerve disorders; submucosal or myenteric plexus neuropathy; aganglionosis of the large bowel; and feline dysautonomia.[2,30–32] Metabolic and endocrine diseases can also be a functional cause of chronic constipation, with young cats with congenital hypothyroidism being particularly predisposed.[2,33,34] Mechanical causes of chronic constipation include luminal obstruction secondary to mural lesions of the large intestine (such as masses or strictures), herniation of large bowel with associated obstruction, and congenital deformities such as atresia ani and atresia coli. Extramural lesions can also result in mechanical obstruction of the large intestine, including malunion pelvic fractures with narrowing of the pelvic canal and extramural masses or neoplasia.[35] Of these differentials, the most common causes in cats are idiopathic megacolon (accounting for approximately 66% of all cases), with an additional 25% of cases being attributed to narrowing of the pelvic canal from malunion fractures.[5] To differentiate constipation from megacolon in cats, a ratio of the maximal diameter of the colon compared to the length of the L5 vertebral body can be used, with a ratio greater than 1.5 suggestive of megacolon.[5] Patients with constipation or obstipation often have fecal material that is increased in opacity compared to that of normal feces, sometimes being mineral opaque, due to excessive water resorption from colon stasis.

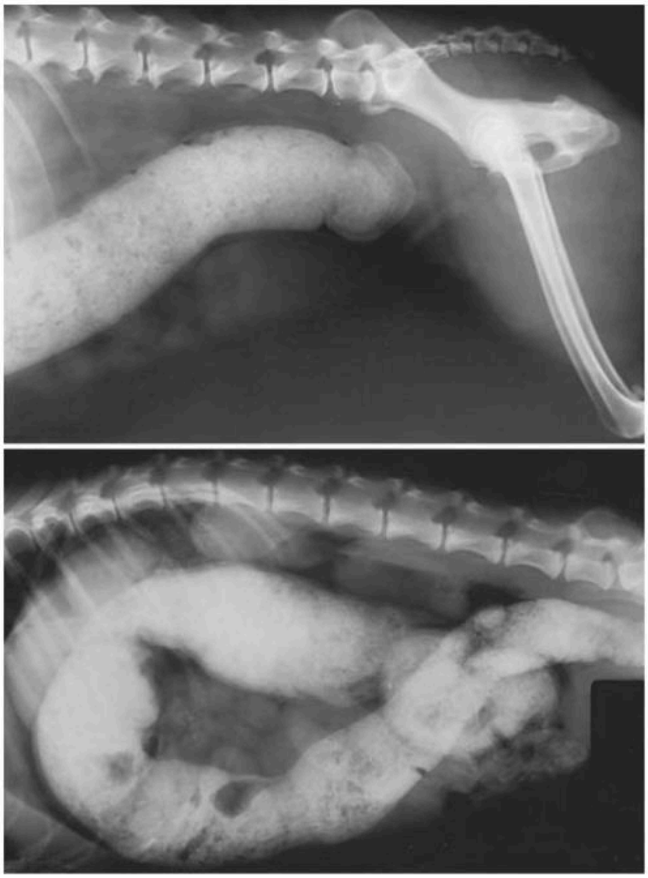
MURAL ABNORMALITIES OF THE LARGE BOWEL

Focal Wall Thickening

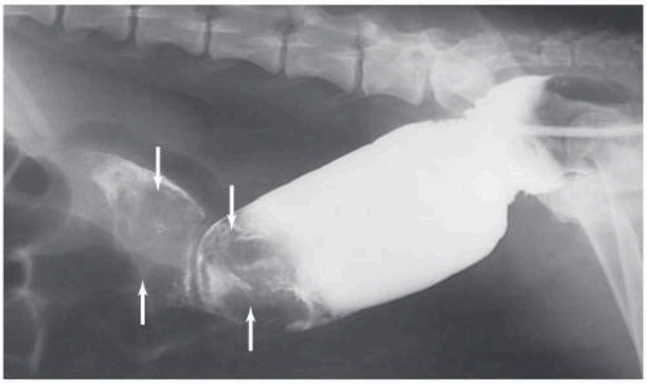
Focal wall thickening and mass lesions of the large intestine occur secondary to infiltration of the wall with cells, most commonly secondary to neoplasia, inflammation, and/or infectious disease. Mass lesions of the large intestine may be visible on radiographs if they are large in size; small lesions are better visualized with ultrasound. Ultrasound findings include focal thickening of the intestinal wall and/or discrete nodules/masses arising from the intestinal wall with alteration or loss of wall layering. While neoplasia is a common cause of these changes, these findings are not specific and there is overlap between neoplastic and inflammatory lesions. Patient signalment, history, clinical signs, and lesion location can sometimes aid in prioritizing differential diagnoses, but ultimately, tissue sampling must be performed for definitive diagnosis.

Malignant Neoplasia of the Large Intestine

The most common colonic neoplasms of dogs are adenocarcinoma and lymphoma, with adenocarcinomas of the large intestine occurring most commonly in the descending colon and rectum.[2] In dogs, gastrointestinal stromal tumors (GISTs) and leiomyosarcomas have a predilection for the cecum (Fig. 47.19, eFig. 47.6).[2] Distinguishing between GISTs and leiomyosarcomas was previously difficult until the advent of new immunohistochemistry stains, leading many historically diagnosed leiomyosarcomas to be reclassified as GISTs.[36] This reclassification may impact the incidence of smooth muscle tumors of the gastrointestinal tract reported in previous studies. In cats, the most common large intestinal neoplasm is also adenocarcinoma, followed by lymphoma (Figs. 47.20 and 47.21, and eFig. 47.7).[37,38] Other etiologies such as mast cell neoplasia and spindle cell tumors are much less common in the large intestine of cats.[37,38]

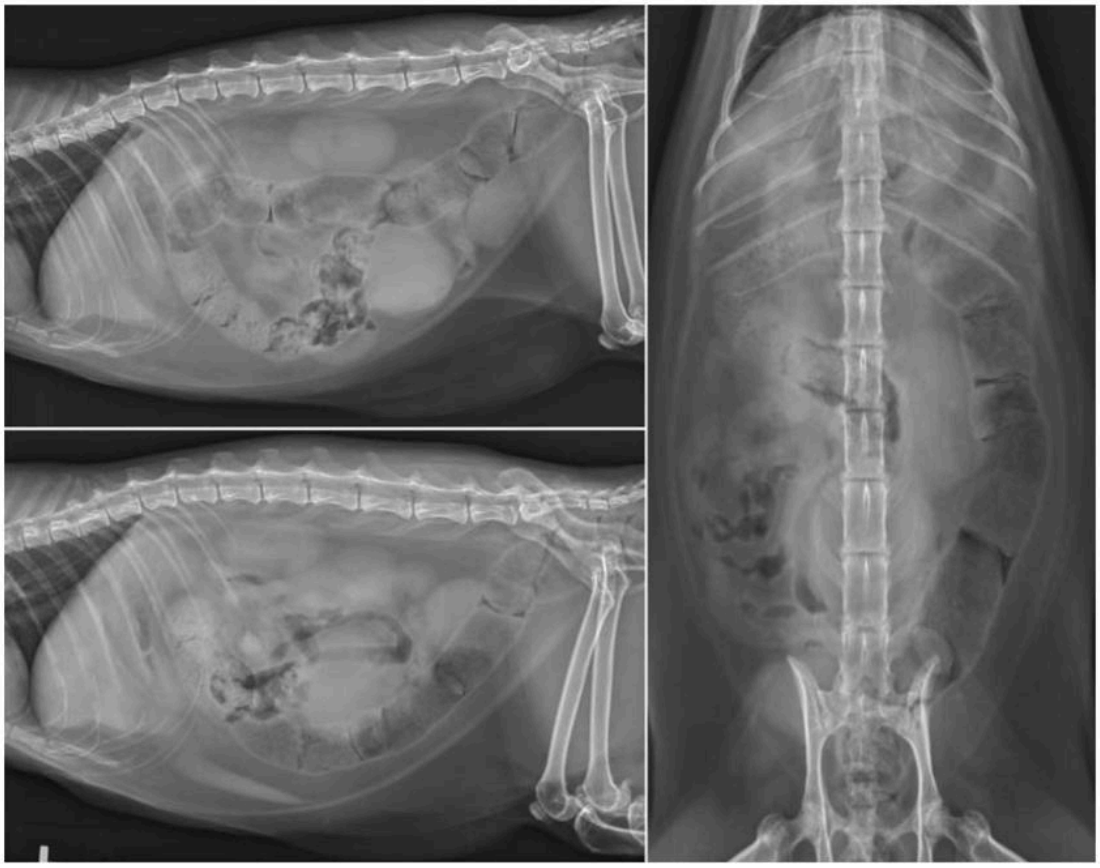


eFig. 47.5 **A,** Survey lateral radiograph of a dog with a pelvic fibroleiomyoma that caused partial colonic obstruction and fecal accumulation. **B,** Generalized megacolon in a young dog caused by Hirschsprung's disease, which is a congenital deficiency in colonic enteric nerves.



eFig. 47.6 A barium enema in a dog with a mass (*arrows*) creating a polypoid filling defect in the midportion of the descending colon. The diagnosis was lymphoma.





eFig. 47.7 Lateral and ventrodorsal views of a cat with a cecal mass. There is a round soft tissue opaque mid-abdominal mass that is located on midline in the ventrodorsal projection. The mass is located immediately caudal to the ascending colon in all views. A small amount of gas is present in the ventral aspect of the mass in the top left image. The location of this mass, internal gas, and lack of associated gastrointestinal mechanical obstruction are all highly suggestive of cecal origin. The histopathologic diagnosis was adenocarcinoma.

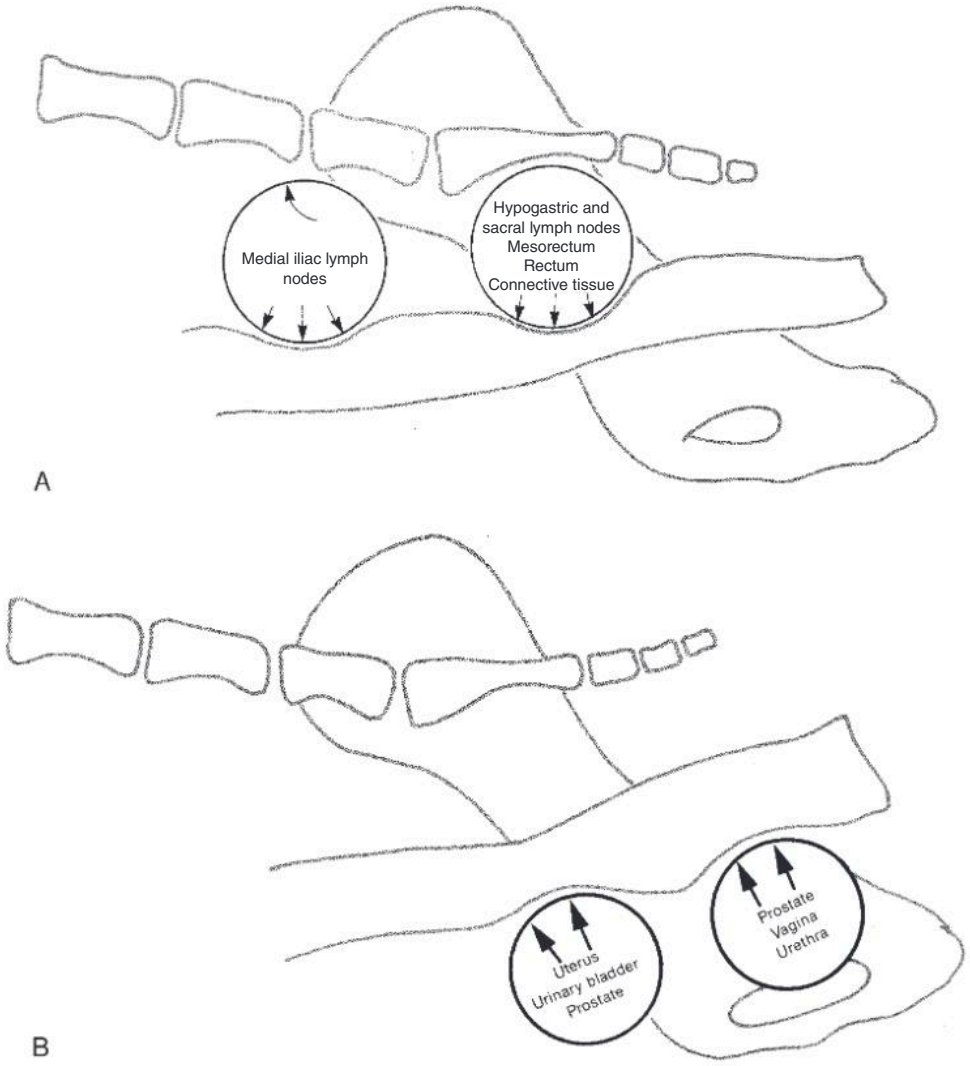


Fig. 47.9 Patterns of displacement of the descending colon and rectum by adjacent organ enlargement. **A,** Ventral displacement of the terminal descending colon and rectum commonly results from medial iliac and sacral lymph node enlargement. Although less common, a hematoma, abscess, or tumor may produce similar displacement alterations. **B,** Dorsal displacement of the rectum commonly results from enlargement of the prostate gland, the uterus, the vagina, or the intrapelvic urinary bladder. (Reproduced with permission from O 'Brien TR. *Radiographic Diagnosis of Abdominal Disorders in the Dog and Cat*. Davis, CA: Covell Park Veterinary; 1981.)

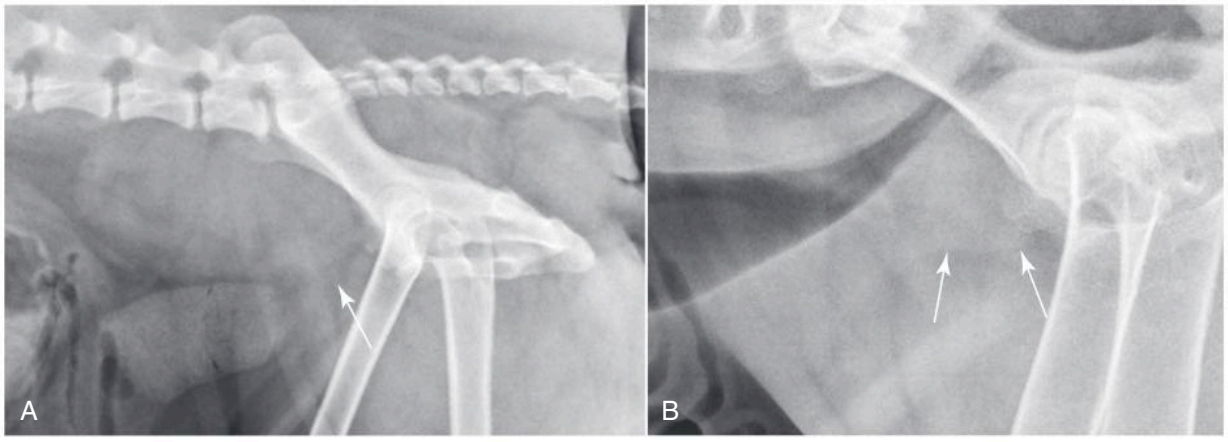


Fig. 47.10 **A,** Lateral radiograph of a dog with anal sac carcinoma metastatic to the medial iliac lymph nodes. The enlarged lymph nodes displace the colon ventrally and there is compression (*arrow*) at the pelvic inlet. **B,** Lateral radiograph of a dog with narrowing of the large bowel at the junction of the descending colon and rectum from an enlarged prostate gland (*arrows*).

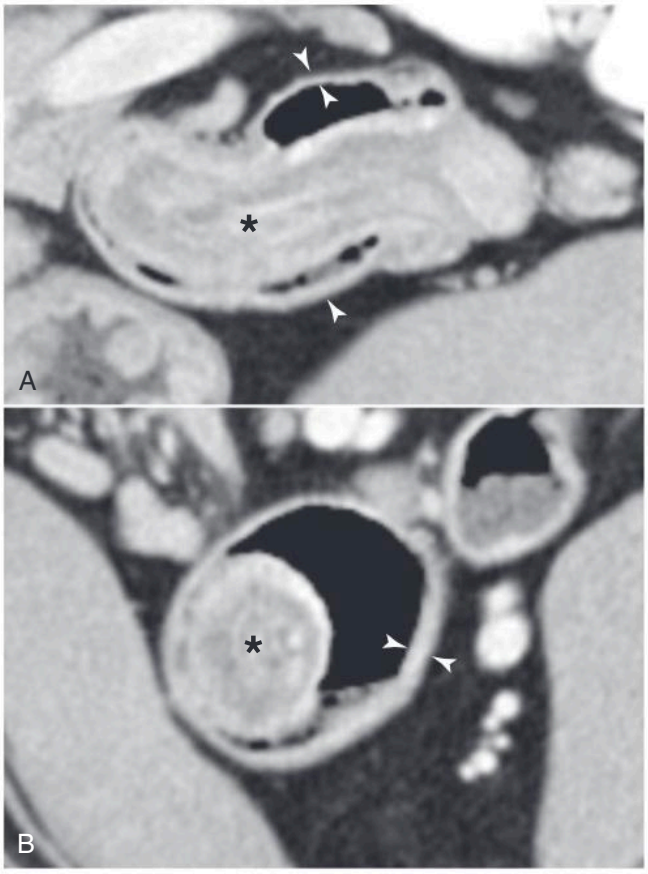


Fig. 47.11 Sagittal **(A)** and transverse **(B)** computed tomography images of a cecocolic intussusception due to large B-cell lymphoma in an older dog. Note the thickened, heterogeneously contrast enhancing cecum (*asterisk*) displaced into the lumen of the ascending colon. The ascending colonic wall is outlined by *arrowheads* and a small amount of luminal gas and fluid outlines the intussusceptum. The lymphoma most likely caused dysmotility that led to cecal inversion and intussusception.

Focal Wall Thickening From Infectious/ Inflammatory Disease

A variety of infectious and inflammatory diseases can result in focal wall thickening or mass lesions of the large intestine with alteration or complete loss of wall layering. In dogs, conditions reported to cause focal masses with loss of wall layering of the colon include pythiosis, fungal disease, and protothecosis.[39–42] Granulomatous colitis can also cause focal wall thickening and masses.[43] Submucosal thickening and mineralization of the colon wall have been reported in dogs secondary to *Heterobilharzia americana* infection, although these changes are often less pronounced than that seen in the small intestine.[44,45] In cats, feline infectious peritonitis, fungal disease, and eosinophilic sclerosing fibroplasia can result in mass lesions and focal thickening of the large intestine.[46,47] In both dogs and cats, bacterial etiologies, such as disseminated mycobacteriosis, can result in focal or multifocal intestinal lesions.[48]

Benign Mass Lesions of the Large Intestine

Benign polyps have been reported in the large intestine of both dogs and cats, and have rarely been associated with intussusception.[21,38,49] Adenomas and leiomyomas are benign neoplasms that can occur within the large intestine, although these are less common than their malignant counterparts (adenocarcinoma and leiomyosarcoma, respectively). Hemorrhage and/or hematoma formation within the wall can also result in focal mass lesions of the large bowel,[50] and cecal mucoceles are a cause of intraluminal mass-like lesions which could be confused for a soft tissue mass.[51]



Fig. 47.12 Survey ventrodorsal abdominal radiograph of a young dog with an ileocecocolic intussusception demonstrating the meniscus sign. The transverse colon is distended by a homogeneous soft-tissue opacity with a curved gas interface caudally (*arrows*), consistent with the leading edge of the intussusceptum. A similar appearance could be seen with a soft tissue opaque foreign body or mass. Ultrasound could be used to distinguish between these differentials if indicated.



Fig. 47.13 Lateral radiograph of a barium enema of a cat with an ileocolic intussusception. The intussusceptum creates a filling defect in the barium. Edema and swelling of the intussusceptum create a coiled-spring appearance to the filling defect; this is typical of the appearance of the intussusceptum in a barium enema.

Diffuse Wall Thickening

Colitis/Typhlitis

With colitis, a gas- or fluid-filled colon may be seen radiographically. On ultrasound, mild diffuse thickening of the wall may be present (Fig. 47.22), usually with preservation of wall layers, in conjunction with echogenic intraluminal fluid. Corrugation of the wall may also be present, characterized by multifocal undulation of luminal margin on radiographs or as numerous small undulations of the mucosa/lumen interface

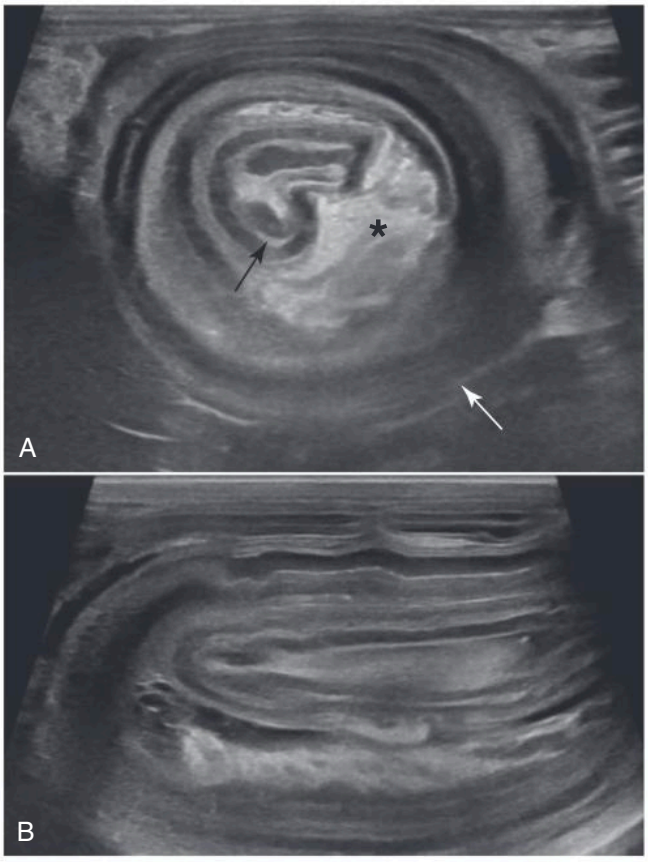


Fig. 47.14 Transverse **(A)** and longitudinal **(B)** ultrasound images of the descending colon of a dog with a jejunocolic intussusception. In **A,** note the target-like or "bullseye" appearance, consisting of multiple hyperechoic and hypoechoic concentric rings, caused by juxtaposition of the walls of the external intussuscipiens (*white arrow*) and internal intussusceptum (*black arrow*) with a hyperechoic center, representative of entrapped mesentery (*asterisk*). In **B,** the same wall layers are now parallel in orientation.

and/or submucosa on ultrasound. Occasionally, small (1–3 mm) ovoid hypoechoic nodules may be seen in the submucosal layer of the colon in patients with diarrhea, thought to represent reactive lymphoid follicles (Fig. 47.23A).[52] Lymphoid follicles can also be visible as coalescing nodules in the cecal mucosa and submucosa, termed the *follicular layer*, in cats with subclinical inflammation.[53] Typhlitis, or inflammation of the cecum, can appear as diffuse wall thickening with loss of wall layering in cats (see Fig. 47.23B).[54] In cat ceca, loss of wall layering is not a reliable predictor of the severity of inflammation or of neoplastic change. The sonographic findings of typhlitis have not been described in dogs, although wall thickening and/or fluid distention of the lumen could be suggestive.

Opacity Changes

Pneumatosis Coli

Pneumatosis coli is the presence of gas within the colon wall. This can occur secondary to a defect in the intestinal mucosa, such as an ulcer, or an increase in intraluminal pressure that allows luminal gas to pass into the bowel wall. Increased intraluminal pressure could occur secondary to large bowel obstruction, as with colonic torsion,[27] or iatrogenically from recent endoscopy.[55] Underlying gastrointestinal necrosis from ischemia or inflammatory disease can also result in introduction of luminal gas into the bowel wall.[55] Anaerobic bacterial infection of the colonic mucosa has also been implicated in the development of pneumatosis coli, namely infection with *Clostridium* species.[55] Radiographically, pneumatosis coli appears as a heterogeneous gas pattern within the wall of the colon. When a large volume of gas is present, it can present as a band of gas that follows the course of the wall (Fig. 47.24). With smaller volumes of gas, it can be difficult to distinguish between intramural gas and intraluminal gas trapped between peripherally located fecal material and the wall. Sonographically, pneumatosis coli is characterized by gas with associated reverberation artifact that originates from the submucosal or subserosal layers of the colonic wall, rather than the lumen (Fig. 47.25).[55,56] Similar to pneumatosis in other regions of the

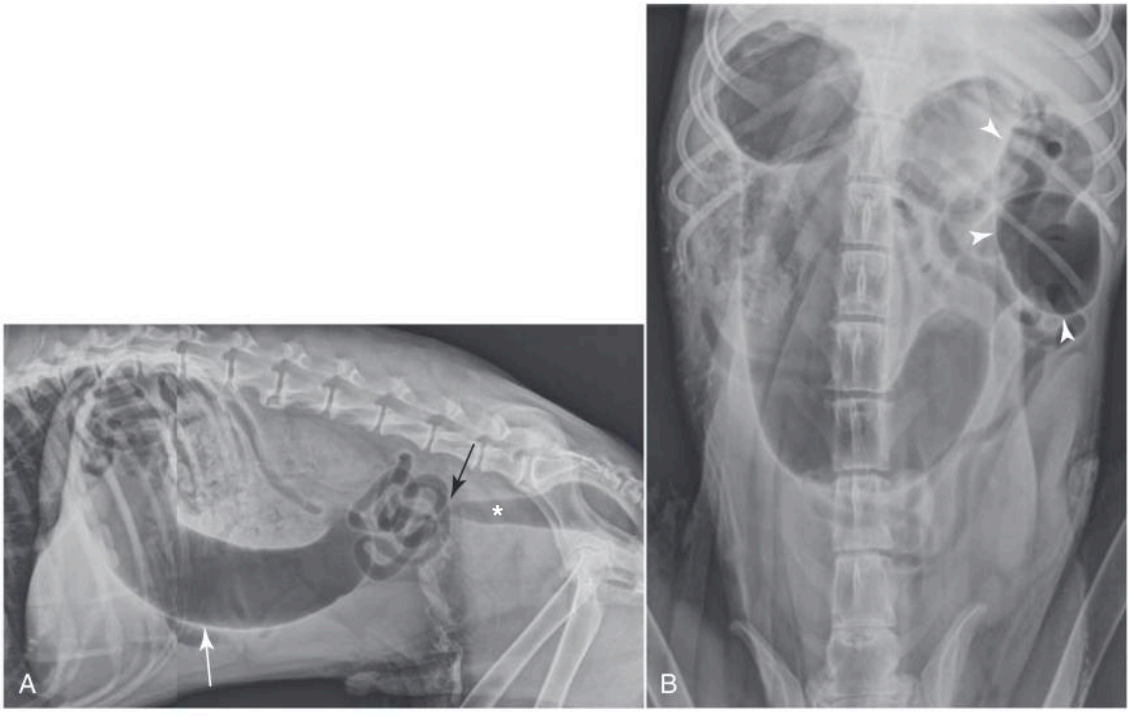


Fig. 47.15 Lateral **(A)** and ventrodorsal **(B)** views of a dog with colonic torsion. Segmental dilation and displacement of the proximal colon (*white arrow*), resulting in a C-shaped distended bowel segment in the cranial abdomen, are typical of colonic torsion. The distal descending colon (*white asterisk*) is nondistended and focally narrows in the caudal abdomen (*black arrow*). In the ventrodorsal view, the cecum (*white arrowheads*) is displaced in the left abdomen.

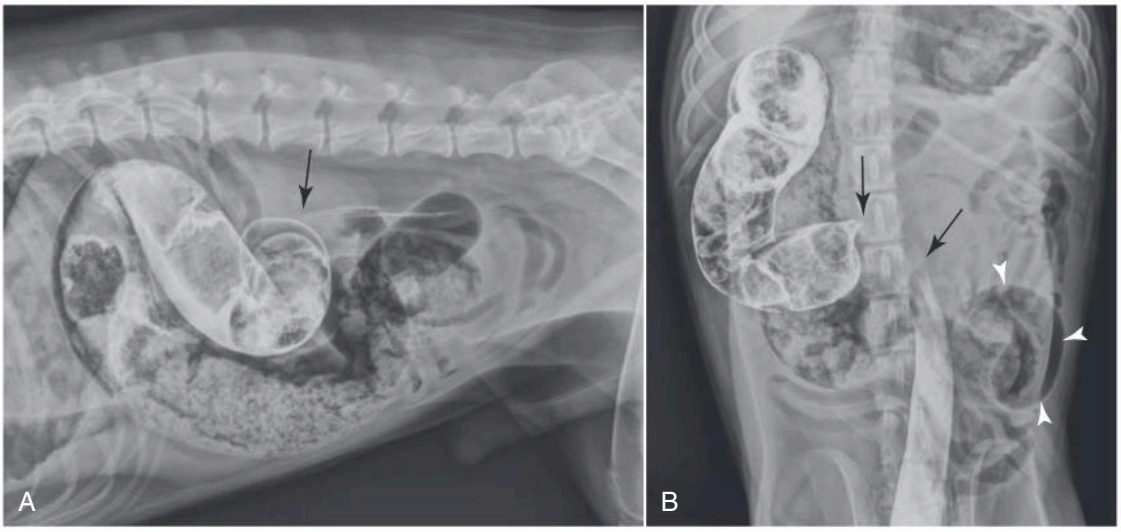


Fig. 47.16 Lateral **(A)** and ventrodorsal **(B)** views following barium enema in a dog with colonic torsion. Note the focal narrowing and longitudinal striations (*black arrows*) in the distal descending colon, which have a somewhat helical pattern in **B**. The cecum is displaced in the left abdomen in the ventrodorsal view (*white arrowheads*).

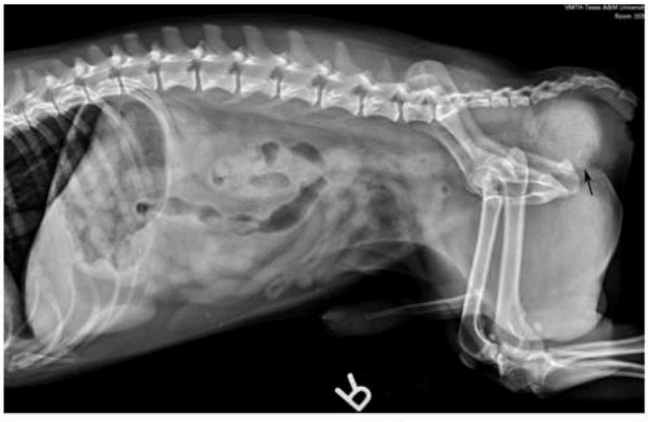


Fig. 47.17 Lateral radiograph of a dog with a perineal hernia. There is herniation of the rectum and colon into the perineal region, with accumulation of desiccated fecal material (*arrow*). Note the increased opacity of the fecal material due to inspissation.

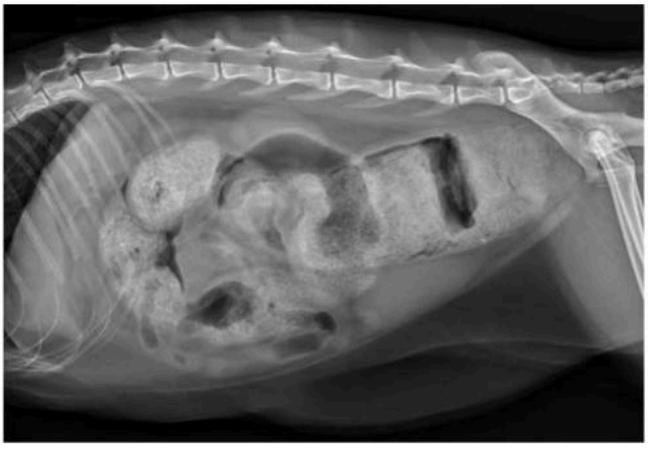


Fig. 47.18 Lateral radiograph of a cat with idiopathic megacolon. There is severe dilation of the entirety of the colon, most severely affecting the descending colon, resulting in ventral displacement of the urinary bladder. Note the increased opacity of the colonic contents, consistent with desiccated fecal material.

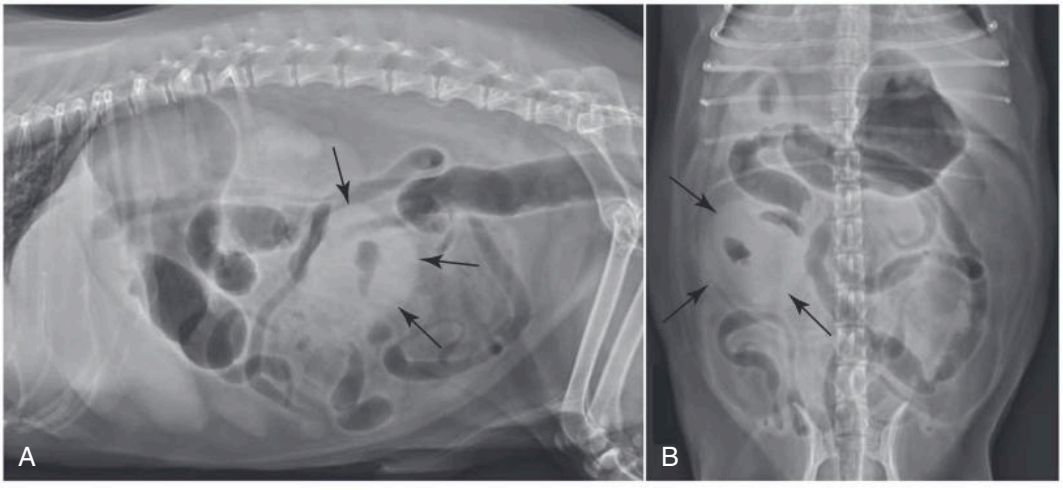


Fig. 47.19 Lateral **(A)** and ventrodorsal **(B)** views of a dog with a cecal mass. There is a round soft tissue opaque midabdominal mass with internal gas (*black arrows*) that localizes to the right of midline in the ventrodorsal projection. The location of this mass, internal gas, and lack of associated gastrointestinal mechanical obstruction are all highly suggestive of cecal origin. This was a gastrointestinal stromal tumor on histopathology.

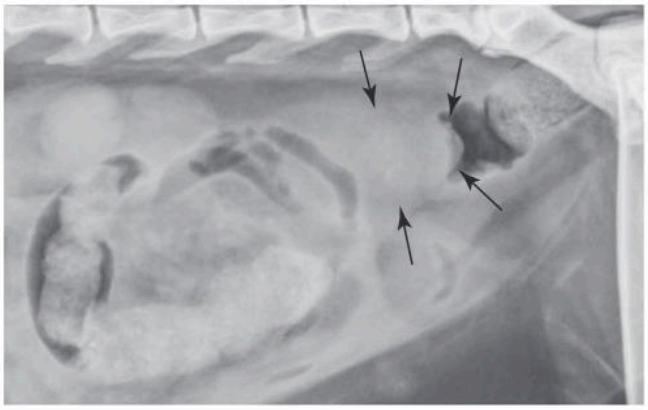


Fig. 47.20 Lateral radiograph of a cat with a descending colonic mass in a cat presented for chronic constipation. There is a large, ovoid soft tissue opaque mass in the region of the distal descending colon (*black arrows*). The caudal margin of the mass is outlined by gas, causing a meniscus sign. The colon proximal to this mass contains mineral opaque fecal material secondary to constipation. There is decreased serosal contrast throughout the ventral abdomen.

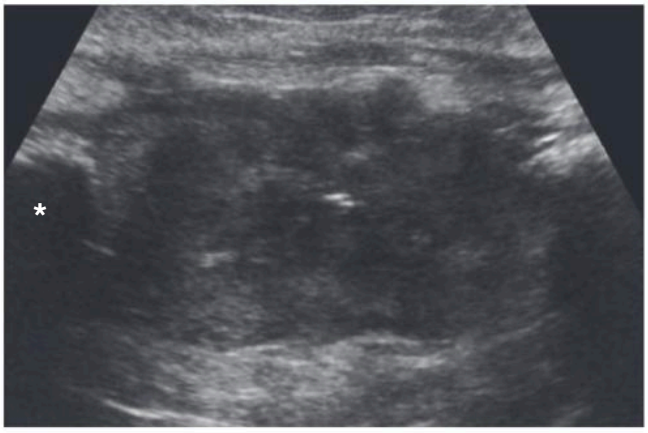


Fig. 47.21 Longitudinal ultrasound image of a cat with a descending colonic mass (same patient as Fig. 47.20). There is a large, hypoechoic, irregularly marginated mass arising from the descending colon with loss of wall layers in this region. Shadowing fecal material is present cranial to the mass (*asterisk*).

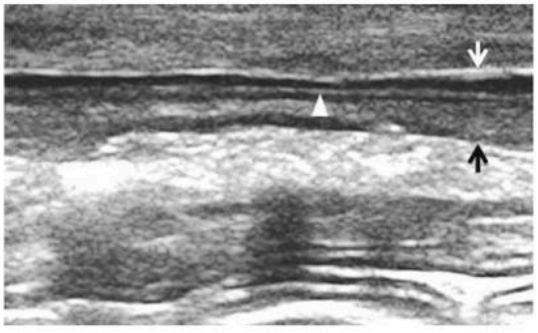


Fig. 47.22 Long-axis ultrasound image of the descending colon of a cat with short colon syndrome and *Campylobacter* colitis. The ascending and transverse colon were absent, the residual descending colon was markedly thickened (*3 mm between arrows*), with reduced wall layering. There is also a hyperechoic line within the tunica muscularis, which can be a normal finding (*arrowhead*).

gastrointestinal tract, gas within the colonic wall can drain into the portal system, resulting in portal venous gas, and sometimes pneumoperitoneum in people.[57,58] There is a wide range of diseases that can result in pneumatosis intestinalis in people, which range from innocuous to fatal.[58,59] Although this is a

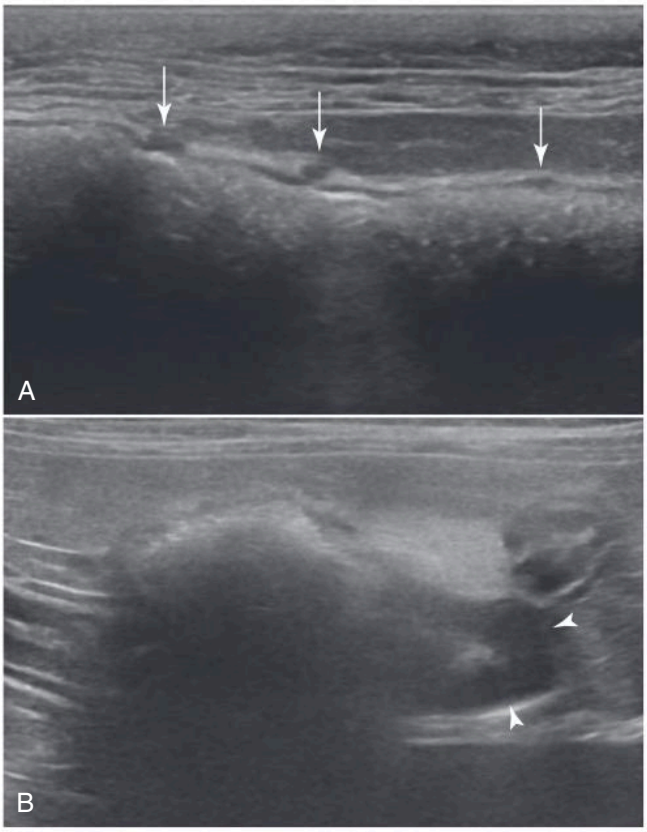


Fig. 47.23 **A,** Longitudinal ultrasound image of the descending colon. There are multifocal small, ovoid, well-defined hypoechoic nodules (*arrows*) in the submucosal layer consistent with lymphoid follicular hyperplasia. **B,** Ultrasound image of the cecum of a cat with presumed typhlitis. The cecal wall (*arrowheads*) is thickened and hypoechoic with loss of wall layering.

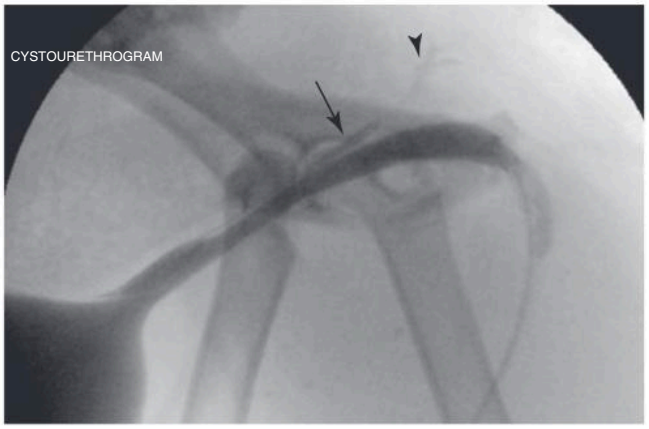
relatively rare condition in dogs, the veterinary literature appears to mirror this as well, with most dogs responding positively to medical therapy upon diagnosis, while others acutely deteriorated and died or were euthanized.[55–57,60,61] Due to the potential serious outcomes associated with this, investigation into the underlying cause should be performed when identified on imaging.

Large Intestinal Perforation

Neoplasia, ulceration, obstipation, trauma from enemas, endoscopic biopsy, and radiation therapy of the pelvic region can all lead to large intestinal perforation.[62–64] Colonic ulceration can occur secondary to primary large intestinal disease, but has also been reported with perforation in association with corticosteroid and nonsteroidal anti-inflammatory drugs.[65–67] Radiographic and ultrasonographic findings of large intestinal perforation are similar to that of perforation of the small intestine.[68]

CONGENITAL LARGE BOWEL DISEASES

Congenital anomalies of the large intestine are rare in dogs and cats. Atresia ani, atresia recti, and atresia coli may be a cause of large intestinal obstruction and obstipation in neonatal animals.[69] Short colon has sporadically been reported in cats and dogs and may be associated with signs of large bowel diarrhea.[70–72] Fistulae, diverticula, and duplication of large intestinal structures can also occur[73–75] (eFig. 47.8). Because of the complexity of many of these congenital anomalies, contrast studies either with radiography, fluoroscopy, and/or CT are often used in their evaluation and treatment planning.



eFig. 47.8 Retrograde urethrography in a male dog with a rectourethral fistula. Note the thin, focal tubular structure filled with contrast medium extending dorsally and caudally from the urethra (*arrow*) and presence of contrast medium within the rectal lumen (*arrowhead*).

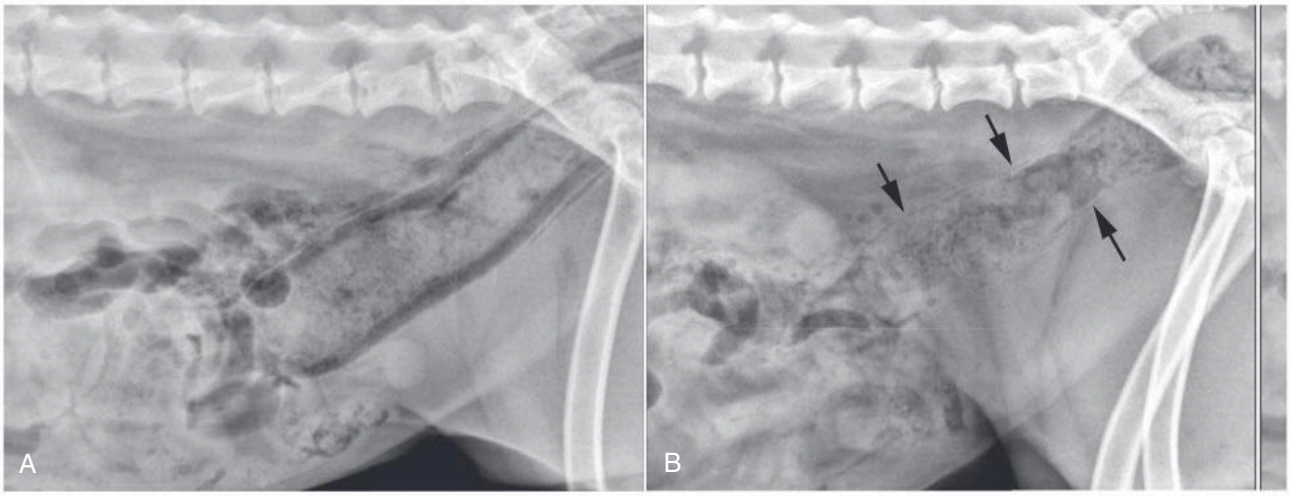


Fig. 47.24 **A,** Lateral radiograph of a dog with tenesmus and hematochezia. There is a large amount of air within the wall of the colon (i.e., pneumatosis coli). **B,** With symptomatic therapy, the clinical signs resolved and the amount of gas in the wall of the colon was markedly reduced (*arrows*) in radiographs acquired 5 days later. The cause of the pneumatosis coli in this patient was not determined but could be related to mucosal ulcerations associated with the large bowel disease.

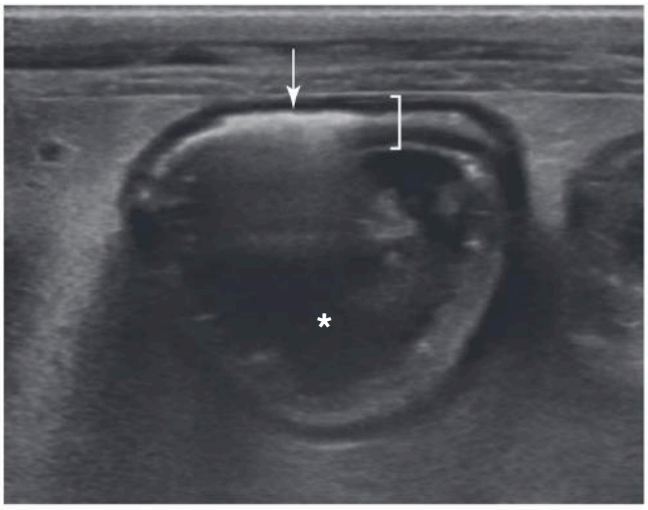


Fig. 47.25 Transverse ultrasound image of the descending colon of a different dog with pneumatosis coli. There is focal hyperechogenicity with reverberation artifact within the wall of the colon (*bracket*), consistent with gas, which obscures the mucosal layer. The colon lumen (*asterisk*) contains fluid.

Acknowledgment

With special thanks to prior authors of this chapter for their contributions.

REFERENCES

1. Evans HE, de Lahunta A. The Digestive Apparatus and Abdomen. In: *Miller and Evan's Anatomy of the Dog*. 4th ed. Philadelphia: Elsevier; 2013.
2. Hall EJ. Diseases of the Large Intestine. In: Ettinger SJ, Feldman EC, Cote E, eds. *Textbook of Veterinary Internal Medicine*. 8th ed. Philadelphia: Elsevier; 2017.
3. Kealy KJ, McAllister H. *Diagnostic Radiology and Ultrasonography of the Dog and Cat*. 5th ed. Philadelphia: WB Saunders; 2010.
4. O'Brien TR. *Radiographic Diagnosis of Abdominal Disorders in the Dog and Cat*. Davis, CA: Covell Park Veterinary; 1981.
5. Trevail T, Gunn-Moore D, Carrera I, et al. Radiographic diameter of the colon in normal and constipated cats and in cats with megacolon. *Vet Radiol Ultrasound*. 2011;52:516.
6. Nyland TG, Ackerman N. Pneumocolon: a diagnostic aid in abdominal radiography. *Vet Radiol*. 1978;19:203–209.
7. Czajkowski PS, Fryer KJ. Colonic torsion in 4 great danes. *J Vet Emerg Crit Care*. 2020;30(5):581–586.
8. Kleine LJ, Lamb CR. Comparative organ imaging: the gastrointestinal tract. *Vet Radiol*. 1989;30:133.
9. Brawner WB, Bartels JE. Contrast radiography of the digestive tract: indications, techniques, and complications. *Vet Clin North Am*. 1983;vol. 13:599.
10. Gremillion CL, Savage M, Cohen EB. Radiographic findings and clinical factors in dogs with surgically confirmed or presumed colonic torsion. *Vet Radiol Ultrasound*. 2018;59(3):272–278.
11. Neelis DA, Mattoon JS, Slovak JE, Sellon RK. Gastrointestinal Tract. In: Mattoon JS, Sellon RK, Berry CR, eds. *Small Animal Diagnostic Ultrasound*. 4th ed. St. Louis: Elsevier; 2021.
12. Gladwin NE, Penninck DG, Webster CRL. Ultrasonographic evaluation of the thickness of the wall layers in the intestinal tract of dogs. *Am J Vet Res*. 2014;75:349.
13. Heng HG, Lim CK, Miller MA, et al. Prevalence and significance of an ultrasonographic colonic muscularis hyperechoic band paralleling the serosal layer in dogs. *Vet Radiol Ultrasound*. 2015;56:666.
14. Spector DL, Fischetti AJ, Kovak-McClaran JR. Computed tomographic characteristics of intrapelvic masses in dogs. *Vet Radiol Ultrasound*. 52:71.
15. Hoey S, Drees R, Hetzel S. Evaluation of the gastrointestinal tract in dogs using computed tomography. *Vet Radiol Ultrasound*. 54:25.
16. Steffey MA, Daniel L, Taylor SL, Chen RX, Zwingenberger AL. Computed tomographic pneumocolonography in normal dogs. *Vet Radiol Ultrasound*. 56(3):278-285.
17. Cheon B, Moon S, Park S, et al. Comparison of contrast media for visualization of the colon of healthy dogs during computed tomography and ultrasonography. *Am J Vet Res*. 2016;77(11):1220–1226.

18. Steffey MA, Zwingenberger AL, Daniel L, Taylor SL. Assessment of 3 bowel preparation protocols for computed tomography pneumocolonography in normal dogs. *Vet Surg*. 2016;45(7):929–935.
19. Lamb CR, Mantis P. Ultrasonographic features of intestinal intussusception in 10 dogs. *J Small Anim Pract*. 1998;39:437.
20. Cinti F. Caecal inversion in association with ileocolic intussusception in a dog. *J Small Anim Pract*. 2021;62(3):233.
21. Boland L, Lindsay S, Brunel L, Podadera J, Bennett P. Caecocolic intussusception associated with a caecal polyp and concurrent hepatocellular carcinoma in a cat. *JFMS Open Rep*. 2017;3(1):2055116917706652.
22. Lansdown ABG, Fox EA. Colorectal intussusception in a young cat. *Vet Record*. 1991;19:429.
23. Patsikas MN, Papazoglou LG, Jakovljevic S, et al. Color Doppler ultrasonography in prediction of the reducibility of intussuscepted bowel in 15 young dogs. *Vet Radiol Ultrasound*. 2005;46:313.
24. Plavec T, Rupp S, Kessler M. Colonic or ileocecocolic volvulus in 13 dogs (2005–2016). *Vet Surg*. 2017;46(6):851–859.
25. Drobatz KJ, Hughes D, Hill C, et al. Volvulus of the colon in a cat. *J Vet Emerg Crit Care*. 1996;6:99.
26. Gagnon D, Brisson B. Predisposing factors for colonic torsion/volvulus in dogs: a retrospective study of six cases (1992-2010). *J Am Anim Hosp Assoc*. 2013;49(3):169–174.
27. Barge P, Fina CJ, Mortier JR, Jones ID. CT findings in five dogs with surgically confirmed colonic torsion. *Vet Radiol Ultrasound*. 2020;61(2):190–196.
28. Hassinger KA. Intestinal entrapment and strangulation caused by rupture of the duodenocolic ligament in four dogs. *Vet Surg*. 1997;26:275.
29. Brand KJ, Lim CK, Cichocki BN. Radiographic and CT features of colonic entrapment due to an omental rent in a dog. *Vet Radiol Ultrasound*. 2021;62(1):E6–E10.
30. Thanaboonnipat C, Kumjumroon K, Boonkwang K, Tangsutthichai N, Sukserm W, Choisunirachon N. Radiographic lumbosacral vertebral abnormalities and constipation in cats. *Vet World*. 2021;14(2):492–498.
31. DeForest ME, Gasrur PK. Malformations and the Manx syndrome in cats. *Can Vet J*. 1979;2:304.
32. Novellas R, Simpson KE, Gunn-Moore DA, Hammond GJ. Imaging findings in 11 cats with feline dysautonomia. *J Feline Med Surg*. 2010;12(8):584–591.
33. Szabo SD, Wells KL. What is your diagnosis? Congenital hypothyroidism. *J Am Vet Med Assoc*. 2007;230(1):29–30.
34. Woodard ML, Constant CE. What is your diagnosis? Congenital hypothyroidism. *J Am Vet Med Assoc*. 2022;260(5):499–501.
35. Matthiesen DT, Scavelli TD, Whitney WO. Subtotal colectomy for the treatment of obstipation secondary to pelvic fracture malunion in cats. *Vet Surg*. 1991;20:113–117.
36. Maas CP, ter Haar G, van der Gaag I, Kirpensteijn J. Reclassification of small intestinal and cecal smooth muscle tumors in 72 dogs: clinical, histologic, and immunohistochemical evaluation. *Vet Surg*. 2007;36(4):302–313.
37. Slawienski MJ, Mauldin GE, Mauldin GN, et al. Malignant colonic neoplasia in cats: 46 cases (1990–1996). *J Am Vet Med Assoc*. 1997;211:878.
38. Kehl A, Törner K, Jordan A, et al. Pathological findings in gastrointestinal neoplasms and polyps in 860 cats and a pilot study on miRNA analyses. *Vet Sci*. 2022;9(9):477.
39. Graham JP, Newell SM, Roberts GD, et al. Ultrasonographic features of canine gastrointestinal pythiosis. *Vet Radiol Ultrasound*. 2000;41:273.
40. Schmiedt CW, Stratton-Phelps M, Torres BT, et al. Treatment of intestinal pythiosis in a dog with a combination of marginal excision, chemotherapy, and immunotherapy. *J Am Vet Med Assoc*. 2012;241(3):358–363.
41. Stenner VJ, Mackay B, King T, et al. Protothecosis in 17 Australian dogs and a review of the canine literature. *Med Mycol*. 2007;45(3):249–266.
42. Chávez-Peón Berle E, KuKanich K, Biller D. Ultrasonographic findings of gastrointestinal histoplasmosis in dogs. *Vet Radiol Ultrasound*. 2021;62(1):108–115.
43. Cordella A, Stock E, Van de Maele I, Willems A, Saunders J. Use of contrast-enhanced ultrasonography and shear-wave elastography in the diagnosis of granulomatous colitis in a French bulldog. *Vet Sci*. 2021;8(7):133.
44. Moshnikova VS, Gilmour LJ, Cook AK, Fabiani M. Sonographic findings of pinpoint hyperechoic foci in the small intestine, liver, and mesenteric lymph nodes are indicative of canine *Heterobilharzia americana* infection. *Vet Radiol Ultrasound*. 2020;61(5):583–591.
45. Corapi WV, Ajithdoss DK, Snowden KF, Spaulding KA. Multi-organ involvement of *Heterobilharzia americana* infection in a dog presented for systemic mineralization. *J Vet Diagn Invest*. 2011;23(4):826–831.
46. Harvey CJ, Lopez JW, Hendrick MJ. An uncommon intestinal manifestation of feline infectious peritonitis: 26 cases (1986-1993). *J Am Vet Med Assoc*. 1996;209(6):1117–1120.
47. Weissman A, Penninck D, Webster C, et al. Ultrasonographic and clinicopathological features of feline gastrointestinal eosinophilic sclerosing fibroplasia in four cats. *J Fel Med Surg*. 2015;15:148.
48. Kukanich KS, Vinasco J, Scott HM. Detection of *Mycobacterium avium subspecies paratuberculosis* from intestinal and nodal tissue of dogs and cats. *ISRN Vet Sci*. 2013;2013:323671.
49. Seiler RJ. Colorectal polyps of the dog: a clinicopathologic study of 17 cases. *J Am Vet Med Assoc*. 1979;174:72.
50. Hsu TC, Lin LS, Chung CS, Chiang C, Chiu HC, Huang PH. Colonic intramural hematoma in a cat: a case report. *Front Vet Sci*. 2022;9:913862.
51. McKenna M, Suárez-Bonnet A, Smith K, Stewart S. Diagnosis and treatment of a caecal mucocoele in a dog. *J Small Anim Pract*. 2021;62(4):305–309.
52. Citi S, Chimenti T, Marchetti V, et al. Micronodular ultrasound lesions in the colonic submucosa of 42 dogs and 14 cats. *Vet Radiol Ultrasound*. 54:646.
53. Hahn H, Freiche V, Baril A, et al. Ultrasonographical, endoscopic and histological appearance of the caecum in clinically healthy cats. *J Fel Med Surg*. 2017;19:85–93.
54. Hahn H, Pey P, Baril A, et al. Ultrasonographic, endoscopic and histological appearances of the caecum in cats presenting with clinical signs of caecocolic disease. *J Fel Med Surg*. 2017;19:94–104.
55. Fisk A, Allen-Durrance A. Pneumatosis coli in a dog. *J Am Anim Hosp Assoc*. 2019;55(4):e55401.
56. Azuma K, Kanemoto H, Ohno K, Fukushima K, Chambers JK, Tsujimoto H. Pneumatosis coli after partial ligation of congenital portosystemic shunt in a dog. *J Vet Med Sci*. 2018;80(10):1549–1552.
57. Cartwright JA, Breheny C, Major AC, Hill TL, Gow AG. Imaging diagnosis-a case of spontaneous hepatic portal vein gas in an 11-month-old west highland white terrier. *Vet Radiol Ultrasound*. 2016;57(5):E54–E57.
58. Lassandro F, Valente T, Rea G, et al. Imaging assessment and clinical significance of pneumatosis in adult patients. *Radiol Med (Torino)*. 2015;120:96.
59. Feczko PJ, Mezwa DG, Farah MC, et al. Clinical significance of pneumatosis of the bowel wall. *Radiographics*. 1992;12:1069.
60. Russell NJ, Tyrrell D, Irwin PJ, et al. Pneumatosis coli in a dog. *J Am Anim Hosp Assoc*. 2008;44:32.
61. Aste G, Boari A, Guglielmini C. What is your diagnosis? Pneumatosis coli. *J Am Vet Med Assoc*. 2005;227(9):1407–1408.

62. Kim J, Yoon H, Eom K. Imaging diagnosis — radiography, ultrasonography, and computed tomography of a giant fecaloma causing stercoral perforation of the colon in a dog with a prostatic abscess. *Vet Radiol Ultrasound.* 2018;59(4):E38–E43.
63. Woolhead VL, Whittemore JC, Stewart SA. Multicenter retrospective evaluation of ileocecocolic perforations associated with diagnostic lower gastrointestinal endoscopy in dogs and cats. *J Vet Intern Med.* 2020;34(2):684–690.
64. Arthur JJ, Kleiter MM, Thrall DE, Pruitt AF. Characterization of normal tissue complications in 51 dogs undergoing definitive pelvic region irradiation. *Vet Radiol Ultrasound.* 2008;49(1):85–89.
65. Toombs JP, Caywood DD, Lipowitz AJ, et al. Colonic perforation following neurosurgical procedures and corticosteroid therapy in four dogs. *J Am Vet Med Assoc.* 1980;177:68.
66. Toombs JP, Collins LG, Graves GM, et al. Colonic perforation in corticosteroid-treated dogs. *J Am Vet Med Assoc.* 1986;188:145.
67. Longley MJ, Baines SJ, Chanoit G. Colonic perforation in 4 dogs following treatment with meloxicam. *J Vet Emerg Crit Care (San Antonio).* 2022;32(3):413–419.
68. Boysen SR, Tidwell AS, Penninck DG. Ultrasonographic findings in dogs and cats with gastrointestinal perforation. *Vet Radiol Ultrasound.* 2003;44(5):556–564.
69. Bredal WP, Thoressen SI, Kvellestad A. Atresia coli in a nine week old kitten. *J Small Anim Pract.* 1994;35:643.
70. Fluke MH, Hawkins EC, Elliott GS, et al. Short colon in two cats and a dog. *J Am Vet Med Assoc.* 1989;195:87.
71. Schlesinger DP, Philbert D, Breur GJ. Agenesis of the cecum and the ascending and transverse colon in a twelve year old cat. *Can Vet J.* 1992;33:544.
72. Le Roux AB, Donovan T, Palma D, et al. Short colon syndrome in cats (abstract). *Vet Radiol Ultrasound.* 2016;57:651.
73. Rahal SC, Vicente CS, Mortari AC, Mamprim MJ, Caporalli EH. Rectovaginal fistula with anal atresia in 5 dogs. *Can Vet J.* 2007;48(8):827–830.
74. Longhofer SL, Jackson RK, Cooley AJ. Hindgut and bladder duplication in a dog. *J Am Anim Hosp Assoc.* 1991;27:97.
75. Shinozaki JK, Sellon RK, Tobias KM, et al. Tubular colonic duplication in a dog. *J Am Anim Hosp Assoc.* 2000;36:209.

ELECTRONIC RESOURCES

Additional information related to the content in Chapter 47 can be found online at eBooks.Health.Elsevier.com.

- Chapter Quiz



Index

Page numbers followed by "*f*" indicate figures, "*t*" indicate tables, and "*b*" indicate boxes.

A
Abaxial fractures, 526
Abdominal cavity, 776f, 778
Abdominal fat, 779, 779f
Abdominal lateral radiography, 837f–838f, 844f
  of chronic hepatitis, 810f
  of hepatic abscessation, 812f
  of hepatocellular carcinoma, 808f
  of left renal enlargement, 844f
  of lymphosarcoma, 807f, 825f
  of mineralized choledocholith, 810f
  of splenic hemangiosarcoma, 826f
  of tubular gas opacities, 788f
Abdominal lymph nodes, 788–790
  abnormalities of, 789–790, 789f–791f
  anatomy of, 788
  computed tomography of, 789
  radiography of, 788
  ultrasound of, 788–789, 789f
Abdominal mass, 772–773
Abdominal radiography, 649, 764–777. *see also specific types of*
  ancillary factors for, 770, 771f
  ancillary view, 770, 770f
  checklist for interpretation of, 777t
  differences between canine and feline, 770–772, 771f–774f
  of equine, 764
  of gallbladder, 805
  interpretation paradigm for, 775
  of nomenclature, 764
  of pancreas, 790, 792f
  positioning for, 765, 765f–767f
  preparation for, 764
  technique, 764–765
Abdominal surface visualization
  decreased, 780–784, 780b
  increased, 784–786
Abdominal testicle, 915, 919f
Abdominal ventrodorsal radiography, 812f, 824f–825f, 837f–838f
  with bilateral renomegaly, 843f
  with chronic hepatitis, 810f
  cranial aspect of, 806f
  with hepatic abscessation, 812f
  with hepatocellular carcinoma, 808f–809f
  with hepatomegaly secondary to steroid hepatopathy, 807f
  of left renal enlargement, 844f
  with lymphosarcoma, 807f
  with radiopaque cholelith, 810f
  with splenic hemangiosarcoma, 826f–827f
Abdominal wall
  abnormalities of, 787–788, 788f
  anal gland adenocarcinoma in, 790f
  of canine, 788f
  lipoma of, 787–788
  normal anatomy and imaging of, 787
Aberrant right subclavian artery, 623–624, 624f
Abnormal fluid accumulations, 190–192, 191f–193f
Abnormal myelogram, 265
Abnormal opacity, of cardiac silhouette, 715–721.e1, 716f
Abnormal renal
  function, 850–851, 851f
  size, 841–844, 842f
  structure, 844–849
Abscesses. *see also specific types of*
  of foot, 557f
Absorbed dose, 4, 5t, 14–15
Absorption, 4, 40. *see also specific types of*
Accessory carpal bone fracture, 480–481, 482f
Accessory lung lobe, 672, 678f
  thoracic radiography of, 581, 587f
Acepromazine, 825, 827–828
Achilles tendon, 416
Acinetobacter, 257
Acoustic enhancement, 47, 48f
Acoustic impedance
  definition of, 40
Acoustic impedance (*Continued*)
  difference in, 40
Acoustic shadow/shadowing. *see also specific types of*
  defined, 47, 47f
  pathologic, 47
Acquired cardiovascular diseases, 716–721.e1
Acquired traumatic hernia, 932–934, 935f
Acquisition hardware, 23–28
Actinomyces, 307
Active periosteal reaction, on radius of horse, 357f
Acute apical periodontitis, 146
Acute discospondylitis, 258f
Acute duodenal obstruction, 966
Acute gaseous distention, 936
Acute gastric dilation, 936–939, 938f
Acute gastritis, 947
Acute lameness, 414f
Acute lung injury, 756
Acute nephropathies, 845, 846f
Acute noncompressive intervertebral disc extrusion, 289, 290f
Acute noncompressive nucleus pulposus extrusion, 283–284
Acute nonprogressive nucleus pulposus extrusion, 254, 267
Acute ptyalism, 628f
Acute pyelonephritis, 849–850
Acute respiratory distress syndrome, 756
Acute rib fractures, 635–636, 637f
Acute tubular necrosis, 845
Addison disease, 698f
Adenomas, 992
Adrenal calcification, 797
Adrenal gland, 795–800
  abnormalities of, 797–800
    decrease in size, 800
    increase in size and/or attenuation, 797–800
  anatomy of, 795
  computed tomography of, 797
  dysfunction of, 797
  enlargement of, 799f
  magnetic resonance imaging of, 797
  masses, differential diagnosis of, 800b
  radiography of, 795
  ultrasound of, 795–797, 796f
Adrenocortical tumor, 798f
Advanced coxofemoral degenerative joint disease, 403f
Aerodigestive disorders, 627
Aerophagia, 600f, 603
Agenesis, 380, 380f. *see also specific types of*
Aggressive bone lesion
  from bacterial bone infection, 361
  causes of, 358, 359t
  of distal tibia, 390f
  versus nonaggressive bone lesions, 348–363, 353t
  radiography of, 257
Aggressive lytic lesion, 359, 359f
Aggressive sternal neoplasia, 640
Aging lungs, 735
Ahead tilt, 200f
Air. *see also specific types of*
  radiation exposure in, 5
Air bronchogram, 735–736, 809
  alveolar pattern in, 735–736
Air bubble
  during cystocentesis, 864f
  from luminal filling defects, 867–868
  tetrahedron of, 49
Air bubble artifacts, 869, 871f
Air trapping, 737
Airway obstruction, 753–754. *See also* Upper airway obstruction
Airways, 724, 726f
  lesions localized to, 730–733
ALARA (as low as reasonably achievable) principle, 6
Aliasing, 52
Alimentary lymphosarcoma, 976
Alternate imaging, of foot, 544
Alternating current, 12–13
Alveolar filling disorders, 737t
Alveolar pattern, 735–736, 736f, 755. *See also* Thorax
  lobar sign as indication for, 735–736
  radiography of, 619f, 736f, 737t
  right middle region of, 736f
  ventral region of, 736f
Alveoli, 724
Amorphous, 377–378
Amorphous mineralization, 639
Amorphous opacity, 696–698, 699f
Amorphous selenium, 26, 26f
Amorphous silicon, 26f
Anal canal, 986f
Anal gland adenocarcinoma, 790f
Analog-to-digital converter (ADC), 64f
Analog *vs.* digital radiography, 29–38
  artificial intelligence, 37
  contrast optimization, 29–34, 31f
  darkroom, elimination of, 29
  exposure latitude, 29, 31f, 33f
  image storage consolidation, 36–37, 36f
  imaging paradigm and, 37–38
  inherent spatial resolution in, 30t, 30b
  portability, enhanced, 37
  postprocessing in, 34–35, 35f
  of skull, 32f
  supply cost, reduced expendable, 29
  thoracic radiographs made with, 32f
  wide contrast resolution of, 31f
Anal sac carcinoma, 991f
Anatomic location, juvenile orthopedic diseases, 366t
Ancillary radiographic projections, 124t
Ancillary view, 123–124, 770, 770f
Anconeal process, ununited, 368, 368f
Anechoic fluid, 782, 782f
Anesthesia, 128
Aneurysmal bone cysts, 220–221, 229f
Angiography. *see also specific types of*
  computed tomography and, 63
  history of, 2
Angiostrongylus, 307
Angle of incidence, 40
Angle of obliquity, of sesamoid bones, 512f
Angle of reflectance, 40
Angular limb deformity, 396, 397f, 452, 473–475, 475f, 475t, 476f
  cartilage retention causing, 378
  chondrodysplasia and, 375
  multiple epiphyseal dysplasia and, 373
Anisotropic back scattering artifacts, 51–52, 52f
Ankylosing arthropathy, 422, 425f
Ankylosing spondylopathy, 422, 424f
Annular array, 41, 59–60
Annulus, 279–280
Annulus fibrosus, 246, 251–254, 258, 258f, 264–265, 267, 273f, 279, 282–284, 292
Anode, 10, 11f
Antebrachial fracture, 393, 394f
Antebrachiocarpal joint, 470, 484–485
  osteoarthritis in, 477–478, 477f
  septic arthritis of, 479f
Antebrachiocarpal subluxation, 396, 397f
Antebrachium
  craniocaudal radiography of, 356f
  lateral radiography of, 357f, 363f
  mediolateral radiography of, 324f
Antecurvatum, 393–394, 395f
Antegrade pyelogram, 842f
Antegrade ultrasound-guided pyelography, 840–841
Anticlinal vertebrae, 128
Antiscatter grid, 30
Aorta, 710
Aortic root mineralization, 715, 716f
Aortic stenosis, 710
Apical fracture, 526f
Apical infections, of cheek teeth, 220, 226f–227f
Apparent diffusion coefficient (ADC), 73f
Appendicular skeleton. *see also individual topics on*
  equine carpus, 470–488
  fetlock joint, 511–529
  foot, 543–575
  fracture healing, 384–400
  metacarpus and metatarsus, 489–510
  neoplastic and infectious bone disease in, 359t
  polyarthropathies affecting, 423b
  principles of radiographic interpretation of
    aggressive *vs.* nonaggressive bone lesions, 348–363, 353t
    checklist for, 364b
    incidental factors, 361–363
    interpretation paradigm, 363, 364t
    oblique projections of, 348, 349t
  radiographic anatomy of, 320–347
  stifle, 428–448
  tarsus, 449–469
Apron, 126
  lead, 10, 15–16
Arachnoid cyst, 187
Arachnoid diverticula, 267–268, 274f, 294
Archiving, of digital images, 36
Array transducers, 41
Arrhythmogenic right ventricular cardiomyopathy (ARVC), 717
Arteries. *see specific types of*
Arterioportal communications, 810–811, 823–824
Arthritis, 401. *see also specific types of*
Arthrography, 515
  cartilage flap, 365
Articular cartilage, 407, 434, 558–560
Articular fracture, 411–412, 414f, 457, 526f, 551, 553f
  of distal phalanx, 553f
Articular process
  cysts of, 296, 297f
  degenerative joint disease of, 253f, 258–260, 259f
  osteophytosis in, 288
  subluxation of, 288
Articular process joint, 244, 279–280, 281f, 288
Articular soft tissue, 403
Artifacts. *see also specific types of*
  anisotropic back scattering, 51–52
  on digital radiographic imaging, 38
  Doppler, 52
  on magnetic resonance imaging, 72–73
  on ultrasound imaging, 46–52
Artificial intelligence (AI), 37
Ascending colon, 842–843, 986, 986f
Aseptic necrosis, 450–452, 454f
  of femoral head, 372, 372f
Aseptic physitis, 452
As low as reasonably achievable (ALARA) principle, 6
Aspergillosis, nasal, 173–174, 173f–174f
Aspergillus felis, 174
Aspergillus fumigatus, 174
Aspergillus riger, 174
Aspiration pneumonia, 619f, 728, 737–738, 750, 758
Asymmetric lung opacity, 738f
Asynchronous growth, 365–368
Atelectasis, 663–664, 667f, 729, 732, 736
  ventrodorsal/dorsoventral view of, 580, 582f
Atlantoaxial instability, 131
Atlantoaxial subluxation, 249–250, 249f–250f
Atrial septal defect, 721.e3–721.e4
Atrophic nonunion fracture, 393
Attached filling defect, 867–870
Attenuation
  of sound wave, 40
  in tissues, 61, 62f
  in x-ray, 22, 24–26, 31f

Avulsion, 461–463
  fracture, 389f
Axial resolution, 41
Axial skeleton. *see also individual topics on*
  brain disease, 187–216
  equine head, 217–243
  principles of radiographic interpretation of, 123–136
  radiographic anatomy of, 110–122
  skull and nasal cavities, 165–186
  spinal cord disease, 279–317
  vertebrae, canine and feline, 244–278

B

Bacterial bronchopneumonia, 739f
Bacterial infection in bone, 361
Bacterial meningoencephalitis, 194–195
Bacterial orchitis, 918f
Bacterial pneumonia, 738
Barium contrast media, 76–77
  adverse effects to, 77
  general information, 76–77
Barium enema, for large bowel, 987–988, 994f
Barium esophagram, 624f, 657f
Barium-food mixtures, 930
Barium-impregnated polyethylene spheres (BIPS), 77, 963–964
Barium paste, 633
Barium sulfate, 76–77, 649
  allergic reactions to, 77
  aspiration of, 77
  for foreign body obstruction, 77f
Barium swallow, 618f–619f, 625f
Beak sign, 939–940
Benign joint disease, 401
Benign mass lesions, of large intestine, 992
Benign strictures, 972–973
Biarticular ulnar carpal bone fracture, 482f
Biceps tendon, 416f
Bicipital tendonitis, 413, 416f
Bicipital tenosynovitis, 413
Bilateral ectopic ureter, 853f–854f
Bilateral paralysis, 658–659
Biliary calculi, 809
Biliary cystadenoma, 816–817
Biliary dilation, 821
Biliary sludge, 814f, 820, 820f
Biliary system disease, 819–821, 819f–822f
Binding energy, 10–11
Biologic injury, 4
Bit depth, 23, 23f–24f
Blackness of film, 16–17, 16f
Bladder and urethra, 860–883
  of canine, 861f
  catheterization of, 861, 864–865, 865f, 870–871
  contusion of, 869f
  cranioventral aspect of, 869f
  filling defects in, 868t
  pathologic process of, 867t
Bladder neck, 860f, 874f
Blastomyces, 307
Blastomycosis, 360, 362f
Block vertebrae, 246, 248f
Blood clots, 871
Bochdalek hernia, 658
Body habitus, 582, 588f–590f, 770
Bone. *see also specific types of*
  abscessation, 459
  development and healing, 384
  disuse atrophy of, 527, 527f, 588f
  formation, 482–483
  infarction of, 359
  opacity of, 379
  shapes, 384
Bone cyst, 220–221, 229f, 401–402. *see also specific types of*
Bone disorder, 379–380. *see also specific types of*
  focal agenesis/malformations, 380–381
  knees and teeth syndrome, 379–380, 380f
  nutritional secondary hyperparathyroidism, 379, 379f
  osteogenesis imperfecta, 379
  osteopetrosis, 379, 379f
Bone filters, 60–61, 62f
Bone formation, 384
Bone infection
  bacterial, 361
  fungal, 360–361
  protozoan, 361
Bone lesions. *See also* Aggressive bone lesion
  aggressive *vs.* nonaggressive, 348–363, 353t
  metastatic bone tumors, 359–360, 360f
Bone lesions (*Continued*)
  subungual tumors *vs.* subungual infections, 360, 361f
Bone marrow lesions (BMLs), 537, 537f, 554–556
Bone proliferation, 637f
Border effacement, 93
Borzoi, 703f
Bowel-associated masses, 978–979, 981f
Bowel dilation, disease resulting in, 965–966, 965t, 966f
Bowel gas, 47–48, 764–765
Boxer cardiomyopathy, 717
Brachycephalic airway obstruction syndrome, 601
Brachycephalic breeds, 165
Brachycephalic syndrome, 595–596, 596f, 596b, 597f
Brain. *See also* Cranium
  computed tomographic examination of, 189–195
  contrast-enhanced transverse computed tomography of, 238f
  developmental conditions of, 190
  developmental morphologic anomalies, 192
  inflammatory conditions of, 194–195, 198f–201f
  magnetic resonance imaging of, 187–189, 187t
    focal intracranial disease, secondary effects of, 188–189, 190f
    normal anatomy of, 190
    sequence selection, rationale for, 187–188, 189f
  metabolism, inherent disorders in, 192–193, 195f
  nutritional, metabolic, and toxic disorders of, 193–194, 196f–197f
Brain disease
  in horses
    cholesterol granulomas, 228–229, 240f
    inflammatory, 228, 238f
    vs. small animals, 228
    traumatic brain injury, 229, 240f
  in small animals, 187–216
    brain neoplasia, 195–209
    invasive extracranial tumor, 207–209
    magnetic resonance imaging of, 187–189, 188f
    miscellaneous disorders of, 195, 202f
    vascular disruption in, 209–210
Brain hemorrhage, 71f
Brain metastases, 207, 209f
Brain neoplasia, 195–209
Braking model of x-ray production, 12f
Braking radiation, 11
Breathing cycle, 725–726
Bremsstrahlung radiation, 11
Bridging callus, 391f, 392–393, 393f
Brightness mode (B-mode), 42
Broad bandwidth technology, 42
Bronchi, 725
Bronchial collapse, 602–603
Bronchial luminal filling, 732f
Bronchial pattern, 730–733, 732f, 754, 754f
Bronchial plugging, 732
Bronchial wall thickening, 730, 732f
Bronchiectasis, 732–733, 733f
Bronchitis, 753–754. *see also specific types of*
Broncholithiasis, 730, 731f
Bronchopneumonia, 728, 750, 751f, 752
Brown fat, 779
Brownian motion, 72, 209–210
Bucky, 18
Butterfly vertebrae, 307

C

Calcaneal osteomyelitis, 460–461, 461f
Calcaneal tuber osteitis, 460–461, 461f
Calcaneus, 358f
Calcification, 569–570. *See also* Ossification. *see also specific types of*
  of soft tissue, 786–787
Calcinosis circumscripta, 443–444, 446f, 486
Calcitonin, 384
Calculi/calculus, 820, 870–871, 872f, 877. *see also specific types of*
Calvarial hyperostosis, 181, 182f
Calvarial hyperostosis syndrome, 381
Cancellous, 384
Cancellous bone, 279–280, 442–443, 445f
Canine and feline. *see also specific topics regarding*
  fracture healing and complications, 384–400
  joint disease of, 401–427
  lungs of, 724–745
  orthopedic diseases of, 365–383
  positioning, 348, 349f, 578, 579f
  radiographic technique for, 578, 579f
  skull and nasal cavities, 165–186
  small bowel of, 956–985
  spinal cord disease of, 279–317
  thoracic radiography, 581–585
    of accessory lung lobe, 581, 587f
    body habitus, 582, 588f–590f
    of cardiac silhouette, 581, 587f
    cutaneous lesions, 584–585, 590f–591f
    of diaphragm, 581, 586f
    of pulmonary vessels, 581, 585f–586f
  vertebrae of, 244–278
Canine and feline dental disease, 137–164
  anatomy and radiographic interpretation, 140–142
  dentoalveolar trauma, 152, 153f–155f
  endodontic disease, 143–147, 146f–149f
  neoplastic disorders, 152–153, 156f–158f
  periodontal disease, 142–143, 145f
  tooth resorption, 147–150, 150f–152f
Canine female genital tract, 895f, 899f
Canine postmyelographic CT image, 264–265, 267f
Canine schistosomiasis, 977
Canine testicular neoplasia, 918–919
Cannon bone, 489, 489f–490f
Capture hardware options, for digital imaging, 28f
Carboxymethylcellulose, 963
Carcinomatosis, 783
Cardia, 656
Cardiac chamber enlargement, 706–710
Cardiac disease, 703–706, 759
Cardiac silhouette, 653, 703–706, 704t–705t, 706f, 706t, 719f, 727f–728f
  abnormal opacity of, 715–721.e1, 716f
  thoracic radiography of, 581, 587f
Cardiogenic pulmonary edema, 715, 717, 741f
Cardiomegaly, 581–584, 717, 720, 720f, 748–749, 759, 759f
  generalized, 709–710
Cardiomyopathies, 716–718
Cardiophrenic ligament, 662–663
Cardiovascular system, 702–703, 702f
Carpal angular limb deformities, 474–475
Carpal bone. *see specific types of*
  sclerosis, 482–483, 483f
  vestigial first and fifth, 471, 473f
Carpal hygroma, 486, 486f
Carpal luxation, 481–482, 482f
Carpal sheath effusion, 485, 485f
Carpal trauma, 406f
Carpometacarpal joint, 470, 484–485, 489
  osteoarthritis in, 478, 479f
Carpus. *see also specific types of radiography of*
  dorsolateral/palmaromedial view of, 348, 352f
  dorsomedial/palmarolateral view of, 348, 353f
  dorsopalmar radiography of, 350f
  entheses around, 404f
  of equine, 470–488
  joint disease of, 416–417, 417f
  lateromedial radiography of, 351f
  lateromedial view of, 348, 351f
  left, 336f
Cartilage, 569–570. *see also specific types of*
Cartilage core, retained, 378, 378f
Cartilage degeneration, 407, 433–434, 516
Cartilage flap, 365
Cartilage retention, 378
Cartilaginous exostoses, 639–640
Cartilaginous fibrillation, 516
Cassette, 125
Cassette holder device, 363
Cat. *See* Feline
Catheterization, of urinary bladder, 861, 864–865, 865f, 870–871
Cathode, 10, 11f
Cauda equina syndrome, 260, 260f–261f, 288
Caudal abdomen, 860f–861f, 863f–864f
Caudal aspect, 132f, 757f, 771f
  of cervical spine, 131f
  of distal radius, 470, 471f
  of esophagus, 622f
  of thoracic spine, 132f
  of thorax, 586f, 590f, 757f
Caudal cervical vertebrae, 122f
Caudal esophagus, 656, 657f
  radiography of, 627f
Caudal fragment, 254f
Caudal lobe pulmonary artery, 713f
Caudal lobe pulmonary vessels
  dorsal *vs.* sternal recumbency, 581, 586f
  ventrodorsal/dorsoventral view of, 581, 586f
Caudal lung lobes, 728
Caudal occipital malformation syndrome (COMS), 166–167, 192, 193f
Caudal region of head, 119f
Caudal thorax, 586f, 633f, 754f
Caudal vena cava (CVC), 579f, 710
Caudal vertebrae, 245, 376
Caudocranial radiography
  of humerus, 321f, 355f
  of shoulder joint, 320f
  of stifle, 438f–443f, 446f
  of stifle joint, 344f
  of tibial diaphysis, 442–443
Caudodorsal alveolar pattern, 755
Caudodorsal aspect, 756f
  of thorax, 628f
Caudodorsal mediastinal masses, 672, 679f
Caudodorsal projection, 746, 747f
Caudodorsal thorax, 621f, 749f
Caudolateral-craniomedial radiography, of stifle, 430f, 432f, 442f, 446f
Caudoventral aspect, of thorax, 579f
Caudoventral mediastinal masses, 672, 678f
Caudoventral mediastinal reflection, 662–663, 666f–667f
Caudoventral projection, 746–747, 748f
Caval foramen hernias, 658
Cavitary tumor, 361f
Cavitated masses, 846–849
Cavitation, 308–309
Cecal mass, 994f
Cecocolic intussusception, 992f
Cecum, 986, 986f–987f
Cellulitis, 638–639
Centering points, 133
Centimeter-gram-second (CGS) system of measures, 4–5, 5t
Central sulci, of foot, 543–544, 543f
Central tarsal bone dorsal slab fractures, 457, 459f
Central tarsal bone sagittal slab fracture, 457, 458f
Centrum, 244
Cerebellar abscess, 200f
Cerebellum, 200f
Cerebrospinal fluid (CSF), 187, 188f–189f, 279, 308
Cervical disc degeneration, 255
Cervical esophagus caudal, 622f
Cervical intervertebral disc disease, 287–288, 288f
Cervical intervertebral disc space, 283f
Cervical lateral radiography, of multiple myeloma, 262f
Cervical mass, radiography of, 594f
Cervical myelogram, 265f
Cervical radiography, 132f
Cervical spine, 131f, 133f, 245f–246f, 250f, 253f, 262f
Cervical spondylolisthesis, 291
Cervical spondylomyelopathy, 291–294
  computed tomography of, 291–292, 292f–293f
  lateral cervical radiography of, 252f–253f
  magnetic resonance imaging of, 292–294, 293f–294f
  sagittal reformatted, 292f
  T2-weighted images of, 252f–253f
  in vertebral column, 250–251, 252f–253f, 254t–259t
Cervical spondylopathy, 291
Cervical vertebrae, 114f, 131f
  caudal, 122f
  cranial, 121f
  instability of, 291
  left-right lateral radiography of, 113f, 121f
  malarticulation of, 291
  malformation of, 291
  middle, 121f
  ventrodorsal radiography of, 114f

Cesium iodide, 26
Characteristic x-rays, 10–11, 11f, 14–15
Charge-coupled device (CCD), 23–24, 27–28, 27f–28f
Chemical fat saturation, 72, 72f
Chevron sign, 146–147
Chiari-like malformation, 166–167
Chip fracture, 525, 525f–526f
Chip fracture fragments, 482f
Choledocholiths, 809, 810f, 820
Cholelith, 809, 810f, 819, 820f
Cholesteatoma, 177
Cholesterol granulomas, 228–229, 240f
Chondrocyte, 376–377
Chondrodysplasia
  of Alaskan malamutes, 375, 375t
  of Norwegian elkhounds, 375t
  and osteochondral dysplasia, 375, 375t
Chondrodystrophic breeds, 255
Chondroids, 224, 233f
Chondrosarcoma, 260–261, 297, 359
Choroid plexus tumor, 197–200, 204f
Chronic bronchitis, 739, 739f, 754f
Chronic cystitis, 866, 872–873
Chronic degenerative joint disease, 517, 519f
Chronic hepatitis, 810f, 815–816, 818, 818f
Chronic laminitis, 567–568, 568f–569f
Chronic nasal discharge, 141f
Chronic nephropathies, 844–845
Chronic partial ileal obstruction, 968f
Chronic periodontitis, 143
Chronic pyelonephritis, 849–850
Chronic pyloric obstruction, 939–940, 941f–942f
Chronic renal disease, 845f
Chronic weight-bearing lameness, 411f
Circular/oval lesions, 728
Cirrhosis, 808, 815–816, 816f
Clavicle, 405f
Clavicular remnant medial, 405f
Cloaca, 396
Cobra-head sign, 867–868
Coccidioides, 307
Coccidioidomycosis, 360, 362f
Cognition, 102–103
Cognitive errors, 105–107
Coherent scattering, 14
Colic flexure, 986, 986f
Colitis, 992–993, 995f
Collateral cartilages, 569–570, 570f
Collateral ligament, 562–563, 565f
  enthesopathy, 461–463, 462f–463f
  injury of, 455f, 483–484, 485f
Collateral sulci, of foot, 543–544, 543f
Collecting system diseases, 849–850
Collimation, 61f, 428
Collimator, 8, 15–16
Collisional interactions, 10–11
Collisional method of x-ray production, 11f
Collisional processes, 15
Colon, 986, 986f–987f. *see also specific parts of*
Colonic mass, 995f
Colonic torsion, 988–989, 993f–994f
Colonic ulceration, 995
Colonic volvulus, 989
Color Doppler, 44–45, 46f, 52, 53f
Color LCD monitors, 29
Columnar periosteal reaction, 396, 398f
Comet tail artifact, 49, 749, 750f, 753–754
Comminuted basisphenoid-basioccipital fracture, 234f
Comminuted fracture, 134f, 389f, 457, 458f, 511–512, 534–535, 536f, 550–551. *see also specific types of*
Complete agenesis, 380
Complete fracture, 386–388, 550–551, 551f
Complete sagittal fractures, 533–534, 533f
Compression fracture, 262f
Compressive hydrated nucleus pulposus extrusion, 290, 291f
Compressive stress, 413
Compton absorption, 15, 15f
Compton electron, 15
Compton scattering, 15, 15f
Computed radiography (CR), 24–26, 25f, 31f
Computed tomography (CT), 58–64, 217. *see also specific types of*
  of abdominal lymph nodes, 789
  of adrenal glands, 797
  of brain, 189–195, 238f
  canine postmyelographic, 264–265, 267f
Computed tomography (CT) (*Continued*)
  of cervical spondylomyelopathy, 291–292, 292f–293f
  components of, 60f
  cone-beam, 64
  contrast-enhanced procedures in, 61–64, 64f
  contrast resolution using, 57f
  of diaphragmatic hernias, 652f
  ear canal tumors, 177, 177f
  of equine head, 218f
  fetlock joint, 513, 514f
  of hepatic masses, 811, 813f
  hyperattenuating nodules, 242f
  image display of, 61, 63f
  image formation of, 56–58, 57f–59f
  of intervertebral disc disease, 284–285, 284f–285f
  kidneys and ureters, 840
  of large bowel, 988, 989f
  of left mandibular squamous cell carcinoma, 172f
  of left tympanic bulla cholesteatoma, 177, 177f
  of liver, 810–811
  of lungs, 725f
  multiplanar reformatting with, 59f
  otitis media, 175, 176f
  of pancreas, 792
  of peritoneum, 780
  of pharynx, larynx, and trachea, 604
  of portosystemic shunts, 810–811
  principles of, 55–75
  of prostate gland, 891, 892f
  of small bowel, 962
  spatial resolution using, 57f
  of spinal cord disease, 279–317
  of stomach, 931, 932f
  system geometry in, 58–60, 60f–62f
  of temporal multilobular osteochondrosarcoma, 173f
  of temporohyoid osteoarthropathy, 236f–237f
  of thorax, 689f
  of urethra, 876–877
  of urinary bladder, 874, 875f
  of uterus, 894
  in veterinary practice, 55–56, 55f–56f
Computed tomography (CT) imaging
  fractures identification, 384–385, 386f
  of stifle, 429, 432f
Computed urethrography of urethra, 876–877
Concurrent disc degeneration, 258
Concurrent rib fractures, 755
Condylar fracture, 397f, 520–525, 525f
Cone-beam computed tomography (CT), 137, 137f
  images of metacarpal condylar subchondral bone disease, 524f
Conformational defects, 220, 225f
Congenital anomalies, 166–167
  hydrocephalus, 166, 166f–167f
  mucopolysaccharidoses, 167
  occipital bone malformation and syringomyelia, 166–167
  occipital dysplasia, 166, 167f
  radiography of, 135
  of spine, 307–308
  temporomandibular joint dysplasia, 167
Congenital cardiovascular diseases, 721.e1
Congenital hydrocephalus, 166, 190, 191f
Congenital hypothyroidism, 372–373, 373f
Congenitally predisposed diaphragmatic hernias, 652, 659f
Congenital radial head luxation, 368, 370f
Congestive heart failure, 714–715, 759
  left-sided, 714–715, 715f
  right-sided, 715, 715f
Constant velocity, 40
Consultation, 37
Continuous-wave Doppler, 44
Contrast
  factors affecting, 19–21
  long scale of, 20
  radiographic technique and, 19–21
  short scale of, 20
Contrast cystography, 863–870
  pitfalls with, 869–870, 871f–872f
  procedures for, 865t
  radiographic signs with, 866–869, 867t
    contrast leakage patterns, from urinary bladder, 868–869, 869f–870f
    filling defects, 867–868, 868t, 869f
    intramural changes, 866, 866f–867f
    mucosal changes, 866–867, 867f–868f
  techniques for, 864–866, 865f–866f
Contrast-enhanced computed tomography, 840
Contrast-enhanced ultrasonography, 818
Contrast-enhanced ultrasound, 46
Contrast examination, of small bowel, 962–964, 962f–964f, 964t–968t
Contrast-induced acute kidney injury (CI-AKI), 81–82
Contrast leakage and retention patterns, 868–869, 869f–870f
Contrast media, 211f, 867–868, 962f
  barium, 76–77
  in diagnostic imaging, 76–89
  dose rate for, 964t–968t
  gadolinium, 83, 84t
  iodinated, in computed tomography, 61–63
  iodine-based, 78–82
  for magnetic resonance imaging, 71, 71f, 83–84
  radiographic, 76
    effects of, on thyroid function, 82
    negative, 76, 77f, 83
    positive, 76, 76f
  for ultrasound, 84–86
Contrast optimization, 29–34, 31f–32f
Contrast radiography
  of esophageal disease, 611–612, 612f
  of large bowel, 987–988
Contrast ratio, iodine-based contrast media, 79
Contrast resolution (CR), 55, 57f, 92–93
Contrast videofluoroscopic swallowing studies, 612–614
Contusion, 251, 283–284
  of bladder, 869f
Conus medullaris, 279
Conventional lateral radiography, 693f
Conventional x-ray machines, 22
Convex array, 41
Core lesion, 564, 565f
Cortex, destruction of, 352–354, 353t, 354f–356f
Cortical bone, 279–280
Cortisone arthropathy, 518, 519f
Cor triatriatum dextrum, 721.e6–721.e7
Cor triatriatum sinistrum, 721.e6–721.e7
Costal cartilage, 633f, 692–695, 695f
Costochondral degeneration, 633f
Costochondral junction, 376, 591f, 631, 632f, 746–747
Costophrenic angle, 689
Coughing, 596f, 600f–601f
Coxofemoral degenerative joint disease, 403f, 408–409
Cranial abdomen, 806f
Cranial aspect, 250f, 408f, 758f–759f, 766f, 770f
Cranial cervical vertebrae, 121f
Cranial cruciate ligament rupture, 106
Cranial mediastinal mass, 593
Cranial mediastinum, 589f, 662, 665f–666f, 758f
Cranial nerve tumors, 203–206, 206f
Craniocaudal fabellae, 410f
Craniocaudal radiography
  of antebrachium, 24f, 324f, 356f
  comminuted fracture of distal tibia, 393f
  of crus, 331f
  distal left humeral diaphysis, 388f
  of elbow joint, 322f, 335f, 385f
  of femur, 329f, 354f–355f
  humeral condylar fracture repair with implant failure, 397f
  of proximal tibia, 362f
  of stifle joint, 330f
Craniocaudal view, 362f, 385f
  of proximal femur, 355f
  of proximal tiba, 362f
Craniodorsal mediastinal masses, 669
Craniodorsal projection, 746, 747f
Craniodorsal thorax, 752f
Craniolateral-caudomedial oblique radiography, of canine elbow joint, 323f
Craniomandibular osteopathy (CMO), 180–181, 180f–181f, 381, 381f
Craniomedial-caudolateral oblique radiography, of canine elbow joint, 323f
Cranioproximal-craniodistal radiograph, 435f, 444f, 446f
Cranioproximal-craniodistal view, of proximal humerus, 349f
Cranioventral aspect, 767f, 783f, 785f
Cranioventral mediastinal mass, 665–669, 668f–673f
Cranioventral mediastinal reflection, 662, 666f
Cranioventral projection, 747, 748f
Cranioventral pulmonary masses, 669
Cranium. *See also* Brain
  drawer sign in, 402–403
Crena margins solaris, 544–545
Cribriform plate, 165
Cricopharyngeal achalasia, 617–618
Cricopharyngeal chalasia, 618, 618f
Cricopharyngeal dysphagia, 616–618
Cricopharyngeal phase, of swallowing, 617
Cricopharyngeal sphincter, 618f, 622f
Cross-sectional imaging of uterus, 894
Cruciate ligament, 407
  cranial, 428
  radiographic signs of, 435–437, 443f
Crus, 331f
Cryptococcus neoformans, 174
Cryptorchidism, 918
C-shaped foreign bodies, 943f
Cuboidal bones, 373, 472–473
Cumulative exposure, 6
Cupula, 646–647, 646f–647f, 650f
Curb, 463, 464f
Curvilinear hyperechoic line, 799f
Cutaneous lesions, 584–585, 770
Cutaneous neoplasms, 540, 540f
Cutaneous structures, 770
Cylindrical bronchiectasis, 733f
Cystadenoma, 817f
Cystic air-filled lesions, 736
Cystic bronchiectasis, 733f
Cystic calculi, 864f, 865t
Cystic duct, 809–810, 821
Cystic endometrial hyperplasia (CEH), 910, 911f
Cystic lesions, of pancreas, 795, 796f
Cystitis, 861, 864f, 866, 872–873, 872f–873f
Cystocentesis, 864f
Cystography. *see also specific types of*
  equipment for, 865f
  interpretation of, 869–870, 871f–872f
  technique for, 864–866, 865f–866f
Cysts
  dentigerous, 227, 237f
  paranasal sinus, 217, 219f

D

Dandy Walker variant, 191, 193f
Decision error, 104–105
Decision making, 102–103, 251, 261
Decreased bone cyst, 401–402
Deep digital flexor tendon (DDFT), 546–548
  injury, 565f
Defect nonunion fracture, 393
Degenerative joint disease, 365, 407–412, 455, 455f–456f, 477–478, 538. *see also specific types of*
  of articular process, 253f, 258–260, 259f
  dorsopalmar radiography of, 519f
  of elbow, 412f
  of femorotibial joint, 433–434, 438f–439f
  hip dysplasia, 406–407
  meniscal ossicles, 412, 413f
  of metacarpophalangeal and metatarsophalangeal articulation, 515–517
  osteoarthritis and, 408–412, 411f, 411b, 412f, 412b
  radiographic changes of, 408–410, 411b
  of stifle, 438f
Degenerative lumbosacral stenosis, 260, 288
Delayed union, 392, 393f
Density, 90
Dental disease, 219–220
  apical infections of cheek teeth, 220, 226f–227f
  cheek teeth fractures, 220, 224f
  conformational defects, 220, 225f
  equine odontoclastic tooth resorption and hypercementosis, 220, 228f
  mandibular, 219
  maxillary/mandibular incisor disease, 219–220, 225f
  normal dentition, 219, 223f
  odontogenic tumors, 220, 227f
  radiographic projections, 219, 224f
Dental fractures, 152
Dental radiography, 137, 140f, 146
Dentigerous cysts, 227, 237f
Dentoalveolar injuries, 146
Dentoalveolar trauma, 152, 153f–155f
Depression fracture, 232f, 238f
Depth of field, 43
Dermoid cyst, 295–296, 296f
Descending colon, 842–843, 844f, 860f, 863f, 986, 986f, 993f, 995f
  displacement of, 991f

Desmopathy, 413–417, 461–463, 563–564, 565f–566f
Detector system, 59–60
Deterministic effect, 6
Developmental laminitis, 567
Developmental lesion, 365
Developmental morphologic anomalies, brain, 192
Developmental orthopedic disease, 365
Diabetic ketoacidosis, 849f
Diagnostic medical imaging, 22
Diagnostic radiology
  basic radiation safety rules for, 10, 10f
  concept of, 15–17
  contrast of, 19–21
  distance in, 7
  distortion of, 19
  image detail during, 17–19
  personnel monitoring in, 8–10
  physics of, 2–21
  practical considerations of, 7–8
  radiation protection during, 4–10
  radiation with matter interaction in, 14–15
  shielding in, 7–8
  time in, 7
  x-rays in, 2–4
Diaphragm, 579f, 646–661
  disease of, 648–659
  gastroesophageal intussusception in, 657, 658f, 658b
  hernia of, 648–650, 650b, 651f–652f, 932–934, 934f
  intact, displacement with, 931–932, 933f, 933t, 934f
  motor disturbance of, 658–659, 660f
  muscular dystrophy of, 649f, 659
  peritoneopleural hernias of, 657–658, 659f
  radiographic anatomy of, 646–647, 646f–647f, 649f
  thoracic radiography of, 581
Diaphragmatic diseases, 648–659, 650t
Diaphragmatic eventration, 658–659
Diaphragmatic flutter, 659
Diaphragmatic hernia, 648–650, 650b, 651f–652f, 757, 757f
Diaphragmatic paralysis, 658–659
Diaphragmatic region, 646f–650f
Diaphysis diseases, 378–379
  panosteitis, 378–379, 378f
Diarthrodial joint, 279–280
Diatrizoate, 80t
Dieffenbachia, 597
Differential absorption, 15
Diffuse disease
  hepatic, 815–816
  of spleen, 827–829, 828f–831f
  of stomach wall, 947–948, 947f–950f
Diffuse lesions, 727
Diffuse parenchymal abnormalities, 844–845
Diffusion-weighted imaging (DWI), 72, 73f
Digital extensor, 485–486
Digital image file, 22
Digital imaging, 28f
  components of, 22–23, 23f–24f
Digital Imaging and Communications in Medicine (DICOM) file, 22, 28, 29f, 36–37
Digital radiographic imaging, 22–39. *See also* Analog *vs.* digital radiography
  acquisition hardware for, 23–28
  artifacts, 38
  charged-coupled device for, 27–28, 27f–28f
  digital image file in, 22
  direct, 26–28
  direct flat-panel detectors for, 26–27, 27f
  of distal humerus, 35f
  image processing/viewing in, 28–29, 29f
  improved image accessibility in, 36–37, 36f
  indirect flat-panel detectors for, 26, 26f
  of lumbar spine, 34f
  of scapular tumor, 35f
  of tarsus, 34f
Digital tumor, 360
Dilated cardiomyopathy (DCM), 715–717, 715f, 718f
Dilated caudal esophagus, 656
Direct bone healing, 389
Direct digital radiography (DDR), 26–28, 31f
Direct flat-panel detectors, 26–27, 27f
Direction of fracture, 386, 388f
Dirofilaria immitis, 307
Discal cyst, 283–284, 294
Discal mineralization, 257
Disc degeneration, 248–249, 255, 257–258, 288
Disc explosion, 283–284
Disc herniation, intervertebral, 266–267, 269b, 270f–273f
Discospondylitis, 258f, 305–306, 306f, 640
Disc protrusion
  type I ventrolateral, 272f
  type II, 251, 267, 273f
  type III intervertebral, 267, 273f
Displacement. *see also specific types of*
  in intact diaphragm, 931–932, 933f, 933t, 934f
  with rupture, 932–934, 934f
  within stomach, 934–936
Display, for ultrasound imaging, 42
Disseminated histiocytic sarcoma, 673
Disseminated idiopathic skeletal hyperostosis (DISH), 262–263, 263f
Distal acoustic shadow/shadowing, 845–846
Distal antebrachium, 24f, 363f
Distal displacement, 410f
Distal epiphysis, 443
Distal femur, 356f
Distal humeral condyle, 370f, 374f
Distal humerus, 35f
  lateral radiography of, 357f, 398f
Distal interphalangeal joint, 546
  collateral ligaments of, 562–563, 565f
  deformity of, 560–561, 563f
  of enthesopathy, 559
  hyperextension of, 560–561
  osteoarthritis of, 558–560, 561f
  in osteochondrosis, 548, 548f
  septic arthritis of, 560, 562f
Distal metacarpal bones, 527f
Distal phalanx, 361f, 543–544, 551–553, 552f–555f
  articular fracture of, 553f
  evaluation, 544t
  extensor process of, 544, 545f
  fractures of, 551–552, 552f
  oblique fracture of lateral wing of, 553f
  OCLLs in, 549
  palmar articular surface fragmentation, 548
  palmar processes of, 547f
  palmar process fracture in, 555f
  of pedal osteitis, 556f
  solar margin contour of toe of, 544–545, 546f
  vascular channel pattern, 546f
Distal radial epiphysis, 470
Distal radial physis, 470, 471f, 474f
Distal ulnar physis, 396, 397f
Distention
  of femorotibial joints, 434
  radiography of, 514–515
  of renal pelvis, 849
  of spinal cord, 308–309
Distinct transition zone, 736f
Distortion in diagnostic radiology, 19
Distraction techniques, 371
Disuse atrophy of bone, 527, 527f, 588f
Diverticula/diverticulum, 981–982. *see also specific types of*
Doberman pinscher, 710f, 716–717
Dog. *See* Canine and feline
Dolichocephalic breeds, 165
Doppler angle, 44
Doppler artifacts, 52
Doppler principle, 43–44
Doppler shift, 43, 52
Doppler techniques, 43–44
Dorsal abdominal mass, 837, 849f
Dorsal articular process, 244f, 248f, 256f
Dorsal aspect, 132f
Dorsal-35 degrees proximal-dorsodistal oblique projection, of carpal bones, 481f
Dorsal longitudinal ligament, 246, 279, 284–285
Dorsal mediastinal masses, 669, 674f–675f
Dorsal plane fractures, 534, 552f
Dorsal recumbency, 586f, 689f
Dorsal soft tissue injuries, 466–467
Dorsal subluxation, 538
Dorsocaudal lung field, 583f
Dorsolateral palmaromedial oblique (DLPaMO) radiography. *see also specific types of*
  of carpus, 337f
  of manus, 326f
  of metacarpophalangeal joint, 341f
  of osseous cyst-like lesion, 523f
  of osteochondral (chip) fracture, 525f
  of septic arthritis, 524f
Dorsolateral-palmaromedial oblique view without sulci, 543f
Dorsolateral-palmaromedial view of carpus, 348, 352f
Dorsolateral/plantaromedial oblique radiography of tarsus, 333f, 346f
Dorsolateral/plantaromedial radiography, of metatarsophalangeal joint, 526f
Dorsomedial/palmarolateral oblique radiography of carpus, 338f
Dorsomedial-palmarolateral view
  of carpus, 348, 353f
  first carpal bone, 473f
Dorsomedial-plantarolateral radiography
  of collateral ligament injury, 455f
  of metacarpus, 490f
  osteochondritis dissecans, 451f
  progressive lameness and plantar swelling, 462f
  tarsal swelling, 457f
  of tarsus, 449–450, 451b
  of tibia, 452f
Dorsopalmar radiography
  of carpus, 325f, 350f, 481f
  of cat, 361f
  of degenerative joint disease, 519f
  of foot, 566–568
  of foredigit, 342f
  of immune-mediated arthropathy, 420f
  of manus, 326f
  of metacarpus, 489f–490f
  of osseous cyst-like lesion, 523f
  of osteomyelitis, 523f
  of proximal interphalangeal joint, 561f
  of septic arthritis, 524f
  of third metacarpal lateral condylar fractures, 525f
Dorsopalmar view
  of carpal valgus, 475f
  comminuted, multiplane, biarticular middle phalanx fracture, 536f
  of distal limb, 530, 531f
  of foot, 569–570, 570f
  of incomplete ossification of cuboidal bones, 474f
  noncomminuted, incomplete, monoarticular long sagittal fracture, 534f
  osteomyelitis, 536f
  proximal interphalangeal sepsis, 539f
  of proximal phalanx, 531, 531f, 534f
Dorsopalmar xeroradiograph, of carpus, 336f
Dorsoplantar radiography, 449–450, 451b
  comminuted articular calcaneal, 457f
  of osteoarthritis, 455f
  of pes, 333f
  point of hock swelling, 465f
  proximal tarsal swelling, 460f
  of tarsus, 332f, 454f, 457f
  tibial malleolar fractures, 458f
Dorsoproximal-dorsodistal radiography. *see also specific types of*
  of equine carpal bones, 338f
  of proximal row of equine carpal bones, 338f
Dorsoproximal-palmarodistal radiography of left equine metacarpophalangeal joint, 340f
Dorsoproximolateral-palmarodistomedial oblique xeroradiography, of left equine foredigit, 343f
Dorsoventral radiography, 220f
  of abdomen, 769f
  of cardiomegaly, 720f
  of caudal region, 119f
  of diaphragmatic region, 647f
  of feline asthma, 719f
  of fluid-filled gastric distention, 941f
  of heart base mass, 721f
  of heartworm disease, 714.e1f–714.e3f
  of left atrial enlargement, 708f
  of maxilla, 851f
  of middle region, 117f
  of paracondylar process fracture, 241f
  of paranasal sinus carcinoma, 221f
  of patent ductus arteriosus, 713f
  of persistent right fourth aortic arch, 623f
  rostral aspect of incisive bone, 225f
  of skull, 224f
  of tension pneumothorax, 699f
  of thorax, 586f
Dorsoventral thoracic radiography, 587f
  of dorsal mediastinal masses, 674f
  of lipoma, 678f
  of obesity, 593f
  of right sided thoracic wall lipoma, 639f
  of subcutaneous emphysema, 636f
  of thorax, 666f
Dorsoventral view, 123, 123f
  of dorsocaudal lung field, 583f
  of pleural fluid, 691f
Dose equivalent, 5–6
Double-contrast cystography/cystogram, 863f–864f, 865–868, 866f, 868f–869f, 871f
Double physis sign, 376
Draining tracts, 486
Dual-phase renal angiography, 840
Dual process theory, 100
Duodenal papilla, 962f
Duodenum, 808–810, 844f, 960–961, 962f
Duplex Doppler image, 44, 45f
Dural tail sign, 203f
Dynamic inspiratory radiography, 602f
Dynamic range, 30–31
Dysphagia
  causes of, 617t
  fluoroscopy findings for, 617t
  types of, 617t
Dyspnea, radiography of, 594f
Dystocia, 907, 907f
Dystrophic calcification
  of abscesses, 827
  of periarticular soft tissues, 514–515
  of soft tissue, 786–787
Dystrophic mineralization, 539, 541, 845–846
  of adrenal glands, 797, 798f

E

Ear, 119f
Ear canal tumors, 177, 177f
Eccentric hypertrophy, 708–709
Echinococcosis infection, 809
Echo detection, 66–67
Echo display, 42
Echo formation, 40
Echogenicity, 43, 43b
Ectatic airways, 733
Ectopic kidney, 838
Ectopic ureters, 849, 853, 853f–854f
Edge enhancement, 28, 394–396
Edge-shadowing artifacts, 51, 51f
Effusion. *see specific types of*
Ehrlichia spp., 307
Elbow, 411f, 415–416
  flexor enthesopathy in dogs, 415–416
  medial epicondylitis in cats, 416, 417f
  with ununited anconeal process, 368f
Elbow dysplasia, 365–368
Elbow joint, 322f–323f, 335f
Elbow sesamoid, 406f
Electric current, 10
Electromagnetic radiation, 2, 3t
Electron, 15
Electronic transducers, 41
Electron volt (eV), 3–4
Elephant foot, 393f
"Elevation" of heart from sternum, 696
Embolization, 864–865
Emphysema, 595, 596f, 737. *see also specific types of*
Emphysematous cholecystitis, 809–810
Emphysematous cystitis, 819–820, 861, 864f, 873, 873f
Emphysematous pyometra, 911, 911f
Encephalitis, 194
  necrotizing, 70f
Encrusted cystitis, 872–873
Endochondral ossification, 365, 384
Endodontic disease, 143–147, 146f–149f
End-on pulmonary vessels, 731f
Endoscopic ultrasonography, of esophageal disease, 624–625
Endotracheal stenting, 603
Enema, for cleansing colon, 840
Enlarged lobar pulmonary arteries
  with normal veins, 714
  and veins, 712
Enlarged lobar pulmonary veins, with normal arteries, 714
Enteritis, 809
Enterococci, 257
Entheses, 403–404, 404f
Enthesitis, 403
Enthesopathy, 258, 450f, 455, 461–463, 466–467
  of distal interphalangeal joint capsule, 559
  soft tissue, 561–562, 564f
Enthesophytes, 403–404, 404f
Eosinophilic bronchitis, 742f
Eosinophilic bronchopneumopathy, 742f
Eosinophilic lung diseases, 741
Eosinophilic meningoencephalitis (EME), 194
Eosinophilic pneumonia, 742f
Ependymoma, 197–200, 296–297

Epidermoid cyst, 295–296, 296f, 549
Epididymitis, 915, 918f
Epidural hemorrhage, 286, 286f
Epidurography, 260
Epiglottic entrapment, 227, 235f
Epiglottic masses, 225, 235f
Epiglottic retroversion, 596–597, 597f
Epiphyseal dysplasias, 372–373, 373f.
See also Chondrodysplasia
Epiphyseal malformation, 373
Epiphysis, 443. *see also specific types of*
proximal, 523f
Epiphysitis, 473, 474f
Epithelial lung tumors, 741
Equine. *see also specific topic regarding*
calcaneus of, 358f
carpus of, 336f, 338f, 470–488
dorsopalmar radiography of, 350f
lateromedial radiography of, 351f
normal anatomical variants and incidental findings, 470–471, 471f–472f
radiographic abnormalities, 472–486
radiographic studies, 470, 471f
caudal cervical vertebrae of, 122f
cranial cervical vertebrae of, 121f
fetlock joint, 511–529
foot, 543–575
guttural pouch of, 120f
head of, 217–243
brain diseases, 228–229
caudal region of, 119f
dental disease, 219–220
ear/hyoid apparatus, 227
larynx/upper airway diseases, 225–227
middle region of, 117f–118f
nasal cavity/paranasal sinuses diseases, 217
occipital region of, 120f
other conditions, 229–230
radiography *vs.* other imaging modalities of, 217, 218f
middle cervical vertebrae of, 121f
positioning of, 348, 349t, 350f–353f, 765
radiographic positioning of, 579–580, 580f
radiographic technique for, 578
skull
positioning of, 123–128
radiographic technique, 126
rostral aspect of, 131f
spine
positioning of, 133–134
radiographic technique, 134–135
temporomandibular joint of, 119f
thorax of, 746–762
Equine digit, 546–548
Equine extremity radiography, 348
Equine herpesvirus type 5 (EHV-5), 753
Equine odontoclastic tooth resorption and hypercementosis (EOTRH), 220, 228f
Equine pastern, 530–542
alternate imaging modalities, 530
hyperextension of proximal interphalangeal joint, 539
normal anatomical and incidental variants, 530–532, 531f, 534f
osseous pathology, 532–537
overview, 530
patient preparation, 530
radiographic abnormalities, 532–541
radiography of, 530
recommended views, 530
Equipment, for urinary bladder catheterization and cystography, 865f
Erosive polyarthropathy, 402f
Errors, radiographic interpretation, 103–107
Esophageal compression, 622, 624f
Esophageal dilation, 619
Esophageal disease, 759
Esophageal endoscopic ultrasound, 627f
Esophageal motility disorders, 618–620
Esophageal neoplasms, 624–625
Esophageal strictures, 624–625, 625f
Esophageal stripe sign, 610–611
Esophageal varices, 627, 628f
Esophagitis, 624
Esophagus, 608–609. *see also specific types of*
anatomic and physiologic features, 608–610
contrast studies of, 611b
dilatation of, 619
diverticula of, 625–627
Esophagus (*Continued*)
enlargement of, 669, 675f
fistula in, 625–627
foreign bodies in, 620–621
hiatal diseases of, 620
inflammatory diseases of, 624–625
lateral radiography of, 619f
radiography of, 610–611
varices in, 627, 628f
vascular ring anomalies of, 622–624
Ethmoid hematoma, 220f
Excitation, in magnetic resonance imaging, 65–66
Excretory urogram/urography, 840
of bilateral ectopic ureter, 853f
functional aspects of, 852b
indications for, 840
kidneys and ureters, 840
of left hydronephrosis, 850f
nephrogram phase of, 840
normal imaging findings in, 840
pyelogram phase of, 856f
technique for, 840
Exercise-induced pulmonary hemorrhage, 754
Exostoses, of caudodistal radius, 483, 484f
Expiratory radiography, 602f, 604f
Exposure, 5, 5t
Exposure dose from ionizing radiation, 7, 7f
Exposure index (EI), 32–33
Exposure latitude, 29–34, 31f, 33f
Exposure standards, 6
Extensive bridging ventral spondylosis, 263f
Extensive costal cartilage mineralization, 633f
Extensor carpi radialis, 404f, 416
Extensor carpi radialis injury, 485–486, 485f
Extensor process
of distal phalanx, 545f
fractures of, 554f
External marking system, 129f
Extra-axial tumor, 195–197, 202f–203f
Extradural tumor, 296–298, 297f–299f
Extrahepatic biliary obstruction (EHBO), 821, 821f–822f
Extrahepatic shunts, 823
Extramural compression, 624–625
Extraoral dental technique, 140f
Extraparenchymal hemorrhage, 304–305
Extrapleural masses, 636–638
Extrapleural sign, 636–638, 639f
Extraskeletal osteosarcoma, 275f
Extratesticular diseases, 915
Extrusion of intervertebral disc, 289, 290f
Exuberant callus, 393f

F

Fabellae, 410f
False thoroughpin, 465
Faraday's law of induction, 64, 64f
Far field, 42
Far lateral disc extrusion, 288–289
Fast spin-echo sequence, 67
Fat. *See* Obesity. *see specific types of*
Fatigue fracture, 386–388
Fat opacity, 789f
Fat pad, 402f, 428, 429f
Fat saturation sequences, 71–72
Federal exposure standards, 6
Feline. *See* Canine and feline
Feline asthma, 714, 719f, 738–739
Feline broncholithiasis, 731f
Feline chronic enteropathy, 976
Feline erosive polyarthritis, 421
Feline gastrointestinal eosinophilic sclerosing fibroplasia (FGESF), 978–979
Feline ischemic encephalopathy, 194–195
Feline nasopharyngeal polyps, 175–177
Feline nonerosive polyarthritis, 421
Feline noninfectious polyarthritis, 421
Feline panleukopenia, 974–975
Feline pleural space, 686–701
Female genital tract diseases, 914–915
Female genital tract radiography
anatomy and normal imaging findings, 895
retrograde vaginography, 894
technique, 894
Female urethra, 874
Femininization syndrome, 918–919
Femoral capital physis, 414f
Femoral epiphysis, 372
Femoral fractures, 442–443, 444f–445f
Femoropatellar joint, 446f
diseases of, 430–433, 432f
Femoropatellar joint (*Continued*)
osteochondrosis of, 430, 432f–434f
osteomyelitis of, 433, 435f
patellar fragmentation of, 430, 435f
patellar luxation of, 430, 435f
upward patellar fixation of, 430
Femorotibial joint, 402f, 428, 436f–438f
degenerative joint disease of, 433–434, 438f–439f
diseases of, 433–437
narrowing of, 433–434
Femur
craniocaudal radiography of, 329f, 354f–355f
lateral radiography of, 354f, 356f, 358f
mediolateral radiography of, 329f
Fetal demise, 906f
Fetal distress, 906–907
Fetlock joint
alternative imaging modalities for, 513–514, 514f–517f
anatomy of, 511
degenerative joint disease of, 515–517, 519f
diseases of, radiographic interpretation of, 514–527
radiographic examination, 511–513, 512f
contrast arthrography, 513
dorsodistal-palmaroproximal projection, 512
dorsoproximal-dorsodistal projection, 513, 514f
flexed dorsopalmar projection, 513, 513f
lateral-palmarodistomedial oblique projection, 511–512
lateromedial projection, 511
palmaroproximal-palmarodistal projection, 512
survey of, 511
tangential projection, 512
Fibrin tag, 757f
Fibrocartilage, 282
Fibrocartilaginous embolism, 304, 304f
Fibroepithelial polyps of urethra, 878–879
Fibroid degeneration, 282
Fibrosarcoma, 170–172, 638–639
Fibrous osteodystrophy, 167
Fibular fractures, 443
Fibularis tertius (FT), 466–467, 466f
50-degree proximal radiography, of articular fracture, 526f
Filament, 10
Filling defects, 867–868, 867f, 868t.
see also specific types of
Filly. *See* Equine
Film
blackness of, 16–17, 16f
contrast of. *See* Contrast
fog/fogging of, 17–19
opacity of, 16–17
Film-screen system, 126, 582, 589f
cassette for, 26
Filum terminale, 279
Fissure, 386–388
Fistula, esophageal, 625–627
Fistulography, 570
Fixation error, 104
Flail chest, 635–636, 638f
FLAIR. *See* Fluid-attenuated inversion recovery (FLAIR) sequence
Flat-panel detectors
direct, 26–27, 26f
indirect, 26, 26f
Flat-panel systems, 26–27
Flexed dorsopalmar radiography, of metacarpophalangeal joint, 522f
Flexed lateromedial radiography
of carpus, 337f
of metacarpophalangeal joint, 340f, 522f
of stifle, 442f, 444f
of tarsus, 451b, 456f
Flexed mediolateral radiography, of canine elbow joint, 322f
Flexor carpi ulnaris, 416
Flexor enthesopathy, 415–416
Flexural deformity, 475, 476f
of interphalangeal joint, 560–561, 563f
Flip angle, 68
Flocculation, 79f
Fluid-attenuated inversion recovery (FLAIR) image, multifocal hyperintensities, 238f
Fluid-attenuated inversion recovery (FLAIR) sequence, 68, 70f, 187, 189f
Fluoroscopy, 749, 853
of dysphagia, 617t
swallowing study using, 612–613
Foal. *See* Equine
Focal agenesis, 380–381
Focal articular cartilage, 407
Focal hepatic disease, 816
Focal hepatomegaly, 808
Focal lesion, 727
Focal or multifocal abnormalities, 845–849
Focal peritarsal cellulitis, 467
Focal point or region, 43
Focal spot, 13
size of, 17, 17f
Focal spot-film distance (FFD), 16
Focal uterine diseases, 912
Focal wall thickening, 990–992
from infectious/inflammatory disease, 992
Focused grids, 18–19, 19f
Fog/fogging, of film image, 17–19
Foot, 543–575
abscesses of, 557f
alternate imaging of, 544
articular pathology, 557–561
distal interphalangeal joint deformity, 560–561, 563f
evaluation, 544t
fractures, 550–553
hoof balance and, 566–567, 568f
indications for radiography, 543
infection of, 554
joints, 546
lameness from, 562f
laminitis in, 567–569, 569f
osseous cyst-like lesions in, 548–549, 549f–550f, 560f
osseous pathology, 548–549
osseous structures, 544–545, 545f–547f
osteoarthritis in, 558–560, 561f
patient preparation, 543–544, 544f
pedal osteitis in, 553–554, 556f
radiographic anatomy of, 544–548
radiographic changes caused by diseases of, 548–557
radiographic measurements for, 569f
recommended views, 544, 544t
soft tissue pathology, 561–565
soft tissue structures, 546–548, 561
sulci of, 543f
technical factors for, 543–544
ungual (collateral) cartilages in, 569–570
unknown trauma in, 562f
Foramenal hernias, 658
Foramen magnum, 166, 190f
Foraminal disc extrusion, 288–289
Foredigit, left equine, 341f–343f
Foreign bodies, 486. *see also specific types of*
in esophagus, 620–621
gastric, 940–942, 943f–944f
intestinal, 970f
linear, 971f–973f
nonobstructing, 964–965, 965f
opaque, 969f
pharyngolaryngeal trauma and, 595, 596f
radiolucent, 969f
in trachea, 599–600, 600f
ultrasound of, 604
in urinary bladder, 871
45-degree ventral 30-degree lateral-caudodorsolateral oblique radiography, 231f
45-degree medial-palmarodistolateral radiography, of articular fracture, 526f
45-degree medial-palmarolateral radiography
of disuse atrophy of bone, 527f
of metacarpophalangeal joint, 520f
of sesamoiditis, 527f
Four standard radiographic views, 746f
Four-view radiography, 580f
Fracture. *see also specific types of*
associated sarcomas, 396, 399f
chronicity of, 388
condylar, 520–525, 525f
direction of, 386, 388f
identification and description of, 384–388
infection, 396, 398f
location of, 385–386
open to closed, 388, 389f
pathologic, 388
in proximal and middle phalanges, 532–535, 533f
Salter-Harris classification, 384–385, 386b
stifle, 437–443
surgical repair of, 392
Fracture classification system, 551, 552f

Fracture healing, 384–400
  age factor, 391–392
  blood supply, 391
  bone development and healing, 384
  classification of, 384–385, 387f
  complication with, 392
  direct (primary) bone healing, 389, 391f
  indirect (secondary) fracture healing, 389, 391b
  infection, 392
  metabolism, 392
  process, 388–389
  radiographic evaluation of, 392, 392f
  remodeling phase, 390–391
  reparative phase, 389
  stability and anatomic reduction, 391
  stress protection and bone atrophy, 392
Fragmented medial coronoid process, 368, 369f, 407, 411f
Free luminal filling defects, 867–868
Free peritoneal fluid, 782f
Free peritoneal gas, 786f
Frequency, 40, 42–43
Frontal sinus, 111f, 125f, 165, 165f, 174
Fully weight-bearing lateral view, of flexural deformities, 475, 476f
Functional ileus, 973–975, 975f
Fundus, 620, 621f
Fungal granuloma, 849
Fungal infection, 194–195
  bone, 360–361, 362f
Fungal osteomyelitis, 360–361, 362f
Fungal pneumonia, 753
Funnel chest, 633–634

G

Gadolinium contrast media, 83, 84t
Gadolinium deposition in tissues, 84
Gain, 42–43
Gallbladder, 812–814
  abdominal radiology of, 805, 806f
  acoustic shadowing by, 812–814, 814f, 820, 820f
  lateral abdominal radiography of, 806f
  ultrasonography of, 813f–814f, 818f–822f
Gallbladder mucocele, 820–821, 820f
Gallbladder wall thickening, 819, 819f
Gamma rays, 3, 3b
Gantry, 58–59
Gas. *see also specific types of*
  opacity, 539
  in palmar soft tissues, 563f
Gastric bleeding, 944–945
Gastric dilation, 809
Gastric dilation volvulus (GDV), 936–939, 939f–940f
Gastric foreign bodies, 940–942, 943f–944f
Gastric neoplasia, 945–947, 946f
Gastric pneumatosis, 938
Gastric ulcers, 942–944, 945f
Gastric wall changes, 942–950
Gastric wall edema, 947, 949f
Gastric wall gas (pneumatosis), 948, 950f
Gastrocnemius muscle, 404f
Gastrocneumius tendinitis, 465–466
Gastroesophageal intussusception, 620, 621f, 657, 658f, 658b, 934
Gastroesophageal reflux, 618–619, 653–656
Gastrography
  positive contrast, 927–930
  of stomach, 926–927, 928b
Gastrointestinal tract, 764, 766f, 842–843, 843f
Gastrothorax, 935f
General anesthesia, 128
Generalized cardiomegaly, 709–710
Generalized hepatomegaly, 807–808, 807f
Generalized osteosclerosis, 379
Gestational age, ultrasonographic calculation of, 906t–907t
Glioma, 201–203, 205f
Glomerulonephritis, 844
Gloves, 8
"Golf tee" pattern, 275f
Golf-tee sign, 299–300
Gradient recalled echo (GRE) sequence, 66, 68–71, 71f, 209f, 212f, 214f
  magnetic susceptibility artifacts in, 74f
  spoiled, 71
Granulation tissue, 372, 549
Granulomatous meningoencephalitis (GME), 194, 198f
Granulomatous urethritis, 878–879
Grating lobes, 49–50, 50f
Gray (Gy), 5
Grayscale display, 29
Gray shades, 23
Greenstick fracture, 386–388, 390f
Grid, 17–19, 126
  malalignment of, 19f
  proper orientation with, 19f
  scatter removal by, 31f
Grid artifact, 30
Grid ratio, 18, 18f, 19t
Guttural pouch, 120f, 223–225
  chondroids, 224, 233f
  empyema, 232f
  fluid, 223–224, 232f
  masses, 224, 234f
  neoplasia, 224–225
  trauma, 225, 234f
  tympany, 225, 234f
Gyromagnetic ratio, 65

H

Hansen type I intervertebral disc disease, 282
Hansen type II intervertebral disc disease, 282
Hansen type III disc disease, 283–284
Harmonics, 42
Harmonic ultrasound techniques, 85–86
Head, 217–243. *See also* Equine
  fractures, 229–230, 241f–242f
  left rostrodorsal-right caudoventral oblique radiographs of, 231f
  middle region of, 116f–118f
  right-left radiography of, 231f
  rostral 45-degree ventral 30-degree lateral-caudodorsolateral oblique radiography, 231f
Head of spleen, 824
Hearing. *see specific types of*
Heart base mass, 720, 721f
Heart base region masses, 672, 676f–677f
Heart, cardiac chamber enlargement in, 706–710
Heart failure, 714–715. *see also specific types of*
Heart to single vertebra ratio (HSVR), 703
Heartworm disease, 714, 714f
Heartworm infection, 710–711
Helical (spiral) scanning, 58–59, 61f
Hemangiosarcoma, 303
Hemarthrosis, 407, 417
Hematoceles, 915
Hematochezia, 996f
Hematogenous bacterial osteomyelitis, 361
Hematogenous infection, 640
Hematogenous osteomyelitis, 444, 535
Hematoma, 213t, 818
Hemilaminectomy, 257
Hemiparalysis, 660f
Hemithorax, 687f, 691f, 694f
Hemivertebrae, 246–248, 248f
Hemoptysis, 596f
Hemorrhage, 741–743. *see specific types of*
Hemorrhagic infarcts, 210, 212f–213f, 213t, 214f
Hemothorax, 755
Hepatic abscess, 810, 812f, 818, 818f
Hepatic abscessation, 812f, 818f
Hepatic carcinoma, 809f, 818f
Hepatic cirrhosis, 808, 815–816
Hepatic cyst, 653, 808, 818
Hepatic disease, 815–816
Hepatic echogenicity, 816
Hepatic granuloma, 809
Hepatic lipidosis, 814f, 815–816
Hepatic mass, 811, 813f
Hepatic neoplasia, 808, 813f, 816–817, 817f
Hepatic opacity, 809–810, 810f–812f
Hepatic parenchyma, 809
Hepatic ultrasound, 808
Hepatic veins, 812, 813f
Hepatitis, 810f, 815–816, 818, 818f
Hepatocellular carcinoma, 808f–809f, 813f, 816–817, 817f
Hepatocutaneous syndrome, 818, 818f
Hepatomegaly, 807–808, 807f. *see also specific types of*
  gastric displacement caused by, 933f
Hepatozoon infection, 361
Hepatozoonosis, 361
Hernia. *see specific types of*
Herniation, 254–255, 658
"Herring bone" appearance, 608–609, 608f
Hertz (Hz), 40
Heterobilharzia americana (HA), 977
Heterotopic polyodontia, 227, 237f
Hiatal diseases, esophageal, 620
Hiatal hernia, 653–656, 656b, 657f, 934, 935f–936f
High-contrast radiography, 20, 20f
High-frequency generator, 14
High-pass filtering, 62f
High-velocity-low-volume disc disease, 283–284
Hilar-region mediastinal masses, 669–672, 675f–677f
Hip dysplasia, 368–371, 370f–372f, 406–407
Hip joint, 343f
Histiocytic sarcoma, 206, 207f, 301–302, 728, 829–830
Histoplasma, 307
Histoplasmosis, 829f
Holoprosencephaly, 192
Homogeneous soft tissue opacity, in peritoneal fluid, 780–781, 780f
Hoof. *See* Foot
Hoof balance, 566–567, 568f
Horizontal-beam lateral thoracic radiography, 582f
Horizontal beam lateral view, 651f
Horizontal-beam radiography, 690–692, 694f, 698
Horizontal-beam ventrodorsal radiography, of thorax, 581f
Horse. *See* Equine
Hounsfield units (HU), 60, 76
  measurements by, 63f
  tissue attenuation determined as, 62f
Human vision, 100
Humeral condyle, incomplete ossification of, 374–375, 374f
Humerus. *see also specific types of*
  caudocranial radiography of, 321f
  mediolateral radiography of, 321f
  proximal, cranioproximal/craniodistal view of, 349f
Hydranencephaly, 191
Hydrocele, 915
Hydrocephalus, 166, 166f–167f
Hydrogen nuclei, 64, 65f
Hydronephrosis, 850, 850f
Hydrophilicity *vs.* lipophilicity, iodine-based contrast media, 79
Hyoid apparatus, 227
Hyoid bone, 592
Hyperadrenocorticism, 228, 239f, 799f
Hyperattenuating hematoma, 240f
Hyperechoic calculus, 852f
Hyperechoic foci, 977
Hyperechoic liver, 815–816
Hyperechoic medullary rim, 845
Hyperechoic mucosal speckles may, 960
Hyperechoic nodule, 799f
Hyperechoic structure, 852–853
Hyperestrogenism, 918–919
Hyperextension of distal interphalangeal joint, 560–561
Hyperinflation, 737
Hyperintensities, 238f
Hyperostosis, 195–197
Hyperparathyroidism, 850–851, 851f
Hypertension, 714–715
Hypertrophic cardiomyopathy (HCM), 717, 719f
Hypertrophic nonunion fracture, 392–393
Hypertrophic osteodystrophy, 376, 377f
Hypertrophic osteopathy, 421, 422f, 486, 539–540
Hypertrophy, 401, 709
Hypervitaminosis A, 423, 424f–425f
Hypoadrenocorticism, 703–706, 705f
Hypoechoic medial iliac lymph node, 791f
Hypoechoic nodules, 815–816, 816f
Hypoperfusion, 737
Hypoplasia, 380
  tracheal, 601, 601f, 604
Hypothyroidism, congenital, 372, 373f
Hypovolemia, 705f

I

Idiopathic bone infarction, 359
Idiopathic megacolon, 990, 994f
Ileocolic intussusception, 992f
Ileocolic lymph node, enlarged, 791f
Ileum, 960–961
Ileus, 965
  functional, 973–975, 975f
Iliopubic sesamoids, 407f
Ill-defined nodular-shaped pulmonary lesions, 734f
Image detail
  factors affecting, 17–19
  focal spot size and, 17, 17f
  grid and, 17–19, 18f
  intensifying screens and, 17, 18f
  motion and, 17
Image matrix, spatial resolution and, 58f
Image reconstruction algorithm, 62f
Images/imaging
  consolidated storage of, 36–37, 36f
  noise in, 33, 34f
  postprocessing of, 34–35, 35f
Imaging modalities, 165, 166f
Imaging time, 72
Immune-mediated polyarthropathies, 419–421
  feline erosive polyarthritis, 421
  feline nonerosive polyarthritis, 421
  feline noninfectious polyarthritis, 421
  hypertrophic osteopathy, 421, 422f
  periosteal proliferative form, 421, 421f
  rheumatoid arthritis, 419–420, 420f
  systemic lupus erythematosus, 420–421
Implant failure
  humeral condylar fracture repair with, 397f
  tarsal arthrodesis with, 394–396, 396f
Implant instability and failure, 394–396, 396f–397f
Inattentional blindness, 105f
Incidental factors, 135
  of bone lesion, 361–363
Incidental reflux, 809–810
Incomplete cuboidal bone ossification, 450–452, 454f
Incomplete fracture, 386–388, 390f
Incomplete sagittal fracture, 533, 533f–534f
  of talus, 457–459, 459f
Increased T2-signal intensity, 187
Indirect flat-panel detectors, 26, 26f
Indirect fracture healing, 389, 391b
Indistinct transition zone, 354, 356, 357f–358f, 360f
Infection. *see specific types of*
  of distal phalanx, 554
  fractures, 396, 398f
  quittor, 570
Infectious arthritis, 401, 424b
Infectious disorders, 173–179
Infectious enteritis, 977
Infectious meningoencephalitis, 194–195
Infectious peritonitis, 194–195, 201f
Infiltrative bowel disease, 975–978, 976f–980f
Inflammation, 915–918
  of pancreas (pancreatitis), 792–794, 792b, 793f, 793b, 794f
Inflammatory airway disease, 638f, 753–754
Inflammatory bowel disease, 977
Inflammatory brain diseases, 228, 238f
Inflammatory/infectious conditions, 257, 262t, 305–307, 360
  of brain, 194–195, 198f–201f
  discospondylitis, 257, 258f, 305–306, 306f
  of esophagus, 624–625
    esophagitis, 624
    strictures, 624–625
  meningomyelitis, 307, 308f
  spinal epidural empyema, 306–307, 307f
  spondylitis, 257, 257f
  vertebral osteomyelitis, 257
  vertebral physitis, 257
Infrapatellar fat pad, 402f
Ingested bone, in pharynx, 616f
Inherent gas, as contrast medium, 962f
Inspiratory difficulty, radiography of, 595f
Inspiratory noise, progressive, 595f
Inspiratory radiography, 604f
Instability, 131, 291
Intensifying screens, 17, 18f
Interarcuate ligaments, 279
Intercapital ligament, 246, 247f, 279
Intercarpal joints, 470
Intercarpal ligament desmopathy, 484
Intercrural cleft, 646–647
Interlobar fissures, 687–688, 690f, 695f
Internal inflammatory resorption, 147
International Commission on Radiological Protection (ICRP), 6
International System of Units (SI units), 4–5
Interphalangeal joint
  flexural deformity of, 560–561, 563f
  hyperextension of, 560–561, 563f
Interphalangeal osteoarthritis, 560f
Interpretation paradigm, 135–136
  of bone lesion, 363
Interstitial opacity, 588f
Interstitial pattern, 733–735, 734f–735f
  structured, 733–734
  unstructured, 733–735, 735f, 735t
Interstitial pneumonia, 751–752
Interstitium, 741

Intervertebral articular process joint space, 255
dorsal, 258–260
Intervertebral disc disease, 282–291
classification of, 282–284, 282f–284f
computed tomography of, 284–285, 284f–285f
intervertebral disc extrusion, 289
magnetic resonance imaging of, 285–286, 285f–287f
regional characteristics of, 287–288
survey radiographic signs of, 256f
of vertebrae, 254–257
Intervertebral disc herniation, 266–267, 269b, 270f–273f
Intervertebral disc, normal, 281f, 282
Intervertebral foramen, 255, 256f
Intestinal foreign bodies, 970f
Intestinal leiomyositis, 975
Intra-abdominal mineral opacity, 786–787, 787f
Intra-articular calcified bodies, 403, 403t
Intra-articular fractures, 478–479
Intra-articular gas, 404–405, 405f, 405b
Intra-axial tumor, 201–203, 205f
Intracranial feline infectious peritonitis, 194–195
Intradural disc herniation, 291
Intradural-extramedullary mass lesion, 268f
Intradural-extramedullary tumors, 298–301
Intrahepatic shunts, 823
Intraluminal tracheal air, 599–600
Intramedullary disc herniation, 291
Intramedullary swelling, 268f
Intramedullary tumors, 301
Intramembranous ossification, 384
Intramural changes, of urinary bladder
in contrast cystography, 866, 867f
in ultrasonography, 870–871, 872f
Intraobserver variability, 107
Intraoral dental radiographs, 137–140
Intraoral dorsoventral radiography, 111f, 126f
Intraparenchymal spinal cord hemorrhage, 304
Intraperitoneal, definition of, 778
Intravenous urography, 863f
Intraventricular gas, 715, 716f
Intussusception, 971–972, 973f–974f
Invasive extracranial tumor, 207–209, 209f
Inverse square law, 16
Inversion recovery sequences, 67–68, 69f–70f
Involucrum, 396
Iodinated contrast medium, in computed tomography, 61–63, 64f
Iodine, 78
Iodine-based contrast media, 76, 78–82
adverse reactions to, 79–82
cardiovascular effects, 81
cellular and vascular effects, 81
chemical composition of, 80f
dose-dependent physiologic reactions, 81
effects on thyroid function, 82
general information, 78
hypersensitivity reactions, 79–81
ionic *vs.* nonionic, 78–79
lower urinary tract effects, 82
neurologic effects, 81
osmolality of, 79
properties of, 78–82
respiratory effects, 81
water soluble, 79
Iodine-induced thyrotoxicosis, 82
Iodixanol, 80t
Iohexol, 80t, 82, 82f, 963
Iomeprol, 80t
Ionic *vs.* nonionic, iodine-based contrast media, 78–79
Ionization, 3–4
Ionization density, 6f
Iopamidol, 80t
Iopromide, 80t
Iothalamate, 80t
Ioversol, 80t
Ioxilan, 80t
Ischemic myelopathy, 304, 304f
Ischemic stroke, 73f

J

Jejunal lymph node, enlarged, 791f
Jejunal volvulus, 975f
Jejunum, 959f–960f, 960–961
Joint, 403, 409t. *see also specific types of*
Joint capsule attachments, 511
Joint disease, 401–427
of articular soft tissue, 403
Joint disease (*Continued*)
aseptic necrosis of femoral head, 372, 372f
bone cyst in, 401–402, 402f
of carpus, 416–417, 417f
congenital radial head luxation, 368, 370f
degenerative, 407–412, 411f, 411b, 412f, 412b, 413f–414f
elbow dysplasia, 365–368
of entheses, 403–404, 404f
of enthesophytes, 403–404, 404f
epiphyseal dysplasia, 372–373
fragmented medial coronoid process, 368, 369f
of hemarthrosis, 417
hip dysplasia, 368–371, 370f–372f
of hypervitaminosis A, 423, 424f–425f
of immune-mediated polyarthropathies, 419–421
intra-articular calcified bodies, 403, 403t
of intra-articular gas, 404–405, 405f, 405b
of joint displacement or incongruency, 403
in joint space, 401, 402f
mucopolysaccharidosis, 372–373, 373f
multiple epiphyseal dysplasia, 373
osseous, 412–413, 414f
osteochondrosis, 365, 366f
osteochondrosis dissecans, 365, 366f
of osteophytes, 403, 403f
of perichondral bone opacity, 402–403, 403f
proximal interphalangeal joint, 537–539
radiographic signs of, 401–405, 401f, 401b
of septic arthritis, 421–423, 423f, 423b, 424f, 424b
of sesamoid bone, 405–407, 405f–408f, 409t
of sesamoid disease, 406–407, 409f–410f
sprain, 413, 415f
of stifle, 417
of subchondral bone opacity, 401–402, 402f
of synovial volume, 401
of synovium, 418–419
of tarsus, 417, 418f
of tendons and ligaments, 413–417
ununited anconeal process, 368, 368f
Joint displacement, 403
Joint effusion, 365, 443f, 484–485, 514–515
Joint incongruency, 403
Joint mouse/mice, 402
Joint neoplasia, 424, 425f–426f
Joints, 546
Joint space, 256f, 401, 402f, 561f
JPEG files, 22, 36–37
Juvenile orthopedic diseases, 472–477
incomplete ossification of cuboidal bones, 472–473, 474f
osseous subchondral cyst-like lesions, 476, 476f
osteochondrosis/osteochondritis dissecans, 476–477
physitis/epiphysitis, 473, 474f

K

Keratoma, 549
Kidneys and ureters, 837–859, 846f
anatomy of, 837–841
antegrade ultrasound-guided pyelography, 840–841
contrast-enhanced computed tomography of, 840
excretory urography of, 840
imaging procedures for, 837–841
lateral radiography of, 838f
magnetic resonance imaging of, 841
with nephroblastoma, 848f
radiographic appearance of, 76f
radiography of, 837–838
renal diseases of, 841–851
scintigraphy of, 841
trauma to, 854–855, 855f–856f
ultrasonography, 838–839, 839f
ureteral diseases, 851–854
Kiloelectron volt (keV), 11
Kilovoltage peak (kVp)
exposure latitude, 32, 33f
in high-contrast radiographs, 20f
setting for, film blackness and, 16, 16f
Kissing lesion, 365
Knees and teeth syndrome, 379–380, 380f

L

Lameness, 411f
in foot, 562f
Lameness (*Continued*)
magnetic resonance imaging of, 516f
osteochondrosis, as cause of, 365
of pelvic limb, 411f
Lamina, 244
Lamina dura, 167, 168f
Laminitis, 567–569
acute, 567
developmental, 567
radiographic evaluation of, 567–569, 569f–570f
Large bowel, 986–998
barium enema for, 987–988
computed tomography of, 988, 989f
contrast radiography of, 987–988
disease of, 988–990
congenital, 995
imaging procedures for, 986–988
large intestinal displacement from mass effect, 988
radiographic findings of, 986–987, 987f
mural abnormalities of, 990–995
diffuse wall thickening, 992–993
focal wall thickening, 990–992
large intestinal perforation, 995
opacity changes, 993–995
radiographic anatomy of, 986–987, 986f–987f
ultrasound of, 988, 988f
Large intestinal displacement, from mass effect, 988
Large intestinal perforation, 995
Large kidneys, 842–844, 843f–844f
Larmor frequency, 65
Laryngeal area, 120f
Laryngeal collapse, ventrodorsal radiography of, 597f
Laryngeal diseases, 225–227
epiglottic entrapment, 227, 235f
epiglottic masses, 225, 235f
mineralization, 225, 235f
palatal dysfunction, 225, 235f
Laryngeal paralysis, 604
Laryngitis, 597
Lateral caudoventral thoracic radiography, 751f
Lateral cervical radiography
of acute ptyalism, 628f
of cricopharyngeal chalasia, 618f
of early ectopic basihyoid thyroid carcinoma, 595f
of ingested bone in pharynx, 616f
of vocalizing, 628f
Lateral decentering, 19, 19f
Lateral digital extensor, 485–486
Lateral digital fluoroscopy
of barium swallow, 618f
of swallowing, 618f
Lateral fabellae, 410f
Lateral meniscus, 402f
Lateral myelogram, 259f
Lateral radiography, 259f, 693f, 746, 771f
of abdomen, 769f, 771f, 808f
of antebrachium, 357f, 363f
of barium esophagram, 624f
of barium swallow, 625f
of block vertebra, 248f
of borzoi, 703f
of canine female genital tract, 895f
of cardiac silhouette, 706f
of carpus, 478f
of cat having dental prophylaxis, 600f
of caudal abdomen, 860f–861f, 863f
of caudal aspect, 131f, 757f, 766f, 770f
of caudal lung, 361f
of caudodorsal aspect of thorax, 628f, 749f
of cervical spine, 133f
of cervicothoracic region, 135f
chondroids in guttural pouches, 233f
of compression fracture, 262f
of conchofrontal sinus, 218f
of costochondral junction, 632f
of cranial abdomen, 660f, 806f
of cranial aspect, 250f, 758f–759f, 766f
of cranial cervical region, 234f
of cranioventral aspect, 767f
of cystic calculi, 864f
of degenerative joint disease, 259f
of depression fracture, 232f
of diaphragmatic hernia, 757f
of discospondylitis, 258f
of distal humerus, 357f
of dorsal aspect, 132f
dorsal calvarial multilobular osteochondrosarcoma, 172f
of dystocia, 907.e1f
of epiglottis, 235f
of esophagus, 619f
of femur, 354f, 356f, 358f
of fluid-filled gastric distention, 941f
Lateral radiography (*Continued*)
of gas, 781f
of gastric foreign body, 943f
of guttural pouch empyema, 232f
of guttural pouch trauma, 225, 234f
of head, 220f
of heartworm disease, 714.e1f
of horse metacarpus, 355f
of humerus, 355f, 357f
of hydrocephalus, 166f
of hypovolemia, 705f
of jejunal crowding, 771f
of jejunal volvulus, 975f
of kidneys, 842f
of Labrador retriever, 181f
of laryngeal region, 235f
of left atrial enlargement, 708f
of left atrium, 706f
of left paranasal sinus cyst, 219f
of lumbar spine, 259f
of mastiff, 182f
of mechanical jejunal obstruction, 967f
of metatarsophalangeal joint, 521f
of midventral aspect, 767f
of mucopolysaccharidosis, 263f
of multiple hemivertebra, 248f
of multiple myeloma, 262f
of nodule, 584f
of nutritional secondary hyperparathyroidism, 263f
opossum with nutritional secondary hyperthyroidism, 168f
of patient hit by car, 255f
of peritoneal effusion, 786f
of peritoneal fluid, 781f, 783f
of persistent right fourth aortic arch, 623f
of pharynx, 592f
of pneumoperitoneum, 785f
of pneumothorax, 696f, 757
of progressive inspiratory noise, 595f
of prostatic carcinoma, 863f
of proximal tibia, 362f
of pulmonary edema, 755f
of pyloric antrum, 940f
of retropharyngeal lymph nodes, 234f
of skull, 32f, 123f, 130f
spinal, 132f
of steroid hepatopathy, 807f
of thoracic inlet, 600f
of thoracic spine, 134f
of thoracic vertebrae, 32f
of thoracolumbar region, 134f
of thorax, 626f, 754f, 757f, 808f
of trachea, 593f
tracheal stent placement, 603f
of traumatic diaphragmatic hernia, 646f, 654f
of tumor, 262f
unilateral temporomandibular luxation, 180f
of urethra, 869f
of urinary bladder, 869f
of volume depletion, 698f
Lateral resolution, 41
Lateral skull radiograph, Labrador retriever, 165f
Lateral soft tissue injuries, 461–463, 462f–463f
Lateral survey radiograph, of thick gastric wall, 948f
Lateral tarsometatarsal sesamoid, 408f
Lateral thoracic radiography
of Borzoi, 703f
of caudal esophageal foreign body, 675f
of caudodorsal thorax, 621f
of cavitary tumor, 361f
of cervical vertebrae, 634f
of chronic healed rib fractures, 632f
of dorsal mediastinal masses, 674f–675f
of esophageal foreign body, 622f
of lung lobes, 724f
of mediastinal mass, 672f
of persistent right fourth aortic arch, 623f
of pleural effusion, 681f
of pneumomediastinum, 682f–684f
of pulmonary blood vessels, 751f
of rib fractures, 632f
of sternal luxation, 638f
of sternal lymph node, 668f
of thoracic esophagus, 621f
of upper airway obstruction, 620f
Lateral trochlea, 365
Lateral trochlear ridge, 434f
Lateral videofluoroscopy, of barium swallow, 618f
Lateral view, 123, 123f, 765–766
of acute gastric dilatation, 940f
of cervicothoracic region, 601f
of diaphragmatic region, 648f

Lateral view (*Continued*)
of distal femur, 390f
of gastric dilation, 938f
of gastric volvulus, 939f
of gastroesophageal intussusception, 658f
of linear foreign body, 971f
of lumbar spine, 646f
of mechanical small bowel obstruction, 967f
of peritoneopericardial diaphragmatic hernias, 655f
of proximal tiba, 362f
of small bowel, 957f
of soft tissue opacity, 657f
of tarsus, 398f
of traumatic diaphragmatic hernia, 651f
of vaginogram, 895f
Lateromedial of proximal metatarsus, 490f
Lateromedial radiography
of calcaneal skyline, 453f
of carpus, 336f, 351f
of cortisone arthropathy, 519f
curb-like swelling, 466f
distal intertarsal degenerative joint disease, 455.e1f
of equine stifle joint, 344f
of foredigit, 341f
of lateral patellar luxation, 435f
of metacarpophalangeal joint, 339f, 518f
of osseous cyst-like lesion, 523f
osteoarthritis, 455f
of osteochondral (chip) fracture, 525f
of osteomyelitis, 523f
of patella, 435f, 446f
of phalanx, 527f
plantar soft tissue swellings, 464f
pont of hock swelling, 465f
regional sclerosis, 450, 453f
of septic arthritis, 446f, 523f
septic physitis, 460, 460f
of stifle, 429f, 432f, 435f, 438f, 440f, 443f, 446f
of tarsus, 346f, 450f, 453f–457f, 459f–461f, 464f–466f
tibial malleolar fractures, 456, 457f
tibiotarsal effusion, 454f
Lateromedial view
of carpus, 348, 351f
comminuted fractures, 535, 536f
cutaneous neoplasms, 540, 540f
gas opacity, 539, 540f
osteoarthritis, 537, 537f
osteomyelitis, 536f
palmar (plantar) eminences fracture, 535, 535f
of proximal phalanx, 531–532, 531f, 534f
septic arthritis, 538, 539f
soft tissue mineralization, 539, 540f
Lattice, 65–66
Leakage, of contrast medium, 868
Left atrial dilation, 717–718
Left atrial enlargement, 706–707, 708f
Left atrium, 706–707, 706f
Left carpus, equine, 336f, 338f
Left caudal aspect, 736f
Left cranial lung lobe torsion, 739f
Left 45-degree dorsal-right ventral oblique (LDRVO) radiography, 130f
Left 20-degree ventral-right dorsal projection, 126f
Left equine carpus, 336f, 338f
Left equine foredigit, 341f–343f
Left equine metacarpophalangeal joint, 339f–341f
Left equine tarsus
dorsomedial-plantarolateral oblique xeroradiograph, 347f
lateromedial xeroradiograph, 346f
Left femur, 360f
Left foredigit, equine, 341f–343f
Left hemipelvis, of dog, ventrodorsal radiography of, 356f
Left hemithorax, 687f
Left hepatic mass, 808
Left hydronephrosis, 850f
Left lateral radiography
of abdomen, 805f, 843f
of cardiomegaly, 720f
of congestive heart failure, 715f
of cranial aspect, 768f
of diaphragmatic region, 646f, 649f
of feline asthma, 719f
of heart base mass, 721f
of hypertrophic cardiomyopathy, 719f
of multinodular pulmonary fibrosis, 753f
of myxomatous tricuspid valve disease, 717f
of peritoneopericardial diaphragmatic hernias, 655f–656f
Left lateral radiography (*Continued*)
of pleural fluid, 692f
of pneumothorax, 697f
Left lateral thoracic radiography
of accessory lung lobe, 678f
of pectus excavatum, 635f
of pneumomediastinum, 670f
of sternal lymph node, 668f
of thorax, 665f
Left lateral view, 764
Left ovarian adenocarcinoma, 909f
Left renal enlargement, 844f
Left-right lateral radiography
of canine head, 110f
of caudal cervical, 122f
of cervical vertebrae, 113f, 121f
of guttural pouch, 120f
of laryngeal area, 120f
of lumbar vertebrae, 115f
of middle region, 118f
of occipital region, 120f
of thoracic vertebrae, 115f
of withers region, 122f
Left-right radiography, 231f, 752f
Left-sided aortic arch, 624f
Left-sided congestive heart failure, 714–715, 715f
Left-sided tension pneumothorax, 699f
Left tarsus, equine, 345f–347f
Left thoracic lateral radiography
of cardiac silhouette, 587f
of caudal thorax, 586f
of caudal vena cava, 579f
of cranial lobe artery, 714.e1f
of dorsocaudal lung field, 583f
in small animals, 580, 581f–584f
of thorax, 585f–586f
Left ventral/rostral right dorsal oblique radiograph, 112f
Left ventricle, 708–709
Left ventricular enlargement, 708–709
Legg-Calvé-Perthes disease. *See* Aseptic necrosis, of femoral head
Leiomyoma, 912, 992
Lesions, localized to airways, 730–733
Level (L), 61, 63f
Ligament damage, collateral, 437, 443f
Ligamentous trauma, 413
Ligamentum flavum, 246, 279–282, 288, 291–292
Light, 100, 101f
Light diffusion, 26
Linear array, 41
Linear attenuation coefficient, 60
Linear foreign body, 942, 944f, 971f–973f
Lipiodol, 79
Lipoma, 678f
of abdominal wall, 787–788, 788f
infiltrative, 297–298, 299f
in retroperitoneal space, 784
Liquid barium sulfate, 77
Lissencephaly, 192, 194f
Liver, 805–836
abnormal ultrasonographic appearance of, 815–819, 815f–819f
biliary system, disease of, 819–821, 819f–822f
cirrhosis of, 816f
computed tomography of, 810–811
with echogenic shadow, 818f
hepatic opacity of, 809–810, 810f–812f
hepatic ultrasound of, 812–824, 813f–815f
hepatomegaly of, 807–808, 807f–809f
microhepatia, 808
mineralized choledocholith in, 810f
radiology of, 805–810, 805f–806f
radiolucencies in, 811f
vascular disease of, 821–824, 822f–824f
vascular malformations, 810–811
Lobar pulmonary vessel changes, 711–714, 712f–713f
Lobar sign, 735–736, 736f
Localizer images, 68
Location of lesion, 728
Loculated fluid, 687
Long-axis ultrasonography, 846f–850f
Long digital extensor tendon (LoDET), 467
Longitudinal ligament, 279
Longitudinal ultrasonograms, of gastric neoplasia, 946f
Longitudinal ultrasonography, 434f
of ascites, 814f, 816f
of biliary sludge, 814f
of cirrhosis, 816f
of cranial extremity, 831f
of cranial portion, 813f
of cystadenoma, 817f
of echogenic shadows, 818f
Longitudinal ultrasonography (*Continued*)
of extrahepatic biliary obstruction, 822f
of gallbladder mucocele, 820f
of hepatic lipidosis, 814f
of hepatocutaneous syndrome, 818f
of hyperechoic hepatic parenchyma, 815–816, 815f
of hyperechoic nodule, 818f
of liver, 814f–815f
of mottled parenchyma, 815f
of spleen, enlarged, 828f
of splenic torsion, 828f
Long plantar desmitis/desmopathy, 463
Long scale of contrast, 20
Low-grade intestinal T-cell lymphoma (LGITL), 976
Lucency sign, 146–147
Lumbar myelogram, 266f
Lumbar myelography, 263–264
Lumbar puncture, 264f
Lumbar spine, 259f, 646f
digital radiography of, 34f
left-right lateral radiography of, 115f
radiography of, 132f
Lumbar vertebrae, 115f
ventrodorsal radiography of, 116f
Lumbosacral disease, 260
Lumbosacral instability, 260
Lumbosacral malarticulation malformation, 260
Lumbosacral stenosis, 260, 288, 289f
Luminal filling defects, 867–868, 868f
Luminance, 100, 101f
Lung aeration, 727f
Lung-digit syndrome, 361f
Lung hyperinflation, 738f
Lung lesions, 726, 728
Lung lobe torsion, 739, 739f, 741f
Lung mass, mediastinal masses *vs.*, 673, 680f–681f
Lung opacity, 729–730
Lung retraction, 688–689, 691f–692f
Lungs, 724–745
anatomy of, 724–725
injury, acute, 756
mineralization in, 731t
nodule in, 584f
radiographic appearance of, 724–725
Lung volume, factors affecting, 725
Luxation, 406, 410f
Lymphadenopathy, 758, 758f
Lymphoma, 206–207, 208f, 302–303, 673, 992f
Lymphosarcoma, 790f, 807f, 816–817, 817f, 825f
in spleen, 828–830

M

Mach lines, 489, 489f
Magnetic field
main, in magnetic resonance imaging, 64, 64f
Magnetic resonance imaging (MRI), 64–73
of adrenal glands, 797
angiography using, 841
artifacts in, 72–73
bone marrow lesions, 537, 537f
of canine and feline spinal cord disease, 279–317
of cervical spondylomyelopathy, 292–294, 293f–294f
contrast media for, 71, 71f, 83–84
adverse reactions of, 83–84
general information, 83, 83f
nephrogenic systemic fibrosis and, 84
diffusion-weighted imaging in, 72, 73f
of equine head, 217
fat saturation sequences, 71–72, 72f
fetlock joint, 513–514, 515f–517f
gradient recalled sequences in, 68–71
image formation in, 56–58, 57f–59f
image quality and imaging time in, 72, 74f
instrumentation for, 64, 64f
of intervertebral disc disease, 285–286, 285f–287f
of kidneys, 841
of lameness, 516f
magnetic field strength in, impact of, 73
main magnetic field and radiofrequency energy in, 64, 64f
of metatarsophalangeal joint, 516f
of pancreas, 792
perfusion-weighted imaging in, 72
of pharynx, larynx, and trachea, 604
planes of, 57–58, 59f
principles of, 55–75
of prostate gland, 891, 892f
role of, in veterinary practice, 55–56, 55f–56f
Magnetic resonance imaging (MRI) (*Continued*)
signal localization in, 66–67
signal-to-noise ratio in, 72, 74f
spin-echo sequences in, 66, 67f–68f selection of, 67–68, 69f–70f
spins, excitation, and relaxation in, 65–66, 65f–67f
of stifle, 429, 432f
system for, components of, 64f
of third metacarpal, 515f
tissue contrast in, 66, 68f–69f
of ureters, 841
of urinary bladder, 874
Magnetic resonance (MR) of brain disease, 187–189, 188f
Magnetic susceptibility artifacts, 72–73, 74f
Magnetization
flipping of, 66
net, 65
Main pulmonary artery, 710–711, 712f
Malarticulation of cervical vertebrae, 291
Male urethra, 874
Malformation
of cervical vertebral, 291
Chiari-like, 308–309, 309f
epiphyseal, 373
Malignant gastric ulcers, 942–943
Malignant melanoma, 170–172
Malignant neoplasia, of large intestine, 990
Malignant (peripheral or cranial) nerve sheath tumor, 203–204
Malignant tumor, of trachea, 598–599
Malunion fracture, 393–394, 395f
Mandible, nondental diseases of, 220–223
Mandibular dental disease, 219
Manus, canine, 326f–327f
Marie's disease, 539–540
Mass, 728, 729f–730f, 912–913
lesions, 639
pharyngolaryngeal, 594–595, 594f, 594b, 595f, 604
Mass effect, 772–773
Mast cell tumor, 816f
Masticatory muscle myositis, 179, 179f
Matter
interaction of radiation with, 14–15
ultrasound wave interaction with, 40
Maxilla, 126f, 851f
nondental diseases of, 220–223
Maxillary dental arcade, 126f
Maxillary/mandibular incisor disease, 219–220, 225f
Maxillary teeth, canine, 112f
Maximum intensity projection (MIP) reformatted transverse computed tomography (CT) angiogram, of cranial abdomen, 812f
Maximum permissible dose (MPD), 6
Mechanical index (MI), 85–86
Mechanical obstruction, of small bowel, 966–973, 967f–971f, 974f
Medial coronoid process, 407, 411f
fragmented, 368, 369f
Medial displacement, 388f
Medial epicondylitis in cats, 416, 417f
Medial fabella, 410f
Medial femorotibial joint, 428, 433
Medial humeral trochlea, osteochondrosis of, 367f
Medial luxation, 410f
Medial soft tissue injuries, 461–463, 462f–463f
Medial tibial malleolus, 462f–463f
Mediastinal cyst, 667, 670f
Mediastinal lymph nodes, 672–673, 679b
Mediastinal masses, 664–673, 668t–670t
caudoventral, 672, 678f
cranioventral, 665–669, 668f–673f
dorsal, 669, 674f–675f
hilar-region, 669–672, 675f–677f
lung mass *versus*, 673, 680f–681f
Mediastinal organs, 663t
Mediastinal pleura, 662
Mediastinal reflection
caudoventral, 662–663, 666f–667f
cranioventral, 662, 666f
Mediastinal serous cavity mesothelioma, 672, 679f
Mediastinal shift, 663–664, 667f
Mediastinum, 662–685
normal anatomy of, 662–663, 663f–667f
Medical digital image, 23
Medical-grade monochrome LCD monitor, 29
Medical imaging, 22

Mediolateral radiography
of antebrachium, 324f
of carpus, 325f
of crus, 331f
of elbow joint, 322f, 335f
of femur, 329f
of humerus, 321f
of manus, 327f
of pes, 334f
of shoulder joint, 320f, 334f
of stifle joint, 330f
of tarsus, 332f
Megacolon, 990, 994f
Megaesophagus, 616f, 619
Megahertz (MHz), 40
Melanomas, 230, 242f
Membranous urethra, 874
Meninges, 279
Meningioma, 69f, 195–197, 299–300, 301f
Meningiti, 307
Meningitis of unknown etiology (MUE), 194
Meningoencephalitis, 194
Meningomyelitis, 307, 308f
Meniscal ligament damage, 434–435, 440f–442f
Meniscal ossicle, 412, 413f
Meniscotibial ligament damage, 434–435, 440f–442f
Meniscus sign, 989, 992f, 995f
Mesaticephalic breeds, 165
Mesenteric root, 778
Mesenteric volvulus, 974–975
Mesentery, 778
Mesocestoides species, in peritoneal masses, 784
Metabolic anomalies, 167–168, 168f
Metacarpophalangeal and metatarsophalangeal articulation
alternative imaging modalities for, 513–514, 514f–517f
anatomy of, 511
degenerative joint disease of, 515–517, 519f
diseases of, radiographic interpretation of, 514–527
radiographic examination, 511–513, 512f
Metacarpophalangeal (MCP) joint, 339f, 513f, 518f–520f, 522f
Metacarpophalangeal sesamoid, 407f
Metacarpus, 489–510
lateral radiographs, 355f
radiographic anatomy and common variants of, 489–493
Metadata tags, 22
Metallic foreign body, 554
Metaphysis diseases, 376–378
hypertrophic osteodystrophy, 376, 377f
multiple cartilaginous exostosis, 376–378, 377f
osteochondroma, 376–378
osteochondromatosis, 376–378
retained cartilage core, 378, 378f
Metastatic bone tumors, 359–360, 360f
Metastatic carcinoma, 830
Metastatic disease, in liver, 816–817
Metastatic neoplasia, 730
Metastatic round cell tumor, 360f
Metastatic tumors, 206–207, 209f
Metatarsophalangeal (MTP) joint, 516f, 521f, 526f
Metatarsophalangeal sesamoid, 407f
Metatarsus, 489–510
radiographic anatomy and common variants of, 489–493
Microbubbles, 84–85, 86t
CEUS, 962
Microcardia, 703–706
Microchips, 73
Microcholelithiasis accumulation, 821
Microhepatia, 808
Microvascular imaging, 46, 46f
Mid-diaphyseal spiral fracture, 388f
Middle carpal joint, 470, 484–485
osteoarthritis in, 477
Middle cervical vertebrae, 121f
Middle ear cholesteatoma, 177
Middle phalanx, 530, 533f, 544, 552f, 559
acute subchondral bone injury of, 538, 538f
fracture of, 534–535, 535f–536f
Middle region of head, 116f–118f
Midventral aspect, 767f
Mild pneumothorax, 696, 696f
Mild uterine distension, 912f
Milliampere-second (mAs), 14, 30
film blackness and, 14
focal spot-film distance and, 17
high-contrast radiographs and, 20
Mineral calculus, 867–868
Mineral ions, in serum, 384
Mineralization
in abdominal wall, 787–788
in adrenal glands, 797, 798f
articular soft tissue, 401–402
of endometrial wall, 912
of fetal structures, 900t–901t
in lung, 731t
in situ, 257
Mineral opacity lesions, 728
Minimally displaced fractures, 456–459
Mirror-image artifacts, 49, 49f
Missile disc, 283–284
Mitral valve dysplasia, 721.e6–721.e6
Mitral valve stenosis, 721.e6–721.e6
Modality worklist, 36
Modified Triadan system, 141, 142f
Monitor quality, 29
Monoarticular fracture, of palmar process of middle phalanx, 552f
Monoarticular sagittal fracture, 533, 534f
Monochrome monitor, 29
Monomers *vs.* dimers, iodine-based contrast media, 79
Moth-eaten lysis, 352–354
Motion, 17
Brownian, 72
Motion mode (M-mode), 41f, 42
Motor disturbance, of diaphragm, 658–659, 660f
Mucocele formation, 820–821
Mucometra, 910
Mucopolysaccharidoses, 167
Mucopolysaccharidosis, 263, 263f, 372–373, 373f
in Alaskan malamute, 373f
Mucosal changes, of urinary bladder, in contrast cystography, 866–867, 867f–868f
Mucus granules, 820–821
Multidetector (multislice) CT scanning, 61f
Multifocal lesion, 727
Multilobular osteochondrosarcoma, 172, 172f–173f
Multinodular pulmonary fibrosis, 753, 753f
Multiplanar reformatting (MPR), 57–58
with computed tomography, 59f
Multiple air bronchogram, 583f, 755f
Multiple cartilaginous exostosis, 376–378, 377f
Multiple epiphyseal dysplasia, 373
Multiple hemivertebra, 248f
Multiple myeloma, 262f
Mummification and ectopic pregnancy, 906, 907f
Mural abnormalities, of large bowel, 990–995
diffuse wall thickening, 992–993
focal wall thickening, 990–992
large intestinal perforation, 995
opacity changes, 993–995
Mural changes, of urinary bladder, in ultrasonography, 871–874
Mural hemorrhage, 873
Mural tracheal masses, 598–599
Muscular dystrophy, 659
Mycotic osteomyelitis, 362f
Myelitis, 307
Myelographic effect, 285–286
Myelographic lesions, classification of, 268f
Myelography, 260, 263–269, 280
arachnoid diverticula, 267–268, 274f
indications for, 263
interpretive principles, 264–266, 264f–268f, 268t, 269f
intervertebral disc herniation, 266–267, 269b, 270f–273f
neoplasia, 269, 275f–276f
synovial cysts, 269, 274f
technique, 263–264, 264f
Myelolipomas, 830, 831f
Myelomalacia, 303, 303f
Myxomatous mitral valve disease, 716
Myxomatous tricuspid valve disease, 716, 717f

N

Nail foreign body, 558f
Nasal aspergillosis, 173–174, 173f–174f
Nasal cavity, 111f
Nasal cavity/paranasal sinuses disease, 217
cysts, 217, 219f
neoplasia, 217–219, 221f–222f
polyps, 219, 222f–223f
progressive ethmoid hematoma, 217, 220f–221f
radiographic projections, 217, 218f
sinusitis, 217, 218f
Nasal foreign bodies, 175
Nasal passages, 165–166, 165f
Nasal tumors, 168–170, 169f–171f, 206f, 207–209
Nasopharyngeal stenosis, 597, 598f
Navicular bone fracture, 550–551, 551f
Navicular bursitis, 565
Navicular syndrome, 556–557, 558f–559f
Near field, 42
Neck pain, radiography of, 602f
Necrotic nonunion fracture, 393
Necrotizing bronchiolitis, 739f
Necrotizing leucoencephalitis (NLE), 194
Negative contrast media, 76, 77f, 83
Negative contrast study, of stomach, 927
Neonatal infectious polyarthritis, 460, 460f
Neoplasia, 720, 721f, 754–755, 918–919
of equine foot, 549
guttural pouch, 224–225
myelographic patterns, 269, 275f–276f
nasal cavity/paranasal sinuses disease, 217–219, 221f–222f
in pancreas, 794–795, 794f
in urinary bladder, 873–874, 873f
vertebral, 260–261, 262f
Neoplasm, esophageal, 624–625
Neoplastic abnormalities, 168–173
cranium, tumors of, 172–173
mandibular and maxillary tumors, 170–172, 171f–172f
multilobular osteochondrosarcoma, 172, 172f–173f
nasal tumors, 168–170, 169f–171f
Neoplastic bone lesions, 360
Neoplastic brain disease, 228, 239f
Neoplastic disorders, 152–153, 156f–158f
Neospora, 194–195
Neospora caninu, 307
Nephroblastoma, 300–301, 302f, 848f
Nephrogenic systemic fibrosis, 84
Nerve root compression, 248–249, 258
Nerve sheath tumor, 203–204
Net magnetization, 65
Neutral lateral radiograph, 415f
New bone formation, 535–537
Newer flat-panel detectors, 26–27
Nocardia, 307
Nodular lymphoid hyperplasia, 830
Nodules, 728
Noise, in image, 33, 34f
Nonaggressive lesion, *vs.* aggressive, 348–363, 353t
Nonarticular fracture, 551
Nonbridging callus, 392
Noncomminuted fracture, 552f
Noncompressive hydrated nucleus pulposus extrusion, 289–290, 290f
Noncompressive intervertebral disc extrusion, 289, 290f
Noncompressive nucleus pulposus extrusion, 283–284
Noncontrast CT, 291–292, 300
Nondental diseases, mandible and maxilla, 220–223
bone cysts, 220–221, 229f
fibro-osseous lesions of craniofacial complex, 221, 230f
fractures, 223, 232f
nondentigerous neoplasia, 221, 229f
suture exostosis, 221–222, 231f
temporomandibular joint abnormalities, 222–223, 231f–232f
Nonobstructing foreign bodies, 964–965, 965f
Nonunion fracture, 392
Nonviable nonunion fracture, 393, 394f
Nuchal ligament, 246
Nuclear Regulatory Commission (NRC), 6
Nuclear scintigraphy, 457–459
fetlock joint, 513
Nucleus pulposus, 281f, 282–284, 289–290, 290f–291f, 296, 304
Nutritional secondary hyperparathyroidism, 263, 263f, 379, 379f

O

Obesity, 593f
Oblique fracture, 386
of lateral wing of distal phalanx, 553f
Oblique radiography, 129f
of dentigerous cyst, 237f
of supraorbital process fracture, 241f
Oblique view, 126
of abdomen, 864f
Oblique xeroradiograph palmaroproximal-palmarodistal, of left equine foredigit, 343f
Occipital bone malformation, 166–167
Occipital dysplasia, 166, 167f
Occipital protuberance, 166f
Occipital region, 120f
Occlusal films, 137
Occlusive infarcts, 209–210, 210f–212f
Occupational radiation exposure, 10
Ocular chondrodysplasia, of Labrador retrievers, 375t
Odontogenic tumors, 220, 227f
Odontoma, 56f
Oligotrophic nonunion fractures, 392–393, 393f–394f
Opacity
of film, 16–17
of subchondral bone, 401–402, 561f
Opaque callus, 379
Opaque foreign bodies, 969f
Open-mouth
left 20-degree ventral-right dorsal projection, 126f
rostrocaudal view, 125f
V20°R-DCdO, 129f
Optimization, of contrast, 29–34, 31f–32f
Oral fibrosarcoma, 170–172
Oral phase dysphagia, 616–617
Orchitis, 915
Orthogonal radiographs, 95
Orthogonal tarsal image, 454f
Orthopedic diseases
in small animals by skeletal distribution and patient demographics, 364t
of young and growing dogs and cats, 365–383
Oslerus (Filaroides) osleri granulomas, 598–599
Osmolality, of iodine-based contrast media, 79
Osseous cyst-like lesions, 520, 523f, 532, 532f, 548–549, 549f–550f, 560f
Osseous cysts, 548–549
Osseous metaplasia, 541
Osseous neoplasia, 541
Osseous structures, 544–545, 545f–547f
Osseous subchondral cyst-like lesions, 476, 476f
Ossification, 569–570, 570f
Osteoarthritis, 258–260, 408–412, 411f, 411b, 412f, 412b, 455, 455f–456f, 477–478, 477f–479f, 515, 517, 532, 537–538, 537f
of distal interphalangeal joint, 558–560, 561f
interphalangeal, 560f
Osteoarthrosis, 515
Osteoblast, 384
Osteochondral dysplasia, 375
Osteochondral fragmentation, 479–480, 480f
Osteochondral fragments, 518, 532
Osteochondritis dissecans, 403, 476–477, 518–520, 520f–522f
of tarsus, 450, 451f–452f
Osteochondrodysplasia, of Scottish Fold cats, 375–376, 376f
Osteochondroma, 376–378, 483, 484f, 639–640
Osteochondromatosis, 376–378
Osteochondrosis, 365, 366f, 434f, 476–477, 518–520, 520f–522f, 531–532
in distal interphalangeal joint, 548, 548f
of femoropatellar joint, 430, 432f–434f
of lateral trochlea, 365
medial humeral trochlea, 367f
of metacarpal III, 522f
radiographic signs of, 365
of shoulder, 366f
of tarsus, 450, 451f–452f
Osteochondrosis dissecans, 365, 366f–367f
Osteoclasts, 384
Osteocyte, 384
Osteodystrophy, hypertrophic, 376, 377f
Osteolysis, 477–478
Osteomyelitis, 396, 398f, 444, 446f, 459–461, 461f, 478, 513, 523f, 535, 536f, 554, 557f–558f
fungal, 360–361, 362f
Osteopenia, 263, 263f, 635–636
Osteopetrosis, 379, 379f
Osteophytes, 259f, 263, 403, 403f, 477–478
Osteophytosis, 288
Osteosarcoma, 358–359, 359f, 549
extraskeletal, 275f
Otitis, 175–177, 176f–177f
Otitis externa, 200f
Otitis interna, 195, 202f

Otitis media, 195, 202f
Ovarian cysts, 908, 908f
Ovarian masses, 908–909
Ovarian neoplasia, 908
Ovarian remnant syndrome, 908
Ovarian stump granuloma, 910f
Ovarian tumors, 908
Ovaries, 894–922
  disease of, 908–909
    abnormal radiographic and ultrasonographic findings in, 908–909
Overexposure, of digital radiographs, 33–34, 35f

P

Pair production, 14
Palatal dysfunction, 225, 235f
Palmar (plantar) eminences fracture, 533f, 535, 535f
Palmaromedial-dorsolateral oblique radiography, of canine manus, 327f
Palmaroproximal-palmarodistal oblique xeroradiography, of left equine foredigit, 343f
Palmar/plantar subluxation, 538
Palmar processes, of distal phalanx, 547f
Palmar process fracture, of foals, 553, 555f
Pancreas, 790–795
  anatomy of, 790
  computed tomography and magnetic resonance tomography of, 792
  cystic lesions of, 795, 796f
  disease of, 792–795
    inflammation of the pancreas (pancreatitis), 792–794, 792b, 793f, 793b, 794f
    neoplasia, 794–795, 794f
  radiography of, 790, 792f
  scintigraphy of, 792
  ultrasound of, 790–792, 792f
Pancreatic abscess, 794f
Pancreatitis, 792–794, 792b, 793f, 793b, 794f, 821
Panosteitis, 378–379, 378f
Paraesophageal hernias, 620
Paraesophageal hiatal hernia, 656
Parallel imaging, 72
Paranasal sinus cysts, 217, 219f
Paranasal sinuses, 165
Paraplegia, 288
Paraprostatic cysts, 885, 886f
Parathyroid hormone, 384
Paravertebral soft tissue tumors, 297–298
Parenchyma, 724
Parenchymal lesions, 733
Parietal peritoneum, 778
Partial agenesis, 380
Parturition date, estimation of, 900
Pasteurella, 307
Patella, 406, 408f, 410f, 428, 435f
Patellar fractures, 437–442, 444f
Patellar fragmentation, 430, 435f
Patent ductus arteriosus, 713f
Pathologic fracture, 379
Pathologic mediastinal conditions, 663–675
Patient hit by car, 255f
Pattern recognition, 100–102, 101f–102f, 105–106, 106f
Pectus carinatum, 633–634, 634f
Pectus excavatum, 633–634, 634f–635f
Pedal osteitis, 553–554, 556f
Pelvic limb monoparesis, 275f
Pelvis, 863f
Penetrating abdominal wounds, 784–785
Penetrating solar injury, 571, 571f
Penile urethra, 874
Percutaneous endoscopic gastrostomy (PEG) tube, 951f
Perforation, of esophagus, 625–627
Perfusion-weighted imaging, 72
Periapical inflammatory lesions, 146
Periarticular connective tissue, 296
Periarticular soft tissue, 402f
  dystrophic calcification of, 514–515
Pericardial effusion, 719–720, 720f
Perichondral bone opacity, 402–403, 403f
Perineal hernia, 990, 994f
Periodontal disease, 142–143, 145f
Periosteal proliferative form, 421, 421f
Periosteal reaction in aggressive bone lesions, 354, 356f–357f, 360f
Periosteum layers, 356f
Peripheral nerve sheath tumors, 298–299, 299f–300f
Perirenal fluid, 846, 847f–848f
Peristalsis, primary, 618–619
Peritarsal soft tissue injuries, 461–467
Peritendinous-periligamentous inflammation, 463
Peritoneal cavity, 778
Peritoneal effusion, 780–782, 780b, 782f, 786f
Peritoneal fluid, 695, 780, 780f–782f
Peritoneal gas, 780–781, 781f, 784–785, 786f
Peritoneal masses, 784
Peritoneal metastasis, 783–784, 783f
Peritoneopericardial diaphragmatic hernia (PPDH), 633–634, 653, 655f, 655b, 656f, 934, 935f–936f
Peritoneopleural hernias, 657–658, 659f
Peritoneum, 778–804
  abdominal surface visualization
    decreased, 780–784, 780b
    increased, 784–786
  anatomy of, 778–779, 778f
  computed tomography of, 780
  peritoneal and retroperitoneal disease, 780–787
    peritoneal masses, 784
    peritoneal metastasis and steatitis, 783–784, 783f
    retroperitoneal fluid, 784, 784f
    retroperitoneal masses, 784
  radiography of, 779, 779f
  ultrasound of, 779–780
Peritonitis, 201f, 781
Permanent lateral patellar luxation, 435f
Persistent right aortic arch, 623f
  fourth, 622–623, 623f
Personal shielding, 7
Personnel monitoring, of radiation, 8–10
Pes, 333f–334f
  radiography of
Phalangeal fractures, 550–553, 552f
  distal phalanx, 551–553
  navicular bone, 550–551, 551f
Pharyngeal collapse, 597, 598f
Pharyngeal constriction ratio (PCR), 613–614, 614f
Pharyngeal dysphagia, 616–618
Pharyngeal phase, of swallowing, 618f
Pharyngitis, 597
Pharyngolarynx, 594–597
  brachycephalic syndrome of, 595–596, 596f, 596b, 597f
  epiglottic retroversion of, 596–597, 597f
  laryngitis of, 597
  masses of, 594–595, 594f, 594b, 595f, 604
  nasopharyngeal stenosis of, 597, 598f
  pharyngeal collapse, 597, 598f
  pharyngitis of, 597
  radiographic technique of, 592–593
  trauma to, 595, 596f
Pharynx, larynx, and trachea, 592–607
  anatomy of, 592, 592f
  computed tomography of, 604
  lateral radiography of, 592f
  magnetic resonance imaging of, 604
  radiographic technique of, 592–593
    pharyngolarynx, 592–593
    trachea, 593, 593f
  ultrasound of, 603–604
  upper airway obstruction of, 603
Photodisintegration, 14
Photoelectric absorption, 15, 21
Photoelectric effect, 14–15
Photographic film, 16
Photon, 3, 14
  scattering of, 17–18
Photostimulable phosphor plate, 24–26, 25f
Photostimulable plates (PSPs), 137, 139f
Phrenicopericardial ligament, 662–663
Physeal dysplasia, 473
Physeal fractures, 534
Physical examination, 384
Physis diseases, 373–376
  chondrodysplasia, 375, 375t
  incomplete ossification of humeral condyle, 374–375, 374f
  osteochondral dysplasia, 375
  osteochondrodysplasia of Scottish Fold cats, 375–376, 376f
  rickets, 375, 375f
  spontaneous capital physeal fracture of cats, 373–374, 374f
Physitis, 473, 474f
Picture Archiving and Communication System (PACS), 36
  rudimentary system for, 36f
Picture elements, 56–57
Piezoelectric crystal, 41
Pituitary-dependent hyperadrenocorticism, 200–201, 799f
Pituitary tumors, 200–201, 204f
Pixels, 22–23, 23f, 56–57
Planck's constant, 3
Planes, of magnetic resonance imaging, 57–58, 59f
Plantar fasciitis, 463
Plantaroproximal/plantarodistal views, 358f
Plantar soft tissue injuries, 463–466
Plant foreign bodies, 912, 913f
Pleural and mediastinal fluid, confounding effects of, 673, 681f
Pleural disease, 756–757
Pleural effusion, 642f, 644f, 718, 808f
Pleural fluid, 687–695, 754, 756–757
  cause of, 687, 688t–690t
  compartmentalization of, 756
  diagnosis of, 692–695, 694f
  distribution of, 690, 694f
  free, roentgen signs of, 690b
  horizontal-beam radiography for, 690–692, 694f, 698
  interlobar fissures with, 687–688
  lung retraction with, 688–689, 693f
  presence of, 756
  radiographic appearance of, 687
  retrosternal soft tissue opacity, 689
  silhouette sign, 689
  simultaneous, 695
Pleural masses, 699, 701f
Pleural neoplasia, 699
Pleural nodules, 699
Pleural space, 686–701
  anatomy of, 686
  pleural fluid in, 687–695
  pneumothorax in, 695–698
  radiographic appearance of, 686–687, 687f
Pleural thickening, 686–687, 699
Pleuritis, 699
Pneumatosis coli, 979, 993–995, 996f
Pneumatosis intestinalis, 979
Pneumocolonography, 987
Pneumocystis carinii, 756
Pneumogastrography, of stomach, 927
Pneumomediastinum, 673–675, 682f–684f, 758, 758f
Pneumonia, 750–753
Pneumoperitoneum, 784–785, 785f–786f, 911
Pneumoretroperitoneum, 674, 684f, 786, 787f
Pneumothorax, 674, 695–698, 757, 757f
  causes of, 695, 695b
  diagnosis of, 698, 700f
  "elevation" of heart from sternum, 696, 698f
  lung retraction from, 696
  radiographic appearance of, 695
  radiographic signs of, 696b
  tension, 696–698, 699f–700f
Podotrochlear apparatus, 564–565
Polyarthropathy, 402f
Polymelia, 380–381, 381f
Polyostotic aggressive bone lesions, 360–361, 362f
Polypoid cystitis, 872–873
Polyps, 945
Porencephaly, 191
Portal hypertension, esophageal varices and, 627, 628f
Portal veins, 812, 813f
Portography, for portosystemic shunts, 810–811
Portosystemic shunts, 810–811, 812f, 823f
Positioning
  appendicular skeleton radiography and, 348
  thoracic radiographic examination and, 578–580
Position of lesion, 728
Positive-contrast arthrogram, of villonodular synovitis, 518f
Positive-contrast cystography, 863–864, 865t, 868, 870f, 872f
Positive contrast enema, 987–988
Positive contrast gastrography
  with barium sulfate suspension, 928b
  findings of, 928–930
  of stomach, 927–930
  technique for, 927–928, 929f
Positive contrast media, 76, 76f
Positive-contrast peritoneogram, 651f
Positive urethro-vaginography, 914
Positron emission tomography (PET), fetlock joint, 514, 517f
Post contrast transverse magnetic resonance (MR) T1-weighted image, 200f
Postcontrast T1-weighted magnetic resonance (MR) image, 213f
Postoperative stomach, 948–950, 950f–951f
Postprocessing, in digital radiographic imaging, 28, 34–35, 35f
Power Doppler, 45–46
Precessional frequency, 71–72
Precontrast T1-weighted magnetic resonance (MR) image, 213f
Pregnancy, 896–900, 899f–900f
  abnormal radiographic and ultrasonographic findings during, 900–907, 901t–905t, 906f
  lateral abdominal radiography during, 900f
Pregnant women, 6
Premature closure and satisfaction, 106, 106f
Premature distal ulnar physeal closure, 397f
Preprocessing, in digital radiographic imaging, 28
Primary bone healing, 389
Primary bone tumors, 358–360, 359f–360f
Primary cardiac disease, 703–706
Primary de novo peritoneal neoplasia, 784
Primary gastric neoplasia, 945
Primary lung tumors, 739–741
Primary metastatic sternebral tumors, 640
Primary peristalsis, 618–619
Primary pulmonary histiocytic sarcoma, 729f
Primary rib tumors, 639
Primary secretory otitis media (PSOM), 175
Primary sinusitis, 217
Primary tumors, 206–207, 206f–208f
Processing, in digital radiographic imaging, 28
Progressive degenerative joint disease, 373
Progressive ethmoid hematoma (PEH), 217, 220f–221f
Progressive inspiratory noise, 595f
Pronounced left atrial dilation, 707f
Prostate gland, 884–893
  anatomy of, 884
  computed tomography of, 891, 892f
  disease of, 884–892
    clinical signs of, 885
    radiographic changes in, 885–887, 886f
  enlargement of, 885f, 887f–888f
  evaluating, 889–891
  magnetic resonance imaging of, 891, 892f
  special radiographic procedures for, 887–889
  ultrasonography for, 889–891, 889f–891f
Prostatic abscess, 885
Prostatic carcinoma, 863f
Prostatic tumors, 885
Prostatic urethra, 874
  small filling defect in, 888f
Prostatitis, 885, 890f–891f
Protein-losing enteropathy (PLE), 978
Proton-density weighted magnetic resonance (MR), 571f
Proton-density (PD) weighting, 66, 68f, 193f
Protons, magnetic resonance imaging and, 64, 65f
Prototheca wickerhamii, 307
Prototheca zopfii, 307
Protozoan bone infection, 361
Protrusion, 254–255
Proximal epiphysis, 523f
Proximal fibular epiphysis, 380f
Proximal humerus, cranioproximal/craniodistal view of, 349f
Proximal interphalangeal joint, 560f–562f
  hyperextension of, 539
    cutaneous neoplasms, 540, 540f
    dystrophic mineralization/osseous metaplasia, 541
    hypertrophic osteopathy, 539–540
    osseous neoplasia, 541
    soft tissue pathology, 539, 540f
  indications for radiography, 530
  osseous pathology, 532–537
    bone marrow lesions, 537, 537f
    fractures, 532–535
    new bone formation, 535–537
    osseous cyst-like lesions, 532, 532f
    osteochondrosis/osteochondral fragments, 532
    osteomyelitis, 535, 536f

Proximal interphalangeal joint (*Continued*)
osteoarthritis, 537–538, 537f
overview, 530
septic arthritis, 538, 539f
subchondral bone trauma, 538, 538f
subluxation/luxation, 535f, 538–539
Proximal intertarsal joints, 449, 455–456
Proximal metatarsus, 490f
Proximal phalanx, 514f, 527f, 530, 533f, 546–548, 552f, 563f, 569
dorsopalmar view, 534f
fractures of, 532–534, 534f
lateromedial view of, 531f
nutrient foramen of, 531, 531f
Proximal sesamoid fractures, 525–527, 526f
Proximal superficial digital flexor tendonitis, 463, 464f
Proximal tiba, lateral view of, 362f
Proximal tibial osteotomy, 391f
Pseudoairway, 600
Pseudofilling defects, 869–870, 872f
Pseudolayering, of stomach wall, 945–946
Pseudoobstruction, 975
Pseudoulcers, 958, 958f, 963
PSPs. *See* Photostimulable plates (PSPs)
Puerperium, 907–908
Pulmonary abscess, 752
Pulmonary alveolar microlithiasis, 730
Pulmonary artery, 710–711, 712f
Pulmonary blood vessels, 751f
Pulmonary contusions, 741–743, 743f, 754
Pulmonary disease
in foals, 755–756, 755f
radiographic assessment of, 726–737
Pulmonary edema, 715, 741, 741f, 754, 755f
Pulmonary hemorrhage, 743, 744f, 754
Pulmonary hypertension, 718–719, 719f
Pulmonary lymphomatoid granulomatosis, 673
Pulmonary mycoses, 673
Pulmonary nodules, 734f
Pulmonary osteomas, 731f
Pulmonary parenchyma, 733–736
Pulmonary vasculature, 725
alterations in, 755
Pulmonary vessels, thoracic radiography of, 581
Pulmonic stenosis, 721.e4–721.e4
Pulsed-wave Doppler, 44, 45f
Pulse echo principle, 42
Pulse repetition frequency (PRF), 41, 52
Pyelogram phase, 856f
Pyelonephritis, 849–850, 850f
Pylorogastric intussusception, 934–936, 937f
Pyoceles, 915
Pyogranulomatous lesions, 978–979
Pyonephrosis, 849–850
Pyothorax, 690
Pythiosis, 978–979

Q

Quality factor, 4
Quantum mottle, 33
Quittor, 570

R

Radial carpal bone, 476f–477f, 479–480, 480f
Radiation
equivalent in man, 6
interaction of matter with, 14–15
pregnant women, limit for, 6
units for, 4–6, 5t
Radiation dosimetry badge, 8–10
Radiation-induced cancer, 6
Radiation-induced cataract, 6
Radiation protection, 4–10
Radiation safety, 6–7, 126
poor practices, 9f
rules for, 10
Radiation supervisor, 8
Radiation therapy, 6
Radiative interaction, 10–11
Radiative model of x-ray production, 12f
Radiofrequency energy, in magnetic resonance imaging, 64
Radiofrequency (RF) pulses, 66, 68f
Radiograph, 90
abnormalities, 95
degree of blackness or whiteness in, 90t
naming and viewing, 91–92, 92f
Radiographic contrast, 93–94, 94f–96f
Radiographic contrast media, 76
Radiographic density, 90
Radiographic geometry, 95–98, 96f–99f
Radiographic interpretation, 90–91, 91f
errors, 103–107
Radiographic opacities, 92–93, 93f, 93t, 94f
Radiography
of abdominal lymph nodes, 788
of antebrachiocarpal joint osteoarthritis, 477f
of brachycephalic syndrome, 598f
of cervical mass, 594f
of chronic partial ileal obstruction, 968f
of coughing, 600f–601f
of dyspnea, 594f
of extremity, 348
of foot, 569f
fracture evaluation, 384, 385f
of inspiratory difficulty, 595f
of interphalangeal osteoarthritis, 560f
of joint, 409t
of large bowel, 986–987, 986f–987f
lateral
of dog antebrachium, 356f, 363f
of dog distal humerus, 357f
of dog femur, 354f, 356f, 358f
of dog humerus, 355f, 357f
of horse metacarpus, 355f
of metastatic round cell tumor, 360, 360f
of neck pain, 602f
of pancreas, 790, 792f
of pelvic, 362f
of peritoneal gas, 784–785, 785f–786f
of peritoneum, 779, 779f
of pharyngeal collapse, 598f
post gastrostomy tube placement, 951f
of seizure, 601f
of small bowel, 956–959, 956f–957f, 957t
of stifle, 436f
of stomach, 923–926
findings of, 924–926, 924f–927f, 927t
indications for, 923–924
technique for, 924
of submandibular mass, 594f
techniques for, 19–21
of temporohyoid osteoarthropathy, 237f
of thoracic, 362f
of uterus, 894–895
vertebral column, inflammatory conditions of, 262t
Radiolucency, 394–396, 396f–398f, 477–478, 531f
in liver, 811f
Radiolucent foreign bodies, 969f
Radiolucent lines, 555f, 569–570
Radiolucent squeeze cage, 612f
Radiopacity of cystic calculi, 865t
Radiopaque urethral calculi, 877
Radio wave, 40
Radon's mathematic principles, 58
Rads, 6
Range ambiguity, 52
Rarefaction, 40
Rebound thymic hyperplasia, 668–669
Receiving coils, 66
Recoil electron, 15
Reconstruction filter, 60–61
Rectum, 986, 986f
displacement of, 991f
Recurrent airway obstruction, 753–754
Recurrent hemarthrosis, 407
Recurrent prostatitis, chronic, 885
Recurvatum fracture, 395f
Redundant array of independent disk (RAID), 37
Redundant esophagus, 620
Reflection, of sound beam, 40
Refraction, 51
Region of interest (ROI), 60–61, 613–614
Relaxation, in magnetic resonance imaging, 65–66
T1, 66f
T2, 67f, 72f
Remodeling phase, 390
Renal abscess, 846
Renal carcinoma, 844f, 848f
Renal cysts, 846, 847f
Renal diseases, 841–851
Renal enlargement, 844f
Renal failure, 851f
Renal function, 851, 851f
Renal lymphoma, 846–849, 848f
Renal mass lesions, 846–849
Renal mineralization, 845–846, 846f
Renal pelvis, 849–850
Renal shape, 844t
Renal size, 841–844, 844t
Renal structure, 844–849
Renomegaly, 842–843
Reparative phase, 389
Resolution, 41
axial, 41
lateral, 41
Resonance, 65
Resorptive atelectasis, 732, 733f
Restrictive and unclassified cardiomyopathies, 718
Retained cartilage core, 378, 378f
Retained testicles, 918, 919f
Reticuloperitonitis, 767f
Retrograde positive-contrast cystography, 863–864, 868
Retrograde urethrography, 876f
Retrograde vaginography, 894
Retroperitoneal, definition of, 778–779
Retroperitoneal fluid, 780, 784, 784f
Retroperitoneal gas, 786, 787f
Retroperitoneal hemorrhage, 784f
Retroperitoneal masses, 784
Retroperitoneal space, 778–779, 782f
Retrosternal soft tissue opacity, 689
Reverberation artifacts, 47–48, 48f
Reversible seizure-associated brain edema, 195
Rhabdomyosarcomas, urinary bladder, 874
Rheumatoid arthritis, 419–420, 420f
Rhinitis, 174, 175f
Rhodococcus equi, 752–753
Rib fractures, 635–636, 635f, 755
segmental, 635–636
spontaneous, 635–636
Rib infection, 640
Rib periostitis, 640
Ribs lesions, 639–640
Rib tumors, 639
Rickets, 375, 375f
Rickettsia rickettsii, 307
Right atrium, 709, 709f
Right cranial lung lobe torsion, 741f
Right femur, 362f
Right hemithorax, 687f, 700f
Right lateral intercostal ultrasound, 814f
Right lateral radiography
of abdomen, 769f
of aortic root mineralization, 715, 716f
of bronchial pattern, 754f
of canine lungs, 724f
of caudodorsal thorax, 749f
of chemodectoma, 677f
of costochondral degeneration, 633f
of cranial aspect, 768f
of cranioventral mediastinal masses, 673f
of cranioventral mediastinum, 671f
of dog, 768f
of esophagus, 622f
of extensive costal cartilage mineralization, 633f
of heart base region masses, 676f
of lipoma, 678f
of pleural fluid, 692f
of soft tissue opacity, 632f
of tracheobronchial lymph node enlargement, 675f–676f
Right lateral thoracic radiography
of caudal esophagus, 627f
of diaphragmatic hernias, 652f, 655f–656f
of diaphragmatic region, 647f, 649f
of peritoneopericardial diaphragmatic hernias, 655f–656f
of trachea, 593f
of traumatic diaphragmatic hernia, 654f
Right lateral view
of congenital diaphragmatic hernia, 659f
of traumatic diaphragmatic hernia, 659f
Right-left caudoventral oblique radiograph, 231f
Right-left lateral radiography, 752f–753f
of canine pelvis, 328f
of middle region, 117f
Right-left view, 764
Right middle region, 736f
Right-sided congestive heart failure, 715, 715f
Right-sided heart failure, 716–717
Right temporomandibular joint, 127f
Right thoracic lateral radiography
of cardiac silhouette, 587f
of caudal thorax, 586f
of caudal vena cava, 579f
of nodular opacity, 590f
of nodule in left lung, 583f
in small animals, 580, 581f–584f
of thorax, 585f–586f
Right tympanic bulla, 127f
Right ventricle, 709
Ring-down artifacts, 49
Rodenticide toxicity, 782f
Roentgen sign, 95, 96b, 110, 690b
of small bowel, 957b
Roentgen, Wilhelm Conrad, 5
Room air, 864–865
Rostral aspect, 131f, 225f–226f, 229f, 231f
Rostral 10-degree ventral-caudodorsal view, 128f
Rostral right/left ventral dorsal oblique radiograph, 112f
Rostrocaudal frontal sinus view, 125f
Rostrodorsal-caudodorsal oblique (RD-CdVO) radiograph, 111f, 119f
Rounded atelectasis, 699
Rudimentary rib, 633–634
Rugae, 923
Rugal folds, 923
Ruptured bicipital tendon, 415, 416f
Ruptured pyometra, 912f

S

Sacrocaudal disc herniation, 288
Sacrocaudal trauma, 260
Sacrum, 245
Safety pin obstruction, 622f
Sagittal computed tomography, 250f, 848f
of esophageal varices, 628f
of temporohyoid osteoarthropathy, 237f
Sagittal reformatted computed tomography (CT) imaging, of nasopharyngeal stenosis, 597, 598f
Sagittal T2-weighted image
of cervical spondylomyelopathy, 252f
of occipital-cervical junction, 190f
Sagittal ultrasound image, 872f–874f
Salter-Harris classification system, 384–385, 386b
Salter-Harris physeal fracture classification, 387f
Salter-Harris type I fracture, 385–386, 386b, 387f
Salter-Harris type II fracture, 385–386, 386b, 387f
Salter Harris type II fracture, 534
Salter-Harris type III fracture, 386b
Salter-Harris type IV fracture, 385f, 386b
Salter-Harris type V fracture, 386b
Scapular tumor, ventrodorsal radiography of, 35f
Scapulohumeral joint, 404f–405f
Scatter-correction software algorithm, 31f
Scattered radiation, 7
Scattering, 40
coherent, 14
of photons, 17–18
Scatter removal, by grid, 31f
Schistosomiasis, 977
Scintigraphy, 841
of pancreas, 792
of stomach, 931
Sclerosis, 482–483
of navicular bone spongiosa, 556
Scottish fold osteochondral dysplasia, 375–376, 376f
Screen capture, 29f
Scrotal testicles, 918
Search error, 104
Secondary fracture healing, 389
Secondary hyperparathyroidism, 851f
Secondary intracranial neoplasia, 207
Secondary sinusitis, 217
Sedation, 125, 128
Segmental rib fractures, 635–636
Seizure, 202f
radiography of, 601f
Septic arthritis, 421–423, 423f, 423b, 424f, 424b, 444, 446f, 459–461, 520, 523f–524f, 538, 539f, 560, 562f
of carpus, 478, 479f
in cats, 423
Septic calcaneal bursitis, 460–461, 461f
Septic osteitis, 554, 557f–558f
Septic osteomyelitis, 461, 462f
Septic (infective) pedal osteitis, 554
Septic physitis, 460, 460f, 473, 535
Sequences, 66
Sequestrum, 396, 398f
Serosal contrast, 782f
Serosal edges, of small intestine, 957f
Sertoli cell tumors, 918–919, 920f
Sesamoid bone, 405–407
of carpal trauma, 406f
clavicular remnant medial, 405f
of elbow, 406f
feline clavicle, 405f
fracture of, 406f, 512, 512f
fragmentation of, 409f

Sesamoid bone (*Continued*)
iliopubic, 407f
lateral tarsometatarsal, 408f
metacarpophalangeal, 407f
metatarsophalangeal, 407f
proximal, 512f, 527f
Sesamoid disease, 406–407, 409f–410f
Sesamoiditis, 527, 527f
Sessile or polypoid masses, in gallbladder, 819–820
Severe hydronephrosis, 850f
Severe pneumoperitoneum, 938f
Shadow, 40
Sharpey fiber, 258f
Shielding, in diagnostic radiology, 7–8
Short colon syndrome, 995f
Short interarcuate ligament, 246
Short inversion time recovery (STIR) sequence, 67–68, 70f, 71–72
Short scale of contrast, 20
Shoulder, 413–415
bicipital tendon in, 413, 416f
osteochondrosis dissecans of, 366f
osteochondrosis of, 366f
ruptured bicipital tendon, 415, 416f
Shoulder joint, 320f, 334f, 405f
Sidebones, 569–570, 570f
Side lobes, 49–50, 50f
Signal averaging, 58f
Signal reception, 68f
Signal-to-noise ratio (SNR), 72, 74f
Signal void, 74f
Silhouette sign, 689
Sine wave, 3, 3f
Single-shot fast spin echo (SSFSE), 282, 285, 285f
Sinonasal neoplasms, 217–219, 221f–222f
Sinuses, 295–296, 296f
Sinusitis, 217, 218f
65-degree proximal-palmarodistal radiography
of distal phalanx, 553f, 555f–556f
dorsal, of left equine foredigit, 342f
of left equine foredigit, 342f
Skull, 123–128
ancillary factors, 126
interpretation paradigm for, 127–128
lateral radiographs of, 32f
positioning of, 123–124
radiograph, 123f
checklist for interpretation of, 131b
radiographic technique of, 126
Skull and nasal cavities, 165–186
anatomy of, 165–166, 165f
diseases of, 180–181
imaging modalities, 165, 166f
inflammatory and infectious disorders of, 173–179
metabolic anomalies of, 167–168, 168f
neoplastic abnormalities of, 168–173
traumatic injuries of, 179–180, 179f–180f
Skull disease, 381
calvarial hyperostosis syndrome, 381
craniomandibular osteopathy, 381, 381f
Slab fractures, 480, 481f
Slice reconstruction interval, 60–61
Slice thickness artifacts, 50–51, 50f
Sliding esophageal hernia, 620
Sliding hiatal hernia, 656, 656b, 657f, 934, 935f–936f
Small bowel, 956–985
abnormal, 964–982
bowel-associated masses of, 978–979, 981f
computed tomography of, 962
contrast examination of, 962–964, 962f–964f, 964t–968t
diseases of, miscellaneous, 979–982
functional ileus of, 973–975, 975f
infiltrative bowel disease of, 975–978, 976f–980f
mechanical obstruction of, 966–973, 967f–974f
radiography of, 956–959, 957f, 957t
roentgen signs in, 957b
ultrasound of, 959–962, 959f–961f, 961t, 962f
Small kidneys, 838, 841
Small lobar pulmonary arteries and veins, 712
Smooth muscle neoplasia, in urinary bladder, 874
SOAP (subjective, objective, assessment, and plan) method, 100–102
Soft tissue, 392
abnormalities, 483–486
calcification of, 786–787
dystrophic calcification of, 786–787
Soft tissue (*Continued*)
pathology, 539
swelling, 388, 389f, 396
thickening, 389
trauma, 388, 486, 486t
Soft tissue emphysema, 595, 596f
Soft tissue enthesopathy, 561–562, 564f
Soft tissue lesions, 638–639
Soft tissue masses, 638–639, 640f
Soft tissue opacity, 632f
Soft tissue pulmonary nodules, 730f
Soft tissue structures, 546–548, 561, 563f
of vertebral column, 245–246
Solar margin contour, of toe of distal phalanx, 544–545, 546f
Solar margin fracture, 551, 569f
Solid-state detectors, for computed tomography, 59–60, 61f
Solid-state intraoral sensor, 137, 139f
Solitary lesion, 727
Sonographic artifacts, 872f
Sonography of uterine leiomyoma, 913.e1f
Sound, 40
Sound beam, reflection of, 40
Sound frequency, change in, 43
Sound waves, 40
attenuation in, 40
penetration of, depth of, 41–42
piezoelectric crystal and, 41
Spatial compounding, 42
Spatial pulse length (SPL), 41
Spatial resolution, 23, 29–30, 55–56, 72
in cone-beam computed tomography, 64
image matrix and, 58f
inherent, 30t, 30b
schematization of, 57f
Spectral broadening, 44
Spectral tracing, 44
Spina bifida, 249, 249f
Spinal arachnoid diverticula, 294–295, 295f
Spinal cord, 128–136, 279
anatomic relationship of, 264f
atrophy, 292
compression of, 246–251, 252f–253f, 259f, 263–265, 264f, 267, 268f, 291–292, 292f
congenital anomalies of, 307–308
contusion of, 251, 283–284
cystic changes of, 294–296
distention of, 308–309
incidental factors, 135
interpretation paradigm, 135–136
normal appearance of, 279–282
radiography of, 132f
tumors of, 269
Spinal cord disease, 279–317
cervical spondylomyelopathy, 291–294
computed tomography of, 279–280, 281f
cystic changes in, 294–296
inflammatory/infectious conditions, 305–307
intervertebral disc disease, 282–291
intradural and intramedullary disc herniation, 291
ischemic myelopathy, 304, 304f
magnetic resonance imaging of, 280–282, 281f
myelomalacia, 303, 303f
normal anatomy of, 279–282, 280f
spinal tumor, 296–303
syringomyelia, 308–309, 309f
vascular pathology, 304–305, 304f
vertebral anomalies, 307–308, 309f
Spinal cord thromboembolism, 304
Spinal epidural empyema, 306–307, 307f
Spinal hemorrhage, 304–305, 305f
Spinal lymphoma, 276f
Spinal nerve root, 279
Spinal trauma, 305, 305f
Spinal tumor, 296–303
Spine
positioning of, 128–131, 132f
radiographic technique of, 134–135
checklist for interpretation of, 136b
Spin-echo sequences, 66, 68f
configuration of, 68f
selection of, 67–68, 69f–70f
Spins, in magnetic resonance imaging, 65–66
precession of, 65, 65f
Spiral fracture, 391f
Spirocerca lupi, 257, 624–625
Spleen
of canine and feline, 805–836
Spleen (*Continued*)
diffuse neoplastic infiltration of, 827–829, 828f–831f
focal disease of, 829–830
head of, 824
normal, 824f
radiology of, 824–827, 824f
size of, 825–827, 825f–826f
splenic sonographic findings in, 827–831
ultrasound of, 827–831, 828f
Splenic abscesses, 830
Splenic congestion, 827–828
Splenic hemangiosarcoma, 826f, 830f
ruptured, 783f
Splenic hematomas, 829–830, 830f
Splenic mass, 826, 826f–827f, 829f–831f
Splenic neoplasia, 829f
Splenic opacity, 827
Splenic parenchyma, 827
Splenic torsion, 825–826, 826f, 828f
Splenitis, 829
Splenomegaly, 825f
Splenosystemic shunts, 823–824
Split spinous process, 249f
Spoiled gradient recalled (SPGR) echo sequence, 71
Spondylitis, 256f, 257
radiographic signs of, 257f
Spondylosis, 257
Spondylosis deformans, 256f, 257–258, 258f–259f
Spontaneous capital physeal fracture of cats, 373–374, 374f
Spontaneous emphysematous splenitis, 827
Spontaneous epidural hematoma, 305f
Sprain, 413, 415f
Squamous cell carcinoma, 170–172
Staphylococcus, 307
Static tracheal collapse, 602
Steatitis, 783–784
Stenosis, tracheal, 600
Stenting, endotracheal, 603
Sternal lymph node, 666–667, 668f
Sternal lymphocenter, 665–666
Sternal osteomyelitis, 640
Sternal recumbency, 586f
Sternebral tumors, 640
Sternocostal junction, 632
Sternum lesions, 639–640
Steroid hepatopathy, 807f
Steroid responsive meningitis-arteritis (SRMA), 194
Stifle, 404f, 410f, 428–448
advanced imaging of, 429, 432f
caudocranial radiography of, 438f–442f
caudolateral/craniomedial radiography of, 446f
caudolateral/craniomedial view of, 428
conditions involving, 443–444
degenerative joint disease of, 438f
femoropatellar joint diseases of, 430–433
femorotibial joint diseases of, 433–437
fractures involving, 437–443
joint disease of, 417
lateromedial radiographs of, 429f, 432f, 435f, 438f, 440f, 443f
malalignment of, 402f
radiographic examination for, 428, 429f–430f
radiographs of, 436f
supplemental stifle imaging of, 428, 431f
Stifle joint, 330f, 344f–345f
Stochastic effect, 6
Stomach, 41f, 923–955
abnormal gastric content of, 940–942
acute gastric dilation of, 936–939, 938f
anatomy of, 923, 923f
changes in position of, differential diagnosis for, 933t
chronic pyloric obstruction of, 939–940, 941f–942f
computed tomography of, 931, 932f
diffuse diseases of, 947–948, 947f–950f
diseases of, 931–936
displacement of, 931–936
distribution of gas and fluid in, 768f
gastric bleeding of, 944–945
gastric foreign bodies in, 940–942, 943f–944f
gastric neoplasia of, 945–947, 946f
gastric scintigraphy of, 931
gastric ulcers of, 942–944, 945f–946f
gastric ultrasound of, 930
gastric wall changes in, 942–950
gastrography of, 926–927, 927t
imaging procedures for, 923–931
postoperative, 948–950, 951f
Stomach (*Continued*)
radiography of, 923–926
shape and size of, changes in, 936–940
Storage diseases, 192–193
Storage, of images, consolidated, 36–37, 36f
Straight sesamoidean ligament, 563f
Streptococcus equi var equi, 223–224
Stress fracture, 386–388
Stress-induced bone injury, 477
Stress radiography, 415f
Strictures, esophageal, 624–625
Structural shielding, 7
Structured interstitial pattern, 733–734, 734t–742t
Stump pyometra, 912
Subchondral bone, 401–402, 402f, 434f, 560, 561f
Subchondral bone cyst, 436f, 476, 476f, 520, 524f, 548–549
Subchondral bone trauma, 538, 538f
Subchondral cystic lesions, 532–533
Subchondral cyst-like lesion, 433, 436f–438f
Subchondral cyst-like osteochondrosis, 548–549
Subchondral osseous cyst-like lesions, 450, 453f–454f
Subcutaneous emphysema, 388, 635–636, 636f
Subfalcine herniation, 188–189
Subluxation, 288, 481–482, 482f
Subluxation/luxation, 538–539
Submandibular mass, radiography of, 594f
Substantial capital outlay, 22
Subtle hepatomegaly, 808
Subungual infections, 360, 361f
Subungual tumor, 360, 361f
Sulci, of foot, 543f
Summation, 95–96
Superficial digital flexor (SDF), 463
luxations, 463–465
subluxation, 463–465, 465f
Superficial digital flexor tendon, 563f
Superimposition, 96–98
Supplemental stifle imaging, 428, 431f
Supracondylar lysis, 515, 518f
Supraorbital process, 241f
Suprasesamoidean location, 564
Survey abdominal radiographs, 865t
Survey radiographic sign, 256f
Survey radiographs, 837
Suspensory enthesopathy, 527
Sustentaculum tali fragmentation, 461, 462f
Suture exostosis, 221–222, 231f
Swallowing, 608
contrast videofluoroscopic evaluation of, 613f
cricopharyngeal phase of, 618f
fluoroscopy of, study using, 612–613
pharyngeal phase of, 618f
radiolucent squeeze cage for examining phase of, 612f
Swiss cheese appearance, 828–829
Synovial cyst, 253f, 269, 294, 294f
with cervical spondylomyelopathy, 274f
Synovial fistula, 486
Synovial hernia, 486
Synovial inflammation, 401
Synovial joints, 244
Synovial osteochondromas, 418–419, 419f–420f
Synovial sepsis, 459
Synovial volume, 401
Synovitis, 484–485
Synovium, 418–419
Syringomyelia, 166–167, 308–309, 309f
Systemic lupus erythematosus, 420–421
System 1 thinking, 100, 103f
System 2 thinking, 100–102, 103f

T

Tail pull injury, 260
Talar ridge, 449
Talocalcaneal ligaments, 463–465
Tangential view, of sesamoid bone, 512, 512f
Target lesions, 816
Tarlov cysts, 294
Tarsal arthrodesis, with implant failure, 394–396, 396f
Tarsal bones, 449, 450f, 457, 459f
Tarsal luxations, 455–456, 456f
Tarsal sheath tenosynovitis, 465, 466f
Tarsus, 449–469
analog radiography of, 33f
anatomy of, 449

Tarsus (*Continued*)
angular limb deformity, 452
aseptic necrosis, 450–452, 454f
aseptic physitis, 452
degenerative and acquired osseous conditions, 455–461
dorsolateral-plantaromedial oblique radiography of, 333f, 347f
dorsoplantar radiography of, 332f
fractures, 456–459, 457f
joint disease in, 417, 418f
lateral view of, 398f
lateromedial radiography of, 346f, 450f, 453f–457f, 459f–461f, 464f–466f
mediolateral radiography of, 332f
neonatal and juvenile, 449, 460f
osteochondritis dissecans of, 450, 451f–452f
osteochondrosis of, 450, 451f–452f
proximal talar tubercle fragmentation, 450, 453f
radiographic examination of, 449–450, 451b
soft tissue compartments, 449, 449b
soft tissue injuries, 461–467
subchondral osseous cyst-like lesions, 450, 453f–454f
variants and incidental findings, 449, 450f
Teeth, 165
deciduous, 141, 141f
developmental abnormalities of, 154–157, 159f–161f
eruption, 141
resorption, 147–150, 150f–152f
Telemedicine, 38
Teleradiology, 38
Temporal resolution, 59–60
in cone-beam computed tomography, 64
Temporohyoid osteoarthropathy (THO), 227, 236f–237f
Temporomandibular joint (TMJ), 119f, 127f, 165, 166f
abnormalities, 222–223, 231f–232f
45-degree ventral 30-degree lateral-caudodorsolateral oblique radiography, 231f
Temporomandibular joint dysplasia, 167
Tendinopathy, 413–417, 463, 464f, 465–466, 485–486, 563–564, 565f–566f
Tendonitis, 413, 416f
Tenesmus, 996f
Tenosynovitis, 413, 485–486
Tenovaginitis, 465, 466f
Tension pneumothorax, 696–698, 699f–700f
Tenting, 647
Teratoma, 909
Testes, 894–922
abnormal CT findings in, 919–920
abnormal radiographic and ultrasonographic findings in, 915–919
imaging procedures for, 915
longitudinal image of, 916f
Testicular seminoma, 920f
Testicular torsion, 919–920
Tetrahedron, of air bubbles, 49
Tetralogy of Fallot, 721.e6–721.e6
T2-fluid-attenuated inversion recovery (FLAIR) sequence, 190f
T2 gradient echo (GRE) sequences, 68–71, 71f
Third metacarpal (MC III), 515f, 522f
Third metacarpal bone, 489, 489f–490f
Third tarsal dorsal slab fractures, 457, 459f
Thoracic esophagus, radiography of, 621f
Thoracic hemivertebrae, 248f
Thoracic inlet, lateral radiography of, 600f
Thoracic radiography
of accessory lung lobe, 581, 587f
ancillary factors, 582
body habitus, 582, 588f–590f
cutaneous lesions, 584–585, 590f–591f
of cardiac silhouette, 581, 587f
of diaphragm, 581, 586f
of dorsocaudal lung field, 583f
of lungs, 725f
multiple pulmonary nodules, 579f
of pulmonary vessels, 581, 585f–586f
Thoracic spine, 132f
left-right lateral radiography of, 115f
Thoracic spinous process, 132f
Thoracic vertebrae, 115f
lateral radiography of, 32f
ventrodorsal radiography of, 115f
Thoracic wall, 631–645
conformation, 631
congenital abnormalities in, 633–634
developmental abnormalities in, 633–634
mass lesions, 636–640
normal, 631–633
radiographic appearance of, 634f
trauma to, 635–636
Thoracolumbar disc extrusion, 288
Thoracolumbar intervertebral disc disease, 288, 288f
Thoracolumbar region, 134f
Thoracolumbar spine, left-right lateral radiography of, 115f
Thorax, 686f, 746–762
alternative imaging modalities, 749–750, 750f
alveolar pattern in, 736f
cardiac disease, 759
caudal aspect of, 586f, 590f, 757f
caudoventral aspect of, 579f
centered over heart, 759f
checklist for, 585, 591b
computed tomography of, 663f, 665f
cranial aspect of, 758f–759f
esophageal disease, 759
four standard radiographic views of, 746f
horizontal-beam ventrodorsal radiography of, 581f
interpretation paradigm of, 585
lateral radiography of, 626f, 757f, 808f
left thoracic lateral radiography of, 580, 581f–584f
mediastinal disease, 758
nomenclature for, 578
normal anatomy of, 747–749
pleural disease, 756–757
with pleural effusion, 808f
with pleural fissures, 687f
pulmonary disease, 750–756
radiographic interpretation of, 578–591
radiographic technique of, 578, 746–747
right thoracic lateral radiography of, 580, 581f–584f
survey radiography of, 610
tracheal disease, 758
transverse computed tomography of, 132f
Three-dimensional, computed tomography (CT) image, of paracondylar process fracture, 241f
Three-dimensional rendering, 244f–246f
Three-dimensional surface rendering, of MTP joint, 521f
Thromboembolism, 304
Thymus, 668–669
T2-hyperintense intramedullary lesion, 304
T2-hyperintense lesion, 187
T2 hyperintensity, 288
Thyroid, function of, effect of iodine-based contrast media on, 82
Thyrotoxicosis, iodine-induced, 82
Tibia, 362f
Tibial agenesis, 380f
Tibial fractures, 442–443, 444f–445f
Tibial lateral malleolus, 449–450, 451f
Tibial malleolar fractures, 456, 457f–458f
TIFF files, 22
Time gain compensation (TGC), 42, 43f
Time, in diagnostic radiology, 7
Time of echo, 66, 68f
Time to repetition, 66, 68f
Tissue attenuation, 62f
Tissue magnetization, 66–67
Torsion, 918
Torsional fracture, 395f
Tortuous pulmonary vessels, 714
Toxoplasma gondii, 307
Toxoplasmosis, 194–195
Trachea, 593, 597–603
avulsion of, 600, 600f
collapse of, 602–603, 602f–603f
cranial lung lobe herniation, 603, 604f
dorsal wall of, 601f
dorsoventral thoracic radiography of, 593f
foreign bodies in, 599–600, 600f
hypoplasia of, 601, 601f
in lateral projection, 599t
masses of, 597–599, 599f, 599t, 600f
redundant tracheal membrane, 601–602, 601f
right lateral thoracic radiography of, 593f
rupture of, 600, 600f
stenosis of, 600, 600f
stent placement in, 603f
tracheitis in, 601, 601f
Tracheal disease, 758
Tracheal stripe sign, 610–611
Tracheitis, 601, 601f
Tracheobronchial lymph nodes, enlargement of, 669–672, 675f
Tracheobronchial lymphocenter, 669
Tracheoesophageal stripe sign, 610–611
Transabdominal ultrasound, 913
Transducers
footprints of, 41
for ultrasound imaging, 41–42
Transitional vertebrae, 248–249
Transition zone, 349–352, 357f–360f, 736f
of bone lesion, 355–356, 358f
Translational fracture, 395f
Transverse colon, 807–808, 986
Transverse computed tomography
of brain, 165f–167f, 238f
of canine thigh, 90f
of cholesterol granulomas, 240f
of hyperattenuating hematoma, 240f
of incomplete ossification of atlas, 251f
of lumbar vertebra, 244f
of mandibular condyle, 232f
of metacarpophalangeal joint, 521f
nasal passage, 165f
soft tissue sarcoma, 166f
of temporohyoid osteoarthropathy, 237f
of thorax, 132f, 609f
Transverse fluid-attenuated inversion recovery images, 238f
Transverse magnetization, 66
Transverse postcontrast computed tomography (CT), of hepatic neoplasia, 813f
Transverse T1-weighted image, of ahead tilt, 200f
Transverse T2-weighted fluid attenuated inversion recovery (T2-FLAIR) sequence, 191f
Transverse T2-weighted image
of cervical spondylomyelopathy, 252f–253f
of congenital hydrocephalus, 191f
of rostral aspect of cerebellum, 210f
Transverse ultrasonography, 434f
of chronic hepatitis, 818f
of fluid bronchogram, 751f
of left thorax, 752f
of liver, 814f
of lung, 749f
of pleural fluid, 751f
of thorax, 752f
of torsion of right medial liver lobe, 819f
of uniformly echoic mass, 758f
Trauma, 210, 215f
foreign body and, 595, 596f, 604
Traumatic antebrachiocarpal joint luxation, 482f
Traumatic brain injury (TBI), 229, 240f
Traumatic diaphragmatic hernia, 650–652, 650b, 651f, 653f–654f, 659f
Traumatic diaphragmatic rupture, 932–934, 935f
Traumatic disc herniation, 283–284
Traumatic disc prolapse, 283–284
Traumatic injuries, 179–180, 179f–180f
Traumatic intervertebral disc extrusion, 283–284
Traumatic orthopedic disease, 478–482
accessory carpal bone fracture, 480–481, 482f
carpal luxation/subluxation, 481–482, 482f
intra-articular fractures, 478–479
osteochondral fragmentation, 479–480, 480f
slab fractures, 480, 481f
Traumatic osteochondral fragmentation, 525
Traumatic osteochondrosis, 520
Traumatic reticuloperitonitis, 767f
Trauma, to ureters and kidney, 854–855, 855f–856f
T2 relaxation, 282
Tricuspid dysplasia, 709, 709f
Tricuspid valve dysplasia, 721.e5–721.e5
Trigeminal nerve, 203–204
Trochlear dysplasia, 430
Trochlear ridge fractures, 456, 457f
True diaphragmatic hernias, 657–658
Tubular gas opacities, 788f
Tubular necrosis, 845
Tumor, 262f
fracture associated, 396, 399f
with variable spinal distribution, 301–303
Tungsten, 15
Turbo spin-echo, 67
T1-weighted image, 281f, 282
T1-weighted magnetic resonance (MR) image, 189f, 198f
T1-weighted post contrast transverse magnetic resonance (MR) image, 200f
T1-weighted pulse sequence, 71
T1-weighted spin-echo sequence, 187
T1-weighting, 66, 68f–69f
T2-weighted fluid-attenuated inversion recovery (T2-FLAIR) sequence, 70f
T2-weighted image, 187, 189f, 281f–282f, 282, 285–286
in dorsal plane, 188f
in sagittal plane, 190f–195f
in transverse plane, 190f–192f
T2-weighted magnetic resonance imaging (MRI), 239f
T2-weighted pulse sequence, 71–72
T2-weighted sagittal magnetic resonance (MR) image, 206f
T2-weighted sequence, 285–286
T2-weighted transverse image, 288
T2-weighting, 66, 68f–69f, 72f
Twinkling artifact, 52
Tympanic bullae, 111f, 123f, 125f, 127f–128f, 165, 165f, 175
Type I cervical intervertebral disc disease, 287–288
Type II herniation, 282
Typhlitis, 992–993
Typical imaging sign, 254t–259t

U

Ulcers, gastric, 942–944, 945f
Ulnar carpal bone, 471, 472f
Ulnar physis, distal, 378
Ultrasonography
of abdominal lymph nodes, 788–789, 789f
of adrenal glands, 795–797, 796f
artifacts on, 46–52
basic scanner controls in, 42–43
of chronic renal disease, 845f
display for, 42
Doppler artifacts in, 52
Doppler modes in, 44–46
Doppler techniques with, 43–44
of duodenum, 960f
fields of view in, 41
gastric, 930, 931f
interpretation of, principles of, 43, 44f
of intestinal foreign bodies, 970f
intraluminal changes in, 870–871, 872f
of intussusception, 974f
of jejunum, 959f–960f
of kidneys and ureters, 839f, 845f, 850f
of leptospirosis, 847f
of linear foreign bodies, 973f
of liver, 812–824, 813f–815f
mural changes in, 871–874
new technologies in, 42
of perinephric pseudocyst, 848f
of peritoneal gas, 785
of peritoneum, 779–780
of pharynx, larynx, and trachea, 604
physics of, 40–54
of prostate gland, 889–891, 889f–891f
of small bowel, 959–962, 961t–963t
of spleen, 827–831, 828f
of stifle, 428, 431f
of stomach, 931f
of tibia, 466f
transducers in, 41–42
ultrasound waves and, physical principles of, 40
of ureterovesicular junction, 874, 874f
of urethra, 876–877, 877f
of urinary bladder, 850f, 870–874, 872f–874f
Ultrasound
of collateral ligament, 458f
dorsal tarsal soft tissue injury, 466f
fetlock joint, 513
gastrocneumius tendinitis, 465–466
of large bowel, 988, 988f
of lateral tibiotarsal collateral ligament, 463f
of medial tibiotarsal collateral ligaments, 462f
proliferative tarsal sheath effusion, 466f
talocalcaneal ligament enlargement, 465f
tarsal soft tissue swelling and pain, 466f
Ultrasound contrast media, 84–86, 85f
adverse reactions to, 86
general information, 84–86
Ultrasound elastography, 46
Ultrasound, genital tract
normal imaging finding, 896

Ultrasound, genital tract (*Continued*)
technique, 895–896
Ultrasound imaging. *See* Ultrasonography
Ultrasound of liver, 812–824, 813f–815f
Ultrasound wave
interaction with matter of, 40
physical principles of, 40
Underexposure, of digital radiographs, 33, 34f
Ungual cartilages, 569–570
ossification/calcification, 569–570, 570f
penetrating solar injuries, 571, 571f
quittor, 570
tears of, 569
Unilateral paralysis, 658–659
Unilateral pneumothorax, 695
Units, for radiation, 4–6, 5t
Unknown trauma, in foot, 562f
Unstructured interstitial pattern, 733–735, 735f, 735t
Ununited anconeal process, 368, 368f
Upper airway collapse, 604
Upper airway obstruction, 603, 754
lateral thoracic radiography of, 620f
Upper esophageal sphincter (UES), 608, 608f, 613–614
Upper gastrointestinal tract film sequence, 964t–968t
Urachal diverticulum, 869f
Ureteral calculi, 852–853, 852f
Ureteral dilation, 850, 852–853
Ureteral diseases, 851–854
Ureteral obstruction, 850f, 852–853, 853f
Ureteral tumor, 854
Ureteroceles, 854, 854f
Ureteroliths, 853
Ureterovesicular junction, 874, 874f
Ureters, 838, 854–855. *See also* Kidneys and ureters
Urethra, 874, 876f
anatomy of, 874
computed tomography, 876–877
computed urethrography, 876–877
diseases of, 877–879
lateral radiography of, 869f
radiography and urethrography of, 874–876, 876f–877f
retrograde urethrography, 875
ultrasonography of, 876–877, 877f
Urethral calculi, 877–878, 878f
Urethral fistulas, 879
Urethral mass lesions, 878–879
Urethral neoplasia and inflammation, 878–879, 879f–880f
Urethral obstruction, 873
Urethral rupture, 879, 880f
Urethral stricture, 879
Urinary bladder
mass, 850f
ultrasonography of, 850f
Urinary bladder and urethra, 860–883
anatomy of, 860, 860f–861f
computed tomography of, 874, 875f
contrast cystography of, 863–870, 865t
contrast leakage patterns from, 868–869, 869f–870f
disease, radiographic signs of, 861–863, 862t, 863f–865f, 865t
lateral radiography of, 867f
magnetic resonance imaging of, 874
post-intravenous contrast, 875f
radiographic visualization of, 860
retrograde urethrography, 876f
ultrasonography of, 870–874, 872f
Urinary tract infection, 849f
Urine, 868, 869f, 870
Uterine adenosquamous carcinoma, 914f
Uterine leiomyoma, 913.e1f
Uterine neoplasia, 912
Uterine neoplastic nodules, 912–913
Uterine nonneoplastic nodules, 912–913
Uterine origin of a mass, 913
Uterine stump disease, 912
Uterine stump granuloma, 915f
Uterine torsion, 912, 913f
Uterus, 894–922, 897t–898t
enlargement in a pregnant bitch, 899f
imaging procedures for, 894–895
during pregnancy, 896
pregnancy and, 900–907
ultrasound of, 894
uterine disease of, 910–913
Uterus masculinus, 873, 885

V

Vacuum phenomenon, 403, 405f, 405b
Vaginal diseases, 913–914
Vaginal leiomyoma, 914f
Vaginogram, 895f
Vaginoscopy, 913
Vaginourethrogram, 854f
Valgus fracture, 395f
Variable signal intensity, 69f
Varus fracture, 395f
Vascular channel, 546f
Vascular disease, of liver, 821–824, 822f–824f
Vascular disruption, 209–210
Vascular malformations, 810–811
Vascular pattern, 736
Vascular ring anomalies, of esophagus, 622–624
Vasogenic edema caudal, 240f
Velocity, 40
of blood flow, 44
constant, 40
Velocity scale, 52
Venous congestion, 821, 822f
Ventral displacement, of gastrointestinal tract, 842–843
Ventral longitudinal ligament, 246, 247f, 279
Ventral region, 736f
Ventricular compression, 207f–208f
Ventricular septal defect, 721.e1–721.e3
Ventro-caudal abdomen, 894f
Ventrodorsal barium gastrogram, of gastric neoplasia, 946f
Ventrodorsal/dorsoventral view
of accessory lung lobe, 587f
of atelectasis, 580, 582f
of cardiac silhouette, 581, 587f
of caudal lobe vessels, 581
Ventrodorsal lateral radiography, of diaphragmatic region, 649f–650f
Ventrodorsal radiography
of abdomen, 766f
of acquired left-sided diaphragmatic hernia, 934f
of canine female genital tract, 899f
of canine pelvis, 328f
of cardiac silhouette, 706f
of caudal aspect of abdomen, 771f
of caudal aspect of thorax, 590f
of caudal esophagus, 627f
of caudal fragment, 254f
of caudal thorax, 633f
of cervical vertebrae, 114f
of congestive heart failure, 715f
with dysplasia, 371f
of esophagus, 619f
of gastric foreign body, 943f
of gastric mineralization, 950f
of gastric ulcer, 945f
of heartworm disease, 714.e1f
of hypertrophic cardiomyopathy, 719f
of hypovolemia, 705f
Ventrodorsal radiography (*Continued*)
of ileocolic intussusception, 973f
of interlobar fissures, 694f
of kidneys, 842f, 850f
of laryngeal collapse, 597f
of left hemipelvis of dog, 356f
of lumbar vertebrae, 116f
of lumbosacral region, 136f
of multiple thoracic hemivertebrae, 248f
of myxomatous tricuspid valve disease, 717f
normal hips, 370f
of pancreatic abscess, 934f
of patient hit by car, 255f
of peritoneal fluid and gas, 781f
of pleural fluid, 692f
of post vehicular trauma, 788f
of pulmonary undercirculation, 714f
of pyloric region, 942f
of retroperitoneal hemorrhage, 784f
of thoracic spine, 248f
of thoracic vertebrae, 116f
of thoracolumbar junction of canine with transitional anomaly, 135f
of thorax, 586f, 626f, 700f
Ventrodorsal thoracic radiography, 587f, 590f
of Borzoi, 703f
of caudal esophageal foreign body, 675f
of chemodectoma, 677f
of costochondral junction, 632f
of cranial abdomen, 660f
of diaphragmatic hernias, 652f
of diaphragmatic region, 647f
of dorsal mediastinal masses, 674f–675f
of extrapleural sign, 639f
of heart base region masses, 676f
of lung lobes, 725f
of mediastinal mass, 672f
of pectus excavatum, 635f
of peritoneopericardial diaphragmatic hernias, 655f
of pleural cavity, 697f
of pneumomediastinum, 670f
of pulmonary undercirculation, 714f
of split spinous process, 249f
of sternal lymph node, 669f
of thorax, 665f–667f
of tracheobronchial lymph node enlargement, 676f
of transitional thoracolumbar vertebral segment, 634f
of traumatic diaphragmatic hernia, 653f–654f
Ventrodorsal view, 123
of congenital diaphragmatic hernia, 659f
of gastroesophageal intussusception, 658f
of pleural fluid, 691f
of traumatic diaphragmatic hernia, 651f, 659f
Ventromedial-dorsolateral oblique radiograph, of equine hip joint, 343f
Vertebrae, 244–278
anatomic considerations of, 244–246, 244f–247f, 247b
degenerative conditions of, 258–260
fractures of, 251–254
inflammatory conditions of, 257
luxation of, 251–254
metabolic conditions of, 262–263
neoplasia of, 260–261, 262f
unclassified conditions of, 262–263
Vertebral anomalies, 307–308, 309f
Vertebral arch, 244
Vertebral canal, 279
Vertebral column, 247b
anomalies of, 246–251
Vertebral column (*Continued*)
atlantoaxial subluxation of, 249–250, 249f–250f
block vertebrae of, 246, 248f
cervical spondylomyelopathy of, 250–251, 252f–253f, 254t–259t
hemivertebrae of, 246–248, 248f
incomplete ossification of atlas, 250, 251f
radiographic technique, 244
spina bifida of, 249, 249f
transitional vertebrae of, 248–249
Vertebral heart scale (VHS), 703
Vertebral left atrial size (VLAS), 707
Vertebral osteomyelitis, 257
Vertebral physitis, 257
Vertebral tumor, 297–298, 297f–298f
Vertebral venus plexus pathology, 304
Vesicoureteral reflux, 868
Vestigial ulna, 470, 471f
Veterinary practice, 7
Viable nonunion fracture, 392–393, 393f
Videofluoroscopic swallowing study (VFSS), 612, 614
Villonodular synovitis, 418, 419f, 515, 518f
Viral pneumonia, 753
Visceral peritoneum, 778
Viscosity, iodine-based contrast media, 79
Vitamin D, 384
Vocalizing, lateral cervical radiography, 628f
Volume depletion, 698f
Volume elements, 56–57
Voxels, 56–57
Voxel-to-pixel translation, 57f

W

Wallerian degeneration, 292–293
Wall-mounted plate holder, 126, 135f
Warmblood, 456f
Water-insoluble contrast media, 79
Wavelength, 40
Wedge force stress, 415f
Wedge-shaped epiphysis, 473, 474f
Weight-bearing lateral views, accessory carpal bone fracture, 482f
Weight-bearing stifle, 428
Weighting factor, 4, 4t
West Highland white terrier, 410f
Wide contrast resolution, 31f
Window width, 61, 63f
Wireless DDR plates, 26–27
Withers region, 122f
Wobbler disease, 291
Wolff's law, 384, 390

X

X-ray, 90
absorption of, 5, 14, 19–20, 26, 32f
attenuation in, 22, 24–26, 31f
basic properties of, 2–4, 3b
biologic injury from, 4
characteristic, 10–11, 11f, 14–15
discovery of, 2
gamma rays and, 2
production of, 10–14, 12f
X-ray beam, 128–129, 130f, 133f
energy of, 19–20
primary, 586f
X-ray dental film sizes, 138t
X-ray dental machines, 137, 138f
X-ray energy, 17
divergence of, 19f
X-ray film, 17, 17f
X-ray generator, 14
X-ray intensifying screen, 26, 26f
X-ray machine, 14, 16
conventional, 22
X-ray tube, 10, 11f, 14

